中国气象局气候研究开放实验室

# 论文汇编

第十七卷

(2014)



LCS

气候研究开放实验室

# 中国气象局气候研究开放实验室

# 论文汇编

## 第十七卷

(2014)

中国气象局气候研究开放实验室

# 内 容 简 介

本文集收录了2014年度中国气象局气候研究开放实验室在国内外核心期刊发表的学术论文61篇。内容涉及气候监测、气候变率的诊断及其机理、气候预测理论和方法、气候模式模拟、气候变化检测及影响评估等研究领域。

# 目　录


1. Climatological characteristics and long-term change of SST over the marginal seas of China …… Bao, B. and G. Y. Ren (1)
2. Urbanization effect on long-term trends of extreme temperature indices at Shijiazhuang station, North China …… Bian, T., G. Y. Ren, B. X. Zhang, et al (12)
3. An observational study of snow aging and the seasonal variation of snow albedo by using data from Col de Porte …… Chen Ajiao, Weiping Li, Weijing Li, et al (24)
4. 基于 Lorenz 系统的数值天气转折期预报理论探索 …… 达朝究　穆　帅　马德山　等 (33)
5. 基于 CMIP5 气候模式的中国地区未来高温风险预估 …… 董思言　徐　影　周波涛　等 (47)
6. IPCC 第五次评估报告关于适应气候变化与可持续发展的新认知 …… 段居琦　徐新武　高清竹 (52)
7. 中国东北区域盛夏雨季的客观识别研究 …… 房一禾　龚志强　赵连伟　等 (58)
8. Dynamic-statistics combined forecast scheme based on the abrupt decadal change component of summer precipitation in East Asia …… Gong Z Q, Zhao J H, Feng G L, et al (70)
9. Influence of the tropical Pacific east-west thermal contrast on the autumn precipitation in South China …… GU wei, Lin WANG, Weijing LI, et al (86)
10. 旋转经验正交函数分解回归方法在东北夏季气温季节预测和成因诊断中的应用 …… 韩荣青　高　辉　李维京 (99)
11. 20 世纪 90 年代末东亚夏季降水年代际变化及其成因初探 …… 胡　泊　乔少博　封国林 (114)
12. Climate Prediction experiment for tropical cyclone genesis frequency using the large0scale circulation forecast by a coupled global circulation model …… JIA Xiaolong,CHEN Lijuan,LUO Jingjia (126)
13. Spatiotemporal distribution and decadal change of the monthly temperature predictability limit in China …… Li Weijing, Jingpeng Liu, Lijuan Chen, et al (135)
14. 中国月平均气温可预报性的时空特征及其年代际变化 …… 李维京　刘景鹏　陈丽娟　等 (144)
15. 资料均一化对沈阳站气温趋势和城市化偏差分析的影响 …… 李　娇　任国玉　任玉玉　等 (152)
16. Simulation and projection of the western Pacific subtropical high in CMIP5 models …… Liu Yunyun, Li Weijing, Zuo Jinqing, et al (159)
17. CMIP5 模式对西太平洋副热带高压的模拟和预估 …… 刘芸芸　李维京　左金清　等 (173)
18. Relationships between interannual and intraseasonal variations of the Asian-western Pacific summer monsoon hindcasted by BCC_CSM1.1(m) …… Liu, Xiangwen, Tongwen Wu, Song Yang, et al (187)
19. An application of hybrid downscaling model to forecast summer precipitation at stations in China … Liu, Y. and Fan, K (201)
20. A hybrid statistical downscaling model for prediction of winter precipitation in China …… Liu, Y. and Ren, H.-L (215)

21. 青藏高原夏季土壤有机质及砾石影响水热传输特性的数值模拟 …… 马 琴 刘 新 李伟平 等 (228)
22. Temporal and spatial variations of global deep cloud systems based on CloudSat and CALIPSO Satellite observations …… Jie PENG, Hua ZHANG, Zhanqing Li (243)
23. 前期西太平洋暖池热含量异常影响长江中下游夏季降水的可能途经 ……
…… 祁 莉 王晓芳 何金海 等 (254)
24. 欧亚北部 2004 年以来频繁冷冬的特征分析及机理初探 …… 乔少博 沈柏竹 王晓娟 等 (267)
25. Urbanization effects on trends of extreme temperature indices of national stations over mainland China, 1961—2008 …… Ren, G. and Y. Zhou (279)
26. 全球陆地表面气温变化研究现状、问题和展望 …… 任国玉 任玉玉 李庆祥 等 (300)
27. Eddy-induced growth rate of low-frequency variability and its mid-late winter suppression in the northern hemisphere …… Ren, Hong-Li, Fei-Fei Jin, and Jong-Seong Kug (313)
28. Application of the analogue-based correction of errors method in ENSO prediction ……
…… Ren, Hong-Li, Ying Liu, Fei-Fei Jin, et al (331)
29. 提高月预报业务水平的动力相似集合方法 …… 任宏利 张培群 李维京 等 (336)
30. 我国北方 TOMS 气溶胶光学厚度与地面沙尘天气频数的比较 …… 任霄玉 任国玉 魏明建 (344)
31. The response of actual evaporation to global warming in China based on six reanalysis datasets …… Su T, Feng G L, Zhou J, Ye M (352)
32. Spatial-temporal variation characteristics of global evaporation revealed by eight reanalyses ……
…… SU T, Feng G L (363)
33. 中国夏季大气水分循环特征及再分析资料对比分析 …… 苏 涛 封国林 (378)
34. 2013 年海洋和大气环流异常对中国气候的影响 …… 司 东 袁 媛 (397)
35. The role of eddy feedback in the excitation of NAO ……
…… Tan, Gui-Rong, Fei-Fei Jin, Hong-Li Ren, et al (405)
36. 海洋模式中垂直混合参数化方案介绍 …… 汪 雷 王彰贵 凌铁军 等 (414)
37. Spatial and Temporal Variations of Regional High Temperature Events in China ……
…… Y. J. Wang, F. M. Ren (426)
38. 2013 年全球重大天气气候事件及其成因 …… 王艳姣 高 蓓 周 兵 等 (438)
39. Improvement of cloud microphysics in the aerosol-climate model BCC_AGCM2.0.1_CUACE/Aero, evaluation against observations and updated aerosol indirect effect ……
…… Zhili Wang, Hua Zhang, and Peng Lu (448)
40. 关于大气臭氧问题的主要研究进展 …… 谢 冰 张 华 (466)
41. 利用 CloudSat 卫星资料分析云微物理和光学性质的全球分布特征 ……
…… 杨冰韵 张 华 彭 杰 等 (475)
42. 1971—2011 年中国县级行政区域热带气旋基本气候特征 …… 尹宜舟 罗 勇 肖风劲 等 (489)
43. Present and projected degree days in China from observation, reanalysis and simulations ……

…… You, Q. L., K. Fraedrich, F. Sielmann. et al (498)
44. Development of the Analogue-Dynamical Method for Error Correction of Numerical Forecasts …
…… YU Haipeng, HUANG Jiangping, LI Weijing, et al (512)
45. 数值预报误差订正技术中相似-动力方法的发展 …… 于海鹏 黄建平 李维京 等 (526)
46. 1981—2010年北京地区极端降水变化特征 …… 尤焕苓 刘伟东 任国玉 (537)
47. 北京"7·21"特大暴雨过程时空特征解析 …… 尤煥玲 任国玉 吴 方 等 (546)
48. 春季马斯克林高压对中国东北地区夏季气温的影响 …… 曾宇星 封国林 赵俊虎 等 (555)
49. Application and evaluation of a new radiation code under McICA scheme in BCC_AGCM2.0.1 Geosci
…… H. Zhang, X. Jing J. Li (564)
50. PM2.5 and tropospheric $O_3$ in China and an analysis of the impact of pollutant emission control …
…… ZHANG H., XIE B., ZHAO S.-Y., et al (582)
51. 中国的PM2.5和对流层臭氧及污染物排放控制对策的综合分析 … 张 华 陈 琪 谢 冰 等 (588)
52. IPCC第五次评估报告关于人为和自然辐射强迫的解读 …… 张 华 黄建平 (596)
53. 多层四流球谐函数的构建及在大气辐射传输模式中的应用 …… 张 华 卢 鹏 (601)
54. Effect of data homogenization on estimate of temperature trend: a case of Huairou station in Beijing
Municipality …… Zhang, L., G. Y. Ren, Y. Y. Ren. et al (613)
55. 武汉异常强降水水汽来源、输送路径分析 …… 张 灵 杜良敏 陈丽娟 等 (622)
56. 无参考序列条件下地面气温观测资料城市化偏差订正方法:以北京站为例 …… 张 媛 任国玉 (628)
57. The Boreal Summer Intraseasonal Oscillation Simulated by Four Chinese AGCMs Participated in the
CMIP5 Project …… Zhao Chongbo, Tianjun Zhou, Lianchun Song, et al (639)
58. Simulating direct effects of dust aerosol on arid and semi-arid regions using an aerosol-climate coupled
system …… Shuyun Zhao, Hua Zhang, Song Feng, et al (653)
59. 气溶胶-气候耦合模式系统BCC_AGCM2.0.1_CAM气候态模拟的初步评估……
…… 赵树云 智协飞 张 华 (662)
60. 城市化对华北地区极端气温事件频率趋势变化的影响 …… 周雅清 任国玉 (675)
61. 冬季大气遥相关和海温关键区的复杂网络性质 …… 左冬冬 龚志强 冯爱霞 等 (685)

Author's personal copy

Continental Shelf Research 77 (2014) 96–106

Contents lists available at ScienceDirect

Continental Shelf Research

journal homepage: www.elsevier.com/locate/csr

Research papers

# Climatological characteristics and long-term change of SST over the marginal seas of China

Baoleerqimuge Bao [a,b,c], Guoyu Ren [c,*]

[a] Chinese Academy of Meteorological Sciences, No. 46, Zhongguancun South Street, Haidian District, Beijing 100081, China
[b] University of Chinese Academy of Sciences, No. 19A Yuquan Road, Beijing 100049, China
[c] Laboratory for Climate Studies, China Meteorological Administration, No. 46, Zhongguancun South Street, Haidian District, Beijing 100081, China

ARTICLE INFO

*Article history:*
Received 9 October 2013
Received in revised form
19 January 2014
Accepted 20 January 2014
Available online 12 February 2014

*Keywords:*
Marginal seas
SST
Climatology
Climate change
Monsoon
Upwelling

ABSTRACT

Based on monthly mean HadISST data, climatological characteristics and long-term changes of sea surface temperature (SST) over marginal seas of China are analyzed for the time period 1870–2011. The results show that (1) The smallest and largest spatial SST differences among various areas are seen in August and January respectively, with the coolest month occurring in February for all of the seas and the warmest month occurring in August for all but South China Sea (SCS); (2) The warming trends of the marginal seas of China during the time periods analyzed are generally larger than the global and hemispheric averages, with the East China Sea seeing the largest warming of all seas; (3) All of the sea areas see significant rising trends of annual mean SST in the last 140 years and the last 50 years, with larger and more significant warming generally occurs in autumn and winter; (4) The last 30 years especially the last 14 years undergo a slowdown of warming in the marginal seas of China, and the slowdown in the last 14 years is more evident than the global and northern hemispheric averages; (5) A weak upwelling current exists in western SCS, and the upwelling intensity has a significant positive correlation with the SCS summer monsoon index, with both seeing a decreasing trend in the last 64 years.

© 2014 Elsevier Ltd. All rights reserved.

## 1. Introduction

Ocean and atmosphere are important components of climate system. Sea–air interaction, especially that occurring between tropical oceans and global atmosphere has been a hot topic in climatology nowadays. There are many studies on global and basin scale SST climatology using different datasets (Reynolds, 1988; Reynolds and Marsico, 1993; Reynolds and Smith, 1995; Smith and Reynolds, 1998). IPCC AR4 showed that global SST exhibits significant increasing trend in recent 100 years, especially in recent 30 years (Trenberth et al., 2007). SST at gulf area and continental shelf area are also studied and dataset is optimized for these areas (Shea and Trenberth, 1992) and relation with large scale change is also analyzed (Belkin, 2009; Takeshige et al., 2013).

The marginal seas of China span tropical, subtropical and temperate zone and exhibit significant geographical diversities. There are many studies about SST change and variability of the region during different time periods (Tang et al., 2009; Huang et al., 2012; Wang et al., 2013). Different datasets are used to study the SST change and variability (Yan and Li, 1997; Hickox et al., 2000; Wu et al., 2005; Song et al., 2007; Jin and Wang, 2011; Liu and Zhang, 2013). It has been shown that the 1990s is the warmest decade of the past 100 years in the marginal seas of China (X.Z. Zhang et al., 2005; Feng and Lin, 2009), and water masses, currents and ENSO might have been the main factors for different modes of SST variability for the East China Sea (ECS) (Song et al., 2007). The SST variability might in turn affect other system, such as East Asian monsoon (Li et al., 2010). Xie et al. (2002) and Yeh and Kim (2010) examined winter SST variability of Yellow/East China Sea in recent years and explained it in terms of the associated atmospheric circulation anomalies and Bathymetric effect.

The previous studies are important for understanding climatological characteristics and change of SST on varied spatial and temporal scales. Most of the previous studies, however, have been limited to given areas or specific time periods. For the marginal seas of China on a whole, the general features of normal climate and climate change of SST over the past more than 100 years have not been well understood, in spite of the fact that a few studies examined the long-term trends of the SST for varied time periods and areas.

In this paper, we use the updated HadISST data to reveal the climatological characteristics and long-term change of SST over the marginal seas of China. Our analysis shows the distinct characteristics of SST climatology and rapid warming of the last 140 years in the region.

* Corresponding author.
*E-mail address:* guoyoo@cma.gov.cn (G. Ren).

http://dx.doi.org/10.1016/j.csr.2014.01.013
0278-4343 © 2014 Elsevier Ltd. All rights reserved.

Author's personal copy



## 2. Study region, data and methods

### 2.1. Study region

In this paper, marginal seas of China are defined as the offshore region of 5–41°N and 105–130°E. The region is further divided into three sub-regions: Bohai Sea and Yellow Sea (BYS, 117–127°E and 35–41°N), East China Sea (ECS, 120–130°E and 22–35°N) and South China Sea (SCS, 105–120°E and 5–22°N) (Fig. 1).

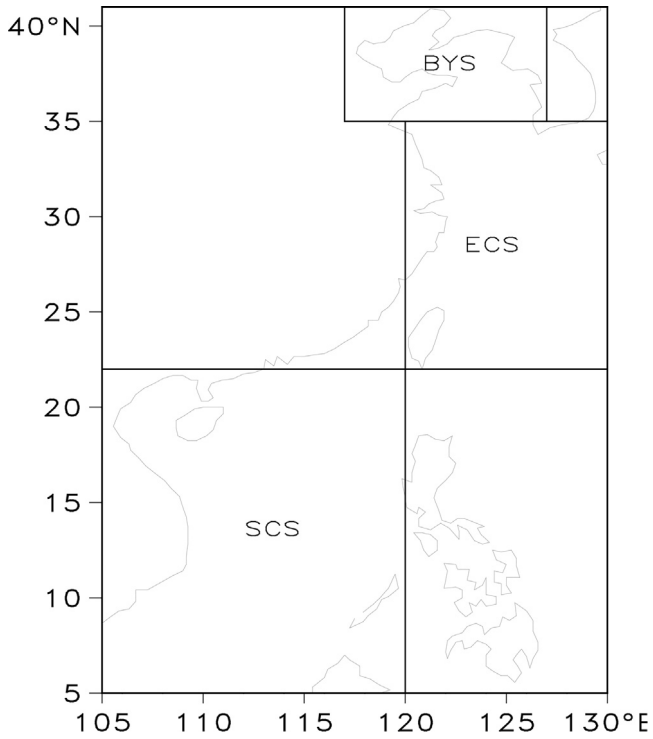


**Fig. 1.** Study regions defined in this paper. BYS: Bohai Sea and Yellow Sea; ECS: East China Sea; SCS: South China Sea.

### 2.2. Data and methods

Monthly SST data and SCS Summer Monsoon index series are used. 1 × 1 monthly HadISST (Rayner et al., 2003) data during 1870–2011 are from Hadley Centre, UK (http://www.metoffice.gov.uk/hadobs/hadisst/data/download.html). This dataset is the longest global historical and real time SST observations with the highest spatial resolution and coverage, and it has been widely used in studies of climate change and variability. In order to examine the relationship between the western SCS upwelling intensity and SCS Summer Monsoon (SCSSM), the SCSSM index data developed by Li et al. (http://ljp.lasg.ac.cn/dct/page/1) from the Institute of Atmospheric Physics, Chinese Academy of Sciences (Li and Zeng, 2002, 2003, 2005) is utilized in this paper. Monthly reanalysis data of 850 hPa zonal wind ($u$), 500 hPa geopotential height (hgt) and sea level pressure (slp) from the National Centers for Environmental Prediction (NCEP) during 1948–2012 are used for calculating the monsoon index series.

We made a quality check of the HadISST data, and found a few quality problems with the data in the Bohai Sea and the Yellow Sea. The absolute values of SST anomalies are larger than 2 times the standard deviation for a few months of 1977, 1980 and 1981 for the grids. These are proved to be wrong records by comparing them to the neighboring grid data. We replace these records with climatological average of the latest climate reference period (1981–2010).

Regional average is calculated by area-weighted averaging the grid data using latitude cosine as weights (Jones and Hulme, 1996). The reference time period 1981–2010 is applied to calculate mean SST values for analyzing climatological characteristics and the time period 1961–1990 as recommended by World Meteorological Organization (WMO) is used as reference time period for calculating SST anomalies for analyzing climate change. We use May, August, November and February as the representative months for spring, summer, autumn and winter respectively as sea water temperature change generally lags by a month or two behind land air temperature. The method of least-squares is used to calculate the linear trends of the SST anomalies series for given time periods, and student $t$-test is used to examine the significance of the linear trends of the time series (Hu, 1996; Von and Francis,

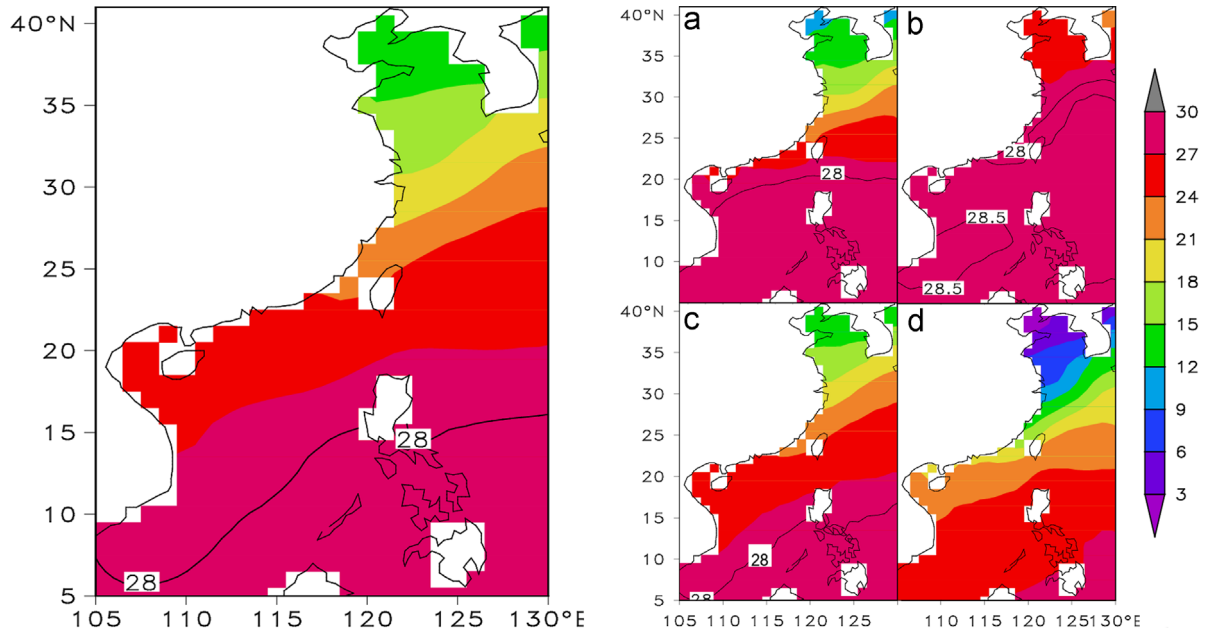


**Fig. 2.** Annual (left) and seasonal (right) mean SST distribution during 1981–2010 in the marginal seas of China. (a): Spring; (b): Summer; (c): Autumn; (d): Winter (Unit: °C).

Author's personal copy



2003; Wei, 2007). Regime shift analysis is based on the method developed by Rodionov (2004) and Rodionov and Overland (2005), in our regime shift analysis, parameters are assigned as: cut-off length equals 10 and probability level is 0.01.

## 3. Results

### 3.1. Spatial and seasonal characteristics

Fig. 2 shows spatial distribution of annual and seasonal mean SST for time period 1981–2010. Annual mean SST decreases with increasing latitude, with high temperature ranging from 24 °C to 28 °C in the south and low temperature ranging from 12 °C to 20 °C in the north. This pattern is closely related to the solar radiation distribution in the offshore region. The isotherm is northeast–southwest oriented and the SST gradient increases as getting closer to the mainland coastal line. It is obvious that the landmass effect in wintertime has contributed to the tilting of the isotherms, which was pointed out by Bao et al. (2002). The ECS exhibits the largest temperature gradient, and the SCS in the tropical zone the lowest temperature gradient.

As a transition season from winter to summer, spring has its unique character (Fig. 2a). Winter northerly wind begins to weaken and the southward coastal current along the coast of the Yellow Sea is not as apparent as in winter. The Yellow Sea SST is latitudinally distributed with smaller gradient. The largest SST gradient occurs in the north, and the SST in the BYS is evidently lower. The SCS SST to the south of the Taiwan Channel is uniformly distributed. The most uniform spatial distribution of SST and the highest seasonal mean temperature appears in most parts of the marginal seas of China during summertime (Fig. 2b). Apparent gradient appears in the joint area of the Yellow Sea and the ECS. The autumn (Fig. 2c) bears a similar spatial distribution of seasonal mean SST to that of annual mean SST (Fig. 2 left). In winter, the temperature gradient largely increases, as a result of the tremendous drop of temperature in the BYS (Fig. 2d). As semi-closed sea, the BYS winter temperature is deeply influenced by the land. The lowest SST, ranging from 0 °C to 3 °C, occurs in the Bohai Sea, and the 27 °C SST isotherm can still be seen in the south of the SCS during wintertime.

There is a unique phenomenon in summer SST of the south-western SCS, characterized by a large area of relative cooler surface water centered to the southeast of the Indochina Peninsula (Fig. 3a, b). This phenomenon was reported in Cai et al. (2001) and Li et al. (2011). The interpretation for its formation is summer southwesterly wind which causes offshore upwelling current. Deep cold water is transported upward and cool the surface water (Cai et al., 2001; Li et al., 2011). In autumn, the cold water area disappears. Weaker upwelling phenomena also appear in the Taiwan Strait and northeast of the Hainan Island in summertime, but they need further investigation by using high-resolution observational data. Under the background of warming during 1981–2010, the upwelling in western SCS still exists in spite of the fact that the SST increases almost everywhere in the SCS (Fig. 3b).

Monthly mean SST generally shows cosine seasonal pattern for the marginal seas, and the range increases with latitude, with the BYS witnessing the largest seasonal variation (Fig. 4). The highest (lowest) SST occurs in August (February) for the BYS and the ECS, and in less extent for the whole region (Fig. 4b). For the SCS, however, the highest SST appears in May and June, about 2–3 months earlier than in the north of the study region, but the lowest SST appears in the same month (February) as other areas. The earlier peak and the flattening pattern of the SCS SST are in large extent related to the northern position of the ITCZ (Inter-Tropical Convergence Zone) and the SCS monsoon in this area during summer (R.H. Zhang et al., 2005; Ding et al., 2008), leading to more cloudy and rainy days, less solar radiation absorbed by the sea surface (Feng et al., 1999) and the upwelling in the off-shore area of the western SCS as described below.

The average annual temperature range is 7.08 °C for the study region, and it is 20.58 °C for the BYS, 11.26 °C for the ECS and 4.03 °C for the SCS. The fastest warming stages within a year occur in different months for different areas, with the whole region in May, the BYS in June, the ECS in May, and the SCS in April. The fastest cooling stage within a year occurs in December for all areas of the region.

### 3.2. Temporal variations in SST

In recent 150 years, all the four areas show increasing trends of annual mean SST anomalies (Fig. 5). The highest annual mean SST anomaly appears in 1998, and the temperature undergoes a decreasing trend since then, in spite of the fact that all of the

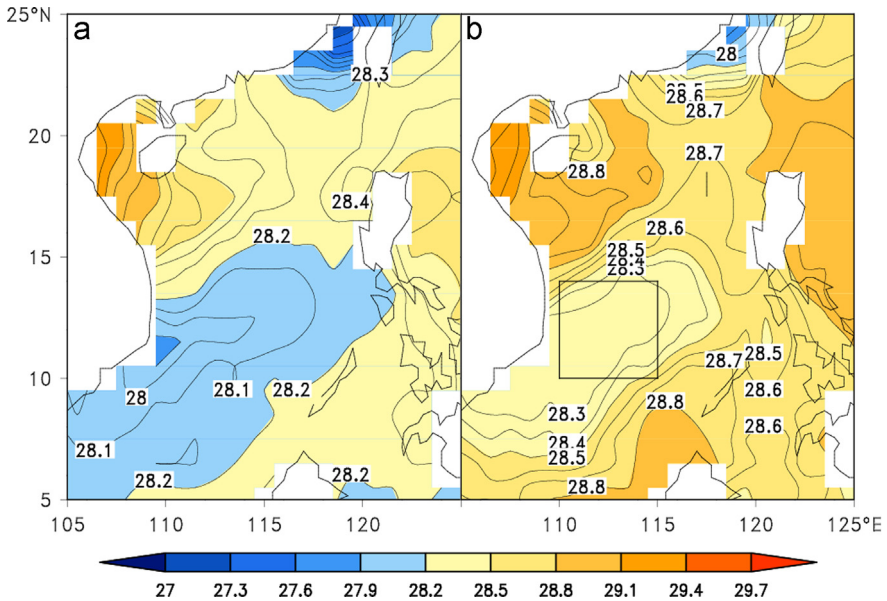


**Fig. 3.** Summer mean SST distribution of the SCS during 1961–1990 (a) and 1981–2010 (b) (Unit: °C).

Author's personal copy



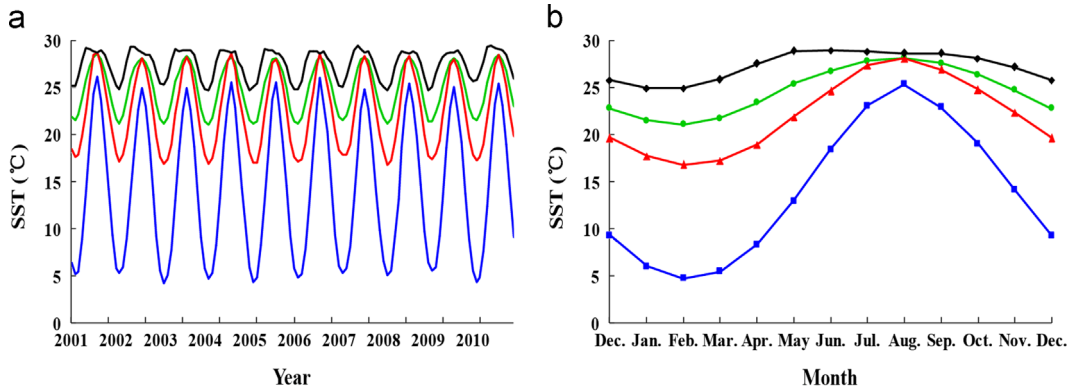


**Fig. 4.** Long term monthly mean SST of the marginal seas of China during 2001–2010 (a) and 1982–2011 (b) for different study areas. Blue: BYS; red: ECS; green: Whole region; black: SCS.

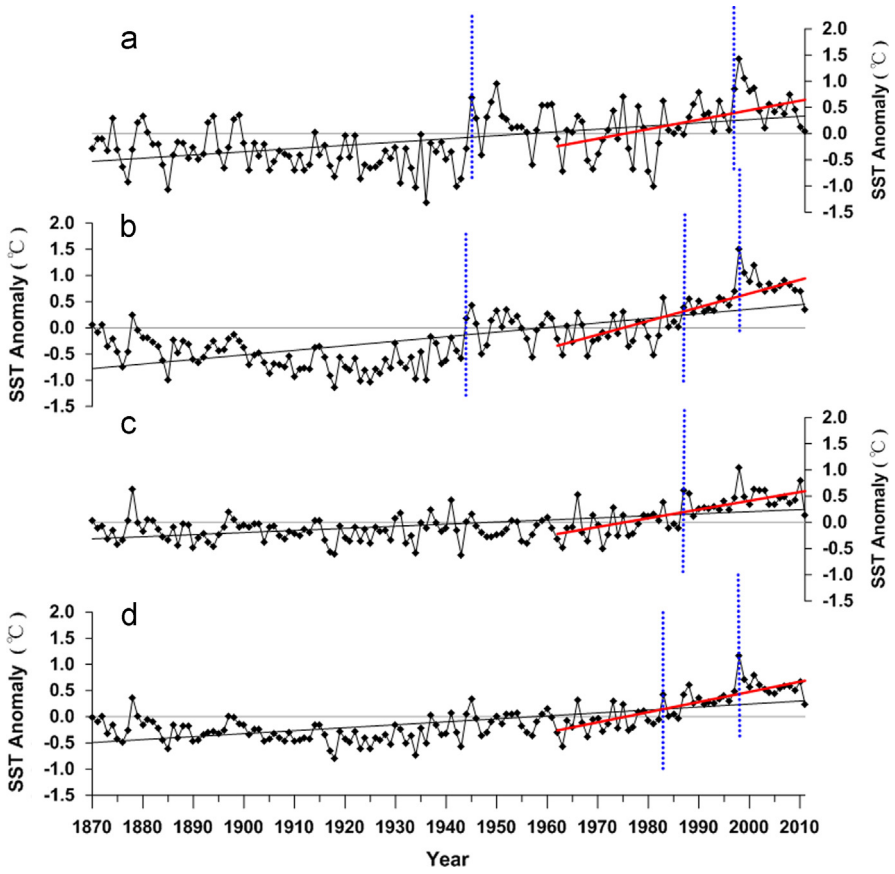


**Fig. 5.** Regional mean annual SST anomalies for marginal seas of China during 1870–2011. Black (red) lines indicate the latest 140 (50) years linear trends; blue dashed lines indicate regime shift years. (a) BYS; (b) ECS; (c) SCS; (d) Whole region. All of the linear trends passed 99% significance test. (For interpretation of the references to color in this figure legend, the reader is referred to the web version of this article.)

areas exhibit positive SST anomalies for continuous 14 years. Averaged annual mean SST anomalies in 1998 are 1.16 °C for the whole region, 1.43 °C for the BYS, 1.51 °C for the ECS and 1.04 °C for the SCS respectively. The increasing trends during 1870–2011 reaches 0.06 °C/10 yr for the whole region, 0.09 °C/10 yr for the ECS, 0.06 °C/10 yr for the BYS, 0.04 °C/10 yr for the SCS, and all of the trends are significant at the 99% confidence level. Fig. 5 also indicates the linear trends of annual mean SST anomalies for the last 50 years, and shows the generally larger warming than for the last 140 years for all the seas.

The marked warming begins in 1940s for the BYS and the ECS, but in 1980s for the SCS as indicated in Fig. 5. There exist decadal to multi-decadal variations in the SST anomalies series, with a general cool period from 1870s to 1930s, a weak warm period from 1940s to 1950s, a weak cool period from 1960s to 1970s, and a recent warm period from 1980s to present. Fig. 5 also shows the climate regime shifts of the SST for different sea areas. The warm (cool) periods and the regime shifts are evident, with the ECS and BYS undergoing the most frequent regime shifts. Besides the BYS, all other sea areas witness significant regime shifts in 1980s, implying an abrupt change to the recent warm period. Meng et al. (2011) also reported the phenomenon of the abnormal warming in the China seas after mid-1980s. The BYS and the ECS see another regime shift in late 1990s. It is clear that the inter-annual to decadal variability is larger in the BYS, and it is smaller in the SCS, indicating an increase in SST variability with latitude.

Author's personal copy



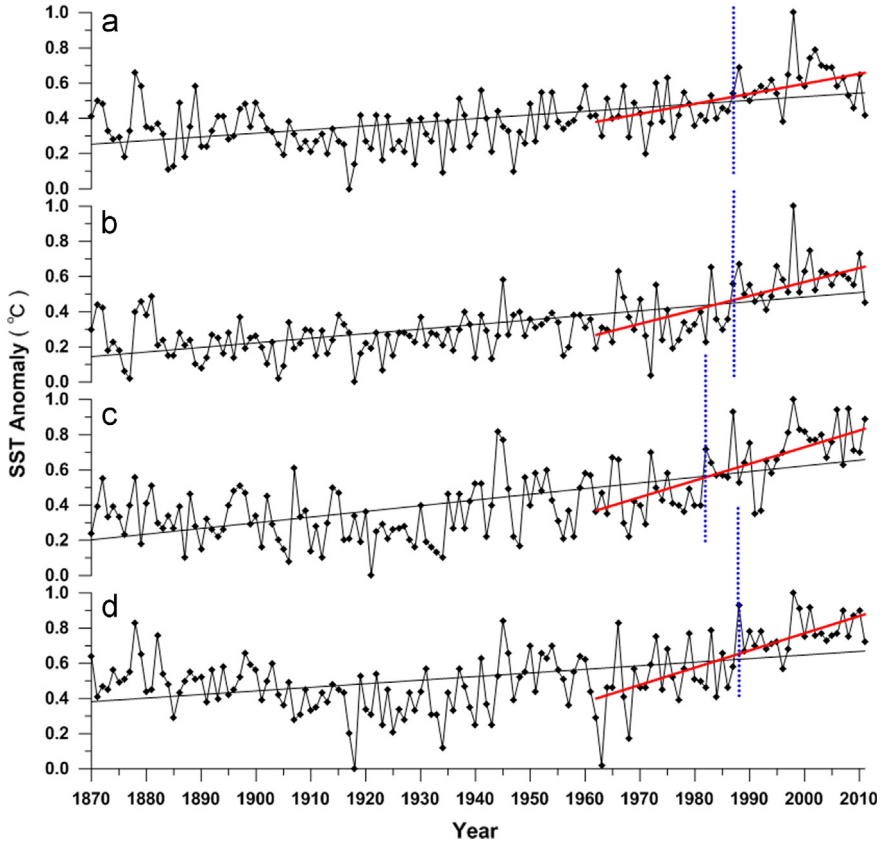


**Fig. 6.** Regional averaged seasonal mean SST anomalies for the marginal seas of China during 1870–2011. Black (red) lines indicate the latest 140 (50) years linear trend; blue dashed lines indicate regime shift years. (a) Spring; (b) Summer; (c) Autumn; (d) Winter. (For interpretation of the references to color in this figure legend, the reader is referred to the web version of this article.)

**Table 1**
Linear trends of SST anomalies for four seasons and year in different areas of the marginal seas of China during 1870–2011 and 1962–2011 (Unit: °C/10 yr).

| | Spring | | Summer | | Autumn | | Winter | | Annual | |
|---|---|---|---|---|---|---|---|---|---|---|
| | 1870–2011 | **1962–2011** | 1870–2011 | **1962–2011** | 1870–2011 | **1962–2011** | 1870–2011 | **1962–2011** | 1870–2011 | **1962–2011** |
| Whole region | 0.047** | **0.129**** | 0.053** | **0.161**** | 0.068** | **0.199**** | 0.057** | **0.273**** | 0.057** | **0.194**** |
| BYS | 0.055** | **0.129**** | 0.036** | **0.122**** | 0.076** | **0.168**** | 0.080** | **0.268**** | 0.061** | **0.181**** |
| ECS | 0.073** | **0.198**** | 0.071** | **0.175**** | 0.108** | **0.302**** | 0.094** | **0.379**** | 0.087** | **0.262**** |
| SCS | 0.033** | **0.093**** | 0.043** | **0.160**** | 0.044** | **0.145**** | 0.035** | **0.225**** | 0.040** | **0.167**** |

** Indicates that the trend is significant at the 99% confidence level.

It is also interesting to note that the latest 30 years see a smaller increasing trend of annual mean SST than that for the last 50 years, indicating a slowdown of warming in the study regions, and the last 14 years actually undergo an evident downward trend especially for the BYS and the ECS. This slowdown of warming in the past decade is found apparent in global scale (Kosaka and Xie, 2013; Smith, 2013). Besides, regional and seasonal characteristics of the phenomenon were also reported (Kosaka and Xie, 2013). Mechanisms for this hiatus were documented in terms of natural climate variability (Kosaka and Xie, 2013; Trenberth and Fasullo, 2013), stratospheric water vapor concentration (Solomon et al., 2010; Held, 2013), solar irradiance (Fröhlich, 2012; Held, 2013), and Pacific Decadal Oscillation (Trenberth and Fasullo, 2013) etc. Kosaka and Xie (2013) studied this global warming hiatus with regard to equatorial Pacific surface cooling and pointed out that natural climate variability caused the hiatus through La-Ninã-like decadal cooling. Solomon et al. (2010) pointed out that stratospheric water vapor concentration decrease lead to the warming slowdown significantly in the last decade. Trenberth and Fasullo (2013) found that negative phase of the Pacific Decadal Oscillation in the last decade is one reason for the hiatus in global warming.

Fig. 6 shows seasonal mean SST anomalies and their trends for the whole region during 1870–2011, and Table 1 gives linear trends of the seasonal and annual mean SST anomalies for various areas and the whole region during 1870–2011 and 1962–2011. For the region on a whole, significant warming occurs in all seasons with those of autumn and winter being the largest, reaching 0.07 °C/10 yr and 0.06 °C/10 yr respectively, and that of spring the smallest. All of the linear trends of seasonal mean SST anomalies for the whole region are significant at the 99% confidence level. The warming in spring and summer begin earlier and exhibit a more monotonous rise, and the increase in SST in autumn and winter begin later and is accompanied by a larger decadal and multi-decadal variability. The same as the annual pattern, seasonal pattern for the latest 50 years shows more significant warming trend than recent 140 years. Caputi et al. (2009) found that austral winter and autumn are more warming than spring and summer for the SST off the lower west coast of Australia.

Author's personal copy



The seasonal mean SST regime shifts are shown in Fig. 6 with blue dashed line. The most significant shifts for four seasons all happened in 1980s. He and Wang (2012) found that there is a decrease in the East Asian Winter Monsoon (EAWM) intensity beginning from 1986, and Ren et al. (2005a, 2005b) reported the rapid increase in annual and winter mean surface air temperature in mainland China beginning around mid-1980s, which are all consistent with the SST regime shift in the marginal seas revealed in this study. Decrease of inter-annual variability of the EAWM intensity after mid-1980s was also reported in other studies (He, 2013; Wang and Fan, 2013). EAWM related systems like Siberian high, Aleutian low, East Asian trough, East Asian jet stream and meridional wind at 850 hPa also show sign of weakening during 1986–2010 compared to 1956–1980 (He, 2013).

Table 1 shows that, except for the SCS, the autumn and winter warming trend is more significant than annual trend in the past 140 years, with the summer and autumn SCS SST experiencing more significant warming than those for the annual SST trend. For recent 50 years, all the sea areas see 3–5 times larger warming trends than those for the past 140 years. These are consistent with the previous analyses of the marginal sea SST (Meng et al., 2011) and of the mainland surface air temperature of eastern China (Ren et al., 2005a; Tang and Ren, 2005).

Among the various areas of the study region, the ECS shows the largest warming trends for all seasons, with the trends for spring, summer, autumn and winter reaching 0.07 °C/10 yr, 0.07 °C/10 yr, 0.11 °C/10 yr and 0.09 °C/10 yr respectively. The trends of autumn and winter SST anomalies in the BYS are also relatively larger, reaching 0.08 °C/10 yr and 0.08 °C/10 yr respectively.

Comparing the results of this analysis with those reported for global and northern hemispheric averages (Table 2), it can be found that the trends of annual mean SST in the marginal seas of China are generally higher than those of global and hemispheric averages for the same time periods (Jones et al., 2012; Trenberth et al., 2007). Except for the SCS for period 1901–2005, all the seas have larger warming rates than global and hemispheric averages during 1901–2005 and 1979–2005. Figs. 5 and 6 show that the slowdown of warming in the marginal seas of China over the last 14 years is also more evident than the global, northern hemispheric and China mainland averages as reported by some recent analyses (Easterling and Wehner, 2009; Jones et al., 2012; Ren et al., 2012; Hartmann et al., 2013). China marginal sea SST is generally influenced by East Asian monsoon system. Studies found that East Asian Winter Monsoon is weakening in recent 60 years and 100 years (Shi et al., 1996; R.H. Zhang et al., 2005; He and Wang, 2012), and this may well explain the rapid warming of the surface water as a result of decline of heat transfer from the air to deep water due to the slugging northerly wind. The unusual warming in East Asia including eastern mainland China may have

**Table 2**
Linear trends of annual mean SST for the study region and the global and northern hemispheric average surface temperature reported by the IPCC AR4 (Trenberth et al., 2007) (Unit: °C/10 yr).

| | Whole region | BYS | ECS | SCS | Global | Northern hemisphere |
|---|---|---|---|---|---|---|
| **1901–2005** | 0.093** | 0.108** | 0.151** | 0.061** | 0.067** | 0.071** |
| **1979–2005** | 0.267** | 0.387** | 0.444** | 0.190** | 0.133** | 0.190** |

** Indicates that the trend is significant at the 99% confidence level.

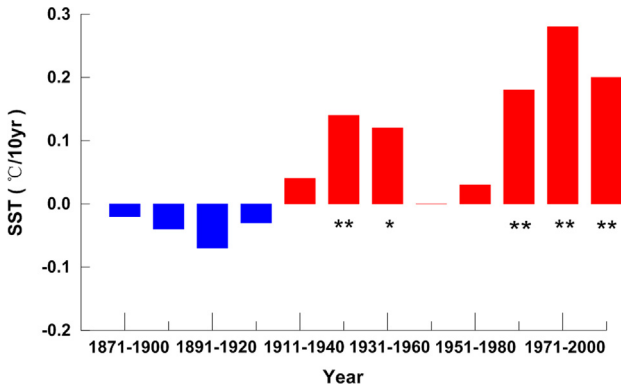


**Fig. 7.** Linear trends of annual mean SST anomaly for every 30 years for the marginal seas of China during 1870–2011. ** and * indicate the trends are significant at 99% and 95% confidence level respectively.

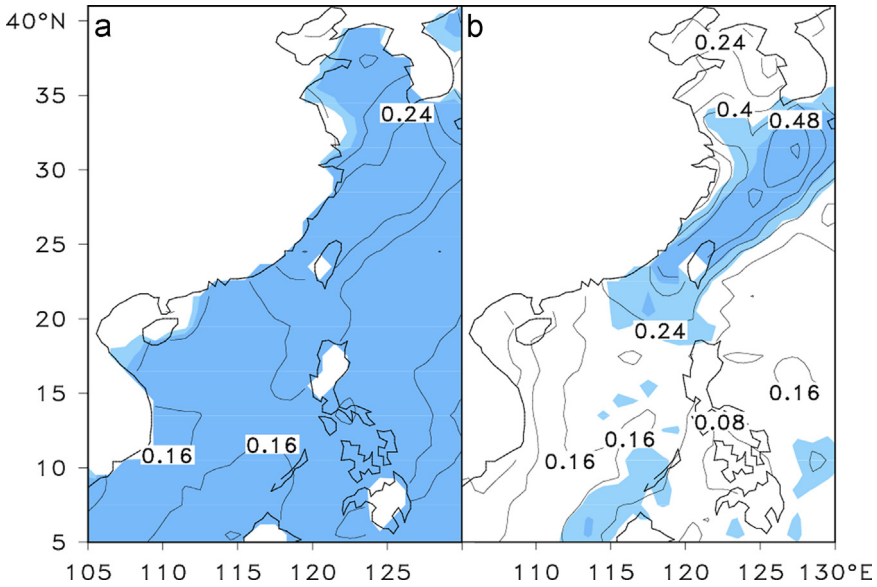


**Fig. 8.** Linear trends of annual mean SST during 1951–2011 (a) and 1979–2011 (b) (Unit: °C/10 yr). Blue color indicates the trends are significant at the 99% confidence level, and light blue indicates the trends are significant at the 95% confidence level.

Author's personal copy



been another reason for the large increase in the marginal sea SST in cold seasons (Ren et al., 2005b, 2012; Ding and Ren, 2008).

Fig. 7 shows the moving trends of annual mean SST anomalies for every 30 years during 1870–2011. The most significant warming for the study region occur in 1921–1950, 1931–1960, 1961–1990, 1971–2000 and 1981–2010, and the trends during these 30-yr periods pass the significance test at the 95% or even 99% confidence level. The largest warming occurs in 1971–2000, almost reaching 0.30 °C/10 yr. It is also clear that the warming occurs in all of the any 30-yr periods since 1911, in spite of the fact that the positive trends for 1911–1940, 1941–1970 and 1951–1980 are not significant at the 95% confidence level. Four of the early 30-yr periods see decreasing trends of annual mean SST, but the decreases did not passed the significant test.

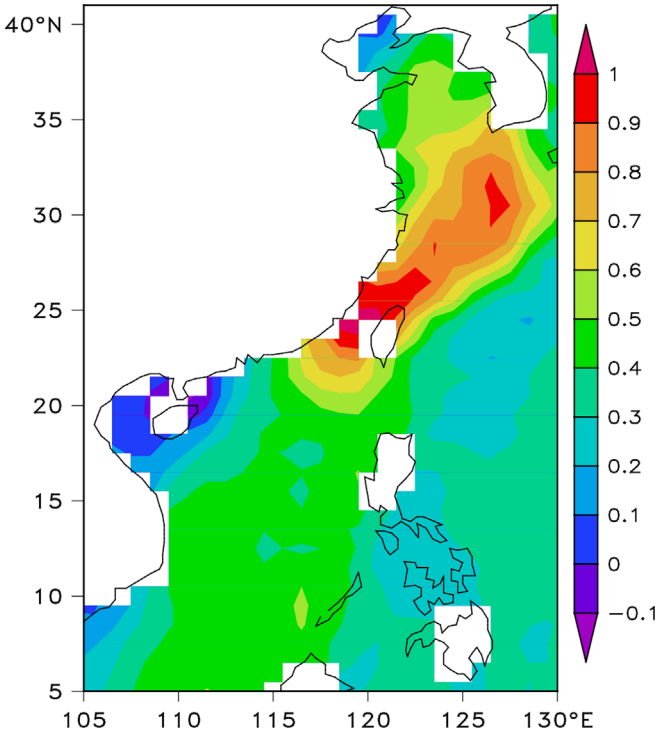


**Fig. 9.** Differences of annual mean SST between climate reference periods 1981–2010 and 1961–1990 over the marginal seas of China.

The detailed spatial pattern of the SST changes during the 140 years is difficult to be identified due to the lack of early-period data. Fig. 8 gives the distributions of the linear trends of annual mean SST for time periods 1951–2011 and 1979–2011 instead, and Fig. 9 shows differences of annual mean SST between climate reference periods 1981–2010 and 1961–1990 over the marginal seas. In the last 60 years and 30 years, the whole region shows increasing trends of annual mean temperature, and almost all of the grids register statistically significant warming. For the last 60 years, there are more grids of the study region where the trends are significant at the 99% confidence level, though the magnitudes of the trends are generally smaller than those for the last 30 years. For both time periods, the most significant warming mainly occurs in the ECS, with the trends usually more than 0.20 °C/10 yr. The weakest warming occurs in central and northern SCS. The most obvious warming is clearly seen in the Taiwan Strait and the ECS, and the weakest warming occurs in northwestern part of the SCS and the Bohai Sea in Fig. 8. The whole study region actually sees significant SST increase in all the seasons in the recent 50 year period, but the most significant trend appears in winter and autumn except for SCS (Table 1).

Fig. 10 exhibits the spatial distributions of linear trends of seasonal mean SST for time periods 1951–2011 and 1979–2011. In the last 60 years, significant warming trends are seen in the whole area, and the largest warming with significance at the 99%

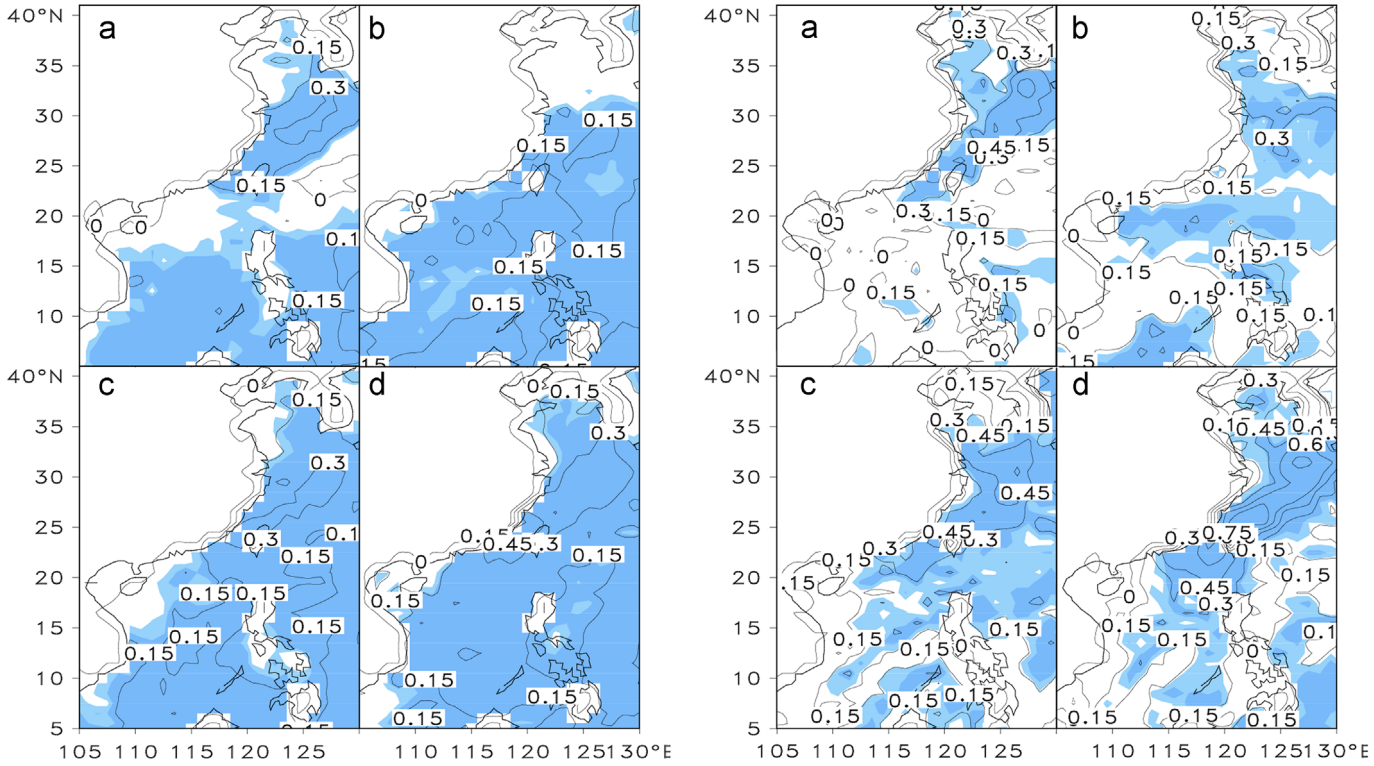


**Fig. 10.** Linear trends of seasonal mean SST during 1951–2011 (left) and 1979–2011 (right) (Unit: °C/10 yr). (a): Spring; (b): Summer; (c): Autumn; (d): Winter. Blue color indicates the trends are significant at the 99% confidence level and light blue indicates the trends are significant at the 95% confidence level.

Author's personal copy



confidence level appears in the ECS, especially for spring, autumn and winter. Most parts of the SCS also see a very significant warming for each of the four seasons. The warming in winter is the largest, with the 0.30 °C/10 yr isotherm surrounding a larger extent than those in other seasons. Less significant warming is seen in the BYS and northern SCS for spring and summer. Change of climatology in four seasons during 1981–2010 comparing to 1961–1990 shows that winter saw the greatest warming in various areas. ECS saw the greatest increase in four seasons compared to other regions. Winter is the most warming season for the whole area (figure is not shown). The seasonal trends of China offshore seas were reported in a few of analyses (Yeh and Kim, 2010; Cai et al., 2011; Meng et al., 2011). Cai et al. (2011) showed that both winter and summer experience warming trend and the climate regime shift in mid-1980. The ECS and the Yellow Sea are among the most significant warming areas. The previous findings are basically consistent with the result of this analysis. It is also realized in the previous studies that winter warming is more significant than that of summer in the East/Japan Sea (Yeh et al., 2010). Zhang et al. (2007) analyzed spring SST in Kuroshio region and found significant warming trend, and they also indicated the abrupt change in SST around 1987.

Similar patterns can be found for the last 30 years (Fig. 10b). The strongest warming trends are in the ECS, with winter mean SST increases reaching more than 0.60 °C/10 yr in the Taiwan Strait and central and eastern ECS. Spring and autumn see less warming trends in most areas. Once again the warming in the BYS and northern SCS is smaller in the last 30 years, and this is especially the case for springtime. The abnormal warming in the Taiwan Strait and the ECS in the last 30 years may be related to the strengthened Kuroshio warm current which may in turn be affected by the multi-decadal variability of the coupled air–sea system in the Pacific Ocean (Feng and Lin, 2009).

## 4. Discussion

Changes and variability of SST have been extensively studied in regional scale (Minobe et al., 2004; Caputi et al., 2009; Goikoetxea et al., 2009; Yeh et al., 2010; Skliris et al., 2012; Takeshige et al., 2013) and global scale (Shea and Trenberth, 1992; Smith and Reynolds, 1998). This paper examines the SST change in the marginal seas of China for the past 140 years.

SST changes of the region show diverse spatial and temporal characteristics. The coastal land area has significant effect on the off-shore sea SST, especially for the Bohai Sea (Yan and Li, 1997; Feng et al., 1999; Bao et al., 2002), and the marginal sea SST also affects the adjacent continent climate (Zhao et al., 2007; Ding et al., 2008). SST of the marginal seas of China is affected by many factors, such as Asian monsoon (Liang et al., 2006), ocean currents including the winter coastal currents, latitudinal locations and solar radiation, discharges of large rivers, and the configuration of the coastal lines (Feng et al., 1999), Kuroshio (Oka and Kawabe, 1998; Ichikawa and Beardsley, 2002; Nonaka and Xie, 2003) and other current systems (Ichikawa and Beardsley, 2002). Annual and seasonal mean SST exhibit different patterns due to the combined influences of the various factors.

Different from other regions, China marginal seas are highly affected by monsoon system. Table 3 shows the correlation coefficients between SST of different seas and the summer and winter monsoon index as formulated by methods which were developed by Q.Y. Zhang et al. (2003) and He and Wang (2012). There is a highly negative correlation between winter monsoon intensity and the SST of all the four sea areas, though the correlation between SST and the summer monsoon index is not so significant. Summer monsoon has less effect on SST in the whole region and the ECS, but the SCS bears a significant negative correlation with the summer monsoon intensity, which can be attributed to the weak upwelling in western SCS during summer monsoon season as discussed in 3.1. Takeshige et al. (2013) analyzed long-term trend of SST in Omura Bay and found that solar radiation is a dominant factor in heating period and air temperature and wind speed are the dominant factors in cooling period. The mechanism mentioned above may give an explanation to highly correlation between the winter monsoon intensity and SST in the marginal seas and the less significant correlation between the summer monsoon intensity and SST. Frequent and intense cold air bursts related to the strong winter monsoon lead to large air–sea heat exchange and apparent impact on off-shore sea SST (Bao et al., 2002). Yeh and Kim (2010) analyzed Yellow/East China Sea SST during 1950–2008 winter and found increase of SST for this area. They also suggested that anomalous anti-cyclonic circulation caused weakening of winter northerly wind is the main cause for the increase of SST. As winter monsoon becomes weaker during the past decades, the marginal seas of China undergo highly significant warming in winter and spring.

**Table 3**
Correlation coefficient between Marginal seas SST and East Asian Monsoon.

| | Whole region | BYS | ECS | SCS |
|---|---|---|---|---|
| Summer | −0.129 | 0.302* | 0.001 | −0.324** |
| Winter | −0.631** | −0.577** | −0.646** | −0.560** |

** and * indicate the trends are significant at 99% and 95% confidence level respectively.

Nevertheless, East Asian Monsoon system is not the only factor influencing the long term trend of marginal seas SST of China. Large-scale factors, like global warming, Pacific Decadal Oscillation and Atlantic Multi-decadal Oscillation may have also affected the long term trends of SST in the marginal seas of China (L.P. Zhang et al., 2010). The mechanism for the linkage, however, is not clear yet at present, and more research is needed to understand the issue.

The low-frequency ENSO variability may have been important in changes of the marginal sea SST (Wu et al., 2005; Song et al., 2007). The maximum values of annual mean SST for all areas of the marginal seas appeared in 1998, when the strongest El Nino event in 20th century occurred (Wang and Gong, 1999; Wolter and Timlin, 2011). ENSO is closely related to East Asian Monsoon (R.H. Zhang et al., 2003; Zhang and Li, 2004), it can lead to weaker than normal East Asian Monsoon (Tomita and Yasunari, 1996; Ji et al., 1997; Wang et al., 2000), and also in favor of an abnormally high SST in the marginal seas. Takeshige et al. (2013) found that 1963 is a strong EAWM year with strong near-surface wind, low air temperature and low SST. In this paper, abnormally low winter SST is also evident in 1963 (Fig. 6). Nevertheless, the winter monsoon intensity in the year seems not so strong (figure is not shown). This difference may be attributed to different definitions and analysis methods used for EAWMI.

The seasonal rhythm of SST obviously results from the effect of solar radiation variation within a year. The absence of the summer peak in the SCS, however, might be related to the prevailing summer southwest monsoon. With the breakout of summer monsoon in late June, upwelling current forms in the western SCS, or offshore area of the Indochina Peninsula, driven by the southwesterly wind. The weak and stable upwelling in the off-shore area of the Indochina Peninsula keeps the summer SST of the whole SCS relatively low. Meanwhile, significant increase of cloudiness and precipitation during summer monsoon season also contribute to the absence of the summer SST peak in the SCS.

We calculate the summer mean SST anomalies of the core upwelling area (10–14°N, 110–115°E, as indicated in Fig. 3b) for

Author's personal copy



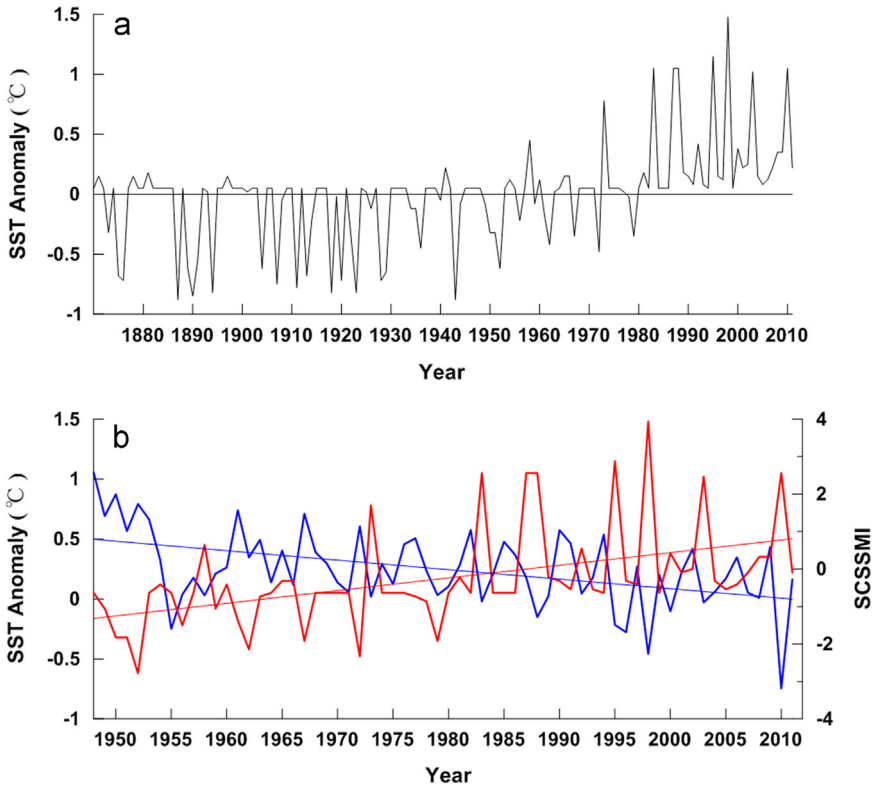


**Fig. 11.** (a) Summer mean SST anomalies of the core upwelling area (10–14°N,110–115°E) for 1870–2011; (b) SCSSMI (blue) and summer mean SST anomalies (red) of the core upwelling area for 1948–2011.

time period 1870–2011, and compare it to the South China Sea Summer Monsoon Index (SCSSMI) defined by Li and Zeng (2002, 2003) for time period 1948–2011. Fig. 11a shows that the SST anomalies undergo a significant increasing trend in the last 50 years, with the SST anomalies for most years shifting from negative to positive values. Correlation coefficient between the summer SST anomalies and SCSSMI is −0.64 (significant at 99.9%), indicating that the weakening of summer monsoon is one of the main reasons for the increase of the SST anomalies in the upwelling area and the decrease of the upwelling intensity.

The observed variations in annual mean SST in the marginal seas of China bear a good similarity to the reported changes in surface air temperature for mainland China for the last 100 years (Tang and Ren, 2005; Ren et al., 2012) and the last half century (Ren et al., 2005a, 2005b). However, the SST trends in the marginal seas are generally smaller than those in the mainland, and the relatively warm period from 1930s to 1940s and the rapidly warming period from 1980s to 2000s found in the mainland air temperature seem much weaker in the study region (Tang and Ren, 2005; Cao et al., 2013).

Compared to the changes in seasonal mean land surface air temperature, the marginal seas of China show more remarkable warming in autumn and winter, and much less increase in temperature in spring and summer. For example, the increases in seasonal mean surface air temperature in mainland China as a whole during 1908–2007 are 0.19 °C/10 yr and 0.16 °C/10 yr for winter and spring, but they are only 0.06 °C/10 yr and 0.01 °C/10 yr for autumn and summer, with the warming in summer insignificant (Tang and Ren, 2005; Ren et al., 2012). The warming in mainland China in the last 50–60 years is also the largest in winter and spring, and the increase in summer temperature is small (Ren et al., 2005, 2012). Therefore, the differences of the trends and decadal variations of annual mean air temperature and seasonal mean SST in the study region from those of mainland surface air temperature are evident. This difference might have partly been caused by the urban bias existing in the land surface air temperature data applied in the current studies (Ren et al., 2008; Jones et al., 2008; A.Y. Zhang et al., 2010) though a further investigation is needed to understand the underlying causes.

It is also worth noting that there are a few of abnormal values in the HadISST dataset used in this paper. We have replaced the records proved wrong with climatological averages. There might be other errors in the dataset, however, and more effort is needed to identify and deal with them. In addition, the spatial resolution of the dataset is relatively low for analyzing climatology of SST in the Bohai Sea and Yellow Sea, and the inefficiency of records of the early years leaves many blank grids for late 19th century and early 20th century, leading to a large uncertainty for the analysis of long-term trends of SST.

## 5. Conclusions

This paper analyzes the spatial characteristics and long-term change of SST over the marginal seas of China for the last 140 years. The following conclusions can be drawn from the analysis. In conclusion, annual mean SST decreases with increasing latitude, with high temperature ranging from 24–28 °C in the south and low temperature ranging from 12–20 °C in the north. Large seasonal shifts mainly occur in the Bohai Sea and the Yellow Sea. The smallest and largest spatial SST differences among various sea areas and latitudinal zones are seen in August and January respectively, and the coolest month is February for the whole region and various areas. Except for the South China Sea for period 1901–2011, the warming trends of the marginal seas of China during 1901–2011 and 1979–2011 are larger than the global and hemispheric averages, with the East China Sea seeing the largest warming of all areas. In recent 140 years or 50 years, all the sea

Author's personal copy



areas see rising trends of annual mean SST, with the East China Sea experiencing the most significant warming. Larger and more significant warming generally occurs in autumn and winter for both time periods 1901–2011 and 1979–2011. An evident slowdown of warming in the marginal seas of China over the last 14 years is found, and the slowdown is characterized by a decreasing trend of annual and seasonal mean SST, indicating that it is more evident than the global, northern hemispheric and China mainland averages. A weak upwelling current exists in western South China Sea, and the upwelling intensity has a significant positive correlation with the SCS summer monsoon index, with both seeing a decrease in recent 64 years.

## Acknowledgments

This work is financially supported by the Ministry of Science and Technology of China (GYHY201206012).

## References

Bao, X.W., Wan, X.Q., Gao, G.P., Wu, D.X., 2002. The characteristics of the seasonal variability of the sea surface temperature field in the Bohai Sea, the Huanghai Sea and the East China Sea from AVHRR data. Acta Oceanol. Sin. 24 (5), 125–133 (in Chinese).

Belkin, I.M., 2009. Rapid warming of large marine ecosystems. Prog. Oceanogr. 81, 207–213.

Cai, R.S., Chen, J.L., Tan, H.J., 2011. Variations of the sea surface temperature in the offshore area of China and their relationship with the East Asian monsoon under the global warming. Clim. Environ. Res. 16 (1), 94–104 (in Chinese with English abstract).

Cai, S.Q., Su, J.L., Gan, Z.J., Liu, Q.Y., 2001. The numerical study on the dynamic mechanism of the South China Sea upper circulation in winter. Acta Oceanol. Sin. 23 (5), 14–23 (in Chinese with English abstract).

Cao, L.J., Zhao, P., Yan, Z.W., Jones, P., Zhu, Y.N., Y., Y, Tang, G.L., 2013. Instrumental temperature series in eastern and central China back to the nineteenth century. J. Geophys. Res.: Atmos. 118, 8197–8207.

Caputi, N., Lestang, S.D., Feng, M., Pearce, A., 2009. Seasonal variation in the long-term warming trend in water temperature off the western Australian coast. Mar. Freshw. Res. 60, 129–139.

Ding, Y.H., Ren, G.Y. (Eds.), 2008. Introduction to Climate Change Science of China. China Meteorological Press, Beijing

Ding, Y.H., Wang, Z.Y., Sun, Y., 2008. Inter-decadal variation of the summer precipitation in East China and its association with decreasing Asian summer monsoon. Part I: Observed evidences. Int. J. Climatol. 28, 1139–1161.

Easterling, D.R., Wehner, M.F., 2009. Is the climate warming or cooling? Geophys. Res. Lett. 36 (L08706), 1–3.

Feng, L., Lin, X.P., 2009. Long-term trend of the East China Sea surface temperature during 1945–2006. Period. Ocean Univ. China 39 (1), 13–18 (in Chinese with English abstract).

Feng, S.Z., Li, F.Q., Li, S.J., 1999. Introduction to Marine Science. Higher Education Press, Beijing, China, pp. 443–457 (in Chinese)

Fröhlich, C., 2012. Total solar irradiance observations. Surv. Geophys. 33, 453–473.

Goikoetxea, N., Borja, Á., Fontán, A., González, M., Valencia, V., 2009. Trends and anomalies in sea-surface temperature, observed over the last 60 years, within the southeastern Bay of Biscay. Cont. Shelf Res. 29, 1060–1069.

Hartmann, D.L., Klein Tank, A.M.G., Rusticucci, M., Alexander, L.V., Brönnimann, S., Charabi, Y., Dentener, F.J., Dlugokencky, E.J., Easterling, D.R., Kaplan, A., Soden, B. J., Thorne, P.W., Wild, M., Zhai, P.M., 2013. Observations: Atmosphere and Surface. In: Climate Change 2013: The Physical Science Basis. Contribution of Working Group I to the Fifth Assessment Report of the Intergovernmental Panel on Climate Change [Stocker, T.F., Qin, D., Plattner, G.-K., Tignor, M., Allen, S.K., Boschung, J., Nauels, A., Xia, Y., Bex, V., Midgley, P.M., (eds.)]. Cambridge University Press, Cambridge, United Kingdom and New York, NY, USA.

He, S.P., 2013. Reduction of the East Asian winter monsoon interannual variability after the mid-1980s and possible cause. Chin. Sci. Bull. 58 (12), 1331–1338.

He, S.P., Wang, H.J., 2012. An integrated East Asian winter monsoon index and its interannual variability. Chin. J. Atmos. Sci. 36 (3), 523–538 (in Chinese with English abstract).

Held, I.M., 2013. Climate science: the cause of the pause. Nature 501, 318–319.

Hickox, R., Belkin, I., Cornilion, P., Shan, Z.Q., 2000. Climatology and seasonal variability of ocean fronts in the East China, Yellow and Bohai seas from satellite SST data. Geophys. Res. Lett. 27 (18), 2945–2948.

Hu, J.F., 1996. Meteorological Statistics Theory and Technique. Qingdao Ocean University Press, Qingdao, China, pp. 34–36 (in Chinese)

Huang, D.J., Ni, X.B., Tang, Q.S., Zhu, X.H., Xu, D.F., 2012. Spatial and temporal variability of sea surface temperature in the Yellow Sea and East China Sea over the past 141 years. Modern Climatology. InTech, Rijeka, Croatia, pp., 213–234

Ichikawa, H., Beardsley, R.C., 2002. The current system in the Yellow and East China Seas. J. Oceanogr. 58, 77–92.

Ji, L.R., Sun, S.Q., Arpe, K., Bengtsson, L., 1997. Model study on the interannual variability of Asian winter monsoon and its influence. Adv. Atmos. Sci. 14 (1), 1–22.

Jin, Q.H., Wang, H., 2011. Multi-time scale variations of sea surface temperature in the China seas based on the HadISST dataset. Acta Oceanol. Sin. 30 (4), 14–23.

Jones, P.D., Hulme, M., 1996. Calculating regional climatic time series for temperature and precipitation: methods and illustrations. Int. J. Climatol. 16, 361–377.

Jones, P.D., Lister, D.H., Li, Q., 2008. Urbanization effects in large-scale temperature records, with an emphasis on China. J. Geophys. Res.: Atmos. 113 (D16122), 1–12.

Jones, P.D., Lister, D.H., Osborn, T.J., Harpham, C., Salmon, M., Morice, C.P., 2012. Hemispheric and large-scale land surface air temperature variations: an extensive revision and an update to 2010. J. Geophys. Res. 117 (D05127), 1–29.

Kosaka, Y., Xie, S.P., 2013. Recent global-warming hiatus tied to equatorial Pacific surface cooling. Nature 501, 403–407.

Li, H.M., Dai, A.G., Zhou, T.J., Lu, J., 2010. Responses of East Asian summer monsoon to historical SST and atmospheric forcing during 1950–2000. Clim. Dyn. 34, 501–514.

Li, J., Zuo, J.C., Li, Y.F., Zhang, B., Chen, Y.H., 2011. Low-frequency variation and influence factors of sea surface temperature in South China Sea. J. Hohai Univ. (Nat. Sci.) 39 (5), 575–582 (in Chinese with English abstract).

Li, J.P., Zeng, Q.C., 2002. A unified monsoon index. Geophys. Res. Lett. 29 (8), 115-1–115-4.

Li, J.P., Zeng, Q.C., 2003. A new monsoon index and the geographical distribution of the global monsoons. Adv. Atmos. Sci. 20 (2), 299–302.

Li, J.P., Zeng, Q.C., 2005. A new monsoon index, its interannual variability and relation with monsoon precipitation. Clim. Environ. Res. 10 (3), 351–365 (in Chinese with English abstract).

Liang, Q.Q., Jian, M.Q., Peng, Y.G., Luo, H.B., 2006. Impacts of East Asian winter monsoon on sea surface temperature in Northwestern Pacific. J. Trop. Oceanogr. 25 (6), 1–7 (in Chinese with English abstract).

Liu, Q.Y., Zhang, Q., 2013. Analysis on long-term change of sea surface temperature in the China Seas. J. Ocean Univ. China (Ocean. Coast. Sea Res.) 12 (2), 295–300.

Meng, Q.J., Shi, J.W., Liu, N., Wang, F., 2011. A comprehensive analysis of the long-term variation of sea surface temperature in the China seas based on historical and satellite data. Mar. Sci. 35 (12), 121–126 (in Chinese with English abstract).

Minobe, S., Sako, A., Nakamura, M., 2004. Interannual to interdecadal variability in the Japan Sea based on a new gridded upper water temperature dataset. J. Phys. Oceanogr. 34, 2382–2397.

Nonaka, M., Xie, S.P., 2003. Covariations of sea surface temperature and wind over the Kuroshio and its extension: evidence for ocean-to-atmosphere feedback. J. Clim. 16, 1404–1413.

Oka, E., Kawabe, M., 1998. Characteristics of variations of water properties and density structure around the Kuroshio in the East China Sea. J. Oceanogr. 54, 605–617.

Rayner, N.A., Parker, D.E., Horton, E.B., Folland, C.K., Alexander, L.V., Rowell, D.P., Kent, E.C., Kaplan, A., 2003. Global analyses of sea surface temperature, sea ice, and night marine air temperature since the late nineteenth century. J. Geophys. Res. 108 (D14), 4407.

Ren, G.Y., Guo, J., Xu, M.Z., Chu, Z.Y., Zhang, L., Zou, X.K., Li, Q.X., Liu, X.N., 2005a. Climate changes of China's mainland over the past half century. Acta Meteorol. Sin. 63 (6), 942–956 (in Chinese with English abstract).

Ren, G.Y., Xu, M.Z., Chu, Z.Y., Guo, J., Li, Q.X., Liu, X.N., Wang, Y., 2005b. Changes of surface air temperature in China during 1951–2004. Clim. Environ. Res. 10 (4), 717–727 (in Chinese with English abstract).

Ren, G.Y., Zhou, Y.Q., Chu, Z.Y., Zhou, J.X., Zhang, A.Y., Guo, J., Liu, X.F., 2008. Urbanization effect on observed surface air temperature trend in North China. J. Clim. 21 (6), 1333–1348.

Ren, G.Y., Ding, Y.H., Zhao, Z.C., Zheng, J.Y., Wu, T.W., Tang, G.L., Xu, Y., 2012. Recent progress in studies of climate change in China. Adv. Atmos. Sci. 29 (5), 958–977.

Reynolds, R.W., 1988. A real-time global sea surface temperature analysis. J. Clim. 1, 75–87.

Reynolds, R.W., Marsico, D.C., 1993. An improved real-time global sea surface temperature analysis. J. Clim. 6, 114–119.

Reynolds, R.W., Smith, T.M., 1995. A high-resolution global sea surface temperature climatology. J. Clim. 8, 1571–1583.

Rodionov, S., Overland, J.E., 2005. Application of a sequential regime shift detection method to the Bering Sea ecosystem. ICES J. Mar. Sci. 62, 328–332.

Rodionov, S.N., 2004. A sequential algorithm for testing climate regime shifts. Geophys. Res. Lett. 31, L09204.

Shea, D.J., Trenberth, K.E., 1992. A global monthly sea surface temperature climatology. J. Clim. 5, 987–1001.

Shi, N., Lu, J.J., Zhu, Q.G., 1996. East Asian winter/summer monsoon intensity indices with their climatic change in 1873–1989. J. Nanjing Inst. Meteorol. 19 (2), 168–177 (in Chinese with English abstract).

Skliris, N., Sofianos, S., Gkanasos, A., Mantziafou, A., Vervatis,V., Axaopoulos, P., Lascaratos, A., 2012. Decadal scale variability of sea surface temperature in the Mediterranean Sea in relation to atmospheric variability. Ocean. Dyn. 62, 13–30.

Smith, D., 2013. Oceanography: has global warming stalled? Nat. Clim. Change 3, 618–619.

Smith, T.M., Reynolds, R.W., 1998. A high-resolution global sea surface temperature climatology for the 1961–90 base period. J. Clim. 11, 3320–3323.

Solomon, S., Rosenlof, K.H., Portmann, R.W., Daniel, J.S., Davis, S.M., Sanford, T.J., Plattner, G.K., 2010. Contributions of stratospheric water vapor to decadal changes in the rate of global warming. Science 327 (5970), 1219–1223.

Author's personal copy



Song, D.H., Yu, H.M., Bao, X.W., 2007. Analysis of the interannual variability of the eastern China seas and its adjacent seas surface temperature. Period. Ocean Univ. China 37, 21–28 (in Chinese with English abstract).
Takeshige, A., Takahashi, T., Nakata, H., Kimura, S., 2013. Long-term trends in sea surface temperature in coastal water in relation to large-scale climate change: a case study in Omura Bay, Japan. Cont. Shelf Res. 66, 73–82.
Tang, G.L., Ren, G.Y., 2005. Reanalysis of surface air temperature change of the past 100 years over China. Clim. Environ. Res. 10 (4), 791–798 (in Chinese with English abstract).
Tang, X.H., Wang, F., Chen, Y.L., Li, M.K., 2009. Warming trend in northern East China Sea in recent four decades. Chin. J. Oceanol. Limnol. 27 (2), 185–191.
Tomita, T., Yasunari, T., 1996. Role of the northeast winter monsoon on the biennial oscillation of the ENSO/monsoon system. J. Meteorol. Soc. Jpn. 74, 399–413.
Trenberth, K.E., Fasullo, J.T., 2013. An apparent hiatus in global warming? Earths Future 1 (1), 19–32.
Trenberth, K.E., Jones, P.D., Ambenje, P., Bojariu, R., Easterling, D., Tank, A. K., Parker, D., Rahimzadeh, F., Renwick, J.A., Rusticucci, M., Soden, B., Zhai, P., 2007. Observations: Surface and Atmospheric Climate Change. In: Climate Change 2007: The Physical Science Basis. Contribution of Working Group I to the Fourth Assessment Report of the Intergovernmental Panel on Climate Change [Solomon, S., Qin, D., Manning, M., Chen, Z., Marquis, M., Averyt, K.B., Tignor, M., Miller, H.L., (eds.)]. Cambridge University Press, Cambridge, United Kingdom and New York, NY, USA.
Von, S.H., Francis, W.Z., 2003. Statistical Analysis in Climate Research. Cambridge University Press, Cambridge, United Kingdom, pp. 150–151
Wang, B., Ren, G.W., Fu, X.H., 2000. Pacific-East Asian teleconnection: how does ENSO affect East Asian climate? J. Clim. 13, 1517–1536.
Wang, F., Meng, Q.J., Tang, X.H., Hu, D.X., 2013. The long-term variability of sea surface temperature in the seas east of China in the past 40 a. Acta Oceanol. Sin. 32 (3), 48–53.
Wang, H.J., Fan, K., 2013. Recent changes in the East Asian Monsoon. Chin. J. Atmos. Sci. 37 (2), 313–318 (in Chinese with English abstract ).
Wang, S.W., Gong, D.Y., 1999. ENSO events and their intensity during the past century. Meteorol. Mon. 25 (1), 9–13 (in Chinese).
Wei, F.Y., 2007. Contemporary Climate Statistical Diagnosis and Forecasting Techniques. China Meteorological Press, Beijing, China (pp. 30–32, 36–38 (in Chinese)
Wolter, K., Timlin, M.S., 2011. El Niño/Southern Oscillation behaviour since 1871 as diagnosed in an extended multivariate ENSO index (MEI.ext). Int. J. Climatol. 31, 1074–1087.
Wu, D.X., Li, Q., Lin, X.P., Bao, X.W., 2005. The characteristics of the Bohai sea SST anomaly interannual variability during 1990–1999. Period. Ocean Univ. China 35 (2), 173–176 (in Chinese with English abstract).
Xie, S.P., Hafner, J., Tanimoto, Y., Liu, W.T., Tokinaga, H., Xu, H.M., 2002. Bathymetric effect on the winter sea surface temperature and climate of the Yellow and East China Seas. Geophys. Res. Lett. 29 (24), 81-1–81-4.
Yan, J.Y., Li, J.L., 1997. East China Sea and adjacent area temperature change in recent 100 years. Acta Oceanol. Sin. 19 (6), 121–126 (in Chinese).
Yeh, S.W., Kim, C.H., 2010. Recent warming in the Yellow_East China Sea during winter and the associated atmospheric circulation. Cont. Shelf Res. 30, 1428–1434.
Yeh, S.W., Park, Y.G., Min, H.S., Kim, C.H., Lee, J.H., 2010. Analysis of characteristics in the sea surface temperature variability in the East/Japan Sea. Prog. Oceanogr. 85, 213–223.
Zhang, A.Y., Ren, G.Y., Zhou, J.X., Chu, Z.Y., Ren, Y.Y., Tang, G.L., 2010. Urbanization effect on surface air temperature trends over China. Acta Meteorol. Sin. 68 (6), 957–966 (in Chinese with English abstract).
Zhang, L.P., Wu, L.X., Lin, X.P., Wu, D.X., 2010. Modes and mechanisms of sea surface temperature low-frequency variations over the coastal China seas. J. Geophys. Res. 115, C08031.
Zhang, Q.Y., Tao, S.Y., Chen, L.T., 2003. The inter-annual variability of East Asian summer monsoon and its association with the pattern of general circulation over East Asia. Acta Meteorol. Sin. 61 (4), 559–568 (in Chinese with English abstract).
Zhang, R.H., Li, Q., 2004. Impact of sea temperature variability of tropical oceans on East Asian Monsoon. Meteorol. Mon. 30 (12), 22–26 (in Chinese with English abstract).
Zhang, R.H., Zhou, G.Q., Chao, J.P., 2003. On ENSO dynamics and its prediction. Chin. J. Atmos. Sci. 27 (4), 674–688 (in Chinese with English abstract).
Zhang, R.H., Liu, J.M., et al., 2005. The roles of ocean and land processes in variations of climate and environment in China. In: Qin, D.H., Ding, Y.H., Su, J.L. (Eds.), Changes of Climate and Environment in China, vol. 1. Science Press, Beijing, pp. 319–357.
Zhang, T.Y., Sun, Z.B., Li, Z.X., Wang, D.Y., 2007. Relation between spring Kuroshio SSTA and summer rainfall in China. J. Trop. Meteorol. 23 (2), 189–195 (in Chinese with English abstract).
Zhang, X.Z., Gong, Y.F., Wu, X.Y., 2005. The long-term change for sea surface temperature in the last 100 years in the offshore sea of China. Clim. Environ. Res. 10 (4), 799–807 (in Chinese with English abstract).
Zhao, P., Zhang, R.H., Liu, J.P., Zhou, X.J., He, J.H., 2007. Onset of southwesterly wind over eastern China and associated atmospheric circulation and rainfall. Clim. Dyn. 28, 797–811.

Author's personal copy

Theor Appl Climatol
DOI 10.1007/s00704-014-1127-x

ORIGINAL PAPER

# Urbanization effect on long-term trends of extreme temperature indices at Shijiazhuang station, North China

**Tao Bian · Guoyu Ren · Bingxiang Zhang · Lei Zhang · Yanxia Yue**

Received: 26 July 2013 / Accepted: 9 February 2014
© Springer-Verlag Wien 2014

**Abstract** Based on daily temperature data from an urban station and four rural stations of Shijiazhuang area in Hebei Province, North China, we analyzed the trends of extreme temperature indices series of the urban station (Shijiazhuang station) and rural stations during 1962–2011 and the urbanization effect on the extreme temperature indices of the urban station. The results showed that the trends of annual extreme temperature indices of the urban station and the rural stations are significantly different in the recent 50 years. Urbanization effect on the long-term trends of hot days, cold days, frost days, diurnal temperature range (DTR), extreme maximum temperature, and extreme minimum temperature at the urban station were all statistically significant, reaching 1.10 days/10 years, −2.30 days/10 years, −2.55 days/10 years, −0.20 °C/10 years, 0.16 °C/10 years, and 0.70 °C/10 years, respectively, with the urbanization contributions to the overall trends reaching 100, 38.0, 42.2, 40.0, 94.1, and 47.0 %, respectively. The urbanization effect on trend of ice days was also significant, reaching −0.47 days/10 years. However, no significant urbanization effect on trends of minimum values of maximum temperature and maximum values of minimum temperature had been detected. The urbanization effects in the DTR and extreme minimum temperature series of Shijiazhuang station in wintertime were highly significant.

## 1 Introduction

Extreme weather and climate phenomena are the small probability events, but they can have major impacts on the human and natural systems, arousing much attention from the governments and academic community. Many researchers examined the long-term change in extreme temperature events (e.g., Karl et al. 1991; Plumner 1996; Easterling et al. 1997; Zhai and Pan 2003; Alexander et al. 2006; Zhou and Ren 2011). They found that the annual mean minimum temperature (Tmin) of global continents and mainland China experienced significant rising trends for the past decades. The annual mean maximum temperature (Tmax) also witnessed rising trends, but they were less significant than the annual mean Tmin. In addition, they also found that the frequency and intensity of extreme cold events generally decreased, but those of extreme warm events mostly increased.

Studies also showed that changing trends of annual mean surface air temperature (SAT) observed by the meteorological stations were clearly influenced by the urban warming in many land areas of eastern Asia including mainland China (Kalnay and Cai 2003; Choi et al. 2003; Chung et al. 2004; Chu and Ren 2005; Ren et al. 2007, 2008; Fujibe 2008; Yang et al. 2011). For example, urbanization effect accounted for more than 38 % of the overall annual mean SAT increase for the national stations in North China during the time period 1960–2000 (Ren et al. 2008). A recent work revealed that urbanization effect on annual mean SAT trends observed by the national reference climatic stations and the national basic meteorological stations in mainland China was also significant, explaining at least 27 % of the overall warming trend (Zhang et al. 2010). Apparently, the urbanization effect on the changing trends of the local and regional annual mean SAT cannot be ignored.

It is natural to assume that the urbanization or the enhanced urban heat island (UHI) effect will also affect the linear trends of frequency and intensity of extreme temperature events due to the close linkage between the mean SAT and the Tmax and Tmin. There is little systematic investigation addressing this issue, however, and the relevant literatures are also scant. Recently, Zhou and Ren (2009) analyzed the urbanization

T. Bian · B. Zhang · Y. Yue
Shijiazhuang Meteorological Bureau, Shijiazhuang 050081, China

T. Bian · G. Ren (✉) · L. Zhang
Laboratory for Climate Studies, National Climate Center, China Meteorological Administration (CMA), Beijing 100081, China
e-mail: guoyoo@cma.gov.cn

Published online: 28 February 2014

Author's personal copy



effect on the changing trends of the mean maximum and minimum temperature for different categories of metrological stations in North China during 1961–2000, and they found significant increasing trends of annual mean Tmin caused by the urbanization for most of the national stations, with the region-averaged urbanization effect for the national stations reaching 0.20 °C/10 years, which accounted for 52.6 % of the overall warming. Zhang et al. (2011) analyzed the urbanization effect on annual and seasonal mean trends of the extreme temperature indices at Beijing Meteorological Station during 1960–2008 and found that urbanization effects on the trends of the indices series related to daily Tmin were all significant, and the contributions of the urbanization effect to the overall changing trends of the Tmin-based annual mean extreme indices series were all as high as 100 %, indicating that the changes caused by the urbanization effect were overwhelming. However, the urbanization effects on the trends of the indices series related to daily Tmax were mostly insignificant at the urban station.

The urban station of Shijiazhuang was originally located in the western suburbs of the city. The observational environment was good and representative for the monitoring of regional climate before the 1980s. The area around the station was desolate, with only a few small villages and barracks of the garrison army being dotted in the vast plain. Since the early 1990s, however, buildings near the station have been increasing gradually as the urbanization process accelerates. At present, the observational ground is well-surrounded by high-rising buildings, and it has now become a typical urban station. The UHI effect near Shijiazhuang station is remarkable, and the urban warming trend in terms of annual mean SAT was estimated to be 0.19 °C/10 years during 1962–2009, accounting for 67.9 % of the overall warming trend (Bian 2010). The urbanization effect on the Tmin trend is more significant, because the largest UHI intensity is registered between 20 and 07 h of nest day Beijing Time.

However, it is unclear if, or in what extent, the rapid urbanization and the increasing UHI intensity around the station have affected the linear trends of the extreme temperature indices. Solving this question or answering this question enables us to better understand the respective trends of the regional and near-station extreme temperature event frequencies and to further explore the mechanism and causes of the regional climate change. We can also provide the accurate observation data for evaluating the climate change impacts on natural ecosystem, water resources, and agricultural production in the area.

Based on daily SAT data from Shijiazhuang station and four nearby rural stations during the past 50 years, we compare the changing trends of the extreme temperature indices of the urban and rural stations and evaluate the urbanization effect on the trends of extreme temperature indices for the urban station. We show that the extreme temperature events recorded by the urban and rural stations experience obviously different trends, indicating a significant urbanization effect at the Shijiazhuang station.

## 2 Data and methods

The daily maximum, minimum, and average temperature records of five meteorological stations during 1962–2011 were used. They were respectively Shijiazhuang, Gaocheng, Yuanshi, Pingshan, and Xinle stations in Shijiazhuang area (Fig. 1). The data had been quality controlled by the Shijiazhuang Meteorological Bureau, and the wrong records caused by manual factors had been corrected. Seasonal division was as follows: spring (3–5 months), summer (6–8 months), autumn (9–11 months), and winter (12 to 2 months of the next year).

Shijiazhuang, the capital city of Hebei Province, is located in the east of the Taihang Mountains and in the west of the North China Plain. It is a large city with a rapid urbanization process during the past 60 years and a permanent population of 2.7 million at present. Shijiazhuang station is located in the mid-west of the city, and it is a typical urban station by any means. It is not only within the built-up areas of the city but also heavily surrounded by the nearby buildings, as seen in Fig. 1. The four rural stations are all located near the four small towns in the east, south, northwest, and northeast of Shijiazhuang station, with a distance of more than 20 km from the urban areas of Shijiazhuang City. The permanent population in the built-up areas is about 0.1 million for each of the small towns (Table 1), and the locations of the observational stations are generally at the periphery zones of the built-up areas. The rural stations have been influenced by the urbanization in some extents as seen in Fig. 1, in spite of the fact that they are the most rural stations available in the study region. A few of the buildings near the rural stations can be seen, but they are usually not tall, and the micro-environment around the observational grounds is somehow good. Real rural stations actually do not exist in any regions of North China Plain. The rural stations have an average altitude of 80.4 m above sea level and an average latitude of 38.09°N, which are close to the altitude and latitude of the urban station (81.0 m and 38.03°N), enabling the direct comparison of the mean temperature and extreme temperature indices between them.

Shijiazhuang station has not been moved since its establishment in 1954. This enables it to be an ideal station for examining the urban climate change and particularly the urbanization effect on mean and extreme temperature trends because there is no major problem with data inhomogeneity probably caused by relocations. This is extremely unusual in mainland China because majority of the large city stations, usually also the national reference climate stations or national basic meteorological stations, have been moved for at least

Author's personal copy



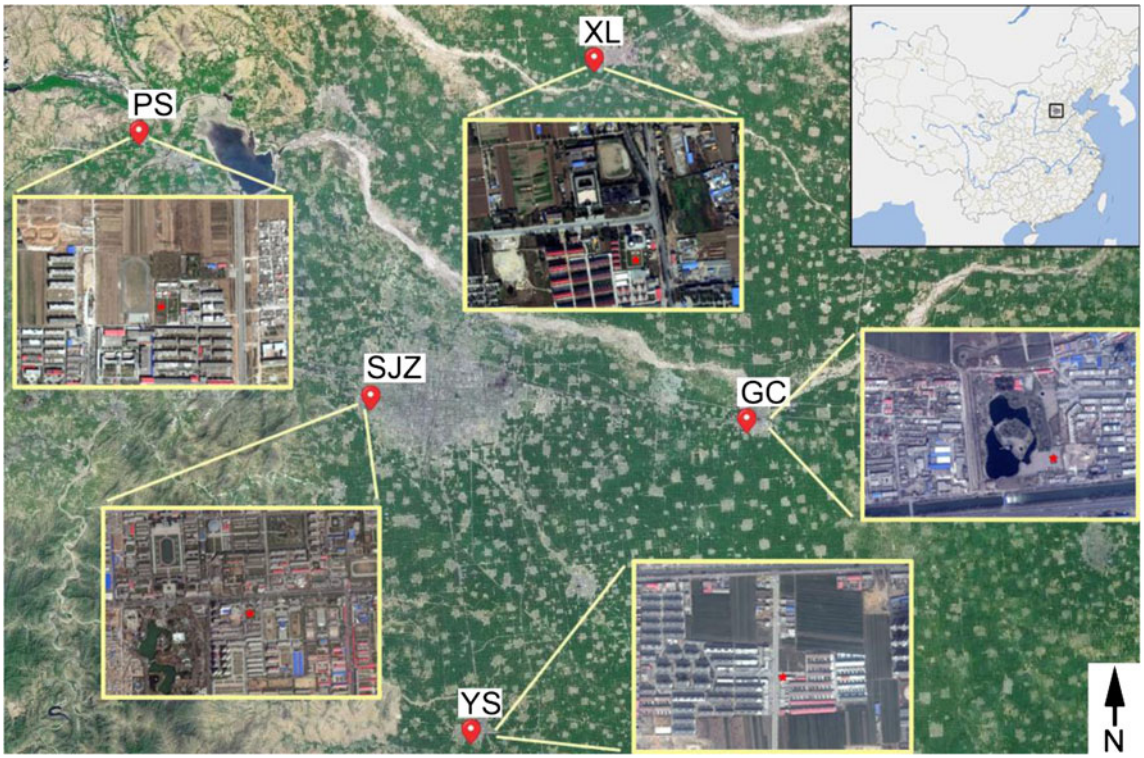


**Fig. 1** Distribution and settings of the five meteorological stations used in this study. *SJZ* Shijiazhuang, *GC* Gaocheng, *YS* Yuanshi, *PS* Pingshan, and *XL* Xinle

one time, leading to obvious temporal inhomogeneities in SAT data (Yan et al. 2001; Li et al. 2004). Therefore, the SAT data from Shijiazhuang station does not need any adjustment for inhomogeneities related to relocation. The introduction of the autonomous weather stations (AWS) around 2004 may in certain extent have affected the SAT data homogeneity, but Wang et al. (2007) showed that the influence was small and could be ignored.

However, each of the four rural stations has been moved, with Xinle station moved for four times (Table 1). The breakpoints of data series caused by relocations were examined for Tmin, Tmax, mean temperature (Tmean), and diurnal temperature range (DTR) for the rural stations. The method was to calculate the difference between each rural station series and the reference series to obtain the difference series and to detect the breakpoints by using moving $t$ test (Fig. 2). The reference series are obtained by averaging the nearby five station data series having the largest correlation coefficients with the target station series, from a bigger dataset in Hebei Province. Based on whether or not the values of $t$ statistics exceed the significance level, locations of the change points could be determined (von Storch and Zwiers 2003; Wei 2007). If the change points could be proved to be real in reference to the metadata, then the adjustments could be made. Here, $n$=60, the length of the subsequences $n1=n2=4$. Given the significant level $\alpha=0.01$, with a freedom degree of $t$ distribution $v=n_1+n_2-2=6$, $t_{0.01}=3.71$ could be obtained.

It was found that the Tmax, Tmean, and DTR series witnessed no significant breakpoint (Figure omitted), but the Tmin series of Pingshan and Yuanshi stations each had a

**Table 1** Information of the five meteorological stations used in this study

| Station | | Longitude (E) | Latitude (N) | Altitude (m.a.s.l.) | Time of starting records | Relocations and time | Population (million) |
|---|---|---|---|---|---|---|---|
| Urban | Shijiazhuang | 114.42° | 38.03° | 81.0 | 1954.12.01 | 0 | 2.70 |
| Rural | Gaocheng | 114.81° | 38.01° | 53.5 | 1958.08.01 | 2 (1969.07, 1999.01) | 0.12 |
| | Yuanshi | 114.53° | 37.75° | 66.4 | 1960.01.01 | 3 (1982.02, 1998.01, 2007.01) | 0.08 |
| | Pingshan | 114.02° | 38.25° | 131.0 | 1959.01.01 | 3 (1961.09, 1964.01, 2000.01) | 0.13 |
| | Xinle | 114.68° | 38.35° | 70.8 | 1959.03.01 | 4 (1961.05, 1963.12, 1989.05, 2003.01) | 0.11 |
| | Rural average | 114.51° | 38.09° | 80.5 | – | – | 0.11 |

Author's personal copy



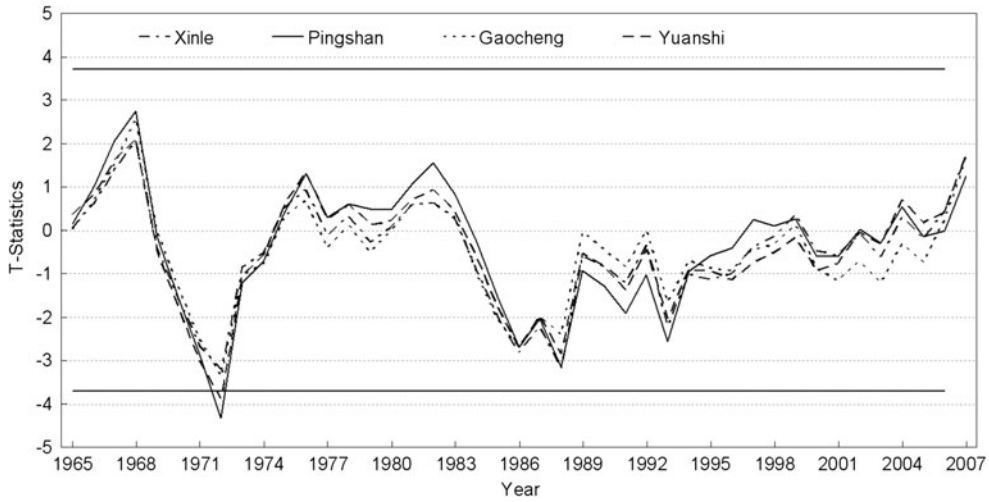


**Fig. 2** Detection of inhomogeneities of annual mean Tmin for four rural stations (*black straight lines* mark the 0.01 significance level) during 1962–2011

breakpoint in 1972. There were no indication for station relocation and instrument change around 1972 for the two stations, however, and the breakpoints were not adjusted in this study.

The extreme temperature indices analyzed are listed in Table 2. These indices were defined with reference to the work of the Expert Team on Climate Change Detection and Indices (ETCCDI) (Alexander et al. 2006) and the operational standards of China Meteorological Administration (CMA). Relative threshold method based on percentile values was not used, but annual counts of days with the actual temperature above certain fix thresholds and the extreme Tmax and Tmin values were adopted. Cold days were defined as the number of days with daily mean temperature equal to or less than 0 °C, according to the local operational standard. Because the study area was relatively small and the distances among the stations were short, a method of simple arithmetic average was applied to calculate average of the extreme temperature indices for the rural stations. The method of least squares was used to calculate the linear trends of the extreme temperature indices series, and Student's *t* test method was used to examine the significance of the linear trends of the time series, with the different significance levels given as $\alpha$=0.05, $\alpha$=0.01, and $\alpha$=0.001 (von Storch and Zwiers 2003).

**Table 2** Definition of the extreme temperature indices applied in this study

| No. | Index | Definition | Unit |
|---|---|---|---|
| 1 | Hot days | Annual count when Tmax≥35 °C | Day |
| 2 | Cold days | Annual count when Tmean≤0 °C | Day |
| 3 | Frost days | Annual count when Tmin< 0 °C | Day |
| 4 | Ice days | Annual count when Tmax<0 °C | Day |
| 5 | DTR | Annual (seasonal) mean difference between Tmax and Tmin | °C |
| 6 | Maximum Tmax | Annual (seasonal) maximum value of Tmax | °C |
| 7 | Minimum Tmin | Annual (seasonal) minimum value of Tmin | °C |
| 8 | Maximum Tmin | Annual (seasonal) maximum value of Tmin | °C |
| 9 | Minimum Tmax | Annual (seasonal) minimum value of Tmax | °C |

In evaluating urbanization effect on trends of the extreme temperature indices, the following terms were defined with reference to Zhou and Ren (2009) and Zhang et al. (2011). The urbanization effect referred to the linear trends in extreme temperature indices recorded at urban station caused by strengthening UHI intensity and/or other local anthropogenic factors, which was expressed as $\Delta Xur$:

$$\Delta Xur = Xu - Xr \quad (1)$$

where $X_u$ was the linear trend of an extreme temperature index series at the urban station, and $X_r$ was the linear trend of the average extreme temperature index series at the rural stations. If $\Delta X_{ur}>0$, the extreme temperature index series at urban station has an upward change related to that of rural station due to the urbanization effect, and if $\Delta X_{ur}<0$, the extreme temperature index series at urban station has a downward change related to that of rural station due to the urbanization effect.

Contribution of urbanization effect or urbanization contribution referred to the proportion of the statistically significant urbanization effect to the overall trend of the extreme temperature index series at the urban station, expressed as $E_u$ (%)

$$Eu = |\Delta Xur/Xu| \times 100\% = |(Xu - Xr)/Xu| \times 100\% \quad (2)$$

Considering the urbanization effect can be negative in some circumstances, absolute value was taken for $E_u$ in order to enable $0 \le E_u \le 100$ %. If $E_u$=0, it denotes that the

Author's personal copy



urbanization effect has no contribution to the overall trend of the extreme temperature index series at the urban station; if $E_u$=100 %, it shows that the linear trend of the extreme temperature index series at the urban station is entirely caused by the urbanization effect. In practical calculations, $E_u$ may exceed 100 % in a few cases, indicating that unknown local anthropogenic factors might have had an effect, but it was adjusted to 100 % in this paper. As indicated in the definition, if the urbanization effect is not statistically significant, the urbanization contribution will not be calculated.

The differences of year-to-year extreme temperature indices between Shijiazhuang station and the four rural station averages were calculated to obtain the difference series, which can be regarded as year-to-year urbanization effect series. Because the altitude difference and latitude difference between Shijiazhuang station and the four rural station averages were only 0.6 m and 0.03°N, the temperature difference caused by the altitude and latitude change can be negligible, and the difference of the extreme temperature indices can well represent the yearly urbanization effect (mainly the UHI effect) on the extreme temperature of Shijiazhuang station. Therefore, the linear trend of the difference series was actually another expression of the urbanization effect as defined in this paper, or it was equal to $\Delta X_{ur}$. The equality had been proved by comparing the values of trends of the difference series with the urbanization effects with regard to the annual and monthly mean temperature series of Shijiazhuang station. For example, the trend of the annual mean difference series was 0.181 °C/10 years, and the difference of trends of the urban station and the reference series was 0.181 °C/10 years. No significant difference was found in estimates obtained by using the two methods.

## 3 The results

### 3.1 Annual mean trends and urbanization effects

Table 3 provides the linear trends of annual extreme temperature indices for all urban station and rural stations and urbanization effect and urbanization contribution for Shijiazhuang station; and Figs. 3, 4, 5, 6 show the yearly values and linear trends of the difference series of extreme temperature indices between Shijiazhuang station and the four rural stations during 1962–2011.

During the past 50 years, hot days of Shijiazhuang station had a weak increasing trend (Fig. 3) at a rate of 0.83 days/10 years, while the hot days of the rural stations experienced a weak decreasing trend at a rate of −0.27 days/10 years, but both were not statistically significant (Table 3). The decrease in hot days of the rural stations might have been caused by the increasing aerosol concentration in the lower troposphere, and the increase in hot days of the urban station might have resulted from the combined influence of the enhanced UHI intensity and the increased aerosol concentration, but this issue needs to be further investigated.

Urban-rural differences of annual hot days significantly increased with time (Table 3 and Fig. 4), indicating that the influence of urbanization on the trend of the hot days series at Shijiazhuang station was large, with an urbanization effect reaching 1.1 days/10 years which was statistically significant at $\alpha$=0.001 confidence level (Table 3). The contribution of urbanization effect to the overall trend of annual hot days was as high as 100 %, indicating that the increase in annual hot days at the urban station had been totally caused by urbanization. Because of the urbanization effect, the frequency of annual hot days at Shijiazhuang station increased by more than 5 days in the last 50 years.

Annual cold days of Shijiazhuang station and the rural stations all decreased during the time period 1962–2011 (Fig. 3), and the decreasing trends, −6.06 and −3.76 days/10 years, respectively, both passed the significance test at $\alpha$=0.001 level. The urban-rural difference series of annual cold days also showed a significant downward trend (Fig. 4) with a rate of −2.3 days/10 years, which passed the significance test at $\alpha$=0.001 level. The contribution of urbanization effect was 38.0 %, indicating that more than one third of the decrease in annual cold days had resulted from urbanization effect. In the recent 50 years, therefore, annual cold days observed at Shijiazhuang station decreased by 32 days, of which at least 12 days were due to the urbanization effect.

Table 3 and Fig. 3 show that annual frost days of Shijiazhuang station and the rural stations also highly significantly decreased during the last 50 years, with linear trends reaching −6.04 and −3.49 days/10 years, respectively. The highly significant downward trend, with a rate of −2.55 days/10 years, can also be seen from the urban-rural difference series (Fig. 4). The contribution of urbanization effect accounted for 42.2 %. Therefore, the overall reduction of annual frost days for the last 50 years at Shijiazhuang station was 31 days, and urbanization effect contributed a portion of at least 13 days.

Although annual ice days for Shijiazhuang station and the rural stations decreased, and a little bit larger reduction can be seen for the urban station, the downward trends had not passed the significance test at $\alpha$=0.05 level (Table 3 and Fig. 3). The urban-rural difference series of the annual ice days showed an obvious downward trend with a rate of −0.47 days/10 years (Fig. 4), which was statistically significant at the $\alpha$=0.05 confidence level. Therefore, the urbanization effect on the long-term trend of annual ice days at Shijiazhuang station was significant. This contrasted the urbanization effect on annual hot days in spite of the fact that the two indices were all defined based on daily Tmax, implying that the increase in Tmax at Shijiazhuang station in the last 50 years was less significant in summer than in other seasons.

Author's personal copy



**Table 3** Linear trends of annual extreme temperature indices for Shijiazhuang station and rural stations (average of four rural stations) and the urbanization effects and urbanization contributions for the time period 1962–2011

| Index | Urban station (days or °C/10 years) | Rural stations (days or °C/10 years) | Urbanization effect (days or °C/10 years) | Urbanization Contribution (%) |
|---|---|---|---|---|
| Hot days | 0.83 | −0.27 | 1.10*** | 100 |
| Cold days | −6.06*** | −3.76*** | −2.30*** | 38.0 |
| Frost days | −6.04*** | −3.49*** | −2.55*** | 42.2 |
| Ice days | −1.08 | −0.60 | −0.47* | 43.5 |
| DTR | −0.50*** | −0.30*** | −0.20*** | 40.0 |
| Maximum Tmax | 0.17 | 0.01 | 0.16** | 94.1 |
| Minimum Tmin | 1.49*** | 0.79*** | 0.70*** | 47.0 |
| Maximum Tmin | 0.28 | 0.21 | 0.07 | – |
| Minimum Tmax | 0.38*** | 0.25*** | 0.14 | – |

*significant at $\alpha$=0.05 confidence level; **significant at $\alpha$=0.01 confidence level; ***significant at $\alpha$=0.001 confidence level

During 1962–2011, highly significant decreasing trends of annual mean DTR occurred for both Shijiazhuang station and the rural stations (Fig. 5), but obviously the decrease was much more evident at the urban station (−0.5 °C/10 years) than the rural stations (−0.3 °C/10 years) (Table 3). The urban-rural difference series of annual mean DTR showed a highly significant downward trend of −0.2 °C/10 years (Fig. 6), which had passed the significance test at $\alpha$=0.001 level (Table 3). Therefore, the urbanization effect on the long-term downward trend of annual mean DTR recorded at Shijiazhuang station was large and highly significant, with almost half of the overall reduction resulting from the urbanization. It is interesting to note that the last decade witnessed a rebound of urban-rural difference of annual mean DTR. This might have been related to the recent urbanization processes around the four rural stations, which might have led to the

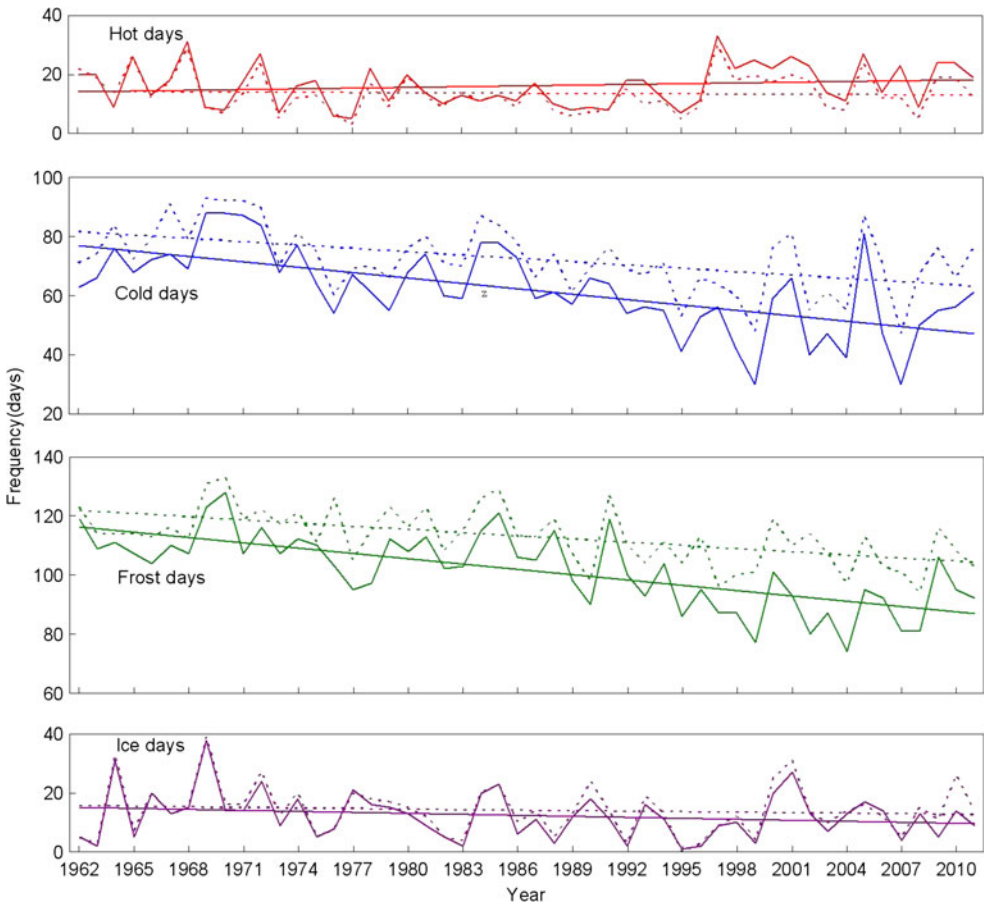


**Fig. 3** Yearly series of hot days, cold days, frost days, and ice days between Shijiazhuang (*solid lines*) and rural stations (average of four rural stations, *dotted lines*) and their trends (*straight lines*) during 1962–2011

Author's personal copy



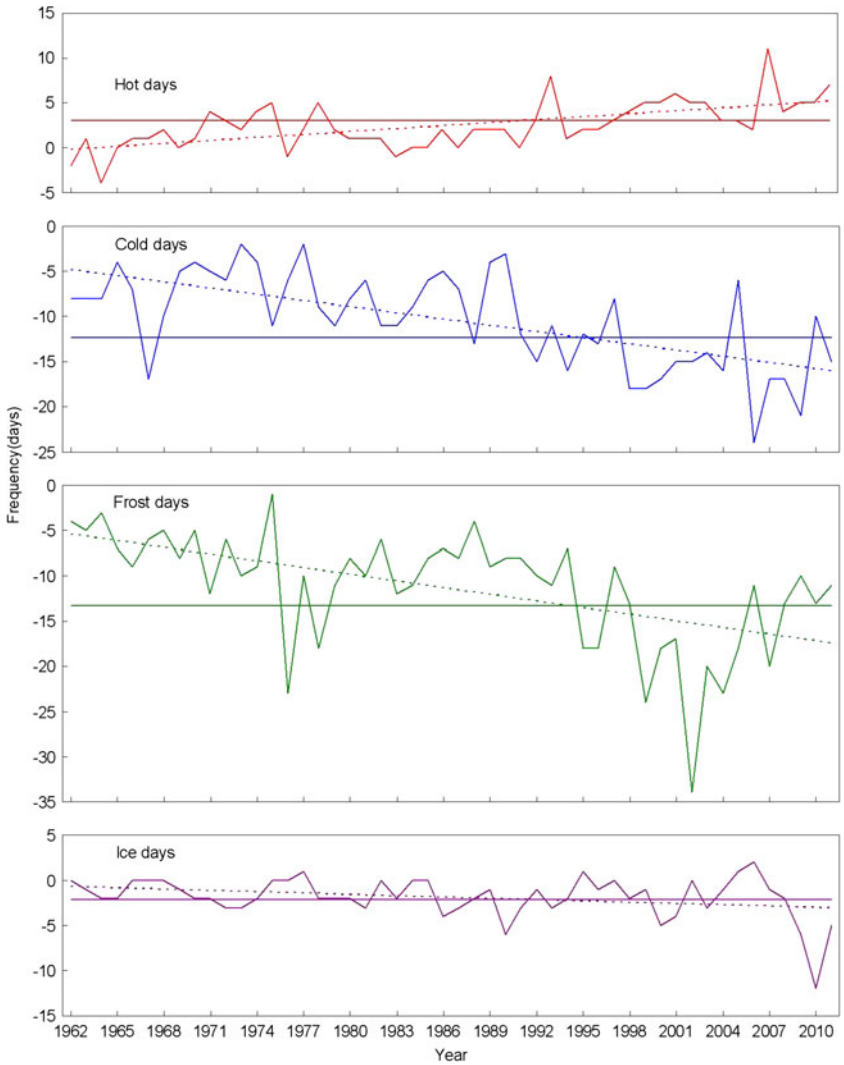


**Fig. 4** Yearly difference series of hot days, cold days, frost days, and ice days (*curve lines*) between Shijiazhuang and rural stations (average of four rural stations) and their trends (*dotted lines*). *Straight lines* denote the averages during 1962–2011

relative increase in Tmin of the rural stations. It is also possible that the decrease in calm weather frequency in winter during the last decade (Jin et al. 2012) was weakening the urban-rural difference of annual mean Tmin and DTR.

During the last 50 years, maximum Tmax of Shijiazhuang station and the rural stations both had insignificant increasing trends at rates of 0.17 and 0.01 °C /10 years, respectively (Fig. 5), with the urban station trend being more obvious than the rural stations, leading to a significant urbanization effect of 0.16 °C/10 years (Table 3 and Fig. 6). The urbanization contribution was large, reaching 94.1 %, indicating that the rise of annual extreme Tmax at Shijiazhuang station had been caused mostly by the urbanization effect. Different from the maximum Tmax, minimum Tmin of both Shijiazhuang station and rural stations showed highly significant increasing trends, reaching 1.49 and 0.79 °C/10 years, respectively, and all passed the significance test at the $\alpha$=0.001 level. The urban-rural difference series of annual minimum Tmin also had an upward trend of 0.7 °C/10 years (Fig. 6), which was highly significant at $\alpha$=0.001 confidence level (Table 3), indicating a larger urbanization effect on the lowest annual Tmin at Shijiazhuang station. The urbanization contribution was estimated to be 47.0 %, or nearly half of the minimum Tmin increase at Shijiazhuang station had been induced by urbanization effect.

Maximum Tmin of Shijiazhuang station and the rural stations increased during the last 50 years (Fig. 5), but the respective trends of 0.28 and 0.21 °C/10 years were not significant at $\alpha$=0.05 confidence level. The linear trend of the urban-rural difference series of maximum Tmin, 0.07 °C/10 years (Fig. 6), was not significant at $\alpha$=0.05 confidence level either, indicating a less obvious urbanization effect on annual maximum Tmin. Although the minimum Tmax of both urban and rural stations experienced highly significant increasing trends, reaching 0.38 and 0.25 °C/10 years, respectively, the upward trend of the urban-rural difference series, 0.14 °C/10 years (Fig. 6), was not significant at the $\alpha$=0.05 confidence level (Table 3), indicating that urbanization was

Author's personal copy



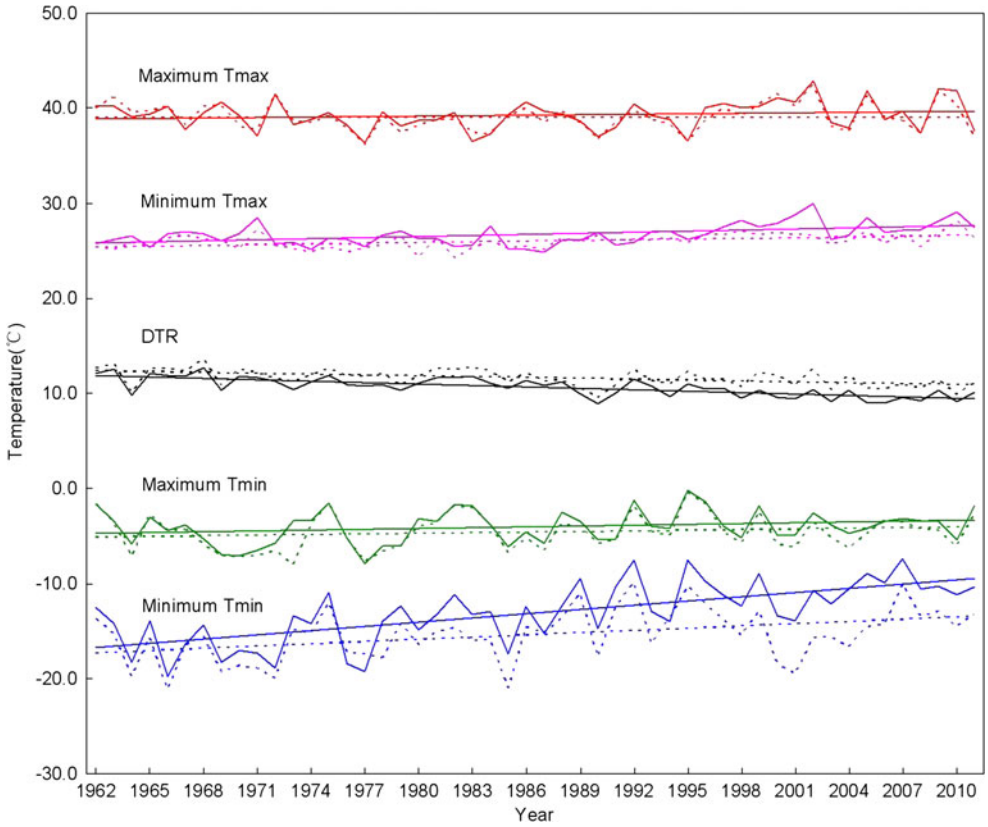


**Fig. 5** Yearly series of DTR, maximum Tmax, minimum Tmin, maximum Tmin, and minimum Tmax between Shijiazhuang (*solid lines*) and rural stations (average of four rural stations, *dotted lines*) and their trends during 1962–2011

not exerting substantial net influence on the change in annual minimum Tmax at Shijiazhuang station.

### 3.2 Seasonal mean trends and urbanization effects

Seasonal analysis was given to DTR and the extreme values of Tmin and Tmax because the other extreme events (cold days, hot days, frost days, and ice days) occurred only on specific seasons. Table 4 shows the seasonal mean trends of the extreme temperature indices for Shijiazhuang station and the rural stations and the urbanization effect and urbanization contribution for Shijiazhuang station.

For every season, the seasonal mean DTR of Shijiazhuang station and rural stations significantly decreased during the time period analyzed (Table 4), and the largest decline of both urban station and rural stations appeared in winter, with summer witnessing the smallest decline. The urban-rural difference series of DTR in every season also showed a clear downward trend, indicating that the urbanization effects were evident at Shijiazhuang station. The urbanization effects were −0.18, −0.10, −0.19, and −0.24 °C/10 years, respectively, for spring, summer, autumn and winter, and the urbanization contributions were 39.1, 32.3, 36.5, and 36.9 %, respectively, for the four seasons (Fig. 7). Although the largest urbanization effect occurred in winter, followed by autumn, spring, and summer, the largest urbanization contribution was recorded in spring, followed by those in winter, autumn, and summer.

During the last 50 years, the trends of maximum Tmax for four seasons at Shijiazhuang station and rural stations were not significant, and they showed only slight increase or decrease. The urban-rural difference series of maximum Tmax in spring and summer showed significant increasing trends at $\alpha$=0.001 confidence level, reaching 0.24 and 0.18 °C/10 years, respectively, and the urbanization contributions were 100 and 72 %, respectively. However, the trends of the urban-rural difference series of maximum Tmax in autumn and winter were very weak and not significant.

Minimum Tmin of four seasons at Shijiazhuang station and rural stations during the last 50 years all showed highly significant increasing trends, and the largest increase appeared in winter and the smallest increase in summer. The urban-rural difference series of minimum Tmin in all the seasons also showed highly significant upward trends, indicating the large and significant urbanization effects in the minimum Tmin series at Shijiazhuang station for every season. The largest urbanization effect occurred in winter, reaching 0.67 °C/10 years, followed by those of spring, summer, and autumn (0.35, 0.31, and 0.29 °C/10 years, respectively). The urbanization contributions in spring, summer, autumn, and winter were 36.5, 37.3, 32.2, and 48.2 %, respectively.

Maximum Tmin of Shijiazhuang station and rural stations showed increasing trends for the seasons except for summer, but only the upward trends of spring and winter for the urban station were statistically significant. Although the maximum

Author's personal copy



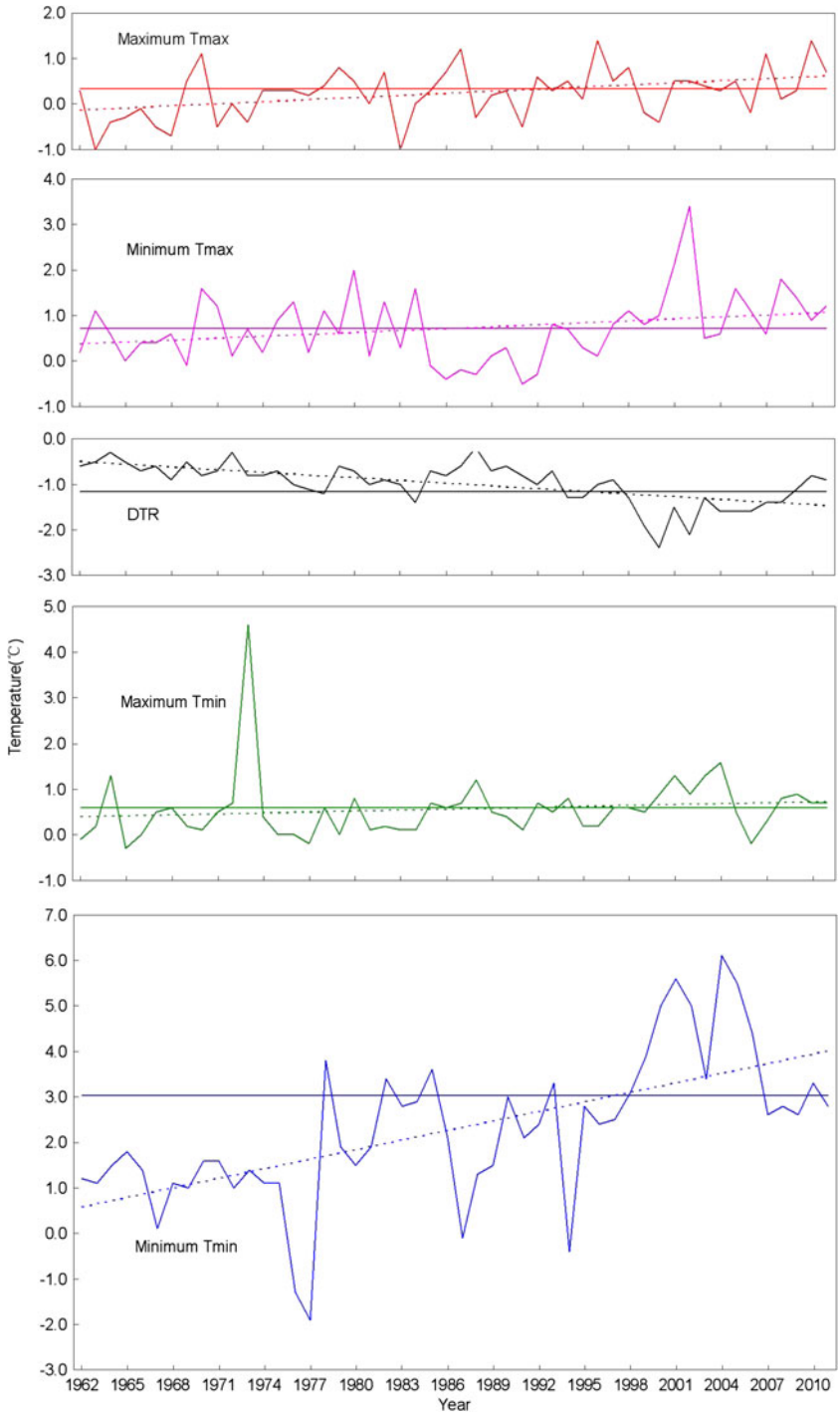


**Fig. 6** Yearly difference series of DTR, maximum Tmax, minimum Tmin, maximum Tmin, and minimum Tmax (*solid lines*) between Shijiazhuang and rural stations (average of four rural stations) and their trends (*dotted lines*). *Straight lines* denote the averages during 1962–2011

Tmin trends of the urban station and the rural stations were not the same in direction for every season, the urbanization effects in maximum Tmin series were significant for all the seasons, with the most significant urban-induced increase occurring in autumn, reaching 0.17 °C/10 years, and the urbanization contributions were 21.3, 100, 68.0, and 52.0 % for spring, summer, autumn, and winter, respectively.

Minimum Tmax of Shijiazhuang station and rural stations showed increasing trends for all the seasons, and the increases were significant except for that of the rural stations in spring. The urban-rural difference series of minimum Tmax in spring and autumn exhibited significant increasing trends at 0.29 and 0.15 °C/10 years, respectively, indicating large urbanization effects in these two seasons, and the urbanization contributions were 58.0 and 25.0 %, respectively. Urbanization effects for minimum Tmax series at the urban station were insignificant for summer and winter.

Author's personal copy



**Table 4** Linear trends of seasonal extreme temperature indices for Shijiazhuang station and rural stations (average of four rural stations) and the urbanization effects and urbanization contributions for the time period 1962–2011

| Index | Season | Urban station (°C/10 years) | Rural station (°C/10 years) | Urbanization effect (°C/10 years) | Urbanization contribution (%) |
|---|---|---|---|---|---|
| DTR | Spring | −0.46*** | −0.28** | −0.18** | 39.1 |
| | Summer | −0.31*** | −0.21** | −0.10*** | 32.3 |
| | Autumn | −0.52*** | −0.33*** | −0.19*** | 36.5 |
| | Winter | −0.65*** | −0.41*** | −0.24*** | 36.9 |
| Maximum Tmax | Spring | 0.09 | −0.15 | 0.24*** | 100 |
| | Summer | 0.25 | 0.07 | 0.18*** | 72.0 |
| | Autumn | 0.04 | 0.01 | 0.03 | – |
| | Winter | −0.07 | −0.01 | −0.06 | – |
| Minimum Tmin | Spring | 0.96*** | 0.61** | 0.35*** | 36.5 |
| | Summer | 0.83*** | 0.52*** | 0.31*** | 37.3 |
| | Autumn | 0.90*** | 0.61** | 0.29** | 32.2 |
| | Winter | 1.39*** | 0.72** | 0.67*** | 48.2 |
| Maximum Tmin | Spring | 0.61* | 0.48 | 0.13* | 21.3 |
| | Summer | −0.08 | −0.21 | 0.13*** | 100 |
| | Autumn | 0.25 | 0.08 | 0.17*** | 68.0 |
| | Winter | 0.25** | 0.12 | 0.13** | 52.0 |
| Minimum Tmax | Spring | 0.50** | 0.21 | 0.29* | 58.0 |
| | Summer | 0.38*** | 0.25** | 0.13 | – |
| | Autumn | 0.61*** | 0.46** | 0.15** | 25.0 |
| | Winter | 0.50* | 0.46** | 0.04 | – |

*significant at $\alpha$=0.05 confidence level; **significant at $\alpha$=0.01 confidence level; ***significant at $\alpha$=0.001 confidence level

It is clear from the description above that the extreme temperature indices associated with Tmin generally showed significant changing trends during the last 50 years, and the changes in urban-rural differences of the indices or urbanization effects were usually large and significant except for minimum Tmax. On the other hand, the trends of the extreme temperature indices associated with Tmax were generally weak and insignificant, but the changes in urban-rural differences of the indices or urbanization effects were not necessarily small, with the urbanization effects on trends of hot days,

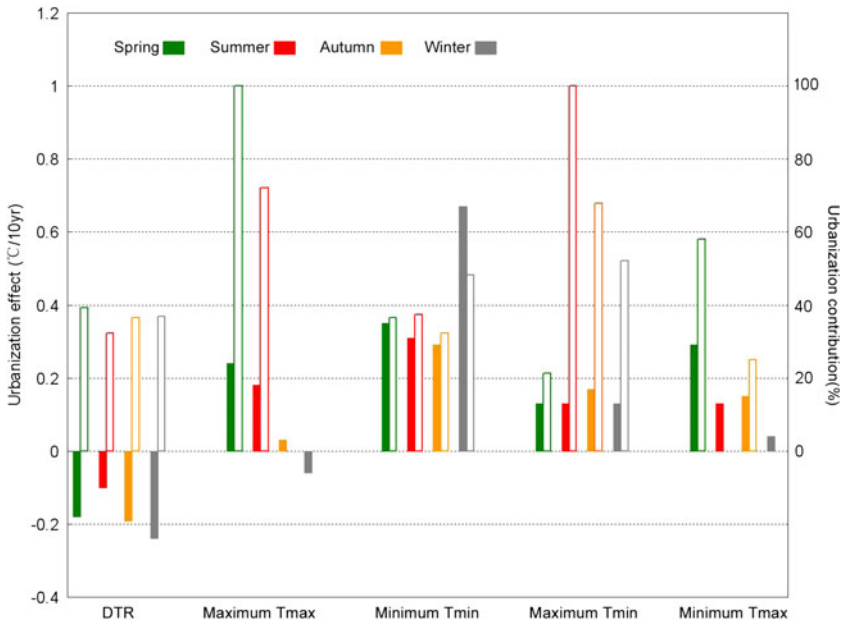


**Fig. 7** Urbanization effects (*solid*) and the urbanization contributions (*blank*) of seasonal DTR, maximum Tmax, minimum Tmin, maximum Tmin, and minimum Tmax for Shijiazhuang station during 1962–2011

Author's personal copy



ice days, and maximum Tmax being statistically significant. Urbanization makes DTR, minimum Tmin, and maximum Tmin of Shijiazhuang station in every season to significantly change with time, among which the trends of DTR and minimum Tmin in winter and the trends of maximum Tmin in autumn were highly significant. The urbanization effects of maximum Tmax were more obvious in spring and summer, and those of minimum Tmax were more significant in spring and autumn.

## 4 Discussion

Little had been done to analyze the urbanization effect on extreme temperature change. Zhang et al. (2011) examined the urbanization effect on trends of extreme temperature indices during 1960–2008 at Beijing Meteorological Station, about 260 km northeast of Shijiazhuang station. They found that, for frost days and DTR, urbanization effects on the linear trends of Beijing station were −5.78 days/10 years and −0.73 °C /10 years, respectively, all statistically significant at the $\alpha$=0.01 confidence level, and the contributions of urbanization effect all reached 100 %, but no significant urbanization effect was detectable for the trends of ice days and hot days. In contrast, although urbanization effects on trends of frost days and DTR at Shijiazhuang station were similarly significant, the urbanization contributions were smaller than those for Beijing station, but urbanization effects on trends of ice days and hot days at Shijiazhuang station were larger and more significant than those for Beijing station. This study revealed that urbanization effects on trends of the extreme temperature indices associated with Tmin were generally larger and more significant than those associated with Tmax at Shijiazhuang station, which is very consistent with the conclusions drawn from the analysis for Beijing station.

Recently, Zhou and Ren (2011) analyzed urbanization effect on the change of the extreme temperature indices and dataset commonly used for analyses of climate change in North China during 1961–2008. They found that urbanization effect had significantly aggravated the linear trends of the cold and warm indices associated with Tmin, and the urbanization contributions to the overall trends of the extreme temperature indices formulated with Tmin for national reference climate stations and basic meteorological stations all reached over 40 %. However, urbanization effects for the indices associated with Tmax were much weaker. These features are well consistent with the analysis results in this paper. Although urbanization effects on the long-term trends of DTR at Shijiazhuang station and the national reference climate stations and basic meteorological stations of North China were all highly significant, the contribution of urbanization effect was only 45.1 % for the former, and it reached 100 % for the latter, more consistent with that obtained for Beijing station (Zhang et al. 2011).

Main uncertainty in the analysis could originate from the data inhomogeneities and the representativeness of the selected rural stations. Although the discontinuous points of the SAT records caused by relocations had been examined, problems probably introduced by the application of automatic weather stations (AWS) in the last decade had not been carefully evaluated. Previous analysis pointed out that, compared with manual stations, Tmax measured by AWS are generally higher, while Tmin are slightly lower (Wang et al. 2007). These biases might have certain influences on the trend estimation of extreme temperature indices and the calculated results of urbanization effects. The rural stations selected in this paper should be representative for long-term record of background climate change and variability in the study area, but these stations are located in small towns around Shijiazhuang station, and inevitably, the SAT records from the rural stations will still be affected by urbanization in a certain extent (Karl et al. 1988; Ren et al. 2008; Zhou and Ren 2009). Actually, the urbanization effects and urbanization contributions estimated for a few of extreme temperature indices in this paper are lower than those reported for Beijing station and the national stations of North China, and this might be related in a large extent to the use of the rural stations in the present analysis. It is therefore safe to point out that the urbanization effects on the trends of the extreme temperature indices series at Shijiazhuang station as given in this paper be regarded as the lowest estimates.

Nevertheless, the results of this analysis showed that urbanization effects on the trends of extreme temperature indices at Shijiazhuang city station were large and mostly significant, especially for those associated with Tmin. Frost days, DTR, and minimum Tmin recorded on Shijiazhuang station, for example, were all significantly reduced due to urbanization. Considering the representativeness of the rural stations, the actual urbanization effects and the contributions of urbanization effects might have been larger. These results indicate that the long-term trends of extreme temperature event frequencies previously estimated based on the data from Shijiazhuang station and from all stations in Shijiazhuang area had been overestimated. There is a need to pay more attention to the urban biases in SAT data in analyses of mean and extreme temperature changes in this area as well as in the whole North China.

## 5 Conclusions

This paper analyzed urbanization effects on the long-term trends of extreme temperature indices at Shijiazhuang station during 1962–2011. The following conclusions were drawn:

1. Urbanization effects on the long-term trends of annual hot days, cold days, frost days, DTR, maximum Tmax, and

Author's personal copy



minimum Tmin at Shijiazhuang station for the time period 1962–2011 were highly significant, reaching 1.1 days/10 years, −2.3 days/10 years, −2.55 days/10 years, −0.2 °C/10 years, 0.16 °C/10 years, and 0.7 °C/10 years, respectively, with contributions of the urbanization effect to the overall trends being 100, 38.0, 42.2, 40.0, 94.1, and 47.0 %, respectively.

2. Urbanization effect on the long-term trend of annual ice days at Shijiazhuang station for the last 50 years was also significant, reaching −0.47 days/10 years, and the contribution of urbanization effect to the overall trend was 43.5 %. Urbanization effects on the trends of annual minimum Tmax and maximum Tmin at Shijiazhuang station for the last 50 years, however, were not statistically significant.
3. The urbanization effect made DTR, minimum Tmin, and maximum Tmin of Shijiazhuang station in every season to significantly change with time, with the downward trend of winter DTR and upward trends of winter minimum Tmin and autumn maximum Tmin being the largest and most significant.
4. The urbanization effects on the trends of extreme temperature indices reported in this paper might have been underestimated, because the selected rural stations are all located in small towns and they cannot fully represent the regional baseline temperature change and variability. The results, however, indicated that the urbanization effects on the trends of extreme temperature indices related to Tmin were large and significant at the urban station examined.

**Acknowledgments** This study is financed by the Ministry of Science and Technology of China (Fund No. GYHY201206012).

## References

Alexander LV, Zhang X, Peterson TC et al (2006) Global observed changes in daily climate extremes of temperature and precipitation. J Geophys Res 111(3):D05109

Bian T (2010) Characteristics of urban climate and climate change in Shijiazhuang City. Master dissertation of Lanzhou University (in Chinese)

Choi J, Chung U, Yun JI (2003) Urban-effect correction to improve accuracy of spatially interpolated temperature estimates in Korea. J Appl Meteorol 42:1711–1719

Chu ZY, Ren GY (2005) Change in urban heat island magnitude and its effect on mean air temperature record in Beijing region. Acta Meteorol Sin 63(4):534–540 (in Chinese)

Chung U, Choi J, Yun JI (2004) Urbanization effect on observed change in mean monthly temperature between 1951–1980 and 1971–2000 in Korea. Clim Chang 66:127–136

Easterling DR, Horton B, Jones PD (1997) Maximum and minimum temperature trends for the globe. Science 277:364–367

Fujibe F (2008) Detection of urban warming in recent temperature trends in Japan. Int J Climatol 29:1811–1822

Jin W, Ren G, Qu Y (2012) Change in surface mean wind speed of Northeast China during 1971–2010. Arid Zone Res 29(4):648–653

Kalnay E, Cai M (2003) Impact of urbanization and land use change on climate. Nature 423:528–531

Karl TR, Diaz HF, Kukla G (1988) Urbanization: its detection and effect in the United States climate record. J Clim 1988(1):1099–1123

Karl TR, Kukla G, Razuvayev VN et al (1991) Global warming: evidence for asymmetric diurnal temperature changes. Geophys Res Lett 18: 2253–2256

Li QX, Liu XN, Zhang HZ, Peterson TC, Easterling DR (2004) Detecting and adjusting on temporal inhomogeneity in Chinese mean surface air temperature data. Adv Atmos Sci 21(2):260–268

Plumner N (1996) Temperature variability and extreme over Australia: part 1-recent observed changes. Aust Meteorol Mag 45:233–250

Ren GY, Chu ZY, Chen ZH, Ren YY (2007) Implications of temporal change in urban heat island intensity observed at Beijing and Wuhan stations. Geophys Res Lett 34, L05711

Ren GY, Zhou YQ, Chu ZY, Zhou JX, Zhan AY, Guo J, Liu XF (2008) Urbanization effects on observed surface air temperature trends in North China. J Clim 21:1333–1350

von Storch H, Zwiers FW (2003) Statistical analysis in climate research. Cambridge University Press, New York, p 504

Wang Y, Liu XN, Ju XH (2007) Differences between automatic and manual observation. J Appl Meteorol Sci 18(6):849–855 (in Chinese)

Wei FY (2007) Diagnosis and forecasting methods of modern climatic statistics (version 2). China Meteorological, Beijing (in Chinese)

Yan ZW, Yang C, Jones PD (2001) Influence of inhomogeneity on the estimation of mean and extreme temperature trends in Beijing and Shanghai. Adv Atmos Sci 18(3):309–322

Yang X, Hou Y, Chen B (2011) Observed surface warming induced by urbanization in east China. J Geophys Res 116:D14113. doi:10.1029/2010JD015452

Zhai PM, Pan XH (2003) Trends in temperature extreme during 1951–1999 in China. Geophys Res Lett 30(17):1–4

Zhang AY, Ren GY, Zhou JX et al (2010) Urbanization effect on surface air temperature trends over mainland China. Acta Meteorol Sin 68(6):957–966 (in Chinese)

Zhang L, Ren GY, Liu J et al (2011) Urbanization effect on trends of extreme temperature indices at Beijing meteorological station. Chin J Geophys 54(5):1150–1159 (in Chinese)

Zhou YQ, Ren GY (2009) Urbanization effect on trends of maximum temperature, minimum temperature and diurnal temperature range in North China. Plateau Meteorol 28(5):1158–1166 (in Chinese)

Zhou YQ, Ren GY (2011) Change in extreme temperature events frequency over mainland China during 1961–2008. Clim Res 50(1–2): 125–139

Chin. Sci. Bull. (2014) 59(34):4881–4889
DOI 10.1007/s11434-014-0429-9

csb.scichina.com
www.springer.com/scp

Article

Atmospheric Science

# An observational study of snow aging and the seasonal variation of snow albedo by using data from Col de Porte, France

**Ajiao Chen · Weiping Li · Weijing Li · Xin Liu**

Received: 10 September 2013 / Accepted: 19 March 2014 / Published online: 15 May 2014
© Science China Press and Springer-Verlag Berlin Heidelberg 2014

**Abstract** An 18-year long (1993–2011) comprehensive dataset of snow and meteorological variables from Col de Porte, France is used to analyze the variation of shortwave broadband albedo with elapsed time after snowfalls (snow aging) during each snow season. The effects of air temperature, snow surface temperature and snow depth on snow albedo are investigated. An index based on the accumulation of air temperature over several consecutive days with daily mean higher than 2.5 °C is proposed to divide each snow-covered period into a dry and the following wet snow season when this index reaches 18 °C. The results indicate that snow surface albedo decreases exponentially with time in both dry and wet snow seasons. Snow albedo reduction with snow aging is small at low surface temperature and the reduction rate increases with the rise of surface temperature. However, the reduction rate is widely scattered within the observed range of temperature, implying a loose relationship between snow albedo and snow surface temperature. Snow albedo in wet snow season is generally smaller and decreases faster than in dry snow season. For Col de Porte site, snow depths to effectively mask the underlying surface are 21 and 33 cm in dry and wet snow season respectively.

**Keywords** Snow aging · Snow albedo · Dry snow season · Wet snow season · Snow surface temperature · Snow depth

## 1 Introduction

Snow albedo is one of the most important parameters in multiple land surface schemes used in various climate models [1–4]. It dominates the energy exchange between the snow surface and overlying atmosphere, exerting strong influences on the atmospheric circulation [5, 6]. The research on Greenland ice sheet by Nolin et al [7] has confirmed that a small change of snow albedo can cause a remarkable perturbation in the energy flux of the ice sheet. The surface energy balance, which is largely determined by snow albedo, controls both the timing and amount of snow melt, and thus affects the seasonal variation of snow cover and consequently the hydrological cycle [8, 9]. The Fourth Assessment Report of the Intergovernmental Panel on Climate Change (IPCC AR4) estimated that the magnitude of polar warming caused by greenhouse gases is 2–3 times that of the average value of the global warming [10]. The alleged positive snow/ice-albedo feedback mechanism is the main reason that causes the amplified polar warming [11, 12]. Therefore, the accurate simulation of snow albedo and appropriate treatment of the snow/ice-albedo feedback mechanism in climate models are essential for the proper simulation of atmospheric circulation and hydrological cycle.

A. Chen
Chinese Academy of Meteorological Sciences, Beijing 100081, China

W. Li (✉) · W. Li
National Climate Center, China Meteorological Administration, Beijing 100081, China
e-mail: liwp@cma.gov.cn

W. Li · W. Li
Laboratory for Climate Studies, China Meteorological Administration, Beijing 100081, China

X. Liu
Laboratory of Tibetan Environment Changes and Land Surface Processes, Institute of Tibetan Plateau Research, Chinese Academy of Sciences, Beijing 100101, China

Snow albedo is dependent on the spectral composition of the incoming solar radiation and essentially determined by snow physical parameters such as snow grain size, impurity concentration, and liquid water content [13–15]. The near infrared albedo decreases with the increase of snow grain size, and the visible albedo is reduced strongly by snow impurities. Liquid water indirectly increases snow albedo by infilling interspace between snow grains and increasing the effective snow grain size. Factors that affect solar radiation include solar zenith angle, the fraction of direct/diffuse radiation, and the spectral composition of incident solar radiation (visible versus near infrared). Besides, when the snowpack is thin, the underlying surface with relatively lower albedo can decrease the snow surface albedo by absorbing more radiation because the snowpack is partly transparent in the visible band region. The surface albedo of a thin snowpack increases with the enhancement of snow depth and consequent volume scattering until the snowpack reaches a certain threshold of depth [16, 17].

Sophisticated radiation transfer models perform well in estimating snow and ice albedo [18, 19], but they are computationally demanding and many model required inputs are hardly available for climate models. Recently, several physically based and computationally economic snow albedo parameterizations have been employed in climate models. For example, based on the theoretical models of Wiscombe and Warren [13, 14] and Toon et al [20], Flanner and Zender [21, 22] developed the two-stream, multilayer Snow, Ice, and Aerosol Radiation model (SNICAR) to calculate snow albedo and solar heating at the surface. The SNICAR has been implemented into NCAR CLM4 [23] to calculate microphysics and radiative properties of snowpack. The Physically Based Snow Albedo Model (PBSAM) established by Aoki et al [24] calculates the broadband albedos as functions of snow grain size and concentration of snow impurities (black carbon and mineral dust). However, these prescribed parameterizations we mention above are not widely used in climate models due to the lack of long-term and representative observations of snow grain size and impurities, which are critical in these parameterizations. At present, relatively simple and less input-demanding empirical parameterizations are widely employed in most climate models. However, snow albedos depend only on surface types (sea ice, land snow) and surface temperature in some empirical schemes. For example, snow albedo is a linear function of surface temperature in ECHAM5 [25]. The snow schemes in the Biosphere-Atmosphere Transfer Scheme (BATS) [26, 27] and Common Land Model (CoLM) [28] are a little bit more complex, with more factors including the zenith angle, the spectral composition of incoming solar radiation, the effects of snow aging, snow grain growth and concentration of impurities being empirically considered.

Since most empirical parameterizations for snow albedo are usually based upon short-term observations at specific sites, the applicability of the prescribed parameters and the schemes are somewhat limited. In this study, we analyze the effects of snow aging, air temperature, snow surface temperature and snow depth on the snow surface albedo using an 18-year (1993–2011) comprehensive snow and meteorological observations at Col de Porte, France. Results of the present study will provide reference for the improvement of empirical snow albedo parameterizations in climate models.

## 2 Data

The Col de Porte observation site (43.30°N, 5.77°E) with an elevation of 1325 m is located in the Chartreuse mountain range of France. All the apparatus are installed within an area of 50 m × 50 m in a grassy meadow. The dataset spans the period from 1 August 1993 to 31 July 2011, consisting of conventional meteorological elements and snow characteristics. The hourly meteorological data include the air temperature, relative humidity, wind speed, downward shortwave and longwave radiation, and precipitation rate. Precipitation are manually partitioned between rain and snow using all possible ancillary information such as air temperature and the information from different rain gauges, snow depth and albedo measurements. The data relevant to snowpack properties (snow depth, albedo, runoff, surface temperature, soil temperature) are provided at hourly interval while the snow water equivalent is at daily resolution. The snow albedo is computed from the ratio between incoming and reflected shortwave radiation. Snow surface temperature is computed from the observed upward longwave radiation [29].

In addition to the regular measurements of snowpack properties, snowpit measurements have been carried out approximately weekly throughout the period. The data collected include the vertical profile of penetration resistance, snow temperature, density, snow type, liquid water content for the natural snow layers [29]. Observational data employed in this study are available on the anonymous ftp server ftp://ftp-cnrm.meteo.fr/pub-cencdp/ or website http://epic.awi.de/30060/. On average the snow cover lasts five months, from November to April. The maximum snow depth experiences evident interannual variation. The highest snow depth can reach up to 2.04 m (1998/1999), while the lowest is only 0.66 m (2006/2007). Owing to the relatively low altitude of the site, surface snowmelt and rainfall events are common in the snow season, but the main and ultimate ablation of snow usually takes place in March or April.

## 3 Results and analysis

### 3.1 Separation of dry snow season and wet snow season

We take the 2005/2006 snow season as an example to illustrate how we divide a snow-covered period into the dry snow season and the wet snow season in this study. Figure 1a shows the observations of snow type from December 2005 to April 2006. Before the end of March 2006 when continuous snow ablation began, the snowpack consisted of dry snow such as New snow (NS), Rounded grains (RG), Faceted crystals (FC), Decomposed particles (DP), Surface hoar (SH) and Depth hoar (DH) [30]. According to the volume water content at the same time, most layers of the snowpack were classified as Dry snow with little Moist snow in the overall 5 categories (Fig. 1b). During this period, the snow depth gradually increased; the snow albedo reached as high as 0.9 when there was a heavy snowfall and decreased slowly after the snowfall (Fig. 2). This period is referred to as the 'accumulating season' or

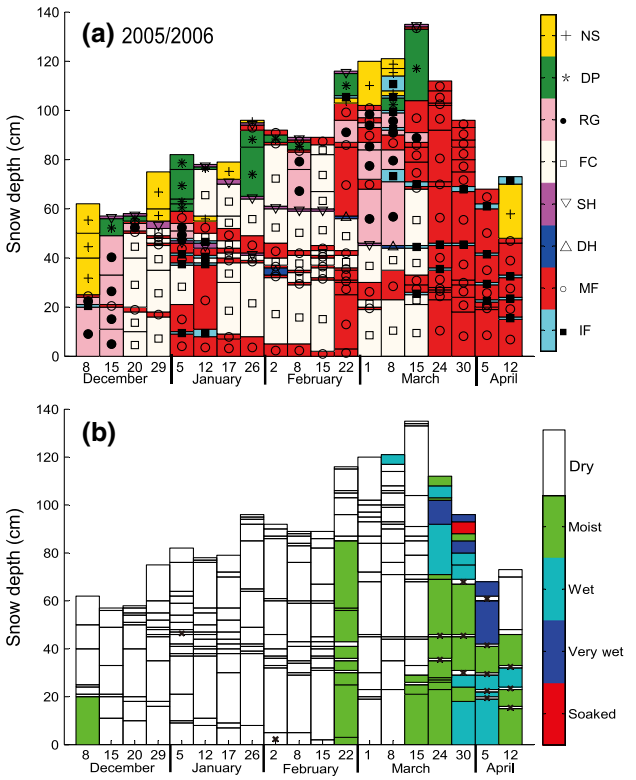


**Fig. 1** Vertical profiles of the major snow type (**a**) and volume water content (**b**) in each layer of the snowpack during 2005/2006 snow season. NS, New snow; DP, Decomposed particles; RG, Rounded grains; FC, Faceted crystals; SH, Surface hoar; DH, Depth hoar; MF, Melt forms; IF, Ice formations; Dry, 0; Moist, 0–3 %; Wet, 3 %–8 %; Very wet, 8 %–15 %; Soaked, >15 %. Missing data are indicated by crosses in (**b**)

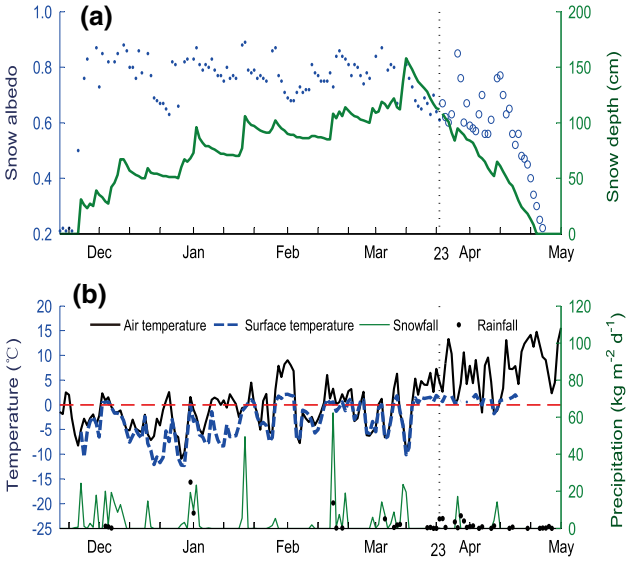


**Fig. 2** Daily variations of **a** snow surface albedo (solid and blank circles) at 12:00 local time (LT) and snow depth (green curve), **b** air temperature (black solid curve), snow surface temperature (blue dashed curve) at 12 LT, and snowfall (green curve) and rainfall (black dots) within 24 h of the albedo observation at 12 LT for 2005/2006 snow season. Vertical dotted line indicates the starting date of wet snow season, March 23, 2006

'dry snow season' due to the quite low water content in the snow pack. Since the end of March 2006, the snow type changed into Melt form (MF); the snowpack layers were classified as Moist, Wet or Very wet snow according to volume water content (Fig. 1b). Meanwhile, the snow depth decreased continually and the reduction rate of snow albedo accelerated (Fig. 2a). We refer to this period as the 'melting season' or 'wet snow season'. Since the snowpit work was conducted at weekly interval, the very beginning of the wet snow season should be determined by weather conditions that are quantified with high quality and high temporal resolution data. Based on a large amount of data analysis, we propose an air temperature index, i.e., the accumulated daytime mean temperature, to determine the starting date of a wet snow season. The temperature is accumulated when the average daytime air temperature is over 2.5 °C in a certain number of consecutive days. If the average daytime air temperature is lower than 2.5 °C in a specific day, the accumulation of temperature is reset to zero at that day. Above procedure is repeated for the next coming days until the threshold of the accumulated daytime mean air temperature is reached. In accordance with the evolution of snow type and liquid water content within a snowpack, we define the threshold of the accumulated daytime mean air temperature as 18 °C for Col de Porte site. Based on above definitions, 23 March 2006 is determined as the starting date of the wet snow season for the 2005/2006 snow-covered period. The snow surface

temperature fluctuated around the snow melting point thereafter (Fig. 2b).

According to the method mentioned above, the starting dates of the wet snow seasons from 1993 to 2011 are identified and listed in Table 1. There exists a large inter-annual variation in the beginning of the wet snow seasons. While 10 out of 18 wet seasons begin in March, 10 February 1997 and 4 April 1995 represent the earliest and the latest starting date of the wet snow season for the period of this study, respectively.

### 3.2 Snow aging

Figure 2 shows that the snow surface albedo increases dramatically to a high value around 0.9 during a snowfall event, then decreases with elapsed time after the snowfall. This is apparently the snow aging effect on surface albedo. Extensive analyses of snow albedo and snowfall events indicate that 3 mm water equivalent of snowfall is a threshold for the new fallen snow to cover the old snow and resets the snow surface albedo to a high value. In this work, a snowfall exceeding 3 mm water equivalent is defined as a "new snow" event, and the hours between two consecutive "new snow" events is counted as the length of elapsed time after the first snowfall. To eliminate the effects of solar zenith angle on snow albedo, only the data at the local noon (12:00 LT) are employed in the following analyses. Besides, to eliminate the effects of underlying surface, only those data with snow depth higher than 30 cm are analyzed, which is further discussed in Sect. 3.3. Considering the differences in snow properties between dry snow season and wet snow season, we perform the statistical analysis separately for these two sub-seasons.

**Table 1** The starting dates of the wet snow season in each snow-covered period from 1993 to 2011

| Year | Date |
|---|---|
| 1993/1994 | Feb 28 |
| 1994/1995 | Apr 4 |
| 1995/1996 | Mar 24 |
| 1996/1997 | Feb 10 |
| 1997/1998 | Feb 12 |
| 1998/1999 | Mar 10 |
| 1999/2000 | Mar 10 |
| 2000/2001 | Feb 25 |
| 2001/2002 | Feb 27 |
| 2002/2003 | Mar 11 |
| 2003/2004 | Mar 17 |
| 2004/2005 | Mar 17 |
| 2005/2006 | Mar 23 |
| 2006/2007 | Feb 19 |
| 2007/2008 | Feb 25 |
| 2008/2009 | Mar 16 |
| 2009/2010 | Mar 18 |
| 2010/2011 | Mar 11 |

Green and red dots in the upper two panels of Fig. 3 represent the albedos with snow surface temperature below and above 0 °C (hereafter referred to as negative/positive temperature), respectively. It shows that the snow albedo decreases as time elapses after a snowfall. In general, the albedo of fresh snow (within 5 h of elapsed time after snowfall) varies from 0.75 to 0.95 in dry snow season and it varies from 0.7 to 0.9 in wet snow season. Statistical analyses indicate that the albedo of fresh snow is independent of the amount of snowfall, but is closely related with the snow surface temperature. The albedo of fresh snow with positive surface temperature is lower than that with negative surface temperature, especially in the wet snow season. The albedo of fresh snow is dependent on snow microstructure which is possibly determined by the physical and chemical variables inside and below the cloud, including the supersaturation and temperature within the cloud, the cloud cooling rate and the temperature and humidity profiles between the cloud and the ground [31]. Therefore, it is difficult to describe the albedo of fresh snow in climate models. Solar radiation is usually weak during a snowfall event, hence the effect of new snow albedo on the surface energy balance is probably weak. However, fresh snow albedo strongly influences the albedos in the following periods. Additionally, in the wet snow season, the big differences between the new and old snow can effectively affect the energy balance of the snowpack as the solar radiation increases continuously. In many parameterizations, fresh snow albedo is set to a fixed value. For example, it is assumed to be 0.85 in the ECMWF model [32]. In the Noah land surface model [4], the prescribed albedo of fresh snow is based on satellite data as proposed by Robinson and Kukla [33] to reflect the spatial heterogeneities of snow albedo.

Snow albedo decreases with time. In the previous literature, the snow aging effect on snow albedo was described either non-linearly [26–28] or linearly [34]. Based on the observational data from the Col de Porte site, the reduction tendency is fitted with a linear line and an exponential curve respectively in Fig. 3, and the statistical parameters are shown in Tables 2, 3. The albedo decreases rapidly within the first 50 h after the snowfall. The correlation coefficients of exponential regression under almost all snow conditions, except for the case of negative snow surface temperature in wet snow season, are larger than that of linear regression, implying that the snow albedo decreases in an exponential rather than a linear way. It also demonstrates the obvious contrast between snow albedo in dry and wet snow seasons (Fig. 3). Within the first 50 h

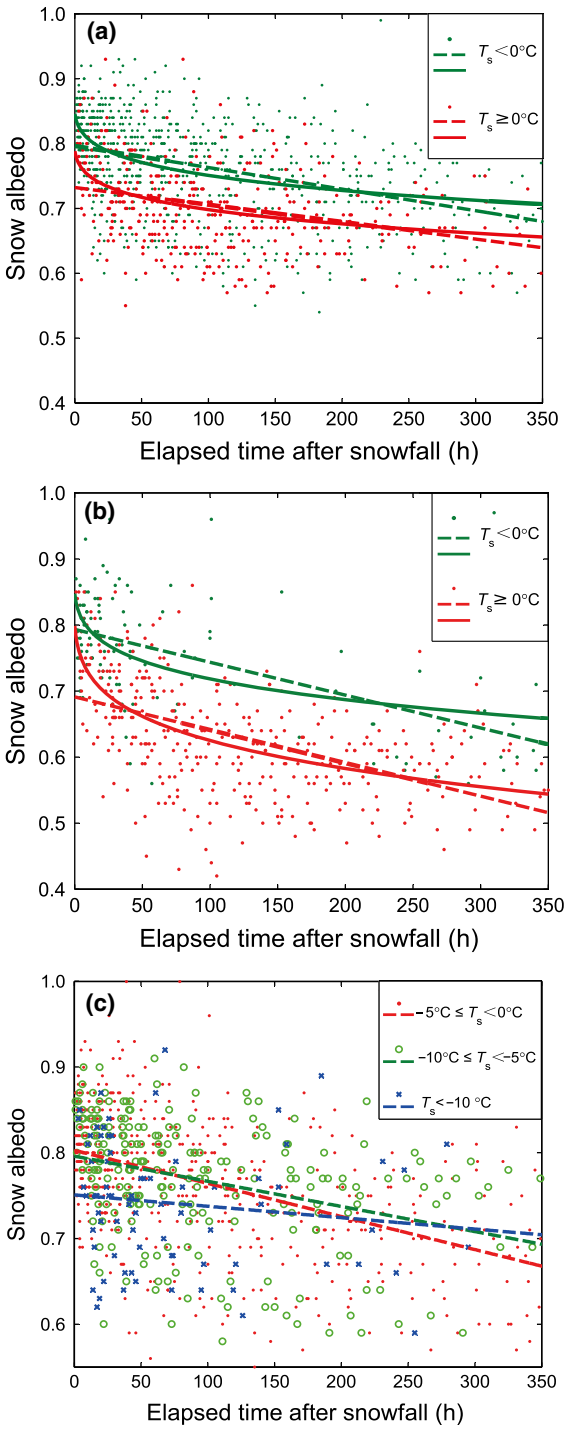


**Fig. 3** Snow albedo as a function of elapsed time after snowfalls exceeding 3 mm water equivalent in **a** dry snow season, **b** wet snow season, and **c** both dry and wet seasons for different ranges of surface temperature below 0 °C. In **a** and **b**, green (red) dots indicate snow surface temperature below (above) 0 °C, solid curves represent exponential regression of the samples. Dashed straight lines in the three panels represent linear regression. Regression functions and coefficients of regression are listed in Tables 2 and 3

after the snowfall, the albedo in wet snow season is relatively lower and decreases more rapidly than in dry snow season. This is partly because the snow grain size is larger in the wet snow season than in the dry snow season, which can be deduced from the snow types in Fig. 1, and partly because the growth rate of snow grains is faster at a relatively warmer snow surface temperature in the wet snow season. In addition, in the wet snow season, snow impurities appear at the surface due to the sublimation/melting of the surface snow and accelerate the albedo reduction. Another difference between the wet and dry snow seasons is that, the dry deposition of atmospheric aerosol onto the snow surface is masked by frequent snowfalls in the dry snow season. The above analyses indicate that it is necessary to parameterize the snow aging and snow albedo variation separately for the dry and wet snow seasons in an empirical snow albedo scheme.

Snow surface temperature is regarded as an important and sometimes even the only dominant parameter in many empirical parameterizations for snow albedo. In the following statistical analysis, we divide the snow albedo under negative surface temperature conditions into three categories and compute the linear reduction rate of albedo for each category to further examine the relationship between the snow surface albedo and snow surface temperature. It can be deduced from the upper two panels of Fig. 3 that most of the samples in Fig. 3c are from the dry snow season. It shows that the albedo reduction with elapsed time after a snowfall is small at low surface temperature (Fig. 3c), and the linear reduction rate increases from $1.33 \times 10^{-4}$ for snow surface temperature lower than −10 °C to $2.93 \times 10^{-4}$ for surface temperature between −10 and −5 °C, and to $3.86 \times 10^{-4}$ for surface temperature between −5 and 0 °C (last three lines in Table 3), implying that the reduction rate of snow albedo increases with the rise of snow surface temperature. It should be pointed out that the albedos of relatively fresh snow (elapsed time less than 20 h) with surface temperature lower than −10 °C are the lowest in these three categories. According to the relevant meteorological and snowpit observations, the air temperature is relatively high for these colder than −10 °C cases. Therefore, the temperature difference between the air and the snow surface is large for these cases, which is favorable for surface hoar to form with snow grain size exceeding 10 mm. As a result, the snow surface albedo decreases. The wide spread of samples and low correlation coefficient of linear regression (0.135) for this below −10 °C category also indicates that snow albedo is more determined by other factors such as snow grain size than by snow surface temperature only. It would cause biases in snow albedo parameterization by using snow surface temperature only.

### 3.3 Snow depth

Solar radiation in visible bands can penetrate a snowpack to a certain depth. Absorption of the visible radiation by the underlying soil and vegetation can influence the snow surface albedo when the snowpack is not thick enough to mask the underlying surface. It has been controversial about the snow depth required to mask the underlying surface. Molga [16] indicated that under the "least favorable" and "most favorable" conditions the penetration depth ranged between 20 and 60 cm. According to the analysis of Baker [17], sufficient snow depths of 5, 7.5, and 15 cm are required to effectively mask the underlying surfaces with bare soil, sod and alfalfa, respectively. Considering the dependence of snow albedo on the conditions and methods of measurement, we try to investigate the effect of snow depth on snow albedo and its seasonal variation by using the newly available long-term comprehensive data from the Col de Porte site. The dry and wet snow seasons are analyzed separately due to their aforementioned different characteristics. For analysis convenience, the albedos of the dry/wet snow season are divided into categories based on snow depth at 3 cm interval. For example, the category of 10 cm consists of those samples with snow depth between 8.5 cm and 11.5 cm. Dataset for the dry/wet snow season are smoothed by Locally Weighted regression Scatterplot Smoothing (LOWESS) to eliminate distortion caused by a small fraction of extremes [35].

The difference between the highest and lowest snow albedos within the same category of snow depth can be as large as 0.5 (Fig. 4), which can be attributed to the differences in snow type and snow age. Snow albedo increases with snow depth at the early stage of snowpack accumulation. There is no evident increase in the mean of surface albedo after it reaches 0.7 (0.6) in the dry (wet) snow season, corresponding to a snow depth of around 20 cm (30 cm). Further statistical analysis indicates that, when the snow depth is more than 21 cm (33 cm) in the dry (wet) snow season, the average of snow surface albedo is usually higher than 0.7 (0.6) and the standard deviation

**Table 2** Non-linear fitting of snow albedo $\alpha$ and elapsed time after snowfall $t$ (h)

| Snow condition | Regression coefficient $a$ | Regression coefficient $b$ | Correlation coefficient | Significance level (%) |
|---|---|---|---|---|
| $T_s < 0$ °C | 0.906 | 0.062 | 0.421 | >99 |
| $T_s \geq 0$ °C | 0.897 | 0.093 | 0.494 | >99 |
| Dry snow season | 0.902 | 0.067 | 0.420 | >99 |
| Wet snow season | 0.955 | 0.124 | 0.631 | >99 |
| $T_s < 0$ °C (Dry snow season) | 0.908 | 0.062 | 0.424 | >99 |
| $T_s \geq 0$ °C (Dry snow season) | 0.847 | 0.059 | 0.374 | >99 |
| $T_s < 0$ °C (Wet snow season) | 0.912 | 0.071 | 0.444 | >99 |
| $T_s \geq 0$ °C (Wet snow season) | 0.917 | 0.115 | 0.627 | >99 |

$\alpha = a - b \times (t+1)^{\frac{1}{3}}$

**Table 3** Linear fitting of snow albedo and elapsed time after snowfall

| Snow condition | Regression coefficient $a$ | Regression coefficient $b$ ($10^{-4}$) | Correlation coefficient | Significance level (%) |
|---|---|---|---|---|
| $T_s < 0$ °C | 0.797 | 3.43 | 0.399 | >99 |
| $T_s \geq 0$ °C | 0.719 | 4.33 | 0.436 | >99 |
| Dry snow season | 0.778 | 3.31 | 0.364 | >99 |
| Wet snow season | 0.724 | 5.77 | 0.534 | >99 |
| $T_s < 0$ °C (Dry snow season) | 0.796 | 3.33 | 0.391 | >99 |
| $T_s \geq 0$ °C (Dry snow season) | 0.732 | 2.65 | 0.313 | >99 |
| $T_s < 0$ °C (Wet snow season) | 0.796 | 4.26 | 0.465 | >99 |
| $T_s \geq 0$ °C (Wet snow season) | 0.696 | 5.08 | 0.535 | >99 |
| $-5$ °C $\leq T_s < 0$ °C | 0.803 | 3.86 | 0.459 | >99 |
| $-10$ °C $\leq T_s < -5$ °C | 0.796 | 2.93 | 0.335 | >99 |
| $T_s < -10$ °C | 0.751 | 1.33 | 0.135 | <90 |

$\alpha = a - b \times t$

of albedo is always less than 0.1, implying that surface albedo is independent of the snow depth if the snowpack is deeper than 21 cm (33 cm) in the dry (wet) snow season.

The non-linear regression curves of snow albedo in the dry (wet) snow season in Fig. 4 explain why we only analyze those data with snow depth more than 30 cm in Sects. 3.2 and 3.3. By this data selection we try to exclude the impact of underlying surface on snow surface albedo. In the following part, we compute the reduction rates of surface albedo with snow depth below and over 30 cm separately. Data in Table 4 indicate that the albedo decreases more rapidly under thinner snowpack condition in both dry and wet snow seasons. The linear reduction rate of snow albedo with snow depth less than 30 cm is almost two times that of snowpack thicker than 30 cm in the first two days after snowfalls. The reduction rate of snow albedo is 30 %–50 % faster within the first 24 h than that within the second 24 h after a snowfall, but the differences between the second and third day are much smaller, suggesting that the snow albedo decreases exponentially in the early hours after a snowfall but decreases much slowly later. The relatively large reduction rate of albedo (0.0045) during the third 24 h after a snowfall in the wet snow season for snowpack less than 30 cm is probably associated with the final ablation of snow cover.

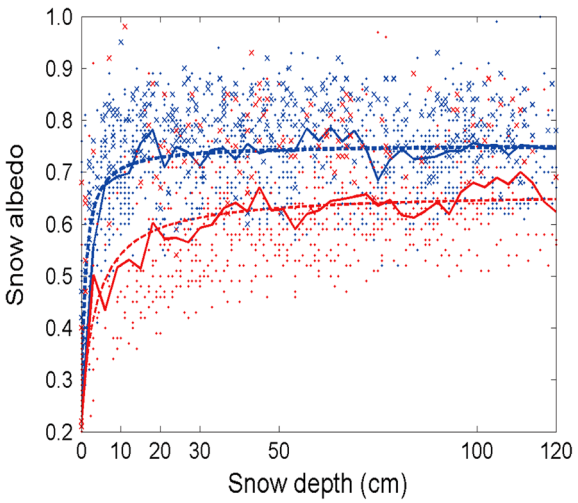


**Fig. 4** Snow albedo as a function of snow depth in dry snow season (blue) and wet snow season (red), crosses indicate fresh snow (snowfall occurred within 24 h before the observation), points indicate old snow. Solid curves are LOWESS-smoothed, dashed curves are non-linear fittings: $(0.75 \times h + 0.22)/(h + 0.97)$ for dry snow season, $(0.66 \times h + 0.79)/(h + 3.66)$ for wet snow season, $h$ is snow depth

**Table 4** Linear reduction rates ($h^{-1}$) of snow albedo in the first three days after snowfalls

| | Snow depth <30 cm | | | Snow depth >30 cm | | |
|---|---|---|---|---|---|---|
| | Day 1 | Day 2 | Day 3 | Day 1 | Day 2 | Day 3 |
| Dry season | 0.0048 | 0.0024 | 0.0021 | 0.0018 | 0.0009 | 0.0004 |
| Wet season | 0.0058 | 0.0030 | 0.0045 | 0.0029 | 0.0019 | 0.0013 |

## 4 Discussion and conclusions

An 18-year long (1993–2011) comprehensive snow and meteorological dataset from Col de Porte, France is used to analyze the seasonal evolution of snow albedo. The reduction rate of snow albedo within different elapsed time after a snowfall (snow aging) is also investigated for different stages of the snow season and under conditions of different surface temperature and snow depth. Effects of the air temperature, snow surface temperature and snow depth on snow surface albedo are explored. Each snow-covered season is divided into a dry snow season and a wet snow season according to the temporal variation of several parameters such as snow type, liquid water content of the snowpack and air temperature. The main conclusions are as follows.

(1) For Col de Porte site, an air temperature index is proposed to determine the starting date of the wet snow season. The temperature is accumulated when the average daytime air temperature is over 2.5 °C in a certain number of consecutive days and the accumulation must be over 18 °C.

(2) After a snowfall, the snow albedo is relatively high (0.7–0.9). It is more determined by the meteorological conditions during the snowfall than by the snowfall amount. The snow albedo decreases exponentially with the elapsed time after the snowfall. It decreases most rapidly within the first 2 or 3 d and gradually slows down afterwards. Significant differences in snow albedo and its variation are found between the dry and wet snow seasons. Snow albedo in the dry snow season is larger than in the wet snow season due to the lower air temperature and smaller effective grain size of snow. Surface albedo decreases more rapidly in the wet snow season than in the dry snow season, for the grain size growth rates and the concentration of impurities that affect the snow surface albedo are significantly higher in the wet snow season.

(3) The albedo reduction with elapsed time after a snowfall is small at low surface temperature and increases with the rise of surface temperature. However, the albedo reduction rates are widely scattered within the observed temperature range, indicating that snow surface albedo is also affected by other factors such as snow grain size instead of by snow surface temperature only.

(4) Visible solar radiation can penetrate the snowpack to a certain depth. When the snowpack is thin, the underlying surface with much lower albedo can reduce the snow surface albedo by absorbing part of the visible solar radiation. Snow surface albedo increases with the enhancement of

snow depth and consequently the volume scattering until the snowpack reaches a certain depth. For Col de Porte site, the thresholds of snow depth to effectively mask the underlying surface in the dry and wet snow seasons are 21 and 33 cm respectively. The reduction rate of surface albedo of a thin snowpack below 21/33 cm is larger than that of a thick snowpack above these thresholds in dry and wet snow seasons.

In current empirical parameterizations for snow albedo, snow surface temperature is considered as an important and sometimes even the only dominant factor. In addition, snow albedo is supposed to decrease linearly with time in some schemes, while the different characteristics of snow aging within a snow season and the effects of snow depth on surface albedo are neglected. However, analysis in our present study indicates that it is necessary to consider the exponential decrease of snow albedo with elapsed time after snowfalls and the different reduction rates of snow albedo in dry and wet snow seasons. The impact of snow depth on snow albedo and its variation should also be considered, especially in the wet snow season when the incoming solar radiation is strong and the snowpack becomes thinner and thinner. Snow albedo in wet snow season might be overestimated by previous unified schemes, which partly explains why the melting rate is weakened and the final ablation of the snow cover is delayed. In order to better represent the reduction of snow albedo with elapsed time after snowfalls, several physical parameters such as air temperature, temperature difference between the air and snow surface, wind speed, and other factors affecting the growth rate of snow grain size and ultimately influencing snow albedo should be taken into account.

**Acknowledgments** This work was supported by the Major National Scientific Research Project on Global Changes (2010CB951902), and the National Natural Science Foundation of China (40975042 and 41175005). Suggestions to improve this manuscript from Professor Jiming Jin of the Utah State University are highly appreciated.

**Conflict of Interest** The authors declare that they have no conflict of interest.

## References

1. Jordan R (1991) A one-dimensional temperature model for a snow cover: technical documentation for SNTHERM.89. Special report 91-16, USA Cold Regions Research and Engineering Laboratory, Hanover, New Hampshire
2. Sun SF, Jin JM, Xue YK (1999) A simple snow-atmosphere soil transfer model. J Geophys Res 104:587–597
3. Slater AG, Schlosser CA, Desborough CE et al (2001) The representation of snow in land-surface schemes: results from PILPS 2(d). J Hydrometeorol 2:7–25
4. Wang Z, Zeng X (2010) Evaluation of snow albedo in land models for weather and climate studies. J Appl Meteorol Climatol 49:363–380
5. Cess RD, Potter GL, Blanchet JP et al (1991) Intercomparison and interpretation of snow climate feedback processes in seventeen atmospheric general circulation models. Science 253:888–892
6. Slater AG, Pitman AJ, Desborough CE (1998) The validation of a snow parameterization designed for use in general circulation models. Int J Climatol 18:595–617
7. Nolin A, Stroeve J (1997) The changing albedo of the Greenland ice sheet: implications for climate change. Ann Glaciol 25:51–57
8. Klok EJ, Oerlemans J (2004) Modeled climate sensitivity of the mass balance of Morteratschgletscher and its dependence on albedo parameterization. Int J Climatol 24:231–245
9. Xue YK, Sun SF, Kahan D et al (2003) Impact of parameterizations in snow physics and interface processes on the simulation of snow cover and runoff at several cold region sites. J Geophys Res 108:8859. doi:10.1029/2002JD003174
10. Solomon S, Qin DH, Manning M et al (eds) (2007) Climate change 2007: the physical science basis. Contribution of working group I to the fourth assessment report of the Intergovernmental Panel on Climate Change. Cambridge University Press, Cambridge
11. Curry JA, Schramm JL, Ebert EE (1995) On the sea ice albedo climate feedback mechanism. J Clim 8:240–247
12. Curry JA, Schramm JL, Perovich DK et al (2001) Applications of SHEBA/FIRE data to evaluation of snow/ice albedo parameterizations. J Geophys Res 106:15345–15355
13. Wiscombe WJ, Warren SG (1980) A model for the spectral albedo of snow. I: pure snow. J Atmos Sci 37:2712–2733
14. Warren SG, Wiscombe WJ (1980) A model for the spectral albedo of snow. II: snow containing atmospheric aerosols. J Atmos Sci 37:2734–2745
15. Hansen J, Nazarenko L (2004) Soot climate forcing via snow and ice albedos. Proc Natl Acad Sci USA 101:423–428
16. Molga M (1962) Agricultural meteorology part II: outline of agrometeorological problems. National Science Foundation, Warsaw
17. Baker DG (1991) Snow depth required to mask the underlying surface. J Appl Meteorol 30:387–392
18. Grenfell TC, Warren SG, Mullen PC (1994) Reflection of solar radiation by the Antarctic snow surface at ultraviolet, visible, and near-infrared wavelengths. J Geophys Res 99:18669–18684
19. Aoki T, Fukabori M, Hachikubo A et al (2000) Effects of snow physical parameters on spectral albedo and bidirectional reflectance of snow surface. J Geophys Res 105:10219–10236
20. Toon OB, McKay CP, Ackerman TP et al (1989) Rapid calculation of radiative heating rates and photodissociation rates in inhomogeneous multiple scattering atmospheres. J Geophys Res 94:16287–16301
21. Flanner MG, Zender CS (2005) Snowpack radiative heating: influence on Tibetan Plateau climate. Geophys Res Lett 32:L06501. doi:10.1029/2004GL022076
22. Flanner MG, Zender CS (2006) Linking snowpack microphysics and albedo evolution. J Geophys Res 111:D12208. doi:10.1029/2005JD006834
23. Oleson KW, Lawrence DM, Bonan GB et al (2010) Technical description of version 4.0 of the community land model (CLM). NCAR technical note NCAR/TN-478+STR, National Center for Atmospheric Research, Boulder, Colorado
24. Aoki T, Kuchiki K, Niwano M et al (2011) Physically based snow albedo model for calculating broadband albedos and the solar heating profile in snowpack for general circulation models. J. Geophys Res 116:D11114. doi:10.1029/2010JD015507
25. Roeckner E, Bäuml G, Bonaventura L et al (2003) The atmospheric general circulation model ECHAM5—part 1: model description. Technical report 349, Max Planck Institute for Meteorology, Hamburg
26. Dickinson RE, Sellers AH, Kennedy PJ (1993) Biosphere–atmosphere transfer scheme (BATS) version 1e as coupled to the

NCAR community climate model. NCAR technical note NCAR/TN-387+STR, National Center for Atmospheric Research, Boulder, Colorado
27. Yang ZL, Dickinson RE, Robock A et al (1997) Validation of the snow submodel of the biosphere–atmosphere transfer scheme with Russian snow cover and meteorological observational data. J Clim 10:353–373
28. Dai YJ, Zeng XB, Dickinson RE et al (2003) The common land model (CLM). Bull Am Meteorol Soc 84:1013–1023
29. Morin S, Lejeune Y, Lesaffre B et al (2012) An 18-yr long (1993–2011) snow and meteorological dataset from a mid-altitude mountain site (Col de Porte, France, 1325 m alt.) for driving and evaluating snowpack models. Earth Syst Sci Data 4:13–21
30. Fierz C, Armstrong RL, Durand Y et al (2009) The international classification for seasonal snow on the ground. IHP-VII technical documents in Hydrology No 83, IACS Contribution No 1, UNESCO-IHP, Paris
31. Taillandier AS, Domine F, Simpson WR et al (2007) Rate of decrease of the specific surface area of dry snow: isothermal and temperature gradient conditions. J Geophys Res 112:F03003. doi:10.1029/2006JF000514
32. Dutra E, Balsamo G, Viterbo P et al (2010) An improved snow scheme for the ECMWF land surface model: description and offline validation. J Hydrometeorol 11:899–916
33. Robinson DA, Kukla G (1985) Maximum surface albedo of seasonally snow-covered lands in the northern hemisphere. J Clim Appl Meteorol 24:402–411
34. Aoki T, Hachikubo A, Hori M (2003) Effects of snow physical parameters on shortwave broadband albedos. J Geophys Res 108:4616. doi:10.1029/2003JD003506
35. Cleveland WS, Devlin SJ (1988) Locally-weighted regression: an approach to regression analysis by local fitting. J Am Stat Assoc 83:596–610

# 基于Lorenz系统的数值天气转折期预报理论探索*

达朝究[1)2)†] 穆帅[1)] 马德山[1)] 于海鹏[2)] 侯威[3)] 龚志强[3)]

1) (西北民族大学数学与计算机科学学院, 兰州 730030)

2) (兰州大学大气科学学院, 兰州 730000)

3) (国家气候中心气候研究开放实验室, 北京 100081)

( 2013 年 8 月 16 日收到; 2013 年 10 月 8 日收到修改稿 )

以 Lorenz 系统为研究对象, 对数值天气转折期预报中的动力学特征进行了理论研究, 通过对 Lorenz 系统平衡点稳定性的讨论, 得到了区分准稳定区域和准不稳定区域的分界曲面, 由此标定出准稳定区域和准不稳定区域. 在准稳定区域, Lorenz 曲线保持相对稳定, 能够在该平衡点周围周期运动; 在准不稳定区域, Lorenz 曲线可能会从这个平衡点周围跃过分界曲面而进入另外一个平衡点周围, 即发生突变, 这是 Lorenz 系统的一个重要动力学特征; 对数值天气转折期预报与气候突变检测、预测给出一种新理论和新方法.

**关键词**: Lorenz 系统, 准稳定区域, 准不稳定区域, 气候突变

**PACS:** 92.40.Cy, 92.60.Aa **DOI:** 10.7498/aps.63.029201

## 1 引 言

1904 年, Bjerknes[1] 用力学、数学和物理学的观点, 制订出天气预报问题的规划, 将天气预报问题转化为一个微分方程组的初值问题. 1922 年, Richardson[2] 首次进行了数值天气预报的尝试, 他详细论述了数值预报的原理和可行性, 使 Bjerknes 的理论成为现实. 由于计算条件的限制, 这种理论的实现距离真实的预报还十分遥远, 但是他无疑是数值天气预报的先驱. 当时, 人们期待许多计算人员能在一个天气工厂内, 像在一个交响乐队指挥下同步进行计算, 从而实现世界的天气预报. 在科学家的不倦探索下, 1950 年, 距 Richardson 的尝试仅 28 年, Charney 等 [3] 利用埃尼阿克 (ENIAC) 电子计算机实现了第一次数值天气预报, 这标志着数值天气预报从理论到现实, 预报成功的基础是电子计算机的飞速发展. 在此基础上, 各国科学家针对自身条件做了大量的研究工作, 取得了丰硕的成果. 中国已故气象学家顾震潮先生在 1958 年指出: 把数值天气预报问题提成初值问题, 只使用一个时刻的资料是一个根本性的缺陷 [4,5]. 1962 年, 丑纪范 [6] 从函数空间的角度将微分方程定解问题变为等价的泛函极值问题, 而后推广了微分方程解的概念, 引进了“广义解”, 利用希尔伯特空间理论论证了“广义解”比原来意义下的“正规解”更接近方程所描述的物理现象的“实况”. 在顾震潮和丑纪范工作的基础上, 邱崇践等 [7]、邵爱梅等 [8] 给出了一种新的资料同化方案; 文献 [9—14] 研究了海气耦合的相似韵律现象, 并建立了利用历史观测数据的相似-动力模式, 得到了很好的预报效果; 封国林等 [15,16] 给出了自忆预测模式的计算方案, 并将其应用到数值天气预报模式上, 得到了很好的结论. 文献 [17—19] 就数值天气预报中历史数据的使用也做了一定的研究工作. 虽然数值天气预报有了长足的发展, 但是转折性天气或气候的预测一直是

* 国家科技支撑计划 (批准号: 2009BAC51B04)、公益性行业 (气象) 科研专项 (批准号: GYHY201206009, GYHY201106016)、全球变化研究国家重大科学研究计划 (批准号: 2012CB955902)、国家自然科学基金 (批准号: 40930952, 41175067, 61162021) 和中央高校基本科研业务费专项资金 (批准号: zyz2012079) 资助的课题.

† 通讯作者. E-mail: jtdcj@163.com

© 2014 中国物理学会 Chinese Physical Society 

科学界没有解决的问题, 现有的数值模式在转折期预报上的能力还是不足[20], 这与大气系统的本质——混沌是关联的. 在数学上处理, 就是微分方程解的不稳定, 或者叫对初值的敏感. 最早发现这一事实的是Lorenz, 他在1963年分析对流运动中的非线性作用, 据大气运动的规律, 建立了一个简化的数学模型, 也就是著名的Lorenz方程组. Lorenz经过研究发现, 当这个方程组的参数取某些值时, 轨线运动会变得复杂和不确定, 导致轨线的行为无法预测, 理论上揭示了气候的突变[21], 加之1979年Lorenz在华盛顿美国科学促进会上讲演中提出的"蝴蝶效应", 使大气系统的混沌特征形象而具体.

大气系统的混沌特性可诱导大气系统的突变, 而大气环流的转折和突变相联系. 气候突变现象及其理论研究是近代气候学的一个新兴研究领域, 许多科学家力图揭示气候突变现象[22−33]. 气候突变又称气候变化的不连续性、气候的跳跃, 是普遍存在于气候系统中的一种重要现象, 是指气候从一种稳定态 (或稳定持续的变化趋势) 跳跃式地转变到另一种稳定态 (或稳定持续的变化趋势) 的过程, 它表现为气候在时空上从一个统计特征到另一种统计特征的急剧变化[22].

近年来, 郑志海等[34−36]将混沌的概念引入全球数值天气预报模式, 揭示了初始时刻不可避免的误差增长规律, 并就其对季节、地区和初始场的依赖性等做了一定的研究.

对气候突变的研究, 以往多采用统计方法, 本文用动力学方法, 以Lorenz 方程组作为研究对象, 对气候突变进行研究, 就Lorenz系统的动力学特征给出定量描述; 对数值天气转折期预报以及气候突变做一定的理论探讨, 期望获得数值天气转折期预报和气候突变的新思路和新方法.

## 2 Lorenz方程轨线在不同平衡态间的跳跃

### 2.1 Lorenz方程组与线性近似方程

Lorenz方程组为

$$\begin{cases} \dfrac{\mathrm{d}x}{\mathrm{d}t} = 10(-x+y) \\ \dfrac{\mathrm{d}y}{\mathrm{d}t} = 28x - y - xz \\ \dfrac{\mathrm{d}z}{\mathrm{d}t} = xy - \frac{8}{3}z \end{cases} . \tag{1}$$

其线性近似方程按如下方法求解, 令

$$\begin{cases} P(x,y,z) \equiv 10(-x+y) = 0 \\ Q(x,y,z) \equiv 28x - y - xz = 0 \\ R(x,y,z) \equiv xy - \dfrac{8}{3}z = 0 \end{cases} , \tag{2}$$

得到Lorenz方程组的三个平衡点, 分别为

$$O(0,0,0), \tag{3a}$$

$$\mathrm{R}(6\sqrt{2}, 6\sqrt{2}, 27), \tag{3b}$$

$$\mathrm{L}(-6\sqrt{2}, -6\sqrt{2}, 27). \tag{3c}$$

本文仅对右平衡点$\mathrm{R}(6\sqrt{2}, 6\sqrt{2}, 27)$和左平衡点$\mathrm{L}(-6\sqrt{2}, -6\sqrt{2}, 27)$做研究. 将动力系统 (1) 在平衡点$(x_0, y_0, z_0)$做Taylor展开, 得

$$\begin{cases} \dfrac{\mathrm{d}x}{\mathrm{d}t} = P(x_0,y_0,z_0) + \left.\dfrac{\partial P}{\partial x}\right|_{(x_0,y_0,z_0)}(x-x_0) + \left.\dfrac{\partial P}{\partial y}\right|_{(x_0,y_0,z_0)}(y-y_0) + \left.\dfrac{\partial P}{\partial z}\right|_{(x_0,y_0,z_0)}(z-z_0) + \cdots \\ \dfrac{\mathrm{d}y}{\mathrm{d}t} = Q(x_0,y_0,z_0) + \left.\dfrac{\partial Q}{\partial x}\right|_{(x_0,y_0,z_0)}(x-x_0) + \left.\dfrac{\partial Q}{\partial y}\right|_{(x_0,y_0,z_0)}(y-y_0) + \left.\dfrac{\partial Q}{\partial z}\right|_{(x_0,y_0,z_0)}(z-z_0) + \cdots \\ \dfrac{\mathrm{d}z}{\mathrm{d}t} = R(x_0,y_0,z_0) + \left.\dfrac{\partial R}{\partial x}\right|_{(x_0,y_0,z_0)}(x-x_0) + \left.\dfrac{\partial R}{\partial y}\right|_{(x_0,y_0,z_0)}(y-y_0) + \left.\dfrac{\partial R}{\partial z}\right|_{(x_0,y_0,z_0)}(z-z_0) + \cdots \end{cases} , \tag{4}$$

只取线性部分, 同时注意到方程 (2), 得

$$\begin{cases} \dfrac{\mathrm{d}x}{\mathrm{d}t} = -10(x-x_0) + 10(y-y_0) \\ \dfrac{\mathrm{d}y}{\mathrm{d}t} = (28-z_0)(x-x_0) - (y-y_0) - x_0(z-z_0) \\ \dfrac{\mathrm{d}z}{\mathrm{d}t} = y_0(x-x_0) + x_0(y-y_0) - \dfrac{8}{3}(z-z_0) \end{cases} . \tag{5}$$

动力系统 (5) 叫做动力系统 (1) 在平衡点$(x_0, y_0, z_0)$处的线性近似方程[37].

## 2.2 Lorenz 系统的稳定性分析

### 2.2.1 系统在右平衡点 $\mathrm{R}(6\sqrt{2},6\sqrt{2},27)$ 的稳定性

动力系统 (1) 在平衡点 $\mathrm{R}(6\sqrt{2},6\sqrt{2},27)$ 的线性近似方程为

$$\begin{cases}\dfrac{\mathrm{d}x}{\mathrm{d}t} &= -10(x-6\sqrt{2})+10(y-6\sqrt{2})\\ \dfrac{\mathrm{d}y}{\mathrm{d}t} &= (x-6\sqrt{2})-(y-6\sqrt{2})-6\sqrt{2}(z-27)\\ \dfrac{\mathrm{d}z}{\mathrm{d}t} &= 6\sqrt{2}(x-6\sqrt{2})+6\sqrt{2}(y-6\sqrt{2})-\dfrac{8}{3}(z-27)\end{cases}. \tag{6}$$

将动力系统 (6) 做平移变换: $\xi=x-6\sqrt{2}$, $\eta=y-6\sqrt{2}$, $\zeta=z-27$, 得到

$$\begin{cases}\dfrac{\mathrm{d}\xi}{\mathrm{d}t} = -10\xi+10\eta\\ \dfrac{\mathrm{d}\eta}{\mathrm{d}t} = \xi-\eta-6\sqrt{2}\zeta\\ \dfrac{\mathrm{d}\zeta}{\mathrm{d}t} = 6\sqrt{2}\xi+6\sqrt{2}\eta-\dfrac{8}{3}\zeta\end{cases}, \tag{7a}$$

用矩阵表示为

$$\begin{pmatrix}\dot{\xi}\\ \dot{\eta}\\ \dot{\zeta}\end{pmatrix}=\boldsymbol{A}_1\begin{pmatrix}\xi\\ \eta\\ \zeta\end{pmatrix}, \tag{7b}$$

(7b) 式中的 $\dot{\xi}$, $\dot{\eta}$ 和 $\dot{\zeta}$ 是导数运算, 矩阵 $\boldsymbol{A}_1$ 为

$$\boldsymbol{A}_1=\begin{pmatrix}-10 & 10 & 0\\ 1 & -1 & -6\sqrt{2}\\ 6\sqrt{2} & 6\sqrt{2} & -\dfrac{8}{3}\end{pmatrix}. \tag{8}$$

求得矩阵 $\boldsymbol{A}_1$ 的特征值分别为

$$\lambda_1=\frac{1}{9}\sqrt[3]{-425537+36\sqrt{140629614}}-\frac{1}{9}\sqrt[3]{425537+36\sqrt{140629614}}-\frac{41}{9}, \tag{9a}$$

$$\lambda_2=-\frac{1}{18}\sqrt[3]{-425537+36\sqrt{140629614}}+\frac{1}{18}\sqrt[3]{425537+36\sqrt{140629614}}-\frac{41}{9}+\left(\frac{\sqrt{3}}{18}\sqrt[3]{-425537+36\sqrt{140629614}}+\frac{\sqrt{3}}{18}\sqrt[3]{425537+36\sqrt{140629614}}\right)\mathrm{i}, \tag{9b}$$

$$\lambda_3=-\frac{1}{18}\sqrt[3]{-425537+36\sqrt{140629614}}+\frac{1}{18}\sqrt[3]{425537+36\sqrt{140629614}}-\frac{41}{9}-\left(\frac{\sqrt{3}}{18}\sqrt[3]{-425537+36\sqrt{140629614}}+\frac{\sqrt{3}}{18}\sqrt[3]{425537+36\sqrt{140629614}}\right)\mathrm{i} \tag{9c}$$

(9) 式中的 $i$ 是虚数单位. 令

$$a=-\frac{1}{18}\sqrt[3]{-425537+36\sqrt{140629614}}+\frac{1}{18}\sqrt[3]{425537+36\sqrt{140629614}}-\frac{41}{9}, \tag{10a}$$

$$b=\frac{\sqrt{3}}{18}\sqrt[3]{-425537+36\sqrt{140629614}}+\frac{\sqrt{3}}{18}\sqrt[3]{425537+36\sqrt{140629614}}, \tag{10b}$$

则 (9b) 和 (9c) 式可写为

$$\lambda_2=a+b\mathrm{i}, \tag{11a}$$

$$\lambda_3 = a - b\mathrm{i}. \tag{11b}$$

矩阵 $\boldsymbol{A}_1$ 与特征值 $\lambda_1$, $\lambda_2$, $\lambda_3$ 对应的特征向量 $\boldsymbol{\alpha}_{11}$, $\boldsymbol{\alpha}_{12}$, $\boldsymbol{\alpha}_{13}$ 分别为 (转置形式)

$$\boldsymbol{\alpha}_{11}^{\mathrm{T}} = \left(\lambda_1^2 + \frac{11}{3}\lambda_1 + \frac{224}{3}, \lambda_1 - \frac{208}{3}, 6\sqrt{2}(\lambda_1 + 2)\right), \tag{12a}$$

$$\boldsymbol{\alpha}_{12}^{\mathrm{T}} = \left(\lambda_2^2 + \frac{11}{3}\lambda_2 + \frac{224}{3}, \lambda_2 - \frac{208}{3}, 6\sqrt{2}(\lambda_2 + 2)\right), \tag{12b}$$

$$\boldsymbol{\alpha}_{13}^{\mathrm{T}} = \left(\lambda_3^2 + \frac{11}{3}\lambda_3 + \frac{224}{3}, \lambda_3 - \frac{208}{3}, 6\sqrt{2}(\lambda_3 + 2)\right). \tag{12c}$$

令

$$\boldsymbol{X} = (\alpha_{11}, \alpha_{12}, \alpha_{13}), \tag{13}$$

则有

$$\boldsymbol{X^{-1}A_1X} = \begin{pmatrix} \lambda_1 & 0 & 0 \\ 0 & \lambda_2 & 0 \\ 0 & 0 & \lambda_3 \end{pmatrix}. \tag{14}$$

由 (9)—(11) 式可知, 一定存在矩阵 $\boldsymbol{P}_1$, 使得 [38]

$$\boldsymbol{P}_1^{-1}\boldsymbol{A}_1\boldsymbol{P}_1 = \begin{pmatrix} \lambda_1 & 0 & 0 \\ 0 & a & -b \\ 0 & b & a \end{pmatrix}. \tag{15}$$

令

$$\boldsymbol{B}_1 = \begin{pmatrix} \lambda_1 & 0 & 0 \\ 0 & a & -b \\ 0 & b & a \end{pmatrix}, \tag{16}$$

则 $\boldsymbol{A}_1$ 与 $\boldsymbol{B}_1$ 相似. 由相似矩阵性质可知, 相似矩阵有相同的特征值, 即 $\lambda_1$, $\lambda_2$, $\lambda_3$ 也是矩阵 $\boldsymbol{B}_1$ 的特征值. 就矩阵 $\boldsymbol{B}_1$ 来说, 与其特征值 $\lambda_1$, $\lambda_2$, $\lambda_3$ 对应的特征向量 $\beta_{11}$, $\beta_{12}$, $\beta_{13}$ 分别为 (转置形式)

$$\boldsymbol{\beta}_{11}^{\mathrm{T}} = (1, 0, 0), \tag{17a}$$

$$\boldsymbol{\beta}_{12}^{\mathrm{T}} = \left(0\frac{\lambda_2 - a}{b}, 1\right), \tag{17b}$$

$$\boldsymbol{\beta}_{13}^{\mathrm{T}} = \left(0\frac{\lambda_3 - a}{b}, 1\right). \tag{17c}$$

令

$$\boldsymbol{Y} = (\boldsymbol{\beta}_{11}, \boldsymbol{\beta}_{12}, \boldsymbol{\beta}_{13}), \tag{18}$$

则

$$\boldsymbol{Y^{-1}B_1Y} = \begin{pmatrix} \lambda_1 & 0 & 0 \\ 0 & \lambda_2 & 0 \\ 0 & 0 & \lambda_3 \end{pmatrix}. \tag{19}$$

结合 (14) 和 (19) 式, 易知

$$\boldsymbol{X}^{-1}\boldsymbol{A}_1\boldsymbol{X} = \boldsymbol{Y}^{-1}\boldsymbol{B}_1\boldsymbol{Y} \tag{20}$$

(20) 式两边分别左乘 $\boldsymbol{Y}$, 右乘 $\boldsymbol{Y}^{-1}$, 可得

$$\boldsymbol{Y}\boldsymbol{X}^{-1}\boldsymbol{A}_1\boldsymbol{X}\boldsymbol{Y}^{-1} = \boldsymbol{B}_1 \tag{21}$$

由 (15), (16) 和 (21) 式, 知

$$\boldsymbol{P}_1 = \boldsymbol{X}\boldsymbol{Y}^{-1} = \begin{pmatrix} \lambda_1^2 + \dfrac{11}{3}\lambda_1 + \dfrac{224}{3} & \lambda_2^2 + \dfrac{11}{3}\lambda_2 + \dfrac{224}{3} & \lambda_3^2 + \dfrac{11}{3}\lambda_3 + \dfrac{224}{3} \\ \times\lambda_1 - \dfrac{208}{3} & \lambda_2 - \dfrac{208}{3} & \lambda_3 - \dfrac{208}{3} \\ 6\sqrt{2}(\lambda_1+2) & 6\sqrt{2}(\lambda_2+2) & 6\sqrt{2}(\lambda_3+2) \end{pmatrix} \begin{pmatrix} 1 & 0 & 0 \\ 0 & \dfrac{\lambda_2 - a}{b} & \dfrac{\lambda_3 - a}{b} \\ 0 & 1 & 1 \end{pmatrix}^{-1}, \tag{22a}$$

$$\boldsymbol{P}_1^{-1} = \boldsymbol{Y}\boldsymbol{X}^{-1} = \begin{pmatrix} 1 & 0 & 0 \\ 0 & \dfrac{\lambda_2 - a}{b} & \dfrac{\lambda_3 - a}{b} \\ 0 & 1 & 1 \end{pmatrix} \begin{pmatrix} \lambda_1^2 + \dfrac{11}{3}\lambda_1 + \dfrac{224}{3} & \lambda_2^2 + \dfrac{11}{3}\lambda_2 + \dfrac{224}{3} & \lambda_3^2 + \dfrac{11}{3}\lambda_3 + \dfrac{224}{3} \\ \lambda_1 - \dfrac{208}{3} & \lambda_2 - \dfrac{208}{3} & \lambda_3 - \dfrac{208}{3} \\ 6\sqrt{2}(\lambda_1+2) & 6\sqrt{2}(\lambda_2+2) & 6\sqrt{2}(\lambda_3+2) \end{pmatrix}^{-1}. \tag{22b}$$

令

$$c_1 = \lambda_1^2 + \frac{11}{3}\lambda_1 + \frac{224}{3}, \tag{23a}$$

$$c_2 = \lambda_2^2 + \frac{11}{3}\lambda_2 + \frac{224}{3}, \tag{23b}$$

$$c_3 = \lambda_3^2 + \frac{11}{3}\lambda_3 + \frac{224}{3}, \tag{23c}$$

和

$$d_1 = \lambda_1 - \frac{208}{3}, \tag{24a}$$

$$d_2 = \lambda_2 - \frac{208}{3}, \tag{24b}$$

$$d_3 = \lambda_3 - \frac{208}{3}, \tag{24c}$$

以及

$$e_1 = 6\sqrt{2}(\lambda_1 + 2), \tag{25a}$$

$$e_2 = 6\sqrt{2}(\lambda_2 + 2), \tag{25b}$$

$$e_3 = 6\sqrt{2}(\lambda_3 + 2), \tag{25c}$$

则

$$\boldsymbol{P}_1^{-1} = \begin{pmatrix} 1 & 0 & 0 \\ 0 & \dfrac{\lambda_2 - a}{b} & \dfrac{\lambda_3 - a}{b} \\ 0 & 1 & 1 \end{pmatrix} \begin{pmatrix} c_1 & c_2 & c_3 \\ d_1 & d_2 & d_3 \\ e_1 & e_2 & e_3 \end{pmatrix}^{-1}. \tag{26}$$

令

$$f = c_1(d_2e_3 - d_3e_2) - c_2(d_1e_3 - d_3e_1) + c_3(d_1e_2 - d_2e_1), \tag{27}$$

则

$$\boldsymbol{P}_1^{-1} = \begin{pmatrix} 1 & 0 & 0 \\ 0 & \dfrac{\lambda_2 - a}{b} & \dfrac{\lambda_3 - a}{b} \\ 0 & 1 & 1 \end{pmatrix} \begin{pmatrix} \dfrac{d_2e_3 - d_3e_2}{f} & -\dfrac{c_2e_3 - c_3e_2}{f} & \dfrac{c_2d_3 - c_3d_2}{f} \\ -\dfrac{d_1e_3 - d_3e_1}{f} & \dfrac{c_1e_3 - c_3e_1}{f} & -\dfrac{c_1d_3 - c_3d_1}{f} \\ \dfrac{d_1e_2 - d_2e_1}{f} & -\dfrac{c_1e_2 - c_2e_1}{f} & \dfrac{c_1d_2 - c_2d_1}{f} \end{pmatrix}. \tag{28}$$

分别令

$$h_1 = \frac{d_2e_3 - d_3e_2}{f}, \tag{29a}$$

$$h_2 = -\frac{c_2e_3 - c_3e_2}{f}, \tag{29b}$$

$$h_3 = \frac{c_2d_3 - c_3d_2}{f}, \tag{29c}$$

与

$$j_1 = -\frac{d_1e_3 - d_3e_1}{f}, \tag{30a}$$

$$j_2 = \frac{c_1e_3 - c_3e_1}{f}, \tag{30b}$$

$$j_3 = -\frac{c_1d_3 - c_3d_1}{f}, \tag{30c}$$

以及

$$k_1 = \frac{d_1e_2 - d_2e_1}{f}, \tag{31a}$$

$$k_2 = -\frac{c_1e_2 - c_2e_1}{f}, \tag{31b}$$

$$k_3 = \frac{c_1d_2 - c_2d_1}{f}, \tag{31c}$$

有

$$\begin{aligned} \boldsymbol{P}_1^{-1} &= \begin{pmatrix} 1 & 0 & 0 \\ 0 & \dfrac{\lambda_2 - a}{b} & \dfrac{\lambda_3 - a}{b} \\ 0 & 1 & 1 \end{pmatrix} \begin{pmatrix} h_1 & h_2 & h_3 \\ j_1 & j_2 & j_3 \\ k_1 & k_2 & k_3 \end{pmatrix} \\ &= \begin{pmatrix} h_1 & h_2 & h_3 \\ \dfrac{(\lambda_2 - a)j_1 + (\lambda_3 - a)k_1}{b} & \dfrac{(\lambda_2 - a)j_2 + (\lambda_3 - a)k_2}{b} & \dfrac{(\lambda_2 - a)j_3 + (\lambda_3 - a)k_3}{b} \\ j_1 + k_1 & j_2 + k_2 & j_3 + k_3 \end{pmatrix}. \end{aligned} \tag{32}$$

取坐标变换 $\begin{pmatrix} \xi \\ \eta \\ \zeta \end{pmatrix} = \boldsymbol{P}_1 \begin{pmatrix} u \\ v \\ w \end{pmatrix}$，有

$$\begin{pmatrix} \dot{u} \\ \dot{v} \\ \dot{w} \end{pmatrix} = \boldsymbol{P}_1^{-1} \begin{pmatrix} \dot{\xi} \\ \dot{\eta} \\ \dot{\zeta} \end{pmatrix} = \boldsymbol{P}_1^{-1}\boldsymbol{A}_1 \begin{pmatrix} \xi \\ \eta \\ \zeta \end{pmatrix} = \boldsymbol{P}_1^{-1}\boldsymbol{A}_1\boldsymbol{P}_1 \begin{pmatrix} u \\ v \\ w \end{pmatrix} = \begin{pmatrix} \lambda_1 & 0 & 0 \\ 0 & a & -b \\ 0 & b & a \end{pmatrix} \begin{pmatrix} u \\ v \\ w \end{pmatrix}, \tag{33a}$$

即

$$\begin{cases} \dfrac{\mathrm{d}u}{\mathrm{d}t} = \lambda_1 u \\ \dfrac{\mathrm{d}v}{\mathrm{d}t} = av - bw \\ \dfrac{\mathrm{d}w}{\mathrm{d}t} = bv + aw \end{cases}, \tag{33b}$$

构造 $\rho = u^2 + v^2 + w^2$ (距离的平方)[37], 可得

$$\frac{1}{2}\frac{\mathrm{d}\rho}{\mathrm{d}t} = \lambda_1 u^2 + av^2 + aw^2 \equiv F_1(u, v, w). \tag{34}$$

注意到平移变换 $\xi = x - 6\sqrt{2}$, $\eta = y - 6\sqrt{2}$, $\zeta = z - 27$, 可得

$$\begin{pmatrix} u \\ v \\ w \end{pmatrix} = \boldsymbol{P}_1^{-1} \begin{pmatrix} \xi \\ \eta \\ \zeta \end{pmatrix} = \boldsymbol{P}_1^{-1} \begin{pmatrix} x - 6\sqrt{2} \\ y - 6\sqrt{2} \\ z - 27 \end{pmatrix}. \tag{35}$$

由 (32) 和 (35) 式, 可得

$$u = h_1 x + h_2 y + h_3 z - 6\sqrt{2}h_1 - 6\sqrt{2}h_2 - 27h_3, \tag{36a}$$

$$v = \frac{(\lambda_2 - a)j_1 + (\lambda_3 - a)k_1}{b}x + \frac{(\lambda_2 - a)j_2 + (\lambda_3 - a)k_2}{b}y + \frac{(\lambda_2 - a)j_3 + (\lambda_3 - a)k_3}{b}z$$
$$- \frac{6\sqrt{2}(\lambda_2 - a)j_1 + 6\sqrt{2}(\lambda_3 - a)k_1 + 6\sqrt{2}(\lambda_2 - a)j_2 + 6\sqrt{2}(\lambda_3 - a)k_2 + 27(\lambda_2 - a)j_3 + 27(\lambda_3 - a)k_3}{b}, \tag{36b}$$

$$w = (j_1 + k_1)x + (j_2 + k_2)y + (j_3 + k_3)z - 6\sqrt{2}(j_1 + k_1) - 6\sqrt{2}(j_2 + k_2) - 27(j_3 + k_3). \tag{36c}$$

(34) 式中的 $F_1(u, v, w)$ 用变量 $x$, $y$, $z$ 表示为

$$\begin{aligned} F_1(x, y, z) =& \left(\frac{1}{9}\sqrt[3]{-425537 + 36\sqrt{140629614}} - \frac{1}{9}\sqrt[3]{425537 + 36\sqrt{140629614}} - \frac{41}{9}\right)(h_1 x + h_2 y + h_3 z \\ & - 6\sqrt{2}h_1 - 6\sqrt{2}h_2 - 27h_3)^2 + \left(-\frac{1}{18}\sqrt[3]{-425537 + 36\sqrt{140629614}} + \frac{1}{18}\sqrt[3]{425537 + 36\sqrt{140629614}} - \frac{41}{9}\right) \\ & \times \left[\frac{(\lambda_2 - a)j_1 + (\lambda_3 - a)k_1}{b}x + \frac{(\lambda_2 - a)j_2 + (\lambda_3 - a)k_2}{b}y + \frac{(\lambda_2 - a)j_3 + (\lambda_3 - a)k_3}{b}z \right. \\ & \left. - \frac{6\sqrt{2}(\lambda_2 - a)j_1 + 6\sqrt{2}(\lambda_3 - a)k_1 + 6\sqrt{2}(\lambda_2 - a)j_2 + 6\sqrt{2}(\lambda_3 - a)k_2 + 27(\lambda_2 - a)j_3 + 27(\lambda_3 - a)k_3}{b}\right]^2 \\ & + \left(-\frac{1}{18}\sqrt[3]{-425537 + 36\sqrt{140629614}} + \frac{1}{18}\sqrt[3]{425537 + 36\sqrt{140629614}} - \frac{41}{9}\right)[(j_1 + k_1)x + (j_2 + k_2)y \\ & + (j_3 + k_3)z - 6\sqrt{2}(j_1 + k_1) - 6\sqrt{2}(j_2 + k_2) - 27(j_3 + k_3)]^2. \end{aligned} \tag{37}$$

$F_1(x, y, z) = 0$ 为区分右平衡点 $\mathrm{R}(6\sqrt{2}, 6\sqrt{2}, 27)$ 的准稳定区域与准不稳定区域的分界曲面.

记 $F_1(x, y, z) < 0$ 的区域为 $U_{\mathrm{R}}^{\mathrm{N}}$, 我们称之为 Nereus[1] 区域, 当 $F_1(x, y, z) < 0$ 时, 即 $\dfrac{\mathrm{d}\rho}{\mathrm{d}t} < 0$, 当 $t$ 增加时, $\rho = u^2 + v^2 + w^2$ 减少, 存在 $\mathrm{R}(6\sqrt{2}, 6\sqrt{2}, 27)$ 的一个邻域 $U_1$, 使得 Lorenz 系统的轨线总保持在 $U_1$ 内, 在 Nereus 区域内, 轨线的动力学特征保持稳定, 轨线始终绕平衡点 $\mathrm{R}(6\sqrt{2}, 6\sqrt{2}, 27)$ 做相对规则的运动, 在该区域内是相对稳定的称之为准稳定区域 [37].

记 $F_1(x, y, z) > 0$ 的区域为 $U_{\mathrm{R}}^{\mathrm{P}}$, 我们称之为 Proteus[2] 区域, 当 $F_1(x, y, z) > 0$ 时, 即 $\dfrac{d\rho}{\mathrm{d}t} > 0$, 在 Proteus 区域内, 当 $t$ 增加时, $\rho = u^2 + v^2 + w^2$ 增加, 轨线表现出不稳定的动力学特征, 存在某些时刻, 轨线穿过分

[1] Nereus, 希腊神话中的海神, 他值得信赖、和蔼可亲、公正善良.
[2] Proteus, 希腊神话中的海神, 他能随意变成各种形状, 变化多端.

界曲面 $F_1(x,y,z)=0$, 到另外一个平衡态去, 所以在该区域是相对不稳定的, 称之为准不稳定区域[37], 在气候动力学上就是所谓的突变, 而对于数值天气预报来说, 就是形式发生改变, 发生转折期, 当然气候突变与数值天气预报中的形式发生改变, 这两者是有时间尺度区分的.

### 2.2.2 系统在左平衡点 $L(-6\sqrt{2},-6\sqrt{2},27)$ 的稳定性

对于左平衡点 $L(-6\sqrt{2},-6\sqrt{2},27)$, 用同样的方法, 可以得到

$$\begin{aligned}F_2(x,y,z)=&\left(\frac{1}{9}\sqrt[3]{-425537+36\sqrt{140629614}}-\frac{1}{9}\sqrt[3]{425537+36\sqrt{140629614}}-\frac{41}{9}\right)(h_1x+h_2y-h_3z\\&+6\sqrt{2}h_1+6\sqrt{2}h_2+27h_3)^2+\left(-\frac{1}{18}\sqrt[3]{-425537+36\sqrt{140629614}}+\frac{1}{18}\sqrt[3]{425537+36\sqrt{140629614}}-\frac{41}{9}\right)\\&\left[\frac{(\lambda_2-a)j_1+(\lambda_3-a)k_1}{b}x+\frac{(\lambda_2-a)j_2+(\lambda_3-a)k_2}{b}y-\frac{(\lambda_2-a)j_3+(\lambda_3-a)k_3}{b}z\right.\\&\left.+\frac{6\sqrt{2}(\lambda_2-a)j_1+6\sqrt{2}(\lambda_3-a)k_1+6\sqrt{2}(\lambda_2-a)j_2+6\sqrt{2}(\lambda_3-a)k_2+27(\lambda_2-a)j_3+27(\lambda_3-a)k_3}{b}\right]^2\\&+\left(-\frac{1}{18}\sqrt[3]{-425537+36\sqrt{140629614}}+\frac{1}{18}\sqrt[3]{425537+36\sqrt{140629614}}-\frac{41}{9}\right)[(j_1+k_1)x+(j_2+k_2)y\\&-(j_3+k_3)z+6\sqrt{2}(j_1+k_1)+6\sqrt{2}(j_2+k_2)+27(j_3+k_3)]^2.\end{aligned}\tag{38}$$

$F_2(x,y,z)=0$ 为区分左平衡点 $L(-6\sqrt{2},-6\sqrt{2},27)$ 的准稳定区域与准不稳定区域的分界曲面, 对于左平衡点 $\mathrm{L}(-6\sqrt{2},-6\sqrt{2},27)$ 有相应的 Nereus 区域 $U_{\mathrm{L}}^{\mathrm{N}}$ 和 Proteus 区域 $U_{\mathrm{L}}^{\mathrm{P}}$, 轨线的运动特征分析与右平衡点 $\mathrm{R}(6\sqrt{2},6\sqrt{2},27)$ 的基本一样.

## 3 数值模拟

本文用四阶、五阶 Runge-Kutta 单步算法求解 Lorenz 方程组 (1), 截断误差为 $(\Delta x)^3$, 初值为 $x_0=12$, $y_0=2$, $z_0=9$.

计算可得, 系数矩阵 $\boldsymbol{A}_1$ 的特征值的数值解为

$$\lambda_1=-13.8546,\tag{39a}$$

$$\lambda_2=0.0940+10.1945\mathrm{i},\tag{39b}$$

$$\lambda_3=0.0940-10.1945\mathrm{i}.\tag{39c}$$

函数 $F_1(u,v,w)$ 为

$$\begin{aligned}\frac{1}{2}\frac{\mathrm{d}\rho}{\mathrm{d}t}&=-13.8546u^2+0.0940v^2+0.0940w^2\\&=F_1(u,v,w),\end{aligned}\tag{40}$$

矩阵 $\boldsymbol{P}_1$ 和 $\boldsymbol{P}_1^{-1}$ 的数值解为

$$\boldsymbol{P}_1=\begin{pmatrix}0.8557&-0.3763&0.4172\\-0.3298&0.0454&0.8048\\-0.3988&-1.0171&0\end{pmatrix},\tag{41a}$$

$$\boldsymbol{P}_1^{-1}=\begin{pmatrix}0.8450&-0.4380&-0.3322\\-0.3313&0.1718&-0.8529\\0.3650&1.0533&-0.0880\end{pmatrix}.\tag{41b}$$

空间 $(x,y,z)$ 到 $(u,v,w)$ 的变换为

$$\begin{cases}u=0.8450x-0.4380y-0.3322z+5.5159\\v=-0.3313x+0.1718y-0.8529z+24.3817\\w=0.3650x+1.0533y-0.0880z-9.6587\end{cases},\tag{42}$$

可得 $F_1(x,y,z)$ 的数值解

$$\begin{aligned}F_1(x,y,z)=&-13.8546(0.8450x\\&-0.4380y-0.3322z+5.5159)^2\\&+0.0940(-0.3313x+0.1718y\\&-0.8529z+24.3817)^2\\&+0.0940(0.3650x+1.0534y\\&-0.0880z-9.6587)^2.\end{aligned}\tag{43}$$

图 1 给出了曲面 $F_1(x,y,z)=0$ ($z1$ 和 $z2$ 曲面) 和 Lorenz 曲线. $z1$ 和 $z2$ 两曲面中间的区域是 $F_1(x,y,z)>0$ 的区域, 也就是 $U_{\mathrm{R}}^{\mathrm{P}}$ 即 Proteus 区域; $z1$ 曲面以上和 $z2$ 曲面以下的区域都是 $F_1(x,y,z)<0$ 的区域, 也就是 $U_{\mathrm{R}}^{\mathrm{N}}$, 即 Nereus 区域. 从 Lorenz 轨线的运动来看, 在 Proteus 区域内轨线有穿过曲面 $F_1(x,y,z)=0$ (这里关键是 $z1$ 曲面) 的可能, 跃入左平衡点周围; 但是在 Nereus 区

域内轨线不会跃入左平衡点周围, 所以在Proteus区域轨线运动不稳定, 是准不稳定区域; 相反在Nereus区域轨线运动相对稳定, 是准稳定区域. 这一数值试验结论佐证了本文前期的理论推导.

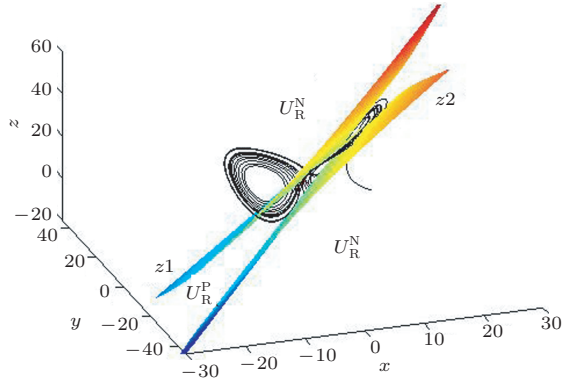


图 1 右平衡点 $\mathrm{R}(6\sqrt{2},6\sqrt{2},27)$ 的准不稳定区域和准稳定区域

为了更清楚地看到Lorenz曲线的运动规律, 图2给出了各个时刻的动态图. 当Lorenz曲线进入准不稳定区域 $U_{\rm R}^{\rm P}$ 时, 运动不稳定, 特别是图中的长方形区域, 表现得极为敏感, 会在某些时刻穿过分界曲面 $F_1(x,y,z)=0$, 跳到另外一个平衡态中去, 离开平衡点 $\mathrm{R}(6\sqrt{2},6\sqrt{2},27)$; 但在稳定区域 $U_{\rm R}^{\rm N}$ 内, 轨线运动稳定, 始终在平衡点 $\mathrm{R}(6\sqrt{2},6\sqrt{2},27)$ 周围运动.

下面再来看左平衡点 $\mathrm{L}(-6\sqrt{2},-6\sqrt{2},27)$ 的情况. 系数矩阵 $\boldsymbol{A}_2$ 的特征值的数值解为

$$\lambda_1=-13.8546, \tag{44a}$$

$$\lambda_2=0.0940+10.1945\mathrm{i}, \tag{44b}$$

$$\lambda_3=0.0940-10.1945\mathrm{i}, \tag{44c}$$

函数 $F_2(u,v,w)$ 为

$$\begin{aligned}\frac{1}{2}\frac{\mathrm{d}\rho}{\mathrm{d}t}&=-13.8546u^2+0.0940v^2+0.0940w^2\\&=F_2(u,v,w),\end{aligned} \tag{45}$$

矩阵 $\boldsymbol{P}_2$ 和 $\boldsymbol{P}_2^{-1}$ 的数值解为

$$\boldsymbol{P}_2=\begin{pmatrix}0.8557&-0.3763&0.4172\\-0.3298&0.0454&0.8048\\0.3988&1.0171&0\end{pmatrix}, \tag{46a}$$

$$\boldsymbol{P}_2^{-1}=\begin{pmatrix}0.8450&-0.4380&0.3322\\-0.3313&0.1718&0.8529\\0.3650&1.0533&0.0880\end{pmatrix}, \tag{46b}$$

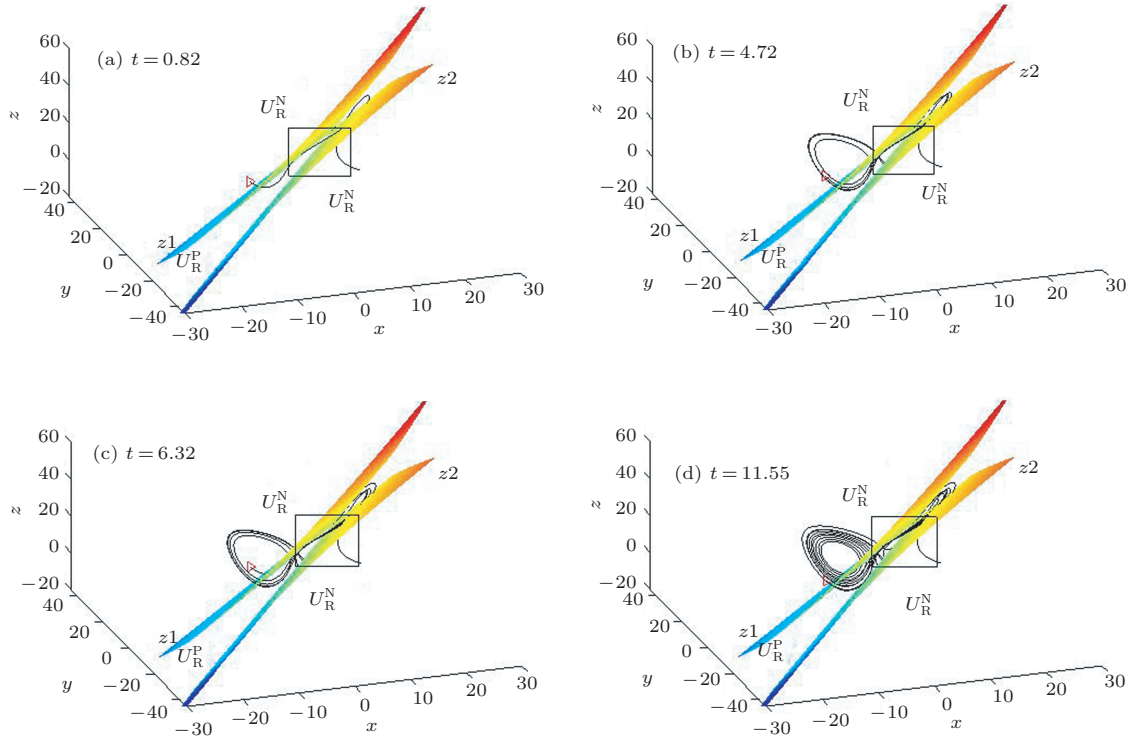


图 2 各个时刻的动态 (a) $t=0.82$; (b) $t=4.72$; (c) $t=6.32$; (d) $t=11.55$

空间 $(x,y,z)$ 到 $(u,v,w)$ 的变换为

$$\begin{cases} u = 0.8450x - 0.4380y + 0.3322z - 5.5159 \\ v = -0.3313x + 0.1718y + 0.8529z - 24.3817 \\ w = 0.3650x + 1.0533y + 0.0880z + 9.6587 \end{cases}, \tag{47}$$

可得 $F_2(x,y,z)$ 的数值解

$$\begin{aligned} F_2(x,y,z) = &-13.8546(0.8450x - 0.4380y \\ &+ 0.3322z - 5.5159)^2 \\ &+ 0.0940(-0.3313x + 0.1718y \\ &+ 0.8529z - 24.3817)^2 \\ &+ 0.0940(0.3650x + 1.0534y \\ &+ 0.0880z + 9.6587)^2. \end{aligned} \tag{48}$$

图 3 给出了曲面 $F_2(x,y,z) = 0$ ($z3$ 和 $z4$) 和 Lorenz 轨线. $z3$ 和 $z4$ 两曲面中间的区域是 $F_2(x,y,z) > 0$ 的区域, 也就是 $U_{\rm L}^{\rm P}$, 即 Proteus 区域; $z3$ 曲面以上和 $z4$ 曲面以下的区域都是 $F_2(x,y,z) < 0$ 的区域, 也就是 $U_{\rm L}^{\rm N}$, 即 Nereus 区域. 从 Lorenz 轨线的运动来看, 在 Proteus 区域内轨线可能穿过曲面 $F_2(x,y,z) = 0$ (这里关键是 $z3$ 曲面), 跃入右平衡点周围; 但是在 Nereus 区域内, 轨线不会跃入右平衡点周围, 轨线运动稳定. 轨线整个的运动规律和右平衡点类似, 不再赘述.

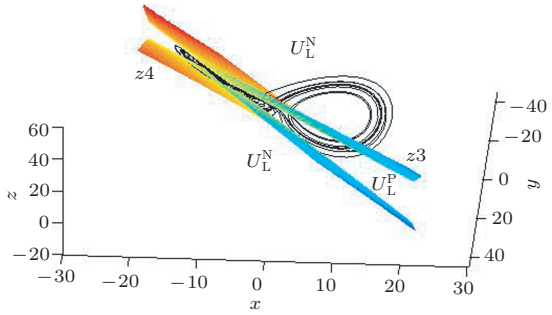


图 3 左平衡点 $\mathrm{L}(-6\sqrt{2},-6\sqrt{2},27)$ 的准不稳定区域和准稳定区域

图 4 给出了左平衡点 $\mathrm{L}(-6\sqrt{2},-6\sqrt{2},27)$ 各个时刻的动态图. 当 Lorenz 曲线进入准不稳定区域 $U_{\rm L}^{\rm P}$ 时, 运动不稳定, 会在某些时刻穿过分界曲面 $F_2(x,y,z) = 0$, 跳到另外一个平衡态中去, 离开平衡点 $\mathrm{L}(-6\sqrt{2},-6\sqrt{2},27)$; 但在稳定区域 $U_{\rm L}^{\rm N}$ 内, 轨线运动稳定, 始终在平衡点 $\mathrm{L}(-6\sqrt{2},-6\sqrt{2},27)$ 周围运动, 这些和图 2 的结论完全一致 (右平衡点 $\mathrm{R}(6\sqrt{2},6\sqrt{2},27)$).

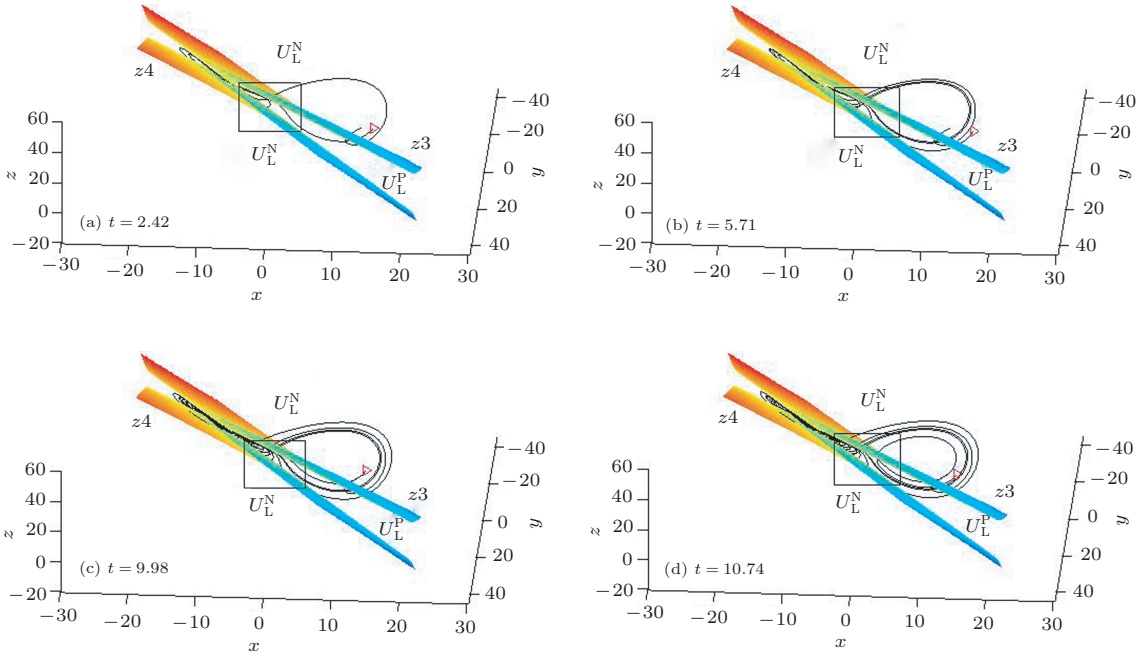


图 4 (a) $t = 2.42$; (b) $t = 5.71$; (c) $t = 9.98$; (d) $t = 10.74$

图 1 和图 2 给出右平衡点的情况; 图 3 和图 4 给出左平衡点的情况, 图 5 给出 Lorenz 曲线的整体情况. 从图中可知: 当轨线在区域 $U_{\rm R}^{\rm N}$ 和区域 $U_{\rm L}^{\rm N}$ 的交集 $U_{\rm R}^{\rm N} \cap U_{\rm L}^{\rm N}$ 内, 轨线一定稳定, 不会跳跃到另外一个平衡点中去; 当轨线在区域 $U_{\rm R}^{\rm P}$ 和区域 $U_{\rm L}^{\rm P}$ 的并集 $U_{\rm R}^{\rm P} \cup U_{\rm L}^{\rm P}$ 内, 轨线可能会跳跃到另外

一个平衡点中去.

若记集合 $U_{\rm R}$ 与 $U_{\rm L}$ 分别为

$$U_{\rm R}=\{(x,y,z)\in R^3|F_1(x,y,z)=0\},\tag{49a}$$

$$U_{\rm L}=\{(x,y,z)\in R^3|F_2(x,y,z)=0\},\tag{49b}$$

则有

$$R^3=U_{\rm R}\cup U_{\rm R}^{\rm N}\cup U_{\rm R}^{\rm P}=U_{\rm L}\cup U_{\rm L}^{\rm N}\cup U_{\rm L}^{\rm P}.\tag{50}$$

集合 $U_{\rm R}$, $U_{\rm R}^{\rm N}$ 和 $U_{\rm R}^{\rm P}$ 两两不交, 集合 $U_{\rm L}$, $U_{\rm L}^{\rm N}$ 和 $U_{\rm L}^{\rm P}$ 也两两不交, 简单计算之后有

$$R^3=(U_{\rm R}^{\rm N}\cap U_{\rm L}^{\rm N})\cup(U_{\rm R}^{\rm P}\cup U_{\rm L}^{\rm P})\cup(U_{\rm R}\cup U_{\rm L}).\tag{51}$$

维恩图 6 中的绿色区域为 $U_{\rm L}^{\rm N}$, 蓝色区域为 $U_{\rm L}^{\rm P}$, 两者中间的分界线为 $U_{\rm L}$; 右斜线区域为 $U_{\rm R}^{\rm N}$, 左斜线区域为 $U_{\rm R}^{\rm P}$, 两者中间的分界线为 $U_{\rm R}$. 区域 $U_{\rm R}^{\rm P}\cup U_{\rm L}^{\rm P}$ 就是红色框中的区域, 当然要把曲线 $U_{\rm L}$ 与 $U_{\rm R}$ 抠出, 区域 $U_{\rm R}^{\rm N}\cap U_{\rm L}^{\rm N}$ 是左上角那块区域.

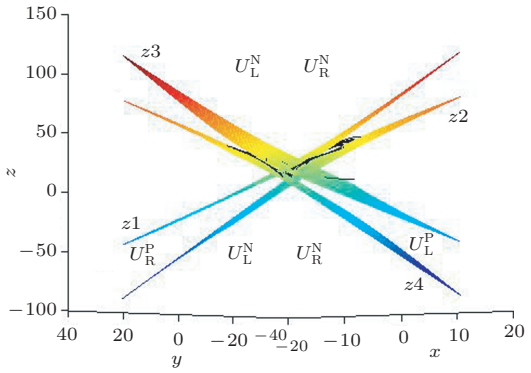


图 5 Lorenz 曲线的准不稳定区域和准稳定区域

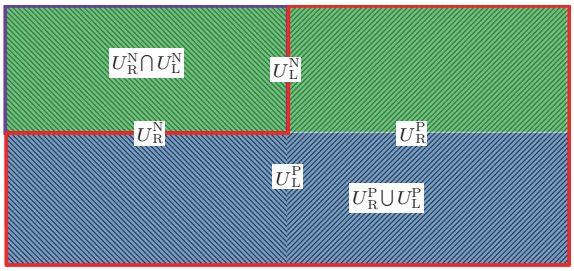


图 6 集合 $U_{\rm R}^{\rm N}\cap U_{\rm L}^{\rm N}$ 与 $U_{\rm R}^{\rm P}\cup U_{\rm L}^{\rm P}$ 维恩图 (概念图)

## 4 数值天气转折期预报和气候突变预报中的使用方法与步骤

本文在理论上为数值天气转折期预报和气候突变预报给出一种新思路与方法. 数值天气预报系统是一个 $n$ 维动力系统

$$\begin{cases}\dfrac{{\rm d}x_1}{{\rm d}t}=f_1(x_1,x_2,\cdots,x_n)\\ \dfrac{{\rm d}x_2}{{\rm d}t}=f_2(x_1,x_2,\cdots,x_n)\\ \cdots\\ \dfrac{{\rm d}x_n}{{\rm d}t}=f_n(x_1,x_2,\cdots,x_n)\end{cases},\tag{52}$$

而 Lorenz 系统是三维动力系统. 在数学理论上来看: 三维动力系统和 $n$ 维动力系统没有本质的区别, 既然上述方法适用于 Lorenz 系统, 自然也会适用于数值天气预报中的 $n$ 维动力系统.

具体可通过以下步骤来进行:

1) 求出数值天气预报中的 $n$ 维动力系统的平衡点

$$\begin{cases}f_1(x_1,x_2,\cdots,x_n)=0\\ f_2(x_1,x_2,\cdots,x_n)=0\\ \cdots\\ f_n(x_1,x_2,\cdots,x_n)=0\end{cases},\tag{53}$$

这一步从理论上没有难度;

2) 求出数值天气预报中的 $n$ 维动力系统在各个平衡点的线性近似方程, 用矩阵表示为

$$\frac{{\rm d}\boldsymbol{X}}{{\rm d}t}=\boldsymbol{A}\boldsymbol{X}+\boldsymbol{B},\tag{54}$$

这里的 $\boldsymbol{X}=(x_1,x_2,\cdots,x_n)$ 是离散之后的大气状态变量, $\boldsymbol{A}$ 是 $n$ 维矩阵, $\boldsymbol{B}$ 是 $n$ 维向量, 矩阵 $\boldsymbol{A}$ 和向量 $\boldsymbol{B}$ 可以算出, 甚至可以通过坐标平移使得向量 $\boldsymbol{B}=0$, 即为

$$\frac{d\boldsymbol{X}}{{\rm d}t}=\boldsymbol{A}\boldsymbol{X};\tag{55}$$

3) 求出矩阵 $\boldsymbol{A}$ 的特征值;

4) 通过矩阵变换和坐标变换, 把 (55) 式写为

$$\begin{pmatrix}\dot\xi_1\\ \dot\xi_2\\ \cdots\\ \dot\xi_n\end{pmatrix}=\boldsymbol{B}\begin{pmatrix}\xi_1\\ \xi_2\\ \cdots\\ \dot\xi_n\end{pmatrix},\tag{56}$$

矩阵 $\boldsymbol{B}$ 往往会有比较好的对角形式, 或者是块对角形式, 具体计算时要用到高阶矩阵的计算;

5) 构造出函数

$$\boldsymbol{F}(\xi_1,\xi_2,\cdots,\xi_n)=\frac{1}{2}\frac{{\rm d}\rho}{{\rm d}t},\tag{57}$$

与

$$F(x_1, x_2, \cdots, x_n) = \frac{1}{2}\frac{\mathrm{d}\hat{\rho}}{\mathrm{d}t}; \tag{58}$$

6) 利用

$$F(x_1, x_2, \cdots, x_n) = 0, \tag{59a}$$

$$F(x_1, x_2, \cdots, x_n) > 0, \tag{59b}$$

$$F(x_1, x_2, \cdots, x_n) < 0, \tag{59c}$$

求出各个各个平衡点的分界曲面、准稳定区域 (Nereus区域) 和准不稳定区域 (Proteus区域);

7) 分析不同区域内的运动特征, 在准不稳定区域 (Proteus区域) 内, 系统轨线不稳定, 将在某些时刻从该平衡点周围穿过分界曲面跳跃到其他平衡点周围, 进入另外一个平衡态中, 即发生突变, 发生突变的区域为敏感区域, 在数值天气预报中转折期预报中, 或气候突变检测上, 可求出Proteus区域, 以此来检测、预测突变; 但在准稳定区域 (Nereus区域) 内, 系统轨线稳定, 不会发生突变.

## 5 结 论

本文通过理论推导, 对Lorenz方程组的平衡点进行稳定性分析: 对于每个平衡点来说, 有分界曲面$F(x, y, z) = 0$, 其把$R^3$分为准稳定区域 (Nereus区域) 和准不稳定区域 (Proteus区域). 在Nereus区域, $F(x, y, z) < 0$, 随时间$t$增加$\rho$减少, 轨线在Nereus区域内的动力学特征保持稳定, 围绕平衡点做相对规则运动, 在该区域内是稳定的. 在Proteus区域内, $F(x, y, z) > 0$, 随时间$t$增加$\rho$增加, 轨线表现出不稳定的动力学特征, 存在某个时刻, 轨线达到Proteus区域的边界, 并穿过曲面$F(x, y, z) = 0$跳到另外一个平衡点周围中, 轨线的动力学特征在该区域内是不稳定的.

本文给出了数值天气转折期预报和气候突变的预报.

虽然本文给出了一种全新方法来预测气候突变, 但真正的使用还很遥远. 首先本文的方法比较粗糙, 不是太精细, 刻画出来的Nereus区域和Proteus区域范围太宽, 特别是Proteus区域, 能否让Proteus区域的范围小一点, 精细一点; 其次理论上的实现到实际使用还有很多技术要克服, 一个无法逃避的现实是数值天气预报对应的动力系统的维数太高, 这就有一个高维矩阵计算问题, 如何解决这个问题? 最后大气系统的混沌度要比Lorenz系统的混沌度高得多, 所以大气系统的非线性和复杂性和Lorenz系统相比, 两者不是一个量级.

## 参考文献


[1] Bjerknes V 1904 *Meteor. Zeit.* **21** 1

[2] Richardson 1922 *The Weather Prediction by Numerical Process* (London: Cambridge University Press)

[3] Charney J G, Fjörtoft R, von Neumann J 1950 *Tellus* **2** 237

[4] Gu Z C 1958 *Acta Meteor. Sin.* **29** 176 (in Chinese)[顾震潮 1958 气象学报 **29** 176]

[5] Gu Z C 1958 *Acta Meteor. Sin.* **29** 93 (in Chinese)[顾震潮 1958 气象学报 **29** 93]

[6] Chou J F 1974 *Sci. China* D **6** 635 (in Chinese) [丑纪范 1974 中国科学 D **6** 635]

[7] Qiu C J, Shao A M, Xu Q, Wei L 2007 *J. Geophys. Res.* **112** D11105

[8] Shao A M, Xi S, Qiu C J, Xu Q 2009 *J. Geophys. Res.* **114** D17114

[9] Huang J P, Chou J F 1989 *Sci. China* B **9** 1001 (in Chinese) [黄建平, 丑纪范 1989 中国科学 B **9** 1001]

[10] Huang J P, Wang S W 1991 *Sci. China* B **21** 216 (in Chinese) [黄建平, 王绍武 1991 中国科学 B **21** 216]

[11] Huang J P, Yi Y H, Wang S W, Chou J F 1993 *Quart. J. Roy Meteor. Soc.* **119** 547

[12] Huang J P, Yi Y H 1991 *Sci. China B* **3** 331 (in Chinese)[黄建平, 衣育红 1991 中国科学 **3** 331]

[13] Huang J P, Yi Y H 1991 *Sci. China* B **34** 1246

[14] Huang J P, North G R 1996 *J. Atmosph. Sci.* **53** 370

[15] Feng G L, Cao H X, Wei F Y 1999 *J. Appl. Meteor. Sci.* **10** 470 (in Chinese) [封国林, 曹鸿兴, 魏凤英 1999 应用气象学报 **10** 470]

[16] Feng G L, Dong W J 2003 *Chin. Phys.* **12** 1076

[17] Zheng Z H 2010 *Ph. D. Dissertation* (Lanzhou: Lanzhou University) (in Chinese) [郑志海 2010 博士学位论文 (兰州: 兰州大学)]

[18] Da C J 2011 *Ph. D. Dissertation* (Lanzhou: Lanzhou University) (in Chinese) [达朝究 2011 博士学位论文 (兰州: 兰州大学)]

[19] Xue H L 2013 *Ph. D. Dissertation* (Lanzhou: Lanzhou University) (in Chinese) [薛海乐 2013 博士学位论文 (兰州: 兰州大学)]

[20] Shabbar A, J Huang, K Higuchi 2001 *Int. J. Climatol.* **21** 355

[21] Lorenz E N 1963 *J. Atmos. Sci.* **20** 130

[22] Fu Z B, Wang Q 1992 *Chin. J. Atmos. Sci.* **16** 482 (in Chinese)[符淙斌, 王强 1992 大气科学 **16** 482]

[23] Ye D Z, Tao S Y, Li M C 1958 *Acta Meteor. Sin.* **29** 249 (in Chinese) [叶笃正, 陶诗言, 李麦村 1958 气象学报 **29** 249]

[24] Feng G L, Gong Z Q, Zhi R 2008 *Acta Meteor. Sin.* **66** 892 (in Chinese)[封国林, 龚志强, 支蓉 2008 气象学报 **66** 892]

[25] Yan P C, Hou W, Hu J G 2012 *Acta Phys. Sin.* **61** 189202 (in Chinese)[颜鹏程, 侯威, 胡经国 2012 物理学报 **61** 189202]

[26] Feng G L, Dai X G, Wang A H, Chou J F 2001 *Acta Phys. Sin.* **50** 606 (in Chinese)[封国林, 戴新刚, 王爱慧, 丑纪范 2001 物理学报 **50** 606]

[27] Wu H, Hou W, Yan P C 2013 *Acta Phys. Sin.* **62** 039206 (in Chinese)[吴浩, 侯威, 颜鹏程 2013 物理学报 **62** 039206]

[28] Feng G L, Hou W, Zhi R 2011 *Research on Detecting, Diagnosing and Predictability of Extreme Climate Events* (Beijing: Science Press) pp350–366 (in Chinese) [封国林, 侯威, 支蓉 2011 极端气候事件的检测、诊断和可预测性研究 (北京: 科学出版社) 第 350—366 页]

[29] Zhao J H, Feng G L, Zhang S X, Sun S P 2011 *Acta Phys. Sin.* **60** 099205 (in Chinese)[赵俊虎, 封国林, 张世轩, 孙树鹏 2011 物理学报 **60** 099205]

[30] Zhao J H, Yang J, Gong Z Q, Zhi R 2013 *Acta Phys. Sin.* **62** 099206 (in Chinese)[赵俊虎, 杨杰, 龚志强, 支蓉 2013 物理学报 **62** 099206]

[31] Wang Q G, Zhang Z P 2008 *Acta Phys. Sin.* **57** 1976 (in Chinese)[王启光, 张增平 2008 物理学报 **57** 1976]

[32] Cui H, He H L, Liu X H, Li Y 2012 *Chin. Phys. B* **21** 109201

[33] Wang Q G, Zhi R, Zhang Z P 2008 *Acta Phys. Sin.* **57** 5343 (in Chinese)[王启光, 支蓉, 张增平 2008 物理学报 **57** 5343]

[34] Zheng Z H, Ren H L, Huang J P 2009 *Acta Phys. Sin.* **58** 7359 (in Chinese)[郑志海, 任宏利, 黄建平 2009 物理学报 **58** 7359]

[35] Wang Q G, Feng G L, Zheng Z H, Zhi R 2011 *Chin. J. Atmos. Sci.* **35** 287 (in Chinese)[王启光, 封国林, 郑志海, 支蓉 2011 大气科学 **35** 287]

[36] Zheng Z H, Huang J P, Feng G L, Chou J F 2012 *Sci. China* D **43** 594 (in Chinese) [郑志海, 黄建平, 封国林, 丑纪范 2013 中国科学 D **43** 594]

[37] Zhang J Y, Feng B Y 2000 *The Geometric and Bifurcation Theory of Ordinary Differential Equations* (Beijing: Beijing University Press) p36 (in Chinese) [张锦炎, 冯贝叶 2003 常微分方程几何理论与分支问题 (北京: 北京大学出版社) 第 36 页]

[38] Gunter Maher, Ke Z Y 1995 Theory of Matrices (Beijing: Higher Education Press) p127 (in Chinese) [甘特马赫尔, 柯召译 1995 矩阵论 (北京: 高等教育出版社) p127]

# The theoretical study of the turning period in numerical weather prediction models based on the Lorenz equations*

Da Chao-Jiu[1)2)†] Mu Shuai[1)] Ma De-Shan[1)] Yu Hai-Peng[2)]
Hou Wei[3)] Gong Zhi-Qiang[3)]

1) (*School of Mathematics and Computer Science Institute, Northwest University for Nationalities, Lanzhou 730030, China*)

2) (*College of Atmospheric Sciences, Lanzhou University, Lanzhou 730000, China*)

3) (*Laboratory for Climate Studies, National Climate Center, China Meteorological Administration, Beijing 100081, China*)

( Received 16 August 2013; revised manuscript received 8 October 2013 )

**Abstract**

Based on the Lorenz equations, the dynamics of the weather turning period is studied about numerical weather prediction. Through the analysis of the stability of equilibrium points of the Lorenz equations, we get the surfaces which separate the quasi-stable region and quasi-unstable region. In the quasi-stable region, the path curve of the Lorenz equations can remain relatively stable around the equilibrium points, however in the quasi-unstable region, the path curve of the Lorenz equations can spring from this equilibrium point to another one. This is one of the important dynamic characteristics of the Lorenz system, and the paper give new method and theory for the detection of the abrupt change of climate.

**Keywords:** Lorenz equations, quasi stabile region, quasi unstabile region, mutation period

**PACS:** 92.40.Cy, 92.60.Aa **DOI:** 10.7498/aps.63.029201

* Project supported by the Key Technologies R&D Program of China (Grant No. 2009BAC51B04), the Meteorological Special Project of China (Grant Nos. GYHY201206009, GYHY201106016), the National Basic Research Program of China (Grant No. 2012CB955902), the National Natural Science Foundation of China (Grant Nos. 40930952, 41175067, 61162021) and the Fundamental Research Funds for the Central Universities, China (Grant No. zyz2012079).

† Corresponding author. E-mail: jtdcj@163.com

www.climatechange.cn



doi:10.3969/j.issn.1673-1719.2014.05.008
董思言 , 徐影 , 周波涛 , 等 . 基于 CMIP5 模式的中国地区未来高温灾害风险预估 [J]. 气候变化研究进展 , 2014, 10 (5): 365-369



# 基于 CMIP5 模式的中国地区未来高温灾害风险预估

董思言[1,2]，徐　影[1]，周波涛[1,3]，侯美亭[4]，
李柔珂[1]，於　琍[1]，　张永香[1]

1 中国气象局国家气候中心，北京 100081；2 中国气象局气候研究开放实验室，北京 100081；
3 南京信息工程大学气象灾害预报预警与评估协同创新中心，南京 210044；
4 中国气象局气象干部培训学院，北京 100081

**摘 要**：本文利用 CMIP5 中 22 个全球气候模式模拟结果和相关社会经济数据，对 RCP8.5 情景下中国未来近期（2016—2035 年）、中期（2046—2065 年）、远期（2080—2099 年）3 个时段高温灾害风险的变化趋势进行了定量预估。结果表明：中国未来不同时期高温致灾危险度可能逐步增加；未来不同时期高温风险也趋于升高。III 级及以上的高温灾害风险等级范围将增大，特别是东北三省、内蒙古、陕西、宁夏、贵州、福建等省（区）处于高风险等级的面积明显增大，山东、河北、河南、安徽在近期将出现 V 级高温灾害风险，中期和远期 V 级高温灾害风险将扩展到江苏、湖南、湖北、江西、四川、广西和广东等省（区）。

**关键词**：RCP8.5 情景；高温灾害风险；未来预估

## 引 言

近年来，高温热浪在世界范围内频发，极端高温事件在中国的出现频率也呈现增高趋势[1]。本文利用 CMIP5 气候模式模拟数据[2]，计算 RCP8.5 情景下中国高温灾害致灾危险度高温指数，在此基础上预估未来高温风险的可能变化，其结果可为极端气候变化引起的灾害风险和未来气候承载力的研究奠定基础，也为中国防灾减灾和气候变化适应提供科学支撑。

## 1　数据与方法

本文选用CMIP5中对中国地区气温变化模拟能力较好的22个全球气候模式（表1）的逐日最高气温模拟试验结果，分析最极端情况（RCP8.5代表全球温室气体高排放情景）下未来中国地区高温灾害风险的变化。与观测资料（CN05资料）的对比[3]结果表明，多模式集合结果能够更准确地描述极端高温事件的时空变化特征。以1986—2005年为基准期，分别计算未来近期（2016—2035年）、中期（2046—2065年）和远期（2080—2099年）的高温灾害风险指数。为便于比较和进行多模式集合，使用双线性插值方法将模式数据统一插值到0.5°×0.5°网格上。

社会经济数据包括人口密度、GDP和耕地面积百分比，其中人口和GDP数据源自奥地利国际应用系统分析研究所（IIASA）研发的GGI情景数据库，

**收稿日期**：2014-02-19；**修回日期**：2014-06-17
**资助项目**：公益性行业（气象）科研专项（GYHY201306019）；国家重点基础研究计划（2010CB950102）；中国清洁发展机制基金赠款项目（121312）；中国气象局气候变化专项（CCSF201339）；国家自然科学基金项目（41275078，41201044）；LCS 气候研究开放课题青年基金 2014 年度资助项目
**作者简介**：董思言，男，助理研究员，主要从事气候变化及气候模拟研究，dongsy@cma.gov.cn

表 1 CMIP5 中 22 个全球气候模式基本信息

Table 1 The basic information of 22 models from CMIP5

| 模式名称 | 单位及所属国家或地区 | 分辨率 | 模式名称 | 单位及所属国家或地区 | 分辨率 |
|---|---|---|---|---|---|
| ACCESS 1.0 | CSIRO-BOM，澳大利亚 | 192 × 145 | NorESM1-M | NCC，挪威 | 144 × 96 |
| BCC-CSM1.1 | BCC，中国 | 128 × 64 | GFDL-ESM2G | NOAA GFDL，美国 | 144 × 90 |
| BNU-ESM | GCESS，中国 | 128 × 64 | GFDL-ESM2M | NOAA GFDL，美国 | 144 × 90 |
| CanESM2 | CCCMA，加拿大 | 128 × 64 | INMCM4 | INM，俄罗斯 | 180 × 120 |
| CCSM4 | NCAR，美国 | 288 × 192 | IPSL-CM5A-MR | IPSL，法国 | 96 × 96 |
| CESM1-BGC | NSF-DOE-NCAR，美国 | 288 × 192 | MIROC5 | MIROC，日本 | 256 × 128 |
| CMCC-CM | CMCC，意大利 | 480 × 240 | MIROC-ESM | MIROC，日本 | 128 × 64 |
| CMCC-CESM | CMCC，意大利 | 480 × 240 | MIROC-ESM-CHEM | MIROC，日本 | 128 × 64 |
| CNRM-CM5 | CNRM-CERFACS，法国 | 256 × 128 | MPI-ESM-LR | MPI-M，德国 | 192 × 96 |
| CSIRO-Mk3-6-0 | CSIRO-QCCCE，澳大利亚 | 192 × 96 | MPI-ESM-MR | MPI-M，德国 | 192 × 96 |
| EC-EARTH | ECMWF，英国 | 320 × 160 | MRI-CGCM3 | MRI，日本 | 320 × 160 |

耕地面积百分比数据源自 Ramankutty 等[4]开发的1700—2002年耕地数据，之后用同样的处理方法将数据延伸到 2007 年。因缺乏未来耕地面积百分比变化数据，本文假定未来该数据与2007年相比变化不大。

采用吴绍洪等[5]使用的研究方法，以致灾危险度指标和承灾体易损度指标估算未来灾害风险度，其中致灾危险度以极端气候指数表示，承灾体易损度则使用人口密度、GDP 和耕地面积百分比数据计算。该方法与国际上通用的以致灾因子、暴露度和脆弱性估算风险的方法相通，其中致灾危险度与致灾因子一致，而承灾体易损度包含了暴露度和脆弱性。各指标具体计算方法如下。

(1) 高温灾害致灾危险度指标。首先利用逐日最高气温模式模拟数据计算极端高温指数，然后综合高温和热浪两种极端高温指数作为高温灾害致灾危险度指标。其中高温日数定义为一年中日最高气温≥35 ℃的总天数，热浪日数定义为日最高气温大于或等于 1961 — 1990 年样本概率分布 97.5% 温度值（≥32 ℃）且至少持续3天的总日数。然后对两个指数进行归一化并赋予权重，叠加后再通过标准化把取值范围限定于[0,1]。最后将高温灾害致灾危险度划分为5个等级：(0～0.1)（I级），[0.1～0.3)（II级），[0.3～0.5)（III级），[0.5～0.8)（IV级）和[0.8～1.0]（V级）；取值为 0 时无高温灾害致灾危险。

(2) 高温灾害承灾体易损度指标。首先对人口密度、GDP 和耕地面积百分比 3 种承灾体物理暴露量指标进行归一化处理，然后根据专家打分法赋予各指标权重，得到高温灾害承灾体易损度指标计算公式：$V_H = 0.4833 \times D_{POP} + 0.2389 \times D_{GDP} + 0.2778 \times P_F$，其中 $V_H$、$D_{POP}$、$D_{GDP}$ 和 $P_F$ 分别为高温灾害承灾体易损度，标准化后的人口密度、GDP 和耕地面积百分比。

(3) 高温灾害风险度指标。按照“风险＝致灾危险度×承灾体易损度”的风险评估基本模型，将高温灾害致灾危险度指标和承灾体易损度指标相乘，再次标准化到[0,1]，即得到中国地区高温灾害风险度，并将高温灾害风险度划分为5个等级：[0～0.02)（I级），[0.02～0.05)（II级），[0.05～0.1)（III级），[0.1～0.2)（IV级）和[0.2～1.0]（V级）。

## 2 分 析

### 2.1 高温灾害致灾危险度时空变化

在基准期，中国地区高温灾害致灾危险度只有I级和II级（表2）。在近期（图 1a），高温灾害致灾危险度增加，II 级高温灾害致灾危险面积扩大到32.5%，新疆、河南、湖北、湖南和广西出现 III 级

www.climatechange.cn



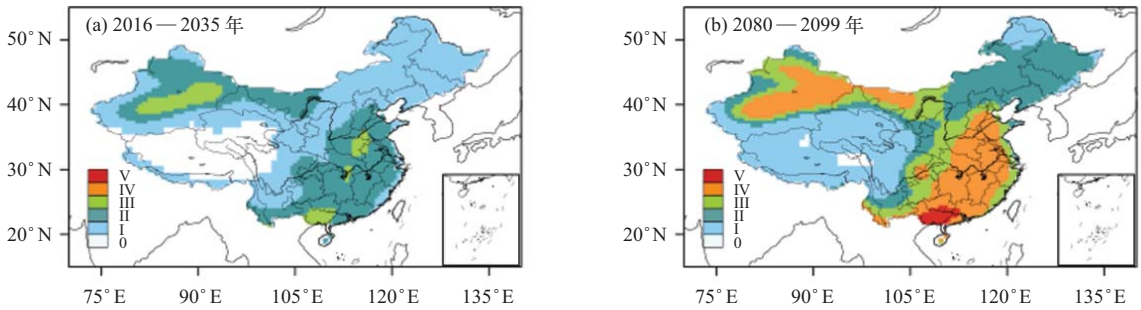


图 1　RCP8.5 情景下高温致灾危险度空间分布

Fig. 1　Spatial patterns of the extreme heat hazard risk over China under RCP8.5

表 2　RCP8.5 情景下高温灾害致灾危险度等级变化

Table 2　The extreme heat hazard risk level change under RCP8.5

%

| 等级 | 基准期 (1986 — 2005) | 近期 (2016 — 2035) | 中期 (2046 — 2065) | 远期 (2080 — 2099) |
|---|---|---|---|---|
| 无 | 19.5 | 18.4 | 12.1 | 1.4 |
| I | 69.1 | 42.4 | 34.3 | 30.5 |
| II | 11.3 | 32.5 | 27.0 | 24.6 |
| III | 0.0 | 6.7 | 22.3 | 15.9 |
| IV | 0.0 | 0.0 | 4.0 | 26.3 |
| V | 0.0 | 0.0 | 0.0 | 1.4 |

高温灾害致灾危险度，达到全国总面积的 6.7%。在中期，高温灾害致灾危险度 II 和 III 级范围呈现出向周边扩散的形态，II 级高温灾害致灾危险度已经延伸到东北地区，III 级高温灾害致灾危险面积扩大到 22.3%，而新疆、河南、湖南和广西等省（区）甚至出现了IV级高温灾害致灾危险度，III级及以上风险面积比例达到 26.3%。在远期（图 1b），无危险等级的地区比例仅为 1.4%，最低风险 I 级危险面积比例缩小到 30.5%，新疆、广西和广东部分地区出现 V 级风险，IV 级及以上风险面积比例达到 27.7%。所以，在 RCP8.5 情景下，中国地区未来高温灾害致灾危险度较气候基准期升高，新疆、河南、湖南及广西尤为明显。总体上是未来时间段越远，高温灾害致灾危险度越大，高等级高温灾害致灾危险度（IV 级和 V 级）的面积也越大。

## 2.2　高温灾害承灾体易损度时空变化

中国地区高温灾害承灾体易损度等级变化在基准期和近期之间差异不是很明显（图 2a），但是随着经济的发展和人口的增长，中国地区未来在中期和远期高温承灾体易损值略微上升，在远期华北地区上升更加突出（图 2b）。从高温灾害承灾体易损度变化可以看出，易损度高值区大多分布在人口稠密、经济较为发达的地区，尤其是华北地区易损度在未来比其他地区都要高，这是因为华北地区人口稠密、经济发达，也是传统的农业区，在全球变暖的背景下该地区的未来高温承灾体易损度将增加。相对于基准期，未来 3 个时段东北等区域高温灾害承灾体易损度整体上有所减小，主要是由于这期间该区域

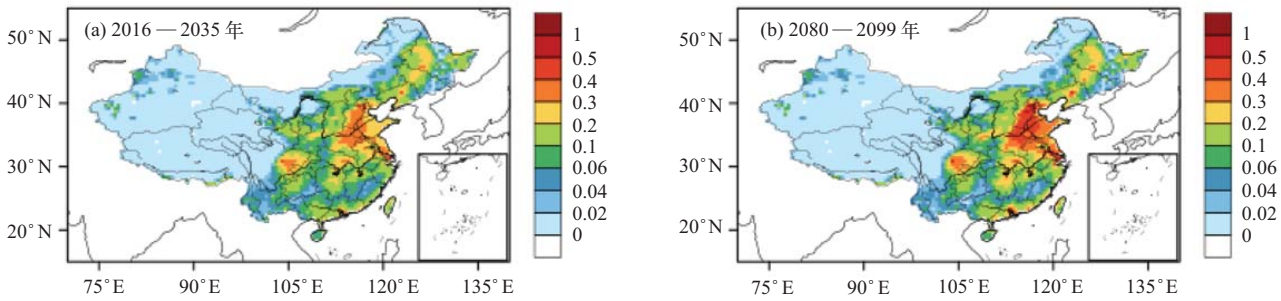


图 2　RCP8.5 情景下高温承灾体易损度空间分布

Fig. 2　Spatial patterns of the extreme heat disaster vulnerability over China under RCP8.5

2007 年耕地面积较 20 世纪 80、90 年代减少。

### 2.3 高温灾害风险预估

在基准期，高温灾害风险区域集中在黄淮平原、长江中下游地区，同时在四川盆地、广东、广西部分地区也有分布。在近期，东北三省出现 II 级风险（图 3a），山东、河北、河南、安徽出现V级风险，中国 III 级及以上高温灾害高风险地区扩大到 13.5%，IV 级风险面积比例由 0.5% 增加到 6.0%，V 级风险面积比例为 2.0%（表 3）。

在中期，高温灾害风险延续近期的风险发展趋势，II级和III级风险在东北三省、内蒙古、陕西、宁夏、贵州、福建等省（区）进一步扩大，V级风险扩展到江苏、湖南、湖北、江西、四川、广西和广东。中国 III 级及以上高温灾害风险面积比例增加到 21.1%，IV 级高风险面积比例为 5.5%，V 级高风险面积比例为 7.8%。

在远期（图 3b），风险进一步增加，其中较突出的特征是，高风险区域（III 级及以上）明显向低风险区域（I级和II级）扩展，这是因为这些区域的高温灾害致灾危险度和高温灾害承灾体易损度都较高的结果，其中陕西、四川、湖南、江西、广东、广西、福建省（区）V 级风险增加明显。中国 III 级及以上高温灾害风险面积比例进一步增加到 33.8%，IV 级和 V 级风险面积比例分别达到 8.0% 和 12.8%。

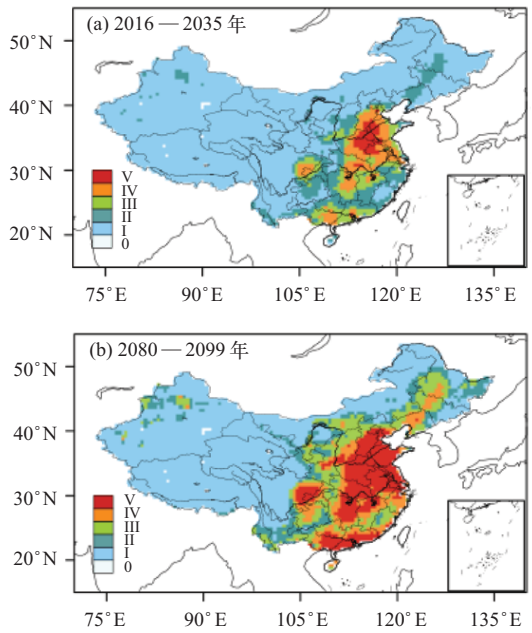


图 3 RCP8.5 情景下高温灾害风险等级空间分布

Fig. 3 Spatial patterns of the extreme heat risk level over China under RCP8.5

表 3 RCP8.5 情景下高温灾害风险等级变化

Table 3 The extreme heat risk level change under RCP8.5

%

| 等级 | 基准期 (1986 — 2005) | 近期 (2016 — 2035) | 中期 (2046 — 2065) | 远期 (2080 — 2099) |
|---|---|---|---|---|
| I | 88.4 | 74.8 | 63.5 | 56.1 |
| II | 7.6 | 11.7 | 15.4 | 10.3 |
| III | 3.5 | 5.5 | 7.8 | 13.0 |
| IV | 0.5 | 6.0 | 5.5 | 8.0 |
| V | 0.0 | 2.0 | 7.8 | 12.8 |

## 3 结论与讨论

在RCP8.5情景下，21世纪中国地区高温灾害风险将趋于增大。其中风险等级高于III级（包括III级）的面积占全国的比例，将从基准期的4.0%增长到未来近期、中期和远期的13.5%、21.1%和33.8%，东北三省、内蒙古、陕西、宁夏、贵州、福建等省（区）的风险增大趋势更为明显。V 级风险未来近期出现在山东、河北、河南、安徽，而未来中期和远期将扩展到江苏、湖南、湖北、江西、四川、广西和广东等省（区）。

在研究过程中也分别计算了RCP2.6（代表低排放情景）和RCP4.5（代表中等排放情景）情景下未来中国地区高温灾害风险变化，结果表明，这两种情景下的高温灾害风险变化，除强度比RCP8.5情景下的稍弱外，空间分布上没有本质差别。

应该承认，本文在高温灾害承灾体易损度指标的计算中，仅考虑了人口密度、GDP 和耕地面积百分比 3 种要素，模型公式中也仅采取了专家打分的半定量方法，这些因素都可能对风险估算结果产生一定影响。需要指出，尽管全球气候模式较过去已有较大程度的发展，但仍存在不确定性[6]，模拟未来中国地区极端高温事件变化的不确定性更大。因此需要进一步研发和改进更加客观合理的技术方法，

www.climatechange.cn



并深入探讨风险变化机理，同时提高指标计算的精细化程度。■

## 参考文献


[1] 王绍武 , 龚道溢 , 陈振华 . 近百年来中国的严重气候灾害 [J]. 应用气象学报 , 1999, 10 (增刊) : 43-53

[2] IPCC. Climate change 2013: the physical science basis [M]. Cambridge: Cambridge University Press, 2013

[3] Xu Y, Gao X J, Shen Y, *et al*. A daily temperature dataset over China and its application in validating a RCM simulation [J]. Adv Atmos Sci, 2009, 26 (4): 763-772

[4] Ramankutty N, Foley J A. Estimating historical changes in global land cover: croplands from 1700 to 1992 [J]. Global Biogeochemical Cycles, 1999, 13 (4): 997-1027

[5] 吴绍洪 , 戴尔阜 , 葛全胜 , 等 . 综合风险防范 : 中国综合气候变化风险 [M]. 北京 : 科学出版社 , 2011

[6] Taylor K E, Stouffer R J, Meehl G A. An overview of CMIP5 and the experiment design [J]. Bull Amer Meteor Soc, 2012, doi: 10.1175/BAMS-D-11-00094.1


# Projected Risk of Extreme Heat in China Based on CMIP5 Models


Dong Siyan[1, 2], Xu Ying[1], Zhou Botao[1, 3], Hou Meiting[4], Li Rouke[1], Yu Li[1], Zhang Yongxiang[1]

1 *National Climate Center, China Meteorological Administration, Beijing* 100081*, China*; 2 *Laboratory for Climate Studies, China Meteorological Administration, Beijing* 100081*, China*; 3 *Collaborative Innovation Center on Forecast and Evaluation of Meteorological Disasters, Nanjing University of Information Science & Technology, Nanjing* 210044*, China*; 4 *China Meteorological Administration Training Centre, China Meteorological Administration, Beijing* 100081*, China*



**Abstract:** Based on the simulations from 22 CMIP5 models and in combination with the socio-economic data, the extreme heat risk change during the near term (2016−2035), medium term (2046−2065) and long term (2080−2099) were projected by quantitative estimation under RCP8.5. The results show that the extreme heat hazard risk will gradually increase during different terms in the future, and extreme heat risk will also tend to increase. Class III and above of the extreme heat risk will increase, especially in the northeast, Inner Mongolia, Shaanxi, Ningxia, Guizhou, Fujian provinces (autonomous region). In Shandong, Hebei, Henan, Anhui provinces, Class V of the extreme heat risk tends to appear in the near term, and it will extend to Jiangsu, Hunan, Hubei, Jiangxi, Sichuan, Guangxi and Guangdong provinces (autonomous region) in the medium and long term.



**Key words:** RCP8.5 scenario; extreme heat risk; projection

www.climatechange.cn



doi:10.3969/j.issn.1673-1719.2014.03.007
段居琦，徐新武，高清竹．IPCC 第五次评估报告关于适应气候变化与可持续发展的新认知 [J]. 气候变化研究进展，2014, 10 (3): 197-202

# IPCC 第五次评估报告关于适应气候变化与可持续发展的新认知

段居琦[1]，徐新武[2]，高清竹[3]

1 中国气象局国家气候中心／中国气象局气候研究开放实验室，北京 100081；
2 中国气象局科技与气候变化司，北京 100081；
3 中国农业科学院农业环境与可持续发展研究所，北京 100081



**摘 要**：IPCC 发布的《气候变化 2014：影响、适应和脆弱性》进一步提升了国际社会对于适应气候变化和可持续发展的认识水平，主要表现在：适应气候变化的研究视角从自然生态脆弱性转向更为广泛的社会经济脆弱性及人类的响应能力；阐明了气候风险与社会发展的关系，明确了适应在气候灾害风险管理中的积极作用；提出了减少脆弱性和暴露度及增加气候恢复能力的有效适应原则；提出了适应极限的概念，指出这一概念对于适应气候变化的政策含义；提出了保障社会可持续发展的气候恢复能力路径；强调要注重适应与减缓的协同作用和综合效应，指出转型适应是应对气候变化影响的必要选择。报告认为，气候变化、影响、适应及社会经济过程不再是一个简单的单向线性关系，需要纳入统一的系统框架下予以认识和理解。

**关键词**：气候变化；影响；适应；风险；可持续发展

## 引 言

应对气候变化，不仅要减少温室气体排放，还要采取积极主动的适应行动，通过加强管理和调整人类活动，充分利用有利因素，减轻气候变化对自然生态系统和社会经济系统的不利影响。可持续发展是既满足当代人的需求，又不对后代人满足其自身需求的能力构成危害的发展。应对气候变化，通过适应措施减少脆弱性和暴露度、增强气候恢复能力，与社会可持续发展密切相关[1]。2007 年 12 月联合国气候变化大会通过的《巴厘行动计划》将适应气候变化与减缓气候变化置于同样重要的位置。2012 年 IPCC 发布的《管理极端事件和灾害风险：推进气候变化适应》特别报告（SREX）指出，不合理的发展过程将加剧灾害风险及其损失，但是采取积极的减灾和适应行动，能够减小灾害风险并促进社会、经济、环境的可持续发展。2014 年 3 月发布的 IPCC 第五次评估报告（AR5）第二工作组报告[2]指出，气候变化已对水资源、陆地和海洋生态系统、农业、农村和城市、人类健康与安全、人们的生计等造成影响，从热带到两极、从小岛到大陆各地区、从最富裕国家到最贫困国家，气候变化的影响遍及全球各个区域。适应气候变化的评估内容贯穿于报告的十个领域和九大区域，其中有 4 章内容专门评估

**收稿日期**：2014-02-11；**修回日期**：2014-04-10
**资助项目**：国家科技支撑计划（2012BAC20B05）；中国气象局气候研究开放实验室开放课题青年基金（420011）；CDM 基金项目
**作者简介**：段居琦，男，工程师，从事应用气象学、气候变化影响评估与适应研究，duanjq@cma.gov.cn；高清竹（通信作者），男，研究员，gaoqzh@ami.ac.cn

适应问题，包括：总结不同领域与区域的适应成果，评估分析适应的需求与选择，适应的规划和实施，综合分析适应的机遇、限制和极限，适应气候变化的经济学问题，最后指出适应气候变化是管理气候灾害风险和增强气候恢复能力的重要组成部分。报告认为[3]，气候变化、影响、适应与社会经济过程等密切关联，需要在系统框架下予以认识和理解。

## 1 适应气候变化与可持续发展主要结论

与第四次评估报告①(AR4)[4]相比，AR5 进一步深化了国际社会对于适应气候变化与可持续发展的认识，其主要内容及科学创新如下。

### 1.1 适应的需求与选择

自 AR4 以来，以风险管理为切入点，适应分析框架已经从关注生态、物理脆弱性拓展到更广泛的社会和经济驱动因子。这些驱动因子包括性别、年龄、健康、社会阶层、个体和群体的社会地位，以及机构在地方、国家、区域和国际上的地位。适应的目标是增强气候恢复能力，这意味着鼓励更广泛的发展目标和更多样化的适应选择，更好地认识人类社会和环境之间的相互作用。

适应需求是指气候变化可能引发的结果与我们期望目标之间的差距。适应需求来自以下方面：自然生态系统的气候变化脆弱性增加，社会组织和个体希望共享适应的经验，私营部门参与适应行动，提升信息服务能力和资源投入等。最迫切的适应需求是气候变化风险引发的安全问题，例如针对未来的气候变化风险及其影响，需要采取适应行动以确保人口、财富和自然资源的安全。

在适应措施选择上，虽然生态系统适应措施、制度和社会层面适应经验（包括为最弱势的群体提供气候安全网）正在增加，但是工程和技术适应措施仍然是最常见的适应选择，包括建设防洪堤、提高灌溉效率、发展节水技术、培育新品种、进行保护性耕作、灾害风险区划、监测及建设预警系统等。适应措施的选择以增量型适应为主，旨在减少气候变化的新增风险及其不利影响从而达到共赢目标。然而，为了应对气候变化影响，有时需要转型适应（transformational adaptation）。此外，有必要运用多种适应方法考虑综合性适应措施而非单一举措。

已有的成功适应经验表明，公私部门的合作是成功适应的重要因素。此外，决策者也需要关注适应行动中存在的不良适应问题（mal-adaptation），即某一地区或部门的政策干预可能会增加另一个地区或部门的脆弱性，或加剧目标群体应对未来气候变化的脆弱性。

### 1.2 适应的规划和执行

适应气候变化正在从关注阶段过渡到社会管理和战略规划阶段。国家和公共机构在促进从规划到执行的适应管理中起着重要作用。适应规划及其实施是一种循环往复、不断改进的学习过程。由于气候变化的影响与发展目标密切相关，降低气候风险的有效适应策略需要充分考虑脆弱性和暴露度的变化及其与发展目标和气候变化的联系。因此，灾害风险管理已成为适应气候变化的前沿问题，一些国家正在把适应整合到可持续发展规划中以应对气候变化可能带来的风险。

决策制定、规划和执行需要有效的工具。适应决策制定的方法包括“自上而下”和“自下而上”的方法。“自上而下”的方法主要是结合专家选择的区域气候情景的降尺度模拟；“自下而上”的方法是通过评估特定部门或群体的气候变化影响／风险和脆弱性，从而作出适应选择。气候变化的不确定性和社会生态系统的复杂性需要采用动态的规划方法，包括动态监测、模拟及空间整合、信息交流沟通及早期预警等。其中整合监测和模拟的地理信息系统（GIS）可以提高适应的前瞻性和实施效果。由于适应气候变化形势的复杂性、多样性和方法路径的制度依赖性，在适应规划及其实施过程中并没有普遍适用的方法。

①此处及下文所提评估报告均指第二工作组报告。

www.climatechange.cn



### 1.3　适应的机遇、限制和极限

风险评估是适应决策的有益基础，旨在评估与人类和自然生态系统适应相关的潜在机遇、限制和极限。自 AR4 以来，对于如何通过社会管理和自然系统适应方式更有效管理气候风险，人们已经加深了认识。跨部门和跨区域的适应政策与行动，已经给许多参与者带来了机遇。

适应气候变化的限制因素包括生物物理、机制、财政、社会和文化等方面。由于气候变化、生物物理和社会经济相互作用的限制，当超过适应目标可承受的风险或影响自然系统的可持续性时，会产生适应的极限（图 1）。适应极限（adaptation limit）是适应者的目标或系统需求不能够通过适应行动避免不可承受风险的临界点。对于不可承受风险的临界点而言，如果无法采取任何适应行动以避免未来的潜在风险，则这一临界点属于硬适应极限；如果仅仅是当前的适应选择不能避免的风险临界点，则是软适应极限。由于减排温室气体可以减少未来气候变化的速率和幅度，适应极限有可能被突破，但目前还不能识别突破适应极限的特定的减缓路径。适应极限为开展气候变化影响和风险评估、制定地区适应和发展规划提供了研究基础。

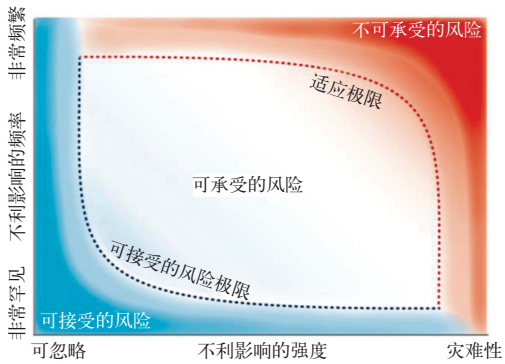


图 1　可接受的、可承受的和不可承受的气候风险及其对适应极限的影响

Fig. 1　Conceptual model of the determinants of acceptable, tolerable and intolerable risks and their implications for limits to adaptation

成功的适应，既需要辨识适应选择和评估它们的价值和效益，也需要利用人类和自然系统来拓展适应能力。自 AR4 以来，一系列新增的文献为适应条件的发展和适应限制的减少提供了指导，通过研究和实践持续发展这些知识可以有效促进适应。但是，由于机会的大小、克服限制、避免极限等可能涉及复杂的管理挑战，因此有必要设立相应的管理机构和改进管理制度，以有效管理多样化的适应参与者和多尺度的气候变化风险。

### 1.4　适应经济学

适应气候变化的成本效益评估已经用于指导适应决策和实际行动。适应的经济学分析包括社会参与者在适应中的作用、适应策略特征、成本投入和收益类型、时间及其他因子的作用等等。

在有限的资源和一定目标下，适应策略的选择要考虑多个政治目标之间的平衡。气候变化适应的经济学分析已经从对适应成本效益的“最经济”分析和识别最优决策转向风险评估和不确定因素下的多目标决策，以便为决策者提供支持。私有和公共部门在适应决策中都扮演着积极的角色，但公共部门的作用更大。适应行动不能消除所有的气候变化影响，适应措施和行动需要随着时间变化和认识提升而随时作出适当调整。

适应的总需求应该考虑国家总体的发展路径，尤其是发展中国家。并非所有的适应行动都是以投资为基础的，政策制定也是适应的重要工具。虽然局地、国家、区域和全球尺度上的风险融资机制有助于增强气候恢复能力，但是在机制设计中应当充分考虑适应投资可能导致的市场失衡和社会公平问题。

适应成本是适应气候变化关注的重要问题。根据估算，全球适应成本总体上高于当前的适应资金投入，尤其在发展中国家，这意味着存在适应资金缺口。根据世界银行最新的全球适应成本评估结果，2010—2050年，发展中国家每年大约需要700～1000亿美元用于适应投资。但是由于数据、方法和测算的范围存在不足，这一估算结果仅能作为初步参考。

### 1.5　气候恢复能力路径和转型适应与可持续发展

气候变化对发展是一种不断增长的威胁，为实

现可持续发展，需要优先判定和寻找具有气候恢复能力的发展路径。气候恢复能力发展路径包括：减少气候变化及其影响的行为；增加或维持有效的风险管理和适应行为。有时，这两者会共同受益，整合可实现双赢。具有气候恢复能力的发展路径在根本上与减缓气候变化的行动具有密切联系。

为了提升气候变化背景下社会经济可持续发展，气候恢复能力路径可能包括转型适应（图2）。转型适应是在作出涉及长期或预期适应决策时需要考虑的重要因素，它可以作为应对适应极限的一个措施。转型适应包括更大尺度和范围的适应，采用新技术或新实践形成新管理结构或新体系，或改变活动地点。与审慎的可持续发展不同，被动或主动的转型会给社会经济系统带来一定的风险，从而对社会治理结构提出新的和更高的要求，以便能够调和相互矛盾的未来目标和愿景。




图2 转型适应的概念分析图
Fig. 2 Conceptual of transformational adaptation

当前我们的世界面临着包含气候变化在内的多重挑战，适应决策和路径选择将决定未来的恢复能力和风险水平。采取高气候恢复能力发展路径将有助于全球提升恢复能力、降低潜在风险，反之采取低气候恢复能力的发展路径将使未来局面难以乐观。延迟当前的适应行动，有可能减少未来可以选择的气候恢复能力发展路径。因此，尽管常常难以确定某一具体适应行为的结果，仍然有必要研究通往具有高气候恢复能力路径的具体方法和行动。

国际社会和各级政府已经开始制定各种适应计划和政策，正在积累跨区域的适应经验。在非洲，大多数国家政府正在启动适应管理系统，但主要以孤立努力、灾害风险管理、改良技术和基础设施、基于生态系统的方法、保护性农业以及生计多样化等方式减少脆弱性。在欧洲，已制定了跨尺度的适应政策，一些适应规划已纳入海岸带、水资源及灾害风险管理领域。在亚洲，适应实践已经带来了一些生计效益，综合水资源管理也促进了适应工作。在澳大利亚，针对海平面上升的适应规划，以及在澳大利亚南部针对可用水量减少的适应规划已被广泛采用，但是在地方和社区层面的转型适应方面还存在行动的障碍。在北美，各国政府正在加强城市地区的适应评估和规划，通过采取前瞻性的适应措施，以推动未来对能源和公共基础设施领域的长期投资。在中美和南美，基于生态系统的适应变得越来越普遍，包括建立保护区、制定保护协议和加强自然保护区管理，这些工作也有助于改善生计和保护传统文化。在北极地区，居民适应气候变化由来已久，但是气候变化速率及其与社会、经济和政治因素的复杂联系给当地居民带来了前所未有的挑战。在各小岛屿国家，适应规划已经综合考虑了多种自然和人类属性，及其对气候相关驱动因子的敏感性。

## 2 科学创新与存在问题

应对气候变化，通过适应措施减少脆弱性和暴露度，提升气候恢复能力，与可持续发展密切相关。与AR4相比，AR5在以下几个方面有明显创新：适应气候变化作为灾害风险管理以构建气候恢复能力路径的措施得到高度重视，适应气候变化的研究视角从自然生态脆弱性转向更广泛的社会经济脆弱性及人类的响应能力；结合IPCC SREX报告中的灾害风险管理框架，深入阐述气候风险与社会发展的关系，明确了适应在气候变化风险管理中的作用，提出了适应气候变化以减少脆弱性和暴露度及增加气候恢复能力的有效适应原则；提出了适应极限的概念，明确了其在适应气候变化中的意义；提出了保障社会可持续发展的气候恢复能力路径，注重适应

www.climatechange.cn



和减缓的协同作用和综合效应，指出转型适应是应对气候变化影响、突破适应极限的必要选择。

整合气候变化减缓、适应和可持续发展是一个较新的挑战，目前学术界还不能提供强有力的适应决策框架和指南，还有很多相关研究工作有待开展。在适应的需求和决策领域，应该更多地关注那些威胁人类生计和生命财产安全的极端灾害事件，研究适应行动的规律和传播心理学。在适应的规划和执行方面，应该更多地关注减小气候变化影响的基础防御设施建设，优化适应策略和方法以更好地利用适应气候变化的资源，将适应措施整合到社会发展中以实现共赢。同时，对于主要的减缓和适应选择，需要对其收益、成本、协同、权衡取舍和限制因素加强认识和研究。在发展路径选择中应坚持气候恢复能力路径，深入研究各种发展路径的驱动因素及其对气候变化的可能影响；充分认识到适应、减缓和发展之间可能存在的反馈和互动效应；研究可能对发展形成特别挑战的潜在的气候变化阈值或临界点；研究减少灾害损失和破坏、支持可持续发展的各种转型适应方法；提升对极端气候事件及其对发展影响的认识，研究受其影响的人类和自然系统所需要的转型适应措施／路径；研究使适应和减缓行动之间产生协同效应的机制措施等等。

## 3　工作启示

中国政府高度重视应对气候变化工作。目前，已建立并逐步形成由国家应对气候变化领导小组统一领导、国家发展和改革委员会归口管理、各有关部门分工负责、各地方各行业广泛参与的应对气候变化管理体制和工作机制。国务院有关部门相继成立了应对气候变化研究中心等工作支持机构，一些高等院校、科研院所成立了气候变化研究机构。2013 年 11 月，在分析中国面临的气候变化威胁形势下，国家发展和改革委员会、中国气象局等 9 部门联合印发了《国家适应气候变化战略》，将适应气候变化问题纳入政府的经济和社会发展规划，明确中国适应气候变化的指导思想、原则和主要目标，指出应在基础设施、农业、水资源、海岸带、森林和其他生态系统、人体健康等领域实施重点适应任务，在城市化地区、农业发展地区、生态安全地区有侧重地实施适应任务，构建区域适应格局等等。上述内容对于中国未来推进适应政策和行动具有很强的战略指导意义。未来应客观认识气候变化影响及其风险，加强减少相关领域暴露度和脆弱性及增加气候恢复能力的机制和方法研究，切实推动适应气候变化，保障自然和社会经济系统可持续发展。■

**参考文献**

[1] IPCC. Managing the risks of extreme events and disasters to advance climate change adaptation: a special report of working groups I and II of the Intergovernmental Panel on Climate Change [M]. Cambridge and New York: Cambridge University Press, 2012: 1-582

[2] IPCC. Climate change 2014: impacts, adaptation, and vulnerability [M/OL]. Cambridge: Cambridge University Press, in press, 2014 [2014-03-20]. http://www.ipcc.ch/report/ar5/wg2/

[3] Stocker T F, Qin D H, Plattner G-K, *et al*. Technical summary [M/OL]// IPCC. Climate change 2014: impacts, adaptation, and vulnerability. Cambridge: Cambridge University Press, in press, 2014 [2014-03-20]. http://cache.cma.gov.cn/files/100900000006547B/ipcc-wg2.gov/AR5/images/uploads/WGIIAR5-TS_FGDall.pdf

[4] IPCC. Climate change 2007: impacts, adaptation, and vulnerability [M]. Cambridge: Cambridge University Press, 2007: 1-976

# Understanding of Climate Change Adaptation and Sustainable Development for IPCC Fifth Assessment Report

Duan Juqi[1], Xu Xinwu[2], Gao Qingzhu[3]

1 *National Climate Center / Laboratory for Climate Studies, China Meteorological Administration, Beijing* 100081*, China*;
2 *Department of Science & Technology and Climate Change, China Meteorological Administration, Beijing* 100081*, China*;
3 *Institute of Environment and Sustainable Development in Agriculture, Chinese Academy of Agricultural Sciences, Beijing* 100081*, China*

**Abstract:** IPCC launched *Climate Change 2014: Impacts, Adaptation, and Vulnerability* and pointed out that since AR4 the framing of adaptation has moved further from a focus on biophysical vulnerability to the wider social and economic drivers of vulnerability and people's ability to respond. It expounded the relationships between climate risk and social development, pointed out how adaptation play an important role in climate-related risk management and that strategies and approaches to climate change adaptation include efforts to decrease vulnerability or exposure and/or increase resilience or adaptive capacity. It presented the concept of adaptation limits and expounded its meaning to climate change adaptation. It put forward climate resilient pathways for sustainable development, significant co-benefits and synergies exist between mitigation and adaptation and between alternative adaptation responses, transformation is a necessary option to cope with climate change. The report considered climate change, impacts, adaptation and social-economics processes are not simple linear relationship and need to be recognized and understood in a compound system.

**Key words:** climate change; impacts; adaptation; risk; sustainable development

# 中国东北区域盛夏雨季的客观识别*

房一禾[1)] 龚志强[2)†] 赵连伟[1)] 赵春雨[1)] 李清泉[2)]

1) (沈阳区域气候中心, 沈阳 110166)

2) (中国气象局国家气候中心开放实验室和监测室, 北京 100081)

( 2014 年 4 月 6 日收到; 2014 年 6 月 6 日收到修改稿 )

鉴于我国东北三省雨季客观识别方法不尽相同, 且无东北区域统一的雨季监测指标. 为了更好地开展区域关键天气过程的客观化识别和监测, 本文从区域角度出发, 采用东北三省 102 站逐日降水量资料, 通过对东北区域多年平均 5 点平滑处理的 4 月 1 日—10 月 31 日逐日降水量序列的综合分析, 及对历年逐日滑动平均雨量的对比试验, 确定了东北盛夏雨季判别的阈值参数及通过阈值后的持续时间参数, 进而研发了适合东北区域盛夏雨季开始和结束日期的客观识别方法. 并采用美国环境预报中心和国家大气研究中心逐日再分析的风场、位势高度场资料, 通过对盛夏雨季前、中、后期不同高度层大气环流场的对比分析, 验证了该客观识别方法的合理性. 结果表明, 东北区域 1981—2010 年气候态平均的盛夏雨季的起止日期分别为每年的 6 月 26 日和 8 月 30 日.

**关键词**: 东北地区, 盛夏雨季, 起止日期, 客观识别

**PACS:** 92.60.Wc **DOI:** 10.7498/aps.63.209202

## 1 引 言

中国处于东亚季风区, 受东亚季风影响, 各地大范围、集中降水开始和结束的时间有较大差别, 例如江南春雨、华南前汛期、梅雨、东北华北雨季、华西秋雨等天气气候现象都表明了中国不同区域降水变化的独特性. 东北三省各自的雨季监测指标也不尽相同, 目前东北地区雨季起止日期尚没有一个统一的、定量的划分标准, 通常只是按一年中雨带的大致变化粗略划分雨季的大概时间. 然而精确的雨季开始和结束日期的监测是气象服务的重要内容, 对于农业生产和政府决策等均有十分重要的作用. 因此, 开展东北雨季尤其是盛夏雨季的客观识别研究有着重要的现实意义.

20 世纪 30 至 40 年代, 竺可桢 [1]、涂长望和黄士松 [2] 就曾指出: 5 到 8 月自南海夏季风爆发后, 雨带的进退形成华南前汛期、江淮梅雨和东北华北雨季, 该结论可作为各地区雨季研究工作的总体参考. 目前, 对华南前汛期和梅雨雨季起止日期划分标准的研究相对较多 [3−6], 而对于其他地区雨季客观识别的研究相对少. 赵汉光 [7] 最早采用旬降水量定义华北雨季, 结果表明, 华北雨季开始期主要集中在 7 月中旬左右, 结束期主要集中在 8 月中旬左右. 采用旬雨量研究雨季起止日期的还包括林之光 [8] 和张家诚 [9]. 强学民等 [10] 指出: 雨季开始和结束与大气环流的季节转换相联系, 因此用候作为划定标准的时间单位最为合适. 此后, 晏红明等 [11] 也采用候雨量为单位对中国西南区域雨季开始和结束日期划分标准进行了研究. 东北雨季方面, 王学忠等 [12] 采用 9 个测站的旬降水量资料, 研究了东北雨季的划分, 结果表明, 东北雨季平均在 7 月中上旬开始, 8 月中上旬结束. 孙欣等 [13] 曾对辽宁雨季和多雨季标准的划分进行过研究, 指出以副热带高压脊线位置作为多雨季划分标准, 可得出辽宁

* 国家自然科学基金 (批准号: 41205040, 41375078)、国家重点基础研究发展计划 (批准号: 2012CB955903) 和公益性行业专项 (批准号: GYHY201306021) 资助的课题.

† 通讯作者. E-mail: gongzq@cma.gov.cn

© 2014 中国物理学会 Chinese Physical Society 

各地雨季、多雨季常年起止时间. 东北地区盛夏降水主要受东亚夏季风影响[14], 前人在东亚夏季风及夏季降水方面研究较多[15−19]. 施能等[20]指出东亚夏季风强度是造成我国夏季气温、降水异常的主要原因. 廉毅等[21]进一步分析了东亚夏季风在中国东北地区建立的标准、日期及其主要特征. 此外, 其他学者也在相关领域进行过研究[22−26], 并得到了有意义的结论.

沈柏竹等[14]指出东北雨季一般分为东北冷涡雨季和盛夏雨季, 初夏(5月和6月)东北地区降水主要受东北冷涡的影响. 随着西太平洋副热带高压的北进, 东北冷涡的影响逐渐减弱, 东亚夏季风在盛夏(7月和8月)开始对东北地区降水产生影响. 因此, 东北雨季应包括冷涡雨季和季风雨季. 本研究主要讨论季风雨季(或称盛夏雨季)的客观识别方法, 冷涡雨季的内容会在另文中分析. 以往对于东北雨季的研究很少, 国家气候监测业务中尚无统一的雨季监测指标. 而且以往对于雨季起止日期的研究多采用旬雨量或候雨量, 这两个时间尺度相对日雨量来讲, 不够精确. 因此, 本研究采用1961—2011年的逐日降水量资料, 基于1981—2010年平均的东北区域平均5点平滑后的逐日降水量序列研究东北雨季的客观识别方法, 并通过对比试验和环流分析来验证其可靠性, 以期为国家气候监测业务提供技术支撑.

## 2 资料和方法

### 2.1 资　料

站点资料方面: 采用由国家气候中心提供的全国2400站高分辨率逐日降水量资料, 经过质量控制得到1961—2011年东北三省102站逐日降水量资料, 站点分布如图1所示. 格点资料方面: 采用美国环境预报中心和国家大气研究中心再分析的逐日位势高度场和风场资料(分辨率为2.5° × 2.5°).

### 2.2 方　法

#### 2.2.1 统计分析方法

本文主要采用5天滑动平均方法对东北区域多年平均的3月30日—11月2日的逐日降水量序列进行平滑, 从而研究东北盛夏雨季的客观识别方法. 其中, 平滑后序列的第一天为4月1日, 最后一日为10月31日. 并采用合成分析及差值$t$检验方法分析东北盛夏雨季前、中、后期的环流差异. 文中提到的多年平均均指1981—2010年的气候平均值.

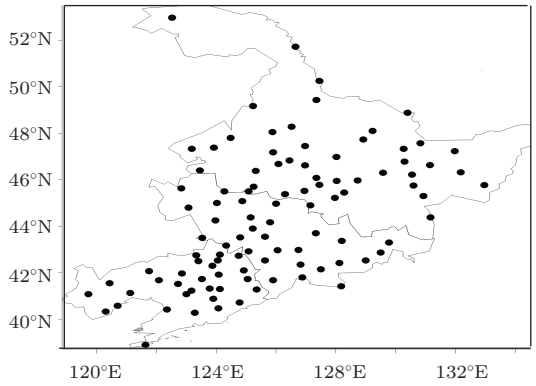


图1　东北区域站点分布图

#### 2.2.2 东北区域多年平均盛夏雨季的客观识别方法

分析东北区域多年平均盛夏雨季客观识别方法是研发东北区域历年盛夏雨季客观识别方法的基础. 设定当$r_i$稳定通过某阈值($yz$)的第一天所在日期为东北区域多年平均盛夏雨季的开始日期(ks)或结束日期(js), 即:

$$\text{当}4\text{月}1\text{日} < i < 7\text{月}31\text{日时}, \ \text{若}r_i > \text{yz}, \ \text{且}r_{i+1} > \text{yz}, \quad \text{则ks} = \min(i); \tag{1}$$

$$\text{当}8\text{月}1\text{日} < i < 10\text{月}31\text{日时}, \ \text{若}r_i < \text{yz}, \ \text{且}r_{i+1} < \text{yz}, \quad \text{则js} = \min(i), \tag{2}$$

其中, $r_i$为东北区域多年平均的逐日5天滑动平均雨量序列 (i为日期, 范围是4月1日—10月31日); 阈值(yz)选取方法有多种[27], 需要后文对$r_i$进行综合分析来确定.

#### 2.2.3 东北区域历年盛夏雨季客观识别的对比试验方案

历年东北区域盛夏雨季的客观识别方法是在多年平均盛夏雨季识别方法的基础上, 进一步通过对比试验确定通过阈值后, 连续超过阈值天数$n$, 从而最终得到的客观识别方法. 连续通过阈值天数$n$需要进行不同标准的对比试验来确定. 对于历年雨季开始日期的识别采用以下4组试验.

从6月1日开始, 当某年某日的$r_{yi} > 2R$, 且东北区域内有50% 以上站点的$r_s > 2\bar{r}$, 则将该日作为盛夏雨季开始的待定日, 如果之后连续$n$天都满足$r_{yi} > 2R$, 则将待定日确定为盛夏雨季开始日(ks1). 其中, $n = 0$为试验一, $n = 3$ 为试验二, $n = 4$为试验三, $n = 5$为试验四.

对于雨季结束日期的识别也采用4组试验. 从7月1日开始, 当某年某日的$r_{yi} < 2R$, 且东北区域内有50% 以上站点的$r_s < 2\bar{r}$, 则将该日作为盛夏雨季结束的待定日, 如果之后连续$n$天都满足$r_{yi} < 2R$, 则将待定日确定为盛夏雨季结束日(js1). 其中, $n = 5$ 为试验一, $n = 6$为试验二, $n = 7$为试验三, $n = 8$为试验四.

其中, $r_{yi}$为东北区域平均的某年逐日5天滑动平均雨量序列($y$为年份, 范围是1961—2011年; $i$为日期, 范围是4月1日—10月31日); $2R$为东北盛夏雨季阈值, 是东北区域多年平均的逐日5天滑动平均雨量(共365天, 剔除闰年2月29日)平均值的2倍; $r_s$为$r_{yi}$对应日期的某日单站逐日5天滑动平均雨量, 下标$s$代表不同站点; $2\bar{r}$为$r_{yi}$对应年份的单站逐日5天滑动平均雨量365天平均值的2倍; $n$为$r_{yi}$第一天通过阈值以后连续通过阈值的天数, 在后文的对比试验中确定.

## 3 东北地区月降水量的分布和演变的气候态特征

应用东北区域盛夏雨季客观识别方法, 确定盛夏雨季开始和结束日期的同时, 有必要分析多年平均雨季可能开始和结束月份(5—10月)的逐月降水量变化和分布特征.

东北地区降水变化的区域差异比较明显. 降水量呈现东南部多于西北部, 即沿海大于内陆的分布特征. 5月东北地区没有出现100 mm以上降水量的站点, 辽宁东部和吉林东部降水量较大, 黑龙江西部、北部及吉林西部降水量较少; 6月降水量较5月整体增加, 辽宁东部和吉林东部降水量最先超过了100 mm, 吉林西部和黑龙江西部、北部降水量较少; 7月和8月东北地区降水量超过100 mm的范围明显扩大, 是降水量最多的两个月. 9月和10月全区降水量较8月整体减少. 从5—10月东北地区逐月降水量的变化来看, 降水量的增加首先出现在东北地区东南部 (即辽宁东部和吉林东部), 然后逐渐向西北扩展, 这一特征在一定程度上反映了东北地区雨季首先从东南沿海开始, 然后逐渐向西北内陆推进的过程. 其中, 6月和7月的降水量分别较上个月有明显的增加, 9月降水量较8月有明显减少, 说明雨季开始日期更倾向于出现在6月底或7月, 结束日期则更倾向于出现在8月底或9月, 盛夏雨季应主要集中在7月和8月.

尽管东北地区东南部和西北部月降水量有一定差异, 但全区域5—10月逐月降水量变化在空间上却有明显的一致性特征. 除7月份第一模态方差贡献率约为30% 以外, 其余月份的方差贡献率均在40% 左右. 各月降水量经验正交函数(EOF)第一模态的空间向量均体现了东北全区域一致的异常变化特征. 说明从整个东北区域的角度来研究东北地区雨季开始和结束日期的划分标准在一定程度上是合理的.

## 4 东北区域多年平均盛夏雨季的客观识别方法

在研究雨季客观识别方法、划分雨季起止日期时, 需要对雨季开始或结束日期的雨量标准进行分析和界定. 到目前为止, 有关雨季起止日期标准的研究多采用日雨量和候雨量的变化来定义[5,6]. 显然, 日雨量相对候雨量来说更加精确, 但日尺度降水的波动较大. 因此, 本研究主要分析逐日雨量5天滑动平均序列的演变特征.

以往的雨季划分研究中[11,13], 通常有两种阈值进行分析: 阈值一(以下简记为$2R$): 采用东北区域多年平均的365日雨量5天滑动平均值的2倍; 阈值二(简记为$R$): 采用东北区域多年平均的365日5天滑动平均雨量的平均值.

图2(a)给出东北区域多年平均的4月1日—10月31日逐日5天滑动平均雨量变化曲线(即$r_i$). 可见, 4月1日—5月21日, $r_i$在波动中缓慢上升; 5月22日—6月30日, $r_i$有两次陡升, 第一次陡升与$R$出现交点, 交点出现在5月26日, 时值初夏, 这次陡升应该与初夏东北冷涡系统对东北地区降水量的影响有关[14]. 第二次陡升与$2R$出现交点(对应第一个阴影区域), 第二次陡升较第一次更为明显, 且第二次陡升与$2R$相交的时间在6月26日, 与前述分析的雨季开始日期可能发生在6月底或7月符合. 由于7月和8月属于盛夏[14], 因此该日期可认为是东北盛夏雨季(为与冷涡雨季对应, 这里称为盛夏雨季)的开始日期. 第二次陡升以后, $r_i$仍在上升, 并在7月下旬到8月初达到峰值. 8月8日—10月31日, $r_i$出现两次陡降和一次缓降, 其中前两次为陡降. 第一次陡降后, 降水量仍较大(大于$2R$), 不适合作为盛夏雨季结束日期的标准. 而第二次陡降(对应第二个阴影区域)过程中, 降水量明显减少, 且$r_i$与$2R$出现两个交点, 稳定小于$2R$的

交点出现在8月30日. 第三次缓降过程应属于雨季结束后降水量的缓慢减少过程.

综上所述, 东北盛夏雨季开始日期应该出现在$r_i$的第二次陡升过程中, 结束日期应该出现在第二次陡降过程中. 结合对$r_i$和阈值的比较分析, 初步把盛夏雨季开始日期定义为第二次陡升过程中, 逐日5天滑动平均雨量稳定超过$2R$的日期, 结束日期定义为第二次陡降过程中, 逐日5天滑动平均雨量稳定小于$2R$的日期. 即东北区域多年平均盛夏雨季开始日期为6月26日, 结束日期为8月30日.

定义一个区域的雨季开始和结束日期, 除考虑降水量的变化外, 很大程度上还要考虑降水范围的大小. 图2 (b)给出东北区域102站单站降水量超过$2R$的站点数占东北区域总站数的百分比. 由图2 (b)可见, 百分比稳定超过(低于) 50% 的日期出现在6月26日(8月30日), 该日期与图2 (a)中$r_i$稳定超过或低于阈值$2R$的日期完全一致. 这进一步证明了之前对于东北盛夏雨季起止日期定义的合理性.

此外, EOF分析的多年平均逐日时间系数变化可以在很大程度上反映季节变化特征. 图3给出东北区域1981—2010年平均的逐日(365天)滑动平均雨量EOF第一模态分布及相应多年平均逐日滑动平均雨量时间系数的变化. 可见, EOF第一模态空间向量反映了全区一致的变化特征. 多年平均的逐日标准化时间系数的变化曲线与图2 (a)给出的东北区域多年平均逐日雨量的变化几乎是一致的. 气候分析中常把标准化时间系数大于1或小于$-1$的情况认为是异常情况. 逐日滑动平均雨量的标准化时间系数大于1的情况可以认为是一年中雨量较多的日期, 标准化时间系数大于1和小于1的情况同样可以理解为雨季和非雨季的差别. 由图3 (b)可见, 标准化时间系数在6月26日稳定大于1, 在8月30日稳定小于1, 这与之前定义的东北雨季开始和结束日期完全一致. 因此, 逐日雨量EOF第一模态分布及相应多年平均逐日标准化时间系数的变化进一步表明了东北区域降水变化的一致性特征及季节变化特征, 同时也进一步说明之前以$2R$作为阈值确定的东北区域多年平均盛夏雨季开始和结束日期的合理性.

通过以上分析, 将$2R$作为判断东北盛夏雨季的阈值, 以$r_i$稳定大于(小于)$2R$的日期来定义东北区域多年平均盛夏雨季的起(止)日期. 东北区域多年平均盛夏雨季ks的客观识别方法可概括为: 当

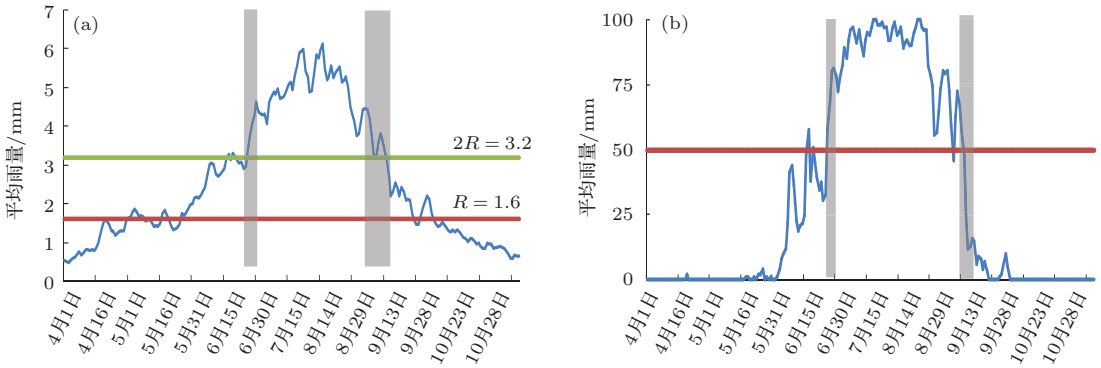


图2 4月1日—10月31日东北区域多年平均 (a) 逐日5天滑动平均雨量曲线(单位为mm); (b) 单站逐日5天滑动平均雨量超过$2R$的站数占总站数的百分比(单位为%)

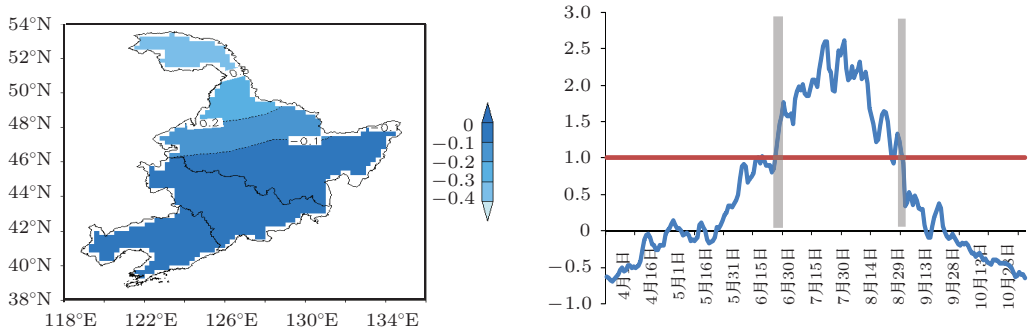


图3 (网刊彩色) 多年平均逐日滑动平均雨量EOF第一模态空间向量及对应的时间系数

4月1日$< i <$ 7月31日时, 若$r_i > 2R$, 且$r_{i+1} > 2R$, 则$\mathrm{ks} = \min(i)$. 东北区域多年平均盛夏雨季js的客观识别方法为: 当8月1日$< i <$10月31日时, 若$r_i < 2R$, 且$r_{i+1} < 2R$, 则$\mathrm{js} = \min(i)$.

基于该客观识别方法, 对东北区域多年平均逐日5天滑动平均雨量曲线进行识别, 可将东北区域多年平均盛夏雨季开始日期定义为6月26日, 结束日期定义为8月30日.

## 5 历年东北区域盛夏雨季的客观识别

由于以上分析的$r_i$经过了区域平均之后再做30年平均, 多次平均之后的结果实际上平滑掉了降水量变化的区域差异和年际波动的信息. 从图2 (a)中$r_i$的变化就可看出, 在6月26日超过$2R$之后一直稳定地大于$2R$, 至8月30日下降至低于$2R$之后也比较稳定, 即波动比较小. 而实际业务中发现, 东北区域历年逐日5天滑动平均雨量围绕$2R$的上下波动是比较明显的. 因此, 在确定逐年雨季开始和结束时间的划分标准时, 逐日滑动平均雨量超过$2R$和低于$2R$的持续时间是必须考虑的重要方面. 那么究竟持续多少日比较合适? 定义的标准太高或太低所得到的结果都会有一定的差异. 这里我们根据日滑动平均雨量连续超过$2R$的日数准备了不同的试验, 通过对比试验来进一步研究合适于东北区域盛夏雨季开始和结束日期的判定标准.

### 5.1 开始日期

根据2.2.3中给出的对比试验方案对盛夏雨季的开始日期进行客观识别. 表1给出采用前述四个对比试验对1961—2011年东北盛夏雨季开始(结束)日期的划分结果, 其中日期序号为盛夏雨季开始(结束)日期距离4月1日的天数加1. 东北区域多年平均盛夏雨季开始日期为6月26日, 日期序号为87. 由1961—2011这51年的平均日期序号可见, 87介于试验三和试验四之间; 从1981—2010这30年的平均日期序号可见, 87介于试验二和试验三之间. 初步认为, 试验三更适合作为判断盛夏雨季开始日期的标准.

表1 不同标准对1961—2011年东北盛夏雨季开始(结束)日期的划分结果

| 年份 | 试验一 | 试验二 | 试验三 | 试验四 |
|---|---|---|---|---|
| | 日期序号 | 日期序号 | 日期序号 | 日期序号 |
| 1961 | 67* (137) | 67* (148) | 67* (160) | 91 (160) |
| 1962 | 66* (156) | 97 (156) | 97 (156) | 97 (156) |
| 1963 | 81 (139) | 81 (139) | 81 (139) | 81 (139) |
| 1964 | 72 (158) | 72 (158) | 72 (158) | 72 (158) |
| 1965 | 89 (142) | 89 (142) | 89 (142) | 99 (142) |
| 1966 | 65* (156) | 65* (156) | 65* (156) | 65* (156) |
| 1967 | 68* (134*) | 68* (134*) | 68* (134*) | 68* (134*) |
| 1968 | 70* (133*) | 70* (150) | 95 (150) | 95 (150) |
| 1969 | 64* (125*) | 89 (125*) | 89 (125*) | 106** (161) |
| 1970 | 85 (136*) | 85 (136*) | 107** (136*) | 107** (136*) |
| 1971 | 71* (183*) | 71* (183**) | 71* (183*) | 71* (183*) |
| 1972 | 78 (144) | 90 (155) | 90 (155) | 113** (155) |
| 1973 | 80 (155) | 80 (155) | 80 (155) | 80 (155) |
| 1974 | 65* (139) | 80 (139) | 80 (139) | 80 (139) |
| 1975 | 69* (131*) | 69* (140) | 86 (140) | 94 (140) |
| 1976 | 71* (148) | 71* (148) | 71* (148) | 71* (148) |
| 1977 | 66* (139) | 74 (139) | 74 (139) | 84 (139) |

表 1 不同标准对 1961—2011 年东北盛夏雨季开始 (结束) 日期的划分结果 (续)

| 年份 | 试验一 日期序号 | 试验二 日期序号 | 试验三 日期序号 | 试验四 日期序号 |
|---|---|---|---|---|
| 1978 | 73 (162) | 73 (162) | 73 (162) | 73 (162) |
| 1979 | 73 (132*) | 89 (132*) | 89 (145) | 89 (145) |
| 1980 | 67* (128*) | 67* (128*) | 75 (128*) | 75 (128*) |
| 1981 | 85 (151) | 85 (151) | 85 (151) | 85 (151) |
| 1982 | 107** (158) | 107** (166) | 107** (166) | 107** (166) |
| 1983 | 69* (136*) | 69* (136*) | 69* (136*) | 69* (136*) |
| 1984 | 70* (156) | 70* (156) | 70* (156) | 70* (156) |
| 1985 | 75 (165) | 75 (165) | 101 (165) | 101 (165) |
| 1986 | 82 (178**) | 82 (178**) | 82 (178**) | 92 (178**) |
| 1987 | 71* (166) | 95 (166) | 95 (166) | 95 (166) |
| 1988 | 69* (130*) | 82 (130*) | 98 (130*) | 98 (130*) |
| 1989 | 80 (130*) | 80 (130*) | 80 (130*) | 80 (130*) |
| 1990 | 75 (132*) | 75 (161) | 75 (161) | 75 (161) |
| 1991 | 77 (140) | 77 (148) | 77 (148) | 77 (148) |
| 1992 | 73 (145) | 73 (145) | 73 (145) | 73 (145) |
| 1993 | 73 (157) | 76 (157) | 76 (157) | 76 (157) |
| 1994 | 93 (155) | 93 (155) | 93 (155) | 93 (184**) |
| 1995 | 88 (166) | 88 (166) | 88 (166) | 88 (166) |
| 1996 | 82 (145) | 82 (145) | 97 (145) | 97 (145) |
| 1997 | 71* (165) | 105** (165) | 130** (165) | 130** (165) |
| 1998 | 79 (157) | 79 (157) | 79 (157) | 79 (157) |
| 1999 | 91 (144) | 91 (163) | 91 (163) | 91 (163) |
| 2000 | 117** (133*) | 117** (164) | 117** (164) | 117** (164) |
| 2001 | 88 (141) | 88 (141) | 103** (141) | 127** (141) |
| 2002 | 79 (142) | 79 (142) | 79 (142) | 79 (142) |
| 2003 | 81 (142) | 81 (142) | 81 (142) | 93 (142) |
| 2004 | 101 (144) | 101 (144) | 101 (144) | 101 (144) |
| 2005 | 73 (153) | 73 (153) | 80 (162) | 80 (162) |
| 2006 | 79 (148) | 79 (148) | 84 (148) | 84 (148) |
| 2007 | 99 (153) | 99 (153) | 99 (153) | 99 (153) |
| 2008 | 89 (138) | 89 (155) | 89 (155) | 89 (155) |
| 2009 | 80 (135*) | 80 (135*) | 80 (135*) | 80 (135*) |
| 2010 | 103** (166) | 103** (166) | 103** (166) | 103** (166) |
| 2011 | 74 (152) | 74 (152) | 74 (152) | 109** (152) |
| 51 年平均 | 78.7 (147.1) | 82.2 (150.2) | 85.8 (150.9) | 89.2 (152.1) |
| 30 年平均 | 83 (149.0) | 85.4 (152.7) | 88.9 (153.0) | 91.5 (154.0) |

注: “*” 代表偏早年; “**” 代表偏晚年.

由表1可见, 东北盛夏雨季开始日期的序号的逐年波动较大, 这里把开始日期序号小于72 (相对多年平均雨季开始日期偏早15天以上) 的年份认为是雨季开始日期偏早年, 把开始日期序号大于102 (相对多年平均雨季开始日期偏晚15天以上) 的年份认为是雨季开始日期偏晚年. 按照该方法, 试验一中有17年属开始日期偏早年, 3年属偏晚年; 试验二中有9年属开始日期偏早年, 4年属偏晚年; 试验三中有7年属开始日期偏早年, 6 年属偏晚年; 试验四中有6年属开始日期偏早年, 9年属偏晚年. 其中试验二和试验三偏早年和偏晚年总数最少, 为13年. 但试验三中偏早年和偏晚年数更为接近, 说明试验三规定的开始日期更为适中. 因此, 选取试验三作为判断东北盛夏雨季开始的标准相对更为合适.

### 5.2 结束日期

同样根据2.2.3中给出的对比试验方案对盛夏雨季结束日期进行客观识别. 由于东北区域多年平均盛夏雨季结束日期为8月30日, 日期序号为152. 从1961—2011年的平均日期序号可见, 152介于试验三和试验四之间; 从1981—2010年的平均日期序号可见, 152介于试验一和试验二之间. 由表1可见, 各种试验的平均结束日期序号相差很小, 这与开始日期的情况有一定差别.

把结束日期序号小于137 (相对多年平均雨季结束日期偏早15天以上) 的年份认为是雨季结束日期偏早年, 把结束日期序号大于167 (相对多年平均雨季结束日期偏晚15天以上) 的年份认为是雨季结束日期偏晚年. 按照该方法, 试验一中有13年属结束日期偏早年, 2年属偏晚年; 试验二中有9年属结束日期偏早年, 2年属偏晚年; 试验三中有8年属结束日期偏早年, 2年属偏晚年; 试验四中有7年属结束日期偏早年, 3年属偏晚年. 其中试验二、试验三和试验四偏早年和偏晚年比较一致, 说明虽然标准不断提高, 但确定的盛夏雨季结束日期已逐渐趋于稳定. 之前分析认为, 试验二或试验三更适合, 而试验三的偏早和偏晚年数总和相对试验二更少. 因此, 选取试验三作为判断东北盛夏雨季结束的标准相对更为合适.

综上所述, 东北盛夏雨季开始 (ks1) 和结束 (js1) 日期的划分标准分别为:

当6月1日$< i <$10月31日时, 若$r_{yi} > 2R$,

且至少50% 站点的$r_{\mathrm{s}} > 2\bar{r}$, 且$r_{yi+n} > 2R$

$$(n = 1-4), \quad \text{则} \quad \mathrm{ks1} = \min(i); \tag{3}$$

当7月1日$< i <$10月31日时, 若$r_{yi} < 2R$,

且至少50% 站点的$r_{\mathrm{s}} < 2\bar{r}$, 且$r_{yi+n} < 2R$

$$(n = 1-7), \quad \text{则} \quad \mathrm{js1} = \min(i). \tag{4}$$

## 6 盛夏雨季前、中、后期的环流场对比分析

### 6.1 500 hPa位势高度场对比

图4分别给出盛夏雨季开始之前一个月 (6月1日—6月25日), 盛夏雨季期间的两个时段 (6月26日—7月31日及8月1日—8月31日), 和盛夏雨季结束后一个月 (9月1—9月30日) 的多年平均500 hPa位势高度场分布图. 由图4 (a) 可见, 6月1日—6月25 日500 hPa位势高度场的多年平均情况是: 西太平洋副热带高压位脊线位于20° N附近, 西伸脊点位于125° E附近. 由图4 (b) 可见, 6月26日—7月31日, 副高脊线北跳至25° N附近, 且略有西伸, 西伸脊点位于122° E附近. 根据孙欣等[13] 的研究, 副高第二次北跳 (通过25° N) 后, 雨带位置开始北推至华北和东北南部. 本文的盛夏雨季开始日期与该结论一致. 由图4 (c) 可见, 8月1日—8月31日, 副高脊线进一步北跳至30° N附近, 更有利于东北地区降水增多. 由图4 (d) 可见, 9月1—9月30 日, 副高脊线已南撤至26° N附近, 并有明显的东退, 西伸脊点位于135° N附近. 即副高的两次北进恰好对应在盛夏雨季期间, 而盛夏雨季之前副高脊线偏南, 盛夏雨季之后副高开始南撤. 可以证明本研究对东北盛夏雨季起止日期的客观识别是合理的.

### 6.2 850 hPa风场对比

图5分别给出盛夏雨季开始之前一个月盛夏雨季期间的两个时段和盛夏雨季结束后一个月的多年平均850 hPa风场分布图. 由图5 (a) 可见, 6月1日—6月25日, 东北地区主要受来自上游中高纬内陆地区的偏西风控制. 由于副高位置偏南, 来自西太平洋绕副高西侧北上的暖湿气流影响日本地区, 东北区域没有充分的水汽输送条件. 东北北

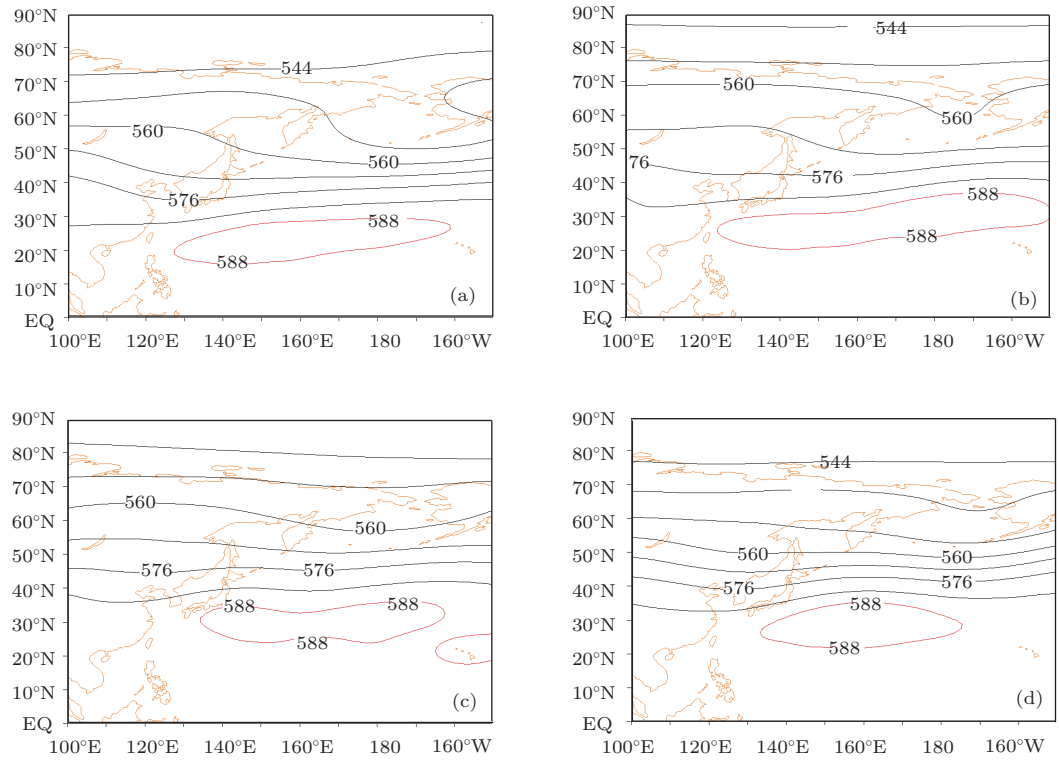


图 4 (a) 6 月 1 日—6 月 25 日, (b) 6 月 26 日—7 月 31, (c) 8 月 1 日—8 月 31 日, (d) 9 月 1—9 月 30 日的 500 hPa 多年气候平均位势高度场 (单位为 hPa)

部上空为一气旋式环流, 该气旋式环流可能是东北冷涡的作用. 这与沈柏竹等[14]的结论: “东北地区初夏 (5 月和 6 月) 降水异常以冷涡活动的影响为主.” 一致. 由图 5 (b) 可见, 6 月 26 日—7 月 31 日, 东北地区开始受西南暖湿气流的控制 (盛夏雨季开始), 此时西南气流主要影响东北地区南部和东部, 而西北部受弱的气旋式环流控制, 可能还受残留东北冷涡的影响. 影响东北地区的西南气流主要来自印度洋, 这主要是受印度季风影响. 而副高西北侧的西南气流对东北地区的影响相对较小. 由图 5 (c) 可见, 8 月 1 日—8 月 31 日, 随着副高进一步北跳, 副高西侧的偏南气流与来自印度洋的西南气流汇合后, 共同影响东北地区中部和南部, 西北部的偏西气流主要是来自印度洋的暖湿气流, 说明雨带进一步到达东北地区西北部. 由图 5 (d) 可见, 9 月 1—9 月 30 日, 控制东北地区上空的西南气流消失, 东北地区重新受到由上游内陆中高纬地区吹来的干冷的偏西气流控制, 盛夏雨季结束.

总体来看, 雨带是呈东北-西南向, 由东北地区东南部向西北部推进, 盛夏雨季期间, 东北地区主要受来自印度洋和副高西北侧的西南气流控制. 而盛夏雨季开始之前和结束之后的一个月, 东北地区主要受来自上游中高纬内陆地区的偏西风控制.

由图 5 (e) 可见, 盛夏雨季前半段的 850 hPa 风场与盛夏雨季前一个月的差值在中国东部为偏南风分量, 由印度洋和太平洋北上到达东北南部的偏南风差值通过了 0.01 信度的显著性检验. 由图 5 (f) 可见, 盛夏雨季结束后一个月与盛夏雨季后半段的 850 hPa 风场差值在中国东部为偏北风分量, 且东北地区上空的西北风差值通过了 0.01 信度的显著性检验. 差值图说明盛夏雨季影响东北地区的偏南风分量要显著强于非雨季. 又因雨季和非雨季时间段均是基于之前定义的盛夏雨季起止日期来选取的, 故也表明东北盛夏雨季起止日期的客观识别是合理的.

### 6.3 200 hPa 纬向风场对比

图 6 分别给出盛夏雨季开始之前一个月盛夏雨季期间的两个时段和盛夏雨季结束后一个月的多年平均 200 hPa 风场分布. 由图 6 (a) 可见, 6 月 1 日—6 月 25 日, 副热带西风急流轴位于 38° N 附近, 处于东北地区南侧, 急流轴强度相对较强, 中心风速大于 30 m/s. 由图 6 (b) 可见, 6 月 26 日—7 月 31 日, 副热带西风急流轴略有北移, 位于 40° N 附近, 急流轴强度相对较弱, 中心风速为 20—30 m/s. 由图 6 (c) 可见, 8 月 1 日—8 月 31 日, 副热带西风急

流轴的南北位置与图8 (b) 的情况相比只有略微北移, 急流轴强度相对较弱, 中心风速为20—30 m/s. 由图6 (d) 可见, 9月1—9月30日, 副热带西风急流轴仍位于40° N附近, 急流轴强度较盛夏雨季期间加强, 中心风速大于30 m/s.

综上分析, 急流轴强度是影响东北地区降水的主要因素. 非雨季急流轴相对较强, 雨季急流轴相对较弱. 图6 (e) 为东风差值, 急流核入口区北侧高空为辐散气流, 导致急流核北侧为上升运动, 有利于降水偏多; 图6 (f) 为西风差值, 西风急流核入口区北侧高空为辐合气流, 导致急流核北侧为下沉运动, 有利于降水偏少[27].

在30° N附近 (东北地区南部), 盛夏雨季前半段与盛夏雨季之前一个月200 hPa纬向风场差值为负, 且通过了显著性检验 (图6 (e)), 说明盛夏雨季期间, 西风急流轴要显著弱于非雨季. 图6 (f) 与 (e) 的情况基本相反, 虽然差值的显著区位置略有北移, 但仍位于东北地区南部. 差值图说明, 雨季的副热带西风急流轴显著弱于非雨季. 同样证明对东北盛夏雨季起止日期客观识别的合理性.

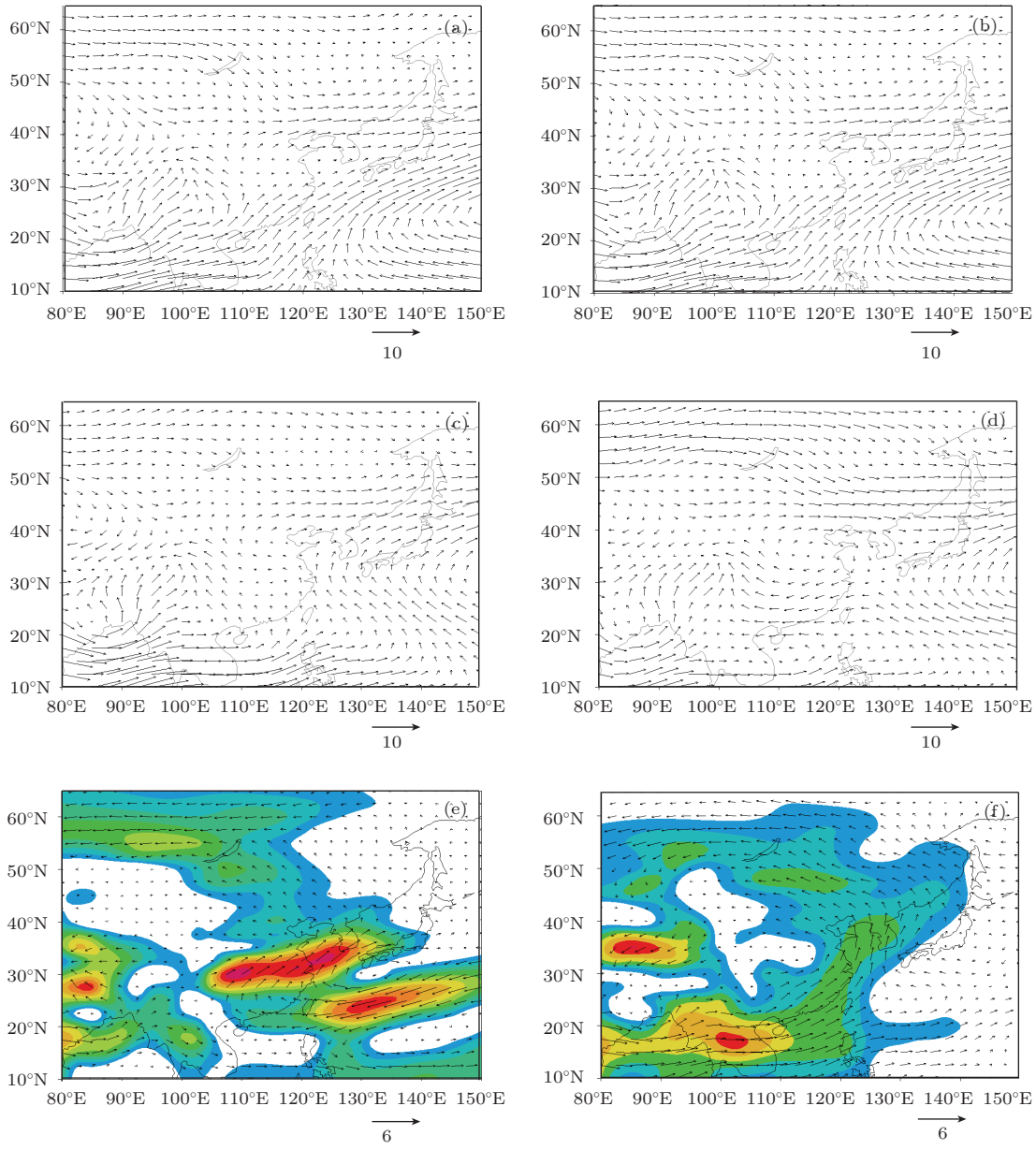


图5 (网刊彩色) (a) 6月1日—6月25日, (b) 6月26日—7月31日, (c) 8月1日—8月31日, (d) 9月1—9月30日的850 hPa多年气候平均风场及 (b)−(a) 的差值检验 (e), (d)−(c) 的差值检验 (f) (单位为m/s)

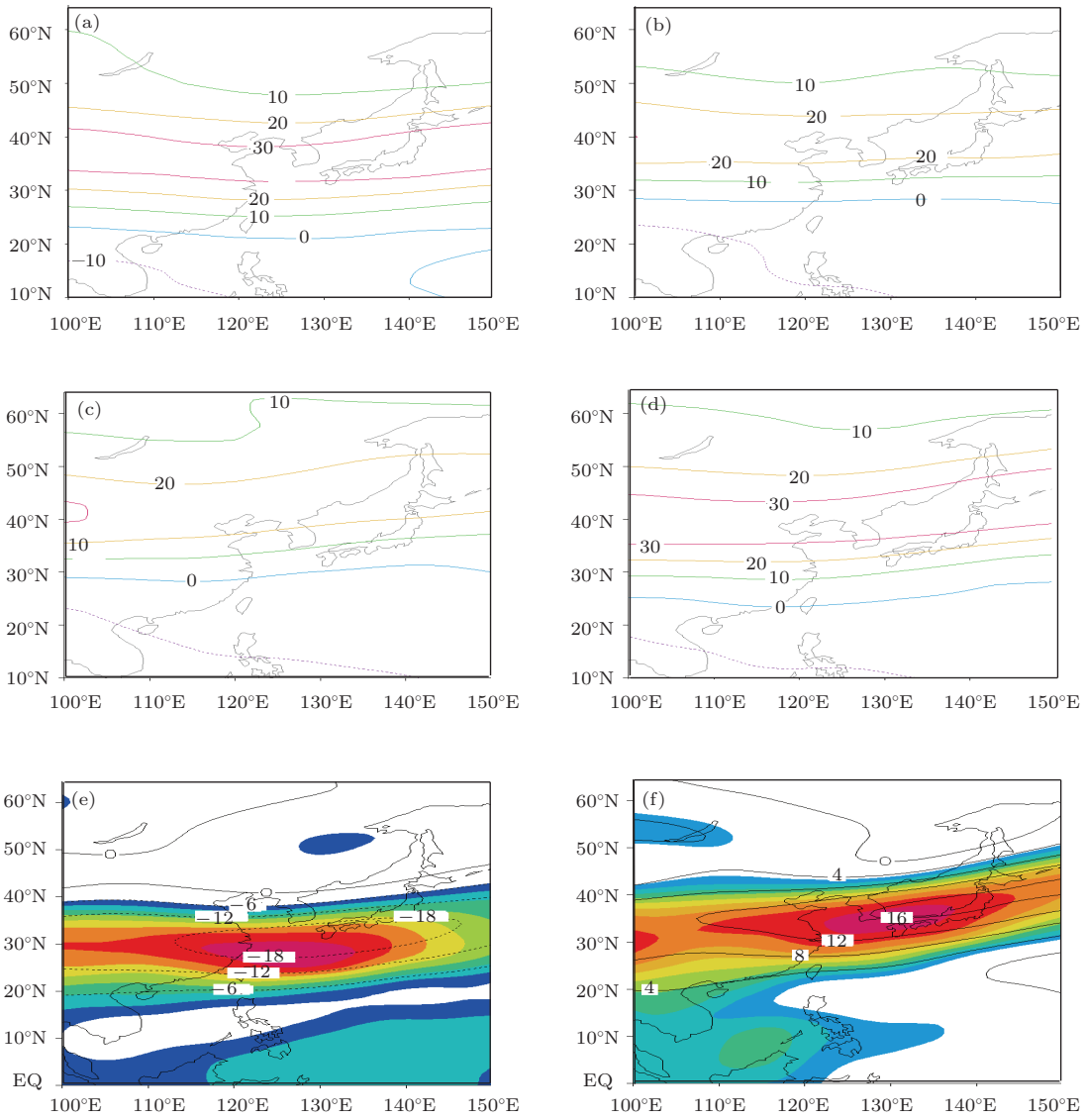


图 6 (网刊彩色) (a) 6 月 1 日—6 月 25 日, (b) 6 月 26 日—7 月 31 日, (c) 8 月 1 日—8 月 31 日, (d) 9 月 1—9 月 30 日的 200 hPa 多年气候平均纬向风场及 (b)−(a) 的差值检验 (e), (d)−(c) 的差值检验 (f) (单位为 m/s)

## 7 结 论

通过对东北区域5—10月降水量的分布和演变特征和逐日5天滑动平均雨量变化的分析, 对东北盛夏雨季前、中、后期各层环流场的对比研究, 以及多种标准的对比试验, 得到以下结论.

1) 综合考虑东北地区降水的逐月分布和演变特征, 并结合对历年东北区域逐日5天滑动平均雨量的综合分析, 研发了东北区域历年盛夏雨季开始和结束日期的客观识别方法. 东北区域历年盛夏雨季开始日期的客观识别: 当6月1日 $< i <$ 10月31日时, 若 $r_{yi} > 2R$, 且至少50% 站点的 $r_s > 2\bar{r}$, 且 $r_{yi+n} > 2R$ ($n$ = 1—4), 则 ks1 = min($i$). 结束日期的客观识别: 当7月1日 $< i <$ 10月31日时, 若 $r_{yi} < 2R$, 且至少50% 站点的 $r_s < 2\bar{r}$, 且 $r_{yi+n} < 2R$ ($n$ = 1—7), 则 js1 = min($i$). 同时, 基于对1981—2010年东北区域逐日降水气候态的分析, 确定了东北区域多年平均盛夏雨季的开始日期为6月26日, 结束日期为8月30日.

2) 500 hPa位势高度场上, 副高的两次北进恰好对应在东北盛夏雨季期间, 而雨季之前副高脊线偏南, 雨季之后副高开始南撤; 850 hPa风场上, 东北盛夏雨季期间, 影响东北地区的偏南风分量要显著强于非雨季期间; 200 hPa纬向风场上, 东北盛夏雨季期间的副热带西风急流轴显著弱于非雨季. 这进一步证明了对东北区域多年平均盛夏雨季起止日期定义的合理性.

基于本文的客观识别方法得到的东北区域多年平均盛夏雨季的开始和结束日期与王遵娅和丁

一汇[28]在采用侯雨量研究全国雨季的气候学特征时, 对于东北地区得出的结论: "东北雨季开始于第38候(7月上旬), 结束于第46候(8月中下旬)" 大体一致. 区别在于采用日滑动平均雨量, 根据本文的方法得到的东北盛夏雨季开始日期略早于上述结论, 说明采用1981—2010年作为气候平均态较1971—2000年作为气候平均态, 东北盛夏雨季开始日期有所提前. 同时该方法是基于一系列确定参数阈值基础上的客观识别, 因此对于科研和气候预报业务均有一定的参考价值.

## 参考文献


[1] Zhu K Z 1934 *Acta Geogr. Sin.* **1** 1 (in Chinese) [竺可祯 1934 地理学报 **1** 1]

[2] Tu C W, Huang S S 1944 *Acta Meteorol. Sin.* **18** 1 (in Chinese) [涂长望, 黄士松 1944 气象学报 **18** 1]

[3] Zheng B, Liang J Y, Lin A L, Li C H, Gu D J 2006 *Chin. J. Atmosph. Sci.* **30** 1207 (in Chinese) [郑彬, 梁建茵, 林爱兰, 李春晖, 谷德军 2006 大气科学 **30** 1207]

[4] Ding Y H, Liu J J, Sun Y, Liu Y J, He J H, Song Y F 2007 *Chin. J. Atmosph. Sci.* **31** 1082 (in Chinese) [丁一汇, 柳俊杰, 孙颖, 柳艳菊, 何金海, 宋亚芳 2007 大气科学 **31** 1082]

[5] Qiang X M, Yang X Q 2008 *Chin. J. Geophys.* **51** 1333 (in Chinese) [强学民, 杨修群 2008 地球物理学报 **51** 1333]

[6] Liang P, Ding Y H, He J H, Chen B M, Lei X T 2010 *Chin. J. Atmosph. Sci.* **34** 418 (in Chinese) [梁萍, 丁一汇, 何金海, 陈伯民, 雷小途 2010 大气科学 **34** 418]

[7] Zhao H G 1994 *Meteorologica* **20** 3 (in Chinese) [赵汉光 1994 气象 **20** 3]

[8] Lin Z G 1985 *Chinese Climate* (Shanghai: Shanghai Scientific and Technical Publishers) p76 (in Chinese) [林之光 1985 中国气候 (上海: 上海科学技术出版社) 第76页]

[9] Zhang J C 1991 *Climate of China* (Beijing: Meteorologica Press) p140 (in Chinese) [张家诚 1991 (北京: 气象出版社) 第140页]

[10] Qiang X M, Yang X Q, Sun C Y 2008 *Meteorologica* **34** 10 (in Chinese) [强学民, 杨修群, 孙成艺 2008 气象 **34** 10]

[11] Yan H M, Li Q Q, Sun C H, Yuan Y, Li D 2013 *Chin. J. Atmosph. Sci.* **37** 1111 (in Chinese) [晏红明, 李清泉, 孙丞虎, 袁媛, 李多 2013 大气科学 **37** 1111]

[12] Wang X Z, Sun Z B, Tan Y K, Hu B H 2006 *Trans. Atmos. Sci.* **29** 203 (in Chinese) [王学忠, 孙照渤, 谭言科, 胡邦辉 2006 大气科学学报 **29** 203]

[13] Sun X, Chen C L, Lu J 2007 *J. Meteor. Environ.* **23** 62 (in Chinese) [孙欣, 陈传雷, 卢娟 2007 气象与环境学报 **23** 62]

[14] Shen B Z, Lin Z D, Lu R Y, Lian Y 2011 *Sci. China: Earth Sci.* **41** 402 (in Chinese) [沈柏竹, 林中达, 陆日宇, 廉毅 2011 中国科学: 地球科学 **41** 402]

[15] Feng G L, Cao H X, Gao X Q, Dong W J, Chou J F 2001 *Adv. Atmos. Sci.* **18** 701

[16] Ye T S, Zhi R, Zhao J H, Gong Z Q 2014 *Chin. Phys. B* **23** 069203

[17] Shen B Z, Zhang S X, Yang H W, Wang K, Feng G L 2012 *Acta Phys. Sin.* **61** 109202 (in Chinese) [沈柏竹, 张世轩, 杨涵洧, 王阔, 封国林 2012 物理学报 **61** 109202]

[18] Yao S X, Huang Q, Zhang Y C, Kuang X Y 2012 *J. Trop. Meteor.* **18** 503

[19] Gong Z Q, Zhao J H, Feng G L 2013 *Acta Phys. Sin.* **62** 099205 (in Chinese) [龚志强, 赵俊虎, 封国林 2013 物理学报 **62** 099205]

[20] Shi N, Zhu Q G, Wu B G 1996 *Chin. J. Atmosph. Sci.* **20** 575 (in Chinese) [施能, 朱乾根, 吴彬贵 1996 大气科学 **20** 575]

[21] Lian Y, Shen B Z, Gao C T, An G, Tang X L 2003 *Acta Meteorol. Sin.* **61** 548 (in Chinese) [廉毅, 沈柏竹, 高枞亭, 安刚, 唐晓玲 2003 气象学报 **61** 548]

[22] He S H, Feng T C, Gong Y C, Hung Y H, Wu C H, Gong Z Q 2014 *Chin. Phys. B* **23** 059202

[23] He W P, Deng B S, Wu Q, Zhang W, Cheng H Y 2010 *Acta Phys. Sin.* **59** 8264 (in Chinese) [何文平, 邓北胜, 吴琼, 张文, 成海英 2010 物理学报 **59** 8264]

[24] Wang X J, Zhi R, He W P, Gong Z Q 2012 *Chin. Phys. B* **21** 029201

[25] Wang Z Y, Ding Y H, Zhang Q, Song Y F 2012 *Acta Meteorol. Sin.* **26** 399

[26] Zheng Z H, Ren H L, Huang J P 2009 *Acta Phys. Sin.* **58** 7359 (in Chinese) [郑志海, 任宏利, 黄建平 2009 物理学报 **58** 7359]

[27] Zhu Q G, Lin J R, Shou S W, Tang D S 2007 *Principle and Methodology of Synoptic Meteorology* (Beijing: Meteorologica Press) p193 (in Chinese) [朱乾根, 林锦瑞, 寿绍文, 唐东昇 2007 天气学原理与方法 (北京: 气象出版社) 第193页]

[28] Wang Z Y, Ding Y H 2008 *Chin. J. Atmosph. Sci.* **32** 1 (in Chinese) [王遵娅, 丁一汇 2008 大气科学 **32** 1]

# Objective identification study of midsummer rainy season in the northeast China*

Fang Yi-He[1)] Gong Zhi-Qiang[2)†] Zhao Lian-Wei[1)] Zhao Chun-Yu[1)] Li Qing-Quan[2)]

1) (*Regional Climate Center of Shenyang, Shenyang 110166, China*)

2) (*Laboratory for Climate Studies and Climate Monitoring and Diagnose, National Climate Center, China Meteorological Administration, Beijing 100081, China*)

( Received 6 April 2014; revised manuscript received 6 June 2014 )

**Abstract**

Owing to the fact that the objective identification methods of rainy season are not totally identical in the three provinces of Northeast China, no unified monitoring criterion of rainy season is available in this area. In order to implement the regional key climate monitoring and to meet the needs of the national weather service, from the angle of the whole region, based on the daily precipitation data of 102 observational stations, by comprehensively analyzing the daily precipitation series disposed by 5-point moving average, the objective identification method of midsummer rainy season in the northeast China is presented in this paper. Then based on the daily reanalysis data of wind field and geopotential height field provided by NCEP/NCAR, the atmospheric circulation fields of different levels before, during and after the midsummer rainy season are contrastively analyzed, and the rationality of the objective identification method is validated. Finally, the partition criterion of the beginning and ending dates are determined. Results show that: the average beginning and ending dates of midsummer rainy season in the northeast China respectively are June 26th and August 30th. The partition criterion of midsummer rainy season in the northeast China by using the objective identification method is reasonable.

**Keywords:** northeast China, midsummer rainy season, beginning and ending dates, objective identification

**PACS:** 92.60.Wc **DOI:** 10.7498/aps.63.209202

* Project supported by the National Natural Science Foundation of China (Grant Nos. 41205040, 41375078), the National Basic Research Program of China (Grant No. 2012CB955203), and the Special Scientific Research Project for Public Interest, China (Grant No. GYHY201006021).

† Corresponding author. E-mail: gongzq@cma.gov.cn

SCIENCE CHINA
Earth Sciences

• RESEARCH PAPER •

March 2015 Vol.58 No.3: 404–419
doi: 10.1007/s11430-014-4967-4

# Dynamic-statistics combined forecast scheme based on the abrupt decadal change component of summer precipitation in East Asia

GONG ZhiQiang[1], ZHAO JunHu[2], FENG GuoLin[1*] & CHOU JiFan[2]

[1] *Laboratory for Climate Studies, National Climate Research Center CMA, Beijing 100081, China;*
[2] *College of Atmospheric Science, Lanzhou University, Lanzhou 730000, China*

Received February 17, 2014; accepted July 6, 2014; published online October 29, 2014

Based on the 1983~2011 CMAP data, the precipitation anomaly in East Asia and its nearby sea regions (hereafter called East Asia for short) demonstrates the "+–+" pattern before 1999 and the "–+–" pattern afterwards; this decadal change is contained principally in the corresponding EOF3 component. However, the NCC_CGCM forecast results are quite different, which reveal the "+–+–" pattern before 1999 and the "–+–+" pattern afterwards. Meanwhile, the probability of improving NCC_CGCM's forecast accuracy based on these key SST areas is discussed, and the dynamic-statistics combined forecast scheme is constructed for increasing the information of decadal change contained in the summer precipitation in East Asia. The independent sample forecast results indicate that this forecasting scheme can effectively modify the NCC_CGCM's decadal change information contained in the summer precipitation in East Asia (especially in the area of 30°N–55°N). The ACC is 0.25 and ACR is 61% for the forecasting result based on the V SST area, and the mean ACC is 0.03 and ACR is 51% for the seven key areas, which are better than NCC_CGCM's system error correction results (ACC is –0.01 and ACR is 49%). Besides, the modified forecast results also provide the information that the precipitation anomaly in East Asia mainly shows the "+–+" pattern before 1999 and the "–+–" pattern afterwards.

**abrupt decadal change, dynamic-statistics combined forecast scheme, summer precipitation, East Asia, sea surface temperature**

**Citation:** Gong Z Q, Zhao J H, Feng G L, et al. 2015. Dynamic-statistics combined forecast scheme based on the abrupt decadal change component of summer precipitation in East Asia. Science China: Earth Sciences, 58: 404–419, doi: 10.1007/s11430-014-4967-4

The monsoon system of East Asia is characterized by typical decadal variations. For example, in the early 1980s, the monsoon of East Asia experienced a distinct decadal variation (Huang et al., 2011; Ding, 2007). Meanwhile, Kwon et al. (2007) pointed out that the summer monsoon of East Asia experienced another distinct variation at the end of 1990s, which was characterized by the obvious increase of the summer precipitation in South China. Si and Ding (2013) identified the decadal variation as a significant northward movement of Meiyu rain belt of East Asian summer monsoon precipitation; Huang et al. (2011) also showed that the decadal variation caused a precipitation mode of abnormally less precipitation in the northern part of Eastern China and more precipitation in the Yangtze River and Jianghuai region.

Meanwhile, as indicated in many researches (Graham, 1994; Zhou and Huang, 2003; Fu et al., 2009; Huang et al., 2011; Gong et al., 2013; Wang, 2012), the anomaly of global sea surface temperature (SST) exerts a significant influence on the monsoon system in East Asia and the decadal variation of summer precipitation anomaly. For example, Gong and Ho (2002) showed that the decadal warming of the SST in the eastern equatorial Pacific at the end of 1970s resulted in the expansion of the western Pacific subtropical high pressure area and the enhancement of its intensity, and

*Corresponding author (email: fenggl@cma.gov.cn)

© Science China Press and Springer-Verlag Berlin Heidelberg 2014

the direct result of its southward withdrawal was the increase of the decadal scale of the summer precipitation of Yangtze River basin in East Asia. Zhou and Huang (2003) suggested that the jump of the decadal variation was closely related to the existence of an obvious decadal "ENSO" phenomenon in the tropical Pacific and that the Pacific Decadal Oscillation (PDO) is an important factor which contributes to the atmospheric circulation of East Asia and the decadal variation of Chinese climate. Zhang et al. (2007) also emphasized the phenomenon that the summer monsoon circulation of East Asia and the decadal variation of summer precipitation pattern in the eastern East Asia share the same turning point with the phase variation of PDO and that the SST of north Pacific may be an important external forcing factor of the East Asian summer monsoon circulation and the decadal variation of summer precipitation in Eastern China. Besides, the meteorologists have also conducted a large number of numerical experiments on the influence of SST anomaly on the East Asian monsoon system and summer precipitation. For example, Xu and Zhu (1999) studied the influence of ENSO events on the precipitation of Eastern China under various decadal backgrounds by means of numerical experiments. Li et al. (2010) conducted numerical experiments, using CAM3 and GFDL AM2.1 models respectively, to investigate the influence of tropical and global SST on summer monsoon of East Asia and summer precipitation of China, and verified that the increase of tropical SST, especially the decadal warming of tropical middle-eastern Pacific, was mainly responsible for the weakening of the East Asian summer monsoon at the end of 1970s. Obviously, we can have a deep understanding of the formation mechanisms of the monsoon system of East Asia and the decadal variation of its precipitation through the researches on the decadal scale variation characteristics of the East Asian monsoon system and its relation with the external forcing such as SST.

However, the main quandaries we have to overcome at present are that the dynamical model is relatively inefficient in forecasting the summer precipitation of East Asia (Li et al., 2005) and particularly that the forecasting ability of the short-term climate forecast model for the decadal variation is quite limited. Therefore, it is an important subject of current climate variation research to explore the possible ways to improve the information of decadal variation in the seasonal forecasts by using the existing research results of diagnostic analyses and numerical simulations based on the dynamical model.

In respect of improving the accuracy of climate forecast, more and more attention is paid to the method which combines dynamics and statistics. This method makes it possible to utilize the merits both in the statistical method and dynamical method, which may lead to a new development in climate forecast research (Chou, 2003). Chou (1986) theoretically discussed the practicability of the combination of statistics and dynamics in the short-term forecast. Pivoting on the development of the dynamic-statistic combined forecast scheme, various forecasting methods have been proposed successively, for example, multi-moment forecasting method using the past evolution information (Chou, 1974), similar dynamical method (Qiu and Chou, 1989; Huang et al., 1993), and the method based on the principle of automatic memory of atmosphere (Cao, 1993; Feng et al., 2001). In recent years, centering on the principles of the methods which combine dynamics and statistics, the young researchers in China have developed a series of forecasting programs and strategies for application (Ren and Chou, 2007; Zheng et al., 2009; Zhao et al., 2011), and extended these methods to the Yangtze River Basin (Wang et al., 2011; Gong et al., 2012), Northeast China (Xiong et al., 2011), North China (Yang et al., 2012), and other regions. Meanwhile, the researches on the precipitation forecast of different seasons such as autumn, spring, and winter (Wang, 2001; Liu and Fan, 2012a, 2012b; Lang and Wang, 2010) as well as the spring dust dynamic-statistics forecast (Lang, 2008) have also been carried out successively. Besides, the forecast method of annual increment takes the interaction of annual and decadal signals into consideration, which is implemented based on the observation information of the previous year, being objective and accurate for both the dynamical model and the observation. This method has been effectively applied to the forecast of the summer precipitation of the middle and lower reaches of the Yangtze River and North China (Fan and Wang, 2009a) as well as the improvement for East Asian summer monsoon forecast of European coupling model (Fan et al., 2009b, 2012).

However, due to the limitation in the length of data, especially model historical forecast (and hindcast) period, currently most of the dynamic-statistics combined forecasts focused on seasonal scale. How to improve the decadal climate variation information in the seasonal forecasts in a combined way of dynamic-statistics is a new scientific issue which deserves further research. Therefore, we attempted to analyze the decadal scale characteristics of summer precipitation in East Asia and its offshore areas (hereafter called East Asia for short), and determine the key sea areas in the global SST field which have a significant correlation with decadal scale component of summer precipitation in East Asia. Based on the analysis above, we identified the forecasting errors of the NCC_CGCM for the decadal variation of summer precipitation in East Asia, and explored the possible reasons. Finally, we designed the dynamic-statistics combined forecast scheme and discussed how to improve the decadal variation information in the East Asian summer precipitation forecasts of NCC_CGCM.

## 1 Data and methods

### 1.1 Data

The National Climate Center (NCC) has established the

short-term climate forecast model, which contains seasonal scale (NCC_CGCM), namely NCC/IAP T63 coupled ocean-atmosphere mode. The horizontal resolution is 1.875°× 1.875°, and the vertical direction is 30 layers. The seasonal forecast is carried out monthly, and the monthly seasonal forecast is the ensemble mean of 48 members. Among them, the initial value of the atmospheric model uses the atmospheric assimilation data of 00Z of the last eight days of the previous month. The ocean initial field is the marine assimilation field obtained through the disturbance of the marine data assimilation system, and the combination of oceanic and atmospheric initial fields constitutes the initial value collection of seasonal forecasts. Note that only ensemble mean results for June–August from the integrations beginning at the end of February (and the forecast is completed in March) in each year are selected (Ding et al., 2002; Li et al., 2005). In this paper, the hindcast and forecast data of a total of 29 years from 1983 to 2011 were generated by NCC_CGCM (the forecast results of summer are directly used after 2005). The average results were interpolated to the space of 2.5°×2.5°. The total precipitation from June to August of the analytical data of CMAP (CPC Merged Analysis of Precipitation) is used as the observation data. The East Asian summer precipitation forecast error field is the difference value field of the two. The SST data of NOAA ERSST (Smith and Reynolds, 2003) from 1961 to 2011 were also used in this paper.

### 1.2 The dynamic-statistics combined forecast scheme of East Asian summer precipitation based on abrupt decadal change component

Generally, the numerical forecast was put forward as the initial value problem of partial differential equations, and the model satisfied by the actual atmosphere can be represented as (Chou, 1986):

$$\frac{\partial \psi}{\partial t} + L(\psi) = E(\psi), \tag{1}$$

where, $\psi$ is model forecast variable, $L$ is the differential operator of $\psi$, and $E$ is the error operator of the model, reflecting the unknown total error term in the model, namely model error. From the dynamical point of view, the historical data mastered by us were a series of special solutions of model forecast variable $\psi$.

The numerical model is a kind of approximation of actual behavior of atmosphere, and the existing models are still far apart from sufficient exactness. People have been trying to make the model have more reliable physical bases and more accurate numerical methods for many years, so as to reduce the model error $E(\psi)$. At the same time, a large number of observation data mastered by us are actually a series of special solutions which satisfy the atmospheric motion equations. Therefore, from the perspective of the inverse problem, the information provided by these observation data can also be used to make up for the defects of the model so as to achieve the purpose of reducing model error. In other words, given the use of the erroneous information of the historical model $\psi'$ which is similar to $\psi$, the forecast field is taken as a small disturbance, which is superimposed on the historical similarity, and the statistically similar methods are taken to estimate the forecast error of the current model.

At the same time, the actual atmosphere contains the interactions of multiple scales such as seasonal and decadal and so on, which may lead to the forecast errors of different scales. Therefore, the model forecast error in eq. (1) can be understood as the superposition of multiple scale errors, as shown in eq. (2),

$$E(\psi) \to f(E_{\text{season}}(\psi),\ E_{\text{decadal}}(\psi),\ E_{\text{other}}(\psi)), \tag{2}$$

where, $f()$ is the superposition function of various scale model error, $E_{\text{season}}(\psi)$ is the forecast error of seasonal scale, $E_{\text{decadal}}(\psi)$ is the forecast error of decadal scale, and $E_{\text{other}}(\psi)$ is the error of other time scales.

In order to verify the contribution of the decadal component in NCC_CGCM and historical actual situations, the wavelet filter method (Rasmusson et al., 1994) is used first to conduct the filter with a scale of 8–10 years for the model historical forecasts (and hindcast) and historical East Asian precipitation of the years from 1983 to 2012, respectively. Then the decadal components with a scale of more than 8–10 years were obtained. Second, the correlation coefficients between the obtained components and the original sequence were calculated, and the spatial distribution map of the correlation coefficients is shown in Figure 1. It can be seen that, whether the actual situation or the model, most correlation coefficients of grid points are above 0.4, and they pass 95% of significance tests, indicating that the role of decadal scale component is very important. Finally, the variances of decadal component and original sequence are calculated, and the spatial distribution of the variance ratio of these two is also shown in Figure 2. It can be seen that, in the actual situations, the corresponding variance ratios of decadal components are basically above 0.1, with ratios above 0.3 in locations, whereas in the model results the variance ratios of decadal scale components basically reach above 0.5. Therefore, it is necessary to consider the corresponding model forecast errors of decadal factors so as to improve the decadal change information contained in the seasonal model forecast results.

The physical basis of climate forecast based on the dynamic-statistic lies in the similar behavior of the dynamic forecast result and forecast error under the condition that the similarity of initial state continues. It contains two aspects, namely, similarity and dynamic model, but the latter should dominate (Chou, 1986; Ren and Chou, 2005). In other words, the similarity of the initial states can last to a later period. In the later period, due to the similarity between the two states, the corresponding dynamic forecast result and

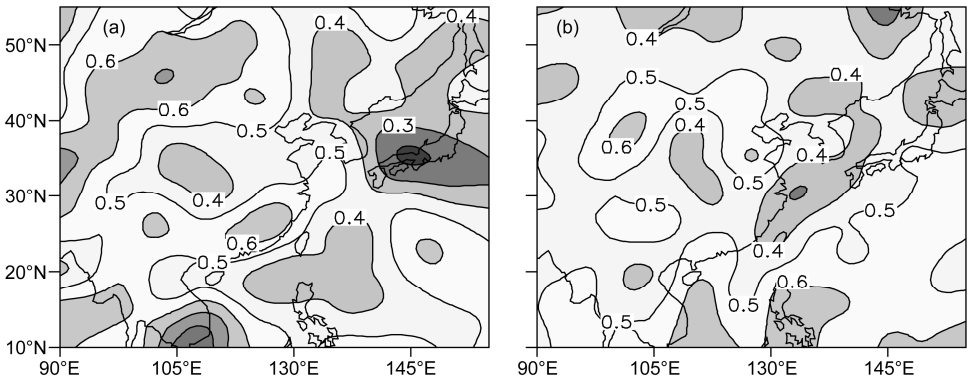


**Figure 1** The Temporal Correlation Coefficients (TCC) distribution maps between low-frequency filter components of East Asian precipitation (a), model forecast (and hindcast) results (b) and the original field for 1983–2011, respectively.

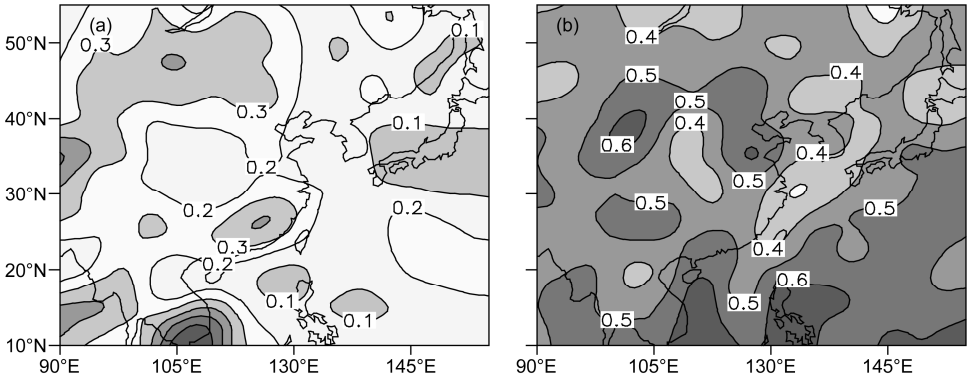


**Figure 2** The variance contribution distribution maps between the low-frequency filter components of East Asian precipitation (a), model forecast (and hindcast) results (b) and the original field for 1983–2011, respectively.

error behavior of the same period will also have similarity, and this belongs to the same period similarity relationship of deterministic system.

The existence of various abnormal patterns in the SST field (i.e., PDO; Atlantic Multi-decadal Occasion, AMO etc.) will inevitably make SST anomalies of some key areas have a significant influence on East Asian monsoon system and its summer precipitation (Graham, 1994; Huang et al., 2011; Zhou and Huang, 2003; Zhang et al., 2007; Fu et al., 2009; Gong et al., 2013). One of the important premises on which NCC_CGCM can be used to correctly forecast the summer precipitation in East Asia must be that the model atmosphere can better respond to the external forcing of some key area SSTs (Liu and Wen, 2008; Wang et al., 2008). In other words, the similarity of key area SST in the early period may last to a late period, and the corresponding forecast error in the same late period has certain similarity. Therefore, if the model has errors in the key area SST forecast, it is possible to improve the forecast error of the model through finding the similar information in historical forecast (and hindcast) based on single or multiple key area SSTs.

On the strength of the above theories, provided here is the East Asian summer precipitation dynamic-statistics combined forecast scheme. Figure 3 shows the flowchart of the corresponding forecast scheme, and the main technical processes are as follows:

(1) Obtaining the forecast error set of the model for East Asian summer precipitation based on CMAP precipitation fields and model forecast field of NCC_CGCM of past years; Conducting EOF decomposition to the East Asian summer precipitation and determining the EOF components which contain the significant characteristics of decadal variations of East Asian summer precipitation and their corresponding time coefficients.

(2) Calculating correlation coefficients between the time coefficients of EOF components and global SST field, and determining the significant correlated key sea areas; Analyzing the correlation between the key area SSTs and the East Asian summer precipitation forecast error set. The better the correlation is, the more likely the area is to be used for the selection of the historically similar error information.

(3) Based on the SST average value curves of the key sea areas, which have good correlations with East Asian summer precipitation forecast error, the historical years which are most similar to the SST status of current actual situation are selected, and the forecast errors of the models of these similar years for East Asian summer precipitation are also extracted.

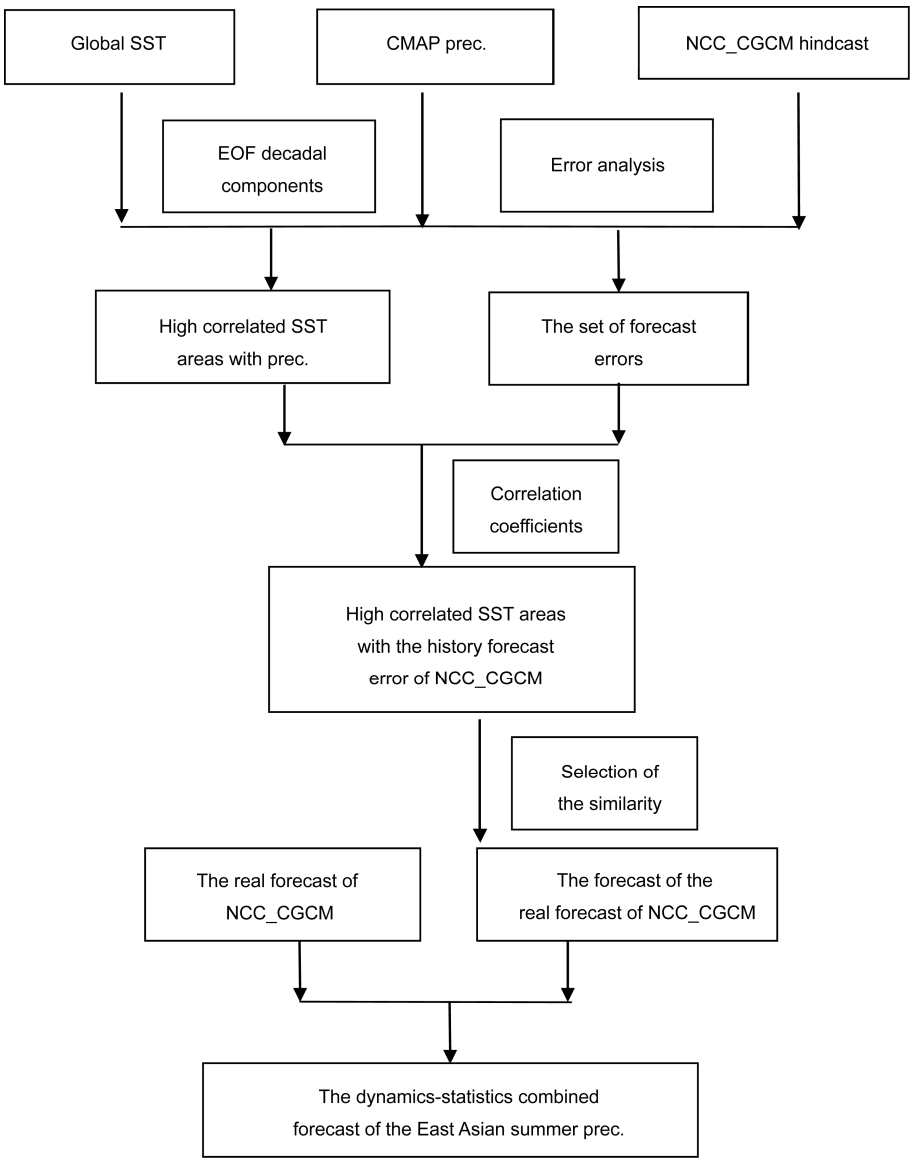


**Figure 3** Flowchart of the dynamic-statistics combined forecast scheme of East Asian summer precipitation bases on decadal scale components.

(4) Compounding the extracted historically similar errors composite with the East Asian summer precipitation forecast result provided by the NCC_CGCM of March of current year, then we can obtain the corrected forecast results.

The error set in this scheme is obtained directly through the result of the forecast (and hindcast) of NCC_CGCM of past years minus the precipitation data of CMAP. Although such processing cannot separate the errors of seasonal scale from those of the other time scales because the key areas of SST selected may have a significant correlation with the decadal EOF components, we will get the years that have the similar decadal characteristics with the current year when we looked for the historically similar years based on the current SST index. In other words, the historical error information of these years will contain the similar decadal variation information. Based on this process, we may achieve the goal to increase the decadal variation information in the seasonal forecast correction results.

## 2 Decadal variation of East Asian summer precipitation

The spatial distribution of the principal components of EOF of the East Asian summer precipitation from 1983 to 2011 in Figure 4(a)–(c) shows: the first mode of the summer precipitation of the region (EOF1) is the land and sea difference mode, and its variance contribution is 16.7%; the second mode (EOF2) is the one that positive and negative appear alternately from north to south, and the variance contribution is 11.2%; the third mode (EOF3) from north to south is the mode of "+−+", and the variance contribution is

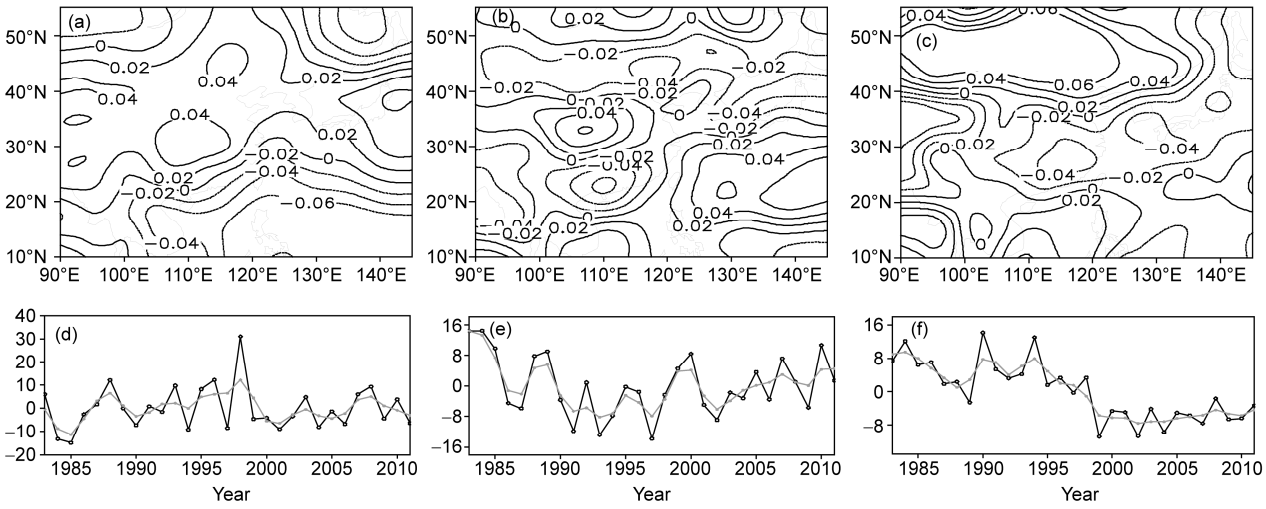


**Figure 4** Spatial distribution maps ((a)–(c)) and time coefficient ((e)–(f)) of principal components of EOF of summer precipitation in East Asia from 1983 to 2011. (a) EOF1, variance contribution 16.7%; (b) EOF2, variance contribution 11.2%; (c) EOF3, variance contribution 8.8%; (d), (e) and (f) is corresponding time coefficient of EOF1, EOF2 and EOF3, respectively, and the grey line is nine-point smooth curve.

8.8%. In the components of EOF2 and EOF3, on the mainland it shows "+–+" and north-south "+–" modes, which is consistent with the relevant conclusions of the researches such as the division of summer rain type of East China provided by Wei and Zhang (1988) and the main mode of summer precipitation of East China given by Huang et al. (2011). The variance contributions of the three modes have passed the Monte_Carlo test with 95% of significance level, namely, each mode is mutually independent.

Figure 4(d)–(f) show the time coefficient curves of EOF1, EOF2 and EOF3. It can be seen that EOF1 and EOF2 are shown more as inter-annual oscillations, whereas the decadal mean value variation characteristics of EOF3 are prominent. We used MTT method to detect the decadal phase adjustment for these three time coefficients (Figure 5(a)). Neither EOF1 nor EOF2 has a significant abrupt change, whereas the abrupt change exists in the time coefficient of EOF3 near 1998, which passes the 95% significance levels. Furthermore, the test results of BG algorithm (Gong et al., 2006) are similar to those of MTT method (Figures not shown). Figure 5(b) and (c) shows the wavelet coefficient figure and wavelet varition of the time coefficient of EOF3. Also it can be seen that the abrupt change that passes 95% of significance levels exists in the time coefficient of EOF3 around 1999.

Figure 6(a) shows the latitude-time cross sections of the anomaly percentage of the East Asian summer precipitation along 90°E–145°E. It can be seen that the characteristics of decadal variation of East Asian summer precipitation anomaly in 30°N–55°N around 1999 are significant. Before 1999, the north (40°N–55°N) was moist, while the south (25°N–40°N) was droughty; from 1999, the north (40°N–55°N) is droughty, while the south (25°N–40°N) is moist. Many researches have also confirmed this kind of characteristics of East Asian summer precipitation (Shi et al., 1996; Zhang et al., 2007; Gong et al., 2012). Figure 6(b) shows the latitude-time cross

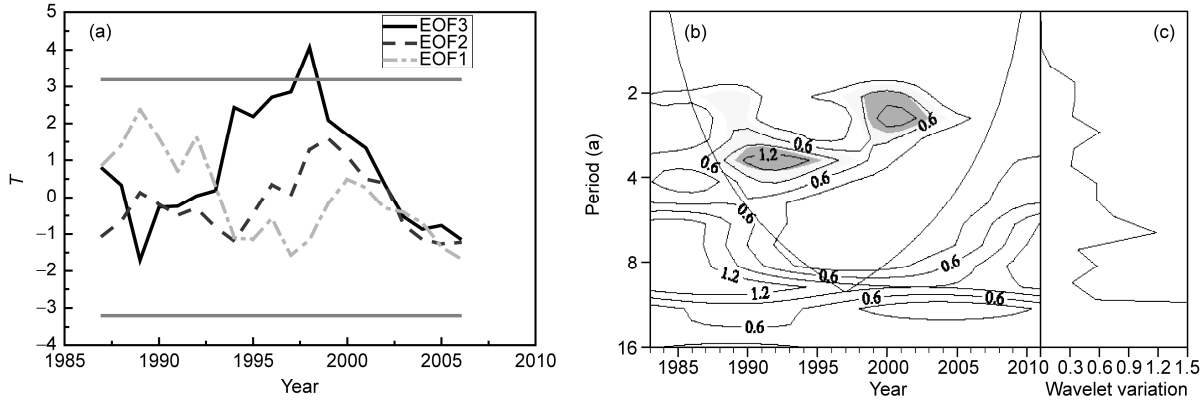


**Figure 5** MTT test of time coefficient of principal components of EOF of summer precipitation in East Asia from 1983 to 2011 (a), wavelet coefficient figure of time coefficient of EOF3 (b), and the correspondingwavelet variation (c). Two parallel straight lines in Figure 5(a) is the threshold value of 95% significance level, the maximal value in Figure 5(b) represents the existence of the corresponding quasi-periodic oscillation of abscissa table, and the shadow represents to pass the 95% of significance test.

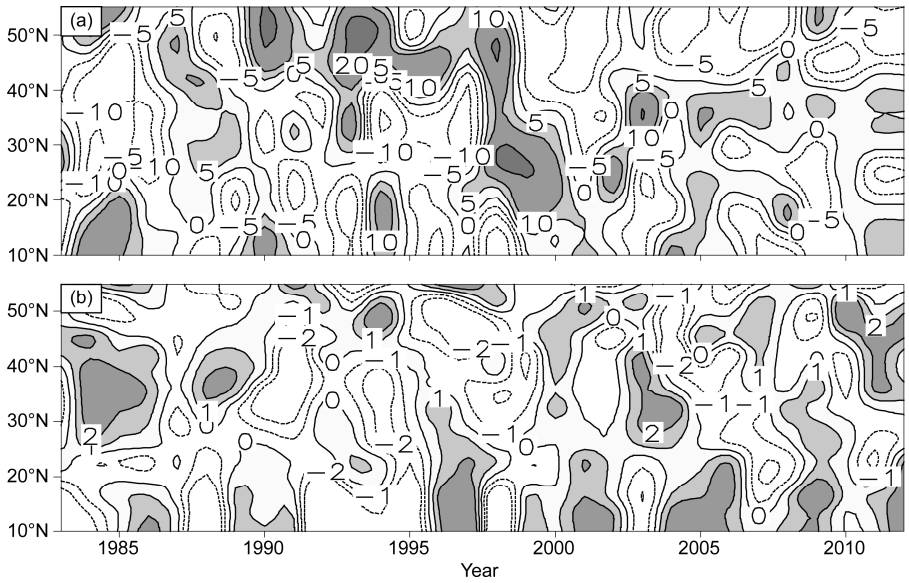


**Figure 6** Latitude-time cross sections of East Asian summer (Jun–Aug) precipitation anomaly percentage (%) along 90°E–145°E. Solid line and dotted line denotes positive and negative anomalies, respectively. Shadow denotes positive anomaly. (a) CMAP data; (b) NCC_CGCM forecast (and hindcast) results.

sections of the anomaly percentage of the East Asian summer precipitation along 90°E–145°E as contained in the forecast (and hindcast) results of NCC_CGCM. It is obvious that the adjustment of the north-south drought and flood situation in the scope of 30°N–55°N around 1999 did not exist. The anomaly correlation coefficient (ACC) of the cross sections of the anomaly percentage in the scope of 30°N–55°N between the CAMP and NCC_CGCM forecast (and hindcast) results is 0.01, and the anomaly symbol consistent rate (ACR) is 49%.

Figure 7 shows CMAP and NCC_CGCM forecast (and hindcast) results of the East Asian summer precipitation anomaly percentage composite maps of two periods of 1983–1998 and 1999–2011. It can be seen that, in CMAP situation, the precipitation anomaly percentage of the former period presents the characteristics of "+–+" from north

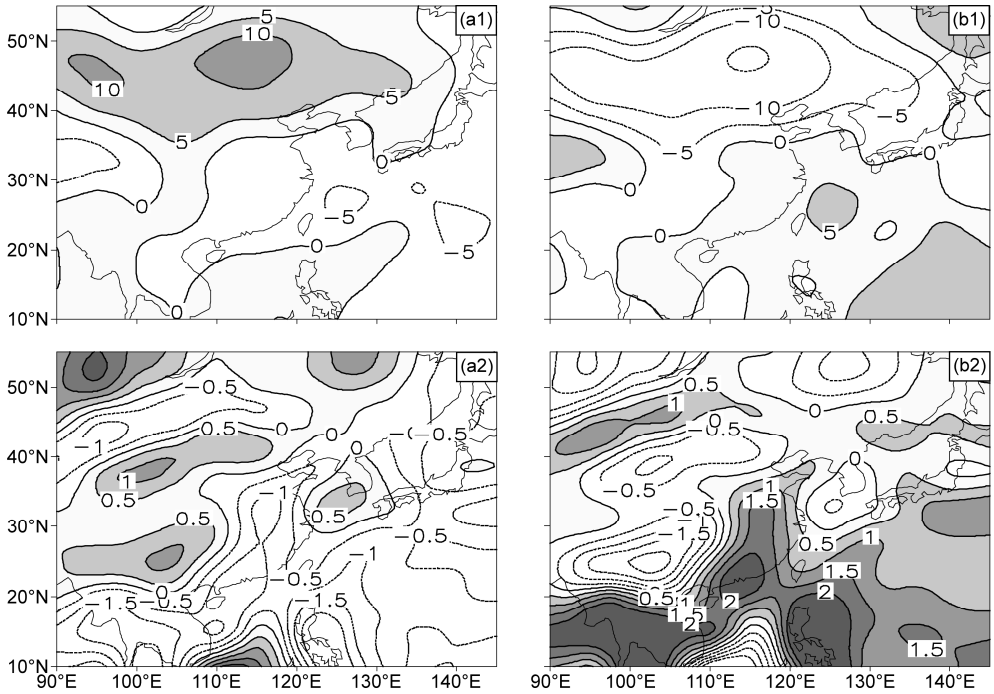


**Figure 7** Composite maps of anomaly percentage (%) of summer precipitation in East Asia. Solid line and dotted line denotes the positive and negative anomalies, respectively. Shadow denotes the positive anomaly. (a1) and (b1) are respectively corresponding to the composite maps of 1983–1998 and 1999–2011 of CMAP data; (a2) and (b2) are same as (a1) and (b1) but for NCC_CGCM forecast (and hindcast) results.

to south (Figure 7(a1)), whereas that of the latter period presents the contrary abnormal characteristics of "–+–" (Figure 7(b1)). In the forecast (and hindcast) results of NCC_CGCM, the precipitation anomaly percentage of the former period presents the characteristics of "+–+–" from north to south (Figure 7(a2)), whereas that of the latter period presents the contrary abnormal characteristics of "–+–+" (Figure 7(b2)). Therefore, it is necessary to improve the decadal variation information contained in the forecasts of NCC_CGCM for the summer precipitation in East Asia.

## 3 Analysis of increasing decadal variation information in East Asian summer precipitation forecast

The decadal adjustment of precipitation in East China is caused by the co-effect of external forcing and internal atmospheric process. To improve the decadal variation information in the forecasts of NCC_CGCM for East Asian summer precipitation, it is essential to analyze the possible causes for the model forecast error. As the decadal variation of the East Asian summer climate has a close relationship with tropical eastern Pacific and north Pacific SSTs (Huang et al., 2007; Zhang et al., 2007; Deng et al., 2009), first the key areas of SST (hereafter referred to as key areas) have to be identified that have significant correlations with the abrupt decadal change components, and the forecast ability of the model for these key area SSTs has to be analyzed. Then we can discuss the possibility of improving decadal variation information in the seasonal forecasts of NCC_CGCM for the East Asian summer precipitation.

In the above-mentioned analysis, the abrupt change characteristics of decadal scale exist in the time coefficients of EOF3, which denote the decadal phase adjustment of East Asian summer precipitation. We calculated the ACCs between the time coefficient of EOF3 and the global SST field in March (mainly considering that the forecast of East Asian summer precipitation is always done in late March) (Figure 8). EOF3 of East Asian summer precipitation is significantly and negatively correlated with SSTs in west wind drift area, western equatorial Pacific, regions of southwestern side of Australia, and southwestern tip of South America; it is significantly and positively correlated with the SSTs in northwest Indian Ocean as well as middle and eastern parts of western equatorial Pacific. Correlations in these areas have passed the confidence degree of 0.05. Therefore, the significantly correlated areas of global SST field can be divided into seven different key areas (Figure 8). The negative correlation areas include Area I (20°N–42°N; 150°E–170°W), Area II (4°S–18°N; 128°E–154°E), Area III (30°S–12°S; 128°E–170°W), Area IV (50°S–30°S; 70°E–110°E), and Area V (64°S–30°S; 94°W–80°W); the positive correlation areas include Area VI (12°S–10°N; 50°E–70°E) and Area VII (8°S–10°N; 168°E–170°W).

On the basis of SST data and SST forecast results of NCC_CGCM of the key areas, we respectively calculated the yearly SST anomaly mean in March from 1983 to 2011 as SST indices and forecast SST indices. As shown in Figure 9, most of the historical anomaly curves of SST indices contain the decadal adjustment characteristics around 1999. On this basis, we calculated ACCs and ACRs of these two types of indices (Table 1). The forecast skills of NCC_CGCM for the SST of Area I, IV, and V are higher, the ACCs pass the 95% significant levels, and the ACRs are also above 65%. However, the forecast skills of NCC_CGCM for the SST of Area II, III, VI, and VII are lower, none of the ACCs of the forecast results passes the 90% significant levels, and the ACRs mostly fluctuate around 50%.

The forecast effects of NCC_CGCM for SSTs of key areas are different, and thus in order to verify the relationship between precipitation forecast and SST forecast of model, it needs not only to consider the key areas with good forecast effects, but also to analyze those with poor forecast effects. According to Figure 9, we respectively selected five years with good forecast effect and five years with poor forecast effect for SSTs of key areas (Table 2). The methods for judging the years with good forecasts and the years with poor forecasts for SSTs of key areas are as follows: As for the former, the SST index anomaly symbol of the forecast results and the actual SST is consistent, and then the absolute

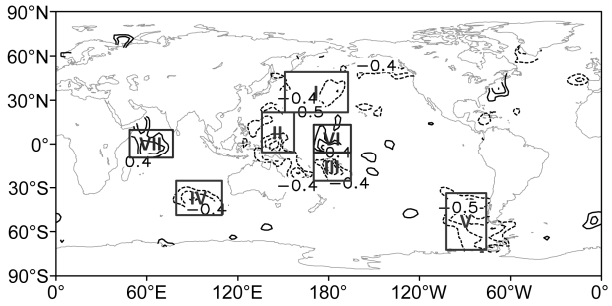


**Figure 8** The distribution of correlation coefficients between time coefficients of EOF3 of East Asia summer precipitation and SST in March during 1983–2011. Area I–V is negative correlated, Area VI–VII is positive correlated.

**Table 1** the ACCs and ACRs between SST indices and forecast SST indices of NCC_CGCM[a)]

| | Area I | Area II | Area III | Area IV | Area V | Area VI | Area VII |
|---|---|---|---|---|---|---|---|
| ACC | 0.46* | 0.12 | 0.04 | 0.34* | 0.69* | 0.17 | –0.05 |
| ACR (%) | 0.69 | 0.61 | 0.54 | 0.67 | 0.75 | 0.44 | 0.53 |

a) * represents the area with good forecast effect.

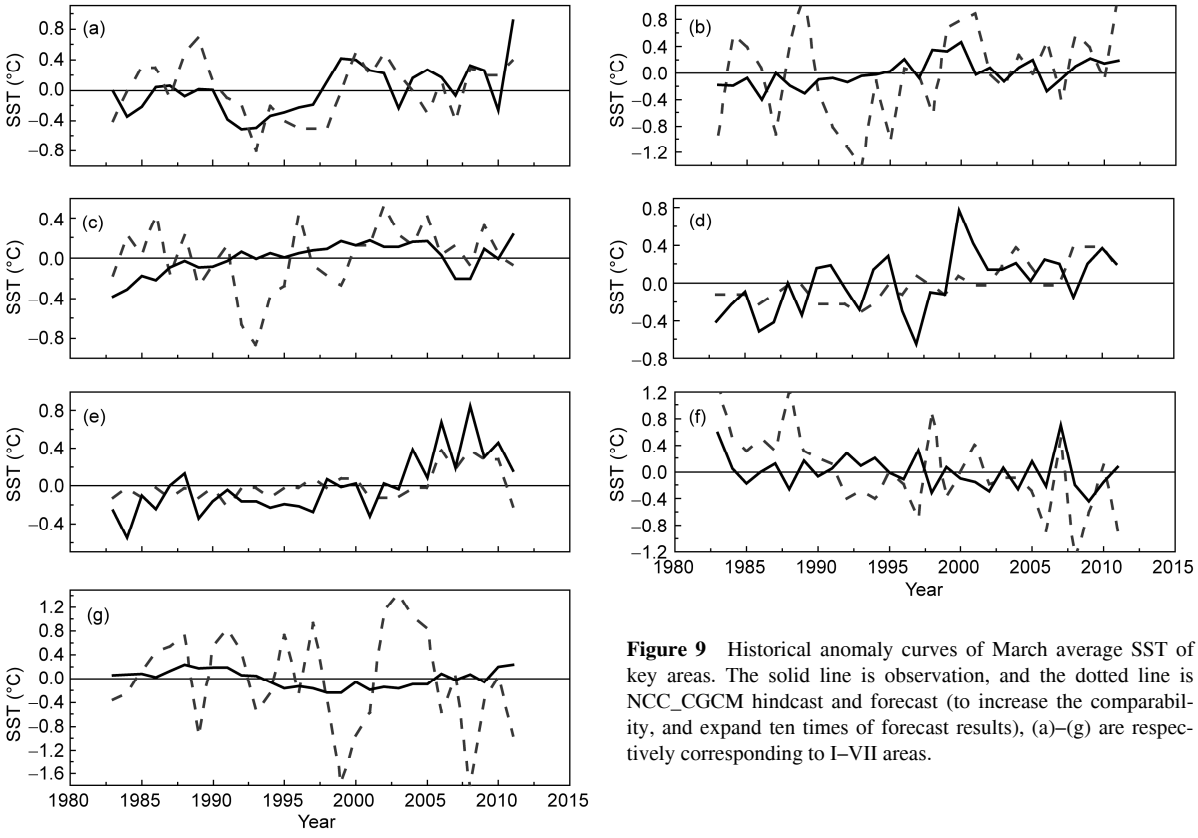


**Figure 9** Historical anomaly curves of March average SST of key areas. The solid line is observation, and the dotted line is NCC_CGCM hindcast and forecast (to increase the comparability, and expand ten times of forecast results), (a)–(g) are respectively corresponding to I–VII areas.

**Table 2** List of years with good and poor forecasts of NCC_CGCM for SSTs of key areas

| Key area | Five years with good forecasts | Five years with poor forecasts |
|---|---|---|
| Area I | 1992, 1993, 1997, 2000, 2011 | 1988, 1985, 2003, 2005, 2010 |
| Area II | 1983, 1992, 2000, 1999, 2011 | 1984, 1986, 1989, 1998, 2006 |
| Area III | 1983, 1987, 2003, 2004, 2005 | 1984, 1986, 1998, 1999, 2007 |
| Area IV | 1983, 1986, 1993, 2004, 2011 | 1990, 1991, 1994, 1997, 2008 |
| Area V | 1983, 1993, 2006, 2008, 2010 | 1984, 1988, 1997, 1999, 2011 |
| Area VI | 1983, 2006, 2007, 2008, 2009 | 1988, 1994, 1998, 2001, 2005 |
| Area VII | 1987, 1988, 1990, 1999, 2001 | 1984, 1989, 2002, 2003, 2008 |

value of anomaly exceeds 0.5 times of standard deviation of index sequence; as for the latter, the SST index anomaly symbol of the forecast results is opposite to the actual situation, and then the absolute value of anomaly exceeds 0.3 times of standard deviation (if taking 0.5 times of variance, some regions cannot reach the conditions, and thus we took 0.3 times). Figure 10 shows East Asian summer precipitation anomaly percentage composite maps which correspond to the years with good and poor forecast for SSTs of key areas. It can be seen that, in the years with good SSTs forecast effects, the positive and negative anomaly centers of the model forecasts of summer precipitation anomalies in East Asia (Figure 10(b1)–(b7)) are mostly consistent with the actual situations (Figure 10(a1)–(a7)), and especially the forecast effect for north-south rain-belt is particularly significant. On the contrary, in the years with poor forecast effects, the positive and negative anomaly centers of precipitation anomalies (Figure 10(d1)–(d7)) are relatively consistent with the actual situations (Figure 10(c1)–(c7)). For the years with the good and poor forecasts effects of NCC_CGCM for SSTs of key areas, Table 3 respectively provides the average value of ACCs and ACRs between the East Asian summer precipitation forecast and actual situation. It can be seen that, except for the individual regions, the ACCs or ACRs of the years with good SSTs forecasts are higher than the situations of the years with poor forecasts. In other words, the overall forecast effects for SSTs of key areas in March may directly determine the forecast errors of summer precipitation.

Through the analyses of Tables 2 and 3, the following two points might preliminarily be verified. First, certain differences exist in the forecasts of the NCC_CGCM for

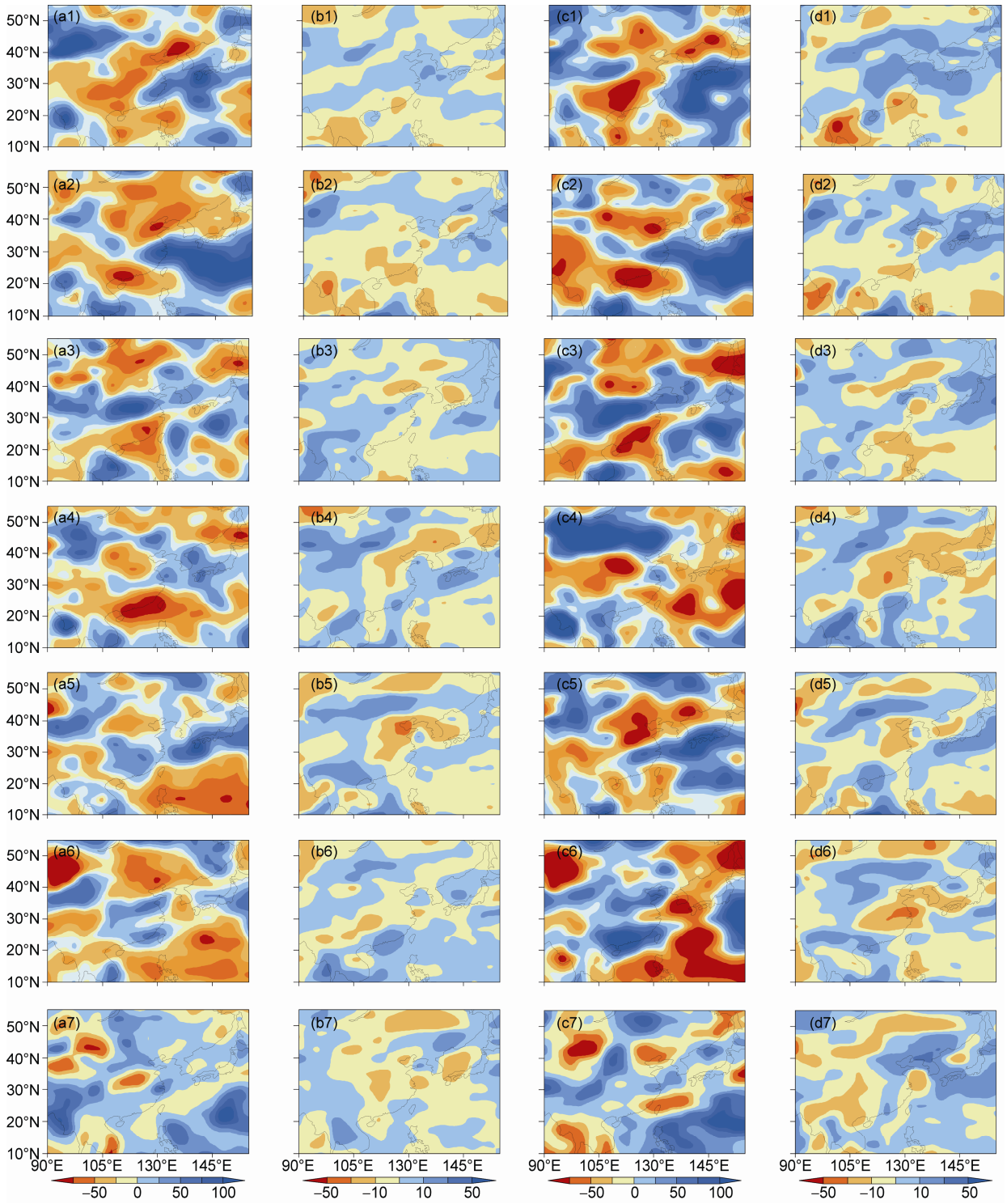


**Figure 10** East Asian (10°N–55°N, 90°E–145°E) summer precipitation anomaly percentage composite maps which correspond to years with good and poor SST forecasts of NCC_CGCM. (a1)–(a7) are respectively corresponding to the CMAP precipitation anomaly percentages of the five years with good SST forecasts (and hindcast) of seven key areas; (b1)–(b7) are respectively corresponding to the model forecast precipitation anomaly percentages of the five years with good SST forecasts (and hindcast) of seven key areas; (c1)–(c7) and (d1)–(d7) are same as (a1)–(a7) and (b1)–(b7) but for poor SST forecasts years.

SSTs of key areas, and these may cause different atmospheric response in the late period, thereby forming East Asian summer precipitation forecast error. Second, as for the situation in which SSTs of key areas forecasts are good, the forecast errors in the late period are relatively small, which means it is possible to carry out the dynamic-statistics combined correction.

Figure 11 shows the correlation distributions between

**Table 3** The average value of ACCs and ACRs of East Asian summer precipitation of five years with good and poor forecasts for SSTs of key areas of NCC_CGCM[a)]

| Circumstances | Method | Area I | Area II | Area III | Area IV | Area V | Area VI | Area VII |
|---|---|---|---|---|---|---|---|---|
| Five years with good forecast effect | ACCs | 0.01 | 0.24* | 0.13* | 0.21* | 0.16* | 0.12* | –0.10 |
| | ACRs (%) | 47 | 53 | 53 | 57 | 61 | 46 | 43 |
| Five years with poor forecast effect | ACCs | –0.10 | 0.26* | 0.08 | 0.21* | 0.11 | 0.15* | –0.15 |
| | ACRs (%) | 42 | 55 | 54 | 57 | 49 | 59 | 47 |

a) The critical correlation value of 95% of significance is 0.11; * represents the situation which exceeds 95% significance levels.

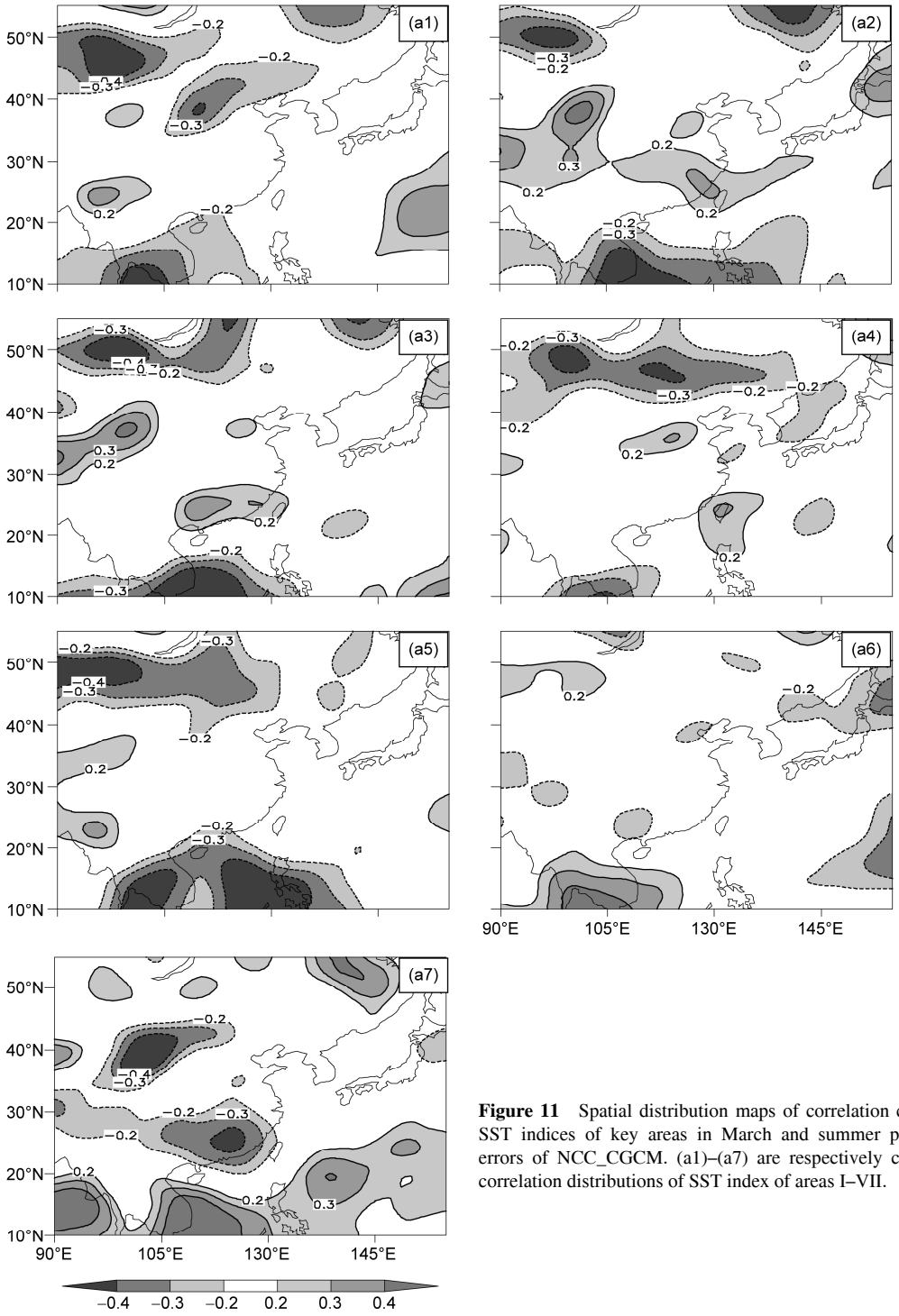


**Figure 11** Spatial distribution maps of correlation coefficients between SST indices of key areas in March and summer precipitation forecast errors of NCC_CGCM. (a1)–(a7) are respectively corresponding to the correlation distributions of SST index of areas I–VII.

SST indices of key areas and summer precipitation forecast errors of NCC_CGCM. Area I has significant and negative correlations with the forecast errors mainly in the northern and southern East Asia, while it has a significant and positive correlation in the locations of sub-tropical western Pacific (Figure 11(a1)). Area II mainly has significant and negative correlations with the regions such as west of the Lake Baikal, northeastern China, southern East Asia and its offshore, while it has significant and positive correlations with the regions such as the Yangtze River Basin and northern Japan (Figure 11(a2)). Area III mainly has significant and negative correlations with the regions such as neighborhood of the Lake Baikal, southern East Asia and its offshore, while it has significant and positive correlations with the regions such as the middle of western East Asia and southeastern coastal areas in China (Figure 11(a3)). Area IV mainly has significant and negative correlations with northern East Asia, while it has significant and positive correlations with the waters near Taiwan (Figure 11(a4)). Area V mainly has significant and negative correlations with the regions such as the neighborhood of the Lake Baikal, southern East Asia and its offshore (Figure 11(a5)). The significant correlation areas of area VI are small, and only exist in the neighborhood of the Indochina Peninsula (Figure 11(a6)). Area VII mainly has significant and negative correlations with the regions such as middle-eastern and southeastern Northwest China, while it has significant and positive correlations with the regions such as northeastern China, southern East Asia, and the sub-tropical western Pacific (Figure 11(a7)).

The poor forecast effects of NCC_CGCM for the SST of key areas in March will cause the errors of late period atmosphere responses to the SST in the model. This process may cause forecast errors of summer precipitation, and this kind of error information may be also contained in the historical results of forecast (and hindcast). Therefore, it can select the historical years in which SSTs of key area in March are similar to the actual situations in new-year, and correct the current model forecast results according to the summer precipitation forecast errors of similar years. This can make up for the late period forecast errors caused by the poor forecast of the model for SSTs of key areas. Chou (1974) also pointed out the importance and feasibility of using past historical data in the numerical weather forecast. Feng et al. (2013) adopted the method of dynamic-statistics combined method, used the historical data for forecast to make up for the defects of the dynamic model, and obtained good results in the real summer precipitation forecasts in China. Therefore, the dynamic-statistics combined forecast scheme in section 2.2 is an effective way in improving the forecast skill of NCC_CGCM for East Asian summer precipitation. Because we mainly considered the components of abrupt decadal change component of East Asian summer precipitation in the selection of key areas, it is possible to use the method to improve the decadal variation information in the year-by-year seasonal forecast results of NCC_CGCM.

## 4 Dynamic-statistics error correction of decadal variation in East Asian summer precipitation forecast

We conducted the independent sample forecast tests of dynamic-statistics error correction of East Asian summer precipitation forecast of NCC_CGCM on the basis of the SST index of each single key area whose purpose was to improve the decadal variation information contained in the model forecast results. As for the selection of similar years of SST index, we mainly calculated the difference between historical and current year, and the smaller the difference is, the more similar the years are. In this paper, we respectively took 1–9 years as the number of similar years and provided the average ACCs and ACRs of the dynamic-statistics error correction of East Asian summer precipitation based on SSTs indices of seven key areas. Figure 12 shows that, when the number of similar years is 1–6, ACR fluctuates; when the number of similar years is greater than 6, it declines rapidly; when the number of similar years is respectively 1, 3 and 5, it has a maximum value. When the number of similar years is 1 or 4–7, the value of ACC is large, and it is relatively more stable when the number is 4–7. Given that if the number of similar years is 1, i.e., only one year of historical similar information is used for correction of the model forecast, it may increase the forecast uncertainty. Therefore, we selected 5 similar years to conduct the dynamic-statistics error correction, and both ACC and ACR are good as this number.

Figure 13(a1)–(a7) respectively show the latitude-time cross section of corrected East Asian summer precipitation anomaly percentage based on SST index of each single key area. In the corrected results of most areas, before 1999 there was a continuously more precipitation in East Asian areas north of 40°N and a continuously less precipitation in the regions between 30°N and 40°N, whereas from the year

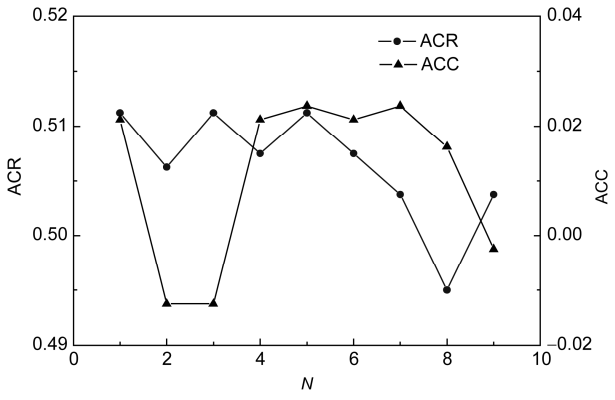


**Figure 12** Changes of ACR and ACC of average result of dynamic-statistics error corrections with selected number of similar years.

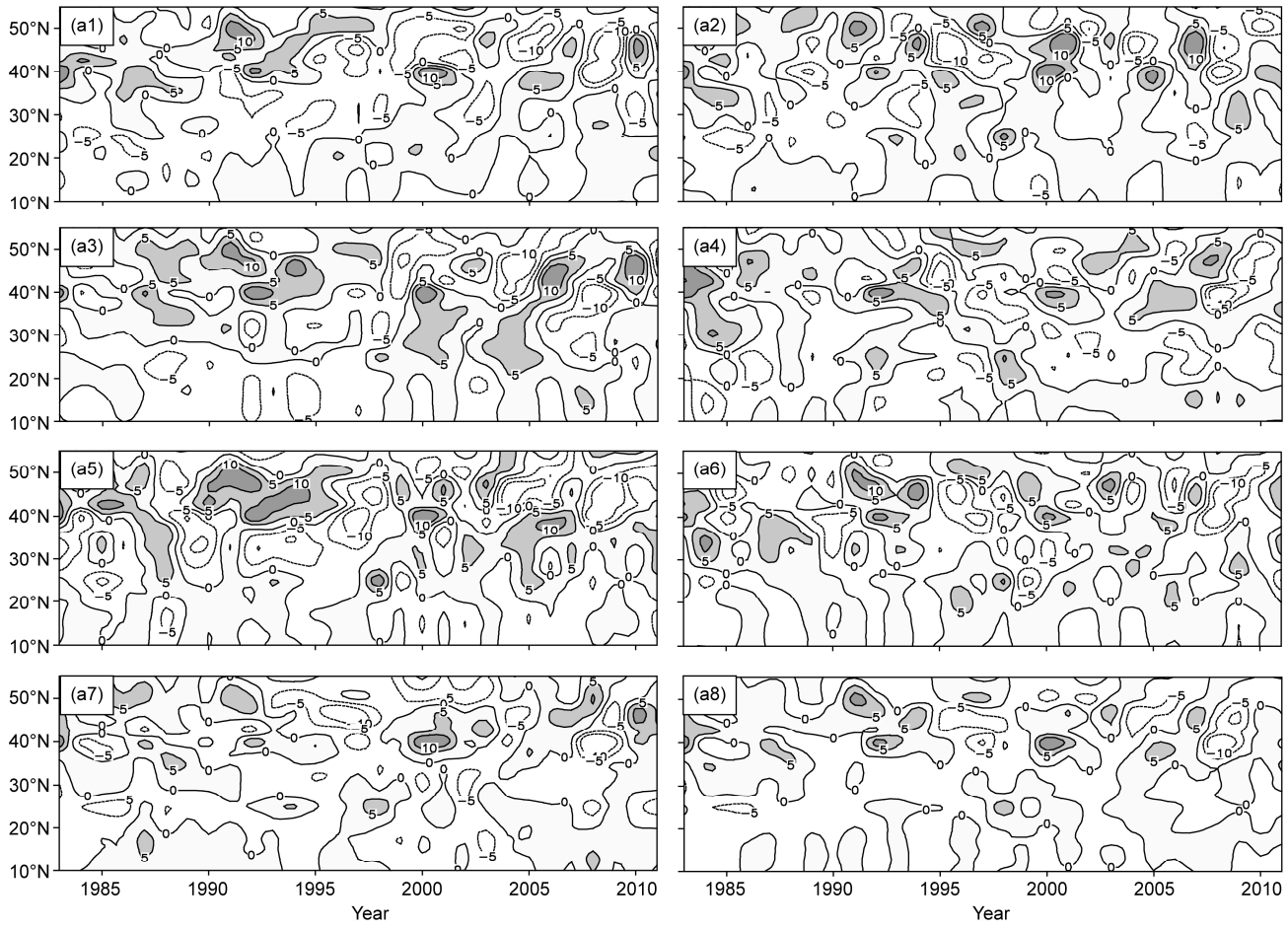


**Figure 13** Latitude-time crosses section of corrected East Asian summer precipitation anomaly percentage (%) along 90°E–145°E. Solid line and dotted line denotes positive and negative anomalies. Shadow denotes positive anomaly. (a1)–(a7) are respectively corresponding to the correction results based on SST index of a single key area, (a8) is the average correction results of seven key areas.

2000 the precipitation in the areas north of 40°N the data changed to be less and in the regions between 30°N and 40°N changed to be more. This characteristic is consistent with the latitude-time cross section of CMAP data in Figure 6(a). Compared with the NCC_CGCM system error correction results in Figure 6(b), this kind of correction represents a certain improvement. Especially the forecast results based on Area V in Figure 13(a5) show the decadal variation characteristics of East Asian summer precipitation that, before 1999, the precipitation anomalies in the northern area was dominated by "+–+", whereas since 2000 they have been dominated by "–+–". Figure 13(a8) shows the average result of the seven forecast tests, which also shows the decadal variation characteristics of the precipitation in East Asian areas. Furthermore, ACCs and ACRs between latitude-time cross section north of 30°N of corrected East Asian summer precipitation anomaly percentage and actual situation are shown in Table 4. Compared with the NCC_CGCM's system error correction results, dynamic-statistics correlated results based on SST index of Area I, III, V, and VI are all improved. Especially the ACC of Area V reaches 0.25, and the ACR reaches 61%. Besides, the corresponding ACC of the average results of the dynamic-statistics corrections of seven areas is 0.03, and the anomaly symbol consistent rate is 51%, which are both better than the –0.01 and 49% of NCC_CGCM's system error correction results.

We provided the corrected East Asian summer precipitation anomaly percentage distributions which correspond to two periods of 1983–1998 and 1999–2011 (Figure 14). The anomaly percentage distributions of the period between 1983 and 1998 partially show the anomaly characteristics of "+–+" from north to south (Figure 14(a1), (a5) and (a8)), whereas the anomaly percentage distributions between 1999 and 2011 partially show the anomaly characteristics dominated by "–+–" from north to south (Figure 14(b1), (b5) and (b8)). Obviously, these results are close to the actual situations of CMAP in Figure 7(a1) and (b1), and are much better than NCC_CGCM's system error correction results in Figure 7(a2) and (b2). Meanwhile, as for ACCs and ACRs of the dynamic-statistics correction results, except for that the result of area VI is not ideal (Table 5), the other results are significantly better than the situations before the correction. The average ACC and ACR of correction results of seven areas in the period of 1983–1998 are 0.70 and 77%,

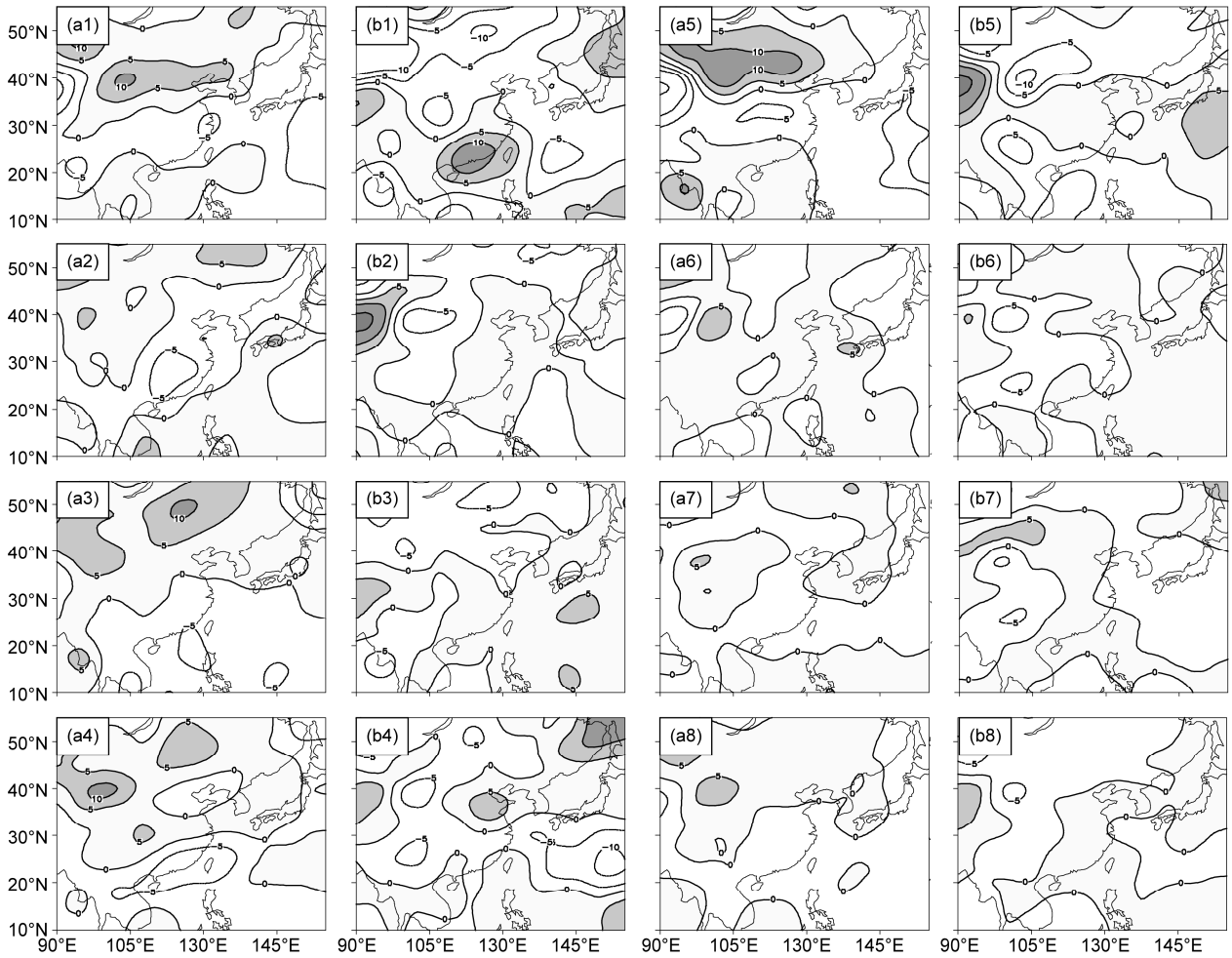


**Figure 14** East Asian summer precipitation anomaly percentage (%) synthesis maps of dynamic-statistics correction in 1983–1998 and 1999–2011. (a1)–(a7) and (b1)–(b7) are respectively corresponding to the dynamic-statistics corrections based on seven key areas, and (a8) and (b8) corresponding to the average results of the dynamic-statistics error corrections of seven key areas. Solid line and dotted line: positive and negative anomalies. Shadow: positive anomaly.

**Table 4** ACCs and ACRs of latitude-time cross section north of 30°N of East Asian summer precipitation anomaly percentage[a)]

| | Area I | Area II | Area III | Area IV | Area V | Area VI | Area VII | Mean | Before correction |
|---|---|---|---|---|---|---|---|---|---|
| ACC | 0.02 | –0.05 | 0.10* | –0.09 | 0.25* | 0.02 | –0.11 | 0.03 | –0.01 |
| ACR (%) | 52 | 49 | 54 | 46 | 62 | 50 | 45 | 51 | 49 |

a) The critical correlation value of 90% of significance is 0.10; * represents the situation that exceeds 90% of significance levels. Independent sample forecast test & actual situation of CMAP.

**Table 5** ACCs and ACRs of East Asian summer precipitation before and after dynamic-statistics corrections[a)]

| Time period | 1983–1998 | | 1999–2011 | |
|---|---|---|---|---|
| Inspection amount | ACC | ACR (%) | ACC | ACR (%) |
| Before correction | 0.03 | 52 | 0.08 | 54 |
| Area I | 0.45* | 69 | 0.77* | 78 |
| Area II | 0.47* | 65 | 0.22* | 64 |
| Area III | 0.57* | 67 | 0.61* | 73 |
| Area IV | 0.49* | 65 | 0.38* | 62 |
| Area V | 0.71* | 76 | 0.38* | 65 |
| Area VI | 0.01 | 46 | 0.05 | 54 |
| Area VII | 0.24* | 58 | 0.02 | 55 |
| Average of seven areas | 0.70* | 77 | 0.60* | 76 |

a) The critical correlation value of 95% of significance is 0.11; * represents the situation that exceeds 95% of significance tests.

and those in the period of 1999–2011 are 0.60 and 76%, which are significantly better than 0.03, 52% and 0.08, 54% before the correction. Therefore, the decadal variation information of East Asian summer precipitation contained in the dynamic-statistics correction results is significantly better than that before the correction.

## 5 Discussions and conclusions

In this paper, based on the CMAP precipitation data from 1983 to 2011, analysis of the decadal variation characteristics of East Asian summer precipitation revealed that the significant decadal adjustment existed in East Asia around 1999. Before 1999, the precipitation anomaly percentage in East Asia showed the distribution pattern of "+–+" from north to south; after 1999, it changed to the pattern of "–+–" from north to south; this kind of decadal variation is mainly reflected in the third model of EOF decomposition. At the same time, in combination with East Asian summer precipitation data of NCC_CGCM forecasts (and hindcast) from 1983 to 2011, we analyzed the forecast ability of the model for the decadal variations of East Asian summer precipitation. The forecast (hindcast) data of NCC_CGCM show that the precipitation anomaly percentage in East Asia presents the distribution pattern of "+–+–" from north to south before 1999, whereas it mainly presents the distribution characteristics of "–+–+" from north to south after 1999. Therefore, the decadal distribution pattern of precipitation of NCC_CGCM is quite different from the actual situations.

Focusing on increasing the decadal variation information in the seasonal forecasts of NCC_CGCM for East Asian summer precipitation, first we discussed the key areas with significant correlations between SSTs and decadal scale components of East Asian summer precipitation. Second, we analyzed the forecast ability of NCC_CGCM for SSTs of key areas, and confirmed that the regional differences of the forecast ability of NCC_CGCM for SSTs of key areas were large and the model forecast errors had important relationships with the SSTs of key areas. This is proved by considering the differences of East Asian summer precipitation forecast, which correspond to the situations with correct forecasts and wrong forecasts for SSTs of key areas. Finally, we provided the research on East Asian summer precipitation dynamic-statistics combined forecast scheme on the basis of the abrupt decadal change components, and conducted the forecast tests for the independent samples from 1983 to 2011. The latitude-time cross section of summer precipitation anomaly percentage in East Asia along 90°E–145°E of dynamic-statistics correction and the spatial distribution maps of precipitation anomaly percentage of two time periods before and after 1999 are both given. Overall, the dynamic-statistics combined forecast scheme can improve the decadal variation information of the precipitation in East Asian areas north of 30°N contained in the seasonal forecasts of the NCC_CGCM. Compared with the model system error correction, the latitude-time cross section of East Asian summer precipitation anomaly percentage of dynamic-statistics corrections based on SST indices of area I, area III, area V, and area VI are obviously improved. Especially the ACC of area V reaches 0.25, and the anomaly symbol consistent rate reaches 61%. Furthermore, the corresponding ACC of the average results of the dynamic-statistics corrections of seven areas is 0.03, and the anomaly symbol consistent rate is 51%, which are both better than the –0.01 and 49% of NCC_CGCM's system error correction results.

In terms of the spatial distribution maps of precipitation anomaly percentage of the two time periods, in the average result of dynamic-statistics corrections and the correction based on area VI, the composite map of the time period 1983–1998 presents the anomaly characteristics of "+–+" from north to south, whereas the composite map of the time period 1999–2011 presents the anomaly characteristics dominated by "–+–". These results are close to the actual situations of CMAP, and are much better than the NCC_CGCM's system error correction results. The ACC and ACR of average correction result of seven areas in the period of 1983–1998 are 0.70 and 77%, and those in the period of 1999–2011 are 0.60 and 76%, which are significantly better than 0.03, 52% and 0.08, 54% before the correction. Therefore, it is helpful to improve the abrupt decadal change information in the forecasts of East Asian summer precipitation by extracting the historical similar forecast errors of NCC_CGCM based on SST indices of key areas.

*This work was supported by the National Basic Research Program of China (Grant No. 2012CB955203), the National Natural Science Foundation of China (Grant Nos. 41205040, 41105055) and the Special Scientific Research Project for Public Interest (Grant No. GYHY201306021).*

Cao H X. 1993. Self-memory equation of atmosphere movement (in Chinese). Sci China Ser B, 23: 104–112

Chou J F. 1974. A problem of using past data in numerical weather forecasting (in Chinese). Sci China Ser A, 6: 635–644

Chou J F. 1986. Why to combine dynamical and statistical methods together and how to combine (in Chinese). Plateau Meteor, 5: 367–372

Chou J F. 2003. Short term climatic prediction: present condition, problems and way out (in Chinese with English Abstract). Bimon Xinjiang Meteorol, 26: 1–4

Deng W T, Sun Z B, Ceng G, et al. 2009. Interdecadal variation of summer precipitation pattern over eastern China and its relationship with the north pacific SST (in Chinese with English Abstract). Sci Atmos Sin, 33: 835–846

Ding Y H, Liu Y M, Song Y J, et al. 2002. The research and test of China short term dynamical climate forecast model systems (in Chinese with English Abstract). Clim Envir Res, 7: 236–246

Ding Y H. 2007. The variability of the Asian summer monsoon. J Metoer Soc Japan, 85B: 21–54

Fan K, Wang H J. 2009a. A new approach to forecasting typhoon frequency over the western North Pacific. Weather Forecas, 24: 974–978

Fan K, Lin M J, Gao Y Z. 2009b. Forecasting the summer rainfall in North China using the year-to-year increment approach. Sci China Ser D-Earth Sci, 52: 532–539

Fan K, Liu Y, Chen H P. 2012. Improving the prediction of the EastAasian summer monsoon: New approaches. Weather Forecast, 27: 1017–1030
Feng G L, Cao H X, Gao X Q, et al. 2001. Prediction of precipitation during summer monsoon with self-memorial model. Adv Atmos Sci, 18: 701–709
Feng G L, Zhao J H, Zhi R, et al. 2013. The latest review on the study of the objective and quantifiable forecasting of precipitation in summer based on dynamical-statistical method (in Chinese with English Abstract). J Appl Meteor, 24: 656–665
Fu J J, Li S L, Luo D H. 2009. Impact of global SST on decadal shift of east summer climate. Adv Atmos Sci, 26: 192–201
Gong D, Ho C. 2002. Shift in the summer rainfall over the Yangtze River valley in the late 1970s. Geophys Res Lett, 29, doi: 10.1007/00703-004-0081-z
Gong Z Q, Feng G L, Wan S Q, et al. 2006. Analysis of Features of climate change of Huabei Area and the global climate change based on heuristic segmentation algorithm (in Chinese with English Abstract). Acta Phys Sin, 55: 477–484
Gong Z Q, Zhao J H, Feng G L. 2013. Analysis of the summer precipitation of 2012 in East China and its possibility of decadal shift (in Chinese with English Abstract). Acta Phys Sin, 62: 099205
Gong Z Q, Zhi R, Zhou L, et al. 2012. Study of tropical middle-eastern Pacific sea surface temperature correlation index and probable correlation with ENSO effects (in Chinese with English Abstract). Acta Meteor Sin, 70: 1074–1083
Graham N E. 1994. Decadal-scale climate variability in the tropical and North Pacific during the 1970s and 1980s: Observations and model results. Clim Dyn, 9: 135–162
Huang J P, Yi Y H, Wang S W, et al. 1993. An analogue-dynamical long-range numerical weather prediction system incorporating historical evolution. Quart J Roy Meteor Soc, 119: 547–565
Huang R H, Chen J L, Liu Y. 2011. Interdecadal variation of the leading modes of summertime precipitation anomalies over eastern China and its association with water vapor transport over East Asia (in Chinese with English Abstract). Sci Atmos Sin, 35: 589–606
Huang R H, Chen J L, Huang G. 2007. Characteristics and variations of the East Asian monsoon system and its impacts on climate disasters in China. Adv Atmos Sci, 24: 993–1023
Kwon M H, Jhun J G, Ha K J. 2007. Decadal change in East Asian summer monsoon circulation in the mid-1990s. Geophys Res Lett, 34: L21706
Lang X, Wang H J. 2010. Improving extra seasonal summer rainfall prediction by merging information from GCMs and observations. Weather Forecast, 25: 1263–1274
Lang X. 2008. Prediction model for spring dust weather frequency in North China. Sci China Ser D-Earth Sci, 51: 709–720
Li W J, Zhang P Q, Li Q Q, et al. 2005. Research and operational application of dynamical climate model prediction system (in Chinese with English Abstract). J Appl Meteor, 16(append): 1–11
Li H M, Dai A G, Zhou T J, et al. 2010. Responses of East Asian summer monsoon to historical SSTand atmospheric forcing during 1950–2000. Clim Dyn, 34: 501–514
Liu Y, Fan K. 2012a. A new statistical downscaling model for autumn precipitation in China. Int J Climatol, 33: 1321–1336
Liu Y, Fan K. 2012b. Improve the prediction of summer precipitation in the southeastern China by a hybrid statistical downscaling model. Meteor Atmos Phys, 117: 121–134
Liu Z, Wen N. 2008. On the assessment of non-local climate feedback part I: Generalized equilibrium assessment. J Clim, 21: 134–148
Qiu C J, Chou J F. 1989. The dynamical-analogue weather forecast method (in Chinese). Chin J Atmos Sci, 13: 22–28
Rasmusson E M, Wang X L, Ropelewski C F. 1994. Secular Variability of ENSO Cycle: Decade to Century Time Scales of Natural Climate Variability. San Diego: Academic Press. 458–569
Ren H L, Chou J F. 2005. Analogue correction method of errors by combining both statistical and dynamical methods together (in Chinese with English Abstract). Acta Meteor Sin, 63: 988–993
Ren H L, Chou J F. 2007. The research on an analogue-dynamical forecast scheme and method (in Chinese with English Abstract). Sci China Ser D-Earth Sci, 37: 1101–1109
Shi N, Zhu Q G, Wu B G. 1996. The East Asian summer monsoon in relation to summer large scale weather-climate anomaly in china for last 40 years (in Chinese with English Abstract). Sci Atmos Sin, 20: 575–583
Si D, Ding Y H. 2013. Decadal Change in the Correlation Pattern between the Tibetan Plateau Winter Snow and the East Asian Summer Precipitation during 1979–2011. J Clim, 26: 7622–7634
Smith T M, Reynolds R W. 2003. Extended reconstruction of global sea surface temperatures based on COADS data 1854–1997. J Clim, 16: 1495–1503
Wang H J, Sun J Q, Lang X M, et al. 2008. Some new results in the research of the interannual climate variability and short-term climate prediction (in Chinese with English Abstract). Sci Atmos Sin, 32: 806–814
Wang H J. 2001. The weakening of the Asian Monsoon Circulation after the End of 1970's. Adv Atmos Sci, 18: 376–386
Wang Q G, Feng G L, Zheng Z H, et al. 2011. A study of the objective and quantifiable forecasting based on optimal factors combinations in precipitation in the middle and lower reaches of the Yangtze River in summer (in Chinese with English Abstract). Scientia Atmos Sin, 35: 287–297
Wang X J, Feng A X, Gong Z Q, et al. 2012. Collective behavior of climate indices in the North Pacific air-sea system and its potential relationships with decadal climate changes. Chin Phys B, 21: 029201
Wei F Y, Zhang X G. 1988. The classification and forecasting of summer rain-belt in the east part of China (in Chinese with English Abstract). Meteor Mon, 14: 15–19
Xiong K G, Feng G L, Huang J P, et al. 2011. Analogue-dynamical prediction of monsoon precipitation in Northeast China based on dynamic and optimal configuration of multiple predictors. Acta Meteor Sin, 25: 316–326
Xu J J, Zhu Q G. 1999. The numerical study of the effect of ENSO and its interdecadal variation on the global and Asian monsoon precipitation (in Chinese with English Abstract). Acta Meteor Sin, 57: 301–215
Yang J, Zhao J H, Zheng Z H, et al. 2012. Estimating the prediction errors of dynamical climate model on the basis of prophase key factors in north China (in Chinese with English Abstract). Sci Atmos Sin, 36: 11–22
Zhang Q Y, Lü J M, Yang L M. 2007. The interdecadal variation of precipitation pattern over china during summer and its relationship with the atmospheric internal dynamic processes and extra-forcing factors (in Chinese with English Abstract). Sci Atmos Sin, 31: 1290–1300
Zhao J H, Feng G L, Wang Q G, et al. 2011. Cause and prediction of summer rainfall anomaly distribution in China in 2010 (in Chinese with English Abstract). Sci Atmos Sin, 35: 1069–1078
Zheng Z H, Huang J P, Ren H L. 2009. Analogue correction of errors based on seasonal climatic predictable components and numerical experiments (in Chinese with English Abstract). Acta Phys Sin, 58: 7359–7367
Zhou L T, Huang R H. 2003. Research on the characteristics of interdecadal variability of summer climate in China and its possible cause (in Chinese with English Abstract). Clim Envir Res, 8: 274–290

INTERNATIONAL JOURNAL OF CLIMATOLOGY
*Int. J. Climatol.* (2014)
Published online in Wiley Online Library
(wileyonlinelibrary.com) DOI: 10.1002/joc.4075

RMetS
Royal Meteorological Society

# Influence of the tropical Pacific east–west thermal contrast on the autumn precipitation in South China

Wei Gu,[a] Lin Wang,[b]* Weijing Li,[a] Lijuan Chen[a] and Chenghu Sun[a]

[a] *Laboratory for Climate Studies, National Climate Center, China Meteorological Administration, Beijing, China*
[b] *Center for Monsoon System Research, Institute of Atmospheric Physics, Chinese Academy of Sciences, Beijing, China*

**ABSTRACT:** Analysis of observational and reanalysis data shows that the autumn precipitation in South China is closely related to the east–west sea surface temperature (SST) contrast in the tropical Pacific. An east–west contrast (EWC) index, defined as the difference of the normalized area-averaged SST between the tropical eastern Pacific (150°W–90°W, 5°S–5°N) and the tropical western Pacific (WP; 110°E–180°E, 5°S–5°N), is proposed to delineate this feature. When the EWC index is positive, the tropical eastern (western) Pacific is warmer (colder) than normal. It would cause significant southerly wind anomalies from the Indochina Peninsula to eastern China, leading to enhanced water vapour convergence and anomalous ascending motion over South China. Therefore, enhanced autumn precipitation is observed in South China. Further analysis suggests that the SST of the tropical WP dominates the lower-tropospheric meridional wind and the resultant water vapour transport and convergence over subtropical East Asia, and that the SST of both the tropical eastern and the tropical WP contributes to the anomalous ascending motions over South China. These results highlight the combined effects of tropical eastern and WP on the autumn precipitation in South China and specifically emphasize the role of tropical WP SST. Given the performance of the EWC index in describing the autumn precipitation as well as the leading time and the persistence of the EWC index, it could be used as a good indicator in the monitoring and prediction of the autumn precipitation in South China, which is demonstrated by a simple statistical prediction model.

KEY WORDS thermal contrast; tropical Pacific; sea surface temperature; autumn precipitation; China

*Received 17 December 2013; Revised 5 April 2014; Accepted 14 May 2014*

## 1. Introduction

The autumn precipitation in South China accounts for about 15–30% of the annual total amount (Wu *et al.*, 2003; Chen *et al.*, 2009). Its interannual variation and associated droughts or flooding could influence the agriculture and activities of the inhabitants in this region, and cause great economic losses due to the reduction of crop products (Chen and Shi, 2003; Niu and Li, 2008; Gu *et al.*, 2012). For example, South China experienced severe autumn droughts in 2009. More than 80 million people were affected, and the direct economic loss has reached up to about 30 billion Chinese Yuan (~4.8 billion US dollars) (Barriopedro *et al.*, 2012; Zhang *et al.*, 2013). Therefore, understanding the variability and mechanism of autumn precipitation over South China is an important issue not only for its scientific significance but also for its social and operational values.

Previous studies on the precipitation in South China were mainly concentrated on the spring and summer seasons (e.g. Chen, 2002; Xin *et al.*, 2006; Huang *et al.*, 2012) whereas those on autumn were less reported. It is a consensus that the El Niño events exert great impacts on the East Asian precipitation especially in summer (Zhang *et al.*, 1999). Such impacts are realized through an anomalous anticyclone around the Philippine Sea (Wang *et al.*, 2000) and the associated anomalous southerly winds (Zhang *et al.*, 1996). The presence of this anomalous anticyclone is originally forced by the sea surface temperature (SST) anomalies of El Niño in the tropical Pacific (Zhang *et al.*, 1996; Wang *et al.*, 2000). This anticyclonic anomaly usually establishes in boreal autumn, peak in winter, and persists to the following summer (Wang and Zhang, 2002). As a result, during the autumn of a developing El Niño year, the precipitation in South China tends to be above normal due to the anomalous Philippine anticyclone, the resultant south wind anomalies and convergence of water vapour flux (Zhang and Sumi, 2002; Wu *et al.*, 2003).

On the basis of the aforementioned studies, the information of El Niño-Southern Oscillation (ENSO) is usually regarded as the most important factor when the operational statistical short-term prediction is performed for South China's autumn precipitation in National Climate Center (NCC), China Meteorological Administration (CMA). However, the effect of this ENSO-based statistical prediction is not satisfactory. For example, South China experienced a severe dry autumn in 2009 although an El Niño event was observed to develop in June and mature around December (NCC/CMA, 2010). Moreover,

* Correspondence to: L. Wang, Center for Monsoon System Research, Institute of Atmospheric Physics, Chinese Academy of Sciences, P.O. Box 2718, Beijing 100190, China. E-mail: wanglin@mail.iap.ac.cn

© 2014 Royal Meteorological Society

an inspection on historical records shows that similar situations were also observed in many other El Niño years such as in 1969, 1991, and 2004 (see Figures 2 and 3 and Section 3). It implies that other factors apart from ENSO may exert stronger influences on the autumn precipitation of South China besides ENSO. Therefore, in this article, we will re-examine the relationship between ENSO and the autumn precipitation in South China. It is proposed that the east–west contrast (EWC) of the tropical Pacific SST shows a much closer relationship with the South China's autumn precipitation than ENSO does, which results from additional information of the SST anomalies over the tropical western Pacific (WP).

Section 2 describes the datasets and methods used in this study. The relationship between ENSO and the autumn precipitation in South China is examined in Section 3. The influences of east–west SST contrast on the autumn precipitation in South China and the possible mechanism are presented in Sections 4 and 5, respectively. On the basis of these results, a preliminary statistical prediction model is proposed and evaluated in Section 6. Finally, a summary and discussion is given in Section 7.

## 2. Data and methods

The rainfall data used in this study are the monthly mean precipitation from 160 Chinese stations for the period 1951–2012, which are archived and updated by the NCC/CMA. The oceanic data are from the global sea ice and SST dataset (HadISST1) maintained by the Met Office Hadley Centre (Rayner *et al.*, 2003), which has a horizontal resolution of 1° by 1° longitude–latitude grid and covers the period 1870–2012. The atmospheric data are from the monthly mean reanalysis dataset provided by the National Centre for Environmental Prediction/National Centre for Atmospheric Research (NCEP/NCAR), which has a 2.5° × 2.5° horizontal resolution and covers the period from 1948 to present (Kalnay *et al.*, 1996). In this study, we focus on the seasonal means where the summer and autumn are defined by averaging the monthly means of June to August (JJA) and September to November (SON), respectively. The time period concerned in this study is from 1951 to 2012. All the anomalies are calculated with respect to the mean of 1951–2012 values.

In this study, the definition of El Niño/La Niña follows that of Climate Prediction Center (CPC) of National Oceanic and Atmospheric Administration (NOAA), i.e. an El Niño/La Niña is identified if 3-month running means of SST anomalies in the Niño3.4 region (5°N–5°S, 120°W–170°W) exceed 0.5 °C/−0.5 °C for 5 months or more. On the basis of these criteria, 21 El Niño autumns were selected: 1951, 1953, 1957, 1958, 1963, 1965, 1968, 1969, 1972, 1976, 1977, 1982, 1986, 1987, 1991, 1994, 1997, 2002, 2004, 2006, and 2009, and 21 La Niña autumns were selected: 1954, 1955, 1956, 1964, 1970, 1971, 1973, 1974, 1975, 1983, 1984, 1988, 1995, 1998, 1999, 2000, 2005, 2007, 2008, 2010, and 2011.

## 3. ENSO and autumn precipitation in South China

Figure 1 shows the long-term mean and interannual standard deviation of autumn precipitation in middle and eastern China. The area to the south of 35°N features large values in both climatology (Figure 1(a)) and interannual variability (Figure 1(b)). The 54 stations over the domain (105°E–125°E, 20°N–32°N) were selected to represent South China. The area to the west of 105°E was not included because it is located over the low-latitude highland (Cao *et al.*, 2014) where the precipitation variability shows quite different features from that in eastern China (Cao *et al.*, 2012).

Figure 2(a) shows the Niño3.4 index and the normalized area-averaged precipitation anomalies of South China (referred to as precipitation index hereafter) in the 21 El Niño autumns. South China is featured with above-normal precipitation in 11 autumns (1951, 1953, 1957, 1963, 1965, 1972, 1976, 1982, 1987, 1997, and 2002; hereafter referred to as wet El Niño autumns) out of the 21 cases concerned. In the rest 10 autumns (1958, 1968, 1969, 1977, 1986, 1991, 1994, 2004, 2006, and 2009; hereafter referred to as dry El Niño autumns), on the contrary, South China experiences below-normal precipitation. During the 21 La Niña autumns, South China is featured with below-normal precipitation in 13 autumns (1954, 1955, 1956, 1964,

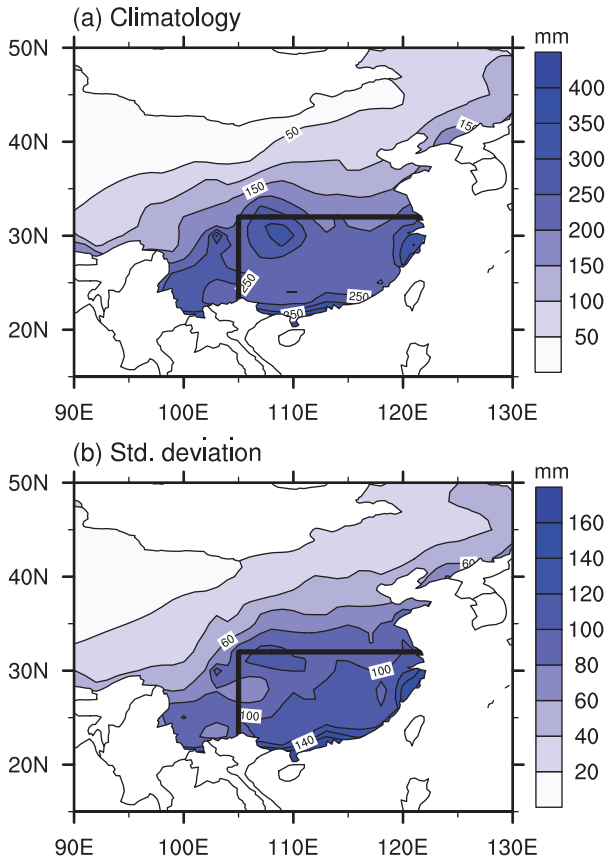


Figure 1. The (a) climatology and (b) interannual standard deviation of autumn mean precipitation in middle and eastern China. CIs are 50 mm in (a) and 20 mm in (b). The target region of this study is located to the southeast of the two black lines.

© 2014 Royal Meteorological Society

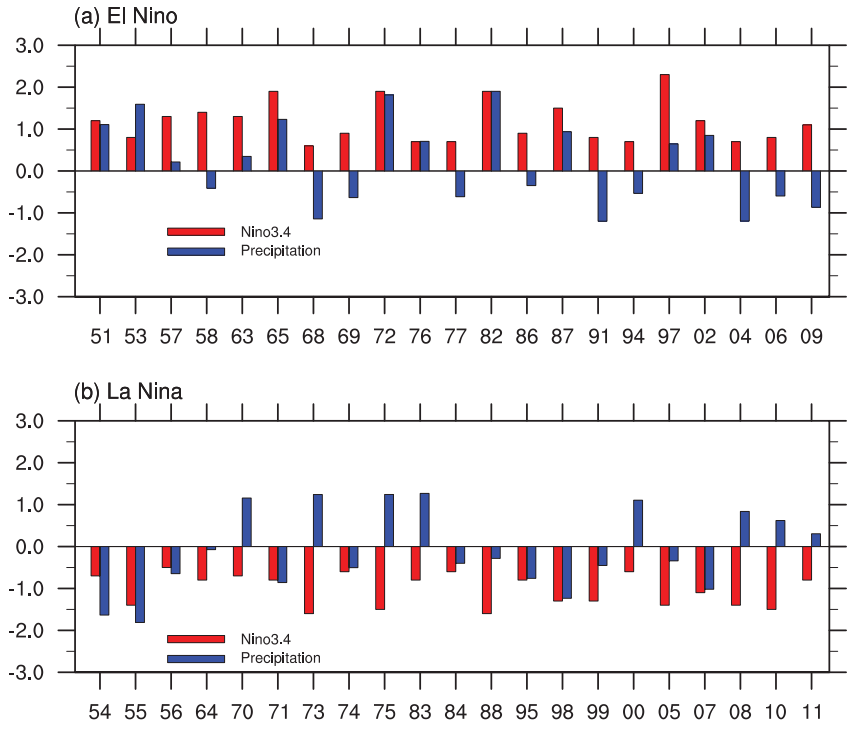


Figure 2. Autumn mean Niño3.4 index and the normalized South China precipitation index in (a) the 21 El Niño and (b) the 21 La Niña years (see text for definitions). X-axis denotes the year.

1971, 1974, 1984, 1988, 1995, 1998, 1999, 2005, and 2007; hereafter referred to as dry La Niña autumns) and above-normal precipitation in 8 autumns (1970, 1973, 1975, 1983, 2000, 2008, 2010, and 2011; hereafter referred to as wet La Niña autumns). It means that over 48% (38%) of the El Niño (La Niña) events do not favour more (less) precipitation in South China, although a statistically significant relationship exists between Niño3.4 index and autumn precipitation in South China (e.g. Wu *et al.*, 2003).

To confirm the above result, the composite spatial distribution of autumn precipitation is shown in Figure 3. Take all of the 21 El Niño autumns as a whole, enhanced precipitation can be observed in South China with more than 60 mm precipitation being observed in the central South China (Figure 3(a)). This pattern quite resembles that reported in previous studies [e.g. Figure 3(c) of Wu *et al.* (2003)], but it only slightly exceeds the 90% confidence level. When the 21 autumns are grouped according to the precipitation index in Figure 2(a), quite distinct features emerge. In the 11 wet El Niño autumns, the precipitation pattern in South China resembles that in Figure 3(a), while the confidence level increases remarkably (Figure 3(b)). Moreover, precipitation anomaly exceeding 120 mm is observed in South China and it almost doubles that in Figure 3(a). In the ten dry El Niño autumns, in contrast, below-normal precipitation is observed in most parts of South China although most of anomalies do not exceed the 90% confidence level (Figure 3(c)). When the 21 La Niña autumns are investigated, similar contrasts are also found (Figure 3(d)–(f)). On one hand, this result suggests that ENSO could exert significant influences on the precipitation in South China, consistent with previous studies (Zhang and Sumi, 2002; Wu *et al.*, 2003). On the other hand, it indicates that a large portion of the variability of autumn precipitation in South China cannot be explained by the SST pattern of ENSO.

## 4. Tropical Pacific east–west SST contrast and autumn precipitation in South China

In order to explore the reason that opposite autumn precipitation is observed in South China during El Niño (or La Niña) years, the SST anomalies were calculated for the wet and dry El Niño autumns, respectively. A most striking feature is that strong negative SST anomalies are observed over the tropical WP during wet El Niño autumns, but not during dry El Niño autumns (Figure 4(a) and (b)). In addition, the magnitude of positive SST anomalies over the tropical eastern Pacific in wet El Niño autumns is larger than that in dry El Niño autumns. The difference between the two cases features a zonal SST dipole in the tropical Pacific (Figure 4(c)). The positive and negative SST anomalies are located mainly to the east of 150°W and to the west of 180°, respectively, suggesting an enhanced Pacific east–west SST contrast in wet El Niño autumns. This SST pattern resembles the second empirical orthogonal function mode of tropical Pacific autumn SST to some extent (not shown). An inspection on the time evolution of this dipolar pattern indicates that it begins to emerge in early spring and then persists and amplifies in summer and autumn (Figure 4(d)). This result suggests that the SST contrast between eastern and western tropical Pacific is the main difference between wet and dry El Niño autumns. Meanwhile, it implies that this east–west SST contrast

© 2014 Royal Meteorological Society

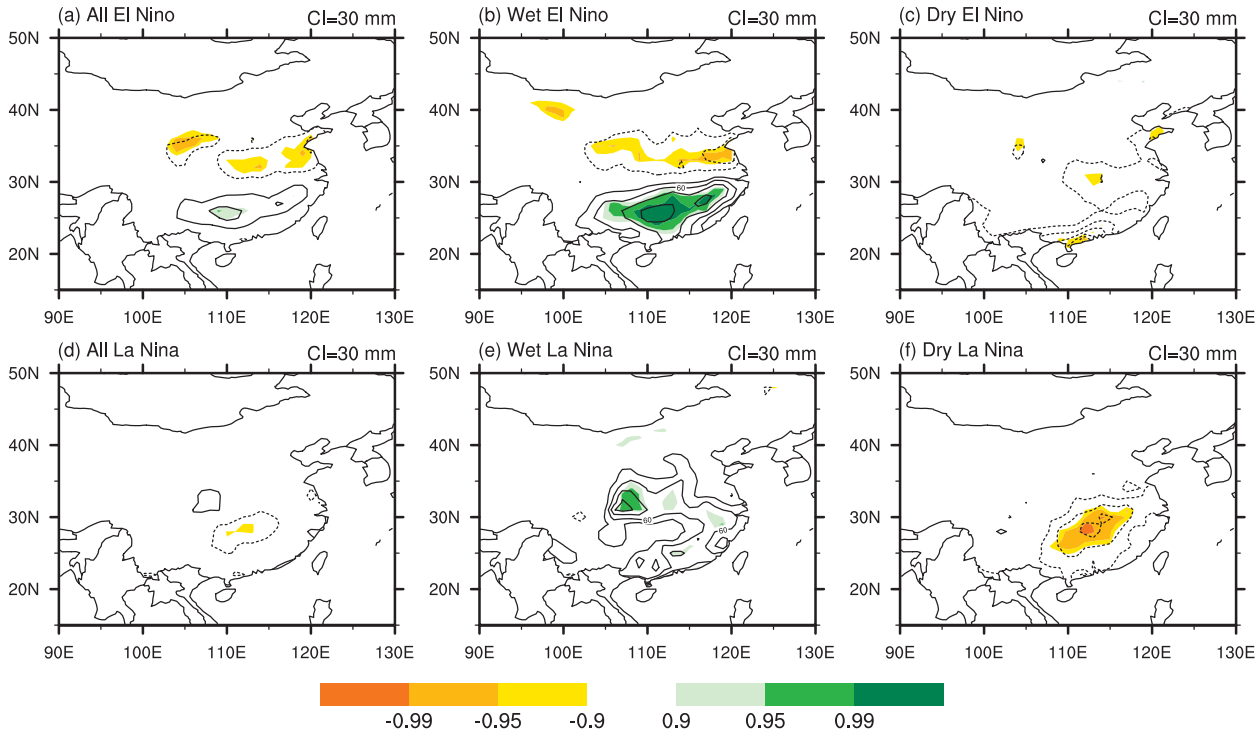


Figure 3. Composite anomalies of precipitation in (a) the total 21 El Niño autumns, (b) the 11 wet El Niño autumns, (c) the 10 dry El Niño autumns, (d) the total 21 La Niña autumns, (e) the 8 wet La Niña autumns, and (f) the 13 dry La Niña autumns. CIs are 30 mm. Zero contours are omitted and contours with negative values are dashed. Dark, middle, and light shading indicate the 99, 95, and 90% confidence levels based on two-tailed Student's *t*-test, respectively.

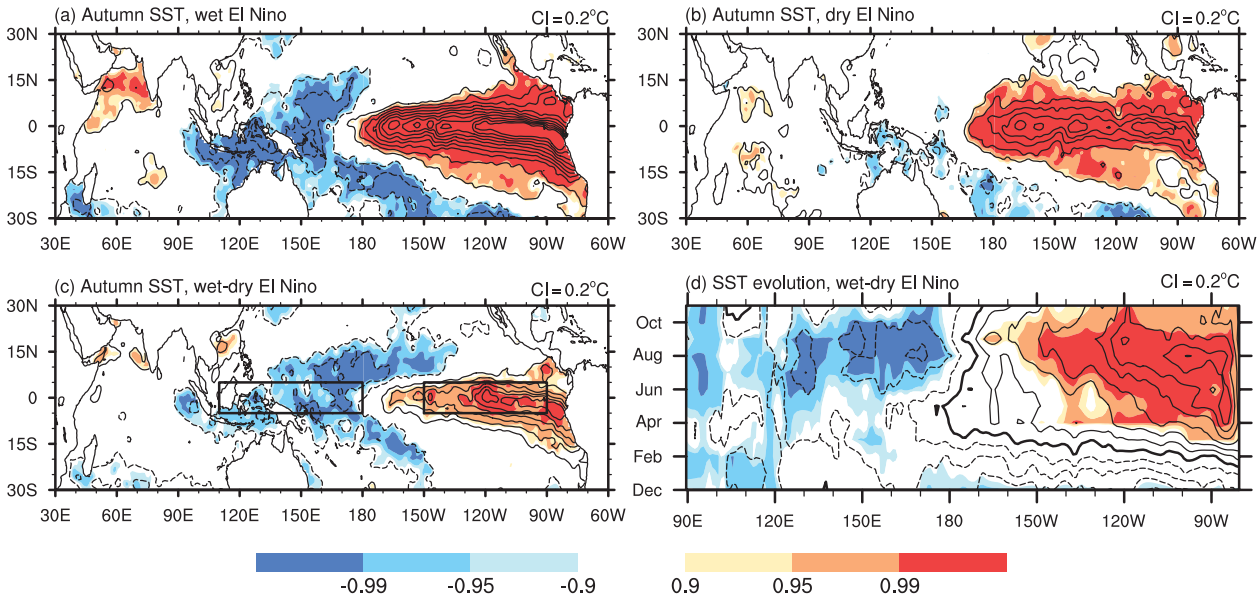


Figure 4. Composite of autumn mean SST anomalies in (a) the 11 wet El Niño autumns, (b) the 10 dry El Niño autumns, and (c) their difference. (d) Composite difference of the monthly evolution of tropical SST averaged over 5°S–5°N between the wet and dry El Niño autumns. CIs are 0.2 °C. Zero contours are omitted in (a)–(c) and bolded in (d). Contours with negative values are dashed. Dark, middle, and light shading indicate the 99, 95, and 90% confidence levels based on two-tailed Student's *t*-test, respectively. The two rectangles in (c) denote the regions to define the EWC index.

may play some role in the interannual variations of the autumn precipitation in South China.

Figure 5 shows the correlation coefficients between the precipitation index and the simultaneous SST in the period 1951–2012. The obtained SST pattern resembles that in the developing phase of El Niño to some extent [e.g. Figure 3 of Feng *et al.* (2011)]. However, the positive SST anomalies are located to the east of 170°W, and the regions that exceed the 90% confidence level are located far more eastward (Figure 5(a)). In contrast, this SST pattern quite resembles the SST dipole shown in Figure 4(c), especially in the tropical Pacific. The Hovmöller diagram

© 2014 Royal Meteorological Society

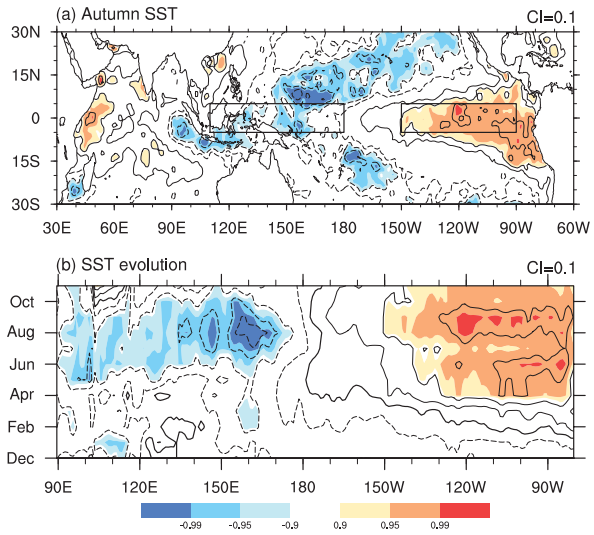


Figure 5. Correlation coefficients between the autumn precipitation index and (a) the autumn mean SST and (b) the monthly tropical SST averaged over 5°S–5°N. CIs are 0.1. Zero contours are omitted in (a) and bolded in (b). Contours with negative values are dashed. Dark, middle, and light shading indicate the 99, 95, and 90% confidence levels based on two-tailed Student's *t*-test, respectively. The two rectangles in (a) denote the regions to define the EWC index.

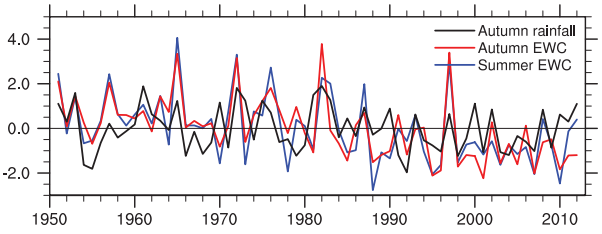


Figure 6. Time series of the autumn mean precipitation index, EWC index, and the summer mean EWC index for the period 1951–2012.

shows that this SST pattern begins to emerge in late spring and becomes significant in summer and autumn (Figure 5(b)). The similarity between Figures 5 and 4(c) and (d) further indicates that this dipole-like SST pattern in the tropical Pacific (Figure 5(a)) is crucial for the variations of the autumn precipitation in China. The key features in Figures 5(a) and 4(c) are the SST contrast between eastern and western tropical Pacific. Therefore, based on Figures 4 and 5, an index reflecting this EWC of the tropical SST is defined as below:

$$I_{EWC} = SST^*_E - SST^*_W$$

where $SST^*_E$ and $SST^*_W$ denote the normalized area-averaged SST in the tropical eastern Pacific (150°W–90°W, 5°S–5°N) and the tropical WP (110°E–180°E, 5°S–5°N), respectively.

Figure 6 shows the normalized EWC index and the normalized precipitation index in autumn for the period 1951–2012. The correlation coefficient between the two indices is 0.40, exceeding the 99% confidence level. The lag correlation reveals that significant correlation coefficient between the autumn precipitation index and the EWC index begins to exceed the 95% confidence level in April and lasts to December, with the maximum 0.46 being observed in both August and September (Figure 7(a)). Although the EWC index shows some downward trend in the period 1951–2012 (Figure 6), the lag correlation remains the same and even slightly higher (0.46 in August and 0.47 in September) when the linear trends are removed (Figure 7(b)). The correlation with summer EWC index is specifically examined because the east–west SST contrast is first observed in summer (Figure 5(b)). It is also expected that the EWC in summer may be useful for the prediction of autumn precipitation in South China. Result indicates that the correlation coefficient between precipitation index and the summer EWC index (Figure 6) is 0.45, which is almost equal to that calculated from the autumn EWC index (0.41). The composite autumn precipitation based on the summer EWC index reveals that significantly enhanced precipitation can be observed in large regions over South China when the EWC index is positive (Figure 8), similar to that based on autumn EWC index (not shown). The area that exceeds the 95% confidence level is even larger than that in wet El Niño autumns (Figure 3(b)). All these results suggest that the autumn precipitation in South China is closely associated with the EWC of the tropical Pacific SST.

In order to further reveal the advantage of the EWC index, a comparison was made between the EWC index and the El Niño indices. In recent years, two flavors of El Niño (i.e. conventional El Niño and El Niño Modoki) were revealed (Ashok *et al.*, 2007), which show different impacts on the East Asian climate (e.g. Feng *et al.*, 2010a, 2010b, 2011; Zhang *et al.*, 2011, 2013). Hence, in addition to the Niño3.4 index, the Niño3 index that is usually used to represent conventional El Niño and the El Niño Modoki index [EMI, Ashok *et al.* (2007)] that is often used to present El Niño Modoki (Table 1) were also included in the comparison (Figure 9). The scatter graphs in Figure 9 present the co-variability of the four SST indices with the autumn precipitation index of South China. Among the four SST indices that take part in the comparison, the autumn precipitation index is most tightly correlated with the EWC index both in autumn (Figure 9(a)) and in summer (Figure 9(e)). This can also be seen from the lag correlations shown in Figure 7(a), which indicates that the correlation with EWC index is the strongest and the most persistent. Although the improvements in correlation coefficients are as small as 0.13 (Figure 9(a) and (b)) and 0.16 (Figure 9(e) and (f)) when the EWC index is used, it corresponds to remarkable increases in the variances of autumn precipitation explained by the SST indices (16.8 *vs* 7.8% for autumn, Figure 9(a) and (b); and 20.3 *vs* 8.4% for summer, Figure 9(e) and (f)). Moreover, taking 0.5 standard deviation as criteria for the precipitation and the four SST indices, the relationship between the four SST indices and the precipitation extremes over South China is best represented by the EWC index (Figure 9). For the 62-year period concerned, the high (low) EWC index in autumn/summer corresponds to 10/10 (9/10) extreme wet

© 2014 Royal Meteorological Society

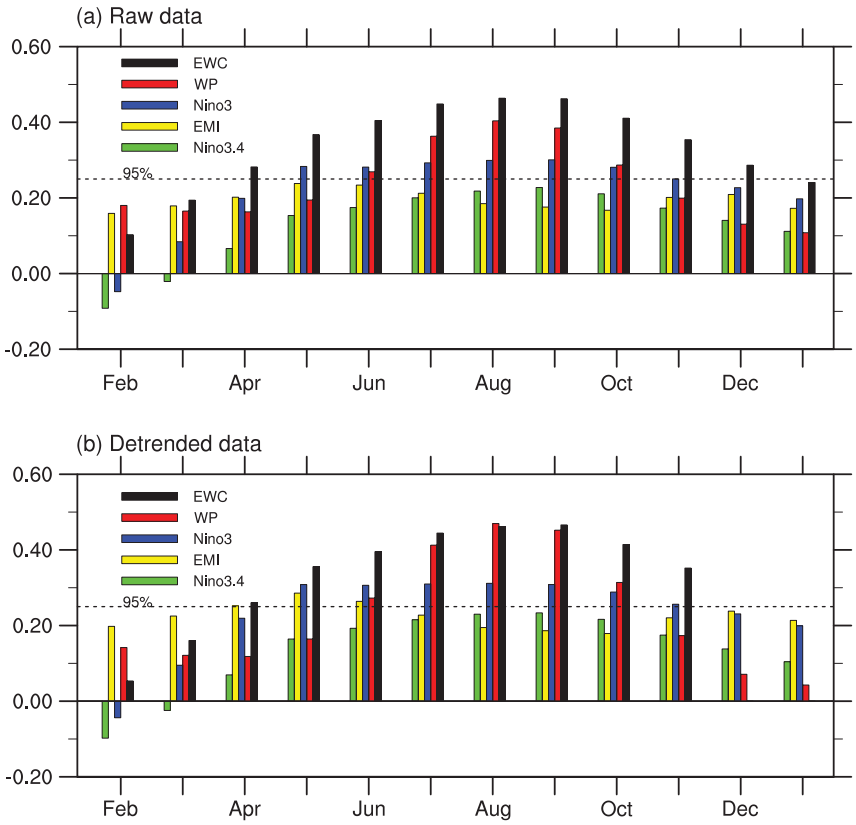


Figure 7. Lag correlations between the autumn mean precipitation index and the EWC index, the Niño3 index, the Niño3.4 index, the negative EMI, and the negative WP index for the period 1951–2012 on the basis of (a) raw data, and (b) data with linear trends removed. All the indices are smoothed by 3-month running mean. Dashed line indicates the 95% confidence level based on two-tailed Student's *t*-test.

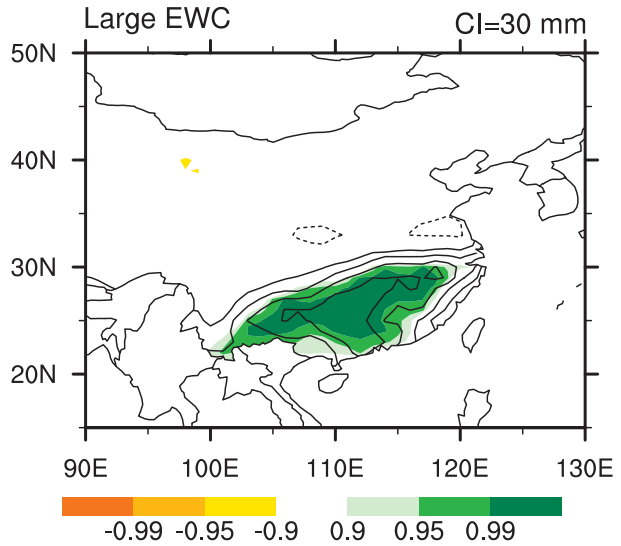


Figure 8. Composite anomalies of autumn precipitation when the summer mean EWC index exceeds 0.6 standard deviation. CIs are 30 mm. Zero contours are omitted and contours with negative values are dashed. Dark, middle, and light shading indicate the 99, 95, and 90% confidence levels based on two-tailed Student's *t*-test, respectively.

(dry) autumns over South China. Hence, all these results suggest that the EWC of the tropical Pacific SST plays a very important role in the interannual variations of the autumn precipitation in South China.

## 5. Possible mechanism

The influences of the tropical Pacific east–west SST contrast on the autumn rainfall over South China need to be realized through the atmospheric circulations and the related moisture transports. In autumn, East Asia is characterized by northeasterly winds in the lower troposphere (Figure 10(a)). An anticyclone is situated over eastern China, where the climatological mean water vapour convergence is relatively weak (Figure 10(b)). Figure 11(a) shows the regressed 850 hPa wind anomalies in autumn onto the simultaneous EWC index. Significant southerly

Table 1. Definitions of indices used in this study. SST* denotes normalized SST.

| Name | Definition |
|---|---|
| EWC index | SST*(150°W–90°W, 5°S–5°N) −SST*(110°E–180°E, 5°S–5°N) |
| Niño3 index | SST (150°W–90°W, 5°S–5°N) |
| Niño3.4 index | SST (170°W–120°W, 5°S–5°N) |
| EMI | SST (165°E–140°W, 10°S–10°N)–0.5 × SST (110°W–70°W, 15°S–5°N)–0.5 × SST (125°E–145°E, 10°S–20°N) |
| WP index | SST (110°E–180°E, 5°S–5°N) |
| Precipitation index | Autumn precipitation averaged over (105°E–125°E, 20°N–32°N) |

© 2014 Royal Meteorological Society

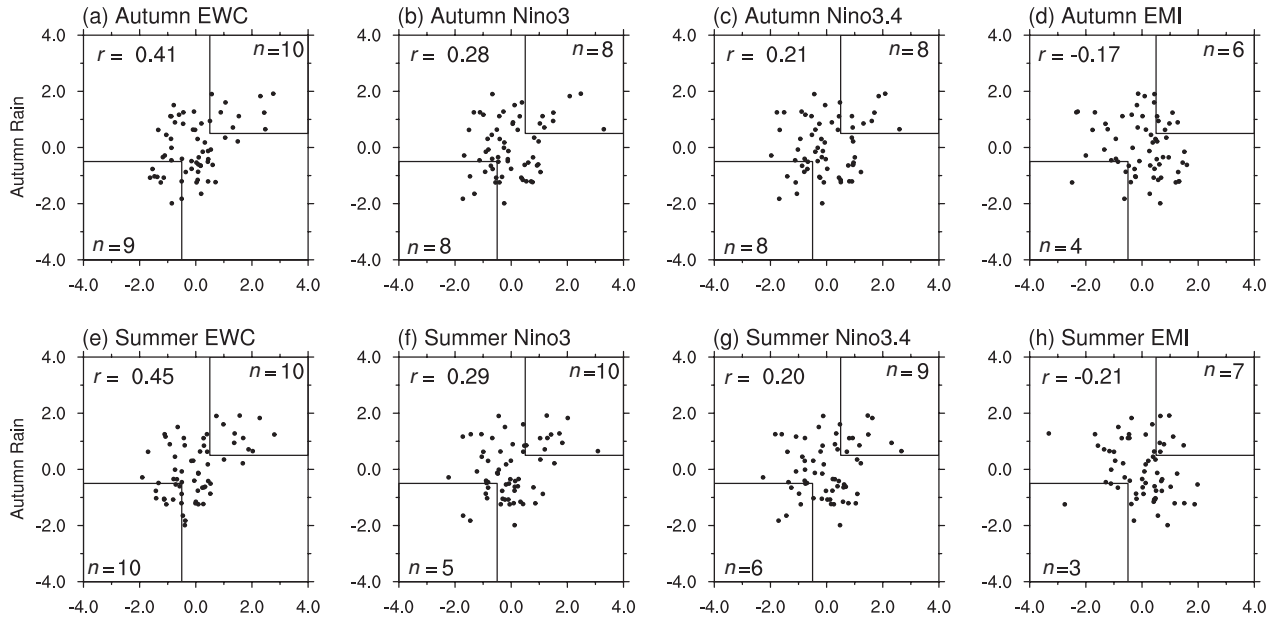


Figure 9. Scatter plot of normalized autumn precipitation index *versus* normalized autumn mean (a) EWC index, (b) Niño3 index, (c) Niño3.4 index, and (d) EMI for the period 1951–2012. The abscissa (ordinate) of each dot in each diagram represents the amplitude and sign of the SST index (the autumn precipitation index) for an individual autumn season. The number of positive (negative) SST index with above-normal (below-normal) autumn precipitation in South China is shown at the upper right (lower left) corner of each diagram. The correlation coefficient between the SST index and autumn precipitation index is shown in the upper left corner of each diagram. (e)–(h) are the same as (a)–(d), but based on autumn precipitation index and summer SST indices.

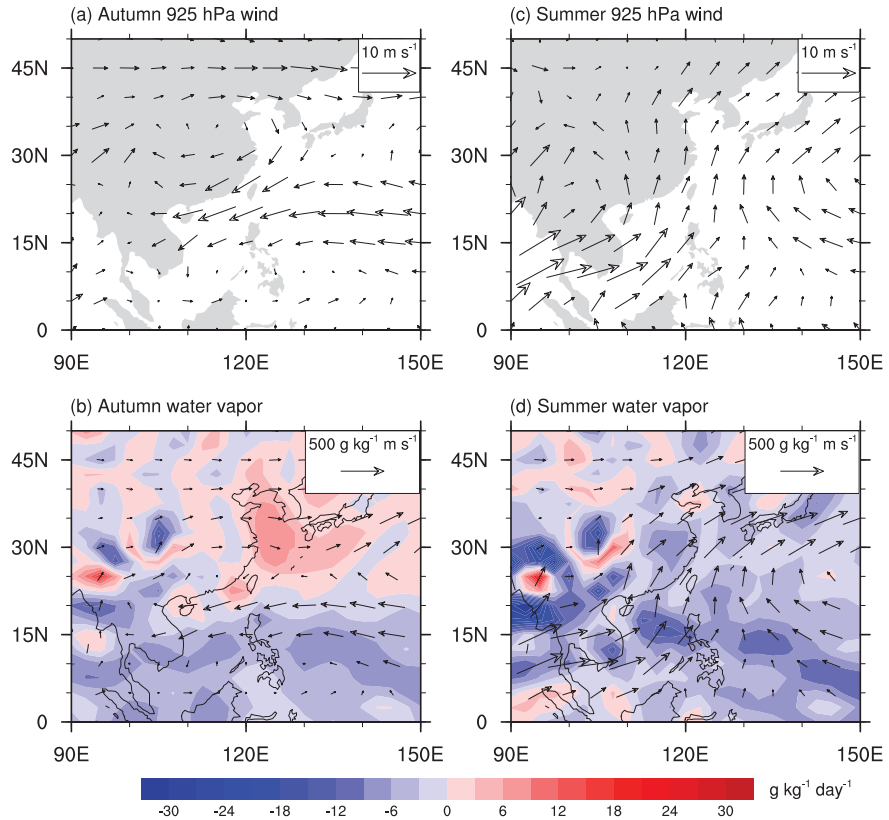


Figure 10. Long-term mean (a) 925 hPa wind and (b) tropospheric vertically integrated water vapour flux (vector; g kg$^{-1}$ ms$^{-1}$) and its divergence (shading; g kg$^{-1}$ day$^{-1}$) in autumn based on the period 1951–2012. (c) and (d) are the same as (a) and (b), but for summer.

© 2014 Royal Meteorological Society

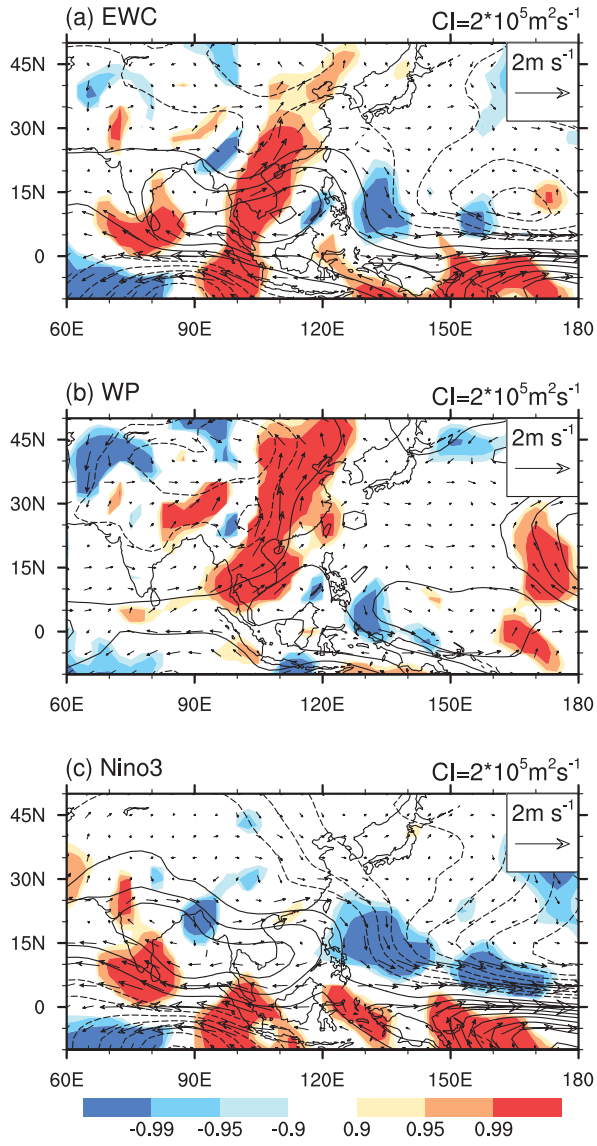


Figure 11. Regression of the autumn mean 850 hPa wind (vector; $ms^{-1}$) and stream function (contour; $CI = 2 \times 10^5\ m^2\ s^{-1}$) onto the normalized simultaneous (a) EWC index, (b) negative WP index, and (c) Niño3 index for the period 1951–2012. Zero contours are omitted and contours with negative values are dashed. Dark, middle, and light shading indicate the 99, 95, and 90% confidence levels of meridional wind component based on two-tailed Student's *t*-test, respectively.

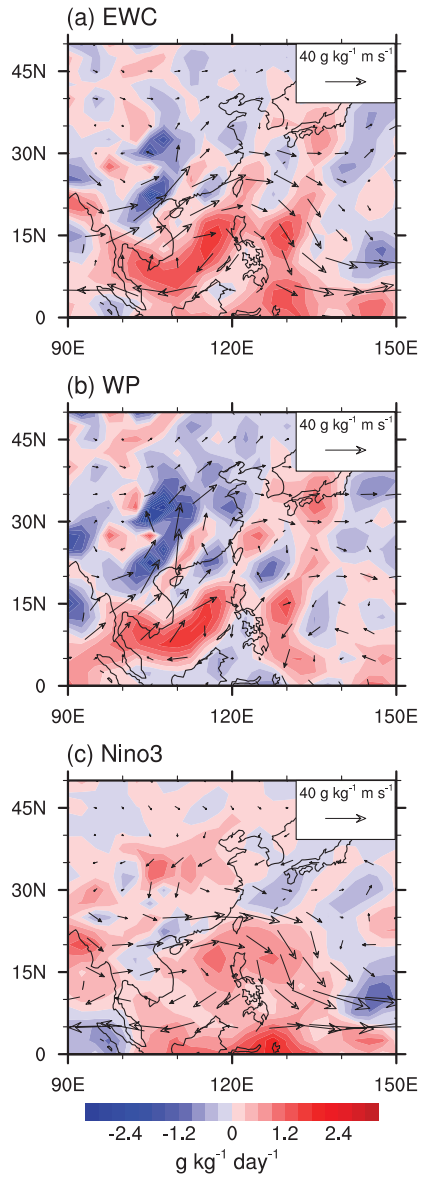


Figure 12. Regression of the autumn mean tropospheric vertically integrated water vapour flux (vector; $g\,kg^{-1}\,ms^{-1}$) and its divergence (shading; $g\,kg^{-1}\,day^{-1}$) onto the normalized simultaneous (a) EWC index, (b) negative WP index, and (c) Niño3 index for the period 1951–2012.

wind anomalies are observed over the Indochina Peninsula and eastern China. This configuration weakens the climatological mean northerly winds (Figure 10(a)) and enhances the water vapour transport to South China, leading to anomalous water vapour convergence in this region (Figure 12(a)). Meanwhile, an inspection on the local meridional circulation indicates anomalous local Hadley circulation. The anomalous descending branch is located in the tropical WP and the anomalous ascending branch is located between 20°N and 30°N (Figure 13(a)), leading to significant ascent anomalies over South China (Figure 13(a) and (b)). Hence, the enhanced water vapour convergence and the anomalous ascent, which are both associated with enhanced tropical Pacific east–west SST contrast, favour enhanced precipitation over South China.

The EWC index consists of the SST in both the tropical eastern Pacific and the tropical WP. So we further examined the potential contributions from the two regions. The eastern box in the definition of EWC index is exactly the Niño3 region. So the Niño3 index and the WP index, defined as the area-averaged SST over the western box in the definition of EWC index (Table 1), were calculated. The correlation coefficient between Niño3 index and WP index is 0.04 in autumn, indicating their independence to each other. The lag correlations with autumn precipitation index suggest that both the Niño3 index and WP index are significantly correlated with the autumn precipitation in South China (Figure 7). The correlation coefficient with WP index is higher than that with Niño3 index from July to October. Given the loose correlation between Niño3 and WP indices, this result indicates that the SST variations in

© 2014 Royal Meteorological Society

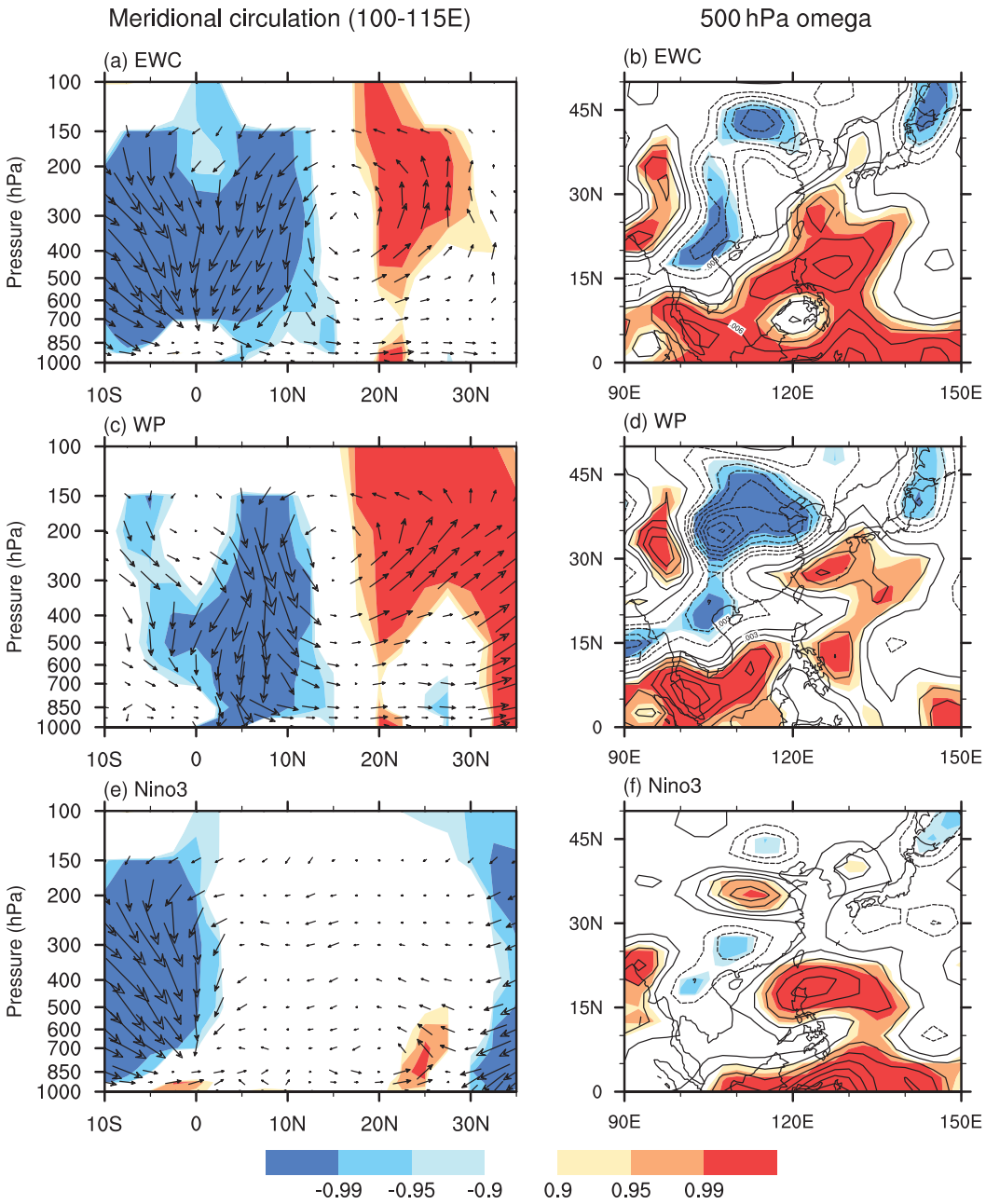


Figure 13. Regression of the autumn mean (a) meridional-vertical circulation averaged over East Asia (100°−115°E) and (b) 500 hPa vertical velocity (contour; CI = 0.0015 Pa $s^{-1}$) onto the normalized simultaneous EWC index for the period 1951–2012. (c, d) and (e, f) are the same and (a, b), but for WP index (multiplied by −1) and Niño3 index, respectively. Zero contours are omitted and contours with negative values are dashed in (b), (d), and (f). Dark, middle, and light shading indicate the 99, 95, and 90% confidence levels of vertical velocity based on two-tailed Student's *t*-test, respectively.

both the tropical eastern and the tropical WP contribute somewhat independently to the autumn precipitation in South China. Moreover, it implies that the SST over tropical WP probably plays a more important role than that over the tropical eastern Pacific.

To verify the above interpretation, the circulation anomalies regressed onto WP and Niño3 indices were further examined. The 850 hPa wind associated with WP index features significant southerly anomalies in the Indochina Peninsula and eastern China, resembling that in Figure 11(a), while the wind anomalies are very weak in the tropics (Figure 11(b)). In contrast, the Niño3 index-related circulation features strong wind anomalies in the tropics and subtropics, with an anticyclonic wind anomaly being located to the west of Philippine, but these wind anomalies are insignificant over South China (Figure 11(c)). Accordingly, the observed water vapour flux and its convergence over South China (Figure 12(a)) are mainly contributed by those associated with the WP index (Figure 12(b)). It is noteworthy that although the Niño3 index-related circulation generally favours divergence of water vapour over East Asia, it facilitates enhanced water vapour convergence over the southernmost part of Mainland China (Figure 12(c)).

© 2014 Royal Meteorological Society

On the other hand, the inspection on the local meridional circulation indicates that the WP index is associated with ascending motion between 20°N and 30°N and descending motion between 0°N and 15°N (Figure 13(c)). It resembles that in Figure 13(a), but significant descending motion that usually suppresses precipitation is observed in the lower troposphere over the northern part of South China (i.e. 25°N–30°N, Figure 13(c)). This anomalous descending motion is mainly located to the east of 112°E (Figure 13(d)). On the contrary, although the Niño3 index-related meridional circulation is much weaker, it is associated with strong descending motion throughout the troposphere over the equatorial region south of the equator and significant ascending motion in the lower and middle troposphere over northern part of South China (Figure 13(e)). The latter is mainly located around 110°E (Figure 13(f)), possibly due to the anomalous lower-tropospheric wind convergence to the north of the anticyclone (Figure 11(c)). It compensates the anomalous descending motion to the east of 112°E shown in Figure 13(d) to some extent (Figure 13(b)), and facilitates enhanced precipitation. Therefore, these results suggest that the SST of tropical WP contributes mostly to the meridional wind over East and Southeast Asia and dominates the water vapour transport and convergence over South China. Meanwhile, the SST of both tropical eastern and WP contributes to the vertical motion over South China and creates a favourable large-scale circulation for enhanced precipitation. As a result, the east–west SST contrast, which is a combination of both the effects, could efficiently influence the interannual variations of the autumn precipitation in South China.

In order to further interpret the formation of the observed circulation anomalies as well as the physical meaning of the EWC index, we analysed the 200 hPa velocity potential and stream function associated with EWC, Niño3, and WP indices (Figure 14), like in Kucharski *et al.* (2011). When the tropical eastern Pacific SST is warmer than normal, an anomalous upper tropospheric divergence (convergence) centre is observed over the tropical eastern (western) Pacific (Figure 14(e)). They roughly superpose the climatological mean centres of divergent circulation (not shown), indicating a weakened Walker circulation. When the tropical WP SST is warmer than normal, in contrast, anomalous upper tropospheric divergence centre is observed around 170°W (Figure 14(c)), indicating a slightly eastward shift of Walker circulation. The combined effect of the two, measured by the EWC index, features upper tropospheric divergence (convergence) around 160°W (100°E) in the tropics (Figure 14(a)). The 200 hPa eddy stream functions associated with the three indices are in quadrature with the corresponding velocity potential anomalies (Figure 14(b), (d) and (f)). It suggests that their stream function maximum lies in the gradient of the velocity potential, which is consistent with the Sverdrup relationship. In this aspect, the WP index-related response is especially important, which shows a large-scale upper-level anticyclone over East Asia continent (Figure 14(d)). This response has baroclinic structure and features a large-scale cyclone at 850 hPa (Figure 11(b)). Hence, significant southerly wind anomalies to the east of this cyclone are observed over East Asia (Figure 11(b)).

## 6. A statistical prediction model for autumn precipitation in South China

Given the good lead–lag relationship between EWC index and South China autumn precipitation (Figure 7), it is meaningful to examine its usefulness in the statistical prediction models and to compare its effect with those based on ENSO in terms of Niño3 and Niño3.4 indices. Here, the summer (JJA) mean indices are employed as predictor to construct a simple linear regression model for the South China's autumn precipitation. The periods 1951–1981 and 1982–2012 are used as calibration period and independent verification period, respectively. Figure 15 shows the observed and predicted precipitation index for the period 1951–2012, where the predicted values in 1951–1981 are obtained via cross-validation. For the independent verification period 1982–2012, the correlation coefficients between predicted and observed precipitation is 0.55 for the EWC model, while it is only 0.34 and 0.20 for the Niño3 and Niño3.4 model, respectively. The predicted variance on the basis of EWC index is 30%, which is much higher than those based on Niño3 and Niño3.4 indices (12 and 4%). This result demonstrates the usefulness of the EWC index in the operational predictions. On the other hand, it is also noteworthy that the precipitation prediction in China is a tough task due to the complex monsoon climate. The statistical prediction model with only one predictor cannot meet the demand of operational predictions. Therefore, a more comprehensive model should be developed and evaluated carefully in the future.

## 7. Summary and discussion

ENSO is usually regarded as the most important factor that influences autumn precipitation in South China with more (less) rainfall in El Niño (La Niña) years. However, a closer inspection suggests that more than 48% (38%) El Niño years (La Niña) are accompanied with autumn drought in South China, implying the inadequacy of explaining the autumn precipitation by ENSO. A revisit of this issue reveals that the east–west SST contrast of the tropical Pacific exerts significant impacts on the autumn precipitation in South China. Accordingly, an EWC index is defined as the difference of the normalized area-averaged SST anomalies between the tropical eastern Pacific (150°W–90°W, 5°S–5°N, the Niño3 region) and the tropical WP (110°E–180°E, 5°S–5°N). Compared with the traditional El Niño indices (Niño3, Niño3.4, and EMI), the EWC index is most tightly related to the precipitation in South China with the significant correlation coefficient persisting from April to December. The leading time and the persistent signal imply the potential usefulness of the EWC index in the prediction of the autumn

© 2014 Royal Meteorological Society

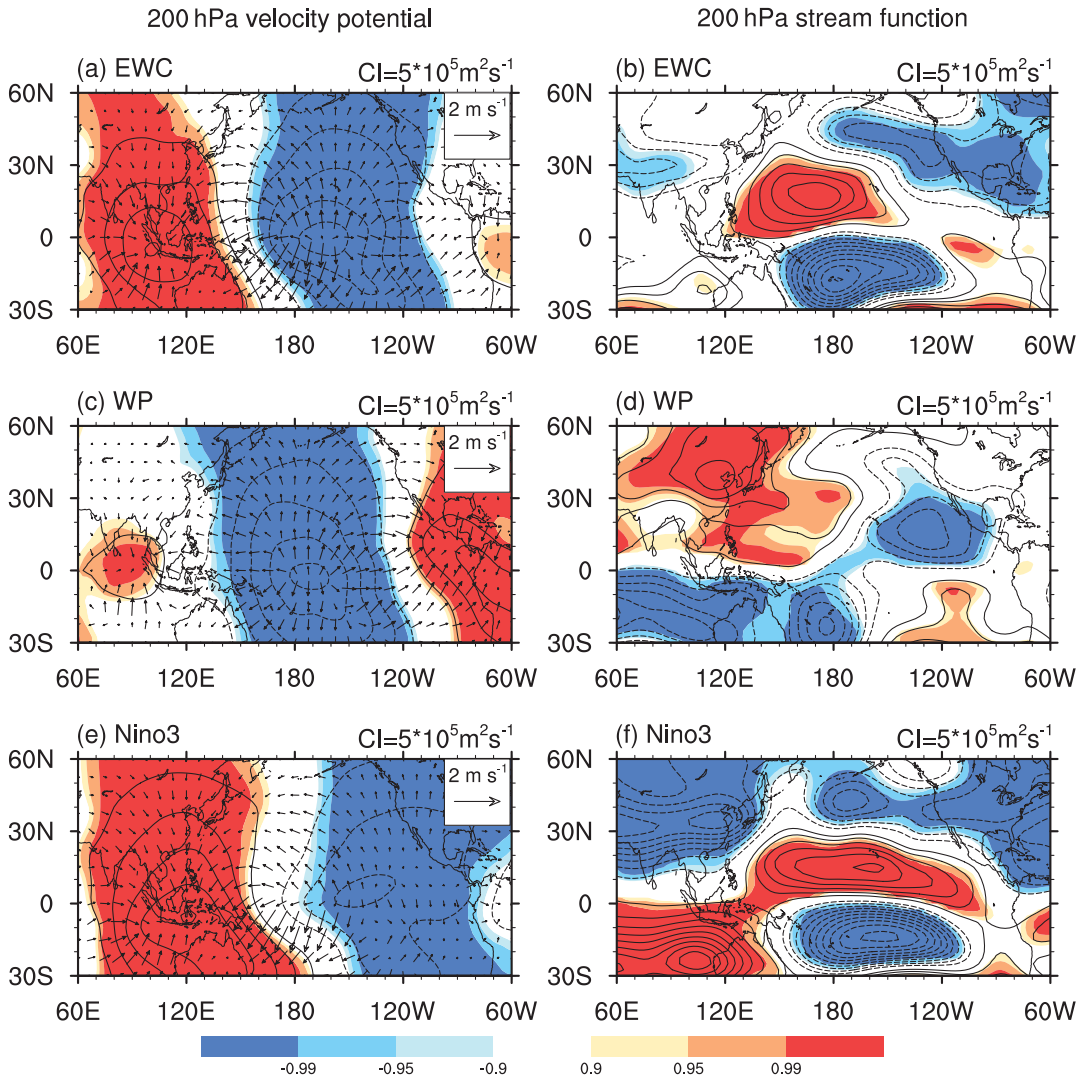


Figure 14. Regression of the 200 hPa autumn mean (a) velocity potential (contour; CI = $5 \times 10^5$ m$^2$ s$^{-1}$) and divergent winds (vector; ms$^{-1}$), and (b) stream function (CI = $5 \times 10^5$ m$^2$ s$^{-1}$) onto the normalized simultaneous EWC index for the period 1951–2012. (c, d) and (e, f) are the same and (a, b), but for WP index (multiplied by −1) and Niño3 index, respectively. Zero contours are omitted and contours with negative values are dashed. Dark, middle, and light shading indicate the 99, 95, and 90% confidence levels based on two-tailed Student's *t*-test, respectively.

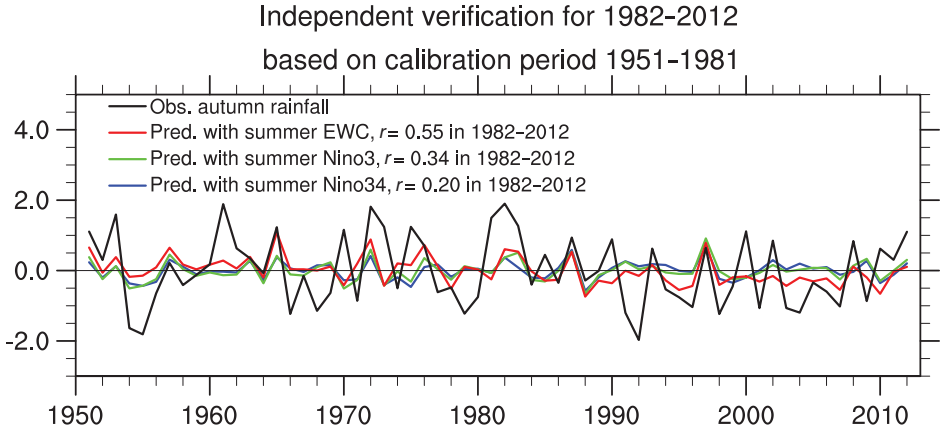


Figure 15. The observed time series of South China autumn mean precipitation index and the reconstructed ones with simple linear regression based on summer mean EWC, Niño3, and Niño3.4 indices. The periods 1951–1981 and 1982–2012 are used as calibration and independent verification periods for the linear regression equation, respectively.

© 2014 Royal Meteorological Society

precipitation in South China, which is demonstrated in a simple statistical prediction model.

The possible mechanism through which the east–west SST contrast influences the precipitation is also analysed. When the EWC index is positive, the tropical eastern (western) Pacific is warmer (colder) than normal. In this situation, the climatological mean Walker circulation is slightly shifted with anomalous upper-level divergence (convergence) being located around 160°W (100°E). The eddy stream function is in quadrature with the corresponding velocity potential anomalies, consistent with Sverdrup relationship. In the lower troposphere, southerly wind anomalies are observed from the Indochina Peninsula to the whole eastern China, which favour water vapour convergence over South China. Meanwhile, the ascending motion over South China is significantly enhanced. Therefore, significant above-normal autumn precipitation is observed. A further inspection suggests that the SST of the tropical WP dominates the lower-tropospheric meridional wind and water vapour transport and convergence over East Asia. In contrast, both the tropical eastern and the tropical WP SST contributes to the anomalous ascending motions over South China. In other words, neither the tropical eastern Pacific nor the tropical WP can explain the precipitation alone. It is their combined effects, i.e. the east–west SST contrast, that lead to significant variations of autumn precipitation in South China.

One may ask why in autumn the anomalous anticyclone (Figures 11(c) and 12(c)) alone cannot lead to significant water vapour convergence and rainfall anomalies as it does in summer (e.g. Huang *et al.*, 2012). It is inferred that this is due to the different climatological mean state between summer and autumn. In summer, strong southwesterly monsoonal wind prevails in the lower troposphere over East Asia (Figure 10(c)). It transports abundant water vapour from the oceans, leading to water vapour convergence over South China (Figure 10(d)). Therefore, with abundant climatological water vapour condition, the circulation anomalies of the anticyclone could easily generate rainfall anomalies. In autumn, on the contrary, northeasterly wind prevails in the lower troposphere over East Asia and an anticyclone dominates eastern China (Figure 10(a)). It blocks water vapour fluxes from the oceans, making the climatological mean water vapour convergence very weak over South China (Figure 10(b)). Hence, the circulation anomalies of the anticyclone alone cannot generate rainfall anomalies in a dry environment. In this situation, the additional water vapour transport induced by the anomalous southerly wind that are associated with the tropical WP SST are crucial to form water vapour convergence and rainfall anomalies over South China (Figures 11(b) and 12(b)).

Given the comparable correlations of summer and autumn EWC indices to the autumn precipitation index (Figure 9(a) and (e)), we also examined the circulation anomalies and water vapour transport associated with summer mean EWC, Niño3, and WP indices like those in Figures 11–13. Quite similar results were obtained with the summer mean EWC index (not shown). Therefore, it is recommended that the summer mean EWC index could be used as a good indicator and potential predictor for the autumn precipitation in South China, as shown in Section 6. In addition, although the EWC index itself shows clear downward trend during the past 62 years (Figure 6), the results of this study do not depend on the long-term trend. On the other hand, it was reported that the NCEP/NCAR reanalysis dataset has some systematic errors over East Asia before the late 1970s (e.g. Wu *et al.*, 2005). Hence, the same analysis was repeated for the period 1982–2012. Although some differences were observed in the areas north of 50°N, almost the same results can be obtained in the subtropical and mid-latitude East Asia, especially over South China. The correlation coefficient between autumn South China precipitation index and summer (autumn) EWC index is 0.55 (0.46) during this period. This is consistent with previous studies that the flaws of the NCEP/NCAR reanalysis dataset are mainly confined in the lower troposphere over Mongolia (e.g. Wu *et al.*, 2005). More importantly, it indicates that the results in this article are not influenced by the systematic errors of the NCEP/NCAR reanalysis dataset.

## Acknowledgements

We thank the three anonymous reviewers for their constructive comments that lead to improvement of the manuscript. This work was supported by the National Basic Research Program of China (2013CB430203), the National Department Public Benefit Research Foundation of China (GYHY201406018), and the National Natural Science Foundation of China (41230527). LW acknowledge the funding from Outstanding Young Scientists Project of Chinese Academy of Sciences. The authors declare no conflict of interest on this manuscript.

## References

Ashok K, Behera SK, Rao SA, Weng H, Yamagata T. 2007. El Niño Modoki and its possible teleconnection. *J. Geophys. Res.* **112**: C11007, DOI: 10.1029/2006JC003798.

Barriopedro D, Gouveia CM, Trigo RM, Wang L. 2012. The 2009/10 drought in China: possible causes and impacts on vegetation. *J. Hydrometeorol.* **13**: 1251–1267, DOI: 10.1175/JHM-D-11-074.1.

Cao J, Hu J, Tao Y. 2012. An index for the interface between the Indian summer monsoon and the East Asian summer monsoon. *J. Geophys. Res.* **117**: D18108, DOI: 10.1029/2012JD017841.

Cao J, Yao P, Wang L, Liu K. 2014. Summer rainfall variability in low latitude highlands of China and subtropical Indian Ocean dipole. *J. Clim.* **27**: 880–892, DOI: 10.1175/JCLI-D-13-00121.1.

Chen W. 2002. Impacts of El Niño and La Niña on the cycle of the East Asian winter and summer monsoon. *Chin. J. Atmos. Sci.* **26**: 595–610.

Chen Y, Shi N. 2003. El Niño/ENSO and climatic anomaly in the autumn of China. *J. Trop. Meteorol.* **19**: 137–146.

Chen W, Wang L, Xue Y, Sun S. 2009. Variabilities of the spring river runoff system in East China and their relations to precipitation and sea surface temperature. *Int. J. Climatol.* **29**: 1381–1394, DOI: 10.1002/joc.1785.

Feng J, Guan ZY, Wang LJ, Yu B. 2010a. Impact of central equatorial Pacific SSTA pattern on precipitation and temperature in East China in summer. *Trans. Atmos. Sci.* **33**: 547–554.

Feng J, Wang L, Chen W, Fong SK, Leong KC. 2010b. Different impacts of two types of Pacific Ocean warming on Southeast Asian rainfall during boreal winter. *J. Geophys. Res.* **115**: D24122, DOI: 10.1029/2010JD014761.

© 2014 Royal Meteorological Society

Feng J, Chen W, Tam CY, Zhou W. 2011. Different impacts of El Niño and El Niño Modoki on China rainfall in the decaying phases. *Int. J. Climatol.* **31**: 2091–2101, DOI: 10.1002/joc.2217.

Gu W, Li WJ, Chen LJ, Jia XL. 2012. Interannual variations of autumn precipitation in China and their relations to the distribution of tropical Pacific sea surface temperature. *Clim. Environ. Res.* **17**: 467–480.

Huang R, Chen J, Wang L, Lin Z. 2012. Characteristics, processes, and causes of the spatio-temporal variabilities of the East Asian monsoon system. *Adv. Atmos. Sci.* **29**: 910–942, DOI: 10.1007/s00376-012-2015-x.

Kalnay E, Kanamitsu M, Kistler R, Collins W, Deaven D, Gandin L, Iredell M, Saha S, White G, Woollen J. 1996. The NCEP/NCAR 40-year reanalysis project. *Bull. Am. Meteorol. Soc.* **77**: 437–471.

Kucharski F, Bracco A, Barimalala R, Yoo JH. 2011. Contribution of the east–west thermal heating contrast to the South Asian Monsoon and consequences for its variability. *Clim. Dyn.* **37**: 721–735.

NCC/CMA. 2010. China Climate Impact Assessment. Report No. 3, National Climate Center, China Meteorological Administration, Beijing, 16pp.

Niu N, Li JP. 2008. Interannual variability of autumn precipitation over South China and its relation to atmospheric circulation and SST anomalies. *Adv. Atmos. Sci.* **25**: 117–125, DOI: 10.1007/s00376-008-0117-2.

Rayner NA, Parker DE, Horton EB, Folland CK, Alexander LV, Rowell DP, Kent EC, Kaplan A. 2003. Global analyses of sea surface temperature, sea ice, and night marine air temperature since the late nineteenth century. *J. Geophys. Res.* **108**: 144407, DOI: 10.1029/2002JD002670.

Wang B, Zhang Q. 2002. Pacific-east Asian teleconnection. Part II: How the Philippine Sea anomalous anticyclone is established during El Niño development. *J. Clim.* **15**: 3252–3265.

Wang B, Wu R, Fu X. 2000. Pacific-East Asian teleconnection: how does ENSO affect East Asian climate? *J. Clim.* **13**: 1517–1536.

Wu RG, Hu ZZ, Kirtman BP. 2003. Evolution of ENSO-related rainfall anomalies in East Asia. *J. Clim.* **16**: 3742–3758.

Wu R, Kinter JL III, Kirtman BP. 2005. Discrepancy of interdecadal changes in the Asian region among the NCEP-NCAR reanalysis, objective analyses, and observations. *J. Clim.* **18**: 3048–3067.

Xin X, Yu R, Zhou T, Wang B. 2006. Drought in late spring of South China in recent decades. *J. Clim.* **19**: 3197–3206, DOI: 10.1175/JCLI3794.1.

Zhang RH, Sumi A. 2002. Moisture circulation over East Asia during El Niño episode in northern winter, spring and autumn. *J. Meteorol. Soc. Jpn.* **80**: 213–227, DOI: 10.2151/jmsj.80.213.

Zhang RH, Sumi A, Kimoto M. 1996. Impact of El Niño on the East Asian monsoon: a diagnostic study of the '86/87 and '91/92 events. *J. Meteorol. Soc. Jpn.* **74**: 49–62.

Zhang RH, Sumi A, Kimoto M. 1999. A diagnostic study of the impact of El Niño on the precipitation in China. *Adv. Atmos. Sci.* **16**: 229–241, DOI: 10.1007/bf02973084.

Zhang W, Jin F-F, Li J, Ren H-L. 2011. Contrasting impacts of two-type El Niño over the Western North Pacific during boreal autumn. *J. Meteorol. Soc. Jpn.* **89**: 563–569, DOI: 10.2151/jmsj.2011-510.

Zhang W, Jin F-F, Zhao J-X, Qi L, Ren H-L. 2013. The possible influence of a nonconventional El Niño on the severe autumn drought of 2009 in Southwest China. *J. Clim.* **26**: 8392–8405, DOI: 10.1175/JCLI-D-12-00851.1.

© 2014 Royal Meteorological Society 

doi:10.11676/qxxb2014.015 气象学报

# 旋转经验正交函数分解回归方法在东北夏季气温季节预测和成因诊断中的应用*

韩荣青 高 辉 李维京
HAN Rongqing GAO Hui LI Weijing

国家气候中心气候研究开放实验室,北京,100081
*Laboratory for Climate Studies, National Climate Center, China Meteorological Administration, Beijing* 100081, *China*
2013-05-31 收稿,2013-11-08 改回.

韩荣青,高辉,李维京. 2014. 旋转经验正交函数分解回归方法在东北夏季气温季节预测和成因诊断中的应用. 气象学报,72(2):291-305

**Han Rongqing, Gao Hui, Li Weijing. 2014. An application of the REOF and stepwise regression to seasonal forecast and cause diagnosis for summer temperature anomaly in northeast China. *Acta Meteorologica Sinica*, 72(2): 291-305**

**Abstract** Based on observed monthly surface air temperatures from the 73 stations in northeastern China from June to August during 1971-2011, the NCEP/NCAR reanalysis Ⅰ monthly height at 500 hPa and the NOAA extended reconstructed monthly Sea Surface Temperature (SST) V3b data during 1971-2012, and employing the statistical prediction idea of principal component regression (PCR), the paper constructed a seasonal forecast model of the modified PCR for classified summer temperatures in northeastern China using the atmospheric circulation and SST of January-May this year as predictors, which made a clear explanation on the early climatic causes of the Northeast summer temperature anomalies. Because of the qualities of smaller sampling errors, significant spatiality structure, but flexible time series of eigenvectors for the Rotated Empirical Orthogonal Function (REOF), the whole time-space series data of surface air temperature from 1971-2011 is analyzed by REOF for gaining full predictand information, the predictors are then diagnosed based on the relationships between REOF eigenvectors and preceding climatic conditions, and at finally the forecast model is built by the multiple stepwise regressions. The training period of the forecast model is the former 30 years of the time series, and the last 11 years in the time series are the period of the independenttest samples, in which the cross hindcast validation and independent test all showed skillful, especially effective for the classified temperature forecast.

The preceding causes of summer temperature anomalies in northeastern China are able to be found by the processes of the built model, and the results show that the certain configured situation of AO/NAO, NPO, and subtropical zonal mode (SZ) of like-signed anomalous pressure in May is significantly responsible for the surface air temperature anomaly of southeastern Northeast in the following June; and the cooperation of AO/NAO, East Pacific Oscillation, and Eurasian pattern type 1 teleconnection wave in March is responsible for the following surface air temperature anomaly of northeastern Inner Magnolia and western Northeast in July; and subtropical zonal mode pattern associated with no apparent planetary wave trains in the mid-high latitudes in May is responsible for the surface air temperature anomaly in the portion of northeastern Inner Magnolia and the central and western part of Heilongjiang Province in coming August, with both of which located in northern Northeast; and, on the other hand, the causes of SST anomaly show that the anomalous SST distribution like El Niño (La Niña) pattern associated with the North Atlantic Tripole pattern in positive (negative) phase is significantly matched with atmospheric circulations leading to the lower (higher) summertime surface air tempertures in Northeast, and Indian Ocean Basin Mode(IOBM) in positive (negative) phase in late spring is related

* 资助课题:国家重点基础研究发展计划 973 项目(2012CB417205)、公益性行业(气象)科研专项(GYHY201306028)、国家自然基金(41075070)、国家科技支撑(2009BAC51B05)和国家气候中心开放实验室青年基金项目。
作者简介:韩荣青,从事短期气候预测工作和大气低频振荡研究。E-mail:hrq@cma.gov.cn

to the circulations leading to the higher (lower) surface air temperature in Northeast in August.

**Key words** Northeast China, Summer-classified temperature, REOF, Stepwise-multiple linear regression, Seasonal forecast model, Forecast verification, Preceding cause diagnosis

**摘 要** 利用中国东北4省/区73个地面气象观测站1971—2011年6—8月月平均气温,以及NCEP/NCAR再分析1971—2011年月平均高度和NOAA月平均海表温度(SST)资料,基于主成分回归(PCR)预测方法的思想,用同年1—5月北半球大气环流和全球SST场建立了东北地区夏季气温的统计预测模型,该建模方法是主成分回归方法的变形,计算方法较为简易,对气温等级的季节预测有较好的预报效果;并用其计算过程做了前期气候成因诊断。考虑到旋转经验正交函数分解样本误差较小、空间模态结构清晰,但特征向量的时间系数在不同时段有所变化的特点,故使用旋转经验正交函数分解整个时段的东北夏季气温场,然后基于旋转经验正交函数分解结果,进行前期影响因子甄别,最后建立多元线性逐步回归预测模型,建模期为前30年,独立样本预报期为后11年。30 a逐年交叉回报检验和11 a独立样本预测效果都显示该模型具有较高的预报技巧,尤其对气温等级的预测具有参考价值。

用预测模型的中间过程诊断了东北夏季各月某一类典型气温异常的前期成因:5月北极涛动和北大西洋涛动(AO/NAO)、北太平洋涛动(NPO)以及副热带纬向一致异常型(SZ)等大气大尺度低频波动对6月吉林和辽宁省气温异常有显著影响;3月北极涛动和北大西洋涛动、东太平洋涛动(EP)及欧亚遥相关型波列对7月内蒙古东北部气温异常有显著影响;5月在北半球中高纬度大尺度低频波列不显著的情况下,SZ型低频波列对8月内蒙古东北部部分地区和黑龙江中、西部等地气温异常有显著影响;前期海温呈厄尔尼诺(拉尼娜)型、同时北大西洋海温三极子为正(负)位相,一般与导致东北6月和7月偏冷(暖)的大气环流型相匹配;春末热带印度洋全区海表温度一致异常模态(IOBM)正(负)位相与导致东北8月偏暖(冷)的大气环流型相匹配。

**关键词** 东北地区,夏季气温等级,旋转经验正交函数分解,多元线性逐步回归,预测模型,预报效果,前期成因诊断
**中图法分类号** P468.0

## 1 引 言

东北地区是中国重要的秋粮产地,5—9月是玉米、水稻和大豆等喜温作物的生长期,此期间的气温变化与秋粮产量关系密切,低温极易使主要农作物遭受冷害而减产。在20世纪50年代至80年代初,东北低温冷害发生较为频繁,致使该地区粮豆产量年际变化较大,产量的年际差异从几十亿千克到几百亿千克,其中1954、1957、1969、1971、1972和1976年的夏季是典型的东北低温冷害年(北方主要作物冷害研究协作组,1981)。东北低温冷害的定义一般用作物生长季(5—9月)的积温距平来定义(丁士晟,1980a,1980b;孙玉亭等,1983;姚佩珍,1995),而低温的定义有多种,有以标准化气温来定义东北低温等级的(刘传凤等,1999),也有把气温距平±0.5℃作为偏暖(冷)异常的分界值的(王绍武等,1985a;李辑等,2006)。低温仅指气温偏低,不与作物受害联系,但低温涵盖低温冷害。20世纪90年代中期以来,夏季高温成为东北地区异常凸出的气候特点,2010年6月大兴安岭就因异常高温诱发了严重的森林火灾,尽管少有冷害发生,但是人们对2009年夏季东北大范围、长时间的严重低温还记忆犹新,同时,东北夏季较大范围的一般性低温也时有发生,如1998、2002和2003年。

20世纪80年代初,中国组建"东北夏季低温预报科研协作组",对东北夏季低温冷害的发生规律、作物冷害类型和低温冷害指标等做了广泛深入的研究,并取得了一系列研究成果(北方主要作物冷害研究协作组,1981;郭裕福等,1983),但关于东北夏季低温冷害的短期气候预测方法的研究成果十分有限,致使短期气候业务缺乏针对性的客观预测方法。统计预测方法常见于将预测因子和预测对象用经验正交函数分解后再作统计关系(Massy,1965;Brunet,et al,1996;Yu,et al,1997),也有的使用统计函数建立预测方程(曹经福等,2013),近年一种新的通过预测预报对象的年际增量来提高季节预报准确率的统计方法被证实在东北冬、夏气温季节预测中较为有效(Fan,2009;Fan, et al, 2010;王会军等,2012)。本研究基于前一类方法,提供一种基于主成分回归方法(Principal Component Regression,简称PCR)的变形预测方法,来预测东北气温各个等级。主成分回归方法由Massy(1965)提出来,该方法使用经验正交函数分解(Empirical Orthogonal Func-

tion, 简称 EOF)结合多元线性回归方法,克服了最小二乘回归方程中因自变量复共线性问题导致的估计效果不稳定性,此后类似于主成分回归的多种变形方法在气候预测中有广泛的应用(施能等,1992;袁景凤等,2000; Tan, et al, 2011; Mo, et al, 2002)。主成分回归方法对预报因子和预报对象都分别进行了经验正交函数分解,然后再用多元线性回归建立预报方程,本研究的预测方法基于主成分回归,但又有所不同,从业务实用角度出发,本着简便有效原则,使用极大方差旋转经验正交函数分解(Rotated Empirical Orthogonal Function, 简称 REOF)仅对预报对象做了时空分解,然后用多元线性逐步回归方法(Stepwise-multiple linear regression,简称 SMLR)建立预报方程。其中旋转经验正交函数分解较好地克服了取样误差,其空间模态结构清晰(魏凤英,2007),特征向量之间线性独立,但旋转经验正交函数分解特征向量的时间系数随样本序列变化而变化,因此本研究使用旋转经验正交函数分解做预报时,将实时预报前一时刻的信息纳入旋转经验正交函数分解,然后诊断分析预报对象旋转经验正交函数分解各模态分别与前期大气、海洋异常的关系,从而利用多元逐步线性回归方法来建立预报模型。预报实验结果表明,该方法在东北夏季气温等级的预测中体现了较高的预报技巧,具备业务实用价值,并且建模的中间过程具有前期气候成因诊断功能。

## 2 数据和方法

### 2.1 数 据

使用中国气象局信息中心公布的中国东北 4 省/区 73 个测站 1971—2011 年 6—8 月月平均地面气温,1971—2011 年美国 NCEP/NCAR reanalysis Ⅰ 500 hPa 高度场月平均资料(Kalnay, et al, 1996)空间水平分辨率为 2.5°×2.5°和美国 NOAA Extended Reconstructed Sea Surface Temperature V3b 准全球月平均海表温度资料(来自 NOAA/OAR/ESRL PSD, Boulder, Colorado, USA, http://www.cdc.noaa.gov/),空间水平分辨率为 2°×2°。

### 2.2 方 法

建立统计预测模型前,先将 1971—2011 年东北 73 站夏季 6—8 月月平均气温资料标准化处理,其中气候平均时段取 1981—2010 年,建模拟合期为前 30 a(1971—2000 年),独立样本预报期为 2001—2011 年共 11 a,前 30 年预测回报检验采用弃一交叉检验方法(Barnston, et al, 1996; 吴洪宝等, 2005)。具体建模方法如下:对于标准化的含有 $m$ 个空间点、$n$ 次观测样本的东北夏季月平均气温矩阵 $X_{mn}$,首先进行极大方差旋转经验正交函数分解,为了消除旋转经验正交函数分解特征向量时间系数的不稳定性,将整个时段的资料做旋转经验正交函数分解,得到 $p$ 个空间特征向量 $V_{mp}$ 和对应的时间权重系数 $T_{pn}$,$X_{mn}$ 是它们的线性组合,即 $X_{mn}=V_{mp}\cdot T_{pn}$,本研究选取的前 7 个($p=7$)旋转经验正交函数分解空间特征向量在旋转前的累积方差达到 95%。因为极大方差旋转是正交旋转,故 7 个矩阵 $T_{pn}$ 可看成是由 7 个正交基函数构成的坐标基,通过前期北半球大气环流($H$)和全球海表温度(SST)场分别与 $p$ 个时间权重系数 $T_{pn}$ 的相关分析,可得到前期气候因子 $H$ 和 SST 影响 $p$ 个($p$ 取 7)特征向量的关键月份,然后按如下计算逐步求得与前期 $H$ 和 SST 相关联的预报因子场(以计算大气环流预报因子场为例):

$$\boldsymbol{C}_{pH}=Cor(H_n,\ T_{pn}) \tag{1}$$

式中,$\boldsymbol{C}_{pH}$ 是张量,表示建模期北半球 500 hPa 高度场 $H_n$ 分别与 $p$ 个旋转经验正交函数分解特征向量时间系数 $T_{pn}$ 的相关场,下标 $n$ 表示时间序列样本数,$H$ 表示北半球高度场空间分布,$p$ 是选取的旋转经验正交函数分解前几个模态个数,本文取 $p=7$,$Cor$ 表示求相关系数的函数。

$$\boldsymbol{C}_{pn}=Cor_n(C_{pH},\ H_n) \tag{2}$$

式中,$\boldsymbol{C}_{pn}$ 表示 $p\times n$ 个相关系数,由 $n$ 个样本逐个样本大气环流场 $H_n$ 分别与 $p$ 个空间场($C_{pH}$)的空间格点相关,$Cor_n$ 表示求 $n$ 次空间场相关的函数。

$$\boldsymbol{A}^k_{mn}=C_{pn}\cdot V_{mp} \tag{3}$$

式中,$\boldsymbol{A}^k_{mn}$ 是预报因子场,即 $p$ 个样本数为 $n$ 的空间场($m$ 为预报对象站点数),由 $p$ 个样本数为 $n$ 的相关系数分别点乘以对应的 $p$ 个旋转经验正交函数分解空间荷载构成,其中 $k=1,\cdots,p$。

类似地,重复以上 3 步计算,可求得 SST 预报因子场,最后得到 $2\times p$ 个与前期大气和前期海表

温度相关联的预报因子场(空间点对应东北站点,时间长度为建模期与独立样本期长度之和)。

在 $2\times p$ 个预报因子场与东北月平均标准化气温场之间建立多元逐步回归预报方程

$$\boldsymbol{Y}_{mn}=\boldsymbol{\beta}^{0}_{mn}+\sum_{k=1}^{2p}(\boldsymbol{\beta}^{k}_{mn}\boldsymbol{A}^{k}_{mn})+\boldsymbol{\varepsilon}_{mn} \tag{4}$$

式中,$\boldsymbol{Y}_{mn}$ 为预报对象矩阵,即东北站点标准化气温,$\boldsymbol{\beta}^{k}_{mn}$ 为回归方程的系数矩阵,$\boldsymbol{\varepsilon}_{mn}$ 为预报误差矩阵,至此完成预报建模。

本研究的目的是气温等级预测建模及其预测能力检验,故预报对象的等级划分并无严格高低温标准,但其中严重低温包含了历史典型低温冷害年份。东北标准化的 6—8 月月平均气温($T_n$)具体分为如下 5 个等级:

(1) 严重低温,$T_n\leqslant -1.3$;

(2) 低温,$-1.3<T_n\leqslant -0.5$;

(3) 正常,$-0.5<T_n\leqslant 0.5$;

(4) 高温,$0.5<T_n\leqslant 1.3$;

(5) 严重高温,$T_n>1.3$。

关于某一等级的预测效果,使用如下等级检验方法:

$$T_S=\frac{N_c}{N_o+N_f-N_c} \tag{5}$$

式中,$T_S$ 为等级预测正确率,其数值越大表示模型预测该等级的能力越强,$N_f$、$N_o$ 分别为某一气温等级的预报站数和实况出现站数;$N_c$ 为某一气温等级预报正确的站数。

## 3 前期气候影响因子

### 3.1 前期气候影响因子的关键期

研究表明(Hastenrath, et al,1977;Moura, et al,1981;Shukla, et al, 1977)海表面温度(SST)在区域降水甚至全球降水变化中起到重要调制作用。统计降尺度季节预测方法研究表明,用前期准全球 SST 和北半球 700 hPa 高度场预测夏威夷和阿拉斯加的气温和降水可以得到较好的预测结果(Barnston, et al, 1996; He, et al, 1996);统计方法对中国冬季气温的预测也得到了较好的效果(Fan, 2009;贾小龙等,2010;王会军等,2012);东北夏季气温与大气环流和海温的异常有密切联系(王绍武等,1985b;廉毅等,1998;王敬方等,1997;贾丽伟等,2006;孙建奇等,2006 年;Fan, et al,2010;沈柏竹等,2011)。因此,本研究将尝试使用前期全球 SST 和北半球高度场来预测东北夏季气温异常。

为了甄别出前期月平均大气环流和海温异常对东北夏季气温影响最密切的关键月份,本研究分别分析了样本序列 1—5 月各月北半球 500 hPa 高度场(0°—80°N 纬度范围共 144×33 格点)和全球海表温度场(72°S—72°N 范围共 180×73 格点),分别与同年夏季各月东北 73 站气温旋转经验正交函数分解前 7 个模态时间序列相关。图 1 给出了 1971—2011 年各相关场通过 $t$ 检验 95% 置信水平的格点数,表明 6 月东北气温各模态与 5 月大气环流场和 5 月海温场显著相关格点最多(图 1a 和 b 中实线);7 月东北气温各模态与 3 月大气环流场和 2 月海温场显著相关格点最多(图 1c 和 d 中实线);8 月东北气温各模态与 5 月大气环流场和 5 月海温场显著相关格点最多(图 1e 和 f 中实线)。

影响因子场的逐年月平均时间序列明显含有年际和年代际变化的气候信息,通过甄别、挑选前期关键影响月,故纳入了气候的季节变化信号,使得季节预报模型的初值信息更为完备。

### 3.2 前期影响因子的甄别

标准化月平均气温旋转经验正交函数分解特征向量的时间系数与前期关键影响月高度或海温场的相关场体现了影响因子的空间分布型态,其中包含了有组织的大尺度大气系统或海温异常现象。下面仅就图 1 中关键影响月份(显著相关格点数最高点)对应的气温旋转经验正交函数分解模态及其可能的前期影响系统做一举例分析。

3.2.1 6 月气温异常成因的典型个例分析

前 5 个月内,大气环流影响 6 月东北气温旋转经验正交函数分解各模态最为关键的时段是 5 月,其中对第 4 模态的影响尤为突出(图 1)。图 2a 和 b 是东北地区 6 月气温旋转经验正交函数分解第 4 模态(方差贡献率为 13%,与第 1 模态方差贡献率 19%相差不大)空间荷载和其时间系数,它们的正(负)对应 6 月东北东部的暖(冷)变化。图 2c 和 d 是第 4 模态时间系数分别与 5 月北半球 500 hPa 高度场和 5 月准全球 SST 的相关分布(1971—2011 年,本文以下同);当第4模态时间系数为正(负)指数

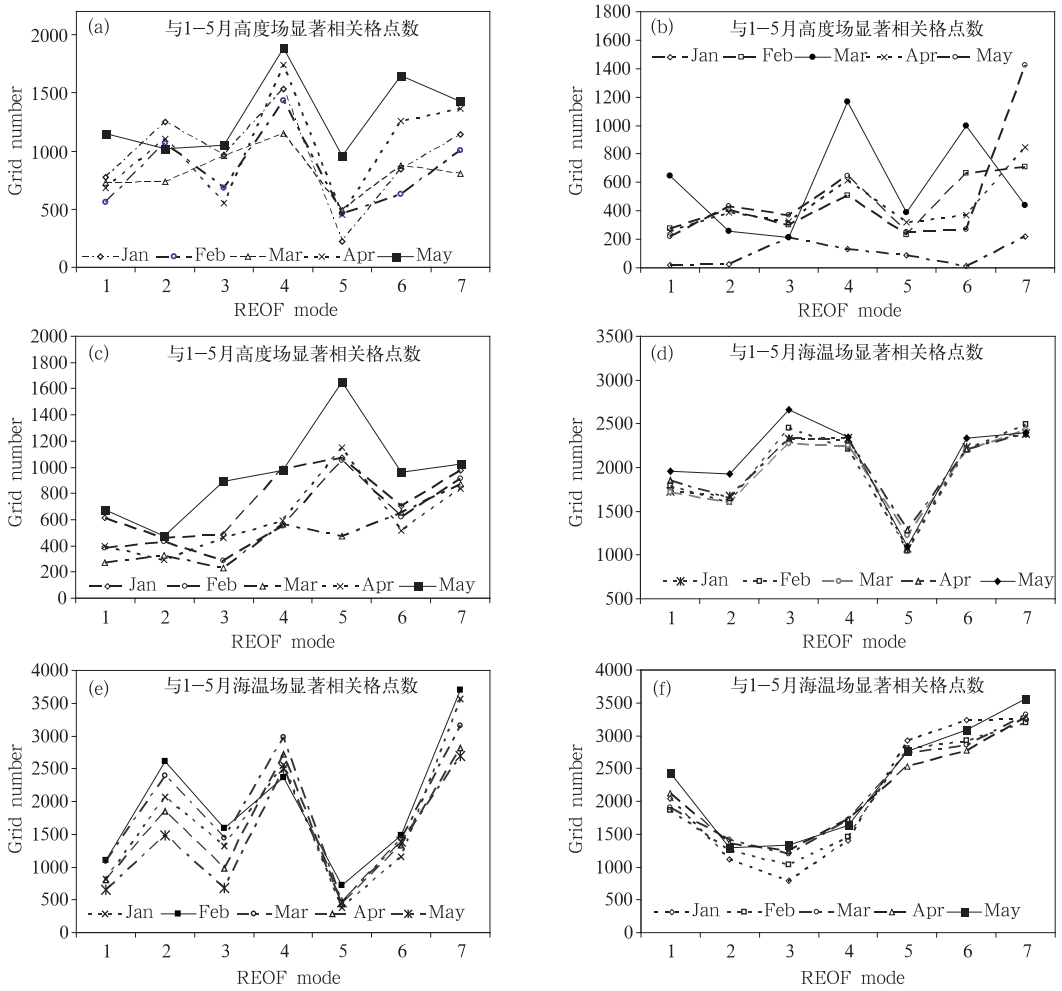


图1 东北夏季6月(a、d),7月(b、e)和8月(c、f)气温前7个旋转经验正交函数分解模态时间序列分别与同年1—5月月平均大气和海温场显著相关的格点数统计

(a、b、c. 500 hPa高度场:0°—80°N,0°—360°E,共144×33格点;d、e、f. 海表温度场:72°S—72°N,0°—360°E,共180×73格点;相关显著性:相关系数通过$t$检验95%置信水平;相关时间序列为1971—2011年)

Fig. 1 Grids' numbers of significant correlation between the first 7 REOF modes' temporal series of series of June (a,d), July (b,e), and August (c,f) surface air temperatures in Northeast and the atmospheric circulation or SST fields of Jan－May this year

(a, b, c. 500 hPa height, 0°－80°N, 0°－360°E, total of 144×33 grids; d, e, f. SST, 72°S－72°N, 0°－360°E, total of 180×73 grids; the correlation coefficients are significant at the 95% confidence level by student test; temporal length of correlation series: 1971－2011)

年时,图2c表明,同年5月500 hPa高度场呈北极涛动处于负(正)位相,北大西洋涛动也呈显著的负(正)位相,北太平洋涛动呈负(正)位相,但在北太平洋涛动南部区域相关不显著,北半球热带至副热带高度场较常年一致偏高(低),其中匹配出现Barnston等(1987)提出的副热带纬向异常一致型遥相关(Subtropical Zonal Pattern,简称SZ),而SST相关场表明(图2d),同年5月热带太平洋海温呈拉尼娜(厄尔尼诺)型分布,且配合北大西洋海温三极子(North Atlantic Tripole,简称NAT,Wu等,2005)呈负(正)位相。

这种5月的大气环流异常型配合海温异常型易导致6月东北地区气温偏高(低)。分别挑选第4模态时间系数极大和极小的各6个年份合成6月500 hPa高度距平(图2e和f),通过$t$检验95%信度的区域表明,高(低)指数年东北地区为正(负)距平

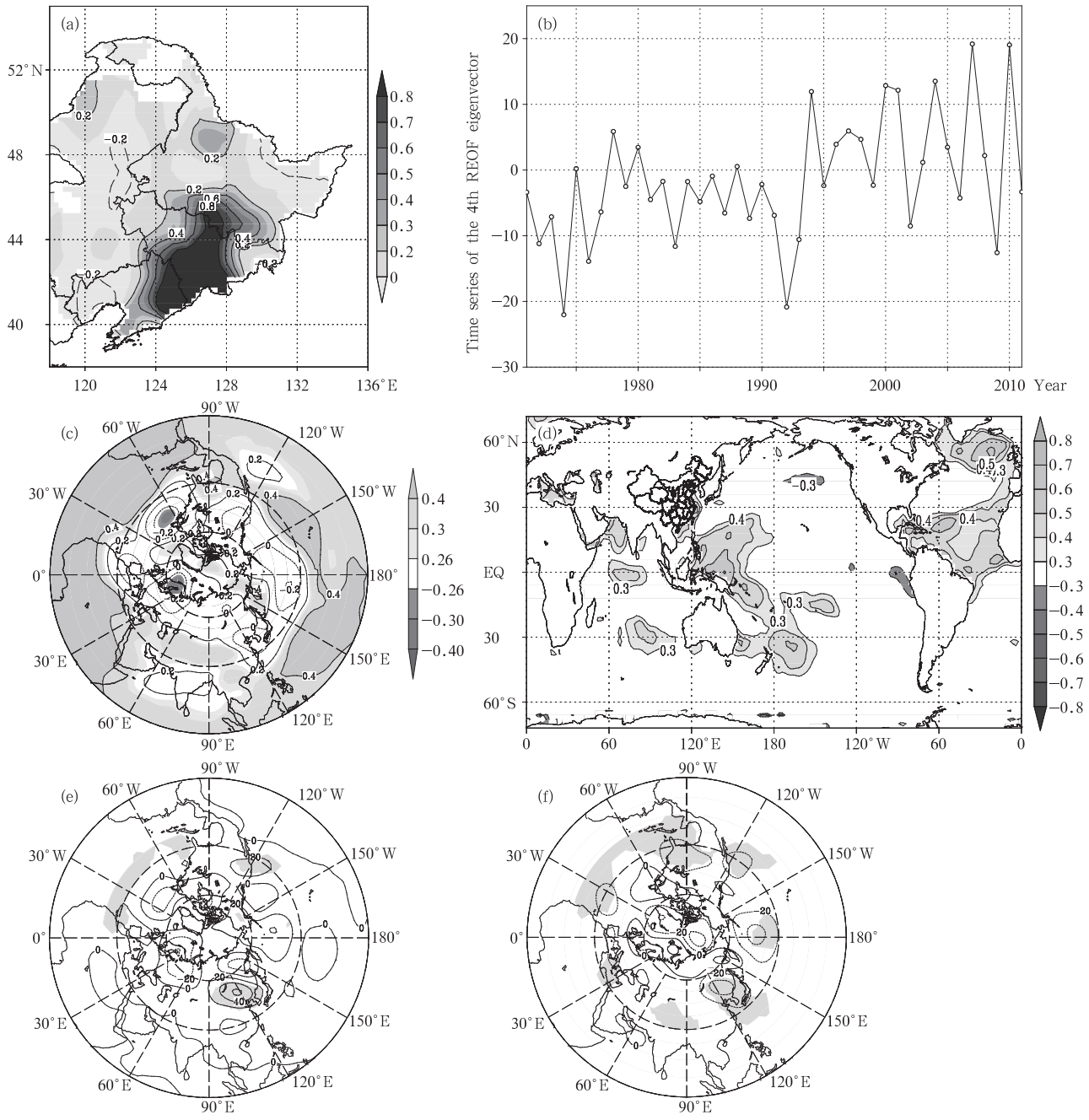


图 2 东北 6 月气温异常成因的典型个例分析

(时段:1971—2011 年;a、b. 6 月东北地区标准化气温旋转经验正交函数分解第 4 空间荷载及其时间系数;c、d. 第 4 空间荷载时间系数分别与同年 5 月 500 hPa 高度场和 SST 相关分布;e、f. 第 4 模态时间系数极大和极小各 6 个年份 6 月 500 hPa 高度距平合成,阴影区通过 $t$ 检验 95%置信水平,单位: m)

Fig. 2 Typical case analysis of the causes of surface air temperatures anomaly in Northeast in June

(statistical time length: 1971 − 2011; a. the 4th REOF spatial load of Northeast surface air temperatures in June; b. time series of the 4th REOF eigenvector; c. correlation distribution between the time series of the 4th REOF eigenvector for June surface air temperatures and 500 hPa height in May with leading one month; d. as in c but for SST; e. and f. are respectively the composites of 500 hPa height anomalies in June for the 6 highest and 6 lowest coefficient years of the time series of the 4th REOF eigenvector, in which shadowed regions are significant at the 95% confidence level by student test and units in meter)

控制,因此导致气温偏高(低)。总之,5月环流北极涛动、北大西洋涛动和北太平洋涛动一致负(正)位相型,配合SST异常呈拉尼娜(厄尔尼诺)及北大西洋海温三极子负(正)位相型,对6月东北地区环流乃至气温有显著性影响。

3.2.2 7月气温异常成因的典型个例分析

Barnston等(1987)用旋转经验正交函数分解北半球700 hPa高度场得到一些典型大气低频模态,指出1—3月东太平洋中低纬度与高纬度存在符号相反的高度异常类型,并称之为EP(东太平洋涛动)型。在同年1—5月,大气环流影响7月东北气温旋转经验正交函数分解各模态最为关键的时段是3月,其中对7月第4模态的影响尤为凸出(图1)。图3a和b分别是东北地区7月气温旋转经验正交函数分解第4空间荷载模态(方差贡献率为14%,而第1模态方差贡献率为18%)和其时间系数,正(负)模态代表东北7月以偏冷(暖)为主;图3c和d是第4模态时间系数分别与同年3月500 hPa高度场和2月准全球SST的相关分布,当第4模态时间系数为正(负)指数年时,图3c表明,同年3月北半球500 hPa高度场北极涛动、北大西洋涛动呈显著的正(负)位相,东太平洋涛动呈显著的负(正)位相(南正北负为正位相),此外,欧洲北部正(负)异常、以北非和地中海西部为中心延伸至大西洋副热带的负(正)异常、伊朗高原至中国西北部负(正)异常、以及日本海附近正(负)异常(不显著)构成了欧亚遥相关波列EU1型(Barnston, et al,1987),而SST相关场表明(图3d),同年2月热带太平洋海温呈厄尔尼诺(拉尼娜)型分布(热带东太平洋区域SST异常不显著),且配合北大西洋三极子呈正(负)位相(北大西洋副热带西部SST异常不显著)。

2月的这种SST异常分布配合3月的上述环流异常型,易导致7月东北地区气温偏低(高)。同样分别挑选第4模态时间系数极大和极小的各6个年份合成7月500 hPa高度距平(图3e和f),通过$t$检验90%信度的区域表明,高(低)指数年东北地区为显著性的负(正)距平控制,从而导致气温偏低(高)。总之,2月准全球SST异常呈拉尼娜(厄尔尼诺)及北大西洋三极子负(正)位相型,配合3月环流北极涛动和北大西洋涛动与东太平洋涛动位相相反以及出现EU1遥相关波列,对7月东北地区环流乃至气温有显著影响。

3.2.3 8月气温异常成因的典型个例分析

在同年1—5月,大气环流影响8月东北气温旋转经验正交函数分解各模态最为关键的时段是5月,其中对8月第5模态的影响尤为突出(图1)。图4a和b分别是东北地区8月气温旋转经验正交分解第5空间荷载模态(方差贡献率为14%,而第1模态方差贡献率为16%)和其时间系数,正(负)模态代表东北8月以偏冷(暖)为主;图4c和d是第5模态时间系数分别与5月500 hPa高度场和准全球SST的相关分布,当第5模态时间系数为正(负)指数年时,图4c表明,5月北半球中高纬度500 hPa高度场已知的遥相关波列不显著,但是北半球热带至副热带高度场较常年一致偏低(高),副热带出现纬向异常一致型遥相关(SZ),而SST相关场表明(图4d),同年5月热带印度洋大部分一致偏冷(暖),即热带印度洋海盆模态(Indian Ocean Basin Mode,简称IOBM)(Yang, et al, 2007)呈负(正)位相,但热带太平洋海温无显著的ENSO形态,北大西洋海温也无明显的北大西洋海温三极子形态。IOBM往往在冬末达到鼎盛,并持续至春夏季,研究认为其由ENSO诱发,并且可延长ENSO的影响(Klein, et al, 1999)。

5月的这种SST和环流异常型易导致8月东北地区气温偏低(高)。分别挑选第5模态时间系数极大和极小的各6 a合成8月500 hPa高度距平(图4e和f),通过$t$检验95%信度的区域表明,高(低)指数年东北地区为显著性的负(正)距平控制,故导致气温偏低(高)。总之,5月SST呈IOBM负(正)位相,且北半球中高纬度环流遥相关波列不显著,副热带出现SZ负(正)位相时,8月东北地区高度场和气温显著性偏低(高)。

综合前期海温对东北夏季气温的影响,可以看出,厄尔尼诺(拉尼娜)型海温异常一般与导致东北偏冷(暖)的大气环流型相匹配,这与已有的研究(王绍武等,1985b)结果一致;同时,北大西洋海洋三极子正(负)位相也与导致东北偏冷(暖)的大气环流型相匹配;春末热带印度洋海温IOBM对东北8月气温影响显著。

## 4 客观预测模型检验

基于前述影响因子甄别结果,按照2.2节介绍的方法,建立季节预测模型。图5是预测模型在

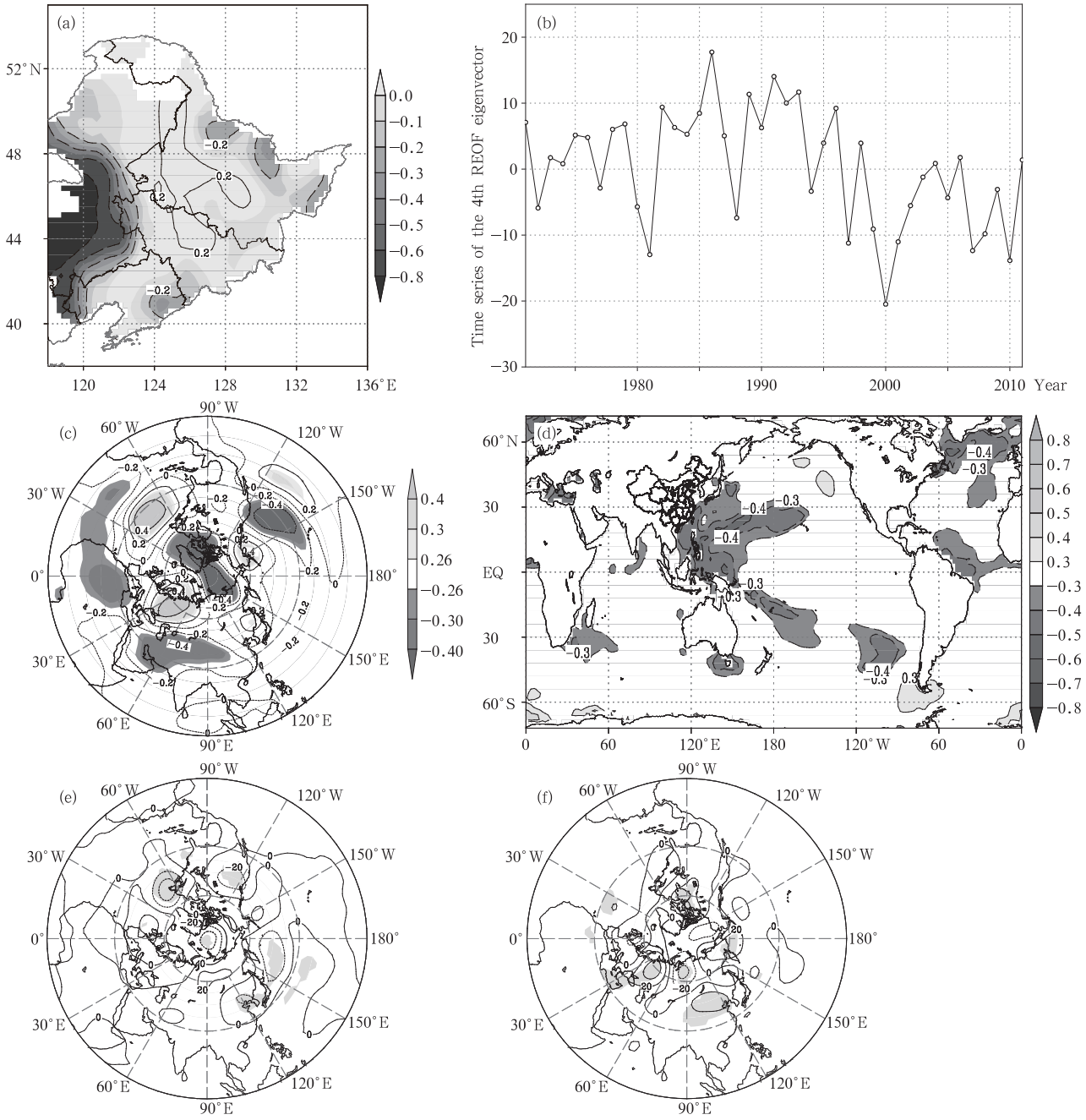


图 3 东北 7 月气温异常成因的典型个例分析

(a、b. 7 月东北地区标准化气温旋转经验正交函数分解第 4 空间荷载及其时间系数;c、d. 第 4 空间荷载时间系数分别与同年 3 月 500 hPa 高度场和 2 月 SST 相关分布; e、f. 第 4 模态时间系数最高和最低各 6 个年份 7 月 500 hPa 高度距平合成,阴影区通过 $t$ 检验 90%置信水平;其余同图 2)

Fig. 3 Typical case analysis of the causes of surface air temperatures anomaly in Northeast in July

(a. the 4th REOF spatial load of Northeast surface air temperatures in July; b. time series of the 4th REOF eigenvector; c. correlation distribution between the time series of the 4th REOF eigenvector for July surface air temperatures and 500 hPa height in March of the same year; d. as in c but for SST in February; e and f. respectively the composites of 500 hPa height anomalies in July for the 6 highest and 6 lowest coefficient years of the time series of the 4th REOF eigenvector, in which shadowed regions are significant at the 90% confidence level by student test. Others are the same as those in Fig. 2)

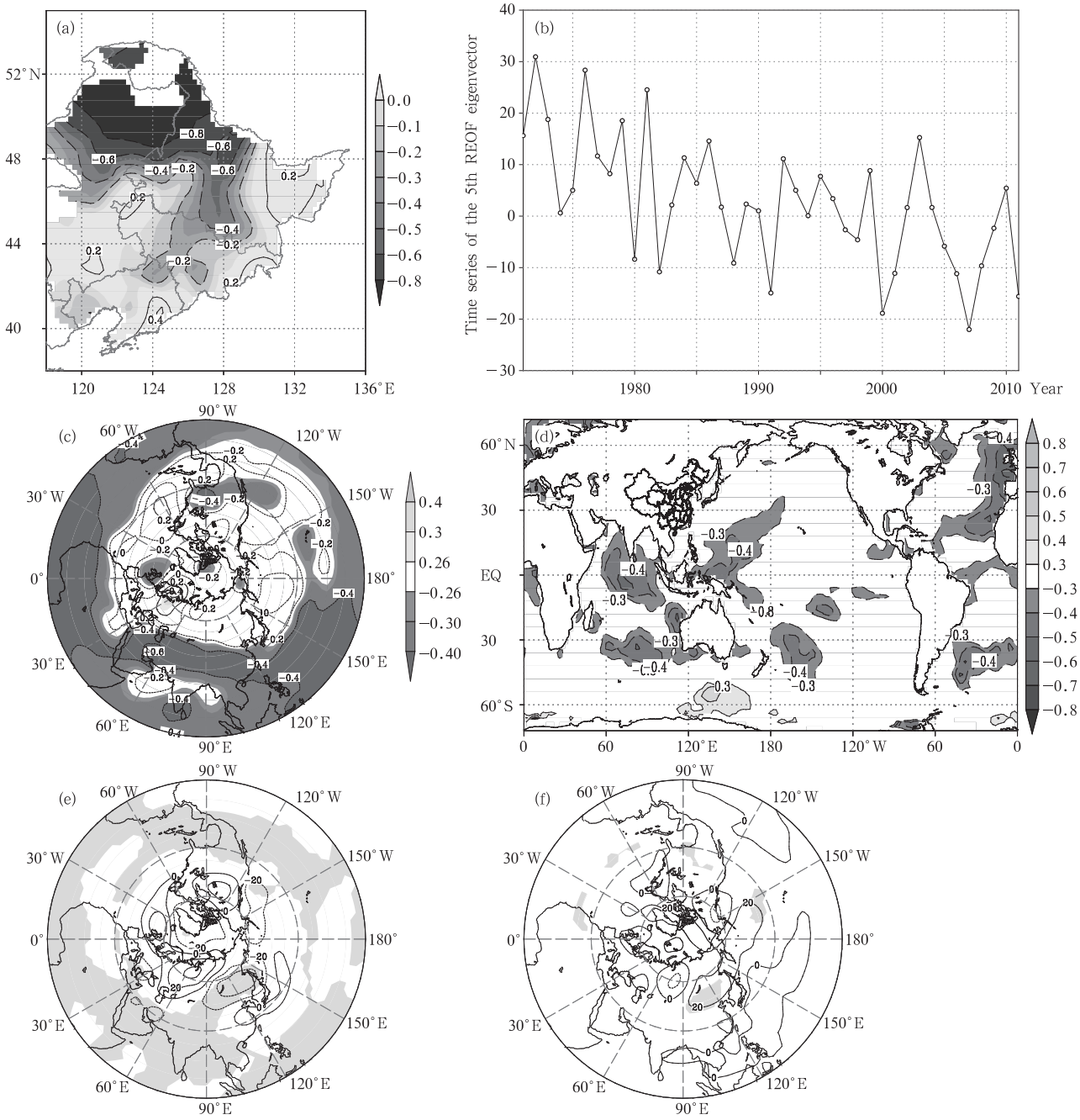


图 4　东北 8 月气温异常成因的典型个例分析

(a、b. 8 月东北地区标准化气温旋转经验正交函数分解第 5 空间荷载及其时间系数;c、d. 第 5 空间荷载时间系数分别与同年 5 月 500 hPa 高度场和 SST 相关分布;e、f. 第 5 模态时间系数最高和最低各 6 个年份 8 月 500 hPa 高度距平合成,阴影区通过 $t$ 检验 95%置信水平;其余同图 2)

Fig. 4　Typical case analysis of the causes of surface air temperatures anomaly in Northeast in August

(a. the 5th REOF spatial load of Northeast surface air temperatures in August; b. time series of the 5th REOF eigenvector; c. correlation distribution between the time series of the 5th REOF eigenvector for August surface air temperatures and 500 hPa height in May of the same year; d. as in c but for SST; e and f. respectively the composites of 500 hPa height anomalies in August for the 6 highest and 6 lowest coefficient years of the time series of the 5th REOF eigenvector, in which shadowed regions are significant at the 95% confidence level by student test. Others are the same as those in Fig. 2)

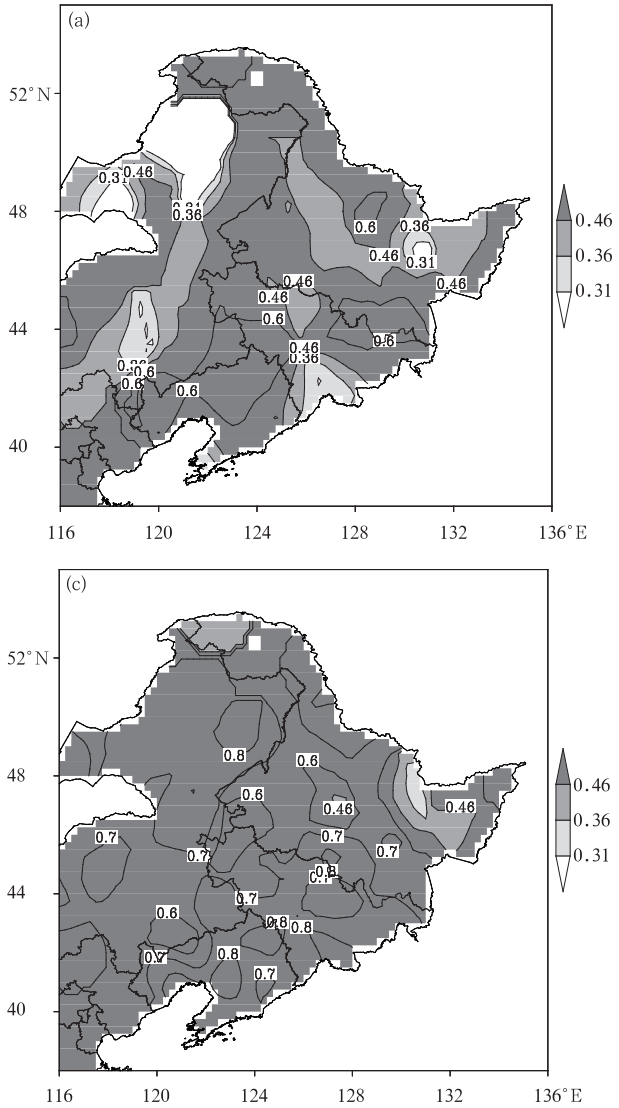


图 5 1971—2000 年夏季 6—8 月(a—c)东北 73 测站气温交叉回报与实况的相关系数分布

Fig. 5 Correlation validation of the cross hindcast of the seasonal forecast model and the actual summer surface air temperatures of the Northeast 73 stations from 1971－2000 (a. June, b. July, c. August)

1971—2000 年 30 a 建模期对 6—8 月各月东北气温的交叉回报与实况的相关系数,可以看出 6—8 月 73 站中的绝大多数相关系数超过了 $t$ 检验 95%置信水平(相关系数≥0.36),大部分站点相关系数超过 $t$ 检验 99%置信水平(相关系数≥0.46)。

图 6 是预测模型对 2001—2011 年独立样本期的站点气温等级预测的正确率(按式(5)计算)。因为模型对 5 个等级中的正常等级的站点预测正确率最高,故本研究不再详述,同时,为了在图 6 中清楚地表示缺省值(指某一气温等级实况出现站数<10 站时,在图中不显示)和预测正确率为 0 的不同,正确率含 0 值时图中纵坐标从负数起始。

如图 6,在 11 a 独立样本预测期中,6 月实况只有 1 a 发生严重低温(仅计出现站数>10 站的情况,下同),站点预测正确率超过 6%,预报技巧虽然不高,但对于小概率事件的预测具有预警参考价值;6 月实况有 6 a 出现低温,其中有 2 a 预报失败(正确率为 0,下同),其余 4 a 预测都有一定参考价值,尤其在低温空间范围发生最大的 2002 和 2009 年站点预测正确率都接近 30%;6 月实况有 4 a 发生了严重高温,站点预测正确率在 20%—70%,尤其是 2010 年 6 月大面积严重高温的站点预测正确率超过 70%;11 a 中有 8 a 在 6 月发生了高温,模型都有一定的预报技巧,除 1 a 正确率较低外,其余 7 a 正确率在 10%至接近 50%;7 月,11 a 中仅发生 1 次严重低温,模型预测失败,但 7 月其余 4 个气温等级预测和 8 月的所有 5 个气温等级预测中,预测模型均有一定的预测技巧,站点等级预测正确率高低分

布类似6月的情况,这里不再赘述。

总之,季节预测模型对严重高温级别的预测技巧要高于严重低温的预测技巧,对高温级别的预测技巧高于低温级别的预测技巧,对东北夏季气温等

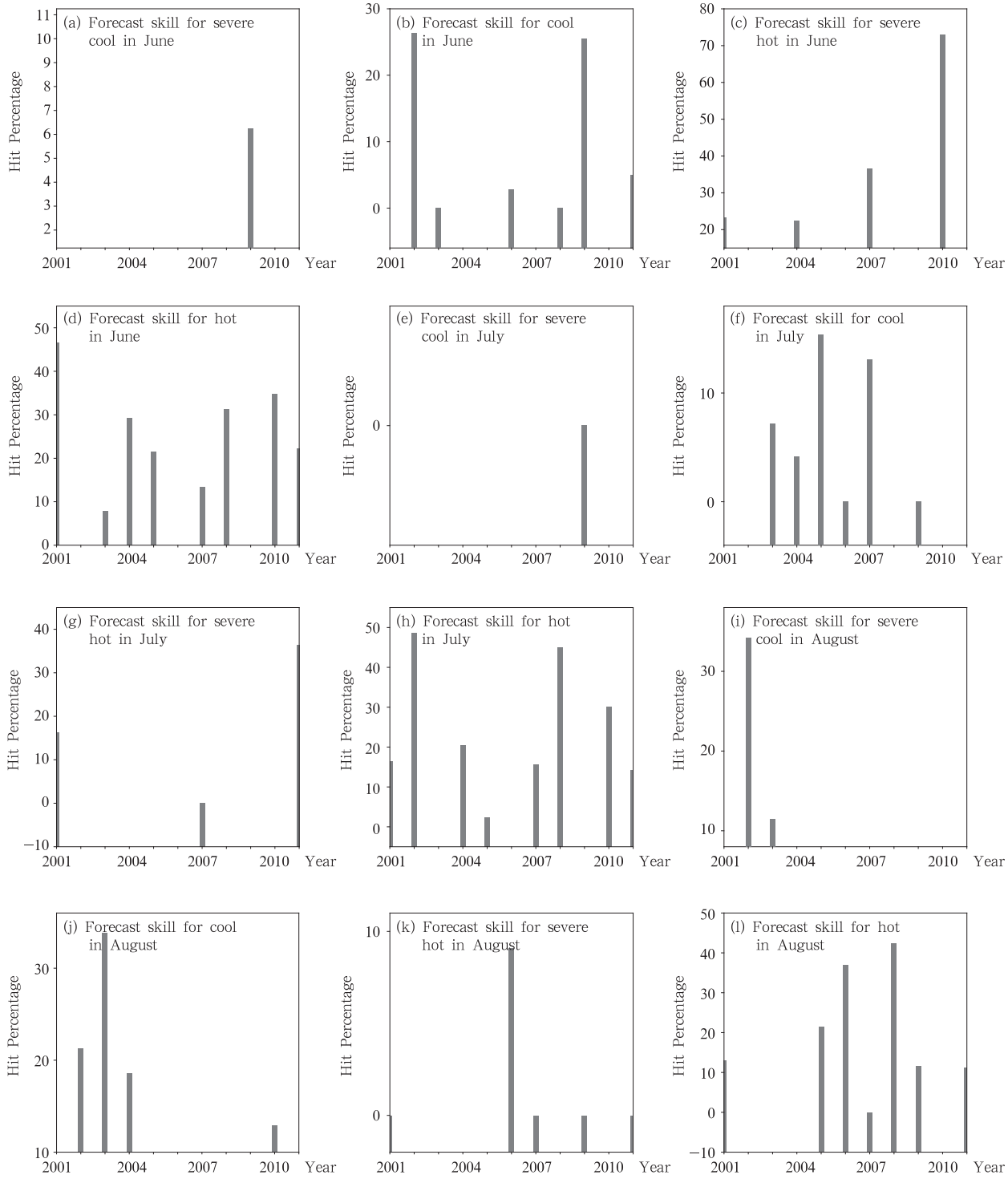


图6 东北夏季气温等级预测检验

(按式(5)计算)

Fig. 6 Forecast validation of summer classified surface air temperatures of Northeast

(calculated based on the formula (5))

级的季节预测具有较高的业务参考价值。

在 11 a 的独立样本预测个例中,挑选了几个大面积发生低温或高温并且预测效果较好的个例,来分析模型对气温等级空间分布的预测能力。图 7 是模型对 2009 年 6 月、2010 年 6 月、2011 年 7 月和 2003 年 8 月东北标准化气温的独立样本预测结果及其实况。对照实况,2009 年 6 月东北地区大部分发生了低温事件,中部和北部大范围地区发生了严重低温事件,模型虽然对部分低温和严重低温区未能正确预测,但预测出了部分低温区和北部局部严重低温区,对极端事件(1994 年至今仅 2009 年发生过严重低温)有预警作用。2010 年 6 月,除辽宁大部分气温属高温等级外,东北其余大部分地区气温达到了严重高温的等级(大兴安岭发生了较严重的森林火灾),模型准确预测出了大部分严重高温区域,高温等级区域与实况也较为一致。2011 年 7 月,东北中部和北部气温达到高温或严重高温等级,而东北西南部大部分地区气温为正常等级,模型预测出了中部和北部严重高温和高温等级,但东北的西南部预测为高温等级与实况不一致。2003 年 8 月,内蒙古东北部、黑龙江、吉林和辽宁北部发生了低温,其中内蒙古东北部部分地区和黑龙江西部气

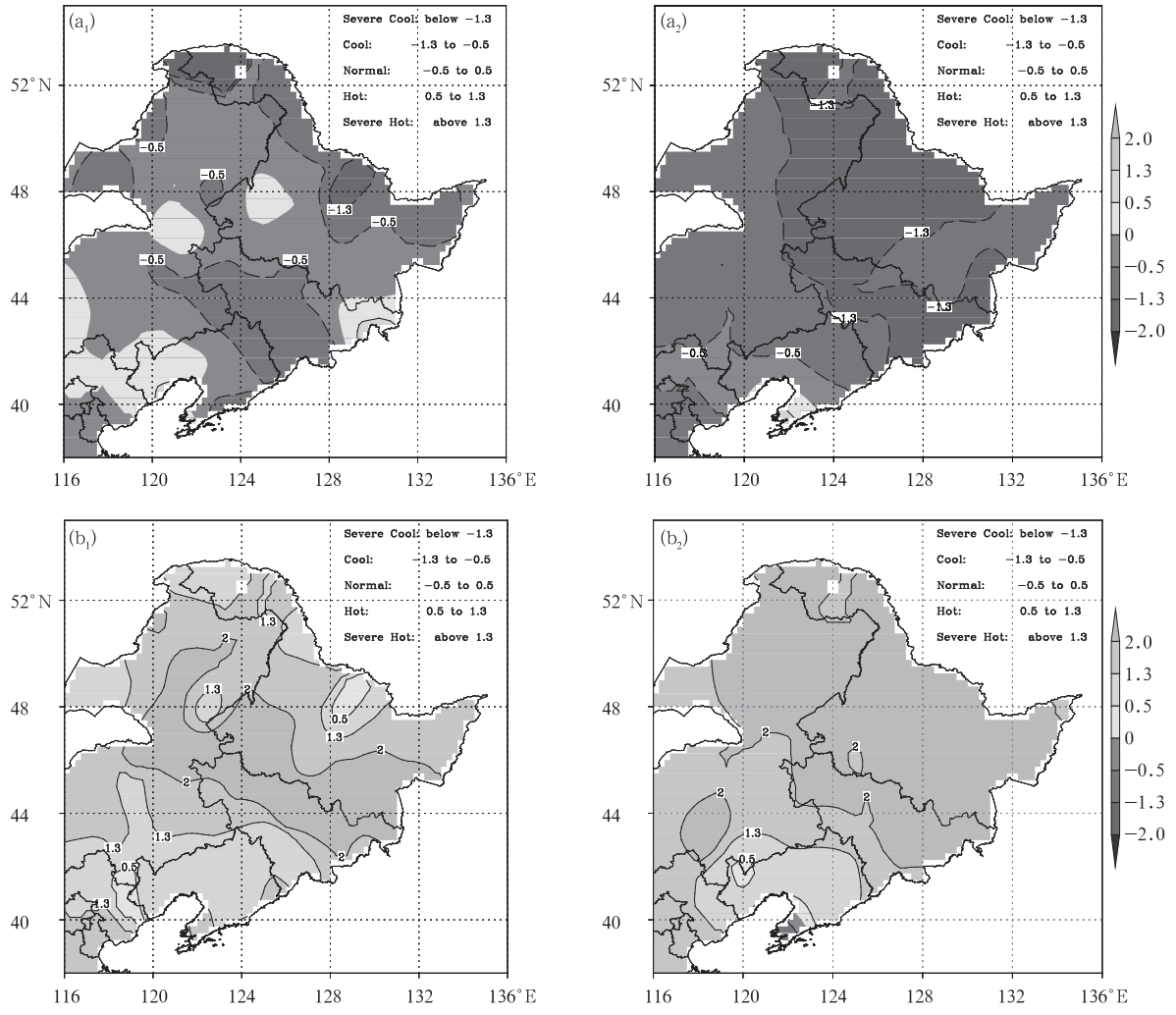


图 7 标准化气温模型预测($a_1$—$d_1$)与实况($a_2$—$d_2$)对比

(a. 2009 年 6 月, b. 2010 年 6 月, c. 2011 年 7 月, d. 2003 年 8 月)

Fig. 7 Example comparison of seasonal forecasts ($a_1$ − $d_1$) with the observation ($a_2$ − $d_2$) on standardized surface air temperatures

(a. June 2009, b. June 2010, c. July 2011, d. August 2003)

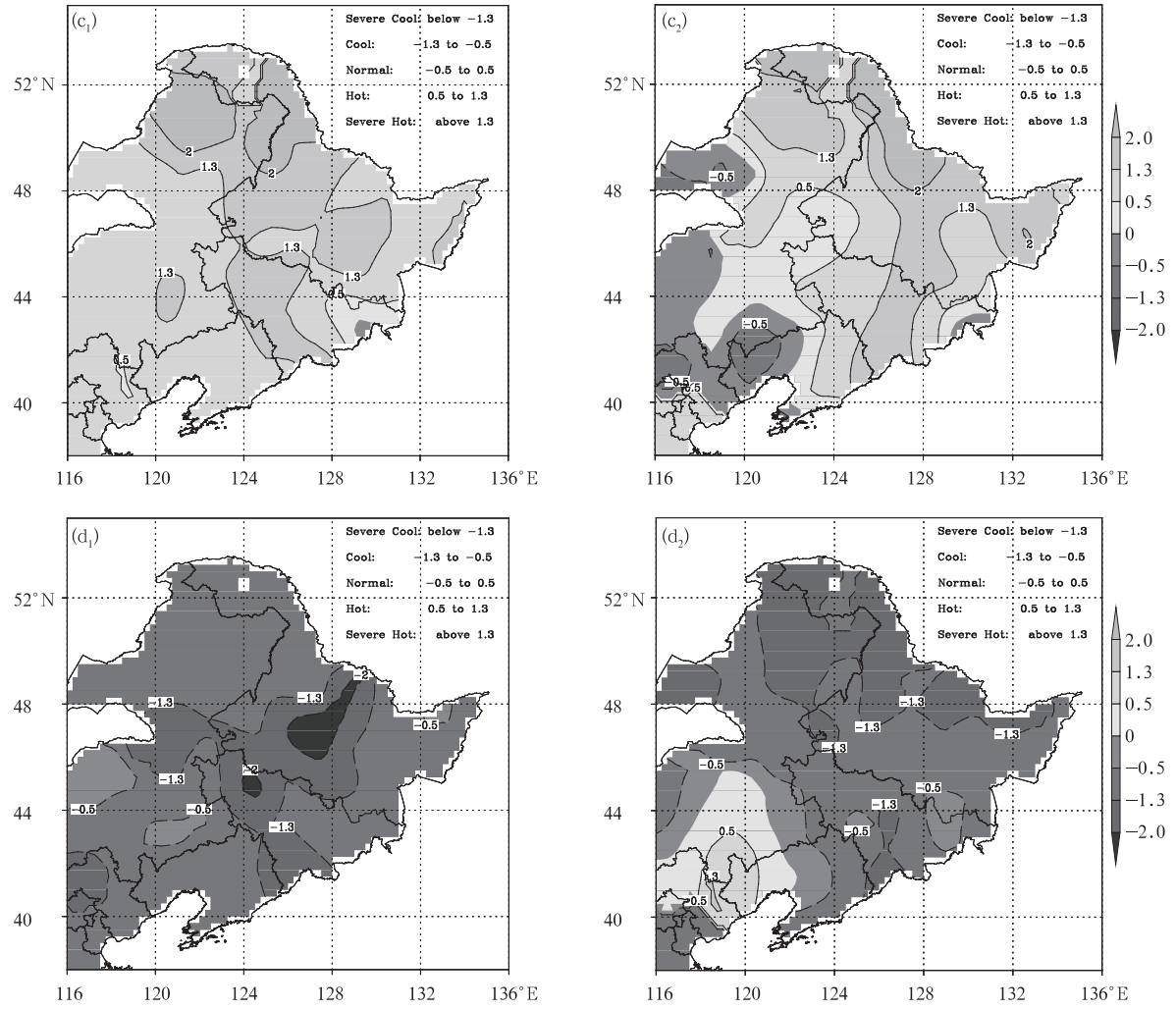


续图 7

Fig. 7 (Continued)

温达到严重高温等级,模型正确预测了上述地区发生的低温等级,但严重高温等级空间位置的预测与实况不符。因此,通过上述预测检验结果可以看出,模型可以对东北夏季气温的 5 个等级进行较有效的预测,有业务参考价值,尤其是对气温偏高的 2 个等级的预测效果要好于气温偏低的 2 个等级的预测;当某一等级的预测正确率等于 10%时,表明预测模型就对将要发生的气温异常有预警作用。

## 5 讨论和结论

本研究首先使用极大方差旋转经验正交函数分解方法处理预报对象,从而可以得到空间分布结构清晰、取样误差较小、线性独立的预报因子场。但由于旋转经验正交函数分解特征向量的时间权重系数反映了空间相关性分布随时间的演变特征,因此,在旋转经验正交函数分解要素的不同时段,时间系数将有所变化,针对这一问题,本研究将整个时段的数据做了旋转经验正交函数分解,以纳入预报对象的所有变化信息。由于预报因子选用前期影响因子,因此,该方法不但可以应用于预测,也可以用于气候成因诊断。但也正是由于没有使用短期气候动力预测模式结果作为预报因子,该预测方法的预测技巧也许还有进一步提高的空间。

本研究的主要工作之一是提供了旋转经验正交函数分解结合逐步回归的一种短期气候预测方法。利用旋转经验正交函数分解将东北夏季各月气温分型,基于夏季之前的实况资料,求出前期大气环流和海表温度场分别与旋转经验正交函数分解模态时间

系数的相关场,并甄别出前期影响关键月份,用前期关键月影响因子场与相关场的相似度乘以对应旋转经验正交函数分解模态的空间荷载系数形成预测因子矩阵,从而建立东北夏季各月标准化气温的逐步回归预测方程,交叉回报的相关系数检验表明该季节预测模型能够较好地预测出气温的异常变化,同时,5个气温等级的独立样本预测结果表明,除了严重低温预测准确率较低外,其余4个气温等级的预测结果都具有较高的业务实用价值,使用该模型可以在4月初对7月东北气温做预测,在6月初可以对6月和8月东北气温做滚动预测。

旋转经验正交函数分解逐步回归季节预测方法还是一种有效的气候成因诊断分析工具。本研究举出了东北夏季各月某一类型气温异常的前期成因:5月中高纬度出现北极涛动和北大西洋涛动与北大西洋涛动一致负(正)位相型,副热带出现SZ遥相关型正(负)位相,相对应SST异常呈拉尼娜(厄尔尼诺)及北大西洋海温三极子负(正)位相型,则易导致6月辽宁大部分地区、吉林大部分地区和黑龙江中部气温偏高(低),其余地区接近正常;2月SST呈厄尔尼诺(拉尼娜)及北大西洋海温三极子正(负)位相型,随后3月大气环流配合北极涛动和北大西洋涛动正(负)位相,东亚-太平洋遥相关为负(正)位相,并且出现EU1型遥相关波列,则7月内蒙古东北部气温显著性偏低(高);5月热带印度洋SST呈IOBM型负(正)位相,而ENSO和北大西洋海温三极子形态不明显,同时,副热带大气环流呈SZ遥相关负(高)位相,而北半球中高纬度环流遥相关波列不明显,则易导致8月内蒙古东北部部分地区、黑龙江中西部、吉林及辽宁北部部分地区气温异常偏低(高),其余地区气温接近常年。

**致谢**:感谢武炳义研究员和张培群研究员对本工作提出的宝贵建议、感谢国家气候中心创新团队的支持!

## 参考文献

北方主要作物冷害研究协作组. 1981. 东北地区粮食作物冷害规律的研究. 气象,(12):20-22

曹经福,江志红,任福民等. 2013. 广义线性统计降尺度方法模拟日降水量的应用研究. 气象学报,71(1):167-175

丁士晟. 1980a. 东北地区夏季低温的气候分析及其对农业生产的影响. 气象学报,38(3):234-242

丁士晟. 1980b. 东北低温冷害和粮食产量. 气象,(5):1-3

郭裕福,邢如楠,巢纪平. 1983. 用滤波模式试做东北夏季温度预报//东北夏季低温长期预报文集. 北京:气象出版社,245-249

贾丽伟,李维京,陈德亮等. 2006. 东北地区月平均大气环流型与哈尔滨气候关系的初步研究. 气象学报,64(2):236-245

贾小龙,陈丽娟,李维京等. 2010. BP-CCA方法用于中国冬季温度和降水的可预报性研究和降尺度季节预测. 气象学报,68(3):398-410

李辑,龚强. 2006. 东北地区夏季气温变化特征分析. 气象与环境学报,22(1):6-10

廉毅,安刚. 1998. 东亚季风El Niño与中国松辽平原夏季低温关系初探. 气象学报,56(6):724-735

刘传凤,高波. 1999. 东北夏季低温冷害气候特征分析. 吉林气象,(1):2-5

沈柏竹,刘实,廉毅等. 2011. 2009年中国东北夏季低温及其与前期海气系统变化的联系. 气象学报,69(2):320-333

施能,曹鸿兴. 1992. 基于所有可能回归的最优气候预测模型. 南京气象学院学报,15(4):459-466

孙建奇,王会军. 2006. 东北夏季气温变异的区域差异及其与大气环流和海表温度的关系. 地球物理学报,49(3):662-671

孙玉亭,王书裕,杨永岐. 1983. 东北地区作物冷害的研究. 气象学报,41(3):313-321

王会军,范可,郎咸梅等. 2012. 我国短期气候预测的新理论、新方法和新技术. 北京:气象出版社,226pp

王敬方,吴国雄. 1997. 持续性东北冷夏的变化规律及相关特征. 大气科学,21(5):523-532

王绍武,赵宗慈. 1985a. 中国夏季低温冷害. 资源科学,(1):254-259

王绍武,朱宏. 1985b. 东亚的夏季低温与厄·尼诺. 科学通报,(17):1323-1325

魏凤英. 2007. 现代气候统计诊断与预测技术(第2版). 北京:气象出版社,117-124

吴洪宝,吴蕾. 2005. 气候变率诊断和预测方法. 北京:气象出版社,131-145

姚佩珍. 1995. 近四十年东北夏季低温冷害的气候特征. 灾害学,10(1):51-56

袁景凤 吴晓曦. 2000. 一种新的多因子综合预报方法及其预测能力评估. 应用气象学报,11(增刊):98-102

Barnston A G, Livezey R E. 1987. Classification, seasonality and persistence of low-frequency atmospheric circulation patterns. Mon Wea Rev, 115(6):1083-1126

Barnston A G, He Y. 1996. Skill of CCA forecasts of 3-month mean surface climate in Hawaii and Alaska. J Climate, 9(10): 2579-2605

Fan K. 2009. Predicting winter surface air temperature in Northeast China. Atmos Oceanic Sci Lett, 2(1):14-17

Fan K, Wang H J. 2010. Seasonal prediction of summer temperature over Northeast China using a Year-to-Year incremental approach. Acta Meteor Sinica, 24(3):269-275

Hastenrath S, Heller L. 1977. Dynamics of climatic hazards in northeast Brazil. Quart J Roy Meteor Soc, 103(435): 77-92

He Y, Barnston A G. 1996. Long-lead forecasts of seasonal precipi-

tation in the tropical Pacific Islands using CCA. J Climate, 9(9): 2020-2035

Kalnay E, Kanamitsu M, Kistler R, et al. 1996. The NCEP/NCAR 40-Year Reanalysis Project. Bull Amer Meteor Soc, 77(3): 437-4721

Klein S A, Soden B J, Lau N C. 1999. Remote sea surface temperature variations during ENSO: Evidence for a tropical atmospheric bridge. J Climate, 12(4): 917-932

Massy W F. 1965. Principal components regression in exploratory statistical research. Amer Statist Assoc, 60(309): 234-256

Moura A D, Shukla J. 1981. On the dynamics of droughts in Northeast Brazil: Observations, theory and numerical experiments with a general circulation model. J Atmos Sci, 38(12): 2653-2675

Mo R P, Straus D M. 2002. Statistical-dynamical seasonal prediction based on principal component regression of GCM ensemble integrations. Mon Wea Rev, 130(9):2167-2187

Shukla J, Misra B N. 1977. Relationships between SST and wind speed over the central Arabian Sea, and monsoon rainfall over India. Mon Wea Rev, 105(8): 998-1002

Wu L X, Liu Z Y. 2005. North Atlantic decadal variability: Air-sea coupling, oceanic memory, and potential Northern Hemisphere resonance. J Climate, 18(2): 331-349

Tan H B, Mao J, Chen H, et al. 2011. A study of a retrieval method for temperature and humidity profiles from microwave radiometer observations based on principal component analysis and stepwise regression. J Atmos Ocean Technol, 28(3): 378-389

Yang J L, Liu Q L, Xie S P, et al. 2007. Impact of the Indian Ocean SST basin mode on the Asian summer monsoon. Geophys Res Lett, 34(2):L02708, doi:10.1029/2006GL028571

Yu Z P, Chu P S, Schroeder T. 1997. Predictive skills of seasonal to annual rainfall variations in the U. S. Affiliated Pacific Islands: Canonical correlation analysis and multivariate principal component regression approaches. J Climate, 10(10): 2586-2599

# 20世纪90年代末东亚夏季降水年代际变化及其成因初探*

胡泊[1)] 乔少博[1)] 封国林[1)2)†]

1) (扬州大学物理科学与技术学院, 扬州 225002)

2) (中国气象局国家气候中心开放实验室, 北京 100081)

( 2014 年 5 月 16 日收到; 2014 年 7 月 15 日收到修改稿 )

基于1983—2011年月总降水量、环流和海温的再分析资料, 给出了20世纪90年代末东亚夏季降水的年代际调整的区域特征, 及其对应的大气环流内部过程和可能的海温外强迫的年代际变化. 研究结果表明, 在20世纪90年代末期东亚北部夏季降水比东亚南部夏季降水由湿向干的表现更为明显, 东亚南部地区夏季降水则是在20世纪90年代初和21世纪初发生年代际的转折. 此外, 东亚地区夏季的500 hPa高度场、850 hPa风场、U200风场、水汽输送场和东亚太平洋遥相关型指数和东亚夏季风指数等在20世纪90年代末期也表现出明显的年代际变化特征. 进而从大气内部过程的角度验证了20世纪90年代末东亚夏季降水发生的年代际调整. 与此同时, 北太平洋和西太平洋海表温度表现出由偏低向偏高的转变, 这可能是导致20世纪90年代末期东亚夏季气候年代际变化的重要外部成因之一.

**关键词**: 降水型, 年代际变化, 环流, 外强迫

**PACS:** 92.60.Wc **DOI:** 10.7498/aps.63.209204

## 1 引 言

东亚是全球最显著的季风气候区, 东亚季风环流在时间尺度上呈现出显著的季节内、季节、年际和年代际变化特征. 由于东亚位于世界上最大的大陆东部, 面临世界上最大的大洋, 海陆差异比较大, 因此东亚夏季降水很容易受到大气内部因素和外强迫因子的影响. 作为东亚占地面积最大的国家, 中国夏季降水的年代际变化很大程度上反映了东亚地区的降水情况. 已有研究表明[1−6], 近几十年来我国夏季降水经过了四次非常明显的年代际变化, 而且表现出了典型的区域性降水形式. 具体事实可归纳为: 1) 严中伟[7] 对北半球夏季气候跃迁的研究表明, 1960s末我国华北地区的夏季降水开始减弱, 马京津等[8] 对华北地区夏季水汽输送研究表明, 从1970s开始水汽输送方向变成以偏西为主; 2) 文献[9—11]研究发现, 1970s末我国长江流域夏季降水增多, 华北地区出现持续性减弱, 与之相对应的东亚夏季风1970s末也出现了显著的年代际变化趋势[12], 我国西北地区夏季降水也表现出增多的趋势[13,14]; 3) 1990s初期, 我国华南地区降水显著性增多[15−18]; 4) 1990s末期, 我国华北和东北地区夏季降水明显减弱[19], 黄河、淮河流域夏季降水增多, 长江流域降水减少[20], 梅雨期降水主雨带北移. 伴随着我国夏季降水的年代际变化, 我国夏季降水异常主模态也出现了年代际转变[21]. 黄荣辉等[19] 的研究结果表明, 我国东部夏季降水主模态在1990s末发生了年代际变化, 由“三极型”向“偶极型”转变, 我国东部夏季降水异常呈现“南正北负”的分布特征. 龚志强等[22] 通过对夏季降水及年代际转型的可能信号分析, 得出在2012年可

* 国家重点基础研究发展计划 (批准号: 2012CB955903)、国家自然科学基金 (批准号: 41205040, 41175067, 41375078) 和公益性行业专项 (批准号: GYHY201306021) 资助的课题.

† 通讯作者. E-mail: fenggl@cma.gov.cn

© 2014 中国物理学会 Chinese Physical Society 

能是中国东部夏季降水的转折点.

此外, 关于东亚地区夏季降水年代际变化可能成因的大量的研究[23−29]表明, El Nino事件(赤道中, 东太平洋海温异常)是全球范围内天气气候年际和年代际变化的一个强有力信号. 东亚夏季气候年代际变化可能是由于热带东太平洋发生了年代际的El Nino现象所引起的. 张庆云等[18]和邓伟涛等[30]的研究表明, 中国地区夏季降水的年代际变化与北太平洋年代际振荡(PDO)有联系. 东亚地区天气变化与东亚季风环流有关[31,32], 同时太平洋海温也是影响东亚地区天气变化的重要原因. 大量的动力统计数值实验都为研究东亚降水做出了贡献[33−37]. Li等[38]通过两种模式研究东亚降水、季风环流调整与热带海温、全球海温、温室效应增加的气溶胶等之间的相互作用. 研究发现, 热带地区海温外强迫能使大多数季风环流减弱; 二氧化碳气体使气溶胶增多, 加强了海陆热力差异, 促进东亚季风环流; 热带地区海温增加, 特别是中东太平洋海温年代际变化是季风消弱的主要原因. Si和Ding[39]研究了青藏高原冬季积雪与东亚夏季降水之间的联系, 发现在1977—1999年青藏高原冬季积雪与我国长江流域、日本南部地区夏季降水相关, 而在2000—2011年青藏高原冬季积雪则与我国淮河流域、朝鲜半岛地区夏季降水联系更大些. 据探测得到的数据显示, 在20世纪90年代末青藏高原温度升高, 而温度升高又与地面热感通量和长波辐射增加有直接关系.

显然与20世纪70年代末的突变相比, 20世纪90年代末发生的东亚地区的夏季降水的调整, 其在空间上表现出的调整显著区域等则略显晦涩. 同时, 这次调整对应的大气内部过程和可能的外部驱动等相关研究也开展较少, 至今没有给出关于20世纪90年代末东亚夏季降水年代际调整的清晰的概念模型图. 因此, 本文尝试根据1983—2011年月总降水量、环流和海温的再分析资料, 利用大气学中常用的统计方法, 探讨了20世纪90年代末东亚夏季降水的年代际调整, 及其对应的大气环流内部过程和可能的海温外强迫的年代际变化. 本文第二节给出资料和方法; 第三节分析东亚夏季降水的年代际变化特征; 第四节分析东亚地区环流系统的调整; 第五节着重分析太平洋海温与东亚夏季降水和东亚环流系统的关系; 第六节总结, 并给出了20世纪90年代末东亚夏季降水调整的概念模型图.

## 2 资料和方法

资料来自美国国家环境预测中心/国家大气研究中心(NCEP/NCAR)发布的1983年6月到2011年8月的全球逐月再分析资料, 包括高度场、风场、比湿$q$、地面气压$p$的月平均资料, 分辨率为2.5° × 2.5°; 1983—2011年NOAA ERSST的海面温度资料, 分辨率为2° × 2°; PREC (The PRECipitation REConstruction data set) 6—8月的总降水量的分析资料.

本文所采用的主要方法是合成分析、相关分析和回归分析. 计算水汽输送主要采用的方法是从地表面($P_s$)到500 hPa厚度的整层纬向水汽输送($Q_u$)、经向水汽输送($Q_v$)的计算方法.

$$Q_v(x,y,t) = \frac{1}{g}\int^{p_s} q(x,y,p,t)v(x,y,p,t)\,\mathrm{d}p, \tag{1}$$

$$Q_u(x,y,t) = \frac{1}{g}\int^{p_s} q(x,y,p,t)u(x,y,p,t)\,\mathrm{d}p, \tag{2}$$

式中: $P_s$为地面气压, $q$为比湿, $u$为纬向风, $v$为经向风, $g$为重力加速度.

为了分析北太平洋和西太平洋平均海温距平指数与东亚地区夏季降水、500 hPa高度场和850 hPa风场之间的关系, 采用了线性回归. 其中相关系数:

$$R_n = \frac{\sum_{i=1}^{n}(x_i-\overline{x})(y_i-\overline{y})}{\sqrt{\sum_{i=1}^{n}(x_i-\overline{x})^2\cdot\sum_{i=1}^{n}(y_i-\overline{y})^2}}. \tag{3}$$

## 3 1990s末东亚夏季降水的年代际变化

图1(a—c)中, 从东亚地区(90° E—145° E, 10° N—55° N) 1983—2011年夏季降水距平经验正交展开(EOF)主分量的空间分布可以看出, 东亚区域夏季降水的第一模态(EOF1)为海陆差异模态, 其方差贡献为16.7%; 第二模态(EOF2)出现由北向南的正负交替的模态, 其方差贡献为11.2%; 第三模态(EOF3)是由北向南的"+ − +"模态, 其方差贡献为8.8%; 在EOF2和EOF3中, 大陆上表现出的"+ − +"和南北向的"+−"模态, 与魏凤英和张先恭[40]关于中国东部夏季雨型的划分、黄荣辉

等[19]研究给出的中国东部地区夏季降水的主要模态等有关结论是一致的, 进而也说明了本文对东亚地区夏季降水EOF展开得到的降水异常模态是可信的.

图1 (d)—(f)中给出的是EOF1, EOF2和EOF3的时间系数. 可以看出, EOF1和EOF2更多地表现出年际振荡, 而EOF3的年代际均值变化的特征相较明显. 利用滑动T检验方法(MTT)分别对EOF1, EOF2和EOF3的时间系数1983—2011年进行年代际位相调整的检验(图2 (a)), 可以看出, EOF1和EOF2均不存在通过0.05信度检验的突变点, 而EOF3的时间系数存在通过0.05 信度检验的突变点, 对应的突变时间在1998年前后. 此外, 龚志强等[41]的启发式分割算法(BG算法)的检测结果与MTT方法的类似(图略). 图2 (b)为对EOF3 的时间系数进行小波分解的方差图. 可以看出, 在对应12—18年左右存在极大值, 即说明EOF3的时间系数存在相应时间尺度的准周期振荡, 这也进一步说明了存在年代际位相调整的可能性.

图3是东亚1983—2011年(6—8)月的降水距平百分率的纬度-时间剖面图. 从图中可以看出明显的年代际的变化特征: 20世纪80年代初到90年代末30° N以北地区降水偏多, 30° N以南地区降水相对于东亚北部地区偏少; 而90年代末至2011年30° N以北地区降水由多变少, 30° N以南降水也相应地由少变多. 而且从图上也可以看出, 东亚北部地区的年代际变化特征更加明显. 为了更容易地看出东亚北部地区夏季降水的年代际变化, 图4 (a) 和(b)分别给出了东亚南部地区夏季降水距平直方图和东亚北部地区夏季降水距平直方图. 从图4可以看出, 东亚北部地区(100° E—130° E, 30° N—55° N)夏季降水在1998 年出现年代际转变, 从正距平转变成负距平, 对应了EOF分解对应的第三模态的时间系数序列. 而东亚南部地区(100° E—130° E, 10° N—30° N)夏季降水在20世纪90 年代初和21世纪初都发生了年代际的转折, 由负距平到正距平再到负距平.

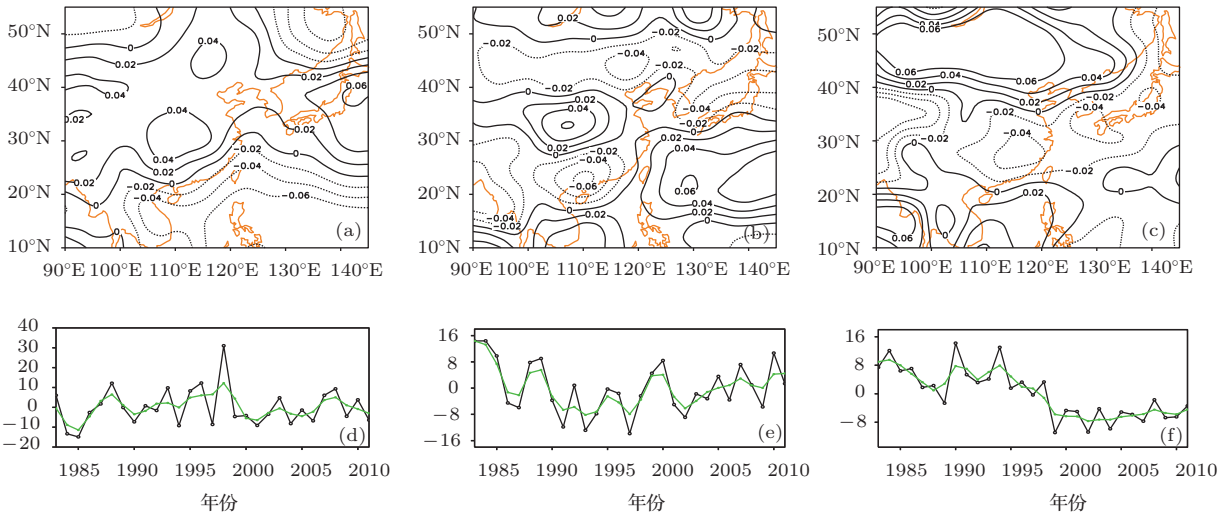


图1 (网刊彩色) 东亚地区1983—2011 年夏季降水的EOF主分量的空间分布 (a)—(c) 和时间系数(d)—(f)
(a) EOF1, 方差贡献16.7%; (b) EOF2, 方差贡献11.2%; (c) EOF3, 方差贡献8.8%; (d) EOF1对应的时间系数; (e) EOF2对应的时间系数; (f) EOF3对应的时间系数

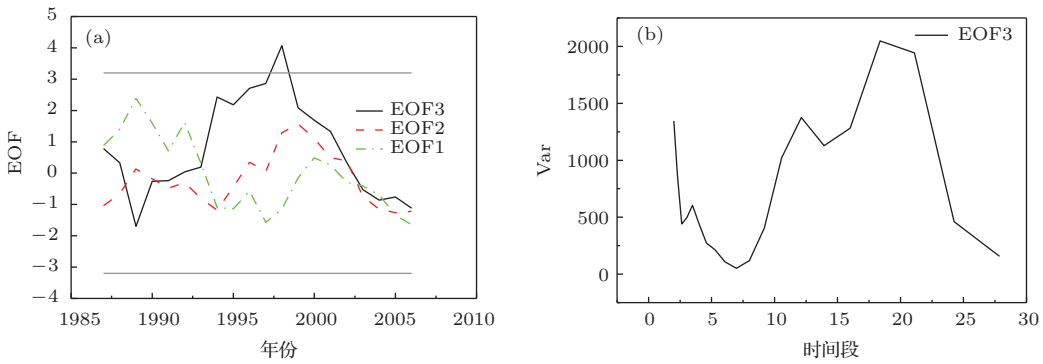


图2 (网刊彩色) 东亚1983—2011年夏季降水的EOF主分量时间系数的MTT检测(a)和EOF3时间系数的小波变化方差(b)

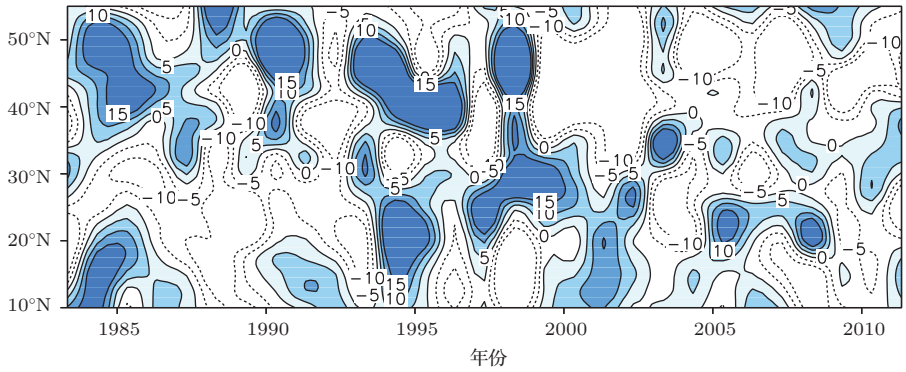


图 3 (网刊彩色) 东亚沿 100° E—130° E 夏季 (6—8 月) 降水距平百分率 (%) 的纬度-时间剖面

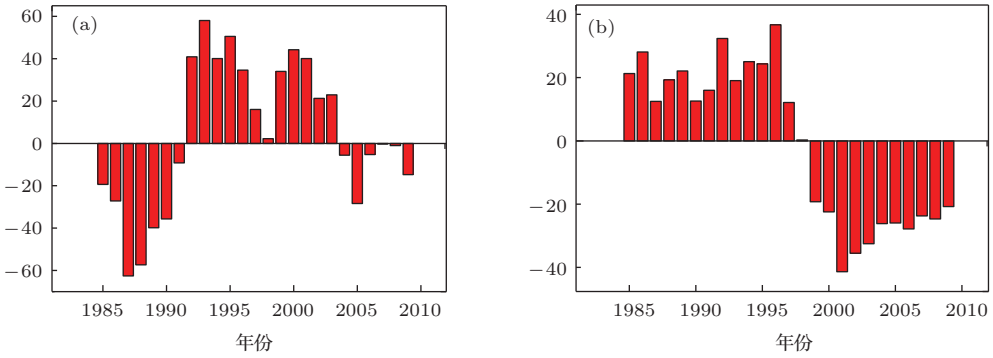


图 4 东亚地区夏季降水距平直方图 (a) 东亚南部地区 (100° E—130° E, 10° N—30° N); (b) 东亚北部地区 (100° E—130° E, 30° N—55° N)

为了更清楚地看出东亚地区夏季降水的年代际变化, 图 5 (a) 和 (b) 分别给出了 1983—1998 年和 1999—2011 年东亚夏季降水距平百分率, 图 5 (c) 是 1983—1998 年和 1999—2011 年降水距平百分率差值图. 从图 5 (a), (b) 中可以看出, 东亚出现非常明显的年代际变化. 1983—1998 年中东亚北部地区降水偏多, 东亚南部地区降水偏少, 呈现明显的“偶极型”的降水特征. 1999—2011 年降水型与 1983—1998 年降水型的情况相反, 东亚北部地区降水偏少, 东亚南部地区降水偏多. 从图 5 (c) 差值图中可以看出, 1983—1998 年与 1999—2011 年降水型几乎一致. 因此, 东亚地区在 20 世纪 90 年代末具有非常明显的年代际变化.

## 4 20 世纪 90 年代末的东亚环流系统的调整

已有研究[42]表明, 中国东部夏季降水异常和年代际的变化都和东亚-太平洋遥相关有很好的联系. 从图 6 可以看出, 90 年代末, 30° N 以北的东亚地区 500 hPa 高度场也出现了年代际的转折. 1983—1998 年东亚北部地区大面积为负值区, 东亚南部地区相对于北部地区为正值区. 1999—2011 年东亚北部地区大面积为正值区, 东亚南部大面积相对于北部地区为负值区. 可以看出, 500 hPa 高度场的这种变化和东亚夏季降水的年代际变化有很好的一致性. 当 500 hPa 高度场为负距平值时, 东亚夏季降水偏多; 当 500 hPa 高度场为正距平值时, 东亚夏季则以降水偏少为主. 图 7 (a)—(c) 分别是 1983—1998 年, 1999—2011 年 500 hPa 高度场距平合成图和 1999—2011 与 1983—1998 年的 500 hPa 高度场距平合成差值图. 可以看出, 1983—1998 年欧亚大陆中高纬度高度场从西到东呈“− + −”分布, 中亚地区到中国东部华南地区为正距平所控制, 在东亚地区从北向南呈现“−+”的偶极分布特征. 这种径向型环流具有相当的正压结构, 有利于水汽向北输送. 1999—2011 年的情况则相反, 欧亚大陆中高纬度高度场从西到东呈“+ − +”分布, 属于“两脊一槽”的分布, 有利于在中亚地区形成阻塞高压频发, 不利于中国夏季的雨带偏北. 差值图则进一步证实了“两脊一槽”的分布特征, 突出了前后两个时期的差异.

图 8 (a), (b) 分别是 1983—1998 年, 1999—2011 年的 850 hPa 风场叠加 U200 风场距平合成

图. 这两幅图最明显的特征就是在 (35° N—55° N, 100° E—130° E) 和 (10° N—30° N, 100° E—130° E) 范围内, 1983—1998 年, 对应的对流层 850 hPa, 东亚北部地区 (35° N—55° N,100° E—130° E) 受异常的气旋控制, 有利于水汽向东亚北部地区输送, 也有利于低层风场辐合, 降水偏多; 而 U200 风场中西风急流偏强, 有利于高层辐散, 这样一种高层辐散, 低层辐合的环流配置给东亚北部等区域带来丰富的降水. 同时, 东亚南部 (10° N—30° N, 100° E—130° E) 受异常的反气旋所控制, 下沉运动增强, 不利于中国东部华南以南地区降水; 而 1999—2011 年的风场则与 1983—1998 年的风场呈现相反的情况, 850 hPa 风场在东亚北部为异常的反异常气旋所控制, 低层风场辐散, 下沉运动增强, U200 风场西风急流偏弱, 风场辐合, 位置较低层的 850 hPa 风场向西倾斜. 这样一种高层辐合、低层辐散、下沉运动增强的高低层环流异常配置不利于该地区降水的产生, 对应着东亚北部地区降水减少. 在东亚南部地区, 低层风场辐合、上升运动增强、高层风场辐散, 有利于降水. 图 9 则是在同期的 500 hPa 垂直速度. 从图 9 (a), (b) 可以看出, 在东亚地区西部, 环流异常表现出从南到北的“+ − +”分布特征. 其中 1983—1998 年, 在 500 hPa 层, 在东亚地区东部, 环流异常表现出南北反相位的“ 偶极型”分布特征. 40° N—55° N 地区为上升运动, 而东亚南部地区 40° N 以南地区为下沉运动所控制, 对应的 200 hPa 风场也大致出现这样的偶极型特征. 在 1999—2011 年, 500 hPa 垂直速度则呈现相反的情况. 因此, 从风场和垂直速度中也可以看出, 在 20 世纪 90 年代末出现年代际变化特征是非常明显的.

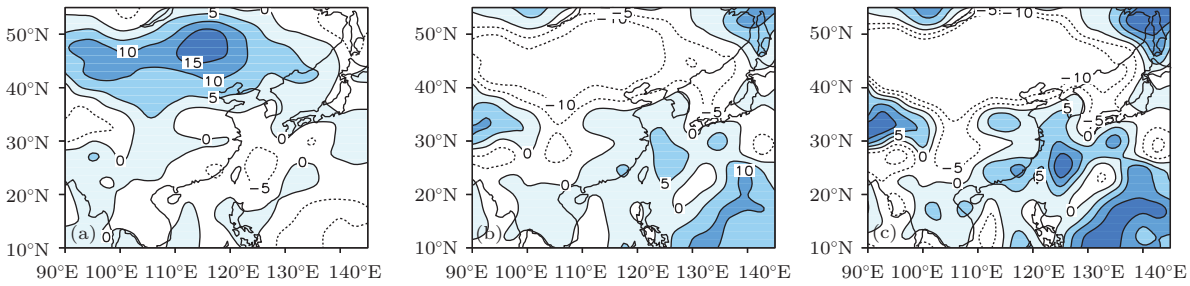


图 5 (网刊彩色) 东亚夏季 (6—8 月) 降水距平百分率 (a) 1983—1998 年; (b) 1999—2011 年; (c) 差值图

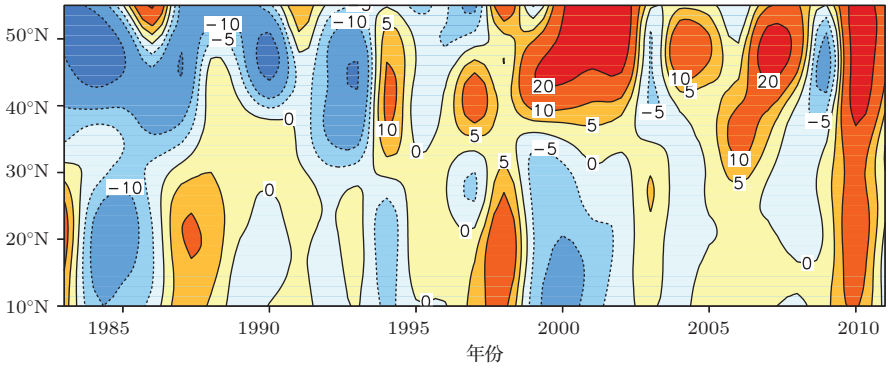


图 6 (网刊彩色) 东亚 500 hPa 高度场距平的纬度-时间剖面

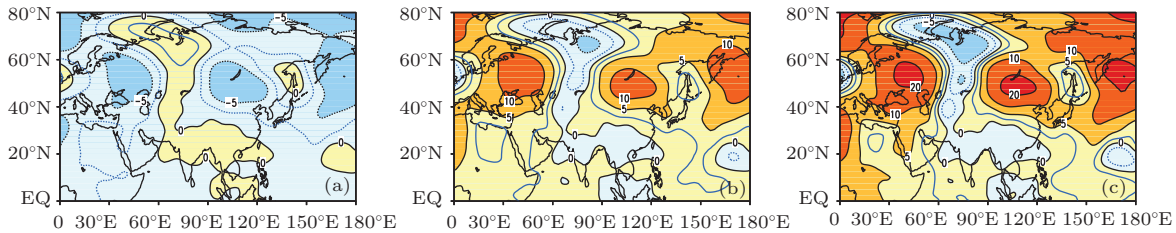


图 7 (网刊彩色) 东亚 500 hPa 高度场距平合成图 (a) 1983—1998 年; (b) 1999—2011 年; (c) 1999—2011 与 1983—1998 年的差值图 (图中蓝色线部分为 $t$ 检验达到 0.05 显著性水平的区域)

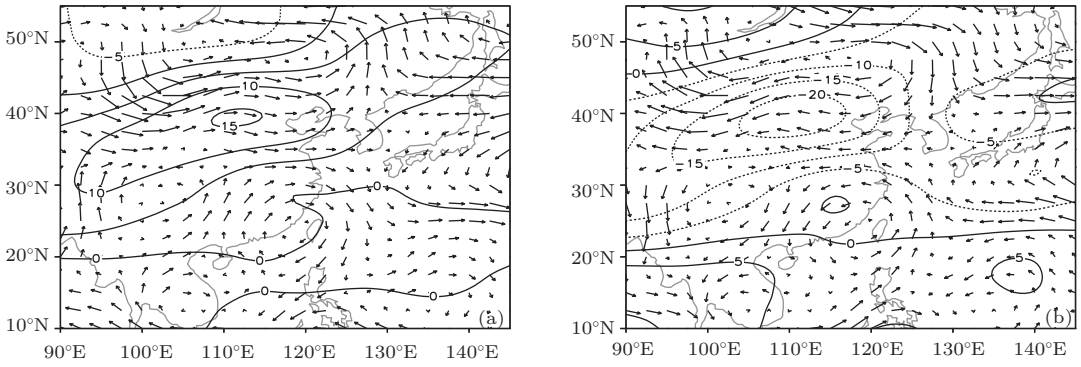


图 8 850 hPa 风场叠加 200 hPa U 风场距平合成 (a) 1983—1998 年; (b) 1999—2012 年

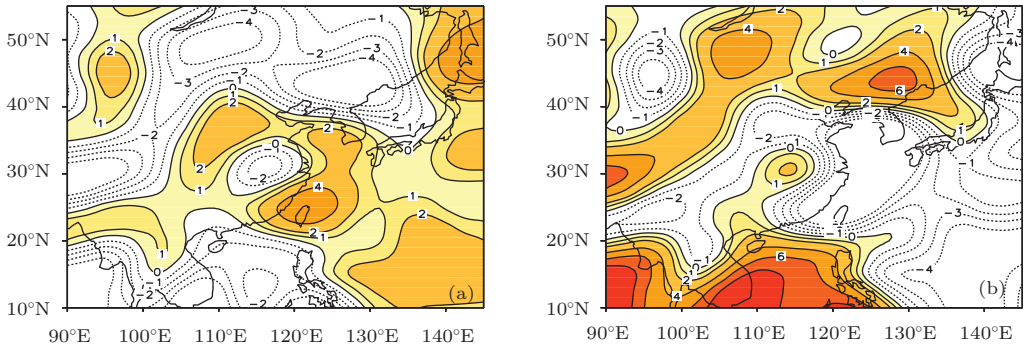


图 9 (网刊彩色) 500 hPa 垂直速度 (a) 1983—1998 年; (b) 1999—2012 年

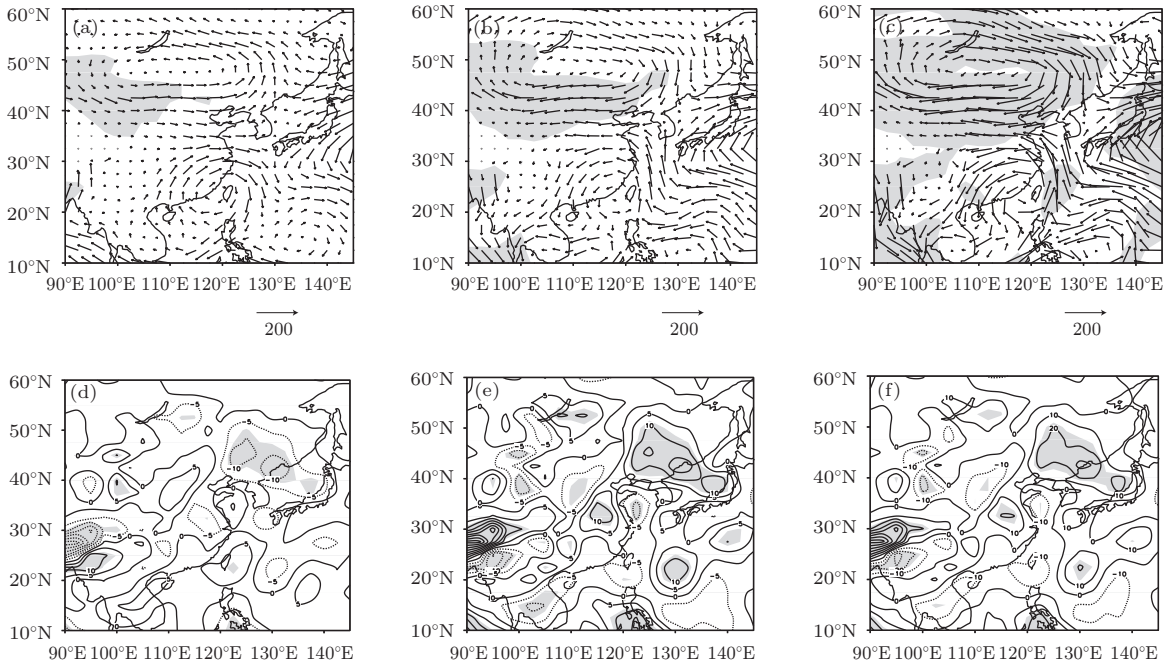


图 10 整层水汽输送通量及其辐合辐散 (a), (d) 1983—1998 年平均与气候态之差; (b), (e) 1999—2011 年平均与气候态之差; (c), (f) 1999—2011 年与 1983—1998 年平均之差 (图中阴影部分是通过信度为 0.05 的显著性检验)

东亚夏季降水与东亚夏季水汽输送有着密切的联系. 图 10 (a)—(c) 分别是 1983—1998 年, 1999—2011 年整层积分的水汽输送的合成图和两时段的整层积分的水汽输送的差值图. 图 10 (d)—(f) 则是与之相对应的辐合辐散场的年代际异常. 从图中可以看出, 1983—1998 年期间, 来自太平洋的水汽在东亚北部地区形成气旋式异常输送, 在气旋南侧 (福建一带) 异常的水汽输送与气候态的输送方向相反, 对应着水汽输送增强, 水汽输送辐合, 有利于东亚北部地区降水. 在东亚南

部, 我国华南地区水汽输送为反气旋式异常. 反气旋式水汽输送伴随着局部地区水汽辐散, 不利于东亚南部地区降水. 而在1999—2011年的水汽输送与前段时间的水汽输送呈现相反的趋势. 东亚北部地区水汽输送形成反气旋式异常输送, 在气旋南侧异常的水汽输送与气候态的输送方向相反, 对应着水汽输送减弱, 水汽输送辐散, 不利于东亚北部地区降水. 在东亚南部, 我国华南地区水汽输送为气旋式异常. 气旋式水汽输送伴随着局部地区水汽辐合, 有利于东亚南部地区降水. 从差值图中也可以看出, 东亚北部地区和东亚南部地区明显的反气旋和气旋变化, 在我国东部地区水汽输送和其辐合辐散呈现南北反相的偶极型分布特征, 这对东亚夏季降水1990s末的年代际异常有着重要的影响, 从侧面也反映了此次水汽输送与东亚夏季降水有着很好的关联.

东亚夏季降水异常与东亚夏季风强度有紧密的关系[43]. 因此, 利用两个常用的东亚夏季风指数研究东亚夏季风强度的年代际变化特征. 这两个指数分别是Huang[44]定义的东亚/太平洋(EAP)遥相关指数和施能等[45]定义的东亚夏季风(EASM)指数. 研究表明两者对于东亚夏季风变化都有很好的描述能力. EAP 指数是基于东亚-太平洋区域存在EAP/PJ大气遥相关型定义的季风环流指数, 反映了东亚地区夏季风水平和垂直环流的异常特征, 包含了热带、副热带和中纬度大气环流变化的特征. 其变率与东亚地区夏季降水和温度异常有着紧密的联系. 施能等定义的EASM指数从大尺度角度出发, 很好地解释了海陆之间海平面气压差与季风之间的关系. 两指数定义分别为

$$\begin{aligned} I_{\mathrm{EAP}} = & -0.25Z_{\mathrm{s}}(60^\circ\ \mathrm{N}, 125^\circ\ \mathrm{E}) \\ & +0.50Z_{\mathrm{s}}(40^\circ\ \mathrm{N}, 125^\circ\ \mathrm{E}) \\ & -0.25Z_{\mathrm{s}}(20^\circ\ \mathrm{N}, 125^\circ\ \mathrm{E}), \end{aligned}$$

其中, $Z_{\mathrm{s}} = (Z - \bar{Z})\sin(45^\circ)/\sin\partial$表征在$\partial$格点夏季平均的500 hPa位势高度场异常标准差.

$$I_t = \sum_{i=1}^{n}(p^*_{1it} - p^*_{2it}), \quad I^*_t = \frac{I_t - \overline{I}}{\sigma_I},$$

$I^*_t$则为标准化的EASM指数, 其中$i$表示纬带, $t$表示年份, $\overline{I}$, $\sigma_I$表示$I$的平均值和均方差, $*$为标准化处理; $p^*_{1it}$, $p^*_{2it}$分别是110° E, 160° E的第$i$纬带第$t$年的标准化海平面气压值.

图11为根据黄刚和施能等定义的指数计算的EAP指数和EASM指数的异常分布. 两个指数都表现出明显的年代际变化和年际变化特征. 在年代际尺度上, EAP指数在20世纪90年代中后期出现了一次明显的年代际变化, 由负相位变为正相位. 这与张庆云等[18]研究20世纪90年代中国华南夏季降水变化相对应, 大致上也与东亚北部地区夏季降水呈现良好的对应关系. 而施能等定义的EASM指数则在1990s初和2000s初出现了两次相位的转变, 与东亚南部地区夏季降水有很好的对应关系. 这两指数都反映了20世纪90年代中后期都发生了年代际的转变, 但两者发生转变的时间并不完全一致, 可能是因为两指数所表征的环流和显著相关的降水的区域不同.

## 5 北太平洋和赤道西太平洋海温的年代际变化

对这次年代际变化的不同时段夏季太平洋海温进行合成分析. 由图12可以发现, 1983—1998年北太平洋中纬度地区海温偏冷, 而赤道中东太平洋海温偏暖, 具有PDO暖相位的特征(图12(a)); 1999—2011年北太平洋中纬度地区海温偏暖, 而赤道中东太平洋海温偏冷, 具有PDO冷相位的特征(图12(b)); 这种PDO由正相位向负相位转变, 通过影响东亚夏季风环流系统, 使得东亚夏季风增强, 从而导致东亚地区降水型的改变. 张庆云等[18]也指出中国东部的夏季降水雨型与大气外部强迫因子北太平洋中纬度海温年代际变化PDO关系密切; Huang[44]的研究表明西北太平洋低层环流存在着明显的年代际变化, 且这种年代际变化表征了西北太平洋夏季风的年代际变化, 并且会影响到东亚夏季风的变化. 大量的研究都表明太平洋海温是影响东亚夏季降水重要的外部因子之一. 1983—2011年东亚夏季降水第三模态的时间系数与夏季海温序列8年滤波低频分量的相关系数分布(图13)可以看出, 在北太平洋地区和西太平洋地区, 两者有着非常显著的相关性.

北太平洋和西太平洋海温是影响东亚夏季降水的重要外强迫因子之一, 对东亚夏季降水起着重要的作用. 因此, 将北太平洋(150° E—150° W, 20° N—40° N)平均海温距平和西太平洋(110° E—116° E, 20° S—20° N)平均海温距平作为指数. 图14(a), (b)分别是北太平洋、西太平洋海温距平指数. 显然, 这两幅图都具有非常明显的

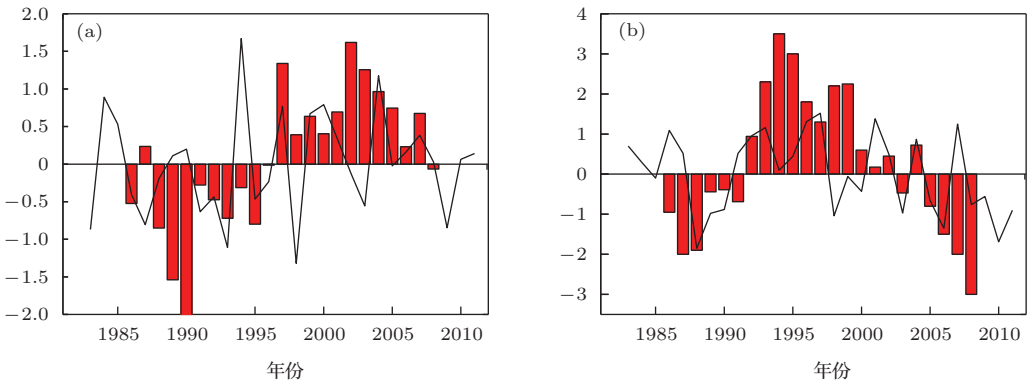


图 11 (a) 和 (b) 分别是 EAP 指数和 EASM 指数 (曲线), 以及相对应的 7 年滑动平均 (柱状图), 其中两指数的 7 年滑动平均扩大了 5 倍

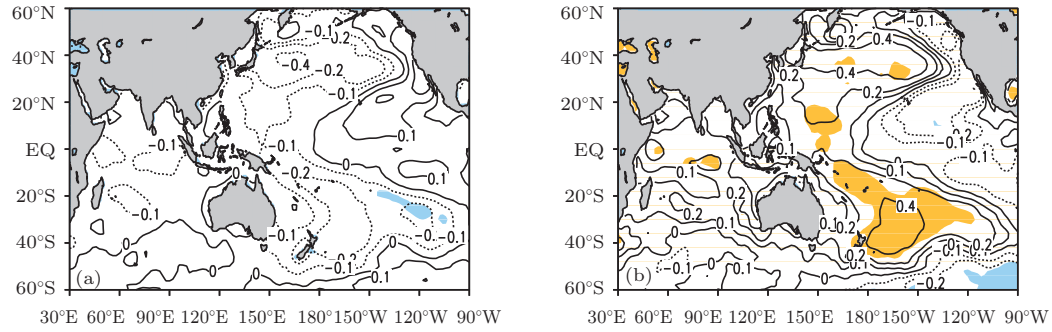


图 12 (网刊彩色) 海温距平合成图 (a) 1983—1998 年; (b) 1999—2011 年

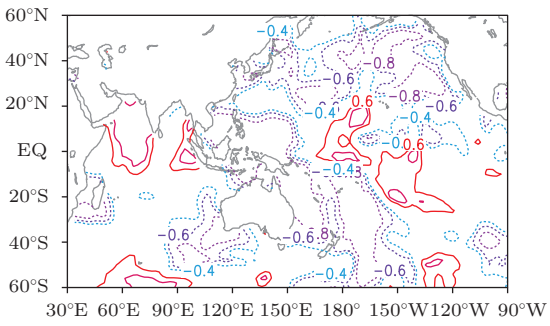

图 13 (网刊彩色) 1983—2011 年东亚夏季降水第三模态的时间系数与夏季海温序列 8 年滤波低频分量的相关系数

年代际变化特征, 在 20 世纪 90 年代中后期之前都是负指数, 在 20 世纪 90 年代中后期之后都转变为正指数. 已有的研究表明, EASM 的强弱直接决定了东亚地区的降水, 而 EASM 强弱的一个重要影响因素在于海陆温差, 而 1999 年之前 (后) 的西太平洋和北太平洋海温以偏冷 (暖) 为主, 海陆温差的加大 (减小), 有利于 EASM 偏强 (弱), 造成东亚北部地区降水偏多 (少).

通过北太平洋海温指数和西太平洋海温指数分别对东亚夏季降水进行相关分析, 图 15 (a1), (a2) 分别是北太平洋海温指数和西太平洋海温指数与东亚夏季降水进行相关分析得出的相关系数; 图 15 (b1) 和 (b2) 分别是北太平洋海温指数和西太平洋海温指数对东亚夏季降水求得的回归场的差

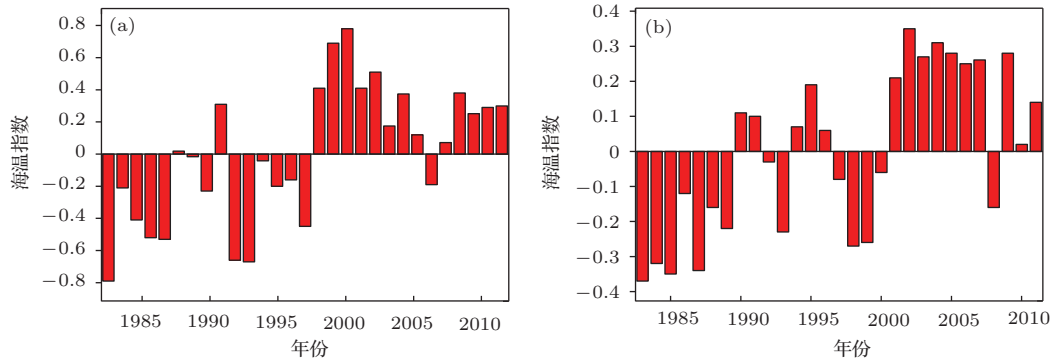


图 14 海温指数分布 (a) 北太平洋海温指数; (b) 西太平洋海温指数

值图. 从图15 (a1) 可以看出, 北太平洋海温指数与东亚北部夏季降水有很好的对应关系, 通过相关系数得出的东亚夏季降水距平百分率回归图 (b1) 与东亚夏季降水距平百分率图相一致. 西太平洋海温与东亚地区大部分都有很好的对应关系. 西太平洋暖池是热带太平洋表面温度场的主要模态, 是调制热带太平洋乃至全球气候的关键因子, 其变化特点一直是人们关注的焦点. 通过西太平洋海温距平指数与东亚夏季降水的相关系数可以看出, 西太平洋海温与东亚地区有很好的对应关系. 因此, 西太平洋海温也是影响东亚夏季降水的重要因子之一.

图16 (a1), (a2) 分别是北太平洋海温指数和西太平洋海温指数对500 hPa高度场进行相关分析得出的相关系数; 图16 (b1), (b2) 分别是北太平洋海

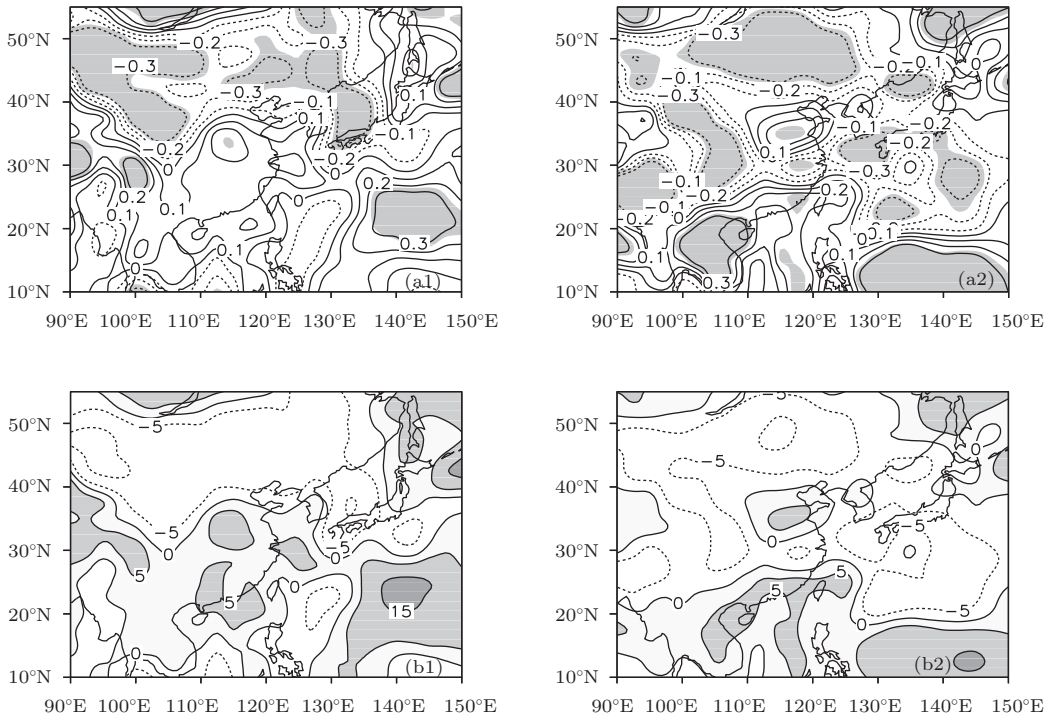


图15 海温指数与东亚夏季降水的相关系数 (a1), (a2) 和东亚夏季降水距平百分率回归图 (b1), (b2), 相关系数图中阴影部分是通过信度为0.10的显著性检验

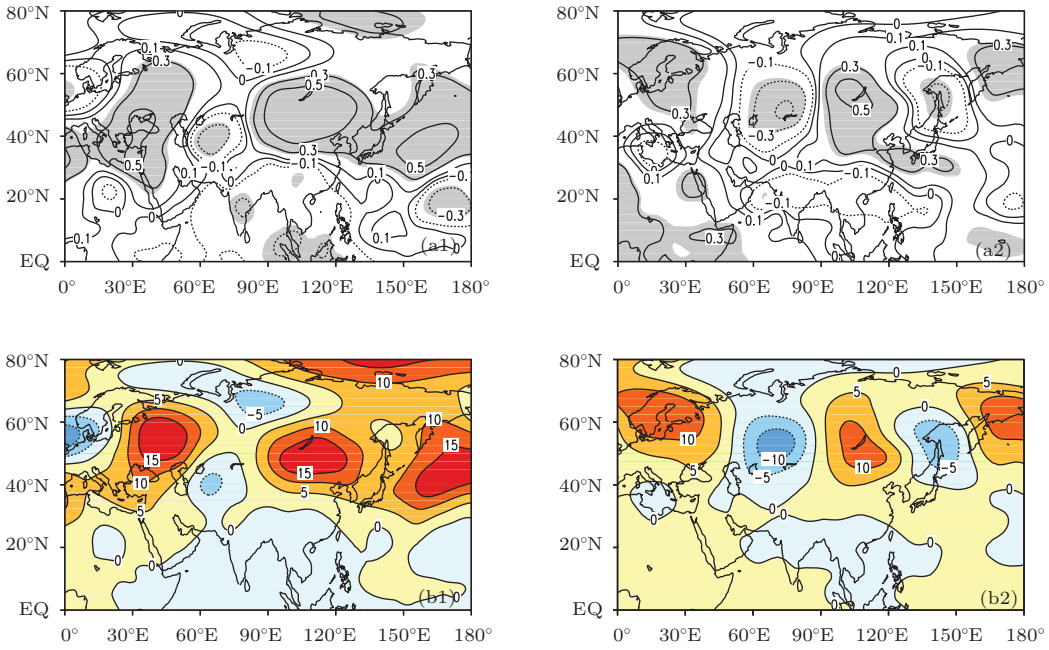


图16 (网刊彩色) 海温指数与500 hPa高度场的相关系数图 (a1), (a2) 和500 hPa高度场距平回归图 (b1), (b2), 相关系数图中阴影部分是通过信度为0.10的显著性检验

温指数和西太平洋海温指数对500 hPa高度场求得的回归场的差值图. 从图16可以发现, 不论是西太平洋海温还是北太平洋海温, 对500 hPa高度场都有很好的对应关系. 通过相关系数回归出的500 hPa回归场也与500 hPa合成距平差值图相一致. 因此, 西、北太平洋海温可能是影响500 hPa高度场发生年代际转折的重要外部强迫因子之一.

## 6 结 论

气候年代际变化是全球海陆气系统相互作用的结果, 天气气候的演变特征受到大气内部动力过程和大气外强迫因子的共同作用. 针对1990s末东亚夏季降水年代际的异常转折, 分析了内在因素——500 hPa高度场, 850 hPa风场, U200风场, 水汽输送和外在因素——海洋等可能的影响, 并对1990s末前后两个时段对比分析了东亚夏季降水的分布特征及其相应的影响因素等, 讨论了1990s末东亚夏季年代际发生转折的可能信号. 得出以下主要结论.

1) 东亚北部夏季降水在20世纪90年代末期发生年代际的转变, 主要表现为由湿向干转变, 而东亚南部夏季降水在20世纪90年代初和21世纪都发生了年代际转变, 降水由干转湿再变干. 从东亚区域宏观的整体角度则更表现为雨型的“+−”型向“−+”型转变.

2) 对应的东亚夏季降水在20世纪90年代末的年代际变化, 东亚地区夏季环流也发生了年代际的转折. 1983—1998年, 500 hPa高度场欧亚大陆从西到东呈“− + −”分布特征, 东亚地区从南到北呈现“+−”的偶极分布特征, 环流具有相当的正压结构; 850 hPa风场在东亚北部形成一气旋, 而U200风场中西风急流偏强, 东亚南部形成一反气旋, 高层辐散, 低层辐合, 有利于东亚北部地区降水; 整层的水汽输送在东亚北部地区气旋式异常输送, 水汽输送辐合, 南部地区形成一反气旋式异常输送, 水汽输送辐散. 1999—2011年的情况则相反, 欧亚大陆中高纬度高度场形成“两脊一槽”的分布, 东亚地区从南到北呈现“−+”的偶极分布特征有利于在中亚地区形成阻塞高压频发; 850 hPa风场在东亚北部为反气旋所控制, 而U200风场辐合, 东亚南部形成一气旋, 高层辐合, 低层辐散; 整层的水汽输送在东亚北部地区反气旋式异常输送, 水汽输送辐散, 南部地区形成一气旋式异常输送, 水汽输送辐合, 有利于东亚南部地区降水. 同时, 两个东亚夏季风指数EAP和EASM都显示了东亚夏季风强度在20世纪中后期出现了明显的年代际变化. 因此, 20世纪90年代末期东亚夏季降水发生年代际调整从大气内动力过程的角度是完全可以解释的.

3) 20世纪90年代末, 太平洋海温也发生了明显的年代际变化. 1983—1998年, PDO偏暖; 1999—2011年与前一段时间相反, PDO偏冷. 通过北太平洋海温指数和西太平洋海温指数对东亚夏季降水和500 hPa高度场进行相关分析: 太平洋海温指数与东亚夏季降水和500 hPa高度场都有很好的对应关系, 因此, 北太平洋海温和西太平洋海温是引起东亚夏季降水和500 hPa 高度场发生年代际变化的重要成因之一. 综合考虑20世纪90年代末东亚夏季降水的调整、同期的大气环流和海温的变化, 给出了20世纪90年代末东亚夏季降水调整的概念模型图(图17).

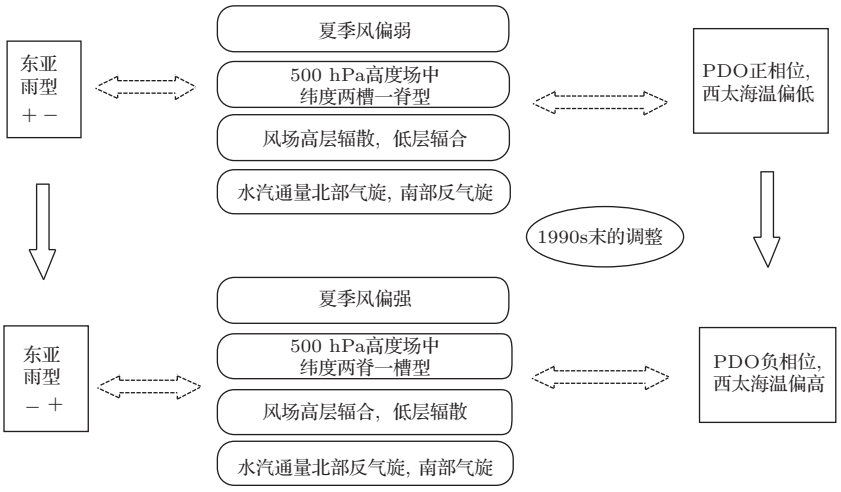


图17 20世纪90年代末东亚夏季降水调整的概念模型图

## 参考文献


[1] Dai X G, Wang P, Chou J F 2004 *Prog. Nat. Sci.* **14** 73

[2] Feng G L, Dong W J 2003 *Chin. Phys.* **13** 413

[3] Gong Z Q, Wang X J, Zhi R, Feng G L 2009 *Acta Phys. Sin.* **58** 4342 (in Chinese) [龚志强, 王晓娟, 支蓉, 封国林 2009 物理学报 **58** 4342]

[4] Huang J P, Yi Y H, Wang S W, Chou J F 1993 *Q. J. Meteorol. Soc.* **119** 547

[5] Dai X G, Wang P, Zhang K J 2012 *Chin. Phys. B* **21** 119201

[6] Kwon M H, Jhun J G, Ha K J 2007 *Geophys. Res. Lett.* **34** L21706

[7] Yan Z W 1992 *Chin. J. Atmos. Sci.* **16** 111 (in Chinese) [严中伟 1992 大气科学 **16** 111]

[8] Ma J J, Gao X Q 2006 *Plateau Meteorology* **25** 893 (in Chinese) [马京津, 高晓清 2006 高原气象 **25** 893]

[9] Huang R H, Xu Y H, Zhou L T 1999 *Plateau Meteorology* **18** 465 (in Chinese) [黄荣辉, 徐予红, 周连童 1999 高原气象 **18** 465]

[10] Ding Y H, Wang Z Y, Sun Y 2008 *Int. J. Climatol.* **28** 1139

[11] Zhang Q Y, We J, Tao S Y 2003 *Climatic and Environmental Research* **8** 307

[12] Wang H 2001 *Adv. Atmos. Sci.* **18** 376

[13] Shi Y F, Shen Y P, Li D L, Zhang G W, Ding Y J 2003 *Quaternary Sci.* **23** 152

[14] Shi Y F, Shen Y P, Kang E, Li D L, Ding Y J, Zhang G W, Hu R J 2007 *Climatic Change* **80** 379

[15] Huang R H, Gu L, Chen J L, Huang G 2008 *Chin. J. Atmospheric Sci.* **32** 691 (in Chinese) [黄荣辉, 顾雷, 陈际龙, 黄刚 2008 大气科学 **32** 691]

[16] Zhang R, Wu B, Zhao P, Han J 2008 *Acta Meteor. Sin.* **22** 435

[17] Qian W H, Lin X, Zhu Y F, Xu Y, Fu J L 2007 *Climatic Change* **84** 167

[18] Zhang Q Y, Lü J M, Yang L M, Wei J, Peng J B 2007 *Chin. J. Atmos. Sci.* **31** 1290 (in Chinese) [张庆云, 吕俊梅, 杨莲梅, 卫捷, 彭京备 2007 大气科学 **31** 1290]

[19] Huang R H, Chen J J, Liu Y 2011 *Chin. J. Atmos. Sci.* **35** 589 (in Chinese) [黄荣辉, 陈际龙, 刘永 2011 大气科学 **35** 589]

[20] Zhu Y, Wang H, Zhou W, Ma J 2010 *Climate Dynamics* **36** 1463

[21] Ye H, Lu R 2011 *J. Climate* **24** 2271

[22] Gong Z Q, Zhao J H, Feng G L 2013 *Acta Phys. Sin.* **62** 099205 (in Chinese) [龚志强, 赵俊虎, 封国林 2013 物理学报 **62** 099205]

[23] Yang L M, Zhang Q Y 2007 *Chin. J. Geophys.* **50** 412 (in Chinese) [杨莲梅, 张庆云 2007 地球物理学报 **50** 412]

[24] Yang P, Hou W, Feng G L 2012 *Chin. Phys. B* **21** 019201

[25] Gong Z Q, Wang X J, Zhi R, Feng G L 2011 *Chin. Phys. B* **20** 079201

[26] Wang X J, Zhi R, He W P, Gong Z Q 2012 *Chin. Phys. B* **21** 029201

[27] Li C Y, Liao Q H 1996 *Climatic and Environmental Research* **1** 124 (in Chinese) [李崇银, 廖清海 1996 气候与环境研究 **1** 124]

[28] Xu J J, Wang D X 2000 *Acta Oceanol. Sin.* **22** 34 (in Chinese) [徐建军, 王东晓 2000 海洋学报 **22** 34]

[29] Li C Y 1998 *Adv. Atmos. Sci.* **15** 31

[30] Deng W T, Sun Z B, Zeng G 2009 *Chin. J. Atmos. Sci.* **33** 835 (in Chinese) [邓伟涛, 孙照渤, 曾刚 2009 大气科学 **33** 835]

[31] Huang R, Zhou L, Chen W 2003 *Adv. Atmos. Sci.* **20** 55

[32] Liu Y 2012 *Ph. D. Dissertation* (Beijing: Chinese Academy of Sciences) (in Chinese) [刘永 2012 博士学位 (北京: 中国科学院)]

[33] Huang J, Yi Y, Wang S, Chou J 1993 *Q. J. Meteorol. Soc.* **119** 547

[34] Feng G L, Gong Z Q, Zhi R, Zhang D Q 2008 *Chin. Phys. B* **17** 2745

[35] He W P, Feng G L, Wu Q, Wan S Q, Chou J F 2008 *Nonlinear Processes in Geophysics* **15** 601

[36] Huang J P, Yi Y H 1991 *Sci. China B* **34** 1246

[37] Huang J P, Wang S W 1992 *Sci. China B* **35** 207

[38] Li H M, Dai A G, Zhou T J, Lu J 2010 *Climate Dynamics* **34** 501

[39] Si D, Ding Y H 2013 *J. Climate* **26** 7622

[40] Wei F Y, Zhang X G 1988 *Meteorological Monthly* **14** 15 (in Chinese) [魏凤英, 张先恭 1988 气象 **14** 15]

[41] Gong Z Q, Feng G L, Wan S Q, Li J P 2006 *Acta Phys. Sin.* **55** 477 (in Chinese) [龚志强, 封国林, 万仕全, 李建平 2006 物理学报 **55** 477]

[42] Chen R D, Wen Z P, Lu R Y, Wu L J 2012 *Chin. J. Atmos. Sci.* **36** 974 (in Chinese) [陈锐丹, 温之平, 陆日宇, 吴丽姬 2012 大气科学 **36** 974]

[43] Shi N, Lu J J, Zhu Q G 1996 *Journal of Nanjing Institute of Meteorology* **19** 168 (in Chinese) [施能, 鲁建军, 朱乾根 1996 南京气象学院学报 **19** 168]

[44] Huang G 2004 *Adv. Atmos. Sci.* **21** 41

[45] Shi N, Zhu Q G, Wu B G 1996 *Chin. J. Atmos. Sci.* **20** 575 (in Chinese) [施能, 朱乾根, 吴彬贵 1996 大气科学 **20** 575]

# Interdecadal variation of precipitation pattern and preliminary studies during the summer of late-1990s in East Asia*

Hu Po[1)] Qiao Shao-Bo[1)] Feng Guo-Lin[1)2)†]

1) (*College of Physical Science and Technology, Yangzhou University, Yangzhou 225002, China*)

2) (*Laboratory for Climate Studies, National Climate Center, China Meteorological Administration, Beijing 100081, China*)

( Received 16 May 2014; revised manuscript received 15 July 2014 )

**Abstract**

Based on the analyses of monthly precipitation, National Centers Environmental Prediction/University Corporation for Atmospheric Research reanalysis dataset, and $2^\circ \times 2^\circ$ sea surface temperature (sst) data of extended reconstructed sea surface temperature during 1983–2011, we discuss the interdecadal variations of precipition around late-1990s in East Asia, the contributions of the atmospheric internal dynamic processes, and the extra-forcing factors such as sst that presents interdecal characteristics corresponding to the results obtained by using regress analysis. The results show that the interdecadal variations of the summer rainfall over Northern East Asia around late-1990s were more obvious than over Southern East Asia, and the summer rainfall over Southern East Asia experienced a notable interdecadal change around early-1990s and early-2000s. The summer geopotential height at 500 hPa, the summer wind at 850 hPa, the summer U-wind at 200 hPa, the water vapor transportation field, the index of EAP and EASM all have the notable characteristics of the interdecadal variations, which further validate the interdecadal change of precipition of late-1990s from the angle of the atmospheric internal dynamic process. At the same time the sea surface temperature interdecadal anomalies of North Pacific and West Pacific may also be one of the important reasons for causing the interdecadal change over East Asia of the late-1990s.

**Keywords:** precipitation pattern, interdecadal variation, circulation, extra-forcing factor

**PACS:** 92.60.Wc **DOI:** 10.7498/aps.63.209204

* Project supported by the National Basic Research Program of China (Grant No. 2012CB955203), the National Natural Science Foundation of China (Grant Nos. 41205040, 41175067, 41375078), and the Special Scientific Research Project for Public Interest, China (Grant No. GYHY201306021).

† Corresponding author. E-mail: fenggl@cma.gov.cn

Article ID: 1006-8775(2014) 02-0103-09

# CLIMATE PREDICTION EXPERIMENT FOR TROPICAL CYCLONE GENESIS FREQUENCY USING THE LARGE-SCALE CIRCULATION FORECAST BY A COUPLED GLOBAL CIRCULATION MODEL

JIA Xiao-long (贾小龙)[1, 2], CHEN Li-juan (陈丽娟)[1], LUO Jing-jia (罗京佳)[3]

(1. National Climate Center, Laboratory for Climate Studies, China Meteorological Administration, Beijing 100081 China; 2. Collaborative Innovation Center on Forecast and Evaluation of Meteorological Disasters, Nanjing University of Information Science & Technology, Nanjing 210044; 3. Climate Variation Predictability and Applicability Research Program, Research Institute for Global Change, Japan Agency for Marine-Earth Science and Technology, Japan)

**Abstract:** Based on an analysis of the relationship between the tropical cyclone genesis frequency and large-scale circulation anomaly in NCEP reanalysis, large-scale atmosphere circulation information forecast by the JAMSTEC SINTEX-F coupled model is used to build a statistical model to predict the cyclogenesis frequency over the South China Sea and the western North Pacific. The SINTEX-F coupled model has relatively good prediction skill for some circulation features associated with the cyclogenesis frequency including sea level pressure, wind vertical shear, Intertropical Convergence Zone and cross-equatorial air flows. Predictors derived from these large-scale circulations have good relationships with the cyclogenesis frequency over the South China Sea and the western North Pacific. A multivariate linear regression (MLR) model is further designed using these predictors. This model shows good prediction skill with the anomaly correlation coefficient reaching, based on the cross validation, 0.71 between the observed and predicted cyclogenesis frequency. However, it also shows relatively large prediction errors in extreme tropical cyclone years (1994 and 1998, for example).

**Key words:** CGCM; large-scale circulation; tropical cyclone; climate prediction

**CLC number:** P435 **Document code:** A

## 1 INTRODUCTION

Being one of the countries most seriously hit by tropical cyclones (TCs), especially landfall TCs, which bring with them abundant amount of rain, China suffers great damages that result in huge economic losses and casualties. As the TCs affecting China are mainly from the western Pacific and South China Sea, predicting the frequency of TCs genesis in the two regions has long been an important operation at National Climate Center of China (NCC). The cyclogenesis, intensity and track of TCs are affected by large-scale atmospheric circulation, which includes tropical sea temperature, atmospheric convection in the tropics, divergence/convergence in the upper and lower atmosphere, and vertical wind shear, which has been much studied at home and abroad[1-11]. In the latest work over the past few years, cyclogenesis in the western Pacific and North Pacific Oscillation[12], the size of sea ice in North Pacific[13], circulation east off Australia[14], and Antarctica Oscillation[15] all are closely related with the issue above. All of the work above has paved solid theoretic basis for predicting the TCs.

Statistical approach has been widely used in predicting the TC season[1, 16-19]. Recently, based on multiple climatological factors, Fan and Wang[20] built a model for statistical predicting the annual genesis of TCs in the northwestern Pacific and with good results. Nicholls[16] used the Southern Oscillation-El Nino index to perform seasonal prediction of the number of TCs in Australia. Klotzbach et al.[18, 19] predicted the frequency of hurricanes in the Atlantic using a statistic prediction model that is based on precursory atmospheric signals. At present, there are only a couple of objective methods based on statistical physics, including the optimized subset and

**Received** 2013-09-11; **Revised** 2014-03-21; **Accepted** 2014-04-15

**Foundation item:** Specialized Science and Technology Project for Public Welfare Industry (GYHY200906015); National Basic Research Program of China (973 Program, 2010CB428606); Key Technologies R&D Program of China (2009BAC51B05)

**Biography:** JIA Xiao-long, associate research fellow, Ph.D., primarily undertaking research on climate prediction and application.

**Corresponding author:** JIA Xiao-long, e-mail: jiaxl@cma.gov.cn



?1994-2014 China Academic Journal Electronic Publishing House. All rights reserved. http://www.cnki.net

mean-generating function methods, at NCC to predict the TC. Statistical physics based prediction cannot take into account the variation of the atmosphere itself in many circumstances while the activity of the TC is closely related with the anomaly of simultaneous atmospheric circulation. Therefore, the anomaly of large-scale tropical atmosphere must be known before the activity pattern of the TC can be predicted and dynamic models have advantages of their own doubtlessly. In 2006, climate models were first put forward to be used in real-time forecasting of the frequency of the TC in western Pacific in the summer of 2006 and the result was consistent with the observation[21]. A nine-layer model from the Atmospheric Physics Institute of Chinese Academy of Sciences was used to study its predictability for large-scale circulation anomaly that was closely related with the TC[22], with the finding that it is capable of performing climatological prediction, with some success, of the TC activity in northwestern Pacific. All of these studies have shown that it is feasible to have observation-based prediction of the TC frequency using dynamic models. Mainly due to relatively weak capabilities of models to predict TC-related circulation anomaly, there has not been any predictive model in the TC forecasting operation of NCC that is based on dynamic models.

The SINTEX-F coupled model has been developed on the basis of SINTEX jointly founded under a Europe-Japan cooperation program[23-26]. As shown in some analyses, the SINTEX-F GCM does well in modeling and predicting the large-scale circulation features of the tropical atmosphere[27]. In view of it, this study attempts to extract a TC-related large-scale circulation field that has high predicting skill as well as observations to set up an objective statistical predictive model of the annual frequency (AF) of the TC in the South China Sea and western Pacific, which is for both forecasting experiment and result verification.

## 2 MODEL, DATA AND METHODS

The atmospheric part of the model is the latest high-resolution version of ECHAM4[28]. It has a horizontal resolution of T106 and 19 vertical layers. The global ocean model is Version 8.2 of Océan Parallélisé that contains the structure of OCRA2[26]. With a horizontal resolution of 2°×2°, the model improves to 0.5° and has 31 vertical layers in areas near the equator. The coupled fields of the model (e.g. sea surface temperature, land surface momentum flux, thermal flux and water vapor flux) are obtained by interpolation and air-sea exchange is executed once every 2 hours through a coupling mechanism that involves the ocean, atmosphere, sea ice and soil[30]. No flux correction is made to the coupled model with only the sea-ice covered area in the OCGCM adjusted towards the observed monthly climatological value. The initial atmospheric condition is determined by integrating for a year under the observed monthly climatological SST. The ensemble forecasting scheme includes nine members that are from three groups of coupled physics (equivalent to three groups of model) and three schemes of initial value formulation. They are combined in pairs of two, totaling at nine groups of forecasting scheme. For detailed introduction to the model, see Roeckner et al.[28], Madec et al.[29] and Valcke et al.[30]. The SINTEX-F model shows high skill in predicting the ENSO, IOD and Asian monsoons[31-36] and does well in the prediction experiments in the past few years[37].

The model data used in this work is the circulation field of May to October from 1982 to 2010 forecast from March 1 by SINTEX-F GCM, which includes the sea level pressure (SLP), zonal winds at 850 and 200 hPa and meridional wind at 850 hPa. The data of TC frequency in northwestern Pacific and South China Sea are all from the *Yearly Book for Typhoons* from China Meteorological Administration. The TCs studied in this work are the ones with near-the-eye wind at Force 8 on the Beaufort scale. The observations used are issued by NCEP/NCAR, which are the monthly mean global reanalysis with the horizontal gridpoint at a resolution of 2.5°×2.5°. The variables include SLP, outgoing longwave radiation (OLR), zonal wind at 1000 and 200 hPa and zonal and meridional wind at 850 hPa.

First, main large-scale circulation conditions are determined that affect the TC activity through the correlation between the annual TC frequency and related NCEP data. Then, correlation analysis is applied to extract information on large-scale circulation field that offers the model with high prediction skill and is closely related with the TC genesis and identify predictors for the key region. And then, large-scale circulation factors forecast with the SINTEX-F model are used to set up a statistical prediction model for the AF of the TC via multivariate regression analysis. The forecast results are cross-verified and experimented through prediction.

## 3 RELATIONSHIP BETWEEN THE TC FREQUENCY AND LARGE-SCALE ATMOSPHERIC CIRCULATION

As the genesis of the TC is closely related with the large-scale circulation, many studies have worked on it. At NCC, the annual typhoon prediction is for the total number of TCs that are formed over the whole year while the TCs in the South China Sea and western Pacific mainly appear from May to October, which take up 80% of the annual cyclogenesis frequency. The series of the TC number from May to



?1994-2014 China Academic Journal Electronic Publishing House. All rights reserved. http://www.cnki.net

October is correlated with that of the whole year at 0.94 while the monthly frequency of TC genesis from January to April is less than one on a multi-year scale. Therefore, the annual TC frequency and May-to-October circulation are selected to set up a statistical relationship between each other by taking into account the operational need for prediction of annual TC frequency and the relationship presented above between the May-to-October time and the whole year as well as the winter-summer circulation contrast. Fig. 1 gives the correlation between the AF and the large-scale circulation averaged over May to October, which include SLP, divergence at 1000 and 200 hPa, vorticity at 850 hPa, vertical shear of the zonal wind at 200 and 850 hPa and the meridional wind at 850 hPa. Fig. 1 gives the correlation between the AF of the TC and the large-scale circulation averaged over May to October, which includes the divergence at 1000 and 200 hPa, vorticity at 850 hPa, vertical shear of the zonal wind at 200 and 850 hPa (|U200 hPa−U850 hPa|) and the meridional wind at 850 hPa. Fig. 1a shows that the AF is much negatively correlated with the SLP in the South China Sea and western Pacific. In the main area of TC activity, low SLP is accompanied with active TCs and otherwise is true. The physical implication of this link is well-defined. Fig. 1b−1d present the relationship between the Intertropical Convergence Zone (ITCZ) and the AF, which indicates that strong low-level convergence (Fig. 1b), upper-level divergence (Fig. 1c) and 850 hPa vorticity (Fig. 1d) are all conducive to large number of TC genesis, which is also easily understood in physics. Fig. 1e gives the relationship between the genesis frequency of the TC and the wind shear between the upper and lower levels of the troposphere. As shown in a number of studies, the vertical wind shear of the source area of the TC has important effects on the TC genesis; the larger the vertical wind shear, the less likely the TC will be generated. Significantly negative correlation is found over an extensive area of 140°E−160°W, 10°−20°N, which is consistent with previous studies. Besides, it is also noted that a large area of significantly positive correlation also exists to the west of it, constituting a well-defined dipole pattern with the eastern area of negative correlation. Such distribution also reflects the effect of the circulation anomaly of the subtropical monsoon in East Asia on the genesis frequency. As the subtropics from the Indian Ocean to the western Pacific is affected by the monsoon, the lower level is with a westerly and the upper level an easterly and a large wind shear between these levels indicates a strong monsoon circulation and thus a strong monsoon trough, making it more likely for the TC to form. In Sun et al.[14], the anomaly of the equatorial westerly upstream of the western part of the western Pacific (125°−150°E) is also focused for its role in affecting the TC cyclogenesis. Therefore, the positive correlation in the corresponding area of Fig. 1e carries its own physical meaning as well. When a cross-equatorial airflow strengthens near 90°E, the westerly in 125°−150°E and 5°−15°N also enhances, increasing the convection east of the Philippines and frequency of the TC in the western Pacific. It can be seen that the genesis frequency is also well linked with the activity of the cross-equatorial flow near 90°E. It is also shown in the correlation between the genesis frequency and the meridional wind at 850 hPa, as indicated in Fig. 1f, with the maximum exceeding 0.4 (surpassing the 99% confidence level). In view of the possibility that the TC series may be erroneous for the time prior to the mid-1970s, the distribution of the correlation is determined once again using the data in 1975−2008. The result showed that main areas of significant correlation still exist as compared with those determined with the 1951−2008 data (figure omitted), suggesting stable correlation for the analysis above.

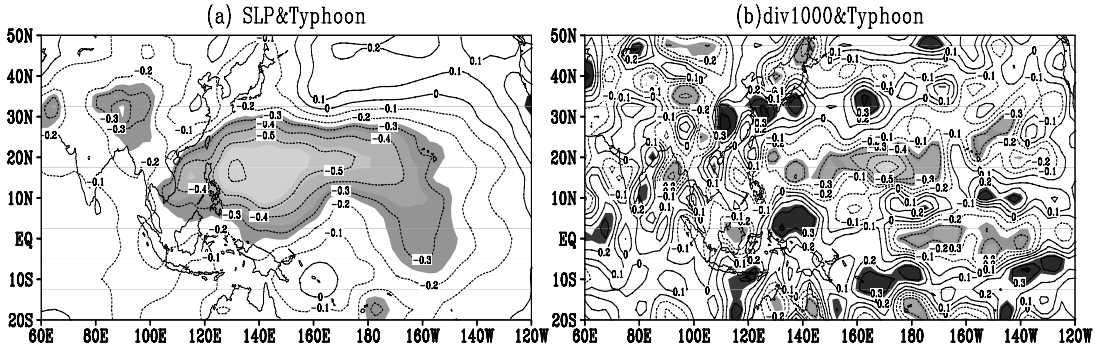




?1994-2014 China Academic Journal Electronic Publishing House. All rights reserved. http://www.cnki.net

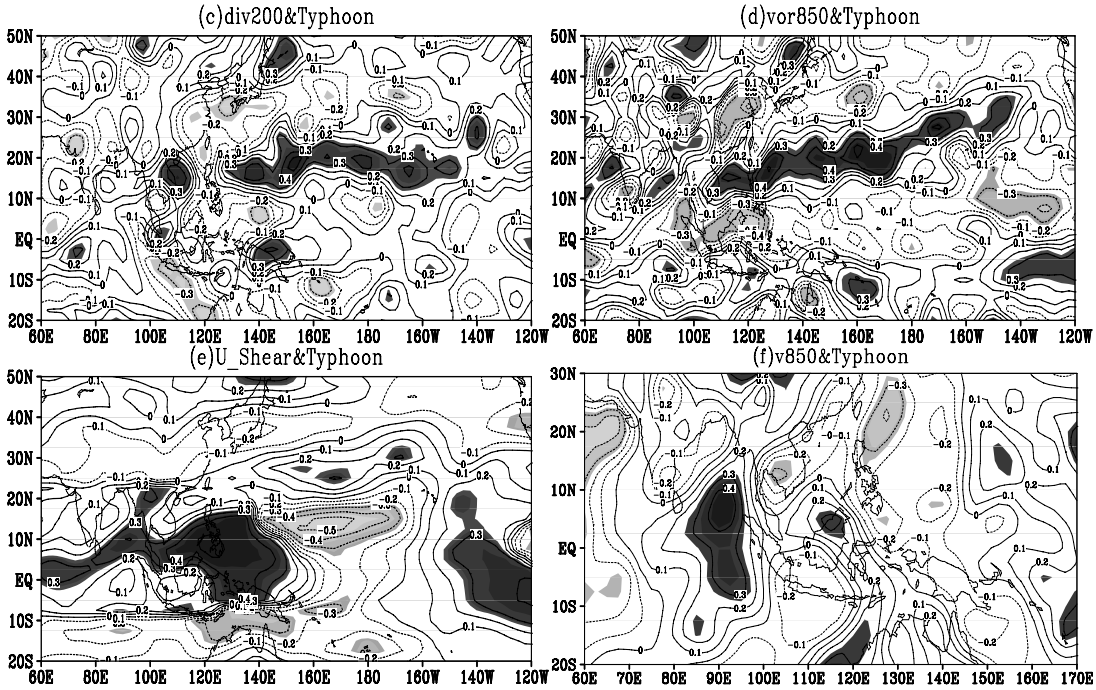


**Figure 1.** Correlation between the AF and large-scale circulation averaged over May to October. Shading indicates areas that pass the 95% confidence test. (a): SLP; (b): divergence at 1000 hPa; (c): divergence at 200 hPa; (d): vorticity at 850 hPa; (e): vertical shear of the zonal wind (|U200 hPa-U850 hPa|); (f): meridional wind at 850 hPa.

Based on the analysis above, six key-region indexes can be constructed as predictors. Table 1 gives the method of calculating the indexes and the area where they distribute. These indexes are good indicators of related features given by Fig. 1. Fig. 2 gives the time series of the six key-area indexes and the genesis frequency. They are correlated at −0.63, −0.65, 0.61, 0.61, 0.57, and 0.38 respectively, all passing the 99.9% test of confidence. If a significant linear trend exists between the two series, their correlation may be caused by the tendency. It is the interannual correlation between series that this work is more concerned about in the prediction of annual TCs. Therefore, the linear trend is removed from the series of the TC and the atmosphere before calculating the correlation again, which are −0.65, −0.64, 0.57, 0.66, 0.54 and 0.33 respectively, suggesting that the high correlation is still there between the two series. It shows that the factors determined for the key region are associated with the TC indeed. The six indexes are then used to set up a multi-variate regression equation for the genesis frequency.

$$y(t) = -0.078 - 0.18 \times x_1(t) - 0.47 \times x_2(t) + 0.29 \times x_3(t) + 0.33 \times x_4(t) - 0.57 \times x_5(t) + 0.18 \times x_6(t)$$

Figure 3 gives the fitting of the series of genesis frequency using the multi-variate regression equation. It shows that the regression equation formulated with the indexes has good fitting of the series and the reconstructed TC series is correlated with the observed ones at a coefficient of 0.73, far surpassing the 99.99% test of confidence and much above the correlation coefficient between each of the index series and TC frequency series. If a circulation model is able to have good prediction of the large-scale environmental field that is closely linked with the TC genesis, the large-scale circulation predicted by models can be used to set up prediction models for the TC frequency. In the next section, on the basis of analyzing the capabilities of the SINTEX-F GCM model in predicting such circulation, model output will be used to set up an objective, statistics-based model to predict the TC frequency over the South China Sea and western Pacific and to run experimental prediction and assessment of the result.

**Table 1.** Computation of the indexes for the key regions of NCEP data.

| Circulation factors | Computation of key regions and indexes |
|---|---|
| SLP | Standardized SLP anomaly averaged over 125°–155°E, 10°–22.5°N |
| Divergence at 1000 hPa (div1000) | standardized divergence anomaly averaged over 160°–180 °E, 15°–22.5°N |
| Divergence anomaly at 200 hPa (div200) | standardized divergence anomaly averaged over 150°–180°E, 17.5°–22.5°N |
| Vorticity at 850 hPa (Vor850) | standardized vorticity anomaly averaged over 140°–170°E, 15°–25°N |
| Zonal wind shear between upper and lower levels (*US*) $US=\|U_{200\ \mathrm{hPa}}-U_{850\ \mathrm{hPa}}\|$ | standardized US differences between the mean for 117.5°–137.5°E, 5°–15 °N and that of 152.5°–177.5°E, 10°–17.5 °N |
| Cross-equatorial airflow at 850 hPa (*V*850) | standardized 850 hPa meridional wind anomaly averaged over 87.5°–92.5°E, 7.5°S–7.5°N |



?1994-2014 China Academic Journal Electronic Publishing House. All rights reserved. http://www.cnki.net

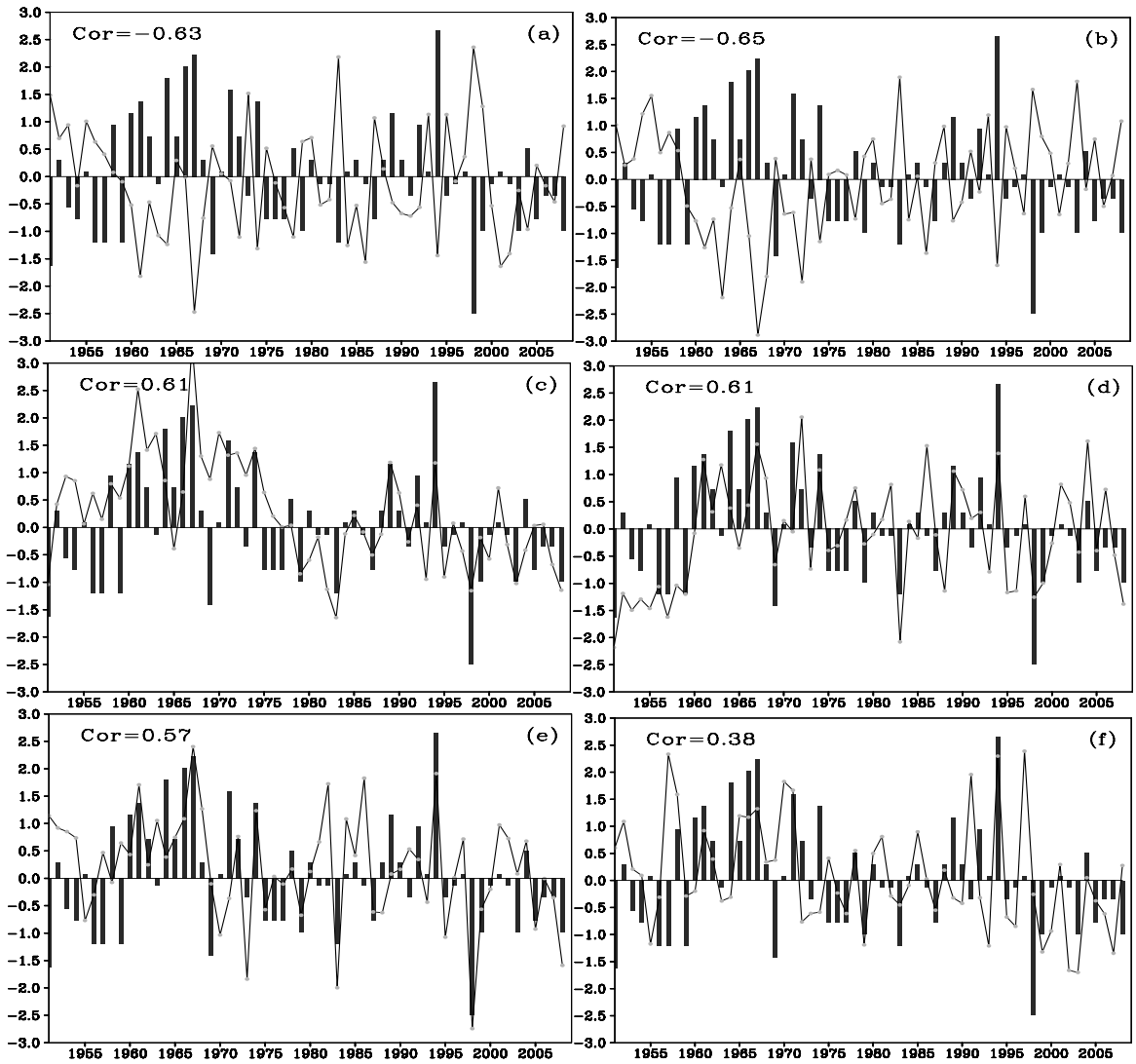


**Figure 2.** Standardized time series of the six key-region indexes (solid curve) and TC frequency (histogram). (The correlation coefficients of the two series are shown in the upper left corner of the curve). (a): SLP; (b): divergence at 1000 hPa; (c): divergence at 200 hPa; (d): vorticity at 850 hPa; (e): vertical shear of zonal wind; (f): meridional wind at 850 hPa. The abscissa is for the year.

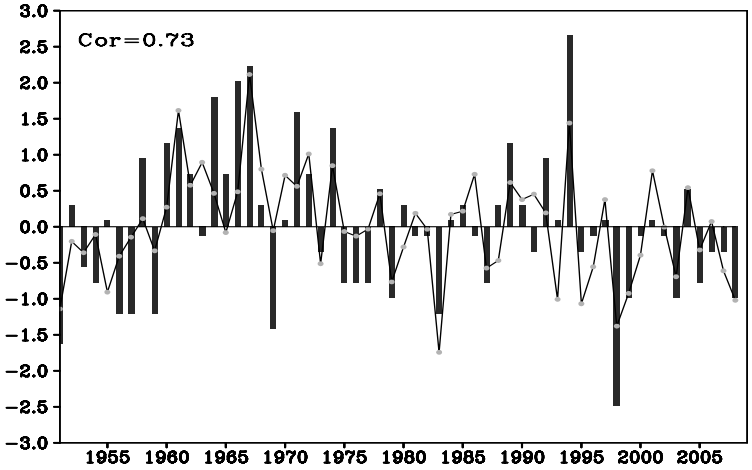


**Figure 3.** Fitting of TC frequency series using the multi-variate equation set up with the six key-region indexes (solid curve) and observations of the series (column). The series are all standardized and their correlation coefficients are shown at the upper left corner.

## 4 PREDICTIVE MODEL BASED ON SINTEX-F AND ITS VERIFICATION

Based on the analysis above on the observations, this work first investigated the capabilities of simulating the correlation between these TC



?1994-2014 China Academic Journal Electronic Publishing House. All rights reserved. http://www.cnki.net

frequencies and the large-scale circulation using the SINTEX-F GCM model. Like the previous section, the correlation is sought between the AF and the May-to-October circulation forecast with the model. As shown in the correlation analysis, the TC frequency's correlation with four of the six large-scale environmental fields presented in the previous sections (including the SLP, vertical wind shear in the troposphere, the cross-equatorial flow at 850 hPa and vorticity at 850 hPa) is well reflected in the model prediction. Fig. 4 gives the correlation between the TC frequency and the four circulations predicted by the model. The model is shown to reproduce main observed patterns of correlation. The correlation between the TC frequency and the predicted SLP is systematically more to the east in distribution as compared to the observation but the overall correlativity is quite significant (Fig. 4a). Consistency and differences both exist between the tropospheric wind shear and the observation as far as the distribution of correlation is concerned, with the simulated correlation for North Pacific and Southern Hemisphere much stronger than the observation (Fig. 4b). Systematic errors are also found between the simulated correlation between the 850 hPa meridional wind (Fig. 4c) and 850 hPa vorticity (Fig. 4d) and the observation, and their main physical characteristics are consistent with it. Based on the distribution of these correlations, the indexes for the four key regions can also be defined following what is presented in the previous text. Table 2 gives the definitions of the indexes. Fig. 5 presents the series of the indexes. They are correlated with the TC frequency by −0.7, 0.79, 0.53, and 0.64 respectively, all passing the test of 99% confidence. With the removal of the linear trend of the series for the TC and the atmosphere, the correlation is 0.65, 0.75, 0.63, and 0.60 respectively, still with significant correlativity.

**Table 2.** Key-region indexes determined with model data.

| Predictors | Key-region indexes determined with model data |
|---|---|
| SLP | Standardized SLP anomaly averaged over 170°E–140°W, 7.5°–22.5°N |
| Zonal wind shear between upper and lower levels (*US*) $US=\|U_{200\ hPa}-U_{850\ hPa}\|$ | Standardized wind shear (US) differences between the mean for 110°–140°E, 2.5°–15.0°N and that of 155°–175°E, 2.5°–15.0°N |
| Cross-equatorial flow at 850 hPa (*V*850) | Standardized 850 hPa meridional wind anomaly averaged over 82.5°–90°E, 10.0°S–2.5°N |
| Vorticity at 850 hPa (Vor850) | Standardized 850 hPa vorticity anomaly averaged over 140°–170°E, 10.0°–17.5°N |

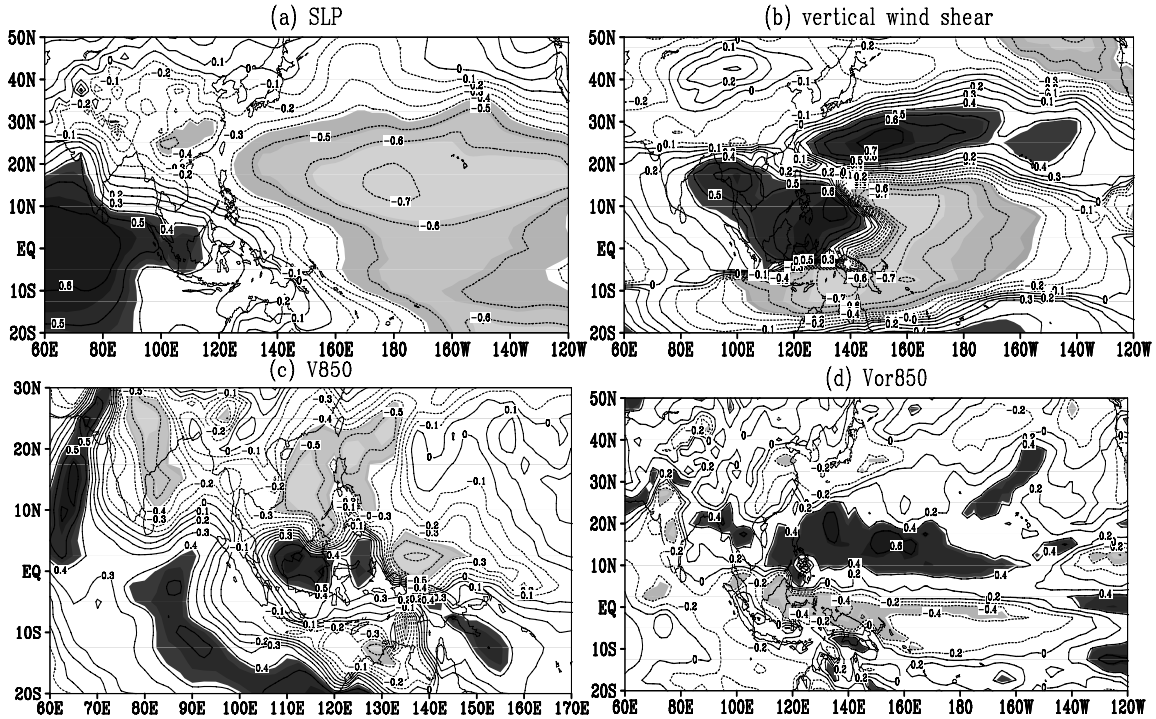


**Figure 4.** Correlation between the AF and model-predicted large-scale circulation. The shading is the area that passes the test of 95% confidence. (a): SLP; (b): vertical shear of meridional wind (|U200 hPa-U850 hPa|); (c): meridional wind at 850 hPa; (d): vorticity at 850 hPa.

The four indexes are used as the predictors to construct a multi-variate regression equation for the AF.

Figure 6 gives the model-fitted and observed anomalies of TC frequency for 1982−2010. They are correlated by a coefficient of 0.8 with a same-sign rate of 86%.



?1994-2014 China Academic Journal Electronic Publishing House. All rights reserved. http://www.cnki.net

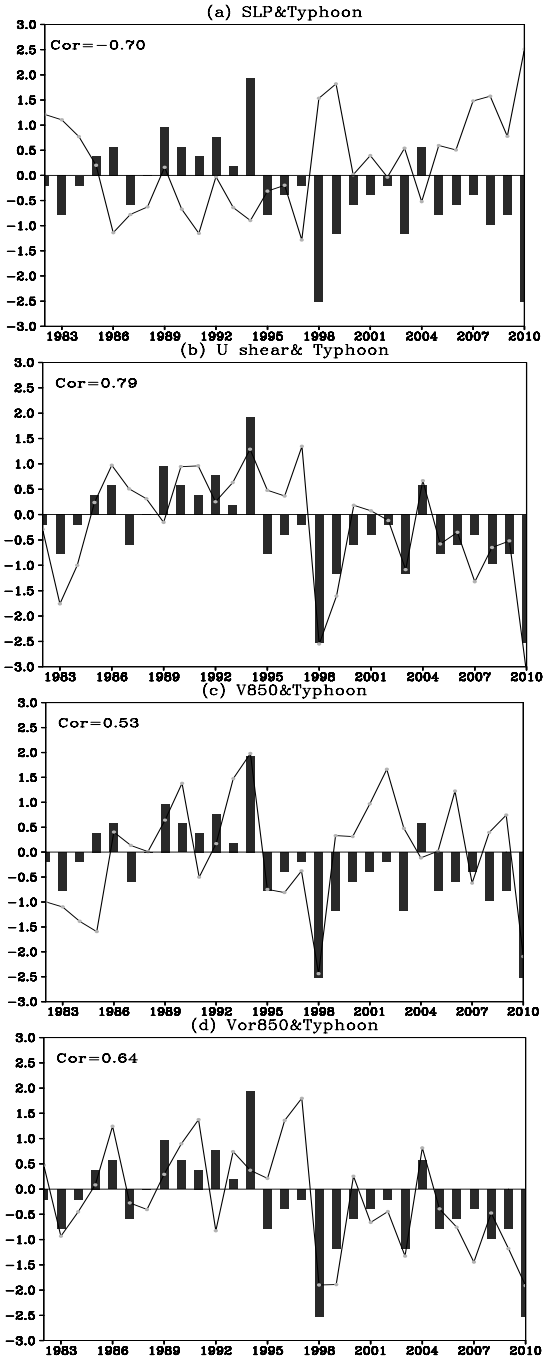


**Figure 5.** Standardized time series of model-predicted indexes of the four key regions (solid curve) and TC frequency (column). The correlation coefficients are shown in the upper left corner of the curve. Other captions are the same as in Fig. 4.

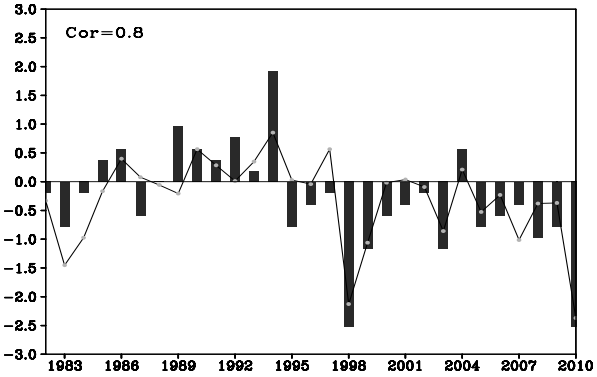


**Figure 6.** Fitting of the TC frequency by the multi-variate regression model set up with the four indexes of model-predicted key regions (curve) and observed series of the TC frequency (column). Both of the series are standardized. Their correlation coefficients are shown at the upper left corner. The abscissa is for the year.

The results of the predictive model are cross-verified as follows. For each of the predictive equations, data from the Mth year (with M taken to be 1, 2, ……, 29) are removed from the set of all available data (for the 29 years from 1982 to 2010). Then, the factors retained for the Mth year are used as the observation in the prediction while what is forecast for the Mth year is used as the observation. Repeat this procedure until M takes all possible values to obtain a series of the predicted value. As the forecast model does not involve predictors for the current year, the forecast so determined is considered one that is based on independent samples. In this way, the verified result of the forecast is close to the real forecast instead of retrospective forecast. Fig. 7 gives a standardized anomaly of the TC frequency derived from the cross verification, which is correlated with the observed frequency by 0.71 and passes the test of 99% confidence. Table 3 gives the TC frequency for each of the years using the cross-verification and the statistics of forecast results over the years. In the result of the cross-verification for the 29 years, the sign of the prediction is the same as that of the observed, or at a rate of 82.8%. There are 16 years for which the absolute forecast error is ±2, taking up 65.5% of the total. 1994 and 1989 are the two years with relatively large forecast errors. The number of TC genesis is anomalously larger, being 37 and 32 respectively, more than any other years since 1951. For the prediction, it is 30 and 25 respectively, or with relative errors at −18.9% and −21.9% respectively. For the years of extremely small frequency (1998 and 2010, both having 14 TCs), the model predicts 17 and 15 TCs respectively, though the relative error is larger for 1998 (21.4%). It is then clear that the forecast error is relatively large for extreme cases. 1994 and 1998 are the years with anomalously more and less TCs, being in extreme situations. For the predictive model that is based on statistical approach, predictive information is mainly from the historical data, which does not predict well if the case is extreme. Extreme events are just the things that cannot be predicted well with the usual statistical methods. In addition, the large-scale circulation field is the main element to build the model with but the large-scale environmental field is just one of the factors affecting the TC genesis. Especially, extreme situations cannot be explained entirely with the large-scale environmental field, which may account for the fact that the model produces large errors in predicting the anomalously more and less TC years.



?1994-2014 China Academic Journal Electronic Publishing House. All rights reserved. http://www.cnki.net

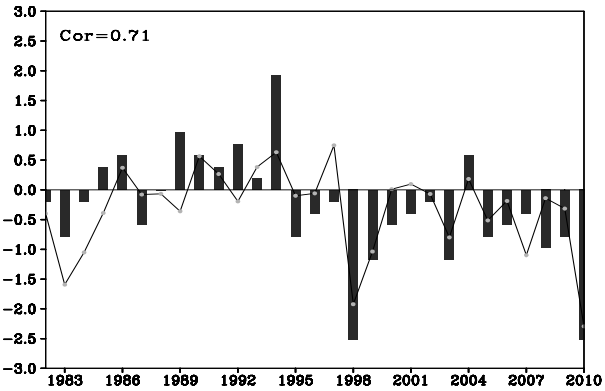


**Figure 7.** Series of TC frequency (results of cross-verification shown in curves) predicted by the multi-variate equation set up with the model-based key-region indexes and that of the observation (column). Both the series are standardized and the correlation coefficients are shown at the upper left corner.

**Table 3.** Cross-verifications of the model prediction of the AF in 1982-2010.

| Year | Observed AF | Predicted AF via Cross-verification | Correct anomaly or not (against a climatological mean of 27 TCs for 1971-2000) | Absolute error of prediction | relative error of prediction/% |
|---|---|---|---|---|---|
| 1982 | 26 | 25 | Y | −1 | −3.8 |
| 1983 | 23 | 19 | Y | −4 | −17.4 |
| 1984 | 26 | 22 | Y | −4 | −15.4 |
| 1985 | 29 | 25 | N | −4 | −13.8 |
| 1986 | 30 | 29 | Y | −1 | −3.3 |
| 1987 | 24 | 27 | Y | 3 | 12.5 |
| 1988 | 27 | 27 | Y | 0 | 0 |
| 1989 | 32 | 25 | N | −7 | −21.9 |
| 1990 | 30 | 30 | Y | 0 | 0 |
| 1991 | 29 | 28 | Y | −1 | −3.4 |
| 1992 | 31 | 26 | N | −5 | −16.1 |
| 1993 | 28 | 29 | Y | 1 | 3.6 |
| 1994 | 37 | 30 | Y | −7 | −18.9 |
| 1995 | 23 | 27 | Y | 4 | 17.4 |
| 1996 | 25 | 27 | Y | 2 | 8.0 |
| 1997 | 26 | 31 | N | 5 | 19.2 |
| 1998 | 14 | 17 | Y | 3 | 21.4 |
| 1999 | 21 | 21 | Y | 0 | 0 |
| 2000 | 24 | 27 | Y | 3 | 12.5 |
| 2001 | 25 | 27 | N | 2 | 8.0 |
| 2002 | 26 | 26 | Y | 0 | 0 |
| 2003 | 21 | 23 | Y | 2 | 9.5 |
| 2004 | 30 | 28 | Y | −2 | −6.7 |
| 2005 | 23 | 24 | Y | 1 | 4.3 |
| 2006 | 24 | 26 | Y | 2 | 8.3 |
| 2007 | 25 | 22 | Y | −3 | −12.0 |
| 2008 | 22 | 26 | Y | 4 | 18.1 |
| 2009 | 23 | 25 | Y | 2 | 8.7 |
| 2010 | 14 | 15 | Y | 1 | 7.1 |

## 5 CONCLUSIONS

Based on analyses of the correlation between the frequency of TC genesis and the large-scale circulation, this work uses the large-scale information from the SINTEX-F air-sea coupled model to extract useful information that is both capable of performing good prediction and closely related with the TC genesis. The results are then used to construct a statistical model for predicting the TC frequency on the basis of dynamic model outputs. Both experiments and verifications were conducted for the prediction.

(1) The genesis of the TC is closely related to the large-scale circulation, which includes the convection in the source area of the TC, wind shear between the upper and lower levels, ITCZ anomaly and the subtropical monsoon upstream of the TC source region and cross-equatorial flows. The predictive model, set up with six key-region factors from the NCEP data, has a fitting rate of 0.73 (correlation coefficient) for the AF of the TC.

(2) The SINTEX-F air-sea coupled model is successful in predicting part of the large-scale circulation patterns closely related to the TC genesis. The patterns include the SLP in the active area of the TC, vertical wind shear in the troposphere, vorticity of the ITCZ and the cross-equatorial flow near 90°E (at 850 hPa for the latter two). The four predictors are well correlated with the TC genesis and the fitting rate of the multi-variate regression model is 0.8 (correlation coefficient, surpassing the test of 99.9% confidence) for the TC genesis.

(3) Cross-verification was conducted of the result of the predictive model set up with the output of the SINTEX-F air-sea coupled model. It is shown that the overall result is good. The cross-verification results are correlated with the real TC frequency at 0.71 (which passes the test of 99% confidence) and the same-sign rate is 82.8%. The predictive model has the largest error for extreme years of the TC. The model's capability can be improved for cases of extremely large or small number of TCs if improvement can be made in introducing factors of extreme conditions in addition to the large-scale circulation.

## REFERENCES:

[1] DING Yi-hui. Large-scale circulation conditions affecting the genesis of typhoons in western Pacific [J]. Acta Oceanol. Sinica, 1983, 5(5): 561-574.

[2] LI Chong-yin. A study on the influence of El Nino upon typhoon action over western Pacific [J]. Acta Meteor. Sinica, 1987, 45: 229-236.

[3] DONG Ke-qin, ZHONG Quan. The correlation between SST for equatorial eastern Pacific and frequency of occurrence for tropical storms in the South China Sea [J]. J. Trop. Meteor., 1989, 5(4): 335-350

[4] CHEN Lian-shou, LUO Zhe-xian. Numerical on the impact of two kinds of factors on tropical cyclone's structure and motion of typhoons [J]. Acta Meteor. Sinica, 1996, 54: 409-415.

[5] LEI Xiao-tu. Advances in the research of the prediction of tropical cyclone frequency and level of operational forecast [J].



?1994-2014 China Academic Journal Electronic Publishing House. All rights reserved. http://www.cnki.net

Atmos. Sci. Res. Appl., 1998, 1: 196-202.
[6] SONG Wen-ling, HE Min. Relationship between convective activity over tropical Pacific and typhoon activity over northwest Pacific [J]. Quart. J. Appl. Meteor., 1998 (Suppl.): 109-118.
[7] CHEN Lie-ting, YAN Zhi-xin. Statistical analysis to the effects of winter-spring snow cover over the Tibetan Plateau on the early summer monsoon [M]. Beijing: Hydraulics and Hydro Electrics Press, 1981: 133-141.
[8] WU Di-sheng, BAI Yi-ping, ZHANG Hong-mei, et al. The influence of variation of subsurface ocean temperature in the equatorial western Pacific warm pool on tropical cyclones [J]. J. Trop. Meteor., 2003, 19(3): 253-259.
[9] LIN Hui-juan, ZHANG Yao-cun. Climatic features of the tropical cyclone influencing China and its relationship with the sea surface temperature in the Pacific Ocean [J]. J. Trop. Meteor., 2004, 20(2): 218-224.
[10] LI Chun-hui, LIU Chun-xia, CHENG Zheng-quan. The characteristics of temporal and spatial distribution of tropical cyclone frequencies over the South China Sea and its affecting oceanic factors in the past 50yrs [J]. J. Trop. Meteor., 2007, 23(4): 341-347.
[11] WANG Yong-mei, LI Wei-jing, REN Fu-min, et al. Study on climatic characteristics of China-influencing typhoons and the interrelations between them and their environmental factors [J]. J. Trop. Meteor., 2007, 23(6): 538-544.
[12] WANG Hui-jun, SUN Jian-qi, FAN Ke. On the relationship between the North Pacific Oscillation and the genesis frequency of typhoons and hurricanes [J]. Sci. China (Ser. D: Earth Sci.), 2007, 37(7): 966-973.
[13] FAN Ke. Is the North Pacific sea ice a predictor for the typhoon genesis in northwestern Pacific? [J]. Sci. China (Ser. D: Earth Sci.), 2007, 37(6): 851-856.
[14] SUN Shu-qing, LIU Ge, ZHANG Qing-yun. The influence of the circulation anomalies in the Southern Hemisphere on the tropical cyclnoe frequency in summer over the western Pacific and its mechanism [J]. Chin. J. Atmos. Sci., 2007, 31(6): 1189-1200.
[15] WANG Hui-jun, FAN Ke. Relationship between the genesis frequency of northwestern Pacific typhoons and the Antarctica Oscillation [J]. Chin. Sci. Bull., 2006, 51(24): 2910-2914.
[16] NICHOLLS N. Recent performance of a method for forecasting Australian season tropical cyclone activity [J]. Aust. Meteor. Mag., 1992, 40: 105-110.
[17] JIANG Guo-rong, SHA Wen-yu. Investigation of the statistical forecast of interannual change of tropical cyclone in the western Pacific by sea surface temperature in the eastern equatorial Pacific [J]. J. Trop. Meteor., 1993, 9(3): 221-228.
[18] KLOTZBACH P J, GRAY W M. Twenty-five years of Atlantic basin seasonal hurricane forecasts (1984–2008) [J]. Geophys. Res. Lett., 2009, 36, L09711, doi:10. 1029/2009GL037580.
[19] KLOTZBACH P J, GRAY W M. Extended range forecast of Atlantic seasonal hurricane activity and landfall strike probability for 2010 [EB/OL]. [2013-09-11] http://hurricane.atmos.colostate.edu.
[20] FAN Ke, WANG Hui-jun. A new approach to forecasting typhoon frequency over the western North pacific [J]. Wea. Forecast., 2009, doi:10.1175/2009WAF2222194.1.
[21] WANG Hui-jun, LONG Xian-mei, FAN Ke, et al. Real-time prediction experiment for the typhoon frequency in the western North Pacific for 2006 [J]. Clim. Environ. Res., 2006, 11(2): 133-137.
[22] LONG Xian-mei, WANG Hui-jun. Can climate models be used to predict the climate background of the activity of typhoons in western North Pacific? [J]. Chin. Sci. Bull., 2008, 53(14): 1702-1708.
[23] GUALDI S, NAVARRA A, GUILYARDI E, et al. Assessment of the tropical Indo-Pacific climate in the SINTEX CGCM [J]. Ann. Geophys., 2003, 46(1): 1-26.
[24] GUILYARDI E, DELECLUSE P, GUALDI S, et al. Mechanism for ENSO phase change in a coupled GCM [J]. J Climate, 2003, 16(8): 1141-1158.
[25] LUO J J, MASSON S, BEHERA S, et al. South Pacific origin of the decadal ENSO-like variation as simulated by a coupled GCM [J]. Geophys. Res. Lett., 2003, 30: 2250, doi:10.029/2003GL018649.
[26] LUO J J, ROECKNER E, MADEC G, et al. Reducing climatology bias in an ocean-atmosphere CGCM with improved coupling physics [J]. J. Climate, 2005, 18(13): 2344-2360.
[27] CHEN Li-juan. Analysis of the predictability of seasonal climate based on air-sea coupled models and interpretation application [D]. Doctoral thesis, Beijing: Graduate School of Chinese Academy of Sciences, 2008.
[28] ROECKNER E, COAUTHORS. The atmospheric general circulation model ECHAM-4: Model description and simulation of present-day climate [R]. Max-Planck-Institut für Meteorologie Rep. 218, Hamburg, Germany, 1996, 90 pp.
[29] MADEC G, DELECLUSE P, IMBARD M, et al. OPA 8.1 ocean general circulation model reference manual [R]. LODYC/IPSL Tech. Rep. Note 11, 1998, Paris, France, 91.
[30] VALCKE S, TERRAY L, PIACENTINI A. The OASIS coupler user guide version 2.4 [R]. CERFACE Tech. Rep. TR/CGMC/00-10, 2000, 85.
[31] LUO J J, MASSON S, BEHERA S, et al. Seasonal climate predictability in a coupled OAGCM using a different approach for ensemble forecasts [J]. J. Climate, 2005, 18(21): 4474–4497.
[32] LUO J J, MASSON S, BEHERA S, et al. Extended ENSO predictions using a fully coupled ocean–atmosphere model [J]. J. Climate, 2008, 21(1): 84-93.
[33] LUO J J, ZHANG R, BEHERA S, et al. Interaction between El Nino and extreme Indian Ocean Dipole [J]. J. Climate, 2010, 23(3): 726-742.
[34] LUO J J, MASSON S, BEHERA S, et al. Experimental forecasts of the Indian Ocean Dipole using a coupled OAGCM [J]. J Climate, 2007, 20 (10): 2178-2190.
[35] JIN E K, COAUTHORS. Current status of ENSO prediction skill in coupled ocean–atmosphere models [J]. Climate Dyn., 2008, 31: 647-664.
[36] WANG B, LEE J Y, KANG I S, et al. How accurately do coupled climate models predict the Asian-Australia monsoon interannual variability? [J]. Climate Dyn., 2008, 31: 605-619.
[37] LUO J J, BEHERA S, MASUMOTO Y, et al. Successful prediction of the consecutive IOD in 2006 and 2007[J]. Geophys Res Lett, 2008, 35, L14S02, doi:10.1029/2007GL032793.
[38] KALNEY E, KANAMITSU M, KISTLER R, et al. The NCEP/NCAR 40-year reanalysis project [J]. Bull. Amer. Meteor. Soc., 1996, 77(3): 437-471.

**Citation:** JIA Xiao-long, CHEN Li-juan, LUO Jing-jia. Climate prediction experiment for tropical cyclone genesis frequency using the large-scale circulation forecast by a coupled global circulation model. *J. Trop. Meteor.*, 2014, 20(2): 103-111.



?1994-2014 China Academic Journal Electronic Publishing House. All rights reserved. http://www.cnki.net

Chin. Sci. Bull. (2014) 59(34):4864–4872
DOI 10.1007/s11434-014-0502-4

csb.scichina.com
www.springer.com/scp

Article

Atmospheric Science

# Spatiotemporal distribution and decadal change of the monthly temperature predictability limit in China

**Weijing Li · Jingpeng Liu · Lijuan Chen · Peiqun Zhang · Hongli Ren**

Received: 6 January 2014 / Accepted: 12 May 2014 / Published online: 12 July 2014
© Science China Press and Springer-Verlag Berlin Heidelberg 2014

**Abstract** Based on the nonlinear Lyapunov exponent and nonlinear error growth dynamics, the spatiotemporal distribution and decadal change of the monthly temperature predictability limit (MTPL) in China is quantitatively analyzed. Data used are daily temperature of 518 stations from 1960 to 2011 in China. The results are summarized as follows: (1) The spatial distribution of MTPL varies regionally. MTPL is higher in most areas of Northeast China, southwest Yunnan Province, and the eastern part of Northwest China. MTPL is lower in the middle and lower reaches of the Yangtze River and Huang-huai Basin. (2) The spatial distribution of MTPL varies distinctly with seasons. MTPL is higher in boreal summer than in boreal winter. (3) MTPL has had distinct decadal changes in China, with increase since the 1970s and decrease since 2000. Especially in the northeast part of the country, MTPL has significantly increased since 1986. Decadal change of MTPL in Northwest China, Northeast China and the Huang-huai Basin may have a close relationship with the persistence of temperature anomaly. Since the beginning of the 21st century, MTPL has decreased slowly in most of the country, except for the south. The research provides a scientific foundation to understand the mechanism of monthly temperature anomalies and an important reference for improvement of monthly temperature prediction.

**Keywords** Monthly temperature · Predictability · Spatiotemporal distribution · Decadal change · Nonlinear Lyapunov Exponent (NLLE)

## 1 Introduction

With expansive territory and complex topography, the temporal and spatial variability of monthly temperature is very great across China. Temperature is not only the most prominent characteristic variable of the climate system, but also the primary indicator of short-term climate prediction. Therefore, it is necessary to study the monthly temperature predictability limit (MTPL) to understand regions in the country with high and low MTPL. This helps to understand the mechanism of monthly temperature anomalies and improve prediction skill for monthly temperature. Under a background of global warming, extreme weather and climate events in China have been frequent [1, 2]. This brings severe challenges to the basic theoretical study of short-term climate prediction. Internal dynamical processes and boundary forcing of the atmosphere have different decadal changes [3] under global warming. Therefore, whether MTPL experiences decadal change with effects from these two factors has attracted much attention among scientists [4, 5]. Wang et al. [4] pointed out that persistent prediction skill of monthly temperature in China increased slowly between 1982 and 2005. Kang et al. [5] indicated that the two 30-year periods 1914–1943 and 1968–1997 had low and high predictabilities, respectively. Further research is still needed to quantitatively investigate the decadal change of MTPL in China.

Qualitative and quantitative methods [6] are the most common in the study of predictability. Qualitative methods aim to estimate the ratio of climatic signal to noise [7–9],

W. Li · J. Liu
Chinese Academy of Meteorological Sciences, Beijing 100081, China

W. Li (✉) · J. Liu · L. Chen · P. Zhang · H. Ren
Laboratory for Climate Studies, National Climate Center, China Meteorological Administration, Beijing 100081, China
e-mail: liwj@cma.gov.cn

but cannot investigate MTPL quantitatively. Quantitative methods include experiential, dynamical, and dynamical-experiential. Among these, dynamical methods are the most widely used and efficient. They can be separated in two branches, by the use of numerical models [10–12] or theory of nonlinear dynamic systems [13–16]. Numerical models cannot construct the real atmosphere because of their limitations [17]. Therefore, the theory of nonlinear dynamic systems can provide methods to estimate MTPL quantitatively, which can remedy the deficiency of qualitative methods [18, 19]. Further, the theory avoids errors caused by differences between the modeled and real atmosphere. Based on the Lyapunov stability theory and criterion of error growth, Lorenz [11] defined the predictability limit as the time over which errors double. The nonlinear Lyapunov exponent (NLLE) proposed by Li et al. [18–21] further developed the Lyapunov stability theory. The NLLE has been widely applied to studying the predictability limit with regard to weather [18–21] and climate [22].

Existing target variables used to estimate predictability are usually located at higher levels of the troposphere and are described by gridded data. Because of limitations of data, theory and methods, there is relatively little quantitative research focusing on surface climatic variables in China. It remains difficult to quantitatively depict characteristics of spatiotemporal change of Chinese monthly climate predictability. Given the complex topography and significant impact of the Asian monsoon in China, the predictability of surface variables there is much different from that in other areas at the same latitude. In this study, using the NLLE method and observed daily station data, we quantitatively investigate the spatiotemporal distribution and decadal change of the monthly temperature predictability limit in China. The data used involves impacts of persistent change of external forcing and of atmospheric inner dynamic processes. Therefore, the estimated predictability using observed data involves dynamical predictability based on initial value and predictability induced by external forcing [22].

By using more intensive and longer observed daily temperature during 1960–2011 from 518 stations in China and dealing with the data appropriately, we quantitatively estimate the MTPL based on NLLE. Then, the spatiotemporal distribution and decadal change of MTPL is described. Two questions will be answered, namely, to what degree can monthly mean temperature be predicted, and whether the MTPL in different regions undergoes interdecadal change.

## 2 Data and method

The datasets used include observed daily temperature during 1960–2011 from 518 stations in China, four times per day temperature fields at 850 hPa from National Centers for Environmental Prediction/National Center for Atmospheric Research (NCEP/NCAR) reanalysis data (1960–2011), observed monthly temperature from 160 stations (1983–2012), and hindcast data of monthly temperature (1983–2012) from the monthly dynamic extended range forecast (DERF) [23]. The quality of the 518-station daily temperature was checked. Missing data never account for more than 5 consecutive days and the total of missing data entries is never more than 60 days within each time series. The missing data are replaced by climatic averages from 1960 to 2011. The spatial density of stations and length of time series are greater than in earlier studies [24, 25]. This assures the reliability of MTPL spatiotemporal distribution to a degree [26]. The annual cycle (using daily average temperature from 1960 to 2011) and linear trend of the time series were removed. Then, the time series were smoothed by 31 days so that the high-frequency part was removed and the time scale limited to months. Finally, the time series were normalized. Anomalies of 160-station observed monthly temperature and hindcasts of monthly temperature were calculated based on climatic values from 1983 to 2012.

On the basis of NLLE [21] and nonlinear error growth theory [27, 28], the monthly predictability of surface temperature is estimated. For vector $x$, the NLLE is defined as

$$\lambda(x(t_0), \delta(t_0), \tau) = \frac{1}{\tau}\ln\left|\frac{\delta(t_0+\tau)}{\delta(t_0)}\right|, \quad (1)$$

where $x(t_0)$ is the initial state of reference orbit in phase space, which means the monthly average temperature of the station-observed time series at time $t_0$; $\delta(t_0)$ is the initial error, which is the difference between temperatures at time $t$ and time $t_0$. Here, time $t$ is searched in the station-observed time series based on local dynamical analogs [21]; $\tau$ is the time accumulated since time $t_0$. The condition $\lambda>0$ means that the distance between the initial similar orbits increases over time and so their correlation weakens with time. The greater the value of $\lambda$, the faster the initial error grows. The mean relative growth of initial error (RGIE) can be obtained by

$$\overline{E}(\delta(t_0), \tau) = \exp(\overline{\lambda}(\delta(t_0), \tau) \cdot \tau). \quad (2)$$

Using the nonlinear error growth theory from Ding and Li [27], we obtain

$$\overline{E}(\delta(t_0), \tau) \xrightarrow{P} c \ (N \to \infty), \quad (3)$$

where constant $c$ can be considered the theoretical saturation level of $\overline{E}(\delta(t_0), \tau)$ when sample number $N$ tends to infinity. Once the error growth reaches the saturation level, almost all similarity information on

initial states is lost and the prediction becomes meaningless. Using the theoretical saturation level, the predictability limit of chaos systems can be quantitatively determined. The monthly temperature predictability limit of the station is defined as

$$\mathrm{MTPL} = \left\{ t | \overline{E}(\delta(t_0), \tau) = 0.99 \cdot c \right\}, \quad (4)$$

where the MTPL is defined as the time at which the error reaches 99 % of its saturation level.

The NLLE of observational data can be estimated using an algorithm based on local dynamical analogs [21]. If the mean relative growth of the initial error of the total time series is calculated by Eq. (2), we can then obtain the annual average MTPL. If the mean relative growth of the initial error of a given month in the time series is calculated by that equation, then we get the monthly average MTPL. Essentially, the MTPL is a dynamical-statistical value. Its physical meaning is the time limit after which the two dynamic similar initial states become absolutely dissimilar. This implies the time for which the monthly temperature can be predicted in advance. By estimating the MTPL at each station, the spatial distribution characteristics of MTPL can be obtained.

## 3 Spatial distribution of MTPL

According to the data processing methods presented above, we calculated the mean RGIE of the total time series with Eq. (2), and then obtained the spatial distribution of annual average MTPL via Eqs. (3) and (4) (Fig. 1a). Figure 1 shows that the MTPL was higher in most areas of northeastern China, northern North China, southwestern Yunnan Province, and eastern Northwest China. In these regions, the MTPL exceeded 30 days in general. The MTPL was lower in the middle and lower reaches of the Yangtze River and Huang-huai Basin, and was about 30 days in general. This implies that as far as its annual average was concerned, MTPL was higher in North and West China and lower in most regions south of the Huang-huai Basin. To further examine the reliability of annual average MTPL estimated by surface-station observation data, we estimated that average at 850 hPa using the four times per day temperature field at that level from the NCEP/NCAR reanalysis data (Fig. 1b). Since temperatures at 850 hPa and the surface are very consistent, the MTPL spatial distribution estimated by the temperature fields at 850 hPa and surface station data are roughly the same theoretically. In fact, the spatial distribution of MTPL shown in Fig. 1b is very similar to that in Fig. 1a. The MTPL from Fig.1b is higher than that in Fig. 1a in most areas of northwestern China, Yunnan and Guizhou Provinces . Therefore, it is reasonable to estimate the spatiotemporal distribution of MTPL using surface observation data. Also, comparison of Fig. 1b and a implies that MTPL at higher levels of the troposphere is greater than that at lower levels in some regions in China.

Figure 2 shows the spatial distribution of MTPL in each month. In December (Fig. 2a), MTPL reached 40–50 days in southwestern and North China. It was generally 30–40 days in most other parts of the country. In January and February (Fig. 2b, c), MTPL was generally 20–30 days. MTPL remained in this range in most regions during March and April (Fig. 2d, e), except for eastern Northeast China, local areas of southwest China, and eastern South China. MTPL reached 30–40 days in the latter region. MTPL increased in May (Fig. 2f), reaching 40–50 days in northern Xinjiang and southern Northwest China, and it was 25–35 days in other regions. In June (Fig. 2g), MTPL was as high as 40–50 days in Xinjiang, western North China, eastern Southwest China, and western South China, and 25–40 days in the rest of the country. The MTPL spatial distribution was similar in July and August, with smaller numbers of days (25–35) in the middle and lower reaches of the Yangtze River and southern Xinjiang. MTPL was 45–60 days in the rest of China, except for maxima of 60–70 days in local areas of Southwest China. Regions where MTPL was lower were strongly connected with active regions of the East Asian summer monsoon and rain belt [29]. In Autumn, MTPL tended to decrease in most parts of the country (Fig. 2j–l). In September (Fig. 2j), MTPL was 50–60 days except for the middle and upper reaches of the Yangtze River, where it remained 30–40 days. In October (Fig. 2k), MTPL was about 40–50 days in southern Northwest China, southern Northeast China, and coastal areas of southern China. MTPL was around 30–45 days in the rest of the country. In November, MTPL was about 30–40 days, except for Southwest China and western South China, where it was still 40–50 days.

In summary, MTPL was lower in the winter half-year (December–May) (Fig. 2a–f) and higher in the summer half-year (June–November) (Fig. 2g–l). This result is different from that of Li and Ding [22], who stated that MTPL of geopotential height and temperature at 500 hPa was higher in winter than in summer on a global scale. The reason might be that China is strongly influenced by the monsoon system, with intraseasonal variability of temperature much greater in winter than in summer. In winter, the effect of atmospheric circulation anomalies is significant and the cold air at mid to high latitudes has strong variability and frequently affects China. This may lead to large intraseasonal variability of surface temperature [24]. Moreover, the frequency and strength of extreme weather events in winter increases at mid to high latitudes in East Asia under global warming. This also leads to greater intraseasonal variability of temperature [30], and MTPL in

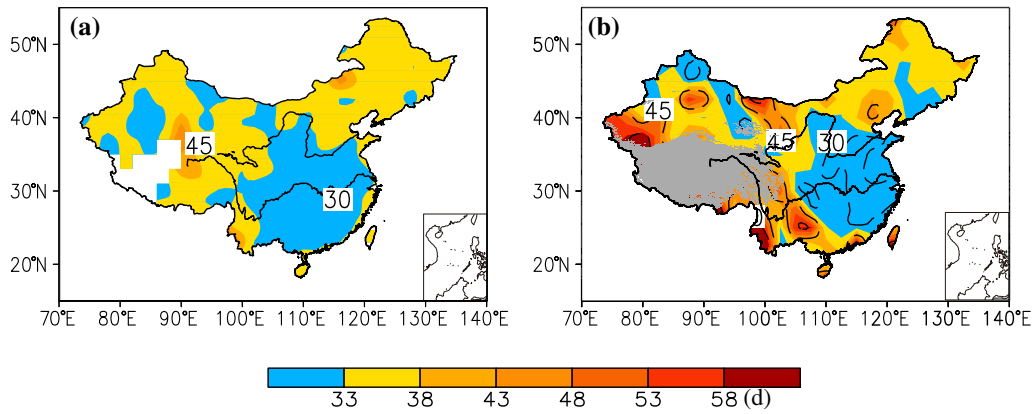


**Fig. 1** Spatial distribution of annual average MTPL. **a** Calculated by surface temperature, **b** calculated by 850 hPa temperature

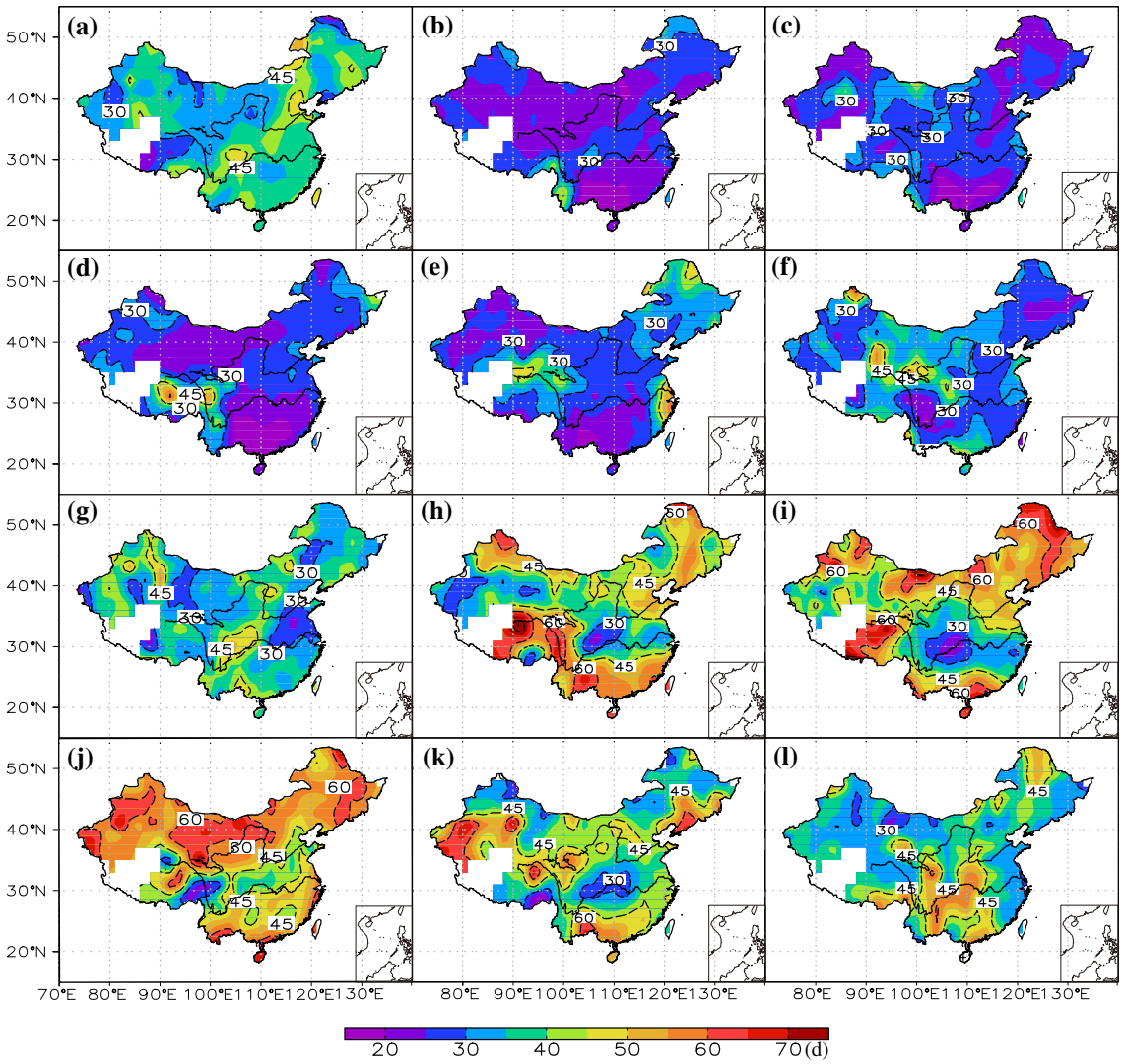


**Fig. 2** Spatial distribution of monthly average MTPL. **a** December, **b** January, **c** February, **d** March, **e** April, **f** May, **g** June, **h** July, **i** August, **j** September, **k** October, **l** November

spring and winter is reduced. In summer and autumn, China is mainly affected by the East Asian summer monsoon. Circulations in tropical and subtropical regions significantly affect the country, but their variability is less than that at mid to high latitudes. Thus, the MTPL in summer and autumn is higher than in winter and spring. Yang et al. [31] obtained the potential predictability of temperature at 850 hPa via model simulations and implied that this predictability is greater in summer but less in winter. This shows that the influence of boundary forcing such as sea surface temperature and soil moisture is strong and that of inner dynamical processes of the atmosphere is weak in summer. As a result, intraseasonal variability of temperature is small [24], which leads to higher MTPL. This conclusion is consistent with the present result. The difference between MTPL in China and other countries at the same latitude shows that the MTPL distribution in China is much more complex.

To further verify the conclusion that the potential predictability of temperature and MTPL in China is higher in summer and lower in winter, we calculated the prediction score (Ps) of monthly temperature anomalies in January and July for 160 stations in the country. The predicted monthly temperature (1983–2012) is given by the DERF, using the first-generation climate model of the National Climate Center. Data used were observed monthly temperature anomalies of 160 stations and predicted monthly temperature anomalies from DERF (both 1983–2012). During that period, if the number ($n$) of years in which the sign of predicted temperature anomalies is consistent with the sign of observational temperature anomalies is $m$, then the prediction score of monthly DERF is defined as

$$\mathrm{Ps} = \frac{m}{n} \times 100\,\%. \tag{5}$$

We obtained the spatial distribution of Ps of monthly DERF in January (Fig. 3a) and July (Fig. 3b) via Eq. (5). Figure 3 shows clearly that Ps was higher in July than in January. This is consistent with the result shown in Figure 2, i.e., MTPL was higher in July (Fig. 2h) than in January (Fig. 2b). The spatial distributions of Ps and MTPL were similar in these two months. This implies that in a month of low (high) MTPL, the DERF Ps is also low (high).

## 4 Decadal change of MTPL in different regions

To obtain the decadal change character of MTPL, the signal on a decadal time scale must be removed. MTPL variations can be analyzed based on an 11-year moving window [32]. Annual mean MTPL can be determined in that window via the NLLE approach. The window moves forward every half year. The time axis indicates the middle year of the windows. Because of the moving window, the range of decadal change obtained is from 1965 to 2006. Figure 4a–e shows MTPL anomalies in various decades relative to the 1965–2006 average (Fig. 4f).

During 1965–2006, the MTPL was higher in North China and West China but lower south of the Huang-huai Basin (Fig. 4f). The MTPL clearly varied by region during each decade. In the 1960s, MTPL was 2 days lower than the climatic average in southern Xinjiang, eastern Northwest China, North China and Northeast China. Meanwhile, MTPL was 2 days higher than the average south of the Huang-huai Basin. In the 1970s, MTPL was about 2 days lower than the average in Northeast and North China and southern Northwest China. During that decade, the MTPL in the rest of China was 2–4 days higher than the average. In the 1980s, the MTPL was about 2 days less than the average in Northeast China, eastern South China, and eastern Tibet. The MTPL was 2–4 days higher than the average in the remainder of China during that decade. In the 1990s, MTPL decreased by about 2 days in most parts of Central and West China, and

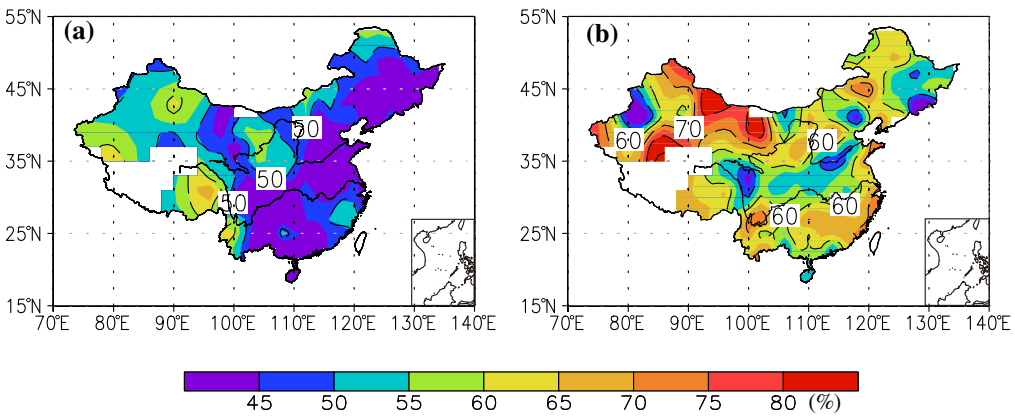


**Fig. 3** Spatial distribution of Ps from DERF in January (**a**) and July (**b**)

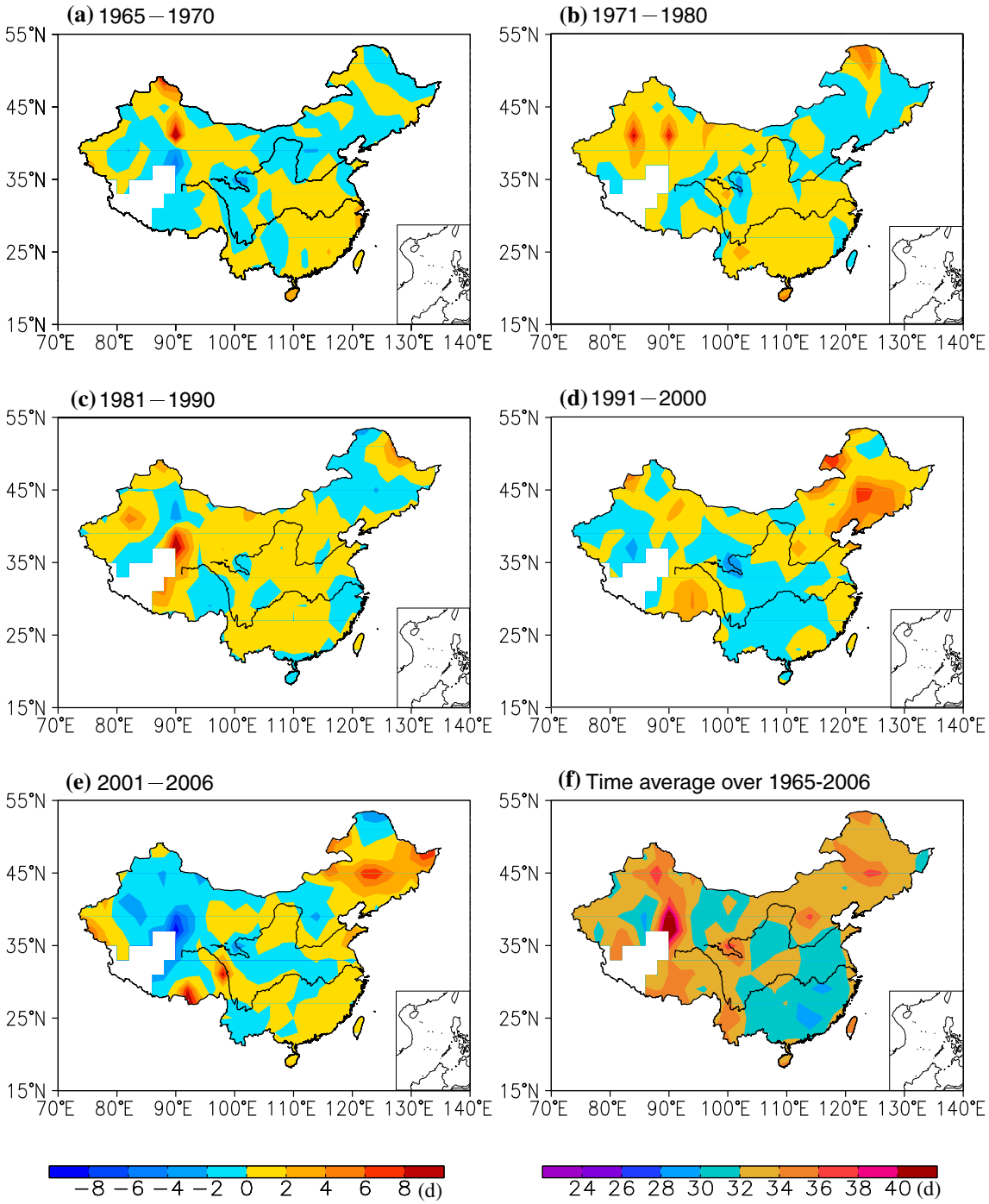


**Fig. 4** MTPL anomalies in different decades (**a**–**e**, color bar at the left) relative to 1965–2006 average (**f**, color bar at the right)

increased by 2–4 days in most parts of North China and East China. In some local areas of Northeast China, the MTPL was 4–6 days higher than the average. After 2000, it was 2 days lower than the average in most of western China. The MTPL decreased by 2–4 days in southern Xinjiang and increased by about 2 days in the rest of China. It was 4–6 days higher than the average in Northeast China.

The MTPL rose significantly after the 1990s in Northeast China. Its decadal change in the rest of China was much more complex. Ding et al. [32] estimated the weather predictability limit (WPL) at different geopotential heights. They demonstrated that during 1953–2000, WPL decreased significantly at mid to high latitudes in Eurasia. However, this study showed that the

characteristics of decadal change are more complex in China, and require further analysis.

To further analyze the inter-decadal change characteristics of MTPL in various regions, China was classified into five subregions (Fig. 5). The regional average MTPL was calculated, thereby obtaining MTPL decadal change in each region (solid lines in Fig. 6).

Figure 6 shows that decadal change characteristics vary with region. The MTPL in Northwest China (region I, Fig. 6a) began to decrease in the mid 1960s and increased slowly in the mid 1970s. It then declined continuously from the early 1980s and began to increase slowly at the end of the 20th century. The MTPL in Southwest China (region II, Fig. 6b) and the Huang-huai Basin (region IV, Fig. 6d) has decreased slowly but insignificantly since the 1980s. The MTPL in Northeast China (region III, Fig. 6c) experienced significant changes, increasing continuously from the 1980s and decreasing significantly since 2000. According to the moving *t*-test and Mann-Kendall test conducted at the 1% level, both methods identified abrupt climate change in 1986. The MTPL in South China (region V, Fig. 6e) decreased in the 1980s, began to increase in the mid 1990s, and is presently increasing. For the entire country (Fig. 6f), the MTPL began to increase in the 1970s and began to decrease after 2000.

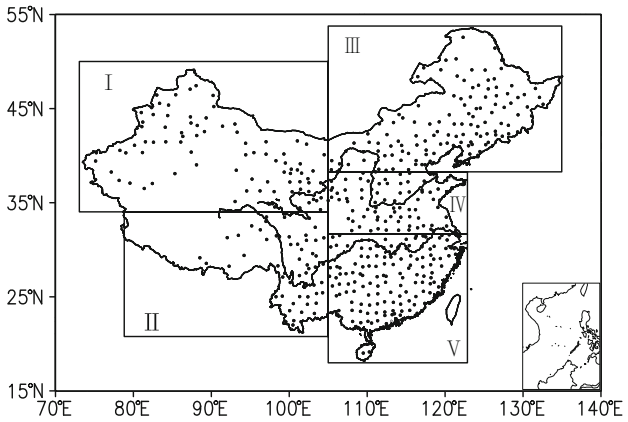


**Fig. 5** Five subregions used to analyze decadal MTPL change. These are Northwest China (region I, 73°–105°E, 34°–50°N), Southwest China (region II, 79°–105°E, 21°–34°N), Northeast China (region III, 105°–135°E, 38°–54°N), Huang-huai Basin (region IV, 105°–123°E, 31°–38°N), and South China (region V, 105°–123°E, 18°–31°N)

To further analyze the reason for inter-decadal change of MTPL, we calculated decadal Ps change of persistent prediction in each region (dashed lines in Fig. 6). The method was as follows. By using the time series of observed daily temperature at 518 stations (1960–2011), the linear trend is first removed from the series, and then monthly temperature anomalies are calculated. Temperature anomalies in this month were considered the predicted anomalies of the subsequent month. If $M$ is the number of stations in which the sign of predicted temperature anomalies was consistent with the sign of observational temperature anomalies, and the total number stations in the

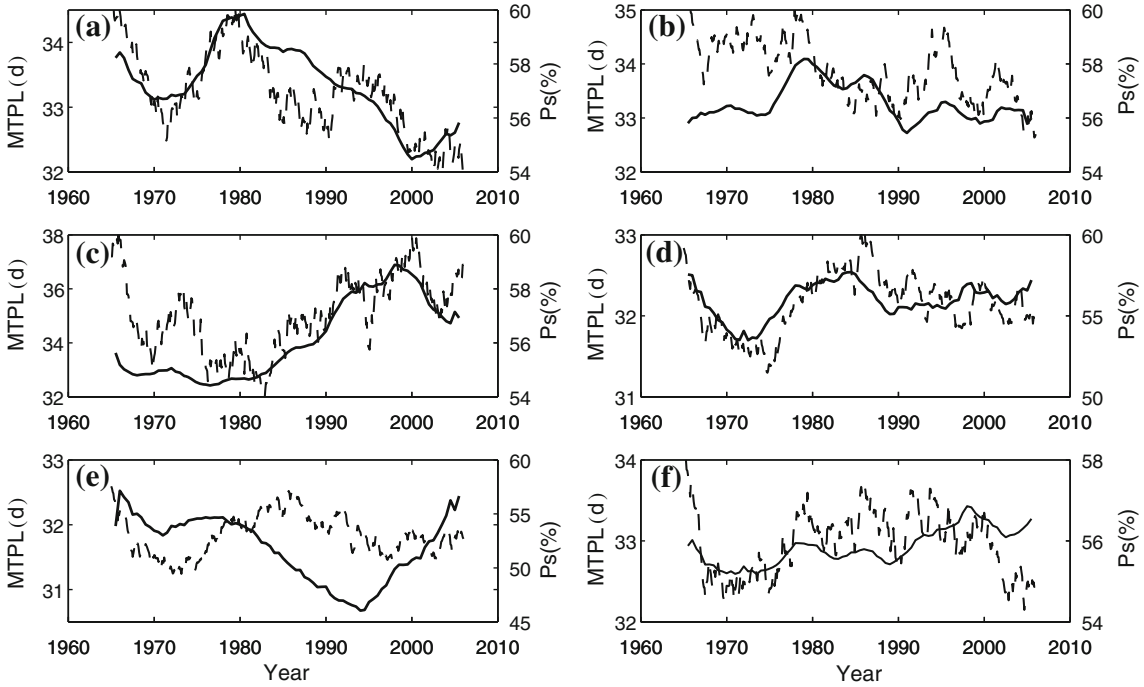


**Fig. 6** Temporal variations of area-averaged MTPL and Ps in the five subregions (**a**–**e**) and entire country (**f**). Nine-year running mean series of MTPL are indicated by solid lines. Eleven-year running mean series of Ps are indicated by dashed lines

region is $N$, then the Ps of persistent prediction can be obtained by

$$\mathrm{Ps} = \frac{M}{N} \times 100\,\%. \quad (6)$$

Thus, we acquired the inter-decadal Ps change of persistent prediction of monthly temperature from 1965 to 2006.

By comparing the solid and dashed lines in Fig. 6, it is obvious that the trends of decadal change of Ps and MTPL are consistent in Northwest China and the Huang-huai Basin (Fig. 6a, d). The trends are consistent in Northeast China after the 1980s (Fig. 6c) and similar from the 1980s to 1990s in Southwest China (Fig. 6b), though quite different in the other decades. They are almost opposite in Southern China (Fig. 6e). From this analysis, we see that the decadal changes of MTPL and Ps of persistent prediction are consistent in certain regions. The reasons for decadal change of MTPL are more complex in other regions. Figure 6 also shows that the MTPL and Ps began to decrease at the beginning of the 21st century in all subregions, except for South China.

## 5 Conclusions

Based on the NLLE and nonlinear error growth dynamics, the MTPL in China was quantitatively investigated. Data used were daily temperature from 1960 to 2011 at 518 stations in China. Principal conclusions are as follows:

(1) The annual average MTPL was higher in North China and West China and lower south of the Huang-huai Basin. The spatial distributions of MTPL varied with month.

(2) MTPL was lower in the winter half-year (December–May) and higher in the summer half-year (June–November). This is mainly because China is strongly affected by the monsoon, and the difference between large-scale atmospheric circulations in these two seasons leads to intraseasonal variability of winter monsoon and summer monsoon.

(3) In general, MTPL began to increase in the 1970s and has decreased since 2000. The decadal change characteristics varied with subregion. The inter-decadal MTPL change was significant in Northeast, Northwest, and South China. That change in Northeast and Northwest China and the Huang-huai Basin was connected with the persistence of monthly temperature. Since the beginning of the 21st century, MTPL showed a decreasing trend in all regions, except South China.

The aforementioned conclusions give a basic understanding for MTPL in China. They help us to know the predictability of different regions in the country, and are important references for the improvement of monthly temperature prediction skill. The reasons and physical mechanisms affecting MTPL in China require further study. The quantitatively estimated MTPL largely relied on the evolution of the data themselves. The methods to deal with the original data, such as the 31-day smoothing and linear trend removal, might have influenced the MTPL values. This problem will be addressed in detail later.

**Acknowledgments** We thank to Jianping Li, Drs. Ruiqiang Ding and Jie Feng from State Key Laboratory of Numerical Modeling for Atmospheric Sciences and Geophysical Fluid Dynamics (LASG) for meaningful advice and instructive discussion. The authors sincerely thank two anonymous reviewers for their questions about the manuscript. This work was supported by the National Basic Research Program of China (2013CB430203), the R&D Special Fund for Public Welfare Industry (meteorology) (GYHY201306033), and the National Key Technologies R&D Program of China (2009BAC51B05).

**Conflict of interest** The authors declare that they have no conflict of interest.

## References

1. Zhai P, Pan X (2003) Trends in temperature extremes during 1951–1999 in China. Geophys Res Lett 30:1913
2. Schär C, Vidale PL, Lüthi D et al (2004) The role of increasing temperature variability in European summer heatwaves. Nature 427:332–336
3. Yang LN, Wu BY (2013) Interdecadal variations of the East Asian winter surface air temperature and possible causes. Chin Sci Bull 58:3969–3977
4. Wang HJ, Chen LJ, Li WJ (2007) Predictability of DERF on monthly mean temperature and precipitation over China. Acta Meteorol Sin 65:725–731 (in Chinese)
5. Kang I-S, Jin EK, An K-H (2006) Secular increase of seasonal predictability for the 20th century. Geophys Res Lett 33:L02703
6. Li JP, Ding RQ, Chen BH (2006) The retrospect and prospect of atmospheric predictability. Paper presented at the fourth frontier academic conference of atmosphere, Beijing, 20–22 September 2006 (in Chinese)
7. Madden RA (1976) Estimates of the natural variability of time-averaged sea-level pressure. Mon Weather Rev 104:942–952
8. Shukla J, Gutzler DS (1983) Interannual variability and predictability of 500 mb geopotential heights over the North hemisphere. Mon Weather Rev 111:1273–1279
9. Ying KR, Zheng XG, Quan XW et al (2013) Predictable signals of seasonal precipitation in the Yangtze-Huaihe River valley. Int J Climatol 33:3002–3015
10. Thompson PD (1957) Uncertainty of initial state as a factor in the predictability of large-scale atmospheric flow patterns. Tellus 9:275–295
11. Lorenz EN (1965) A study of the predictability of a 28-variable atmospheric model. Tellus 17:321–333
12. Lorenz EN (1982) Atmospheric predictability experiments with a large numerical model. Tellus 34:505–513
13. Mu M, Duan WS (2003) A new approach to studying ENSO predictability: conditional nonlinear optimal perturbation. Chin Sci Bull 48:1045–1047

14. Mu M, Duan WS (2005) Conditional nonlinear optimal perturbation and its applications to the studies of weather and climate predictability. Chin Sci Bull 50:2401–2407
15. Mu M, Duan WS, Wang JC (2002) The predictability problems in numerical weather and climate prediction. Adv Atmos Sci 19:191–204
16. Mu M, Duan WS, Chou JF (2004) Recent advances in predictability studies in China (1999–2002). Adv Atmos Sci 21:437–443
17. Zheng F, Wang H, Zhu J (2009) ENSO ensemble prediction: initial error perturbations vs. model error perturbations. Chin Sci Bull (Chin Ver) 54:2395–2401 (in Chinese)
18. Chen BH, Li JP, Ding RQ (2006) Nonlinear local Lyapunov exponent and atmospheric predictability research. Sci China Ser D Earth Sci 49:1111–1120
19. Ding RQ, Li JP (2007) Nonlinear finite-time Lyapunov exponent and predictability. Phys Lett A 364:396–400
20. Ding RQ, Li JP (2009) Spatiotemporal distributions of weather predictability of different variables. Acta Meteorol Sin 67: 343–354 (in Chinese)
21. Li JP, Ding RQ (2011) Temporal-spatial distribution of atmospheric predictability limit by local dynamical analogs. Mon Weather Rev 139:3265–3283
22. Li JP, Ding RQ (2008) Spatiotemporal distributions of predictability limit of short-term climate. Chin J Atmos Sci 32:975–986 (in Chinese)
23. Li WJ, Zhang PQ, Li QQ et al (2005) Research and operational application of dynamical climate model prediction system. J Appl Meteorol Sci 16:1–11 (in Chinese)
24. Yue Q, Cao JW, Lin ZS et al (1999) Climatic noise and potential predictability of monthly mean temperature over China. Acta Meteorol Sin 57:604–612 (in Chinese)
25. Zhao XC (2008) Estimate of potential predictability of monthly and seasonal mean temperature and precipitation in China. Dissertation, Nanjing University of Information Science & Technology (in Chinese)
26. Tang GL, Ding YH, Wang SW et al (2009) Comparative analysis of the time series of surface air temperature over China for the last 100 years. Adv Clim Change Res 5:71–78 (in Chinese)
27. Ding RQ, Li JP (2007) Nonlinear error dynamics and predictability study. Chin J Atmos Sci 31:571–576 (in Chinese)
28. Ding RQ, Li JP (2008) Application of nonlinear error growth dynamics in studies of atmospheric predictability. Acta Meteorol Sin 67:241–249 (in Chinese)
29. Wang B (2002) Rainy season of the Asian-Pacific summer monsoon. J Clim 15:386–398
30. Wu BY, Handorf D, Dethloff K et al (2013) Winter weather patterns over northern Eurasia and Arctic sea ice loss. Mon Weather Rev 141:3786–3800
31. Yang XQ, Anderson JL, Stern WF (1998) Reproducible forced modes in AGCM ensemble integrations and potential predictability of atmospheric seasonal variations in the extratropics. J Clim 11:2942–2959
32. Ding RQ, Li JP, Ha KJ (2008) Trends and interdecadal changes of weather predictability during 1950s–1990s. J Geophys Res 113:D24112

科学通报 2014 年 第 59 卷 第 25 期：2520 ~ 2527
论 文 www.scichina.com csb.scichina.com
《中国科学》杂志社
SCIENCE CHINA PRESS

# 中国月平均气温可预报性的时空特征及其年代际变化

李维京[①②*], 刘景鹏[①②], 陈丽娟[②], 张培群[②], 任宏利[②]

① 中国气象科学研究院, 北京 100081;
② 国家气候中心, 中国气象局气候研究开放实验室, 北京 100081
* 联系人, E-mail: liwj@cma.gov.cn

2014-01-06 收稿, 2014-05-14 接受, 2014-08-04 网络版发表
国家重点基础研究发展计划(2013CB430203)、公益类行业(气象)专项(GYHY201306033)和国家科技支撑计划(2009BAC51B05)资助

**摘要** 利用中国 1960~2011 年资料比较完整的 518 站逐日气温观测资料, 采用非线性局部 Lyapunov 指数(NLLE)和非线性误差增长理论, 定量分析了中国区域月时间尺度平均气温可预报性期限(MTPL)的时空分布和年代际变化特征. 分析发现: 多年平均的 MTPL 空间分布存在明显的地域差异, 总体来看, 东北大部、云南西南部和西北地区东部为可预报性高值区, 长江中下游地区及黄淮流域为可预报性低值区; MTPL 在各月份的空间分布存在明显的季节变化, 总体上表现为冬半年可预报性较低, 而夏半年较高; MTPL 还具有明显的年代际变化特征, 就全国而言, 从 1970 年以来, MTPL 具有上升的趋势, 在 2000 年前后出现下降的趋势, 尤其是东北地区在 1986 年之后可预报性显著提高. 西北、黄淮、东北 MTPL 的年代际变化可能与气温的持续性有关. 进入 21 世纪, 除南方地区外, 大部分地区的 MTPL 有降低趋势. 上述结果为进一步认识我国月尺度气温异常的机理奠定科学基础, 并为提高月尺度气温预测能力提供参考.

**关键词**
月平均气温
可预报性
时空分布特征
年代际变化
非线性局部 Lyapunov 指数

我国地域辽阔、地形复杂, 月平均气温的时空变率很大, 而气温是气候系统最显著的特征量之一, 又是短期气候预测的主要预报对象, 因此开展对月平均气温可预报性的研究, 清楚地认识我国哪些区域月平均气温具有较高的可预报性, 哪些区域的可预报性较低, 对于认识影响月尺度气温异常的机理以及提高预测能力具有重要的科学意义和应用价值. 另外, 在全球气候变暖的背景下, 极端天气和气候事件频发[1,2], 给短期气候预测的基础理论研究和业务带来了更大挑战. 在全球变暖的背景下, 大气内部动力过程和外强迫因子表现出不同的年代际变化特征[3]. 月时间尺度平均气温的可预报性受这两种因素的影响, 是否发生了年代际变化, 也是国内外科学家关注的重点[4,5]. 王会军等人[4]指出, 中国区域月尺度气温的持续性预报技巧在 1982~2005 年间有一定的提升. Kang 等人[5]指出, 全球地表气温潜在可预报性在 1914~1943 年为低值期, 而在 1968~1997 年为高值期. 如何定量描述中国月时间尺度平均气温的可预报性的年代际变化特征, 目前的研究工作还很少.

常用于研究可预报性有定性和定量方法[6]. 定性方法一般是基于估计外部信号和系统内部噪音的相对大小[7~9], 不能给出气候变量确切的可预报性时效. 定量方法主要有经验方法、动力学方法和动力学-经验方法. 其中的动力学方法是定量估计可预报性期限研究中使用最多和最有效的方法, 这种方法又有两大分支: 利用数值模式进行数值试验[10~12]和利用非线性动力系统理论[13~16]的方法. 而数值模式的缺陷[17]使得其无法刻画实际大气, 因此利用非线性动力系统理论的方法既可以定量地给出可预报性的估计[18,19], 弥补了定性分析的不足, 又避免了模式大气

**引用格式**: 李维京, 刘景鹏, 陈丽娟, 等. 中国月平均气温可预报性的时空特征及其年代际变化. 科学通报, 2014, 59: 2520–2527
**英文版见**: Li W J, Liu J P, Chen L J, et al. Spatiotemporal distribution and decadal change of the monthly temperature predictability limit in China. Chin Sci Bull, 2014, 59, doi: 10.1007/s11434-014-0502-4

和实际大气差异造成的误差问题. Lorenz[11]从Lyapunov 稳定性理论和误差增长的观点出发, 提出将误差倍增的时间作为可预报性的期限. Ding 和 Li[19,20]提出的非线性局部 Lyapunov 指数(NLLE)进一步发展了 Lyapunov 稳定性理论. NLLE 已经广泛用于研究天气尺度可预报性[18~21]及短期气候可预报性[22].

然而, 已有的可预报性研究变量一般是基于格点的对流层中高层变量. 但是, 由于受资料、理论和方法所限, 对于我国地表气候变量的可预报性的定量研究较少, 到目前还不能定量地给出我国月尺度气候(温度和降水)可预报性的时空变化特征. 由于我国地形复杂, 并且是显著的季风气候区, 因此地表变量的可预报性可能与全球其他同纬度地区有较大的差异. 本文拟采用NLLE方法并利用逐日站点观测资料来研究我国月尺度平均气温可预报性的时空分布及年代际变化问题. 而这些逐日站点观测资料实际上包含了各种外强迫缓慢变化的影响和大气内部各种过程相互影响结果的所有信息, 因此基于观测资料的可预报性分析实际上包含了依赖于初值条件的动力学可预报性和外强迫下的可预报性两类问题[22].

本文采用更密集更完整的台站逐日气温观测资料, 基于非线性局部 Lyapunov 指数(NLLE)方法, 通过合理处理观测资料, 定量研究月尺度平均气温的可预报性期限, 获得可预报性的时空分布和年代际变化特征. 目的是力求回答 2 个问题: 全国月尺度平均气温在哪些区域、什么月份、多大程度上可以预报? 不同地区气温的可预报性是否发生了年代际的变化?

## 1 数据和方法

本文使用的资料有: 中国区域 1960~2011 年 518 个台站的日平均气温资料, 该资料经过质量控制(连续缺测不超过 5 d, 总缺测不超过 60 d, 缺测数据用 1960~2011 年计算得到的平均态补齐). 这 518 站的日平均气温资料的空间分布密度以及资料序列的长度较以往的研究都要丰富[23,24], 一定程度上保证了计算结果的时空代表性[25]; NCEP/NCAR 提供的 1960~2011 年 850 hPa 逐日 4 次气温场, 水平分辨率为 2.5°×2.5°经纬度; 国家气候中心提供的 160 站 1983~2012 年的月平均温度及月动力延伸预报的月平均温度资料[26], 分别取 1983~2012 年 30 年月平均气温值作为气候场, 得到各月份月动力延伸预报和观测的月平均温度距平值.

为了更好地研究月尺度气温的可预报性问题, 对逐日气温资料做了如下处理: 首先, 去除了站点气温观测资料的线性趋势项和季节循环(采用 1960~2011 年资料计算得到逐日气温平均值); 其次, 对逐日观测资料序列进行 31 d 的滑动平均处理, 滤去序列的高频部分, 获得月时间尺度的资料序列; 最后, 对月时间尺度的资料序列做标准化处理.

基于非线性局部 Lyapunov 指数(NLLE)[21]和非线性误差增长理论[27,28]计算地面气温月时间尺度可预报性. 对于变量 $x$, 定义非线性局部 Lyapunov 指数(NLLE)为

$$\lambda(x(t_0),\delta(t_0),\tau)=\frac{1}{\tau}\ln\left|\frac{\delta(t_0+\tau)}{\delta(t_0)}\right|, \tag{1}$$

$x(t_0)$为相空间中参考轨道的初始状态, 这里指站点气温观测序列中 $t_0$时刻的月时间尺度平均气温; $\delta(t_0)$为初始误差, 是通过在气温观测序列中寻找与$t_0$时刻气温未来演变局部动力相似的时刻 $t$[21], 则 $t$ 时刻气温与 $t_0$ 时刻气温的差值即为初始误差; $\tau$ 为演变时间, 这里指对 $t_0$ 时刻月时间尺度平均气温的演变时长. $\lambda>0$ 表示临近初始轨道间的距离随时间增长, 它们之间的相关性随时间减弱; 指数值越大表示误差发展越快. 平均的误差相对增长率 $\bar{E}(\delta(t_0),\tau)$ 可以通过平均的非线性局部 Lyapunov 指数 $\bar{\lambda}(\delta(t_0),\tau)$ 获得, 即

$$\bar{E}(\delta(t_0),\tau)=\exp(\bar{\lambda}(\delta(t_0),\tau)\cdot\tau). \tag{2}$$

利用丁瑞强和李建平[27]提出的非线性误差增长理论, 可得

$$\bar{E}(\delta(t_0),\tau)\xrightarrow{P}c \quad (N\to\infty), \tag{3}$$

即当样本数 $N$ 趋于无穷多时, $\bar{E}(\delta(t_0),\tau)$ 趋于其理论饱和值 $c$. 误差增长达到饱和, 意味着系统的初始相似信息全部丢失, 预测失去意义. 因此利用这个饱和值, 能够定量地确定混沌系统的可预报期限. 可以将平均的误差相对增长率达到理论饱和值的 99%时所对应的演变时间 $t$ 作为该站点月尺度气温可预报性期限(monthly temperature predictability limit, MTPL), 即

$$\mathrm{MTPL}=\left\{t\left|\bar{E}(\delta(t_0),\tau)=0.99\cdot c\right.\right\}. \tag{4}$$

采用局部动力类比的思想, 可以实现用NLLE计算月时间尺度平均气温可预报性期限的目的[21]. 若采用(2)式计算全序列平均误差相对增长率, 可得到全年平均的 MTPL, 若采用(2)式计算各月份平均的误差相对增长率, 可相应得到各月份平均的 MTPL. MTPL 本质上是一个动力统计量, 它的物理含义是:

在月时间尺度条件下，初始动力相似的两种状态，在多长时间后变的完全不具有相似性，这个时间期限即为 MTPL. 它表示在动力学意义下，可以提前多少天对月尺度气温进行预测. 通过计算各站点的 MTPL，即可获得其空间分布特征.

## 2 月时间尺度平均气温可预报性的空间分布

根据前述资料处理方法，用(2)式计算了全序列平均误差相对增长率后，由(3)~(4)式得到的全年平均的月尺度平均气温可预报性的空间分布(图 1(a)). 从图 1(a)可见，在东北大部、华北北部、云南地区、青藏高原以及西北大部分地区均为 MTPL 的高值区，可预报性期限一般在 30 d 以上；而在黄淮流域、江淮地区、江南地区，均为 MTPL 低值区，可预报性期限一般在 30 d 左右. 这表明就全年平均而言，我国北方以及西部地区月尺度平均气温可预报性较高，而黄淮以南大部地区可预报性较低. 为进一步验证采用地面站点数据计算全年平均的 MTPL 的可靠性，另外采用 NCEP 提供的 850 hPa 一日 4 次的气温再分析格点资料计算了全年平均的 MTPL(图 1(b)). 由于 850 hPa 气温和地面气温的变化具有较高的一致性，由其计算得到的 MTPL 的空间分布理论上应与采用地面观测资料计算的 MTPL 的空间分布大致相同. 而图 1(b)的 MTPL 的空间分布特征与图 1(a)的空间分布十分相似，主要在西北大部及云贵地区可预报性有所提高. 表明本文选用地面气温站点资料分析 MTPL 的时空分布特征具有代表性，同时也表明某些地区高层温度变量的可预报性比低层温度的高.

图 2 给出 1~12 月的月尺度平均温度可预报性(MTPL)的空间分布. 12 月(图 2(a))西南和华北部分地区的 MTPL 达 40~50 d，其余大部地区的 MTPL 一般在 30~40 d，1 月和 2 月(图 2(b), (c))全国大部地区的 MTPL 一般在 20~30 d, 3~4 月份(图 2(d), (e))除东北东部、西南局部、江南东部的 MTPL 在 30~40 d 外，全国其余地区的 MTPL 均在 20~30 d. 5 月份(图 2(f))，全国的 MTPL 有所提高，新疆北部、西北南部的 MTPL 在 40~50 d，其余大部分地区的 MTPL 在 25~35 d. 6 月份(图 2(g))，新疆大部、华北西部、西南东部、华南西部的 MTPL 可达 40~50 d，其余大部地区的 MTPL 一般在 25~40 d. 7~8 月(图 2(h), (i))，MTPL 的空间分布特征十分相似，长江中下游、新疆南部的 MTPL 较低，一般为 25~35 d，全国其余大部分地区的 MTPL 一般在 45~60 d，西南局部地区可达 60~70 d，这里长江中下游地区的 MTPL 低值区与东亚夏季风及雨带的活跃区相对应[29]. 秋季(图 2(j)~(l))全国 MTPL 趋向减小，9 月份(图 2(j))，除长江中上游 MTPL 值在 30~40 d 外，其余大部地区在 50~60 d. 10 月(图 2(k))西北南部、东北南部及南部沿海的 MTPL 一般在 40~50 d，全国其余大部地区在 30~45 d. 11 月(图 2(l))，除西南大部、华南西部 MTPL 达到 40~50 d，全国其余地区均在 30~40 d.

综上所述，我国月尺度平均气温可预报性 MTPL 在 12 月到次年 5 月的冬半年(图 2(a)~(f))都比较低，而在 6~11 月的夏半年(图 2(g)~(l))比较高. 这个结论同李建平和丁瑞强[22]分析全球 500 hPa 高度场和温度场得出的可预报性冬季略高于夏季的结论有所不同. 其主要原因可能是我国为著名的季风气候国家，冬春季节我国主要受冬季风影响，中高纬度大气环

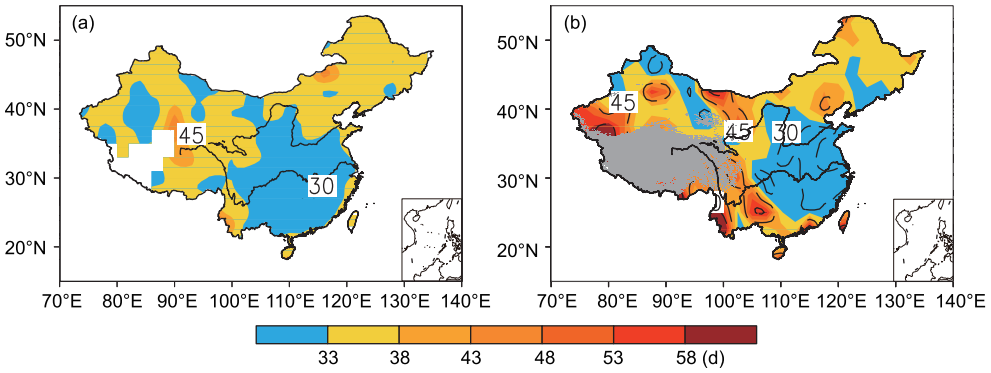


**图 1 月尺度平均气温可预报性的空间分布**

(a)和(b)分别为地面气温和 850 hPa 气温计算结果

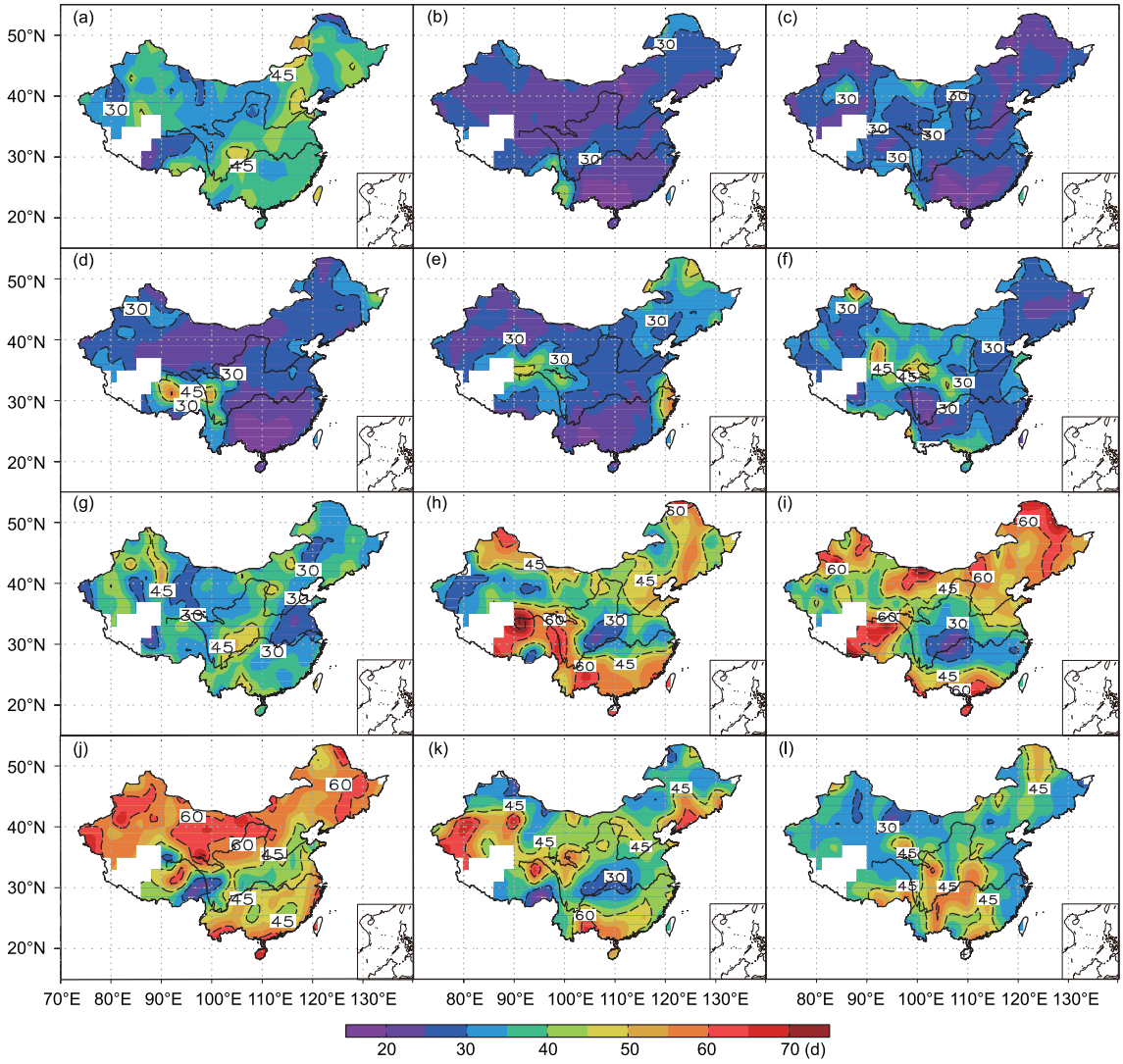


**图 2　各月份月尺度平均气温可预报性 MTPL 分布图**

(a)~(c)为 12 月、1 月、2 月; (d)~(f)为 3~5 月; (g)~(i)为 6~8 月; (j)~(l)为 9~11 月

流异常的影响显著，而中高纬度冷空气影响频繁、变率大，加之我国地形复杂，使得我国的地表气温有比较大的季节内变率[23]，并且在全球变暖背景下，东亚中、高纬度冬季的极端天气事件发生频率增多，强度增大，也同样导致气温的季节内变率加大[30]，从而降低了冬春季气温的 MTPL. 而夏秋季，我国主要受东亚夏季风的影响，受热带海洋和副热带大气环流异常影响显著，热带和副热带系统相对于中高纬度系统变率小，因此夏秋季气温的 MTPL 比冬春季节明显偏高. Yang 等人[31]通过模式模拟分析得到的全球 850 hPa 气温的季节潜在可预报性也表明，中国区域气温潜在可预报性在夏季较高，冬季较低. 认为夏季海温、土壤湿度等下边界强迫作用比较强，而大气内部动力过程的作用比较弱，气温季节内变率较小[23]，便导致了夏季气温 MTPL 比较高的值，与本文结论是一致的. 中国气温与全球同纬度其他地区气温可预报性的差异也表现出我国气温可预报性分布的复杂性.

为了进一步说明中国区域气温潜在可预报性在夏季较高和冬季较低以及 MTPL 的空间分布的合理性，采用国家气候中心提供的第一代气候模式对 1983~2012 年的月动力延伸预测结果，计算了全国 1 月和 7 月 160 站月平均气温距平预报准确率. 计算方法如下：利用 1983~2012 年全国 160 站月动力延伸预

测温度和观测温度的距平场, 若某站在 30 年($n$ 年)内预报值和观测值的符号一致的年份数为 $m$, 则该站点的月动力延伸预报准确率为

$$Ps=\frac{m}{n}\times 100\%. \tag{5}$$

利用(5)式分别计算了月动力延伸预报对 1 月(图 3(a))和 7 月(图 3(b))平均气温的预报准确率的空间分布(计算时段为 1983~2012 年). 由图 3 可知, 7 月份的月动力延伸预报准确率要明显高于 1 月份, 这与 7 月 MTPL(图 2(h))明显高于 1 月 MTPL(图 2(b))很一致. 并且 $Ps$(prediction score)与 MTPL 在 1(7)月的空间分布型也较为一致. 表明可预报性较低(高)的月份, 月动力延伸预报准确率也较低(高).

## 3 不同区域月尺度平均气温可预报性的年代际变化

为得到月尺度平均气温可预报性期限的年代际变化特征, 需要滤去年代际以下时间尺度的变率信息. 取 11 年的滑动窗口[32], 采用(2)~(4)式计算窗口区平均的 MTPL, 将其作为窗口区中间年份的 MTPL. 当窗口遍历整个观测序列, 就得到了该站点 MTPL 的年代际变化曲线. 由于滑动窗口取为 11 年, 因此年代际变化曲线范围为 1965~2006 年. 图 4(a)~(e)为地面气温各个年代相对 1965~2006 年平均的 MTPL 距平值的空间分布, 图 4(f)为采用 1965~2006 年序列时段计算得到的气候月尺度平均气温可预报性的空间分布.

由图 4(f)可知, 1965~2006 年这段时间, 平均来讲我国北方以及西部地区 MTPL 较高, 而黄淮以南大部地区 MTPL 较低. 而在不同年代, 不同区域的 MTPL 有显著变化. 图 4(a)显示, 20 世纪 60 年代, 新疆南部、河套、华北大部及东北北部和南部 MTPL 较气候值(1965~2006 年平均)降低约 2 d, 黄淮及其以南地区的 MTPL 升高约 2 d 以上; 20 世纪 70 年代, 东北、华北大部、西北南部的 MTPL 减少约 2 d, 而全国其余大部地区的 MTPL 增加约 2~4 d; 20 世纪 80 年代, 东北、江南东部、西藏东部的 MTPL 降低约 2 d, 而全国其余大部地区的 MTPL 升高约 2~4 d; 20 世纪 90 年代, 我国中西部大部地区的 MTPL 降低约 2 d, 而北方和东部大部地区 MTPL 升高约 2~4 d, 其中东北局部地区 MTPL 升高达 4~6 d; 2000 年以后, 我国西部大部地区的 MTPL 降低约 2 d, 其中新疆南部降低 2~4 d, 而全国其余大部地区的 MTPL 升高约 2 d, 其中东北部分地区升高约 4~6 d.

整体而言, 东北地区在 20 世纪 90 年代之后 MTPL 有明显的提高, 而全国其余地区的 MTPL 的年代际变化比较复杂. Ding 等人[32]对各层位势高度的天气尺度可预报性的年代际变化的分析发现, 1953~2000 年间, 天气尺度可预报性在欧亚大陆的中高纬度地区有明显的下降趋势. 而中国区域 MTPL 呈现出更加复杂的年代际变化特征, 值得进一步分析.

为了更好地分析不同区域 MTPL 的年代际变化特征, 将全国划分为 5 个子区域(图 5), 分别计算各区域平均的 MTPL, 获得每个区域 MTPL 的年代际变化曲线(图 6 中实线).

分别为西北区(Ⅰ区, 73°~105°E, 34°~50°N)、西南区(Ⅱ区, 79°~105°E, 21°~34°N)、东北区(Ⅲ区, 105°~135°E, 38°~54°N)、黄淮区(Ⅳ区, 105°~123°E, 31°~38°N)、南方区(Ⅴ区, 105°~123°E, 18°~31°N)

图 6 表明不同区域月尺度平均气温可预报性 MTPL 具有不同的年代际变化特征. 我国西北地区的 MTPL(Ⅰ区, 图 6(a))在 20 世纪 60 年代中期开始下降,

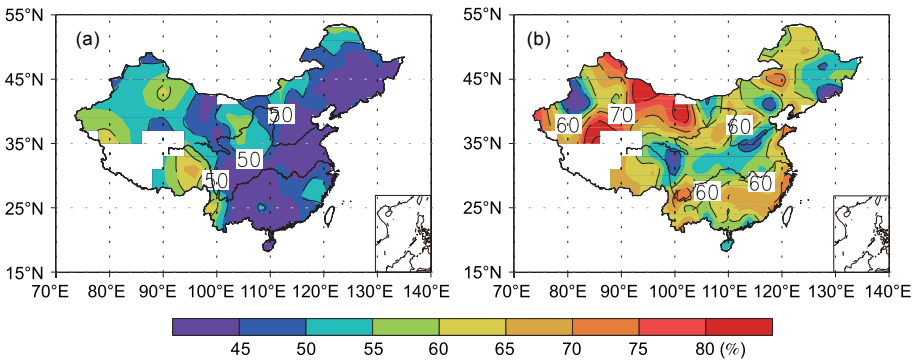


**图 3 月动力延伸预报对 1 月(a)和 7 月(b)平均气温的预报准确率($Ps$)的空间分布**

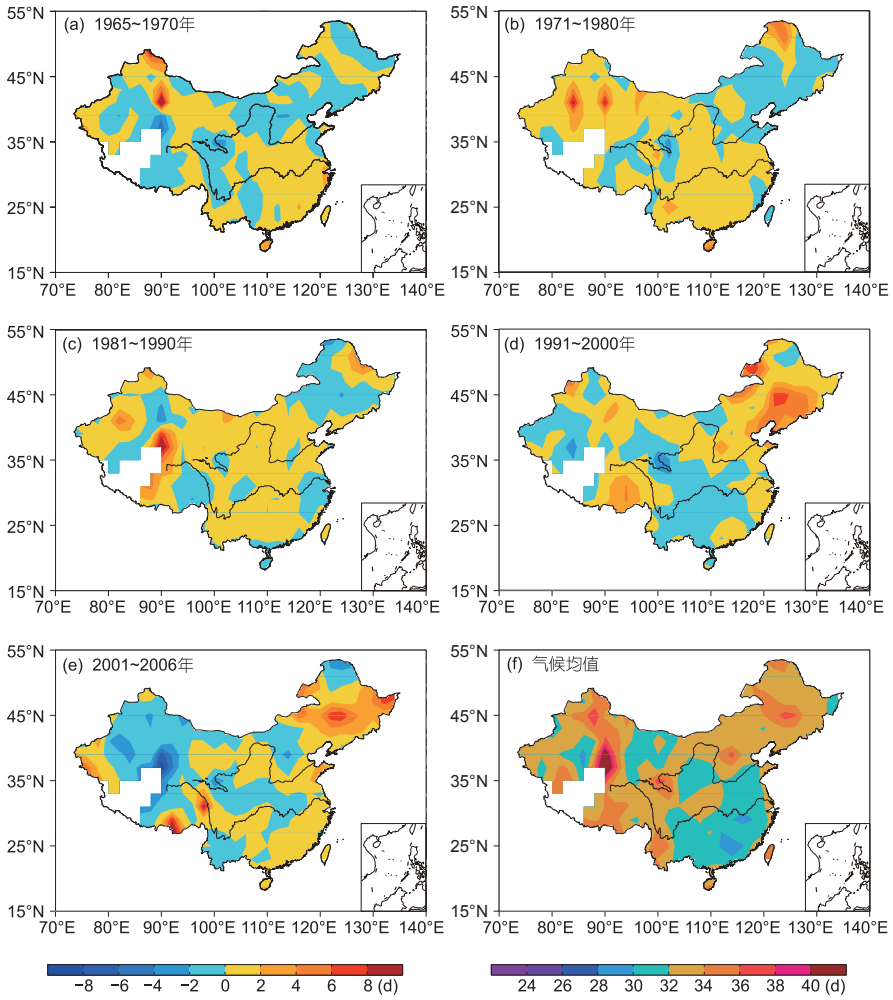


**图 4　不同年代((a)~(e))MTPL 距平的空间分布以及气候平均值(f)**

左边色标代表各个年代距平值，右边色标代表 1965~2006 年气候平均值

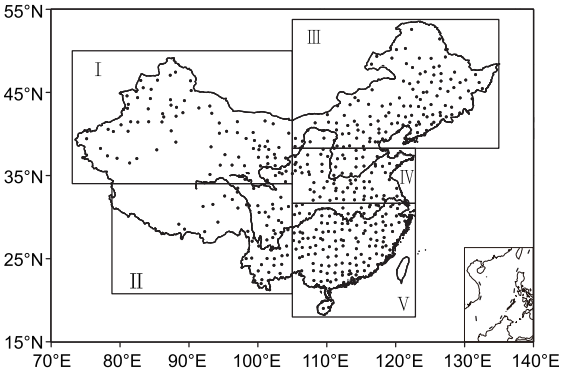


**图 5　分析年代际变化采用的 5 个子区域示意图**

到 70 年代中期缓慢回升，80 年代初期之后持续下降，20 世纪末之后缓慢回升. 我国西南(Ⅱ区，图 6(b))和黄淮地区(Ⅳ区，图 6(d))的 MTPL 在 1980 年以来 MTPL 有缓慢下降的变化趋势，但变化不显著. 东北地区(Ⅲ区，图 6(c))MTPL 的年代际变化尤其明显，在 80 年代以来 MTPL 持续上升，而 2000 年之后，明显下降；经过滑动 *t* 检验和 *M-K* 检验的气候突变检验分析，均发现东北地区的 MTPL 在 1986 年出现气候突变(通过 0.01 的信度检验). 南方区(Ⅴ区，图 6(e))的 MTPL 在 80 年代初期开始下降，到 90 年代中期开始上升，目前处于可预报性增大的阶段. 就全国平均而言(图 6(f))，从 70 年代以来，MTPL 总体具有上升的年代际变化趋势，在 2000 年前后出现下降的趋势.

为了进一步分析本文计算的不同区域 MTPL 年代际变化特征的可能原因，又计算了各个区域的月尺度气温持续性预报准确率的年代际变化(图 6 中虚线)进行对比. 具体计算过程如下：利用全国 1960~2011 年中国区域 518 站的逐日平均气温，去掉趋势项后求出月平均气温距平序列，将本月的气温距平

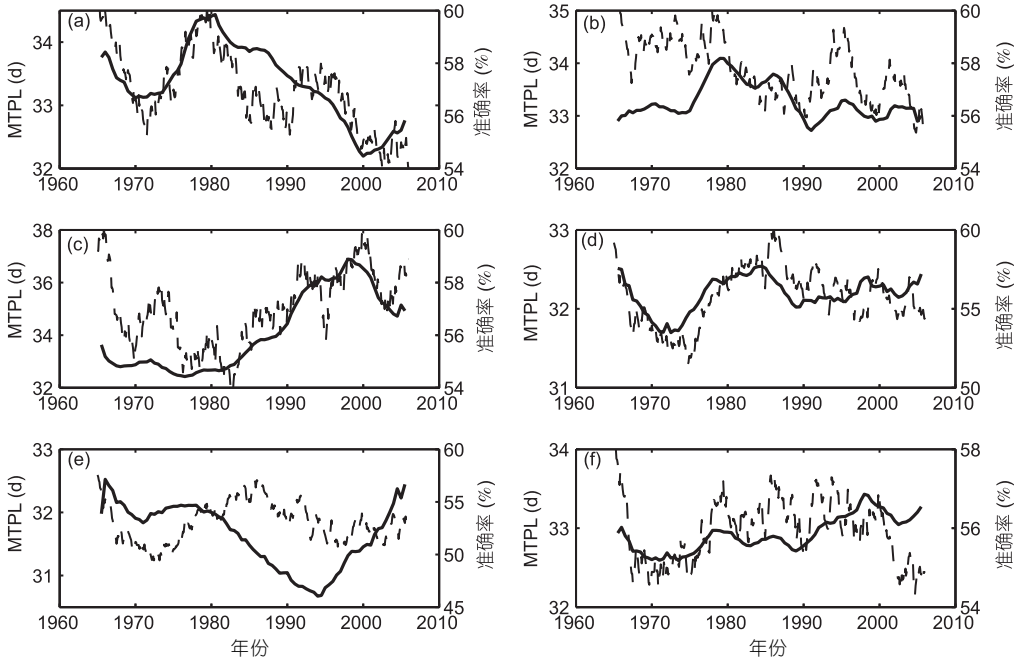


**图 6 各区平均的 MTPL(实线)及持续性预报准确率(虚线)的年代际变化曲线图**

(a)~(e)分别为Ⅰ~Ⅴ区, (f)为全国, MTPL 做了 9 点平滑, 持续性预报准确率做了 11 年平滑

作为下个月的气温距平预报值, 若区域内预报值和实测值的符号一致的站点数为 $M$, 区域内总的站点数为 $N$, 则该月份的持续性预报准确率为

$$Ps = \frac{M}{N} \times 100\%, \tag{6}$$

进而可得到 1965~2006 年月平均气温持续性预报准确率的年代际变化曲线.

比较图 6 中的实线和虚线可以看出, 西北区和黄淮区(图 6(a), (d))气温持续性预报准确率的年代际变化与 MTPL 的年代际变化呈现较一致的变化趋势; 东北区(图 6(c))在 20 世纪 80 年代之后两者的变化趋势比较一致; 西南区(图 6(b))在 20 世纪 80~90 年代比较一致, 而其余时段差异较大; 南方区(图 6(e))预报准确率的年代际变化与 MTPL 的年代际变化几乎相反. 可见, 有的区域的 MTPL 的年代际变化与气温持续性的变化趋势是一致的, 而有的区域 MTPL 的年代际变化原因比较复杂. 从图 6 还可以看出, 目前 5 个区域中除去南方区(图 6(e))外, 其余区域的 MTPL 和月尺度气温持续性预报准确率在进入 21 世纪以后均有不同程度的下降.

## 4 结论

本文利用我国 1960~2011 年较为密集和完整的 518 个站点逐日气温观测资料, 采用非线性局部 Lyapunov 指数和非线性误差增长理论, 探讨了月尺度平均气温的可预报性, 主要结论如下.

(1) 总体平均而言, 我国北方以及西部地区月尺度平均气温可预报性较高, 而黄淮以南大部地区可预报性较低, 具体到各月还有明显的空间差异.

(2) 我国月尺度平均气温可预报性在 12 月到次年 5 月的冬半年相对较低, 而在 6~11 月的夏半年比较高. 这可能与我国的季风气候以及造成冬季风变率和夏季风变率的大尺度环流特征的差异有密切关系.

(3) 从全国平均来看, 20 世纪 70 年代以来, 月尺度平均气温可预报性总体具有上升的年代际变化趋势, 在 2000 年前后出现下降的趋势. 但是不同区域月尺度平均气温可预报性具有不同的年代际变化特征, 特别是我国东北、西北和华南地区具有比较显著的年代际变化. 西北、黄淮、东北的可预报性的年代际变化可能与气温的持续性有关. 进入 21 世纪, 除了华南区域外, 全国大部分地区月尺度平均气温可预报性有下降的趋势.

上述结果仅仅是对月尺度平均气温可预报性的初步认识, 初步了解中国哪些区域的气温具有较高的可预报性, 哪些区域气温的可预报性较低, 从而为气候预测提供一定的科学参考. 对于影响我国不同

区域月尺度平均气温可预报性的原因及其物理机制还需要进一步研究. 本研究主要依据数据自身的演变规律, 来定量化讨论气温预测的可预报性. 因此, 数据资料的处理方式, 如去掉线性趋势和 31 d 滑动平均等, 很可能会对计算结果产生一定的影响, 这个问题将另文进行详细分析.

## 参考文献


1 Zhai P, Pan X. Trends in temperature extremes during 1951–1999 in China. Geophys Res Lett, 2003, 30: 1913
2 Schär C, Vidale P L, Lüthi D, et al. The role of increasing temperature variability in European summer heatwaves. Nature, 2004, 427: 332–336
3 杨柳妮, 武炳义. 东亚冬季气温的年代际变化及其可能成因分析. 科学通报, 2013, 58: 2728–2736
4 王会军, 陈丽娟, 李维京, 等. 中国区域月平均温度和降水的模式可预报性分析. 气象学报, 2007, 65: 725–732
5 Kang I-S, Jin E K, An K-H. Secular increase of seasonal predictability for the 20th century. Geophys Res Lett, 2006, 33: L02703, doi: 10.1029/2005GL024499
6 李建平, 丁瑞强, 陈宝花. 大气可预报性研究的回顾与展望. 见: 国家自然科学基金委员会地球科学部, 中国科学院资源环境科学与技术局, 中国气象局科技发展司, 等, 编. 21 世纪初大气科学前沿与展望——第四次全国大气科学前沿学科研讨会论文集. 北京: 气象出版社, 2006. 96–103
7 Madden R A. Estimates of the natural variability of time-averaged sea-level pressure. Mon Weather Rev, 1976, 104: 942–952
8 Shukla J, Gutzler D S. Interannual variability and predictability of 500 mb geopotential heights over the northern hemisphere. Mon Weather Rev, 1983, 111: 1273–1279
9 Ying K R, Zheng X G, Quan X W, et al. Predictable signals of seasonal precipitation in the Yangtze-Huaihe river valley. Int J Climatol, 2013, 33: 3002–3015
10 Thompson P D. Uncertainty of initial state as a factor in the predictability of large-scale atmospheric flow patterns. Tellus, 1957, 9: 275–295
11 Lorenz E N. A study of the predictability of a 28-variable atmospheric model. Tellus, 1965, 17: 321–333
12 Lorenz E N. Atmospheric predictability experiments with a large numerical model. Tellus, 1982, 34: 505–513
13 穆穆, 段晚锁. ENSO 可预报性研究的一个新方法: 条件非线性最优扰动. 科学通报, 2003, 48: 747–749
14 穆穆, 段晚锁. 条件非线性最优扰动及其在天气和气候可预报性研究中的应用. 科学通报, 2005, 50: 2695–2701
15 Mu M, Duan W S, Wang J C. The predictability problems in numerical weather and climate prediction. Adv Atmos Sci, 2002, 19: 191–204
16 Mu M, Duan W S, Chou J F. Recent advances in predictability studies in China (1999–2002). Adv Atmos Sci, 2004, 21: 437–443
17 郑飞, 王慧, 朱江. 初始误差和模式误差对 ENSO 集合预报的影响. 科学通报, 2009, 54: 2395–2401
18 陈宝花, 李建平, 丁瑞强. 非线性局部 Lyapunov 指数与大气可预报性研究. 中国科学 D 辑: 地球科学, 2006, 36: 1068–1076
19 Ding R Q, Li J P. Nonlinear finite-time Lyapunov exponent and predictability. Phys Lett A, 2007, 364: 396–400
20 丁瑞强, 李建平. 天气可预报性的时空分布. 气象学报, 2009, 67: 343–354
21 Li J P, Ding R Q. Temporal-spatial distribution of atmospheric predictability limit by local dynamical analogs. Mon Weather Rev, 2011, 139: 3265–3283
22 李建平, 丁瑞强. 短期气候可预报期限的时空分布. 大气科学, 2008, 32: 975–986
23 乐群, 曹俊武. 中国月平均温度的气候噪声和潜在可预报性. 气象学报, 1999, 57: 605–612
24 赵晓川. 中国月季平均温度和降水量的潜在可预报性估计. 硕士学位论文. 南京: 南京信息工程大学, 2008. 7–27
25 唐国利, 丁一汇, 王绍武, 等. 中国近百年温度曲线的对比分析. 气候变化研究进展, 2009, 5: 71–78
26 李维京, 张培群, 李清泉, 等. 动力气候模式预测系统业务化及其应用. 应用气象学报, 2005, 16: 1–11
27 丁瑞强, 李建平. 误差非线性的增长理论及可预报性研究. 大气科学, 2007, 31: 571–576
28 丁瑞强, 李建平. 非线性误差增长理论在大气可预报性中的应用. 气象学报, 2009, 67: 242–249
29 Wang B. Rainy season of the Asian-Pacific summer monsoon. J Clim, 2002, 15: 386–398
30 Wu B Y, Handorf D, Dethloff K, et al. Winter weather patterns over northern Eurasia and Arctic sea ice loss. Mon Weather Rev, 2013, 141: 3786–3800
31 Yang X Q, Anderson J L, Stern W F. Reproducible forced modes in AGCM ensemble integrations and potential predictability of atmospheric seasonal variations in the extratropics. J Clim, 1998, 11: 2942–2959
32 Ding R Q, Li J P, Ha K J. Trends and interdecadal changes of weather predictability during 1950s–1990s. J Geophys Res, 2008, 113: D24112, doi: 10.1029/2008JD010404

李娇,任国玉,任玉玉,等.2014.资料均一化对沈阳站气温趋势和城市化偏差分析的影响[J].大气科学学报,37(3):297-303.
Li Jiao,Ren Guo-yu,Ren Yu-yu,et al.2014.Effect of data homogenization on temperature trend estimation and urban bias at Shenyang station[J].Trans Atmos Sci,37(3):297-303.(in Chinese)

# 资料均一化对沈阳站气温趋势和城市化偏差分析的影响

李娇[1,2,3],任国玉[2],任玉玉[2],张雷[2]
(1.南京信息工程大学 大气科学学院,江苏 南京 210044;2.中国气象局 气候研究开放实验室,北京 100081;
3.铁岭市气象局,辽宁 铁岭 112000)

**摘要**:利用国家气象信息中心 2013 年发布的逐日均一化气温资料,对沈阳站资料均一化处理前后平均气温和极端气温指数序列的线性趋势及其城市化影响偏差进行了比较评价。结果表明:1)资料均一化处理对日最高气温及其衍生的极端气温指数序列趋势估计的影响较弱,但对日最低气温及其衍生的极端气温指数序列趋势估计具有显著影响。2)经资料均一化处理后,平均气温序列中的城市化影响偏差有所增大,平均最低气温序列中的城市化影响偏差增大尤其明显;与冷事件有关的极端气温指数序列的城市化影响偏差数值有所减小,与暖事件有关的极端气温指数序列的城市化影响偏差数值有所增加。3)资料均一化处理有效纠正了因迁站等原因造成的地面气温观测记录中的非均一性,但却在很大程度上还原了城市站地面气温观测记录中的城市化影响偏差。

**关键词**:气温资料;均一化;极端气温指数;城市化影响;气候变化
**中图分类号**:P467 **文献标志码**:A **文章编号**:1674-7097(2014)03-0297-07

# Effect of data homogenization on temperature trend estimation and urban bias at Shenyang station

LI Jiao[1,2,3],REN Guo-yu[2],REN Yu-yu[2],ZHANG Lei[2]
(1.School of Atmospheric Sciences,NUIST,Nanjing 210044,China;
2.Laboratory for Climate Studies,CMA,Beijing 100081,China;
3.Tieling Meteorological Bureau,Tieling 112000,China)

**Abstract**:Based on the homogeneous daily surface air temperature dataset in 2013 from the National Meteorological Information Center,the linear trends of mean temperature and extreme temperature indices and their urban biases at Shenyang station before and after homogenization were compared and evaluated.The result shows that homogeneity of temperature series exerts weak effect on the daily maximum temperature and the relevant extreme temperature indices trend estimation.Meanwhile,it exerts obvious effect on the daily minimum temperature and the relevant extreme temperature indices trend estimation.The result also indicates that the urban bias of annual mean temperature increases after homogenization,especially that of annual mean minimum temperature.However,the urban bias of extreme temperature indices relevant to cold events reduces while that relevant to warm events increases after homogenization.Therefore,homogenization can correct the non-uniformity of surface temperature observation data effectively such as relocation of weather stations but it also brings new urban bias to the observation records to a certain extent.

**Key words**:temperature series;homogeneity;extreme temperature indices;urban effect;climate change

**收稿日期**:2013-10-09;**改回日期**:2014-02-25
**基金项目**:公益性行业(气象)科研专项(GYHY201206012)
**通信作者**:任国玉,博士,研究员,研究方向为气候变化,guoyoo@cma.gov.cn.

# 0 引言

在国内的单站和区域尺度气候变化研究中,近年来对采用均一化地面观测资料给予了高度重视(Yan and Yang,2001;任国玉,2003;Li et al.,2004;任国玉等,2005;Yan et al.,2010;曹丽娟和严中伟,2011;周建平等,2013)。中国气象局国家气象信息中心发布的中国地面气温均一化数据集(Li et al.,2004),在国内气候变化研究中得到广泛应用。2013 年发布了这个数据集的更新版本。Li and Yan(2009)根据中国气象局国家气象信息中心的地面气温资料开展了资料均一化研究,获得了均一化的最高和最低气温资料数据集。

气候变化分析采用均一化资料是必要的。但是,最近利用早期版本均一化地面气温资料开展的研究,发现位于城市附近的台站,在资料均一化处理后,其平均和极端气温指数序列中的城市化影响偏差变得更明显了(任国玉等,2010;张雷等,2011;Zhang et al.,2014)。造成这个问题的可能原因是,在 2004 年以前我国地面气温观测记录中的非均一性主要是由于城镇附近台站迁移造成的(Li et al.,2004;任国玉等,2010)。目前还不清楚,在最新版本的均一化气温资料中,是否仍然存在着城市化影响偏差被还原或增大的问题。

沈阳作为东北大城市的代表站,历史上经历较多的站址迁移。选取沈阳站作为案例城市,采用最新版本的均一化地面气温观测数据及经过质量控制的原始数据,探讨资料均一化处理过程对沈阳站平均气温和极端气温指数序列趋势的影响,着重比较评价均一化处理前后各个气温指数序列中城市化影响偏差的不同。

# 1 资料和方法

## 1.1 数据来源

沈阳站的逐日气温数据来自国家气象信息中心 2013 年发布的升级版均一化气温数据集。沈阳站对比气温数据、乡村站气温数据以及历史沿革资料同样来自国家信息中心,对比资料经过严格质量控制,但未做均一化处理。

## 1.2 分析方法

极端气温指数采用气候变化监测、检测和指数专家组的定义(Frich et al.,2002)。以 1971—2000 年为参考期,使用 R-climdex 软件进行计算。本文选取其中的 10 个极端气温指数作为研究对象(表 1)。根据指数计算方法,将霜冻日数、炎热夜数、结冰日数、夏季日数定义为绝对指数;冷(暖)夜(昼)日数定义为相对指数;暖(冷)日持续指数定义为持续时间指数。

**表 1 本文所用的极端气温指数**

Table 1 Extreme temperature indices used in this study

| 名称 | 定义 | 单位 |
|---|---|---|
| 霜冻日数 | 日最低气温<0 ℃的全部日数 | d |
| 结冰日数 | 日最高气温<0 ℃的全部日数 | d |
| 夏季日数 | 日最高气温>25 ℃的全部日数 | d |
| 炎热夜数 | 日最低气温>20 ℃的全部日数 | d |
| 冷夜日数 | 日最低气温<10%分位值的日数 | d |
| 冷昼日数 | 日最高气温<10%分位值的日数 | d |
| 暖夜日数 | 日最低气温>90%分位值的日数 | d |
| 暖昼日数 | 日最高气温>90%分位值的日数 | d |
| 热日持续指数 | 每年至少连续 6 d 日最高气温>90%分位值的日数 | d |
| 冷日持续指数 | 每年至少连续 6 d 日最低气温<10%分位值的日数 | d |

将城市站和乡村站气温变化速率的差值作为城市化影响偏差,即城市化增温引起的绝对趋势偏差;将城市化影响偏差与城市站气温趋势的比值作为城市化贡献率(周雅清和任国玉,2005)。从城市化影响偏差和城市化贡献率两个方面探讨资料均一化处理对沈阳站地面气温趋势估计的影响。

参考站的选取综合考虑了资料序列长度、迁站情况、站址所在辖区人口数据、与目标站的距离、观测场附近探测环境等因素(任国玉等,2010),选取沈阳站附近的法库、康平站作为乡村站。两个观测站的站址信息如表 2 所示。康平站在 1982 年 9 月 1 日迁至康平县东关乡苏家岗村;法库站在 1973 年 11 月 1 日由法库县小东门外迁至南门村。采用滑动 $t$ 检验法对这两个站点的年平均、平均最低、平均最高气温序列进行均值突变检验。两站的平均气温和最低气温的不连续点出现在 1987—1989 年,平均最高气温无不连续点,该突变主要是由背景气候增暖引起的。但两站在迁站年份附近并未出现不连续点,这表明迁站对两站气温序列的均一性未造成显著影响,可以认为两站的气温序列是相对均一的。年平均(逐日)参考序列的建立方法采用两站与沈阳站均一化后的年平均(逐日)气温序列相关系数的平方值作为权重系数,加权平均获得。

**表 2　用于本文研究的站址信息**

Table 2　Information of the weather stations in this study

| 站号 | 站名 | 经度/E | 纬度/N | 海拔高度/m | 记录起始年份 | 迁站记录 | 台站类型 | 2000 年人口/个 | 站址环境 |
|---|---|---|---|---|---|---|---|---|---|
| 54342 | 沈阳 | 123°31′ | 41°44′ | 45.2 | 1953 年 | 1970-10、1976-10、1989-01、2006-06 | 国家站 | 601 489 | 城市郊区 |
| 54244 | 康平 | 123°2′ | 42°45′ | 119.6 | 1959 年 | 1982-09 | 一般站 | 54 245 | 县郊 |
| 54245 | 法库 | 123°24′ | 42°3′ | 98.6 | 1957 年 | 1973-11 | 一般站 | 52 218 | 县郊 |

## 2　均一化处理对气温趋势的影响

### 2.1　均一化处理前后平均气温趋势差异

图 1 给出了沈阳站均一化处理前后的年平均、平均最高、最低气温序列。其中,平均气温取为最高、最低气温的均值。可以看出,平均最低气温的订正幅度最大,平均最高气温的订正幅度微弱。订正后气温序列时间变化特征与气温非均一性的订正方法有关,城市不断发展导致气象台站逐渐向郊区迁移,使得气温下降,将气温值订正到目前台站所处位置后,造成迁站年份之前气温递减。年平均和平均最低气温订正前后的曲线交点出现在 2006 年,即沈阳站最后一次迁站出现的时间;平均最高气温的曲线交点出现在 1989 年,沈阳站在 1989 年 1 月由沈河区文化路 2 段 2 号迁至沈阳市东陵区五三乡营盘路 12 号,这说明 1989 年迁站对最高气温造成的影响较为明显,2006 年的迁站对最高气温影响甚微。

表 3 给出了 1951—2012 年沈阳站气温均一化处理前后的线性趋势对比。将订正后与订正前的线性趋势差值定义为绝对偏差;绝对偏差与订正后趋势百分比的绝对值定义为相对偏差。订正前年平均、平均最高、平均最低气温的线性趋势较微弱,除平均气温外均未通过显著性检验;订正后增温趋势则变得十分明显,分别为 0.460、0.257、0.591 ℃/(10 a),均通过了 0.05 信度的显著性检验。其中,平均最低气温的绝对偏差和相对偏差最大,分别为 0.444 ℃/(10 a)和 75.13%;平均最高气温的绝对偏差和相对偏差最小,分别为 0.132 ℃/(10 a)和 51.36%。就沈阳站来说,资料非均一性使得平均气温的线性趋势被低估。

**表 3　1951—2012 年沈阳站均一化处理前后年平均、平均最高和最低气温趋势差异**

Table 3　The differences of trends of annual mean temperature, mean maximum temperature and mean minimum temperature before and after homogenization during 1951—2012 at Shenyang station

| 气温 | 订正前趋势/(℃·(10 a)$^{-1}$) | 订正后趋势/(℃·(10 a)$^{-1}$) | 绝对偏差/(℃·(10 a)$^{-1}$) | 相对偏差/% |
|---|---|---|---|---|
| 平均气温 | 0.195[1)] | 0.460[1)] | 0.265 | 57.61 |
| 平均最高气温 | 0.125 | 0.257[1)] | 0.132 | 51.36 |
| 平均最低气温 | 0.147 | 0.591[1)] | 0.444 | 75.13 |

注:1)表示通过了 0.05 信度的显著性检验.

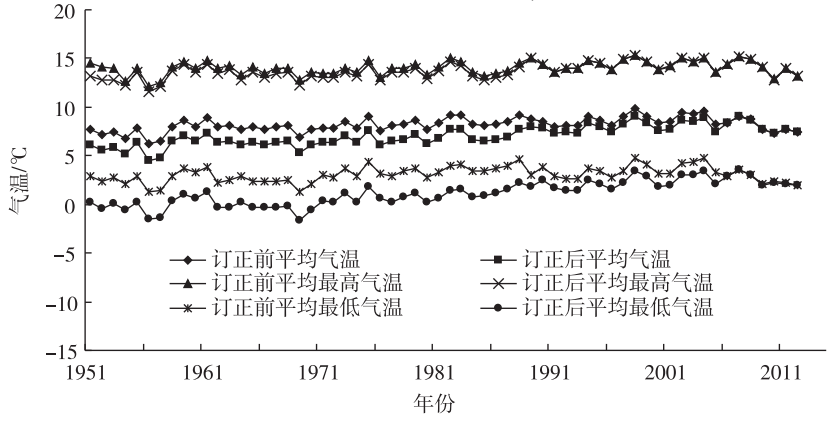


图 1　沈阳站均一化处理前后的平均气温序列(单位:℃)

Fig.1　The annual mean temperature series before and after homogenization at Shenyang station(units:℃)

### 2.2 均一化处理前后极端气温指数趋势差异

订正前后极端气温指数线性趋势的对比(图 2)表明:无论订正前后,与冷事件有关的指数都呈下降趋势,如霜冻日数、结冰日数、冷夜日数、冷昼日数、冷日持续指数;与暖事件有关的指数都呈增加趋势,如夏季日数、炎热夜数、暖夜日数、暖昼日数、暖日持续指数。这与以往的研究相一致(Zhai and Pan, 2003;Qian and Lin, 2004;Ren et al., 2012)。同时,订正后的趋势变化更为显著。斜线直方图表明:订正后极端气温指数的线性趋势均通过了 0.05 信度的显著性检验;订正前除夏季日数和冷昼、冷(暖)夜日数外,均未通过检验。

表 4 给出均一化处理前后,1951—2012 年各个极端气温指数的线性趋势变化情况。就趋势大小来说,资料非均一性使得沈阳站冷指数的趋势变化被高估,绝对偏差为负;暖指数的趋势变化被低估,绝对偏差为正。其中,冷夜日数和暖夜日数的绝对偏差较大,绝对值分别为 8.80 和 7.17 d/(10 a),结冰日数、夏季日数和暖日持续指数的绝对偏差大小要小于 1.0 d/(10 a),一方面是这些指数的趋势变化原本就很微弱,另一方面说明资料非均一性对该指数趋势变化影响较小。霜冻日数、炎热夜数、冷(暖)夜日数、冷日持续指数以及暖昼日数的相对偏差均大于 70%。可见,订正前后,与最低气温有关的极端气温指数绝对(相对)偏差较大,与最高气温有关的极端气温指数绝对(相对)偏差较小。

**表 4 1951—2012 年沈阳站均一化处理前后极端气温指数的线性趋势及差值**

Table 4 The linear trends and differences of extreme temperature indices before and after homogenization during 1951—2012 at Shenyang station

| 指数 | 订正前趋势/(℃·(10 a)$^{-1}$) | 订正后趋势/(℃·(10 a)$^{-1}$) | 绝对偏差/(℃·(10 a)$^{-1}$) | 相对偏差/% |
|---|---|---|---|---|
| 霜冻日数 | −0.74 | −4.48[1)] | −3.74 | 83.48 |
| 炎热夜数 | 0.47 | 3.54[1)] | 3.07 | 86.72 |
| 结冰日数 | −1.48 | −2.43[1)] | −0.95 | 39.09 |
| 夏季日数 | 1.70[1)] | 2.52[1)] | 0.82 | 32.54 |
| 冷夜日数 | −3.28[1)] | −12.08[1)] | −8.8 | 72.85 |
| 暖夜日数 | 2.55[1)] | 9.72[1)] | 7.17 | 73.77 |
| 冷昼日数 | −2.85[1)] | −4.86[1)] | −2.01 | 41.36 |
| 暖昼日数 | 1.08 | 4.53[1)] | 3.45 | 76.71 |
| 热日持续指数 | 0.67 | 1.63[1)] | 0.96 | 58.90 |
| 冷日持续指数 | −0.5 | −2.64[1)] | −2.14 | 81.06 |

注:1)表示通过了 0.05 信度的显著性检验.

## 3 均一化处理对城市化偏差分析的影响

### 3.1 均一化处理前后平均气温序列城市化影响差异

图 3 给出均一化订正前后平均气温的城市化影响偏差与标准误差线。均一化处理前,年平均气温的城市化影响偏差均为负,均一化处理后,均为正值。但无论订正前后,城市化影响偏差的绝对值以平均最低气温最大,平均最高气温最小。这与最低

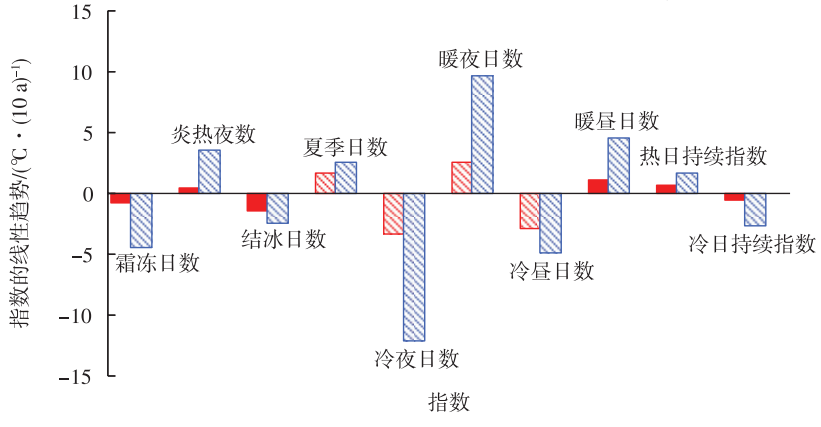


图 2 沈阳站均一化处理前后极端气温指数序列的线性趋势对比(单位:℃·(10 a)$^{-1}$;红色:订正前;蓝色:订正后;斜线:通过 0.05 信度的显著性检验)

Fig.2 The comparison of linear trends of extreme temperature indices before and after homogenization (units: ℃·(10 a)$^{-1}$; red: before homogenization; blue: after homogenization; slant: significance of over 95% confidence level)

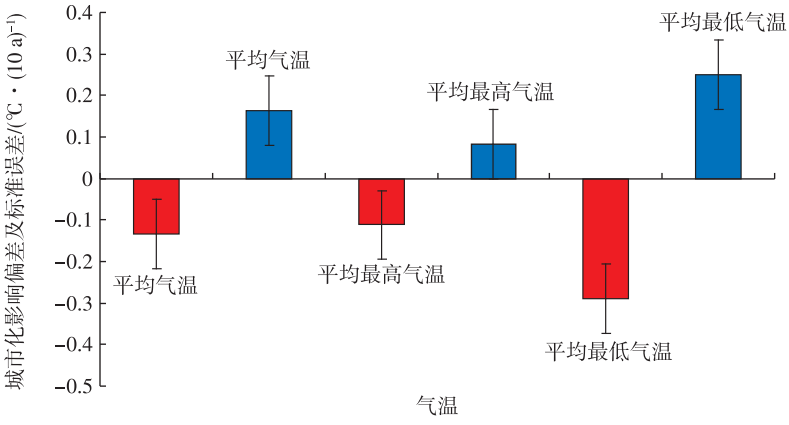


图 3　沈阳站均一化订正前后年平均气温趋势变化的城市化影响偏差及标准误差线(单位:℃·(10 a)$^{-1}$;柱状图:城市化影响偏差;黑实线:标准误差;红色:订正前;蓝色:订正后)

Fig.3　The urban bias of annual mean temperature before and after homogenization and its standard error (units: ℃ · (10 a)$^{-1}$; histogram: urban bias; black solid line: standard error; red: before homogenization; blue: after homogenization)

气温受城市化影响明显的认识相一致(司鹏等,2010)。订正前后平均最低气温的城市化影响偏差分别为-0.289、0.249 ℃/(10 a);平均最高气温的城市化影响偏差分别为-0.112、0.084 ℃/(10 a);年平均气温的城市化影响偏差分别为-0.135、0.163 ℃/(10 a)。就沈阳站来说,资料非均一性对平均气温的城市化偏差定量估计在 0.196~0.538 ℃/(10 a)之间。就标准误差的绝对大小来说,订正前后平均气温城市化影响偏差估计的可信区间相差不大,参数估计精度近似。

均一化处理前沈阳站的城市化影响偏差均为负值,作为一个城市建设不断发展,城市规模不断扩大,人口数量众多的大城市,订正前的城市化负偏差并不符合城市站气温增暖趋势高于乡村站的一般认识。迁站等因素造成的非均一性显然对沈阳站城市化影响指标造成较大影响,采用未经均一化的数据来评估城市化对趋势变化造成的影响显然会造成错误的认知。但值得注意的是,均一化处理后的气温序列在一定程度上恢复了城市化造成的增温趋势(任国玉等,2010;Zhang et al.,2014),这也给订正数据加入了新的系统性误差。

表 5 分析了均一化后沈阳站与参考站年平均气温的线性趋势差异。参考站年平均、平均最高(最低)气温的增温趋势分别为 0.246、0.122、0.370 ℃/(10 a),沈阳站订正后的增温趋势则可以达到 0.409、0.206、0.619 ℃/(10 a)。可见,城市站年平均气温(包括平均最高、最低)序列的增温趋势均要高于参考站。除参考站的最高气温外,平均气温序列均通过 0.05 信度的显著性检验。均一化处理后,平均气温的城市化影响偏差在 0.084~0.249 ℃/(10 a);城市化贡献率在 40%左右。

**表 5　城市化对沈阳站平均气温序列趋势变化的影响(均一化处理后)**

Table 5　The influence of urbanization on the linear trends of average mean temperature after homogenization at Shenyang station

| 气温 | 参考站趋势/(℃·(10 a)$^{-1}$) | 沈阳站趋势/(℃·(10 a)$^{-1}$) | 城市化影响偏差/(℃·(10 a)$^{-1}$) | 城市化影响贡献率/% |
|---|---|---|---|---|
| 平均气温 | 0.246[1)] | 0.409[1)] | 0.163[1)] | 39.85 |
| 平均最高气温 | 0.122 | 0.206[1)] | 0.084[1)] | 40.78 |
| 平均最低气温 | 0.370[1)] | 0.619[1)] | 0.249[1)] | 40.23 |

注:1)表示通过了 0.05 信度的显著性检验.

### 3.2　均一化处理前后极端气温指数序列城市化影响差异

图 4 给出资料均一化处理前后,极端气温指数城市化影响偏差的对比情况及标准误差线,可以清楚地反映城市化对不同指数趋势变化造成的不同影响以及同一指数在均一化处理前后城市化影响偏差变化情况。指数位于 0 值线以上代表城市化影响偏差为正;位于 0 值线以下代表城市化影响偏差为负;红色代表订正前;蓝色代表订正后。可见,均一化订正后,与冷事件有关的极端气温指数序列的城市化

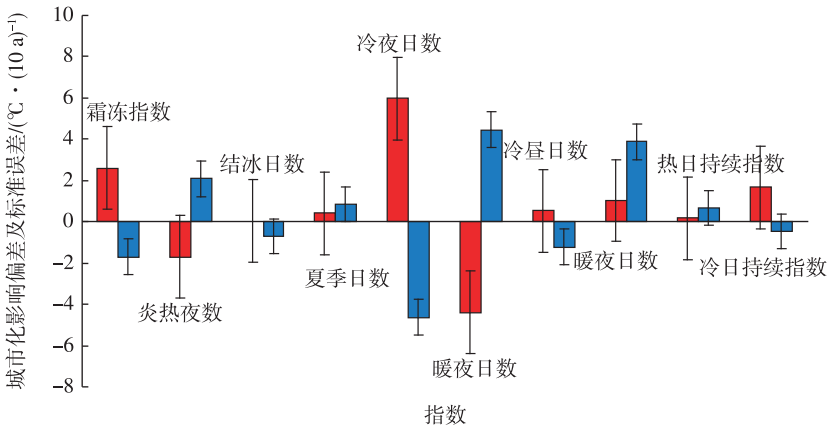


图 4 沈阳站均一化订正前后极端气温指数趋势变化的城市化影响偏差及标准误差线(单位:℃·(10 a)$^{-1}$;柱状图:城市化影响偏差;黑实线:标准误差;红色:订正前;蓝色:订正后)

Fig.4 The urban bias of extreme temperature indices before and after homogenization and its standard error(units:℃·(10 a)$^{-1}$;histogram:urban bias;black solid line:standard error;red:before homogenization;blue:after homogenization)

影响偏差均为负值,如霜冻日数、结冰日数、冷夜(昼)日数、冷日持续指数;与暖事件有关的极端气温指数序列的城市化影响偏差均为正值,如炎热夜数、夏季日数、暖夜(昼)日数、暖日持续指数;符合中国大陆区域各极端气温指数城市化影响偏差整体上的数值特征(Ren and Zhou,2013),但订正前极端气温指数的城市化影响偏差分布无规律性。

均一化处理前后同一指数的城市化影响偏差数值表明:均一化后,冷指数的城市化影响偏差数值有所减小;暖指数的城市化影响偏差数值有所增加。但极端气温指数城市化影响偏差的绝对大小分布在订正前后并无规律性。从标准误差线可以看出:订正后极端气温指数序列的城市化影响偏差参数估计的精度远远高于订正前。

资料非均一性对沈阳站冷指数的城市化偏差影响的定量估计(订正后减去订正前)在 −0.74 ~ −10.63 d/(10 a)之间;暖指数在 0.45 ~ 8.863 d/(10 a)之间;对与最低气温有关指数的城市化偏差的绝对影响(订正前后绝对差值)为 2.13 ~ 10.63 d/(10 a);对与最高气温有关指数的绝对影响为 0.45 ~ 2.85 d/(10 a)。

表 6 反映了均一化后沈阳站及参考站的极端气温指数趋势变化情况对比。可以看出,与城市化对平均气温序列造成的增温趋势不同,城市化对极端气温指数趋势变化的影响呈现不同符号。订正后冷指数的城市化影响为负值;暖指数的城市化影响为正值。同时,参考站极端气温指数趋势变化的大小都要小于沈阳站的趋势,因此城市化实际上加剧了沈阳站极端气温指数的趋势变化幅度。就沈阳站来说,相对于本地背景气候变化,城市化使得冷指数的趋势变化被低估;使得暖指数的趋势变化被高估,并不能反映本地大尺度背景下极端气温指数序列真实的趋势变化。这与资料非均一性对极端气温指数趋势变化的影响相反。

对于参考站,各极端气温指数的趋势变化在 −7.31 ~ 6.68 d/(10 a)之间,除结冰日数、夏季日数和暖昼(夜)日数外,其他指数的趋势变化均通过了 0.05 信度的显著性检验;沈阳站(订正后),各极端气温指数的趋势变化在 −11.95 ~ 11.14 d/(10 a)之间,除结冰日数外,各极端气温指数趋势变化均通过显著性检验。

城市化影响偏差以相对指数为最大,绝对指数次之,持续时间指数最小。因此,就同类指数而言,城市化对与最低气温有关的极端气温指数趋势变化影响相对较大(霜冻日数、炎热夜数、冷(暖)夜日数);对与最高气温有关的极端气温指数趋势变化影响相对较弱(结冰日数、夏季日数、冷(暖)昼日数)。虽然选取的极端气温指数略有不同,但这与周雅清和任国玉(2010)、张雷等(2011)、Zhou and Ren(2011)的研究相一致。此外,城市化对持续时间指数的影响较为微弱。显著性检验结果表明:结冰日数、夏季日数、冷(暖)日持续指数的城市化影响偏差未通过显著性检验。

**表 6　城市化对沈阳站极端气温指数序列趋势变化的影响(均一化处理后)**

Table 6　The influence of urbanization on the linear trends of extreme temperature indices after homogenization at Shenyang station

| 指数 | 参考站趋势/(℃·(10 a)$^{-1}$) | 沈阳站趋势/(℃·(10 a)$^{-1}$) | 城市化影响偏差/(℃·(10 a)$^{-1}$) | 城市化影响贡献率/% |
|---|---|---|---|---|
| 霜冻日数 | −3.21[1)] | −4.91[1)] | −1.70[1)] | 34.62 |
| 炎热夜数 | 2.22[1)] | 4.31[1)] | 2.09[1)] | 48.49 |
| 结冰日数 | −0.65 | −1.35 | −0.70 | 51.85 |
| 夏季日数 | 1.46 | 2.32[1)] | 0.86 | 37.07 |
| 冷夜日数 | −7.31[1)] | −11.95[1)] | −4.64[1)] | 38.83 |
| 暖夜日数 | 6.68[1)] | 11.14[1)] | 4.46[1)] | 40.04 |
| 冷昼日数 | −1.74 | −2.96[1)] | −1.22[1)] | 41.22 |
| 暖昼日数 | 1.28 | 5.16[1)] | 3.88[1)] | 75.19 |
| 热日持续指数 | 1.21[1)] | 1.88[1)] | 0.67 | 35.64 |
| 冷日持续指数 | −1.26[1)] | −1.73[1)] | −0.47 | 27.17 |

注:1)表示通过了 0.05 信度的显著性检验.

## 4　结论

1)资料均一化处理对日最高气温及其衍生的极端气温指数序列趋势影响较弱,但对日最低气温及其衍生的极端气温指数序列趋势影响很大。

2)沈阳站是由于城市扩张导致迁站降温的典型案例,经资料均一化处理后,平均气温序列的城市化影响偏差有所增大,平均最低气温序列城市化影响偏差增大尤其明显。资料非均一性对沈阳站平均气温的城市化偏差影响定量估计为 0.196~0.538 ℃/(10 a),同样以对最低气温的影响最大,最高气温的影响最小。

3)均一化处理前后沈阳站同一指数的城市化影响偏差表明:订正后冷指数的城市化影响偏差数值较订正前有所减小;暖指数的城市化影响偏差数值有所增加。资料非均一性对冷指数的城市化偏差影响定量估计为−0.74~−10.63 d/(10 a);暖指数为 0.450~8.863 d/(10 a);对与最低气温有关指数的城市化偏差的绝对影响为 2.13~10.63 d/(10 a);对与最高气温有关指数的绝对影响为 0.45~2.85 d/(10 a)。

4)资料均一化处理有效纠正了因迁站等原因造成的地面气温观测记录中的非均一性,但却在很大程度上还原了城市站地面气温观测记录中的城市化影响偏差,给数据加入新的系统误差。

## 参考文献:


曹丽娟,严中伟.2011.地面气候均一性研究进展[J].气候变化研究进展,7(2):129-135.

任国玉.2003.器测时期地面气温变化研究的现状和问题[J].气象,29(8):3-7.

任国玉,郭军,徐铭志,等.2005.近五十年中国地面气候变化基本特征[J].气象学报,63(6):942-956.

任国玉,张爱英,初子莹,等.2010.我国地面气温参考站点遴选的依据、原则和方法[J].气象科技,38(1):85-98.

司鹏,李庆祥,李伟,等.2010.城市化对深圳气温变化的贡献[J].大气科学学报,33(1):110-116.

张雷,任国玉,刘江,等.2011.城市化对北京气象站极端气温指数趋势变化的影响[J].地球物理学报,54(5):1150-1159.

周建平,孙照渤,倪东鸿,等.2013.中国气象台站迁移对年平均气温均一性的影响[J].大气科学学报,36(2):139-146.

周雅清,任国玉.2005.华北地区地表气温观测中城镇化影响的检测和订正[J].气候与环境研究,10(4):743-753.

周雅清,任国玉.2010.中国大陆 1956~2008 年极端气温事件变化特征分析[J].气候与环境研究,15(4):406-417.

Frich P, Alexander L V, Della-Marta P, et al. 2002. Observed coherent changes in climatic extremes during the second half of the twentieth century[J]. Climate Res, 19: 193-212.

Li Q X, Liu X N, Zhang H Z, et al. 2004. Detecting and adjusting on temporal inhomogeneity in Chinese mean surface air temperature data[J]. Adv Atmos Sci, 21(2): 260-268.

Li Z, Yan Z W. 2009. Homogenized daily mean/maximum/minimum temperature series for China from 1960—2008[J]. Atmos Oceanic Sci Lett, 2(4): 237-243.

Qian W H, Lin X. 2004. Regional trends in recent temperature and indices in China[J]. Climate Res, 27: 119-134.

Ren G Y, Zhou Y Q. 2013. Urbanization effect on trends of extreme temperature indices of national stations over Mainland China, 1961—2008[J]. J Climate, 27: 2340-2360.

Ren G Y, Ding Y H, Zhao Z C, et al. 2012. Recent progress in studies of climate change in China[J]. Adv Atmos Sci, 29(5): 958-977.

Yan Z W, Yang C. 2001. Influence of inhomogeneity on the estimation of mean and extreme temperature trends in Beijing and Shanghai[J]. Adv Atmos Sci, 18(3): 309-321.

Yan Z W, Li Z, Li Q X, et al. 2010. Effects of site change and urbanization in the Beijing temperature series 1977—2006[J]. Int J Climatol, 30: 1226-1234.

Zhai P M, Pan X H, 2003. Trends in temperature extremes during 1951—1999 in China [J]. Geophys Res Lett, 30 (17): 1913. doi: 10.1029/2003GL018004.

Zhang L, Ren G Y, Ren Y Y, et al. 2014. Effect of data homogenization on estimate of temperature trend: A case of Huairou station in Beijing Municipality[J]. Theor Appl Climatol, 115(3): 365-373.

Zhou Y Q, Ren G Y. 2011. Change in extreme temperature event frequency over mainland China, 1961—2008 [J]. Climate Res, 50: 125-139.


(责任编辑:张福颖)

# Simulation and Projection of the Western Pacific Subtropical High in CMIP5 Models

LIU Yunyun[1*] (刘芸芸), LI Weijing[1] (李维京), ZUO Jinqing[1] (左金清), and HU Zeng-Zhen[2]

1 *Laboratory for Climate Studies, National Climate Center, China Meteorological Administration, Beijing* 100081, *China*

2 *Climate Prediction Center, NCEP/NWS/NOAA, College Park* 20740, *USA*

(Received October 19, 2013; in final form February 16, 2014)

**ABSTRACT**

This work examined the performance of 26 coupled climate models participating in the Coupled Model Intercomparison Project Phase 5 (CMIP5) in the simulation of the present-day temporal variability and spatial pattern of the western Pacific subtropical high (WPSH). The results show that most models are able to capture the spatial distribution and variability of the 500-hPa geopotential height and zonal wind fields in the western subtropical Pacific, but with underestimated mean intensity of the WPSH. The underestimation may be associated with the cold bias of sea surface temperature in the tropical Indian and western Pacific oceans in the models. To eliminate the impact of the climatology biases, the climatology of these models is replaced by that of the NCEP/NCAR reanalysis in the verification, and the models reproduce the WPSH's enhancement and westward extension after the late 1970s. According to assessment of the simulated WPSH indices, it is found that some models (CNRM-CM5, FGOALS-g2, FIO-ESM, MIROC-ESM, and MPI-ESM-P) are better than others in simulating WPSH. Then, the ensemble mean of these better models is used to project the future changes of WPSH under three representative concentration pathway scenarios (RCP8.5, RCP4.5, and RCP2.6). The WPSH enlarges, strengthens, and extends westward under all the scenarios, with the largest linear growth trend projected in RCP8.5, smallest in RCP2.6, and in between in RCP4.5; while the ridge line of WPSH shows no obvious long-term trend. These results may have implications for the attribution and prediction of climate variations and changes in East Asia.

**Key words:** western Pacific subtropical high (WPSH), simulation and projection, CMIP5, RCP scenarios

**Citation:** Liu Yunyun, Li Weijing, Zuo Jinqing, et al., 2014: Simulation and projection of the western Pacific subtropical high in CMIP5 models. *J. Meteor. Res.*, **28**(3), 327–340, doi: 10.1007/s13351-014-3151-2.

## 1. Introduction

Western Pacific subtropical high (WPSH) is one of the most important atmospheric circulation systems over East Asia. Its variability in the location and intensity has important impacts on the summer rainfall anomaly over China (Xu et al., 2001; Tao and Wei, 2006). Abundant moisture from the tropical oceans transports to eastern China through the southerly flow from its western boundary, then converges with the cold air from the high latitude and conforms the front, causing rain belts at the northwestern margin of the WPSH and hot and drought summer under its covered area (Han and Wang, 2007). Clearly, its interannual variability causes droughts and floods over East China (Wu et al., 2002), while its interdecadal variability modulates the drought and flood pattern over East Asia (Hu, 1997; Xiong, 2001). Liu et al. (2013) noted that the biennial component of the WPSH in intensity and zonal position also has the obvious interdecadal transition in the late 1970s, with larger amplitudes during the recent 30 years. As a result, great attention has been given to variations of WPSH on the interannual and interdecadal timescales, since understanding the variations will help us to improve the forecast of summer climate anomaly in East Asia.

Supported by the National (Key) Basic Research and Development (973) Program of China (2010CB950501 and 2013CB430202), National Natural Science Foundation of China (41005037), and China Meteorological Administration Special Public Welfare Research Fund (GYHY201306024 and GYHY201306033).

*Corresponding author: liuyuny@cma.gov.cn.

©The Chinese Meteorological Society and Springer-Verlag Berlin Heidelberg 2014

To simulate and project climate change, climate model becomes one of the main quantitative tools now. Due to a lot of uncertainties and biases in the climate models and in order to improve model simulations, the Coupled Model Intercomparison Project (CMIP) has been proposed by the World Climate Research Program (WCRP). The last phase of CMIP (CMIP5) involves about 30 climate modeling groups around the world, aiming to advance our knowledge of climate variability and climate change and projection, and to provide simulations for evaluation in the IPCC Fifth Assessment Report (AR5) (Taylor et al., 2012). Compared with the models used in the previous phase of CMIP simulations (such as CMIP3), most models in CMIP5 have been improved in many aspects, including physical processes and coupled carbon cycle. Thus, it will be interesting to assess the performance of CMIP5 models in the simulation of WPSH mean state and variability. Also, it is meaningful to project the possible changes of WPSH under different climate warming scenarios in the future.

In this work, the capacities of 26 CMIP5 models in simulating WPSH are evaluated from various aspects based on a set of reconstructed indices that describe the WPSH objectively (Liu et al., 2012). It is expected to provide some valuable information for the model development and improvement in the future by comparisons between the simulations and observations, and among the models. Finally, the models with good performance are identified and selected to project the possible evolution of WPSH in the future, which is expected to provide implication for future trends of the East Asian summer climate over China.

## 2. Data and CMIP5 models

Table 1 gives the basic description of the 26 coupled climate models participating in CMIP5. The simulation data used in this study include the data from two groups of model runs. (1) Historical runs, which are initiated from an arbitrary point of a quasi-equilibrium control run and integrated longer than 156 yr (1850–2005). The historical run is forced by time-evolving greenhouse gases, ozone, aerosols, and a so-

**Table 1.** Description of the 26 coupled climate models participating in the CMIP5

| Model name | Institute/country | Resolution |
|---|---|---|
| ACCESS1-0 | CAWCR/Australia | 1.875°×1.25° |
| BCC-CSM1-1 | BCC/China | 2.8°×2.8° |
| CanESM2 | CCCMA/Canada | 2.8°×2.8° |
| CCSM4 | NCAR/USA | 1.25°×0.94° |
| CESM1-CAM5-1-FV2 | NSF-DOE-NCAR/USA | 2.5°×1.9° |
| CNRM-CM5 | CNRM-CERFACS/France | 1.4°×1.4° |
| FGOALS-g2 | LASG-CESS/China | 2.8°×2.8° |
| FIO-ESM | FIO/China | 2.8°×2.8° |
| GFDL-CM3 | NOAA GFDL/USA | 2.5°×2.0° |
| GFDL-ESM2G | NOAA GFDL/USA | 2.5°×2.0° |
| GFDL-ESM2M | NOAA GFDL/USA | 2.5°×2.0° |
| GISS-E2-H | NASA GISS/USA | 2.5°×2.0° |
| GISS-E2-R | NASA GISS/USA | 2.5°×2.0° |
| HadCM3 | MOHC/UK | 3.75°×2.5° |
| HadGEM2-AO | NIMR/Korea | 1.875°×1.25° |
| HadGEM2-CC | MOHC/UK | 1.875°×1.25° |
| HadGEM2-ES | MOHC/UK | 1.875°×1.25° |
| INMCM4 | INM/Russia | 2.0°×1.5° |
| IPSL-CM5A-LR | IPSL/France | 3.75°×1.875° |
| IPSL-CM5A-MR | IPSL/France | 2.5°×1.25° |
| MIROC5 | MIROC/Japan | 1.4°×1.4° |
| MIROC-ESM | MIROC/Japan | 2.8°×2.8° |
| MPI-ESM-LR | MPI-M/Germany | 1.9°×1.9° |
| MPI-ESM-P | MPI-M/Germany | 1.9°×1.9° |
| MRI-CGCM3 | MRI/Japan | 1.1°×1.1° |
| NorESM1-M | NCC/Norway | 2.5°×1.875° |

lar constant that are consistent with the observations, and for the first time, time-evolving land cover/land use pattern is included (Taylor et al., 2012). (2) Future climate change projection runs, which are forced with three typical representative concentration pathways (RCPs), i.e., RCP2.6, RCP4.5, and RCP8.5. Every emission scenario has a set of specified concentration of greenhouse gases, aerosols and other chemistry gases, and land cover/land use pattern (Moss et al., 2010; Xin et al., 2012).

Atmospheric monthly reanalysis (Kalnay et al., 1996) provided by NCEP/NCAR and the Extended Reconstructed SST dataset (ERSSTv3b) (Smith et al., 2008) from NOAA are used in this study. Hereafter we refer to these observation-based datasets as observations. The analysis period of the historical runs and observations is from 1951 to 2005, and the period of the future projection runs is from 2006 to 2099. The model output atmospheric fields are interpolated to the regular grids with a horizontal resolution of 2.5° × 2.5°, and SST fields are interpolated to the regular grids with a horizontal resolution of 2° × 2° for facilitating the comparison among CMIP5 models.

Normally, WPSH is represented in the weather chart as the region surrounded by the contour of 5880 gpm at 500-hPa level within 10°–45°N, 110°E–180°. In order to quantitatively describe the variation of WPSH in the intensity and position, the monthly WPSH indices are computed based on NCEP/NCAR reanalysis, including the area, intensity, ridge line, and western boundary indices (Liu et al., 2012). It is well known that WPSH is strongest in summer, with significant impacts on the summer rainfall over East Asia (Nitta and Hu, 1996; Wu et al., 2002). Therefore, we will examine the WPSH in summer (June, July, and August) in terms of its spatial distribution, amplitude variation, and interdecadal and interannual variations, while the entire time series of the monthly data is used only in power spectrum analysis.

To assess the model's ability in simulating current climate, Taylor diagram (Taylor, 2001) is used to centralize multi-model related information. The correlation coefficient between the model simulations and observations represents the model's capability to simulate climatic variability in the concerned region. The root-mean-square error (RMSE) indicates deviation of the model from the observations (the closer to zero the RMSE is, the higher simulation capability the model has). The standard deviation ratio of model simulation relative to the observation indicates the model's ability in simulating the amplitude of variability. These three assessment indicators displayed in a Taylor diagram can reflect the overall performance of the model. Therefore, Taylor diagram is used in this study to evaluate the 26 CMIP5 models, where both the self-correlation coefficient and the standard deviation of the observations are 1, and RMSE is 0.

## 3. Climatology of WPSH

### *3.1 Spatial distribution*

According to the definition of WPSH, the simulated geopotential height (H500) and zonal wind fields at 500 hPa (u500) by CMIP5 are examined first. Note that the model biases present in the spatial pattern, coverage, as well as intensity of WPSH relative to the observations (Fig. 1). The simulated H500 in CCSM4, CESM1-CM5, and FIO-ESM models is stronger than the observations, with a larger coverage area surrounded by the 5880-gpm contour. In the other CMIP5 models, however, the simulated H500 is much weaker than the observations, without the 5880-gpm isoline over the subtropical western Pacific in summer when WPSH is seasonally strongest in the observation; even no 5840-gpm isoline presents at H500 in HadGEM2-CC and IPSL-CM5A-LR models. Furthermore, the simulation of u500 = 0 m $s^{-1}$ is not good as well (figure omitted). Most of the models fail to capture the position of the WPSH ridge line except three models which reproduce the 5880-gpm contour. It is also noted that the simulated easterly wind belt on the south of WPSH is much weaker than the observation. This is consistent with the overall weak WPSH simulated by these models.

Systematic errors usually exist in the simulated atmospheric circulation in current global atmosphere-ocean coupled models (also known as the model climate drift; Sun and Ding, 2008; Huang and Qu, 2009; Feng and Li, 2012). These biases in simulating the WPSH are common in most state-of-the-art GCMs,

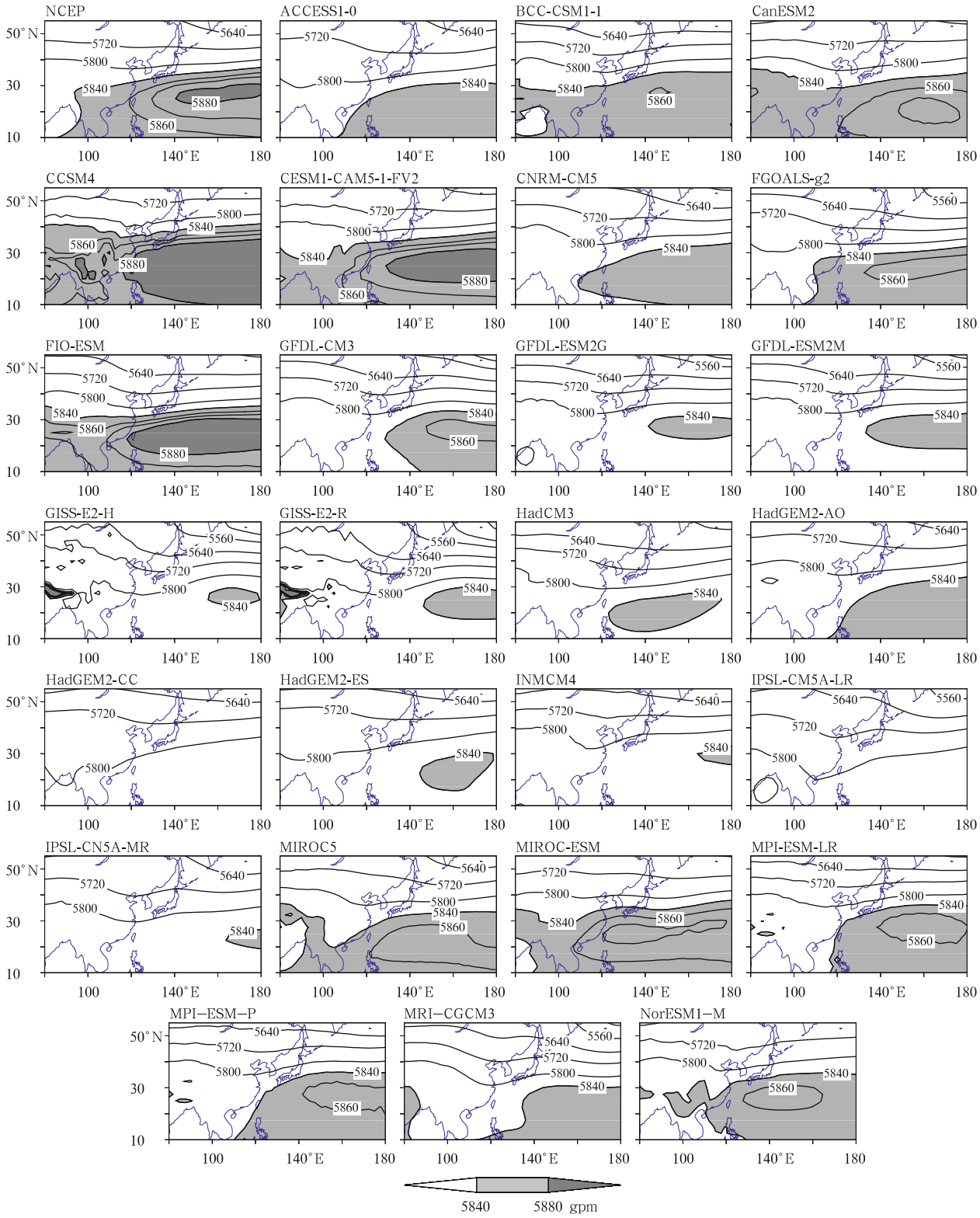


**Fig. 1.** Climatological means of H500 in summer from the observation (NCEP/NCAR reanalysis) and CMIP5 model simulations. Light and dark shaded areas denote H500 larger than 5840 and 5880 gpm, respectively.

implying a challenge in simulating and predicting summer climate variability over East Asia (Zhang and Chen, 2011a, b). Considering that the intensity and spatial pattern of WPSH are influenced by the thermal anomalies from underlying surface, especially the sea surface temperature (SST) in the tropical Pacific and Indian Ocean (Nitta, 1987; Huang and Sun, 1994; Nitta and Hu, 1996; Wu et al., 2002), we plot the observed and simulated climatological tropical SST in summer and the model biases relative to the observations in Fig. 2. The result shows that the SST in both tropical Pacific warm pool and Indian Ocean is above 28°C in summer, which is favorable to the maintenance of the WPSH. However, compared to the observations, the simulated regions surrounded by the contour of SST = 28℃ in most CMIP5 models are much smaller, indicating cold biases in the tropical Indian Ocean and Pacific warm pool. This consists with the underestimated H500 over the western Pacific in the simulations. Nevertheless, the three models (CCSM4, CESM1-CAM5, and FIO-ESM), which have produced realistic H500, also reproduce the SSTs in the tropical Indian and Pacific oceans with smaller cold biases. These results may suggest a connection in simulating the spatial distribution of tropical SST and in simulating the WPSH.

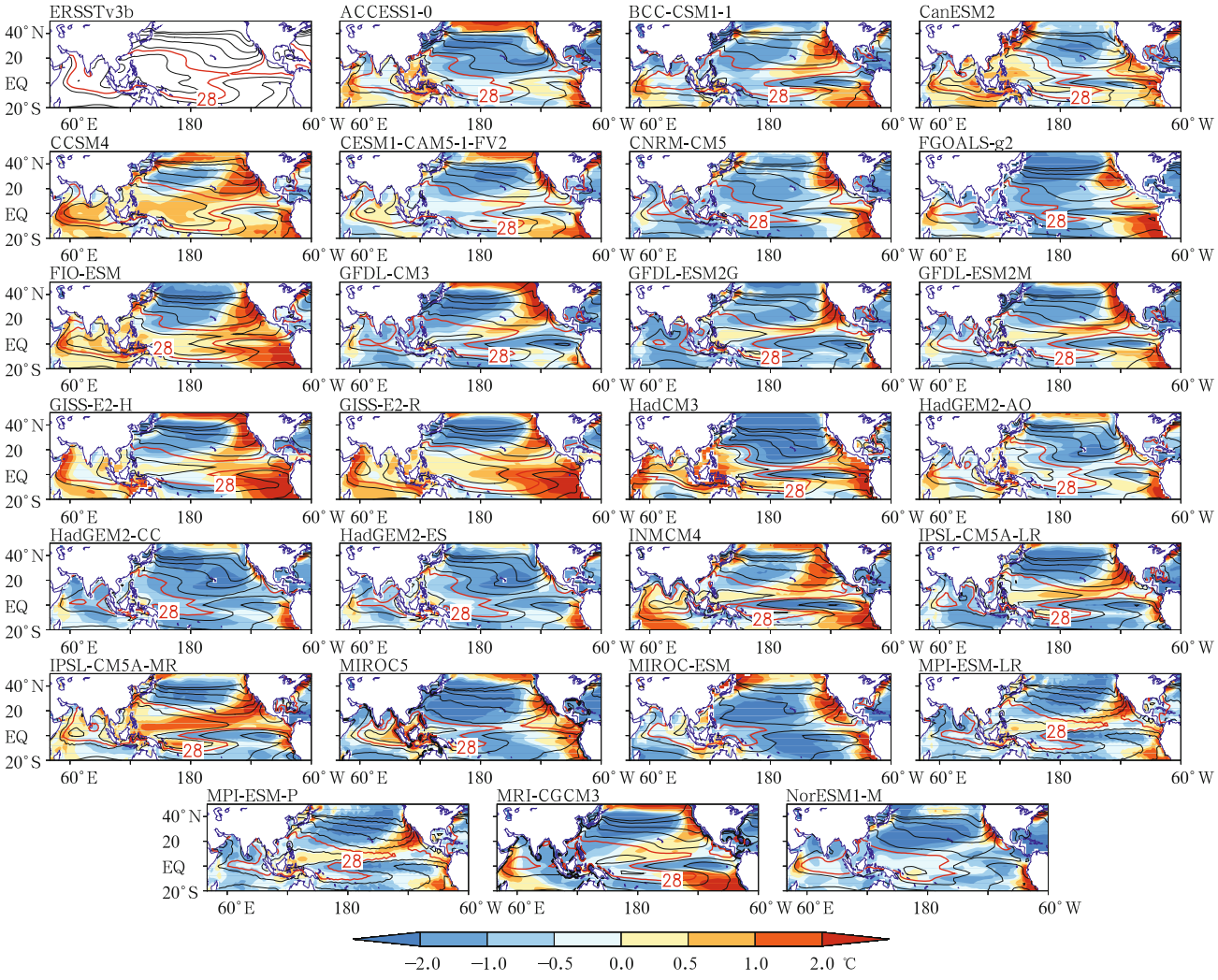


**Fig. 2.** Climatological mean of SST (contours; °C) in summer from the observation (ERSSTv3b) and CMIP5 model simulations, with the model biases shaded. The contour interval is 2℃. The red line is isoline of 28℃.

### *3.2 Climatology calibration*

The Taylor diagram of the climatological H500 over the western Pacific in summer compared to the observation (Fig. 3a) shows that the simulations of the spatial pattern of H500 are similar to the observation, with the correlation coefficient above 0.96, even 0.99 in 5 models. RMSEs of all models are within 1 gpm. The high correlations and small RMSEs indicate good simulations of the spatial distribution of H500 over the western Pacific. It is also noted that the amplitude of H500 is also well captured, with standard deviation of the models ranging from 0.6 to 1.6 gpm. Figure 3b is the Taylor diagram of the simulated climatological u500. All of the correlation coefficients with the observation are above 0.90, RMSEs are less than 0.5 m $s^{-1}$, and the standard deviations are from 0.5 to 1.5 m $s^{-1}$, which imply decent performances of the 26 CMIP5 models in capturing the spatial distribution and amplitude of u500.

We note that although there are significant model biases in simulating H500 and u500 (Fig. 1), possibly associated with cold SST biases in the tropical Indian and Pacific oceans (Fig. 2), the spatial pattern and variability of H500 and u500 over the western Pacific are well reproduced in all of the 26 CMIP5 models (Fig. 3). To correct the climatology biases in the simulations, the simulated climatology of H500 and u500 from all of the models is replaced by that from the observations. In other words, all the model outputs are calibrated to the same climatic state, and then superimposed with each model's own variability of H500 and u500. For example, the calibration of H500 for a model (the same in u500) is:

$$h'_{\rm model} = \left(h_{\rm model} - \overline{h}_{\rm model}\right) + \overline{h}_{\rm ncep}, \qquad (1)$$

where $h_{\rm model}$ represents an H500 simulation value from a specified model, $\overline{h}_{\rm model}$ represents the model climatology of H500, and $\overline{h}_{\rm ncep}$ denotes the climatology of H500 from the observation. In the following, the verification of WPSH is based on the outputs from climatology calibrated runs.

## 4. Variability of WPSH

### *4.1 WPSH indices*

To characterize the variability of WPSH in intensity and position objectively, Fig. 4 shows the 9-yr

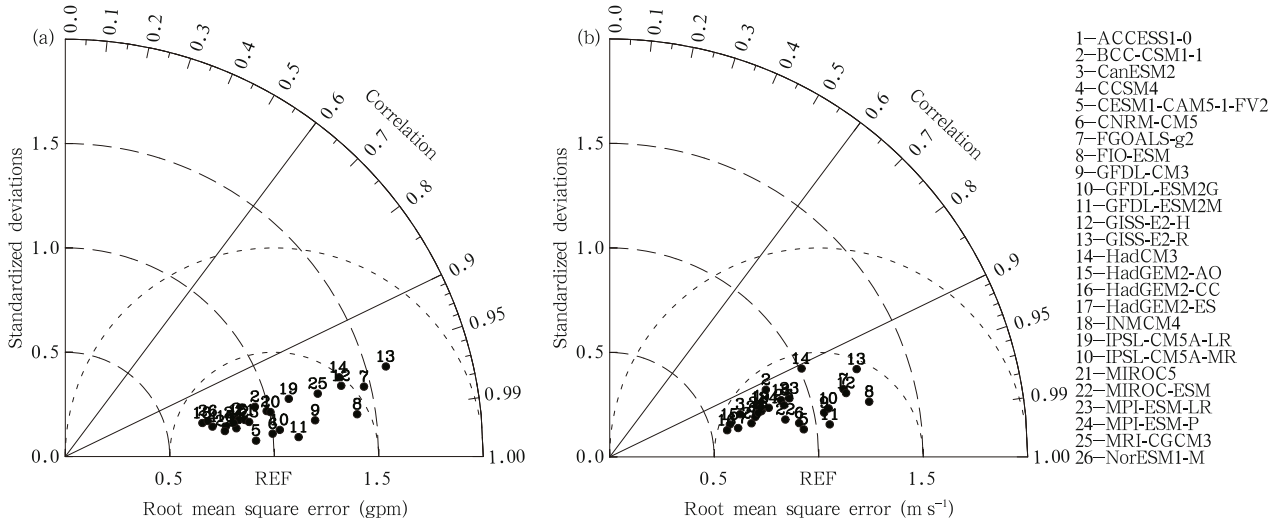


**Fig. 3.** Taylor diagrams of (a) simulated climatological H500 and (b) u500 over the western Pacific in summer compared to the observation. REF indicates the reference value of 1. The radial distance of the model code pointing from the origin is the standard deviation ratio of the model relative to the observation. The correlation coefficient of spatial pattern between model and observation is shown by the cosine of the azimuthal angle of model code point, and their root-mean-square error is given by the distance of model code pointing from the REF.

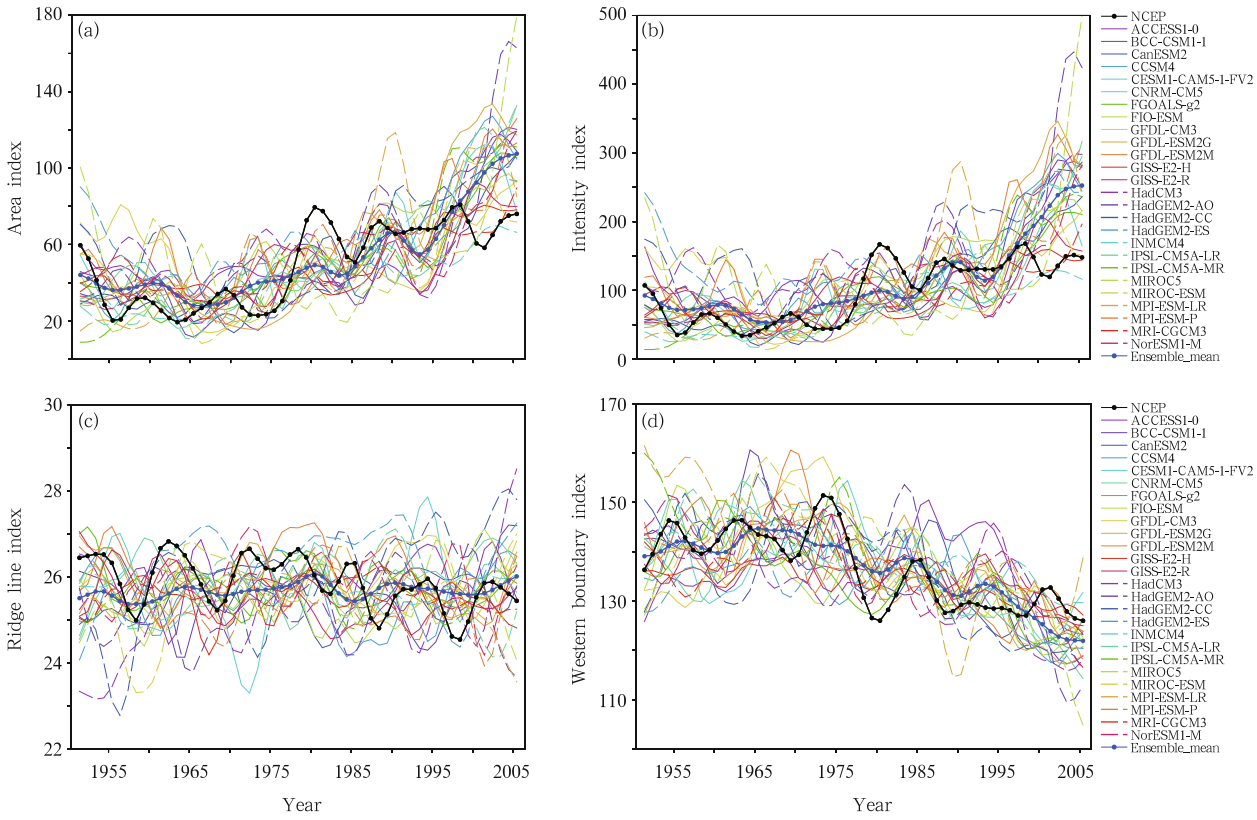


**Fig. 4.** Time series of the WPSH indices in summer from the observation (thick black line) and calibrated model simulations (thin colored lines) for the period from 1951 to 2005. (a) Area index, (b) intensity index, (c) ridge line index, and (d) western boundary index. The thick blue line is the ensemble mean of the 26 CMIP5 models.

running mean time series of the WPSH indices, including the area, intensity, ridge line, and western boundary indices from both observation and calibrated model simulations. The observation curves show that the area and intensity indices of WPSH increase significantly and the western boundary index decreases after the late 1970s, i.e., WPSH becomes stronger and more westward-extending during the recent 30 years. Such an interdecadal shift of WPSH has also been noted in previous works (Hu, 1997; Huang et al., 2006; Zhao et al., 2007; Liu and Ding, 2012). Interestingly, there is a slightly downward trend in the observed ridge line index (Fig. 4c), suggesting that WPSH slightly shifts southward after the late 1970s, consistent with Nitta and Hu (1996) and Hu (1997).

Compared with the observations, all the calibrated model results capture the interdecadal shift of WPSH in the late 1970s. In these simulations, the observed greenhouse gases, ozone, aerosols, and solar constant, and the variability of land cover are all taken into account in the models (Taylor et al., 2012). Thus, it is suggested that these external forcing factors may have played an important role in causing the interdecadal variability of WPSH, although the internal variability of the atmospheric circulation over the western Pacific may also be influenced by the local atmosphere-ocean interaction (Wang et al., 2005; Zhu and Shukla, 2013).

### *4.2 Interdecadal variability of WPSH in spatial pattern*

To display visually the interdecadal shift of WPSH in its spatial pattern, distributions of the contours of H500 = 5880 gpm and u500 = 0 m $s^{-1}$ averaged in two periods of 1951–1960 and 1996–2005 are computed and compared (Fig. 5). During the period of 1951–1960, WPSH is relatively weaker and eastward, with the observed 5880-gpm contour between

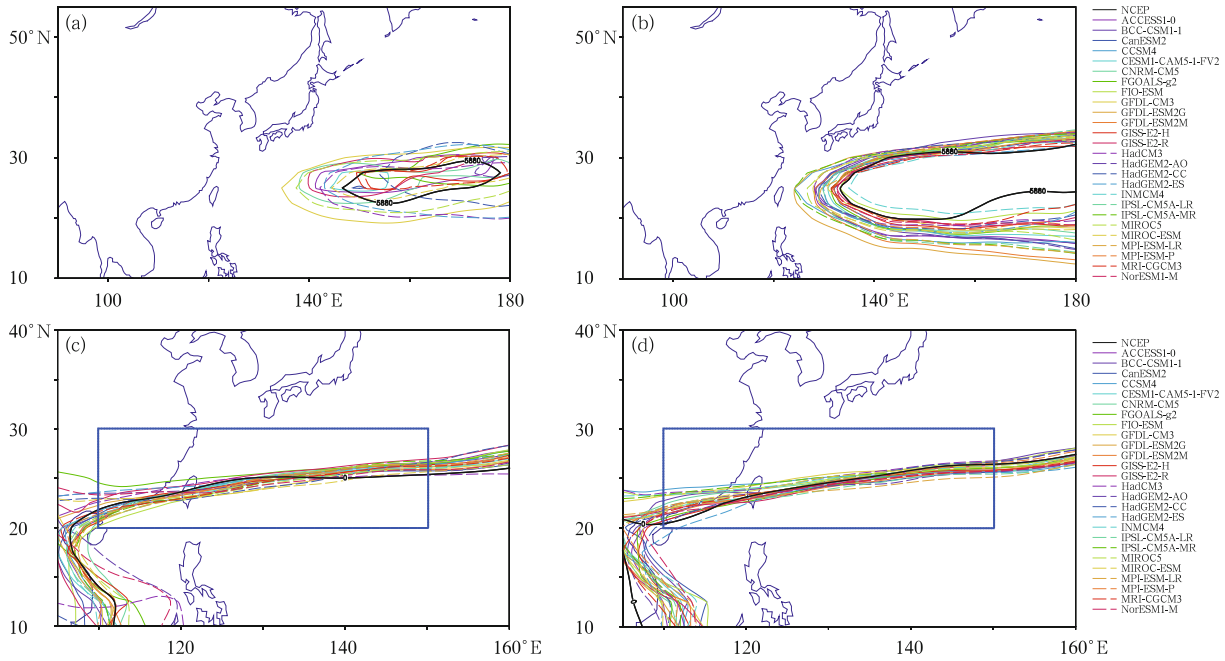


**Fig. 5.** Distributions of the contour of (a, b) H500 = 5880 gpm and (c, d) u500 = 0 m s$^{-1}$ averaged in (a, c) 1951–1960 and (b, d) 1995–2005 from the observation (thick black line) and calibrated model simulations (thin colored lines).

20° and 30°N, and its western boundary no more than 140°E (Fig. 5a). The observed ridge line is near 25°N, with a northeastern-southwestern direction (Fig. 5c). Most of the calibrated simulations are able to reproduce WPSH, i.e., the 5880-gpm contour, much better than the model results before climatology calibration (Fig. 1). Unfortunately, there are still 10 models failing to capture the 5880-gpm contours. Compared with simulation of the 5880-gpm contour line, the ridge lines of WPSH are better simulated, except near the coastland of China of about 115°E.

In the period of 1996–2005, WPSH becomes stronger and more westward, the area of the observed WPSH increases, with its southern and northern borders extending to 18° and 32°N, and the western boundary to 135°E (Fig. 5b). The calibrated model results well simulate the interdecadal shift of WPSH. The area and intensity indices of WPSH increase significantly relative to the period of 1951–1960 in the model simulations (Figs. 5b and 5d).

### *4.3 Linear trend and standard deviation of WPSH indices*

In order to quantitatively assess the capabilities of the CMIP5 models in simulating WPSH indices, linear trends of each WPSH index from all the CMIP5 models are calculated, except for the ridge line index (trend too small) (see Fig. 6). The observed results show that the linear ascending trend of WPSH area and intensity indices are more than 20% per decade, and the trend of the western boundary is –2.7% per decade, at the significance level of 0.01. Compared to the observations, all the models well simulate the tendency of enhancing and westward extension of WPSH during 1951–2005, but with large quantitative differences. Some are larger than the observation in the intensity of WPSH, such as IPSL-CM5A-LR and GFDL-ESM2G, while others are weaker than the observations, such as GFDL-CM3 and HadGEM2-ES. Taking all the three WPSH indices into account, it is found that the simulations of nine models, i.e., CESM1-CAM5-1-FV2, CNRM-CM5, FGOALS-g2, FIO-ESM, HadCM3, HadGEM2-CC, MIROC-ESM, MPI-ESM-P, and NorESM1-M, are better than others in capturing the linear trend of WPSH indices.

The standard deviation of WPSH indices can be used to measure the capability of the models in simulating the interannual variability of WPSH. Figure 7 shows the simulated standard deviation ratio of the WPSH indices relative to the observations. The closer

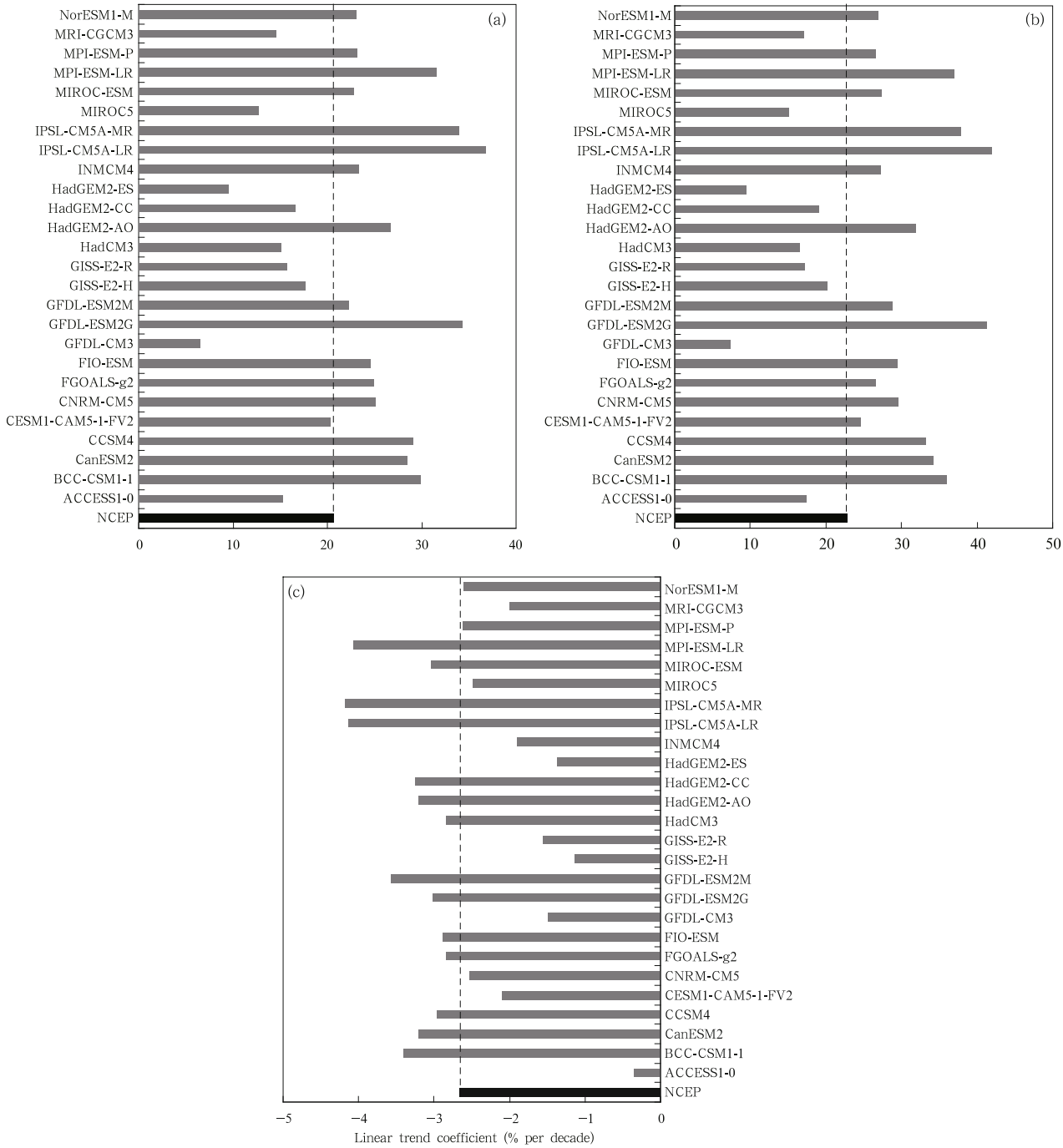


**Fig. 6.** Linear trend coefficients of the WPSH indices in summer from the observation (black bar) and CMIP5 model simulations (grey bars) for the period 1951–2005. (a) Area index, (b) intensity index, and (c) western boundary index.

to 1 the ratio is, the better to simulate the interannual variability of WPSH indices the model is. The grey bars in Fig. 7 denote the accumulated distance between the ratios of these four WPSH indices and the reference value of 1. The smaller the accumulated distance is, the closer to observations the simulated WPSH index is, which provides a measurement of the model performance in simulating the overall feature of WPSH. It is noted that most of the standard deviation ratios of the calibrated simulations to the observations

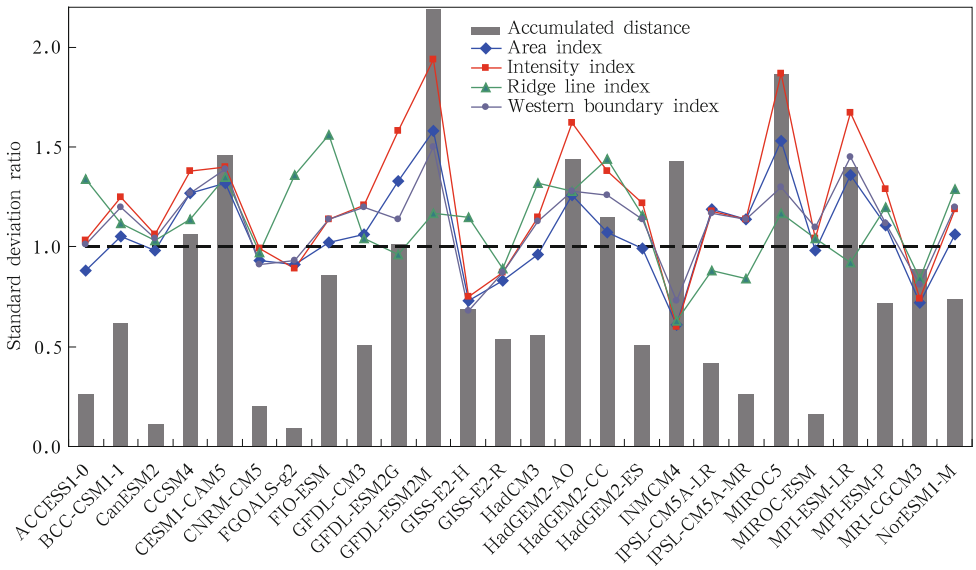


**Fig. 7.** Standard deviation ratios of the simulated WPSH indices relative to the observation. The grey bars are the accumulated distance of the standard deviation ratio of the four WPSH indices from the reference value of 1. The smaller the grey bar is, the closer to the observation the simulated result is.

are larger than the reference value, indicating an overestimation of the amplitudes of WPSH indices in the models. GFDL-ESM2M, MIROC5, and INMCM4 models have relatively poor simulations in the interannual variability of WPSH, because of the too large accumulated ratios in the GFDL-ESM2M and MIROC5, and the too small one in INMCM4. According to Fig. 7, it is found that six models: ACCESS1-0, CanESM2, CNRM-CM5, FGOALS-g2, IPSL-CM5A-MR, and MIROC-ESM, perform relatively better.

### *4.4 Interannual variability of WPSH*

The interannual variability is another important feature to describe the characteristics of WPSH. Figure 8 shows the power spectrum of the monthly WPSH intensity index in the entire analysis period from the observation and 26 CMIP5 models. Considering that seasonal variability of WPSH is more significant than other timescales, a low-pass filter is firstly used to remove the seasonal variability (cycle of 11 months) from the raw data for highlighting the interannual signals.

It is known that significant tropospheric biennial oscillation (TBO) exists over the East Asian monsoon region on interannual timescales (Nitta and Hu, 1996). Being one of the dominant members of the East Asian monsoon system, WPSH has a TBO component on the interannual timescale as well (Liu et al., 2013). The observation shows that there are two interannual periods, i.e., the quasi-four-year (36–60-month) and the quasi-biennial-year (24–36-month) period, and both pass the 0.05 significance level of the red noise test. The period of the quasi-biennial variation is consistent with the TBO component of WPSH and the monsoon rainfall in China (Chang and Li, 2000; Chang et al., 2000; Ding, 2007). The power spectra in the CMIP5 model simulations exhibit obvious differences from each other on the interannual timescales (Fig. 8). To some extent, only ACCESS1-0, GFDL-CM3, HadGEM2-CC, and HadGEM2-ES can capture both the quasi-four-year period and the TBO period.

Comparison of the 26 CMIP5 model simulations with the observations shows that most of the simulated H500 values in the western subtropical Pacific region are weaker than observation, and even the calibrated results of some models still fail to capture the spatial and temporal characteristics of WPSH. According to the overall simulations of the distributions of SST, H500, and u500, and the quantitative assessment of the WPSH indices, it is noted that CNRM-CM5, FGOALS-g2, FIO-ESM, MIROC-ESM, and MPI-ESM-P models are better than others. Due to the unavailability of the MPI-ESM-P model for the

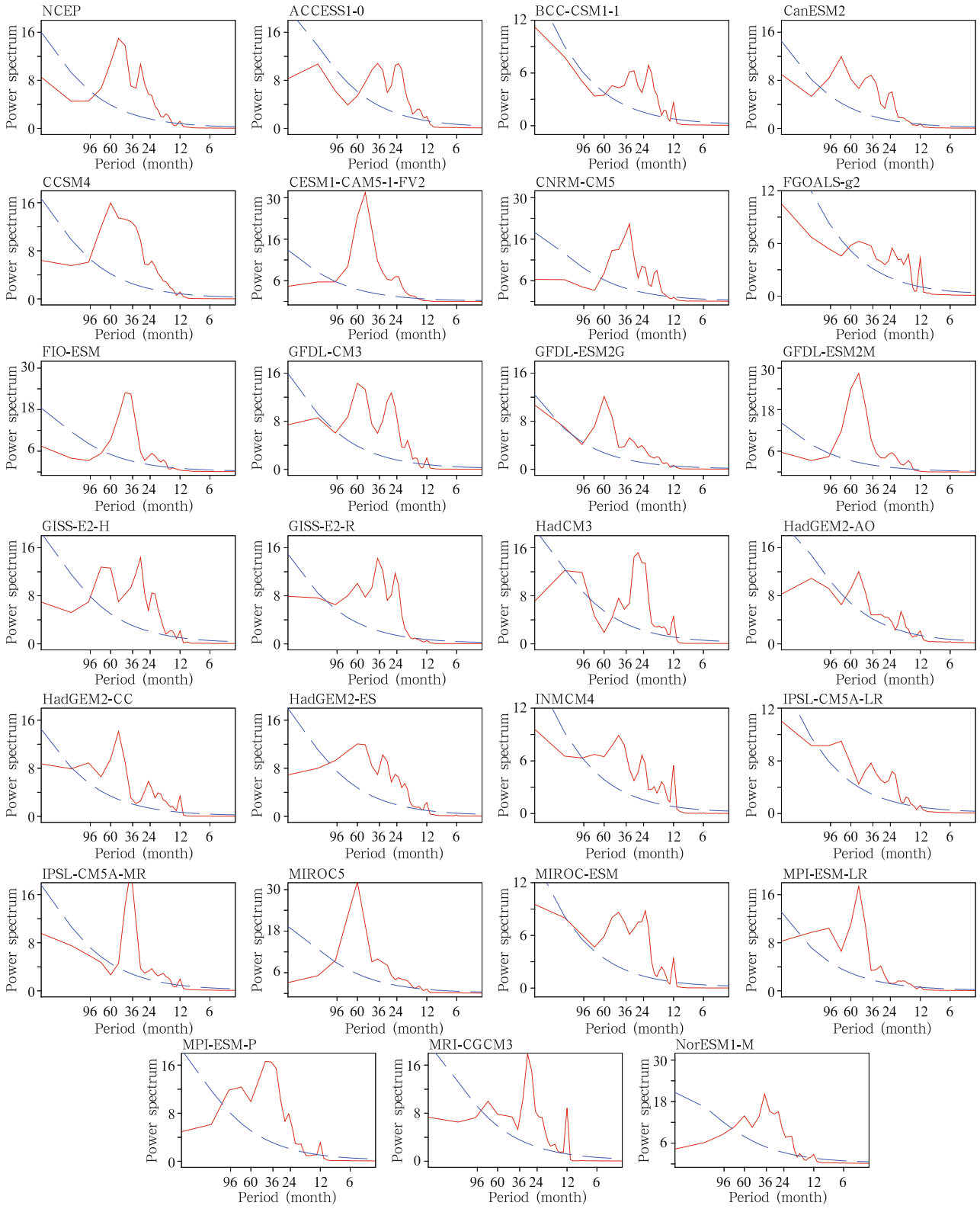


**Fig. 8.** Power spectra (red solid line) of the monthly WPSH intensity index from the observation and CMIP5 model simulations. Blue dashed line indicates the 0.05 significance level of the red noise test.

RCP scenarios, the ensemble mean results of the four models (CNRM-CM5, FGOALS-g2, FIO-ESM, and MIROC-ESM) are selected to project the evolution of WPSH in the future under different RCP scenarios.

## 5. Possible changes of WPSH in different RCP scenarios

To investigate the possible changes of WPSH under three typical RCP scenarios in the 21st century, long-term integration (2006–2099) of H500 and u500 from the four selected models is averaged firstly as the climatological state, and then the anomaly of each model is added to calculate the time series of the WPSH indices; an approach similar to that in Section 2.2. Next, the 9-yr running mean of WPSH indices from 2006 to 2099 under different RCP scenarios from these four models' ensemble mean is used to project the possible changes of WPSH in the future. It is noted that all the simulated area, intensity, and western boundary indices of WPSH display significantly interdecadal variations in the different RCP scenarios (Fig. 9).

Under the RCP2.6 scenario, both the WPSH area and intensity increase and extend westward obviously. After 2050, the linear trends of the WPSH area, intensity, and western boundary indices gradually approach zero. The linear ascending trends of WPSH under the RCP4.5 scenario are similar to those under the RCP2.6, but the period of significant growth lasts until about 2070, and then the growth trends weaken. Similar long-term variations of WPSH show up with faster growth in the period and a relatively smaller trend in the latter period under the RCP8.5 scenario. Interestingly, the western boundary index of WPSH maintains at 90°E since the late 2050s. In fact, the most western boundary of the 5880-gpm contour extends westward to the west of 90°E after the late 2050s. In that case, the definition of the western boundary of WPSH is limited as 90°E (Liu et al., 2012).

Overall, WPSH enlarges, strengthens, and ex-

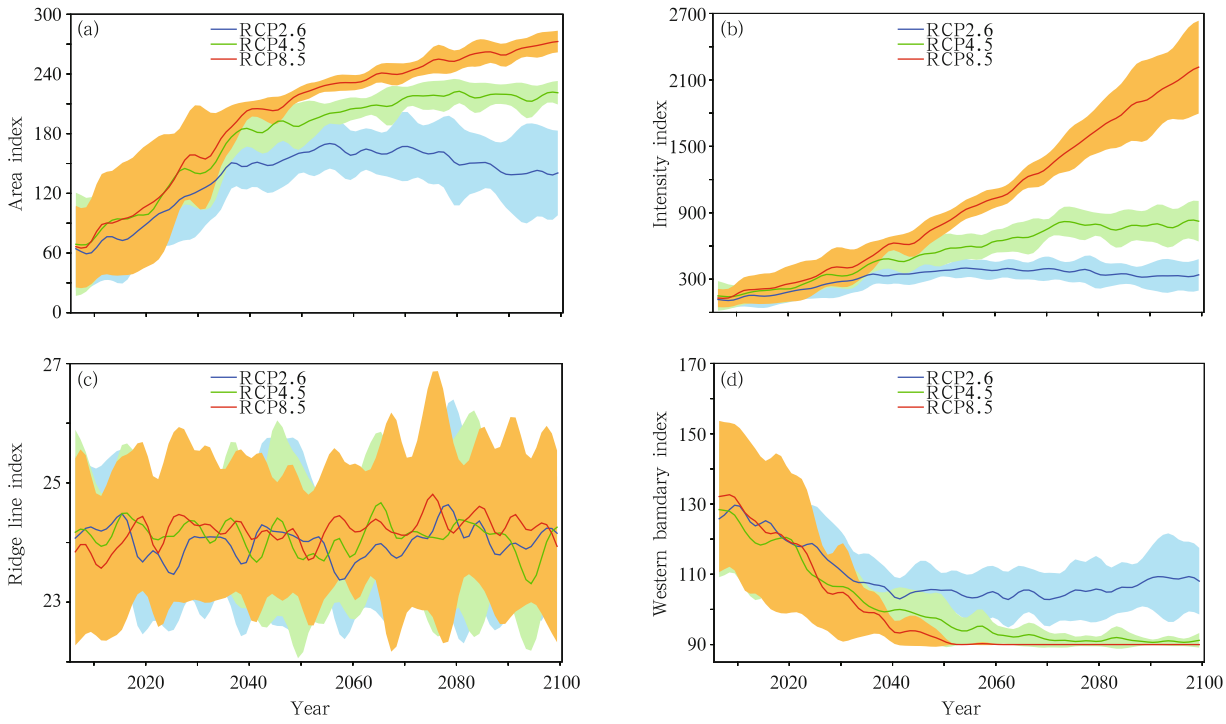


**Fig. 9.** Nine-yr running mean of the WPSH indices in summer from 2006 to 2099 under different RCP scenarios from four CMIP5 models' ensemble mean. (a) Area index, (b) intensity index, (c) ridge line index, and (d) western boundary index. Shaded areas represent one standard deviation from the multi-model mean.

tends westward under different RCP scenarios, with the largest linear growth trend projected in RCP8.5, weakest in RCP2.6, and in between in RCP4.5. The ridge line of WPSH has no obvious long-term trend in the three RCP scenarios. These results have implications for the attribution and projection of climate changes in East Asia in using the CMIP5 model output.

## 6. Summary and discussion

The performances of 26 coupled climate models participating in the Coupled Model Intercomparison Project Phase 5 (CMIP5) in the simulation of the present-day temporal variability and spatial pattern of the WPSH are assessed. Then, the ensemble mean of four selected models is used to project the future possible changes of WPSH under three typical representative concentration pathways (RCPs). The results are as follows.

(1) The intensity of WPSH is underestimated in most CMIP5 model simulations, which may be associated with colder SST biases in the tropical Indian and western Pacific oceans in the models. Nevertheless, spatial distribution and variability of H500 and u500 are reasonably captured. To eliminate the impact of the model climatology biases, the model climatology is replaced with that of NCEP/NCAR reanalysis, which makes the model results more realistic, and without any change in temporal variability.

(2) The climatology-calibrated model results reproduce the observed interdecadal shift of WPSH (enhancement and westward extension after the late 1970s). According to overall assessment of the WPSH indices, it is identified that CNRM-CM5, FGOALS-g2, FIO-ESM, MIROC-ESM, and MPI-ESM-P have better performances than other models in simulating the WPSH.

(3) The selected models' simulations suggest that WPSH will enlarge, strengthen, and extend westward under the three RCP scenarios, with the highest linear growth trend projected in RCP8.5, in between in RCP4.5, and weakest in RCP2.6. The simulated ridge line of WPSH has no obvious long-term trend in the scenarios.

It is easily noticed that the model defaults, such as the systemic biases in the western subtropical regions, may affect the credibility of these projections. Thus, it is necessary to explore the reasons resulting in the biases as well as their connection with the cold biases of the models in the tropical Indian and western Pacific oceans. It is also an interesting topic to examine possible changes of the East Asian summer rain belt under the projection of strengthening and westward extending WPSH associated with the increasing concentration of greenhouse gases in the future. Furthermore, the mechanism for the projected enhancing and westward-extending WPSH under the global warming scenarios is also worthy of further analysis.

***Acknowledgments.*** Many thanks to the support of the National Innovation Team of Climate Prediction of the China Meteorological Administration. Thanks also go to the contribution of the WCRP's Working Group on Coupled Modeling. NCEP/NCAR reanalysis and NOAA ERSSTv3b data are downloaded from NOAA website at http://www.esrl.noaa.gov/psd/.

## REFERENCES

Chang, C. P., and T. Li, 2000: A theory for the tropical tropospheric biennial oscillation. *J. Atmos. Sci.*, **57**, 2209–2224.

——, Y. S. Zhang, and T. Li, 2000: Interannual and interdecadal variations of the East Asian summer monsoon and tropical Pacific SSTs. Part I: Roles of the subtropical ridge. *J. Climate*, **13**, 4310–4325.

Ding, Y. H., 2007: The variability of the Asian summer monsoon. *J. Meteor. Soc. Japan*, **85B**, 21–54.

Feng Juan and Li Jianping, 2012: Evaluation of IPCC AMIP models in simulating monsoon-like southwest Australian circulation. *Climatic and Environ. Res.*, **17**, 409–421. (in Chinese)

Han Jinping and Wang Huijun, 2007: Features of interdecadal changes of the East Asian summer monsoon and similarity and discrepancy in ERA-40 and NCEP/NCAR reanalysis. *Chinese J. Geophys.*, **50**, 1444–1453. (in Chinese)

Hu, Z.-Z., 1997: Interdecadal variability of summer climate over East Asia and its association with 500-hPa height and global sea surface temperature. *J. Geo-*

*phys. Res.*, **102**(D16), 19403–19412.

Huang Gang and Qu Xia, 2009: Meridional location of West Pacific subtropical high in summer in IPCC AR4 simulation. *Trans. Atmos. Sci.*, **32**, 351–359. (in Chinese)

Huang Ronghui and Sun Fengying, 1994: Impacts of the thermal state and the convective activities in the tropical western warm pool on the summer climate anomalies in East Asia. *Chinese J. Atmos. Sci.*, **36**, 673–685. (in Chinese)

——, Cai Rongshuo, Chen Jilong, et al., 2006: Interdecadal variations of drought and flooding disasters in China and their association with the East Asian climate system. *Chinese J. Atmos. Sci.*, **30**, 730–743. (in Chinese)

IPCC, 2007: *Climate Change 2007: The Physical Scientific Basis*. Solomon, S., D. Qin, M. Manning, et al., Eds., Cambridge University Press, Cambridge, United Kingdom and New York, NY, USA, 996 pp.

Kalnay, E., M. Kanamitsu, R. Kistler, et al., 1996: The NCEP/NCAR 40-year reanalysis project. *Bull. Amer. Meteor. Soc.*, **77**, 437–472.

Liu, Y. Y., Y. H. Ding, H. Gao, et al., 2013: Tropospheric biennial oscillation of the western Pacific subtropical high and its relationship with the tropical SST and atmospheric circulation anomalies. *Chinese Sci. Bull.*, **58**, 3664–3672.

Liu Yunyun and Ding Yihui, 2012: Analysis of the leading modes of the Asian-Pacific summer monsoon system. *Chinese J. Atmos. Sci.*, **36**, 673–685. (in Chinese)

——, Li Weijing, Ai Wanxiu, et al., 2012: Reconstruction and application of the monthly western Pacific subtropical high indices. *J. Appl. Meteor. Sci.*, **23**, 414–423. (in Chinese)

Moss, R. H., J. A. Edmonds, K. A. Hibbard, et al., 2010: The next generation of scenarios for climate change research and assessment. *Nature*, **46**, 747–756.

Nitta, T., 1987: Convective activities in the tropical western Pacific and their impact on the Northern Hemisphere summer circulation. *J. Meteor. Soc. Japan*, **65**, 373–390.

——, and Z.-Z. Hu, 1996: Summer climate variability in China and its association with 500-hPa height and tropical convection. *J. Meteor. Soc. Japan*, **74**, 425–445.

Smith, T. M., R. W. Reynolds, T. C. Peterson, et al., 2008: Improvements to NOAA's historical merged land-ocean surface temperature analysis (1880–2006). *J. Climate*, **21**, 2283–2296.

Sun Ying and Ding Yihui, 2008: Validation of IPCC AR4 climate models in simulating interdecadal change of East Asian summer monsoon. *Acta Meteor. Sinica*, **66**, 765–780. (in Chinese)

Tao Shiyan and Wei Jie, 2006: The westward, northward advance of the subtropical high over the West Pacific in summer. *J. Appl. Meteor. Sci.*, **17**, 513–525. (in Chinese)

Taylor, K. E., 2001: Summarizing multiple aspects of model performance in a single diagram. *J. Geophys. Res.*, **106**(D7), 7183–7192.

——, R. J. Stouffer, and G. A. Meehl, 2012: An overview of CMIP5 and the experiment design. *Bull. Amer. Meteor. Soc.*, **93**, 485–498.

Wang, B., Q. H. Ding, X. Fu, et al., 2005: Fundamental challenges in simulation and prediction of summer monsoon rainfall. *Geophys. Res. Lett.*, **32**, L15711. doi: 10.1029/2005GL022734.

Wu Guoxiong, Chou Jifan, Liu Yimin, et al., 2002: *Dynamics of the Formation and Variation of Subtropical Anticyclones*. Science Press, Beijing, 1–20. (in Chinese)

Xin Xiaoge, Wu Tongwen, and Zhang Jie, 2012: Introduction of CMIP5 experiments carried out by climate system model. *Adv. Climate Change Res.*, **8**, 378–382. (in Chinese)

Xiong Anyuan, 2001: Analysis on background of climatic variation for extremely rainy over the middle reaches of the Yangtze River in the 1990s. *J. Appl. Meteor. Sci.*, **12**, 113–117. (in Chinese)

Xu Haiming, He Jinhai, and Zhou Bing, 2001: The features of atmospheric circulation during Meiyu onset and possible mechanisms for westward extension (northward shift) of Pacific subtropical high. *J. Appl. Meteor. Sci.*, **12**, 150–158. (in Chinese)

Zhang Hongfang and Chen Haishan, 2011a: Evaluation of summer circulation simulation over East Asia by 21 climate models. Part I: Climatology. *Scientia Meteor. Sinica*, **31**, 119–128. (in Chinese)

—— and ——, 2011b: Evaluation of summer circulation simulation over East Asia by 21 climate models. Part II: Interannual variability. *Scientia Meteor. Sinica*, **31**, 247–257. (in Chinese)

Zhao, P., Y. N. Zhu, and R. H. Zhang, 2007: An Asian-Pacific teleconnection in summer tropospheric temperature and associated Asian climate variability. *Climate Dyn.*, **29**, 293–303.

Zhu, J. S., and J. Shukla, 2013: The role of air-sea coupling in seasonal prediction of Asian-Pacific summer monsoon rainfall. *J. Climate*, **26**, 5689–5697.

doi:10.11676/qxxb2014.025 气象学报

# CMIP5 模式对西太平洋副热带高压的模拟和预估*

刘芸芸[1] 李维京[1] 左金清[1] 胡增臻[2]
LIU Yunyun[1] LI Weijing[1] ZUO Jinqing[1] HU Zengzhen[2]

1. 国家气候中心 气候研究开放实验室,北京,100081
2. 美国海洋和大气管理局 气候预测中心,大学公园市,20740
1. *Laboratory for Climate Studies, National Climate Center, China Meteorological Administration, Beijing* 100081, *China*
2. *Climate Prediction Center, NOAA, College Park* 20740, *USA*
2013-07-19 收稿,2013-12-16 改回.

刘芸芸,李维京,左金清,胡增臻. 2014. CMIP5 模式对西太平洋副热带高压的模拟和预估. 气象学报,72(2):277-290
**Liu Yunyun, Li Weijing, Zuo Jinqing, Hu Zengzhen. 2014. Simulations and projections of the western Pacific subtropical high in CMIP5 models. *Acta Meteorologica Sinica*, 72(2): 277-290**

**Abstract** This work examined the performance of 26 coupled climate models participating in the Coupled Model Intercomparison Project Phase 5 (CMIP5) in the simulation of the present-day temporal variability and spatial pattern of the western Pacific subtropical high (WPSH). Results show that most models are able to capture the spatial distribution and variability of the 500 hPa geopotential height and zonal wind fields in the western subtropical Pacific, with the underestimation of the mean intensities of WPSH. The underestimation may be associated with the cold bias of sea surface temperature in the tropical Indian and western Pacific Oceans in the models. To eliminate the impact of the climatology biases, the climatology of these models is replaced by that of the NCEP/NCAR reanalysis in the verification. It is noted that at interdecadal time scales, the models reproduce the shift of WPSH with enhancement and westward extension after the late 1970s. According to assessment of the simulations of the WPSH indices, it is found that some models (CNRM-CM5, FGOALS-g2, FIO-ESM, MIROC-ESM and MPI-ESM-P) are better than others in simulating WPSH. Then the ensemble mean of these better models are used to project the future changes of WPSH under three typical Representation Concentration Pathway scenarios (RCP8.5, RCP4.5, RCP2.6). It is suggested that the WPSH enlarges and strengthens, and its position extends westward under the scenarios, with the largest linear growth trend in RCP8.5, smallest in RCP2.6, and in between in RCP4.5; while the ridge line of WPSH does not show obvious long-term trend. These results may have implications for the attribution and prediction of climate variations and changes in East Asia.
**Key words** CMIP5, Western Pacific subtropical high (WPSH), Simulation and projection, RCP scenarios

**摘 要** 利用国际耦合模式比较计划第五阶段(CMIP5)26 个模式的模拟结果,从空间分布和振幅变化、年际周期及年代际趋势等方面,初步评估了 CMIP5 模式对西太平洋副热带高压(副高)的模拟能力。在此基础上,还对未来不同典型浓度路径(RCPs)情景下副高的可能变化给出了定性的预估。CMIP5 模式历史试验结果显示,大多数模式对 500 hPa 位势高度气候平均值的模拟有明显误差,这主要是由于模式对热带印度洋和西太平洋地区海表温度(SST)的模拟普遍较观测值低,从而导致模式对副高的模拟能力有限。但大多数模式对高度场和纬向风场变化的空间形态与振幅都有较强的模拟能力。因此,通过用 NCEP/NCAR 再分析资料的气候平均值替代 CMIP5 模式气候平均值的简单方法,对 CMIP5 模拟结果进行了订正。经订正后的模式结果均有能力刻画副高指数的历史时间序列,且能够反映出 20 世纪 70 年代末期之后,副高面积增大、强度增强和

* 资助课题:国家重点基础研究发展计划(2010CB950501、2013CB430202)、国家自然科学基金项目(41005037)、公益性行业(气象)科研专项(GYHY201306024、GYHY20130633)。
作者简介:刘芸芸,主要从事气候变化和气候预测工作。E-mail:liuyuny@cma.gov.cn

显著西伸的变化趋势。此外,通过对副高指数的长期趋势、年际周期及标准差等的定量评估,注意到 CNRM-CM5、FGOALS-g2、FIO-ESM、MIROC-ESM 和 MPI-ESM-P 这 5 个模式对副高的模拟能力较强。未来气候预估试验中,副高面积和强度均增大,且显著西伸;其线性增长趋势在 RCP8.5 情景下最高,RCP4.5 情景下次之,RCP2.6 情景下最弱。有趣的是副高脊线指数在 3 种排放情景下都没有明显的长期变化趋势。这些结果为选取和利用 CMIP5 模式进行东亚地区气候变化的归因分析和未来预估提供了一定的科学依据。

**关键词** CMIP5,西太平洋副热带高压,模拟和预估,典型浓度路径情景

**中图法分类号** P467

## 1 引 言

西太平洋副热带高压(副高)是影响东亚天气气候最主要的大气环流系统之一,中国的地理位置决定了受副高的影响很大,其位置和面积(强度)的变化对中国汛期降水有重要影响(徐海明等,2001;陶诗言等,2006)。副高西面的偏南风引导海洋上的丰富水汽向中国大陆地区输送,与来自中高纬度地区的冷空气交汇,形成锋面,造成副高西北外围地区出现降水带,而受到副高控制的地区出现高温少雨天气(韩晋平等,2007)。夏季副高的年际变化决定了中国东部旱涝的出现(吴国雄等,2002),而副高等环流因子的年代际变化则为中国旱涝格局的重新分配提供了气候背景(Hu, 1997;熊安元,2001)。最近的研究还发现副高的强度和东西位置表现出的准 2 a 振荡分量在 20 世纪 70 年代末期也表现出显著的年代际转折(Liu, et al, 2013)。副高的年际-年代际变化特征一直是中国气象工作者非常关心的问题,对副高年际-年代际变化的归因、未来情景分析、敏感性试验等将有助于进一步深入认识和理解它对中国汛期降水的影响机理。

对气候变化模拟和预测的主要定量工具就是气候模式,而就目前的水平,模式尚存在很大不确定性,模式本身误差较大,且模式之间的差异也较大。最近的 CMIP 计划(即 CMIP5),已于 2008 年 9 月由世界气候研究计划(WCRP)下的耦合模式工作组(WGCM)组织启动,全球近 30 个模式开发机构参与该计划。CMIP5 模式将为气候变化机理研究和未来预估提供重要的数值模拟数据。相关评估结果则为政府间气候变化专门委员会(IPCC)第 5 次评估报告(AR5)提供重要的科学依据(Taylor, et al, 2012)。与前几个阶段的 CMIP 模式相比,大部分 CMIP5 模式在物理过程、耦合碳循环等方面有明显的改进。那么,这些当今国际上最先进的耦合模式对副高的平均状态和变率的模拟能力如何?还有,在未来不同的气候变暖情景下,副高会有什么样的可能变化呢?为了回答这些问题,本研究基于一套能够客观描述西太副高系统的重建指数(刘芸芸等,2012b),从多方面评估了 26 个 CMIP5 模式对副高的模拟能力,期望通过模式与观测、模式与模式之间的比较,为模式的发展和模式未来的改进提供一些依据;最后通过选取模拟能力较强的模式,对未来情景下副高指数的可能演变进行了预估,从而为东亚夏季风系统和中国夏季降水雨带位置的未来变化趋势提供参考信息。

## 2 模式和资料简介

表 1 给出了参与 CMIP5 试验的 26 个耦合模式的基本信息。本文所采用的数值模拟数据包括:(1)历史试验(Historical),该试验是在工业革命前控制试验的基础上选取初始场,然后对模式进行不少于 156 a(1850 年开始)的积分,强迫场除了观测的温室气体、臭氧、气溶胶和太阳常数外,还首次加入了随时间变化的土地覆盖(Taylor, et al, 2012);(2)21 世纪气候变化预估试验,包含 3 种温室气体和气溶胶等排放的典型浓度路径(Representation Concentrtaion Pathways, RCPs),分别为 RCP2.6/4.5/8.5。每种情景对应一套温室气体、气溶胶和化学活性气体的排放浓度变化,以及土地利用/土壤覆盖的时间路线(Moss, et al, 2010;辛晓歌等,2012)。

此外,本研究用 NCEP/NCAR(National Centers for Environmental Prediction/ National Center for Atmospheric Research)提供的逐月大气再分析资料(Kalnay, et al, 1996)和美国国家海洋大气管理局(NOAA)发布的扩展重建的海表温度资料(ERSSTv3b,Smith, et al, 2008)作为“观测资料”,尽管大气再分析资料并非严格意义上的观测资料。本研究中历史试验和观测资料时段均为 1951—

2005年,预估试验时段为2006—2099年。为了便于模式间的比较,将模式输出结果中的环流场都插值到水平分辨率为2.5°×2.5°的规则网格上,海温场插值到水平分辨率为2°×2°的规则网格上。

本研究所关注的副高是指出现在西北太平洋上的副热带高压系统,500 hPa高空天气图上用(10°—45°N,110°E—180°)范围内的5880 gpm等值线所包围的区域来表示。为了定量描述副高的强度和位置等变化特征,基于NCEP/NCAR再分析资料,计算了逐月的重建副高指数(刘芸芸等,2012b)作为描述副高变化的观测事实,包括面积指数、强度指数、脊线指数和西伸脊点。由于夏季副高的强度及位置变率最大,且对中国东部地区降水的影响最为显著(吴国雄等,2002),所以本研究主要分析夏季(6—8月)副高的空间分布和振幅变化、年代际演变趋势及年际周期等。在对副高指数序列进行功率谱分析时,则是利用了整个研究时段中全年所有月份的数据。

表1 参与CMIP5试验的26个耦合模式主要信息

Table 1 Description of the 26 coupled climate models participating in the CMIP5

| 模式名称 | 所属机构/国家 | 水平分辨率(经度×纬度) |
|---|---|---|
| ACCESS1-0 | CAWCR/Australia | 1.875×1.25 |
| BCC-CSM1-1 | BCC/China | 2.8×2.8 |
| CanESM2 | CCCMA/Canada | 2.8×2.8 |
| CCSM4 | NCAR/USA | 1.25×0.94 |
| CESM1-CAM5-1-FV2 | NSF-DOE-NCAR/USA | 2.5×1.9 |
| CNRM-CM5 | CNRM-CERFACS/France | 1.4×1.4 |
| FGOALS-g2 | LASG-CESS/China | 2.8×2.8 |
| FIO-ESM | FIO/China | 2.8×2.8 |
| GFDL-CM3 | NOAA GFDL/USA | 2.5×2.0 |
| GFDL-ESM2G | NOAA GFDL/USA | 2.5×2.0 |
| GFDL-ESM2M | NOAA GFDL/USA | 2.5×2.0 |
| GISS-E2-H | NASA GISS/USA | 2.5×2.0 |
| GISS-E2-R | NASA GISS/USA | 2.5×2.0 |
| HadCM3 | MOHC/UK | 3.75×2.5 |
| HadGEM2-AO | NIMR/Korea | 1.875×1.25 |
| HadGEM2-CC | MOHC/UK | 1.875×1.25 |
| HadGEM2-ES | MOHC/UK | 1.875×1.25 |
| INMCM4 | INM/Russia | 2.0×1.5 |
| IPSL-CM5A-LR | IPSL/France | 3.75×1.875 |
| IPSL-CM5A-MR | IPSL/France | 2.5×1.25 |
| MIROC5 | MIROC/Japan | 1.4×1.4 |
| MIROC-ESM | MIROC/Japan | 2.8×2.8 |
| MPI-ESM-LR | MPI-M/Germany | 1.9×1.9 |
| MPI-ESM-P | MPI-M/Germany | 1.9×1.9 |
| MRI-CGCM3 | MRI/Japan | 1.1×1.1 |
| NorESM1-M | NCC/Norway | 2.5×1.875 |

泰勒图方法(Taylor,2001)能够将多模式的相关信息集中表示。其中,模式模拟值与观测值的相关系数可表示模式对所关注区域的气候变率的模拟能力,均方根误差表示模拟相对于观测值的偏差(均方根误差越接近0,表示模拟能力越高),模拟与观测序列的标准差之比则表示模式对变率振幅的模拟能力。将这3个评估指标显示在一张图中可以较全面地反映多个模式的模拟能力。本文选用泰勒图方法对模式结果进行评估,其中观测资料的自相关和标准差均为1,均方根误差为0。

## 3 模式对500 hPa环流场和海温场的模拟及订正

### 3.1 空间分布

在定量描述副高强度和位置等变化特征的重建副高指数中,面积指数、强度指数和西伸脊点都与

500 hPa 位势高度场的 5880 gpm 等值线密切相关，而脊线指数则由 500 hPa 等压面上 $u=0$ 等值线的纬度位置所决定(刘芸芸等,2012a)。因此,首先关注 CMIP5 模式对 500 hPa 高度场和纬向风场的模拟能力。结果显示,26 个 CMIP5 模式模拟的副高空间分布及其范围和强度均与观测资料有较大差别(图 1)。CCSM4、CESM1-CAM5 和 FIO-ESM 这 3 个模式的 500 hPa 位势高度值偏强,5880 gpm 所包围的面积比观测值大,其中以 CCSM4 最为明显。而其他模式的 500 hPa 位势高度值则较观测资料明显偏弱,在副高最强的夏季,西太平洋上空均没有 5880 gpm 等值线。其中 HadGEM2-CC 和 IPSL-CM5A-LR 模拟的 500 hPa 高度场上甚至没有 5840 gpm 等值线。另外,CMIP5 模式对 500 hPa 等压面上 $u=0$,且 $\partial u/\partial y\geqslant 0$ 的纬向风切变线的模拟也不十分成功(图略)。仅有在 500 hPa 高度场上能够模拟出 5880 gpm 等值线的 3 个模式,对纬向风切变线位置的模拟与 NCEP/NCAR 较为接近;而其他模式的脊线位置则多为偏南。不少 CMIP5 模式对副高南侧的东风带强度模拟偏弱,从而导致纬向风 $u=0$ 的等值线不能西伸至 110°E 附近,与观测值相差较大。

目前全球海-气耦合模式对整个大气环流的模拟均存在不同程度的系统性误差(亦称模式的气候漂移)(孙颖等,2008;黄刚等,2009;冯娟等,2012)。大多数模式对东亚地区夏季大气环流系统模拟整体偏弱(张宏芳等,2011a,2011b),而少数模式具有系统性偏强的特点。对于副高来说,其强度与空间分布受下垫面热力异常影响较大,特别是与 ENSO 相联系的热带太平洋和印度洋的海表温度(SST)异常(Nitta, 1987; 黄荣辉等,1994; 吴国雄等,2002)。因此,图 2 给出了对应的多年平均的夏季热带海温的空间分布及模式与观测的差值。观测资料显示,夏季热带印度洋和西太平洋暖池区 SST 均在 28℃以上,暖性的下垫面,使得 500 hPa 副高系统得以维持(图 2)。与观测资料相比,大多数模式模拟的海表温度 28℃等温线所包围的范围较观测小,对西北太平洋和印度洋地区的 SST 模拟显著偏低,对应的 500 hPa 位势高度值则较观测资料明显偏弱,西太平洋上空均没有 5880 gpm 等值线;相反的,对 500 hPa 位势高度值模拟偏强的 CCSM4、CESM1-CAM5 和 FIO-ESM 模式,其模拟的赤道印度洋或太平洋地区 SST 则相对较高。可见,模式是否能够准确刻画热带海温的空间分布将直接影响其对副热带高压系统的模拟能力。

### 3.2 对 500 hPa 高度场和风场的订正

西太平洋地区夏季平均的 500 hPa 高度场与观测值的泰勒图显示(图 3a),26 个 CMIP5 模式对该地区 500 hPa 高度场空间形态的模拟结果与观测结果均非常相似,其空间相关系数均在 0.96 以上,有 5 个模式的相关系数达到 0.99。而均方根误差也都在 1 gpm 以内。各模式的相关系数较高,而均方根误差相对较小,说明模式对西太平洋地区 500 hPa 高度场整体形态的模拟能力较好。模式的标准差范围在 0.6—1.6 gpm,表明模式模拟的位势高度值的空间振幅与观测资料的较为接近。图 3b 为夏季平均的 500 hPa 纬向风与观测值的泰勒图,其相关系数均在 0.90 以上,均方根误差也都在 0.5 m/s 以内,而标准差范围在 0.5—1.5 m/s,表明模式对西太平洋副热带地区 500 hPa 纬向风的空间形态和空间振幅也与观测较为接近,具备较强的模拟能力。

以上分析表明,尽管由于 CMIP5 模式对热带印度洋和西北太平洋海温模拟偏低,导致其对500 hPa 位势高度气候平均值的模拟有明显误差,但模式对高度场和纬向风场变化的空间形态与振幅都有较强的模拟能力。为了让不同模式的输出结果能够更好地反映出西太平洋上空的副高系统,将所有模式输出的 500 hPa 位势高度和纬向风的气候平均值替换成观测资料的气候平均值,即将所有的模式输出结果校正到同一个气候态上,然后叠加上各模式自身的位势高度及纬向风的距平值,这样对原始数据的处理既不改变模式结果的时间变率,又能够让模式结果优势得以更充分利用。对于某一模式的 500 hPa 位势高度值(纬向风类似),其处理办法为

$$h'_{\text{model}}=(h_{\text{model}}-\overline{h}_{\text{model}})+\overline{h}_{\text{NCEP}}$$

式中,$h'_{model}$ 为经气候态订正后的分析结果,$h_{\text{model}}$ 表示模式中 500 hPa 等压面上某一个格点上某一年的夏季位势高度值,$\overline{h}_{\text{model}}$ 表示该模式该格点 1951—2005 年多年平均的夏季位势高度值,$\overline{h}_{\text{NCEP}}$ 表示观测资料的 500 hPa 等压面上该格点 1951—2005 年多年平均的夏季位势高度值。以下对副高的模式评估均是基于经气候态订正后的分析结果。

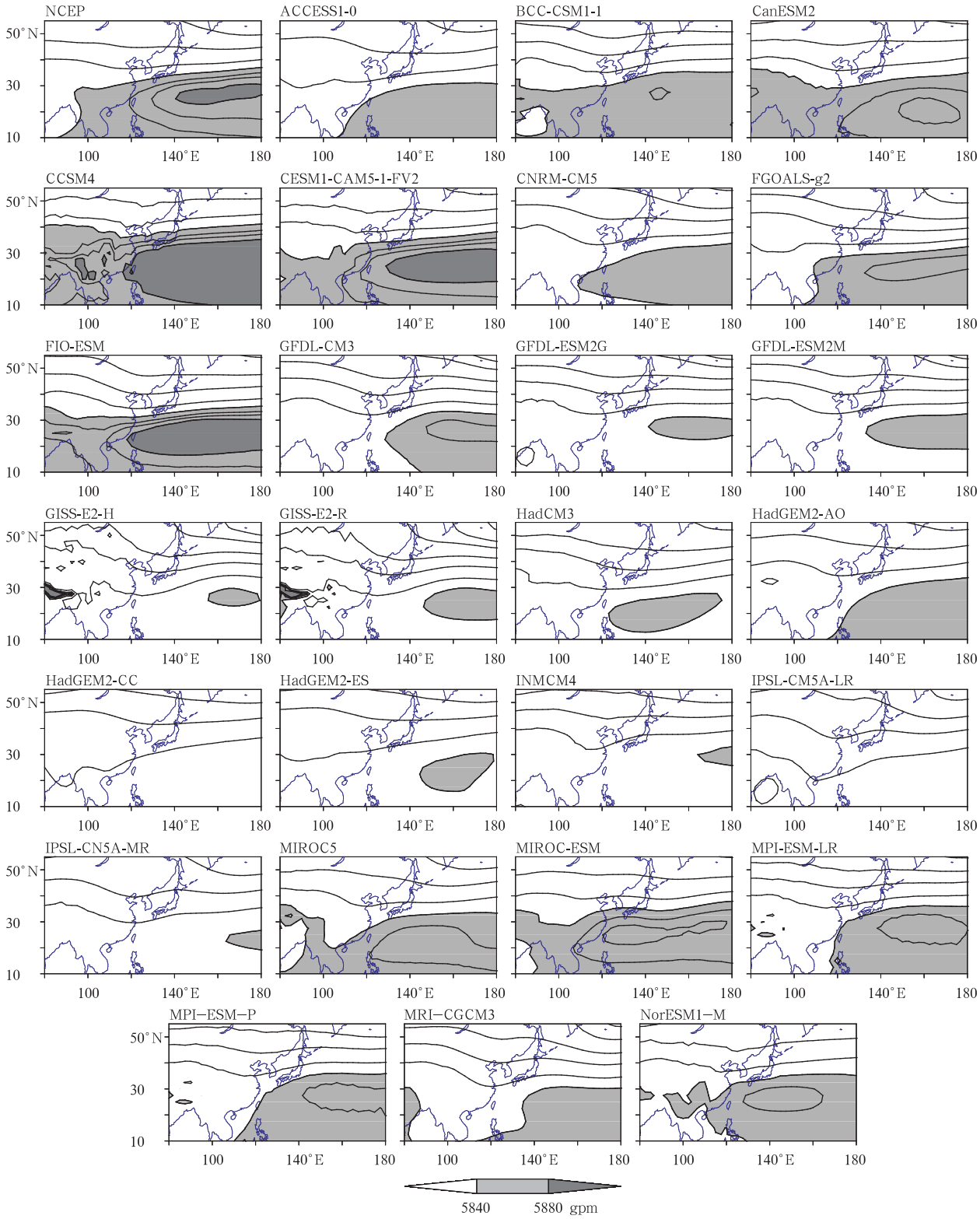


图 1 1951—2005 年多年平均的观测(NCEP/NCAR 再分析资料)和 CMIP5 模式中夏季 500 hPa 位势高度场的空间分布

(浅色阴影和深色阴影分别代表大于 5840 gpm 和 5880 gpm 等值线的区域,图上边为模式名称)

Fig. 1 Climatological mean of 500 hPa geopotential height in Summer from the CMIP5 model simulations and the observation (the NCEP/NCAR reanalysis)

(light and dark shaded areas indicate the geopetential height larger than 5840 and 5880 gpm, respectively)

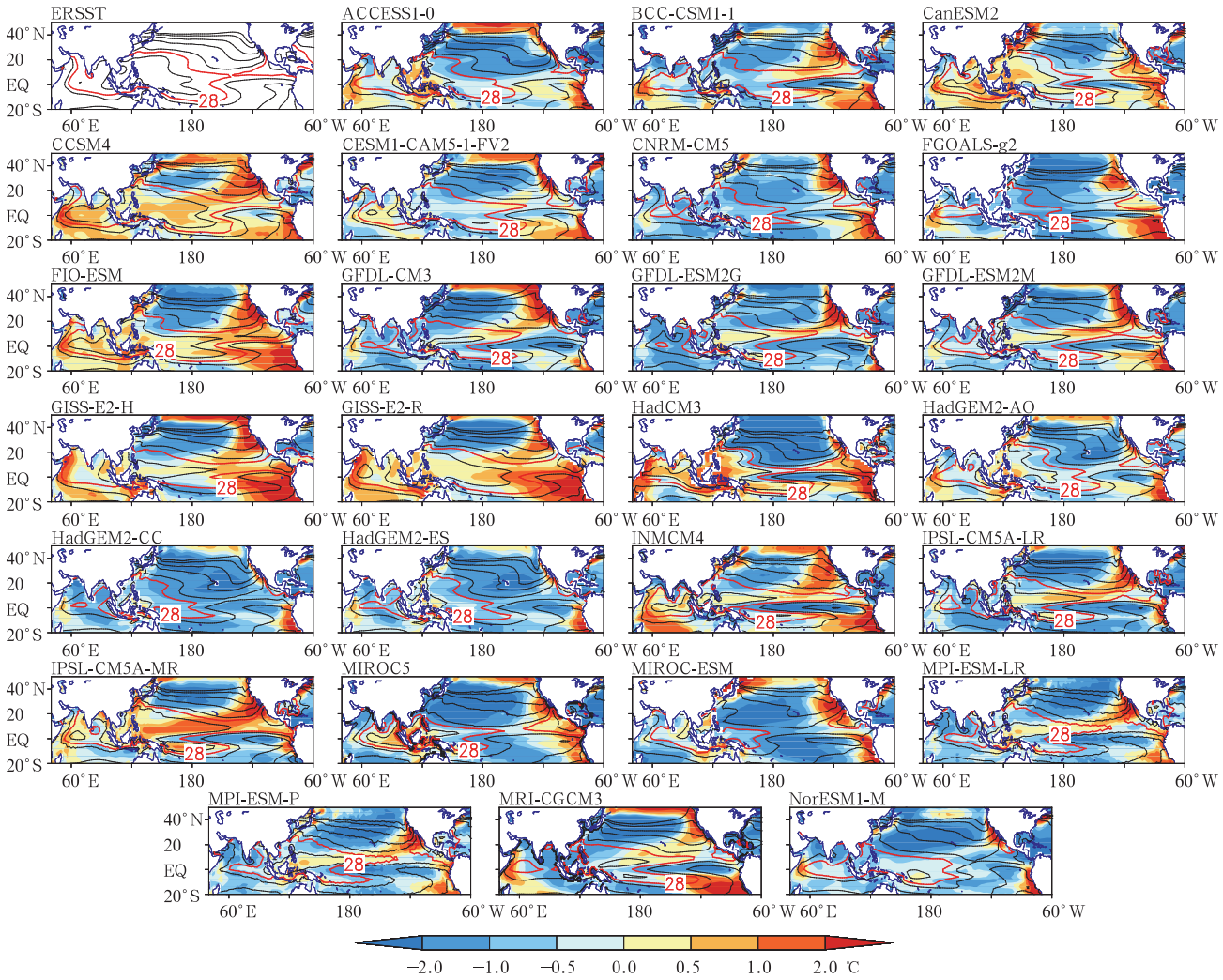


图 2 1951—2005 年多年平均的观测(ERSSTv3b)和 CMIP5 模式模拟的夏季 SST 空间分布
(等值线,单位:℃)及模式与观测的差值(阴影)(图上边为模式名)

Fig. 2 Climatological mean of SST in Summer from the CMIP5 model simulations and the observation (ERSSTv3b, contours, ℃), with the model biases (shading)

## 4 模式对副高气候特征的模拟

### 4.1 夏季副高指数历史序列

副高指数可以客观地表征其强度和位置异常变化特征,图 4 给出了 9 a 滑动平均的夏季副高面积指数、强度指数、脊线指数和西伸脊点指数序列。观测资料得到的副高指数显示,20 世纪 70 年代后期副高的面积和强度指数明显增大,而西伸脊点指数则在 20 世纪 70 年代后期呈现下降趋势,表明副高在 20 世纪 70 年代末之后明显增强西伸,副高的这种年代际转折特征与已有的研究结果一致(Hu, 1997;黄荣辉等,2006;Zhao, et al, 2007;刘芸芸等, 2012a)。而副高脊线指数在 1951—2005 年没有明显的变化趋势。与观测结果相比,经订正后的 CMIP5 模式结果基本都能够反映出 20 世纪 70 年代末期之后,副高面积和强度增强、西伸脊点偏西的变化趋势;从 26 个模式集合平均的结果也能看出副高的年代际转折特征。在这些历史试验中,模式考虑了观测的温室气体、臭氧、气溶胶和太阳常数,以及土地覆盖随时间的变化(Taylor, et al, 2012),模式较好地模拟出了副高的年代际变化。这意味着这些外强迫因子可能是导致副高发生年代际变化的原因之一,尽管海-气相互作用对西北太平洋的气候年际变率至关重要(Wang, et al, 2005; Zhu, et al, 2013)。

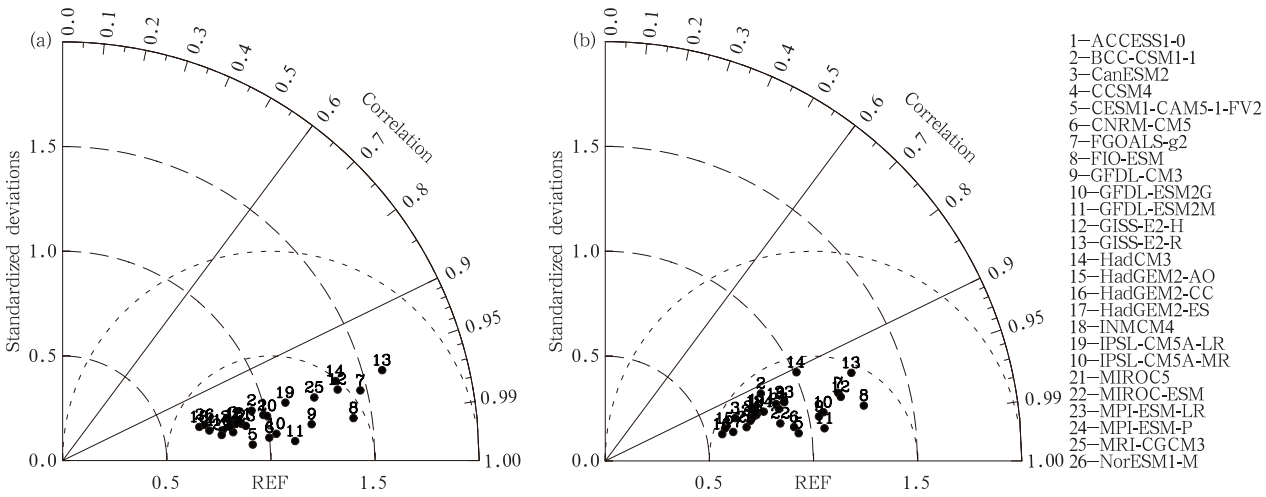


图 3 CMIP5 模式的西太平洋副热带地区夏季平均 500 hPa 高度场(a)和纬向风场(b)与观测资料的泰勒图

(图中 REF 参考点代表观测资料,各模式到原点的半径代表其相对于观测值的标准差,模式在图中方位角的余弦代表模式场与观测值的相关系数,模式到参考点的距离代表其均方根误差)

Fig. 3 Taylor diagrams of the simulated climatological 500 hPa geopotential height (a) and zonal wind (b) over the western Pacific in Summer compared to the observation

(REF indicates the reference value of 1. The radial distance of the model code point from the origin is the standardized deviation ratio of the models relative to observation. The correlation coefficient of spatial pattern between the model outputs and the observation is shown by the cosine of the azimuthal angle of model code point, and their root mean square error is given by the distance of model code point from the REF)

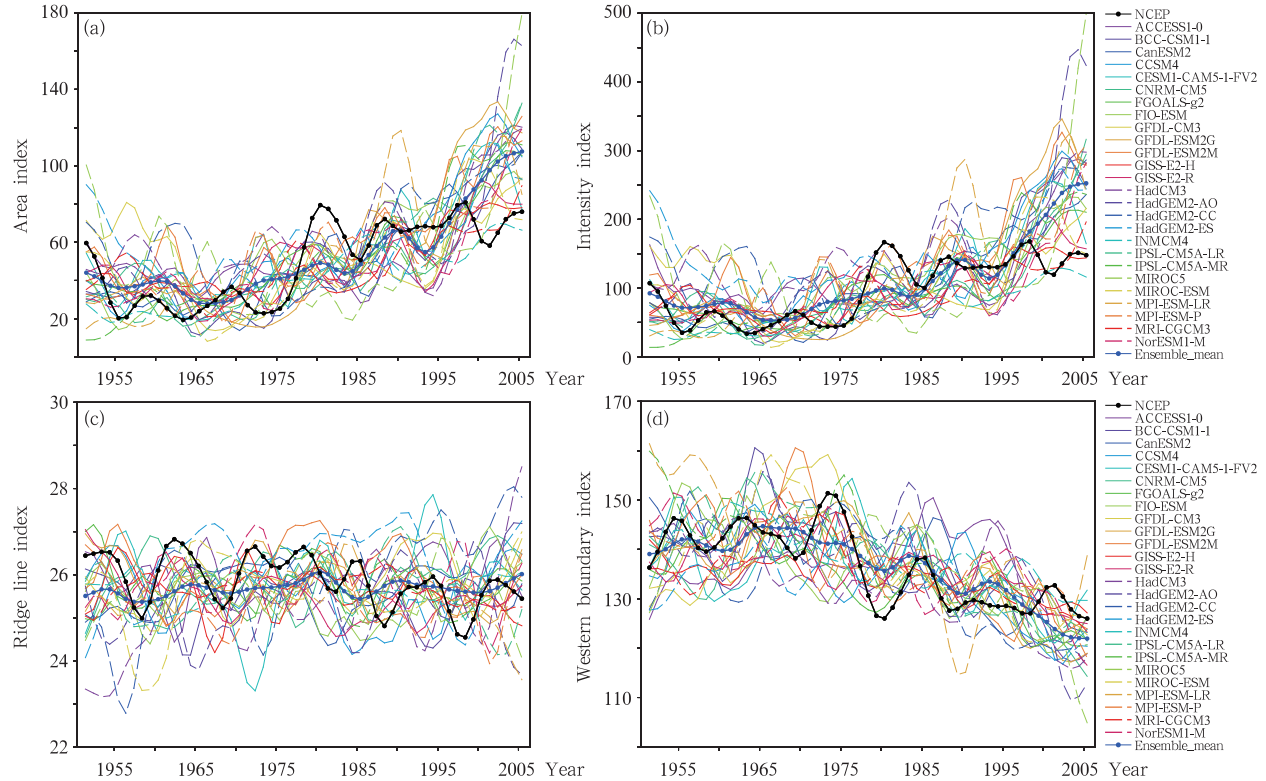


图 4 1951—2005 年观测(黑粗线)和 CMIP5 模式(彩色细线)的经 9 a 滑动平均的夏季副高指数

(a. 面积指数, b. 强度指数, c. 脊线指数, d. 西伸脊点;蓝粗线为 26 个模式平均结果)

Fig. 4 Time series of the WPSH indices in Summer from the calibrated model simulations (thin colored lines) and the observation (thick black line) for the period from 1951 to 2005

(a. area index, b. intensity index, c. ridge line index, d. western boundary index; the thick blue line is for the 26 models ensemble mean)

### 4.2 副高空间形态的年代际变化

为了更直观地显示副高在空间形态上所呈现的年代际转折特征，对 1951—1960 年和 1996—2005 年这两个典型时段中 5880 gpm 和 $u=0$ 等值线的空间分布进行了对比分析(图 5)。1951—1960 年，副高处于偏弱偏东的年代际背景下，观测的 5880 gpm 等值线位于 20°—30°N，且西伸不超过 140°E(图 5a)；对应的副高脊线在 25°N 附近呈现东北—西南走向(图 5c)。经订正的 CMIP5 模式结果已较图 1 有了明显的改善，能够模拟出副高(5880 gpm 等值线)的大致范围，但在副高相对偏弱的这段时期，仍然还有 10 个模式的 500 hPa 位势高度值偏弱到不能模拟出 5880 gpm 等值线；副高脊线的模拟与观测值较为接近，在靠近中国沿海附近(115°E)各模式的差异稍大，这可能会对中国南方降水异常区域的模拟产生一定影响。

1996—2005 年，副高则处于偏强偏西的背景下，观测的 5880 gpm 等值线所围成的范围显著增大，南北边界扩至 18°—32°N，且西伸至 135°E(图 5b)；而对应的副高脊线仍然位于 25°N 附近，与 1951—1960 年相比没有明显的南北偏移(图 5d)。经订正后的 CMIP5 模式的模拟结果在空间分布上也较好地反映了副高的年代际变化特征，较 1951—1960 年副高面积明显增大，其强度也相应增强。大部分模式模拟结果都与观测值较为接近，或者略偏大偏西，最西可达 125°E 附近。该时段副高脊线的模拟依然与观测资料较为接近，仅是在 115°E 附近各模式的差异稍大一些。可见，尽管 CMIP5 模式对副高本身的空间分布有一些偏差，但基本都能在空间上较好地抓住副高在年代际时间尺度上增大西伸的变化特征。

### 4.3 夏季副高指数的线性趋势特征

为了定量评估 CMIP5 模式对副高指数的模拟能力，还进一步计算了各个模式的副高指数线性趋势系数(图 6)。由于副高脊线的线性趋势不显著，这里暂不考虑。观测结果显示，1951—2005 年，副高面积和强度的线性增长趋势均超过 20%/(10 a)，而西伸脊点的西伸趋势达到 2.7%/(10 a)，其线性趋势系数均通过 0.01 的显著性水平。与观测资料相比，所有的模式都能够模拟出副高在1951—2005年

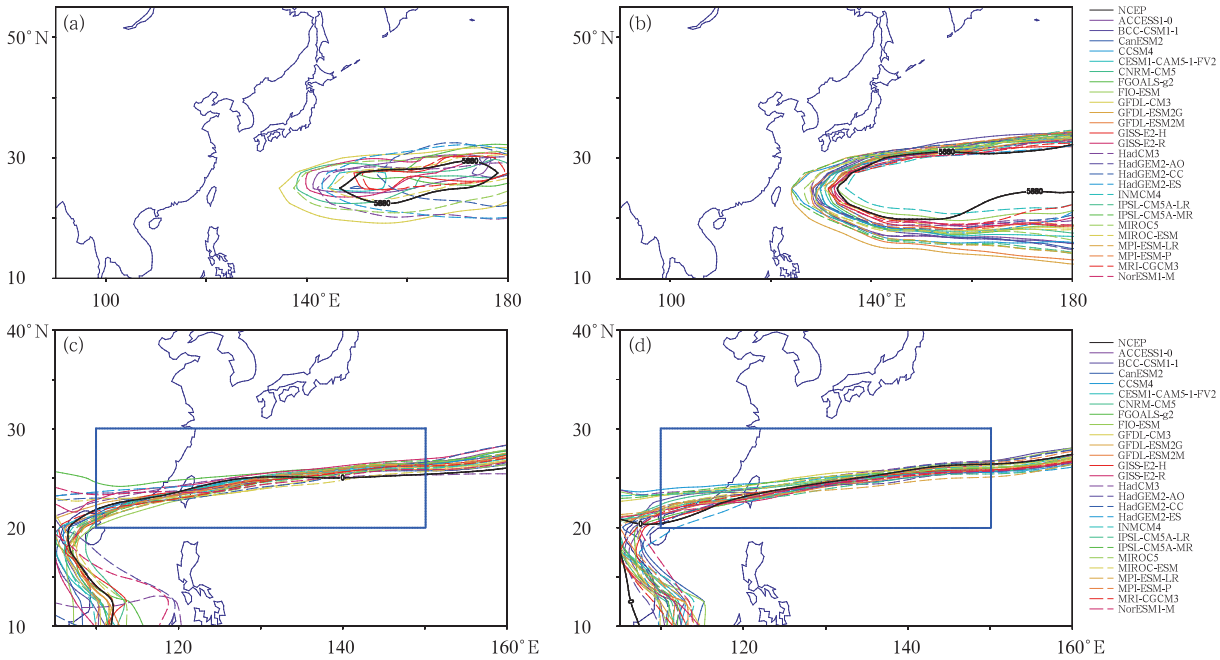


图 5 观测(粗黑线)和 CMIP5 模式(彩色细线)中经校正后的 5880 gpm 等值线(a、b)和 $u=0$ 等值线(c、d)的分布

(a、c. 1951—1960 年；b、d. 1996—2005 年)

Fig. 5 Distributions of the 5880 gpm isoline (a, b) and the $u=0$ isoline (c, d) from the calibrated model simulations (thin colored lines) and the observation (thick black lines) (a, c. the period of 1951—1960; b, d. the period of 1996—2005)

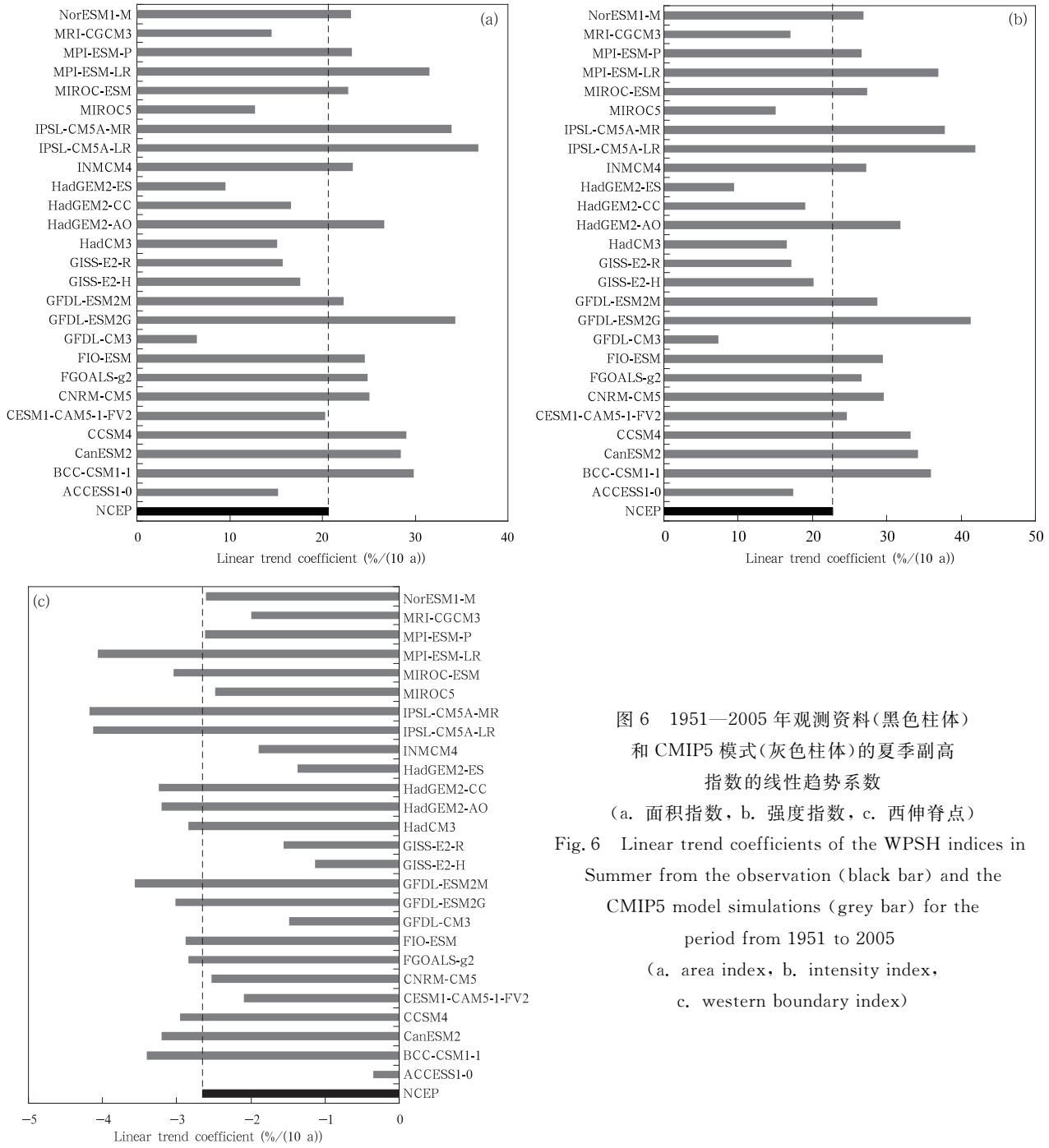


图 6 1951—2005 年观测资料(黑色柱体)和 CMIP5 模式(灰色柱体)的夏季副高指数的线性趋势系数

(a. 面积指数, b. 强度指数, c. 西伸脊点)

Fig. 6 Linear trend coefficients of the WPSH indices in Summer from the observation (black bar) and the CMIP5 model simulations (grey bar) for the period from 1951 to 2005

(a. area index, b. intensity index, c. western boundary index)

表现出增大增强且西伸的变化趋势,但各模式模拟的指数趋势系数差异较大,有的模式模拟的副高强度增强趋势过于显著,如 IPSL-CM5A-LR 和 GFDL-ESM2G;有的则增强趋势明显不足,如 GFDL-CM3 和 HadGEM2-ES。综合 3 个指数线性趋势系数与观测结果的接近程度,其中,CESM1-CAM5-1-FV2、CNRM-CM5、FGOALS-g2、FIO-ESM、HadCM3、HadGEM2-CC、MIROC-ESM、MPI-ESM-P、NorESM1-M 这 9 个模式模拟的副高线性趋势系数与 NCEP/NCAR 最为接近。

### 4.4 夏季副高指数的标准差

副高指数的标准差能够衡量模式对副高指数逐年变化振幅的模拟能力。图 7 中折线是 CMIP5 模式计算得到的副高指数标准差与观测的副高指数标

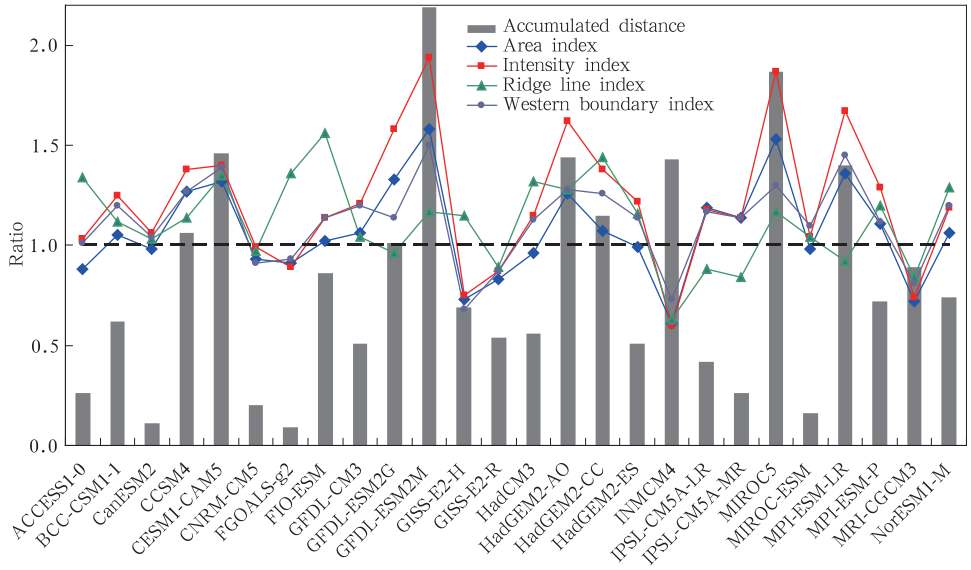


图 7 CMIP5 模式副高指数标准差与观测结果的比值

(灰色柱状值表示 4 个副高指数的标准差比值与标准值 1 的距离之和,距离越小,表示与观测越接近)

Fig. 7 Standard deviation ratios of the simulated WPSH indices relative to the observation

(the gray bars are the accumulated distance of the standard deviation ratio of the four WPSH indices from the reference value of 1. Smaller the distance is, closer to the observation the simulated result is)

准差的比值,比值越接近 1,表示模式模拟指数的逐年变化振幅与观测结果越接近。图中灰色柱状表示副高 4 个指数标准差比值与标准值 1 的距离之和,该值越小,则表示副高的 4 个指数与观测结果越接近。由图 7 可知,大多数经订正后的模式副高指数标准差与观测结果的比值均大于 1,表明模式指数的逐年变化振幅比观测结果大,其中 GFDL-ESM2M 和 MIROC5 模拟的副高指数变幅最大,而 INMCM4 模式模拟结果变幅最小,表明其对副高的模拟能力相对较差。综合考虑模式对副高 4 个指数标准差的模拟情况,ACCESS1-0、CanESM2、CNRM-CM5、FGOALS-g2、IPSL-CM5A-MR、MIROC-ESM 这 6 个模式模拟结果与观测最为接近。

### 4.5 副高的年际周期

模式对年际周期的模拟也是评估模式能否真实反映气候特征的一个重要评估指标。图 8 为观测资料和 CMIP5 模式的逐月副高强度指数在整个分析时段的功率谱。由于副高的季节变率较强,远比其他周期的变化显著。因此,为了突出年际尺度信号,首先利用低通滤波器滤掉了季节变化(11 个月以下的周期变化),再对滤波后的序列做功率谱分析,最大落后长度为 150 个月(序列长度为 660 个月)。

东亚季风区在年际尺度上存在显著的准 2 a 振荡周期,作为东亚季风系统中一个重要组成成员,副高的准 2 a 振荡周期是年际时间尺度上的一个重要分量(Liu, et al, 2013)。观测结果显示,副高存在明显的准 4 a(36—60 个月)和准 2 a(24—36 个月)这两个年际尺度的周期,且均通过 0.05 显著性水平的红噪声检验;其中副高的准 2 a 周期分量与东亚及中国夏季季风降水准 2 a 振荡的年际周期(Chang, et al, 2000a, 2000b; Ding, 2007)一致。CMIP5 模式结果对副高年际周期的模拟能力差异较大,仅有 ACCESS1-0、GFDL-CM3、HadGEM2-CC 和 HadGEM2-ES 模式能够同时抓住准 4 a 和准 2 a 这两个年际周期,其余大部分模式则只能抓住其中一个年际周期,有的夸大了准 4 a 周期,或仅有准 2 a 周期,还有的模式结果中存在 5—8 a 的周期峰值。

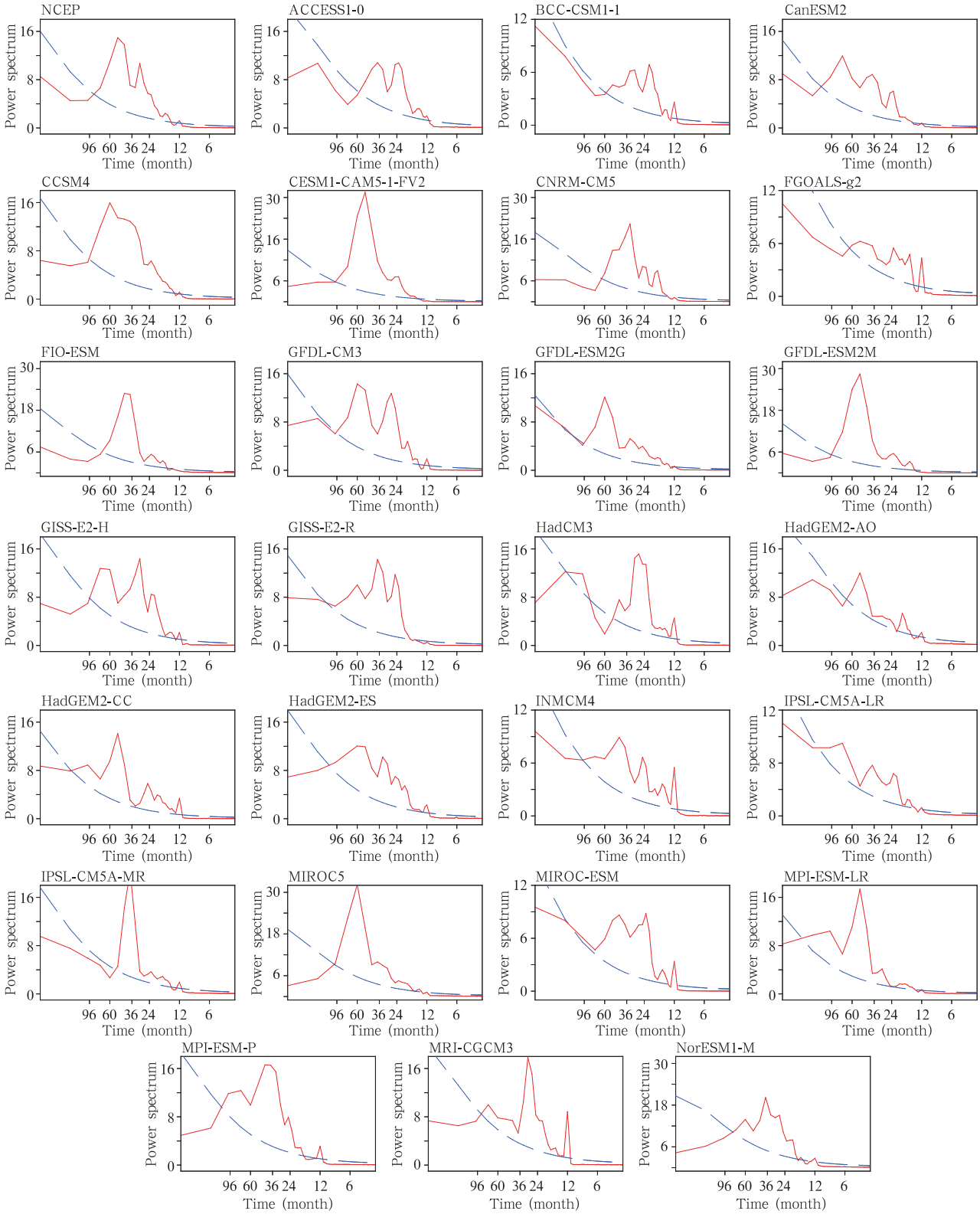


图 8　观测资料和 CMIP5 模式中经校正后的副高强度指数序列的功率谱(实线),虚线为 0.05 显著性水平对应的红噪声检验

Fig. 8　Power spectrum (solid line) for the monthly WPSH intensity index from the the Observation and the CMIP5 model simulations

(The dashed line indicates that it is significant at the 0.95 confidence level of red noise test)

综合前面 26 个 CMIP5 模式历史试验的模拟结果对副高空间分布、年际周期、年代际尺度特征等方面的对比分析,可以看到大多数模式对 500 hPa 位势高度场模拟偏弱,经订正后也几乎没有一个模式能够较为全面地表现出副高的时空特征,多数模式仅仅只能抓住副高的某些特征。综合 26 个 CMIP5 模式对海温、500 hPa 高度场和风场的空间形态以及副高指数的多项指标模拟能力,发现 CNRM-CM5、FGOALS-g2、FIO-ESM、MIROC-ESM 和 MPI-ESM-P 对副高的综合模拟结果表现较好。为了在一定程度上减少未来情景预估的不确定性,下面就选取以上模式的集合平均结果预估 21 世纪副高的演变趋势。遗憾的是,MPI-ESM-P 模式暂时没有提供未来情景模拟试验的结果,因此,只能利用其他 4 个对副高模拟能力较强的模式进行集合平均。

## 5 未来情景下副高的可能变化趋势

为了考察 3 种典型浓度路径下 21 世纪副高的可能变化趋势,本研究利用与 2.2 节类似的方法,以 4 个模式的多年平均值作为标准值,然后将各模式自身的距平值加上校准值得到的各模式副高指数的时间序列,经 9 a 滑动平均后的集合平均来表征未来变化,预估其年代际变化趋势(图 9)。由图可以看到,在不同典型浓度路径情景下,副高面积、强度和西伸脊点都呈现出显著的年代际变化特征。

在 RCP2.6 情景下,副高先随着辐射强迫的稳定增长到 3 W/m$^2$ 而面积增大、强度增强,且显著西伸。到 2050 年后,由于辐射强迫逐渐减至 2.6 W/m$^2$,副高面积、强度和西伸脊点的线性趋势系数也逐渐趋于 0。在 RCP4.5 情景下副高的长期变化趋势与 RCP2.6 类似,只是显著增长的时段一直持续至 2070 年前后,此后增长趋势减小。RCP8.5 情景下,副高面积指数和西伸脊点同样呈现出前期增长迅速,后期增长减缓的特征。西伸脊点在 21 世纪 50 年代后期就一直维持在 90°E,这表明副高(5880 gpm 等值线)已经西伸超过 90°E,甚至在副热带地区成带状,在这种情况下,西伸脊点就规定

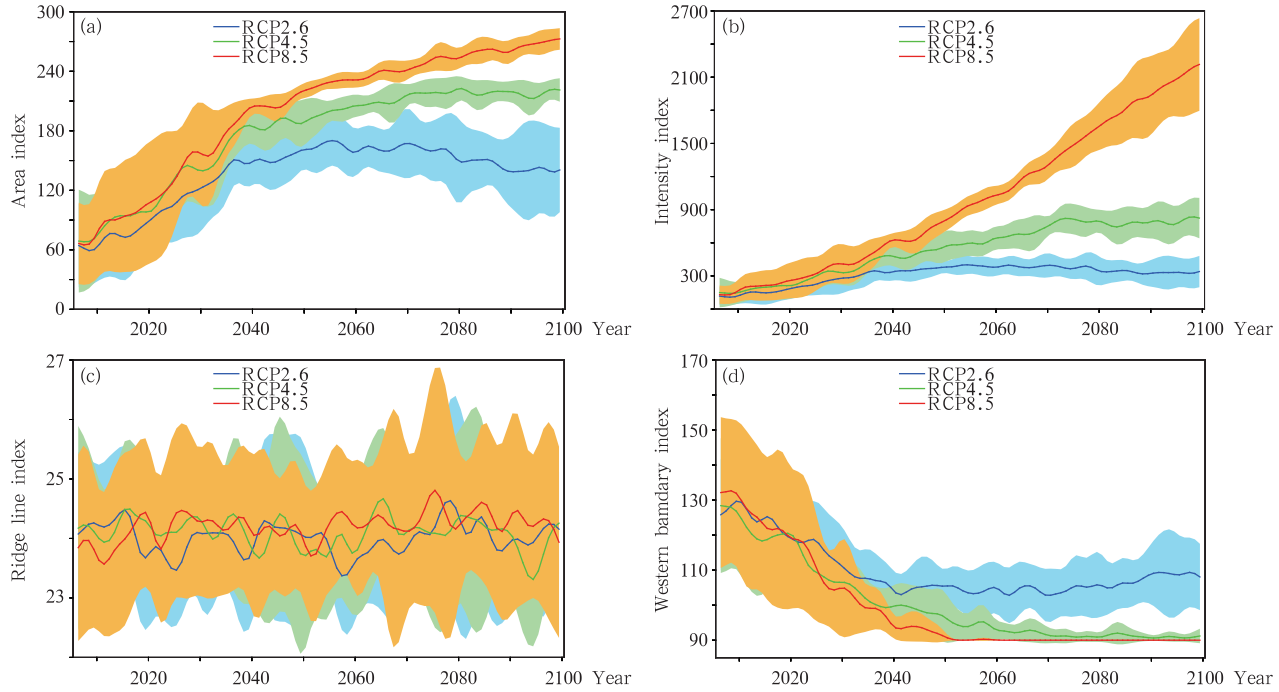


图 9 3 种不同排放情景下 4 个 CMIP5 模式集合平均预估的 2006—2099 年夏季副高指数的 9 a 滑动平均演变

(a. 面积指数, b, 强度指数, c. 脊线指数, d. 西伸脊点; 阴影为模式间平均的 1 个标准差范围)

Fig. 9 9-year running mean of the WPSH indices in Summer from 2006 to 2099 under different RCP scenarios from the four CMIP5 models ensemble mean

(a. area index, b. intensity index, c. ridge line index, d. western boundary index; shaded areas represent one standard deviation from the multi-model mean)

为 90°E(刘芸芸等,2012a);而副高强度指数则在 2006—2099 年一直维持显著增长的趋势。

总体来说,未来随着温室气体浓度的升高,副高面积和强度均增大,且显著西伸;其线性增长趋势在 RCP8.5 情景下最高,RCP4.5 情景下次之,RCP2.6 情景下最弱。副高脊线指数在 3 种排放情景下都没有明显的长期变化趋势。这些结果为选取和利用 CMIP5 模式进行东亚地区气候变化的归因分析和未来预估提供了一定的参考依据。

## 6 结论和讨论

利用国际耦合模式比较计划第 5 阶段(CMIP5) 26 个模式的模拟结果,从空间分布和变化振幅、年际周期及年代际趋势等方面评估了 CMIP5 模式对副高的模拟能力。在此基础上,还对未来不同典型浓度路径情景下副高的可能变化趋势给出了定性的预估。结果发现:

(1) CMIP5 模式历史试验结果显示,大多数模式对 500 hPa 位势高度气候平均值的模拟偏弱,这主要是由于模式对热带印度洋和西太平洋地区海表温度的模拟普遍较观测值低造成的。但模式对高度场和纬向风场的空间形态和振幅有较强的模拟能力,因而利用 NCEP/NCAR 再分析资料的气候平均值替代 CMIP5 模式气候平均值的简单方法进行了模式系统误差的订正,该订正方法不改变模式结果的时间变率,且能够让模式结果优势得到更充分的利用。

(2) 经订正后的模式结果均有能力刻画副高指数的历史演变特征,且能够反映出 20 世纪 70 年代末期之后,副高面积和强度增强、西伸脊点偏西的变化趋势。通过对副高指数的长期趋势、标准差及年际周期等的定量评估,发现 CNRM-CM5、FGOALS-g2、FIO-ESM、MIROC-ESM 和 MPI-ESM-P 这 5 个模式对副高的模拟能力较强。

(3) 在不同典型浓度路径情景下,副高指数的变化特征各不相同。综合 3 种不同情景,未来随着温室气体浓度的升高,副高面积和强度均增大,且显著西伸;其线性增长趋势在 RCP8.5 情景下最高,RCP4.5 情景下次之,RCP2.6 情景下最弱。副高脊线指数在 3 种排放情景下都没有明显的长期变化趋势。

以上的分析结果表明,未来随着温室气体浓度的升高,副高将显著增大增强且西伸,其对未来中国夏季主要雨带和旱涝的分布,乃至对东亚季风区气候异常的影响机理需要进一步研究。而在未来全球变暖的背景下,副高增强西伸的机制也值得深入分析。先前的研究表明,20 世纪 70 年代末西太平洋副热带高压呈现出加强西伸的特征,通过数值试验证实热带印度洋和西太平洋的变暖是导致副高西伸的重要因子,并给出了两种影响机制(Zhou, et al, 2009)。在未来不同典型浓度路径情景下,热带印度洋和西太平洋的变暖程度将有所差异(IPCC, 2007),副高增强西伸的响应也各不相同,因此两者之间的关系与反馈作用需要更加定量化的研究。

**致谢**:感谢中国气象局短期气候预测国家级创新团队提供的技术指导。感谢世界气候研究计划耦合模式工作组和各模式机构为 CMIP5 试验所作的贡献,感谢美国 NOAA 提供的 NCEP/NCAR 大气再分析资料和扩展重建的海表温度资料(ERSSTv3b)。

## 参考文献

冯娟, 李建平. 2012. IPCC AMIP 模式对西南澳类季风环流的模拟. 气候与环境研究, 17(4): 409-421

韩晋平, 王会军. 2007. 东亚夏季风年代际变化的若干重要特征及两份大气再分析资料的异同. 地球物理学报, 50(6): 1666-1676

黄刚, 屈侠. 2009. IPCC AR4 模式中夏季西太平洋副高南北位置特征的模拟. 大气科学学报, 32(3): 351-359

黄荣辉, 孙凤英. 1994. 热带西太平洋暖池的热状态及其上空的对流活动对东亚夏季气候异常的影响. 大气科学, 18(2): 141-151

黄荣辉, 蔡榕硕, 陈际龙等. 2006. 我国旱涝气候灾害的年代际变化及其与东亚气候系统变化的关系. 大气科学, 30(5): 730-743

刘芸芸, 丁一汇. 2012a. 亚洲-太平洋夏季风系统的基本模态特征分析. 大气科学, 36(4): 673-685

刘芸芸, 李维京, 艾孜秀等. 2012b. 月尺度西太平洋副热带高压指数的重建与应用. 应用气象学报, 23(4): 414-423

孙颖, 丁一汇. 2008. IPCC AR4 气候模式对东亚夏季风年代际变化的模拟性能评估. 气象学报, 66(5): 765-780

陶诗言, 卫捷. 2006. 再论夏季西太平洋副热带高压的西伸北跳. 应用气象学报, 17(5): 513-525

吴国雄, 丑纪范, 刘屹岷等. 2002. 副热带高压形成和变异的动力学问题. 北京: 科学出版社, 1-20

辛晓歌, 吴统文, 张洁. 2012. BCC 气候系统模式开展的 CMIP5 试验介绍. 气候变化研究进展, 8(5): 378-382

熊安元. 2001. 90 年代长江中游异常多雨的气候变化背景分析. 应用气象学报, 12(1): 113-117

徐海明，何金海，周兵. 2001. 江淮入梅前后大气环流的演变特征和西太平洋副高北跳西伸的可能机制. 应用气象学报，12(2)：150-158

张宏芳，陈海山. 2011a. 21个气候模式对东亚夏季环流模拟的评估 I：气候态. 气象科学，31(2)：119-128

张宏芳，陈海山. 2011b. 21个气候模式对东亚夏季环流模拟的评估 II：年际变化. 气象科学，31(3)：247-257

Chang C P, Li T. 2000a. A theory for the tropical tropospheric biennial oscillation. J Atmos Sci, 57(14): 2209-2224

Chang C P, Zhang Y S, Li T. 2000b. Interannual and interdecadal variations of the East Asian summer monsoon and tropical Pacific SSTs. Part I: Roles of the subtropical ridge. J Climate, 13(24): 4310-4340

Ding Y H. 2007. The variability of the Asian summer monsoon. J Meteor Soc Japan, 85: 21-54

Hu Z Z. 1997. Interdecadal variability of summer climate over East Asia and its association with 500 hPa height and global sea surface temperature. J Geophys Res, 102(D16): 19403-19412

IPCC. 2007. Climate Change 2007: The Physical Scientific Basis// Solomon S, Qin D, Manning M, et al. Contribution of Working Group I to the Forth Assessment Report of the Intergovernmental Panel on Climate Change. Cambridge, United Kingdom and New York, NY, USA: Cambridge University Press, 996pp

Kalnay E, Kanamitsu M, Kistler R, et al. 1996. The NCEP/NCAR 40-year reanalysis project. Bull Amer Meteoro Soc, 77: 437-472

Liu Y Y, Ding Y H, Gao H, et al. 2013. Tropospheric biennial oscillation of the western Pacific subtropical high and its relationship with the tropical SST and atmospheric circulation anomalies. Chin Sci Bull, 58(30): 3664-3672

Moss R H, Edmonds J A, Hibbard K A, et al. 2010. The next generation of scenarios for climate change research and assessment. Nature, 463(7282): 747-756

Nitta T. 1987. Convective activities in the tropical western Pacific and their impact on the Northern Hemisphere summer circulation. J Meteor Soc Japan, 65(3): 373-390

Smith T M, Reynolds R W, Peterson T C, et al. 2008. Improvements to NOAA'S historical merged land-ocean surface temperature analysis. (1880－2006). J Climate, 21:2283-2296

Taylor K E. 2001. Summarizing multiple aspects of model performance in a single diagram. J Geophys Res, 106(D7): 7183-7192

Taylor K E, Stouffer R J, Meehl G A. 2012. An overview of CMIP5 and the experiment design. Bull Amer Meteoro Soc, 93: 485-498

Wang B, Ding Q H, Fu X, et al. 2005. Fundamental challenge in simulation and prediction of summer monsoon rainfall. Geophys Res Lett, 32(15): L15711, doi:10.1029/2005GL022734

Zhao P, Zhu Y N, Zhang R H. 2007. An Asian-Pacific teleconnection in summer tropospheric temperature and associated Asian climate variability. Climate Dyn, 29(2-3): 293-303

Zhou T J, Yu R C, Zhang J, et al. 2009. Why the western Pacific subtropical high has extended westward since the late 1970s. J Climate, 22: 2199-2215

Zhu J S, Shukla J. 2013. The role of air-sea coupling in seasonal prediction of Asian-Pacific summer monsoon rainfall. J Climate, 26(15): 5689-5697

ADVANCES IN ATMOSPHERIC SCIENCES, VOL. 31, SEPTEMBER 2014, 1051–1064

# Relationships between Interannual and Intraseasonal Variations of the Asian–Western Pacific Summer Monsoon Hindcasted by BCC_CSM1.1(m)

LIU Xiangwen*[1], WU Tongwen[1], YANG Song[2], LI Qiaoping[1], CHENG Yanjie[1], LIANG Xiaoyun[1], FANG Yongjie[1], JIE Weihua[1], and NIE Suping[1]

[1]*National Climate Center, China Meteorological Administration, Beijing* 100081

[2]*Department of Atmospheric Sciences, Sun Yat-sen University, Guangzhou* 510275

(Received 9 October 2013; revised 6 January 2014; accepted 24 February 2014)

ABSTRACT

Using hindcasts of the Beijing Climate Center Climate System Model, the relationships between interannual variability (IAV) and intraseasonal variability (ISV) of the Asian–western Pacific summer monsoon are diagnosed. Predictions show reasonable skill with respect to some basic characteristics of the ISV and IAV of the western North Pacific summer monsoon (WNPSM) and the Indian summer monsoon (ISM). However, the links between the seasonally averaged ISV (SAISV) and seasonal mean of ISM are overestimated by the model. This deficiency may be partially attributable to the overestimated frequency of long breaks and underestimated frequency of long active spells of ISV in normal ISM years, although the model is capable of capturing the impact of ISV on the seasonal mean by its shift in the probability of phases.

Furthermore, the interannual relationships of seasonal mean, SAISV, and seasonally averaged long-wave variability (SALWV; i.e., the part with periods longer than the intraseasonal scale) of the WNPSM and ISM with SST and low-level circulation are examined. The observed seasonal mean, SAISV, and SALWV show similar correlation patterns with SST and atmospheric circulation, but with different details. However, the model presents these correlation distributions with unrealistically small differences among different scales, and it somewhat overestimates the teleconnection between monsoon and tropical central-eastern Pacific SST for the ISM, but underestimates it for the WNPSM, the latter of which is partially related to the too-rapid decrease in the impact of El Niño–Southern Oscillation with forecast time in the model.

**Key words**: interannual variability, intraseasonal variability, western North Pacific summer monsoon, Indian summer monsoon

**Citation**: Liu, X. W., and Coauthors, 2014: Relationships between interannual and intraseasonal variations of the Asian–western Pacific summer monsoon hindcasted by BCC_CSM1.1(m). *Adv. Atmos. Sci.*, **31**(5), 1051–1064, doi: 10.1007/s00376-014-3192-6.

## 1. Introduction

Because of its complex variability and significant economic and social impacts, prediction of monsoon has long been an important yet challenging task. As an important approach, dynamical prediction of monsoon has drawn much attention from both academic and operational communities. However, monsoon prediction with climate models suffers from many limitations, such as initial condition errors, imperfect model physics, incomplete forecast methods, among others. Therefore, monsoon prediction by state-of-the-art climate models still shows an inability to capture the climatological mean state (e.g., Lee et al., 2010; Li et al., 2012; Liu et al., 2013), spatial and temporal variability (e.g., Wang et al., 2008; Xue et al., 2010; Liu et al., 2014), and relationships between monsoon and other climate systems (e.g., Yang et al., 2008; Drbohlav and Krishnamurthy, 2010; Rajeevan et al., 2012). Thus, assessing the skills and diagnosing the deficiencies of dynamical monsoon prediction are important for improving monsoon prediction and model development.

As the strongest monsoon system in the world, the Asian–western Pacific summer monsoon is marked by significant multiscale variability. In particular, its interannual variability (IAV) and intraseasonal variability (ISV), known by their important impacts on many prominent climate and weather phenomena both inside and outside the monsoon region, have received much research interest (e.g., Wang et al., 2008; Xavier et al., 2008; Zhou et al., 2009; Yoo et al., 2010). Although with respective mechanisms and representations, the IAV and the ISV of monsoon are connected with each other and with other climate systems. The predictability of IAV

* Corresponding author: LIU Xiangwen
Email: xwliu@cma.gov.cn

© Institute of Atmospheric Physics/Chinese Academy of Sciences, and Science Press and Springer-Verlag Berlin Heidelberg 2014

of tropical monsoon is supposed to be originated from external forcing, such as SST, soil moisture, and snow cover (Charney and Shukla, 1981), while the ISV of monsoon often serves as an important but less predictable internal component (e.g., Goswami, 1998; Kang and Shukla, 2006; Suhas et al., 2012). However, it has also been hypothesized that the IAV of monsoon is determined by the shift in the probability density function of ISV toward either active or break phases, in which external boundary forcing may act as an essential modulating factor (Palmer, 1994; Ferranti et al., 1997; Sperber et al., 2000; Goswami and Ajaya Mohan, 2001). In this scenario, significant correlation between seasonal mean monsoon and ISV has been found for the South Asian summer monsoon (e.g., Lawrence and Webster, 2001; Waliser et al., 2004; Goswami et al., 2006; Qi et al., 2008; Fujinami et al., 2011), and the relationship between the ISV of summer monsoon and El Niño–Southern Oscillation (ENSO) has also been revealed (Teng and Wang, 2003; Kim et al., 2008; Qi et al., 2008). At present, it is still worth further exploring whether the ISV of monsoon is not entirely internal variability, but instead partially related to external components.

Also, as revealed by previous studies on the South Asian summer monsoon, the IAV of the seasonal mean consists of two independent parts: a large-scale seasonally persistent mean component, and an average of the ISV; and the predictability of the seasonal mean monsoon depends on the relative magnitudes of seasonal averages of the persistent component and the intraseasonal component (Krishnamurthy and Shukla, 2000, 2007, 2008). In this context, both observations and model simulations have proved the presence of a large-scale seasonally persistent structure that is attributable to external forcing and largely determines the IAV of seasonal mean monsoon, while the nature of ISV is less dependent on the IAV of monsoon (Achuthavarier and Krishnamurthy, 2010).

Although the connection and interaction between the IAV and ISV of monsoon is still a controversial issue, a reasonable reproduction of the relationship between IAV and ISV by climate models is indispensable for the skillful seasonal prediction of monsoon. Thus, in this study, we explore the relationships between the IAV and ISV of the Asian–western Pacific monsoon by comparisons between observations and model hindcasts, and between the western North Pacific summer monsoon (WNPSM) and the Indian summer monsoon (ISM). The following questions are addressed: are there significant relationships between the IAV and ISV of monsoon over this monsoon region? In what way and to what degree are the IAV and the ISV of monsoon connected with external forcing and background circulation? What are the differences in the above features between the WNPSM and ISM? How well can models reproduce the observed features?

In section 2, a brief overview of the model output, observational data, and analysis methods is provided. In sections 3–5, we analyze the predictions of basic monsoon features, the relationship between the ISV and IAV of monsoon, and the links with external forcing and atmospheric circulation, respectively. A summary and further discussion are presented in section 6.

## 2. Model, data and methods

The model used in this study is an updated version of the Beijing Climate Center (BCC) Climate System Model version 1.1 (BCC_CSM1.1; Wu et al., 2013) with a moderate atmospheric resolution [BCC_CSM1.1(m)]. The atmospheric component in BCC_CSM1.1(m) is the BCC Atmospheric General Model version 2 with a T106 horizontal resolution and 26 hybrid sigma/pressure layers in the vertical direction (Wu et al., 2010). The oceanic component is the Geophysical Fluid Dynamics Laboratory (GFDL) Modular Ocean Model version 4 with a tripolar grid in the horizontal direction and 40 levels in the vertical direction, and the sea ice component is the GFDL Sea Ice Simulator. The land model is the BCC Atmosphere and Vegetation Interaction Model version 1.0. The different components are coupled without any flux correction. The BCC_CSM1.1(m) and the BCC_CSM1.1 are two of the climate system models joining phase five of the Coupled Model Intercomparison Project (CMIP5). The reasonable performance of BCC_CSM1.1(m) in climate simulation and projection has been revealed by a fair number of studies listed on the website http://cmip.llnl.gov/cmip5/publications/model?exp=BCC-CSM1.1-m.

Some experiments aimed at boreal summer climate prediction are implemented using BCC_CSM1.1(m). The hindcasts are initiated from 1 March of each year from 1991 to 2010 and end with a 7-month integration. The atmospheric initial conditions are obtained from the winds, air temperature, and surface pressure of the National Centers for Environmental Prediction (NCEP) Reanalysis with four-times-daily output, and oceanic initial conditions are from the sea temperature of the NCEP Global Oceanic Data Assimilation System. These reanalysis data are used to initialize the model by a nudging strategy, which operates from late 1980 to the beginning of a certain retrospective forecast. Each hindcast includes 15 members, produced by a combination of lagged average forecasting on atmospheric and oceanic initials, and singular vector perturbing on initials of SST at the end of February in the hindcast year.

The observations used for model verification include various variables from the NCEP Reanalysis 2 (Kanamitsu et al., 2002), the Optimum Interpolation SST (Reynolds et al., 2002), and the daily mean outgoing longwave radiation (OLR; Liebmann and Smith, 1996) from the National Oceanic and Atmospheric Administration (NOAA), and the global monthly precipitation from the Climate Prediction Center Merged Analysis (Xie and Arkin, 1997).

The IAV of monsoon for a particular year refers to the difference of the June–July–August–September (JJAS) mean between the specific year and the climatology from 1991 to 2010, and the ISV is computed based on the daily mean series in that year with a subtraction of daily climatology and a subsequent filtering on the intraseasonal component, unless otherwise indicated. For the model output, the length of the daily anomaly series (daily means minus daily clima-

tologies) in each year is only 214 days (from 1 March to 30 September), which is unfavorable for using a Lanczos band-pass filter to extract the intraseasonal part. Thus, a Fourier harmonic analysis is performed on the time series and the leading three harmonics (period $> 70$ days) are first deducted as part of long-wave variability, followed by a 5-day running average on the residue to get the part of the ISV. Then, the results from June to September are chosen for the ISV in boreal summer. The same process is also used to extract observed ISV in each year from 1991 to 2010.

To focus on the variability of the WNPSM and ISM, two dynamical monsoon indices are used in our analyses. The WNPSM index (WNPSMI) and the ISM index (ISMI) are defined as the differences in area-averaged 850-hPa zonal wind between (5°–15°N, 100°–130°E) and (20°–30°N, 110°–140°E), and between (5°–15°N, 40°–80°E) and (20°–30°N, 70°–90°E), respectively (Wang et al., 2001). All the summer means, ISV and long-wave variability of each monsoon index are calculated with the methods mentioned above.

Additionally, we compute the direct correlations between predictions and observations using ensemble-averaged variables to better depict the performance of ensemble prediction. However, to objectively assess the model's ability, for comparisons of any feature between the predictions and observations, computations are first performed for individual members before averages are made.

## 3. Predictions of basic monsoon features

Figure 1 shows the climatologies of JJAS mean precipitation and 850-hPa winds for prediction, observations, and model biases. The model captures the major low-level features of the distribution of the Asian–western Pacific summer monsoon. It also captures the overall locations and magnitude of major rainfall and winds in many places. However, apparent systematic biases of the model are also found, which include a dry bias over most of the Bay of Bengal, a wet bias over the west coast of the Indo-China Peninsula, and a cyclonic wind bias over the northwestern Pacific associated with a wet bias over the central zone of the wind bias and dry biases over the South China Sea and the western edge of the Western Pacific Subtropical High (WPSH). With overall weaker magnitude, these biases also appear in the NCEP Climate Forecast System (e.g., Yang et al., 2008; Drbohlav and Krishnamurthy, 2010), and also some multi-model ensembles of the DEMETER and ENSEMBLES EU projects (e.g., Lee et al., 2010; Rajeevan et al., 2012), suggesting some common deficiencies of state-of-the-art climate models. Besides, significant convergence wind bias over the central tropical North Indian Ocean and divergence wind bias over the eastern tropical South Indian Ocean, along with wet and dry bias, respectively, exist in BCC_CSM1.1(m).

Despite the obvious systematic biases, a reasonable prediction skill of the model for monsoon variability is still expected. Figure 2 shows the temporal correlations between predictions and observations for interannual variations of JJAS mean 850-hPa zonal wind and precipitation. Significant skills for the forecast of low-level winds are mainly found over most of the tropical western North Pacific and East Asia, covering the majority of areas along the western edge of the WPSH. The model seems to perform better in predicting the WNPSM and East Asian summer monsoon than the South Asian summer monsoon, at least for atmospheric circulation. In contrast, except for some sparse regions near the equator, the prediction of rainfall shows little skill over most areas (Fig. 2b), consistent with previous results showing that the forecasting of precipitation often exhibits quicker error growth and shorter time in approaching the upper limit of predictability than circulation (e.g., Xie et al., 2012; Liu et al., 2014).

As important measures of monsoon variability, the intensities of the ISV and IAV of 850-hPa zonal wind, given by their respective standard deviations, are further explored (Fig. 3). The model reasonably reproduces the observed features of the distribution of ISV intensity with maximums over the extratropical North Pacific and areas from the Bay of Bengal to the Philippine Sea, as well as the distribution of IAV intensity with a magnitude center over the tropical western North Pacific induced by ENSO. Nevertheless, compared to observations, obviously stronger ISV intensity over most places and a more extensive and too-far-east center of magnitude are found. Meanwhile, the IAV shows a larger central intensity

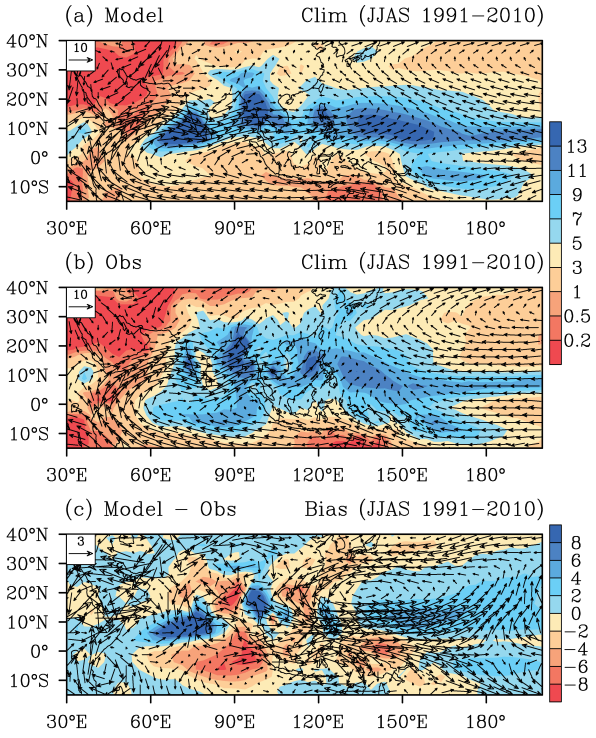


**Fig. 1.** 20-year means of precipitation (shading; units: mm $d^{-1}$) and 850-hPa winds (vectors; units: m $s^{-1}$) for (a) hindcasts, (b) observations, and (c) biases (predictions minus observations) averaged from June to September.

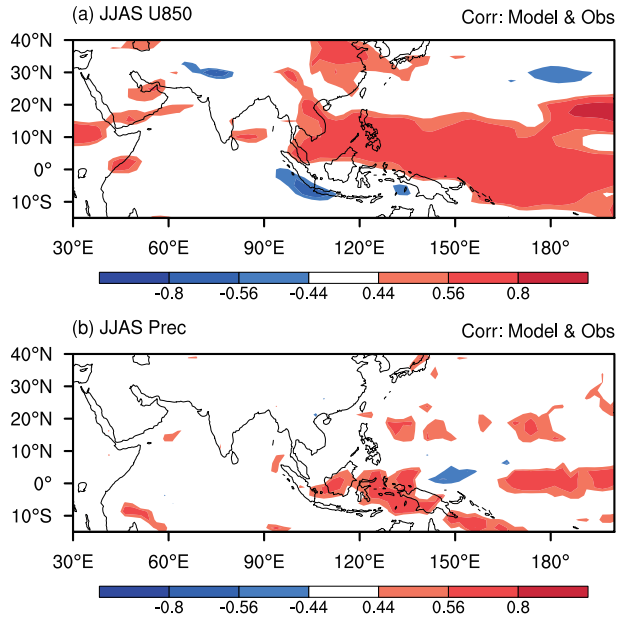


**Fig. 2.** Spatial distributions of temporal correlations between predictions and observations for summer-averaged (a) 850-hPa zonal wind and (b) precipitation from 1991 to 2010. The shading levels above 0.44 and 0.56 represent the statistical significance of correlation above the 95% and 99% confidence levels, respectively, and the same hereafter.

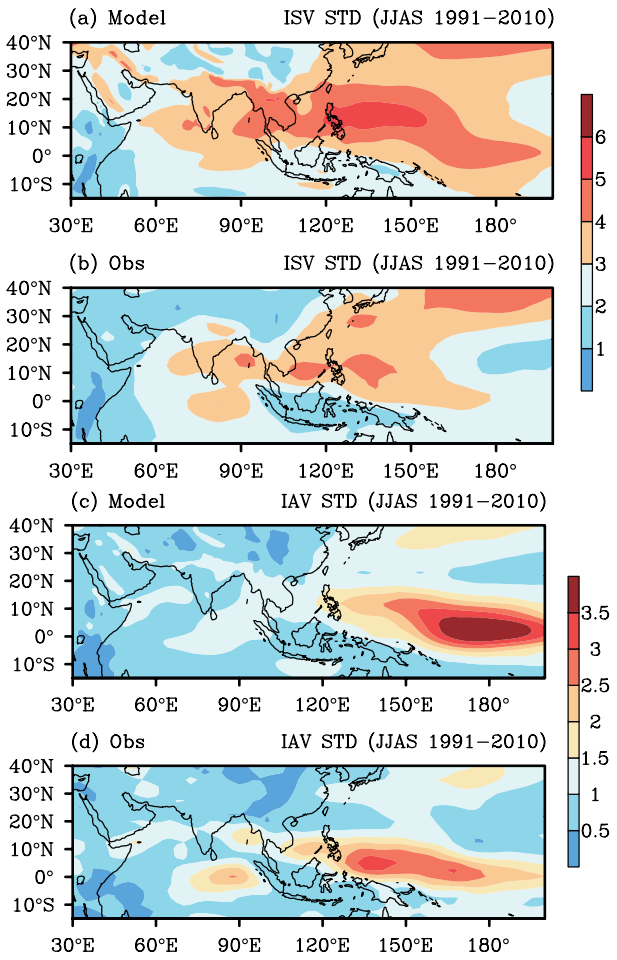


**Fig. 3.** Ensemble mean standard deviation (units: m $s^{-1}$) of intraseasonal variability in summer (top two rows) and interannual variability of summer mean (bottom two rows) for 850-hPa zonal wind from 1991 to 2010. Panels (a) and (c) are for the model, and (b) and (d) are for observations.

with a farther southeastward shift toward the dateline over the western Pacific in the model. In addition, because the ISV and IAV of monsoon may be governed by a common spatial mode of variability (Ferranti et al., 1997; Sperber et al., 2000; Goswami and Ajaya Mohan, 2001), the observed features given in Figs. 3b and d both show high intensity over the Bay of Bengal, the South China Sea, and the Philippine Sea, even though this is not well captured by the model for the false shifts of variability centers in Figs. 3a and c.

Next, we discuss some basic characteristics of ISV before exploring the relationships among different time scales. A similar-to-observed vertical structure (Figs. 4a and b) and northward propagation (Figs. 4e and f) are found for the ISV of the WNPSM in the model, albeit with a somewhat smaller range of the vorticity center and a faster propagation speed than in observations. For the ISV of the ISM, the model captures a slightly faster northward propagation (Figs. 4g and h) and a more northward center of vertical vorticity (Figs. 4c and d) compared to observations. Furthermore, the broadband spectrum of ISV and its resulting aperiodicity is one of the important characteristics in generating a non-trivial seasonal mean ISV anomaly, which partially acts as a bridge to connect the ISV and IAV of monsoon (Goswami and Xavier, 2005; Goswami et al., 2006). Thus, the spectral features of the ISV of the WNPSM and ISM are specifically examined in Fig. 5. Narrower-than-observed spectral bands are captured by the model for both the WNPSM and ISM. In particular, the predicted ISV does not show a significant period of near 50 days, which is the spectral peak found in observations. Besides, similar results can be derived by power spectral analyses for regionally averaged OLR over the WNPSM region (10°–25°N, 110°–140°E) and the ISM region (7.5°–22.5°N, 60°–90°E) (figures not shown). This feature is unfavorable for the seasonally accumulated quantity of ISV anomaly to contribute to the seasonal mean in the model since a narrow band may be periodic and its accumulation should show little residue in the whole season.

## 4. Relationship between the ISV and IAV of monsoon

In this section, the relationship between the ISV and IAV of the Asian–western Pacific summer monsoon is explored with a focus on the intensity, seasonally averaged anomaly, frequency of occurrence of positive (negative) phase, and frequency of consecutive break or active spells of ISV.

Figures 6a and b show the interannual correlations between the intensity of ISV and the summer mean for 850-hPa zonal wind in the model and observations. The intensity of ISV in boreal summer shows a significant positive correlation

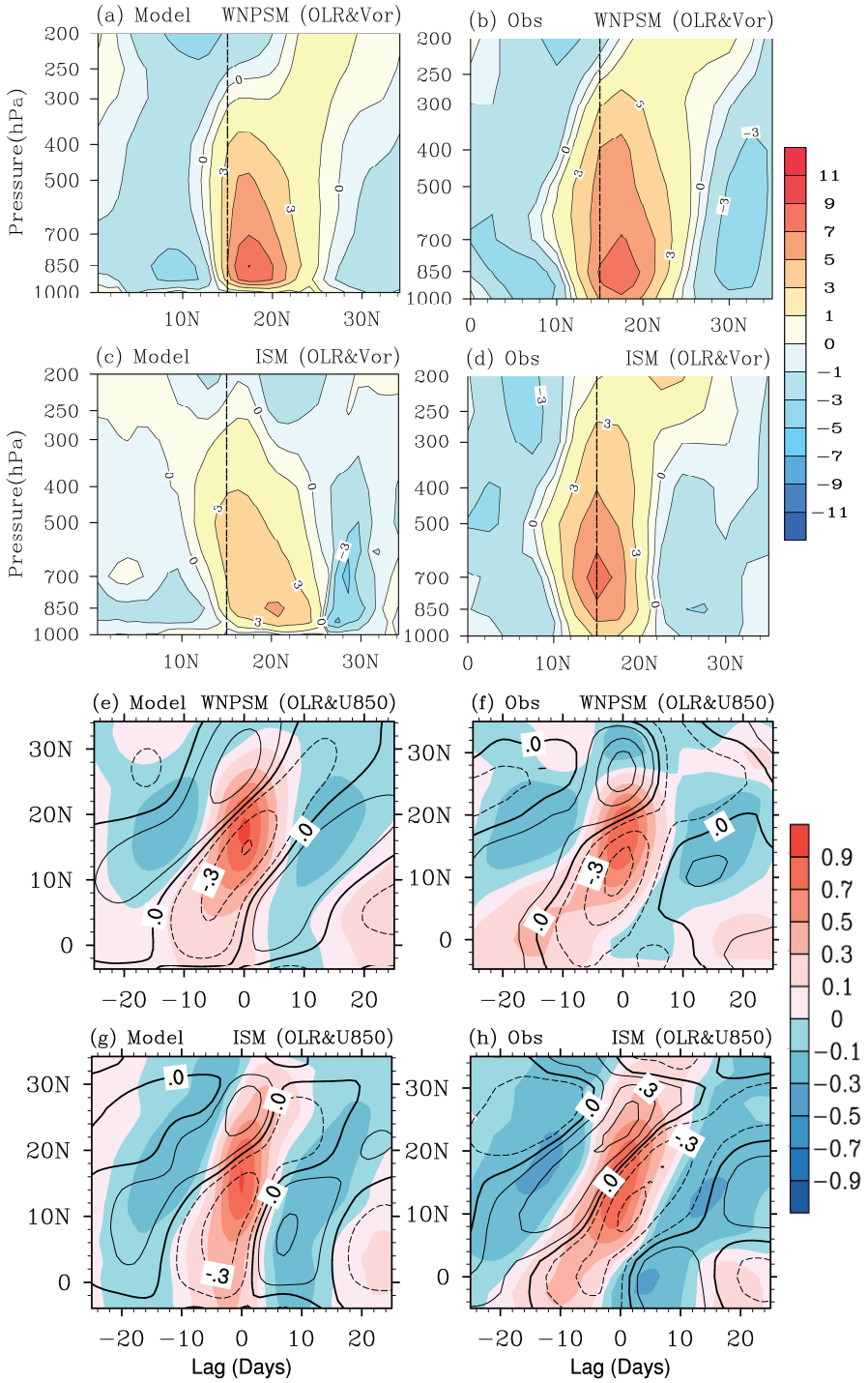


**Fig. 4.** (a–d) Meridional–vertical structure of intraseasonal vorticity (units: $10^{-6}$ s$^{-1}$) along 110°–140°E/60°–90°E for the WNPSM/ISM. (e–h) Latitude–lag correlations of intraseasonal OLR (10°–25°N, 110°–140°E)/(7.5°–22.5°N, 60°–90°E) with 850-hPa zonal wind (contours) and OLR (shaded) along 110°–140°E/60°–90°E for the WNPSM/ISM. Predictions by the model and observations are shown in the left and right columns, respectively. The dashed lines in (a–d) represent the position of the maximum convection center.

with the summer mean over the tropical western Pacific (Fig. 6b), which is attributed to their sensitivity to ENSO variability (Teng and Wang, 2003; Lin and Li, 2008). To a certain extent, the prediction captures this relationship, but with a more eastward range of significant correlation distributed over the tropical central Pacific (Fig. 6a).

The interannual correlations between seasonally averaged ISV anomaly (SAISV) and the JJAS mean of 850-hPa zonal wind are further shown in Figs. 6c and d. Observations present significant positive correlation over most of

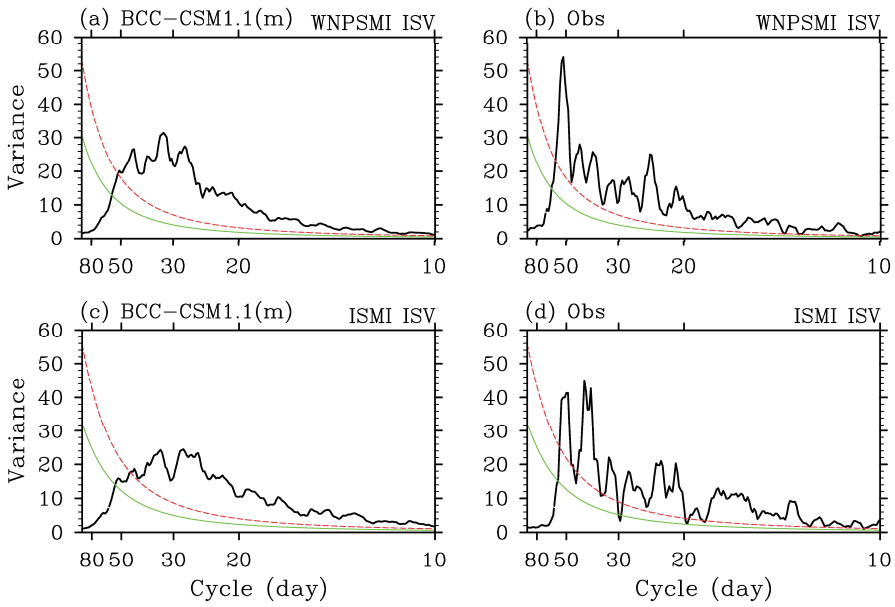


**Fig. 5.** Power spectra of the intraseasonal variability of (a, b) WNPSMI and (c, d) ISMI for model (left column) and observations (right column). The green and red lines denote red noise spectrums and 95% confidence bounds, respectively.

Asia and the western Pacific, especially the tropical western Pacific, where areas with correlation coefficients above 0.9 extend from the South China Sea to the east of the dateline (Fig. 6d). In contrast, relatively weaker correlation appears over the area from the tropical western South Indian Ocean across Somalia to the southern Arabian Sea and India (Fig. 6d), corresponding to an insignificant correlation between the SAISV and summer mean for the OLR over the Bay of Bengal and southern Indo-China Peninsula (figure not shown). This feature partially supports the result about the South Asian summer monsoon that the ISV anomaly itself may have little linear link with the summer mean (e.g., Qi et al., 2008; Achuthavarier and Krishnamurthy, 2010). The model, however, evidently overestimates the relationship between the SAISV and summer mean over the tropical central Pacific, and near Somalia and the southern Arabian Sea (Fig. 6c).

Table 1 further examines the interannual variation of the summer mean, intensity of ISV, and the SAISV for the WNPSMI and ISMI. Measured by the correlations between predictions and observations, prominent prediction skills are found only for the summer mean and SAISV of the WNPSMI with a correlation coefficient of about 0.7, but little skill for any of the other items of the WNPSMI and ISMI. Compared to observations, the model underestimates the connection between the summer mean and the intensity of ISV for both the WNPSMI and ISMI. Also, significant positive correlations between the summer mean and the SAISV are found for the above two dynamical monsoon indices in both prediction and observation, and a stronger-than-observed connection is especially captured by the model for the ISMI, as already partially revealed in Fig. 6.

A narrower-than-observed spectral band of ISV (Fig. 5) and an exaggerated relationship between the SAISV and summer mean of the ISM (Fig. 6 and Table 1) coexist in the model. To explore this feature, the frequencies of ISV anomalies in different monsoon years for the ISMI, as well as for the WNPSMI, are examined (Fig. 7). The strong, weak and normal monsoon years for a specific observed monsoon index are distinguished by a standardized anomaly of the JJAS mean index above 0.8, below −0.8, and between −0.8 and 0.8, respectively. According to these criteria, there are 5, 5, and 10 (4, 4, and 12) strong, weak and normal years for the observed WNPSMI (ISMI) from 1991 to 2010. Both the ensemble average and individual members of predictions show a similar proportion of frequency of certain

**Table 1.** Interannual correlations between predictions and observations for some relevant items of western North Pacific summer monsoon index (WNPSMI) and Indian summer monsoon index (ISMI), and correlations between two of the items for model and observations. Values in bold font exceed the confidence level of 99%.

| | Model & Obs | | | ISV Std & JJAS mean | | SAISV & JJAS mean | |
|---|---|---|---|---|---|---|---|
| | JJAS mean | ISV Std | SAISV | Model | Obs | Model | Obs |
| NPSMI | **0.69** | 0.36 | **0.71** | −0.06 | 0.33 | **0.91** | **0.92** |
| ISMI | −0.17 | 0.30 | 0.27 | 0.09 | 0.33 | **0.88** | **0.75** |

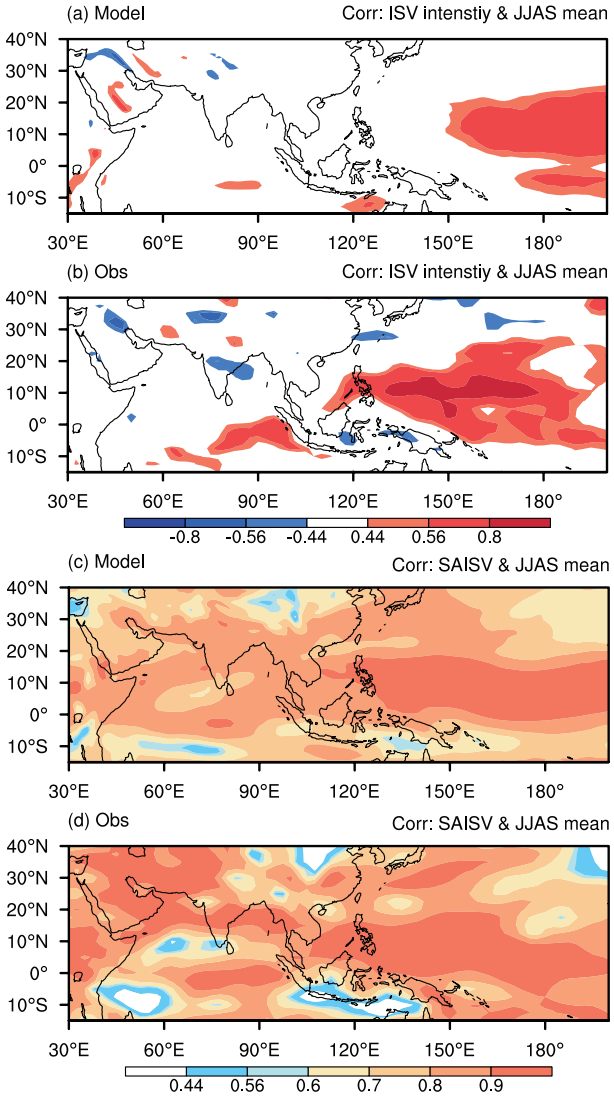


**Fig. 6.** Spatial distributions of temporal correlations between (a, b) the intensity of intraseasonal variability and summer mean and (c, d) the seasonal average of intraseasonal variability and summer mean from 1991 to 2010 for 850-hPa zonal wind in (a, c) the model and (b, d) observations.

monsoon years in general; however, only about 40%, 40% and 60% (25%, 25% and 67%) of strong, weak and normal WPNSM (ISM) years in observations are consistently captured by the model. Here, the statistics of ISV and IAV anomalies for each one of the 15 members are individually computed before showing the general ensemble features. Figure 7 indicates that, in both the model and observations, the phase of ISV is often characterized by a shift towards more frequent active (break) events in the strong (weak) summer monsoon years, and a smaller change in the normal monsoon years. This feature suggests that the frequency of active and break cycles of ISV is distinguishable between a strong and weak monsoon year, which supports the hypothesis that the IAV of seasonal mean monsoon may partially result from the shifts in the probability of the phase of the ISV (e.g., Palmer, 1994; Sperber et al., 2000; Goswami and Ajaya Mohan, 2001).

Although the model exhibits a reasonable prediction skill in the link between IAV and the frequency of ISV phases, it may not be necessary to support a reliable contribution of ISV to the summer mean monsoon. The very-long-duration active or break phases of ISV can act as a common seminal factor for generating anomalous seasons (Joseph et al., 2009; Krishnan et al., 2009; Joseph et al., 2010) and are rather important for the non-triviality of SAISV in a whole summer. Thus, the frequency of long break (active) spells and the strong/normal/weak monsoon years co-occurring with long break (active) spells are further explored in Table 2. The long break (active) spells here are identified as break (active) phases of ISV with consecutive standardized anomalies below $-1.0$ (above 1.0) and a duration of at least 10 days for the WNPSMI or ISMI. Statistics for the predictions are based on all ensemble members. As seen from columns b and d in Table 2, about 50% of the long break (active) spells occur in weak (strong) monsoon years and the sum of long break (active) spells during weak (strong) and normal monsoon years stands at around 90%, as indicated by both the model prediction and observations. Further, columns a and c in Table 2 show that a considerable proportion of normal and weak (strong) monsoon years is associated with long break (active) spells. For the more frequent occurrence and higher consistency between forecasts and observations for normal monsoon years compared to weak and strong monsoon years, the overestimated frequency of long breaks and underestimated frequency of long active spells in normal ISM years favor the non-triviality of SAISV in those years and further contribute to the summer mean, which may be part of the reason why a stronger-than-observed relationship between the SAISV and IAV of the ISM is captured by the model.

## 5. Link with external forcing and circulation

The links of the WNPSMI and ISMI on various forms [i.e., summer mean, SAISV, and seasonally averaged longwave variability (SALWV)] with summer mean SST, low-level winds and precipitation are further explored.

The correlations between JJAS mean SST and the summer mean, SAISV, and SALWV of the WNPSMI for the model and observations are given in Figs. 8a–f. Also, the connections between the WNPSMI of different forms and JJAS mean circulation are shown in Figs. 9a–f. It is observed that a stronger-than-normal summer mean WNPSMI is associated with a positive SST anomaly over the equatorial central Pacific and a negative SST anomaly over the northeast of Australia, eastern Indonesian Islands, and region from the eastern Bay of Bengal to the Philippine Sea (Fig. 8b). It not only corresponds to a belt of westerly wind anomaly across the Maritime Continent and the tropical western Pacific surrounded by anomalies of cyclonic wind convergence over its both sides in the two hemispheres, but also is coupled with more precipitation over the tropical western Pacific and less precipitation over a cross-equatorial sloping belt from Aus-

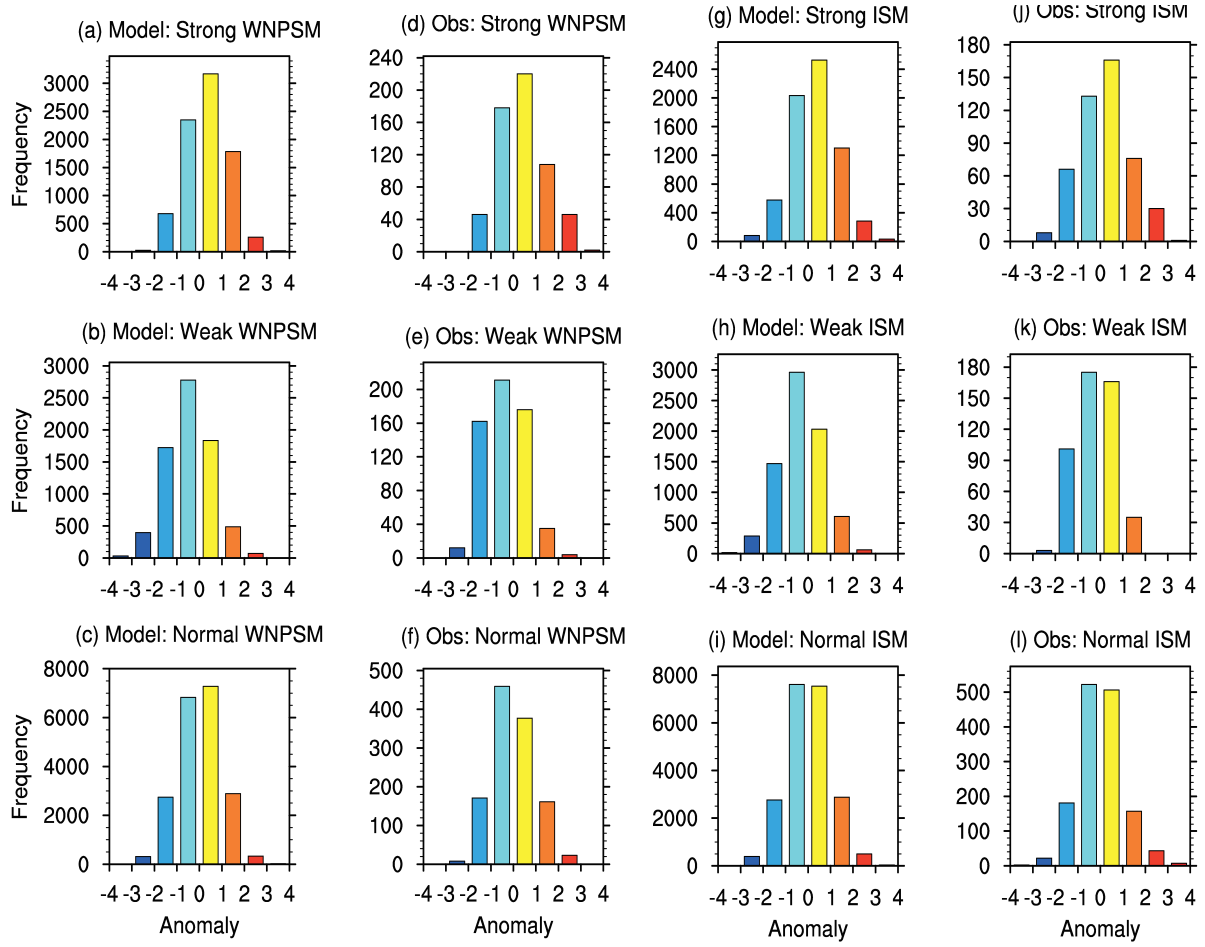


**Fig. 7.** Frequencies of intraseasonal anomalies of (a–f) WNPSMI and (g–l) ISMI in strong (upper row), weak (middle row) and normal (bottom row) monsoon years for (a–c; g–i) the model and (d–f; j–l) observations.

**Table 2.** The frequencies (units: %) of long break/active spells (LBS/LAS) and anomalous summer monsoon years co-occurring with LBS/LAS. Monsoon years are classified into weak, normal and strong ones according to the magnitude of standardized anomalies of the summer-mean WNPSMI and ISMI.

| | (a) Certain monsoon years with LBS/sum of these monsoon years | | (b) LBS occurring in certain monsoon years/sum of LBS | | (c) Certain monsoon years with LAS/sum of these monsoon years | | (d) LAS occurring in certain monsoon years/sum of LAS | |
|---|---|---|---|---|---|---|---|---|
| | Model | Obs | Model | Obs | Model | Obs | Model | Obs |
| Weak WNPSM | 85.2 | 60.0 | 57.5 | 50.0 | 8.2 | 20.0 | 3.9 | 9.1 |
| Normal WNPSM | 30.0 | 40.0 | 39.7 | 50.0 | 30.6 | 40.0 | 50.0 | 45.5 |
| Strong WNPSM | 5.8 | 0.0 | 2.8 | 0.0 | 59.4 | 60.0 | 46.1 | 45.4 |
| Weak SASM | 59.7 | 50.0 | 53.1 | 57.1 | 4.8 | 0.0 | 5.5 | 0.0 |
| Normal SASM | 21.5 | 16.7 | 42.7 | 28.6 | 19.9 | 33.3 | 54.2 | 57.1 |
| Strong SASM | 7.0 | 25.0 | 4.2 | 14.3 | 42.1 | 75 | 40.3 | 42.9 |

tralia across Indonesia to India (Fig. 9b). Similar to the findings by Wang et al. (2000), the above features may be supported by air–sea interaction processes, in which the strengthening westerly wind (weakening easterly trade) over the east (west) of the Philippine Sea encourages the cooling (warming) SST by enhanced (suppressed) evaporation and entrainment cooling over respective regions. The distribution of SST anomalies over the tropical western Pacific in turn favors the persistence of wind anomalies through an atmospheric thermal response. Although sharing a similar correlation pattern as above, the SAISV and SALWV of the WNPSMI are correlated with SST with different priorities, in which the former is related more to the SST over the region from the Bay of Bengal to the Philippine Sea and less to the SST over the equatorial central Pacific, while the latter often shows a very similar connection with SST to that of the summer-mean WNPSMI

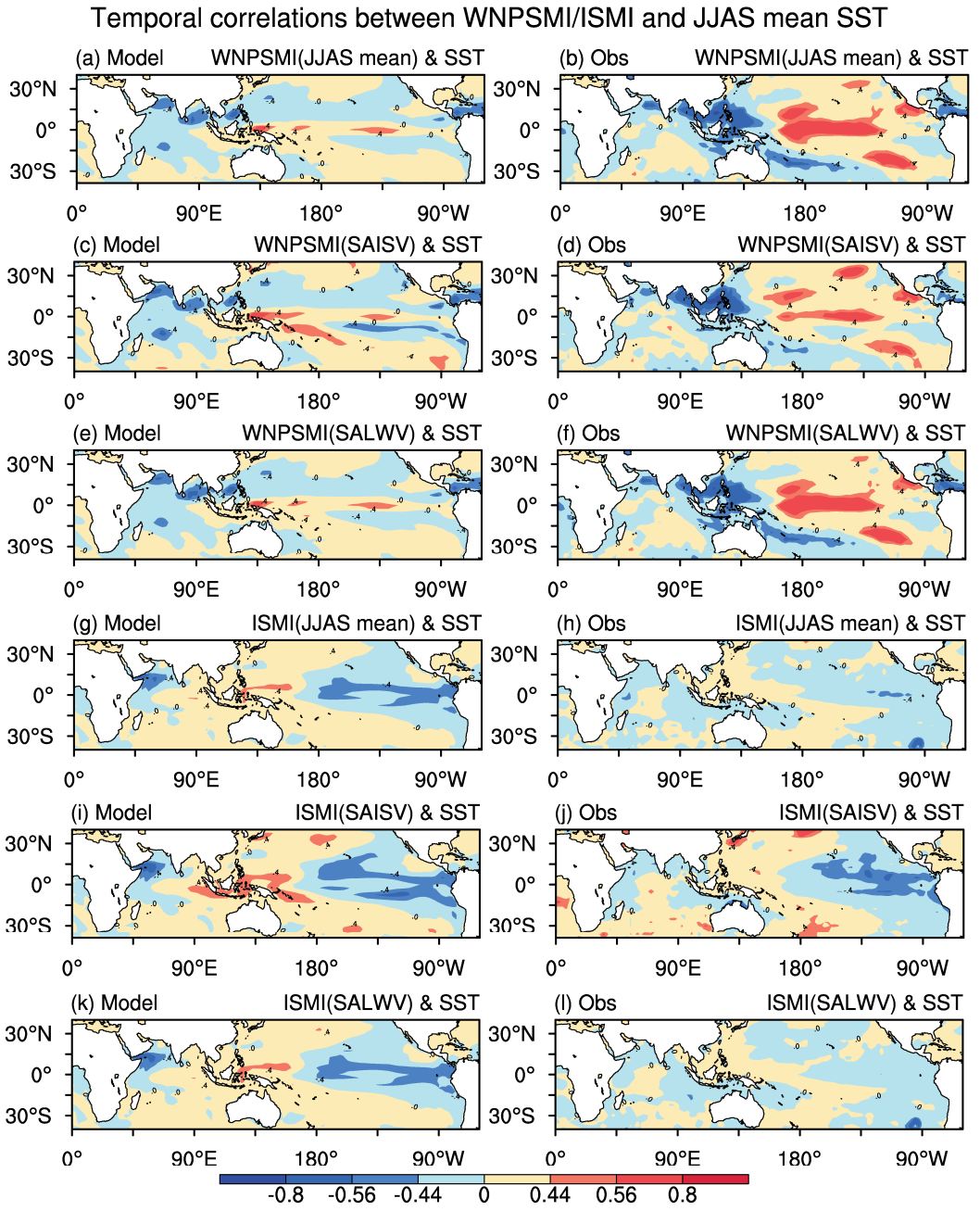


**Fig. 8.** Patterns of correlations between summer-mean SST and WNPSMI/ISMI for the model (left column) and observations (right column). The monsoon index is examined by the summer mean (a, b; g, h), seasonal average of intraseasonal variability (c, d; i, j), and seasonal average of long-wave variability (e, f; k, l), respectively. The shading levels above 0.44 and 0.56 (below −0.44 and −0.56) represent the statistical significance of correlation above the 95% and 99% confidence levels, respectively.

(Figs. 8d, f). In association, a significant response feature of low-level winds is confined to the west of the dateline for the SAISV, while it extends into the tropical central Pacific for the SALWV (Figs. 9d and f).

The summer-mean WNPSMI in the model almost shows no significant connections with SST except over some very small and sparse regions in the tropical Indian Ocean and western Pacific (Fig. 8a). Meanwhile, a regional cyclonic wind response over the western Pacific is captured by the model (Fig. 9a). These features are almost equivalently reproduced by the results for the SAISV and SALWV of the WNPSMI, indicating that the seasonal contributions of monsoon variability with different scales tend to show a common link with external forcing and circulation rather than a selective connection (Figs. 8c, e, 9c and e).

The links of predicted and observed summer mean, SAISV and SALWV of the ISMI with JJAS mean SST are presented in Figs. 8g–l, and with JJAS mean 850-hPa winds

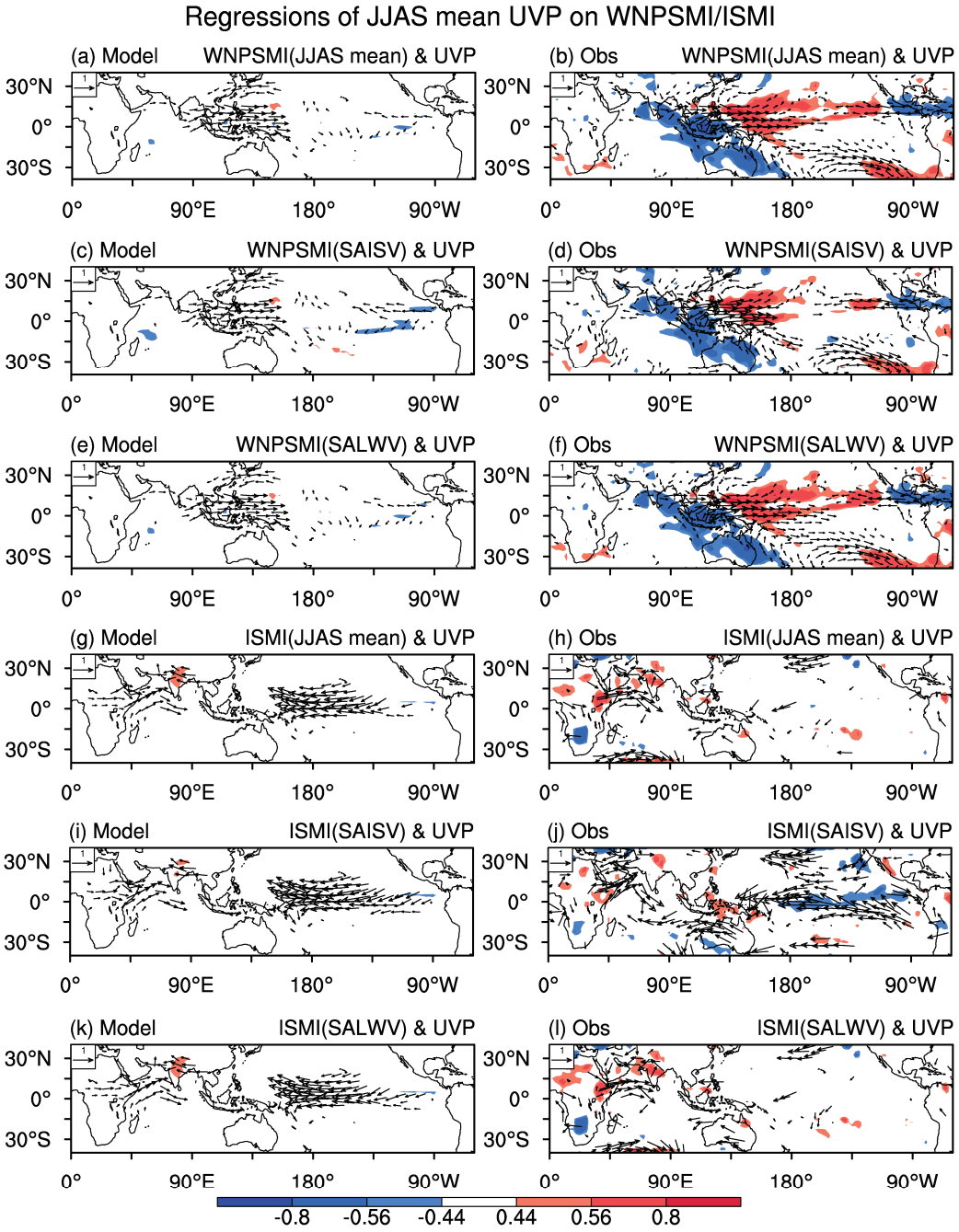


**Fig. 9.** Patterns of regressions (vectors) of summer-mean 850-hPa winds on WNPSMI/ISMI and correlations (shading) between summer-mean precipitation and WNPSMI/ISMI for the model (left column) and observations (right column). The monsoon index is examined by the summer mean (a, b; g, h), seasonal average of intraseasonal variability (c, d; i, j), and seasonal average of long-wave variability (e, f; k, l), respectively. The shading and vectors represent the statistical significance of correlation above the 95% confidence level.

and precipitation in Figs. 9g–l. The summer mean of ISMI shows a negative but insignificant correlation with the SST over the tropical central and eastern Pacific and the tropical western North Indian Ocean (Fig. 8h), in association with a significant correlation with zonal wind over most of the Arabian Sea (Fig. 9h). These observational features essentially indicate a degree of teleconnection between ENSO and ISM, although overtaken by an obvious decline since the 1980s in contrast to before that time (e.g., Kumar et al., 1999; Wang et al., 2001; Kripalani et al., 2003). Similar to the results for the WNPSMI, the SAISV and SALWV of the ISMI are also correlated with SST with similar patterns but different details. In particular, over the tropical eastern Pacific, the SAISV is more apparently and negatively correlated with SST and low-

level zonal wind than the SALWV and summer mean (Figs. 8j and 9j), implying a strong link between ENSO and the ISV of the ISM.

For the ISM in the model, however, the summer mean, SAISV and SALWV are all significantly related to SST and circulation over the tropical central and eastern Pacific and the differences among them are small (Figs. 8g, i, k, 9g, i, and k). Additionally, the negative correlations with SST in the tropical eastern Pacific and western Indian Ocean, as well as the horseshoe patterns of positive correlation in the western Pacific and part of the tropical eastern Indian Ocean are similar to the La Niña SST anomaly distribution. To some extent, these features indicate an overestimation of the link between the ISM and ENSO.

Given the critical role of ENSO in seasonal climate forecasts, we assess the prediction skills for ENSO and its impact on monsoon circulation. If the interannual departures of Niño3.4 SST above 0.5°C or below −0.5°C in each month from March to September in the 20 years are chosen as significant anomalies of ENSO, 64 and 68 anomalous months are observed and predicted, respectively, and 41 of them are consistently captured by both the model and observations. The correlation between prediction and observation in all forecast months is 0.78, suggesting a reasonable skill for ENSO forecasting. However, the observed connections between monsoon and SST in the Niño region are limitedly reproduced by the model as presented in Figs. 8 and 9. Due to the small differences among the multiscale responses of monsoon to tropical SST and circulation in the model, we further examine the impact of ENSO on seasonal mean circulation. Figures 10a–d show the simultaneous relationships between the Niño3.4 SST index and the 850-hPa winds and precipitation for both predictions and observations in summer and spring. Also, the correlations between the Niño3.4 SST index and tropical SST are shown in Figs. 10e–h. In summer, when ENSO is in a developing or decaying stage, significant large-scale atmospheric responses are mainly observed over the subtropical South Pacific and the tropical region from the eastern Indian Ocean to the eastern Pacific (Fig. 10b), associated with an in-phase SST anomaly over the eastern Pacific and a horseshoe-pattern response over the western Pacific (Fig. 10f). However, the model evidently underestimates the responses of winds and precipitation over most of the tropical Pacific and the tropical eastern Indian Ocean (Fig. 10a), in association with narrower-than-observed significant correlation of SST over the central-eastern Pacific (Fig. 10e). Compared to that in summer, the model basically reproduces the connections between the Niño3.4 index and tropical SST and circulation in spring (Figs. 10c, d, g, and h). Therefore, the too-rapid decrease in the impact of ENSO with forecast time should be partially responsible for the apparent underestimation of the relationship of the WNPSM with SST and circulation.

## 6. Summary and discussion

In this study, we have explored the relationship between the IAV and ISV of the Asian–western Pacific monsoon using retrospective forecasts initialized at the end of February by the BCC_CSM1.1(m).

The model exhibits reasonable skill in its predictions of climatologies and the IAV of monsoon, in spite of some apparent systematic biases, and it performs better with respect to the IAV of the WNPSM than that of the ISM. In terms of the standard deviations of the ISV and IAV of summer monsoon, the model also reasonably reproduces the observed features of spatial distribution, but with larger amplitude and a farther eastward position of the central strength for both. Besides, narrower-than-observed spectral bands for the WNPSM and ISM on the intraseasonal scale are found in the model since the predicted spectral variances are mainly limited to the bands with periods of less than 50 days.

The model shows positive interannual correlation between the summer mean and intensity of ISV over the western Pacific, but with a more eastward shift of significant correlation compared to observation. Also, the predictions show a stronger-than-observed connection between the summer mean and SAISV over the tropical central Pacific and near Somalia and the southern Arabian Sea. The statistics on the frequencies of ISV anomalies in strong, weak, and normal WNPSM and ISM years indicate that the seasonal anomalies of summer monsoon are to a certain extent determined by the shifts in probability of ISV towards either an active or break phase. Although the model can basically reproduce this feature, it still overestimates the frequency of long breaks and underestimates the frequency of long active spells in normal Indian monsoon years, which may partially contribute to the stronger-than-observed relationship between the SAISV and seasonal mean of the ISM.

Furthermore, the interannual links of the seasonal mean, SAISV and SALWV of the WNPSMI and ISMI with summer mean SST, low-level winds and precipitation have been explored. Observations reveal that, the seasonal mean, SAISV and SALWV of summer monsoon all show similar correlation patterns with summer SST but with different details. For the WNPSMI, both seasonal mean and SALWV are significantly and positively correlated with SST over the equatorial central Pacific but negatively correlated with SST over the northeast of Australia, eastern Indonesian Islands, and regions from the eastern Bay of Bengal to the Philippine Sea. The correlation between SAISV and SST is concentrated more in the region from the Bay of Bengal to the Philippine Sea and less in the equatorial central Pacific. However, the predicted seasonal mean, SAISV, and SALWV of the WNPSMI present highly similar links with SST, and the correlations are insignificant except over some small and sparse regions in the tropical Indian Ocean and the western Pacific. It is supposed that the excessive decline of the impact of ENSO with forecast time should partially account for the apparent underestimation of the relationship of the WNPSM with SST and circulation. For the ISMI, the observed seasonal mean and SALWV show similar but insignificant correlations with the SST over most tropical areas, while significant correlation between SAISV and tropical eastern Pacific SST is found. Nevertheless, not only stronger-than-observed

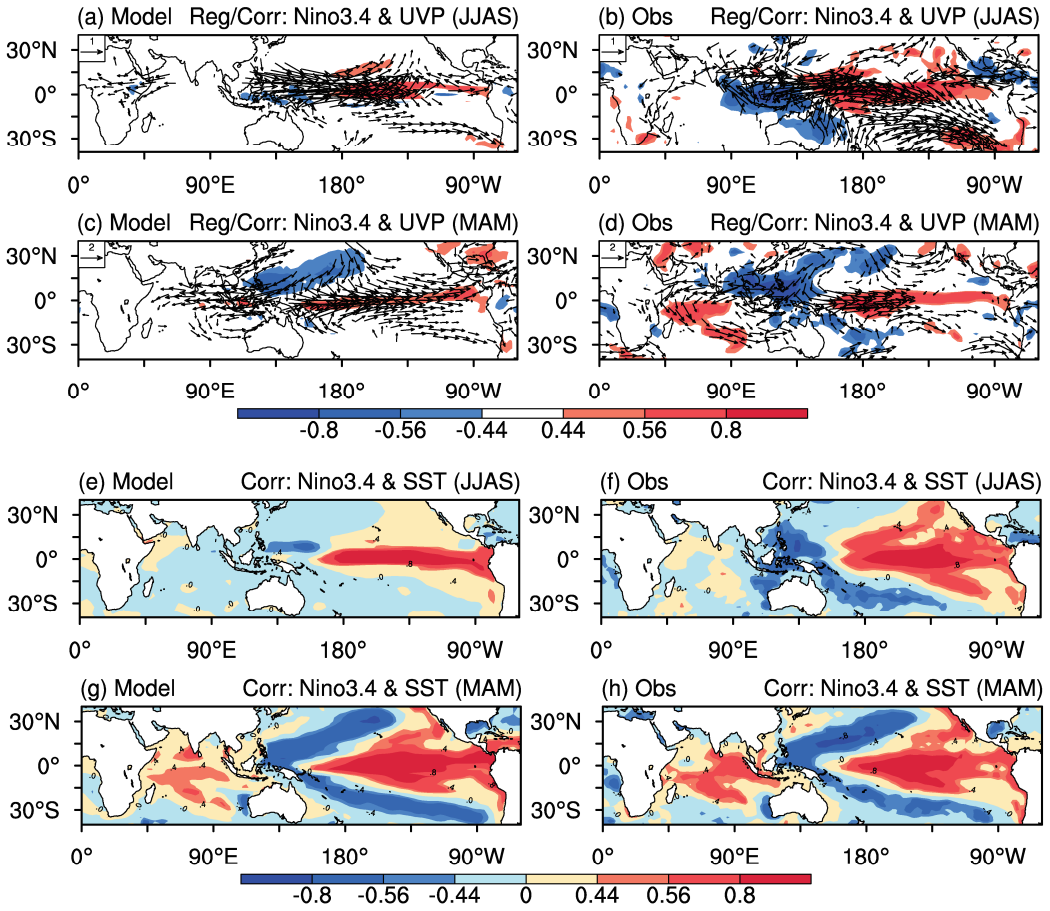


**Fig. 10.** (a–d) Patterns of regressions (vectors) of seasonal mean 850-hPa winds on Niño3.4 SST index and correlations (shading) between precipitation and Niño3.4 SST index for the (a, c) model and (b, d) observations. The features for the summer (June to September) and spring (March to May) are given in (a, b) and (c, d), respectively. Panels (e–h) are the same as (a–d), but only for the correlations between SST and Niño3.4 index.

relationships with SST over the tropical eastern Pacific, but also very small differences among these correlation distributions for the seasonal mean, SAISV and SALWV of the ISMI are captured by the model, implying an overestimated link between the ISM and ENSO. The features of low-level circulation and precipitation also match the above results.

The BCC_CSM1.1(m) shows reasonable but limited skill in capturing the observed relationships between the ISV and IAV of summer monsoon. However, this may gradually improve with a decrease in the lead time of prediction given that the current hindcasts initialized at the end of February most likely suffer from a spring predictability barrier. Thus, more experiments and evaluations on this subject should be implemented in future work. Meanwhile, our analyses have revealed some shortcomings of the model in forecasting the relationships between the ISV and IAV of monsoon and have preliminarily explored the possible causes, suggesting that we should pay attention to further improving the model's ability in capturing ENSO events and their links with atmospheric circulation, as well as in reproducing monsoon ISV with accurate spectral characteristics and reasonable frequencies of long breaks or active spells.

In addition, it should be noted that the ensemble prediction of the WNPSM exhibits more skill than that of the ISM, as demonstrated in section 3, which is also found in predictions of the Asian summer monsoon by the NCEP Climate Forecast System (e.g., Jiang et al., 2013). Two factors may account for this feature. First, compared to the ISM, the WNPSM is more highly correlated with ENSO and large-scale circulation on the interannual scale (e.g., Wang et al., 2000; Xie et al., 2009), which can be relatively better captured by the ensemble prediction of models. Secondly, the interannual variability of the ISM is affected not only by ENSO, but also by local SST (e.g., the Indian Ocean dipole) and thermal conditions over the surrounding lands such as the Tibetan Plateau, leading to more complex and less skillful prediction of the ISM. Further studies on this issue are undoubtedly necessary.

***Acknowledgements.*** The authors thank the three anonymous reviewers for their constructive comments, which improved the overall quality of this paper. This study was partially supported by the National Natural Science Foundation of China (Grant Nos. 41305057, 41275076, 41105069, and 41375081), the National Ba-

sic Research Program of China (Grant Nos. 2010CB951903 and 2014CB953900) and the LCS Youth Fund (2014).

## REFERENCES


Achuthavarier, D., and V. Krishnamurthy, 2010: Relation between intraseasonal and interannual variability of the South Asian monsoon in the national Centers for Environmental Predictions forecast systems. *J. Geophys. Res.*, **115**, D08104, doi: 10.1029/2009JD012865.

Charney, J. G., and J. Shukla, 1981: Predictability of monsoons. *Monsoon Dynamics*, J. Lighthill and R. P. Pearce, Eds., Cambridge University Press, Cambridge, 99–109.

Drbohlav, H., and V. Krishnamurthy, 2010: Spatial structure, forecast errors, and predictability of the South Asian monsoon in CFS monthly retrospective forecasts. *J. Climate*, **23**, 4750–4769.

Ferranti, L., J. M. Slingo, T. N. Palmer, and B. J. Hoskins, 1997: Relations between interannual and intraseasonal monsoon variability as diagnosed from AMIP integrations. *Quart. J. Roy. Meteor. Soc.*, **123**, 1323–1357.

Fujinami, H., and Coauthors, 2011: Characteristic intraseasonal oscillation of rainfall and its effect on interannual variability over Bangladesh during boreal summer. *Int. J. Climatol.*, **31**, 1192–1204.

Goswami, B. N., 1998: Interannual variation of Indian summer monsoon in a GCM: External conditions versus internal feedbacks. *J. Climate*, **11**, 501–522.

Goswami, B. N., and R. S. Ajaya Mohan, 2001: Intraseasonal oscillations and interannual variability of the Indian summer monsoon. *J. Climate*, **14**, 1180–1198.

Goswami, B. N., and P. K. Xavier, 2005: Dynamics of "internal" interannual variability of the Indian Summer Monsoon in a GCM. *J. Geophys. Res.*, **110**, D24104, doi: 10.1029/2005JD006042.

Goswami, B. N., G. Wu, and T. Yasunari, 2006: The annual cycle, intraseasonal oscillations, and roadblock to seasonal predictability of the Asian summer monsoon. *J. Climate*, **19**, 5078–5099.

Jiang, X., S. Yang, Y. Li, A. Kumar, X. Liu, Z. Zuo, and B. Jha, 2013: Seasonal-to-interannual prediction of the Asian summer monsoon in the NCEP Climate Forecast System Version 2. *J. Climate*, **26**, 3708–3727.

Joseph, S., A. K. Sahai, and B. N. Goswami, 2009: Eastward propagating MJO during boreal summer and Indian monsoon droughts. *Climate Dyn.*, **32**, 1139–1153.

Joseph, S., A. K. Sahai, and B. N. Goswami, 2010: Boreal summer intraseasonal oscillations and seasonal Indian monsoon prediction in DEMETER coupled models. *Climate Dyn.*, **35**, 651–667.

Kanamitsu, M., W. Ebisuzaki, J. Woollen, S. K. Yang, J. J. Hnilo, M. Fiorino, and G. L. Potter, 2002: NCEP-DEO AMIP-II Reanalysis (R-2). *Bull. Amer. Meteor. Soc.*, **83**, 1631–1643.

Kang, I. S., and J. Shukla, 2006: Dynamic seasonal prediction and predictability of the monsoon. *The Asian Monsoon*, Springer, 585–612.

Kim, H. M., I. S. Kang, B. Wang, and J. Y. Lee, 2008: Interannual variations of the boreal summer intraseasonal variability predicted by ten atmosphere-ocean coupled models. *Climate Dyn.*, **30**, 485–496.

Kripalani, R. H., A. Kulkarni, S. S. Sabade, and M. L. Khandekar, 2003: Indian monsoon variability in a global warming scenario. *Nat. Hazards*, **29**, 189–206.

Krishnamurthy, V., and J. Shukla, 2000: Intraseasonal and interannual variability of rainfall over India. *J. Climate*, **13**, 4366–4377.

Krishnamurthy, V., and J. Shukla, 2007: Intraseasonal and seasonally persisting patterns of Indian monsoon rainfall. *J. Climate*, **20**, 3–20.

Krishnamurthy, V., and J. Shukla, 2008: Seasonal persistence and propagation of intraseasonal patterns over the Indian monsoon region. *Climate Dyn.*, **30**, 353–369.

Krishnan, R., V. Kumar, M. Sugi, and J. Yoshimura, 2009: Internal feedbacks from monsoon–midlatitude interactions during droughts in the Indian summer monsoon. *J. Atmos. Sci.*, **66**, 553–578.

Kumar, K. K., B. Rajagopalan, and M. A. Cane, 1999: On the weakening relationship between the Indian monsoon and ENSO. *Science*, **284**, 2156–2159.

Lawrence, D. M., and P. J. Webster, 2001: Interannual variations of the intraseasonal oscillation in the South Asian summer monsoon region. *J. Climate*, **14**, 2910–2922.

Lee, J. Y., and Coauthors, 2010: How are seasonal prediction skills related to models' performance on mean state and annual cycle? *Climate Dyn.*, **35**, 267–283.

Li, C., R. Lu, and B. Dong, 2012: Predictability of the western North Pacific summer climate demonstrated by the coupled models of ENSEMBLES. *Climate Dyn.*, **39**, 329–346.

Liebmann, B., and C. A. Smith, 1996: Description of a complete (interpolated) outgoing longwave radiation dataset. *Bull. Amer. Meteor. Soc.*, **77**, 1275–1277.

Lin, A., and T. Li, 2008: Energy spectrum characteristics of boreal summer intraseasonal oscillations: climatology and variations during the ENSO developing and decaying phases. *J. Climate*, **21**, 6304–6320.

Liu, X. W., S. Yang, A. Kumar, S. Weaver, and X. W. Jiang, 2013: Diagnostics of subseasonal prediction biases of the Asian summer monsoon by the NCEP Climate Forecast System. *Climate Dyn.*, **41**, 1453–1474, doi: 10.1007/s00382-012-1553-3.

Liu, X. W., S. Yang, Q. P. Li, A. Kumar, S. Weaver, and S. Liu, 2014: Subseasonal forecast skills and biases of global summer monsoons in the NCEP Climate Forecast System version 2. *Climate Dyn.*, **42**, 1487–1508, doi: 10.1007/s00382-013-1831-8.

Palmer, T. N., 1994: Chaos and predictability in forecasting the monsoons. *Proc. Indian Natl. Sci. Acad.*, **60A**, 57–66.

Qi, Y. J., R. H. Zhang, T. Li, and M. Wen, 2008: Interactions between the summer mean monsoon and the intraseasonal oscillation in the Indian monsoon region. *Geophys. Res. Lett.*, **35**, L17704, doi: 10.1029/2008GL034517.

Rajeevan, M., C. K. Unnikrishnan, and B. Preethi, 2012: Evaluation of the ENSEMBLES multi-model seasonal forecasts of Indian summer monsoon variability. *Climate Dyn.*, **38**, 2257–2274.

Reynolds, R. W., N. A. Rayner, T. M. Smith, D. C. Stokes, and W. Wang, 2002: An improved in situ and satellite SST analysis for climate. *J. Climate*, **15**, 1609–1625.

Sperber, K. R., J. M. Slingo, and H. Annamalai, 2000: Predictability and relationship between subseasonal and interannual variability during the Asian summer monsoon. *Quart. J. Roy. Meteor. Soc.*, **126**, 2545–2574.

Suhas, E., J. M. Neena, and B. N. Goswami, 2012: Interannual

variability of Indian summer monsoon arising from interactions between seasonal mean and intraseasonal oscillations. *J. Atmos. Sci.*, **69**, 1761–1774.

Teng, H., and B. Wang, 2003: Interannual variations of the boreal summer intraseasonal oscillation in the Asian-Pacific region. *J. Climate*, **16**, 3572–3584.

Waliser, D. E., R. Murtugudde, and L. E. Lucas, 2004: Indo-Pacific Ocean response to atmospheric intraseasonal variability. Part II: boreal summer and the intraseasonal oscillation. *J. Geophys. Res.*, **109**, C03030, doi: 10.1029/2003JC002002.

Wang, B., R. Wu, and X. Fu, 2000: Pacific-East Asia teleconnection: How does ENSO affect East Asian climate? *J. Climate*, **13**, 1517–1536.

Wang, B., R. Wu, and K. M. Lau, 2001: Interannual variability of Asian summer monsoon: Contrast between the Indian and western North Pacific-East Asian monsoons. *J. Climate*, **14**, 4073–4090.

Wang, B., and Coauthors, 2008: How accurately do coupled climate models predict the leading modes of Asian–Australian monsoon interannual variability? *Climate Dyn.*, **30**, 605–619.

Wu, T., and Coauthors, 2010: The Beijing Climate Center atmospheric general circulation model: Description and its performance for the present-day climate. *Climate Dyn.*, **34**, 123–147.

Wu, T. W., and Coauthors, 2013: Global carbon budgets simulated by the Beijing Climate Center climate system model for the last century. *J. Geophys. Res.*, **118**, 1–22, doi: 10.1002/jgrd.50320.

Xavier, P. K., J. P. Duvel, and J. D. Francisco, 2008: Boreal summer intraseasonal variability in coupled seasonal hindcasts. *J. Climate*, **21**, 4477–4497.

Xie, P., and P. A. Arkin, 1997: Global precipitation: A 17-year monthly analysis based on gauge observations, satellite estimates, and numerical model outputs. *Bull. Amer. Meteor. Soc.*, **78**, 2539–2558.

Xie, S., K. Hu, J. Hafner, H. Tokinaga, Y. Du, G. Huang, and T. Sampe, 2009: Indian Ocean capacitor effect on Indo-western Pacific climate during the summer following El Niño. *J. Climate*, **22**, 730–747.

Xie, S., H. Ma, J. Boyle, S. Klein, and Y. Zhang, 2012: On the correspondence between short- and long-time-scale systematic errors in CAM4/CAM5 for the year of tropical convection. *J. Climate*, **25**, 7937–7955.

Xue, Y., and Coauthors, 2010: Intercomparison and analyses of the climatology of the West African monsoon in the West African monsoon modeling and evaluation project (WAMME) first model intercomparison experiment. *Climate Dyn.*, **35**, 3–27.

Yang, S., Z. Zhang, V. Kousky, R. W. Higgins, S. H. Yoo, J. Liang, and Y. Fan, 2008: Simulations and seasonal prediction of the Asian summer monsoon in the NCEP Climate Forecast System. *J. Climate*, **21**, 3755–3775.

Yoo, J. H., W. R. Andrew, and I. S. Kang, 2010: Analysis of intraseasonal and interannual variability of the Asian summer monsoon using a hidden Markov model. *J. Climate*, **23**, 5498–5516.

Zhou, T., B. Wu, and B. Wang, 2009: How well do atmospheric general circulation models capture the leading modes of the interannual variability of the Asian–Australian monsoon? *J. Climate*, **22**, 1159–1173.

Atmospheric Research 143 (2014) 17–30

Contents lists available at ScienceDirect

Atmospheric Research

journal homepage: www.elsevier.com/locate/atmos

# An application of hybrid downscaling model to forecast summer precipitation at stations in China

Ying Liu [a,b,c], Ke Fan [c,b,*]

[a] Laboratory for Climate Studies, National Climate Center, China Meteorological Administration, Beijing 100081, China
[b] Collaborative Innovation Center on Forecast and Evaluation of Meteorological Disasters, Nanjing University of Information Science & Technology, Nanjing 210044, China
[c] Nansen-Zhu International Research Centre, Institute of Atmospheric Physics Chinese Academy of Sciences, Beijing 100029, China

ARTICLE INFO

*Article history:*
Received 19 November 2012
Received in revised form 20 January 2014
Accepted 28 January 2014
Available online 7 February 2014

*Keywords:*
Summer precipitation
Stations
China
Downscaling model

ABSTRACT

A pattern prediction hybrid downscaling method was applied to predict summer (June–July–August) precipitation at China 160 stations. The predicted precipitation from the downscaling scheme is available one month before. Four predictors were chosen to establish the hybrid downscaling scheme. The 500-hPa geopotential height (GH5) and 850-hPa specific humidity (q85) were from the skillful predicted output of three DEMETER (Development of a European Multi-model Ensemble System for Seasonal to Interannual Prediction) general circulation models (GCMs). The 700-hPa geopotential height (GH7) and sea level pressure (SLP) were from reanalysis datasets. The hybrid downscaling scheme (HD-4P) has better prediction skill than a conventional statistical downscaling model (SD-2P) which contains two predictors derived from the output of GCMs, although two downscaling schemes were performed to improve the seasonal prediction of summer rainfall in comparison with the original output of the DEMETER GCMs. In particular, HD-4P downscaling predictions showed lower root mean square errors than those based on the SD-2P model. Furthermore, the HD-4P downscaling model reproduced the China summer precipitation anomaly centers more accurately than the scenario of the SD-2P model in 1998. A hybrid downscaling prediction should be effective to improve the prediction skill of summer rainfall at stations in China.

© 2014 Elsevier B.V. All rights reserved.

## 1. Introduction

China is located in East Asia, and the variability of its summer (June–July–August) precipitation is largely dominated by the East Asian Summer Monsoon (EASM). The monsoon system is characterized not only by unique seasonal changes but also by the interannual and interdecadal variability of the winter and summer monsoons (Tao and Chen, 1987; Wang et al., 2001; H.J. Wang, 2001, 2002). Furthermore, the EASM often leads to severe disasters, which makes accurate predictions on the interannual variability of EASM important for both the society and economy of China. General Circulation Models (GCMs) have become one important tool for conducting seasonal predictions. GCMs can predict large-scale atmospheric circulation systems better, but they show a relatively low overall ability to simulate the EASM precipitation (Wang, 1997; Wang et al., 2000, 2004; Sperber et al., 2001; Kang et al., 2002; Gao et al., 2011).

Different downscaling techniques had been developed as tools for interpolating large-scale information into local or regional variables. Statistical downscaling (SD) was a popular approach that uncovered the stable relationship between one or several large-scale meteorological variables (predictors), such as atmospheric circulation, and local-scale variables (predictand). This relationship was exploited to predict regional elements by projecting large-scale information onto local-scale variables (Zorita and Von Storch, 1999; Fernández-Ferrero et al., 2009). A SD scheme can use both GCM outputs and the

* Corresponding author at: IAP–CAS, China.
*E-mail addresses:* liuying@cma.gov.cn (Y. Liu), fanke@mail.iap.ac.cn (K. Fan).

0169-8095/$ – see front matter © 2014 Elsevier B.V. All rights reserved.
http://dx.doi.org/10.1016/j.atmosres.2014.01.024

preceding atmospheric circulation variables of observations as predictors to make predictions (e.g., Wang and Qian, 2010). Thus, local precipitation can be forecasted by well-predicted large-scale circulation data from GCMs and the observational variables that are strongly correlated with the predictand (Wu et al., 2012). Statistical downscaling is widely used because it can largely eliminate the impact of model biases and capture the statistical relation using predictors from GCM and observational data, respectively.

Most SD schemes were based on regression or similar methods (Fan et al., 2012; Giorgi et al., 2001; Benestad, 2004; Lang and Wang, 2010; Guo et al., 2011; Liu et al., 2011). Murphy (2000) established a SD method based on linear regression relationships between surface temperature or precipitation and a range of atmospheric predictor variables to predict climate change in Europe. Chu et al. (2008) used 500-hPa geopotential height and sea level pressure as predictors of downscale precipitation over north Taiwan. Singular Value Decomposition (SVD) and Canonical Correlation Analysis (CCA) have the advantage of selecting pairs of spatial patterns that are optimally covariated and correlated, respectively, among the linear statistical methods. Uvo et al. (2001) applied SVD to estimate the average rainfall over some parts of Japan and concluded that the major rainfall features had been captured. Paul et al. (2008) developed a SVD-based regression model to downscale the monthly rainfall over East Asia, and they predicted the annual rainfall tendency at the end of the 21st century. A number of studies have focused on the seasonal precipitation and temperature over regions (Mao and Li, 1997; Huang and Huang, 2000; Zhang et al., 2006; Jia et al., 2010) and stations of China (Chen et al., 2012; Sun and Chen, 2012). However, few studies have used both the previous and simultaneous predictors to predict the summer rainfall in China with the coupled patterns of statistical correlation (e.g., SVD) between the predictor and predictand. Thus, this study aims to develop a hybrid SD to forecast the summer precipitation at stations over China. In particular, the downscaling scheme was developed to estimate summer rainfall based on the establishment of links between large-scale circulation patterns and regional rainfall with the SVD method. The predictors were chosen from simulated GCM outputs and reanalysis variables. The results of the downscaling method based on multi-predictor experimental datasets will be analyzed.

Section 2 introduced the GCMs, the observational data and the method used to establish the downscaling scheme. The relationship between the predictors and predictand was analyzed in Section 3. The GCMs' prediction skill evaluations of two of the predictors were shown in Section 4. Section 5 analyzed results of the downscaling. The conclusions and discussions were presented in Section 6.

## 2. Data and method

### 2.1. Data

The predictand was the summer precipitation at 160 stations over China, the locations of which were shown in Fig. 1(a). Station-based observed monthly rainfall data from 1960 to 2001 were obtained from the National Climate Center of the China Meteorological Administration. The observed data were used not only to develop the SD technique but also to validate the skill of the prediction scheme.

The simultaneous predictor data were taken from three global coupled ocean–atmosphere DEMETER (Development of a European Multi-model Ensemble System for Seasonal to Interannual Prediction) model outputs. The DEMETER project was conceived to produce nine ensemble members of 6-month long predictions by running a number of state-of-the-art global coupled ocean–atmosphere models on a single supercomputer with common archiving and diagnostic software (Palmer et al., 2004). The initial conditions for the atmospheric and land states in the DEMETER models were provided by the ECMWF 40-yr Reanalysis (ERA-40) (Uppala et al., 2005) four times each year on the 1st day of February, May, August and November with a spatial resolution of 2.5° in latitude and longitude. Starting from 1 May, the hindcast data used in the study were the outputs of three selected DEMETER models: CNRM (Centre National de Recherches Météorologiques, France), ECMWF (European Centre for Medium-Range Weather Forecasts, UK) and UKMO (Met Office, UK). These models were chosen because they have more extensive hindcast data than the other models of the

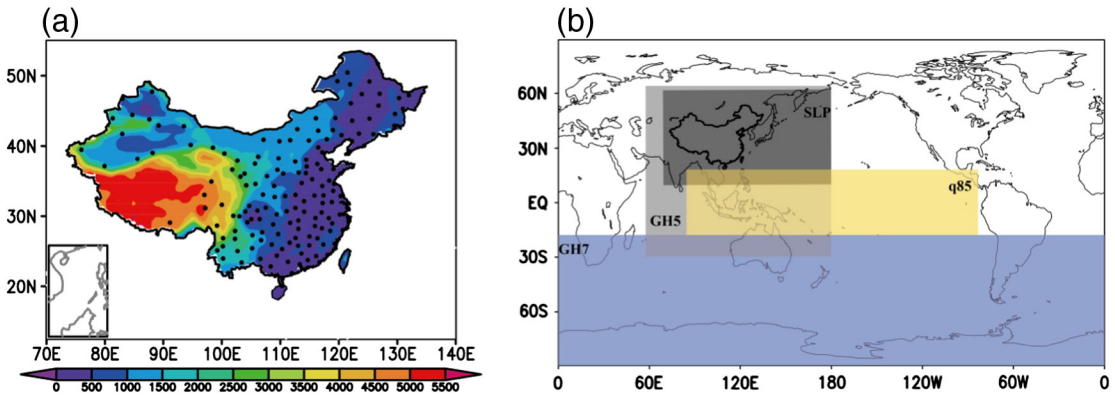


**Fig. 1.** A China topography map with 160 station locations. Shading in China denotes the topography (m), and the dots show the locations of 160 stations over China. The gray, dark gray, yellow and blue rectangles represent domains of predictors GH5, SLP, q85 and GH7, respectively. (For interpretation of the references to color in this figure legend, the reader is referred to the web version of this article.)

DEMETER project. Multi-model ensemble (MME) denotes the average of the hindcasts generated by CNRM, ECMWF and UKMO. Two simultaneous predictors were taken from the variables of the GCM outputs: 500-hPa geopotential height (GH5) and 850-hPa specific humidity (q85). The hindcast data also span the 42-yr period from the summer of 1960 to the summer of 2001.

The ECMWF 40-year reanalysis project dataset was also used to define the other two preceding predictors with a resolution of 2.5° × 2.5°. The reanalyzed data from ERA-40 are 700-hPa geopotential height (GH7) and sea level pressure (SLP), and these data were available in April of 1960–2001 and winter of 1959–2000, respectively. In addition, GH5 and q85 in summer from the ERA-40 reanalysis dataset were used to evaluate the predictive skill of simultaneous predictors from DEMETER.

In addition, the summer precipitation data with a resolution of 2.5° × 2.5° from the GCMs (i.e., CNRM, ECMWF, and UKMO) were interpolated into the 160 stations in China. Then, the downscaling method and the GCMs were compared based on the observational data. In the interpolated method, the original GCM precipitation data in 160 stations were assigned by the nearest GCM grid data (Im et al., 2007; Yang et al., 2010).

### 2.2. Method

In this study, a combination of Empirical Orthogonal Function (EOF) analyses, Singular Value Decomposition (SVD) analyses and multi linear regression analyses were used to obtain stable statistical relationships between large-scale circulation and regional precipitation. Before downscaling was performed, the predictors and predictand were reconstructed using the respective EOFs and principal components as a means of noise filtering during the training period (Liu and Fan, 2012a, 2012b). The criterion of the retained EOF modes referred to the Kaiser's rule (Wilks, 2006):

$$\lambda_m > \frac{T}{K}\sum_{k=1}^{K} s_{k,k} \tag{1}$$

where $\lambda_m$ represents the retained eigenvalue of EOF, $s_{k,k}$ is the variance of the $k$th element of the variable field, and T is a threshold parameter, here T = 0.7 (Jolliffe, 1972, 2002). Based on Eq. (1), first 12 EOF modes for the predictand (rainfall) and the first 3, 4, 3 and 7 EOF modes for GH5, SLP, q85 and GH7 were retained, respectively.

SVD was then used to extract coupled patterns between large-scale circulation and regional precipitation during the fitting time span (Bretherton et al., 1992). Additionally, different stations should have different weights in this step. The detail of the process of SD model was shown in Appendix A.

In this study, more than one predictor was selected into the SD model and the detail will be discussed in Section 4. After the calculation of the SD results based on different predictors, the final predicted rainfall was obtained by weighting the downscaling prediction based on different predictors optimally as follows:

$$R_{SD}(x,t) = \beta_0(x,t) + \sum_{i=1}^{k} \beta_i(x,t) R_i(x,t) \tag{2}$$

where $R_{SD}(x,t)$ indicates the final downscaled precipitation, $R_i(x,t)$ is the downscaling result based on individual predictor, $k$ is the total number of the downscaling predictions (i.e., $k = 2$ or $k = 4$), $\beta_i(x,t)$ indicates the regression coefficients of multiple linear regression analysis, and $x$ and $t$ represent the station point and forecast time, respectively.

Both the cross-validation for the 1960–2001 (42 yr) period and the independent hindcasts for the 1990–2001(12 yr) period were performed to verify the capability of the downscaling scheme. In cross-validation, the rainfall data of one year were excluded from the dataset, and the rainfall data of the other years were defined in the training period. Then a prediction based on the training period was made for the excluded year (Michaelsen, 1987). This procedure was repeated 42 times until rainfall predictions for 42 years were generated for validation. The cross-validation scheme was called Scheme-CV. In the independent hindcasts during the 1990–2001 (12 yr) period, the downscaling scheme was established on the moving 30 yr (i.e., the first 30 years from 1960 to 1989) period to predict the rainfall for the following year. This procedure was repeated 12 times. The scheme that depended on independent hindcasts was named Scheme-IH. The corresponding climatology and anomaly fields for both the predictor and predictand were redefined at the same time as the training period in both of the aforementioned downscaling Schemes.

## 3. Predictors

### 3.1. Choice of predictors

Statistical downscaling used long-term general circulation variables and regional variables to derive a robust relationship between the predictors and predictand. In this study, the simultaneous and previous predictors were both considered in the downscaling scheme. Here, the GH5 in the summer during the 1960–2001 period was considered over the 30°S–65°N, 60°–180°E (Pan-East Asian) region, which covers Baikal, the western North Pacific, the EASM and the Somali jet, among other areas. These related and important atmospheric systems strongly influence the rainfall over China (Chen and Zhao, 2000; Wang et al., 2001). In addition, as Nitta and Hu (1996) and Hu (1997) demonstrated, the variation of the summer rainfall in China has a strong link with the geopotential height anomaly at 500 hPa.

The SVD analysis was used to unveil the leading mode of covariability between the GH5 and station rainfall data (Prohaska, 1976). Fig. 2 gave the spatial pattern of the first SVD mode for rainfall over China and the GH5 over Pan-East Asia as the input data. For the GH5 field, a tripole pattern dominated this region. In addition, a north–south distribution shaped the Pacific–Japan (PJ) pattern (Nitta, 1987; Nitta and Hu, 1996) over the central North Pacific Ocean (Fig. 2b). The PJ wave-train, which is closely related to the west Pacific subtropical high and summer monsoon over East Asia, can give influence on summer rainfall over China (Huang and Li, 1987; Kosaka and Nakamura, 2006). The corresponding rainfall pattern was characterized by a typical 'more, less, more' (vice versa) summer rainfall distribution over East China (Fig. 2a). The time coefficients corresponding to the leading SVD mode for precipitation and GH5 were given in Fig. 2(c). High correlation between the time coefficients

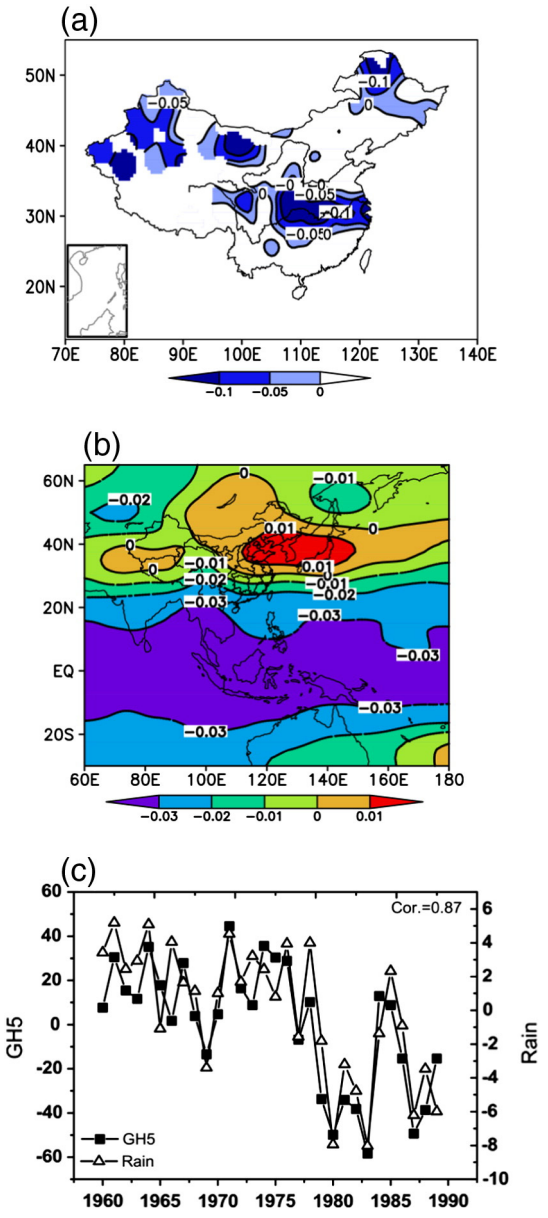


**Fig. 2.** The leading SVD mode spatial patterns of (a) the observed station rainfall in China and (b) the reanalyzed GH5 in Pan-East Asia during the summer. (c) The normalized time coefficients corresponding to rainfall and GH5. Data for the 1960–1989 period were used.

suggested that the leading rainfall and GH5 patterns were coupled to the interannual and interdecadal variability (e.g., the shift around the end of the 1970s) (Hu, 1997; S.W. Wang, 2001; Gong and Ho, 2003). Additionally, the Squared Covariance Fraction explained by the first pair of SVD patterns was approximately 65%. Overall, the result indicated that the typical summer rainfall distribution over China was associated with a large-scale tripole pattern in the GH5 field. Therefore, we chose GH5 over the Pan-East Asian region as a simultaneous predictor of China summer rainfall.

The humidity from oceans is a key factor influencing rainfall (S.W. Wang, 2001). Wang and Fan (2009) proposed the 'tropical analog' idea to predict the rainfall in the East Asian and Western Pacific regions. The predictability of the models is higher in the tropics than in the extratropics (Branković et al., 1994). Therefore, Wang and Fan (2009) designed a new scheme that uses the tropical rainfall prediction skill to improve East Asian rainfall prediction. In addition, the specific humidity at 850-hPa over the tropical Pacific Ocean region (20°S–20°N, 80°E–180°W) was closely related to the precipitation in the tropical Pacific Ocean. The systems that exist in the eastern tropical Pacific and Philippines are important components of the ENSO and PJ patterns (Nitta and Hu, 1996), which have close relationships with the summer rainfall over East Asia. Based on their works, q85 in this region was selected as the other simultaneous predictor.

In this study, the other two variables, GH7 and SLP, from the atmospheric circulation, were used as the previous predictors, and the extratropics in the Southern Hemisphere (90°–20°S, 0°–357.5°E) and East Asia (10°–60°N, 70°–180°E), respectively, were chosen as their domains. The Antarctic Oscillation (AAO) (GH7) was the dominant mode in the Southern Hemisphere, which was characterized by a large-scale seesaw oscillation of atmospheric circulations between the middle and high latitudes of the Southern Hemisphere (Rogers and van Loon, 1982; Kidson, 1988). Gong and Wang (1999) and Thompson and Wallace (2000) defined the AAO based on the oscillation between middle and high latitudes in Southern Hemisphere. The AAO in spring can impact the East Asian summer monsoon rainfall through atmospheric teleconnection, the western Pacific subtropical High and the tropical convection (Xue et al., 2004; Sun et al., 2009; Wang and Fan, 2005). Therefore, the AAO had been applied in the development of some effective statistical models of the summer rainfall in China (Wang and Fan, 2005; Fan, 2006; Fan and Wang, 2006). According to the above studies, the April AAO was an important preceding predictor of the summer rainfall over China. Additionally, the correlation coefficient between the principal component of the China summer rainfall EOF1 and that of the April GH7 was 0.45 (above 99% confident level) from 1960 to 1989. Therefore, the AAO in April derived from GH7 was an important predictor of the summer rainfall in China.

In boreal winter, monsoonal northwesterly winds prevail over Eurasia and northwestern Pacific Ocean. These winds are accompanied by the development of the Siberian High and Aleutian Low systems at sea level (Yoshiike and Kawamura, 2009). If the East Asian Winter Monsoon (EAWM) is enhanced, the associated northwesterly winds strengthen and supply additional cold air to the south of Eurasia. The EAWM is believed to provide a mechanism that generates the ENSO (El Niño and Southern Oscillation) phenomena (Li et al., 1987; Li, 1988). In particular, the anomalous atmospheric circulation in winter (i.e., EAWM) through ocean–atmosphere interactions (i.e., ENSO) influences the western Pacific subtropical high and the rainfall over China in the following summer (Sun and Sun, 1994; Chen et al., 2000). In addition, the correlation coefficient between the principal component of the China summer rainfall EOF1 and that of the winter SLP was 0.52 (above 99% confident level) from 1960 to 1989. Therefore, the SLP in winter over East Asia had a close relationship with EAWM and a delaying influence on the later summer precipitation over China. Overall, four predictors from the

simultaneous and previous large-scale circulation were chosen, and their domains are shown in Fig. 1(b). In addition, Table 1 showed the basic descriptions of the four predictors, the time span, the datasets and the domains covered.

### 3.2. Forecasting skill of the predictors by the GCMs

According to this SD scheme, the improved prediction effect of summer rainfall over China was dependent on the model forecast of GH5 and q85 to some extent.

First, the GH5 prediction skill of the GCMs and MME was evaluated. For all of the GCMs and MME, the multi-year average of spatial anomaly correlation coefficients (ACCs) for GH5 was larger than 0.18 (above 95% confidence level) (Fig. 3). The temporal CCs between the GCMs data and reanalysis data (ERA-40) of GH5 during the summers of 1960–2001 were computed (not shown). The significantly positive CCs between the observed and model-predicted GH5 field mainly covered the mid-low latitude regions of both hemispheres for these GCMs (i.e., CNRM, ECMWF and UKMO) and MME. The high CCs were centralized within 40°N–40°S (Lang and Wang, 2005). It was also found that the GCMs show good skill over most of the region over Pan-East Asian, which was the domain of the GH5 predictor.

To estimate whether the GH5 from the GCM outputs can capture the interannual variability of the reanalysis data over Pan-East Asia, this study performed an EOF analysis during the summers of the 1960–1989 period for the GH5 anomaly (not shown). The CCs between the reanalysis EOF1 and GCM EOF1 patterns of the GH5 anomaly were 0.41, 0.34, 0.49 and 0.43 for CNRM, ECMWF, UKMO and MME, respectively. In addition, the spatial pattern covering the central North Pacific was also shaped like the PJ pattern, as shown in Fig. 2(b). Overall, the GH5 from CNRM, ECMWF, UKMO and MME over Pan-East Asia can provide favorable circulation information for the SD scheme in this study.

Next, the same evaluation techniques were carried out on the other simultaneous predictor, q85. For all of the GCMs and MME, the multi-year average of the ACCs for q85 was larger than 0.36 (above 99% confidence level) (Fig. 4). It was noted that positive correlations of q85 are found at low latitudes (not shown), where the interannual climate variability was dominated by the anomalies of lower boundary forces, between the reanalysis and GCMs at a 90% confidence level (Charney and Shukla, 1981). The predictor q85 from the GCMs and MME in the region covering the tropical Pacific Ocean (in the rectangle) had stronger and more positive correlations. Similar to GH5, the EOF analysis during the summers of the 1960–2001 period for q85 was also performed (not shown). The corresponding CCs between the reanalysis EOF1 and GCM EOF1 patterns of the q85 anomaly were 0.49, 0.44, 0.54 and 0.52, respectively. Overall, the good prediction skill of GH5 and q85 from the models suggested that these two predictors are available and suitable for the downscaling Scheme.

**Table 1**
Description of the predictors.

| Predictors | Period | Datasets | Domains |
|---|---|---|---|
| GH5 | 1960–2001 summer | CNRM,ECMWF, UKMO | 30°S–65°N,60°–180°E |
| q85 | 1960–2001 summer | CNRM,ECMWF, UKMO | 20°S–20°N,80°E–80°W |
| GH7 | 1960–2001 Apr. | ERA-40 | 90°–20°S,0°–357.5°E |
| SLP | 1959–2000 winter | ERA-40 | 10°–60°N,70°–180°E |

## 4. Verification of the statistical downscaling schemes

Because four predictors (from GCMs and reanalysis data) were selected for the downscaling scheme, the contribution of the predictors will be estimated by involving the predictors step by step. First, each predictor was involved in the downscaling scheme. For example, the GH5 predictor is used in the downscaling model abbreviated as the "GH5 model", and the same was true for the other predictor downscaling models. Second, SD models based on two simultaneous predictors derived from GCMs (e.g., GH5 and q85) (abbreviated as the "SD-2P model") and a hybrid statistical model (HD) including two simultaneous predictors in SD-2P and two previous predictors from observation (abbreviated as the "HD-4P model") are established as shown in Eq. (2).

The downscaling results based on each of the above models were compared in Scheme-CV. Here, the RMSE skill score indicated the difference between the RMSE of the original GCMs and the RMSE of the downscaling models with the division of the former (Wilks, 2011). A positive RMSE skill score indicated an improved prediction skill. The performance of the different downscaling models involving different predictors of Scheme-CV for MME was shown in Fig. 5. The spatial RMSE skill score for all of the downscaling models was larger than zero during the whole period. The multi-year average RMSE skill score was approximately 35% for the downscaling models involving any individual predictor. In addition, the multi-year average RMSE skill score in SD-2P model had been more than 37%, but for the HD-4P model, it reached more than 40% (Table 2). Furthermore, the differences between multi-year average RMSE skill score of 4P model and 2P model (individual predictor model) are significant at 90% (95%) from *t*-test. It was demonstrated that HD-4P downscaling model performs better than the single-predictor downscaling models.

Finally, downscaling results based on the SD-2P model and the HD-4P model were estimated and compared with the original GCM outputs. And two schemes (i.e., Scheme-CV and Scheme-IH) were performed to compare the downscaling summer precipitation over China between SD-2P model and HD-4P model.

### 4.1. Downscaling prediction of the station rainfall by Scheme-CV

The spatial anomaly correlation between the observational data and the GCM-simulated or Scheme-CV downscaling HD-4P model's predictions of rainfall at 160 stations was shown in Fig. 6. All of the GCMs showed much lower skill than the downscaling scheme in predicting China station rainfall. The multi-year average ACCs between the observational rainfall over China 160 stations and that from original GCMs were 0.04, 0.05, −0.01 and 0.0.03 for CNRM, ECMWF, UKMO and MME, respectively. The corresponding ACCs of HD-4P model all increased to approximately 0.23. In addition,

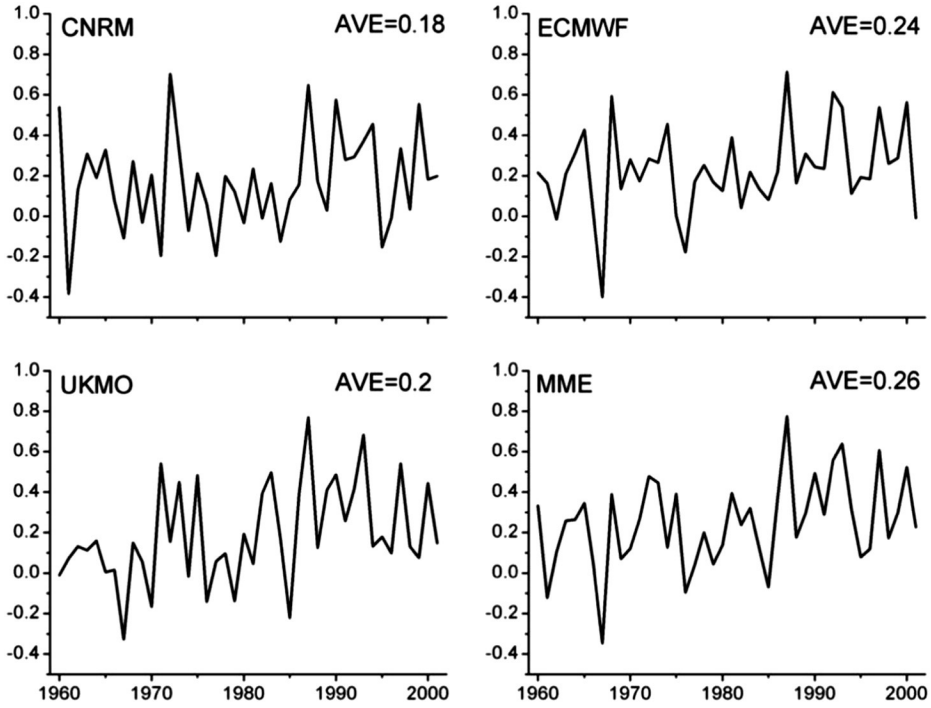


**Fig. 3.** The spatial anomaly correlation coefficient of GH5 over Pan-East Asia between the analysis and the GCMs during the summers of 1960–2001. The model name and multi-year average ACCs are shown at the top left and right of each panel, respectively.

the spatial ACCs for all of the GCMs of downscaling SD-2P model were relatively lower than those of the HD-4P model (Scheme-CV in Table 3). The downscaling HD-4P model products based on Scheme-CV also made significant progress with respect to the temporal anomaly correlation coefficients (ACCs) (Fig. 7 showed the use of the Cressman interpolation

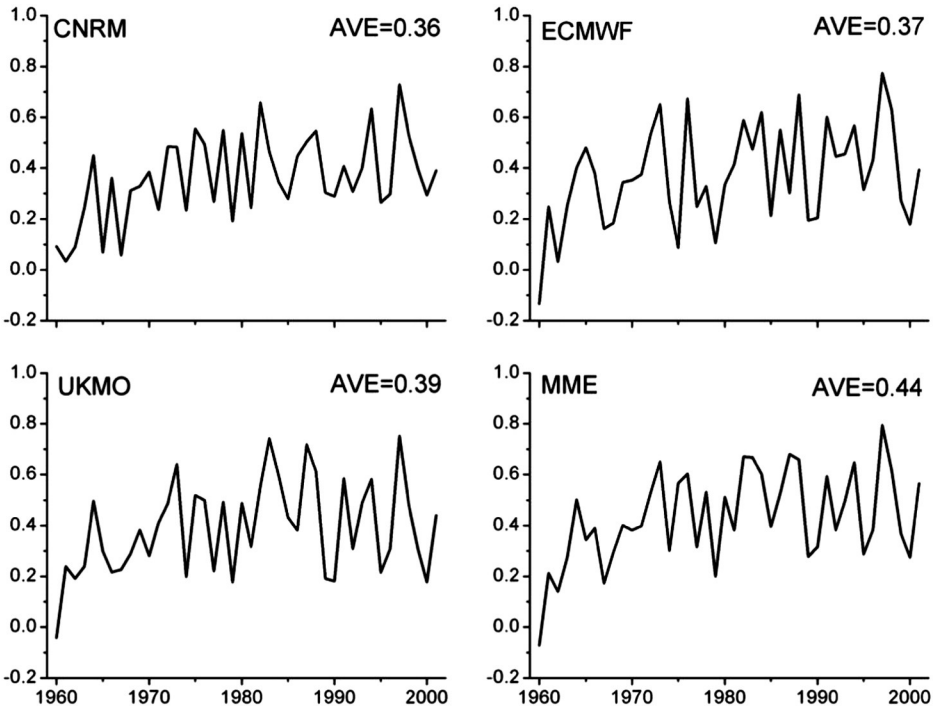


**Fig. 4.** Same as Fig. 3 but for q85 in the tropical Pacific Ocean.

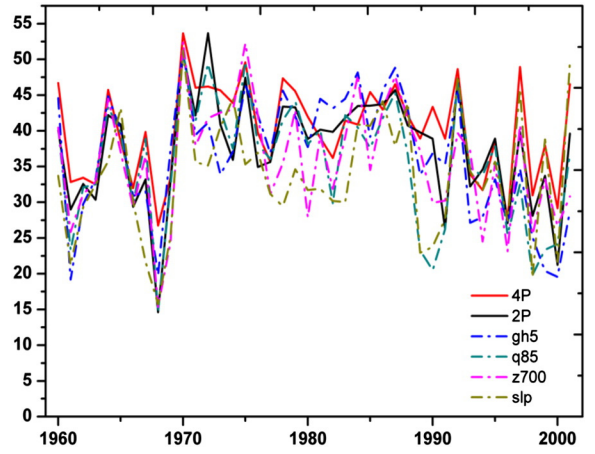


**Fig. 5.** The spatial RMSE skill score based on the MME downscaling (a) GH5 model, (b) q85 model, (c) GH7 model, (d) SLP model, (e) SD-2P model and (f) HD-4P model. Unit: %.

method for mapping and the same below) (Gilchrist and Cressman, 1954; Cressman, 1959). The temporal ACC spatial distributions for the individual original GCMs were only greater than 0.25 (90% confident level) in several small regions that were mainly centralized in the Jianghuai Valley (left column of Fig. 7). The predicted rainfall of the Scheme-CV downscaling model showed higher skill in the ACCs between the observational rainfall and the downscaling HD-4P model's predictions of rainfall in the summers of 1960–2001. For all of the GCMs and MME, the temporal ACCs (above 99% confidence level) performed well over most parts of China, especially for most parts of Xinjiang, Northeast China, the Ordos Region and the Yangtze River Valley (right column of Fig. 7). The spatial features of the predicted precipitation ACCs were consistent with that of Ke et al. (2009). In particular, the ACC patterns of CNRM and ECMWF performed better than those of other models. However, it can be seen that the hindcasts of CNRM and ECMWF failed to provide the highest correlation between the leading EOF mode of observation and the GCMs in the GH5 and q85 fields. The results demonstrated that the preceding predictors (i.e., AAO and SLP) in the downscaling HD-4P model contributed to the prediction skill in the downscaling results regarding China summer rainfall.

The RMSE skill score was used to evaluate the magnitude of the model's prediction skill regarding summer rainfall. The spatially and temporally improved RMSE skill score was evaluated in this study. The interannual variability of the spatial RMSE skill score in the HD-4P model was given in Fig. 8. The 42-yr averages of the RMSE skill score for the summer rainfall over China in CNRM, ECMWF, UKMO and MME for the Scheme-CV downscaling HD-4P model were 42.58%, 29.23%, 40.71% and 40.16%, respectively, which were comparable with those of the SD-2P model (not shown).

**Table 2**
Multi-year average of spatial RMSE skill score for different downscaling models (different predictors involved) of Scheme-CV in Fig. 5.

| | GH5 model | q85 model | GH7 model | SLP model | SD-2P model | HD-4P model |
|---|---|---|---|---|---|---|
| RMSE skill score | 35.83% | 35.62% | 35.16% | 33.83% | 37.50% | **40.16%** |

The comparison between the spatial pattern of the temporally improved RMSE skill score for the Scheme-CV downscaling HD-4P model and the original model simulation was shown in the left column of Fig. 9. The differences between the RMSE skill score based on the HD-4P model and SD-2P model are also examined (right column in Fig. 9). For all of the GCMs and MME, the spatial patterns of the temporal RMSE skill score of the HD-4P model are all much larger than zero in most stations over China. In comparison with the rainfall hindcast from the original GCMs, the RMSE decreased in northern China and parts of southern China. The largest RMSE skill score nearly reached 70%. The RMSE skill scores were negative over some stations near Yangtze River. The right column of Fig. 9 compared the HD-4P model and the SD-2P model. In particular, when the predictors AAO and SLP were incorporated into the downscaling model, the RMSE skill scores increase (compared with those of the SD-2P model) in most parts of China, excluding some stations over Ordos region, south of Yangtze River Valley and Southwest China. Approximately 80% of the stations cover China, where the differences between the RMSE skill scores of the HD-4P model and the SD-2P model were larger than zero for all of the GCMs and MME (Fig. 9, right column).

In the summer of 1998, several floods occurred in the Yangtze River, the Pearl River and the Songhua River Valley. Rainstorms together with flood peaks generated the great flood event. The multi-scale atmospheric systems of the subtropical high in the Western Pacific, the EASM, the cold air activity at mid-high latitudes and the Tibet Plateau dynamic effect, among others, caused serious flooding in the Yangtze River Valley (Tao et al., 1998; Zhang et al., 2001). Therefore, we compare the observed precipitation to the predictions based on the Scheme-CV downscaling model in 1998.

Fig. 10 showed the spatial pattern of the summer precipitation anomaly in 1998. Here, the anomaly precipitation referred to the deviations relative to the 1960–2001 average. A positive rainfall anomaly was centered in the Yangtze River Valley and Northeast China, whereas South China was the negative center (Fig. 10 OBS). For the original output from MME, the rainfall anomaly had the opposite sign, which corresponded to the observation over South China and the Yangtze River Valley. After downscaling based on the SD-2P model and HD-4P model, MME can capture the main spatial pattern shown in the observational data. However, the details of the spatial pattern of the 1998 summer rainfall anomaly in the SD-2P model and HD-4P model were inconsistent. For the SD-2P model, the larger and smaller rainfall centers in the Yangtze River Valley and South China are consistent with the observational pattern, but an abnormal negative anomaly appeared in Southwest China (Fig. 10 MME-2Pmodel). In contrast, the Southwest China was changed to a positive anomaly in the HD-4P model, and the negative center over South China was also shrinking, which was comparable with the scenario in the observational data (Fig. 10 MME-4Pmodel), the anomaly correlation coefficient between the observation and the 4P downscaling result reached 0.43 (for SD-2P model was 0.31) in 1998 summer. In addition, the amplitude of both models is comparable of the observation. Furthermore, the AAO was strengthened in April of 1998, which may have led the western Pacific subtropical high to be positioned in the far

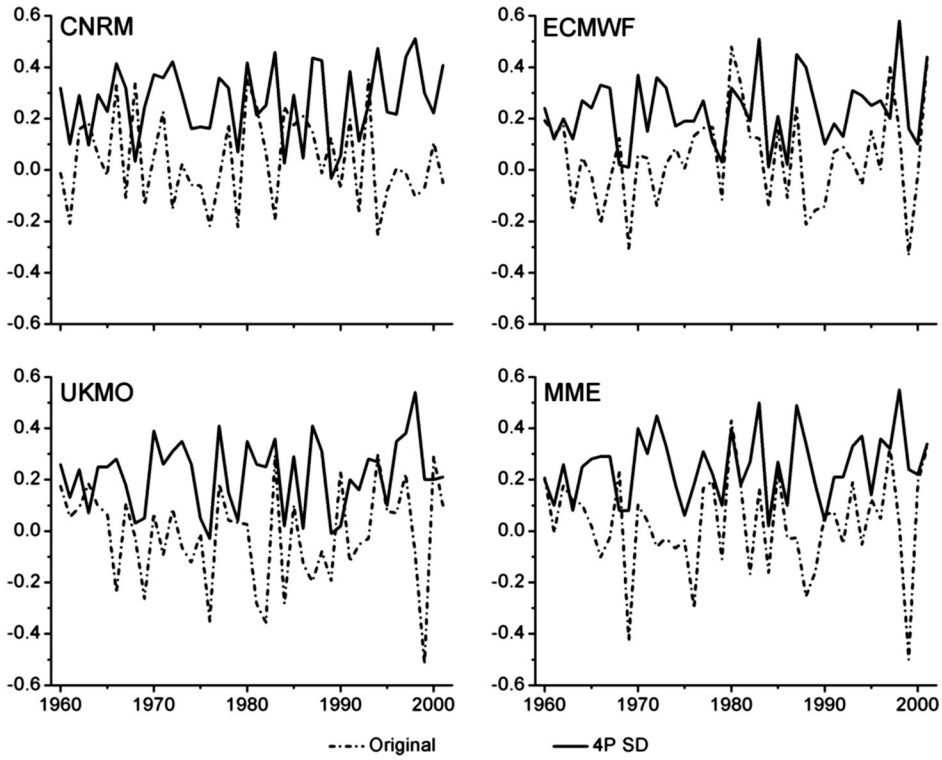


**Fig. 6.** The spatial anomaly correlation coefficients between the observed summer rainfall and predicted rainfall from the original models (dot line) or the Scheme-CV downscaling HD-4P model (solid line).

south and had brought more water vapor to East China such that more rainfall appeared over the Yangtze River Valley (Xue et al., 2004). Meanwhile, the EAWM was weak in the 1997 winter, which shifted the western Pacific subtropical high southward, and more rainfall also occurred over the Yangtze River Valley in the 1998 summer (Chen et al., 2000).

Based on the examination of the CCs and RMSE skill scores from 1960 to 2001, both downscaling models performed much better than the original GCMs with respect to rainfall hindcasts generally. In particular, the downscaling HD-4P model showed better results than those of the SD-2P model based on the RMSE skill scores and the hindcast of the summer rainfall anomaly over China in 1998.

### *4.2. Downscaling prediction of station rainfall by Scheme-IH*

After examining the skill of the Scheme-CV downscaling model, this study now evaluated and compared the results generated in Scheme-IH. For each GCM, the multi-year average ACCs increased to approximately 0.25 (based on the downscaling HD-4P model) from approximately 0.01 (based on the original GCM outputs) (Scheme-IH in Table 3).

The percentage of spatial and temporal RMSE skill score was also examined when comparing the performance of the Scheme-IH downscaling results with that of the original GCM hindcasts (not shown). During the independent period (1990–2001), the 12-year averages of the HD-4P model's RMSE skill score were at least 30% for all of the GCMs and MME.

The RMSE skill scores in most stations were larger than zero for all of the GCMs and MME (not shown). In addition, the RMSE skill scores over Western China were larger than those in other parts of China. In approximately 70% stations, the RMSE skill scores of the HD-4P model were larger than those of the SD-2P model, especially over the Yangtze River Valley, Northeast China and Xinjiang. According to the results

**Table 3**
The multi-year average ACCs of original GCMs and downscaling models (SD-2P model and HD-4P model) in Scheme-CV and Scheme-IH.

| GCMs | Scheme-CV (1960–2001) | | | Scheme-IH (1990–2001) | | |
|---|---|---|---|---|---|---|
| | Original GCMs | Downscaling models | | Original GCMs | Downscaling models | |
| | | SD-2P | HD-4P | | SD-2P | HD-4P |
| CNRM | 0.04 | 0.20 | 0.27 | −0.01 | 0.21 | 0.24 |
| ECMWF | 0.05 | 0.25 | 0.23 | 0.07 | 0.22 | 0.24 |
| UKMO | −0.01 | 0.20 | 0.22 | 0.04 | 0.24 | 0.26 |
| MME | 0.03 | 0.21 | 0.25 | 0.06 | 0.20 | 0.22 |

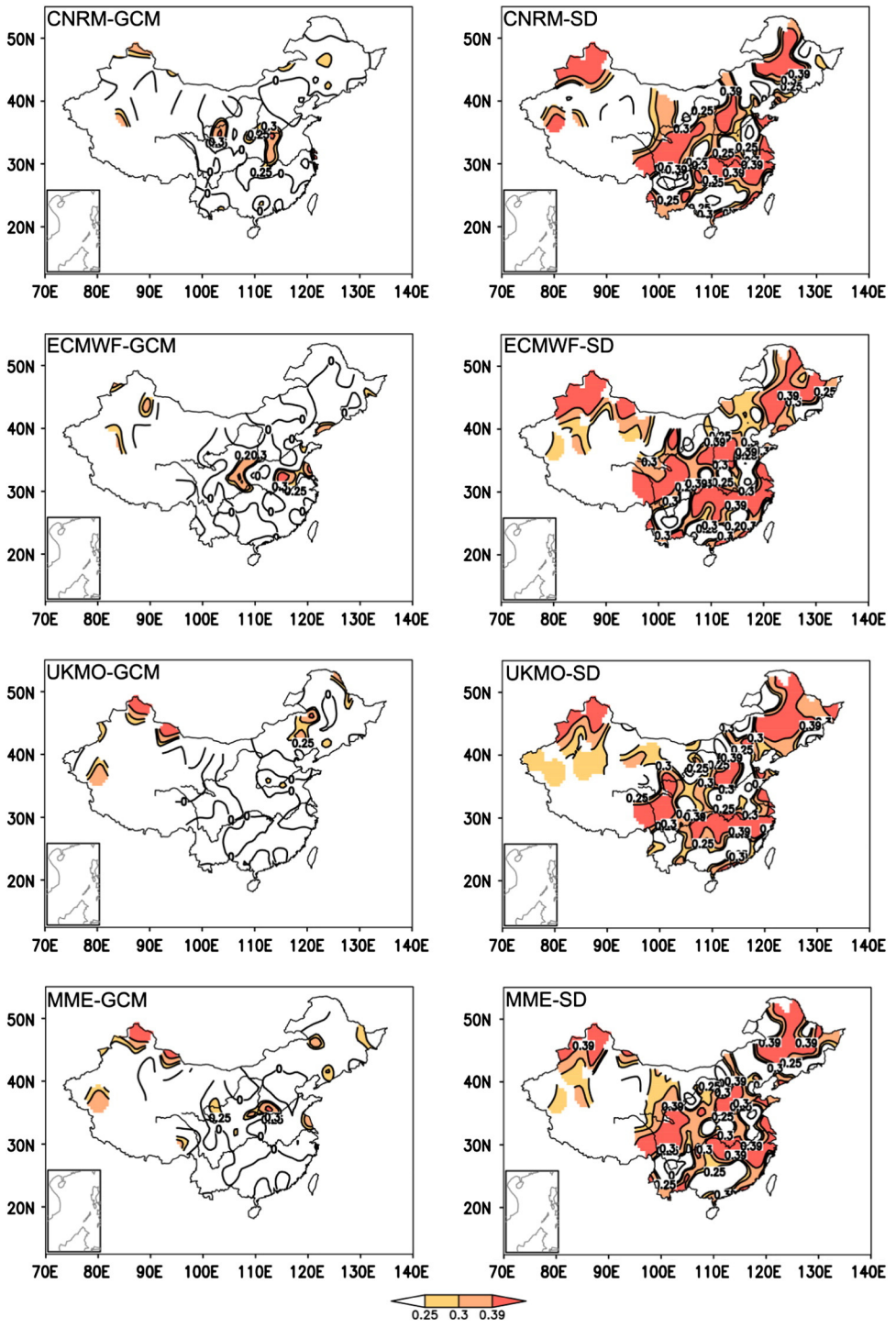


**Fig. 7.** The spatial pattern of the anomaly correlation coefficients between the observed summer precipitation and the predicted summer rainfall from the original models (left column) or the Scheme-CV downscaling HD-4P model (right column). The shaded areas with yellow, orange and red correspond to 90%, 95% and 99% confidence levels, respectively. (For interpretation of the references to color in this figure legend, the reader is referred to the web version of this article.)

of the CCs and RMSE skill scores, the Scheme-IH downscaling model based on the SD-2P model and HD-4P model increased the CCs and decreased the RMSE compared with the original GCM results from 1990 to 2001. In addition, based on the comparison of RMSE skill scores, the downscaling HD-4P model performed significantly better than the SD-2P model.

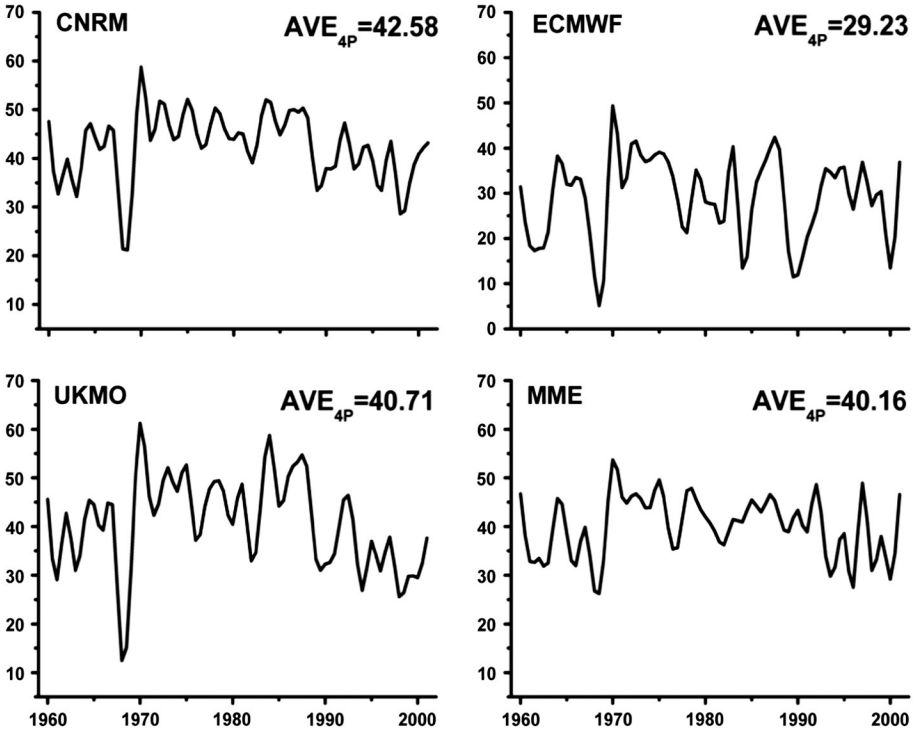


**Fig. 8.** The spatial RMSE skill score for Scheme-CV. The model name and multi-year average RMSE skill score of the downscaling HD-4P model are shown at the top left and right of each panel, respectively. Unit: %.

Overall, our study demonstrates that the downscaled precipitation based on large-scale variables was useful for making regional predictions based on these two Schemes.

## 5. Conclusions and discussions

In this study, two SD schemes based on the GCM outputs and observational data of large-scale circulation patterns were used to predict station rainfall over China. Two predictors (GH5 and q85) from three different DEMETER GCMs and two predictors (GH7 and SLP) from the observations were applied to the downscaling schemes step by step. The downscaling model based on any single predictor showed lower prediction skill than the multi-predictor downscaling models (SD-2P model and HD-4P model). The original GCM outputs and the results of the downscaling models were compared in Scheme-CV and Scheme-IH.

Scheme-CV was used as a cross-validation method to downscale the summer rainfall for the 1960–2001 periods. For every GCM, Scheme-CV had higher skill in predicting rainfall than the corresponding original outputs. The spatial and temporal CCs of both downscaling models increased significantly compared with those of the original GCMs. In addition, the downscaling spatial and temporal RMSE decreased greatly compared with the RMSE of the original GCM hindcasts, and the predictions of the downscaling HD-4P model were better than those based on the SD-2P model. Furthermore, the downscaling HD-4P model better reproduced the 1998 summer rainfall anomaly pattern than the downscaling SD-2P model. Scheme-IH was carried out as an independent hindcast to predict the summer precipitation during 1990–2001. The spatial and temporal CCs and RMSE skill score also improved significantly for all of the GCMs, and the prediction skill of the downscaling predictions based on the HD-4P model is higher than those based on the 2P model.

All the above downscaling RMSE skill scores were calculated based on each GCM, respectively, but not a uniform reference. Therefore, it's difficult to tell which GCM had absolute increased prediction skill through downscaling approach. Here, a new reference based observational precipitation was defined as follows:

$$\mathrm{RMSE}_{\mathrm{ref}} = \sqrt{\frac{\sum_{i=1}^{N}\left(R_i^{obs} - \overline{R}\right)^2}{N}} \tag{3}$$

where $R_i^{obs}$ and $\overline{R}$ indicate the observed rainfall and that of the climatology, respectively. Here, the RMSE skill score indicated the difference between the $\mathrm{RMSE}_{\mathrm{ref}}$ and the RMSE of the downscaling models with the division of the former (Table 4). It is shown that the HD-4P performed better than SD-2P (Table 4). Meanwhile, with the comparison of each GCM downscaling, all of them have comparable improved RMSE skill score.

It is well known that original GCM precipitation has systematic bias which will affect the RMSE calculation but can be removed statistically. The GCM precipitation forecast rainfall removing systematic bias ($R$) in target year can be expressed as follows:

$$\begin{aligned} R &= R_0 - R' \\ R' &= \frac{1}{n}\sum_{i=1}^{n}\left[(R_0)_i - R_i^{obs}\right] \end{aligned} \tag{4}$$

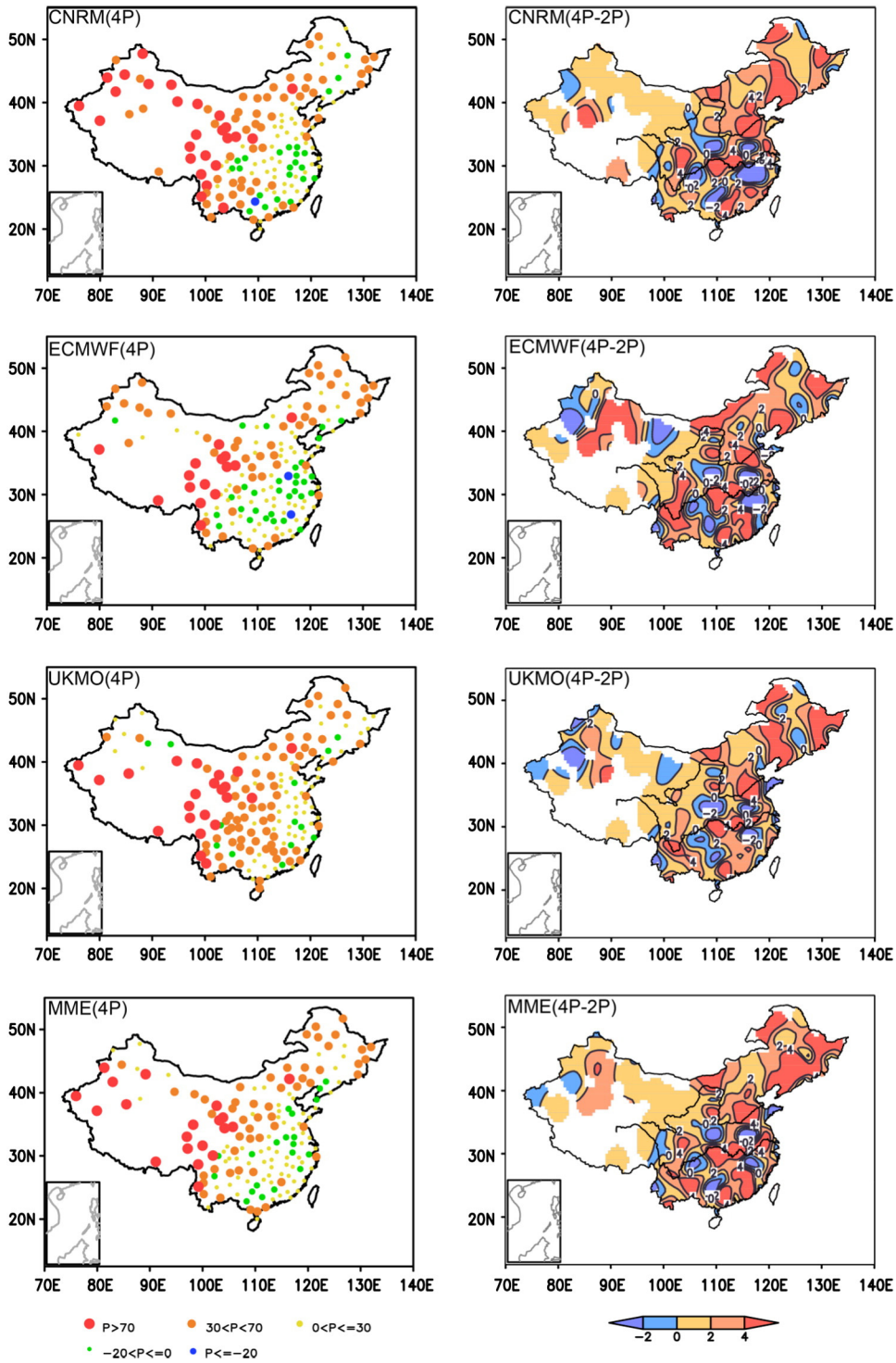


**Fig. 9.** The pattern of temporal RMSE skill score based on the downscaling HD-4P model (left column) and the differences in RMSE skill score between the HD-4P model and the SD-2P model (right column) in Scheme-CV. P denotes the values of RMSE skill score in 160 stations. The names of the GCMs are shown at the top left of each panel. Unit: %.

where $R_0$, $R^{obs}$ and $n$ denote the original GCM precipitation, the observational data and the fitting years respectively. The cross validation RMSE skill score of downscaling with the reference of removing the systematic bias of GCM was shown in Table 5. RMSE skill score was larger than zero for all the GCMs, and can reach 8%, but much lower than the scenario of

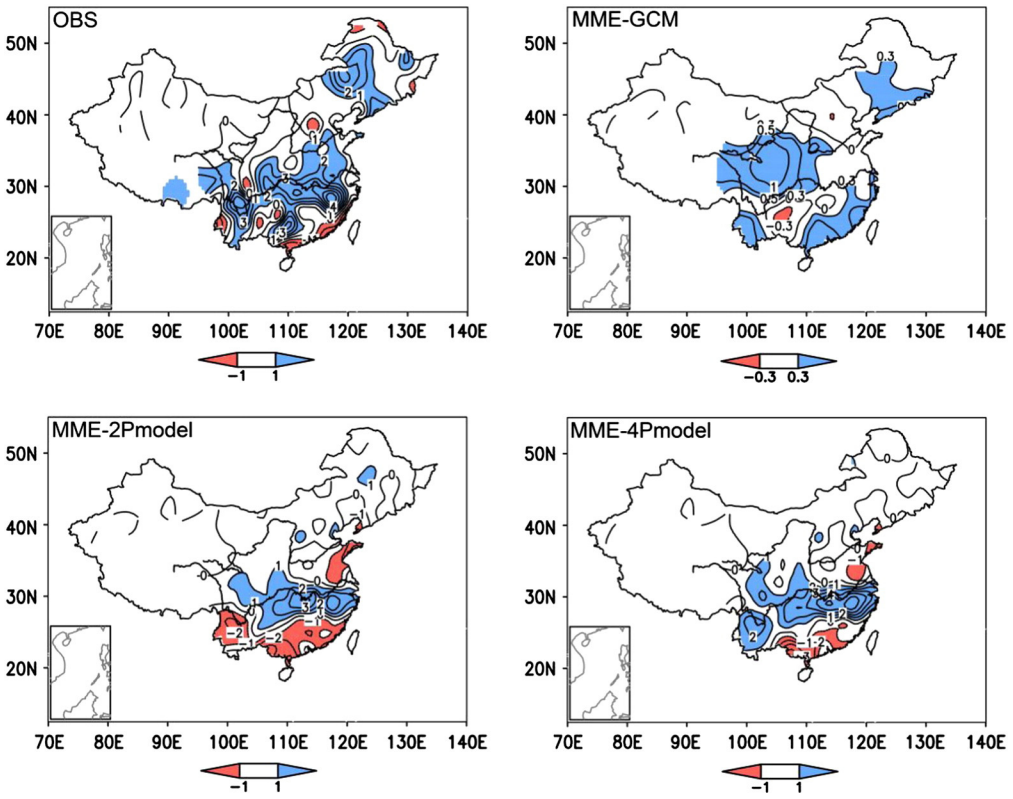


**Fig. 10.** The precipitation anomaly spatial patterns of the observations, original model outputs and Scheme-CV downscaling model in the summer of 1998. The dataset sources are given at the top left of each panel. MME-GCM, MME-2P model and MME-4P model denote the MME original hindcast, the downscaled rainfall anomaly based on the SD-2P model and the downscaled rainfall anomaly based on the HD-4P model, respectively. Unit: mm/d.

the downscaling result. Therefore, the downscaling method in the current work is also superior to the systematic bias correction.

In general, the downscaling predictions based on the HD-4P model gave higher scores than those based on the model using GH5 and q85 as the predictors. This difference may be due to the inability of some GCMs to represent a realistic coupled pattern between station precipitation and the GH5 and q85 predictors. Conversely, the April AAO and winter SLP seemed to be better captured because of the data source of the GH7 and SLP predictors and the important influence of previous AAO and SLP signals on summer precipitation in particular years. Overall, the combination of previous (i.e., GH7 and SLP) and simultaneous (i.e., GH5 and q85) predictors favors the acquisition of more information regarding delayed and synchronous effect from atmospheric systems for summer rainfall over China. The combination of the previous observation and current skillful prediction of output of the GCMs should be effective to improve the SD prediction of summer rainfall at stations in China.

## Acknowledgments

The authors are grateful to the anonymous reviewers for their valuable comments and good advises. This research was jointly supported by the National Basic Research Program of China (Grant No. 2010CB950304), and the National Nature Science Foundation for Distinguished Young Scientists of China (Grant No. 41325018), the National Nature Science Foundation of China (Granted 41175071) and the Special Fund for public welfare industry (meteorology) (GYHY200906018).

**Table 4**
The multi-year average RMSE skill score (with the reference of $RMSE_{ref}$) based on observation precipitation in Scheme-CV.

| GCM | SD-2P | HD-4P |
|---|---|---|
| CNRM | −15.27% | −9.35% |
| ECMWF | −16.43% | −10.39% |
| UKMO | −16.82% | −11.07% |
| MME | −19.44% | −13.06% |

**Table 5**
The multi-year average RMSE skill score of original GCMs based on bias correction and downscaling models (HD-4P model) in Scheme-CV.

| GCM | HD-4P | Bias Correction |
|---|---|---|
| CNRM | 42.58% | 7.52% |
| ECMWF | 29.23% | 7.91% |
| UKMO | 40.71% | 3.69% |
| MME | 40.16% | 8.94% |

## Appendix A. The downscaling approach

In SVD, the coupled patterns mentioned above can be expressed in the following equation:

$$Y(t,x) = \sum_{i=1}^{m} R_i(x)K_i(t)$$

$$X(t,x) = \sum_{i=1}^{m} U_i(x)S_i(t).$$

Here, m is the total number of SVD modes. $Y(t,x)$ and $X(t,x)$ are the predictand and predictor, respectively. $R_i(x)$ and $U_i(x)$ indicate the singular vector of the predictand and predictor, respectively, in the $i$th mode. $K_i(t)$ and $S_i(t)$ denote, respectively, the time expansion coefficient of the $i$th SVD mode for the regional predictand and the large-scale predictor.

The following linear regression will be used.

$$\hat{K}_i(t) = \beta_i S_i(t) + \varepsilon_i, i = 1, \ldots, n$$

Here, $\hat{K}_i(t)$ indicates the regressed time expansion from $S_i(t)$, $\beta_i$ is the linear regression coefficient, $\varepsilon_i$ is the residual and n denotes the total number of SVD modes retained. In this study, the first six modes are retained. Finally, the forecasted precipitation $Y(t + \Delta t, x)$ in the target year can be written as:

$$Y(t+\Delta t,x) = \sum_{i=1}^{n} R_i(x)\left(\hat{K}_i(t+\Delta t)\right).$$

## References


Benestad, R.E., 2004. Empirical-statistical downscaling in climate modeling. EOS Trans. Am. Geophys. Union 85 (42), 417–422. http://dx.doi.org/10.1029/2004EO420002.

Branković, Č., Palmer, T.N., Ferranti, L., 1994. Predictability of seasonal atmospheric variations. J. Clim. 7, 217–237.

Bretherton, C.S., Smith, C., Wallace, J.M., 1992. An intercomparison of methods for finding coupled patterns in climate data. J. Clim. 5, 541–560.

Charney, J.G., Shukla, J., 1981. Predictability of monsoons. In: Lighthill, J., Pearce, R. (Eds.), Monsoon Dynamics. Cambridge University Press (735 pp.).

Chen, X.F., Zhao, Z.G., 2000. Study and application on prediction of rainfall over China in flood season. (in Chinese) Meteor. Press (241 pp.).

Chen, W., Graf, H.F., Huang, R.H., 2000. The interannual variability of East Asian winter monsoon and its relation to the summer monsoon. Adv. Atmos. Sci. 17 (1), 48–60.

Chen, H.P., Sun, J.Q., Wang, H.J., 2012. A statistical downscaling model for forecasting summer rainfall in China from DEMETER hindcast datasets. Weather Forecast. 27, 608–628.

Chu, J.L., Kang, H., Tam, C.Y., Park, C.K., Chen, C.T., 2008. Seasonal forecast for local precipitation over northern Taiwan using statistical downscaling. J. Geophys. Res. 113, D12118. http://dx.doi.org/10.1029/2007JD009424.

Cressman, G.P., 1959. An operational objective analysis system. Mon. Weather Rev. 87, 367–374.

Fan, K., 2006. Atmospheric circulation anomalies in the Southern Hemisphere and summer rainfall over Yangtze River Valley. Chin. J. Geophys. 49 (3), 672–679 (in Chinese).

Fan, K., Wang, H.J., 2006. Antarctic Oscillation anomaly and forecast of 2006 summer precipitation in eastern China. J. Appl. Meteorol. Sci. 17 (3), 383–384 (in Chinese).

Fan, K., Liu, Y., Chen, H., 2012. Improving the prediction of the East Asian summer monsoon: new approaches. Weather Forecast. 27, 1017–1030. http://dx.doi.org/10.1175/WAF-d-11-000921.

Fernández-Ferrero, A., Sáenz, J., Ibarra-Berastegi, G., Fernández, J., 2009. Evaluation of statistical downscaling in short range precipitation forecasting. Atmos. Res. 94, 448–461.

Gao, H., Yang, S., Kumar, A., Hu, Z.Z., Huang, B., Li, Y., Jha, B., 2011. Variations of the East Asian Mei-yu and simulation and prediction by the NCEP Climate Forecast System. J. Clim. 24, 94–108.

Gilchrist, B., Cressman, G.P., 1954. An experiment in objective analysis. Tellus 6 (4), 309–318.

Giorgi, F., et al., 2001. Regional climate simulation–evaluation and projections. In: Houghton, J.T. (Ed.), Climate Change 2001: The Scientific Basis. Cambridge Univ. Press, New York (944 pp.).

Gong, D.Y., Ho, C.H., 2003. Detection of large-scale climate signals in spring vegetation index (normalized difference vegetation index) over the Northern Hemisphere. J. Geophys. Res. 108 (D16), 4498. http://dx.doi.org/10.1029/2002JD002300.

Gong, D.Y., Wang, S.W., 1999. Definition of Antarctic Oscillation index. Geophys. Res. Lett. 26, 459–462.

Guo, Y., Li, J.P., Li, Y., 2011. Statistically downscaled summer rainfall over the middle-lower reaches of the Yangtze River. Atmos. Ocean. Sci. Lett. 4, 191–198.

Hu, Z.Z., 1997. Interdecadal variability of summer climate over East Asia and its association with 500 hPa height and global sea surface temperature. J. Geophys. Res. 102 (D16), 19403–19412. http://dx.doi.org/10.1029/97JD01052.

Huang, M.Y., Huang, J.Y., 2000. Forecasting experiments and diagnostic results of the CCA model on summer precipitation of China. (in Chinese) Q. J. Appl. Meteorol. 11, 31–39 (Suppl.).

Huang, R.H., Li, W.J., 1987. Influence of the heat source anomaly over the western tropical Pacific on the subtropical high over East Asia. Proc. International conference on the general circulation of East Asia, pp. 40–51.

Im, E., Kwon, W., Ahn, J., Giorgi, F., 2007. Multi-decadal scenario simulation over Korea using a one-way double-nested regional climate model system. Part 1: recent climate simulation (1971–2000). Clim. Dyn. 28 (7), 759–780.

Jia, X.L., Chen, L.J., Li, W.J., Chen, D.L., 2010. Statistical downscaling based on BP-CCA: predictability and application to the winter temperature and precipitation in China. Acta Meteorol. Sin. 68 (3), 398–410.

Jolliffe, I.T., 1972. Discarding variables in a principal component analysis, I: artificial data. Appl. Stat. 21, 160–173.

Jolliffe, I.T., 2002. Principal Component Analysis, 2nd ed. Springer (487 pp.).

Kang, I.S., Jin, K., Wang, B., Lau, K.M., Shukla, J., Krishnamurthy, V., Schubert, S., Wailser, D., Stern, W., Kitoh, A., 2002. Intercomparison of the climatological variations of Asian summer monsoon precipitation simulated by 10 GCMs. Clim. Dyn. 19, 383–395. http://dx.doi.org/10.1007/s00382-002-0245-9.

Ke, Z.J., Zhang, P.Q., Dong, W.J., Wang, J., 2009. An application of optimal subset regression in seasonal climate prediction. Chin. J. Atmos. Sci. 33 (5), 994–1002 (in Chinese).

Kidson, J.W., 1988. Interannual variations in the Southern Hemisphere circulation. J. Clim. 1, 1177–1198.

Kosaka, Y., Nakamura, H., 2006. Structure and dynamics of the summertime Pacific–Japan teleconnection pattern. Q. J. R. Meteorol. Soc. 132, 2009–2030.

Lang, X.M., Wang, H.J., 2005. Seasonal differences of model predictability and the impact of SST in the Pacific. Adv. Atmos. Sci. 22 (1), 103–113.

Lang, X.M., Wang, H.J., 2010. Improving extraseasonal summer rainfall prediction by merging information from GCMs and observations. Weather Forecast. 25, 1263–1274.

Li, C.Y., 1988. Frequent activities of stronger aero troughs in East Asia wintertime and occurrence of the El Niño event. Sci. China Ser. B-Earth Sci. 31, 976–985.

Li, M.C., Hu, Y.F., Huang, J.Y., 1987. The research on the interaction between the atmospheric circulation of East Asia and El Niño. Chin. J. Atmos. Sci. 11 (4), 359–364 (in Chinese).

Liu, Y., Fan, K., 2012a. A new statistical downscaling model for autumn precipitation in China. Int. J. Climatol. http://dx.doi.org/10.1002/joc.3514.

Liu, Y., Fan, K., 2012b. Prediction of spring precipitation in China using a downscaling approach. Meteorol. Atmos. Phys. 118, 79–93.

Liu, Y., Fan, K., Wang, H.J., 2011. Statistical downscaling prediction of summer precipitation in southeastern China. Atmos. Ocean. Sci. Lett. 4 (3), 173–180.

Mao, H.Q., Li, X.Q., 1997. Short-term climate forecast experiment of winter temperature in China using Canonical Correlation Analysis. (in Chinese) Q. J. Appl. Meteorol. 8 (4), 385–392.

Michaelsen, J., 1987. Cross-validation in statistical climate forecast models. J. Appl. Meteorol. Sci. 26 (11), 1589–1600.

Murphy, J., 2000. Predictions of climate change over Europe using statistical and dynamical downscaling techniques. Int. J. Climatol. 20, 489–501.

Nitta, T., 1987. Convective activities in the tropical western Pacific and their impact on the Northern Hemisphere summer circulation. J. Meteorol. Soc. Jpn. 65, 373–390.

Nitta, T., Hu, Z.Z., 1996. Summer climate variability in China and its association with 500-hPa height and tropical convection. J. Meteorol. Soc. Japan 74, 425–445.

Palmer, T.N., et al., 2004. Development of a European Multimodel Ensemble System for Seasonal-to-Interannual Prediction (DEMETER). Bull. Am. Meteorol. Soc. 85, 853–872.
Paul, S., Liu, C.M., Chen, J.M., Lin, S.H., 2008. Development of a statistical downscaling model for projecting monthly rainfall over East Asia from a general circulation model output. J. Geophys. Res. 113, D15117. http://dx.doi.org/10.1029/2007JD009472.
Prohaska, J.A., 1976. A technical for analyzing the linear relationships between two meteorogical fields. Mon. Weather Rev. 104, 1345–1353.
Rogers, J.C., van Loon, H., 1982. Spatial variability of sea level pressure and 500 mb height anomalies over the Southern Hemisphere. Mon. Weather Rev. 110, 1375–1392.
Sperber, K.R., et al., 2001. Dynamical Seasonal Predictability of the Asian Summer Monsoon. Mon. Weather Rev. 129, 2226–2248.
Sun, J.Q., Chen, H.P., 2012. A statistical downscaling scheme to improve global precipitation forecasting. Meteorol. Atmos. Phys. 117, 87–102. http://dx.doi.org/10.1007/s00703-012-0195-7.
Sun, B.M., Sun, S.Q., 1994. The analysis on the feature of the atmospheric circulation in preceding winter for the summer drought and flooding in the Yangtze and Huaihe River valley. Adv. Atmos. Sci. 11, 79–90.
Sun, J.Q., Wang, H.J., Yuan, W., 2009. A possible mechanism for the co-variability of the boreal spring Antarctic Oscillation and the Yangtze River valley summer rainfall. Int. J. Climatol. 29, 1276–1284.
Tao, S.Y., Chen, L.X., 1987. A review of recent research on the East Asian summer monsoon in China. In: Chang, C.P., Krishnamurti, T.N. (Eds.), Monsoon Meteorology. Oxford University Press, pp. 60–92.
Tao, S.Y., Zhang, Q.Y., Zhang, S.L., 1998. The Great Floods in the Changjiang River Valley in 1998 (in Chinese). Clim. Environ. Res. 3 (4), 290–299.
Thompson, D.W.J., Wallace, J.M., 2000. Annular modes in the extratropical circulation: part I: month-to-month variability. J. Clim. 13, 1000–1016.
Uppala, et al., 2005. The ERA-40 re-analysis. Q. J. R. Meteorol. Soc. 131, 2961–3012. http://dx.doi.org/10.1256/qj.04.176.
Uvo, C.B., Olsson, J., Morita, O., Jinno, K., Kawamura, A., Nishiyama, K., Koreeda, N., Nakashima, T., 2001. Statistical atmospheric downscaling for rainfall estimation in Kyushu Island, Japan. Hydrol. Earth Syst. Sci. 5 (2), 259–271.
Wang, H.J., 1997. A Preliminary study on the uncertainty of short-term climate prediction. (in Chinese) Clim. Environ. Res. 2 (4), 333–338.
Wang, H.J., 2001a. The weakening of the Asian monsoon circulation after the end of 1970's. Adv. Atmos. Sci. 18, 376–386.
Wang, S.W., 2001b. Progress of Modern Climate Research. (Chapter 11) China Meteorology Press (In Chinese).
Wang, H.J., 2002. Instability of the East Asian Summer monsoon-ENSO relations. Adv. Atmos. Sci. 19, 1–11.
Wang, H.J., Fan, K., 2005. Central-North China precipitation as reconstructed from the Qing dynasty: signal of the Antarctic Atmospheric Oscillation. Geophys. Res. Lett. 32, L24705. http://dx.doi.org/10.1029/2005GL024562.
Wang, H.J., Fan, K., 2009. A New scheme for improving the seasonal prediction of summer precipitation anomalies. Weather Forecast. 24, 548–554.
Wang, H.J., Qian, Z.L., 2010. a potential high-score scheme for the prediction of Atlantic storm activity. Atmos. Ocean. Sci. Lett. 3 (2), 116–119.
Wang, H.J., Matsuno, T., Kurihara, Y., 2000. Ensemble hindcast experiments for the flood period over China in 1998 by use of the CCSR/nies atmospheric general circulation model. J. Meteorol. Soc. Jpn. 78 (4), 357–365.
Wang, B., Wu, R., Lau, K.M., 2001. Interannual variability of the Asian summer monsoon: contrasts between the Indian and the western North Pacific East Asian monsoons. J. Clim. 14, 4073–4090.
Wang, B., Kang, I.S., Lee, J.Y., 2004. Ensemble simulation of Asian–Australian monsoon variability by 11 AGCMs. J. Clim. 17, 803–818.
Wilks, D.S., 2006. Statistical Methods in the Atmospheric Sciences, 2nd ed. Academic Press (627 pp.).
Wilks, D.S., 2011. On the reliability of the rank histogram. Mon. Weather Rev. 139, 311–316.
Wu, W.L., et al., 2012. Statistical downscaling of climate forecast system seasonal predictions for the Southeastern Mediterranean. Atmos. Res. 118, 346–356.
Xue, F., Wang, H.J., He, J.H., 2004. Interannual variability of Mascarene high and Australian high and their influences on East Asian summer monsoon. J. Meteorol. Soc. Jpn. 82 (4), 1173–1186.
Yang, H.L., Xu, Y.L., Zhang, L., Pan, J., Tao, S.C., 2010. Projected Change in Mean and Extreme Climate over China in the Late 21st Century from PRECIS Under SRES A2 Scenario. (in Chinese) Adv. Clim. Chang. Res. 6 (3), 157–163.
Yoshiike, S., Kawamura, R., 2009. Influence of wintertime large-scale circulation on the explosively developing cyclones over the western North Pacific and their downstream effects. J. Geophys. Res. 114, D13110. http://dx.doi.org/10.1029/2009JD011820.
Zhang, S.L., Tao, S.Y., Zhang, Q.Y., Zhang, X.L., 2001. Meteorological and hydrological characteristics of severe flooding in China during the summer of 1998. (in Chinese) Q. J. Appl. Meteorol. 12 (4), 442–457.
Zhang, Y.Q., Wu, S.G., Ding, Y.G., He, T., Gao, Q.Z., 2006. Forecast of summer precipitation based on SVD iteration model. (in Chinese) Acta Meteorol. Sin. 64 (1), 121–127.
Zorita, E., Von Storch, H., 1999. The analog method as a simple statistical downscaling technique: comparison with more complicated methods. J. Clim. 12, 2474–2489.

INTERNATIONAL JOURNAL OF CLIMATOLOGY
*Int. J. Climatol.* (2014)
Published online in Wiley Online Library
(wileyonlinelibrary.com) DOI: 10.1002/joc.4058

RMetS
Royal Meteorological Society

# A hybrid statistical downscaling model for prediction of winter precipitation in China

Ying Liu[a,b] and Hong-Li Ren[a]*

[a] *Laboratory for Climate Studies, National Climate Center, China Meteorological Administration, Beijing, China*
[b] *Collaborative Innovation Center on Forecast and Evaluation of Meteorological Disasters, Nanjing University of Information Science & Technology, China*

**ABSTRACT:** Downscaling techniques can effectively improve the coarse resolution and poor representation of precipitation predicted by general circulation model (GCM). In this study, a statistical downscaling (SD) method, based on the singular value decomposition (SVD), is proposed for better representing the coupled variation between predictors and winter precipitation in China. By comparing current predictors from Climate Forecast System version 2 (CFSv2) of National Centers for Environmental Prediction and previous predictors from observation, the two best appropriate predictors, the winter sea level pressure (SLP) from the CFSv2 and the autumn sea-ice concentration (SIC) from observation, are selected to construct the SD model for prediction of winter precipitation in China. Three downscaling schemes are developed by involving the SLP, SIC, and both of them (i.e. SLP-scheme, SIC-scheme, and SS-scheme), respectively. Validations for the schemes show a considerable improvement of performance in predicting China winter precipitation, compared with the original CFSv2 output. The temporal and spatial anomaly correlation coefficient (ACC) and root mean square errors (RMSE) were estimated. For the cross validation, the spatial ACC are increased from ~0.01 of the CFSv2 to >0.3 of the downscaling model. For the independent validation, the temporal RMSE from the downscaling schemes are all decreased more than 30%. In particular, the results using the SS-scheme showed relatively smaller RMSE than those of either the SLP-scheme or SIC-scheme, and hence can reproduce the precipitation anomaly in 2011 and 2012 winters more accurately.

KEY WORDS winter precipitation; statistical downscaling; CFSv2; SVD

*Received 12 December 2013; Revised 30 March 2014; Accepted 29 April 2014*

## 1. Introduction

General circulation models (GCMs) are the primary tool for understanding and predicting how global climate may vary in the future. However, the current GCMs are usually not able to provide reliable information on regional scales (Huth, 1999; Lang *et al.*, 2003). Hence, to more reliably predict seasonal precipitation in regional domains, the relatively coarse scale information from the GCM is not enough apparently. To overcome this difficulty, downscaling approach attempts to resolve the scale discrepancy between large-scale variables and the local precipitation required for prediction, based on the assumption that large-scale climate exhibits a strong influence on local-scale climate. In general, there are two downscaling approaches coexisting (Christensen *et al.*, 2007). One is the dynamical downscaling, which, through nesting a regional climate model (RCM) into the GCM, can represent atmospheric physics with a higher spatial resolution within a limited area of interest (Gao *et al.*, 2001, 2006; Ju and Lang, 2011). The other is the statistical downscaling (SD) which establishes statistically some empirical linkages between large-scale variables and observed local-scale variables (Wigley *et al.*, 1990; Widmann and Bretherton, 2003). The relatively low computational demand makes the SD an attractive approach for climate projection and prediction (Schoof, 2013).

Under the background of winter climate changes in recent years, the impacts of winter precipitation, such as snowstorm, on China has caused widespread concerns and raised an important scientific question. As shown in Figure 1, the climatological winter precipitation increases from the northern to southern China, however, at the top corner of the northwestern (NW) China, there is more precipitation than over the adjacent regions. This indicates that winter precipitation typically occurs on finer and more regional spatial scales in China, and thus that it is usually a hard topic to predict the winter precipitation in China. Therefore, it is essential and important for decreasing losses of economy and lives to improve accuracy of the China winter precipitation prediction (e.g. using the SD model).

Previous studies have concerned the winter precipitation prediction in China using different prediction approaches. For example, a statistical method named year-to-year increment prediction has been proposed (Fan *et al.,* 2008) as an effective method to improve the prediction skill of East Asian climate (Fan *et al.,* 2012) and hurricane activity

* Correspondence to: H.-L. Ren, Laboratory for Climate Studies, National Climate Center, China Meteorological Administration, Beijing 100081, China. E-mail: renhl@cma.gov.cn

© 2014 Royal Meteorological Society

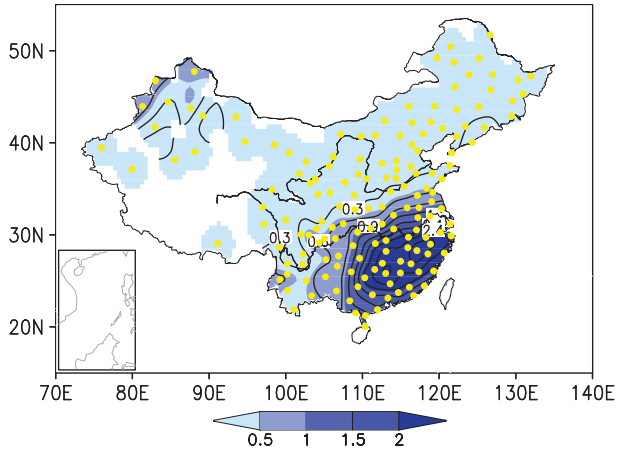


Figure 1. The climatology of winter precipitation rate (mm day$^{-1}$) of 160 station locations from 1982 to 2012. Shading denotes the precipitation rate (mm day$^{-1}$), and the dots show the locations of the 160 stations in China.

(Fan, 2011), and was further applied to prediction of wintertime heavy snow activity in Northeast China (Fan and Tian, 2013). Recently, in terms of the idea of downscaling, a few studies have applied the SD approaches to the winter precipitation in China using only current GCM information (Yan *et al.*, 2008; Jia *et al.*, 2010) or previous observational signals (Lang, 2011). However, either information source is definitely not enough to provide a significant performance of predicting the winter precipitation in China and it is probably a more effective way to combine both the information sources (Liu *et al.,* 2013). Therefore, this study will focus on a new hybrid SD model for predicting the winter precipitation in China based on different informative predictors from both GCM and observation. Particularly, we will explore to design the procedure of selecting predictors and to verify the performance of different SD models in the hybrid model based on different predictors. The aim of this study is to select suitable predictors and establish an effective hybrid SD model to notably improve the predictive capability of winter precipitation in China. This study is reported as follows: Section 2 introduces the used datasets and the SD model. Section 3 analyses the candidate predictors and then selects the optimal ones. The analysis results of the SD models based on different predictors are described in Section 4. Section 5 presents a summary and some discussions.

## 2. Data and method

### 2.1. Data

The GCM hindcast used in this study was from the Climate Forecast System version 2 (CFSv2) of the National Centers for Environmental Prediction (NCEP). CFSv2 is a fully coupled dynamical prediction system that has been an important component of the monthly to seasonal prediction system of the NCEP's Climate Prediction Center (CPC) since it became operational in 2011, replacing its predecessor, CFS version 1 (CFSv1) (Saha *et al.*, 2013). CFSv1 has been particularly successful in seasonal-to-interannual climate forecasting, both retrospectively and operationally (Saha *et al.*, 2006). In CFSv2, the oceanic and atmospheric components exchange surface momentum, heat and freshwater fluxes every 30 minutes. Here, sea level pressure (SLP) and precipitation during 1982–2012 winters are used to define the current predictor with a $1^\circ \times 1^\circ$ latitude–longitude spatial resolution. The CFSv2 datasets used in this study were initialized on November, and ensemble of forecast for every lead day from initial time was done to produce the winter variables.

The observed SLP, which was derived from the joint reanalysis data of the NCEP and National Centers for Atmospheric Research (NCAR), were compiled on a $2.5^\circ \times 2.5^\circ$ regular latitude–longitude grid (Kalnay *et al.,* 1996). The National Oceanic and Atmospheric Administration's (NOAA) Precipitation Reconstruction Dataset (PREC) was used as the observation of monthly global precipitation. The datasets are defined by interpolation of gauge observations over land (PREC/L) and by empirical orthogonal function (EOF) reconstruction of historical observations over ocean (PREC/O) (Chen *et al.*, 2002). It is composed of $2.5^\circ \times 2.5^\circ$ global grid. The sea-ice concentration (SIC) data, obtained from Met Office Hadley Centre's sea-ice and sea surface temperature data set version 1 (HadISST1) (Rayner *et al.,* 2003), includes globally complete monthly fields on a $1^\circ \times 1^\circ$ latitude–longitude grid. Monthly precipitation at the 160 standard stations was obtained from National Climate Center of China Meteorological Administration. The locations of the 160 stations are shown in Figure 1.

The common period for all the datasets is spanning from 1982 to 2012. For each year, we generated autumn (September–October–November) and winter (December–January–February) averages.

### 2.2. Method

The first method is a 1-year-out cross validation. One year of predictor and predictand data were excluded from the respective data set, and the data from the residual years were used in the training period. Next, a prediction based on the training period was made for the remaining years (Michaelsen, 1987). This cross-validated procedure was performed 31 times to produce precipitation predictions from 1982 to 2012 for the validation. The other method is an independent validation for the period from 1982 to 2012, in which, the downscaling scheme used a moving 25 years for the fitting. Therefore, the precipitation prediction for the targeted year is completely independent of the training period.

In this article, singular value decomposition (SVD) analysis (Bretherton *et al.,* 1992) was used to statistically describe the link between precipitation and its predictors. We chose this method to objectively determine coupled anomaly patterns in the predictor and predictand fields. During the training period, the predictors and predictand were reconstructed using the respective EOF modes and

© 2014 Royal Meteorological Society

Table 1. Descriptions of the candidate predictors.

| Predictors | SLP | SIC | Precipitation |
|---|---|---|---|
| Domain | 15°N–60°N; 70°E–180°E | 60°N–90°N; 0°–360°E | 15°N–55°N; 70°E–140°E |
| Dataset | CFSv2 | HadISST1 | CFSv2 |
| Period | 1982–2012 winter | 1982–2012 autumn | 1982–2012 winter |

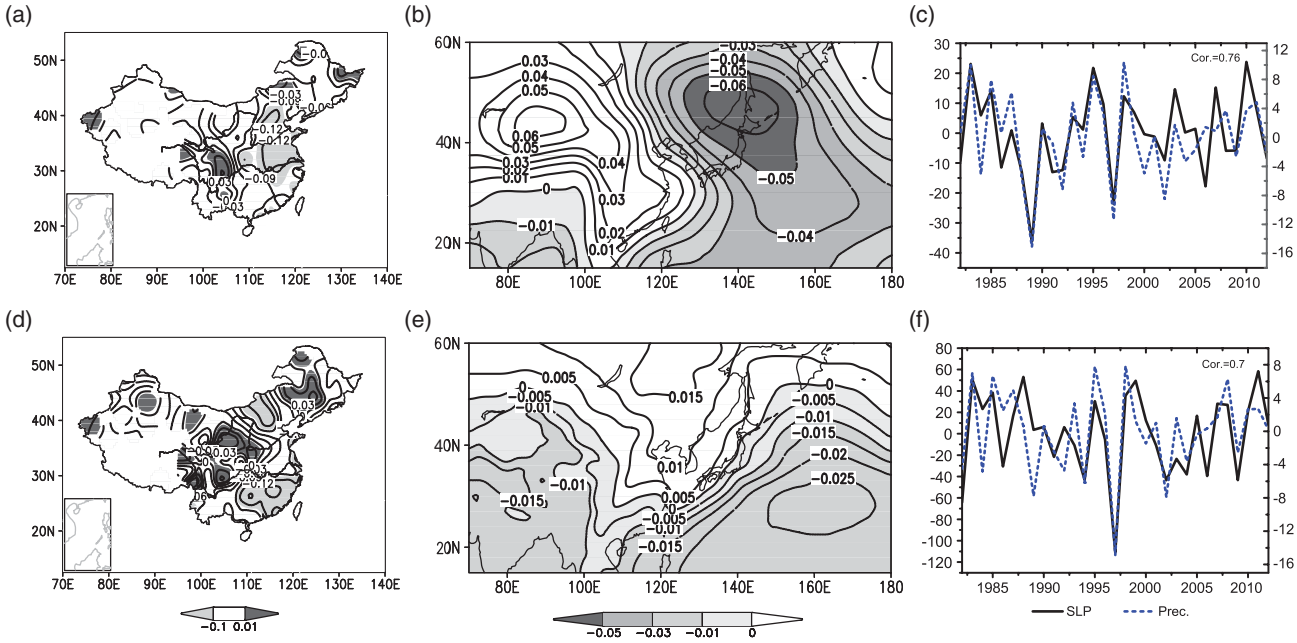


Figure 2. The heterogeneous correlation patterns of the first leading SVD for the observed precipitation in China (a, d) and SLP (b, e); as well as time series of extension coefficients for precipitation and SLP (c, f) in the boreal winter during 1982–2012, where SLP in (b) and (e) are based on the NCEP and CFSv2 data, respectively.

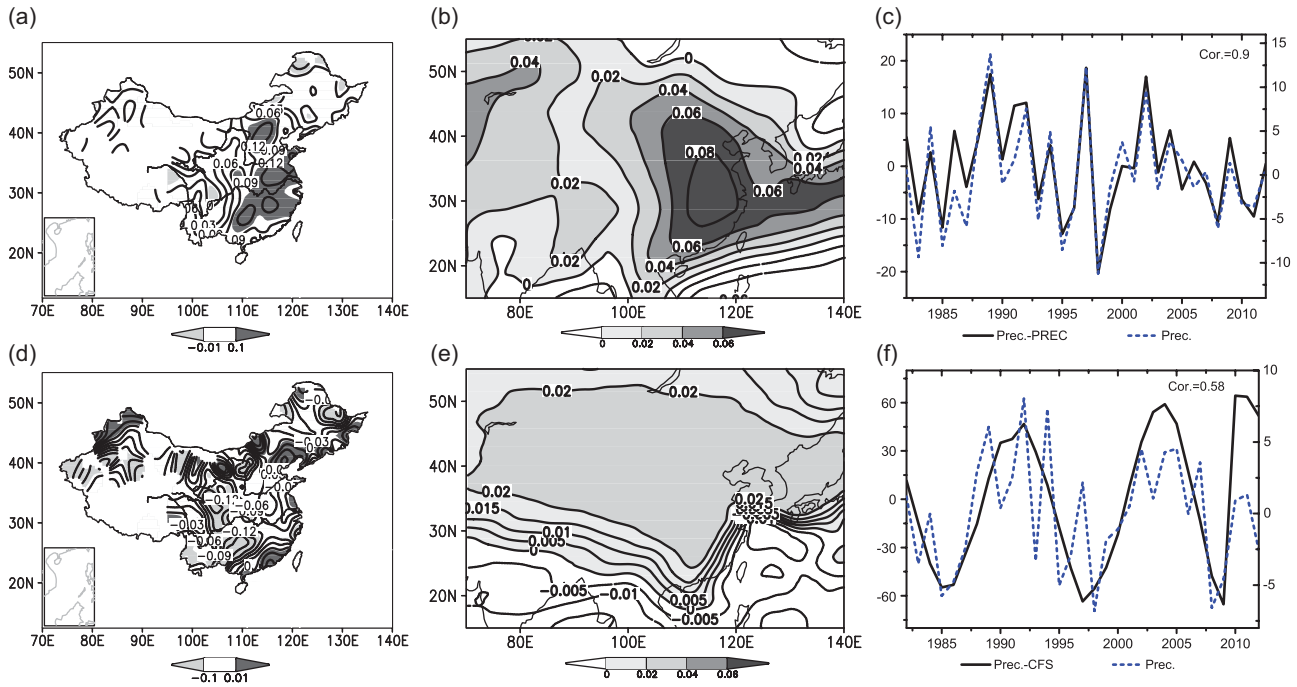


Figure 3. The heterogeneous correlation patterns of the first leading SVD for the observed precipitation in China (a, d) and precipitation over eastern Asia (b, e); as well as time series of extension coefficients for precipitation and precipitation over eastern Asia (c, f) in the boreal winter during 1982–2012, where precipitation over eastern Asia in (b) and (e) are based on the PREC and CFSv2 data, respectively.

© 2014 Royal Meteorological Society

the principal components of the two fields to filter out the noise. Then, SVD was applied to extract coupled patterns between observed precipitation and large-scale variables. Next, during the prediction period, the linear regression was used to forecast the time expansion coefficients of the SVD for the predictand based on that of the large-scale predictors. Finally, the predictand in the target year was predicted by the time expansion coefficient at the forecasting time and the singular vector of the SVD mode in training time for the predictand. More details of the procedure of the SD can be referred from Liu and Fan (2012, 2013).

Here, we defined a decreased root mean square error percentage (RMSEP) as measuring the difference between the root mean square error (RMSE) of the original CFSv2 and the downscaling model to quantify the ability of the SD model in predicting the winter precipitation anomalies. The RMSE and RMSEP can be expressed with the following equations:

$$\mathrm{RMSE} = \sqrt{\frac{\sum_{i=1}^{N}\left(y_i - y_{oi}\right)^2}{N}} \quad (1)$$

$$\mathrm{RMSEP} = \frac{\mathrm{RMSE}_{\mathrm{CFSv2}} - \mathrm{RMSE}_{\mathrm{SD}}}{\mathrm{RMSE}_{\mathrm{CFSv2}}} \times 100\% \quad (2)$$

In Equation 1, $y_i$ is the output of original CFSv2 or downscaling, and $y_{oi}$ is the observational data. $N$ presents total number of stations in China or forecast period according to the spatial or temporal RMSE. In Equation 2, $\mathrm{RMSE}_{\mathrm{CFSv2}}$ and $\mathrm{RMSE}_{\mathrm{SD}}$ indicated the RMSE of original CFSv2 and RMSE of SD result, respectively. That is, positive (negative) RMSEP indicates the SD model has higher (lower) predictive capability than the CFSv2. The spatial and temporal RMSEP (or RMSE) and the Pearson correlation between the observations and the CFSv2 output were used to measure performances of the downscaling models.

## 3. Predictors

### 3.1. Candidates of the predictors related to winter precipitation over China

A pool of candidate predictors for precipitation will be selected based on the previous studies and superior influential processes with physical mechanisms. Local changes in meteorological parameters in mid-latitudes, including precipitation, are mainly controlled by atmospheric circulation (Parker *et al.*, 1994). Meanwhile, the predicted precipitation from the GCM output is the product of interactions between lots of the model physical processes which are closely related to occurrences of the precipitation. Autumn Arctic sea-ice is another one of the important predictor for winter climate. Decreases in the autumn Arctic sea-ice have affected climate variation in atmospheric circulation during boreal winter (Honda *et al.*, 2009), especially recent years with the accelerated decrease of the Arctic sea-ice. Therefore, three candidate predictors, namely the SLP and precipitation in current winter from CFSv2 and the SIC in previous autumn from observation, were considered to be involved into the SD model of the winter precipitation in China.

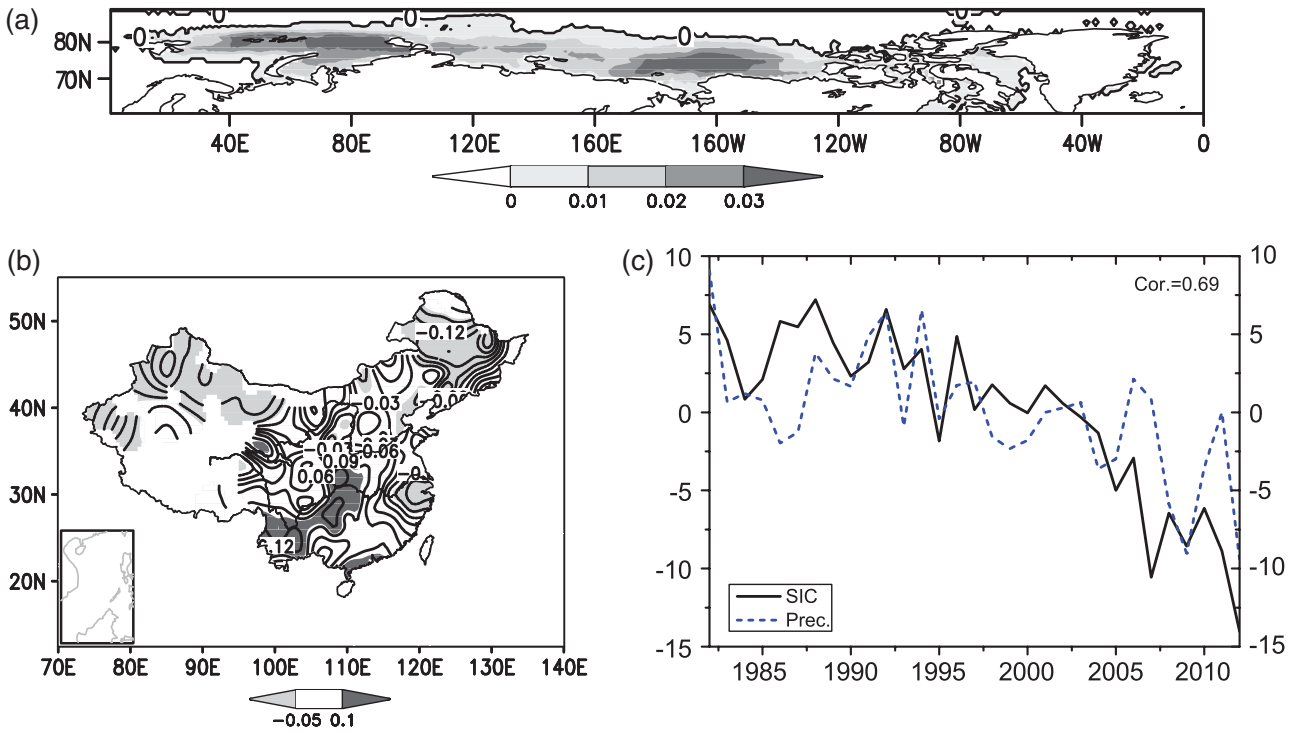


Figure 4. The heterogeneous correlation patterns of the first leading SVD for the observed SIC in autumn (a); winter precipitation in China (b); and time series of extension coefficients for precipitation and SIC (c) over the period 1982–2012.

© 2014 Royal Meteorological Society

Table 2. Multi-year average of the spatial RMSE and ACC in the cross validation and independent validation.

| | Cross-validation (1982–2012) | | Independent-validation (2007–2012) | |
|---|---|---|---|---|
| | RMSE (mm day$^{-1}$) | ACC | RMSE (mm day$^{-1}$) | ACC |
| Original CFSv2 | 1.67 | 0.01 | 1.47 | −0.01 |
| SLP-scheme | 0.48 | 0.33 | 0.55 | 0.31 |
| Precipitation-scheme | 0.54 | 0.30 | 0.61 | 0.25 |
| SIC-scheme | 0.49 | 0.38 | 0.52 | 0.39 |
| SS-scheme | 0.40 | 0.42 | 0.49 | 0.44 |

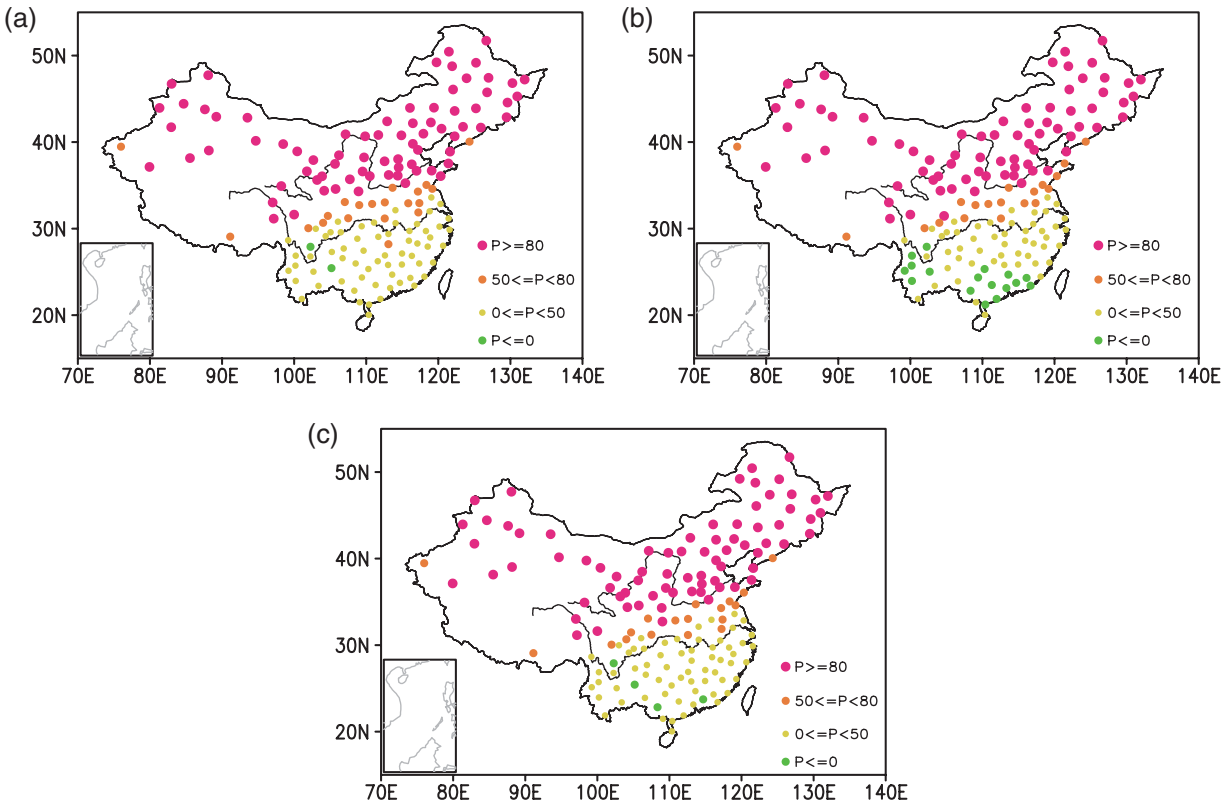


Figure 5. The temporal RMSEP pattern of SD based on SLP-scheme (a), precipitation-scheme (b), and SIC-scheme (c) in the cross validation during 1982–2012 winters. The solid circles in pink, orange, and yellow represent the decreased RMSE compared with the original CFSv2 output with different threshold values, respectively. The green solid circles represent the increased RMSE compared with the original CFSv2. *P* denotes the RMSEP (unit: %).

In boreal winter, the SLP field over Asia and North Pacific is featured by the East Asian Winter Monsoon (EAWM) (Shi and Zhu, 1996). In addition, the movements of cold air, as a necessary condition for forming precipitation, can be seen in the SLP over the mid-high latitudes. EAWM has prominent impacts on the winter precipitation in China (Xu and Chan, 2002; Wang and He, 2013). Therefore, the SLP over East Asia and northeastern (NE) Pacific, which represents the EAWM, can be selected as a candidate predictor (Table 1). Figure 2 depicts the spatial patterns of precipitation and SLP associated with their leading SVD modes for the observation/reanalysis and CFSv2 data, respectively. Over the entire region, the reanalysis data showed that the first SVD mode of SLP had an east–west oriented dipole pattern. In particular, the pattern of SLP is characterized by relatively lower (higher) anomalies over the NW Pacific and higher (lower) anomalies over the East Asian continent (Figure 2(b)). The pattern just represents the Aleutian low over the North Pacific and the Siberian high over the Asian mainland. The gradient in the SLP anomalies determines variations of the EAWM to make impacts on the winter precipitation in China (Tao and Chen, 1987; Xu *et al.*, 1998). A similar spatial pattern is found for features of the CFSv2 SLP in the northern East Asian mainland and the NW Pacific (Figure 2(e)). However, some details of the dipole pattern for the reanalysed SLP anomalies failed to be reproduced by the CFSv2. For instance, a shrinking and weakened negative anomaly over NW Pacific and a further eastward positive anomaly centre emerge in the first SVD mode of CFSv2.

The corresponding precipitation pattern for the reanalysed SLP showed a decreased precipitation in China, excluding the NE and southwestern (SW) China (Figure 2(a)). For the CFSv2, the first precipitation SVD mode reproduced the primary spatial characteristics,

© 2014 Royal Meteorological Society

except the expansible negative domain over the SW China (Figure 2(d)). The correlation coefficients between the precipitation expansion coefficients and SLP (i.e. 0.7) are lower for CFSv2, compared with the reanalysis (i.e. 0.76). Furthermore, the correlation coefficient between the SLP expansion coefficients of the CFSv2 and reanalysis reaches 0.51 and that between the precipitation expansion coefficients of them is 0.89. On the basis of the above results, the predictive performance of the SLP from CFSv2 as a predictor is comparable to that from the reanalysis.

The GCM precipitation, to some extent, integrates all relevant large-scale predictors, in which more physical processes are involved than any single circulation variable. Deviations between the large-scale GCM precipitation and regional precipitation are due to biases from systematic errors of the GCM. Moreover, such a choice of predictor is less vulnerable to nonstationarities in the predictor–predictand relationship, because GCM biases are usually less variable than relationships to circulation indices (Widmann *et al.,* 2003). Some studies have identified GCM precipitation fields as the predictors for precipitation downscaling. Schmidli *et al.* (2006) applied the SD to precipitation over the European Alps taking the GCM precipitation as the predictor. The simulated precipitation from NCEP–NCAR reanalysis was also used as a predictor to develop a SD model (Widmann and Bretherton, 2003). In this study, the predicted winter precipitation over China and adjacent regions (Table 1) from the CFSv2 was considered as a predictor for regional winter precipitation over China. The first SVD mode between the CFSv2 winter precipitation and the observed station precipitation can catch some characteristics of observation, but also miss more. The strength of the anomaly centres from the CFSv2 is much weaker than that of the PREC, and the position even moves far away (Figure 3). In addition, the correlation between the expansion coefficients of the predictand and predictor is 0.58 for CFSv2 which is much lower compared with that of the PREC dataset (i.e. 0.9).

During 1979–2006, the linear trends in Arctic sea-ice extent are negative in every month, especially the larger trend in September. The loss of the ice cover can affect the atmospheric circulation and precipitation in middle latitudes (Mark *et al.,* 2007). Recently, Liu *et al.* (2012) have indicated that the decrease of Arctic sea-ice tends to result in anomaly snowfall and severe cold in mid-high latitude. The autumn SIC anomalies could persist in the following winter and the winter Arctic sea-ice anomalies, which is memorized from the autumn Arctic sea-ice anomalies, includes the signal induced by winter atmospheric circulation variability (Song *et al.*, 2012). Therefore, the autumn Arctic SIC is the third candidate predictor for winter precipitation in China.

The spatial patterns of winter precipitation and the autumn SIC associated with the leading SVD mode during 1982–2012 are shown in Figure 4. The SIC pattern is almost positive in the entire domain (Figure 4(a)). In particular, the relatively larger anomaly centres are located over the regions adjacent to the Barents–Kara Seas and Beaufort Sea, where the SIC decreased rapidly these years (Petoukhov and Semenov, 2010; Tivy *et al.*, 2011). The corresponding precipitation pattern shows positive values for most parts of the northern China, southern China, except the middle-lower reach of Yangtze River which has negative anomalies for the first observed SVD mode (Figure 4(b)). The coupled patterns between the SIC and precipitation illustrates that, the decreased sea-ice over

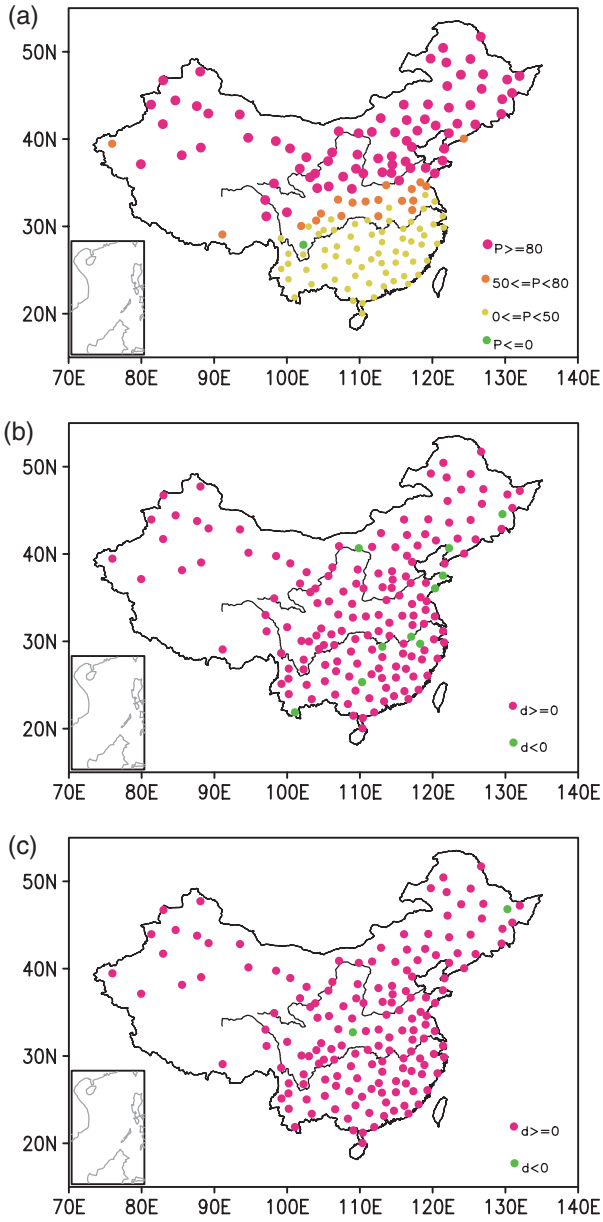


Figure 6. The patterns of temporal RMSEP of SD based on SS-scheme (a), difference of temporal RMSEP between SS-scheme and SLP-scheme (b) or SIC-scheme (c) in the cross validation during 1982–2012 winters (unit: %). In (a), the solid circles in pink, orange, and yellow represent the decreased RMSE compared with the original CFSv2 output with different threshold values, respectively. The green solid circles represent the increased RMSE compared with the original CFSv2. *P* denotes the RMSEP. In (b, c), the solid circles in pink (green) represent the positive (negative) difference of RMSEP which is calculated by the RMSEP of SS-scheme minuses that of SLP-scheme or SIC-scheme. (d) It denotes the difference of RMSEP.

© 2014 Royal Meteorological Society

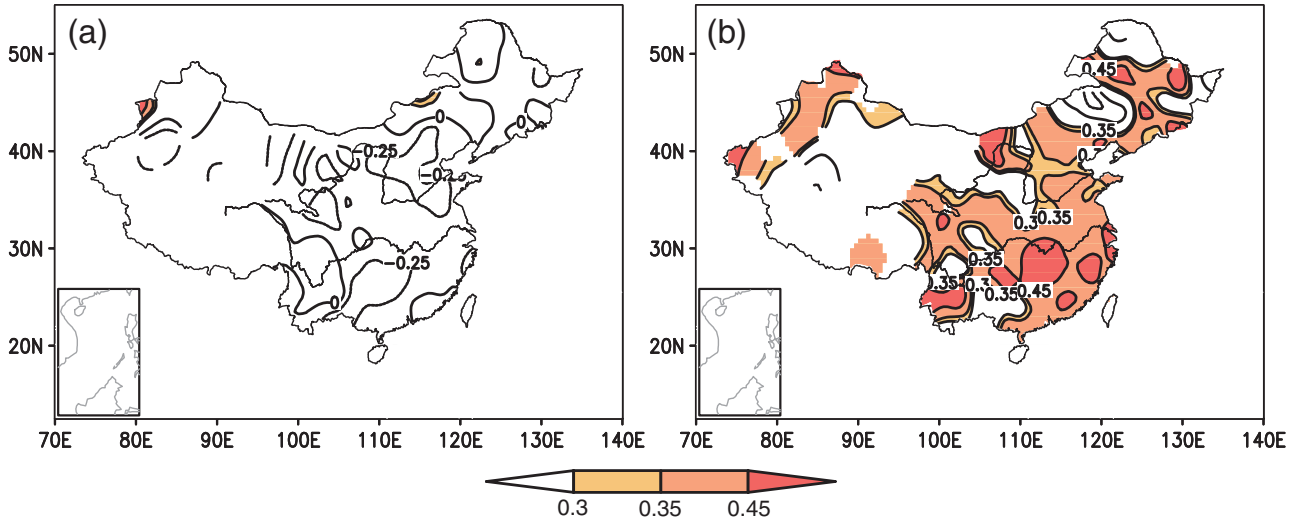


Figure 7. The spatial pattern of ACCs between the observed autumn precipitation and either the hindcasts from original CFSv2 (a) or cross-validation downscaling based on the SS-scheme (b). The shaded areas from light to dark correspond to 90, 95, and 99% confidence levels, respectively.

Arctic (especially Barents–Kara Seas and Beaufort Sea) tends to induce more precipitation in the northern China and less precipitation in the southern. Some studies have demonstrated that the sea-ice over Kara Sea and Beaufort Sea can influence the precipitation over North China and the middle-lower reach of Yangtze River (Wang *et al.*, 1992; Bai *et al.*, 2000). Decreased autumn-winter Arctic SIC in the eastern Arctic and Eurasian marginal seas could produce enhanced Siberian High (Wu *et al.*, 2011) and more open water, which can provide more water vapour for more precipitation through southward flow (Wang and Fan, 2013). Meanwhile, the correlation coefficient between the expansion coefficients of the predictand and predictor is 0.69.

### 3.2. Predictors selected into the SD model

It is crucial for developing a SD model to select suitable predictors. On the basis of the above analyses, three variables were determined for candidate predictors, the winter SLP, winter precipitation, and autumn SIC. Here, the SD model involved SLP was abbreviated as SLP-scheme and so on for other predictors (i.e. precipitation-scheme and SIC-scheme). Although the candidate predictors have close relationship with winter precipitation of China, the downscaling result is usually determined by more other factors, such as the performance of the GCM. Therefore, the cross validation during 1982–2012 winters and independent validation from 2007–2012 winters were carried out to verify the SD model involving the different predictors, respectively. The purpose of the above two validations is to determine the predictors more applicable for downscaling the winter precipitation in China. The multi-year average of the spatial RMSE and spatial anomaly correlation coefficient (ACC) of precipitation anomaly in every individual SD scheme is shown in Table 2. For the original CFSv2, the RMSE is 1.67 mm day$^{-1}$, whereas after downscaling, the RMSEs of the SD results were all decreased largely, i.e. 0.48, 0.54, and 0.49 mm day$^{-1}$ from the SLP, precipitation, and SIC SD schemes, respectively. And the ACC of all the SD schemes increased to >0.3 from ∼0.01 of the original CFSv2. For the independent validation, the RMSE of SD schemes (i.e. ∼0.6 mm day$^{-1}$) is much smaller than that of the original CFSv2 (i.e. 1.47 mm day$^{-1}$). Meanwhile, the ACC of all the SD schemes increased largely compared with the original CFSv2 result. Overall, all the SD schemes performed much better than the original CFSv2, but the precipitation-scheme SD model has slightly larger RMSE and smaller ACC than the two others.

As shown in Figure 5, the temporal RMSEP of precipitation anomaly was investigated. The SLP-scheme and SIC-scheme of the SD model have positive RMSEP over 98.7 and 97.7% stations. In contrast, the precipitation-scheme has less than 89.4% stations with positive RMSEP located over the southern China. On the basis of these results of the cross-validation, the precipitation-scheme SD models has relatively lower prediction skill than the SLP-scheme and SIC-scheme of the SD model, therefore, the predictors of SLP and SIC are ultimately selected to downscale the winter precipitation in China.

## 4. SD results

In this study, two validation methods (an independent validation and a 1-year-out cross validation) were applied to assess the SD models for the winter precipitation in China. Here, predictors SLP and SIC were involved into the SD model, respectively. And then, both predictors were all put into the SD model (abbreviated as SS-scheme). Finally, three schemes (i.e. SLP-scheme, SIC-scheme, and SS-scheme) have been established in this study. The performances of the SD models can be verified comparing each SD model with original CFSv2.

© 2014 Royal Meteorological Society

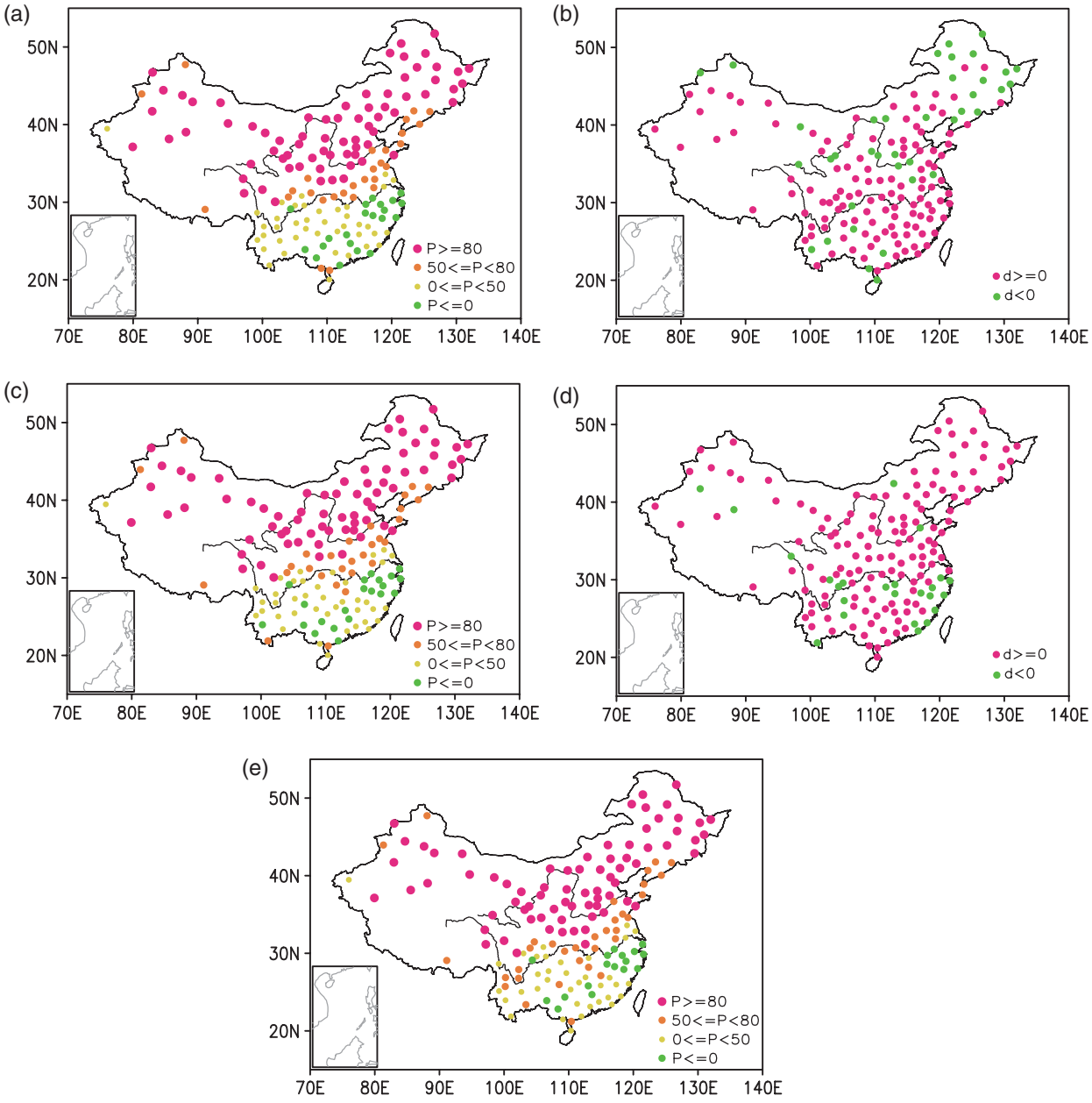


Figure 8. The patterns of temporal RMSEP of SD based on SLP-scheme (a), SIC-scheme (c), SS-scheme (e), difference of temporal RMSEP between SS-scheme and SLP-scheme (b) or SIC-scheme (d) in the independent validation during 2007–2012 winters (unit: %). In (a, c, e), the solid circles in pink, orange, and yellow represent the decreased RMSE compared with the original CFSv2 output with different threshold values, respectively. The green solid circles represent the increased RMSE compared with the original CFSv2. *P* denotes the RMSEP. In (b, d), the solid circles in red (green) represent the positive (negative) difference of RMSEP which is calculated by the RMSEP of SS-scheme minuses that of SLP-scheme or SIC-scheme. (d) It denotes the difference of RMSEP.

The precipitation in the original CFSv2 was interpolated to the 160 stations in China, and then, is compared with the observations. In this case, the original CFSv2 precipitation data in the 160 stations are assigned by the nearest CFSv2 grid data (Im *et al.,* 2007; Yang *et al.,* 2010). In the following, we compare the skill of precipitation predictions by the SD models relative to the original CFSv2 output with the above two validations.

### 4.1. Cross validation from 1982–2012

Now, we show the specific comparisons between the original CFSv2 and the downscaling results. The patterns of the temporal RMSEP between the RMSEs of original CFSv2 and the SD result were shown in Figures 5(a), (c) and 6(a). For all the three schemes of the SD model, RMSEPs are overall positive over most of the stations in China, except some stations in the SW China. The RMSEPs in the northern China are larger than those in the southern China. One possible reason for the phenomenon is that the magnitude of precipitation in the northern China is relatively uniform, compared with that in the southern China (refer to Figure 1). For the individual scheme, there are 158, 156, and 159 stations (more than 97% of total stations) which have positive RMSEPs, for the

© 2014 Royal Meteorological Society

SLP-scheme, SIC-scheme, and SS-scheme, respectively (Figures 5(a), (c) and 6(a)). Furthermore, the difference between the RMSEP of SS-scheme and that of the SLP-scheme or SIC-scheme was investigated, and the positive values are located in most of China (Figure 6(b) and (c)). It is demonstrated that the SS-scheme has higher prediction skill that the two other schemes.

The temporal ACCs of the downscaling results only based on the SS-scheme in terms of cross validation was examined in Figure 7. The downscaling model shows a significant improvement of prediction skill, compared with the original CFSv2 output (see right column of Figure 7). The ACCs are all larger than 0.35 (significant at the 95% confidence level) over China, except some parts of the NW China. The ACC reaches 0.6 over the middle reach of Yellow River. As a contrast, the temporal ACCs for the original CFSv2 are greater than 0.3 (significant at the 90% confidence level) only in some small regions (left column of Figure 7). Meanwhile, the multi-year average of the spatial RMSE and ACC in cross validation was investigated in Table 2. The ACC and RMSE of SS-scheme are 0.42 and 0.40 mm day$^{-1}$, respectively. Therefore, it is evident that the SS-scheme is superior to other two SD schemes in the cross validation during 1982–2012 winters.

### 4.2. Independent validation from 2007–2012

We here further examine the predictive skill of the downscaling model by conducting independent validation. The spatial patterns of the temporal RMSEPs based on the different schemes are shown in Figure 8(a), (c) and (e). Similar to the cross-validation results, the performances of the SD model in terms of RMSEPs are better over the northern China than the southern China, but the difference is there are more negative dots here, compared with the cross-validation. In details, the negative RMSEPs are located in the lower reach of Yangtze River and over some parts of South China. The SS-scheme, comparing the schemes with each other, has the most stations with positive RMSEPs (∼90% stations, Figure 8(e)) than the SLP-scheme (∼86% stations, Figure 8(a)) and SIC-scheme (∼86% stations, Figure 8(c)). The difference between the RMSEP of SS-scheme and that of the SLP-scheme or SIC-scheme is shown in Figure 8(b) and (c). The SS-scheme has superior prediction skill compared with the other schemes over most of China stations. Meanwhile, the ACC of all the SD schemes is much higher than that of the original CFSv2 from 2007–2012 winters, and the ACC is the highest in 2008 winter (figure not shown). The multi-year average of the spatial RMSE and ACC from SS-scheme in independent validation is 0.49 and 0.44 mm day$^{-1}$, respectively (Table 2).

Also, the temporal variation of the spatial RMSE is evaluated in Figure 9. For the whole period of the independent validation (from 2007 to 2012), the SS-scheme shows the lowest RMSE for 5 of 6 years (red bar), the SIC-scheme has the medium performance (blue bar), while the SLP-scheme performs the best only in 2009 but the worst in other years (yellow bar). For all the schemes, the downscaling model has much less RMSE (i.e. ∼0.2–0.8 mm day$^{-1}$) in predictions than the original CFSv2 (i.e. ∼1.2–1.6 mm day$^{-1}$) every year. On the basis of the above results, it is clear that the SD scheme with the combination of the predictors (i.e. SS-scheme) has the best performance than the scheme with either predictor for the independent validation. Therefore, we used the SS-scheme to do the prediction of the winter precipitation anomaly in China.

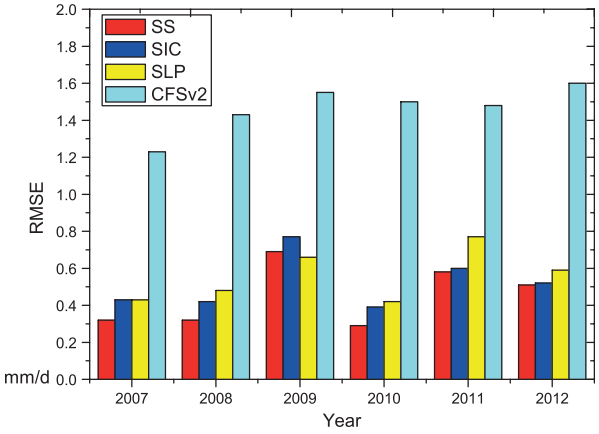


Figure 9. The spatial RMSE of SD based on SLP-scheme (yellow), SIC-scheme (blue), SS-scheme (red), and original CFSv2 (light blue) in the independent validation during 2007–2012 (unit: mm day$^{-1}$).

Finally, we examine the hindcast of winter precipitation anomaly over China in the nearest years (i.e. 2011 and 2012) based on the SS-scheme to investigate the predicted capability of SS-scheme. As seen in Figure 9, original CFSv2 and SS-scheme SD result are verified using the station observations.

In 2011 winter, positive precipitation anomaly centres were located in the southeastern (SE) and western China, and negative anomalies in the middle reach of Yangtze River and Huang-Huai River (Figure 10(a)). The original CFSv2 output failed to capture the details of large precipitation anomaly centres; it simply predicted more precipitation over most regions of the northern China (Figure 10(c)). The downscaling output based on the SS-scheme reproduced the opposite precipitation anomalies between the southern China and the SE or SW China, and especially the negative centre located in the middle reach of Yangtze River (Figure 10(e)). The right column of Figure 10 gives the spatial pattern of the precipitation anomaly in 2012 winter. The eastern (western) part of East China had positive (negative) precipitation anomalies with the largest centres located in the lower reach of Yangtze River (Figure 10(b)). However, the original CFSv2 was unable to reproduce the pattern of large precipitation anomalies centred over East China, as seen in the observations. In contrast, the downscaling prediction with the SS-scheme SD did capture the main pattern of the precipitation anomalies over East China, e.g. the large centres of precipitation anomalies located in the Yangtze River Valley (Figure 10(f)). It is notable there was less sea-ice over Arctic in 2012 autumn than in 2011 autumn

© 2014 Royal Meteorological Society

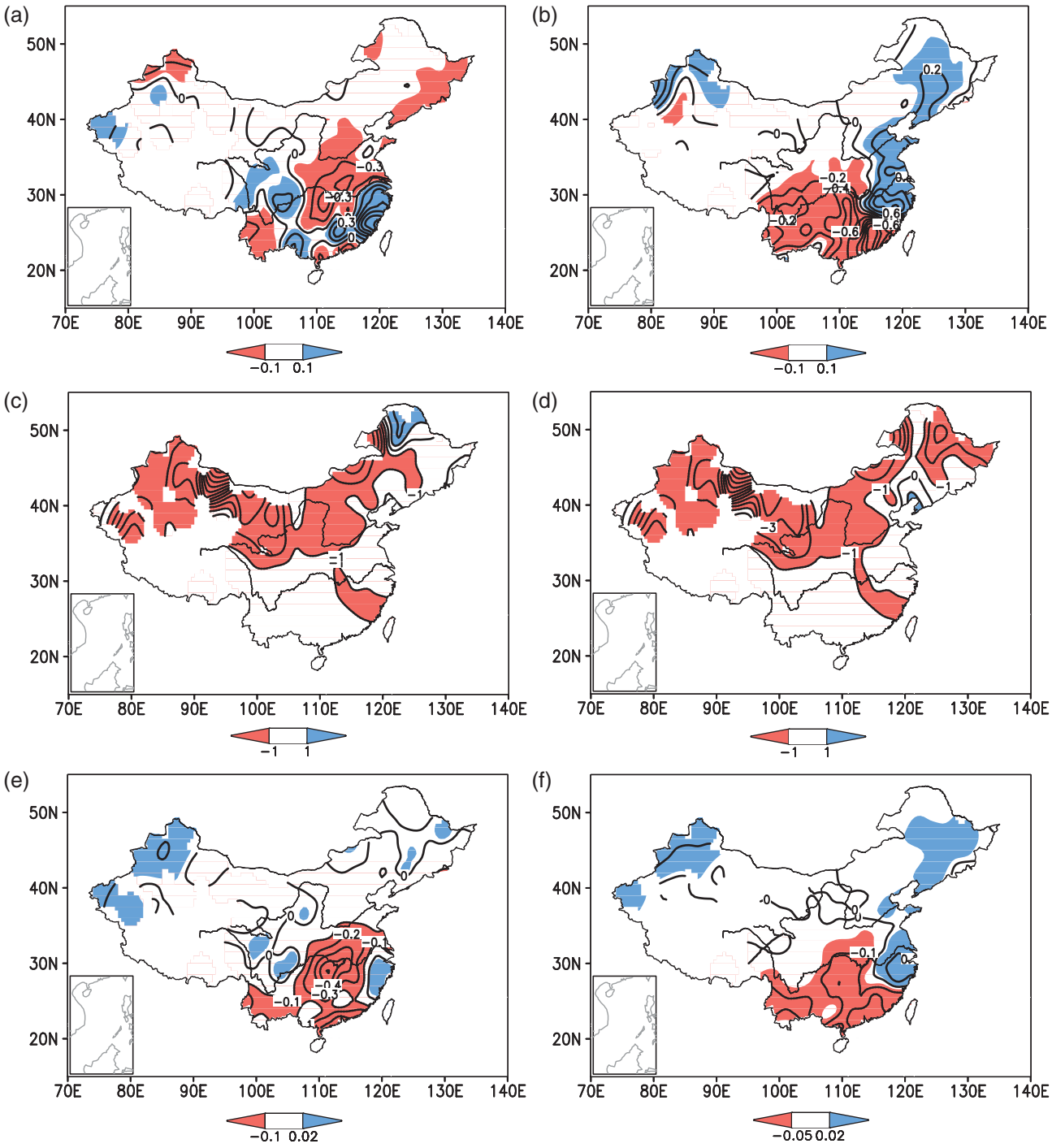


Figure 10. The spatial pattern for the precipitation anomaly of observations (a, b); original CFSv2 outputs (c, d); downscaling based on SS-scheme (e, f) in 2011(left) and 2012 winter (right). Red and blue represent the negative and positive precipitation anomaly, respectively (unit: mm day$^{-1}$).

(Figure 4c), which would favour more water vapour transportation into China region (Ma *et al.*, 2012). Therefore, more precipitation emerged over China region in 2012 winter than in 2011 winter (Figure 10(a) and (b)). Furthermore, the SS-scheme can capture the locations of the anomaly centres over eastern China in the other 4 years (i.e. during 2007–2010, figure not shown).

A decline of the Arctic sea-ice extent has been particular strong in recent years (Comiso *et al.*, 2008) and can significantly impact other components of the climate system, including the Northern Hemisphere atmospheric circulation (Wu *et al.*, 1999), and then makes impact on the winter precipitation in China (Figure 1). Peings and Magnusdottir (2014) examined the wintertime Northern Hemisphere atmospheric circulation response to 2007–2012 Arctic sea-ice decline using Community Atmospheric Model, they found that the surface forcing leads to a weaker polar vortex and more turbulences in mid-latitude. Therefore, the decreased Arctic sea-ice could influence the variability of winter climate in China and improve the prediction

© 2014 Royal Meteorological Society

skill of SD model during 2007–2012 winters. Overall, this study demonstrates that the downscaled precipitation based on the large-scale variables from the CFSv2 is fairly useful in regional climate prediction, which improves coarse resolution forecast products from GCM. Furthermore, the previous signals from additional climatic variables (e.g. autumn SIC) can also increase the prediction skill of the SD model to some extent.

## 5. Conclusion and discussion

Direct outputs of current GCMs are usually so coarse that regional precipitation anomalies cannot be well predicted through these outputs. Under the condition of such a GCM level, the studies on prediction strategies are well known to be effective to improve the performance of short-term climate prediction (e.g. Ren and Chou 2005, 2007; Ren 2008; Zheng *et al.,* 2009). Many of previous studies have confirmed that the SD method can be a useful approach to producing more skillful regional climate prediction (e.g. Sun and Chen, 2012; Wang, 2011; Chen *et al.*, 2012). In this study, a hybrid SD model based on the CFSv2 outputs and observational data of the large-scale circulation variables has been developed to predict the station winter precipitation over China. After the procedure of selecting predictor, the winter SLP from the CFSv2 and the previous autumn SIC from observation were used as predictors, respectively. Downscaling based on the SLP-scheme, SIC-scheme, and SS-scheme has been shown to considerably outperform global GCM in predicting regional precipitation. It is notable that, the SS-scheme SD model had relatively higher prediction skill than both the SLP-scheme and SIC-scheme.

In the cross-validation during 1982–2012 winters, the downscaling results based on the SLP-scheme, SIC-scheme, and SS-scheme all performed much better than that of the original CFSv2. The spatial patterns of the temporal RMSEP from the different schemes have positive values over more than 97% stations in China. Even more, the significant ACCs of downscaling output covers most parts of China. In the hindcast of the independent validation from 2007 to 2012, the positive temporal RMSEP of downscaling based on the different schemes were located over ∼87% stations in China. The spatial RMSE demonstrates that the downscaling using the different schemes perform superior to the original CFSv2. Meanwhile, the SS-scheme has the best performance among the three schemes. Moreover, compared with the observation, the SD based on the SS-scheme can predict the 2011 and 2012 winter precipitation anomalies much better than the output of original CFSv2.

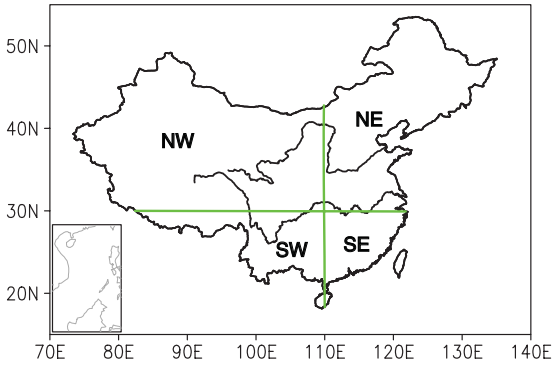


Figure 11. Sub-regions in China. NE, SE, SW, and NW represent the northeastern, southeastern, southwestern, and northwestern China, respectively.

In this study, the prediction skill of three SD schemes was estimated not only over the whole China but also different sub-regions. As shown in Figure 11, the whole region of China was divided into four sub-regions, which are NE, SE, SW and NW China, respectively. The regional average RMSEP of the three SD schemes is shown in Table 3. The RMSEP over NE and NW of all the three schemes is comparable with each other in cross validation and independent validation. Over SE and SW, the RMSEP of SS-scheme is relatively larger than that of SLP-scheme and SIC-scheme.

In general, downscaling predictions using the SS-scheme can give higher scores than those only based on one predictor (i.e. SLP-scheme or SIC-scheme). One reason is that CFSv2 may be able to represent climate anomaly variation, but unable to produce a realistic coupled pattern between SLP and station precipitation. On the other hand, SIC is an important previous predictor for winter precipitation in China, but beside the seasonal timescale, the feedback period of winter climate from autumn SIC may have other timescales in different years. Therefore, these results illustrate that the combination of current and preceding signals can provide more useful prediction information for winter precipitation prediction than either individual predictor. Overall, the hybrid SD model established in this study can be a useful tool for extracting useful information on large-scale climate

Table 3. Regional average of RMSEP from different schemes over subregions of China for cross validation and independent validation (unit: %).

| | Cross validation | | | Independent validation | | |
|---|---|---|---|---|---|---|
| | SLP-scheme | SIC-scheme | SS-scheme | SLP-scheme | SIC-scheme | SS-scheme |
| NE | 77.91 | 79.11 | 79.71 | 72.51 | 70.29 | 75.9 |
| SE | 20.89 | 19.09 | 24.11 | −9.3 | 1.07 | 5.91 |
| SW | 14.25 | 15.95 | 17.7 | 18.93 | 17.38 | 27.34 |
| NW | 88.06 | 87.93 | 88.2 | 86.22 | 85.47 | 88.98 |

© 2014 Royal Meteorological Society

variation from both GCM output and observation to downscale onto local-scale climate variable anomalies.

## Acknowledgements

The work is jointly supported by National Basic Research Program (973) of China (grant nos. 2010CB950404, 2010CB950304), China Meteorological Special Project (GYHY201206016), and National Natural Science Foundation grants of China (41375062, 41275078). The authors are grateful to the anonymous reviewers for their valuable comments and useful advises.

## References

Bai JY, Xu XD, Miao QJ. 2000. The Arctic sea-ice 'strong-signal' region (in Chinese). *Acta Meteorol. Sin.* **4**: 485–491.

Bretherton CS, Smith C, Wallace JM. 1992. An intercomparison of methods for finding coupled patterns on climate data. *J. Clim.* **5**: 541–560.

Chen HP, Sun JQ, Wang HJ. 2012. A statistical downscaling model for forecasting summer rainfall in China from DEMETER hindcast datasets. *Weather Forecast*. **27**: 608–628.

Chen MP, Xie JEJ, Arkin PA. 2002. Global land precipitation: a 50-yr monthly analysis based on gauge observation. *J. Hydrometeorol.* **3**: 249–266.

Christensen JH, Hewitson B, Busuioc A, Chen A, Gao XJ, Held I, Jones R, Kolli RK, Kwon WT, Laprise R, Magaña Rueda V, Mearns L, Menéndez CG, Räisänen J, Rinke A, Sarr A, Whetton P. 2007. Regional climate projections, Chapter 11. In *Climate Change 2007: The Physical Science Basis. Contribution of WGI to the IPCC AR4*, Solomon S, Qin D, Manning M, Chen Z, Marquis M, Averyt KB, Tignor M, Miller HL (eds). Cambridge University Press: Cambridge, UK and New York, NY, 847–940.

Comiso J, Parkinson C, Gersten R, Stock L. 2008. Accelerated decline in the Arctic sea ice cover. *Geophys. Res. Lett.* **35**: L01703.

Fan K. 2011. A statistical scheme for the seasonal forecasting of North China's surface air temperature during winter. *Atmos. Oceanic Sci. Lett.* **4**: 81–85.

Fan K, Liu Y, Chen HP. 2012. Improving the Prediction of the East Asian Summer Monsoon: New Approaches. *Weather Forecast.* **27**: 1017–1030.

Fan K, Tian BQ. 2013. Prediction of wintertime heavy snow activity in northeast China. *Chin. Sci. Bull.* **58**: 1420–1426.

Fan K, Wang HJ, Choi YJ. 2008. A physically-based statistical forecast model for the middle-lower reaches of the Yangtze River Valley summer rainfall. *Chin. Sci. Bull.* **53**: 602–609.

Gao XJ, Zhao ZC, Ding YH, Huang RH, Giorgi F. 2001. Climate change due to greenhouse effects in China as simulated by a regional climate model. *Adv. Atmos. Sci.* **18**: 1224–1230.

Gao XJ, Xu Y, Zhao ZC, Pal JS, Giorgi F. 2006. On the role of resolution and topography in the simulation of East Asia precipitation. *Theor. Appl. Climatol.* **86**: 173–185, DOI: 10.1007/s00704-005-0214-4.

Honda M, Inoue J, Yamane S. 2009. Influence of low Arctic sea-ice minima on anomalously cold Eurasian winters. *Geophys. Res. Lett.* **36**: L08707, DOI: 10.1029/2008GL037079.

Huth R. 1999. Statistical downscaling in central Europe: evaluation of methods and potential predictors. *Clim. Res.* **13**: 91–103.

Im E, Kwon W, Ahn J, Giorgi F. 2007. Multi-decadal scenario simulation over Korea using a one-way double-nested regional climate model system. Part 1: recent climate simulation (1971–2000). *Clim. Dyn.* **28**: 759–780.

Jia XL, Chen LJ, Li WJ, Chen DL. 2010. Statistical downscaling based on BP-CCA: predictability and application to the winter temperature and precipitation in China (in Chinese). *Acta Meteorol. Sin.* **68**: 398–410.

Ju LX, Lang XM. 2011. Hindcast experiment of extraseasonal shortterm summer climate prediction over China with RegCM3 IAP9LAGCM. *Acta Meteorol. Sin.* **25**(3): 376–385, DOI: 10.1007/s13351-011-0312-4.

Kalnay E, Kanamitsu M, Kistler R, Collins W, Deaven D, Gandin L, Iredell M, Saha S, White G, Woollen J, Zhu Y, Leetmaa A, Reynolds R, Chelliah M, Ebisuzaki W, Higgins W, Janowiak J, Mo KC, Ropelewski C, Wang J, Jenne R, Joseph D. 1996. The NCEP/NCAR 40-year reanalysis project. *Bull. Amer. Meteorol. Soc.* **77**(3): 437–471.

Lang XM. 2011. A hybrid dynamical-statistical approach for predicting winter precipitation over eastern China. *Acta Meteorol. Sin.* **25**: 272–282.

Lang XM, Wang HJ, Jiang D. 2003. Extraseasonal ensemble numerical prediction of winter climate over China. *Chin. Sci. Bull.* **48**: 2121–2125.

Liu Y, Fan K. 2012. Prediction of spring precipitation in China using a downscaling approach. *Meteorol. Atmos. Phys.* **118**: 79–93.

Liu Y, Fan K. 2013. A new statistical downscaling model for autumn precipitation in China. *Int. J. Climatol.* **33**: 1321–1336, DOI: 10.1002/joc. 3514.

Liu JP, Curry JA, Wang HJ, Song M, Horton RM. 2012. Impact of declining Arctic sea ice on winter snowfall. *Proc. Natl. Acad. Sci. U.S.A.* **109**: 4074–4079.

Liu Y, Fan K, Yan YP. 2013. A new statistical downscaling scheme for predicting winter precipitation in China *Atmos. Oceanic Sci. Lett.* **6**:332–336.

Ma JH, Wang HJ, Zhang Y. 2012. Will boreal winter precipitation over China increase in the future? An AGCM simulation under summer "ice-free Arctic" conditions. *Chin. Sci. Bull.* **57**: 921–926, DOI: 10.1007/s11434-011-4925-x.

Mark CS, Marika MH, Stroeve J. 2007. Perspectives on the Arctic's shrinking sea-ice cover. *Science* **315**(5818): 1533–1536, DOI: 10.1126/science.1139426.

Michaelsen J. 1987. Cross-validation in statistical climate forecast models. *J. Clim. Appl. Meteorol.* **26**: 1589–1600.

Parker D, Jones PD, Folland CK, Bevan A. 1994. Interdecadal changes of surface temperature since the late nineteenth century. *J. Geophys. Res.* **99**: 14373–14399.

Peings Y, Magnusdottir G. 2014. Response of the wintertime Northern Hemisphere atmospheric circulation to current and projected Arctic sea ice decline: a numerical study with CAM5. *J. Clim.* **27**: 244–264.

Petoukhov V, Semenov VA. 2010. A link between reduced Barents-Kara sea ice and cold winter extremes over northern continents. *J. Geophys. Res.* **115**: D21111, DOI: 10.1029/2009JD013568.

Rayner NA, Parker DE, Horton EB, Folland CK, Alexander LV, Rowell DP, Kent EC, Kaplan A. 2003. Global analyses of sea surface temperature, sea ice, and night marine air temperature since the late nineteenth century. *J. Geophys. Res.* **108**: 4407, DOI: 10.1029/2002JD002670.

Ren H. 2008. Predictor-based error correction method in short-term climate prediction. *Prog. Nat. Sci.* **18**(1): 129–135, DOI: 10.1016/j.pnsc.2007.08.003.

Ren H, Chou J. 2005. Analogue correction method of errors by combining statistical and dynamical methods. *Acta Meteorol. Sin.* **20**(3): 367–373.

Ren H, Chou J. 2007. Strategy and methodology of dynamical analogue prediction. *Sci. Chin. Ser. D. Earth Sci.* **50**(10): 1589–1599.

Saha S, Nadiga S, Thiaw C, Wang J, Wang W, Zhang Q, Van den Dool HM, Pan HL, Moorthi S, Behringer D, Stokes D, Peña M, Lord S, White G, Ebisuzaki W, Peng P, Xie P. 2006. The NCEP climate forecast system. *J. Clim.* **19**: 3483–3517.

Saha S, Moorthi S, Wu X, Wang J, Nadiga S, Tripp P, Behringer D, Hou YT, Chuang HY, Iredell M, Ek M, Meng J, Yang R, Peña M, Van den Dool H, Zhang Q, Wang W, Chen M, Becke E. 2013. The NCEP climate forecast system version 2. *J. Clim.* **27**: 2185–2208, DOI: 10.1175/JCLI-D-12-00823.1.

Schmidli J, Frei C, Vidale PL. 2006. Downscaling from GCM precipitation: a benchmark for dynamical and statistical downscaling methods. *Int. J. Climatol.* **26**: 679–689.

Schoof JT. 2013. Statistical downscaling in climatology. *Geog. Compass.* **7**: 249–265, DOI: 10.1111/gec3.12036.

Shi N, Zhu Q. 1996. An abrupt change in the intensity of the East Asian summer monsoon index and its relationship with temperature and precipitation over East China. *Int. J. Climatol.* **16**: 757–764.

Song M, Liu JP, Liu HL, Ren XB, Wang XC. 2012. Associations between the autumn Arctic sea ice and North American winter precipitation. *Atmos. Ocean. Sci. Lett.* **5**: 212–218.

Sun JQ, Chen HP. 2012. A statistical downscaling scheme to improve global precipitation forecasting. *Meteorol. Atmos. Phys.* **117**: 87–102, DOI: 10.1007/s00703-012-0195-7.

Tao SY, Chen L. 1987. A review of recent research on the East Asian monsoon in China. In *Monsoon Meteorology*. Oxford University Press: Oxford, UK, 60–92.

Tivy A, Howell SEL, Alt B, McCourt S, Chagnon R, Crocker G, Carrieres T, Yackel JJ. 2011. Trends and variability in summer sea

© 2014 Royal Meteorological Society 

ice cover in the Canadian Arctic based on the Canadian Ice Service Digital Archive, 1960–2008 and 1968–2008. *J. Geophys. Res.* **116**: C03007, DOI: 10.1029/2009JC005855.

Wang HJ. 2011. A new prediction model for tropical storm frequency over the western North Pacific using observed winter-spring precipitation and geopotential height at 500 hPa. *Acta Meteorol. Sin.* **25**(3): 262–271.

Wang HJ, Fan K. 2013. Recent changes in the East Asian monsoon (in Chinese). *Chin. J. Atmos. Sci.* **37**(2): 313–318.

Wang HJ, He SP. 2013. The increase of snowfall in Northeast China after the mid 1980s. *Chin. Sci. Bull.* **58**: 1350–1354.

Wang XL, Peng G, Pan Z, Zhou E. 1992. Connection of the flood-season runoff of the upper-middle Yangtze River with Arctic sea ice indices (in Chinese). *Acta Meteorol. Sin.* **50**: 126–128.

Widmann M, Bretherton CS. 2003. Statistical precipitation downscaling over Northwestern United States using numerically simulated precipitation as a predictor. *J. Clim.* **16**: 799–816.

Widmann M, Bretherton CS, Salathé EP. 2003. Statistical precipitation downscaling over the Northwestern United States using numerically simulated precipitation as a predictor. *J. Clim.* **16**: 799–816.

Wigley TML, Jones PD, Briffa KR, Smith G. 1990. Obtaining subgrid scale information from coarse-resolution general circulation model output. *J. Geophys. Res.* **95**: 1943–1953.

Wu BY, Huang RH, Gao DY. 1999. The impact of variation of sea-ice extent in the Kara Sea and the Barents Seas in winter on the winter monsoon over East Asia (in Chinese). *Chin. J. Atmos. Sci.* **3**: 267–275.

Wu BY, Su JZ, Zhang RH. 2011. Effects of autumn-winter Arctic sea ice on winter Siberian High. *Chin. Sci. Bull.* **56**: 3220–3228, DOI: 10.1007/s11434-011-4696-4.

Xu J, Chan JCL. 2002. Interannual and interdecadal variability of winter precipitation over China in relation to global sea level pressure anomalies. *Adv. Atmos. Sci.* **19**: 914–926.

Xu JJ, Zhu Q, Sun Z. 1998. Interrelation between East-Asian winter monsoon and Indian/Pacific SST with the interdecadal variation. *Acta Meteorol. Sin.* **12**: 75–287.

Yan XD, Wu ZP, Ma ZF, Gu SH, Yan HS. 2008. Application of a new downscaling model to winter temperature and rainfall prediction over Guizhou (in Chinese). *Plateau Meteorol.* **17**: 169–715.

Yang HL, Xu YL, Zhang L, Pan J, Tao SC. 2010. Projected change in mean and extreme climate over china in the late 21st century from PRECIS Under SRES A2 scenario (In Chinese). *Adv. Clim. Change Res.* **6**(3): 157–163.

Zheng Z, Ren H, Huang J. 2009. Analogue correction of errors based on seasonal climate predictable components and numerical experiments (in Chinese). *Acta Phys. Sin.* **58**: 7359–7367.

© 2014 Royal Meteorological Society

马琴, 刘新, 李伟平, 等. 2014. 青藏高原夏季土壤有机质及砾石影响水热传输特性的数值模拟 [J]. 大气科学, 38 (2): 337–351, doi:10.3878/j.issn.1006-9895.2013.13119. Ma Qin, Liu Xin, Li Weiping, et al. 2014. Simulation of thermal and hydraulic properties affected by organic and gravel soil over the Tibetan Plateau during summer [J]. Chinese Journal of Atmospheric Sciences (in Chinese), 38 (2): 337–351.

# 青藏高原夏季土壤有机质及砾石影响水热传输特性的数值模拟

马琴[1, 2] 刘新[1] 李伟平[3] 丁宝弘[1, 2]

1 中国科学院青藏高原研究所青藏高原环境变化与地表过程实验室，北京 100011

2 中国科学院大学，北京 100049

3 中国气象局国家气候中心气候研究开放实验室，北京 100081

**摘 要** 本文针对青藏高原部分地区土壤有机质和砾石含量较高的特点，在前人工作的基础上，发展了一个新的参数化方案以描述土壤有机质和砾石对土壤导热率、导水率的影响。通过对通用陆面模式 CoLM 中的土壤水、热参数化方案以及地表蒸发阻抗三方面的逐步改进，对青藏高原藏东南站和纳木错站两种不同下垫面进行单点数值模拟分析。对比原方案与最终优化方案的模拟结果表明：采用新方案的 CoLM 模式对藏东南站土壤湿度模拟性能明显提高，平均偏差减小到 0.04，而对纳木错站浅层 20 cm 以上土壤湿度的模拟偏差略微增大。新方案在藏东南站对土壤内部温度的模拟改善较为显著，平均偏差减小了 0.2°C；而在纳木错站 40 cm 以上有所改进。新参数化方案较好地模拟了两个观测站表面能量通量的时间变化，纳木错站 7、8 月份的潜热通量改进尤为明显，比原方案减少大约 20 W $m^{-2}$，与观测结果较为接近。

**关键词** 青藏高原 CoLM 模式 有机质砾石 参数化方案

**文章编号** 1006–9895(2014)02–0337–15 **中图分类号** P461 **文献标识码** A

**doi:**10.3878/j.issn.1006-9895.2013.13119

# Simulation of Thermal and Hydraulic Properties Affected by Organic and Gravel Soil over the Tibetan Plateau during Summer

MA Qin[1, 2], LIU Xin[1], LI Weiping[3], and DING Baohong[1, 2]

1 *Laboratory of Tibetan Environment Changes and Land Surface Processes* (*TEL*), *Institute of Tibetan Plateau Research*, *Chinese Academy of Sciences*, *Beijing* 100011

2 *University of Chinese Academy of Sciences*, *Beijing* 100049

3 *Laboratory for Climate Studies*, *National Climate Center, China Meteorological Administration*, *Beijing* 100081

**Abstract** The soil of some parts of the Tibetan Plateau contains an abundance of organic matter and gravel. On the basis of previous research, a new parameterization scheme has been developed to consider the influences of these material on soil thermal and hydrological conductivities. Sensitivity experiments conducted by using the Common Land Model to improve the parameterizations of soil temperature, hydraulic conductivities, and soil surface resistance are compared with simulation results from off-line numerical experiments reported by Southeast Tibet and Namco stations. By using the new

**收稿日期** 2013–01–25，2013–05–13 收修定稿

**资助项目** 全球变化研究重大科学研究计划项目 2010CB951703、2010CB951902，国家自然科学基金项目 41175005、41275075

**作者简介** 马琴，女，1987 年出生，硕士，主要从事陆面过程模拟研究。E-mail: maqin@itpcas.ac.cn

**通讯作者** 刘新，E-mail: lx@itpcas.ac.cn

parameterization scheme, the average deviation of the simulated soil moisture reported by the former station decreased by 0.04; however, the value showed a slight increase above the layer of 20 cm at the latter station. Although the average deviation of soil temperature, except at the surface, is decreased by 0.2°C at the Southeast Tibet station, the biases decrease above the layer of 40 cm at the Namco station. With the new parameterization, the discrepancies of soil net radiation and surface sensible and latent heat fluxes are reduced. In particular, the surface latent heat flux at the Namco station in July and August is reduced by about 20 W $m^{-2}$, which is closer to the observation value than that obtained by using the original parameterization.

**Keywords** Tibetan Plateau, Common Land Model, Soil organic matter, Gravel, Parameterization scheme

## 1 引言

青藏高原是全球气候变化的敏感区，其动力和热力作用对大气环流、气候变化和灾害性天气形成发展有十分重要的影响（卞林根等，2001），而且高原上能量和水分循环对亚洲季风的形成与演化也具有十分重要的作用，所以加深对青藏高原陆面过程的了解，是改善大气环流模式对亚洲季风以及全球天气和气候预报效果的关键（王介民，1999）。其中土壤温度、湿度是检验陆面过程的重要指标，而土壤温湿等理化性质及模式模拟的水分循环和热通量等都与土壤质地有关（赵勇和钱永普，2007；梁晓和戴永久，2008）。近年来我国的陆面过程研究水平不断提高，但是在高原地区的模拟仍存在着一些问题：Yang et al.（2009）通过对比简单生物圈模式 SiB2、通用陆面模式 CoLM、Noah 三个陆面模式在高原中东部高寒草甸的模拟，发现三个模式均低估了表层土壤水分；罗斯琼等（2008）利用陆面模式 CoLM 在青藏高原中部 Bujiao（BJ）站进行单点数值模拟试验，指出在模式中没有考虑砾石对青藏高原土壤水热性质的影响, 这是模拟存在偏差的一个原因。除此之外，其他研究（刘少锋和林朝晖，2005；王澄海和师锐，2007）也指出陆面模式在高原地区的模拟有待进一步改进。

青藏高原地区较于同纬度地区温度偏低，有机质分解慢，从而导致土壤表层根系发达、有机质累积，在平均深度为 72 cm 的土层中积累了 $38.4\times10^9$ t 的有机碳，约占全国土壤总碳库的 21%（方精云等，1996）；而面积为 $1.60\times10^8$ $hm^2$ 的草地生态系统，其土壤有机碳储量达到 $33.5\times10^9$ t，其中，以高原草甸土和高原草原土有机碳积累量为主（王根绪等，2002）。土壤有机质的水热传输特性与矿物质相比有很大的区别。有机质能够改变土壤水分常数、水分特征曲线、饱和导水率等土壤水动力学参数，提高土壤的有效持水量（单秀芝等，1998），从而增强土壤吸热的能力，提高土壤温度（Lawrence and Slater，2008）。目前已有众多学者考虑有机质对土壤水热特性带来的变化，例如 Letts et al.（2000）和 Beringer et al.（2001）在加拿大和美国阿拉斯加州冻土地带估算了纯泥炭的影响，但是并没有考虑矿物质对土壤特性的作用；Lawrence and Slater（2008）在 Farouki（1981）参数化方案的基础上将矿物质和有机质进行了权重分配，但是土壤热参数化方案的适用性并没有经过严格的验证；Chen et al.（2012）通过 34 个站点的 77 个土壤样品分析了土壤有机碳对土壤孔隙度、热传输参数等的影响，进而提出了新的土壤热参数化方案并进行了验证，但是并没有考虑有机质对水传输特性的作用以及该参数化方案在模式中的适用性。

在高原的局部地区不仅含有较高的有机质，而且砾石含量也较高。砾石是指粒径大于 2 mm，相对独立、不易破碎的矿物质颗粒（Miller and Guthrie，1984）。青藏高原土壤砂土含量较大, 粘、壤土含量较少，局部地方石块和砾石含量较多；从表层向下，随着土壤深度增加, 土质越粗砾石越多（罗斯琼等，2008）。土壤中砾石的存在不仅会影响温度等物理特性（Mehuys et al.，1975），并且对土壤的孔隙度、导热率、含水量和入渗特性存在影响（Hanson and Blevins，1979；Box，1981；Cerdà，2001）。目前在 CoLM 模式的土壤分析中并没有考虑有机质和砾石的影响，但它们的存在对青藏高原土壤的水热性质的作用不能够忽视，因此，本文将改进的参数化方案引入该模式中，选取高原上不同类型下垫面的站点观测资料，进行单点数值模拟试验，考察新参数化方案对改进陆面模式 CoLM 在高原地区的模拟能力有何效果。

## 2 资料选取

本文选取中国科学院藏东南高山环境综合观测研究站（简称藏东南站）和纳木错多圈层综合观

测研究站（简称纳木错站）为研究对象。藏东南站（29°46′N，94°44′E）位于西藏自治区林芝县鲁朗镇北 6 km 左右的鲁朗河谷，海拔高度 3327 m，属于高山草地；纳木错站（30°46′N，90°59′E）位于当雄县纳木错乡纳木错湖东南岸，海拔高度 4730 m，下垫面为高寒草甸。目前两个站都建立了大气边界层塔站观测系统和大气湍流观测系统，其中藏东南站的土壤温度和湿度观测垂直分为 4 cm、10 cm、20 cm、60 cm 和 100 cm 五层，而纳木错站的土壤观测垂直分为 10 cm、20 cm、40 cm、80 cm 和 160 cm 五层。分别选取 2008 年和 2009 年夏季 6 月 1 日至 8 月 31 日三个月的观测资料，并根据模式输入的需要，整理出时间步长为 30 分钟的向下长波辐射、向下短波辐射、降水速率、温度、$u$ 风速、$v$ 风速、气压、比湿共八项气象要素，对于缺测资料我们采取线性插值方法补齐。模式各层土壤温度、湿度初值根据实测结果在垂直方向线性插值得到，而模式结果则线性插值到相应观测所在层析以便于比较。

表 1 列出了两个站点土壤成分的观测值，其中砂粒和粘粒百分比是指在细土颗粒（粒径小于 2 mm）中所占的比例，有机碳和砾石百分比是在整个土壤中的比例。从表中我们可以看出藏东南站浅层 20 cm 及以上的土层有机碳含量（$m_{\mathrm{soc}}$）明显高于中层，浅层砾石含量极少；而纳木错站有机碳含量低于藏东南站，砾石含量越往下层越多。因为泥炭的容重较矿物质的小很多，所以，Chen et al.（2012）采用有机碳的体积百分比（$V_{\mathrm{soc}}$），这样能够突出土壤有机质的比重，并且通过有机碳的体积百分比来计算砾石的体积百分比：

$$V_{\mathrm{soc}}=\frac{\rho_{\mathrm{p}}(1-\theta_{\mathrm{sat,m}})m_{\mathrm{soc}}}{\left(\rho_{\mathrm{soc}}(1-m_{\mathrm{soc}})+\rho_{\mathrm{p}}(1-\theta_{\mathrm{sat,m}})m_{\mathrm{soc}}+(1-\theta_{\mathrm{sat,m}})\dfrac{\rho_{\mathrm{soc}}m_{\mathrm{g}}}{(1-m_{\mathrm{g}})}\right)},\quad(1)$$

$$V_{\mathrm{g}}=\frac{\rho_{\mathrm{soc}}(1-\theta_{\mathrm{sat,m}})m_{\mathrm{g}}}{(1-m_{\mathrm{g}})\left(\rho_{\mathrm{soc}}(1-m_{\mathrm{soc}})+\rho_{\mathrm{p}}(1-\theta_{\mathrm{sat,m}})m_{\mathrm{soc}}+(1-\theta_{\mathrm{sat,m}})\dfrac{\rho_{\mathrm{soc}}m_{\mathrm{g}}}{(1-m_{\mathrm{g}})}\right)},\quad(2)$$

式中，

$$\theta_{\mathrm{sat,m}}=0.489-0.00126V_{\mathrm{s}},\quad(3)$$

其中，$\theta_{\mathrm{sat,m}}$ 指矿物质土壤的孔隙度，$V_{\mathrm{sand}}$（%sand）是指土壤中砂粒体积百分比含量，$\rho_{\mathrm{p}}$=2700 kg m$^{-3}$ 是矿物质密度，$\rho_{\mathrm{sc,\,max}}$=130 kg m$^{-3}$ 是泥炭的容重，$m_{\mathrm{g}}$ 是指土壤中的砾石含量，$V_{\mathrm{g}}$ 指砾石的体积百分比，最后计算结果见表 1。由于两个观测站的土壤成分数据分别只到 40 cm 和 30 cm，所以在模式土壤参数设定时采用与其最接近的观测深度处的值，对于深层则进行插值或者根据土壤观测来确定。同时 因为青藏高原土壤发育较差，土层较薄（李燕等，2012），我们将 40 cm 以下土壤有机质含量设为 0。另外，由于地表温度受到观测仪器的影响，使得观测误差较大（尤其是藏东南站），所以我们采用地面长波辐射的计算公式进行反演，从而得到地表温度，具体表达式为

$$T_{\mathrm{sfc}}=\left[\left(R_{\mathrm{lw}}^{\uparrow}-\left(1-\varepsilon_{\mathrm{g}}\right)R_{\mathrm{lw}}^{\downarrow}\right)\Big/\left(\varepsilon_{\mathrm{g}}\sigma\right)\right]^{1/4},\quad(4)$$

其中，$\varepsilon_{\mathrm{g}}$ 表示地表发射率，在藏东南站、纳木错站分别为 0.98、0.97（由观测者给出的经验值）；$R_{\mathrm{lw}}^{\uparrow}$、$R_{\mathrm{lw}}^{\downarrow}$ 分别指向上和向下长波辐射（直接采用观测值）；$\sigma=5.67\times10^{-8}$ W m$^{-2}$ K$^{-4}$ 是 Stefan-Boltzmann 常数。

## 3 参数化方案

### 3.1 CoLM 模式及其参数化方案

CoLM 模式是 Dai et al（2003，2004）发展的新一代通用陆面过程模式，它考虑了陆面的生态、水文等过程，对土壤—植被—积雪—大气之间的能

**表 1 两个观测站的土壤成分**

**Table 1 The composition of soil at two stations**

| 地点 | 深度/cm | 细土颗粒① | $1-V_{\mathrm{g}}-V_{\mathrm{sol}}$（粒径≤2 mm） | 砾石粒径（>2 mm） | | 有机质 | |
|---|---|---|---|---|---|---|---|
| | | 粘粒 | 粘粒 | $m_{\mathrm{g}}$ | $V_{\mathrm{g}}$ | $m_{\mathrm{soc}}$ | $V_{\mathrm{soc}}$ |
| 藏东南站 | 10 | 53.95% | 1.16% | 0.00% | 0.00% | 7.38% | 42.81% |
| | 20 | 46.28% | 2.06% | 0.00% | 0.00% | 4.59% | 32.10% |
| | 30 | 66.05% | 0.00% | 0.00% | 0.00% | 0.59% | 5.62% |
| | 40 | 61.52% | 0.00% | 0.00% | 0.00% | 0.41% | 3.87% |
| 纳木错站 | 10 | 91.88% | 0.40% | 18.50% | 9.41% | 2.46% | 22.56% |
| | 20 | 95.00% | 0.00% | 24.50% | 14.57% | 1.61% | 14.99% |
| | 30 | 93.07% | 0.29% | 34.86% | 23.26% | 1.54% | 13.01% |

注：① 细土颗粒由砂粒、粉粒和粘粒构成。

量与水分的传输进行了较好的描述。CoLM 包括 1 层植被、10 层土壤（距离表面 0.007、0.028、0.062、0.119、0.212、0.366、0.620、1.038、1.728 和 2.865 m），地面若有积雪，依据雪盖厚度分层，最多分为 5 层，下垫面类型采用的是 25 类 USGS 植被覆盖、17 类土壤质地和 8 种土壤颜色。模式中的土壤热传导率参数化方案来自于 Farouki（1981），导水率及土壤水势参数化方案来自 Clapp and Hornberger（1978）以及 Cosby et al.（1984）。

在矿物质土壤中，饱和土壤基质热传导率 $\lambda_{s,m}$（单位：W m$^{-1}$ K$^{-1}$）表示为

$$\lambda_{s,m}=\frac{8.8V_{sand}+2.921V_{clay}}{V_{sand}+V_{clay}}, \quad (5)$$

其中，$V_{sand}$ 和 $V_{clay}$ 分别为土壤中砂粒及粘粒的百分比含量。干土壤热传导率 $\lambda_{dry,m}$ 是土壤干密度 $\rho_d$ 的函数：

$$\lambda_{dry,m}=\frac{0.135\rho_d+64.7}{2700-0.94\rho_d}. \quad (6)$$

其中，干密度表达式为

$$\rho_d=2700(1-\theta_{sat,m}). \quad (7)$$

土壤固体热容量 $C_{s,m}$（单位：J m$^{-3}$ K$^{-1}$）表示为

$$C_{s,m}=\frac{2.128V_{sand}+2.385V_{clay}}{V_{sand}+V_{clay}}\times10^6, \quad (8)$$

模式中对于土壤水力学性质的描述采用的是 Clapp and Hornberger（1978）的参数化方案。在矿物质土壤中，土壤饱和导水率 $k_{sat,m}$、饱和基质势 $\Psi_{sat,m}$ 以及 Clapp-Hornberger 指数 $b_m$ 的表达式分别为

$$k_{sat,m}=0.007056\times10^{-0.884+0.0153V_{sand}}, \quad (9)$$

$$\psi_{sat,m}=-10.0\times10^{1.88-0.0131V_{sand}}, \quad (10)$$

$$b_m=2.91+0.156V_{clay}\ \ b_m=2.91+0.156(\%clay). \quad (11)$$

从以上公式我们可以看出，CoLM 模式中的参数化方案都是关于矿物质土壤的函数，并没有考虑有机碳和砾石对土壤的影响。由于观测区域不仅土壤有机碳含量较高，而且砾石含量也较高，尤其是往土壤下层越高（例如表 1 纳木错站），所以不能够忽略其作用。

### 3.2 新参数化方案

土壤孔隙度 $\theta_{sat}$ 是土壤的主要物理特征之一，对很多自然物理过程都有影响，如径流、土壤渗水容量、土壤持水量等，因此孔隙度计算的准确与否直接关系到模式的模拟效果。在土壤中，砾石的体积百分比对土壤有效含水量通常有负面的影响(Hanson and Blevins，1979)，其饱和含水量最低可以近似看为零（Poesen and Lavee，1994）。所以在计算土壤饱和含水量 $\theta_{sat}$ 时，可以看作砾石部分含水量为零，只有细土颗粒和有机质部分能够持水：

$$\theta_{sat}=(1-V_{soc}-V_g)\theta_{sat,m}+V_{soc}\theta_{sat,sc}, \quad (12)$$

其中，$\theta_{sat,sc}$=0.9，是泥炭饱和含水量（Lawrence and Slater，2008）。

#### 3.2.1 土壤热参数化方案

Chen et al.（2012）提出了一个新的热参数化方案，该方案综合了 Farouki（1981）、Johansen（1975）和 Yang et al.（2005）的土壤热参数化方案，比模式中 Farouki（1981）方案计算的土壤热传导率小，能够较好地描述土壤热参数性质，所以我们在该方案的基础上稍作改进。同时因为砾石的导热率同砂粒相似，我们采用简单的方式考虑砾石的作用，即增大砂粒的含量而减少粘土的含量：

$$V_{sand\text{-}new}=\frac{(1-V_{soc}-V_g)V_{sand}+V_g}{(1-V_{soc})}, \quad (13)$$

$$V_{sand\text{-}new}=\frac{(1-V_{soc}-V_g)V_{clay}}{(1-V_{soc})}, \quad (14)$$

土壤饱和热传导率：

$$\lambda_s=\lambda_q^q\lambda_{soc}^{V_{soc}}\lambda_o^{1-q-V_{soc}}, \quad (15)$$

干土壤热传导率：

$$\lambda_{dry}=(1-V_{soc})\lambda_{dry,m}+V_{soc}\lambda_{dry,sc}, \quad (16)$$

土壤固体热容量：

$$C_s=(1-V_{soc})C_{s,m}+V_{soc}C_{s,sc}. \quad (17)$$

Kensten 数用指数形式表示，避免了负值的出现：

$$K_e=\exp[K_T(1-1/S_r)], \quad (18)$$

其中 $K_T$=0.36 是一个经验系数（Yang et al.，2005）。

对于 $\lambda_s$、$\lambda_{dry}$、$C_s$、$K_e$ 的计算，本文采用 Chen et al.（2012）的参数化方案，其中 $\lambda_{soc}$=0.25 W m$^{-1}$ K$^{-1}$ 是泥炭热传导率；$\lambda_q$ 和 $\lambda_o$ 为石英热传导率和其他物质热传导率；分别等于 7.7 W m$^{-1}$ K$^{-1}$ 和 2.0 W m$^{-1}$ K$^{-1}$；$q$=0.5$V_{sand\text{-}new}$ 为土壤中石英含量；$\lambda_{dry,sc}$=0.05 W m$^{-1}$ K$^{-1}$ 是泥炭的干土壤热传导率；$C_{s,sc}$=2.5×10$^6$ W m$^{-1}$ K$^{-1}$ 是泥炭热容量（Lawrence and Slater，2008，表 1）。

3.2.2 土壤水参数化方案

在泥炭土的参数中饱和导水率具有较大的变化性，对于纤维、半分解和高分解泥炭土，其饱和导水率至少相差一个量级（Lawrence and Slater，2008）。Lawrence and Slater（2008）发展了一个新的水传输参数化方案，采用的是土壤有机碳的密度百分比，考虑到有机碳的密度较小，本文采用体积百分比以突出土壤有机碳的作用。而土壤中砾石的存在对导水率和对入渗规律的影响较为复杂，目前尚未有人研究砾石土/砾质土的非饱和导水率（符素华，2005；李燕等，2006），因此我们仍采用简单的方式考虑砾石的作用（公式 12、13），土壤饱和导水率可以表示为

$$k_{\mathrm{sat}}=(1-V_{\mathrm{soc}})k_{\mathrm{sat,m}}+V_{\mathrm{soc}}k_{\mathrm{sat,sc}}, \quad (19)$$

其中 $k_{\mathrm{sat,sc}}$ 是指泥炭的饱和导水率。对于饱和基质势和 $b$ 指数也是相同的形式：

$$\psi_{\mathrm{sat}}=(1-V_{\mathrm{soc}})\psi_{\mathrm{sat,m}}+V_{\mathrm{soc}}\psi_{\mathrm{sat,sc}}, \quad (20)$$

$$b=(1-V_{\mathrm{soc}})b_{\mathrm{m}}+V_{\mathrm{soc}}b_{\mathrm{sc}}, \quad (21)$$

其中 $\Psi_{\mathrm{sat,\,sc}}$ 和 $b_{\mathrm{sc}}$ 分别指泥炭的饱和基质势和分布指数。

关于泥炭水水分参数的选取，Letts et al.（2000）总结了很多文献中提出的值，并将其分为低分解、半分解和完全分解三种泥炭。在青藏高原藏东南地区其植被覆盖度较高，降雨较多，温度较高，有机质分解相较于纳木错地区分解度更高，所以我们选择了一个较小的值 $k_{\mathrm{sat,\,sc}}=1.0\times10^{-1}$mm s$^{-1}$，而纳木错地区海拔相对较高，植被覆盖较为稀疏，有机质分解较为缓慢，因此我们选择低分解泥炭的一个中值 $k_{\mathrm{sat,\,sc}}=2.8\times10^{-1}$mm s$^{-1}$，对于不同的观测站，我们选取的 $\Psi_{\mathrm{sat,\,sc}}$ 和 $b_{\mathrm{sc}}$ 也不一样，具体见表 2。

**表 2 两个观测站在水参数化方案中的数值确定**

**Table 2 The values of hydraulic parametrization over two stations**

| 地点 | $k_{\mathrm{sat,\,sc}}$/mm s$^{-1}$ | $\Psi_{\mathrm{sat,\,sc}}$/mm | $b_{\mathrm{sc}}$ |
|---|---|---|---|
| 藏东南站 | $1.0\times10^{-1}$ | 10.2 | 6.1 |
| 纳木错站 | $2.8\times10^{-1}$ | 10.1 | 2.7 |

另外，许多陆面模式因为没有考虑土壤内部水分向地表迁移的阻抗，在土壤湿度较小的地区高估了土壤表面的蒸发（Kondo et al., 1990），CoLM 也不例外。地表蒸发阻抗是表面蒸发以及上层土壤含水量计算的一个重要参数，缺乏该参数将造成模拟的潜热通量变化剧烈（Yang et al., 2009），所以我们在CoLM方案的基础上增加地表蒸发阻抗并采用 SSiB 中的计算方法（孙菽芬，2005），增加部分如下：

$$R_{\mathrm{S}}=101840\times(1-w^{0.0027}), \quad (22)$$

其中，$R_{\mathrm{S}}$ 反映的是下层土壤到地表的蒸发阻抗，$w$ 是表层土壤湿度。

我们将新参数化方案计算的孔隙度和导热率同观测值和原参数化方案进行对比。从表 3 中可以看出在藏东南站原方案对孔隙度的计算值偏小，平均偏低 11.24%，新方案的计算更接近观测值，浅层土壤 10 cm 和 20 cm 比观测值平均高出 6.5%，30 cm 和 40 cm 平均偏低 8.38%；纳木错站对孔隙度的计算原方案平均偏低 2%，新方案平均偏高 0.49%，更接近实测值。

**表 3 土壤孔隙度的观测值与新、旧方案计算结果的对比**

**Table 3 Comparison of soil porositiescalculated from new, old parameterizations and observations**

| | 藏东南站 $\theta_{\mathrm{sat}}$ | | | 纳木错站 $\theta_{\mathrm{sat}}$ | | |
|---|---|---|---|---|---|---|
| 深度/cm | 观测值 | 旧方案 | 新方案 | 观测值 | 旧方案 | 新方案 |
| 10 | 54.91% | 42.10% | 62.61% | 44.80% | 37.27% | 45.69% |
| 20 | 52.75% | 43.07% | 58.13% | 38.38% | 36.27% | 39.50% |
| 30 | 52.49% | 40.58% | 44.00% | 35.45% | 37.09% | 35.40% |
| 40 | 51.70% | 41.15% | 43.43% | | | |

另外，由于只有土壤热传导率的观测值，所以通过计算干土壤热传导率 $\lambda_{\mathrm{dry}}$ 和饱和基质土壤热传导率 $\lambda_{\mathrm{s}}$，我们可以得到土壤热传导率 $\lambda$ 的计算结果。图 1 给出了两个观测站土壤热传导率新旧参数化方案的计算值与观测值的对比。从图中可以看出新方案比旧方案更接近实测值：藏东南站土壤含水量 $\theta_{\mathrm{liq}}$ 在 0.2～0.5 之间，土壤热传导率的平均值为 0.629 W m$^{-1}$ K$^{-1}$，新方案由于考虑土壤有机质的低导热性，计算均值为 0.594 W m$^{-1}$ K$^{-1}$，比原方案减小许多，更接近观测值。纳木错站土壤含水量 $\theta_{\mathrm{liq}}$ 较低，在我们的观测时间内大多数含水量在 0.1 左右甚至更低，在含水量小于 0.1 时，计算的热传导率平均值为 0.241 W m$^{-1}$ K$^{-1}$，比观测值高出 0.043 W m$^{-1}$ K$^{-1}$；当 $\theta_{\mathrm{liq}}$ 大于 0.1，新方案计算的平均值比观测值高 0.356 W m$^{-1}$ K$^{-1}$，但相较于与原方案更接近观测值（图 1b）

### 3.3 试验设计

本文主要针对模式中的土壤水、热参数化方案以及地表蒸发阻抗三方面进行了优化。由于本文改进了土壤孔隙度参数化方案，而孔隙度的大小直接影响土壤水热的传输，所以本文在孔隙度参数化方案的基础上逐步改进，首先考虑土壤热参数化方案

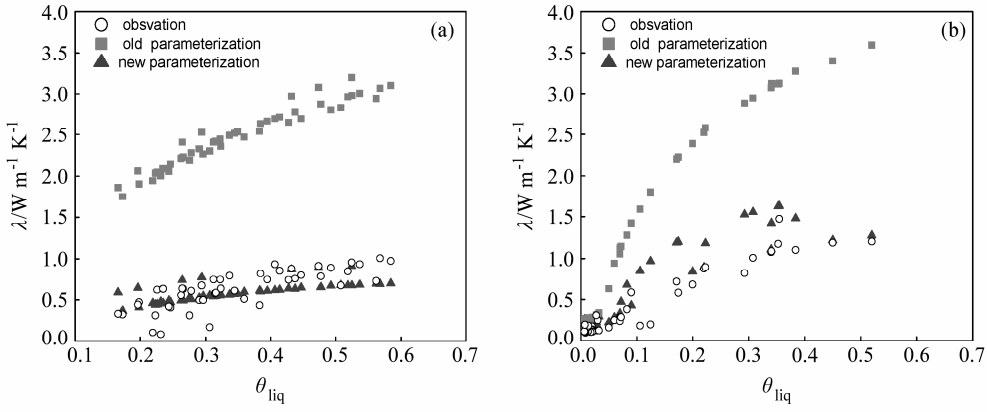


图 1 两个观测站的土壤热传导率对比：（a）藏东南站；（b）纳木错站

Fig. 1 Comparison between soil thermal conductivities at two stations: (a) Southeast Tibet station; (b) Namco station

的引进对模式的影响，并设计了敏感性试验 1（test1）；然后又引入了新的水传输参数，作为敏感性试验 2（test2）；最后综合考虑三者的共同作用（test3）。本文共进行了四组试验（详见表 4），其中控制试验 CTL（ConTroL）是用原模式进行的数值模拟。

**表 4 试验设计**

**Table 4 Design of experiments**

| 模拟试验 | 新热参数化方案 | 新水参数化方案 | 地表蒸发阻抗 |
|---|---|---|---|
| CTL | No | No | No |
| test1 | Yes | No | No |
| test2 | Yes | Yes | No |
| test3 | Yes | Yes | Yes |

## 4 新参数化方案在数值模式中的应用

我们将新的参数化方案用于 CoLM 陆面模式中，利用观测资料来驱动原始和修改后的模式，对藏东南站和纳木错站进行单点数值模拟试验。其中藏东南植被覆盖度取为 0.6，纳木错站为 0.25（由观测者给出的经验值）。

### 4.1 土壤湿度的模拟

土壤湿度作为表征土壤水分状况的重要参量，是陆气相互作用中的一个重要物理参量，能够改变土壤表面的反照率、热容量和植被生长状况等（马柱国等，2001；林朝晖等，2001）。对土壤湿度空间分布和时间变化的准确模拟有助于了解大尺度能量和水分交换过程，改善季节到年际时间尺度的气候和降水预报（Koster et al.，2004）。

图 2 给出了藏东南观测站日平均降水率和各层土壤含水量的对比。从图中可以看出，每组试验均能模拟出土壤含水量的变化趋势，并且土壤水分的跳跃性增大和降水事件能够较好地对应，只是原模式（CTL）模拟偏干，随着参数化方案的逐步优化，模式对于土壤湿度的模拟有明显改善：（1）在优化土壤热参数化方案后（test1 试验），20 cm 以上土壤含水量的模拟有所改善，但是在降雨事件发生后，含水量快速下降，这主要是新方案孔隙度计算值较大（见表 3），而土壤的持水能力不够。（2）在试验 1 的基础上优化水参数化方案后（test2 试验），模拟结果更加接近实测值，主要的改进在于降水过后含水量下降趋势减缓，这是由于藏东南站 20 cm 往上的浅层土壤有机质含量较大（表 1），持水性更好。（3）在综合考虑了土壤水、热参数化方案以及地表蒸发阻抗后（test3），模式在 4 cm 和 10 cm 的平均偏差分别减小了 0.14，0.13，五层的平均偏差由 0.106 减小到 0.04，更接近实测值，因为加入地表蒸发阻抗而减少了表面蒸发，使得土壤含水量增加，但是较实测值仍然偏小（表 5）；60 cm 以下的模拟稍微偏低，可能是因为我们假设 40 cm 以下土壤有机质含量为零，导致下层孔隙度和持水能力偏低。60 cm 土壤水分观测值不连续，可能观测本身也存在问题，需要慎重对待。总的来说，三组试验相对于原方案对 20 cm 以上土壤含水量的模拟是逐步改进的。

对于纳木错站的模拟却不如藏东南站，从图 3 中我们可以看到，随着新方案的逐步优化，模式对土壤含水量的模拟并非都有所改进：（1）试验 1 对含水量的模拟明显偏高，这主要是因为新方案计算的孔隙度相较于原方案虽然更接近实测值，但是略微偏高，在这种误差的累积下，使得含水量模拟较高。（2）在改进土壤水传输参数后（test2），对于

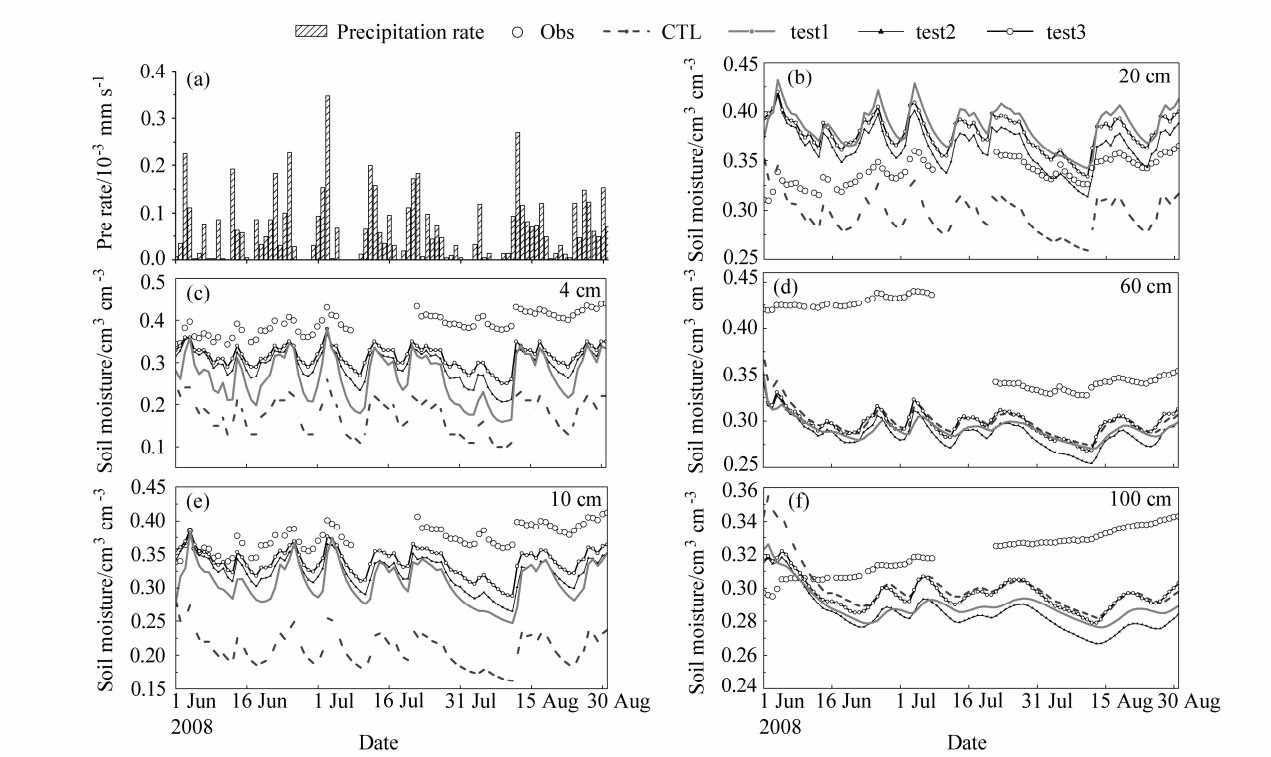


图 2 藏东南观测站日平均（a）降水率和（b–f）各层土壤含水量变化

Fig. 2 The daily average values of (a) precipitation rate and (b–f) soil moisture at different depth at Southeast Tibet station

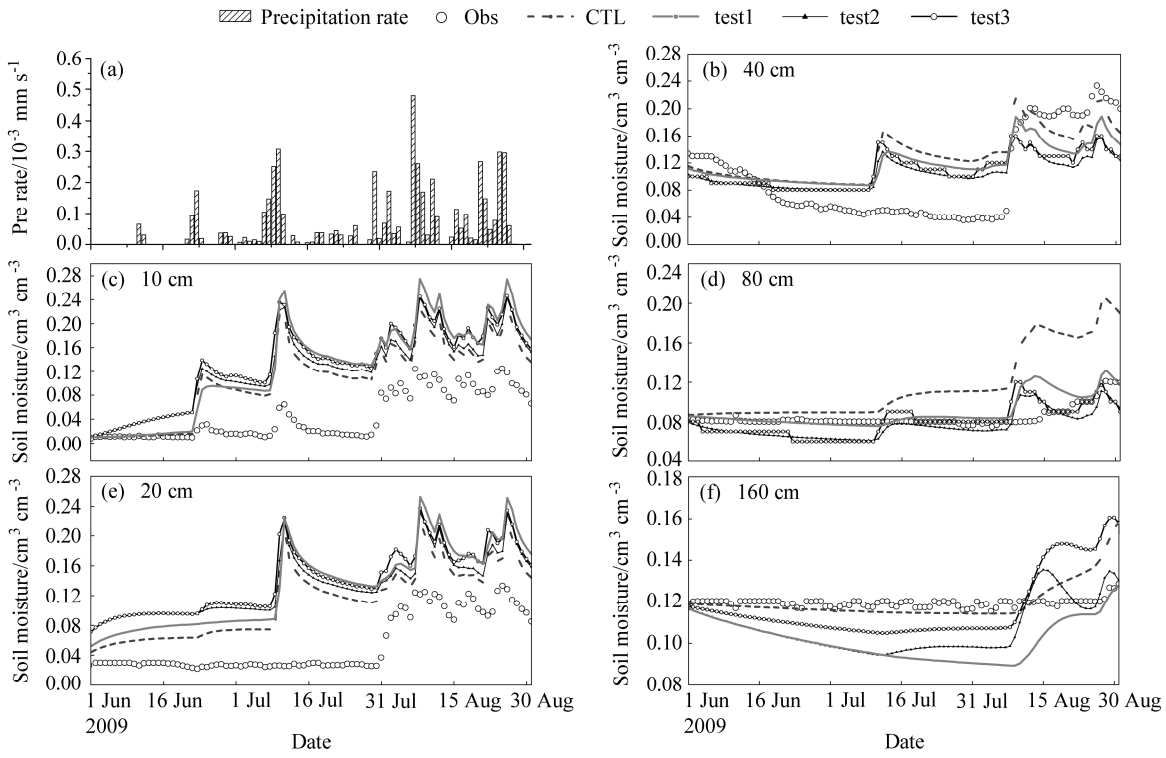


图 3 同图 2，但为纳木错站

Fig. 3 The same as Fig. 3, but for Namco station

10 cm 和 160 cm 土壤含水量的模拟相较于原模式（CTL）略有增大，对其他土壤层湿度的模拟更接近观测值，平均偏差约减小 0.01。（3）增大地表蒸发阻抗以后（test3）相较于试验 2 没有显著改进，相较于原模式浅层 20 cm 以上土壤湿度的模拟偏差略微增大。可能是模式中加入了地表蒸发阻抗以后，地表蒸发减小，也可能是对于表层土壤水分入渗考虑较为简单，高估了土壤的持水能力，以致对土壤湿度模拟偏大。总的来讲，新的参数化方案更适用于像藏东南站有机质含量较高的地区。

### 4.2 土壤温度的模拟

土壤温度尤其是地表温度是检验陆面过程模式模拟性能的重要指标，因为一个陆面过程模式中土壤温度计算的准确性关系到陆面与大气之间的能量和物质交换（周锁铨等，2004）；土壤温度异常会影响地表能量平衡，进而影响大气环流（Luo et al.，2009）。目前，已有许多研究指出土壤温度的变化对气候产生的重要影响（王万秋，1991；Zheng et al.，2002；Zhang et al.，2005；房云龙等，2010）。因此，正确模拟土壤温度是陆面过程模式数值模拟过程的一个重要环节。

图 4a 给出了藏东南观测站各层土壤温度的观测值和模拟值的日平均变化情况。原模式模拟上层偏暖，尤其是 7 月中旬和 8 月中旬的两个少雨时段，10 cm 以下的中下层则偏冷。试验 1 模拟的表层略偏暖，其他各层都略微偏冷。改进了水参数化方案之后，test2 试验模拟的温度变化趋势要平缓一些，这主要是因为含水量模拟增大，使得土壤热容增大。试验 1 和试验 2 模拟的土壤内部 10 cm 及以下的温度模拟相较于原模式偏小，主要是因为新的热参数化方案计算的导热率较小（见图 1a）。test3 的模拟结果最接近观测值，虽然试验 3 对地表温度的模拟偏高，平均偏高 2.7°C，但是中层的温度模拟有不同程度的改进，相较于原模式模拟结果与观测的偏差，中层 10 cm、20 cm 的平均偏差分别减少 0.5°C、0.3°C，下层 60 cm、100 cm 的平均偏差则分别增大 0.1°C 和 0.3°C（表 6）。相对而言，那木错站各层的温度模拟都比观测值偏低，尤其是 10 cm 至 40 cm 的中层土壤温度显著偏低（图 4b），这与该站土壤水分模拟偏高导致各层土壤热容偏大有关（图 3）。对整个模拟时间段求平均，试验 1 相较于原模式的模拟结果冷偏差增大，与考虑土壤有机质使得表层能量向下传播受阻相一致。test2 试验比 CTL 和 test1 试验对 20 cm 以上各层温度的模拟有所改进，test3 试验模拟的 40 cm 以上各层温度都比 CTL 有所改进（表 6）。

**表 5 两个观测站土壤各层含水量的模拟值与观测值平均偏差**

**Table 5 Comparison of bias between observation and simulation of soil moisture over two stations**

| 站点 | 模拟试验 | 不同深度的平均偏差/$cm^3\ cm^{-3}$ | | | | | |
|---|---|---|---|---|---|---|---|
| | | 4 cm | 10 cm | 20 cm | 40 cm（藏东南为 60 cm） | 80 cm（藏东南为 100 cm） | 160 cm |
| 藏东南站 | CTL | −0.22 | −0.17 | -0.04 | −0.08 | −0.02 | |
| | test1 | −0.13 | −0.07 | 0.05 | −0.08 | −0.03 | |
| | test2 | −0.10 | −0.05 | 0.03 | −0.09 | −0.04 | |
| | test3 | −0.08 | −0.04 | 0.04 | −0.08 | −0.02 | |
| 纳木错站 | CTL | | 0.06 | 0.06 | 0.03 | 0.03 | −0.001 |
| | test1 | | 0.08 | 0.07 | 0.02 | 0.005 | −0.02 |
| | test2 | | 0.07 | 0.06 | 0.01 | −0.008 | 0.01 |
| | test3 | | 0.07 | 0.07 | 0.01 | −0.004 | −0.002 |

**表 6 两个观测站土壤各层温度的模拟值与观测值平均偏差**

**Table 6 Comparison of bias between observation and simulation of soil temperature over two stations**

| 站点 | 模拟试验 | 不同深度的平均偏差/°C | | | | | | |
|---|---|---|---|---|---|---|---|---|
| | | 0 cm | 4 cm | 10 cm | 20 cm | 40 cm（藏东南为 60 参谋） | 80 cm（藏东南为 100） | 160 cm |
| 藏东南站 | CTL | 2.0 | 0.2 | −1.2 | −0.8 | −0.3 | −0.2 | |
| | test1 | 1.5 | −0.4 | −2.0 | −1.7 | −1.3 | −1.1 | |
| | test2 | 1.2 | −0.6 | −2.0 | −1.7 | −1.1 | −0.8 | |
| | test3 | 2.7 | 0.8 | −0.7 | −0.5 | −0.4 | −0.5 | |
| 纳木错站 | CTL | −1.8 | | −3.0 | −2.7 | −2.0 | −0.6 | 0.5 |
| | test1 | −2.1 | | −3.8 | −3.8 | −3.5 | −2.2 | −1.1 |
| | test2 | −1.2 | | −2.0 | −2.1 | −2.1 | −1.2 | −0.4 |
| | test3 | −0.6 | | −2.2 | −2.2 | −1.9 | −1.0 | −0.6 |

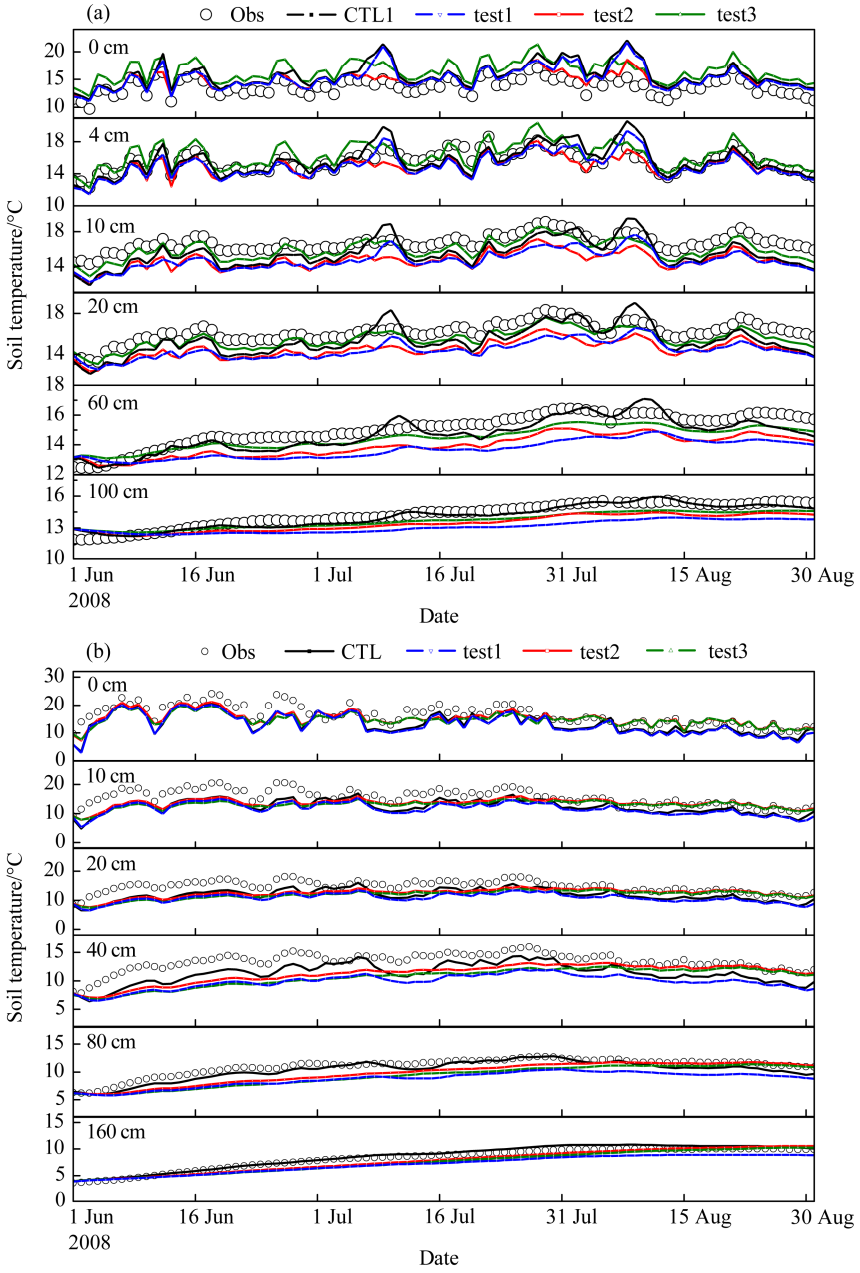


图 4 两个观测站日平均各层土壤温度变化：（a）藏东南站；（b）纳木错站

Fig. 4 The daily average values of soil temperature at different depthat two stations: (a) Southeast Tibet station; (b) Namco station

从前面分析可知，综合考虑三种因素的 test3 试验结果较好，下面分析该方案与原方案模拟的土壤温度剖面。图 5 是藏东南站日平均土壤温度的时间—深度剖面图。藏东南站表面土壤温度较低，最高温度位于 10 cm 深度附近，温度波动随着季节向下传播的特征明显，表层的多个低温时间段都与图 2 所示的降水过程对应。原方案（CTL）模拟的土壤温度偏差主要表现在表层偏暖，7 月 7 日前后以及 8 月上旬少雨时段的暖偏差可传至 20 cm 甚至更深，由 10 cm 处暖中心向上、向下的热传导导致该层附近在大多数时段偏冷（图 5b）。在采用新方案后（test3），由于土壤导热率减小，从 10 cm 处暖中心向上、向下的热传导减弱，该层的冷偏差因而减弱，而上述两个少雨时段表层的暖偏差及其向下传播的深度都减弱（图 5c）。从图 5b 和 c 中可以看出，新旧方案对于表层温度模拟的暖偏差较大，除了模式中表面通量的计算误差以外，也可能是因为观测站点植被覆盖的影响导致土壤表层温度的观测值偏低。

图 6 给出了纳木错站土壤温度的时间—深度剖

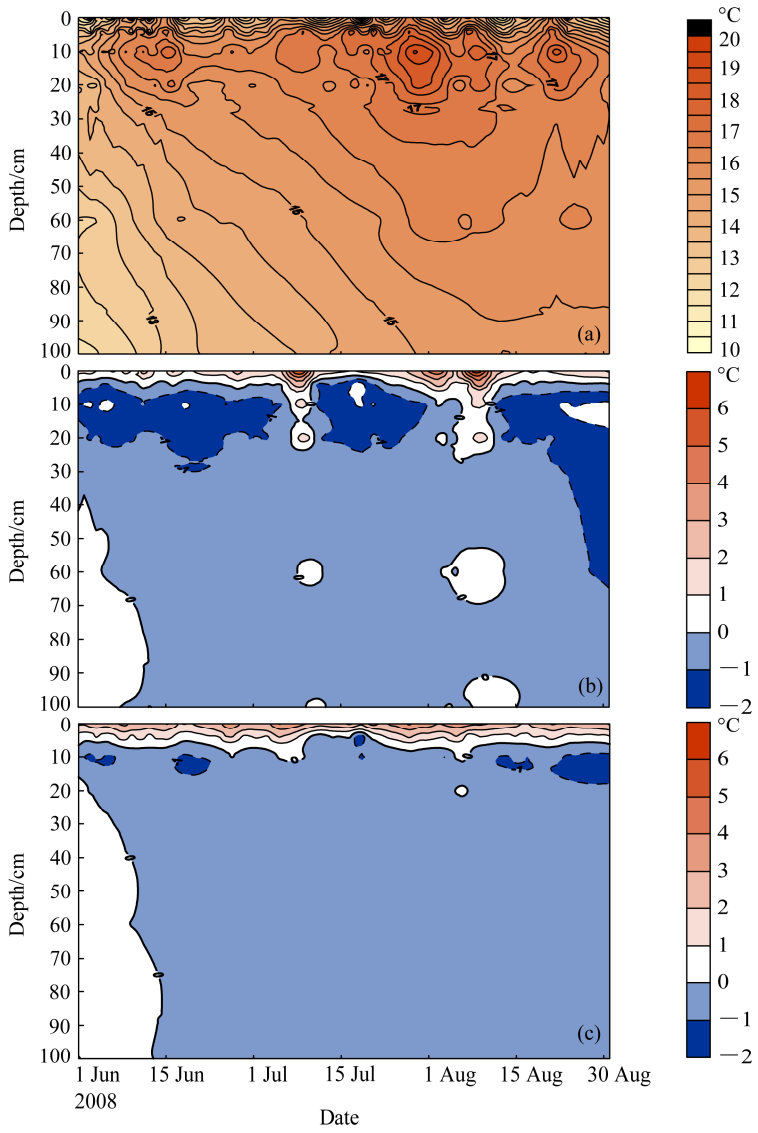


图 5 藏东南站日平均土壤温度的时间—深度剖面：（a）观测值；（b）CTL 模拟值与观测值的差值；（c）test3 模拟值与观测值的差值

Fig. 5 The time–depth crosssections of daily mean soil temperature at Southeast Tibet station: (a) Observation; (b) differences between CTL and observation; (c) differences between expttest3 and observation

面图。纳木错站植被稀疏，表层土壤温度最高，在初夏少雨时期，偶然的降水事件导致表层土壤温度降低，比如 6 月下旬、7 月中旬（图 6a）。原方案（CTL）对于纳木错站土壤温度的模拟偏差表现为 120 cm 以上偏冷，可能原因是土壤湿度模拟偏高而导致的土壤热容偏大，深层略微偏暖（图 6b）。而采用新方案后（test3），由于孔隙度的计算较原方案更接近实测值（见表 3），而且有机质的热传导率较低，以致计算得到的土壤热传导率较低，从图 6c 中可以看出试验 3 模拟的冷偏差略有加大。但是在降水较多的 8 月份，因为试验 3 减少了表面蒸发而提高了表层温度，所以下层土壤温度模拟的冷偏差有较明显的改进。当然，新参数化方案仍存在一些问题，土壤内部温度模拟没有明显改善，需要进一步研究。

### 4.3 能量通量的模拟

图 7 给出了藏东南站净辐射（向下的短波辐射与长波辐射之和减去向上的短波辐射与长波辐射之和）、感热通量和潜热通量的日平均值变化。从图中可以看出，在该站夏季的表面能量收支中，潜热通量起主要作用。随着方案改进程度的逐步递进，各个能量通量的模拟也更加接近观测值：对于净辐射的模拟，各个试验模拟结果相近，与观测值相比偏差不大。模式对辐射通量的模

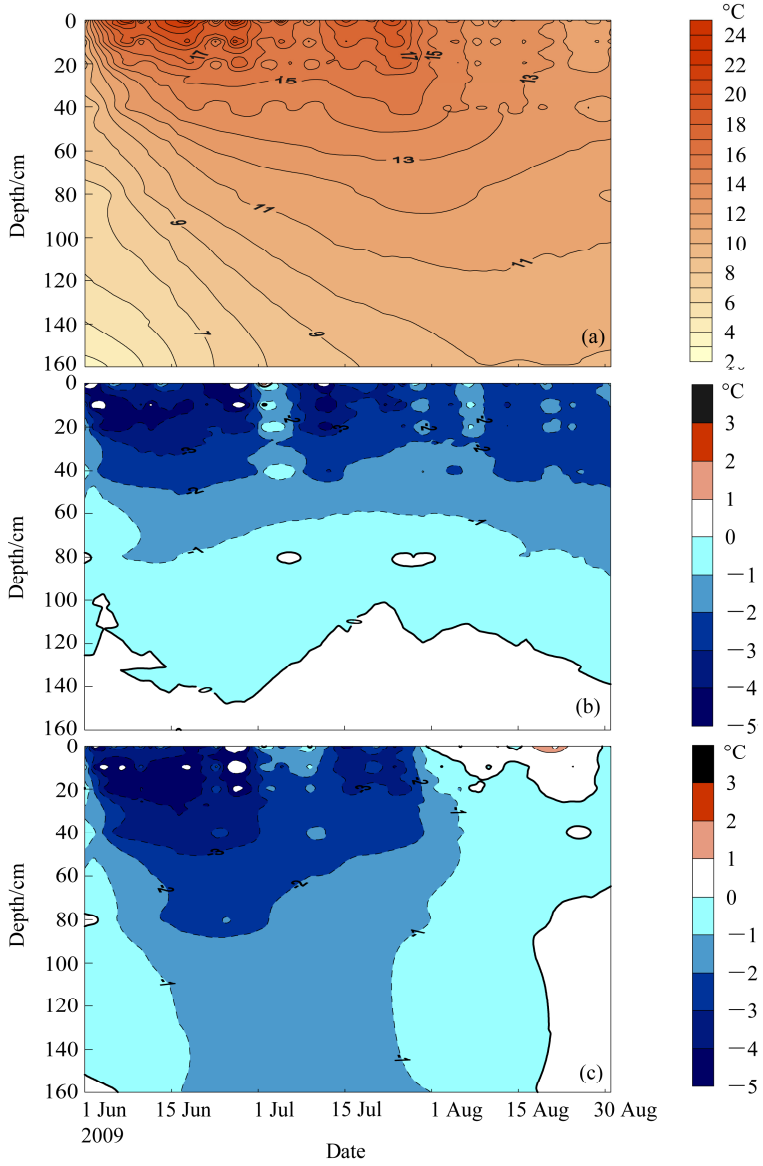


图 6 同图 5，但为纳木错站

Fig.6 The same as Fig.5, but for Namco station

拟直接影响到对地表能量平衡的模拟，同时关系到净辐射在感热通量和潜热通量之间的分配。整个模拟时段平均而言，新参数化方案（test3）对各个能量通量的模拟均偏高，净辐射、感热通量和潜热通量分别偏高 14.1 W $m^{-2}$、2.6 W $m^{-2}$ 和 34.6 W $m^{-2}$。虽然 test3 对净辐射的模拟偏差比 CTL 试验略微增大，但是与观测结果的决定系数提高到 0.985；对感热通量的模拟相对于原方案的提高约 0.2，表面感热通量偏大主要是因为地表温度的模拟偏高。各组试验对于潜热通量的模拟整体偏高，test3 试验加入地表蒸发阻抗以后，对蒸发潜热的模拟有明显改进，普遍比原方案减弱，更接近观测值，与观测值的相关系数的平方达到 0.87（表 7）。

图 8 给出了纳木错站净辐射、感热通量和潜热通量的日平均值变化，从图中可以看出 CTL 与 test3 的模拟结果较为接近。新方案（test3）对三个通量的模拟值与观测的决定系数分别为 0.882、0.703 和 0.568，都比原方案的模拟有所提高。对于净辐射的模拟，新旧方案的模拟均偏大，但是新方案更接近观测值，平均偏差减小近 10 W $m^{-2}$；新方案对潜热通量模拟的改进最为明显，平均偏差减小了 20.2 W $m^{-2}$，虽然两种方案对土壤含水量的模拟都比观测值大，但是因为纳木错站土壤含水量较低，新方案表面蒸发阻抗较大，导致潜热通量模拟降低，更接近观测值。

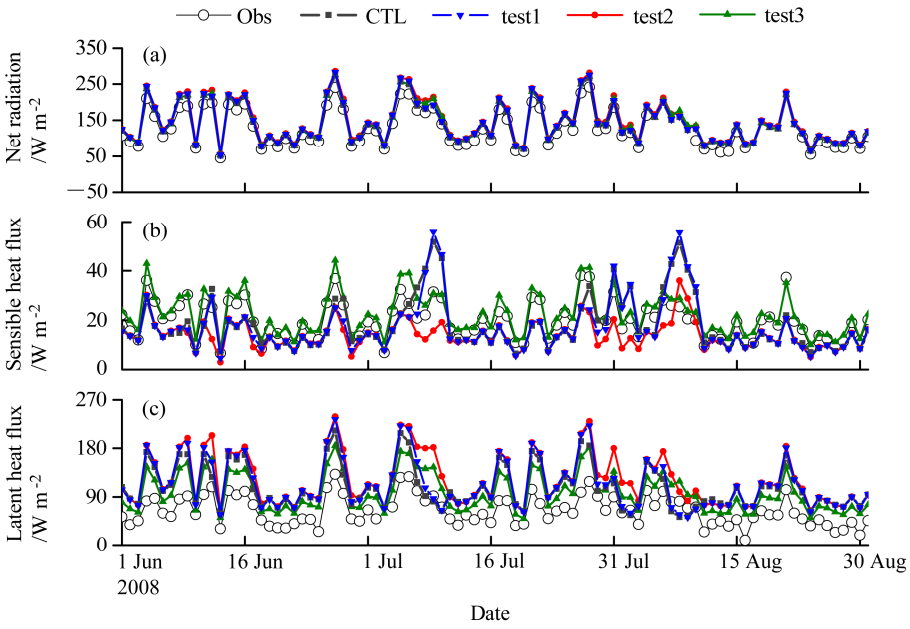


图 7 藏东南站（a）净辐射、（b）感热和（c）潜热的日平均值变化

Fig. 7 The daily average values of (a) net radiation, (b) sensible heat flux, and (c) latent heat flux over Southeast Tibet station

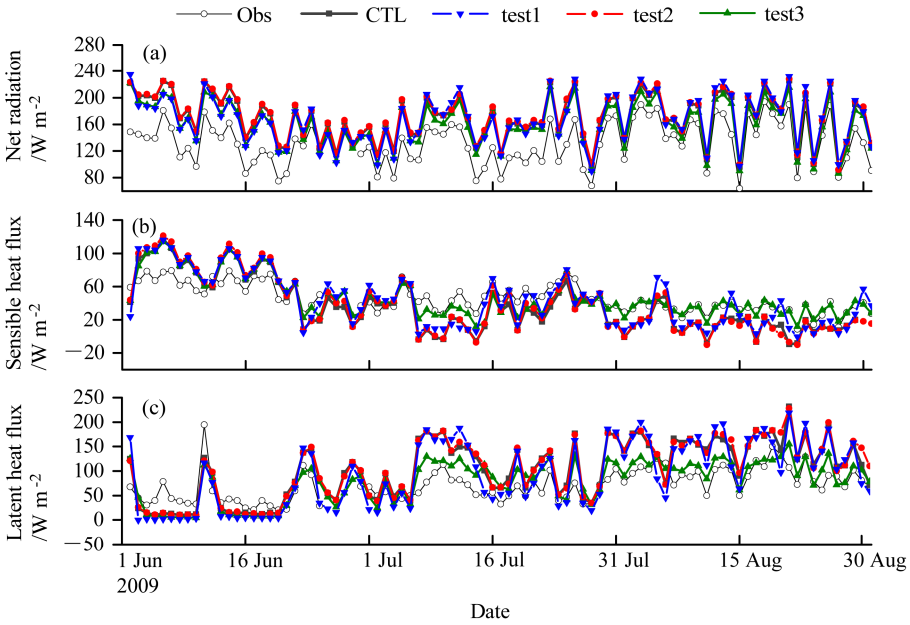


图 8 同图 7，但为纳木错站

Fig.8 The same as Fig. 8,but for Namco station

## 5 结论与讨论

青藏高原具有独特的地理位置和地形高度，其陆面过程相较其他地区存在着一定的特殊性。高原地区土壤发育较差，土壤层较薄，东南部地区较同纬度其他地区温度偏低，土壤有机质含量高，且土壤质地较粗,局部地方石块和砾石含量较多。根据这个特点，我们在 Chen et al.（2012）的土壤热参数化方案和 Lawrence and Slater（2008）的水传输特性参数化方案的基础上，发展了一个新的参数化方案以描述土壤有机质和砾石对土壤水热传输的影响，并用站点的实测资料对新方案进行了检验。本文对 CoLM 陆面模式中的土壤水、热参数化方案以及地表蒸发阻抗三方面进行了改进，并对青藏高原藏东南站和纳木错站进行了单点数值模拟试验。通过对比分析，主要得到以下几点结论：

**表 7 新旧方案模拟的能量通量与观测值的决定系数和平均偏差**

**Table 7 The coefficient of determination ($R^2$) and the simulated bias between observation and simulation of energy flux over two stations**

| 观测站 | 模拟试验 | 净辐射 | | 感热 | | 潜热 | |
|---|---|---|---|---|---|---|---|
| | | $R^2$ | 偏差/W m$^2$ | $R^2$ | 偏差/W m$^2$ | $R^2$ | 偏差/W m$^2$ |
| 藏东南站 | CTL | 0.982 | 13.5 | 0.747 | −2.0 | 0.745 | 44.3 |
| | Test1 | 0.982 | 16.9 | 0.725 | −2.5 | 0.796 | 49.3 |
| | Test2 | 0.984 | 19.5 | 0.924 | −5.7 | 0.836 | 58.0 |
| | Test3 | 0.985 | 14.1 | 0.945 | 2.6 | 0.870 | 34.6 |
| 纳木错站 | CTL | 0.873 | 35.1 | 0.674 | −4.0 | 0.479 | 21.9 |
| | test1 | 0.881 | 33.3 | 0.648 | −2.8 | 0.519 | 24.6 |
| | test2 | 0.874 | 38.1 | 0.676 | −2.3 | 0.483 | 22.6 |
| | test3 | 0.882 | 29.1 | 0.703 | 4.3 | 0.568 | 1.7 |

（1）藏东南站的砂粒含量相较于纳木错站较低，20 cm 以上土壤层粘粒含量较高，有机质含量大约是纳木错站的 2 倍，20 cm 以下有机质含量极少，40 cm 以上砾石含量很低，可以忽略不计；而纳木错站砂粒含量很高，粘粒含量几乎为零，20 cm 以下砾石含量超过 25%，比有机质所占比例要高出很多。

（2）新参数化方案计算的藏东南站土壤孔隙度较实测值平均偏高 5.7%，浅层土壤 10 cm 和 20 cm 比观测值平均高出 6.5%，30 cm 和 40 cm 土壤层平均偏低 8.38%，更接近观测值；纳木错站原方案对孔隙度的计算平均偏低 2%，新方案略偏高 0.49%，更接近观测值。

（3）新方案计算的藏东南站的热传导率均值为 0.594 W m$^{-1}$ K$^{-1}$，较观测值稍微偏低，但是比原方案更接近观测值。而对于纳木错站，在土壤含水量低于 0.1 时，热传导率平均值为 0.241 W m$^{-1}$ K$^{-1}$，比观测值高出 0.043 W m$^{-1}$ K$^{-1}$；当含水量大于 0.1 时，新方案计算的平均值比观测值高 0.356 W m$^{-1}$ K$^{-1}$，但相较于与原方案更接近观测值。

（4）各个控制试验对藏东南站土壤湿度的模拟都有所改善，其中在所有参数优化后（test3）的模拟改进效果显著：五层的平均偏差由 0.106 减小到 0.04，更接近实测值；而新方案对纳木错站浅层 20 cm 以上土壤含水量的模拟相较于控制试验 CTL 的模拟偏差略微增大。

（5）参数方案优化后模式均能较好模拟出日平均温度变化，但是仍存在着一定的偏差，在藏东南站新参数化方案对表层土壤温度模拟偏高，可能是因为净辐射的模拟偏高，另外，新方案考虑土壤有机质的低导热率，使得夏季地表面的净辐射不易向深层土壤传导而在表面积累，从而导致表面温度模拟偏高。10 cm 以下土壤温度的模拟值较观测值稍微偏低，比原方案模拟的平均误差减小 0.1°C。对纳木错站而言，新方案对地表温度的模拟有较明显的改进，平均偏差从−1.8°C 减小到−0.6°C，中层土壤温度模拟的冷偏差也有不同程度的改善。

（6）参数化方案优化后，模式对两个观测站能量通量的模拟有不同程度的改进。藏东南站净辐射、感热通量和潜热通量的模拟相较于观测值分别偏高 14.1、2.6 和 34.6 W m$^{-2}$，从模拟值与观测值的决定系数来看，净辐射、感热通量、潜热通量的相关系数的平方分别达到 0.985，0.945，0.87，其中感热通量的模拟改进最显著，相较于原方案提高约 0.2；纳木错站对能量通量的日变化模拟也较好，相关系数的平方分别为 0.882、0.703 和 0.568，但改进效果不如藏东南站。

（7）模式在改进土壤热参数化方案后（test1），对有机质含量较多的藏东南站土壤湿度的模拟结果有所改进，而对比较干燥且有机质含量较少的纳木错站土壤湿度的改进效果不明显，该站土壤温度的模拟反而更差；进一步改进土壤水参数化方案后（test2），对两个观测站土壤温、湿度的模拟有一定程度的改进，但是对地表通量的模拟并不理想；将所有参数化方案优化后的试验（test3）对地表能量通量的模拟有显著改善，相较于 test2 对土壤温、湿度的模拟则没有明显改进。总的来讲，test3 相较于其他模拟试验的模拟结果更接近观测值。

虽然新的参数化方案对于两个观测站的模拟有不同程度的提高，但仍存在着一些问题：一方面，新的参数化方案更适用于有机质含量较高的地区，而对于像纳木错站这样有机质含量较低的地区，更要考虑砾石对土壤水热传输特性的影响。砾石含量高的土壤通透性好，导致土壤水分下渗量大。但土壤

中砾石含量对导水率的影响较为复杂，而我们的参数化方案对砾石的考虑较为简单，需要进一步改善。另一方面，模式中地表蒸发阻抗增大后，土壤浅层含水量以及土壤内部温度的模拟结果在纳木错站并不理想。由于地表蒸发阻抗无法用实验仪器进行直接观测，所以参数化方案的选用给模式带来了很大的不确定性。

## 参考文献（References）


Beringer J, Lynch A H, Chapin F S, et al. 2001. The representation of arctic soils in the land surface model: The importance of mosses [J]. J. Climate, 14 (15): 3324–3335.

卞林根, 陆龙骅, 逯昌贵, 等. 2001. 1998 年夏季青藏高原辐射平衡分量特征 [J]. 大气科学, 25 (5) 577–588. Bian L G, Lu L H, Lu C G, et al. 2001. The characteristics of radiation balance components of the Tibetan Plateau in the summer of 1998 [J]. Chinese Journal of Atmospheric Sciences (in Chinese), 25 (5): 577–588.

Box J E. 1981.The effects of surface slaty fragments on soil erosion by water [J]. Soil Sci. Soc. Am. J., 45 (1): 111–116.

Cerdà A. 2001. Effects of rock fragment cover on soil infiltration, interrill runoff and erosion [J]. European Journal of Soil Science, 52 (1): 59–68.

Chen Y Y, Yang K, Tang W J, et al. 2012. Parameterizing soil organic carbon's impacts on soil porosity and thermal parameters for eastern Tibet grass-lands [J]. Sci. China Earth Sci., 55 (6): 1001–1011.

Clapp R B, Hornberger G M. 1978. Empirical equations for some soil hydraulic properties [J]. Water Resour. Res., 14 (4): 601–604.

Cosby B J, Hornberger G M, Clapp R B, et al. 1984. A statistical exploration of the relationships of soil moisture characteristics to the physical properties of soils [J]. Water Resour. Res., 20 (6): 682–690.

Dai Y J, Zeng X B, Dickinson R E, et al. 2003.The common land mode1 [J]. Bull. Amer. Meteor. Soc., 84 (8): 1013–1023.

Dai Y J, Dickinson R E, Wang Y P. 2004.A two-big-leaf model for canopy temperature, photosynthesis and stomatal conductance [J]. J. Climate, 17 (12): 2281–2299.

Farouki O T. 1981. The thermal properties of soils in cold regions [J].Cold. Reg. Sci. Technol., 5 (1): 67–75.

方精云, 刘国华, 徐嵩龄. 1996. 中国陆地生态系统的碳库 [C]// 王庚辰, 温玉璞. 温室气体浓度和排放监测及相关过程. 北京: 中国环境科学出版社, 109–128. Fang J Y, Liu G H, Xu S L. 1996. Carbon reservoir of terrestrial eco system in China [C]// Wang Gengchen, Wen Yupu, Eds. Monitoring and Relevant Process of Greenhouse Gas Concentration and Emission (in Chinese). Beijing: China Environment Sciences Publishing House, 109–128.

房云龙, 孙菽芬, 李倩, 等. 2010. 干旱区陆面过程模型参数优化和地气相互作用特征的模拟研究 [J]. 大气科学, 34 (2): 290–306. Fang Y L, Sun S F, Li Q, et al. 2010. The optimization of parameters of land surface model in arid region and the simulation of land–atmosphere interaction [J]. Chinese Journal of Atmospheric Sciences (inChinese), 34 (2): 290–306.

符素华. 2005. 土壤中砾石存在对入渗影响研究进展 [J]. 水土保持学报, 19 (1): 171–175. Fu S H. 2005. Effect of soil containing rock fragment on infiltration [J]. Journal of Soil and Water Conservation, 19 (1): 171–175.

Hanson C T, Blevins R L. 1979.Soil water in coarse fragments [J]. Soil Sci. Soc. Am. J., 43 (4): 819–820.

Johansen O. l975.Thermal conductivity of soils [D]. Ph. D. dissertation. University of Trondheim.

Kondo J, Nobuko S, Takeshi S. 1990. A parameterization of evaporation from bare soil surfaces [J]. J. Appl. Meteor., 29 (5): 385–389.

Koster R D, Dirmeyer P A, Guo Z C, et al. 2004.Regions of strong coupling between soil moisture and precipitation [J]. Science, 305 (5687): 1138–1140.

Lawrence D M, Slater A G. 2008.Incorporating organic soil into a global climate model [J]. Climate Dyn., 30 (2–3): 145–160.

Letts M G, Roulet N T, Comer N T, et al. 2000. Parametrization of peatland hydraulic properties for the Canadian Land Surface Scheme [J]. Atmos. Ocean, 38 (1): 141–160.

李燕, 高明, 魏朝富, 等. 2006. 土壤砾石的分布及其对水文过程的影响 [J]. 中国农学通报, 22 (5): 271–276. Li Y, Gao M, Wei C F, et al. 2006. Spatial distribution of rock fragment and its influences on soil hydrological processes [J]. Chinese Agricultural Science Bulletin (in Chinese), 22 (5): 271–276.

李燕, 刘新, 李伟平. 2012. 青藏高原地区不同下垫面陆面过程的数值模拟研究 [J]. 高原气象, 31 (3): 581–591. Li Y, Liu X, Li W P. 2012. Numerical simulation of land surface process at different underlying surfaces in Tibetan Plateau [J]. Plateau Meteorology (in Chinese), 31 (3): 581–591.

梁晓, 戴永久. 2008. 通用陆面模式对土壤质地和亮度的敏感性分析 [J]. 气候与环境研究, 13 (5): 585–597. Liang X, Dai Y J. 2008.A sensitivity study of the Common Land Model on soil texture and soil brightness [J]. Climatic and Environmental Research (in Chinese), 13 (5): 585–597.

林朝晖, 杨小松, 郭裕福. 2001. 陆面过程模式对土壤含水量初值的敏感性研究 [J]. 气候与环境研究, 6 (2): 240–248. Lin Z H, Yang X S, Guo Y F. 2001. Sensitivity of land surface model to the initial condition of soil moisture [J]. Climatic and Environmental Research (in Chinese), 6 (2): 240–248.

刘少锋, 林朝晖. 2005. 通用陆面模式 CLM 在东亚不同典型下垫面的验证试验 [J]. 气候与环境研究, 10 (3): 684–699. Liu S F, Lin Z H. Validation of common land model using field experiment data over typical land cover types in East Asia [J]. Climatic and Environmental Research (in Chinese), 10 (3): 684–699.

罗斯琼, 吕世华, 张宇, 等. 2008. CoLM 模式对青藏高原中部 BJ 站陆面过程的数值模拟 [J]. 高原气象, 27 (2): 259–271. Luo S Q, Lü S H, Zhang Y, et al. 2008. Simulation analysis on land surface process of BJ site of central Tibetan Plateau using CoLM [J]. Plateau Meteorology (in Chinese), 27 (2): 259–271.

Luo S Q, Lü S H, Zhang Y. 2009. Development and validation of the frozen soil parameterization scheme in Common Land Model [J]. Cold Regions Science and Technology, 55 (1): 130–140.

马柱国, 符淙斌, 谢力, 等. 2001. 土壤湿度和气候变化关系研究中的某些问题 [J]. 地球科学进展, 16 (4): 563–568. Ma Z G, Fu C B, Xie L,

et al. 2001. Some problems in the study on the relationship between soil moisture and climatic change [J].Advancesin Earth Science (in Chinese), 16 (4): 563–568.

Mehuys G R, Stolzey L H, Letey J, et al. 1975. Effect of stones on the hydraulic conductivity of relatively dry desert soils [J]. Soil Science Society of America Journal, 39 (1): 37–42.

Miller F T, Guthrie R L. 1984. Classification and distribution of soils containing rock fragments in the United States [J]. Soil Science Society of America Journal, 13: 1–6.

Poesen J, Lavee H. 1994. Rock fragments in top soils: Significance and processes [J]. CATENA, 23 (1–2): 1–28.

单秀芝, 魏由庆, 严慧峻,等. 1998. 土壤有机质含量对土壤水动力学参数的影响 [J]. 土壤学报, 35 (1): 1–9. Shan X Z, Wei Y Q, Yan H J, et al. 1998. Influence of organic matter content on soil hydrodynamic parameters [J]. Acta Pedologica Sinica (in Chinese), 35 (1): 1–9.

孙菽芬. 2005. 陆面过程的物理、生化机理和参数化模型 [M]. 北京: 气象出版社, 303pp. Sun S F. 2005. Parameterization Study of Physical and Biochemical Mechanism in Land Surface Process (in Chinese) [M]. Beijing: China Meteorological Press, 303pp.

王澄海, 师锐. 2007. 青藏高原西部陆面过程特征的模拟分析 [J]. 冰川冻土, 29 (1): 73–81. Wang C H, Shi R. 2007. Simulation of the land surface processes in the western Tibetan Plateau in summer [J]. Journal of Glaciology and Geocryology (in Chinese), 29 (1): 73–81.

王根绪, 陈国栋, 沈永平. 2002. 青藏高原草地土壤有机碳库及其全球意义 [J]. 冰川冻土, 24 (6): 693–700. Wang G X, Chen G D, Shen Y P. 2002. Soil organic carbon pool of grasslands on the Tibetan Plateau and its global implication [J]. Journal of Glaciology and Geocryology (in Chinese), 24 (6): 693–700.

王介民. 1999. 陆面过程实验和地气相互作用研究——从 HEIFE 到 IMGRASS 和 GAME-Tibet/TIPEX [J]. 高原气象, 18 (3): 280–294. Wang J M. 1999. Land surface process experiments and interaction study in China—From HEIFE to IMGERASS and GAME-Tibet/TIPEX [J]. Plateau Meteorology (in Chinese), 18 (3): 280–294.

王万秋. 1991. 土壤温湿异常对短期气候影响的数值模拟试验 [J]. 大气科学, 15 (5): 115–123. Wang W Q. 1991. Numerical experiments of the soil temperature and moisture anomaliesp' effects onthe short term climate [J]. Chinese Journal of Atmospheric Sciences (Scientia Atmospherica Sinica) (in Chinese), 15 (5): 115–123.

Yang K, Koike T, Ye B S, et al. 2005. Correction to "Inverse analysis of the role of soil vertical heterogeneity in controlling surface soil state and energy partition" [J]. J. Geophys. Res., 110 (D13): D08101, doi:10.1029/2004JD005500.

Yang K, Chen Y Y, Qin J. 2009. Some practical notes on the land surface modeling in the Tibetan Plateau [J]. Hydrol. Earth Syst. Sci., 13 (5): 687–701.

Zhang Y, Chen W J, Smith S L, et al. 2005. Soil temperature in Canada during the twentieth century: Complex responses to atmospheric climate change [J]. J. Geophys. Res., 110 (D3): D03112, doi:10.1029/2004JD004910.

赵勇, 钱永甫. 2007. 青藏高原地表热力异常与我国江淮地区夏季降水的关系 [J]. 大气科学, 31 (1): 145–154. Zhao Y, Qian Y F. 2007. Relationships between the surface thermal anomalies in the Tibetan Plateau and the rainfall in the Jianghuai area in summer [J]. Chinese Journal of Atmospheric Sciences (in Chinese), 31 (1): 145–154.

Zheng Y Q, Qian Y F, Yu G, et al. 2002. Simulations of the effects of soil temperature and humidity disturbances on regional climate of China [J]. Meteor. Atmos. Phys., 81 (1–2): 85–102.

周锁铨, 张翠, 王小宁, 等. 多层土壤温度模拟及其检验 [J]. 南京气象学院学报, 2004, 27 (2): 200–209. Zhou S Q, Zhang C, Wang X N, et al. 2004.Simulation of soil temperature with a multi-layer model and its verification [J]. Journal of Nanjing Institute of Meteorology (in Chinese), 27 (2): 200–209.

ADVANCES IN ATMOSPHERIC SCIENCES, VOL. 31, MAY 2014, 593–603

# Temporal and Spatial Variations of Global Deep Cloud Systems Based on CloudSat and CALIPSO Satellite Observations

PENG Jie[1,2], ZHANG Hua*[3], and Zhanqing LI[1,4]

[1]*College of Global Change and Earth System Science, Beijing Normal University, Beijing* 100875
[2]*Shanghai Meteorological Bureau, Shanghai* 200030
[3]*Laboratory for Climate Studies, China Meteorological Administration, National Climate Center, Beijing* 100081
[4]*Department of Atmospheric and Oceanic Sciences & Earth System Science Interdisciplinary Center, University of Maryland, College Park, MD* 20740, *USA*

(Received 11 March 2013; revised 12 August 2013; accepted 19 August 2013)

ABSTRACT

The spatial and temporal global distribution of deep clouds was analyzed using a four-year dataset (2007–10) based on observations from CloudSat and CALIPSO. Results showed that in the Northern Hemisphere, the number of deep cloud systems (DCS) reached a maximum in summer and a minimum in winter. Seasonal variations in the number of DCS varied zonally in the Southern Hemisphere. DCS occurred most frequently over central Africa, the northern parts of South America and Australia, and Tibet. The mean cloud-top height of deep cloud cores (TDCC) decreased toward high latitudes in all seasons. DCS with the highest TDCC and deepest cores occurred over east and south Asian monsoon regions, west-central Africa and northern South America. The width of DCS (WDCS) increased toward high latitudes in all seasons. In general, DCS were more developed in the horizontal than in the vertical direction over high latitudes and vice versa over lower latitudes. Findings from this study show that different mechanisms are behind the development of DCS at different latitudes. Most DCS at low latitudes are deep convective clouds which are highly developed in the vertical direction but cover a relatively small area in the horizontal direction; these DCS have the highest TDCC and smallest WDCS. The DCS at midlatitudes are more likely to be caused by cyclones, so they have less vertical development than DCS at low latitudes. DCS at high latitudes are mainly generated by large frontal systems, so they have the largest WDCS and the smallest TDCC.

**Key words**: deep cloud, deep cloud core, aerosol invigoration effect

**Citation**: Peng, J., H. Zhang, and Z. Q. Li, 2014: Temporal and spatial variations of global deep cloud systems based on CloudSat and CALIPSO satellite observations. *Adv. Atmos. Sci.*, **31**(3), 593–603, doi: 10.1007/s00376-013-3055-6.

## 1. Introduction

Clouds and their interactions with atmospheric circulation, shortwave and longwave radiation, and the surface are very important components of both weather and climate. Serving as one of the most important elements of hydrological and energy circulation, clouds have a crucial impact not only on radiation budgets at the surface and the top-of-the-atmosphere, but also on heating profiles within the atmosphere and the spatial and temporal distribution of precipitation around the globe. Usually accompanied by precipitation, deep cloud systems (DCS) have a more direct impact on hydrologic circulation, and absorb much more surface longwave radiation and reflect more shortwave solar radiation than do shallow clouds. Satellite-based studies (Ramanathan et al., 1989; Harrison et al., 1990; Hartmann et al., 1992; Kiehl, 1994; Hartmann et al., 2001; Futyan and Del Genio, 2007) have revealed that the mean net radiative forcing of DCS over large spatial scales and over long time periods is close to zero because of the cancellation of strong negative shortwave forcing and strong positive longwave forcing. Yuan and Li (2010) and Yuan et al. (2010) used moderate resolution imaging spectroradiometer (MODIS) data to study macro- and micro-physical properties of deep convective clouds. They found that the optical depth of deep convective clouds varies slightly over the course of a year and that the particle size of ice crystals at the top of deep convective clouds are positively correlated to the brightness temperature, although the correlation varied over time and space. They also developed a method to estimate glaciation temperatures inside deep convective clouds. Using a combination of CloudSat and atmospheric infrared sounder data, as well as output from the Global Data Assimilation System model, Savtchenko (2009) found that deep convective clouds humidified the upper level of the troposphere and reduced the

* Corresponding author: ZHANG Hua
Email: huazhang@cma.gov.cn

© Institute of Atmospheric Physics/Chinese Academy of Sciences, and Science Press and Springer-Verlag Berlin Heidelberg 2014

amount of outgoing longwave radiation under all-sky conditions. Sassen et al. (2009) explored the correlation between deep convective clouds and cirrus clouds over tropical regions. Using data from the A-train constellation of satellites, Iwasaki et al. (2010) estimated the mean radius of ice crystals and the mean ice water content above a level with a potential temperature of 380 K (near the top of the troposphere) in deep convective clouds to be $23.0 \pm 4.9$ $\mu$m and $7.2 \pm 8$ mg m$^{-3}$, respectively. Yuan and Houze (2010) and Yuan et al. (2011) analyzed the 3D structure of deep convective cloud anvils on a global scale, based on MODIS/Advanced Microwave Scanning radiometer observations. Takahashi and Luo (2012) analyzed the level of neutral buoyancy for deep convective clouds based on CloudSat data. While interactions between clouds, aerosols, radiation and precipitation contribute toward one of the largest uncertainties in the field of climate change, recent studies (Rosenfeld et al., 2008; Li et al., 2011) suggest that aerosols could also influence the development of DCS.

Aerosols can serve as cloud condensation nuclei, so they can modify cloud radiative and dynamical properties. The effect of aerosols on cloud life time and precipitation is often referred to as the "aerosol indirect effect". Studies (Albrecht, 1989; Radke et al., 1989; Rosenfeld, 2000; Ramanathan et al., 2001; Andreae et al., 2004; Li et al., 2011) have suggested that, with a fixed amount of water, an influx of aerosols could lead to the formation of more but smaller cloud droplets, thus suppressing collision and coalescence processes. The number of cloud droplets that could grow large enough to start rainfall would then be reduced, resulting in less precipitation. When deep mixed-phase clouds are formed under suitable dynamical conditions, more aerosols could enhance the development of these clouds in the following way. In the presence of a high concentration of aerosols, smaller cloud droplets could weaken, or even completely shut down, downdrafts within the cloud. Updrafts could then move these cloud droplets higher into the cloud. Once they pass the freezing level and start condensing, more latent heat would be released which would allow the cloud to grow more vigorously. This mechanism is the so-called aerosol invigoration effect (AIE) (Rosenfeld et al., 2008). Although both modeling and observational studies (Khain et al., 2005; Koren et al., 2005; Tao et al., 2007; Lee et al., 2010; Li et al., 2011; Freud and Rosenfeld, 2012; Niu and Li, 2012) have reported evidence to support the AIE and pointed out that it is particularly important for mixed-phase deep clouds, more work is still needed to further understand the AIE and its possible impact on climate and extreme weather. As modeling studies have shown (Khain et al., 2005; Tao et al., 2007), the AIE is more significant under certain conditions, such as with sufficient water vapor supply and weaker wind shear, but it is much weaker under opposite conditions, and such conditions are different for mixed-phase deep clouds at different geo-locations/time periods. Thus, better understanding of the temporal and spatial distribution of global DCS will help to reveal the best time and location to study the AIE. Therefore, in the present reported study, the global distribution of DCS was analyzed using four years' worth of CloudSat/Cloud-Aerosol Lidar and Infrared Pathfinder Satellite Observation(CALIPSO) data in order to build the foundation for a future, more in-depth study on the large-scale AIE. Section 2 describes the algorithm developed to identify DCS. The global frequency of DCS and the global distribution of the macro-physical properties of DCS are presented in sections 3 and 4, respectively. Conclusions and a discussion are given in section 5.

## 2. Algorithm for identifying DCS

### 2.1. *CloudSat data*

CloudSat is a polar-orbiting satellite and is a member of National Aeronautics and Space Administration (NASA)'s A-train constellation, launched in April 2006. The satellite carries a 94-GHz nadir-view cloud profiling radar (CPR) that can objectively observe clouds at a high vertical resolution. It is in a sun-synchronous orbit at an altitude of 705 km with an orbit period of about 98.9 minutes during which time approximately 37 081 profiles are generated. The resolution for each pixel in the horizontal direction is 1.1 km along the orbit swath tracking and 1.4 km perpendicular to the orbit tracking and 0.24 km in the vertical direction. With the combination of observations from CloudSat and CALIPSO, as well as reanalysis data from the European Centre for Medium-Range Weather Forecasts (ECMWF), CloudSat standard products provide the macro/micro-physical and radiative properties of cloud as well as the meteorological parameters in each pixel.

In our studies, 2B-GEOPROF and 2B-GEOPROF-LIDAR were used to determine the location of DCS. Both products provide the cloud geometry information but measured from different instruments. 2B-GEOPROF provides the radar echo in each pixel from the CPR, which has strong penetrability and can therefore detect low-level cloud with thick cloud above. 2B-GEOPROF-LIDAR contains information from the Cloud-Aerosol Lidar with Orthogonal Polarization (CALIOP) aboard CALIPSO, which can observe very thin ice cloud that the CPR cannot. Therefore, a combination of both products has the benefit of both radar and lidar data and thus provides more accurate cloud detections.

Using cloud mask, cloud fraction and radar reflectivity data from the 2B-GEOPROF and 2B-GEOPROF-Lidar products, pixels were identified as clear or cloudy. The cloud mask indicates that each pixel is detected by the CPR and that the threshold for cloud existing is larger than 20. The cloud fraction contains the percentage within each pixel that is identified by the lidar as cloud. The radar reflectivity is the radar echo from the CPR within each pixel. Since the minimum detectable signal of the CPR is approximately $-30$ dB$Z$, if the pixel has a cloud mask flag $< 20$ and a cloud fraction $\geqslant 50\%$ or a reflectivity $\geqslant -30$ dB$Z$ and a cloud mask flag $\geqslant 20$, the pixel is cloudy; in all other cases the pixel is clear (Zhang et al., 2013; Peng et al., 2013).

### 2.2. *Identifying DCS*

No universal definition of DCS has been established even though related studies about DCS have been published by

others. In this study, which focuses on how deep mixed-phase clouds might be affected by the AIE, cloud top and base heights were used to define DCS. CloudSat records cloud information continuously along its orbital track, so it provides not only single profile information but also information on the cross-section formed by the combination of adjacent profiles. Following the method used in Luo et al. (2010), we first identified a cloudy profile which was strongly developed in the vertical direction and defined it as a deep cloud core (DCC); the DCC and adjacent cloudy pixels in the cross-section were then defined as DCS. The AIE is most significant in deep mixed-phase clouds with cloud bases lower than 2 km (Li et al., 2011), so only those DCC that are single-layered with a cloud-top height $>$ 10 km and with a distance $<$ 2 km between the surface and the cloud base were considered. Once a DCC was identified, adjacent profiles in both forward and backward directions along track were examined and if there were cloudy pixels at the same altitude in connected profiles, they were deemed associated with the same deep cloud. This process continued in expanding directions until no cloudy pixels in connecting profiles were found; at this point, a DCS had been identified.

An example of a DCS is shown in Fig. 1, taken from CloudSat orbit 4108 on 4 February 2007. This DCS includes 214 DCC and covers a horizontal range of 1841.1 km.

Studies (Huang et al., 2005, 2006) have demonstrated the importance of multi-layer clouds to the radiation budget and have developed algorithms for the identification of multi-layer clouds and the retrieval of their properties. So if any deep cloud is overlapped by other cloud, such as cirrus, it is not considered as a DCC, which leads to an underestimate of the number of global DCS. All data were checked to estimate the uncertainties. If the lowest-layer cloud of any multi-layer cloudy profile had a cloud-top height $>$ 10 km and a distance $<$ 2 km between the surface and the cloud base, the multi-layer profile was considered to be a miss-identified DCC. According to the geographical location and UTC time of the misidentified DCC, we found that most of them were included in the currently identified DCS. Then, we checked all misidentified DCC that were not included in the current DCS, and if the number of continuously misidentified DCC not included in the current DCS was larger than five, they were considered to be missed-DCS. So, the ratio of the number of missed-DCS to the number of DCS was considered to be the underestimate of global DCS, which ranged from about 5% in low latitudes to about 2% in high latitudes.

## 3. Global distribution and seasonal trends in DCS

The global distribution of DCS and seasonal trends in the number of DCS (NDCS) are examined in this section. First, the Southern and Northern Hemispheres (SH and NH, respectively) were each divided into zones: low latitude (LL: 0°–30°), midlatitude (ML: 30°–60°) and high latitude (HL: 60°–90°). Seasons were defined as follows:

(1)December, January and February for winter in the NH and summer in the SH;

(2) March, April and May for spring in the NH and autumn in the SH;

(3) June, July and August for summer in the NH and winter in the SH;

(4) September, October and November for autumn in the

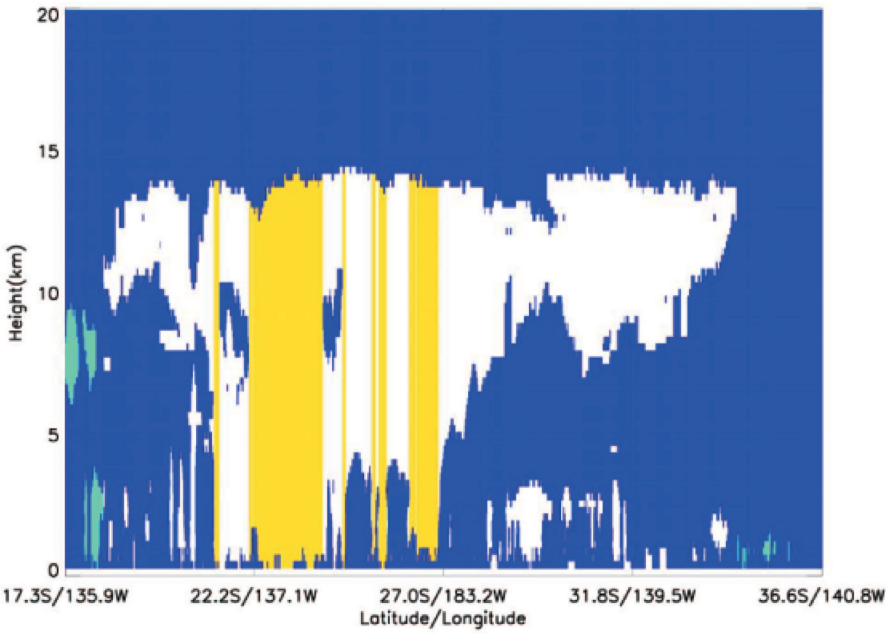


**Fig. 1.** Example of a DCS identified on 4 Feb 2007. White and yellow areas represent the DCS (the yellow area is the DCC) and blue regions are clear sky; green areas represent cloudy pixels not classified as part of the DCS.

NH and spring in the SH.

The mean latitude and longitude of all the DCC in each DCS was used to represent the location of the DCS; they were calculated over $5^\circ \times 5^\circ$ grid boxes. The NDCS was calculated as the sum of the DCS in each grid box per season over the four-year period. Figure 2 shows the monthly time series of NDCS in different zonal bands. In the NH, the NDCS changes significantly with season in all zonal bands; the maximum NDCS occurs in summer and the minimum in winter (Fig. 2a). In the LL zone of the SH, the maximum NDCS also occurs in summer and the minimum in winter; in the HL zone in the SH, the reverse is seen (Fig. 2b). The NDCS remains generally the same year-round in the ML zone of the SH. Globally, for any single month over the four-year period, the maximum NDCS (4221) occurred in August 2007 and the minimum NDCS (561) occurred in April 2010.

Convective instability caused by radiative heating is the main contributing factor toward the generation of DCS in the LL zone of both hemispheres, which explains why the NDCS in this zonal band is large in summer and small in winter. Figures 2c–f demonstrate how different underlying surfaces can lead to large differences in the seasonal variation of the NDCS in the ML and HL zones of both hemispheres. The seasonal variations of the NDCS over land and over the ocean in the LL zone are the same. The much larger NDCS over the ocean than over land is because many tropical cyclones are generated over the ocean in the LL zone. The seasonal variation of the NDCS over land in the NH (Fig. 2c, dash–

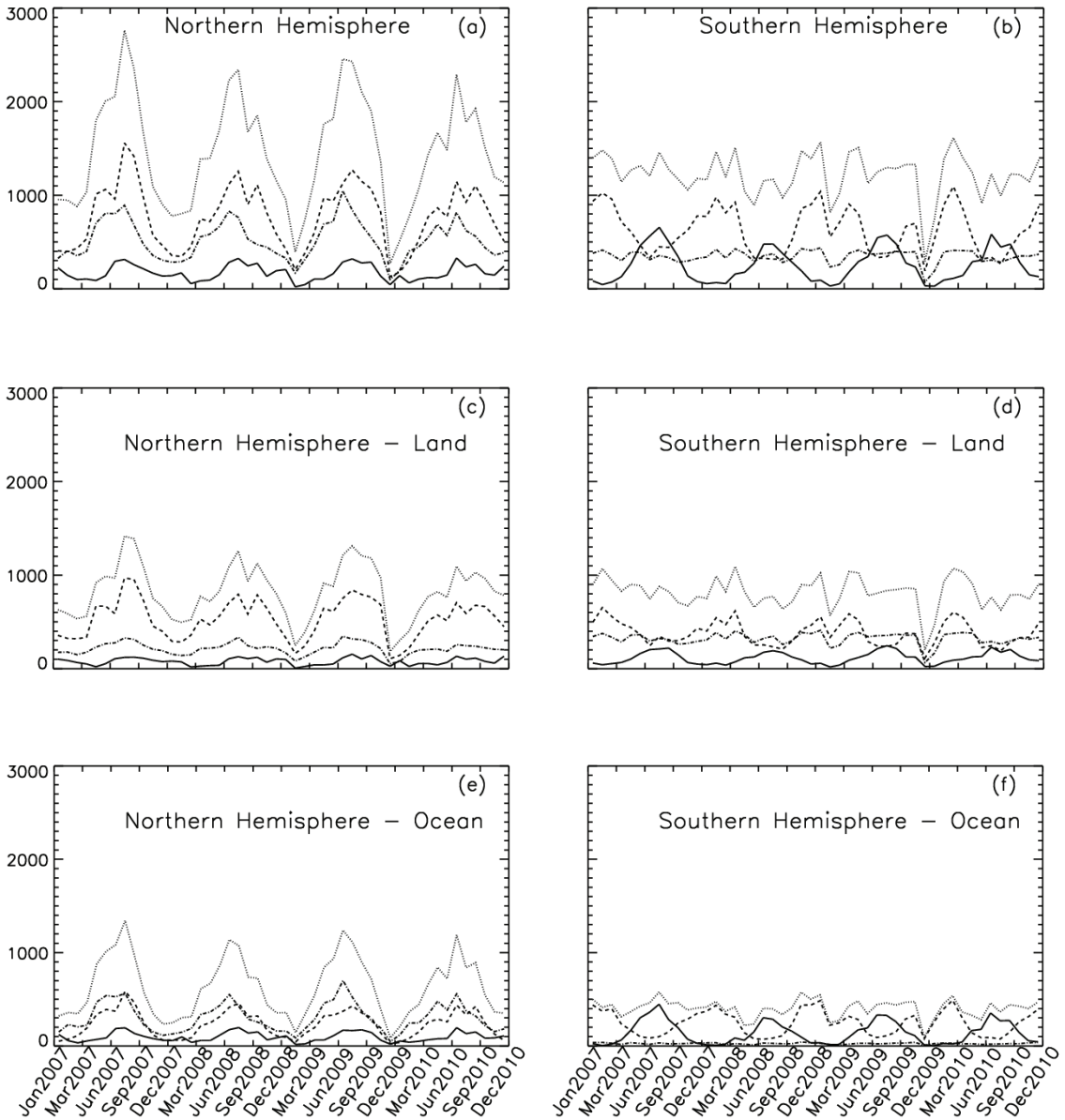


**Fig. 2.** Total NDCS per month in different zonal bands for (a) the NH, (b) the SH, (c) the NH over land, (d) the SH over land, (e) the NH over the ocean, and (f) the SH over the ocean. The dotted line represents the NDCS over all zonal bands; the dashed line is for 0°–30°; the dash–dot line is for 30°–60°; and the solid line is for 60°–90°.

dot line) is much more significant than over the oceans (Fig. 2e, dash–dot line) because cloud development over land is more complex. Oceans dominate in the ML zone of the SH so cloud formation is a simpler process over this surface and little seasonal variation is seen in the NDCS (Fig. 2f). The largest NDCS in the HL zone occurs in the SH where the sub-polar low is located. DCS here are formed from the convergence of cold air from the polar region and warm air from the subtropical region.

The NDCS for different zonal regions and seasons is summarized in Table 1; the global distribution of NDCS for each season is shown in Fig. 3. The global distribution of NDCS are consistent with previous deep-cloud-related studies (Sassen et al., 2009; Savtchenko, 2009), which indicate that the representation according to CloudSat/CALIPSO's observations is still reasonable despite the limited spatial and temporal resolution. The maximum NDCS (39 343) occurs in the NH summer/SH winter and the minimum NDCS (23 827) occurs in the NH winter/SH summer. The highest density of DCS occurs in central Africa, northern South America, Indonesia and Tibet, with the maximum values of NDCS in a single grid box within each of these regions over the four-year period being 86, 112, 87 and 154, respectively. Note the significant increase in the NDCS over the Antarctic polar region during NH summer/SH winter (Fig. 3b).

## 4. Macrophysical properties of DCS on a global scale

AIE-related studies have reported that deep mixed-phase clouds tend to have higher cloud-top heights and lower cloud-top temperatures under polluted conditions than under clean conditions (Li et al., 2011; Niu and Li, 2012). Using a

**Table 1.** Total number of DCS in different zonal regions for different seasons over the period 2007–10.

| | LL/NH | ML/NH | HL/NH | Total/NH | LL/SH | ML/SH | HL/SH | Total/SH |
|---|---|---|---|---|---|---|---|---|
| Spring NH/Autumn SH | 7971 | 6063 | 1107 | 15 141 | 9414 | 4454 | 1917 | 15 785 |
| Summer NH/Winter SH | 13 006 | 9367 | 2968 | 25 341 | 4222 | 4076 | 5705 | 14 003 |
| Autumn NH/Spring SH | 11 524 | 5954 | 2543 | 20 021 | 6759 | 4145 | 3709 | 14 613 |
| Winter NH/Summer SH | 4296 | 3563 | 1711 | 9570 | 9479 | 3977 | 801 | 14 257 |

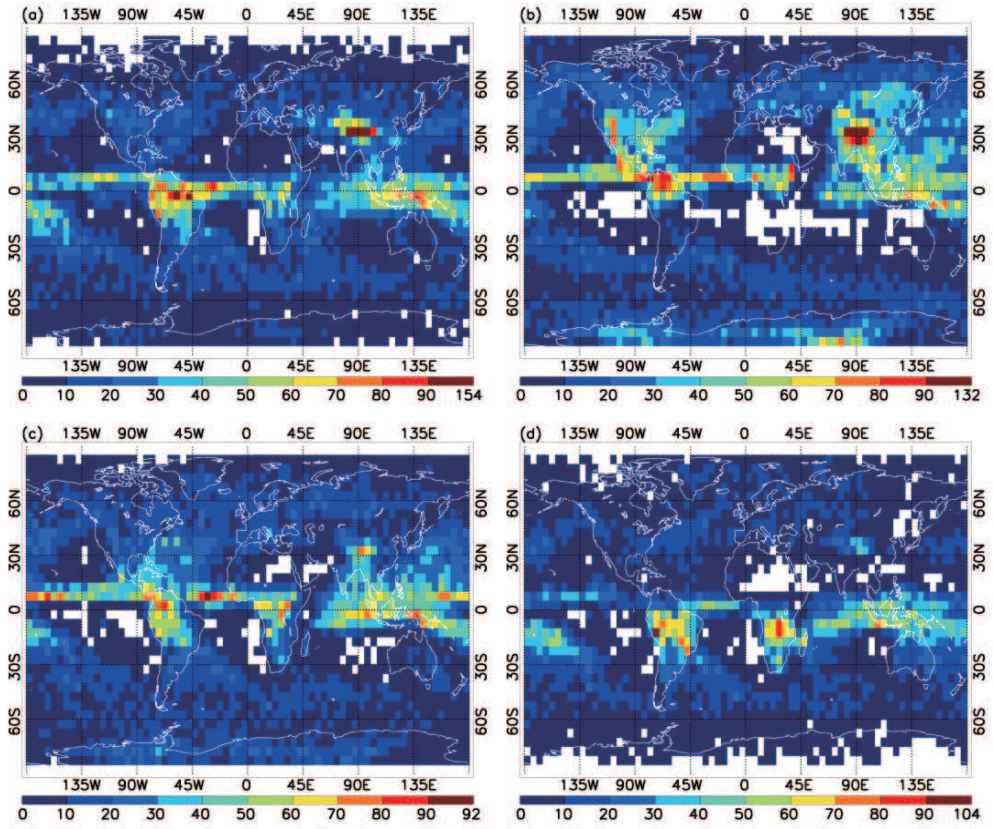


**Fig. 3.** Total number of DCS in each $5^\circ \times 5^\circ$ grid box over the four-year period for (a) NH spring/SH autumn, (b) NH summer/SH winter, (c) NH autumn/SH spring, and (d) NH winter/SH summer. White grid boxes signify that no DCS were identified in that box.

combination of MODIS retrievals and Goddard Chemistry Aerosol Radiation and Transport model simulations, Khain et al. (2005) found that when the aerosol optical depth increases, the ratio of clouds with large optical depths to those with small optical depths decreases. They explained that with an increase in aerosol loading, the most vertically developed part of a DCS (high optical depth) would intensify, and the horizontal extent of the anvil (small optical depth) would increase. These findings suggest that both the vertical and horizontal macrophysical properties of a DCS can be modified through the AIE. The mean distance between the top of each DCC and the surface within a single DCS (cloud-top height of deep cloud cores; TDCC) and the mean depth of the deep cloud core (DDCC) are used to describe the strength of the vertical development. The horizontal development of a DCS is expressed as the cross-sectional width of the DCS (WDCS).

### 4.1. *Global distribution and seasonal trends in TDCC*

Figure 4 shows the monthly time series of the mean TDCC over the four-year period. There is little seasonal variation in the mean TDCC in the LL and HL zones of the NH. The mean TDCC in the ML zone of the NH reaches a maximum in summer (10.59 km) and a minimum in winter (9.89 km). In the SH, the highest TDCC occurs in the LL and ML zones in summer (13.51 km and 11.03 km, respectively) and the lowest TDCC occurs in these regions in winter (13.00 km and 10.77 km). The mean TDCC in the HL zone of the SH varies greatly from month-to-month (Fig. 4b) but there is little difference in TDCC between different seasons (Table 2). Global distributions of TDCC and DDCC for different seasons are shown in Figs. 5 and 6, respectively. The TDCC decreases toward higher latitudes in both hemispheres; the mean TDCCs from the HL to the LL zone are 9.97 km, 10.47 km and 13.24 km. The lowest TDCC and smallest DDCC can be seen over Tibet, Greenland, the Antarctic continent and Chilean plateaus. Because TDCC is defined as the distance between the cloud top and the surface and DCC is defined as a single-layered cloud with top heights greater than 10 km above mean sea level, the DCC over these elevated land surfaces have the lowest TDCC. The DCS with the highest TDCC (up to 16 km) and largest DDCC ($\sim$ 15 km) occur over south and eastern Asian monsoon regions, west-central Africa and northern South America. Note that the DCS grows thicker and higher in the winter over the Antarctic (Figs. 5b and 6b).

### 4.2. *Global distribution and seasonal trends in WDCS*

Figure 7 shows the monthly time series of the mean WDCS over the four-year period; Table 3 summarizes the mean WDCS for different zonal regions and seasons. The maximum and minimum WDCS in the NH are 1055.9 km (in winter) and 645.2 km (in summer), respectively. Large-scale circulation in winter is mainly in the form of frontal systems, which are much larger in scale than summertime convective cloud systems, so although fewer DCS are seen in the NH during winter (Table 1), they are much larger in horizontal extent. In the SH, the maximum WDCS occurs in the HL zone in the autumn (1364.7 km) and the minimum WDCS can be seen in the LL zone in the winter (585.7 km).

The global distribution of WDCS is shown in Fig. 8. The main feature that can be seen is the increase in WDCS to-

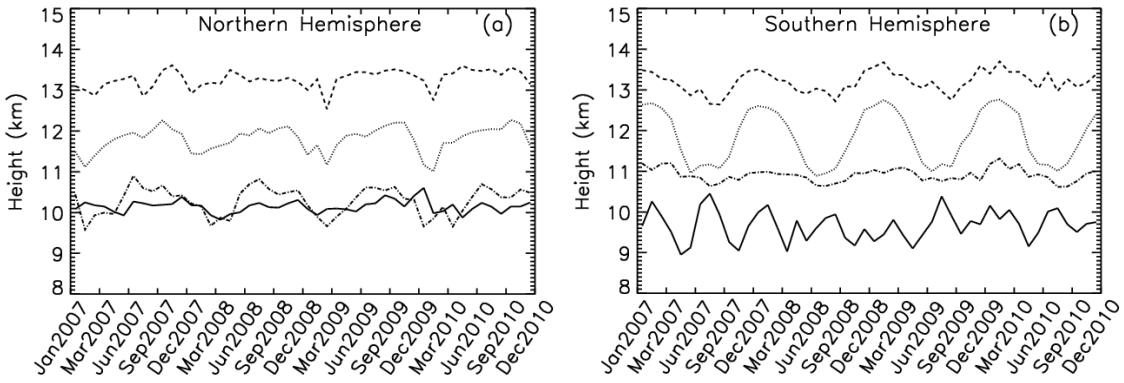


**Fig. 4.** Monthly time series of mean TDCC over the four-year period for different zonal bands in (a) the NH and (b) the SH. The dotted line represents TDCC over all zonal bands; the dashed line is for 0°–30°; the dash–dot line is for 30°–60°; and the solid line is for 60°–90°.

**Table 2.** Mean TDCC in different zonal regions for different seasons over the period 2007–10 (units: km).

| | LL/NH | ML/NH | HL/NH | Total/NH | LL/SH | ML/SH | HL/SH | Total/SH |
|---|---|---|---|---|---|---|---|---|
| Spring NH/Autumn SH | 13.22 | 10.14 | 10.04 | 11.64 | 13.26 | 11.02 | 9.50 | 12.15 |
| Summer NH/Winter SH | 13.34 | 10.59 | 10.15 | 11.95 | 13.00 | 10.77 | 9.81 | 11.08 |
| Autumn NH/Spring SH | 13.40 | 10.49 | 10.18 | 12.12 | 13.03 | 10.81 | 9.57 | 11.55 |
| Winter NH/Summer SH | 13.12 | 9.89 | 10.22 | 11.49 | 13.51 | 11.03 | 9.79 | 12.60 |

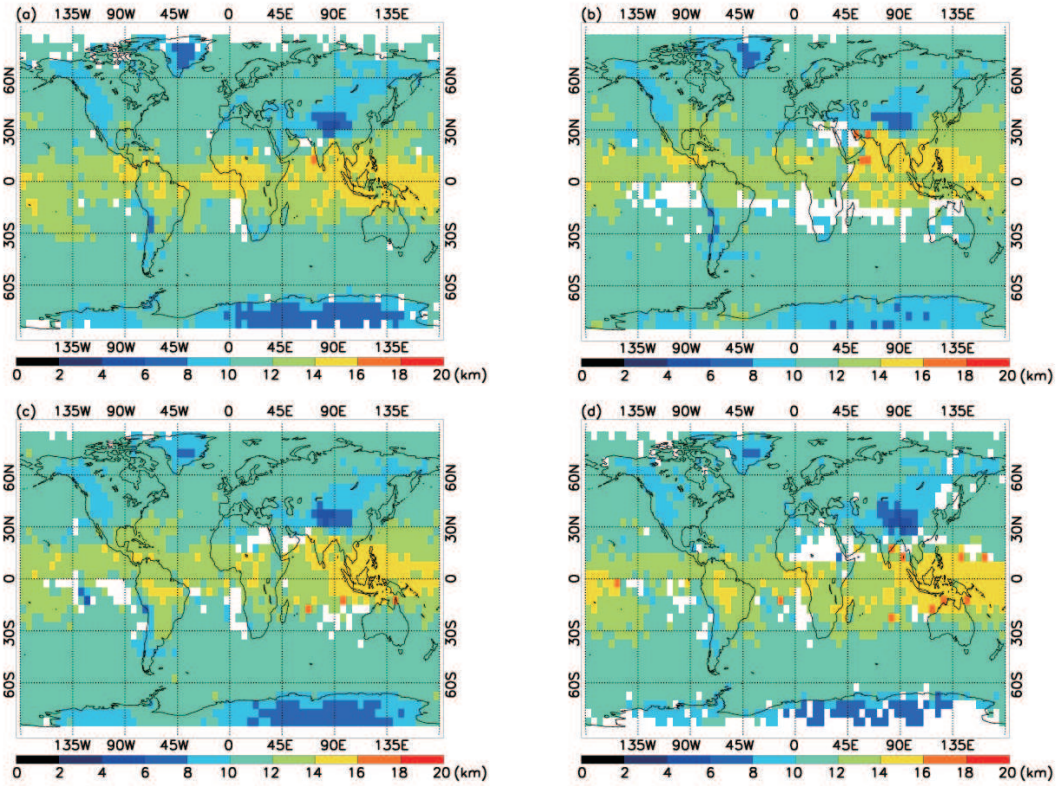


**Fig. 5.** Mean TDCC in each $5^\circ \times 5^\circ$ grid box over the four-year period for (a) NH spring/SH autumn, (b) NH summer/SH winter, (c) NH autumn/SH spring, and (d) NH winter/SH summer. White grid boxes signify that no DCS were identified in that box.

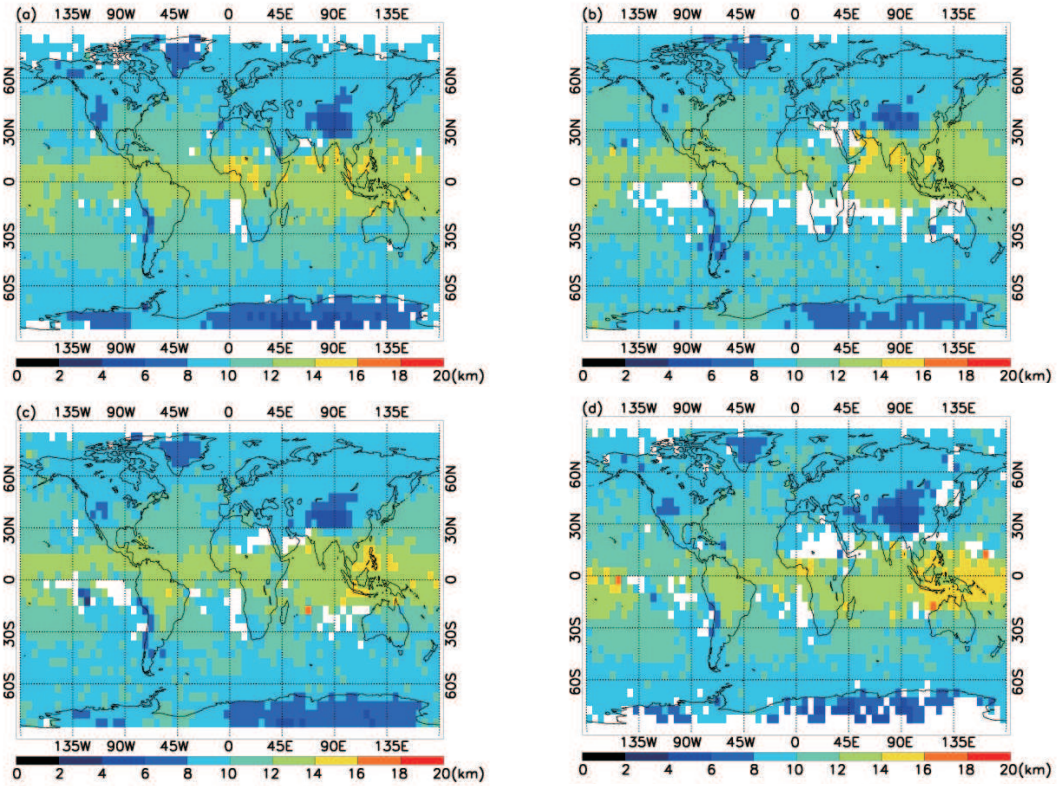


**Fig. 6.** Same as Fig. 5 but for mean DDCC.

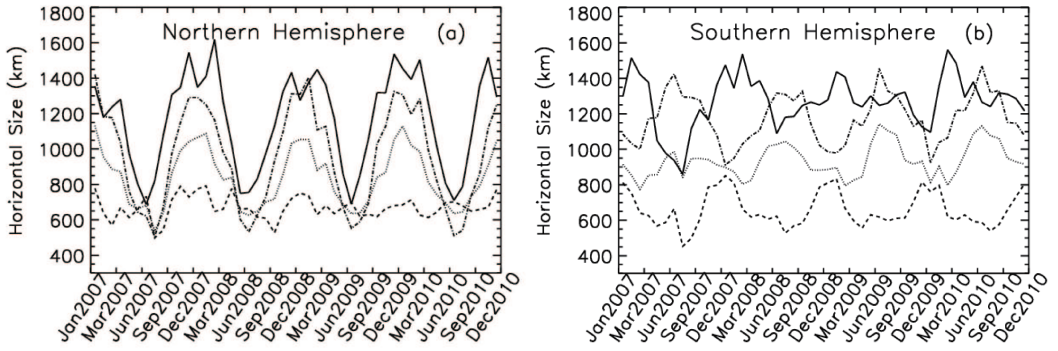


**Fig. 7.** Monthly time series of mean WDCS over the four-year period for different zonal bands in (a) the NH and (b) the SH. The dotted line represents WDCS over all zonal bands; the dashed line is for 0°–30°; the dash–dot line is for 30°–60°; and the solid line is for 60°–90°.

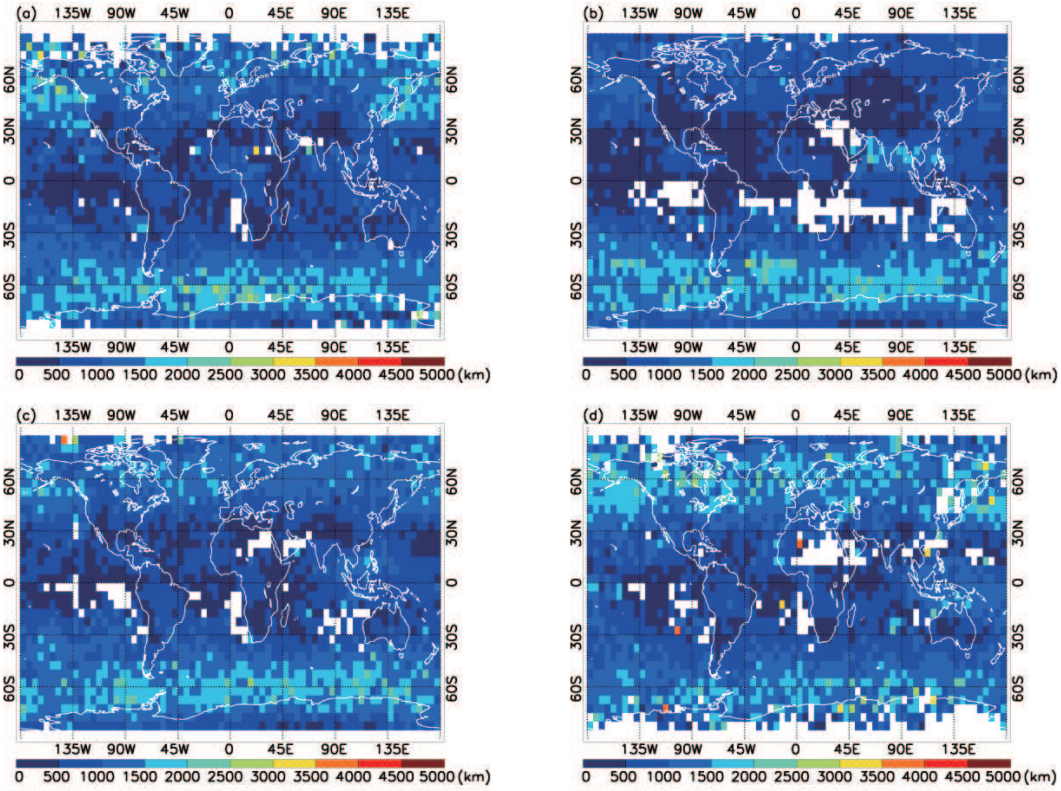


**Fig. 8.** Mean WDCC in each 5°×5° grid box over the four-year period for (a) NH spring/SH autumn, (b) NH summer/SH winter, (c) NH autumn/SH spring, and (d) NH winter/SH summer. White grid boxes signify that no DCS were identified in that box.

**Table 3.** Mean WDCS in different zonal regions for different seasons over the period 2007–10 (units: km).

| | LL/NH | ML/NH | HL/NH | Total/NH | LL/SH | ML/SH | HL/SH | Total/SH |
|---|---|---|---|---|---|---|---|---|
| Spring NH/Autumn SH | 647.2 | 1017.4 | 1263.8 | 844.1 | 618.5 | 1115.4 | 1364.7 | 846.4 |
| Summer NH/Winter SH | 657.9 | 588.8 | 779.7 | 645.2 | 585.7 | 1337.5 | 1168.8 | 1036.8 |
| Autumn NH/Spring SH | 643.6 | 925.9 | 1232.2 | 801.0 | 633.9 | 1230.4 | 1245.1 | 964.2 |
| Winter NH/Summer SH | 730.8 | 1295.0 | 1383.1 | 1055.9 | 802.8 | 1021.1 | 1313.4 | 890.5 |

ward higher altitudes; the mean WDCS in the LL, ML and HL zones in both hemispheres is 665.05 km, 1066.44 km and 1218.85 km, respectively. Over the four-year period, the DCS with the largest WDCS are seen in the HL zone of the SH; this is attributed to the presence of the sub-polar low and the resulting generation of large-scale DCS. Worth to note that, when we calculate the WDCS for any particularly grid, the profile not in the grid may also be taken into the consideration as long as it belongs to the DCS that the averaged latitude and longitude of its DCCs lies in the grid. Therefore, although the length of each grid is different in different latitudes, it will not influence the result of WDCS.

### 4.3. *Reasons behind the distribution of macrophysical properties of DCS*

Seasonal variations of TDCC and DDCC in different zonal regions are mainly due to the different mechanisms for generating DCS at different latitudes. Using reanalysis data from the ECMWF, convective available potential energy (CAPE) was calculated; this quantity is often used to represent convective intensity. Figure 9 shows the monthly time series of mean CAPE over the four-year period for different zonal bands. In general, the TDCC is positively correlated to CAPE at different latitudes. The DCS in the LL zone are mainly deep convective clouds, highly developed in the vertical direction but covering a relatively small area in the horizontal direction. The generation of clouds in the ML zone is highly impacted by mesoscale weather systems, so many DCS are formed along fronts; strong monsoons also influence the generation of DCS. In the ML zone of the NH, the significant increase in the number of deep cumulonimbi during the summer results in an increase in TDCC. In the SH, oceans are the dominant surface in the ML zone, so there is much less variation in conditions producing DCS throughout the year. Convection is weakest in the HL zone in both hemispheres, so DCS are mainly generated by large-scale frontal systems; TDCC (WDCS) decreases (increases) toward higher latitudes.

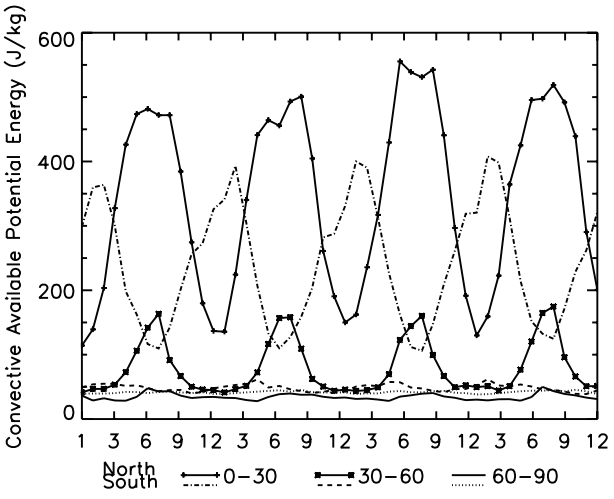


**Fig. 9.** Monthly time series of mean CAPE over the four-year period for different zonal bands.

## 5. Discussion and conclusions

Using four years' worth of CloudSat and CALIPSO data (2007–10), DCS were identified and the global distribution of the number of DCS, TDCC, DDCC and WDCS was analyzed. The main conclusions are as follows:

(1) The greatest concentration of DCS occurred in central Africa, northern South America, northern Australia and Tibet; the maximum values of NDCS in a single grid box within each of these regions over the four-year period were 86, 112, 87 and 154, respectively. There was a significant increase in the NDCS over the Antarctic polar region during NH summer/SH winter. In the NH, the fewest NDCS were seen in winter (9570) and the greatest NDCS occurred in summer (25 341); the total number of DCS in spring and autumn were 15 141 and 20 021. There was more seasonal and zonal variation in NDCS in the SH. The maximum NDCS seen in the LL zone occurred in summer (9479) and the minimum in winter (4222); in the HL zone in the SH, the reverse was seen (winter: 5705, summer: 801). The NDCS remained generally the same year-round in the ML zone of the SH.

(2) TDCC decreased toward higher latitudes in both hemispheres. The DCS with the highest TDCC (up to 16 km) and largest DDCC ($\sim$ 15 km) occurred over south and eastern Asian monsoon regions, west-central Africa and northern South America. There was little seasonal variation in the mean TDCC in the LL and HL zones of the NH. The mean TDCC in the ML zone of the NH reached a maximum in summer (10.59 km) and a minimum in winter (9.89 km). In the SH, the highest TDCC occurred in the LL and ML zones in summer (13.51 km and 11.03 km, respectively) and the lowest TDCC occurred in these regions in winter (13.00 km and 10.77 km). The mean TDCC in the HL zone of the SH varied greatly from month-to-month but there was little difference in TDCC between different seasons.

(3) The WDCS increased in magnitude toward higher latitudes; the mean WDCS in the LL, ML and HL zones of both hemispheres was 665.05 km, 1066.44 km and 1218.85 km, respectively. Over the four-year period, the DCS with the largest WDCS were found in the HL zone of the SH. The maximum and minimum WDCS in the NH was 1383.1 km (winter) and 645.2 km (summer), respectively. The WDCS in the LL zone of the SH was largest in summer (802.8 km) and smallest in winter (585.7 km). In the ML zone of the SH, the maximum (minimum) WDCS (1337.5 km; 1021.1 km) occurred in winter (summer). The largest and smallest WDCS were seen in autumn and winter in the HL zone of the SH (1364.7 km and 1168.8 km, respectively).

(4) Seasonal variations of TDCC and DDCC in different zonal regions are mainly due to the different mechanisms for generating DCS at different latitudes. The DCS in the LL zone are mainly deep convective clouds, highly developed in the vertical direction but covering a relatively small area

in the horizontal direction. Most DCS in the ML zone are formed by frontal systems, so they have smaller TDCC than those in the LL zone. The NDCS in the ML zone of the NH (SH) increases significantly in summer (winter) because of the monsoon circulation. The DCS in the HL zone are mainly generated by large frontal systems, so have the largest WDCS and smallest TDCC.

Future work will focus on examining the AIE in DCS at a global scale.

***Acknowledgements.*** The authors would like to thank the NASA CloudSat project for providing the CloudSat data used in this study and AAS editors for their English improvements to the whole text. This work was supported by the National Natural Science Foundation of China (Grant No. 41375080) and the National Program on Key Basic Research Project of China (Grant Nos. 2011CB403405 and 2013CB955804) and the US Department of Energy Atmospheric System Research Program (DESC0007171).

## REFERENCES

Albrecht, B. A., 1989: Aerosols, cloud microphysics, and fractional cloudiness. *Science*, **245**, 1227–1230.

Andreae, M. O., D. Rosenfeld, P. Artaxo, A. A. Costa, G. P. Frank, K. M. Longo, and M. A. F. Silva-Dias, 2004: Smoking rain clouds over the Amazon. *Science*, **303**, 1337–1342.

Freud, E., and D. Rosenfeld, 2012: Linear relation between convective cloud drop number concentration and depth for rain initiation. *J. Geophys. Res.*, **117**, D02207, doi: 10.1029/2011JD016457.

Futyan, J. M., and A. D. Del Genio, 2007: Deep convective system evolution over Africa and the tropical Atlantic. *J. Climate*, **20**, 5041–5060.

Harrison, E. F., P. Minnis, B. R. Barkstrom, V. Ramanathan, R. D. Cess, and G. G. Gibson., 1990: Seasonal-variation of cloud radiative forcing derived from the Earth Radiation Budget Experiment. *J. Geophys. Res.*, **95**(D11), 18 687–18 703.

Hartmann, D. L., M. E. Ockert-Bell, and M. L. Michelsen, 1992: The effect of cloud type on earths' energy-balance: Global analysis. *J. Climate*, **5**, 1281–1304.

Hartmann, D. L., L. A. Moy, and Q. Fu, 2001: Tropical convection and the energy balance at the top of the atmosphere. *J. Climate*, **14**, 4495–4511.

Huang, J. P., P. Minnis, B. Lin, Y. H. Yi, M. M. Khaiyer, R. F. Arduini, A. Fan, and G. G. Mace, 2005: Advanced retrievals of multilayered cloud properties using multispectral measurements. *J. Geophys. Res.*, **110**(D15), D15S18, doi: 10.1029/2004JD005101.

Huang, J. P., P. Minnis, B. Lin, Y. H. Yi, T. F. Fan, S. Sun-Mack, and J. K. Ayers, 2006: Determination of ice water path in ice-over-water cloud systems using combined MODIS and AMSR-E measurements. *Geophys. Res. Lett.*, **33**(21), L21801, doi: 10.1029/2006GL027038.

Iwasaki, S., T. Shibata, J. Nakamoto, H. Okamoto, H. Ishimoto, and H. Kubota, 2010: Characteristics of deep convection measured by using the A-train constellation. *J. Geophys. Res.*, **115**, D06207, doi: 10.1029/2009JD013000.

Khain, A., D. Rosenfeld, and A. Pokrovsky, 2005: Aerosol impact on the dynamics and microphysics of deep convective clouds. *Quart. J. Roy. Meteor. Soc.*, **131**, 2639–2663, doi: 10.1256/qj.04.62.

Kiehl, J. T., 1994: On the observed near cancellation between longwave and shortwave cloud forcing in tropical regions. *J. Climate*, **7**, 559–565.

Koren, I., Y. J. Kaufman, D. Rosenfeld, L. A. Remer, and Y. Rudich, 2005: Aerosol invigoration and restructuring of Atlantic convective clouds. *J. Geophys. Res.*, **32**, L14828, doi: 10.1029/2005GL023187.

Lee, S. S., L. Donner, and J. E. Penner, 2010: Thunderstorm and stratocumulus: How does their contrasting morphology affect their interactions with aerosols? *Atmos. Chem. Phys.*, **10**, 6819–6837, doi: 10. 5194/acp-10-6819-2010.

Luo, Y. L., R. H. Zhang, W. M. Qian, Z. Z. Luo, and H. Xin, 2010: Intercomparison of deep convection over the Tibetan Plateau-Asian monsoon region and subtropical North America in boreal summer using CloudSat/CALIPSO data. *J. Climate*, **24**, 2164–2177, doi: 10.1175/2009JCLI4032.1.

Niu, F., and Z. Q. Li, 2012: Systematic variations of cloud top temperature and precipitation rate with aerosols over the global tropics. *Atmos. Chem. Phys.*, **12**, 8491–8498, doi: 10.5194/acp-12-84910-2012.

Li, Z. Q., F. Niu, J. W. Fan, Y. G. Liu, D. Rosenfeld, and Y. N. Ding, 2011: Long-term impacts of aerosols on the vertical development of clouds and precipitation. *Nat. Geosci.*, **4**, 888–894, doi: 10.1038/ngeo1313.

Peng, J., H. Zhang, and X. Y. Shen, 2013: Analysis of vertical structure of clouds in East Asia with CloudSat data. *Chinese J. Atmos. Sci.*, **37**(1), 91–100, doi: 10.3878/j. issn.1006-9895.2012.11188. (in Chinese)

Radke, L. F., J. A. Coakley Jr., and M. D. King, 1989: Direct and remote sensing observations of the effects of ships on clouds. *Science*, **246**, 1146–1149.

Ramanathan, V., R. D. Cess, E. F. Harrison, P. Minnis, B. R. Barkstrom, E. Ahmad, and D. Hartmann, 1989: Cloud-radiative forcing and climate: Results from the Earth Radiation Budget Experiment. *Science*, **243**, 57–63.

Ramanathan, V., P. J. Crutzen, J. T. Kiehl, and D. Rosenfeld, 2001: Aerosols, climate, and the hydrological cycle. *Science*, **294**, 2119–2124.

Rosenfeld, D., 2000: Suppression of rain and snow by urban and industrial air pollution. *Science*, **287**, 1793–1796.

Rosenfeld, D., U. Lohmann, G. B. Rage, C. D. O'Dowd, M. Kulmala, S. Fuzzi, A. Reissell, and M. O. Andreae, 2008: Flood or drought: How do aerosols affect precipitation? *Science*, **321**, 1309–1313.

Sassen, K., Z. E. Wang, and D. Liu, 2009: Cirrus clouds and deep convection in the tropics: Insights from CALIPSO and CloudSat. *J. Geophys. Res.*, **114**, D00H06, doi: 10.1029/2009JD011916.

Savtchenko, A., 2009: Deep convection and upper-tropospheric humidity: A look from the A-Train. *Geophys. Res. Lett.*, **36**, L06814, doi: 10.1029/2009GL037508.

Takahashi, H., and Z. J. Luo, 2012: Where is the level of neutral buoyancy for deepconvection? *Geophys. Res. Lett.*, **39**, L15809, doi: 10.1029/2012GL052638.

Tao, W. K., X. W. Li, A. Khain, T. Matsui, S. Lang, and J. Simpson, 2007: Role of atmospheric aerosol concentration on deep convective precipitation: Cloud-resolving model simulations. *J. Geophys. Res.*, **112**, D24S18, doi: 10.1029/2007JD008728.

Yuan, J., and R. A. Houze Jr., 2010: Global variability of mesoscale convective system anvil structure from A-Train satellite data. *J. Climate*, **23**, 5864–5888, doi:

10.1175/2010JCLI3671. 1.

Yuan, J., R. A. Houze Jr., and A. J. Heymsfield, 2011: Vertical structures of anvil clouds of tropical mesoscale convective systems observed by CloudSat. *J. Atmos. Sci.*, **68**, 1653–1674, doi: 10.1175/2011JAS3687.1.

Yuan, T. L., and Z. Q. Li, 2010: General macro- and microphysical properties of deep convective clouds as observed by MODIS. *J. Climate*, **23**, 3457–3473, doi: 10.1175/2009JCLI3136.1.

Yuan, T. L., J. V. Martins, Z. Q. Li, and L. A. Remer, 2010: Estimating glaciation temperature of deep convective clouds with remote sensing data. *Geophys. Res. Lett.*, **37**, L08808, doi: 10.1029/2010GL042753.

Zhang, H., J. Peng, X. W. Jing, and J. N. Li, 2013: The features of cloud overlapping in Eastern Asia and their effect on cloud radiative forcing. *Sci. China* (*Earth*), **56**, 737–747, doi: 10.1007/s11430-012-4489-x.

祁莉,王晓芳,何金海等.前期西太平洋暖池热含量异常影响长江中下游夏季降水的可能途经.地球物理学报,57(6):1769-1781,doi:10.6038/cjg20140609.

Qi L, Wang X F, He J H, et al. The approach of the previous anomalous heat content in the western Pacific warm pool affecting the summer rainfall over the middle and lower reaches of the Yangtze River. *Chinese J. Geophys.* (in Chinese), 57(6):1769-1781, doi:10.6038/cjg20140609.

# 前期西太平洋暖池热含量异常影响长江中下游夏季降水的可能途经

祁莉[1],王晓芳[2*],何金海[1],张文君[1],吴捷[3]

1 南京信息工程大学 气象灾害预报预警与评估协同创新中心,气象灾害省部共建教育部重点实验室,南京 210044

2 中山市气象局,广东中山 528401

3 国家气候中心 气候研究开放实验室,北京 100081

**摘要** 利用日本气象厅历史海温资料、NCEP/NCAR 再分析资料、海表温度和降水资料,研究了 1951—2010 年前期西太平洋暖池(简称暖池)热含量异常与长江中下游夏季降水的关系,及其可能影响途径.结果表明,前期暖池热含量与长江中下游夏季降水存在超前 2 个季节的显著负相关关系,前期 11—1 月(即上年 11 月—当年 1 月,下同)暖池关键区(166.5°E—173.5°W,7.5°S—3.5°N)0～200 m 热含量的偏低(高)对长江中下游夏季降水偏多(少)的预测有重要指示意义.前期暖池热含量异常的持续存在,及其外强迫作用激发的具有一定斜压性结构的夏季东亚—太平洋型遥相关(EAP),可能是影响长江中下游夏季降水的主要原因.暖池热含量在前期 11—1 月异常偏低导致其西北侧菲律宾异常反气旋形成并维持,夏季菲律宾异常反气旋向西北方向扩展加强,东亚沿岸 EAP 波列形成,使得长江中下游及其以东的西北太平洋副热带地区受异常气旋控制,且长江中下游地区为北方冷空气与南方暖湿气流的交汇区.同时,对流层高层东亚沿岸亦存在位置较中低层向西北偏移的 EAP 波列,长江中下游及其以南地区为异常偏强高压,高层辐散与中低层辐合相配合,有利于长江中下游地区对流发展和降水增多;反之亦然.

**关键词** 西太平洋暖池;热含量;长江中下游夏季降水;前兆信号;遥相关

doi:10.6038/cjg20140609 **中图分类号** P461 **收稿日期** 2013-08-01,2014-01-12 收修定稿

# The approach of the previous anomalous heat content in the western Pacific warm pool affecting the summer rainfall over the middle and lower reaches of the Yangtze River

QI Li[1], WANG Xiao-Fang[2*], HE Jin-Hai[1], ZHANG Wen-Jun[1], WU Jie[3]

1 *Collaborative Innovation Center on Forecast and Evaluation of Meteorological Disasters, Key Laboratory of Meteorological Disaster of Ministry of Education, Nanjing University of Information Science and Technology, Nanjing* 210044, *China*

2 *Zhongshan Meteorological Bureau, Guangdong Zhongshan* 528401, *China*

3 *Laboratory for Climate Studies, National Climate Center of China Meteorological Administration, Beijing* 100081, *China*

**Abstract** The relationship between the previous heat content anomaly in the western Pacific warm pool (WPWP) and summer rainfall over the middle and lower reaches of the Yangtze

**基金项目** 国家重点基础研究发展计划(973 计划)项目(2012CB417403),江苏高校优势学科建设工程资助项目(PAPD),长江学者和创新团队发展计划(PCSIRT)资助.



**作者简介** 祁莉,主要从事季风、海陆气相互作用与短期气候预测的研究.E-mail:qili@nuist.edu.cn

* **通讯作者** 王晓芳,女,硕士,主要从事海陆气相互作用与短期气候预测的研究.E-mail:catharine0607@sina.com

River, and the way how heat content anomaly probably affects the summer rainfall are studied by using the historical ocean temperature analysis data provided by Japan Meteorological Agency, NCEP/NCAR reanalysis dataset, sea surface temperature and rainfall data. The results indicated that there is a significant two-season lead negative correlationship between the previous heat content of the WPWP and the summer rainfall over the middle and lower reaches of the Yangtze River, and it is an important indicator for prediction that the smaller anomalies of the 0～200 m heat content averaged from November to January in the key area (166.5°E—173.5°W, 7.5°S—3.5°N) are followed by more rain in the middle and lower reaches of the Yangtze River. The baroclinic East Asia-Pacific (EAP) teleconnection stimulated by the previous heat content anomaly for its persistence in the WPWP may be the main reason that influences the summer rainfall in the middle and lower reaches of the Yangtze River. The negative heat content anomaly between the previous November and January in the key area leads to the formation and persistence of anomalous Philippine Sea anticyclone. In summer, the anticyclone expands northwestward and strengthens, and then the EAP teleconnection appears along the East Asian coast, which makes the middle and lower reaches of the Yangtze River and the area to its east in the Northwest Pacific subtropical region under the control of anomalous cyclone, and thus the middle and lower reaches of the Yangtze River becomes the area where cold air from the North and warm air from the South join together. At the same time, there exists a wave train of EAP pattern in the upper troposphere tilting to northwest compared to the middle and lower troposphere, so that the middle and lower reaches of the Yangtze River and the area to its south is under the control of anomalously stronger high, which is conducive to more rain in the middle and lower reaches of the Yangtze River with upper tropospheric divergence as well as middle and lower tropospheric convergence, and vice versa.

**Keywords** Western Pacific warm pool; Heat content; Summer rainfall over the middle and lower reaches of the Yangtze River; Precursory signal; Teleconnection

## 1 引言

长江中下游地区是我国东部经济发达地区之一,素有"鱼米之乡"之称,也是重要的工业基地,夏季旱涝与该地区经济的发展关系密切.例如,1998年长江大洪灾造成了3000亿人民币的经济损失(李春,2008),2011年的罕见干旱则推动了食品价格的大幅上涨.长江中下游夏季降水一直是我国实际业务预测工作的重点和难点,有关研究已经开展了很多,然而目前,无论是基于统计模式还是动力模式,我国汛期降水的短期气候预测业务的平均水平仅达60%～70%,而长江中下游地区的预测水平近十年来提高不大(Fan et al.,2008).

长江中下游夏季降水受到如太阳活动、地球自转速率、海气相互作用(魏凤英,2006)、北极涛动(龚道溢,2003;魏凤英,2006)、马斯克林高压和澳大利亚高压(Xue et al.,2003)、西太平洋副高(He et al.,2001)等诸多因子的影响,物理过程复杂,这给它的预测带来了困难.考虑到中国毗邻太平洋,而海洋是影响中国东部汛期降水的强信号,气象学者们给予了西太平洋海域热状况对长江中下游夏季降水的影响越来越多的关注.西太平洋暖池(简称暖池)是全球大洋海温最高的海域,也是全球大气对流最强烈和海气能量交换总量最大的地区(张启龙和翁学传,1999),它对于维持Walker环流的能量循环(Cornejo-Garrdo and Stone,1977;Hartmann et al.,1984)和驱动局域Hadley环流异常(Hu,1997)都有重要作用.暖池热状态变化对东亚气候异常有着重要影响,暖池上空对流活动异常可在北半球夏季激发出东亚—太平洋遥相关型(EAP或PJ型)(Nitta,1987;Huang and Wu,1989;Huang and Lu,1989),从而影响到西太平洋副高和我国东部夏季降水(Huang and Sun,1992;黄荣辉和孙凤英,1994a,1994b).Wang等(2000)强调了西北太平洋冷海温在菲律宾异常反气旋形成中的作用,该异常反气旋

持续存在进而影响到东亚副热带锋区降水. Ping 等(2006)指出暖池海温异常是影响长江流域汛期降水年际变化的关键因子. 李春(2008)研究表明长江中下游夏季降水和西北太平洋海温之间存在密切的耦合关系,这种耦合模态反映出东亚—太平洋地区上空低层风场为自南向北的 EAP 遥相关波列.

近年来,气象学者们开始引入热含量来表征暖池热状态. 因为,相比于海表温度,暖池区热含量具有更好的稳定性(王丽娟等,2011),不会出现因持续性显著下降而造成的"春季障碍"现象(McPhaden,2003). 另外,暖池热含量年际变率更大(陈永利和胡敦欣,2003),对太平洋大尺度海-气事件的响应也更加敏感(林传兰,1990),暖池热含量变异会对其上空的环流和气候产生重要作用(陈永利和胡敦欣,2003). 早期黄荣辉和孙凤英(1994a)及翁学传等(1996)已经注意到存在于暖池次表层海温和热含量中超前西太平洋副高和我国东部汛期降水变化的预测信息,卢楚翰等(2014)进一步提出前期冬季暖池区热含量可以作为夏季西太平洋副高变化和西北太平洋夏季风强度的有效预测因子. 那么,具体到长江中下游地区,暖池热含量与该地区夏季降水是否存在显著的超前相关关系,前期暖池热含量异常与长江中下游夏季降水关系到底如何,其影响夏季降水的前兆强信号是什么,以及影响长江中下游夏季旱涝的具体过程又如何? 本文以上述问题为着眼点,讨论了前期暖池热含量异常与长江中下游夏季降水的关系,提取出了夏季降水的预测信号,并对前期暖池热含量异常影响夏季降水的可能途径进行了探讨.

## 2　资料

本文所用资料有:日本气象厅提供的 1949—2010 年月平均历史海温资料(Ishii et al., 2006),水平分辨率为 1°×1°,垂直深度共 24 层,根据研究需要仅选取了海水上部的 16 层(0、10、20、30、50、75、100、125、150、200、250、300、400、500、600、700 m). 参考白虹和胡敦欣(1989)的方法,利用海温资料计算得到全球各格点上从海水深度 $z_0$ 到 $z_1$($z_0<z_1$)范围单位面积水柱所含的热含量,单位为 $W\cdot s\cdot m^{-2}$;大气资料取自 NCEP/NCAR 的月平均再分析数据集(Kalnay et al., 1996),水平分辨率为 2.5°×2.5°,时间跨度为 1950—2010 年;1951—2010 年全中国 160 站逐月降水资料由中国国家气候中心提供,并将 6—8 月的和作为夏季降水. 为考察中国区域以外地区的降水分布,还使用了美国国家海洋和大气管理局(NOAA)提供的 1951—2010 年月平均降水重建数据集(PREC)资料(Chen et al., 2002),该数据集来源于台站观测和卫星资料,已为降水距平,水平分辨率为 2.5°×2.5°,夏季降水也是 6—8 月之和;此外,还采用了英国 Hadley 中心提供的 1950—2010 年月平均海表温度资料(Rayner et al., 2003),水平分辨率为 1°×1°,以及 CPC(NOAA 气候预测中心)提供的 1950—2010 年逐月的 Niño3.4 指数.

## 3　长江中下游夏季降水的时空分布特征

旋转经验正交函数(REOF)分解得到的各分量能够着重表现空间要素场的局部相关结构,使单个空间型的分布特征简明直观,相应的方差贡献只集中在某一局部区域,而使其他区域的方差贡献尽量减小,旋转后各分量方差贡献率也要比旋转前均匀分散,而不像经验正交函数(EOF)分解那样将大部分的方差贡献集中在前几个模态上.

对中国东部地区(105°E 以东)120 个台站夏季降水进行 REOF 分解,得到第 1 模态(按方差贡献从大到小的顺序排列)解释了总方差的 7.73%,空间型载荷分量大值区位于长江中下游地区,如图 1a 中阴影区所示,与金啟华等(2012)选取的表征区域基本一致,28°N 附近为载荷分量达 0.8 的正中心,局地方差贡献率达 64%以上,第 1 模态对应的时间系数(以下称 Rpc1)如图 1b 所示. 为验证 Rpc1 作为长江中下游夏季降水序列的可靠性,计算图 1a 阴影区内 11 个站(杭州、屯溪、九江、岳阳、常德、宁波、衢县、浦城、贵溪、南昌和长沙站)的夏季平均降水量,求得其与 Rpc1 的相关系数高达 0.95,通过了 0.001 信度的 t 检验(以下信度检验均采用 t 检验方法). 如图 1b,二者随时间的变化高度一致,并呈现出明显的年际变化特征,20 世纪 50 年代初长江中下游夏季降水略偏少,1954、1955 年突然增加,随后直到 60 年代末期降水偏少,基本以负距平为主,70 年代初期到 90 年代初期降水波动起伏变化较大,降水距平正负交替,从 1993 年开始转为正距平,降水显著增强,2003 年之后转为负距平,直到 2008 年开始转为正距平. 以上表明 Rpc1 可以代表长江中下游夏季降水的变化情况.

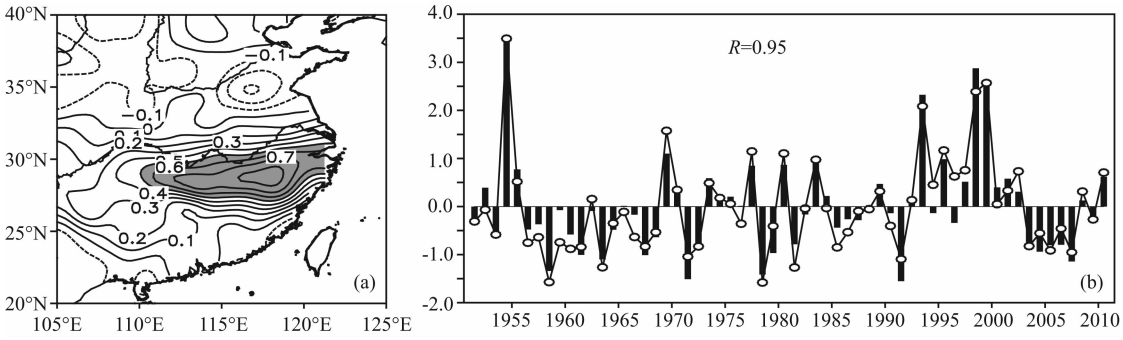


图1 1951—2010年中国东部夏季降水REOF第1模态空间型(阴影代表载荷分量≥0.5的区域)(a)及其时间系数Rpc1(柱状图)与标准化的11个台站夏季平均降水量(曲线)时间演变(b)

Fig. 1 First REOF mode of summer rainfall during 1951—2010 in eastern China

(a) Spatial pattern; (b) Corresponding time series Rpc1 (bars) and standardized average summer precipitation of 11 stations (curve). Shadings in (a) denote loading values no less than 0.5.

## 4 长江中下游夏季降水与暖池热含量的关系

为了提取长江中下游夏季降水的前兆信号,利用相关分析方法,来确定暖池区热含量影响长江中下游夏季降水的关键区、海水深度范围及关键时段.为方便叙述,本文将Rpc1(1951—2010年)对应年份的前一年称为上年,对应年份的当年称作当年.

首先计算Rpc1与前期各月(上年1月—当年5月)中国近海热含量的相关,发现从上年春季开始,暖池海域一直存在显著的负相关区,东海地区从当年1月开始也存在显著的正相关区,但范围没有暖池区大,持续时间也不比暖池区的长.图2(为0～200 m热含量情形,其他海水深度范围热含量与之类似)仅给出了上年11月到当年4月的相关分布,由图2可见上年12月暖池区热含量与长江中下游夏季降水的相关最好(图2b),因此选取图2b中位于暖池南部的赤道中太平洋海区(166.5°E—173.5°W,7.5°S—3.5°N)(黑色方框)作为前期暖池区热含量影响长江中下游夏季降水的关键区.

然后计算Rpc1与上年1月到当年5月关键区各海水深度范围热含量及海表温度的相关系数,如图3a所示,仅展示了有代表性的相关系数曲线.可见,前期各月关键区热含量与Rpc1的相关系数在各海水深度范围的变化趋势基本一致,海表温度和浅层海水(50 m以浅)热含量相关性较弱,其大小在−0.1～0.1之间变化,其他海水深度范围热含量均呈现出不同程度的负相关关系,随着海水深度的不断加深,相关性不断增强并趋于稳定,其中以0～200 m热含量与Rpc1的相关性最好,相关系数从上年7月到当年5月均超过了0.01信度检验,最大值达到−0.53,出现在上年12月,超过了0.001信度检验.此外,200 m也恰好代表了暖池区温跃层的大致深度(Meinen and McPhaden, 2000;陈永利等,2003),因此本文选取0～200 m作为前期暖池关键区热含量影响长江中下游夏季降水的关键海水深度范围.通过关键区12月0～200 m热含量的时滞自相关曲线(图3b)发现,暖池关键区热含量可从与基准月(12月)同年份的5月维持至来年11月,保持19个月之久,与基准月(12月)相关最好的月份有同年的11、12月以及来年的1、2、3和4月.

进而计算Rpc1与关键区前期各月(上年11月—当年4月)及滑动起止月平均的0～200 m热含量的相关系数,如表1(相关系数均通过了0.01信度检验)所示.若滑动开始月为上年11月,滑动终止月为当年1月,那么相关系数−0.5184即为Rpc1与关键区上年11月到当年1月平均的0～200 m热含量的相关系数,以此类推.由表1可知,最好的3个相关时段分别为:上年12月、上年11—12月和上年11—当年1月,鉴于上年11—当年1月时间跨度为3个月,更加稳定,因此本文选取上年11—当年1月作为暖池关键区热含量影响长江中下游夏季降水的关键时段.

根据上述分析,将关键区(166.5°E—173.5°W,7.5°S—3.5°N)关键时段(上年11月—当年1月)0～200 m热含量标准化,定义为暖池热含量指数(HCI).由HCI与Rpc1随时间的变化(图4a)可见,二者存在显著的负相关关系,相关系数达到了−0.52,我们也计算对比了去掉线性趋势前后前期11—1月暖池关键区0～200 m热含量与长江中下游11个站夏季平均降水量的相关系数,分别为−0.42和−0.43,显著通过了0.01信度检验.而前期冬季(上年12

月—当年 2 月平均)Niño3.4 指数与 Rpc1 相关系数仅有 0.16,并未通过 0.05 信度检验.这再次说明了西太平洋暖池热含量较 ENSO 对长江中下游夏季降水的影响和预测的优越性.

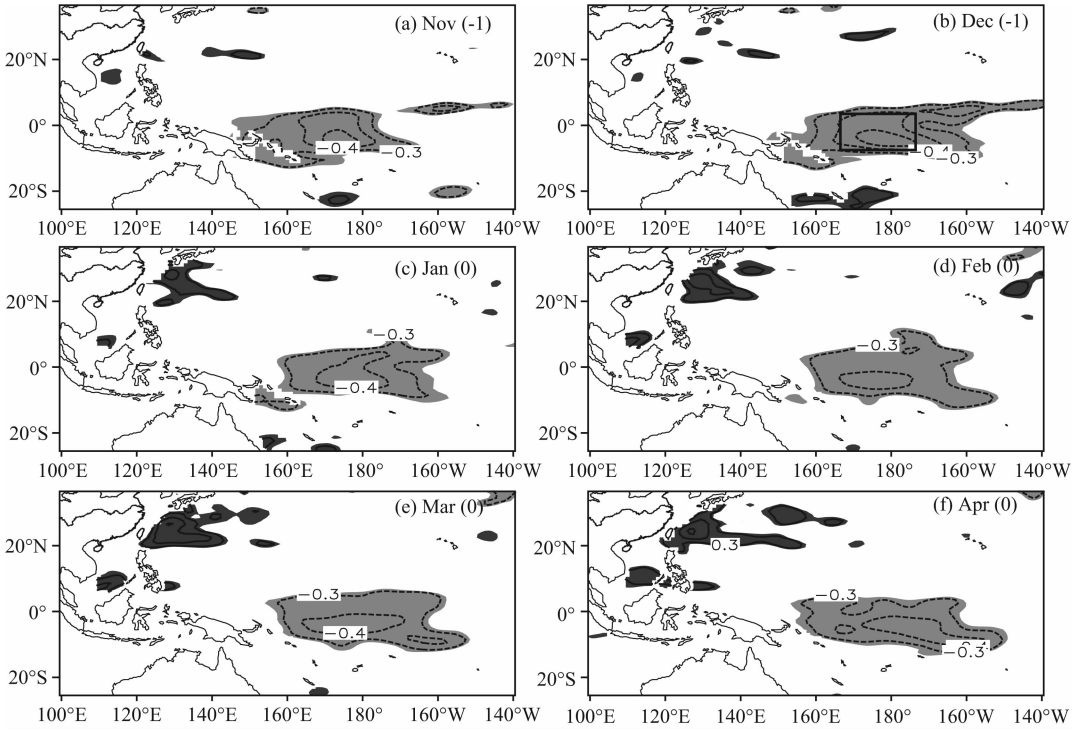


图 2　Rpc1(1951—2010 年)与上年 11 月—当年 4 月(a—f)0～200 m 热含量的相关分布图

等值线表示相关系数绝对值≥0.3,间隔为 0.1;深(浅)色阴影为通过 0.05 信度检验的正(负)相关区域.

Fig. 2　Distributions of monthly correlation coefficients between Rpc1 (1951—2010) and 0～200 m heat content for the period from previous November to simultaneous April (a—f)

Contours indicate absolute values of correlation coefficients exceeding 0.3 with an interval of 0.1. Dark (light) shadings indicate positive (negative) correlation areas that are significant at the 95% confidence level.

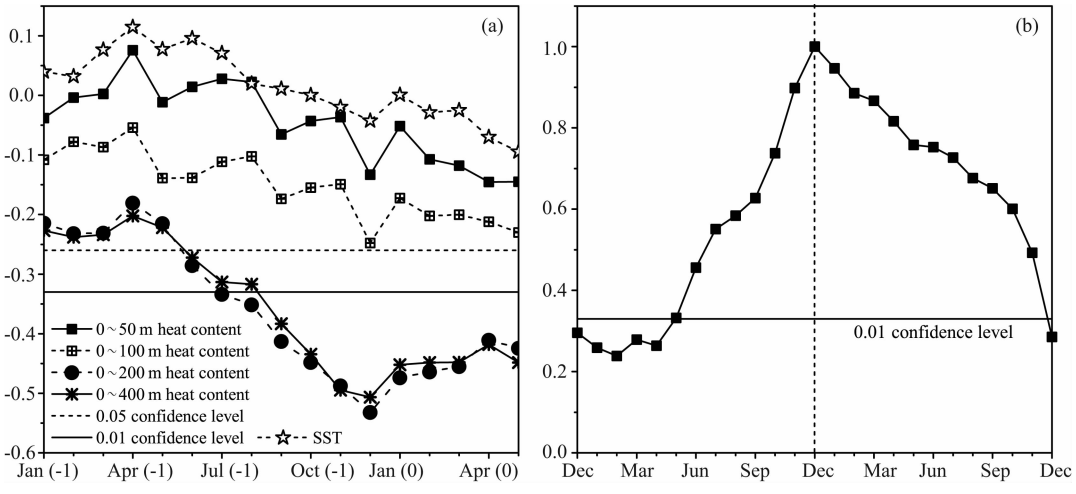


图 3　Rpc1(1951—2010 年)与关键区(166.5°E—173.5°W,7.5°S—3.5°N)各海水深度范围热含量及海表温度(上年 1 月—当年 5 月)的相关系数(a)和以 12 月(1950—2009 年)为基准月(已由竖直虚线标出)关键区 0～200 m 热含量的超前、同时、滞后自相关系数(b)

Fig. 3　Correlation coefficients between Rpc1 (1951—2010) and heat content from sea surface to various water depths and SST for each month from previous January to simultaneous May in the key area (166.5°E—173.5°W, 7.5°S—3.5°N) (a), and monthly lead, contemporary and lag self-correlations of 0～200 m heat content in the key area relative to December (1950—2009) which is used as the base month marked by the vertical dashed line (b)

**表 1 Rpc1(1951—2010 年)与关键区(166.5°E—173.5°W,7.5°S—3.5°N)前期各月及滑动起止月平均的 0～200 m 热含量的相关系数**

**Table 1 Correlation coefficients between Rpc1 (1951—2010) and 0～200 m heat content in the key area (166.5°E—173.5°W, 7.5°S—3.5°N) for the previous each month (i. e. the previous November, December, simultaneous January, February, March and April) against itself and each of the following months till simultaneous April inclusive of this month**

| 滑动开始月 | 滑动终止月 | 相关系数(Rpc1,热含量) | 滑动开始月 | 滑动终止月 | 相关系数(Rpc1,热含量) |
|---|---|---|---|---|---|
| 上年 11 月 | 上年 11 月 | −0.4874 | 当年 1 月 | 当年 1 月 | −0.4738 |
| | 上年 12 月 | −0.5214 | | 当年 2 月 | −0.4726 |
| | 当年 1 月 | −0.5184 | | 当年 3 月 | −0.4711 |
| | 当年 2 月 | −0.5145 | | 当年 4 月 | −0.4617 |
| | 当年 3 月 | −0.5093 | 当年 2 月 | 当年 2 月 | −0.4640 |
| | 当年 4 月 | −0.4995 | | 当年 3 月 | −0.4632 |
| 上年 12 月 | 上年 12 月 | −0.5319 | | 当年 4 月 | −0.4511 |
| | 当年 1 月 | −0.5077 | 当年 3 月 | 当年 3 月 | −0.4552 |
| | 当年 2 月 | −0.4991 | | 当年 4 月 | −0.4378 |
| | 当年 3 月 | −0.4929 | 当年 4 月 | 当年 4 月 | −0.4108 |
| | 当年 4 月 | −0.4824 | | | |

以 0.9$\sigma$ 为阈值,HCI 高于 0.9$\sigma$ 的 9 个暖异常年(1967/1968、1978/1979、1980/1981、1989/1990、1990/1991、1996/1997、2001/2002、2003/2004、2004/2005)中,只有 2 年(1996/1997 和 2001/2002)Rpc1 为正;HCI 低于 −0.9$\sigma$ 的 8 个冷异常年(1965/1966、1982/1983、1983/1984、1987/1988、1991/1992、1992/1993、1997/1998、1998/1999)中,只有 1 年(1965/1966)Rpc1 为负.表明前期 11—1 月暖池区热含量偏高(低)时,对应着长江中下游夏季降水偏少(多).

以 Rpc1 大于 1(小于−1)的标准来选取长江中下游夏季多(少)雨年,其结果列于表 2 中.多雨年中仅有 1 年(1969 年)HCI 为正距平,其余 5 年 Rpc1 均与 HCI 反相对应,反号率达 83.3%.少雨年中有 4 年 HCI 为正距平,反号率为 50%,其余 4 年(1958、1967、1971 和 1978 年)Rpc1 与 HCI 同号,而这 4 个少雨年对应的 HCI 值在 −0.20～−0.002 之间,此时夏季降水的偏少可能受其他因子影响更大.可见,相比于前期 11—1 月暖池区热含量异常偏高的前兆信号,其异常偏低对随后长江中下游夏季降水偏多的影响更加显著.

将冷异常年(1982/1983、1983/1984、1987/1988、1991/1992、1992/1993、1997/1998 和 1998/1999 年,共 7 年)与暖异常年(1967/1968、1978/1979、1980/1981、1989/1990、1990/1991、2003/2004 和 2004/2005 年,共 7 年)夏季降水作差值,由 160 站降水资料得出的结果(图 4b)来看,整个中国东部地区,仅长江中下游地区存在大范围显著的降水正距平区,其南北分别为负距平区.根据 PREC 降水资料(图 4c),中国东部降水距平分布与图 4b 基本一致,并且长江中下游地区的降水正距平一直延伸至日本东部洋面,日本南部的降水中心区达到了 0.05信度水平,与 6、7 月发生在中国长江中下游及日本的梅雨分布相似.总言之,前期 11—1 月暖池区 0～200 m 热含量的冷暖异常对长江中下游夏季降水、及占主要贡献的梅雨有重要的预测意义,特别是对长江中下游夏季降水多寡的预测有一定的针对性.

**表 2 1951—2010 年夏季长江中下游地区多、少雨年**

**Table 2 The years of wet and dry summers in the middle and lower reaches of the Yangtze River for 1951—2010**

| | | | | | | | | |
|---|---|---|---|---|---|---|---|---|
| 多雨年(共 6 年) | 1954* | 1969 | 1983* | 1993* | 1998* | 1999* | | |
| 少雨年(共 8 年) | 1958 | 1961* | 1963* | 1967 | 1971 | 1978 | 1991* | 2007* |

注:* 表示 Rpc1 与 HCI 反相对应的年份.

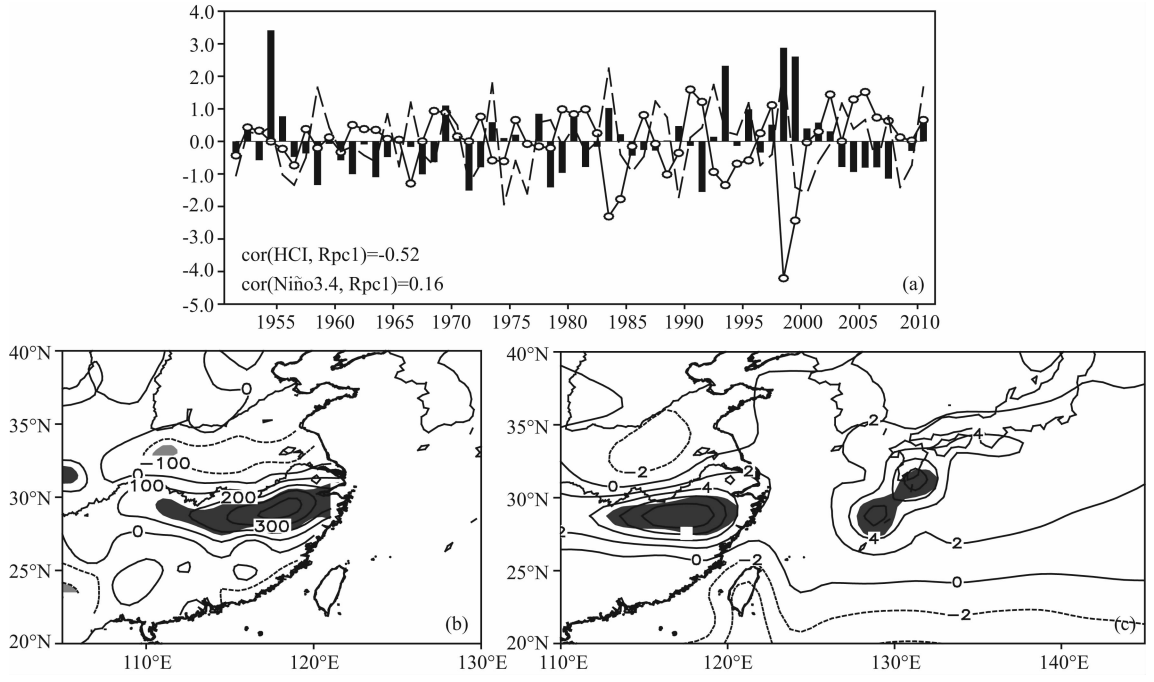


图 4　1951—2010 年 HCI(曲线)、冬季 Niño3.4 指数(虚线)和 Rpc1(柱状图)随时间的变化(a)和冷异常年与暖异常年夏季降水差值图(b. 国家气候中心160站降水资料，单位：mm；c. PREC，单位：mm·d$^{-1}$；深(浅)阴影表示通过0.05信度检验的正(负)降水距平)

Fig. 4　Time series of HCI (curve), preceding DJF Niño3.4 index (dashed line), and Rpc1 (bars) for 1951—2010 (a), and composite differences of summer rainfall between the anomalous cold and warm years in the key area obtained according to precipitation data of 160 stations provided by National Climate Centre (unit: mm) (b) and PREC (unit: mm·d$^{-1}$) (c). Dark (light) shadings indicate positive (negative) precipitation anomalies that are significant at the 95% level of confidence

## 5　前期暖池区热含量异常影响长江中下游夏季旱涝的可能原因

由暖池关键区 0～200 m 热含量(1—12 月)时滞(+)1 至(+)12 个月的自相关系数分布(图略)可以看出，暖池区热含量几乎全年每个月都可保持至少 7 个月的显著相关，秋、冬季持续性最好，可保持超前 11～12 个月的显著联系，夏季次之，春季有所下降. 可见，暖池关键区热含量异常具有较好的持续性，前期 11—1 月的热含量异常可保持 11～12 个月的超前自相关，从而持续到夏季.

前期 11—1 月暖池区热含量异常约两个季节的持续存在，必然会对东亚—太平洋地区大气环流造成持续的影响. 图 5 为前期冬(上年 12 月—当年 2 月平均)、春季(当年 3—5 月平均)和当年夏季(当年 6—8 月平均)逐个季节 850 hPa 风场异常分布，由负 HCI 回归的结果(图 5a—5c)可见，前期冬季西太平洋广大海域上空为异常反气旋，我国华南地区上空出现异常气旋，日本海上空异常反气旋正在形成(图 5a)；春季西太平洋上空异常反气旋中心位于菲律宾以东洋面，位于华南地区的异常气旋依然存在，日本海上空出现异常反气旋(图 5b)；当年夏季菲律宾异常反气旋向西北扩展至我国华南沿海地区并加强，呈东西向带状分布，原位于华南上空的异常气旋则移至华东及其以东洋面，日本海上空异常反气旋向北移至鄂霍次克海地区附近. 从而，东亚大陆沿岸(110°E—150°E)形成经向拉长的类似 EAP 型遥相关波列(Nitta，1987；Huang and Wu，1989；Huang and Lu，1989). 长江中下游及其以东的西北太平洋副热带地区都受到异常气旋的控制，有利于水汽在该区域辐合，同时，长江中下游地区为河套东部东北风距平与西太平洋副高西北侧西南风距平的交汇区，为降水的偏多创造了条件(图 5c)；当前期暖池区热含量为正异常时，则相反. 冷异常年与暖异常年(图 5d—5f)、多雨年与少雨年(图 5g—5i)差值图的季节演变特征与上述负 HCI 回归结果基本一致. 前期冬季至当年夏季 500 hPa 环流异常(图略)特征与 850 hPa 类似，不再赘述. 中低层风场异常分布特征随季节的演变存在一定的连续性，位于暖池西北侧菲律宾异常反气旋的持续存在正是前期暖池区热含量异常通过Gill响应持续影响大气环流的结果，夏

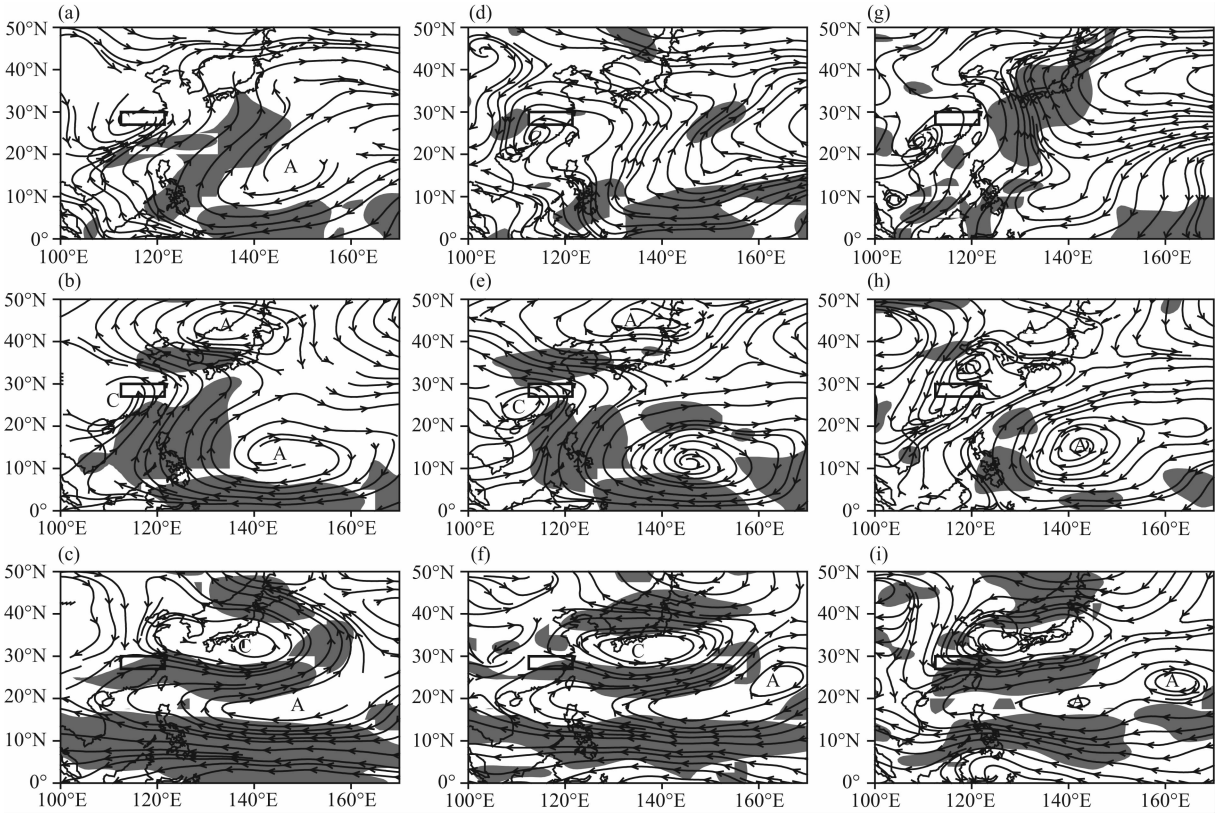


图 5 前期冬(a,d,g)、春季(b,e,h)和当年夏季(c,f,i)850 hPa 风场异常

(a—c)对负 HCI 回归的结果;(d—f)冷异常年与暖异常年的差值;(g—i)多雨年与少雨年的差值.

阴影表示通过 0.05 信度检验,矩形框表示长江中下游地区.

Fig. 5 Wind anomalies at 850 hPa for pre-winter (a,d,g), pre-spring (b,e,h) and simultaneous summer (c,f,i) obtained by regression onto reversed HCI (a—c), subtracting anomalous warm years from cold ones (d—f), and subtracting dry years from wet years (g—i)

Shadings indicate the wind anomalies pass the 95% significance level, and the rectangle boxes denote the area of the middle and lower reaches of the Yangtze River.

季菲律宾异常反气旋向西北方向扩展加强,东亚沿岸 EAP 型遥相关波列形成,直接影响长江中下游夏季降水的变化.

从前期冬季到当年夏季,高层 200 hPa 高度场异常上表现出不同于对流层中低层的环流分布特征,如图 6 所示,前期冬季东亚—西太平洋地区以 40°N 附近为界,呈现"南正北负"的位势高度异常分布,南海南部的菲律宾以西地区出现了位势高度正距平(图 6a,6d 和 6g);春季南海南部的位势高度正距平略向西北方向移动,冷、暖异常年的差值图(图 6e)上,位置更偏北,位于中南半岛上空.北太平洋中部(160°E,20°N)开始出现位势高度负距平,但强度较弱(−5～0 gpm),并有向北扩展的趋势(图 6b,6e 和 6h);当年夏季南海上空的位势高度正距平进一步北移至我国南部地区,强度加强.北太平洋中部的位势高度负距平增强,向北扩展,与贝加尔湖至日本海地区的位势高度负距平合并.50°N 以北的东北亚地区则出现了位势高度正距平(图 6c,6f 和 6i).从而东亚沿岸形成与对流层中低层相对应的类似 EAP 型的经向波列,但位置向北偏移约 10 个经度,且中心偏西,表现出一定的斜压性结构.中国南部地区及东海海域上空受异常偏强的高压控制,为长江中下游地区上空的对流提供了很好的辐散场.

在负 HCI 回归的结果,冷、暖异常年以及多、少雨年的差值图上,前期冬季到当年夏季东亚—西太平洋地区整层大气环流异常演变特征几乎一致,即前期暖池区热含量异常引起的环流异常与导致长江中下游夏季降水变化的环流异常能够较好吻合,前期暖池区热含量异常对长江中下游夏季降水影响显著.

上述分析中夏季东亚沿岸经向波列随高度的变化差异在对负 HCI 回归的沿 110°E—150°E 平均的垂直剖面涡度场异常上(图 7a)也有清晰体现,可以看出,对于冷异常年,对流层中低层(500 hPa 以下)

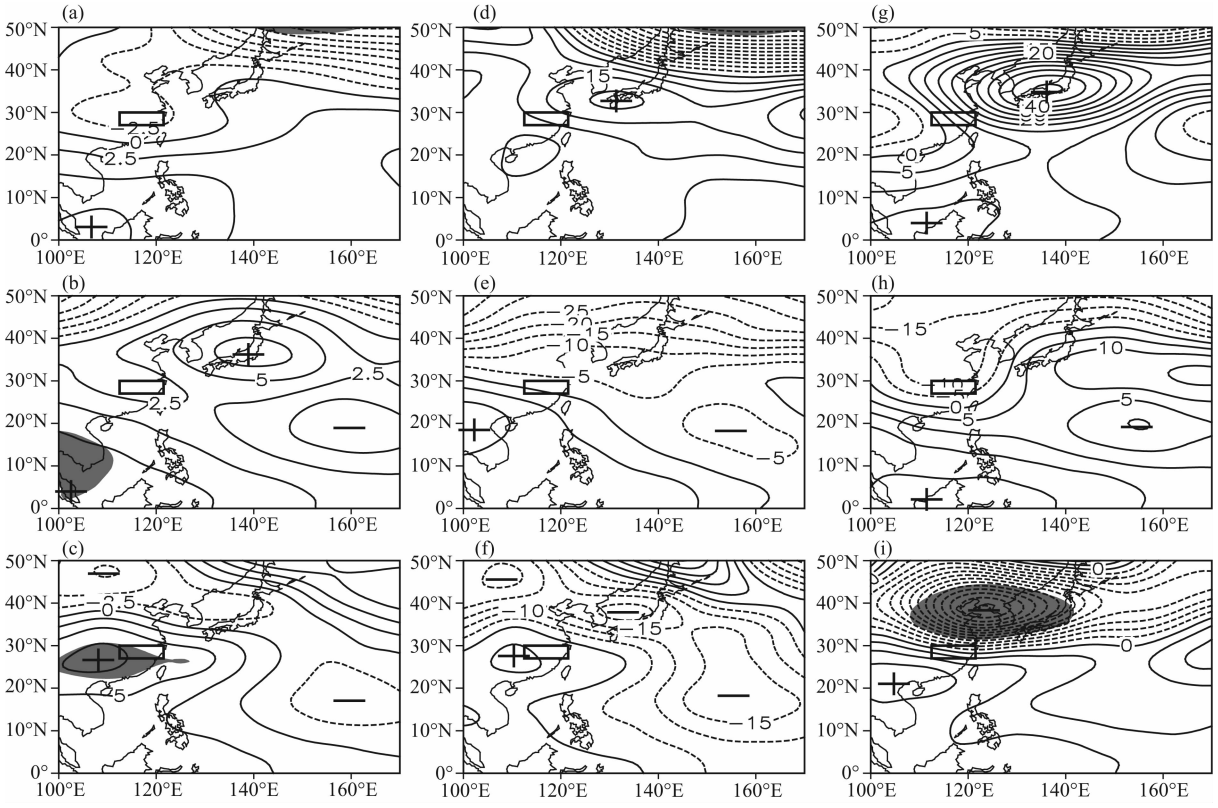


图 6　同图 5，但为 200 hPa 位势高度场异常

阴影表示通过 0.05 信度检验.(a—c)间隔 2.5 gpm；(d—i)间隔 5 gpm.

Fig. 6　As in Fig. 5 but for geopotential height anomalies at 200 hPa

Shadings indicate the geopotential height anomalies pass the 95% significance level, and the interval of contour is 2.5 gpm in (a—c) and 5 gpm in (d—i).

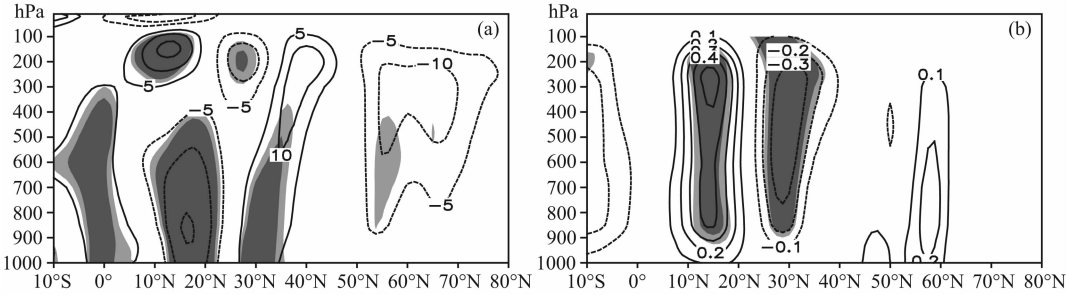


图 7　对负 HCI 回归的沿 110°E—150°E 平均的垂直剖面涡度场异常(单位：$\times 10^{-7}\,s^{-1}$)(a)和垂直速度 $\omega$ 场异常(单位：0.01 $Pa \cdot s^{-1}$)(b)

0 线已省略，深(浅)色阴影表示通过 0.05(0.10)信度检验.

Fig. 7　Vertical cross section of the vorticity anomalies (unit: $\times 10^{-7}\,s^{-1}$) (a) and vertical velocity $\omega$ anomalies (unit: 0.01 $Pa \cdot s^{-1}$) (b) averaged over 110°E—150°E regressed upon reversed HCI

The zero contour is omitted, and dark (light) shadings indicate the vorticity anomalies in (a) and $\omega$ anomalies in (b) pass the 95% (90%) significance level.

0°—70°N 和高层(200 hPa 附近)10°N—70°N 各有一个经向波列. 在对流层中低层赤道、15°N、30°N 和 55°N 附近分别存在一个显著的正、负、正、负的涡度异常中心，而对流层高层涡度异常中心与中低层存在约 10 个经度的向北偏移，表现出一定向北倾斜的斜压性结构，以中低纬地区更加明显. 长江中下游及其以南的地区高层为负涡度异常，与中低层相反，这种高层辐散中低层辐合的配置，使得长江中下游地区上空整层大气出现异常上升气流(图 7b)，有利于该地区对流的发展和降水的增多；对于暖异常年，则

相反.

为了进一步揭示冷、暖异常年夏季东亚沿岸经向波列是否具备 EAP 遥相关波列的特性,以及暖池区热含量异常在 EAP 波列形成中所起的作用,我们计算了 Takaya 和 Nakamura(2001)在准地转框架下提出的波作用通量,它与 Rossby 波群速度相平行,几乎独立于位相,能够用来诊断 Rossby 波能量的传播特征,波作用通量散度对于波源的位置也有较好的指示作用.

冷异常年合成的夏季 850 hPa 涡度场异常和波作用通量如图 8a 所示,可见涡度场异常上沿东亚沿岸(110°E—150°E)赤道西太平洋地区、菲律宾以东洋面(15°N)、中国长江中下游—日本南部一带(30°N)、东北亚地区(50°N)为"+−+−"的经向波列分布,波作用通量则由赤道西太平洋沿该经向波列向北指向中国长江中下游—日本一带附近,然后转向东北方向经过中国东北地区、鄂霍次克海到达阿留申地区.在暖异常年夏季,如图 8c 所示,东亚沿岸(110°E—150°E)涡度异常与冷异常年(图 8a)位相相反,只是中国长江中下游—日本一带负涡度异常强度偏弱,中心偏向日本以南.波作用通量表现出与冷异常年基本一致的特征,但是由热带西太平洋向北指向长江中下游的波作用通量强度比冷异常年夏季弱,随后 Rossby 波能量向北的传播也明显减弱.可见,无论冷异常年还是暖异常年夏季,赤道西太平洋的暖池区都是波作用通量的源地(或者外强迫源),这在冷、暖异常年合成的夏季 850 hPa 波作用通量散度场(图略)上也得以证实,暖池区为波作用通量辐散区,Rossby 波能量由该地区向北频散出去.

冷异常年合成的夏季 200 hPa 涡度场异常和波作用通量如图 8b 所示,涡度场异常上也表现出与低层 850 hPa(图 8a)较一致的"+−+−"的经向波列

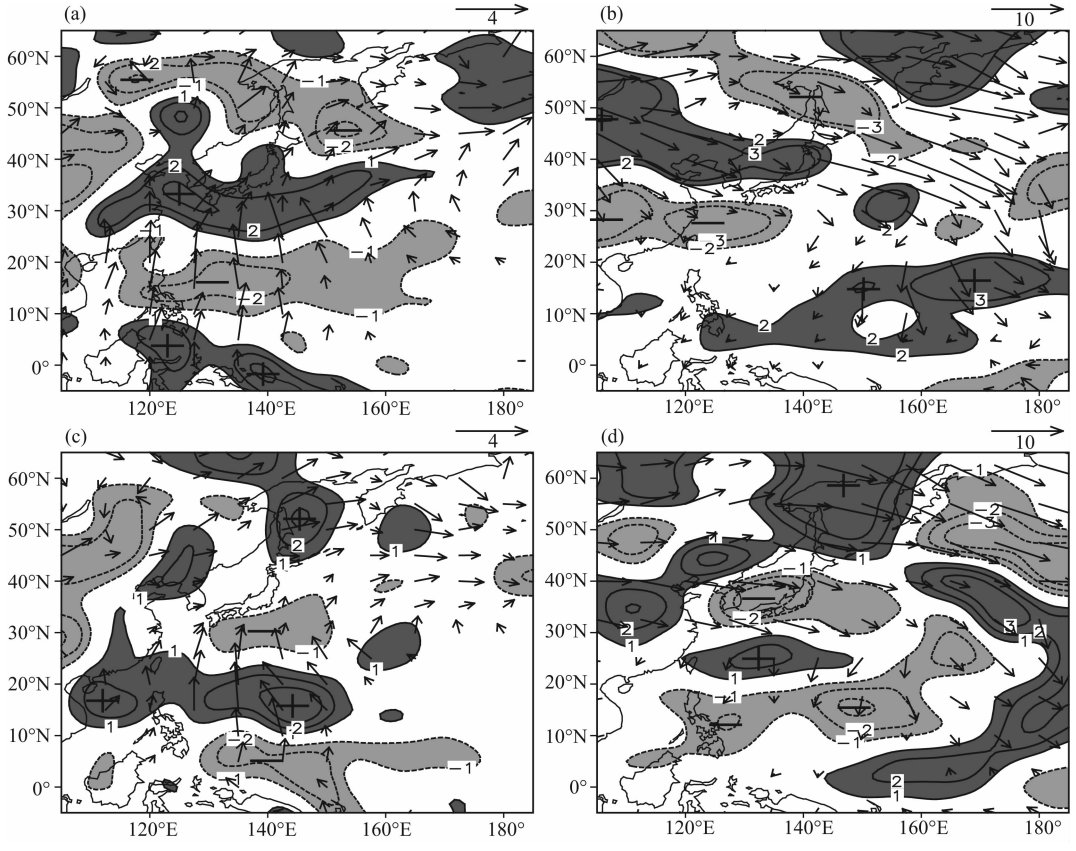


图 8 冷(a,b)、暖(c,d)异常年合成的夏季 850 hPa(a,c)和 200 hPa(b,d)涡度场异常(等值线,单位:$\times10^{-6}s^{-1}$,间隔:$1\times10^{-6}s^{-1}$,0 线已省略,且(b)图省略了$\pm1\times10^{-6}s^{-1}$,深(浅)色阴影表示正(负)涡度异常)和波作用通量(矢量,单位:$m^2\cdot s^{-2}$,小于 0.5 $m^2\cdot s^{-2}$时不显示)

Fig. 8 Composite vorticity anomalies (contours, unit: $\times10^{-6}s^{-1}$) and wave activity flux (vectors, unit: $m^2\cdot s^{-2}$) at 850 hPa (a,c) and 200 hPa (b,d) in the summers of cold (a,b) and warm (c,d) years in the key area. Solid and dashed lines denote positive and negative values with contour intervals of $1\times10^{-6}s^{-1}$. Zero contour lines in all panels and $\pm1\times10^{-6}s^{-1}$ contour lines in (b) are omitted. Dark (light) shadings indicate the positive (negative) vorticity anomalies. Fluxes smaller than 0.5 $m^2\cdot s^{-2}$ are not plotted

分布特征,但是中心位置向北向西偏移.而波作用通量则与低层有着明显不同,东亚沿岸的波作用通量由中纬度向南指向低纬度地区,这种 Rossby 波能量从中纬度地区向南频散可能与经向基本气流有关(Takaya and Nakamura,2001).亚洲大陆中高纬地区波作用通量向东指向贝加尔湖附近,然后分为两支,分别向东北和东南方向传播至阿留申地区和太平洋.在暖异常年夏季,如图 8d,涡度场异常上东亚沿岸(120°E—150°E)出现与冷异常年夏季(图 8b)符号相反的"－＋－＋"经向波列,中心位置较低层 850 hPa(图 8c)也向北向西偏移,但向西偏移不如冷异常年明显.波作用通量表现出与冷异常年(图 8b)基本一致的特征,但东亚沿岸特别是西北太平洋地区 Rossby 波能量的向南频散更强烈.

冷、暖异常年夏季东亚沿岸低层波作用通量向北传播(图 8a 和 8c),高层向南传播(图 8b 和 8d),证实了东亚沿岸经向波列具备 EAP 波列在对流层高、低层表现出的显著特征(Kosaka and Nakamura,2006);而暖池区热含量异常正是激发出夏季 EAP 型遥相关波列的外强迫源.

## 6　结论和讨论

本文针对长江中下游夏季降水与暖池热含量的关系以及前期暖池热含量异常影响长江中下游夏季降水的可能原因进行了探讨,主要结论如下:

(1)前期暖池热含量与长江中下游夏季降水存在超前 2 个季节的显著负相关关系,前期 11—1 月暖池关键区(166.5°E—173.5°W,7.5°S—3.5°N)0～200 m热含量的偏低(高)对长江中下游夏季降水偏多(少)的预测有重要指示意义.

(2)从前期冬季到当年夏季,在负 HCI 回归的结果,冷、暖异常年以及多、少雨年的差值图上,东亚—西太平洋地区整层大气环流异常演变特征几乎一致,即前期暖池区热含量异常引起的环流异常与导致长江中下游夏季降水变化的环流异常能够较好吻合,前期暖池区热含量异常对长江中下游夏季降水影响显著.

(3)前期 11—1 月暖池区热含量异常约两个季节的持续存在,对东亚—太平洋地区大气环流造成持续的影响.前期暖池热含量异常偏低导致其西北侧异常反气旋形成,冬季该异常反气旋位于广阔的西太平洋海域,春季位于菲律宾以东洋面,夏季菲律宾异常反气旋向西北方向扩展加强,东亚沿岸 EAP 型遥相关形成,使得长江中下游及其以东的西北太平洋副热带地区受到异常气旋的控制,有利于水汽辐合,而长江中下游地区又是北方冷空气与南方暖湿气流的交汇区,为降水的偏多创造了条件.同时,对流层高层东亚沿岸亦存在经向分布的 EAP 波列,但位置较中低层向西北偏移,使得 EAP 波列在整层大气表现出一定的斜压性结构.长江中下游及其以南为异常偏强高压,为长江中下游地区上空的对流提供了很好的辐散场,这种高层辐散中低层辐合的配置,有利于该地区对流的发展和降水的增多;反之亦然.前期暖池热含量异常的持续存在,及其外强迫作用激发的具有一定斜压性结构的夏季 EAP 型遥相关,可能是影响长江中下游夏季降水的主要原因.

值得注意的是,本文讨论的降水模态是利用 REOF 方法对中国东部夏季降水分区得到的,能够反映长江中下游夏季降水地域性特点的一个典型模态,其他降水异常分布型与暖池热含量关系如何,需要进一步研究.长江中下游夏季降水影响因子众多,过程复杂,因此在预测时比较困难.本文只是讨论了前期暖池热含量异常对长江中下游夏季降水的影响,仍然不排除其他海域热含量的影响.在暖池热含量异常年份,对流层高层中高纬度波作用通量向东传播,继而在贝加尔湖附近转向东南传播(图 8b 和 8d),对长江中下游夏季降水可能也有所影响,那么前期暖池热含量与夏季中高纬度环流以及长江中下游夏季降水之间的可能联系,也是下一步值得探讨和分析的.

## References


Bai H, Hu D X. 1989. A preliminary analysis of the heat content distribution and change in the Philippine sea. *Marine Sciences* (in Chinese), (3): 7-12.

Chen M Y, Xie P P, Janowiak J E, et al. 2002. Global land precipitation: A 50-yr monthly analysis based on gauge observations. *Journal of Hydrometeorology*, 3(3): 249-266.

Chen Y L, Hu D X. 2003. The relation between the South China Sea summer monsoon onset and the heat content variations in the tropical western Pacific warm pool region. *Acta Oceanologica Sinica* (in Chinese), 25(3): 20-31.

Chen Y L, Bai X Z, Zhao Y P. 2003. Relationship between summer rainfall anomalies over Shandong and the western tropical Pacific warm pool areas thermal state and summer monsoon variability. *Studia Marina Sinica* (in Chinese), (45): 29-39.

Cornejo-Garrido A G, Stone P H. 1977. On the heat balance of the Walker circulation. *J. Atmos. Sci.*, 34(8): 1155-1162.

Fan K, Wang H J, Choi Y J. 2008. A physically-based statistical forecast model for the middle-lower reaches of the Yangtze River valley summer rainfall. *Chinese Science Bulletin*, 53(4): 602-609.

Gong D Y. 2003. Arctic Oscillation's significance for prediction of East Asian summer monsoon rainfall. *Meteorological Monthly* (in Chinese), 29(6): 3-6.

Hartmann D L, Hendon H H, Houze R A Jr, et al. 1984. Some implications of the mesoscale circulations in tropical cloud clusters for large-scale dynamics and climate. *J. Atmos. Sci.*, 41(1): 113-121.

He J H, Zhou B, Wen M, et al. 2001. Vertical circulation structure, interannual variation features and variation mechanism of western Pacific subtropical high. *Advances in Atmospheric Sciences*, 18(4): 497-510.

Hu Z Z. 1997. Interdecadal variability of summer climate over East Asia and its association with 500 hPa height and global sea surface temperature. *J. Geophys. Res.*, 102(D16): 19403-19412.

Huang R H, Wu Y F. 1989. The influence of ENSO on the summer climate change in China and its mechanism. *Adv. Atmos. Sci.*, 6(1): 21-32.

Huang R H, Lu L. 1989. Numerical simulation of the relationship between the anomaly of subtropical high over East Asia and the convective activities in the western tropical Pacific. *Adv. Atmos. Sci.*, 6(2): 202-214.

Huang R H, Sun F Y. 1992. Impacts of the tropical western Pacific on the East Asian summer monsoon. *J. Meteor. Soc. Japan*, 70(1): 243-256.

Huang R H, Sun F Y. 1994a. Impacts of the thermal state and the convective activities in the tropical western warm pool on the summer climate anomalies in East Asia. *Scientia Atmospherica Sinica* (in Chinese), 18(2): 141-151.

Huang R H, Sun F Y. 1994b. Impact of the convective activities over the western tropical Pacific warm pool on the intraseasonal variability of the East Asian summer monsoon. *Scientia Atmospherica Sinica* (in Chinese), 18(4): 456-465.

Ishii M, Kimoto M, Sakamoto K, et al. 2006. Steric sea level changes estimated from historical ocean subsurface temperature and salinity analyses. *Journal of Oceanography*, 62(2): 155-170.

Jin Q H, Wang H, Jiang H, et al. 2012. Impacts of the variations in the intensity of the northern Pacific subtropical ocean circulation on the rainfalls over the middle and lower reaches of the Changjiang River. *Acta Oceanologica Sinica* (in Chinese), 34(1): 64-70.

Kalnay E, Kanamitsu M, Kistler R, et al. 1996. The NCEP/NCAR 40-year reanalysis project. *Bull. Amer. Meteor. Soc.*, 77(3): 437-471.

Kosaka Y, Nakamura H. 2006. Structure and dynamics of the summertime Pacific-Japan teleconnection pattern. *Quart. J. Roy. Meteor. Soc.*, 132(619): 2009-2030.

Li C. 2008. Coupling mode analysis of summer precipitation in mid-low valley of Yangtze River and sea surface temperature in northwest Pacific. *Journal of Tropical Oceanography* (in Chinese), 27(4): 38-44.

Lin C L. 1990. Some features of heat content changes of the ocean upper layer in northwest Pacific during 1964-1982. *Tropic Oceanology* (in Chinese), 9(2): 78-85.

Lu C H, Huang L, He J H, et al. 2014. Interannual variability of heat content in western Pacific warm pool and its impact on the eastern Asian climatic anomaly. *Journal of Tropical Meteorology* (in Chinese), 30(1): 64-72.

McPhaden M J. 2003. Tropical Pacific ocean heat content variations and ENSO persistence barriers. *Geophysical Research Letters*, 30(9), 1480, doi: 10.1029/2003GL016872.

Meinen C S, McPhaden M J. 2000. Observations of warm water volume changes in the equatorial Pacific and their relationship to El Niño and La Niña. *Journal of Climate*, 13(20): 3551-3559.

Nitta T. 1987. Convective activities in the tropical western Pacific and their impact on the northern hemisphere summer circulation. *J. Meteor. Soc. Japan*, 65(3): 373-390.

Ping F, Luo Z X, Ju J H. 2006. Differences between dynamics factors for interannual and decadal variations of rainfall over the Yangtze River valley during flood seasons. *Chinese Science Bulletin*, 51(8): 994-999.

Rayner N A, Parker D E, Horton E B, et al. 2003. Global analyses of sea surface temperature, sea ice, and night marine air temperature since the late nineteenth century. *J. Geophys. Res.*, 108(D14), 4407, doi: 10.1029/2002JD002670.

Takaya K, Nakamura H. 2001. A formulation of a phase-independent wave-activity flux for stationary and migratory quasigeostrophic eddies on a zonally varying basic flow. *J. Atmos. Sci.*, 58(6): 608-627.

Wang B, Wu R G, Fu X H. 2000. Pacific-East Asian teleconnection: How does ENSO affect East Asian climate? *Journal of Climate*, 13(9): 1517-1536.

Wang L J, Wang H, Jin Q H, et al. 2011. A preliminary analysis on the relationship between the South China Sea summer monsoon onset and the upper heat content during the previous period in this region. *Acta Oceanologica Sinica* (in Chinese), 33(4): 49-61.

Wei F Y. 2006. Relationships between precipitation anomaly over the middle and lower reaches of the Changjiang River in summer and several forcing factors. *Chinese Journal of Atmospheric Sciences* (in Chinese), 30(2): 202-211.

Weng X C, Zhang Q L, Yan T Z. 1996. Variation of the subsurface water heat content in the tropical western Pacific warm pool area and its relation to precipitation in eastern China and to the western Pacific subtropical high. *Studia Marina Sinica* (in Chinese), (37): 1-9.

Xue F, Wang H J, He J H. 2003. Interannual variability of Mascarene high and Australian high and influence on summer rainfall over East Asia. *Chinese Science Bulletin*, 48(5): 492-

497.

Zhang Q L, Weng X C. 1999. Analysis of heat content of the tropical western Pacific warm pool. *Plateau Meteorology* (in Chinese), 18(4): 584-589.

## 附中文参考文献

白虹, 胡敦欣. 1989. 菲律宾海热含量分布及其变化的初步探讨. 海洋科学, (3): 7-12.

陈永利, 胡敦欣. 2003. 南海夏季风爆发与西太平洋暖池区热含量及对流异常. 海洋学报, 25(3): 20-31.

陈永利, 白学志, 赵永平. 2003. 山东夏季降水与西太平洋暖池区海洋热状态及夏季风异常. 海洋科学集刊, (45): 29-39.

龚道溢. 2003. 北极涛动对东亚夏季降水的预测意义. 气象, 29(6): 3-6.

黄荣辉, 孙凤英. 1994a. 热带西太平洋暖池的热状态及其上空的对流活动对东亚夏季气候异常的影响. 大气科学, 18(2): 141-151.

黄荣辉, 孙凤英. 1994b. 热带西太平洋暖池上空对流活动对东亚夏季风季节内变化的影响. 大气科学, 18(4): 456-465.

金啟华, 王辉, 姜华等. 2012. 北太平洋副热带海洋环流强度异常对长江中下游夏季降水的影响. 海洋学报, 34(1): 64-70.

李春. 2008. 长江中下游夏季降水与西北太平洋海温的耦合模态分析. 热带海洋学报, 27(4): 38-44.

林传兰. 1990. 1964—1982 年热带西北太平洋海洋上层热含量的变化特征. 热带海洋, 9(2): 78-85.

卢楚翰, 黄露, 何金海等. 2014. 西太平洋暖池热含量年际变化及其对东亚气候异常的影响. 热带气象学报, 30(1): 64-72.

王丽娟, 王辉, 金啟华等. 2011. 南海夏季风爆发与冬春季南海上层海洋热含量关系的初探. 海洋学报, 33(4): 49-61.

魏凤英. 2006. 长江中下游夏季降水异常变化与若干强迫因子的关系. 大气科学, 30(2): 202-211.

翁学传, 张启龙, 颜廷壮. 1996. 热带西太平洋暖池域次表层水热含量变化及其与我国东部汛期降水和副高的相关关系. 海洋科学集刊, (37): 1-9.

张启龙, 翁学传. 1999. 热带西太平洋暖池表层热含量分析. 高原气象, 18(4): 584-589.

(本文编辑　何燕)

doi:10.11676/qxxb2014.067 气象学报

# 欧亚北部2004年以来频繁冷冬的特征分析及机理初探*

乔少博[1] 沈柏竹[2] 王晓娟[3] 封国林[1,4]
QIAO Shaobo[1] SHEN Baizhu[2] WANG Xiaojuan[3] FENG Guolin[1,4]

1. 扬州大学物理科学与技术学院,扬州,225002
2. 吉林省气象科学研究所,长春,130062
3. 常熟理工学院物理与电子工程学院,常熟,215500
4. 国家气候中心气候研究开放实验室,北京,100081
1. *College of Physical Science and Technology, Yangzhou University, Yangzhou* 225002, *China*
2. *Jilin Meteorological Science Institute, Changchun* 130062, *China*
3. *College of Physics and Electronic Project, Changshu Institute of Technology, Changshu* 215500, *China*
4. *Laboratory for Climate Studies, National Climate Center, China Meteorological Administration, Beijing* 100081, *China*
2013-12-19 收稿,2014-06-05 改回.

乔少博,沈柏竹,王晓娟,封国林. 2014. 欧亚北部2004年以来频繁冷冬的特征分析及机理初探. 气象学报,72(6):1143-1154
**Qiao Shaobo, Shen Baizhu, Wang Xiaojuan, Feng Guolin. 2014. Feature analysis and preliminary causes study of the frequent cooling winter in northern Eurasia since 2004. *Acta Meteorologica Sinica*, 72(6):1143-1154**

**Abstract** By using the monthly NCEP/NCAR reanalysis datasets of 1961－2013, anomalous features and potential causes of the frequent cooling winter in northern Eurasia (40°－65°N, 50°－120°E) since 2004 are analyzed in this paper. The results show that: Cooling winters took place frequently in northern Eurasia since 2004, but there is a notable difference in the distribution of temperature anomalies, especially the cold center position. It shows that 2005, 2009, 2010 and 2012 appear as whole-region-colder years, while 2004, 2007 and 2011 as south-region-colder years. The whole-region-colder years are mainly caused by the significant negative phase of the Arctic Oscillation (AO), and the corresponding SST features are zonally distributed with a Northeast-Southwest "positive-negative-positive" pattern from high latitudes, middle latitudes to low latitudes in the North Atlantic, which is beneficial to continuous negative phase of the Arctic Oscillation/North Atlantic Oscillation (AO/NAO). While south-region-colder ones were caused by the enhanced Ural-Baikal (UB) blocking with the AO/NAO generally in the weak positive phase, which mainly corresponds to the warm SST in the middle latitudes of the North Atlantic, and secondly to "similar La Niña events" under the Pacific Decadal Oscillation (PDO) negative phase. Both of the SST anomalies above can accelerate the Rossby waves which is similar to the Eurasian Teleconnections pattern and is helpful to enhanced UB blocking and trough activities in central Aisa. Either in the circulation or SST anomalies, the two types of cooling winters in northern Eurasia since 2004 are similar to the corresponding typical years in history.
**Key words** Northern Eurasia, Frequent cooling winter, AO, North Atlantic

**摘 要** 利用1961—2013年NCEP/NCAR发布的月平均全球再分析资料,分析了欧亚北部(40°—65°N,50°—120°E)2004年以来频繁冷冬的异常特征及形成机理。结果表明:欧亚北部2004年以来冷冬频繁发生,但温度异常的空间分布,尤其中心冷

* 资助课题:国家自然科学基金(41375078、41175067、41305075、41105055)、国家重点基础研究发展计划项目(2012CB955902、2013CB430204)。
作者简介:乔少博,主要从事冬季冷事件等研究。E-mail: qiaoshbokuailemore@163.com
通讯作者:封国林,主要从事短期气候预测等研究。E-mail: fenggl@cma.gov.cn

区的位置有显著差异,主要表现为全区偏冷型(2005、2009、2010、2012 年)和南部偏冷型(2004、2007、2011 年)。全区偏冷年主要由北极涛动(AO)显著负位相所致,对应海表温度特征为北大西洋高、中、低纬度成东北—西南走向的"+、-、+"带状分布,该分布有利于北极涛动/北大西洋涛动(AO/NAO)负位相维持和增强;南部偏冷年大气内部活动异常为乌拉尔—贝加尔湖阻塞高压偏强,北极涛动/北大西洋涛动以弱正位相为主,对应主要海表温度特征为北大西洋中部偏高,其次则为太平洋年代际振荡(PDO)负位相下"类拉尼娜事件",上述海表温度异常均可促进类似欧亚遥相关的罗斯贝波列形成,有利于乌拉尔—贝加尔湖阻塞高压偏强、亚洲中部多低槽活动。2004 年以来欧亚北部两种类型冷冬的大气环流与海表温度均表现出与历史典型年相类似的特征。

**关键词** 欧亚北部,频繁冷冬,北极涛动,北大西洋

**中图法分类号** P434 P429

## 1 引 言

在全球变暖的背景下,中国乃至欧亚大部分地区的气温成显著升高的趋势(赵宗慈等,2005;唐国利等,2009)。然而近年来欧亚地区冬季大范围极端低温事件却频繁发生。例如,2004/2005 年冬季,中国出现了两次大范围寒潮过程,改变了 1986 年以来大部分地区连续出现 18 个暖冬的局面(马晓青等,2008);2005/2006 年欧洲经历近一个世纪最冷冬季(Scaife, et al, 2008);2008 年 1 月,中国南方出现了历史罕见的持续性冰冻雨雪灾害(王凌等,2008);2009/2010、2010/2011 年冬季,极端低温/暴雪侵袭了北半球大部分国家和地区(孙诚等,2012;Wang, et al, 2013);2012 年 1—2 月,寒流横扫欧亚大陆,一些地区甚至出现了近百年来的最低气温记录(兰晓青等,2013)。

冬季大范围持续性极端低温事件给人们的生活和生产活动带来了极大的破坏,对此类事件的成因进行分析,并对其提前进行预测具有重大意义。近年来围绕冬季低温频发的情况开展了大量研究,如围绕 2004/2005 年冬季两次大寒潮过程、2007/2008 年冬季低温雨雪冰冻事件等个例分析(马晓青等,2008;陶诗言等,2008;丁一汇等,2008;王东海等,2008;杨贵名等,2008;陶祖钰等,2008;王亚非等,2008;曾明剑等,2008;顾雷等,2008;Zhou, et al, 2009;谭桂容等,2010;Bueh, et al, 2011a;王阔等,2012);围绕近年来冬季区域性低温事件频繁发生对应的异常特征及其与历史类似时期的环流系统对比分析研究(Peng, et al, 2011;沈柏竹等,2012;Liu, et al, 2012;龚志强等,2012;王晓娟等,2012,2013);冬季持续较长的区域性低温事件形成对应大气系统中的大型的斜脊斜槽(Bueh, et al, 2011b),低频扰动(张宗婕等,2011;钱维宏,2012),阻塞高压配置(龚志强等,2013)等。但是,从季节尺度上来看,21 世纪初尤其 2004 年以来频繁冷冬温度异常分布情况差异显著,有的年份表现为整个欧亚大陆偏冷,有的年份仅仅局部地区偏冷,这种差异如何来区分,其形成的机理又有何异同。对这些问题的进一步深入研究,将有助于更好地认识和理解当前频繁冷冬的特征。鉴于此,选取 2004 年以来显著变冷的欧亚北部,对该区域冷冬主要类型进行划分,并就其形成可能机理开展初步探究。

## 2 资料和方法

所用资料来自 NCEP/NCAR 发布的全球逐月再分析资料,包括 2 m 温度场、分辨率为 2.5°×2.5°的海平面气压场和垂直方向自 1000 hPa 至 10 hPa 共 17 层的位势高度场、风场资料;分辨率为 2.0°×2.0°的 NOAA ERSST 的逐月海表温度资料(Smith, 2003);CPC 网站(ftp://ftp.cpc.ncep.noaa.gov/cwlinks)逐月的北极涛动、北大西洋涛动、Nino3.4 指数资料;时间均为 1961 年 1 月—2013 年 2 月;文中冬季定义为当年 12 月至次年 2 月,气候态取 1981—2010 年。

主要方法为经验正交函数分解(EOF),另外,还采用了合成分析以及相关分析的方法,并采用 $F$、$t$ 检验来检验其显著性。

## 3 2004 年以来冬季低温显著影响区

为了得到 2004 年以来冬季低温显著影响区,对 2004—2012 年冬季地面气温距平进行合成,得到图 1。由图 1 可知,40°N 以南除青藏高原、非洲东北部等显著升高外其他区域不明显;40°N 以北欧亚大陆以降低为主,最显著影响区域位于欧亚北部,气温距平低于 -1.0℃范围为 50°—120°E。因此,以气温距平低于 -1.0℃为标准,选取欧亚北部(40°—65°N,50°—120°E)作为气温异常典型区,并研究该区域 2004 年以来频繁出现冷冬的异常特征。

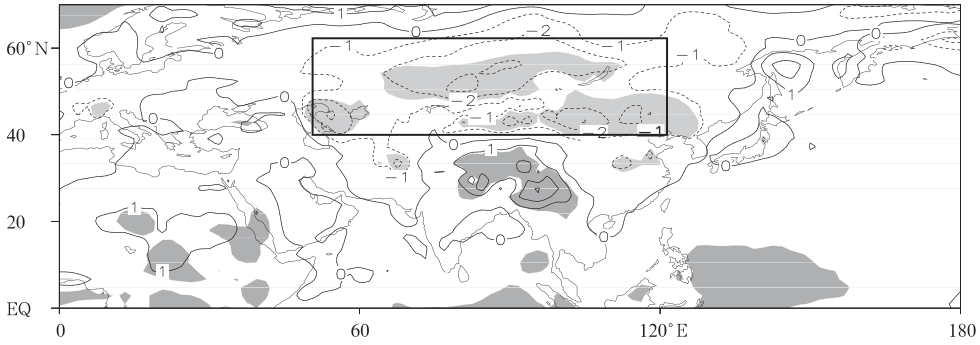


图1 2004—2012年冬季地面气温距平合成分布

(单位:℃;阴影区域表示通过信度为0.05的统计检验)

Fig. 1 Horizontal distribution of the composite surface air temperature anomalies (SATA) during the 2004－2012 winter seasons

(unit: ℃; the shaded area is significant at the confidence level of 0.95)

图2给出了1961—2012年冬季欧亚北部地面气温距平时间序列。由图2可知,欧亚北部总体成变暖趋势,线性趋势为0.16℃/(10 a),表现出明显"偏冷—偏暖—偏冷"的年代际变化特征。20世纪60—70年代气温显著偏低,其中1965—1979年出现11个偏冷年,20世纪80年代至21世纪初以偏高为主,其中1980—2003年出现20个偏暖年,2004年以来9 a出现7个偏冷年,近4年连续偏冷,冷冬进入频发期。经过11 a滑动平均处理后也表现出类似的年代际变化特征,两次转折分别发生在1982、2005年前后。

## 4 2004年以来欧亚北部两种类型冷冬对比

### 4.1 欧亚北部冬季气温异常的两个主模态

为了得到欧亚北部冬季气温异常的主要分布特征,对1961—2012年欧亚北部冬季地面气温距平进行经验正交函数分解。前两个模态解释方差达79%,按照North等(1982)的准则,这两个主分量彼此可分,并且可以和其他主分量区分开,因此可以表征该区域的冬季气温异常的主要分布型。从图3a的EOF1空间分布可以看出,第1模态表现为全区一致变化,变化幅度由北至南递减。结合图3b可知,$PC_1$正位相代表全区偏冷,负位相相反。与图2类似,$PC_1$年代际变化特征明显,20世纪60—70年代以偏冷为主,80—90年代以偏暖为主,21世纪以来气温下降趋势明显。从图3c的EOF2空间分布可以看出,第2模态表现为约以55°N为分界线南北气温成反相变化,南部变化幅度最大区域位于50°N以南,北部位于最北端。结合图3d可知,$PC_2$正位相代表55°N以南偏冷,以北偏暖,负位相相反。$PC_2$最大值出现在2011年,为2.61,最小值出现在1978年,为－2.61。

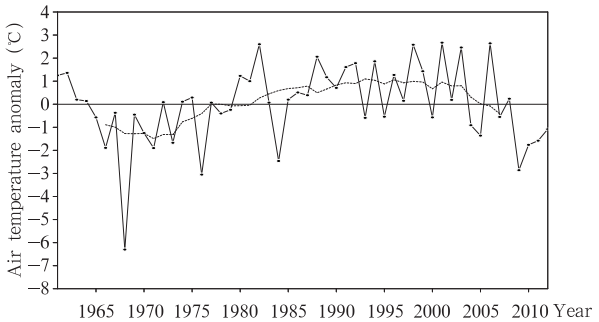


图2 1961—2012年冬季欧亚北部(40°—65°N,50°—120°E)地面气温距平时间序列

(单位:℃;虚线为11 a滑动平均序列)

Fig. 2 Time series of winter SATA in northern Eurasia (40°－65°N, 50°－120°E) for the period of 1961－2012

(unit: ℃; dotted line means the 11 years moving-average)

具体到一个特定年份的总方差而言,每个模态都有一定量解释方差。为了进一步区分前两个模态在任意年份的作用大小,如果该年第1模态(第2模态)解释方差为所有模态中最大,且解释方差超过35%,即表明这一具体年份气温异常主要表示第1模态(第2模态)的特征,这样即可挑选出所有以第1模态(第2模态)为主模态的典型年。进一步从这些年份中筛选出$PC_1$($PC_2$)大于0的年份,则为全区偏冷年(南部偏冷年),相反则为全区偏暖年(南部偏暖年)。

采用该定义后计算发现,52 a中以第1模态为

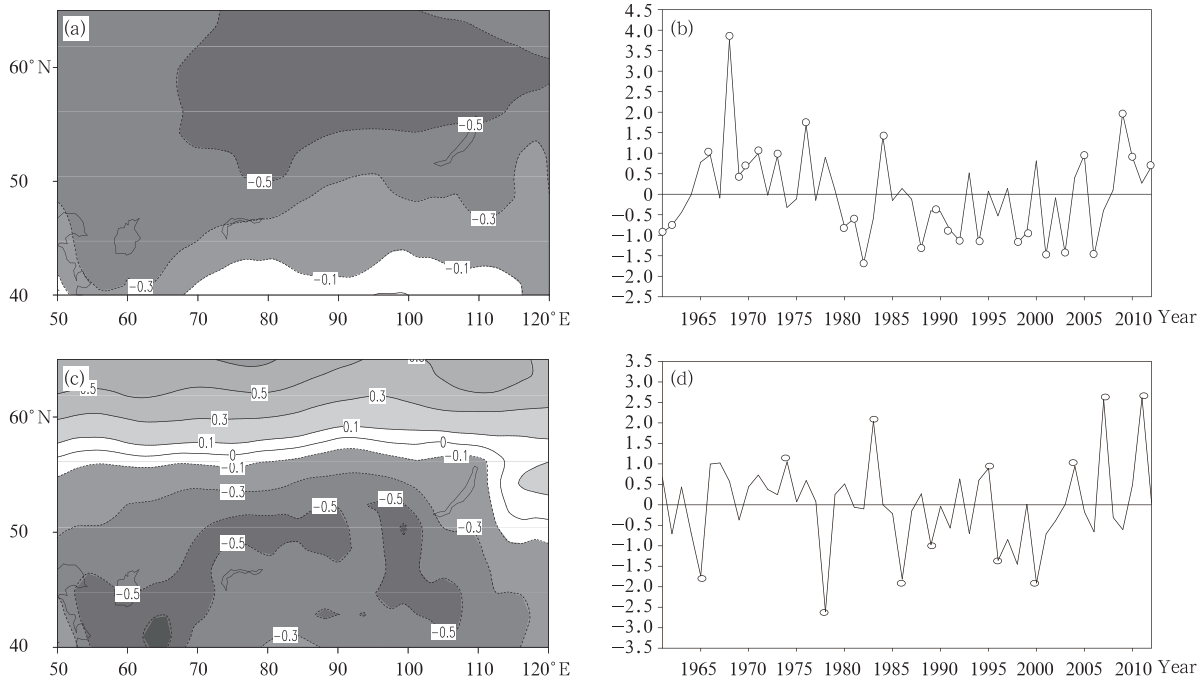


图 3 欧亚北部冬季气温距平场经验正交函数分解的前两个主模态

(a、b 分别为经验正交函数分解第 1 模态的空间分布型和对应标准化时间系数;c、d 同 a、b,但为第 2 模态)

Fig. 3 Two leading EOF modes of the winter air temperature anomalies in northern Eurasia: (a) Spatial pattern; (b) the corresponding normalized time coefficient of the first EOF mode; and (c) and (d) as in (a) and (b), respectively but for the second mode

主模态年份共有 27 个,全区偏冷年 12 个,全区偏暖年 15 个,平均解释方差达 72.2%;以第 2 模态为主模态年份为 12 个,南部偏冷、暖年均为 6 个,平均解释方差为 54.6%。前两个模态典型年分别以圆圈标记在图 3b、3d 中。欧亚北部 2004 年以来 9 a 中出现 7 个偏冷年(图 2),其中 2005、2009、2010、2012 年为第 1 模态典型年,均为全区偏冷年(图 3b),第 1 模态解释方差分别为 71%、87%、71% 及 56%;2004、2007、2011 年为第 2 模态典型年,均为南部偏冷年,第 2 模态解释方差分别达到 37%、78%、87%。

表 1 进一步给出欧亚北部 585 个格点所有全区偏冷年、南部偏冷年地面气温距平场与对应主模态距平相关系数(ACC)分布。从表中可以发现,所有典型年与对应主模态间距平相关系数大都在 0.5 以上,远超信度为 0.001 的统计检验,表明 2004 年以来全区偏冷年、南部偏冷年气温异常分布均与历史典型年非常相似。因此,下文分别对所有全区偏冷年、南部偏冷年做合成,对两种类型冷冬进行全面比较。

表 1 所有全区偏冷年、南部偏冷年地面气温距平场与对应主模态距平相关系数分布

Table 1 The ACC between the whole-region-colder years/south-region-colder years' SATA and the corresponding main mode for all the years

| EOF1 + 年份 | 1966 | 1968 | 1969 | 1970 | 1971 | 1973 |
|---|---|---|---|---|---|---|
| ACC 系数 | 0.34 | 0.93 | 0.73 | 0.58 | 0.50 | 0.52 |
| EOF1 + 年份 | 1976 | 1984 | 2005 | 2009 | 2010 | 2012 |
| ACC 系数 | 0.74 | 0.79 | 0.77 | 0.87 | 0.48 | 0.55 |
| EOF2 + 年份 | 1974 | 1983 | 1995 | 2004 | 2007 | 2011 |
| ACC 系数 | 0.65 | 0.92 | 0.71 | 0.54 | 0.93 | 0.94 |

### 4.2 欧亚北部两种类型冷冬温度场与环流场对比

图4分别给出了全区偏冷年与南部偏冷年地面气温距平合成分布。全区偏冷年气温距平场表现为显著偏低区域位于40°N以北的欧亚大陆,偏低中心位于60°N附近,气温距平低于-2.0℃范围为20°—130°E,40°N以南以偏高为主,比较显著区域位于非洲北部及青藏高原(图4a);南部偏冷年气温距平场约以55°N为分界线从北至南成"+、-"分布,60°N以北显著偏高,中心位于极区,50°N以南的亚洲大陆显著偏低,中心位于40°N附近,气温距平低于-2.0℃范围为50°—100°E(图4b)。从图4还可以看出,两个主模态不仅为欧亚北部两个主要异常气温分布类型,也可表征整个欧亚大陆异常温度主要分布特征。

气温异常与大气环流密切相关,图5分别给出了全区偏冷年与南部偏冷年环流距平场合成分布。在对流层上层200 hPa上,全区偏冷年45°N以北为东风异常带,中心位于60°N附近,表明极地急流偏弱,20°—40°N为西风异常带,显著区域位于北大西洋—地中海及中国西北(图5a);南部偏冷年表现出欧亚地区与北大西洋不一致的变化特征,欧亚地区在50°N附近为东风异常带,30°N附近为西风异常带,表明西、东亚副热带急流偏强,北大西洋表现为20°—45°N东风异常,45°—70°N西风异常(图5b)。在对流层中层500 hPa上,全区偏冷年从北至南呈"+、-"形势,60°N以北几乎全为显著正距平,中心位于极区,最大强度超过60 gpm。中纬度存在两个显著负距平中心,并且呈现出带状的分布特征,中心分别位于西欧沿岸和贝加尔湖,表明西欧沿岸高压脊偏弱、东亚大槽偏西偏强;南部偏冷年也表现出欧亚地区与北大西洋不一致的变化特征,欧亚地区在50°N以北地区为显著正距平,范围为50°—120°E,中心位于(65°N,80°E)附近,最大强度超过60 gpm,表明乌拉尔阻塞高压与贝加尔湖阻塞高压均偏强,两个显著负距平中心分别位于里海以东和日本中部,表明中亚多低压槽活动及东亚大槽偏强,北大西洋则表现为格陵兰岛南部为负距平,北大西洋中部为显著正距平(图5d)。在对流层底层海平面气压场上,全区偏冷年约以50°N为分界线从北至南成"+、-"分布,西伯利亚高压略偏强但位置偏北,北大西洋涛动区异常对应北大西洋涛动负位相(图5e);南部偏冷年欧亚大陆除青藏高原外均为正距平,显著正距平中心位于50°N附近,表明西伯利亚高压偏强,东亚冬季风加强,北太平洋中部为显著负距平,北大西洋涛动区异常对应北大西洋涛动正位相(图5f)。无论是全部偏冷年还是南部偏冷年,各层环流异常表现出相当正压结构。对欧亚北部的影响而言,全区偏冷年对流层上层60°N附近西风偏弱、40°N附近西风偏强有利于对流层中下层在50°N附近形成气旋式环流,相应西伯利亚高压略偏强,位置偏北;南部偏冷年对流层上层50°N附近西风偏弱、30°N附近西风偏强有利于对流层中、下层乌拉尔—贝加尔湖阻塞高压及西伯利亚高压显著偏强。

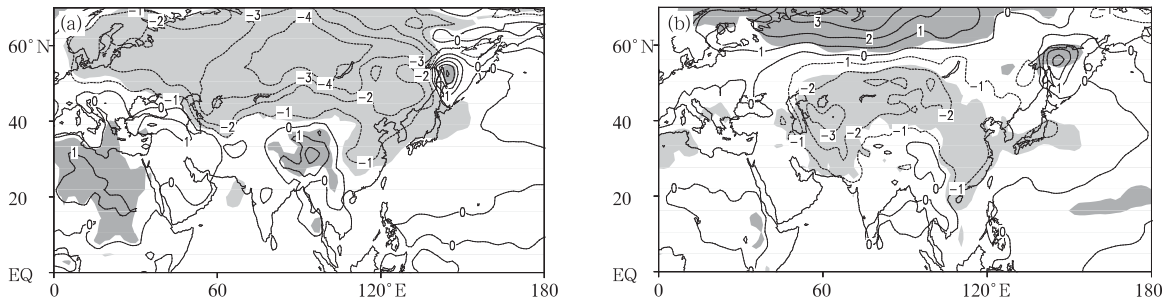


图4 (a) 全区偏冷年地面气温距平场合成分布,(b)同(a),但为南部偏冷年

(单位:℃;阴影区域表示通过信度为0.05的统计检验)

Fig. 4 (a) Horizontal distribution of SATA in whole-region-colder years, (b) as in (a) but for south-region-colder years

(unit: ℃; the shaded area is significant at the confidence level of 0.95)

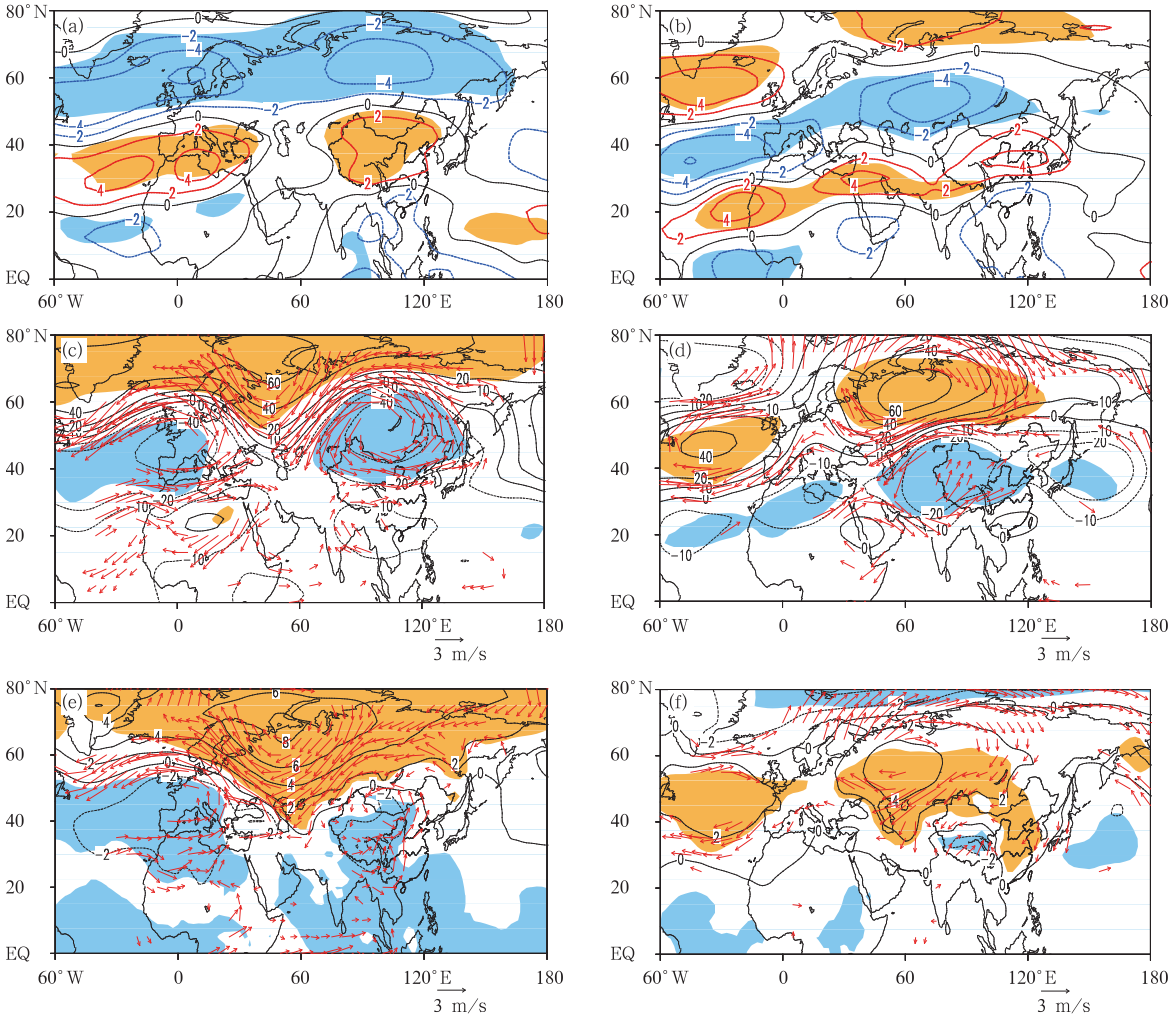


图 5 全区偏冷年大气环流距平场合成分布

(a. 200 hPa 纬向风场(m/s), c. 500 hPa 高度场(gpm)与风场(m/s), e. 海平面气压场(hPa)与 850 hPa 风场(m/s);
b、d、f 同 a、c、e,但为南部偏冷年环流距平场合成分布;阴影区域表示通过信度为 0.05 的统计检验)

Fig. 5 Horizontal distribution of the atmospheric circulation anomalies

(a) 200 hPa zonal wind (m/s), (c) 500 hPa geopotential height (gpm) and wind (m/s), and
(e) sea level pressure (hPa) and 850 hPa wind (m/s); (b), (d), (f) as in (a),
(c), (e) but for south-region-colder years

(The shaded area is significant at the confidence level of 0.95)

## 5 2004 年以来欧亚北部 4 个全区偏冷年形成机理初探

### 5.1 全区偏冷年显著大气内部异常活动特征及与海表温度的联系

从图 5 的分析可以看出,两种类型冷冬均对应北大西洋涛动区环流异常,而北极涛动在保留北大西洋涛动特征基础上对北半球热带外气候更具有代表性(Thompson, et al, 1998)。此外,相关研究表明,ENSO 对东亚冬季风强弱有较好指示意义,拉尼娜(厄尔尼诺)年有利于东亚冬季风偏强(偏弱),这种影响在中低纬度地区尤为明显(Li, 1990; Wang, et al, 2000, 2010)。因此,表 2 给出了 1961—2012 年 $PC_1$、$PC_2$ 与北极涛动、北大西洋涛动及 Nino3.4 指数同期相关系数,可以看出 $PC_1$ 与北极涛动、北大西洋涛动指数成显著负相关,尤其是北极涛动指数,相关系数达到 −0.64,通过了信度为 0.001 的统计检验 ,对 12 个全区偏冷年北极涛动指数与 $PC_1$

进行统计分析后发现,12 a中二者反位相变化年份有11个,准确率达到92%,且往往$PC_1$越大对应北极涛动负位相强度越高(图略),表明全区偏冷年与北极涛动关系确实密切。

表2 1961—2012年$PC_1$、$PC_2$与北极涛动、北大西洋涛动及Nino3.4指数同期相关系数分布

Table 2 The correlation coefficients between the time series of $PC_1/PC_2$ and AO/NAO/ Niño3.4 in the winters for the period of 1961-2012

(*, **, *** correspond to 0.10, 0.05, 0.001 significance levels)

| | 北极涛动 | 北大西洋涛动 | Nino3.4 |
|---|---|---|---|
| $PC_1$ | -0.64*** | -0.53*** | -0.01 |
| $PC_2$ | 0.25* | 0.30** | -0.26* |

上标*,**,***分别表示通过信度为0.10、0.05、0.001的统计检验

为了具体探究全区偏冷年与北极涛动负位相关系,图6给出了1961—2012年冬季北极涛动指数的相反数对同期环流场及海表温度场线性回归分布。从图中可以发现,当冬季北极涛动指数呈显著负位相时,500 hPa风场上从格陵兰岛、中西欧、乌拉尔山至贝加尔湖附近依次形成"+、-、+、-"的罗斯贝波列分布,对应高纬度西风减弱,极涡减弱,欧亚北部地区为异常气旋式环流(图6a),有利于极地冷空气南下并在欧亚北部聚集,从而导致全区偏冷(图6b),这与Hurrell(1995, 1996)、Thompson等(1998,2000)、龚道溢等(2000)、陈文等(2006)、谭本馗等(2007)、所玲玲等(2009)的相关研究是类似的。有关该过程的物理机制,李建平(2005a,2005b)、孙诚等(2012)指出,负位相的北极涛动会使费雷尔环流减弱,欧亚北部因异常北风及经向冷平流作用而降温。因此,北极涛动负位相是导致全区偏冷年的主要大气内部活动因子。

作为大气系统最主要的外强迫之一,海表温度一直是气象学家关注的重点。从图6a中冬季北极涛动指数的相反数回归的同期海表温度分布可以看出,北极涛动负位相时海表温度特征主要表现为北大西洋海表温度高、中、低纬度呈现出明显东北—西南走向的"+、-、+"带状分布以及太平洋年代际振荡正位相。对于北大西洋海表温度高、中、低纬度呈现出东北—西南走向的"+、-、+"带状分布而言,根据热成风原理,可通过非绝热加热造成北大西洋中、低(高)纬度间温度梯度增大(减小),西风增强(减弱),有利于北大西洋涛动/北极涛动负位相维持和增强,相互间存在一个正反馈过程(Watanabe, et al,2000)。对于太平洋年代际振荡正位相而言,有利于北太平洋出现显著气旋式环流,高纬度地区出现纬向东风异常,加强贝加尔湖附近气旋式环流,间接加强北极涛动负位相。因此,北大西洋海表温度高、中、低纬度成东北—西南走向的"+、-、+"带状分布有利于北极涛动负位相,太平洋年代际振荡正位相也产生一定影响。

### 5.2 2004年以来4个全区偏冷年北极涛动及海表温度实况特征

具体到2004年以来4个全区偏冷年显著大气内部活动异常而言,2005、2009、2010、2012年冬季北极涛动指数分别为-0.81、-3.42、-0.91、-1.12,均表现为显著负位相。图7则给出了4个全区偏冷年海表温度距平分布,其中2009、2010年冬季北大西洋高、中、低纬度海表温度成东北—西南走向的"+、-、+"带状分布特征非常显著,2005、2012年虽然北大西洋中纬度地区海表温度为正常态,但高、低纬度暖海表温度非常明显,同样类似于高、中、低纬度成东北—西南走向的"+、-、+"带状分布,但4个全区偏冷年太平洋年代际振荡指数差异较大,正、负位相均为2 a。因此,2004年以来4个全区偏冷年对应北极涛动负位相与北大西洋海表温度高、中、低纬度成东北—西南走向的"+、-、+"带状分布特征与历史上典型年是类似的,是导致4个全区偏冷年的重要原因。

## 6 2004年以来3个南部偏冷年形成机理初探

### 6.1 南部偏冷年显著大气内部异常活动特征及与海表温度的联系

由表1还可以看出,$PC_2$与同期北极涛动/北大西洋涛动指数为正相关,与Nino3.4指数为负相关,均通过了信度为0.10的统计检验。具体到2004年以来3个南部偏冷年可以发现,北极涛动/北大西洋涛动指数分别为0.11/0.59、0.86/0.38、0.65/1.05,Nino3.4指数距平值分别为0.53、-1.76、-0.92,即3个南部偏冷年中北极涛动/北大西洋涛动指数均为弱正位相,赤道中东太平洋出

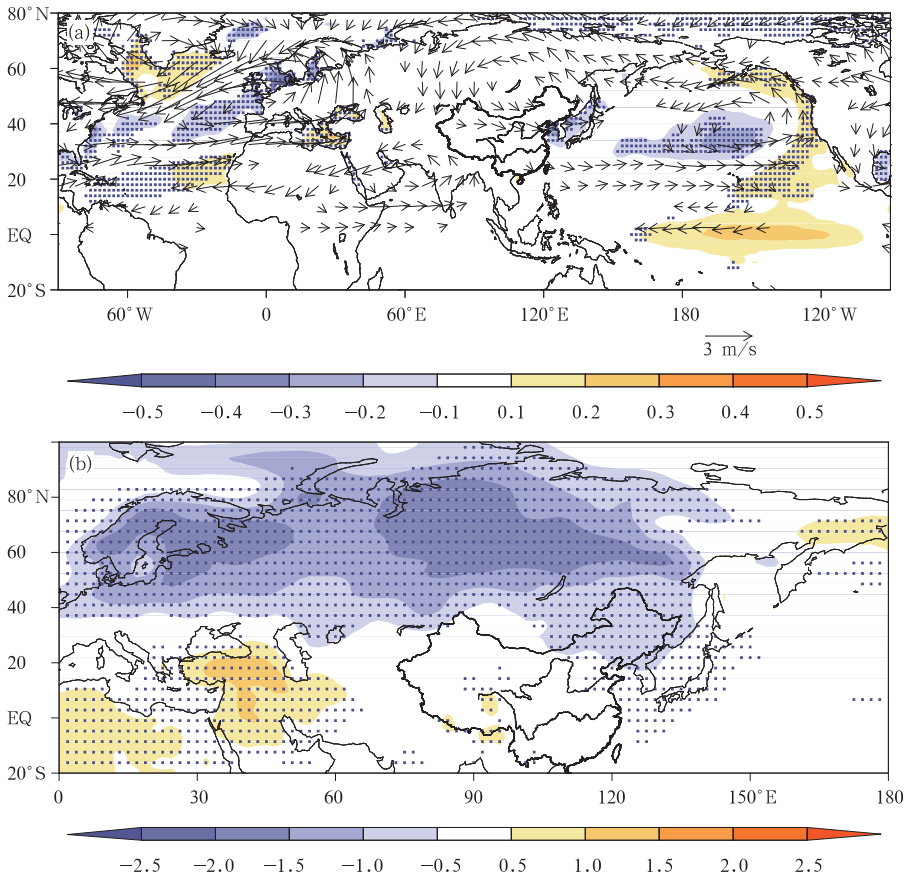


图 6 1961—2012 年冬季北极涛动指数的相反数对(a)500 hPa 风场(矢量箭头),海表温度(℃,阴影部分)及(b)地面气温场(℃)线性回归分布

(黑点表示通过信度为 0.05 的统计检验)

Fig. 6 Regression maps for (a) 500 hPa wind (m/s, vectors), SST (℃, shadings) and (b) surface air temperature (℃) on the inverted AO index for the 1961 − 2012 winter seasons

(black symbols are significant at the confidence level of 0.95)

现 2 个拉尼娜事件,对应关系较好。但如果采用北极涛动/北大西洋涛动指数为正位相且 Nino3.4 指数为显著负位相(距平低于 − 0.5℃)作为南部偏冷年发生判据的话,满足条件的 8 个年份有 4 a 为南部偏冷年,准确率只有 50%。因此,仅仅从北极涛动/北大西洋涛动弱正位相及持续拉尼娜事件来描述南部偏冷年特征既不充分也不够准确,应该关注更显著的大气内部活动异常及其对应整个海表温度背景。

对流层中层的环流系统是影响冷空气活动及气温变化的重要因子。从上文对图 5d 的分析可知,南部偏冷年 500 hPa 高度场最显著的环流特征表现为“北高南低”形势分布,乌拉尔—贝加尔湖阻塞高压偏强,亚洲中纬度地区多低槽活动,与南部偏冷年“北暖南冷”气温异常有很好的对应关系。因此以图 5d 中通过信度为 0.05 的统计检验区域为标准,定义指数 $I_{UB} = H^{*}_{(55°—70°N,40°—110°E)}$、$I_{MA} = -H^{*}_{(30°-45°N,60°-160°E)}$ 分别代表乌拉尔—贝加尔湖阻塞高压、亚洲中纬度低槽强度,这里 $H^{*}$ 代表 500 hPa 高度场区域平均的标准化值。分别计算 $PC_2$ 与上述两个指数相关系数发现,$PC_2$ 与 $I_{UB}$、$I_{MA}$ 关系非常密切,相关系数分别达到 0.65、0.54,均通过信度为 0.001 的统计检验。与此同时,$I_{UB}$、$I_{MA}$ 也有很强相关关系,相关系数为 0.75,远超过信度为 0.001 的统计检验。鉴于 $I_{UB}$ 与 $PC_2$ 相关系数更高且 $I_{UB}$ 基本可以反映 $I_{MA}$ 情况,因此选 $I_{UB}$ 作为南部偏冷年最显著大气内部活动异常因子。

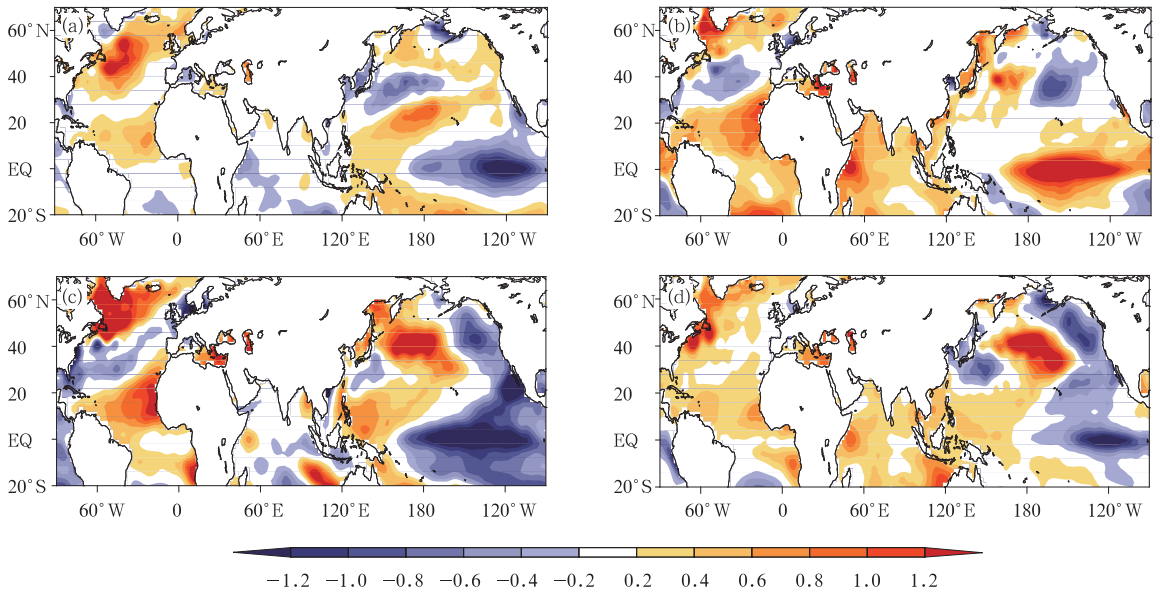


图 7 (a)2005、(b)2009、(c)2010、(d)2012 年冬季海表温度距平分布(阴影,℃)

Fig. 7 Horizontal distribution of SSTA in (a) 2005, (b) 2009, (c) 2010, and (d) 2012 winter season (shadings, ℃)

同样地,图 8 给出了 1961—2012 年冬季 $I_{UB}$ 对同期环流场及海表温度线性回归分布。从图 8a 可以发现,$I_{UB}$ 正异常时 500 hPa 风场从北大西洋中部至中东欧、乌拉尔—贝加尔湖地区、东北亚地区存在一个类似欧亚遥相关的"+、−、+、−"罗斯贝波列,欧亚地区 50°N 附近纬向西风减弱,东亚副热带急流轴大幅度增强,有利于南部偏冷年 50°N 以南亚洲大部分偏冷,55°N 以北欧亚地区由于异常反气旋活动反而偏暖(图 8b),这与龚志强等(2013)的相关研究是一致的。

从图 8a 中 $I_{UB}$ 回归的同期海表温度可以看出,$I_{UB}$ 正异常时北大西洋中部海表温度特征表现为 40°N 附近显著偏高,太平洋海表温度表现为"类拉尼娜事件"及太平洋年代际振荡显著负位相。当北大西洋中部海表温度偏高时,该地区上空出现显著反气旋式环流,对类似于欧亚遥相关的"+、−、+、−"罗斯贝波列产生起重要作用,有利于乌拉尔—贝加尔湖阻塞高压偏强,这与 Gambo 等(1983);顾雷等(2008)、Li 等(2012)的相关研究是一致的;当赤道太平洋表现出"类拉尼娜事件"时,会造成东亚副热带西风急流增强(Yang, et al, 2002),50°N 附近纬向西风相应减弱,有利于乌拉尔—贝加尔湖阻塞高压建立,且作用效果在太平洋年代际振荡负位相时更加显著(Wang, et al, 2008)。因此,乌拉尔—贝加尔湖阻塞高压偏强对应海表温度特征为北大西洋中部显著偏暖,其次则为太平洋年代际振荡负位相下"类拉尼娜事件"。

### 6.2 2004 年以来 3 个南部偏冷年 $I_{UB}$ 及海表温度实况特征

具体到 2004 年以来 3 个南部偏冷年显著大气内部活动异常而言,2004、2007、2011 年冬季 $I_{UB}$ 分别为 1.37、0.85、2.99,均表现为明显正异常。图 9 则给出了 3 个南部偏冷年海表温度距平分布,2004、2007 年北大西洋中部海表温度均为异常偏高,2011 年偏高程度稍弱甚至小范围偏低,但其上空异常反气旋式环流十分显著(图略),是造成 3 个南部偏冷年的重要原因。与此同时,2007、2011 年还为太平洋年代际振荡负位相下显著拉尼娜事件,相应南部偏冷程度更强($PC_2$ 均高于 2.5)。

## 7 结论和讨论

选取 2004 年以来冬季显著变冷的欧亚北部地区,并从历史相似角度分析了该区域频繁冷冬的异常特征及形成机理,得到以下结论:

(1) 2004 年以来冷冬频繁发生,显著影响区位于欧亚北部,1961—2012 年冬季欧亚北部气温表现出明显的"偏低-偏高-偏低"年代际变化特征。

(2)欧亚北部2004年以来频繁冷冬的温度异

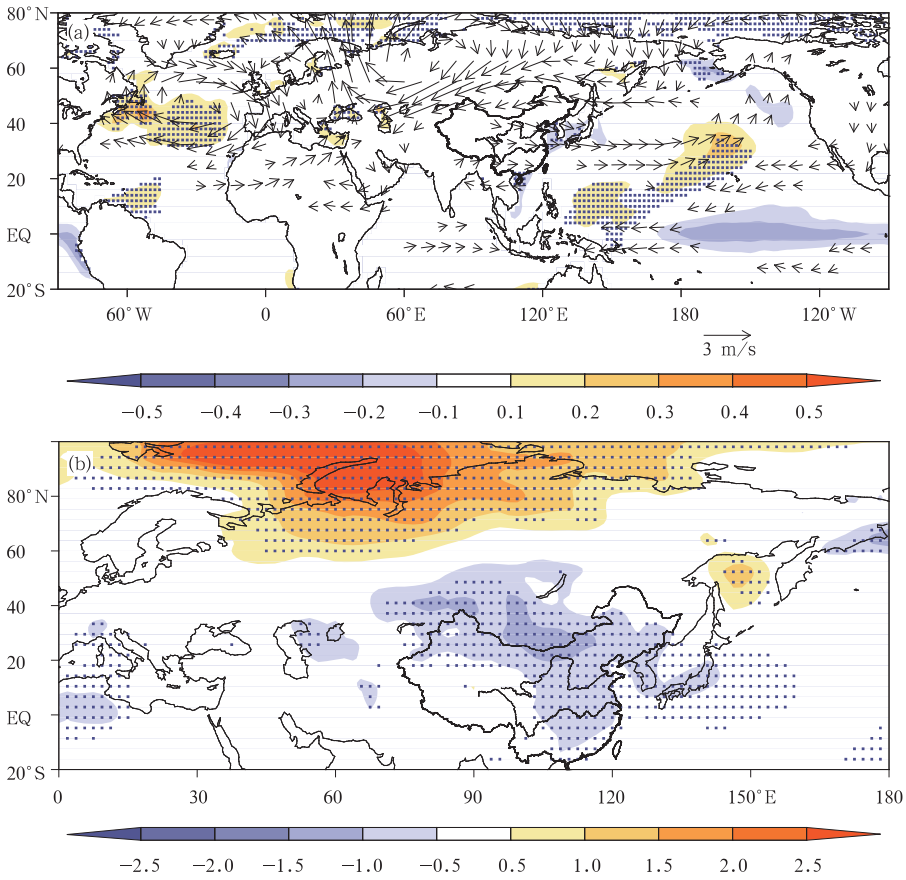


图 8 1961—2012 年冬季 $I_{UB}$ 对(a)500 hPa 风场(矢量箭头,m/s),海表温度(阴影,℃)及(b)地面气温场(℃)线性回归分布

(黑点表示通过信度为 0.05 的统计检验)

Fig. 8 Regression maps for (a) 500 hPa wind (vectors, m/s), SST (shadings, ℃) and (b) surface air temperature (℃) on the AO index for the 1961－2012 winter seasons

(black symbols are significant at the confidence level of 0.95)

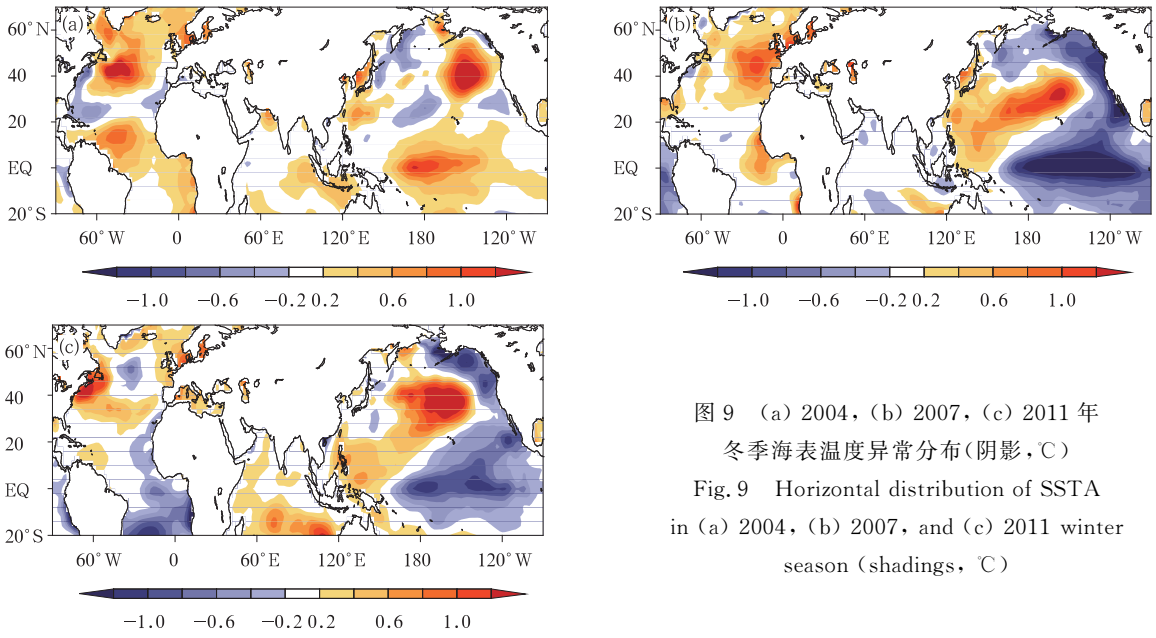


图 9 (a) 2004,(b) 2007,(c) 2011 年冬季海表温度异常分布(阴影,℃)

Fig. 9 Horizontal distribution of SSTA in (a) 2004, (b) 2007, and (c) 2011 winter season (shadings, ℃)

常有所差异。2005、2009、2010、2012年表现为全区偏低,全区偏低年气温场表现为40°N以北欧亚大陆显著偏低,中心位于60°N附近。2004、2007、2011年表现为50°N以南显著偏低,偏低中心位于40°N附近,60°N以北显著偏高。

(3) 全区偏冷年主要由北极涛动显著负位相所致,主要外强迫海表温度特征为北大西洋高、中、低纬度成东北—西南走向的"+、-、+"带状分布,该分布有利于北极涛动/北大西洋涛动负位相维持和增强;南部偏冷年北极涛动/北大西洋涛动特征不明显且以弱正位相为主,主要大气内部活动异常为乌拉尔—贝加尔湖阻塞高压偏强,主要外强迫海表温度特征为北大西洋中部海表温度偏高,其次则为太平洋年代际振荡负位相下"类拉尼娜事件",上述海表温度异常均可促进类似欧亚遥相关的罗斯贝波列活动,有利于乌拉尔—贝加尔湖阻塞高压偏强、亚洲中部多低槽活动。2004年以来欧亚北部两种类型冷冬在大气环流与外强迫海表温度上均表现出与历史典型年相类似的特征。

值得注意的是,进入21世纪以来全球变暖进入停滞期(唐国利等,2012;Jeff,2014),当前欧亚北部频繁冷冬存在一些新的特征,如北极海冰减少与欧亚北部频繁冷冬存在密切联系(Liu,et al,2012)。在新的背景下,对全球变暖停滞期频繁冷冬与历史相似年间外强迫进行系统比较是下一步探索的重点。

## 参考文献


陈文,康丽华. 2006. 北极涛动与东亚冬季气候在年际尺度上的联系:准定常行星波的作用. 大气科学,30(5):863-870

丁一汇,王遵娅,宋亚芳等. 2008. 中国南方2008年1月罕见低温雨雪冰冻灾害发生的原因及其与气候变暖的关系. 气象学报,66(5):808-825

龚道溢,王绍武. 2000. 近百年北极涛动对中国冬季气候的影响. 地理学报,58(4):559-568

龚志强,王晓娟,崔冬林等. 2012. 区域性极端低温事件的识别及其变化特征. 应用气象学报,23(2):195-204

龚志强,王晓娟,任福民等. 2013. 亚欧中纬度关键区正位势高度距平场配置与中国冬季区域性极端低温事件的联系. 大气科学,37(6):1274-1286

顾雷,魏科,黄荣辉. 2008. 2008年1月我国严重低温雨雪冰冻灾害与东亚季风系统异常的关系. 气候与环境研究,13(4):405-417

兰晓青,陈文. 2013. 2011—2012年冬季欧亚大陆低温严寒事件与平流层北极涛动异常下传的影响. 大气科学,37(4):863-872

李建平. 2005a. 北极涛动的物理意义及其与东亚大气环流的关系//俞永强,陈文等. 海气相互作用对我国气候变化的影响. 北京:气象出版社,169-176

李建平. 2005b. 海气耦合涛动与中国气候变化//秦大河. 中国气候与环境演变(上卷). 北京:气象出版社,324-333

马晓青,丁一汇,徐海明等. 2008. 2004/2005年冬季强寒潮事件与大气低频波动关系的研究. 大气科学,32(2):380-394

钱维宏. 2012. 天气尺度瞬变扰动的物理分解原理. 地球物理学报,55(5):1439-1448

沈柏竹,廉毅,张世轩等. 2012. 北极涛动、极涡活动异常对北半球欧亚大陆冬季气温的影响. 气候变化研究进展,8(6):434-439

孙诚,李建平. 2012. 2009/2010年北半球冬季异常低温分析. 气候与环境研究,17(3):259-273

所玲玲,谭本馗,黄嘉佑. 2009. 北半球环状模异常时温度场异常的成因再探讨. 科学通报,54(6):798-803

谭本馗,所玲玲,黄嘉佑. 2007. 各层北半球环形模态异常与地面大气温度的关系研究. 气象学报,65(5):718-724

谭桂容,陈海山,孙照渤等. 2010. 2008年1月中国低温与北大西洋涛动和平流层异常活动的联系. 大气科学,13(1):175-183

唐国利,丁一汇,王绍武等. 2009. 中国近百年温度曲线对比分析. 气候变化研究进展,5(2):1673-1719

唐国利,罗勇,黄建斌等. 2012. 气候变暖在继续. 气候变化研究进展,8(4):235-242

陶诗言,卫捷. 2008. 2008年1月我国南方严重冰雪灾害过程分析. 气候与环境研究,13(4):337-350

陶祖钰,郑永光,张小玲. 2008. 2008年初冰雪灾害和华南准静止锋. 气象学报,66(5):850-854

王东海,柳崇健,刘英等. 2008. 2008年1月中国南方低温雨雪冰冻天气特征及其天气动力学成因的初步分析. 气象学报,66(3):405-422

王阔,封国林,孙树鹏等. 2012. 基于2008年1月中国南方低温雨雪冰冻事件10-30天延伸期稳定分量的研究. 物理学报,61(10):109201-1-109201-10

王凌,高歌,张强等. 2008. 2008年1月我国大范围低温雨雪冰冻灾害分析Ⅰ:气候特征与影响评估. 气象,34(4):95-100

王晓娟,龚志强,任福民等. 2012. 1960—2009年中国冬季区域性极端低温事件的时空特征. 气候变化研究进展,8(1):8-15

王晓娟,龚志强,沈柏竹等. 2013. 近50年中国区域性极端低温事件频发期的气候特征对比分析研究. 气象学报,71(6):1061-1073

王亚非,李琰,李萍云等. 2008. 2008年初中国南方雪灾大尺度环流背景分析. 气象学报,66(5):826-835

杨贵名,孔期,毛冬艳等. 2008. 2008年初"低温雨雪冰冻"灾害天气的持续性原因分析. 气象学报,66(5):836-849

曾明剑,陆维松,梁信忠等. 2008. 2008年初中国南方持续性冰冻雨雪灾害形成的温度场结构分析. 气象学报,66(6):1043-1052

张宗婕,钱维宏. 2012. 中国冬半年区域持续性低温事件的前期信号. 大气科学,36(6):1269-1279

赵宗慈，王绍武，徐影等. 2005. 近百年我国地表气温趋势变化的可能原因. 气候与环境研究，10(4)：808-817

Bueh C，Fu X，Xie Z W. 2011a. Large-scale circulation features typical of wintertime extensive and persistent low temperature events in China. Atmos Oceanic Sci Lett，4(4)：235-241

Bueh C，Shi N，Xie Z W. 2011b. Large-scale circulation anomalies associated with persistent low temperature over Southern China in January 2008. Atmos Sci Lett，12(3)：273-280

Gambo K，Kudo K. 1983. Three-dimensional teleconnections in the zonally asymmetric height field during the Northen Hemisphere winter. J Meteor Soc Japan，61：36-52

Hurrell J W. 1995. Decadal trends in the North Atlantic Oscillation：Regional temperature and precipitation. Science，269(5224)：676-679

Hurrell J W. 1996. Influence of variations in extratropical wintertime teleconnections on Northern Hemisphere temperature. Geophys Res Lett，23(6)：665-668

Jeff T. 2014. Climate change：The case of the missing heat. Nature，505(7483)：276-278

Li C Y. 1990. Interaction between anomalous winter monsoon in East Asia and El Niño events. Adv Atmos Sci，7(1)：36-46

Li C Y，Zhang Q Y，Ji L R，et al. 2012. Interannual variations of the Blocking High over the Ural Mountains and its association with the AO/NAO in boreal winter. Acta Meteor Sinica，26(2)：163-175

Liu J P，Curry J A，Wang H J，et al. 2012. Impact of declining Arctic sea ice on winter snowfall. Proc Natl Acad Sci USA，109(11)：4074-4079

North G R，Bell T L，Cahalan R F，et al. 1982. Sampling errors in the estimation of empirical orthogonal functions. Mon Wea Rev，110(7)：699-706

Peng J B，Bueh C. 2011. The definition and classification of extensive and persistent extreme cold events in China. Atmos Oceanic Sci Lett，4(5)：281-286

Scaife A A，Knight J R. 2008. Ensemble simulations of the cold European winter of 2005－2006. Quart J Roy Meteor Soc，134(636)：1647-1659

Smith T M，Reynolds R W. 2003. Extended reconstruction of global sea surface temperatures based on COADS data (1854－1997). J Climate，16(10)：1495-1510

Thompson D W J，Wallace J M. 1998. The Arctic Oscillation signature in the wintertime geoptential height and temperature fields. Geophys Res Lett，25(9)：1297-1300

Thompson D W J，Wallace J M. 2000. Annular modes in the extratropical circulation. Part Ⅰ：Month-to-month variability. J Climate，13(5)：1000-1016

Wang B，Wu R G，Fu X H. 2000. Pacific-East Asia teleconnection：How does ENSO affect East Asian climate?. J Climate，13(9)：1517-1536

Wang B，Wu Z W，Chang C P，et al. 2010. Another look at interannual-to-interdecadal variations of the East Asian winter monsoon：The Northern and Southern Temperature Modes. J Climate，23(6)：1495-1512

Wang K，Feng G L，Zeng Y X，et al. 2013. Analysis of stable components in the extended-range forecast for the coming 10－30 days in winter 2010 and 2011. Chin Phys B，22(12) 129202

Wang L，Chen W，Huang R H. 2008. Interdecadal modulation of PDO on the impact of ENSO on the East Asian winter monsoon. Geophys Res Lett，35(20)：L20702，doi：10.1029/2008GL035287

Watanabe M，Kimoto M. 2000. Atmosphere-ocean thermal coupling in the North Atlantic：A positive feedback. Quart J Roy Meteor Soc，126(570)：3343-3369

Yang S，Lan K M，Kim K M. 2002. Variations of the East Asian-Pacific-American winter climate anomalies. J Climate，15(3)：306-325

Zhou W，Chan J C L，Chen W，et al. 2009. Synoptic-scale controls of persistent low temperature and icy weather over southern China in January 2008. Mon Wea Rev，137(11)：3978-3991

# Urbanization Effect on Trends of Extreme Temperature Indices of National Stations over Mainland China, 1961–2008

GUOYU REN

*Laboratory for Climate Studies, National Climate Center, China Meteorological Administration, Beijing, China*

YAQING ZHOU

*Laboratory for Climate Studies, National Climate Center, China Meteorological Administration, Beijing, and Jinzhong Meteorological Bureau of Shanxi Province, Jinzhong, China*

(Manuscript received 8 July 2013, in final form 9 December 2013)

ABSTRACT

Understanding the long-term change of extreme temperature events is important to the detection and attribution of climate change. It is unclear, however, how much effect urbanization has had on trends of the extreme temperature indices series constructed based on the commonly used datasets on a subcontinental scale. Applying a homogenized daily temperature dataset of the national reference climate stations and basic meteorological stations, and a rural station network previously developed, urbanization effects on trends of extreme temperature indices in mainland China for the time period 1961–2008 are evaluated. It is found that 1) the country-averaged annual- and seasonal-mean extreme temperature indices series generally experience statistically significant trends; 2) annual-mean urbanization effects in the country as a whole are statistically significant for daily minimum temperature (Tmin), maximum temperature (Tmax), and mean temperature of Tmin and Tmax (Tavg), reaching 0.070°, 0.023°, and 0.047°C $(10\,\mathrm{yr})^{-1}$, respectively, with the largest values for annual-mean Tmin occurring in north China; 3) annual- and seasonal-mean urbanization effects for the declining diurnal temperature range (DTR) are highly significant, and the largest seasonal-mean DTR decline because of urbanization occurs in winter and spring; 4) annual-mean urbanization effects for the lowest Tmin, summer days, tropical nights, and frost days series are significant, but an insignificant urbanization effect is detected for icing days series; 5) urbanization has led to a highly significant decline of annual cold nights at a rate of $-1.485$ days $(10\,\mathrm{yr})^{-1}$ and a highly significant increase of annual warm nights at a rate of 2.264 days $(10\,\mathrm{yr})^{-1}$. Although urbanization effects are also significant for cold days and warm days, they are relatively smaller, and 6) the smallest absolute values of annual-mean urbanization effects for most of the indices series are found to dominantly appear during 1966–76, a well-known deurbanization period resulting from the Cultural Revolution.

## 1. Introduction

An understanding of long-term change of extreme temperature events is of importance to the detection and attribution of climate change and to the assessment of climate change impacts on natural and human systems. It is unclear in the present, however, whether or to what extent the urbanization has affected the long-term trends of the extreme temperature indices series constructed based on the frequently used observational datasets on a subcontinental to global scale.

Many studies on changes in extreme climate events were conducted in the past decade, and almost all of them showed coherent changes in the temperature indices series over the post-1950 time periods in the continents or countries, with the warm extreme temperature indices witnessing significant increasing trends and cold extreme temperature indices witnessing significant decreasing trends (Easterling et al. 2000; Frich et al. 2002; Alexander et al. 2006; Ding et al. 2006; Solomon et al. 2007; Peterson et al. 2008; Choi et al. 2009; Shi et al. 2009; Zhou and Ren 2011; Ren et al. 2011; L. Zhang et al. 2011). Alexander et al. (2006) showed significant changes in temperature extremes associated with climate warming from 1951 to 2003, for example, indicating that more than 70% of the global land area underwent a significant decrease in frequency of cool nights and

*Corresponding author address:* G. Y. Ren, Laboratory for Climate Studies, National Climate Center, China Meteorological Administration, 46 Zhongguancun Nandajie, Beijing, 100081, China. E-mail: guoyoo@cma.gov.cn

DOI: 10.1175/JCLI-D-13-00393.1



© 2014 American Meteorological Society

a significant increase in frequency of warm nights. Klein Tank and Konnen (2003), Vincent et al. (2005), and Choi et al. (2009), respectively, reported the similar long-term changes in extreme temperature indices in Europe, South America, and the Asian–Pacific region.

Studies for mainland China also evidenced the countrywide reduction in frequency of cold waves, frost days, and cool days (nights) and a general increase in frequency of hot events and warm days (nights), though some differences still existed among the trend estimates because of the varied time periods, areas analyzed, and the different criteria used (Yan el al. 2002; Zhai and Pan 2003; Ma et al. 2003; Qian and Lin 2004; Gong and Han 2004; Liu et al. 2006; You et al. 2008). Recently, Zhou and Ren (2011) updated the analysis of spatial and temporal changes in extreme temperature events in mainland China based on a homogeneity-adjusted daily temperature dataset of 526 stations for period 1961–2008, showing that, across the country, frost days and ice days significantly reduced and annual highest daily maximum temperature (Tmax) and daily minimum temperature (Tmin) (TXX and TNX) and annual lowest Tmax and Tmin (TXN and TNN) generally rose. The analysis also found that cool nights (days) significantly decreased at a rate of $-8.23$ days $(10\,\mathrm{yr})^{-1}$ [$-3.26$ days $(10\,\mathrm{yr})^{-1}$], and warm nights (days) significantly increased at a rate of 8.16 days $(10\,\mathrm{yr})^{-1}$ [5.22 days $(10\,\mathrm{yr})^{-1}$] in the country as a whole. These latest results are generally consistent with those reported in the previous studies for mainland China except for the slightly higher estimates mainly due to updated data series.

An important issue in the studies, however, is whether or not, or to what extent, the urban warming near the weather stations has affected the estimates of trends of the extreme temperature indices on a large spatial scale. Many studies for mainland China and other eastern Asian countries in the past decade have evidenced the significant urbanization effect on area-averaged annual- and seasonal-mean surface air temperature (SAT) trends over the post-1950 periods as estimated from the commonly applied observational datasets (e.g., Zhao 1991; Choi et al. 2003; Kalnay and Cai 2003; Zhou et al. 2004; Chung et al. 2004; Ren et al. 2005, 2008; Chen et al. 2005; Tang et al. 2008; Fujibe 2009; Zhang et al. 2010; Yang et al. 2011, 2012; Wu and Yang 2013; He et al. 2013; Li et al. 2013). A recent and comprehensive study by Zhang et al. (2010) used data from all of the weather stations for selecting reference stations to evaluate the urbanization effect on SAT trends in mainland China, and they showed that, in the warming trend of annual-mean SAT estimated based on the dataset of national Reference Climatic and Basic Meteorological Stations (RCBMS or National Stations hereafter) in 1961–2004, annual-mean urban warming ranged mostly among 0.06°–0.09°C $(10\,\mathrm{yr})^{-1}$, contributing 27% to the overall warming over the country as a whole. The urban heat island (UHI) effect therefore had a significant effect on the increasing SAT trends of the country as estimated by the observational records from the RCBMS. Since the enhanced UHI magnitude has obviously contributed to the overall increasing trends of mean SAT in mainland China, it must have exerted some influence on trends of Tmax and Tmin and the trends of the extreme temperature indices series based on the Tmax and Tmin as well.

Chen et al. (2005) analyzed the urbanization effect on area-averaged Tmax and Tmin trends in Hubei Province, central China, for the time period 1960–2004 and showed a large proportion of urban warming in annual- and seasonal-mean Tmin trends. Similar results were reported by Hua et al. (2008) for mainland China and by Zhou and Ren (2009) for north China, with the latter indicating a 53% contribution of urbanization to the long-term trend of annual-mean Tmin during 1961–2000. L. Zhang et al. (2011) and Zhou and Ren (2011) were among the first studies to further evaluate the urbanization effect on long-term trends of the commonly applied extreme temperature indices in Beijing Municipality and north China, and they all reported significant urbanization effects on the indices series related to daily Tmin including frost days, cold nights, warm nights, the lowest and highest Tmin, and diurnal temperature range (DTR). The urbanization effects on the negative trends of frost days, DTR, cool nights, and cool days, and the positive trends of summer days, tropical nights, TNX, TNN, and warm nights calculated based on the data of RCBMS for the time period 1961–2008 in north China were all statistically significant at the 0.05 confidence level (Zhou and Ren 2011).

It is unclear at present, however, how much effect the rapid urbanization, especially the increased UHI magnitudes, has had on the long-term trends of the extreme temperature indices series of the RCBMS in mainland China as a whole. The RCBMS dataset has been frequently used by researchers in China for analyzing the long-tern changes in mean and extreme climate (Ren et al. 2008, 2012), and it is desirable to identify the nature and extent of the urbanization contribution in the dataset after the urbanization effect on trends of regional-averaged annual- and seasonal-mean temperature series in mainland China has been well understood. In this paper, we apply a homogeneity-adjusted daily temperature dataset and a reference SAT network previously developed by Ren et al. (2010b) to evaluate the urbanization effects on trends of the extreme temperature indices in mainland China. Our investigation shows a similarly significant urbanization effect across the country,

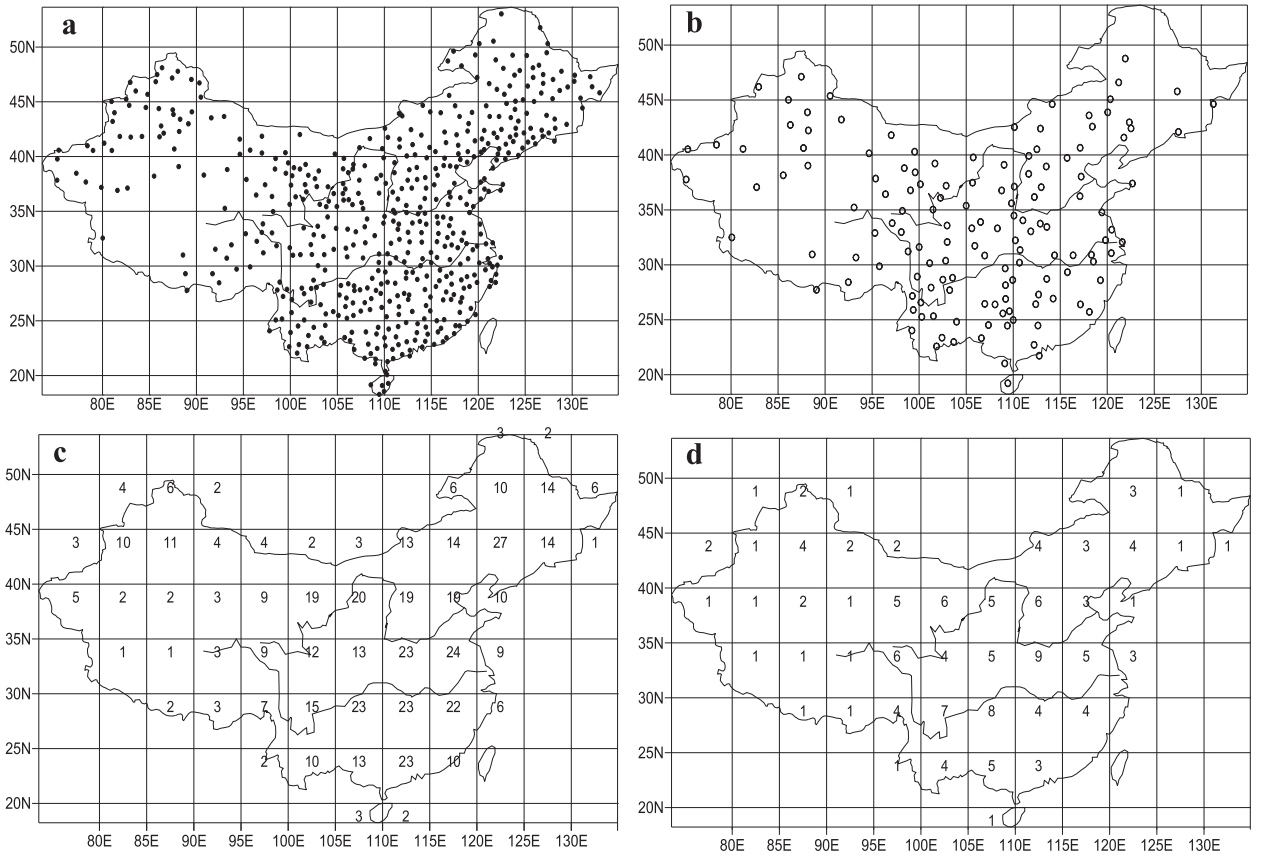


FIG. 1. Distribution of the (a) RCBMS and the (b) reference/rural stations in mainland China, and the numbers of stations within the 5° × 5° latitude–longitude grids for the (c) RCBMS and the (d) reference/rural stations.

despite the effect being somewhat smaller in magnitude than that found for north China.

## 2. Data and methods

### *a. Selection of reference temperature stations*

It is crucial to have a set of representatively rural stations for evaluating the urbanization effect on trends of SAT and the related extreme indices series (Hansen et al. 2001; Pielke et al. 2007; Ren et al. 2008). Ren et al. (2010b) developed a rural/reference temperature station (reference station hereafter) network for use in studies of urbanization effect on SAT in mainland China, applying a comprehensive procedure and all the available weather stations of approximately 2300. The procedure took a consideration of spatial distribution and density of stations, length and complicity of records, times and distance of relocations, population in the nearby cities/towns, proportion of built-up areas around the stations (within 12 $km^2$ around the observational grounds), and straight distance from the center of the cities and towns. For example, the population in the built-up areas of the cities and towns where the stations are located must be less than 20 000 in central and western China and be less than 70 000 for 16 provinces (municipalities) in the eastern plain areas of China; station relocations must occur no more than two times since 1961, and the relocation distance must be within 5 km; and the percentage of the built-up areas within a radius of 2 km (or within about 12 $km^2$) around the observational grounds must be less 33%. These criteria were forged and adopted to account for the different influences on SAT observations from local anthropogenic activities in varied spatial scales. A detailed description of the procedure for selecting the reference stations was given in Ren et al. (2010b), and a brief introduction to the comprehensive method and the comparison with that of remote sensing–based land surface brightness temperature were also given in Ren and Ren (2011).

A total of 143 stations were finally chosen by applying the procedure (Fig. 1), among which 68 are from the RCBMS managed by the China Meteorological Administration (CMA), and 75 are from the Ordinary Meteorological Stations (OMS) previously overseen by provincial meteorological bureaus but now are also

overseen by the CMA. We used 141 reference stations of the network because the records from 2 stations have not been updated. A brief description of the RCBMS and OMS including how they are used for climatic researches in mainland China is given in section 2b.

Overall, the reference stations are well spatially distributed, though they are still relatively smaller in number in northern northeast China, northwest China, and the western Qinghai–Tibetan Plateau. As an example, the grid where northern Beijing City is located contains three reference stations (Figs. 1b,d): Shangdianzi, Beijing; Gangzi, Inner Mongolia; and Linxi, Inner Mongolia. An OMS, Shangdianzi station is located on a hill slope at an elevation of 287 m above mean sea level (MSL), and it is near a mountain village with a population less than 9000 in 2000; Gangzi station is also an OMS, but Linxi station is one of the RCBMS, and both are located in the Inner Mongolian Plateau with elevations 961 and 800 m MSL, respectively, and a population of 9200 and 11 000, respectively, in 2000. This station network was compared to another reference network of 138 stations developed by using the surface brightness temperature data retrieved from the remote sensing of satellite, and it was found to have similar country-averaged trends of annual- and seasonal-mean SAT and the magnitudes of urban warming of the RCBMS for the same time periods (Ren and Ren 2011). It has been applied already for identifying and adjusting the urban biases of mean SAT of the RCBMS in mainland China (Zhang et al. 2010; Zhou and Ren 2011). In this study, we use the daily temperature data of the reference station network for examining urbanization effects on an extreme temperature indices series in mainland China.

### *b. Data and processing*

Daily temperature data are from the National Meteorological Information Center (NMIC) of the CMA. There are different historical datasets available in the CMA for use in studies of climate change, but the most frequently applied historical SAT dataset has been the observational records from the RCBMS, consisting of about 730 stations approximately evenly distributed across the country but more located near cities and towns. As a subset of the dataset, the national Reference Climate Stations (RCS) consisting of 143 stations (160 stations for a variant in some publications) more evenly distributed spatially and nearer big cities have also been used by climatologists. The readings at the RCS were made 24 times a day before the application of the autonomous weather station (AWS) system around 2004 in mainland China. Another subset of the dataset is the national Basic Meteorological Stations (BMS, about 580 stations), manually observed eight times a day before the AWS system, also mostly situated near cities or towns (Ren et al. 2008; Zhang and Xu 2008). In the last decade, the historical temperature records of the RCS and BMS were merged and inhomogeneity-adjusted to meet the increasing demand for climate change studies (Li et al. 2004; Ren et al. 2005, 2012; Ding et al. 2006). The RCBMS include almost all the stations with long-term records in mega and large cities of mainland China, and few are really located in rural areas. In addition, there are about 1600 OMS that are mostly located near small cities, towns, and villages, but the observations were manually made only three times (0800, 1400, and 2000 local time) a day before about 2004, and they have been seldom applied so far in large-scale analyses of climate change.

The objective of this study is to investigate into the nature and magnitude of the urbanization effect on the estimates of trends of the commonly used extreme temperature indices obtained from data of all the RCBMS. These stations are regarded as problematic ones in this work, as evidenced in many previous studies, and they are to be evaluated in terms of the systematic bias of mean SAT and extreme temperature indices series induced by urbanization. The urbanization effect may result from a complex matrix of influential factors including poor siting on the microscale, urban heat island effect, enhanced precipitation in or near built-up areas, and increased concentration of atmospheric aerosols in the urban boundary layer. For example, most of these stations are characterized by being too close to the built-up areas of cities and the poor siting or deteriorative microsettings immediately around the observational grounds. The unqualified microsettings are one of the many problems related to urbanization. One of the more important issues in addition to the poor microsettings would be the enhanced urban island intensity near the observational sites that is more associated with the size and population of the cities where the stations are located. By applying the ''good'' reference stations, as described in section 2a, we could evaluate the overall urbanization effect on the trends of the extreme temperature indices series at the ''poor'' RCBMS.

Daily temperature data of 1951–2004 from the RCBMS were inhomogeneity-adjusted by the NMIC (Li et al. 2004). The method of Easterling and Peterson (1995) was adopted to conduct the detection and adjustment of the inhomogeneities of the monthly-mean data, and the monthly average adjustments were then applied to daily records to obtain the homogenized daily temperature data. The discontinuous points mainly caused by relocations had been adjusted to the latest observational locations, and the historical SAT records from the 730 stations can be considered as being relatively homogenous after the adjustments (Li et al. 2004;

TABLE 1. Extreme temperature indices used in this study [modified from Zhang and Yang (2004) and Zhou and Ren (2011)].

| Category | Abbreviation | Term | Definition (unit) |
|---|---|---|---|
| Mean and extreme value | TN | Tmin | Mean value of daily Tmin (°C) |
| | TX | Tmax | Mean value of daily Tmax (°C) |
| | TM | Tavg | Mean value of Tmax and Tmin (°C) |
| | DTR | Diurnal temperature range | Difference between Tmax and Tmin (°C) |
| | TNX | Highest Tmin | Monthly maximum value of Tmin (°C) |
| | TXX | Highest Tmax | Monthly maximum value of Tmax (°C) |
| | TNN | Lowest Tmin | Monthly minimum value of Tmin (°C) |
| | TXN | Lowest Tmax | Monthly minimum value of Tmax (°C) |
| Absolute threshold | FD0 | Frost days | Annual count when daily Tmin $<$ 0°C (day) |
| | SU25 | Summer days | Annual count when daily Tmax $>$ 25°C (day) |
| | ID0 | Icing days | Annual count when daily Tmax $<$ 0°C (day) |
| | TR20 | Tropical nights | Annual count when daily Tmin $>$ 20°C (day) |
| Relative threshold | TN10p | Cool nights | Days when daily Tmin $<$ 10th percentile (day) |
| | TX10p | Cool days | Days when daily Tmax $<$ 10th percentile (day) |
| | TN90p | Warm nights | Days when daily Tmin $>$ 90th percentile (day) |
| | TX90p | Warm days | Days when daily Tmax $>$ 90th percentile (day) |

Li and Dong 2009). The homogenized monthly and daily SAT datasets have been frequently used in studies and services of regional climate change in China (Ren et al. 2005, 2012; Tang et al. 2005; Ding et al. 2006; You et al. 2012). We update the data to 2008, and the after 2004 records are simply connected to the adjusted data series, with an assumption that the inhomogeneities in the last 4 yr are negligible. The assumption is somehow debatable because although the relocations might have little influence, the nationwide applications of the AWS around 2004 might have caused some discontinuities in the daily temperature records. However, Wang et al. (2007) compared the country-averaged annual- and seasonal-mean SAT of the AWSs with those of the manual observations and found an insignificant difference, despite the fact that the maximum (minimum) temperature of the AWSs somehow exhibits systematically higher (lower) values in the country as a whole.

Among the records of 74 stations of the OMS in the reference station network, which had already been quality controlled by the NMIC, only nine with annual-mean SAT series are found to be inhomogeneous due to the moves of observational locations, and the monthly and daily temperature data of the nine stations are therefore adjusted by using the same method as that used by Li et al. (2004) for the data of the RCBMS. The significant inhomogeneities have not been found or verified for the SAT data series from the other OMS sites, and they are assumed as homogeneous and, together with the adjusted data, are simply merged with the RCBMS data of the reference station network for use in this study.

Most of the stations actually started routine observations after the mid-to-late 1950s, and there also existed missing records in the entire data series of some stations. We take 1961 as the beginning year and choose those stations with records suffering from missing values less than 2% of the total days of 1961–2008 for the analysis. The records of 526 stations in the RCBMS dataset can meet the requirement (Fig. 1). It is clear from Fig. 1 that the stations selected for use in this study are approximately evenly distributed across the country, despite observations in the northwestern deserts and western Tibetan Plateau still being small in number due to the lack of weather stations.

Finally, we recheck the quality of the daily SAT data of all stations used with RClimDex software developed by Zhang and Yang (2004) and find that 10 records from six stations are not reasonable with the temperature values larger than 4 times that of standard deviations of the data series. These wrong records are treated as missing values, which account for about $4 \times 10^{-6}$ of the total daily SAT records.

### c. *Definition of extreme temperature indices*

We use a set of total 16 temperature indices, including 15 extreme temperature indices (ETIs), among which 13 are adopted, with no modification, from the definitions by the Expert Team on Climate Change Detection and Indices (ETCCDI), and the remaining 2 are monthly-mean Tmax and Tmin. Monthly-mean temperature is also applied. Definitions and units of the temperature indices are shown in Table 1. They can be broadly divided into three categories: absolute threshold indices, relative threshold indices, and the mean and extreme value indices.

The mean and extreme value indices are simply the mean and extreme values of Tmax and Tmin during a certain period, including mean Tmax and Tmin, the highest Tmax (TXX) and Tmin (TNX), the lowest Tmax

(TXN) and Tmin (TNN), DTR, and monthly- and annual-mean SAT or Tavg (TM).

The absolute threshold indices are those directly determined based on original daily data and fixed thresholds, including frost days (FD0), summer days (SU25), ice days (ID0), and tropical nights (TR20). For these indices, there will be some stations without records of extremes for some or even all years of the time period analyzed. In this case, we determine that if a station has no record of extremes for 1/3 yr of the 48-yr period, the linear trend of the index series for the station is regarded as being insignificant, and the station is no longer included in the statistics of the index time series.

The relative threshold indices are defined based on relative (floating) thresholds, including cool days (nights) and warm days (nights). We take the 90th (10th) percentile values of daily Tmax (Tmin) data in a certain station from 1971 to 2000 as the upper (lower) thresholds. If the daily Tmax (Tmin) is greater (less) than the upper (lower) threshold, the day (night) is considered as a warm (cool) day (night) event.

### d. Analysis methods

We apply a method of comparing average ETI series between the RCBMS and the reference stations on a basis of longitude by latitude grids. The size of grids is $5° \times 5°$. Only those grids with both the RCBMS and the reference stations are analyzed, and there are thus a total of 42 grids in the study region (Fig. 1). The eight grids that own only the RCBMS but no reference stations are all located along the national boundaries or coastal lines and are of incomplete grids. In addition, there are three grids in which the RCBMS and the reference stations are at the same sites in the northwestern Qinghai–Tibetan Plateau resulting from the lack of observations, and they are not included in the analysis either. Therefore, each of the grids analyzed owns at least one station of the RCBMS and one reference station, with those of the eastern parts of the study region generally having more observational records.

The following terms are used in this paper, referring to Chu and Ren (2005), Ren et al. (2008), and L. Zhang et al. (2011).

The urbanization effect ($\Delta T_{u-r}$) refers to the impact of urbanization on SAT trends. It is here defined as the linear trend of the ETI of a station or a group of stations, caused by the strengthening UHI effect and other local anthropogenic factors near the stations, and is expressed as

$$\Delta T_{u-r} = T_u - T_r, \tag{1}$$

where $T_u$ is the linear trend of any ETI of an urban/town station or stations of the RCBMS within a grid, and $T_r$ is the linear trend of any ETI of reference stations within the grid. A value of $\Delta T_{u-r} > 0$ indicates that the ETI relatively increases at the urban/town station or stations of the RCBMS because of the urbanization effect, mainly to the enhanced UHI effect; $\Delta T_{u-r} < 0$ implies that the ETI at the urban/town station or stations of the RCBMS relatively decreases because of the urbanization effect, including the local anthropogenic factors other than the UHI effect.

Urbanization contribution ($C_u$) is defined as the proportion that the statistically significant urbanization effect accounts for the overall ETI trend at an urban/town station or stations of the RCBMS (Chu and Ren 2005; Ren et al. 2008). It can be expressed as

$$C_u = \left| \frac{\Delta T_{u-r}}{T_u} \right| \times 100\%. \tag{2}$$

Generally, $\Delta T_{u-r}/T_u$ is a positive value less than 1; the absolute value is taken because in a few circumstances it assumes negative value resulting from the effects of local factors other than increasing UHI intensity. If $C_u = 100\%$, then it shows that the ETI trend of the urban station is entirely caused by urbanization; if $C_u$ is more than 100%, it implies that the extra trend might have been caused by other local factors not yet identified or the errors of data, but it is regarded as 100% in this study. As the definition implies, urbanization contribution is not calculated if the urbanization effect is not statistically significant.

The grid-averaged annual and seasonal ETIs series of the RCBMS and reference stations for each of the 42 grids are first calculated, respectively, for the 48 yr. With the period 1971–2000 taken as reference period, RClimDex software (Zhang and Yang 2004) is used to calculate the time series of the ETIs for each of the stations. The grid-averaged ETIs series are then obtained by simply averaging all values within the grids for each of the 48 yr. The respective linear trends of the ETIs for the RCBMS and reference stations are calculated using the least squares method. This requires the calculation of the linear regression coefficients between any grid-averaged ETIs and ordinal numbers of time (e.g., $i = 1, 2, 3, \ldots, 48$ for 1961–2008). Once the grid-averaged ETIs series and their trends are obtained, $\Delta T_{u-r}$ and the $C_u$ then can be calculated for each of the grids by applying Eqs. (1) and (2). (The annual values in Figs. 5, 7, 9, and 11 have been obtained this way.) The country-averaged ETIs series of the RCBMS and reference stations are obtained by area-weighted averaging of the values of all the grids, with the weights assigned as the cosine midlatitude values of the grids (Figs. 2, 3) (Jones and Hulme 1996). Linear trends of the country-averaged

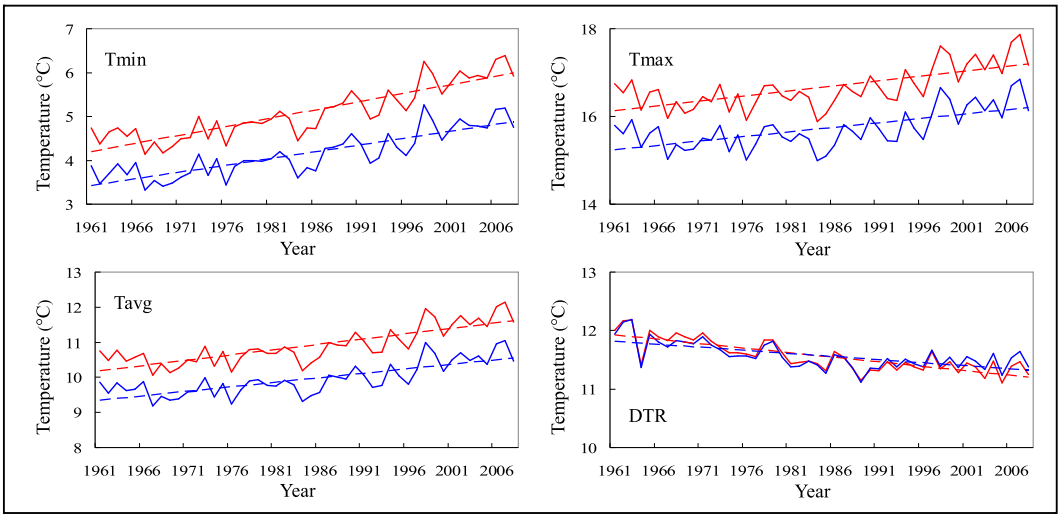


(a)

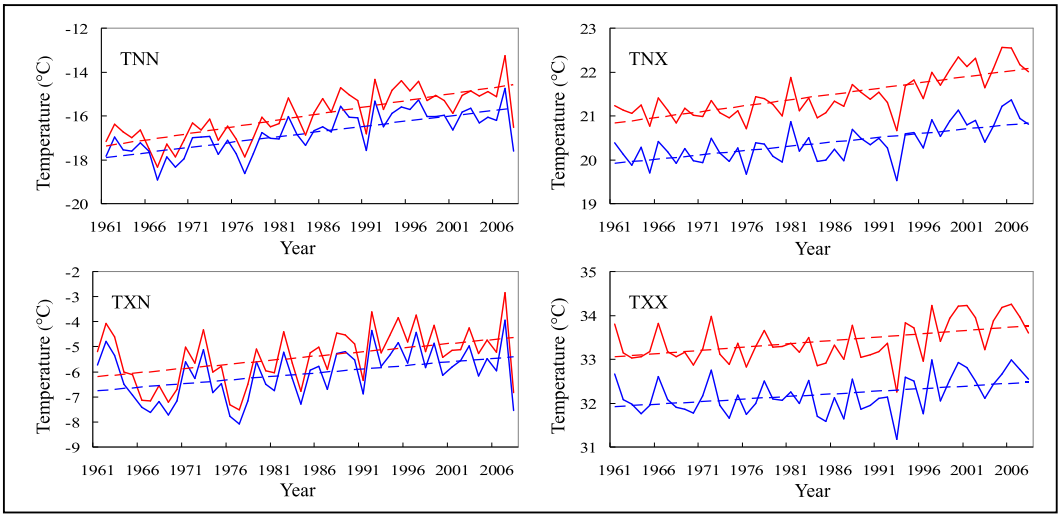


(b)

FIG. 2. Changes in mean and extreme value indices for the RCBMS (red) and the reference/rural stations (blue) in mainland China over 1961–2008 for (a) Tmin, Tmax, Tavg, and DTR; and (b) TNN, TNX, TXN, and TXX. Straight dashed lines denote linear trends.

ETIs series are then calculated for the RCBMS and the reference stations (Table 2), and the country-averaged $\Delta T_{u-r}$ and $C_u$ of the RCBMS are obtained by applying Eqs. (1) and (2). The annual and seasonal values in Tables 3 and 4 have thus been obtained.

To visualize the temporal change in the country-averaged $\Delta T_{u-r}$, we also construct on the basis of the grids the difference value series of the grid-averaged ETIs between the RCBMS and reference stations and then obtain the time series of the country-averaged difference values of the ETIs between the RCBMS and the reference stations applying an area-weighted averaging method. The annual country-averaged difference value series visually exhibit the temporal variation in country-averaged annual $\Delta T_{u-r}$ for the ETIs of the RCBMS. (Figures 4, 6, 8, and 10 have been drawn based on the values of the annual $\Delta T_{u-r}$.)

Kendall's tau nonparametric test method is applied for examining the statistical significance of the linear trends and $\Delta T_{u-r}$ (Kendall and Gibbons 1990; von Storch and Zwiers 2003). Meteorological seasons are adopted for the analysis of seasonality, and they are respectively spring (March–May), summer (June–August), autumn (September–November), and winter (December–February). Annual-mean (total) values (counts) are those from January to December.

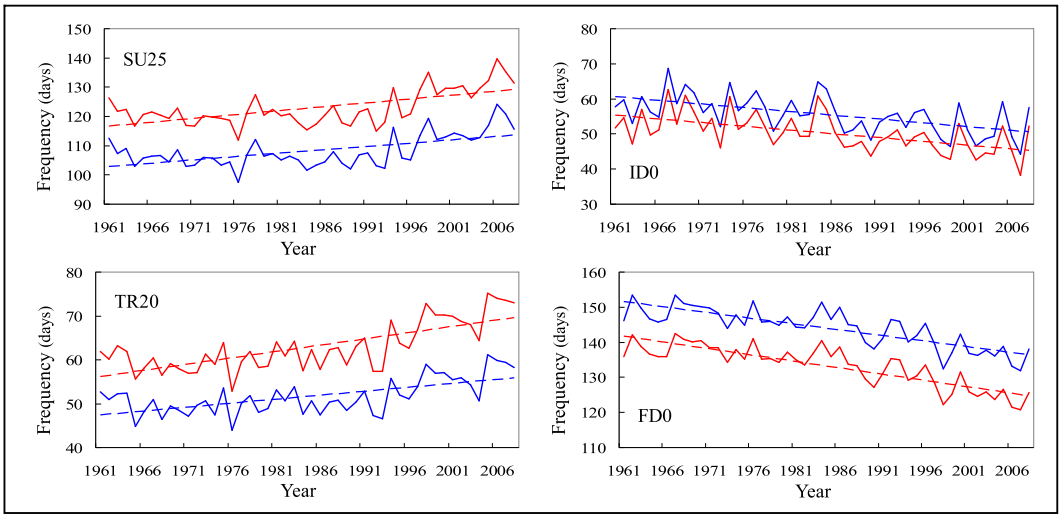


(a)

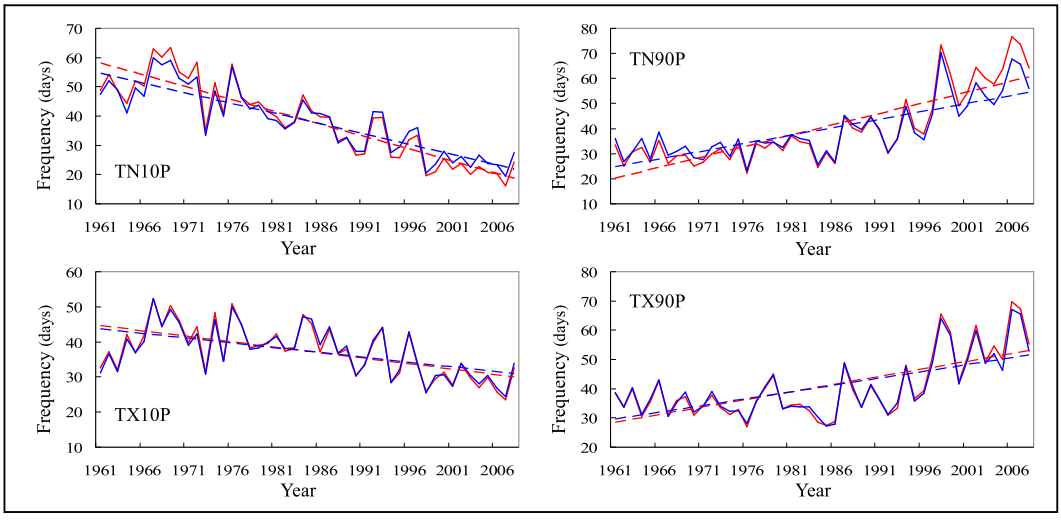


(b)

FIG. 3. As in Fig. 2, but for absolute and relative threshold indices: (a) SU25, ID0, TR20, and FD0; and (b) TN10p, TN90p, TX10p, and TX90p.

## 3. ETIs trends of the RCBMS

Table 2 shows the annual- and seasonal-mean linear trends in the ETIs series for the RCBMS in mainland China over the time period 1961–2008. Statistically significant changes can be found for all of the annual-mean ETIs series and for seasonal-mean trends of the ETIs series except for the increases in spring TXN and summer TXX. Larger and more significant trends generally occur in the ETIs series relative to the daily minimum temperature. With regard to the annual-mean trends, the largest changes are seen for the increase in the lowest Tmin and warm nights, reaching 0.596°C (10 yr)$^{-1}$ and 8.584 days (10 yr)$^{-1}$, respectively, and the decrease in cold nights at a rate of −8.409 days (10 yr)$^{-1}$, all related to the minimum temperature. The largest changes of seasonal-mean ETIs occur in the decrease of cold nights in winter and the increase of warm nights in summer, reaching −11.108 and 10.184 days (10 yr)$^{-1}$, respectively.

Figures 2 and 3 show changes in the ETIs of the RCBMS and reference stations in mainland China over the period 1961–2008. Extremely good correlations between the two datasets can be seen, especially for interannual variability of the ETIs. The linear trends of the ETIs series of the RCBMS exhibit the consistent

TABLE 2. Trends in extreme temperature indices series for the national RCBMS in mainland China over 1961–2008. Units are degrees Celsius per decade [°C (10 yr)$^{-1}$] for Tmin, Tmax, Tavg, DTR, TNN, TNX, TXN, and TXX, and days per decade for TN10p, TN90p, TX10p and TX90p. An asterisk denotes that the trends are statistically significant at the 0.05 confidence level.

| | Tmin | Tmax | Tavg | DTR | TNN | TNX | TXN | TXX |
|---|---|---|---|---|---|---|---|---|
| Annual | 0.381* | 0.228* | 0.305* | −0.154* | 0.596* | 0.264* | 0.331* | 0.150* |
| Spring | 0.364* | 0.200* | 0.282* | −0.167* | 0.444* | 0.253* | 0.180 | 0.131* |
| Summer | 0.279* | 0.138* | 0.209* | −0.144* | 0.493* | 0.218* | 0.151* | 0.105 |
| Autumn | 0.339* | 0.264* | 0.301* | −0.074* | 0.544* | 0.338* | 0.389* | 0.327* |
| Winter | 0.542* | 0.311* | 0.426* | −0.230* | 0.565* | 0.435* | 0.321* | 0.330* |
| | SU25 | ID0 | TR20 | FD0 | TN10p | TN90p | TX10p | TX90p |
| Annual | 2.622* | −2.140* | 2.884* | −3.579* | −8.409* | 8.584* | −3.113* | 5.230* |
| Spring | | | | | −7.532* | 8.599* | −1.892* | 4.830* |
| Summer | | | | | −7.495* | 10.184* | −1.496* | 4.906* |
| Autumn | | | | | −7.854* | 7.871* | −4.305* | 5.941* |
| Winter | | | | | −11.108* | 7.870* | −5.074* | 5.353* |

patterns of changes with those shown in Table 2, but they usually witness larger trends than those of the reference stations, in particular for the ETIs formulated from minimum temperature, such as Tmin, DTR, TNN, TN10p), and TN90p. The systematically higher annual values and mean values of the RCBMS than those of the reference stations for the absolute threshold and extreme value indices might have been induced mainly by different average altitudes of the two observational networks and might have also been related to the urbanization effects to some extent.

Trends of the temperature indices of the RCBMS shown in Table 2, Figs. 2 and 3 are almost all consistent with the recent analyses (Zhou and Ren 2011; Ren et al. 2011; You et al. 2013) and well comparable with earlier studies conducted for mainland China, including those by Zhai et al. (1999), Yan et al. (2002), Zhai and Pan (2003), Qian and Lin (2004), and Gong and Han (2004), despite the fact that the stations, the data processing procedures, and the time periods applied in the analyses bear some differences from the present study. Our analysis results are also broadly consistent with those reported for larger spatial-scale studies outside mainland China (e.g., Easterling et al. 2000; Alexander et al. 2006; Solomon et al. 2007; Choi et al. 2009). The next issue is whether or not, or to what extent, the significant changes for the various ETIs in mainland China have been caused by the locally anthropogenic interferences or urbanization.

## 4. Urbanization effects and contributions

### *a. Extreme value indices*

Table 3 gives annual- and seasonal-mean urbanization effects and contributions of the RCBMS for Tmin, Tmax, Tavg, and DTR over the time period 1961–2008. Annual- and seasonal-mean urbanization effects for mainland China as a whole are all statistically significant at the 0.05 confidence level for Tmin, Tmax, and Tavg, with the annual-mean urbanization effects for the three indices reaching 0.070°, 0.023°, and 0.047°C (10 yr)$^{-1}$, respectively, and the urbanization contributions reaching 18.4%, 10.1%, and 15.4%, respectively. Larger urbanization effects are found for Tmin for winter and spring,

TABLE 3. Urbanization effect (UE) and urbanization contribution (UC) of the RCBMS of mainland China for Tmin, Tmax, Tavg, DTR, TNN, TNX, TXN, and TXX over the time period 1961–2008. An asterisk denotes that the trends are statistically significant at the 0.05 confidence level.

| | | Tmin | Tmax | Tavg | DTR | TNN | TNX | TXN | TXX |
|---|---|---|---|---|---|---|---|---|---|
| Annual | UE [°C (10 yr)$^{-1}$] | 0.070* | 0.023* | 0.047* | −0.049* | 0.118* | 0.069* | 0.045* | 0.034* |
| | UC (%) | 18.4 | 10.1 | 15.4 | 31.8 | 19.8 | 26.1 | 13.6 | 22.7 |
| Spring | UE [°C (10 yr)$^{-1}$] | 0.072* | 0.015* | 0.044* | −0.060* | 0.112* | 0.052* | 0.016 | 0.012 |
| | UC (%) | 19.8 | 7.5 | 15.6 | 35.9 | 25.2 | 20.6 | | |
| Summer | UE [°C (10 yr)$^{-1}$] | 0.057* | 0.028* | 0.043* | −0.031* | 0.100* | 0.057* | 0.019 | 0.016 |
| | UC (%) | 20.4 | 20.3 | 20.6 | 21.5 | 20.3 | 26.1 | | |
| Autumn | UE [°C (10 yr)$^{-1}$] | 0.063* | 0.022* | 0.043* | −0.043* | 0.082* | 0.029 | 0.031 | 0.005 |
| | UC (%) | 18.6 | 8.3 | 14.3 | 58.1 | 15.1 | | | |
| Winter | UE [°C (10 yr)$^{-1}$] | 0.083* | 0.024* | 0.054* | −0.061* | 0.102* | 0.036* | 0.032 | 0.004 |
| | UC (%) | 15.3 | 7.7 | 12.7 | 26.5 | 18.1 | 8.3 | | |

TABLE 4. As in Table 3, but for SU25, ID0, TR20, FD0, TN10p, TN90p, TX10p, and TX90p.

| | | SU25 | ID0 | TR20 | FD0 | TN10p | TN90p | TX10p | TX90p |
|---|---|---|---|---|---|---|---|---|---|
| Annual | UE [days (10 yr)$^{-1}$] | 0.335* | −0.013 | 1.090* | −0.360* | −1.485* | 2.264* | −0.390* | 0.561* |
| | UC (%) | 12.8 | | 37.8 | 10.1 | 17.6 | 26.4 | 12.5 | 10.7 |
| Spring | UE [days (10 yr)$^{-1}$] | | | | | −1.526* | 2.292* | −0.037 | 0.263 |
| | UC (%) | | | | | 20.3 | 26.7 | | |
| Summer | UE [days (10 yr)$^{-1}$] | | | | | −1.310* | 3.435* | −0.580* | 0.956* |
| | UC (%) | | | | | 17.5 | 33.7 | 38.8 | 19.5 |
| Autumn | UE [days (10 yr)$^{-1}$] | | | | | −1.332* | 2.029* | −0.332* | 0.730* |
| | UC (%) | | | | | 17.0 | 25.8 | 7.7 | 12.3 |
| Winter | UE [days (10 yr)$^{-1}$] | | | | | −1.865* | 1.343* | −0.588* | 0.307* |
| | UC (%) | | | | | 16.8 | 17.1 | 11.6 | 5.7 |

reaching 0.083° and 0.072°C (10 yr)$^{-1}$, respectively, and the smallest urbanization effect and contribution, 0.015°C (10 yr)$^{-1}$ and 7.5%, respectively, are seen for Tmax for spring, which might have been related to the higher average wind speeds and the generally weakened urban heat island intensity of the afternoons in the season (Zhang and Lin 1992; Gao et al. 2013; Yang et al. 2013). Overall, the annual- and seasonal-mean urbanization contributions for Tmin, Tmax, and Tavg for the 48 yr range from 7.5% to 20.6%, with the largest seasonal-mean contributions occurring in summertime. Table 3 also shows that annual- and seasonal-mean urbanization effects for DTR in mainland China as a whole are all statistically significant at the 0.05 confidence level. The largest decline of seasonal-mean DTR because of urbanization are found in winter and spring, reaching −0.061° and −0.060°C (10 yr)$^{-1}$, respectively, but the largest urbanization contributions appear in autumn and spring, reaching 58.1% and 35.9%, respectively, for the study region as a whole.

Figure 4 shows the temporal variation in annual-mean urbanization effects as calculated based on the differences between the RCBMS and reference stations in mainland China as a whole for Tmin, Tmax, Tavg, and DTR over the time period 1961–2008. The annual differences have very similar interannual and long-term variations for Tmin and Tavg, with the significant increase obviously occurring after 1976, and the lowest values are almost all found in the time period 1966–76 when an unprecedented deurbanization process occurred across mainland China during the Cultural Revolution (1966–76). Although a significant increase in the annual urbanization effects is also seen for Tmax, they experience a larger interannual and decadal variability. A highly significant decline occurs in the DTR difference series, with the largest values found once again during 1966–76 and the smallest ones in the last 6 yr. It is also notable that, except for the DTR, average values of the annual differences between the RCBMS and reference stations for the first years of the indices

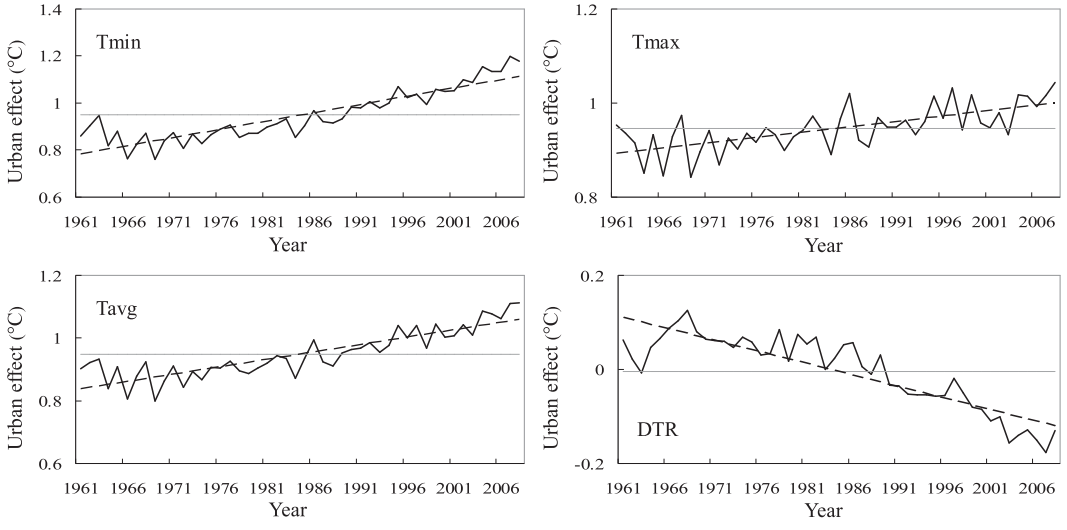


FIG. 4. Temporal variations in annual differences between the RCBMS and reference stations for Tmin, Tmax, Tavg, and DTR in mainland China over the time period 1961–2008.

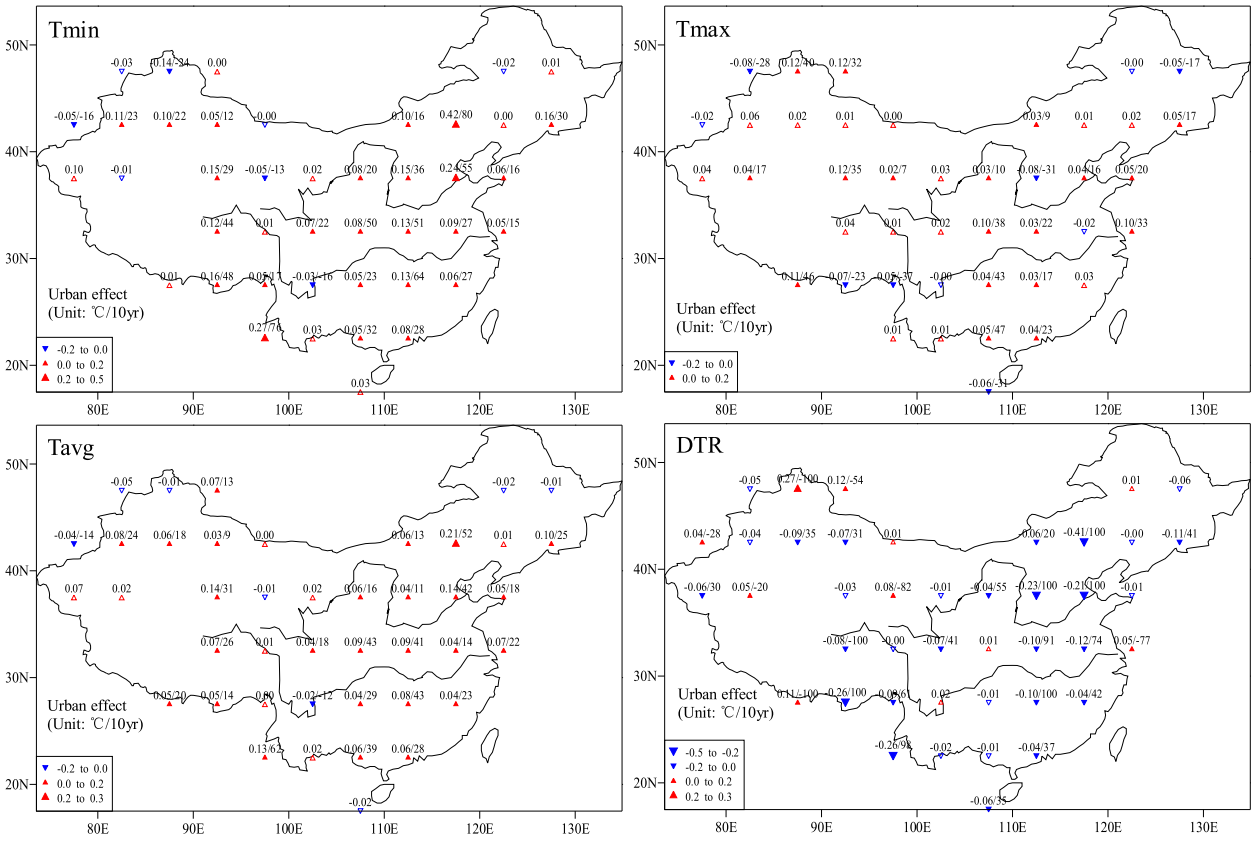


FIG. 5. Spatial distributions of urbanization effects and contributions of annual-mean Tmin, Tmax, Tavg, and DTR in mainland China over the time period 1961–2008. The solid (hollow) triangle denotes that the urbanization effect is (is not) significant at the 0.05 confidence level. The value to the left is urbanization effect [°C (10 yr)$^{-1}$] and to the right is urbanization contribution (%).

series are well above zero, with those of Tmin and Tavg close to 0.80°–0.90°C, implying that either the RCBMS are generally lower in heights than the reference stations, or the urbanization effects for the RCBMS actually began well before 1961.

In view of the spatial distributions of urbanization effects and contributions (Fig. 5), the largest and more significant urbanization effects for Tmin occur in north China, generally ranging from 0.10° to 0.30°C (10 yr)$^{-1}$, with the urbanization contributions generally ranging from 20% to 60%. Most of the grids registers the significant positive urbanization effects for annual-mean Tmin in mainland China, but almost half of the grids in arid northwestern China witness negative urbanization effects with half of them being significant at the 0.05 confidence level. By contrast, there are fewer grids where significant positive urbanization effects are spotted for annual-mean Tmax, despite the fact that most of the grids similarly have positive values of urbanization effects and the significant negative values in a few grids are more evenly distributed across the country. Annual-mean SAT sees a similar spatial pattern, and the largest and more significant urbanization effects, mostly ranging from 0.06° to 0.14°C (10 yr)$^{-1}$, are found in the grids of north China and the lower Yangtze basin. There is a relatively coherent distribution of the DTR urbanization effects across mainland China, and most of the grids experience a decrease because of urbanization, with more than 80% of them registering a significant urbanization effect. The largest urban-induced decrease in the annual-mean DTR are seen in north China and the southeastern Tibetan Plateau, and a 100% urbanization contribution appears in five grids of the two regions, indicating a thorough urbanization effect on the decrease of the annual-mean DTR during the past 48 yr in these areas.

Table 3 also shows annual- and seasonal-mean urbanization effects and contributions of the RCBMS for TNN, TNX, TXN, and TXX over the time period 1961–2008, and Fig. 6 shows the temporal changes in annual-mean urbanization effects as calculated based on the differences between the RCBMS and reference stations in mainland China as a whole for the four indices for the same time period. It is evident that all of the annual

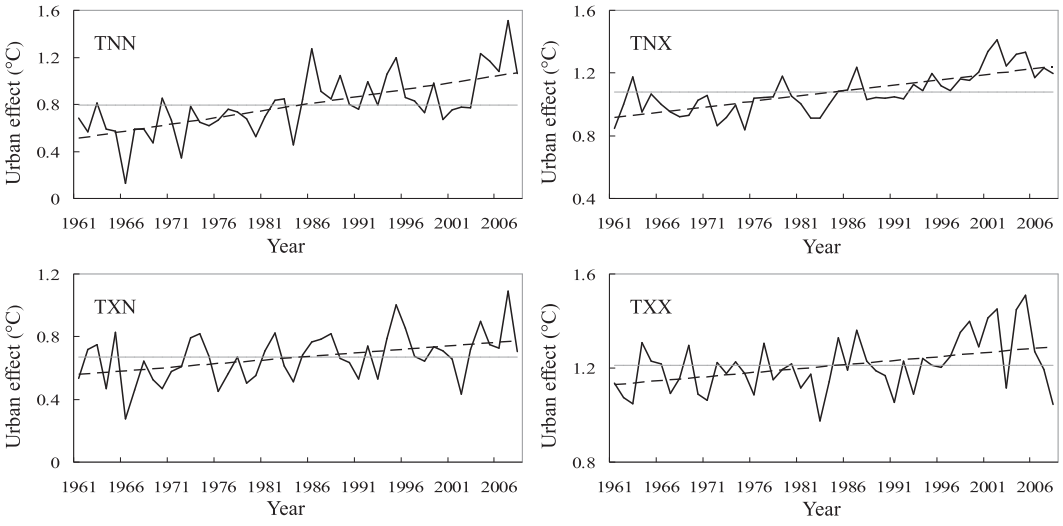


FIG. 6. As in Fig. 4, but for TNN, TNX, TXN, and TXX.

extreme values of Tmin and Tmax experience upward trends, and more significant increases can be seen for TNN and TNX, despite the fact that a larger interannual variability appears in the four indices compared to Tmin, Tmax, Tavg, and DTR. Annual- and seasonal-mean urbanization effects for TNN are all statistically significant at the 0.05 confidence level, with the annual value reaching $0.118°C\,(10\,yr)^{-1}$ and the annual-mean urbanization contribution reaching 19.8%. Although the seasonal-mean urbanization effects for TXN and TXX are all positive for the four seasons, none of them are statistically significant at the 0.05 confidence level (Table 3).

Figure 7 shows spatial distributions of annual-mean urbanization effects and contributions for TNN, TNX, TXN, and TXX over the time period 1961–2008. Most of the grids witness increases, and the largest and more significant increases, generally above $0.150°C\,(10\,yr)^{-1}$ for urbanization effect, are seen for TNN in north China and the northern Qinghai–Tibet Plateau. The positive urbanization effects are also seen for TNX in north China and southeastern China to a lesser extent. The annual-mean urbanization effects for TXN and TXX, however, are usually not so significant with the exceptions of a few of grids in the coastal regions and southeast China. Overall, a more heterogeneous distribution of urbanization effects can be seen for the four indices especially for TXN and TXX, as compared to the spatial uniformity for Tmin, Tmax, Tavg, and DTR.

### *b. Absolute threshold indices*

Table 4 and Fig. 8 exhibit urbanization effects of the RCBMS for SU25, ID0, TR20, and FD0 for the time period 1961–2008. Urbanization leads to an increase in annual total days of SU25 and TR20, but to a decrease in annual total days of ID0 and FD0, and the annual effects are statistically significant except for ID0, with the upward trend reaching $1.090\,days\,(10\,yr)^{-1}$ for the tropical night frequency and an urbanization contribution as high as 37.8%. Urbanization effects are $-0.360$ and $0.335\,days\,(10\,yr)^{-1}$, respectively, for frost days and summer days, and the urbanization contributions are 10.1% and 12.8%, respectively, for the two indices. An insignificant urbanization effect has been detected for ice days over mainland China as a whole, consistent with the insignificant change in annual-mean Tmax. Figure 8 also shows that the linear trends of TR20 and FD0 are larger and more significant, especially after 1976 when the 10-yr Cultural Revolution ended and the economic growth and urbanization of mainland China began to accelerate.

Figure 9 shows spatial distributions of urbanization effects and contributions of annual-mean SU25, ID0, TR20, and FD0 over the time period 1961–2008. With the exception of ID0, the indices exhibit coherent urbanization effects in the regions where the trends can be analyzed. SU25 or summer days are generally characterized by positive urbanization effects, and the most remarkable urbanization-induced increases in summer days, with trends ranging from 0.60 to $1.50\,days\,(10\,yr)^{-1}$ and contributions ranging from 20% to 50%, occur in northern and central China. More spatially coherent distributions of urbanization effects are seen for TR20 and FD0, with the TR20 urbanization effects mostly exhibiting significantly positive trends of $1.00–3.00\,days\,(10\,yr)^{-1}$ and urbanization contributions ranging from 30% to 100% in north China and southeastern China, and the FD0 urbanization effects showing significantly negative

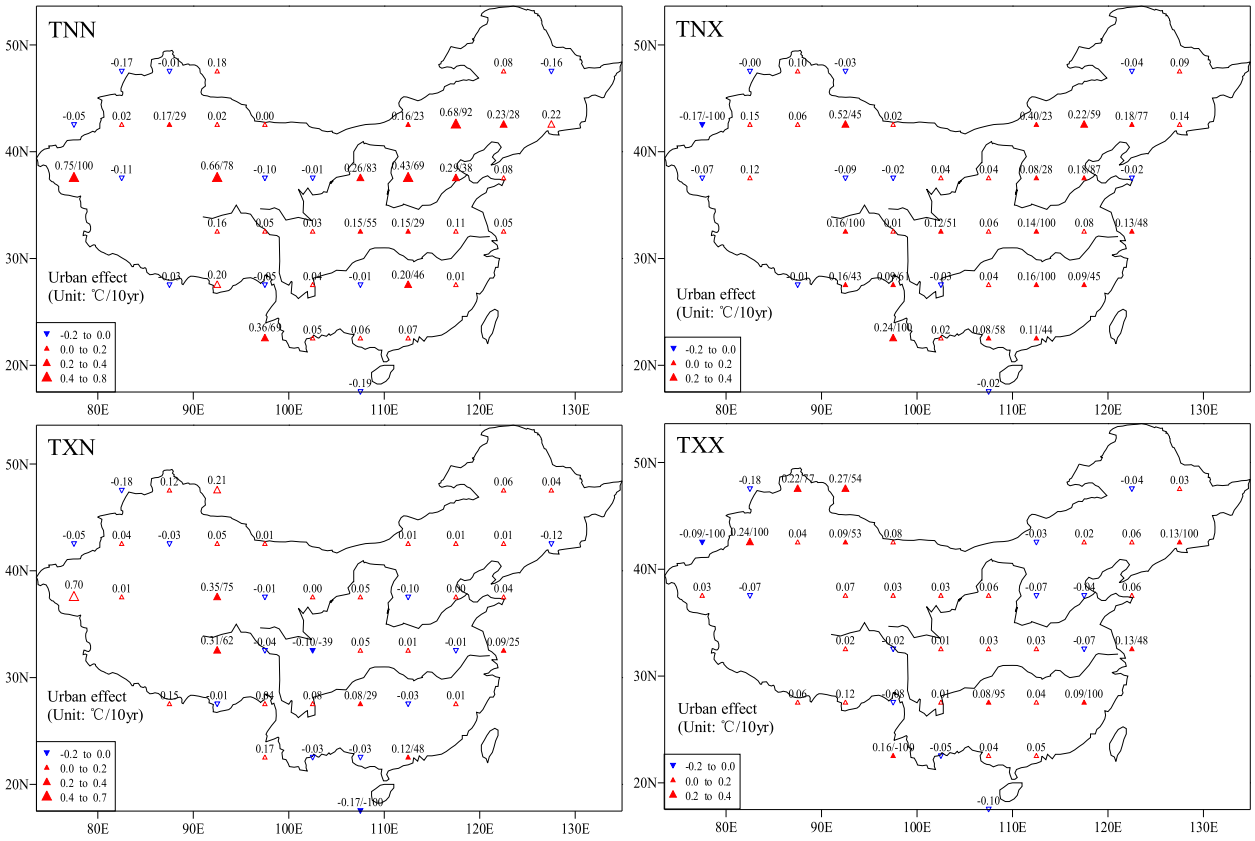


FIG. 7. As in Fig. 5, but for TNN, TNX, TXN, and TXX.

trends from $-1.00$ to $-3.00$ days $(10\,\mathrm{yr})^{-1}$ and urbanization contributions ranging from 20% to 80% in north China. The coherent urbanization effects are not found for ID0 or ice days despite the fact that more negative values can be seen in northwestern China, which is well consistent with the insignificant trend detected in the country-averaged annual ID0 difference series between the RCBMS and reference stations.

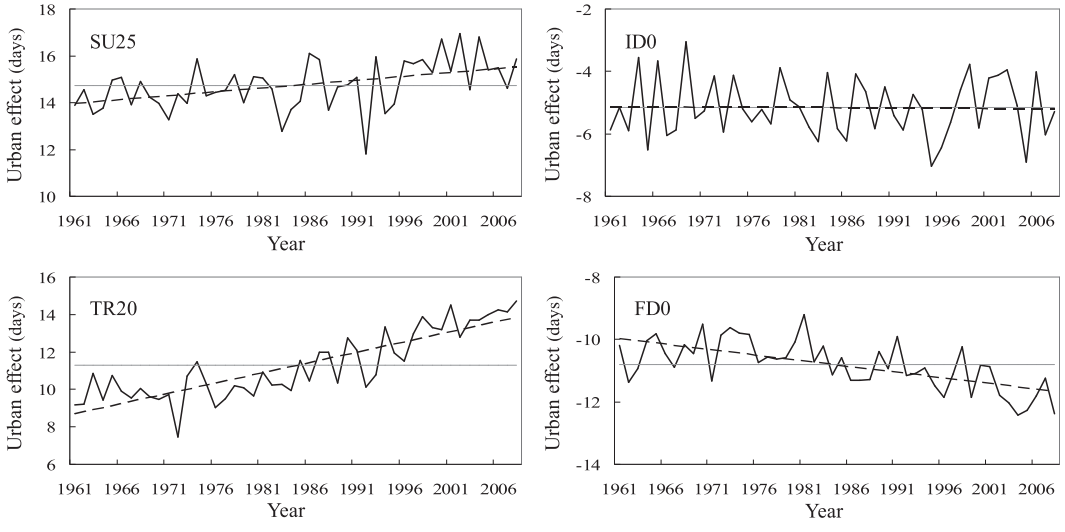


FIG. 8. As in Fig. 4, but for SU25, ID0, TR20, and FD0.

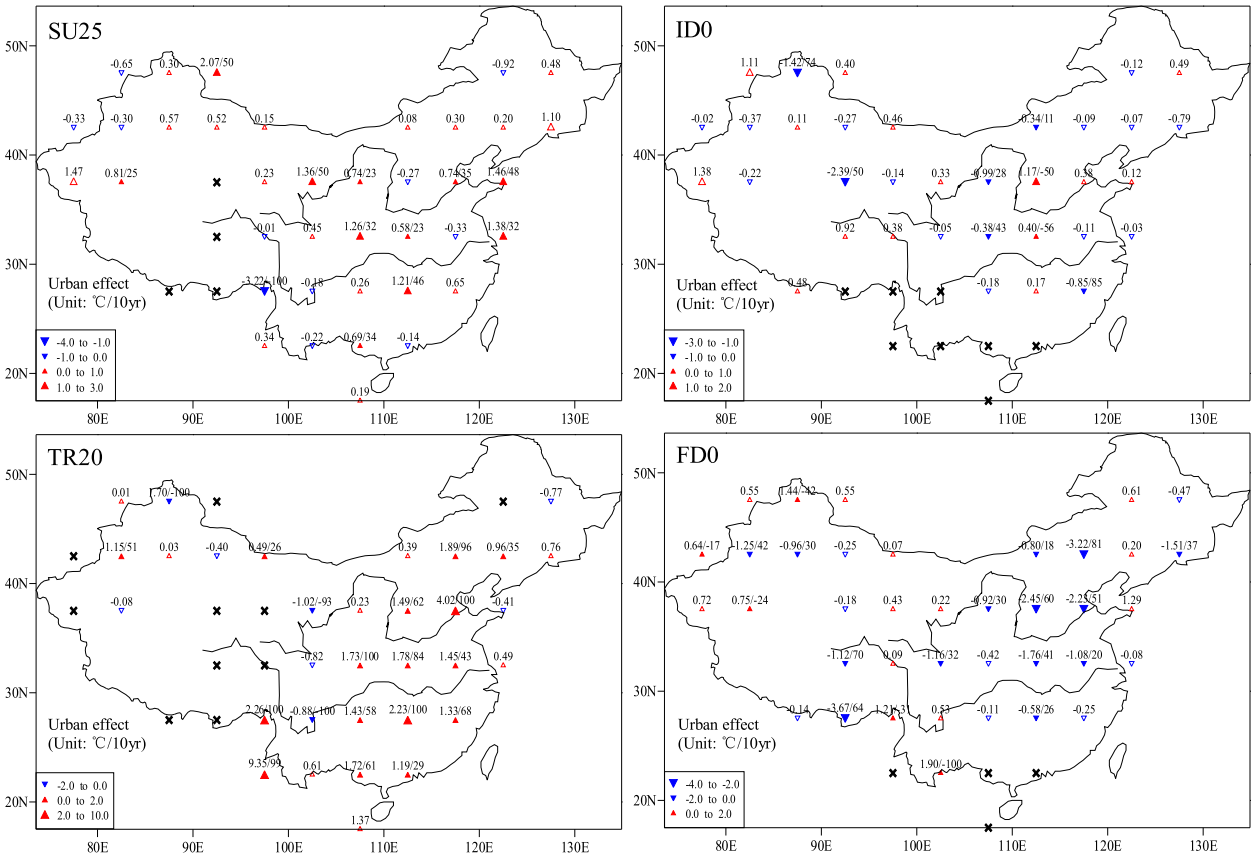


FIG. 9. As in Fig. 5, but for SU25, ID0, TR20, and FD0. Black diagonal crosses indicate the grids where urbanization effects cannot be analyzed because of lacking or incomplete time series of the index.

### c. *Relative threshold indices*

Table 4 also gives urbanization effects and contributions of the RCBMS for TN10p, TN90p, TX10p, and TX90p for the time period 1961–2008, and Fig. 10 shows the temporal change in annual-mean urbanization effects as calculated based on the differences between the RCBMS and reference stations in mainland China for TN10p, TN90p, TX10p, and TX90p for the same time period. The annual-mean urbanization effects are all statistically significant for the four indices over mainland China. Urbanization has led to a highly significant decline of annual-mean cold night frequency at a rate of $-1.485$ days $(10\,\mathrm{yr})^{-1}$, which accounts for 17.6% of the overall decrease as observed in the RCBMS, and a tremendous increase of annual-mean warm night frequency at a rate of 2.264 days $(10\,\mathrm{yr})^{-1}$, which accounts for 26.4% of the overall increase as observed in the RCBMS. The urbanization-induced decline of cold nights mainly occurred after 1976, and the urbanization-induced increase of warm nights dominantly appeared after the beginning of the 1990s. Although the urbanization effects are also statistically significant for cold days and warm days, they are relatively smaller and less significant as compared to cold nights and warm nights. It is interesting to note that the decline of the cold indices (TN10p and TX10p) generally began about 20 yr earlier than the increase of the warm indices (TN90p and TX90p), probably related to the earlier popularization of heating in winter than the widespread application of air conditioning in summer in cities of mainland China.

Seasonal-mean urbanization effects are statistically significant for all of the relative indices and seasons except for cold days and warm days of spring. The largest seasonal-mean trend because of urbanization is seen for warm nights of summer, reaching 3.435 days $(10\,\mathrm{yr})^{-1}$ with an urbanization contribution of 33.7%. The positive urbanization effects are also larger for warm nights of spring and autumn. Reasons for the insignificant urbanization effects for cold days and warm days of spring need to be further examined, but they might have been related to the weakest afternoon UHI intensity resulting from the larger number of days with strong wind during

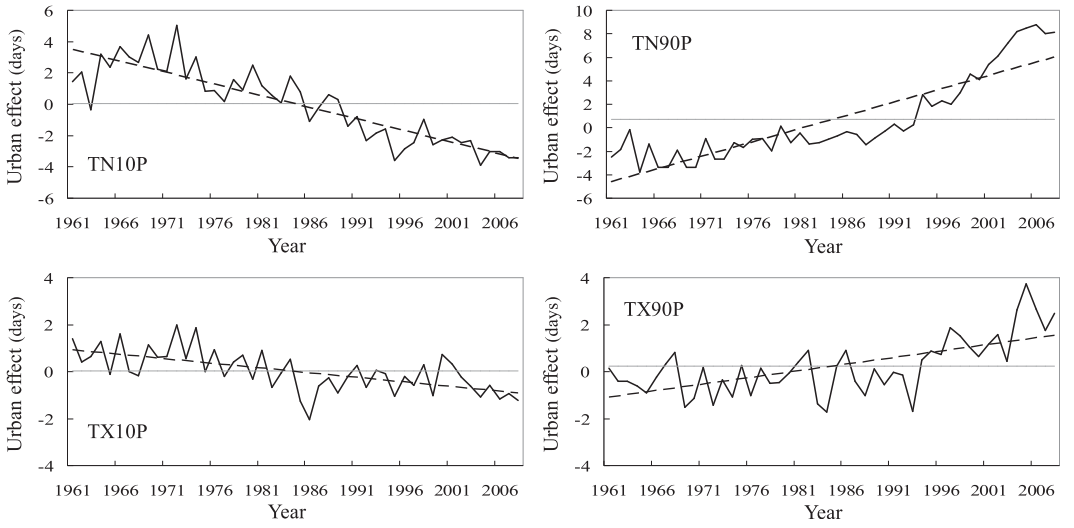


FIG. 10. As in Fig. 4, but for TN10p, TN90p, TX10p, and TX90p.

the season of a year, especially in northern China (Gao et al. 2013; Yang et al. 2013).

Figure 11 shows spatial distributions of urbanization effects and contributions of annual-mean TN10p, TN90p, TX10p, and TX90p in mainland China over the time period 1961–2008. Both cold nights and warm nights exhibit highly coherent urban-induced trends across mainland China. The negative (positive) TN10p (TN90p) urbanization effects are statistically significant for most grids, indicating the tremendous decrease (increase) in cold nights (warm nights) because of the rapid urbanization near the National Stations during the 48-yr period. A few exceptions mainly occur in the northwestern and northeastern parts of the country, consistent with the spatial patterns of the urbanization effects of annual-mean Tmin (Fig. 5). The largest urbanization effects for both TN10p and TN90p, usually ranging from 1.50 to 5.00 days $(10\,\mathrm{yr})^{-1}$ for absolute values with urbanization contributions mostly ranging from 20% to 60%, are seen in north China, the mid-to-lower Yangtze basin, and the eastern part of the Qinghai–Tibet Plateau. Although the TN10p sees larger urbanization effects in northern regions, the TN90p experiences somewhat larger urban-induced warming in southern grids.

Similar to the urbanization effects of the annual-mean Tmax, and obviously different from those of annual-mean Tmin, the annual-mean TX10p and TX90p urbanization effects exhibit generally less spatial coherence across the country than the annual-mean TN10p and TN90p (Fig. 11). Significant decrease (increase) of cold days (warm days) because of urbanization usually appears in northern, central, and southern China, with the absolute values mostly reaching 0.50–2.00 days $(10\,\mathrm{yr})^{-1}$ and the urbanization contributions reaching 10%–50%. The insignificant urbanization effects are seen mainly in western regions and northern northeast China.

## 5. Discussion

Statistically significant changes in extreme temperature indices during the past half a century have been reported for all continents except the Antarctic region (e.g., Karl et al. 1993; Easterling et al. 2000; Manton et al. 2001; Frich et al. 2002; Alexander et al. 2006; Solomon et al. 2007; Qian et al. 2007; Ren et al. 2010a, 2011; X. B. Zhang et al. 2011). These changes are closely related to the significant increase in the global and regional average annual-mean SAT, as both the extreme temperature indices and the mean temperature are dependent on daily maximum and minimum temperature records. The previous studies examined urbanization effects on annual- and seasonal-mean SAT trends as observed in the commonly used datasets or in the records from urban stations in some regions of the global continents and found significant urban warming in the regional average temperature series (e.g., Karl et al. 1988; Hansen et al. 2001; Zhou et al. 2004; Ren et al. 2005, 2008, 2012; Fujibe 2009; Zhang et al. 2010; Fall et al. 2010; Yang et al. 2011). It is therefore natural to assume that urbanization also exerts an nonnegligible effect on the trends of the extreme temperature indices.

Chen et al. (2005) analyzed the urbanization effects on regional trends of annual- and seasonal-mean Tmin and Tmax in Hubei Province, China, and found generally larger urbanization effects in the Tmin series than in the Tmax series. Hua et al. (2008) reported large urbanization effect in minimum temperature series of city stations of the RCBMS in winter over mainland China,

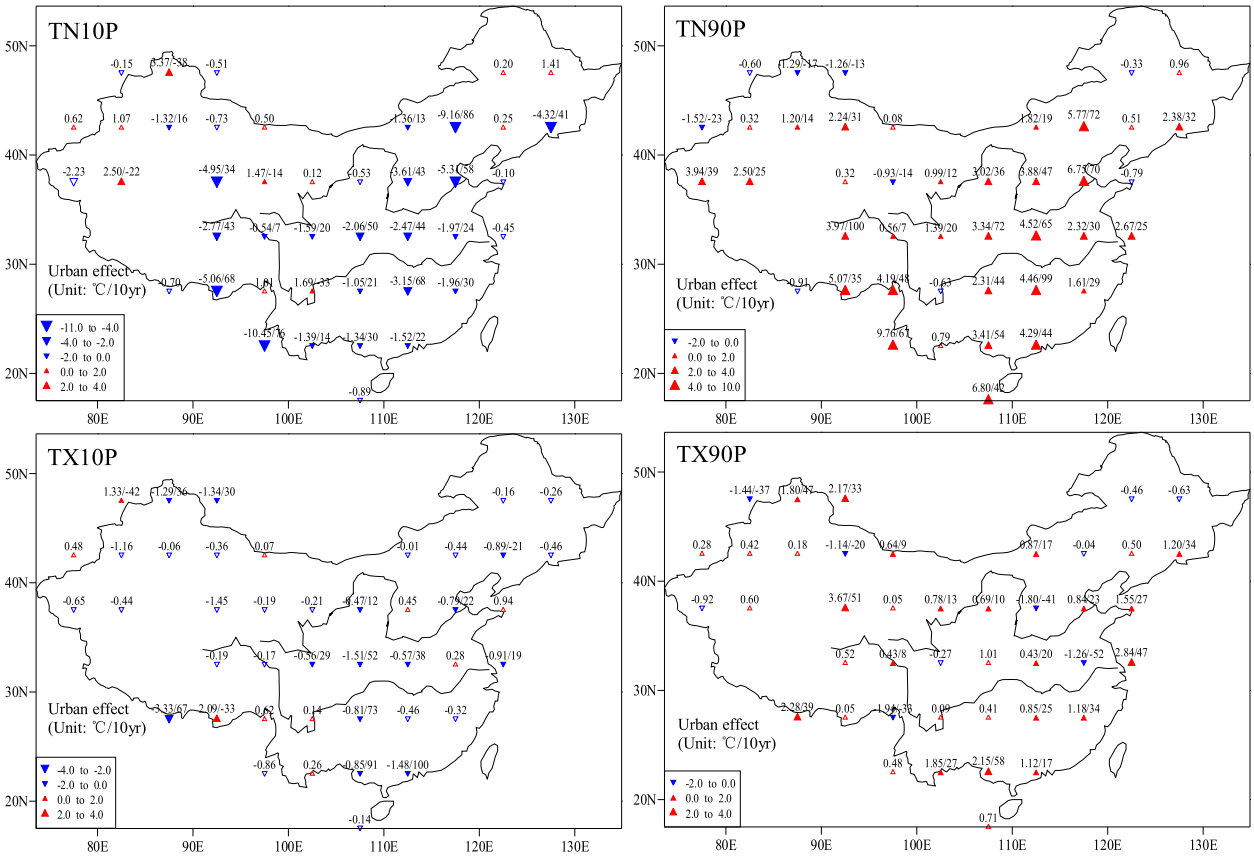


FIG. 11. As in Fig. 5, but for TN10p, TN90p, TX10p, and TX90p.

despite the evident regional differences of the urban warming. Zhou and Ren (2009) analyzed annual- and seasonal-mean urbanization effects on linear trends of Tmax, Tmin, and DTR for the RCBMS in north China and found highly significant urbanization effects in the regional average annual- and seasonal-mean Tmin and DTR series, with the urbanization contributions reaching 53% for annual-mean Tmin and 100% for annual-mean DTR. Zhou and Ren (2011) estimated urbanization effects on trends of different extreme temperature indices for the RCBMS in north China for the time period 1961–2008 and revealed highly significant urbanization effects in the ETIs series related to Tmin, with urbanization contributions reaching 44% and 48%, respectively, for frequencies of annual cold nights and annual warm nights and once again 100% for annual-mean DTR. Zhang et al. (2010) showed that north China is among the regions that experience the largest and most significant urbanization effects on annual-mean temperature trends of the past half a century over mainland China, though significant urban warming also occur in the other regions, except for northern Xinjiang of northwestern China.

Our analysis in this paper shows that urbanization effects in the country-averaged annual- and seasonal-mean Tmin and the Tmin-based ETIs series are also highly significant during the past half a century over mainland China, but magnitudes of the urbanization effects and the contributions to overall changes in the Tmin-based ETIs series are generally smaller than those reported for north China (Zhou and Ren 2011), probably due to the offset effect from the less developed regions in western China and northern northeast China. The largest urbanization effects and contributions of annual-mean DTR are found in north China and the southeastern Tibetan Plateau with five grids witnessing a thorough urbanization contribution to the decrease of the annual-mean DTR, which is well consistent with that reported for north China by Zhou and Ren (2009, 2011) and Zhang et al. (2010). The universally more significant urbanization effects in the Tmin-based ETIs series are also well consistent with those reported before for many regions and are understandable because the UHI intensity and its increase with time near the urban stations are dominantly larger during nighttime than during daytime in temperate and subtropical regions (Landsberg

1981; Oke 1987; Xie et al. 2006; Pielke et al. 2007; Yang et al. 2013). However, the results given in this paper are different from those reported for north China (Zhou and Ren 2011) in that a few of ETIs related to daily Tmax records, such as Tmax, TX10p, and TX90p, also witness significant urbanization effects in mainland China as a whole. This happens probably due to the larger and more significant urbanization effects on the Tmax-based ETIs trends in the southern parts of the country where the use of air conditioning during summer becomes more usual than before as economy grows and people's living standard rises, leading to a generally increasing UHI intensity near the observational sites.

In northwestern and northeastern China, there are a few grids where unexpectedly negative urbanization effects for some ETIs series, obviously for Tmin, Tavg, DTR, TR20, FD0, TN10p, and TN90p, are found. The ''paradox'' has been pointed out for northern northwest China by Zhang et al. (2010) in their study of mainland China. The urban stations of the RCBMS are mostly located in oasis areas in the northwestern arid region. The cool island effect in summer over the oases was reported (Su and Hu 1988). With urban growth, the oasis areas will expand, and SAT observations will be affected not only by increased UHI intensity or urbanization, but also by the oasis development and increasing cool island effect. It is thus possible that the stations near large cities, compared to those near rural and small towns, have undergone relative cooling trends with urbanization and oasis expansion (Zhang et al. 2010). Another reason for the distinct urbanization effects found in northwestern China might have been the relatively poor representativeness of the reference stations, as a few of them in the plains and basins had to be chosen from small cities or towns that might have undergone a rapider urbanization than big cities in the last decades.

Average values of the annual differences of the mean and extreme value indices and absolute threshold indices between the RCBMS and reference stations for the first years of the ETIs series are obviously deviated from zero, with those of Tmin, Tmax, Tavg, TNX, and TXX well above +0.8°C. This is related to the generally lower elevations of the RCBMS stations than the reference stations. Table 5 gives the average latitudes, longitudes, and heights of the RCBMS and reference stations. The average height is calculated from the area-weighted average grid values as done for SAT data. It is clear that little difference of average latitudes exists between the RCBMS and reference stations, but the average height of the RCBMS is about 327 m lower than that of the reference stations, leading to a generally higher SAT temperature in the RCBMS data. It is also possible that the urbanization effects on the extreme temperature indices had actually been felt by the very beginning years of the time period analyzed.

TABLE 5. Average latitudes, longitudes, and heights of the RCBMS and reference stations and the differences between the two networks. Note that mMSL refers to meters above sea level.

| | Latitude (°N) | Longitude (°E) | Elevation (mMSL) |
|---|---|---|---|
| RCBMS | 34.67 | 109.70 | 1258.56 |
| Reference stations | 34.00 | 105.69 | 1585.94 |
| Difference | 0.67 | 4.01 | −327.38 |

Except for DTR and the four relative threshold indices, the smallest absolute values of the annual-mean urbanization effects or the annual differences of the ETIs between the RCBMS and reference stations in the country as a whole dominantly occur during the time period 1966–76. This is especially true for Tmin, Tavg, Tmax, TNN, TXN, TR20, and FD0. The 10-yr period is known as the Cultural Revolution when the country was in its unprecedented chaos and a measurable proportion of urban dwellers including the middle school graduates and university students were sent to the countryside for ''reeducation by farmers.'' The well-known deurbanization process across mainland China might have affected the UHI intensity near the urban stations, leading to the abnormally small urbanization effects as observed from the RCBMS. After the end of Cultural Revolution in 1976, the Chinese central government initiated the ''reform and opening up'' policy, the intellectual youth and other originally urban dwellers returned to cities, and economic growth and urbanization accelerated, leading to the increasing urbanization effects as detected from the country-averaged ETIs series of the RCBMS.

A major source of uncertainty is related to the dataset of the reference stations. Although great efforts had been made to select the reference stations (Ren et al. 2010b; Zhang et al. 2010), and a relatively high-quality dataset of 143 stations had been developed, there are still areas (grids) where no reference station is available. Furthermore, some reference stations in the northeast China plain, north China plain, and northwestern China had to be chosen from small cities and towns because of the lack of real rural stations with sufficient length of records. A consequence of the lowered standard for selecting reference stations is that the urbanization effects on the ETIs series of the RCBMS in this study must have been somehow underestimated. The underestimates for each of the indices series of the RBCMS need to be investigated in the future. In addition, even if the reference stations are truly located in rural areas, there might be more local effects of siting quality of observational

grounds on surface air temperature trends (Fall et al. 2011; McNider et al. 2012), leading to extra nighttime warming for some of the stations. This issue, however, might be more serious for the RCBMS than for the reference stations, but the siting effect might have been included in the estimated urbanization bias of the ETIs series of the RCBMS in a large extent. Although improvement is needed to select more representatively reference stations, the 141 reference stations as used in this work are the best ones we are able to obtain at present.

Despite the uncertainties mentioned above, the urbanization effects in most of the ETIs series of the commonly applied climate dataset in mainland China are of significance, and they are not negligible, especially for those indices series related to daily minimum temperature records in the relatively developed areas of north China, central China, the mid-to-lower reaches of the Yangtze basin, and the southeastern coastal zone. It is also obvious from our analysis that urbanization effects cannot account for the overall changes in the ETIs in mainland China as a whole over the time period 1961–2008, and other factors or processes in addition to the local human influence would be important. These might include the increased concentration of greenhouse gases and aerosols in atmosphere, large-scale land use and land cover change, and the multidecadal natural variability of the climatic system mainly related to the ocean surface temperature variations.

## 6. Conclusions

Applying a homogeneity-adjusted daily temperature dataset of the Chinese national Reference Climate and Basic Meteorological Stations (RCBMS), and a reference station network previously developed by our group, we evaluate the urbanization effects on trends of the extreme temperature indices of the RCBMS for the time period 1961–2008. The following conclusions can be drawn from this study.

1) All the country-averaged annual- and seasonal-mean extreme temperature indices series for the RCBMS experience statistically significant trends, except for the increases in spring of the lowest Tmax and in summer of the highest Tmax. Larger and more significant trends occur in the indices series relative to minimum temperature and the largest positive annual trends are seen for the lowest Tmin and warm nights, reaching $0.596°C\,(10\,yr)^{-1}$ and $8.584\,days\,(10\,yr)^{-1}$, respectively. Decrease of cold nights in winter and increase of warm nights in summer are among the largest seasonal changes of the indices.
2) The annual-mean urbanization effect for mainland China as a whole is 0.070°, 0.023°, and $0.047°C\,(10\,yr)^{-1}$, for Tmin, Tmax, and Tavg, respectively, all statistically significant at the 0.05 confidence level, with urbanization contributions being 18.4%, 10.1%, and 15.4%, respectively. Urbanization effects in winter and spring Tmin series are larger, reaching 0.083° and $0.072°C\,(10\,yr)^{-1}$, respectively. Overall, seasonal-mean urbanization contributions for Tmin, Tmax, and Tavg range from 7.5% to 20.6%. The largest urbanization effects for annual-mean Tmin occur in north China, mostly ranging from 0.10° to $0.30°C\,(10\,yr)^{-1}$, and the urbanization contributions generally from 20% to 60%.
3) Annual- and seasonal-mean urbanization effects for DTR in mainland China as a whole are all highly significant. The largest seasonal-mean DTR decline because of urbanization occurs in winter and spring, reaching −0.061° and $-0.060°C\,(10\,yr)^{-1}$ respectively, but the largest contributions appear in autumn and spring, being 58.1% and 35.9%, respectively. There is a spatially coherent distribution of the DTR urbanization effects across mainland China, and most of the regions experience a decrease because of urbanization. A 100% urbanization contribution is registered in a few areas of the country.
4) Annual extreme values of Tmin and Tmax experience upward trends because of urbanization, and more evident urbanization effects appear in the TNN and TNX series, but a larger interannual variability exists in the indices compared to Tmin, Tmax, Tavg, and DTR. Annual- and seasonal-mean urbanization effects for TNN are statistically significant. However, seasonal-mean urbanization effects for TXN and TXX for all the seasons are not significant. The larger urbanization effects for annual-mean TNN occur in north China and the northern Qinghai–Tibet Plateau. The urbanization effects for annual-mean TXN and TXX, however, are generally not significant.
5) The country-averaged annual-mean SU25, TR20, and FD0 series also see significant urbanization effects. The urbanization effects and contribution are $1.090\,days\,(10\,yr)^{-1}$ and 37.8% for tropical nights, $-0.360\,days\,(10\,yr)^{-1}$ and 10.1% for frost days, and $0.335\,days\,(10\,yr)^{-1}$ and 12.8% for summer days. An insignificant urbanization effect has been detected for ice days over mainland China as a whole. Spatially coherent urbanization effects are seen for TR20 and FD0, with the TR20 urbanization effects mostly exhibiting significantly positive trends of 1.00–2.00 $days\,(10\,yr)^{-1}$ in north China and southeastern China, and the FD0 urbanization effects showing significantly negative trends from $-1.00$ to $-3.00\,days\,(10\,yr)^{-1}$ in north China.
6) Urbanization has led to a highly significant decline of annual-mean cold nights at a rate of

$-1.485$ days $(10\,\text{yr})^{-1}$, accounting for 17.6% of the overall decrease as observed in the RCBMS, and a tremendous increase of annual-mean warm nights at a rate of 2.264 days $(10\,\text{yr})^{-1}$, accounting for 26.4% of the overall increase as observed in the RCBMS. The urbanization-induced decline of cold nights mainly occurred after 1972, but the increase in warm nights because of urbanization dominantly appeared after the early 1990s. Although the urbanization effects are also statistically significant for cold days and warm days, they are relatively smaller in magnitude. Seasonal-mean urbanization effects are statistically significant for the relative threshold indices and for all seasons except for the cold days and warm days of spring.

The negative (positive) TN10p (TN90p) urbanization effects are statistically significant for most regions, indicating the tremendous decrease (increase) in cold nights (warm nights) because of urbanization near the RCBMS. The largest urbanization effects for both TN10p and TN90p, usually ranging from 1.50 to 5.00 days $(10\,\text{yr})^{-1}$ for absolute values with urbanization contributions mostly from 20% to 60%, appear in north China, the mid-to-lower Yangtze basin, and the eastern part of the Qinghai–Tibet Plateau. Larger urbanization effects are in northern regions for TN10p, but in the south for TN90p. The annual-mean TX10p and TX90p urbanization effects exhibit generally less spatial coherence.

7) Except for DTR and the four relative threshold indices, the smallest absolute values of annual-mean urbanization effects or the annual differences of the ETIs between the RCBMS and reference stations in the country as a whole generally occur during the time period 1966–76. This is especially true for Tmin, Tavg, Tmax, TNN, TXN, TR20, and FD0. The 10-yr Cultural Revolution and the resulting deurbanization might have led to the abnormally small urbanization effects observed from the RCBMS. After that, urbanization effects rapidly and stably increased.
8) The urbanization effects reported for all the indices series in this paper should be regarded as the lowest estimates resulting from the compromise for selecting quality reference stations in a few areas in the country. It is therefore clear that urbanization effects on the long-term trends of the frequently used extreme temperature indices series of the observational data commonly applied in mainland China are of significance, despite the fact that they are generally smaller compared to the regional background changes, probably resulting from other factors and processes. The larger and more significant urbanization effects are especially notable for the indices related to daily minimum temperature in relatively developed areas of the country.

*Acknowledgments.* This study is financially supported by the Ministry of Science and Technology of China (Grant GYHY201206012). We appreciate the contributions to the previous study of selecting reference stations from Z. Y. Chu, A. Y. Zhang, and Y. Y. Ren. We also appreciate the constructive comments and suggestions by the four anonymous reviewers.

## REFERENCES

Alexander, L. V., and Coauthors, 2006: Global observed changes in daily climate extremes of temperature and precipitation. *J. Geophys. Res.,* **111,** D05109, doi:10.1029/2005JD006290.

Chen, Z. H., H. J. Wang, G. Y. Ren, H. Xiang, and L. Xue, 2005: Change of urban heat intensity and its effect on regional temperature series: A case study in Hubei Province (in Chinese). *Climate Environ. Res.,* **10,** 771–779.

Choi, G., and Coauthors, 2009: Changes in means and extreme events of temperature and precipitation in the Asia-Pacific network region, 1955–2007. *Int. J. Climatol.,* **29,** 1906–1925.

Choi, J., U. Chung, and J. I. Yun, 2003: Urban-effect correction to improve accuracy of spatially interpolated temperature estimates in Korea. *J. Appl. Meteor.,* **42,** 1711–1719.

Chu, Z. Y., and G. Y. Ren, 2005: Effect of enhanced urban heat island magnitude on average surface air temperature series in Beijing region (in Chinese). *Acta Meteor. Sin.,* **63,** 534–540.

Chung, U., J. Choi, and J. I. Yun, 2004: Urbanization effect on observed change in mean monthly temperature between 1951-1980 and 1971-2000 in Korea. *Climatic Change,* **66,** 127–136.

Ding, Y. H., and Coauthors, 2006: National assessment report on climate change (I): Climate change in China and its future trend (in Chinese). *Adv. Climate Change Res.,* **2,** 3–8.

Easterling, D. R., and T. C. Peterson, 1995: A new method for detecting and adjusting for undocumented discontinuities in climatological time series. *Int. J. Climatol.,* **15,** 369–377.

——, J. L. Evans, P. Ya. Groisman, T. R. Karl, K. E. Kunkel, and P. Ambenje, 2000: Observed variability and trends in extreme climate events: A brief review. *Bull. Amer. Meteor. Soc.,* **81,** 417–425.

Fall, S., D. Niyogi, A. Gluhovsky, R. A. Pielke Sr., E. Kalnay, and G. Rochon, 2010: Impacts of land use land cover on temperature trends over the continental United States: Assessment using the North American Regional Reanalysis. *Int. J. Climatol.,* **30,** 1980–1993.

——, A. Watts, J. Nielsen-Gammon, E. Jones, D. Niyogi, J. Christy, and R. A. Pielke Sr., 2011: Analysis of the impacts of station exposure on the U.S. Historical Climatology Network temperatures and temperature trends. *J. Geophys. Res.,* **116,** D14120, doi:10.1029/2010JD015146.

Frich, P., L. V. Alexander, P. Della-Marta, B. Gleason, M. Haylock, A. M. G. Klein Tank, and T. Peterson, 2002: Observed coherent changes in climatic extremes during the second half of the twentieth century. *Climate Res.,* **19,** 193–212.

Fujibe, F., 2009: Detection of urban warming in recent temperature trends in Japan. *Int. J. Climatol.,* **29,** 1811–1822, doi:10.1002/joc.1822.

Gao, G., and Coauthors, 2013: Climatological characteristics of China. *Climate of China,* Y. H. Ding et al., Eds., Scientific Press, 327–391.

Gong, D. Y., and H. Han, 2004: Extreme climate events in northern China over the last 50 years (in Chinese). *Acta Geophys. Sin.,* **59,** 230–238.

Hansen, J., R. Ruedy, M. Sato, M. Imhoff, W. Lawrence, D. Easterling, T. Peterson, and T. Karl, 2001: A closer look at United States and global surface temperature change. *J. Geophys. Res.,* **106** (D20), 23 947–23 963.

He, Y. T., G. S. Jia, Y. H. Hu, and Z. J. Zhou, 2013: Detecting urban warming signals in climate records. *Adv. Atmos. Sci.,* **30,** 1143–1153, doi:10.1007/s00376-012-2135-3.

Hua, L. J., Z. G. Ma, and W. D. Guo, 2008: The impact of urbanization on air temperature across China. *Theor. Appl. Climatol.,* **93,** 179–194.

Jones, P. D., and M. Hulme, 1996: Calculating regional climatic time series for temperature and precipitation: Methods and illustrations. *Int. J. Climatol.,* **16,** 361–377.

Kalnay, E., and M. Cai, 2003: Impact of urbanization and land use change on climate. *Nature,* **423,** 528–531.

Karl, T. R., H. F. Diaz, and G. Kukla, 1988: Urbanization: Its detection and effect in the United States climate record. *J. Climate,* **1,** 1099–1123.

——, and Coauthors, 1993: A new perspective on recent global warming: Asymmetric trends of daily maximum and minimum temperature. *Bull. Amer. Meteor. Soc.,* **74,** 1007–1023.

Kendall, M. G., and J. D. Gibbons, 1990: *Rank Correlation Methods.* 5th ed. Oxford University Press, 272 pp.

Klein Tank, A. M. G., and G. P. Konnen, 2003: Trends indices of daily temperature and precipitation extremes in Europe, 1946–99. *J. Climate,* **16,** 3665–3680.

Landsberg, H. E., 1981: *The Urban Climate.* Academic Press, 275 pp.

Li, Q. X., and W. J. Dong, 2009: Detection and adjustment of undocumented discontinuities in Chinese temperature series using a composite approach. *Adv. Atmos. Sci.,* **26,** 143–153.

——, X. N. Liu, H. Z. Zhang, T. C. Peterson, and D. R. Easterling, 2004: Detecting and adjusting temporal inhomogeneity in Chinese mean surface air temperature data. *Adv. Atmos. Sci.,* **21,** 260–268.

Li, Y., L. Zhu, X. Zhao, S. Li, and Y. Yan, 2013: Urbanization impact on temperature change in China with emphasis on land cover change and human activity. *J. Climate,* **26,** 8765–8780.

Liu, X. D., Z. Y. Yin, X. M. Shao, and N. S. Qin, 2006: Temporal trends and variability of daily maximum and minimum, extreme temperature events, and growing season length over the eastern and central Tibetan Plateau during 1961–2003. *J. Geophys. Res.,* **111,** D19109, doi:10.1029/2005JD006915.

Ma, Z. G., C. B. Fu, X. B. Ren, and C. Yang, 2003: Trend of annual extreme temperature and its relationship to regional warming in northern China. *Acta Geogr. Sin.,* **58** (Suppl.), 11–20.

Manton, M. J., and Coauthors, 2001: Trends in extreme daily rainfall and temperature in Southeast Asia and the South Pacific: 1961–1998. *Int. J. Climatol.,* **21,** 269–284.

McNider, R. T., and Coauthors, 2012: Response and sensitivity of the nocturnal boundary layer over land to added longwave radiative forcing. *J. Geophys. Res.,* **117,** D14106, doi:10.1029/2012JD017578.

Oke, T. R., 1987: *Boundary Layer Climates.* Methuen, 435 pp.

Peterson, T. C., X. Zhang, M. Brunet-India, and J. L. Vázquez-Aguirre, 2008: Changes in North American extremes derived from daily weather data. *J. Geophys. Res.,* **113,** D07113, doi:10.1029/2007JD009453.

Pielke, R. A., Sr., and Coauthors, 2007: Documentation of uncertainties and biases associated with surface temperature measurement sites for climate change assessment. *Bull. Amer. Meteor. Soc.,* **88,** 913–928.

Qian, W. H., and X. Lin, 2004: Regional trends in recent temperature indices in China. *Climate Res.,* **27,** 119–134.

——, J. Fu, W. Zhang, and X. Lin, 2007: Changes in mean climate and extreme climate in China during the last 40 years (in Chinese). *Adv. Earth Sci.,* **22,** 673–684.

Ren, G. Y., and Coauthors, 2005: Recent progresses in studies of regional temperature changes in China (in Chinese). *Climatic Environ. Res.,* **10,** 701–716.

——, Y. Q. Zhou, Z. Y. Chu, J. X. Zhou, A. Zhang, J. Guo, and X. Liu, 2008: Urbanization effect on observed surface air temperature trend in north China. *J. Climate,* **21,** 1333–1348.

——, G. L. Feng, and Z. W. Yan, 2010a: Progresses in observation studies of climate extremes and changes in mainland China (in Chinese). *Climate Environ. Res.,* **15,** 337–353.

——, A. Y. Zhang, Z. Y. Chu, J. X. Zhou, Y. Y. Ren, and Y. Zhou, 2010b: Principles and procedures for selecting reference surface air temperature stations in China (in Chinese). *Meteor. Sci. Technol.,* **38,** 78–85.

——, Z. Guan, X. Shao, and D. Y. Gong, 2011: Change in climatic extremes over mainland China. *Climate Res.,* **50,** 105–111, doi:10.3354/cr01067.

——, Y. H. Ding, Z. C. Zhao, J. Y. Zheng, T. W. Wu, G. Tang, and Y. Xu, 2012: Recent progress in studies of climate change in China. *Adv. Atmos. Sci.,* **29,** 958–977.

Ren, Y. Y., and G. Y. Ren, 2011: A remote-sensing method of selecting reference stations for evaluating urbanization effect on surface air temperature trends. *J. Climate,* **24,** 3179–3189.

Shi, J., Y. H. Ding, and L. L. Cui, 2009: Climatic characteristics of extreme maximum temperature in East China and its causes (in Chinese). *Chin. J. Atmos. Sci.,* **33,** 347–358.

Solomon, S., D. Qin, M. Manning, Z. Chen, M. Marquis, K. Averyt, M. Tignor, and H. L. Miller Jr., Eds., 2007: *Climate Change 2007: The Physical Science Basis.* Cambridge University Press, 996 pp.

Su, C. X., and Y. Q. Hu, 1988: Cold island effect over oasis and lake. *Chin. Sci. Bull.,* **10,** 756–758.

Tang, G. L., G. Y. Ren, and J. X. Zhou, 2008: Change of urban heat island intensity and its effect on surface air temperature records in southwest China (in Chinese). *J. Appl. Meteor.,* **19,** 722–730.

Tang, H. Y., P. M. Zhai, and Z. Y. Wang, 2005: On change in mean maximum temperature, minimum temperature and diurnal range in China during 1951-2002 (in Chinese). *Climatic Environ. Res.,* **10,** 728–735.

Vincent, L. A., and Coauthors, 2005: Observed trends in indices of daily temperature extremes in South America 1960–2000. *J. Climate,* **18,** 5011–5023.

Von Storch, H., and F. W. Zwiers, 2003: *Statistical Analysis in Climate Research.* Cambridge University Press, 484 pp.

Wang, Y., X. N. Liu, and X. H. Ju, 2007: Differences between automatic and manual observation (in Chinese). *J. Appl. Meteor. Sci.,* **18,** 849–855.

Wu, K., and X. Q. Yang, 2013: Urbanization and heterogeneous surface warming in eastern China. *Chin. Sci. Bull.,* **58,** 1363–1373, doi:10.1007/s11434-012-5627-8.

Xie, Z., J.-L. Cui, D.-G. Chen, and B.-K. Hu, 2006: The annual, seasonal and monthly characteristics of diurnal variation of urban heat island intensity in Beijing (in Chinese). *Climatic Environ. Res.,* **11,** 69–75.

Yan, Z., and Coauthors, 2002: Trends of extreme temperatures in Europe and China based on daily observations. *Climatic Change,* **53,** 355–392.

Yang, P., G. Y. Ren, and W. D. Liu, 2013: Spatial and temporal characteristics of Beijing urban heat island (UHI) intensity. *J. Appl. Meteor. Climatol.,* **52,** 1803–1816.

Yang, X., Y. Hou, and B. Chen, 2011: Observed surface warming induced by urbanization in east China. *J. Geophys. Res.,* **116,** D14113, doi:10.1029/2010JD015452.

Yang, Y. J., and Coauthors, 2012: Impacts of urbanization and station-relocation on surface air temperature series in Anhui Province, China. *Pure Appl. Geophys.,* **170,** 1969–1983, doi:10.1007/s00024-012-0619-9.

You, Q.-L., S.-C. Kang, C.-L. Li, Y.-P. Yan, and S.-Y. Yan, 2008: Change in extreme temperature over Sanjiangyuan region in the period from 1961 to 2005 (in Chinese). *Res. Environ. Yangtze Basin,* **17** (2), 233–236.

You, Q. L., K. Fraedrich, G. Ren, N. Pepin, and S. Kang, 2012: Variability of temperature in the Tibetan Plateau based on homogenized surface stations and reanalysis data. *Int. J. Climatol.,* **33,** 1337–1347, doi:10.1002/joc.3512.

——, G. Y. Ren, K. Fraedrich, S. C. Kang, Y. Y. Ren, and P. L. Wang, 2013: Winter temperature extremes in China and their possible causes. *Int. J. Climatol.,* **33,** 1444–1455.

Zhai, P. M., and X. H. Pan, 2003: Trends in temperature extremes during 1951–1999 in China. *Geophys. Res. Lett.,* **30** (17), 1913–1916.

——, A. J. Sun, F. M. Ren, X. N. Liu, B. Gao, and Q. Zhang, 1999: Chances of climate extremes in China. *Climatic Change,* **42,** 203–218.

Zhang, A. Y., G. Y. Ren, J. X. Zhou, Z. Y. Chu, Y. Y. Ren, and G. L. Tang, 2010: Urbanization effect on surface air temperature trends over China (in Chinese). *Acta Meteor. Sin.,* **68,** 957–966.

Zhang, J. C., and Z. G. Lin, 1992: *Climate of China.* Wiley, 376 pp.

Zhang, L., G. Y. Ren, J. Liu, Y. Q. Zhou, Y. Y. Ren, A. Y. Zhang, and Y. W. Feng, 2011: Urbanization effect on trends of extreme temperature indices at Beijing station (in Chinese). *Chin. J. Geophys.,* **54,** 1150–1159.

Zhang, R. H., and X. D. Xu, 2008: *China Climatic Observational System.* China Meteorological Press, 291 pp.

Zhang, X. B., and F. Yang, 2004: *RClimDex (1.0) User Manual.* Climate Research Branch, Environment Canada.

——, L. Alexander, G. C. Hegerl, P. Jones, A. K. Tank, T. C. Peterson, B. Trewin, and F. W. Zwiers, 2011: Indices for monitoring changes in extremes based on daily temperature and precipitation data. *Wiley Interdiscip. Rev.: Climate Change,* **2,** 851–870, doi:10.1002/wcc.147.

Zhao, Z. C., 1991: Temperature change of the past 39 years and the impact of urbanization on it (in Chinese). *Meteor. Mon.,* **17** (4), 14–17.

Zhou, L. M., R. E. Dickinson, Y. H. Tian, J. Y. Fang, Q. X. Li, R. K. Kaufman, C. J. Tucker, and R. B. Myneni, 2004: Evidence for a significant urbanization effect on climate in China. *Proc. Natl. Acad. Sci. USA,* **101,** 9540–9544.

Zhou, Y. Q., and G. Y. Ren, 2009: The effect of urbanization on maximum, minimum temperature and daily temperature range in north China (in Chinese). *Plateau Meteor.,* **28,** 1158–1166.

——, and ——, 2011: Change in extreme temperature events frequency over mainland China during 1961–2008. *Climate Res.,* **50,** 125–139, doi:10.3354/cr01053.

任国玉,任玉玉,李庆祥,等. 全球陆地表面气温变化研究现状、问题和展望[J]. 地球科学进展,2014,29(8):934-946,doi:10.11867/j.issn.1001-8166.2014.08.0934. [Ren Guoyu, Ren Yuyu, Li Qingxiang, et al. An overview on global land surface air temperature change[J]. Advances in Earth Science,2014,29(8):934-946,doi:10.11867/j.issn.1001-8166.2014.08.0934.]

# 全球陆地表面气温变化研究现状、问题和展望*

任国玉[1],任玉玉[1],李庆祥[2],徐文慧[2]
(1. 中国气象局气候研究开放实验室,国家气候中心,北京 100081;
2. 中国气象局国家气象信息中心,北京 100081)

**摘 要**: 气候变化模拟、预估、影响评价和适应行动,均需深入了解全球陆地及不同区域地面平均气温、极端气温变化的基本观测事实和精准时空规律。长期以来,近百年全球陆地表面气温序列的构建和分析主要由英国和美国少数几家研究机构垄断。这些机构研制的长序列全球陆地表面气温变化分析产品成为气候变化科学的基石。然而,现有全球陆地表面气温资料数据及分析结果还存在明显不足,其中突出的问题包括: ①中国及周边国家、地区观测覆盖不充分,早期资料覆盖严重匮乏; ②对城市化影响偏差重视不够,没有对其进行系统研究和订正。另一方面,我国气象部门目前已初步建立了全球陆地表面气温观测资料数据集,中国科学家也在城市化对地面气温趋势影响偏差评价和订正方面开展了系统研究。但迄今为止,我国还没有研制出高质量、覆盖全球各个大陆的地表气温资料数据集及其分析产品。如何完善业已建成的地表气温观测资料数据集,系统分析、评价全球陆地城镇观测站地面气温序列中的城市化影响性质和程度,发展客观的方法订正城市化影响偏差,建立中国自己的高质量全球陆地长序列地面气温资料数据集,构建和分析全球陆表平均和极端气温时间序列,监测和揭示全球陆地及不同区域地面气温变化的精细规律,已成为我国气候变化和全球变化科学的重要任务。

**关 键 词**: 全球气候变化; 地表气温; 基础数据; 城市化影响
**中图分类号**: P54 **文献标志码**: A **文章编号**: 1001-8166(2014)08-0934-13

## 1 引 言

全球气候变化或气候变化,因其高度的政治、环境、经济意义和较高的科学上的不确定性,引起社会各界、特别是学术界相关领域学者的广泛关注。

气候变化成为科学研究的热点是因为近 100 多年地球表面温度的显著上升,即全球气候变暖,以及由此引起了地球气候系统其他圈层要素的明显变化[1~5]。研究指出,过去 100 年特别是过去 50 年全球陆地表面气温比海洋表层水温升高明显得多,最显著的气候变暖区域位于亚洲中高纬度地带[3~4,6],包括中国东北、华北、西北和青藏高原地区[7~14]。研究还表明,全球气候变暖,特别是大陆中高纬度的显著变暖,可能已对生态系统、水文循环和农业生产造成了深刻影响[15~18]。因此,全球陆地及其关键区域现代地面气温长期变化趋势的监测和检测,是气候变化研究的重要基础性工作[19]。

开展全球陆地表面气温变化规律研究,将为我国全球气候变化监测业务提供基础数据、理论和方法支持,也将为国家制定应对气候变化策略和行动

收稿日期: 2014-06-16; 修回日期: 2014-07-21.
* 基金项目: 国家公益性行业(气象)专项"近百年全球陆地气候变化监测技术与应用"(编号: GYHY-201206012)资助.
作者简介: 任国玉(1958-),男,辽宁沈阳人,研究员,主要从事气候变化研究. E-mail: guoyoo@cma.gov.cn

?1994-2014 China Academic Journal Electronic Publishing House. All rights reserved. http://www.cnki.net

方案提供准确的科学信息。

国家相关部门十分重视全球气候变化研究。国家自然科学基金委员会发起的《全球变化及其区域响应》计划,重点支持围绕全球气候变化机制的若干重大基础科学问题研究; 科技部发布的《国家中长期科学和技术发展规划纲要(2006—2020 年)》和《中国应对气候变化科技专项行动》均把全球和区域气候变化监测、检测研究作为未来我国气候变化科技发展的优先领域或重点任务。

我国学者在中国和东亚地区气候变化检测研究方面取得了系列成果,为深入理解区域气候变化的原因和机理、制定气候变化应对政策,做出了贡献[5,7,20~22]。但是,迄今为止,国内针对地面气温等关键气候要素的监测和检测研究,主要还局限于中国大陆地区[23~32],对于整个亚洲地区特别是全球陆地气温长期变化的研究还很少[33,34],业已开展的全球陆地分析亦未采用我国自己发展的气温观测数据资料,无法建立独立的全球陆地平均气温序列。研究区域的局限性不利于对全球变化时空规律监测信息的完整掌握,削弱了建立在观测事实基础上的全球变化机制和预估研究能力,对于和气候变化政策相关的若干重大科学问题缺少原创性认识[35,36]。

从满足国家需求的角度看,不论是确立气候谈判的国家策略和立场,还是同其他国家特别是发展中国家和地区合作开展气候变化适应工作,政府决策者和各利益相关方都需要准确及时了解中国以外的亚洲、非洲以及其他大陆各主要国家和地区的气候变化监测信息,分析评价各主要国家、地区气候变化政策、立场形成的背景和深层次因素,增强气候谈判策略制定的科学性,同时有针对性地开展应对特别是适应气候变化的国际合作。

## 2　研究现状

长期以来,开展全球陆地近地面气温变化监测和分析的国际研究机构主要有: 英国东英吉利大学气候研究中心(Climate Research Unit, CRU)、美国国家海洋—大气管理局(National Ocean-Atmosphere Administration, NOAA)的国家气候资料中心(National Climate Data Center, NCDC)和美国国家航空—航天管理局(National Aeronautics and Space Administration, NASA) Goddard 空间研究所(Goddard Institute for Space Studies, GISS)。CRU 建立了全球陆地地面气温格点数据集(CRUTEM-3,4); NCDC 建立了全球历史气候网数据集(GHCN-3); GISS 则在 GHCN 数据集基础上通过订正城市热岛效应偏差,增加南极大陆部分观测资料,建立了自己的全球陆地气温数据集(GISTEMP)。利用这 3 个机构数据集获得的过去 100 多年全球陆地地面气温长期变化趋势的分析结果[6,37~40],是政府间气候变化专门委员会(Intergovernmental Panel on Climate Change, IPCC)历次评估报告的关键科学凭据[3,4,41],也为全球和区域尺度气候变化检测、预估和影响评估研究提供了基本观测数据。最近,美国伯克利地球表面温度项目(Berkeley Earth Surface Temperature Project)发展了一套新的全球陆地气温序列[4,42],日本气象厅也公布了全球陆地和海洋表层温度变化监测序列[43],但这 2 套资料序列的陆地部分几乎完全是在 GHCN 月平均气温资料基础上建立起来的,前者则采用了不同的区域平均方法,目前还不是学术界公认的独立全球陆表气温数据集。

应用上述数据集获得的过去全球陆地平均地面气温距平序列,均表明了显著的气候变暖趋势(表 1)。如在 1900—2005 年期间,根据 CRU,GHCN 和 GISS 数据集资料,全球陆地平均气温增加速率分别为(0.08 ± 0.02),(0.06 ± 0.02)和(0.07 ± 0.02) ℃/10a,CRU 的估算结果最大,GHCN 和 GISS 结果相近,但均反映出显著变暖趋势; 1901—2012 年,CRU,GHCN 和 GISS 数据集给出的全球陆地年平均气温上升速率分别为(0.10 ± 0.02),(0.11 ± 0.02)和(0.10 ± 0.02) ℃/10a,相互差异很小; 而根据 1979—2005 年的 3 套资料分析获得的全球陆地平均气温上升速率分别为(0.27 ± 0.07),(0.32 ± 0.09)和(0.19 ± 0.07) ℃/10a,表现出加速变暖现象,但不同估计值之间的差异较大,NCDC 最高,GISS 最低[3,37,38,43,44]。近年 GISS 数据集中增补了北极地区遥感观测数据,给出了与原来不同的结果[45,46],各个时期的增温趋势都有增加,其中 1979 年以来的增温趋势比他们原来的估计值显著增大。造成前后估算结果差异的主要原因是,GISS 数据集增加北极地区遥感温度观测资料覆盖后,明显增大了全球陆地最近几十年快速增暖区域所占比例,如果仅分析检验 20 世纪 80 年代以来全球陆表温度的变化,这样处理是可以的; 但由于 20 世纪早、中期没有卫星遥感数据,对于建立和分析过去 100 多年全球陆表温度的时间序列,这种处理方法就有失妥当了。

此外,在 1951—2012 年期间,根据 CRU(CRUTEM4.1.1.0),GHCN(v3.2.0)和 GISS 更新数据集获得的全球陆表年平均气温上升速率分别为



?1994-2014 China Academic Journal Electronic Publishing House. All rights reserved.　http://www.cnki.net

表 1 全球陆表年平均气温不同时期变化趋势估计值比较(单位: ℃/10a)

Table 1 Comparison of long-term trends of global land annual mean surface air temperature estimated based on different datasets(unit: ℃/10a)

| 数据集 | 起讫时间 | 时长/a | 趋势及信度区间 | 参考文献 |
|---|---|---|---|---|
| CRUTEM | 1900—2005 年 | 106 | 0.08 ±0.02 | [40,43] |
| | 1979—2005 年 | 27 | 0.27 ±0.07 | |
| | 1901—2012 年 | 112 | 0.10 ±0.02 | |
| | 1951—2012 年 | 62 | 0.18 ±0.04 | |
| | 1979—2012 年 | 34 | 0.25 ±0.05 | |
| GHCN | 1900—2005 年 | 106 | 0.06 ±0.02 | [38,39] |
| | 1979—2005 年 | 27 | 0.32 ±0.09 | |
| | 1901—2012 年 | 112 | 0.11 ±0.02 | |
| | 1951—2012 年 | 62 | 0.20 ±0.03 | |
| | 1979—2012 年 | 34 | 0.27 ±0.05 | |
| GISS | 1900—2005 年 | 106 | 0.07 ±0.02 | [44,45] |
| | 1979—2005 年 | 27 | 0.19 ±0.07 | |
| | 1901—2012 年 | 112 | 0.10 ±0.02 | |
| | 1951—2012 年 | 62 | 0.19 ±0.03 | |
| | 1979—2012 年 | 34 | 0.27 ±0.05 | |
| Berkeley | 1901—2012 年 | 112 | 0.10 ±0.02 | [42] |
| | 1951—2012 年 | 62 | 0.18 ±0.03 | |
| | 1979—2012 年 | 34 | 0.25 ±0.05 | |

注: 趋势估计误差为 90% 信度区间(1 倍标准差),仅包括采样不确定性范围

(0.18 ±0.04),(0.20 ±0.03) 和(0.19 ±0.03) ℃/10a (表 1);基于所有数据集构建的全球陆表年平均气温序列在最近 15 年左右(1998 年以后) 均呈现出明显的变暖趋缓现象[4]。

可见,利用不同数据集获得的百年增温速率估算结果之间差异较小,这主要和他们包含着较高比例的共同观测站点有关。CRUTEM-4 包括 4 891 站经过均一化的月气温数据,空间分布较均匀,用以计算距平的气候基准期(1961—1990 年) 内观测记录相对较完整; GHCN-3 包括 7 280 站月平均气温数据和近 5 000 站的月平均最高(最低) 气温数据,尽管均一化处理后的数据量要少些,但站点数量仍比 CRUTEM-4 数据集多。后者站点绝大部分来自 GHCN 数据集; GISS 则几乎完全使用 GHCN 数据,仅在南极大陆增加了少量来自南极研究科学委员会(Scientific Committee on Antarctic Research, SCAR) 公布的观测资料,目前全部站点数约 6 300 个,但对美国以外地区的城市化偏差做了初步订正。

站点数量及其覆盖范围的不同,以及空间平均方法的差异,可能是造成不同数据集全球陆地平均气温序列趋势估计值存在差别的部分原因。CRUTEM 和 GHCN 数据集中不同的均一化处理方法对个别区域(如美国本土区域) 平均地面气温趋势变化有一定影响,但对全球陆地平均气温序列趋势估计值的影响不大[3,4]。

对全球陆地平均气温序列趋势估计值或误差范围的影响主要来自城市化造成的系统偏差和早期观测资料的缺乏。就城市化偏差来看,Hansen 等[37]对其给予了一定考虑。他们利用人口资料和卫星遥感资料分类气象台站,确定气温参考站,并订正其他站的城市化偏差。利用他们早期订正获得的数据集构建全球陆地平均气温序列,其趋势变化估计值确实较基于其他数据集的分析结果偏低,在 1979—2005 年偏小尤为显著[3,44],大约比 CRU 和 NCDC 序列揭示的增温趋势分别减少 30% 和 41%,说明对城市台站地面气温序列进行城市化偏差订正,其分析结果比其他 2 套气温数据集更接近区域和全球背景变暖趋势。如前所述,GISS 最新估计得到的 1979—2012 年全球陆地增温速率明显增大,主要是在北极地区采用了卫星遥感资料造成的。在更长时间尺度上,GISS 数据集全球陆地气温序列趋势与其他数据集相差不大[3,4]。

## 3 存在问题

上述 3 套数据集及其分析产品为全球气候变化研究提供了陆地气温观测基础资料,对气候变化科学的发展产生了深远影响。但是,这 3 套全球陆地气温数据资料也存在若干明显的问题和缺陷。其中最突出的问题包括: ①亚洲等发展中国家和地区观测覆盖不充分,早期资料尤其匮乏; ②没有对城市化影响偏差给予足够重视。

现有全球地面气温数据分析产品的一个缺陷是,观测站点在北美和欧洲密集,但在亚洲、非洲和南美洲等地区台站分布稀疏,特别是在 1950 年以前资料覆盖率较低,1990 年以后许多地区资料覆盖率下降。

在 19 世纪末 20 世纪初,所有数据集的观测站点都很少,其中亚洲的中国及其周边地区尤其稀疏。即使在 20 世纪后期和现在,亚洲、非洲和南美等大陆站点稀缺的状况依然严重。如 CRUTEM 长期以来在中国地区仅有 160 余站,这些台站的观测记录大部分始于 20 世纪 50 年代以后,早期特别是 20 世纪初期资料十分稀缺; GHCN 和 GISTEMP 尽管采用了中国 1997 年以前 500 余站的资料,但 1997 年后的数据没有更新,数据完整的仅有不足 100 个站。同时,在 GHCN 和 GISTEMP 数据集



?1994-2014 China Academic Journal Electronic Publishing House. All rights reserved. http://www.cnki.net

中,北亚、蒙古、西亚、巴基斯坦和朝鲜等地区资料稀少,蒙古和西亚大片区域几乎没有月平均最高、最低气温数据(图 1),青藏高原资料也极少。在 1990 年前后和 2005 年以后,GHCN 数据集中台站数大幅下降,中国、加拿大、俄罗斯西部、非洲和南美洲等地区下降尤其明显。

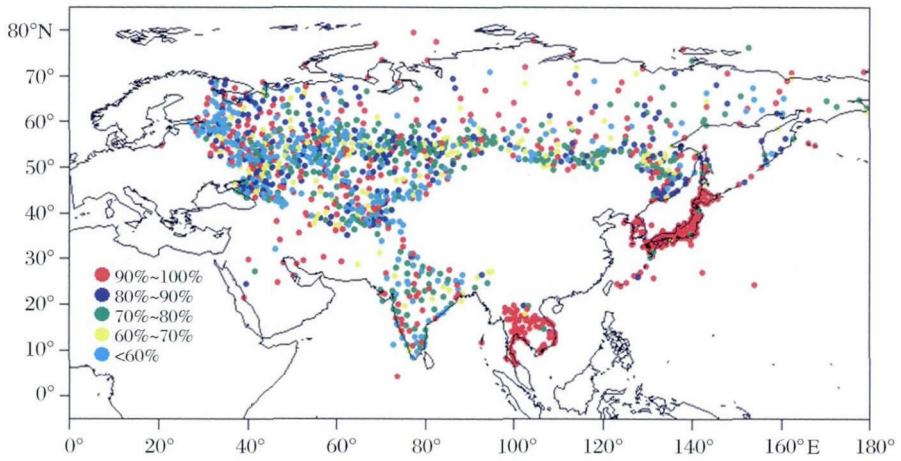


**图 1　NCDC 数据集中国以外亚洲区域具有月平均最高气温记录的台站分布**

**Fig. 1　Distribution of stations of the NCDC/GHCN monthly temperature dataset outside China**

**彩色圆圈表示资料完整性,红色表示缺测率最低,浅蓝色表示缺测率最高**

The color circles denote the completeness of the records, with red the lowest missing rate and light blue the highest missing rate

因此,CRU,NCDC 和 GISS 数据集在亚洲等广大发展中地区的代表性均不理想,20 世纪早期和后期(90 年代)、21 世纪初期在全球很多地区观测站点覆盖率显著偏低,给区域和全球陆地气温变化监测、研究带来较大不确定性。

现有全球陆地地面气温数据及其分析结果的另一个重要缺陷是没有对城市化偏差进行深入、系统研究和合理订正[27,47~49]。CRUTEM 数据集由于该缺陷对其相关分析产品产生了一定影响,并长期受到批评[50~53]。尽管 CRUTEM 开发者声称,他们已经认真考虑了这个问题,选用了非城市观测站资料,但实际上大部分长序列站点资料均来自各类城市站; GHCN 数据集虽对美国气温资料做了订正,但对全球其他地区观测资料的城市化偏差未予考虑; GISS 数据集对城市化偏差做了一定处理,包括通过利用卫星遥感夜光强度资料寻找乡村站点,订正城市站的城市化偏差,但其订正结果仅在美国本土地区具有较高可信性,对其他地区的处理不尽合理[32,37,54]。

CRUTEM 和 GHCN 数据集的开发和使用者之所以未对资料进行城市化偏差订正,是因为他们认为,在全球陆地范围内城市化偏差极其微小,比实际观测到的全球陆地和区域平均增温趋势小一个量级[3,41,55~61],因而可忽略不计,无需订正。基于这个认识,在做全球和区域分析时,研究者仅在平均气温序列的误差估计中对城市化偏差予以考虑。IPCC 第二次、第三次和第四次报告对城市化偏差的处理几乎完全一致,即认为 1900 年以来全球陆地上城市化引起的增温趋势不超过 0.006 ℃/10a,在全球陆地—海洋平均气温序列中则不超过 0.002 ℃/10a[3,4]。这一认识在很大程度上依赖于 Jones 等[55]早期对中国东部、澳大利亚东部、俄罗斯和美国本土 4 个区域资料截止到 20 世纪 80 年代中后期的案例研究结论。IPCC 第五次评估报告开始吸收中国等国家科学家的研究成果,首次承认城市化增温偏差在经济快速发展区域有较明显的表现,但认为在半球和全球陆地尺度上影响仍然很小[4]。

然而,采用更为完整观测资料序列的研究表明,全球陆地许多地区特别是中国地区,气象台站记录的单站和区域平均气温变化趋势中,城市化的影响比原来的估计要显著得多[27,32,54,62,63]。在这些地区包括当年 Jones 等[55]研究中作为个例的中国东部,城市化增温率与实际观测到的总体增温趋势多处于同一量级上。北半球大陆平均气温序列中的城市化影响也比原来的估计值偏大。因此,城市化对区域、半球甚至全球陆地等大范围地面平均气温序列的真实影响,需要给予足够关注。

赵宗慈[64]对国家基准站中不同规模城市站 39



?1994-2014 China Academic Journal Electronic Publishing House. All rights reserved.　http://www.cnki.net

年地面气温序列中的城市化影响进行了分析，发现所有城市站相对乡村站增温速率均明显偏高，大城市站偏高最多；Kalnay 等[65] 对比 1980s 和 1990s 美国大陆 775 个城市站和 167 个乡村站，得出平均热岛强度变化为 0.18 ℃；黄嘉佑等[66] 选取中国华南区 42 个测站 1950—2001 年的月气温资料，按 2001 年人口数将测站分为 6 类，发现特大城市站的年平均气温比特小城市站高 1.0 ℃，全部城市站热岛效应增温速率约为 0.05 ℃/10a；在华北地区，在国家基准气候站和基本气象站网记录的 1961—2000 年区域年平均气温增加趋势中，城市化因素引起的增暖达到 0.11 ℃/10a，对全部增温趋势的贡献达到 39% 以上[62,67]；Yang 等[68] 采用城市减乡村和观测减再分析 2 种方法的分析表明，1981—2007 年华东地区城市化因素对现有地面气温观测趋势的影响很显著，达到整个区域年平均总体增温的 24.2%；Wang 等[69] 利用遥感方法划分土地利用变化和台站类型，发现相对于乡村站，1980—2009 年中国各类城市站年平均地面气温序列中的城市化偏差达 0.09 ℃/10a，城市化增温贡献率为 20% 。

张爱英等[70] 采用任国玉等[71] 发展的综合指标和客观标准，从 2 400 个国家气象站网中遴选地面气温参考站，应用经过均一化订正的月平均气温数据，通过对比分析中国 614 个国家基准气候站、基本气象站与参考站地面气温变化趋势，发现 1961—2004 年国家基准、基本站年平均地面气温序列中的城市化增温率为 0.076 ℃/10a，占同期全部增温速率的 27.3% 。所有季节的城市化增温率均很显著（表 2）。年平均城市化增温率在江淮地区最明显，达到 0.086 ℃/10a，对同期全部增温的贡献达到 55.5% 。除北疆外，其他地区城市化造成的增温趋势均很明显[70] 。最近，任国玉等[32] 采用相同参考站网及国家基准气候站和基本气象站网均一化日气温资料的研究表明，城市化对 1961—2008 年中国大陆地区年和季节平均最低气温（$T_{min}$）、平均气温（$T_{avg}$）、气温日较差（*DTR*）及其常用的极端气温指数序列趋势变化也具有十分显著的影响，对 $T_{min}$ 长期上升趋势和 *DTR* 长期下降趋势的影响尤为突出（图 2），说明在次大陆尺度上城市化不仅显著改变了地面气温均值序列趋势，而且对目前常用的主要

表 2 1961—2004 年国家基准和基本站网全国平均年、季城市化增温率及其城市化增温贡献率[70]

Table 2 Annual and seasonal mean urbanization effects and contributions in long-term temperature trends of the national reference and basic stations in mainland China over 1961-2004[70]

| | 年 | 冬季 | 春季 | 夏季 | 秋季 |
|---|---|---|---|---|---|
| 城市化增温率/(℃/10a) | 0.076＊＊ | 0.093＊＊ | 0.089＊＊ | 0.068＊＊ | 0.059＊＊ |
| 城市化贡献率/% | 27.33 | 18.20 | 34.63 | 38.53 | 23.51 |

注：＊＊表示增温趋势通过了 0.01 显著性水平检验，城市化贡献率是指城市化增温率与总体增温率的百分比值

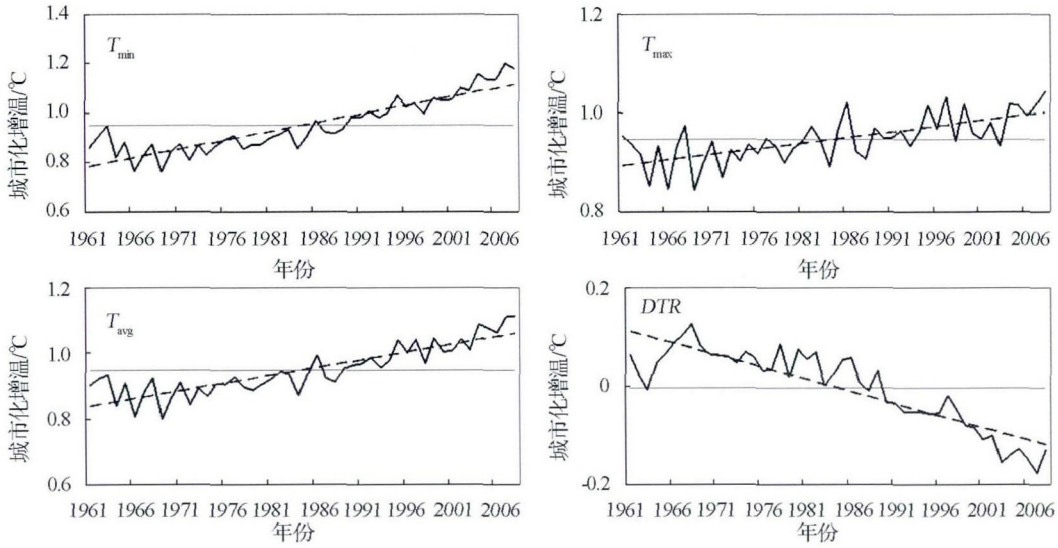


图 2 1961—2008 年中国大陆地区国家基准气候站和基本气象站网（RCBMS）与参考站网年平均最低（$T_{min}$）、最高气温（$T_{max}$），平均气温（$T_{avg}$）和气温日较差（*DTR*）差值序列及其趋势变化[32]

Fig. 2 Temporal variations in annual differences between the national reference and basic stations (RCBMS) and reference stations for $T_{min}$, $T_{max}$, $T_{avg}$ and *DTR* in mainland China over the time period 1961-2008[32]



?1994-2014 China Academic Journal Electronic Publishing House. All rights reserved. http://www.cnki.net

极端气温指数序列的趋势变化也具有明显的影响。华北地区过去几十年冬季极端最低气温指数序列中的显著城市化影响,也得到 Li 等[72]研究的证实。

国内其他相关研究报道了城市化对单站和区域性地面平均气温和最高、最低气温趋势估计的显著影响[32,68,73~81];在东亚的日本、韩国和台湾地区,研究发现城市化对城镇气象站和气候变化分析中常用的气象站网资料序列影响显著[82~85];城市化对欧洲地区气象站网观测记录的影响在最近几十年较弱,但在 19 世纪后期和 20 世纪早中期十分明显[86]。

因此,在现有的全球陆地气温数据集中,世界许多地区还不同程度地保留着城市化增温造成的系统偏差。该认识与以 Jones 等[55,57]、Peterson[59]和 Parker[60]等为代表的先前研究结论有较大差异。中国、日本和韩国等国家学者的研究表明,不仅在局地和区域尺度上,而且可能在大陆和半球尺度上,城市化偏差很可能导致原来给出的区域平均气温趋势变化估计值偏高,并可能致使原来对于近半个世纪全球陆地表面升温空间分布型式的认识出现较大偏差。IPCC 第五次评估报告比过去任何一次报告都更为客观地评价了针对中国等国家的区域性研究工作,但给出的评估结论仍偏于保守[4]。目前没有解决的问题是,在大陆到全球尺度上,城市化引起的地面气温序列系统偏差究竟有多大?其在全球各个大陆和国家的空间变异性如何?在同一地点和同一地区的不同时期内城市化偏差有什么差异?这些问题迫切需要进行深入研究,并做出合理的解释和订正。

如前所述,Hansen 等[37]对全球陆地资料中的城市化影响给予了一定考虑,但他们对美国以外地区的订正,采用 GHNC/NCDC 提供的 1980 年前后人口统计数据遴选参考站。20 世纪后期部分地区城市化发展迅速,城市人口快速增加,利用 1980 年前后人口数据进行判别,可能会将发展迅速地区的部分小城市站选为参考站。研究指出,小城镇附近的台站仍然可以感受到明显的城市化增温[62,64,87]。同时,仅用台站附近居民点人口数据遴选参考站,方法本身也有很大局限性。

Hansen 等[45]后来认识到他们对美国以外地区城镇台站城市化偏差的处理比较粗糙,改用卫星夜间灯光(夜光)强度资料划分乡村站和城市站,并把全球陆地所有城镇台站气温资料进行了"标准夜光订正"。通过调整夜光"亮区"台站气温趋势到邻近的"暗区"台站趋势上,他们认为只能将全球(陆地加海洋) 1900—2009 年的平均温度增加值从 0.71 ℃降到 0.70 ℃,差异非常小。但是,由于经济发展阶段、消费观念、文化传统等差异,具有相同卫星夜光强度的城镇,其实际人口数量或经济发展水平可能迥然不同,城镇建成区及其附近真实的热环境差异很大,世界不同地区和不同国家之间的卫星夜光强度无法真实反映城市站附近城市热岛强度及其随时间变化情况。严格地说,夜光强度指标在不同国家和地区之间缺乏可比性。

## 4　机遇和挑战

全球和大陆尺度地面气温变化观测研究是气候变化科学的重要基础性工作。长期以来,国内外的科学研究和评估工作几乎完全依赖于英国 CRU、美国 NOAA/NCDC 和 NASA/GISS 等机构发展的全球陆地表面气温观测数据产品,早期也曾参考前苏联(俄罗斯)的全球陆地表面气温序列,近年来美国伯克利地球表面温度数据集也得到一定程度的关注。不同于全球气候模式,在 IPCC 过去和最新的评估报告中,很少引用中国科学家在基础观测数据分析上的重要成果,这与我国地球科学和大气科学当前快速发展的现状和地位不相称。

在国内开展全球陆地、各大陆、主要国家和地区近地面气温变化趋势研究,建立我国自己的全球陆地及主要区域平均气温曲线,为未来的 IPCC 评估报告及其他国内外重要相关咨询评估工作提供科学支持,促进我国全球气候变化研究工作上一个新台阶,是中国科学家义不容辞的任务。

为此,首先应该进一步挖掘早期观测资料,充分利用中国及其周边地区和其他发展中地区的近几十年历史观测站点,填补全球陆地特别是亚洲地区早期和现代观测资料分布上的空缺,并对多来源气温资料进行融合、优选和均一化处理,建立合理密度和均衡分布的全球陆地气温资料数据集,是气候变化监测和研究中的重要任务。

2012 年 2 月,科技部和中国气象局启动的公益性行业(气象)科研专项"近百年全球陆地气候变化监测技术与应用",其研究内容侧重在全球陆地气温、降水资料的融合、均一化检验和订正技术,亚洲地区月气温资料的城市化影响评价与订正技术,陆地降水的风速"低捕获"偏差订正技术,全球陆地气温和降水长期气候变化监测技术,以及气温和降水监测数据及产品存储管理的标准化、规范化技术等方面,研究成果将为我国气候变化监测业务系统建设提供技术支撑。



?1994-2014 China Academic Journal Electronic Publishing House. All rights reserved.　http://www.cnki.net

目前这项工作的基础数据集建设已基本完成，初步建立了经过质量控制和均一化处理的我国第一套全球陆地月平均气温资料数据集和亚洲地区日气温资料数据集[88]；预计到 2014 年底、2015 年初，将完成亚洲地区日气温资料的均一化处理，全球陆地和亚洲地区气温观测资料数据集研制工作将初步完成。图 3 表明，新的全球陆地月平均气温数据集在亚洲及南美洲等地区的站点密度和序列长度较其他主要数据集有明显改进。

未来几年，应继续充实完善已经初步建立起来的我国全球陆地表面气温资料数据集，包括根据新的元数据资料完善部分站点资料的均一化处理工作。与此同时，应结合国际地球大气环流重建计划（The Atmospheric Circulation Reconstructions over the Earth（ACRE） Initiative）的全球早期气候资料拯救任务，组织开展中国地区 20 世纪前期气象观测记录的归档、图像化、数字化和质量控制工作，发掘新的早期地面气温观测资料；通过 ACRE 国际合作渠道，获取英国、德国、法国和日本等国家相关研究机构业已完成的亚洲等大陆区域早期数字化气温资料；对通过各种渠道获取的中国和亚洲地区早期观测资料进行质量控制和均一化处理，补充到中国气象局现有的全球陆地和亚洲地面气温数据集中，有效改善中国东部和东南亚等地区 20 世纪上半叶的资料覆盖度和序列完整性。

在获取空间覆盖完好的陆地气温资料的基础上，还应该进一步对城镇台站地面气温序列中的城市化偏差进行科学评价，发展单站城市化偏差订正方法，对城镇站气温资料的城市化偏差进行合理订正，建立消除城市化偏差的全球陆地地面气温历史资料数据集，分析揭示全球陆地、亚洲地区平均气温和极端气温变化的时空规律。

在城市化对地面气温序列影响评价中，关键在于遴选有代表性的地面气温参考站。任国玉等[71,89]发展了一个遴选气温参考站的多指标方法，综合考虑台站具体位置、记录年限、资料缺测、迁站信息、附近居民点人口和台站周围建成区相对比例等多重信息，最后建立一个由 143 个站构成的中国地面气温参考站网。利用这个参考站网资料的分析研究，获得了对中国地区城市化影响性质和程度的全面认识[70,90,91]。但是，这种方法运用于全球陆地研究有一定困难，主要因为对中国以外的其他国家和地区无法获取其详尽的台站观测环境信息。

采用卫星遥感资料反演台站附近地面亮度温度，生成亮度温度空间分布场，然后依据站点在该温度场中的具体位置，确定台站是否代表区域背景温

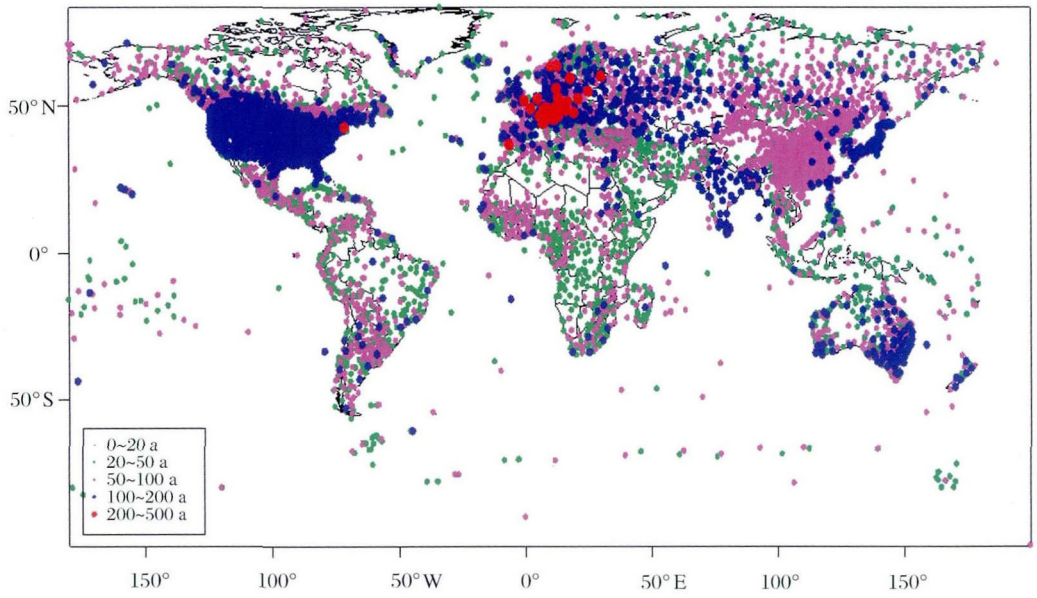


**图 3 全球陆地和岛屿月平均气温观测资料站点分布情况**

**Fig. 3 Distribution of stations of the newly developed global lands（islands） monthly mean temperature dataset**

彩色圆圈表示具有不同观测记录长度（年数）的站点

The colors denote the lengths（years） of records



?1994-2014 China Academic Journal Electronic Publishing House. All rights reserved. http://www.cnki.net

度和气候条件,进而分类所有台站,选取气温参考站,是可以在全球陆地范围采用的方法[90];同时,利用卫星遥感可见光等影像资料,发展其他的气象站点周围建成区面积和观测环境识别方法,对全球陆地气象站进行客观分类,遴选气温参考站[69,80,92,93],也具有潜在的应用价值。

城市化偏差的订正目前国际上还没有成熟的方法。Karl 等[87] 和 Hansen 等[37] 对美国本土地区的研究分别采用人口与台站温度之间的相关性和回归方程以及城市站与乡村站之间的分段趋势差值订正方法,对城镇站地面气温序列进行趋势偏差订正。他们均没有对日气温资料序列进行城市化偏差订正。Karl 等[87] 的方法由于台站气温和附近居民区人口的相关性比较弱,城市化影响在很大程度上取决于气象台站相对城市中心区的具体位置,以及观测场附近一定范围内建成区的面积和建筑物高度等复杂因素,因此不具有推广价值。Hansen 等[37] 的方法有一定的借鉴意义,但对于美国以外参考站序列的建立存在缺陷,因为城市卫星夜光强度还与历史、文化和经济发展阶段等多种因素有关,难以客观反映台站附近真实人类活动影响强度。黄嘉佑等[66] 根据台站地面气温与大气环流特征量的相关性,建立回归模型,订正城市化影响偏差。这种方法依赖于再分析资料,而再分析资料在长期趋势变化上存在着比地面实际观测资料大的误差; 同时 20 世纪早期也没有高质量的再分析资料,因此无法用于近百年全球陆地范围的研究。

相对来说,最客观、可靠和有效的办法,仍然是利用邻近若干(3 ~ 5 个) 乡村站建立参考气温序列,通过参考站与城镇站气温序列趋势比较获得某一时段内总的订正值和逐年订正值。参考站网与城市化影响评价研究中所用参考站网可以完全一致,也可以在站点稀疏区域考虑利用部分已订正台站资料补充作为参考气温序列。进一步,还需要考虑如何确定每个具体目标站附近的参考站点,如何建立针对每个目标站的平均参考气温序列,以及如何处理上百年单站气温资料序列中城市化偏差的年代和多年代变异性。

全球和区域平均地面气温距平序列的构建和分析方法比较成熟。国际上常用的几种方法,包括 CRU 全球气温数据分析组发展的距平值网格面积加权平均方法[6,94] 和 Peterson 等[95] 提出的第一差分参考序列方法,以及其他各种距平值内插格点化和面积加权平均方法,都具有参考价值。最近,Wang 等[96] 发展了一种基于最优无偏估计(BLUE) 理论的统计方法,构建了中国区域长期地面气温序列,交叉验证显示能够有效降低区域平均序列估计的误差水平。总体来看,不同的格点化(内插) 和面积加权平均方法对大区域平均的地面气温趋势估算结果影响很小,采用各种方法获得的全球和大尺度地面气温变化分析结果,没有明显差异。

## 5　结　语

全球陆地和区域尺度表面气温时间序列构建、分析是气候变化研究的基础性工作,在过去 30 多年得到了各方面的高度关注,也取得了许多研究成果。但是,这项工作还受到早期观测资料覆盖缺乏、部分地区近几十年观测资料覆盖不足以及城镇台站地面气温序列中的城市化影响偏差难以分离和订正等诸多问题的困扰。

改进和完善现有的观测资料数据集,分析、评价城镇观测站地面气温序列中的城市化影响性质和程度,合理订正城市化影响偏差,建立消除城市化偏差的全球陆地长序列地面气温资料数据集,精准监测和分析全球陆表平均气温的长期趋势变化规律,是摆在我国和世界气候变化或全球变化科学工作者面前的极富挑战性的任务。

在国家若干重大科技计划项目支持下,经过科学工作者多年的不懈努力,我国相关部门和研究机构在陆表气温变化观测研究方面培养了一批人才,产出了一系列成果,积累了丰富的经验,形成了自己的特色,已经具备了开展全球性研究的工作基础和条件。今后,在相关部门和基金机构的支持下,完全可以建成一套我国自己的高质量全球陆表气温观测资料数据集,提供新的全球和区域平均陆表气温时间序列,加深科学界对全球气候变化速率和空间变异性的认识。

实现上述目标,对于全球和区域气候变化检测、归因、模拟、预估和影响评估研究,科学、协调应对全球气候和环境变化,具有重要的理论和实际意义,同时也将实质性拓宽我国的气候变化或全球变化基础科学领域,进一步提升我国相关研究在国际上的地位。

**致谢**: 感谢课题组成员周雅清、张雷、张爱英、郭军、初子莹、李娇、张媛的技术支持。

**参考文献(References)**:

[1]　Zhang Lansheng, Fang Xiuqi, Ren Guoyu. Global Change [M].



?1994-2014 China Academic Journal Electronic Publishing House. All rights reserved.　http://www.cnki.net

Beijing: Higher Education Press, 2000. [张兰生,方修琦,任国玉. 全球变化 [M]. 北京: 高等教育出版社, 2000.]

[2] An Zhisheng, Fu Zongbin. Progresses in global change science [J]. *Advances in Earth Science*, 2001, 16(5): 671-680. [安芷生,符淙斌. 全球变化科学的进展 [J]. 地球科学进展, 2001, 16(5): 671-680.]

[3] IPCC. Climate Change 2007: The Physical Science Basis [M] // Solomon S, Qin D, Manning M, *et al*, eds. Contribution of Working Group I to the Fourth Assessment Report of the IPCC. New York: Cambridge University Press, 2007: 1 056.

[4] Stocker T F, Qin D, Plattner G K, *et al*. Climate Change 2013: The Physical Science Basis [M]. New York: Cambridge University Press, 2013.

[5] Ding Yihui, Ren Guoyu. Introduction to Climate Change Science of China [M]. Beijing: China Meteorological Press, 2008: 281. [丁一汇,任国玉. 中国气候变化科学概论 [M]. 北京: 气象出版社, 2008: 281.]

[6] Jones P D, Moberg A. Hemispheric and large-scale surface air temperature variations: An extensive revision and update to 2001 [J]. *Journal of Climate*, 2003, 16: 206-223.

[7] Wang Shaowu, Dong Guangrong. Environmental characteristics and change in western China (Vol. One) [M] // Qin Dahe, ed. Assessment on Environment of Western China. Beijing: Science Press, 2002: 71-145. [王绍武, 董光荣. 中国西部环境特征及其演变(第一卷) [M] // 秦大河,编. 中国西部环境评估. 北京: 科学出版社, 2002: 71-145.]

[8] Zhai P M, Pan X H. Trends in temperature extremes during 1951-1999 in China [J]. *Geophysical Research Letters*, 2003, 30, doi: 10.1029/2003GL018004.

[9] Qian W, Lin X. Regional trends in recent temperature indices in China [J]. *Climate Research*, 2004, 27(5): 119-134.

[10] Wang Zunya, Ding Yihui, He Jinhai. A re-analysis of climate change characteristics during the past 50 years in China [J]. *Acta Meteorologica Sinica*, 2004, 62(2): 228-236. [王遵娅,丁一汇,何金海. 近 50 年来中国气候变化特征的再分析 [J]. 气象学报, 2004, 62(2): 228-236.]

[11] Ren Guoyu, Guo Jun, Xu Mingzhi, *et al*. Climate changes of mainland China over the past half century [J]. *Acta Meteorologica Sinica*, 2005, 63(6): 942-956. [任国玉,郭军,徐铭志,等. 近五十年中国地面气候变化基本特征 [J]. 气象学报, 2005, 63(6): 942-956.]

[12] Zhou T, Yu R. 20th century surface air temperature over China and the globe simulated by coupled climate models [J]. *Journal of Climate*, 2006, 19: 5 843-5 858.

[13] Duan A, Wu G X, Zhang Q, *et al*. New proofs of the recent climate warming over the Tibetan Plateau as a result of the increasing greenhouse gas emissions [J]. *Chinese Science Bulletin*, 2006, 51(11): 1 396-1 400.

[14] Wang H J, Sun J Q, Chen H P, *et al*. Extreme climate in China: Facts, simulation and projection [J]. *Meteorologische Zeitschrift*, 2012, 21: 279-304.

[15] Zhang Xinshi, Zhou Guangsheng, Gao Qiong. Terrestrial forest-steppe profile of Northeast China in the IGBP program [J]. *Earth Science Frontiers*, 1997, 4: 145-152. [张新时,周广胜,高琼. 全球变化中研究的中国东北森林—草原陆地样带 [J]. 地学前缘, 1997, 4: 145-152.]

[16] Parmesan C, Yohe G. A globally coherent fingerprint of climate change impacts across natural systems [J]. *Nature*, 2003, 421: 37-42.

[17] Qin Dahe, Ding Yihui, Su Jilan. Climate and Environmental Change of China (Vol. One) [M]. Beijing: Science Press, 2005: 562. [秦大河,丁一汇,苏纪兰. 中国气候与环境演变(上卷) [M]. 北京: 科学出版社, 2005: 562.]

[18] Perry A L, Low P J, Ellis J R, *et al*. Climate change and distribution shifts in marine fishes [J]. *Science*, 2005, 308: 1 912-1 915.

[19] Overpack J T, Meehl G A, Bony S, *et al*. Climate data challenges in the 21th century [J]. *Science*, 2011, 331: 700-702.

[20] Wang Shaowu, Wu Rongsheng, Yang Xiuqun, *et al*. Change in climate of China [M] // Qin Dahe, Ding Yihui, Su Jilan, eds. Climate and Environmental Change of China (Vol. One). Beijing: Science Press, 2005: 63-103. [王绍武,伍荣生,杨修群,等. 中国的气候变化 [M] // 秦大河,丁一汇,苏纪兰,编. 中国气候与环境演变(上卷). 北京: 科学出版社, 2005: 63-103.]

[21] Committee of National Assessment Report on Climate Change. 2007: China National Assessment Report on Climate Change [M]. Beijing: Science Press, 2007. [气候变化国家评估报告编委会. 气候变化国家评估报告 [M]. 北京: 科学出版社, 2007.]

[22] Committee of National Assessment Report on Climate Change. China National Assessment Report on Climate Change (Vol. One) [M]. Beijing: Science Press, 2012. [气候变化国家评估报告编委会. 气候变化国家评估报告(第一卷) [M]. 北京: 科学出版社, 2012.]

[23] Ren G Y, Ding Y H, Zhao Z C, *et al*. Recent progress in studies of climate change in China [J]. *Advance in Atmospheric Sciences*, 2012, 29(5): 958-977.

[24] Li Q X, Dong W J. Detection and adjustment of undocumented discontinuities in Chinese temperature series using a composite approach [J]. *Advance in Atmospheric Science*, 2009, 26: 143-153.

[25] Wang Xihong, Shi Guangyu, Ma Xiaoyan. Anthropogenic forcings of tropospheric sulfate aerosols and their influence on temperature in East Asia [J]. *Chinese Journal of Atmospheric Science*, 2002, 26(6): 751-760. [王喜红,石广玉,马晓燕. 东亚地区对流层人为硫酸盐辐射强迫及其温度响应 [J]. 大气科学, 2002, 26(6): 751-760.]

[26] Hua Lijuan, Ma Zhuguo, Luo Dehai, *et al*. Analysis of diurnal temperature range over China during 1961-2000 [J]. *Acta Goegraphica Sinica*, 2004, 59(5): 680-688. [华丽娟,马柱国,罗德海, 等. 1961—2000 年中国区域气温较差分析 [J]. 地理学报, 2004, 59(5): 680-688.]

[27] Ren Guoyu, Xu Mingzhi, Chu Ziying, *et al*. Recent progresses in studies of regional temperature changes in China [J]. *Climatic*



?1994-2014 China Academic Journal Electronic Publishing House. All rights reserved. http://www.cnki.net

*and Environmental Research*, 2005, 10(4): 701-716. [任国玉, 徐铭志, 初子莹, 等. 中国气温变化研究的最新进展 [J]. 气候与环境研究, 2005, 10(4): 701-716.]

[28] Qian Weihong, Fu Jiaolan, Zhang Weiwei, *et al*. Changes in mean climate and extreme climate in China during the last 40 years [J]. *Advances in Earth Science*, 2007, 22(7): 673-684. [钱维宏, 符娇兰, 张玮玮, 等. 近 40 年中国平均气候与极值气候变化的概述 [J]. 地球科学进展, 2007, 22(7): 673-684.]

[29] Li Lijuan, Wang Bin, Zhou Tianjun. Integrated influence of external forcings on global warming of 20th century [J]. *Chinese Science Bulletin*, 2007, 52(15): 1 820-1 825. [李立娟, 王斌, 周天军. 外强迫因子对 20 世纪全球变暖的综合影响 [J]. 科学通报, 2007, 52(15): 1 820-1 825.]

[30] Zhang Renhe, Xu Xiangde. China Climatic Observational System [M]. Beijing: China Meteorological Press, 2008: 291. [张人禾, 徐祥德. 中国气候观测系统 [M]. 北京: 气象出版社, 2008: 291.]

[31] Li Qingxiang, Dong Wenjie, Li Wei, *et al*. Estimate of uncertainties in temperature change of China over the last 100 years [J]. *Chinese Science Bulletin*, 2010, 55(16): 1 544-1 554. [李庆祥, 董文杰, 李伟, 等. 近百年中国气温变化中的不确定性估计 [J]. 科学通报, 2010, 55(16): 1 544-1 554.]

[32] Ren G Y, Zhou Y Q. Urbanization effects on trends of extreme temperature indices of national stations over mainland China, 1961-2008 [J]. *Journal of Climate*, 2014, 27(6): 2 340-2 360.

[33] Wei Fengying, Cao Hongxing. Abrupt change and trends of surface temperature in China, northern hemisphere and globe [J]. *Chinese Journal of Atmospheric Science*, 1995, 19(2): 140-148. [魏凤英, 曹鸿兴. 中国, 北半球和全球的气温突变分析及其趋势预测研究 [J]. 大气科学, 1995, 19(2): 140-148.]

[34] Jiang Zhihong, Li Jianping, Wang Meihua, *et al*. Regional characteristics of the trend change for global temperature field during the last century [J]. *Climatic and Environmental Research*, 2004, 9(3): 422-434. [江志红, 李建平, 王梅华, 等. 20 世纪全球温度场趋势变化的区域特征分析 [J]. 气候与环境研究, 2004, 9(3): 422-434.]

[35] Zheng Qiuhong, Hu Ying, Qin Lianxia. Analysis of citation for research institutes in the IPCC SREX [J]. *Advances in Meteorological Science and Technology*, 2013, 3(5): 63-69. [郑秋红, 胡英, 秦连霞. IPCC SREX 报告中来自专门机构的引文分析 [J]. 气象科技进展, 2013, 3(5): 63-69.]

[36] Wu Guoxiong, Lin Hai, Zou Xiaolei, *et al*. Global climate change studies and scientific data [J]. *Advances in Earth Science*, 2014, 29(1): 15-22. [吴国雄, 林海, 邹晓蕾, 等. 全球气候变化研究与科学数据 [J]. 地球科学进展, 2014, 29(1): 15-22.]

[37] Hansen J, Ruedy R, Sato M, *et al*. A closer look at United States and global surface temperature change [J]. *Journal of Geophysical Research*, 2001, 106: 23 947-23 964.

[38] Smith T M, Reynolds R W. A global merged land and sea surface temperature reconstruction based on historical observations (1880-1997) [J]. *Journal of Climate*, 2005, 18: 2 021-2 036.

[39] Lawrimore J H, Menne M J, Gleason B E, *et al*. An overview of the global historical climatology network monthly mean temperature data set, version 3 [J]. *Journal of Geophysical Research*, 2011, 116, doi: 10.1029/2011jd016187.

[40] Jones P D, Lister D H, Osborn T J, *et al*. Hemispheric and large-scale land surface air temperature variations: An extensive revision and an update to 2010 [J]. *Journal of Geophysical Research*, 2012, 117: D05127, doi: 10.1029/2011JD017139.

[41] IPCC. Climate change 2001: The scientific basis [M] // Houghton J T, Ding Y H, eds. Contribution of Working Group I to the Third Assessment Report of the IPCC. Cambridge: Cambridge University Press, 2001.

[42] Rohde R, Muller R A. Berkeley earth temperature averaging process [J]. *Geoinformatics & Geostatistics: An Overview*, 2013, doi: 10.4172/gigs.1000103.

[43] Brohan P. Uncertainty estimates in regional and global observed temperature changes: A new dataset from 1850 [J]. *Journal of Geophysical Research*, 2006, 111: D12106, doi: 10.1029/2005JD006548.

[44] Hansen J, Sato M, Ruedy R, *et al*. Global temperature change [J]. *Proceedings National Academy of Sciences*, 2006, 103: 14 288-14 293.

[45] Hansen J, Ruedy R, Sato M, *et al*. Global surface temperature change [J]. *Review of Geophysics*, 2010, 48: RG4004, doi: 10.1029/2010RG000345.

[46] Wang Shaowu, Luo Yong, Zhao Zongci, *et al*. Global warming does not stale in the 21st century [J]. *Advance in Climate Change Research*, 2013, 9(5): 386-387. [王绍武, 罗勇, 赵宗慈, 等. 21 世纪气候变暖并未停滞 [J]. 气候变化研究进展, 2013, 9(5): 386-387.]

[47] Gong Daoyi, Wang Shaowu. Uncertainties of studies on global climate warming [J]. *Earth Science Frontiers*, 2002, 9(2): 371-376. [龚道溢, 王绍武. 全球气候变暖研究中的不确定性 [J]. 地学前缘, 2002, 9(2): 371-376.]

[48] Ren Guoyu. History, current state and uncertainty of studies of climate change attribution [J]. *Advances in Earth Science*, 2008, 23(9): 16-23. [任国玉. 气候变暖成因研究的历史、现状和不确定性 [J]. 地球科学进展, 2008, 23(9): 16-23.]

[49] Fall S, Watts A, Nielsen-Gammon J, *et al*. Analysis of the impacts of station exposure on the U.S. Historical Climatology Network temperatures and temperature trends [J]. *Journal of Geophysical Research*, 2011, 116: D14120, doi: 10.1029/2010JD015146.

[50] Pielke R A Sr. Unresolved issues with the assessment of multidecadal global land surface temperature trends [J]. *Journal of Geophysical Research*, 2007, 112: D24S08, doi: 10.1029/2006JD008229.

[51] Zhao Zongci, Wang Shaowu, Luo Yong, *et al*. Analysis of uncertainties in climate warming of the past 100 years [J]. *Science and Technology Review*, 2009, 27(23): 41-48. [赵宗慈, 王绍武, 罗



?1994-2014 China Academic Journal Electronic Publishing House. All rights reserved.　http://www.cnki.net

勇,等. 近百年气候变暖的不确定性分析[J]. 科技导报,2009,27(23):41-48.]

[52] Wang Fang, Ge Quansheng, Chen Panqin. Uncertainty on observational data of temperature change in the IPCC reports[J]. *Acta Geographica Sinica*, 2009, 64(7): 828-838. [王芳,葛全胜,陈泮勤. IPCC 评估报告气温变化观测数据的不确定性分析[J]. 地理学报,2009,64(7): 828-838.]

[53] Heffernan O. "Climategate" scientist speaks out[J]. *Nature Climate Change*, 2010, 4: 26-27.

[54] Ren Yuyu, Ren Guoyu, Zhang Aiying. An overview of researches of urbanization effect on land surface air temperature trends[J]. *Progress in Geography*, 2010, 29(11): 1 301-1 310. [任玉玉,任国玉,张爱英. 城市化对地面气温变化趋势影响研究综述[J]. 地理科学进展,2010,29(11):1 301-1 310.]

[55] Jones P D, Groisman P Y, Coughlan M, *et al*. Assessment of urbanization effects in time series of surface air temperature over land[J]. *Nature*, 1990, 347: 169-172.

[56] Jones P D, New M, Parker D E, *et al*. Surface air temperature and its variations over the last 150 years[J]. *Reviews of Geophysics*, 1999, 37: 173-199.

[57] Jones P D, Lister D H, Li Q. Urbanization effects in large-scale temperature records, with an emphasis on China[J]. *Journal of Geophysical Research*, 2008, 113: D16122, doi: 10.1029/2008JD009916.

[58] Peterson T C, Gallo K P, Lawrimore J, *et al*. Global rural temperature trends[J]. *Geophysical Research Letters*, 1999, 26(3): 329-332.

[59] Peterson T C. Assessment of urban versus rural in situ surface temperatures in the contiguous United States: No difference found[J]. *Journal of Climate*, 2003, 16: 2 941-2 959.

[60] Parker D E. A demonstration that large-scale warming is not urban[J]. *Journal of Climate*, 2005, 19: 2 882-2 895.

[61] Li Q X, Li W, Si P, *et al*. Assessment of surface air warming in northeast China, with emphasis on the impacts of urbanization[J]. *Theoretical and Applied Climatology*, 2010, 99, doi: 10.1007/s00704-009-0155-4.

[62] Ren G Y, Zhou Y Q, Chu Z Y, *et al*. Urbanization effects on observed surface air temperature trends in North China[J]. *Journal of Climate*, 2008, 21: 1 333-1 348.

[63] Qian Weihong. Atlas of Climate Change and China Extreme Climatic Events[M]. Beijing: China Meteorological Press, 2011: 111-124. [钱维宏. 气候变化与中国极端气候事件图集[M]. 北京:气象出版社,2011:111-124.]

[64] Zhao Zongci. The changes of temperature and the effects of urbanization in China in the last 39 years[J]. *Meteorological Monthly*, 1991, 17(4): 14-17. [赵宗慈. 近 39 年中国气温变化与城市化影响[J]. 气象,1991,17(4): 14-17.]

[65] Kalnay E, Cai M. Impact of urbanization and land-use change on climate[J]. *Nature*, 2003, 423: 528-531.

[66] Huang Jiayou, Liu Xiaoning, Li Qingxiang. Study on relationship between urban heat island effect and population in southern coastal region of China[J]. *Journal of Tropical Meteorology*, 2004, 20(6): 713-722. [黄嘉佑,刘小宁,李庆祥. 中国南方沿海地区城市热岛效应与人口的关系研究[J]. 热带气象学报,2004,20(6): 713-722.]

[67] Zhou Yaqing, Ren Guoyu. Identifying and correcting urban bias in regional surface air temperature trends of North China over time period 1961-2000[J]. *Climate and Environmental Research*, 2005, 10(4): 743-753. [周雅清,任国玉. 华北地区地表气温观测中城镇化影响的检测和订正[J]. 气候与环境研究,2005,10(4): 743-753.]

[68] Yang X C, Hou Y L, Chen B D. Observed surface warming induced by urbanization in east China[J]. *Journal of Geophysical Research*, 2011, 116: D14113, doi: 10.1029/2010JD015452.

[69] Wang F, Ge Q S. Estimation of urbanization bias in observed surface temperature change in China from 1980 to 2009 using satellite land-use data[J]. *Chinese Science Bulletin*, 2012, 57: 1 708-1 715.

[70] Zhang Aiying, Ren Guoyu, Zhou Jiangxing, *et al*. Impacts of urbanization on trends of surface air temperature change in China[J]. *Acta Meteorologica Sinica*, 2010, 68(6): 957-966. [张爱英,任国玉,周江兴,等. 中国地面气温变化趋势中的城市化影响偏差[J]. 气象学报,2010,68(6): 957-966.]

[71] Ren Guoyu, Zhang Aiying, Chu Ziying, *et al*. Principles and procedures for selecting reference surface air temperature stations in China[J]. *Meteorological Science and Technology*, 2010, 38(1): 78-85. [任国玉,张爱英,初子莹,等. 我国地面气温参考站点遴选的依据、原则和方法[J]. 气象科技,2010,38(1): 78-85.]

[72] Li Q X, Huang J Y, Jiang Z H, *et al*. Detection of urbanization signals in extreme winter minimum temperature changes over northern China[J]. *Climatic Change*, 2014, doi: 10.1007/s10584-013-1013-z.

[73] Zhou L, Dickinson R E, Tian Y, *et al*. Evidence for a significant urbanization effect on climate in China[J]. *Proceedings National Academy of Sciences*, 2004, 101: 9 540-9 544.

[74] Zhang J, Dong W, Wu L, *et al*. Impact of land use changes on surface warming in China[J]. *Advances in Atmospheric Sciences*, 2005, 22(3): 343-348.

[75] Lin Xuechun, Yu Shuqiu, Tang Guoli. A study of relationship between urbanization process and urban heat island intensity in Beijing[J]. *Advance in Natural Sciences*, 2005, 15(7): 882-886. [林学椿,于淑秋,唐国利. 北京城市化进展与热岛强度关系的研究[J]. 自然科学进展,2005,15(7): 882-886.]

[76] Chu Ziying, Ren Guoyu. Effect of enhanced urban heat island magnitude on average surface air temperature series in Beijing region[J]. *Acta Meteorologica Sinica*, 2005, 63(4): 534-540. [初子莹,任国玉. 北京地区城市热岛强度变化对区域温度序列的影响[J]. 气象学报,2005,63(4): 534-540.]

[77] Hua L J, Ma Z G, Guo W D. The impact of urbanization on air temperature across China[J]. *Theoretical and Applied Climatology*, 2008, 93: 179-194.

[78] Tang Guoli, Ren Guoyu, Zhou Jiangxing. Change of urban heat island intensity and its effect on surface mean air temperature re-



?1994-2014 China Academic Journal Electronic Publishing House. All rights reserved. http://www.cnki.net

cords in Southwest China [J]. *Chinese Journal of Applied Meteorology*, 2008, 19 (6): 722-730. [唐国利,任国玉,周江兴. 西南地区城市热岛强度变化对地面气温序列的影响 [J]. 应用气象学报, 2008, 19 (6): 722-730.]

[79] Zhou Yaqing, Ren Guoyu. Urbanization effect on trends of mean maximum, minimum temperature and daily temperature range in North China [J]. *Plateau Metrology*, 2009, 28 (5): 1 158-1 166. [周雅清,任国玉. 城市化对华北地区最高,最低气温和日较差变化趋势的影响 [J]. 高原气象, 2009, 28 (5): 1 158-1 166.]

[80] He Y T, Jia G S, Hu Y H, *et al*. Detecting urban warming signals in climate records [J]. *Advances in Atmospheric Sciences*, 2013, doi: 10.1007/s00376-012-2135-3.

[81] Wu K, Yang X Q. Urbanization and heterogeneous surface warming in eastern China [J]. *Chinese Science Bulletin*, 2013, 58: 1 363-1 373.

[82] Choi J, Chung U, Yun J I. Urban-effect correction to improve accuracy of spatially interpolated temperature estimates in Korea [J]. *Journal of Applied Meteorology*, 2003, 42: 1 711-1 719.

[83] Chung U, Choi J, Yun J I. Urbanization effect on observed change in mean monthly temperature between 1950-1980 and 1971-2000 in Korea [J]. *Climate Change*, 2004, 66: 127-136.

[84] Fujibe F. Detection of urban warming in recent temperature trends in Japan [J]. *International Journal of Climatology*, 2009, 29: 1 811-1 822.

[85] Lai W L, Cheng W L. Air temperature change due to human activities in Taiwan for the past century [J]. *International Journal of Climatology*, 2010, 30: 432-444.

[86] Ren Yuyu. Effect of Urbanization on Observational Records of Land Surface Air Temperature in Northern Hemisphere [D]. Beijing: Beijing Normal University, 2008. [任玉玉. 城市化对北半球陆地气温观测记录的影响 [D]. 北京: 北京师范大学, 2008.]

[87] Karl T R, Diaz H F, Kukla G. Urbanization: Its detection and effect in the United States climate record [J]. *Journal of Climatology*, 1988, 1: 1 099-1 123.

[88] Xu Wenhui, Li Qingxiang, Xu Yan. A survey of global land surface air temperature dataset [J]. *Advance in Climate Change Research*, 2014, in press. [除文慧,李庆祥,许艳. 近百年全球地表气温数据集的概况与初步整合 [J]. 气候变化研究进展, 2014, 待刊.]

[89] Ren G Y, Li J, Ren Y Y, *et al*. Determination of reference stations for evaluating and adjusting urbanization bias in surface air temperature data over mainland China [J]. *Journal of Climate*, 2014, in press.

[90] Ren Y Y, Ren G Y. A remote-sensing method of selecting reference stations for evaluating urbanization effect on surface air temperature trends [J]. *Journal of Climate*, 2011, 24 (7): 3 179-3 189.

[91] Zhou Y Q, Ren G Y. Change in extreme temperature events frequency over mainland China during 1961-2008 [J]. *Climate Research*, 2011, 50 (1/2): 125-139.

[92] Sun Chaoyang, Shao Quanqin, Liu Jiyuan, *et al*. Analysis of characteristics of meteorological observations and temperature change under the urban expansion [J]. *Climatic and Environmental Research*, 2011, 16(3): 337-346. [孙朝阳,邵全琴,刘纪远,等. 城市扩展影响下的气象观测和气温变化特征分析 [J]. 气候与环境研究, 2011, 16(3): 337-346.]

[93] Yang Y J, Wu B W, Shi C E, *et al*. Impacts of urbanization and station-relocation on surface air temperature series in Anhui Province, China [J]. *Pure and Applied Geophysics*, 2012, doi: 10.1007/s00024-012-0619-9.

[94] Jones P D. Adjusting for sampling density in grid-box land and ocean surface temperature time series [J]. *Journal of Geophysical Research-Atmospheres*, 2001, 106: 3 371-3 380.

[95] Peterson T C, Vose R S. An overview of the global historical climatology network temperature data base [J]. *Bulletin of the American Meteorological Society*, 1997, 78: 2 837-2 849.

[96] Wang J, Xu C, Hu M, *et al*. A new estimate of the China temperature anomaly series and uncertainty assessment in 1900-2006 [J]. *Journal of Geophysical Research*, 2014, 119, doi: 10.1002/2013JD020542.



?1994-2014 China Academic Journal Electronic Publishing House. All rights reserved.　http://www.cnki.net

# An Overview on Global Land Surface Air Temperature Change

Ren Guoyu[1], Ren Yuyu[1], Li Qingxiang[2], Xu Wenhui[2]
(1. *Laboratory for Climate Studies, National Climate Center, China Meteorological Administration, Beijing* 100081, *China*; 2. *National Meteorological Information Center, China Meteorological Administration, Beijing* 100081, *China*)

**Abstract:** Understanding of tempo-spatial pattern and the systimatic bias of the obeserved decadal to multi-decadal variability and long-term trends of global land Surface Air Temperature (SAT) is needed for climate change studies and policy-making. This paper summarizes the state and problems of the current studies of global land SAT change, and points out the necessarty and possibility to launch a new study of global and regional SAT dataset and analyzing products. It is obvious from the overview that there exist some problems with the current three global data-sets under use in global climate change research, and a major issue would be the inefficient treatments of the urban-ization bias in the land SAT series. It is proposed that the Chinese global land SAT dataset developed in the China Meteorological Administration (CMA) be improved and completed, and the urbanization effect on SAT trends of global land stations be evaluated and adjusted. Based on the urban-bias adjusted SAT datasets, global and regional SAT series could be constructed and analyzed to reveal the spatial and temporal patterns of SAT variablity and change. Chinese scientists could paly a more important role in the endouvour facing climate community.

**Key words:** Climate change; Temperature; Dataset; Urbanization effect.

# *Nature*: 气候变暖使全球干旱地区面积显著扩大

2014 年 7 月 1 日,*Nature* 发表题为《气候变暖使陆地碳固定的干燥控制区扩展》(Warming Climate Ex-tends Dryness – Controlled Areas of Terrestrial Carbon Sequestration) 的文章,指出气候变化引起的干燥、温暖区域面积的扩展可能会加速全球变暖。

在生物群系尺度,陆地碳吸收主要受控于天气变化。来自全球监测网络的观测数据表明,在 16 ℃阈值时陆地碳汇对年平均温度($T$) 的变化不再敏感,高于 16 ℃时地面 $CO_2$ 通量由干燥度而不是温度控制。纽约市立大学(City University of New York) 的研究人员利用美国国家大气研究中心下属的国家环境预报中心(NCEP/NCAR) 的每月平均地表温度数据,计算了 1948—2012 年 $T \geqslant 16$ ℃区域的陆地面积并检测以下假设——随着地球表面变暖,16 ℃阈值纬度带极向移动,因此陆地 $CO_2$ 通量受干燥度控制的区域($T > 16$ ℃的区域) 正在扩大,该研究还对气候变暖引起的干燥度控制区扩展对气候变化产生的潜在后果进行了分析。结果表明,自 1948 年以来气候变暖已使 16 ℃温度维度带向极地方向移动。碳吸收的调节因素主要受干燥度而不是温度控制的 $T > 16$ ℃区域的陆地表面积已经增加了 6%,预计到 2050 年将增加至少 8%。受到这种变暖影响的大部分陆地面积是干旱或半干旱生态系统,这些区域极易受到干旱和土地退化的影响。相较于温度和干燥度($T < 16$ ℃) 调节植物生产力的地区,目前受干燥度控制的区域碳净吸收能力要降低 27%。这种气候变暖引起的干燥度控制区的扩展可能会对全球变暖的加速产生正反馈。$T > 16$ ℃的陆地面积继续增加,不仅对气候变化有正反馈作用,也会影响生态系统的完整性和土地覆盖,尤其会影响贫瘠土地的牧民。

(裴惠娟 编译)

**原文题目:** Warming Climate Extends Dryness-Controlled Areas of Terrestrial Carbon equestration

**来源:** Nature,2014,doi:10.1038/srep05472



?1994-2014 China Academic Journal Electronic Publishing House. All rights reserved. http://www.cnki.net

# Eddy-Induced Growth Rate of Low-Frequency Variability and Its Mid- to Late Winter Suppression in the Northern Hemisphere

HONG-LI REN

*Laboratory for Climate Studies, National Climate Center, China Meteorological Administration, Beijing, China*

FEI-FEI JIN

*Laboratory for Climate Studies, National Climate Center, China Meteorological Administration, Beijing, China, and Department of Meteorology, School of Ocean and Earth Sciences and Technology, University of Hawai'i at Mānoa, Honolulu, Hawaii*

JONG-SEONG KUG

*School of Environmental Science and Engineering, Pohang University of Science and Technology, Pohang, South Korea*

(Manuscript received 23 July 2013, in final form 20 February 2014)

ABSTRACT

Synoptic eddy and low-frequency flow (SELF) feedback plays an important role in reinforcing low-frequency variability (LFV). Recent studies showed that an eddy-induced growth (EIG) or instability makes a fundamental contribution to the maintenance of LFV. To quantify the efficiency of the SELF feedback, this study examines the spatiotemporal features of the empirical diagnostics of EIG and its associations with LFV. The results show that, in terms of eddy vorticity forcing, the EIG rate of LFV is generally larger (smaller) in the upper (lower) troposphere, whereas, in terms of eddy potential vorticity forcing, it is larger in the lower troposphere to partly balance the damping effect of surface friction. The local EIG rate shows a horizontal spatial distribution that corresponds to storm-track activity, which tends to be responsible for maintaining LFV amplitudes and patterns as well as sustaining eddy-driven jets. In fact, the EIG rate has a well-defined seasonality, being generally larger in cold seasons and smaller in the warmest season, and this seasonality is stronger in the Northern Hemisphere than in the Southern Hemisphere. This study also reveals a mid- to late winter (January–March) suppression of the EIG rate in the Northern Hemisphere, which indicates a reduced eddy feedback efficiency and may be largely attributed to the eddy kinetic energy suppression and the midlatitude zonal wind maximum in the midwinter of the Northern Hemisphere.

## 1. Introduction

In the extratropical stormy atmosphere, the slow-varying low-frequency flow with planetary-scale patterns is well developed in the monthly- and seasonal-mean fields. Over recent decades, much attention has been paid to such low-frequency variability (LFV) as it accounts for a large proportion of atmospheric variability and significantly impacts on global weather and climate. However, a fundamental question remains unanswered: how is the LFV maintained amid the transient atmospheric circulation? Previous studies have concluded that the LFV is internal to atmospheric dynamics. The internal dynamics in atmospheric models without external forcing can display significant LFV and the pure nonlinear eddy–mean flow interactions can generate a substantial amount of LFV (e.g., Held 1983; Egger and Schilling 1983; Hendon and Hartmann 1985; Cai and Mak 1990; Cai and van den Dool 1991; Lau and Nath 1991; Robinson 1991; Branstator 1995; Whitaker and Barcilon 1995; Limpasuvan and Hartmann 1999, 2000). The dynamical feedback between short-lived atmospheric synoptic eddies and low-frequency planetary-scale flow has long been recognized as essential to the maintenance of the extratropical atmospheric LFV (Kok et al. 1987; Lau 1988; Cai and Mak 1990).

*Corresponding author address:* Dr. Hong-Li Ren, Laboratory for Climate Studies, National Climate Center, China Meteorological Administration, 46 Zhongguancun Nandajie St., Haidian District, Beijing 100081, China.
E-mail: renhl@cma.gov.cn

DOI: 10.1175/JAS-D-13-0221.1

© 2014 American Meteorological Society

Lau (1988) first found high covariations between monthly-mean flow anomalies and anomalies of variance fields of synoptic eddy flow and thus suggested a positive feedback between synoptic eddy and low-frequency flow (SELF). Subsequently, a number of studies have shown that the SELF feedback is vital for the generation and maintenance of zonal indices and dominant climate modes and that synoptic eddies are major supplier of energy to the LFV (e.g., Cai and van den Dool 1991; Lau and Nath 1991; Robinson 1991, 2000; Branstator 1992, 1995; Lee and Feldstein 1996; Limpasuvan and Hartmann 1999, 2000; Lorenz and Hartmann 2001, 2003).

To better understand the dynamics of the general SELF feedback, Jin et al. (2006a,b) and Pan et al. (2006) proposed a linear dynamical closure scheme in which the slowly varying part of eddy feedback can be expressed directly by low-frequency flow through a formulated linear operator. Following their studies, many diagnostic analyses revealed a left-hand preference in the direction of eddy fluxes relative to that of low-frequency flow (Kug and Jin 2009; Ren et al. 2009, 2011, 2012; Kug et al. 2010a,b). In particular, both eddy-vorticity and transformed eddy potential vorticity (TEPV) fluxes are preferentially directed to the left-hand side of the low-frequency flow, which shows that the left-hand preference is a convenient diagnostic indicator of the positive SELF feedback as it relates anomalies in the mean synoptic eddy forcing to mean-flow anomalies.

Recently, Jin (2010) proposed a theory of eddy-induced instability for LFV and predicted theoretically the eddy-induced growth (EIG) of LFV through a simple formula. Based on this theory, Ren et al. (2011) defined an empirical EIG rate to conveniently measure the efficiency of the positive SELF feedback. This EIG rate, originated from the dynamical closure and the new instability theory of the LFV, provides a good indicator for the nature of the two-way SELF interaction. It reflects the fact that only a portion of total synoptic eddy forcing is available as the energy of maintaining the LFV because the portion can be explained by the LFV itself. In this study, to further reveal implications of the EIG rate in quantifying the degree that maintenance or persistence of the general LFV (not only climate modes) can be extended by contributions of the positive synoptic eddy feedback, we will apply the EIG rate to quantitatively examine spatiotemporal features of the eddy-induced instability of the LFV and its associations with LFV.

In addition, the synoptic eddy feedback is intimately associated with the intensity of eddy activity. As revealed in previous studies, storm-track intensity in the North Pacific was observed as being suppressed in midwinter—namely, the phenomenon of the midwinter suppression of North Pacific storminess, which was first pointed out by Nakamura (1992) and has since attracted much research interest (e.g., Zhang and Held 1999; Chang 2001; Nakamura and Sampe 2002; Deng and Mak 2005; Park et al. 2010; Penny et al. 2010; Lee et al. 2013). Thus, we will also examine the relationship of the EIG with the storm-track activity as well as mean zonal flow in the climatological sense. The remainder of the paper is organized as follows. Section 2 is a brief introduction to the data and method used. Basic features of the empirical EIG rate are outlined in section 3 and horizontal spatial features of the local EIG rate are shown section 4. Main features of seasonal variations of the EIG are examined in section 5 and its possible associations with storm-track activity are in section 6. Finally, a summary and discussion are given in section 7.

## 2. Data and method

National Centers for Environmental Prediction–National Center for Atmospheric Research (NCEP–NCAR v1) reanalysis data are used for monthly and daily-mean 30-yr datasets from January 1978 to February 2008 (Kalnay et al. 1996). The variables used are geopotential height, zonal wind, meridional wind, and potential temperature derived from air temperature. The fields on 12 normal pressure levels (1000–100 hPa) are used. Streamfunction and vorticity fields are calculated from zonal and meridional wind. The low frequency is defined as monthly mean. The boreal spring, summer, autumn, and winter seasons are taken as averages of March–May (MAM), June–August (JJA), September–November (SON), and December–February (DJF), respectively. The LFV is further defined in this paper as the monthly- or seasonal-mean anomalies of a variable. To separate the synoptic eddy component, the daily-mean fields are bandpass filtered using a 2–8-day Lanczos filter with 41 weights (Duchon 1979). Here, the so-called low-frequency eddy is excluded though it may indirectly contribute to the LFV (Zhang et al. 2012).

The focus of this study is on the projection of the eddy forcing onto the LFV to measure the efficiency of the synoptic eddy feedback. The eddy forcing can be expressed conventionally in terms of the geopotential tendencies induced by the anomalous eddy fluxes. In this paper, the geopotential tendencies, which are induced by anomalous eddy vorticity fluxes and eddy potential vorticity (PV) fluxes, can be defined by conducting the 2D and 3D Laplacian inversions, respectively, as follows:

$$f\chi_2 = \Delta_2^{-1}(-\nabla \cdot \mathbf{F}^{\mathrm{VORT}}), \quad \text{and}$$
$$f\chi_3 = \Delta_3^{-1}(-\nabla \cdot \mathbf{F}^{\mathrm{PV}}), \tag{1}$$

where $\nabla \cdot ( )$ is horizontal divergence operator, $\Delta$ (or $\nabla^2$) is Laplacian operator, $\Delta_2^{-1}$ and $\Delta_3^{-1}$ are the 2D and 3D inverse Laplacian operators, and $f$ is the Coriolis parameter. The methods for these Laplacian inversions and calculations of the eddy fluxes can be referred to the paper of Ren et al. (2011). In Eq. (1), the anomalous eddy vorticity and eddy PV fluxes are defined as

$$\mathbf{F}^{\mathrm{VORT}} = (\overline{u'\zeta'}^a, \overline{v'\zeta'}^a) \quad \text{and}$$
$$\mathbf{F}^{\mathrm{PV}} = (\overline{u'q'}^a, \overline{v'q'}^a), \tag{2}$$

where $u'$, $v'$, $q'$, and $\zeta'$ denote the bandpass-filtered zonal wind, meridional wind, quasigeostrophic PV, and relative vorticity; $\overline{( )}^a$ denotes monthly-mean anomaly, defined as the deviation of a variable from its climatological mean at each month. In addition, the storm track here is expressed as monthly mean of $v'^2$.

## 3. Empirical EIG rate and its basic features

To quantitatively examine the efficiency of the synoptic eddy feedback onto the low-frequency flow, we use the empirical diagnostics developed by Ren et al. (2011) to measure the EIG of LFV for the eddy vorticity feedback and eddy PV feedback cases (refer to appendix for the details of the EIG rate definition), as follows:

$$\lambda_2 = \frac{\iint_S f\overline{\Phi}^a \chi_2 \, dx \, dy}{\iint_S \overline{\Phi}^a \overline{\Phi}^a \, dx \, dy}, \tag{3}$$

$$\lambda_3 = \frac{\iint_S f\overline{\Phi}^a \chi_3 \, dx \, dy}{\iint_S \overline{\Phi}^a \overline{\Phi}^a \, dx \, dy}. \tag{4}$$

Here, $f\chi_2$ and $f\chi_3$ are the geopotential tendency induced by the eddy vorticity forcing in terms of the 2D inversion and the eddy PV forcing in terms of the 3D inversion, respectively, as defined in Eq. (1), and the domain of horizontal integration $S$ here is specified over the annular mid- and high-latitude areas (30°–70°N, 0°–360°E). In addition, we may define more kinds of EIG rate if other kinds of eddy-induced tendencies can be provided, such as those produced by linear or nonlinear models.

We applied Eqs. (3) and (4) at each vertical level to estimate the EIG rates $\lambda_2$ and $\lambda_3$ (also denoted as $\lambda_{\mathrm{VORT}}$ and $\lambda_{\mathrm{PV}}$) for the eddy vorticity feedback and eddy PV feedback, respectively. It is noteworthy that the definitions here are exactly the same as those by Ren et al. (2011) even though they emphasized more the conception of TEPV flux, which is linearly transformed from the eddy PV flux. Therefore, we will uniformly use the expression of the EIG rate derived from the eddy PV flux forcing. Unit of the EIG rate is per day in this paper.

Figure 1 shows the relationship between the variance of LFV and the covariance of eddy forcing and LFV, which correspond to the denominator and numerator of the two definitions of the empirical EIG rate in Eqs. (3) and (4). It is clear in Fig. 1 that high correlations are between the denominator and numerator, which exist in both the NH and SH extratropics, although the correlations in the NH are higher than those in the SH. These high correlations indicate that the total variance of LFV may be well explained by the eddy-induced part of the LFV in the sense of its vertical average. The slope of the lines fitted to the data points in Fig. 1 actually represents the EIG rate according to its definition in the climate-mean sense.

We further examine the relationships between the denominator and numerator at all the pressure levels and show vertical profiles of the correlations in Fig. 2; in general, high correlations are evident at most levels. The eddy-induced LFV that only involves the effect of eddy vorticity forcing has larger values at the upper levels, whereas the eddy-induced LFV that combines the effects of eddy vorticity and eddy heat forcing has larger values at the mid- to lower levels. Noting the seasonality in the relationships between the numerator and denominator in Fig. 1, we also show the vertical profiles of correlations for the different seasons in Fig. 2. Almost all seasons have positive correlations throughout all levels, indicating that the eddy-induced forcing that projects onto the low-frequency flow may play an important role in maintaining the variance of LFV. In addition, the correlations in warm seasons are lower, compared with cold seasons, probably reflecting a stronger SELF interaction during the latter than the former. However, it is interesting that the highest correlations do not appear in the boreal winter.

Figure 3 uses mass weighting to compare the vertically integrated $\lambda_2$ and $\lambda_3$ for all months to examine the coherence between them. The EIG rate in each month is almost always positive, reflecting the positive feedback of eddies onto LFV. A good relationship exists between the two growth rates in terms of the eddy vorticity and eddy PV forcing, respectively, and the correlation is stronger in the NH than in the SH. Such a good coherence between the two EIG rates indicates the predominance of the dynamical eddy vorticity feedback in the positive eddy feedback, particularly at upper level, and the eddy heat flux tends to favor the formation of a barotropic structure of the extratropical LFV (e.g.,

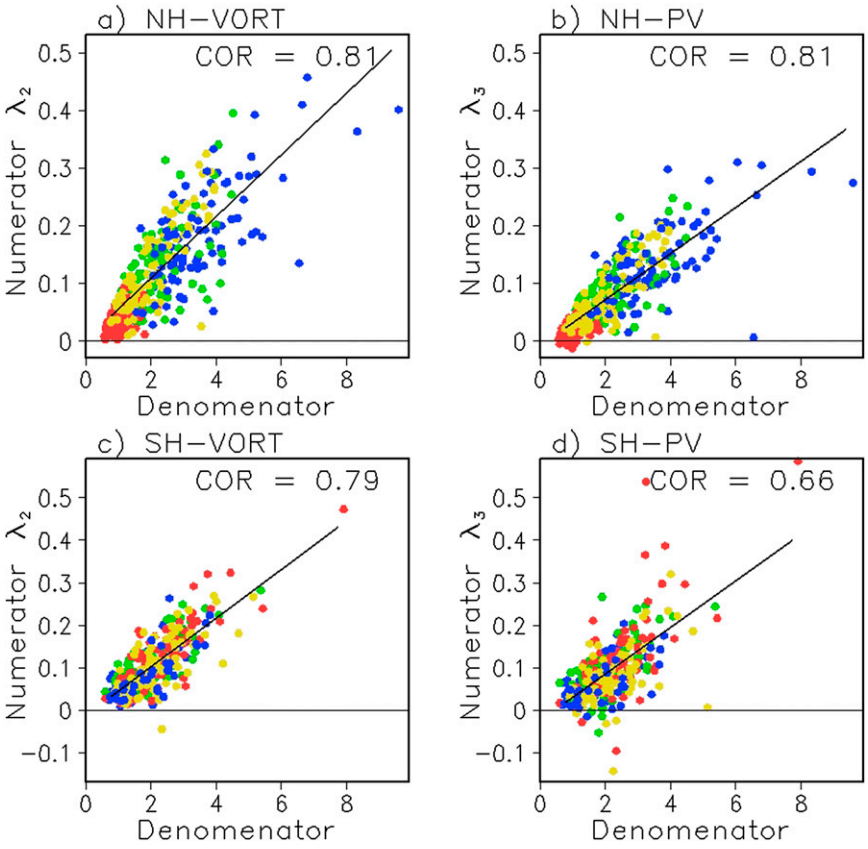


FIG. 1. Scatter diagrams between the vertically integrated (from 1000 to 100 hPa) variances of low-frequency flow and the vertically integrated projections of the eddy forcing derived from the (a),(c) eddy vorticity flux forcing and (b),(d) PV flux forcing for MAM (green), JJA (red), SON (yellow), and DJF (blue) in the (a),(b) NH and (c),(d) SH. Latitudes of the NH and SH are both taken as 30°–70°.

Lau and Nath 1991; Kug et al. 2010a). Moreover, as first noted by Ren et al. (2011), $\lambda_2$ is typically smaller than $\lambda_3$, which is much clearer in the SH than in the NH. This implies that the forcing induced by the eddy heat flux may positively contribute to the eddy feedback although its effect tends to be largely canceled out by the vertical integration.

To examine the seasonal dependency of the empirical EIG rates at different levels, Fig. 4 shows the vertical structures of the climatological-mean growth rates. All of the profiles are positive at all levels, and in all seasons, except at the 100-hPa level in Fig. 4b, indicating that the LFV catches a positive growth induced by synoptic eddies throughout the entire troposphere. The warmest season typically shows the minimum growth rate, indicating that it not only has a weak variance of LFV but also a weak EIG. This seasonal variation in the EIG rate appears to be much larger in the NH than in the SH, presumably because the SH has more oceanic areas to modulate a moderate seasonality. In addition, it is more interesting that the EIG rate in the NH cold season (DJF) is not at its maximum, whereas the SH has its maximum in the cold season (JJA).

The positive growth of LFV due to eddy feedback actually accords the left-hand preference that has been found in the directing of the eddy vorticity flux and TEPV flux (Kug et al. 2010a; Ren et al. 2011). As seen in Figs. 4a and 4c, the eddy vorticity–induced growth rate peaks at upper levels where the dynamical feedback dominates. In contrast, the eddy PV–induced growth rate (Figs. 4b and 4d) decreases with height, which can be essentially attributed to the offset effect of the eddy heat feedback. That is to say, the divergence (convergence) of eddy heat fluxes induces local cooling (warming) and downward (upward) secondary circulation, which tends to weaken the eddy vorticity feedback at upper levels but strengthen it at lower levels, and may contribute to inducing the barotropic structure of the low-frequency flow.

To further understand the role of the EIG in maintaining the LFV, it is necessary to clarify what the value of

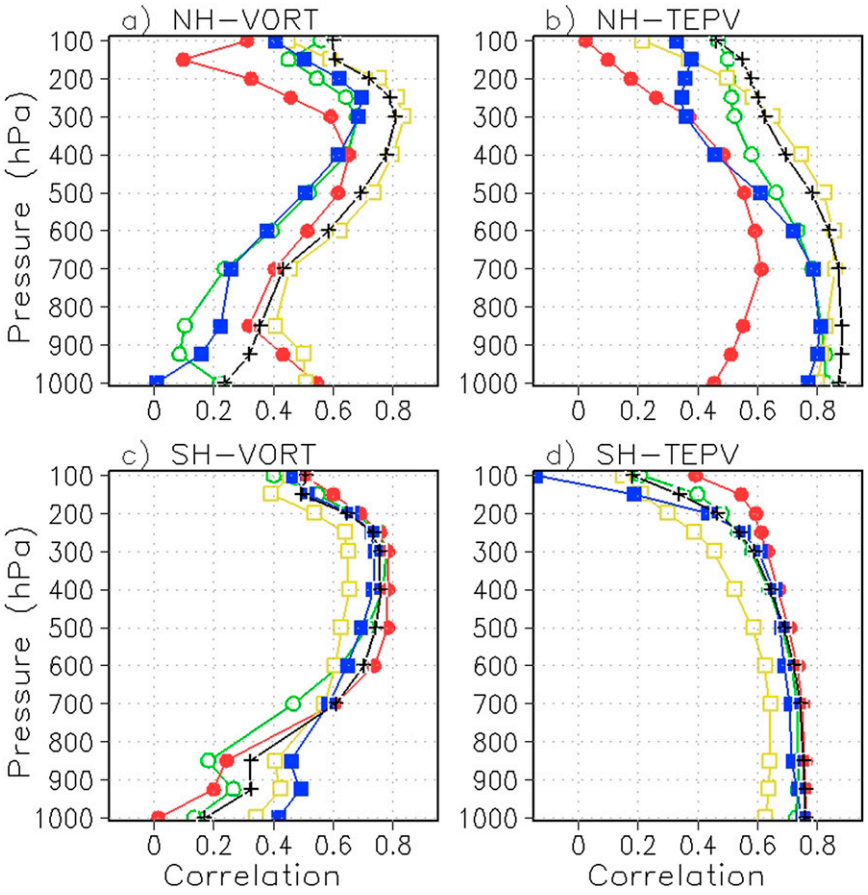


FIG. 2. Correlations between the variances of low-frequency flow and the projections of the eddy forcing derived from the (a),(c) eddy vorticity flux forcing and (b),(d) eddy PV flux forcing for all seasons (black), MAM (green), JJA (red), SON (yellow), and DJF (blue) in the (a),(b) NH and (c),(d) SH.

the EIG rate dynamically means. As seen in Figs. 3 and 4, the vertically integrated EIG rate is about 0.04–0.05, averaged at all seasons, corresponding to an *e*-folding time scale on the order of 20–25 days, which is consistent with the results of Lau (1988). This EIG is usually insufficient to overcome the linear damping, where the damping rate at the surface corresponds to the damping time scale of about 3.5–5 days (Jin 2010; Barnes and Hartmann 2010), but it can significantly reduce the damping from surface friction. For example, in cold seasons, the observed EIG rate, $\lambda_2$ at the 300-hPa level or $\lambda_3$ near the surface, reaches about 0.08–0.10, representing the time scale on the order of about 10–12 days. In contrast, the *e*-folding time scale of the dominant low-frequency variability; for example, the first four low-frequency modes as revealed by Simmons et al. (1983), has been estimated to be on the order of 7–15 days without external forcing effect. The intercomparison between these three time scales clearly indicates the significant contribution of the EIG to reducing the linear damping and thus surviving the LFV. Thus, it can be seen that the value of the EIG rate actually reflects the time scale of the LFV induced by eddies, which has obtained a quantitative support by the above-mentioned results.

As referred to in Eq. (A6), the contribution of the linear advection terms will be zero if we take integration over a global area or a regional domain without lateral boundary flow. In this case, the growth induced by the eddy and external forcing would together act to overcome the linear damping and enhance the LFV. However, the way to define the empirical EIG rate may not be suitable to an estimation of the growth by the external forcing only based on an observational analysis but without numerical solution. Jin et al. (2006a) and Pan et al. (2006) quantitatively demonstrated the fundamental importance of the eddy forcing, compared with the external forcing, to the Pacific–North America (PNA)-like pattern by numerically solving their linearized barotropic and baroclinic models with the eddy feedback operators. Once the feedback of eddy is closed, the amplitude of the PNA-like

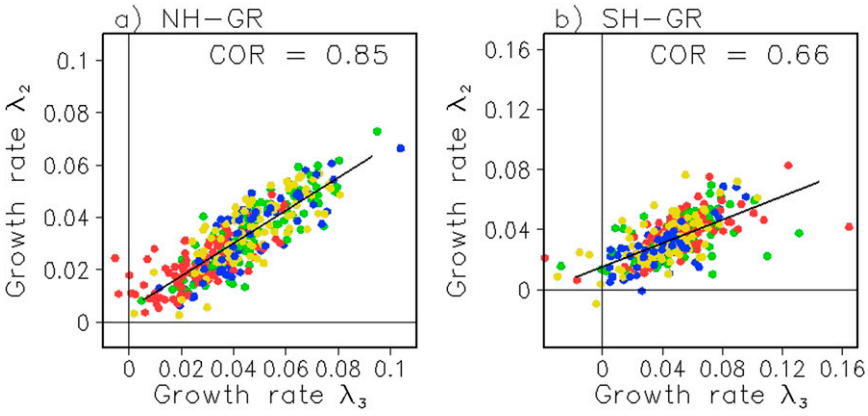


FIG. 3. Scatter diagrams with each dot indicating the vertically integrated (from 1000 to 100 hPa) EIG rate (day$^{-1}$, the same hereafter) derived from the eddy PV flux forcing ($x$ axis) and eddy vorticity flux forcing ($y$ axis) during the period from January 1978 to February 2008 in the (a) NH and (b) SH.

pattern in extratropics as a response to the tropical external forcing will be more than 50% weakened. This clearly suggests the important role of the EIG to the LFV maintenance through the way that the synoptic eddy forcing not only directly sustains the LFV but also forms a singularity condition favoring the effective response of extratropical atmosphere to the tropical external forcing (Jin 2010).

## 4. Spatial features of the local growth rate

The differences between the results from the two hemispheres shown in Figs. 1–4 imply a geographical dependency of the EIG of LFV. To examine the horizontal spatial features of the EIG rate, we devise a localized approach based on Eqs. (3) and (4):

$$\tilde{\lambda}_j = S_f(\lambda_j), \tag{5}$$

where $j = 2$ or 3, $S_f$ denotes a spatial definition operator with a sliding window. Here, to estimate the local growth rate (LGR) of LFV, the size of the sliding window is taken as 40° longitude × 20° latitude, by which the relatively stable results can be obtained.

Figure 5 shows distributions of the climate-mean LGR. Similar patterns of the LGR appear on the upper, middle, and lower levels, and the amplitudes of the patterns change with height—consistent with what is shown in Fig. 4. The EIG rate is almost always positive over all extratropical regions. In the mid- to high latitudes, the LGR patterns reach a meridional maximum and are mainly centered over oceanic regions, which are similar to the distribution of the midlatitude storm tracks (e.g., Chang et al. 2002). It is noted that the LGR has an essentially zonally annular structure, which may be linked with the NH and SH annular modes because their maintenance is intimately associated with the synoptic eddy feedback (e.g., Lorenz and Hartmann 2001, 2003). The annular patterns of LGR, which are more symmetric in the SH than in the NH, further confirm that the EIG plays a key role in forming the two dominant hemispheric annular modes. Moreover, the growth rate reaches the regional maximum over the North Pacific and North Atlantic, where synoptic eddy activity is the strongest and several climate modes dominate. Overall, the LGR has climatological spatial patterns and regional centers that are fairly similar to those of the variances of LFV, referred to in Fig. 9b of Jin (2010), indicating that the EIG plays an important role in maintaining the patterns and amplitudes of LFV. Also, it is noteworthy that the major centers of $\tilde{\lambda}_2$ and $\tilde{\lambda}_3$ at the upper level appear be located downstream of the corresponding centers at the lower level.

Figure 6 shows how the LGR varies with seasons where the 300- and 850-hPa levels are taken as representing $\tilde{\lambda}_2$ and $\tilde{\lambda}_3$, respectively. In the NH, the LGR has similar patterns and amplitudes in spring, autumn, and winter, whereas summer is distinct, with considerably poleward-contracted patterns and relatively small amplitudes. In the SH, the austral summer is also characterized by poleward-contracted patterns and relatively small amplitudes when compared with the other seasons. Overall, the warmest season has a much weaker EIG of LFV than the cold seasons. Nevertheless, the climatic LGR is positive in all four seasons, indicating a positive eddy feedback onto the local LFV. Moreover, in Fig. 6 the major LGR centers at the upper level tend to be downstream of those at the lower level. Based on the theory of Jin (2010),

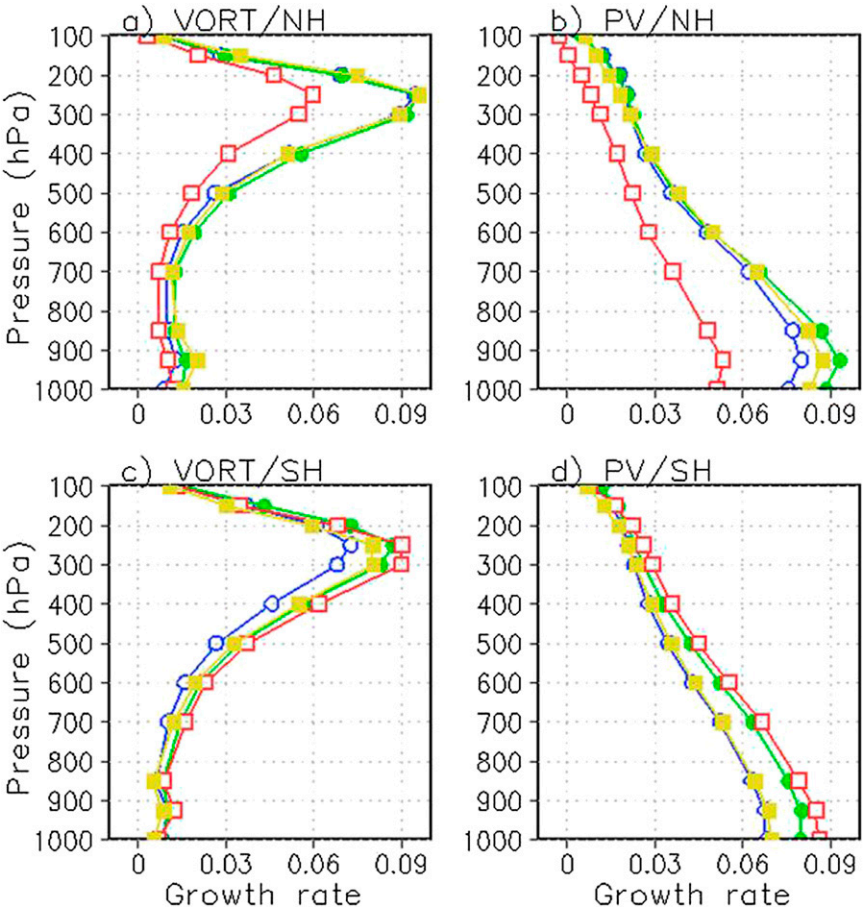


FIG. 4. Vertical profiles of the climatological EIG rates derived from the (a),(c) eddy vorticity flux forcing and (b),(d) eddy PV flux forcing for MAM (green), JJA (red), SON (yellow), and DJF (blue) in the (a),(b) NH and (c),(d) SH.

this is presumably due to the observed fact that the midlatitude major storm-track centers at the upper level are usually located downstream of the centers at the lower level (not shown).

Here, we take the North Atlantic region as an example to illustrate the time scale reflected by the EIG rate that has the largest values in this region. As seen in Figs. 5 and 6, the EIG rate over the region can reach about 0.14–0.16, corresponding to the time scale on the order of 6–7 days, which means the strongest synoptic eddy feedback in the globe. That is the major reason that the North Atlantic Oscillation (NAO), the dominant climate model in the NH, is gestated in this region. Barnes and Hartmann (2010), based on a vorticity budget analysis using observations, showed that the upper-tropospheric eddy vorticity forcing act to counteract the effect of the large-scale advection terms at the upper level and to indirectly maintain the low-level vorticity anomalies against frictional drag through generating a large-scale vertical circulation cell. They further demonstrated that the eddy forcing contributes to a significant extension of the persistence of the NAO vorticity anomaly owing to the fact that the decay time scale of the NAO can be extended from 3.5 to 13.2 days as a result of positive synoptic eddy feedback. In the similar way, our results show that the decay time scale of the North Atlantic LFV can be extended from 3.5–5 to 8–20 days to the biggest degree because of the eddy feedback.

To present comprehensively the vertical structure and seasonality of the LGR, we here take zonal means of the patterns in Fig. 6. As seen in Fig. 7, the EIG rate of LFV is mostly positive in the extratropics but weakly negative in the tropics. The dynamical eddy vorticity feedback contributes to a strongly positive LGR at upper levels and in the subpolar regions, serving to maintain the so-called eddy-driven jet (e.g., Athanasiadis et al. 2010). In contrast, the eddy PV feedback generates a downward positive LGR by involving the eddy heat forcing effect and induced vertical secondary circulation, which acts to partly balance surface friction

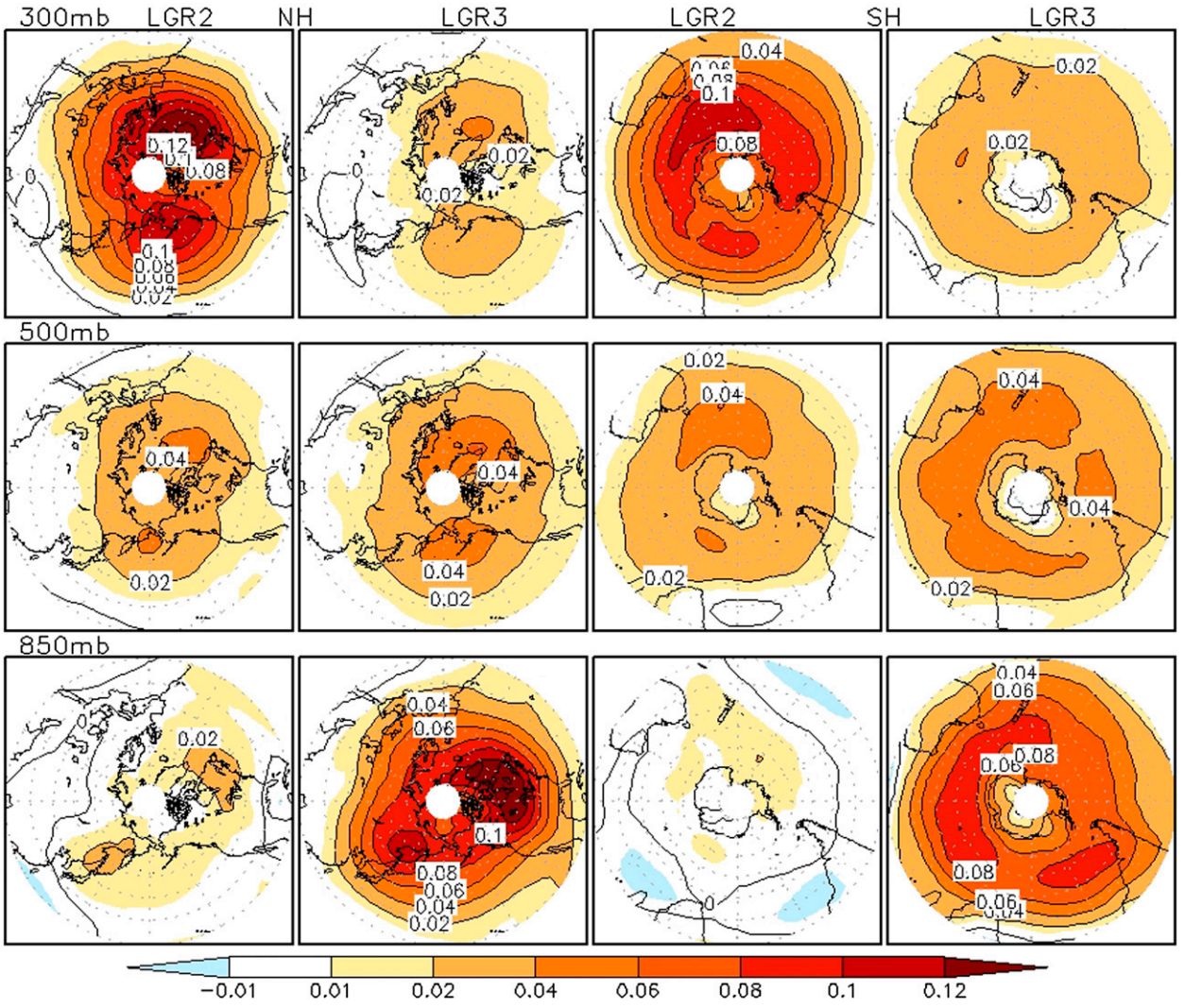


FIG. 5. Maps of the LGR derived from the eddy vorticity flux forcing (LGR2) and eddy PV flux forcing (LGR3) in the (left) NH and (right) SH for (top) 300, (middle) 500, and (bottom) 850 hPa using all months of data.

damping and contributes to generating a barotropic structure in the LFV (e.g., Ren et al. 2011). In fact, $\tilde{\lambda}_2$ and $\tilde{\lambda}_3$ become similar when they are taken as vertical integrations (not shown). It is also evident that the NH shows a stronger seasonality in the LGR amplitude and meridional location than the SH; that is, the LGR centers become weaker and more poleward during the warm season.

## 5. Seasonal variations of the EIG rate and its mid- to late winter suppression in the NH

It is well known that the LFV usually has a larger amplitude in colder seasons, as indicated in Fig. 1 and, hence, a higher EIG rate would be expected. However, a comparison of Figs. 4 and 7 shows that the highest EIG rate in the NH does not occur in winter, which differs from the situation in the SH. For example, as seen in Fig. 7, the amplitude of the EIG rate mostly maximizes in spring or autumn for either of the EIG rates. That is to say, the EIG rate of LFV in the NH might be subject to suppression in winter, in the sense of seasonal variation, even though, at the same time, the LFV reaches its maximum amplitude and projection of the eddy forcing onto it, as revealed in Fig. 1.

To confirm that the boreal EIG rate tends to be suppressed in the winter, Fig. 8 shows the seasonal variations of the zonal-mean monthly climatological LGR, which is vertically averaged throughout the troposphere. It is most interesting to see that the NH growth rate peaks in autumn to early winter and spring, while, in contrast, the SH growth rate essentially peaks during

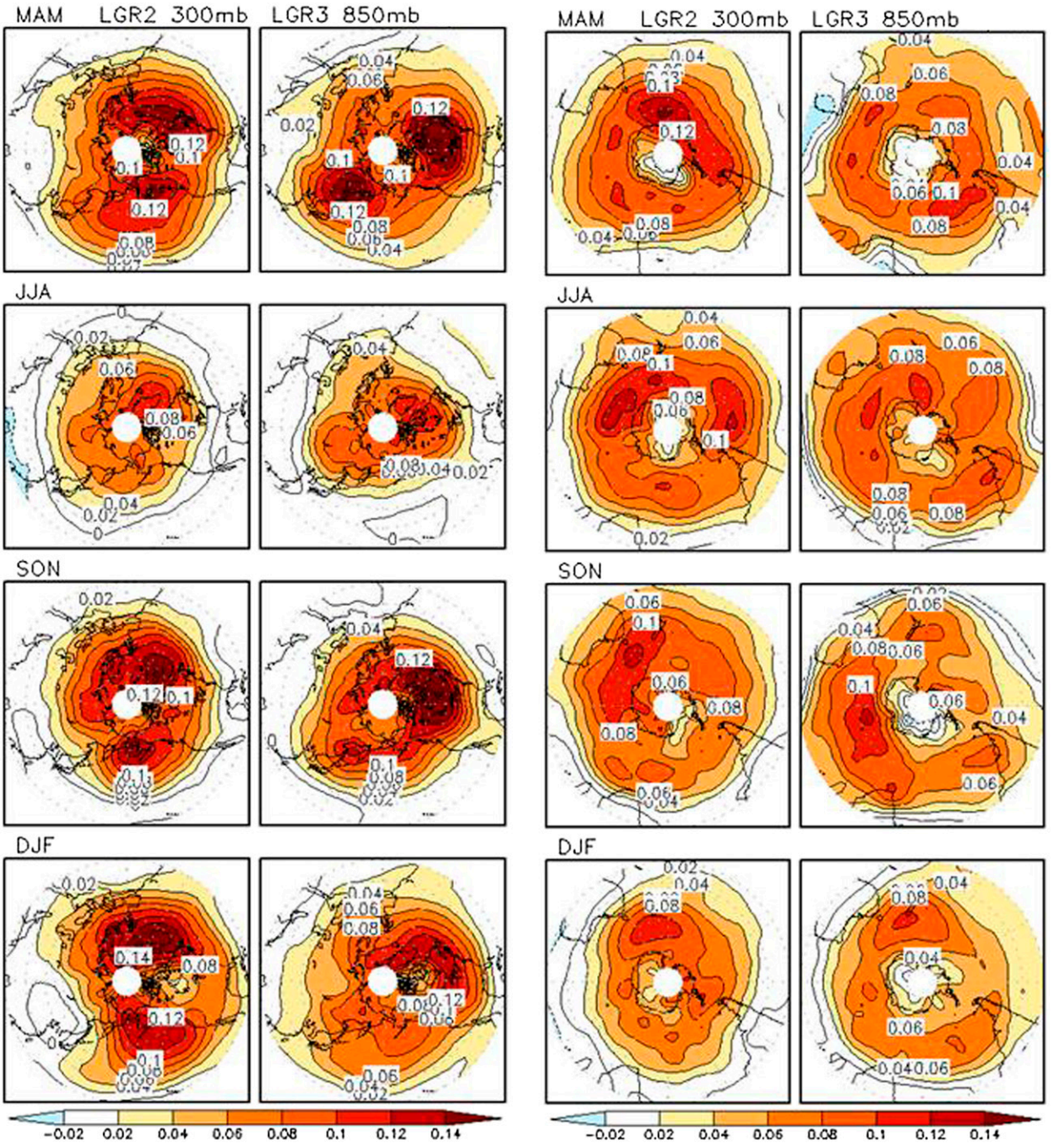


FIG. 6. As in Fig. 5, but for (top to bottom) MAM, JJA, SON, and DJF in the (left) NH and (right) SH, where LGR2 is shown at the 300-hPa level and LGR3 at the 850-hPa level.

austral winter, which is the case for both of the EIG rate definitions. Furthermore, seasonal variations of the mid- to high-latitude-averaged growth rate in the NH experience a general mid- to late winter (January–March) suppression (MLWS), which is well defined in the North Pacific, Eurasian, and North Atlantic regions. In addition, the $\tilde{\lambda}_2$ and $\tilde{\lambda}_3$ patterns are similar, but the latter is about one-third larger than the former. It is also noted that the SH EIG rate has a much smaller seasonal variation than in the NH, particularly in $\tilde{\lambda}_2$.

To confirm the observed MLWS phenomenon, Fig. 9 presents the extratropics-averaged LGR from the vertical levels for the NH and SH, and at all levels the EIG rate in the SH reaches a maximum during the austral

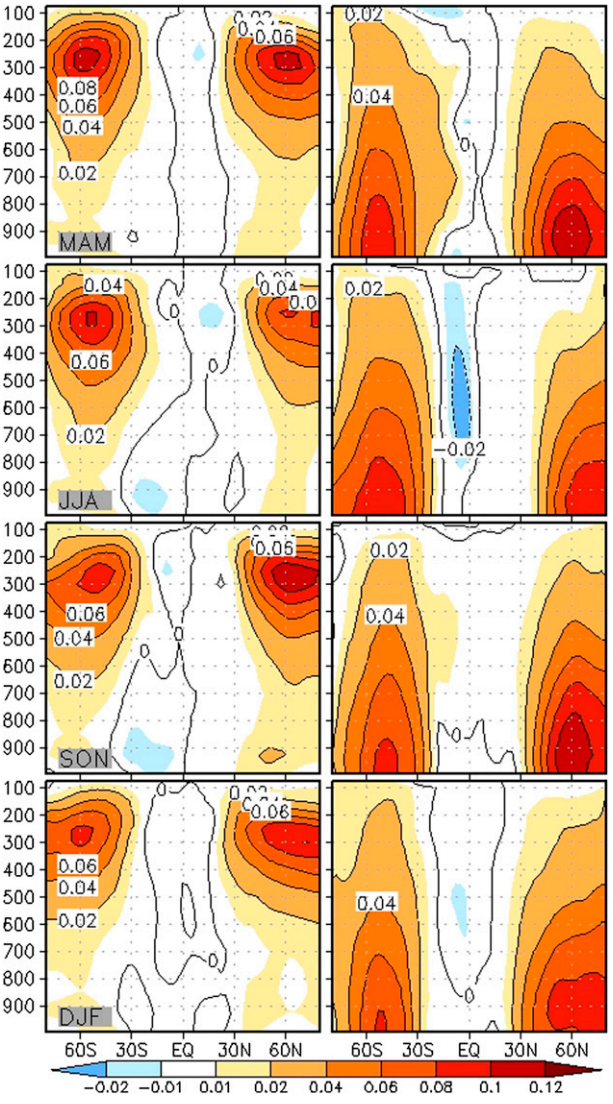


FIG. 7. The zonal-averaged LGR derived from the (left) eddy vorticity flux forcing and (right) eddy PV flux forcing for (top to bottom) MAM, JJA, SON, and DJF.

winter despite some other weaker peaks being present, whereas the situation in the NH is very different. That is, the NH EIG rate at all levels tends to peak in autumn to early winter and springtime and lessen in the mid- to late winter when the rate may have been expected to peak as it does in the SH. We also further examine the contributions from different sectors in the NH to the MLWS in the EIG of LFV, such as the LGR averaged over the North Pacific, Eurasian, and North Atlantic regions (not shown). The North Pacific sector shows the most similarity to the EIG patterns of the NH, indicating its dominant contribution to the NH MLWS in the EIG of LFV. The North Atlantic sector makes a positive, but relatively weak contribution to the MLWS, and the Eurasian sector, in spite of smaller values, still shows the MLWS, interestingly, with the minimum EIG rate in mid- to late winter rather than in summer.

The major features of the seasonal variations in the EIG are highlighted by the vertically integrated LGR curves shown in Fig. 10. All of the three main sectors in the NH extratropics (i.e., North Pacific, Eurasia, and North Atlantic) contribute positively to the observed NH MLWS phenomenon. The weakest EIG of LFV in the extratropics occurs during the Eurasian winter, which is induced by the upper-level eddy vorticity forcing, as also seen in Fig. 8. In addition, the suppression of EIG in the North Pacific tends to occur in midwinter, while that in the North Atlantic occurs in late winter. Another prominent feature of the NH EIG rate curves is that the largest values are always anchored in April, compared with the broad range of September–December peaks.

## 6. Possible causes of the MLWS of EIG

The MLWS phenomenon in the EIG of the NH LFV presumably develops because the coldest season usually has the largest amplitude LFV, which may reduce the EIG rate in terms of its definition, even though the relevant eddy forcing and its projection onto the LFV are also the largest, as indicated by Fig. 1 (and further, more clearly shown in Fig. A1). This probably indicates that the efficiency of the positive eddy feedback is dependent on the amplitude of the LFV. Watanabe (2009) found a nonlinear self-limitation of the positive eddy feedback to the North Atlantic Oscillation–like zonal flow anomalies in eddy life cycle experiments, where the dipole-type zonal-flow anomalies with extremely large amplitude cannot be efficiently intensified by the baroclinic wave feedback. This means that the eddy feedback may be suppressed nonlinearly when the amplitude of the LFV increases to some degree. Our current observations strongly reflect such a self-limitation in the NH but not in the SH. Consequently, we must consider what the possible causes of the MLWS of the EIG may be.

To address this question, it is naturally thought that the synoptic eddy feedback is closely related to the mid- to high-latitude eddy activity intensity, which is usually referred to as the storm track. In other words, the seasonal variations in storm activity can influence those of the synoptic eddy feedback. Similar to Fig. 8a, in Fig. 11 the storm-track statistics ($v'^2$) show that the zonal-mean storm-track intensity peaks in autumn to early winter and spring are similar to the seasonal variations of the zonal-mean EIG rate in the NH. The longitudinal distributions of seasonal storm-track variations in Fig. 11b

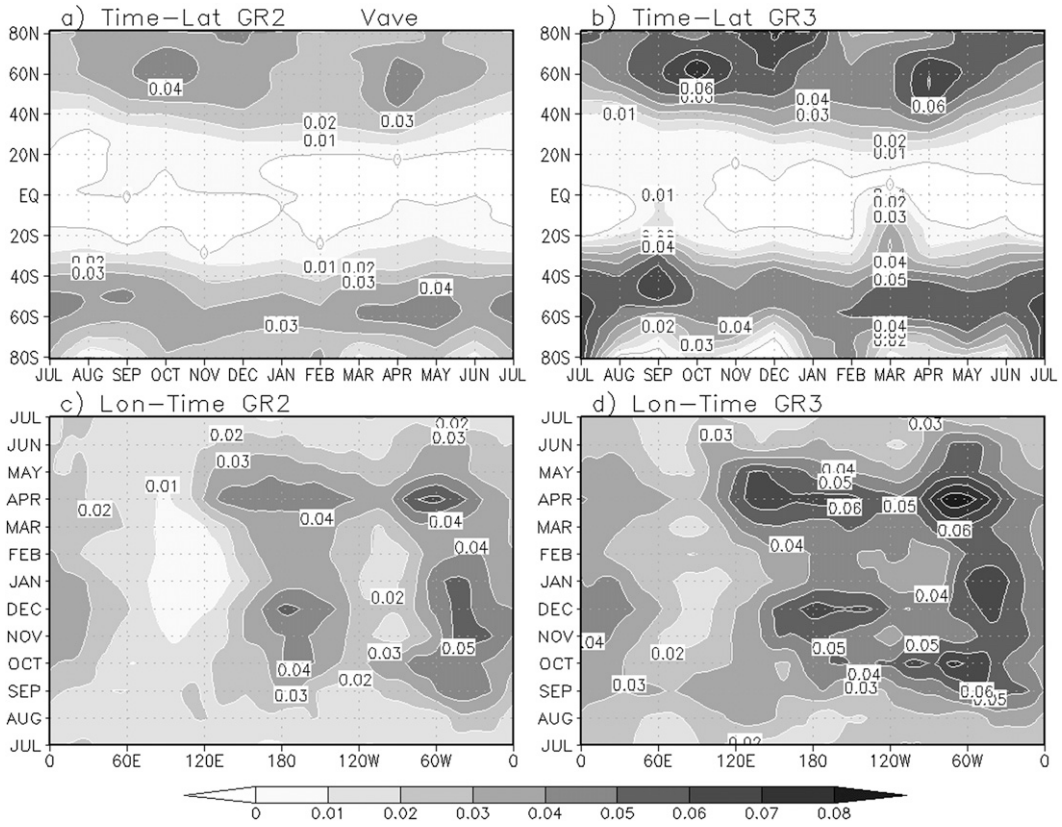


FIG. 8. Seasonal variations of the (a),(b) climatological vertically averaged zonal-mean LGR and (c),(d) extratropical NH (30°–80°N)-mean LGR.

further reflect the phenomenon of midwinter suppression of North Pacific storm-track activity. However, our results show that such a midwinter suppression of storminess not only occurs in the North Pacific but also in the Eurasian region, to which Ren et al. (2010) noted a similar situation in the East Asia. It is even possible to identify a weak signal of the late winter suppression in the North Atlantic. Therefore, the MLWS of the EIG may be attributed to the midwinter suppression of storm-track activity in the NH.

To further understand the possible dynamical causes of the observed MLWS of the NH EIG, the theory proposed by Jin (2010) regarding the eddy-induced instability of LFV is conceptually employed here. His study proved theoretically that EIG is intimate to the climatological eddy kinetic energy (EKE) and zonal-mean zonal flow under certain conditions, as described by his Eq. (8):

$$e_M \sim D\tau_r^{-1}(C_r^2 + C_g^2)^{-1}, \qquad (6)$$

where $D = (u'^2 + v'^2)/2$ is the climatological mean of the synoptic EKE, $\tau_r^{-1}$ is the summation of the typical synoptic eddy autodecay rate, $C_r$ is a constant on the order of $10\,\mathrm{m\,s^{-1}}$, and $C_g$ is a group velocity for synoptic Rossby waves, which depends on the zonal-mean zonal flow and is on the order of $10$–$20\,\mathrm{m\,s^{-1}}$. It is shown in Eq. (6) that the EIG rate tends to be directly proportional to the synoptic EKE and inversely proportional to the zonal-mean zonal flow squared. Note that as this equation was derived by Jin (2010) based on a linear dynamically closed barotropic model for the low-frequency flow, we consequently use either the 300-hPa or vertically averaged EIG rate and eddy statistics from Fig. 8 to the following figures. Our purpose is to make that the observed empirical EIG rate features can be well captured by Eq. (6) in a barotropic sense.

For attribution of the MLWS of the EIG in terms of Eq. (6), Fig. 12 presents the zonal-mean extratropical EKE and zonal flow over the different regions. It shows that the climatological EKE at mid- to high latitudes in the different NH regions all tends to be at a secondary minimum (to different extents) in mid- to late winter, around February. This feature is particularly clear in North Pacific, which is coincident with the occurrence of the midwinter suppression of storminess. It indicates that the midwinter suppression of the synoptic EKE in the NH may be the dominant factor controlling the MLWS of the

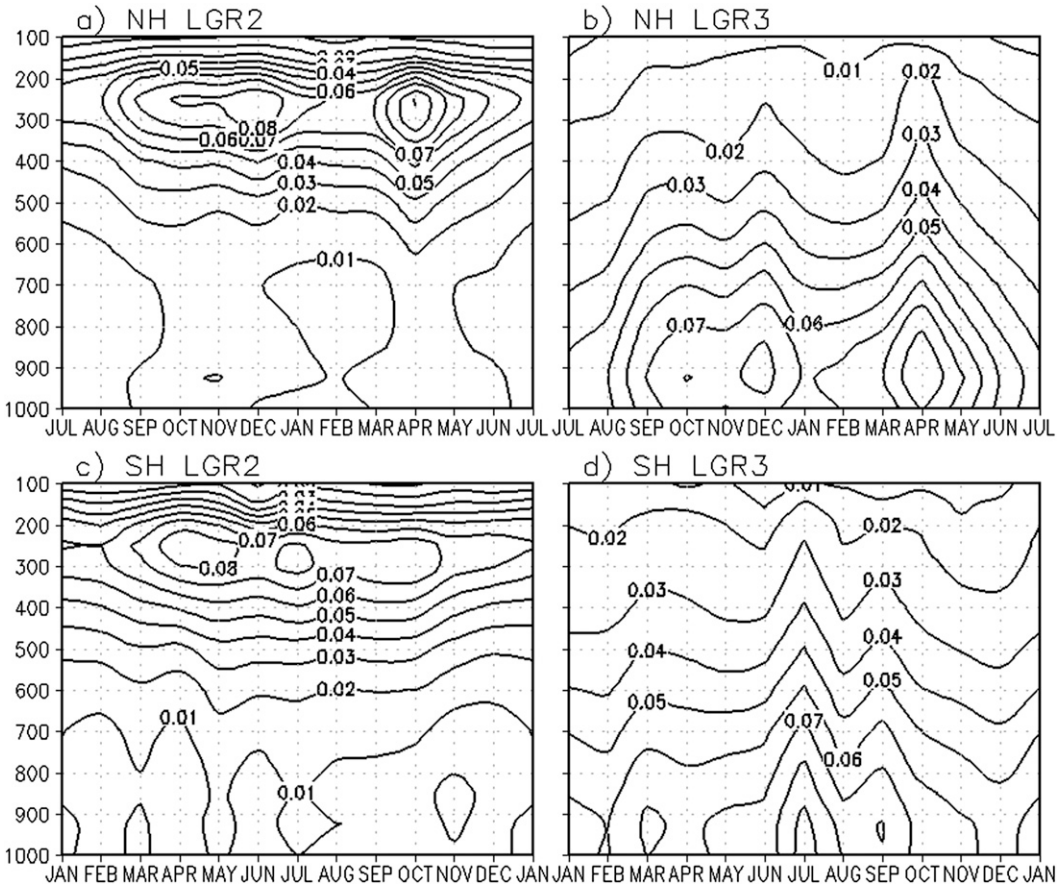


FIG. 9. Seasonal variations of the climatological LGR of LFV calculated over the (a),(b) NH and (c),(d) SH regions.

EIG of LFV in the NH. In contrast, the climatological zonal flow in Fig. 12 normally peaks in the coldest months and can also contribute to the MLWS of the EIG since the growth rate in Eq. (6) is inversely proportional to the mean flow squared via $C_g$. In addition, as Eq. (6) implies, the EIG rate may be dependent upon the eddy autodecay rate as well; that is, a smaller growth rate will be predicted as long as eddies in mid- to late winter have a longer lifespan. This remains an open question and requires further study.

Figure 13 further extracts the mid- to high-latitude means of the EKE and zonal flow over the different regions to highlight the fact that the EKE reaches its minimum and the zonal wind reaches its maximum around February, both of which favor generation of a mid- to late winter suppression of the EIG rate. That is, both the weakening of eddy activity and the strengthening of group velocity of synoptic Rossby waves can yield the suppression of the efficiency of SELF interaction. However, the LFV intensity reaches the maximum in mid- to late winter, although, meanwhile, the covariance between eddy forcing and LFV reaches the maximum in the NH. Evidently, the former has a larger speed to grow up than the latter, which may be due to the fast-increasing contributions of external forcing in low latitudes. In contrast, the storm tracks or EKE are somehow weakened and then the eddy forcing becomes weaker, suggesting that the efficiency of the SELF feedback on the LFV (viz., the EIG rate) will be smaller.

Indeed, many of mechanisms have been raised in previous studies for explaining the occurrence of the midwinter suppression of storminess in the North Pacific based on diagnosing data from observation and climate models. These mechanisms have reflected different aspects of dynamics, mainly including advection of the storminess suppression by strong westerly jets (Nakamura 1992; Harnik and Chang 2004), diabatic heating effect (Chang 2001), trapping effect of higher-altitude baroclinic waves by stronger subtropical jet (Nakamura and Sampe 2002), weakened eddy seeding–feeding processes associated with downstream development (Chang 2001; Zurita-Gotor and Chang 2005), the barotropic wind shear effect (Deng and

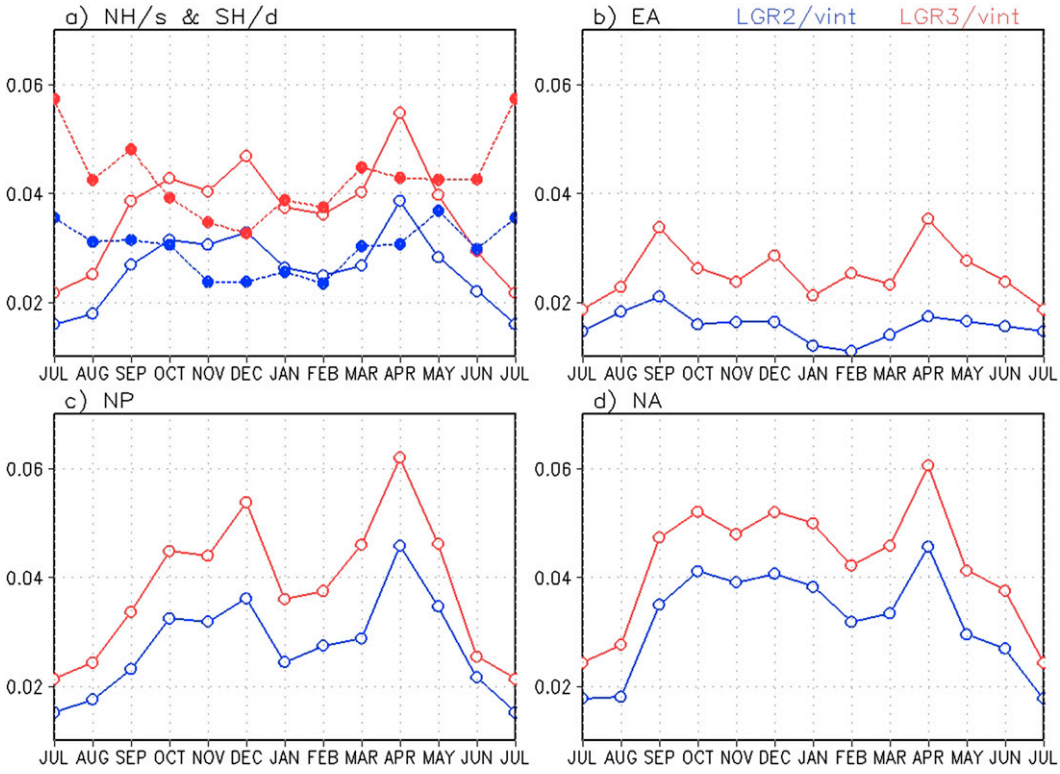


FIG. 10. Seasonal variations of the climatological vertically integrated LGR2 (blue) and LGR3 (red) averaged over the (a) NH (30°–80°N, 0°–360°E) and SH (30°–80°S, 0°–360°E), (b) Eurasia (30°–80°N, 30°–120°E), (c) North Pacific (30°–80°N, 120°E–100°W), and (d) North Atlantic (30°–80°N, 100°W–30°E). The dashed–dotted lines in (a) are for the SH.

Mak 2005), and impacts of the central Asian mountains and Tibetan Plateau (Park et al. 2010; Lee et al. 2013).

It is interesting that these mechanisms for explaining the midwinter suppression of storm-track intensity in North Pacific may provide more clues to interpret the MLWS in the EIG. Particularly, these mechanisms can be used to explain the suppression of the EKE, which is the controlling factor for the MLWS of the EIG. However, Chang (2001) also suggested the enhanced group velocity of eddy propagation as a result of the strong jet may contribute to a slower downstream growth of eddy energy over the North Pacific, which further yields an interannual variability in the reduction of the storm-track intensity. In contrast, we may find a similar story in Eq. (6): the climatologically strongest westerly jet in midwinter corresponds to the fastest group velocity of synoptic Rossby waves in the meanwhile, which tends to generate a relatively slow downstream growth of eddy energy over North Pacific and hence the midwinter suppression of storm-track intensity. Also, the zonal-mean EKE and zonal wind curves in the SH have been put into Fig. 13a, which, similar to those of the EIG rate, does not exhibit a suppression of the EKE in the austral midwinter. According to the effects of big mountains on the midwinter suppression, the presumable suspects for the differences between the hemispheres are more land–sea contrast and pronounced topography of the NH than the SH. Further demonstrations for the mechanism implied in Eq. (6) are still needed in future studies.

## 7. Summary and discussion

A number of past studies have also concluded that the SELF feedback plays an indispensable role in reinforcing LFV, as outlined in the introduction to this paper. The feedback that is induced by synoptic eddies can contribute to the growth or instability of the LFV (Jin et al. 2006a,b; Pan et al. 2006; Jin 2010). Therefore, how to quantitatively measure the EIG or instability of the LFV, caused by the SELF feedback, is an important issue. In this paper, we have completed a fundamental study with the aim of examining the climatological spatial features and seasonal variations of the empirical EIG rate, which is able to quantify the efficiency of the SELF feedback by projecting the eddy-induced forcing onto the LFV.

Our results show that the eddy forcing projected onto the LFV, and the variability of the LFV, are closely related in the extratropics, and their ratio has been defined

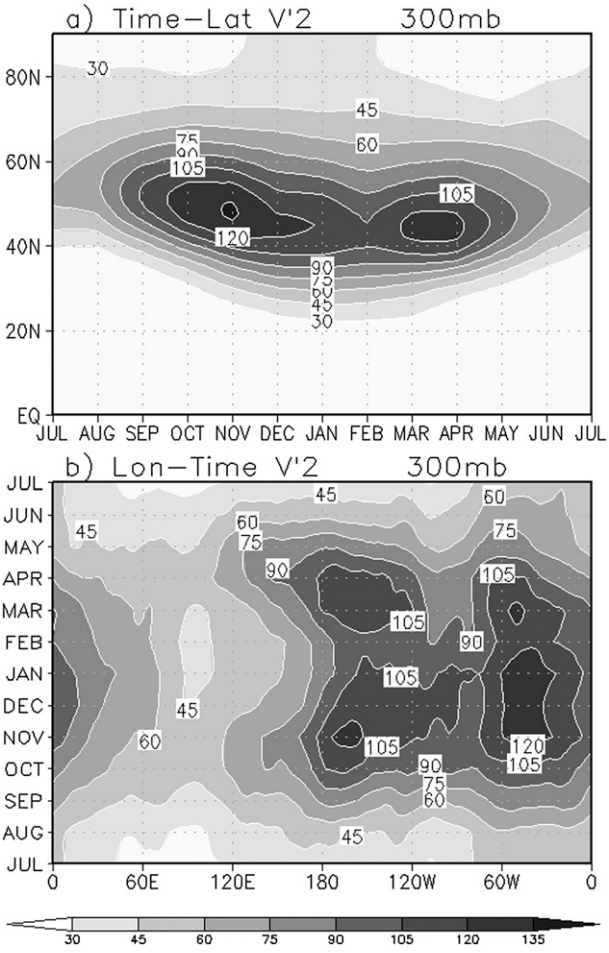


FIG. 11. Seasonal variations of the (a) climatological 300-hPa zonal-mean and (b) extratropical NH (30°–80°N) mean storm-track statistics ($m^2 s^{-2}$).

as the empirical EIG rate of LFV. Generally speaking, the EIG rate, which is derived from the eddy vorticity flux forcing, is dominant in the upper troposphere, whereas the EIG rate, which is derived from the eddy PV flux forcing, is dominant in the lower troposphere. This downward redistribution of the EIG rate is mainly due to the eddy heat flux effect, which is important to balance the surface frictional damping to some degree, and may also contribute to the barotropic structure of LFV. Further results show that the local growth rate has climatological spatial patterns and regional centers that are similar to those of the LFV variances, indicating that the EIG plays an important role in maintaining the patterns and amplitudes of LFV. The vertical structures of the LGR reflect the contributions that the eddy-induced growth makes to both sustaining the eddy-driven jets and overcoming the surface friction. The SH tends to have a more uniform distribution of the local EIG rate than that in the NH, which may favor the more zonally symmetric annular mode in the SH than in the NH.

The EIG rate of LFV shows a general seasonality, with a maximum in cold seasons and minimum in the warmest season, which may explain why the warmest season has a lower-amplitude LFV when compared with the colder seasons. This seasonality appears stronger in the NH than in the SH and may account for the seasonality in the variability of LFV to some degree. Further results show that the seasonal variations of the EIG rate in the NH are more complicated than those in the SH. The EIG rate of LFV is subject to suppression in the NH mid- to late winter, although this is also the time when the LFV experiences its maximum amplitude and projection of eddy forcing onto it. This mid- to late winter suppression of the EIG in the NH essentially represents suppression of eddy feedback efficiency and may be attributed largely to the midwinter suppression of the storm-track activity (EKE) in the NH, probably implying a nonlinear self-limitation of the eddy feedback for large-amplitude LFV.

However, the attribution of the observed MLWS of the EIG remains an open question. As discussed in the context of Eq. (6), the eddy autodecay rate may play a role in suppressing the mid- to late winter EIG. In addition, the dynamics associated with the baroclinic eddy equilibration during the boreal winter (Zhang and Stone 2010) may offer an alternative interpretation of the MLWS of the eddy feedback efficiency. Furthermore, the good agreement between the seasonal variations of the empirical EIG rate and the EKE indicate that the former may be expected to agree well with the theoretical EIG rate as predicted by the theory of eddy-induced instability of LFV proposed by Jin (2010), which would validate this theory to a great degree. All of these points will be considered further in future studies. In addition, note the fact that the eddy vorticity and heat fluxes can make different contributions to the EIG of the LFV; we may distinguish the different roles of the two kinds of eddy fluxes by examining the growth rate $\lambda_3$ generated from the eddy vorticity part and from the eddy heat part in the eddy PV flux, respectively. Also, we may further examine the roles of the eddy-induced vertical secondary circulation in contributing eddy feedback by comparing the difference between $\lambda_2$ and $\lambda_3$ derived from the eddy vorticity flux forcing. These will be further studied in the future.

This study directly quantified the features of the positive synoptic eddy feedback onto the LFV in extratropics. On one hand, the positive EIG provided by eddies, serving as an important energy source for LFV, may substantially offset the natural frictional and thermal damping. Thus, an improved understanding of the SELF feedback, as indicated in this study, may enable us to

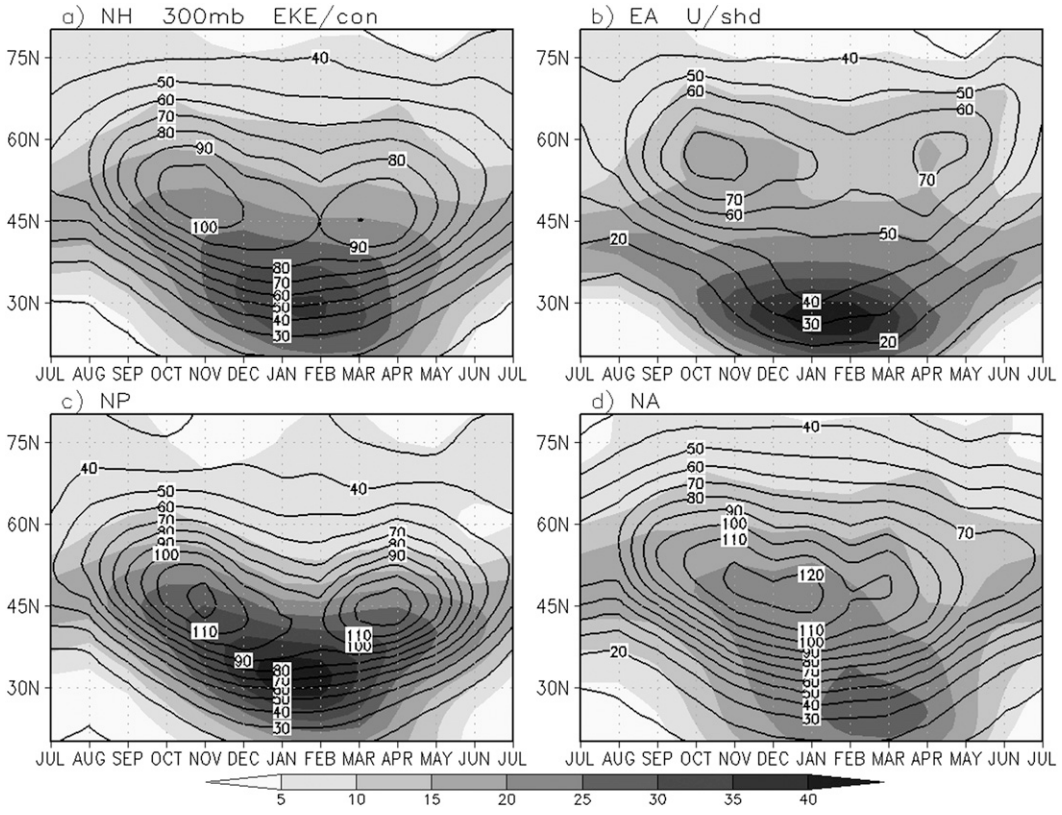


FIG. 12. Seasonal variations of the climatological 300-hPa EKE (contours; $m^2 s^{-2}$) and zonal wind (shaded; $m s^{-1}$), zonally averaged over regions defined in Fig. 10.

better utilize the systematic low-frequency information. By diagnosing the EIG rate, such low-frequency information can be gleaned from transient synoptic eddies and eventually increase our ability to improve monitoring and prediction of climate variability in the mid- to high latitudes. On the other hand, the EIG rate, as the diagnostic to measure the efficiency of the SELF interaction, also represents the degree that the persistence of the LFV can be extended by the positive eddy feedback. Indeed, the relative importance of the EIG in reinforcing and maintaining LFV, compared to other factors, such as linear advection terms, external forcing, low-frequency eddy, and so on, remains an open question notwithstanding some previous studies.

*Acknowledgments.* This work is jointly supported by National Science foundation (NSF) Grant of China (41375062), China Meteorological Special Projects (GYHY201406022, GYHY201206016), U.S. NSF Grant (ATM 1034439), and 973 Program Grant of China (2010CB950404). JSK was supported by the National Research Foundation of Korea (Grant NRF-2009-C1AAA001-2009-0093042) funded by the South Korean government (MEST).

## APPENDIX

### Eddy-Induced Growth Rate of Low-Frequency Variability

As usual, the geopotential tendency induced by the eddy vorticity flux forcing and the eddy PV flux forcing, respectively, can be expressed as follows:

$$\frac{1}{f}\left(\frac{\partial\overline{\Phi}^{a}}{\partial t}\right)_{\mathrm{ed}} = -\Delta_2^{-1}(\nabla\cdot\mathbf{F}^{\mathrm{VORT}}) = \chi_2, \qquad \text{(A1)}$$

$$\frac{1}{f}\left(\frac{\partial\overline{\Phi}^{a}}{\partial t}\right)_{\mathrm{ed}} = -\Delta_3^{-1}(\nabla\cdot\mathbf{F}^{\mathrm{PV}}) = \chi_3. \qquad \text{(A2)}$$

Here, the anomalous eddy fluxes and their induced anomalous geopotential tendencies are the same as the definitions in Eqs. (1) and (2). Equation (A1) indicates that the tendency is estimated from the eddy vorticity forcing based on the vorticity equation framework, and Eq. (A2) indicates that the tendency is obtained from the eddy PV forcing under the quasigeostrophic PV equation framework, referring to the paper of Lau and Holopainen (1984). Using either the 2D or 3D inversion operator is

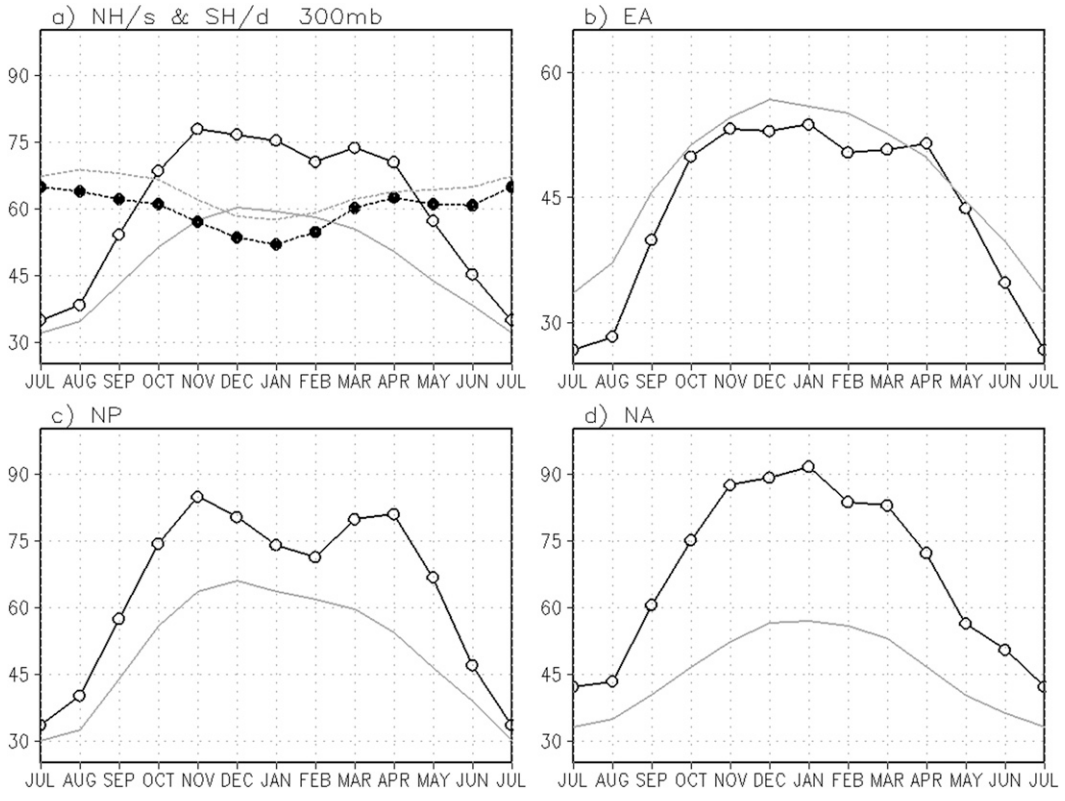


FIG. 13. Seasonal variations of the climatological 300-hPa EKE (black) and zonal wind (gray) averaged over the regions defined in Fig. 10. The dashed–dotted lines in (a) are for the SH.

just dependent on the purpose to do diagnosis, as many previous studies did (e.g., Lau 1988; Lau and Nath 1991; Kug et al. 2010a). In this paper, we, still along this line, aim to define the two kinds of EIG rate using the 2D and 3D Laplacian inversions, respectively.

Lau (1988) demonstrated the close association between anomalies in the monthly-mean-flow field and systematic anomalies in the monthly-mean eddy statistics such as the eddy forcing. Jin et al. (2006a) further hypothesized that part of the eddy forcing can be directly related to the low-frequency flow via a dynamical closure between the two fields, which, in a barotropic framework, can be expressed as

$$\chi_2 \approx \frac{1}{f} L_f \overline{\Phi}^a, \tag{A3}$$

where $L_f$ is the linear operator representing synoptic eddy feedback. Therefore, a linear barotropic geopotential equation, similar to the version as derived by Jin et al. (2006a), can be expressed as

$$\frac{\partial \overline{\Phi}^a}{\partial t} = L\overline{\Phi}^a + r\overline{\Phi}^a + L_f\overline{\Phi}^a + \overline{F}^a. \tag{A4}$$

Here, $L$ is the linear advection operator, $r$ the damping coefficient ($<0$), and $\overline{F}^a$ is the external forcing. Based on the dynamic closure, Jin (2010) proposed a theory on the eddy-induced instability of low-frequency variability and formulated a theoretical eddy-induced growth rate by which the contribution of $L_f$ can be simply expressed as a constant.

Motivated by abundant observed evidence for the positive eddy feedback, Ren et al. (2011) assumed the linear relationship between the eddy vorticity–induced forcing and low-frequency flow as

$$\chi_2 = \lambda_2 \overline{\Phi}^a / f + R_2, \tag{A5}$$

where $\lambda_2$ is a linear coefficient for the bulk growth rate ($>0$) or damping rate ($<0$), representing the positive or negative eddy feedback, and $R_2$ is the residual term, representing the remainder of eddy forcing that is not explained by low-frequency flow. If we approximately take $R_2$ as zero, then Eq. (A4) can be changed into

$$\frac{\partial \overline{\Phi}^a}{\partial t} = L\overline{\Phi}^a + r\overline{\Phi}^a + \lambda_2\overline{\Phi}^a + \overline{F}^a. \tag{A6}$$

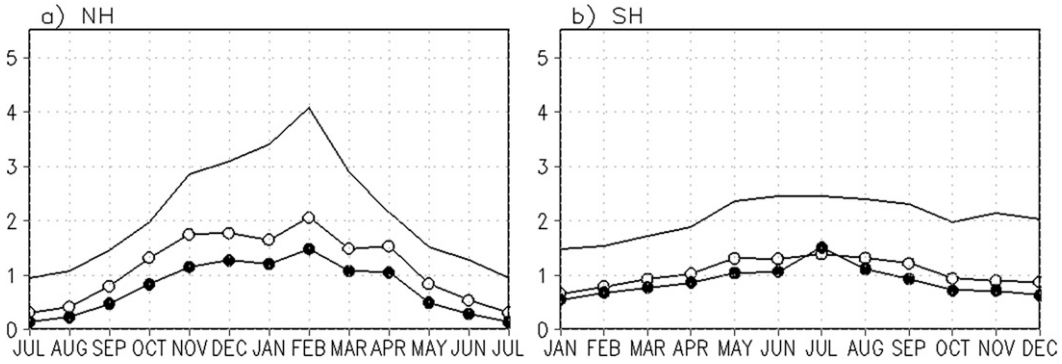


FIG. A1. Seasonal variations of the climatological vertically integrated denominator (black lines) of Eq. (6) and the corresponding numerators of $\lambda_2$ (open-circle lines) and $\lambda_3$ (filled-circle lines).

It is indicated in Eq. (A6) that the total derivative of low-frequency flow is determined by the contrast between $r$ and $\lambda_2$, given that $\overline{F}^a = 0$.

Then, it can be similarly assumed that

$$\chi_3 = \lambda_3 \overline{\Phi}^a / f + R_3, \tag{A7}$$

where $\lambda_3$ represents the growth rate ($>0$) or damping rate ($<0$) induced by the eddy PV forcing, and $R_3$ is the residual term.

To quantify the eddy-induced growth for the low-frequency flow, as written in Eqs. (A5) and (A7), Ren et al. (2011) adopted an empirical expression as follows:

$$\lambda_j = \frac{\iint_S f \overline{\Phi}^a \chi_j \, dx \, dy}{\iint_S \overline{\Phi}^a \overline{\Phi}^a \, dx \, dy}, \tag{A8}$$

where $j = 2$ and 3 denotes the eddy vorticity and eddy PV feedback cases, respectively. It is clearly seen in the definition equation that the EIG rate will be positive (negative) when the eddy forcing pattern is in phase (out of phase) with the LFV pattern, which is actually used as a diagnostic to measure the SELF feedback efficiency instead of its intensity. Moreover, the maintenance of the LFV generated from the eddy forcing also expresses to what degree the persistence of the LFV can be extended by the positive eddy feedback. In addition, we here show the seasonal variations of the climatological vertically integrated denominator of Eq. (A8) and the corresponding numerators of $\lambda_2$ and $\lambda_3$, as shown in Fig. A1. It is quite clear that both the denominator and numerators are the biggest during February in the NH and during July in the SH.

## REFERENCES

Athanasiadis, P. J., J. M. Wallace, and J. J. Wettstein, 2010: Patterns of wintertime jet stream variability and their relation to the storm tracks. *J. Atmos. Sci.,* **67,** 1361–1381, doi:10.1175/2009JAS3270.1.

Barnes, E. A., and D. L. Hartmann, 2010: Dynamical feedbacks and the persistence of the NAO. *J. Atmos. Sci.,* **67,** 851–865, doi:10.1175/2009JAS3193.1.

Branstator, G., 1992: The maintenance of low-frequency atmospheric anomalies. *J. Atmos. Sci.,* **49,** 1924–1946, doi:10.1175/1520-0469(1992)049<1924:TMOLFA>2.0.CO;2.

——, 1995: Organization of storm track anomalies by recurring low-frequency circulation anomalies. *J. Atmos. Sci.,* **52,** 207–226, doi:10.1175/1520-0469(1995)052<0207:OOSTAB>2.0.CO;2.

Cai, M., and M. Mak, 1990: Symbolic relation between planetary and synoptic-scale waves. *J. Atmos. Sci.,* **47,** 2953–2968, doi:10.1175/1520-0469(1990)047<2953:SRBPAS>2.0.CO;2.

——, and H. M. van den Dool, 1991: Low-frequency waves and traveling storm tracks. Part I: Barotropic component. *J. Atmos. Sci.,* **48,** 1420–1436, doi:10.1175/1520-0469(1991)048<1420:LFWATS>2.0.CO;2.

Chang, E. K. M., 2001: GCM and observational diagnoses of the seasonal and interannual variations of the Pacific storm track during the cool season. *J. Atmos. Sci.,* **58,** 1784–1800, doi:10.1175/1520-0469(2001)058<1784:GAODOT>2.0.CO;2.

——, S. Lee, and K. L. Swanson, 2002: Storm track dynamics. *J. Climate,* **15,** 2163–2183, doi:10.1175/1520-0442(2002)015<02163:STD>2.0.CO;2.

Deng, Y., and M. Mak, 2005: An idealized model study relevant to the dynamics of the midwinter minimum of the Pacific storm track. *J. Atmos. Sci.,* **62,** 1209–1225, doi:10.1175/JAS3400.1.

Duchon, C., 1979: Lanczos filtering in one and two dimensions. *J. Appl. Meteor.,* **18,** 1016–1022, doi:10.1175/1520-0450(1979)018<1016:LFIOAT>2.0.CO;2.

Egger, J., and H.-D. Schilling, 1983: On the theory of the long-term variability of the atmosphere. *J. Atmos. Sci.,* **40,** 1073–1085, doi:10.1175/1520-0469(1983)040<1073:OTTOTL>2.0.CO;2.

Harnik, N., and E. K. M. Chang, 2004: The effects of variations in jet width on the growth of baroclinic waves: Implications for midwinter Pacific storm track variability. *J. Atmos. Sci.,* **61,** 23–40, doi:10.1175/1520-0469(2004)061<0023:TEOVIJ>2.0.CO;2.

Held, I. M., 1983: Stationary and quasi-stationary eddies in the extratropical troposphere: Theory. *Large Scale Dynamical Processes in the Atmosphere,* B. Hoskins and R. Pearce, Eds., Academic Press, 127–169.

Hendon, H. H., and D. L. Hartmann, 1985: Variability in a nonlinear model of the atmosphere with zonally symmetric

forcing. *J. Atmos. Sci.,* **42,** 2783–2797, doi:10.1175/1520-0469(1985)042<2783:VIANMO>2.0.CO;2.

Jin, F.-F., 2010: Eddy-induced instability for low-frequency variability. *J. Atmos. Sci.,* **67,** 1947–1964, doi:10.1175/2009JAS3185.1.

——, L.-L. Pan, and M. Watanabe, 2006a: Dynamics of synoptic eddy and low-frequency flow interaction. Part I: A linear closure. *J. Atmos. Sci.,* **63,** 1677–1694, doi:10.1175/JAS3715.1.

——, ——, and ——, 2006b: Dynamics of synoptic eddy and low-frequency flow interaction. Part II: A theory for low-frequency modes. *J. Atmos. Sci.,* **63,** 1695–1708, doi:10.1175/JAS3716.1.

Kalnay, E., and Coauthors, 1996: The NCEP/NCAR 40-Year Reanalysis Project. *Bull. Amer. Meteor. Soc.,* **77,** 437–471, doi:10.1175/1520-0477(1996)077<0437:TNYRP>2.0.CO;2.

Kok, C. J., J. D. Opsteegh, and H. M. van den Dool, 1987: Linear models: Useful tools to analyze GCM results. *Mon. Wea. Rev.,* **115,** 1996–2008, doi:10.1175/1520-0493(1987)115<1996:LMUTTA>2.0.CO;2.

Kug, J.-S., and F.-F. Jin, 2009: Left-hand rule for synoptic eddy feedback on low-frequency flow. *Geophys. Res. Lett.,* **36,** L05709, doi:10.1029/2008GL036435.

——, ——, J.-H. Park, H.-L. Ren, and I.-S. Kang, 2010a: A general rule for synoptic-eddy feedback onto low-frequency flow. *Climate Dyn.,* **35,** 1011–1026, doi:10.1007/s00382-009-0606-8.

——, ——, and H.-L. Ren, 2010b: Role of synoptic eddies on low-frequency precipitation variation. *J. Geophys. Res.,* **115,** D19115, doi:10.1029/2009JD013675.

Lau, N.-C., 1988: Variability of the observed midlatitude storm tracks in relation to low-frequency changes in the circulation pattern. *J. Atmos. Sci.,* **45,** 2718–2743, doi:10.1175/1520-0469(1988)045<2718:VOTOMS>2.0.CO;2.

——, and E. O. Holopainen, 1984: Transient eddy forcing of the time-mean flow as identified by geopotential tendencies. *J. Atmos. Sci.,* **41,** 313–328, doi:10.1175/1520-0469(1984)041<0313:TEFOTT>2.0.CO;2.

——, and M. J. Nath, 1991: Variability of the baroclinic and barotropic transient eddy forcing associated with monthly changes in the midlatitude storm tracks. *J. Atmos. Sci.,* **48,** 2589–2613, doi:10.1175/1520-0469(1991)048<2589:VOTBAB>2.0.CO;2.

Lee, S., and S. B. Feldstein, 1996: Mechanism of zonal index evolution in a two-layer model. *J. Atmos. Sci.,* **53,** 2232–2246, doi:10.1175/1520-0469(1996)053<2232:MOZIEI>2.0.CO;2.

Lee, S.-S., J.-Y. Lee, K.-J. Ha, B. Wang, A. Kitoh, Y. Kajikawa, and M. Abe, 2013: Role of the Tibetan Plateau on the annual variation of mean atmospheric circulation and storm-track activity. *J. Climate,* **26,** 5270–5286, doi:10.1175/JCLI-D-12-00213.1.

Limpasuvan, V., and D. L. Hartmann, 1999: Eddies and the annular modes of climate variability. *Geophys. Res. Lett.,* **26,** 3133–3136, doi:10.1029/1999GL010478.

——, and ——, 2000: Wave-maintained annular modes of climate variability. *J. Climate,* **13,** 4414–4429, doi:10.1175/1520-0442(2000)013<4414:WMAMOC>2.0.CO;2.

Lorenz, D. J., and D. L. Hartmann, 2001: Eddy-zonal flow feedback in the Southern Hemisphere. *J. Atmos. Sci.,* **58,** 3312–3327, doi:10.1175/1520-0469(2001)058<3312:EZFFIT>2.0.CO;2.

——, and ——, 2003: Eddy-zonal flow feedback in the Northern Hemisphere winter. *J. Climate,* **16,** 1212–1227, doi:10.1175/1520-0442(2003)16<1212:EFFITN>2.0.CO;2.

Nakamura, H., 1992: Midwinter suppression of baroclinic wave activity in the Pacific. *J. Atmos. Sci.,* **49,** 1629–1641, doi:10.1175/1520-0469(1992)049<1629:MSOBWA>2.0.CO;2.

——, and T. Sampe, 2002: Trapping of synoptic-scale disturbances into the North-Pacific subtropical jet core in midwinter. *Geophys. Res. Lett.,* **29,** doi:10.1029/2002GL015535.

Pan, L.-L., F.-F. Jin, and M. Watanabe, 2006: Dynamics of synoptic eddy and low-frequency flow interaction. Part III: Baroclinic model results. *J. Atmos. Sci.,* **63,** 1709–1725, doi:10.1175/JAS3717.1.

Park, H.-S., J. C. H. Chiang, and S.-W. Son, 2010: The role of the central Asian mountains on the midwinter suppression of North Pacific storminess. *J. Atmos. Sci.,* **67,** 3706–3720, doi:10.1175/2010JAS3349.1.

Penny, S., G. H. Roe, and D. S. Battisti, 2010: The source of the midwinter suppression in storminess over the North Pacific. *J. Climate,* **23,** 634–648, doi:10.1175/2009JCLI2904.1.

Ren, H.-L., F.-F. Jin, J.-S. Kug, J.-X. Zhao, and J. Park, 2009: A kinematic mechanism for positive feedback between synoptic eddies and NAO. *Geophys. Res. Lett.,* **36,** L11709, doi:10.1029/2009GL037294.

——, ——, ——, and L. Gao, 2011: Transformed eddy-PV flux and positive synoptic eddy feedback onto low-frequency flow. *Climate Dyn.,* **36,** 2357–2370, doi:10.1007/s00382-010-0913-0.

——, ——, and L. Gao, 2012: Anatomy of synoptic eddy–NAO interaction through eddy-structure decomposition. *J. Atmos. Sci.,* **69,** 2171–2191, doi:10.1175/JAS-D-11-069.1.

Ren, X., X. Yang, and C. Chu, 2010: Seasonal variations of the synoptic-scale transient eddy activity and polar-front jet over East Asia. *J. Climate,* **23,** 3222–3233, doi:10.1175/2009JCLI3225.1.

Robinson, W. A., 1991: The dynamics of low-frequency variability in a simple model of the global atmosphere. *J. Atmos. Sci.,* **48,** 429–441, doi:10.1175/1520-0469(1991)048<0429:TDOLFV>2.0.CO;2.

——, 2000: A baroclinic mechanism for the eddy feedback on the zonal index. *J. Atmos. Sci.,* **57,** 415–422, doi:10.1175/1520-0469(2000)057<0415:ABMFTE>2.0.CO;2.

Simmons, A. J., J. M. Wallace, and G. W. Branstator, 1983: Barotropic wave propagation and instability, and atmospheric teleconnection patterns. *J. Atmos. Sci.,* **40,** 1363–1392, doi:10.1175/1520-0469(1983)040<1363:BWPAIA>2.0.CO;2.

Watanabe, M., 2009: Self-limiting feedback between baroclinic waves and a NAO-like sheared zonal flow. *Geophys. Res. Lett.,* **36,** L08803, doi:10.1029/2009GL038520.

Whitaker, J. S., and A. Barcilon, 1995: Low-frequency variability and wavenumber selection in models with zonally symmetric forcing. *J. Atmos. Sci.,* **52,** 491–503, doi:10.1175/1520-0469(1995)052<0491:LFVAWS>2.0.CO;2.

Zhang, Y., and P. Stone, 2010: Baroclinic eddy equilibration under specified seasonal forcing. *J. Atmos. Sci.,* **67,** 2632–2648, doi:10.1175/2010JAS3392.1.

——, X. Yang, Y. Nie, and G. Chen, 2012: Annular mode like variation in a multi-layer QG model. *J. Atmos. Sci.,* **69,** 2940–2958, doi:10.1175/JAS-D-11-0214.1.

Zhang, Y. Q., and I. M. Held, 1999: A linear stochastic model of a GCM's midlatitude storm tracks. *J. Atmos. Sci.,* **56,** 3416–3435, doi:10.1175/1520-0469(1999)056<3416:ALSMOA>2.0.CO;2.

Zurita-Gotor, P., and E. K. M. Chang, 2005: The impact of zonal propagation and seeding on the eddy-mean flow equilibrium of a zonally varying two-layer model. *J. Atmos. Sci.,* **62,** 2261–2273, doi:10.1175/JAS3473.1.

ATMOSPHERIC AND OCEANIC SCIENCE LETTERS, 2014, VOL. 7, NO. 2, 157–161

# Application of the Analogue-Based Correction of Errors Method in ENSO Prediction

REN Hong-Li[1], LIU Ying[1], JIN Fei-Fei[2], YAN Yu-Ping[1], and LIU Xiang-Wen[1]

[1] *Laboratory for Climate Studies, National Climate Center, China Meteorological Administration, Beijing 100081, China*
[2] *Department of Meteorology, School of Ocean and Earth Sciences and Technology, University of Hawaii at Manoa, Honolulu, Hawaii 96822, USA*

Received 12 October; revised 21 November 2013; accepted 4 December 2013; published 16 March 2014

**Abstract** In this study, a method of analogue-based correction of errors (ACE) was introduced to improve El Niño-Southern Oscillation (ENSO) prediction produced by climate models. The ACE method is based on the hypothesis that the flow-dependent model prediction errors are to some degree similar under analogous historical climate states, and so the historical errors can be used to effectively reduce such flow-dependent errors. With this method, the unknown errors in current ENSO predictions can be empirically estimated by using the known prediction errors which are diagnosed by the same model based on historical analogue states. The authors first propose the basic idea for applying the ACE method to ENSO prediction and then establish an analogue-dynamical ENSO prediction system based on an operational climate prediction model. The authors present some experimental results which clearly show the possibility of correcting the flow-dependent errors in ENSO prediction, and thus the potential of applying the ACE method to operational ENSO prediction based on climate models.

**Keywords:** ENSO, climatic prediction, error correction
**Citation:** Ren, H.-L., Y. Liu, F.-F. Jin, et al., 2014: Application of the analogue-based correction of errors method in ENSO prediction, *Atmos. Oceanic Sci. Lett.*, **7**, 157–161, doi:10.3878/j.issn.1674-2834.13.0080.

## 1 Introduction

The El Niño-Southern Oscillation (ENSO), as the dominant mode of natural climate variability in the tropical Pacific on interannual timescales, has a major impact on the global climate and particularly East Asian climate variability (e.g., Rasmusson and Carpenter, 1982; Zhang et al., 1996, 2012; Wang et al., 2000). In the past three decades, a number of international efforts have been made to find a good method to predict the ENSO phenomenon, and many prediction methods have been proposed, such as statistical models and simplified dynamic air-sea coupled models, as well as fully coupled general circulation models (GCMs) (e.g., Cane et al., 1986; Zebiak and Cane, 1987; Chen et al., 1995, 2004; Luo et al., 2005, 2008; Zheng et al., 2006, 2009; Cheng et al., 2010; Izumo et al., 2010). Following these works, much progress has been made in improving methods for ENSO prediction. There is no doubt that such achievements can be largely attributed to improvements in the understanding of ENSO, climate modelling, and ocean data assimilation (Moore and Kleeman, 1996; Latif et al., 1998; Kirtman, 2003; Jin et al., 2008; Barnston et al., 2012).

However, there are still many GCMs that are incapable of adequately simulating ENSO and reasonably assimilating ocean initial states. Particularly, when such models are applied to operational ENSO prediction, their prediction performance can be expected to be relatively low. The question is: how do we improve the capability of such models with low performance in predicting ENSO? An efficient way is to develop empirical/statistical correction methods of model prediction errors (e.g., Wang et al., 2000; Chen and Lin, 2006; Zeng, 2009). Generally speaking, the predictions based on coupled GCMs are subject to biases and the raw outputs of the models include systematic errors due to model deficiencies. This kind of systematic bias used to be regarded as a constant and may be largely reduced using model climatology in generating climate anomalies. Nevertheless, the errors in model predictions are flow-dependent with changing climate states, which are correlated to physical predictors and further statistically estimated by them (Ren, 2008).

Many studies have focused on developing effective methods/schemes to correct such flow-dependent errors in model predictions (c.f., Ren and Chou, 2007a). In our previous studies, we proposed the method of analogue-based correction of errors (ACE) in model predictions, based on the hypothesis that the flow-dependent errors are to some degree similar under analogous historical states (Ren and Chou, 2005, 2007b; Ren et al., 2009). With this method, we can empirically estimate the unknown errors of the current prediction using the known prediction errors that can be produced by the same model with historical analogue states. Since 2006, this method has been continually developed with different schemes for applications in seasonal climate prediction. In this paper, we propose a new idea to empirically improve ENSO prediction performance in an operational climate model by applying the ACE method, and report results from an idealized experiment conducted to test the idea.

## 2 Methodology and ENSO prediction system

Here, we briefly introduce the basic idea behind the strategy and methodology of dynamical analogue prediction (Ren and Chou, 2007b). To effectively use analogous

Corresponding author: REN Hong-Li, renhl@cma.gov.cn

information from historical data in climate prediction based on complicated models, a method of ACE in model prediction has been proposed in previous studies (Ren and Chou, 2005, 2007b). The main idea of the method can be simply expressed by the equation of analogue correction of errors as follows:

$$\hat{P}_{\mathrm{M}}(\psi_0) = P_{\mathrm{M}}(\psi_0) + \tilde{P}_{\mathrm{M}}(\tilde{\psi}_j) - P_{\mathrm{M}}(\tilde{\psi}_j). \quad (1)$$

The term on the left side of Eq. (1) is the corrected model prediction, and those on the right side are the direct model prediction, historical analogue, and its corresponding prediction with the same model, where M denotes the time integration or time mean prediction, and the wave denotes the analogue. It is clearly seen from Eq. (1) that the question of conducting the model prediction can be transformed into the question of prediction error estimation by extracting information about the model prediction errors from the historical analogue and further correcting the current prediction of the same model.

In fact, the estimated prediction errors can be made much more stationary and acceptable using many historical analogues (Ren and Chou, 2007b). Therefore, Eq. (1) can be further developed into

$$\hat{P}_{\mathrm{M}}(\psi_0) = P_{\mathrm{M}}(\psi_0) + \sum_{j=1}^{m} w_j \left[ \tilde{P}_{\mathrm{M}}(\tilde{\psi}_j) - P_{\mathrm{M}}(\tilde{\psi}_j) \right], \quad (2)$$

where $m$ denotes many historical analogues and $w_j$ is the weight function. Based on Eqs. (1) and (2), we can take $P_{\mathrm{M}}$ as the monthly ENSO prediction, such as SST anomalies, and establish an analogue-dynamical ENSO prediction system (ADEPS). Figure 1 shows the schematic diagram for constructing the ADEPS and illustrating its main procedures.

## 3 Experiment and results

To validate the idea of applying the ACE method to ENSO prediction, we designed an idealized experiment based on the ADEPS assuming that we could find perfect historical analogues. That is, the best analogues could be determined by directly using the current analysis field that actually emerged after the initial time and needed to be predicted, instead of using the initial analysis field as usual. Through such an experiment, as we will see, we were able to demonstrate the potential of the ACE method to be used in ENSO prediction.

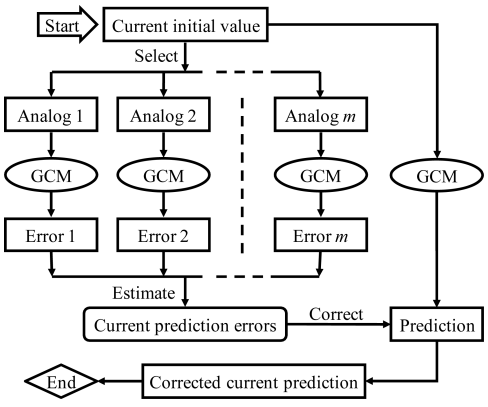


**Figure 1** Schematic diagram of the analogue-dynamical ENSO prediction system.

In the experiment, a 30-yr hindcast dataset for the period 1983–2012, produced by the operational air-sea coupled GCM at the Beijing Climate Center (BCC CGCM1) (Ding et al., 2002) was used; specifically, the March to August ensemble-mean data of 48 members predicted at the end of February. In addition, the initial values of the atmospheric model were generated at 0000 UTC on the last eight days of February from the National Centers for Environmental Prediction/National Center for Atmospheric Research (NCEP/NCAR) reanalysis dataset (NNRA). The initial values of the oceanic model were generated from the global ocean data assimilation system of the BCC, and were further perturbed and combined into 48 ensemble members of dynamical seasonal prediction. The monthly sea surface temperature (SST) dataset employed in this study was the global sea ice and sea surface temperature analyses from the Hadley Center (HadISST) (Rayner et al., 2003). The traditional Niño3.4 index can be calculated by taking an average of the SST anomalies in the region of (5°S–5°N, 120–170°W).

The scheme for the experiment applying the ADEPS was designed as: 1) March to August SST anomalies were extracted from the 30-yr hindcast and HadISST analysis datasets for selecting the historical analogues and verifying predictions; 2) the root-mean-square distance between two SST anomaly fields was taken as the metric to measure their analogy and the first four best analogues were used to estimate the prediction errors with equal weighting; 3) an independent validation was conducted for target years from 1993 to 2012, and for each target year all of the data prior to the target year were used to define the climatology and select historical analogues; 4) prediction skill scores were taken as the temporal correction coefficient (TCC) and root-mean-square error (RMSE) between the predicted and observed Niño3.4 SST anomaly indices.

Figure 2 compares the predicted time series of the Niño3.4 indices with the observed indices at different lead months. It is clear that the direct model predictions tend to have a lower amplitude, presumably due to the strong damping effect in the operational BCC CGCM1. This situation becomes more apparent as the lead months increase, and even after three months, the directly predicted indices have become so weak that they are almost not able to provide a useful signal any more. In contrast, the predicted indices generated in the idealized experiment are perfectly consistent with the observed indices. Under the condition of prescribing the historical analogue information, the ADEPS based on the ACE method can extract those prediction errors which are similar in the analogues, and empirically estimate the current prediction error. The correction originated from historical analogues using the same prediction model, not only calibrate well the climate variability signals in the ENSO prediction, but also recover the amplitude of the ENSO variability predicted directly by the model to a large degree.

To quantitatively present the potential ability of the ACE method to improve the performance of ENSO pre-

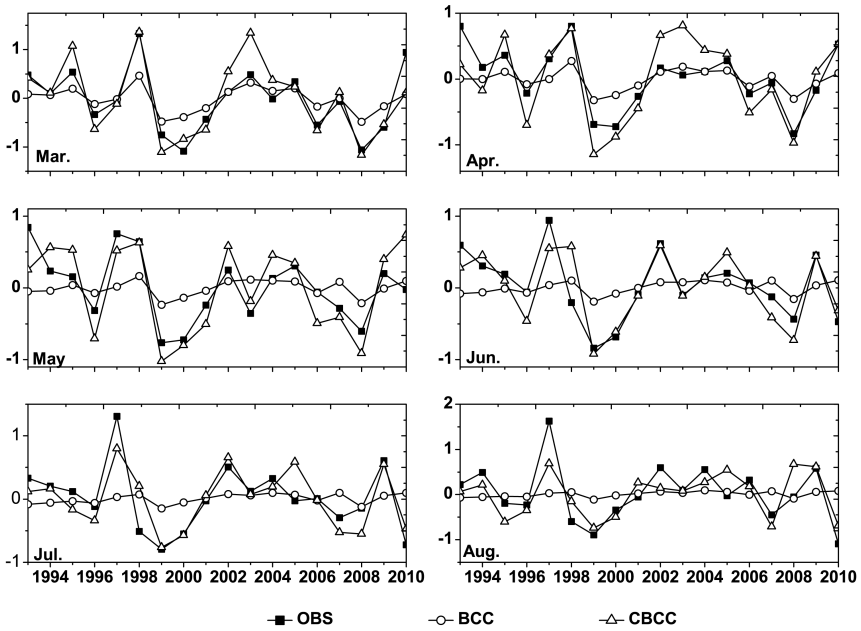


**Figure 2** Niño3.4 indices from the observation (square line), direct model prediction (circle line), and corrected model prediction (triangle line) in different forecast months.

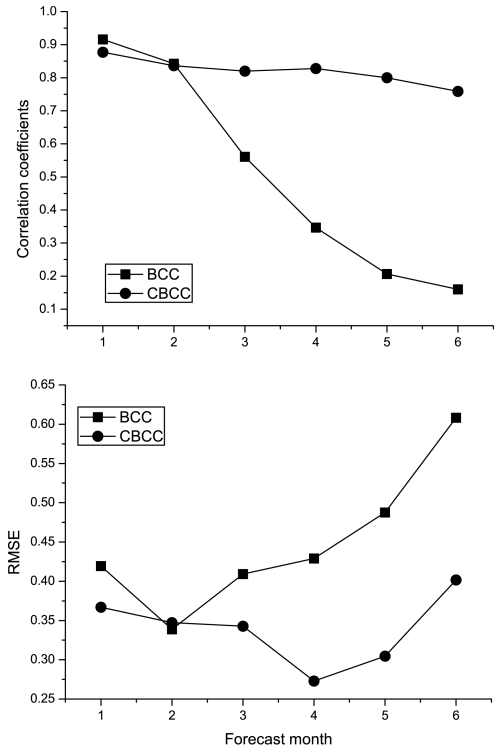


**Figure 3** Prediction skill scores as a function of forecast month: the temporal correlation coefficients TCCs (upper) and RMSE (lower), for direct model prediction (square line) and corrected model prediction (circle line).

diction, Fig. 3 further give the two traditional prediction skill scores—TCC and RMSE—which are widely used in the verification of ENSO prediction. It is quite evident in Fig. 3 that the TCC scores of the direct model prediction appear to be very low, compared with those of the corrected prediction. The former is subject to a quick decrease of values after three lead months, which is probably attributable to the poorly represented air-sea coupling over the tropical ocean in the model. Although, in the last decade, this climate model prediction system has been established and developed on the operational platform of the BCC, the deficiencies in the model coupling processes and ocean data assimilation make this model hard to use to predict ENSO adequately.

In contrast to the direct model prediction, as seen in Fig. 3, the TCC score profile of the corrected prediction based on the ADEPS shows quite a slow decrease as the lead months increase. The TCC at a lead of six months is close to 0.8, although that at a lead of one month is slightly lower than the uncorrected value. Alongside this, the RMSE scores are also much smaller in the corrected prediction than the direct model prediction. Further, the ACE method can be applied to each spatial point in the entire domain. Figure 4 presents the distributions of the TCC scores over the tropical Pacific region. Compared with the low TCC scores in the direct model predictions (not shown), the scores in the analogue-corrected predictions become systematically higher.

Indeed, the prediction skill scores shown in Figs. 3 and 4 outline an upper limit of predictability using the ACE method for ENSO prediction, in terms of the designed idealized experiment. That is, once the historical analogues have been identified adequately, the unknown current model prediction error can be estimated to some degree by the known prediction errors that the same model made based on the historical analogues. In reality, it is not possible to capture perfect historical analogues using only the information prior to the initial time. Thus, one of the most challenging technical questions in the ACE method is always how to select adequate analogues a priori.

## 4 Summary and discussion

Climate prediction, such as ENSO prediction, based on

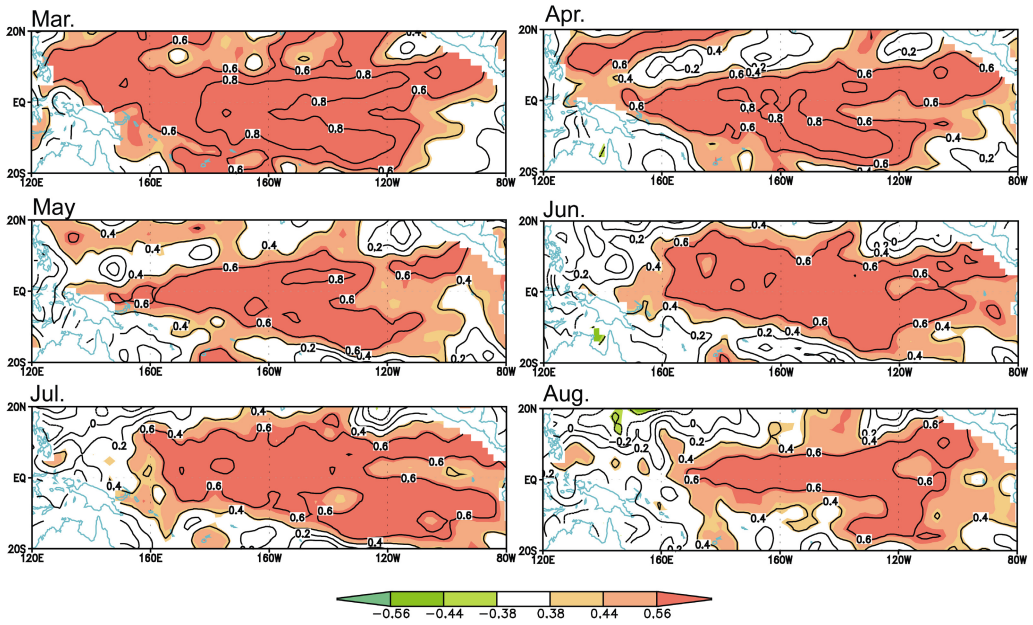


**Figure 4** Spatial distributions of TCCs of the corrected model prediction for March to August, where the skill scores are calculated with data during 1983–2012.

numerical models is usually subject to model biases. Raw model outputs include systematic errors due to deficiencies in climate models. This kind of systematic bias is usually regarded as a constant and can be reduced by a systematic bias correction using model climatology in defining climatic anomalies. However, model prediction errors are known to be flow-dependent, and difficult to eliminate as a constant. In this paper, we introduced the method of analogue-based correction of errors into an operational climate prediction model which has a poor air-sea coupling, and further exhibited the potential of the ACE method to improve the performance of model ENSO prediction.

The ACE method is based on the hypothesis that the flow-dependent errors are similar to some degree under analogous climate states. Using this method, we were able to empirically estimate the unknown current prediction errors using the known prediction errors that can be produced by the same model with historical analogue states, and thus effectively correct the current model prediction with the estimated prediction error. To apply the ACE method to improving ENSO prediction, we developed an analogue-dynamical ENSO prediction system based on the operational climate prediction model of the BCC, and performed an idealized experiment using the multi-year hindcast data with this model, in order to test whether the system could be applied to the operational model. The experimental results showed an encouraging performance of the ACE method in increasing prediction skill and reducing the prediction errors of ENSO.

This study demonstrated the potential of the ACE method to effectively correct ENSO prediction in low-performing operational climate prediction models. However, we assumed that all the historical analogues are known a priori, and examined the predictability of the ACE method. We are working to develop effective schemes for selecting historical analogues through diagnosing the statistical relationship between initial conditions and model prediction errors. Further results from using this correction method in improving ENSO prediction performance will be presented in another paper. In summary, the current study clearly suggests that the strategy of using the ACE method provides deeper insights into how to improve the performance of ENSO prediction based on the current level of models and data.

**Acknowledgements.** This work was jointly supported by the Integration and Application Project for Key Meteorology Techniques in China Meteorological Administration (Grant No. CMAGJ2014M64), the China Meteorological Special Project (Grant No. GYHY2012 06016), and the National Basic Research Program of China (973 Program, Grant No. 2010CB950404).

## References

Barnston, A. G., M. K. Tippett, M. L. L'Heureux, et al., 2012: Skill of real-time seasonal ENSO model predictions during 2002–11: Is our capability increasing? *Bull. Amer. Meteor. Soc.*, **93**(5), 631–651.

Cane, M. A., S. E. Zebiak, and S. C. Dolan, 1986: Experimental forecasts of El Niño, *Nature*, **321**, 827−832.

Chen, D., M. A. Cane, A. Kaplan, et al., 2004: Predictability of El Niño over the past 148 years, *Nature*, **428**, 733–736, doi:10.1038/nature02439.

Chen, D., S. E. Zebiak, A. J. Busalacchi, et al., 1995: An improved procedure for El Niño forecasting: Implications for predictability, *Science*, **269**, 1699−1702.

Chen, H., and Z. H. Lin, 2006: A correction method suitable for dynamical seasonal prediction, *Adv. Atmos. Sci.*, **23**(3), 425–430.

Cheng, Y. J., Y. M. Tang, X. B. Zhou, et al., 2010: Further analysis of singular vector and ENSO predictability in the Lamont model—Part I: Singular vector and the control factors, *Climate Dyn.*, **35**, 807−826.

Ding, Y. H., Y. M. Liu, Y. J. Song, et al., 2002: Research and experiments of the dynamical model system for short-term climate prediction, *Climatic Environ. Res.* (in Chinese), **7**(2), 236–246.

Izumo, T., J. Vialard, M. Lengaigne, et al., 2010: Influence of the state of the Indian Ocean Dipole on the following year's El Niño, *Nature Geosci.*, **3**(3), 168–172, doi:10.1038/ngeo760.

Jin, E. K., J. L. Kinter, B. Wang, et al., 2008: Current status of ENSO prediction skill in coupled ocean-atmosphere models, *Climate Dyn.*, **31**(6), 647–664.

Kirtman, P. B., 2003: The COLA anomaly coupled model: Ensemble ENSO prediction, *Mon. Wea. Rev.*, **131**, 2324–2341.

Latif, M., D. Anderson, T. Barnett, et al., 1998: A review of the predictability and prediction of ENSO, *J. Geophys. Res.*, **103**, 14375−14393.

Luo, J.-J., S. Masson, S. Behera, et al., 2005: Seasonal climate predictability in a coupled OAGCM using a different approach for ensemble forecasts, *J. Climate*, **18**, 4474–4497.

Luo, J.-J., S. Masson, S. K. Behera, et al., 2008: Extended ENSO predictions using a fully coupled ocean-atmosphere model, *J. Climate*, **21**(1), 84–93.

Moore, A. M., and R. Kleeman, 1996: The dynamics of error growth and predictability in a coupled model of ENSO, *Quart. J. Roy. Meteor. Soc.*, **122**, 1405–1446.

Rasmusson, E. M., and T. H. Carpenter, 1982: Variations in tropical sea surface temperature and surface wind fields associated with the Southern Oscillation/El Niño, *Mon. Wea. Rev.*, **110**, 354–384.

Rayner, N. A., D. E. Parker, E. B. Horton, et al., 2003: Global analyses of sea surface temperature, sea ice, and night marine air temperature since the late nineteenth century, *J. Geophys. Res.*, **108**(D14), 4407, doi:10.1029/2002JD002670.

Ren, H., 2008: Predictor-based error correction method in short-term climate prediction, *Prog. Nat. Sci.*, **18**(1), 129–135, doi:10.1016/j.pnsc.2007.08.003.

Ren, H., and J. Chou, 2005: Analogue correction method of errors by combining statistical and dynamical methods, *Acta Meteor. Sinica*, **20**(3), 367–373.

Ren, H., and J. Chou, 2007a: Study progress in prediction strategy and methodology on numerical model, *Adv. Earth Sci.* (in Chinese), **22**(4), 376–385

Ren, H., and J. Chou, 2007b: Strategy and methodology of dynamical analogue prediction, *Sci. China Ser. D-Earth Sci.*, **50**(10), 1589–1599.

Ren, H., J. Chou, J. Huang, et al., 2009: Theoretical basis and application of analogue-dynamical model in the Lorenz system, *Adv. Atmos. Sci.*, **26**(1), 67–77.

Wang, B., R. Wu, and X. Fu, 2000: Pacific-East Asian teleconnection: How does ENSO affect East Asian climate? *J. Climate*, **13**, 1517–1536.

Wang, H. J., G. Q. Zhou, and Y. Zhao, 2000: An effective method for correcting the seasonal-interannual prediction of summer climate anomaly, *Adv. Atmos. Sci.*, **17**(2), 234−240.

Zebiak, S. E., and M. A. Cane, 1987: A model El Niño-Southern Oscillation, *Mon. Wea. Rev.*, **115**, 2262−2278.

Zeng, Q.-C., 2009: Progress and challenge of the short-term climate prediction, *Atmos. Oceanic Sci. Lett.*, **2**, 267−270.

Zhang, R., A. Sumi, and M. Kimoto, 1996: Impact of El Niño on the East Asia monsoon: A diagnostic study of the '86/87 and '91/92 events, *J. Meteor. Soc. Japan*, **74**, 49–62.

Zhang, W., F.-F. Jin, H.-L. Ren, et al., 2012: Differences in teleconnection over the North Pacific and rainfall shift over the USA associated with two types of El Niño during boreal autumn, *J. Meteor. Soc. Japan*, **90**(4), 535–552, doi:10.2151/jmsj.2012-407.

Zheng, F., H. Wang, and J. Zhu, 2009: ENSO ensemble prediction: Initial error perturbations vs. model error perturbations, *Chinese Sci. Bull.*, **54**(14), 2516–2523.

Zheng, F., J. Zhu, R.-H. Zhang, et al., 2006: Ensemble hindcasts of SST anomalies in the tropical Pacific using an intermediate coupled model, *Geophys. Res. Lett.*, **33**, L19604, doi:10.1029/2006GL026994.

doi:10.11676/qxxb2014.055 气象学报

# 提高月预报业务水平的动力相似集合方法*

任宏利 张培群 李维京 陈丽娟
REN Hongli ZHANG Peiqun LI Weijing CHEN Lijuan

中国气象局国家气候中心,气候研究开放实验室,北京, 100081
*Laboratory for Climate Studies, National Climate Center, China Meteorological Administration, Beijing* 100081, *China*
2013-12-17 收稿,2014-03-28 改回.

任宏利,张培群,李维京,陈丽娟. 2014. 提高月预报业务水平的动力相似集合方法. 气象学报, 72(4): 723-730
**Ren Hongli, Zhang Peiqun, Li Weijing, Chen Lijuan. 2014. The dynamical-analogue ensemble method for improving operational monthly forecasting. *Acta Meteorologica Sinica*, 72(4): 723-730**

**Abstract** Focusing on the monthly forecasting problem based on the Atmospheric General Circulation Model (AGCM), a method of the dynamical-analogue ensemble forecasting (DAEF) is proposed to effectively reduce prediction errors and increase prediction skills. This method aims to the intrinsic combination of the dynamical model and statistical-empirical methods, which can establish perturbation members for ensemble forecasting by extracting the historical analogue information of the atmospheric general circulation, parameterizing empirically model errors and generating the multi-time-independent analogue forcing. Applying this new ensemble method to the operational AGCM in Beijing Climate Center (BCC AGCM1), a 10-yr monthly forecasting experiment under a quasi-operational condition shows encouraging results. Compared with the operational ensemble forecasts by the BCC AGCM1, the DAEF method is capable to improve effectively prediction skills of the monthly-mean and daily atmospheric circulation forecasts in which the former almost reaches the standard, available in the BCC operation, through effectively improving predictions of the zonal mean, ultra-long waves and long waves of the circulation. The results also show that prediction errors for the DAEF are significantly reduced and its spread of the ensemble members is reasonably increased, indicating an improvement in the relationship between the prediction errors and the spread. This study suggests a big potential application of the DAEF method in the BCC monthly forecasting operation.
**Key words** Monthly forecasting, Ensemble method, Dynamical Analogue, Error parameterization

**摘 要** 针对基于大气环流模式的月预报问题,提出了一种能有效减小预报误差并提高预报技巧的动力相似集合预报新方法。该方法着眼于动力模式与统计经验的内在结合,在模式积分过程中通过提取大气环流历史相似性信息,对模式误差进行参数化处理,形成多个时变的相似强迫量来扰动生成预报的集合成员。将这一集合新方法应用到中国国家气候中心业务大气环流模式(BCC AGCM1.0),一组 10 a 准业务环境下回报试验结果显示,相比于业务集合预报,动力相似集合预报方法能有效改进模式对于大气环流的纬向平均、超长波和长波预报,从而有效提高了月平均环流预报技巧(几乎达到业务可用标准)和逐日环流预报技巧,并显著降低了预报误差,合理增加集合离散度,使二者配置关系得以改善,有望在业务预报中应用。
**关键词** 月预报,集合方法,动力相似,误差参数化
**中图法分类号** P435

* 资助课题:公益类行业(气象)科研专项(GYHY201406022)、国家重点基础研究发展计划 973 项目(2010CB950404、2013CB430203)、国家自然科学基金项目(41375062)。
作者简介:任宏利,主要从事气候动力学与短期气候预测研究。E-mail:renhl@cma.gov.cn

## 1 引 言

伴随着数值模式性能和观测资料状况的日益改善,国际上天气预报和短期气候预测水平不断提高。相对于数值天气预报取得的巨大成功、以及季节气候预测的长足发展,介于二者之间的月预报问题一直是学界关注的重点(李维京等,2000)。然而,这一"过渡"时间尺度的预报受到逐日大气可预报上限(大约2—3周)的制约,尽管中外学者进行了大量努力和尝试,但基于数值模式的热带外大气环流预报技巧总体偏低,始终无法形成有效的业务预报能力(王绍武,2001;任宏利等,2007a)。近些年来,随着气候变化背景下全球持续性异常事件频繁发生,防灾减灾的巨大需求推动了中外学者对月预报方法的新一轮研究热潮(郑志海,2013)。例如,欧美主要气象业务中心陆续将月预报的着眼点转向了具有较高可预报性的大气季节内振荡,预报水平稳步提高(Weigel, et al,2008;Hirschi,et al,2012;Jia,et al,2013;Liu,et al,2013;Vitart,2014)。这种预报对象的转变能在一定程度上避开月尺度一般性大气环流可预报性偏低的困难,但仍需要从预报方法论创新方面开展深入研究。

当前,数值模式已逐渐成为天气-气候预报的主要工具,但即便如此,围绕如何有效运用数值模式进行预报的策略和方法仍是提高预报水平的重要手段,中外大量研究工作已经开展(任宏利等,2007a;郑志海,2013),例如,集合预报技术以及模式预报误差订正等已为世人所熟知。事实上,预报策略和方法研究的基本思路就是寻求动力模式和统计经验两种基本方法的结合使用,但对于怎样实现二者有效结合的问题尚需深入研究。中国学者在这方面做出了很多独具特色的研究,开辟了改进数值预报的新途径(顾震潮,1958;郑庆林等,1973;丑纪范,1974;巢纪平等,1979;黄建平等,1991;曹鸿兴,1993;Zeng,et al,1994;Wang,et al,2000;陈伯民等,2003;鲍名等,2004)。近年来,围绕如何将历史资料相似性信息有效运用到复杂模式预报中的科学问题,发展了动力相似预报策略和方法(例如,相似误差订正方法)(任宏利等,2005,2006,2007a, 2007b;Ren,et al,2009,2014;郑志海等,2009),其提升模式预报能力的有效性被大量数值试验证实,正式的业务应用尚不足。本研究将探索基于动力相似预报策略的月预报方法及其在业务模式上的应用。

多年实践表明,无论数值天气预报还是短期气候预测,集合预报都是提高预报技巧、降低预报误差的强有力工具。然而,在将天气尺度预报中富有成效的集合方法(如奇异向量法等)延伸到用于月预报时,通常会出现初始集合扰动衰减过快、集合预报离散度偏小的问题(Palmer,2000)。目前,通过随机扰动物理过程、边界条件以及采用多模式等途径构建集合,虽然能在一定程度上改进预报,但也面临着模式中可扰动对象过多、敏感性参数/过程选择的主观性大等问题。为此,本研究将利用现有业务预报模式,通过在模式积分过程中引入历史资料相似性信息,对未知的模式误差进行经验性参数化,以此形成多个"相似强迫量"驱动模式来生成集合扰动成员,发展适用于月预报的新集合方法,并进行准业务环境下的预报检验。

## 2 基于模式误差参数化的动力相似集合预报方法

数值天气预报问题在数学上一般可以作为偏微分方程初值问题的形式表示为

$$\frac{\partial \psi}{\partial t} = L(\psi) \tag{1}$$

$$\psi(t_0) = \psi_0$$

式中,$\psi(t)$为模式预报变量,$t$为时间;$L$为$\psi$的微分算子,用于表示实际数值模式。$t_0$为初始时刻,$\psi_0$代表初值,当$t>t_0$时,可由初值进行数值积分得到$\psi$或者它的泛函数$P(\psi)$。假设实际大气满足的准确模式可表示为

$$\frac{\partial \psi}{\partial t} = L(\psi) + L_e(\psi) \tag{2}$$

式中,$L_e$是$\psi$的泛函数,表征了模式过程与真实大气过程的误差,反映了数值模式中未知的总误差项,即模式误差。历史观测资料是满足式(2)的一系列特解$\hat{\psi}$或者它的泛函数。

通常有两种途径可以减小模式误差,一是直接发展模式来削减$L_e(\psi)$,通过不断的改进,可以得到多个模式算子$L_1$、$L_2$…;另一是从反问题角度利用历史资料信息估计和减小模式误差$L_e(\psi)$,使用某个$L$和不同的历史观测数据,就可得到多个误差算子$L_{e1}$、$L_{e2}$…,数学上等价于得到了多个模式算子。可见,在线性化意义下(或忽略模式非线性项的假设

下),这两种途径改进模式的效果是一致的。那么,在给定模式条件下如何发展预报策略和方法呢?由于对大气或气候系统的认识还很不够,模式中大量参数和过程仍是未知的,即更多的是需要求解反问题估计未知项,然后再做预报。按照这一思路,可采用经验方式对模式未知总误差项进行参数化估计。本研究发展了一种基于历史相似的模式误差参数化方案(Analogue-based Model Error Parameterization, AMEP),其基本思路来源于动力相似预报策略中运用历史资料相似性信息对模式积分进行过程订正(任宏利,2006)。在式(2)中,模式误差项可以通过历史相似状态提供的已知误差项来估计,从而得到经过订正或"扰动"的新的右端项

$$L_j(\hat{\psi}) = L(\hat{\psi}) + L_e(\tilde{\psi}_j) \tag{3}$$

式中,$\tilde{\psi}$ 为特解 $\hat{\psi}$ 的历史相似,$j$ 表示了多个相似。可见 $L_e(\tilde{\psi}_j)$ 为附加在模式预报方程中的相似强迫项。此时,改变相似状态便能得到不同的模式算子。

AMEP 包含 3 个组成部分:(1)相似初值驱动(在历史资料中选取与当前模式状态具有相似边界条件并处于同一季节的相似初值,驱动模式进行历史再预报);(2)采集模式预报误差(采集模式以历史相似为初值进行积分的预报误差);(3)生成相似强迫量(利用预报误差,生成模式积分所需的相似强迫量,并按需要插值到特定间隔的积分时间步上去)。图 1 给出 AMEP 的概念流程,输入的是模式预报变量,输出的是变量的时间强迫项,其中 $t_1 - t_2$ 或 PAU(Period of Analogue Updating)为相似更新周期,IAF(Interval of Analogue Forcing)为相似强迫间隔。

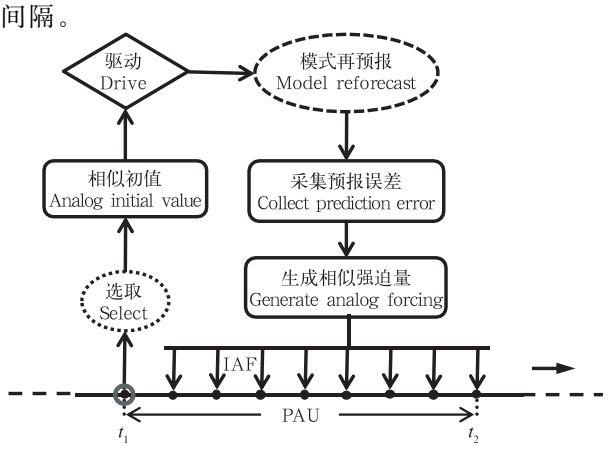


图 1 基于历史相似的模式误差参数化方案概念流程

Fig. 1 Schematic diagram of the analogue-based model error parameterization

由式(3)可见,AMEP 生成的相似强迫量不仅可以通过弥补模式未知部分来减小模式误差项,更重要的是多个历史相似的使用可为模式算子提供一组相似的强迫扰动,由于模式状态在积分过程中会不断地向这些相似强迫适应,有效地模拟了模式行为在状态 $\psi$ 附近的不确定性。在此基础上提出了动力相似集合预报(Dynamical Analogue Ensemble Forecasting, DAEF)方法:针对当前预报初值选取一组历史相似状态,分别以这些相似状态驱动 AMEP 输出多个时变的相似强迫量,进一步对当前模式积分过程进行强迫扰动,由此产生的多个扰动预报作为成员形成集合。考虑到每个成员来源于不同历史相似对模式误差项的一种形式估计,这样构建的集合能在一定程度上充分反映模式的不确定性。此外,也应看到,历史相似强迫如用于以后 IAF 间隔,由于未来基态不同,同样的强迫会产生不同的结果,这是需要注意的问题。

## 3 预报试验和结果分析

将动力相似集合预报方法运用到中国国家气候中心的业务大气环流模式(BCC_AGCM1.0)(丁一汇等,2002)中,在准业务环境下进行月预报试验,并与中国国家气候中心业务集合预报(李维京等,2005)进行直接比较。试验方案设计:(1)使用全球 500 hPa 高度场计算的场距离作为相似选取指标(任宏利等,2006);(2)选用 4 个最好的历史相似,并与纯动力控制预报一起按照两种误差诊断方案构建动力相似集合预报的 11 个集合预报成员,这里考虑到所用模式为谱模式,相似强迫将由各模式变量以谱系数形式添加到各个预报方程右端,在积分过程中取 6 h 间隔在所有垂直层次上对各模式变量进行强迫,更多技术细节可参阅任宏利(2006);(3)月平均环流预报直接使用 30 d 逐日预报的算术平均,无其他后处理;(4)预报评分采用世界气象组织推荐的距平相关系数(ACC)和均方根误差(RMSE)(Murphy, et al, 1989)。上述预报试验方案与业务集合预报的比较列于表 1 中。

供选相似使用的历史数据集为 1968 年以来的美国 NCEP 逐日再分析资料(Kalnay, et al, 1996)。预报试验检验所展示的是 2003 年 9 月 20 日—2013 年 8 月 20 日共 10 a 120 个预报个例在北半球热带外地区(20°—90°N)的 500 hPa 高度场预报结果的评分情况。

表 1 预报试验方案

Table 1 The schemes for the prediction experiments

| 试验方案 | DAEF 准业务环境回报试验 | 业务预报(OPRF) |
|---|---|---|
| 下边界海温种类 | 初始时刻前期持续性海温 | 初始时刻前期持续性海温 |
| 初始场资料集 | 中国国家气象中心全球客观分析场 | 中国国家气象中心全球客观分析场 |
| 集合成员 | 11 个动力相似集合预报成员 | 40 个集合成员(LAF,SVD) |
| 起报时间 | 每月 20 日 12 时起报 | 这里仅选取同期的预报结果 |
| 预报时效 | 未来 30 d | 未来 45 d |
| 检验气候场 | 中国国家气象中心全球客观分析场 | 模式气候场 |

### 3.1 月平均环流回报检验

图 2 直接比较了月平均环流(500 hPa 高度场)的 DAEF 和 OPRF 集合平均的检验评分结果。散点图直观地展现了 DAEF 的优势:距平相关系数图上的散点绝大多数位于右下方,而均方根误差图上的散点几乎都位于左上方(仅有 5 个个例除外),这清楚地表明 DAEF 具有比 OPRF 更大的距平相关系数和更小的均方根误差。从考察距平相关系数大于 0.5 的个例数比例来看,DAEF 约有 50%,而 OPRF 仅约 30%。由此可见,对于月平均环流预报而言,DAEF 相比于 OPRF 有效提高了预报技巧,减小了预报误差,其中对于误差的削减效果更为凸出一些。

表 2 首先比较了所有个例平均的预报检验评分。可以看到,基于动力相似集合方法的月平均环流预报效果明显好于业务集合预报。DAEF 的距平相关系数达到 0.48,这对于准业务环境下的多年平均预报技巧而言并不容易,虽然略低于 0.5 的业务标准,但相比于 OPRF 的 0.39 提高了 23%,预报技巧提高明显。对月平均环流的均方根误差而言,DAEF 平均比 OPRF 降低了 13.7 gpm。同时,也比较了 120 个例中 DAEF 的预报评分高于 OPRF 的个例数,DAEF 对应的距平相关系数有 86 个高于 OPRF,预报技巧提高率为 72%,DAEF 对应的均方根误差有 115 个低于 OPRF,预报误差降低率是 96%。这表明,就所关注的北半球热带外地区而言,11 个成员的动力相似集合预报方法显著优于 40 个成员的业务集合预报。

从表 2 中还可以看到,冬半年平均的预报技巧明显高于夏半年。这种差距在业务预报中约有0.1,而 DAEF 中仅为 0.04,这说明动力相似集合方法大幅度提高了对夏半年的预报技巧。而且,DAEF 在冬半年距平相关系数达到 0.5 的业务可用标准,显示出令人鼓舞的业务应用前景;即便是在夏半年也有应用潜力,其距平相关系数达到 0.46,接近业务可用。相比之下,OPRF 在冬半年的预报技巧明显低于 DAEF,而夏半年则比 DAEF 低 0.12。对于预报误差,DAEF 在冬半年均方根误差比 OPRF 减小约 17 gpm,夏半年减小约 10 gmp,误差降低幅度分别为 27%和 24%。上述结果反映出冬半年的环流预报一般要好于夏半年。

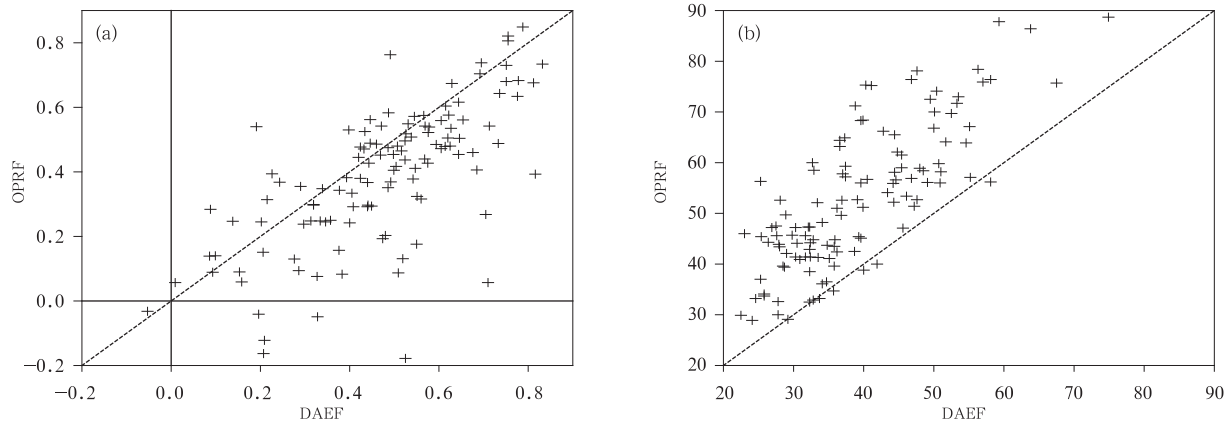


图 2 月平均环流预报的距平相关系数(a)和均方根误差(b,单位:gpm)评分散点

Fig. 2 Scatter maps for ACC (a) and RMSE (b, unit: gpm) of the monthly mean circulation predictions between DAEF and OPRF

表 2 个例平均的全年、冬半年和夏半年的预报评分

Table 2 The prediction skill scores in terms of the case means for the whole year, wintertime and summertime

| 预报方案 | 全年 | | 冬半年(Oct20—Mar20) | | 夏半年(Apr20—Sep20) | |
|---|---|---|---|---|---|---|
| | 距平相关系数 | 均方根误差(gpm) | 距平相关系数 | 均方根误差(gpm) | 距平相关系数 | 均方根误差(gpm) |
| OPRF | 0.39 | 52.9 | 0.44 | 63.3 | 0.34 | 42.5 |
| DAEF | 0.48 | 39.2 | 0.50 | 46.2 | 0.46 | 32.3 |
| DAEF－OPRF | 0.09 | －13.7 | 0.06 | －17.1 | 0.12 | －10.2 |

特别地,针对东亚—西太平洋区域(0°—60°N,100°E—160°W)的环流进行了检验,对于月平均环流,DAEF 的所有个例平均距平相关系数技巧(0.44)与业务集合预报(0.36)相比有明显提高,而其平均均方根误差(28.5 gpm)与业务预报(43.2 gpm)相比有显著降低。

总体而言,动力相似集合方法在降低月平均环流预报误差和提高预报技巧两方面都展示出不错的能力,特别是在预报误差削减方面更为显著一些,这与动力相似预报策略着眼于减小模式误差的基本思想(任宏利,2006)是一致的。

### 3.2 逐日环流回报检验

为考察新集合方法对于月内逐日预报的性能,图3a给出了所有个例平均的逐日集合平均预报距

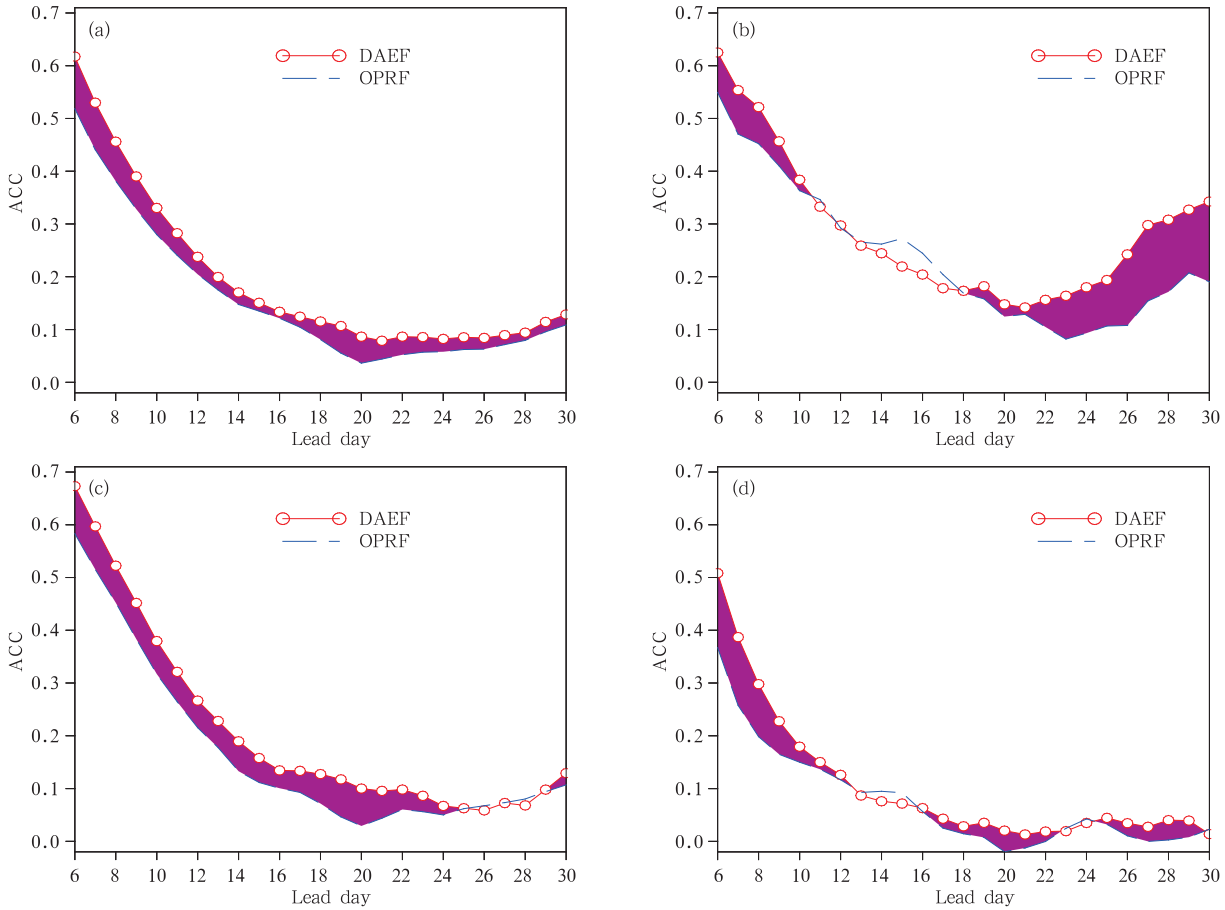


图 3 不同尺度波逐日预报与实况的距平相关系数(a—d)和均方根误差(e)对比

(a.全波,b.纬向平均(0波),c.超长波部分(1—3波),d.天气尺度波部分(4－9波);

紫色阴影表示 DAEF 评分优于 OPRF)

Fig. 3 Comparisons of ACC (a－d) and RMSE (e) between the daily prediction and the observation in terms of the different spatial scales. (a) All waves, (b) zonal mean (wave 0), (c) ultra long wave part (waves 1－3), and (d) synoptic scale wave part (waves 4－9). The purple areas denote that the skill of DAEF is superior to OPRF

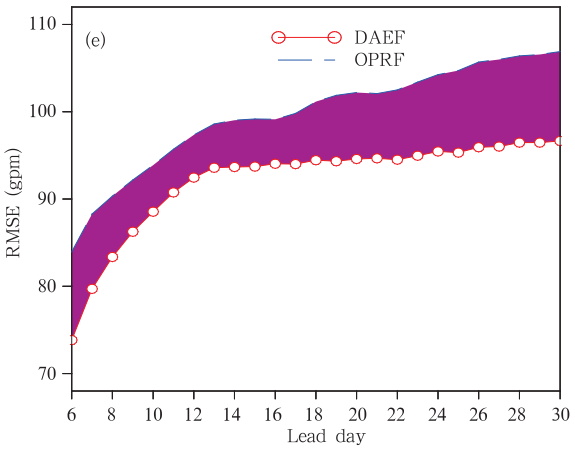


图 3 续

Fig. 3 (Continued)

平相关系数。可以看到,DAEF 相对 OPRF 对距平相关系数评分在 6—30 天均有一定提高,但由于模式自身性能和大气可预报性所限,超过两周的技巧依然较低。图 3e 给出了逐日集合平均预报均方根误差,DAEF 相对于 OPRF 对逐日预报均方根误差的降低非常显著,特别是在两周以后。总体来看,相对于业务集合预报,DAEF 对逐日环流预报技巧有一定程度提高,对预报误差则有显著削减作用。下面进一步通过纬向傅立叶分解针对不同空间尺度逐日预报来考察 DAEF 性能。图 3b—d 分别给出了不同纬向波动的逐日预报距平相关系数。

从图 3 可以看到,DAEF 相对于 OPRF,对于纬向平均部分预报效果的改善主要发生在 10 天之前和 18 天之后,对于超长波部分的改进几乎涵盖了所有预报时段,而对于长波部分的改进主要集中在预报 12 天之前和 16 天之后。这些结果表明,DAEF 对于月内全波以及各尺度的逐日预报都有不同程度改善,特别是对持续性较好的 0 波和超长波的改进最为明显,这可能与加入相似强迫后大尺度环流能够得到更好的模拟有关,但仍需要深入进行归因研究。

图 4 进一步给出了东亚—西太平洋区域的逐日环流检验评分。可以看到,DAEF 仍能提高预报技巧,大幅削减预报误差。但同时也应看到,这一区域的技巧评分要略低于北半球热带外整体的评分,反映出在东亚—西太平洋地区进行月尺度预报的难度很大。

### 3.3 集合预报性能检验

集合平均的预报误差与集合预报离散度的关系是衡量集合预报系统可靠性的一个重要标准,一个理想集合预报系统的集合平均均方根误差应与集合离散度基本一致(Palmer,2000)。然而,实际中的集合预报系统普遍存在集合离散度偏小的问题,这就增加了对极端事件预报的难度。为此,进一步考察了模式预报系统对于月平均和逐日环流的预报误差及离散度的对应关系(图 5)。可以看到,业务集合预报离散度远小于集合平均均方根误差,相比之下,DAEF 方法的集合平均预报则大幅削减了均方根误差,而且集合离散度相对于业务预报也有了合理的提升,使预报误差和离散度的配置关系得到改善。这表明,DAEF 不但能提高预报技巧、削减预报误差,还可以改进集合预报系统可靠性。

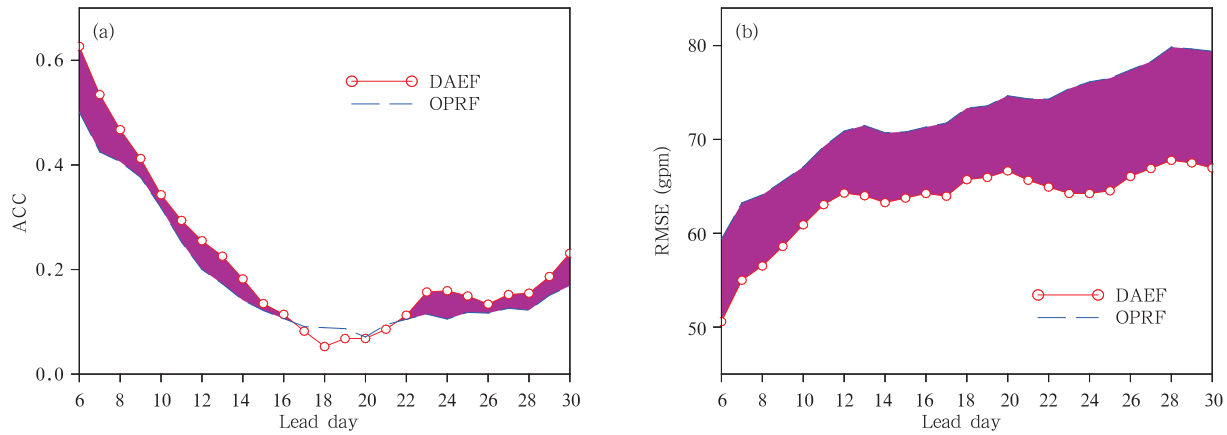


图 4 东亚—西太平洋区域逐日环流预报的距平相关系数(a)和均方根误差(b)
(紫色阴影表示 DAEF 评分优于 OPRF)

Fig. 4 ACC and RMSE of the daily circulation prediction in the East Asian-Western Pacific region,
(The purple area denotes that the skill of DAEF therein is superior to OPRF)

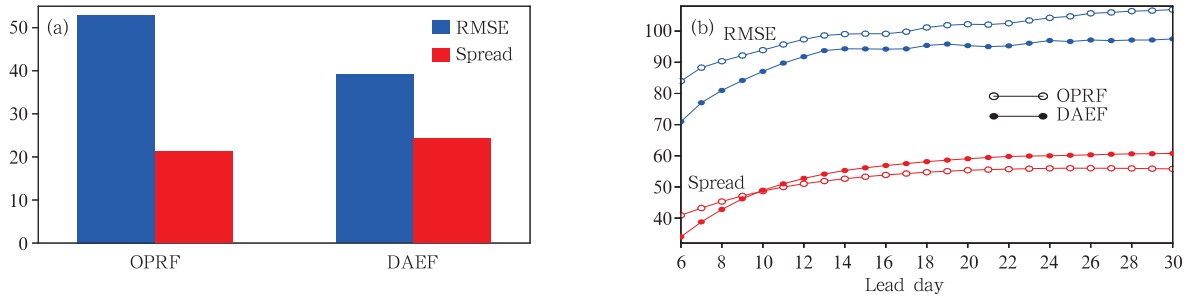


图 5 月平均环流(a)和逐日环流(b)对应的集合平均均方根误差与集合离散度(单位:gpm)

Fig. 5 Ensemble mean RMSE and ensemble spread (unit: gpm) of the monthly mean circulation (a) and the daily circulation (b)

## 4 结论与讨论

针对基于大气环流模式的月预报提出了一种能有效提高预报技巧和减小预报误差的动力相似集合预报新方法。基本思路是发展一个基于历史相似的模式误差参数化方案,利用不同历史相似提供的相似强迫量,对预报模式积分过程分别进行扰动,从而形成预报集合成员。该方法通过不同历史相似可以生成不同的模式误差估计,其效果相当于产生多个不同的预报模式,再将这些预报值进行集合,从而实现"虚拟多模式集合"。将这一集合方法应用到业务大气环流模式中,10 a 的实时准业务环境预报和回报试验结果显示,相对于业务集合预报,动力相似集合预报能够显著提高月预报技巧(月平均环流预报几乎达到业务可用标准,其中冬半年已业务可用,夏半年预报技巧提升也很明显),大幅度降低预报误差,合理增加集合离散度,这主要归功于该集合新方法对大气环流纬向平均、超长波和长波预报均有显著改进,其所体现的集合理念以及改善预报效果的性能和潜力具有良好的业务应用前景。

对于月尺度所关注的预报对象,其可预报性问题与特定时空尺度可能存在密切联系(李建平等,2008),模式预报必然受到大气流型变化的显著影响,DAEF 也不例外,这与模式预报性能以及受大气可预报性时空变化的影响有关。事实上,预报检验评分结果是对众多在月尺度上可预报个例和大量不可预报个例的总体平均。需要指出的是,本预报试验仅是基于单一方法来考察预报水平相对于业务的提高,若结合采用其他有效的预报信息提取技术,有望进一步提升预报技巧。另外,模式所用的资料可能对于预报结果有很大影响,DAEF 试验与实时业务预报要求(海温和模式)完全一致,但由于历史资料集不得不使用 NCEP 再分析资料,而实时预报初始场使用了中国国家气象中心客观分析资料,这可能引起初值与历史相似的资料不匹配问题。上述诸多问题在接下来工作中仍需要进一步加以研究。

## 参考文献

鲍名,倪允琪,丑纪范. 2004. 相似-动力模式的月平均环流预报试验. 科学通报,49(11):1112-1115

曹鸿兴. 1993. 大气运动的自忆性方程. 中国科学(B 辑),23(1):104-112

巢纪平,季劲钧,朱志辉等. 1979. 长期数值天气预报的滤波方法. 中国科学,22(1):75-84

陈伯民,纪立人,杨培才等. 2003. 改善月动力延伸预报水平的一种新途径. 科学通报,48(5):513-520

丑纪范. 1974. 天气数值预报中使用过去资料的问题. 中国科学,17(6):635-644

丁一汇,刘一鸣,宋永加等. 2002. 我国短期气候动力预测模式系统的研究及试验. 气候与环境研究,7(2):236-246

顾震潮. 1958. 天气数值预报中过去资料的使用问题. 气象学报,29(3):176-184

黄建平,王绍武. 1991. 相似-动力模式的季节预报试验. 中国科学(B 辑),21(2):216-224

李建平,丁瑞强. 2008. 短期气候可预报期限的时空分布. 大气科学,32(4):975-986

李维京,纪立人. 2000. 月动力延伸预报研究. 北京:气象出版社,171pp

李维京,张培群,李清泉等. 2005. 动力气候模式预测系统业务化及其应用. 应用气象学报,16(增刊):1-11

任宏利,丑纪范. 2005. 统计-动力相结合的相似误差订正法. 气象学报,63(6):988-993

任宏利. 2006. 动力相似预报的策略和方法[D]. 兰州:兰州大学,1-171

任宏利,张培群,李维京等. 2006. 基于多个参考态更新的动力相似预报方法及应用. 物理学报,55(8):4388-4396

任宏利,丑纪范. 2007a. 数值模式的预报策略和方法研究进展. 地

球科学进展，22(4)：376-385

任宏利，丑纪范. 2007b. 动力相似预报的策略和方法研究. 中国科学(D辑)，37(8)：1101-1109

王绍武. 2001. 现代气候学研究进展. 北京：气象出版社，306-311

郑庆林，杜行远. 1973. 使用多时刻观测资料的数值天气预报新模式. 中国科学，16(2)：289-297

郑志海，任宏利，黄建平. 2009. 基于季节气候可预报分量的相似误差订正方法和数值实验. 物理学报，58(10)：7359-7367

郑志海. 2013. 月动力延伸预报研究进展回顾. 气象科技进展，3(1)：25-30

Hirschi M，Spirig C，Weigel A P，et al. 2012. Monthly weather forecasts in a pest forecasting context：Downscaling，recalibration，and skill improvement. J Appl Meteor Climatol，51(9)：1633-1638

Jia X L，Yang S，Li X，et al. 2013. Prediction of global patterns of dominant quasi-biweekly oscillation by the NCEP Climate Forecast System version 2. Climate Dyn，41(5-6)：1635-1650

Kalnay E，Kanamitsu M，Kistler R，et al. 1996. The NCEP/NCAR 40-year reanalysis project. Bull Amer Meteor Soc，77(3)：437-471

Liu X W，Yang S，Kumar A，et al. 2013. Diagnostics of subseasonal prediction biases of the Asian summer monsoon by the NCEP climate forecast system. Climate Dyn，41(5-6)：1453-1474

Murphy A H，Epstein E S. 1989. Skill scores and correlation coefficients in model verification. Mon Wea Rev，117(3)：572-581

Palmer T N. 2000. Predicting uncertainty in forecasts of weather and climate. Reports on Progress in Physic，63(2)：71-116

Ren H L，Chou J F，Huang J P，et al. 2009. Theoretical basis and application of an analogue-dynamical model in the Lorenz system. Adv Atmos Sci，26(1)：67-77

Ren H L，Liu Y，Jin F F，et al. 2014. Application of the analogue-based correction of errors Method in ENSO Prediction. Ocean Atmos Sci Lett，7(2)：157-161

Vitart F. 2014. Evolution of ECMWF sub-seasonal forecast skill scores. Quart J Roy Meteor Soc，doi：10.1002/qj.2256

Wang H J，Zhou G Q，Zhao Y. 2000. An effective method for correcting the seasonal-interannual prediction of summer climate anomaly. Adv Atmos Sci，17(2)：234-240

Weigel A P，Baggenstos D，Liniger M A，et al. 2008. Probabilistic verification of monthly temperature forecasts. Mon Wea Rev，136(12)：5162-5182

Zeng Q C，Zhang B L，Yuan C G，et al. 1994. A note on some methods suitable for verifying and correcting the prediction of climatic anomaly. Adv Atmos Sci，11(2)：121-127

doi:10.13866/j.azr.2014.05.15

# 我国北方TOMS气溶胶光学厚度与地面沙尘天气频数的比较①

任霄玉[1,2]， 任国玉[2]， 魏明建[1]
(1.首都师范大学资源环境与旅游学院,北京 100048; 2.中国气象局气候研究开放实验室,国家气候中心 北京 100081)

**摘 要:** 利用卫星监测和反演沙尘天气频率或沙尘气溶胶光学厚度,检验卫星监测和反演结果是否与地面观测一致。采用地面观测记录获得全部沙尘天气事件频数(*DF*)资料,对1979—2002年TOMS(臭氧总量绘图系统)反演的气溶胶光学厚度指数(*AI*)进行检验分析。结果表明:① *AI*高值区基本与我国北方地面观测的沙尘天气频数高值分布区一致,两者均在我国西北部极端干旱的盆地和高原地区出现最高值,相对低值一般分布在气候湿润的东部地区,但东北平原和华北平原*AI*值相对较高,冬季尤其明显,与地面沙尘观测差异很大;② *AI*和*DF*年内变化也具有很高的一致性,均在春季最大,4月达到峰值以后减小,但前者在冬季12月和1月出现次高值,而后者冬季为全年低谷;③ 相关性分析表明,*AI*和*DF*相关系数一般在夏季最大,冬季最小,年和季节的相关系数具有随时间呈下降的趋势;④ TOMS *AI*数据在反映我国北方沙尘天气频数时空变化特征方面,区域上西北干旱区效果最好,东部季风区的华北和东北较差;季节上夏季、初秋和春季较好,冬季效果较差。同时还对*AI*和*DF*资料时空分布差异的可能原因及其潜在应用意义进行了讨论。

**关键词:** TOMS(臭氧总量绘图系统); 气溶胶; 光学厚度; 沙尘天气; 时空分布; 北方地区; 中国

沙尘天气是我国北方干旱、半干旱地区经常发生的低能见度天气现象。频繁的冷空气和气旋活动是引起我国北方春季沙尘天气频繁发生的直接原因[1-6],而大范围气候变暖及其由此引起的中纬度地带大气环流纬向性加强、径向性减弱、近地面平均风速和大风频率减小、降水量增多,则构成了我国北方最近半个世纪沙尘天气发生频率下降的气候背景[1,7-9]。沙尘天气现象传统上利用地面气象站网通过瞬时风速和能见度来进行观测及分析[4,10],或者通过卫星遥感技术监测单一沙尘天气过程。近年来,卫星遥感由于其较高的空间覆盖率,成为沙尘监测和研究中不可或缺的技术,得到广泛应用。卫星遥感技术可采用近红外或可见光以外光谱探测器反演沙尘气溶胶光学厚度。1999年12月发射的EOS-Terra卫星以及2002年初发射的Aqua卫星搭载的MODIS传感器,已被用来监测和反演陆地气溶胶的光学厚度[11-12],并通过地面不同的气溶胶性质来区分气溶胶类型。

利用卫星监测和反演沙尘天气频率或沙尘气溶胶光学厚度,一个关键的问题是监测和反演结果是否与观测一致,是否能够明确反映实际的沙尘天气发生频率的时空特征。地球观测科学计划(earth observation science,EOS)的Terra卫星平台搭载的多角度成像光谱仪(multi-angle imaging spectra radiometer,MISR),通过云筛选等算法反演覆盖陆地和水域的大气中气溶胶光学厚度(aerosol optical depth,AOD),没有区分沙尘气溶胶、生物燃烧气溶胶、火山灰以及当地产生的烟雾,陆地反演结果较水上好一些,但在区分气溶胶类型上还需要改进[13]。Gonzalez等[14]通过将ERS-2ESA反演的欧洲气溶胶资料与模式计算结果对比,得到两者监测结果具有可互补的结论。Levy等[15]比较了AERONET中的AOD以及搭载在CLAMS卫星上的MODIS传感器反演的海陆气溶胶数据,发现两者在海洋的相关性较好,误差在允许范围内,但在陆地的相关性没有达到预期。

美国国家航空航天局(NASA)利用Nimbus和地球探测器EPtoms卫星遥感资料搭载的臭氧总量

① **收稿日期:** 2013-11-27; **修订日期:** 2014-02-24
**基金项目:** 国家公益性行业专项(GYHY201206012)和北京市自然科学基金重点项目(KZ201210028034)共同资助
**作者简介:** 任霄玉(1987-),女,硕士研究生,研究方向为第四纪地质专业. E-mail: 714195363@qq.com
**通讯作者:** 任国玉. E-mail: guoyoo@cma.gov.cn

绘图系统(total ozone mapping spectrometer,TOMS),通过近紫外射线的方法,反演获得一套几乎覆盖全球海洋和陆地的沙尘及碳质气溶胶光学厚度指数(*AI*)长序列资料集。Torres 等[16]曾比较了这套数据集与气溶胶自动观测网(AERONET)的分析结果,发现在不同气溶胶类型占主导的区域中,该数据集基本能够再现实际的气溶胶含量,但不同地区反演效果差异比较明显。迄今,已有一些研究者利用这套资料或其他卫星资料,分析了中国部分区域和特定时段沙尘气溶胶时空分布规律,并和实际观测的沙尘气溶胶资料进行了比较[17-27],发现 TOMS 在西北地区反演结果较好,但在东部沿海等区域可能由于黑碳气溶胶影响结果不太理想。对于我国北方地区,这套卫星资料在多大程度上能代表实际的沙尘天气发生频率的时空分布特征,目前还没有开展系统研究。

本文利用 TOMS 光学厚度长序列资料,以及同期地面气象站观测获得的沙尘天气日数记录,比较分析中国北方卫星反演光学厚度与沙尘天气频率的时间和空间分布特征,希望进一步了解 TOMS 反演数据在代表中国北方沙尘气溶胶方面的可靠性,为进一步改进卫星反演技术和利用卫星资料分析我国北方沙尘天气频率和沙尘气溶胶光学厚度时空分布规律提供科学依据。

## 1　资料和方法

卫星资料来自于 NASANimbus 7(1979—1992 年)和地球探测器(Earth-Probe)(1996—2005 年)上搭载的 TOMS 逐日气溶胶光学厚度长序列资料集。由于航天器故障,1994 年和 1995 年资料缺失,2000 年资料存在严重质量问题,因此,在 2 套资料的处理过程中,用多年逐月平均值代替缺失的 2 a 资料和 2000 年的资料。

沙尘天气地面观测资料来源于中国气象局国家气象信息中心的国家基准、基本站逐月沙尘日数数据集,时间长度为 1954—2002 年。这套数据包括逐月浮尘日数、扬沙日数和沙尘暴日数。本文利用该数据集中北方地区 495 个站点观测资料(图 1)。由于浮尘、扬沙和沙尘暴天气均可造成大气沙尘气溶胶含量或光学厚度上升,能见度下降,取 3 种天气事件发生日数的总和,称沙尘天气频数(*DF*),与卫星资料比较。北方地区是指我国 30° N 以北区域(图 1)。

卫星反演资料为 1979—2005 年 1.25° ×1°网格点逐日光学厚度,而站点沙尘天气频数观测资料则为 1954—2002 年的逐月统计结果,统一取 1979—2002 年为研究时段,并将站点观测资料转换成与卫星资料相同尺寸和格式的网格点资料。采用简单算术平均方法分别统计 2 套资料的逐年月、季和年的要素值,然后计算整个时期多年平均月、季、年要素值。利用相关系数方法对 2 套资料序列做月、季、年的相关性分析。四季划分采用气候学定义,即春季为 3—5 月,夏季为 6—8 月,秋季为 9—11 月,冬季则为 12 月至翌年 2 月。年是指一年的 12 个月。

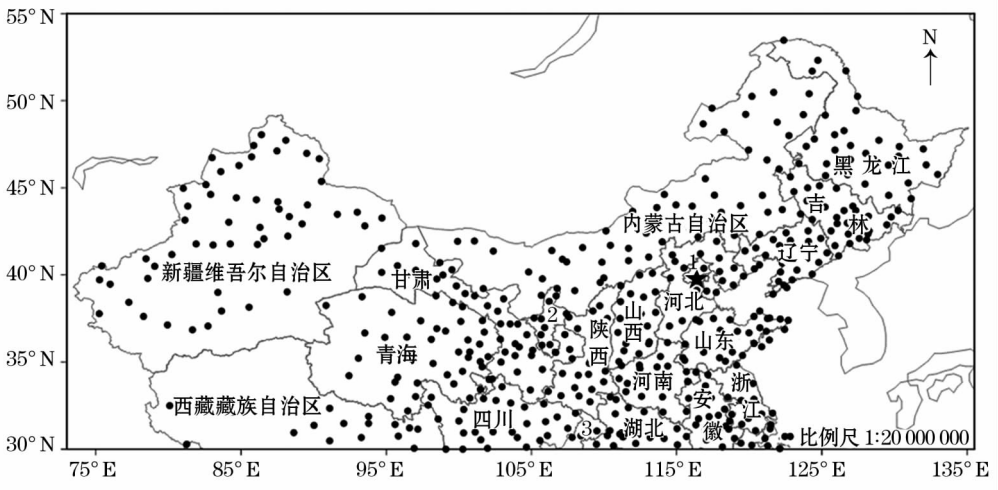


1 代表北京市,五角星代表北京站位置;2 代表宁夏回族自治区;3 代表重庆市。

图 1　研究区范围及其地面气象观测站点分布

Fig. 1　The study area and the distribution of meteorological stations

## 2 结果分析与讨论

图 2 给出了 1979—2002 年多年平均 TOM *AI* 和地面沙尘天气频数的空间分布情况。高值区的分布基本一致,均位于南疆盆地和内蒙古西部。地面观测资料的高值区域还包括青藏高原北部地区。在其他地区,2 套资料的差别较大,主要表现在 *DF* 的次高值区分布范围很小,局限于内蒙古中西部和南疆盆地外围地区;而 *AI* 次高值区位于更广大的区域,能够代表大气背景值的区域范围很小,主要在川、青、藏交界地带。*AI* 分布在华北平原和东北平原形成明显的相对高值区域,达到 0.5 ~ 0.6,略低于内蒙古高原西部。造成两者空间分布不一致的原因,可能是卫星资料不仅反映了沙尘气溶胶,还包含碳质气溶胶的影响,是沙尘和碳质气溶胶的综合作用产物[16]。东部地区特别是华北平原和东北平原等地区,人类排放的碳质气溶胶浓度高,致使 *AI* 呈现出相对高值。

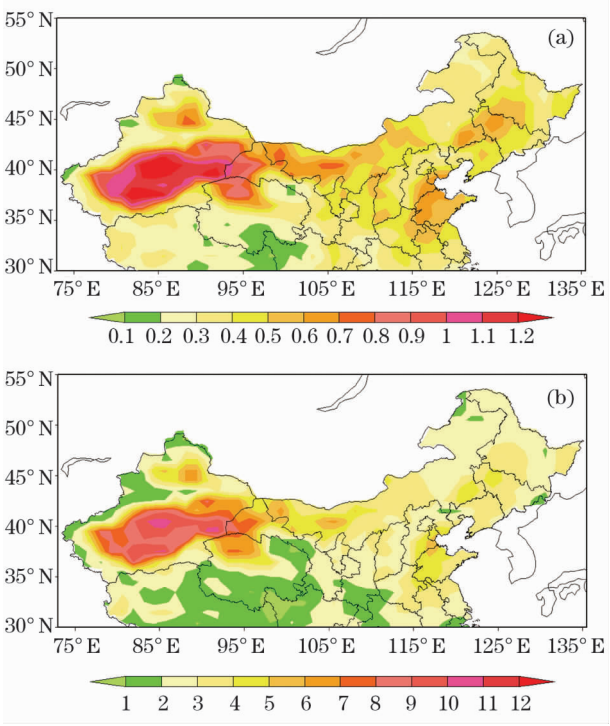


图 2 1979—2002 年多年平均 TOMS 气溶胶光学厚度( *AI* )(a)和地面观测沙尘天气频数( *DF* )(b)的空间分布

Fig. 2 Annual optical depth index of aerosols (a) and spatial distribution of frequency of dust weather (b) during the period of 1979 – 2002

由图 3 可以看出,春季是我国北方沙尘天气现象最频繁的季节,总体上看,1979—2002 年四季 TOMS *AI* 指数和 *DF* 的高值和低值分布基本一致,高值均位于南疆盆地及其甘肃西部、青海柴达木盆地等极端干旱地区,*AI* 值在 0.8 以上,*DF* 值一般在 9 d 以上。西部地区存在一些微小差异,主要包括 *AI* 的高值范围一般比 *DF* 要小,在塔里木盆地周边没有延伸到北部的天山山脉和南部的昆仑山脉,内蒙古西部分布也比较狭窄,且量值比高值区要小得多。造成这一差异的原因可能与地形等因素有关。*AI* 指示卫星传感器感应的整个大气柱内沙尘气溶胶厚度,在盆地区域较大,山地和高原区域较小;而地面观测仅记录近地表的大气能见度和沙尘天气现象,在高山和高原区域仍然会有较低的能见度和较频繁的沙尘天气,但沙尘物质可能仅集中在近地面较薄的大气层,卫星探测的气溶胶光学厚度可能不大。同样,内蒙古西部的差异可能也与高原地形导致的 *AI* 值相对较小有关。

在北方的东部地区,两者差异比较大。*AI* 值在内蒙古中东部、东北西部和华北大部特别是山东半岛等地也较高,达到 0.5 以上,个别地区甚至超过 0.8。*DF* 的较高值区位于内蒙古中部、黄土高原、科尔沁沙地及其南部,而 *AI* 的较高值分布范围要大得多,且量值也较 *DF* 大,几乎涵盖了东部所有地区,一般在 0.3 以上。形成这一差异的原因一个是地形影响,东北平原和华北平原等区域一般气溶胶光学厚度比较大;另一个原因可能是东部人口密集,城市较多,经济相对发达,区域人类活动排放的碳质气溶胶数量大,导致 *AI* 值偏高。因此,东部地区 TOMS *AI* 资料用来反映沙尘气溶胶浓度和沙尘天气频率具有较大偏差。

夏季 *AI* 和 *DF* 空间分布与春季有相似性,两者高低值分布态势的差异是所有季节中最小的,具有较高的一致性。高值区仍均位于西部的干旱盆地和高原,东部和东南部数值较小。卫星资料在东部的平原和黄土高原地区仍维持次高值,仅东北北部、青海南部、四川西北部以及青藏高原东北部等小部分地区接近大气背景区域,*AI* 值很小,而 *DF* 值在季风区域都很小。这个差异主要与季风区夏季处于雨季,地面沙尘发生频率很低,但人类排放的碳质气溶胶仍然比较多,致使东部平原和半干旱区 *AI* 值仍旧偏高。

从秋季平均 *AI* 和 *DF* 空间分布看,2 套资料高值区域均呈明显的减小趋势。*DF* 分布与夏季相似,高值区域范围甚至比夏季还小。*AI* 高值区域范围缩

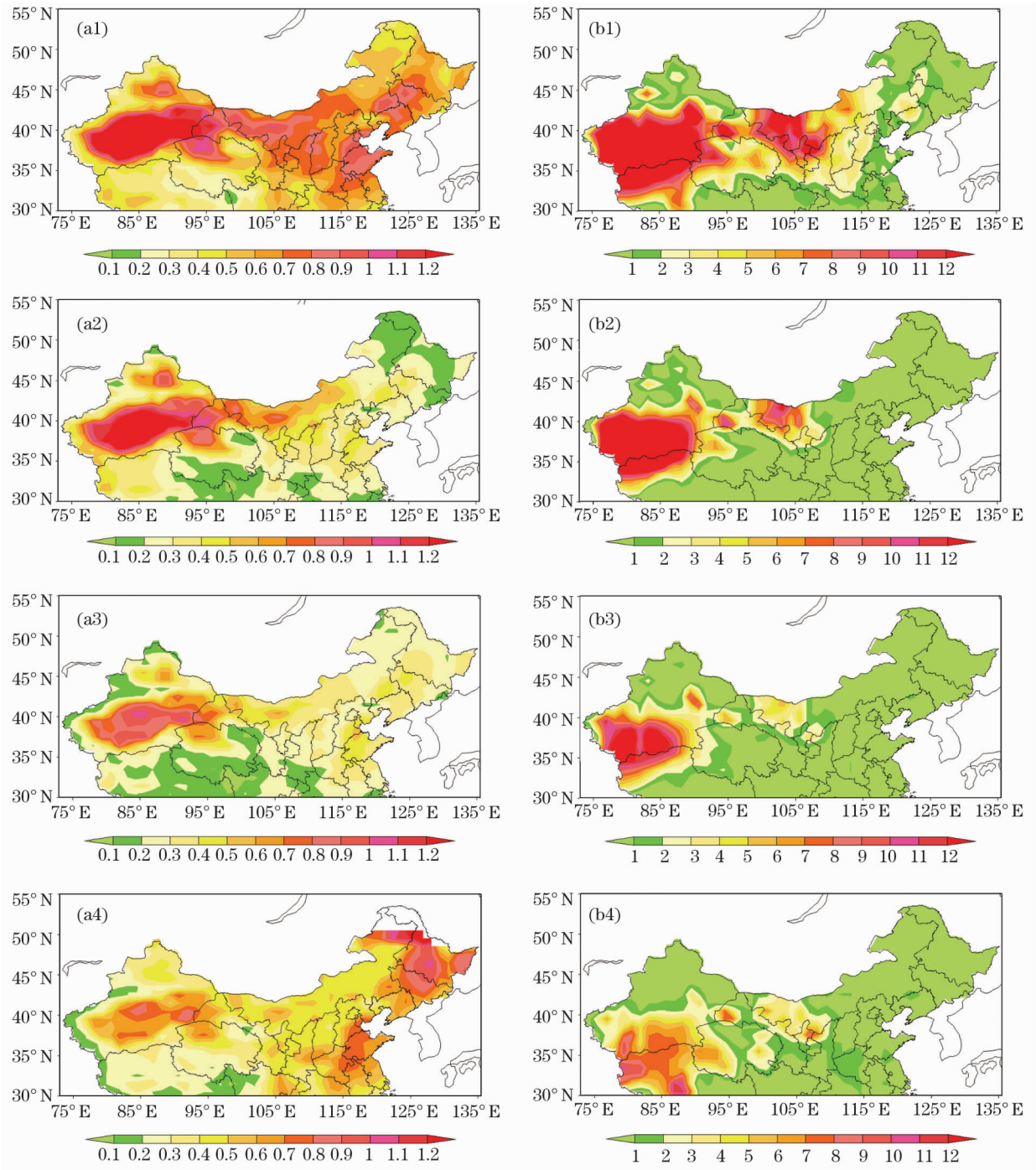


a1 ~ a4 和 b1 ~ b4 分别代表 *AI* 和 *DF* 春、夏、秋、冬四季平均值。

图 3　1979—2002 年四季 TOMS 气溶胶光学厚度(*AI*)(a)和地面观测沙尘天气频数(*DF*)(b)的空间分布

Fig. 3　Seasonal optical depth index of aerosols(a) and spatial distribution of frequency of dust weather(b) during the period of 1979 – 2002

小不明显,但减小趋势比 *DF* 大。两者次高值区范围也呈减小趋势,低值区域范围增大。*DF* 次高值区基本位于南疆盆地周边地区以及内蒙古西部,而 *AI* 次高值区分布较 *DF* 广泛,包括准噶尔盆地、内蒙古高原、东北平原、青海西北部、黄土高原以及东部沿海地区,可能与东南部人类排放的碳质气溶胶有关。

冬季平均 *AI* 值和 *DF* 值空间分布的差异最大。*AI* 高值区移至东北北部,华北平原也是相对高值区,而 *DF* 的高值区则南移至青藏高原北部和塔里木盆地南部。冬季卫星资料和地面沙尘天气频率资料几乎相反的空间分布格局,可能与季节性取暖燃煤排放更多的碳质气溶胶有关,也与东北地区近地

面大气强烈发展的逆温层等因素有联系。这表明，*AI* 在冬季难以用来代表沙尘天气频率，也难以表征大气里沙尘气溶胶浓度或光学厚度。

就整个北方地区来看（图 4），沙尘天气的频发季节为春季，因此，*DF* 值从 2 月开始明显增大，4 月达到最高，平均达 4.5 d，此后连续下降，最低值出现在秋冬季节。*AI* 高值月份也出现在春季，同样 4 月最高，4月和 5月*AI*值均超过0.5，但最低值发生在秋季，冬季则是除春季外 *AI* 值的次高峰。可见，除冬季外，我国北方地区月平均 *AI* 和 *DF* 值年内变化具有较好的一致性。冬季 *AI* 值的相对峰值可能是东部区域人类活动排放大量碳质气溶胶，造成卫星反演结果异常偏高。

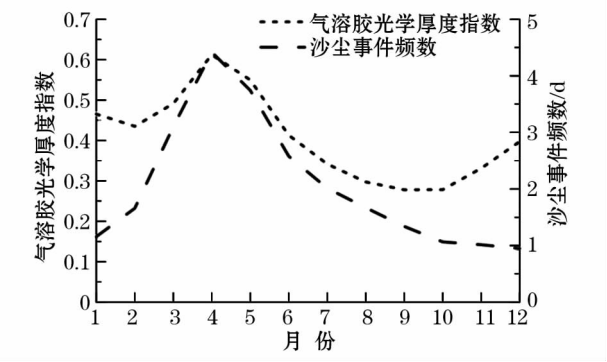


图 4 1979—2002 年北方地区月平均气溶胶光学厚度（*AI*）和地面观测沙尘天气频数（*DF*）的年内变化

Fig. 4 Monthly optical depth index of aerosols and monthly frequency of dust weather in north China during the period of 1979 – 2002

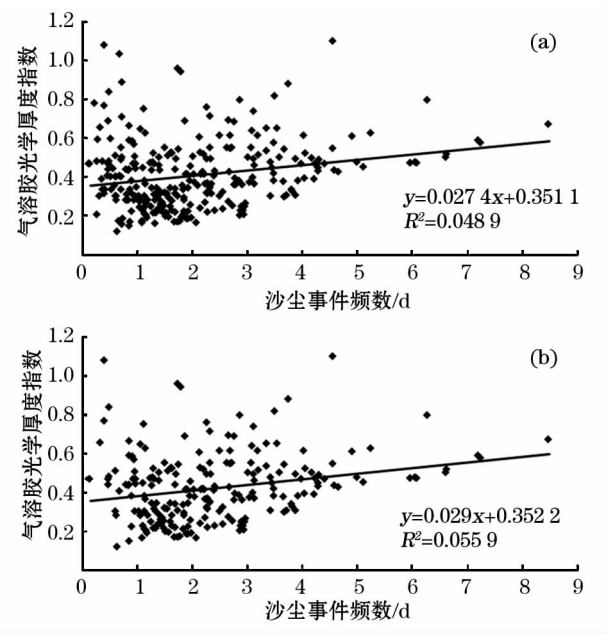


（a）全年所有月；（b）除冬季（12、1、2 月）外其余月份。

图 5 1979—2002 年北方地区 TOMS 气溶胶光学厚度（*AI*）和地面观测沙尘天气频数（*DF*）月均值散点图

Fig. 5 Scatter diagram of monthly optical depth index of aerosols and monthly frequency of dust weather in north China during the period of 1979 – 2002

由图 5 可以看到，两者在沙尘天气频数高的月份关系较好，而在沙尘频数低的月份分布较分散，关系比较差；另一个特点是，在 *AI* 值偏小的月份，两者关系常常很好，而在 *AI* 值较大的月份，两者关系较差。由于沙尘发生频次高的月份一般在春季和夏季，此时东部地区碳质气溶胶浓度较低，因此 *AI* 和 *DF* 关系较好；*AI* 值较高的情形在东部主要出现在冬季，此时 *DF* 值很低，是造成两者关系不佳的主要原因。

总体上看，各月平均 *AI* 和 *DF* 之间存在显著正相关关系，*T* – 检验均达到 0.01 的显著性水平。不考虑冬季的 12、1、2 月，两者的正相关性有所增加（图 5b），在一定程度上说明由于冬季东部地区碳质气溶胶排放等原因，削弱了 TOMS 气溶胶光学厚度与地面观测沙尘天气频数的对应关系。图 6 给出了北方地区各月沙尘天气频数与 *AI* 值的相关系数年内变化情况。春季虽为沙尘天气的高发季节，但两者相关系数并不是最高的，4—5 月高于 0.3，未通过 0.05 的显著性水平检验。相关系数最高季节在夏季和初秋，7—9 月均在 0.4 以上，通过了 0.05 的显著性水平检验。冬季特别是 12 月和 1 月相关系数最低，没有通过显著性水平检验。总体上，月平均 *AI* 和 *DF* 的相关性比预期的要小，*AI* 值在春季、夏季和秋季大致可以反映沙尘天气事件频率的时空变化，但与地面气象观测的沙尘天气还有一定差异。造成这种现象的原因，可能与地面观测站点比较稀疏以及地面观测仅局限于近地表很浅大气层次有关，也与沙尘天气定义比较严格，没有包括部分地区和季节程度较轻、但频数很高的大气含尘现象有关。

由图 7 可见，多数年份，特别是 20 世纪 80 年代早、中期和 90 年代中期以后，*AI* 和 *DF* 之间的相关系数较高，达到 0.30 以上，通过了 0.01 显著性水平检验。逐年相关系数总体呈下降趋势，这与人为碳质气溶胶排放增加，*AI* 值越来越受到人类活动干预的事实相符。20 世纪 80 年代后期和 90 年代初期，两者关系最差，多数年份没有通过统计显著性检验，可能与我国北方甚至全球尺度大气“变暗”现象有

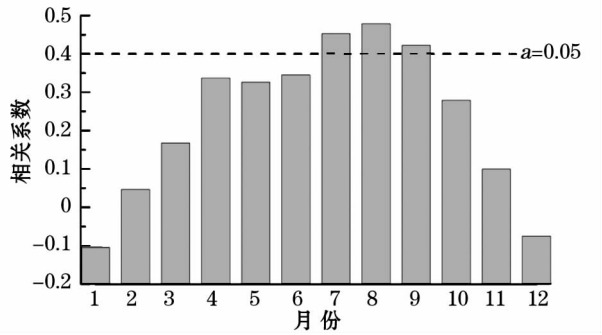


图 6　1979—2002 年北方地区沙尘天气频数与卫星资料 *AI* 值的逐月相关系数

Fig. 6　Correlation coefficients between frequency of dust weather and optical depth index of aerosols in north China during the period of 1979 – 2002

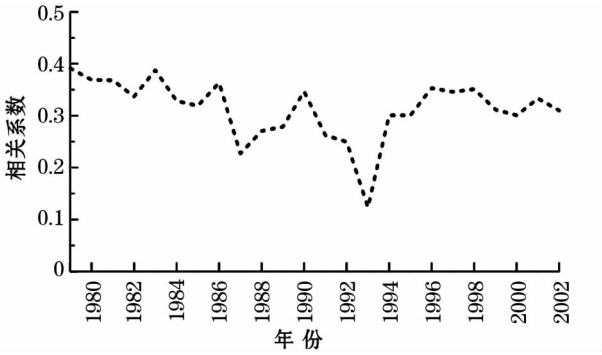


图 7　1979—2002 年北方地区沙尘天气频数与卫星资料 *AI* 值相关系数逐年变化

Fig. 7　Annual change of correlation coefficients between frequency of dust weather and optical depth index of aerosols in north China during the period of 1979 – 2002

关[28-30]。1993 年相关系数出现明显的低谷,可能与卫星的转换有关,也可能与 1991 年皮纳图博火山喷发[31]的后续影响有关,需要进一步调查。值得说明的是,在资料处理过程中,发现 2000 年的 *AI* 和 *DF* 相关系数接近 0,根据年内变化规律分析判断,应该是当年卫星数据有误,因此,本文用多年平均值代替 2000 年的月平均 *AI* 值。

## 3　结 论

利用 1979—2002 年美国 NASA TOMS 反演的 *AI* 资料及其中国地面观测的逐月沙尘日数资料,比较分析了卫星反演沙尘气溶胶及碳质气溶胶光学厚度与地面沙尘天气频数的时空分布特征,得到以下结论:

(1) *AI* 高值区与 *DF* 高值区分布一致,尤其在中国西北部极端干旱区,两者对应很好;相对低值区主要分布在东部地区,但东北平原和华北平原的 *AI* 值明显高于 *DF* 值,且 *AI* 高值分布范围大于 *DF*,这种情况在冬季尤为明显。造成分布不一致的原因可能是受东部平原地区碳质气溶胶排放的影响。

(2) 春、夏季,2 套资料高值区均分布在南疆盆地及其甘肃西部、青海柴达木盆地等气候干燥地区,空间分布特征基本一致,但北方地区的东部 *AI* 次高值区范围大于 *DF*;秋季,2 套资料高值区域范围明显减小,*AI* 高值区的减小趋势比 *DF* 大;冬季 2 套资料高低值空间分布差异较大,*AI* 高值区移至东北北部,华北地区也是相对高值区;而 *DF* 的高值区移至青藏高原北部、塔里木盆地南部。

(3) 就整个北方地区的年内变化来看,*DF* 与 *AI* 高值均出现在春季以及初夏季节,最高在 4 月和 5 月;*DF* 的低值出现在秋、冬季,但 *AI* 最低值发生在秋季,冬季是除春季外的次高峰。因此,除冬季外,北方地区月均 *AI* 和 *DF* 值年内变化具有较好的一致性。

(4) 北方地区 *DF* 与 *AI* 值的月相关只在夏季和初秋通过了 0.05 的显著性检验,春季的相关性也较高,冬季相关最差。总体来看,两者相关性要比预期的小,*AI* 值在春、夏、秋季大致可以反映地面沙尘天气事件频数的时空变化特征,但与地面观测仍有较大的不一致性。

(5) 2 套资料的逐年相关系数年际变化总体表现出下降趋势,这与人为碳质气溶胶排放增加的事实相符,其年代变化也与大气“变暗”和“变亮”的观测事实基本一致。

综上所述,TOMS 反演的 *AI* 资料与地面观测的沙尘天气频数资料各自均有优缺点。*AI* 资料的不足主要是卫星转换等造成的资料序列时间非均一性和不完整性,也难以完全分离自然沙尘气溶胶和人为碳质气溶胶,但能够反映出从地面到大气高层整层气柱的光学厚度;而地面观测的主要缺陷是对轻度和高频的沙尘天气现象没有记录,也无法反映近地面层以上整个气柱的气溶胶浓度和分布情况,但大体反映了与人类活动关系密切的地面附近空气质量,并具有连续的较长时间序列。合理使用两类观测资料,对于沙尘天气气候研究和业务具有现实意义。

**参考文献(References):**

〔1〕 叶笃正,丑纪范,刘纪远,等. 关于我国华北沙尘天气的成因与治理对策〔J〕. 地理学报, 2000, 55(5): 513 – 521. 〔Ye

Duzheng, Chou Jifan, Liu Jiyuan, et al. Causes of sand-stormy weather in northern China and control measures〔J〕. Acta Geographica Sinica, 2000, 55(5): 513 – 521.〕

〔2〕 吴晓京,陆均天,张晓虎,等. 2001 年春季沙尘天气分析〔J〕. 国土资源遥感, 2001, 13(3): 8 – 10, 24 – 25.〔Wu Xiaojing, Lu Juntian, Zhang Xiaohu, et al. Synoptic analysis on the sand-dust storm in spring, 2001〔J〕. Remote Sensing for Land and Resources, 2001, 13(3): 8 – 10, 24 – 25.〕

〔3〕 方翔,郑新江,陆均天,等. 2002 年春季北京沙尘天气成因及源地分析〔J〕. 国土资源遥感, 2002, 14 (4): 17 – 22.〔Fang Xiang, Zheng Xinjiang, Lu Juntian, et al. Origin and source region of the dust storm in fluencing Beijing in spring of 2002〔J〕. Remote Sensing for Land and Resources, 2002, 14(4): 17 – 22.〕

〔4〕 陆均天,邹旭恺,王锦贵,等. 近 3 年我国沙尘天气较频繁发生的原因分析〔J〕. 气候与环境研究, 2003, 8(1): 107 – 113.〔Lu Juntian, Zou Xukai, Wang Jingui, et al. Analyses of the causes for frequent dust weather occurred in China during the last three years〔J〕. Climatic and Environmental Research, 2003, 8(1): 107 – 113.〕

〔5〕 韩忠辉,郑军. 我国北方地区沙尘天气的起因及预防〔J〕. 林业勘查设计, 2010, 30(4): 58 – 59.〔Han Zhonghui, Zheng Jun. The causes and prevention measures of sand-dust weather of Northern China〔J〕. Forestry Prospect and Design, 2010, 30(4): 58 – 59.〕

〔6〕 薛占金,秦作栋,孟宪文,等. 2010 年 3 月我国沙尘天气的若干特征〔J〕. 干旱区研究, 2011, 28(4): 694 – 698.〔Xue Zhanjin, Qin Zuodong, Meng Xianwen, et al. Characteristics of sandstorm weather in China in march 2010〔J〕. Arid Zone Research, 2011, 28(4): 694 – 698.〕

〔7〕 张莉,任国玉. 中国北方沙尘暴频数演化及其气候成因分析〔J〕. 气象学报, 2003, 61(6): 744 – 750.〔Zhang Li, Ren Guoyu. Change in dust storm frequency and the climatic controls in Northern China〔J〕. Acta Meteorologica Sinica, 2003, 61(6): 744 – 750.〕

〔8〕 孟猛,宗美娟. 中国 20 世纪干旱化趋势分析〔J〕. 干旱区研究, 2012, 29(4): 705 – 712.〔Meng Meng, Zong Meijuan. Study on aridity trend in China in 20th century〔J〕. Arid Zone Research, 2012, 29(4): 705 – 712.〕

〔9〕 朱晓炜,杨建玲,崔洋,等. 1961—2009 年西北地区东部降水时空分布及成因〔J〕. 干旱区研究, 2013, 30(6): 1 094 – 1 099.〔Zhu Xiaowei, Yang Jianling, Cui Yang, et al. The spatial and temporal distribution of the precipitation in the east of northwest China from 1961 to 2009〔J〕. Arid Zone Research, 2013, 30(6): 1 094 – 1 099.〕

〔10〕 钱正安,蔡英,刘景涛,等. 中国北方沙尘暴研究的若干进展〔J〕. 干旱区资源与环境, 2004, 18(增刊): 1 – 8.〔Qian Zheng'an, Cai Ying, Liu Jingtao, et al. Some advances in dust storm researchs in Northern China〔J〕. Journal of Arid Land Resources and Environment, 2004, 18(Suppl.): 1 – 8.〕

〔11〕 Chu D A, Kaufman Y J, Ichoku C. et al. Validation of MODIS aerosol optical depth retrieval over land〔J〕. Geophysical Research Letter, 2002, 29 (12): MOD2 – 1 – MOD2 – 4.

〔12〕 Levy R C, Remer L A, Oleg D. Global aerosol optical properties and application to moderate resolution imaging spectroradiometer aerosol retrieval over land〔J〕. Journal of Geophysical Research, 2007, 112(D13210).

〔13〕 Martonchik J V, Diner D J, Crean K A, et al. Regional aerosol retrieval results from MISR〔J〕. Geoscience and Remote Sensing, 2002, 40(7): 1 520 – 1 531.

〔14〕 Gonzalez C Robles, Schaap M, de Leeuw G, et al. Spatial variation of aerosol properties over Europe derived from satellite observations and comparison with model calculations〔J〕. Atmospheric Chemistry and Physics, 2003, 3: 521 – 533.

〔15〕 Levy R C, Remer L A, Martins J V, et al. Evaluation of the MODIS aerosol retrievals over Ocean and land during CLAMS〔J〕. Journal of the Atmospheric Sciences-Special Section, 2005, 62: 974 – 992.

〔16〕 Torres O, Bhartia P K, Herman J R, et al. Derivation of aerosol properties from satellite measurements of backscattered ultraviolet radiation: Theoretical basis〔J〕. Journal of Geophysical Research, 1998, 103(D14): 17 099 – 17 110.

〔17〕 Li Chengcai, Mao Jietai, Kai-Hon Alexis Lau, et al. Characteristics of distribution and seasonal variation of aerosol optical depth in eastern China with MODIS products〔J〕. Chinese Science Bulletin, 2003, 48(22): 2 488 – 2 495.

〔18〕 张鹏,石广玉. 从反射太阳光谱反演大气气溶胶体积谱分布的理论研究〔J〕. 气象学报, 2003, 61(1): 85 – 94.〔Zhang Peng, Shi Guangyu. The theoretic study on the retrieval of aerosols' volume distribution from solar spectral reflectance〔J〕. Acta Meteorologica Sinica, 2003, 61(1): 85 – 94.〕

〔19〕 Xu Jin, Bergin M H, Liu X Y, et al. Measurement of aerosol chemical, physical and radiative properties in the Yangtze delta region of China〔J〕. Atmospheric Environment, 2002, 36(2): 161 – 173.

〔20〕 David G Streets, Carolyne Yu, Ye Wu, et al. Aerosol trends over China, 1980 – 2000〔J〕. Atmospheric Research, 2008, 88(2): 174 – 182.

〔21〕 Wen Mi, Zhanqing Li, Xiangao Xia, et al. Evaluation of the moderate resolution imaging spectroradiometer aerosol products at two aerosol robotic network stations in China〔J〕. Journal of Geophysical Research, 2007, 112(D22S08).

〔22〕 Lin I-I, Chen Jenping, George T F, et al. Aerosol input to the South China Sea: Results from the moderate resolution imaging spectroradiometer, the quick scatterometer, and the measurements of pollution in the troposphere sensor〔J〕. Deep Sea Research Part II: Topical Studies in Oceanography, 2007, 54(14/15): 1 589 – 1 601.

〔23〕 申彦波,王标,石广玉. 2006 年春季我国东部海域气溶胶光学厚度与沙尘天气〔J〕. 地球科学进展, 2008, 23(3): 290 – 298.〔Shen Yanbo, Wang Biao, Shi Guangyu. Aerosol optical depth and dusty weather over Eastern China seas in spring of 2006〔J〕. Advances in Earth Science, 2008, 23(3): 290 – 298.〕

〔24〕 朱爱华,李成才,刘桂青,等. 北京地区 MODIS 卫星遥感气溶胶资料的检验与应用〔J〕. 环境科学学报, 2004, 24(1): 86 – 90.〔Zhu Aihua, Li Chengcai, Liu Guiqing, et al. Validation and application of MODIS remote aerosol information in Beijing〔J〕. Acta Scientiae Circumstantiae, 2004, 24(1): 86 – 90.〕

〔25〕 黄珏,陈晓玲,田礼乔,等. 渤海海域 CALIOP 与 MODIS 气溶胶光学厚度相关性分析〔J〕. 海洋科学, 2013, 37(1): 113 – 118.〔Huang Jue, Chen Xiaoling, Tian Liqiao, et al. Correlational research on aerosol optical depths from CALIPSO and MODIS/Aqua over the Bohai Sea〔J〕. Marine Scienes, 2013, 37(1): 113 –

118.〕

〔26〕郑新江,陈渭民,方翔,等. 利用 NOAA 卫星资料估算陆地沙尘量的方法〔J〕. 国土资源遥感,2008,20(2):35 – 38.〔Zheng Xinjiang, Chen Weimin, Fang Xiang, et al. A method for estimating the amount of air borne sand over the land〔J〕. Remote Sensing for Land and Resources, 2008, 20(2): 35 – 38.〕

〔27〕吴序鹏,杨军,车慧正,等. 塔克拉玛干沙漠地区气溶胶光学厚度卫星遥感产品验证〔J〕. 气候与环境研究,2012,17(2):149 – 159.〔Wu Xupeng, Yang Jun, Che Huizheng, et al. Verification for the satellite remote sensing products of aerosol optical depth in Taklimakan desert area〔J〕. Climatic and Environmental Research, 2012, 17(2): 149 – 159.〕

〔28〕Shi G Y, Hayasaka T, Ohmura A, et al. Data quality assessment and the long-term trend of ground solar radiation in China〔J〕. Journal of Applied Meteorology and Climatology, 2008, 47: 1 006 – 1 016.

〔29〕申彦波,赵宗慈,石广玉. 地面太阳辐射的变化、影响因子及其可能气候效应的最新研究进展〔J〕. 地球科学进展,2008,23(9):915 – 923.〔Shen Yanbo, Zhao Zongci, Shi Guangyu. The progress in variation of surface solar radiation, factors and probable climatic effects〔J〕. Advances in Earth Science, 2008, 23(9): 915 – 923.〕

〔30〕You Q L, Sanchez-Lorenzo A, Wild M, et al. Decadal variation of surface solar radiation in the Tibetan Plateau from observations, reanalysis and model simulations〔J〕. Climate Dynamics, 2013, 40(7/8): 2 073 – 2 086.

〔31〕陈洪滨,吕达仁,许丽生. 利用 SAGE Ⅱ 资料分析皮纳图博火山爆发前后平流层气溶胶的变化特征〔J〕. 科学通报,1994,39(22):2 084 – 2 087.〔Chen Hongbin, Lv Daren, Xu Lisheng. Using the SAGE Ⅱ to analyze the variation of stratospheric aerosol before and after Pinatubo eruption〔J〕. Chinese Science Bulletin, 1994, 39(22): 2 084 – 2 087.〕

# Comparison between TOMS Optical Depth Index of Aerosol and Dust Weather Frequency in North China

REN Xiao-yu[1,2], REN Guo-yu[2], WEI Ming-jian[1]

(1. *College of Resources, Environment and Tourism, Capital Normal University, Beijing* 100048, *China*;
2. *Open Laboratory for Climate Studies, National Climate Center, China Meteorological Administration, Beijing* 100081, *China*)

**Abstract**: It is necessary to examine whether the satellite monitoring results are consistent with the ground-based observations if satellite data are used in studying dust weather frequency (*DF*) or dust aerosol optical thickness. In this paper, the dust weather frequency data from the ground-based observations and the values of aerosol optical thickness index (*AI*) from TOMS for the time period of 1979 – 2002 were analyzed. The results are as follows: ① The areas with high *AI* value were basically consistent with those with high *DF* value in north China, these areas were located in the extremely arid basins and plateaus in northwest China; the areas with low value were generally distributed in humid east China except the Northeast Plain and North China Plain where the *AI* value was relatively high, especially in winter; ② Change of monthly *AI* and *DF* values was highly consistent, the highest *AI* and *DF* values occurred in spring, the second highest *AI* values occurred in December and next January; ③ The correlation coefficient between *AI* and *DF* was generally the highest in summer but lowest in winter; ④ The TOMS *AI* data could be used to ideally reflect the spatiotemporal patterns of *DF* in arid northwest China but poorly in north China and northeast China.

**Key words**: TOMS; aerosol; optical depth; dust weather; spatiotemporal distribution; north China

INTERNATIONAL JOURNAL OF CLIMATOLOGY
*Int. J. Climatol.* (2014)
Published online in Wiley Online Library
(wileyonlinelibrary.com) DOI: 10.1002/joc.4203

RMetS
Royal Meteorological Society

# The response of actual evaporation to global warming in China based on six reanalysis datasets

Tao Su,[a] Guolin Feng,[b]* Jie Zhou[c] and Min Ye[c]

[a] *College of Atmospheric Sciences, Lanzhou University, China*
[b] *National Climate Center, Laboratory for Climate Studies of China Meteorological Administration, Beijing, China*
[c] *College of Physical Science and Technology, Yangzhou University, China*

**ABSTRACT:** In this paper, we present the response of actual evaporation to global warming in China based on the National Centers for Environmental Prediction-National Center for Atmospheric Research (NCEP/NCAR) reanalysis 1, the NCEP-Department of Energy (NCEP/DOE) reanalysis 2, 40-year ECMWF Re-Analysis (ERA-40), ECMWF-Interim Re-Analysis (ERA-Interim), Modern-Era Retrospective Analysis for Research and Applications (MERRA), and Climate Forecast System Reanalysis (CFSR). Rotated empirical orthogonal function (REOF) analysis was applied to reveal the coherent pattern of the change in reanalysis evaporation (RE). According to the first four REOF modes in NCEP/NCAR, we subdivided China into six climatic regions, and found that RE increased significantly in central and southeast of China from 1979 to 2012, especially during the sub-period of 1985–2004. Various estimates of linear trend are statistically consistent, and most of them are significant at the 95% confidence level. Conversely, RE decreased in northern and northeast although the magnitude of decreasing trends is inconsistently among the reanalysis. Moreover, there is a general tendency of RE to increase in northwest, but mostly RE trends are not significant. In the dry northwest and northern regions, rainfall is an important factor affecting the changing of RE, while RE is less sensitive to the change of temperature. However, RE rates are dominated by temperature in the humid central and southeast regions. These results support the view that the sensitivity of RE to global warming largely depends on the environment. In view of data availability, despite the general similarity, differences exist among the various reanalysis, especially in NCEP/NCAR and CFSR. In summary, it can be concluded that the quality of RE values is higher in central and southeast, while even greater uncertainties lie in the estimates of RE in northwest China and Qinghai-Tibet Plateau.

KEY WORDS actual evaporation; global warming; reanalysis; linear trend

*Received 28 March 2014; Revised 9 October 2014; Accepted 12 October 2014*

## 1. Introduction

Changes in the rates of evaporation would be of great significance for water resource planning, irrigation control, agricultural and ecosystems (Cohen *et al.*, 2002; Zuo *et al.*, 2005; Jhajharia *et al.*, 2009). Evaporation is an essential part of the hydrologic cycle, together with precipitation and runoff, which is an important process in determining the weather and climate on global and regional scales (Mariotti, 2010; Lorenz and Kunstmann, 2012). Precipitation and runoff are intermittent and nonlinear processes whereas evaporation occurs every day and is a much better time integrator of regional climate change. Furthermore, evaporation plays a key role in the global energy budget (Pearlmutter *et al.*, 2009; Bosilovich *et al.*, 2011). Therefore, changes of evaporation have a great impact on global hydrologic cycle and energy budget (Cong *et al.*, 2009), it is critical for predicting changes in surface climate (Chattopadhyay and Hulme, 1997; Goyal, 2004), including heatwaves and droughts. Global warming has become a popular topic for governments and general public. It is reported that the surface temperature of the Earth was increasing at a rate of about 0.13°C decade$^{-1}$ over the past 50 years (IPCC, 2007). Global warming is expected to intensify the global hydrological cycle (Huntington, 2006), with an increase of both evaporation and precipitation. However, the magnitude and spatial distribution of this global and annual mean response remains highly uncertain (Douville *et al.*, 2013). Understanding and exploring the interannual and interdecadal variability of evaporation under global warming have been an essential part of the task of assessing global hydrological cycle climate variability and possible change.

However, contrary to expectations, lots of observations show that the rate of pan evaporation had been consistently decreasing throughout the world over the past 50 years (Lawrimore and Peterson, 2000; Liu *et al.*, 2004; Cong *et al.*, 2009; Shen *et al.*, 2010). The contrast between expected and observed trends of pan evaporation rate is called 'pan evaporation paradox' or 'evaporation paradox' (Roderick and Farquhar, 2002). Several researchers have carried out studies on changes in pan evaporation around China. Recently, Cong *et al.* (2009) reported that pan

* Correspondence to: G. Feng, National Climate Center, Laboratory for Climate Studies of China Meteorological Administration, China Meteorological Administration, 46 Zhongguancun Nan Da Jie, Haidian District, Beijing 100081, China. E-mail: fenggl@cma.gov.cn

© 2014 Royal Meteorological Society

evaporation paradox exists in China and pan evaporation kept decreasing during the period of 1956–2005. According to the statistics, the annual pan evaporations of about 66% Chinese routine meteorological stations hold descend trend, and the biggest descent reaches −24.9 mm $a^{-2}$ from 1961 to 2000 (Zuo *et al.*, 2005), nevertheless the rate was highest in the northwest and lowest in the southwest (Liu *et al.*, 2004). Evidence for a decrease of potential evapotranspiration has also been reported from China using estimates made with Penman's combined radiation balance and aero-dynamic equation (Thomas, 2000; Chen *et al.*, 2005; Wang *et al.*, 2007). There are many interpretations of the possible cause for 'pan evaporation paradox', however, at present these competing explanations remain controversial (Lawrimore and Peterson, 2000; Roderick and Farquhar, 2002; Liu *et al.*, 2004). It is generally accepted that from a surface in which there is abundant moisture, actual evaporation equals potential evaporation and is also equivalent to the amount of pan evaporation multiplied by a pan coefficient (Lawrimore and Peterson, 2000; Kirono *et al.*, 2009; Jacobs *et al.*, 2010). Conversely, in a region without adequate moisture, potential evaporation cannot be sustained. It is important to distinguish between potential evaporation, pan evaporation and actual evaporation.

As it is very hard to measure the actual evaporation accurately, long-term and large-scale datasets do not exist. Studies on changes in actual evaporation have been few and limited due to the lack of station-based measurements. For now, estimation of actual evaporation is often made by using information about potential evaporation and soil moisture. A full accounting of projected changes in actual evaporation requires an extension system analysis. Hence, additional data and analysis will be necessary to explain the response of evaporation to global warming in China. Fortunately global and regional atmospheric retrospective analysis models (reanalysis) play a crucial role in today's hydrological and hydrometeorological research (Trenberth *et al.*, 2011; Lorenz and Kunstmann, 2012). The object of reanalysis is to optimally combine atmospheric observations with an atmospheric general circulation model (AGCM) to produce the best estimate of the global atmospheric state (Kinter *et al.*, 2004). Reanalysis evaporation (RE) has been widely used in many research works. Much of the current climate knowledge on evaporation has been gained from studies using global reanalysis (Mariotti, 2010; Trenberth *et al.*, 2011; Lorenz and Kunstmann, 2012).

Although evaporation in reanalysis and actual evaporation are not exactly the same, however, RE can roughly characterize the variability of actual evaporation (Lorenz and Kunstmann, 2012). Therefore, we extracted the main characteristics of actual evaporation over China from six different reanalysis. Note that multi-reanalysis datasets are applied to avoid data dependence of the results. In this paper a new analysis of RE trends due the global warming over the past 60 years will be presented. To further explore the predominant factors to control the dynamic of RE, sensitivity of RE has been studied in terms of change in surface temperature and rainfall. The significance of these historic trends and their possible threat to managing water resources are discussed. Moreover, another purpose of this study is to estimate the uncertainties incorporated in these reanalysis, it will afford valuable information to improve the quality of the reanalysis.

## 2. Data and methods

### 2.1. Data

The National Centers for Environmental Prediction (NCEP) and the National Center for Atmospheric Research (NCAR) produced a 50-year analysis of the global atmospheric circulation (Kalnay *et al.*, 1996) whose length makes it an attractive database for discovering and quantifying decadal time scale climate variations. Numerous studies have made use of reanalysis products to evaluate many aspects of atmospheric variability, including several recent contributions examining the secular variations and decadal regime shifts in the atmosphere (Kinter *et al.*, 2004). However, the NCEP-NCAR (called NCEP-R1) had the substantial problems that limit their use, particularly for global climate change and variability studies. A second limited version of the NCEP reanalysis (called NCEP-R2) was run to address some problems (Kanamitsu *et al.*, 2002). The NCEP-R2 used an updated version of the original GSM, and besides a few physical parameterization changes, a number of notable bugs in the NCEP-R1 analysis were also fixed.

The European Centre for Medium-range Weather Forecasts (ECMWF) reanalysis (called ERA-40) addressed some of the shortcomings of the earlier reanalysis, but many of the problems tied to observing system changes and model deficiencies remain. Substantial problems were again revealed in the ERA-40. ERA-Interim (called ERA-I) is the latest global atmospheric reanalysis produced by the ECMWF. ERA-I was intended to cover the period from 1989 to the present to provide a bridge between ECMWF's previous reanalysis ERA-40 (Uppala *et al.*, 2005) and forthcoming next-generation reanalysis. Recently, ERA-I has been extended to cover the satellite period from 1979 to the present. A key objective was to address several difficult data assimilation problems encountered in ERA-40, mostly related to the use of satellite data, resulting in an improved representation of the hydrological cycle, a more realistic stratospheric circulation, and better temporal consistency on a range of time-scales (Dee *et al.*, 2011).

The Modern Era Retrospective-Analysis for Research and Applications (MERRA) was stimulated by the recognition that various aspects of the hydrologic cycle represented in previous generations of reanalysis were not adequate for climate and weather studies (Bosilovich *et al.*, 2011). MERRA proposed to improve upon the water cycle as a contribution to the science community and to reanalysis research. Additionally, the other objective of MERRA is to provide a climate context for the NASA satellite observing system. A new reanalysis of the atmosphere, ocean, sea ice and land has been produced by NCEP under

© 2014 Royal Meteorological Society

a project referred to CFSR. It is worth noting that the analysis system used in CFSR for the atmosphere, the GSI scheme, is nearly the same as the one used by MERRA at the NASA GSFC. Obviously, the near-parallel development and execution of the reanalysis (CFSR and MERRA) can provide value-added results. Table 1 provides further details about these global reanalysis relevant to the study (details available online at http://rda.ucar.edu/).

In addition, the monthly temperature and rainfall data were provided by the China Meteorological Administration from 160 stations for the period of 1951–2012. The stations are well distributed across China including the Tibetan plateau, but it must be declared that the meteorological stations are sparse and insufficient in western China.

### 2.2. Computation of reanalysis evaporation

For evaporation fields, there are directly outputs for ERA-I, ERA-40 and MERRA, but not for NCEP-R1, NCEP-R2 and CFSR. However, these fields can be transformed from latent heat flux, which is given in energy flux form (Lorenz and Kunstmann, 2012). The turbulent flux of heat from the Earth's surface to the atmosphere that is associated with evaporation or condensation of water vapour at the surface. Evaporation is the process of a liquid becoming vaporized, energy will be absorbed during evaporation. The lower the rates of evaporation of water to the air, the lesser the latent heat flux to the air. Because latent heat flux is proportional to RE, thus we calculate the RE field for NCEP-R1, NCEP-R2 and CFSR using the latent heat flux (Jacobson, 2007; Lorenz and Kunstmann, 2012). The relation between latent heat flux $\lambda E$ (unit: W m$^{-2}$) and surface evaporation $E$ (unit: mm day$^{-1}$) can be written as

$$E = \frac{\lambda E}{L_e}, \tag{1}$$

$$L_e \approx 2.501 \times 10^6 - 2370 T_c, \tag{2}$$

here $T_c$ is the near-surface temperature in degrees Celsius (°C). The data such as latent heat flux, land surface temperature, are all at daily time scale in NCEP-R1, NCEP-R2 and CFSR. All global latent heat flux data are estimated using a bulk formula; latent heat flux $\lambda E$ in reanalysis is a product of the wind speed, surface temperature and specific humidity (Kubota *et al.*, 2003; Trenberth *et al.*, 2011).

### 2.3. Methodology

For easy comparison and for computation purposes, all reanalysis data are interpolated onto a same 2.5° × 2.5° grid by using a bilinear interpolation technique. From these fields, area-weighted averages were computed over different regions. In order to depict low-frequency variations of RE on decadal time scales, a Gaussian Low-pass filter (10-year) was applied to suppress high-frequency variations in the original series (Thomas, 2000). The Gaussian filter modifies the input signal by convolution with a Gaussian function, and a low-pass filter has a smoothly declining frequency response that remains low at frequencies higher than specified threshold frequency. Moreover, linear trends of annual mean values are also computed to quantify long-term changes in RE (Shi *et al.*, 2003). Although the focus is on these variations, annual mean values are displayed for selected datasets as an indicator of interannual variability.

Evaporation is a complex dynamic process affected by many environmental factors. Partial correlation can measure the degree of association between two random variables, with the effect of a set of controlling random variables removed. Therefore, partial correlation analysis was used to analyse the level of agreement of RE with rainfall and surface temperature. A variety of different reanalysis are used in this study, annual mean RE values are distinct and the results will vary in different years. We used the coefficient of variation (CV) to measure the substantial uncertainties in reanalysis. CV is a normalized measure of dispersion of a probability distribution or frequency distribution (Jacobs *et al.*, 2010). The standard deviation and the mean are denoted respectively by $S$ and $M$, which CV can be written as

$$\mathrm{CV} = \frac{S}{M} \times 100\%. \tag{3}$$

To reveal the coherent pattern of the change in RE, both conventional empirical orthogonal function (EOF) analysis and rotated empirical orthogonal function (REOF) analysis are used in this study. The essence of EOF analysis is to identify and extract the spatiotemporal modes that are ordered in terms of their representations of data variance (Shi, 2009). On the other hand, it is noted that the objective of REOF is to minimize the mode complexity by making the large loadings larger and the small loadings smaller. The synthetic experiments indicate that REOF analysis is overwhelmingly a better choice in terms of accuracy and effectiveness, especially for picking up localized patterns (Lian and Chen, 2012).

## 3. Results

### 3.1. Time evolution of reanalysis evaporation in China

To investigate the temporal characteristics of RE in China, Figure 1 illustrates the interannual and interdecadal variations of RE obtained from different reanalysis. For China as a whole, RE decreased from 1948 to 1980 according to NCEP-R1 and ERA-40. However, the interannual variations of these two datasets disagree in some years. Most of reanalysis show a roughly similar behaviour after 1979. Overall, RE has a sharp decrease at about 1982, after that there is a steady increased from 1985 to 2004, with RE remaining high in the early 21st century and then rapidly decrease after 2004. Nevertheless, the increase over this period varies significantly among different reanalysis. NCEP-R1 and CFSR reveals large differences in terms of interdecadal variations; NCEP-R1 RE shows a slight decrease for the1979–2012 period. Notably,

© 2014 Royal Meteorological Society

Table 1. Reanalysis products used in the study, with the horizontal resolution, the starting and ending dates, the assimilation method, the approximate vintage of the products and the current status.

| Reanalysis | Horizontal resolution | Period | Assimilation method | Vintage | Status |
|---|---|---|---|---|---|
| NCEP-R1 | T62 | 1948–2012 | 3D VAR | 1995 | Ongoing |
| NCEP-R2 | T62 | 1979–2012 | 3D VAR | 2001 | Ongoing |
| ERA-40 | T159 | 1958–2002 | 3D VAR | 2004 | Completed |
| ERA-I | T255 | 1979–2012 | 4D VAR | 2009 | Ongoing |
| MERRA | 2/3° × 1/2° | 1979–2012 | 3D VAR | 2009 | Ongoing |
| CFSR | T382 | 1979–2010 | 3D VAR | 2009 | Ongoing |

pan evaporation increased during the period 1986–2006 according to Cong *et al.* (2009), which is consistent with RE in NCEP-R2, ERA-I, ERA-40 and MERRA, while different on interannual timescales. Despite the general similarity, differences exist among the various estimates, owing in part to the changing amount of assimilated observational data, and different data assimilation methods, and different model equations and assumptions, results of reanalysis models deviate significantly, even if they should be similar in principle (Lorenz and Kunstmann, 2012). There are highly uncertainties lie in the estimates of RE because it is seldom measured, and instead is estimated from bulk flux formulas (Kubota *et al.*, 2003; Trenberth *et al.*, 2011). Multi-reanalysis datasets are applied to avoid data dependence of the results.

To analyse the agreement of interannual variability between two datasets, time correlations were computed for further analysis. The time correlation coefficients in Figure 2 show that NCEP-R1 presents positive correlation with other reanalysis, however, mostly are not significant. This may be due significant negative variation trend in the NCEP-R1 RE during the period between 1990 and 2002. Similarly, CFSR also differ from the other reanalysis, because the CFSR series show a distinctive interannual and interdecadal change pattern. In contrast to NCEP-R1 and CFSR, NCEP-R2, ERA-I, ERA-40 and MERRA correlate well with other reanalysis, we got positive correlations of them. Of particular note NCEP-R2 and MERRA are highly positive correlated with the other reanalysis.

### 3.2. Rotated EOF results of reanalysis evaporation in NCEP-R1

To analyse the spatial-temporal variability of RE in China, here we use EOF method to get the dominant RE patterns. Only the NCEP-R1 is available going back to the 1940s, according to NCEP-R1, the normalized annual mean RE field in China is decomposed using the EOF method. Then, all EOF components are sorted according to their variances in a descending order. The first ten EOF modes can explain about 81.5% of the variance, which is a good representation of the total variance. According to the rule given by North *et al.* (1982), all of the ten EOF modes are statistically distinguishable from each other and the rest of the eigenvectors. Taking into account that the contribution to the variance from each additional mode is small beyond mode 10, thereby rotating the first ten modes can remain identical.

The REOF modes capture localized centres of variability that contribute to the larger-scale spatial patterns of the unrotated modes. In the following section we present and describe the first four leading REOF modes in NCEP/NCAR. Our reasons for only using the first four leading REOF modes in this analysis are based on both theoretical and practical considerations. From a theoretical point of view, the first four leading REOF modes account for about 60% of the variance, thus they can represent the major spatial variability of RE. From a practical point of view, another purpose of this section is to subdivide China into different regions according to the dominant mode of the change in RE. However, results indicate that there are no obvious regional characteristics in the rest REOF modes. As described above, the analysis focuses on RE changes in the first four leading REOF modes are reliably and practical. Figure 3 depicts major typical spatial structures of the first four REOF modes, respectively. The first REOF mode (Figure 3(a)) reproduced the obviously negative anomalies in Qinghai–Tibet Plateau and positive anomalies in northwest, north and central regions of China. However, this structure is almost contrary to the second REOF mode (Figure 3(b)). Finally, the third (Figure 3(c)) and fourth (Figure 3(d)) REOF mode can reasonably reproduce the anomalous positive pattern in the Qinghai–Tibet Plateau and northeast China, respectively.

According to the first four REOF modes of RE in NCEP/NCAR, the coherent spatial pattern of RE over China presented significant regional characteristics. The major localized centres of variability are located in Northwest, North China, Northeast, Qinghai–Tibet Plateau, Central and Eastern regions and South China. From these results, China can be roughly divided into six climatic regions. The six regions are defined by latitude and longitude and named NW (Northwest region), NC (North China), NE (Northeast Region), QT (Qinghai–Tibet Plateau), CE (Central and Eastern regions) and SC (South China), respectively. Interestingly, the six climatic regions are roughly consistent with the moisture conditions in China (Wu *et al.*, 2006), since a clearly southeast–northwest gradient is shown. China occupies a vast area and is characterized by diverse soils, precipitation, vegetation, together with the unique altitude. Moreover, the concept of water- and energy-limited evaporation has long been used to understand the role of evaporation in the water balance. The location of the climatological annual-average energy- and water-limited landscapes is given in McVicar *et al.* (2012).

© 2014 Royal Meteorological Society

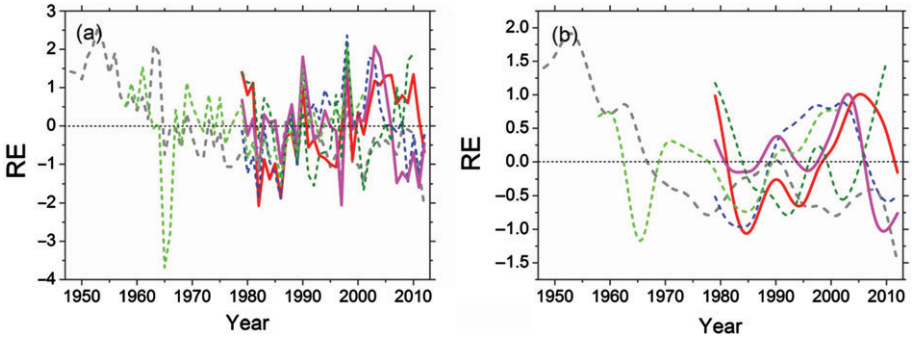


Figure 1. Normalized RE variability on interannual (a) and interdecadal (b) time scales over China obtained from NCEP-R1 (grey dash), NCEP-R2 (red solid), ERA-I (blue dash), ERA-40 (green dash), MERRA (magenta solid) and CFSR (olive dash) datasets.

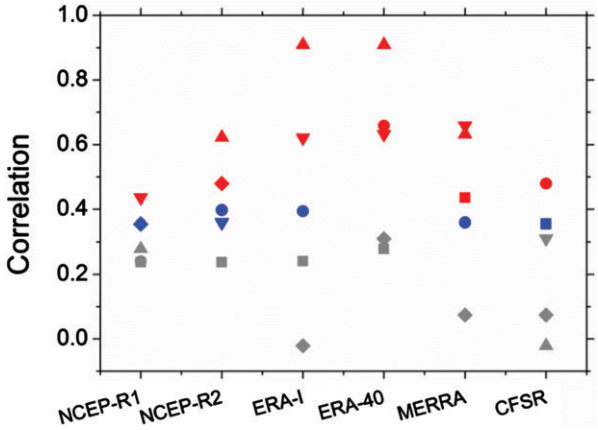


Figure 2. Time correlation coefficients between annual mean RE fields in China obtained from NCEP-R1, NCEP-R2, Interim, ERA-40, MERRA and CFSR datasets. Red dots are at the 99% confidence level, blue dots are significant at the 95% confidence level.

In general, CE and SC belong to energy-limited landscapes, while the rest of China belongs to water-limited landscapes.

The climatological estimates of RE computed by averaging all six reanalysis are also shown in Figure 4. From the spatial dimension, RE gradually decreases from southeast coastal to northwest inland regions of China, indicating that the spatial distribution of RE is similar to precipitation. Moreover, RE also decreases with the increase of altitude, as well as differences in meridional direction, which is consistent with the distribution of energy. The spatial distribution of pan evaporation (Zuo *et al.*, 2005), reference evapotranspiration (Chen *et al.*, 2005), and RE (Figure 4) in China showed significant regional differences. Pan evaporation displayed a consistent regional pattern with reference evapotranspiration, gradually increased from southeast coastal to northwest inland regions of China, which is just the opposite to RE. Moreover, pan evaporation is higher than RE in most parts of China, especially in the arid region. This provides direct evidence that actual evaporation is limited by the supply of water (rainfall) in a dry environment; result in actual evaporation cannot reach the values of pen evaporation (Matsoukas *et al.*, 2011). Conversely, in a wet environment, such as CE and SC, pan evaporation, reference evapotranspiration and RE show a quite similar distribution. In fact, actual evaporation in these regions will be greatly influenced by energy supply (Zhang *et al.*, 2012).

### 3.3. Interdecadal variations of regional reanalysis evaporation

To see whether there are spatial differences in the change of RE within China, we explored the interdecadal variations of RE for China's six climatic regions (Figure 5). Overall RE decreased gradually from 1970s to about 1985 and subsequently increased rapidly in NW (Figure 5(a)). NCEP-R2, MERRA and ERA-40 are in general agreement with each other, while NCEP-R1 and CFSR present different change characteristics. Interdecadal variation of RE in NCEP-R2, MERRA and ERA-40 agree well with pan evaporation in Shen *et al.* (2010). In contrast to NW, most of the six reanalysis decreased significantly during the period of 1985–2004 in NE, but the decrease over this period varies significantly among datasets (Figure 5(b)). Similarity, RE also showed a decreasing trend in NC (Figure 5(c)). The six reanalysis except for NCEP-R1 RE increased from 1985 to 2002 in QT (Figure 5(d)), nonetheless, the magnitudes of six different reanalysis also vary significantly and uncertainties are high. All reanalysis show a roughly similar behaviour in CE and SC, RE decreased from 1948 to early 1980s, then increased and peaked in about 2005. Evaporation process involves many physical factors, and many material fluxes on the earth surface would have an impact on it. The topography, vegetation and climate conditions are diverse in China. Climate and environmental forcing variables control energy and energy partitioning, therefore the change of the RE showed distinct regional characteristics. The interdecadal variations of RE vary significantly in different regions of China may be mainly due to the above factors.

The long-term annual mean RE obtained from different reanalysis are presented in Table 2. The NCEP-R1 gives value of China RE is 2.09 mm day$^{-1}$, significantly higher than the values of other reanalysis. Liu *et al.* (2011) and Cong *et al.* (2009) reported that annual pan evaporation over China is 4.2–4.9 mm day$^{-1}$, however, RE is much smaller, only about half of pan evaporation. NCEP-R2 is slightly higher than NCEP-R1 in CE and

© 2014 Royal Meteorological Society

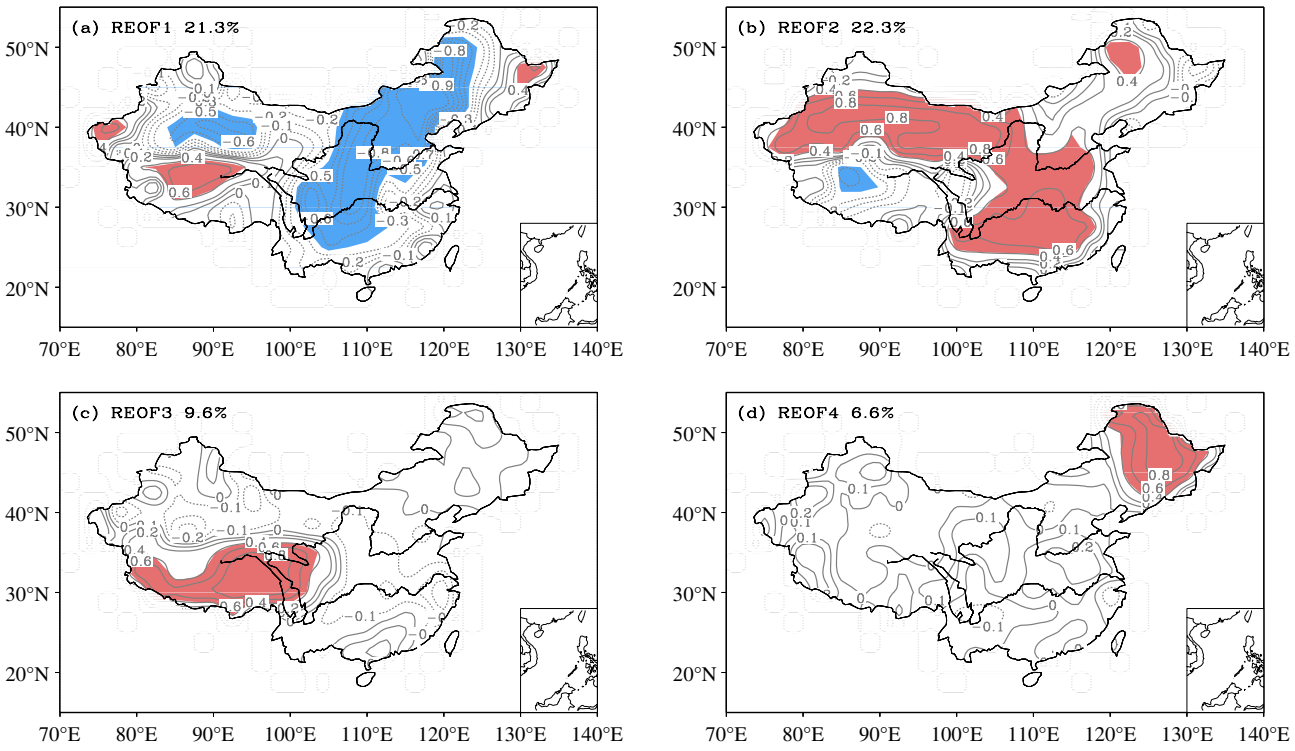


Figure 3. The first four REOF modes of the normalized annual mean RE fields in China calculated from the NCEP-R1 dataset for the period of 1948–2012. (a) REOF1 21.3%, (b) REOF2 22.3%, (c) REOF3 9.6% and (d) REOF4 6.6%. High values are shaded and the numbers on top of the panels show the explained variance of each mode.

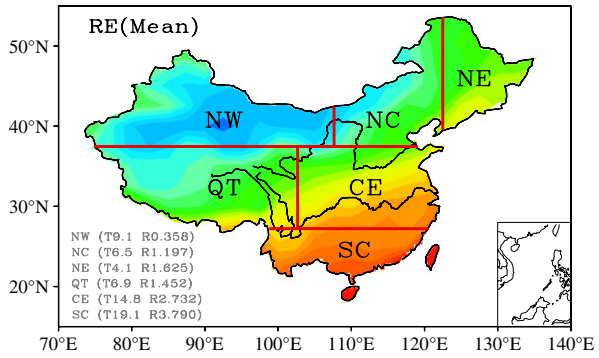


Figure 4. Six climatic regions in China and the climatological estimates of RE computed by averaging all six reanalysis (unit: mm day$^{-1}$) with the annual area-averaged air temperature (T, °C) and rainfall (R, mm day$^{-1}$) for each climatic region.

SC, as the NCEP-R2 values are 2.90 and 4.10 mm day$^{-1}$, respectively. Moreover, comparisons of these datasets reveal large discrepancies in NW, mean amounts in NCEP-R1 and ERA-40 differ by about 50%. In contrast, the datasets intercomparison highlights qualitative agreement among the reanalysis in NC and CE. Among the caveats is that many of the analysed datasets, and especially the satellite-based ones, share common data sources, although data are often diversely processed and combined. Other datasets instead use reanalysis for their derivation, and hence are not purely observational (Mariotti, 2010). Inevitably, the lack of ground-based measurements result in the uncertainties in these estimates is not well determined.

The CV can be used to compare distribution of RE values obtained from different reanalysis. Figure 6 shows the annual CVs of each climatic region and China. The magnitude of CV in different climatic region varied from about 15–30%. On average, CVs for China roughly remained stable from 1979 to 2012, at the rate of about 20%. CVs for NW are highest with about 30% during the period of 1979–2012. In contrast, CVs for NC and CE are relatively small, but there is a general tendency of CV to increase from 1996 for NC. Similarity, CV for NE in 1990s is about 22%, and subsequently increase leading up to the current period. Moreover, CVs for SC are quite stable and have no significant trends from 1980 to 2001, but show a steep decrease from early 21st century. Considering that annual mean value is an important indicator for selected datasets, it should be noted that RE values vary significantly in NW and NE, the quality of reanalysis dataset needs to be improved in these domains.

### 3.4. Linear trends of annual mean reanalysis evaporation

Since the early 20th century, the global air and sea surface temperature has increased about 0.8°C, with about two-thirds of the increase occurring since 1980 (National Research Council, 2011). On the other hand, only the NCEP-R1 and ERA-40 datasets are available going back to the 1950s. Therefore, linear trends of annual mean RE during the period 1979–2012 are computed in order to quantify long-term changes of annual mean RE (Table 3). The positive and negative values of climate tendency rate

© 2014 Royal Meteorological Society

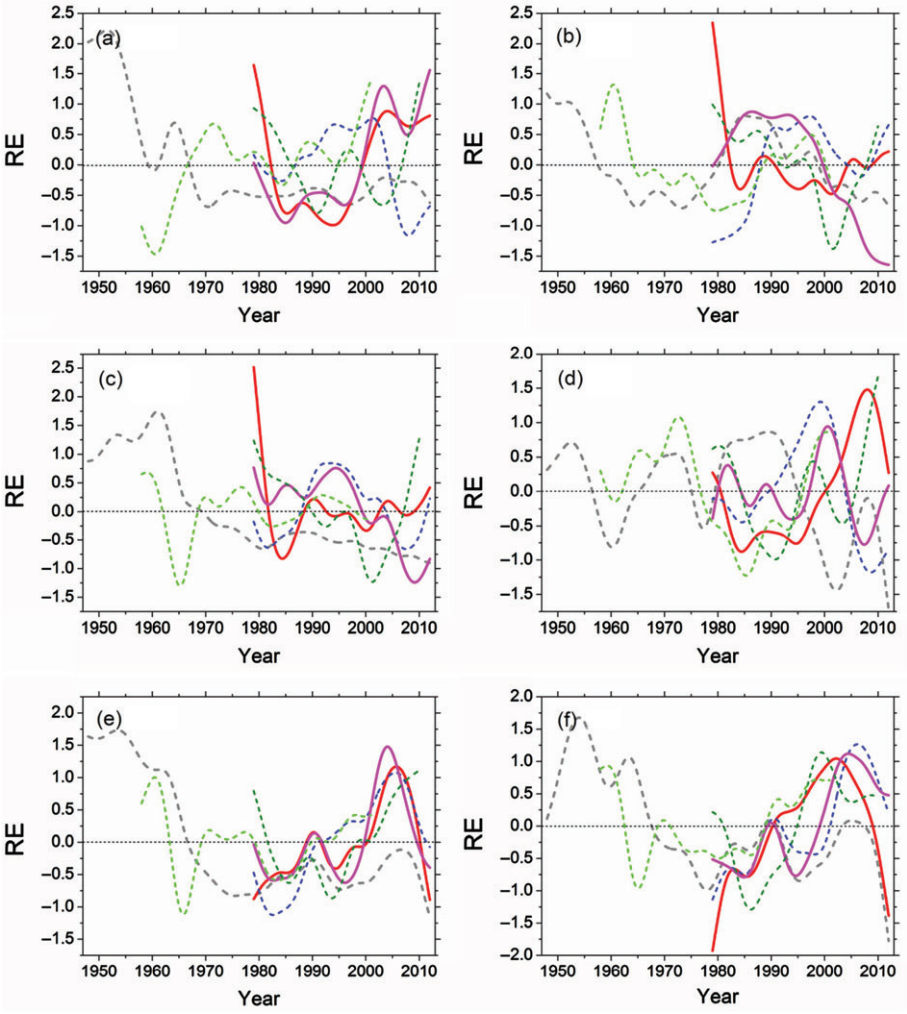


Figure 5. As in Figure 1(b), but for (a) NW, (b) NE, (c) NC, (d) QT, (e) CE and (f) SC region, respectively.

indicate increasing and decreasing trends, respectively. Except for NCEP-R1 and MERRA, the other reanalysis unanimously show an increase in RE for China. However, the increase over this period varies significantly among reanalysis, with ERA-40 giving the highest increase and CFSR the lowest. Linear trends of annual mean RE for NW obtained from different reanalysis are inconsistently, MERRA increased significantly at the rate of about 1.483 mm $a^{-2}$, while ERA-I and CFSR have decrease trend of $-0.284$ and $-0.379$ mm $a^{-2}$, respectively. Comparison of linear trends in NE reveals larger differences among the reanalysis, ERA-40 and ERA-I increased significantly at the 95% confidence level, and the other reanalysis decrease significantly instead. In addition, this situation is similar in QT. ERA-40 also showed increase trend in NC, which is different with the other reanalysis. Various estimates of linear trends are statistically consistent in SC, and rates of increase in SC are in the range of 0.037–2.232 mm $a^{-2}$, most of them are significant at the 99% confidence level. Similarity, the increase rates of RE in CE are in the range of 0.397–1.477 mm $a^{-2}$, and lots of these trends are significant. Analysis of the shorter but more consistent time series of RE in different reanalysis demonstrates a more obvious increase in RE between 1982 and 2005.

Table 2. Long-term annual mean RE obtained from different reanalysis for each climatic region and China.

| Reanalysis | RE (mm $day^{-1}$) | | | | | | |
|---|---|---|---|---|---|---|---|
| | CHN | NW | NE | NC | QT | CE | SC |
| NCEP-R1 | 2.09 | 0.89 | 2.48 | 1.51 | 1.78 | 2.86 | 3.98 |
| NCEP-R2 | 1.97 | 0.76 | 2.21 | 1.42 | 1.46 | 2.90 | 4.10 |
| ERA-40 | 1.33 | 0.45 | 1.40 | 1.14 | 1.12 | 1.96 | 2.29 |
| ERA-I | 1.38 | 0.52 | 1.46 | 1.15 | 1.11 | 2.01 | 2.44 |
| MERRA | 1.60 | 0.49 | 1.57 | 1.10 | 1.43 | 2.35 | 3.25 |
| CFSR | 1.49 | 0.54 | 1.69 | 1.05 | 1.01 | 2.21 | 3.17 |

RE that is separately area averaged over China gives distinctive linear trends during the period 1979–2012 (Table 3). By subdividing China into six climatic regions, we found that RE increased significantly in SC and CE under global warming, but decreased in NE and NC although the magnitude of decreasing trends is inconsistently among the reanalysis. Moreover, there is a general tendency of RE to increase in NW, although mostly RE trends are not significant. In summary, it can be concluded

© 2014 Royal Meteorological Society

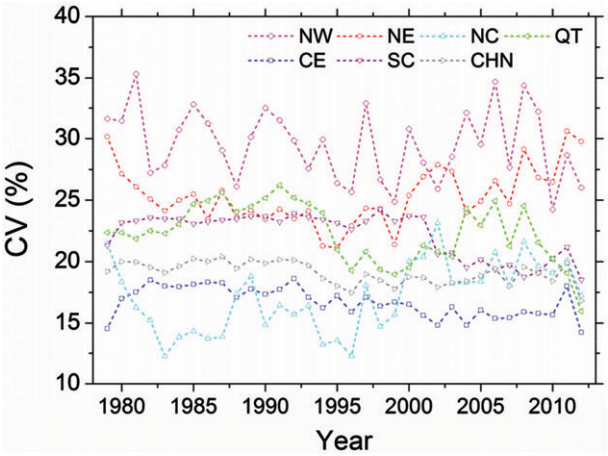


Figure 6. Time series of the annual CVs of RE obtained from different reanalysis for each climatic region and China.

that the quality of RE values in CE and SC is higher, while even greater uncertainties lie in the estimates of RE in NW and QT.

### 3.5. Analysis of the impact of global warming on reanalysis evaporation

Water on the Earth's surface will evaporate into the atmosphere as energy is absorbed by liquid water. The evaporation of water from soil is controlled mainly by the available energy and the soil moisture conditions. Because soil moisture is often difficult to obtain, annual mean rainfall can be used as an indicator of soil moisture (Lawrimore and Peterson, 2000). It is well-known that surface temperature is the most widely used indicator of climatic changes both on global and regional scales. In fact equilibrium evaporation is very insensitive to changes in surface temperature while it is directly proportional to changes in the surface radiation balance (Cohen *et al.*, 2002). Over the past 60 years, temperature of China showed a trend of increase from late 1970s, while there is no significant trend of rainfall (Figure 7). However, rainfall gives similar pattern of change to the variation of RE during the period of 1985–1998 (see Figure 1). As climate changes, emphasis in this section is given to the influence of surface temperature on the RE in different regions of China.

Table 4 summarizes linear trends of annual mean temperature and rainfall for each climatic region and China. It should be noted that the trends of temperature in these six climatic regions are all significant at the 99% confidence level. However, no statistically significant trend in rainfall was observed for each climatic region. Rainfall increases in NW, QT and CE at the rate of 0.733, 1.568, 0.353 mm $a^{-2}$, respectively, but slightly decreases in NE, NC and SC, especially for SC the linear trend reaches −1.048 mm $a^{-2}$. The concurrent occurrences of RE increases and temperature increases were found in SC and CE, while the concurrent occurrences of RE decreases and rainfall decreases were found in NE and NC.

To identify the dominant variables associated with RE changes, partial correlation method was applied. Because RE will be influenced by temperature and rainfall at the same time, therefore we use partial correlation coefficient to quantify the correlation between RE and temperature when conditioning on rainfall (Table 5). Except for NCEP-R1, the other RE showed positive correlation with temperature for China. Partial correlation coefficients of NCEP-R2 and ERA-I are all significant at the 99% confidence level. Similarity, temperature and RE have a strongly positive correlation for CE and SC, and most of partial correlation coefficients are significant at the 99% confidence level. However, for the other regions of China, the partial correlations exhibit a wider range among the reanalysis. Furthermore, the low spatial density of meteorological data in western China makes it challenging to separate local changes from regional or even continental-scale changes. Meanwhile, interannual variability of RE varies significantly among the six reanalysis for these regions. Therefore it is difficult to determine the exact relationship between RE and temperature.

Partial correlation coefficients between RE and rainfall were given in Table 6. RE showed positive correlation with rainfall over most regions of China, for example, partial correlation coefficients are mostly significant at the 99% confidence level for NW and NC. Similarity, this relationship is also consistent for CE, but only NCEP-R1, ERA-40 and CFSR RE showed significant correlation with rainfall at the 95% confidence. It can also be noticed that RE may be less sensitive to rainfall for SC, as the partial correlation coefficients vary from −0.495 to 0.470. There are considerable differences in the annual means and trends in RE derived from the six reanalysis, however, the relationship between RE and rainfall are consistent in NW,

Table 3. Linear trends of annual mean RE for each climatic region and China during the period 1979–2012 obtained from different reanalysis.

| Reanalysis | RE trend rate (mm $a^{-2}$) | | | | | | |
|---|---|---|---|---|---|---|---|
| | CHN | NW | NE | NC | QT | CE | SC |
| NCEP-R1 | −0.481 | 0.214 | **−1.189** | −0.726 | *−1.506* | 0.397 | 0.037 |
| NCEP-R2 | **0.887** | 1.100 | −1.039 | −0.295 | *1.328* | **1.253** | **2.232** |
| ERA-40 | *0.894* | 0.456 | **1.056** | 0.243 | *0.923* | **1.230** | *1.386* |
| ERA-I | 0.278 | −0.284 | **0.661** | −0.001 | −0.169 | *1.335* | *1.055* |
| MERRA | −0.206 | *1.483* | *−4.380* | *−2.049* | −0.148 | 1.101 | *1.091* |
| CFSR | 0.136 | −0.379 | **−2.608** | −1.474 | 0.543 | 1.477 | *1.997* |

Italics values are significant at the 99% confidence level; bold values are significant at the 95% confidence level.

© 2014 Royal Meteorological Society

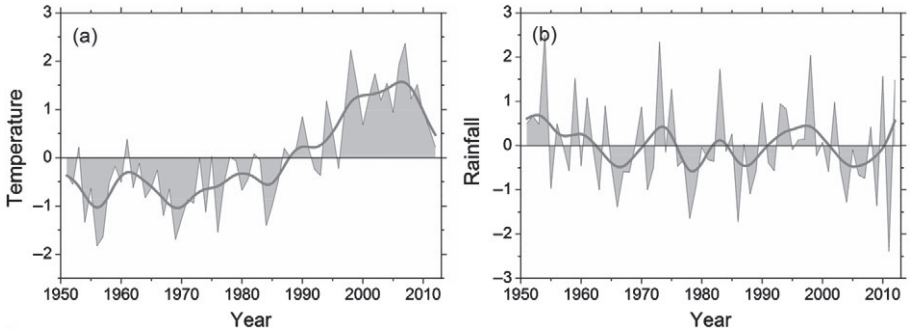


Figure 7. Normalized surface temperature (a) and rainfall (b) variability on interannual and interdecadal (grey solid lines) time scales over China.

Table 4. Linear trends of annual mean temperature (T) and rainfall (R) for each climatic region and China during the period 1979–2012.

| Regions | CHN | NW | NE | NC | QT | CE | SC |
|---|---|---|---|---|---|---|---|
| T (°C $a^{-1}$) | *0.033* | *0.039* | *0.028* | *0.034* | *0.039* | *0.037* | *0.023* |
| R (mm $a^{-2}$) | −0.015 | 0.733 | −0.359 | −0.422 | 1.568 | 0.353 | −1.048 |

Italics values are significant at the 99% confidence level.

NC, NE and CE. Therefore, rainfall is an important factor affecting the changing of RE, and it is plausible that the relationships of RE and rainfall are strong and dependable, especially in NW and NC.

As evidenced by partial correlation coefficients in Table 5, how changes in surface temperature impact the evaporative process in energy-limited and water-limited landscapes is distinct. In the dry NW and NC regions, rainfall is an important factor affecting the changing of RE, while RE is less sensitive to the change of temperature. However, on examining RE's relationship with temperature in SC and CE, it is observed that they all show a concurrent increase in RE and an increase in temperature, although there is a slightly decrease trend of rainfall in SC. Increasing temperature might be the main contributor to increasing RE in SC and CE. These results support the view that the sensitivity of RE to global warming largely depends on the environment, pan evaporation and actual evaporation can be inversely related (Lawrimore and Peterson, 2000).

Linear trends of annual mean RE and pan evaporation differ significantly in some regions. Liu *et al.* (2011) explored recent changes in pan evaporation dynamics in China, found the observed pan evaporation increased in most stations from 1992 to 2007. During these years, RE decreased in NC and NE, while increased in SC, CE and NW. It can be seen that change in RE and pan evaporation are consist in humid regions, whereas differ in arid regions. Change of annual RE in arid regions is projected to follow a similar pattern as precipitation, and partial correlation coefficients between RE and rainfall in NW, NC and NE have evidenced this view directly. Evaporation is driven essentially by meteorological variables, mediated by vegetation and soil characteristics, and constrained by the amount of available water. The relationship between pan evaporation and actual evaporation might be complementary with water control and proportional with energy control (Yang *et al.*, 2006). Consequently, it can be seen that actual evaporation would be restricted by the available energy and the soil moisture conditions deeply.

The identification of RE trends in response to changing climatic conditions could help to quantify the potential impacts of climate change on actual evaporation. In fact the reported changes in rainfall and RE are large enough for the consequent changes in surface moisture balance to be readily observed. Droughts are likely to become more frequent and severe in some regions as higher air temperatures increase the potential for evaporation. It is high time to think in terms of expected change in water requirement due to global warming while planning for development of future water resources in the humid regions, such as SC and CE. The present study provides a contemporary view on future water requirement of this region in context of global warming.

## 4. Conclusions and discussion

The focus of this paper is given to the response of RE to global warming in China. With the motivation to reveal whether a warming climate would lead to an intensified hydrological cycle, the climatology, interannual variation and long-term trend of RE derived from six sets of reanalysis data are assessed. In a globally warming climate, there are a number of climatic responses that are tightly coupled to the temperature response. The temporal characteristics of RE trends in different regions of China under global warming are studied based on six different reanalysis. We can get these conclusions:

1. By subdividing China into six climatic regions, we found that RE increased significantly in CE and SC of China from 1979 to 2012, various estimates of linear trend are statistically consistent, and most of them are significant at the 95% confidence level. Conversely, RE

© 2014 Royal Meteorological Society

Table 5. Partial correlation coefficient between temperature and RE with the effect of rainfall removed.

| Reanalysis | Partial correlation coefficient | | | | | | |
|---|---|---|---|---|---|---|---|
| | CHN | NW | NE | NC | QT | CE | SC |
| NCEP-R1 | **−0.286** | −0.204 | 0.121 | **−0.307** | −0.036 | −0.091 | 0.029 |
| NCEP-R2 | *0.515* | 0.277 | **−0.355** | −0.006 | *0.667* | *0.552* | *0.515* |
| ERA-40 | 0.237 | 0.198 | *0.394* | 0.196 | **0.357** | 0.296 | 0.199 |
| ERA-I | *0.544* | −0.290 | **0.480** | *0.505* | −0.225 | *0.796* | *0.504* |
| MERRA | 0.106 | **0.406** | −0.145 | −0.081 | −0.084 | *0.496* | *0.609* |
| CFSR | 0.108 | −0.265 | −0.307 | −0.302 | **0.362** | *0.473* | *0.662* |

Italics values are significant at the 99% confidence level; bold values are significant at the 95% confidence level.

Table 6. Partial correlation coefficient between rainfall and RE with the effect of temperature removed.

| Reanalysis | Partial correlation coefficient | | | | | | |
|---|---|---|---|---|---|---|---|
| | CHN | NW | NE | NC | QT | CE | SC |
| NCEP-R1 | *0.335* | 0.124 | *0.382* | *0.440* | −0.133 | **0.322** | −0.184 |
| NCEP-R2 | 0.021 | **0.379** | −0.035 | **0.402** | −0.140 | 0.256 | 0.175 |
| ERA-40 | *0.414* | *0.499* | **0.348** | *0.641* | −0.004 | **0.331** | 0.111 |
| ERA-I | *0.518* | *0.546* | 0.243 | *0.781* | 0.271 | 0.245 | −0.219 |
| MERRA | 0.267 | *0.605* | 0.229 | *0.626* | 0.276 | 0.267 | *−0.495* |
| CFSR | 0.269 | **0.427** | **0.437** | *0.542* | −0.065 | **0.434** | *0.470* |

Italics values are significant at the 99% confidence level; bold values are significant at the 95% confidence level.

decreased in NE and NC although the magnitudes of decreasing trends are inconsistently among the reanalysis. Moreover, there is a general tendency of RE to increase in NW.

2. In the dry NW and NC regions, rainfall is an important factor affecting the changing of RE, while RE is less sensitive to the change of temperature. However, it is observed that they all show a concurrent increase in RE and an increase in temperature in SC and CE, although there is a slightly decrease trend of rainfall in SC. These results support the view that the sensitivity of evaporation to global warming largely depends on the environment.
3. In view of data availability, despite the general similarity, differences exist among the various reanalysis, especially NCEP-R1 and CFSR. The lack of ground-based measurements result in the uncertainties in these estimates is not well determined. In summary, it can be concluded that the quality of RE values in CE and SC is higher, while even greater uncertainties lie in the estimates of RE in NW and QT.
4. Interdecadal variability of RE showed some similar characteristics with pan evaporation in China, while varied significantly on interannual timescales. Moreover, RE is much smaller, only about half of pan evaporation. From the spatial dimension, RE gradually decreases from southeast coastal to northwest inland regions in China, which is just the opposite to pan evaporation. During the sub-period of 1992–2007, linear trends of annual mean RE and pan evaporation are consist in humid regions, whereas differ in arid regions.

The climate is dominated by diverse and changeable natural processes over a wide range of time and space scales. It should be noted that global warming could be due to natural variability, anthropogenic effects or more likely a combination of both. In addition, there are a number of climatic responses that are tightly coupled to the temperature response. Hence, although temperature or rainfall plays a critical role in changing evaporation, other parameters could influence or mediate their effect, not to mention anthropogenic climate change has not been well established.

## Acknowledgements

The authors thank three anonymous reviewers and editors for beneficial and helpful suggestions for this manuscript. This research was jointly supported by the National Basic Research Program of China (Grant No. 2013CB430204 and 2012CB955900), National Natural Science Foundation of China (Grant Nos. 41375078 and 41175084) and Special Scientific Research Fund of Meteorological Public Welfare Profession of China (Grant Nos. GYHY201106016).

## References

Bosilovich MG, Robertson FR, Chen JY. 2011. Global energy and water budgets in MERRA. *J. Clim.* **24**: 5721–5739.

Chattopadhyay N, Hulme M. 1997. Evaporation and potential evapotranspiration in India under conditions of recent and future climate change. *Agric. For. Meteorol.* **87**: 55–73.

Chen DL, Gao G, Xu CY, Guo J, Ren GY. 2005. Comparison of the Thornthwaite method and pan data with the standard Penman-Monteith estimates of reference evapotranspiration in China. *Clim. Res.* **28**: 123–132.

Cohen S, Ianetz A, Stanhill G. 2002. Evaporative climate changes at Bet Dagan, Israel, 1964–1998. *Agric. For. Meteorol.* **111**: 83–91.

Cong ZT, Yang DW, Ni GH. 2009. Does evaporation paradox exist in China? *Hydrol. Earth Syst. Sci.* **13**: 357–366.

© 2014 Royal Meteorological Society 

Dee DP, Uppala SM, Simmons AJ, Berrisford P, Poli P, Kobayashi S, Andrae U, Balmaseda MA, Balsamo G, Bauer P, Bechtold P, Beljaars ACM, van de Berg L, Bidlot J, Bormann N, Delsol C, Dragani R, Fuentes M, Geer AJ, Haimberger L, Healy SB, Hersbach H, Holm EV, Isaksen L, Kallberg P, Kohler M, Matricardi M, McNally AP, Monge-Sanz BM, Morcrette JJ, Park BK, Peubey C, de Rosnay P, Tavolato C, Thepaut JN, Vitart F. 2011. The ERA-Interim reanalysis: configuration and performance of the data assimilation system. *Q. J. R. Meteorol. Soc.* **137**: 553–597.

Douville H, Ribes A, Decharme B, Alkama R, Sheffield J. 2013. Anthropogenic influence on multidecadal changes in reconstructed global evapotranspiration. *Nat. Clim. Change* **3**: 59–62.

Goyal RK. 2004. Sensitivity of evapotranspiration to global warming: a case study of arid zone of Rajasthan (India). *Agric. Water Manag.* **69**: 1–11.

Huntington TJ. 2006. Evidence for intensification of the global water cycle: review and synthesis. *J. Hydrol.* **319**: 83–95.

IPCC. 2007. *Climate Change 2007: The Physical Science Basis. Contribution of Working Group I to the Fourth Assessment*. Cambridge University Press: New York, NY.

Jacobs AFG, Heusinkveld BG, Holtslag AAM. 2010. Eighty years of meteorological observations at Wageningen, the Netherlands: precipitation and evapotranspiration. *Int. J. Climatol.* **30**: 1315–1321.

Jacobson MZ. 2007. *Fundamentals of Atmospheric Modeling*. Cambridge University Press: Cambridge, UK and New York, NY.

Jhajharia D, Shrivastava SK, Sarkar D, Sarkar S. 2009. Temporal characteristics of pan evaporation trends under the humid conditions of northeast India. *Agric. For. Meteorol.* **149**: 763–770.

Kalnay E, Kanamitsu M, Kistler R, Collins W, Deaven D, Gandin L, Iredell M, Saha S, White G, Woollen J. 1996. The NCEP/NCAR 40-year reanalysis project. *Bull. Am. Meteorol. Soc.* **77**: 437–471.

Kanamitsu M, Ebisuzaki W, Woollen J, Yang SK, Hnilo JJ, Fiorino M, Potter GL. 2002. NCEP–DOE AMIP-II Reanalysis (R-2). *Bull. Am. Meteorol. Soc.* **83**: 1631–1643.

Kinter JL III, Fennessy MJ, Krishnamurthy V, Marx L. 2004. An evaluation of the apparent interdecadal shift in the tropical divergent circulation in the NCEP-NCAR reanalysis. *J. Clim.* **17**: 349–361.

Kirono DGC, Jones RN, Cleugh HA. 2009. Pan-evaporation measurements and Morton-point potential evaporation estimates in Australia: are their trends the same? *Int. J. Climatol.* **29**: 711–718.

Kubota M, Kano A, Muramatsu H, Tomita H. 2003. Intercomparison of various surface latent heat flux fields. *J. Clim.* **16**: 670–678.

Lawrimore JH, Peterson TC. 2000. Pan evaporation trends in dry and humid regions of the United States. *J. Hydrometeorol.* **1**: 543–546.

Lian T, Chen DK. 2012. An evaluation of rotated EOF analysis and its application to tropical Pacific SST variability. *J. Clim.* **25**: 5361–5373.

Liu B, Xu M, Henderson M, Gong W. 2004. A spatial analysis of pan evaporation trends in China, 1955–2000. *J. Geophys. Res.* **109**: D15102, doi: 10.1029/2004JD004511.

Liu X, Luo Y, Zhang D, Zhang M, Liu C. 2011. Recent changes in pan-evaporation dynamics in China. *Geophys. Res. Lett.* **38**: L13404.

Lorenz C, Kunstmann H. 2012. The hydrological cycle in three state-of-the-art reanalysis: intercomparison and performance analysis. *J. Hydrometeorol.* **13**: 1397–1420.

Mariotti A. 2010. Recent changes in the Mediterranean water cycle: a pathway toward long-term regional hydroclimatic change? *J. Clim.* **23**: 1513–1525.

Matsoukas C, Benas N, Hatzianastassiou N, Pavlakis KG, Kanakidou M, Vardavas I. 2011. Potential evaporation trends over land between 1983–2008: driven by radiative fluxes or vapour-pressure deficit? *Atmos. Chem. Phys.* **11**: 7601–7616.

McVicar TR, Roderick ML, Donohue RJ, Li LT, Van Niel TG, Thomas A, Grieser J, Jhajharia D, Himri Y, Mahowald NM, Mescherskaya AV, Kruger AC, Rehman S, Dinpashoh Y. 2012. Global review and synthesis of trends in observed terrestrial near-surface wind speeds: implications for evaporation. *J. Hydrol.* **416–417**: 182–205.

National Research Council. 2011. *America's Climate Choices*. The National Academies Press: Washington, DC.

North GR, Bell TL, Cahalan RF, Moeng FJ. 1982. Sampling errors in the estimation of empirical orthogonal functions. *Mon. Weather Rev.* **110**: 699–706.

Pearlmutter D, Kruger EL, Berliner P. 2009. The role of evaporation in the energy balance of an open-air scaled urban surface. *Int. J. Climatol.* **29**: 911–920.

Roderick ML, Farquhar GD. 2002. The cause of decreased pan evaporation over the past 50 years. *Science* **298**: 1410–1411.

Shen Y, Liu C, Liu M, Zeng Y, Tian C. 2010. Change in pan evaporation over the past 50 years in the arid region of China. *Int. J. Climatol.* **24**: 225–231.

Shi N. 2009. *Meteorological Statistical Forecast*. China Meteorological Press: Beijing.

Shi N, Huang X, Yang Y. 2003. Spatiotemporal features of the trend variation of global land annual rainfall fields from 1948–2000. *Chin. J. Atmos. Sci.* **27**: 971–982.

Thomas A. 2000. Spatial and temporal characteristics of potential evapotranspiration trends over China. *Int. J. Climatol.* **20**: 381–396.

Trenberth KE, Fasullo JT, Mackaro J. 2011. Atmospheric moisture transports from ocean to land and global energy flows in reanalysis. *J. Clim.* **24**: 4907–4924.

Uppala SM, Kallberg PW, Simmmons AJ, Andrea U, da Costa BV, Fiorino M, Gibson JK, Haseler J, Hernandez A, Kelly GA, Li X, Onogi K, Saarinen S, Sokka N, Allan RP, Andersson E, Arpe K, Balmaseda MA, Beljaars ACM, Van De Berg L, Bidlot J, Bormann N, Caires S, Chevallier F, Dethof A, Dragosavac M, Fisher M, Fuentes M, Hagemann S, Holm E, Hoskin BJ, Isaken L, Janssen PAEM, Jenne R, McNally AP, Mahfouf JF, Morcrette JJ, Rayner NA, Saunders RW, Simon P, Sterl A, Trenberth KE, Untch A, Vasiljevic D, Viterbo P, Woollen J. 2005. The ERA-40 re-analysis. *Q. J. R. Meteorol. Soc.* **131**: 2961–3012.

Wang Y, Jiang T, Bothe O, Fraedrich K. 2007. Changes of pan evaporation and reference evapotranspiration in the Yangtze River basin. *Theor. Appl. Climatol.* **90**: 13–23.

Wu S, Yin Y, Zheng D, Yang Q. 2006. Moisture conditions and climate trends in China during the period 1971–2000. *Int. J. Climatol.* **26**: 193–206.

Yang DW, Sun FB, Liu ZY, Cong ZT, Lei ZD. 2006. Interpreting the complementary relationship in non-humid environments based on the Budyko and Penman hypotheses. *Geophys. Res. Lett.* **33**: L18402.

Zhang YQ, Leuning R, Chiew FHS, Wang EL, Zhang L, Liu CM, Sun FB, Peel MC, Shen YJ, Jung M. 2012. Decadal trends in evaporation from global energy and water balances. *J. Hydrometeorol.* **13**: 379–391.

Zuo HC, Li DL, Hu YQ, Bao Y, Lu S. 2005. Characteristics of climatic trends and correlation between pan-evaporation and environmental factors in the last 40 years over China. *Chin. Sci. Bull.* **50**: 1235–1241.

© 2014 Royal Meteorological Society 

SCIENCE CHINA
Earth Sciences

• RESEARCH PAPER •

February 2015 Vol.58 No.2: 255–269
doi: 10.1007/s11430-014-4947-8

# Spatial-temporal variation characteristics of global evaporation revealed by eight reanalyses

SU Tao[1] & FENG GuoLin[1,2*]

[1] *College of Atmospheric Sciences, Lanzhou University, Lanzhou 730000, China;*
[2] *Laboratory for Climate Studies, National Climate Center, China Meteorological Administration, Beijing 100081, China*

Received December 17, 2013; accepted July 23, 2014; published online December 5, 2014

On the basis of eight atmospheric reanalyses, we analyzed the spatial-temporal characteristics of global evaporation and also briefly evaluated the eight reanalyses. The results indicate that the long-term mean annual evaporation obtained from different reanalyses are consistent over most regions, with significant maritime-continental contrasts, as well as differences in meridional directions, and the land evaporation generally decreases with the increase of altitude. In addition, the temporal evolution of global evaporation varies significantly among the datasets, MERRA, ERA-Interim, NCEP-NCRA, and NCEP-DOE are very similar, whereas CFSR agrees best with ERA-40. Comparison of the inter-annual to inter-decadal variability of land evaporation reveals large differences among the reanalyses, whereas MERRA, CFSR, and NCEP-DOE are exactly similar. The temporal variation of evaporation over the oceans showed a relatively high consistency, which indicates that the quality of the reconstructed evaporation values over the oceans is higher, and even greater uncertainties lie in the estimates of evaporation over the land. In general, MERRA and NCEP-DOE may appropriately reflect the spatial-temporal characteristics of global evaporation, showing strong representativeness. The CFSR and ERA-40 are capable of revealing the characteristics of land evaporation, whereas ERA-Interim, NCEP-NCAR, OAFlux, and HOAPS are relatively applicable for research focused on the evaporation over the oceans. According to ERA-40, NCEP-NCAR, and OAFlux, global evaporation significantly decreased for the period of 1958–1978. In contrast, most of the eight reanalyses show a significant linear increase for the period of 1979–2011, and evaporation over the oceans was even more pronounced. Furthermore, the results are presented for the mean annual cycle of global evaporation, the changes at the low latitudes in the Northern Hemisphere are most distinct, and the monthly variation amplitude of the land evaporation was higher than that of the evaporation over the oceans.

**evaporation, reanalyses, spatial-temporal variation, linear trend, annual cycle**

**Citation:** Su T, Feng G L. 2015. Spatial-temporal variation characteristics of global evaporation revealed by eight reanalyses. Science China: Earth Sciences, 58: 255−269, doi: 10.1007/s11430-014-4947-8

The proportion of water vapor in the atmosphere is very small, but its activities seriously affect the water ecological environment on the Earth's surface and the survival of human beings (Zhang et al., 2010). Water in the atmosphere originates mainly from the free evaporation of the water surface and soil evaporation, as well as plant evapotranspiration (Liu et al., 2011). Landscapes depend greatly on the peculiarities of water cycle distribution on the land surface, where evaporation is one of the main links of the water cycle, together with precipitation and runoff (Guo et al., 2005), which is an important process in determining the weather and climate of various areas (Wang et al., 2005; Wang et al., 2010). At the same time, climate change will also affect evaporation, because, as the temperature increases, so does the process of evaporation. The moisture holding capacity of the atmosphere increases with the temperature, resulting in an increase in the evaporation of land surface and water

*Corresponding author (email: fenggl@cma.gov.cn)

© Science China Press and Springer-Verlag Berlin Heidelberg 2014

(IPCC, 2001). In addition, water vapor is the dominant greenhouse gas, providing a positive feedback mechanism with the temperature variation, as water vapor increase would intensify the greenhouse effect, thereby causing an increase in the temperature along with the water-holding capacity, which is compensated by evaporation to close the water budget (Huang et al., 2010). In fact, the precipitation in China originates from the evaporation from around the world, and the water vapor transport of the Indian Ocean, South China Sea, northwestern area of the Western Pacific, cross equatorial flow, and westerly belt of the Northern Hemisphere would have a certain impact on the precipitation in China (Zhang et al., 2003; Lian et al., 2003; Fan et al., 2006). Apparently, evaporation plays a crucial role in the Earth's climate and environment, and thus it is important to study the variation of global evaporation.

At present there are many methods for estimating evaporation from landscapes, regions and larger geographic extents, among which the most direct method is the instrument-measurement method. Much progress has been made in gaining insight into local-scale evaporation processes through accurate point measurements such as evaporating pan and terrestrial evaporator. Although evaporation values are seldom measured over most regions, they are estimated from empirical formulas, such as the Penman formula (Penman, 1948) and Kuzmin formula (Kuzmin, 1957). However, because the different underlying surface conditions and water vapor content have large differences, evaporation estimates are significantly influenced by the spatial-temporal conditions of meteorological data, and thus a large number of derived formulas applicable to different regions have been presented (Monteith, 1981; Shen et al., 2008; Summer et al., 2005). In addition, assuming that the perceptible water would remain approximately constant in a certain time scale, the evaporation could be estimated according to the water balance equation (Yi et al., 1996; Zhang et al., 2007). Each of the above methods has its respective advantages, but there are uncertainties and limitations associated with these estimation methods, such as the instrument-measurement method's susceptibility to the restrictions of the observational environment and measurement instruments, and the global evaporation observing system does not exist. However, the variations of the actual evaporation and pan evaporation are inconsistent, as the pan evaporation has a relationship with the land evaporation, but differ significantly in some aspects (Guo et al., 2005). In some areas, the time variations of them even present a negative correlation (Xie et al., 2009). When empirical methods such as the Penman formula are used, it is necessary to consider the physical conditions of various areas, and thus it is difficult to use this formula for research focusing on global evaporation. Although the estimation of evaporation through the water balance equation ensures the moisture conservation and follows the laws of physics, the uncertainties of the evaporation estimations are quite large (Zhang et al., 2007). Because of the limitations presented above, most studies regarding global evaporation deal with only some specific aspects. There are many regional or basin-scale synthesized analyses of evaporation (Zuo et al., 2005). Relatively few studies have attempted to provide a synthesized, quantitative view of the spatial-temporal variation characteristics of global evaporation.

Regional hydrometeorological and hydroclimatological applications require long-term, consistent datasets for analysis, particularly those with the capability to provide a reliable estimate of the annual mean global energy and water cycles. Retrospective analyses (reanalyses) are often used for these purposes. Numerical reanalyses have been useful to making historical record more homogeneous and accessible for many applications (Zhao et al., 2010). Reanalyses fields provide a unique opportunity to examine the water cycle at the high spatial-temporal scales, and thus have been widely used in weather and climate studies. However, because of the changing amount of assimilated observational data, different data assimilation methods, and different model equations and assumptions, the results of reanalyses models deviate significantly, even if they should be similar in principle. The lack of ground-based measurements of evaporation has meant that problems with reanalyses evaporation estimates are still unknown. For comparison, eight different global atmospheric reanalyses are used to analyze the spatial-temporal distribution of global evaporation. The reanalyses are evaluated by comparing quantities with each other. Differences in the total amount, spatial variability, and distribution of evaporation are analyzed in order to estimate the uncertainties incorporated in these datasets. The differences of global fields must be considered as uncertainty ranges, which can be expected when using such datasets for validation purposes. This not only provides a useful commentary on the quality and usability of the reanalyses, but also affords valuable information to improve the quality of the reanalyses.

## 1 Data and methods

### 1.1 Reanalyses data

From the 1990s metaphase, atmospheric reanalyses have been produced by the major meteorological centers (NCEP (NOAA), ECMWF, JMA, and NASA) (Zhao et al., 2010; Zhu et al. 2012). Several new reanalyses have recently become available, and those currently ongoing are given in Table 1. The first-generation atmospheric reanalyses in the mid- to late 1990s at NCEP (National Centers for Environmental Prediction), called NCEP-NCAR (National Center for Atmospheric Research) and referred to as NCEP-R1, had the substantial problems that limit their use, particularly for global climate change and variability studies. A second limited version of the NCEP reanalyses (called NCEP-DOE or NCEP-R2) was run to address some problems but is still

**Table 1** Summary of the eight reanalyses

| Reanalysis | Data range | Horizontal resolution | Period | Output times |
|---|---|---|---|---|
| MERRA | Global | 2/3°×1/2° | 1979–2011 | 1 h, daily, month |
| CFSR | Global | 2.5°×2.5° | 1979–2010 | 1 h, 6 h, month |
| Interim | Global | 1.5°×1.5° | 1979–2011 | 6 h, month |
| ERA-40 | Global | 2.5°×2.5° | 1958–2002 | 6 h, month |
| NCEP-R1 | Global | T62 | 1948–2011 | 6 h, daily |
| NCEP-R2 | Global | T62 | 1979–2011 | 6 h, daily |
| OAFlux | Ocean | 1.0°×1.0° | 1958–2011 | month |
| HOAPS | Ocean | 0.5°×0.5° | 1987–2005 | month |

the first-generation reanalyses. The NCEP-R1 used the NCEP global spectral model (GSM), or medium-range forecast (MRF) model, which is used for making the four times daily global data assimilation system (GDAS) analysis and for making the MRF predictions. The data assimilation and the model used are identical to the global system implemented operationally at the NCEP. The database has been enhanced with many sources of observations unavailable in real time for operations, provided by different countries and organizations, which included the Global rawinsonde data, COADS surface marine data, aircraft data, surface land synoptic data, satellite sounder data, SSM/I surface wind data, and satellite cloud drift winds. The NCEP-R2 used an updated version of the original GSM, and besides a few physical parameterization changes, a number of notable bugs in the NCEP-R1 analysis were also fixed. The NCEP-R1 and NCEP-R2 reanalyses of precipitation and evaporation are likely to be more different since these quantities depend more heavily upon the intrinsic model parameterizations (Roads, 2003; Trenberth et al., 2011).

The European Centre for Medium-range Weather Forecasts (ECMWF) reanalyses (ERA-40) covers the period from September 1957 to August 2002. The ERA-40 analysis also uses the 3D-Var variational method, where a cost function is minimized in relation to observations and background model field. The spreading of observations in the horizontal and the vertical is controlled by horizontal and vertical correlation of the background errors. Most satellite observations are used by computing radiances from the model fields and by comparing them with the satellite radiances. The analysis system uses a wide range of other observations, from conventional radiosonde and synoptic (SYNOP) observations, to ocean winds from satellite scatterometry. ERA-Interim (Interim) is the latest global atmospheric reanalyses produced by the ECMWF. Interim was intended to cover the period from 1989 to the present to provide a bridge between ECMWF's previous reanalyses ERA-40 (Uppala et al. 2005) and forthcoming next-generation reanalyses. Recently, Interim was extended to cover the years between 1979 and 1989 as well. Interim is produced with the ECMWF IFS, which incorporates a forecast model with three fully coupled components for the atmosphere, land surface, and ocean waves. Interim incorporates many important model improvements such as resolution and physics changes, the use of four-dimensional variational (4D-Var) data assimilation, and various other changes in the analysis methodology. A key objective was to address several difficult data assimilation problems encountered in ERA-40, mostly related to the use of satellite data, resulting in an improved representation of the hydrological cycle, a more realistic stratospheric circulation, and better temporal consistency on a range of time-scales (Dee et al., 2011).

The Modern Era Retrospective-Analysis for Research and Applications (MERRA) has recently been produced by the National Aeronautics and Space Administration's (NASA) Global Modeling and Assimilation Office (GMAO). The objectives of MERRA are to provide a climate context for the NASA satellite observing system and to improve the representation of the water cycle in reanalyses. MERRA was made using the data assimilation system component of the Goddard Earth Observing System and covers the modern satellite era from 1979 to the present. The assimilation system utilizes the GEOS model, version 5 (GEOS-5), a finite-volume atmospheric general circulation model (AGCM) that is used for routine numerical weather prediction. MERRA uses a 3D-Var analysis algorithm based on the Grid point Statistical Interpolation scheme with a 6-h update cycle. The GSI originally developed at NCEP and now jointly developed by NCEP and the GMAO includes a number of advancements over the previously used 3D-Var algorithms. MERRA was run in three separate data streams, each of which was initialized with spun up states from a long climate model simulation, then two years of coarse-resolution data assimilation followed by at least four years of data assimilation for the last two data streams (Rienecker et al., 2011; Bosilovich et al., 2011). Furthermore, the analysis system used in CFSR (Climate Forecast System reanalyses) for the atmosphere, the Gridpoint Statistical Interpolation (GSI) scheme, is nearly the same as the one used by MERRA at NASA GSFC, and GEOS-5 uses an incremental analysis update (IAU) procedure in which the analysis correction is applied to the forecast model gradually. The CFSR dataset succeeds the widely used NCEP–NCAR reanalyses. The novelties of these reanalyses are the coupling to the ocean during the generation of the 6-h guess field, an interactive sea ice model, and the assimilation of satellite radiances for the entire period (Saha et al., 2010). CFSv2 (Climate Forecast System version 2) was the extended product of the CFSR data (Yuan et al., 2013).

The Objectively Analyzed Air-sea Heat Fluxes (OAFlux) project products are constructed not from a single data source, but from an optimal blending of satellite retrievals and three atmospheric reanalyses (NCEP-R1, NCEP-R2, and ERA-40). Daily fluxes are computed from the optimally estimated variables using the COARE bulk flux algorithm 3.0. Subsequent evaluation revealed good agreement with *in situ* buoy data (Trenberth et al., 2011). The HOAPS (Hamburg Ocean Atmosphere Parameters and Fluxes from Satel-

lite Data), based on SSM/I data, provides turbulent fluxes, and the latest HOAPS-3 update covers the period from 1987. Daily and monthly products of latent heat fluxes at 1° resolution provided by the GSSTF data have been updated in 2010 (Andersson et al., 2011).

Reanalyses combine model fields with observations distributed irregularly in space and time into a spatially complete gridded meteorological dataset, with an unchanging model and analysis system spanning the historical data record (Xu et al., 2001). These reanalyses can be used to analyze the global climate system, atmosphere, and land surface processes on large to continental scales and to understand exchange processes between these different regimes. However, the beginning times of the eight reanalyses were inconsistent and the spatial distribution was not uniform (Table 1), which would cause a certain impact on the continuity of the reanalyses in time and space. For example, some reanalyses cover the satellite period from 1979 to the present, while ERA-40 covers the period of 1957–2002. Furthermore, the assimilation of humidity information in ERA-40 led to excessive rainfall over tropical oceans and a generally poor representation of the global transport of moisture in the atmosphere (Hagemann et al., 2005). In order to obtain accurate results, it is necessary to validate the eight different reanalyses. Therefore, we analyzed the similarities and differences of the spatial-temporal variation of evaporation obtained from the eight reanalyses, and discussed their applicability at different regional scales in different time scales.

### 1.2 Computation of evaporation

Note that MERRA, Interim, and ERA-40 also provide the sublimation fields. However, NCEP-R1, NCEP-R2, and CFSR did not provide the evaporation fields. Therefore, these fields can be computed from latent heat flux, which is given in energy flux form. Evaporation is the process of a liquid becoming vaporized, as the phase change of water vapor needs to absorb energy, which is namely the latent heat of evaporation $L_e$ (J kg$^{-1}$), and will change with the temperature (Jacobson et al., 2007). The latent heat flux $\lambda E$ (W m$^{-2}$) that could be transformed into units of mm was performed via (Jacobson et al., 2007; Lorenz et al., 2012):

$$E = \frac{\lambda E}{L_e}. \tag{1}$$

On the other hand, the evaporation generated by the sublimation of water in solid forms such as ice and snow should be considered at the same time, and eq. (1) can be further written as

$$E = \frac{\lambda E}{L_e} + \frac{\lambda S}{L_s}, \tag{2}$$

where $\lambda S$ is the sublimation (W m$^{-2}$), and $L_s$ indicates the latent heat of sublimation (J kg$^{-1}$). The data such as latent heat flux and sublimation, as well as land surface temperature and SST, are all at daily time scale in NCEP-R1, NCEP-R2, and CFSR, and the daily mean evaporation corresponding to the above datasets was calculated according to eq. (2).

### 1.3 Methodology

For the validation of the reanalyses evaporation estimates, all fields were remapped to the resolution of the ERA-40 dataset (2.5°×2.5°) using the bilinear interpolation method. The bilinear interpolation is an extension of linear interpolation for interpolating functions of two variables (e.g., $x$ and $y$) on a regular 2D grid. The key idea is to perform linear interpolation first in one direction, and then again in the other direction. Although each step is linear in the sampled values and in the position, the interpolation as a whole is not linear but rather quadratic in the sample location. In computer vision and image processing, bilinear interpolation is one of the basic resampling techniques, and the interpolation result is able to maintain the continuity of the original field effectively. In order to compare the differences among the evaporation values among the datasets, the mean absolute difference MAD and deviation MD were calculated, which are defined as (Zhu et al., 2012):

$$\mathrm{MAD} = \left[\sum_{i=1}^{n} |x_i - y_i|\right] \Big/ n, \tag{3}$$

$$\mathrm{MD} = \left[\sum_{i=1}^{n} x_i - y_i\right] \Big/ n, \tag{4}$$

where $x$ and $y$ are the evaporation values of the different reanalyses, and $i$ indicates the grid point number.

The climate tendency coefficient can quantitatively describe the inter-decadal variation of meteorological elements, and test the climate tendency coefficient by using the common correlation coefficient statistical test method or Monte Carlo Method (Shi et al., 2003). Similarly, the climate tendency rate can represent the variation rate of the meteorological factors every 10 a (Shen et al., 2008). The climate tendency coefficient and the climate tendency rate of annual mean values are computed in order to quantify long-term changes of the evaporation.

The correlation coefficient can give a measure of the strength and direction of the linear relationship between two variables, which is defined as the (sample) covariance of the variables divided by the product of their (sample) standard deviations. In addition, in order to analyze the agreement of spatial patterns between two datasets, spatial similarity coefficient and the least square fitting method are used for further analysis (Shi et al., 2009).

## 2 Spatial distribution of global evaporation

This section depicts the 1981–2010 mean values of evaporation from the eight different reanalyses, and analyzes the main spatial characteristics of global evaporation. In view of data availability, we also compute the mean absolute difference MAD and deviation MD of global mean evaporation (referred to as $E_G$), land mean evaporation (referred to as $E_L$), and mean evaporation over the oceans (referred to as $E_O$).

### 2.1 Distribution of long-term mean evaporation

As shown in Figure 1, the spatial distribution of global evaporation obtained from different reanalyses is in good agreement over most regions, with the following four main characteristics: first, there were significant differences in the evaporation over the land and oceans. Actual evaporation depends on the availability of water, and therefore more water is evaporated from oceans than from dry soil in general, as most of the evaporation over the oceans remained 3–7 mm $d^{-1}$, and the land evaporation stayed at 1–3 mm $d^{-1}$,

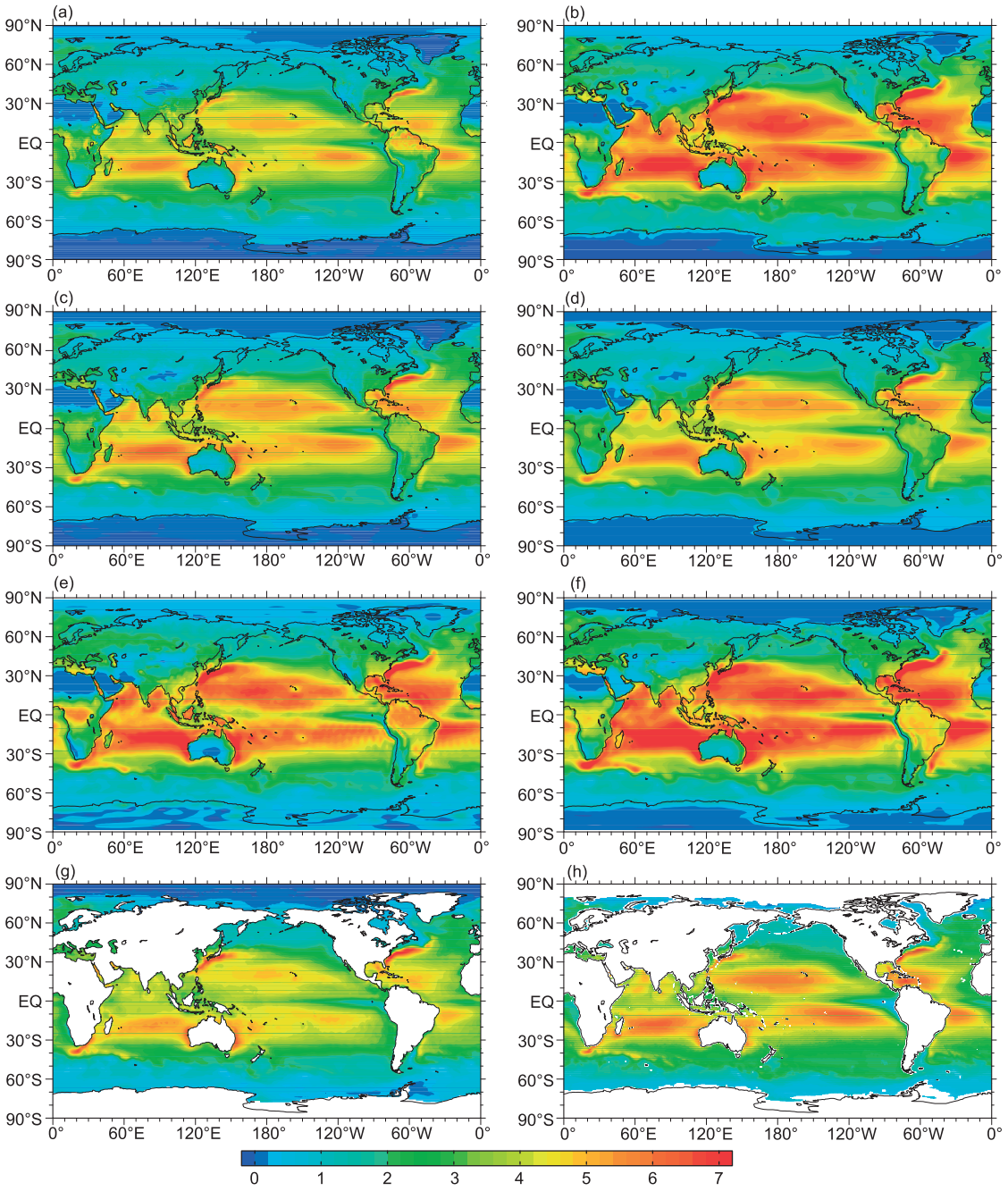


**Figure 1** Long-term mean annual evaporation from MERRA (a), CFSR (b), Interim (c), ERA-40 (d), NCEP-R1 (e), NCEP-R2 (f), OAFlux (g), and HOAPS (h) (unit: mm $d^{-1}$).

with approximately 2–3 times the difference. Humid regions like tropical rain forests have higher evaporation rates than arid regions. Evaporation is the process of a liquid becoming vaporized. In other words, a change in phase in the atmosphere occurs when substances change from a liquid to a gaseous (or vaporous) form. Evaporation in the atmosphere is a crucial step in the water cycle. Water on the Earth's surface will evaporate into the atmosphere as energy is absorbed by liquid water. Water in the soil can be absorbed by plants and is then transferred to the atmosphere by a process known as transpiration. Water from the soil can also be evaporated into the atmosphere. These processes are collectively known as evapotranspiration. The evaporation of water from soil is controlled mainly by the available energy and the soil moisture conditions. Compared with the water surface evaporation, the amount of water that evaporates from the land surface depends on the amount that is contained in the soil, which is the main reason for the large difference in the evaporation over ocean and land. On the ice-free oceans, the rate of evaporation depends mainly on factors such as saturated vapor pressure difference, air saturation deficit, wind speed, temperature, and relative humidity (Zuo et al., 2005; Ren et al., 2006). Second, the global evaporation showed the characteristics of meridional distribution, evaporation decrease from the equator toward the poles. The values of evaporation over oceans between the Equator to the latitudes of 30°S and 30°N are generally over 5 mm $d^{-1}$, while less than 0.5 mm $d^{-1}$ in the polar regions. This is consistent with the distribution of global energy, indicating that the evaporation is highly dependent on energy. Third, the land evaporation generally decreases with the increase of altitude, such as the Qinghai-Tibet Plateau, the Mongolia Plateau, the Iran Plateau, the Arabia Plateau, the East African Plateau, the Rocky Mountains, the Mexico Plateau, and the Andes, because the atmospheric temperature would decrease with the increase of elevation. The physical processes of evaporation and transpiration require a large amount of energy, which is why the evaporation in the high altitude areas was relatively small. Finally, the evaporation over the oceans in the equatorial regions was smaller than that in the areas on either side, whereas the land showed the opposite effect, which also reflected the important influence of the underlying surface physical conditions on the evaporation.

### 2.2 Differences of evaporation from the eight reanalyses

In order to demonstrate major differences between the datasets, this section takes the average values of the long-term mean evaporation obtained from the eight reanalyses (referred to as AVE), and then calculates the differences between the AVE and the eight reanalyses, as well as the similarity coefficient on every latitude circle (Figure 2). Figure 2(a) shows that the differences between MERRA and AVE mainly in the ocean, especially in the low latitude regions between the Equator to 30°S and 30°N, such as the southeastern coast of China, eastern American Ocean, and coast of Australia, have a negative bias of about 1 mm $d^{-1}$. The land evaporation differences are located mainly in the south-central South America. The similarity coefficients on every latitude circle are all above 0.9, indicating that the spatial distribution of MERRA is consistent with the AVE. Over the tropical Pacific, the USA, Japan, the east coast of Brazil, and the Somali Peninsula and its western region, significant positive biases in CFSR are found. The Interim evaporation estimates seem to have a negative bias especially in the land, such as southern China, North America, northern South America, and the Eastern European Plain. ERA-40 and Interim exhibit similar biases in addition to the Congo Basin. A significant positive bias between NCEP-R1 and AVE can be observed over the Congo Basin and its surrounding area, southern China, eastern USA, central and northern South America, and the Tropical Ocean. Comparison of evaporation estimates from the eight reanalyses reveals that the large differences between NCEP-R2 and the AVE, especially in the oceans at the middle and low latitudes, show a positive bias of about 2 mm $d^{-1}$, and even so, their spatial distribution is still highly consistent. OAFlux has a negative bias that extends over most of the oceans, while the differences between HOAPS and the AVE are distributed mainly over the Pacific around 30°N and 30°S. In general, the major differences between the datasets are located mainly in the tropical Pacific, southern China, northern North America, the Eastern European Plain, the Congo Basin, and south-central South America.

Table 2 shows the spatial MAD (absolute difference) and MD (deviation) of $E_G$, $E_L$, $E_O$, and AVE from the eight reanalyses. For $E_G$, Interim shows the lowest MAD (~0.195 mm $d^{-1}$) and MD (~ −0.166 mm $d^{-1}$); the error rate was approximately 6%; thus its spatial distribution was closest to the AVE. In contrast, the differences between NCEP-R2 and the AVE are significant with a high spatial MAD (~0.525 mm $d^{-1}$) and MD (~0.486 mm $d^{-1}$). For $E_L$, MERRA and CFSR match well with the AVE with an average spatial MAD (~0.225 mm $d^{-1}$, ~0.206 mm $d^{-1}$, respectively) and MD (~0.107 mm $d^{-1}$, ~0.115 mm $d^{-1}$, respectively), whereas NCEP-R1 shows MAD of ~0.364 mm $d^{-1}$ and MD of ~0.313 mm $d^{-1}$. Interim and ERA-40 agree better with the AVE of $E_O$, resulting in a low spatial MAD (~0.170 mm $d^{-1}$, ~0.162 mm $d^{-1}$, respectively) and MD (~0.155 mm $d^{-1}$, ~0.132 mm $d^{-1}$, respectively). However, the greatest differences in spatial variability can be found between NCEP-R2 and the AVE.

To analyze the agreement of spatial patterns between two datasets, the least-square linear fitting method is used for further analysis. The average values of variance explained by the linear fitting among the eight different reanalyses were all above 0.89 (Figure 3). This indicates that the spatial distribution of the evaporation obtained from the different

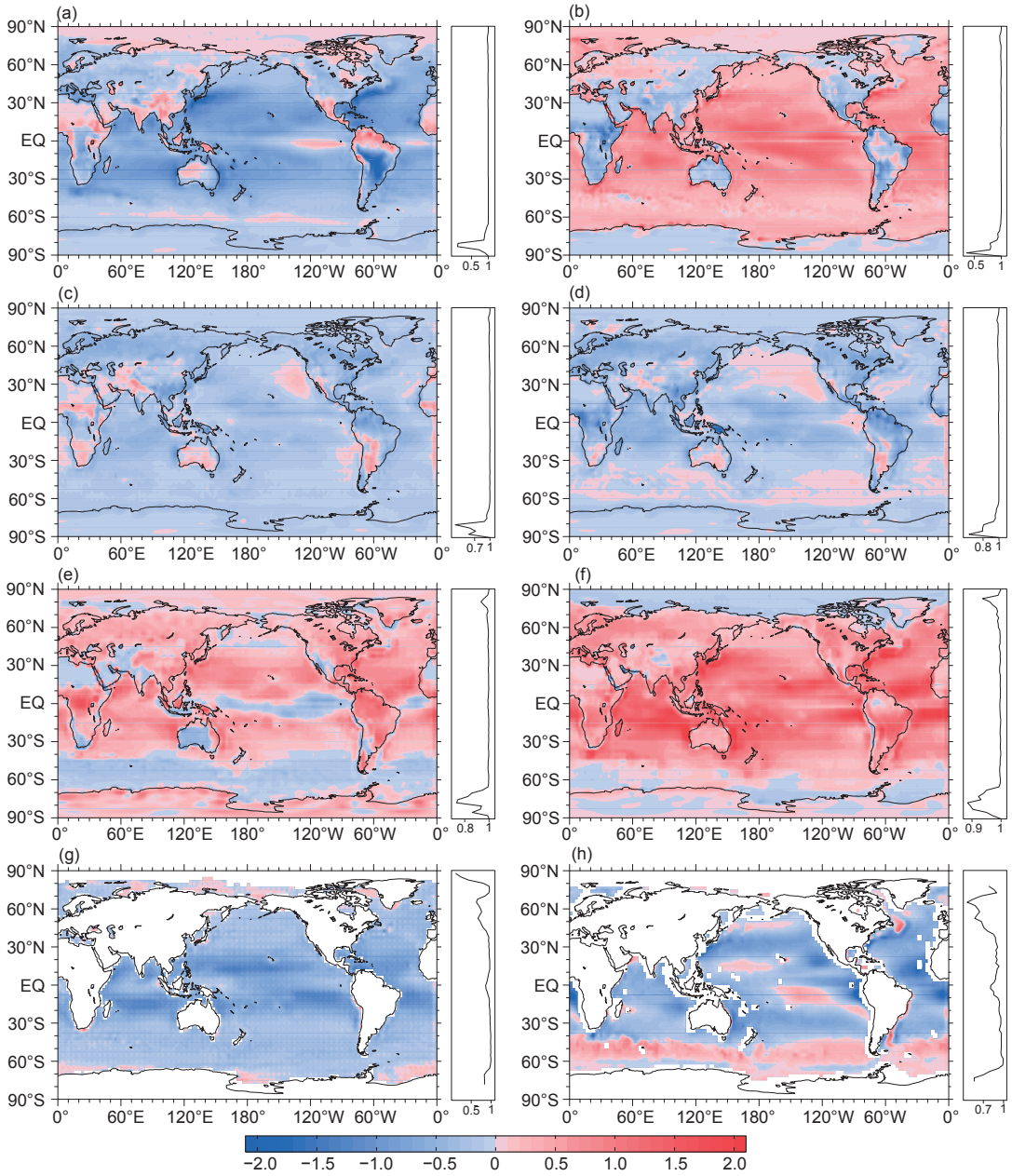


**Figure 2** Differences of the mean annual evaporation between AVE and MERRA (a), CFSR (b), Interim (c), ERA-40 (d), NCEP-R1 (e), NCEP-R2 (f), OAFlux (g), and HOAPS (h). Unit: mm $d^{-1}$; similarity coefficient on every latitude circle is given to the right of each panel.

**Table 2** MAD and MD of $E_G$, $E_L$, $E_O$ between average value (AVE) and MERRA, CFSR, Interim, ERA-40, NCEP-R1, NCEP-R2, OAFlux, and HOAPS (unit: mm $d^{-1}$)

| | $E_G$ | | $E_L$ | | $E_O$ | |
|---|---|---|---|---|---|---|
| | MAD | MD | MAD | MD | MAD | MD |
| MERRA | 0.362 | −0.308 | 0.225 | −0.107 | 0.432 | −0.410 |
| CFSR | 0.408 | 0.293 | 0.206 | −0.115 | 0.511 | 0.502 |
| Interim | 0.195 | −0.166 | 0.245 | −0.187 | 0.170 | −0.155 |
| ERA-40 | 0.197 | −0.168 | 0.267 | −0.239 | 0.162 | −0.132 |
| NCEP-R1 | 0.323 | 0.236 | 0.364 | 0.313 | 0.302 | 0.198 |
| NCEP-R2 | 0.525 | 0.486 | 0.347 | 0.332 | 0.616 | 0.565 |
| OAFlux | | | | | 0.405 | −0.374 |
| HOAPS | | | | | 0.431 | −0.261 |

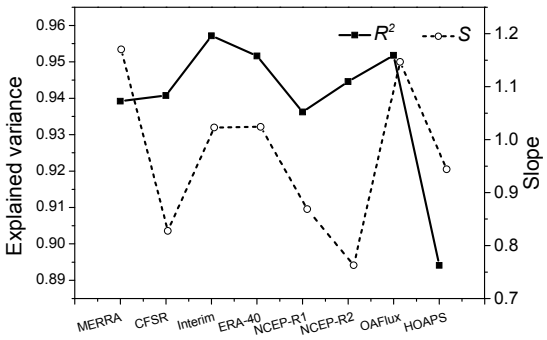


**Figure 3** Average values of linear fitting variance explained ($R^2$) and slope ($S$) for spatial distribution of evaporation between different reanalyses.

reanalyses was in good agreement. Interim agrees best with the other datasets, it shows the highest average values of variance explained (approximately 0.96), and the average values of the linear fitting slope was close to 1, demonstrating that interim could represent the spatial distribution of the global evaporation to a certain degree. In addition, the OAFlux average value of the variance explained reaches 0.952, and the average value of the slope is 1.15, indicating that it has good representativeness on the spatial distribution of evaporation over the oceans.

## 3 Temporal variation of global evaporation

### 3.1 Time evolution of global evaporation

Time series of annual mean evaporation for the globe, ocean, and land domain from the eight different reanalyses are given in Figure 4. It can be seen from Figure 4(a) that MERRA, Interim, NCEP-R1, and NCEP-R2 show a roughly similar behavior, whereas CFSR agrees quite well with ERA-40. The MERRA values are quite small and have significant inter-decadal variations. $E_G$ is about 2.56 mm $d^{-1}$ in 1979, then begins to gradually increase, and peaks in 1998 (~2.73 mm $d^{-1}$), after which there is a steady decrease up until 2011. Interim and MERRA are in good agreement except the Interim values are slightly higher. Only NCEP-R1 is available since the 1940s, according to this dataset, $E_G$ gradually increases in 1948–1961, then decreases in 1963–1979, and subsequently increases again after 1980. ERA-40 is broadly similar to NCEP-R1 from 1958 to 1979, but agrees better with CFSR after 1979. CFSR shows high amplitude of intra-annual variation, and there is no significant trend during 1979–2010. However, NCEP-R2 is characterized by substantial inter-decadal variations and a positive long-term trend.

Figure 4(b) shows the time series of annual mean evaporation for the land domain. The MERRA values are quite stable and have no significant trends, around approximately 1.7 mm $d^{-1}$. CFSR and NRCP-R2 are in good agreement with MERRA, but they showed significant inter-annual variations. The Interim values appear to be very stable. ERA-40 gives an overall increase trend in 1958–2002, and these trends are significant and statistically consistent. NCEP-R1 also shows significant inter-decadal variation.

According to Figure 4(b), the intra-annual variation of the evaporation over the oceans has similar overall features to the global mean evaporation (Figure 4(a)). MERRA, Interim, NCEP-R1, NCEP-R2, and OAFlux are in good agreement, and inter-annual fluctuations are also quite consistent among these datasets. ERA-40 is similar to NCEP-R1 before 1979, but shows a significant difference after 1979. The HOAPS values remained constant in 1987–1990, followed by a rapid decrease in 1991, and then increased significantly since 1992.

The black dashed line in Figure 4 shows the average value (AVE) of the evaporation obtained from the eight reanalyses. The correlation coefficients between the AVE and the eight reanalyses are shown in Table 3. The global, continental, and oceanic MERRA and NCEP-R2 evaporation values are in very good agreement with the AVE, with

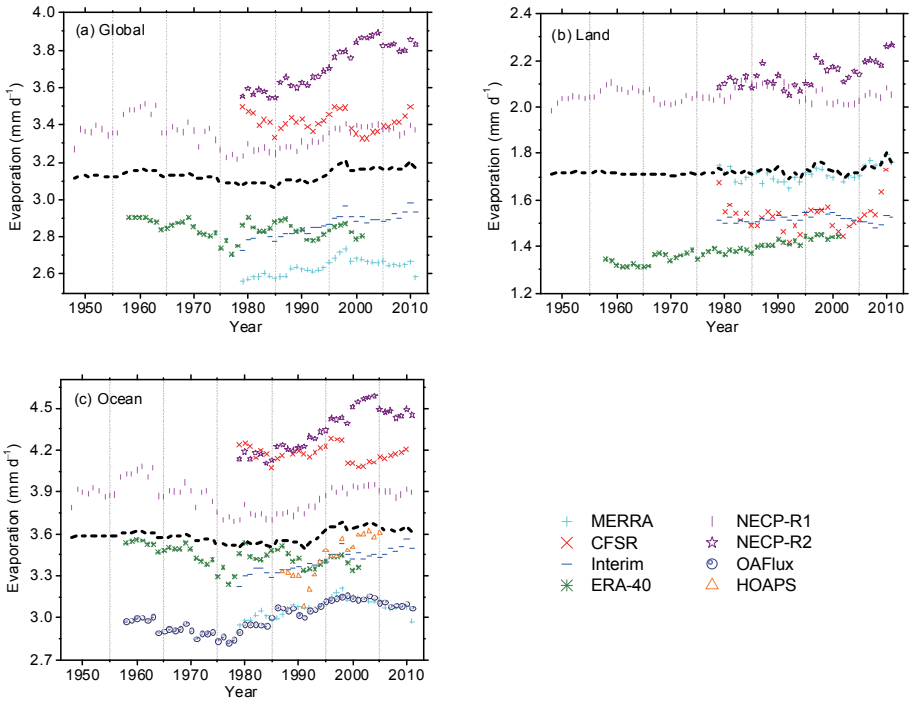


**Figure 4** Time series of $E_G$ (a), $E_L$ (b), and $E_O$ (c) from MERRA, CFSR, Interim, ERA-40, NCEP-R1, NCEP-R2, OAFlux, and HOAPS. Black dashed lines indicate the average value.

**Table 3** Time correlation coefficient ($\rho_G$, $\rho_L$, $\rho_O$) in mean annual $E_G$, $E_L$ and $E_O$ between AVE and MERRA, CFSR, Interim, ERA-40, NCEP-R1, NCEP-R2, OAFlux, HOAPS [a)]

| Reanalysis | $\rho_G$ | $\rho_L$ | $\rho_O$ |
|---|---|---|---|
| MERRA | 0.835 | 0.785 | 0.753 |
| CFSR | 0.158 | 0.810 | −0.004 |
| Interim | 0.927 | 0.351* | 0.851 |
| ERA_40 | 0.409 | 0.562 | 0.330* |
| NCEP_R1 | 0.773 | 0.230 | 0.765 |
| NCEP_R2 | 0.919 | 0.813 | 0.931 |
| HOAPS | | | 0.939 |
| OAFlux | | | 0.716 |

a) _ passing the inspection of 0.01 credibility, * passing the inspection of 0.05 credibility.

**Table 4** Long-term mean $E_G$, $E_L$, $E_O$ ($\mu$) and the standard deviation ($\sigma$) (unit: mm $d^{-1}$)

| | $E_G$ | | $E_L$ | | $E_O$ | |
|---|---|---|---|---|---|---|
| | $\mu$ | $\sigma$ | $\mu$ | $\sigma$ | $\mu$ | $\sigma$ |
| MERRA | 2.64 | 0.04 | 1.71 | 0.03 | 3.07 | 0.06 |
| CFSR | 3.41 | 0.05 | 1.53 | 0.06 | 4.17 | 0.06 |
| Interim | 2.86 | 0.06 | 1.52 | 0.02 | 3.40 | 0.08 |
| ERA-40 | 2.85 | 0.05 | 1.38 | 0.04 | 3.44 | 0.08 |
| NCEP-R1 | 3.35 | 0.07 | 2.05 | 0.03 | 3.87 | 0.10 |
| NCEP-R2 | 3.72 | 0.12 | 2.14 | 0.05 | 4.34 | 0.15 |
| OAFlux | | | | | 3.01 | 0.10 |
| HOAPS | | | | | 3.43 | 0.15 |
| AVE | 3.13 | 0.033 | 1.722 | 0.018 | 3.585 | 0.047 |

the correlation coefficients all being greater than 0.75 (statistically significant). CFSR agrees well with the AVE over land with a correlation coefficient >0.8, while CFSR evaporation for the globe and ocean domain shows deviations from the AVE. In contrast, Interim and NCEP-R1 are consistent with the AVE for $E_G$ and $E_O$, but show a large difference for $E_L$. The ERA-40 $E_G$, $E_L$ and $E_O$ values are similar to the AVE, but with a generally lower correlation. HOAPS and OAFlux show a reasonable agreement with the AVE, indicating that HOAPS and OAFlux could reveal the temporal variation characteristics of the evaporation over the oceans to a certain extent.

The correlation coefficients between the eight different reanalyses are also computed, the global MERRA, Interim, NCEP-R1 and NCEP-R2 evaporation values are highly consistent, while CFSR agrees better with ERA-40. Over land, MERRA, CFSR, and NCEP-R2 show similar features, while Interim, ERA-40, and NCEP-R1 are very different from them. In contrast to the evaporation over land, the MERRA, Interim, NCEP-R1, NCEP-R2, OAFlux, HOAPS, and ERA-40 evaporation values over oceans are in very good agreement. In general, it can be concluded that the evaporation over oceans estimates are in much better agreement than the land evaporation.

### 3.2 Long-term mean annual evaporation

Table 4 shows the annual mean ($\mu$) and standard deviation ($\sigma$) of the evaporation for the globe, ocean, and land domain. The global mean evaporation ($E_G$) values obtained from different data sources are ordered from largest to smallest as follows: NECR-R2, CFSR, NCEP-R1, Interim, ERA-40, and MERRA, in which NCEP-R2 shows the largest standard deviation up to 0.12 mm $d^{-1}$, while the smallest is MERRA (about 0.04 mm $d^{-1}$), indicating the global mean evaporation values are quite stable and have no significant inter-annual variation. The global mean evaporation values over land ($E_L$) are ordered from largest to smallest as follows: NECR-R2, NCEP-R1, MERRA, CFSR, Interim, and ERA-40, which ranges from 1.52 to 2.14 mm $d^{-1}$, and CFSR had the largest standard deviation. The global mean evaporation values over oceans ($E_L$) are ordered from largest to smallest as follows: NECR-R2, CFSR, NCEP-R1, ERA-40, HOAPS, Interim, MERRA, and OAFlux. In addition, note that the order of $E_G$, $E_L$, and $E_O$ obtained from the eight reanalyses was inconsistent, the MERRA $E_G$ value was smallest, but the MERRA $E_L$ value was relatively large. The proportions of evaporation over the oceans in the global total evaporation were respectively 80.8%, 86.8%, 84.8%, 86.1%, 82.4%, and 83.6% , with an average value of approximately 84.1%, which implies that the oceans are the source of 84.1% of the global evaporation and are a key component of the global water cycle. As noted above, the annual mean and standard deviations of the evaporation obtained from different reanalyses show certain differences; evaporation is generally higher in NCEP2 than that of the other datasets, which was mainly because NCEP-R2 generally has a higher latent heat flux (Betts et al., 2006), resulted in an overestimation of the evaporation. This indicates that the quality of the reanalyses still requires further improvement, and it is necessary to correct the systematic measuring errors of the reanalyses. These biases in the climatology of the reanalyses, as well as the uncertainties in the data sets which we have compared them with, must be considered by users.

### 3.3 Long-term mean evaporation changes

We now explore long-term global evaporation changes for the period since 1958. For the period of 1979–2011, a variety of evaporation data sources are available. However, only the NCEP-R1, ERA-40, and OAFlux datasets are available going back to the 1950s (Table 1). As shown in Table 5, all datasets show a decrease in evaporation over the oceans during 1958–1978, while the evaporation over land shows a significant increase trend in ERA-40, with a significant decrease trend in NCEP-R1. In contrast, the linear trend of the evaporation varies significantly among datasets for the periods of 1979–2011, the evaporation for the globe and ocean domain in MERRA, NCEP-R2, Interim and NCEP-R1 shows a significant linear increase, while ERA-40 is characterized by a negative long-term trend. In addition, the

**Table 5** Linear trends of annual mean $E_G$, $E_L$, $E_O$ for the periods of 1959–1978 and 1979–2011 using various datasets [a)]

| Reanalysis | $E_G$ | $E_L$ | $E_O$ |
|---|---|---|---|
| 1958–1978 | | | |
| ERA-40 | −0.863 | 0.755 | −0.891 |
| NCEP-R1 | −0.898 | −0.708 | −0.881 |
| OAFlux | | | −0.863 |
| AVE | −0.916 | −0.008 | −0.907 |
| 1979–2011 | | | |
| MERRA | 0.627 | 0.458 | 0.515 |
| CFSR | −0.158 | 0.073 | −0.235 |
| Interim | 0.888 | 0.101 | 0.904 |
| ERA-40 | −0.425* | 0.930 | −0.577 |
| NCEP-R1 | 0.857 | −0.456 | 0.837 |
| NCEP-R2 | 0.917 | 0.660 | 0.898 |
| OAFlux | | | 0.757 |
| HOAPS | | | 0.852 |
| AVE | 0.848 | 0.379* | 0.804 |

a) _ passing the inspection of 0.01 credibility, * passing the inspection of 0.05 credibility.

evaporation over land in MERRA, ERA-40, and NCEP-R2 also shows a significant trend of linear increase, but this is in a marked contrast to NCEP-R1 with a trend coefficient of −0.456. Besides, there are no significant trends in CFSR and Interim. Hence, the evaporation obtained from the eight reanalyses shows a significant trend of linear decrease in 1958–1978, while showing a significant increase in 1979–2011.

### 3.4 Linear trends for evaporation during 1979–2011

Long-term mean evaporation changes for the period of 1979–2011 are presented in Figure 5. As discussed in section 3.3, decadal variations characterize the low-frequency variability of the global evaporation during 1979–2011. These are quite similarly represented in the various datasets. MERRA displays increases over northwestern China, the middle and lower reaches of the Yangtze River, the East African Plateau, the South African Plateau, south-central South America, northern Australia, the Mediterranean, the central Pacific Ocean at low southern latitudes, and the central north Atlantic waters. According to CFSR, these regions showed a significant trend, such as the central Pacific Ocean, the western Peru Sea, the central north Atlantic waters, the Arabian Sea, and the Mediterranean, as well as the waters off eastern Brazil between the Equator and 30°S, with the climate tendency rate of at least 0.4 mm $d^{-1}$ $decade^{-1}$; similar to MERRA, the evaporation over the middle and lower reaches of the Yangtze River and areas near the Lake Baikal increase significantly. Interim evaporation trends give similar patterns of change as those described above, except a broader space distribution; the Mediterranean, the tropical Pacific, the Indian Ocean, and some parts of the Atlantic Ocean see an increase of at least 0.2 mm $d^{-1}$ $decade^{-1}$. Over land, annual mean increases are found mainly in Eurasia, the Congo Basin, Midwestern USA, as well as southwest China and the middle and lower reaches of the Yangtze River. It can be seen from Figure 5(d) that the spatial pattern of the linear evaporation trend in ERA-40 is mainly distributed in the tropical Pacific, the tropical Indian Ocean, the central Atlantic Ocean, Western Europe, the Congo Basin, and the Lake Baikal extending to its northern area. NCEP-R1 and NCEP-R2 evaporation give similar results, and there are significant evaporation trends over the oceans, except that NCEP-R2 displays significant increases in northeastern North America, South Africa, and the South Peninsula. Based on OAFlux (Figure 5(g)), there is a significant linear trend of evaporation over the southeastern coast of China, the Mediterranean, the Pacific Ocean near Hawaii, the tropical Indian Ocean, and the tropical Pacific. During 1987–2005, HOAPS behavior is quite similar to that depicted by the other datasets, and evaporation is seen to increase significantly over the Subtropical oceans, with the climate tendency rate exceeding 0.4 mm $d^{-1}$ $decade^{-1}$.

Overall, the greatest annual evaporation increases during 1979–2006 can be seen over the oceans, such as the central Pacific Ocean, the tropical Indian Ocean, the central North Atlantic, the Mediterranean, and the Northwest Pacific Ocean. The amplitude of the variations for the evaporation over the land tends to be generally smaller, and there are significant linear trends over the Lake Baikal and its surrounding areas, the Congo Basin, the Amazon Basin, and the middle and lower reaches of the Yangtze River.

## 4 Annual cycle results

The earth seasonal climate variation occurs as a result of minute changes in our planet's distance from the sun during orbit; therefore, the seasonal and latitudinal distribution of solar radiation received at the Earth's surface also varies. Solar radiation is more than the light and heat that we perceive from the sun. Solar radiation and temperature are the thermal sources that cause water to evaporate from the earth's surface (Liu, 2011). The climatological annual cycle characteristics of global evaporation will be given in this section.

### 4.1 Annual cycle of zonal mean evaporation

As discussed in section 2.1, the global evaporation showed the characteristics of meridional distribution. And to show this, we take zonal means evaporation of the various fields that have gone into these figures (Figure 6) and contrast the results from the eight different reanalyses. Maps of the zonal mean evaporation show striking similarities, with the main characteristics as follows: the evaporation near the equator was approximately 4 mm $d^{-1}$, with a relatively small monthly difference, reaching the minimum from February to April, then increasing gradually, reaching the maximum from May to September, and decreasing again.

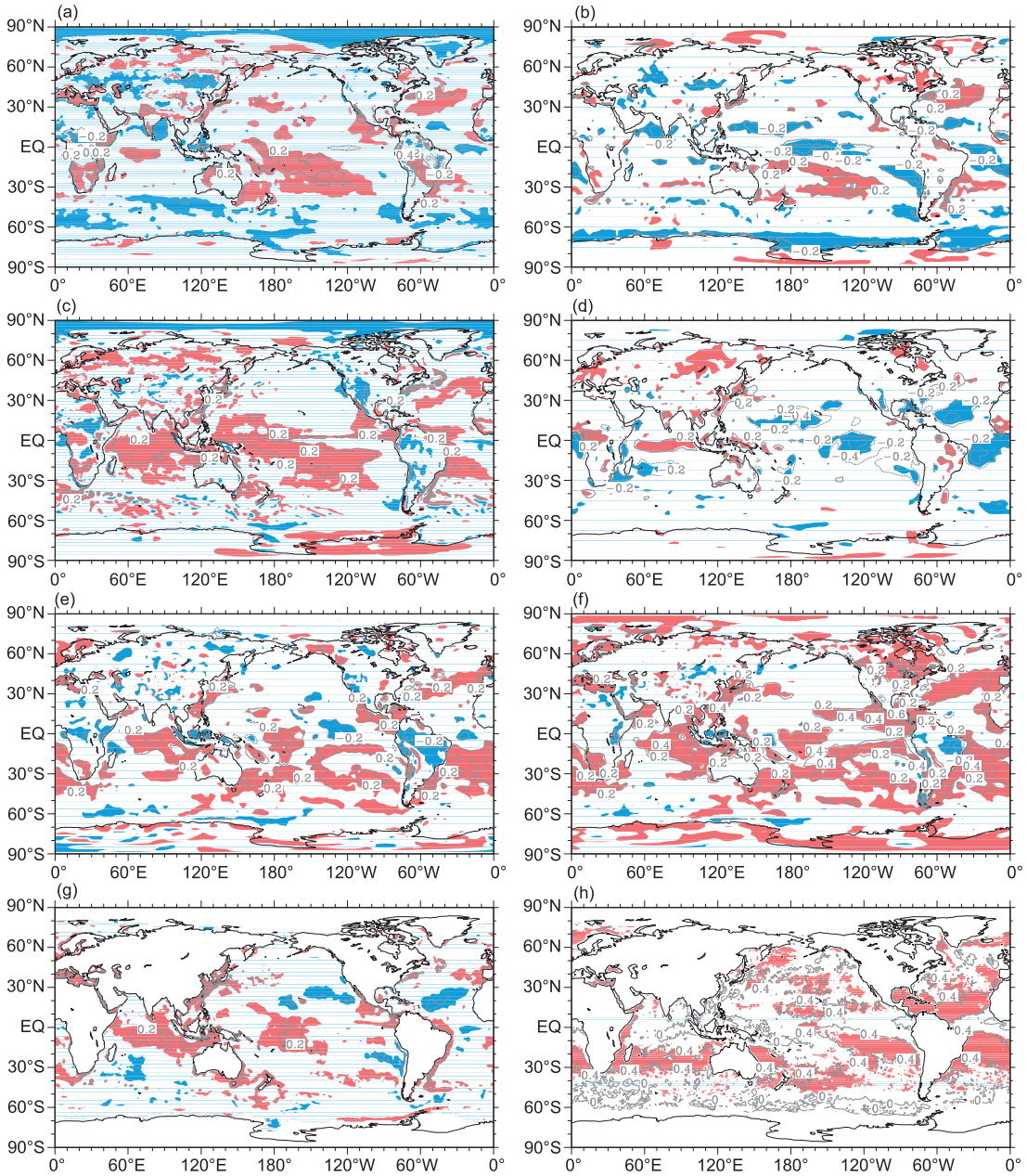


**Figure 5** Linear trends for evaporation for the period of 1979–2011 from MERRA (a), CFSR (b), Interim (c), ERA-40 (d), NCEP-R1 (e), NCEP-R2 (f), OAFlux (g), and HOAPS (h). Statistically significant results are in shadow; red indicates linear increase; blue indicates linear decrease; and the contour was the climate tendency rate (unit: mm $d^{-1}$ $decade^{-1}$).

The monthly variation of evaporation at the low latitudes in the Northern Hemisphere was significant, being large from November to February, and various sets of dataset were approximately 5 mm $d^{-1}$, then decreased gradually, at approximately 4 mm $d^{-1}$ from March to April, then increased slowly after May, and decreased once again after August. The monthly variation of evaporation at low latitudes in the Southern Hemisphere was small, increasing gradually from January to June, up to approximately 5 mm $d^{-1}$ from July to August, and even over 6 mm $d^{-1}$ in some areas in CFSR and NCEP-R2, and then decreasing gradually from August to September. The monthly variation of the evaporation at the middle latitudes in the Northern Hemisphere was similar to that of the low latitudes in the Southern Hemisphere, reaching the maximum from June to August, and being relatively small in the other months. For the middle latitudes in the Southern Hemisphere, the evaporation is fairly stable over time, reaching the maximum from May to July and changing little in the other months. The evaporation at high latitudes in both hemispheres was very small, without significant monthly variation, and the evaporation in June was the maximum in the Northern Hemisphere, whereas the maximum of the evaporation is in December in the Southern Hemisphere. Figure 6(g) and (h) shows the monthly variation

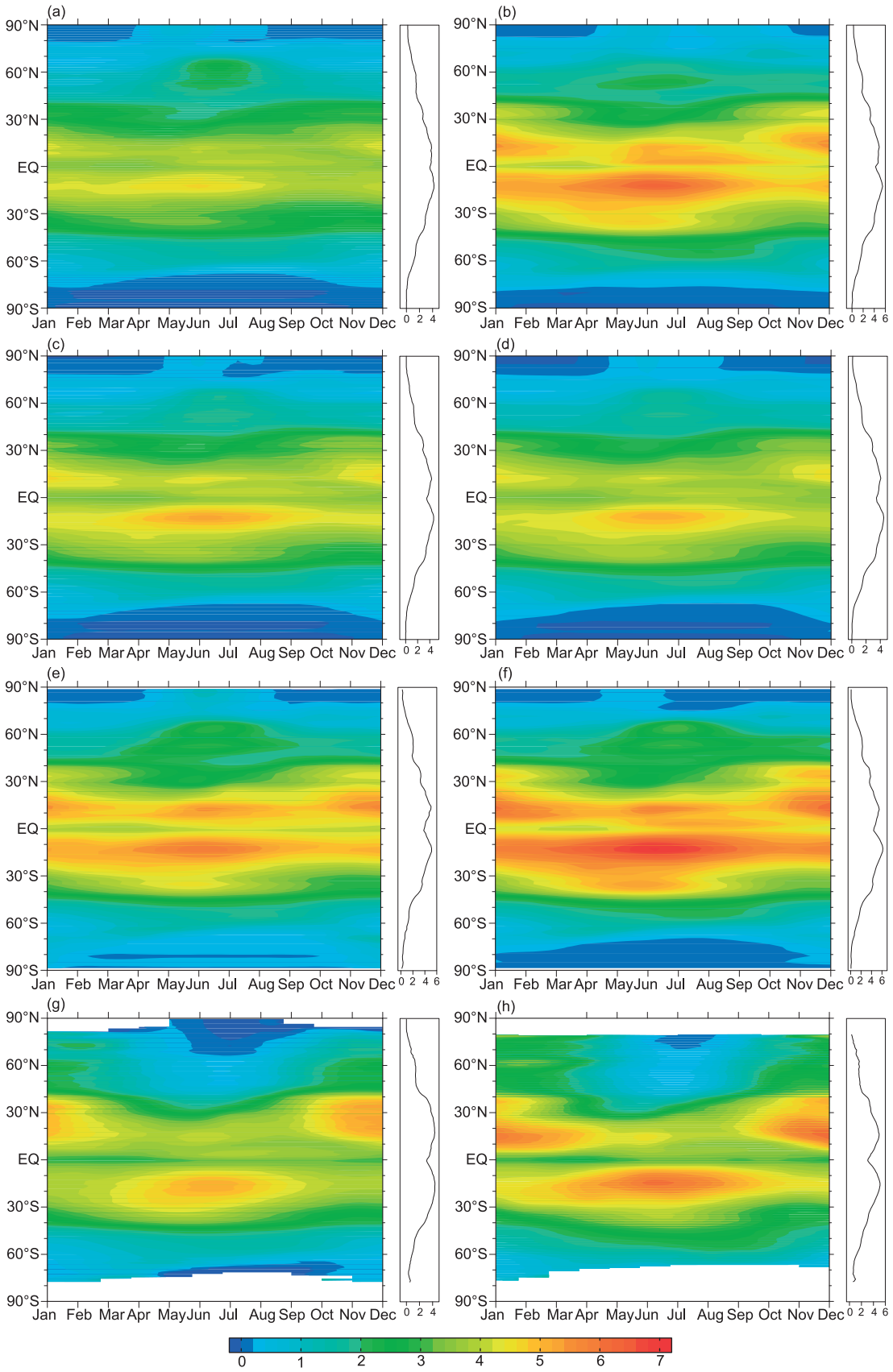


**Figure 6** Zonal mean evaporation for the climatological mean annual cycle from MERRA (a), CFSR (b), Interim (c), ERA-40 (d), NCEP-R1 (e), NCEP-R2 (f), OAFlux (g), and HOAPS (h) (unit: mm $d^{-1}$).

of the zonal mean evaporation over the oceans, quite similar to that depicted above. Despite the general similarity, differences exist at the mid-latitudes in the Northern Hemisphere especially, in which the evaporation was relatively high from November to February, and smaller from May to September. Overall, there are significant monthly variations of evaporation at different latitudes, especially at the low latitudes in the Northern Hemisphere, and the results obtained from the different reanalyses are in good agreement.

### 4.2 Monthly variations of evaporation

The climatological seasonal cycles of area-averaged evaporation for the globe, ocean, and land domain are given in this section. Figure 7 shows the monthly variation of $E_G$, $E_L$, and $E_O$ from the eight different reanalyses, and it can be seen from Figure 7(a) that the $E_G$ decreased from January to March, increased gradually from April to June, reaching the maximum in June and July, and then gradually decreased from July to October, followed by a slowly increased from October to December. The monthly variation amplitude of the $E_L$ was relatively large (Figure 7(b)) and consistent across the reanalyses. The monthly variations of the $E_L$ can be remarkably approximated by an inverted V-type, increasing gradually from January to June, reaching the maximum in June and July, and gradually decreasing from August to December. The climatological seasonal cycle of area-averaged evaporation for the ocean domain can be approximated by a W-type, there are three peaks in January, June, and December respectively and two troughs in April and September in CFSR, Interim, NCEP-R1, NCEP-R2, OAFlux, ERA-40, and HOAPS, and the difference between peaks and troughs are about 0.2 mm $d^{-1}$. In addition, the ERA-40 and HOAPS values are higher in June and July than that in January and December. MERRA is inconsistent with the other reanalyses in that the $E_O$ value was substantially lower in December. Therefore, the climatological annual cycles of $E_G$, $E_L$, and $E_O$ obtained from the eight different reanalyses presented significant characteristics. Moreover, the monthly variation amplitude of the $E_L$ was higher than that of the $E_O$.

## 5 Conclusions

Evaporation is an important process in the global water cycle, it involves many factors, and many material fluxes on the earth surface would have an impact on it. The global topography, vegetation, and climate conditions are diverse; climate and environmental forcing variables control energy and energy partitioning, so it is very difficult to estimate the evaporation value. Based on the eight different reanalyses, we have given a broad overview on the spatial-temporal characteristics of global evaporation, and a brief evaluation of the eight reanalyses is also given. The main conclusions can be outlined as follows.

(1) The spatial distributions of global evaporation obtained from different reanalyses are in good agreement over most regions; there were significant differences in the

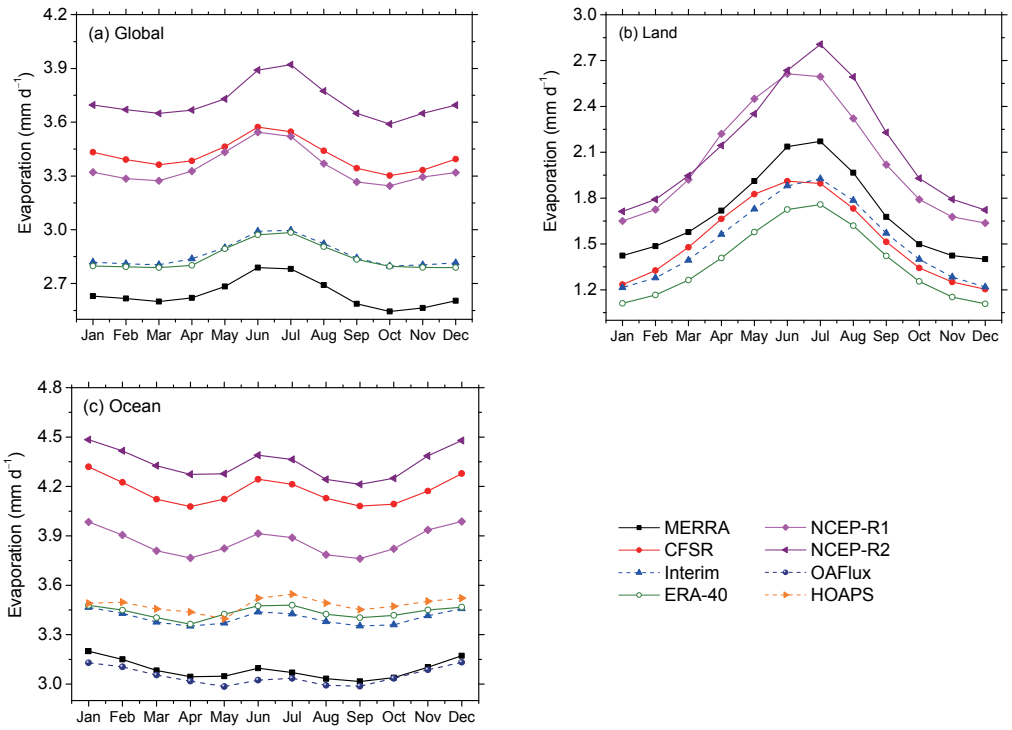


**Figure 7** Mean annual cycle of $E_G$ (a), $E_L$ (b), and $E_O$ (c) from different reanalyses.

evaporation over the land and oceans with a difference of approximately 2–3 times. The global evaporation showed the characteristics of meridional distribution, evaporation decrease from the equator toward the poles. The land evaporation generally decreases with the increase of altitude. In general, the major differences between the datasets are located mainly in the tropical Pacific, southern China, northern North America, the Eastern European Plain, the Congo Basin, and south-central South America.

(2) The time evolution of global evaporation varies significantly among the datasets, among which MERRA, Interim, NCEP-R1, and NCEP-R2 are highly consistent, while CFSR agrees better with ERA-40. Over land, MERRA, CFSR, and NCEP-R2 show similar features, while Interim, ERA-40, and NCEP-R1 are very different from them. In contrast to the evaporation over land, the MERRA, Interim, NCEP-R1, NCEP-R2, OAFlux, HOAPS, and ERA-40 evaporation values over oceans are in very good agreement. Overall, the estimates of evaporation over oceans are in much better agreement than those of the land evaporation.

(3) In general, MERRA and NCEP-R2 could appropriately reflect the spatial-temporal characteristics of global evaporation, showing strong representativeness. The CFSR and ERA-40 are capable of revealing the characteristics of land evaporation, whereas ERA-Interim, NCEP-R1, OAFlux, and HOAPS are relatively applicable for research focuses on the evaporation over the oceans.

(4) The annual mean evaporation of various sets of dataset shows a significant linear decrease trend in 1958-1978, and a linear increase throughout most of 1979–2011, especially over the oceans, such as the central Pacific Ocean at low southern latitudes, the equatorial India Ocean, the central north Atlantic waters, the Mediterranean, and southeastern coast of China; the areas with significant linear trends of land evaporation were located mainly in the Lake Baikal, the Congo Basin, the Amazon Basin, and the middle and lower reaches of the Yangtze River.

(5) Overall, there are significant monthly variations of evaporation at different latitudes, especially at the low latitudes in the Northern Hemisphere, and the results obtained from the different reanalyses are in good agreement. Moreover, the monthly variation amplitude of the land evaporation was higher than that of the evaporation over the oceans.

The dataset inter-comparison highlights qualitative agreement among the datasets. However, despite the general similarity, differences exist among the various estimates. This is because there is no global evaporation observation system. Reanalyses represent an approximation of the real world, thus we extracted the main characteristics of the spatial-temporal variation of global evaporation from the eight reanalyses. Because of the limitations presented, the performance of all eight reanalyses in reproducing the evaporation still causes doubts in the use of such models for climate trend analyses and long-term studies.

*This work was supported by the National Basic Research Program of China (Grant Nos. 2013CB430204, 2012CB955900), the National Natural Science Foundation of China (Grant Nos. 41375078, 41175084) and the Special Scientific Research Fund of Meteorological Public Welfare Profession of China (Grant No. GYHY201106016).*

Andersson A, Klepp C, Fennig K, et al. 2011. Evaluation of HOAPS-3 ocean surface freshwater flux ccomponents. J Appl Meteorol Clim, 50: 379–398

Betts A K, Zhao M, Dirmeyer P A, et al. 2006. Comparison of ERA40 and NCEP/DOE near-surface data sets with other ISLSCP-II data sets. J Geophys Res, 111: D22S04-1-D22S04-20

Bosilovich M G, Robertson F R, Chen J. 2011. Global energy and water budgets in MERRA. J Clim, 24: 5721–5739

Dee D P, Uppala S M, Simmons A J, et al. 2011. The ERA-Interim reanalyses: Configuration and performance of the data assimilation system. Quart J R Meteor Soc, 137: 553–597

Fan K, Wang H J. 2006. Studies of the relationship between southern hemispheric atmospheric circulation and climate over East Asia (in Chinese). Chin J Atmos Sci, 30: 402-412

Guo J, Ren G Y. 2005. Recent change of pan evaporation and possible climate factors over the Huang-Huai-Hai watershed, China (in Chinese). Adv Water Resour, 16: 666–672

Hagemann S, Arpe K, Bengtsson L. 2005. Validation of the hydrological cycle of ERA-40. ERA Rep Series, ECMWF, 42

Huang J P, He M, Yan H R, et al. 2010. A study of liquid water path and precipitable water vapor in Lanzhou area using ground-based microwave radiometer (in Chinese). Chin J Atmos Sci, 34: 548–558

IPCC. Climate Change 2001: The Scientific Basis, Contribution of Working Group I to the Third Assessment Report of the Intentional Panel on Climate Change. In: Hongbton J T, ed. New York: Cambridge University Press. 193–227

Jacobson M Z. 2007. Fundamentals of Atmospheric Modeling. 2nd ed. New York: Cambridge University Press. 53–62

Kalnay E, Kanamitsu M, Kistler R, et al. 1996. The NCEP/NCAR 40-year reanalyses project. Bull Amer Meteorol Soc, 77: 437–471

Kuzmin P O. 1957. Hydrophysical investigations of land waters. Int Assoc Sci Hydrol Publ, 3: 468–478

Lian Y, Shen B Z, Gao Z T, et al. 2003. The study of the on-set criterion and the date of East Asian summer monsoon in northeast China and its main characteristic analysis (in Chinese). Acta Meteorol Sin, 61: 548–558

Liu Y B. 2011. Hydroclimatology: Perspectives and Applications (in Chinese). Beijing: Higher Education Press. 69–79

Lorenz C, Kunstmann H. 2012. The hydrological cycle in three state-of-the-art reanalyses: Intercomparison and performance analysis. J Hydrometeorol, 13: 1397–1420

Monteith J L. 1981. Evaporation and surface temperature. Quart J R Meteor Soc, 107: 1–27

Penman H L. 1948. Natural evaporation from open water, bare soil, and grass. Proc Roy Soc Lond A, 193: 120–145

Rienecker M M, Suarez M J, Gelaro R, et al. 2011. MERRA: NASA's modern-era retrospective analysis for research and applications. J Clim, 24: 3624–3648

Ren G Y, Guo J. 2006. Change in pan evaporation and the influential factors over China: 1956–2000 (in Chinese). J Nat Res, 21: 31–44

Roads J. 2003. The NCEP-NCAR, NCEP-DOE, and TRMM tropical atmosphere hydrologic cycles. J Hydrol, 4: 826–840

Saha S, Moorthi S, Pan H L, et al. 2010. The NCEP climate forecast system reanalyses. Bull Amer Meteorol Soc, 91: 1015–1057

Shen S H, Sheng Q.2008. Changes in pan evaporation and its cause in China in the last 45 years (in Chinese). Acta Meteorol Sin, 66: 452–460

Shi N, Huang X X, Yang Y. 2003. Spatiotemporal features of the trend variation of global land annual rainfall fields from 1948 to 2000 (in Chinese). Chin J Atmos Sci, 27: 971–982

Shi N. 2009. Meteorological Statistical Forecast (in Chinese). Beijing: China Meteorological Press. 15–34

Summer D M, Jacobs J M. 2005. Utility of Penman-Monteith, Priestley-

Taylor, reference evapotranspiration, and pan evaporation methods to estimate pasture evapotranspiration. J Hydrol, 308: 81–104
Trenberth K E, Fasullo J T, Mackaro J. 2011. Atmospheric moisture transports from ocean to land and global energy flows. J Clim, 24: 4907–4924
Uppala S M, Kallberg P W, Simmons A J, et al. 2005. The ERA-40 re-analysis. Quart J R Meteorol Soc, 131: 2961–3012
Wang Y J, Jiang T, Xu C Y, et al. 2005. Trends of Evapotranspiration in the Yangtze River Basin in 1961–2000 (in Chinese). Adv Clim Change Res, 1: 99–105
Wang H J. 2010. Preliminary results of the 973 Project on the energy and water cycle and their role in extreme climate of China (in Chinese). Adv Earth Sci, 25: 643–670
Xie P, Chen X H, Wang Z L, et al. 2009. Comparison of actual evapotranspiration and pan evaporation (in Chinese). Acta Geogr Sin, 64: 270–277
Xu Y, Ding Y H, Zhao Z C. 2001. Confidence analysis of NCEP/NCAR 50 year global reanalyzed data in climate change research in China (in Chinese). J Appl Meteorol, 12: 337–347
Yi L, Tao S Y. 1996. Water balance in land-atmospheric system over the East Asian monsoon region (in Chinese). Clim Environ Res, 1: 63–80
Yuan X, Wood E F, Roundy J K, et al. 2013. CFSv2-based seasonal hydroclimatic forecasts over the conterminous United States. J Clim, 26: 4828–4847
Yu L, Jin X Z, Weller R A. 2008. Multidecade Global Flux Datasets from the Objectively Analyzed Air-sea Fluxes (OAFlux) Project: Latent and Sensible Heat Fluxes, Ocean Evaporation, and Related Surface Meteorological Variables. Technical Report. OAFlux Project Technical Report (OA-2008-01). Woods Hole Oceanographic Institution
Zhang X W, Zhou S X. 2010. Preliminary Study of Air Hydrology (in Chinese). Beijing: China Meteorological Press. 1–9
Zhang Q Y, Tao S Y, Zhang S L. 2003. The persistent heavy rainfall over the Yangtze River Valley and its associations with the circulations over East Asian during summer (in Chinese). Chin J Atmos Sci, 27: 1018–1030
Zhang W J, Zhou T J, Yu R C. 2007. A preliminary analysis on the moisture budget of East China (in Chinese). Chin J Atmos Sci, 31: 329–345
Zhao T B, Fu C B, Ke Z J, et al. 2010. Global atmosphere reanalyses datasets: Current status and recent Advances (in Chinese). Adv Earth Sci, 25: 242-254
Zhu Y L, Ling C, Chen H B, et al. 2012. Comparison of two reanalyses data with the RS92 radiosonde data (in Chinese). Clim Environ Res, 17: 381–391
Zuo H C, Li D L, Hu Y Q, et al. 2005. Characteristics of climatic trends and correlation between pan-evaporation and environmental factors in the last 40 years over China. Chin Sci Bull, 50: 1235–1241

# 中国夏季大气水分循环特征及再分析资料对比分析*

苏涛[1)] 封国林[2)†]

1) (兰州大学大气科学学院, 兰州 730000)

2) (国家气候中心, 中国气象局气候研究开放实验室, 北京 100081)

( 2014 年 6 月 24 日收到; 2014 年 8 月 8 日收到修改稿 )

大气水分循环过程耦合了降水、蒸发、水汽输送等多个环节. 本文利用 ERA-Interim 与 MERRA 再分析资料, 研究了中国 1979—2012 年夏季大气水分循环的时空变化特征及其对全球气候变化的响应, 并对两套再分析资料在中国地区的适用性进行了评估. 结果表明: 1) 中国夏季降水、蒸发、可降水量均自东南沿海地区向西北内陆递减; 降水与蒸发相互联系、相互制约, 由于不同地区下垫面物理条件的差异, 它们之间同时存在正、负反馈的影响机制, 可降水量主要集中在地面至 700 hPa 高度, 约占总量的 75%; 2) 近 34 年大气水分循环显著变化的区域主要集中在西部和东北地区, 西部内陆地区可降水量显著增加, 北方大部分地区纬向水汽输送通量显著减小, 西北北部地区经向水汽输送通量显著增大, 蒸发量与水汽输送的气候变化可能是造成可降水量增加的主要原因; 3) Interim 与 MERRA 资料对降水量时空变化特征的再现能力要优于蒸发量, 此外, 它们对降水与蒸发气候变化趋势的模拟结果差别较大, 使用时应该慎重; 两套资料对可降水量与水汽输送通量的时空变化特征以及气候变化趋势的模拟比较一致, 可信度较高; 4) Interim 资料对西南、东南以及东北区域夏季水循环均有较好的描述能力; 而 MERRA 资料更适用于研究西南和西北区域的水汽收支情况.

**关键词**: 大气水分循环, 再分析资料, 大气水汽收支, 气候变化趋势

**PACS:** 92.40.Zg, 92.60.Ry **DOI:** 10.7498/aps.63.249201

## 1 引 言

水循环是一个涉及降水、蒸发、水汽输送以及径流等环节的动态系统, 其变化深刻地影响着全球水资源系统和生态环境系统的结构和演变, 并且对各地区的天气与气候变化起着重要的作用, 旱涝降水异常就与水循环存在直接联系 [1,2]; 此外, 水循环还与人类经济社会活动息息相关 [3,4], 人类活动也在很多方面影响水循环过程 [5]. 水循环包括了大气分支与陆地分支 [6], 大气分支是水循环系统最活跃的部分, 主要指海洋和陆地上空的水汽输送和陆地不同区域上空的水分交换 [7]. 大气中的水分所占的比例非常小, 但是它的活动严重影响着地球表层的生态环境和人类的生存 [8], 水汽既是大气降水的物质基础, 也是大气中主要的温室气体 [9]. 由于大气观测资料相对较少, 陆地蒸发与降水数据也存在一定程度的不确定性, 近代关于水循环的研究, 还主要侧重于其陆面过程 [10]. 为了更加全面地认识不同时空尺度上的水循环特征, 仍需要对大气水分循环进行深入研究.

近年来, 国内学者针对大气水分循环已经开展了一些工作. 崔一峰和刘国纬 [11] 利用 1983 年探空气象资料及地面水文资料, 计算了中国大陆及六大区域水汽收支的分布特征; Zhai 和 Eskridge[12]

* 国家重点基础研究发展计划 (批准号: 2012CB955902, 2013CB430204) 和公益性行业科研专项 (批准号: GYHY201106016) 资助的课题.

† 通讯作者. E-mail: fenggl@cma.gov.cn

© 2014 中国物理学会 Chinese Physical Society 

探讨了中国地区上空大气水汽的分布特征; 施小英和施晓晖[13]研究了夏季青藏高原东南部水汽收支的气候特征及其影响效应; 赵瑞霞和吴国雄[6]定量分析了长江流域水分收支各分量的季节循环、年际变化以及线性趋势变化; 伊兰和陶诗言[14]根据水平衡方法尝试对东亚季风区进行蒸发与土壤和地下水含量估算及总的水量平衡分析; 张文君等[15]同样基于水汽平衡方程估算了华北、长江流域和华南三个典型区域的水分收支情况. 综上可见, 以往的研究大多针对中国局部地区或部分水循环要素进行分析, 还缺少对中国地区大气水分循环的系统分析.

再分析资料是资料同化的产物, 具有空间分布均匀、时间尺度长且连续、动力、热力一致性等特点[16]. 由于前几代再分析资料水文循环数据在很多方面逐渐难以满足水循环的天气与气候研究, 最近欧洲中期天气预报中心(ECMWF)与美国国家航空航天局(NASA)分别发展了两套新一代再分析资料. ERA-Interim与MERRA是目前全球最先进的大气再分析资料同化系统[17], 它们对前几代再分析资料的水文循环过程做出了重要改进, 其中, ERA-Interim与ERA-40相比在很多方面都有一定的提高, 尤其是在水分收支和能量循环方面有了显著改善[18]. 同时, MERRA的主要目标也是改善前几代再分析资料中的水文循环数据问题. 但是ERA-Interim与MERRA资料目前在中国地区的应用较少, 正确认识和评价这两套再分析资料的质量并在实际研究中合理应用是一个亟待解决的问题. 中国地处东亚季风区, 年内降水主要集中在夏季, 因此本文结合ERA-Interim与MERRA再分析资料对中国夏季大气水分循环进行了系统研究, 并探讨了其对全球气候变化的响应, 同时鉴定了这两套再分析资料在中国各地区的适用性与局限性, 这不仅能为中国地区水资源综合管理提供重要的理论支持, 也对再分析资料的改进提供了科学的参考依据.

## 2 资料与方法

### 2.1 资料说明

ERA-Interim (简称Interim)是ECMWF发布的一套新型再分析资料, 它解决了ERA-40系统同化卫星资料时存在的一些问题, 同时为ECMWF发展下一代数值同化系统奠定了基础[19]. Interim资料采用四维变分同化技术(4D-VAR), 利用一个以12 h为周期的连续数据同化方法, 在每个同化周期中, 观测资料都会与预报模型(IFS)的初始数据结合在一起估计全球大气与地表的变化. 此外, NASA全球模式与同化办公室(GMAO)开发了新一代数值同化产品MERRA, 它有两个主要目标: 一是把来自NASA的地球观测卫星数据作为气候背景, 二是改善前几代再分析资料中的水文循环数据[20]. MERRA使用GEOS-5大气模式与资料同化系统, 资料同化应用的是美国国家环境预报中心(NECP)发展的以6 h为周期的格点统计插值系统(GSI, 观测资料在进行同化之前均进行了质量控制与误差订正, 在三种相互独立的数据上进行增量分析得到全球再分析数据. 由此可见, Interim与MERRA资料所使用的同化系统、同化方案以及同化的资料均有所不同. 本文使用了Interim与MERRA资料降水量($P$)、蒸发量($E$)、比湿($q$)、风场($u$, $v$)、地面气压($p$)等要素的日平均数据, 其中比湿($q$)与风场($u$, $v$)资料包括由1000 hPa至50 hPa共24层的数据, 以及国家气候中心整编的中国160站月降水资料.

### 2.2 水汽平衡方程

一般情况下, 在任意时段内, 某一地区大气的水汽收支情况需要满足水汽平衡方程[21,22], 如(1)式所示:

$$\frac{\partial W}{\partial t}+\nabla\cdot[\boldsymbol{Q}_\lambda\boldsymbol{Q}_\varphi]=E-P, \tag{1}$$

$$W=\frac{1}{g\rho_{\mathrm{w}}}\int_{p=0}^{p_{\mathrm{s}}}q\,\mathrm{d}p, \tag{2}$$

$$\boldsymbol{Q}_\lambda=\frac{1}{g\rho_{\mathrm{w}}}\int_{p=0}^{p_{\mathrm{s}}}qu\,\mathrm{d}p, \tag{3}$$

$$\boldsymbol{Q}_\varphi=\frac{1}{g\rho_{\mathrm{w}}}\int_{p=0}^{p_{\mathrm{s}}}qv\,\mathrm{d}p, \tag{4}$$

其中, $P$为降水量, $E$为蒸发量, $W$为大气可降水量, $\boldsymbol{Q}_\lambda$与$\boldsymbol{Q}_\varphi$分别为纬向与经向的水汽输送通量, $u$是纬向风分量, $v$是经向风分量, $g$是重力加速度, $\rho_{\mathrm{w}}$是液态水的密度, $q$表示比湿, $p_{\mathrm{s}}$表示地表面气压. 水汽收支平衡是大气水分循环能够持续的基本前提, 蒸发、降水、水汽输送等环节通过水汽平衡方程紧密地联系为统一的整体.

表 1 Interim 与 MERRA 再分析资料的概况

| 再分析资料 | 水平分辨率 | 同化方案 | 数据时次 | 垂直层次 |
|---|---|---|---|---|
| Interim | T255 (~ 78 km) | 4DVAR | 6 h, daily, monthly | 37 |
| MERRA | 1/2° × 2/3° | 3DVAR | 1 h, 6 h, daily, monthly | 42 |

### 2.3 研究与处理方法

本文使用 Jones 网格面积加权平均法[23]计算了各要素逐年的区域平均值, 并进一步分别求得各要素逐年变化的相关系数[24]. Jones 等[23]网格面积加权平均法的公式为

$$S_k = \sum_{i=1}^{n} \cos(W_i) S_{ik} \Big/ \sum_{i=1}^{n} \cos(W_i), \qquad (5)$$

式中, $S_{ik}$ 表示第 $i$ 个网格第 $k$ 年的值, $W_i$ 表示第 $i$ 网格上的纬度值, $S_k$ 表示某区域第 $k$ 年的区域平均值, $N$ 为某区域包含的格点数目.

Interim 与 MERRA 资料水平分辨率并不一致(表 1), 为了比较两套再分析资料的差异, 本文采用双线性插值方法将它们统一成相同的格点形式, 然后计算了它们的相似系数与均方根误差[24,25], 这可以反映出两套再分析资料大气水分循环要素空间分布的相似程度. 此外, 通过趋势系数[26]可以了解气象要素的长期趋势变化, 适用于研究大范围气象场的长期变化, 而气候倾向率能够表征气象要素每 10 a 的变化率, 因此本文结合气候趋势系数与气候倾向率研究了大气水分循环的气候变化特征.

## 3 中国夏季大气水分循环的时空变化特征

蒸发与降水是地表与大气之间的水分通量, 蕴藏在海洋、冰雪、陆地和植被等下垫面的固态水与液态水通过蒸发进入大气, 大气中过饱和水汽上升冷凝后形成降水回到地面, 大气水汽输送则将时空分布不均的蒸发重新输送到各个地区. 大气可降水量是一个重要的气象参数, 它是产生降水的物质基础, 对降水的形成、辐射能的吸收和放射以及气候的形成与变化都有重要的影响. 降水、蒸发、水汽输送以及可降水量是水汽平衡方程中的基本参数, 同时也是大气水分循环的基本要素, 因此本节重点分析中国夏季上述各要素时空分布的主要特征, 并对比分析两套再分析资料的时空相似性.

### 3.1 降水量与蒸发量的时空特征

中国受夏季风的影响, 降水呈现出明显的地域性差异, 降水量 ($P$) 自东南沿海地区向西北内陆递减 (图 1), 对于 Interim 资料而言 (图 1 (a)), 华南、江南、西南南部、四川盆地、西藏东南部以及江汉等地区 $P$ 相对较大, 均在 10 mm/d 左右, 西藏东南部地区甚至超过 18 mm/d, 西藏东北部、西南中北部、江淮、黄淮以及东北东南部等地区 $P$ 有所减少, 在 6 mm/d 左右, 西藏中北部、华北、内蒙古中东部以及西北东南部等地区 $P$ 进一步减少至大约 2 mm/d, 而西北中北部的大部分地区都要小于 0.5 mm/d. MERRA 与 Interim 资料 $P$ 的分布形势基本一致 (图 1 (b)), 相似系数达到 0.947, 但是 MERRA 资料华南与江南地区 $P$ 更大, 而西藏与江汉地区 $P$ 相对较小.

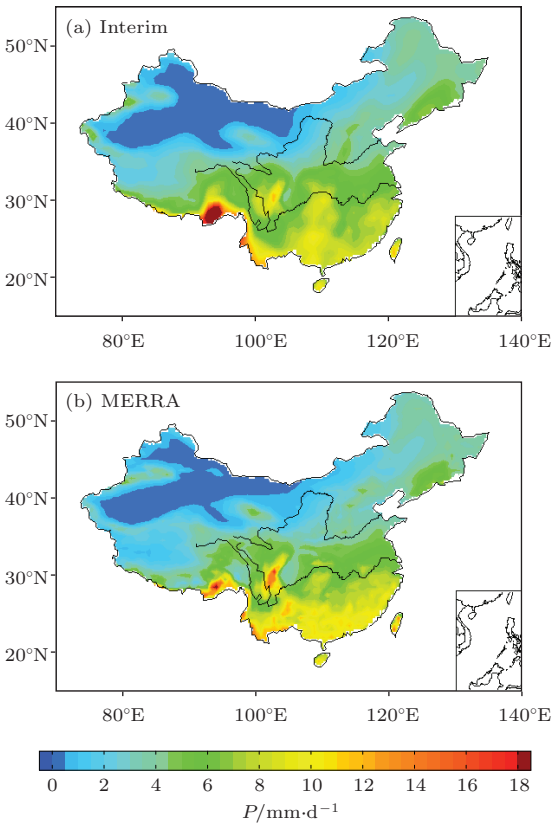


图 1 中国大陆夏季 (a) Interim 与 (b) MERRA 资料日平均降水量 ($P$) 的空间分布形势 (单位为 mm/d)

蒸发量($E$)的分布形势也具有显著的地域性特征. Interim资料(图2(b)) $E$较高的地区主要分布在华南、江南、江淮、黄淮、华北以及东北东部等地区, 均在4 mm/d左右; 西藏、西南、东北西部、内蒙古东部以及西北东南部等地区相对较小, 大约在2—3 mm/d; 西北中北部地区最小, 尤其是塔里木盆地及其附近地区, 仅为0.2 mm/d左右. MERRA资料(图2(b))江南至华南中北部地区的$E$都在5 mm/d左右, 明显高于Interim资料; 此外, 在西藏东南部、西南以及东北东部等地区也相对更大, 但华北、东北西部、西藏中西部以及西北局部地区$E$略低. 整体来说, Interim与MERRA资料$P$的空间分布形势比较一致, 差别较大的地区主要位于西藏、江南、华南以及江汉地区, 而$E$的空间分布差异较大, 尤其是江南、西南等地区, 差值达到1 mm/d左右.

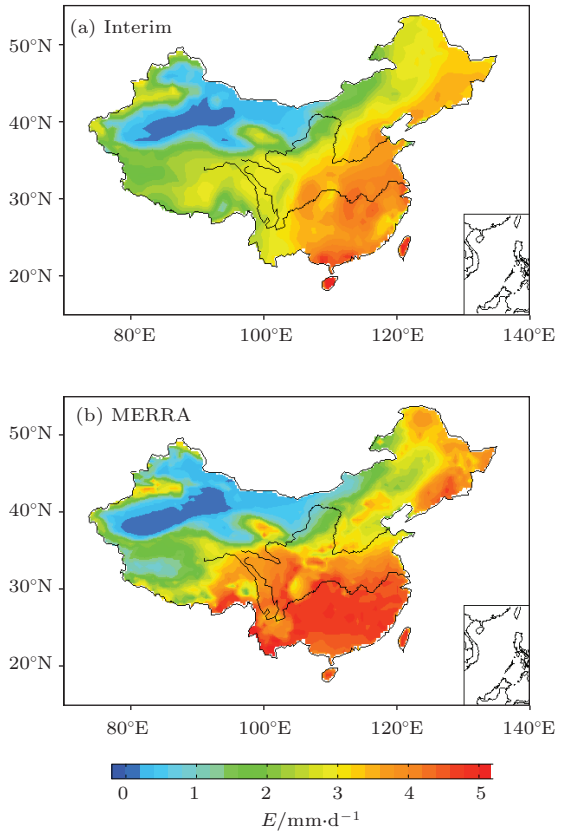


图2 中国大陆夏季(a) Interim与(b) MERRA资料日平均蒸发量($E$)的空间分布形势(单位为mm/d)

图3(a)给出了$P$在1979—2012年逐年变化的时间序列, 可见Interim与MERRA资料$P$的逐年变化形势基本相同, 相关系数为0.850, 此外, 它们与中国160站降水观测资料的相关系数分别达到0.745, 0.709, 置信水平均超过99%, 说明再分析资料对中国夏季降水逐年变化的再现能力较好, 可信度较高. 其中, 1979—1990年$P$在4.2 mm/d左右, 1990—1998年$P$逐渐增大, 在1998年达到最大值, 1999年之后有明显的线性减少趋势. 由图3(b)可知, 夏季$E$逐年变化的幅度较小, Interim资料$E$略低于MERRA资料, 相关系数为0.498, 达到了99%的置信水平, 可见两套再分析资料$P$逐年变化的相关性要优于$E$.

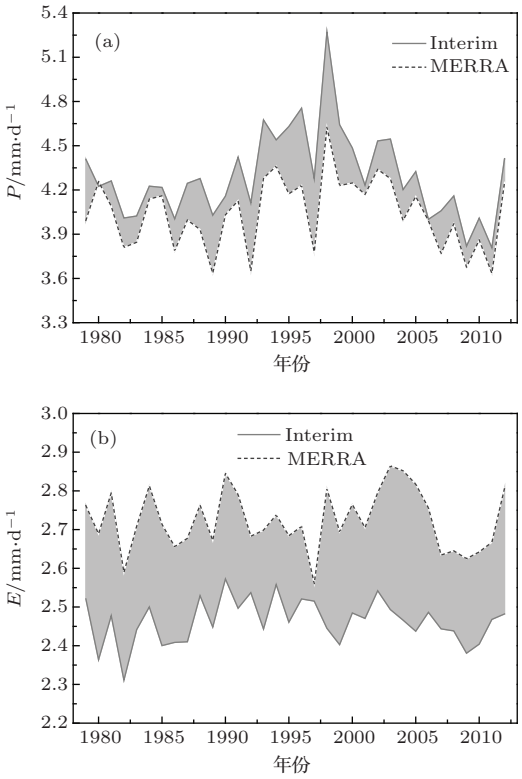


图3 中国1979—2012年夏季降水量($P$)与蒸发量($E$)的逐年变化时间序列(单位为mm/d)

中国夏季$P$与$E$空间分布的地域性差异显著(图1、图2), 为了研究再分析资料$P$与$E$在不同地区的适用性, 本文参考中国气象地理区划标准, 将中国地区依110°E, 35°N为界划分为四个区域, 分别为西南(WS)、东南(ES)、西北(WN)与东北(EN)区域. 表2分别是中国地区(CHN)及各区域Interim与MERRA资料$P$与$E$逐年变化的相关系数($\rho$)与空间分布的相似系数($S$)和均方根误差(RMSE). 对于WS区域, $P$逐年变化的相关系数为0.830, 空间分布的相似系数达到0.938, 置信水平均达到99%, RMSE则为2.65 mm, 表明WS区域$P$的时空分布均基本一致, 但是在量值上存在一定的差别; $E$的相似系数为0.965, 但相关系数仅有0.327. 可见两套资料在WS区域$E$的空间分布

非常接近, 但 $E$ 逐年变化形势差别较大. ES 区域 $P$ 与 $E$ 逐年变化与空间分布均具有较高的一致性, RMSE 也相对较小, 说明再分析资料在 ES 区域的适用性较好. WN 区域 $P$ 与 $E$ 逐年变化的形势差别较大, 相关系数分别为 0.257, 0.221, 相似系数与其他区域相比也明显较低, 表明再分析资料对 WN 区域 $P$ 与 $E$ 时空演变特征的再现能力较弱. EN 区域 $P$ 的逐年变化形势非常接近, 相关系数高达 0.980, RMSE 也仅有 0.79 mm; $E$ 的逐年变化也较为一致, 相关系数为 0.423, 置信水平达到 95%. 综上可知, Interim 与 MERRA 资料对中国夏季 $P$ 时空变化特征的再现能力要优于 $E$, 特别是 WS 与 WN 区域 $E$ 的逐年变化形势差别较大, 空间分布的相似度较低.

表 2 中国各区域 Interim 与 MERRA 资料降水量 ($P$) 和蒸发量 ($E$) 逐年变化的相关系数 ($\rho$) 及空间分布的相似系数 ($S$) 与均方根误差 (RMSE)

| 区域 | $P$ | | | $E$ | | |
|---|---|---|---|---|---|---|
| | $\rho$ | $S$ | RMSE/mm·d$^{-1}$ | $\rho$ | $S$ | RMSE/mm·d$^{-1}$ |
| WS | **0.830** | **0.938** | 2.65 | 0.327 | **0.965** | 1.17 |
| ES | **0.785** | **0.976** | 1.63 | **0.750** | **0.979** | 0.86 |
| WN | 0.257 | **0.889** | 0.82 | 0.221 | **0.931** | 0.55 |
| EN | **0.928** | **0.980** | 0.79 | 0.423* | **0.976** | 0.70 |
| CHN | **0.850** | **0.947** | 1.72 | **0.498** | **0.962** | 0.87 |

注: 粗体置信水平达到 99%, "*" 置信水平达到 95%.

## 3.2 大气可降水量与水汽输送的时空特征

图 4 为中国大陆夏季大气可降水量 ($W$) 的空间分布形势, 由此可见, Interim 与 MERRA 资料具有很高的一致性, 华南、江南、江淮以及四川盆地等地区 $W$ 均在 50—60 mm 左右, 华北、西南南部等地区约为 40 mm, 东北、内蒙古、西北东部与西部等地区 $W$ 在 20—30 mm 之间, 而西藏地区的可降水量相对较少, 仅为 10 mm 左右.

为了研究不同高度大气可降水量的分布特征, 表 3 进一步计算了中国地区各层次大气水汽含量的平均值及其逐年变化的相关系数与空间分布的相似系数和均方根误差, 两套再分析资料地表至 50 hPa 大气的水汽含量非常接近, 平均值分别为 25.58, 25.57 mm, 逐年变化的相关系数达到 0.746, 空间分布的相似系数高达 0.999. 地面至 700 hPa 的大气水汽含量分别为 19.17, 19.02 mm, 约占据整层大气水汽含量的 75%. 其余层次的大气水汽含量相对较少, 并且时空变化也基本一致. 由此可知, Interim 与 MERRA 资料各层次大气水汽含量的时空分布特征均具有非常高的一致性, 中国夏季大气可降水量主要集中在地面至 700 hPa 高度.

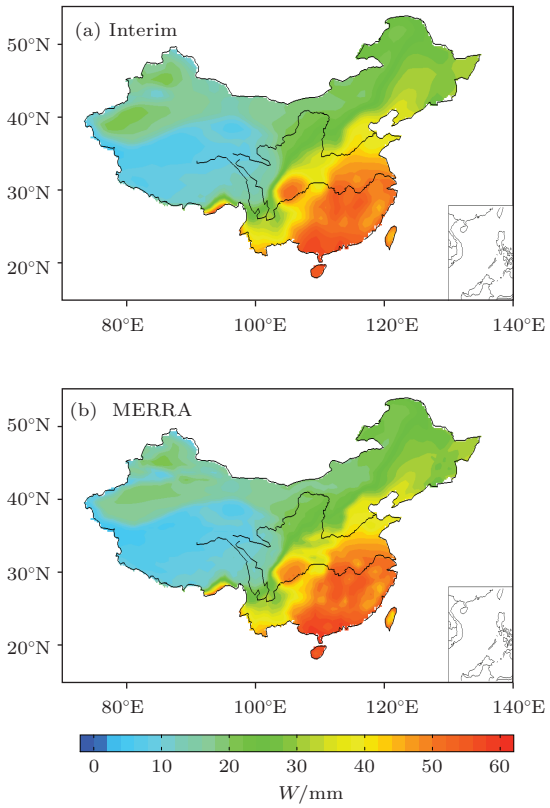


图 4 中国大陆夏季 (a) Interim 与 (b) MERRA 资料大气可降水量 ($W$) 的空间分布形势 (单位为 mm)

图 5 给出了中国大陆地区大气水汽输送及其散度的分布形势, 可见 Interim 与 MERRA 资料基本相同, 经向与纬向水汽输送通量场的相似系数分别为 0.969, 0.971, 只是江南、台湾以及西北局部地

区的水汽输送散度存在一定差别. 主要特征表现为华南、江南、江淮、东北东部等地区的水汽输送均较强, 其中华南地区以经向输送为主, 江南、江淮以及东北东部等地区的纬向水汽输送有所增强, 而西藏、内蒙古中西部以及西北地区基本受纬向水汽输送控制.

表 3 中国夏季 Interim 和 MERRA 资料各层次大气平均水汽含量 ($W$) 及其分别对应的相关系数 ($\rho$)、相似系数 ($S$) 与均方根误差 (RMSE)

| 层 | $W_{\text{Interim}}$/mm | $W_{\text{MERRA}}$/mm | $\rho$ | $S$ | RMSE/mm |
|---|---|---|---|---|---|
| 地表—700 hPa | 19.17 | 19.02 | **0.795** | **0.999** | 1.20 |
| 700—500 hPa | 8.71 | 8.88 | 0.419* | **0.999** | 0.56 |
| 500—300 hPa | 3.12 | 3.21 | **0.930** | **0.998** | 0.25 |
| 300—50 hPa | 0.24 | 0.25 | **0.674** | **0.996** | 0.03 |
| 地表—50 hPa | 25.58 | 25.57 | **0.746** | **0.999** | 1.40 |

注: 粗体置信水平达到 99%, "*" 置信水平达到 95%.

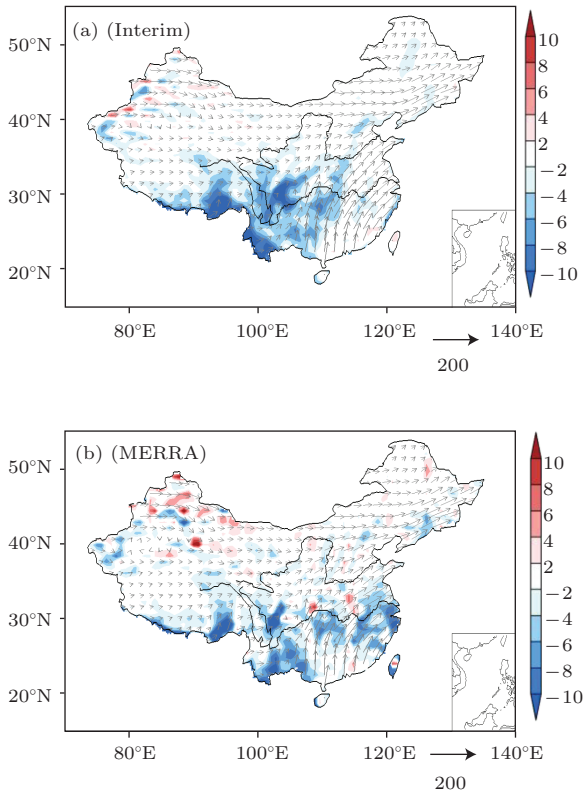


图 5 中国大陆夏季水汽输送通量 (矢量, 单位为 kg·m$^{-1}$·s$^{-1}$) 与水汽输送通量散度 (阴影区, 单位为 $10^{-8}$ kg·s$^{-1}$·m$^{-2}$) 的空间分布形势

## 3.3 中国各区域夏季大气水分循环要素逐月的平均分布

再分析资料对于全球或区域尺度上水分平衡的描述具有一定的局限性, 当利用再分析资料研究大气水分循环特征时, 必须引入残差项 (res) 才能严格地满足水汽平衡方程[21,22], 如 (6) 式所示:

$$\frac{\partial W}{\partial t} + \nabla \cdot [\boldsymbol{Q}_\lambda, \boldsymbol{Q}_\varphi] = E - P + \text{res}. \qquad (6)$$

图 6 是根据 (6) 式计算得到的中国各区域夏季 (JJA) 以及 6, 7, 8 月份 $P$, $E$、水汽输送通量散度 (div$Q$)、可降水量随时间变化项 ($\partial w/\partial t$) 以及残差项 (res) 的分布, 由此可见, WS 区域 (图 6 (a), (b)), 大气水分循环各要素均能较好地满足水汽平衡方程, 各月份 $W$ 基本保持不变, res 相对较小, $P$ 与 $E$ 的差值较大, 但是水汽输送具有很强的辐合趋势, 为该地区的降水提供了良好的水汽条件. ES 区域 (图 6 (c), (d)) $W$ 也比较稳定, 但 res 较大, 特别是 MERRA 资料, 夏季 res 平均值约为 1.8 mm/d, 其中以 7 月份最大, $P$, $E$ 以及 div$Q$ 均相对较大, 水汽输送辐合趋势明显; 值得注意的是, Interim 资料 7 月份降水量低于 8 月份, 而 MERRA 资料 7 月份降水量高于其他月份, 这可能是 MERRA 资料 7 月份残差相对较大的原因. WN 区域 (图 6 (e), (f)) 各要素量值较小, $P$ 与 $E$ 大致相等, MERRA 资料各要素基本满足水汽平衡方程, 但是 Interim 资料在各个月份残差值均较大, Interim 资料 res 与 div$Q$ 均高于 MERRA 资料, res 各月平均值均与 div$Q$ 接近, 因此 Interim 资料 res 可能与 div$Q$ 紧密相关. Interim 资料各要素在 EN 区域基本保持平衡 (图 6 (g)), $P$ 与 $E$ 在 7 月份大体相等, 但在 8 月份相差较大; MERRA 资料 EN 区域 $P$, $E$ 以及 div$Q$ 的逐月分布与 Interim 资料基本一致, Interim 与 MERRA 资料 div$Q$ 相差较大, MERRA 资料 div$Q$ 明显较大, 同时 res 也相对更大 (图 6 (h)). 综上可知, Interim 资料对西南、东南以及东北区域夏季水汽平衡均有较好的描述能力; 而 MERRA 资料比较适用于研究西南和西北区域的大气水汽收支情况, 水循环各要素能够很好地保持平衡, 并且 div$Q$ 与 res 存在很大的联系.

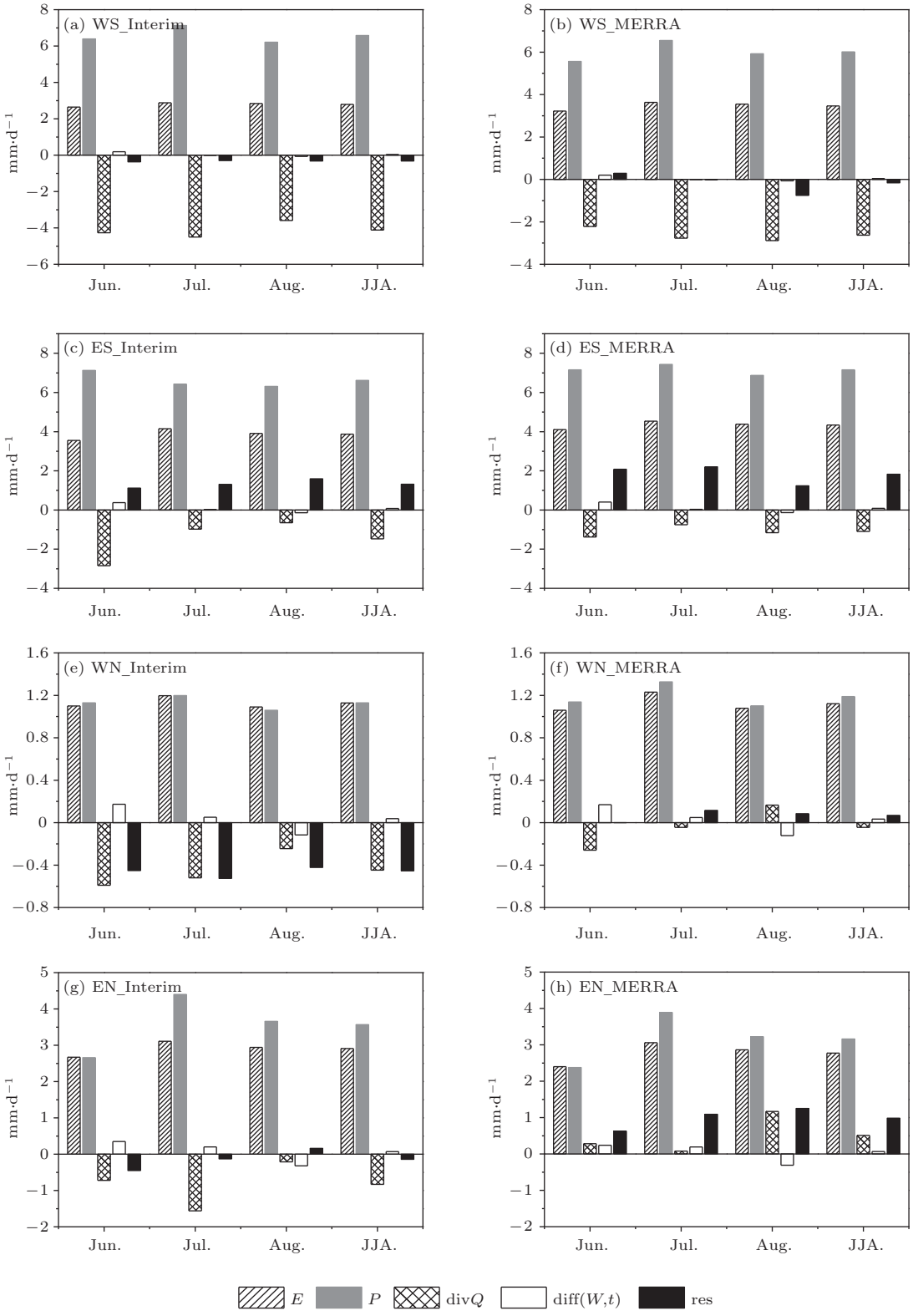


图 6 中国各区域夏季大气水分循环各要素的逐月平均值分布 (单位为 mm/d)

## 4 中国夏季大气水分循环的气候变化特征

水循环对全球气候有重要的调节作用, 而气候是水循环重要的驱动因子[27], 气候变化可以直接影响水资源[28], 全球变暖可能导致水循环强度增大, 降水量、蒸发量以及大气水汽含量显著增加[5,29]. 因此本节计算了中国夏季大气水分循环各要素的趋势系数与气候倾向率, 然后进一步分析了各要素的气候变化特征, 并评估两套再分析资料在

研究中国地区水循环长期气候变化中存在的一些质量问题.

### 4.1 降水量与蒸发量的线性变化趋势

图7是中国大陆地区1979—2012年夏季$P$与$E$以及($P$-$E$)值线性变化趋势的空间分布, 由此可见, 对于Interim资料, 西藏中东部、西北中部以及西南局部地区$P$呈现显著的线性增加趋势(图7(a)), 而西藏东南部、塔里木盆地中西部、内蒙古中东部以及西南南部等地区$P$具有显著的线性减少趋势, 气候倾向率基本都在0.2 mm·d$^{-1}$·decade$^{-1}$, 局部地区甚至超过0.6 mm·d$^{-1}$·decade$^{-1}$; 塔里木盆地中西部、华北西部以及内蒙古局部地区的$E$也具有显著的线性减少趋势(图7(c)), 西北中东部局部地区和东部北部地区$E$呈现显著的线性增加趋势; 此外, ($P$-$E$)值的气候变化趋势也非常明显(图7(e)), 并且($P$-$E$)值与$P$线性变化显著的区域分布在整体上基本一致. MERRA资料$P$, $E$, ($P$-$E$)值的线性变化趋势与Interim有所不同, 西北、西南北部和江淮东部等地区$P$具有显著的线性增加趋势, 而西藏中东部、东北北部与华北北部等地区$P$呈现显著的线性减少趋势, $E$线性变化显著的区域分布与$P$基本一致, 只是江南与西南南部地区$E$也具有显著的线性增加趋势; ($P$-$E$)值线性变化显著的区域主要分布在西北、西藏中东部、江淮、黄淮东部等地区. 综上可知, 中国夏季$P$, $E$, ($P$-$E$)值线性变化显著的区域主要分布在西北和东北地区, 表明上述地区$P$, $E$, ($P$-$E$)值对气候变化的响应较为敏感, 并且$P$与$E$显著性变化区域的空间分布形势基本一致, 但是Interim与MERRA资料$P$, $E$, ($P$-$E$)的气候趋势变化在一些地区存在明显的差别, 部分地区甚至呈现反位相, 也说明再分析资料对中国夏季$P$与$E$气候变化趋势的模拟还存在一定的问题.

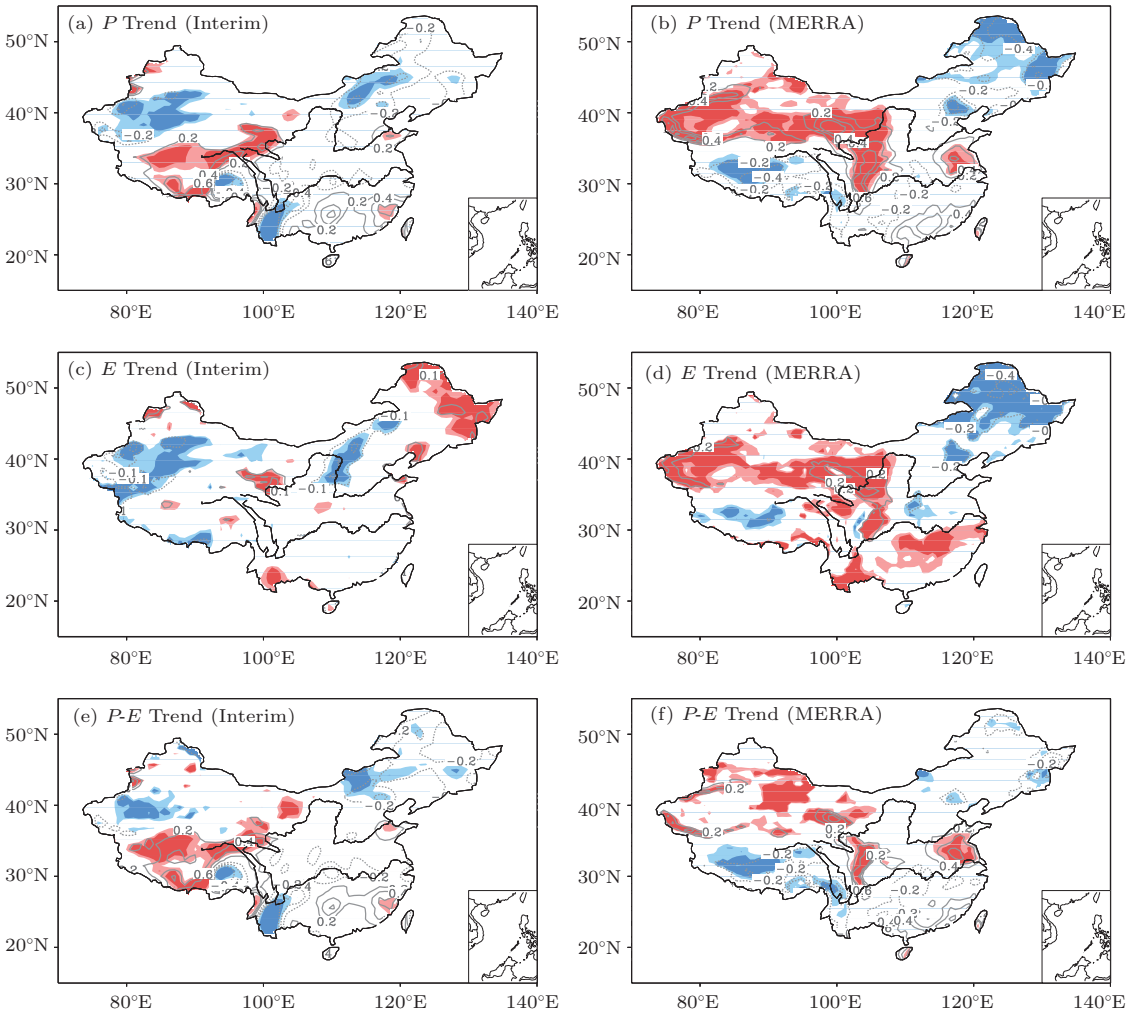


图7 中国大陆夏季降水量($P$)、蒸发量($E$)以及($P$-$E$)值的线性变化趋势(阴影区是趋势系数置信水平分别达到95%, 99%的区域, 红色表示线性增加, 蓝色表示线性减少, 等值线是气候倾向率, 单位为 mm·d$^{-1}$·decade$^{-1}$)

### 4.2 大气可降水量与水汽输送的线性变化趋势

如图8所示, 中国大陆地区1979—2012年夏季 $W$ 以及纬向 ($Qu$) 与经向 ($Qv$) 水汽输送通量也具有显著的线性变化趋势. 其中, 如图8 (c), (d) 所示, $Qu$ 线性变化显著的区域分布基本一致, 主要集中在西北、内蒙古中西部和华北西北部等地区, 气候倾向率在5—15 g·cm$^{-1}$·s$^{-1}$·decade$^{-1}$ 之间. 此外, $Qv$ 线性变化显著的区域也主要分布在西北地区, 尤其是西北北部地区, 呈现显著的线性增加趋势; 内蒙古东部、东北西部、华北西部以及华南局部地区 $Qv$ 呈现显著的线性减少趋势. $W$ 线性变化趋势显著的区域也主要分布在西部地区, Interim 资料西藏、西北中东部等地区 $W$ 线性变化趋势的置信水平均达到了99%, 气候倾向率超过0.5 mm·decade$^{-1}$ (图8 (a)), 而MERRA资料西北、西藏北部、内蒙古西部、华南、黄淮东部等地区 $W$ 均呈现显著的线性增加趋势 (图8 (b)); $W$ 主要受到本地区的蒸发和水汽输送形势的影响, 西部内陆地区受纬向水汽输送控制, $Qu$ 能够对该地区 $W$ 产生重要影响, 近34年夏季西部内陆地区 $E$ 显著增加, 而 $Qu$ 显著减小, 因此 $W$ 也相应的显著增加, 可见 $E$ 与 $Qu$ 的气候变化是造成 $W$ 显著增加的主要原因. 另外, Interim 与 MERRA 资料对空中水循环要素气候变化趋势的

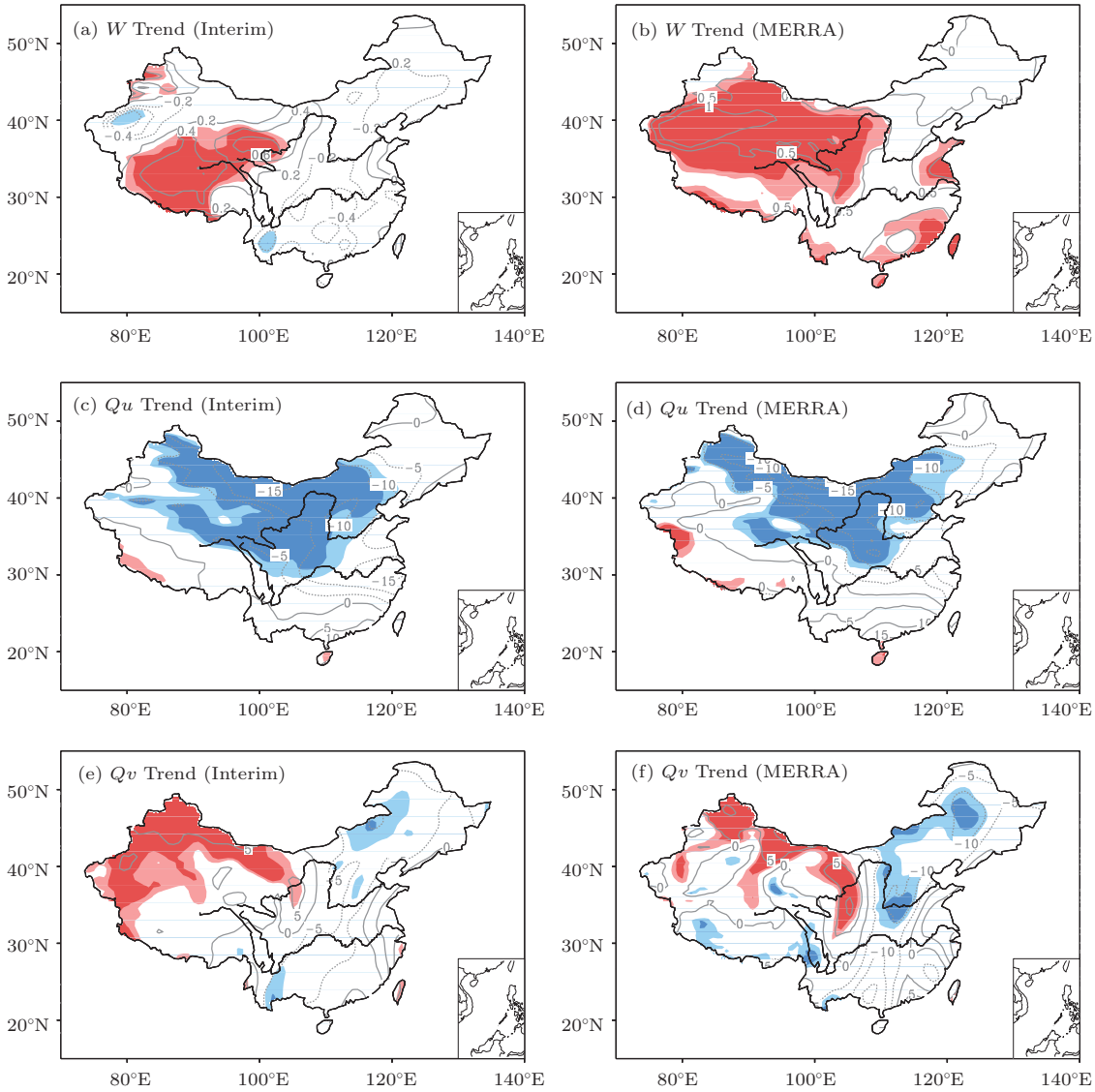


图8 中国大陆夏季可降水量 ($W$) 和纬向 ($Qu$) 与经向 ($Qv$) 水汽输送通量的线性变化趋势 (阴影区是气候趋势系数置信水平分别达到95%, 99% 的区域, 红色表示线性增加, 蓝色表示线性减少, 等值线是气候倾向率, 单位分别为: mm·decade$^{-1}$, g·cm$^{-1}$·s$^{-1}$·decade$^{-1}$)

再现能力更强, 线性变化趋势显著的区域分布基本一致.

本节的研究表明, 中国1979—2012年夏季大气水分循环要素线性变化显著的区域主要分布在中国西北、西藏和东北地区, 体现出上述地区的水循环要素对气候变化的响应程度相对较高, 但是两套再分析资料陆地水循环要素 ($P$, $E$) 的气候变化趋势差别较大, 而空中水循环要素 ($W$, $Qu$, $Qv$) 比较接近, 说明再分析资料对空中水循环要素气候变化趋势的模拟更加准确, 可信度更高.

## 5 中国夏季大气水分循环的机理分析

大气水分循环各要素紧密相连 (图9), 蒸发不仅是大气中水汽的最终来源, 而且蒸发过程中伴随的能量收支变化也为大气环流提供了动力, 水汽随大气环流运动, 影响大气可降水量的空间分布, 进而决定各地区的降水分布, 因此全球气候变化能够从各个方面影响大气水分循环过程, 西部内陆地区 $E$ 与 $Qu$ 的气候变化就是造成 $W$ 显著增加的主要原因 (图8). 相关性研究表明, 中国夏季 $P$ 与 $W$ 的逐年变化呈现显著的正相关关系, Interim 与 MERRA 资料 $P$ 与 $W$ 的相关系数分别为0.711, 0.552, 置信水平均达到了99%, $P$ 与 $W$ 空间分布的相似系数分别为0.834, 0.876, 表明充足的水汽供应是形成降水的必要条件之一. 而某一地区大气的 $W$ 主要来源于外界的水汽输送和本地区的蒸发, 中国东部地区经向水汽输送较强, 而西部地区主要受纬向水汽输送控制, MERRA 资料 WN 区域 $P$ 与 $Qu$ 的相关系数为 $-0.415$, 呈现显著的负相关关系, 这可能是由于 $Qu$ 较小时, 该地区向其他区域的水汽输送较弱, 转化为 $P$ 的水汽相应增多, 导致 $P$ 较大; 而对于ES区域, $P$ 与 $Qv$ 的相关性更高, 说明 $Qv$ 对该区域 $P$ 的影响更大; EN区域 $P$ 同时受到 $Qu$, $Qv$ 的共同影响, $P$ 与 $Qu$, $Qv$ 均存在显著的正相关关系.

降水与蒸发是水循环的两个基本过程, 大气降水所需要的水汽最终来自于蒸发, Interim 与 MERRA 资料中国夏季 $P$ 与 $E$ 的相关系数分别为0.263, 0.576, 后者置信水平达到99%, 尤其是在WN与EN区域 $P$ 与 $E$ 相关系数的置信水平均超过99%, 另外Interim与MERRA资料 $P$ 与 $E$ 空间分布的相似系数分别为0.854, 0.945, 并且 $P$ 与 $E$ 线性变化趋势显著性区域的空间分布也基本一致 (图7), 这体现出了 $P$ 与 $E$ 之间存在正反馈机制; 但是在WS, ES区域 $P$ 与 $E$ 逐年变化的相关性较低, 甚至存在显著的负相关关系 (WS). 蒸发量的变化主要受到两个方面的影响: 供水条件与能量条件. 首先, 陆地蒸发主要包括土壤蒸发以及植物的蒸散, 其中土壤蒸发是发生在土壤孔隙中的水的蒸发现象, 供水条件的差异是导致蒸发量不同的重要因素. WN 与EN 区域相对较为干旱, 土壤含水量较低, 供水条件是制约该地区蒸发量大小的主要原因, 大部分降水又会通过蒸发重新回归大气, 进而导致大气可降水量增加, 因此降水与蒸发可以相互促进; 而WS, ES区域比较湿润, 供水条件对该地区 $E$ 的影响相对较小, 蒸发量主要受到饱和水汽压

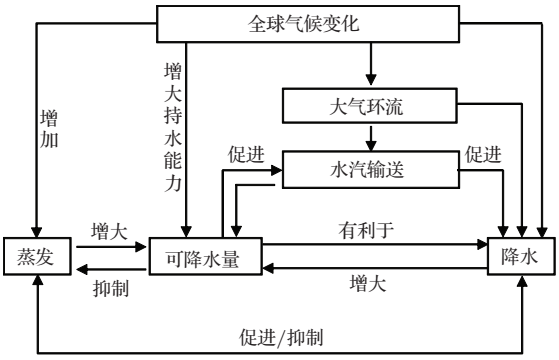


图9 大气水分循环的机理分析及其对全球气候变化的响应

表4 中国各区域Interim与MERRA资料降水量 ($P$) 与其余大气水分循环要素逐年变化的相关系数

| 区域 | Interim | | | | MERRA | | | |
|---|---|---|---|---|---|---|---|---|
| | $E$ | $W$ | $Qu$ | $Qv$ | $E$ | $W$ | $Qu$ | $Qv$ |
| WS | −0.429* | **0.707** | 0.161 | 0.116 | 0.299 | **0.612** | 0.098 | 0.135 |
| ES | −0.293 | **0.570** | 0.152 | 0.357* | −0.239 | **0.519** | −0.024 | 0.319 |
| WN | **0.855** | **0.602** | 0.064 | −0.010 | **0.954** | **0.856** | −0.415* | 0.215 |
| EN | **0.457** | **0.513** | 0.293 | **0.483** | **0.881** | **0.449** | 0.360* | **0.561** |
| CHN | 0.263 | **0.706** | 0.132 | 0.297 | **0.576** | **0.550** | 0.035 | 0.254 |

注: 粗体置信水平达到99%, "*" 置信水平达到95%.

差、空气饱和差、风速、相对湿度等其他因子的影响[30], 因此$P$与$E$的相关性较低, $P$反而会对$E$产生负作用. 可见由于不同地区下垫面物理条件的差异, 降水与蒸发相互联系、相互制约, 同时存在正、负反馈的影响机制(见图9). 需要指出的是, 全球变暖背景下江南与华南地区蒸发量呈现显著的增加趋势, 这与温度的变化是比较一致的, 体现出湿润地区蒸发量的变化与温度也存在着重要联系.

## 6 结 论

本文结合Interim与MERRA再分析资料, 运用水汽平衡方程研究了中国1979—2012年夏季大气水分循环的时空变化特征, 并对两套资料降水、蒸发、可降水量以及水汽输送通量等要素的时空分布进行了对比分析, 主要结论如下.

1) 中国大气水分循环各要素大小存在显著的地域性差异, 均自东南沿海地区向西北内陆递减; 降水与蒸发相互联系、相互制约, 由于不同地区下垫面物理条件的差异, 它们之间同时存在正、负反馈的影响机制; 大气可降水量主要集中在地面至700 hPa高度, 约占总量的75%.

2) 大气水分循环呈现显著的气候变化特征, 特别是西北、西藏和东北地区, 近34年大气可降水量显著增加, 纬向水汽输送强度显著减弱, 局部地区经向水汽输送显著增强, 蒸发量与水汽输送的气候变化是造成可降水量增加的主要原因; 降水与蒸发也发生了显著变化, 并且线性变化显著的区域分布基本一致.

3) Interim与MERRA资料对中国夏季降水量时空变化特征的再现能力要优于蒸发量, 另外对降水与蒸发气候变化趋势的模拟结果差别较大, 使用时应该慎重; 但是它们对可降水量与水汽输送通量的时空变化特征以及气候变化趋势的模拟结果比较一致, 可信度较高.

4) 再分析资料对中国不同区域水循环的描述能力存在一定的差别, Interim资料对西南、东南以及东北区域夏季水汽平衡均有较好的描述能力; 而MERRA资料适用于研究西南和西北区域的大气水汽收支情况, 水循环各要素能够很好地保持平衡.

通过对比分析Interim与MERRA资料中国夏季大气水分循环的时空变化特征, 可以评估上述资料对中国地区水循环过程的再现能力及其局限性, 为利用再分析资料研究中国地区水循环特征提供一定的参考依据. 目前, 获取全球或区域尺度上的水循环大气气候观测资料仍存在一定的难度, 而不同再分析资料也存在明显的差别, 针对这些问题仍需要开展进一步的深入研究.

## 参考文献


[1] Ye M, Wu Y P, Zhou J, Wu H, Tu G 2014 *Acta Phys. Sin.* **63** 129201 (in Chinese) [叶敏, 吴永萍, 周杰, 吴浩, 涂钢 2014 物理学报 **63** 129201]

[2] Feng G L, Yang H W, Zhang S X, Wang K, Shen B Z 2012 *Chin. J. Atmos. Sci.* **36** 1009 (in Chinese) [封国林, 杨涵洧, 张世轩, 王阔, 沈柏竹 2012 大气科学 **36** 1009]

[3] Shen B Z, Zhang S X, Yang H W, Wang K, Feng G L 2012 *Acta Phys. Sin.* **61** 109202 (in Chinese) [沈柏竹, 张世轩, 杨涵洧, 王阔, 封国林 2012 物理学报 **61** 109202]

[4] Boucher O, Myhre G, Myhre A 2000 *Climate Dyn.* **22** 597

[5] IPCC 2013 *Climate Change 2013 The Physical Science Basis* (Cambridge: Cambridge University Press) p403

[6] Zhao R X, Wu G X 2007 *Acta Meteor. Sin.* **65** 416 (in Chinese) [赵瑞霞, 吴国雄 2007 气象学报 **65** 416]

[7] Wu Y P 2011 *Ph. D. Dissertation* (Lanzhou: Lanzhou University) (in Chinese) [吴永萍 2011 博士学位论文 (兰州: 兰州大学)]

[8] Zhang X W, Zhou S X 2010 *Preliminary Study of Air Hydrology* (Beijing: Higher Education Press) p18 (in Chinese) [张学文, 周少祥 2010 空中水文学初探 (北京: 高等教育出版社) 第18页]

[9] Bengtsson L 2010 *Environ. Res. Lett.* **5** 025002

[10] Liu G W 1997 *Atmospheric Processes in Hydrologic Cycle* (Beijing: Science Press) pp19–24 (in Chinese) [刘国纬 1997 水文循环的大气过程 (北京: 科学出版社) 第19—24页]

[11] Cui Y F, Liu G W 1990 *J. China Hydrol.* **4** 22 (in Chinese) [崔一峰, 刘国纬 1990 水文 **4** 22]

[12] Zhai P M, Eskridge R E 1997 *J. Climate* **10** 2643

[13] Shi X Y, Shi X H 2008 *J. Appl. Meteorol. Sci.* **19** 41 (in Chinese) [施小英, 施晓晖 2008 应用气象学报 **19** 41]

[14] Yi L, Tao S Y 1996 *Climat. Environ. Res.* **1** 63 (in Chinese) [伊兰, 陶诗言 1996 气候与环境研究 **1** 63]

[15] Zhang W J, Zhou T J, Yu R C 2007 *Chin. J. Atmos. Sci.* **31** 329 (in Chinese) [张文君, 周天军, 宇如聪 2007 大气科学 **31** 329]

[16] Zhao T B, Fu C B, Ke Z J, Guo W D 2010 *Adv. Earth Sci.* **25** 242 (in Chinese) [赵天保, 符淙斌, 柯宗建, 郭维栋 2010 地球科学进展 **25** 242]

[17] Lorenz C, Kunstmann H 2012 *J. Hydrometeor.* **13** 1397

[18] Dee D P, Uppala S M, Simmons A J, *et al.* 2011 *Q. J. R. Meteorol. Soc.* **137** 553

[19] Uppala S M, Kallberg P W, Simmons A J 2005 *Q. J. R. Meteorol. Soc.* **131** 2961

[20] Rienecker M M, Suarez M J, Gelaro R 2011 *J. Climate* **24** 3624

[21] Su T, Lu Z Y, Zhou J, Hou W, Li Y, Tu G 2014 *Acta Phys. Sin.* **63** 099201 (in Chinese) [苏涛, 卢震宇, 周杰, 侯威, 李悦, 涂钢 2014 物理学报 **63** 099201]

[22] Bisselink B, Dolman A J 2008 *J. Hydrometeor.* **9** 1973

[23] Jones P D, Groisman P Y, Coughlan M, Plummer N, Wang W C, Karl T R 1990 *Nature* **347** 169

[24] Shi N 2009 *Meteorological Statistical Forecast* (Beijing: China Meteorological Press) pp15–34 (in Chinese) [施能 2009 气象统计预报 (北京: 气象出版社) 第15—34页]

[25] Zhou J, Wu Y P, Feng G L, Hu J G 2013 *Acta Phys. Sin.* **62** 199202 (in Chinese) [周杰, 吴永萍, 封国林, 胡经国 2013 物理学报 **62** 199202]

[26] Shi N, Huang X X, Yang Y 2003 *Chin. J. Atmos. Sci.* **27** 971 (in Chinese) [施能, 黄先香, 杨扬 2003 大气科学 **27** 971]

[27] Liu Y B 2011 *Hydroclimatology: Perspectives and Applications* (Beijing: Higher Education Press) pp3–37 (in Chinese) [刘元波 2011 水文气候学——视角与应用 (北京: 高等教育出版社) 第3–37页]

[28] Mariotti A 2010 *J. Climate* **23** 1513

[29] Douville H, Ribes A, Decharme B, Alkama R, Sheffield J 2013 *Nature Climate Change* **3** 59

[30] Zuo H C, Li D L, Hu Y Q, Bao Y, Lü S H 2005 *Chin. Sci. Bull.* **50** 1125 (in Chinese) [左洪超, 李栋梁, 胡隐樵, 鲍艳, 吕世华 2005 科学通报 **50** 1125]

# The characteristics of the summer atmospheric water cycle over China and comparison of ERA-Interim and MERRA reanalysis*

Su Tao[1)] Feng Guo-Lin[2)†]

1) (*College of Atmospheric Sciences, Lanzhou University, Lanzhou 730000, China*)

2) (*Laboratory for Climate Studies of China Meteorological Administration, National Climate Center, Beijing 100081, China*)

( Received 24 June 2014; revised manuscript received 8 August 2014 )

**Abstract**

Atmospheric water cycle process includes precipitation, evaporation, water vapor transport and other links. The temporal and spatial characteristics of the atmospheric water cycle over China in summer are investigated by using the ERA-Interim and MERRA reanalysis from 1979 to 2012. Comparison and performance analyses of these two reanalysis data are given. The obtained results are as follows. 1) the spatial distributions of precipitation, evaporation and precipitable water are highly similar to each other, and all gradually decrease from southeast coast to northwest inland regions. Because the differences in physical condition, precipitation and evaporation among different underlying surfaces, mutually promot or mutually restrict each other, the interactions among them have positive and negative feedback mechanisms. Precipitable water mainly concentrates in the ground to the 700 hPa height, accounts for about 75% of the total quantity. 2) All of the atmospheric water cycle elements have obvious characteristics of climate change, especially in these areas like Northwest China, Tibet and Northeast China. The zonal flux of water vapor transport significantly decreases in most parts of the northern, while the meridional flux of water vapor transport significantly increases in the northern region of Northwest China. 3)The reproduction ability to change characteristics of precipitation is better than that of evaporation based on these reanalyses. The temporal and spatial distribution characteristics of moisture transport situation and the various levels of atmospheric water vapor content are highly consistent with each other. The simulations of flux climate change trend of precipitation and water vapor transport are more accurate and more reliable. 4) Interim reanalysis is applicable to the study of the southwest, Southeast and northeast regional atmospheric water balance, water cycle elements can maintain balance well, while MERRA reanalysis is more reasonable in Southwest and northwest.

**Keywords:** atmospheric water cycle, reanalysis data, moisture budget of atmospheric, climatic variation trend

**PACS:** 92.40.Zg, 92.60.Ry **DOI:** 10.7498/aps.63.249201

* Project supported by the National Basic Research Program of China (Grant Nos. 2012CB955902, 2013CB430204) and the Special Scientific Research Fund of Meteorological Public Welfare Profession of China (Grant No. GYHY201106016).

† Corresponding author. E-mail: fenggl@cma.gov.cn

# ACTA PHYSICA SINICA

## Vol. 63, No. 24, December 2014

## CONTENTS

### GENERAL

240201 **Homotopic mapping solving method of transfers model with a class of generalized femtosecond pulse laser for nano metal**
*Xie Feng  Lin Wan-Tao  Mo Jia-Qi*

240202 **Expanded four-dimensional variatiaonal data assimilation method to optimize model physical parameters**
*Wang Yun-Feng  Gu Cheng-Ming  Zhang Xiao-Hui  Wang Yu-Shun  Han Yue-Qi  Wang Yun-Feng*

240301 **Analytical solutions to pulsed eddy current field excited by a differently oriented probe coil outside a conducting ferromagnetic pipe**
*Chen Xing-Le  Lei Yin-Zhao*

240302 **Differential quotient rules of operator in composite function and its applications in quantum physics**
*Xu Shi-Min  Xu Xing-Lei  Li Hong-Qi  Wang Ji-Suo*

240303 **Influences of mesoscale sandstorm on the quantum satellite communication channel and performance simulation**
*Nie Min  Shang Peng-Gang  Yang Guang  Zhang Mei-Ling  Pei Chang-Xing*

240501 **Microblog propagation network model based on mean-field theory**
*Wu Teng-Fei  Zhou Chang-Le  Wang Xiao-Hua  Huang Xiao-Xi  Chen Zhi-Qun  Wang Rong-Bo*

240502 **Thermodynamical properties of a three-dimensional free electron gas confined in a one-dimensional harmonical potential**
*Shao Zong-Qian  Chen Jin-Wang  Li Yu-Qi  Pan Xiao-Yin*

240503 **Generation and application of non-ergodic noise**
*Liu Yan  Bao Jing-Dong*

240504 **Modeling and analysis of piezoelectric vibration energy harvesting system using permanent magnetics**
*Tang Wei  Wang Xiao-Pu  Cao Jing-Jun*

240505 **Wien-bridge chaotic oscillator based on fisrt-order generalized memristor**
*Yu Qing  Bao Bo-Cheng  Hu Feng-Wei  Xu Quan  Chen Mo  Wang Jiang*

240506 **A novel four-dimensional multi-wing hyper-chaotic attractor and its application in image encryption**
*Peng Zai-Ping  Wang Chun-Hua  Lin Yuan  Luo Xiao-Wen*

240507 **Doppler power spectrum density and multi-antenna system performance in three-dimensional environment**
*Zhou Jie  Wang Ya-Lin  Hisakazu Kikuchi*

(*Continued*)

240508 **The shape regulation of probability density function for stochastic systems**
*Yang Heng-Zhan Qian Fu-Cai Gao Yun Xie Guo*

240509 **Analysis of scale-free characteristic on sharp variation point of traffic flow**
*Zhang Yong Li Shi-Gao*

240601 **Cross-phase modulation typed frequency resolved optical gating measurement for ultra-short pulses using a single mode fiber**
*Ma Xiao-Lu Li Pei-Li Guo Hai-Li Zhang Yi Zhu Tian-Yang Cao Feng-Jiao*

240701 **Refractive index sensing characteristic of a hybrid-Fabry-Perot interferometer based on an in-fiber ellipsoidal cavity**
*Wang Ting-Ting Ge Yi-Xian Chang Jian-Hua Ke Wei Wang Ming*

240702 **A new approach to designing circular grating focusing reflector**
*Ma Chang-Lian Huang Yong-Qing Duan Xiao-Feng Ren Xiao-Min Wang Qi Wang Jun Zhang Xia Cai Shi-Wei*

## ATOMIC AND MOLECULAR PHYSICS

243101 **Structural and electronic properties of the $B_nY$ ($n = 1$–$11$) clusters**
*Ruan Wen Yu Xiao-Guang Xie An-Dong Wu Dong-Lan Luo Wen-Lang*

243102 **First-principles study of electronic structure and optical properties of $TiO_2$ nanotubes**
*Xie Zhi Cheng Wen-Dan*

243601 **Generations of energetic deuterons and neutrons from the Coulomb explosion of deuterated ethane clusters**
*Dai Li-Jiao Li Hong-Yu*

## ELECTROMAGENTISM, OPTICS, ACOUSTICS, HEAT TRANSFER, CLASSICAL MECHANICS, AND FLUID DYNAMICS

244101 **Modified equivalent current approximation and graphical electromagnetic computing method of analyzing radar cross section of missile target scatterer covered with thermal protection layer**
*Zhu Yan-Ju Jiang Yue-Song Hua Hou-Qiang Zhang Chong-Hui Xin Can-Wei*

244102 **Design of a novel wideband directivity patch antenna**
*Guo Rong Cao Xiang-Yu Yuan Zi-Dong Xu Xue-Fei*

244103 **Experimental study on multiple-ring vortex beams**
*Huang Su-Juan Gu Ting-Ting Miao Zhuang He Chao Wang Ting-Yun*

244201 **Analysis and improvement of reconstruction phase error in the image plane digital holography**
*Shi Bing-Chuan Zhu Zhu-Qing Wang Xiao-Lei Xi Si-Xing Gong Li-Ping*

244202 **Measuring topology charge of vortex beam using digital holography**
*Wang Lin Yuan Cao-Jin Nie Shou-Ping Li Chong-Guang Zhang Hui-Li Zhao Ying-Chun Zhang Xiu-Ying Feng Shao-Tong*

244203 **Construction of a strongly coupled cavity quantum electrodynamics system with easy accessibility of single or multiple intra-cavity atoms**
*Wen Rui-Juan Du Jin-Jin Li Wen-Fang Li Gang Zhang Tian-Cai*

(*Continued*)

244204 **Acquiring narrow linewidth microwave signals based on an optical injection semiconductor laser under subharmonic microwave modulation**
*Mao Song Wu Zheng-Mao Fan Li Yang Hai-Bo Zhao Mao-Rong Xia Guang-Qiong*

244205 **Single-atom transfer in a strongly coupled cavity quantum electrodynamics: experiment and Monte Carlo simulation**
*Li Wen-Fang Du Jin-Jin Wen Rui-Juan Yang Peng-Fei Li Gang Zhang Tian-Cai*

244206 **Detections and analyses of aerosol optical properties under different weather conditions using multi-wavelength Mie lidar**
*Di Hui-Ge Hou Xiao-Long Zhao Hu Yan Lei-Jie Wei Xin Zhao Huan Hua Deng-Xin*

244207 **Tamm state of semi-infinite photonic crystal based on surface defect cavity with porous silicon and its refractive index sensing mechanism**
*Chen Ying Fan Hui-Qing Lu Bo*

244208 **Optical control of the vibrational excitation of the polyatomic ions via strong field multi-photon ionization**
*Liu Yu-Zhu Gerber Thomas Knopp Gregor*

## CONDENSED MATTER: STRUCTURAL, MECHANICAL, AND THERMAL PROPERTIES

246101 **Molecular dynamics study of epitaxial compressive strain influence on the radiation resistance of $BaTiO_3$ ferroelectrics**
*Wang Yu-Zhen Ma Ying Zhou Yi-Chun*

246102 **Shock response and evolution mechanism of brittle material containing micro-voids**
*Yu Yin He Hong-Liang Wang Wen-Qiang Lu Tie-Cheng*

246103 **Optical properties and laser damage performance of $SiO_2$ irradiated by high-power pulsed electron beam**
*Zhong Mian Yang Liang Ren Wei Xiang Xia Liu Xiang Lian You-Yun Xu Shi-Zhen Guo De-Cheng Zheng Wan-Guo Yuan Xiao-Dong*

246801 **Effect of titanium ion energy on surface structure during the amorphous titanium dioxide film deposition**
*Chen Xian Wang Yan-Wu Wang Xiao-Yan An Shu-Dong Wang Xiao-Bo Zhao Yu-Qing*

## CONDENSED MATTER: ELECTRONIC STRUCTURE, ELECTRICAL, MAGNETIC, AND OPTICAL PROPERTIES

247101 **First-principles study of $Ag_2ZnSnS_4$ as a photocatalyst**
*Huang Dan Ju Zhi-Ping Li Chang-Sheng Yao Chun-Mei Guo Jin*

247301 **New super junction lateral double-diffused MOSFET with electric field modulation by differently doping the buffered layer**
*Duan Bao-Xing Cao Zhen Yuan Song Yuan Xiao-Ning Yang Yin-Tang*

247501 **Evolution of vortex configuration for superconducting ring in the presence of an externally applied field**
*Shi Liang-Ma Zhou Ming-Jian Zhu Ren-Yi*

247502 **Static magnetization and demagnetizing field distribution of the amorphous wire in non-uniform applied field**
*Zhao Yin Xu Hong-Guang Zhang Qin-Yu*

(*Continued*)

247801 **Spectroscopic properties of $\sim$ 2 μm emissions of $Tm^{3+}$-doped germanate-tellurite glasses**
*Gao Song Wang Xin Fan Xiao-Kang Li Ke-Feng Liao Mei-Song Hu Li-Li*

247802 **Origin of nanopore alumina film photoluminescence: three kinds of defect centers**
*Li Guo-Dong Wang Qian Deng Bao-Xia Zhang Ya-Jing*

247803 **Nanocrystalline aluminum studied by positron annihilation lifetime spectroscopy**
*Li Yu Luo Jiang-Shan Wang Zhu Yang Meng-Sheng Xing Pi-Feng Yi Yong Lei Hai-Le*

## INTERDISCIPLINARY PHYSICS AND RELATED AREAS OF SCIENCE AND TECHNOLOGY

248101 **First-principles study of the effect of lanthanum on the Cu diffusion mechanism in bcc-Fe**
*Gao Xue-Yun Wang Hai-Yan Li Chun-Long Ren Hui-Ping Li De-Chao Liu Zong-Chang*

248102 **Calculation methods of InGaAsSb quaternary alloy band gap**
*Liu Chao Wei Zhi-Peng An Ning He Bin-Tai Liu Peng-Cheng Liu Guo-Jun*

248103 **Process parameters of large single crystal graphene prepared by chemical vapor deposition**
*Han Lin-Zhi Zhao Zhan-Xia Ma Zhong-Quan*

248104 **Effect of additive zinc on larger diamond crystal growth**
*Zhou Zhen-Xiang Jia Xiao-Peng Li Yong Yan Bing-Min Wang Fang-Biao Fang Chao Chen Ning Li Ya-Dong Ma Hong-An*

248105 **Nano-scale lithography and *in-situ* electrical measurements based on the micro-chips in a transmission electron microscope**
*Zhang Chao Fang Liang Sui Bing-Cai Xu Qiang Wang Hui*

248106 **Syntheses of negative thermal expansion materials $Sc_2(MO_4)_3$ ($M$ = W, Mo) with a $CO_2$ laser and their Raman spectra**
*Liang Yuan Xing Huai-Zhong Chao Ming-Ju Liang Er-Jun*

248107 **Phase transition and structure of $LuTaO_4$**
*Xing Xue Wang Xiao-Fei Zhang Qing-Li Sun Gui-Hua Liu Wen-Peng Sun Dun-Lu Yin Shao-Tang*

248201 **An optimization method for ion etching yield modeling combined with factual etching data**
*Gao Yang-Fu Sun Xiao-Min Song Yi-Xu Ruan Cong*

248401 **Multi-period analysis of current-mode pulse-train controlled continuous conduction mode converter**
*Sha Jin Xu Jian-Ping Xu Li-Jun Zhong Shu*

248402 **Outline design and performance analysis of navigation constellation near earth-moon libration point**
*Meng Yun-He Chen Qi-Feng*

248403 **Efficiency improvement in organic solar cells by doping cholesteric liquid crystal**
*Li Meng Niu He-Ying Yao Lu-Yan Wang Dong-Liang Zhou Zhong-Po Ma Heng*

248501 **Realization and experiment of vertical multijunction integrated photovoltaic Si X-ray detector**
*Zhang Zhi-Guo*

(*Continued*)

248502 **Two-dimensional model of symmetrical double-gate strained Si single Halo metal-oxide semiconductor field effect transistor with gate stack dielectric**
*Xin Yan-Hui Liu Hong-Xia Wang Shu-Long Fan Xiao-Jiao*

248503 **Three-dimensional simulation study of bias effect on single event effects of SiGe heterojunction bipolar transistor**
*Zhang Jin-Xin He Chao-Hui Guo Hong-Xia Tang Du Xiong Cen Li Pei Wang Xin*

248504 **Influence of horizontal static magnetic field on the stability of electromagnetic levitated Cu molten droplet**
*Song Qi-Hui Shi Wan-Yuan*

248701 **Phase noise induced single or double coherence resonances of neural firing**
*Ding Xue-Li Li Yu-Ye*

248702 **Magnetocardiac signal analysis based on multiple time windows beamformer method**
*Wang Wei-Yuan Jiang Shi-Qin Zhou Da-Fang Zhu Jia-Chen Yan Yu-Rui Quan Wei-Wei*

248801 **A first principles study on the synergistic catalytic mechanism of anion, cation ions in $TiF_3$, $TiCl_3$ catalysts for $LiBH_4$ hydrogen-storage materials**
*Liu Gui-Li Zhang Guo-Ying Bao Jun-Shan Zhang Hui*

248901 **Congestion control in complex network based on local routing strategy**
*Liu Wei-Yan Liu Bin*

## GEOPHYSICS, ASTRONOMY, AND ASTROPHYSICS

249201 **The characteristics of the summer atmospheric water cycle over China and comparison of ERA-Interim and MERRA reanalysis**
*Su Tao Feng Guo-Lin*

# 公 告

为实现录用稿件的提前在线全文出版, 我刊采用单篇论文给定编码的目录方案, 编码的设定按照文章的 PACS 代码的前两位数字及稿件录用时间的先后排序.

《物理学报》已加入“中国知网”优先数字出版, 录用文章将先于印刷版期刊在中国知网 www.cnki.net 在线优先发布, 如果作者不愿优先出版可在版权协议里补充说明, 如无补充说明, 编辑部将视为同意授权.

《物理学报》编辑部


**物 理 学 报 ( WULI XUEBAO )**

( 半月刊, **1933 年创刊** )

2014 年 12 月 第 63 卷 第 24 期

**ACTA PHYSICA SINICA**

**( Semimonthly First Published in 1933 )**

Vol. 63 No. 24 December 2014



**版 权 所 有**

**© 2014 Chinese Physical Society**



| | |
|---|---|
| 编 辑 | 物理学报编辑委员会<br>(北京 603 信箱 邮政编码 100190) |
| 主 编 | 欧阳钟灿 |
| 主 管 | 中国科学院 |
| 主 办 | 中国物理学会<br>中国科学院物理研究所<br>(北京 603 信箱 邮政编码 100190) |
| 出 版 | 中国物理学会 |
| 印刷装订 | 北京科信印刷有限公司 |
| 总发行处 | 北京报刊发行局 |
| 订 购 处 | 全国各邮电局 |
| 国外总发行 | 中国国际图书贸易总公司<br>(北京 399 信箱 邮政编码 100044) |

广告经营许可证 京海工商广字第0335号

Edited by the Editorial Board of ACTA PHYSICA SINICA

Address of the Editorial Board
c/o P. O. Box 603, Beijing 100190, China
apsoffice@iphy.ac.cn http://wulixb.iphy.ac.cn

Editor-in-Chief Ouyang Zhong-Can

Published by Chinese Physical Society and Institute of Physics, Chinese Academy of Sciences
P. O. Box 603, Beijing 100190, China

Distributed by China International Book Trading Corporation
P. O. Box 399, Beijing 100044, China

ISSN 1000-3290
国内邮发代号: 2-425

国内统一刊号: CN11-1958/O4
国外发行代号: M52 定价: 120 元

公 开 发 行

司东，袁媛，崔童，等. 2014. 2013 年海洋和大气环流异常及对中国气候的影响. 气象，40(4)：494-501.

# 2013 年海洋和大气环流异常及对中国气候的影响*

司 东[1,2] 袁 媛[1] 崔 童[1] 孙 冷[1] 王东阡[1]
柳艳菊[1] 郭艳君[1] 王遵娅[1]

1 中国气象局气候研究开放实验室，北京 100081
2 南京信息工程大学气象灾害预报预警与评估协同创新中心，南京 210044

**提 要**：本文对 2013 年海洋和大气环流异常特征进行分析，讨论这些异常特征对中国气温和降水的主要影响。结果表明：2012/2013 年冬季，北极涛动持续维持负位相，500 hPa 位势高度场上，欧亚大陆中高纬环流呈“两槽一脊”的环流形势，乌拉尔山的高压脊持续偏强，而东亚槽也异常偏强，导致全国平均气温较常年同期偏低。季内，西伯利亚高压强度变化显著，与之相对应，我国气温季内阶段性变化大，前冬冷、后冬暖。进一步研究表明，前秋北极海冰的大幅偏少是造成东亚冬季风偏强的重要原因。2013 年冬季至夏季，赤道中东太平洋海温异常偏低而海洋性大陆至西太平洋海温异常偏高，受此影响，夏季西太平洋副热带高压位置明显偏北，导致我国北方夏季多雨。与此同时，受西太平洋副热带高压下沉气流的控制，我国南方大部高温持续。2013 年南海夏季风爆发偏早两候，结束偏晚 4 候，强度偏弱。

**关键词**：海温，大气环流，气候异常
**中图分类号**：P461 **文献标志码**：A **doi**：10.7519/j.issn.1000-0526.2014.04.012

# Anomalies of Ocean and Atmospheric Circulation in 2013 and Their Impacts on Climate in China

SI Dong[1,2] YUAN Yuan[1] CUI Tong[1] SUN Leng[1] WANG Dongqian[1]
LIU Yanju[1] GUO Yanjun[1] WANG Zunya[1]

1 Laboratory for Climate Studies, China Meteorological Administration, Beijing 100081
2 Collaborative Innovation Centre on Forecast and Evaluation of Meteorological Disasters, Nanjing University of Information Science and Technology, Nanjing 210044

**Abstract**: Anomalies of oceanic and atmospheric circulations are analyzed and their impacts on temperature and precipitation anomalies of 2013 in China are discussed. The results show that the Arctic Oscillation (AO) experienced negative phase during the 2012/2013 winter. At 500 hPa, a “two troughs and one ridge” anomalous geopotential height pattern dominated the mid-high latitudes in Eurasia, leading to an enhanced ridge and trough over Urals and East Asia, respectively, and further leading to be colder than normal situation over China. While the Siberian high exhibited strong intra-seasonal variations, the temperature over China had two-stage variations last winter, warmer in the early winter and colder in the late winter. Further research indicates that the reduced Arctic sea ice extent in the last autumn was responsible for the stronger East Asian winter monsoon. During the period from winter to summer 2013, the anomalous low sea surface temperature (SST) was observed in the tropical central and eastern Pacific, while abnormal high SST in tropical western Pacific and oceanic continent. As a response of atmospheric circulation to the

* 国家重点基础研究发展(973)计划(2013CB430202 和 2012CB955203)及中国气象局气候研究开放实验室 2012/2013 年度开放青年基金资助项目共同资助
2014 年 1 月 21 日收稿； 2014 年 2 月 23 日收修定稿
第一作者：司东，主要从事气候诊断研究. Email：sidong@cma.gov.cn

anomalous tropical oceanic condition, the western Pacific subtropical high extended further north, leading to more precipitation over the northern part of China during the summer. Meanwhile, the northward extending of the western Pacific subtropical high dominated most southern part of China, causing higher temperature and less precipitation than normal in the region in summer. In 2013, onset of South China Sea summer monsoon was 2 pentads earlier than normal and the ending was 4 pentads later than normal, and the intensity was weaker than normal.

**Key words**: sea surface temperature, general circulation, climatic anomaly

## 引　言

在全球变暖背景下,极端天气、气候事件频繁发生,对重大天气、气候事件的成因分析已经成为气候业务服务的重要内容之一(李清泉等,2013)。了解和掌握气候系统关键异常信号及其气候影响机理,分析气候异常的成因,对正在发生或刚发生过的气候异常事件及时进行诊断分析(高辉等,2008;张培群等,2009;艾婉秀等,2010;贾小龙等,2011;王朋岭等,2012;王遵娅等,2013a),有利于加深对气候异常形成机制或机理的认识,同时为气候预测提供参考。

2013 年,我国极端天气气候事件较前一年少,但局地气象灾害较重。2013 年,降水总体偏多,但时空分布不均,前少后多、北多南少;气温总体偏高,但东北偏低。全国平均降水量 653.6 mm,较常年偏多 4%,比 2012 年略偏少;冬季降水偏少,春、夏、秋三季偏多。全国平均气温较常年偏高 0.7℃,为 1961 年以来第四暖年,较 2012 年偏高 0.8℃;冬季气温偏低,春、夏、秋三季偏高。2013 年汛期,我国主要多雨带位置偏北。华南前汛期开始早、结束晚、雨量多,长江中下游入梅晚、出梅早、雨量少;华北雨季早、雨量偏多;华西秋雨开始早、结束晚、雨量多;西南雨季开始早、结束晚、雨量少。从区域情况看,东北、华北、西北、华南降水偏多,其中东北偏多 22%、华北偏多 14%,长江中下游和西南偏少。

本文将主要从海温异常和大气环流异常两方面来分析产生我国 2013 年气候异常的原因,揭示其可能的成因机制。

## 1　资　料

本文主要使用了国家气候中心的"气候系统监测—诊断—预测—评估系统"提供的资料和产品及 1961—2013 年 NCEP/NCAR 的 2.5°×2.5°水平分辨率的逐日高度场、温度场、风场和比湿场等再分析资料。中国地区的气温、降水资料来源于中国气象局国家气象信息中心整编的中国地区台站观测气候数据集。本文使用的各要素的气候平均值为 1981—2010 年平均值。

## 2　海温异常及其影响

### 2.1　赤道太平洋海温

2013 年,赤道中东太平洋大部海温呈弱冷水状态。

2013 年 1—3 月,赤道中东太平洋大部海温维持前期的弱冷水状态,并呈现出逐渐减弱的趋势;4 月起,赤道中东太平洋冷海温再次发展,5—7 月发展到最强,Niño Z 指数(李晓燕等,2000)在 7 月达到−0.5℃,但冷海温向西扩展的范围并不大,低于−0.5℃的冷水区域一直维持在赤道中东太平洋东部(150°W 以东);9—12 月,冷海温明显减弱。在赤道中东太平洋冷水波动的过程中,赤道西太平洋海温一直维持较明显的偏暖状态(图1)。年内,尽管

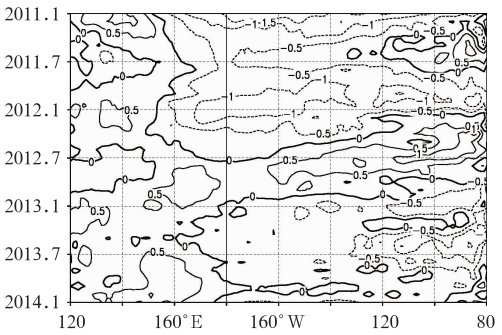


图 1　赤道太平洋(5°S～5°N)海表温度距平时间-经度剖面(单位:℃)

Fig. 1　Time-longitude section of monthly mean equatorial (5°S～5°N) sea surface temperature anomalies of Pacific Ocean (unit: ℃)

赤道中东太平洋的冷水状态没有发展成一次 La Niña 事件，但大气仍较明显地表现出了对冷水波动的响应。主要表现在夏季西太平洋副热带高压（简称西太副高）位置偏北，导致夏季我国南方大部分地区持续受异常下沉运动控制，对流活动受到抑制，降水偏少，高温持续发展。相反，受西太副高偏北影响，我国东北、华北夏季降水异常偏多。

### 2.2 印度洋海温

2013 年 5—8 月，热带印度洋呈现出中东部暖而西部正常的异常海温分布[印度洋偶极子（IOD）负位相]。定义热带印度洋海温偶极子指数为热带西印度洋（10°S～10°N、50°～70°E）的海温距平与热带东南印度洋（10°S～0°、90°～110°E）的海温距平差（Saji et al，1999；Webster et al，1999）。可以发现，5 月的偶极子指数已超过－0.5，而 8 月的偶极子指数也在－0.5 以下（图 2）。

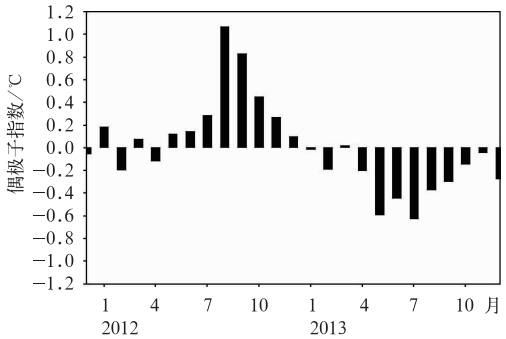


图 2 热带印度洋偶极子指数逐月变化

Fig. 2 Monthly variation of tropical Indian Ocean dipole (IOD) index

## 3 北半球大气环流异常及其影响

### 3.1 2011/2012 年冬季

2012/2013 年冬季，全国平均气温为－3.7℃，较常年同期（－3.4℃）偏低 0.3℃（王东阡等，2013）。与常年同期相比，东北大部、内蒙古东部、华北大部、华东大部、华中大部、新疆北部和中部、西藏西部部分地区气温偏低，其中东北大部、内蒙古东部、华北东北部、新疆北部和西藏西部局部地区偏低 2～4℃，局部偏低 4℃以上。

2012/2013 年冬季，北极涛动（AO）指数持续维持负位相，有利于极地的冷空气向南侵袭影响我国。500 hPa 位势高度场上，欧亚大陆中高纬环流呈“两槽一脊”的环流形势，乌拉尔山的高压脊持续偏强，而东亚槽也异常偏强，有利于冷空气沿高空槽南下影响我国（图 3）。Wu 等（2013）研究发现，该异常环流型与冬季极端天气型的盛行模态非常相似，有利于我国冬季极端低温天气的出现。而该异常环流型的出现与前期秋季北极海冰异常偏少也存在密切联系。Wu 等（2011）研究发现，前期海冰偏少有利于欧亚大陆北部地区出现异常阻塞环流异常，导致西伯利亚高压阶段性加强，进而导致我国出现极端阶段性低温。观测显示，自 2012 年夏季开始，北极海冰覆盖范围持续异常偏小，偏小幅度超过气候态两倍标准差，这一状况一直持续到 2012/2013 年冬季；其中 8 月中旬至 10 月中旬，海冰覆盖面积持续低于自有观测资料以来年海冰覆盖面积的最小纪录——2007 年同期海冰覆盖面积（图略）。而从海冰范围距平分布来看（图 4），秋季北极大部分地区海冰范围较常年明显偏少，巴伦支海北部、喀拉海、拉普捷夫海、楚科奇海、波弗特海和巴芬湾等海域海冰范围较常年同期偏低 20%～60%，其中喀拉海北部和波弗特海偏低 60%以上。因此，前期秋季北极海冰的减少有利于欧亚地区高纬的冷空气南下影响我国，导致冬季我国东北、内蒙古东部、华北、华东等地大范围低温的出现。

季内，我国气温变化呈现前冬冷，后冬暖的阶段性变化特征。前冬是过去 27 年中我国经历的最冷的冬季，东北、华北地区气温均创近 40 年新低；而到后冬又迅速转暖，全国除东北和内蒙古东部偏冷外，其余大部地区气温以偏暖为主。季内，西伯利亚高压强度变化显著，前冬西伯利亚高压偏强，后冬西伯利亚高压偏弱（图 5），这可能是导致我国冬季前冬冷、后冬暖的主要原因。

### 3.2 春季

2013 年春季，全国平均气温较常年同期偏高 1.0℃，平均降水量较常年同期偏多 8.3%，但气温和降水空间分布不均，东北气温持续偏低，华北出现区域性气象干旱。

从图 6a 中可以看到，春季我国大部尤其是西北至华北一带受异常高压脊的控制，盛行下沉气流，不利于降水的产生但有利于气温偏高。图 6b 还显示，在我国西北至华北一带，为水汽的弱辐散区，表明水汽条件不利于这一地区降水的出现，加之气温持续

偏高,使得气象干旱发展。值得注意的是,自冬季以来 AO 持续负位相,尤其在 2013 年 3 月负位相显著加强。这在中高层异常环流场上表现为欧亚中高纬

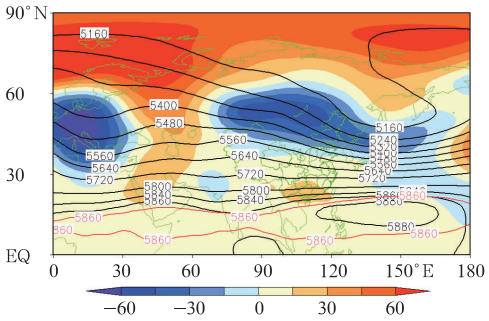


图 3　2012 年 12 月至 2013 年 2 月 500 hPa 平均位势高度(等值线)和距平场(阴影)分布(单位:gpm)

Fig. 3　500 hPa mean geopotential height (contour) and anomalies (shaded areas) from December 2012 to February 2013 (unit: gpm)

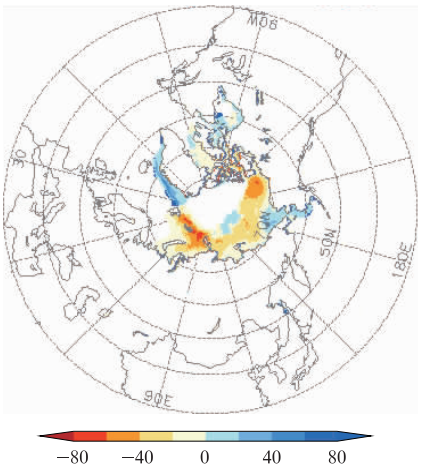


图 4　2012 年秋季北极海冰范围距平分布

Fig. 4　Distribution of sea ice extension anomalies in autumn 2012

地区维持一宽阔的异常低压带而极地区域则为高气压所盘踞,我国东北地区正好处于异常低槽的控制下(图 6a),冷空气频繁影响从而引发持续低温。

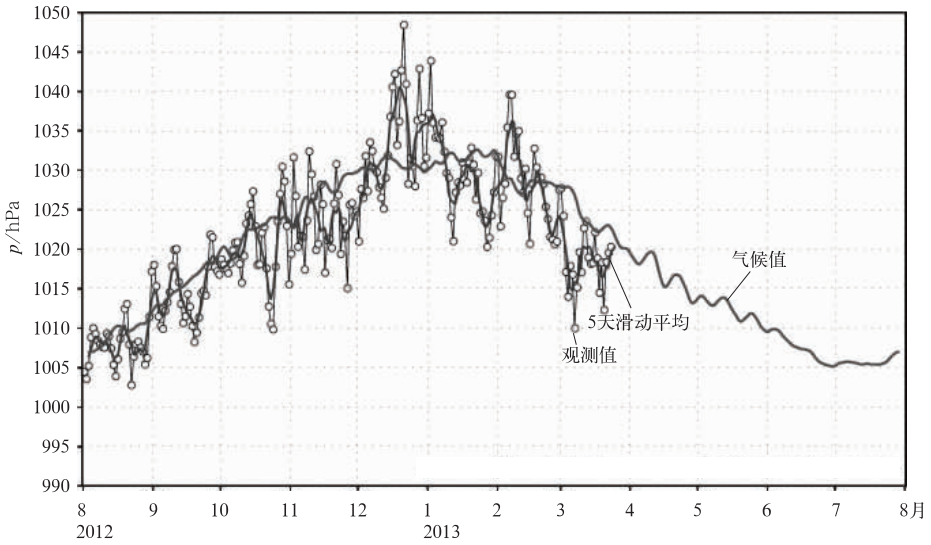


图 5　2012/2013 年冬季西伯利亚高压强度逐日演变(单位:hPa)

Fig. 5　Daily variation of Siberian high intensity index in winter 2012/2013 (unit: hPa)

东北冷涡是我国东北地区特有的天气系统,对东北地区的天气气候有很大影响,是造成东北低温的重要因子。统计发现,2013 年春季东北冷涡活跃且总体偏强,其中 3 月出现 24 次过程,4 月出现 29 次过程,均较常年同期明显偏多,并且该两月冷涡的强度均较常年同期偏强,有利于我国东北地区气温偏低。另外,我国东北地区自 2012 年秋季以来积雪持续偏多,通过增加地表长波辐射,有利于东北温度偏低。并且春季东北积雪季节性融雪消耗热量导致东北气温偏低加剧(王遵娅等,2013b)。

### 3.3　夏季

2013 年夏季,受热带太平洋海洋的影响,西太副高异常偏北,使得东亚夏季风雨带明显偏北。

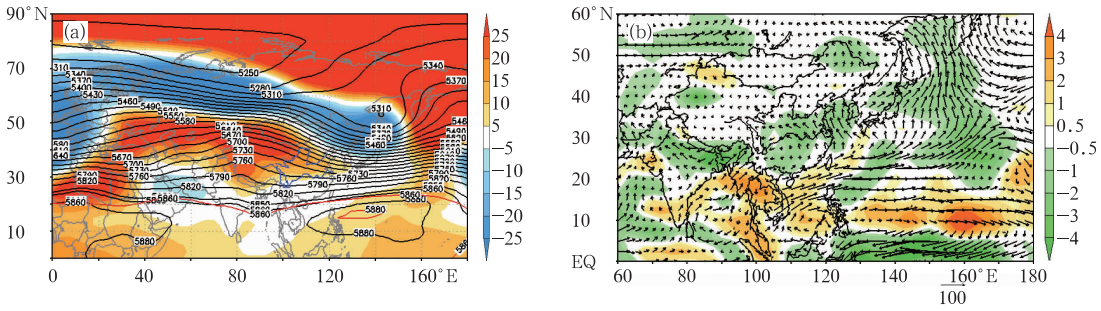


图 6 2013 年 3—5 月平均 500 hPa 位势高度
(a,等值线,单位:gpm)和距平场(a,阴影区,单位:gpm),整层积分的水汽输送通量距平
(b,箭头,单位:kg·s$^{-1}$·m$^{-1}$)和散度距平场(b,阴影区,单位:10$^{-5}$ kg·s$^{-1}$·m$^{-2}$)

Fig. 6 500 hPa mean geopotential height (a, contour, unit: gpm) and anomalies (a, shaded areas, unit: gpm) and moisture transport anomalies vertically integrated from 1000 to 300 hPa (b, vector, unit: kg·s$^{-1}$·m$^{-1}$) and anomalies of divergence and convergence of moisture transport (b, shaded areas, unit: 10$^{-5}$ kg·s$^{-1}$·m$^{-2}$) from March to May 3013

2013 年夏季,500 hPa 高度及距平场上,欧洲大部至西伯利亚西北部为正高度距平控制,而欧洲东南部至东亚北部为宽广的低槽区,这种环流型有利于高纬冷空气南下影响中国北方地区。季内,热带中东太平洋海温偏低而热带西太平洋海温偏高,偏高的热带西太平洋海温有利于热带西太平洋地区对流活跃,气旋式异常环流发展,而热带西太平洋地区偏强的对流活动也可以通过激发异常偏强的局地 Hadley 环流圈,使得西太副高位置偏北(Si et al, 2012);此外,夏季我国西部(四川部分地区)的降水异常偏多,有利于凝结潜热释放,在西太副高西侧激发反气旋性涡度发展,有利于副高的西伸(司东等, 2008)。副高西侧偏南气流与来自南方偏强的季风水汽汇合后,向我国北方地区输入异常偏多的暖湿水汽(图 7b),冷空气和暖湿气流在我国北方地区交汇辐合,造成我国北方地区夏季降水异常偏多。季内,欧亚中高纬度地区的低压槽相对较浅薄,不利于北方地区的冷空气深入南下影响我国的南方地区(图 7a);同时,受西太副高位置偏北、偏西影响,西太副高持续稳定控制我国南方大部分地区,导致该地区持续受异常下沉运动控制,对流活动受到抑制,夏季降水偏少,高温持续以及秋季干旱的出现。

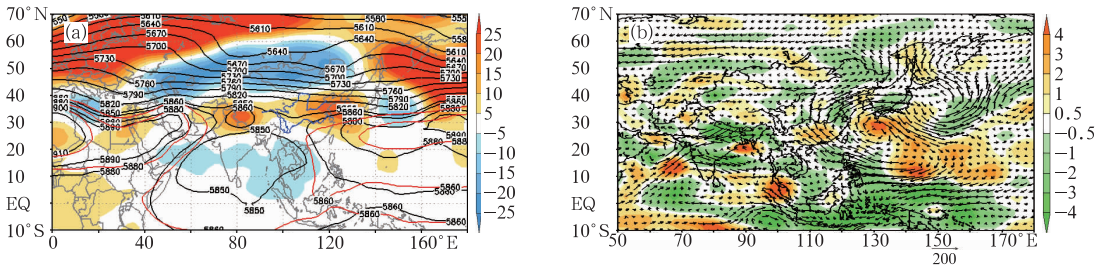


图 7 同图 6,但时间为 2013 年 6—8 月

Fig. 7 Same as Fig. 6, but for the period from June to August 2013

### 3.4 秋季

2013 年秋季,受 AO 正位相、东亚大槽偏弱等因素的影响,秋季我国大部气温偏高。此外,西太副高位置偏北,西北太平洋东南水汽输送异常偏强北伸,造成我国东北、华北一带降水偏多。

2013 年秋季,AO 总体处于正位相,但季内变化显著,其中 9 月中旬至 10 月 AO 处于弱的负位相,而 10 月底以来 AO 维持明显正位相。在此背景下,500 hPa 位势高度场上,亚洲地区以纬向型环流为主,在东亚中高纬呈北低南高的异常环流型,东亚大槽偏弱(图 8a),西伯利亚高压强度偏弱。这样的环流形势不利于中高纬度地区的冷空气南下,我国大部气温接近常年或偏高。季内,西太副高较常年同

期明显偏弱、西伸脊点偏东,脊线位置偏北(图 8a)。受其影响,来自西北太平洋异常的东南风水汽输送明显偏北(图 8b),与北方的冷空气共同作用导致我国秋季东北和华北等地降水偏多,而东南部地区降水偏少。此外,受孟加拉湾热带风暴及西太平洋热带气旋活动影响,四川西部、华南西部等地降水偏多。

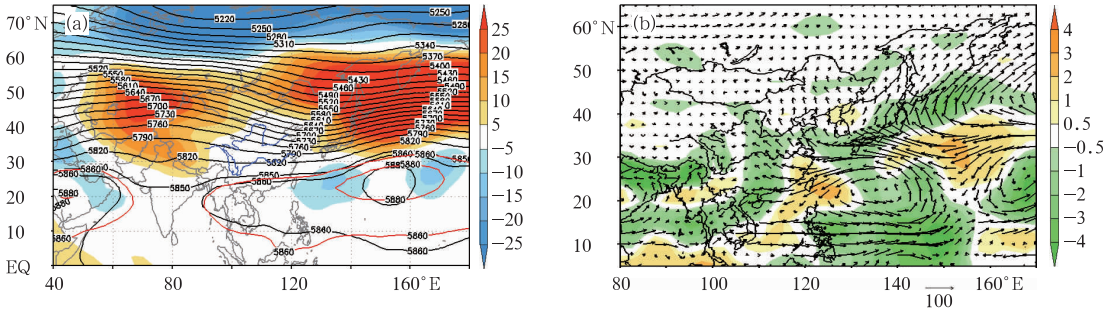


图 8　同图 6,但时间为 2013 年 9—11 月

Fig. 8　Same as Fig. 6, but for the period from September to November 2013

## 4　亚洲夏季风

2013 年南海夏季风爆发偏早 2 候,结束偏晚 4 候,强度偏弱。

### 4.1　南海夏季风

2013 年南海夏季风于 5 月第三候爆发,较常年偏早 2 候。5 月 3 候,对流层低层(850 hPa)赤道印度洋西风加强东伸并北抬,南海地区为热带西南风控制,对流活动明显增强,西太副高撤出南海,南海夏季风环流形势基本建立。同时,南海季风监测区主要监测指标从这一候开始连续 3 候超过季风爆发时的临界值,即监测区内平均纬向风由偏东风转为偏西风、假相当位温大于 340 K(图 9)。

2013 年南海夏季风于 10 月第四候结束,较常年偏晚 4 候,也是连续第八年结束偏晚。10 月 4 候,对流层低层,索马里及 105°E 附近的越赤道气流及赤道印度洋的西风明显减弱,南海地区主要受较强的偏东风控制。同时,监测区内两个主要监测指标从这一候开始连续 2 候下降到临界值以下,即监测区内平均纬向风由偏西风转为偏东风、假相当位温小于 340 K(图 9)。

2013 年南海夏季风强度指数为−1.29,较常年明显偏弱。南海夏季风强度的逐候演变显示(图 10),自 5 月 3 候南海夏季风爆发后,强度呈波动性变化,其中 5 月 3～4 候、6 月 4～5 候、8 月 3～5 候、9 月 3～5 候、10 月 2 候偏强,而其余时段以偏弱为主。

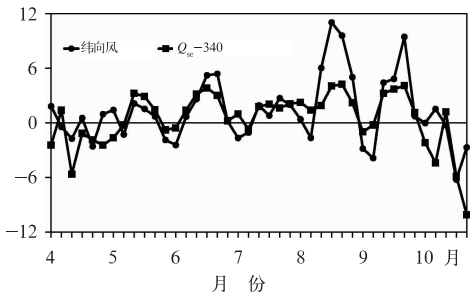


图 9　南海地区(10°～20°N、110°～120°E)纬向风(单位:m·s$^{-1}$)和假相当位温与 340 K 的差值(单位:K)的逐候演变

Fig. 9　Pentad evolution of zonal winds (unit: m·s$^{-1}$) and pseudo-equivalent potential temperature (unit: K) over South China Sea (10°−20°N, 110°−120°E)

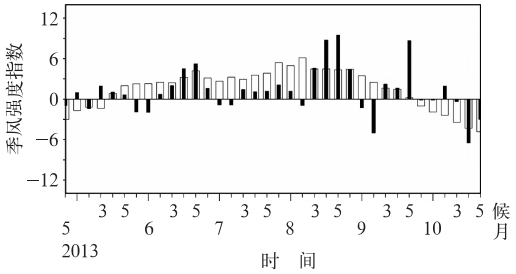


图 10　2013 年 5—10 月逐候南海季风强度指数演变

(空心柱为气候平均值)

Fig. 10　Pentad evolution of South China Sea monsoon index (hollow column: climate averge) from May to October 2013

### 4.2 东亚夏季风

2013 年 6 月，索马里越赤道气流明显偏强；7 月，这支异常的越赤道气流加强东伸展至中南半岛地区，同时西北太平洋地区为异常反气旋性环流控制；8月，索马里越赤道气流明显减弱，西北太平洋地区异常反气旋性环流东撤、南压（图略）。从整个夏季平均的情况看，印度洋西部为异常南风，反映索马里急流偏强，而西北太平洋为异常反气旋性环流（图 11），同时也有利于西太副高加强西伸。受西北太平洋异常反气旋环流的影响，来自西北太平洋的东南风水汽输送明显偏强，有利于我国北方大部地区异常水汽辐合，而我国长江以南大部地区为水汽辐散。

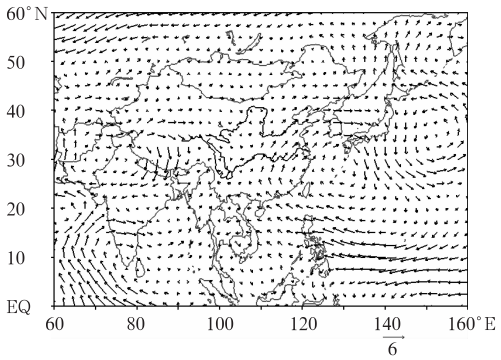


图 11 2013 年 6—8 月平均 850 hPa 异常风场（单位：m·s$^{-1}$）

Fig. 11 Anomalous 850 hPa mean wind field (unit: m·s$^{-1}$) from June to August 3013

### 4.3 夏季风雨带进退特征

2013 年 5 月 3 候至 6 月 1 候，东亚副热带夏季风主要维持在我国华南至江南一带；之后，随着西太副高北推并持续偏北，江南地区率先入梅，6 月我国东部主雨带维持在江淮地区；7 月上旬末至 8 月上旬，我国东部主雨带位于华北地区；8 月中旬起，东部主雨带位置明显南落至 35°N 以南地区；8 月下半月至 9 月中旬，东亚季风明显减弱，伴随西太副高南落以及季风的南撤，雨带有所南移。9 月下旬，东亚季风再次加强，水汽输送明显偏北，造成我国东部出现明显降水。10 月起，随着北方冷空气南下影响我国华南沿海和南海地区，南海地区的热力性质出现明显改变，夏季风开始撤离南海地区，中国东部降水明显减少。10 月 4 候，南海夏季风结束（图 12）。

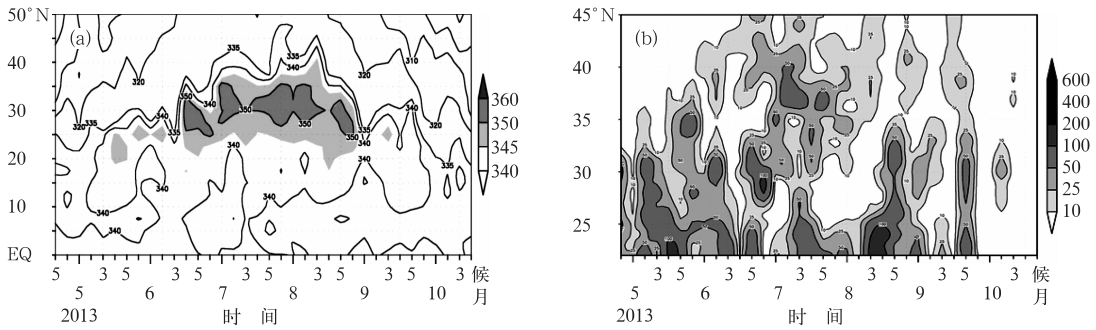


图 12 110°～120°E 候平均假相当位温（a，单位：K）和降水量（b，单位：mm）的纬度-时间剖面

Fig. 12 Time-latitude section of pentad mean pseudo-equivalent potential temperature (a, unit: K) and precipitation (b, unit: mm) averaged over 110°－120°E

### 4.4 雨季特征

根据国家气候中心各雨季监测指标监测显示，2013 年，华南前汛期 3 月 28 日开始，7 月 3 日结束，历时 97 d，累计雨量 830.3 mm。与常年相比，开始偏早，结束偏晚，雨季偏长，雨量偏多。西南雨季 5 月 15 日开始，10 月 19 日结束，历时 157 d，总降雨量 831.1 mm。与常年相比，开始偏早 11 d，结束偏晚 5 d，雨季偏长 16 d，雨量偏少。长江中下游地区梅雨 6 月 23 日入梅，6 月 29 日出梅。入梅偏晚，出梅偏早，梅雨期仅为 6 d，较常年显著偏短，与 1990 年、1971 年并列为 1885 年来历史最短年份。华北雨季 7 月 9 日开始，8 月 13 日结束，历时 35 d；开始与结束时间均较常年偏早，长度偏长；累计降雨量 205.9 mm，较常年偏多。华西秋雨 8 月 31 日开始，11 月 6 日结束，历时 68 d。与常年相比，开始偏早，结束晚，累计雨量 258.8 mm，较常年偏多。

## 5 台风活动异常

2013 年，西北太平洋和南海上共有 31 个台风生成，生成个数较常年同期偏多 7 个；9 个台风在我

国登陆,较常年偏多 2 个。初台和终台登陆时间均偏早;5 个台风登陆时风力在 12 级或以上,强度明显偏强;登陆点均在华南沿海,其中福建 4 个、广东 3 个、海南 2 个,登陆位置总体偏南。全年台风共造成 199 人死亡,67 人失踪,直接经济损失 1262.8 亿元。与 1990—2012 年平均值相比,死亡人数偏少,但直接经济损失为 1990 年以来最大。总体而言,2013 年台风灾情偏重。2013 年登陆我国的 9 个台风中,除 1305 号"贝碧嘉"、1306 号"温比亚"、1308 号"西马仑"、1309 号"飞燕"以外,其余 5 个登陆时强度均在 12 级或以上(其中有 4 个登陆时达强台风级别),其中 1319 号"天兔"登陆时中心最大风力 14 级,是 2013 年登陆我国大陆地区强度最强的台风,也是近 40 年来登陆粤东沿海的最强台风。

造成 2013 年台风生成与登陆均偏多且影响偏南的主要原因有以下几方面。首先是台风活跃季节内,赤道西太平洋暖池海温较常年同期偏暖,对流活动异常偏强,有利于台风生成,且在近海风切偏小,有利于台风加强,使台风登陆强度偏强。另外,由于热带西太平洋地区对流活动偏强以及西太副高的位置偏北,导致季风槽的位置明显偏北,使得活动在西北太平洋和我国南海的台风多偏西或西北路径,而且由于登陆和影响我国的台风生成位置明显偏西(多数在 130°E 以西),这导致台风更容易登陆或影响我国,从而造成台风影响偏南。

## 6　结　论

对 2012/2013 年冬季至 2013 年秋季的主要海洋和大气环流异常及其对中国气温、降水的影响分析发现:

(1) 2013 年冬季至夏季,赤道中东太平洋处于冷水状态,尽管没有发展成一次 La Niña 事件,但大气仍较明显地表现出了对冷水波动的响应。受此影响,夏季西太副高脊线位置明显偏北。西太副高西北侧的强东南气流携带丰沛的水汽深入我国北方,导致我国北方尤其是东北、华北夏季多雨。与此同时,受西太副高下沉气流的控制,我国南方大部高温持续。

(2) 2012/2013 年冬季,北极涛动持续维持负位相。500 hPa 位势高度场上,欧亚大陆中高纬环流呈"两槽一脊"的环流形势,乌拉尔山的高压脊持续偏强,而东亚槽也异常偏强,有利于冷空气沿高空槽南下,导致我国东部长江以北地区的东北、华北、内蒙古东部以及黄淮地区气温偏低。季内,西伯利亚高压强度变化显著,与之相对应,我国气温季内阶段性变化大,前冬冷、后冬暖。进一步研究表明,前秋北极海冰的大幅偏少是造成东亚冬季风偏强的重要原因。

(3) 2013 年南海夏季风于 5 月第三候爆发,较常年偏早 2 候。于 10 月第四候结束,较常年偏晚 4 候,强度偏弱。受东亚夏季风活动影响,我国长江中下游地区于 6 月 23 日入梅,6 月 29 号出梅。7 月 9 日华北雨季开始,8 月中旬季风雨带开始南落,8 月 13 日华北雨季结束。8 月 31 日华西秋雨开始。

## 参考文献


艾婉秀,孙林海,宋文玲. 2010. 2009 年海洋和大气环流异常及对中国气候的影响. 气象,36(4):101-105.

高辉,王永光. 2008. 2007 年海温和大气环流异常对我国气候的影响. 气象,34(4):107-112.

贾小龙,陈丽娟,龚振淞,等. 2011. 2010 年海洋和大气环流异常及对中国气候的影响. 气象,37(4):446-453.

李清泉,孙丞虎,袁媛,等. 2013. 近 20 年我国气候监测诊断业务技术的主要进展. 应用气象学报,24(6):666-676.

李晓燕,翟盘茂. 2000. ENSO 事件指数与指标研究. 气象学报,58(1):102-109.

司东,温敏,许海明. 2008. 2005 年 6 月华南暴雨期间西太平洋副高西伸过程分析. 热带气象学报,24(2):169-175.

王东阡,周兵,孙丞虎,等. 2013. 2012/2013 年东亚冬季风活动特征及其可能成因分析. 气象,39(7):930-937.

王朋岭,周兵,韩荣青,等. 2012. 2011 年海洋和大气环流异常及对中国气候的影响. 气象,38(4):472-479.

王遵娅,任福民,王东阡,等. 2013a. 2012 年海洋和大气环流异常及其对中国气候的影响. 气象,39(4):508-515.

王遵娅,周兵,王艳姣,等. 2013b. 2013 年春季我国气候异常特征及其可能原因. 气象,39(10):1374-1378.

张培群,贾小龙,王永光. 2009. 2008 年海洋和大气环流异常对中国气候的影响. 气象,35(4):112-117.

Saji N H, Goswami B N, Vinayahandran P N, et al. 1999. A dipole mode in the tropical Indian Ocean. Nature, 401: 360-363.

Si Dong, Ding Yihui. 2012. A numerical simulation of the impact of tropical western Pacific SST anomalies on the decadal shift of the Meiyu belt. Acta Meteor Sin, 26(4): 467-475.

Webster P J, Moore A M, Loschnigg J P, et al. 1999. Coupled ocean-atmosphere dynamics in the Indian Ocean during 1997－98. Nature, 401: 356-360.

Wu B, Handorf D, Dethloff K, et al. 2013. Winter weather patterns over Northern Eurasia and Arctic Sea Ice Loss. Mon Wea Rev, 141: 3786-3800.

Wu B, Su J, Zhang R. 2011. Effects of autumn-winter Arctic sea ice on winter Siberian high. Chinese Sci Bull, 56. doi: 10.1007/s11434-011-4696-4.

METEOROLOGICAL APPLICATIONS
*Meteorol. Appl.* **21**: 768–776 (2014)
Published online 2 August 2013 in Wiley Online Library
(wileyonlinelibrary.com) DOI: 10.1002/met.1415

RMetS
Royal Meteorological Society

# The role of eddy feedback in the excitation of the NAO

Gui-Rong Tan,[a,b]* Fei-Fei Jin,[b] Hong-Li Ren[b,c] and Zhao-Bo Sun[a]

[a] *Jiangsu Key Laboratory of Meteorological Disaster, Nanjing University of Information Science and Technology, Nanjing, China*
[b] *Department of Meteorology, University of Hawaii, Honolulu, HI, USA*
[c] *Laboratory for Climate Studies, National Climate Center, China Meteorological Administration, Beijing, China*

**ABSTRACT:** In this paper, the role of eddy feedback in the formation and excitation of the NAO (North Atlantic Oscillation) is examined in a linear barotropic model with an empirical closure for synoptic eddy and low-frequency flow (SELF) feedback. The EOF-space based model captures the linear dynamics of the barotropic model linearized with respect to climatological mean flow very accurately with relative low-order truncations. The parameterized empirical linear low-dimension SELF-feedback operator also depicts the relation between eddy-induced streamfunction tendencies and the large-scale circulation to a reasonable degree. Singular vector analysis (SVD) is performed on the linear low-dimension dynamic operator with SELF-feedback to exam the leading low-frequency mode of the system. It is shown that the leading SVD mode (the left vector) of the linear low-dimension dynamic operator with smallest SVD value resembles the observed NAO pattern. The role of eddy feedback in the excitation and maintenance of NAO is then further examined by relating the effective external forcing patterns to the right vector of the leading SVD mode of the linear dynamic operator. It is shown that local dipolar external forcing at middle latitudes over North Atlantic is effective in exciting the NAO-like anomaly pattern, whereas the effectiveness of the external forcing over different areas sensitively depends on the eddy feedback.

KEY WORDS formation and excitation of the NAO; eddy feedback; low-dimension linear operator

*Received 5 September 2012; Revised 7 April 2013; Accepted 12 May 2013*

## 1. Introduction

The North Atlantic Oscillation (NAO), as one of the most prominent modes of Northern Hemisphere (NH) atmospheric variability, is well known for its great impacts on the climate variation over the middle and high latitudes of the NH (e.g., Walker and Bliss, 1932; Van Loon and Rogers, 1978; Wallace and Gutzler, 1981; Thompson *et al.*, 2002). A number of studies also demonstrated NAO variability response to the global warming (Hurrell, 1995; Hurrell *et al.*, 2003). Therefore, the low-frequency modes of atmospheric circulation, particularly the NAO and its related northern annular mode (NAM) or Arctic Oscillation (AO) (Thompson and Wallace, 2000), have been subjects of many studies. One focus of these studies is the role of synoptic eddies in the generation of the low-frequency variability of the extratropical atmospheric circulation (e.g., Lau, 1988; Cai and van den Dool, 1991; Lau and Nath, 1991; Robinson, 1991a, 1991b, 2000; Branstator, 1992, 1995; Limpasuvan and Hartmann, 1999, 2000; Vallis *et al.*, 2004). There exists a two-way interaction between synoptic eddies and low-frequency flow (e.g., Cai and Mak, 1990; Qin and Robinson, 1992; Whitaker and Barcilon, 1992a, 1992b, 1995). Most results suggest that positive feedback of synoptic eddy is important in maintaining low-frequency flow variability associated with prominent climate modes (e.g., Nakamura and Wallace, 1990; Hoerling and Ting, 1994; Lorenz and Hartmann, 2001, 2003). The low-frequency variability has been shown not only to be maintained by transient eddy forcing, but also to organize systemically the eddy activity for generating such kind of eddy forcing (e.g., Lau, 1988; Lee and Feldstein, 1996; Kimoto *et al.*, 2001; Feldstein, 2003; Watanabe and Jin, 2004). High-frequency synoptic activity interacts with low-frequency variability through nonlinear rectification (Egger and Schilling, 1983; Lau and Holopainen, 1984; Lau and Nath, 1991). The SELF-feedback has been recognized as playing an essential role in generating the dominant modes of the low-frequency variability (Limpasuvan and Hartmann, 2000; Robinson, 2000).

One dynamic approach to gain insight in the dynamics of synoptic eddy and low-frequency flow (SELF) feedback is to develop a linear dynamic closure for the SELF-feedback (Jin *et al.*, 2006a, 2006b; Pan *et al.*, 2006; Jin, 2010). They proposed a linear dynamic framework that includes both dynamic processes linearized with respect to climate mean flow and an approximate but dynamically deduced linear closure for the SELF-feedback. This new linear framework with the inclusion of linear dynamics for the SELF-feedback was shown to be a useful tool for exploring the dynamics of the low frequency mode. Using this framework, it was shown thorough eigen value and singular value analyses that SELF-feedback is responsible for the emergence of leading modes which resemble the known atmospheric low-frequency patterns such as AO/NAO, AAO and PNA (Jin *et al.*, 2006a, 2006b). Analytical results deduced from this linear framework demonstrate that a scale-selective eddy-induced low-frequency dynamic instability is the underlying fundamental mechanism for the origin of the extratropical low-frequency variability (Jin, 2010).

* Correspondence: G-. R. Tan, Key Laboratory of Meteorological Disaster of Ministry of Education, Nanjing University of Information Science and Technology, Nanjing 210044, China. E-mail: tanguirong@nuist.edu.cn

© 2013 Royal Meteorological Society

The key hypothesis of the linear dynamic closure is that the low-frequency flow anomalies can systematically alter the statistical nature of synoptic eddies such that the so-called anomalous eddy forcing onto the low-frequency flow is to a large extent slaved by the low-frequency flow itself. Kug and Jin (2009) and Kug *et al.* (2010a, 2010b) investigated the scale interaction between synoptic eddies and low-frequency flow and pointed out that the synoptic eddy feedback is a key process to sustain the low-frequency flow through a positive SELF-feedback process that can be diagnostically depicted by the so-called 'Left-Hand Rule'. Observational studies by Ren *et al.* (2009, 2011, 2012) following this approach depicted clearly systematical changes in statistical eddy structure associated with NAO. Moreover, they demonstrated that these changes in eddy activity are to a large extent generated by and linearly related to the NAO on one hand; they are also responsible for generating the anomalous eddy forcing that maintains the NAO, on the other hand. These observations supported the view that SELF-feedback to a certain extent can be by and large viewed as a linear dynamic process.

The linear dynamic framework with SELF-feedback has also been used to examine the role eddy feedback plays in shaping the atmospheric remote response to external forcing, thus shaping the atmospheric teleconnections (Peng *et al.*, 2005; Jin *et al.*, 2006a). In fact, numerous studies have demonstrated that both tropical and extra-tropical anomaly forcing can induce NAO-like patterns in the winter atmosphere (e.g., Palmer and Anderson, 1994; Trenberth *et al.*, 1998; Rodwell *et al.*, 1999; Watanabe and Kimoto, 2000; Cassou and Terray, 2001; Hoerling and Kumar, 2002; Peng *et al.*, 2002, 2003, 2005; Greatbatch *et al.*, 2003; Gerber and Vallis, 2005; Pozo-Vasquez *et al.*, 2001, 2005). However, atmospheric responses are often found to be sensitive to specific features of the external forcing (Sutton and Hodson, 2003; Mathieu *et al.*, 2004) because these forced responses are heavily regulated by the eddy feedback (Ting and Sardeshmukh, 1993; Peng and Whitaker, 1999; Peng *et al.*, 2002; Li *et al.*, 2006; Pan *et al.*, 2006).

This paper builds upon the approaches taken by Peng *et al.* (2005) and Jin *et al.* (2006a,b) and uses a linear barotropic framework to examine the role of SELF feedback in the formation and external excitation of the NAO. The linear dynamic framework of Jin *et al.* (2006a,b) and subsequent numerical and observational studies (Pan *et al.*, 2006; Ren *et al.*, 2009; Kug *et al.*, 2010a, 2010b) suggested that the linear dynamical closure for SELF-feedback is largely valid. However, such a dynamic closure is somewhat complicated. Peng *et al.* (2005) proposed a simple empirical closure for the SELF-feedback and it worked remarkably well in the simulations of NAO. Thus, a low-dimension linear framework is proposed that includes two parts: (1) the classic linear dynamics cast in low-dimension by projecting the linear model onto EOF bases, and (2) a simple empirical SELF-feedback closure also expressed using the EOF bases. With adequate yet still relatively small numbers of EOF bases, this linear low-dimension dynamic framework can efficiently capture the linear dynamics of low-frequency variability through the approaches of Peng *et al.* (2005) and Jin *et al.* (2006a,b). The relatively low-dimension of this approach provides an efficient way of exploring optimal excitations of the NAO or singular patterns of linear dynamics with considerations of SELF-feedback.

This paper is organized as follows. Section 2 describes an empirical closure for SELF-feedback, based on observed monthly streamfunction and corresponding eddy induced streamfunction tendency. Section 3 gives a low-dimension EOF-space representation of linear dynamics and a linear barotropic model with empirical SELF-closure. The leading SVD modes of the reconstructed linear dynamic model are then explored to elucidate the role of eddy feedback on the formation of a leading low frequency pattern. Section 4 presents the optimal forcing of leading modes to illustrate the role of eddy feedback on the excitation of the NAO-like pattern. The sensitivity of the forced atmospheric response with eddy feedback to the remote forcing over different areas is also examined in this section. The conclusions are given in Section 5.

## 2. An empirical closure for SELF-feedback

### 2.1. Description of the empirical operator

Following the approaches of (Peng *et al.*, 2003; Jin *et al.*, 2006a, 2006b; Pan *et al.*, 2006), the linearized barotropic model with the closure of SELF-feedback can be written as:

$$\frac{\partial \Delta\psi^a}{\partial t} + J\left(\overline{\psi}^c, \Delta\overline{\psi}^a\right) + J\left(\overline{\psi}^a, \Delta\overline{\psi}^c + f\right) + \gamma\Delta\overline{\psi}^a + \overline{J\left(\psi', \Delta\psi'\right)}^a = \overline{Q}^a \quad (1)$$

Here, $r$ is a linear damping rate, $\overline{\psi}^c$, $\overline{\psi}^a$ denote the monthly climatological mean and anomaly streamfunction, $\overline{Q}^a$ denotes monthly-mean anomalies in the external forcing and $f$ is the Coriolis parameter. Monthly mean eddy forcing $\overline{J\left(\psi', \Delta\psi'\right)}^a$ is hypothesized directly related to $\overline{\psi}^a$ by a linear SELF–feedback operator $L^*_f$ (Jin *et al.*, 2006a) as:

$$\overline{J\left(\psi', \Delta\psi'\right)}^a \approx L^*_f\overline{\psi}^a \quad (2)$$

and a linear operator $L^*$ is defined as:

$$L^*\overline{\psi}^a = J\left(\overline{\psi}^c, \Delta\overline{\psi}^a\right) + J\left(\overline{\psi}^a, \Delta\overline{\psi}^c + f\right) + \gamma\Delta\overline{\psi}^a \quad (3)$$

Since here the streamfunction is used instead of the vorticity, so the linear operator $L$ is defined as

$$L\overline{\psi}^a = \Delta^{-1}J\left(\overline{\psi}^c, \Delta\overline{\psi}^a\right) + \Delta^{-1}J\left(\overline{\psi}^a, \Delta\overline{\psi}^c + f\right) + \gamma\overline{\psi}^a \quad (4)$$

and the eddy-induced streamfunction forcing are related to $\overline{\psi}^a$ by a linear SELF–feedback operator $L_f$:

$$-\Delta^{-1}\overline{J\left(\psi', \Delta\psi'\right)}^a \approx -\Delta^{-1}\left(\nabla \bullet \overline{V'\zeta'}^a\right) \approx L_f\overline{\psi}^a \quad (5)$$

Here $\overline{V'\sigma'}^a$ denotes the monthly-mean anomalies of synoptic eddy vorticity fluxes ($V'$, $\sigma'$, $\psi'$ denote the 2–8 days band-pass filtered winds, relative vorticity and streamfunction), $\Delta^{-1}$ is a Lapalacian inversion operator, and $J$ means the Jacobian operator defined as $J(a,b) = \frac{\partial a}{\partial x}\frac{\partial b}{\partial y} - \frac{\partial a}{\partial y}\frac{\partial b}{\partial x}$. To separate the synoptic-eddy component, the daily mean zonal and meridional winds are band-pass filtered in the period of 2–8 days using a Lanczos filter (using 41 weights, Duchon, 1979). The low-frequency variability is defined as the monthly mean value. Empirical orthogonal functions (EOF) are used to expand $\overline{\psi}^a$

© 2013 Royal Meteorological Society

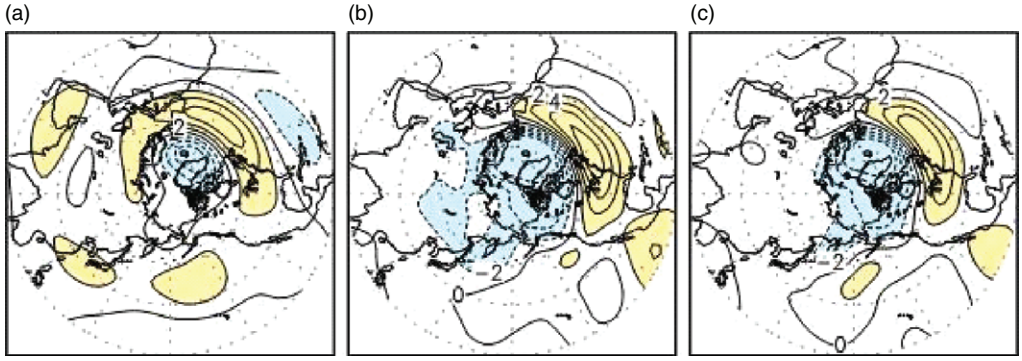


Figure 1. The NAO patterns of low-frequency variability. (a) Obtained by regressing the anomalous monthly stream function at 300 hPa(1952–2008) onto the NAO indices; (b) eddy-induced stream function obtained by regressing the monthly averaged anomalies of eddy vorticity forcing to the NAO indices; (c) eddy forcing patterns for NAO by applying the SELF-closure on to the monthly streamfunction anomalies. The unit is $10^6$ m$^2$ s$^{-1}$, contour interval is 2.

and the streamfunction tendencies $-\Delta^{-1}\overline{J\left(\psi', \Delta\psi'\right)}^a$ which is further denoted as $\overline{\chi}^a$ as follows:

$$\overline{\psi}^a = \sum_{k=1}^{N_\psi} E_{\psi k} A_k \tag{6}$$

$$\overline{\chi}^a = \sum_{k=1}^{N_\chi} E_{\chi k} B_{0k} \approx \sum_{k=1}^{N_\chi} E_{\psi k} B_k \tag{7}$$

where $E_\psi$, $E_\chi$ are leading spatial EOF patterns of $\overline{\psi}^a$ and $\overline{\chi}^a$, $A_k$, $B_{0k}$ and $B_k$ are associated time coefficients of the $k^{\text{th}}$ leading EOF modes, but $B_{0k}$ and $B_k$ mean the time coefficients of $\overline{\chi}^a$ projecting on the EOF modes of the streamfunction tendencies and streamfunction respectively. $N_\psi$, $N_\chi$ are the numbers of the truncated EOF modes for $\overline{\psi}^a$ and $\overline{\chi}^a$. The SELF operator is here mainly for the study of the Northern Hemisphere, the domain of the data for EOF analysis is in the area over (2.5–90 °N; 0–357.5 °E). Based on the linear framework of Jin *et al.* (2006a), $\overline{\chi}^a$ can be directly related to $\overline{\psi}^a$ through a dynamic relationship between the two fields as $\overline{\chi}^a \approx L_f \overline{\psi}^a$, namely, $E_\psi B \approx E_\psi L_f A$. To derive the closure operator empirically, a simple multiple linear regression method is used to establish the relation between $A_k$ and $B_k$, which is defined as $B = L_s A + \varepsilon_s$ ,where $L_s$ is the linear regression operator, and $\varepsilon_s$ is the error. $B \approx E_\psi^T E_\psi L_f A \approx L_s A$. Because $E_\psi^T E_\psi = I$ (where $I$ is identity matrix), the $L_f$ closure operator can be obtained from those data as $L_f \approx L_s$.

In reality, the monthly anomalous streamfunction tendency is not completely a linear function of the monthly mean streamfunction fields. There is a number of sources that may contribute to the residual term $\varepsilon_s$, including truncation error and neglected nonlinearities as well as sampling fluctuations. All of these may hinder the accuracy of the empirically derived linear closure operator. Nevertheless, as shown in Peng *et al.* (2003) and also later in this section, such an empirical model tends to capture SELF-feedback reasonably well, especially for the leading low-frequency mode.

### 2.2. Validating of the empirical operator

To construct the empirical closure operator, the 300 hPa streamfunction fields of the reanalysis data from national Centers for Environmental Prediction/National Center for Atmospheric Research (December 1951 to February 2008) with $2.5^\circ \times 2.5^\circ$ horizontal resolution (Kalnay *et al.*, 1996) is used. The synoptic eddy fields are derived from band-pass filtered daily data as mentioned in the above section, and the low-frequency variability is defined as the monthly mean anomaly field with respect to monthly mean climatology.

To examine the accuracy of the empirical closure $L_f$, the relation between a leading mode of atmospheric low-frequency variability such as the NAO and its associated eddy forcing is examined. The observed patterns of the NAO derived from the monthly mean anomaly fields of the 300 hPa streamfunction fields $\overline{\psi}^a$ is shown in Figure 1(a), whereas the corresponding observed eddy forcing fields $\overline{\chi}^a$ are shown in Figure 1(b). These patterns are obtained by linearly regressing the observed cold-season monthly mean anomaly fields $\overline{\psi}^a$ and $\overline{\chi}^a$ onto the monthly time series of the NAO indices from Climate Prediction Center (http://www.cpc.ncep.noaa.gov/products/precip/CWlink).

The synoptic eddy forcing (Figure 1(b)) associated with the NAO projects positively onto the streamfunction anomaly patterns (Figure 1(a)). Moreover, the eddy forcing associated with the NAO is mostly concentrated in the Atlantic sector and is much weaker over the other half of the NH. These results are well known and they indicate a positive SELF-feedback as noted by many authors in earlier studies (e.g. Lau, 1988; Jin *et al.*, 2006a).

With the empirical closure of eddy feedback, the observed low-frequency flow $\overline{\psi}^a$ can be used to estimate the eddy forcing by $L_f \overline{\psi}^a$. The results, as shown in Figure 1(c), are very similar to the observed eddy forcing in Figure 1(b). The pattern correlation between the parameterized eddy forcing $L_f \overline{\psi}^a$ and the observed $\overline{\chi}^a$ is 0.92 for the NAO, which is higher than those obtained by dynamically derived closure in Jin *et al.* (2006a). This result is also consistent with that obtained by Peng *et al.* (2005) who obtained excellent empirical parameterization for the NAO related to eddy forcing. In the parameterized eddy forcing associated with the NAO, not only the positive projections of stream function tendency pattern onto the streamfunction are captured, but also the magnitudes of these eddy-induced stream function forcings are well expressed in the mid-latitude and Polar regions. Only the magnitudes of parameterized negative forcing in the Polar regions are somewhat weaker than the observed (see Figure 1(c)).

To further illustrate the validity of the empirical closure for the SELF-feedback, the parameterized eddy forcing patterns

© 2013 Royal Meteorological Society

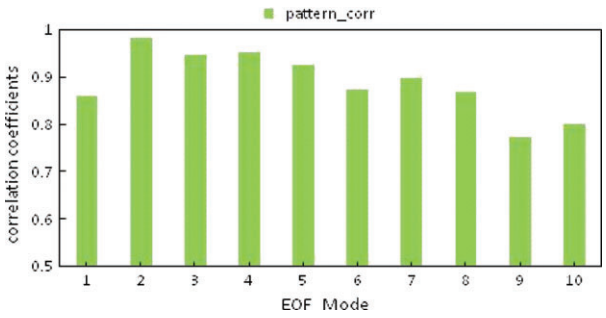


Figure 2. Pattern correlations of the observed and parameterized eddy forcing associated with the first 10 leading EOFs of the monthly mean anomalies of the streamfunction field during the cold seasons of 1979–2008 for northern hemisphere.

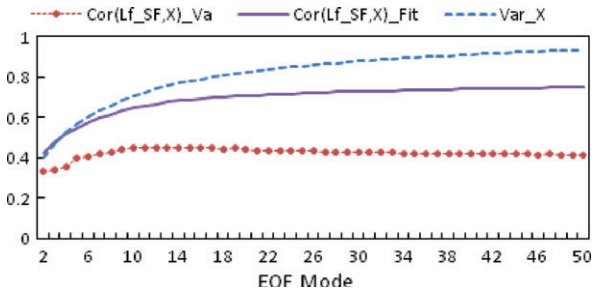


Figure 3. Cross-validated skill of linear SELF operator as a function of the number of retained EOF modes of December to February 300 mb stream-function anomalies and related tendency. Solid line: correlation of the observed $\overline{\chi}^a$ and the estimated by SELF linear operator for fitting skill; dashed line: explaining variance of the truncated EOF modes; dashed line with real circle marks: correlation of the observed $\overline{\chi}^a$ and the estimated by SELF linear operator for cross-validated skill.

of $L_f\overline{\psi}^a$ associated with each EOF pattern of $\overline{\psi}^a$ for the period 1979–2008 is calculated. The observed eddy forcing patterns corresponding to these EOF modes of monthly-mean anomalies of streamfunction are obtained by regressing $\overline{\chi}^a$ onto the time coefficients associated with each EOF of $\overline{\psi}^a$. The spatial correlations of the parameterized and observed eddy forcing patterns for the first 10 EOFs of $\overline{\psi}^a$, which explain about 78% of the total variance of the low-frequency variability of $\overline{\psi}^a$, are shown in Figure 2. It can be seen that the correlations are all above 0.8, also higher than those in Jin *et al.* (2006a). However, it should be noted that these skills of the empirical closure operator are not cross validation skills whereas the skill from dynamic closure operator derived in Jin *et al.* (2006a) is a truly independent skill.

The errors of $L_f$ include truncation error, nonlinearities as well as sampling fluctuations. The truncation error, which depends on the truncated EOF modes of both streamfunction and eddy forcing in terms of streamfunction tendencies, can be estimated before the empirical operator is finally established. The accuracy of the EOF-based empirical operator $L_f$ is shown in Figure 3. The more EOF modes are retained, the largest the variance of eddy induced forcing can be explained by EOF expansion, and the correlation coefficients between the resolved forcing $L_f\overline{\psi}^a$ and actual $\overline{\chi}^a$ are also increasing steadily. However, when the retained EOF modes are larger than 10, the cross validation errors increase as the truncation errors decrease. Therefore, only 10 EOF modes for $\overline{\chi}^a$ were retained. The cross validation error also depends on the number of EOF modes of the streamfunction. The EOF mode number of the streamfunction is set at 50 and the accuracy of the SELF-operator $L_f$ is not higher with more EOF modes selected.

To cross validate the empirical closure of the SELF-feedback, the empirical operator was established using the data about 40 years of December, January and February (DJF) from 1951/1952 to 1990/1991. The correlation distribution between the observed monthly-mean eddy-induced streamfunction forcing $\overline{\chi}^a$ and that estimated by applying the empirical operator onto $\overline{\psi}^a$ for DJF from 1991/1992 to 2007/2008 are then calculated. The correlation between the observed seasonal-mean eddy-induced streamfunction forcing and that estimated by applying the empirical operator but onto the seasonal-mean anomalous streamfunction field for all 57 winters from 1951/1952 to 2007/2008 is also examined. The correlation coefficients (171 months and 57 winters) are positive with the highest values over 0.8 in both Atlantic and Pacific storm track areas and the seasonal map shows even a few broad areas of higher correlation (not shown). The empirical operator shows reasonable ability in expressing the observed eddy-induced streamfunction forcing for each month and each season through the entire 57 winters. There are significant fluctuations in pattern correlations for monthly data, indicating that the significant portion of month-mean anomalous eddy forcing cannot be linearly parameterized by the closure. These fluctuations are less for seasonal mean data, although the empirical operator may still fail for some years. Nevertheless, the correlation score is similar for the entire period, indicating that the empirical operator stands for cross validation. Overall, the parameterized empirical SELF-feedback operator captures the linear relation between eddy forcing and the large scale circulation.

## 3. Leading low-frequency modes of a linear barotropic model with empirical SELF-closure

### 3.1. EOF-space representation of linear dynamics

To study the linear dynamics of low-frequency atmospheric flow dynamics, a set of fully nonlinear primitive equations numerically linearized with respect to climatological mean are often used to derive the related linear dynamical operator (*cf* Hoskins and Karoly, 1981; Watanabe and Jin, 2004). However, this kind of linear operator is often expressed in terms of a matrix whose rank depends on model resolution. Here it is proposed to project the linear operator onto the EOFs so that the linear operator has a low-dimension in a reduced phase-space.

Following Jin *et al.* (2006a), the linearized barotropic model with the closure of SELF-feedback can be written as:

$$\frac{\partial\overline{\psi}^a}{\partial t} + L\overline{\psi}^a + L_f\overline{\psi}^a = \overline{Q}^a \tag{8}$$

where $\overline{Q}^a$ denotes external forcing, and $L_f$ is the SELF-feedback operator, and $L$ is the linear operator, which are obtained in Section 2.

Here, $r$ is a linear damping rate, $\overline{\psi}^c$ denotes the monthly climatological mean streamfunction. The monthly mean value is calculated for winter months (DJF) from 1951/1952 to 2007/2008 and $f$ is the Coriolis parameter.

To obtain the linear operator $L$, the numerical method proposed by Hoskins and Karoly (1981) is used with the difference that each EOF pattern of the streamfunction, instead of each spherical harmonic function, is the perturbation streamfunction field. The model is then used to evaluate and compute the tendency corresponding to each EOF pattern (*cf* Appendix

© 2013 Royal Meteorological Society

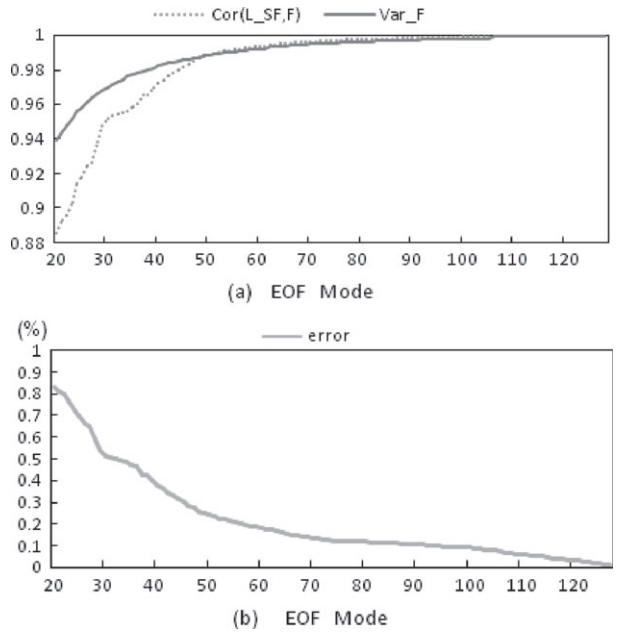


Figure 4. Cross-validated skill of linear dynamic operator. (a) Cross-validated skill of linear dynamic operator as a function of the number of retained EOFs of December to February 300 mb streamfunction anomalies and related tendency. Solid line: explaining variance of the truncated EOF modes for external forcing; dashed line: correlation of the observed tendency and the estimated by space reduced linear dynamic operator. (b) The errors as a function of the number of the retained EOFs.

A). The linear operator in the EOF-based space can then be obtained. For instance, if all tendencies are denoted as $F_E$, then $F_E = LE_\psi$, so $L$ can be obtained by projecting $F_E$ onto the EOF base as $L = E_\psi^T F_E$. It should be pointed out that this method is not limited to the barotropic model and can be easily extended to any primitive equation models. In fact, in the latter case, the advantage of this method in terms of great reduction in the size of matrix for linear dynamic operator will become even more significant.

The accuracy of the EOF-based linear operator $L$ is shown in Figure 4. When more EOF modes are retained, larger variance of the low-frequency-induced tendency $F$ can be explained by the EOF expansion, and the correlation coefficients between the resolved forcing $LE_\psi$ and actual $F$ also increase steadily. The first 50 EOF modes can explain 98.8% of the total variance of $F$, and the correlation coefficient between the observed $F$ and the resolved portion $LE_\psi$ arrives at about 0.996 when all the 50 EOF modes are included (Figure 4(a)). The errors are given in the Equation (9):

$$\varepsilon = \sqrt{\sum_i \left(F_{oi} - \widehat{F}_i\right)^2} \Big/ \left|\sum_i F_{oi}\right| \times 100\% \qquad (9)$$

where $F_{oi}$ is the observed external forcing, and $\widehat{F}_i$ is the estimated. The errors also decrease as the EOF modes increase, and the error is less than 0.25% when 50 EOFs are considered (Figure 4(b)). It suggests that the EOF-space-based linear operator $L$ is a very accurate approximation of the linear dynamical system for low-frequency flow variability.

With the linear dynamic operator expressed in the EOF-space and the empirical operator $L_f$, the linear dynamic operator is $L + L_f$. Since the dimension of the two linear operators is different, in order to add them together, $L_f$ is expanded by simply adding zeros to make it to a full matrix with ranks the same as the $L$ operator. The reduced model is then tested with a localized external forcing. Results show that the linear dynamic system can capture the remote forcing pattern in the mid-latitudes, which is similar to Jin *et al.* (2006a). Thus, this operator with a much reduced degree of freedom captures the essential linear dynamics for low-frequency variability, similar to the full linear barotropic model with an approximate dynamic SELF-closure (Jin *et al.*, 2006b).

### 3.2. NAO-like SVD modes with and without SELF feedback

It was suggested in an earlier study (Jin *et al.*, 2006b) that leading SVD modes (left v vector) of the linear operator $L + L_f$ resemble the observed leading patterns of extratropical low-frequency variability of the atmospheric circulation. Following this approach, the role of the SELF-feedback in the formation of the leading modes is examined by tracing the dependence of the leading SVD modes of the linear matrix for $L + \mu L_f$ on the control parameter $\mu$ (see Figures 5 and 6).

When $\mu = 1.0$, the leading SVD mode resembles the observed pattern (Figure 5(c) and (f)). As $\mu$ decreases from 1.0 toward zero (Figure 5(a) and (d)), the NAO-like leading SVD mode not only loses some of its pattern resemblance (the pattern correlation between the observed pattern and SVD pattern is 1.0 and 0.29 as $\mu = 1.0$ and $\mu = 0.0$, respectively), but also the corresponding singular value $\lambda_\mu$ increases significantly with the eddy feedback (Figure 6). It suggests that SELF-feedback is important not only in the formation of the NAO pattern but also in increasing the singularity of the NAO mode.

The increase of growth rate of the NAO due to SELF feedback is consistent with the well known notion that SELF-feedback for the NAO is strongly positive (e.g., Lorenz and Hartmann, 2001, 2003; Jin *et al.*, 2006a, 2006b; Pan *et al.*, 2006; Ren *et al.*, 2009). It is the strong positive feedback that tends to bring the NAO close to criticality or singularity and this increase of singularity due to the SELF-feedback greatly increases the variance of the NAO (Jin, 2010). To further demonstrate this point, the change in pattern of the ratio between the observed NAO pattern and the diagnosed NAO with the reduction of the SELF-feedback is examined. This ratio is defined as $< \widetilde{\psi}, \psi_{NAO} > / < \psi_{NAO}, \psi_{NAO} >$. It is a function of $\mu$. When $\mu = 0.0$, this value is about 0.28 (Figure 6), indicating that without SELF-feedback, the NAO will lose more than a half of its identity in terms of its pattern.

## 4. Excitation of NAO mode

Although eddy fluxes are central to the forcing and maintenance of the NAO, external excitation is also essential in maintaining the NAO variability. Since the leading left-vector of the linear dynamic operator is related to the spatial structure of the NAO, the corresponding right-vector is examined to study the optimal forcing for the NAO-like mode. The optimal forcing patterns in terms of streamfunction tendency for the case with and without SELF-feedback are shown in Figure 5. The main loadings of the patterns are similar, apart from that the ranges of centre variation are different for different eddy feedback. The main loading of the forcing pattern for the NAO is over the Atlantic and eastern Pacific sectors. However, those forcings over the Indian Ocean and western Pacific become more apparent, and those over the tropical area shift to the higher latitude area in

© 2013 Royal Meteorological Society

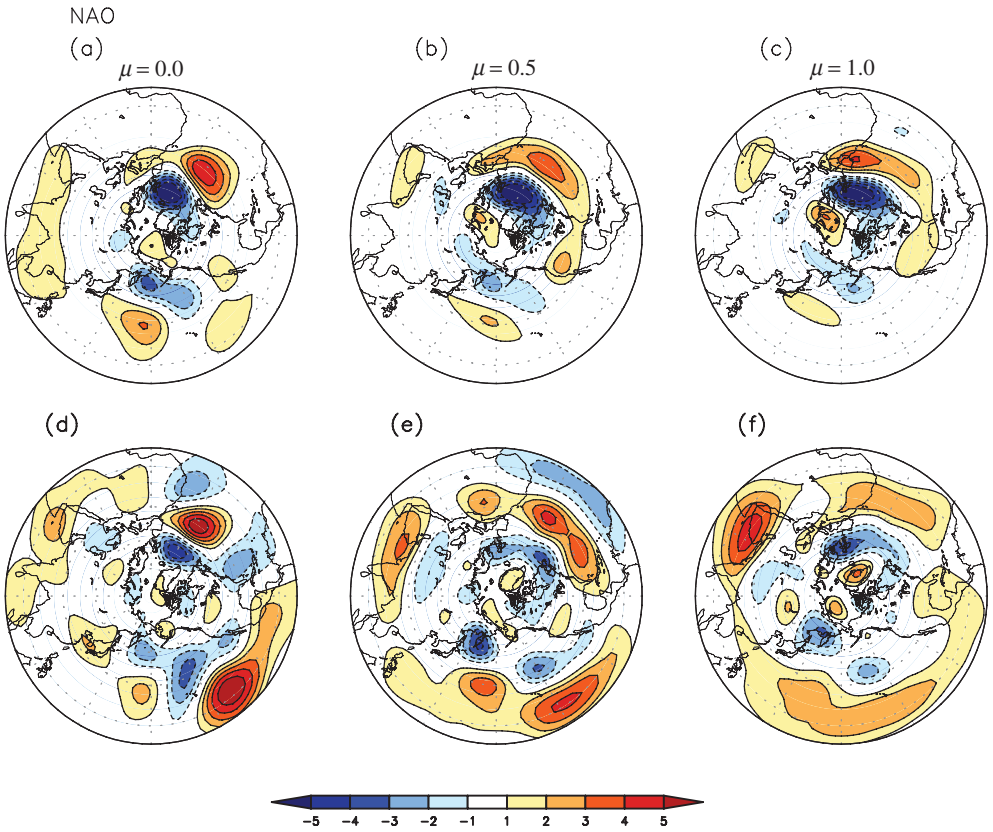


Figure 5. The leading SVD vectors of the linear system with (a), (d) none ($\mu = 0.0$); (b), (e) middle ($\mu = 0.5$) and (c), (f) strong ($\mu = 1.0$) SELF feedback for the NH cold season basic flow. The contour interval is 1.0. (a), (b) and (c) are the left v-vectors for NAO-like pattern, while (d), (e) and (f) are associated right u-vectors for NAO-like pattern of the linear system. The contour interval is $1 \times 10^{-2}$.

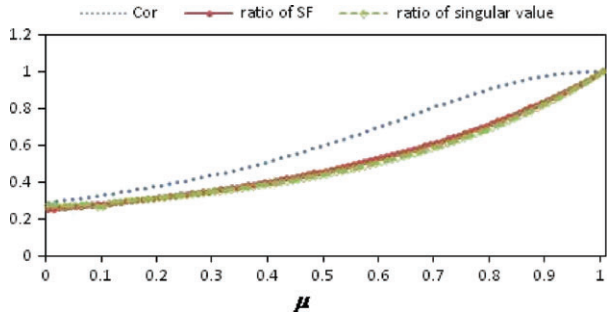


Figure 6. Structure variation of NAO pattern as a function of eddy feedback. Dotted line, real line and dashed line denotes the pattern correlation, $< \widetilde{\psi}, \psi_{NAO} > / < \psi_{NAO}, \psi_{NAO} >$ and ratio of singular values $\sqrt{\lambda_\mu}/\sqrt{\lambda_{\mu=1}}$, respectively.

the Atlantic with the SELF-feedback (Figure 5(d)–(f)), while the forcings in the east Pacific also expand to the central and western Pacific. The significant differences remain in terms of the amplitudes over the centre areas of forcing patterns. In tropical Indian Ocean to Western Pacific, and mid- and high-Atlantic regions, the dependence of the sign and amplitudes in the optimal forcing on the SELF-feedback suggest that it not only serves as a positive feedback to amplify the NAO but also alters the way the NAO might be excited. It suggests that with the SELF- feedback, anomalous forcing over the Indian Ocean to the west Pacific and subtropical to higher-latitude Atlantic are easier to excite the NAO pattern than the case without SELF-feedback. The forcing anomalies over the tropical Atlantic may become less important in exciting the NAO pattern with the participation of the SELF-feedback.

To illustrate further the role of the SELF-feedback in the excitation of the NAO, a set of experiments were conducted with isolated forcing in the regions with significant loadings in the optimal forcing pattern (Figure 5). The areas of forcing having absolute values greater than 2 in Figure 5 are chosen as the effect's forcing sites. When the isolated forcing is located over the Indian Ocean sector, though there is a wave train induced from the resource area with a positive anomaly centre over the North Atlantic and a negative one over the Polar area, the response is weak and the anomalous range is small in the case without eddy feedback. With the eddy feedback (Figure 7(c)), the atmospheric remote response to the Indian Ocean forcing becomes much stronger, with a negative variation in the Polar area and the positive one over the North Atlantic as nearly four times large as in Figure 7(a). It suggests that anomaly forcing over the Indian Ocean may contribute to the formation of the NAO pattern with positive phase and it is largely owing to the eddy feedback.

When the isolated forcing is located over the east Pacific sector (Figure 7(d)–(f)), there is a PNA-like wave train which appears from the resources area. Though the amplitude changes not so greatly as that in Figure 7(b)–(c), the anomalous range in the response tends to increase and expand to the regions further away.

When the isolated forcing is located over the tropical Atlantic sector (Figure 7(g)–(i)), an NAO-like pattern can be induced without eddy feedback and the amplitude increases as eddy feedback increases to moderate intensity but decreases as

© 2013 Royal Meteorological Society

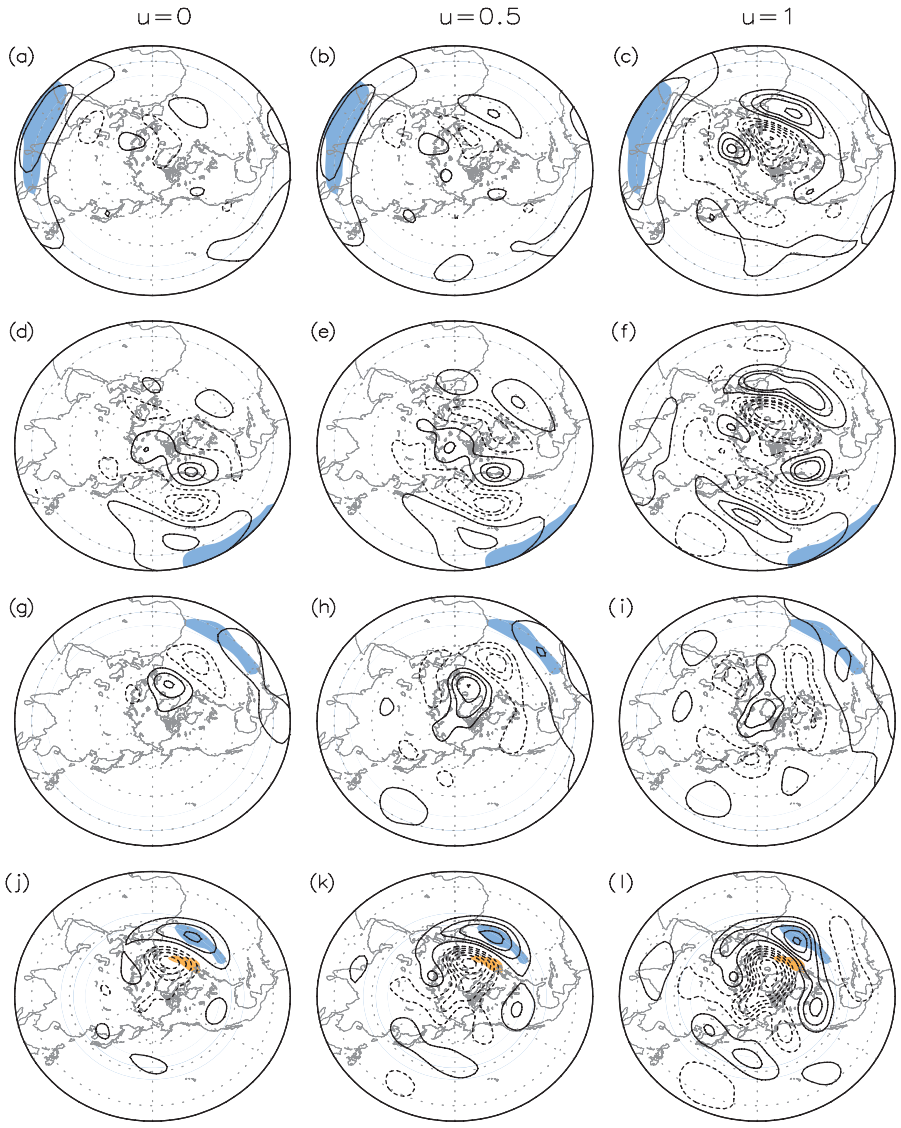


Figure 7. The direct response of the streamfunction fields to the stable forcing in different areas with none ($\mu = 0.0$), middle ($\mu = 0.5$) and strong ($\mu = 1.0$) SELF feedback for the NH.(a), (b) and (c) for the forcing in the Indian Ocean; (d), (e) and (f) for the forcing in the east Pacific; (g), (h) and (i) for the forcing at low-latitude Atlantic; (j), (k) and (l) for the forcing at mid- and high-latitudes of the Atlantic. Blue (yellow) shaded areas denote the positive (negative) anomaly divergence stable forcing. The contour interval is $0.5 \times 10^6$ m$^2$ s$^{-1}$, but for (a)–(i) two lines with contour value $-0.25 \times 10^6$ m$^2$ s$^{-1}$ and $0.25 \times 10^6$ m$^2$ s$^{-1}$ are added.

eddy feedback becomes very strong. This is not surprising because the optimal excitation in the tropical Atlantic area may disappear under the strong eddy feedback (see Figure 5). A dipolar anomaly forcing in the Atlantic tends to generate a significant NAO-like response more effectively with eddy feedback (Figure 7(j)–(l)).

As all the amplitudes of the forcings used here are identical, the anomalies of the response are comparable. Both the extra-tropical anomaly forcing and tropical forcing can induce NAO-like patterns in the winter atmosphere. However, under the condition of no eddy feedback, the most effective excitation for NAO-like mode in the tropical is the eastern tropical Atlantic forcing. For moderate eddy feedback, forcings over tropical eastern Pacific and Indian Ocean become important in exciting the NAO-like mode, while with the full strength of eddy feedback the most important forcing in the tropics is the one over the Indian Ocean for the excitation of the NAO-like mode. In the extra-tropics, the local dipolar forcing can induce a significant NAO-like response.

## 5. Conclusion and discussion

In this work, a low-dimension linear model is proposed whose classic linear dynamics is derived from a dynamic model linearized with respect to the climatological mean, then projected onto the EOF-bases and additional empirical linear closure for synoptic eddy and low frequency feedback. This simple model is useful for understanding the role of eddy feedback on the excitation and formation of low frequency mode. This approach may be extended to 3-demensional models.

The observed NAO-like pattern can be qualitatively reproduced by the proposed linear system, where the SELF-feedback plays a central role in the generation of NAO-like mode. Though the NAO-like mode can be produced owing to the internal linear dynamics, the external forcing is also important in its excitation. The importance of the external forcing in the excitation of the NAO-like pattern depends on the eddy feedback. Those forcings over the tropical Indian Ocean to the

© 2013 Royal Meteorological Society

west Pacific and east Atlantic area have little influence on the excitation of the NAO-like mode if there is no eddy feedback, indicating the essential role of eddy feedback in enhancing atmospheric teleconnections. As for the NAO-like mode, the most effective excitation for the NAO-like mode is the one over the Indian Ocean and the dipolar forcing over the North Atlantic. More work is needed to further test these results in a baroclinic framework.

## Acknowledgements

This work was supported by National Science foundation(NSF) Grant ATM1034439, the National Key Technology R&D Program (2012CB955200), the Special Foundation for Public Welfare Industry (GYHY 201206016, GYHY201306028), and the Priority Academic Program Development of Jiangsu Higher Education Institutions (PAPD) of China.

### Appendix A: The linear advection operator in EOF space

The streamfunction field is denoted as $\psi(j)$ or in vector form $\Psi$. Using the linear barotropic vorticity equation, the streamfunction tendency due to linear advection and friction can be obtained, which shall be denoted as $F(j)$ or in vector form $F$. Then the linear equation can be written as

$$\frac{\partial \Psi}{\partial t} = F = L^* \Psi \tag{A.1}$$

The linear operator $L^*$ *is* $J^*J$ matrix and is normally very large in grid space. Here we propose to truncate the $L^*$ matrix using the EOF of the streamfunction as the base functions. With a set of EOFs of $\Psi$, which is denoted as $E_n(j)$ or in matrix form $E$, then we can express

$$\Psi = EA + R_\psi \tag{A.2}$$

here $A$ is principle component vector and $A_n(t)$ is the time coefficient of $n^{\text{th}}$ EOFs, and $R_\psi$ is truncation error. The tendency term can also be expressed as

$$F = EB + R_F \tag{A.3}$$

where $B$ is principle component vector derived from the tendency and $R_F$ is the residual part that could not be expressed in the EOF space of $\Psi$. We then can get a relation:

$$B = L^* A + E^T \left( L^* R_\psi - R_F \right) \tag{A.4}$$

In practice, we first use each EOF as the perturbation pattern of stream function field and then use the linear barotropic model to compute $F_E$. We then can get the linear operator by projecting $F_E$ onto EOF base, then we have

$$B = L_E A + E^T \left( L R_\psi{}^E - R_F \right) \tag{A.5}$$

The truncation error in both streamfunction field and tendency field will have impact on the accuracy of representation of $F$. Let $\widetilde{\mathrm{F}} = E\,\widetilde{\mathrm{B}}$ and $\widetilde{\mathrm{B}} = L_E A$. Then the error is

$$F - \widetilde{\mathrm{F}} = R_F + EE^T \left( L_E R_\psi - R_F \right) \tag{A.6}$$

The error should be small as long as $R_\psi$ and $R_F$ are small, thus the EOF base is sufficiently accurate in expressing both streamfunction and tendency fields with adequate number of EOF bases in the truncation.

## References

Branstator G. 1992. The maintenance of low-frequency atmospheric anomalies. *J. Atmos. Sci.* **49**: 1924–1945.
Branstator G. 1995. Organization of storm track anomalies by recurring low-frequency circulation anomalies. *J. Atmos. Sci.* **52**: 207–226.
Cai M, van den Dool HM. 1991. Low-frequency waves and traveling storm tracks. Part I: barotropic component. *J. Atmos. Sci.* **48**: 1420–1436.
Cai M, Mak M. 1990. Symbolic relation between planetary and synoptic-scale waves. *J. Atmos. Sci.* **47**: 2953–2968.
Cassou C, Terray L. 2001. Oceanic forcing of the wintertime low-frequency atmospheric variability in the North Atlantic European sector: a study with the ARPEGE model. *J. Clim.* **14**: 4266–4291.
Duchon C. 1979. Lanczos filtering in one and two dimensions. *J. Appl. Meteorol.* **18**: 1016–1022.
Egger J, Schilling H-D. 1983. On the theory of the long-term variability of the atmosphere. *J. Atmos. Sci.* **40**: 1073–1085.
Feldstein SB. 2003. The dynamics of NAO teleconnection pattern growth and decay. *Q. J. R. Meteorol. Soc.* **129**: 901–924.
Gerber EP, Vallis GK. 2005. A stochastic model for the spatial structure of annular patterns of variability and the North Atlantic Oscillation. *J. Clim.* **18**: 2102–2118.
Greatbatch RJ, Lin H, Lu J, Peterson KA, Derome J. 2003. Tropical/extratropical forcing of the AO/NAO: a corrigendum. *Geophys. Res. Lett.* **30**: 1738, DOI: 10.1029/2003 GL017406.
Hoerling MP, Kumar A. 2002. Atmospheric response patterns associated with tropical forcing. *J. Clim.* **15**: 2184–2203.
Hoerling M, Ting M. 1994. Organization of extratropical transients during El Niño. *J. Clim.* **7**: 745–766.
Hoskins BJ, Karoly DJ. 1981. The steady linear response of a spherical atmosphere to thermal and orographical forcing. *J. Atmos. Sci.* **38**: 1179–1196.
Hurrell JW. 1995. Decadal trends in the North Atlantic Oscillation: regional temperatures and precipitation. *Science* **269**: 676–679.
Hurrell JW, Kushnir Y, Ottesen G, Visbeck M (eds). 2003. An overview of the North Atlantic Oscillation. In *The North Atlantic Oscillation: Climate Significance and Environmental Impact*, Geophysical Monograph Series, Vol. **134**. American Geophysical Union: Washington, DC; 1–35.
Jin F-F, Pan L-L, Watanabe M. 2006a. Dynamics of synoptic eddy and low-frequency flow interaction. Part III: baroclinic model results. *J. Atmos. Sci.* **63**: 1709–1725.
Jin F-F, Pan L-L, Watanabe M. 2006b. Dynamics of synoptic eddy and low-frequency flow interaction. Part II: a theory for low-frequency modes. *J. Atmos. Sci.* **63**: 1695–1708.
Jin FF. 2010. Eddy-induced instability for low-frequency variability. *J. Atmos. Sci.* **67**, DOI: 10.1175/2009JAS3185.1.
Kalnay E, Kanamitsu M, Kistler R, Collins W, Deaven D, Gandin L, Iredell M, Saha S, White G, Woollen J, Zhu Y, Leetmaa A, Reynolds R, Chelliah M, Ebisuzaki W, Higgins W, Janowiak J, Mo CK, Ropelewski C, Wang J, Jenne R, Joseph D. 1996. The NCEP/NCAR 40-year reanalysis project. *Bull. Am. Meteorol. Soc.* **77**: 437–470.
Kimoto M, Jin F-F, Watanabe M, Yasutomi N. 2001. Zonal-eddy coupling and a neutral mode theory for the Arctic Oscillation. *Geophys. Res. Lett.* **28**: 737–740.
Kug J-S, Jin F-F. 2009. Left-hand rule for synoptic eddy feedback on low frequency flow. *Geophys. Res. Lett.* **36**: L05709, DOI: 10.1029/2008GL036435.
Kug J-S, Jin F-F, Park J-H, Ren H-L, Kang I-S. 2010a. A general rule for synoptic-eddy feedback onto low-frequency flow. *Clim. Dyn.* **35**: 1011–1026, DOI: 10.1007/s00382-009-0606-8.
Kug J-S, Jin F-F, Ren H-L. 2010b. Role of synoptic eddies on low-frequency precipitation variation. *J. Geophys. Res.* **115**: D19115, DOI: 10.1029/2009JD013675.
Lau N-C. 1988. Variability of the observed midlatitude storm tracks in relation to lowfrequency changes in the circulation pattern. *J. Atmos. Sci.* **45**: 2718–2743.
Lau N-C, Holopainen EO. 1984. Transient eddy forcing of the time-mean flow as identified by geopotential tendencies. *J. Atmos. Sci.* **41**: 313–328.
Lau N-C, Nath MJ. 1991. Variability of the baroclinic and barotropic transient eddy forcing associated with monthly changes in the midlatitude storm tracks. *J. Atmos. Sci.* **48**: 2589–2613.
Lee S, Feldstein SB. 1996. Mechanism of zonal index evolution in a two-layer model. *J. Atmos. Sci.* **53**: 2232–2246.

© 2013 Royal Meteorological Society

Li S, Hoerling MP, Peng S, Weickmann KM. 2006. The annular response to tropical Pacific SST forcing. *J. Clim.* **19**: 1802–1819.
Limpasuvan V, Hartmann DL. 1999. Eddies and the annular modes of climate variability. *Geophys. Res. Lett.* **26**: 3133–3136.
Limpasuvan V, Hartmann DL. 2000. Wave-maintained annular modes of climate variability. *J. Clim.* **7**: 1144–1163.
Lorenz DJ, Hartmann DL. 2001. Eddy-zonal flow feedback in the Southern Hemisphere. *J. Atmos. Sci.* **58**: 3312–3327.
Lorenz DJ, Hartmann DL. 2003. Eddy-zonal flow feedback in the northern hemisphere winter. *J. Clim.* **16**: 1212–1227.
Mathieu P-P, Sutton RT, Tong B, Collins M. 2004. Predictability of winter climate over the North Atlantic European region during ENSO events. *J. Clim.* **17**: 1953–1974.
Nakamura H, Wallace JM. 1990. Observed changes in baroclinic wave activity during the life cycles of low-frequency circulation anomalies. *J. Atmos. Sci.* **47**: 1100–1116.
Palmer T, Anderson D. 1994. The prospects for seasonal forecasting – a review paper. *Q. J. R. Meteorol. Soc.* **120**: 755–793.
Pan L-L, Jin F-F, Watanabe M. 2006. Dynamics of synoptic eddy and low-frequency flow interaction. Part III: baroclinic model results. *J. Atmos. Sci.* **63**: 1709–1725.
Peng S, Robinson WA, Li S, Hoerling MP. 2005. Tropical Atlantic SST forcing of coupled north Atlantic seasonal responses. *J. Clim.* **18**(3): 480–496.
Peng S, Whitaker JS. 1999. Mechanisms determining the atmospheric response to midlatitude SST anomalies. *J. Clim.* **12**(5): 1393–1408, DOI: DOI:10.1175/1520-0442(1999)012%3c1393:MDTART%3e2.0.CO;2.
Peng S, Whitaker JS, Li S. 2002. North Atlantic SST forcing of the NAO and relationships with intrinsic hemispheric variability. *Geophys. Res. Lett.* **29**: 1276, DOI: 10.1029/2001GL014043.
Peng S, Whitaker JS, Li S. 2003. Mechanisms for the linear and nonlinear NAO response to the North Atlantic SST tripole. *J. Clim.* **16**: 1987–2004.
Pozo-Vasquez D, Esteban-Parra M, Rodrigo F, Castro-Diez Y. 2001. The association between ENSO and winter atmospheric circulation and temperature in the North Atlantic region. *J. Clim.* **14**: 3408–3420.
Pozo-Vasquez D, Gamiz-Fortis SR, Tovar-Pescador J, Esteban-Parra M, Castro-Diez Y. 2005. North Atlantic winter SLP anomalies based on the autumn ENSO state. *J. Clim.* **18**: 97–103.
Qin J, Robinson WA. 1992. Barotropic dynamics of interactions between synoptic and low-frequency eddies. *J. Atmos. Sci.* **49**: 71–79.
Ren H-L, Jin F-F, Gao L. 2012. Anatomy of synoptic eddy-NAO interaction through eddy-structure decomposition. *J. Atmos. Sci.* **69**(7): 2171–2191, DOI: 10.1175/JAS-D-11-069.1.
Ren H-L, Jin F-F, Kug J-S, Zhao J-X, Park J. 2009. A kinematic mechanism for positive feedback between synoptic eddies and NAO. *Geophys. Res. Lett.* **36**: L11709, DOI: 10.1029/2009GL037294.
Ren H-L, Jin F-F, Kug J-S, Gao L. 2011. Transformed eddy-PV flux and positive synoptic eddy feedback onto low-frequency flow. *Clim. Dyn.* **36**(11): 2357–2370, DOI: 10.1007/s00382-010-0913-0.
Robinson WA. 1991a. The dynamics of low-frequency variability in a simple model of the global atmosphere. *J. Atmos. Sci.* **48**: 429–441.
Robinson WA. 1991b. The dynamics of the zonal index in a simple model of the atmosphere. *Tellus* **43A**: 295–305.
Robinson WA. 2000. A baroclinic mechanism for the eddy feedback on the zonal index. *J. Atmos. Sci.* **57**: 415–422.
Rodwell MJ, Rowell DP, Folland CK. 1999. Oceanic forcing of the wintertime North Atlantic Oscillation and European climate. *Nature* **398**: 320–323.
Sutton RT, Hodson DLR. 2003. Influence of the ocean on North Atlantic climate variability 1971–1999. *J. Clim.* **16**: 3296–3313.
Thompson DWJ, Lee S, Baldwin MP. 2002. Atmospheric processes governing the Northern Hemisphere Annular Mode/North Atlantic Oscillation. In *The North Atlantic Oscillation: Climatic Significance and Environmental Impact*, *Geophysical Monograph Series*, Vol. **34**. American Geophysical Union: Washington, DC; 81–112.
Thompson DWJ, Wallace JM. 2000. Annular modes in the extratropical circulation. Part I: month-to-month variability. *J. Clim.* **13**: 1000–1016.
Ting M, Sardeshmukh PD. 1993. Factors determining the extratropical responses to equatorial diabatic heating anomalies. *J. Atmos. Sci.* **50**: 907–918.
Trenberth KE, Branstator GW, Karoly D, Kumar A, Lau N-C, Ropelewski C. 1998. Progress during TOGA in understanding and modeling global teleconnections associated with tropical sea surface temperatures. *J. Geophys. Res.* **103**: 14291–14324.
Vallis GK, Gerber EP, Kushner PJ, Cash BA. 2004. A mechanism and simple dynamical model of the North Atlantic Oscillation and annular modes. *J. Atmos. Sci.* **61**: 264–280.
Van Loon H, Rogers JC. 1978. The seesaw in winter temperatures between Greenland and northern Europe. Part I: general description. *Mon. Weather Rev.* **106**: 296–310.
Walker GT, Bliss EW. 1932. World weather V. *Mem. R. Meteorol. Soc.* **4**: 53–84.
Wallace JM, Gutzler DS. 1981. Teleconnection in the geopotential height field during the Northern Hemisphere winter. *Mon. Weather Rev.* **109**: 111–125.
Watanabe M, Jin F-F. 2004. Dynamical prototype of the Arctic Oscillation as revealed by a neutral singular vector. *J. Clim.* **17**: 2119–2138.
Watanabe M, Kimoto M. 2000. Atmosphere–ocean thermal coupling in the North Atlantic: a positive feedback. *Q. J. R. Meteorol. Soc.* **126**: 3343–3369.
Whitaker JS, Barcilon A. 1992a. Type B cyclogenesis in a zonally varying flow. *J. Atmos. Sci.* **49**: 1877–1892.
Whitaker JS, Barcilon A. 1992b. Genesis of mobile troughs in the upper westerlies. *J. Atmos. Sci.* **49**: 2097–2107.
Whitaker JS, Barcilon A. 1995. Low-frequency variability and wavenumber selection in models with zonally symmetric forcing. *J. Atmos. Sci.* **52**: 491–503.

© 2013 Royal Meteorological Society 

DOI:10.11737/j.issn.1003-0239.2014.05.015

# 海洋模式中垂直混合参数化方案介绍

汪雷[1,2]，王彰贵[2]，凌铁军[2]，左金清[3]

（1. 北京大学物理学院，北京 100871；2. 国家海洋环境预报中心 国家海洋局海洋灾害预报技术研究重点实验室，北京 100081；3. 中国气象局国家气候中心 中国气象局气候研究开放实验室，北京 100081）

**摘 要：** 介绍了海洋垂直混合过程参数化方案的发展，以及不同参数化方案在海洋模式中的应用情况。首先，介绍不同垂直混合参数化方案的物理问题、理论依据、数学表达和特征，并对不同参数化方案进行了比较。其次，针对中尺度涡、亚中尺度涡以及波浪、潮流混合参数化的最新研究进展进行了总结并对垂直混合参数化的未来发展提出了一些建议。

**关键词：** 湍流闭合方案；中尺度涡混合；亚中尺度涡混合；波浪混合；潮流混合

**中图分类号：** P731 **文献标识码：** A **文章编号：** 1003-0239（2014）05-0093-12

## 1 引言

地球流体原始方程组通常描述了一定时空范围平均的流体运动行为。由于受到计算资源的限制，在数值计算中往往需要在更大的时空尺度上求解流体运动方程。更小尺度运动的效应，常以湍流通量散度形式出现[1]，它们需要利用大尺度变量来参数化以闭合方程，这些过程常被称作次网格尺度物理过程。

海表混合层是海洋上层中直接与上覆大气、海冰相互作用的部分。一个完备的海表混合层参数化[2]，必须模拟海风搅拌驱动的混合、不稳定浮力强迫、流切变不稳定、湍流平流、非局地混合，例如密集羽流渗入层流、重力内波破碎等物理过程。海洋内部温盐等属性沿位密面的传输主要通过大尺度洋流和中尺度涡来实现，而海洋内部跨密度混合发生在重力内波破碎区域[3]，大部分波能量来源于海底反射的潮流、小尺度地形下重力波产生和辐射对地转运动的耗散、以及斜压不稳定的失稳。随着观测增多、模式发展和分辨率的提高，中尺度涡、亚中尺度涡以及波浪、潮流等过程对海洋混合的影响受到越来越多的关注。图1给出了海洋中小尺度混合过程的示意图。

海洋垂直混合是海洋混合中的重要部分，受到模式分辨率的限制，其在模式中需要进行参数化。海洋垂直混合参数化方案，根据混合系数的选取可分为：常混合系数、依赖Richardson数的方案和湍流动能模型等[1]。常混合系数方案，动量垂直粘性和示踪物垂直扩散系数在整个海洋设定为常数。由Richardson数决定的混合方案，利用观测资料寻找垂直湍流活动和大尺度海洋结构之间的联系，通过模型诊断出垂直混合系数与大尺度变量之间的关系。湍流闭合模型，则是一种基于湍流动能诊断方程和湍流特征长度闭合假设的模型。随着观测的增多和理论的发展，许多小尺度物理过程得到了更精确的刻画。

范植松[4]回顾了大洋内部、浅海内部混合的主要过程和一些参数化方法。近十年来，随着海洋模式的发展，国内外涌现出了一些新的海洋垂直混合参数化方案。本文将介绍影响重大的海洋垂直混合参数化方案、以及该领域最新的进展，并进行系统的总结与展望。

**收稿日期：** 2014-06-02

**基金项目：** 国家重点基础研究发展计划(2010CB950303)；国家自然科学基金(41376016，41205058)；国家重点基础研究发展计划(2014CB745004)

**作者简介：** 汪雷（1984-），男，助理研究员，主要从事扰动位能、季风、海洋模式研究。E-mail: wangl@nmefc.gov.cn



?1994-2014 China Academic Journal Electronic Publishing House. All rights reserved. http://www.cnki.net

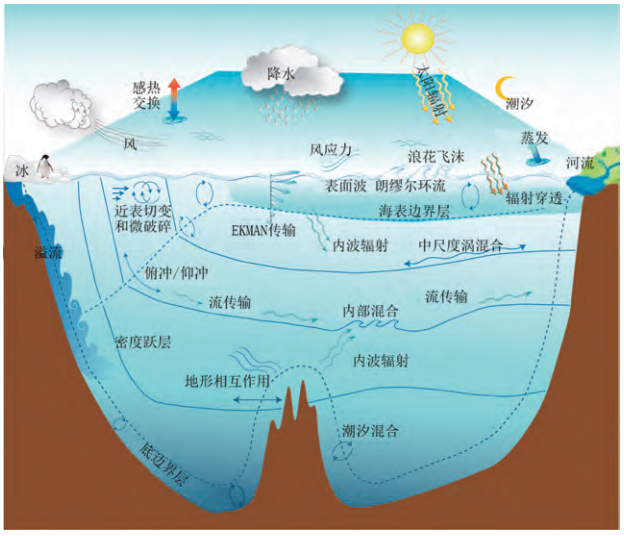


图1 海洋中的小尺度混合过程示意图
(引自:http://www.gfdl.noaa.gov/ocean-mixing)

## 2 海洋垂直混合参数化方案

海洋模式旨在求解大尺度速度和温盐度的运动学方程,其中,动量、温盐通量是由速度、温盐扰动量的非线性相互作用所引起的。在局地湍流模型中,动量、温盐通量常表示为大尺度变量梯度的函数。模式分辨率通常大于切变不稳定、内波破碎等垂向湍流发生的主要源汇尺度,湍流运动一般未能显式求解,而是需要对其进行参数化处理。海洋上层的垂直混合过程是大气和海洋之间热量、水、动量交换的重要方式,下面我们将介绍一些具有代表性的垂直混合参数化方案。

### 2.1 KT67混合层模型(The Kraus-Turner mixed layer model)

研究对象:Kraus和Turner[5]考察了海表过程如辐射穿透、海表冷却和风搅拌所引起的层结过程。在盛夏,辐射穿透引起的对流混合与风搅拌作用具有相同的量级;在冬季,混合层厚度和稳定性主要由海表冷却控制,辐射穿透或风搅拌的作用相对较小。

理论依据:假定影响水柱的热量和机械能不受水平速度、平流或旋转的显著影响,而在海表附近向下穿透,Turner和Kraus[6]建立了一个简单的季节温跃层模型。在热量给定时,所有搅拌动能用于改变系统的位能,充分混合后得到表层混合厚度和温度。

表达形式:混合层是垂直均质水层,在假定外源、汇平衡后略去时间倾向项,得到湍流动能诊断方程,求解水层厚度。通过热量平衡以及动能平衡方程得到水层厚度[5]:

$$h = 2(k - \varepsilon + S_R l^{-1})(S_R + I_R)^{-1}$$

式中,$k, \varepsilon, S_R, I_R, l$分别与风输入动能、耗散、太阳辐射、红外辐射和长度尺度有关。

混合层底的厚度是模式预报量。在密度坐标系模式中,KT67混合层模式的混合层底与模式垂直坐标吻合,但卷出过程很难处理。

在混合坐标海洋模式如HYCOM[7]中,KT67混合层模式兼容的困难之处在于,需要记录混合层底的浮力变化以近似混合层夹卷对湍动能平衡的贡献,和热力、动力变量不连续以计算混合层夹卷对其影响。完整KT67方案,设计unmixing方案以减少混合层和海洋内部属性的数值交换。由于unmixing方案十分复杂,简化KT67方案通过松弛混合层底为预报量这一条件,在计算效率提高和数值误差增长之间权衡。

特征:KT67模型[5]仅仅控制表面混合层,使用时需同时加入考虑内部跨密度混合算法。HYCOM[8]提供了该参数化方案选项。

### 2.2 PWP86动力不稳定模型(Price-Weller- Pinkel dynamical instability model)

研究对象:海洋上层的热含量存在着众所周知的日循环,午后的温度、速度廓线表现出海表混合、分层剪切的上下两层结构。在海表加热和风应力已知时,预报海洋日循环的关键在于热量"陷阱"的确定。Price等[9]发展了一个对加热和风混合响应的上层海洋简单模式,以模拟日循环。

理论依据:在仅仅使用混合层夹卷时,整体混合层模式可给出合理的表面强迫,但对过渡层的模拟存在突变和偏浅的问题。在仅仅使用梯度混合时,模式对表面强迫的模拟也相对合理,只是无法模拟风驱动的海表混合层,加入自由对流过程后可得到改善。通过构造海表混合层,并且考虑混合层下的层流混合,可得到相当真实的廓线结构[9-10]。

表达形式:混合由三步完成:

(1)自由对流。海表热量损失出现静力不稳定



?1994-2014 China Academic Journal Electronic Publishing House. All rights reserved. http://www.cnki.net

时($\partial_z\rho \geqslant 0$),发生自由对流,对流混合至对流深度(日循环的典型值小于1 m);

(2)整体混合层夹卷。当整体Richardson数($Ri_b$)小于临界值(0.65)时,混合层夹卷相邻下层,在新形成的混合层中使所有的变量均质,其中 $Ri_b = g\Delta\rho h/\{\rho_0[(\Delta u)^2+(\Delta v)^2]\}$;

(3)相邻层结垂直切变不稳定混合。若Richardson数($Ri$)小于临界值(0.25)时,界面上下层混合,其中 $Ri = N^2/|\partial_z u|^2$,Brunt-Väisälä频率 $N^2 = -g\rho_0^{-1}\partial_z\rho$,$\rho$为位密。

在日循环中,后两种混合在垂直混合过程中占优势,由于Richardson数中出现的速度完全是由风驱动的,从这种意义上来说,可视为风-混合过程。

特征:PWP86方案[9]丢失了混合层特征,如对数廓线和非局地输送;在对流稳定条件下,该方案无法描述在混合层以下层结区由对流引起的额外夹带。PWP86方案提供了表面混合层以下的切变不稳定混合,未给出内波破碎等引起的背景混合。HYCOM[8]使用PWP86方案时,同时启动显式跨密度混合算法。

### 2.3 BL79方案(Bryan-Lewis water mass model)

研究对象:考察海洋环流在地球热平衡中的作用时发现,温跃层厚度对次网格尺度运动的参数化方案十分敏感,其中温跃层的平均厚度与全球有效位能成正比[11]。

理论依据:在地转条件下,即使闭合参数不同,有效位能和总动能也保持一个几乎恒定的比例。浮力强迫做功使动能转化为位能,浮力做功引起能量传输的方向取决于能量库的耗竭情况,即耗散、风做功供给和非均匀加热的差异[12]。温跃层厚度与参数变化之间有明确的格局,当参数改变使得风做功增加或者耗散减小时,海洋环流的总能量增加,这意味着密度层结更大的偏移和模式中更深的温跃层。

表达形式:温盐控制方程为:

$$\partial_t(\theta,S) + v\cdot\nabla(\theta,S) + w\partial_z(\theta,S) = \partial_z[K_\rho\partial_z(\theta,S)] + K_{\rho H}\nabla^2(\theta,S)$$

式中,水平粘性系数$K_{mH}$和垂直粘性系数$K_m$取为常数。水平扩散系数$K_{\rho H}$是垂直坐标的函数 $K_{\rho H}(z) = K_{\rho HB} + (K_{\rho HS} - K_{\rho HB})e^{-0.002z}$。垂直混合系数是稳定度的函数,不稳定时,系数无限大,不稳定水柱温盐彻底混合;稳定时取为垂直坐标的简单函数。垂直扩散系数$K_\rho$在温跃层最小且随深度增加而增大,其计算方程考虑了风搅拌对上层海洋的作用:

$$K_\rho(z) = 10^4\{0.8 + (1.05/\pi)\tan^{-1}[4.5\times10^{-3}(z-2500)]\}$$

特征:在海洋环流数值模式尤其是气候模式中,通常采用BL79方案[11]来确定背景垂直湍扩散系数。该方案给出的垂直湍扩散系数只是深度z的函数。MOM[13]等加载了BL79方案。

### 2.4 PP81混合方案(Pacanowski-Philander mixing scheme)

研究对象:海表混合过程非常重要,KT67模型[5]考虑了风搅拌和跨混合层的夹带作用,但是忽略了海洋对风场变化的动力响应,故KT67模型在局地通量占主的区域效果不错。而在风场再分布效果大于局地作用的热带地区,KT67模型表现不佳。在热带海洋的上层,表面通量和对风场变化的动力响应都是重要的。

理论依据:观测表明,混合过程受到平均流剪切的强烈影响[14-15]。通过经验研究,Jones等人[16]给出了黏性/扩散系数与Richardson数的关系。PP81混合方案[17]主要应用在热带海洋,扩散系数依赖于Richardson数。由于该方案能够较合理地描述强垂直切变与黏性之间的关系,它可以更好地模拟赤道温跃层和赤道潜流。

表达形式:垂直扩散系数和粘性系数是Richardson数($Ri$)的函数。式中,垂直粘性系数$K_m$为:$K_m = K_{mb} + K_{m0}/(1+\alpha Ri)^n$;垂直扩散系数$K_\rho$为:$K_\rho = K_{\rho b} + K_m/(1+\alpha Ri)$。背景值$K_{mb}$、$K_{\rho b}$由运行时间决定。在POP中,$\alpha = 5$,$n = 2$。

特征:海洋混合过程极其复杂,PP81混合方案[17]只是简单地把垂直混合系数设为Richardson数的函数,而忽略了其它的混合过程,造成该方案在中高纬度的模拟结果不佳。由于湍流动能耗散率与Richardson数的关系随深度变化,PP81方案依赖于Richardson数的简单混合参数化方法并非对所有深度有效。采用该方案的模式有LICOM[18]、MOM[13]、NEMO[1]、POP[19]等。



?1994-2014 China Academic Journal Electronic Publishing House. All rights reserved.　http://www.cnki.net

### 2.5 MY82 湍流闭合方案 (Mellor-Yamada Turbulence Closure Model)

研究对象：湍流粘性或混合长假说对二维湍流边界层有可观的预测能力。无压力梯度、热传输时，平均速度场闭合模型采用常数参数的平坦湍流层，无法预测层结效应。平均湍流场闭合模型由平均湍流能量模型和平均雷诺应力(MRS)模型组成时，虽然成功用于中性层，但是对于分层流MRS的计算量惊人。

理论依据：将湍流理论扩展到层结流体，Mellor[20]建立了湍流闭合模型。为了实现准确性和计算速度的优化，Mellor和Yamada[21]利用观测对湍流模型进行了简化。从四阶到二阶模型，求解的偏微分方程数量由十个降到两个，而结果十分相似。为便于其在三维大气和海洋模型中的应用，Mellor和Yamada[22]对三阶模型简化得到2.5层模型。

表达形式：温度扩散方程可写为：

$$\partial_t(TD)+\partial_x(TDU)+\partial_y(TDV)+\partial_\sigma(T\omega)=$$
$$\partial_\sigma[(K_\rho/D)\partial_\sigma T]+F_T-\partial_z R$$

式中，粘性系数$K_m$和扩散系数$K_\rho$取决于湍流速度尺度$q$、特征长度$l$以及反映层结的Richardson数$Ri$[22]：

$$K_m=qlS_m\ ,\ K_\rho=qlS_\rho\ ,$$

湍动能$k$和预报量$kl$，由下列方程控制：

$$\partial_{t_s}(k\partial_s p)+\nabla_s\cdot(Vk\partial_s p)-\nabla_s\cdot[A_H\partial_s p\nabla_s k]+$$
$$\partial_s(k\partial_s p ds/dt)=\zeta_k$$
$$\partial_{t_s}(kl\partial_s p)+\nabla_s\cdot(Vkl\partial_s p)-\nabla_s\cdot[A_H\partial_s p\nabla_s(kl)]+$$
$$\partial_s(kl\partial_s p ds/dt)=\zeta_l$$

方程右端代表局地过程的作用。左侧第二至四项分别为水平平流、水平扩散、坐标转换时跨坐标引起的通量。温、盐项的局地作用表现为垂直扩散和海表强迫。湍动能和预报量的局地作用表现为边界层强迫、垂直扩散以及垂直切变产生、与位能的相互转化以及耗散。$S_\rho$，$S_m$与$Ri$的有关：

$$S_\rho[1-(3A_2B_2+18A_1A_2)Ri]=A_2(1-6A_1/B_1)$$
$$S_M(1-9A_1A_2Ri)-S_H[(18A_1+9A_1A_2)Ri]=$$
$$A_1(1-3C_1-6A_1/B_1)$$

特征：MY82方案[20-22]产生从海表到海底的混合，弱混合发生在海洋内部，强混合产生在海表边界层，增强混合在洋底。该方案对混合层动力过程的模拟较好，但混合层厚度可能偏浅[23]，在对流夹带偏弱、稳定密度梯度情况下混合偏小[24]。MY82方案的湍动能和预报量，在POM[25]中是垂直交界面变量，而在HYCOM[8]中是层变量。

### 2.6 GGL90 湍流闭合方案 (Gaspar-Grégoris-Lefevre TKE Turbulent Closure Scheme)

研究对象：对于那些垂直扩散系数为常系数或依赖Richardson数的简单参数化方案，上混合层模拟往往较差。简单整体模型如KT67[6]计算高效，但是仅适用于边界层。复杂的湍流闭合方案如MY82[21]，提供了更加真实的垂直湍流混合，但在湍流主长度尺度的确定上存在不足。

理论依据：GGL90湍流闭合方案[26]是一种基于湍流动能诊断方程和湍流长度尺度闭合假设的参数化方案。Bougeault和Lacarrère[27]最早提出了简单、物理意义清晰的大气湍流闭合模型，Gaspar等[26]将其应用到海洋模式中，Madec等[28]对混合长度尺度的公式进行了改进。

表达形式：湍流动能的时间演变是垂直切变制造、层结破坏、垂直扩散和Kolmogorov耗散共同作用的结果[26]：

$$\partial_t k=K_m k^{-2}\cdot[(\partial_z u)^2+(\partial_z v)^2]-K_\rho N^2+k^{-1}\cdot$$
$$\partial_z[K_m k^{-1}\partial_z k]-c_\varepsilon l_\varepsilon^{-1}k^{3/2}$$

式中，海表湍动能由风应力场确定，当考虑表面波破碎时，使用较大的值。假设底层湍动能为紧邻上层湍动能的值。其中，垂直涡粘性和涡扩散系数分别为：

$$K_m=C_\kappa l_\kappa k^{1/2}\ ,\ K_\rho=K_m/P_{rt}\ ,$$

$l_\varepsilon$和$l_k$分别为粘性、混合长度尺度，Prandtl数($P_{rt}$)依赖于局地Richardson数。简化的湍流长度尺度：$l_\kappa=l_\varepsilon=N^{-1}\sqrt{2k}$，以到海表$l_u$、海底$l_d$、或局地垂直尺度因子为界，仅适用于层结稳定区域。针对局地层结不稳定，考虑长度尺度的垂直梯度项[28]：$k^{-1}|\partial_z l|\leqslant 1$，$l=l_\kappa=l_\varepsilon$，即长度尺度的垂直变化不大于深度变化。

通过修正表面长度尺度和湍动能的数值以及海气拖曳系数来参数化表面波破碎能量效应[29-30]。GGL90上边界条件为[29]：$k_0=2^{-1}(15.8\alpha_{CB})^{2/3}\rho_0^{-1}|\tau|$，$\alpha_{CB}$是取决于“波龄”的常数。湍流长度尺度的上边



?1994-2014 China Academic Journal Electronic Publishing House. All rights reserved. http://www.cnki.net

界条件: $l_0 = g^{-1}\rho_0^{-1}V_C C_c|\mathbf{s}|$ , $V_C$是von Karman常数, $C_C$是Charnock常数。

特征: GGL90方案[26]指定了两种不同的特征尺度来分别表示混合和耗散,由于它们与所有深度的湍流长度相关,所以得到的混合参数化并不限于上边界层,而是可以应用在海洋整层。MITGCM[31]、NEMO[1]等模式采用了该参数化方案。

### 2.7 GISS01混合层模式(Goddard Institute for Space Studies)

研究对象:海洋混合过程的模拟通常采用单点湍流闭合模型,特别是MY82方案[22]开创了1980年代最先进的湍流模型。该方案使用了较小的临界Richardson数,且假定湍流不受旋转影响。随着湍流模型的发展,一些关键物理过程的模拟,如临界Richardson数取值、非局地分层和剪切、旋转、混合层下的混合等,都需要得到进一步的提高[32]。

理论依据:GISS01混合层模式根据实验观测来调整临界Richardson数(约为1),并通过求解动力系统三阶方程而得到包含分层和剪切作用的表达式。在混合层下的开洋面上考虑内波破碎等,地形附近则考虑潮耗散或地热加热作用。提出了雷诺应力模式的热、动量扩散系数表达式[32],并对双扩散过程[33]进行了完善。

表达形式:扩散系数 $K_\rho(r_\rho, N, Ri, \varepsilon)$ 取决于密度比 $r_\rho$、Brunt-Väisälä频率 $N$、Richardson数 $Ri$ 和动能耗散率$\varepsilon$, 其中下标$\rho$=($m$,$h$,$s$)分别代表动量、热量和盐度, $r_\rho = \alpha\partial_z\bar{\theta}/(\beta\partial_z\bar{S})$ 。

密度比和Brunt-Väisälä频率由海洋环流模式的大尺度场计算得到。剪切作用由Richardson数表征,混合层内主要为风驱动的大尺度剪切,混合层之下则是小尺度剪切如内波为主。耗散率表示混合相关的物理过程,混合层内主要为风搅拌作用;在混合层下的开洋面上考虑内波破碎等,地形附近则考虑潮耗散或地热加热作用。GISS01方案适用于双稳定、双不稳定、盐指和对流扩散情况:

双稳定 ($\partial_z T>0$, $\partial_z S<0$, $r_\rho<0$ , $Ri^T>0$ )

双不稳定 ($\partial_z T<0$, $\partial_z S>0$, $r_\rho>0$ , $Ri^T<0$ )

盐指 ($\partial_z T>0$, $\partial_z S>0$, $r_\rho>0$ , $Ri^T>0$ )

扩散对流 ($\partial_z T<0$, $\partial_z S<0$, $r_\rho>0$ , $Ri^T>0$ )

特征:GISS01方案[32-33]适用于混合层及其以下的垂直混合参数化。该方案首先计算压力网格点上的粘性、扩散系数,随后使用隐式方案求解垂直扩散方程,并将粘性廓线水平插值到速度网格点,最后求解动量的垂直扩散方程。GISS01方案未对非局地效应进行参数化。HYCOM[8]加载了该参数化方案。

### 2.8 GLS03湍流闭合方案(Generic Length Scale scheme )

研究对象:海洋模式中雷诺–应力模型的应用在湍流长度尺度的选择上存在争议。所有雷诺-应力和两阶-方程模型都采用了经典串级模型: $\varepsilon \propto k^{3/2}l^{-1}$ 。在物理上,使用($l$,$\varepsilon$)中某变量并无客观优势,而在数学和计算上,模式性质受到长度尺度变量的很大影响。

理论依据:GLS03湍流闭合方案[34-35]包含两个预测方程:湍动能方程$k$和通用尺度$\psi$方程。通过适当的变换,GLS03方案可以复原一系列著名的湍流闭合方案,如MY82的$k$-$kl$方案[22]、Rodi的$k$-$\varepsilon$方案[36]和Wilcox的$k$-$\omega$方案[37]等。

表达形式:湍动能由湍流传输 $T_k$、切变产生 $G_S$、浮力制造 $G_B$和耗散项 $\varepsilon$ 确定:

$$\partial_t k + u_i\partial_{x_i}k = T_k + G_S + G_B - \varepsilon$$

通用尺度 $l_\psi$与湍动能和耗散相关 $l_\psi = \tilde{l}_\psi(k,\varepsilon)$ ,方程可写为:

$$\partial_t l_\psi + u_i\partial_{x_i}l_\psi = T_\psi + l_\psi k^{-1}\cdot(c_{\psi 1}G_S + c_{\psi 3}G_B - c_{\psi 2}\varepsilon)$$

式中, $T_\psi$ 为传输项, $c_{\psi 1}$ 、$c_{\psi 1}$ 和 $c_{\psi 1}$ 是模式常数。进一步假定 $l_\psi$依赖于 $k$ 和 $\varepsilon$ 的乘积: $l_\psi = C_{0\mu}{}^p k^m \varepsilon^n$ ,通过适当变换$p$、$m$和$n$的值,通用尺度方程可复原一系列著名的模型(见表1)。

**表1　通用尺度中定义的$p$、$n$和$m$及其与著名二阶方程模型的关系[34]**

| $l_\psi$ | 两阶方程 | $p$ | $m$ | $n$ |
|---|---|---|---|---|
| $\omega$ | Wilcox (1988) | −1 | 1/2 | −1 |
| $kl$ | Mellor and Yamada (1982) | 0 | 1 | 1 |
| $\varepsilon$ | Rodi (1987) | 3 | 3/2 | −1 |
| $k\tau$ | Zeierman and Wolfshtein (1986) | −3 | 1/2 | 1 |

在一定条件下,GLS03方程组可以化为[1]:

$$\partial_t k = K_m\sigma_k^{-1}k^{-1}\cdot[(\partial_z u)^2 + (\partial_z v)^2] - K_\rho N^2 + k^{-1}\cdot$$
$$\partial_z[K_m k^{-1}\partial_z k] - \varepsilon$$



?1994-2014 China Academic Journal Electronic Publishing House. All rights reserved.　http://www.cnki.net

$$\partial_t l_\psi = l_\psi k^{-1}\cdot\{C_1 K_m \sigma_\psi^{-1} k^{-1}[(\partial_z u)^2+(\partial_z v)^2]-C_3 K_\rho N^2 - C_2\varepsilon F\omega\}+k^{-1}\cdot\partial_z[K_m k^{-1}\partial_z l_\psi]$$

粘性、扩散系数和耗散分别为：$K_m = C_\mu l k^{1/2}$，$K_\rho = C_\mu l k^{1/2}$，$\varepsilon = C_{0\mu} l^{-1} k^{3/2}$，常数$C$由模式给定。

特征：GLS03方案[34-35]既可以用来分析已有模式，本身又可作为广义模式方程。对于制造等于耗散的传统标准流动情况，GLS03方案与传统模式表现相当。但对于无切变情形，耗散由湍流传输平衡的情况，此时除Wilcox的 *k-ω*方案[37]外模拟效果都不好。传统模式对边界附近廓线的模拟存在困难。另外，GLS03方案解析解指出，模式参数间相互依赖很强。当合理使用这些参数时，模式在均质层结、切变流中表现良好。NEMO[1]等模式采用了该参数化方案。

### 2.9 KPP94参数化(K-Profile Parameterization)

研究对象：海洋垂直混合过程可分为海表边界层和海洋内部两种截然不同的混合型。通常使用的混合方案未考虑某些潜在重要的边界层物理过程，需要发展新的参数化方案代表这些物理过程。

理论依据：在海表边界层，KPP94方案对风驱动混合、表面浮力通量和对流不稳定进行参数化。在海表强迫下，边界层混合增强，这使得边界层属性渗透到温跃层。海洋内部混合由切变不稳定、背景内波破碎和双扩散控制。另外，该方案还对温、盐非局地混合作用进行了参数化，允许逆梯度通量的发展。

表达形式：KPP94方案[38-39]为半隐式，需要多步迭代过程。首先，在模式界面和网格上计算内部混合系数。其次，诊断出网格上的边界层深度。第三，计算网格上的边界层混合系数，代替初始值。最终得到网格上的平均系数。

海表通量：初始海表热力、动量通量在上层设为均匀分布[8]。

海洋内部跨密度面扩散：$\overline{\omega'\theta'} = -\nu_\rho \partial_z \bar{\theta}$，温盐扩散系数由可分辨切变不稳定$\nu_\rho^s$、背景内波引起的不可分辨切变不稳定$\nu_\rho^w$、双扩散$\nu_\rho^d$组成：$\nu_\rho = \nu_\rho^s + \nu_\rho^w + \nu_\rho^d$。其中，$\nu_\rho^s$由Richardson数($Ri$)确定。$\nu_\rho^w$取经验系数。$\nu_\rho^d$依赖于双扩散密度比：$r_\rho = \alpha\partial_z\bar{\theta}/(\beta\partial_z\bar{S})$。

海表边界层厚度由整体Richardson数($Ri_b$)确定。

模式界面处海表边界层扩散廓线：$\overline{\omega'\theta'} = -K_\rho(\partial_z\bar{\theta}+\gamma_\theta)$，混合系数$K_\rho(\sigma) = h_b\omega_\theta(\sigma)G_\theta(\sigma)$，平滑形状函数$G_\theta$满足Monin-Obukhov相似率，且使模式界面处与海洋内部值一阶连续。在海表强迫失稳时，启动非局地通量项$\gamma_\theta$和$\gamma_S$。

垂直混合：通过水平平流、扩散、动量和通量方程得到每个网格点变量值，将垂直扩散视为海表、底边界上零通量的纯一维问题求解。

特征：非局地KPP 94方案[38-39]是非刚盖混合层模型，统一了垂直混合中的多种未解析过程[31]，以处理海洋边界层、海洋内部的不同混合过程。KPP94方案有效地刻画了从海洋边界层到海洋内部混合系数减小的特点，可以应用在较粗网格和不平坦地形情况[8]，在HYCOM[8]、MITGCM[31]、MOM[13]、NEMO[1]、POP[19]等模式中使用。

### 2.10 GM90中尺度涡参数化(Gent-McWilliams Parameterization)

研究对象：中尺度涡是涡旋场中最有活力的部分，支配着物质属性的等密度面混合。前人提出的涡扩散通量是沿等密度面的方向，而这不满足平均密度平衡。GM90方案[40]针对非涡分辨海洋环流模式，将次网格中尺度涡混合参数化，以描述中尺度涡对于大尺度位温、盐度及其它示踪物的影响。

理论依据：绝热和风驱动环流的精细数值解表明，平均速度导致的大尺度密度通量散度由中尺度涡诱发的密度通量散度平衡。GM90方案利用准绝热参数化的构想，在粗分辨率模式中保持平均示踪物浓度在等密度面上守恒。等密度层厚度沿等密度面进行混合，对示踪物附加平流和扩散项来实现中尺度涡对示踪物传输的参数化。将大尺度速度与涡诱发速度之和视为“有效速度”，得出与绝热模型相似的解[41]。

表达形式：示踪物传输方程为[19]：

$$\partial_t\varphi+(u+u^*)\cdot\nabla\varphi+(w+w^*)\partial_z\varphi = R(\varphi)+D_V(\varphi)$$

式中，中尺度涡诱发的推注速度：$u^* = \nu\nabla\rho/\rho_z$，$w^* = -\nabla(\nu\nabla\rho/\rho_z)$。方程右侧第一项采用等中性扩散算子[42]：$R(\varphi) = \nabla_3(\boldsymbol{K}\cdot\nabla_3\varphi)$，$\boldsymbol{K}$代表沿等密度面扩散的对称张量。在POP模式中，将推注速度写为



?1994-2014 China Academic Journal Electronic Publishing House. All rights reserved. http://www.cnki.net

偏斜通量形式[43]:

$u_3^* \cdot \nabla_3 \varphi = \nabla_3 \cdot (u_3^* \varphi) = -\nabla_3 \cdot (B \cdot \nabla_3 \varphi)$ ,B 代表反对称张量。

传输方程可以重新写为:

$$\partial_t \varphi + u \cdot \nabla \varphi + w \partial_z \varphi = \bar{R}(\varphi) + D_V(\varphi),$$

$$\bar{R}(\varphi) = \nabla_3 \cdot (K + B) \cdot \nabla_3 \varphi ,$$

新公式对中性坡度的描述避免了非线性不稳定的激发。

在MITGCM中,涡参数化方案调用GM90方案前,首先使用Redi涡参数化方案[42],利用沿局地等熵面的扩散算子实现示踪物属性沿等熵面的混合。

特征:GM90方案[40]要求将背景扩散项中的水平扩散部分去掉,这是因为它有可能产生不适当的穿过等位密度面的扩散。对于次网格尺度的物理过程,GM90方案给定的侧向涡旋系数对大尺度度特征实际变化的反映并不理想,且未考虑跨密度混合。使用该方案的有LICOM[18]、MITGCM[31]、MOM[13]、NEMO[1]、POP[19]。

### 2.11 FKFH08亚中尺度涡参数化(Fox-Kemper-Ferrari-Hallberg restratification effects by submesoscale eddies)

研究对象:典型的海洋层化和切变允许两种斜压不稳定:贯穿整个深度的深厚中尺度不稳定,以及限于弱层结海表混合层的浅薄亚中尺度不稳定[44]。浅混合层不稳定是非地转斜压不稳定,以其快速增长率、小尺度区别于深厚中尺度不稳定,且前者在强混合事件后上层海洋的再层化中发挥重要作用。

理论依据:对于FKFH08方案[45-46],海洋混合层亚中尺度涡再层化效应发生的时间尺度远小于由中性物理参数化的中尺度涡。有限振幅斜压不稳定驱动了混合层的再层化,等密度面发生由垂直向水平的倾斜。参数化过程引入了翻转流函数,它正比于水平密度梯度、混合层深度平方和惯性周期的乘积。

表达形式:FKFH08参数化[45]是通过引入矢量流函数来实现:

$$\Psi = (C_e \mu h^2 g \Delta s \Big/ \rho_0 L_f \sqrt{f^2 + \tau^{-2}}) \hat{z} \wedge \nabla \overline{\gamma}^z ,$$

式中,$C_e$ 为无量纲数,$\mu$混合层垂直结构函数,$h$混合层厚度,$g$重力加速度,$\Delta s$水平网格距,$\rho_0$ 为Boussinesq密度常数,$L_f$亚中尺度涡宽度尺度,$f$科氏力参数,$\tau$ 亚中尺度涡的时间尺度,$z=\delta-d$,$d$为海水深度,$\delta$为自由海表偏差,$\nabla \overline{\gamma}^z$ 是混合层平均参考位密水平梯度。写为分量形式:

$$\Psi = \Gamma \mu (-\overline{\partial_y \gamma}^z, \overline{\partial_x \gamma}^z, 0), \Gamma = C_e h^2 g \Delta s \Big/ \rho_0 L_f \sqrt{f^2 + \tau^{-2}}$$

这些公式适用于混合层,利用水平浮力梯度进行参数化:$-\rho_0 \nabla b = g \nabla \gamma = g(\partial_\theta \gamma \nabla \theta + \partial_S \gamma \nabla S)$ ,这与局地位密梯度有关。锋的尺度可以是常数,或通过斜压Rossby半径计算得到:$L_f = h\bar{N}^z \Big/ f$ ,$\bar{N}^z$ 混合层平均的浮力频率。

示踪物浓度受流函数的影响:

$$F = (\psi^{(y)} \partial_z C, -\psi^{(x)} \partial_z C, -\psi^{(y)} \partial_x C + \psi^{(x)} \partial_y C)$$

涡诱发速度表示为:

$$v^* = (-\partial_z \psi^{(y)}, \partial_z \psi^{(x)}, \partial_x \psi^{(y)} - \partial_y \psi^{(x)})$$

特征:在稳定层结情况下,FKFH08方案[45]的涡传输与GM90等[41]诱导速度传输不同。Fox-Kemper[47]等评估了FKFH08方案对全球海洋气候模拟的影响。MOM[13]加入了该方案,对近海表混合层层化的弱偏差有改善。风-锋、对流-锋相互作用和锋生过程等其它亚中尺度效应,目前尚未参数化。

### 2.12 CB94波浪增强混合(Craig-Banner wave-enhanced turbulence)

研究对象:在海洋表面,风将动量传输给海水。动量首先进入到表面波,通过波破碎传递给表面流场。相邻海面的湍动能随之增强,通过动量混合影响邻近海表的洋流廓线。海表波动的潜在影响包括:产生斯托克斯漂移和雷诺应力[48],影响平均流,以及波破碎时释放混合下传的湍动能。

理论依据:观测表明,表面几米的子层,湍流在海表波动作用下增强,该层的耗散率随深度以3—4.6幂数递减。CB94方案[29]将涡耗散表示为湍流速度和长度尺度的乘积,对波破碎的影响以海表能量源的形式进行参数化。在此波强化层,湍动能向下的通量由耗散平衡。

表达形式:湍动能方程为:

$$\partial_t k = \partial_z (K_\rho \partial_z k) + K_m S^2 - 2^{3/2} k^{3/2} \Big/ M_C l$$

式中,$k$为湍动能,$K_\rho$为湍流扩散系数,$K_m$为湍流粘性系数,$S^2 = (\partial_z u)^2 + (\partial_z v)^2$ 为切变产生项,l为长度尺度,$M_C$为模式常数。Mellor和Blumberg[30]在以上方程右端加入浮力项作用$-K_H N^2$ 。



?1994-2014 China Academic Journal Electronic Publishing House. All rights reserved. http://www.cnki.net

海表湍动能的边界条件为：

$$K_\rho \partial_z k = \alpha_{CB} u_s^3, z = 0$$

上式等价于 $\overline{k_0} = 2^{-1}(15.8\alpha_{CB})^{2/3}|\varsigma|/\rho_0$，式中，$\alpha_{CB}$是取决于波龄的常数，不考虑波破碎的情形设为零。$\varsigma$为风应力矢量，$\rho_0$为参考密度，$\rho_0^{-1}\varsigma = u_s^2$。

湍流长度尺度的上边界条件为 $l_0 = g^{-1}\rho_0^{-1}V_C C_C|\varsigma|$，$V_C$是von Karman常数，$C_C$是Charnock常数。

Mellor等[30]对湍动能闭合模型进行了调整，以包含表面波破碎能量的效应，校正作用于表面长度尺度、湍动能取值和海–气托曳系数。

特征：当混合层相对较浅时，使用CB94方案[29]对夏天海表温度虚高的偏差有改进。NEMO[1]等模式采用了该参数化方案。

### 2.13 QYY04波致混合方案(Qiao-Yuan-Yang wave-induced vertical viscosity)

研究对象：近海温度的垂直结构存在明显的季节变化。模式模拟的夏季海表温度通常偏高，上混合层偏浅，这可能是由上层混合强度不足导致的。波浪破碎在上层混合中发挥重要作用[29, 49-50]，然而海洋模式对其模拟能力尚待提高。

理论依据：基于波流耦合模型[51]，假定波致混合项为波数谱的函数，得到波浪和潮流混合方案[52-53]。通过海浪的波数谱数值模式积分得到波浪方向谱，计算出随时空变化的波致垂直粘性系数，将它作为垂直混合的一部分叠加到不同的湍流混合模型中，引入波浪运动对环流速度、温度和盐度的混合作用。

表达形式：将速度、温度、盐度等物理量分解为平均和脉动两部分[52]：$U_i = \overline{U_i} + u_i$，$\Theta = \bar{\Theta} + \theta$，$S = \bar{S} + s$，其中脉动速度进一步分解为湍流部分和波致扰动：$u_i = u_{ic} + u_{iw}$。温盐扩散通量可表示为：

$$-\overline{u_i\theta} = -\overline{u_{ic}\theta} - \overline{u_{iw}\theta}\ ,\ -\overline{u_i s} = -\overline{u_{ic}s} - \overline{u_{iw}s}$$

波致速度扰动可以用下式表示：

$$u_{iw} = \{\iint_k (n_x/n) f d\vec{n}, \iint_n (n_y/n) f d\vec{n}, \iint_n -i f d\vec{n}\},$$

式中，$f = A_f A(\vec{n})\exp(nz)\exp[i(\vec{n}\cdot\vec{x} - A_f t)]$，$A(\vec{n})$为波振幅，$A_f$为波角频率，$n$为波数，$z$为垂直坐标。

波致混合的温盐通量可表示为：

$$-\overline{u_{iw}\theta} = K_\rho \partial_z \bar{T}\ ,\ -\overline{u_{iw}s} = K_\rho \partial_z \bar{S}\ ,$$

参数$K_\rho$定义为波致垂直运动学粘性/扩散系数，依赖于混合长和波质点位移：

$$K_\rho = \alpha \iint_n E(\vec{n})\exp(2nz) d\vec{n} \partial_z \cdot [\iint_{\vec{n}} A_f^2 E(\vec{n})\exp(2nz) d\vec{n}]^{1/2}$$

$K_\rho$是决定波致混合的关键因子，应该考虑加入到海洋环流模式中。

特征：QYY04波致混合方案[52]对PP81和KPP94垂直混合方案均有显著提升，可减小太平洋冷舌偏冷和过于西伸的偏差，对海洋上层温度的模拟也有改善作用。

### 2.14 SJL04潮能耗散混合(Simmons-Jayne-Laurent Mixing related to tidal energy dissipation)

研究对象：在层结海洋粗糙地形中，正压潮和潮流会诱发内波之间的动量交换。其中，重力内波破碎能量来自潮与粗糙海底地形作用时正压潮向内潮的能量散射；当潮流遇到大陆架时，发生底部拖曳摩擦。潮流模拟需要垂向几米、水平1—10 km的分辨率，在全球气候模式中难以实现，故有必要对其进行参数化处理。

理论依据：基于St Laurent等的理论[54]，Simmons等[55]将dianeutral参数化方案引入海洋环流模式，假定混合发生在一单位Prandtl数，强化等量的dianeutral示踪扩散和动量粘性。当能量在小尺度耗散时，引起dianeutral混合。

表达形式：内潮破碎引起额外的垂直扩散项，表达为正压潮向斜压潮转换的能量E的函数[54]：

$$A_{tides}^{vT} = \eta\Gamma E(x,y)\mu(z)/\rho N^2$$

式中，$\eta$为潮耗散效率，典型取值为$\eta$=1/3，是局地耗散的部分内波能量通量，剩余部分作为低频内波模态贡献于背景内波场；$\Gamma$为混合效率，经常取值$\Gamma$=0.2。内波能量通量 $E(x,y) = 2^{-1}\rho_0 N_b n A_m^2 \langle u^2 \rangle$，$\rho_0$为海水的参考密度，$N_b$是沿海床的浮力频率，$(n, A_m)$为地形粗糙度的波数和振幅，$u$为正压潮速度，内波能量图谱通过潮流正压模型得出。描述湍流混合的垂直结构函数为：

$$\mu(z) = e^{-(H+z)/\xi}(1 - e^{-H/\xi})^{-1}\zeta^{-1}$$

$H$为水柱总深度，$\zeta$为湍流垂直耗散尺度。

海底拖曳引起的dianeutral扩散[13]可表示为：

$$K_{drag} = K_{\max}(1 + \sigma Ri)^{-\chi}$$

式中，$\sigma$和$\chi$分别为无量纲参数。

特征：SJL04方案[55]显式给出了混合的潮能量，其混合系数随时空变化。相比水平/垂直系数均一



?1994-2014 China Academic Journal Electronic Publishing House. All rights reserved. http://www.cnki.net

方案,SJL04方案会显著降低温度、盐度模拟的偏差。MOM[13]和NEMO[1]都采用了该方案。

## 3 讨论与结论

本文通过对海洋垂直混合过程参数化方案的回顾,总结了常用参数化类型的理论依据、数学表达及应用情况等。

在模式混合层的设定上,海洋垂直混合参数化方案可分为整体混合模型和连续混合层模型两类[2]。整体模型假定海表边界层完全湍流,在混合层厚度中速度、示踪物分布均匀,如KT67方案[5]和PWP86方案[9]。结合KT67整体模型和PWP86模型中的梯度Richardson数判据,Chen等[56]提出了一种混合方案。由于整体方案无法分辨边界层中的垂直结构,不能计算非局地混合,故其性能受到限制。

连续混合可以较好的反映混合层细节特征。在BL79方案[11]中,垂直混合系数不随时间变化,仅为深度的简单函数。另外一些方案将垂直湍流混合与大尺度海洋结构相联系,例如,PP81方案[17]将这些系数规定为梯度Richardson数的函数。根据实验观测,GISS01模型[32-33]对Richardson数的取值进行了调整。值得注意的是,K理论在垂直混合方案中应用广泛,它将垂直混合参数化为涡扩散和涡粘性系数(K)与平均量垂直梯度的乘积。MY82方案[22]引入多阶预报方程求解不同湍流场,首先计算湍流混合长和速度尺度,然后确定垂直扩散和粘性系数。由于MY82方案[22]使用了相同的粘性和扩散长度尺度,GGL90方案[26]对其进行了改进,对粘性和扩散系数采用了不同的尺度。基于GLS03方案[34-35]的模拟结果表明,湍流长度尺度的选择存在约束条件,该方案既可用做广义长度尺度方案,还可以用来分析比较已有的模型。由于湍流混合模型计算较为复杂,KPP94方案[38-39]将大气模式常用的K-profile parameterization (KPP)[57]方案引入海洋模式,旨在建立一个包含所有重要过程的参数化方案,它在相对粗糙的垂直网格上运行良好。

随着观测、理论和数值方法的发展以及硬件条件的提高,对于海洋的模拟越来越精细化,海洋中小尺度过程如中尺度涡旋、内波等过程的参数化受到人们的关注。GM90中尺度涡参数化提高了大多数z坐标模式的物理完整性。另外,FKFH08亚中尺度涡参数化对海洋上层的层结模拟有明显改进。然而,目前中尺度涡、亚中尺度涡参数化仍然存在一些问题[3],例如海洋内部中尺度涡闭合与边界层方案的匹配问题、亚中尺度涡中的风-锋相互作用、能量串级在模式中尚未考虑。更精确的卫星海面观测对于中尺度涡的参数化过程有帮助。内波混合目前尚未有成熟的参数化方案,有待于进一步研究。

在海洋表面,波破碎对于动量由大气风场向海洋流场的传递具有重要作用。CB94和QYY04分别发展了波浪混合参数化方案,对海洋上层温度模拟的偏差有改善作用,并且加入QYY04方案还提高了PP81、KPP94参数化方案的性能。在海底地形作用下,正压潮流的能量向斜压潮流转化,增强海洋底层物理要素的混合。SJL04方案将潮流耗散加入到混合过程参数化,改善了温盐的模拟,对大洋深海层结的模拟有重要作用。在海洋垂直混合过程中,一些模式也考虑了双扩散[1, 58],溢流[13]等过程的影响。

当前海洋垂直混合参数化方案众多,模式开发者一般选择偏好的参数化方案并直接编码进入模式。2014年在Breckenridge Colorado举行的海洋模式工作组/通用地球系统模式 (OMWG/CESM)会议上,Levy等人[59]提出了通用海洋垂直混合 (CVMix)的构想,目标是建立一种包含一系列参数化方案的易用程式库,最终实现参数化库的独立驱动。

随着数值计算的发展,国内外涌现出了一些新的海洋模式[60]。如MITGCM[31]采用了非静力框架,使其可以模拟多种尺度的流体现象,还使用了结构守恒映射,通过一种流体力学内核既可用于描述大气又可用于海洋。在今后的工作中,我们将对这些模式进行详细介绍。

致谢:论文的前期工作,受到与史珍博士共同调研工作的启发,作者深表感谢。

**参考文献:**

[1] Madec G. NEMO ocean engine[M]. Note du Pole de modélisation, Institut Pierre-Simon Laplace (IPSL), France, 2008, 27: 1288-1619.

[2] Griffies S M, Böning C, Bryan F O, et al. Developments in ocean climate modelling[J]. Ocean Modelling, 2000, 2(3-4): 123-192.

[3] Griffies S M, Adcroft A J, Banks H, et al. Problems and prospects in large-scale ocean circulation models. In: Proceedings of



?1994-2014 China Academic Journal Electronic Publishing House. All rights reserved. http://www.cnki.net

OceanObs' 09: Sustained Ocean Observations and Information for Society[C]. Venice, Italy, 2010.

[4] 范植松. 海洋内部混合研究基础[M]. 北京: 海洋出版社, 2002.

[5] Kraus E B, Turner J S. A one-dimensional model of the seasonal thermocline II. The general theory and its consequences[J]. Tellus, 1967, 19(1): 98-106.

[6] Turner J S, Kraus E B. A one-dimensional model of the seasonal thermocline I. A laboratory experiment and its interpretation[J]. Tellus, 1967, 19(1): 88-97.

[7] Wallcraft A, Metzger E, Carroll S. Software Design Description for the HYbrid Coordinate Ocean Model (HYCOM), Version 2. 2[Z]. DTIC Document, 2009.

[8] Bleck R. An oceanic general circulation model framed in hybrid isopycnic-Cartesian coordinates[J]. Ocean Modelling, 2002, 4(1): 55-88.

[9] Price J F, Weller R A, Pinkel R. Diurnal cycling: Observations and models of the upper ocean response to diurnal heating, cooling, and wind mixing[J]. Journal of Geophysical Research: Oceans (1978-2012), 1986, 91(C7): 8411-8427.

[10] Price J F, Mooers C N K, Van Leer J C. Observation and simulation of storm-induced mixed-layer deepening[J]. Journal of Physical Oceanography, 1978, 8(4): 582-599.

[11] Bryan K, Lewis L J. A water mass model of the world ocean[J]. Journal of Geophysical Research: Oceans (1978-2012), 1979, 84 (C5): 2503-2517.

[12] Holland W. Energetics of barcoclinic oceans. In: Numerical Models of Ocean Circulation: Proceedings of a Symposium [C]. Washington, DC: National Academy of Sciences, 1975.

[13] Griffies S M. Elements of mom4p1[R]. GFDL Ocean Group Techical Report 6, 2010: 444.

[14] Crawford W R, Osborn T R. Microstructure measurements in the Atlantic equatorial undercurrent during GATE[J]. Deep-Sea Research, 1979, 26: 285-308.

[15] Osborn T R, Bilodeau L E. Temperature microstructure in the equatorial Atlantic[J]. Journal of Physical Oceanography, 1980, 10 (1): 66-82.

[16] Jones J H. Vertical mixing in the Equatorial Undercurrent[J]. Journal of Physical Oceanography, 1973, 3(3): 286-296.

[17] Pacanowski R C, Philander S G H. Parameterization of vertical mixing in numerical models of tropical oceans[J]. Journal of Physical Oceanography, 1981, 11(11): 1443-1451.

[18] 刘海龙, 俞永强, 李薇, 等. LASG/IAP 气候系统海洋模式 (LICOM1.0)参考手册[M]. 北京: 科学出版社, 2004.

[19] Smith R, Gent P. Reference manual for the Parallel Ocean Program (POP), ocean component of the Community Climate System Model (CCSM2. 0 and 3. 0) [R]. Technical Report LA-UR-02-2484, Los Alamos National Laboratory, Los Alamos, NM, 2002.

[20] Mellor G L. Analytic prediction of the properties of stratified planetary surface layers[J]. Journal of the Atmospheric Sciences, 1973, 30(6): 1061-1069.

[21] Mellor G L, Yamada T. A hierarchy of turbulence closure models for planetary boundary layers[J]. Journal of the Atmospheric Sciences, 1974, 31(7): 1791-1806.

[22] Mellor G L, Yamada T. Development of a turbulence closure model for geophysical fluid problems[J]. Reviews of Geophysics, 1982, 20(4): 851-875.

[23] Martin P J. Simulation of the mixed layer at OWS November and Papa with several models[J]. Journal of Geophysical Research: Oceans (1978-2012), 1985, 90(C1): 903-916.

[24] Kantha L H, Clayson C A. An improved mixed layer model for geophysical applications[J]. Journal of Geophysical Research: Oceans (1978-2012), 1994, 99(C12): 25235-25266.

[25] Mellor G L. User's guide for a three-dimensional, primitive equation, numerical ocean model[M]. Princeton, NJ: Atmospheric and Oceanic Sciences Program, Princeton University, 1998.

[26] Gaspar P, Grégoris Y, Lefevre J M. A simple eddy kinetic energy model for simulations of the oceanic vertical mixing: Tests at station Papa and Long-Term Upper Ocean Study site[J]. Journal of Geophysical Research: Oceans (1978-2012), 1990, 95(C9): 16179-16193.

[27] Bougeault P, Lacarrere P. Parameterization of Orography-Induced Turbulence in a Mesobeta--Scale Model[J]. Monthly Weather Review, 1989, 117(8): 1872-1890.

[28] Madec G, Delecluse P, Imbard M, et al. OPA 8.1, ocean general circulation model reference manual[M]. Note du Pôle de modélisation, Institut Pierre-Simon Laplace, 1998, 11: 97.

[29] Craig P D, Banner M L. Modeling wave-enhanced turbulence in the ocean surface layer[J]. Journal of Physical Oceanography, 1994, 24(12): 2546-2559.

[30] Mellor G, Blumberg A. Wave breaking and ocean surface layer thermal response[J]. Journal of Physical Oceanography, 2004, 34 (3): 693-698.

[31] Adcroft A, Campin J M, Dutkiewicz S, et al. MITgcm user manual [M]. MIT Department of EAPS, Cambridge, 2008.

[32] Canuto V M, Howard A, Cheng Y, et al. Ocean Turbulence. Part I: One-Point Closure Model-Momentum and Heat Vertical Diffusivities[J]. Journal of Physical Oceanography, 2001, 31(6): 1413-1426.

[33] Canuto V M, Howard A, Cheng Y, et al. Ocean turbulence. Part II: Vertical diffusivities of momentum, heat, salt, mass, and passive scalars[J]. Journal of Physical Oceanography, 2002, 32(1): 240-264.

[34] Umlauf L, Burchard H. A generic length-scale equation for geophysical turbulence models[J]. Journal of Marine Research, 2003, 61(2): 235-265.

[35] Umlauf L, Burchard H. Second-order turbulence closure models for geophysical boundary layers. A review of recent work[J].



?1994-2014 China Academic Journal Electronic Publishing House. All rights reserved. http://www.cnki.net

Continental Shelf Research, 2005, 25(7-8): 795-827.

[36] Rodi W. Examples of calculation methods for flow and mixing in stratified fluids[J]. Journal of Geophysical Research: Oceans (1978 2012), 1987, 92(C5): 5305-5328.

[37] Wilcox D C. Reassessment of the scale-determining equation for advanced turbulence models[J]. AIAA Journal, 1988, 26(11): 1299-1310.

[38] Large W G, McWilliams J C, Doney S C. Oceanic vertical mixing: A review and a model with a nonlocal boundary layer parameterization[J]. Reviews of Geophysics, 1994, 32(4): 363-403.

[39] Large W G, Danabasoglu G, Doney S C, et al. Sensitivity to surface forcing and boundary layer mixing in a global ocean model: Annual-mean climatology[J]. Journal of Physical Oceanography, 1997, 27(11): 2418-2447.

[40] Gent P R, Mcwilliams J C. Isopycnal mixing in ocean circulation models[J]. Journal of Physical Oceanography, 1990, 20(1): 150-155.

[41] Gent P R, Willebrand J, McDougall T J, et al. Parameterizing eddy-induced tracer transports in ocean circulation models[J]. Journal of Physical Oceanography, 1995, 25(4): 463-474.

[42] Redi M H. Oceanic isopycnal mixing by coordinate rotation[J]. Journal of Physical Oceanography, 1982, 12(10): 1154-1158.

[43] Griffies S M. The gent-mcWilliams skew flux[J]. Journal of Physical Oceanography, 1998, 28(5): 831-841.

[44] Boccaletti G, Ferrari R, Fox-Kemper B. Mixed layer instabilities and restratification[J]. Journal of Physical Oceanography, 2007, 37 (9): 2228-2250.

[45] Fox-Kemper B, Ferrari R, Hallberg R. Parameterization of mixed layer eddies. Part I: Theory and diagnosis[J]. Journal of Physical Oceanography, 2008, 38(6): 1145-1165.

[46] Fox-Kemper B, Ferrari R. Parameterization of mixed layer eddies. Part II: Prognosis and impact[J]. Journal of Physical Oceanography, 2008, 38(6): 1166-1179.

[47] Fox-Kemper B, Danabasoglu G, Ferrari R, et al. Parameterization of mixed layer eddies. III: Implementation and impact in global ocean climate simulations[J]. Ocean Modelling, 2011, 39(1-2): 61-78.

[48] Phillips O M. The dynamics of the upper ocean[M]. Cambridge: Cambridge University Press, 1977.

[49] Mellor G L. One-dimensional, ocean surface layer modeling: A problem and a solution[J]. Journal of Physical Oceanography, 2001, 31(3): 790-809.

[50] Mellor G. The three-dimensional current and surface wave equations[J]. Journal of Physical Oceanography, 2003, 33(9): 1978-1989.

[51] Yuan Y, Qiao F, Hua F, et al. The development of a coastal circulation numerical model: 1. Wave-induced mixing and wave-current interaction[J]. Journal of Hydrodynamics, Ser. A, 1999, 14: 1-8.

[52] Qiao F L, Yuan Y, Yang Y Z, et al. Wave-induced mixing in the upper ocean: Distribution and application to a global ocean circulation model[J]. Geophysical Research Letters, 2004, 31(11).

[53] 乔方利, 马建, 夏长水, 等. 波浪和潮流混合对黄海、东海夏季温度垂直结构的影响研究[J]. 自然科学进展, 2004, 14(12): 1434-1441.

[54] St Laurent L C, Simmons H L, Jayne S R. Estimating tidally driven mixing in the deep ocean[J]. Geophysical Research Letters, 2002, 29(23): 21-1-21-4.

[55] Simmons H L, Jayne S R, St Laurent L C, et al. Tidally driven mixing in a numerical model of the ocean general circulation[J]. Ocean Modelling, 2004, 6(3-4): 245-263.

[56] Chen D, Rothstein L M, Busalacchi A J. A hybrid vertical mixing scheme and its application to tropical ocean models[J]. Journal of Physical Oceanography, 1994, 24(10): 2156-2179.

[57] Holtslag A A M, Boville B A. Local versus nonlocal boundary-layer diffusion in a global climate model[J]. Journal of Climate, 1993, 6(10): 1825-1842.

[58] Merryfield W J, Holloway G, Gargett A E. A global ocean model with double-diffusive mixing[J]. Journal of Physical Oceanography, 1999, 29(6): 1124-1142.

[59] Levy M, Danabasoglu G, Griffies S, et al. Community Ocean Vertical Mixing (CVMix) Status Update[Z]. OMWG Meeting. Breckenridge, CO, 2014.

[60] 郑沛楠, 宋军, 张芳苒, 等. 常用海洋数值模式简介[J]. 海洋预报, 2008, 25(4): 108-120.



?1994-2014 China Academic Journal Electronic Publishing House. All rights reserved. http://www.cnki.net

# Review of vertical mixing parameterization in ocean climate modeling

WANG Lei[1,2], WANG Zhang-gui[2], LING Tie-jun[2], ZUO Jin-qing[3]

*(1. School of Physics, Peking University, Beijing 100871 China; 2. Key Laboratory of Research on Marine Hazards Forecasting, NMEFC, Beijing 100081 China; 3. Laboratory for Climate Studies, National Climate Center, China Meteorological Administration, Beijing 100081 China)*

**Abstract**: In ocean climate models, the parameterization schemes of vertical mixing processes are introduced. Firstly, the corresponding physical issues, theoretical basis, numerical expressions and characteristics of various vertical mixing parameterization schemes are introduced, and the evolutions of different schemes are shown. Secondly, the latest advancement about vertical mixing parameterization, owing to considering the contribution from the mesoscale eddies, submesoscale eddies, wave and tidal are summarized. Finally, we propose some suggestions on the future development in vertical mixing models.

**Key words**: turbulence closure scheme; mesoscale eddies mixing; submesoscale eddies mixing; wave induced mixing; tidal induced mixing



?1994-2014 China Academic Journal Electronic Publishing House. All rights reserved. http://www.cnki.net

INTERNATIONAL JOURNAL OF CLIMATOLOGY
*Int. J. Climatol.* **34**: 3054–3065 (2014)
Published online 23 December 2013 in Wiley Online Library
(wileyonlinelibrary.com) DOI: 10.1002/joc.3893

RMetS
Royal Meteorological Society

# Spatial and temporal variations of regional high temperature events in China

Yanjiao Wang,[a] Fumin Ren[b]* and Xuebin Zhang[c]

[a] *Laboratory for Climate Studies, National Climate Center, China Meteorological Administration, Beijing 100081, China*
[b] *State key Laboratory of Severe Weather (LaSW), Chinese Academy of Meteorological Sciences (CAMS), Beijing 100081, China*
[c] *Climate Research Division, Environment Canada, Toronto, Ontario M3H 5T4, Canada*

**ABSTRACT:** An objective identification technique is applied to identify Regional High Temperature Events (RHTE) in China using daily maximum temperature data at 642 stations from 1961 to 2010. There are 213 RHTE identified. These events in general occur from May to September, with months from June to August being high season and the peak frequency appearing in July. Over the space, these events mainly occur in regions east of 90°E, with higher frequencies and stronger intensities in the middle and lower valleys of the Yangtze River. Extreme and severe RHTE are more frequent in southern, central and eastern China and are less frequent in northern China. Statistics that characterize the regional events including annual frequency, annual sum of integrated index, annual sum of single indices (e.g. duration, accumulated high temperature intensity, accumulated impacted area and extreme high temperature) and annual maximum values of these single indices suggest that the RHTE are becoming more severe in both space and time and impacting more areas. A further analysis shows that the distribution patterns of the trend change of China RHTE, i.e. RHTE becoming more frequent and stronger in most China especially in northern China, but less frequent and weaker in eastern regions between the Yangtze River and the Yellow River during the past 50 years, is mainly a regional response to global warming. Meanwhile, the increasing trends in frequency and accumulated intensity of the RHTE in southern China may also be partly due to the western Pacific subtropical high westward extension and intensification in summer during the past decades.

KEY WORDS regional high temperature event; objective identification technique; spatial and temporal variations; China

*Received 30 May 2013; Revised 30 October 2013; Accepted 11 November 2013*

## 1. Introduction

Significant progress has been made over the past three decades on the understanding of characteristics and changes in extreme high temperature events. In the early 1980s, Karl *et al.* (1984) first studied extreme temperatures and diurnal temperature range. Subsequent studies, such as Karl *et al.* (1991 and 1993) and Horton (1995), focused on trends in daily temperature range, asymmetric diurnal temperature change and changes in extreme temperatures. Since the late 1990s, many more observational studies examined the changes in extreme temperature at regional scale as well as their regional differences (e.g., Easterling *et al.*, 1997; Zhai and Ren, 1997; Plummer *et al.*, 1999; Kysely *et al.*, 2000; Frich *et al.*, 2002; Nasrallaha *et al.*, 2004; Vincent *et al.*, 2005; Parey *et al.*, 2007; Brito-Castillo *et al.*, 2009 and Safar *et al.*, 2011).

Almost all these studies focus on temperature extremes at individual sites (observing sites or sometimes gridded values). Generally, extreme temperature events such as the 2003 European summer heat wave and the 2010 Russian heat wave are typically regional phenomena, i.e. they occur over an extended period affecting a large area. Recently, there has been some attention to such regional high-temperature events. Huang *et al.* (2009) studied the regional characteristics of extreme temperatures using daily maximum temperature data from 738 stations in China for 1961–2002. They analysed cumulative frequency distribution (CFD) of extreme temperatures and showed that extreme maximum temperatures occurred frequently in South China, regions between the Yangtze and the Huaihe Rivers, North China and Northeast China. Ding *et al.* (2010, 2011) analysed geographical patterns and temporal variations of regional dry and wet heat wave events in China (dry heat waves are calculated in terms of daily maximum temperature alone, while wet heat waves are calculated by temperature and relative humidity). They found that the frequencies and intensities of dry and wet heat waves in China have significantly increased since the 1960s.

For regional high-temperature events, both their spatial extents and their intensities may change within the life spans of such events. Therefore, it is important to develop suitable methods to identify such highly dynamical events and characterize them. Ren *et al.* (2012) proposed an objective identification technique for regional extreme event (OITREE). Here, we apply this method to observed

* Correspondence to: F. Ren, State key Laboratory of Severe Weather (LaSW)/CAMS, Beijing 100081, China. E-mail: fmren@163.com

© 2013 Royal Meteorological Society

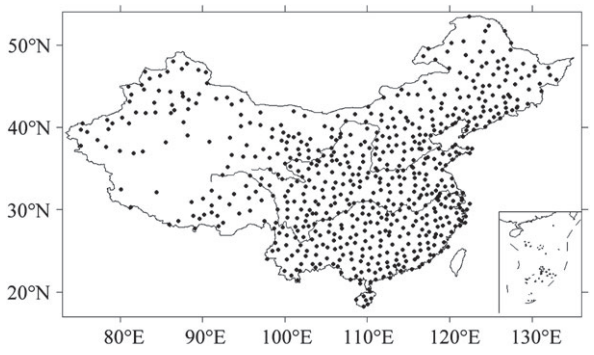


Figure 1. Geographical distribution of the 642 stations in China.

temperature data over China for 1961–2010, establishing suitable parameters to identify such events, and examine their temporal and spatial characteristics.

## 2. Data

The daily maximum temperatures at 723 stations in China for the period 1961–2010 are available for this study. Processes of quality control and homogeneity analysis have been carried out for this dataset (Li *et al.*, 2004, Li and Li, 2007). In addition, another simple data quality control procedure was used to this study to identify stations with extended missing values. We consider stations with more than 20% missing values to be of poor temporal coverage and discarded data from these stations. Consequently, data at 642 stations have been retained for the subsequent analysis. None of these stations is located in Taiwan and the geographical distribution of the 642 stations in China is shown in Figure 1.

## 3. Method

Using the new model of 'the string of candied fruits' proposed by Ren *et al.* (2012), the natural daily abnormal belts were reasonably stringed into a string of daily impacted areas to constitute a complete regional event. The technique includes five steps: (1) to select a daily index for each individual point (station), (2) to partition natural daily abnormality belts, (3) to distinguish the event's temporal continuity, (4) to construct the index system for regional events, and (5) to judge extremity for regional events.

Among these steps, steps (2) and (3) are the most important. Partitioning natural daily abnormality belts starts from a structural analysis of the daily abnormality distribution. Then, the abnormality distribution can be separated into different natural daily abnormality belts. This step includes three sub-steps – to judge abnormality for individual stations, to judge spatial continuity of the abnormality and to get natural daily abnormality belts. Meanwhile, distinguishing the event's temporal continuity starts from an analysis of the spatial distributions of different natural daily abnormality belts between adjacent dates by analysing their spatial overlap to evaluate the temporal continuity of an event, which is further divided into three sub-steps – to confirm ongoing events, to judge spatial overlap between every ongoing event and the belts in each day, and to identify the ongoing event's temporal continuity.

The OITREE method is applied in this study and after a lot of tests to identify China regional high temperature events (RHTE), values of the parameters in the method, which are listed in Table 1, have been set up. The parameters are described in detail in five steps as following.

### 3.1. To select a daily high temperature index for individual stations

This step selects one climate variable to represent high temperature. Both daily minimum and daily maximum temperature could be used. In this study, we use daily maximum temperature.

### 3.2. To partition natural daily high temperature belts

This step requires three parameters: The threshold for defining daily high temperature for a site is set to be the 90th percentile of all daily temperature for summer (June–July–August), while threshold for the distance to define neighbour sites and threshold for the number of sites in a daily high temperature belt are 250 km and 20, respectively.

### 3.3. To distinguish the temporal continuity of an event

This step uses two parameters. Threshold for the number of days for a gap in an event is set to be zero which means no gap is allowed in an event, while threshold for the ratio of overlapping sites for a daily high temperature belt is chosen to be 0.3.

### 3.4. To establish the index system for regional high temperature events

The indices in the index system have been divided into three types: the type-I indices are for the whole event process, the type-II indices provide daily conditions, and the type-III indices present extreme information for a station during the duration of the high temperature event. The content of the index system is as follows:

#### *3.4.1. Single indices*

The five type-I single indices for the whole high temperature event are duration ($D$), extreme high temperature ($I_1$), accumulated high temperature intensity ($I_2$), accumulated impacted area ($A_s$) and maximum impacted area ($A_m$).The formulas of the five single indices are as follows.

$$D = K \tag{1}$$

© 2013 Royal Meteorological Society

Table 1. Values of the parameter of the OITREE method for identifying China RHTE.

| Step | Parameter name | Code | Meaning | Value |
|---|---|---|---|---|
| Step 1: to select a daily high temperature index for individual stations | The daily index for individual stations | $T_m$ | It can represent the state of temperature for individual stations | Daily maximum temperature |
| Step 2: to partition natural daily high temperature belts | Threshold for defining daily high temperature for individual stations | $T_t$ | Abnormality occurs at individual stations only when $T_m$ is above or equals $T_t$ | The 90th percentile of $T_m$ |
| | Threshold for the distance to define neighbour stations | $d_0$ | For a station, all other stations within $d_0$ are defined as its neighbour stations | 250 km |
| | Threshold for the number of stations in a daily high temperature belt | $M_0$ | Only when the number of stations in a daily high temperature belt is above or equals $M_0$, the belt is called a formal daily high temperature belt | 20 |
| Step 3: to distinguish the temporal continuity of an event | Threshold for the number of days for a gap in an event | $M_{\text{gap}}$ | Only when the number of days for a gap is less than or equals $M_{\text{gap}}$, the gap is allowed to exist in an event | 0 |
| | Threshold for the ratio of overlapping stations for a daily high temperature belt | $C$ | Only if the ratio of overlapping stations for a high temperature belt with an ongoing event the day before is above or equals $C$, the belt belongs the ongoing event | 0.3 |
| Step 4: to establish the index system for regional high temperature events | The five weight coefficients in the integrated index | $e_1$, $e_2$, $e_3$, $e_4$ and $e_5$ | The five weight coefficients in the formula $Z = \mathrm{F}(I_1, I_2, A_S, A_m, D) = e_1 {I_1}^{\%} + e_2 {I_2}^{\%} + e_3 {A_S}^{\%} + e_4 {A_m}^{\%} + e_5 D^{\%}$ | 0.08, 0.26, 0.25, 0.16, and 0.25 |
| Step 5: to judge extremity for China regional high temperature events | The index and its threshold for defining a China regional high temperature event | Integrated intensity index $Z$ and its threshold of $Z_0$ | An event can be defined as a China regional high temperature event only when $Z$ is above or equals $Z_0$ | $Z_0$, 0.25 |
| | Thresholds for classifying China regional high temperature events | $Z_1$, $Z_2$ and $Z_3$ | The three thresholds can be applied in defining the four intensity categories by proportion 10% (extreme, $Z \geq Z_1$), 20% (severe, $Z_1 > Z \geq Z_2$), 40% (moderate, $Z_2 > Z \geq Z_3$), and 30% (slight, $Z_3 > Z$) | 3.6, 1.7, and 0.6 |

© 2013 Royal Meteorological Society

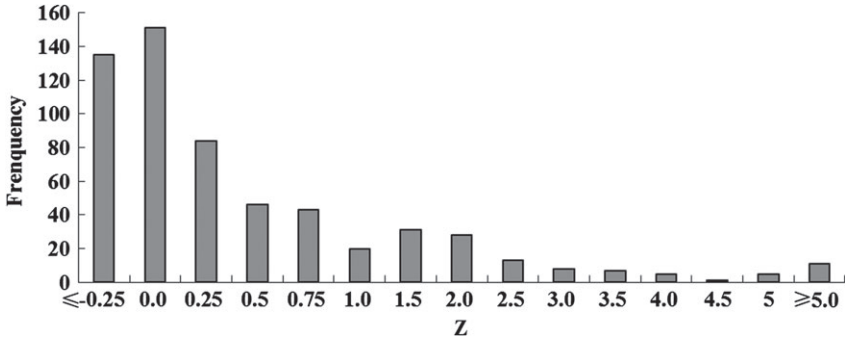


Figure 2. The frequency distributions of integrated index for 576 events.

where $K$ is the duration of a RHTE in days.

$$A_s = \sum_{k=1}^{K} A_k = \sum_{k=1}^{K} \text{Area}\,(S_k) \tag{2}$$

$$A_m = \text{Area}\left(\bigcup_{k=1}^{K} S_k\right) \tag{3}$$

where $S_k$ is the distribution of the impacted stations for day $k$, and $A_k$, (Area($S_k$)) means the area of $S_k$.

$$I_1 = \underset{k=1,K}{\text{Max}}\left(\underset{i=1,J_k}{\text{Max}}\,(T_{ki})\right) \tag{4}$$

$$I_2 = \sum_{k=1}^{K}\sum_{i=1}^{J_k}(T_{ki} - T_{ki}|_c) \tag{5}$$

where $J_k$ is the number of impacted stations for day $k$ and $T_{ki}$ is the value of the daily maximum temperature for station $i$ on day $k$, while $T_{ki}|_c$ is the threshold (the 90th percentile) of $T_{ki}$ for defining high temperature.

For a day (the day $k$), the three type-II indices are daily extreme temperature ($I_{1k}$), accumulated daily intensity ($I_{2k}$) and daily impacted area ($A_k$).

$$I_{1k} = \underset{i=1,J_k}{\text{Max}}\,(T_{ki}) \tag{6}$$

$$I_{2k} = \sum_{i=1}^{J_k}(T_{ki} - T_{ki}|_c) \tag{7}$$

where the parameters have the same meanings as before, while $A_k$ can be directly calculated by gridding the impacted area.

For the extreme values for a station during the duration of the event, formulas of the two indices of type-III named station extreme temperature ($I_1|_j$) and station accumulated intensity ($I_2|_j$) are as follows:

$$I_1|_j = \underset{k=1,K}{\text{Max}}\left(T_{kj}\right) \tag{8}$$

$$I_2|_j = \sum_{k=1}^{K}\left(T_{kj} - T_{kj}|_c\right) \tag{9}$$

where $T_{kj}$ and $T_{kj}|_c$ are defined analogously to $T_{ki}$ and $T_{ki}|_c$, respectively but considered from the perspective of the number of impacted stations for the whole event process.

### 3.4.2. *The integrated index*

The integrated index, i.e. the integrated intensity, is defined on the basis of the single indices. The integrated index is for the whole event process and it is developed as a function of the five single indices.

$$\begin{aligned} Z &= F\,(I_1, I_2, A_s, A_m, D) \\ &= e_1 I_1^{\%} + e_2 I_2^{\%} + e_3 A_s^{\%} + e_4 A_m^{\%} + e_5 D^{\%} \end{aligned} \tag{10}$$

where $I_1{}^{\%}, I_2{}^{\%}, A_s{}^{\%}, A_m{}^{\%}$ and $D^{\%}$ are standardized $I_1, I_2, A_s, A_m$ and D, respectively, and $e_1, e_2, e_3, e_4$ and $e_5$ are their coefficients.

It is recommended (Ren *et al.*, 2012) that the five coefficients need to be objectively and carefully determined, to make sure the integrated index $Z$ and the five products – $e_1 I_1{}^{\%}, e_2 I_2{}^{\%}, e_3 A_s{}^{\%}, e_4 A_m{}^{\%}$ and $e_5 D^{\%}$ – have the same nature: the greater the intensity of the event

Table 2. Information of the Top three China RHTE during 1961–2010.

| Order of the RHTE | Beginning time | Ending time | Extreme high temperature $I_1$(°C) | Accumulated intensity $I_2$(°C) | Maximum impacted area $A_m$ ($10^4$km$^2$) | Duration $D$ (days) | Integrated index $Z$ | Location of the RHTE |
|---|---|---|---|---|---|---|---|---|
| No. 1 | 30 June 2000 | 30 July 2000 | 47.7 | 9992.3 | 520.3 | 31 | 11.4 | Northern China |
| No. 2 | 11 July 2003 | 11 August 2003 | 43.2 | 6354.7 | 399.1 | 32 | 8.2 | Southern China |
| No. 3 | 16 July 2010 | 5 August 2010 | 46.8 | 6611.8 | 677.6 | 21 | 7.7 | Most China |

© 2013 Royal Meteorological Society

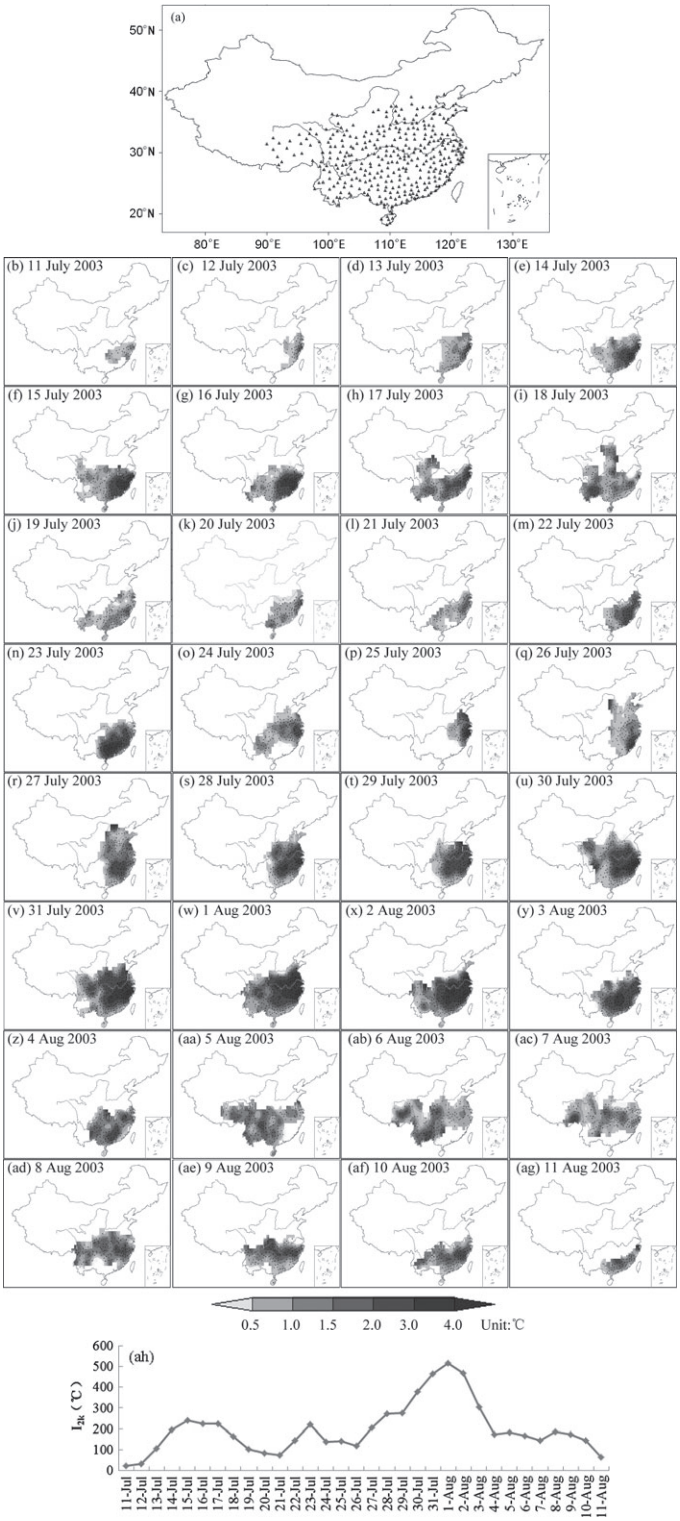


Figure 3. Results for No. 2 regional extreme high temperature event in China (a) Distribution of the maximum impacted area of the regional high temperature event during 11 July to 11 August 2003; (b)-(ag) distributions of the daily impacted area and intensity from 11 July to 11 August 2003, respectively; (ah) variations of accumulated daily intensity ($I_{2k}$) during the duration.

the greater the $Z$ value and the product values. In this study, the objective method to gain the five weighting coefficients is as follows: (1) the series of each index is normalized by the mean and standard deviation of 1971–2000, (2) The standardized series of each indices rank in descending order, and the ratio of the sum of the top 10th percentile values divided by the sum of all values for each index is calculated, and (3) The five coefficients are obtained by that ratio for each index divided by the sum of the five ratios, and the five coefficients are 0.08, 0.26, 0.25, 0.16 and 0.25, respectively. The coefficients indicate that the proportions of the extreme high values

© 2013 Royal Meteorological Society 

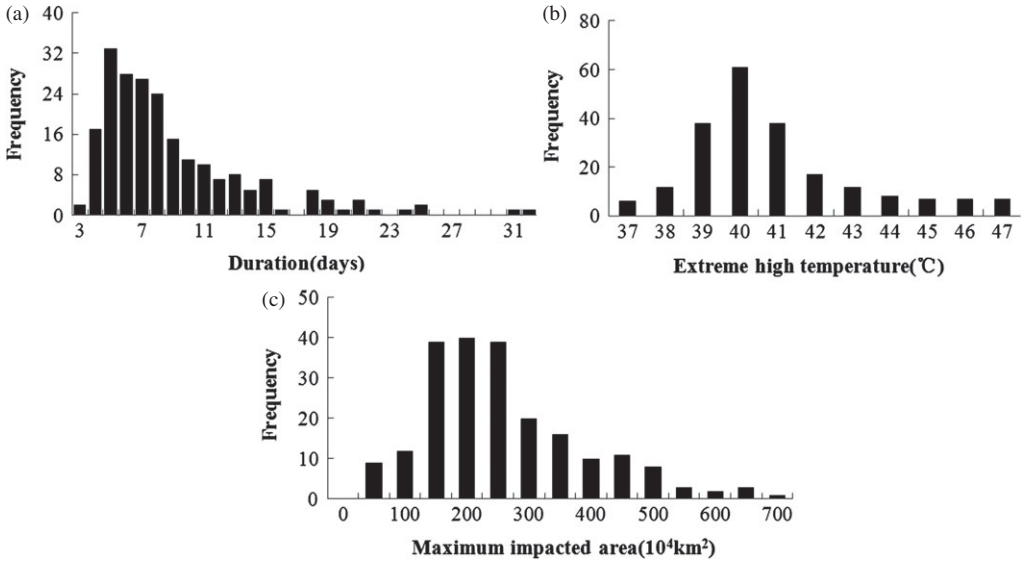


Figure 4. Frequency distributions of single indices for the 213 China RHTE (a) Duration, (b) extreme high temperature, and (c) maximum impacted area.

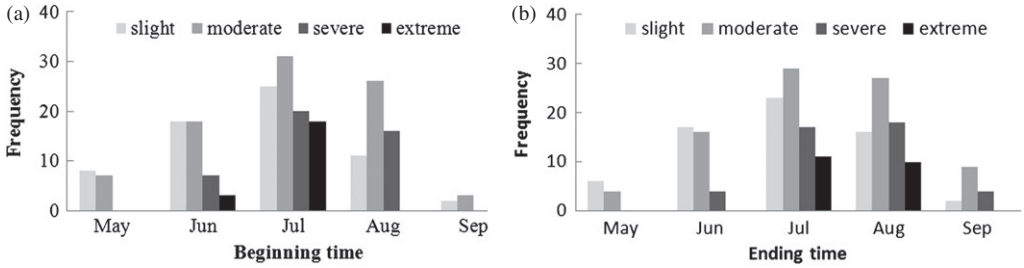


Figure 5. Frequency distributions of the beginning time (a) and the ending time (b) of the four category China RHTE.

for each index are larger, the extremity of each index is larger, and the influence to the integrated index is greater.

### 3.5. To judge extremity for China regional high temperature events

Using OITREE, 576 events with durations longer or equal to 3 days are identified during 1961–2010. Figure 2 displays the integrated index $Z$-frequency statistics for these events. The range of $Z$ is between −0.68 and 11.4, and it is obvious that the frequencies of small values of $Z$ (lower than 0.25) are higher, which means that many events are weak with small values of single indices. In this study, our main concern is on strong events, and according to the suggestion of Ren *et al.* (2012) the integrated index ($Z$) and 0.25 have been selected respectively as the index and its threshold to define a regional event for China as a whole. This leads to a total of 213 China RTHEs. Following the suggestion of proportions such as 10% (extreme), 20% (severe), 40% (moderate) and 30% (slight) (Ren *et al.*, 2012) for classifying China RHTE, the thresholds of the integrated index ($Z$) for classifying China RHTE are 3.6, 1.7 and 0.6, respectively, with the numbers of extreme China RHTE, severe China RHTE, moderate China RHTE and slight China RHTE being 21, 43, 85 and 64, respectively.

## 4. Effect of the identification

According to the integrated index, the top three extreme China RHTE during the past 50 years are as follows: (1) No. 1 event lasted 31 days from 30 June to 30 July 2000 occurred in most northern China, with the integrated index being 11.4, (2) No. 2 event occurred in most southern China during 11 July–11 August 2003, with the integrated index being 8.2 and (3) No. 3 event occurred in most China during 16 July–5 August 2010, with the integrated index being 7.7. Table 2 details the information for the three extreme China RHTE. Other researches (Bian, 2000; Ma *et al.*, 2004; Ding *et al.*, 2007; Zhao *et al.*, 2011) indicated that extreme high temperature occurred with serious economic losses and a number of deaths during each of the above three time periods and regions.

In addition, Figure 3 shows the result for No. 2 China RHTE in detail. Figure 3(a) is the distribution of the maximum impacted area of the event during 11 July–11 August 2003, while Figure 3(b)-(ag) display the distributions of the daily impacted extent and intensity during the period, and Figure 3(ah) presents the evolution of accumulated daily intensity ($I_{2k}$) during the duration. It is easy to see that the whole event influenced a large area in most southern China, and during the period the

© 2013 Royal Meteorological Society

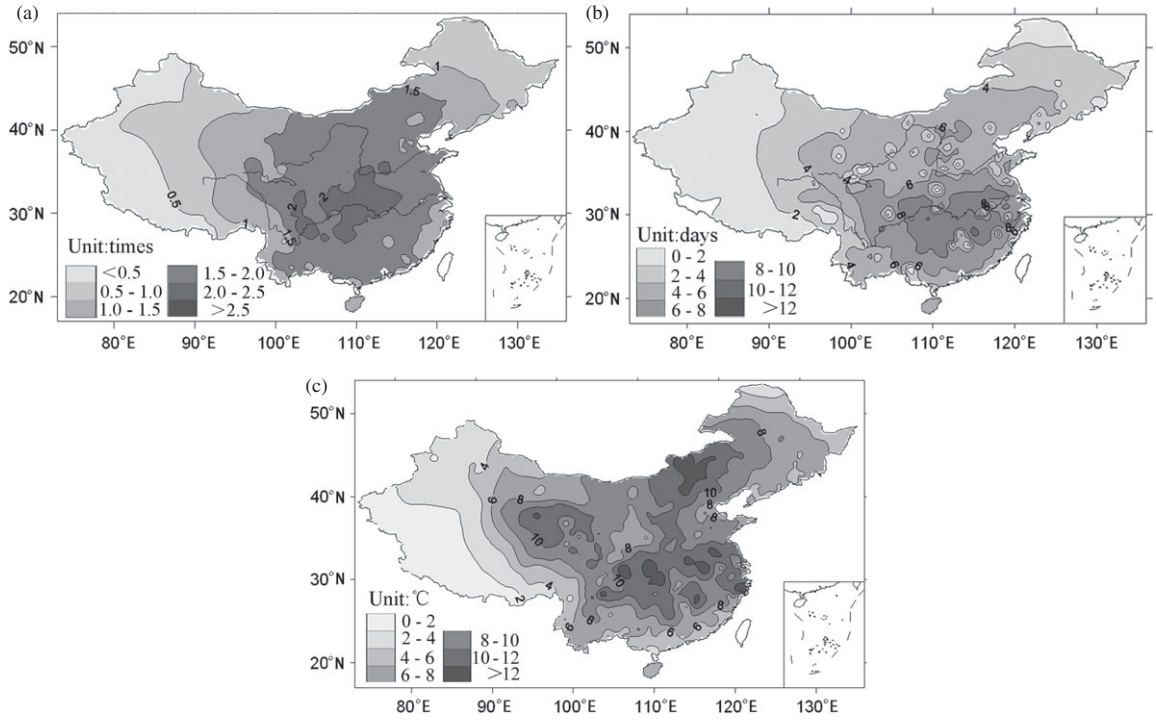


Figure 6. Spatial distributions of variable averages of the China RHTE during 1961 to 2010 (a) Frequency, (b) number of days, and (c) station accumulated intensity ($I_2|_j$).

daily impacted area and intensity varied day by day with accumulated daily intensity peaking on 1 August. In short, the results look quite reasonable.

## 5. Results

Figure 4 shows frequency distributions of single indices for the 213 China RHTE. Duration varies from 3 to 32 days, with a peak frequency of 33 at 5 days (Figure 4(a)). In Figure 4(b), extreme high temperatures for the 213 China RHTE range from 37 to 47 °C, with a peak frequency of 61 at 40 °C. Maximum impacted area changes from $5.0 \times 10^5$ to $7.0 \times 10^6$ km$^2$, with a peak frequency of 40 at about $2.0 \times 10^6$ km$^2$ (Figure 4(c)).

To understand the season when the RHTE occur, Figure 5 presents frequency distributions of the beginning time and the ending time of the four category China RHTE. It is easy to see that generally China RHTE occur from May to September, with the period from June to August being frequent and a peak frequency in July. The extreme China RHTE generally begin only in June and July and end only in July and August, while the slight and moderate China RHTE with low frequencies mainly occur in May and September.

Figure 6 displays spatial distributions of variable averages of the China RHTE during 1961 to 2010. Frequency averages (Figure 6(a)) are more than 1.0 time in most regions east to 90°E except for parts of Northeast China, with values of above 2.0 times in the western regions between the Yangtze River and the Yellow River and most of the Sichuan Basin.

On the basis of distribution of station accumulated intensity ($I_2|_j$) for each event, statistics of frequencies of the four category China RHTE for different regions are shown in Table 3. The 213 RHTE have been divided into eight kinds according to different regions, and the order of frequency is North China and Northeast China

Table 3. Statistics of frequencies of the four category China RHTE for different regions.

| Regions/Categories | Extreme | Severe | Moderate | Slight | Total |
|---|---|---|---|---|---|
| North China and Northeast China | 0 | 6 | 26 | 22 | 54 |
| Southeast China | 2 | 5 | 26 | 12 | 45 |
| Southwest China | 2 | 2 | 9 | 19 | 32 |
| Most southern China | 5 | 12 | 11 | 0 | 28 |
| Northwest China | 0 | 5 | 6 | 9 | 20 |
| Most central and eastern China | 5 | 5 | 5 | 0 | 15 |
| Most northern China | 3 | 3 | 2 | 2 | 10 |
| Most China | 4 | 5 | 0 | 0 | 9 |
| Total | 21 | 43 | 85 | 64 | 213 |

© 2013 Royal Meteorological Society

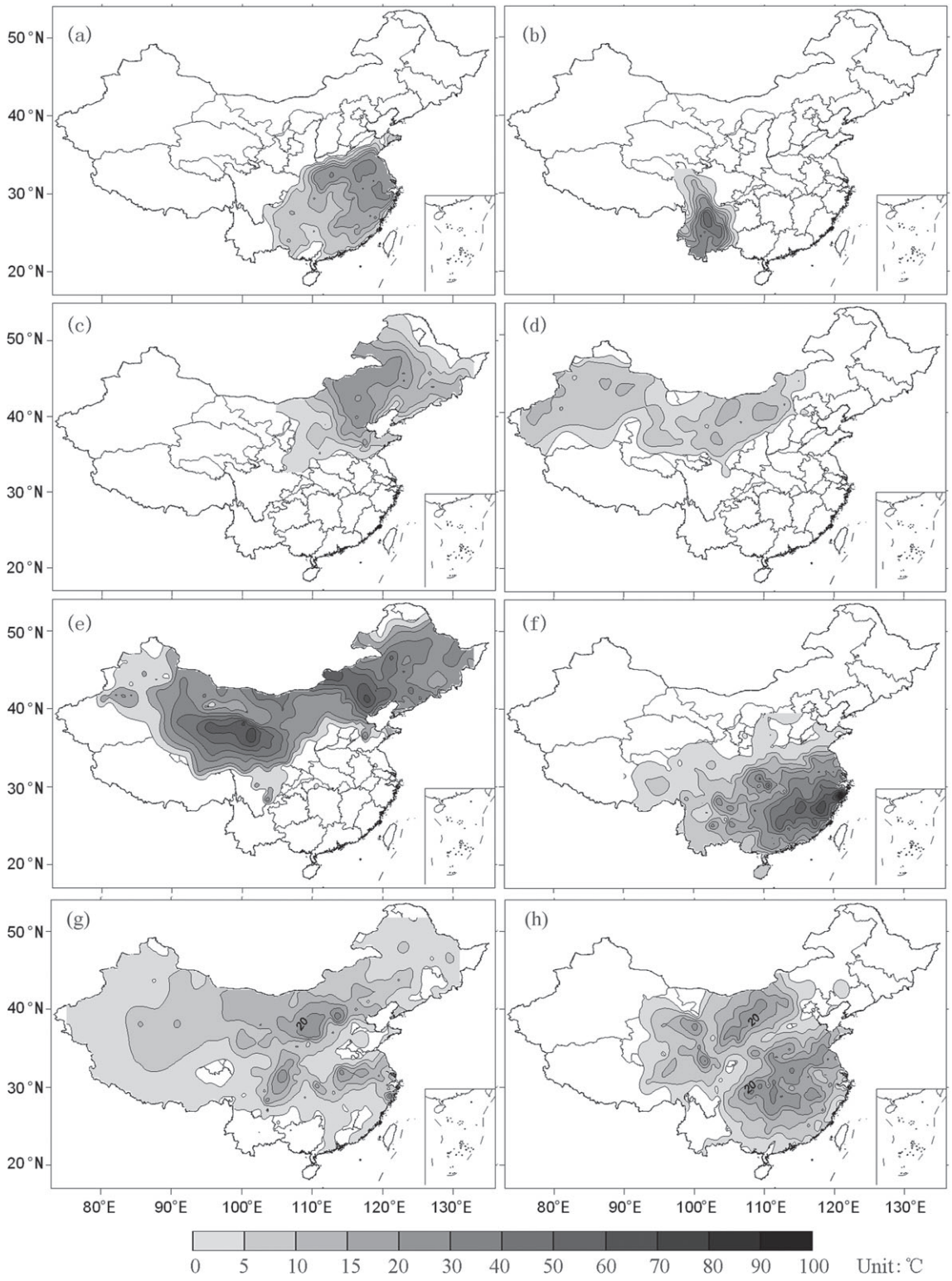


Figure 7. Distributions of station accumulated intensity ($I_{2|j}$) for typical China RHTE cases in eight regions. (a) Southeast China during 3–20 July 1988; (b) Southwest China during 8–23 May 1969; (c) North China and Northeast China during 8–16 July 1997; (d) Northwest China during 11–17 July 1975; (e) most northern China during 30 June–30 July 2000; (f) most southern China during 11 July–11 August 2003; (g) most China during 10–30 July 2001; (h) most central and eastern China during 10–27 July 1971.

(54 times), Southeast China (45 times), Southwest China (32 times), most southern China (28 times), Northwest China (20 times), most central and eastern China (15 times), most northern China (10 times) and most China (9 times). During the past 50 years, extreme RHTE occur frequently in most southern China (5 times), most central and eastern China (5 times) and most China (4 times), while no extreme RHTE occur only in North China and Northeast China (0 times) and Northwest China (0 times). Meanwhile, severe RHTE are observed most frequently

© 2013 Royal Meteorological Society

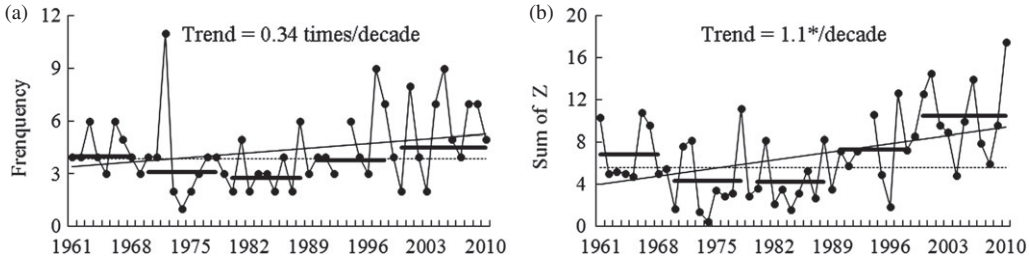


Figure 8. Variations of annual frequency (a) and annual sum of integrated index $Z$ (b) for the China RHTE. Dotted curve is the annual values of variable, straight line is the trend line, dotted line is the zero line, and short thick line is the average values of variable per decade. Asterisks (*) denote the significance of trends at the 0.05 confidence level by Mann–Kendall test.

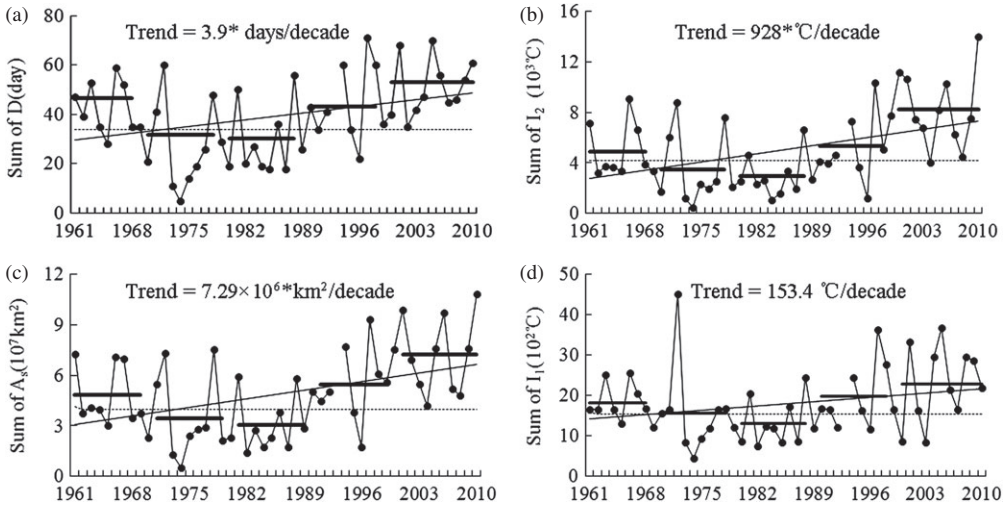


Figure 9. Variations of annual sum of single indices for the China RHTE (a) duration (D), (b) accumulated high temperature intensity($I_2$), (c) accumulated impacted area ($A_s$), and (d) extreme high temperature ($I_1$). Asterisks (*) denote the significance of trends at the 0.05 confidence level by Mann–Kendall test.

in most southern China (12 times), and frequently in North China and Northeast China (6 times), Southeast China (5 times), Northwest China (5 times), most central and eastern China (5 times) and most China (5 times).

Figure 6(b) shows that annual averages of the number of days within the RHTE are generally greater than 4 days in most China east to 90°E except for parts of Northeast China, parts of western Yunnan with values of above 8 days in the middle and lower valley of the Yangtze River. The distribution of annual average of station accumulated intensity ($I_{2|j}$) (Figure 6(c)) is similar to that of the number of days with the RHTE (Figure 6(b)), and the averages are stronger in most regions east to 90°E except for parts of eastern Northwest China, parts of Northeast China and southern South China.

Figure 7 shows the distributions of station accumulated intensity ($I_{2|j}$) for typical China RHTE cases in the eight regions. The eight cases are those of Southeast China during 3–20 July 1988, Southwest China during 8–23 May 1969, North China and Northeast China during 8–16 July 1997, Northwest China during 11–17 July 1975, most northern China during 30 June–30 July 2000, most southern China during 11 July–11 August 2003, most China during 10–30 July 2001 and most central and eastern China during 10–27 July 1971.

Variations of annual variables of the China RHTE are presented in Figures 8–10. During the past 50 years, frequency of the RHTE shows an increasing trend with a mean rise of 0.34 times per decade. Frequency also displays obvious inter-decadal variations with high values in the1960s, 1990s and 2000s and low values in the 1970s and 1980s, the top three annual frequencies being 11 times in 1972, 9 times in both 1997 and 2005, and no RHTE in 1993 (Figure 8(a)). Annual sum of integrated index displays a significant increasing trend with a mean rise of 1.1 per decade and similar inter-decadal variations to that of frequency with the top three values of the sum in 2010, 2001 and 2006 (Figure 8(b)). Above results indicate that the RHTE are becoming more frequent and stronger during the past 50 years.

For the single indices (Figure 9(a)–(d)), annual sum of single indices (duration, accumulated high temperature intensity, accumulated impacted area and extreme high temperature) show increasing trends in the past 50 years with similar inter-decadal variations to these frequencies and sum of integrated index, the trends of duration, accumulated high temperature intensity and accumulated impacted area pass significant Mann–Kendall rank test at 0.05 level (Figure 9(a)–(c)). Figure 10(a)–(d) displays the variations of the annual maximum of duration,

© 2013 Royal Meteorological Society 

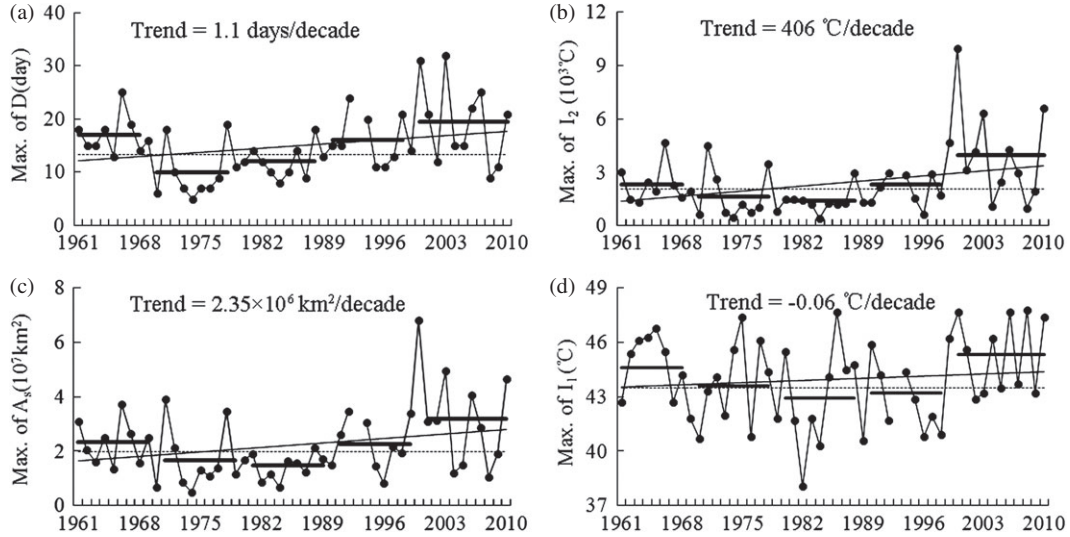


Figure 10. Variations of annual maximum values of single indices for the China RHTE (a) duration (D), (b) accumulated high temperature intensity($I_2$), (c) accumulated impacted area ($A_s$), and (d) extreme high temperature($I_1$).

accumulated high temperature intensity, accumulated impacted area and extreme high temperature. It can be seen that all annual maximum of single indices show increasing trends with similar inter-decadal variations to these in Figures 8 and 9.

To further understand the trend changes of China RHTE, the trends of annual frequency and accumulated intensity ($I_{2|j}$) with time for individual station are computed by linear regression (shown in Figure 11). Figure 11(a) displays that during 1961–2010 the increasing trends of RHTE frequency exist in most China especially in northern China, while decreasing trends mainly appear in eastern regions between the Yangtze River and the Yellow River. For accumulated intensity, the distribution pattern is similar to that of frequency, with increasing trends in most China, especially in northern China and western regions between the Yangtze River and the Yellow River, and decreasing trends in eastern regions between the Yangtze River and the Yellow River (Figure 11(b)).

The significant trend test by the Mann–Kendall shows that increasing trends of annual frequency and accumulated intensity are significant in most of northern China, parts of western regions between the Yangtze River and the Yellow River and parts of the coast areas of South and Southeast China (Figure 11).

In addition, trend distributions of summer mean temperatures from 1961 to 2010 are also analysed. Figure 12 shows that increasing temperature trends exist in most China especially in northern China, while decreasing temperature trends mainly appear in eastern regions between the Yangtze River and the Yellow River, which is a very similar distribution pattern to that in Figure 11. It is well known that a local or regional response can be complex and perhaps even counter-intuitive (IPCC, 2007) and the temperature trend distribution pattern in Figure 12 is a regional response to global warming during the past 50 years in summer in China (SNCCAR Writing Committee, 2011), and then the trend changes of China RHTE are mainly a regional response to global warming, too. In addition, some recent studies (Wu *et al.*, 2005; Zhou *et al.*, 2009) note that the western Pacific subtropical high (WPSH) shows a westward extension and intensification in summer during the past decades especially since the late 1970s. The WPSH is an important weather system that influences southern China, when the WPSH strengthens and extends westward that will cause high temperature weather in regions that controlled by it. Then it can be understood that besides the regional response to the global warming, the increasing trends in RHTE frequency and accumulated intensity in southern China may also be partly due to the WPSH westward extension and intensification in summer during the past decades.

## 6. Conclusions and discussions

Through the above analyses and discussions, the main conclusions are given below.

1. The OITREE method is applied in identifying China RHTE and a suitable set of parameters of OITREE has been determined. Tests of effect of the identification show that the results are quite reasonable.
2. There are totally 213 China RHTE during 1961–2010, including 21 extreme RHTE, 43 severe RHTE, 85 moderate RHTE and 64 slight RHTE. China RHTE generally occur from May to September, with the period from June to August being frequent and peak frequency in July.
3. All the annual variables for the 213 China RHTE, such as annual frequency, annual sum of integrated index, annual sum of single indices (duration, accumulated high temperature intensity, accumulated impacted area and extreme high temperature) and annual maximum values of the single indices, show increasing trends during the past 50 years, with

© 2013 Royal Meteorological Society

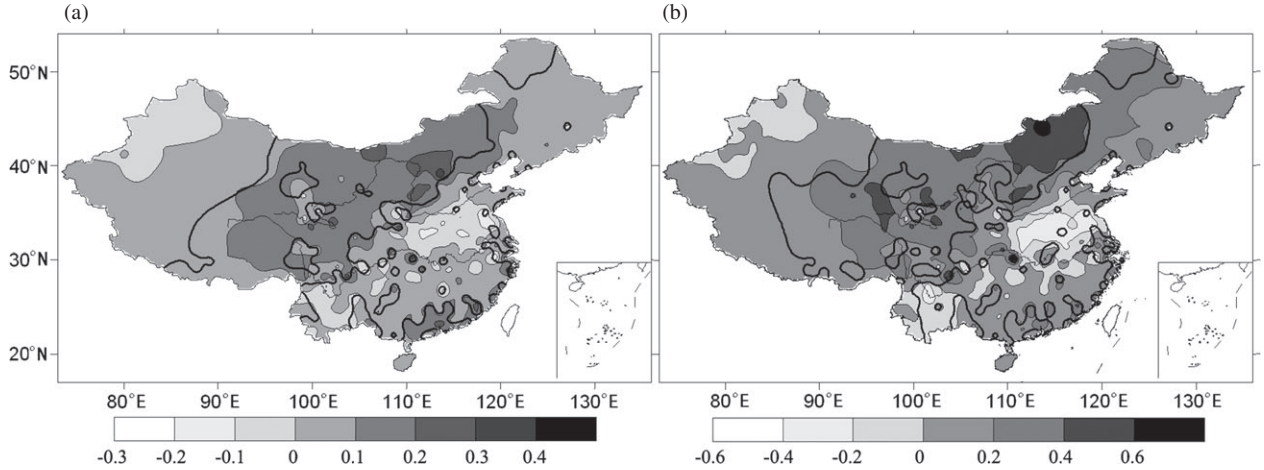


Figure 11. The linear trend distributions of annual frequencies (Unit: times $yr^{-1}$) (a) and accumulated intensities (Unit: $^{\circ}C\ yr^{-1}$) (b) of RHTE in China (shaded), with the thick black lines being the significance lines at 0.05 confidence level by the Mann–Kendall test.

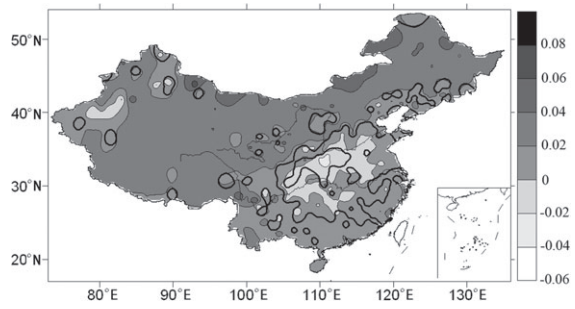


Figure 12. Trend distribution of summer mean temperatures from 1961 to 2010 (Unit: $^{\circ}C\ yr^{-1}$), with the black solid lines being the significance lines at 0.05 confidence level by the Mann–Kendall test.

significant increasing trends in annual sum of integrated index, annual sum of duration, annual sum of accumulated impacted area and annual sum of accumulated high temperature intensity.

4. A further analysis of the trend change for China RHTE reveals that RHTE are becoming more frequent and stronger in most China especially in northern China, but less frequent and weaker in eastern regions between the Yangtze River and the Yellow River during the past 50 years. This distribution pattern of trend change of China RHTE is mainly a regional response to global warming. Meanwhile, the increasing trends in RHTE frequency and accumulated intensity in southern China may also be partly due to the westward extension and intensification in summer during the past decades.

In this study, the daily maximum temperature data from 642 stations and the OITREE method were applied in identifying China RHTE. As the station distribution is uneven with dense stations in Southeast China and spare stations in Northwest China, a question about which we care is that how big the uneven distribution can influence the results. Two parameters in OITREE which are relative to the station distribution are threshold for the distance to define neighbour stations (parameter 1) and threshold for the number of stations in a daily high temperature belt (parameter 2), and considering the question, a lot of tests for the two parameters have been carried out. Analyses show that parameter 1 has little influence to the results with a value variation of the parameter between 200 and 400 km. For parameter 2, although the influence on the original results is obvious with a value variation of the parameter between 5 and 20 (stations), selecting only relatively strong events with big integrated index (such as $Z \geq 0.25$ in this study) as a China RHTE limits the influence. Above analysis suggests that when we pay attention to RHTE in a smaller region such as Northwest China, the two parameters need to change to suitable values.

Undoubtedly, this study suggests that OITREE shows skilful capability in identifying RHTE. Compared with some existing identification methods of RHTE (Ding *et al.*, 2010, 2011), the OITREE method has some distinctive features: (1) basing on the theoretical model of a string of candied fruits, (2) being more objective with more detailed introduction, and (3) more easily being applied in researches and climate operations, such as a special website of monitoring RHTE in China (http://cmdp.ncc.cma.gov.cn/extreme/hightemp.php?product=hightemp_moni&monicat=regional) in Chinese.

## Acknowledgements

This work was supported jointly by the Major State Basic Research Development Program of China (973 program) (Grant No.2013CB430201), the National Natural Science Foundation of China (Grant No.41175075, Grant No.41301458) and Meteorological Specialty Foundation of China (Grant No.GYHY201206013).

## REFERENCES

Bian ZQ. 2000. Abnormal high temperature and extremely hot in most China and floods in Huaihe River. *Meteorolo. Mon.* **26**(10): 58–61.

Brito-Castillo L, Castro S, Herrera R. 2009. Observed tendencies in maximum and minimum temperature in Zacatecas, Mexico and possible causes. *Int. J. Climatol.* **29**(2): 211–221.

© 2013 Royal Meteorological Society

Ding HJ, Zhou LL, Zha B, Zhai GQ. 2007. An analysis on the abnormal high temperature weather in the south Yangtze Valley during summer 2003. *J. Zhejiang Univ. Sci.* **34**(1): 100–105.

Ding T, Qian W, Yan Z. 2010. Changes in hot days and heat waves in China during 1961–2007. *Int. J. Climatol.* **30**(10): 1452–1462.

Ding T, Qian WH. 2011. Geographical patterns and temporal variations of regional dry-wet heat wave events in China during 1960–2008. *Adv. Atmos. Sci.* **28**(2): 322–337.

Easterling DR, Horton B, Jones PD, Peterson TC, Karl TR, Parker DE, Salinger MJ, Razuvayev VN, Plummer N, Jamason P, Folland CK. 1997. Maximum and minimum temperature trends for the globe. *Science* **277**: 364–367.

Frich P, Alexander LV, DellaMarta P. 2002. Observed coherent changes in climatic extremes during the second half of the twentieth century. *Climate Res.* **19**(193): 212.

Horton B. 1995. Geographical distribution of changes in maximum and minimum temperatures. *Atmos. Res.* **37**: 101–117.

Huang TQ, Qian YP. 2009. The analysis method of regional characteristics of extreme temperature and its results. *J. Nanjing Univ.* **45**(6): 715–723.

IPCC. 2007. *IPCC Fourth Assessment Report: Climate Change 2007 (AR4)*. Cambridge University Press: Cambridge, UK/New York, NY.

Karl TR, Kukla G, Gavin J. 1984. Decreasing diurnal temperature range in the United States and Canada from 1941–1980. *J. Climate Appl. Meteorol.* **23**: 1489–1504.

Karl TR, Kukla G, Razuvayev VN, Changery MJ, Quayle RG, Heim RR, Easterling DR, Fu CB. 1991. Global warming: evidence for asymmetric diurnal temperature change. *Geophys. Res. Lett.* **18**: 2253–2256.

Karl TR, Jones PD, Knight RW, Kukla G, Plummer N, Razuvayev VN, Gallo KP, Lindseay J, Charlson RJ, Peterson TC. 1993. A new perspective on recent global warming: asymmetric trends of daily maximum and minimum temperature. *Bull. Am. Meteorol. Soc.* **74**(6): 1007–1023.

Kysely J, Kalvova J, Kveton V. 2000. Heat waves in the south Moravian region during the period 1961 1995. *Studia geoph. Et geod.* **44**(57): 72.

Li QX, Li W. 2007. Construction of the gridded historic temperature dataset over China during the recent half century. *Acta Meteorologica Sinica* **65**(2): 293–300.

Li Q, Liu X, Zhang H, Peterson TC, David R. 2004. Detecting and adjusting temporal inhomogeneity in Chinese mean surface air temperature data. *Adv. Atmos. Sci.* **21**: 260–268.

Ma Z, Zhang Q, Xiao F, Li B. 2004. Characteristic of meteorological disasters and its influence in 2003 in China. *J. Catastrophology* **19**(supplement): 2–7.

Nasrallaha HA, Nieplovab E, Ramadan E. 2004. Warm season extreme temperature events in Kuwait. *J. Arid Environ.* **56**(357): 371.

Parey S, Malek F, Laurent C, Dacunha-Castelle D. 2007. Trends and climate evolution: Statistical approach for very high temperatures in France. *Clim. Change* **81**(331): 352.

Plummer N, Salinger MJ, Nicholls N. 1999. Changes in climate extremes over the Australian region and New Zealand during the twentieth century. *Clim. Change* **42**(183): 202.

Ren F, Cui D, Gong Z, Wang Y, Zou X, Li Y, Wang S, Wang X. 2012. An objective identification technique for regional extreme events. *J. Clim.* **25**: 7015–7027.

Safar M, Mohammad MS, Kurosh M, Mohammadi K, Sabziparvar AA, Abyaneh HZ. 2011. Investigation of meteorological extreme events over coastal regions of Iran. *Theor. Appl. Climatol.* **103**: 401–412.

SNCCAR Writing Committee. 2011. *The Second National Climate Change Assessment Report (SNCCAR) in China*. China Science Press: Beijing, China.

Vincent LA, Peterson TC, Barros VR, Marino MB, Rusticucci M, Carrasco G, Ramirez E, Alves LM, Ambrizzi T, Berlato MA, Grimm AM, Marengo JA, Molion L, Moncunill DF, Rebello E, Anunciacao YMT, Quintana J, Santos JL, Baez J, Coronel G, Garcia J, Trebejo I, Bidegain M, Haylock MR, Karoly D. 2005. Observed trends in indices of daily temperature extremes in South America 1960 2000. *J. Climate* **18**(5011): 5023.

Wu L, Wang B, Geng S. 2005. Growing typhoon influence on East Asia. *Geophys. Res. Lett.* **32**(18): L18703, DOI: 10.1029/2005GL022937.

Zhai PM, Ren FM. 1997. On changes of China's maximum and minimum temperatures in the recent 40 years. *Acta Meteorologica Sinica* **55**(4): 418–429.

Zhao QY, Huang JP, LÜ P, Zhang W, Cheng P. 2011. Abnormal high temperature phenomena and causes in summer 2010 over the Northern Hemisphere. *J. Lanzhou Univ. (Natural Sciences)* **47**(1): 52–56.

Zhou T, Yu R, Zhang J, Drange H, Cassou C, Deser C, Hodson D, Sanchez-Gomez E, Li J, Keenlyside N, Xin X, Okumura Y. 2009. Why the western pacific subtropical high has extended westward since the late 1970s. *J. Clim.* **22**: 2199–2215.

© 2013 Royal Meteorological Society

王艳姣，高蓓，周兵，等. 2014. 2013 年全球重大天气气候事件及其成因. 气象，40(6)：759-768.

# 2013 年全球重大天气气候事件及其成因*

王艳姣 高 蓓 周 兵 姜 彤 龚志强 司 东

国家气候中心气候研究开放实验室，北京 100081

**提 要**：2013 年，全球气温持续偏高，与 2007 年并列为第六个最暖年份，其中气温异常偏高的地区主要位于澳大利亚、北美洲北部、南美洲东北部、非洲北部以及欧亚大陆的大部地区。年内，赤道中东太平洋基本维持弱冷水状态，北极海冰范围仍处于记录中最低水平之一，而南极海冰范围则创历史新高。受大气环流异常以及海洋和海冰等外强迫因子的共同影响，世界范围内出现了显著的气候异常和极端事件，年初寒流和暴风雪袭卷亚洲、欧洲部分地区和北美洲，澳大利亚出现了极端高温天气；6—9 月中欧、亚洲和北美洲部分地区遭受暴雨洪涝的袭击，期间北半球大部地区则发生了极端高温天气；6 月以来多个强台风袭击东亚、东南亚和北美洲东海岸。分析指出，大气环流异常是上述全球重大天气气候事件的直接原因，而太平洋海温异常通过海气相互作用对大气环流异常产生重要影响。此外，在全球升温的过程中，伴随着气温平均值和变幅增大，致使发生极端天气气候事件的概率增加，这为全球许多国家和地区出现异常天气提供了有利的气候背景条件。

**关键词**：全球表面气温，暴风雪，洪涝，高温，热带气旋

**中图分类号**：P458 **文献标志码**：A **doi**：10.7519/j.issn.1000-0526.2014.06.013

# Global Significant Weather and Climate Events in 2013 and the Possible Causes

WANG Yanjiao GAO Bei ZHOU Bin JIANG Tong GONG Zhiqiang SI Dong

Laboratory for Climate Studies, National Climate Centre, Beijing 100081

**Abstract**: In 2013, above-average temperatures affected most of the global land surface areas. This is the sixth warmest year since records began in 1850, which is the same as 2007, and abnormal high temperatures were observed in Australia, northern North America, northeastern South America, northern Africa and most Eurasia. During the year, the weak cold water continually dominated the most of the eastern and central equatorial Pacific, and sea ice extent in the Arctic was still at one of the lowest levels in records, while the Antarctic sea ice extent has reached a new record. Affected by the anomalous atmospheric circulation combined with the external forcing factors of ocean and sea ice, notable climate anomalies and extreme events occurred worldwide in 2013. In early 2013, extreme cold waves and snowstorm attacked parts of Asia, Europe and North America while Australia experienced extreme high temperatures; from June to September, the Central Europe, parts of the Asia and North America suffered rainstorms and floods, while the hot weather hits the most of the Northern Hemisphere in same period. Since June, tropical storms and hurricanes attacked the East Asia, Southeast Asia and the east coast of America. The analysis results show that atmospheric circulation anomalies are the main causes for the above global extreme weather and climate events, and the Pacific sea surface temperature anomalies contribute to the atmospheric circulation anomalies by air-sea interaction. In addition, during the process of global warming, the aver-

* 国家重点基础研究发展计划项目(2013CB430201)、国家自然科学基金重点项目(41301458)和公益性行业(气象)科研专项(GYHY201206013)共同资助

2014 年 1 月 13 日收稿； 2014 年 4 月 16 日收修定稿

第一作者：王艳姣，研究方向为气候变化及遥感应用. Email：wangyj@@cma.gov.cn

age temperature and its amplitudes of variation are all increasing, resulting in the increase of the frequencies of extreme weather and climate events, which has provided the favorable conditions for the occurrence of abnormal weathers in many countries and regions of the world.

**Key words**: global surface air temperature, snowstorm, flood, high temperature, tropical cyclone

## 引 言

一年一度的《世界气象组织全球气候状况声明》(WMO,2013)中指出,2013 年全球陆地和海洋表面气温持续偏高,比 1961—1990 年平均值高约0.5℃,与 2007 年并列为 1850 年以来第六个最暖年份。2013 年既没有出现拉尼娜现象,也没有出现厄尔尼诺现象,赤道中东太平洋基本维持弱冷水状态,太平洋年代际振荡(PDO)呈冷位相。2013 年北极海冰范围仍处于记录中最低水平之一,而南极海冰范围创历史新高,并且比 1981—2010 年的平均值高了 2.6%。受大气环流异常以及海洋和海冰等外强迫因素的共同影响,2013 年世界范围内出现了显著的气候异常和极端事件,其中北半球部分地区多次受到天气气候极端事件的袭击(王遵娅等,2013;民政部国家减灾中心,2013a;2013b;秦苗苗,2013a;2013b;2013c;2013d;2013e;龚志强等,2014;国家气候中心气候与气候变化服务室,2013)。

本文重点对 2013 年全球发生的重大天气气候事件及其造成的影响进行综述,并对一些重大气候事件的成因进行分析。使用的资料包括:NCEP/NCAR 再分析资料、国家气象信息中心、国家气候中心 GDCN1.0 数据集和美国国家气候资料中心提供的全球逐日最高气温、最低气温和降水资料。

## 1 全球重大天气气候事件分述

### 1.1 全球气温

2013 年全球陆地和海洋表面气温为 14.5℃,比 1961—1990 年全球平均气温值(14.0℃)高约 0.5℃,比 2001—2010 年全球平均气温高 0.03℃,与 2007 年并列为 1850 年以来第六个最暖年份(图 1;WMO,2013)。其中温度偏高最显著地区包括澳大利亚、北美洲北部、南美洲东北部、非洲北部以及欧亚大陆的多数地区。在西南太平洋,澳大利亚报告称 2013 年 1 月是该国观测到的最热月份,1 月 7 日,还创下了该国按面积加权平均的日最高温度 40.3℃的新纪录,在南澳大利亚的蒙巴日最高温度达 49.6℃,异常高温导致该国出现有记录以来最热的夏季(12 月至次年 2 月)。此外,澳大利亚全年温度持续高于平均值,从 2012 年 11 月至 2013 年 10 月是该国有史以来最暖的 12 个月。在亚洲,日本出现了有记录以来最热的夏季。中国则出现了有记录以来最热的 8 月(与 2006 年持平)。韩国观测到其第四最暖的 7 月和最暖的 8 月,创下了夏季高温纪录(WMO, 2013)。

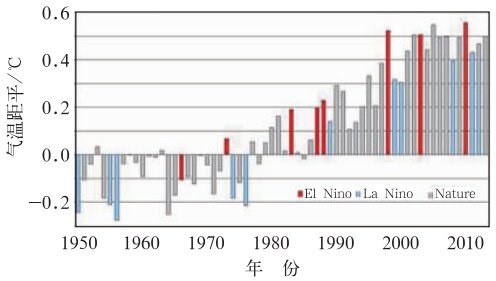


图 1 1950—2013 年全球表面气温距平序列(引自 WMO,2013)

Fig. 1 Time series of the global combined sea surface and land temperature anomalies during 1950−2013 (from WMO,2013)

### 1.2 南北极海冰

在 2012 年出现前所未有的大范围融化之后,北极海冰范围略有恢复,但 2013 年仍处在记录中最低水平之一。根据美国国家冰雪数据中心(NSIDC)的记录,3 月 15 日北极海冰范围达到了年最高值 1513 万 $hm^2$,比 1981—2010 年平均值还低约 50 万 $hm^2$。9 月 13 日北极海冰范围达到了其年周期的最低值 510 万 $hm^2$,成为记录中第六最小值,比 1981—2010 年的平均值减少了 18%(近 110 万 $hm^2$),但比 2012 年 9 月创纪录的低值增加了 341 万 $hm^2$。2013 年,南极海冰范围连续第二年于 9 月达到了创纪录的最高值 1947 万 $hm^2$,比 2012 年创下的原纪录约大了 3 万 $hm^2$,并且比 1981—2010 年的平均值高了 2.6%(WMO,2013)。

### 1.3　暴风雪频繁袭击亚洲、北美和欧洲

1 月上旬,亚洲西部遭遇暴风雪袭击,造成至少 4 人遇难,50 多人受伤,交通受阻,房屋倒塌;印度北部遭严寒袭击,造成至少 114 人死亡;孟加拉国遭遇寒潮,造成数十人死亡。中旬,日本关东地区遭暴风雪袭击,造成 2 人死亡,3 人失踪,近 900 人受伤;中下旬,英国遭大雪袭击,造成至少 10 人死亡;下旬,美国遭寒流袭击,造成至少 4 人死亡。1 月,波兰遭严寒袭击,共造成 31 人死亡。

2 月上旬,暴风雪袭击加拿大安大略省南部地区,造成至少 3 人死亡;同期,暴风雪袭击美国东北部,造成至少 12 人死亡,60 人受伤;下旬,美国中南部各州遭受严重的暴风雨雪袭击,造成至少 5 人死亡。

3 月上旬,日本北海道遭暴风雪袭击,导致 8 人死亡;同期,美国中东部地区也受暴风雪吹袭导致 4 人遇难,20 万户居民断电,1900 余航班停飞。中旬,欧洲大部遭受暴风雪袭击,多国进入紧急状态,大雪导致法国 2 人死亡,多国交通瘫痪,工厂停工,学校关闭。

4 月中旬,美国中西部和南部多州遭暴风雪袭击,造成至少 3 人死亡,数人受伤,道路封闭,数以万计家庭断电。

5 月上旬,美国科罗拉多遭遇倒春寒,降雪量超过 1 ft(1 ft=0.3048 m);下旬,暴雪袭击美国新英格兰地区北部和纽约州北部高海拔山区,部分地区积雪近 1 m。

11 月下旬,美国西部遭暴风雪袭击,致 13 人死亡。12 月中旬,中东地区多国遭遇强暴风雪袭击,其中以色列因灾死亡 4 人。12 月下旬,美国及加拿大部分地区遭受暴风雨雪和冻雨袭击。受此恶劣天气影响,两国至少 24 人丧生(其中美国境内死亡 14 人),50 多万户家庭或商家断电,全美超过 2 万个航班延误或取消。

### 1.4　澳大利亚、美国和亚洲多国遭受高温热浪袭击

2013 年初,巴西东北部地区降水持续偏少,部分地区遭受 50 年来最严中的干旱。同期,新西兰北部和东部受异常高温天气影响,降雨量显著偏少,遭受了近几十年来最严重的干旱。

1 月上旬,澳大利亚遭热浪袭击,6 个州中有 5 个发生火情,其中塔斯马尼亚州山火造成 100 多座房屋被烧毁,新南威尔士州高温引发火灾,上万只羊被烧死;中旬,热浪再袭澳大利亚,新南威尔士州和维多利亚州山林大火一度失控。

3 月,印度西部发生 40 年来最严重干旱,数百万人受灾。

6 月中旬,美国阿拉斯加州反常高温,18 日当地最高温度破 1969 年最高纪录。

7 月,日本遭高温热浪袭击,造成至少 41 人死亡;美国东北部和中西部地区遭高温热浪袭击,造成至少 6 人死亡;英国遭高温袭击,造成至少 760 人死亡;中国江南及重庆等地出现持续高温,造成至少 10 人死亡。

8 月上中旬,奥地利高温天气造成 1 人死亡;日本因高温天气造成 9815 人中暑入院,其中 17 人死亡;美国西部连日高温、干燥和强风天气造成多个州森林野火肆虐,已烧毁至少 800 英亩(1 英亩≈0.004069 $km^2$)土地。

### 1.5　北半球多国遭受暴雨洪涝袭击

#### 1.5.1　亚洲

1 月,印度尼西亚多个地区发生暴雨洪水,造成至少 53 人死亡,18 人失踪;上旬,以色列遭暴雨袭击,多个地区洪水泛滥,造成 3 人死亡。

3 月下旬,印度尼西亚爪哇岛遭洪水袭击,并引发山体滑坡,造成至少 11 人死亡。

4 月上旬,日本遭暴风雨袭击,造成 3 人死亡,至少 11 人受伤;下旬,阿富汗北部遭洪水袭击,造成 15 人死亡,数百人无家可归。

5 月中旬,斯里兰卡东部和南部沿海地区遭暴风雨袭击,造成至少 7 人死亡,10 人受伤。

6 月上旬,尼泊尔东北部连降暴雨导致滑坡,导致 7 人死亡,4 人失踪,2 人重伤;中旬,印度北部遭遇暴雨袭击,暴雨引发洪水,造成至少 807 人死亡,近 6000 人失踪,超过 10 万人被疏散。

7 月,印度北方邦遭暴雨袭击,造成至少 150 人死亡,50 万人被迫转移;上中旬,中国四川、陕西、甘肃和山西等省发生暴雨洪涝及滑坡泥石流灾害,共造成至少 100 人死亡,直接经济损失超过 200 亿元人民币;同期,尼泊尔遭暴雨洪水袭击,导致至少 60 人死亡;中旬,土耳其南部哈塔伊省遭暴雨袭击,造成 5 人死亡,10 人受伤;中下旬,韩国中部地区遭暴雨袭击,造成 5 人死亡,2 人失踪;同期,朝鲜遭暴雨洪水袭击,造成 15 人死亡;下旬,日本遭暴雨袭击,

造成1人死亡,2人失踪。

8月上旬,阿富汗遭暴雨洪水袭击,造成至少84人死亡,上百栋房屋被摧毁;上中旬,巴基斯坦遭遇洪水袭击,导致多地洪水泛滥,造成至少165人丧生,66000人受灾,数百房屋倒塌。

9月上中旬,越南北部和中部遭受暴雨袭击,引发洪水和山体滑坡,造成至少23人死亡,12人失踪,许多房屋被淹没;9月中旬,泰国遭洪水袭击,截至9月27日,受灾人口达210余万;柬埔寨遭遇持续的洪灾影响,造成至少168人死亡,经济损失约5亿美元。

10月上旬,菲律宾遭遇暴雨袭击,造成11人死亡,逾9万人逃离家园;下旬,印度遭遇暴雨袭击,造成至少45人死亡。

11月中旬,沙特频遭大雨和暴雨袭击,造成至少15人死亡,8人失踪;下旬,印度因连降大雨造成房屋倒塌,导致5人死亡。11月底至12月初,印度尼西亚苏门答腊不拉士达易火山区连降暴雨,引发洪水和山体滑坡灾害,造成9人死亡。

12月中旬,中国南方多地遭遇暴雨袭击,造成3人死亡。

1.5.2 欧洲

6月上旬,中欧多国遭受洪水肆虐,导致16人死亡,各国损失严重。

7月,俄罗斯远东地区遭洪水袭击,超过10万人受灾,道路和电力系统被摧毁。

8月上旬,英国遭遇暴雨袭击,大雨导致海滩消失、道路淹没,数百房屋受损;俄罗斯遭遇严重洪灾,直接经济损失超过30亿美元。

11月中旬,意大利西南部岛屿遭洪水袭击,导致17人死亡。

12月下旬,欧洲多国遭暴风雨袭击,其中英法两国因灾死亡6人,超过10万户家庭断电。

1.5.3 美洲

3月,巴西里约热内卢遭遇暴雨袭击,并引发山体滑坡,造成至少31人死亡,1人失踪,1400多人无家可归;厄瓜多尔西南部暴雨引发洪灾,造成至少8人丧生。4月上旬,阿根廷首都布宜诺斯艾利斯市及其周边省份遭受暴雨袭击,造成35万人受到影响,58000座建筑物被摧毁,至少59人死亡,直接经济损失超过5亿美元。5月初,美国东南部多地普降大雨,暴雨引发山洪,导致1人死亡,上千用户断电。

6月下旬,加拿大西部遭遇特大洪水,10万人被疏散,1人失踪。7月上旬,加拿大多伦多遭受暴雨袭击,造成交通大面积阻塞,30万用户停电。8月上旬,美国遭遇暴雨肆虐,导致至少3人死亡;下旬,巴西南部遭遇暴雨袭击,导致近7000人受灾,其中2000多人无家可归。

9月上旬,墨西哥维拉克鲁斯州连降大雨引发山体滑坡和洪水灾害,造成14人死亡;中旬,美国科罗拉多州连日暴雨引发洪灾,导致8人死亡,600人失踪,1.7万处房屋受损。11月底至12月初,古巴首都哈瓦那连降暴雨,造成100多栋建筑倒塌,导致2人死亡。12月中旬,巴西东南部连降暴雨引发严重洪灾,截至26日已导致至少44人死亡,超6万人无家可归。

1.5.4 非洲

1月中旬,莫桑比克大部分地区连降暴雨,导致洪水泛滥,造成12人死亡。4月中下旬,肯尼亚遭洪水袭击,造成63人死亡,超过3.4万人无家可归。

8月上旬,苏丹多个州普降暴雨,酿成洪涝灾害,已夺去了数十人的生命,8万栋房屋倒塌,10多万人受灾。

11月中旬,南非连遭暴雨袭击,造成至少8人死亡。

12月中旬,肯尼亚东南部遭遇洪水侵袭,导致至少12人死亡。

### 1.6 全球热带气旋活动接近常年同期

1.6.1 太平洋

8月中旬,菲律宾遭超强台风尤特和热带风暴潭美袭击,多地普降大到暴雨,导致许多地方发生洪水和山体滑坡,造成至少18人死亡,5人失踪,41人受伤。

9月初,日本琦玉县和千叶县遭龙卷风袭击,导致67人受伤,547幢建筑受损;中旬,日本遭强热带风暴万宜袭击,造成2人死亡,4人失踪,交通受到严重影响;下旬,强台风天兔登陆中国华南,造成至少34人死亡,直接经济损失超过220亿元人民币。

10月上旬,强台风菲特登陆中国,造成至少10人死亡,直接经济损失623.3亿元;中旬,台风百合

登陆菲律宾,造成至少 12 人死亡,210 万人断电;热带气旋费林袭击印度,造成 14 人死亡;强台风韦帕袭击日本,造成至少 18 人死亡,47 人失踪。

11 月上中旬,超强台风海燕横扫菲律宾中部地区,造成严重灾害,菲律宾全国至少有 5598 人死亡,1759 人失踪,近 3 万人受伤;中国广西、广东和海南遭"海燕"袭击,造成 9 人死亡,4 人失踪,直接经济损失超过 40 亿元人民币;越南北部遭"海燕"袭击,导致至少 10 人死亡,4 人失踪,84 人受伤;15 日,越南中部遭台风杨柳袭击,导致 36 人死亡,9 人失踪,8 万人无家可归。

1.6.2　大西洋

1 月下旬,美国南部部分地区遭龙卷风袭击,导致至少 2 人死亡。

2 月中旬,强龙卷风侵袭美国密西西比、阿拉巴马等南部多州,造成 60 余人受伤。5 月中旬,美国德州遭受至少 10 场龙卷风吹袭,造成 6 人死亡,超过 100 人受伤;20 日,多场龙卷风吹袭俄克拉荷马及其周边城镇,造成至少 24 人死亡;22 日,龙卷风袭击了俄罗斯中部地区,导致 15 人受伤,大量房屋倒塌。

6 月上旬,热带风暴安德莉亚登陆美国佛罗里达洲,并北上影响美国东部沿海地区,给当地带来强风暴雨。

8 月中旬,德国遭遇龙卷风袭击,导致 27 人受伤,其中包括 16 名儿童。

9 月中旬,墨西哥遭双风暴夹击,并引发暴雨、洪灾和泥石流,造成至少 139 人死亡,35 人受伤,53 人失踪,近 24 万人遭受重大财产和住房损失,受灾总人数约达 120 万人,经济损失超过 60 亿美元。

10 月下旬,欧洲多国遭遇强风暴袭击,造成至少 16 人遇难。11 月中旬,美国中西部遭到龙卷风及强风暴袭击,导致 8 人死亡,约 1 万人受到影响,经济损失超过 10 亿美元。

1.6.3　印度洋

3 月下旬,孟加拉东部地区遭龙卷风袭击,造成 20 人死亡,200 多人受伤,数百座房屋倒塌,上千棵树木折断。5 月中旬,气旋风暴马哈森在孟加拉南部沿海登陆下,导致 10 人死亡,百万民众被迫转移。

综合以上分析可见,受大气环流异常以及海洋和海冰等外强迫因子的共同影响,2013 年世界范围内出现了显著的气候异常和极端事件。年初寒流和暴风雪袭卷亚洲、北美洲和欧洲部分地区,造成至少 200 多人死亡,而澳大利亚则出现了极端高温天气;6—9 月亚洲、欧洲和北美洲部分地区遭受暴雨洪涝的袭击,造成至少 1700 多人死亡,期间北半球大部地区则发生了极端高温天气;2013 年全球热带气旋活动接近常年同期,其中多个强台风袭击东亚、东南亚和北美洲东海岸,造成至少 5000 多人死亡。图 2 为 2013 年全球重大天气气候事件示意图.

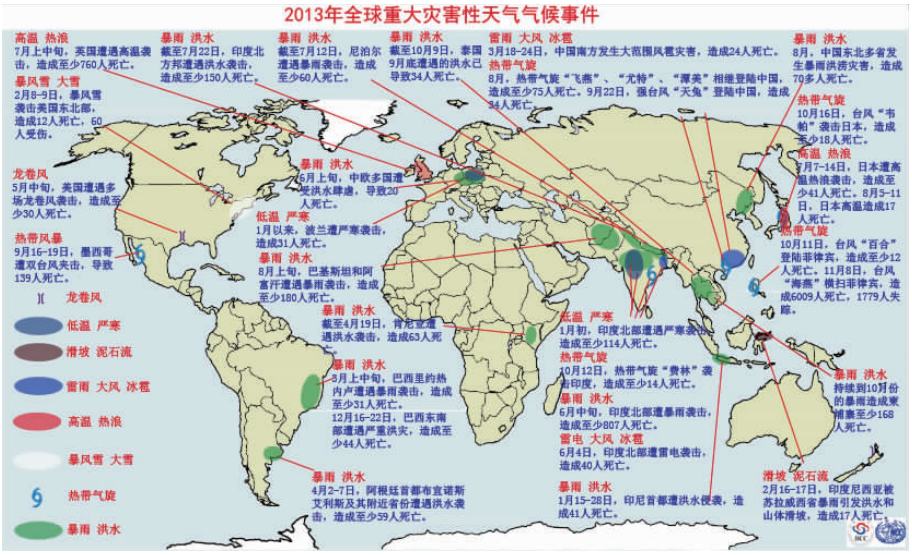


图 2　2013 年全球重大天气气候事件示意图

Fig. 2　Diagram of global significant weather and climate events in 2013

## 2 全球极端天气气候事件指标监测

全球极端天气气候事件监测指标采用世界气象组织(WMO)世界气候研究计划(WCRP)项目中专家组(ETCCDMI)推荐使用的极端天气气候事件监测指标,包括暖昼、暖夜、冷昼、冷夜、降水强度、极端降水量和极端强降水日数等指标(Peterson,2005)。各指标的详细定义参见文献(王东阡等,2013)。

2013 年,全球极端温度事件监测显示,亚洲、欧洲、非洲和南美洲等地出现极端偏暖事件的站点数多于极端偏冷事件的站点数;而北美洲地区则呈现极端偏冷事件相对较多的特征。极端偏暖事件主要出现在欧亚大陆大部,北美洲西部、南部和东部,南美洲南部,非洲南部和西部等地;极端偏冷事件主要出现在北美洲中部和南部、欧洲西部、东亚大部、南亚局部和南美洲中南部等地。极端强降水事件则主要集中在东亚东部、南亚、澳大利亚北部、欧洲南部、非洲西部和东部、北美洲东南部、南美洲西部和中南部等地区。

全球暖昼(TX90p)和暖夜(TN90p)指标监测表明,2013 年,欧洲大部、东亚大部、南亚南部、西亚北部、非洲北部和南部的局部、北美洲西北和南部、南美洲南部以及澳大利亚局部等地极端偏高的暖昼日数一般在 10 d 以上,其中中国中东部、南亚南部、东南亚局部、澳大利亚局部和南美洲南部的局部等地区暖昼日数超过 20 d(图 3);欧洲大部、东亚大部、中亚北部、南亚南部、西亚北部、非洲北部的局部、北美洲西部和东部及南美洲南部的局部等地区夜间温度极端偏高的暖夜日数在 10 d 以上,其中中国中东部、东北亚局部、东南亚局部和北美洲东北部局部等地超过 20 d(图 4)。

全球冷昼(TX10p)和冷夜(TN10p)指标监测显示,2013 年,白天温度极端偏冷的冷昼日数在欧洲中西部、东亚东北部和南部、北美洲中西部和东部、南美洲中东部等地区为 10 d 以上,其中北美洲中西部和东部局部等地区超过 20 d(图 5)。夜间温度极端偏冷的冷夜日数在欧洲西部、东亚东部、南亚、非洲北部和南部局部、北美洲中部、东南部和西北部、南美洲南部以及环澳大利亚的局部等地区达 10 d 以上,其中东亚东北部局部、南亚西部局部和北美洲中部的局部等地区达 20 d 以上(图 6)。

全球极端强降水量(R95p)和极端强降水日数(R95d)指标监测显示,2013 年,欧洲西部、东亚东南部和东北部的局部、南亚大部、东南亚北部和南部、北美洲东部、南美洲西部和南部的局部等地区极端降水量在 300 mm 以上,其中东亚东南部的局部、印度大部和东南亚局部等地区极端降水量达 1000 mm 以上(图 7)。同时,欧洲西部和北部的局部、东亚东南部和东北部局部、南亚南部、东南亚局部、北美洲东部局部、南美洲西部和东南部局部等地区极端强降水日数达 10 d 以上,其中部分地区达 20 d 以上(图 8)。上述大部地区的降水强度指数(SDII)均超过了 10 mm·d$^{-1}$,其中东亚的东南部局部、南亚的西部和北部局部、非洲西部局部及北美洲南部局部等地区超过 20 mm·d$^{-1}$(图 9)。

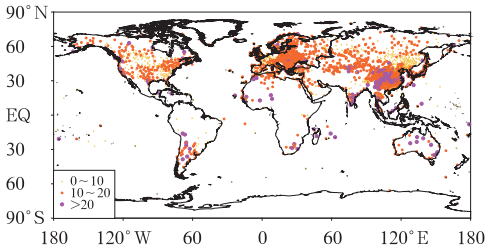


图 3 2013 年全球暖昼日数分布图(单位:d)

Fig. 3 Global distribution of warm days (TX90p) in 2013 (unit: d)

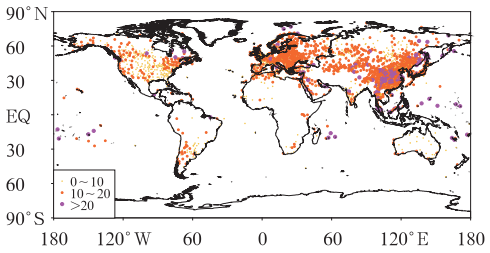


图 4 2013 年全球暖夜日数分布图(单位:d)

Fig. 4 Global distribution of warm nights (TN90p) in 2013 (unit: d)

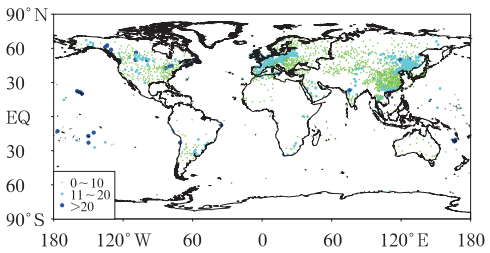


图 5 2013 年全球冷昼日数分布图(单位:d)

Fig. 5 Global distribution of cool days (TX10p) in 2013 (unit: d)

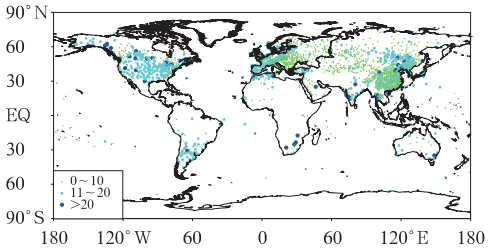


图 6　2013 年全球冷夜日数分布图(单位:d)

Fig. 6　Global distribution of cool nights (TN10p) in 2013 (unit: d)

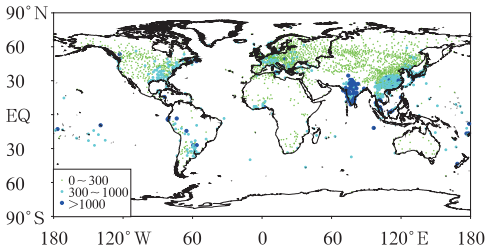


图 7　2013 年全球极端强降水量分布图(单位:mm)

Fig. 7　Global distribution of heavy precipitation amounts (R95p) in 2013 (unit: mm)

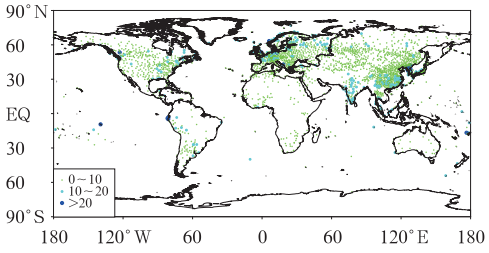


图 8　2013 年全球极端强降水日数分布图(单位:d)

Fig. 8　Global distribution of heavy precipitation days (R95d) in 2013 (unit: d)

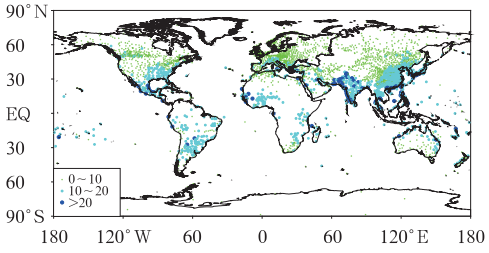


图 9　2013 年全球降水强度指数分布图(单位:mm·d$^{-1}$)

Fig. 9　Global distribution of simple daily intensity index (SDII) in 2013 (unit: mm·d$^{-1}$)

# 3　重大天气气候事件可能成因分析

## 3.1　俄罗斯远东地区最大洪灾

2013 年 7—9 月,俄罗斯远东地区的出现持续性降水,该区累积降水量较常年同期普遍偏多 5 成至 2 倍,局部偏多 2～4 倍,且降水极端性突出。异常偏多的降水导致俄罗斯远东地区出现 120 年来最大洪灾,造成 10 万多人受灾,3.2 万当地居民被疏散,经济损失高达数十亿美元(国家气候中心气候监测室,2013)。

2013 年 7—9 月,持续性环流异常是导致俄罗斯远东地区洪灾的最直接原因。7—9 月 500 hPa 高度及距平场上,受欧亚中高纬度切断性低压的影响,欧亚大陆西北部上空为异常正高度距平区,而欧洲东南部至俄罗斯东南部和东亚北部为宽广的低槽区,这种环流型有利于高纬冷空气南下影响俄罗斯远东地区;同时,鄂霍次克海地区阻塞异常发展有利于这种环流型的持续稳定维持(图 10)。与高度场相匹配,850 hPa 距平风场上,在贝加尔湖以东地区为一异常气旋性环流,西北太平洋地区存在一异常反气旋性环流,气旋性环流东侧偏南气流与反气旋环流西侧的偏南气流将西北太平洋和低纬度的暖湿空气向异常偏北的地区输送。在低纬度地区,西太平洋副热带高压(以下简称副高)持续控制中国东南部地区,且副高脊线位置异常偏北,副高西侧偏西南气流将低纬度地区的水汽持续向中高纬度地区输送。异常偏多的暖湿水汽与来自极地的冷空气在俄罗斯远东地区交汇,造成该区降水异常偏多(图 11)。

另一方面,2013 年东亚季风指数的逐日监测表明,6—9 月东亚夏季风总体偏强(图略)。东亚夏季风的持续偏强也有利于低纬度水汽向北方地区输送,加之受贝加尔湖以东地区异常气旋性环流和西北太平洋异常反气旋以及副高持续偏北的影响,来自西北太平洋的水汽与来自低纬度地区的水汽持续不断的向俄罗斯远东地区输送,有利于该区降水的异常偏多。

综合以上分析可见,在低纬度系统和中高纬度系统的共同调制作用下,7—9 月俄罗斯远东地区出现持续异常偏多的降水,造成该区出现 120 年来最大洪灾。

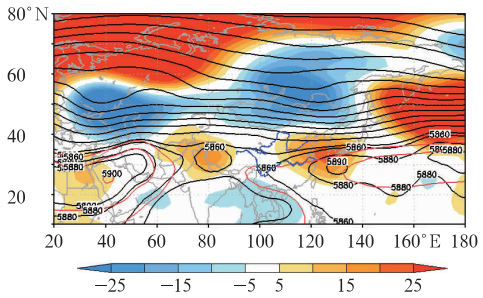


图 10 2013 年 7—9 月 500 hPa 位势高度(等值线)及距平场(阴影区)分布(单位:gpm,红色等值线为气候态下 5860 和 5880 线)

Fig. 10 500 hPa geopotential height (contours) and anomalies (shaded) from July to September in 2013 (unit: gpm, red lines: 5860 and 5880 gpm of climatology)

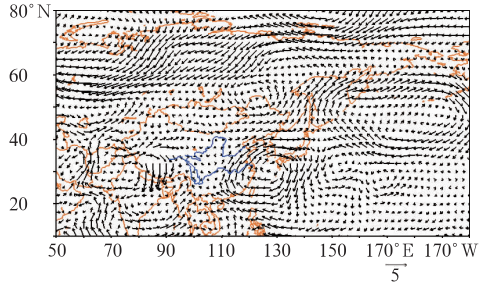


图 11 2013 年 7—9 月 850 hPa 风场距平(单位:$m \cdot s^{-1}$)

Fig. 11 850 hPa wind anomalies from July to September in 2013 (unit: $m \cdot s^{-1}$)

### 3.2 夏季北半球极端高温

2013 年夏季,北半球许多国家和地区出现持续高温天气。在亚洲,日本出现了有记录以来最热的夏季;中国出现了有气象记录以来最热的八月;韩国则创下了夏季高温纪录。此外,在欧洲和北美洲的多地也遭受了异常高温天气的袭击。2013 年夏季,北半球许多国家和地区出现持续高温天气的主要原因包括以下几方面:

(1) 全球气候变暖是大背景。IPCC 第五次评估报告指出,1880—2012 年,全球地表平均温度大约上升了 0.85℃。在北半球,1983—2012 年可能是过去 1400 年中最暖的 30 年(IPCC, 2013)。全球温度变化是人类活动引起的温室气体增暖效应和气候系统内部变率耦合作用的结果,自然气候变化驱动因子(如太阳活动、火山活动和大洋环流等)同样对温度变化产生影响,且其主要表现为年际或年代际尺度的变化。在全球升温的过程中,伴随着气温的平均值和变幅增大,致使发生极端温度天气的概率增加,这为夏季北半球许多国家和地区出现持续高温天气提供有利的气候背景条件。

(2) 海温异常是重要的外强迫因子。已有的研究指出,海温异常将通过海气相互作用对全球气候产生重要的影响(朱益民,2003;黄荣辉等,2006;张庆云等,2007;邓伟涛等,2009)。2013 年夏季(主要在 7—8 月),赤道西太平洋和海洋性大陆区的海温明显偏暖,尤其是海洋性大陆区南部海温增暖更为显著(图 12)。受异常暖海温影响,海洋性大陆区的对流活动也显著偏强。而在赤道中东太平洋大部,弱的冷海温持续发展也使得日界线附近对流活动明显偏弱(图 13)。由此,热带地区的 Walker 环流较常年同期显著偏强,赤道西太平洋为异常上升运动控制,而赤道中太平洋日界线附近为异常下沉运动控制。通过经向垂直运动,赤道西太平洋的异常上升运动激发异常下沉运动控制在东亚东部上空(图 14),从而使得副高不断增强并持续控制东亚东部地区,造成中国、日本和韩国等亚洲国家出现持续异常高温天气。

(3) 北半球中高纬异常大气环流影响。北极涛

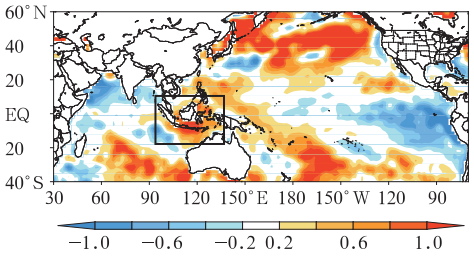


图 12 2013 年 7—8 月全球海温异常分布(单位:℃)

Fig. 12 Distribution of global sea surface temperature anomalies from July to August 2013 (unit: ℃)

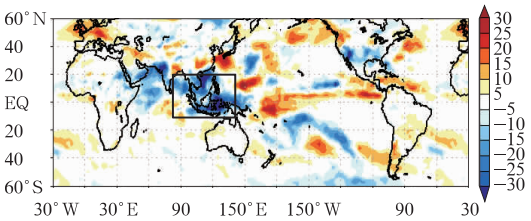


图 13 2013 年 7—8 月热带射出长波辐射异常分布(单位:$W \cdot m^{-2}$)

Fig. 13 Distribution of tropic Outgoing Longwave Radiation (OLR) anomalies from July to August 2013 (unit: $W \cdot m^{-2}$)

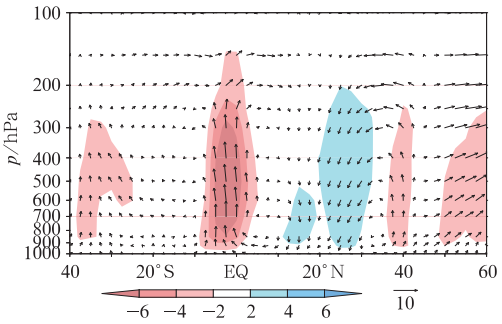


图 14　东亚东部(120°～140°E)平均经向垂直速度剖面图

(阴影区表示垂直速度异常，单位：$10^{-2}$ Pa·$s^{-1}$)

Fig. 14　The average meridional vertical velocity section (shaded is the vertical velocity anomalies, unit: $10^{-2}$ Pa·$s^{-1}$) in the eastern part of East Asia (120°—140°E)

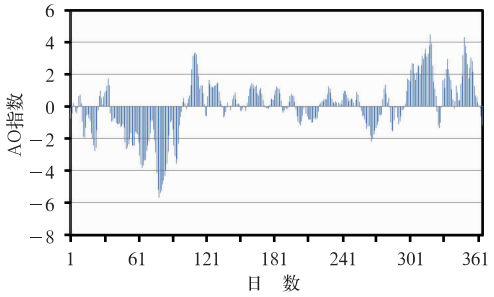


图 15　2013 年 AO 指数日变化

Fig. 15　Variations of daily AO index in 2013

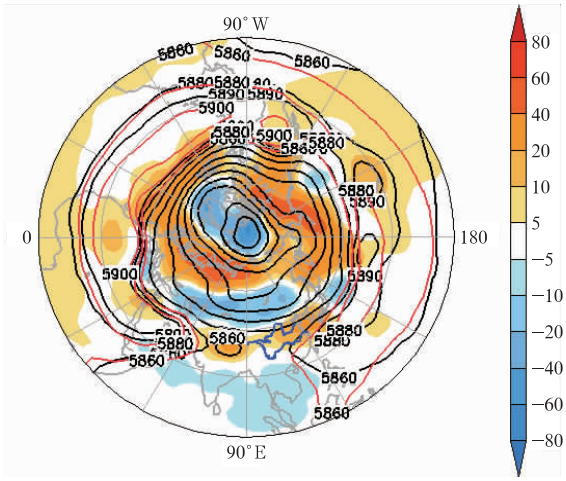


图 16　2013 年 6—8 月 500 hPa 高度场(等值线)及距平场(阴影)分布

(单位：gpm，浅色等值线为气候态下的 5860 和 5880 线)

Fig. 16　500 hPa geopotential height (contours) and anomalies (shaded) from June to August in 2013 (unit: gpm, light lines: 5860 and 5880 gpm of climatology)

动(AO)作为半球尺度的气候系统，对北半球气候有重要的影响(武炳义等，2004；琚建华等，2004；2006；龚道溢等，2003)。2013 年 4—8 月 AO 持续以正位相为主(图 15)，由于北极地区通常受低气压系统支配，当北极涛动持续处于正位相时，极地的冷空气不断堆积，冷低压不断增强，同时中纬度地区暖高压也不断增强，限制了极地冷空气向南扩展。这一方面使得北半球中纬度地区冷空气活动较弱，不容易促使北半球副热带地区高压减弱和东退；另一方面使得北半球中高纬度地区持续受异常高压控制(图 16)，这是导致今年夏季北半球中高纬度地区出现大范围高温异常天气的另一重要原因。

可见，在全球变暖的背景下，AO 持续正位向和赤道太平洋海温异常是造成北半球夏季大部地区出现异常高温天气的主要原因。

## 4　结　论

2013 年的全球陆地和海洋表面温度持续偏高，比 1961—1990 年平均值高约 0.5℃，与 2007 年并列为第六个最暖年份。在全球持续偏暖的背景下，2013 年世界范围内出现了显著的气候异常和极端事件，其中北半球部分地区受到多重天气气候极端事件的袭击。年初，寒流和暴风雪袭卷亚洲、欧洲部分地区和北美洲，而澳大利亚则出现了极端高温天气；6—9 月中欧、亚洲和北美洲部分地区遭受暴雨洪涝的袭击，期间北半球大部地区则发生了高温热浪天气；6 月以来多个强台风袭击东亚、东南亚和北美洲东海岸，其中超强台风海燕菲律宾全国有 5598 人死亡，1759 人失踪，近 3 万人受伤。

2013 年 7—9 月，中高纬度地区受欧亚中高纬度切断性低压的影响，欧亚大陆西北部上空为异常正高度距平区，而欧洲东南部至俄罗斯东南部和东亚北部为宽广的低槽区，这种环流型有利于高纬冷空气南下影响俄罗斯远东地区；同时，鄂霍次克海地区阻塞的异常发展有利于这种环流型的持续稳定维持。低纬度地区，西太平洋副热带高压持续控制中国东南部地区，且副高脊线位置异常偏北；另一方面，7—9 月东亚夏季风持续偏强，东亚夏季风的持续偏强有利于低纬度水汽向北方地区输送，加之受西北太平洋异常反气旋以及副高持续偏北的影响，来自西北太平洋与来自低纬度地区的水汽不断向俄罗斯远东地区输送。暖湿气流与来自高纬度地区冷

空气在俄罗斯远东地区汇合，使得7—9月俄罗斯远东地区出现持续异常偏多的降水，造成该区出现120年来最大洪灾。

在全球持续增暖的背景下，受北极涛动持续正位相和赤道太平洋海温异常的共同影响，2013年夏季，东亚东部、北美洲和欧洲等地持续受高压系统的控制，大气以下沉气流为主，天气晴好，地面容易接收更多的太阳辐射。太阳辐射的强烈加热作用，导致大气温度持续偏高，使得北半球大部地区出现异常高温天气。

## 参考文献


邓伟涛，孙照渤，曾刚，等. 2009. 中国东部夏季降水型的年代际变化及其与北太平洋海温的关系. 大气科学，33(4)：835-846.

龚道溢，王绍武. 2003. 近百年北极涛动对中国冬季气候的影响. 地理学报，58(4)：559- 568.

龚志强，王艳姣，王遵娅，等. 2014. 2013年夏季气候异常特征及成因简析. 气象，40(1)：119-125.

国家气候中心气候监测室. 2013. 2013年7月以来俄罗斯东南部降水异常特征及成因简析. 气候监测快报，18：1-2.

国家气候中心气候与气候变化服务室. 2013. 中国气候公报.

黄荣辉，蔡榕硕，陈际龙，等. 2006. 我国旱涝气候灾害的年代际变化及其与东亚气候系统变化的关系. 大气科学，30(5)：730-743.

琚建华，吕俊梅，任菊章. 2006. 北极涛动年代际变化对华北地区干旱化的影响. 高原气象，25(1)：74- 81.

琚建华，任菊章，吕俊梅. 2004. 北极涛动年代际变化对东亚北部冬季气温增暖的影响. 高原气象，23(4)：492-434.

民政部国家减灾中心. 2013a. 全国自然灾害基本情况分析_2013年一季度. 中国减灾，5：64.

民政部国家减灾中心. 2013b. 全国自然灾害基本情况分析_2013年5月. 中国减灾，7：64.

秦苗苗. 2013a. 2013年1月国内外主要灾害统计. 生命与灾害，2：44-46.

秦苗苗. 2013b. 2013年2月国内外主要灾害统计. 生命与灾害，3：43-46.

秦苗苗. 2013c. 2013年6月国内外主要灾害统计. 生命与灾害，7：43-46.

秦苗苗. 2013d. 2013年7月国内外主要灾害统计. 生命与灾害，8：44-46.

秦苗苗. 2013e. 2013年8月国内外主要灾害统计. 生命与灾害，9：44-46.

王东阡，王腾飞，任福民，等. 2013. 2012年全球重大天气气候事件及其成因. 气象，39(4)：516-525.

王遵娅，周兵，王艳姣，等. 2013. 2013年春季我国气候异常特征及其可能原因. 气象，39(10)：1374-1378.

武炳义，卞林根，张人禾. 2004. 冬季北极涛动和北极海冰变化对东亚气候变化的影响. 极地研究，16(3)：211-220.

张庆云，吕俊梅，杨莲梅，等. 2007. 夏季中国降水型的年代际变化与大气内部动力过程及外强迫因子关系. 大气科学，30(6)：1290-1300.

朱益民，杨修群. 2003. 太平洋年代际振荡与中国气候变率的联系. 气象学报，61(6)：641-654.

IPCC. 2013. Climate Change 2013：The Physical Science Basis：Fifth Assessment Report.

Peterson T C. 2005. Climate Change Indices. WMO Bulletin，54(2)：83-86.

WMO. 2013. WMO Provisional Statement on the State of Global Climate in 2013. http：// www. wmo. int/pages/mediacentre/press_releases/documents/981_zh. pdf.

http：// www. wmo. int/pages/mediacentre/press_releases/pr_983_en. html.

AGU PUBLICATIONS

JGR

Journal of Geophysical Research: Atmospheres

RESEARCH ARTICLE
10.1002/2014JD021886

Special Section:
Fast Physics in Climate Models: Parameterization, Evaluation and Observation

# Improvement of cloud microphysics in the aerosol-climate model BCC_AGCM2.0.1_CUACE/Aero, evaluation against observations, and updated aerosol indirect effect

**Zhili Wang[1,2], Hua Zhang[3,2], and Peng Lu[4]**

[1]Chinese Academy of Meteorological Sciences, Beijing, China, [2]Collaborative Innovation Center on Forecast and Evaluation of Meteorological Disasters, Nanjing University of Information Science and Technology, Nanjing, China, [3]Laboratory for Climate Studies, National Climate Center, China Meteorological Administration, Beijing, China, [4]Jiangsu Climate Center, Nanjing, China

**Key Points:**
- Two-moment cloud microphysical scheme is implemented into a climate model
- Modeling results for aerosols and cloud properties are evaluated
- Anthropogenic aerosol indirect effect is estimated based on this model

**Correspondence to:**
H. Zhang,
huazhang@cma.gov.cn

**Citation:**
Wang, Z., H. Zhang, and P. Lu (2014), Improvement of cloud microphysics in the aerosol-climate model BCC_AGCM2.0.1_CUACE/Aero, evaluation against observations, and updated aerosol indirect effect, *J. Geophys. Res. Atmos.*, *119*, 8400–8417, doi:10.1002/2014JD021886.

Received 9 APR 2014
Accepted 16 JUN 2014
Accepted article online 19 JUN 2014
Published online 14 JUL 2014

**Abstract** A two-moment cloud microphysical scheme, to predict both the mass and number concentrations of cloud droplets and ice crystals, is implemented into the aerosol-climate model BCC_AGCM2.0.1_CUACE/Aero. The model results for aerosols, cloud properties, and meteorological fields are evaluated, and the anthropogenic aerosol indirect effect (AIE) is estimated. The new model simulates more realistic aerosol mass concentrations and optical depth compared with the original version using a one-moment bulk cloud microphysical scheme. The global annual mean column cloud droplet number concentration (CDNC) from the new model is $3.3\times10^{10}\,\mathrm{m}^{-2}$, which is comparable to the $4.0\times10^{10}\,\mathrm{m}^{-2}$ from satellite retrieval. The global annual mean cloud droplet effective radius at the cloud top from the new model is 8.1 μm, which is smaller than the 10.5 μm from observation. The simulated liquid water path (LWP) in the new model is significantly lower than that in the original model. In particular, the annual mean LWP is lower in the new model by more than $100\,\mathrm{g\,m}^{-2}$ in some midlatitude regions and hence much more consistent with satellite retrievals. Cloud radiative forcing and precipitation are improved to some extent in the new model. The global annual mean radiation budget at the top of the atmosphere is $-0.6\,\mathrm{W\,m}^{-2}$, which is considerably different from the value of $1.8\,\mathrm{W\,m}^{-2}$ in the original model. The global annual mean anthropogenic AIE is estimated to be $-1.9\,\mathrm{W\,m}^{-2}$ without imposing a lower bound of CDNC, whereas it is reduced significantly when a higher lower bound of CDNC is prescribed.

## 1. Introduction

Clouds do not only reflect solar radiation and reduce the radiation flux reaching the surface but also absorb thermal radiation and decrease the energy loss in the Earth-atmosphere system. Therefore, any change in cloud properties can greatly disturb the energy balance of the Earth-atmosphere system [*Boucher et al.*, 2013]. Anthropogenic aerosols can alter cloud microphysical and optical properties such as the cloud droplet size distribution, cloud albedo, and cloud lifetime by serving as cloud condensation nuclei (CCN) or ice nuclei [*Twomey*, 1977; *Albrecht*, 1989]. This may indirectly affect atmospheric radiation, temperature, circulation, and the hydrological cycle.

Aerosol-cloud interactions, including the aerosol indirect effect (AIE), are one of the greatest sources of uncertainty in projections of future climate change [*Boucher et al.*, 2013]. Many uncertainties remain in the study of AIE, and our understanding of it is still very limited. For example, recent studies have indicated large uncertainty ranges of $-0.3$ to $-1.5\,\mathrm{W\,m}^{-2}$ for the cloud albedo effect and 0 to $-1.2\,\mathrm{W\,m}^{-2}$ for the aerosol-cloud interactions due to anthropogenic aerosols [*Lohmann et al.*, 2010; *Boucher et al.*, 2013]. The estimation of anthropogenic AIE is affected by many parameters, such as natural and anthropogenic aerosol emissions, aerosol precursor gas emissions, microphysical processes, preindustrial CCN concentration, preindustrial accumulation mode radius, width of the accumulation mode, size of primary particles, and cloud thickness [*Carslaw et al.*, 2013; *Ghan et al.*, 2013].

Satellite and field observations during the past decade have greatly improved our understanding of how aerosols affect cloud processes at regional and global scales. Field observations have revealed a positive correlation between an increase in cloud reflectance and an enhanced ambient aerosol concentration [*Brenguier et al.*, 2000]. A strong positive correlation between the liquid water path (LWP) and the boundary layer CCN was also observed based on the measurements during the VAMOS Ocean-Cloud-Atmosphere-Land



©2014. American Geophysical Union. All Rights Reserved.

Study-Regional Experiment [*Zheng et al*., 2010]. Analysis of a 10 year data set of aerosol, cloud, and meteorological variables showed that cloud-top height and thickness as well as rain in deep clouds that had high liquid-water content increased with aerosol concentration in mixed phase clouds with a warm and low base, but no change was found in cloud-top height and precipitation with aerosol concentration in clouds without ice or with cool bases [*Li et al*., 2011]. At regional scales, long-term observational data and cloud-resolving model simulations have revealed that the significant increase in aerosol concentrations due to air pollution was at least partly responsible for the decreased number of light rain events observed in China over the past 50 years [*Qian et al*., 2009].

Aerosol-cloud interactions include a variety of complicated processes, and it is therefore very difficult to quantitatively determine the effect of aerosols on cloud, radiation, or climate through observations. However, a global climate model (GCM) including complete atmospheric, dynamic, and thermodynamic processes is a powerful tool to study these effects [*Lohmann et al*., 2007; *Gettelman et al*., 2008; *Ghan et al*., 2012]. Previously, most GCMs adopted the one-moment cloud microphysical scheme, which only predicts the cloud droplet and cloud ice mass concentrations. Thus, the empirical formulae for the relationship between aerosol mass or number concentration and cloud droplet number concentration (CDNC) obtained from observations were used to study the AIE in these models [e.g., *Boucher and Lohmann*, 1995; *Hansen et al*., 2005; *Menon and Rotstayn*, 2006]. These empirical relationships are based on limited amounts of observed data and have significant limitations. Furthermore, many real physical processes in clouds are neglected in these formulae, such as the subgrid vertical velocity, size distribution, supersaturation, and aerosol activation, leading to great uncertainty in the study of AIE. For example, AIE values ranged from $-0.3$ to $-4.36\,\mathrm{W\,m^{-2}}$ when GCMs were combined with simple relationships [e.g., *Boucher and Lohmann*, 1995; *Menon et al*., 2002; *Ming et al*., 2005; *Quaas et al*., 2006; *Wang et al*., 2010].

Some fairly sophisticated two-moment cloud microphysical schemes based on cloud physics have been developed and implemented into GCMs in recent years. These schemes take the cloud droplet and ice crystal mass and number concentrations as prognostic variables [e.g., *Ghan et al*., 1997; *Lohmann et al*., 1999; *Nenes and Seinfeld*, 2003; *Lohmann et al*., 2007; *Morrison and Gettelman*, 2008; *Ghan et al*., 2012]. *Morrison et al*. [2005a, 2005b] developed a two-moment bulk cloud microphysics scheme to predict the mass and number concentrations of four hydrometeor species (cloud droplet, cloud ice, rain, and snow). This scheme includes more cloud microphysical processes, such as treatments of homogeneous and heterogeneous ice nucleation, droplet activation allowing for simulating aerosol-cloud interactions, and the dispersion of the droplet size distribution, than single-moment schemes do. The parameterization was then improved to be more suitable for large-scale GCMs [*Morrison and Gettelman*, 2008; *Gettelman et al*., 2008]. The scheme of *Abdul-Razzak and Ghan* [2000] is adopted for the activation of cloud droplets as a function of aerosol chemical and physical parameters, temperature, and updraft speed, and the ice nucleation is a function of temperature based on *Cooper* [1986] in this parameterization. The prediction of both mass and number concentrations using the two-moment scheme allows the cloud droplet effective radius (CDER) to much more realistically evolve and takes into account more robust aerosol-cloud interactions [*Morrison and Gettelman*, 2008] compared with the use of a one-moment scheme that specifies the CDNC or CDER. This is also important for the improved description of the cloud microphysical and aerosol-cloud interaction processes in GCMs.

A one-moment bulk cloud microphysical scheme was used in the BCC_AGCM2.0.1 (Atmospheric General Circulation Model of Beijing Climate Center) coupled with an aerosol model of CUACE/Aero (China Meteorological Administration Unified Atmospheric Chemistry Environment for Aerosols) (hereafter BCC_AGCM2.0.1_CUACE/Aero) developed by *Zhang et al*. [2012a], which only included prognostic variables for cloud liquid and ice mass concentrations. The CDNC and CDER are specified for treating large-scale cloud precipitation and cloud-radiation interactions in the model, respectively [*Collins et al*., 2004]. The CDNCs are set to be $400\,\mathrm{cm^{-3}}$ over land, $150\,\mathrm{cm^{-3}}$ over ocean, and $75\,\mathrm{cm^{-3}}$ over sea ice and to an interpolation of these values in coastal regions. The CDERs are specified to be 14 μm over ocean and sea ice, and are 8 μm and 14 μm over land when the temperatures are above −10°C and below −30°C, respectively, but are determined by using a linear ramp between 8 μm and 10 μm between −30°C and −10°C over land [*Collins et al*., 2004]. The model lacks an accurate description of cloud microphysical and aerosol-cloud interaction processes. Therefore, there is a considerable uncertainty when estimating the AIE with this model [*Wang et al*., 2010]. This study attempts to improve these cloud microphysical processes and the aerosol-cloud interactions in the BCC_AGCM2.0.1_CUACE/Aero.




©2014. American Geophysical Union. All Rights Reserved.

In this study, we first implemented the two-moment bulk cloud microphysical scheme developed by *Morrison and Gettelman* [2008] and *Gettelman et al.* [2008] (hereafter the MG08 scheme) into the BCC_AGCM2.0.1_CUACE/Aero, which enabled our model to predict both cloud liquid and ice crystal mass and number concentrations from online simulated dynamic aerosol mass concentrations. Then, we changed some individual parameters in the MG08 scheme to make them more compatible with our model. Finally, we fully evaluated the model results for aerosol mass concentration and optical depth, CDNC, CDER, LWP, cloud radiative forcing and precipitation and estimated the anthropogenic AIE. In section 2, we introduce the aerosol-climate model and cloud microphysical scheme. In section 3, we present a detailed comparison of the simulated aerosol concentrations and optical depth, cloud properties, and some primary climate variables with the corresponding observations. In section 4, we estimate anthropogenic AIE. Finally, a discussion and summary are presented in section 5.

## 2. Model and Scheme

### 2.1. Aerosol-Climate Model

BCC_AGCM2.0.1, developed by the Beijing Climate Center of China Meteorological Administration, coupled with an aerosol model (CUACE/Aero), developed by the Institute of Atmospheric Composition of Chinese Academy of Meteorological Sciences, was used in this study. The aerosol-climate model is detailed in *Zhang et al.* [2012a] and *Wang et al.* [2013a, 2013b], and thus we only give a brief description here. BCC_AGCM2.0.1 is based on the Eulerian spectral formulation of dynamical equations and employs a horizontal T42 spectral resolution (approximately $2.8° \times 2.8°$) and a terrain-following hybrid vertical coordinate having 26 levels, with a top located at about 2.9 hPa. The time step is 20 min. The cloud fraction diagnostic scheme given by *Slingo* [1987] was used. The main features of BCC_AGCM2.0.1 were described by *Wu et al.* [2010]. However, the cloud-radiation processes in BCC_AGCM2.0.1 are currently being improved. The cloud overlap scheme of the Monte Carlo independent column approximation (McICA) [*Pincus et al.*, 2003] with the new BCC_RAD (Beijing Climate Center RADiation transfer model) developed by *Zhang et al.* [2003a, 2006a, 2006b] was adopted [*Jing and Zhang*, 2013]. These schemes have improved the accuracy of the subgrid cloud structure and its radiative transfer process [*Zhang et al.*, 2014]. The optical properties of water and ice clouds were taken from *Nakajima et al.* [2000] and *Zhang et al.* [2014], respectively. Aerosol optical properties are given by *Wei and Zhang* [2011] and *Zhang et al.* [2012b].

The atmospheric aerosol model CUACE/Aero, based on the Canadian Aerosol Module (CAM) developed by *Gong et al.* [2002, 2003], is a comprehensive module incorporating emission, gaseous chemistry, transport, removal, and size-segregated multicomponent aerosol algorithms. *Zhou et al.* [2012] gave a detailed description of the improvements of CAM in CUACE/Aero. The five types of tropospheric aerosol are included in the model, i.e., sulfate, black carbon (BC), organic carbon (OC), sea salt, and soil dust. Each aerosol type is divided into 12 bins as a geometric series for a radius between 0.005 and 20.48 μm. The emissions of sea salt and soil dust are calculated online [*Zhang et al.*, 2012a]. Aerosols are removed by dry deposition, below-cloud scavenging, and in-cloud processes [*Gong et al.*, 2003].

BCC_AGCM2.0.1_CUACE/Aero simulates the aerosol mass concentrations and optical properties well [*Zhang et al.*, 2012a] and has joined the AeroCom Phase II [*Myhre et al.*, 2013]. It has been used to study aerosol radiative forcing and the subsequent effects on climate [*Zhang et al.*, 2012a; *Wang et al.*, 2013a, 2013b].

### 2.2. Cloud Microphysical Scheme

A one-moment bulk cloud microphysical scheme developed by *Rasch and Kristjánsson* [1998] with an improvement by *Zhang et al.* [2003b] (hereafter the RK98 scheme) was used in the original BCC_AGCM2.0.1_CUACE/Aero. The model with the RK98 scheme only predicted the cloud liquid and ice crystal mass concentrations. Both CDNC and CDER were specified in the model [*Collins et al.*, 2004]. These limitations generated great uncertainties in the estimation of AIE. Therefore, we initially incorporated the MG08 scheme into the BCC_AGCM2.0.1_CUACE/Aero instead of the RK98 scheme to predict both cloud liquid and ice crystal mass and number concentrations using the online-predicted aerosol mass concentrations. The model then has the ability to calculate the CDER with the forecasted CDNC. Additionally, the threshold size separating cloud ice from snow was set to 240 μm instead of the value of 200 μm in the original MG08 scheme to make the simulated cloud radiative forcing more realistic, which changes the radiation balance at the top of the atmosphere (TOA) from 0.8 W $m^{-2}$ to −0.6 W $m^{-2}$ in




©2014. American Geophysical Union. All Rights Reserved.

**Table 1.** Comparison of Global Annual Means of Simulated Aerosol Column Burdens and Optical Depth at 550 nm With Those From AeroCom Models[a]

| | BCC_MG08 | BCC_RK98 | AeroCom_Med | Max (Min) |
|---|---|---|---|---|
| M (mg m$^{-2}$) | | | | |
| SU | 3.2 | 1.8 | 3.9 | 5.3 (1.8) |
| BC | 0.17 | 0.14 | 0.39 | 1.0 (0.09) |
| OC | 1.6 | 1.3 | 2.4 | 3.6 (0.64) |
| DU | 43.0 | 44.6 | 39.1 | 57.8 (8.8) |
| SS | 14.1 | 14.5 | 12.6 | 27.5 (3.0) |
| $AOD_{550\ nm}$ | 0.11 | 0.08 | 0.13, 0.135[b], 0.151[c], 0.16[d] | 0.15 (0.06) |

[a]AeroCom_Med, Max and Min are global annual average of the median-ranked model, annual averaged maximum and minimum among AeroCom models, respectively [*Kinne et al*., 2006]. M = aerosol column burden, SU = sulfate, BC = black carbon, OC = organic carbon, DU = dust, SS = sea salt, and AOD = aerosol optical depth.
[b]Mean values from AERONET given by *Kinne et al*. [2006].
[c]Mean values from combinations of MISR over land and MODIS over ocean given by *Kinne et al*. [2006].
[d]Mean values from combinations of MISR over land and MODIS over ocean given by *van Donkelaar et al*. [2010].

the model. These modifications gave our model the ability to estimate AIE quantitatively. Following *Gettelman et al*. [2008], we adopted *Vavrus and Waliser's* [2008] changes to the diagnostic scheme of cloud fraction presented by *Slingo* [1987] to reduce Arctic cloud biases. Currently, no aerosol effect is taken into account in the microphysics for convective clouds in our model, but the convective detrainment of cloud water and ice is addressed by the MG08 scheme. The number concentrations of detrainment were obtained by assuming mean volume radii of 8 μm and 32 μm for cloud droplets and ice crystals, respectively [*Morrison and Gettelman*, 2008].

The cloud droplet and ice size distributions are given by gamma functions in the MG08 scheme. The main microphysical processes include the activation of CCN or deposition/condensation-freezing nucleation on ice nuclei to form droplets or cloud ice, condensation/deposition, evaporation/sublimation, autoconversion of cloud droplets and ice to form rain and snow, accretion of cloud droplets and ice by rain, accretion of cloud droplets and ice by snow, heterogeneous freezing of droplets to form ice, homogeneous freezing of cloud droplets, melting, sedimentation and convective detrainment. The subgrid vertical velocity and CCN concentration are the two key variables in the cloud droplet activation scheme given by *Abdul-Razzak and Ghan* [2000]. The subgrid vertical velocity ($w'$) is derived from the turbulent diffusion coefficient following *Morrison et al*. [2005a] ($w' = K_d/l_c$, where $K_d$ is the turbulent diffusion coefficient and $l_c = 30$ m is the mixing length). The subgrid cloud water variability is considered in accordance with a probability density function that follows a gamma distribution function based on observations of the optical depth in marine boundary layer clouds [*Barker*, 1996; *Barker et al*., 1996; *Pincus et al*., 1999]. However, the subgrid variability for cloud ice, precipitation, and cloud droplet number concentration is neglected. The descriptions for these processes are detailed by *Morrison and Gettelman* [2008].

### 2.3. Data and Simulation Design

The National Centers for Environmental Prediction reanalysis climatological data on a Gaussian grid was used by BCC_AGCM2.0.1_CUACE/Aero as the initial condition. The sea ice and surface temperature boundary data were prescribed based on the 21 year (1981–2001) Hadley Centre Sea Ice and Sea Surface Temperature climatological mean data set. These data can be obtained from http://www.cesm.ucar.edu/models/atm-cam/download/. First, two simulations were performed with the model including the RK98 cloud microphysical scheme (hereafter BCC_RK98) and the MG08 cloud microphysical scheme (hereafter BCC_MG08), using the AeroCom emissions for present-day conditions [*Dentener et al*., 2006]. To estimate anthropogenic AIE, two additional simulations were performed with the model including the MG08 scheme but completely ignoring the aerosol direct effect (the aerosol-radiation interaction was turned off), using the AeroCom aerosol emissions for present-day conditions (hereafter PD) and preindustrial conditions (hereafter PI) [*Dentener et al*., 2006]. Some models used a lower bound of CDNC that possibly reduced the simulated AIE [*Hoose et al*., 2009]. Therefore, two groups of sensitivity simulations were performed with the new model to test the change of anthropogenic AIE, where the lower bound of CDNC was set to 10 cm$^{-3}$ and 20 cm$^{-3}$ instead of to the default


©2014. American Geophysical Union. All Rights Reserved.

**Table 2.** Global Budgets for Aerosols and Cloud Water (CW)[a]

| | BCC_MG08 | | | | BCC_RK98 | | | |
|---|---|---|---|---|---|---|---|---|
| | Source | Burden | Sink | Lifetime | Source | Burden | Sink | Lifetime |
| SU | 70.2 | 0.97 | 20.2 (D), 52.9 (W) | 5.0 | – | 0.69 | 16.7 (D), 55.4 (W) | 3.6 |
| BC | 7.7 | 0.084 | 4.9 (D), 2.6 (W) | 4.0 | – | 0.069 | 4.7 (D), 2.8 (W) | 3.3 |
| OC | 66.1 | 0.79 | 39.1 (D), 26.6 (W) | 4.4 | – | 0.68 | 38.0 (D), 27.3 (W) | 3.8 |
| DU | 3846.4 | 20.7 | 3049.0 (D), 799.2 (W) | 1.96 | 5535.6 | 21.3 | 4080.3 (D), 1459.1 (W) | 1.4 |
| SS | 33320.3 | 7.2 | 31171.4 (D), 2154.7 (W) | 0.079 | 34737.4 | 7.4 | 31688.5 (D), 3046.2(W) | 0.078 |
| CW | $6.3\times10^7$ | $4.2\times10^7$ | $4.0\times10^7$ | 243.3 | $25.7\times10^7$ | $7.1\times10^7$ | $8.7\times10^7$ | 100.8 |

[a]Units in source, burden, sink and lifetime are Tg $yr^{-1}$, Tg, Tg $yr^{-1}$, and days, respectively, but are Tg S $yr^{-1}$ and Tg S for SU. D and W in parentheses are dry and wet depositions, respectively.

value of 0. Each simulation was run for 30 years, and the simulation data of the last 20 years were averaged and analyzed in this study.

The data sets used for evaluating the model that include the cloud data from International Satellite Cloud Climatology Project (ISCCP) [*Rossow and Schiffer*, 1999] and the moderate resolution imaging spectroradiometer (MODIS) [*King et al*., 2003], the LWP from National Aeronautics and Space Administration Water Vapor Project (NVAP) [*Randel et al*., 1996] and Special Sensor Microwave Imager (SSMI) [*Wentz*, 1997], the precipitation rate from Climate Prediction Center merged analysis of precipitation (CMAP) [*Xie and Arkin*, 1996], and the radiation flux at the TOA and cloud radiative forcing from Earth Radiation Budget Experiment (ERBE) [*Kiehl and Trenberth*, 1997] and Clouds and Earth's Radiant Energy System (CERES) (http://ceres.larc.nasa.gov/) are from the Atmospheric Model Working Group diagnostics package of National Center for Atmospheric Research (http://www.cgd.ucar.edu/cms/rneale/tools/amwg_diagnostics.html).

## 3. Model Evaluation and Analysis

### 3.1. Aerosol Mass Concentration and Optical Depth

Table 1 shows a comparison of global annual means of the simulated aerosol column burdens with those from AeroCom models. The global burdens of sulfate, BC, OC, sea salt, and dust in BCC_MG08 are 3.2 mg $m^{-2}$, 0.17 mg $m^{-2}$, 1.6 mg $m^{-2}$, 14.1 mg $m^{-2}$, and 43.0 mg $m^{-2}$, respectively. Three of the anthropogenic aerosol burdens in BCC_MG08 are obviously larger than those in BCC_RK98, but they are closer to the AeroCom_Medians. It can be seen from Table 2 that the cloud water lifetime in BCC_MG08 is significantly longer than that in BCC_RK98, resulting in longer lifetimes and larger burdens of aerosols in BCC_MG08. The changes in dust and sea salt burdens between the two simulations were not noticeable. This is because wet deposition is less important for these particles than for accumulation mode particles (Table 2).

The distribution of the aerosol column burden has been detailed by *Zhang et al*. [2012a] with a one-moment scheme. Here we emphasize the comparisons between BCC_MG08 and BCC_RK98. The distributions of the aerosol burden simulated by BCC_MG08 and BCC_RK98 are similar, but the differences in magnitude between the simulations are considerable. The aerosol mass concentrations simulated by BCC_MG08 generally increase (data not shown). *Zhang et al*. [2012a] indicated that sulfate, BC, and OC mass concentrations are underestimated by the model with a one-moment scheme. Therefore, the use of the

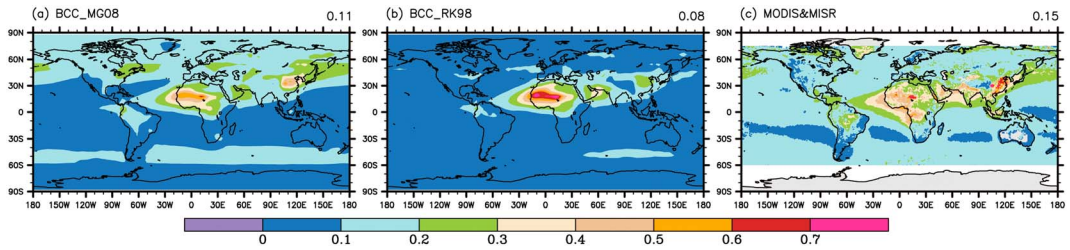


**Figure 1.** Global distributions of simulated and observed annual mean AOD at 550 nm. (a) BCC_MG08, (b) BCC_RK98, and (c) MODIS and MISR [*van Donkelaar et al*., 2010].




©2014. American Geophysical Union. All Rights Reserved.

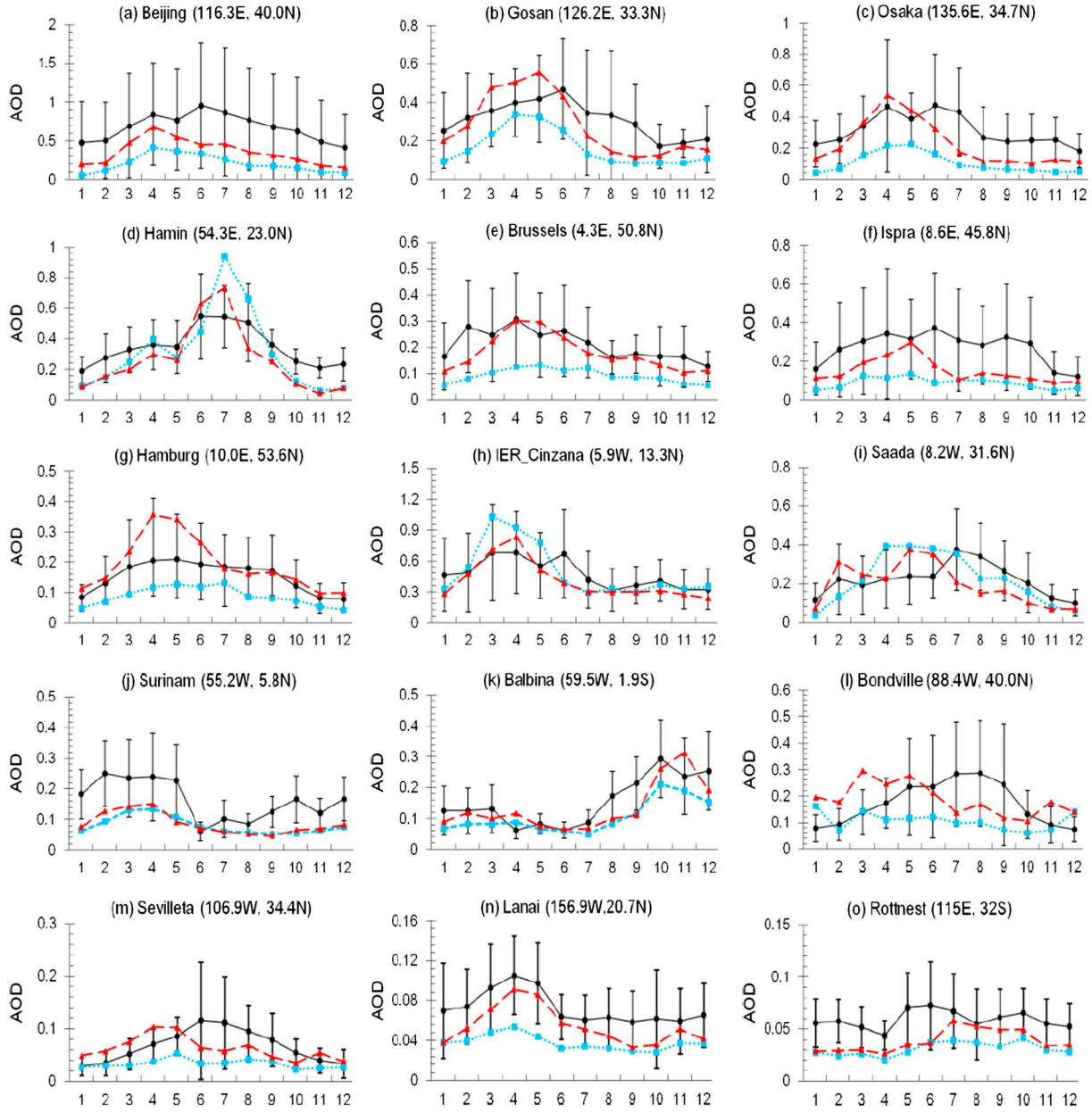


**Figure 2.** Comparisons of simulated AOD with those measured at 550 nm at 15 AERONET sites. The solid line is AERONET values, and the error bar is the standard deviation of observed values. The long and short dashed lines are the values from BCC_MG08 and BCC_RK98, respectively.

MG08 scheme in the model can improve the simulation of these aerosols to some extent probably due to the more reasonable descriptions of cloud microphysical processes.

The global annual mean aerosol optical depth (AOD) at 550 nm in BCC_MG08 is 0.11, which is larger than the value of 0.08 in BCC_RK98, and closer to both the 0.135 given by AERONET from a global (land and ocean) estimation [*Kinne et al.*, 2006] and the 0.16 retrieved by the combination of Multiangle Imaging Spectroradiomete (MISR) over land and MODIS over ocean (A. van Donkelaar et al., personal communication, 2010) (Table 1). A larger aerosol mass concentration generally produces a larger AOD. Figures 1 and 2 show comparisons of simulated AODs with satellite retrievals and ground-based sun photometer measurements from AERONET at 550 nm, respectively. The AERONET data can be obtained from http://aeronet.gsfc.nasa.gov/cgi-bin/climo_menu_v2_new. The global distribution of simulated AOD in BCC_MG08 is generally improved, and it is more consistent with observations, especially in the areas mainly affected by




©2014. American Geophysical Union. All Rights Reserved.

**Table 3.** Global Annual Mean Values of Cloud Properties, Precipitation, and Energy Budget at the TOA[a]

| | BCC_MG08 | BCC_RK98 | OBS |
|---|---|---|---|
| $CLD_{tot}$ (%) | 62.3 | 61.2 | 62–67 |
| LWP ($g\,m^{-2}$) | 83.1 | 139.0 | 64–122 |
| IWP ($g\,m^{-2}$) | 8.4 | 18.7 | |
| $N_d$ ($10^{10}\,m^{-2}$) | 3.3 | | 4 |
| $R_{eff}$ (μm) | 8.1 | | 10.5 |
| $P_{tot}$ ($mm\,d^{-1}$) | 2.66 | 2.72 | 2.69 |
| $P_{strat}$ ($mm\,d^{-1}$) | 0.8 | 0.97 | |
| $P_{conv}$ ($mm\,d^{-1}$) | 1.86 | 1.75 | |
| SWCF ($W\,m^{-2}$) | −48.5 | −50.0 | −49 to −54 |
| LWCF ($W\,m^{-2}$) | 27.3 | 28.6 | 27–30 |
| FSNT ($W\,m^{-2}$) | 239.1 | 235.8 | 234.0–243.5 |
| FLUT ($W\,m^{-2}$) | 238.5 | 237.6 | 233.9–238.9 |
| Energy budget ($W\,m^{-2}$, +upward) | −0.6 | 1.8 | |

[a]The total cloud cover ($CLD_{tot}$) observation is obtained from ISCCP [*Rossow and Schiffer*, 1999] and MODIS [*King et al*., 2003] data. The cloud liquid water path (LWP) observation is from MODIS [*King et al*., 2003] and AVHRR [*Han et al*., 1998] data. The column cloud drop number concentration ($N_d$) and cloud droplet effective radius at cloud top ($R_{eff}$) observations are from the AVHRR data [*Han et al*., 1998]. The total precipitation rate ($P_{tot}$) observation is from CMAP data [*Xie and Arkin*, 1996]. The shortwave cloud forcing (SWCF), longwave cloud forcing (LWCF), net solar flux at the TOA (FSNT), and upwelling longwave flux at the TOA (FLUT) observations are from CERES (http://ceres.larc.nasa.gov/) and ERBE (Earth Radiation Budget Experiment) data [*Kiehl and Trenberth*, 1997].

anthropogenic aerosols such as East Asia, Western Europe, and North America and also over the Sahara, which is predominantly affected by dust. However, the model underestimates the AOD over South Asia, eastern China, and Northern Hemisphere (NH) tropical oceans. These errors could be caused by a variety of factors such as uncertainty in the aerosol sources, coarse model resolution, and the uncertainties of physical processes in the model. Additionally, the absence of nitrate and ammonium aerosols and secondary organic aerosol in the model could lead to an underestimation of AOD in some areas too [*Zhang et al*., 2012a].

### 3.2. Cloud Properties and Meteorological Fields

#### 3.2.1. Global Mean Statistics

Table 3 shows a comparison of the global annual means of simulated physical variables with the corresponding observational values. The global annual mean of column CDNC in BCC_MG08 is $3.3\times10^{10}\,m^{-2}$, slightly less than the value of $4.0\times10^{10}\,m^{-2}$ from the Advanced Very High Resolution Radiometer (AVHRR) retrieval. However, the AVHRR data may treat some dust as cloud droplets, leading to these larger values [*Han et al*., 1998]. The global annual average value of CDER at the cloud top in BCC_MG08 is 8.1 μm, which is consistent with the value of 7.7 μm calculated by *Gettelman et al*. [2008] but 23% less than the AVHRR retrieval. The values for the first cloud level (counting down from the model top) for more than 1 ppm of condensate are output as appropriate values at the cloud top for either liquid or ice at each time step, according to the method of *Gettelman et al*. [2008]. However, a direct comparison between satellite and modeled results at the cloud top is complicated due to differences in the vertical scale between the satellite retrievals (much less than 1 km) and model (a vertical level of about 1 km), as well as by the need to distinguish between convective cloud and rain particles [*Gettelman et al*., 2008]. The higher sensitivity of the retrieval to cloud-top than to cloud-base properties can also lead to a large difference between model and satellite retrievals [*Barahona et al*., 2011]. Additionally, the differences in internal assumptions between satellite retrievals and model output is another important factor [*Pincus et al*., 2012].

The total cloud cover in BCC_MG08 is slightly greater than that in BCC_RK98 and is close to the lower limit of 62% obtained from observations. The global annual mean LWP retrieved by satellite ranges between 64 and $122\,g\,m^{-2}$ (Table 3). The satellite estimations of LWP vary substantially, because it cannot be retrieved reliably [*Lohmann et al*., 2007]. The global annual mean LWP in BCC_RK98 is $139\,g\,m^{-2}$, which is higher than the observational maximum. However, the global annual mean LWP in BCC_MG08 is only $83.1\,g\,m^{-2}$. *Gettelman et al*. [2008] also found a large reduction in LWP when they switched from RK98 to MG08.

The global annual means of longwave and shortwave cloud forcing in BCC_MG08 are $27.3\,W\,m^{-2}$ and $-48.5\,W\,m^{-2}$, respectively, and both absolute values are about $1.5\,W\,m^{-2}$ less than those in BCC_RK98. This is




©2014. American Geophysical Union. All Rights Reserved.

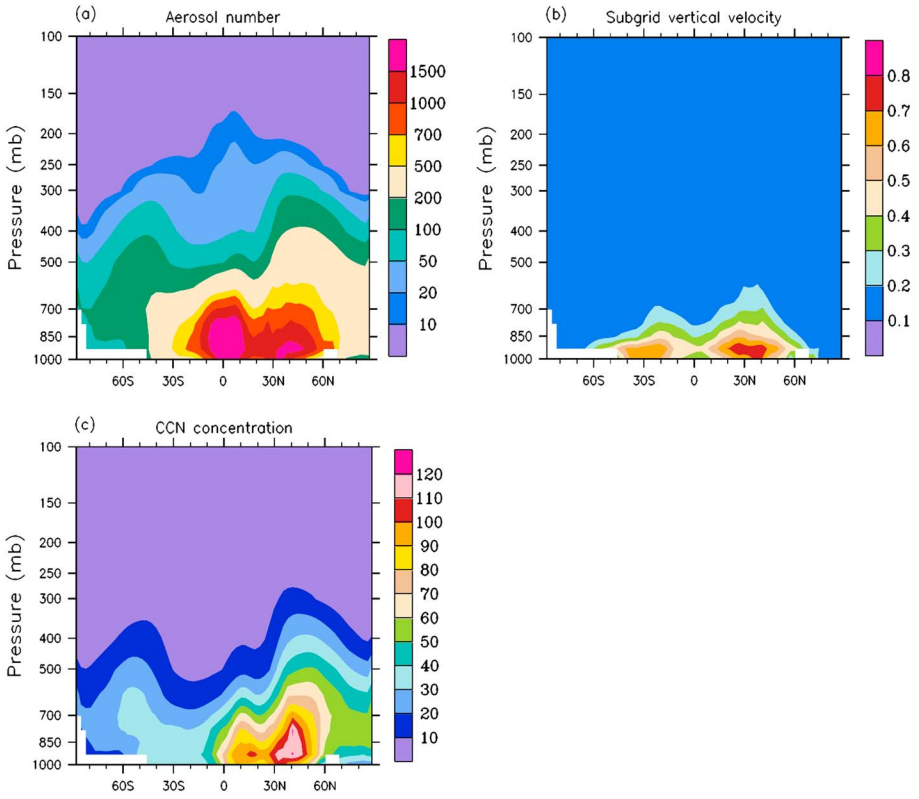


**Figure 3.** Annual zonal mean latitude versus pressure plots of (a) aerosol number concentration (unit: $cm^{-3}$), (b) subgrid vertical velocity (unit: $m\ s^{-1}$), and (c) CCN concentration (unit: $cm^{-3}$) at 0.1% supersaturation in BCC_MG08.

likely to be due to the lower LWP in BCC_MG08. These values are closer to the values of 27.1 $W\ m^{-2}$ and $-49.0\ W\ m^{-2}$ from the CERES data. All of the simulated longwave and shortwave cloud forcings are within the uncertainty of the radiation measurements of $\pm 5\ W\ m^{-2}$ given by *Kiehl and Trenberth* [1997]. Moreover, the global annual average radiation budget at the TOA is significantly changed in BCC_MG08 ($-0.6\ W\ m^{-2}$) compared with BCC_RK98 ($1.8\ W\ m^{-2}$).

The global annual means of total precipitation rate in BCC_MG08 and BCC_RK98 are 2.66 mm $day^{-1}$ and 2.72 mm $day^{-1}$, respectively. Both are consistent with the value of 2.69 mm $day^{-1}$ from the CMAP data, whereas the stratiform precipitation rate with the MG08 scheme is about 20% less than that with the RK98 scheme due to the significantly reduced conversion rate of condensate to precipitation, especially in the tropics and subtropics (Figure 10b). The decrease of stratiform precipitation rate is made up by the increase of convective precipitation rate, which agrees with the result obtained by *Gettelman et al.* [2008].

### 3.2.2. Cloud Microphysical Properties

Figure 3 shows the annual zonal mean aerosol number concentration, subgrid vertical velocity, and CCN concentration at 0.1% supersaturation in BCC_MG08. The high aerosol number concentrations mainly occur in the middle and low troposphere over the equator and midlatitude regions of the NH, with values exceeding 700 $cm^{-3}$ due to the contribution from anthropogenic fine aerosol particles. The aerosol number concentrations decline rapidly with height (Figure 3a). The largest subgrid vertical velocities are located at 30°S and 30°N, with values close to 0.8 $m\ s^{-1}$ (Figure 3b). The larger aerosol loading leads to larger CCN concentrations in the midlatitudes of the NH (Figure 3c).

A comparison of annual mean column CDNC between the BCC_MG08 simulation and MODIS retrieval is presented in Figure 4. The column CDNC from MODIS data is calculated following *Han et al.* [1998]. The MODIS data can be obtained from ftp://laadsweb.nascom.nasa.gov/NetCDF/L3_Monthly/V02/ [*Pincus et al.*, 2012]. The simulated column CDNC is higher in the regions with higher aerosol emissions in the NH as well as in their downwind areas, with the largest value exceeding $7 \times 10^{10}\ m^{-2}$. The column CDNC is above




©2014. American Geophysical Union. All Rights Reserved.

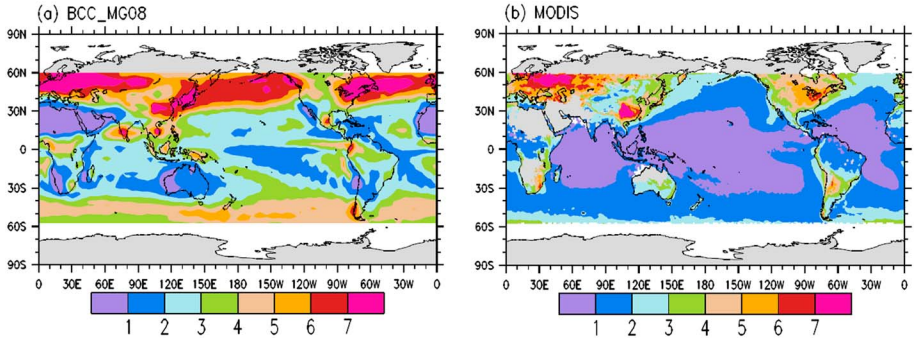


**Figure 4.** Annual mean distributions of column cloud droplet number concentration (unit: $10^{10}\,m^{-2}$). (a) BCC_MG08 and (b) MODIS.

$3\times10^{10}\,m^{-2}$ in the midlatitudes of the Southern Hemisphere (SH) due to the effects of sulfate and sea salt. The model captures the spatial features of the column CDNCs compared with MODIS retrieval, but there are clear discrepancies in some regions. The model underestimates the column CDNCs off the western coasts of USA, South America, southern Africa, and Australia, whereas strongly overestimates the column CDNCs in the downwind areas of Western Europe, East Asia, and North America and over the subtropical oceans of the SH. The simulated CDNCs in southern India and Southeast Asia are also higher than those from MODIS data. It is found that the differences in low cloud fraction greatly contribute to the differences in column CDNC between the simulation and satellite retrieval (data not shown). Additionally, the discrepancies could be caused by many factors such as uncertainty in the modeled aerosol concentration, cloud thickness, CCN activation scheme, and model resolution.

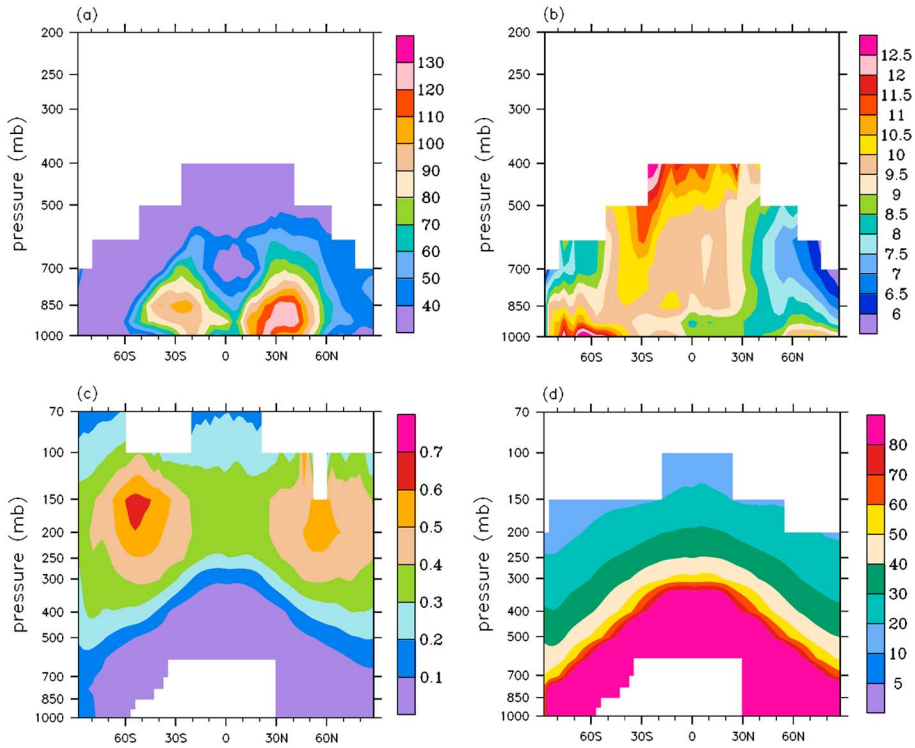


**Figure 5.** Annual zonal mean latitude versus pressure plots of (a) in-cloud droplet number concentration (unit: $cm^{-3}$), (b) cloud droplet effective radius (unit: μm), (c) in-cloud ice number concentration (unit: $cm^{-3}$), and (d) cloud ice effective radius (unit: μm) in BCC_MG08.




©2014. American Geophysical Union. All Rights Reserved.

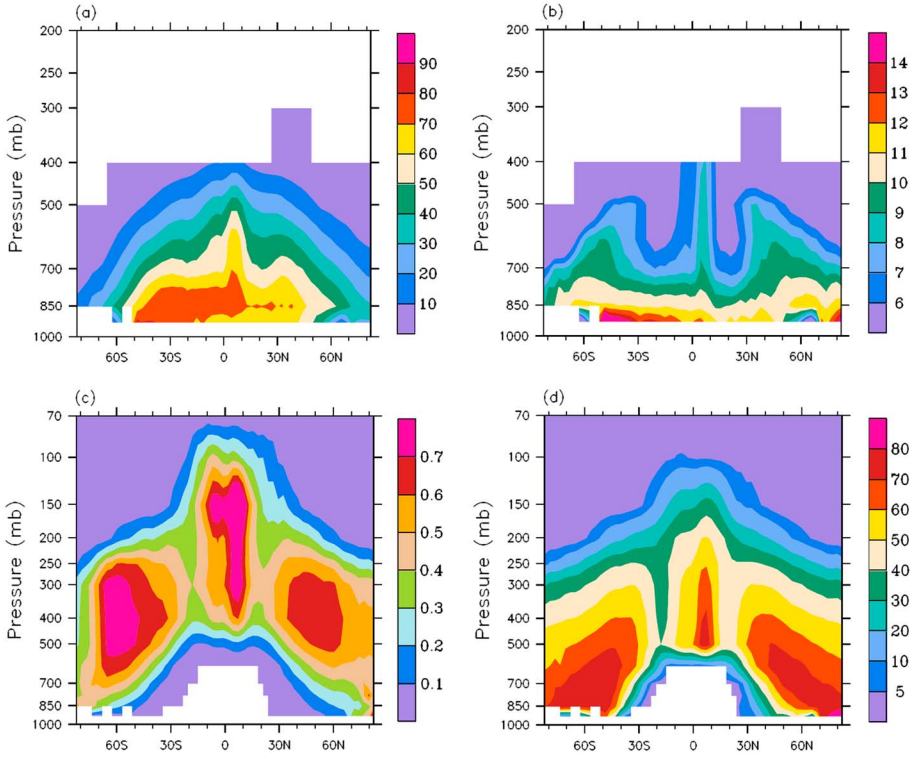


**Figure 6.** Same as Figure 5, but for retrievals from CloudSat 2B-CWC-RO data (http://www.cloudsat.cira.colostate.edu/dataSpecs.php?prodid=70).

The annual zonal mean in-cloud droplet number concentration (ICDNC), CDER, in-cloud ice number concentration (ICINC), and cloud ice effective radius (CIER) in BCC_MG08 are shown in Figure 5. Higher CCN concentrations due to higher aerosol concentrations result in larger ICDNCs in the mid and low latitudes of the NH. The largest ICDNC occurs at heights of 850 to 900 hPa in the midlatitudes of the NH, with a value of about 130 $cm^{-3}$ (Figure 5a). A region with a high droplet number concentration also exists in the tropical lower troposphere of the SH due to the transportation of hygroscopic sulfate and OC from central Africa, South America, and Southeast Asia. Higher ICDNCs lead to smaller CDERs at low altitudes in the tropics (Figure 5b). The ICINC peaks at 150–250 hPa in storm track regions, with a maximum value of 0.6 $cm^{-3}$ (Figure 5c). The distribution of CIER is comparatively uniform, and values decrease as altitude and latitude increase (Figure 5d).

Annual zonal means of ICDNC, CDER, ICINC, and CIER from the CloudSat 2B-CWC-RO product are presented in Figure 6. The retrieval algorithm of the 2B-CWC-RO product can be obtained at http://www.cloudsat.cira.colostate.edu/dataICDlist.php?go=list&path=/2B-CWC-RO. The horizontal and vertical resolutions of CloudSat data are 2.8° × 2.8° and 240 m, respectively. We selected data during the period of January 2007 to December 2010 and interpolated the values for comparison with our model levels. As can be seen from Figures 5 and 6, the simulated and retrieved patterns appear to be similar, but there are clear differences in the magnitude of ICDNC and CDER in some regions, e.g., ICDNC values in the lower troposphere in the midlatitudes of the NH and CDER values in the tropical midtroposphere. The difference in ICDNC between the NH and the SH suggests a much larger anthropogenic aerosol effect in BCC_MG08 than the CloudSat retrieval does, which is consistent with the modeled results given by *Lohmann et al.* [2007] and *Gettelman et al.* [2008]. The MODIS data also showed that the ICDNCs are larger over the NH than the SH due to the greater number of CCNs [*Quaas et al.*, 2006; *Bennartz*, 2007]. The CloudSat data appear to be inconsistent with the other results, and the cloud droplet numbers from the CloudSat data must be expected to be strongly biased toward regions where mainly large droplets exist. Therefore, the accuracy of observational data is an important factor to consider when evaluating the model. The simulated ice number appears to be too low, and its distribution is very different from the observation. For example, the model produces a much lower ice




©2014. American Geophysical Union. All Rights Reserved.

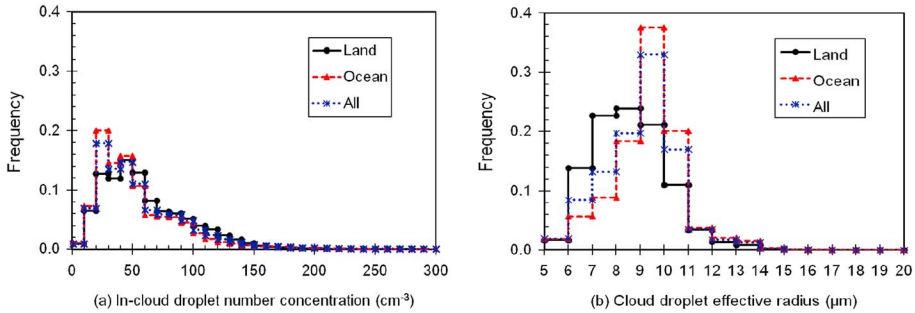


**Figure 7.** Probability density functions of annual mean (a) in-cloud droplet number concentration and (b) cloud droplet effective radius in BCC_MG08.

number concentration over the equator than the CloudSat data show, and does not produce the ice number concentrations around 40°N and 60°S like CloudSat. A possible reason for this is that no aerosol effect is taken into account in the ice crystal nucleation and microphysics for convective clouds in the model. Further improvement is required. Additionally, the coarse model resolution and the differences in the sampling of liquid and ice particles also have an effect. For example, the cloud droplet size can change from 6 μm to 12 μm within a vertical distance of 250 m in a cloud [*Brenguier et al*., 2003]. Therefore, the performance of the model can be more intuitively presented by the comparisons of cloud macrophysical properties such as LWP and cloud radiative forcing with satellite retrievals (section 3.2.3).

The probability density functions of ICDNC and CDER in BCC_MG08, given in Figure 7, show that the differences in ICDNC and CDER between ocean and land are significant, with higher droplet number concentrations and smaller particles over land. The number concentrations are generally within 150 $cm^{-3}$, peaking at 20–70 $cm^{-3}$ over land and 20–30 $cm^{-3}$ over ocean in BCC_MG08. The simulated CDERs are

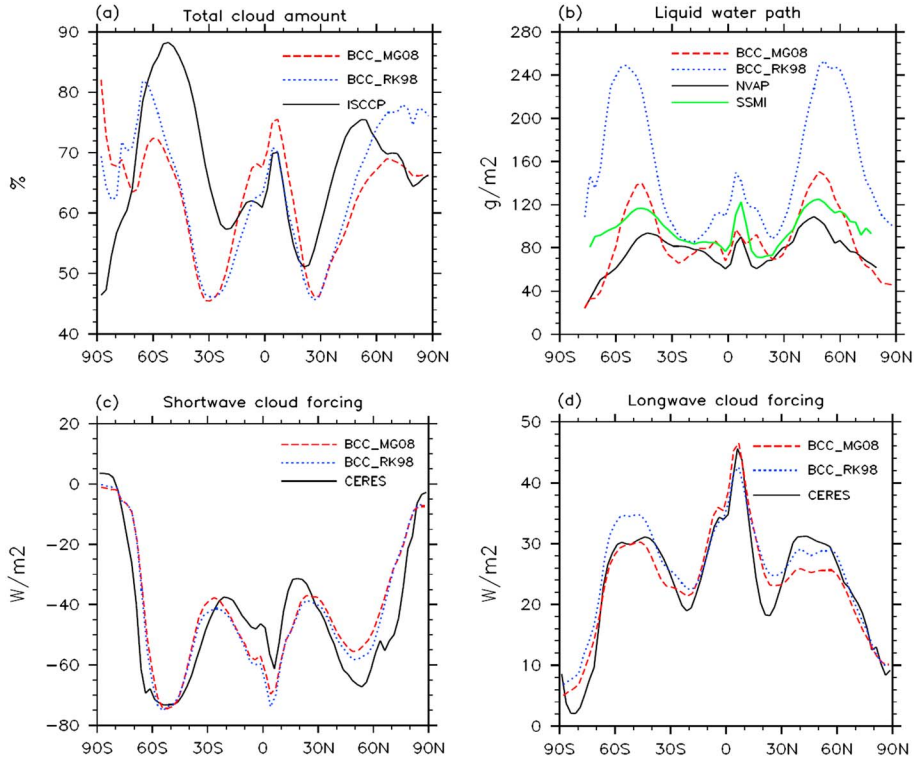


**Figure 8.** Annual zonal means of (a) total cloud cover, (b) liquid water path, (c) shortwave cloud forcing, and (d) longwave cloud forcing from BCC_MG08 (long dashed line), BCC_RK98 (short dashed line), and satellite retrievals (solid line), respectively.




©2014. American Geophysical Union. All Rights Reserved.

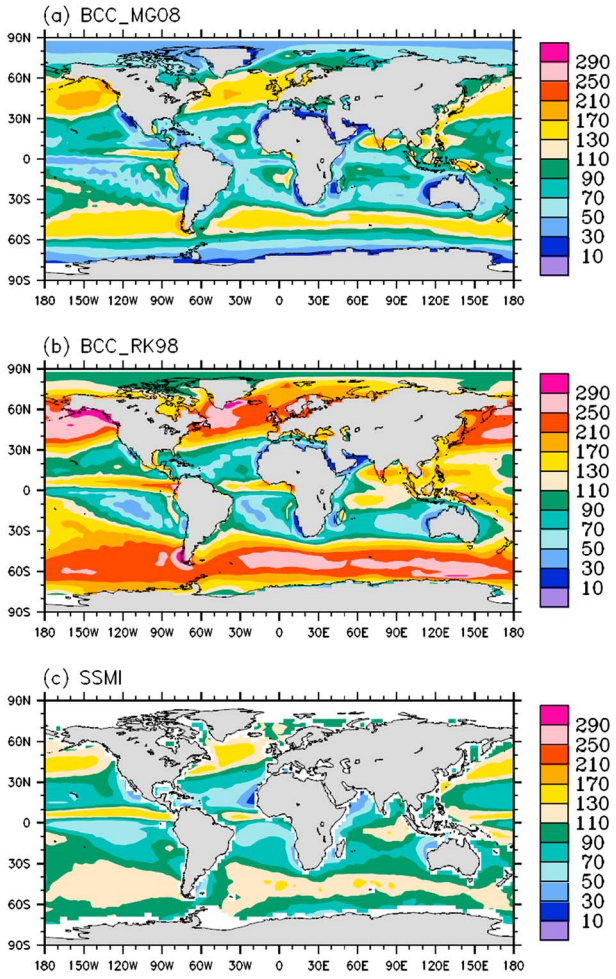


**Figure 9.** Annual mean distributions of liquid water path from (a) BCC_MG08, (b) BCC_RK98, and (c) satellite retrievals (units: g $m^{-2}$), respectively.

generally less than 15 μm, and their peaks range between 6 μm and 10 μm over land and between 7 μm and 11 μm over ocean. The simulated values of CDNCs of 60–180 $cm^{-3}$ are comparable to the mean values of 90–167 $cm^{-3}$ observed from aircraft measurements by *Gultepe and Isaac* [2004] over the Bay of Fundy, Ontario, Newfoundland, and Ottawa from the three field projects including the Alliance Icing Research Study (AIRS), the Radiation Aerosols and Climate Experiment, and the First International Regional Experiment Arctic Cloud Experiment. The simulated values of CDERs of 6–8 μm are consistent with the values of 6 ± 2 μm in polluted conditions for stratocumulus from flights around the Beijing area [*Deng et al*., 2009]. Additionally, the CDERs in BCC_MG08 are consistent with the reported ranges of 4–10 μm in polluted conditions and 7–13 μm in pristine conditions over the subtropical North-East Atlantic during the Second Aerosol Characterization Experiment, the eastern Pacific off the southern coast of California, the South and North Atlantic, and over the sea areas around the British Isles from flight measurements [*Martin et al*., 1994; *Brenguier et al*., 2003; *Pawlowska et al*., 2006]. A similar range of 6–12 μm is given by the ground-based retrievals of liquid cloud effective radii in the boundary layer at the Southern Great Plains site [*Sengupta et al*., 2003; *Kim et al*., 2003]. Most of the global CDERs are 8–11 μm in BCC_MG08, comparable to the values of 9–11 μm from the CloudSat data given by *Yang et al*. [2014]. However, the most frequent effective radii are 9–10 μm, which is less than the range of 10–11 μm from the CloudSat Data. Both simulated ICDNCs and CDERs are smaller in BCC_MG08 than the assumed values in BCC_RK98.

### 3.2.3. Cloud Macrophysical Properties

Figure 8 shows a comparison of annual zonal means of cloud macrophysical properties from simulations and satellite retrievals. A difference in total cloud cover between BCC_MG08 and BCC_RK98 appears in the high latitudes of both hemispheres (Figure 8a). BCC_MG08 simulates less cloud cover in the Arctic, which is much closer to ISCCP observations. However, BCC_MG08 simulates more cloud cover in the latitudes of higher than 75°S than BCC_RK98 and the observations. This is a consequence of the change in the cloud fraction scheme from that of *Slingo* [1987] to that of *Vavrus and Waliser* [2008]. BCC_MG08 overestimates the cloud cover in the tropics, which is likely to be due to the differential treatment of cirrus and anvil cloud microphysics in BCC_MG08 and BCC_RK98 [*Gettelman et al*., 2008]. The LWP in BCC_MG08 is significantly reduced due to a weaker conversion rate of condensate to precipitation compared with that in BCC_RK98, especially over the storm tracks in midlatitude regions (Figures 8b and 9). The decreased LWPs are consistent with NVAP and SSMI data. In particular, the locations of three LWP peak values (10°N, 50°N, and 45°S) in BCC_MG08 are more consistent with those from observations.

The zonal mean tendencies of shortwave and longwave cloud forcing in BCC_MG08 and BCC_RK98 agree well with CERES retrievals (Figures 8c and 8d). The longwave cloud forcing in the middle and high




©2014. American Geophysical Union. All Rights Reserved.

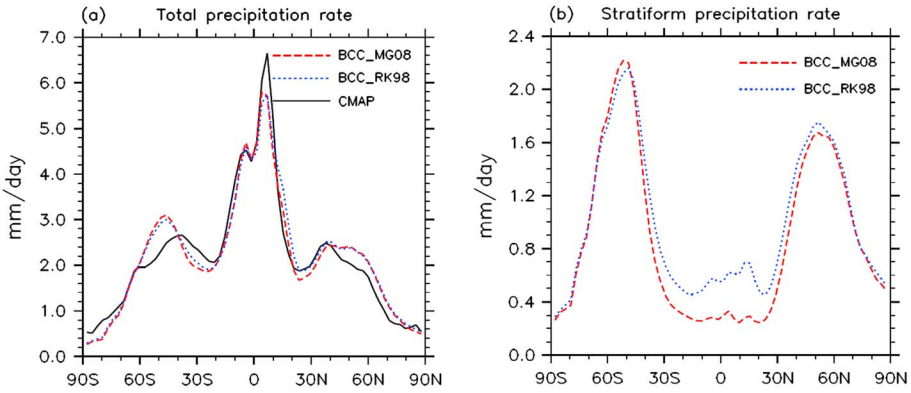


**Figure 10.** Annual zonal means of (a) total precipitation rate and (b) stratiform precipitation rate from BCC_MG08 (long dashed line), BCC_RK98 (short dashed line), and (c) CMAP data (solid line), respectively.

latitudes of the SH and longwave and shortwave cloud forcing in the tropics are improved in BCC_MG08 compared with those in BCC_RK98. However, the bias in shortwave cloud forcing between BCC_MG08 and observation is increased in the midlatitudes of the NH, although the simulated LWP is significantly improved. These biases are caused not only by the different microphysical schemes but also by changes in the cloud cover.

### 3.2.4. Precipitation

Figure 10 shows a comparison of the simulated annual mean precipitation rate with CMAP observations. The total precipitation rate in BCC_MG08 is less than that in BCC_RK98 in the tropics of the NH and at about 30°S because of the decrease in stratiform precipitation rate. The simulated total precipitation rate is slightly improved in the tropics, but becomes worse at about 30°S and 30°N in BCC_MG08.

## 4. Anthropogenic AIE

Anthropogenic AIE was then investigated using the above model with the MG08 scheme in this work. Table 4 shows the global annual mean values of AOD, cloud properties, and radiation flux in PD and PI as well as the corresponding differences between PD and PI (PD minus PI). Anthropogenic AIE is defined as the difference in net radiation flux at the TOA between PD and PI that allows the rapid adjustment of the atmosphere and land surface [*Ghan et al.*, 2012]. The aerosol direct effect is not taken into account in these simulations. The global annual mean AOD is increased by 0.04 from PI to PD, which agrees with the result given by *Lohmann et al.* [2007]. The increase in aerosols enhances the global annual mean LWP, column CDNC and total cloud cover by 6.4 g m$^{-2}$, $0.8 \times 10^{10}$ m$^{-2}$, and 0.06%, respectively, whereas the total precipitation rate is reduced slightly. The global annual mean value of net anthropogenic AIE in the

**Table 4.** Global Annual Mean Values of Aerosol Optical Depth, Cloud Properties, Precipitation Rate, and Radiation Flux (Positive Values Mean Incoming) in PD and PI

| | PD | PI | PD − PI |
|---|---|---|---|
| Aerosol optical depth at 550 nm | 0.12 | 0.08 | 0.04 |
| Liquid water path (g m$^{-2}$) | 82.2 | 75.8 | 6.4 |
| Ice water path (g m$^{-2}$) | 8.51 | 8.47 | 0.04 |
| Column cloud droplet number ($10^{10}$ m$^{-2}$) | 3.3 | 2.5 | 0.8 |
| Total cloud cover (%) | 62.13 | 62.07 | 0.06 |
| Shortwave cloud forcing (W m$^{-2}$) | −51.3 | −49.0 | −2.3 |
| Longwave cloud forcing (W m$^{-2}$) | 27.9 | 27.6 | 0.3 |
| Total precipitation rate (mm day$^{-1}$) | 2.675 | 2.677 | −0.002 |
| Net shortwave radiation at TOA (W m$^{-2}$) | 238.8 | 241.3 | −2.5 |
| Net longwave radiation at TOA (W m$^{-2}$) | −238.2 | −238.8 | 0.6 |
| Net radiation at TOA (W m$^{-2}$) | | | −1.9 |




©2014. American Geophysical Union. All Rights Reserved.

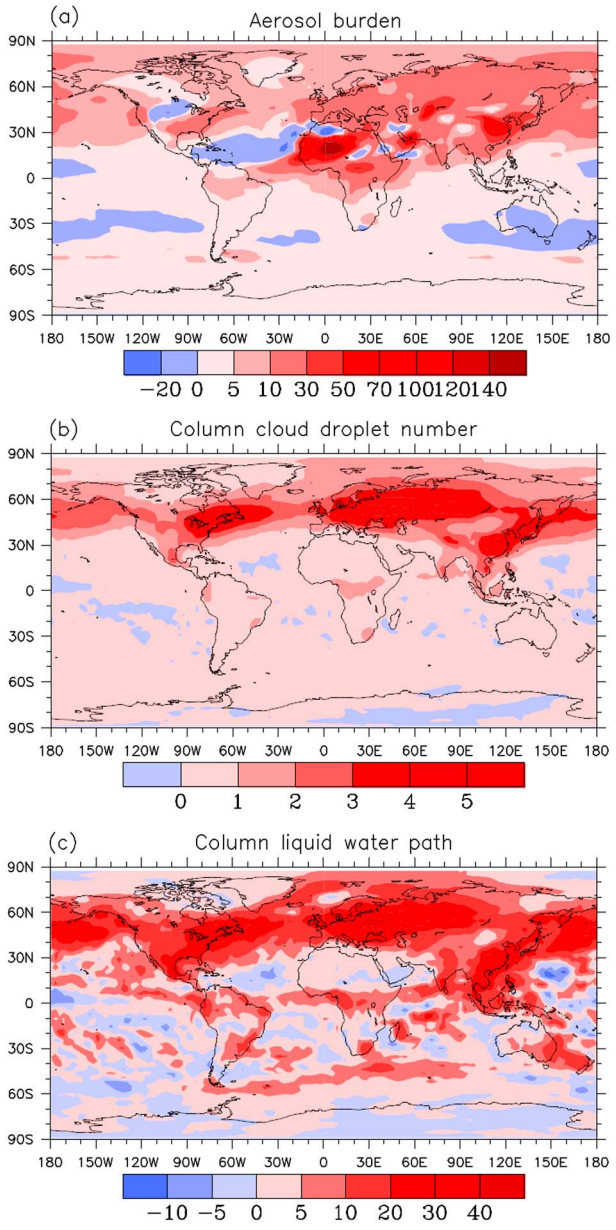


**Figure 11.** Global distributions of annual mean changes of (a) aerosol burden (unit: mg $m^{-2}$), (b) column cloud droplet number concentration (unit: $10^{10}$ $m^{-2}$), and (c) liquid water path (unit: g $m^{-2}$) from PI to PD.

total wavelength region is estimated to be $-1.9\,W\,m^{-2}$ in this study. This value is obtained without imposing a lower bound of CDNC. The net anthropogenic AIE becomes $-1.6\,W\,m^{-2}$ and $-1.2\,W\,m^{-2}$ when the lower bound of CDNC is set to $10\,cm^{-3}$ and $20\,cm^{-3}$, respectively, in our tests. The results are consistent with those given by *Hoose et al*. [2009]. Many models applied different lower bounds of CDNC due to simulated too low CDNCs or as a proxy for natural background aerosols which are not included in models, such as setting $40\,cm^{-3}$ in the European Centre/Hamburg 5 [*Lohmann et al*., 2007], $20\,cm^{-3}$ in IMPACT-CAM [*Wang and Penner*, 2009], and $15\,cm^{-3}$ in CAM-Oslo [*Kirkevag et al*., 2008]. However, prescribing any bound of CDNC can be unphysical [*Hoose et al*., 2009]. There are poor observations to verify the assumption over remote oceans, especially in PI. Therefore, the estimation of AIE by GCMs still has large uncertainty.

Figure 11 presents the global distributions of annual mean changes in the aerosol burden, column CDNC, and LWP from PI to PD. The aerosol loading has grown considerably due to human activities. Particularly, the increase in the aerosol burden is greater than $10\,mg\,m^{-2}$ in East Asia, South Asia, eastern America, Europe, and north and central Africa (Figure 11a). A higher aerosol loading leads to a higher CCN concentration and CDNC and hence a higher LWP. The largest increases in CDNC and LWP appear over areas with significant human activities such as Western Europe, North America, and East and South Asia (Figures 11b and 11c).

Figure 12 gives the annual mean distributions of anthropogenic AIE in the shortwave, longwave, and total wavelength regions, respectively. AIE distributions vary widely among regions, from a regional cooling exceeding $15\,W\,m^{-2}$ to a warming exceeding $5\,W\,m^{-2}$. The spatial variability of AIE in the shortwave region is associated with changes in LWP and CDNC. The strongest cooling occurs in South Asia, North America, and Eurasia and in their downwind areas. Some regions over oceans in the tropics and middle and high latitudes of the SH undergo shortwave warming to differing extents (Figure 12a). The quick adjustment of the atmosphere leads to changes in clouds and longwave radiation. Longwave warming is typically seen over the regions where the strongest shortwave cooling occurs due to the increase in cloud cover (Figure 12b); thus, they partly compensate for each other (Figure 12c). The regions of greatest net cooling caused by AIE are in East Asia, North America, and Europe (Figure 12c). The distributions and magnitudes of anthropogenic AIE are broadly consistent with the results given by *Ghan et al*. [2012].




©2014. American Geophysical Union. All Rights Reserved.

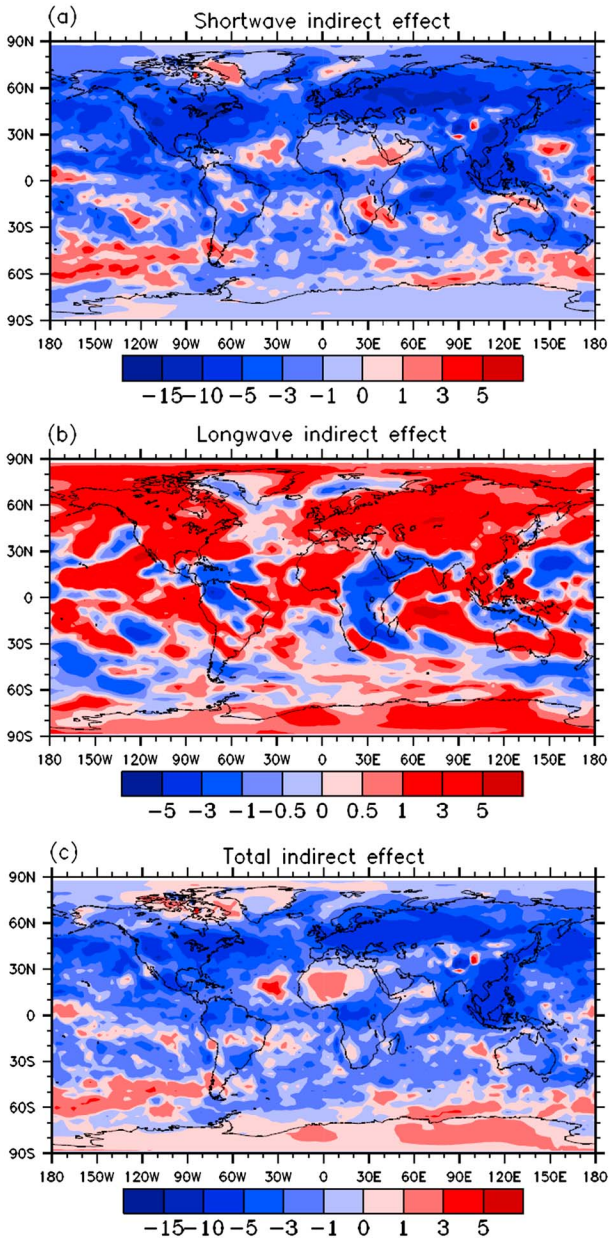


**Figure 12.** Global distributions of annual mean AIE in (a) shortwave, (b) longwave, and (c) total wavelength regions (units: W $m^{-2}$) from PI to PD.

## 5. Discussion and Summary

A two-moment bulk cloud microphysical scheme was implemented into the aerosol-climate model BCC_AGCM2.0.1_CUACE/Aero instead of the one-moment bulk cloud microphysical scheme in the original model. Then, we adjusted the threshold size separating cloud ice from snow in the two-moment scheme to make our new model describe cloud microphysics and aerosol-cloud interaction processes more accurately. Based on the above, we examined differences in the aerosols, cloud properties, and precipitation and temperature fields between the new and original models in detail and finally estimated the anthropogenic AIE. The specific conclusions are summarized as follows:

Compared with the original model, the aerosol column burdens simulated by the new model become more consistent with AeroCom_Medians. The global annual mean and distribution of AOD given by the new model are in better agreement with the ground-based and satellite observations. In particular, the AODs are significantly improved in the areas that are mainly affected by anthropogenic aerosols and over the Sahara, which is affected by dust.

The new model more realistically describes the differences in CDNC and CDER between ocean and land, with higher cloud number concentrations and smaller particles over land. The model captures the spatial features of column CDNC compared with MODIS data, but there are also clear discrepancies in some regions, e.g., underestimates CDNC values off the western coasts of USA, South America, southern Africa, and Australia, and overestimates the CDNC values in the downwind areas of Western Europe, East Asia, and North America and over the subtropical oceans of the SH, southern India, and Southeast Asia. The peak of simulated global annual mean CDER is comparable to that from CloudSat data. The simulated CDNC and CDER values in the new model are significantly lower than the assumed values in the original model, but are consistent with corresponding aircraft observations and ground-based retrievals.

The LWP value in the new model is also significantly less than that in the original model but is closer to NVAP and SSMI observations. Particularly, the locations of LWP peak values match the corresponding observations better. The global annual mean longwave and shortwave cloud forcings simulated by the new model are more consistent with CERES observations. The longwave cloud forcing in the middle and high latitudes of the SH and longwave and shortwave cloud forcing in the tropics are improved, but the shortwave cloud forcing becomes worse in the midlatitudes of the NH in the new model.




©2014. American Geophysical Union. All Rights Reserved.

The total precipitation rates in both simulations are consistent with values from CMAP observations. However, the stratiform precipitation rate simulated by the new model is nearly 20% lower than that produced by the original model, and this difference is especially great in the tropics and subtropics. The total precipitation rate is improved in the tropics, but it becomes worse at about 30°S and 30°N in the new model.

The global annual mean of anthropogenic AIE is estimated to be $-1.9\,\mathrm{W\,m^{-2}}$ when using the new model without imposing a lower bound of CDNC, whereas it decreases significantly when setting a higher lower bound of CDNC. The uncertainties associated with such an estimate are still large.

In conclusion, the descriptions of cloud microphysics and aerosol-cloud interaction processes are improved in the BCC_AGCM2.0.1_CUACE/Aero model. The new model produces better simulations for aerosol, cloud properties, precipitation, and radiation budget at the TOA and has better ability to simulate climate change due to human activity. This work could be a useful reference by some other models that still adopt the single-moment cloud microphysical scheme, since it clearly shows how a significant improvement can be achieved by replacing a single-moment scheme with a two-moment scheme. However, the comparison between simulation and observation indicates that there are still some biases in the model results. Further work is required to eliminate these effects.

**Acknowledgments**

This work was funded by the National Basic Research Program of China (2011CB403405), Public Meteorology Special Foundation of MOST (GYHY201406023), National Natural Science Foundation of China (41205116), and CAMS Basis Research Project (2012Y003). We thank the principal investigators and their staff for establishing and maintaining the AERONET sites used in this investigation. The authors would like to give many thanks to the anonymous reviewers for their helpful suggestions.

## References

Abdul-Razzak, H., and S. J. Ghan (2000), A parameterization of aerosol activation: 2. Multiple aerosol types, *J. Geophys. Res.*, *105*, 6837–6844, doi:10.1029/1999JD901161.

Albrecht, B. (1989), Aerosols, cloud microphysics, and fractional cloudiness, *Science*, *245*, 1227–1230, doi:10.1126/science.245.4923.1227.

Barahona, D., R. Sotiropoulou, and A. Nenes (2011), Global distribution of cloud droplet number concentration, autoconversion rate, and aerosol indirect effect under diabatic droplet activation, *J. Geophys. Res.*, *116*, D09203, doi:10.1029/2010JD015274.

Barker, H. (1996), A parameterization for computing grid-averaged solar fluxes for inhomogeneous marine boundary layer clouds. Part I: Methodology and homogeneous biases, *J. Atmos. Sci.*, *53*, 2289–2303.

Barker, H., B. A. Weilicki, and L. Parker (1996), A parameterization for computing grid-averaged solar fluxes for inhomogeneous marine boundary layer clouds. Part II: Validation using satellite data, *J. Atmos. Sci.*, *53*, 2304–2316.

Bennartz, R. (2007), Global assessment of marine boundary layer cloud droplet number concentration from satellite, *J. Geophys. Res.*, *112*, D02201, doi:10.1029/2006JD007547.

Boucher, O., and U. Lohmann (1995), The sulfate-CCN-cloud albedo effect: A sensitivity study using two general circulation models, *Tellus*, *47B*, 281–300.

Boucher, O., et al. (2013), Clouds and aerosols, in *Climate Change 2013: The Physical Science Basis. Contribution of Working Group I to the Fifth Assessment Report of the Intergovernmental Panel on Climate Change*, edited by T. F. Stocker et al., pp. 573–632, Cambridge Univ. Press, Cambridge, U. K., and New York.

Brenguier, J. L., H. Pawlowska, L. Schüller, R. Preusker, J. Fischer, and Y. Fouquart (2000), Radiative properties of boundary layer clouds: Droplet effective radius versus number concentration, *J. Atmos. Sci.*, *57*, 803–821.

Brenguier, J. L., H. Pawlowska, and L. Schüller (2003), Cloud microphysical and radiative properties for parameterization and satellite monitoring of the indirect effect of aerosol on climate, *J. Geophys. Res.*, *108*(D15), 8632, doi:10.1029/2002JD002682.

Carslaw, K. S., et al. (2013), Large contribution of natural aerosols to uncertainty in indirect forcing, *Nature*, *503*, 67–71, doi:10.1038/nature12674.

Collins, W. D., et al. (2004), Description of the NCAR community atmosphere model (CAM3.0), *Tech. Rep. NCAR/TN-464STR*, Natl. Cent. for Atmos. Res., 226 pp.

Cooper, W. A. (1986), Ice initiation in natural clouds, in *Precipitation Enhancement—A Scientific Challenge*, Meteor. Mongr., No.43, pp. 29–32, American Meteor Society, Boston.

Deng, Z. Z., C. S. Zhao, Q. Zhang, M. Y. Huang, and X. C. Ma (2009), Statistical analysis of microphysical properties and the parameterization of effective radius of warm clouds in Beijing area, *Atmos. Res.*, *93*(4), 888–896.

Dentener, F., et al. (2006), Emissions of primary aerosol and precursor gases in the years 2000 and 1750 prescribed data-sets for AeroCom, *Atmos. Chem. Phys.*, *6*, 4321–4344, doi:10.5194/acp-6-4321-2006.

Gettelman, A., H. Morrison, and S. J. Ghan (2008), A new two-moment bulk stratiform cloud microphysics scheme in the community atmosphere model, version 3 (CAM3). Part II: Single-column and global results, *J. Clim.*, *21*, 3660–3679.

Ghan, S. J., L. R. Leung, and Q. Hu (1997), Application of cloud microphysics to NCAR community climate model, *J. Geophys. Res.*, *102*, 16,507–16,527, doi:10.1029/97JD00703.

Ghan, S. J., X. Liu, R. C. Easter, R. Zaveri, P. J. Rasch, J.-H. Yoon, and B. Eaton (2012), Toward a minimal representation of aerosols in climate models: Comparative decomposition of aerosol direct, semidirect, and indirect radiative forcing, *J. Clim.*, *25*, 6461–6476.

Ghan, S. J., S. J. Smith, M. Wang, K. Zhang, K. Pringle, K. Carslaw, J. Pierce, S. Bauer, and P. Adams (2013), A simple model of global aerosol indirect effects, *J. Geophys. Res. Atmos.*, *118*, 6688–6707, doi:10.1002/jgrd.50567.

Gong, S. L., L. A. Barrie, and M. Lazare (2002), Canadian Aerosol Module (CAM): A size-segregated simulation of atmospheric aerosol processes for climate and air quality models 2. Global sea-salt aerosol and its budgets, *J. Geophys. Res.*, *107*(D24), 4779, doi:10.1029/2001JD002004.

Gong, S. L., et al. (2003), Canadian Aerosol Module: A size-segregated simulation of atmospheric aerosol processes for climate and air quality models 1. Module development, *J. Geophys. Res.*, *108*(D1), 4007, doi:10.1029/2001JD002002.

Gultepe, I., and G. A. Isaac (2004), Aircraft observations of cloud droplet number concentration: Implications for climate studies, *Q. J. R. Meteorol. Soc.*, *130*, 2377–2390, doi:10.1256/qj.03.120.

Han, Q., W. B. Rossow, J. Chou, and R. W. Welch (1998), Global variation of column droplet concentration in low-level clouds, *Geophys. Res. Lett.*, *25*, 1419–1422, doi:10.1029/98GL01095.





©2014. American Geophysical Union. All Rights Reserved.

Hansen, J., et al. (2005), Efficacy of climate forcings, *J. Geophys. Res.*, *110*, D18104, doi:10.1029/2005JD005776.
Hoose, C., J. E. Kristjansson, T. Iversen, A. Kirkevag, Ø. Seland, and A. Gettelman (2009), Constraining cloud droplet number concentration in GCMs suppresses the aerosol indirect effect, *Geophys. Res. Lett.*, *36*, L12807, doi:10.1029/2009GL038568.
Jing, X. W., and H. Zhang (2013), Application and evaluation of McICA scheme in BCC_AGCM2.0.1, *AIP Conf. Proc.*, *1531*, 756–759, doi:10.1063/1.4804880.
Kiehl, J. T., and K. E. Trenberth (1997), Earth's annual global mean energy budget, *Bull. Am. Meteorol. Soc.*, *78*, 197–208.
Kim, B.-G., S. E. Schwartz, M. A. Miller, and Q. Min (2003), Effective radius of cloud droplets by ground-based remote sensing: Relationship to aerosol, *J. Geophys. Res.*, *108*(D23), 4740, doi:10.1029/2003JD003721.
King, M. D., W. P. Menzel, Y. J. Kaufman, D. Tanre, B. C. Gao, S. Platnick, S. A. Ackerman, L. A. Remer, R. Pincus, and P. A. Hubanks (2003), Cloud and aerosol properties, precipitable water, and profiles of temperature and water vapor from MODIS, *IEEE Trans. Geosci. Remote Sens.*, *41*, 442–458.
Kinne, S., et al. (2006), An AeroCom initial assessment–optical properties in aerosol component modules of global models, *Atmos. Chem. Phys.*, *6*, 1815–1834, doi:10.5194/acp-6-1815-2006.
Kirkevag, A., T. Iversen, Ø. Seland, J. B. Debernard, T. Storelvmo, and J. E. Kristjansson (2008), Aerosol-cloud-climate interactions in the climate model CAM-Oslo, *Tellus A*, *60*, 492–512.
Li, Z., F. Niu, J. Fan, Y. Liu, D. Rosenfeld, and Y. Ding (2011), Long-term impacts of aerosols on the vertical development of clouds and precipitation, *Nat. Geosci.*, *4*, 888–894, doi:10.1038/ngeo1313.
Lohmann, U., J. Feichter, C. C. Chuang, and J. E. Penner (1999), Predicting the number of cloud droplets in the ECHAM GCM, *J. Geophys. Res.*, *104*, 9169–9198, doi:10.1029/1999JD900046.
Lohmann, U., P. Stier, C. Hoose, S. Ferrachat, S. Kloster, E. Roeckner, and J. Zhang (2007), Cloud microphysics and aerosol indirect effects in the global climate model ECHAM5-HAM, *Atmos. Chem. Phys.*, *7*, 3425–3446, doi:10.5194/acp-7-3425-2007.
Lohmann, U., L. Rotstayn, T. Storelvmo, A. Jones, S. Menon, J. Quaas, A. M. L. Ekman, D. Koch, and R. Ruedy (2010), Total aerosol effect: Radiative forcing or radiative flux perturbation?, *Atmos. Chem. Phys.*, *10*, 3235–3246.
Martin, G. M., D. W. Johnson, and A. Spice (1994), The measurement and parameterization of effective radius of droplets in warm stratocumulus clouds, *J. Atmos. Sci.*, *51*, 1823–1842.
Menon, S., and L. Rotstayn (2006), The radiative influence of aerosol effects on liquid-phase cumulus and stratiform clouds based on sensitivity studies with two climate models, *Clim. Dyn.*, *27*(4), 345–356, doi:10.1007/s00382-006-0139-3.
Menon, S., A. D. Del Genio, D. Koch, and G. Tselioudis (2002), GCM simulations of the aerosol indirect effect: Sensitivity to cloud parameterization and aerosol burden, *J. Atmos. Sci.*, *59*, 692–713.
Ming, Y., V. Ramaswamy, P. A. Ginoux, L. W. Horowitz, and L. M. Russell (2005), Geophysical Fluid Dynamics Laboratory general circulation model investigation of the indirect radiative effects of anthropogenic sulfate aerosol, *J. Geophys. Res.*, *110*, D22206, doi:10.1029/2005JD006161.
Morrison, H., and A. Gettelman (2008), A new two-moment bulk stratiform cloud microphysics scheme in the Community Atmosphere Model, version 3 (CAM3). Part I: Description and numerical tests, *J. Clim.*, *21*(15), 3642–3659.
Morrison, H., J. A. Curry, and V. I. Khvorostyanov (2005a), A new double-moment microphysics parameterization for application in cloud and climate models. Part I: Description, *J. Atmos. Sci.*, *62*(6), 1665–1677.
Morrison, H., J. A. Curry, M. D. Shupe, and P. Zuidema (2005b), A new double-moment microphysics parameterization for application in cloud and climate models. Part II: Single-column modeling of Arctic clouds, *J. Atmos. Sci.*, *62*(6), 1678–1693.
Myhre, G., et al. (2013), Radiative forcing of the direct aerosol effect from AeroCom Phase II simulations, *Atmos. Chem. Phys.*, *13*, 1853–1877, doi:10.5194/acpd-12-22355-2012.
Nakajima, T., M. Tsukamoto, Y. Tsushima, A. Numaguti, and T. Kimura (2000), Modeling of the radiative process in an atmospheric general circulation model, *Appl. Opt.*, *39*(27), 4869–4878, doi:10.1364/AO.39.004869.
Nenes, A., and J. H. Seinfeld (2003), Parameterization of cloud droplet formation in global climate models, *J. Geophys. Res.*, *108*(D14), 4415, doi:10.1029/2002JD002911.
Pawlowska, H., W. W. Grabowski, and J.-L. Brenguier (2006), Observations of the width of cloud droplet spectra in stratocumulus, *Geophys. Res. Lett.*, *33*, L19810, doi:10.1029/2006GL026841.
Pincus, R., S. A. McFarlane, and S. A. Klein (1999), Albedo bias and the horizontal variability of clouds in subtropical marine boundary layers: Observations from ships and satellite, *J. Geophys. Res.*, *104*, 6183–6191, doi:10.1029/1998JD200125.
Pincus, R., H. W. Barker, and J.-J. Morcrette (2003), A fast, flexible, approximate technique for computing radiative transfer in inhomogeneous cloud fields, *J. Geophys. Res.*, *108*(D13), 4376, doi:10.1029/2002JD003322.
Pincus, R., S. Platnick, S. A. Ackerman, R. S. Hemler, and R. J. P. Hofmann (2012), Reconciling simulated and observed views of clouds: MODIS, ISCCP, and the limits of instrument simulators, *J. Clim.*, *25*, 4699–4720.
Qian, Y., D. Gong, J. Fan, L. R. Leung, R. Bennartz, D. Chen, and W. Wang (2009), Heavy pollution suppresses light rain in China: Observations and modeling, *J. Geophys. Res.*, *114*, D00K02, doi:10.1029/2008JD011575.
Quaas, J., O. Boucher, and U. Lohmann (2006), Constraining the total aerosol indirect effect in the LMDZ and ECHAM4 GCMs using MODIS satellite data, *Atmos. Chem. Phys.*, *6*, 947–955, doi:10.5194/acp-6-947-2006.
Randel, D. L., T. J. Greenwald, T. H. Vonder Haar, G. L. Stephens, M. A. Ringerud, and C. L. Combs (1996), A new global water vapor dataset, *Bull. Am. Meteorol. Soc.*, *77*, 1233–1246.
Rasch, P. J., and J. E. Kristjánsson (1998), A comparison of the CCM3 model climate using diagnosed and predicted condensate parameterizations, *J. Clim.*, *11*, 1587–1614.
Rossow, W. B., and R. A. Schiffer (1999), Advances in understanding clouds from ISCCP, *Bull. Am. Meteorol. Soc.*, *80*, 2261–2287.
Sengupta, M., E. E. Clothiaux, T. P. Ackerman, S. Kato, and Q. Min (2003), Importance of accurate liquid water path for estimation of solar radiation in warm boundary layer clouds: An observational study, *J. Clim.*, *16*, 2997–3009.
Slingo, J. M. (1987), The development and verification of a cloud prediction scheme for the ECMWF model, *Q. J. R. Meteorol. Soc.*, *113*, 899–927, doi:10.1002/qj.49711347710.
Twomey, S. A. (1977), The influence of pollution on the shortwave albedo of clouds, *J. Atmos. Sci.*, *34*, 1149–1152.
van Donkelaar, A., R. V. Martin, M. Brauer, R. Kahn, R. Levy, C. Verduzco, and P. J. Villeneuve (2010), Global estimates of ambient fine particulate matter concentrations from satellite-based aerosol optical depth: Development and application, *Environ. Health Perspect.*, *118*(6), 847–855, doi:10.1289/ehp.0901623.
Vavrus, S., and D. Waliser (2008), An improved parameterization for simulating Arctic cloud amount in the CCSM3 climate model, *J. Clim.*, *21*, 5673–5687.
Wang, M., and J. E. Penner (2009), Aerosol indirect forcing in a global model with particle nucleation, *Atmos. Chem. Phys.*, *9*, 239–260, doi:10.1029/1998JD200125.




©2014. American Geophysical Union. All Rights Reserved.

Wang, Z. L., H. Zhang, X. S. Shen, S. L. Gong, and X. Y. Zhang (2010), Modeling study of aerosol indirect effects on global climate with an AGCM, *Adv. Atmos. Sci.*, *27*(5), 1064–1077, doi:10.1007/s00376-010-9120-5.

Wang, Z. L., H. Zhang, X. W. Jing, and X. D. Wei (2013a), Effect of non-spherical dust aerosol on its direct radiative forcing, *Atmos. Res.*, *120*, 112–126.

Wang, Z. L., H. Zhang, J. Li, X. W. Jing, and P. Lu (2013b), Radiative forcing and climate response due to the presence of black carbon in cloud droplets, *J. Geophys. Res. Atmos.*, *118*, 3662–3675, doi:10.1002/jgrd.50312.

Wei, X. D., and H. Zhang (2011), Analysis of optical properties of nonspherical dust-like aerosols, *Acta Opt. Sin.*, *31*(5), 0501002-1-8.

Wentz, F. J. (1997), A well-calibrated ocean algorithm for special sensor microwave / imager, *J. Geophys. Res.*, *102*, 8703–8718, doi:10.1029/96JC01751.

Wu, T., R. C. Yu, F. Zhang, Z. Z. Wang, M. Dong, L. Wang, X. Jin, D. Chen, and L. Li (2010), The Beijing Climate Center atmospheric general circulation model: Description and its performance for the present-day, *Clim. Dyn.*, *34*, 123–147, doi:10.1007/s00382-009-0594-8.

Xie, P., and P. A. Arkin (1996), Analyses of global monthly precipitation using gauge observations, satellite estimates, and numerical model predictions, *J. Clim.*, *9*, 840–858.

Yang, B. Y., H. Zhang, J. Peng, Z. L. Wang, and X. W. Jing (2014), Analysis on global distribution characteristics of cloud microphysical and optical properties based on the CloudSat data, *Plateau Meteorol.*, *33*(3), doi:10.7522/j.issn.1000-0534.2013.00026.

Zhang, H., T. Nakajima, G.-Y. Shi, T. Suzuki, and T. Imasu (2003a), An optimal approach to overlapping bands with correlated *k* distribution method and its application to radiative calculations, *J. Geophys. Res.*, *108*(D20), 4641, doi:10.1029/2002JD003358.

Zhang, H., G.-Y. Shi, T. Nakajima, and T. Suzuki (2006a), The effects of the choice of the *k*-interval number on radiative calculations, *J. Quant. Spectros. Radiat. Transfer*, *98*, 31–43, doi:10.1016/j.jqsrt.2005.05.090.

Zhang, H., T. Suzuki, T. Nakajima, G.-Y. Shi, X.-Y. Zhang, and Y. Liu (2006b), Effects of band division on radiative calculations, *Opt. Eng.*, *45*(1), 016002, doi:10.1117/1.2160521.

Zhang, H., et al. (2012a), Simulation of direct radiative forcing of typical aerosols and their effects on global climate using an online AGCM-aerosol coupled model system, *Clim. Dyn.*, *38*, 1675–1693, doi:10.1007/s00382-011-1131-0.

Zhang, H., Z. P. Shen, X. D. Wei, M.-G. Zhang, and Z. Li (2012b), Comparison of optical properties of nitrate and sulfate aerosol and the direct radiative forcing due to nitrate in China, *Atmos. Res.*, *113*, 113–125.

Zhang, H., X. W. Jing, and J. Li (2014), Application and evaluation of a new radiation code under McICA scheme in BCC_AGCM2.0.1, *Geosci. Model Dev.*, *7*, 737–754, doi:10.5194/gmd-7-737-2014.

Zhang, M., W. Lin, C. Bretherton, J. Hack, and P. J. Rasch (2003b), A modified formulation of fractional stratiform condensation rate in the NCAR Community Atmospheric Model (CAM2), *J. Geophys. Res.*, *108*(D1), 4035, doi:10.1029/2002JD002523.

Zheng, X., B. Albrecht, P. Minnis, K. Ayers, and H. Jonson (2010), Observed aerosol and liquid water path relationships in marine stratocumulus, *Geophys. Res. Lett.*, *37*, L17803, doi:10.1029/2010GL044095.

Zhou, C. H., S. Gong, X.-Y. Zhang, H. L. Liu, M. Xue, G. L. Cao, X. Q. An, H. Z. Che, Y. M. Zhang, and T. Niu (2012), Towards the improvements of simulating the chemical and optical properties of Chinese aerosols using an online coupled model-CUACE/Aero, *Tellus B*, *64*, 18965.





©2014. American Geophysical Union. All Rights Reserved.

第14卷 第8期 2014年3月
1671—1815(2014)08-0000-05

科 学 技 术 与 工 程
Science Technology and Engineering

Vol. 14 No. 8 Mar. 2014
ⓒ 2014 Sci. Tech. Engrg.

地球科学

# 关于大气臭氧问题的主要研究进展

谢 冰[1,2] 张 华[2]

(兰州大学大气科学学院,半干旱气候变化教育部重点实验室[1],兰州 730000;
中国气象局气候研究开放实验室国家气候中心[2],北京 100081)

**摘 要** 大气臭氧是非常重要的温室气体,其在全球的分布具有不均匀性,受到人类活动的显著影响,近几十年来由于对流层臭氧增加造成正的辐射强迫会增加大气温室效应,而平流臭氧减少会使其吸收的紫外线辐射减少,为负的辐射强迫,使得平流层大气降温。因此关于大气臭氧 浓度变化及其对气候的影响是非常复杂的,一直是科学界研究的热点和难点问题。自从20世纪50年代末到70年代就发现臭氧浓度有减少的趋势。1985年英国南极考察队在南纬60°地区观测发现存在大气臭氧层空洞;自此开始,大气臭氧问题引起了世界各国的极大关注,并给予很多研究。目前,平流层和对流层臭氧浓度的观测仍然是研究的重点。鉴于对流层臭氧浓度持续升高和平流层臭氧浓度的不断下降,以及他们在对流层和平流层大气温度中所起的不同作用,本文将主要针对近五年来大气臭氧相关的研究进展进行简要的综述,包括对流层和平流层臭氧浓度及其观测研究,和人类活动的影响等方面进行分述。最后给出目前研究工作的不足和未来工作展望。

**关键词** 大气臭氧 对流层 平流层 研究进展
**中图法分类号** 421.33; **文献标志码** A

臭氧是地球大气中重要的气体,90%集中在10~30 km的平流层,仅有10%左右的臭氧分布在对流层中。平流层臭氧对太阳紫外辐射有强烈的吸收,从而起到保护地球生物圈的作用;在对流层,臭氧是一种重要的温室气体(通过吸收地气系统的长波辐射而加热大气);也是污染气体(高浓度的地面臭氧将引发城市光化学烟雾,影响人类健康)。尽管臭氧总量中只有10%左右臭氧在对流层,但对流层臭氧变化所引起的气候效应却能与平流层扰动作用不相上下。林磊等(2012)[1]利用Fu-Liou模式和南半球的臭氧观测数据发现,臭氧浓度垂直廓线的改变影响着Brewer-Dobson环流的流速。平流层中的臭氧主要集中在臭氧层(平流层中臭氧浓度相对较高的部分,大多分布在离地20~50 km的高空),平流层臭氧主要以紫外线打击双原子的氧分子,把它分为两个原子,然后每个原子和没有分裂的氧分子合并成臭氧分子;臭氧分子不稳定,紫外线照射之后又分为$O_2$和O,形成一个连续的过程$O_3$—$O_2$循环过程,如此产生臭氧层。对流层中臭氧的来源问题,国内外学者主要有两种观点:一是平流层动力下传以及平流层与对流层之间的相互交换;二是对流层中发生的光化学反应。在过去的二十年中,科学家们已就臭氧总量随纬度变化的差异以及臭氧总量随季节的变化进行了深入而广泛的研究,最近几年研究结果表明[2],臭氧总量具有年际和年代际的变化,而且季风对臭氧的浓度变化具有显著的影响[3—6]。自"大气臭氧空洞"现象被发现以来,平流层臭氧损耗就成为广大国内外学者关注的热点问题,其中平流层臭氧损耗对气候的影响,平流层臭氧含量与温度湿度的相互作用等问题是近年来关注的焦点。随着经济的快速发展,人类活动对臭氧的影响也是不可小觑的。王革丽等(2009)[7]研究发现飞机排放的二氧化碳、水汽、氮氧化物氮氧化物、硫酸盐和煤烟粒子等对臭氧层有潜在的影响。如前所述臭氧也是一种重要的温室气体,Lorenzo和Polvani(2011)[8]发现臭氧损耗所造成的增温是其作为温室气体所造成的增温的3到4倍,对流层臭氧能引起植物气孔关闭、光合组织结构和功能的破坏,从而影响自然界对二氧化碳的吸收,这一间接作用会增加0.2~0.4 W/m$^2$的二氧化碳辐射强迫,差不多使对流层臭氧的辐射强迫增加了一倍。Daniel和Jacob(2009)[9]发现在夏季,仅气候变暖就会使全球地表臭氧浓度升高$1\sim10\times10^{-9}$(ppb),其中最主要的影响发生在受污染的城市地区。

2013年8月23日收到,10月25日修改 国家自然科学基金面上项目(41075014)资助

第一作者简介:谢 冰,男,1986年生,研究生,主要从事气候方面的研究工作,E-mail:bubba@126.com。



## 1 大气臭氧的浓度变化

全球范围内,大气臭氧总量分布自赤道向南北

极却呈低-高-低型,这主要是大气环流和涡旋输送的结果;低纬度地区臭氧柱总量较低,高纬度地区臭氧柱总量较高。全球平均臭氧柱总量有明显的季节变化和纬度变化。平均臭氧柱总量在春季达到最大值,秋季达到最小值。据 WMO(2010)臭氧评估报告[10],2006 ~2009 年平均臭氧总量与过去十年相比基本持平,全球范围内臭氧总量与 1964 ~1980 年平均值相比低 3.5%,而 60°S ~60°N 范围内臭氧总量与 1964 ~1980 年平均值相比低 2.5%。在 2006 ~2009 年间南半球中纬度地区臭氧柱含量与过去十年基本相同,与 1964 ~1980 年平均值相比大约低 6%;同时期北半球中纬度地区臭氧柱含量也与 1998 -2005 年期间大致相当,与 1964 - 1980 年平均值相比大约低 3.5%。模式模拟的臭氧柱含量随纬度的变化趋势与观测得到的结果基本相符,在南半球中高纬度地区和北半球中纬度地区有明显的下降趋势。我国科研工作者也为全球臭氧的研究做出了很大的贡献,朱乾根和郭品文(2000)[11]指出 1987 年前后北半球 40°N 以北的中高纬地区春季大气臭氧柱总量的趋势变化存在明显的突变,大部分地区突然减少。张金强和王振会(2007)[12]利用 1989 ~2000 年期间每年逐日臭氧总量数据进行平均计算,得出对应的南北纬度带地区,北纬臭氧总量要高于南纬,并且随着纬度的增加,这个差值将变大。东亚地处全球最显著的季风区,有着全球最大的海陆差异,是臭氧浓度高值区,不仅受中高纬天气系统的影响,低纬地区天气系统的影响也不可忽略。吴国雄等(2006)[13]提出了“亚印太交汇区”的概念,指出该地区是影响我国短期气候变异的关键海气相互作用区。郭世昌等(2007)[14]利用 1979 ~1992 年和 1997 ~2008 年两个时间段的 TOMS 对臭氧总量月平均网格资料进行了较为详细的对比研究,结果表明:1979 ~1992 年较 1997 ~2008 年东亚低伟地区大气臭氧浓度低;其受地形和环流影响显著。由于我国地理位置和地形等原因,中国地区臭氧浓度变化一直是许多科学家关注的焦点。早在 20 世纪 90 年代,魏鼎文等(1994)[15]指出 70 年代以来我国臭氧总量有减少的趋势。近年来,该方面的工作又有了显著地进展,韦惠红(2006)[16]根据臭氧总量的地理分布特征把我国划分成 7 个区域,利用卫星观测资料分析,发现东部地区的臭氧总量常年大于西部地区,青藏高原、西北高原与东部同纬度地区相比,在夏季差别最大,冬季最小。作为地球“第三极”青藏高原地区的大气臭氧浓度变化引起了人们的关注。周秀骥等(1995)[17]发现青藏高原上空存在臭氧浓度“低谷”现象。卞建春(2009)[18]利用卫星资料对青藏高原的臭氧低谷现象进行研究发现 1990 年以前,低谷现象只在 1987 年的 11 月到 12 月期间发生过,但在 1990 年之后该现象发生次数明显增多。刘传熙等(2010)[19]研究发现低谷现象是由于青藏高原地区对流层顶的升高与热带臭氧浓度较低的空气向北输送。通过对臭氧卫星观测资料及大气环流资料的分析,邹捍等(2011)[20]研究了青藏高原上空臭氧年际变化中的 ENSO 信号,在厄尔尼诺年青藏高原臭氧总量增加,在拉尼娜年青藏高原臭氧总量减小。青藏高原对流层中部臭氧低谷现象(TMTOM,tibetan middle tropospheric ozone minimum),是在六月份青藏高原上空臭氧层下部与对流层中部出现的异常现象。刘毅等(2009)[21]用卫星资料研究发现 TMTOM 发生在青藏高原东部地区上空 8 ~13 km 处,且常常伴随着亚洲夏季风的发生。大气臭氧不仅随空间变化,随时间也呈现出多种变化。史久恩等(1996)[22]对中国地区大气臭氧总量的研究表明,中国南部地区臭氧变化也表现出显著的准两年振荡。郭世昌等(2007)[14]应用 Morlet 小波分析方法对欧亚地区 30 年的大气臭氧总量月平均资料加以研究,发现臭氧存在明显的年际变化和年代际变化,其年际变化的特征时间尺度为 2 年和 5 年,年代际变化的特征时间尺度为 12 年。刘毅等(2011)[23]利用卫星资源对臭氧随高度与纬度的年际间异常变化就行了分析,发现动力转输作用是控制臭氧浓度变化准两年震荡的主要因素。

### 1.1　平流层臭氧

由于平流层臭氧占全球臭氧总量的 90%,而在平流层内有两个海拔高度带对臭氧柱总量的长期变化具有重要影响[10]。表 1 给出了 WMO(2010)对平流层臭氧浓度廓线的近几十年的观测结果的评估。(1)平流层上层(35 ~45 km),从 1979 年至 20 世纪 90 年代中期在这一高度层内的臭氧含量有一个显著性下降(每十年 6% ~8% ),之后为略微增加的趋势,这主要是由于卤素催化消耗臭氧所造成的。(2)平流层低层(20 ~25 km),在中纬度地区,臭氧含量也经历了一个显著的下降,在 1979 年至 20 世纪 90 年代中期的下降速度约为每十年 4% ~5%,这主要是由于溴和含氯化合物的作用。大部分的臭氧损耗与溴和氯的化合物(氟氯化碳和替代品)有关,除了一氧化二氮都与人类活动有关;之后为稳定或略有增加的趋势(每十年 2% ~3% )。直到 2010 年,虽然平流层臭氧含量略有回升但仍比 1964 ~1980 年平均值低 2.5%。

**表 1 平流层臭氧浓度廓线的近几十年的观测结果 WMO(2010)**

| | 臭氧柱含量 | 12 ~ 15 km | 20 ~ 25 km | 35 ~ 45 km |
|---|---|---|---|---|
| 数据来源 | 地基观测<br>卫星资料 | 臭氧探空仪 | 臭氧探空仪卫星资料傅里叶变换红外光谱 | 卫星资料傅里叶变换红外光谱 Umkehrs |
| 1980 ~ 1996 年北半球中纬度 | 大约减少了 6% | 大约减少了 9% | 大约减少了 7% | 大约减少了 10% |
| 1996 ~ 2009 年北半球中纬度 | 从 1998 年的最低值增长 2% 后几乎保持不变 | 大约增长了 6% | 大约增加了 2.5% | 增加了 1% ~ 2%<br>不确定性较大 |
| 1980 ~ 1996 年南半球中纬度 | 减少了 6% | 没有资料 | 大约减少了 67% | 大约减少了 10% |
| 1969 ~ 2009 年南半球中纬度 | 几乎保持不变 | 没有明显变化 | 没有明显变化 | 增加了 1% ~ 3%<br>不确定性较大 |

平流层温度变化也会对平流层化学反应速度产生影响,从而造成平流层化学成分的变化,尤其对平流层臭氧浓度的影响很大,臭氧浓度的变化也将反过来影响平流层温度场。21 世纪的平流层温度变化将主要取决于两个相反的因素,一个是温室气体增加导致的平流层变冷,另一个是臭氧恢复造成的平流层温度升高[24]。研究表明由于人为因素的影响,温室气体持续增加使得海温不断上升,而在南半球高纬度地区海平面温度与平流层温度成正相关关系,从而大大影响了南极臭氧空洞的恢复[25]。王卫国等(2006)[26]利用 1958 ~ 2001 年的 ECMWF 资料(European Center for Medium-Range Weather Forecasts)及参数化方法,计算了对流层顶臭氧含量的时空分布,结果表明臭氧含量分布的空间梯度从赤道指向两极,而加热率则是分别由高纬和低纬指向副热带。胡春娟(2007)[27]应用改进后的 CCM1(R15L12)动力气候模式,以国家气象中心 1991 年 1 月 16 日的全球客观分析资料为初始场,研究了南极高空臭氧含量减少对平流层温度场影响的数值模拟,认为臭氧减少可造成平流层各层的温度降低,从而影响到平流层的大气环流及输送过程。胡永云等(2009)[28]研究发现在温室气体增加和臭氧恢复的双重作用下,平流层中层变冷,而平流层低层却变暖。陈月娟等(2009)[29]采用大气环流模式模拟了不考虑臭氧作用时水汽和 $CO_2$ 等温室气体对温度的影响,结果表明与实际温度场不符,从而证明了臭氧加热的重要性。用臭氧吸收解释热力状态的研究表明,下平流层增温主要是臭氧吸收的短波辐射引起,而冷却效应是臭氧吸收长波辐射造成的。近 10 年来,平流层低层温度呈现上升趋势,与臭氧柱含量的升高是一致的。施春华等(2009)[30]采用一个包含平流层化学、辐射、动力相互作用的二维模式,检验了达成“蒙特利尔议定书”框架协议到 20 世纪 90 年代平流层变冷趋势减缓 0.6 K。关于臭氧和平流层爆发性增温之间的关系很早就引起了学者们的关注,研究表明某地平流层温度和当地的臭氧总量成正比。William(1993)[31]指出平流层爆发性增温的发生使低纬的臭氧减少,高纬的臭氧增加,同时中低纬臭氧的变化是与平流层爆发性增温相联系的大气环流圈的表现形式,平流层下层臭氧的变化是受动力传输控制,而上层受光化学影响,更为有意义的是,他指出了低纬度臭氧的传输是受纬向平均的垂直运动所控制。刘毅等(2009)[32]研究发现在平流层爆发性增温的过程中,极地涡旋和行星波对平流层臭氧的空间分布和平流层底与对流层上层的臭氧通量起着重要的作用。

由于人为排放臭氧消耗物造成的平流层臭氧减少在短波波段有正的辐射强迫(增加了到对流层的辐射通量),而在长波波段有负的辐射强迫。在较低的平流层中长波效应往往较大,而在较高的平流层中短波效应占主导地位。因此,平流层臭氧损耗的净辐射强迫是正是负取决于垂直廓线的变化。WMO(2010)对 1979 年至 2005 观测到的臭氧变化和多个模式模拟的从 20 世纪 70 年代至 2004 年年平均的辐射强迫进行了评估[10]。观测和模式模拟的平均臭氧变化所产生的辐射强迫的符号不同。大气化学模式比较计划 ACCMIP(Atmospheric Chemistry Climate Model Intercomparison Project)中具有平流层化学的模式算出臭氧变化的辐射强迫为 $-0.05 \pm 0.2$ W/m$^2$,这一结果与 WMO (2010)的模拟结果相一致[33,34]。Forster 等(2007)[35]观测得出 1979 至 1998 期间臭氧辐射强迫为 $-0.05$ W/m$^2$。Hansen 等(2005)[36]从 1979 年至 1998 年的观测数据中得到平流层的臭氧辐射强迫有 $-0.05 \pm 0.1$ W/m$^2$ 的增加趋势,其中甲烷氧化所产生的平流层水汽的辐射强迫为 $0.07 \pm 0.05$ W/m$^2$。自从政府间气候变化委员会(简称 IPCC; intergovernmental panel on climate change)第一次评估报告就开始对平流层和对流层的臭氧辐射强迫有一些初步的研究,到目前 WMO(2010)平流层臭氧评估报告中用多模式的研究平流层臭氧的辐射强迫,同时 ACCMIP 利用多模式也对平流层与对流层臭氧的辐射强迫有了进一步的研究,其结果为:臭氧总量的辐射强迫($RF$)是 $0.30 \pm 0.2$ W/m$^2$[10];根据高度或强迫因子的不同得到对流层臭氧 $RF = 0.40 \pm 0.2$ W/m$^2$,平流层臭氧 $RF = -0.10 \pm 0.15$ W/m$^2$;或臭氧前体物 $RF = 0.50 \pm 0.2$ W/m$^2$,臭氧层 $RF = -0.20$ ($-0.3$ ~ $0.0$) W/m$^2$[31,37]。

### 1.2　对流层臭氧

对流层臭氧是一种短寿命的痕量气体,来源于平流层的下传或者对流层自然和人为的前体物质的光化学反应。对流层臭氧的化学源和汇的估计不明朗,化学因素净产生的臭氧量(产生减去消耗)约每年为 300 Tg[38]。自从 IPCC 第四次评估报告[29]以来,由于烃化物的加入模拟全球臭氧的产生与消耗的结果出现了持续性的增长。在为第四次 IPCC 评估报告进行的大气成分变化-欧洲网络优秀多模式研究(简称 ACCENT -AR4:atmospheric composition change,the european network of excellence multi-model study for the fourth Assessment report)中模式模拟得到对流层顶传输进入对流层的臭氧净流量为每年 636 ± 273 Tg[39],而同时地表臭氧沉积量估计是在每年 902 ± 255 Tg 的范围内[40]。对流层臭氧是一种重要的气候影响因子,另外地面臭氧浓度的升高还会影响人类和植被健康。经观测得到的地表臭氧含量从热带太平洋地区上空的不到 $10 \times 10^{-6}$(ppb)至高排放地区的下风向地区超过 $100 \times 10^{-6}$(ppb)。对流层中臭氧的寿命受到季节和地点的强烈影响:它在热带边界层可能只有 1 天,而对流层上层可高达 1 年,全球臭氧的平均寿命约 25 天[41]。由于对流层臭氧平均寿命只有几个星期,缺乏长期测量,使得评估全球臭氧变化的长期趋势具有很大的难度。由于人类活动排放的臭氧前体物的增加,从工业革命以来,全球对流层臭氧浓度显著升高,其全球年平均辐射强迫效应仅次于二氧化碳和甲烷的效应。另外,欧洲和北美地区对流层臭氧浓度已经经历了长时间的显著上升过程,目前虽然上升速度有所减缓,但上升趋势并没有扭转。与此同时,其它经济快速发展地区,臭氧浓度上升趋势也显现出来。考虑到这些地区经济发展的潜力和能源消耗增长的速度,21 世纪的对流层臭氧水平将可能进一步上升。ACCMIP 估计对流层臭氧从 1850 年至 2000 年间增加了约 98 Tg[35]。自从 2000 年以来,模式评估的全球年平均对流层量约为 330 ± 50 Tg,对流层顶定义的不同造成模式间的差异约为 10%[42]。卫星观测得到在热带中纬度地区对流层臭氧柱含量北半球比南半球更大。在北半球,臭氧高峰期在夏季,在 35°N ~40°N 的纬度带上臭氧浓度增加最为明显,从美国东部一直延伸到欧洲南部,从东亚延伸到北太平洋西部。在南半球,高峰出现在 25°S ~30°S 的春季,从巴西东至澳大利亚的带状范围内[43]。在少数的对流层臭氧柱含量趋势分析中,Beig 和 Singh (2007)[44]分析 1979 年至 2005 年太平洋的观测资料,没有发现对流层臭氧柱含量有太多的变化趋势,但在南大西洋的热带、印度、中国南部、东南亚、印尼和中国北部下风向等广大地区发现了显着增加的趋势。

ACCMIP 估计从 1850 年至 2000 年平均的对流层臭氧辐射强迫为 0.34 W/m$^2$。Skeie 等(2010)[45]发现从 1750 年至 1850 年的工业革命前对流层臭氧的辐射强迫为 0.04 W/m$^2$。归一化的辐射强迫(NRF,normalized radiative forcing)表示臭氧柱辐射强迫的改变,单位为 W × m − 2 × DU − 1 或 W × mol − 1。NRF 对于臭氧浓度的垂直变化较敏感,对于臭氧纬度变化敏感度较小。Stevenson 等(2012)[36]和 Søvde 等(2012)[46]给出了臭氧的 NRF 为 0.041 ± 0.005 W × m$^{-2}$ · DU$^{-1}$(83 W · mol$^{-1}$)值稍低于 IPCC 第三次评估报告中给出的 0.042 W · m$^{-2}$ × DU$^{-1}$(94 W · mol$^{-1}$)。还有一小部分研究集中在人类活动排放物所造成的臭氧浓度及辐射强迫的变化。Søvde 等(2012)[46]报告了对流层臭氧辐射强迫为 0.38 W/m$^2$,其中臭氧前体物辐射强迫贡献为 −0.06 W/m$^2$ 而平流层臭氧耗损对对流层辐射强迫贡献为 0.44 W/m$^2$。Shindell 等(2012)[47]计算得到消耗臭氧物质对对流层臭氧辐射强迫的贡献是 −0.08 ~0.10 W/m$^2$ 之间。Stevenson 等(2012)[32]估计 1750 至 2010 年对流层臭氧辐射强迫为 0.40 W/m$^2$。其中甲烷、氮氧化物、一氧化碳和挥发性有机化合物的排放所造成的辐射强迫分别为 0.19 W/m$^2$,0.12 W/m$^2$,0.06 W/m$^2$ 和 0.04 W/m$^2$。

国内科学家在观测、模式研究等方面开展了我国对流层臭氧及其前体物的大量研究工作,周秀骥(2004)[48]建立了二维空气质量模型来研究长三角地区臭氧的分布和变化。廖宏和常文渊等人[49—51]模拟得出对流层臭氧在大气层顶的辐射强迫为 +0.53 W/m$^2$,而在地表的辐射强迫是 +0.07 W/m$^2$。江芳等(2007)[52]研究了云顶以下臭氧对 TOMS 反演臭氧总量的影响。郑永光等(2008)[53]利用 NCEP 再分析资料、日本 GMS −5 地球静止卫星水汽云图资料对中国南部对流层中上层臭氧浓度的影响进行了详细分析,结果表明臭氧垂直廓线的多个极小与极大值,对流层中上层位势涡度分布以及卫星水汽图像分析都表明大气中的多尺度运动对臭氧垂直分布特征有显著影响。周艳明等人(2008)[54]对广州市城区边界层臭氧浓度进行了分析,发现臭氧的日平均浓度与 PM10 和气温有正相关而与 $NO_X$、NO、CO 存在负相关。徐晓斌等(2010)[55]用卫星数据分析了我国全境及不同区域对流层臭氧柱含量,结果表明对流层臭氧柱含量在夏季有微弱的上升趋势,其他季节呈下降趋势,但总体变化趋势并

不显著。王永等人(2012)[56]利用臭氧无线电探测仪的探测资料和大尺度化学模式对 2000 ~ 2010 年北京地区臭氧变化趋势尽享了分析,发现在过去的十年间北京地区对流层春季和夏季的臭氧浓度主要是由光化学作用所控制。白建辉等人(2008)[57]利用兴隆站的观测资料获得了臭氧等气体组分浓度发现臭氧在 6 月、9 月出现高值。

## 2 臭氧观测

地基和卫星观测是监测大气臭氧总量的主要平台。1978 年 Nimbus-7 卫星的 TOMS (Total Ozone Mapping Spectrometer)和 SBUV(Scatter Backward Ultra-Violet)仪器正式提供臭氧总量产品。在过去 30 年里,卫星臭氧总量观测仪器已经从固定波长狭缝型光谱观测转变到高分辨率紫外-可见光波段的连续光谱观测,前者代表性的仪器是 TOMS 系列和 SBUV,我国已经发射的风云三号卫星臭氧总量观测就是采取这种仪器。后者包括了 GOME(Global Ozone Monitoring Experiment),SCIAMACHY (Scanning Imaging Absorption spectrometer for Atmospheric Chartongraphy) 和 OMI(Ozone Monitoring Instrument)。在反演方法上,也从不断改进 TOMS 反演方法逐步过渡到 TOMS 和 DOAS ( Differential Optical Absorption Spectroscopy)并存的局面。潘亮和牛生杰(2008)[58]对 AIRS(Atmospheric Infrared Sounder)/TOVS(The TIROS Operational Vertical Sounder)/TOMS 反演的臭氧总量进行了对比分析,指出 TOMS 在赤道地区反演值比 AIRS 和 TOVS 的反演值高;在其它地区,TOMS 的反演值低于 AIRS 和 TOVS 的反演值;AIRS 的反演值相对较高,在南北纬 50°之外,特别是在南极地区,出现了很明显的偏差。云的出现使得后向紫外散射增强,因此,不可避免的给基于卫星后向紫外散射测量所反演的臭氧总量精确度带来了干扰。随着 TOMS 卫星版本的不断升级,考虑了云对臭氧的影响,提高了臭氧总量数据的精度。郑向东(2008)[59]根据卫星和地基观测,比较了自 1979 年以来我国香河、昆明、瓦里关和龙凤山四个站点臭氧总量的变化。结果表明卫星与地基观测的臭氧总量长期变化趋势比较一致,但是卫星与地基各自观测的值仍存在着显著的差别。江芳等(2009)[60,61]在反演臭氧方面做了许多深入的研究,得出:云的出现使得云顶以下,特别是云内光程增强,导致紫外波段的臭氧吸收衰减增大,造成反演偏大,并且云上臭氧误差和云下臭氧误差比较大,且两者总是相互叠加在一起,他们的研究结果有利于臭氧反演精度的提高。我国大陆地区分别从 1979, 1980 年利用 Dobson 光谱仪正式在香河、昆明开展了臭氧总量观测; 20 世纪 90 年代我国又在青海瓦里关、黑龙江龙凤山、浙江临安和南极中山站利用 Brewer 光谱仪开展臭氧总量及垂直分布的反演观测,同时也在拉萨进行短期地基臭氧总量观测以验证青藏高原的“臭氧低谷”分布[62,63]。陶玉龙等人(2010)[64]用 FY-3 SBUS 数据和 NOAA SBUV/2 臭氧的垂直廓线数据进行对比研究,结果表明两组数据具有较好的相对偏差。

## 3 人类活动对臭氧的影响

地面臭氧浓度的增加会对人体健康及动植物的生长造成一系列负面影响,甚至严重威胁生态系统的平衡。起初人们认为这主要是平流层臭氧向下输送造成的,最近的研究表明低层大气中的光化学反应也是臭氧的一个重要来源。臭氧的化学性质十分的活泼,很容易和其他物质发生化学反应,氮氧化物、可挥发性有机化合物($VOC_s$)、甲烷、水汽、气溶胶等物质都会对臭氧产生显著的影响。氮氧化物与可挥发性有机化合物($VOC_s$)是光化学反应过程中生成臭氧的首要前体物,臭氧生成量和生成速率不仅与氮氧化物 、可挥发性有机化合物的浓度有关,还与其比值($VOC_s$/ $NO_X$)有很强的非线性关系。国内外研究表明[65,66]:在低氮氧化物条件下(氮氧化物控制区),臭氧浓度随一氧化氮的增加而增加,而可挥发性有机化合物浓度改变对臭氧影响不大; 在高氮氧化物条件下(可挥发性有机化合物控制区),氮氧化物的增加会引起臭氧浓度的降低,可挥发性有机化合物的增大会使臭氧浓度升高。Ravishankara(2009)[67]研究表明未来的一百年内,一氧化二氮是影响臭氧浓度最主要的气体。对一氧化二氮的控制不但可以使臭氧层得到恢复,同时也可以减少人为辐射强迫。可挥发性有机化合物早期的研究主要侧重于工业源、交通源等人类活动产生的污染源。近年来研究发现[68],自然源排放的可挥发性有机化合物( 生物可挥发性有机化合物,主要是异戊二烯)也不容忽视。西方科学家[69]利用数值模式研究了生物可挥发性有机化合物对地面臭氧形成的影响,指出生物可挥发性有机化合物在臭氧生成过程中起重要作用。屈玉等(2009)[70]采用因子分离方法和改进后的区域空气质量模式(RAQM,Regional Air Quality Model)计算了人为氮氧化物( 氮氧化物 = 一氧化氮 + 二氧化氮)、人为可挥发性有机化合物($AVOC_s$)以及生物可挥发性有机化合物($BVOC_s$)对春季东亚地区地面臭氧浓度的协同贡献及总贡献,同时平流层臭氧对氮氧化物具有非线性的影

响[71]。漏嗣佳等(2010)[72]利用 GEOS(Goddard Earth Observing System)化学模式进行数值试验,研究中国地区氮氧化物和两类可挥发性有机化合物对臭氧质量浓度分布及其化学机理的影响表明,控制地面臭氧质量浓度时,中国西部主要考虑氮氧化物的减排,东部 35°N 以北主要考虑人为可挥发性有机化合物的减排,而 30°~35°N 应同时考虑人为可挥发性有机化合物和生物可挥发性有机化合物的减排,在 30°N 以南的地区,则需要全面考虑氮氧化物和可挥发性有机化合物的减排。甲烷对臭氧的变化有着双重的影响,一方面甲烷在平流层被氧化生成水汽,并进一步形成氢氧根(OH),它有利于臭氧损耗;另一方面,甲烷是氯原子的汇,甲烷和氯原子反应生成稳定的盐酸并沉降出平流层,从而有利于臭氧恢复,两方面总的效应是有利于臭氧恢复。Jason(2007)[73]利用三维全球臭氧大气化学模式(MOZART-2:model for ozone and related chemical tracers)和中层大气通用气候模式(CCM - MACCM3:community climate model-middle atmosphere community climate model)耦合发现通过改变甲烷的浓度来实现长期的地表臭氧变化,会导致氮氧化物与一氧化碳浓度的减小。在研究臭氧时,还应该重视水汽的作用。自然界中水汽造成的臭氧损失约占其自然损失的 30% ~40%,水汽在近地面臭氧化学、光化学过程中同样具有重要作用。实际上,对流层臭氧的破坏和氢氧根自由基的产生过程与水汽和紫外线是密不可分的。田文寿等(2009)[74]研究发现在化学方面,水汽增加 2 ppmv 会引起全球平均臭氧柱含量降低 1.5 DU,在辐射方面,增加 $2\times10^{-6}$(ppmv)水汽会导致全球臭氧柱含量增加 4.8 DU。同样值得关注的是,发生在气溶胶表面的非均相过程对臭氧具有明显影响。研究表明,平流层硫酸盐气溶胶、极地平流层云等通过非均相化学反应对臭氧的损耗起着重要作用。季节性的生物体燃烧会导致南大西洋、非洲南部、南美洲、东南亚以及香港等地区对流层中下层的臭氧增加。生物体燃烧释放大量燃烧产物如一氧化碳、二氧化碳、甲烷、非甲烷碳氢化合物(NMHC)和氮氧化物等到大气中,这些化学物质在太阳光的作用下能够生成高浓度的臭氧。郑永光等(2004)[75]发现东南亚地区的生物体燃烧产物能够使得昆明、香港等地的对流层中下层臭氧浓度升高。郑永光(2007)[76]还使用 NCEP(national centers for environmental prediction)分析资料、中尺度数值模式 MM5 模拟的大气环流数据、卫星观测的东南亚地区的生物体燃烧状况、气溶胶指数等资料,分析了生物体燃烧产生的烟尘轨迹,结果发现:昆明对流层低层高浓度的臭氧来源于有生物体燃烧的南亚地区。人为排放臭氧前体物的变化趋势与该地区的台站观测到臭氧的变化趋势并不一致。东亚是人为排放前体物增长最快的地区,几乎所有东亚地表测站都观测到臭氧浓度的增加。然而,虽然在美国西部人为排放量少,春季沿海农村地区的网站和许多内陆农村的站点都能观测到臭氧浓度的增加,可能是由于这些台站位于亚洲下风向[77],来自亚洲臭氧输送引起。而在美国东部近一半的农村网站臭氧浓度在冬季增大,造成该现象的原因还未知。在欧洲,从 20 世纪 50 年代到大约 2000 年的臭氧浓度一直处在增加的趋势中。在欧洲和北美人为排放前体物的不断增加直到 20 世纪 80 年代,然后趋于稳定,在 20 世纪 90 年代开始下降,但在 20 世纪 90 年代欧洲臭氧的浓度出乎意料的增加[78]。

## 4　臭氧研究的不足和展望

现阶段关于臭氧的研究还存在很多问题有待解决,无论是从观测、模拟还是理论研究都有待改进。对流层臭氧也随海拔高度变化,其性质难以用卫星反演来进行评估。目前,在地表和自由对流层的具体高度上,臭氧浓度变化的长期趋势只能从高质量站点的外场测量中得到。很多站点都只是集中在少数地区,而大多数地区,特别是在热带和南半球站点分布稀疏。在未来的研究中,模式必须包含完整平流层以及考虑平流层辐射和动力因素与大气化学之间的耦合,同时在对未来臭氧恢复的研究过程中应该更加重视水汽的作用。在模式模拟全球气候效应的时候,臭氧的精确模拟也是决定模拟结果精度的重要因素。Aghedo(2006)[79]利用四种化学气候模式(AM2-Chem, CAM-Chem, ECHAM5-MOZ 和 GISS-PUCCINI)模拟对流层臭氧的瞬时辐射强迫,他们的研究表明模式中精确模拟臭氧的空间分布和量级是非常重要的,因为如极地对流层顶看到的,高浓度的臭氧产生较大的瞬时辐射强迫,也许会弥补出射长波辐射(OLR)对臭氧的低敏感度。一方面温室气体增加的辐射效应是造成地面和对流层变暖,但它却导致平流层变冷,而另一方面,事实表明平流层臭氧有可能在 21 世纪恢复到 1979 年以前的水平,臭氧恢复的直接辐射效应将导致平流层变暖。胡永云等(2011)[80]利用 IPCC-AR4 模式与大气化学模式相耦合模拟发现,考虑到臭氧恢复现象,在 21 世纪上半叶对流层的增温现象更加明显。温室气体增加和臭氧恢复如何影响平流层和对流层的温度变化还需要给予进一步的研究。

## 参 考 文 献


1 Lin L, Fu Q, Zhang H, *et al*. Upward mass fluxes in tropical upper troposphere and lower stratosphere derived from radiative transfer calculations. Journal of Quantitative Spectroscopy & Radiative Transfer, 2012;117 (2013) :114—122

2 马鹏里,张 强,杨兴国,等. 大气化学研究进展-臭氧、气溶胶研究综述. 干旱气象,2003;21(4) :66—70

3 Hu Y, Xia Y, Fu Q. Tropospheric temperature response to stratospheric ozone recovery in the 21st century. Atmos Chem Phys, 2011;(11) : 7687—7699

4 贾 龙,葛茂发,徐永春,等. 大气臭氧 化学研究进展. 化学进展, 2006;18(11) :1565—1574

5 纪 飞,秦 瑜. 对流层臭氧 研究进展. 气象科学,1998(4) : 17—24

6 胡永云. 平流层极地臭氧损耗影响对流层气候的研究进展. 北京大学学报(自然科学版),2006;42(5) :561—568

7 王革丽,吕达仁,杨培才. 人类活动对大气臭氧 层的影响. 地球科学进展,2009;24(3) :331—337

8 Polvani L M. Stratospheric ozone depletion: the main driver of twentieth-century atmospheric circulation changes in the southern hemisphere. American Meteorological Society, 2011:795—812

9 Jacob D J. Effect of climate change on air quality. Atmospheric Environment, 2009;(43) :51—63

10 World Meteorological Organization Global Ozone Research and Monitoring Project, Report No. 52 , Scientific Assessment of Ozone Depletion: 2010

11 朱乾根,郭品文. 北半球春季大气臭氧变化特征及其对大气温度和环流场的影响. 应用气象学报,2000;11(4) : 448—454

12 张金强,王振会. 臭氧总量的纬度带变化特征分析. 科技信息, 2007;16:1—2

13 吴国雄,李建平,周天军,等. 影响我国短期气候异常的关键区: 亚印太交汇区 . 地球科学进展,2006;21(11) : 1109—1118

14 郭世昌,常有礼,张利娜. 北半球中纬度地区大气臭氧的年际和年代际变化研究 . 大气科学,2007;31(3) : 418— 424

15 魏鼎文,赵延亮,秦 芳,等. 中国北京和昆明地区大气臭氧层的异常变化. 科学通报,1994;39(16) : 1509—1511

16 韦惠红. 我国臭氧总量的时空分布特征。南京气象学院学报, 2006;29(3) :390—395

17 周秀骥,罗 超,李维亮,等. 中国地区臭氧总量变化与青藏高原低值中心. 科学通报,1995;40(15) :1396—1398

18 Bian J C. Features of ozone mini-hole events over the Tibetan Plateau. Adv Atmos Sci,2009;26(2) :305—311

19 Liu C, Liu Y, Cai Z, *et al*. Dynamic formation of extreme ozone minimum events over the Tibetan Plateau during northern winters 1987—2001, J Geophys Res,2010,115(D18) :311—325

20 Zou Han, Ji Chongpi, Zhou Libo, *et al*. ENSO signal in total ozone over tibet. Advances in Atmospheric Sciences, 2011; 18 (2) : 231—238

21 Liu Yi, Wang Yong, Liu Xiong, *et al*. Tibetan middle tropospheric ozone minimum in June discovered from GOME observations. Geophysical Reseapch Letters, 2009;36(5) : 814—820

22 史久恩,周秀骥,任福民. 中国地区大气臭氧 变化的若干特征. 中国地区大气臭氧 变化及其对气候环境的影响(一),北京: 气象出版社,1996: 239—245

23 Liu Yi, Lu Chunhui, Wang Yong. The quasi-biennial and semi-annual oscillation features of tropical $O_3$, $NO_2$, and $NO_3$ revealed by GOMOS satellite observations for 2002—2008. Chinese Science Bulletin, 2011;56(18) :1921—1929

24 胡永云,夏 炎,高 梅,等. 21 世纪平流层温度变化和臭氧恢复. 气象学报,2008;66(6) :880—891

25 Hu Y, Fu Q. Stratospheric warming in southern hemisphere high latitudes since 1979. Atmos Chem Phys,2009,9: 4329—4340

26 王卫国,樊雯璇,吴 洞,等. 全球平流层-对流层之间臭氧通量的时空演变研究. 地球物理学报,2006;49: 1595—1607

27 胡春娟. 南极高空臭氧 含量减少对平流层温度场影响的数值模拟. 西北大学学报: 自然科学版,2007;37(3) : 479—482

28 Hu Yongyun, Xia Yan, Gao Mei, *et al*. Stratospheric temperature changes and ozone recovery in the 21st century. Acta Meteor. Sinica,2009; 23(3) :263—275

29 陈月娟,易明建,毕 云,等. 平流层微量气体变化趋势的研究。地球科学进展,2009;24(3) :308—319

30 施春华,郑 彬,陈月娟. 平流层臭氧 对地表有机氯排放的多耦合响应. 大气科学学报,2009;32(4) : 522—529

31 William J R. Global variations of zonal mean ozone during Stratospheric warming events. J Atmos Sci,1993; 50: 3308—3321

32 Liu Y, Liu C X, Wang H P, *et al*. Atmospheric tracers during the 2003—2004 stratospheric warming event and impact of ozone intrusions in the troposphere. Atmospheric Chemistry and Physics,2009; 9: 2157—2170

33 Conley A J, Lamarque J F, Vitt F, *et al*. PORT, a CESM tool for the diagnosis of radiative forcing. Geos Model Devel, 2012

34 Stevenson D S, Young P J, Naik V, *et al*. Tropospheric ozone changes, attribution to emissions and radiative forcing in the atmospheric chemistry and climate model intercomparison project (ACCMIP). ACP/GMD Inter-Journal SI,2012

35 Forster P, Ramaswamy V, Artaxo P, *et al*. Changes in Atmospheric Constituents and in Radiative Forcing. Climate Change 2007: The Physical Science Basis. Contribution of Working Group I to the Fourth Assessment Report of the Intergovernmental Panel on Climate Change , Cambridge University Press, 2007

36 Hansen J, Sato M, Ruedy R, *et al*. Efficacy of climate forcings. Journal of Geophysical Research-Atmospheres, 2005, 110, D18

37 Skeie R, Berntsen T, Myhre G, Tanaka K, *et al*. Anthropogenic radiative forcing time series from pre- industrial times until 2010. Atmospheric Chemistry and Physics, 2011;11:11827— 11857

38 IPCC. Climate Change 2007: The Physical Science Basis. Working Group I Contribution to the Intergovernmental Panel on Climate Change Fourth Assessment Report. Solomon S, Qing D H, *et al*. Eds. , Cambridge University Press, Cambridge, United Kingdom and New York, NY, USA, 2007

39 Young P J, Archibald A T, Bowman K W, *et al*. Preindustrial to end 21st century projections of tropospheric ozone from the Atmospheric Chemistry and Climate Model Intercomparison Project (ACCMIP). Atmos Chem Phys,2013;13:2063—2090

40 Wu S L, Mickley L J, Jacob D J, *et al*. Why are there large differences between models in global budgets of tropospheric ozone? Journal of Geophysical Research-Atmospheres, 2007; 112 (D05) : 302—320

41 Stevenson D S, Dentener F J, Schultz M G, *et al*. Multimodel en-

semble simulations of present-day and near-future tropospheric ozone. Journal of Geophysical Research-Atmospheres,2006, 111, D8

42 Wild O. Modelling the global tropospheric ozone budget: exploring the variability in current models. Atmospheric Chemistry and Physics,2007;7 :2643—2660

43 Ziemke J R, Chandra S, Labow G J, *et al*. A global climatology of tropospheric and stratospheric ozone derived from Aura OMI and MLS measurements. Atmos Chem Phys, 2011; 11 (17): 9237—9251

44 Beig G, Singh V. Trends in tropical tropospheric column ozone from satellite data and MOZART model. Geophys Res Lett, 2007; 34 (17)801—806

45 Skeie R, Berntsen T, Myhre G, *et al*. Anthropogenic radiative forcing time series from pre-industrial times until 2010. Atmospheric Chemistry and Physics,2011;11:11827—11857

46 Sovde O, Hoyle C, Myhre G, *et al*. The $HNO_3$ forming branch of the $HO_2$ + NO reaction: pre -industrial-to-present trends in atmospheric species and radiative forcing s. Atmospheric Chemistry and Physics, 2011; 11: 8929— 8943

47 Shindell D, Faluvegi G, Nazarenkno L, *et al*. Attribution of historical whole atmosphere ozone forcing to anthropogenic emissions. Nature Climatic Change,2013;6(3):567—570

48 周秀骥. 长江三角洲低层大气与生态系统相互作用. 北京:气象出版社,2004: 130—146

49 Chang Wenyuan, Liao Hong, Wang Huijun. Climate responses to direct radiative forcing of anthropogenic aerosols, tropospheric ozone, and long-lived greenhouse gases in eastern China over 1951—2000. Advances in Atmospheric Sciences, 2009; 26(4):748—762

50 Chang Wenyuan, Liao Hong. Anthropogenic direct radiative forcing of tropospheric ozone and aerosols from 1850 to 2000 estimated with IPCC AR5 emissions inventories. Tmospheric and Oceanic Science Letters, 2009; 2(4): 201—207

51 Liao Hong, Seinfeld J H, Adams P J, *et al*. Global radiative forcing of coupled tropospheric ozone and aerosols in a unified general circulation model. Journal of Geophysical Research, 2004; 109(D16): 207—240

52 江　芳,王英鉴,刘振兴,等. 云顶以下臭氧对 TOMS 反演臭氧总量的影响及反演方法的理论研究. 地球物理学报,2007;50(2): 364—369

53 郑永光,陈　炯,陈尊裕,等. 中国南部对流层中上层臭氧增加的气象场判识及臭氧 变化的多尺度特征. 地球物理学报,2008;51(3):668—681

54 周艳明,刘厚凤,吴保庆. 边界层臭氧浓度变化特征及相关因子分析. 气象与环境学报,2008;24(1): 63—66

55 徐晓斌,林伟立. 卫星观测的中国地区 1979—2005 年对流层臭氧变化趋势. 气候变化研究进展,2010;6(2):100—105

56 Wang Y, Konopka P, Liu Y, *et al*. Tropospheric ozone trend over Beijing from 2002—2010: ozone sound measurements and modeling analysis. Atmos Chem Phys, 2012, 12, 8389—8399

57 白建辉,王普才,王庚辰. 北京周边地区主要微量气体的基本特征. 科学技术与工程,2008;(9):2323—2330

58 潘　亮,牛生杰. AIRS/TOVS/TOMS 反演的臭氧总量的对比分析. 遥感学报,2008;12(1):54—63

59 郑向东. 云对中国区域卫星观测臭氧总量精度影响的检验分析. 大气科学,2008;32(6): 1431—1444

60 江　芳. 云顶高度对紫外辐射反演臭氧总量的影响. 高原气象,2009;28(3):647—651

61 江　芳. 紫外线后向散射探测臭氧总量的反演误差研究. 空间科学学报,2010;30(1):35—42

62 王革丽, 杨培才. 平流层臭氧对人类活动排放氯化物及氮氧化物的非线性响应. 地球物理学报, 2007;50(1): 5 1—57

63 肖钟湧,江　洪. 利用遥感监测青藏高原上空臭氧总量 30 a 的变化. 环境科学,2010;31(11):2569—2574

64 陶玉龙,陈胜波,张恭正,等. FY-3 SBUS 数据和 NOAA SBUV/2 数据对比研究. 科学技术与工程,2010;10(5):1118—1123

65 Solomon P, Cowling E, Hidy G, *et al*. Comparison of scientific findings from major ozone field studies in North America and Europe. Atmospheric Environment,2000;34: 1885—1920

66 朱　彬,安俊岭,王自发,等. 光化学臭氧日变化特征与其前体物关系的探讨. 南京气象学院学报,2006;29 (6): 744—749

67 Ravishankara A R. Nitrous oxide ($N_2O$): the dominant ozone-depleting substance emitted in the 21st century. Science, 2009; 326: 123—125

68 Guenther A, Geron C, Pierce T, *et al*. Natural emissions of non-methane volatile organic compounds, carbon monoxide, and oxides of nitrogen from North America. Atmospheric Environment, 2000; 34: 2205—2230

69 Tao Z, Larson S M, Wuebbles D J, *et al*. A summer simulation of biogenic contributions to ground-level ozone over the continental United States. J Geophys Res, 2003, 108(D14):4404—4419

70 屈　玉,安俊岭,周　慧,等. 人为和生物排放量对春季东亚地面臭氧 的协同贡献. 大气科学,2009;33(4): 670—680

71 陶玉龙. 青藏高原地区大气臭氧时空变化及其温度响应研究. 吉林大学,2010

72 漏嗣佳,朱　彬,廖　宏. 中国地区臭氧前体物对地面臭氧 的影响. 大气科学学报,2010;33(4): 451—459

73 West J J. Ozone air quality and radiative forcing consequences of changes in ozone precursor emissions. Geophysical Research Letters,2007;34(6):806—811

74 Tian W S, Chipperfield M P, lu D R. Impact of increasing stratospheric water vapor on ozone depletion and temperature change. AdvAtmos Sci,2009;26(3): 423—437

75 郑永光,朱佩君,陈尊裕,等. 2001 年春季东南亚地区生物体燃烧对华南地区对流层中下层臭氧浓度影响的个例分析. 地球物理学报,2004;47((5): 767—775

76 郑永光. 南亚地区生物体燃烧对昆明地区对流层中下层臭氧 浓度的影响. 北京大学学报(自然科学版),2007;43(3):330—337

77 Cooper O R. Long-term ozone trends at rural ozone monitoring sites across the United States, 1990—2010. J Geophys Res, 2012; 117 (D22):307—331

78 Logan J A, Staehelin J, Megretskaia I A, *et al*. Changes in ozone over Europe since 1990: analysis of ozone measurements from sondes, regular Aircraft (MOZAIC), and alpine surface sites. Journal Geophysical Research,2012;117(D9):301—324

79 Aghedo A M. The vertical distribution of ozone instantaneous radiative forcing from satellite and chemistry climate models. Journal of Geophysical Research, 2011; 116(D1):305—321

80 Hu Y, Xia Y, Fu Q. Tropospheric temperature response to stratospheric ozone recovery in the 21st century. Atmos Chem Phys, 2011;11:7687—7699

# Main Progresses in the Research on Ozone

XIE Bing[1,2], ZHANG Hua[2]

(Key Laboratory for Semi-Arid Climate Change of the Ministry of Education, College of Atmosphere Science, Lanzhou University[1], Lanzhou 730000, P. R. China;
Laboratory for Climate Studies, National Climate Center, China Meteorological Administration[2], Beijing, 100081, China)

[**Abstract**] Tropospheric Ozone is a very important greenhouse gas and its global distribution is affected by human activities significantly. The radiative forcing (RF) of increasing tropospheric ozone will strengthen atmospheric greenhouse effect and the depletion of stratospheric ozone will reduce ultraviolet radiation absorption, which is negative RF leading to stratospheric cooling. Therefore, change in the concentration of atmospheric ozone and its impact on the climate has become a key issue. The decrease in the concentration of stratospheric ozone was found between late 1950s and the 1970s. In 1985, the observation of the stratospheric ozone hole at 60°S made by British Antarctic Expedition raised attentions and studies around the word. Currently, the concentration of ozone is still increasing in the troposphere and declining in the stratosphere, thus ozone plays different roles in the troposphere and stratosphere temperature change. Therefore, observations of tropospheric and stratospheric ozone concentration are still hot topics. This paper will overview studies on atmospheric ozone briefly over the past five years, including tropospheric and stratospheric ozone concentration, ozone observation, the impact of human activities and the insufficiency of current ozone researches.

[**Key words**] atmospheric ozone troposphere stratosphere progresses

杨冰韵, 张华, 彭杰, 等. 利用 CloudSat 卫星资料分析云微物理和光学性质的分布特征[J]. 高原气象, 2014, 33(4): 1105－1118, doi: 10.7522/j.issn.1000-0534.2013.00026.

# 利用 CloudSat 卫星资料分析云微物理和光学性质的分布特征

杨冰韵[1-3], 张 华[2], 彭 杰[4], 王志立[1], 荆现文[2]

(1. 中国气象科学研究院, 北京 100081; 2. 中国气象局 气候研究开放实验室/国家气候中心, 北京 100081; 3. 国家卫星气象中心, 北京 100081;
4. 上海市气象局上海气象科学研究所, 上海 200030)

**摘要**: 利用 2007 年 1 月－2010 年 12 月高垂直分辨率 CloudSat 卫星的 2B 数据产品, 对云微物理特征量(包括云中液态水/冰水含量、液态水/冰水路径、云滴有效半径等)以及云光学参数(云光学厚度等)的全球分布和季节变化进行了统计分析, 并研究了云微物理性质对光学性质的影响。结果表明, 冰水路径分布在北美南部、南美大陆、非洲大陆、澳大利亚和南亚的陆地上空, 以及太平洋、大西洋和印度洋的洋面上空, 高值区最大值达 600 g·m$^{-2}$以上; 垂直方向上, 高值区位于赤道地区 8 km 附近以及中纬度地区 4～8 km 高度上。液态水路径在 300 g·m$^{-2}$以上的高值区主要位于太平洋、印度洋和大西洋的中低纬度海域上空, 垂直上液态水含量随高度递减。冰云有效半径在高纬度地区近地面层达 200 μm 以上, 在赤道附近 4～8 km 上有 1 个高值区, 南北半球中纬度地区 2～4 km 上有 2 个高值区, 最大值均达到 80 μm 以上。在 1 km 以下的边界层水云有效半径值较大, 达到 12 μm 以上。总云光学厚度在全球大部分地区 <40, 高值区普遍位于中高纬度的广阔地区和低纬度靠近大陆的洋面上空; 垂直方向上, 云光学厚度的高值集中在 2 km 以下的边界层。云光学厚度的分布受云量、云水含量和云滴有效半径的影响, 云量大的地区基本为云光学厚度的大值区。

**关键词**: CloudSat; 云光学厚度; 云滴有效半径; 云水含量

**文章编号**: 1000-0534(2014)04-1105-14 **中图分类号**: P426.5 **文献标志码**: A

**doi**: 10.7522/j.issn.1000-0534.2013.00026

## 1 引言

地球上超过 50% 的区域都覆盖着云, 云是地气系统中辐射收支最重要的调节器[1]。云可以通过直接影响大气中长波和短波辐射的传输, 调节全球或局地的总能量收支和能量在大气层中的垂直分布, 从而影响全球和区域气候[2-6]。与此同时, 全球气候的变化也会引起云的调整, 如云量及其分布、云的高度、云光学厚度、云水含量和云的微物理特性等因子。因此, 研究云的各种物理特性, 对深入了解云、辐射和气候之间复杂的相互作用, 进而更好地认识气候变化有着极为重要的意义。

国际上对于云的观测手段包括地面观测、飞机观测、轮船观测和卫星观测等[7]。卫星观测由于具备覆盖范围广、重复率高、客观真实性强、云参数完备、信息源可靠等诸多优势, 成为目前云研究中越来越重要的手段之一[8-10]。太阳极轨卫星作为观测卫星中的一种, 其观测能够覆盖全球大部分区域, 在研究大尺度特别是全球范围内云特性时有很大的优势。以往卫星观测仅提供云顶信息, 而对云内部及三维结构信息非常有限, 因此无法了解云整体变化所需要的细节。CloudSat 是第一颗专门用于

**收稿日期**: 2012-05-30; **定稿日期**: 2013-03-06

**资助项目**: 国家重点基础研究计划课题(2011CB403405); 国家自然科学基金项目(41375080, 41075056, 41205116); 科技部公益性行业(气象)科研专项项目(GYHY201406023); 中国气象科学研究院基本科研业务费(2012Y003)

**作者简介**: 杨冰韵(1989－), 女, 河南南阳人, 硕士, 主要从事卫星遥感资料分析、云－辐射相互作用研究
E-mail: byyang0110@126.com

**通讯作者**: 张华. E-mail: huazhang@cma.gov.cn

观测云的太阳极轨卫星，其上搭载的 94 GHz 毫米波云廓线雷达(Cloud Profile Rada)具有垂直分辨率高的特点，可以实现对全球云三维结构的观测。

目前利用 CloudSat 卫星资料对云的研究主要集中于云的分布以及云的特征量分析两个方面。Kenneth et al[11]用 CloudSat 和 CALIPSO 的探测结果研究了全球范围内卷云的分布情况，结果发现全球平均卷云发生率为 16.7%，研究主要侧重于云的分布规律。Gerald et al[12]使用 CloudSat 的 2B－GROPROF 资料分析了全球降水的覆盖范围和发生率，结果发现降水在全球覆盖比例达 0.5，降水发生率的垂直分布也揭示了云与大气环流的密切联系，但研究主要侧重于云对降水等天气现象的影响。此外，还有一些研究通过与其他云探测卫星资料对比，进一步研究云参数的分布和物理规律。Patrick et al[13]通过分析 CloudSat 和 CALIPSO 资料研究了极地薄冰云中云参数的分布规律以及气溶胶分布，并进一步证实了气溶胶的间接效应，该工作涉及了气溶胶、云和辐射的相互作用，有助于进一步了解极地气候的变化；Dong et al[14]根据 Aura 卫星搭载的探测器 MLS 得到的资料计算了对流层高层的冰水含量，并与 CloudSat 资料进行对比。Dong et al[15]通过对比 MLS、CloudSat 和 ECMWF、MODIS、AMSU－B 等数据，分析了全球冰云的物理量参数分布情况。但是，这些研究侧重于比较不同卫星资料的差异，并没有系统地分析云物理量参数的空间和时间分布特点。相比之下，国内有关 CloudSat 的研究还较少，主要侧重于云量的分布方面。王帅辉等[16]分析了中国及周边地区的云垂直结构分布特征，并根据气候特征的地域差异从该区域选出 8 个子区域，逐区统计了云的垂直结构特征。彭杰等[17]对 CloudSat 卫星观测资料加以统计分析，将东亚地区划分为 5 个子区域，进一步细化了对东亚地区云的垂直分布特征。张华等[18]结合 CloudSat 资料分析了东亚地区云的垂直结构特征，计算了在气候模式的云辐射过程中表征云的垂直结构特征的抗相关厚度，为气候模式云辐射物理过程的改进提供了相关的卫星观测反演结果。李静等[19]利用 MODIS 卫星反演云水含量和云顶温度、CloudSat 反演云团雷达反射率因子和冰相粒子含量对降水云团的宏观特征及内部垂直结构特征进行分析，结果表明卫星监测得到的云团特征与降水区域对应较好，研究工作涉及云光学参数，但侧重于天气特征。

上述研究加深了对小尺度空间范围内云的空间分布及云团特征的理解，并对模式模拟研究提供了依据。然而，对于全球范围内云的微物理和光学特性的空间分布和季节变化的研究还较少，特别是详细分析 CloudSat 高垂直分辨率资料的相关参数的时空分布，而该工作对改进气候模式中云的光学和微物理特征的模拟非常关键。因此，本文通过统计分析 2007 年 1 月－2010 年 12 月 CloudSat 卫星提供的全球范围内云的观测资料，研究云微物理和光学性质的全球分布特征，以期对气候模式中云辐射物理过程的描述及其参数化改进提供参考依据。

## 2 资料选取和方法介绍

### 2.1 CloudSat 资料简介

CloudSat 卫星于 2006 年 4 月 28 日在美国发射升空，是 A－Train 卫星观测系统的成员之一。A－Train 卫星观测系统由 Aqua、CloudSat、CALIPSO、PASASOL 和 Aura 五颗卫星组成，这些卫星互相配合在同一轨道上实现了准同步主、被动多波段对地球的观测[20]。

CloudSat 卫星首次从空间采用主动毫米波遥感对云体垂直结构进行探测，能够提供云体的垂直廓线及云中粒子的相关特性。它搭载的遥感探测器是云廓线雷达 CPR(Cloud Profile Radar)，该雷达为 94 GHz 毫米波雷达，灵敏度是标准天气雷达的 1000 倍，CPR 向地球发射能量并按距离函数计算由云返回的能量[21]。该卫星位于 705 km 高度的太阳同步轨道上，卫星绕地球一周称为一个扫描轨道，一个轨道的扫描时间约为 99 min，扫描长度约为 40022 km，每轨有 36383 个星下像素点，每个像素点的星下点波束覆盖宽度的沿轨分辨率是 2.5 km，横轨分辨率是 1.4 km，垂直分辨率是 500 m[22]。每个垂直剖面上共有 125 个垂直层，每层厚度为 240 m。主要有两类数据，标准数据和辅助数据[23]。标准数据按反演程度分为两个等级，即：level－1 是通过卫星搭载的云雷达直接得到的数据产品；level－2 是根据 level－1 产品结合其他卫星产品反演得到的。产品主要包括雷达回波强度，云覆盖和雷达反射率，云的分类，液态水/冰水含量，辐射通量和加热率等(表 1)。

### 2.2 统计方法

所用 CloudSat 资料中主要描述了云光学厚度的2B－TAU和雷达可以探测到的液态水/冰水含量的2B－CWC－RO数据产品(算法及物理意义

**表 1　CloudSat 主要的数据产品**

**Table 1　The major data products of CloudSat**

| 名称 | 内容 |
|---|---|
| 1B-CPR | 1B 平台下获得的回波强度(CPR:云廓线雷达) |
| 2B-GEOPROF | 云覆盖和雷达反射率 |
| 2B-CLDCLASS | 云的分类 |
| 2B-CWC-RO | 雷达探测到的液态水/冰水含量 |
| 2B-TAU | 云的光学厚度 |
| 2B-CWC-RVOD | 雷达和可见光学厚度探测的液态水/冰水含量 |
| 2B-FLXHR | 辐射通量和加热率 |
| 2B-GEOPROF-Lidar | 云廓线雷达和毫米波雷达探测的云覆盖 |

详见 http://www. cloudsat. cira. colostate. edu. html)[24]，分析的物理量有 2B－TAU 中提取的总云光学厚度、分层云光学厚度以及 2B－CWC－RO 中提取的冰水含量、冰水路径、冰云有效半径、液态水含量、液态水路径和水云有效半径。

确定物理量后，由于卫星探测在南北纬 83°以上区域没有扫描廓线，将南北纬 83°之间的区域按经纬度划分为 2.8°×2.8°的网格，一共 128×60 个网格区域。根据星下点位置，筛选出每个网格内的 CloudSat 卫星扫描的廓线，然后选取所需要的云物理量进行网格内平均，统计出这些量在全球范围内的月平均分布。参考彭杰等[17]的工作，本文将 2007 年 1 月－2010 年 12 月进行划分：3－5 月为北半球春季，6－8 月为北半球夏季，9－11 月为北半球秋季，12 月－次年 2 月为北半球冬季；南半球与之相反，最终统计出各个物理量在不同季节的全球分布。

此外，研究总云光学厚度时，采用 2007 年 1 月－2010 年 12 月 MODIS 云产品资料(http://modis. gsfc. nasa. gov. html)，季节划分与 CloudSat 资料的处理方法一致。

### 2.3　因子选取

#### 2.3.1　云水含量

云的冰水含量是 2B－CWC－RO 产品中的物理量，反映了冰云中整体所含的冰晶质量，是冰云的重要光学参数。用公式可以表示为

$$\mathrm{IWC} = \int_0^\infty V\rho_i n(L)\,\mathrm{d}L \quad , \tag{1}$$

其中：IWC 为云的冰水含量；$\rho_i$ 为冰的密度；$L$ 为冰晶的最大尺寸[1]；$n(L)$为冰晶的尺度分布[1]。

冰水路径 IWP 是冰水含量的整层积分量，即：

$$\mathrm{IWP} = \int_0^z\int_0^\infty V\rho_i n(L)\,\mathrm{d}L\mathrm{d}z \quad . \tag{2}$$

云的液态水含量 LWC 反映了水云中的含水量，即：

$$\mathrm{LWC} = \frac{4\pi}{3}\rho_w\int a^3 n(a)\,\mathrm{d}a \quad , \tag{3}$$

其中：$\rho_w$ 为水的密度；$a$ 为水滴半径。

液态水路径是液态水含量的整层积分，反映了整层大气中液态水含量的水平分布，其表达式为

$$\mathrm{LWP} = \frac{4\pi}{3}\rho_w\int_0^z\int_0^\infty a^3 n(a)\,\mathrm{d}a\mathrm{d}z \quad . \tag{4}$$

#### 2.3.2　云滴有效半径

冰云有效半径反映了冰云粒子的平均有效尺度。其表达式为

$$D_e = \frac{\int V_n(L)\,\mathrm{d}L}{\int A_n(L)\,\mathrm{d}L} \quad , \tag{5}$$

其中：$L$ 为冰晶的最大尺寸；$V$ 为体积；$A$ 为冰晶在垂直于入射光束的平面上的几何投影面积[1]。

水云有效半径反映了水云中云滴的尺度大小，其定义为

$$a_e = \frac{\int \pi a^3 n(a)\,\mathrm{d}a}{\int \pi a^2 n(a)\,\mathrm{d}a} \quad , \tag{6}$$

其中云滴的截面作为权重因子来考虑，不管云滴尺度的具体分布如何，反射和透射的太阳光主要由有效半径来决定[1]。有效半径的减小会使云的反照率增大[25]。

#### 2.3.3　云光学厚度

云光学厚度是研究云光学性质的一个重要参数，描述了云的消光作用。其定义为

$$\tau = \Delta z\int Q_e\pi a^2 n(a)\,\mathrm{d}a \quad , \tag{7}$$

其中：$Q_e$ 为消光效率因子，是云滴半径、波长和折射率的函数；$\Delta z$ 为云层厚度；$n(a)$为单位体积内半径为 $a$ 的粒子数浓度。在可见光波段，当云粒子尺度增大到一定值时，$Q_e \to 2$，则有：

$$\tau = \Delta z 2\pi\int a^2 n(a)\,\mathrm{d}a \quad . \tag{8}$$

这时云光学厚度与单位体积云滴浓度、云滴半径以及云厚有关。结合式(4)、(6)、(8)可得：

$$\tau = \frac{3}{2\rho_w}\frac{\mathrm{LWP}}{a_e} \quad . \tag{9}$$

式(9)将光学厚度与 LWP 和云滴半径联系起来。当两块云的 LWP 相同时，含有较小云滴的云将具有较大的光学厚度，可以反射较多的太阳光[1]。气溶胶可以增加云滴数量，从而减小云粒子半径，即

气溶胶的间接效应[25]。对于冰云来说同样可以得到三者的关系：

$$\tau \approx \mathrm{IWP}\left(c + \frac{b}{D_e}\right) \quad , \qquad (10)$$

其中：$b$、$c$ 均为与冰晶形状有关的参数。式(9)、(10)为水云和冰云的微物理参量分布和光学特征量分布之间的关系提供了理论依据。

## 3 结果分析

### 3.1 云水含量及路径分布和季节变化

#### 3.1.1 冰水含量及路径

冰水含量是描述冰云微物理特性的重要物理量。纬圈平均的冰水含量值大部分在 150 mg · m$^{-3}$ 以下。从纬圈平均冰水含量的垂直分布的季节变化(图 1)中可以看出，在 17 km 以上没有分布，在 5 km 以下 30°S－30°N 的低纬度地区上空冰水含量很小，这是因为该区域位于热带地区，温度较高，不利于冰云形成。高值区主要分布在 4～15 km 之间，最大值均达到 90 mg · m$^{-3}$ 以上，具体分为四部分：4～8 km 位于 20°N－40°N、20°S－40°S 附近有 2 个高值区，最大值达 105 mg · m$^{-3}$；赤道地区上空有 2 个高值区，在 8 km 附近有一高值区，最大值可达 120 mg · m$^{-3}$ 以上，另一高值区在 14 km 处，最大值和范围均较小。

值得注意的是，除了这 4 个主要高值区外，北极上空 3 km 以下的边界层也存在 1 个较强的高值区，中心最大值达 150 mg · m$^{-3}$ 以上，甚至高出赤道上空中层的值，这可能与北极地区近地面水汽充沛且温度有利于冰云形成有关。从季节分布的差异来看，北半球冬、春季赤道地区的两个高值区位置偏向赤道以南，而北半球夏、秋季则移到赤道以北；中纬度地区的 2 个次高值中心位置和范围也存在差异，北半球夏季 40°N 附近的高值区位置比冬季高，南北移动不明显；而 40°S 附近的高值区比北半球冬季低、位置偏南，2 个高值区的覆盖范围在北半球夏季比冬季大。从高值区最大值的季节变化来看，北极地区的高值中心最大值在北半球夏季略

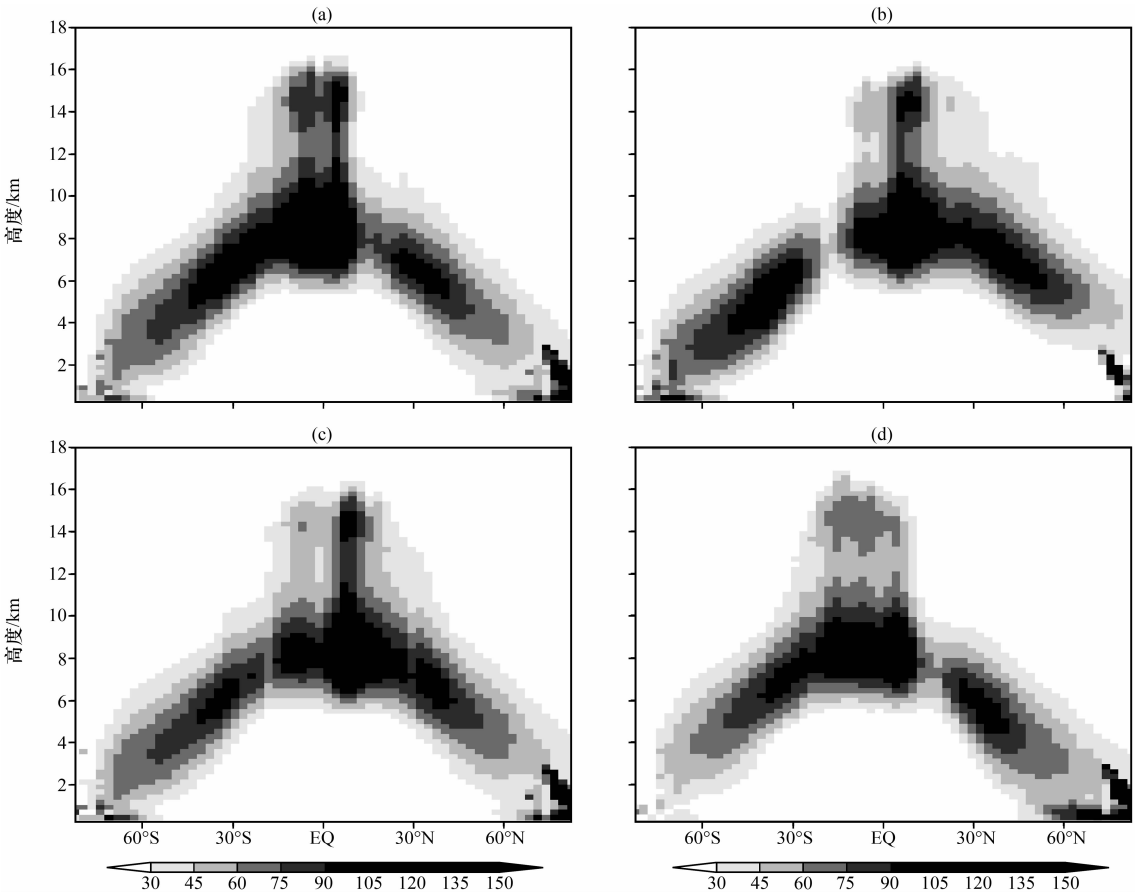


图 1 北半球四季纬圈平均冰水含量的垂直分布(单位：mg · m$^{-3}$)

(a) 春季，(b) 夏季，(c) 秋季，(d) 冬季

Fig. 1 Vertical distribution of mean cloud ice water content in different seasons of the northern hemisphere. Unit: mg · m$^{-3}$. (a) spring, (b) summer, (c) autumn, (d) winter

小，其他季节差异不大；另外，中低纬度上空的 4 个高值区在北半球冬季比其他季节偏小，但程度不明显。整体来看，赤道地区的 2 个高值区位置偏向南、北半球夏季，可能因为夏季温度高，蒸发进入大气的水汽相对较多，冰云中的含水量也相对较大。

从冰水路径在全球分布的季节变化(图 2)中可以看出，冰水路径在全球大部分 $< 800\ g \cdot m^{-2}$，中、低纬地区均有高值分布，海陆差异并不明显，陆地上主要分布在北美南部、南美大陆、非洲大陆、澳大利亚和南亚地区上空；洋面上则主要在太平洋、大西洋和印度洋上空，高值区最大值达 $600\ g \cdot m^{-2}$以上，分布位置随季节不同有所差异。西太平洋的高值区有很明显的季节变化，其中在北半球的夏、秋季高值中心偏向北半球，夏季的范围已经扩展到亚洲东部和南部的大部分地区；北半球的冬、春季高值中心偏向南半球，范围扩展到澳大利亚地区。美洲和非洲大陆上的高值区也随季节存在南北位置的变化，北半球夏季高值中心偏向北美和非洲中部，冬季偏向南美和南非地区。总的来说，冰水路径的分布呈偏向南北半球夏季的特点，原因与夏季蒸发量大有关。

### 3.1.2 液态水含量及路径

水云对降水的发生有重要作用，研究水云中的含水量可以更好地认识降水的物理过程。图 3 给出了不同季节液态水含量纬圈平均的垂直分布。液态水含量大部分在 $400\ mg \cdot m^{-3}$以下，从图 3 中可以看出，分布的集中区域在 8 km 以下，呈拱形，上部基本没有值出现，6 ~ 8 km 随高度分层递减。在 2 km 以下液态水含量较高，达 $250\ mg \cdot m^{-3}$以上，南北半球分布较均匀，没有明显集中的纬度带。导致该分布的原因与水云分布的位置有关，水云的形成受温度影响一般都集中在对流层中低层，近地层由于温度较高且下垫面蒸发量大，故液态水含量也较大。从季节分布的差异来看，北半球夏季高值区的位置偏北，冬季偏南，春秋两季基本呈以赤道为中心南北对称分布。总体而言，液态水含量呈偏向南北半球夏季分布，该分布规律同样受温度影响较大。

图 4 给出的是不同季节液态水路径分布。从图 4 中可以看出，全球大部分地区液态水路径的值 $< 500\ g \cdot m^{-2}$，主要分布在中低纬度地区，高值区在海洋上分布较多，主要位于太平洋、印度洋和大西洋的中低纬度海域，最大值在 $300\ g \cdot m^{-2}$以上。南美洲北部、亚洲南部地区和澳大利亚北部也有高值区存在，除了亚洲南部液态水路径较大外，大部分地区陆地上空的值比洋面小。从季节变化来看，液态水路径在全球范围内的季节分布差异不大，但

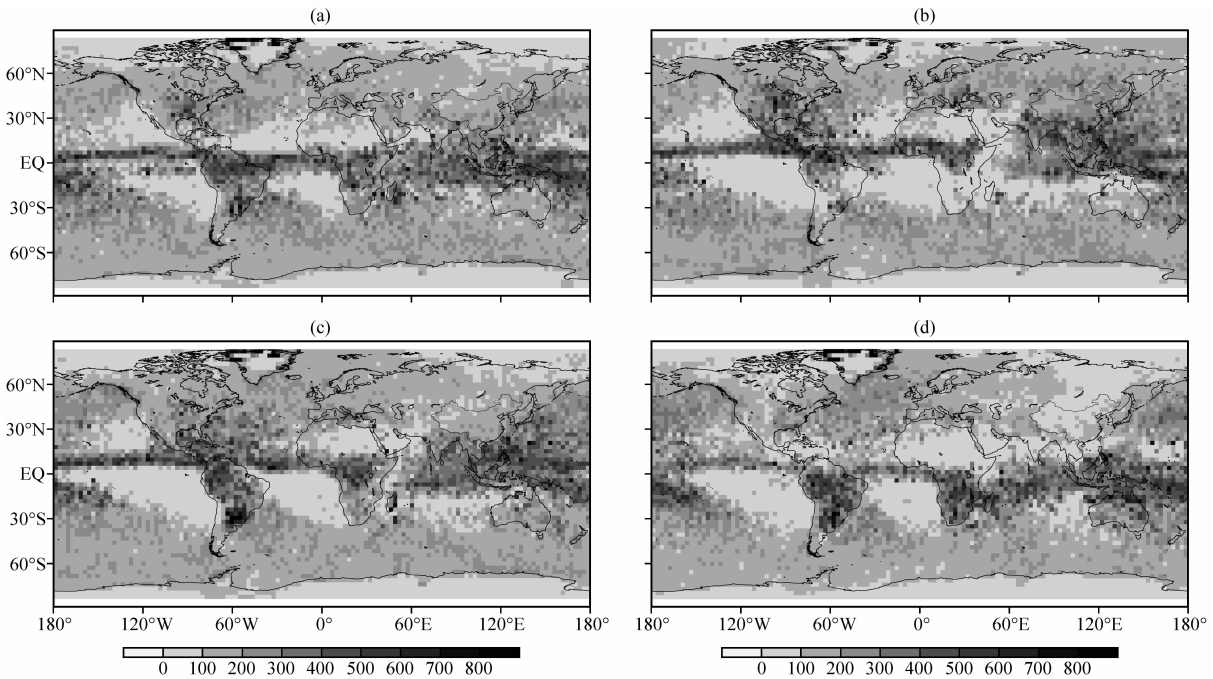


图 2　北半球四季冰水路径的水平分布(单位：$g \cdot m^{-2}$)

(a) 春季，(b)夏季，(c)秋季，(d) 冬季

Fig. 2　Horizontal distributions of cloud ice water path in different seasons of the northern hemisphere. Unit: $g \cdot m^{-2}$. (a) spring, (b) summer, (c) autumn, (d) winter

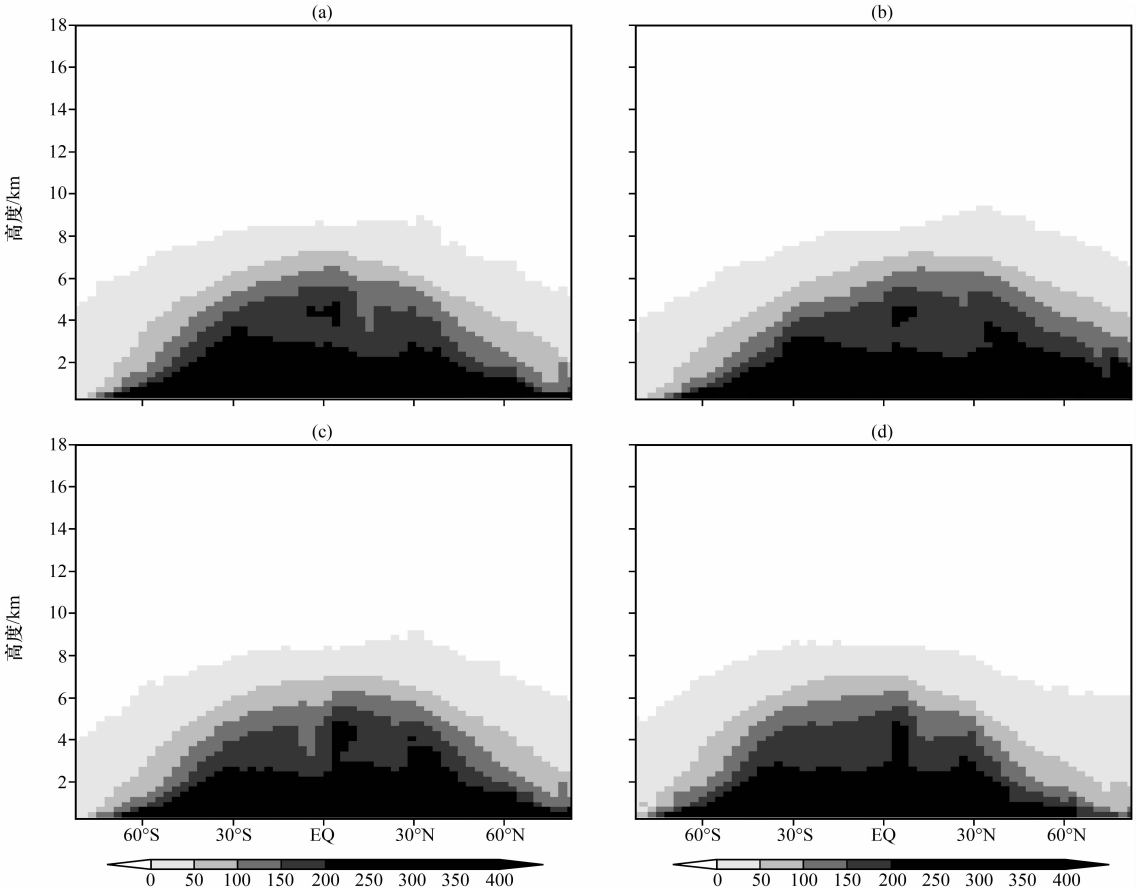


图 3 同图 1，但为液态水含量(单位：mg · m$^{-3}$)

Fig. 3 The same as Fig. 1, but for cloud liquid water content. Unit: mg · m$^{-3}$

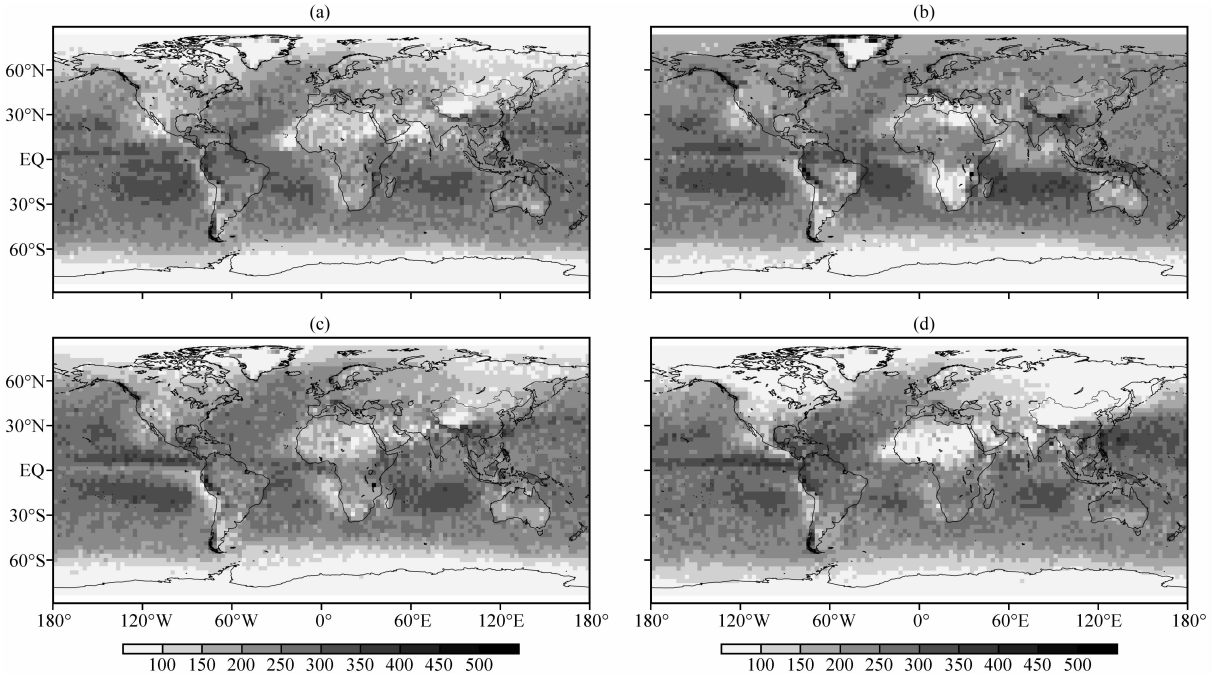


图 4 同图 2，但为液态水路径(单位：g · m$^{-2}$)

Fig. 4 The same as Fig. 2, but for cloud liquid water path. Unit: g · m$^{-2}$

有海陆差异存在，其中冬季液态水路径的分布相比之下更集中在海洋上空，这可能是由于冬季海洋比大陆暖，大气含水量也比大陆多。东亚地区夏季高值区位于中国西南地区，这可能与夏季该地区云量较大有关；而冬季受暖洋面影响，高值区位于西北太平洋洋面。

### 3.2　云滴有效半径的分布及季节变化

云滴有效半径是重要的云物理特征参量，从宏观上考虑，它可以影响云层的散射特性。对于给定的液态水含量或冰水含量而言，具有较小的水云有效半径或冰云有效半径的云将反/散射较多的太阳辐射[1]。从微观层面来说，云滴有效半径还会影响云微物理过程。陈英英等[26]研究发现，对于明显的降水来说，云滴的有效半径至少要达到 12 μm。

#### 3.2.1　冰云有效半径

冰云有效半径也称平均有效尺度，用来代表非球形冰晶粒子的尺度分布。图 5 为不同季节纬圈平均的冰云有效半径的垂直分布。从图 5 中可以看出，纬圈平均的冰云有效半径的值大部分在 100 μm 以下，垂直分布呈拱形，低层(2 ~4 km)主要分布在高纬度地区，热带地区在 4 km 以下基本没有值出现，随着高度逐渐增大，分布区逐渐向中低纬度移动，到高空基本集中在低纬度地区。在高纬度地区的近地面 0.4 ~0.6 km 高度上，冰云有效半径很大，最大可达 200 μm 以上。自近地层随高度迅速减小，2 km 以上存在 3 个高值区，低层有 2 个，中层(4 ~8 km)有一个，最大值达 80 μm 以上。低层的 2 个高值区分别位于 30°S －55°S 和 30°N －55°N 之间，中层的高值区位于赤道附近 10 ~20 个纬距内，高值区的位置和最大值随季节有所差异。8 km 以上基本不存在高值区，其值随高度递减，16 km 以上的值较小，基本可以忽略不计。研究发现冰云有效半径是冰水含量和温度的函数[27]，在垂直高度上，冰水含量大的地方冰云有效半径一般较大，在 8 km 以上冰水含量较小，这时冰云有效半径的值主要受温度影响呈分层递减，温度相对越高则半径一般越大。从季节变化来看，北半球春季中低层的 3 个高值区位置基本以赤道为中心南北对称分布，低层的 2 个高值区位于 30°S －55°S 和 30°N －55°N之间，中层的高值区位于10°S －10°N之

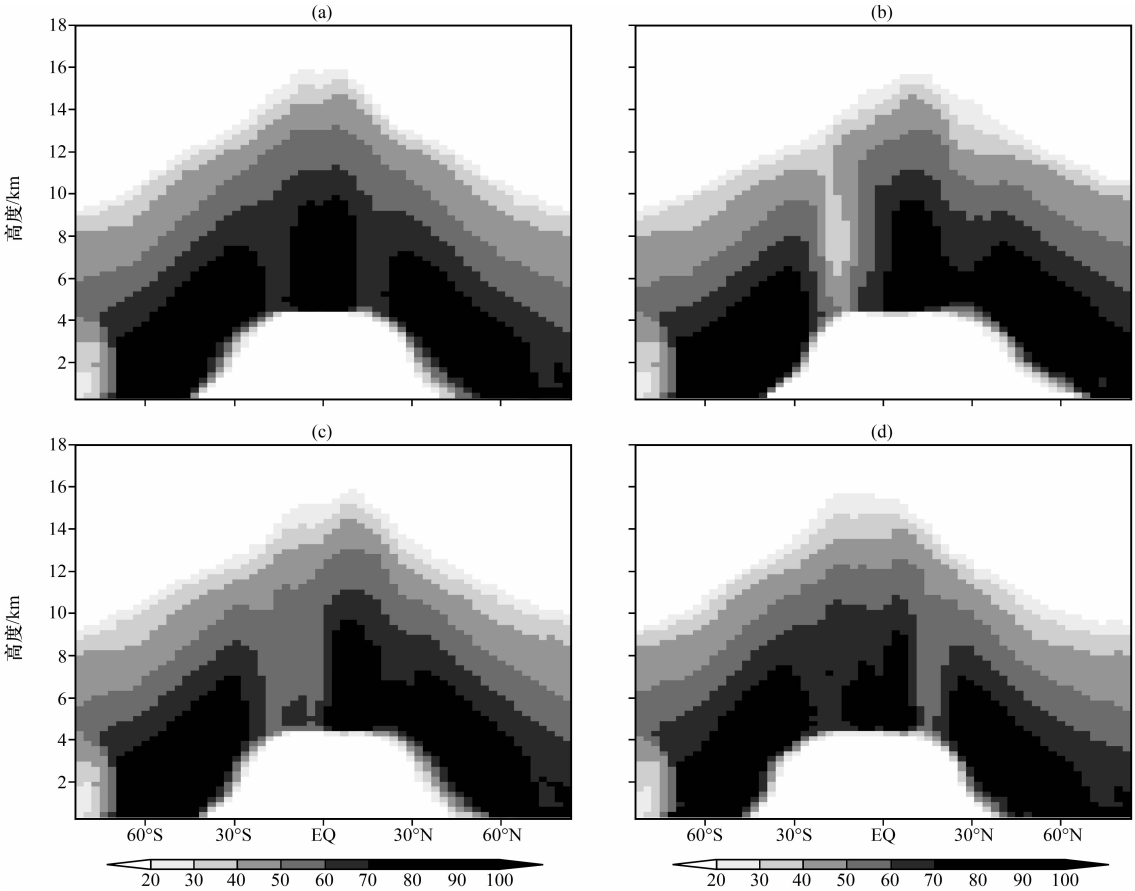


图 5　同图 1，但为冰云有效半径(单位：μm)

Fig. 5　The same as Fig. 1, but for cloud ice effective radius. Unit: μm

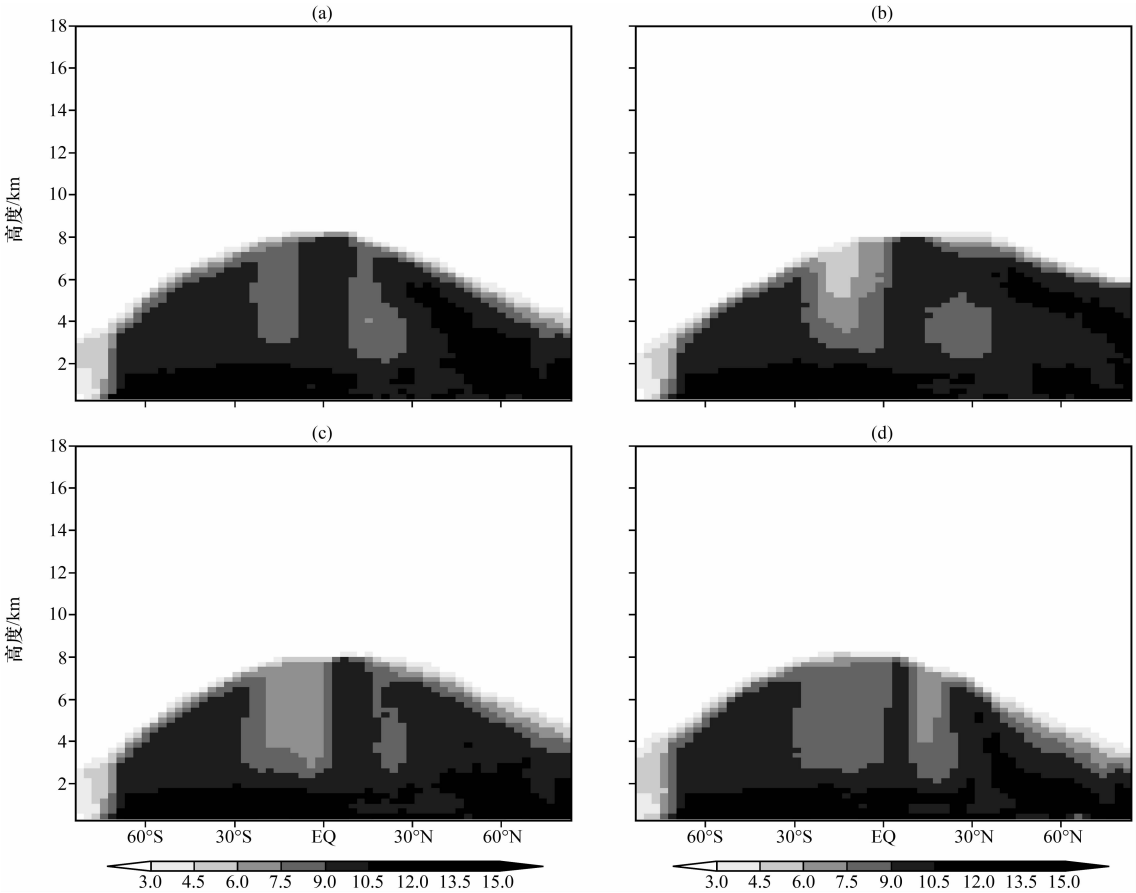


图 6 同图 1，但为水云有效半径(单位：μm)

Fig. 6 The same as Fig. 1, but for cloud liquid effective radius. Unit: μm

间；北半球夏季 3 个高值区明显向北半球偏移，其中低层的高值区位置没有变化，中层则完全移到赤道以北，但纬度范围减小，集中在 0°－15°N 之间；秋季 3 个高值区仍然偏向北半球，大小和位置与之前差别不大；冬季 3 个高值区最大值都有所减弱，位置均略微向南半球偏移。从整体来看，冰云有效半径高值区呈偏向南北半球夏季的分布特点，原因可能是夏季温度较高，冰云有效半径较大[27]，这与冰水含量的分布基本一致。

### 3.2.2 水云有效半径

水云有效半径大部分 < 15 μm，从不同季节水云有效半径的垂直分布(图 6)中可以看出，主要分布在 8 km 以下，呈拱形，两极分布的高度比赤道地区低。水云有效半径高值区在南北半球的分布有所不同，北半球从 0 ~ 6 km 高度均有高值区分布，南半球高值区基本集中在 2 km 以下，高值区最大值达 10 μm 以上；南北半球在 1 km 以下的边界层分布的值较大，达 12 μm 以上；南北半球的低纬度地区在 2 km 以上的高空有两个 < 9 μm 的低值区。这种拱形的分布情况与液态水含量有关，大部分地区的值随高度减小。从季节变化来看，水云有效半径的值在南北半球夏季的大小和范围普遍比冬季大，夏季拱形的上部位置比冬季高；北半球夏季在 4 ~ 6 km 的高空出现明显的高值区，冬季的高值区则集中在 4 km 以下，南半球冬、夏季高值区范围的变化没有北半球显著；低纬度两个低值区的分布也呈冬季强度比夏季小的特点。

### 3.2.3 云滴有效半径

图 7 给出了不同季节南北半球冰(水)云有效半径的 PDF 分布，统计对象是所有层上的数据。从图 7 中可以看出，冰云有效半径值的范围比水云有效半径大，两者范围分别为 300 μm 和 45 μm 以下，与之前垂直分布中得出的结论相一致。冰云有效半径的值大多集中在 100 μm 以下，100 μm 以上较少，水云有效半径则主要分布在 15 μm 以下。北半球冰云有效半径的值分布比南半球集中，高峰区间所占比例较大。具体来看，冰云有效半径在北半球春、夏、秋、冬季的值分布最高峰分别集中在 50 ~ 60、70 ~ 80、50 ~ 60 和 40 ~ 50 μm 范围内，高峰区间的频率分别达 0.190，0.185，0.175 和 0.191，

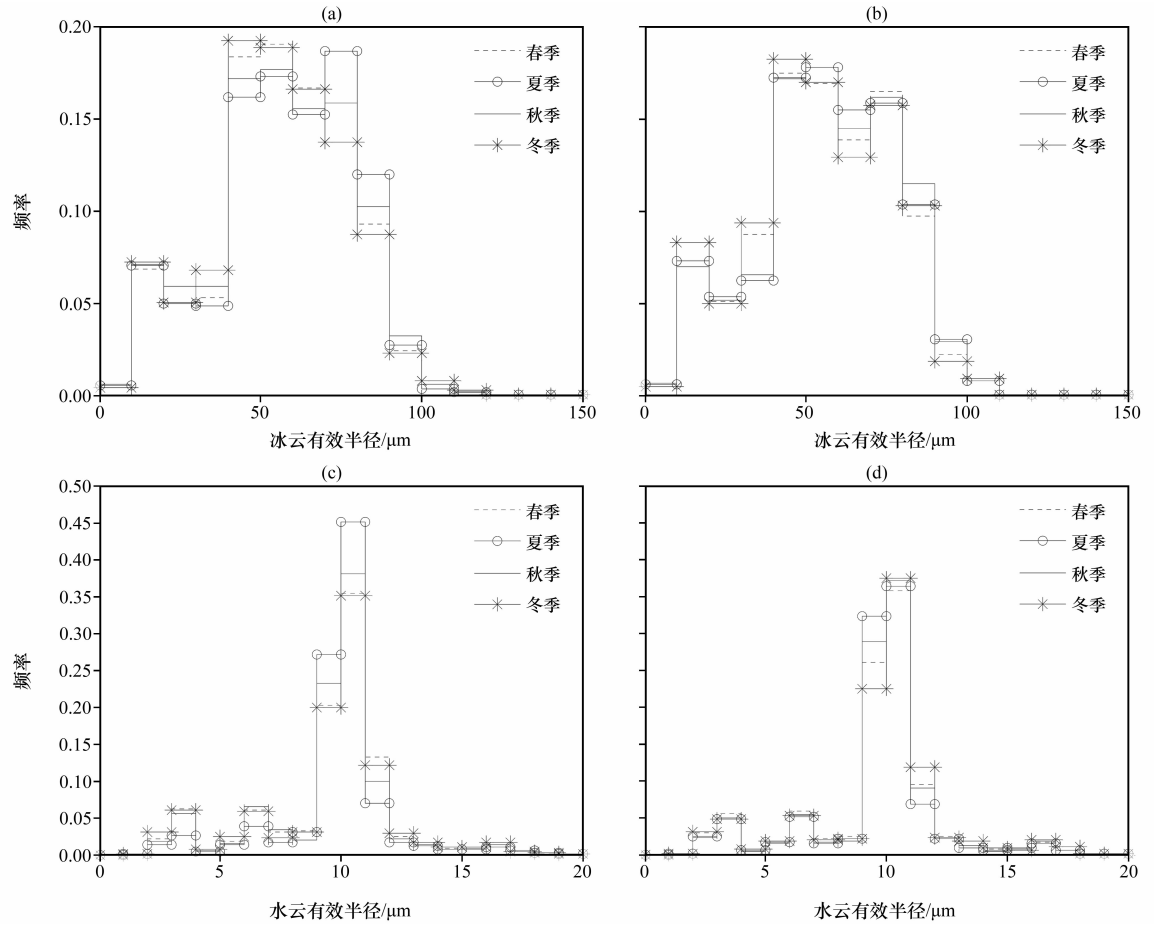


图 7　不同季节北半球(a, c)、南半球(b, d)冰云(a, b)和水云(c, d)有效半径的 PDF 分布

Fig. 7　Seasonal changes of PDF distributions of cloud ice(a, b)and cloud liquid(c, d) effective radius in the northern(a, c) and southern(b, d) hemispheres

南半球四季的值依次集中在 40 ~ 50、40 ~ 50、50 ~ 60 和 40 ~ 50μm，高峰区间的频率分别为 0. 175，0. 171，0. 178 和 0. 181；四季水云有效半径在北半球分布最集中的区间均为 10 ~ 11 μm，频率依次为 0. 350，0. 450，0. 355 和 0. 350，南半球则为 10 ~ 11 μm，频率依次为 0. 351，0. 352，0. 354 和 0. 355，相差较小。由此可知，北半球冰云和水云有效半径的季节差异均比南半球大，不同季节冰云有效半径分布最集中的区间比水云有效半径分散。

### 3.3　云光学厚度的分布及季节变化

#### 3.3.1　总云光学厚度

云的物理光学特性对地气系统的辐射收支有很大影响，云光学厚度作为描述云的重要物理量，不仅可以影响辐射平衡，还会影响地面能见度[28]。图 8 给出了不同季节总云光学厚度的水平分布。从图 8 中可以看出，全球总云光学厚度的值大部分在 40 以下，分布的高值区普遍位于中高纬度的广阔地区和低纬度靠近大陆的洋面上空。具体来说，四季中普遍存在的高值区位于南北纬中高纬度的广阔洋面、北美和欧亚大陆北部、中国的西南地区，以及低纬度的北美、南美、南非的西部海域，高值区最大值可达 15 以上，高纬度部分地区达 30 以上。从季节变化来看，北半球夏季高纬度地区总云光学厚度的值偏小，低纬度地区则偏大，高值区位置偏北；冬季海陆差异较大，高值区位置偏南。影响总云光学厚度分布的主要因子是云量，参照 ISCCP(http://isccp. giss. nasa. gov. html)网站提供的全球总云量分布(图略)可以看出，云量分布的高值区与上述总云光学厚度的高值区基本相一致，原因是云量大的地方整层云的消光作用强。中高纬度高值区位置偏向于南北半球夏季，原因是夏季极地地区处于极昼，蒸发加大，使云量增多，致使光学厚度的值变大。此外，除极地外的几个高值区冰云和水云有效半径的值也相对较小，根据式(9)可知光学厚度的值相对变大。

对比 2007 年 1 月－2010 年 12 月 MODIS 资料

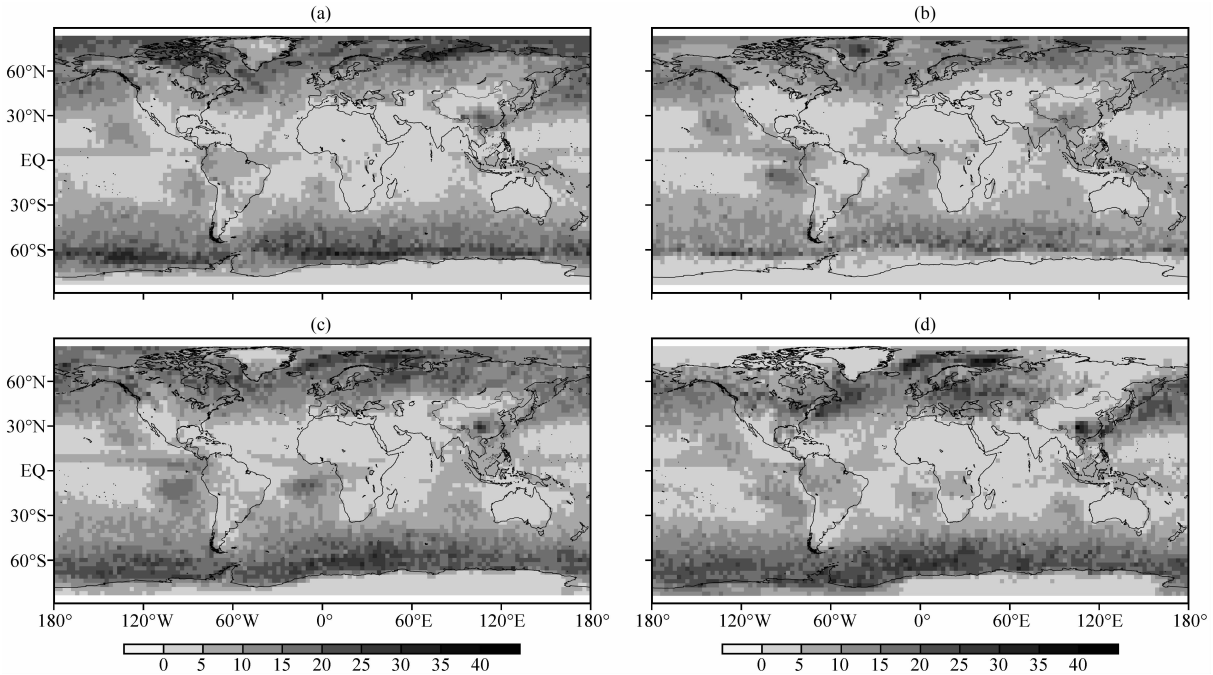


图 8 同图 2，但为总云光学厚度

Fig. 8 The same as Fig. 2, but for total cloud optical depth

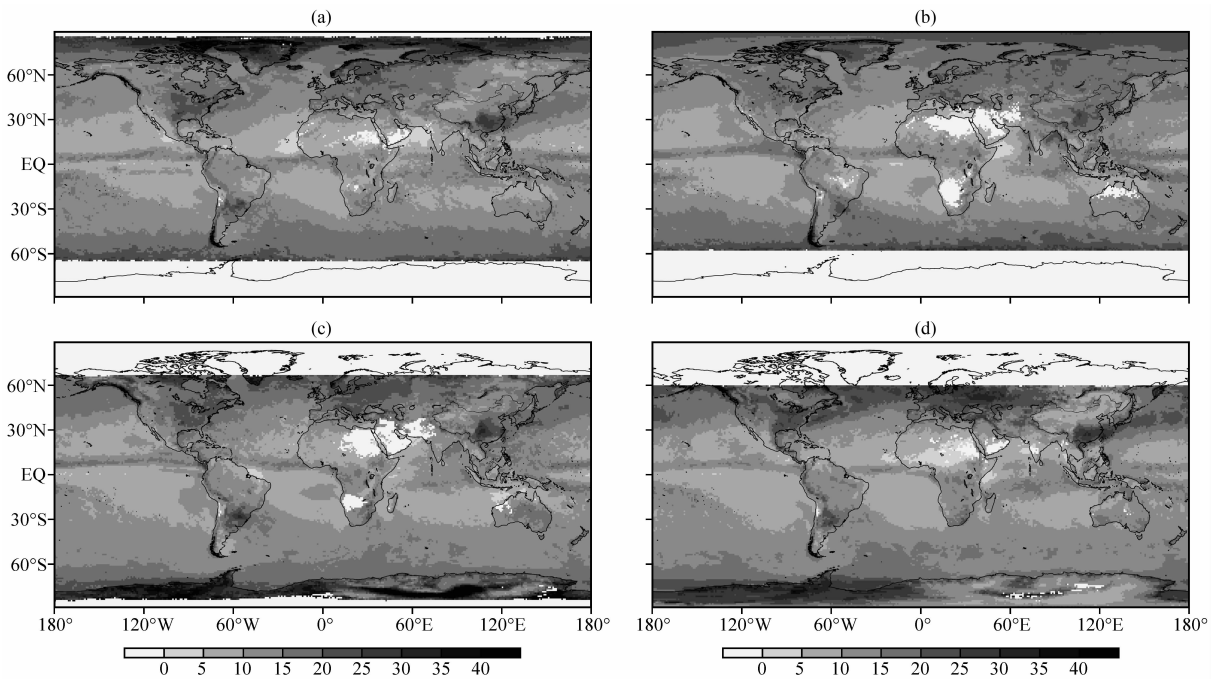


图 9 同图 2，但为 MODIS(2007 年 1 月－2010 年 12 月)总云光学厚度

Fig. 9 The same as Fig. 2, but for total cloud optical depth from MODIS (from January 2007 to December 2010)

的全球总云光学厚度的季节分布(图 9)可以看出，CloudSat 资料能够很好地反映总云光学厚度在全球的分布，与 MODIS 资料有较好的一致性，两种资料得出的全球大部分地区的总云光学厚度的值均在 40 以下，主要高低值中心位置也基本一致。但由于探测仪器不同(CloudSat 上搭载的 CPR 为主动遥感，MODIS 传感器为被动遥感)，两者的结果也存在一定差异：从全球范围来看，MODIS 资料得出的

总云光学厚度的值普遍比 CloudSat 资料高，特别是陆面上的差异更为显著；在南半球春、夏季（即北半球秋、冬季），CloudSat 资料在 60°S 附近的值很高，而 MODIS 资料的高值区与 CloudSat 相比偏南，位于南极地区。

### 3.3.2　云光学厚度

CloudSat 资料的最大优点是可以反演云信息的垂直分布。云光学厚度在不同高度上值的范围大部分在 4.0 以下，图 10 给出了纬圈平均的云光学厚度垂直分布的季节变化，从图 10 中可以看出，在垂直高度上光学厚度的值集中在 4 km 以下，2 km 以下的边界层中值最大，达 4.0 以上；在 4 km 以上，光学厚度的值普遍减少，范围在 0.2 ~ 1.2 之间，在 4 km 以上区域的值很小，原因主要与云的形成有关，云主要在 2 km 以下的边界层中产生、发展。赤道附近云光学厚度存在一个低值带，约 10 个纬距，值在 1.2 以下，这与云量的分布相对应，云量在这个区域也相对较少。南北半球的中高纬度地区分别有两个高值区，最大值可以达 4.0 以上，都位于近地面层，但中心位置随季节的不同有所差异。该分布与液态水含量的垂直分布相似，可能受其影响较大，由式(9)可知液态水含量越大，光学厚度越大。一方面，中高纬度的云量比较大；另一方面，水云的光学厚度一般大于冰云，因此对光学厚度的贡献较大。整体来看，高值区位置偏向南北半球的夏季，春、秋两季高值区基本以赤道为中心南北对称分布，主要是因为夏季蒸发量大，云水含量较大，从而云量较大，消光作用较强。

图 11 给出了不同高度各个物理量的平均值随高度的变化。从图 11 中可以看出，各个物理量的垂直分布规律与之前分析的结论基本一致，在南北半球夏季值普遍偏大，而冬季则偏小，其中北半球的季节变化比南半球显著。

从图 11 中可以清晰地看出，云水含量和云滴有效半径与云光学厚度之间的关系。整层平均的液态水含量在 600 mg · $m^{-3}$以下，冰水含量则集中在 80 mg · $m^{-3}$以下，云的总含水量中液态水含量所占的比重较大。液态水含量主要分布在 8 km 以下，冰水含量可以达到 18 km。整层平均后的冰云有效半径比水云有效半径大，分别为80 μm以下和14

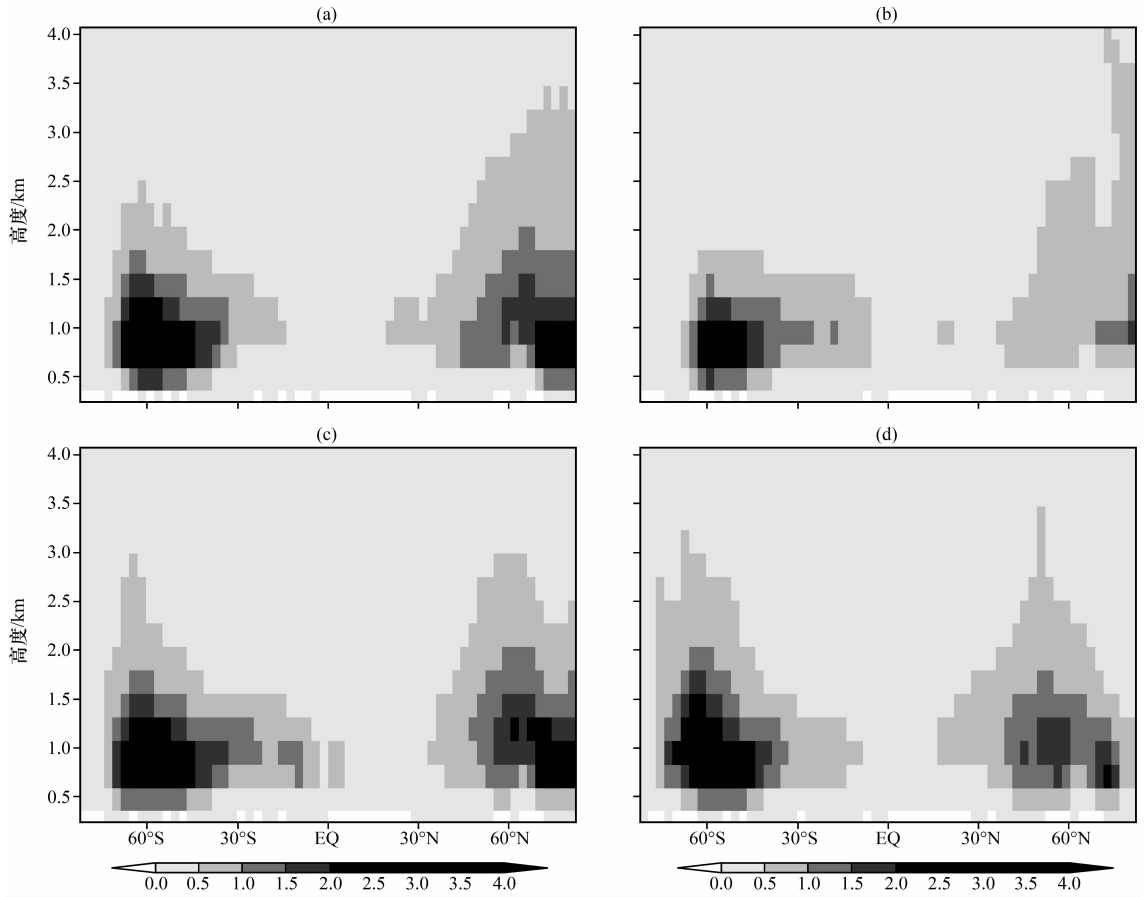


图 10　同图 1，但为云光学厚度

Fig. 10　The same as Fig. 1, but for cloud optical depth

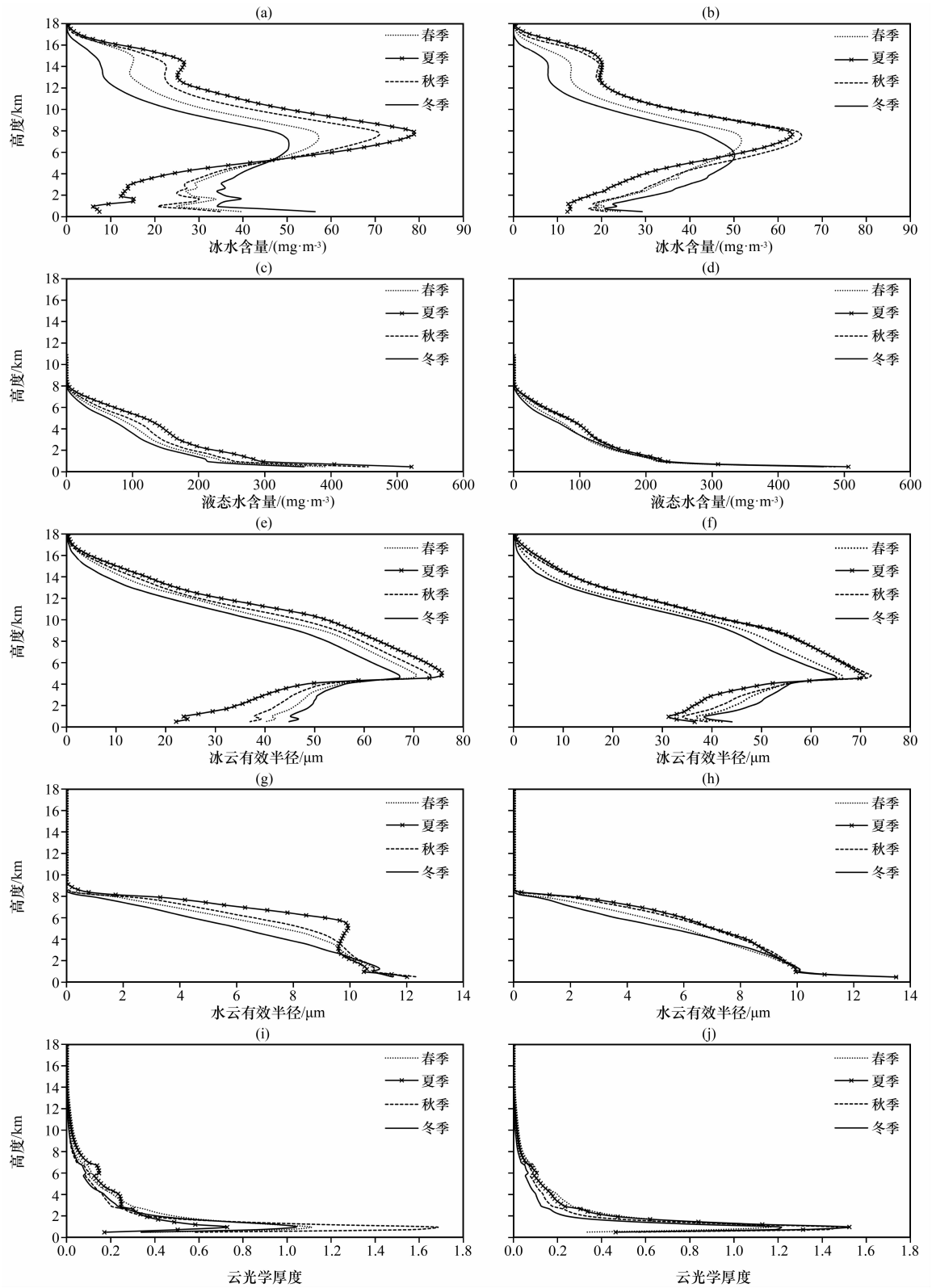


图 11 不同季节南半球(右)、北半球(左)的冰(a, b)/液态(c, d)水含量、冰(e, f)/水(g, h)云有效半径和云光学厚度(i, j)的垂直分布

Fig. 11 The vertical distributions of the total amount of cloud ice(a, b)/liquid(c, d) water content, cloud ice(e, f)/liquid(g, h) effective radius and cloud optical depth(i, j) in the northern(left) and southern(right) hemispheres in different seasons

μm 以下，分布高度分别为 18 km 和 8 km 以下。冰云有效半径在 5 km 以下随高度增大，在 5 km 以上随高度减小；水云有效半径在 8 km 以下都随高度减小。云光学厚度在 14 km 以下随高度的增大单调递减，近地面可以达到 1.4 以上。总体看来，冰云和水云总云光学厚度随高度的变化与液态水含量随高度的变化一致，说明液态水含量的变化对总的云光学厚度的贡献更大；而云滴有效半径随高度的变化与云光学厚度的关系不明显。

## 4　结论

利用 CloudSat 卫星资料对云微物理特征量（云中液态水/冰水含量、液态水/冰水路径、云滴有效半径等）以及云光学参数（云光学厚度等）在全球的分布和季节变化进行了统计分析，并研究了云微物理特征量对云光学参数的影响，得到以下主要结论：

（1）　冰水路径的值在 800 g·m$^{-2}$以下，主要分布在北美南部、南美大陆、非洲大陆、澳大利亚、南亚地区以及太平洋、大西洋、印度洋上空，最大值达到 600 g·m$^{-2}$以上；在垂直方向上，冰水含量的最大值在赤道上空 8 km 附近，达 120 mg·m$^{-3}$以上，其次在中纬度地区 4～8 km 高度上有 2 个高值区，最大值达 105 mg·m$^{-3}$以上。液态水路径的值大部分在 500 g·m$^{-2}$以下，高值区主要位于中低纬度的太平洋、印度洋和大西洋上空；在垂直方向上，液态水含量随高度递减。冰水含量和液态水含量的高值区位置都偏向南北半球夏季。

（2）　冰云有效半径在高纬度地区近地层的值最大，达 200 μm 以上，对流层中低层有 3 个 >80 μm 的高值区，分别位于赤道地区 4～8 km 上，南、北半球的中纬度地区 2～4 km 上。水云有效半径的值分布在 8 km 以下，最大值位于 1 km 以下的边界层，达 12 μm 以上，中低纬度地区上空受副热带高压影响有两个 <9 μm 的低值区。冰/水云有效半径在南北半球夏季均比冬季大，分布也呈偏向南北半球夏季的特点。北半球冰云和水云有效半径的值的季节差异均比南半球大，不同季节冰云有效半径分布最集中的区间比水云有效半径分散。

（3）　总云光学厚度在全球大部分地区的值在 40 以下，分布的高值区位于中高纬度的广阔地区和低纬度靠近大陆的洋面上空。从垂直分布来看，高值区集中在 2 km 以下的边界层中，南北半球的中高纬度地区分别有 2 个高值区，最大值达 4 以上。云光学厚度的分布受云量、云水含量和云滴有效半径的影响，云量大的地区基本为云光学厚度的大值区，从垂直变化来看，云光学厚度的变化受液态水含量随高度的变化影响较大。

本研究侧重于云微物理量和云光学参数在全球不同地区和高度上的气候态分布特征及季节变化规律，主要为气候模式模拟和检验这些参数提供依据，以便改进气候模式中相关物理过程的参数化方案。

**参考文献：**


[1] Liou K N. 大气辐射学导论[M]. 北京：气象出版社，2004.

[2] 吴伟，王式功. 中国北方云量变化趋势及其与区域气候的关系[J]. 高原气象，2011，30(3)：651－658.

[3] 王胜杰，何文英，陈洪滨，等. 利用 CloudSat 资料分析青藏高原、高原南坡及南亚季风区云高度的统计特征量[J]. 高原气象，2010，29(1)：1－9.

[4] 牛晓瑞，王淑瑜. 华北地区低云量的变化特征及其影响因子分析[J]. 高原气象，2012，31(5)：1340－1347.

[5] 杜川利，余兴，李星敏，等. 过去 60 年中国秦岭地区云量变化及原因分析[J]. 高原气象，2012，31(2)：446－455.

[6] 张丁玲，黄建平，刘玉芝，等. 利用 CERES(SYN) 资料分析青藏高原云辐射强迫的时空变化[J]. 高原气象，2012，31(5)：1192－1202.

[7] 彭杰，沈新勇，王志立，等. 中国地区云的观测研究进展[J]. 安徽农业科学，2010，38(24)：13070－13073.

[8] 刘瑞霞，刘玉洁. 中国云气候特征的分析[J]. 应用气象学报，2004，15(4)：468－476.

[9] 戴进，余兴，刘贵华，等. 青藏高原雷暴弱降水云微物理特征的卫星反演分析[J]. 高原气象，2011，30(2)：288－298.

[10] 刘贵华，余兴师，春香，等. FY－3A/VIRR 反演云微物理特征及与 TERRA/MODIS 反演结果的比较[J]. 高原气象，2011，30(2)：461－470.

[11] Kenneth S，Zhien W，Dong L. Global distribution of cirrus clouds from CloudSat/Cloud－Aerosol Lidar and Infrared Pathfinder Satellite Observations (CALIPSO) measurements[J]. J Geophys Res，2008，113：D00A12，doi：10.1029/2008JD009972.

[12] Gerald G M，Roger M，Qiquing Z，et al. Global hydrometeor occurrence as observed by CloudSat：Initial observations from summer[J]. Geophys Res Lett，2007，34：L09808，doi：10.1029/2006GL029017.

[13] Patrick G，Jean－Pierre B，Munoz－Alpizar R. Study of polar thin ice clouds and aerosols seen by CloudSat and CALIPSO during midwinter 2007[J]. J Geophys Res，2009，114：D09201，doi：10.1029/2008JD010927.

[14] Wu D L，Jonathan H J，William G R，et al. Validation of the Aura MLS cloud ice water content measurements[J]. J Geophys Res，2008，113：D15S10，doi：10.1029/2007JD008931.

[15] Wu D L，Austin R T，Deng M，et al. Comparisons of global

cloud ice from MLS, CloudSat, and correlative data sets[J]. J Geophys Res, 2009, 114: D00A24, doi: 10.1029/2008JD009946.
[16] 王帅辉, 韩志刚, 姚志刚, 等. 基于 CloudSat 资料的中国及周边地区云垂直结构统计分析[J]. 高原气象, 2011, 30(1): 38-52.
[17] 彭杰, 张华, 沈新勇. 东亚地区云垂直结构的 CloudSat 卫星观测研究[J]. 大气科学, 2013, 37(1): 91-100.
[18] 张华, 彭杰, 荆现文, 等. 东亚地区云的垂直重叠特性及其对云辐射强迫的影响[J]. 中国科学, 2013, 43(4): 523-535.
[19] 李静, 肖子牛, 刘奇俊, 等. 基于 MODIS 和 CloudSat 云产品分析降水云系特征[J]. 科技信息, 2009(11): 36-37.
[20] Graeme L S, Deborah G V, Simone T, et al. CloudSat mission: Performance and early science after the first year of operation[J]. J Geophys Res, 2008, 113: D00A18, doi: 10.1029/2008JD009982.
[21] 马占山, 刘奇俊, 秦琰琰, 等. 云探测卫星 CloudSat[J]. 气象, 2008, 34(8): 104-112.
[22] 周毓荃, 赵姝慧. CloudSat 卫星及其在天气和云观测分析中的应用[J]. 南京气象学院学报, 2008, 31(5): 603-614.
[23] 王帅辉, 韩志刚, 姚志刚. 基于 CloudSat 和 ISCCP 资料的中国及周边地区云量分布的对比分析[J]. 大气科学, 2010, 34(4): 767-779.
[24] Igor N P, Laurent C, Steve C, et al. Level 2 cloud optical depth product process description and interface control document[R]. Cooperative Institute for Research in the Atmosphere Colorado State University, 2008.
[25] 段婧, 毛节泰. 气溶胶与云相互作用的研究进展[J]. 地球科学进展, 2008, 23(3): 252-261.
[26] 陈英英, 周毓荃, 毛节泰. 利用 FY-2C 静止卫星资料反演云粒子有效半径的试验研究[J]. 气象, 2007, 33(4): 29-34.
[27] Klaus W. The Effective Radius in Ice Clouds[J]. J Climate, 1998, 11(7): 1793-1802.
[28] 邓军, 白洁, 刘健文. 基于 EOS_MODIS 的云雾光学厚度和有效粒子半径反演研究[J]. 遥感技术与应用, 2006, 21(3): 220-226.

# Analysis on Global Distribution Characteristics of Cloud Microphysical and Optical Properties Based on the CloudSat Data

YANG Bingyun[1-3], ZHANG Hua[2], PENG Jie[4], WANG Zhili[1], JING Xianwen[2]

(1. *Chinese Academy of Meteorological Science*, *Beijing* 100081, *China*; 2. *Laboratory for Climate Studies*, *China Meteorological Administration*, *National Climate Center*, *Beijing* 100081, *China*; 3. *National Satellite Meteorological Center*, *Beijing* 100081, *China*; 4. *Shanghai Meteorogical Science institute*, *Shanghai Meteorological Bureau*, *Shanghai* 200030, *China*)

**Abstract**: The global distribution and seasonal variation of the cloud physical characteristics (including the cloud liquid and ice water content, liquid and ice water path, the effective radius, etc.) and cloud optical parameters (the cloud optical depth, etc.) were analyzed by the CloudSat data from January 2007 to December 2010. The results show that: The distribution of ice water path is mainly over the North America, South America, Africa, Australia and the South Asia, as well as the Pacific, Atlantic and Indian Ocean, with the highest values reaching 600 $g \cdot m^{-2}$ or more. In the vertical direction, the high values of ice water content are located near the height of 8 km over the equatorial regions and from 4 to 8 km over the middle latitude regions. The high values of liquid water path are located over the Pacific Ocean, the Indian Ocean and the middle and low latitudes of Atlantic. In the vertical direction, the value of liquid water content decreases with height. The ice effective radius reaches its maximum of over 200 μm near the surface at high latitudes, while having a maximum of over 80 μm at 4 ~ 8 km in the equatorial region and at 2 ~ 4 km in the mid-latitude. The liquid effective radius maximizes under 1 km, with a value of over 12 μm. The total cloud optical depth is below 40 around the globe, with largest values located in the vast middle and high latitudes as well as the oceans off the west coasts of low-latitude continents. Large cloud optical depths are concentrated below the boundary layer. The distribution of the cloud optical depth is closely linked to cloud amount, which is in good spatial accordance with the former, and also to cloud water content, and cloud effective radius. The latest analysis of satellite observation data for the climate models, and improvement of the cloud optical parameterizations and cloud microphysical schemes of the models are provided.

**Key words**: CloudSat; Cloud optical depth; Cloud effective radius; Cloud water content

尹宜舟，罗勇，肖风劲，等. 1971—2011年中国县级行政区域热带气旋基本气候特征[J]. 热带气象学报，2014，30(6): 1 089-1 097.

**文章编号**：1004-4965(2014)06-1 089-09

# 1971—2011年中国县级行政区域热带气旋基本气候特征

尹宜舟[1,2,3]，罗勇[3]，肖风劲[2]，朱鑫君[4]

(1. 中国气象局气候研究开放实验室，北京 100081；2. 中国气象局国家气候中心，北京 100081；
3. 清华大学地球系统科学研究中心，北京 100084；4. 江宁区气象局，江苏 南京 211100)

**摘　　要**：借助ArcGis软件获取了1971—2011年中国县级行政区域内热带气旋活动的基本信息，包括经纬度、持续时间、强度等，并对这些信息进行了统计。结果显示，中国县域内热带气旋活动最多频次为台湾省花莲县，平均每年0.78次；最大平均强度出现在台湾省宜兰县，达到35 m/s；持续时间最长的为海南省乐东县，平均每年 2.2 h；受热带气旋潜在影响程度最高的为台湾省台东县，年平均 YTCPI(Yearly Tropical Cyclone Potential Impact Index)达到15 106。与此同时，对6—10月各月中国县域内的热带气旋活动特征进行了详细分析。结论有助于进一步了解中国县域受热带气旋影响的基本特征，为有关部门防台减灾提供参考。

**关 键 词**：气候学；统计特征；地理信息系统；热带气旋；县级特征；防台减灾

**中图分类号**：P444　　**文献标识码**：A　　**Doi**：10.3969/j.issn.1004-4965.2014.06.009

## 1 引　　言

热带气旋灾害是中国主要的自然灾害之一，据不完全统计(且不含台湾省)，每年因灾造成的直接经济损失约占GDP的0.4%左右，死亡人口达400～500人[1−5]。在社会经济快速发展的背景下，直接经济损失将呈现上升的趋势[3−4]，与此同时，随着中国热带气旋监测预警预报技术水平的提升[6−8]，以及公众防灾意识的增强，死亡人口呈现出下降趋势[3−4]。而在全球变暖背景下，极端事件频发，且不确定性因素增多，“超乎寻常”的热带气旋时有发生[9]，这进一步促使有关热带气旋研究向更细致的方向发展[10−11]。

目前对于中国热带气旋基本气候特征的研究已取得较多的进展[12−18]，雷小途等[9]总结指出在影响或登陆中国的热带气旋频数、强度及登陆位置变化等方面的结论较一致，即频数呈现弱减少趋势，但是登陆强度显著增加，且登陆点趋于向中国海岸线中部地带集中。由于中国沿海省区受热带气旋影响比较严重，因此研究较多的为广西区、海南省、广东省、福建省、台湾省、浙江省等，或者以大的区域作为研究对象，如华南、东南、华东等[19]。这些研究均有利于人们了解相应地区受热带气旋影响的基本特征，且很多研究者在此基础上，进一步分析这些基本特征(特别是频数)在年际或季节尺度上变化的影响因子，进而对相应地区热带气旋的频数进行预测。

由于热带气旋对生命安全、经济发展和社会稳定造成的影响十分严重，人们渴望了解到更多更细的有关热带气旋影响的信息。比如，某个县的热带气旋基本特征(频数、持续时间、影响强度等)，这是细致化分析的基础，但是主要困难在于获取较小区域范围内的热带气旋活动信息。基于此，本文以县级行政区域(以下简称县域)为研究对象，利用ArcGis软件以及有关方法获取中国各

**收稿日期**：2013-09-27; **修订日期**：2014-02-18

**资助项目**：LCS气候研究开放课题青年基金2014年度资助项目；国家自然科学基金项目(41275076、40905046)共同资助

**通讯作者**：尹宜舟，男，安徽省人，副研究员，研究方向：台风气候及风险分析，E-mail: ship2001691@sohu.com

县域内热带气旋活动的基本信息。对这些信息进行统计，最终得出中国县域内热带气旋活动的持续时间、强度、频数以及综合特征的空间分布图，为以后的研究奠定基础。

## 2 资料方法

### 2.1 资料来源

本文采用了中国气象局上海台风研究所热带气旋最佳路径资料(http://www.typhoon.gov.cn/index.php?controller=spage&pid=169)，该套资料包含热带气旋活动的时间、经纬度位置、强度等每 6 h 一次的信息，由于早期热带气旋路径资料可信度存疑，因此本文的研究时段为 1971—2011 年。2006 年中国采用了新的热带气旋等级国家标准(GB/T19201—2006)[20]，以其底层中心附近最大平均风速为标准，分为热带低压(10.8 ~ 17.1 m/s)、热带风暴(17.2 ~ 24.4 m/s)、强热带风暴(24.5 ~ 32.6 m/s)、台风(32.7 ~ 41.4 m/s)、强台风(41.5 ~ 50.9 m/s)和超强台风(≥51.0 m/s)6 个等级。另外研究中采用的地理信息系统的地图底图来自于国家基础地理信息系统网的“国家基础地理信息系统全国 1∶400 万数据库”(http://nfgis.nsdi.gov.cn/nfgis/chinese/c_xz.htm)，编制时间为 1997 年(在线咨询)。

### 2.2 县域热带气旋活动信息获取方法

由于热带气旋资料是每 6 h 记录一次其中心位置，时间跨度比较大，难以判定热带气旋是否经过某县域。基于此，将两个相邻记录位置确定的线段称为热带气旋 6 h 路径段，在该路径段上另外再等间距地插入 8 个点，这样每个 6 h 路径段对应有 10 个点，这些点称之为热带气旋点(图 1，见下页)。通过线性插值得出插入的 8 个点对应的经纬度位置、中心风速，即相当于得到了每 0.6 h 一次的记录。这大大缩小了时间跨度，有利于我们判断经过县域的热带气旋情况。利用 ArcGis 软件获取了各县域内的热带气旋点信息，最终依据这些信息进行统计分析。

### 1.3 热带气旋综合指数介绍

为了更全面了解热带气旋的影响，本文采用了 TCPI(Tropical Cyclone Potential Impact Index)指数[21−23]来进行分析。TCPI 指数以热带气旋 6 h 路径段为基础，充分考虑了热带气旋对某一区域(如县域)的影响频数、强度、范围、持续时间等，将在邻近区域活动的热带气旋对该区域的影响也包含在内。可见，TCPI 指数反映了热带气旋对该区域的潜在影响程度，可用于热带气旋风险区划。将某区域一年之内的 TCPI 累加和称为年 TCPI (YTCPI)，一月之内的累加和称为月 TCPI (MTCPI)。

## 3 结果分析

### 3.1 经过频数

统计 1971—2011 年各县域内的热带气旋点数，每相同热带气旋编号的点仅保留一次，最终得出各县域内经过的热带气旋频数(图 2)。

从图 2 中 41 年来总频数分布可看出，中国东部及南部大部分县域都有热带气旋经过，而东北三省及内蒙古等北方部分县、西南部的贵州、云南省的部分县也有热带气旋经过的历史。频数较多的是广西、广东、海南、台湾、福建、浙江等沿海省区，而在内陆以江西省居多，安徽、湖南、湖北次之。频数最多的县域为台湾省花莲县，达到 32 次，平均每年 0.78 次；台湾省频数较多的县域还有宜兰县(26 次)、台北县(25 次)和台东县(23 次)；海南省较多的频数分别出现在三亚市(31 次)、琼中县(28 次)、东方市(27 次)、乐东县(27 次)、万宁市(27 次)、文昌市(26 次)；广东省较多的频数分别出现在电白县(27 次)，且另外有 6 个县市频数在 20 次以上。广西区有 5 个县市频数在 20 次以上，分别为灵山县和博白县(均为 23 次)、合浦县(22 次)、钦州市(21 次)、陆川县(21 次)；福建省有 2 个县市频数在 16 次及以上，分别为南安市(19 次)、安溪县(17 次)；浙江省频数最多的县市出现在台州市市辖区(14 次)；内陆以江西省兴国县经过的频数最多，达到 16 次，图 3 给出了经过兴国县的 16 个热带气旋路径，可以发现兴国

县处在台湾-福建-江西和广东-江西两路热带气旋　　的交汇处。

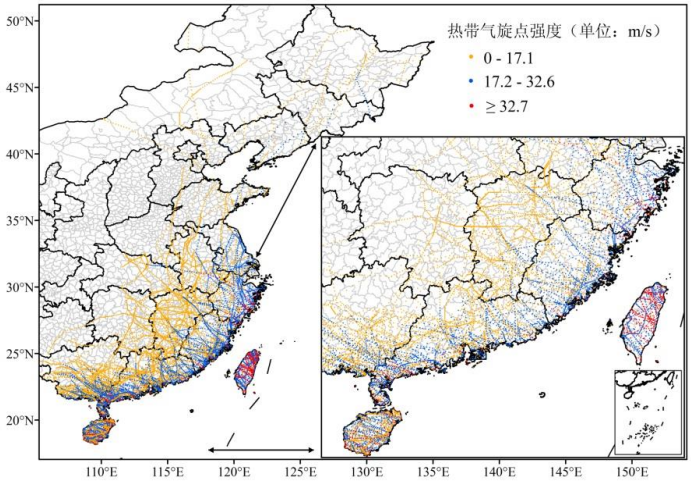


图 1　1971—2011 年热带气旋路径点示意图

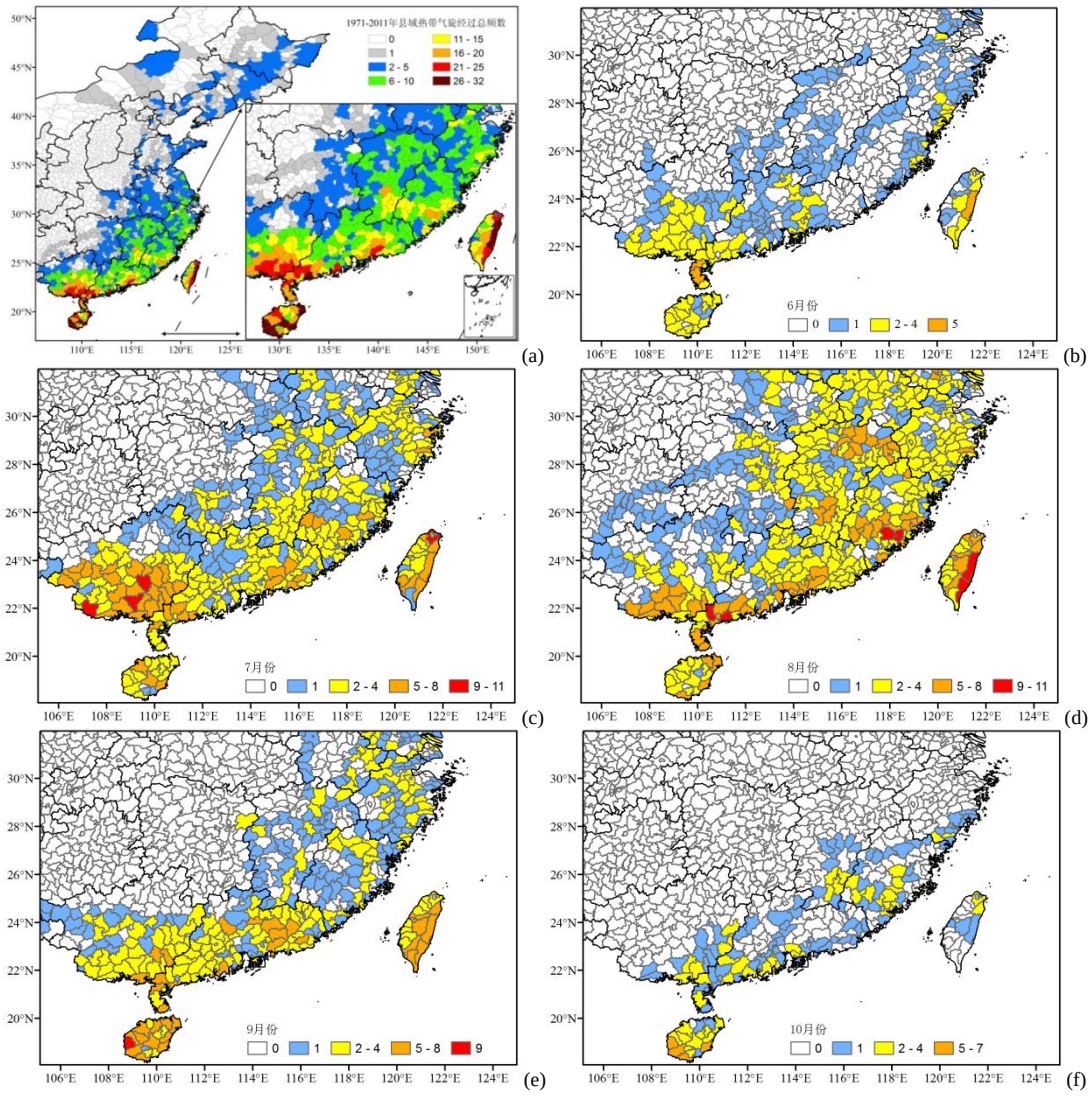


图 2　1971—2011 年中国县域经过的热带气旋年总频数及分月累计频数

a. 年总频数；b. 6 月；c.7 月；d. 8 月；e. 9 月；f. 10 月。

6月和10月由于登陆中国的热带气旋频数较少，因此有热带气旋经过的县域相对较少。6 月主要集中在海南及广东西南部和广西东南部、台湾东部沿海，最多频数出现在广东省雷州市和遂溪县以及台湾省的花莲县，均为5次。10月频数最多的县为海南省三亚市(7次)；除海南省外，广东和广西两省区的县域经过的热带气旋频数较 6月明显减少，与此同时，台湾东部-福建西北部-江西东南部分布相对较多。7 月频数较多(5 次及以上)县市主要分布在广西东南部以及台湾东部沿海，最大频数为 11 次(台湾省台北县)。8 月频数较多县市分布在广西中部沿海至广东中西部沿海一带、台湾-福建西南部-江西南部一带以及江西北部，最大频数出现在台湾省花莲县(11 次)。9月较多频数县比较密集地分布在海南省、广东东部以及台湾，最大频数出现在海南省东方市(9次)。

从 7—9 月的分布可以隐约地看出这三个月的月登陆中国热带气旋的路径变化，7 月以西行路径为主且较多地深入广西境内，且转向型路径较少，8 月西行和转向型热带气旋并存，且转向型路径数量达到鼎盛，且在江西省境内出现两处转向型路径的交集区。9月转向型路径数量减少，以西行路径为主，在福建东部以及浙江东部出现2～4 次的密集带，即 9 月较多地经过台湾-福建东部一带，然后转出，或经过浙江东部一带然后转出。

### 3.2 持续时间

由于客观条件的限制，各县域内热带气旋活动的确切持续时间难以获取，只能借助于 2.2 节中提到的热带气旋点。在某县域内的点数越多，表明在该县域内热带气旋活动的持续时间越长。基于此，本节统计分析了 1971—2011 年各县域内的热带气旋总点数以及 6—10 月各月内的总点数(图 4)。

经统计，1971—2011 年，海南省有 5 个县市(儋州市 126 个、琼中县 137 个、东方市 133 个、乐东县 148 个、三亚市 134 个)以及广西区有 3 个县市(钦州市 146 个、合浦县 138 个、博白县 109 个)境内热带气旋总点数达到 100 个以上，最多的点数为乐东县的148个。若按照每点次代表0.6 h，则热带气旋在该县内活动的时长达到 88.8 h，平均每年 2.2 h。另外广东省、台湾省、福建省、浙江省县域内最多的热带气旋点数分别为 93 个(雷州市和台山市)、91 个(花莲县、南投县)、67 个(南安市)、39 个(永嘉县)。内陆出现点数较多的分别为江西省境内的鄱阳县(58 个)、吉水县(43 个)、兴国县(42 个)、安徽省境内的东至县(52 个)和六安市市辖区(44 个)、湖北省的随州市(43 个)。

6 月热带气旋点数最多仅 18 个(约 10.8 h)，出现在广东省雷州市和广西区合浦县，且较大值基本上出现在 110 °E 附近的华南部分县市，这与6月的热带气旋以西北行路径为主有关。7—9 月分布范围比较广，且较大值密集区在雷州半岛及周边地区，各月最大点数分别出现在广西钦州市(49 个，约 29.4 h)、福建南安市(39 个，约 23.4 h)、台湾南投县(54 个，约 32.4 h)。据统计，8 月内陆省区出现 9 个县市热带气旋点数在 21 个及以上，且中国北部点数在 11 个以上的有 6 个县市，均明显多于其他月，表明 8 月热带气旋在中国内陆停留时间更持久。台湾省内最多点数为 9 月的 54 个，出现在南投县，多于 7 月的 39 个(台北县)和 8 月的 29 个(花莲县)，且 54 个为中国县域热带气旋点累积数的月份最大值。10 月分布范围明显缩小，尽管如此，海南省东方市点数达到 53 个(约 31.8 h)，且有 4 个县市点数在 21 个及以上。

综上所述，以雷州半岛为中心的周边县市地区是热带气旋活动密集区，持续时间相对较长，而内陆县市以 8 月持续时间较长。内陆县市之所以出现较长的持续时间，除与面积及热带气旋自身特性因素外，还可能与中高纬度天气系统与热带气旋的相互作用有关，减缓了热带气旋的推进。

### 3.3 平均强度

如前文所述，在得到热带气旋点的同时，通过线性内插得到了各新增点对应的强度。在此基础上，将各县域内 41 年来热带气旋点对应的强度进行平均，同时对 6—10 月各县域内点强度分别进行平均，在计算过程中，为了使结果更具针对

性，将强度为 0 的热带气旋点排除在外。最终结　　果如图 5 所示。

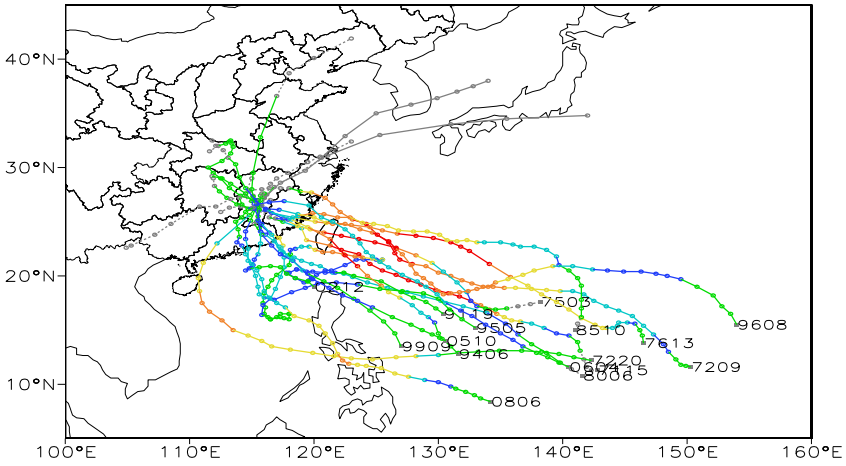


图 3　1971—2011 年经过江西兴国县的热带气旋路径

灰色：未达热带低压强度；绿色：热带低压；蓝色：热带风暴；青色：强热带风暴；黄色：台风；桔黄：强台风；红色：超强台。

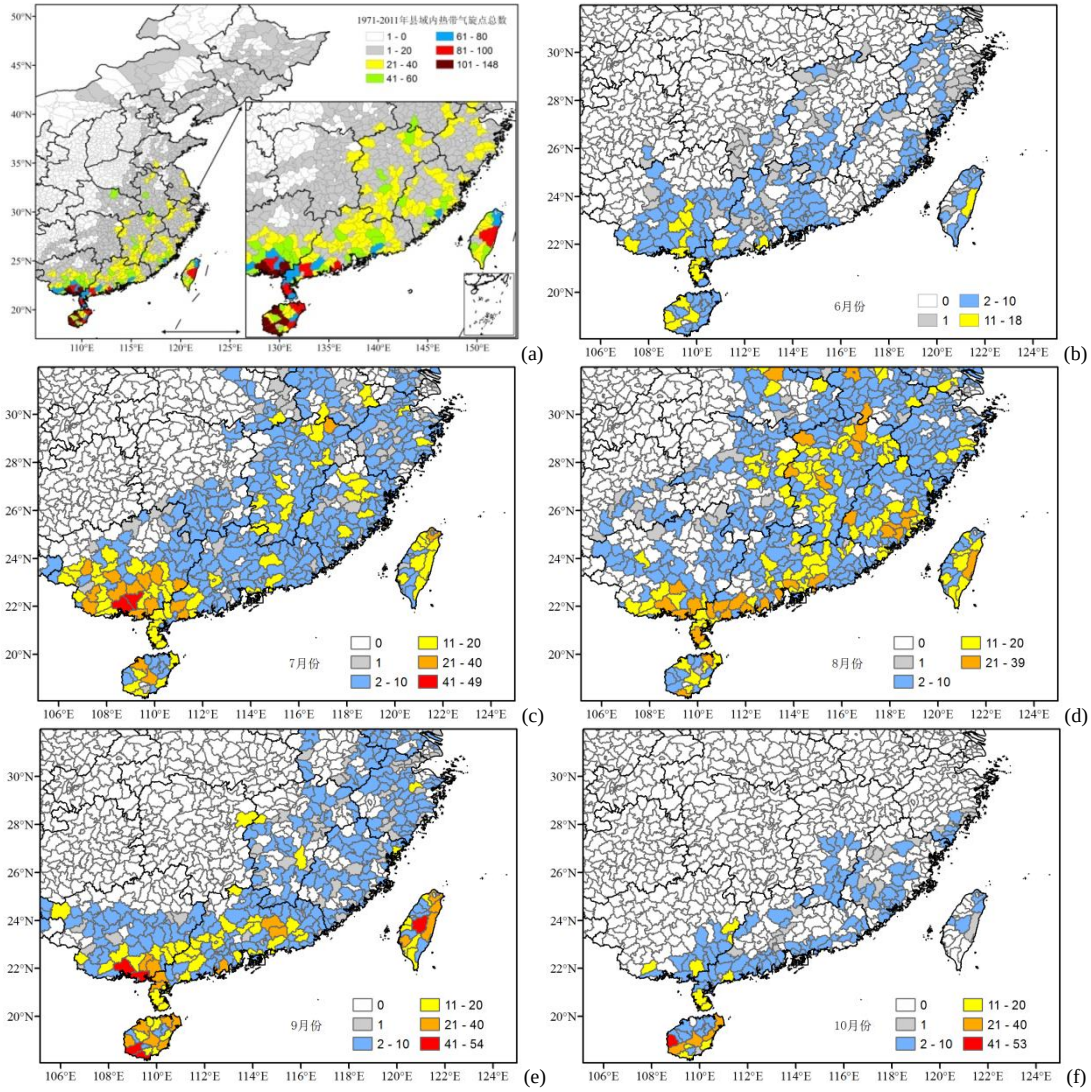


图 4　1971—2011 年中国县域内出现的热带气旋总点数及分月累计点数

持续时间，每点约代表 0.6 h。a. 年总点数；b. 6 月；c.7 月；d. 8 月；e. 9 月；f. 10 月。

41 年来,平均强度在 17.2 m/s 以上(热带风暴及以上级别)的县域主要分布在沿海各省区(主要分布在台湾、浙江、福建三省内),内陆省区县域平均强度几乎在 17.2 m/s 以下,最大值出现在安徽省泾县(27.6 m/s)。台湾省有四个县域平均强度在台风级别,分别为宜兰县(35.0 m/s)、桃园县(34.8 m/s)、花莲县(34.6 m/s)、新竹县(33.7 m/s),且宜兰县的 35.0 m/s 是中国县域的最大值。对比图 4 不难发现,虽然广西、海南、广东三省区 41 年来的总点数大值县域明显多于福建、台湾、浙江三省,但是平均强度较大值的县域基本分布在福建、台湾、浙江三省。

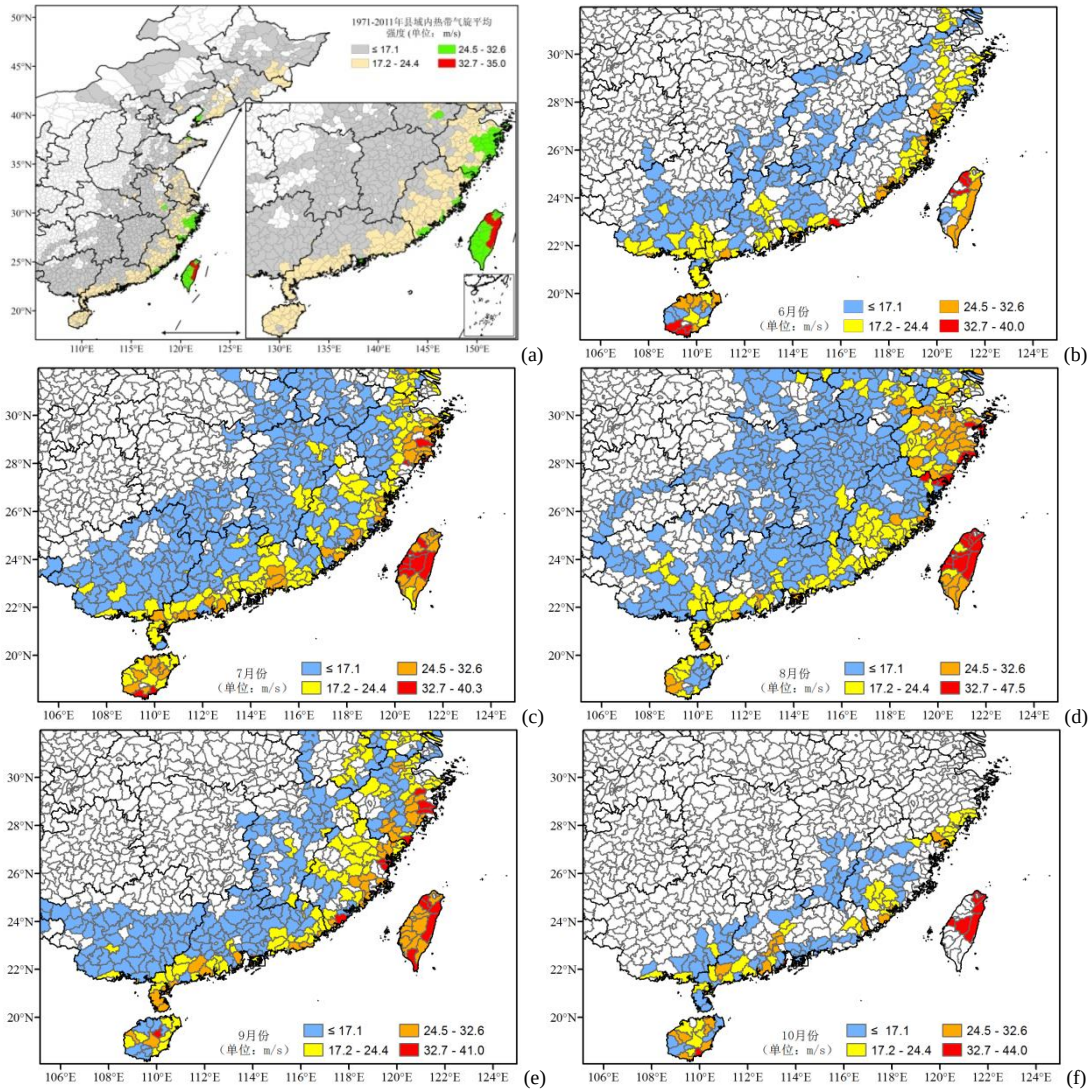


图 5 1971—2011 年中国县域内热带气旋平均强度 单位：m/s。a. 年平均；b. 6 月；c.7 月；d. 8 月；e. 9 月；f. 10 月。

分月来看，6 月以台湾省台中县 37 m/s 为最大，另外有 7 个县域平均强度达到台风级别，台湾东部以及海南北部多数县域平均强度达到强热带风暴级别。7 月强热带风暴及以上级别的县域数量增加，且以海南陵水县 40.3 m/s 为最大；台风级别县域达到 12 个,主要集中在台湾省中部地区。8 月强热带风暴级别的县域主要集中在浙江省，且该省内有 7 个县域达到台风级别；另外台湾省北部县域以台风级别为主，而南部以强热带风暴级别为主；8 月有 2 个县域强度达到强台风级别，分别为福建省的福鼎市(47.5 m/s)和柘荣县(43.8 m/s)。9 月以福建省漳浦县 41 m/s 为最大，台风级别的县域有 14 个,强热带风暴级别的县域主要集中在福建中东部至浙江中东部一带以及台

湾省。10 月由于热带气旋影响点数的减少，具有强度标示的县市也明显减少，强度最大值为 44 m/s(台湾省宜兰县、花莲县)，仅次于 8 月；强热带风暴级别的县域主要分布在广东和海南两省；台湾省仍有 4 个县市强度为强台风级别(台北县 42 m/s、宜兰县 44 m/s、花莲县 44 m/s、南投县 42 m/s)，2 个县市强度在台风级别。

### 3.4　综合指数

以上比较全面地分析了经过中国县域的热带气旋基本特征，即持续时间、平均强度、频数。众所周知，热带气旋本身特性对地区的影响是一个综合的过程，即多因素的合力，仅单独分析这三个方面是不够全面的，为此本节利用 TCPI 指数来进一步作探讨。

图 6 为年平均 YTCPI 及 6—10 月平均 MTCPI 的分布，全年受热带气旋潜在影响最严重的县域(平均 YTCPI 在 5 000 以上)主要分布在台湾省以及海南省(最大值为台湾台东县的 15 106)，其次分布在广西区东南部至浙江省东南部邻近海洋一带以及海南省西部。

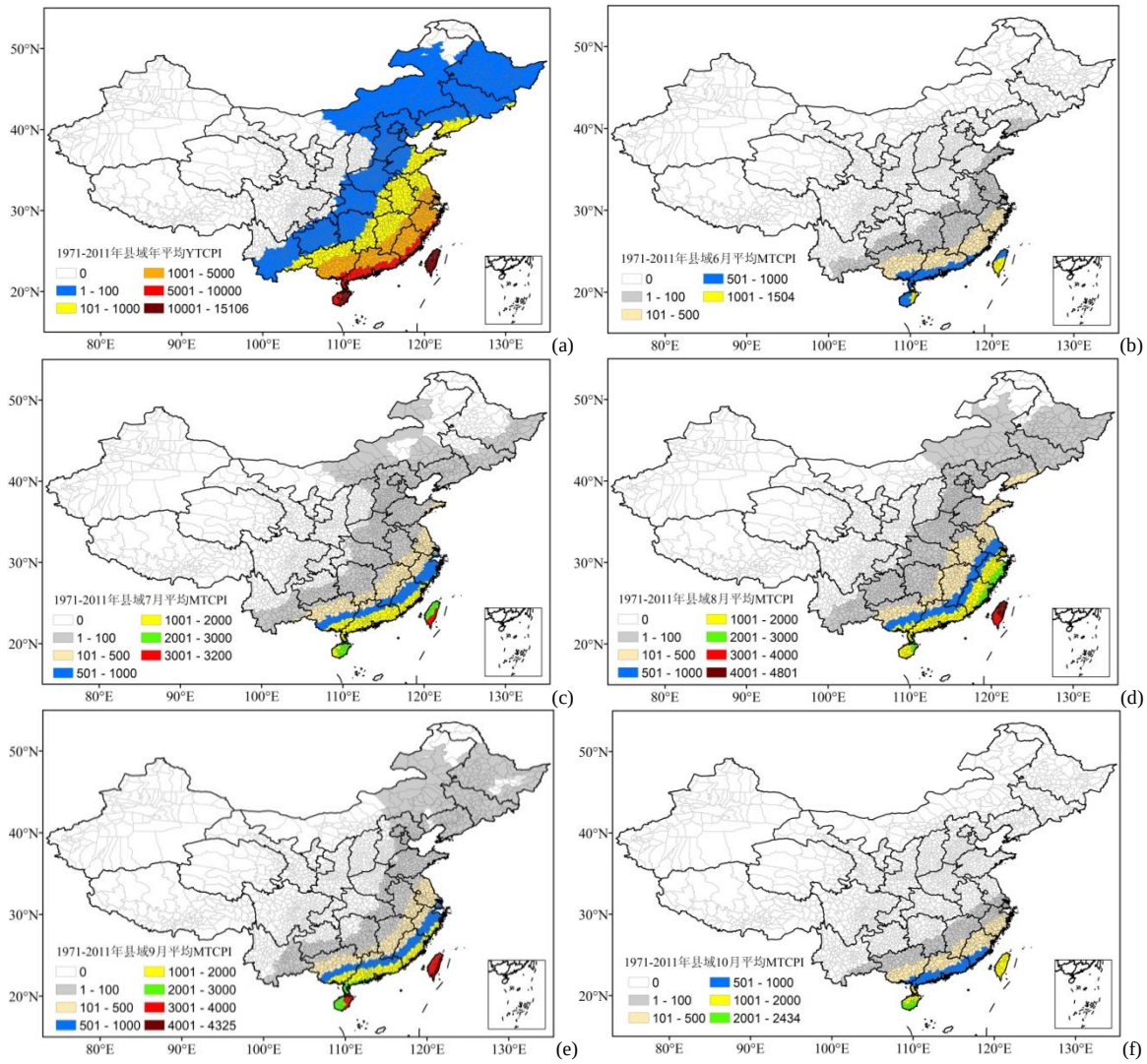


图 6　1971—2011 年中国平均 YTCPI 及 MTCPI 分布　a. 年平均；b. 6 月；c.7 月；d. 8 月；e. 9 月；f. 10 月。

以上这些区域往往是热带气旋影响最直接、最易造成灾害损失的地区。较为严重的地区(平均 YTCPI 在 1 001～5 000 之间)主要分布在广西东南部、广东福建内陆、江西南部及东部、浙江大部分地区、江苏东南部以及安徽湖南极少数县域。其中内陆县域，受热带气旋深入内陆后与地形以

及中高纬度天气系统相互作用，使得潜热迅速释放，也极易造成强对流天气。处于严重地区的沿海县域，由于常年登陆的热带气旋频数或者强度等不存在优势，使得平均 YTCPI 指数与沿海其他县市不在一个水平。平均 YTCPI 处于 101～1 000 区间的县域主要是云南东南部、广西北部、湖南南部及东部、江西中部北部大部分地区、湖北东部、河南东南部、安徽大部分地区、江苏中部及北部、山东东部以及辽宁南部，这些地区受热带气旋潜在影响较轻。数值在 100 以下的县域，主要是 41 年来偶尔几次热带气旋经过该县或在邻近地区，造成灾害损失的几率较小。

6 月受热带气旋潜在影响的县域主要集中在海南、台湾以及广西东南部至福建中部一带近海地区，特别是台湾中部及南部和海南东部县域 MTCPI 在 1 000 以上，其中最大值出现在台湾屏东县(1 504)。7—9 月，MTCPI 大于 100 的区域分布呈现出先扩大后再缩小的特征，8 月达到顶峰，基本上覆盖华东华南大部分县域以及辽宁和华中部分县域。501～1 000 区域在 7 月的基础上，8 月其东段向西北推移至江西东部以及安徽东南部，且向东扩展至江苏中部，9 月再回落至 7 月位置。1 001～2 000 的区域分布变化类似于 501～1 000，7 月主要分布于广西东南部县域至福建省临近海洋的县域一带，8 月向东扩展至浙江省，9 月再退至浙江中部沿海地区，且浙江和福建两省内的分布出现明显缩小。2 000 以上的区域在 7 月主要分布于海南省以及台湾省，且仅有台湾南部 4 个县市数值在 3 000～3 652 之间，最大值为屏东县的 3 200。8 月，台湾县市均在 3 000 以上，且最大值出现在基隆市(4 801)；2 001～3 000 区间主要分布在福建中部沿海至浙江东部沿海一带，海南仅东部 4 个县域在此区间。9 月台湾县域仍分别在3 000以上，以台东县的4 325为最大；海南东部县域在 3 001～4 000 区间，西部为 2 001～3 000 区间，较 8 月受热带气旋的潜在影响明显增大；雷州半岛至广东中部部分沿海县市数值在 2 001～3 000 之间。10 月潜在影响范围出现明显的南缩，且仅海南中南部地区数值在 2 001～2 434 之间，而台湾县域均在 1 001～2 000 之间，501～1 000 区间地区主要分布在广西东南部至福建南部一带。

## 4 结 论

对于热带气旋的基本特征分析，一般以整个中国以及省级为研究对象，鉴于此，本文以县级行政区域作为研究单元，分析了 1971—2011 年中国县域内受热带气旋影响的基本特征，包括热带气旋在县域内活动的持续时间、平均强度、经过频次以及综合指数，包括年及 6—10 月各月情况。

(1) 1971—2011 年，县域经过频次最多的为台湾省花莲县，达到 32 次，平均每年 0.78 次；平均强度最大值为台湾省宜兰县的 35 m/s；热带气旋活动累积持续时间最长的为海南省乐东县，初步估算累积时长为 88.8 h，平均每年 2.2 h。

(2) 经统计，6—10 月县域内热带气旋最多经过频次分别为 5 次(广东省雷州市和遂溪县、台湾省花莲县)、11 次(台湾省台北县)、11 次(台湾省花莲县)、9 次(海南省东方市)、7 次(海南省三亚市)；平均强度最大值分别为 37 m/s(台湾省台中县)、40.3 m/s(海南省陵水县)、47.5 m/s(福建省福鼎市)、41 m/s(福建省漳浦县)、44 m/s(台湾省花莲县)；持续时间最长的分别为 10.8 h(广东省雷州市和广西区合浦县)、29.4 h(广西区钦州市)、23.4 h(福建省南安市)、32.4 h(台湾省南投县)、31.8 h(海南省东方市)。

(3) 文中根据年平均 YTCPI 数值对我国受热带气旋潜在影响程度进行了划分，年平均 YTCPI 最大值出现在台湾省台东县(15 106)，即该县受热带气旋潜在影响最严重。6—10 月的平均 MTCPI 分布呈现先扩大后收缩的特征，在 8 月分布范围达到顶峰。

(4) 对于了解热带气旋精细化的气候特征、灾害风险评估分析等具有一定的价值。由于 10 余年来，部分县市行政区划出现变动，因此在获取最新的基础地理信息数据库后，作者将继续采用本文方法进一步更新有关图表。与此同时，各

级地方气象部门可以借助本文的方法更加详细地　　分析本地区精细化的热带气旋活动特征。

## 参 考 文 献：


[1] 王凌，罗勇，徐良炎，等. 近 35 年登陆我国台风的年际变化特征及灾害特点[J]. 科技导报，2006，24(11)：23-25.

[2] ZHANG Q, LIU Q F, WU L G. Tropical cyclone damages in China 1983–2006[J]. Bull AMS, 2009, 90(4)：489-495.

[3] 雷小途，陈佩佩，杨玉华，等. 中国台风灾情特征及其灾害客观评估方法[J]. 气象学报，2009，67(5)：875-883.

[4] XIAO F J, XIAO Z N. Characteristics of tropical cyclones in China and their impacts analysis[J]. Nat Hazards，2010，54(3)：827-837.

[5] 张娇艳，吴立广，张强. 全球变暖背景下我国热带气旋灾害趋势分析[J]. 热带气象学报，2011，27(4)：442-454.

[6] 陈联寿. 热带气旋研究和业务预报技术的发展[J]. 应用气象学报，2006，17(6)：672-681.

[7] 端义宏，金荣花. 我国现代天气业务现状及发展趋势[J]. 气象科技进展，2012，2(5)：6-11.

[8] 钱传海，端义宏，麻素红，等. 我国台风业务现状及其关键技术[J]. 气象科技进展，2012，2(5)：36-43.

[9] 雷小途，徐明，任福民. 全球变暖对台风活动影响的研究进展[J]. 气象学报，2009，67(5)：679-688.

[10] 王会军，范可，孙建奇，等. 关于西太平洋台风气候变异和预测的若干研究进展[J]. 大气科学，2007，31(6)：1 076-1 081.

[11] 雷小途. 全球气候变化对台风影响的主要评估结论和问题[J]. 中国科学基金，2011，25(2)：85-89.

[12] 王小玲，王咏梅，任福民，等. 影响中国的台风频数年代际变化趋势: 1951-2004 年[J]. 气候变化研究进展, 2006，5 (3)：135-138.

[13] 王小玲，任福民. 1957-2004 年影响我国的强热带气旋频数和强度变化[J]. 气旋变化研究进展, 2007，3(6)：345-349.

[14] 任福民，王小玲，董文杰，等. 登陆中国初、终热带气旋的变化[J]. 气候变化研究进展，2007，3(4)：224-228.

[15] 王咏梅，李维京，任福民，等. 影响中国台风的气候特征及其与环境场关系的研究[J]. 热带气象学报，2007，23 (6)：538-544.

[16] 王小玲，任福民. 1951—2004 年登陆我国热带气旋频数和强度的变化[J]. 海洋预报，2008，25(1)：65-73.

[17] 杨玉华，应明，陈葆德. 近 59 年来登陆中国热带气旋气候变化特征[J]. 气象学报，2009，67(5)：689-696.

[18] 赵珊珊, 王小玲. 影响中国的热带气旋极端事件年代际变化[J]. 气候变化研究进展，2012，8(1)：16-21.

[19] 应明，杨玉华，陈葆德，等. 近 50 年影响中国热带气旋的气候变化特征[J]. 中国科学：地球科学，2011，41(9)：1 352-1 364.

[20] 中国标准化管理委员会. 热带气旋等级国家标准(GB/T 19201—2006)[S]. 北京: 中国国家标准化出版社，2006: 1-3.

[21] 尹宜舟，肖风劲，罗勇，等. 我国热带气旋潜在影响力指数分析[J]. 地理学报，2011，66(3)：367-375.

[22] 尹宜舟. 我国热带气旋潜在影响力分析[D]. 北京：中国科学院研究生院, 2011: 46-76.

[23] 尹宜舟，罗勇，肖风劲，等. 热带气旋年潜在影响力指数[J]. 中国科学：地球科学，2013, 43(12)：2 086-2 098.


# BASIC CLIMATIC CHARACTERISTICS OF TROPICAL CYCLONES IN COUNTY-LEVEL ADMINISTRATIONS OF CHINA DURING 1971—2011


YIN Yi-zhou[1, 2, 3], LUO Yong[3], XIAO Feng-jing[2], ZHU Xin-jun[4]

(1. Laboratory for Climate Studies, China Meteorological Administration, Beijing 100081, China;
2. National Climate Center, China Meteorological Administer, Beijing 100081, China;
3. Center for Earth System Science, Tsinghua University, Beijing 100084, China;
4. Jiangning Meteorological Bureau, Jiangsu Province, Nanjing 211100, China)



**Abstract:** By using the ArcGis software, the basic information for the activity of tropical cyclones in county-level administrative regions of China from 1971 to 2011 is obtained, including longitude and latitude, duration, and intensity, among others. With it, it is possible to study the influence the tropical cyclone makes on these regions. Results showed that the Hualian County in Taiwan province has the most frequency of tropical cyclones that pass through it, with an annual frequency of 0.78. The maximum average intensity appears in Yilan county Taiwan province, up to 35 m/s. The longest accumulative duration of the tropical cyclone activity is 2.2 h per year in average in Ledong county Hainan province. The most serious potential impact by tropical cyclone occurs in Taidong county Taiwan province as the Yearly Tropical Cyclone Potential Impact Index (YTCPI) is 15 106. Moreover, the monthly characteristics are analyzed during the typhoon season in this paper. Helpful in learning about the basic characteristics of the influences by tropical cyclones in the county-level administrations of China, the conclusions in this paper can be provided to the department concerned.



**Key words:** climatology; statistical characteristic; basic geographic information system; tropical cyclone; county characteristics; typhoon disaster prevention and reduction

Clim Dyn (2014) 43:1449–1462
DOI 10.1007/s00382-013-1960-0

# Present and projected degree days in China from observation, reanalysis and simulations

**Qinglong You · Klaus Fraedrich · Frank Sielmann · Jinzhong Min · Shichang Kang · Zhenming Ji · Xiuhua Zhu · Guoyu Ren**

Received: 23 August 2013 / Accepted: 30 September 2013 / Published online: 8 October 2013
© Springer-Verlag Berlin Heidelberg 2013

**Abstract** Degree days are usually defined as the accumulated daily mean temperature varying with the base temperature, and are one of the most important indicators of climate changes. In this study, the present-day and projected changes of four degree days indices from daily mean surface air temperature output simulated by Max Planck Institute, Earth Systems Model of low resolution (MPI-ESM-LR) model are evaluated with the high resolution gridded-observation dataset and two modern reanalyses in China. During 1979–2005, the heating degree days (HDD) and the numbers of HDD (NHDD) have decreased for observation, reanalyses (ERA-Interim and NCEP/NCAR) and model simulations (historical and decadal experiments), consistent with the increasing cooling degree days (CDD) and the numbers of CDD (NCDD). These changes reflect the general warming in China during the past decades. In most cases, ERA-Interim is closer to observation than NCEP/NCAR and model simulations. There are discrepancies between observation, reanalyses and model simulations in the spatial patterns and regional means. The decadal hindcast/forecast simulation performance of MPI-ESM-LR produce warmer than the observed mean temperature in China during the entire period, and the hindcasts forecast a trend lower than the observed. Under different representative concentration pathway (RCP) emissions scenarios, HDD and NHDD show significant decreases, and CDD and NCDD consistently increase during 2006–2100 under RCP8.5, RCP4.5 and RCP2.6, especially before the mid-21 century. More pronounced changes occur under RCP8.5, which is associated with a high rate of radiative forcing. The 20th century runs reflect the sensitivity to the initial conditions, and the uncertainties in terms of the inter-ensemble are small, whereas the long-term trend is well represented with no differences among ensembles.

**Keywords** Degree days · MPI-ESM-LR · NCEP/NCAR and ERA-Interim · China

Q. You (✉) · J. Min
Key Laboratory of Meteorological Disaster, Ministry of Education, Nanjing University of Information Science and Technology, Nanjing 210044, China
e-mail: yqingl@126.com

Q. You · K. Fraedrich · F. Sielmann · X. Zhu
Max Plank Institute for Meteorology, KlimaCampus, 20144 Hamburg, Germany

S. Kang
State Key Laboratory of Cryospheric Science, Chinese Academy of Sciences (CAS), Lanzhou 730000, China

S. Kang · Z. Ji
Laboratory of Tibetan Environment Changes and Land Surface Processes, Institute of Tibetan Plateau Research, Chinese Academy of Sciences (CAS), Beijing 100085, China

G. Ren
Laboratory for Climate Studies, National Climate Center, China Meteorological Administration (CMA), Beijing 100081, China

## 1 Introduction

According to the Intergovernmental Panel on Climate Change (IPCC) Fourth Assessment Report (AR 4), the global average surface air temperature has risen by $0.74 \pm 0.18$ °C during 1906–2005, and most of the observed increase in globally averaged temperature since the mid-20th century is very likely due to the observed increase in anthropogenic greenhouse gas concentrations (IPCC 2007). However, trends of temperature always

exhibit temporal variations. In China, the warming is very evident, supporting by the proxy indices such as the ice core and tree ring (Wang and Gong 2000). Based on 740 observational stations, the surface air temperature in China's mainland as a whole rose by about 1.1 °C for the last 50 years, with a warming rate of about 0.22 °C/decade, which is more rapid than the average values of the world and Northern Hemisphere. Moreover, the most evident warming has occurred in winter and spring, and the Northeast China, North China and Northwest China experienced more significant warming in terms of annual mean temperature (Ding et al. 2007; Ren et al. 2005, 2011a, b). Thus, the trends in annual mean temperatures show a large spatial heterogeneity and regional differences across China, which may be explained by the feedbacks of cold waves and snow cover change (Wang et al. 2010). Except for the warming of surface temperature, both the low-level atmospheric temperature and the middle-upper troposphere air temperatures have changed responding to the global warming (Wang et al. 2012).

The impact of climate change in China has been observed in many records and is discussed in the previous studies (Wang et al. 2010, 2012). For example, the glacier areas in China have shrunk about 2–10 % over the past four decades, and the total glacier area has receded by about 5.5 % (Li et al. 2008; Yao et al. 2012). The permafrost in China is significantly degenerating, indicated by shrinking areas of permafrost, increasing depths of the active layer, rising of lower limit of permafrost and thinning areas of the seasonal frost depth (Li et al. 2008; Zhang 2007). In addition, the spatial pattern and variability of snow cover in China has changed, mainly explained by the linear variations of snowfall and snow season temperature (Qin et al. 2006). Meanwhile, the climate extreme is also accompanied by climate change in China, and the previous studies have addressed the observed and projected trends in frequency and intensity of climate extremes (Ren et al. 2011b; You et al. 2011; Zhai and Pan 2003). Twelve indices of extreme temperature have been analyzed during 1961–2003, which reflect the consistent warming (You et al. 2011). This is in good agreement with the previous results that the frequency of warm nights significantly has increased, and the cool nights decreased over most China (Zhai and Pan 2003). A new climate extreme index with evident climatological and socio-economic significance is developed, which has been composed with the country-averaged frequencies of high temperature, low temperature, intense precipitation, dust storm and strong wind events, meteorological drought area percentage, and number of land-falling tropical cyclones (Ren et al. 2011b).

To summarize, the previous temperature studies focus on the seasonal and annual temperature, and the consequences of climate change in China. However, there are no results about degree days in China under the representative concentration pathway (RCP) scenarios (Moss et al. 2010). Degree days can be defined as a measure of heating or cooling, and are usually considered as one of the important indicators of global climate change. As degree days indices are a measure to indicate the demand for energy to heat or cool building. The monthly and/or annual cooling and heating requirements of specific buildings in different locations can be estimated by means of the degree days concept. The methods assure that the energy needs of a building are proportional to the difference between the mean daily temperature and a base temperature. The base temperature is the outdoor temperature below or above which heating or cooling is needed (Büyükalaca et al. 2001).

Traditionally, heating degree days (HDD) are calculated at a base temperature of 18 °C and cooling degree days (CDD) are determined at a base temperature of 22 °C. However, the base temperature varied widely from one building to another due to different building characteristics, it has been questioned by a number of authors and must be employed with caution (Büyükalaca et al. 2001; Jiang et al. 2009; OrtizBeviá et al. 2012; Rehman et al. 2011). In Turkey, the base temperature for HDD are selected in the range of 18–28 °C, which is from 18 to 28 °C for cooling degree day (Büyükalaca et al. 2001). In Saudi Arabia, a heating base temperature in the range of 14–22 °C is suitable, and the recommended cooling base temperature is between 23 and 25.5 °C for buildings without insulation and between 25.5 and 27.8 °C for well-insulated buildings (Rehman et al. 2011). In China, 18 °C is usually accepted as the base temperature for HDD and 24 °C for CDD (Jiang et al. 2009). In this study, the base temperature of 18 and 24 °C is used for heating and CDD, respectively. The present and projected degree days in China are studied by the outputs of a global climate model (GCM), which contribute to the IPCC AR5 under the different emissions scenario. The comparison between reanalysis and model outputs has also been evaluated. The objective of this study is to provide a reliable basis for decision making and formulation of environmental policy in China.

## 2 Data and methods

For the coming IPCC AR 5, the simulations from the new generation of state-of-the-art GCMs are available for analysis within the Coupled Model Intercomparison Project Phase 5 (CMIP5) (Taylor et al. 2012). Compared with the previous models, CMIP5 includes more comprehensive global climate modes such as earth system models with generally higher spatial resolution, and have been used to evaluate the extreme climate and weather events on the

global scales (Sillmann et al. 2013a, b). The model used in this study is the latest version of Max Planck Institute for Meteorology (MPI-M), Earth Systems Model (MPI-ESM), Hamburg, Germany, performed with the version of MPI-ESM coupled model of low resolution (MPI-ESM-LR). The model outputs by MPI-ESM-LR have been organized by the Program for Climate Model Diagnosis and Intercomparison (PCMDI) for the IPCC AR 5. The historical, decadal and long-term experiments simulations are selected in this study. The historical experiments are aimed at reproducing the climate evolution of the twentieth century as accurately as possible, by considering all major natural and anthropogenic forcing, such as changes in atmospheric greenhouse gases, aerosol loadings, solar output and land use (Wild et al. 2013). Most historical experiments start around 1860 and end around 2005. The decadal experiments will be possible to assess the skill of the forecast system in predicting climate statistics for times when the initial climate state may exert some detectable influences, which is a set of 10-year hindcasts initialized from observed climate states near the years 1960, 1965, and every 5 years to 2005 (Taylor et al. 2012). The long-term experiments are forced by observed atmospheric composition changes (reflecting both anthropogenic and natural sources) and include time-evolving land cover. The long-term experiments have three future projection simulations forced with specified concentrations, consistent with a high emissions scenario (RCP8.5), a midrange mitigation emissions scenario (RCP4.5), and a low emissions scenario (RCP2.6) (Taylor et al. 2012). The CMIP5 projections of climate change are driven by concentration or emission scenarios consistent with the RCPs (Moss et al. 2010). In contrast to the scenarios described in the IPCC "Special Report on Emissions Scenarios" (SRES) used for CMIP3, which did not include policy intervention, the RCPs are mitigation scenarios that assume policy actions will be taken to achieve certain emission targets (Taylor et al. 2012). For example, RCP8.5 emission scenarios mean that radiative forcing increases throughout the 21st century before reaching a level of about 8.5 W $m^{-2}$ at the end of the century.

In addition to the CMIP5 models, daily mean surface temperatures estimated from NCEP/NCAR and ERA-Interim reanalysis are selected. NCEP/NCAR reanalysis is provided by the National Oceanic and Atmospheric Administration (NOAA)/Earth System Research Laboratory (ESRL)/Physical Sciences Division (PSD), Boulder, Colorado, USA, from their website at http://www.cdc.noaa.gov/. The datasets cover January 1948 to the present with a spatial resolution of 2.5° × 2.5° (Kalnay et al. 1996), and are initialized with a wide variety of weather observations, including ships, planes and satellite. The ERA-Interim reanalysis data are obtained from the European Centre for Medium-Range Weather Forecasts (ECMWF) website (http://www.ecmwf.int/), available from January 1979 to the present with a spatial resolution of 1.5° × 1.5° (Dee et al. 2011). It includes a large variety of 3-h surface parameters, describing weather as well as ocean-wave and land-surface conditions, and 6-h upper-air parameters covering the troposphere and stratosphere (Dee et al. 2011). Compared with ERA-40 (Uppala et al. 2005), ERA-Interim has been improved on the representation of the hydrological cycles, the quality of the stratospheric, and the consistency in time of reanalyzed geophysical fields.

**Table 1** Definitions of four degree days indices used in this study

| Index | Descriptive name | Definition | Units |
|---|---|---|---|
| HDD | Heating degree day | Sum of absolute TG where TG < 18 °C | °C |
| CDD | Cooling degree day | Sum of TG where TG > 18 °C | °C |
| NHDD | Number of heating degree day | Account number of days where TG < 24 °C | day |
| NCDD | Number of cooling degree day | Account number of days where TG > 24 °C | day |

TG is daily mean temperature

For the purpose of reanalyses (NCEP/NCAR and ERA-Interim) and MPI-ESM-LR climate model validation (history and decadal experiments), we use the 0.5° × 0.5° daily temperature datasets in China for the period of 1979–2005 (Xu et al. 2009). The dataset is primarily developed for the validation of climate models, and has potential applications in the studies such as climate, hydrology and ecology.

Four indices of degree days are used and detailed descriptions are provided in Table 1. The HDD, the numbers of HDD (NHDD), the CDD and the numbers of CDD (NCDD) are based on the daily mean temperatures from multi-datasets. In order to validate the indices from model simulations and reanalyses, they are compared with observations during 1979–2005. After that, indices from the long-term experiments under RCP8.5, RCP4.5 and RCP2.6 are analyzed from 2006 to 2100. Due to different resolutions between CMIP5 output, reanalyses and observations, all the indices are interpolated into a common 144 × 73 grid (2.5° × 2.5°) using the bilinear interpolation procedure implemented in the Climate Data Operators (http://code.zmaw.de/projects/cdo). To produce the values for the whole China, there are 190 grid points covering the entire region (Fig. 1).

The Mann–Kendall test for a trend and Sen's slope estimates are used to detect trends in degree days indices series (Sen 1968). A trend is considered to be statistically significant if it is significant at the 5 % level. Three statistical metrics are used to quantify the accuracy of the reanalysis and simulations: Relative bias (RB), root-mean-square error (RMSE) and correlation coefficient (R).

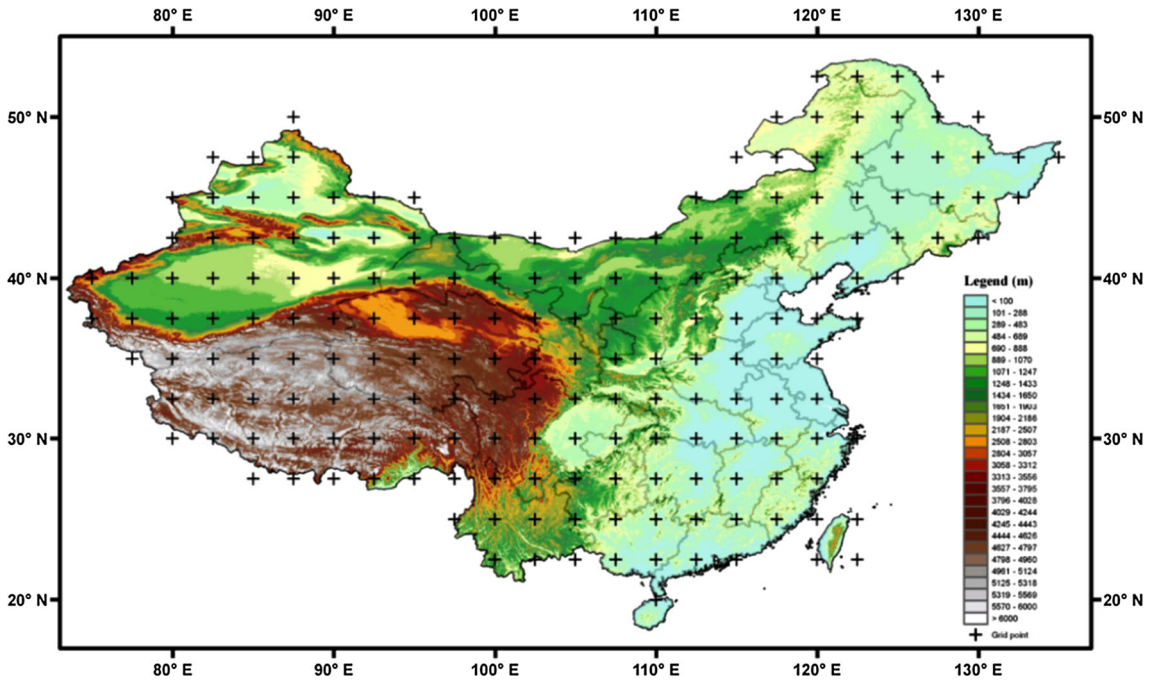


**Fig. 1** Topography of China and the distribution of 190 grid points used in this study

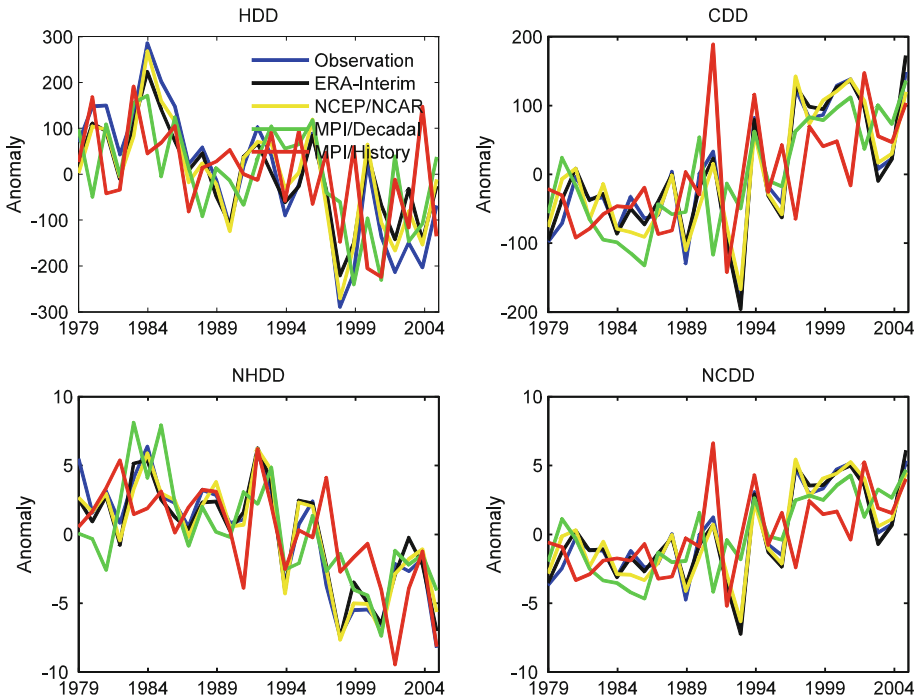


**Fig. 2** Anomalies of HDD, CDD, NHDD and NCDD from observation, ERA-Interim, NCEP/NCAR reanalysis data, the historical and decadal experiments simulation outputs in China during 1979–2005

## 3 Results: past and future changes of degree days

Figure 2 shows the regional changes of HDD, CDD, NHDD and NCDD from observation, two reanalyses and two experiments simulations in China on the annual basis during 1979–2005. The spatial patterns of trends for HDD, CDD, NHDD and NCDD from multi-datasets in China during 1979–2005 are shown in Figs. 3, 4 and 5, respectively. The seasonal and annual trends of each series of indices calculated by Mann–Kendall slope estimator (Sen 1968) are summarized in Table 2. The correlation coefficients between multi-datasets are listed in Table 3.

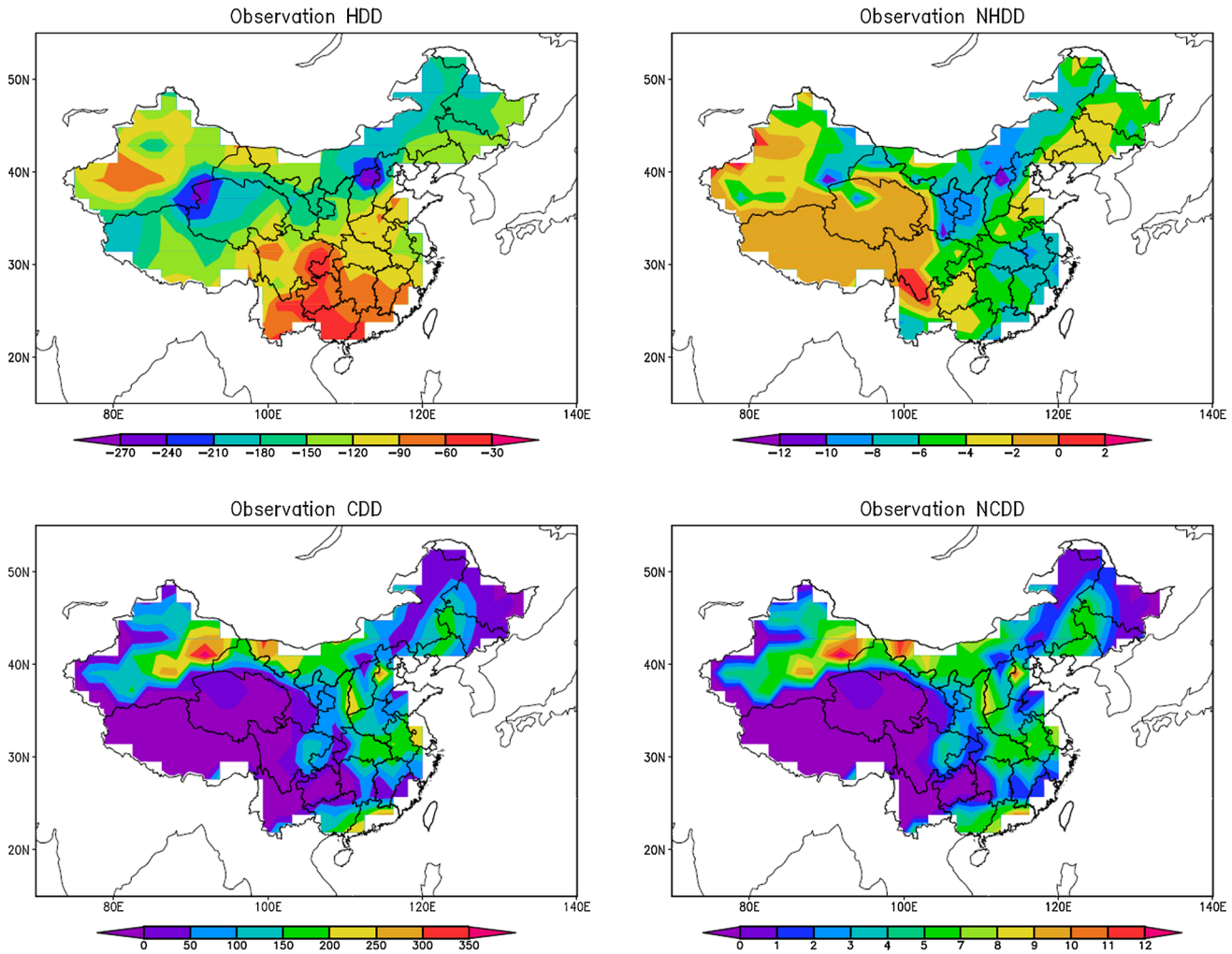


**Fig. 3** Spatial trends of HDD, NHDD, CDD and NCDD from observation in China during 1979–2005. The unit is °C/decade for HDD and CDD, and is day/decade for NHDD and NCDD, respectively

### 3.1 Heating degree days (HDD)

It can be seen from Fig. 2 that the HDD from multi-datasets has decreased during the studied period. The decreasing rates are −130.97, −82.48, −80.52, −65.45 and −69.48 °C/decade for observation, ERA-Interim, NCEP/NCAR, the decadal experiments and historical experiments, respectively. The HDD from both ERA-Interim and NCEP/NCAR reanalyses is closer to observation than the decadal experiment than the historical experiments, indicated by the high correlation coefficients ($R > 0.9$). There are some differences of the season with the largest trend magnitudes. The largest decreasing trends for observation, ERA-Interim and NCEP/NCAR occur in the transition season of spring and autumn, respectively, while both the decadal experiments and historical experiments reveal largest decreasing trends in winter. Overall, the multi-datasets show large decreasing trend magnitudes in the high terrain (such as the Tibetan Plateau) and in high latitude regions (such as the northeastern China), with the exception of the historical experiments. Due to the lower altitudes and latitudes, southeastern China has smallest decreasing trends for all the used datasets. It should be noted that the historical experiments show greatest increases in the northern China, which is not consistent with the observed global warming in the region (Liu et al. 2004).

### 3.2 Cooling degree days (CDD)

In contrast to HDD, the decreasing trends of CDD are significant for all datasets during 1979–2005, and the observed trend magnitude is 76.91 °C/decade on the annual basis. The correlation coefficients between observation, reanalyses and simulations are higher ($R > 0.45$), and reanalyses are very well captured than the simulations. In most cases, the pronounced increases occur in spring and autumn. For the spatial patterns, the southeastern China have larger increasing trends and the Tibetan Plateau have

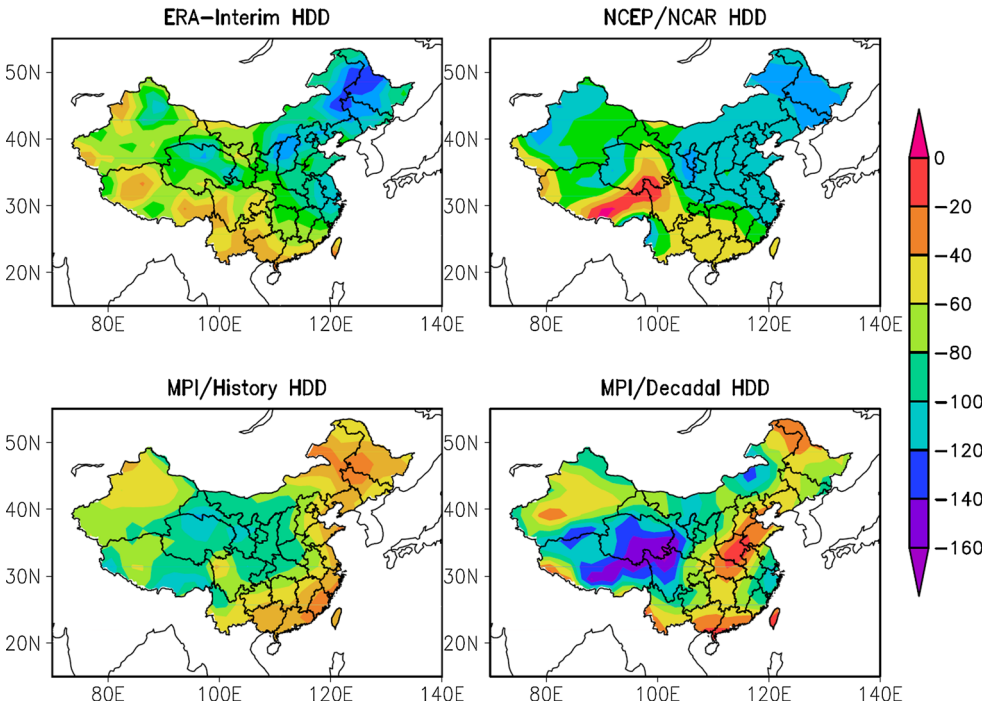


**Fig. 4** Spatial trends of HDD from ERA-Interim, NCEP/NCAR reanalysis data and the historical and decadal experiments simulation outputs in China during 1979–2005. The unit is °C/decade

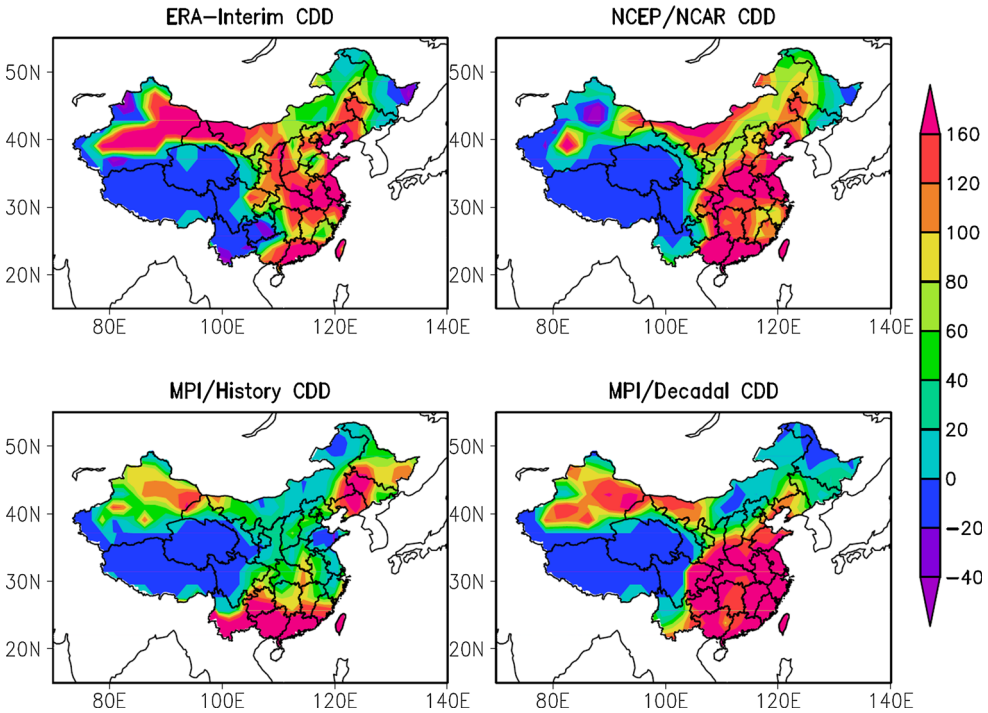


**Fig. 5** Same as Fig. 4, but for CDD

the smaller increases, and the differences between reanalyses and model simulations exist in the northeastern TP.

### 3.3 Number of degree days (NHDD and NCDD)

For NHDD and NCDD, the decreased NHDD and increased NCDD are clear during 1979–2005 for observation, reanalyses and model simulations. Compared with observation, ERA-Interim data reproduce the variabilities of NHDD and NCDD better than NCEP/NCAR, as reflected by the mean anomalies and correlation coefficients. NCEP/NCAR overestimate NHDD and underestimate NCDD, due to the data assimilation in the model system (Ma et al. 2008). On the annual basis, the

**Table 2** Regional trend of HDD, CDD, NHDD and NCDD from observation, ERA-Interim, NCEP/NCAR reanalysis data and the simulation outputs under different run experiments in China during 1979–2005 on the annual and seasonal basis

| Index | Unit | Annual | Spring | Summer | Autumn | Winter |
|---|---|---|---|---|---|---|
| Observation | | | | | | |
| HDD | °C/decade | **−130.97** | **−43.61** | −2.17 | **−37.71** | −40.32 |
| CDD | °C/decade | **76.91** | 6.18 | **53.26** | **12.27** | 0 |
| NHDD | Day/decade | **−3.84** | **−1.30** | **−1.45** | **−1.09** | −0.13 |
| NCDD | Day/decade | **2.83** | 0.23 | **1.86** | **0.47** | 0 |
| ERA-Interim | | | | | | |
| HDD | °C/decade | **−82.48** | **−33.52** | −0.93 | −19.25 | −21.81 |
| CDD | °C/decade | **74.95** | 6.68 | **44.14** | **14.97** | **0.59** |
| NHDD | Day/decade | **−2.99** | **−0.94** | **−0.90** | **−0.93** | −0.26 |
| NCDD | Day/decade | **2.67** | 0.26 | **1.68** | **0.56** | 0.02 |
| NCEP/NCAR | | | | | | |
| HDD | °C/decade | **−80.52** | **−19.06** | **11.80** | **−30.29** | −31.67 |
| CDD | °C/decade | **64.64** | **5.75** | **43.54** | **12.86** | 0.13 |
| NHDD | Day/decade | **−3.22** | **−0.68** | **−1.10** | **−1.18** | −0.30 |
| NCDD | Day/decade | **2.47** | **0.22** | **1.55** | **0.49** | 0.01 |
| MPI/decadal | | | | | | |
| HDD | °C/decade | **−65.45** | **−25.81** | **−12.98** | −3.77 | −35.15 |
| CDD | °C/decade | **76.93** | 0.52 | **56.73** | **22.66** | **1.84** |
| NHDD | Day/decade | **−2.66** | **−0.79** | −0.93 | −0.92 | −0.29 |
| NCDD | Day/decade | **2.73** | 0.02 | **2.01** | **0.87** | **0.08** |
| MPI/history | | | | | | |
| HDD | °C/decade | **−69.48** | −1.37 | **−20.04** | **−20.19** | −21.75 |
| CDD | °C/decade | **55.49** | **21.04** | **27.86** | 4.41 | 0.01 |
| NHDD | Day/decade | **−2.80** | **−0.72** | −0.93 | **−1.05** | −0.07 |
| NCDD | Day/decade | **2.01** | **0.74** | **0.95** | 0.17 | 0 |

The linear trends of all series are calculated by Mann–Kendall slope estimator. Trends at the 5 % level are marked in bold

decreasing trends of NHDD for observation, ERA-Interim, NCEP/NCAR, the historical and decadal experiments are −3.84, −2.99, −3.22, −2.66 and −2.80 day/decade, respectively, which are mostly contributed by winter. Meanwhile, the increased annual trends of NHDD for observation, ERA-Interim, NCEP/NCAR, the historical and decadal experiments are 2.83, 2.76, 2.47, 2.73 and 2.01 day/decade, respectively, which are slightly larger than NHDD with the exception of the historical experiments. For the spatial patterns of NHDD, the multi-datasets reveal the negative trends in the western China, and positive trends in the southern China. The differences between ERA-Interim and NCEP/NCAR are found in the Tibetan Plateau, where the pronounced upward trends occur in NCEP/NCAR and slight downward trends for ERA-Interim. In most regions, both the historical and decadal experiments show similar spatial patterns of trends, while they differ for ERA-Interim and NCEP/NCAR in the northeastern China. For the spatial trends of NCDD, the multi-datasets show slight increases in the southern China, and larger increases in the northeastern China. The differences between ERA-Interim and NCEP/NCAR occur in the Tibetan Plateau, similar to NHDD, and both reanalyses depict pronounced positive trends in the northeastern China. Both the historical and decadal experiments of NCDD show consistencies, which differ from renalyses in the northeastern China.

### 3.4 Future changes

Figure 6 shows the regional changes of HDD, CDD, NHDD and NCDD from the long-term simulations in China during 2006–2100 under RCP8.5, RCP4.5 and RCP2.6. The spatial patterns of trends for HDD, CDD, NHDD and NCDD under RCP8.5 and RCP2.6 are displayed in Figs. 7 and 8, respectively. The seasonal and annual trends of HDD, CDD, NHDD and NCDD are summarized in Table 4.

During the period 2006–2100, HDD and NHDD in China display significant decreases under RCP8.5, with the rates of −142.17 °C/decade and −5.11 day/decade, respectively, mostly contributed by winter. Both HDD and NHDD show

**Table 3** Correlation coefficients between observation, ERA-Interim, NCEP/NCAR reanalysis data and the simulation outputs under different run experiments in China in China during 1979–2005 on the annual basis

| | Observation | ERA-Interim | NCEP/NCAR | MPI/decadal | MPI/history |
|---|---|---|---|---|---|
| HDD | | | | | |
| Observation | 1.00 | | | | |
| ERA-Interim | 0.97 | 1.00 | | | |
| NCEP/NCAR | 0.96 | 0.97 | 1.00 | | |
| MPI/decadal | 0.61 | 0.52 | 0.59 | 1.00 | |
| MPI/history | 0.33 | 0.24 | 0.27 | 0.34 | 1.00 |
| CDD | | | | | |
| Observation | 1.00 | | | | |
| ERA-Interim | 0.99 | 1.00 | | | |
| NCEP/NCAR | 0.96 | 0.97 | 1.00 | | |
| MPI/decadal | 0.70 | 0.72 | 0.75 | 1.00 | |
| MPI/history | 0.49 | 0.47 | 0.45 | 0.34 | 1.00 |
| NHDD | | | | | |
| Observation | 1.00 | | | | |
| ERA-Interim | 0.96 | 1.00 | | | |
| NCEP/NCAR | 0.97 | 0.98 | 1.00 | | |
| MPI/decadal | 0.73 | 0.74 | 0.73 | 1.00 | |
| MPI/history | 0.64 | 0.63 | 0.64 | 0.45 | 1.00 |
| NCDD | | | | | |
| Observation | 1.00 | | | | |
| ERA-Interim | 0.99 | 1.00 | | | |
| NCEP/NCAR | 0.96 | 0.97 | 1.00 | | |
| MPI/decadal | 0.70 | 0.72 | 0.75 | 1.00 | |
| MPI/history | 0.49 | 0.46 | 0.45 | 0.34 | 1.00 |

larger decreasing trends in the northeastern China and the Tibetan Plateau, and slight changes in the southeastern China. Contrarily, CDD and NCDD in China represent the positive trends, with the rates of 154.66 °C/decade and 5.12 day/decade, respectively. The variabilities of HDD, NHDD, CDD and NCDD under RCP4.5 are similar to those under RCP8.5 before the mid-21 century, turning to mild changes afterwards, which lead to rates of −51.75 °C/decade, −1.91 day/decade, 46.31 °C/decade and 1.61 day/decade, respectively. Meanwhile, the spatial patterns of trends are also closer to those under RCP8.5. Under RCP2.6, the variability of HDD, NHDD, CDD and NCDD is closer to both RCP 4.5 and RCP 8.5 before 2050, which turns into opposite directions afterwards. Thus, the annual rates of the four indices during 2006–2011 are not significant, and most regions in China have no change for these indices.

## 4 Discussions and conclusion

In this study, the HDD, numbers of HDD (NHDD), CDD and the numbers of CDD (NCDD) have been analyzed in China from Max Planck Institute, Earth Systems Model of low resolution (MPI-ESM-LR) model in the CMIP5. To evaluate how the realistic the models are in simulating the recent past, the historical and decadal experiments simulations are compared to observation, ERA-Interim and NCEP/NCAR reanalyses. Four degree days indices are calculated as the accumulated of daily mean temperature and the numbers of days during the period in which daily mean temperature is above/below base temperatures. In this study, the base temperature of 18 and 24 °C is used for heating and CDD, respectively. The degree days indices provide a good supplement for the 27 temperature and precipitation indices for climate extremes defined by the Expert Team on Climate Change Detection and Indices (ETCCDI) (IPCC 2007); they are relevant parameters to study the climate change, especially for the cryospheric region (Kang et al. 2010; Li et al. 2008).

During 1979–2005, both HDD and NHDD have decreased for observation, reanalyses (ERA-Interim and NCEP/NCAR) and model simulations (historical and decadal experiments), consistent with the increased CDD and NCDD. These changes of the four degree days reflect the general warming in China during the past decades, identified by observations and model simulations (Wang et al. 2012). The variability of four degree days is also in accordance with the temperature extremes from observation in China. During 1961–2003, for the majority of stations, significant increases in warm nights/days and significant decreases in cold nights/days are observed in China, consistent with a long-term decrease in diurnal temperature range (You et al. 2011). On the global scale, the widespread significant changes in temperature extremes are associated with warming, especially for those indices derived from daily minimum temperature (Alexander et al. 2006). In the previous studies, the over 10 °C accumulated temperature is regarded as an indicator to study various crop development stages and the threshold for cold invasion, which also has increased in the northeastern China in recent decades (Yan et al. 2011). Thus, degree days keep consistency with other temperature indices and

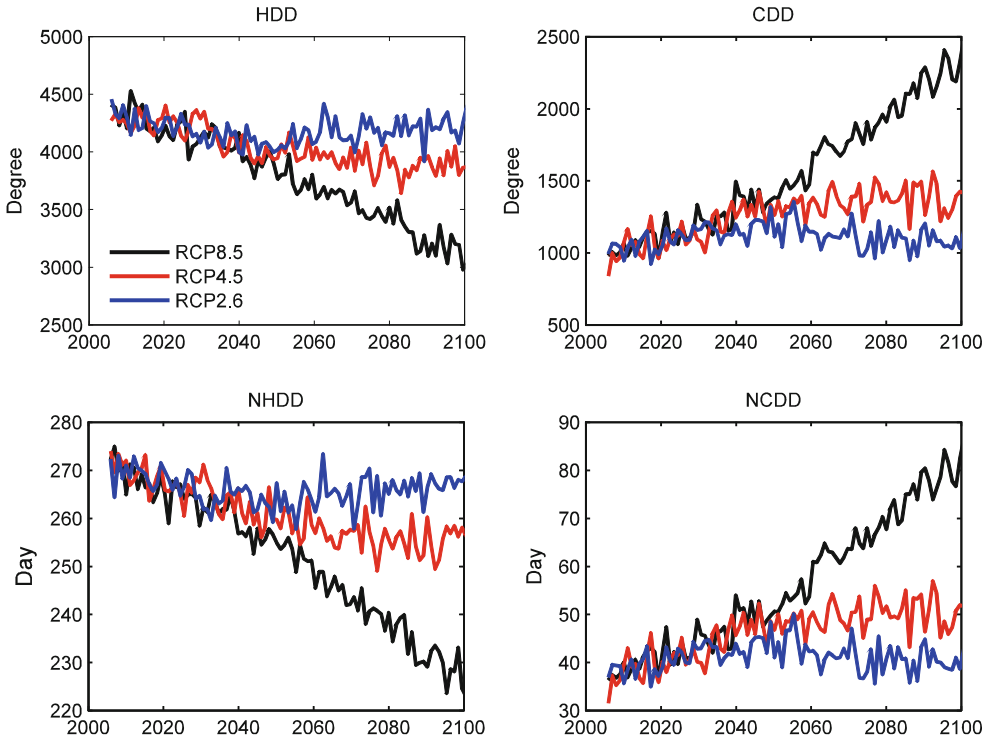


**Fig. 6** Regional change of HDD, CDD, NHDD and NCDD from the simulation outputs in China 2006–2100 under RCP8.5, RCP4.5 and RCP2.6

accumulated temperature, and can be used as an indicator to detect climate changes in China.

In most cases, both the decadal experiments and historical experiments can represent the decadal variability of HDD, NHDD, CDD and NCDD shown by observation, ERA-Interim and NCEP/NCAR, and correlation coefficients among them are very high. For the decadal experiments and historical experiments, the spatial patterns of trends for NHDD and NCDD are similar. For spatial patterns of HDD and CDD, the discrepancy between the decadal experiments and historical experiments occurs in the northeastern China, probably due to the CMIP5 strategy of two experiments about aspects of climate model forcing, response, and processes (Taylor et al. 2012). Meanwhile, the historical experiments initialize from the end of freely evolving simulations of the historical period, which in some cases may be coupled to a carbon cycle model, while the decadal experiments will be initialized with observed ocean state and sea-ice (Taylor et al. 2012).

The actual prediction skill of natural climate variability on decadal timescales has received great attention. The CMIP5 has devised an innovative experimental design to assess the predictability and prediction skill at decadal time scales of state-of-the-art climate models. The MPI-ESM-LR decadal hindcasts and forecasts have been conducted. The data consist of simulations over a 10 year period that are initialized every five years during the period 1960/1961 to 2005/2006 (Taylor et al. 2012). The model prediction skill is examined by comparing the annual mean surface temperature from observation, ERA-Interim, NCEP/NCAR reanalysis data, the historical and the ensemble-mean of the MPI-ESM-LR 10 year hindcast/forecast during 1979–2005 (initialized every 5 years) (Fig. 9). During the entire period, MPI-ESM-LR model simulate higher mean surface temperature in China than the observation and NCEP/NCAR, and lower mean surface temperature than ERA-Interim. At the same time, MPI-ESM-LR model simulate close mean surface temperature as the historical simulations. Thus, the decadal hindcast/forecast simulation performance of MPI-ESM-LR produce warmer than the observed mean temperature in China during the entire period. This is consistent with other seven state-of-the-art-ocean–atmosphere coupled models (Kim et al. 2012). The skill in decadal forecasting is associated with boundary conditions (mainly greenhouse gas concentrations but also tropospheric and stratospheric aerosol distributions) and initial conditions (mainly the ocean state) (Kim et al. 2012; Smith et al. 2012; van Oldenborgh et al. 2012).

Besides the differences of degree days from two experiments simulations, there are discrepancies between ERA-Interim and NCEP/NCAR on the spatial patterns and the regional means, which have been confirmed in the study of hydrological process of temperature, precipitation and evaporation, surface radiation and cloud fields (Betts et al. 2009). Compared with two experiments simulations and ERA-Interim, NCEP/NCAR underestimates CDD and NCDD, and overestimates NHDD, suggesting that the cold biases exist for the temperature for NCEP/NCAR. This is

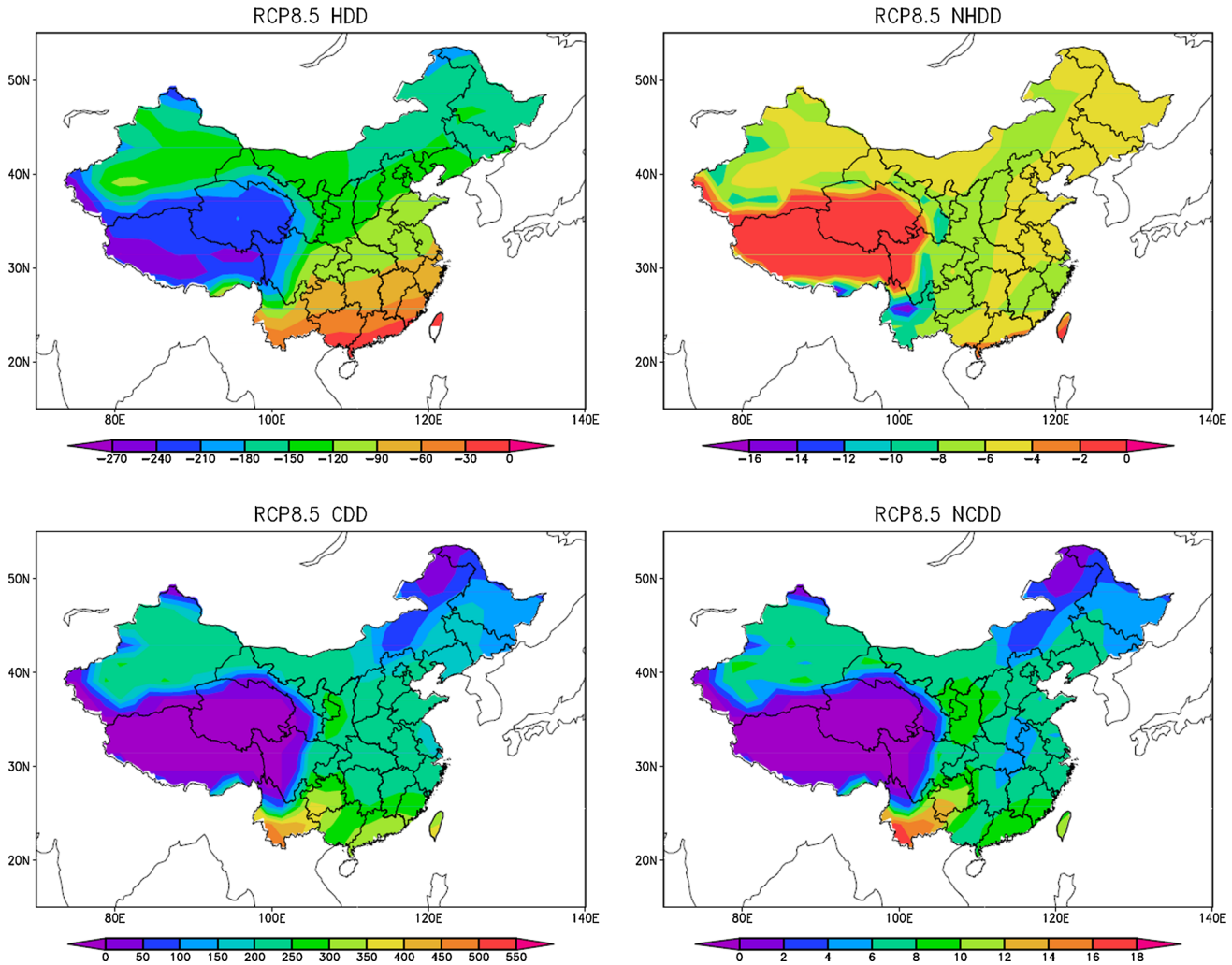


**Fig. 7** Spatial trends of HDD, CDD, NHDD and NCDD from the simulation outputs in China during during 2006–2100 under RCP8.5 scenario

in accordance with the previous studies that ERA-40 temperatures correspond closely to the observations than NCEP/NCAR, and the biases are due mainly to the elevation differences in the model assimilation (Ma et al. 2008; You et al. 2010). Moreover, ERA-Interim uses mostly the sets of observations acquired for ERA-40, supplemented by data for later years from the European Centre for Medium-Range Weather Forecasts (ECMWF) operational archive (Dee et al. 2011), and could capture the observations better than ERA-40 and NCEP/NCAR.

Under different RCP emissions scenarios in the CMIP5, HDD and NHDD show significant decreases, and both CDD and NCDD consistently increase during 2006–2100 under RCP8.5, RCP4.5 and RCP2.6, especially before the mid-21 century. More pronounced changes of degree days indices occur in most regions in China under RCP8.5. The variability of HDD, NHDD, CDD and NCDD has good agreements with the radiative forcing trajectories in RCP, which can reflect various possible combinations of economic, technological, demographic, and policy developments (Moss et al. 2010). For example, the RCP2.6 scenario is designed to meet the 2 °C global average warming target compared to pre-industrial conditions, and it has a peak in the radiative forcing at approximately 3 W/m$^2$ (440 ppm $CO_2$) before 2050 and then declines to 2.6 W/m$^2$ by the end of 2100 (330 ppm $CO_2$). Radiative forcing in RCP4.5 peaks at about 4.5 W/m$^2$ (540 ppm $CO_2$) in 2100, which is comparable to the "Special Report on Emissions Scenarios" (SRES) scenarios B1 with similar $CO_2$ concentrations and median temperature increases by 2100. RCP8.5 assumes a high rate of radiative forcing increasing, peaking at 8.5 W/m$^2$ (940 ppm $CO_2$) in 2100 (Rogelj et al. 2012). The degree days indices are results of daily mean temperature influenced by the radiative forcing.

Models lose their memory of the initial conditions and create their own climates and trends. As shown by Bordi et al. (2010) for ECMWF model forecasts, a trend mismatch between observations and model occurs at midlatitudes,

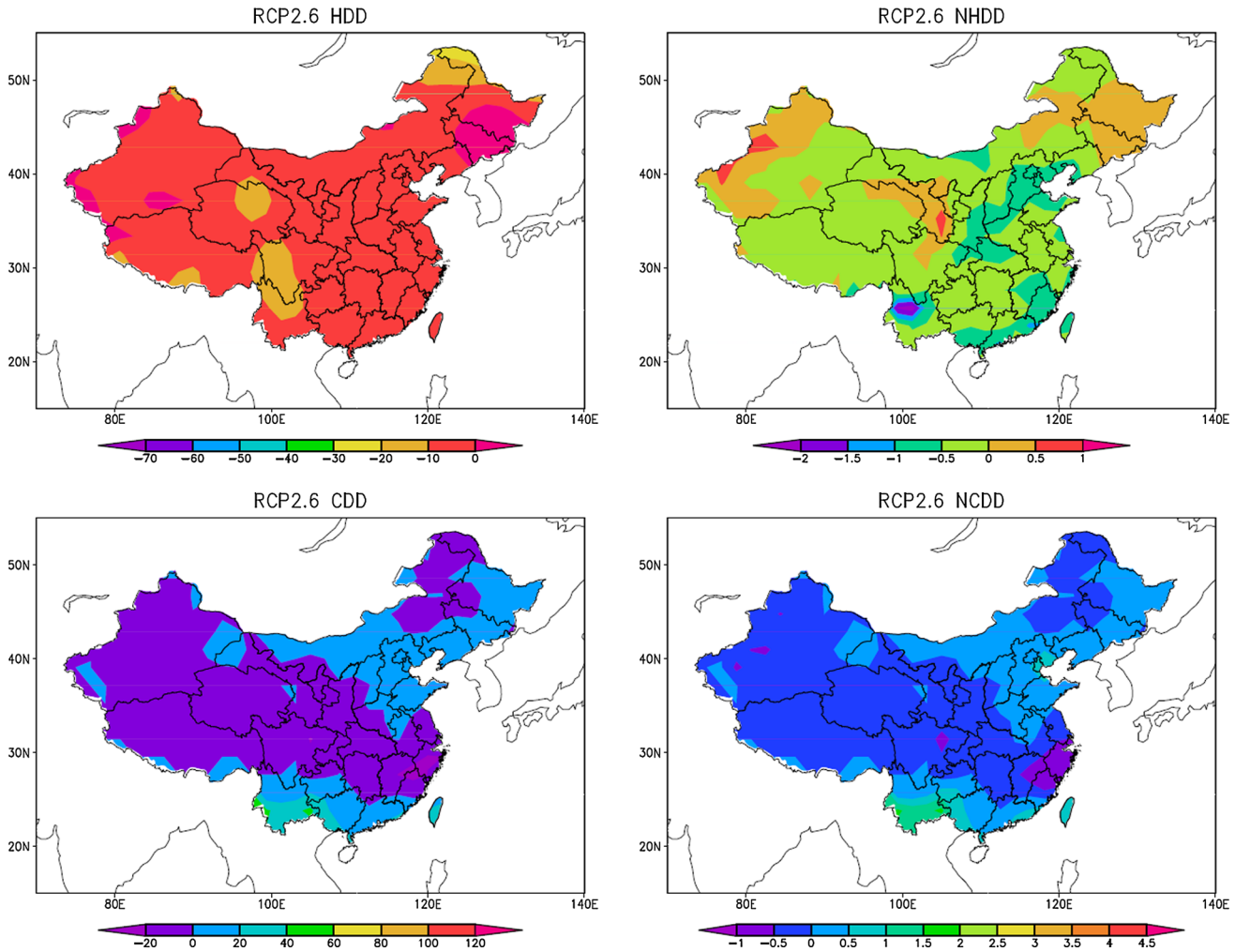


**Fig. 8** Spatial trends of HDD, CDD, NHDD and NCDD from the simulation outputs in China during 2006–2100 under RCP2.6 scenario

which might be connected with the model dynamic response rather than with the variations in the imposed external forcing (Bordi et al. 2010). That is, climate extrapolation by simply using climate models may be affected by different trends that observations and models have even at short lead time. Thus, both reanalyses and short-term forecasts by GCMs are required, if the climate has to be predicted. That is, appears to be more important to comprehend the statistics of the short-term tendencies rather than the forecast accuracy of long-term averages. A first step in this direction is the detailed use of the lead-time dependent climate predictions based on the five year updated forecasts. Such analysis needs to be supported by dynamical underpinning as, for example, the dynamics of stationary waves and the stratosphere–troposphere interaction.

There is considerable interest in exploring the degree days to which future climate states depend on the initial climate state, focusing in particular on whether we can more accurately predict the actual trajectory of future climate (including both forced and unforced change) if we initialize the models with at least the observed ocean state (and perhaps also sea ice and land surface) (Taylor et al. 2012). Hence, the differences of decadal runs and the 20th century runs simply reflect the sensitivity to the initial conditions, as stated above. Addressing these uncertainties, that are an intrinsic feature of all climate models, being the main motivation for decadal predictions. To estimate the uncertainty of decadal experiment, the three ensembles are taken showing the time series of annual mean surface temperature in China for the mean of MPI decadal hindcasts and forecasts during 1979–2005 (Fig. 10). For three ensembles, the decadal hindcasts and forecasts are consistent and similar, indicating there is no strong positive/negative deviations from the ensemble mean temperature. The uncertainties in terms of the inter-ensemble root mean square difference are in a range of some tenth of a degree, whereas the long-term trend is well represented and showing no difference among ensembles.

**Table 4** Regional trend of HDD, CDD, NHDD and NCDD from the simulation outputs under RCP8.5, RCP4.5 and RCP2.6 in China during 2006–2100 on the annual and seasonal basis

| Index | Unit | Annual | Spring | Summer | Autumn | Winter |
|---|---|---|---|---|---|---|
| RCP8.5 | | | | | | |
| HDD | °C/decade | **−142.17** | **−30.38** | **−9.10** | **−38.62** | **−54.00** |
| CDD | °C/decade | **154.66** | **25.65** | **93.97** | **29.26** | **4.34** |
| NHDD | Day/decade | **−5.11** | **−1.40** | **−1.71** | **−1.63** | **−0.33** |
| NCDD | Day/decade | **5.12** | **0.89** | **2.97** | **1.03** | **0.17** |
| RCP4.5 | | | | | | |
| HDD | °C/decade | **−51.75** | **−12.18** | **−3.73** | **−12.42** | **−20.74** |
| CDD | °C/decade | **46.31** | **9.09** | **27.43** | **8.00** | **1.22** |
| NHDD | Day/decade | **−1.91** | **−0.51** | **−0.72** | **−0.53** | **−0.12** |
| NCDD | Day/decade | **1.61** | **0.33** | **0.93** | **0.28** | **0.05** |
| RCP2.6 | | | | | | |
| HDD | °C/decade | −3.51 | −1.63 | 0.32 | −0.08 | −1.57 |
| CDD | °C/decade | 1.12 | 1.80 | −0.28 | −0.56 | 0.25 |
| NHDD | Day/decade | −0.14 | **−0.11** | 0.01 | −0.04 | −0.05 |
| NCDD | Day/decade | 0.04 | 0.06 | −0.01 | −0.02 | 0.01 |

The linear trends of all series are calculated by Mann–Kendall slope estimator. Trends at the 5 % level are marked in bold

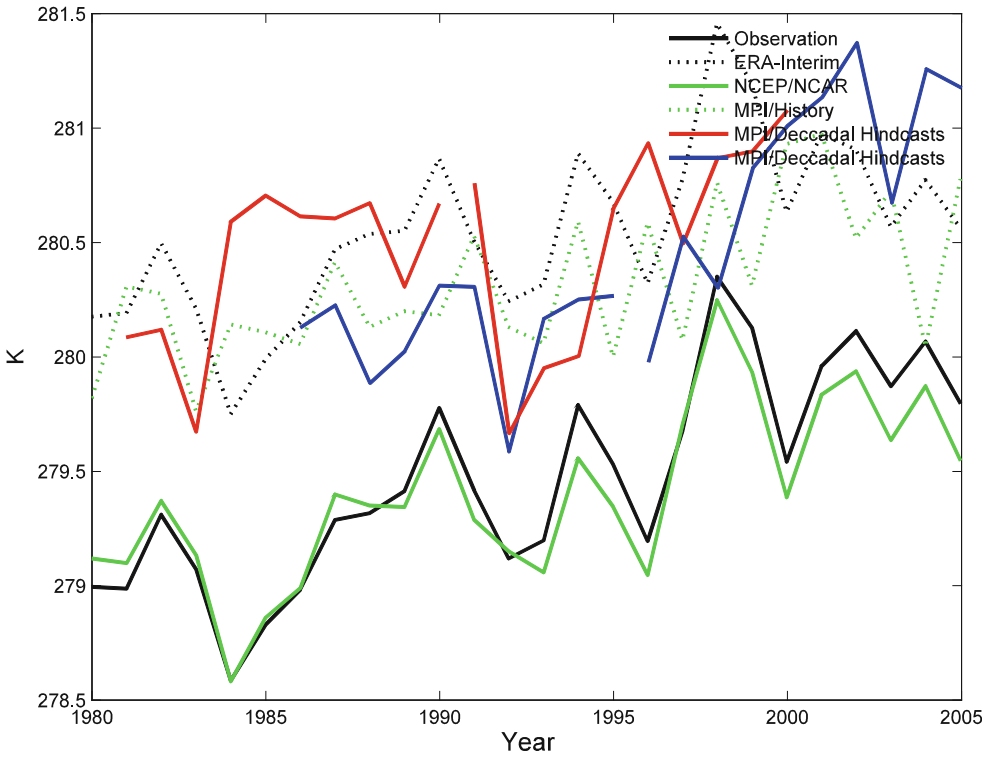


**Fig. 9** Time series of averaged annual mean surface temperature (K) in China for observation, ERA-Interim, NCEP/NCAR reanalysis data, the historical and the ensemble-mean of MPI decadal hindcasts and forecasts (*Red* and *blue line*) during 1979–2005. It is 5-year decadal forecasts with 0-year lead for every 5 years during 1979–2005

In this study, the differences of degree days between CMIP3 and CMIP5 are not evaluated, while the main results should be the same from both CMIP3 and CMIP5. The previous studies have addressed that for the temperature indices, the performance of the CMIP3 and CMIP5 multi-model ensembles is similar in regard to their ensemble mean and median, but that the spread amongst CMIP3 models tends to be larger than amongst CMIP5 models, probably due to higher spatial resolution and more comprehensive GCMs of CMIP5 (Sillmann et al. 2013a, b).

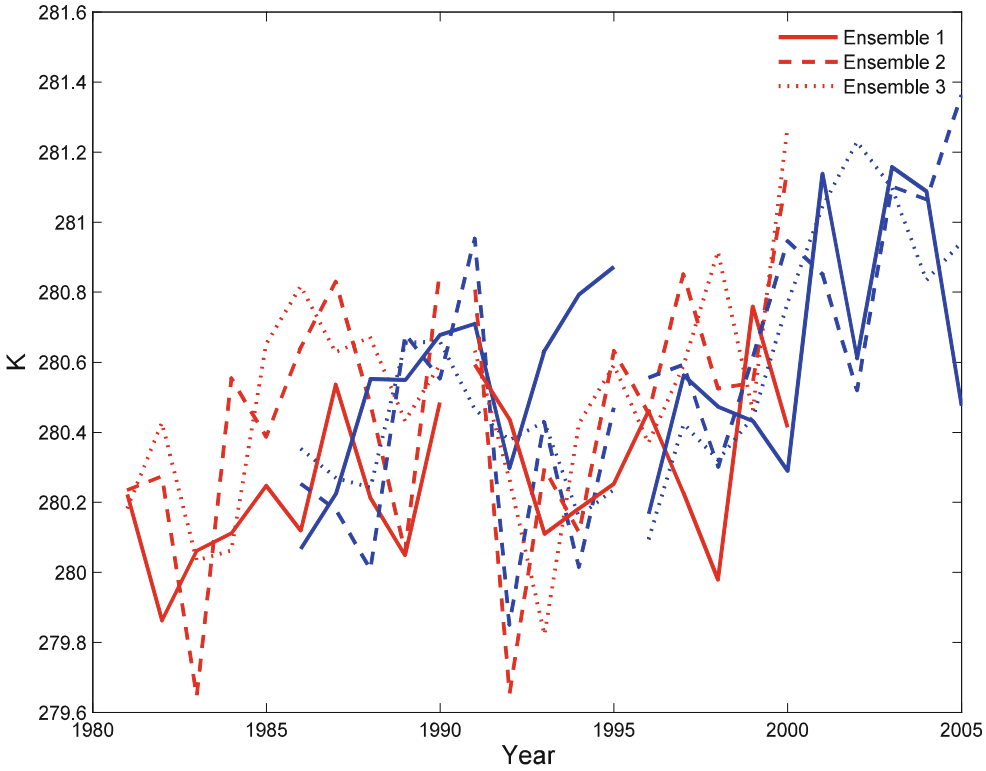


**Fig. 10** Time series of averaged annual mean surface temperature (K) in China for three ensembles for the mean of MPI decadal hindcasts and forecasts (*Red* and *blue line*) during 1979–2005. It is 5-year decadal forecasts with 0-year lead for every 5 years during 1979–2005

More attention should be paid to the relationship between degree days and the cryosphere, to improve the understanding and predictability of cryosphere in China in the context of future climate change.

**Acknowledgments** This study is supported by the National Natural Science Foundation of China (41201072). The authors thank the National Climate Center, China Meteorological Administration, for providing the meteorological data for this study. QY and KF acknowledge support of the Max Planck Fellowship. This study is also funded by the Ministry of Science and Technology of China (Grand No. GYHY201206012) and "the Priority Academic Program Development of Jiangsu Higher Education Institutions" (PAPD). We are very grateful to the reviewers for their constructive comments and thoughtful suggestions.

## References

Alexander LV et al (2006) Global observed changes in daily climate extremes of temperature and precipitation. J Geophys Res-Atmos 111:D05109

Betts AK, Kohler M, Zhang YC (2009) Comparison of river basin hydrometeorology in ERA-Interim and ERA-40 reanalyses with observations. J Geophys Res-Atmos 114:D02101

Bordi I, Fraedrich K, Sutera A (2010) Northern Hemisphere climate trends in reanalysis and forecast model predictions: the 500 hPa annual means. Geophys Res Lett 37:L11809

Büyükalaca O, Bulut H, Yılmaz T (2001) Analysis of variable-base heating and cooling degree-days for Turkey. Appl Energy 69(4):269–283

Dee DP et al (2011) The ERA-Interim reanalysis: configuration and performance of the data assimilation system. Q J R Meteorol Soc 137(656):553–597

Ding YH, Ren GY, Zhao ZC, Xu Y, Luo Y, Li QP, Zhang J (2007) Detection, causes and projection of climate change over China: an overview of recent progress. Adv Atmos Sci 24(6):954–971

IPCC (2007) Summary for policymakers of climate change 2007: the physical science basis. Contribution of working group I to the fourth assessment report of the Intergovernmental Panel on Climate Change. Cambridge University Press, Cambridge

Jiang F, Li X, Wei B, Hu R, Li Z (2009) Observed trends of heating and cooling degree-days in Xinjiang Province, China. Theor Appl Climatol 97(3–4):349–360

Kalnay E et al (1996) The NCEP/NCAR 40-year reanalysis project. Bull Am Meteorol Soc 77(3):437–471

Kang SC, Xu YW, You QL, Flugel WA, Pepin N, Yao TD (2010) Review of climate and cryospheric change in the Tibetan Plateau. Environ Res Lett 5(1):015101

Kim HM, Webster PJ, Curry JA (2012) Evaluation of short-term climate change prediction in multi-model CMIP5 decadal hindcasts. Geophys Res Lett 39:L10701

Li X, Cheng GD, Jin HJ, Kang E, Che T, Jin R, Wu LZ, Nan ZT, Wang J, Shen YP (2008) Cryospheric change in China. Glob Planet Change 62(3–4):210–218

Liu BH, Xu M, Henderson M, Qi Y, Li YQ (2004) Taking China's temperature: daily range, warming trends, and regional variations, 1955–2000. J Clim 17(22):4453–4462

Ma LJ, Zhang TJ, Li QX, Frauenfeld OW, Qin DH (2008) Evaluation of ERA-40, NCEP-1, and NCEP-2 reanalysis air temperatures with ground-based measurements in China. J Geophys Res-Atmos 113:D15115

Moss RH et al (2010) The next generation of scenarios for climate change research and assessment. Nature 463(7282):747–756

OrtizBeviá M, Sánchez-López G, Alvarez-Garcìa F, RuizdeElvira A (2012) Evolution of heating and cooling degree-days in Spain: trends and interannual variability. Glob Planet Change 92:236–247

Qin DH, Liu SY, Li PJ (2006) Snow cover distribution, variability, and response to climate change in western China. J Clim 19(9):1820–1833

Rehman S, Al-Hadhrami LM, Khan S (2011) Annual and seasonal trends of cooling, heating, and industrial degree-days in coastal regions of Saudi Arabia. Theor Appl Climatol 104(3–4):479–488

Ren GY, Gu J, Xu MZ, Li QX, Liu XN (2005) Climate changes of China's mainland over the past half century. Acta Meteorol Sinica 63:942–956 (in Chinese with English abstract)

Ren GY, Guan ZY, Shao XM, Gong DY (2011a) Changes in climatic extremes over mainland China. Clim Res 50:105–111

Ren GY, Chen Y, Zou X, Zhou KYQ, Ren YY, Jiang Y, Ren FM, Zhang Q, Wang XL, Zhang L (2011b) Change in climatic extremes over mainland China based on an integrated extreme climate index. Clim Res 50:113–124

Rogelj J, Meinshausen M, Knutti R (2012) Global warming under old an new scenarios using IPCC climate sensitivity range estimates. Nat Clim Change 2(4):248–253

Sen PK (1968) Estimates of Regression Coefficient Based on Kendalls Tau. J Am Stat Assoc 63(324):1379–1389

Sillmann J, Kharin V, Zhang X, Zwiers F, Bronaugh D (2013a) Climate extremes indices in the CMIP5 multimodel ensemble: part 1. Model evaluation in the present climate. J Geophys Res-Atmos 118:1716–1733

Sillmann J, Kharin V, Zwiers F, Zhang X, Bronaugh D (2013b) Climate extremes indices in the CMIP5 multimodel ensemble: part 2. Future climate projections. J Geophys Res-Atmos 118:2473–2493

Smith DM, Scaife AA, Boer GJ, Caian M, Doblas-Reyes FJ, Guemas V, Hawkins E, Hazeleger W, Hermanson L, Ho CK (2012) Real-time multi-model decadal climate predictions. Clim Dyn. doi:10.1007/s00382-012-1600-0

Taylor KE, Stouffer RJ, Meehl GA (2012) An overview of CMIP5 and the experiment design. Bull Am Meteorol Soc 93(4):485–498

Uppala SM et al (2005) The ERA-40 re-analysis. Q J R Meteorol Soc 131(612):2961–3012

van Oldenborgh GJ, Doblas-Reyes FJ, Wouters B, Hazeleger W (2012) Decadal prediction skill in a multi-model ensemble. Clim Dyn 38(7–8):1263–1280

Wang SW, Gong DY (2000) Enhancement of the warming trend in China. Geophys Res Lett 27(16):2581–2584

Wang SP, Wang ZH, Piao SL, Fang JY (2010) Regional differences in the timing of recent air warming during the past four decades in China. Chin Sci Bull 55(19):1968–1973

Wang HJ, Sun JQ, Chen HP, Zhu YL, Zhang Y, Jiang DB, Lang XM, Fan K, Yu ET, Yang S (2012) Extreme climate in China: facts, simulation and projection. Meteorol Zeitschrift 21(3):279–304

Wild M, Folini D, Schaer C, Loeb N, Dutton EG, Koenigh-Langlo G (2013) The global energy balance from a surface perspective. Clim Dyn 40:3107–3134

Xu Y, Gao XJ, Yan SY, Xu CH, Shi Y, Giorgi F (2009) A daily temperature dataset over China and its application in validating a RCM simulation. Adv Atmos Sci 26(4):763–772

Yan M, Liu X, Zhang W, Li X, Liu S (2011) Spatio-temporal changes of >= 10° accumulated temperature in northeastern China since 1961. Chin Geogr Sci 21(1):17–26

Yao T et al (2012) Different glacier status with atmospheric circulations in Tibetan Plateau and surroundings. Nat Clim Change 2(9):663–667

You QL, Kang SC, Pepin N, Flugel WA, Yan YP, Behrawan H, Huang J (2010) Relationship between temperature trend magnitude, elevation and mean temperature in the Tibetan Plateau from homogenized surface stations and reanalysis data. Glob Planet Change 71(1–2):124–133

You QL, Kang SC, Aguilar E, Pepin N, Flugel WA, Yan YP (2011) Changes in daily climate extremes in China and their connection to the large scale atmospheric circulation during 1961–2003. Clim Dyn 36:2399–2417

Zhai PM, Pan XH (2003) Trends in temperature extremes during 1951–1999 in China. Geophys Res Lett 30(17):1913

Zhang TJ (2007) Perspectives on environmental study of response to climatic and land cover/land use change over the Qinghai-Tibetan plateau: an introduction. Arct Antarct Alp Res 39:631–634

# Development of the Analogue-Dynamical Method for Error Correction of Numerical Forecasts

YU Haipeng[1] (于海鹏), HUANG Jianping[1*] (黄建平), LI Weijing[2] (李维京), and FENG Guolin[2] (封国林)

1 *College of Atmospheric Sciences and Key Laboratory for Semi-Arid Climate Change, Lanzhou University, Lanzhou* 730000

2 *Laboratory for Climate Studies, National Climate Center, China Meteorological Administration, Beijing* 100081

(Received March 31, 2014; in final form July 22, 2014)

**ABSTRACT**

Due to the increasing requirement for high-level weather and climate forecasting accuracy, it is necessary to exploit a strategy for model error correction while developing numerical modeling and data assimilation techniques. This study classifies the correction strategies according to the types of forecast errors, and reviews recent studies on these correction strategies. Among others, the analogue-dynamical method has been developed in China, which combines statistical methods with the dynamical model, corrects model errors based on analogue information, and effectively utilizes historical data in dynamical forecasts. In this study, the fundamental principles and technical solutions of the analogue-dynamical method and associated development history for forecasts on different timescales are introduced. It is shown that this method can effectively improve medium- and extended-range forecasts, monthly-average circulation forecast, and short-term climate prediction. As an innovative technique independently developed in China, the analogue-dynamical method plays an important role in both weather forecast and climate prediction, and has potential applications in wider fields.

**Key words:** analogue-dynamical method, numerical model, error correction, historical data

**Citation:** Yu Haipeng, Huang Jianping, Li Weijing, et al., 2014: Development of the analogue-dynamical method for error correction of numerical forecasts. *J. Meteor. Res.*, **28**(5), 934–947, doi: 10.1007/s13351-014-4077-4.

## 1. Introduction

Since numerical forecasts were successfully realized by Charney et al. (1950), their capability has been much developed (Chen and Xue, 2004). While forecast errors are still significant, the forecast accuracy for high-impact weather events remains very low (Wu et al., 2007). The two factors restricting the accuracy of numerical forecasts are initial error and model error (Zhong et al., 2011), so improving the quality of the initial field and reducing model errors are two ways to improve forecast capability. In recent years, numerical forecasts have been developed in the direction of elaborate models and accurate initial fields. This trend has resulted in more intensive observational data, more sophisticated assimilation technology, more elaborate numerical models, and more reasonable parameterization. These efforts have much improved forecasting accuracy, but with the increasing economic and social development, current forecasting capabilities still cannot satisfy the growing demand (Wu et al., 2007).

No matter how elaborate the model, forecast errors are inevitable, and the efforts required to make further improvements are considerably greater. Along with the development of assimilation technology, another effective way to improve forecast accuracy is to conduct error correction. Much work has been done in developing error correction technology, and it is worth mentioning that Chinese scientists combined statisti-

Supported by the China Meteorological Administration Special Public Welfare Research Fund (GYHY201206009), National Basic Research Program of China (2012CB955301), and China University Research Talents Recruitment Program (B13045).

*Corresponding author: hjp@lzu.edu.cn.

©The Chinese Meteorological Society and Springer-Verlag Berlin Heidelberg 2014

cal and dynamical methods (Chou, 1986) and obtained a series of innovative theories and methods (Gu, 1958a, b; Zheng and Du, 1973; Chou, 1974; Qiu and Chou, 1990; Huang and Yi, 1991; Zhang and Chou, 1991; Cao, 1993; Zhang and Chou, 1997; Gu, 1998). Particularly, by combining the analogue evolution law of the atmosphere and the dynamic model, the analogue-dynamical method (ADM) was developed (Chou, 1979). This has played an important role in improving the prediction theory and raising the level of operational forecast capability. Error correction technology using the ADM has been widely used in medium-range, extended-range, and short-term climate predictions.

This paper first reviews the progress in research on error correction strategies in Section 2. The principle and evolution of the implementation scheme of the ADM, and its development on different-scale weather and climate forecasts are systematically introduced in Section 3. Finally, a summary is provided in Section 4.

## 2. Progress in research of the error correction technology

Generally, forecast errors can be divided into systematic and non-systematic errors (Shao et al., 2009). The former is independent of time variation, can usually be calculated by the time average of some forecast errors, and represents the bias between the equilibrium of the numerical model and the actual climate state. The latter is flow-dependent (dependent on atmospheric state) and includes random errors. Focusing on both types of errors, correction techniques can also be divided into systematic and flow-dependent correction (Dalcher and Kalnay, 1987).

### *2.1 Systematic correction*

The size of systematic correction is independent of model variable, and the common method is to calculate the mean of a large amount of hindcast errors (considering seasonal and diurnal variations) and to add them to the corresponding forecast results. Zeng et al. (1990) adopted a convenient method to remove climate drift by replacing the forecast climate mean with the actual climate mean, then adding the anomaly of the forecast field to the actual climate mean to give the corrected forecast field. Afterwards, they proposed a series of error correction schemes (Zeng et al., 1994), such as the maximum-likelihood correction, minimum bias correction, empirical orthogonal function (EOF) correction, and so on, applied them in the Institute of Atmospheric Physics (IAP) two-level atmospheric circulation model, and obtained some reasonable results (Lin et al., 1998; Zhao et al., 1999; Zhou et al., 1999; Wang et al., 2000; Li et al., 2005). Moreover, establishing statistical relations on the basis of hindcast data and historical actual data is also common, such as the approach using Perfect Prediction (PP) and Model Output Statistics (MOS) (Klein et al., 1959; Klein, 1971; Glahn, 1972), which are forecasted by establishing the relationship between the circulation pattern and the weather phenomena. These methods are all postprocessings after numerical integration, and are usually called after-the-fact correction (Danforth et al., 2007). This is widely used for its convenient operation, while its shortcoming is not considering the nonlinear interaction between external and internal errors in model integration (Danforth et al., 2007).

The online correction differs by adding a forcing term in the numerical integration to offset the model tendency error and to restrain the nonlinear growth of the forecast error (Danforth et al., 2008a). As it corrects the variation tendency of the model variable in the integration, it is also called the tendency error correction. The most common technique for tendency error correction is nudging, which originates in data assimilation by adding a nudging term to bring the forecast close to the observational data (Hoke and Anthes, 1976; Jeuken et al., 1996). Some scholars have compared the nudging with the after-the-fact corrections, and the result indicates that these two types of correction can both improve forecast abilities, but uncertainty exists in the correction performance. Danforth et al. (2008a) indicated that nudging was better beyond one day; Saha (1992) indicated that nudging had no superiority for forecast skills; Johansson and Saha (1989) indicated that nudging had better effects on small scales, but may destroy the conservativeness

of transient energy. These differences illustrate that the performances of these two correction methods are largely dependent on the model used, and when the magnitude of the forcing term in the online correction is too large, coordination among model variables may be destroyed (Danforth et al., 2008a).

To reasonably estimate the magnitude of the forcing term, Klinker and Sardeshmukh (1992) used the mean result of one-step integration to estimate the tendency error, by closing each parameterization in turn to obtain the contribution of each term, and found that the gravity wave parameterization played an important role. Kaas et al. (1999) nudged some low-resolution global circulation models (GCMs) toward a high-resolution GCM to obtain the empirical interaction function of the horizontal diffusion, and reduced the large-scale systematic errors. The above two methods are complex in operation, and empirical estimation is usually adopted in practical numerical models, i.e., the ensemble mean of the ratios of some forecast errors and forecast time is set as the forcing term. This method assumes that the forecast error grows linearly (Yang et al., 2008), and it demands that the forecast time be not too long. As for the selection of forecast time, different investigations have shown different results. Danforth et al. (2007) set it to 6 h, same as the interval of the reanalysis dataset, and averaged all of the 6-h forecast errors from the same month from the previous 5 years as the estimation. To avoid the influence of diurnal variation, Saha (1992) averaged all the 24-h forecast errors from the month before the initial time. Yang et al. (2008) averaged a large amount of 6-, 12-, 18-, and 24-h forecast errors from different years, to estimate the current forecast error, which avoids the variation in the tendency error from different forecast times.

The above empirical correction method is easy to realize, but cannot ensure that the introduced forcing term is optimal. The optimal is usually related to variation assimilation. In the traditional four-dimensional variational data assimilation (4DVar) system, the model is assumed to be perfect, and the effect of model errors is not considered. The weak-constraint 4DVar developed by Bennett et al. (1996, 1997) has considered the existence of model errors. By introducing a term of tendency model error, both the initial error and model error are reduced. This kind of technique has achieved remarkable effects in both simple and complex numerical models (Derber, 1989; Zupanski, 1993; Trémolet, 2007; Akella and Navon, 2009), but the format of the tendency error needs to be assumed as a priori and tested by experiments. Additionally, the solution of 4DVar is usually restricted by the necessity to establish an adjoint model, and the appended term of the model error undoubtedly increases the calculation load.

### *2.2 Flow-dependent correction*

Some studies (Saha, 1992; DelSole and Hou, 1999; DelSole et al., 2008) have indicated that systematic correction can reduce systematic errors, but has little effect on non-systematic errors, which makes it necessary to develop flow-dependent correction.

Leith (1978) established the relationship between tendency errors and state variables using a statistical approach, which expressed the forcing term as the linear function of the state variables, and provided a statistical model with a large number of samples. Though the derivation was under a linear assumption, the results showed that it also had effects on nonlinear models. Delsole and Hou (1999) applied this method in a quasi-geostrophic model and effectively improved the forecast results, but the error covariance matrix required a large amount of calculation. Danforth et al. (2007) and Danforth and Kalnay (2008a, b) reduced the dimension of this method by using singular value decomposition (SVD). The 6-h forecast results from a quasi-geostrophic model indicated that this method could reduce errors in some areas with high values, but the global improvement is little. A common step in the above studies is to establish an error covariance matrix by using a large number of training samples, meaning that the established statistical relationship depends highly on the selected samples, and the stability is difficult to ensure. Once the forecast model is changed or corrected, the rebuilding of the error covariance matrix needs large amounts of computation and is difficult to transplant (Zheng, 2013).

With a linear system, establishing the statistical relationship is an effective approach, and the more the samples, the more stable the relationship. With a nonlinear system, the relationship between the correction effect and the samples is not stable, and a larger number of samples may not be better. Therefore, the selection of samples is important (Chou and Ren, 2006).

The analogue phenomenon exists widely in the evolution of atmosphere and ocean (Zhao et al., 1982; Wang et al., 1983). For two similar atmospheric states, their evolutions are usually similar. This phenomenon provides a reference for selecting samples. For example, Chen and Ji (2003) and Chen et al. (2006a, b) utilized phase space reconstruction theory and a prediction method based on nonlinear time series, searched for the analogue history information to forecast the current state. They thus constructed a regional nonlinear dynamic forecast model on zonal average on the monthly scale, and conducted the correction in the process of model integration. The results indicated that it not only reduced the zonal averaged error, but also had effects on some wave components. They showed that the analogue phenomenon has reference values for improving model forecasting ability.

Based on the above ideas, some investigators combined the analogue phenomenon with the dynamical models, and developed an analogue-dynamical method (ADM) to correct forecast errors. In the following section, the principle and evolution of this method will be systematically introduced, with a focus on its development in different forecast ranges.

## 3. Development of the ADM

### *3.1 Analogue phenomenon and forecast*

The analogue phenomenon exists in the atmosphere and ocean, and the analogue forecast based on this phenomenon has long been used widely. The basis of this method is, for two similar initial fields, when the atmosphere is in a stable flow pattern, the analogue will be maintained on synoptic timescales. On monthly and seasonal scales, the analogue rhythm phenomenon also exists; i.e., the atmosphere circulation experiences an alternate process of analogue-disanalogue-analogue in the long-term evolution, while the formation of this phenomenon is different from the law of analogue on synoptic scales. As for the dynamical form, Huang and Chou (1990), Huang (1991), and Huang et al. (1990a) studied this form with a coupled ocean-atmosphere model. Their results showed that the analogous rhythm is a non-uniform oscillation of analogous deviation disturbance, caused by the nonlinear coupled interaction of the ocean-atmosphere system and the seasonal variation of monthly mean circulation. They found that the analogue phenomenon is not formed by the evolution of atmosphere or ocean, but that the ocean-atmosphere interaction plays an important role and the seasonal variation of monthly mean circulation increases the amplitude of the disturbance markedly. They also indicated that the ocean and the seasonal variations are important factors when choosing analogues.

Analogue forecasting is widely used in weather and climate forecasting. Lorenz (1969) used natural analogue samples to study the predictability of forecast error growth, and showed that finding strict analogue samples is difficult. This conclusion was confirmed by Van den Dool (1994). While this does not mean that analogue forecasting lacks scope, Van den Dool sequentially proposed regional analogue (Van den Dool, 1989, 1991), construction analogue (Van den Dool et al., 2003), and other methods. Barnett and Preisendorfer (1978) reduced the dimensions of the state space by EOF, and extracted the "analogue climate state vectors," which are used to describe the climate system evolution to select analogues. The analogue forecast was put into operation at NCEP as reported by Livezey and Barnston (1988).

It may be too simple to regard the future state as a repetition of past states (Ren and Chou, 2007a). By combining the analogue forecast and dynamical models, the ADM became an effective means for improving the accuracy of numerical forecasts.

### *3.2 Principle of the ADM*

The ADM was proposed in 1979, and the basic thought was "regarding the forecast field as a small disturbance superimposed on historical analogue fiel-

ds, so historical analogue errors can be used to estimate and correct forecast errors" (Chou, 1979). This method acknowledged the existence of tendency error, and estimated it by historical analogues. Its principle is as follows.

The numerical forecast is proposed as the initial problem of a partial differential equation, expressed as:

$$\frac{\partial \psi}{\partial t} = L(\psi), \tag{1}$$

$$\psi(t_0) = \psi_0, \tag{2}$$

where $\psi$ is the model state variable, $L$ is the numerical model operator, $t_0$ is the initial time, and $\psi_0$ is the initial value. Because of the existence of model errors, the evolution of model atmosphere is different from that of the actual atmosphere. By expressing the tendency of the model error as $E$, the evolution of the actual state variable $\varphi$ can be described as:

$$\frac{\partial \varphi}{\partial t} = L(\varphi) + E(\varphi), \tag{3}$$

where $E$ is the functional of the state variable, which is consistent with the view of Leith (1978). Comparing Eqs. (1) with (3), it can be seen that, if $E(\varphi)$ is known, adding it to the model can force the model tendency in each step toward the actual state. An analogue state can be found in the historical dataset, and the current state variable is regarded as a disturbance of the historical analogue, i.e., $\varphi = \tilde{\varphi} + \hat{\varphi}$, where $\tilde{\varphi}$ is the analogue state variable, and $\hat{\varphi}$ is the analogue deviation. With consideration of the historical evolution of the actual atmosphere, the analogue reference state satisfies:

$$\frac{\partial \tilde{\varphi}}{\partial t} = L(\tilde{\varphi}) + E(\tilde{\varphi}). \tag{4}$$

Subtracting Eq. (4) from Eq. (3), the deviation equation becomes:

$$\frac{\partial \hat{\varphi}}{\partial t} = L(\tilde{\varphi} + \hat{\varphi}) - L(\tilde{\varphi}) + E(\tilde{\varphi} + \hat{\varphi}) - E(\tilde{\varphi}). \tag{5}$$

Calculating the tendency error is difficult; to avoid calculating it, the ADM replaces the current tendency error with the tendency error of historical analogues, resulting in

$$\frac{\partial \hat{\varphi}}{\partial t} = L(\tilde{\varphi} + \hat{\varphi}) - L(\tilde{\varphi}). \tag{6}$$

The control variable of Eq. (6) has changed from $\varphi$ to $\hat{\varphi}$. After obtaining $\hat{\varphi}$ by solving Eq. (6), adding it to the $\tilde{\varphi}$ produces the current forecast field. Comparing Eqs. (1), (4), and (6) reveals a clear difference: the original forecast Eq. (1) has omitted the whole tendency error, while Eq. (6) has omitted the difference between the current tendency error and the tendency error of the analogue reference state. Equation (6) considers the effect of the analogue evolution of the circulation anomaly, and thus theoretically has higher accuracy. Meanwhile, it identifies certain analogue selections, i.e., analogous initial value, analogous climate state, and analogous boundary (Qiu and Chou, 1989).

### *3.3 Early development of the ADM*

Qiu and Chou (1989) introduced forcing errors, topography height errors, and subgrid errors into a quasi-geostrophic barotropic vorticity equation model, and showed that the ADM could reduce the mean square errors. By defining an analogue index, this method need not be hugely analogous, though the improvement is increased by an increase in both the forecast time and the degree to which it is analogous.

Being a stationary wave (Yi et al., 1990), the atmospheric circulation anomaly has the characteristic of barotropy (Huang and Chou, 1988; Zhou et al., 1989; Huang et al., 1990b; Yang et al., 1990), and is analogue in the long-term evolution. Huang (1990) introduced these features into the long-term range numerical forecasts, developed a quasi-geostrophic baroclinic ocean-atmosphere coupled model (Huang, 1992), and established the corresponding analogue deviation equation. They first used the ADM to perform experimental seasonal forecasts (Huang et al., 1993a), monthly forecasts (Huang and Wang, 1991a), and flood season forecasts. Their results indicated that the anomaly centers at 500 hPa were precisely produced. The 8-yr mean results (Huang and Wang, 1991b) in summer (August), forecasted from winter (January), indicated that the accuracy rate (represented by the consistency of anomaly symbols) was 56.8% for the 500-hPa height field, and 55.4% for surface temperature. The 8-yr mean results (Huang et al., 1993b) in winter (February), forecasted

from summer (July), indicated that the accuracy rate was 57% for the 500-hPa height field, and 55.7% for surface temperature. The forecast effect was obviously better than the traditional analogue forecast. The advantage was more evident with increasing forecast time. This study provided a new method for seasonal forecasting.

The above work was based on a simple model. To investigate the effectiveness in complex models and improve the accuracy of monthly operational forecasts, Bao et al. (2004) applied this method to the T63L16 monthly extended-range operational model (Li et al., 2005) of the National Climate Center (NCC) of China, and established an analogue-dynamical monthly forecast model. They selected multiple analogue reference states in the historical dataset to create the analogue-dynamical forecast. The results indicated that the ensemble mean had a better effect than a single analogue member. The global averaged anomaly correlation coefficient (ACC) was improved by 0.2, and the root mean square error (RMSE) was reduced by 12 gpm. From the results of different regions and scales, the tropics and subtropics had the most obvious correction effect; the correction effect on the planetary scale was improved beyond the 15-day forecast, while the accuracy was not improved on the synoptic scale.

### *3.4 The simplified analogue correction*

Besides the development of ADM, D'Andrea and Vautard (2000) (abbreviated as DV2000) independently proposed a tendency error estimating method by historical analogues. They adopted the 4DVar technique to obtain the optimal estimation of tendency model errors of analogue samples, and added them to the equation as the approximation of the current forcing term. The basic idea was equivalent to the ADM; i.e., they approximately replaced the current tendency error with that of analogue reference states. The difference is, this method adopted the variational technique to solve Eq. (4) to obtain $E(\tilde{\varphi})$ and then used it in Eq. (3), while the ADM subtracted Eq. (4) from Eq. (3), and established a new equation. This means that the ADM is a reasonable and effective method and some related early leading work has been completed (Ren, 2006).

The heavy computation load of the 4DVar restricted application of the DV2000 method in the quasi-geostrophic baroclinic model. The DV2000 method was also difficult to be applied in sophisticated operational models. Though the early-developed ADM has avoided compiling an adjoint model, an analogue deviation equation still needs to be established, which is also too complex to facilitate its application in operational models.

Aiming at this problem, Ren et al. (2009) simplified the early ADM by replacing the analogue of the tendency error with the analogue of the forecast error. That is, assuming analogue samples have analogous forecast errors, the current forecast error can be estimated by that of analogues, thus avoiding the calculation of tendency error. In practice, the forecast time is divided into intervals. At each interval, the ensemble mean of the forecast errors of some analogue samples is superposed on the current forecast results, i.e., the forcing is not by step and the after-the-fact correction is done at intervals of some steps. As the duration of the analogue is limited, the analogues are reselected after some time. These simplifications have avoided the rebuilding of a new model, have enhanced the operability, and are easier to transport to other sophisticated models. A total of 24 cases were selected to perform the monthly forecast experiment with the T63L16 model (Ren et al., 2006). The results indicated that the global mean ACC was improved by 0.1, and the RMSE was reduced by 7.49 gpm; the improvement was more evident in the tropics. The improvement of daily forecasting was concentrated beyond 7 days and on the scale of planetary wave; there was no improvement on synoptic scales. Additionally, the precipitation forecast for summer has been examined by using the NCC/IAP T63 ocean-atmosphere coupled model (Ren and Chou, 2007b); the mean result of 23 cases revealed that the global pattern correlation coefficient was improved by 0.092, and by 0.124 for eastern Asia.

The above sections systematically introduced the fundamentals of the ADM and the evolution of practical schemes. When the ADM is applied to different

forecast fields, it needs to be further adjusted based on the characteristics of the particular field. The following section describes application of the ADM to different range forecasts.

### *3.5 Application of the ADM in extended-range forecasts*

For the ADM and traditional analogue forecasts, the selection of analogue fields is always the core problem. On the one hand, the numerical model is sensitive to the initial field, and it is difficult to ensure the consistency of the forecast error evolution between the current state and the analogue state. On the other hand, the numerical model has a large degree of freedom, and it is difficult to choose ideal initial analogue values (Zheng et al., 2013).

Based on the chaotic characteristic of the atmosphere, Chou et al. (2010) proposed a theory to separate the predictable components that are not sensitive to initial error from the random components that cannot be predicted. Based on this theory, Zheng et al. (2009, 2010) extracted the basis of the climate attractor (Huang et al., 1989; Wang et al., 1989) by decomposing the historical data with EOF. The model variable was expanded, the predictable components were retained, and the random components were filtered. The ADM was developed, based on the predictable components, to avoid the impact of rapid growth of small-scale component errors. As the predictable components are not sensitive to the initial errors and have a small degree of freedom, using them to select analogues can avoid the two difficulties mentioned in the preceding paragraph. A 6–15-day forecast experiment was carried out with the T63L16 model (Zheng et al., 2013). Comparison results showed that the ADM, based on predictable components, improved the forecast accuracy beyond 10 days, and offerred a slight improvement on synoptic scales. This contrasts with the result described in the preceding section. The reason for this may be that this method can to some extent restrain the growth of small-scale components errors. It may also be that the improvement on planetary scales can partly restrain the error growth on synoptic scales by the interaction between high and low frequencies. As for the random components, the probability distribution can be calculated by using a large amount of historical data. Compared with the operational extended-range ensemble forecast system of the NCC (Zheng et al., 2012), the mean ACC of 6–15 days was improved by 0.12, and the RMSE was reduced by 12.36 gpm.

The above study used the climate attractor from the historical data as the basis, which is easy to operate. There is a climate drift between the model atmosphere and the actual atmosphere, and their climate attractors are naturally different. No time evolution of the atmospheric pattern can be considered when fixing the climate attractor (Wang et al., 2014). As a result, the large-scale components determined by the historical data do not correspond to the model components, whose errors grow slowly. To solve this problem, Wang et al. (2012a) calculated the levels of the predictable components under given initial values using conditional nonlinear optimal perturbation (CNOP) (Mu et al., 2003; Wang and Tan, 2009). The analogue-dynamical correction was conducted for the predictable components, and the random components corresponding to the historical analogues were averaged. The combination of these two parts formed the corrected forecast results. The 10–30-day forecast experiments were also conducted with the T63L16 model (Wang et al., 2014), and the global mean ACC of the 500-hPa field was improved from 0.06 to 0.32. As for different scales, the effect on the planetary scale was the most marked.

### *3.6 Application of the ADM in short-range climate forecasts*

The summer precipitation forecast is an important aspect of short-range climate forecasting, as it relates to the prevention and reduction of flood disasters. So far, this practice has been difficult. The ADM plays an important role in improving the forecast accuracy for the flood season. Unlike the above monthly and extended-range forecasts, the flood season forecast is a boundary problem affected most by external forcing, and presents as low frequency. Therefore, selecting the initial field as the analogue factor is not suitable, and the external forcing and low-frequency variation should be considered. Feng et al. (2013)

used the forecast errors of analogue years to estimate and correct the forecast errors of the current year, based on the Beijing Climate Center's coupled general circulation model (BCC-CGCM), and developed a dynamical-statistical quantitative precipitation forecast method for the flood season. The core of this method is the filter and combinatorial arrangements of analogue forecast factors. In normal years, the corrections are conducted by optimal multi-factor combination; when these factors are unusual, the abnormal factors correction scheme is adopted. Working in different regions, Wang et al. (2011, 2012b) established the dynamical-statistical ensemble forecast schemes for the middle and lower reaches of the Yangtze River, Xiong et al. (2011, 2012) established the optimal multi-factor forecast scheme in Northeast China, and Yang et al. (2011, 2012) established the multi-factor combination forecast scheme in North China. This forecast system has provided good predictions of the location of the main summer rain band in China, as confirmed by the verification following the annual national conference on the flood season in 2009. The mean of the predictive scores (PS) from 2009 to 2012 was 73, and the corresponding ACC was 0.16, both higher than the systematic corrected forecast results of the BCC-CGCM (the mean PS score was 63 and the mean ACC was 0.01) (Feng et al., 2013). The dynamical-statistical integrated forecasting system for seasonal precipitation (FODAS1.0), based on this method was also put into operational forecasting (Feng et al., 2013). In the flood season forecast of 2013, the forecast result had a PS of 74 and an ACC of 0.20; it generally captured the location of the summer drought and flood of China in 2013. After the flood season of each year, the forecast results from this method were checked and summarized, and the reason for any climatic anomaly was diagnosed (Zhao et al., 2011, 2013a, 2014). In addition to the above flood season forecast, this method has also been applied to the seasonal forecast of geopotential height field for some critical regions of China, and it reduced the forecast errors to some extent (Zhao et al., 2013b).

The El Ninõ–Southern Oscillation (ENSO) is one of the strongest indicators of climate change and is associated with an anomalous change in atmosphere circulation. Sun et al. (2006) applied the ADM to the ENSO forecast, and conducted some experiments using the Ninõ3 index with the simplified ocean-atmosphere coupled model of the NCC. With regard to the particularity of the ENSO forecast, the partial analogue selection, which considered only sea surface temperature (SST), and the entire analogue selection, which considered both SST and surface wind field, were compared. The results indicated that the entire analogue selection more accurately reflected the analogue degree of the ocean-atmosphere coupled system than did the partial analogue selection. When selecting five analogue samples, and setting the oceanic analogue update period as 20 days and the atmospheric analogue update period as 10 days, the best effect was achieved. The experiment with the Ninõ3 index from 1998 to 2003 indicated that the ADM had a greater effect than the control forecast for the whole forecast time. It had a mean ACC of 0.45 and an accumulative absolute error of 10.69℃, while the corresponding accuracy of the control forecast was 0.29 and 13.78℃.

### *3.7 Application of the ADM in medium-range forecasts*

From the above discussion, it can be seen that the ADM has effectively improved the accuracy in short-term climate, monthly mean, and extended-range forecasts, but its improvement in the medium range is not evident, as indicated by Ren et al. (2006). This can be attributed to the essence of ADM, which considers the dynamical process of analogue circulation anomalies. This process has a large timescale, the impact of the initial field is small, and the low-frequency variation is evident, the analogue evolution of which is easy to grasp. Regarding medium-range forecasts, these are sensitive to initial values, the internal error grows nonlinearly, and it is much more difficult to carry the flow-dependent correction by analogues. Therefore, developing and realizing the ADM for medium-range forecasting is urgently needed.

Working on this problem, Yu et al. (2014) modified the ADM to correct the medium-range operational forecast model. The above simplified ADM assumed

that analogous samples have analogous forecast errors, which is more of an approximation to that in the early ADM; the reason of this needs to be verified. By introducing the continuity theorem of forecast errors, it is proved under some assumptions that forecast errors can constitute a continuous curved surface in hyperspace when the volume of the historical data is large enough. It is also shown that the current forecast error can be interpolated with the corresponding hindcast errors of some selected analogue reference states, which means that the simplification is reasonable. In extreme conditions, the analogue-dynamical correction can be converted into control forecast and systematic correction. In the operational scheme, considering that the medium-range forecast is sensitive to the initial field and the global model is dependent on the SST, the seasonal and diurnal variations, atmospheric circulation pattern, and SST pattern are all considered when choosing analogue samples. To avoid the nonlinear growth of errors that could destroy the analogue, the optimal update period was selected as 5 days in sensitivity experiments. Forty cases were selected from summer and winter to carry out 10-day forecast experiments with GRAPES (Global and Regional Assimilation and Prediction System; Chen et al., 2009). The results (Yu et al., 2014) demonstrated that this method extended the period of validity of the global 500-hPa height field by 0.8 day, the most remarkable being 1.25 days in the tropical region. The correction effect became more significant as the lead time increased. Although the analogues were selected by using the height field at 500 hPa, the forecast ability at all vertical levels was improved. The average increase in ACC was 0.07, and RMSE decreased by 10 gpm, on average, at a lead time of 10 days. The magnitude of errors for most forecast fields such as height, temperature, and kinetic energy decreased considerably by inverse correction. These all show the effectiveness of the method for medium-range forecasts.

## 4. Summary

The development of numerical models does not conflict with the development of error correction technology; on the contrary, they supplement each other. On the one hand, the forecast error is not a simple superposition of internal error (initial error) and external error (model error), but the result of their nonlinear interaction (Chen and Ji, 1990). It is difficult to locate the error origin from the forecast output and to correct it positively, thus it is necessary to change the point of view. This needs to acknowledge the existence of forecast errors, summarize their evolution pattern, and establish the empirical relationship to estimate and correct the errors. On the other hand, the numerical forecast treats the atmosphere as a certain system (Chen, 2007); i.e., the future state is determined by the current state and certain physical rules. Actually, both the numerical model and the initial field are approximate descriptions of the real atmospheric state and have large uncertainties; thus, the forecasted future state must also have a large uncertainty. In contrast, the statistical forecast admits the future uncertainties, and infers the future state probability from the information on current and historical states. The disadvantage of this line of thoughts is that the physical rules are not considered. Therefore, the dynamical and statistical methods have respective advantages and disadvantages, and combining them (Chou, 1986) to develop a better error correction technique is naturally advantageous.

To this end, the ADM was developed by combining the statistical method with dynamical models and utilizing the analogue information from historical data. This paper reviewed the creation and development of this method, and discussed associated key issues, corresponding solutions, and improvement of this method for forecasts on different timescales.

This review and related discussion indicate that the ADM has been developed and modified considerably over several decades. It has greatly improved the ability of numerical models in medium-range, extended-range, monthly mean circulation, and short-range climate forecasts, and has shown broad application potentials. This method not only considers systematic errors but also includes the information on the evolution of flow-dependent model errors, avoiding the

establishment of the statistical relationship between forecast error and model variable, and is easy to operate and translate to other sophisticated models (Li et al., 2013).

By comparing the recent ADM with the earlier one, the recent method has been shown to be simplified for application to sophisticated models through replacing tendency errors with forecast errors and replacing the online correction with after-the-fact correction. These simplifications also induce a problem; i.e., there is no consideration of the interaction between external and internal errors (Danforth and Kalnay, 2008a). Therefore, a meaningful direction for future research is to combine the advantages of both recent and earlier methods, and further improve the ADM to make it easy to operate while still restraining the nonlinear growth of forecast errors.

***Acknowledgments.*** We thank Academician Chou Jifan for his efforts in carefully reviewing the manuscript and providing valuable suggestions.

## REFERENCES

Akella, S., and I. M. Navon, 2009: Different approaches to model error formulation in 4D-Var: A study with high-resolution advection schemes. *Tellus A*, **61**, 112–128.

Bao Ming, Ni Yunqi, and Chou Jifan, 2004: The monthly averaged circulation forecast experiments of Analogue-Dynamical Model. *Chin. Sci. Bull.*, **49**, 1112–1115. (in Chinese)

Barnett, T. P., and R. W. Preisendorfer, 1978: Multifield analog prediction of short-term climate fluctuations using a climate state vector. *J. Atmos. Sci.*, **35**, 1771–1787.

Bennett, A. F., B. S. Chua, and L. M. Leslie, 1996: Generalized inversion of a global numerical weather prediction model. *Meteor. Atmos. Phys.*, **60**, 165–178.

——, ——, and ——, 1997: Generalized inversion of a global numerical weather prediction model. II: Analysis and implementation. *Meteor. Atmos. Phys.*, **62**, 129–140.

Cao Hongxing, 1993: Self-memorization equation of atmospheric motion. *Sci. China (Ser. B)*, **23**, 104–112. (in Chinese)

Charney, J. G., R. Fjörtoft, and J. Neumann, 1950: Numerical integration of the barotropic vorticity equation. *Tellus*, **2**, 237–254.

Chen Bomin and Ji Liren, 2003: A new approach to improve the monthly dynamical extended forecast. *Chin. Sci. Bull.*, **48**, 513–520. (in Chinese)

——, ——, Yang Peicai, et al., 2006a: Monthly extended predicting experiments with nonlinear regional prediction. Part I: Prediction of zonal mean flow. *Acta Meteor. Sinica*, **20**, 283–294.

——, ——, and ——, et al., 2006b: Monthly extended predicting experiments with non-linear regional prediction. Part II: Improvement of wave component prediction. *Acta Meteor. Sinica*, **20**, 295–305.

Chen Dehui and Xue Jishan, 2004: An overview on recent progresses of the operational numerical weather prediction models. *Acta Meteor. Sinica*, **62**, 623–633. (in Chinese)

——, ——, Yang Xuesheng, et al., 2009: New generation of multi-scale NWP system (GRAPES): General scientific design. *Chin. Sci. Bull.*, **53**, 2396–2407. (in Chinese)

Chen Minghang and Ji Liren, 1990: Error growth in numerical prediction and atmospheric predictability. *Acta Meteor. Sinica*, **4**, 147–155.

Chou Jifan, 1974: A problem of using past data in numerical weather forecasting. *Sci. China*, **6**, 635–644. (in Chinese)

——, 1979: Some problems in long-term range numerical forecast. *Anthology of Medium and Long Term Hydro-Meteorology Forecast*. Water Resources and Electric Power Press, Beijing, 216–221. (in Chinese)

——, 1986: Why and how to combine dynamics and statistics. *Plateau Meteor.*, **5**, 367–372. (in Chinese)

——, 2007: An innovative road to numerical weather prediction—From initial value problem to inverse problem. *Acta Meteor. Sinica*, **65**, 673–682. (in Chinese)

—— and Ren Hongli, 2006: Numerical weather prediction-necessity and feasibility of an alternative methodology. *J. Appl. Meteor. Sci.*, **17**, 240–244. (in Chinese)

——, Zheng Zhihai, and Sun Shupeng, 2010: The think about 10–30 days extended-range numerical weather prediction strategy—Facing the atmosphere chaos. *Scientia Meteor. Sinica*, **30**, 569–573. (in Chinese)

Dalcher, A., and E. Kalnay, 1987: Error growth and predictability in operational ECMWF forecasts. *Tellus A*, **39**, 474–491.

D'andrea, F., and R. Vautard, 2000: Reducing systematic errors by empirically correcting model errors. *Tellus A*, **52**, 21–41.

Danforth, C. M., E. Kalnay, and T. Miyoshi, 2007: Estimating and correcting global weather model error. *Mon. Wea. Rev.*, **135**, 281–299.

——, and ——, 2008a: Impact of online empirical model correction on nonlinear error growth. *Geophys. Res. Lett.*, **35**, L24805.

——, and ——, 2008b: Using singular value decomposition to parameterize state-dependent model errors. *J. Atmos. Sci.*, **65**, 1467–1478.

DelSole, T., and A. Y. Hou, 1999: Empirical correction of a dynamical model. Part I: Fundamental issues. *Mon. Wea. Rev.*, **127**, 2533–2545.

——, M. Zhao, P. A. Dirmeyer, et al., 2008: Empirical correction of a coupled land-atmosphere model. *Mon. Wea. Rev.*, **136**, 4063–4076.

Derber, J. C., 1989: A variational continuous assimilation technique. *Mon. Wea. Rev.*, **117**, 2437–2446.

Feng Guolin, Zhao Junhu, Zhi Rong, et al., 2013: Recent progress on the objective and quantifiable forecast of summer precipitation based on dynamical statistical method. *J. Appl. Meteor. Sci.*, **24**, 656–665. (in Chinese)

Glahn, H. R., and D. A. Lowry, 1972: The use of model output statistics (MOS) in objective weather forecasting. *J. Appl. Meteor.*, **11**, 1203–1211.

Gu Xiangqian, 1998: A spectrum model based on atmosphere self-memorization theory. *Chin. Sci. Bull.*, **43**, 1–9. (in Chinese)

Gu Zhenchao, 1958a: On the equivalency of formulations of weather forecasting as an initial value problem and as an "evolution" problem. *Acta Meteor. Sinica*, **29**, 93–98. (in Chinese)

——, 1958b: On the utilization of past data in numerical weather forecasting. *Acta Meteor. Sinica*, **29**, 176–184. (in Chinese)

Hoke, J. E., and R. A. Anthes, 1976: The initialization of numerical models by a dynamic-initialization technique. *Mon. Wea. Rev.*, **104**, 1551–1556.

Huang, J. P., Y. H. Yi, S. W. Wang, et al., 1993a: An analogue-dynamical long-range numerical weather prediction system incorporating historical evolution. *Quart. J. Roy. Meteor. Soc.*, **119**, 547–565.

Huang Jianping, 1990: The spatial and temporal characteristic of circulation anomaly and the design of long-term range numerical model circulation. *Meteor. Sci. Technol.*, (3), 27–32. (in Chinese)

——, 1991: The dynamical mechanism of analogous evolution for circulation anomaly. *Acta Sci. Nat. Uni. Pek.*, **27**, 99–108. (in Chinese)

——, 1992: *Theoretical Climate Models*. China Meteorological Press, Beijing, 152–178. (in Chinese)

—— and Chou Jifan, 1988: On the annual variation of the barotropic and baroclinic kinetic energy of monthly mean circulation over the mid-high latitude of the Northern Hemisphere. *Plateau Meteor.*, **7**, 260–264. (in Chinese)

——, ——, and Yi Yuhong, 1989: The macro-description of the evolution of 500-hPa monthly anomaly field. *Acta Meteor. Sinica*, **47**, 484–487. (in Chinese)

—— and ——, 1990: Studies on the analogous rhythm phenomenon in coupled ocean-atmosphere system. *Sci. China (Ser. B)*, **33**, 851–860. (in Chinese)

——, Gao Jidong, and Chou Jifan, 1990a: The analogous rhythms phenomena of monthly mean circulation over the Northern Hemisphere. *Plateau Meteor.*, **9**, 88–92. (in Chinese)

——, Guo Xueliang, and Chou Jifan, 1990b: The dynamical and statistical analysis of the proportion of the barotropic and baroclinic kinetic energy of monthly mean circulation. *Anthology of Long Term Weather Forecast*. China Meteorological Press, Beijing, 53–62. (in Chinese)

—— and Wang Shaowu, 1991a: The monthly prediction experiments using a coupled analogy-dynamical model. *Acta Meteor. Sinica*, **5**, 8–15.

—— and ——, 1991b: The experiment of seasonal prediction using the analogy-dynamical model. *Sci. China (Ser. B)*, **2**, 216–224. (in Chinese)

—— and Yi Yuhong, 1991: Inversion of a nonlinear dynamical model from the observation. *Sci. China (Ser. B)*, **34**, 331–336. (in Chinese)

——, ——, and ——, 1993b: The seasonal prediction experiments using the analogue-dynamical model–Prediction for winter months. *Acta Meteor. Sinica*, **51**, 118–121. (in Chinese)

Jeuken, A. B. M., P. C. Siegmund, L. C. Heijboer, et al., 1996: On the potential of assimilating meteorological analyses in a global climate model for the purpose of model validation. *J. Geophys. Res. Atmos.*, **101**, 16939–16950.

Johansson, A., and S. Saha, 1989: Simulation of systematic error effects and their reduction in a simple model of the atmosphere. *Mon. Wea. Rev.*, **117**, 1658–1675.

Kaas, E., A. Guldberg, W. May, et al., 1999: Using tendency errors to tune the parameterization of unresolved dynamical scale interactions in atmospheric general circulation models. *Tellus A*, **51**, 612–629.

Klein, W. H., 1971: Computer prediction of precipitation probability in the United States. *J. Appl. Meteor.*, **10**, 903–915.

——, B. M. Lewins, and I. Enger, 1959: Objective prediction of five-day mean temperatures during winter. *J. Meteor.*, **16**, 672–682.

Klinker, E., and P. D. Sardeshmukh, 1992: The diagnosis of mechanical dissipation in the atmosphere from large-scale balance requirements. *J. Atmos. Sci.*, **49**, 608–627.

Leith, C. E., 1978: Objective methods for weather prediction. *Annu. Rev. Fluid Mech.*, **10**, 107–128.

Li Fang, Lin Zhongda, Zuo Ruiting, et al., 2005: The methods for correcting the summer precipitation anomaly predicted extraseasonally over East Asian monsoon region based on EOF and SVD. *Climatic Environ. Res.*, **10**, 658–668. (in Chinese)

Li Weijing, Zhang Peiqun, Li Qingquan, et al., 2005: Research and operational application of dynamical climate model prediction system. *J. Appl. Meteor. Sci.*, **16**(S1), 1–11. (in Chinese)

——, Zheng Zhihai, and Sun Chenghu, 2013: Improvements to dynamical analogue climate prediction method in China. *Chinese J. Atmos. Sci.*, **37**, 341–350. (in Chinese)

Lin Zhaohui, Li Xu, Zhao Yan, et al., 1998: An improved short-term climate prediction system and its application to the extraseasonal prediction of rainfall anomaly in China for 1998. *Climatic Environ. Res.*, **3**, 339–348. (in Chinese)

Livezey, R. E., and A. G. Barnston, 1988: An operational multifield analog/antianalog prediction system for United States seasonal temperatures. 1: System design and winter experiments. *J. Geophys. Res.*, **93**, 10953–10974.

Lorenz, E. N., 1969: Atmospheric predictability as revealed by naturally occurring analogues. *J. Atmos. Sci.*, **26**, 636–646.

Mu, M., W. S. Duan, and B. Wang, 2003: Conditional nonlinear optimal perturbation and its applications. *Nonlinear Proc. Geophy.*, **10**, 493–501.

Qiu Chongjian and Chou Jifan, 1989: The analogue-dynamical method for weather forecasting. *Chinese J. Atmos. Sci.*, **13**, 22–28. (in Chinese)

—— and ——, 1990: An optimization method for the parameters of forecast models. *Sci. China (Ser. B)*, **2**, 218–224. (in Chinese)

Ren Hongli, 2006: Strategy and methodology of dynamical analogue prediction. Ph. D. dissertation, Lanzhou University, 52 pp. (in Chinese)

——, Zhang Peiqun, and Li Weijing, et al., 2006: A new method of dynamical analogue prediction based on multi-reference-state updating and its application. *Acta Phys. Sinica*, **55**(8), 4388–4396. (in Chinese)

—— and Chou Jifan, 2007a: Study progress in prediction strategy and methodology on numerical model. *Adv. Earth Sci.*, **22**, 376–385. (in Chinese)

—— and ——, 2007b: Strategy and methodology of dynamical analogue prediction. *Sci. China (Ser. D)*, **50**, 1589–1599.

——, Chou Jifan, Huang Jianping, et al., 2009: Theoretical basis and application of an analogue-dynamical model in the Lorenz system. *Adv. Atmos. Sci.*, **26**, 67–77.

Saha, S., 1992: Response of the NMC MRF model to systematic-error correction within integration. *Mon. Wea. Rev.*, **120**, 345–360.

Shao Aimei, Xi Shuang, and Qiu Chongjian, 2009: The variational method to correct nonsystematic errors of numerical foreasting. *Sci. China (Ser. D)*, **2**, 235–244. (in Chinese)

Sun Chenghu, Li Weijing, Ren Hongli, et al., 2006: A dynamic-analogue error correction model for ENSO prediction and its initial hindcast verification. *Chinese J. Atmos. Sci.*, **30**, 965–976. (in Chinese)

Trémolet, Y., 2007: Model-error estimation in 4D-Var. *Quart. J. Roy. Meteor. Soc.*, **133**, 1267–1280.

Van den Dool, H. M., 1989: A new look at weather forecasting through analogues. *Mon. Wea. Rev.*, **117**, 2230–2247.

——, 1991: Mirror images of atmospheric flow. *Mon. Wea. Rev.*, **119**, 2095–2106.

——, 1994: Searching for analogues, how long must we wait? *Tellus A*, **46**, 314–324.

——, J. Huang, and Y. Fan, 2003: Performance and analysis of the constructed analogue method applied to U.S. soil moisture over 1981–2001. *J. Geophys. Res. Atmos.*, **108**, 8617, doi: 10.1029/2002JD003114.

Wang Bin and Tan Xiaowei, 2009: A fast algorithm for solving CNOP and associated target observation tests. *Acta Meteor. Sinica*, **67**, 175–188. (in Chinese)

Wang Huijun, Zhou Guangqing, and Zhao Yan, 2000: An effective method for correcting the interannual prediction of summer precipitation and atmospheric general circulation. *J. Appl. Meteor. Sci.*, **11**(A06), 40–50. (in Chinese)

Wang Qiguang, Feng Guolin, Zheng Zhihai, et al., 2011: A study of the objective and quantifiable forecasting based on optimal factors combinations in precipitation in the middle and lower reaches of the Yangtze River in summer. *Chinese J. Atmos. Sci.*, **35**, 287–297. (in Chinese)

——, ——, ——, et al., 2012a: The preliminary analysis of the procedures of extracting predicable components in numerical model of lorenz system. *Chinese J. Atmos. Sci.*, **36**, 539–550. (in Chinese)

——, ——, Zhi Rong, et al., 2012b: A study of the error field of the flood period precipitation of the mid-lower reaches of the Yangtze River as predicted by an operational numerical prediction model. *Acta Meteor. Sinica*, **70**, 789–796. (in Chinese)

——, Chou Jifan, and Feng Guolin, 2014: Extracting predictable components and forecasting techniques in extended-range numerical weather prediction. *Sci. China (Ser. D)*, **57**, 1525–1537.

Wang Shaowu, Zhao Zongci, and Chen Zhenhua, 1983: The persistence and the rhythm of anomalies of monthly mean atmospheric circulation in relation to ocean-atmospheric interactions. *Acta Meteor. Sinica*, **41**, 33–42. (in Chinese)

Wang Shouhong, Huang Jianping, and Chou Jifan, 1989: Some properties of the solutions of large-scale atmospheric motion equations. *Sci. China (Ser. B)*, **3**, 308–336. (in Chinese)

Wu Rongsheng, Tan Zhemin, and Wang Yuan, 2007: Discussions on the scientific and technological development of Chinese operation weather forecast. *Scientia Meteor. Sinica*, **27**, 112–118. (in Chinese)

Xiong Kaiguo, Feng Guolin, Huang Jianping, et al., 2011: Analogue-dynamical prediction of monsoon precipitation in Northeast China based on dynamic and optimal configuration of multiple predictors. *Acta Meteor. Sinica*, **25**, 316–326.

——, Zhao Junhu, Feng Guolin, et al., 2012: A new method of analogue-dynamical prediction of monsoon precipitation based on analogue prediction principal components of model errors. *Acta Phys. Sinica*, **61**, 149204. (in Chinese)

Yang Chengbin, Huang Jianping, and Zhou Qinfang, 1990: The vertical structure of monthly mean atmospheric circulation anomaly. *Anthology of Long Term Weather Forecast*. China Meteorological Press, Beijing, 99–106. (in Chinese)

Yang Jie, Wang Qiguang, Zhi Rong, et al., 2011: Dynamic optimal multi-indexes configuration for estimating the prediction errors of dynamical climate model in North China. *Acta Phys. Sinica*, **60**, 029204. (in Chinese)

——, Zhao Junhu, Zheng Zhihai, et al., 2012: Estimating the prediction errors of dynamical climate model on the basis of prophase key factors in North China. *Chinese J. Atmos. Sci.*, **36**, 11–21. (in Chinese)

Yang, X. S., T. DelSole, and H. L. Pan, 2008: Empirical correction of the NCEP global forecast system. *Mon. Wea. Rev.*, **136**, 5224–5233.

Yi Yuhong, Pan Tao, Huang Jianping, et al., 1990: The teleconnection analysis of latitude anomaly field of Northern Hemisphere in January and July. *Plateau Meteor.*, **9**, 43–52. (in Chinese)

Yu, H. P., J. P. Huang, and J. F. Chou, 2014: Improvement of medium-range forecasts using the analogue-dynamical method. *Mon. Wea. Rev.*, **142**, 1570–1587.

Zhang Banglin and Chou Jifan, 1991: The application of empirical orthogonal function in climate numerical modeling. *Sci. China (Ser. B)*, **4**, 442–448. (in Chinese)

Zhang Peiqun and Chou Jifan, 1997: A method improving monthly extended range forecasting. *Plateau Meteor.*, **16**, 376–388. (in Chinese)

Zhao Junhu, Feng Guolin, Wang Qiguang, et al., 2011: Cause and prediction of summer rainfall anomaly distribution in China in 2010. *Chinese J. Atmos. Sci.*, **35**, 1069–1078. (in Chinese)

——, Yang Jie, Feng Guolin, et al., 2013a: Causes and dynamic statistical forecast of the summer rainfall anomaly over China in 2011. *J. Appl. Meteor. Sci.*, **24**, 43–54. (in Chinese)

——, ——, Gong Zhiqiang, et al., 2013b: The experiments of transseasonal prediction by combining together the dynamical and statistical methods of the geopotential height fields on the blocking high in the Eurasian mid-high latitudes. *Acta Phys. Sinica*, **62**, 099206. (in Chinese)

——, Zhi Rong, Shen Xi, et al., 2014: Prediction and cause analysis of summer rainfall anomaly distribution in China in 2012. *Chinese J. Atmos. Sci.*, **38**, 237–250. (in Chinese)

Zhao Yan, Li Xu, Yuan Chongguang, et al., 1999: Quantitative assessment and improvement to correction technology on prediction system of short-term climate anomaly. *Climatic Environ. Res.*, **4**, 353–364. (in Chinese)

Zhao Zongci, Wang Shaowu, and Chen Zhenhua, 1982: The rhythm and long-term range prediction. *Acta Meteor. Sinica*, **40**, 464–474. (in Chinese)

Zeng Qingcun, Yuan Chongguang, Wang Wanqiu, et al., 1990: Experiments in numerical extraseasonal prediction of climate anomalies. *Chinese J. Atmos. Sci.*, **14**, 10–25. (in Chinese)

——, Zhang Banglin, Yuan Chongguang, et al., 1994: A note on some methods suitable for verifying and correcting the prediction of climatic anomaly. *Adv. Atmos. Sci.*, **11**, 121–127.

Zheng Qinglin and Du Xingyuan, 1973: A new numerical weather prediction model utilized multiple observational data. *Sci. China*, **16**, 289–297. (in Chinese)

Zheng Zhihai, 2013: Review of the progress of dynamical extended-range forecasting studies. *Adv. Meteor. Sci. Technol.*, **3**, 25–30. (in Chinese)

——, Ren Hongli, and Huang Jianping, 2009: Analogue correction of errors based on seasonal climatic predictable components and numerical experiments. *Acta Phys. Sinica*, **58**, 7359–7367. (in Chinese)

——, Feng Guolin, Chou Jifan, et al., 2010: Compression for freedom degree in numerical weather prediction and the error analogy. *J. Appl. Meteor. Sci.*, **21**, 139–148. (in Chinese)

——, ——, Huang Jianping, et al., 2012: Predictability-based extended-range ensemble prediction method and numerical experiments. *Acta Phys. Sinica*, **61**, 199203. (in Chinese)

——, Huang Jianping, Feng Guolin, et al., 2013: Forecast scheme and strategy for extended-range predictable components. *Sci. China (Ser. D)*, **56**, 878–889.

Zhong Jian, Huang Sixun, Fei Jianfang, et al., 2011: Dynamics of model errors: Accounting for parameters error and physical processes lacking error. *Chinese J. Atmos. Sci.*, **35**, 1169–1176. (in Chinese)

Zhou Guangqing, Zeng Qingcun, and Zhang Huarong, 1999: An improved ocean-atmosphere coupled model and its numerical modeling. *Prog. Nat. Sci.*, **9**, 542–551. (in Chinese)

Zhou Qinfang, Huang Jianping, and Yang Chengbin, 1989: The vertical structure feature of the Northern Hemisphere wintertime general circulation anomalies. *Acta Meteor. Sinica*, **47**, 173–179. (in Chinese)

Zupanski, M., 1993: Regional four-dimensional variational data assimilation in a quasi-operational forecasting environment. *Mon. Wea. Rev.*, **121**, 2396–2408.

# 数值预报误差订正技术中相似-动力方法的发展*

于海鹏[1,2] 黄建平[1] 李维京[3] 封国林[3]
YU Haipeng[1,2] HUANG Jianping[1] LI Weijing[3] FENG Guolin[3]

1. 兰州大学大气科学学院,半干旱气候变化教育部重点实验室,兰州,730000
2. 中国人民解放军93811部队86分队,兰州,730020
3. 国家气候中心,中国气象局气候研究开放实验室,北京,100081
1. *College of Atmospheric Sciences and Key Laboratory for Semi-Arid Climate Change, Lanzhou University, Lanzhou* 730000, *China*
2. *Unit* 86 *of No.* 93811 *PLA, Lanzhou* 730020, *China*
3. *Laboratory for Climate Studies, National Climate Center, Chinese Meteorological Administration, Beijing* 100081, *China*

2014-03-31收稿,2014-07-14改回.

于海鹏,黄建平,李维京,封国林.2014.数值预报误差订正技术中相似-动力方法的发展.气象学报,72(5):1012-1022
**Yu Haipeng, Huang Jianping, Li Weijing, Feng Guolin. 2014. Development of the analogue-dynamical method for error correction of numerical forecasts. *Acta Meteorologica Sinica*, 72(5): 1012-1022**

**Abstract** Due to the increasing requirement for high-level weather and climate forecasting accuracy, it is necessary to exploit a strategy for model error correction while developing numerical modeling and data assimilation techniques. This study classifies the correction strategies according to the types of forecast errors, and reviews recent studies on these correction strategies. Among others, the analogue-dynamical method has been developed in China, which combines statistical methods with the dynamical model, corrects model errors based on analogue information, and effectively utilizes historical data in dynamical forecasts. In this study, the fundamental principles and technical solutions of the analogue-dynamical method and associated development history for forecasts on different timescales are introduced. It is shown that this method can effectively improve medium- and extended-range forecasts, monthly-average circulation forecast, and short-term climate prediction. As an innovative technique independently developed in China, the analogue-dynamical method plays an important role in both weather forecast and climate prediction, and has potential applications in wider fields.

**Key words** Analogue-dynamical method, Numerical model, Error correction, Historical data

**摘 要** 随着对天气和气候预测准确率要求的提高,在发展数值模式和资料同化技术的同时,很有必要在现有数值模式基础上开发误差订正技术。基于预报误差的不同类型对订正技术进行了分类,回顾了目前误差订正技术的研究进展。中国学者在该领域研究中将统计方法和动力模式相结合,发展了一种基于历史相似信息进行误差订正的相似-动力方法,实现了动力预报中历史资料的有效运用。重点介绍了该方法的基本原理、技术方案的演变过程,及其在不同时间尺度的天气和气候预测中的发展,结果表明该方法在中短期预报、延伸期预报、月平均环流预报和短期气候预测等各个时间尺度中均能够有效提高预报技巧。作为一项中国自主研发的创新技术,在天气预报和气候预测中发挥了重要作用,展现出广阔的应用前景。

**关键词** 相似-动力方法,数值模式,误差订正,历史资料

---

* 资助课题:公益性行业专项(GYHY201206009)、国家重大科学研究计划项目(2012CB955301)和高等学校学科创新引智计划项目(B13045)。

作者简介:于海鹏,主要从事数值预报方法研究。E-mail: hpyu09@lzu.edu.cn
通讯作者:黄建平,主要从事天气动力学和全球变化研究。E-mail: hjp@lzu.edu.cn

**中图法分类号** P456.7

## 1 引 言

在《国家中长期科学和技术发展规划纲要(2006—2020年)》的“公共安全”重点领域及其优先主题“重大自然灾害监测与防御”中明确指出:“重点研究开发地震、台风、暴雨、洪水、地质灾害等监测、预警和应急处置关键技术,森林火灾、溃坝、决堤险情等重大灾害的监测预警技术以及重大自然灾害综合风险分析评估技术。”而就各种灾害性天气的预报而言,其关键技术是数值天气预报技术。自从Charney等(1950)第一次成功实现数值预报以来,经过60年的发展,数值预报水平取得了很大进步(陈德辉等, 2004),但预报误差仍然显著地存在,对重大天气灾害的预测准确率仍然很低(伍荣生等, 2007),需要进一步提高预报能力。制约数值天气预报准确率的两个基本因素是初值误差和模式误差(钟剑等, 2011),因此提高初值场质量和减小模式误差自然成为提高预报水平的两个努力方向。近年来数值预报也一直朝着数值模式精细化、初始条件准确化的方向发展,在此发展趋势下,观测资料更加密集,同化技术更加完善,数值模式更加精密,参数化方案更加合理,这些努力大大提高了数值预报的准确率,但经济社会和国防建设的发展对业务预报的要求越来越高(伍荣生等, 2007),而目前的预报水平还不能满足人们日益增长的需求。

无论是何等精细的模式,误差总是不可避免,在现有的预报水平上做出改进需要付出的努力也会越来越大。同时,中国业务预报水平与发达国家相比仍有一定差距,因此,在提高中国模式精度和改进资料同化技术的同时,要进一步提高预报水平,一个有效且可行的方向是在现有数值模式基础上针对预报误差开展订正技术。这样既能依靠模式本身,利用现有模式的发展成果;又不对模式本身做过多改动,实施时简便可行。中外在发展订正技术方面已开展了大量工作,值得一提的是,中国学者在这方面的研究中,将统计和动力相结合(丑纪范, 1986),取得了一系列创新性的理论和方法(顾震潮, 1958a, 1958b; 丑纪范, 1974; 郑庆林等, 1973; 邱崇践等, 1990; 黄建平等, 1991b; 张邦林等, 1991; 曹鸿兴, 1993; 张培群等, 1997; 谷湘潜, 1998)。特别是将大气的相似演变规律和动力模式相结合,突破国际上统计相似预报的局限性,提出了相似-动力方法(丑纪范, 1979),并开展了大量探索性的工作,在创新预报理论和提高实际预报水平等方面发挥了重要作用。如今,在相似-动力方法基础上发展起来的预报订正技术已经在中短期预报、延伸期预报、短期气候预测等各个时间尺度上有效提高了预报技巧,展现出了较好的应用前景。

## 2 误差订正技术研究进展

一般预报误差可以分为系统性误差和非系统性误差两种(邵爱梅等, 2009),前者是不随时间变化的部分,常由大量预报误差的时间平均得到,表征了模式平衡态相对于实际气候态的漂移;后者则是随流型变化的部分,即依赖于大气状态变量,又包含随机误差。针对不同的误差,订正方法也可相应地分为两类:系统订正和依流型订正(Dalcher, et al, 1987)。

### 2.1 系统订正

系统订正的订正量不依赖于模式变量,常用的方法是计算大量回报误差的平均值(考虑季节变化和日变化),将其叠加到对应预报时效的当前输出结果上。曾庆存等(1990)在短期气候预测中采取了一种简便有效的方法去除模式的气候漂移,即将预报场的气候平均用实况的气候平均代替,将预报场的距平叠加到实况的气候平均上作为预测值。之后又提出了一系列误差订正方案(Zeng, 1994),如最大似然、最小偏差、经验正交函数分解(EOF)订正法等,并在中国科学院大气物理研究所两层大气环流模式中取得了订正效果(林朝晖等, 1998; 赵彦等, 1999; 周广庆等, 1999; 王会军等, 2000; 李芳等, 2006)。此外,根据大量回报和历史实况资料建立统计关系的方法在预报中也较为常用,例如早期发展的PP法和MOS法(Klein, et al, 1959; Klein, 1971; Glahn, et al, 1972),利用历史观测或预报结果建立环流场与天气实况之间的统计关系进行预报。这些方法均是在预报完成后对结果的后处理,一般称之为事后订正(Danforth, et al, 2007)。因

其操作简便,得到了广泛的应用,但缺点是没有考虑模式积分过程中内部误差和外部误差的非线性相互作用(Danforth, et al, 2007)。

与之不同的是过程订正,即在模式积分过程中加入强迫项以抵消倾向误差,从而抑制误差的非线性增长(Danforth, et al, 2008a)。由于订正的是模式变量在积分过程中的变化倾向,因此又叫倾向误差订正。这其中最为常用的是张弛逼近技术,它来源于资料同化,通过在预报方程中增加一个强迫项使预报接近观测值(Hoke, et al, 1976; Jeuken, et al, 1996)。有学者将张弛逼近技术和事后订正方法进行了对比,表明二者均能有效提高预报技巧,但在二者效果的优劣上存在不确定性。Danforth 等(2008a)的研究表明在 1 天后张弛逼近技术相对于事后订正表现出更好的订正效果;Saha(1992)结果表明张弛逼近技术在预报技巧上并没有体现出优势;而 Johansson 等(1989)的结果表明,张弛逼近技术对小尺度有更好的改进效果,但可能会破坏瞬变能量的守恒性。这些差异说明二者的订正性能很大程度上依赖于所采用的模式,而过程订正中强迫项的量级过大易破坏模式变量间的协调性(Danforth, et al, 2008a)。

为了对强迫项给出合理估计,Klinker 等(1992)利用一步积分的平均结果估计倾向误差,通过依次关闭每个独立的参数化方案以得到各项的贡献,并发现重力波参数化过程起主导作用;Kaas 等(1999)将几个低分辨率的大气环流模式向一个高分辨率的大气环流模式进行张弛逼近以得到水平扩散的经验作用函数,从而使得动能谱和观测更加接近,并减小了大尺度系统误差。以上两种方法操作上较为复杂,对实际预报模式而言一般采取经验估计的方式,即将大量预报误差和对应预报时间的比值进行集合平均作为强迫项。这类方法实际上是假设预报误差随时间线性增长(Yang, et al, 2008),这就要求预报时效不宜过长。对于预报时效的取法,不同研究有差异。Danforth 等(2007)将其设为与分析资料间隔一致的 6 h,将近 5 年内相同月份的所有 6 h 预报误差进行平均;Saha(1992)将预报起始时刻前 1 个月内所有 24 h 预报误差进行平均,以避免日变化的影响;Yang 等(2008)则是将多年的 6、12、18 和 24 h 的预报误差进行平均,从而避免了倾向误差在不同预报时段内变化的影响。

上述经验性订正易于实现,但并不能保证所加入的强迫项是最优的。最优往往和变分方法相联系,在传统的四维变分同化(4DVar)中假定模式是准确的,无法考虑模式误差的作用;Bennett 等(1992, 1996, 1997)发展的弱约束四维变分同化考虑了模式误差的存在,通过在目标函数中加入模式倾向误差项达到同时减小初值误差和模式误差的目的。该类方法通过一些简单模式和复杂模式的试验取得了显著的订正效果(Derber, 1989; Zupanski, 1993; Trémolet, 2007; Akella, et al, 2009),但该方法需要先验地给定倾向误差的形式,在应用中需要针对模式反复试验进行确定。另外,四维变分同化的求解受到伴随模式的限制,而模式误差项的加入更增加了计算量,这无疑增大了该方法的推广难度。

### 2.2 依流型订正

有部分研究(Saha, 1992; DelSole, et al, 1999, 2008)表明,系统订正仅能有效减小系统误差,对非系统误差作用较小,这意味着发展依流型订正是非常必要的。

Leith(1978)利用统计方法建立了倾向误差和模式状态变量距平的关系,即将强迫项表达为状态变量的线性函数,通过大量样本给出了统计模型。虽然是在线性假设下进行的推导,但试验表明对非线性模式的误差也有改进效果。这一著名工作被后续进行了深入研究,Delsole 等(1999)将该方法应用到一个准地转模式中,有效提高了预报效果,但误差协方差矩阵的计算对计算量要求很高。Danforth 等(2007,2008a,2008b)通过奇异值分解对该方法进行了降维处理,从而大大降低了计算量。在准地转模式上进行的 6 h 预报试验结果表明,该方法能够在误差大值区有效减少误差,但全球的提高量相对较小。上述方法的共同点是需要一个训练样本序列以建立误差协方差矩阵,这意味着所建立的统计模型严重依赖于所选取的样本,其稳定性难以保证;一旦模式有了改进或者变动,误差协方差矩阵的重建需要重新进行大量计算和调试,不便于移植(郑志海, 2013)。

对于线性系统而言,建立统计关系是一个有效的解决方案,并且样本量越大,其可靠性越高;但对于非线性系统,改进效果和样本之间的关系变得不稳定,也并非样本量越大效果越好,因此,样本的选取非常重要(丑纪范等, 2006)。在大气和海洋的演变中广泛存在相似现象(赵宗慈等, 1982; 王绍武等, 1983),对于相似的两个大气状态,其演变规律往往相似,这种现象为订正样本的选取提供了参考。例如,陈伯民等(2003, 2004a, 2004b)基于相空间重构理论和非线性时空序列预测方法,寻找历史相似状态的信息预报当前状态,构建了纬向平均月尺度逐候非线性动力学区域预报模型,并用非线性预报结果在模式积分过程中实施过程订正。试验表明不仅减少了纬向平均误差,对部分波分量也有明显改进,这表明相似现象对提高预报效果具有参考价值。

基于上述考虑,中国学者将相似现象与动力模式相结合,发展出一套用于误差订正的相似-动力方法。下面将对该方法的基本原理和演化过程进行系统介绍,并重点讨论其在不同预报领域中的发展。

## 3 相似-动力方法的发展

### 3.1 相似现象与相似预报

大气和海洋中广泛存在相似现象,基于这种现象进行的相似预报方法很早就已经形成并被广泛采用。该方法的依据是对于两个相似的初始状态,当大气处于稳定流型时,由于大气的连续演变性,这种相似性可以在天气时间尺度内得以维持。而在月和季节尺度中,也存在明显的相似韵律现象,即大气环流在长期演变中存在相似—不相似—相似的交替过程,这种现象的成因与上述天气尺度的规律不同。对于其形成的动力学机制,黄建平等(1989a, 1990a, 1991)通过海-气耦合模式进行了研究,认为这种现象的产生是由于在月平均环流季节变化的强迫下,海-气系统非线性反馈造成的相似离差扰动的不均匀振荡,这种不均匀振荡和大气环流的不均匀变化密切相关。首次发现相似现象不是大气或海洋自身的演变形成的,海-气耦合作用在相似形成中起了关键作用,而月平均环流季节变化显著增大了离差扰动的振幅。该研究表明海洋和季节变化是相似选取时需要考虑的重要因素,对相似预报具有实际指导意义。

相似预报被广泛应用于天气和气候预测。Lorenz(1969)曾用自然相似样本来研究预报误差增长的可预报性,其结果同时表明,找到较严格的相似样本是非常困难的,这一结论被 Van den Dool (1994)证实。但这并不意味着相似性在天气预报中无用武之地,Van den Dool(1989, 1991)相继提出了区域相似、构造相似(Van den Dool, et al, 2003)等概念,而 Barnett 等(1978)通过经验正交分解对多维状态空间进行降维,提取出描述气候系统演变的"相似气候状态向量"进行相似选取。相似预报的不断发展使其在 NCEP 实现了业务化(Livezey, et al, 1988)。

将未来状态看作过去状态的重复再现,这种考虑过于简化(任宏利等, 2007a)。在相似预报基础上发展起来的相似-动力方法,将相似方法与动力模式相结合,成为提高数值预报技巧的一个途径。

### 3.2 相似-动力方法的提出

相似-动力方法最早于 1979 年提出,其基本思想是"把要预报的场视为叠加在历史相似上的一个小扰动,就可以把天气学的预报经验吸收到数值预报中来"(丑纪范, 1979)。相对于经典的数值预报而言,该方法承认了倾向误差的存在,并通过历史相似对倾向误差进行估计。

数值预报是作为偏微分方程的初值问题提出来的,可以表示为

$$\frac{\partial \psi}{\partial t} = L(\psi) \tag{1}$$

$$\psi(t_0) = \psi_0 \tag{2}$$

式中,$\psi$ 为模式状态变量,$L$ 为数值模式算子,$t_0$ 为预报初始时刻,$\psi_0$ 为模式初值。由于模式误差的存在,模式大气与实际大气的状态演变不同。将模式倾向误差算子表示为 $E$,则实际大气的状态变量 $\varphi$ 的演变可描述如下

$$\frac{\partial \varphi}{\partial t} = L(\varphi) + E(\varphi) \tag{3}$$

这里将 $E$ 视为状态变量的函数,这与 Leith(1978)的观点是一致的。对比式(1)和(3)发现,假定模式倾向误差可以得到,将其加入模式中可以在每一时间步对模式倾向进行强迫,使模式状态向实际状态

接近。从历史资料中选择一个相似参考态,将当前状态变量视为叠加在历史相似上的一个扰动,即 $\varphi=\tilde{\varphi}+\hat{\varphi}$,$\tilde{\varphi}$ 为相似状态变量,$\hat{\varphi}$ 为相似离差。相似参考态作为大气的历史演变,满足以下关系

$$\frac{\partial\tilde{\varphi}}{\partial t}=L(\tilde{\varphi})+E(\tilde{\varphi}) \tag{4}$$

将式(3)和(4)相减,可以得到离差方程

$$\frac{\partial\hat{\varphi}}{\partial t}=L(\tilde{\varphi}+\hat{\varphi})-L(\tilde{\varphi})+E(\tilde{\varphi}+\hat{\varphi})-E(\tilde{\varphi}) \tag{5}$$

求解倾向误差本身是非常困难的,为了避免倾向误差的计算,相似-动力方法做了如下近似,将当前的倾向误差项用历史相似对应的倾向误差近似代替,即得到相似-动力模式

$$\frac{\partial\hat{\varphi}}{\partial t}=L(\tilde{\varphi}+\hat{\varphi})-L(\tilde{\varphi}) \tag{6}$$

该方程的控制变量不再是预报变量本身,而是当前变量相对于相似状态变量的扰动。根据该方程求解得到扰动变量的演变规律后,叠加到相似状态变量上即得到当前预报场。将式(1)和(6)与(4)对比可以发现,该方法与原预报的差别在于,原预报式(1)将整个倾向误差项全部省略,而该方法式(6)省去的仅仅是当前倾向误差和相似参考态倾向误差之间的差别,考虑了环流异常相似演变的作用,因此在理论上有更高的精度。这同时对相似的选取提出了要求,在初值相似的同时,尽量保证气候环境和边界状况相近(邱崇践等, 1989)。

### 3.3 相似-动力方法的早期发展

方法提出后,首先考察了参考态在多高的相似度下,新方法会优于原预报。邱崇践等(1989)在一个准地转正压涡度方程中分别引入强迫源误差、地形高度误差和次网格误差,试验表明相似-动力方法均能有效减少预报的均方差。通过定义一个相似指标发现该方法对参考态与预报量之间的相似度要求不高,但对相似度有依赖性,提高量随相似度的提高而增大,随预报时效的延长而增大。

环流异常在长期演变过程中具有正压性(周琴芳等, 1989; 杨成彬等, 1990; 黄建平等, 1988; 1990b)、驻波性(衣育红等, 1990)和相似性等特点,黄建平等(1990)将其引入到长期数值模式中,发展了一套准地转斜压海-气耦合模式(黄建平等, 1992, 1993),并建立了对应的相似离差方程,首次采用相似-动力方法进行了季节预测试验(Huang, et al, 1993)、月预报试验(Huang, et al, 1991)和汛期洪涝预测(黄建平等, 1993b)。采用预报与实况的距平同号率作为评分,结果显示能够较准确地反映 500 hPa 主要距平中心。冬季(1 月)报夏季(8 月)的 8 年平均预测结果(黄建平等, 1991a)表明,500 hPa 平均准确率达 56.8%,地表温度达55.4%;夏季(7 月)报冬季(2 月)的 8 年平均预测结果(黄建平等, 1993a)表明,500 hPa 平均准确率达 57%,地表温度达 55.7%。预报效果明显优于传统的相似预报,且随着预报时效的延长,优势更明显。该工作为预报技巧较低的季节预测提供了新思路。

简单模式的试验成功表明了相似-动力方法的有效性。为考察该方法在复杂模式中的可行性和提高月尺度业务预报水平,鲍名等(2004)将该方法应用到中国国家气候中心 T63L16 月动力延伸业务预报模式(李维京等, 2005)中,以该模式为动力核建立了相似-动力月预报模式。突破了选取单个相似成员的局限,从历史资料中选取了多个样本进行相似-动力预报,并将预报结果进行集合平均。将 2002 年 12 个月作为试验对象,结果显示引入集合平均后效果优于单个相似成员预报,全球距平相关系数(ACC)平均提高 0.2,均方根误差(RMSE)减少 12 gpm。从不同区域和不同尺度的对比发现,热带、副热带地区改进最为明显;行星尺度波的改进效果在预报 15 日以后较控制预报有所改善,但天气尺度波预报技巧没有改进。这表明,该方法对预报技巧的提高主要体现在延伸期。

### 3.4 方法的简化——相似预报误差订正

在中国学者发展相似-动力方法之后,D'Andrea 等(2000)独立提出了一种利用历史相似估计倾向误差的方法。该方法使用四维变分同化技术得到历史相似样本的倾向误差的最优估计,将其作为当前预报的强迫项加入到模式中。可见其思想是和相似-动力方法等价的,都是将当前倾向误差用相似参考态对应的倾向误差近似代替。不同之处在于该方法利用变分技术求解式(4)得到 $E(\tilde{\varphi})$ 后代入式(3)中进行预报;而相似-动力方法将式(3)和(4)作差,并建立了新的方程。这也同时表明相似-动力方法是一种合理并有效的误差订正技术,中国学者较

早地领先其他国家开展了这方面的研究(任宏利,2006)。

四维变分同化技术巨大的计算量使得 D'Andrea 的方法仅仅在准地转斜压模式上进行了试验,难以应用到复杂业务模式。而上述相似-动力方法虽然避免了编写伴随模式来求解强迫项,但需要重新建立相似离差方程,这很大程度上限制了在复杂模式中的应用。

针对此问题,Ren 等(2009)对原有的相似-动力方法进行了简化,由原有的倾向误差相似简化为预报误差相似,即认为相似样本具有相似的预报误差,进而利用若干相似样本对应的预报误差估计当前预报误差,以避免求解倾向误差。预报过程中将预报时段分为若干订正间隔,在每个间隔处用对应相似样本的预报误差的集合平均叠加到当前预报结果上。不再是在每个时间步长上进行强迫,而是每隔若干时间步长进行一次事后订正。考虑到相似持续时间有限,每隔一定时间后重新选取相似。这些改进避免了重新建立数值模式,增强了方法的可操作性和可移植性。选取 24 个个例在中国国家气候中心 T63L16 模式上进行了月平均预报试验(任宏利等,2006b),全球距平相关系数平均提高 0.1,均方根误差降低了 7.49 gpm,对热带地区的改善最为明显。从预报不同时段看,对逐日预报技巧的提高主要在一周以后,且主要集中在行星尺度波部分,对天气尺度波几乎无提高。此外,通过 NCC/IAP T63 海-气耦合模式进行了夏季降水的预测试验(任宏利等,2007b),23 个个例平均结果表明对夏季降水的全球距平相关系数提高 0.092,对东亚地区提高 0.124。

### 3.5 延伸期预报中的发展——基于可预报分量的相似-动力方法

对相似-动力方法以及传统的相似预报而言,相似场的选取始终是核心问题。一方面,数值模式对初值敏感,难以保证相似初值之间预报误差演变规律的一致性;另一方面,数值模式具有很大自由度,选取理想的相似初值很困难(郑志海等,2013b)。

丑纪范等(2010)针对大气系统的混沌特性,从误差增长的角度给出了分离延伸期可预报分量(对初值误差不敏感的分量,可用数值模式预报)和不可预报的随机分量的方法。郑志海等(2009,2010)基于此理论,通过将历史资料作经验正交函数分解提取出气候吸引子(汪守宏等,1989;黄建平等,1989b)基底,对模式变量以此基底展开后滤除随机分量,保留可预报分量,针对可预报分量进行数值预报,并发展了基于可预报分量的相似-动力方法。避免了小尺度分量预报误差快速增长的影响,更能针对可预报分量进行确定性预报。由于可预报分量对初值不敏感且自由度小,用它进行相似选取避免了上述两方面的困难。在 T63L16 模式上进行了 6—15 d 中期预报试验(郑志海等,2013b),将基于可预报分量的相似-动力方法和可预报分量数值模拟结果进行了对比,结果表明相似-动力方法对 10 d 以后预报技巧有提高作用。但其具体表现与上述研究结果不同:第一,对环流场的距平相关系数提高最明显的区域在南半球热带外,而并非在热带地区;第二,对天气尺度波预报效果略有提高,这表明基于可预报分量的相似-动力方法可能在一定程度上抑制小尺度分量预报误差的增长,也可能是由于行星波尺度的改善通过高低频相互作用部分制约了天气尺度波误差的增长。而对于不可预报的随机分量,利用历史资料中相似的强迫给出可能的概率分布。针对两种分量的不同特性,采用历史相似分别估计可预报分量的预报误差,并将历史相似对应的随机分量相加形成集合预报。与中国国家气候中心的业务动力延伸集合预报系统的对比(郑志海等,2012)表明,6—15 d 平均的距平相关系数评分提高了 0.12,均方根误差减少了 12.36 gpm。

上述研究从历史实况资料中提取气候吸引子作为基底,这种方法易于操作。但实际上模式大气与实况大气之间存在气候漂移,其气候吸引子也不相同;而且将气候吸引子基底固定,不能考虑大气流型的特殊性和时间演变(王启光等,2014)。因此,利用历史资料确定的大尺度分量,与数值模式中误差增长较慢的分量并不能保证对应。为解决此问题,王启光等(2012a,2012b)基于条件非线性最优扰动(CNOP)方法(Mu,et al,1999;王斌等,2009)提取出数值模式在给定初值下误差增长较慢的可预报分量基底,对数值模式中可预报分量进行了相似-动力订正,并将历史相似对应的随机分量进行了集合

平均,将二者相加形成延伸期预报结果。基于T63L16模式对10—30 d 500 hPa平均环流场的预报效果进行了比较(王启光等,2014),全球平均距平相关系数由0.06提高到0.32,对不同区域也都有一定提高,其中北半球热带外和热带地区提高明显,南半球热带外改进较小,这可能与所选取的个例为北半球冬季(1月)有关。从不同尺度波的预报效果看,各尺度均有改进效果,行星尺度波最为明显。

### 3.6 相似-动力方法在短期气候预测中的发展

夏季降水预测是短期气候预测的重点和难点,直接关系到国家防灾、减灾的重大需求,而相似-动力方法在提高汛期预测技巧方面发挥了重要作用。与上述月平均预报和延伸期预报不同,汛期预测是边值问题,主要受外源强迫作用,体现出低频信号特征。因此,在选取相似因子时,不宜仅以初始场为指标,而应综合考虑外源强迫和海-气低频变化。封国林等(2013)基于中国国家气候中心业务模式——BCC-CGCM,利用相似年的预报误差信息对预报年的预报误差进行估计和订正,发展了汛期降水动力-统计客观定量化预测方法。该方法的核心为相似预报因子的筛选和组合配置,在正常年份选取最优多因子组合进行订正,当预报年前期因子出现异常时,采用异常因子订正方案。针对不同区域影响因素的差异,王启光等(2011,2012b)、熊开国等(2012a,2012b)、Xiong等(2011)和杨杰等(2011,2012)从不同角度分别建立了针对长江中下游地区、东北地区和华北地区的动力-统计集成预测方案、最优多因子动态预测方案和动态多因子组合预测方案。该方法自2009年开始参加中国夏季汛期会商以来,连续5年较好地把握了中国夏季的主雨带特征。其中2009—2012年PS评分平均为73分,距平相关系数平均为0.16,相比BCC_CGCM模式系统订正的预测结果(PS平均分63分,距平相关系数平均0.01)有较大的提高(封国林等,2013)。基于该方法研发的动力-统计集成的季节气候预测系统1.0版本(FODAS1.0)于2012年投入业务运行(封国林等,2013),并在多个地区进行了推广。在2013年的汛期预测中,该系统预测结果的PS平均分74分,距平相关系数平均0.20(赵俊虎等,2014a),对夏季旱涝分布的大体形势预测基本正确。在每年的汛期结束之后,对该方法的预测结果进行了检验和总结,并对气候异常成因进行了诊断分析(赵俊虎等,2011,2013a,2013b,2014a,2014b)。除上述汛期预测外,该方法也被应用到关键区域高度场的跨季度预测中,一定程度上减小了预报误差(赵俊虎等,2013a,2013b)。

ENSO循环作为年际气候变化中最强信号之一,与大气环流异常变化有关,对中国气候有重要指示意义。孙丞虎等(2006)将相似-动力方法应用到ENSO预测中,以中国国家气候中心的简化海-气耦合模式为平台对Nino3指数进行了12个月的预报试验。在选取相似时,考虑了ENSO预测的特殊性,将部分相似(仅考虑海表温度)和全相似(考虑海表温度和风场)进行了对比,结果表明全相似比部分相似更能反映海-气耦合系统的相似程度,且在相似样本个数为5个、海洋相似更新周期设为20 d、大气更新周期设为10 d时,预报效果最佳。通过对1980—2003年Nino3指数的回报试验发现,相似-动力方法的预报效果在整个预报时段均好于控制预报,12个月内控制预报的平均距平相关系数和累计绝对误差分别为0.29和13.78℃,而相似-动力方法对应的预报技巧分别为0.45和10.69℃。

### 3.7 相似-动力方法在中短期预报中的发展

通过以上讨论可以发现,相似-动力方法在提高短期气候预测、月平均预报和延伸期预报领域有效提高了预报水平,但对中短期预报改进效果不明显(任宏利等,2006b)。这归因于相似-动力方法的理论基础,即考虑了环流异常相似演变的动力过程。这种过程时间尺度大,初始场作用相对较小,低频变化特征明显,其相似演变规律易于把握。而对于中短期预报,对初值极为敏感,且存在内部误差的非线性增长,要通过相似方法进行依流型订正的难度很大,实现此方法显得尤为迫切。发展中短期预报的相似-动力方法,将能拓展应用领域,是对该方法的补充和完善。

针对这一问题,Yu等(2014)发展了用于改进中短期天气业务预报模式的相似-动力方法。首先,上述简化后的相似-动力方法认为相似样本具有相似的预报误差,这与早期的相似-动力方法相比无疑是更大程度的近似,其合理性需要从理论上进行检

验。通过引入预报误差的连续性定理,在一些假定条件下,证明了当历史资料足够多时,预报误差可以构成超空间的连续曲面,当前预报误差可以由曲面上某邻域内若干点(即相似样本对应的预报误差)插值得到,从而证明了近似的合理性,并指明了相似-动力订正可以蜕化为控制预报和系统订正。在其实施过程中,根据中短期天气预报对初值敏感和全球模式对海温强迫依赖的特点,从季节变化、日变化、大气环流型和海温类型等方面对相似选取作了严格要求;同时为避免误差非线性增长对相似性的破坏,通过敏感性试验确定出中短期预报中最优相似更新周期为5 d。选取了冬季和夏季的40个个例在中国自主研发的GRAPES全球中期预报系统(陈德辉等,2009)上进行了回报试验(Yu, et al, 2014),结果表明相似-动力方法将500 hPa全球可用预报时效延长了0.8 d,最为显著的热带地区延长了1.25 d,且随着预报时效的延长,提高效果逐渐增强。通过各层高度场的距平相关系数和均方根误差的对比发现,相似-动力方法在垂直各层均有稳定的改进效果,预报第10天各层平均距平相关系数相对于控制预报提高0.07,而系统订正相对于控制预报的平均提高量为0.03。除了高度场,对温度场和风场动能也进行了对比分析,发现相似-动力方法能够准确识别各物理量误差的高值区,并能够削弱误差量级。这充分表明了相似-动力方法在中短期预报中的有效性。

## 4 总 结

数值模式的发展与误差订正技术的发展并不矛盾,反而相辅相成。一方面,预报误差不仅仅是内部误差(初始误差)和外部误差(模式误差)的简单叠加,而是二者非线性相互作用的结果(陈明行等,1989),要从预报结果中确定误差根源以针对性地正面改进是非常困难的,因此改变观点很有必要,即承认预报误差的客观存在,总结其演变规律,建立经验关系对预报误差进行估计和订正;另一方面,作为动力方法的数值预报将大气视为一个确定论系统(丑纪范,2007),即未来状态是由现在状态和满足的物理规律所决定的,但数值模式和初值实际上都是大气真实状态的近似描述,本身存在很大的不确定性,预报得到的未来状态也必然存在很大的不确定性,与动力方法不同,统计方法承认未来的不确定性,依据历史资料和现在状态中所包含的信息对未来状态进行概率推断,但缺点是没有考虑应满足的物理规律。可见,动力方法和统计方法各有长短,将动力与统计相结合(丑纪范,1986),发展误差订正技术是十分必要的。

在误差订正技术研究方面,中国学者将统计方法与动力模式有机结合,开展了一系列独具特色的工作,发展了一种基于相似误差订正的预测方法,实现了在动力预报中有效运用历史资料的相似信息。本研究回顾了该方法的提出和发展过程,讨论了针对不同时间尺度预报时需要解决的问题、对应的技术思路,以及预报技巧改进情况。

通过回顾和讨论可以看到,相似-动力方法经过几十年的努力,逐步发展完善,形成了一套有中国特色的预报技术方法。从理论提出,到简单模式的试验成功,再到复杂模式上取得改进效果,最后在中短期预报、延伸期预报、月平均环流预报和短期气候预测等各个时间尺度的业务模式上均有效提高了预报技巧,展现出广阔的应用前景。该方法利用历史相似提供的预报误差对预报误差进行预报,不但考虑了模式的系统性误差,还包含了与相似初值相近流型的模式误差演变信息,且避免了建立预报误差与模式变量统计关系的困难,具有良好的可操作性和可移植性(李维京等,2013)。

同时,对比近期和早期的相似-动力方法可以发现,为了便于在复杂模式上应用和推广,近期的方法对早期的方法做了简化,用预报误差取代了倾向误差,用事后订正取代了过程订正。这样虽然使得方法能够移植到任意复杂模式,但也带来了问题,即无法考虑内部误差和外部误差的非线性相互作用(Danforth, et al, 2008a)。因此,一个有意义的发展方向是,吸取近期方法和早期方法的优势,发展既简便易行,又能够抑制误差非线性增长的相似-动力方法,进一步提高模式预报水平,为中国数值预报业务发挥更大作用。

**致谢**:感谢丑纪范院士细致地审阅了初稿并提出了很有意义的修改意见。

## 参考文献

鲍名,倪允琪,丑纪范. 2004. 相似-动力模式的月平均环流预报试

验. 科学通报，49(11)：1112-1115
曹鸿兴. 1993. 大气运动的自忆性方程. 中国科学(B辑)，23(1)：104-112
陈伯民，纪立人. 2003. 改善月动力延伸预报水平的一种新途径. 科学通报，48(5)：513-520
陈伯民，纪立人，杨培才等. 2004a. 与非线性区域预测方法结合的月延伸预报试验I：纬向平均环流的预报. 气象学报，62(1)：1-10
陈伯民，纪立人，杨培才等. 2004b. 与非线性区域预测方法结合的月延伸预报试验II：对波动分量预报的改进. 气象学报，62(1)：11-19
陈德辉，薛纪善. 2004. 数值天气预报业务模式现状与展望. 气象学报，62(5)：623-633
陈德辉，薛纪善，杨学胜等. 2009. GRAPES新一代全球/区域多尺度统一数值预报模式总体设计研究. 科学通报，53(20)：2396-2407
陈明行，纪立人. 1989. 数值天气预报中的误差增长及大气的可预报性. 气象学报，47(2)：147-155
丑纪范. 1974. 天气数值预报中使用过去资料的问题. 中国科学，(6)：635-644
丑纪范. 1979. 长期数值天气预报的若干问题//中长期水文气象预报文集. 北京：水利电力出版社，216-221
丑纪范. 1986. 为什么要动力-统计相结合？——兼论如何结合. 高原气象，5(4)：367-372
丑纪范，任宏利. 2006. 数值天气预报——另类途径的必要性和可行性. 应用气象学报，17(2)：240-244
丑纪范. 2007. 数值天气预报的创新之路——从初值问题到反问题. 气象学报，65(5)：673-682
丑纪范，郑志海，孙树鹏. 2010. 10～30 d延伸期数值天气预报的策略思考——直面混沌. 气象科学，30(5)：569-573
封国林，赵俊虎，支蓉等. 2013. 动力-统计客观定量化汛期降水预测研究新进展. 应用气象学报，24(6)：656-665
谷湘潜. 1998. 一个基于大气自忆原理的谱模式. 科学通报，43(9)：909-917
顾震潮. 1958a. 作为初值问题的天气形势数值预报与由地面天气历史演变作预报的等值性. 气象学报，29(2)：93-98
顾震潮. 1958b. 天气数值预报中过去资料的使用问题. 气象学报，29(3)：176-184
黄建平，丑纪范. 1988. 北半球中高纬月平均环流正压斜压动能的年变化特征. 高原气象，7(3)：264-268
黄建平，丑纪范. 1989a. 海气耦合系统相似韵律现象的研究. 中国科学(B辑)，19(9)：1001-1008
黄建平，丑纪范，衣育红. 1989b. 500 hPa月平均距平场演变的宏观描述. 气象学报，47(4)：484-487
黄建平. 1990. 环流异常的时空特征与长期数值预报模式设计. 气象科技，(3)：27-32
黄建平，郜吉东. 1990a. 北半球月平均环流异常演变的相似韵律现象. 高原气象，9(1)：88-92
黄建平，郭学良，丑纪范. 1990b. 北半球月平均环流正压斜压动能的比重以及各自特点的动力统计分析//长期天气预报论文集. 北京:气象出版社，53-62
黄建平. 1991. 环流异常相似性演变的动力学机制. 北京大学学报(自然科学版)，(1)：99-108
黄建平，王绍武. 1991a. 相似-动力模式的季节预报试验. 中国科学(B辑)，(2)：216-224
黄建平，衣育红. 1991b. 利用观测资料反演非线性动力模型. 中国科学(B辑)，(3)：331-336
黄建平. 1992. 理论气候模式. 北京：气象出版社，152-178
黄建平，衣育红，王绍武. 1993a. 相似-动力模式的由夏季报冬季的季节预报试验. 气象学报，51(1)：118-121
黄建平，衣育红，王绍武等. 1993b. 1991年江淮大涝环流形势的季节预报//王绍武等. 长江黄河旱涝灾害发生规律及其经济影响的诊断研究. 北京：气象出版社，228pp
黄建平. 1993. 相似-动力季节数值预报模式//王绍武等. 气候预测与模拟研究. 北京：气象出版社，99-147
李芳，林中达，左瑞亭等. 2006. 基于经验正交函数和奇异值分解对东亚季风区跨季度夏季降水距平的订正方法. 气候与环境研究，10(3)：658-668
李维京，张培群，李清泉等. 2005. 动力气候模式预测系统业务化及其应用. 应用气象学报，16(1)：1-11
李维京，郑志海，孙丞虎. 2013. 近年来我国短期气候预测中动力相似预测方法研究与应用进展. 大气科学，37(2)：341-350
林朝晖，李旭，赵彦等. 1998. 中国科学院大气物理研究所短期气候预测系统的改进及其对1998年全国汛期旱涝形势的预测. 气候与环境研究，3(4)：339-348
邱崇践，丑纪范. 1989. 天气预报的相似-动力方法. 大气科学，13(1)：22-28
邱崇践，丑纪范. 1990. 预报模式的参数优化方法. 中国科学(B辑)，20(2)：218-224
任宏利. 2006. 动力相似预报的策略和方法[D]. 兰州：兰州大学，52pp
任宏利，张培群，李维京等. 2006. 基于多个参考态更新的动力相似预报方法及应用. 物理学报，55(8)：4388-4396
任宏利，丑纪范. 2007a. 数值模式的预报策略和方法研究进展. 地球科学进展，22(4)：376-385
任宏利，丑纪范. 2007b. 动力相似预报的策略和方法研究. 中国科学(D辑)，37(8)：1101-1109
邵爱梅，希爽，邱崇践. 2009. 修正数值天气预报的非系统性误差的变分方法. 中国科学(D辑)，39(2)：235-244
王斌，谭晓伟. 2009. 一种求解条件非线性最优扰动的快速算法及其在台风目标观测中的初步检验. 气象学报，67(2)：175-188
王会军，周广庆，赵彦. 2000. 降水和大气环流距平年际预测的一个高效的修正方案. 应用气象学报，11(A06)：40-50
王启光，封国林，郑志海等. 2011. 长江中下游汛期降水优化多因子组合客观定量化预测研究. 大气科学，35(2)：287-297
王启光，封国林，郑志海等. 2012a. 基于Lorenz系统提取数值模式可预报分量的初步试验. 大气科学，36(3)：539-550
王启光，封国林，支蓉等. 2012b. 长江中下游汛期降水数值预报业务模式误差场预报研究. 气象学报，70(4)：789-796
王启光，丑纪范，封国林. 2014. 数值模式延伸期可预报分量提取及预报技术研究. 中国科学(D辑)，44(2)：343-354
汪守宏，黄建平，丑纪范. 1989. 大尺度大气运动方程组解的一些性质：定常外源强迫下的非线性适应. 中国科学(B辑)，(3)：328-336
王绍武，赵宗慈，陈振华. 1983. 月平均环流异常的持续性与韵律性和海气相互作用. 气象学报，41(1)：33-42
伍荣生，谈哲敏，王元. 2007. 我国业务天气预报发展的若干问题思考. 气象科学，27(1)：112-118
熊开国，封国林，黄建平等. 2012a. 最优多因子动态配置的东北汛期降水相似动力预报试验. 气象学报，70(2)：213-221

熊开国,赵俊虎,封国林等. 2012b. 汛期降水相似动力预报:模式误差主分量相似预报方法. 物理学报,61(14):149204,doi:10.7498/aps.61.149204

孙丞虎,李维京,任宏利等. 2006. 一个 ENSO 动力-相似误差订正模式及其后报初检验. 大气科学,30(5):965-976

杨成彬,黄建平,周琴芳. 1990. 月平均大气环流异常的垂直结构//长期天气预报论文集.北京:气象出版社,99-106

杨杰,王启光,支蓉等. 2011. 动态最优多因子组合的华北汛期降水模式误差估计及预报. 物理学报,60(2):029204,doi:10.7498/aps.61.029204

杨杰,赵俊虎,郑志海等. 2012. 华北汛期降水多因子相似订正方案与预报试验. 大气科学,36(1):11-21

衣育红,潘桃,黄建平等. 1990. 北半球1月和7月纬偏场遥相关结构分析.高原气象,9(1):43-52

曾庆存,袁重光,王万秋等. 1990. 跨季度气候距平数值预测试验. 大气科学,14(1):10-25

张邦林,丑纪范. 1991. 经验正交函数在气候数值模拟中的应用. 中国科学(B辑),21(4):442-448

张培群,丑纪范. 1997. 改进月延伸预报的一种方法. 高原气象,16(4):376-388

赵俊虎,封国林,王启光等. 2011. 2010 年我国夏季降水异常气候成因分析及预测. 大气科学,35(6):1069-1078

赵俊虎,杨杰,封国林等. 2013a. 2011 年我国夏季降水动力统计预测与异常成因.应用气象学报,24(1):43-54

赵俊虎,杨杰,龚志强等. 2013b. 欧亚中高纬阻塞高压关键区高度场动力-统计跨季度预测试验.物理学报,62(9):099206,doi:10.7498/aps.62.099206

赵俊虎,封国林,杨杰. 2014a. 2013 年中国夏季降水动力-统计预测回顾及存在问题探讨.气象科技进展,录用待刊

赵俊虎,支蓉,申茜等. 2014b. 2012 年我国夏季降水预测与异常成因分析.大气科学,38(2):237-250

赵彦,李旭,袁重光等. 1999. IAP 短期气候距平预测系统的定量评估及订正技术的改进研究. 气候与环境研究,4(4):353-364

赵宗慈,王绍武,陈振华. 1982. 韵律与长期天气预报. 气象学报,40(4):464-474

郑庆林,杜行远. 1973. 使用多时刻观测资料的数值天气预报新模式. 中国科学,16:289-297

郑志海,任宏利,黄建平. 2009. 基于季节气候可预报分量的相似误差订正方法和数值实验. 物理学报,58(10):7359-7367

郑志海,封国林,丑纪范等. 2010. 数值预报中自由度的压缩及误差相似性规律. 应用气象学报,21(2):139-148

郑志海,封国林,黄建平等. 2012. 基于延伸期可预报性的集合预报方法和数值试验. 物理学报,61(19):199203,doi:10.7498/aps.61.199203

郑志海. 2013. 月动力延伸预报研究进展回顾. 气象科技进展,3(1):25-30

郑志海,黄建平,封国林等. 2013. 延伸期可预报分量的预报方案和策略. 中国科学(D辑),43(4):594-605

钟剑,黄思训,费建芳等. 2011. 模式误差动力特征:模式参数误差和物理过程描绘缺失误差. 大气科学,35(6):1169-1176

周广庆,曾庆存,张荣华. 1999. 一个改进的海气耦合模式及其数值模拟. 自然科学进展,9(6):542-551

周琴芳,黄建平,杨成彬. 1989. 北半球冬季环流异常的垂直结构特征. 气象学报,47(2):173-179

Akella S, Navon I M. 2009. Different approaches to model error formulation in 4D-Var: A study with high-resolution advection schemes. Tellus A, 61(1): 112-128

Barnett T, Preisendorfer R W. 1978. Multifield analog prediction of short-term climate fluctuations using a climate state vector. J Atmos Sci, 35(10):1771-1787

Bennett A F. 1992. Inverse Methods in Physical Oceanography. Cambridge:Cambridge University Press

Bennett A F, Chua B S, Leslie L M. 1996. Generalized inversion of a global numerical weather prediction model. Meteor Atmos Phys, 60(1-3): 165-178

Bennett A F, Chua B S, Leslie L M. 1997. Generalized inversion of a global numerical weather prediction model, II: Analysis and implementation. Meteor Atmos Phys, 62(3-4): 129-140

Charney J G, Fjörtoft R, Neumann J. 1950. Numerical integration of the barotropic vorticity equation. Tellus, 2(4): 237-254

Dalcher A, Kalnay E. 1987. Error growth and predictability in operational ECMWF forecasts. Tellus A, 39(5):474-491

D'andrea F, Vautard R. 2000. Reducing systematic errors by empirically correcting model errors. Tellus A, 52(1):21-41

Danforth C M, Kalnay E, Miyoshi T. 2007. Estimating and correcting global weather model error. Mon Wea Rev, 135(2):281-299

Danforth C M, Kalnay E. 2008a. Impact of online empirical model correction on nonlinear error growth. Geophys Res Lett, 35: L24805, doi: 10.1029/2008GL036239

Danforth C M, Kalnay E. 2008b. Using singular value decomposition to parameterize state-dependent model errors. J Atmos Sci, 65(4):1467-1478

DelSole T, Hou A Y. 1999. Empirical correction of a dynamical model. Part I: Fundamental issues. Mon Wea Rev, 127(11): 2533-2545

DelSole T, Zhao M, Dirmeyer P A, et al. 2008. Empirical correction of a coupled land-atmosphere model. Mon Wea Rev, 136(11):4063-4076

Derber J C. 1989. A variational continuous assimilation technique. Mon Wea Rev, 117(11): 2437-2446

Glahn H R, Lowry D A. 1972. The use of model output statistics (MOS) in objective weather forecasting. J Appl Meteor, 11(8):1203-1211

Hoke J E, Anthes R A. 1976. The initialization of numerical models by a dynamic-initialization technique. Mon Wea Rev, 104(12): 1551-1556

Huang J P, Wang S W. 1991. The monthly prediction experiments using a coupled analogy-dynamical model. Acta Meteor Sinica, 5(1):8-15

Huang J P, Yi Y H, Wang S W, et al. 1993. An analogue-dynamical long-range numerical weather prediction system incorporating historical evolution. Quart J Roy Meteor Soc, 119(511): 547-565

Jeuken A B M, Siegmund P C, Heijboer L C, et al. 1996. On the potential of assimilating meteorological analyses in a global climate model for the purpose of model validation. J Geophys Res, 101(D12): 16939-16950

Johansson A, Saha S. 1989. Simulation of systematic error effects and their reduction in a simple model of the atmosphere. Mon

Wea Rev, 117(8):1658-1675

Kaas E, Guldberg A, May W, et al. 1999. Using tendency errors to tune the parameterization of unresolved dynamical scale interactions in atmospheric general circulation models. Tellus A, 51(5):612-629

Klein W H, Lewins B M, Enger I. 1959. Objective prediction of five-day mean temperatures during winter. J Meteor, 16(6): 672-682

Klein W H. 1971. Computer prediction of precipitation probability in the United States. J Appl Meteor, 10(5):903-915

Klinker E, Sardeshmukh P D. 1992. The diagnosis of mechanical dissipation in the atmosphere from large-scale balance requirements. J Atmos Sci, 49(7):608-627

Leith C. 1978. Objective methods for weather prediction. Annu Rev Fluid Mech, 10(1):107-128

Livezey R E, Barnston A G. 1988. An operational multifield analog/antianalog prediction system for United States seasonal temperatures: 1. System design and winter experiments. J Geophys Res, 93(D9):10953-10974

Lorenz E N. 1969. Atmospheric predictability as revealed by naturally occurring analogues. J Atmos Sci, 26(4):636-646

Mu M, Duan W S, Wang B. 1999. Conditional nonlinear optimal perturbation and its applications. Nonlinear Proc Geoph, 10(6): 493-501

Ren H L, Chou J F, Huang J P, et al. 2009. Theoretical basis and application of an analogue-dynamical model in the Lorenz system. Adv Atmos Sci, 26(1): 67-77

Saha S. 1992. Response of the NMC MRF model to systematic-error correction within integration. Mon Wea Rev, 120(2):345-360

Trémolet Y. 2007. Model-error estimation in 4D-Var. Quart J Roy Meteor Soc, 133(626): 1267-1280

Van den Dool H M. 1989. A new look at weather forecasting through analogues. Mon Wea Rev, 117(10): 2230-2247

Van den Dool H M. 1991. Mirror images of atmospheric flow. Mon Wea Rev, 119(9): 2095-2106

Van den Dool H M. 1994. Searching for analogues, how long must we wait? Tellus A, 46(3):314-324

Van den Dool H M, Huang J, Fan Y. 2003. Performance and analysis of the constructed analogue method applied to US soil moisture over 1981 - 2001. J Geophys Res, 108(D16), doi: 10.1029/2002JD003114

Xiong K G, Feng G L, Huang J P, et al. 2011. Analogue-dynamical prediction of monsoon precipitation in Northeast China based on dynamic and optimal configuration of multiple predictors. Acta Meteor Sinica, 25(3): 316-326

Yang X, DelSole T, Pan H L. 2008. Empirical correction of the NCEP global forecast system. Mon Wea Rev, 136(12):5224-5233

Yu H, Huang J, Chou J. 2014. Improvement of medium-range forecasts using the analogue-dynamical method. Mon Wea Rev, 142(4): 1570-1587

Zeng Q C, Zhang B L, Yuan C G, et al. 1994. A note on some methods suitable for verifying and correcting the prediction of climatic anomal. Adv Atmos Sci, 11(2): 121-127

Zupanski M. 1993. Regional four-dimensional variational data assimilation in a quasi-operational forecasting environment. Mon Wea Rev, 121(8): 2396-2408

尤焕苓, 刘伟东, 任国玉. 2014. 1981～2010 年北京地区极端降水变化特征 [J]. 气候与环境研究，19 (1): 69–77，doi:10.3878/j.issn.1006-9585.2012.12143. You Huanling, Liu Weidong, Ren Guoyu. 2014. Variation characteristics of precipitation extremes in Beijing during 1981–2010 [J]. Climatic and Environmental Research (in Chinese), 19 (1): 69–77.

# 1981～2010 年北京地区极端降水变化特征

尤焕苓[1]　刘伟东[1]　任国玉[2]

1 中国气象局北京城市气象研究所，北京 100089
2 中国气象局气候研究开放实验室，国家气候中心，北京 100081

**摘　要**　采用北京地区 20 个常规气象站 1981～2010 年逐日降水数据，对北京地区极端降水的空间分布特征进行了分析。得到以下主要结论：1981～2010 年，北京地区极端降水百分位数（第 90、95 和 99 个百分位数）阈值表现出较一致的空间分布特征，以第 95 个百分位数阈值计算的极端降水日数与降水阈值和降水量的分布有较大差异，极端降水量对总降水量的贡献可达 30%～37%，极端降水强度分布与极端降水阈值分布相似。近 30 年，北京地区多数站点的极端降水量、降水日数和降水强度呈下降趋势，极端降水量以上甸子、怀柔、平谷和观象台下降较为明显，可达到 40 mm (10 a)$^{-1}$ 以上，极端降水强度以顺义、海淀、观象台、大兴和上甸子等站下降较为显著，每 10 a 降水强度减小趋势可达 4 mm d$^{-1}$，极端降水日数变化分布与极端降水量变化分布类似，极端降水强度变化与降水量和降水日数变化的分布有明显不同。

**关键词**　极端降水　降水日数　降水强度　北京
**文章编号**　1006–9585（2014）01–0069–09　　**中图分类号**　P446　　**文献标识码**　A
doi:10.3878/j.issn.1006-9585.2012.12143

# Variation Characteristics of Precipitation Extremes in Beijing during 1981–2010

YOU Huanling[1], LIU Weidong[1], and REN Guoyu[2]

1 *Institute of Urban Meteorology*, *Beijing*, *China Meteorological Administration*, *Beijing* 100089
2 *Laboratory for Climate Studies*, *China Meteorological Administration*, *National Climate Center*, *Beijing* 100081

**Abstract**　Daily precipitation data of 20 national stations in Beijing area during 1981–2010 are used to study the extreme precipitation exceeding relative thresholds (upper 90th, 95th, and 99th percentiles of precipitation for local sites and given time). The results show that the relative thresholds of 90th, 95th, and 99th percentiles have a similar spatial distribution. The distribution of extreme precipitation days shows a significant difference from the precipitation amount and relative threshold calculated as the upper 95th percentile. The extreme precipitation amount can account for 30%–37% of the total precipitation amount. The distribution of extreme precipitation intensity is consistent with the extreme precipitation threshold. In the recent 30 years, the extreme precipitation amount, days, and intensity of most stations in Beijing area have shown apparent decreasing trends. In Shangdianzi, Huairou, Pingu, and Guanxiangtai stations, the decreasing trend of extreme precipitation amount is obvious, reaching a value of 40 mm (10 a)$^{-1}$. In Shunyi, Haidian, Guanxiangtai, Daxing, and Shangdianzi stations, the decreasing trend of extreme precipitation intensities is more pronounced, with precipitation intensity being as low as 4 mm d$^{-1}$ (10 a)$^{-1}$. The distribution trend of extreme precipitation amount is positively related to the precipitation frequency and that of extreme precipitation intensity is inconsistent with the precipitation amount,

**收稿日期**　2012–08–12 收到，2013–03–03 收到修定稿
**资助项目**　中国科学院战略性先导科技专项 XDA05090202，国家自然科学基金项目 40975066、41375069
**作者简介**　尤焕苓，女，1973 年出生，硕士，高级工程师，研究方向为城市气象服务等。E-mail: you_hl@sohu.com

frequency, and patterns of distribution.

**Keywords** Extreme precipitation, Precipitation day, Precipitation intensity, Beijing

## 1 引言

极端降水事件常与洪涝灾害密切相关。为掌握中国极端降水事件的变化规律，许多学者利用不同的指标，对降水量、降水频率、降水强度的极值变化做了大量的研究。任国玉等（2010）研究表明，在气候变化背景下，总降水量增大的区域，极端强降水事件出现的机率有可能增加；即使平均总降水减少的区域，一些地点的强降水量及其降水频数也有增加。翟盘茂等（2007）、王小玲和翟盘茂（2008）的研究表明，近 50 年来我国多数地区极端强降水量或暴雨降水量在总降水量中的比重有所增加，极端强降水或暴雨级别的降水强度增强，年降水日数趋于减少，有暴雨出现地区的年平均暴雨日数呈微弱增多趋势，但其时空差异较大。Zhai et al.（2005）采用超过气候标准期中日降水量序列的第 95 个百分位数的天数，作为台站极端强降水气候事件的度量，发现中国地区年极端强降水日数的趋势变化的空间分布特征与年降水量和暴雨日数相似。王萃萃和翟盘茂（2009）研究发现，我国北方尤其是在华北南部，大城市极端降水强度和频数增加的趋势比周围大，华北东南部大城市极端降水强度呈较明显的增强趋势。Wang and Zhou（2005）利用 1961～2001 年我国的台站资料，发现西南、西北北部和华东极端降水事件频率有增加趋势，华北、华中有减少趋势，而且这种趋势与平均降水变化趋势空间分布一致。Alexander et al.（2006）的研究也发现了华北极端降水事件频率有减少趋势。张爱英等（2008）分析了近 45 年来华北中北部极端降水事件频率变化时空特征，发现平均年最大日降水量呈下降趋势，强降水事件频率变化不大，但其在总降水日数中的比重有所增大，20 世纪 90 年代中期以后这种现象比较明显。王冀等（2012）利用华北地区 84 个气象台站 1961～2009 年的资料分析得到了华北地区极端降水量、降水次数和降水强度均呈下降趋势的结论。Tu et al.（2010）对华北降雨进行研究指出，华北 1954～2006 年降水及频次均减少，但大暴雨频次并未减少。郭军等（2010）利用环渤海地区 60 个测站 1961～2008 年逐日降水资料，发现山东南部、河北西南部、辽宁西部与河北东北部等区域具有较高极端降水值。

虽然很多研究者在极端气候方面做了大量的研究，但对于北京这样一个地形复杂、城市化高速发展的较小的区域，通常仅采用北京观象台站的极端气候特征作为北京地区的特征，而对于北京地区各站极端气候事件的相关研究较少。因此，本文选取北京地区 1981～2010 年的 20 个常规气象站日降水资料对北京地区极端降水特征进行研究，以期了解北京地区极端降水量、降水日数和降水强度等的变化特征，从一个新的角度分析北京地区极端降水的特征，对于深入理解北京地区降水变化规律以及评估区域气候特征、提高城市适应气候变化能力等具有重要意义。

## 2 资料与方法

本文采用北京地区 20 个常规气象站 1981～2010 年逐日降水数据，分析极端降水事件变化趋势和极端事件的空间分布。北京地区地形复杂，气候的地域差异明显，仅用绝对阈值定义日降水极端事件，在各个区县之间缺乏可比性。因此，本文采用国际上在气候极值变化研究中常见的将某个百分位值作为极端值的阈值检验方法，定义基于日降水量的极端降水指数。具体采用 1981～2010 年日降水量大于 0.1 mm 的按升序排列的第 90%、95%、99%的降水量值作为该测站极端降水量的阈值，年极端降水日数指一年中日降水量超过该极端降水阈值的日数，年极端降水强度指超过极端降水阈值的年极端降水总量与年极端降水日数的比值。以极端降水事件为例，95%极端降水阈值的计算方法为：把 1981～2010 年逐年日降水量大于 0.1 mm 的降水量按升序排列，将第 95 个百分位值的降水量值定义为极端降水事件的阈值，当某站某日降水量超过了该站的阈值时，就称该日该站出现了极端降水事件。具体算法为：

参照 Bonsal et al.（2001）的方法，如果某个气象要素有 $n$ 个值，将这 $n$ 个值按升序排列，某个值小于 $x_1, x_2,\ldots, x_m,\ldots, x_n$ 或等于 $x_m$ 的概率为：

$$P=(m-0.31)/(n+0.38), \quad (1)$$

其中，$m$ 为 $x_m$ 的序号，$n$ 为某个气象要素值的个数，如果有 100 个值，那么第 95 个百分位上的值为排序后的 $x_{95}$（$P$=94.3%）和 $x_{96}$（$P$=95.3%）的线性插值。

## 3 结果与分析

### 3.1 极端降水事件空间分布

从表 1 可以看出，对于第 90 百分位的极端降水事件，降水阈值为 16.8～24.8 mm，均在中雨雨量范围内，对于第 95 百分位的极端降水事件，降水阈值为 23.9～37.5 mm，除延庆站外均在大雨雨量范围，第 99 百分位的降水阈值为 43.1～79.6 mm，除延庆、佛爷顶、汤河口和斋堂站外，降水阈值均处在暴雨雨量范围。几种降水阈值都表现出类似的分布特征，即在北京地区东部和南部地区以及城区降水阈值较大，而在北京西部及其西北部山区，降水阈值较小（图 1）。尤莉等（2010）统计了内蒙古 116 个单站 1961～2008 年的逐日降水量，发现第 90 和第 95 百分位的极端降水阈值分别为 2.1～14.2 mm 和 4.0～23.8 mm。总体可见，北京地区极端降水阈值明显高于内蒙古地区。极端强降水阈值的空间分布与年降水量的分布相似，说明极端强降水与年降水量关系密切。同时，相对阈值方法检测出了西部山区暴雨以下量级但可能形成一定灾害的极端降水。因第 90 个、第 95 个和第 99 个百分位的降水极端事件的阈值空间分布相近，以下主要针对第 95 个百分位的降水极端事件进行分析。

**表 1 1981～2010 年北京地区 20 个气象站第 90、95 和 99 个百分位数的极端降水阈值**

**Table 1 The upper 90th, 95th, and 99th percentile extreme precipitation threshold in Beijing during 1981–2010** mm

| 站名 | 第 90 百分位 | 第 95 百分位 | 第 99 百分位 |
|---|---|---|---|
| 顺义 | 22.90 | 35.55 | 79.70 |
| 海淀 | 22.93 | 35.39 | 71.81 |
| 延庆 | 16.70 | 24.70 | 42.72 |
| 佛爷顶 | 17.24 | 25.69 | 46.75 |
| 汤河口 | 16.80 | 25.74 | 48.61 |
| 密云 | 23.04 | 36.40 | 80.20 |
| 怀柔 | 24.30 | 35.10 | 74.20 |
| 上甸子 | 21.51 | 33.00 | 66.19 |
| 平谷 | 24.50 | 37.00 | 73.51 |
| 通州 | 22.30 | 34.30 | 64.06 |
| 朝阳 | 24.30 | 34.73 | 73.71 |
| 昌平 | 18.50 | 28.08 | 67.62 |
| 斋堂 | 16.80 | 23.20 | 46.86 |
| 门头沟 | 22.92 | 33.30 | 74.44 |
| 观象台 | 22.38 | 32.85 | 65.35 |
| 石景山 | 21.77 | 33.90 | 66.32 |
| 丰台 | 21.90 | 35.43 | 68.73 |
| 大兴 | 21.99 | 32.87 | 67.93 |
| 房山 | 20.70 | 34.18 | 66.70 |
| 霞云岭 | 21.20 | 34.08 | 72.52 |

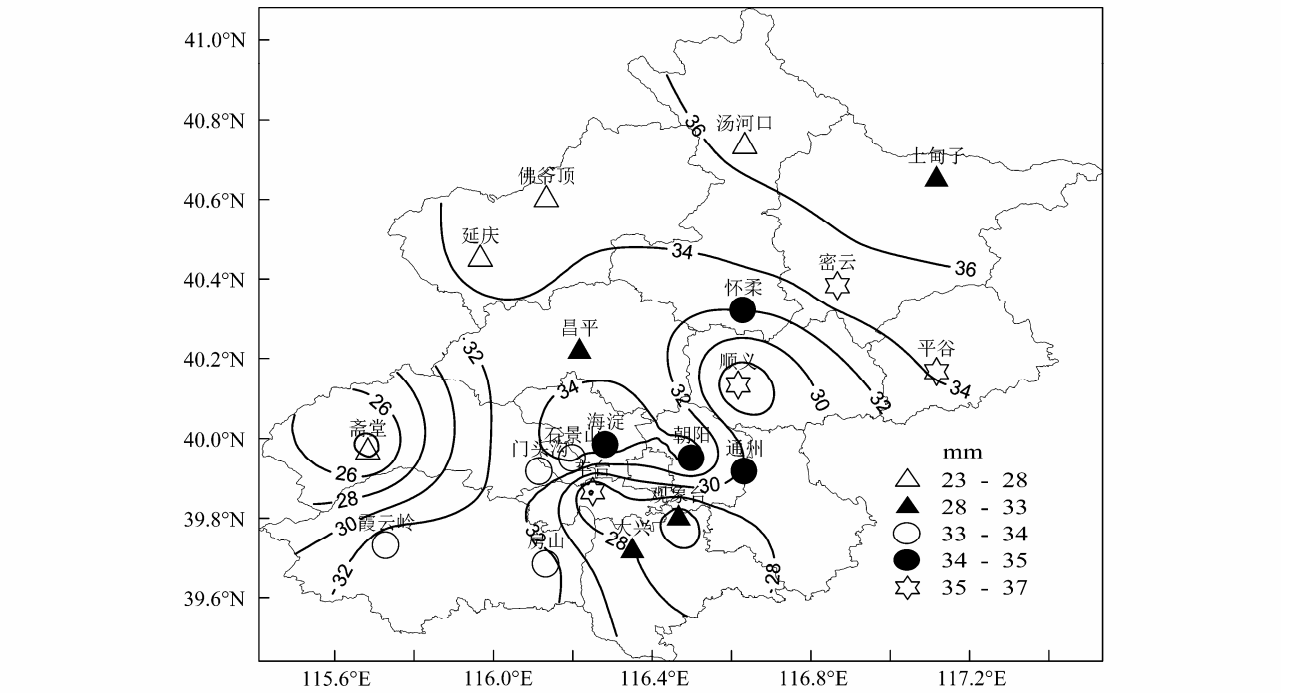


图 1 北京地区 1981～2010 年第 95 百分位降水量阈值

Fig. 1 Distribution of the 95th percentile extreme precipitation threshold in Beijing during 1981–2010

由图 2 可以看到，北京地区极端降水量从西南部到东北部以及城区较强，极端降水量可达 190 mm 以上，而在西部和东南部逐渐减少，降水量在 180 mm 以下。极端降水量大值区主要分布在北京的上甸子、密云、海淀、朝阳、门头沟、丰台和房山等站。这种分布和降水的气候平均态以及大雨和暴雨分布较为类似，也反映了极端降水对于降水的贡献非常大，用百分位方法确定的极端降水阈值是合理的。同时可以看出，在北京城区、城区东北部盛行风下风方向和城区西部、东南部郊区的降水差异，北京地区主城区下风方的东北区降水量最大，表现出明显的“城市雨岛效应”，这主要是由于夏季北京地区多处于北支低槽区域和副高控制下西南暖湿气流的冷暖空气交汇处，有利于降水频繁发生。另外北京城市化产生的城市热岛、建筑物对天气系统移动减速及更多凝结核对暴雨起增幅作用所引起的（陈静和刘琳，2011）。

北京地区极端降水日数平均为每年 3.16～4.24 d（图 3），极端降水日数与极端降水阈值和极端降水量的分布有较大差异，表现出极端降水阈值小的站点其极端降水日数较多。从西南至北部，沿山区分布，极端降水日数较大，如佛爷顶站极端降水日数大约在 4 d 左右，而在城区及其附近降水日数较少，大约在 3.4 d 左右，对应极端降水量分布，表明这些站点极端降水量大而极端降水日数小。对于佛爷顶站，其极端降水量不大，但极端降水日数较多。对于密云、平谷和门头沟等站，其极端降水量大、极端降水日数少的特点更加显著。这主要是由于北京西部和北部山区受北方频发的冷空气影响，与来自北京东南的暖湿空气受燕山、太行山的抬升，在山前迎风坡形成多雨区，而背风坡则形成少雨区，造成系统性降水过程增多，从而导致降雨日数多的原因（徐宗学等，2006）。

极端降水量对年总降水量的贡献可以通过年极端降水量在全年总降水量中所占的比例来衡量，在一定程度上反映了一个地区降水量年内分布情况。北京地区极端降水量对总降水量的贡献为 30%～38%（见图 4），其中霞云岭、房山、昌平、顺义、门头沟等站点极端降水对总降水量贡献较大，达到了 36%以上，说明这些地区的极端降水在更大程度上决定了该地区总降水量的大小。而延庆、汤河口、佛爷顶和斋堂这些山区站，极端降水对总降水量的贡献较小，不到 33%。同郭军等（2010）得出的京津唐地区极端降水量对年降水量的贡献超过了 30%的结论比，与本研究的结果基本一致，其差异主要同极端降水阈值的确定时限、研究站点和所研究的时期有关。

极端降水强度是衡量极端降水的重要指标，强

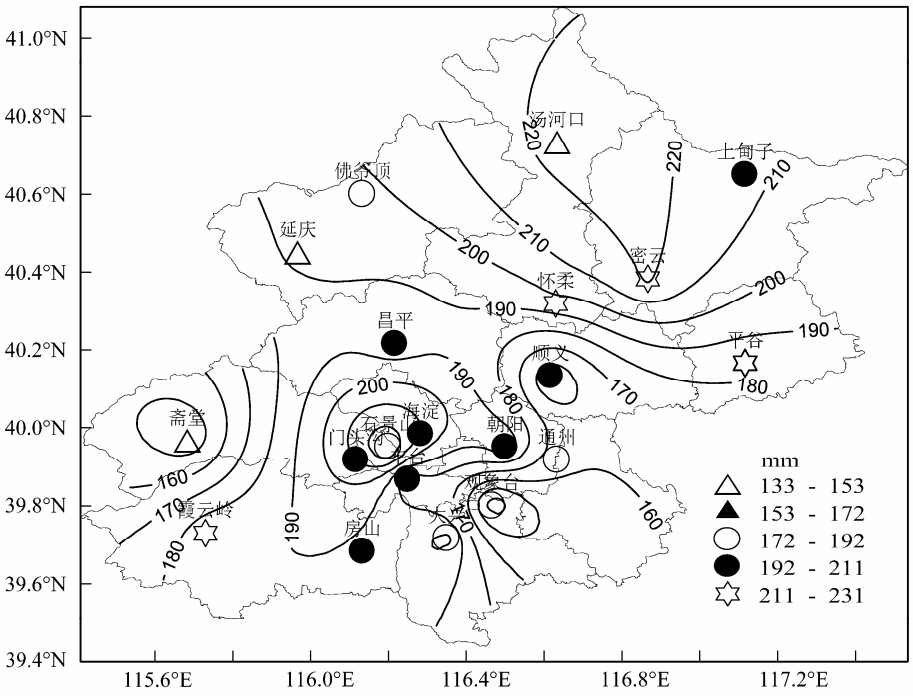


图 2 北京地区 1981～2010 年年平均极端降水量分布

Fig. 2 Distribution of annual extreme precipitation amount in Beijing during 1981–2010

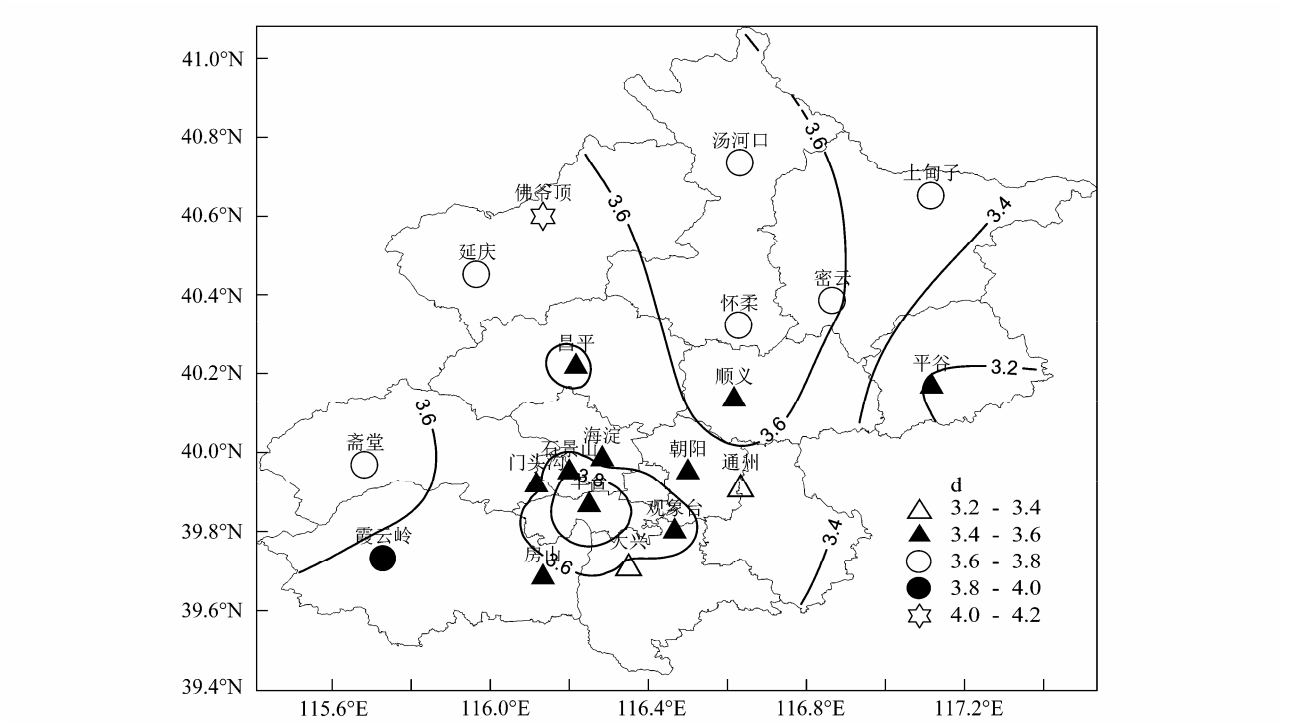


图 3　北京地区 1981～2010 年极端降水日数年平均空间分布

Fig. 3　Distribution of annual extreme precipitation days in Beijing during 1981–2010

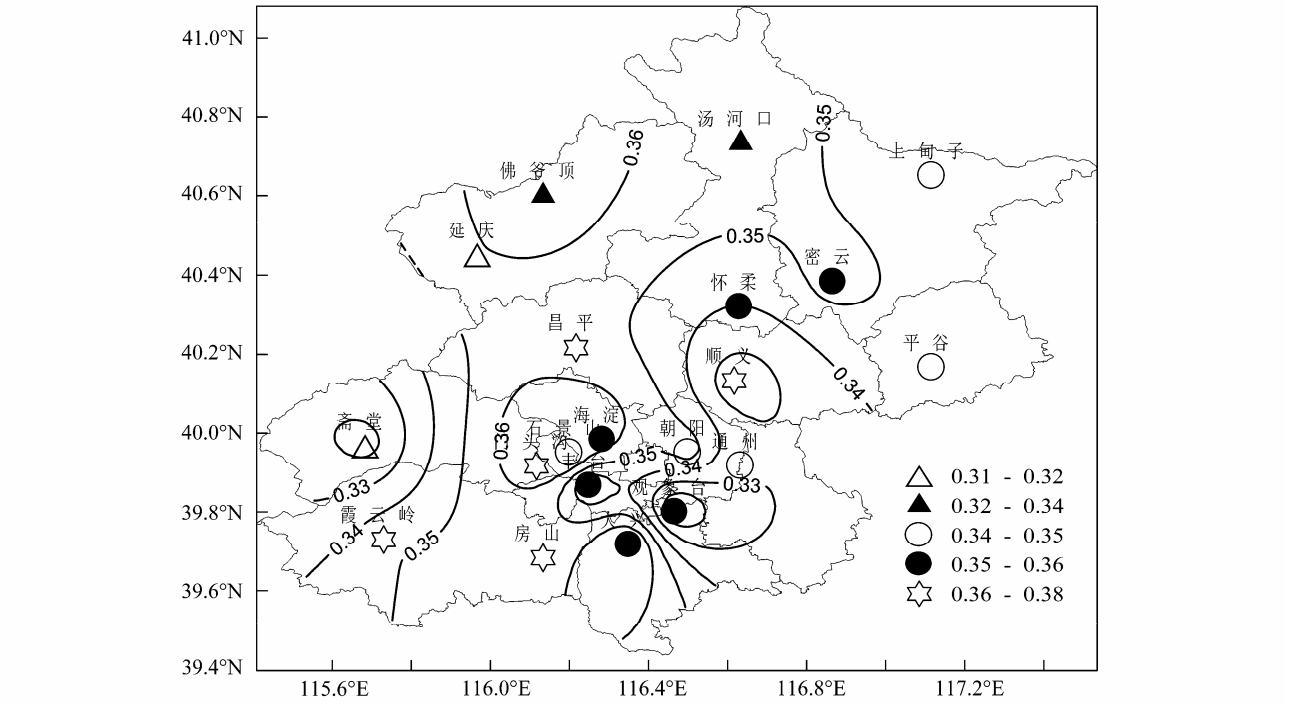


图 4　北京地区 1981～2010 年极端降水量对总降水量的贡献

Fig. 4　Contribution of the extreme precipitation amount to total precipitation in Beijing during 1981–2010

度越大造成灾害的可能性越大。图 5 所示，北京地区多年平均年极端降水强度分布与极端降水阈值分布相似，即在东北部和城区降水强度较大，可达 56 mm $d^{-1}$，而在北京西部、北部山区降水强度较小，低于 48 mm $d^{-1}$。其中在顺义、密云、怀柔、平谷和霞云岭等地高于 60 mm $d^{-1}$，而在延庆、汤河口、佛爷顶和斋堂等地低于 41 mm $d^{-1}$。由于北京受地形和城市的影响，造成其降水强度分布不均匀。结合阈值分布，说明阈值大的地方，其降水强度也大，形成灾害的风险也大。

### 3.2 极端降水事件时间变化

近 30 年北京地区极端降水量变化趋势（图 6）表明，大部分站点的极端降水量均呈现出下降趋势，而以上甸子、怀柔、平谷和观象台下降最为明显，大于 40 mm（10 a）$^{-1}$，佛爷顶、延庆站则有小幅上升，大约在 10 mm（10 a）$^{-1}$，其它站点的极端降水量变化在－40～0 mm（10 a）$^{-1}$ 范围内。总体上看，北京东北部、顺义、昌平和城区极端降水量下降较多。极端降水日数变化是造成极端降水量变化的主要因素之一，极端降水日数变化分布（图 7）与极端降水量变化分布相似。可以推知，北京地区极端降水量的减少原因之一是因为极端降水日数

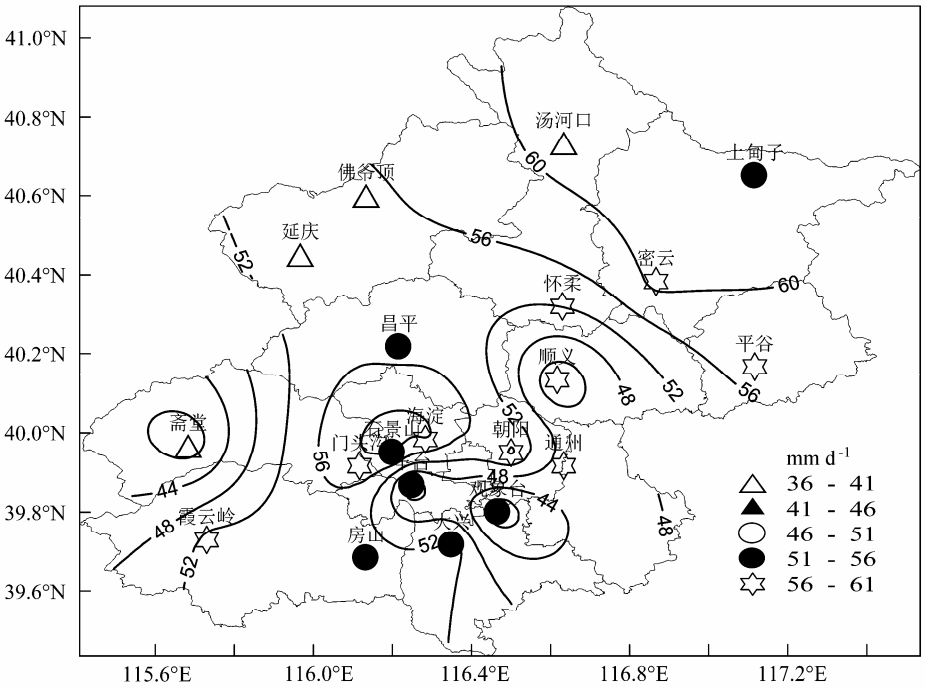


图 5 北京地区 1981～2010 年平均极端降水强度分布

Fig. 5 Distribution of the mean extreme precipitation intensities in Beijing during 1981–2010

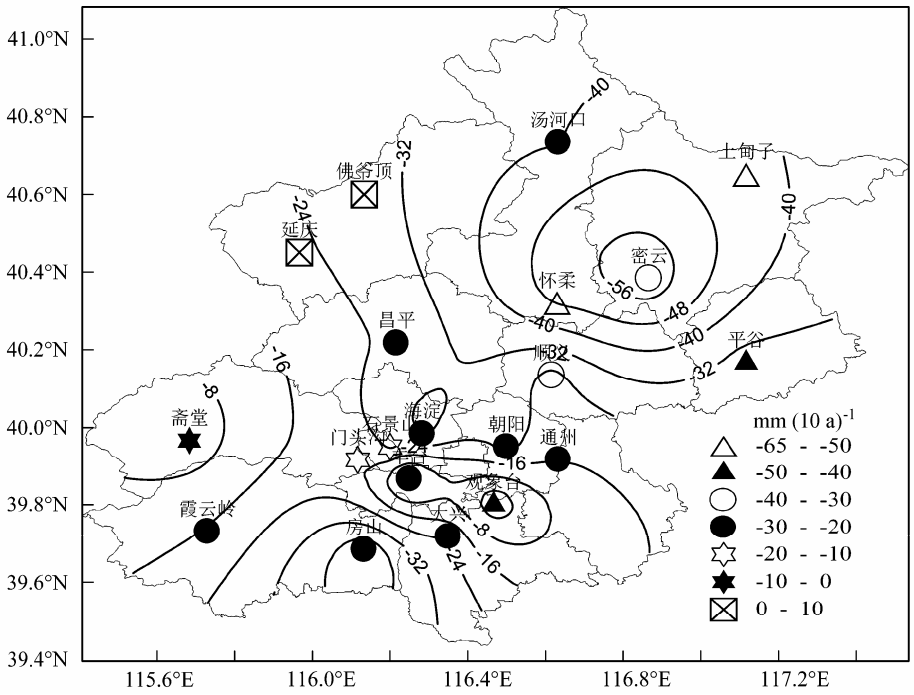


图 6 北京地区 1981～2010 年年平均极端降水量变化趋势

Fig. 6 The trend of annual extreme precipitation amount in Beijing during 1981–2010

减少所造成的。该结论与王冀等（2012）利用华北地区 84 个气象台站 1961～2009 年资料分析得到的华北地区极端降水量、降水次数和降水强度均呈下降趋势的结论一致。但这与 Tu et al.（2010）研究得出的华北地区 1954～2006 年大暴雨频次并未减少的结论有所不同，其主要原因是所研究的时段、降雨量级和区域的范围等不同所造成的。

图 8 所示的极端降水强度变化趋势与极端降水量和极端降水日数变化趋势的分布有明显不同，可以看出在北京西部、西北部、北部和东部多数地区

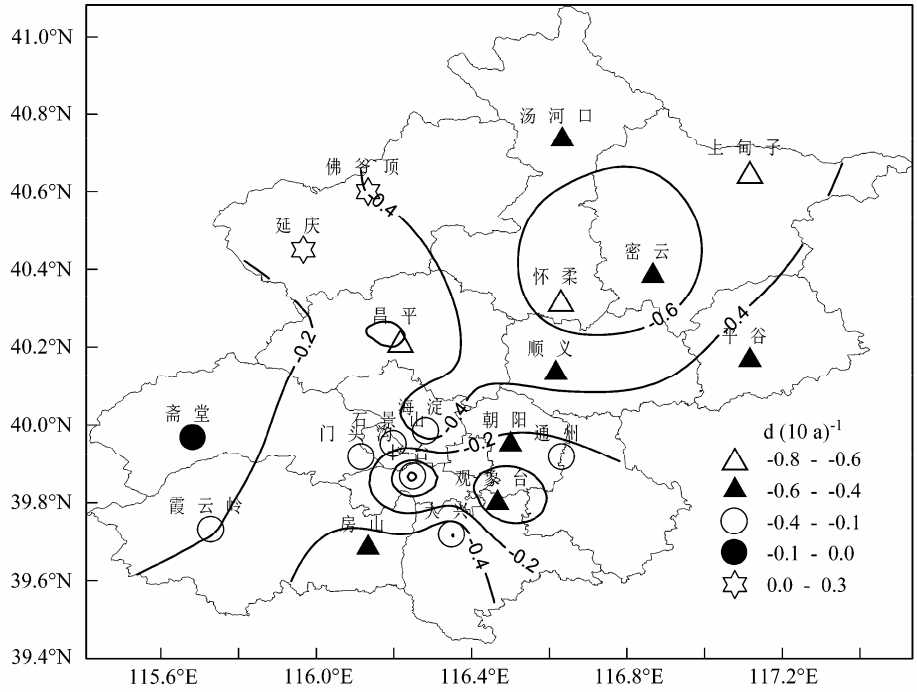


图 7　北京地区 1981～2010 年年平均极端降水日数变化趋势

Fig. 7　The trend of annual extreme precipitation days in Beijing during 1981–2010

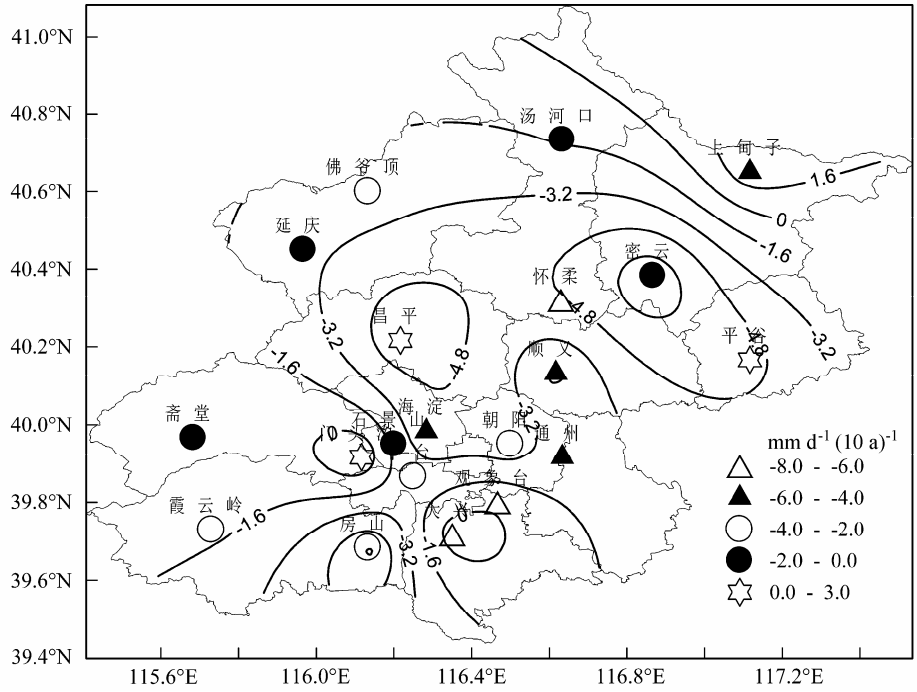


图 8　北京地区 1981～2010 年极端降水强度变化趋势空间分布

Fig. 8　The trend of mean extreme precipitation intensities in Beijing during 1981–2010

极端降水强度减小，其中顺义、海淀、观象台、大兴和上甸子等 5 个站每 10 a 降水强度减小趋势大于 4 mm $d^{-1}$；而在北京平谷、昌平和门头沟等台站，极端降水强度有弱增强趋势。总体上看，在西南部平原地区，降水强度减小明显，而在西部北部山区，降水强度减小不明显。

## 4 结论与讨论

本文采用北京地区 20 个常规气象站 1981～2010 年逐日降水数据，分析了北京地区 1981～2010 年极端降水阈值、极端降水量、极端降水日数、极端降水强度及其变化趋势的分布，得到以下结论：

（1）对于北京地区 1981～2010 年的极端降水阈值，降水量最强的 10%极端降水阈值均在中雨雨量范围内；对于降水量最强的 5%，其极端降水阈值除延庆站均在大雨雨量范围；而对于降水量最强的 1%的极端降水阈值，除延庆、佛爷顶、汤河口和斋堂，其降水阈值均处在暴雨雨量范围。几种降水阈值均表现出一致的分布特征，即在北京地区东部和南部地区以及城区降水阈值较大，而在北京西部及其西北部山区，降水阈值较小。

（2）北京地区极端降水气候平均分布表现为从西南到东北以及城区较强，而在西部和东南部逐渐减少。与降水的气候平均态以及大雨和暴雨分布较为类似，极端降水的多寡在很大程度上影响该地区降水量大小。最强的 5%极端降水量对北京地区总降水量的贡献为 30%～38%，多年平均年极端降水强度分布与极端降水阈值分布非常一致，阈值大的地方，极端降水强度也大。

（3）近 30 年北京大部分地区极端降水量均呈下降趋势，极端降水日数变化趋势分布与极端降水量变化趋势分布相同。极端降水强度变化趋势与极端降水量和极端降水日数变化趋势的分布有明显不同，在北京西部、西北部、北部和东部多数地区极端降水强度减小，而在北京平谷、昌平和门头沟极端降水强度有增强趋势。

北京地区极端降水总量的减少主要是由于降水强度和降水日数减少共同作用所造成的，极端降水总量的减少是造成北京地区近些年来干旱化的一个可能的原因。北京地区极端降水变化在空间分布上的不均匀性极其复杂，可以通过进一步分析北京地区的天气气候背景、地形和城市热岛特征上得到一些合理解释。本文的分析对城市规划建设、管理和理念方面的思考，以及为科学制定城市规划可提供一些借鉴作用。

### 参考文献（References）

Alexander L V, Zhang X, Peterson T C, et al. 2006. Global observed changes in daily climate extremes of temperature and precipitation [J]. J. Geophys. Res., 111 (3): D05109, doi: 10.1029/2005JD006290.

Bonsal B R, Zhang X, Vincent L A, et al. 2001. Characteristics of daily and extreme temperatures over Canada [J]. J. Climate, 14(9): 1959–1976.

陈静, 刘琳. 2011. 2011 年汛期北京城市暴雨特征及其灾害成因初步分析 [J]. 暴雨灾害, 30 (3): 282–287. Chen Jing, Liu Lin. 2011. Characteristics of urban rainstorm and its disaster cause over Beijing in flood season of 2011 [J]. Torrential Rain and Disasters (in Chinese), 30 (3): 282–287.

郭军, 任国玉, 李明财. 2010. 环渤海地区极端降水事件概率分布特征 [J]. 气候与环境研究, 15 (4): 425–432. Guo Jun, Ren Guoyu, Li Mingcai. 2010. Characteristics of the probability distribution of the extreme precipitation events around the Bohai Bay [J]. Climatic and Environmental Research (in Chinese), 15 (4): 425–432.

任国玉, 封国林, 严中伟. 2010. 中国极端气候变化观测研究回顾与展望 [J]. 气候与环境研究, 15 (4): 337–353. Ren Guoyu, Feng Guolin, Yan Zhongwei. 2010. Progresses in observation studies of climate extremes and changes in mainland China [J]. Climatic and Environmental Research (in Chinese), 15 (4): 337–353.

Tu K, Yan Z W, Dong W J. 2010. Climatic jumps in precipitation and extremes in drying North China during 1954–2006 [J]. J. Meteor. Soc. Japan, 88 (1): 29–42.

王萃萃, 翟盘茂. 2009. 中国大城市极端强降水事件变化的初步分析 [J]. 气候与环境研究, 14 (5): 553–560. Wang Cuicui, Zai Panmao. 2009. Changes of precipitation extremes in Chinas large cities [J]. Climatic and Environmental Research (in Chinese), 14 (5): 553–560.

王冀, 蒋大凯, 张英娟. 2012. 华北地区极端气候事件的时空变化规律分析 [J]. 中国农业气象, 33(2): 166–173. Wang Ji, Jiang Dakai, Zhang Yingjuan. 2012. Analysis on spatial and temporal variation of extreme climate events in North China [J]. Chinese Journal of Agrometeorology (in Chinese), 33 (2): 166–173.

王小玲, 翟盘茂. 2008. 1957～2004 年中国不同强度级别降水的变化趋势特征 [J]. 热带气象学报, 24 (5): 459–466. Wang Xiaoling, Zai Panmao. 2008. Changes in China's precipitation in various categories during 1957–2004 [J]. Journal of Tropical Meteorology (in Chinese), 24 (5): 459–466.

Wang Y Q, Zhou L. 2005. Observed trends in extreme precipitation events in China during 1961–2001 and the associated changes in large-scale circulation [J]. Geophys. Res. Lett., 32 (5): L09707.

徐宗学, 张玲, 阮本清. 2006. 北京地区降水量时空分布规律分析 [J]. 干旱区地理, 29 (2): 186–192. Xu Zongxue, Zhang Ling, Ruan Benqing. 2006. Analysis on the spatiotemporal distribution of precipitation in the Beijing region [J]. Arid Land Geography (in Chinese),

29 (2): 186–192.

尤莉, 戴新刚, 张宇. 2010. 1961～2008 年内蒙古降水极端事件分析 [J]. 气候变化研究进展, 6 (6): 411–416. You Li, Dai Xingang, Zhang Yu. 2010. Extreme precipitation events in Inner Mongolia in 1961–2008 [J]. Advances in Climate Change Research (in Chinese), 6 (6): 411–416.

翟盘茂, 王萃萃, 李威. 2007. 极端降水事件变化的观测研究 [J]. 气候变化研究进展, 3 (3): 144–148. Zai Panmao, Wang Cuicui, Li Wei. 2007. A review on study of change in precipitation extremes [J]. Advances in Climate Change Research (in Chinese), 3 (3): 144–148.

Zhai P M, Zhang X B, Wan H, et al. 2005. Trends in total precipitation and frequency of daily precipitation extremes over China [J]. J. Climate, 18 (7): 1096–1108.

张爱英, 高霞, 任国玉. 2008. 华北中部近 45 a 极端降水事件变化特征 [J]. 干旱气象, 26 (4): 46–50. Zhang Aiying, Gao Xia, Ren Guoyu. 2008. Characteristic of extreme precipitation events change in central North China in recent 45 years [J]. Arid Meteorology (in Chinese), 26 (4): 46–50.

# 北京“7·21”特大暴雨过程时空特征解析

尤焕苓[1,2,3] 任国玉[2*] 吴方[1,3] 刘伟东[1] 杨萍[4]

(1 北京市气象局,北京 100089; 2 中国气象局气候研究开放实验室,国家气候中心,北京 100081;
3 中国气象局北京城市气象研究所,北京 100089; 4 中国气象局气象干部培训学院,北京 100081)

**摘要** 利用高密度自动站观测记录和长序列气象站观测资料,对 2012 年 7 月 21 日北京地区特大暴雨过程的时空演化规律进行了分析。结果表明:“7·21”特大暴雨期间,全市累积降雨量大于 100 mm 的站数达到 211 个,占全部测站数的 92%,96 个站累积雨量大于 200 mm,12 个站大于 300 mm;多数地区降雨时长超过 16 h,密云大成子站降水时间最长,达到 20 h,强降雨时长在西南房山和门头沟最大;最大小时雨强中心出现在东北和西南区域,东北部最大雨强中心较突出;平均雨强高值阶段出现在 21 日 18:00—21:00,其中 19 :00 雨强最大,达到 22 mm/h,但最大雨强在 70 mm/h 以上的高强度降雨发生在 21 日 13:00—14:00(门头沟龙泉站)和 19:00—22:00,20:00—21:00 平谷挂甲峪站高达 100.3 mm/h;城区及其附近地带 20 mm 以上量级的小时降雨强度较大,同时傍晚阶段平均累积雨量增长速率快,平均小时降水强度偏大;房山站 21 日雨量位居 1961 年以来逐年最大日降水量第 2 位,仅次于 1979 年 7 月 18 日降雨量,而全市 15 站平均 21 日雨量打破了 1961 年以来的最大日降水量记录,比处于第 2 位的 1963 年 8 月 9 日平均雨量高出 43 mm。

**关键词** 特大暴雨 累积雨量 降雨时长 降雨强度 城市热岛效应

## 引言

2012 年 7 月 21—22 日,北京地区出现历史罕见的特大暴雨过程,简称“7·21”特大暴雨。“7·21”特大暴雨始于 21 日上午 10:00,结束于 22 日清晨 06:00,持续近 20 h。在本次降雨过程中,北京市大部分地区出现大暴雨到特大暴雨,暴雨引发房山地区山洪暴发,引起重大人员伤亡和经济损失。研究表明,近 50 年北京不同量级的降水均呈下降趋势,大雨和暴雨雨强减小趋势明显[1],暴雨或强降水日数总体表现为波动式的缓慢下降,20 世纪 90 年代后期以来强降水事件发生频率和降水量减少尤其显著[2];观测研究还表明,近几十年北京市夏季降水发生了结构性调整,短持续性降水的降水总量逐步增多,而长持续性降水事件的降水总量却大幅减少[3]。在这样的年代到多年代尺度气候变异背景下,发生持续时间长、雨强大的“7·21”特大暴雨,非同寻常。深入分析、了解这场特大暴雨过程的时空演化规律及其成因,是改进北京地区极端强降水预报技术的基础性工作。本文根据北京地区自动站和国家站地面观测记录,对此次特大暴雨过程的时空演化规律进行了分析,对其孕育和发生发展过程获得了比较清晰的认识。

## 1 资料和方法

资料包括北京地区 241 个自动气象站 2012 年 7 月 21 日 10:00 到 7 月 22 日 06:00 降水及 15 个常规气象站 1961 年 1 月至 2012 年 7 月日降水观测数据(图 1)。城区范围包括城 6 区(朝阳、海淀、丰台、石景山、东城、西城),共有自动站 55 个,常规站 4 个,分别为朝阳、海淀、丰台和石景山站。房山区自动站 13 个,常规站 2 个(房山站和霞云岭站)。15 个常规气象站长序列日降水资料经过严格质量控制,241 个自动站降水资料经过质量检查和确认。



国家公益性行业专项(GYHY201206012,GYHY201206031)资助

作者简介:尤焕苓,女,1973 年生,高级工程师,主要从事应用气象及城市气象服务等研究,Email: you_hl@sina.cn

收稿日期:2013 年 10 月 8 日;定稿日期:2014 年 3 月 10 日

* 通信作者, Email: guoyoo@cma.gov.cn

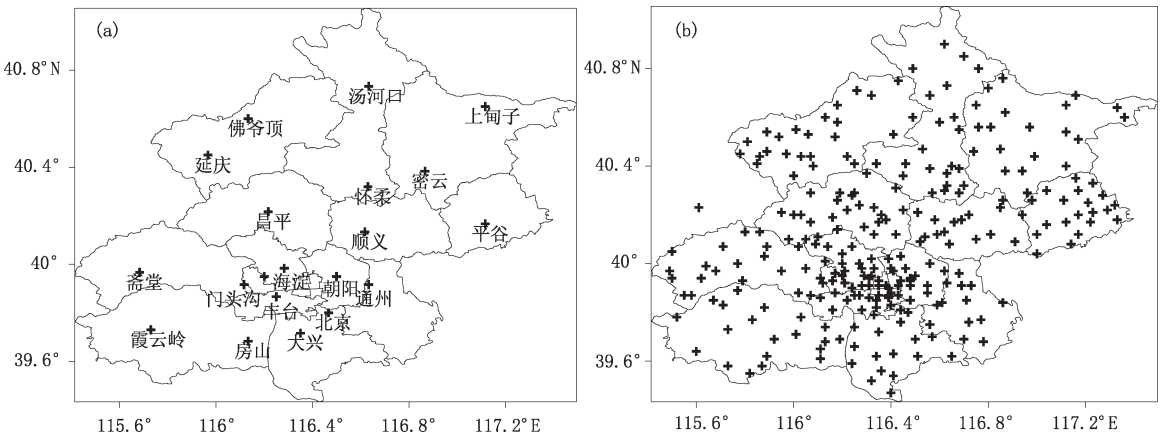


图 1　北京地区气象观测站分布：(a)常规观测气象站，(b)自动气象站

本文中的降水量为每小时大于等于 0.1 mm 的累积降水量，降水时长为降水持续过程的小时数，降水强度为单位时间(h)内的降水量。为了比较区域降水差异，分别统计分析了 2012 年 7 月 21 日10:00 到 7 月 22 日 06:00 房山、北京城区和北京全市的面积平均小时雨量特征值，包括小时雨量、总雨量、降水时长和平均降水强度，绘制了单站和区域平均累积雨量时间演变曲线图以及平均逐时降雨量演变曲线图、特征时刻累积雨量等值线分布图、特征降水量的等时线分布图、不同强度降水时长等值线分布图等。门头沟区的龙泉站记录到本次降水过程最大降雨量，将其单独进行分析，并与各个区域平均序列进行比较。

此外，为了解本次降水过程的历史地位，还统计分析了 1961 年 1 月至 2012 年 7 月期间全市 15 个常规站平均和房山站逐年最大日降水量时间序列。

## 2　结果分析

### 2.1　降水量

图 2 表示不同区域范围内累积水量的时间演变过程。可以看出，北京地区降水时间始于 7 月 21 日 10:00 以后，房山地区开始最早，城区略晚；13:00—21:00 是各地区累积雨量迅速增长时期，此期间降雨量达到或超过总降雨量的 2/3；房山区平均降雨结束时间最早，在 22 日 01:00，龙泉站在 22 日 02:00左右，城区平均大约在 22 日 03:00—04:00，到 22 日 06:00 全市降雨结束。整个降雨过程中，房山降雨量都明显高出城区，门头沟龙泉站降雨量在 21 日 13:00 以后一直显著高于房山区和城区，18:00以后与房山和城区的累积雨量差值更大，到 22 日 03:00，龙泉站累积降雨量接近 400 mm，为城区平均累积雨量的近 2 倍。

门头沟龙泉站降水快速增长主要发生在 21 日 12:00—14:00、16:00—19:00 和 22 日 00:00—02:00三个阶段，其中 21 日 16:00—19:00 呈持续快速增长趋势，在 3 h 内累积雨量从 150 mm 左右急速增加到 330 mm 左右。这种阶段性快速增长特点也在一定程度上出现在北京城区，但似乎比龙泉站延迟 1 h 左右，而且平均增长速率更为和缓。在 21 日 18:00 之前，城区降水量累积曲线与全市平均十分接近，但此后二者出现明显分叉，主要和 18:00—20:00 之间城区降水的相对快速增长有关。

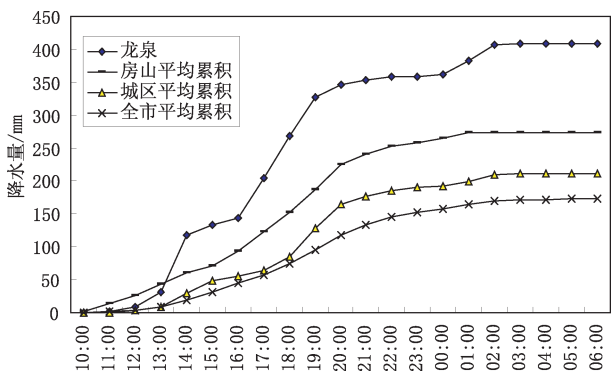


图 2　北京地区 21 日 10:00 至 22 日 06:00 平均累积降水量的时间变化

图 3(彩页)给出从 21 日 10:00 开始的不同时段累积降水量等值线分布形势。西南部地区于 7 月 21 日 10:00 左右首先出现降雨，10:00—12:00 出现明显累积降水量中心，降雨区域自西南向东北方向

扩展，降雨范围覆盖北京西部、南部及城区，10 mm以上降雨范围覆盖房山大部分地区，房山西南部多数站雨量在25～50 mm，其中张坊和南窖雨量超过50 mm(图3a)。

到21日15:00，降雨范围迅速扩展到全市。超过50 mm的累积降水量的有61个自动站，6个站累积雨量超过100 mm，主要集中在房山、门头沟和城区南部，门头沟龙泉镇降雨最大，达到134 mm(图3b)；到21日18:00，暴雨区继续扩大，累积降水量超过100 mm的观测站站达到70个，6个站累积雨量大于200 mm，同样集中分布在房山、门头沟和城区南部，房山南窖雨量最大，为276.5 mm(图3c)；到当日21:00，累积降水量大于200 mm的站点已经达到37个，有3个站超过300 mm，分别是房山的坨里355.4 mm、门头沟龙泉镇353.6 mm和丰台北宫森林公园320.8 mm，此时累积降水量大于50 mm的范围已经达到北京市面积的2/3，大于100 mm的范围超过了1/2(图3d)。

此后，暴雨范围继续扩大，但扩展速率明显减小，从22日00:00至22日06:00，特定累积降水量等值线范围变化比较小(图3e～g)。到22日00:00，累积降水量大于200 mm的区域在东北部明显增大，6个站雨量超过300 mm，门头沟龙泉最大，为361.7 mm；截止22日03:00，大部分地区降雨结束；到06:00，累积降水量大于100 mm的站数为211个，除西北部的延庆外均出现了100 mm以上的大暴雨，其中有96个站累积雨量大于200 mm，12个站累积雨量大于300 mm。

图4(彩页)表示25 mm、50 mm和100 mm 3个特征累积降水量值的等时线分布。可以看出，累积降水量达到25 mm、50 mm和100 mm的时间均自西南向东北方向推移。累积降水量达到25 mm的时间，在西南部是21日14:00以前，由此向东和东北逐渐推迟；累积降水量达到50 mm的时间，在西南部是21日15:00，城区发生在16:00—19:00，东南部和东部推迟至21:00—23:00；累积降水量达到100 mm的时间，西南部在21日19:00之前，城区出现在19:00—20:00，而东北部推迟到22日00:00—02:00。

就代表站的降水来看，房山张坊站在11:00降雨量达到58.1 mm，12时强降雨在房山霞云岭、南窖等地迅速扩展，南窖、张坊雨量都超过了50 mm；100 mm降雨首先在14:00出现于门头沟龙泉和南窖，龙泉更大，为118.4 mm；房山南窖、佛子庄和门头沟龙泉早在17:00出现200 mm以上的累计降雨量；龙泉在21日19:00降水量首先超过300 mm，达到327.3 mm。

### 2.2 降水时长

图5(彩页)给出北京地区小时雨量大于等于0.1 mm、10 mm和20 mm等不同量级降水时长等值线分布。对于雨量大于等于0.1 mm的量级，全市多数地区降水时长达到或超过16 h，西南门头沟、房山等地一般在17 h或以上，密云大成子降水时间最长，达到20 h，门头沟龙泉为19 h；西北延庆和东南通州、大兴等地小于16 h。结合本次过程累积降水量空间分布分析，可以看到降雨量分布与降水时长分布存在一定的正相关。

小时雨量大于等于10 mm和20 mm较强量级降水时长空间分布情况具有不同特点。10 mm降水时长在西南房山和门头沟构成高值中心，房山霞云岭、石景山老山、海淀五棵松达到了10 h，房山龙泉和潭柘寺为9 h，降水时长分布自西南向东北方向逐渐递减，北部山区最短，其分布态势与累积降水量分布更为相似；小时雨量大于等于20 mm的强降水时长分布，除了在西南房山和门头沟仍为最大中心外，在东北部平谷、顺义、密云等地区分布有次高值中心。门头沟龙泉和大台20 mm以上小时降水达到7 h，房山14个观测站平均达到近4 h，其中坨里有3 h雨量超过50 mm，龙泉和大兴南各庄则有4 h雨量超过50 mm。

由此可见，西南部地区不但累积降水量大，而且较强量级的降水时间长，暴雨和大暴雨持续时间久，成为本次过程最高和最强降水中心。一个有趣的现象是，西南地区尽管10 mm以上量级降水时长最大中心发生在最西南端，但20 mm以上量级降水时长却出现在以龙泉站为中心的门头沟、石景山和丰台三区交界处。这个现象在一定程度上也出现在累积降水量空间分布上(图3d～g)。另一个有趣的现象是，城区及其附近地带20 mm以上降水时长比较小，短于3 h，成为次级低值中心。由于这种现象在累积降水量分布上并不明显，说明城区及其附近地带20 mm以上量级的降水强度较大。此外，相比于西南部地区，另一高值降水中心东北部地区无论弱降雨还是强降雨，其降水时长均相对较短，其中10 mm以上量级降水时长明显偏短。

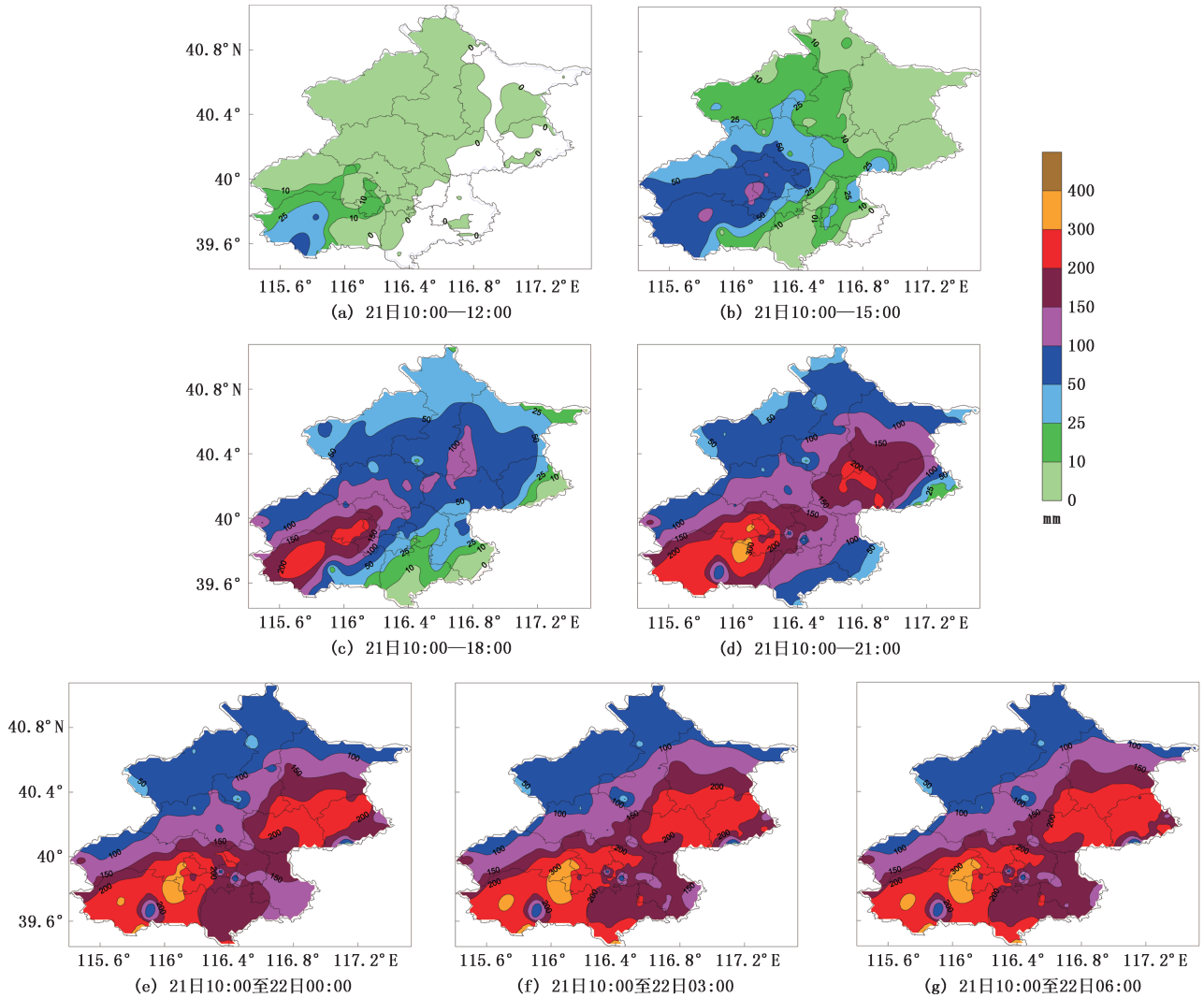


图 3　不同时段累积降水量(mm)等值线分布

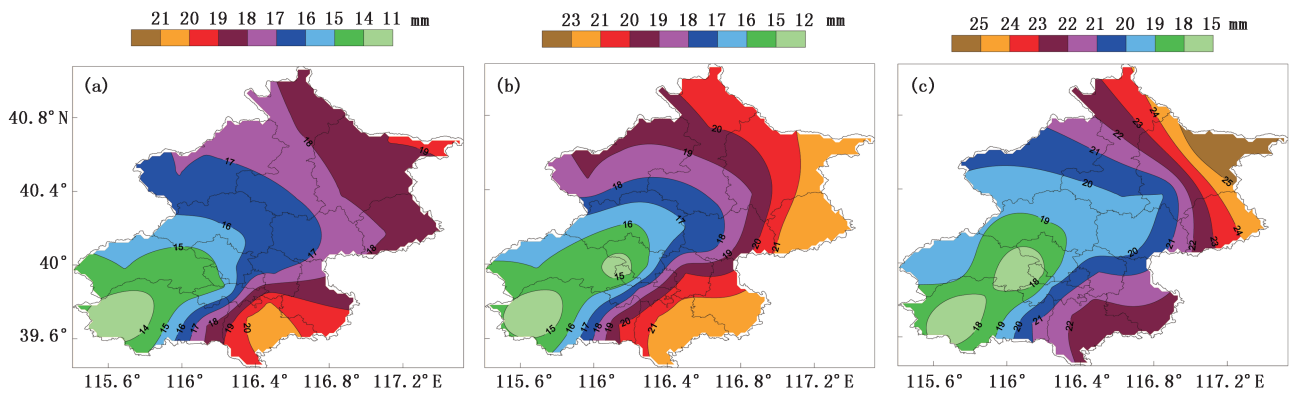




图 4　3 个特征累积降水量值等时线分布(图中数字为 7 月 21 日整时时间):
(a) 25 mm,(b) 50 mm,(c) 100 mm

### 2.3 降水强度

不同区域平均和龙泉站逐时降水量(即小时降雨强度)时间演变曲线(图 6)表明,全市、城区和房山区域平均曲线均为单峰型,龙泉站则为 3 峰型。全市平均降雨最强时期在 18:00—21:00,雨强达到 20 mm/h 左右,19 h 雨强最大,达到 22 mm/h;房山平均雨强在 16:00—21:00 雨强较大,超过 20 mm/h,20 h 降雨强度最大为 39 mm/h;城区在 18:00—20:00 雨强较大,平均雨强超过了 20 mm/h,19 h 降雨强度最大为 45 mm/h;城区和房山共同的降雨最强时间段为 18:00—20:00,平均降雨强度达到 30～40 mm/h;龙泉站 13:00—14:00 雨强达到 86 mm/h,此时强降雨集中在龙泉和石景山模式口、八大处等区域,16:00—19:00 龙泉雨强第 2 次达到峰值,为 60 mm/h 左右。在本次强降雨过程中,各地 15:00—16:00 及 21 h 以后降雨强度都较小,仅龙泉站在 22 日 01:00—02:00 降雨强度出现第 3 次峰值,达到 20～22 mm/h。

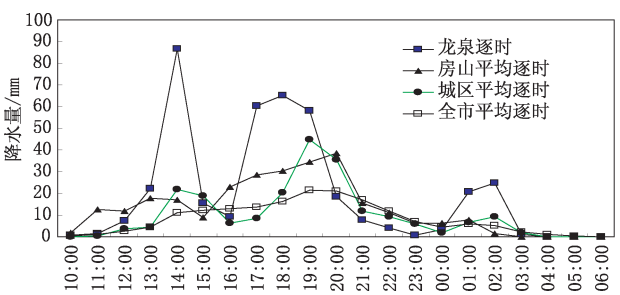


图 6 全市、城区、房山平均和龙泉站逐时降水量变化曲线

一个值得注意的现象是,在 18:00—21:00 之间,城区平均小时降水强度比全市平均明显偏大,19:00 也比房山区域平均偏大。这个现象不能用各个区域台站数量差异和平均方法解释,因为城区自动站分布最为密集,数量达到 55 个,远远多于房山区。造成这个现象的原因可能与城市热岛强度在傍晚开始明显增加以及城区下垫面粗造度较大等因素有关[1,4-5]。另一个异常现象是,门头沟龙泉站在 14:00 左右表现出整个过程最大的降雨强度,14:00 附近雨强高达 86 mm/h,经核实不是仪器故障所致,可能与当时中低空强盛的东南气流和其所处地理位置和地形特点有关[6-8],但具体机制还有待进一步研究。

从平均降雨强度等值线分布图(图 7,彩页)可以看出,本次过程平均降雨强度整体呈自东南向西北递减趋势,与累积降雨量的空间分布有较明显一致性,尤其是西南部大值中心对应累积降水量高值中心,房山大部分地区平均降雨强度超过了 16 mm/h,城区东北部形成次大值中心,平均降雨强度超过 14 mm/h,北部山区和山间盆地降雨强度最小,不足 6 mm/h。城区平均降雨强度比其西南和东北部区域小。为了进一步分析高强度降水分布情况,图 8(彩页)给出了各站大于等于 20 mm/h 平均降雨强度等值线分布情况。在这个级别上,平均降雨强度超过 50 mm/h 的高值中心也主要集中在房山为主的南部和城区东北部。后者比弱降雨强度更为明显,与南部中心区一样,均超过 50 mm/h。

从各站最大小时雨强的空间分布(图 9,彩页)可以看出,最大雨强分布存在东北和西南两个高值中心,这与累积降雨量的分布大体一致,但东北部最大雨强中心表现得更为明显。大于 70 mm/h 的最大雨强发生在以房山东北为核心的西南部地区和东北部的平谷、密云地区,西北和北部山区最大雨强一般低于 30 mm/h。从全市和各区最大小时雨强的时间演变来看,最大雨强在 70 mm/h 以上的高强度降雨发生在两个时间段,分别是下午 13:00—14:00(门头沟龙泉站)和 19:00—22:00,20:00—21:00 平谷挂甲峪降雨强度达到了 100.3 mm/h,成为此次降水过程中的最大降雨强度。最大雨强 50 mm/h 以上的强降雨在北京近 1/2 地区出现,全市共有 33 个站点最大雨强超过 70 mm/h,占全部有观测记录台站数的 13%。

### 2.4 历史记录

由于精细观测资料的限制,要了解 2012 年 7 月 21 日北京特大暴雨过程的精确历史地位,目前还有困难。本文根据 1961—2012 年全市 15 个站长序列逐年最大日降水量观测资料,对“7·21”特大暴雨期间单日极端最大降水量的历史地位进行初步探讨。

图 10 表示北京地区 1961 年以来 15 个站平均、观象台和房山站逐年最大日(24 h)降水量时间序列。房山站 61 年间最大日降水量存在较大的年际和年代际波动,20 世纪 60 至 80 年代出现较多最大日降水量高值年份,年际之间波动幅度也较大,90 年代以后高值年份较少,年际之间波动较小,2012 年 7 月 21 日 24 h 降水量陡然上升,达到 180 mm,成为 1980 年代以来的最大值,仅比 1979 年的次高值 182 mm 小 2 mm(表 1)。因此,从 24 h 最大降水

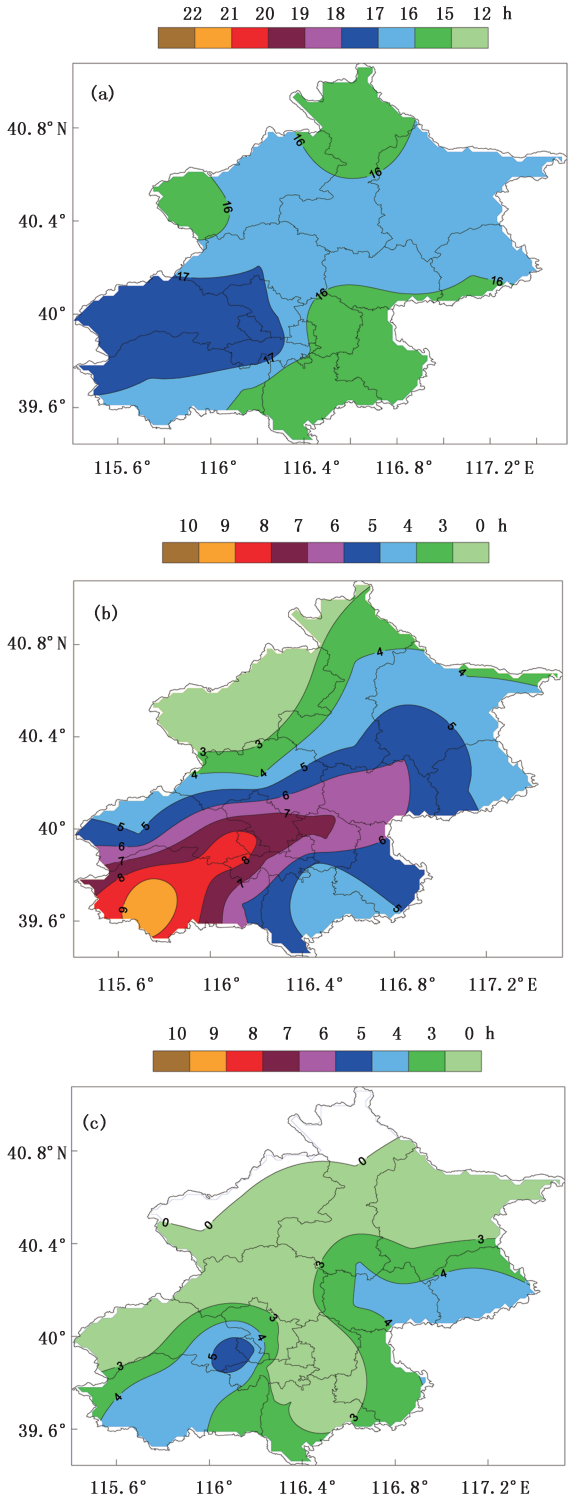


图 5　北京地区降水时长等值线分布:
(a)小时雨量≥0.1 mm,(b)小时雨量≥10 mm,
(c)小时雨量≥20 mm

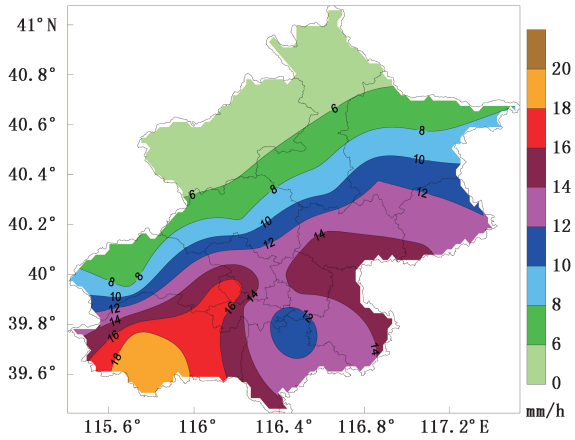


图 7　大于等于 0.1 mm/h 平均降雨强度等值线分布

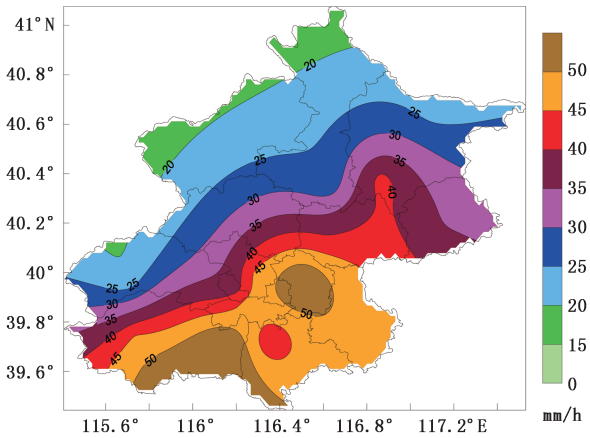


图 8　大于等于 20 mm/h 平均降雨强度等值线分布

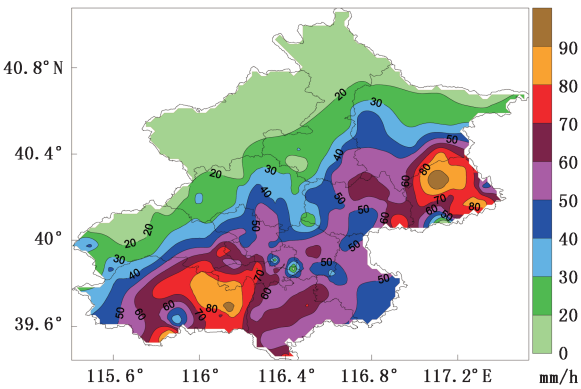


图 9　北京地区 7 月 21 日 10:00 至 7 月 22 日 06:00
各站最大雨强空间分布

量来看，“7·21”特大暴雨期间房山站观测尚未突破历史记录，但它确实终结了 2001 年以来缺少特大暴雨的枯、平水期历史。

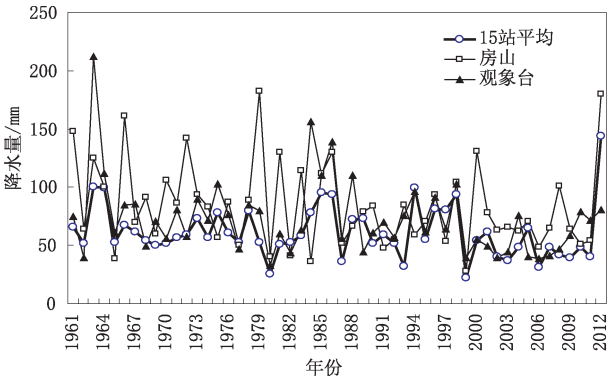


图 10 北京地区 15 站平均、观象台、房山站 1961 年以来逐年最大日降水量时间变化

南郊北京观象台 61 年间最大日降水量年际变化更为明显。20 世纪 60 年代初期和 80 年代中期为明显的高值期，日最大降水量超过 100 mm，其中 1963 年 8 月 9 日降水量达到了最高值 212 mm，其他时期都相对波动平缓，多在 50～100 mm 之间。进入 21 世纪，出现了连续多年极端日最大降水量不足 50 mm 的情况，与全市 15 站平均时间变化相近。与全市和房山站不同，在 2012 年“7·21”暴雨过程中，南郊观象台 21 日降水量仅为 81 mm，在 1961 年以来历史排序中表现平平，历史上年极端日最大降水量从大到小排序的前 5 位都在 110 mm 以上（表 1）。因此，如果以南郊观象台记录看，“7·21”暴雨的极端性并不突出。造成这个现象的原因主要是南郊观象台远离“7·21”特大暴雨中心区域。

全市 15 站平均年最大日降水量与观象台和房山站有较好的关系，但平均后年际和年代际波动幅度较小。1965—1976 年之间最大日降水量年际波动尤其不明显，是一个缺少大暴雨和特大暴雨的时期，20 世纪 70 年代末到 90 年代末，年际和年代际波动增大，但进入 21 世纪以后再次比较平静，缺少全区性大暴雨和特大暴雨。2012 年“7·21”特大暴雨从根本上扭转了这种平静形势，21 日 15 站平均降水量达到 144 mm，打破了 1961 年以来的年最大日降水量记录，比位于第 2 位的 1963 年 8 月 9 日 101 mm 高出 43 mm。

因此，从单日极端最大降水量历史演化来看，房山站和北京站 2012 年 7 月 21 日 24 h 降水量都不是有完整观测记录以来最大的，前者仅排第 2 位，后者则没有进入前 5 名；但全市平均的 7 月 21 日 24 h 降水量很可能是 1961 年以来的最大值。

**表 1 北京 15 站平均、观象台、房山站 1961 年以来最大日降水量前 5 位排序（括号内数字为出现日期）** mm

| | 1 | 2 | 3 | 4 | 5 |
|---|---|---|---|---|---|
| 15 站平均 | 143.9<br>(2012-07-21) | 101<br>(1963-08-09) | 99.7<br>(1994-07-13) | 99.5<br>(1964-08-01) | 98.1<br>(1963-08-08 |
| 观象台 | 212.2<br>(1963-08-09) | 156.2<br>(1984-08-09) | 139.2<br>(1986-06-27) | 125.2<br>(1963-08-08) | 111.8<br>(1964-08-01) |
| 房山 | 182.6<br>(1979-07-18) | 180.2<br>(2012-07-21) | 161.1<br>(1966-08-14) | 148.3<br>(1961-08-22) | 142.2<br>(1972-07-19) |

## 3 讨论

对于“7·21”特大暴雨的环流条件和天气成因，已有若干分析研究。谌芸等[9]、孙军等[10]和方翀等[11]对北京“7·21”特大暴雨的降水特点、水汽特点、中尺度对流系统的环境场条件和发生发展过程进行了分析，指出这次过程发生在高层辐散、中低层低涡切变和地面辐合线等高低空系统耦合的背景下。俞小鼎[12]分析了北京“7·21”特大暴雨的成因，认为高空低槽伴随地面冷锋东移，东南风/南风低空急流输送的充分水汽，起源于河套地区低层涡旋的中尺度对流系统的发展等，都对此次极端降水过程的形成起到关键作用。孙继松等[6]分析指出，高空急流与对流层中低层的低涡、切变线及地面倒槽构成的深厚辐合区，副热带高压外围的东南水汽通道和西南低空急流的水汽输送，边界层内长时间维持的东南风与山地地形相互作用，都是造成此次特强降水特别是北京西南部山区降水过程维持和发展的

重要条件。

本文侧重分析北京“7·21”特大暴雨过程中降水本身的时空演化规律，没有探讨此次天气过程的成因。但是，本文分析结果将有助于今后深入认识这次特大暴雨过程维持和发展的影响因子及其相互作用。例如，本文分析发现，北京城区及其附近地带 20 mm 以上量级的小时降水强度明显偏大，同时在 7 月 21 日 18:00—21:00 之间城区平均累积降雨量增长速率较快，平均小时降水强度也比全市平均明显偏大，19:00 比房山区域平均偏大。这些观测事实与北京 6 环以内建成区城市热岛效应在午后和傍晚迅速加强的规律一致[13]，说明尽管“7·21”特大暴雨过程主要起源于各种尺度的异常天气系统及其与地形的相互作用，但城市热岛效应和下垫面粗造度等因素可能仍具有一定影响[14]，值得今后开展进一步研究。

关于城市化对夏季降水的影响，已经有研究从气候学角度进行了分析。例如，Li 等[15]发现北京地区夏季傍晚降水以短持续时间事件为主，且这种类型降水事件频率有随时间增加趋势。Yin 等[16]通过分析降水和风向观测资料建议，北京城区夏季降水可能受到山谷风和城市热岛环流的共同作用。Yang 等[5]利用高密度自动站资料分析了北京夏季降水的气候学特征，验证了 Li 等[15]发现北京地区夏季小时降水量和降水强度以及短历时强降水频率等降水指标在市区及其附近出现明确的高值中心，说明城市化因素对夏季降水影响可能确实存在。识别城市热岛效应、下垫面粗造度和边界层气溶胶浓度等因素在北京地区单个重大天气过程中的作用具有更大难度，但可以结合多种观测手段和数值模拟技术进行探索。

## 4　结论

根据北京市高密度自动站观测资料和长序列国家站观测记录，对 2012 年 7 月 21 日特大暴雨过程的时空演化规律进行了分析，得到以下结论：

(1)本次降雨过程始于 7 月 21 日 10:00，13:00—21:00 累积雨量迅速增长。降雨和暴雨区域自西南向东北扩展，西南部于 21 日 10:00 首先出现降雨和累积降雨量中心，到 15 :00 降雨范围迅速扩展到全市，到 21:00 累积降雨量大于 200 mm 的站点达到 37 个，22 日 06:00 全市所有地区降雨结束。整个过程中累积降雨量大于 100 mm 的站数达到 211 个，占全部测站数的 92%，仅西北部的延庆没有出现大暴雨。

(2)全市多数地区降雨时长超过 16 h，西南门头沟、房山等地达 17 h 或以上，密云大成子降水时间最长，达到 20 h。雨量大于等于 20 mm 的强降水时长在西南房山和门头沟为大值中心，在东北部平谷、顺义、密云等地存在次高值中心。西南部地区不仅累积降水量大，而且较强量级的降水持续时间长，成为本次过程最高和最强降水中心。

(3)全市平均雨强高值阶段出现在 21 日 18:00—21:00，19:00 雨强最大，达到 22 mm/h；房山平均雨强在 20:00 最大，为 39 mm/h；城区雨强在 19:00 最大，为 45 mm/h。平均雨强自东南向西北递减，房山大部分地区超过 16 mm/h。整个过程的最大平均雨强中心出现在东北和西南两个区域。全市最大雨强在 70 mm/h 以上的高强度降雨发生在 21 日 13:00—14:00(龙泉站)和 19:00—22:00，其中 20:00—21:00 平谷挂甲峪站达到 100.3 mm/h，成为此次过程的最大点降雨强度。

(4)从 1961—2012 年单日极端最大降水量历史记录来看，房山站和北京站 2012 年 7 月 21 日 24 h 降水量都不是最大的，前者排第 2 位，仅次于 1979 年 7 月 18 日降雨量，后者则没有进入前 5 名；但 2012 年 7 月 21 日全市 15 个站平均 24 h 降水量为 144 mm，成为 1961 年以来观测到的最大值，比 1963 年 8 月 9 日平均雨量高出 43 mm。

(5)北京城区及其附近地带强降水强度偏大，7 月 21 日 18:00—21:00 城市热岛强度加强期间平均累积降雨量增长速率快，平均小时降水强度也较大，说明此次特大暴雨过程中城区及其附近区域降水可能仍在一定程度上受到了城市化因素的影响。

## 参考文献

[1] 尤焕苓，任国玉，刘伟东. 1961—2010 年北京地区降水变化特征[J]. 沙漠与绿洲气象，2012，6(4)：13-20.

[2] 孙澈. 北京地区暴雨气候特征及其变化分析[J]. 气候与环境研究，2010，15(5)：672-676.

[3] 李建，宇如聪，王建捷. 北京市夏季降水的日变化特征[J]. 科学通报，2008，53(7)：829-832.

[4] 孙继松、舒文军. 北京城市热岛效应对冬夏季降水的影响研究[J]. 大气科学，2007，31(2)：311-320.

[5] Yang P, Ren G Y, Hou W, et al. Spatial and diurnal charac-

teristics of summer rainfall over Beijing Municipality based on a high-density AWS dataset [J]. International Journal of Climatology, 2013, 33(13): 2769-2780.

[6] 孙继松,何娜,王国荣,等."7·21"北京大暴雨系统的结构演变特征及成因初探[J]. 暴雨灾害, 2012, 31(3): 218-225.

[7] 丁青兰,王令,卞素芬. 北京局地降水中地形和边界层辐合线的作用[J]. 气象科技,2009,37(2):152-156.

[8] 王从梅,吴智杰,刘瑾,等. 城市短时降雨中尺度观测特征分析[J]. 气象科技,2011,39(6):678-684.

[9] 谌芸,孙军,徐胥,等. 北京 721 特大暴雨极端性分析及思考(一)观测分析及思考[J]. 气象,2012,38(10):1255-1266.

[10] 孙军,谌芸,杨舒楠,等. 北京 721 特大暴雨极端性分析及思考(二)极端性降水成因初探及思考[J]. 气象,2012, 38(10): 1267-1277.

[11] 方翀,毛冬艳,张小雯,等. 2012 年 7 月 21 日北京地区特大暴雨中尺度对流条件和特征初步分析[J]. 气象,2012, 38(10): 1278-1287.

[12] 俞小鼎. 2012 年 7 月 21 日北京特大暴雨成因分析[J]. 气象,2012,38(11):1313-1329.

[13] Yang P, Ren G, Liu W. 2013 Spatial and temporal characteristics of Beijing urban heat island intensity [J]. Journal of Applied Meteorology and Climatology, 2013, 52(8): 1803-1816.

[14] 田晨,周伟灿,苗峻峰. 中国下垫面特征对强对流天气影响研究进展[J]. 气象科技,2012,40(2):207-212.

[15] Li J, Yu R C, Wang J J. Diurnal variations of summer precipitation in Beijing [J]. Chinese Science Bulletin, 2008, 53 (12): 1933-1936.

[16] Yin S Q, Li W J, Chen D L, et al. Diurnal variations of summer precipitation in the Beijing area and the possible effect of topography and urbanization [J]. Advances in Atmospheric Sciences, 2011, 28(4): 725-734.

# Spatial and Temporal Characteristics of a Summer Rainstorm in 2012 in Beijing

You Huanling[1,2,3] Ren Guoyu[2] Wu Fang[1,3] Liu Weidong[1] Yang Ping[4]

(1 Beijing Meteorological Service, Beijing 100089; 2 Laboratory for Climate Studies, China Meteorological Administration (CMA), National Climate Center, Beijing 10081; 3 Institute of Urban Meteorology, CMA, Beijing 100089; 4 CMA Training Center, Beijing 100081)

**Abstract:** Based on the high-density precipitation data of automatic weather stations (AWS), the spatial-temporal characteristics of extremely intensive precipitation on 21and 22 July 2012 over the Beijing area are analyzed. The results show that during the rainstorm, there were 211 stations recorded greater than 100 mm cumulative rainfall except for Yanqing Station, 96 stations recorded greater than 200 mm cumulative precipitation, and 12 stations greater than 300 mm. In most regions, the durations of precipitation were above 16 hours, with the largest in the southwestern Beijing, and the secondary in the northeast of Beijing. The average precipitation intensity exceeded 16 mm/h in Fangshan, and 14 mm/h in northeastern parts of the urban zone, in spite of the fact that precipitation intensities were less than 6 mm/h in the mountains of the north and northwest. The maximum hourly precipitation intensity was found in the northeast of Beijing and the second in the southwest. The larger average precipitation intensities occurred during 18:00–21:00 of 21 July, with the maximum of 22 mm/h recorded at 19:00. Abnormally strong precipitation intensities of more than 70 mm/h appeared during 19:00–22:00 over the whole city and 13:00–14:00 at Longquan Station. The analysis also shows that the 24-h maximum precipitation of Fangshan on 21 July 2012 ranks the second for the time period of 1961 to 2012. The average 24-h maximum precipitation of 15 stations broke the record of Beijing since 1961, much larger than the second (9 August 1963).

**Key words:** rainstorm, accumulated rainfall, precipitation duration, precipitation intensity, urban heat island effect

曾宇星, 封国林, 赵俊虎, 等. 春季马斯克林高压对中国东北地区夏季气温的影响[J]. 高原气象, 2014, 33(5): 1374－1382, doi: 10.7522/j.issn.1000-0534.2013.00078.

# 春季马斯克林高压对中国东北地区夏季气温的影响

曾宇星[1-2], 封国林[2], 赵俊虎[1-2], 沈柏竹[1-2]

(1. 兰州大学大气科学学院, 兰州 730000; 2. 国家气候中心气候研究开放实验室, 北京 100081)

**摘要**: 利用中国东北地区26个站点的月平均温度资料和NCEP/NCAR月平均高度场、风场、海温场资料, 研究了春季马斯克林高压(下称马高)对中国东北夏季气温的影响及其途径。结果表明: (1)春季马高与后期东北地区夏季气温呈明显的正相关关系。春季马高偏强年, 后期夏季北半球盛行纬向环流, 东北地区与阿留申群岛南侧为主要的正距平中心, 东北地区上空为高压系统所控制, 总云量偏少, 气流辐散下沉, 冷空气不易南下, 造成该区域的高温天气。春季马高偏弱年则相反, 后期夏季东北地区为高度场的负距平中心, 受低压影响, 总云量偏多, 高纬冷空气与低纬气流辐合上升, 使该区域气温容易偏低; (2)春季马高异常会引起印度洋中部地区的海温异常, 并持续到夏季且进一步加强, 从而在200 hPa纬向风场上激发出一个从南半球中高纬到北半球中高纬的经向遥相关波列, 通过该波列可以影响到东北地区夏季500 hPa高度场, 进而影响东北地区的夏季气温; (3)春季马高偏强时还可以通过增强后期夏季的索马里越赤道气流与80°E附近的越赤道气流, 从而减弱赤道印度洋上的异常西风, 使西太平洋副热带高压加强西伸, 造成东北地区的夏季高温天气, 春季马高偏弱年则相反。

**关键词**: 马斯克林高压; 东北地区; 夏季气温; 遥相关; 越赤道气流

**文章编号**: 1000-0534(2014)05-1374-09 **中图分类号**: P461 **文献标志码**: A

**doi**: 10.7522/j.issn.1000-0534.2013.00078

## 1 引言

东北地区是中国最重要的粮食生产地之一, 属于东亚季风气候区。其地处我国的最北与最东部, 纬度较高, 无霜期短, 夏季气候异常对粮食生产具有重要的影响[1-3]。因此, 研究和了解东北地区夏季气温的时空变化规律及其主要的影响因子对预测东北地区夏季气温有着重要意义。一些研究表明, 在全球变暖的背景下, 我国东北地区夏季气温有明显上升的趋势[4-8]。张茜等[9]对东北夏季气温异常的特征和不同空间型的大气环流进行了分析, 结果发现我国东北夏季气温异常主要有全区一致型和东北—西南反位相分布型, 且1990年以后东北地区增温明显, 区域差异主要表现在东北部升温早而西南部晚。

影响东北地区夏季气温的因子包括西太平洋副热带高压(下称西太副高)、阻塞高压(下称阻高)、冷涡、西风槽等。符淙斌[10]揭示了冬春季北半球积雪面积和大西洋海冰状况与我国东北地区夏季气温的密切关系: 当冬春季北半球积雪面积和大西洋海冰面积增大时, 夏季东北地区温度偏低; 反之, 冰雪面积缩小时, 夏季东北地区温度偏高。王敬方等[11]利用时滞相关分析发现, 东北夏季气温与西太平洋暖池以及印度洋地区的海温相关性不好, 而与黑潮区域夏季的海温有较好相关关系, 东北冷夏年, 黑潮海温偏低。汪宏宇等[12]研究发现20世纪90年代之前, 东北夏季低温与El Nino的对应关系较好, 但之后这种关系遭到破坏, 东北夏季气温与Nino3区的海温关系不显著。由于这些研究都集中在北半球, 南半球的环流系统对东北夏季气温是否存在影响还不得而知。

由于东北地区处于东亚季风区, 其夏季气温还受到了东亚夏季风的影响[13]。黄士松等[14-15]在陈隆勋[16]研究基础上提出了新的东亚夏季风体系框

**收稿日期**: 2012-11-05; **定稿日期**: 2013-05-03

**资助项目**: 全球变化研究重大科学研究计划(2013CB430204); 国家自然科学基金项目(40930952, 41175067, 41275096)

**作者简介**: 曾宇星(1988－), 男, 湖南岳阳人, 硕士研究生, 主要从事天气和气候研究. E-mail: z275525111@126.com

**通讯作者**: 封国林. E-mail: fenggl@cma.gov.cn

架，认为马斯克林高压（下称马高）是与西太副高同等重要的东亚夏季风系统成员，其对我国东部地区包括华南前汛期降水[17]、长江流域夏季降水[18]等都有很大的影响。因此，本文主要选取南半球的马高作为研究重点，探究春季马高对中国东北地区夏季气温的影响。

## 2　资料选取和方法介绍

选用 1948－2012 年 NCEP/NCAR 月平均风场和高度场 2.5°×2.5°再分析资料；美国国家海洋和大气管理局（NOAA）提供的 1948－2012 年海温扩展重建资料，分辨率为 2.0°×2.0°；以及 1948－2012 年月平均高斯格点的总云量再分析资料。

中国气象局国家气候中心整理的 1951 年 1 月－2011 年 12 月 160 个测站月平均气温资料中选取位于东北地区的 26 个测站（图 3）的资料以及 74 项环流指数。

文中分析均采用季平均值，冬季为 12 月—次年 2 月，春季为 3－5 月，夏季为 6－8 月。取 1981－2010 年平均值为气候值。

使用的方法主要有经验正交函数分解（EOF），此方法已经广泛应用于气候研究的各领域[19－21]。并用滤波[22－23]方法提取年际分量去掉年代际分量，还采用相关分析以及合成分析等气象统计常用的方法，并对其结果进行显著性检验[24]。

## 3　春季马高的基本特征

崔锦等[25]研究发现马高在 850 hPa 等压面上表现最强，无论是从高度场还是从环流场来看，850 hPa 最能表现马高的特征。所以本文选取崔锦等[25]定义的 850 hPa 位势高度场上 0°—45°S，15°E－110°E 范围内大于或等于 1540 gpm 的格点之和为马高面积指数，本文选取春季平均的马高面积指数进行研究。

从图 1 中可以看出，春季马高表现出明显的年际及年代际变化，其中年代际转折最为明显，其距平累加值的变化表明马高在 20 世纪 70 年代中后期发生了年代际的突变。小波分析结果表明，马高在年际尺度上存在着准 8 年的周期，而在年代际尺度上则以 28 年左右的周期为主（图略）。

## 4　春季马高对东北地区夏季气温的可能影响

图 2 为 1951－2011 年间东北地区夏季平均气温变化。从图 2 中可以看出，东北地区夏季气温存在着明显的年代际变化，而且转变时间晚于马高。在 20 世纪 80 年代之前，东北地区夏季气温偏低；80 年代－90 年代初期，偏低的趋势趋于平缓；之后，东北地区夏季气温完全转入正相位阶段，气温明显偏高。

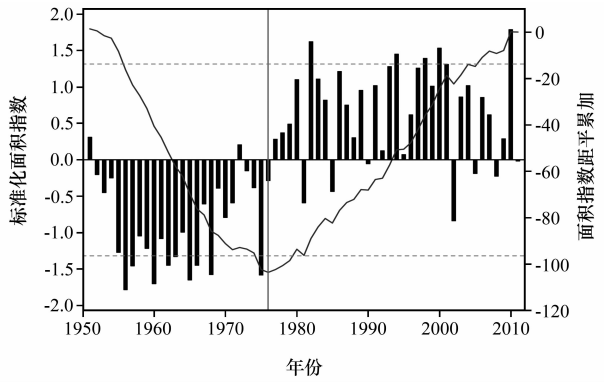


图 1　春季马高标准化面积指数（直方柱）以及马高面积指数距平累加值除以 10（实线）的时间演变

Fig. 1　The temporal evolution of spring Mascarene high standardized area index (histogram) and index anomalies accumulated value (divided by ten, solid line)

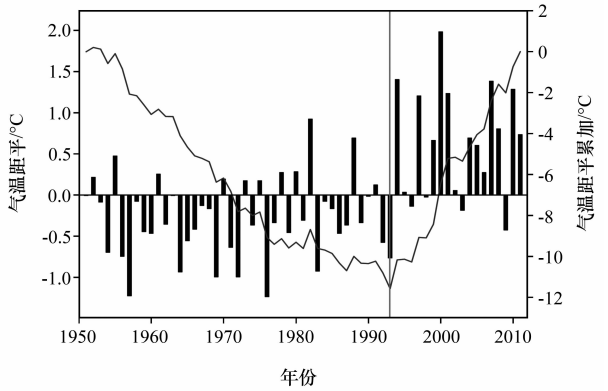


图 2　东北夏季气温距平（直方柱）与气温距平累加（实线）的时间演变

Fig. 2　The temporal evolution of summer air temperature anomalies in Northeast China (histogram) and its anomalies accumulated value (solid line)

1951－2011 年春季马高面积指数与东北夏季平均气温的相关系数为 0.45，通过了 0.001 的显著性水平检验。但春季马高与夏季东北地区平均气温均存在明显的年代际变化，要研究二者的年际变化则需要对指数进行处理，滤除年代际分量。本文使用高通滤波器滤除掉指数 10 年以上的年代际分量。滤波之后两个指数年际分量的相关系数减为 0.191，没有通过显著性检验，而年代际分量之间

的相关系数则高达 0.703。考虑到马高在 1976 年之后先发生突变，再选取 1977－2011 年 35 年间二者年际分量的指数求相关，发现相关系数提升到了 0.329，通过了 0.05 的显著性水平检验。

将春季马高面积指数与夏季我国东北地区 26 个测站月平均气温进行相关分析。从图 3 中可以看出，东北地区为一致的变化情况，春季马高与东北地区均为正相关关系，但显著的高相关区主要位于东北中东部地区。这表明当春季马高偏强（偏弱）时，东北大部分地区的当年夏季气温容易偏高（偏低）。

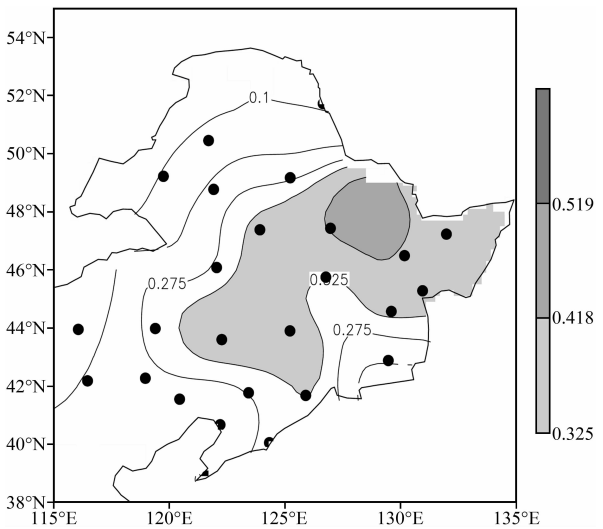


图 3 东北地区 26 个测站分布（黑点）及其夏季气温距平场与春季马高面积指数的相关分布（等值线）
阴影区由浅到深分别表示通过 0.05，0.01 和 0.001 的显著性水平检验

Fig. 3 Distribution of 26 stations in northeast China (black dots) and correlation coefficient distribution of temperature departure in summer and the spring Mascarene high area index (isoline). The shaded area from shallow to deep have passed the significance level at 0.05, 0.01 and 0.001, respectively

为了检验该结果的准确性，对 1977－2011 年东北地区 26 个测站滤波之后的夏季平均气温进行 EOF 分解，前三个模态的解释方差分别为 71%，10% 和 5%，已占总的方差贡献率的 86%，收敛十分迅速。其中，第一模态 EOF1 表示为东北地区全区一致的气温变化分布型。春季马高面积指数年际分量与 EOF1 的时间系数的相关系数为 0.352，通过了 0.05 的显著性水平检验，而与其他两个模态的时间系数的相关系数非常弱，均没有达到显著性水平。表明春季马高的确仅对东北地区全区一致的气温变化产生影响。所以本文主要对东北地区的夏季平均气温进行研究，将东北夏季平均气温定义为这 26 个站点夏季平均气温的平均值。

选取 1977 年之后马高标准化面积指数滤波后 $>0.5$ 时为马高偏强年，一共有 5 年，分别为 1982，1986，1994，2000 和 2010 年；$<-0.5$ 时为马高偏弱年，一共有 8 年，分别为 1981，1985，1990，1992，1995，2002，2008 和 2011 年。在马高偏强的 5 年中有 4 年的东北夏季气温为正异常，占 80%；而在马高偏弱的 8 年中，东北夏季气温为负异常的有 6 年，占 75%。若将马高的强弱划分标准提高到 $\pm0.7$，则在马高偏强时东北夏季气温全偏高，而马高偏弱时则全偏低。将马高偏强的 5 年中国夏季平均气温减去马高偏弱的 8 年平均气温（图 4），仅东北地区为 1℃以上的正温度距平，且通过了 0.05 的显著性水平检验。这说明虽然东北夏季气温受到很多因子的影响，但前期春季马高强度对后期东北夏季气温仍有比较重要的预测意义。

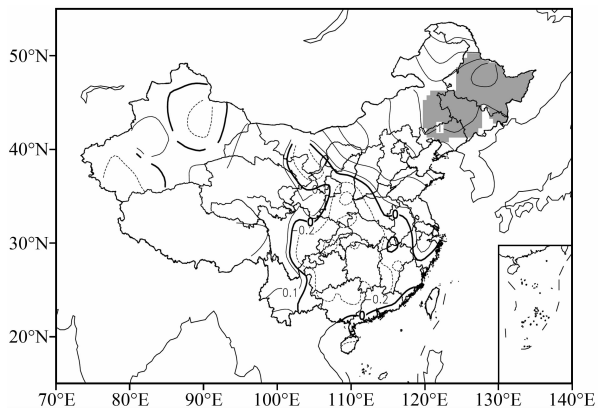


图 4 春季马高偏强年减去偏弱年后期中国夏季气温距平差值场（单位：℃）
阴影区表示通过 0.05 的显著性水平检验

Fig. 4 Differences of air temperature over China in summer between the positive and the negative Mascarene high area index phases. Unit: ℃. The shaded area has passed the significance level at 0.05

### 4.1 马高强弱年夏季环流形势

由春季马高偏强年减去偏弱年后期夏季 500 hPa 高度场距平与 850 hPa 风场距平的差值合成（图 5a）可以看出，在春季马高偏强年，环绕极区大部分为负距平，北半球中高纬度地区为环状的正距平地带，中国东北地区与阿留申群岛南侧为主要的正距平中心，表明北半球盛行纬向环流，冷空气不易南下，东北地区气温容易偏高；而在春季马高偏

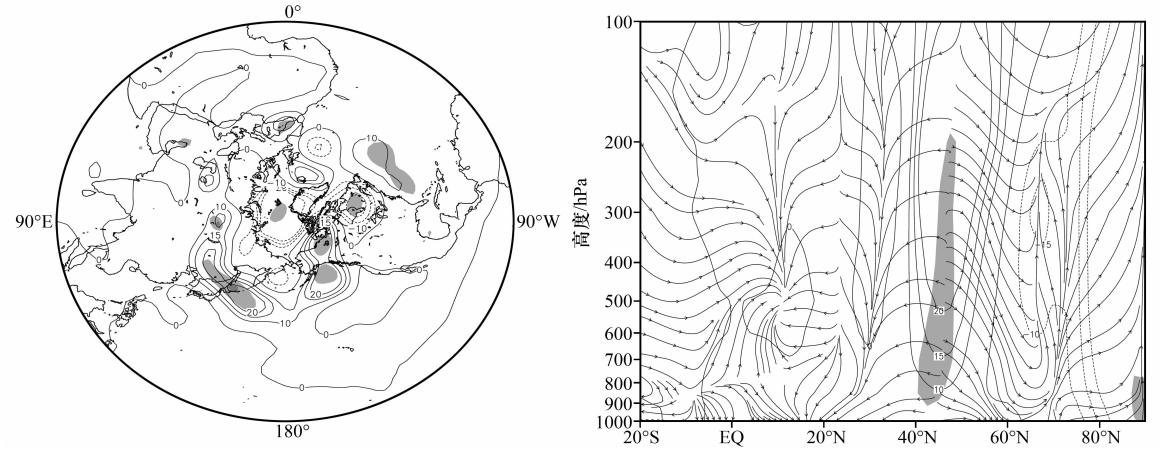


图 5　春季马高偏强年与偏弱年后期夏季 500 hPa 高度场距平的差值分布(a)与平均经圈(115°E－135°E)风场流线和高度场距平差值的垂直剖面(b)(单位：gpm)
浅、深阴影区分别表示通过 0.05 和 0.01 的显著性水平检验

Fig. 5　The difference of 500 hPa geopotential height anomaly in summer(a) and the section of difference distribution of average (115°E－135°E) meridional streamlines and geopotential height anomaly(b) between the strong years and weak years of spring Mascarene high. Unit: gpm. The gray and dark shaded area have passed the significance level at 0.05 and 0.01, respectively

弱年则相反，环绕极区为正距平控制，我国东北地区负距平中心，表明北半球经向环流较强，冷空气可以扩散到中纬度地区，东北地区气温容易偏低。

图 5b 为春季马高偏强年减去偏弱年平均经圈(115°E－135°E)风场距平和高度场距平的差值垂直剖面。春季马高偏强年东北上空的高压系统异常深厚，强辐散下沉气流贯穿整个对流层，容易造成东北地区的高温天气；而春季马高偏强年则相反，东北上空的负高度距平区域几乎达到对流层顶，近似垂直的正压结构，高纬地区的冷空气与来自低纬的气流在 50°N 附近交汇辐合上升，使东北地区受冷空气影响容易出现低温天气。

## 4.2　总云量的异常

气温变化除了与降水有关之外，还受云量显著影响[26]。云对太阳短波辐射有散射和反射的作用，可以减少到达地面的辐射量，从而使气温保持在一个低的状态。Robert et al[27] 认为云可以通过反射太阳的短波辐射达到使气候系统变冷的作用。从图 6a 中可以看出，春季马高与夏季总云量分布的正相关区域包括整个东北地区，但显著相关的区域主要

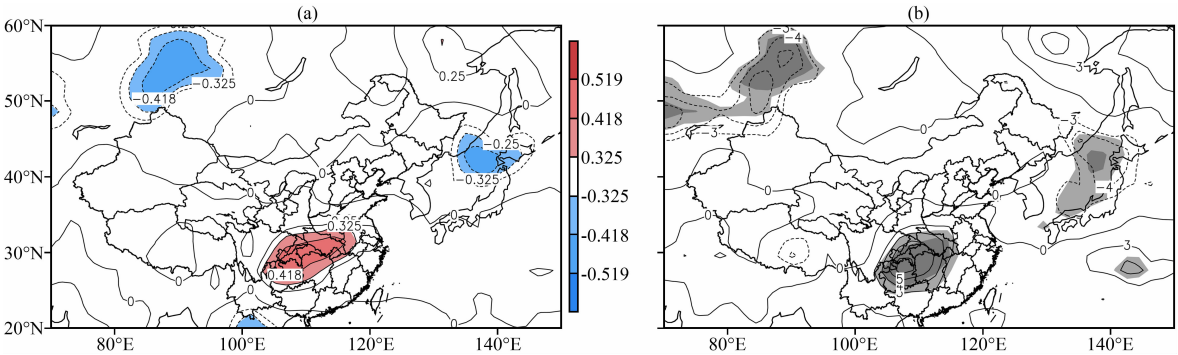


图 6　春季马高面积指数与后期夏季总云量的相关系数分布(a，阴影区由浅到深分别表示通过 0.05、0.01、0.001 的显著性水平检验)以及总云量的差值分布(b，春季马高强减弱年，单位：%，阴影区由浅到深分别表示通过 0.05 和 0.01 的显著性水平检验)

Fig. 6　Distribution of correlation coefficient between spring Mascarene high area index and the lag summer total cloud amount(a, the shaded area from shallow to deep have passed significance level at 0.05, 0.01 and 0.001, respectively) and the differences of total cloud amount between the positive and the negative Mascarene high area index phases(b, unit: %, the gray to dark area have passed the significance level at 0.05 and 0.01, respectively)

位于东北东部地区，春季马高偏强时东北地区上空夏季总云量偏少，到达地面的太阳短波辐射增加，地面发射的长波辐射也相应增加，造成东北地区气温偏高；而春季马高偏弱时则相反，东北地区上空夏季总云量偏多，大气系统的辐射加热减少，造成东北地区气温偏低。而春季马高偏强年减去偏弱年后期夏季总云量的差值分布情况高值中心（图 6b）与图 6a 的高相关中心基本一致，同样显示了春季马高偏强东北夏季总云量偏少，而春季马高偏弱年夏季东北总云量偏多的情况。

## 5 可能的影响途径

众所周知，春季是重要的转换季节，已有研究[18, 28-29]表明春季的环流形势异常会对后期夏季我国的天气气候造成很大的影响。而南半球为全球气候系统变化的关键区[30-31]，其环流异常必然导致北半球大气环流产生某种应激变化[18, 28-29]。所以春季马高的变化也必然会造成后期环流的调整。

### 5.1 遥相关的影响

将春季马高面积指数与夏季全球 200 hPa 纬向风场计算相关系数（图 8a）。从图 8a 中可以看出，春季马高异常的后期夏季在东半球后期夏季 200 hPa 纬向风场上 60°E－150°E 之间存在一个从南半球中高纬到北半球中高纬的正负相间的经向遥相关波型，但是在北半球中高纬不是很显著。

而海温异常可以对大气环流产生直接影响。从马高偏强年与偏弱年同期及后期夏季印度洋海温的差值（图 7）上可以看出，春季马高偏强年印度洋东北部地区海温偏低，而中部地区海温偏高，这种情况一直持续到夏季，并且进一步加强，夏季通过了 0.05 的显著性水平检验。取 30°S－40°S、75°E－90°E 的平均海温表示印度洋中部地区的海温状况，同样对其进行滤波处理，夏季海温与春季马高面积指数的年际分量间相关系数为 0.344，通过了 0.05 的显著性水平检验，春季海温则与马高面积指数的年际分量也呈正相关关系但并不显著，且其和同期 200 hPa 纬向风场的相关情况与图 8a 相比几乎一致。所以可以认为这个经向遥相关型可能为印度洋中部地区的海温异常所激发，而春季马高则通过对这一区域海温的影响来间接控制。

Namias[32]研究指出月平均气温的异常在很大程度上取决于对流层中层的月平均高度场；沈柏竹等[33]也认为 500 hPa 大气环流系统的演变可以作为东北夏季气温诊断和预测的核心层。所以为了检验该经向遥相关波列对于东北地区大气环流的影响，选取 37.5°N－55°N，115°E－135°E 范围内（完全包括整个东北地区）的夏季 500 hPa 高度场的平均值代表东北地区的高度，其年际分量与东北地区夏季气温的年际分量间相关系数高达 0.773。且与东北夏季气温相对应，东北乃至整个亚洲大陆的 500 hPa 高度场同样存在着明显的年代际突变，且与马高的年代际转变时间差不多，70 年代后期高度场抬升均 >20 gpm[34]，使这些地区气温容易偏高，特别是东北地区（见图 2）。

同样的将东北地区夏季平均高度指数和夏季全球200 hPa纬向风场计算相关系数（图 8b）。从图

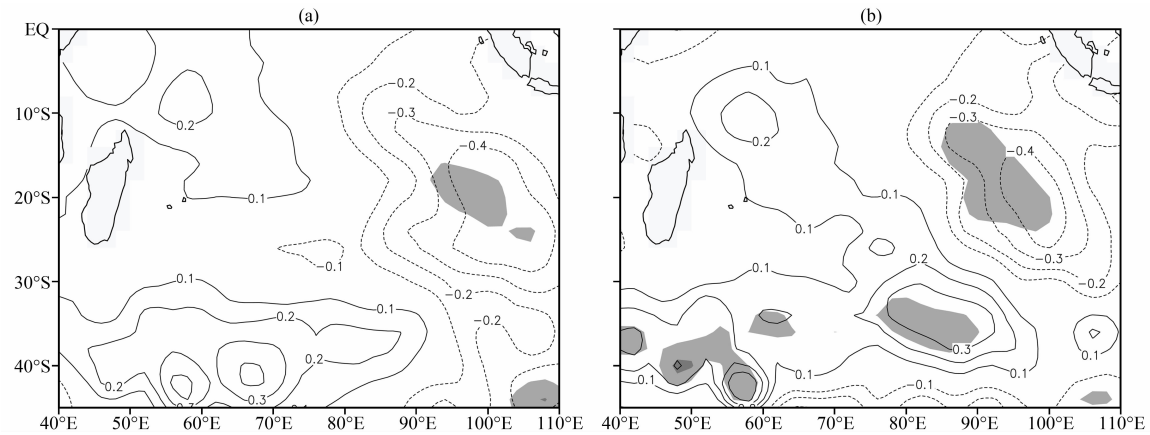


图 7 春季马高偏强年减去偏弱年同期（a）与后期夏季（b）印度洋海温差值场（单位：℃）
浅、深阴影区分别表示通过 0.05 和 0.01 的显著性水平检验

Fig. 7 Differences of Indian Ocean SST between the positive and the negative Mascarene high area index phases in the same period（a）and the lag summer（b）. Unit：℃. The shaded area from gray to dark have passed the significance level at 0.05 and 0.01, respectively

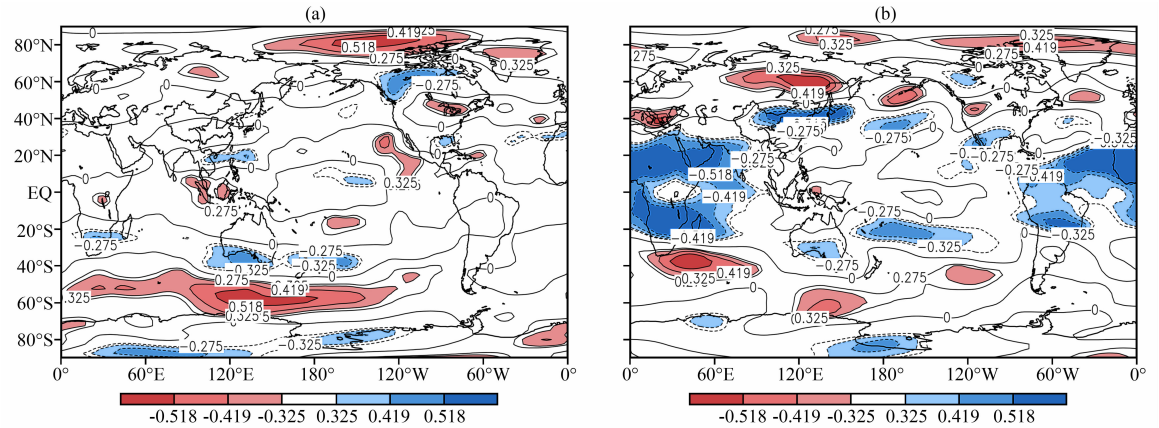


图 8　春季马高面积指数年际分量(a)和夏季东北地区 500 hPa 平均位势高度年际分量(b)与滤波后的夏季 200 hPa 纬向风场的相关分布

阴影区由浅到深分别表示通过 0.05，0.01 和 0.001 的显著性水平检验

Fig. 8　Distribution of correlation between the spring Mascarene high area index interannual component(a), the summer 500 hPa mean geopotential height interannual component over northeast China(b) and 200 hPa zonal wind field after smoothing in summer. The shaded area from shallow to deep have passed the significance level at 0.05, 0.01 and 0.001, respectively

8a 中可以看出，从南半球中高纬一直到北半球中高纬的正负相间的高相关中心，与图 8a 相比位置基本一致，但是在南半球通过信度检验的区域明显比图 8a 偏小。

春季马高偏强年减去偏弱年后期夏季 200 hPa 纬向风场差值分布(图 9)显示出相似的结果，从南半球高纬一直到北半球中高纬存在 5 个明显的大气环流中心(图 9 中 A 表示)，但急流轴在南半球不显著，仅东北地区东风轴通过了显著性检验。所以，当春季马高异常时，可以通过对后期印度洋中部地区海温的影响，在 200 hPa 纬向风场上激发出一个从南半球中高纬一直到北半球中高纬的经向遥相关波列，通过这个波列可以影响到东北地区夏季 500 hPa 高度场(图 5)，进而影响东北地区的夏季气温。东北地区平均高度场年际分量与春季马高面积指数年际分量也为正相关关系，但相关系数为 0.287，只通过了 0.1 的显著性水平检验。

## 5.2　越赤道气流的影响

越赤道气流对南北半球环流间的相互作用产生重要的影响[35-37]，其中索马里越赤道气流与澳大利亚以北 105°E 越赤道气流的最为重要。从图 10 上可以看出，春季马高面积指数与同期东半球的越赤道气流相关均不显著；春季马高与夏季的索马里越赤道气流为正相关关系，但通过显著性检验的区域较小，与 80°E 越赤道气流也为正相关关系，且比较显著，说明春季马高对这两条越赤道气流主要是滞后的影响。春季马高越强(越弱)，后期夏季索马里越赤道气流越强(越弱)，80°E 越赤道气流越强(越弱)。

而在夏季当索马里越赤道气流偏强，且 80°E 附近的越赤道气流增强时，对流层中下层赤道印度洋上的西风异常减弱，仅延伸到印度半岛附近(图略)，使得西太副高加强西伸[38-39](图 5a)，从我国

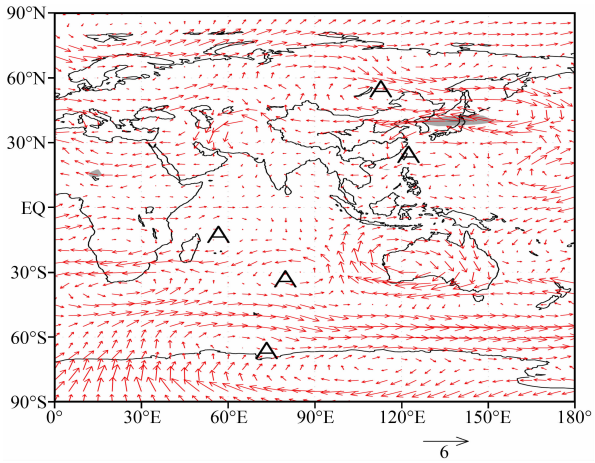


图 9　春季马高偏强年减去偏弱年夏季 200 hPa 纬向风场差值分布(单位：$m \cdot s^{-1}$)

阴影区表示通过 0.05 和 0.01 的显著性水平检验

Fig. 9　Distribution of differences of 200 hPa zonal wind field in summer between the positive and the negative Mascarene high area index phases. Unit: $m \cdot s^{-1}$. The shaded area from gray to dark have passed the significance level at 0.05 and 0.01, respectively

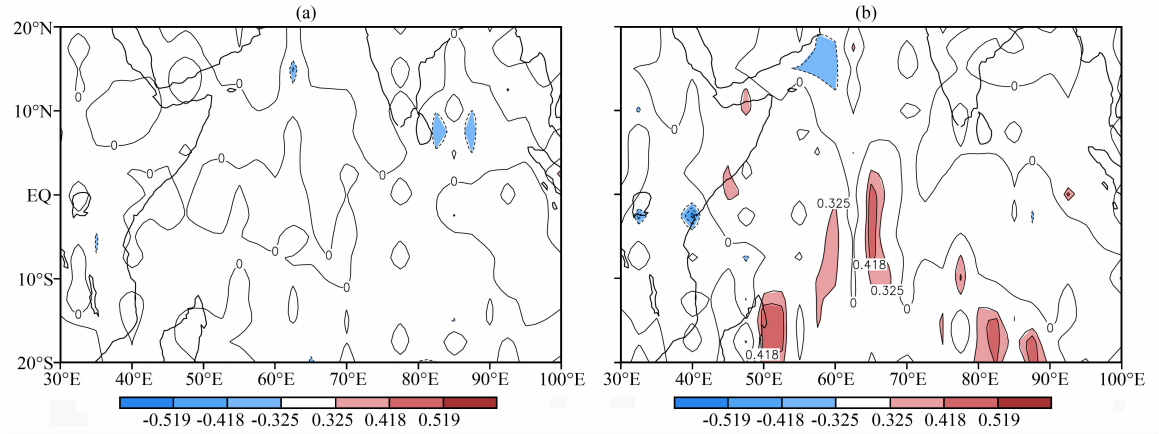


图 10 春季马高面积指数年际分量分别与同期(a)和夏季(b)850 hPa 经向风年际分量的相关分布

阴影区由浅到深分别表示通过 0.05, 0.01 和 0.001 的显著性水平检验

Fig. 10 Distribution of correlation between the spring Mascarene high area index interannual component and 850 hPa Meridional wind interannual component in the same period(a) and the lag summer(b), respectively. The shaded area from shallow to deep have passed the significance level at 0.05, 0.01 and 0.001, respectively

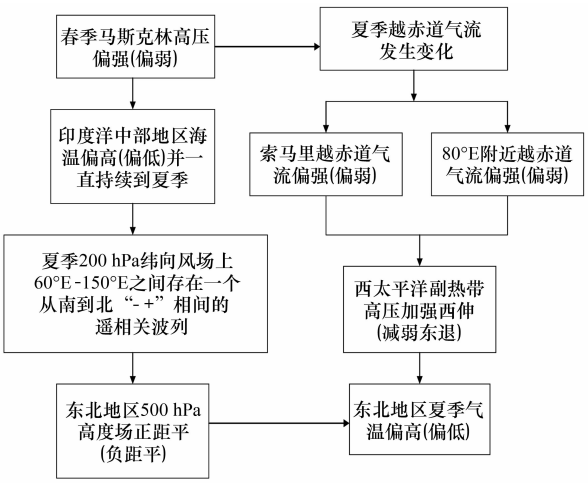


图 11 春季马高对东北地区夏季气温的影响示意图

Fig. 11 The influencing process of the spring Mascarene high on air temperature over Northeast China in summer

南海一直到菲律宾以东海域均为高度场正异常区，这种情况下夏季东北地区容易出现高温天气[40-42]。春季马高偏弱年则相反，夏季当索马里越赤道气流偏弱，80°E 附近的越赤道气流同样偏弱，使得西太副高减弱东退，东北地区夏季气温容易偏低。

所以，春季马高偏强年可以通过增强后期夏季的索马里越赤道气流与 80°E 附近的越赤道气流，从而减弱赤道印度洋上的西风异常，使得西太副高加强西伸，造成东北地区的夏季高温天气，春季马高偏弱年则相反。

通过前面的分析，可以得到春季马高影响东北地区夏季气温的示意图(图 11)。

## 6 结论

(1) 春季马高与后期东北地区夏季气温呈正相关关系，显著的高相关区主要位于东北中东部地区。春季马高偏强年，后期夏季北半球盛行纬向环流，中国东北地区与阿留申群岛南侧为主要的正距平中心，东北地区上空为高压系统所控制，总云量偏少，气流辐散下沉，造成这一区域的高温天气。春季马高偏弱年则相反，后期夏季北半球以经向环流为主，东北地区受低压系统影响，总云量偏多，高纬冷空气与低纬气流在此辐合上升，使得这一区域气温容易偏低。

(2) 春季马高偏强时，受其控制印度洋中部地区海温偏强，这种影响一直持续到夏季且进一步加强，从而通过海温的强迫在 200 hPa 纬向风场上激发出一个从南半球高纬到北半球高纬的经向遥相关波列，并通过这个遥相关波列影响到东北地区夏季 500 hPa 高度场，进而造成东北地区的夏季气温偏高；马高偏弱年则相反。

(3) 春季马高偏强年可以通过增强后期夏季的索马里越赤道气流与 80°E 附近的越赤道气流，从而减弱西北印度洋到南海上的赤道西风带，使得西太副高加强西伸，造成东北地区的夏季高温天气；春季马高偏弱年则相反。

综上所述，本文通过相关分析基本揭示了春季马高对于东北夏季气温可能的影响以及作用途径，

能够为预测东北夏季气温提供一定的参考，但其物理过程和机制还不是很清楚，有待进一步的研究。

## 参考文献：


[1] 东北低温协作组. 东北地区冷夏、热夏长期预报的初步研究[J]. 气象学报, 1979, 37(3): 44 –58.

[2] 丁士晟. 东北地区夏季低温的气候分析及其对农业生产的影响[J]. 气象学报, 1980, 38(3): 234 –242.

[3] 汤懋苍, 汤池. 历史上气候变化对我国社会发展的影响初探[J]. 高原气象, 2000, 19(2): 159 –165.

[4] 李栋梁, 吴洪宝, 章基嘉. 中国夏季月平均气温异常研究[J]. 高原气象, 1995, 14(2): 165 –175.

[5] 左洪超, 吕世华, 胡隐樵. 中国近 50 年气温及降水量的变化趋势分析[J]. 高原气象, 2004, 23(2): 238 –244.

[6] 屠其璞, 邓自旺, 周晓兰. 中国气温异常的区域特征研究[J]. 气象学报, 2000, 58(3): 288 –296.

[7] 沈柏竹, 廉毅, 杨涵洧, 等. 中国东北夏季温度年代际变化特征[J]. 地理科学, 2012, 32(6): 739 –745.

[8] 周小珊, 陈力强, 李辑, 等. 全球气候变暖条件下沈阳若干气候特征的变化[J]. 高原气象, 2005, 24(5): 823 –828.

[9] 张茜, 李栋梁. 东北及邻近地区夏季气温异常的新特征及对大气环流的响应[J]. 高原气象, 2011, 30(6): 1604 –1614.

[10] 符淙斌. 北半球冬春冰雪面积变化与我国东北地区夏季低温的关系[J]. 气象学报, 1980, 38(2): 187 –192.

[11] 王敬方, 吴国雄. 持续性东北冷夏的变化规律及相关特征[J]. 大气科学, 1997, 21(5): 523 –532.

[12] 汪宏宇, 龚强, 孙凤华, 等. 东北和华北东部气温异常特征及其成因的初步分析[J]. 高原气象, 2005, 24(6): 1024 –1033.

[13] 廉毅, 安刚. 东亚季风、El Nino 与中国松辽平原夏季低温关系初探[J]. 气象学报, 1998, 56(6): 724 –735.

[14] 黄士松, 汤明敏. 论东亚夏季风体系的结构[J]. 气象科学, 1987, 7(3): 1 –16.

[15] 黄士松, 汤明敏. 西北太平洋和南印度洋上环流系统的中期振荡与遥相关[J]. 气象科学, 1988, 8(4): 1 –13.

[16] 陈隆勋. 东亚季风环流系统的结构及其中期变动[J]. 海洋学报, 1984, 6(6): 744 –758.

[17] 施能, 朱乾根. 南半球澳大利亚、马斯克林高压气候特征及其对我国东部夏季降水的影响[J]. 气象科学, 1995, 15(2): 20 –27.

[18] 薛峰, 王会军, 何金海. 马斯克林高压和澳大利亚高压的年际变化及其对东亚夏季风降水的影响[J]. 科学通报, 2003, 46(3): 287 –292.

[19] 魏红, 韦志刚, 刘慧, 等. 我国北方 500 hPa 春、夏季平均长波年际异常的 EOF 分析[J]. 高原气象, 2012, 31(1): 102 –112.

[20] 严华生, 董慧林, 程建刚, 等. 近 51 年 500 hPa 上北极涛动的时空[J]. 高原气象, 2005, 24(2): 187 –195.

[21] 邹立尧, 丁一汇. 1961 –2005 年东北暴雨气候特征分析[J]. 高原气象, 2010, 29(5): 1314 –1321.

[22] 帅嘉冰, 郭品文, 庞子琴. 中国冬季降水与 AO 关系的年代际变化[J]. 高原气象, 2010, 29(5): 1128 –1136.

[23] 曹杰, 尤亚磊, 黄玮. 夏季西太副高脊面年际变化与太平洋海温关系的研究[J]. 高原气象, 2009, 28(2): 411 –418.

[24] 施能, 古文保. 大气环流异常分析中使用合成方法的一个问题[J]. 气象, 1993, 19(9): 32 –34.

[25] 崔锦, 杨修群. 马斯克林高压的变化及其与 ENSO 的关系[J]. 气象科学, 2005, 25(5): 441 –449.

[26] 张蓬勃, 管兆勇, 蔡佳熙. SVD 分析揭示的澳大利亚高压年际变化对中国夏季气温的可能影响[J]. 大气科学学报, 2010, 33(1): 58 –66.

[27] Robert D C, Zhang M H, Wielicki B A, et al. The influence of the 1998 El Nino upon cloud-radiative forcing over the Pacific warm pool[J]. J Climate, 2001, 14(9): 2129 –2137.

[28] 南素兰, 李建平. 春季南半球环状模与长江流域夏季降水的关系：Ⅰ基本事实[J]. 气象学报, 2005, 63(6): 837 –846.

[29] 南素兰, 李建平. 春季南半球环状模与长江流域夏季降水的关系：Ⅱ印度洋和南海海温的“海洋桥”作用[J]. 气象学报, 2005, 63(6): 847 –856.

[30] 范可. 南半球环流异常与长江中下游夏季旱涝的关系[J]. 地球物理学报, 2006, 49(3): 672 –679.

[31] 范可, 王会军. 有关南半球大气环流与东亚气候的关系研究的若干新进展[J]. 大气科学, 2006, 30(3): 402 –412.

[32] Namias J. Evolution of monthly mean circulation and weather patters[J]. Trans Amer Geophys, 1948, 29: 777 –788.

[33] 沈柏竹, 刘实, 廉毅, 等. 2009 年中国东北夏季低温及其与前期海气系统变化的联系[J]. 气象学报, 2011, 69(2): 320 –333.

[34] 曾红玲, 高新全, 戴新刚. 近20 年全球冬、夏季海平面气压场和500hPa 高度场年代际变化特征分析[J]. 高原气象, 2002, 21(1): 66 –73.

[35] Ding Y H, He C. The summer monsoon onset over the tropical eastern Indian Ocean: The earliest onset process of the Asian summer monsoon[J]. Adv Atmos Sci, 2006, 23(6): 940 –950.

[36] 王会军, 薛峰. 索马里急流的年际变化及其对半球间水汽输送和东亚夏季降水的影响[J]. 地球物理学报, 2003, 46(1): 18 –25.

[37] 刘向文, 孙照渤, 倪东鸿, 等. 105°E 和 125°E 越赤道气流与南、北半球环流变化的关系[J]. 大气科学, 2009, 33(3): 443 –458.

[38] 薛峰, 何卷雄. 南半球环流变化对西太平洋副高东西振荡的影响[J]. 科学通报, 2005, 50(15): 1660 –1662.

[39] 刘向文, 孙照渤, 李维京, 等. 澳洲北部强/弱越赤道气流对应的环流配置[J]. 大气科学, 2009, 33(6): 1348 –1362.

[40] 崔锦, 李辑, 张爱忠, 等. 东北夏季低温的研究进展[J]. 气象, 2007, 33(4): 3 –9.

[41] 王静. 东北地区夏季冷暖年大气环流异常的空间特征及演变[J]. 气象科学, 2002, 22(4): 394 –401.

[42] 李菲, 李辑, 管兆勇. 我国东北夏季气温年代际变化特征及与太平洋海温异常关系的研究[J]. 气象与环境学报, 2010, 26(3): 19 –26.

# Impacts of Spring Mascarene High on Air Temperature over Northeast China in Summer

ZENG Yuxing[1-2], FENG Guolin[2], ZHAO Junhu[1-2], SHEN Baizhu[1-2]

(1. *College of Atmospheric Sciences, Lanzhou University, Lanzhou* 730000, *China*;
2. *Laboratory for Climate Studies of China Meteorological Administration, National Climate Center, Beijing* 100081, *China*)

**Abstract**: Based on the monthly average data of air temperature at 26 stations in Northeast China and the NCEP/NCAR monthly reanalysis data of wind spead and geopotential height from 1951 to 2011, the impacts of Spring Mascarene High (SMH) in summer air temperature over Northeast China are studied. The results show that SMH is positively related to the summer temperature over Northeast China. In a stronger SMH year, Northeast China region is controlled by the deep high-pressure system in summer, which lead to the divergence and sinking of air flow and the decreasing of total cloud amount, which cause the air temperature in this region is higher than the conventional year. On the contrary, when the SMH is weaker than the conventional year, Northeast China region is controlled by the low-pressure system in summer, the cold air in high-latitude and the warm air flow in low-latitude are converged in this region, which cause the increasing of total cloud amount, and the air temperature is lower than the conventional year. In addition, the SMH anomaly can cause in the middle of the Indian Ocean SST anomaly, and continue until the summer and further strengthen, the meridional teleconnection wave train which is vitalized by the summer Indian Ocean SST anomaly on 200 hPa zonal wind field have effect on 500 hPa geopotential over Northeast China, which can be used for explain the variation of air temperature in this region. Besides, SMH can also enhance summer Somali Jet and cross-equatorial flow at 80°E, which thereby enhance the convective activity in surrounding areas of the Philippines, then intensify the subtropical northwestern Pacific high, and make it extend southwestward, which also contribute to the change of air temperature over Northest China.

**Key words**: Mascarene high; Northeast China; Summer temperature; Teleconnection; Cross-equatorial flow

Geosci. Model Dev., 7, 737–754, 2014
www.geosci-model-dev.net/7/737/2014/
doi:10.5194/gmd-7-737-2014
© Author(s) 2014. CC Attribution 3.0 License.



Geoscientific Model Development
Open Access

# Application and evaluation of a new radiation code under McICA scheme in BCC_AGCM2.0.1

**H. Zhang**[1,2], **X. Jing**[1,2], **and J. Li**[3]

[1]Laboratory for Climate Studies, National Climate Center, China Meteorological Administration, Beijing, China
[2]Collaborative Innovation Center on Forecast and Evaluation of Meteorological Disasters, Nanjing University of Information Science & Technology, Nanjing, China
[3]Canadian Center for Climate Modeling and Analysis, University of Victoria, Victoria, British Columbia, Canada

*Correspondence to:* H. Zhang (huazhang@cma.gov.cn)

Received: 26 July 2013 – Published in Geosci. Model Dev. Discuss.: 16 September 2013
Revised: 10 March 2014 – Accepted: 10 March 2014 – Published: 6 May 2014

**Abstract.** This research incorporates the correlated *k* distribution BCC-RAD radiation model into the climate model BCC_AGCM2.0.1 and examines the change in climate simulation by implementation of the new radiation algorithm. It is shown that both clear-sky radiation fluxes and cloud radiative forcings (CRFs) are improved. The modeled atmospheric temperature and specific humidity are also improved due to changes in radiative heating rates, which most likely stem from the revised treatment of gaseous absorption.

Subgrid cloud variability, including vertical overlap of fractional clouds and horizontal inhomogeneity in cloud condensate, is addressed by using the Monte Carlo Independent Column Approximation (McICA) method. In McICA, a cloud-type-dependent function for cloud fraction decorrelation length, which gives zonal mean results very close to the observations of CloudSat/CALIPSO, is developed. Compared to utilizing a globally constant decorrelation length, the maximum changes in seasonal CRFs by the new scheme can be as large as 10 and 20 W m$^{-2}$ for longwave (LW) and shortwave (SW) CRFs, respectively, mostly located in the tropics. The inclusion of an observation-based horizontal inhomogeneity of cloud condensate has also a significant impact on CRFs, with global means of $\sim$ 1.5 W m$^{-2}$ and $\sim$ 3.7 Wm$^{-2}$ for LW and SW CRFs at the top of atmosphere (TOA), respectively. Generally, incorporating McICA and horizontal inhomogeneity of cloud condensate in the BCC-RAD model reduces global mean TOA and surface SW and LW flux biases in BCC_AGCM2.0.1.

These results demonstrate the feasibility of the new model configuration to be used in BCC_AGCM2.0.1 for climate simulations, and also indicate that more detailed real-world information on cloud structures should be obtained to constrain cloud settings in McICA in the future.

## 1 Introduction

Radiation process is crucial for climate simulations. Over the past 2 decades, a lot of progress has been made in atmospheric radiation. For example, in most radiation schemes the traditional band model for gaseous transmittance has been replaced by the correlated *k* distribution (CKD) method (Fu and Liou, 1992; Mlawer et al., 1997; Zhang et al., 2003; Li and Barker, 2005; Shi et al., 2009, and others). In principle, CKD can be applied to a single absorption line while band models utilize mean values for entire bands. Thus, CKD shows considerable promise in simulating atmospheric radiation accurately and efficiently. The breakthrough in nonspherical scattering makes it possible to accurately calculate ice cloud optical properties (Mishchenko et al., 2002). In an ice cloud optical property parameterization, the full set of single-scattering properties is provided by considering three-dimensional random orientations for multiple ice crystal habits following the observations of CALIPSO (Yang et al., 2005, 2013; Baum et al., 2011). All this progress has been included in the Beijing Climate Center Radiation transfer model (BCC-RAD), which is used in the general circulation model (GCM) of Beijing Climate Center (i.e., BCC_AGCM2.0.1).

How to deal with cloud vertical overlap and cloud internal inhomogeneity has been a very difficult task for atmospheric radiation. This arises mostly from the relatively coarse spatial resolution of GCMs (dozens to hundreds of kilometers), which leaves cloud-relevant processes and inherent subgrid variations of clouds unresolved (Barker and Räisänen, 2005; Zhang et al., 2013). Typically, cloud condensate (water and ice) is treated as horizontally homogeneous (the plane parallel homogeneous, or PPH, assumption) within a GCM grid cell. Additionally, certain predetermined assumptions about the vertical overlap of fractional clouds are required (traditionally maximum-random overlap, or MRO) (Tian and Curry, 1989). Computing on a cloud system resolving model (CSRM) data set, Barker and Räisänen (2005) found that, by a small change to the standard deviation of cloud condensate distribution, zonal mean shortwave (SW) cloud radiative forcing (CRF) could change up to $25\,\mathrm{W\,m^{-2}}$ at certain latitudes (with a global mean of $\sim 8\,\mathrm{W\,m^{-2}}$). The radiative sensitivity to cloud overlap is of similar magnitude for global averages. Oreopoulos et al. (2012) included a beta distribution function and a latitude-/day-dependent cloud overlap function, both derived from CloudSat/CALIPSO data, in the GEOS-5 atmospheric general circulation model. SW and longwave (LW) CRFs showed significant changes compared to the traditional PPH and maximum-random overlap setup, but the magnitude of changes depends also on the cloud scheme utilized. All of these studies have emphasized the importance of faithfully addressing subgrid cloud variability in GCMs.

To make the representation of subgrid cloud properties flexible and modularized and to maintain computational efficiency, a scheme named the Monte Carlo Independent Column Approximation (McICA) method was developed (Pincus et al., 2003). McICA is a method that does fast spectral integration over given cloudy subcolumns within a domain. The cloud subcolumns required by McICA can be supplied from certain subgrid cloud generators (Räisänen and Barker, 2004) or cloud-resolving models (Hill et al., 2011). The advantages of McICA are that it facilitates adjustment or alteration of both cloud structure and radiative transfer and thus accelerates future development of GCMs.

Though McICA has been extensively studied, there lacks a detailed description on cloud-type-related vertical overlap. An e-folding relationship of cloud overlap has been developed to quantitatively represent cloud overlap for different types of clouds and over different regions (Hogan and Illingworth, 2000; Mace and Benson-Troth, 2002). In current GCMs, a global mean constant value of decorrelation length (hereinafter $L_{\mathrm{cf}}$), a critical parameter in this overlap algorithm, is often used. Usually, convective cloud has well-organized structures with large vertical correlation due to strong upward motion. Therefore, $L_{\mathrm{cf}}$ for convective cloud should be larger than for the other types of clouds. To address the climate impact by distinguishing the cloud-type-related $L_{\mathrm{cf}}$ in McICA is one goal of this work. We here incorporate the McICA scheme and a stochastic cloud generator (SCG; Räisänen et al., 2004) into the BCC_AGCM2.0.1 model with the BCC-RAD radiation algorithm.

This work contains two parts: first, we report the improvements on climate simulation by introducing the new BCC-RAD radiation algorithm. Second, we analyze the impact of cloud overlap assumption and cloud condensate inhomogeneity through the McICA scheme. Most attention will be paid to the cloud-type-related decorrelation length by comparing with the results of using a globally constant value. This preliminary work aims to document the impact of the modifications in cloud-radiation process on simulated climate and the model response to these changes and thereby provide suggestions for future development. In Sect. 2, the BCC_AGCM2.0.1 model, the BCC-RAD radiation scheme and the McICA scheme are briefly described. The design of experiments is given in Sect. 3. Results of the simulations with various model configurations are described in Sect. 4. In Sect. 5, we conclude with a brief summary.

## 2 Model description

### 2.1 Description of BCC_AGCM2.0.1

BCC_AGCM2.0.1 was developed by the Beijing Climate Center (BCC) at the China Meteorological Administration (CMA) based on the Community Atmosphere Model Version 3 (CAM3) of the National Center for Atmospheric Research (NCAR) (Wu et al., 2010). The model runs at T42 spectral resolution (approximately $2.8^\circ \times 2.8^\circ$) horizontally, and it uses vertical hybrid $\delta$-pressure coordinates including 26 layers with the top located at about 2.9 hPa. An additional layer is added above the topmost layer in the radiative calculation to prevent excessive heating. The default timestep is 20 min, and the radiation code is invoked every three timesteps.

Relative to CAM3, several revisions have been made to improve the physics of the model. These include new reference atmosphere and surface pressures; a revised convection scheme (Zhang and Mu, 2005) that significantly improves the tropical rainfall simulation; a different function for calculating the snow-cover fraction that influences the resulting surface albedo, especially in polar and plateau regions (Wu and Wu, 2004); a new adiabatic adjustment originated by Yan (1987); and new methods for calculating turbulent fluxes over ocean surface that remove the systematic biases in the wind stress and sensible and latent heat fluxes in CAM3. A more detailed description of BCC_AGCM2.0.1 can be found in Wu et al. (2010). In the present research, the interactive Canadian Aerosol Module (CAM) (Gong et al., 2003) with updated aerosol emission sources (Zhou et al., 2012) is used to predict atmospheric aerosol burdens (Zhang et al., 2012).

**Table 1.** Comparison of the new and old schemes.

| | Old | New |
|---|---|---|
| Absorbing gases in LW | $H_2O$, $CO_2$, and $O_3$<br>$CH_4$, $N_2O$, CFC11, CFC12 | The same as in Old |
| Absorbing gases in SW | $H_2O$, $CO_2$, $O_3$, and $O_2$ | $H_2O$, $CO_2$, $O_3$, $N_2O$, and $O_2$ |
| Range of LW | 0–2000 $cm^{-1}$ | 0–2680 $cm^{-1}$ |
| Range of SW | 2000–50 000 $cm^{-1}$ | 2110–49 000 $cm^{-1,*}$ |
| Band transmittance scheme | Band model (LW: Kiehl and Briegleb, 1991) (SW: Briegleb, 1992) | CKD scheme (Zhang et al., 2003, 2006a, b) |
| RT solver in LW | Absorptivity/emissivity formulations (Ramanathan and Downey, 1986) | Two-stream approximation (Nakajima et al., 2000) |
| RT solver in SW | $\delta$-Eddington method (Briegleb, 1992) | $\delta$-Eddington method (Coakley et al., 1983) |
| Cloud fraction parameterization | Diagnostic scheme (Rasch and Kristjansson, 1998) | The same as in Old |
| Cloud optics | LW: emissivity formulations (Ebert and Curry, 1992); SW: formulas of Slingo (1989) for liquid and of Ebert and Curry (1992) for ice | Ice cloud: computed using data from Fu (1996), Yang et al. (2005), and Hong et al. (2009); liquid cloud: Nakajima et al. (2000) |
| Cloud effective radius | Ice cloud: Kristjansson et al. (2000); Liquid cloud: Kiehl et al. (1994) | Ice cloud: Wyser (1998); Liquid cloud: the same as in Old |
| Cloud overlap | Maximum random overlap (MRO) (Collins, 2001) | McICA (Räisänen and Barker, 2004; Barker et al., 2008) |
| Aerosol–radiation coupling scheme | BCC_AGCM2.0.1_CAM (Zhang et al., 2012) | BCC_AGCM2.0.1_CAM (Zhang et al., 2012) |

* In the new scheme, contributions from the solar spectrum and terrestrial emission are mixed within 2110–2680 $cm^{-1}$.

### 2.2 Description of radiation schemes

In this work, we incorporate the CKD model by Zhang et al. (2003, 2006a, b), i.e., the Beijing Climate Center Radiation transfer model (BCC-RAD), into BCC_AGCM2.0.1. The BCC-RAD model is substantially different from the previous radiation scheme used in BCC_AGCM2.0.1. To explain the importance of this radiation scheme in modulating climate simulation, it is necessary to describe this revision in advance. A detailed comparison between the old and new schemes is provided in Table 1.

The previous radiation scheme in BCC_AGCM2.0.1 is basically a band model. Although some band models simulated well the broadband fluxes and heating rates, this may have been partly fortuitous because of band overlap effects (Ellington et al., 1991). Another defect of band models is the use of a scaling procedure to account for inhomogeneous atmospheric paths, although these can be made arbitrarily accurate for a homogeneous atmosphere (Kratz, 1995). Therefore, there has been a trend over the past decades to replace band models with CKD methods in GCMs.

The 10–49 000 $cm^{-1}$ (0.204–1000 µm) spectral range in BCC-RAD is divided into 17 bands (8 LW and 9 SW). Five major greenhouse gases (GHGs) – $H_2O$, $CO_2$, $O_3$, $N_2O$, and $CH_4$ – as well as chlorofluorocarbons (CFCs) are considered. The major absorbers in the solar bands are $H_2O$ (including continuum absorption), $CO_2$, $N_2O$, $O_3$, and $O_2$. The HITRAN2000 database (Rothman et al., 2003) was used to provide line parameters and cross sections. Lu et al. (2012) compared the line parameters in different HITRAN versions and found that the difference in the simulated radiative fluxes between the updated HITRAN2008 and HITRAN2000 is very small, so the use of HITRAN2000 should not affect the final modeled climates in this research. In BCC-RAD, the effective absorption coefficients of CKD are calculated based on the line-by-line radiative transfer model (LBLRTM; Clough and Iacono, 1995) with a spectral interval of one-fourth the mean half-width and a 25 $cm^{-1}$ cutoff for line wings over each band (Clough and Iacono, 1995). The thermal radiation transfer calculation is solved with a two-stream algorithm developed by Nakajima et al. (2000), and the solar radiation transfer is solved with the $\delta$-Eddington method (Coakley et al., 1983). SW radiation model comparisons, including BCC-RAD, are given in Randles et al. (2013).

Cloud and aerosol optical properties in BCC-RAD are also different from those in the original scheme. The optical properties of cloud droplets are from Nakajima et al. (2000), and those of ice crystals are calculated based on several data sets: observational size distribution data from Fu (1996), optical properties of single particles of different shapes from Yang et al. (2005), and the fractional mixing of particles of various shapes suggested by Baum et al. (2005). Aerosol optical properties are from Wei and Zhang (2011) and Zhang et al. (2012).

### 2.3 Description of the McICA scheme

The McICA scheme is based on the ICA algorithm for the computation of domain mean radiation fields. It greatly and

effectively reduces computation time while maintaining the accuracy of ICA from a statistical perspective. The basic principles of McICA were first explained in detail by Pincus et al. (2003); Räisänen and Barker (2004) then provided additional ways to diminish the induced noise. For clarity and completeness, we provide a brief summary here.

Conceive a domain $R$ (a GCM grid). The subgrid clouds could be represented by a certain number of subcolumns, which contain individual cells in each layer that are either clear or overcast. Moreover, the domain mean of these subcolumns should hold the cloud profile provided by the GCM. Given these subcolumns, radiative computation can be liberated from the description of partial clouds and their vertical overlap. The required subcolumns could be derived through SCG with consideration of certain overlap and horizontal distribution rules for clouds. For a thorough methodology of SCG, one can refer to Räisänen et al. (2004).

Within the domain $R$ composed of subcolumns, the domain-averaged radiative fluxes can be accurately given by ICA as

$$\left\langle F^{\mathrm{ICA}}\right\rangle = \int S(\lambda)\left\{\iint\limits_{R} F(x,y,\lambda)\mathrm{d}x\mathrm{d}y\right\}\mathrm{d}\lambda, \tag{1}$$

where $x$ and $y$ are subcolumn counters along the zonal and meridional axis, respectively, $S(\lambda)$ is the spectral weight at wavelength $\lambda$, and $F(x,y,\lambda)$ denotes the radiative flux at location $(x,y)$ and wavelength $\lambda$.

If $R$ is partially cloudy, $\left\langle F^{\mathrm{ICA}}\right\rangle$ can be split into clear $\left\langle F^{\mathrm{clr}}\right\rangle$ and cloudy $\left\langle F^{\mathrm{cld}}\right\rangle$ parts weighted by the cloud fraction Ac:

$$\left\langle F^{\mathrm{ICA}}\right\rangle = (1-\mathrm{Ac})\left\langle F^{\mathrm{clr}}\right\rangle + \mathrm{Ac}\left\langle F^{\mathrm{cld}}\right\rangle. \tag{2}$$

The most time-consuming part of Eq. (2) is $\left\langle F^{\mathrm{cld}}\right\rangle$ due to the full spectral integration in all cloudy subcolumns. To diminish the computational burden, Pincus et al. (2003) reduced the two-dimensional integration to a single dimension by introducing a Monte Carlo (random sampling) process:

$$\left\langle F^{\mathrm{cld}}\right\rangle \approx \int S(\lambda)\, F^{\mathrm{cld}}(s_{\mathrm{rnd}},\lambda)\,\mathrm{d}\lambda, \tag{3}$$

where $s_{\mathrm{rnd}}$ is a randomly selected cloudy subcolumn number for radiative calculation at $\lambda$. Equation (3) tremendously reduces computation time compared with Eq. (2) and represents the kernel of McICA.

It should be noted that the random selection of $s_{\mathrm{rnd}}$ in Eq. (3) inevitably introduces random noise. Although this may yield deviated results for a single calculation, averaging over a number of calculations generates almost unbiased results with respect to ICA (Barker et al., 2008). One method for reducing the noise is to increase the number of $s_{\mathrm{rnd}}$ for optically critical spectral intervals (Räisänen and Barker, 2004). To date, the McICA scheme has already been operationally utilized in several climate models and numerical weather prediction models (Morcrette et al., 2008; Räisänen and Järvinen, 2010; Neale et al., 2010).

## 3 Experimental design

We now have considered two model configurations: the new one with McICA and BCC-RAD to handle the cloud-radiative procedure and the old one with the traditional overlap treatment by Collins et al. (2001) and radiation scheme described in Briegleb (1992). The details of these are listed in Table 1. Experiments were designed to reveal (a) the differences in simulated climate between the two configurations and (b) the impact of changing subgrid cloud structures on simulated climate within the new configuration. For all the following experiments, the sea surface temperature (SST) data are from the global Hadley Centre Sea Ice and Sea Surface Temperature (HadISST) data set (Rayner et al., 2003) for years up to 1981 and the Reynolds et al. (2002) for years after 1981; the greenhouse gases are set the same by using the current values; aerosols are produced by a coupled aerosol model (named CAM) that is described in detail in Zhang et al. (2012). All of the experiments are integrated from September 1979 to December 1990, and the results of the last 10 years are used for analysis.

### 3.1 Experiments comparing the new and old model configurations

First, an experiment with the old scheme, denoted OLD, was performed as a control run. Second, a McICA experiment denoted N_MRO, utilizing PPH and the MRO assumptions to be consistent with the OLD run, was done. The comparison between N_MRO and OLD illustrates differences in the climate response due to changes in radiation scheme other than subgrid cloud variation.

### 3.2 Experiments exploring the impacts of subgrid cloud structures

As the McICA scheme is flexible in depicting subgrid cloud structures, three more experiments were implemented to test the model's sensitivity to cloud-structure variations.

First, the impact of changing cloud overlap assumption was tested by including the so-called general overlap (hereafter GenO) (Mace and Benson-Troth, 2002). In GenO, the vertically projected cloud fraction of the two cloud layers $k$ and $l$ ($C_{k,l}$) is defined as the linear combination of maximum ($C_{k,l}^{\mathrm{max}}$) and random overlap ($C_{k,l}^{\mathrm{ran}}$):

$$C_{k,l} = \alpha_{k,l} C_{k,l}^{\mathrm{max}} + \left(1-\alpha_{k,l}\right) C_{k,l}^{\mathrm{ran}}, \tag{4}$$

where

$$C_{k,l}^{\mathrm{max}} = \max\left(C_k, C_l\right), \tag{5}$$

$$C_{k,l}^{\mathrm{ran}} = C_k + C_l - C_k C_l, \tag{6}$$

and the overlap parameter $\alpha_{k,l}$ is prescribed via an exponential decay function of altitude separation between cloud layers:

$$\alpha_{k,l} = \exp\left[-\int_{z_k}^{z_l} \frac{\mathrm{d}z}{L_{\mathrm{cf}}(z)}\right]. \quad (7)$$

The Eq. (4) is applied to both continuous and discontinuous clouds as in Mace and Benson-Troth (2002). The lapse rate of the decay of $\alpha_{k,l}$ is controlled by the "decorrelation length" ($L_{\mathrm{cf}}$ in Eq. 7), which has a global mean value of about 2 km (Barker, 2008). We term the scheme of using a globally constant $L_{\mathrm{cf}} = 2$ km as N_GO2. In reality, $L_{\mathrm{cf}}$ is highly related to cloud type and atmospheric dynamics (Naud et al., 2008). Usually, convective cloud has well-organized structure (convective tower) with large vertical correlation due to strong upward motion. Therefore, $L_{\mathrm{cf}}$ for convective cloud should be larger than for other types of clouds. Generally, $L_{\mathrm{cf}}$ is about 5 km to 10 km for convective cloud and is much smaller (around 1 km) for other types of clouds (H. Barker, personal communication, 2013). In a GCM grid cell, we simply define the grid-scale mean result as

$$L_{\mathrm{cf}} = \left[L_{\mathrm{cf}_1} \times f_{\mathrm{con}} + L_{\mathrm{cf}_2} \times (f_{\mathrm{tot}} - f_{\mathrm{con}})\right] / f_{\mathrm{tot}}, \quad (8)$$

where $L_{\mathrm{cf}_1}$ and $L_{\mathrm{cf}_2}$ are the decorrelation lengths for deep convective cloud and all other types of clouds, and $f_{\mathrm{con}}$ and $f_{\mathrm{tot}}$ are the cloud fractions for deep convective cloud and total cloud in a model layer. Though both deep and shallow convective clouds are diagnosed in the BCC_AGCM2.0.1 model, we reserve $L_{\mathrm{cf}_1}$ to deep convective cloud, because the decorrelation length for shallow convective cloud (mostly near the boundary layer) is likely to be very small as demonstrated by previous studies (Neggers et al., 2011). Besides deep and shallow convective clouds, stratiform cloud and marine stratocumulus are also diagnosed in the BCC_AGCM2.0.1 model, based on relative humidity. As $f_{\mathrm{con}}$ depends directly on updraft mass flux in the diagnosis, the new cloud overlap scheme is also related to updraft mass flux. The test studies show that if $L_{\mathrm{cf}_1} = 10$ km and $L_{\mathrm{cf}_2} = 1$ km, the global mean $L_{\mathrm{cf}}$ is $\sim 1.7$ km (see Sect. 4.2 for more details), which is close to the result of Barker (2008). We term the scheme of Eq. (8) as N_GOF. This can also be called as convective–stratiform contrast scheme, since the stratiform cloud dominates all the other types of cloud in cloud fraction.

Additionally, the impact of breaking the default PPH assumption is addressed by perturbing the horizontal distribution of cloud condensate (water and ice) with an ideal distribution function. The gamma function of cloud condensate applied by Shonk et al. (2010) is used here. In such distribution, the magnitude of inhomogeneity is constrained by the fractional standard deviation ($f$), which is defined as

$$f = \frac{\sigma_c}{\bar{c}}, \quad (9)$$

where $\bar{c}$ is the layer mean cloud condensate ignoring the cloud phase, and $\sigma_c$ is the standard deviation of the condensate. In this work, $f$ was set to be 0.75 for both the liquid and ice phases, as was obtained by Shonk et al. (2010) from an extensive collection of observations. This inhomogeneity setup was tested with $L_{\mathrm{cf}}$ given as Eq. (8), denoted as N_GOF_IH. Because the cloud overlap assumptions are consistent for N_GOF and N_GOF_IH, any discrepancies illustrate the impact of including horizontally inhomogeneous clouds.

In this study, the decorrelation length for cloud condensate in GenO is set to be 1 km in all tests. The variation of the decorrelation length for cloud condensate has smaller influence and is less important than that for the overlap of cloud fractions (Barker and Räisänen, 2005).

## 4 Results

This section reports the results in two parts: (i) first, results from OLD and N_MRO are provided to clarify the differences between the new and old model configurations; (ii) second, results from N_GO2, and N_GOF and N_GOF_IH are presented to show the impacts of cloud overlap variations and changing the horizontal distribution of cloud condensate within the McICA scheme.

### 4.1 Comparison between the new and old model configurations

#### 4.1.1 Radiation budget

We first investigate the difference between the old and new schemes under the same subgrid cloud structure setups. Figure 1 shows the global annual mean radiation fields for various simulations at the top of atmosphere (TOA) and at the surface (SFC) with a comparison against the satellite-derived 11-year (2000–2010) mean CERES_EBAF data sets (http://ceres.larc.nasa.gov/order_data.php) (Loeb et al., 2009). We focus on the results of OLD and N_MRO in this section.

The central column of Fig. 1 shows that the new scheme obtains much improved net all-sky LW and SW TOA radiative fluxes. This is due to improvements in both the revised cloud optics and the net clear-sky fluxes calculated by the new radiation scheme.

Compared with CERES_EBAF data, the OLD run shows notable discrepancies in TOA LW and SW CRFs (right column of Fig. 1), which are overestimated by $\sim 3\,\mathrm{W\,m^{-2}}$ and $\sim 7\,\mathrm{W\,m^{-2}}$, respectively. The N_MRO run shows large reductions in these biases, with TOA LW and SW CRFs errors reduced to $\sim 1.5$ and $\sim 3\,\mathrm{W\,m^{-2}}$, respectively. As the same cloud overlap assumptions are used, the improved CRFs in N_MRO should come mainly from the revised cloud optics (see Table 1).

As for the clear-sky net fluxes at TOA ($F^{\mathrm{clr}}$, the left column in Fig. 1), the OLD run overestimates LW and SW $F^{\mathrm{clr}}$

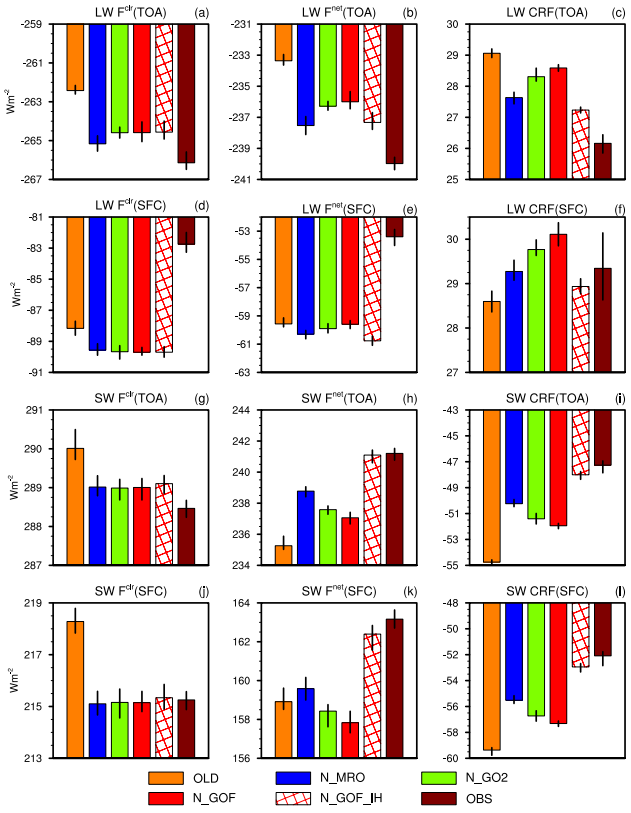


**Fig. 1.** Global annual mean clear-sky net fluxes ($F^{\mathrm{clr}}$, left panels), all-sky net fluxes ($F^{\mathrm{net}}$, central panels), and CRFs (right panels) for TOA LW (upmost row), surface LW (second row), TOA SW (third row), and surface SW (bottom row) from the various simulations and CERES_EBAF observations. The error bars are the ranges between the maximum and minimum annual mean values for the simulated or observed decades.

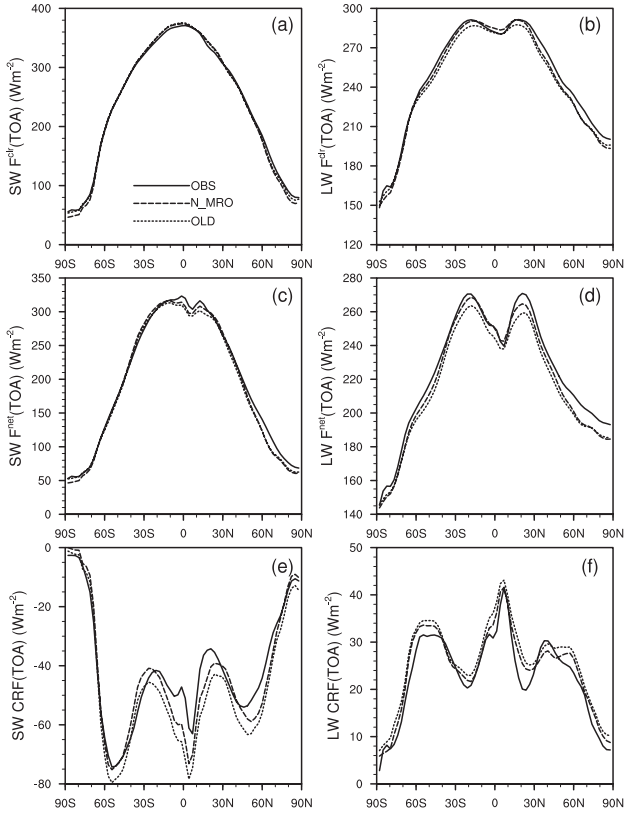


**Fig. 2.** $F^{\mathrm{clr}}$ (top), $F^{\mathrm{net}}$(central), and CRFs (bottom) at the TOA for LW (left) and SW (right) from OLD, N_MRO, and CERES_EBAF observations.

by $\sim 5$ and $\sim 1.5\,\mathrm{W\,m^{-2}}$, respectively. The biases at the surface are also large, up to $\sim 4\,\mathrm{W\,m^{-2}}$ for SW $F^{\mathrm{clr}}$. Again, N_MRO produces clear-sky fluxes much closer to the observations (except for LW $F^{\mathrm{clr}}$ at surface). The differences between the simulated TOA LW $F^{\mathrm{clr}}$ and SW $F^{\mathrm{clr}}$ and those from CERES_EBAF observations are reduced to $\sim 1$ and $\sim 0.5\,\mathrm{W\,m^{-2}}$, respectively, for N_MRO.

The improvements in both $F^{\mathrm{clr}}$ and CRFs suggest that the implementation of the new radiation scheme fares much better at modeling the inner balance between the radiation components from clear and cloudy regimes. Thus, the new configuration behaves in a more physically coherent manner than the original one in BCC_AGCM2.0.1, and it predictably yields more reasonable all-sky net fluxes ($F^{\mathrm{net}}$, central column of Fig. 1).

Figure 2 displays zonal annual mean $F^{\mathrm{clr}}$, $F^{\mathrm{net}}$, and CRFs at the TOA from the OLD, and N_MRO runs, as well as the CERES_EBAF data set. The simulated zonal distributions of these variables are all in reasonable agreement with observations. However, the N_MRO run gives LW and SW $F^{\mathrm{net}}$ much closer to observations, especially at mid–low latitudes (Fig. 2c, d). This occurs mainly because the vast overestimation of LW and SW CRFs by the OLD scheme is reduced overall by the new scheme (Fig. 2e, f). Moreover, N_MRO also shows notable improvement in LW $F^{\mathrm{clr}}$ in the subtropics and mid-latitudes (Fig. 2a). The SW $F^{\mathrm{clr}}$ is calculated well at most latitudes in all experiments, except at the polar regions where there are noticeable underestimations. This may be linked to the enhanced solar albedo over snow surfaces compared with observations in the Community Land Model version 3 (CLM3) used in the BCC_AGCM2.0.1 model (Oleson et al., 2003), which results in an overestimated solar energy loss to space.

Figure 3 shows the global distribution of errors in annual mean SW and LW CRFs relative to CERES_EBAF, as well as the differences between N_MRO and OLD. The OLD run exhibits negative biases in SW CRF at most low and mid-latitudes (see Fig. 3a). The N_MRO run significantly reduces these errors (see Fig. 3c), but the enhanced positive biases appear over subtropical oceans near the west coasts of continents and over East Asia. Figure 3e shows that the differences in SW CRF between the new and old configurations are located mainly in the intertropical convective zone (ITCZ), with maximum values of over $14\,\mathrm{W\,m^{-2}}$, as

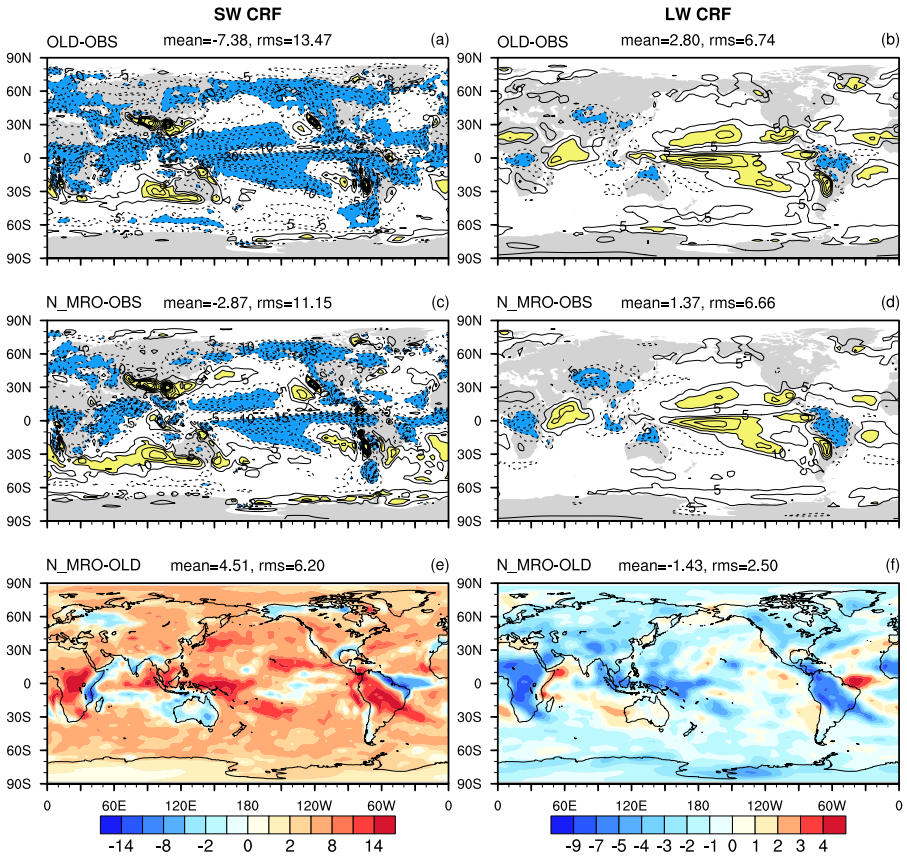


**Fig. 3.** The annual mean differences in SW CRF (left) and LW CRF (right). Differences larger (smaller) than 10 ($-10$) W m$^{-2}$ are shaded in yellow (blue). The global mean and root mean square values of each figure are also shown.

abundant high-level ice clouds exist in all the ITCZ regions. Differences in SW CRF over mid–high latitudes are much smaller. There are only minor differences in areas with large SW CRF along 60° S, where a large number of low-level clouds (mostly liquid) exist, because the liquid cloud optics in the two configurations are almost equivalent for CRF calculation. Consequently, the changes in ice cloud optical properties are the main cause of the changes in SW in the run with the new configuration when maximum-random overlap of plane-parallel horizontally homogeneous clouds is assumed.

In the OLD run, LW CRF is overestimated over most of the tropical and subtropical oceans with very few exceptions, but it is underestimated over intensively convective tropical regions such as the central Africa, the west Pacific warm pool, and the Amazon forests of South America (Fig. 3b). The N_MRO run produces similar distributions of these biases; however, the positive biases in the tropical and subtropical oceans are reduced, whereas the negative biases are enhanced somewhat (Fig. 3d). The differences in LW CRF between the new and old configurations (see Fig. 3f) show a quite similar geographic distribution to those of SW CRF (see Fig. 3e), with a maximum value of more than $-9$ W m$^{-2}$ in the tropical east Pacific. Again, variations in ice cloud optics play a critical role in causing these differences.

The cooling effect by SW CRF and heating effect by LW CRF at the TOA in tropical deep convective regions have been shown to be nearly linearly correlated and generally compensate for each other (Kiehl and Ramanathan, 1990), which means that the (SW CRF) / (LW CRF) ratio is about $-1$. This ratio is often used as a criterion for showing the performance of modeled CRF. The (SW CRF) / (LW CRF) ratios in the Indonesian region (10° S–20° N, 110–160° E) for the OLD and N_MRO simulations and CERES_EBAF observations are given in Table 2. The table shows that the OLD run overestimates the (SW CRF) / ( LW CRF) ratios for the annual and seasonal means. N_MRO shows a generally noticeable decrease in SW CRF, especially for the annual and summer (JJA) means. This results in decreased (SW CRF) / (LW CRF) ratios (Table 2). However, previous offline comparisons (not shown here) give very similar results for the new and old schemes. Thus, it can be inferred that the two versions of radiation scheme are comparable for diagnosing the (SW CRF) / (LW CRF) ratio, whereas the climate feedback evidently changes the simulated cloud fractions or cloud condensate.

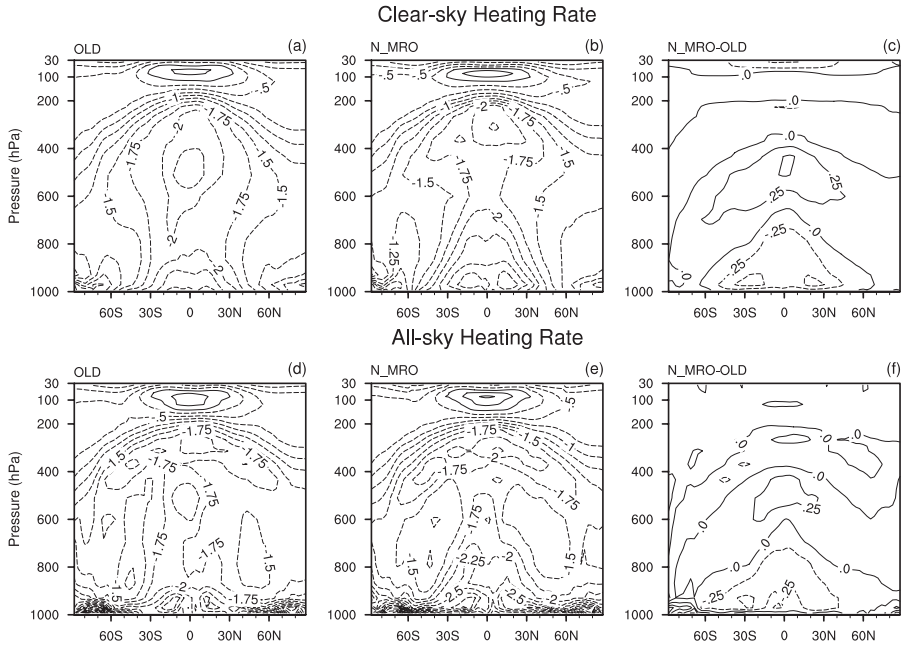


**Fig. 4.** Zonal annual mean clear-sky and all-sky LW heating rates for OLD **(a, d)**, N_MRO **(b, e)** and the differences between N_MRO and OLD **(c, f)** (units: K day$^{-1}$).

**Table 2.** The modeled and observed (SW CRF / LW CRF) ratios in the tropical warm pool region (10° S–20° N, 110–160° E).

| | OLD | N_MRO | OBS |
|---|---|---|---|
| ANN | −1.17 | −0.94 | −1.13 |
| DJF | −1.55 | −1.34 | −1.14 |
| JJA | −1.83 | −1.51 | −1.09 |

Radiative heating/cooling within the atmosphere is a critical driving factor in climate simulations. Figure 4 compares the clear-sky and all-sky LW heating rates (HRs) of N_MRO and OLD, respectively. The differences in SW HR are much smaller than those in LW HR (figure not shown). For the clear-sky condition, N_MRO shows a remarkable (more than 10 %) increased radiative cooling in the lower troposphere within 60° S–60° N and a reduced radiative cooling in most of the middle troposphere. These may be related to the different treatments of greenhouse gases, especially $O_3$ and water vapor. The difference in the all-sky LW HR (see Fig. 4f) is similar to the pattern shown in Fig. 4c, indicating that the differences in the HR of clouds are less important for determining the all-sky HR differences in this case. This pattern tends to increase the stability of the atmosphere below 600 hPa but enhance vertical mixing above 600 hPa.

As shown above, the application of the BCC-RAD radiation scheme, without tuning the subgrid cloud structures, remarkably influences the radiation budget at both boundaries and within the atmosphere. These changes will extensively affect the final simulated climate.

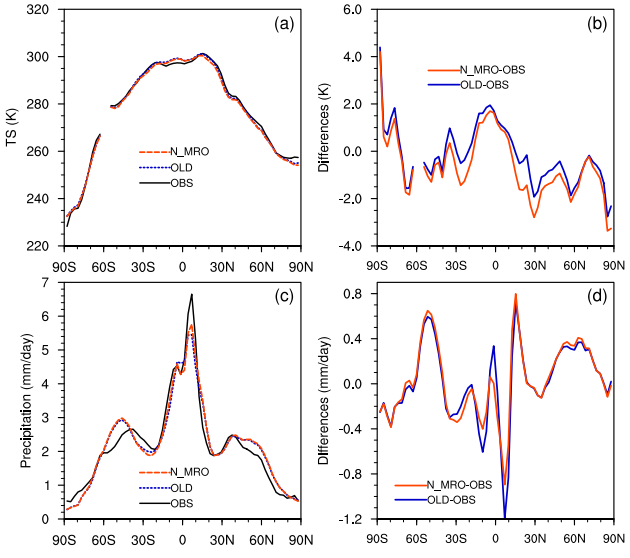


**Fig. 5.** Zonal annual mean **(a)** surface temperature and **(c)** precipitation from N_MRO, OLD, and observation data, as well as **(b, d)** the differences between N_MRO and observations (red solid lines) and between OLD and observations (blue solid lines). The observation data for temperature are from the ERA-Interim reanalysis, and those for precipitation are from the Xie and Arkin (1997) data set.

### 4.1.2 Surface climatology

In this subsection, the simulated surface temperature and precipitation are evaluated.

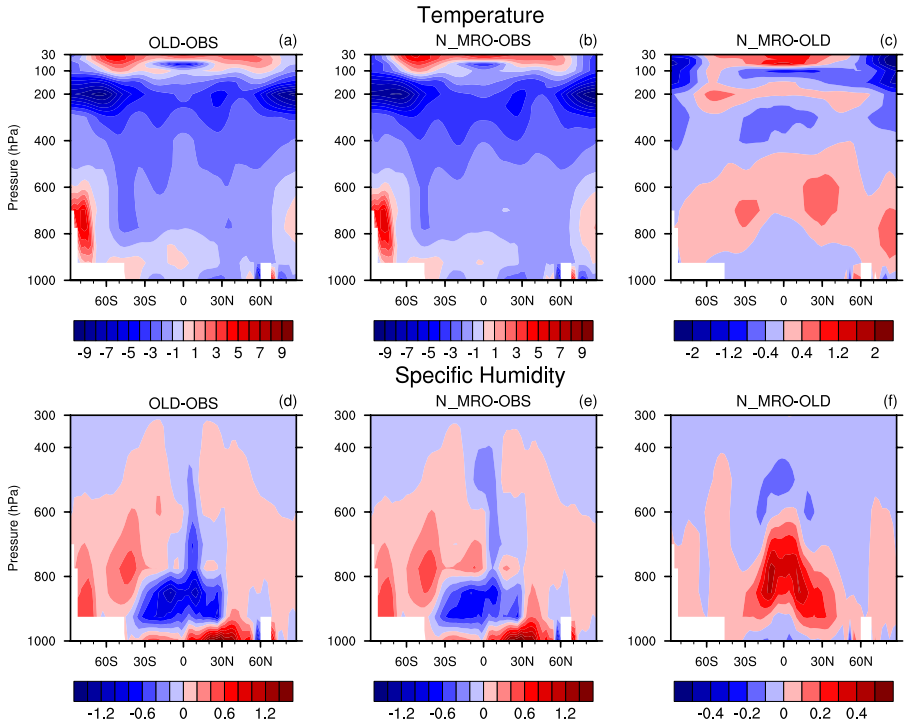


**Fig. 6.** Biases in zonal annual mean atmospheric temperature and specific humidity compared with the ERA-Interim reanalysis for **(a, d)** OLD and **(b, e)** N_MRO simulations and **(c, f)** the differences between N_MRO and OLD.

Zonal comparisons of surface temperature (ST, for land only) and precipitation rate are shown in Fig. 5. There are substantial differences between the simulations and the ERA-Interim reanalysis (Uppala et al., 2005), which is averaged over the same period as the simulations. For instance, simulated STs are underestimated by about 1.5 K in the mid-latitudes and by about 3 K around the North Pole (see Fig. 5b), but overestimated by about 2 K and 4 K over the tropics and South Pole, respectively. The global distributions of surface temperature biases for the N_MRO and OLD runs are quite similar (figures not shown), with local maximum differences between the N_MRO and OLD runs reaching ±2–4 K. The differences between the simulations and observations are much larger than the differences between the N_MRO and OLD simulations. It should be noted that the SSTs used here are prescribed, which limited the model response.

Similar to Fig. 5a and b, Fig. 5c and d show comparisons of the precipitation rate. Both the N_MRO and OLD simulations capture the main features of the meridional distribution of precipitation, such as the maximum in the tropics and secondary maxima at the mid-latitude storm tracks. However, errors are also clear relative to the observation, especially in the tropics. The two simulations are comparable in the simulation of the zonal mean distribution of precipitation, but there are noticeable local differences in the tropical and subtropical regions (figures not shown). These differences probably stem from the altered atmospheric thermodynamics and dynamics caused by the changes in radiation budget. The increases and decreases in precipitation often coincide with the decreases and increases in surface temperature (figures not shown), respectively; thus, the changes in precipitation also obviously influence the surface energy balance.

### 4.1.3 Atmospheric states

Simulated atmospheric temperature and specific humidity are analyzed in this subsection.

Figure 6 shows the comparisons of the latitude–height distribution of atmospheric temperature and specific humidity. Notable cold biases relative to ERA-Interim, about 1–2 K in the low–mid troposphere, exist throughout almost the entire troposphere in the OLD case (see Fig. 6a). The N_MRO simulation inherits most of these biases, but the relative warming (up to 0.4–0.8 K) within the middle troposphere (800 ∼ 500 hPa) is a desirable change compared with OLD (see Fig. 6c). This is definitely related to the reduced LW cooling rate in the middle troposphere, as shown in Fig. 4.

In addition to the improvements in tropospheric temperature, there are favorable changes in specific humidity. Compared with ERA-Interim, the OLD run is subject to considerable dry biases in the tropical lower troposphere (see Fig. 6d). This is likely caused by LW heating rate biases related to the LW parameterization of water vapor (Collins et al., 2002). Due to changes in heating rate, as shown in Fig. 4,

the N_MRO run notably increases the specific humidity in the tropics, typically reducing the original biases by about 30 %.

The changes in atmospheric temperature and specific humidity exert influences on the formation and maintenance of cloud water and ice (figures not shown), affecting the modeled local radiation budget, such as altering the (SW CRF) / (LW CRF) ratio mentioned above.

Overall, the incorporation of the new scheme influences radiative fluxes and heating rates remarkably. Due to these changes, the simulated surface and atmospheric climate are comparable or improved relative to the old model configuration. Therefore, the new scheme used here has been demonstrated to be a viable option for long-term climate simulation.

It should also be mentioned that the differences in simulated climate between the two model configurations are relatively smaller than those between the simulations and observations. Nevertheless, the much more flexible cloud structure and internal consistency of the new configuration will benefit further development of model physics. In regard to the convenience of the McICA scheme for modifying subgrid clouds, the impacts of the cloud structure variations are assessed as follows.

### 4.2 The impacts of altering subgrid cloud structures

In this subsection, we discuss the impacts of altering overlapping scheme of fractional clouds and breaking the traditional PPH assumption on simulated radiation and climate.

#### 4.2.1 The impact of altering cloud overlap

In Fig. 7, the top panels show the zonal mean distributions of the fractional contribution by deep convective cloud to total cloud ($f_{\mathrm{con}}/f_{\mathrm{tot}}$) in GCM grid cells. $f_{\mathrm{con}}/f_{\mathrm{tot}}$ has the maximum value in the upper tropics, then decreases sharply with latitude. There is a seasonal variation as shown in DJF and JJA. In the second row of Fig. 7, the latitude–height distributions of the grid-cell mean $L_{\mathrm{cf}}$ calculated using Eq. (8) are shown. In general, $L_{\mathrm{cf}}$ reaches its maximum value in upper tropics, and decreases with latitude, similar to the distribution of $f_{\mathrm{con}}/f_{\mathrm{tot}}$. That the decorrelation length tends to increase upwards has also been alluded by Barker (2008) and Räisänen et al. (2004).

In the bottom panels of Fig. 7, the zonal mean vertically averaged $L_{\mathrm{cf}}$ (solid lines) is shown. Also shown is the Shonk et al. (2010) function result based merely on latitude (dashed lines). It is found that $L_{\mathrm{cf}}$ not only depends on geographical location but also has seasonal variation as indicated in DJF and JJA. Therefore, it is difficult to parameterize $L_{\mathrm{cf}}$ only based on latitude. Though the scheme of N_GOF is not directly from observations, the result shown is very close to that derived from CloudSat/CALIPSO observations (see Fig. 1 in Oreopoulos et al., 2012). Through comparison with

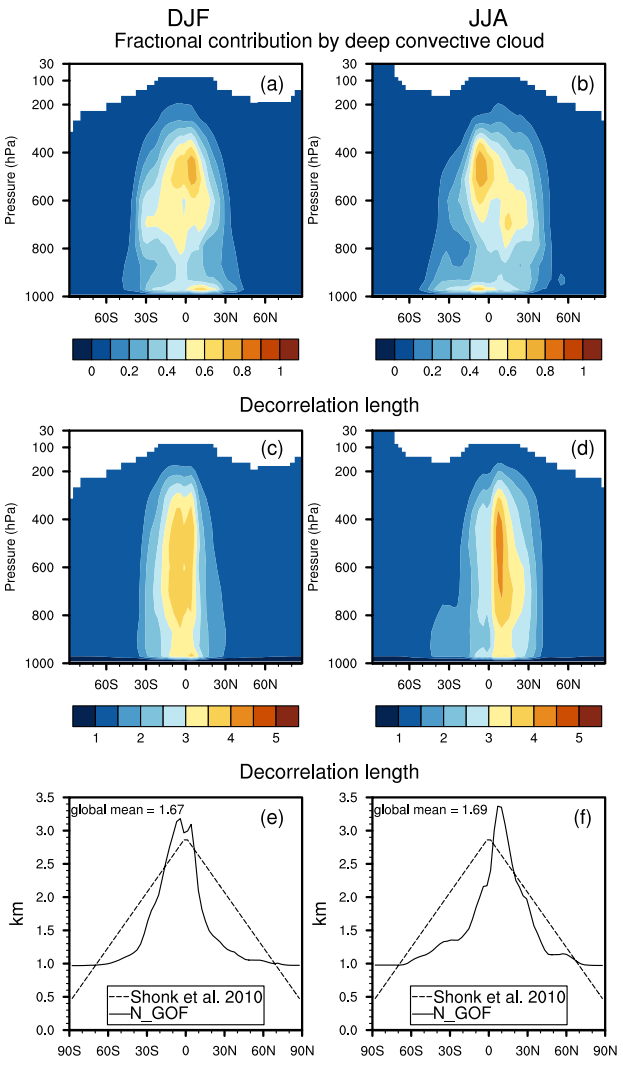


**Fig. 7.** Zonal annual mean **(a, b)** fractional contribution by deep convective cloud fraction ($f_{\mathrm{con}}/f_{\mathrm{tot}}$) and **(c, d)** $L_{\mathrm{cf}}$ calculated using Eq. (8) from the N_GOF run, as well as **(e, f)** the vertically averaged $L_{\mathrm{cf}}$ for N_GOF (solid lines) and that used by Shonk et al. (2010) (dashed lines), for DJF (left) and JJA (right).

the standard scheme of N_GO2, the impact of cloud-type-related $L_{\mathrm{cf}}$ can be explored.

In the upper panels of Fig. 8, the changes in total cloud fraction between N_GOF and N_GO2 are shown for DJF and JJA. Compared to N_GO2, N_GOF yields fewer clouds in low latitudes of the summer hemisphere, and generally produces more clouds in the middle and high latitudes. This is clearly seen in the zonal mean results presented in the lower panels (black lines). In the regions with more strongly convective clouds, the larger $L_{\mathrm{cf}}$ causes a larger possibility for maximum overlap, which leads to less cloud fraction. The same argument applies to the regions with fewer convective clouds. In the lower panels, the changes in zonal mean cloud fraction by N_GOF–N_GO2 for low, middle and

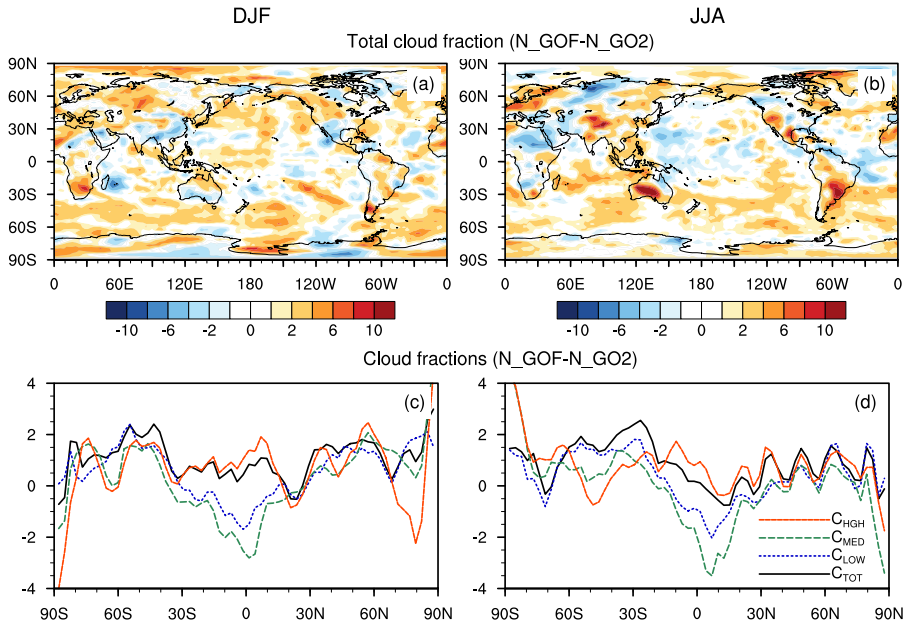


**Fig. 8.** Differences in **(a, b)** total cloud fraction between N_GOF and N_GO2, and **(c, d)** zonal mean differences in total ($C_{\mathrm{TOT}}$), low ($C_{\mathrm{LOW}}$), middle ($C_{\mathrm{MED}}$), and high ($C_{\mathrm{HGH}}$) cloud fractions between N_GOF and N_GO2, for DJF (left) and JJA (right).

high clouds are presented separately. For the low and middle clouds, it is found that the cloud fraction generally decreases in the tropics and increases in the middle and high latitudes, which is consistent with the total cloud fraction. However, for high clouds, N_GOF generally produces a larger cloud fraction compared to N_GO2 even in the tropics. As the cloud fractions in individual layers do not change notably, the increased high cloud fraction is mostly because the decorrelation length in the upper troposphere is smaller in N_GOF than in N_GO2. Fewer low/middle clouds in the tropics causes more solar radiation to reach the lower atmosphere and surface, because high clouds have smaller impact on solar radiation compared to the low/middle clouds. The extra solar heating in the lower atmosphere and surface can enhance the surface evaporation and atmospheric convection, which then can produce more cirrus clouds (Emmanuel, 1994).

In the top panels of Fig. 9, the differences in SW CRF between N_GOF and N_GO2 are shown. The differences in SW CRF can exceed $15\,\mathrm{W\,m^{-2}}$ over a large domain in the tropical regions. In the regions with more convective clouds (for instance, the summer northern Indian Ocean and tropical Atlantic Ocean), the larger chance of maximum overlap leads to less cloud solar reflection, and thereby less SW CRF (positive differences between N_GOF and N_GO2). Similarly, in the regions with fewer convective clouds (for instance, the summer Arctic and winter Southern Hemisphere oceans), the difference between the two schemes becomes negative. The zonal mean results show that SW CRF generally increases in the tropics and decreases in the middle and high latitudes.

The middle panels of Fig. 9 show the differences in LW CRF between N_GOF and N_GO2. In the regions with more convective clouds, the smaller cloud fraction shades less longwave radiation from reaching outer space, thereby causing less LW CRF. Similarly, in the regions of fewer convective clouds, LW CRF is increased. The zonal mean results show that the LW CRF is generally increased by N_GOF in the middle and high latitudes. However the change in the tropics is small. LW CRF is strongly dependent on high clouds. As shown in Fig. 8, the change in high cloud fraction in the tropics is different from that in low/middle clouds.

The changes of SW and LW CRFs are generally opposite. For example, over the summer northern Indian Ocean and tropical Atlantic Ocean, a positive SW CRF difference corresponds to a negative LW CRF difference. However, the solar effect is generally stronger than that of longwave. The net effect in the total CRF does not cancel out. In the lower panels of Fig. 9, the differences in total CRF are shown. From the zonal mean result, a more strongly positive CRF in the summer Arctic is clearly seen. Despite the obvious differences of CRFs at the TOA in different latitudes, the global mean differences in net fluxes are small (Fig. 1b, h) at the TOA, due to compensation between latitudes.

By using diagnostic calculations, Shonk and Hogan (2010) and Oreopoulos et al. (2012) found that more maximum-like cloud overlap leads to decreases in the magnitude of SW and LW CRFs with local maximum shift on an order of $10\,\mathrm{W\,m^{-2}}$, which is consistent with our convective–stratiform contrast scheme. One advantage of the cloud-dependent decorrelation length described in this article is

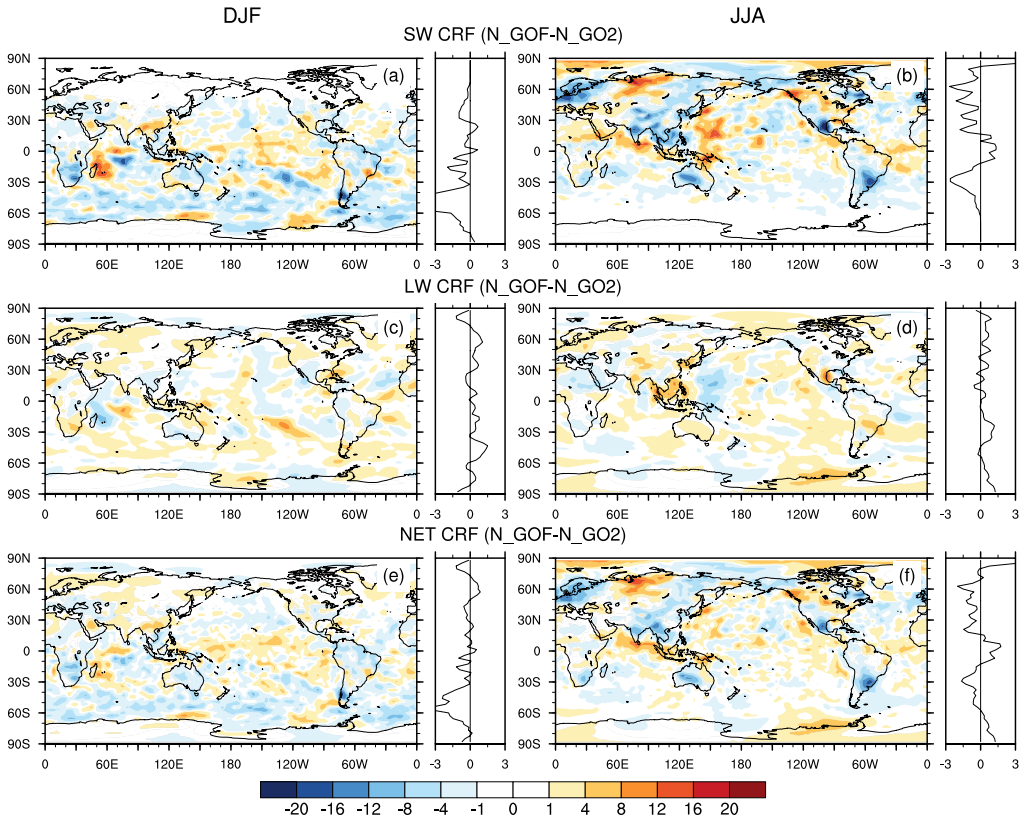


**Fig. 9.** Differences in **(a, b)** SW CRF, **(c, d)** LW CRF, **(e, f)** net CRF at the TOA between N_GOF and N_GO2, for DJF (left) and JJA (right).

that it can respond to climate change (i.e., if the distribution of convective cloud changes in a climate change experiment, so will the decorrelation length). This is not the case for the latitude-dependent and Julian-day-dependent decorrelation parameterizations of Shonk and Hogan (2010) and Oreopoulos et al. (2012).

In Fig. 10, the top panels show the change in net radiative flux at the TOA, which is equivalent to the change in energy balance at the TOA. It is found that the energy balance at the TOA has been considerably affected by addressing the cloud-type-related $L_{\mathrm{cf}}$. N_GOF leads to an obvious increase of net flux in the tropics (especially for the JJA season) and high-latitude regions. In the subtropical high-pressure regions, the change in net flux is relatively small because the cloud fraction is low there. The change in energy balance from the tropics to the subtropical high regions can influence Hadley circulation. The same as the result at TOA, the largest changes in surface energy balance occur in the tropics and high latitudes. It is worth emphasizing that the change in energy balance in Arctic is large, which should have very strong impact on the evolution of sea ice. Investigating the impact on polar climate by N_GOF will be a subsequent work for us.

Figure 11a and b are the land surface temperature differences between N_GOF and N_GO2. The patterns are similar to those of the differences in net CRF at the surface as shown in Fig. 10c and d over land. For DJF, most land surfaces are simulated warmer by N_GOF than by N_GO2, as net CRF over these areas is more positive for N_GOF. The JJA season sees more negative differences between N_GOF and N_GO2. The range of differences is generally between $-3$ and 3 K.

### 4.2.2 The impact of breaking the PPH assumption

In this subsection, we briefly consider the impact of breaking the traditional PPH assumption on the simulated radiation and climate by comparing the N_GOF_IH and N_GOF tests, where N_GOF_IH employs the same vertical overlap scheme as N_GOF but with consideration of the horizontal inhomogeneity in cloud condensate as discussed in Sect. 3.

From a global mean perspective, the changes in CRFs and net fluxes caused by including horizontally inhomogeneous cloud condensate (Eq. 9) are as large as or even larger than the changes from altering the cloud overlap assumptions (see N_GOF_IH in Fig. 1), which has also been shown by calculations from cloud-resolving models (Barker and Räisänen, 2005). The global mean reductions in LW and SW CRFs at the TOA are about 1.5 and 3.7 $\mathrm{W\,m^{-2}}$, respectively. These are a little smaller than the 2.02 and 6.15 $\mathrm{W\,m^{-2}}$ in Shonk and Hogan (2010) using the ERA-40 data set, but larger than the 0.7 and 2.2 $\mathrm{W\,m^{-2}}$ in Räisänen et al. (2007) using the

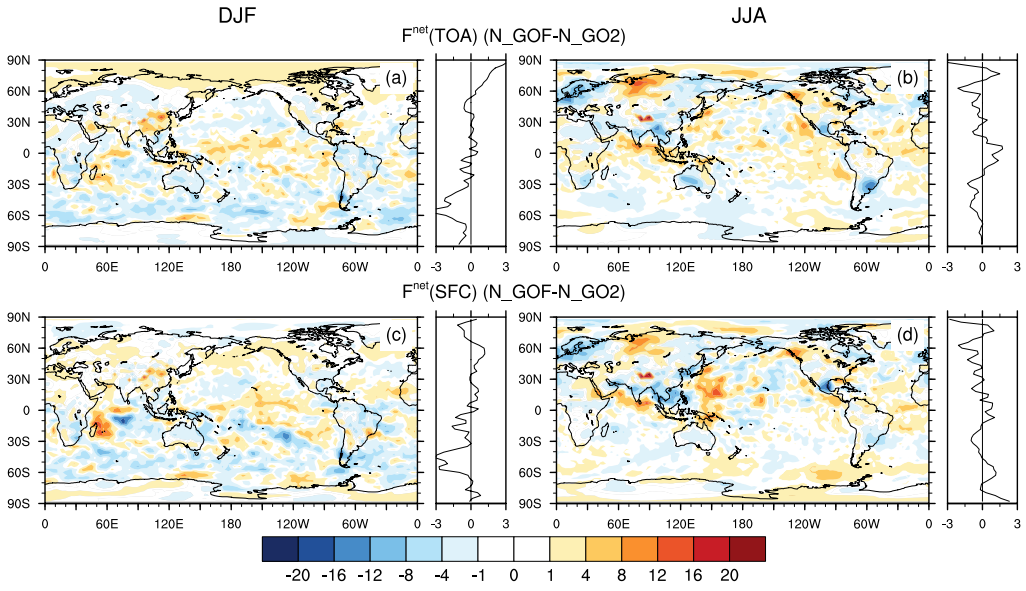


**Fig. 10.** Differences in net radiative budget **(a, b)** at the TOA and **(c, d)** at the surface between N_GOF and N_GO2, for DJF (left) and JJA (right).

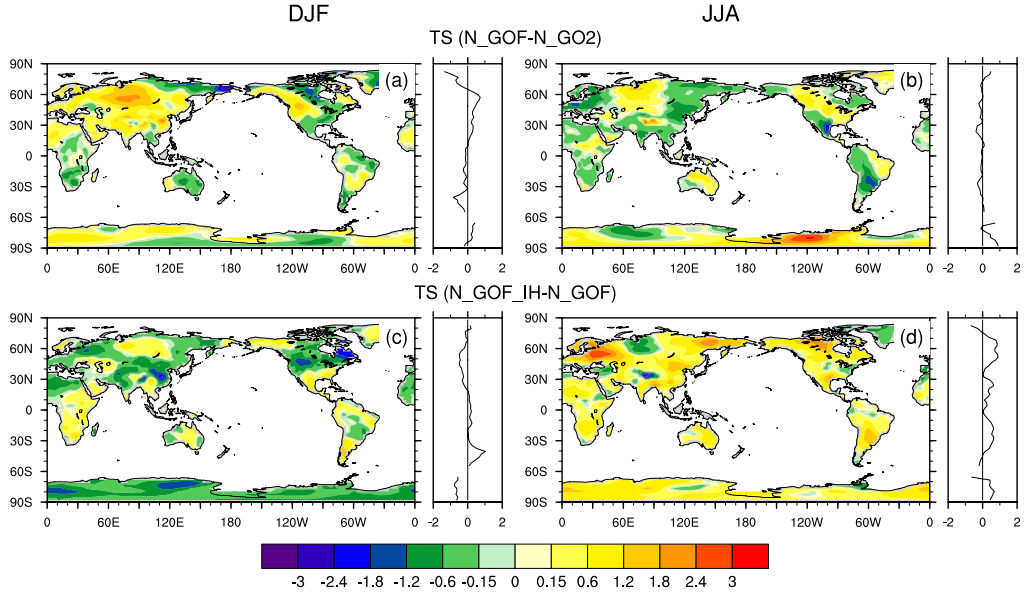


**Fig. 11.** Differences in simulated surface temperature **(a, b)** between N_GOF and N_GO2 and **(c, d)** between N_GOF_IH and N_GOF, for DJF (left) and JJA (right).

ECHAM5 data set. Both of these two are offline calculations; thus no climate interactions are included. The consideration of horizontally inhomogeneous clouds here brings the global mean CRFs and $F^{\text{net}}$ much closer to observations. In general, N_GOF_IH is the best among all the simulations in terms of the global mean radiative fluxes. However, the spatial distributions of CRF biases of N_GOF_IH are similar to those of other simulations (see Fig. 12), which requires revision of not only the radiation scheme but also the other parts of the model.

Figure 13 shows the differences in LW and SW CRFs between N_GOF_IH and N_GOF for DJF and JJA. It is seen that the inclusion of cloud horizontal inhomogeneity weakens the negative SW CRF nearly everywhere, with local maximum increase of more than 20 W m$^{-2}$ over the western Pacific warm pool region. This is qualitatively consistent with the well-accepted conclusion that the PPH assumption of

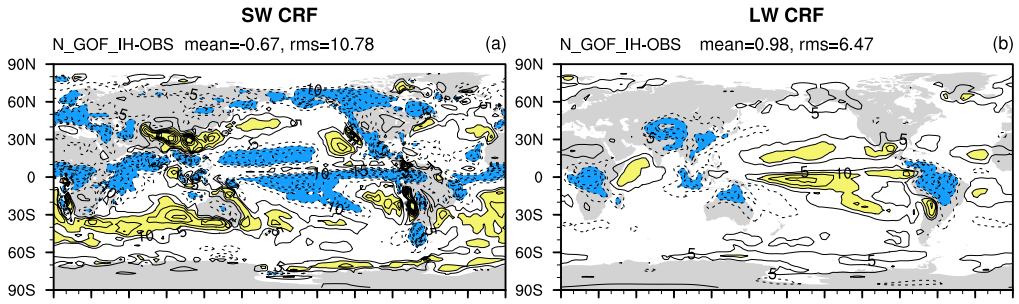


**Fig. 12.** The same as Fig. 3 **(c, d)**, but for the simulation N_GOF_IH.

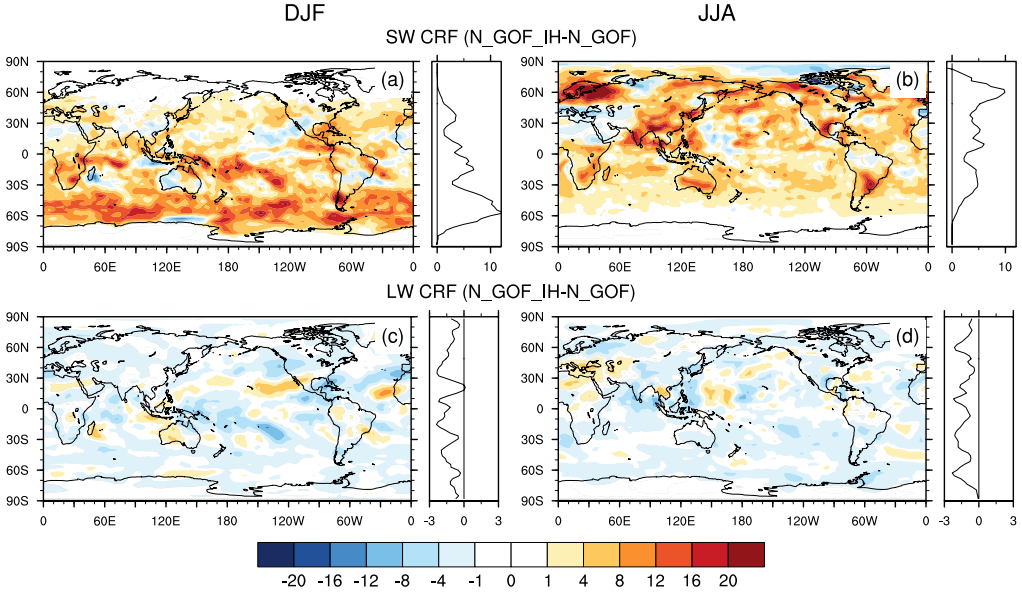


**Fig. 13.** Differences in **(a, b)** SW CRF and **(c, d)** LW CRF between N_GOF_IH and N_GOF, for DJF (left) and JJA (right).

cloud condensate generally overestimates solar reflectance (Carlin et al., 2002). The zonal mean results show that enhancements of SW CRF mostly happen in high latitudes for both the boreal summer and austral summer. Barker and Räisänen (2005) got very similar zonal distribution of SW sensitivity to cloud inhomogeneity by computing on a CSRM data set, with zonal maximum of as large as $\sim 25\,\mathrm{W\,m^{-2}}$ around 60° S.

The inclusion of horizontal inhomogeneity of cloud condensate generally reduces LW CRF all over the globe (Fig. 13c, d). This is because the PPH assumption of cloud condensate generally overestimates the LW emissivity upwards (Pomroy and Illingworth, 2000). The patterns of change in SW and LW CRFs are very similar. However, the zonal mean results of LW CRF do not show very special features in the boreal or austral summer. This is also similar to results of Barker and Räisänen (2005). LW CRF shows less dependence on season probably because LW CRF does not increase proportionally with the incoming solar flux at the TOA.

The magnitude of the local change of CRFs by addressing cloud inhomogeneity is about the same as changing $L_{\mathrm{cf}}$ (compared with Fig. 10). Thus, it is of great importance to address the cloud water/ice horizontal distribution together with the overlap of fractional clouds in GCMs.

The consideration of cloud horizontal inhomogeneity has a noticeable influence on surface temperature (see Fig. 11c, d). In the middle and high latitudes of the Northern Hemisphere, there is a remarkable decrease in surface temperature during DJF and an increase during JJA. These changes arise mainly from competition between LW cooling and SW heating. When inhomogeneous clouds succeed homogeneous ones, more LW flux is emitted outward, and more SW flux penetrates to the surface (see Fig. 1). The surface energy budget is then the net effect of the two fluxes.

In general, the modifications of cloud subgrid configurations have distinct impacts on the simulated radiation budget and surface temperature. Considering the improved LW and SW budget for clear-sky and all-sky conditions, the new

model configuration can be used in BCC_AGCM2.0.1 to improve physical processes and perform climate simulations.

It should be noted that, in this work, we altered only the subgrid cloud structures used in the radiation calculation, whereas those in precipitation parameterization were not changed. Physically, cloud overlap assumptions in the radiation and precipitation processes should be consistent with each other, but the latter may have a larger effect on the simulated precipitation (Morcrette and Jakob, 2000). However, this is beyond the scope of this study.

## 5 Discussion and conclusions

In this work, the BCC-RAD radiation algorithm was incorporated into the BCC_AGCM2.0.1 GCM as a replacement for the original radiation algorithm. The new radiation is entirely distinct from the original one, by including the advanced treatments of gaseous absorption, cloud optics and radiation transfer. The results show that the new scheme markedly improves the representation of the SW and LW radiation budget for both clear-sky and all-sky conditions, whether in the global mean or in geographic distribution. The simulated relationship between SW and LW CRFs in deep convective regions is improved by the new scheme as well. The modeled temperature and specific humidity benefited from changes in the LW heating rate, resulting in a reduction in temperature biases by 0.4–0.8 K at the middle troposphere and a reduction in moisture biases by one-third in the tropical lower troposphere relative to the ERA-Interim reanalysis. This shows the superiority of a CKD radiation algorithm to the band-model-based CAM3 radiation scheme. All these results indicate that using the BCC-RAD radiation scheme makes the cloud-radiation process more intrinsically coherent and reasonable.

The McICA scheme was applied to the BCC-RAD radiation algorithm to deal with cloud subgrid variability. This new configuration is flexible for treating arbitrarily complex subgrid cloud structures, including the vertical overlap of fractional clouds and the horizontal distribution of cloud condensate. The impact of altering cloud overlap within the McICA scheme was assessed by including a so-called "general overlap" with a global constant $L_{cf}$ of 2 km. In this work we have also considered a cloud-type-related $L_{cf}$, which especially distinguishes the deep convective cloud from other types of clouds. This scheme yields a similar zonal mean distribution of $L_{cf}$ compared to the CloudSat/CALIPSO result demonstrated by Oreopoulos et al. (2012). One advantage of the cloud-dependent decorrelation length described in this article is that it can respond to climate change. The new cloud-type-related $L_{cf}$ has remarkable effect on local radiation budget compared to the scheme of constant $L_{cf}$. In the regions of frequent convection such as South Asia monsoon region and ITCZ, CRF is most notably influenced, with local differences of $> 20\,\mathrm{W\,m^{-2}}$ for SW CRF and $> 10\,\mathrm{W\,m^{-2}}$ for LW CRF. Generally, more net energy reaches surface around the tropics while less reaches the surface in mid–high latitudes. This could enhance the simulated Hadley circulation. Therefore, a constant value of $L_{cf}$ could lead to large biases in climate simulations.

The effect of the horizontal inhomogeneity of cloud condensate was then considered by including an observation-based gamma function in an additional test. The changes compared with its PPH counterpart were strikingly significant, with decreases in the global mean TOA LW and SW CRFs of $\sim 1.5\,\mathrm{W\,m^{-2}}$ and $\sim 3.7\,\mathrm{W\,m^{-2}}$, respectively, making the simulation much closer to observations. This emphasizes the importance of addressing the cloud horizontal distribution in GCMs along with the cloud overlap issue.

For simulated climate, the changes in cloud structures showed a notable effect on surface temperatures in mid–high latitudes, with the largest zonal mean differences being about 1 K, exceeding the differences between the new and old radiation scheme configurations when both use the maximum-random overlap and PPH assumptions. This will exert an effect on the evolution of sea ice. In this work, we did not include sea–atmosphere interaction, which could enlarge the effect of the signal imposed by the changing cloud structures.

This study shows that N_GOF_IH is the current best choice for climate simulations, and it will be adopted in BCC_AGCM2.0.1.

This study also provided a direction for future improvement of the McICA. More realistic cloud overlap assumption or cloud horizontal distribution, achieved from satellite observations or any other objective sources, could be used to constrain the generation of cloud-type-related $L_{cf}$ and the horizontal distribution of cloud condensate.

*Acknowledgements.* This work was financially supported by National Basic Research Program of China (2011CB403405 & 2012CB955303), the National Natural Science Foundation of China (grant nos. 41075056) and Public Meteorology Special Foundation of MOST (GYHY201406023). The authors would like to thank Howard W. Barker and Jason N. Cole for providing the McICA and SCG codes, and thank the two anonymous reviewers for their helpful and constructive suggestions.

Edited by: W. Hazeleger

## References

Barker, H. W.: Overlap of fractional cloud for radiation calculations in GCMs: A global analysis using CloudSat and CALIPSO data. J. Geophys. Res., 113, D00A01, doi:10.1029/2007JD009677, 2008.

Barker, H. W. and Räisänen, P.: Radiative sensitivities for cloud structural properties that are unresolved by conventional GCMs, Q. J. Roy. Meteorol. Soc., 131, 3103–3122, 2005.

Barker, H. W., Cole, J. N. S., Morcrette, J. J., Pincus, R., Räisänen, P., von Salzen, K., and Vaillancourt, P. A.: The Monte Carlo

independent column approximation: an assessment using several global atmospheric models, Q. J. Roy. Meteorol. Soc., 134, 1463–1478, 2008.

Baum, B. A., Heymsfield, A. J., Yang, P., and Bedka, S. T.: Bulk Scattering Properties for the Remote Sensing of Ice Clouds. Part I: Microphysical Data and Models, J. Appl. Meteorol., 44, 1885–1895, 2005.

Baum, B. A., Yang, P., Heymsfield, A. J., Schmitt, C., Xie, Y., Bansemer, A., Hu, Y. X., and Zhang, Z.: Improvements to shortwave bulk scattering and absorption models for the remote sensing of ice clouds, J. Appl. Meteorol. Clim., 50, 1037–1056, 2011.

Briegleb, B. P.: Delta-Eddington approximation for solar radiation in the NCAR Community Climate Model, J. Geophys. Res., 97, 7603–7612, 1992.

Carlin, B., Fu, Q., Lohmann, U., Mace, G. G., Sassen, K., and Comstock, J. M.: High-Cloud Horizontal Inhomogeneity and Solar Albedo Bias, J. Climate, 15, 2321–2339, 2002.

Clough, S. A. and Iacono, M. J.: Line-by-line calculation of atmospheric fluxes and cooling rates 2: Application to carbon dioxide, ozone, methane, nitrous oxide and the halocarbons, J. Geophys. Res., 100, 16519–16535, 1995.

Coakley, J. A., Cess, R. D., and Yurevich, F. B.: The Effect of Tropospheric Aerosols on the Earth'sRadiation Budget: A Parameterization for Climate Models, J. Atmos. Sci., 40, 116–138, 1983.

Collins, W. D.: Parameterization of Generalized Cloud Overlap for Radiative Calculations in General Circulation Models, J. Atmos. Sci., 58, 3224–3242, 2001.

Collins, W. D., Hackney, J. K., and Edwards, D. P.: An updated parameterization for infrared emission and absorption by water vapor in the National Center for Atmospheric Research Community Atmosphere Model, J. Geophys. Res., 107, 4664, doi:10.1029/2001JD001365, 2002.

Ebert, E. E. and Curry, J. A.: A Parameterization of Ice Cloud Optical Properties for Climate Models, J. Geophys. Res., 97, 3831–3836, 1992.

Ellingson, R. G., Ellis, J., and Fels, S.: The Intercomparison of Radiation Codes Used in Climate Models: Long Wave Results, J. Geophys. Res., 96, 8929–8953, 1991.

Emmanuel, K. A.: Atmospheric Convection, Oxford: Oxford University Press, 580 pp., 1994.

Fu, Q.: An Accurate Parameterization of the solar radiative properties of cirrus clouds for climate models, J. Climate, 9, 2058–2082, 1996.

Fu, Q. and Liou, K. N.: On the Correlated $k$-Distribution Method for Radiative Transfer in Nonhomogenecous Atmospheres, J. Atmos. Sci., 49, 2139–2156, 1992.

Gong, S. L., Barrie, L. A., Blanchet, J. P., von Salzen, K., Lohmann, U., Lesins, G., Spacek, L., Zhang, L. M., Girard, E., Lin, H., Leaitch, R., Leighton, H., Chylek, P., and Huang, P.: Canadian Aerosol Module: A size-segregated simulation of atmospheric aerosol processes for climate and air quality models 1. Module development, J. Geophys. Res., 108, 4007, doi:10.1029/2001JD002002, 2003.

Hill, P. G., Manners, J., and Petch, J. C.: Reducing noise associated with the Monte Carlo Independent Column Approximation for weather forecasting models, Q. J. Roy. Meteorol. Soc., 137, 219–228, 2011.

Hogan, R. J. and Illingworth, A. J.: Deriving cloud overlap statistics from radar, Q. J. Roy. Meteorol. Soc., 128, 2903–2909, 2000.

Hong, G., Yang, P., Baum, B. A., Heymsfield, A. J., and Xu, K. M.: Parameterization of Shortwave and Longwave Radiative Properties of Ice Clouds for Use in Climate Models, J. Climate, 22, 6287–6312, 2009.

Kiehl, J. T. and Briegleb, B. P.: A new parameterization of the absorptance due to the 15 µm band system of carbon dioxide, J. Geophys. Res., 96, 9013–9019, 1991.

Kiehl, J. T. and Ramanathan, V.: Comparison of Cloud Forcing Derived From the Earth Radiation Budget Experiment with That Simulated by the NCAR Community Climate Model, J. Geophys. Res., 95, 11679–11698, 1990.

Kiehl, J. T., Hack, J. J., and Briegleb, B. P.: The simulated Earth radiation budget of the National Center for Atmospheric Research Community Climate Model CCM2 and comparisons with the Earth Radiation Budget Experiment (ERBE), J. Geophys. Res., 99, 20815–20827, 1994.

Kratz, D. P.: The correlated $k$-distribution technique as applied to the AVHRR channels, J. Quant. Spectrosc. Ra., 53, 501–517, 1995.

Kristjansson, J. E., Edwards, J. M., and MitChell, D. L.: Impact of a new scheme for optical properties of ice crystals on climates of two GCMs, J. Geophys. Res., 105, 10063–10079, 2000.

Li, J. and Barker, H. W.: A Radiation Algorithm with Correlated-k Distribution. Part I: Local Thermal Equilibrium, J. Atmos. Sci., 62, 286–309, 2005.

Loeb, N. G., Wielicki, B. A., Doelling, D. R., Smith, G. L., Keyes, D. F., Kato, S., Manalo-Smith, N., and Wong, T.: Toward optimal closure of the Earth's top-of-atmosphere radiation budget, J. Climate, 22, 748–766, 2009.

Lu, P., Zhang, H., and Jing, X. W.: The effects of different HITRAN versions on calculated long-wave radiation and uncertainty evaluation, Acta Meteorol. Sin., 26, 389–398, 2012.

Mace, G. G. and Benson-Troth, S.: Cloud-Layer Overlap Characteristics Derived from Long-Term Cloud Radar Data, J. Climate, 15, 2505–2515, 2002.

Mishchenko, M. I., Travis, L. D., and Lacis, A. A.: Scattering, Absorption, and Emmision of Light by Small Particles, Cambridge University press, 2002.

Mlawer, E. J., Taubman, S. J., Brown, P. D., Iacono, M. J., and Clough, S. A.: Radiative transfer for inhomogeneous atmospheres: RRTM, a validated correlated-k model for the longwave, J. Geophys. Res., 102, 16663–16682, 1997.

Morcrette, J. J. and Jakob, C.: The Response of the ECMWF Model to Changes in the Cloud Overlap Assumption, Mon. Weather Rev., 128, 1707–1732, 2000.

Morcrette, J. J., Barker, H. W., Cole, J. S., Iacono, M. J., and Pincus, R.: Impact of a new radiation package, McRad, in the ECMWF Integrated Forecasting System, Mon. Weather Rev., 136, 4773–4798, doi:10.1175/2008MWR2363.1, 2008.

Nakajima, T., Tsukamoto, M., Tsushima, Y., Numaguti, A., and Kimura, T.: Modeling of the Radiative Process in an Atmospheric General Circulation Model, Appl. Optics, 39, 4869–4878, 2000.

Naud, C. M., Del Genio, A., Mace, G. G., Benson, S., Clothiaux, E. E., and Kollias, P.: Impact of Dynamics and Atmospheric State on Cloud Vertical Overlap, J. Climate, 21, 1758–1770, 2008.

Neale, R. B., Chen, C. C., Andrew, G., Lauritzen, P. H., Park, S., Williamson, D. L., Conley, A. J., Garcia, R., Kinnison, D., Lamarque, J. F., Marsh, D., Mills, M., Smith, A. K., Tilmes, S., Vitt, F., Morrrison, H., Cameron-Smith, P.,

Collins, W. D., Iacono, M. J., Easter, R. C., Ghan, S. J., Liu, X., Rasch, P. J., and Taylor, M. A.: Description of the NCAR Community Atmosphere Model (CAM 5.0). NCAR Tech. Note TN-486, available at: http://www.cesm.ucar.edu/models/cesm1.2/cam/docs/description/cam5_desc.pdf (last access: 30 April 2014), 2010.

Neggers, R. A. J., Heus, T., and Siebesma, A. P.: Overlap statistics of cumuliform boundary-layer cloud fields in large-eddy simulations, J. Geophys. Res., 116, D21202, doi:10.1029/2011JD015650, 2011.

Oleson, K. W., Bonan, G. B., Schaaf, C., Gao, F., Jin, Y., and Strahler, A.: Assessment of global climate model land surface albedo using MODIS data, Geophys. Res. Lett., 30, 1443, doi:10.1029/2002GL016749, 2003.

Oreopoulos, L., Lee, D., Sud, Y. C., and Suarez, M. J.: Radiative impacts of cloud heterogeneity and overlap in an atmospheric General Circulation Model, Atmos. Chem. Phys., 12, 9097–9111, doi:10.5194/acp-12-9097-2012, 2012.

Pincus, R., Barker, H. W., and Morcrette, J. J.: A fast, flexible, approximate technique for computing radiative transfer in inhomogeneous cloud fields, J. Geophys. Res., 108, 4376, doi:10.1029/2002JD003322, 2003.

Pomroy, H. R. and Illingworth, A. J.: Ice cloud inhomogeneity: Quantifying bias in emissivity from radar observations, Geophys. Res. Lett., 27, 2101–2104, 2000.

Räisänen, P. and Barker, H. W.: Evaluation and optimization of sampling errors for the Monte Carlo Independent Column Approximation, Q. J. Roy. Meteorol. Soc., 130, 2069–2085, 2004.

Räisänen, P. and Järvinen, H.: Impact of cloud and radiation scheme modifications on climate simulated by the ECHAM5 atmospheric GCM, Q. J. Roy. Meteorol. Soc., 136, 1733–1752, 2010.

Räisänen, P., Barker, H. W., Khairoutdinov, M. F., Li, J., and Randall, D. A.: Stochastic generation of subgrid-scale cloudy columns for large-scale models, Q. J. Roy. Meteorol. Soc., 130, 2047–2067, 2004.

Räisänen, P., Järvenoja, S., Järvinen, H., Giorgetta, M., Roeckner, E., Jylhä, K., and Ruosteenoja, K.: Tests of Monte Carlo Independent Column Approximation in the ECHAM5 Atmospheric GCM, J. Climate, 20, 4995–5011, 2007.

Ramanathan, V. and Downey, P.: A nonisothermal emissivity and absorptivity formulation for water vapor, J. Geophys. Res., 91, 8649–8666, 1986.

Randles, C. A., Kinne, S., Myhre, G., Schulz, M., Stier, P., Fischer, J., Doppler, L., Highwood, E., Ryder, C., Harris, B., Huttunen, J., Ma, Y., Pinker, R. T., Mayer, B., Neubauer, D., Hitzenberger, R., Oreopoulos, L., Lee, D., Pitari, G., Di Genova, G., Quaas, J., Rose, F. G., Kato, S., Rumbold, S. T., Vardavas, I., Hatzianastassiou, N., Matsoukas, C., Yu, H., Zhang, F., Zhang, H., and Lu, P.: Intercomparison of shortwave radiative transfer schemes in global aerosol modeling: results from the AeroCom Radiative Transfer Experiment, Atmos. Chem. Phys., 13, 2347–2379, doi:10.5194/acp-13-2347-2013, 2013.

Rasch, P. J. and Kristjansson, J. E.: A comparison of the CCM3 model climate using diagnosed and predicted condensate parameterizations, J. Climate, 11, 1587–1614, 1998.

Rayner, N. A., Parker, D. E., Horton, E. B., Folland, C. K., Alexander, L. V., Powell, D. P., Kent, E. C., and Kaplan, A.: Global analyses of sea surface temperature, sea ice, and night marine air temperature since the late nineteenth century, J. Geophys. Res., 108, 4407, doi:10.1029/2002JD002670, 2003.

Reynolds, R. W., Rayner, N. A., Smith, T. M., Stokes, D. C., and Wang, W.: An improved in situ and satellite SST analysis for climate, J. Climate, 15, 1609–1625, 2002.

Rothman, L. S., Barbe, A., Chris Benner, D., Brown, L. R., Camy-Peyret, C., Carleer, M. R., Chance, K., Clerbaux, C., Dana, V., Devi, V. M., Fayt, A., Flaud, J. M., Gamache, R. R., Goldman, A., Jacquemart, D., Jucks, K. W., Lafferty, W. J., Mandin, J. Y., Massie, S. T., Nemtchinov, V., Newnham, D. A., Perrin, A., Rinsland, C. P., Schroeder, J., Smith, K. M., Smith, M. A. H., Tang, K., Toth, R. A., Vander Auwera, J., Varanasi, P., and Yoshino, K.: The HITRAN molecular spectroscopic database: edition of 2000 including updates through 2001, J. Quant. Spectrosc. Ra., 82, 5–44, 2003.

Shi, G.-Y., Xu, N., Wang, B., Dai, T., and Zhao, J.-Q.: An improved treatment of overlapping absorption bands based on the correlated *k* distribution model for thermal infrared radiative transfer calculations, J. Quant. Spectrosc. Ra., 110, 435–451, 2009.

Shonk, J. K. P. and Hogan, R. J.: Effect of improving representation of horizontal and vertical cloud structure on the Earth's global radiation budget. Part II: The global effects, Q. J. Roy. Meteorol. Soc., 136, 1205–1215, 2010.

Shonk, J. K. P., Hogan, R. J., Edwards, J. M., and Mace, G. G.: Effect of improving representation of horizontal and vertical cloud structure on the Earth's global radiation budget. Part I: Review and parametrization, Q. J. Roy. Meteorol. Soc., 136, 1191–1204, 2010.

Slingo, A.: A GCM Parameterization for the Shortwave Radiative Properties of Water Clouds, J. Atmos. Sci., 46, 1419–1427, 1989.

Tian, L. and Curry, J. A.: Cloud Overlap Statistics, J. Geophys. Res., 94, 9925–9935, 1989.

Uppala, S. M., KÅllberg, P. W., Simmons, A. J., Andrae, U., da Costa Bechtold, V., Fiorino, M., Gibson, J. K., Haseler, J., Hernandez, A., Kelly, G. A., Li, X., Onogi, K., Saarinen, S., Sokka, N., Allan, R. P., Andersson, E., Arpe, K., Balmaseda, M. A., Beljaars, A. C. M., Van De Berg, L., Bidlot, J., Bormann, N., Caires, S., Chevallier, F., Dethof, A., Dragosavac, M., Fisher, M., Fuentes, M., Hagemann, S., Hólm, E., Hoskins, B. J., Isaksen, L., Janssen, P. A. E. M., Jenne, R., McNally, A. P., Mahfouf, J. F., Morcrette, J. J., Rayner, N. A., Saunders, R. W., Simon, P., Sterl, A., Trenberth, K. E., Untch, A., Vasiljevic, D., Viterbo, P., and Woollen, J.: The ERA-40 re-analysis, Q. J. Roy. Meteorol. Soc., 131, 2961–3012, 2005.

Wei, X. D. and Zhang, H.: Analysis of optical properties of nonspherical dust aerosols, Acta Optica. Sinica, 31, 0501002, doi:10.3788/aos201131.0501002, 2011.

Wu, T. W. and Wu, G. X.: An empirical formula to compute snow cover fraction in GCMs, Adv. Atmos. Sci., 21, 529–535, 2004.

Wu, T., Yu, R., Zhang, F., Wang, Z., Dong, M., Wang, L., Jin, X., Chen, D., and Li, L.: The Beijing Climate Center atmospheric general circulation model: description and its performance for the present-day climate, Clim. Dynam., 34, 123–147, doi:10.1007/s00382-008-0487-2, 2010.

Wyser, K.: The Effective Radius in Ice Clouds, J. Climate, 11, 1793–1802, 1998.

Xie, P. and Arkin, P. A.: Global Precipitation: A 17-Year Monthly Analysis Based on Gauge Observations, Satellite Estimates, and

Numerical Model Outputs, B. Am. Meteorol. Soc., 78, 2539–2558, 1997.

Yan, H.: The design of a nested fine-mesh model over complex topography part 2: parameterization of sub grid physical processes, Plateau Meteorol., 6, 64–139, 1987 (in Chinese).

Yang, P., Wei, H., Huang, H. L., Baum, B. A., Hu, Y. X., Kattawar, G. W., Mishchenko, M. I., and Fu, Q.: Scattering and absorption property database for nonspherical ice particles in the near-through far-infrared spectral region, Appl. Optics., 44, 5512–5523, 2005.

Yang, P., Bi, L., Baum, B. A., Liou, K. N., Kattawar, G. W., Mishchenko, M. I., and Cole, B.: Spectrally consistent scattering, absorption, and polarization properties of atmospheric ice crystals at wavelengths from 02 to 100 µm, J. Atmos. Sci., 70, 330–347, 2013.

Zhang, F., Liang, X. Z., Li, J., and Zeng, Q.: Dominant roles of subgrid-scale cloud structures in model diversity of cloud radiative effect, J. Geophys. Res., 118, 7733–7749, doi:10.1002/jgrd.50604, 2013.

Zhang, G. and Mu, M.: Effects of modification to the Zhang-Mcfarlane convection parameterization on the simulation of the tropical precipitation in the National Center for Atmosphere Research Community Climate Model, Version 3, J. Geophys. Res., 110, D09109, doi:10.1029/2004JD005617, 2005.

Zhang, H., Nakajima, T., Shi, G., Suzuki, T., and Imasu, R.: An optimal approach to overlapping bands with correlated $k$-distribution method and its application to radiative calculations, J. Geophys. Res., 108, 4641, doi:10.1029/2002JD003358, 2003.

Zhang, H., Shi, G., Nakajima, T., and Suzuki, T.: The effect of the choice of the $k$-interval number on radiative calculation, J. Quant. Spectrosc. Ra., 98, 31–43, 2006a.

Zhang, H., Suzuki, T., Nakajima, T., Shi, G., Zhang, X., and Liu, Y.: Effects of band division on radiative calculations, Opt. Eng., 45, 016002, doi:10.1117/1.2160521, 2006b.

Zhang, H., Wang, Z., Wang, Z., Liu, Q., Gong, S., Zhang, X., Shen, Z., Lu, P., Wei, X., Che, H., and Li, L.: Simulation of direct radiative forcing of aerosols and their effects on East Asian climate using an interactive AGCM-aerosol coupled system, Clim. Dynam., 38, 1675–1693, 2012.

Zhou, C. H., Gong, S. L., Zhang, X. Y., Liu, H. L., Xue, M., Cao, G. L., An, X. Q., Che, H. Z., Zhang, Y. M., and Niu, T.: Towards the improvements of simulating the chemical and optical properties of Chinese aerosols using an online coupled model CUACE/Aero, Tellus B, 64, 18965, doi:10.3402/tellusb.v64i0.18965, 2012.

Available online at www.sciencedirect.com

ScienceDirect

Advances in Climate Change Research 5 (2014) 136–141

www.keaipublishing.com/en/journals/accr/

# PM2.5 and tropospheric $O_3$ in China and an analysis of the impact of pollutant emission control

ZHANG Hua[a,*], XIE Bing[a,b], ZHAO Shu-Yun[a,c], CHEN Qi[a,c]

[a] *Laboratory for Climate Studies of China Meteorological Administration, National Climate Center, China Meteorological Administration, Beijing 100081, China*
[b] *Key Laboratory for Semi-Arid Climate Change of the Ministry of Education, College of Atmospheric Sciences, Lanzhou University, Lanzhou 730000, China*
[c] *Chinese Academy of Meteorological Sciences, Beijing 100081, China*

Received 20 February 2014; revised 26 March 2014; accepted 25 April 2014
Available online 19 December 2014

**Abstract**

This study reviewed the status of PM2.5 and tropospheric $O_3$ observations in China (15–55°N, 72–136°E). Initially, the distribution of tropospheric $O_3$ over the globe and China was determined based on satellite observations made during 2010–2013. The annual mean values were 29.78 DU and 33.97 DU over the globe and China, respectively. The distribution of PM2.5 and seasonal changes in concentrations in China were then simulated using an aerosol chemistry–climate coupled model system, with an annual mean value of $0.51 \times 10^{-8}$ kg m$^{-3}$. The contributions from five different aerosols to the simulated PM2.5 concentrations in different seasons were also determined. The relationships among the emissions of aerosols, greenhouse gases and their precursors and radiative forcings were determined with reference to the (IPCC AR5) Intergovernmental Panel on Climate Change the Fifth Assessment Report. From these relationships, the possible effects of controlling $O_3$ precursors and (PM) particulate matter on the climate were considered. The influence of the control of $O_3$ precursors was not totally clear, and reducing emissions of short-lived greenhouse gases and black carbon was considered a secondary measure for short-term (the next 50 years) climate-change mitigation. Reducing emissions of $CO_2$ is still the best strategy for meeting the target of a global average rise in surface air temperature of less than 2 °C. Near- and short-term emission reduction strategies are important for both effective environmental protection and climate-change mitigation.

*Keywords:* Tropospheric $O_3$; PM2.5; Greenhouse gas; Air pollution; Climate change

## 1. Introduction

As society has developed since the industrial revolution, economic productivity has significantly increased. However, the resulting anthropogenic emissions are not only damaging the environment but also dramatically changing the climate. In recent decades, globalization has led to a rapid increase in the emissions of GHGs, which are implicated in the melting of icebergs, a rise in sea levels, and the increased occurrence of extreme weather. Increased emissions of some gases and aerosols have exacerbated pollution problems. In China, the frequent occurrence of large scale smog events in recent years has seriously affected public health. With our environment worsening, a social consensus has emerged suggesting that we should protect the environment and slow the pace of climate change. In its sixteenth session, the Conference of the Parties to the (UNFCCC) United Nations Framework Convention on Climate Change agreed that, to avoid dangerous impacts on the climate system, the increase in the global mean

* Corresponding author.
*E-mail address:* huazhang@cma.gov.cn (ZHANG H.).

Peer review under responsibility of National Climate Center (China Meteorological Administration).

Production and Hosting by Elsevier on behalf of KeAi

http://dx.doi.org/10.1016/j.accre.2014.11.005

1674-9278/Copyright © 2014, National Climate Center (China Meteorological Administration). Production and hosting by Elsevier B.V. on behalf of KeAi. This is an open access article under the CC BY-NC-ND license (http://creativecommons.org/licenses/by-nc-nd/3.0/).

This is an English translational work of an article originally published in Advances in Climate Change Research (Chinese). The original article can be found at: 10.3969/j.issn.1673-1719.2014.04.010.

temperature from the preindustrial level should not exceed 2 °C. Under the difficulty of reducing the emissions of long-lived (GHGs) greenhouse gases in the near future of 50 years, controlling (SLCPs) short lived climate pollutants (such as tropospheric $O_3$, $CH_4$ and BC) may not only effectively slow down climate change, but also improve the environment and protect human health.

## 2. Air pollutants

Large amounts of domestic and industrial waste gases are emitted into the atmosphere by human activities. Air pollution is generated when the accumulation of these substances threatens the survival, health, and development of humans and other organisms. Air pollutants are mainly emitted from transportation and industrial sources (Shindell et al., 2004). Pollutants can be divided into man-made and natural pollutants and also into primary and secondary pollutants. Primary pollutants refer to substances discharged directly from sources, such as carbon monoxide (CO), nitrogen oxide ($N_2O$), sulfur dioxide ($SO_2$), and (PM) particulate matter, whereas secondary pollutants are generated in the atmosphere through chemical and/or photochemical reactions involving primary pollutants. The physical and chemical properties of secondary pollutants, such as sulfate aerosols, nitrate aerosols, and $O_3$, are very different from those of their precursors.

In this study, the distribution of observed and simulated global and Chinese tropospheric $O_3$ and PM2.5 were examined. We considered the need to reduce emissions of aerosol particles, tropospheric $O_3$, and their precursors to control air pollution. The effect on the climate of reducing these air pollutants and means for achieving this aim were also investigated. A simple introduction to PM2.5 and SLCPs (tropospheric $O_3$, BC, and $CH_4$) is given in the following section.

### 2.1. PM2.5

Aerosols are suspended particles or droplets in the atmosphere (Zhang and Wang, 2011), also referred to as PM. PM2.5, which is currently receiving significant attention, is defined as that fraction of PM with an aerodynamically equivalent diameter of 2.5 μm or less (Shindell et al., 2004). PM2.5 can be inhaled into the lungs when breathing. PM2.5 can contain poisonous and harmful substances, and due to its small size and large specific surface area, its impact can be great. It also has a long residence time in the atmosphere, and it can be transported for long distances. Therefore, PM2.5 has a large influence on the atmospheric environment and on human health.

### 2.2. Tropospheric $O_3$

Ozone plays an important role in regulating the Earth's climate. About 90% of atmospheric ozone is distributed in the stratosphere, at 10−30 km above the surface of the Earth, with the remainder located in the troposphere. Stratospheric $O_3$ is crucial for life on the Earth because it absorbs incoming solar ultraviolet radiation. Tropospheric $O_3$ is an important GHG because it absorbs infrared radiation from the surface and heats the atmosphere. Because it is a key component of photochemical smog, tropospheric $O_3$ is also an important air pollutant. There are two main sources of $O_3$ in the troposphere; the first is from the reactions of its precursors ($CH_4$, CO, VOCs, $NO_x$, etc.), and the second is the downward transport of $O_3$ from the stratosphere.

### 2.3. BC

(BC) black carbon aerosol, with a particle size of about 0.01−1 μm, results from the incomplete combustion of fossil fuels, wood, and other biomass. The main sources of BC include industrial coal, automobile exhaust, kitchen smoke, burning forests, and crops. Zhang and Wang (2011) summarized the published research regarding BC and reported that it was a strong absorber of solar and infrared radiation, which can heat the atmosphere. It can also affect cloud formation and reduce snow albedo (Zhang and Wang, 2011; Zhang et al., 2012a; Wang et al., 2011). BC can absorb toxic substances and have an impact on human health when inhaled. In practice, combustion is rarely complete due to technological constraints, and together with BC, CO, (VOCs) volatile organic compounds, and non-volatile organic compounds and (OC) organic carbon aerosol besides $CO_2$, can also be released into atmosphere simultaneously. Of which, BC has tightly relationship with OC. However, unlike BC, OC in the atmosphere has a strong cooling effect, and therefore the mixing ratio of the two forms of carbon from different emission sources is important to understand.

### 2.4. Methane

Methane is an atmospheric trace gas. It is commonly agreed that $CH_4$ is the second most important GHG after $CO_2$. Its atmospheric concentration is far less than $CO_2$, but its growth rate is much larger (the growth rates for $CO_2$ and $CH_4$ since the industrial revolution are 40% and 150% respectively) (Alexander et al., 2013). Methane is a very effective absorber of infrared radiation, and it then reemits infrared radiation with its temperature, thus producing a greenhouse effect in the atmosphere. Furthermore, $CH_4$ is also an important $O_3$ precursor. Therefore, reducing anthropogenic emissions of $CH_4$ would not only slow down the rate of global warming but also protect the environment and human health.

## 3. Distribution of the major air pollutants

### 3.1. Observed air pollutants

Smog events occurred frequently in central and eastern China during January and February 2013. The smog events in 2013 were of a large scale and long duration, and they severely affected the lives of the exposed urban population. The Chinese government has expressed determination to cut the emissions of air pollutants. Recent smog events were not

completely natural phenomena, but were closely related to aerosol particles (PM10 and PM2.5) emitted by human activities (Zhang et al., 2013). Many studies of aerosols have been undertaken in the area based on both the observation and simulation of aerosols. Kim Oanh et al. (2006) selected six cities (Bangkok, Beijing, Chennai, Bandung, Manila, and Hanoi), all of which are influenced by the Asian monsoon, and studied nearly 3,000 air samples from 2001 to 2004. In their study, each city was divided into six representative areas, and each year was divided into dry and wet seasons (wet season: May to October; dry season: the rest of the year). They found that Beijing had the highest concentrations of PM2.5 and PM10 during both the dry and wet seasons. Zhang et al. (2012b) analyzed PM10 samples collected from 2006 to 2007 at 16 stations in China and found that mineral particles accounted for the largest portion (35%) of the material collected (dust, coal smoke, and dust from cities), with sulfate aerosol and OC each accounting for about a further 15%. The main reason for the high concentration of sulfate aerosols was that 70% of the power consumed in China is produced by coal consumption. BC in the PM10 accounted for only about 3.5% of the total sample, with little difference among the different regions. In addition to biomass burning, coal and oil consumption are also important sources of BC (Cao, et al., 2011). Zhang et al. (2013) also measured mass concentrations of PM2.5 in eastern China during the period of 1−16 January, 2013, and found that static stable weather and high aerosol concentrations favored the formation of smog.

Tropospheric $O_3$ absorbs infrared radiation and consequently acts as a strong GHG. Near the surface, $O_3$ is also harmful to human health and plants. There is strong evidence that tropospheric $O_3$ has an adverse effect on plant physiological processes (Ashmore, 2005). In this study, we used $O_3$ profile data collected during 2010−2013 by the Ozone Monitor Instrument to calculate the (TOCC) tropospheric ozone column concentration (shown in Fig. 1). The Ozone Monitor Instrument is housed onboard the Aura spacecraft (AURA satellite data URL: http://aura.gsfc.nasa.gov/), which was launched by the National Aeronautic and Space Administration on 15 July, 2004, as part of the Earth Observing System. The TOCC is influenced by anthropogenic $O_3$ precursors; it is small in equatorial and polar regions and relatively large in the mid-latitudes. The TOCC in the Northern Hemisphere is much larger than that in the Southern Hemisphere. The TOCC maximum value in the Northern Hemisphere is located in bands between 30°N and 60°N, where two low centers exists: the Tibetan Plateau and western North America. In China, the TOCC increases from west to east, with a maximum located in the East China Sea. The TOCC trough in the Tibetan Plateau is due to the increased height of the tropopause in the region and dilution by air with a low $O_3$ concentration from tropical areas (Liu et al., 2010). Liu et al. (2009) reported that the Tibetan Middle Tropospheric Ozone Minimum often occurred at an altitude of 8−13 km over the eastern Tibetan Plateau, accompanied by the Asian summer monsoon. Yin et al. (2006) and An et al. (2007; 2010) studied near-surface $O_3$ concentrations in Jinan, Beijing, and Nanjing, and found that the urban $O_3$ concentration reached a minimum in winter and maximum in summer. During a typical day, the highest concentration of $O_3$ was recorded around 14:00 pm, and the lowest concentration was recorded around 5:00 am. According to the joint report of the World Meteorological Organization and the United Nations Environment Programme (Shindell et al., 2004), China is the largest contributor to global $CH_4$ emissions, accounting for about 18% of the global total, with the total Asian emissions accounting for 45%. The important sources of $CH_4$ are coal exploitation and agricultural activities.

### 3.2. Simulated PM2.5

In this study, we used an aerosol−climate coupled model, BCC_AGCM2.0.1_CUACE/Aero (Zhang et al., 2012a; Zhao et al., 2014), to simulate the aerosol concentration and the distribution of PM2.5 in China and its seasonal variation. BCC_AGCM2.0.1_CUACE/Aero comprises the aerosol model CUACE/Aero that was developed by the Institute of Atmospheric Composition, Chinese Academy of Meteorological Sciences, and the general circulation model BCC_AGCM2.0.1, which was developed by the Beijing Climate Center, China Meteorological Administration. Here, we give a brief description of the aerosol−climate model; more detail can be found in Zhang et al. (2012a) and Zhao et al. (2014). The dynamical equations are an Eulerian spectral formulation. The model has a horizontal T42 spectra resolution (approximately 2.8° × 2.8°) and vertical hybrid δ-pressure coordinates, including 26 layers, with the top located at about 2.9 hPa. Five different tropospheric aerosols were included in the model: sea salt, soil dust, sulfate, OC, and BC. Each type of aerosol was divided into 12 bins as a geometric series, with radii between 0.005 and

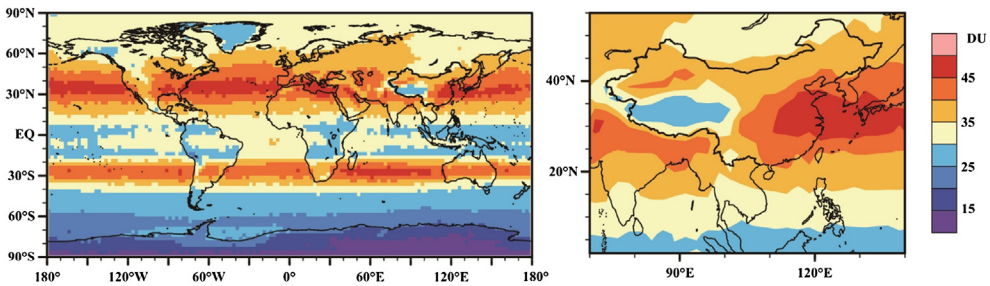


Fig. 1. Distribution of the tropospheric ozone column concentration observed by satellite during 2010−2013.

20.48 μm. The emission data were primarily from AeroCom and included observations of BC (Bond et al., 2004), OC (van der Werf et al., 2004), $SO_2$ and sulfate (van der Werf et al., 2004; Cofala et al., 2005), and dimethyl sulfide (Kettle and Andreae, 2000; Nightingale et al., 2000). Other emission data used were from the Emission Database for Global Atmospheric Research version 3.2, 1995 (Olivier et al., 2002). Sea salt and soil dust emission schemes were developed by Gong et al. (2002) and Marticorena and Bergametti (1995). The simulated distribution of anthropogenic PM2.5 aerosols in China is shown in Fig. 2; the maximum and minimum values of PM2.5 are located in the north and northwest of China. The concentration of anthropogenic aerosol changes obviously with season and is notably high in spring and summer. Additionally, the simulated concentrations of the five typical aerosols in China and the proportion of PM2.5 within them are shown in Table 1. The sulfate and dust aerosols have the largest PM2.5 content (about 85%); dust aerosol has a PM2.5 proportion that is higher than 50% in winter and spring, and reaches 52% as an annual mean. It is likely that dust aerosol is the main constituent of PM2.5 in China. The high concentration of dust aerosol is mainly derived from the deserts located in Mongolia and Northwest China, such as Taklimakan and Badain Jaran. The high concentration of sulfate aerosol is due to power production in China, which is largely dependent on coal. It is estimated that coal will still be the main source of power until 2050 (Kim Oanh et al., 2006). The proportion of sea salt in PM2.5 is less than 5%, which is a consequence of China's geographic location. The annual mean proportion of BC in PM2.5 is 6%, with a stable concentration >0.4 μg $m^{-3}$ year round. The high aerosol concentrations in China can be attributed to the consumption of coal and fuel and domestic emissions associated with the increased economic development and social activities. Zhang et al. (2012a) simulated the global averaged radiative forcing for the five typical aerosols at the top of the atmosphere and at the surface. Only the radiative forcing of BC was positive (heating the atmosphere) at the top of the atmosphere. The radiative forcing of the anthropogenic aerosols in a cloudy atmosphere was −0.23 W $m^{-2}$, which cooled the earth–atmosphere system. Scientists have simulated the distribution of future global PM2.5 using multi-models and found that both

Table 1
The seasonal mean concentrations of five aerosol species in China (unit: μg $m^{-3}$; percentage contribution of each component to the total PM2.5 in brackets).

| Aerosol | Spring | Summer | Autumn | Winter | Annual |
|---|---|---|---|---|---|
| Sulfate | 2.74 (29%) | 2.80 (45%) | 2.22 (40%) | 1.96 (35%) | 2.43 (36%) |
| BC | 0.45 (5%) | 0.43 (7%) | 0.40 (7%) | 0.41 (7%) | 0.42 (6%) |
| OC | 0.26 (3%) | 0.25 (4%) | 0.21 (4%) | 0.18 (3%) | 0.23 (3%) |
| Dust | 5.82 (60%) | 2.40 (39%) | 2.57 (45%) | 2.93 (52%) | 3.43 (52%) |
| Sea salt | 0.14 (2%) | 0.29 (5%) | 0.22 (4%) | 0.14 (3%) | 0.20 (3%) |

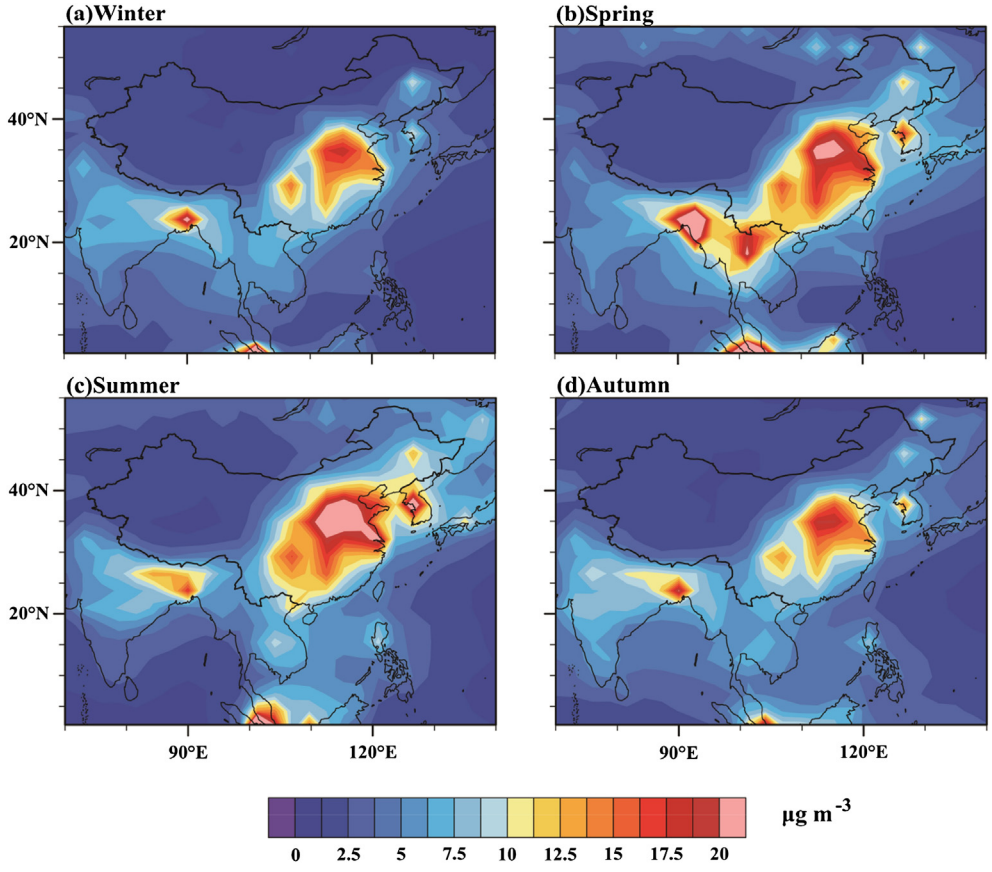


Fig. 2. Distribution of simulated PM2.5 (including only anthropogenic aerosols).

global and regional PM2.5 will be decreased at the end of the 21st century, under four representative concentration pathways (RCP2.6 RCP4.5 RCP6.0, and RCP8.5) used by the IPCC AR5, especially in East Asia (Fiore et al., 2012; Zhao et al., 2013).

## 4. The effects of air pollution mitigation on climate change

### *4.1. Air pollutants and radiative forcing*

The IPCC AR5, released in 2014, related radiative forcing to emissions of GHGs, aerosols, and their precursors for the first time (Qin et al., 2014). The IPCC AR5, directly and indirectly, provides the radiative forcings of air pollutants composed of tropospheric $O_3$, aerosols, and their precursors. Relative to 1750, the total radiative forcing is positive, with the increase in $CO_2$ concentrations being the largest contributor (1.68 [1.33−2.03] W $m^{-2}$) to global warming. The total radiative forcing in 2011 relative to 1750 due to anthropogenic activities was 2.29 [1.13−3.33] W $m^{-2}$, and it has been accelerating since 1970. The total of well-mixed GHGs [$CO_2$, $CH_4$, $N_2O$, and (CFCs) chlorofluorocarbon] is 3.00 [2.22−3.78] W $m^{-2}$. Some of the well-mixed GHGs can be transformed into other components through a series of complex chemical reactions. The total radiative forcing due to the change in their concentration is 2.83 [2.26−3.40] W $m^{-2}$. The radiative forcing due to changes in the $CH_4$ concentration is 0.48 [0.38−0.58] W $m^{-2}$, whereas that due to $CH_4$ emissions is 0.97 [0.74−1.20] W $m^{-2}$, as its effects on tropospheric $O_3$ and stratospheric $H_2O$ double its warming energy. Among the GHGs with a short atmospheric residence time, CO has a warming effect on climate, whereas, $NO_x$ has a negative radiative forcing of −0.15 [−0.34−0.03] W $m^{-2}$. The total radiative forcing of aerosols (including aerosol−cloud interactions) is −0.90 W $m^{-2}$. Most aerosols have negative radiative forcings, with the exception of BC.

### *4.2. The possible effects of the mitigation of $O_3$ precursors and PM on climate change*

To decrease the concentrations of tropospheric $O_3$ and aerosols, efforts should be made to reduce the emissions of important gases and aerosols. As shown in Fig. 3, to control the concentration of tropospheric $O_3$ we must reduce the emissions of $CH_4$, CO, VOCs, and $NO_x$, and to control the concentrations of aerosols, the emissions of $NO_x$, VOCs, $NH_3$, BC, OC, and $SO_2$ must be reduced. However, some contradictory effects should be noted. For example, reducing the emissions of $O_3$ precursors can suppress the $O_3$ concentration, resulting in a cooling effect. Furthermore, of the $O_3$ precursors, $NO_x$ can control the lifetime of $CH_4$ and inhibit the production of aerosols. Consequently, the reduction of $NO_x$ emissions leads to global warming. The mitigation of aerosols leads to overall warming, but there is strong evidence that BC mitigation has a direct cooling effect. The indirect effects of BC, caused by its interaction with clouds, are still unknown and require further study.

## 5. Conclusions

For effective environmental protection, there is a need to reduce emissions of tropospheric $O_3$ and PM2.5 to effectively protect public health, food, water, and the ecosystems on which our survival depends, and to reduce atmospheric pollution events. From the perspective of short-term climate protection, the comprehensive reduction of emissions of SLCPs (including tropospheric $O_3$, $CH_4$, and BC) in the next 50 years may slow down the rate of climate change and reduce future global warming by 0.2−0.7 °C (Shindell et al., 2004). This measure would also protect glaciers and snowfields in Polar Regions, including the Himalayas, from rapid melting.

To reduce the concentration of tropospheric $O_3$, the mitigation of $O_3$ precursors should be considered. Methane, one of the $O_3$ precursors, is also an important GHG, and the reduction of $CH_4$ emissions would provide both global warming

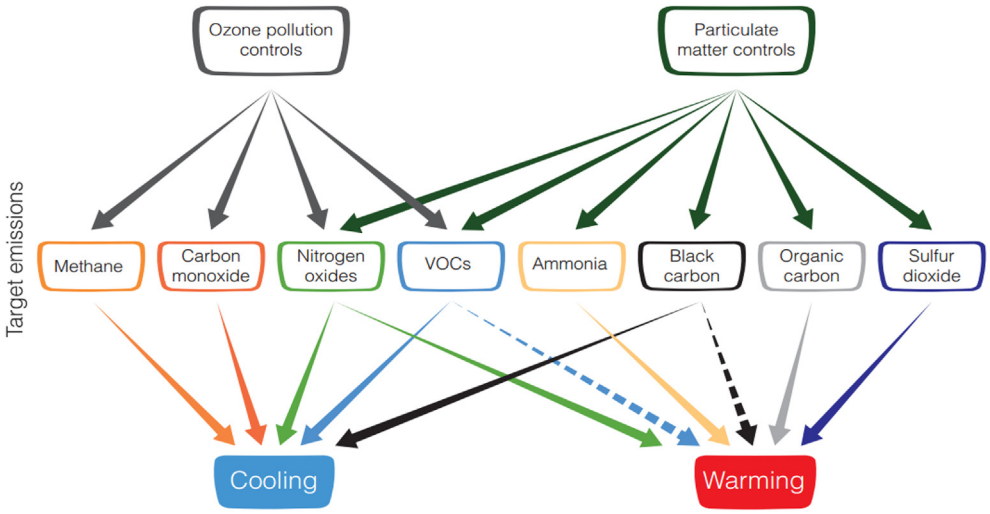


Fig. 3. Schematic diagram of the impacts of pollution control on specific emissions and on climate (from IPCC AR5 (Myhre et al., 2013); the solid black line indicates the known impact, and the dashed line indicates an uncertain impact).

mitigation and environmental protection. The influence of reducing other $O_3$ precursor emissions on the climate is not as clear. The indirect effect of reducing BC emissions requires further studies, but the mitigation of other aerosols will lead to an increase in the global average surface temperature.

It should be noted that reducing the emission of SLCPs is a helpful measure in short-term, whereas the reduction of $CO_2$ emissions remains the best long-term strategy to ensure that the increase in global average temperature does not exceed 2 °C. Both short- and long-term emission reduction strategies are vitally important for effective environmental protection and climate-change mitigation.

## Acknowledgements

This work was funded by the National Basic Research Program of China (2011CB403405).

## References

Alexander, L., Allen, S., Bindoff, N.L., et al., 2013. Summary for policy makers, in IPCC, Climate Change 2013: The Physical Science Basis, Working Group I Contribution to the IPCC Fifth Assessment Report. Accessed http://www.climatechange2013.org/images/uploads/WGIAR5_WGI-12Doc2b_FinalDraft_SPM.pdf.

An, J.L., Wang, Y.S., Li, X., et al., 2007. Analysis of the relationship between NO, $NO_2$ and $O_3$ concentrations in Beijing. Environ. Sci. 28 (4), 706−711 (in Chinese).

An, J.L., Hang, Y.X., Zhu, B., et al., 2010. Observational study of ozone concentrations in northern suburb of Nanjing. Ecol. Environ. Sci. 19 (6), 1383−1386 (in Chinese).

Ashmore, M.R., 2005. Assessing the future global impacts of ozone on vegetation. Plant Cell Environ. 28, 949−964.

Bond, T.C., Streets, D.G., Yarber, K.F., et al., 2004. A technology-based global inventory of black and organic carbon emissions from combustion. J. Geophys. Res. 109, D14203.

Cao, G.L., Zhang, X.Y., Gong, S.L., et al., 2011. Main particulate matter and pollutant emission source list of China. Chin. Sci. Bull. 56, 261−268 (in Chinese).

Cofala, J., Amann, M., Klimont, Z., et al., 2005. Scenarios of World Anthropogenic Emissions of $SO_2$, $NO_x$, and Coup to 2030, Internal Report of the Tran Boundary Air Pollution Programme. International Institute for Applied Systems Analysis, Laxenburg, Austria.

Fiore, A.M., Naik, V., Spracklen, D.V., et al., 2012. Global air quality and climate. Chem. Soc. Rev. 41, 6663−6683.

Gong, S.L., Barrie, L.A., Lazare, M., 2002. Canadian aerosol module (CAM): a size-segregated simulation of atmospheric aerosol processes for climate and air quality models 2, global sea-salt aerosol and its budgets. J. Geophys. Res. 107 (D24), 4779.

Kettle, A.J., Andreae, M.O., 2000. Flux of dimethyl sulfide from the oceans: a comparison of updated data sets and flux models. J. Geophys. Res. 105, 26793−26808.

Kim Oanh, N.T., Upadhya, N., Zhuang, Y.H., et al., 2006. Particulate air pollution in six Asian cities: spatial and temporal distributions, and associated sources. Atmos. Environ. 40, 3367−3380.

Liu, C.X., Liu, Y., Cai, Z.N., et al., 2010. Dynamic formation of extreme ozone minimum events over the Tibetan Plateau during northern winters 1987−2001. J. Geophys. Res. 115 (D18), 311−325.

Liu, Y., Wang, Y., Liu, X., et al., 2009. Tibetan middle tropospheric ozone minimum in June discovered from GOME observations. Geophys. Res. Lett. 36 (5), 814−820.

Marticorena, B., Bergametti, G., 1995. Modeling the atmospheric dust cycle: 1. Design of a soil-derived dust emission scheme. J. Geophys. Res. 100, 16415−16430.

Myhre, G., Shindell, D., Bréon, F.M., et al., 2013-09-30 [2013-11-30]. Anthropogenic and natural radiative forcing, in IPCC, Climate Change 2013: The Physical Science Basis, Working Group I Contribution to the IPCC Fifth Assessment Report. Accessed http://www.climatechange2013.org/images/uploads/WGIAR5_WGI-12Doc2b_FinalDraft_Chapter08.pdf.

Nightingale, P., Malin, G., Law, C., et al., 2000. Upstill-Goddard RC in situe valuation of air-sea gas exchange parameterizations using novel conservative and volatile tracers. Glob. Biogeochem. Cycles 14, 373−387.

Olivier, J., Berdowski, J., Peters, J., et al., 2002. Applications of EDGAR Including a Description of EDGAR V3.0: Reference Database with Trend Data for 1970−1995. R. NRP Report, 410200051. RIVM, Bilthoven, the Netherlands.

Qin, D.-H., Stocker, T., 259 authors and TSU, 2014. Highlights of the IPCC working group I fifth assessment report. Progressus Inquisitiones DE Mutatione Climatis 10 (1), 1−6 (in Chinese).

Shindell, D., Ramanathan, V., Raes, F., et al., 2004. Integrated Assessment of Black Carbon and Tropospheric Ozone. R. ISO 14001. UNON Publishing Services Section, Nairobi.

van der Werf, G.R., Randerson, J.T., Collatz, G.J., et al., 2004. Continental-scale partitioning of fire emissions during the 1997 to 2001 El Niño/La Niña period. Science 303, 73−76.

Wang, Z.L., Zhang, H., Shen, X.Y., 2011. Radiative forcing and climate response due to black carbon in snow and ice. Adv. Atmos. Sci. 28 (6), 1336−1344.

Yin, Y.Q., Shan, W.B., Ji, X., et al., 2006. Characteristics of atmospheric ozone in the urban area of Ji'nan. Environ. Sci. 11, 2299−3004 (in Chinese).

Zhang, H., Wang, Z.L., 2011. Advances in the study of black carbon effects on climate. Adv. Clim. Change Res 2 (1). http://dx.doi.org/10.3724/SP.J.1248.2011.00023.

Zhang, H., Wang, Z.L., Wang, Z.Z., et al., 2012a. Simulation of direct radiative forcing of aerosols and their effects on East Asia climate using an interactive GCM-Aerosol coupled system. Clim. Dyn. 38, 1675−1693.

Zhang, X.-Y., Wang, Y.-Q., Niu, T., et al., 2012b. Atmospheric aerosol compositions in China: spatial/temporal variability, chemical signature, regional haze distribution and comparisons with global aerosols. Atmos. Chem. Phys. 11, 26571−26615.

Zhang, X.-Y., Sun, J.-Y., Wang, Y.-Q., et al., 2013. Factors contributing to haze and fog in China. Chin. Sci. Bull. 58, 1178−1187 (in Chinese).

Zhao, S.-Y., Zhi, X.-F., Zhang, H., et al., 2014. Primary assessment of the simulated climatic state using a coupled aerosol-climate model BCC_AGCM2.0.1_CAM. Clim. Environ. Res. 19 (3), 265−277 (in Chinese).

Zhao, Z.-C., Luo, Y., Huang, J.-B., 2013. Projections of PM2.5 change. Progressus Inquisitiones DE Mutatione Climatis 9 (3), 223−224 (in Chinese).

第 10 卷 第 4 期
2014 年 7 月
气 候 变 化 研 究 进 展
PROGRESSUS INQUISITIONES DE MUTATIONE CLIMATIS
Vol. 10 No. 4
July 2014

doi:10.3969/j.issn.1673-1719.2014.04.010
张华 , 陈琪 , 谢冰 , 等 . 中国的 PM2.5 和对流层臭氧及污染物排放控制对策的综合分析 [J]. 气候变化研究进展 , 2014, 10 (4): 289-296



# 中国的 PM2.5 和对流层臭氧及污染物排放控制对策的综合分析

张 华[1,2], 陈 琪[1,2], 谢 冰[1,3], 赵树云[1,2]

1 中国气象科学研究院, 北京 100081;
2 中国气象局气候研究开放实验室 / 中国气象局国家气候中心, 北京 100081;
3 兰州大学大气科学学院半干旱气候变化教育部重点实验室, 兰州 730000

**摘 要**：本文首先对中国 PM2.5 和近地面臭氧浓度的观测进行了简要的综述；并利用 2010—2013 年全球对流层臭氧的卫星观测数据给出了对流层臭氧浓度在全球和中国地区的分布特征，其平均值分别为 29.78 DU 和 33.97 DU。然后，利用一个气溶胶大气化学－全球气候双向耦合模式模拟了中国地区 PM2.5 的浓度分布和季节变化，其年平均值为 $0.51 \times 10^{-8}$ kg/m$^3$。在此基础上又分析了 5 种典型气溶胶对 PM2.5 总浓度在不同季节的贡献。结合 IPCC 第五次评估报告（AR5），讨论了气溶胶和温室气体及其前体物的排放与辐射强迫的联系，以及减排大气臭氧前体物和气溶胶颗粒物质（PM）对气候变化的可能影响。指出减排臭氧前体物对气候的影响还不完全清楚，对短寿命的温室气体和黑碳气溶胶的减排是一种短期（未来 50 年）的辅助措施；为了保证全球平均温度增长不超过 2 ℃，减少二氧化碳的排放仍是我们需要坚持的长期战略。短期和长期的减排战略对于保护环境和减缓气候变化都是至关重要的。

**关键词**：对流层臭氧；PM2.5；温室气体；大气污染；气候变化

## 引 言

自工业革命以来，随着人类社会的飞速发展，生产效率有了质的飞越，人类活动排放的污染物不仅破坏了我们赖以生存的地球环境，同时也改变着地球气候。近几十年来，随着经济的迅速全球化，温室气体排放迅速增多，造成冰雪消融、海温升高、极端天气气候事件频发，同时造成的污染问题也日渐严重，特别是近年来在中国频发的大面积雾霾天气事件，严重影响了我们的生活和身体健康。面对我们生存环境的不断恶化，保护环境和减缓气候变化已经成为社会的共识。同时，《联合国气候变化框架公约》（UNFCCC）第 16 次缔约方大会已经达成共识，只有全球平均地表温度与工业革命前相比升高不超过 2 ℃才能有效地避免气候系统变化发展到对人类生产生活可能造成危险的状态。近年来致力于减排长寿命温室气体的努力已经无法满足近期控制全球升温的需要，而控制某些短寿命的气候污染物（如对流层臭氧、黑碳气溶胶和甲烷等）的浓度不仅可以在短期内有效减缓气候变化，也可以改善我们生存的环境并保护我们的健康。

**收稿日期**：2014-02-19；**修回日期**：2014-03-26
**资助项目**：国家重点基础研究发展计划（2011CB403405）
**作者简介**：张华，女，研究员，主要从事大气辐射传输模式、温室气体和气溶胶辐射强迫与气候效应研究，huazhang@cma.gov.cn

## 1 大气污染物

人类活动将大量的工业、生活废气和烟尘等物质排放到大气中，当这些物质浓度达到影响人类的正常生存发展，危害生物健康时，我们称之为大气污染。其中交通运输和工业生产活动是大气污染物的主要来源[1]。除了按照人为污染物和天然污染物来划分外，大气污染物还可以划分成一次污染物和二次污染物。一次污染物是指直接从源排放出来的污染物质，如一氧化碳、一氧化氮、二氧化硫和颗粒物等；二次污染物是指由一次污染物在大气中经过化学或光化学反应等相互作用而产生的物理、化学性质均不同的新的大气污染物，如硫酸盐气溶胶、硝酸盐气溶胶和臭氧等。

本文对观测和模拟的全球和中国地区对流层臭氧和中国地区 PM2.5 的浓度分布进行了分析，讨论了控制空气污染物排放就需要控制对流层臭氧及其前体物排放以及颗粒物排放，由此对未来气候可能产生的影响及相应的对策。以下分别简单介绍 PM2.5 和短寿命的气候污染物（对流层臭氧、黑碳气溶胶和甲烷）。

### 1.1 PM2.5

气溶胶是除地球大气中的气体成分之外，悬浮在大气中的粒子或液滴[2]，也被称为颗粒物（PM: particulate matter）。现在广受大家关注的PM2.5通常被称为细颗粒物，代表了空气中气体动力学当量直径<2.5 μm的颗粒物[1]。PM2.5也被称为可入肺颗粒物，由于它粒径小、面积大、活性强，所以极易附带有毒、有害物质，同时 PM2.5 在大气中的停留时间较长、输送距离远，因此对大气环境质量和人类健康的影响很大。

### 1.2 对流层臭氧（$O_3$）

臭氧是地球大气中重要的组成部分，在 10～30 km 的平流层内集中了约 90% 臭氧，仅有约 10% 的臭氧分布在对流层中。平流层臭氧通过对太阳紫外辐射的强烈吸收从而保护地球上的生命，使我们可以正常地生产生活；对流层臭氧通过吸收地气系统的长波辐射，对大气产生加热作用，从而成为了重要的温室气体，同时对流层臭氧由于可以引发城市光化学烟雾而成为污染气体。在平流层中，氧分子因高能量的辐射而分解为氧原子，而氧原子与另一氧分子结合，即生成臭氧。而对流层中，臭氧的来源问题是国内外学者讨论的热点问题，主要有两种观点：一是由臭氧前体物（甲烷、一氧化碳、可挥发性有机化合物、氮氧化物等）经过光化学反应产生的；二是平流层动力下传。

### 1.3 黑碳气溶胶（BC）

黑碳气溶胶是由化石燃料、木材或其他生物质不完全燃烧而产生的，粒径为 0.01～1 μm。它的来源主要包括工业用煤、汽车尾气排放、住宅灶火、森林和农作物燃烧等。张华等[2]综述了黑碳气溶胶的研究进展，指出黑碳气溶胶通过吸收太阳和红外辐射对大气具有很强的加热作用，同时它还可以影响云的形成和降低积雪的反照率[2-4]。黑碳气溶胶不但影响气候，而且影响人类健康。黑碳气溶胶的表面能够吸附其他污染物，随着呼吸过程，黑碳气溶胶会夹带吸附的有毒物质进入人体，对人类身体健康造成危害。由于技术方面的原因，在生产生活当中燃烧不均匀、燃料与空气配合不当等因素的存在，不完全燃烧现象不可避免，此时除了二氧化碳，伴随着黑碳气溶胶生成的还有一氧化碳、可挥发性有机物和有机碳气溶胶。其中有机碳与黑碳气溶胶的关系十分密切，二者经常是同时产生的；不同于黑碳气溶胶，有机碳气溶胶对大气具有较强的降温作用，因此我们较为关注不同的排放源中二者的混合比例。

### 1.4 甲烷（$CH_4$）

甲烷是大气中的痕量气体，是一种公认的仅次于二氧化碳的重要温室气体。它与二氧化碳相比在大气中的浓度虽小得多，但增长率却大得多（二氧化碳与甲烷自工业革命以来增长率分别是 40% 和 150%）[5]。甲烷能够强烈吸收红外辐射，然后再向外发射红外辐射，因而对大气具有增温作用。甲烷不但是温室气体，同时也是重要的臭氧前体物，因此减少人为甲烷排放不但可以减缓全球变暖，还可以

www.climatechange.cn



减小空气污染，保护环境和人类健康。

## 2　主要大气污染物的分布

### 2.1　观测的大气污染物的分布

2013 年 1 月和 2 月在我国中东部地区出现了多次雾霾天气事件，而且2013年全年出现的雾霾天气事件，发生的范围大、持续时间长，对人们的生活造成了严重的影响，目前中国政府正以前所未有的决心治理大气污染。当今发生的雾霾天气，都已经不是完全的自然现象了，其产生的原因都与人类活动产生的气溶胶粒子（例如 PM10，PM2.5）息息相关[6]。国内外许多科学家就气溶胶粒子进行了大量的观测和模拟研究。Kim Oanh 等[7]选择了受亚洲季风影响的具有代表性的 6 个城市（曼谷、北京、金奈、万隆、马尼拉、河内），对2001—2004年近3000个样本进行了研究，在研究过程中他们将每个城市分为 6 个代表性区域进行观测，并将一年分为干湿两季（湿润季为 5 — 10 月，干燥季为一年中除 5 — 10月剩下的月份）。观测结果表明无论是干季还是湿季，北京是这6个城市中PM2.5与PM10浓度最高的城市。Zhang 等[8]在对2006和2007年我国16个观测站的干PM10滤膜气溶胶样品的分析中发现，其中含量最大的成分是矿物气溶胶(沙尘、煤烟尘和城市逸散性粉尘等)，约占 35%；其次是硫酸盐气溶胶和有机碳气溶胶，各占 15%。我国大气中硫酸盐浓度较高主要是因为我国产能 70% 靠燃煤提供。而黑碳气溶胶在观测的 PM10 中只占约 3.5%，而且在全国各个区域变化不大，黑碳气溶胶的主要来源除了生物质燃烧外，燃煤和燃油也有很大贡献[9]。同时他们还对 2013 年 1 月 1 — 16 日中国中东部地区的 PM2.5 质量浓度进行了观测，发现静稳型天气和高浓度的气溶胶有利于雾霾的形成[6]。

对流层中的臭氧除了会使全球增温外，在近地面高浓度的臭氧还会对人体和农作物造成很大危害，强有力的证据显示对流层臭氧对植物生理过程有不利影响[10]。本文利用美国国家航天局（NASA）为地球观测系统发射的AURA卫星上携带的臭氧监测仪观测到的臭氧廓线数据，计算了2010—2013年对流层臭氧柱浓度（TOCC）的分布（图1）。在全球范围内，由于人类活动而产生的臭氧前体物影响对流层臭氧的分布，TOCC 随着纬度呈现出两极和赤道地区较小，而中高纬度地区较高的分布，并且北半球的数值明显高于南半球。TOCC 在 30° ～60° N 之间的臭氧高值区中存在两个低值中心，分别位于亚洲大陆中部（中国青藏高原）和北美大陆中西部。在中国所在地区范围内 TOCC 自东向西递减，青藏高原为低值中心，高值中心位于东部海域。Liu 等[11]研究发现青藏高原成为TOCC的低值中心主要是由于该地区对流层顶的升高与热带臭氧浓度较低的空气向北输送造成的。Liu 等[12]用卫星资料研究发现青藏高原对流层中部臭氧低谷现象常发生在青藏高原东部地区上空 8 ～13 km 处，且伴随着亚洲夏季风发生。殷永泉等[13]以及安俊琳等[14-15]分别对济南、北京和南京的近地面臭氧浓度进行了观测研究，发现在城市范围内冬季的臭氧浓度最低，夏季最高；

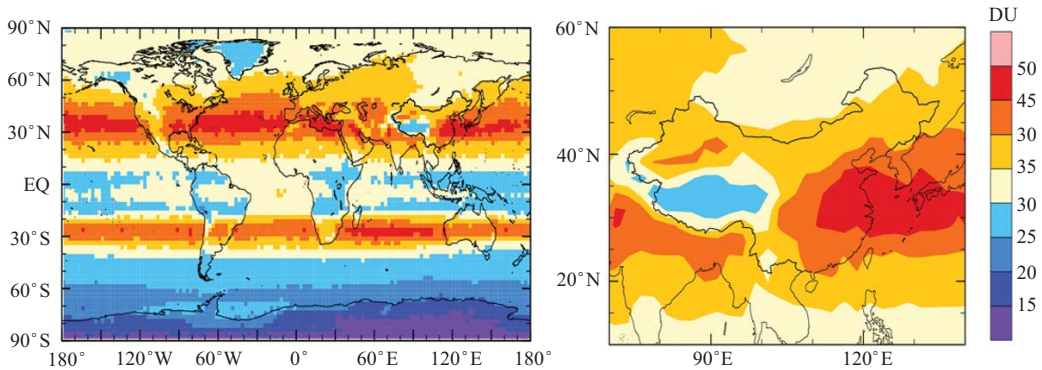


图 1　卫星观测的 2010 — 2013 年对流层臭氧柱浓度分布

Fig. 1　Distribution of tropospheric ozone column concentration observed by satellite in 2010−2013

在日变化过程中，无论任何季节，臭氧浓度最高值都出现在14时前后，而最低值出现在清晨5时前后。在众多臭氧前体物中，甲烷是最受大家关注的。减少甲烷排放可以有效减少对流层臭氧的生成。根据世界气象组织（WMO）和联合国环境规划署（UNEP）的联合报告[1]，中国是甲烷最大的源，大约占整个甲烷排放量的18%，而整个亚洲排放的甲烷占总量的45%。由于甲烷最主要的两个来源是煤的开采和农业活动，这就决定了亚洲成为全球最主要的甲烷排放源。

### 2.2 模式模拟的PM2.5分布

本文还运用中国气象局国家气候中心的气溶胶大气化学－气候双向耦合模式BCC_AGCM2.0.1_CUACE/Aero[3,16]模拟了气溶胶浓度和PM2.5在中国地区（15°～55°N，72°～136°E）的分布和季节变化特征。其中，大气模式采用42波三角截断的水平方案（T42，近似于2.8°×2.8°），并以欧拉谱动力核为基础，垂直方向共26层，采用混合$\sigma$-$p$坐标系，模式顶层为2.9 hPa；气溶胶模式包含5种典型气溶胶（黑碳、有机碳、硫酸盐、海盐、沙尘），并按粒径大小分为12档（0.005～20.48 μm）。气溶胶的排放资料（包括自然和人为排放）主要来自气溶胶观测和模式比较项目AeroCom，包括黑碳和有机碳[17-18]、二氧化硫和硫酸盐[18-19]、二甲基硫[20-21]。其他排放数据资料来自于EDGAR3.2 1995年资料[22]。海盐和沙尘排放方案分别来自Gong等[23]和Marticorena等[24]的研究。模式模拟了中国地区人为气溶胶PM2.5的分布（图2），可以看出：中国华北地区是人为气溶胶PM2.5的高值区，而西北部地区是低值区；季节不同，人为气溶胶PM2.5浓度也呈明显的变化，其中春季和夏季是人为气溶胶PM2.5浓度较高的季节。另外，运用该模式系统模拟的中国地区5种典型气溶胶浓度及其在PM2.5中所占的比例见表1，在中国地区硫酸盐和沙尘气溶胶是PM2.5中含量最大的两种气溶胶，大约占整体的85%。在冬季和春季，沙尘气溶胶的含量高达50%以上，而从全年平均来看，沙尘气溶胶也达到52%，是中国PM2.5中的主要成分。沙尘气溶胶的高浓度主要与位于中国西北部蒙古地区的沙漠有关，其中塔克拉玛干与巴丹吉林沙漠是最主要的沙尘气溶胶的源；而硫酸盐气溶胶的高浓度与中国能源消费主要依靠煤炭有关，经测算到2050年燃煤仍将是中国产能的主要方式[7]。由于地理位置的原因，海盐气溶胶在整个PM2.5中所占

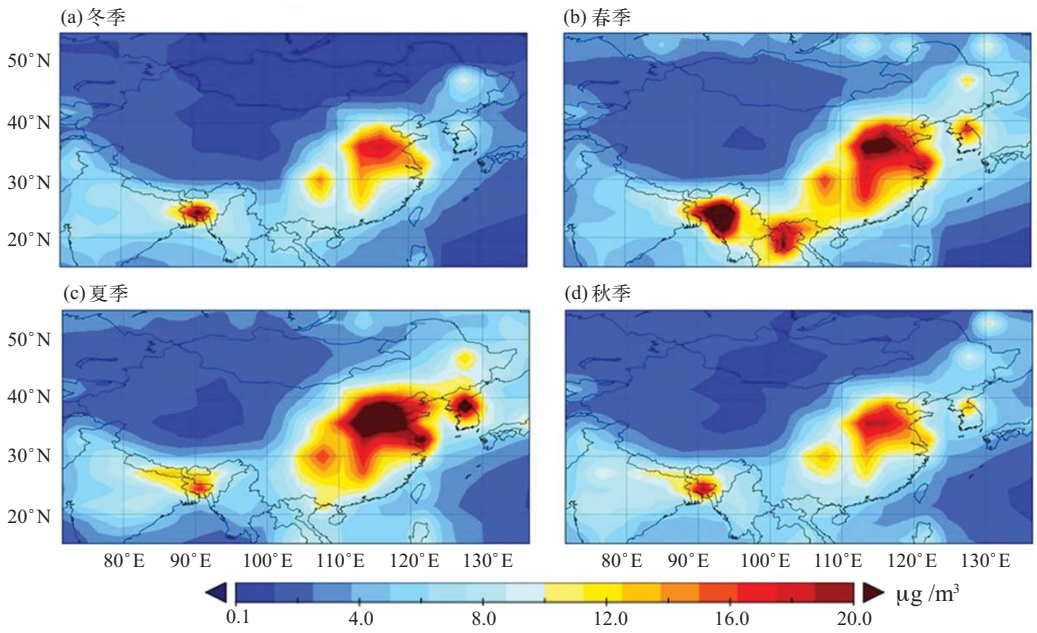


图2 模式模拟的PM2.5（仅包括人为气溶胶）的分布

Fig. 2 Distribution of simulated PM2.5 (only including anthropogenic aerosols)

www.climatechange.cn



表 1　中国地区 5 种典型气溶胶的季节平均浓度（单位：μg /m³；括号中为各种成分占 PM2.5 的比例）
Table 1 The seasonal mean concentrations of 5 aerosol species in China (unit: μg /m³; contribution percentage of each components to PM2.5 in brackets)

| 气溶胶 | 春季 | 夏季 | 秋季 | 冬季 | 全年 |
|---|---|---|---|---|---|
| 硫酸盐 | 2.74 (29%) | 2.80 (45%) | 2.22 (40%) | 1.96 (35%) | 2.43 (36%) |
| 黑碳 | 0.45 (5%) | 0.43 (7%) | 0.40 (7%) | 0.41 (7%) | 0.42 (6%) |
| 有机碳 | 0.26 (3%) | 0.25 (4%) | 0.21 (4%) | 0.18 (3%) | 0.23 (3%) |
| 沙尘 | 5.82 (60%) | 2.40 (39%) | 2.57 (45%) | 2.93 (52%) | 3.43 (52%) |
| 海盐 | 0.14 (2%) | 0.29 (5%) | 0.22 (4%) | 0.14 (3%) | 0.20 (3%) |

的比例最小，不超过 5%。在中国地区，黑碳气溶胶年平均含量达到 6%，仅次于硫酸盐和沙尘气溶胶，其浓度全年稳定在 0.4 μg/m³以上。中国气溶胶较高的浓度水平与维持中国经济发展和社会活动的燃煤、燃油和居民生活排放是密不可分的。Zhang 等[3]模拟了 5 种典型气溶胶全球平均的大气层顶和地表的直接辐射强迫。其中只有黑碳气溶胶在大气层顶的辐射强迫是正值，对地球大气具有加热作用，而其他 4 种气溶胶均为负值。有云大气条件下人为气溶胶的辐射强迫约为 −0.23 W/m²，对地气系统起着冷却作用。而国内外科学家运用多模式模拟 PM2.5 未来全球浓度的分布，发现在IPCC第五次评估报告（AR5）给出的未来4种排放路径（RCP2.6、RCP4.5、RCP6.0、RCP8.5）下，到21世纪末全球和分区的PM2.5均有所下降，其中东亚地区减少较为明显[24-26]。

## 3　减排空气污染物对气候变化的影响

### 3.1　空气污染与辐射强迫

2014年发布的AR5第一次把温室气体和气溶胶及其前体物的排放和辐射强迫建立了联系[27]。由于对流层臭氧及其前体物和气溶胶及其前体物构成了大气污染物，这样 AR5 就直接和间接地给出了大气污染物质的辐射强迫。与 1750 年相比，总的辐射强迫都为正值，净的作用都导致全球气候系统变暖，其中贡献最大的仍是由于二氧化碳浓度的增加而产生的辐射强迫（1.68 [1.33～2.03] W/m²）。相对于 1750 年，2011 年的整体人为辐射强迫为2.29 [1.13～3.33] W/m²，而且从 1970 年以来的近几十年间，人为辐射强迫的增长速度正在加快。排放到大气中的均匀混合的温室气体（二氧化碳、甲烷、一氧化二氮和卤化物）总的辐射强迫为 3.00 [2.22～3.78] W/m²，但是由于排放在空气中的这些气体经过复杂的化学过程而产生了其他物质，所以这些均匀混合的温室气体的浓度变化所产生的辐射强迫为2.83 [2.26～3.40] W/m²。其中甲烷由于浓度变化所产生的辐射强迫只有 0.48 [0.38～0.58] W/m²，但甲烷的排放所造成的辐射强迫为 0.97 [0.74～1.20] W/m²。这主要是由于甲烷会影响臭氧和平流层水汽的浓度，从而加倍了它对大气的加热能力。而短寿命的温室气体（一氧化碳、非甲烷挥发性有机物和氮氧化物）中，一氧化碳会对气候产生较明显的加热作用，而氮氧化物却会产生负的辐射强迫 −0.15 [−0.34～0.03] W/m²。在考虑了与云的相互作用后，气溶胶总的辐射强迫为−0.9 W/m²，其中绝大多数的气溶胶辐射强迫为负值，而只有黑碳气溶胶的辐射强迫为正值。

### 3.2　减排臭氧前体物和PM对气候变化的可能影响

为了降低对流层中臭氧和大气中的气溶胶颗粒物的浓度，我们应努力减少几种重要气体和颗粒物的人为排放。如图 3 所示，为了控制对流层中臭氧的浓度，就要减排甲烷、一氧化碳以及可挥发性有机化合物并合理控制氮氧化物的浓度；而为了控制气溶胶颗粒物的浓度，就要减少氮氧化物、可挥发性有机化合物、氨、黑碳气溶胶、有机碳气溶胶和二氧化硫的人为排放。正如图 3 所示，通过减排臭氧前体物从而降低对流层臭氧浓度，使得全球平均温度下降。由于氮氧化物可以有效地控制甲烷的生

命期和气溶胶的生成，所以减排氮氧化物同时会造成全球平均温度的升高。减排气溶胶颗粒物主要会对大气起加热的作用，但已经有充分的证据证明减排黑碳气溶胶的直接效应会使大气冷却[2]，而其中黑碳气溶胶和云相互作用造成的间接效应是不确定的，需要进一步的研究。

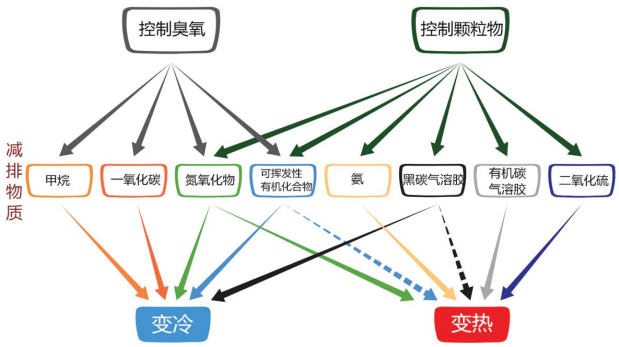


图 3 减排特定排放物对气候变化的影响示意图 [28]
（实线表示已知的影响，虚线表示不确定的影响）
Fig. 3 Schematic diagram of the impacts of pollution controls on specific emissions and climate impact (Solid line indicates known impact, dashed line indicates uncertain impact)[28]

## 4 应对措施

为了能够更好地保护环境，节能减排，国家和区域政策上的保障是必不可少的。在过去的 10 年中，随着汽车数量的增多，汽车尾气已经成为空气污染和 PM2.5 的主要来源之一。在中国大气污染防治法的支持下，已经建立起了一系列严格的控制汽车尾气和化石燃料燃烧的排放标准，通过监督和检查制度以及建立低排放区来保护空气质量。在法律法规的保障和我们的共同努力下，在过去的10年间，中国已经实现减排碳氢化合物总量 445 万 t、一氧化碳 2.387 亿 t，、氮氧化物 380 万 t 及 PM 70 万 t[1]。同时国家与地区之间应该更好地相互协助，这样才能更好地改善跨地区的气候和空气质量问题。

从保护环境的策略上，应减少对流层臭氧和 PM2.5 的排放，有效地保护公共健康、人类赖以生存的水和食物以及生态系统，减少大气污染事件的发生。从短期保护气候的战略上，全面实施减排短寿命气候污染物（包括对流层臭氧、甲烷和黑碳气溶胶）在未来的 50 年可能会减缓气候变化的速率，并可能会使未来全球变暖降低0.5 [0.2～0.7] ℃ [1]；同时该措施也可以减缓极地、喜马拉雅山脉及其他冰川和积雪的快速消融。

为了减少对流层中臭氧的浓度，我们应该致力于减少几种人为臭氧前体物的排放。其中甲烷不但影响对流层臭氧的生成而且也是非常重要的温室气体，因此控制甲烷的排放是一项保护环境和减缓全球变暖的双赢策略。而减排臭氧其他前体物对气候的影响还不完全清楚。减排黑碳气溶胶的直接影响会冷却大气系统，但是黑碳气溶胶的间接效应需要给予进一步的研究。减排其他气溶胶，会使全球平均地表温度升高。

需要说明的是，对短寿命气候污染物的减排只是一种短期内的辅助措施，而为了保证全球平均温度增长不超过 2 ℃，减少二氧化碳的排放仍是我们需要坚持的长期战略。短期和长期的减排战略对于保护环境和减缓气候变化都是至关重要的。■

### 参考文献

[1] Shindell D, Ramanathan V, Raes F, *et al*. Integrated assessment of black carbon and tropospheric ozone [R]. ISO 14001. Nairobi: UNON Publishing Services Section, 2004

[2] 张华，王志立．黑碳气溶胶气候效应的研究进展 [J]. 气候变化研究进展，2009, 5 (6): 311-317

[3] Zhang H, Wang Z L, Wang Z Z, *et al*. Simulation of direct radiative forcing of aerosols and their effects on East Asia climate using an interactive GCM-aerosol coupled system [J]. Climate Dynamics, 2012, 38: 1675-1693

[4] Wang Z L, Zhang H, Shen X S. Radiative forcing and climate response due to black carbon in snow and ice [J]. Advances in Atmospheric Sciences, 2011, 28 (6):1336-1344

[5] Alexander L, Allen S, Bindoff N L, *et al*. Summary for policy makers [M/OL]// IPCC. Climate change 2013: the physical science basis. Cambridge: Cambridge University Press, 2013 [2013-11-30]. http://www.climatechange2013.org/images/uploads/WGIAR5_WGI-12Doc2b_FinalDraft_SPM.pdf

[6] 张小曳，孙俊英，王亚强，等．我国雾－霾成因及其治理的思考 [J]. 科学通报，2013, 58: 1178-1187

www.climatechange.cn



[7] Kim Oanh N T, Upadhya N, Zhuang Y H, *et al*. Particulate air pollution in six Asian cities: spatial and temporal distributions, and associated sources [J]. Atmospheric Environment, 2006, 40: 3367-3380

[8] Zhang X Y, Wang Y Q, Niu T, *et al.* Atmospheric aerosol compositions in China: spatial/temporal variability, chemical signature, regional haze distribution and comparisons with global aerosols [J]. Atmospheric Chemistry and Physics, 2012, 11: 26571-26615

[9] 曹国良 , 张小曳 , 龚山陵 , 等 . 中国区域主要颗粒物及污染气体的排放源清单 [J]. 科学通报 , 2011, 56: 261-268

[10] Ashmore M R. Assessing the future global impacts of ozone on vegetation [J]. Plant Cell and Environment, 2005, 28: 949-964

[11] Liu C X, Liu Y, Cai Z N, *et al*. Dynamic formation of extreme ozone minimum events over the Tibetan Plateau during northern winters 1987−2001 [J]. Journal of Geophysical Research, 2010, 115 (D18): 311-325

[12] Liu Y, Wang Y, Liu X, *et al.* Tibetan middle tropospheric ozone minimum in June discovered from GOME observations [J]. Geophysical Research Letters, 2009, 36 (5): 814-820

[13] 殷永泉 , 单文坡 , 纪霞 , 等 . 济南大气臭氧浓度变化规律 [J]. 环境科学 , 2006, 11: 2299-3004

[14] 安俊琳 , 王跃思 , 李昕 , 等 . 北京大气中 NO、$NO_2$ 和 $O_3$ 浓度变化的相关性分析 [J]. 环境科学 , 2007, 28 (4): 706-711

[15] 安俊琳 , 杭一纤 , 朱彬 , 等 . 南京北郊大气臭氧浓度变化特征 [J]. 生态环境学报 , 2010, 19 (6): 1383-1386

[16] 赵树云, 智协飞, 张华, 等. 气溶胶−气候耦合模式系统BCC_AGCM2.0.1_CAM气候态模拟的初步评估[J]. 气候与环境研究, 2014, 19 (3): 265-277, doi:10.3878/j.issn.1006-9585.2012.12015

[17] Bond T C, Streets D G, Yarber K F, *et al*. A technology-based global inventory of black and organic carbon emissions from combustion [J]. Journal of Geophysical Research, 2004, 109, D14203

[18] van der Werf G R, Randerson J T, Collatz G J, *et al*. Continental-scale partitioning of fire emissions during the 1997 to 2001 El Niño/La Niña period [J]. Science, 2004, 303: 73-76

[19] Cofala J, Amann M, Klimont Z, *et al*. Scenarios of world anthropogenic emissions of $SO_2$, $NO_x$, and CO up to 2030 [R]. Internal report of the Tran Boundary Air Pollution Programme. Laxenburg: International Institute for Applied Systems Analysis, 2005

[20] Kettle A J, Andreae M O. Flux of dimethyl sulfide from the oceans: a comparison of updated data sets and flux models [J]. Journal of Geophysical Research, 2000, 105: 26793-26808

[21] Nightingale P, Malin G, Law C, *et al*. Upstill-Goddard RC in situ valuation of air-sea gas exchange parameterizations using novel conservative and volatile tracers [J]. Global Biogeochemical Cycles, 2000, 14: 373-387

[22] Olivier J, Berdowski J, Peters J, *et al*. Applications of EDGAR including a description of EDGAR V3.0: reference database with trend data for 1970−1995 [R]. NRP report, 410200051, RIVM, Bilthoven, the Netherlands, 2002

[23] Gong S L, Barrie L A, Lazare M. Canadian aerosol module (CAM): a size-segregated simulation of atmospheric aerosol processes for climate and air quality models 2, global sea-salt aerosol and its budgets [J]. Journal of Geophysical Research, 2002, 107(D24), 4779, doi:10. 1029/2001JD002004

[24] Marticorena B, Bergametti G. Modeling the atmospheric dust cycle: 1. Design of a soil-derived dust emission scheme [J]. Journal of Geophysical Research, 1995, 100: 16415-16430

[25] Fiore A M, Naik V, Spracklen D V, *et al*. Global air quality and climate [J]. Chemical Society Reviews, 2012, 41: 6663-6683

[26] 赵宗慈 , 罗勇 , 黄建斌 . 预估 PM2.5 的变化 [J]. 气候变化研究进展 , 2013, 9 (3): 223-224

[27] 秦大河 , Stocker T, 259 名作者和 TSU(驻伯尔尼和北京). IPCC 第五次评估报告第一工作组报告的亮点结论 [J]. 气候变化研究进展, 2014, 10 (1): 1-6

[28] Myhre G, Shindell D, Bréon F M, *et al*. Anthropogenic and natural radiative forcing [M/OL]//IPCC. Climate change 2013: the physical science basis. Cambridge: Cambridge University Press, 2013 [2013-11-30]. http://www.climatechange2013.org/images/uploads/WGIAR5_WGI-12Doc2b_FinalDraft_Chapter08.pdf

# PM2.5 and Tropospheric Ozone in China and Pollutant Emission Controlling Integrated Analyses

Zhang Hua[1, 2], Chen Qi[1, 2], Xie Bing[1, 3], Zhao Shuyun[1, 2]

1 *Chinese Academy of Meteorological Sciences, Beijing* 100081, *China*; 2 *Laboratory for Climate Studies of China Meteorological Administration, National Climate Center, China Meteorological Administration, Beijing* 100081, *China*; 3 *Key Laboratory for Semi-Arid Climate Change of the Ministry of Education, College of Atmosphere Science, Lanzhou University, Lanzhou* 730000, *China*

**Abstract:** This work reviewed the observational status of PM2.5 and tropospheric ozone in China firstly; the distribution of the concentration of tropospheric ozone over the globe and China were given based on the satellite observation during the period of 2010−2013. The annual mean values are 29.78 DU and 33.97 DU in the globe and China region, respectively. Then, the distribution of PM2.5 concentration and their seasonal changes in China were simulated by an aerosol chemistry-climate coupled model system, with annual mean value of $0.51 \times 10^{-8}$ kg/m$^3$. The contributions from five kinds of aerosols to the simulated PM2.5 concentrations in different seasons were also analyzed. Then, the relations between the emissions of aerosol, greenhouse gases and their precursors and their radiative forcings were illustrated referring to the IPCC AR5. For these relations, the possible effects of controlling ozone precursors and particle matter on the climate were given, of which, the former is not totally clear, while reducing emissions of short lived greenhouse gases and black carbon is a secondary measure for short term (the future 50 years) climate change mitigation. Reducing emission of $CO_2$ is still our main strategy to promise the target of global average surface air temperature rise less than 2 ℃. The strategies of pollutant emission control for near term and long term are all important for the prospects of both environment protection and climate change mitigation.

**Key words:** tropospheric ozone; PM2.5; GHG; air pollution; climate change

第 10 卷 第 1 期 气 候 变 化 研 究 进 展 Vol. 10 No. 1
2014 年 1 月 PROGRESSUS INQUISITIONES DE MUTATIONE CLIMATIS January 2014

doi:10.3969/j.issn.1673-1719.2014.01.009
张华，黄建平．对 IPCC 第五次评估报告关于人为和自然辐射强迫的解读 [J]. 气候变化研究进展，2014, 10 (1): 40-44

# 对 IPCC 第五次评估报告关于人为和自然辐射强迫的解读

# Interpretation of the IPCC Fifth Assessment Report on Anthropogenic and Natural Radiative Forcing

张 华[1]，黄建平[2]

1 中国气象局气候研究开放实验室／中国气象局国家气候中心，北京 100081；
2 兰州大学大气科学学院教育部半干旱气候变化重点实验室，兰州 730000

人为辐射强迫是气候变化的驱动力之一，因此，对人为和自然辐射强迫的评估[1]是IPCC第五次评估报告（AR5）第一工作组科学部分的重要内容。AR5在指出了IPCC第四次评估报告（AR4）及其之前所用的辐射强迫概念的优点和局限性后，为了涵盖影响云的快速过程，给出了新的辐射强迫——有效辐射强迫的概念，并与之前使用的瞬时辐射强迫和平流层调整的辐射强迫进行了比较。此外，为了定量比较各种排放对气候的影响，AR5首次定义并使用了基于排放的辐射强迫概念，并对衡量温室气体排放的两个概念，即全球增温潜势（GWP）和全球温变潜势（GTP）进行了全面的评价。

AR5有关人为和自然辐射强迫的结论是，人类活动导致的混合温室气体①（WMGHGs）增加已经大幅度地加强了温室效应，其导致的强迫将继续增加。气溶胶部分地抵消了WMGHGs的强迫，是气候变化中总的人为强迫的最不确定部分。

## 1 辐射强迫的概念

与前几次IPCC报告一样，AR5使用了辐射强迫（RF）概念，同时引入了有效辐射强迫（ERF）的新概念。传统的辐射强迫概念中，所有的地面和对流层的条件都是固定的，而这里给出的有效辐射强迫的计算允许所有物理量对扰动进行响应（除了与海洋和海冰有关的物理量外）[2-3]。这些调整使得有效辐射强迫能更好地成为最终温度响应的指示器。图1比较了各种辐射强迫概念。

## 2 自工业革命以来的人为辐射强迫

自工业革命以来的总人为有效辐射强迫值为2.3 (1.1～3.3) W/m$^2$。自1970年以来，总的人为有效辐射强迫比之前10年增加更为迅速。由于气溶胶辐射强迫的减少以及温室气体辐射强迫的继续增加，2011年的总人为有效辐射强迫的估计值比AR4中2005年相应的估计值高44%（图2），其中除了温室气体和气溶胶的浓度自2005年有所变化外，采用了新的辐射强迫概念和不同的计算方法可能是造成上述估计变化的另一个原因。

由图2可见，混合温室气体的辐射强迫为2.83 (2.54～3.12) W/m$^2$，与2005年的AR4相比，其辐射强迫增加了0.20 (0.18～0.22) W/m$^2$ (8%)。从AR4到现在，变化部分是由$CO_2$辐射强迫增加了近10%造

收稿日期：2013-11-27；修回日期：2013-12-18
资助项目：国家重点基础研究发展计划项目（2011CB403405，2012CB955301）
作者简介：张华，女，研究员，从事大气辐射传输模式、温室气体与气溶胶辐射强迫及其气候效应研究，huazhang@cma.gov.cn
①混合温室气体指在大气中均匀混合的温室气体，包括$CO_2$、$CH_4$、$N_2O$和卤代烃。

www.climatechange.cn



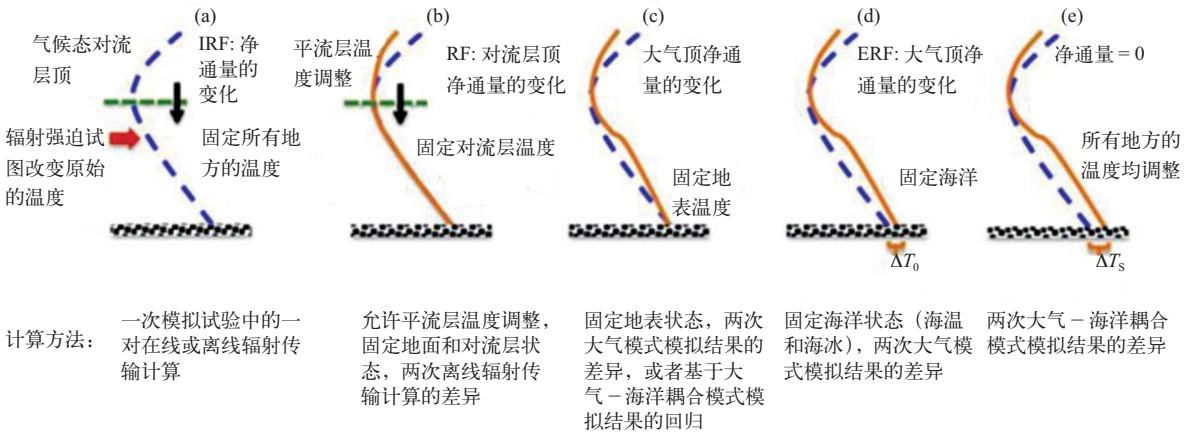


图 1　辐射强迫比较（来源于 Hansen 等 [4] 的工作。每种类型辐射强迫的计算方法已经列出。$\Delta T_0$ 代表陆地温度响应，$\Delta T_S$ 代表全部地表温度响应）(a) 瞬时辐射强迫，(b) 允许对流层温度响应时的辐射强迫，(c) 全球表面温度处于定值时的辐射通量变化（一种计算有效辐射强迫的方法），(d) 允许大气和陆面温度响应，但海洋边界条件固定的有效辐射强迫，(e) 对各种辐射强迫因子响应达到平衡态

Fig. 1　Cartoon comparing (a) instantaneous RF, (b) RF, which allows stratospheric temperature to adjust, (c) flux change when the surface temperature is fixed over the whole Earth (a method of calculating ERF), (d) the ERF calculated allowing atmospheric and land temperature to adjust while ocean conditions are fixed, (e) the equilibrium response to the climate forcing agent. The methodology for calculation of each type of forcing is also outlined. $\Delta T_0$ represents the land temperature response, while $\Delta T_S$ is the full surface temperature response. Updated by Hansen *et al.* [4]

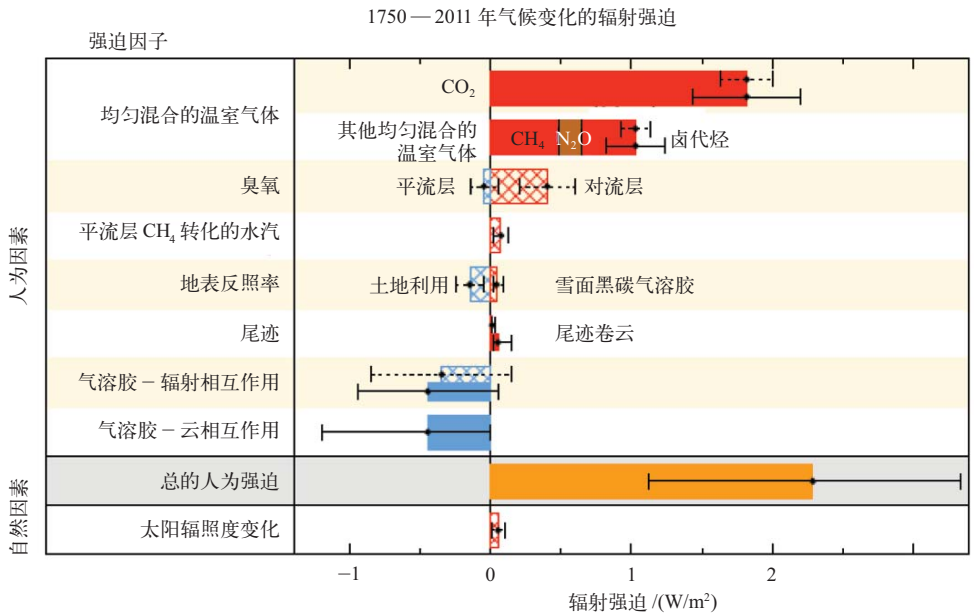


图 2　1750—2011 年间辐射强迫（网格线）和有效辐射强迫（实心）的条形图，图中给出了辐射强迫（点状线）和有效辐射强迫（实线）的不确定性（置信度区间为 5%～95%）[1]

Fig. 2　Bar chart for RF (hatched) and ERF (solid) for the period 1750−2011. Uncertainties (5%−95% confidence range) are given for RF (dotted lines) and ERF (solid lines) [1]

成的。在工业革命时期，$CO_2$ 的辐射强迫只有 1.82 (1.63～2.01) W/m²。$CO_2$ 是最大的全球平均辐射强迫的组分，在过去的 10 年中，$CO_2$ 的辐射强迫增加了 0.27 (0.24～0.30) W/m²。

从 2005 年的 AR4 以来，除 $CO_2$ 以外的混合温室气体的净强迫有小幅增加。其中，$CH_4$ 浓度的少量增加使其辐射强迫增加 2%，AR5 的估计值变为 0.48 (0.43～0.53) W/m²，对辐射强迫的贡献仅次于 $CO_2$。而 $N_2O$ 的辐射强迫增加了 6%，现在已达到 0.17 (0.15～0.19) W/m²。在过去的几十年中，对辐射强迫贡献排第三的均匀混合温室气体 CFC-12，在《蒙特利尔协议》及其修正案限制下排放逐渐停止，因此，自 2011 年以来，$N_2O$ 已经成为对辐射强迫贡献排第三的混合温室气体。在氟氯烃的辐射强迫减少而氟氯烃的许多替代物的辐射强迫增加的情况下，所有的卤代烃的辐射强迫（0.36 W/m²）和 AR4 的值相差不大。4 种卤代烃（CFC-11、CFC-12、CFC-113 和 HCFC-22）大约占卤代烃总辐射强迫的 85%。在过去的 5 年里，前 3 种化合物的辐射强迫有所降低，而这种降低被 HCFC-22 辐射强迫的相应增加所弥补。自 AR4 以来，虽然所有氢氟碳化物（HFCs）的辐射强迫量已经接近翻一番，但其数值仍然只有 0.02 W/m²。具有*很高信度*的结果表明，由于非 $CO_2$ 气体辐射强迫的增加率减小，来自所有混合温室气体的辐射强迫总增加率在过去 10 年里比 20 世纪 70、80 年代的增长率小。

$O_3$ 和平流层水汽对总的辐射强迫有很大贡献[5]。从模拟的 $O_3$ 变化估计得到的总辐射强迫是 0.35 (0.15～0.55) W/m²，其中对流层 $O_3$ 变化导致的辐射强迫为 0.40 (0.20～0.60) W/m²，而平流层 $O_3$ 变化导致的辐射强迫为 −0.05 (−0.15～0.05) W/m²。$O_3$ 不是直接排放的产物，而是由光化学反应形成的。对流层 $O_3$ 辐射强迫大部分是由人为排放 $CH_4$、$NO_X$、CO 和非 $CH_4$ 挥发性有机化合物造成的，而平流层 $O_3$ 辐射强迫主要源自卤代烃导致的 $O_3$ 消耗。AR5 同时提供了由排放的化合物造成的辐射强迫。$O_3$ 消耗物质（ODS）导致的 $O_3$ 辐射强迫为 −0.15 (−0.30～0.00) W/m²，其中部分是在对流层。对流层 $O_3$ 前体物导致的 $O_3$ 辐射强迫为 0.50 (0.30～0.70) W/m²，其中部分在平流层，这个值要比 AR4 的值大。强有力的证据显示对流层 $O_3$ 对植物生理过程有不利影响[6]，因而影响植物吸收 $CO_2$ 的能力，但是这种间接效应的定量化估计具有*低信度*。$CH_4$ 氧化产生的平流层水汽的辐射强迫为 0.07 (0.02～0.12) W/m²。$O_3$ 和平流层水汽辐射强迫最佳估计值与 AR4 完全相同或与其范围一致。

自 AR4 以来，气溶胶强迫的绝对值在减小。由气溶胶－辐射相互作用产生的辐射强迫（也称之为气溶胶的直接效应）的最佳估计为 −0.35 (−0.85～0.15) W/m²，冰雪表面的黑碳造成的辐射强迫为 0.04 (0.02～0.09) W/m²。由气溶胶－辐射相互作用产生的有效辐射强迫为 −0.45 (−0.95～0.05) W/m²，总的气溶胶－云相互作用产生的有效辐射强迫为 −0.45 (−1.2～0.0) W/m²，总的气溶胶有效辐射强迫估计值为 −0.9 (−1.9～−0.1) W/m²。气溶胶有效辐射强迫估计中存在较大不确定性是造成自工业革命以来总的净强迫估计值不确定性的主要因素。自 AR4 以来在模式中包含了更多的气溶胶过程，但模式和观测之间的差异持续存在，导致气溶胶强迫估计的不确定性与 AR4 相同。尽管存在大的不确定范围，还是有*很高信度*显示气溶胶已经抵消了很大部分由混合温室气体造成的全球平均辐射强迫。

强有力的证据表明人类活动造成的土地利用变化增加了地表反射率[7-9]，其导致的辐射强迫为（−0.15 ± 0.10）W/m²。由于对自然和人为的地表反照率以及 1750 年前土地利用变化的比例有不同假定，辐射强迫的估计值存在一个较大的变化范围。土地利用变化也导致其他非辐射变化来影响地表温度，尤其是通过水文循环，这些更不确定且难以量化，但都趋向于抵消地表反照率改变产生的影响。因此，对由土地利用变化导致的全球平均温度的升高或降低还不确定。

把强迫归因于排放提供了从人类活动到强迫的更直接联系。由 $CH_4$ 排放导致的辐射强迫（约 1.0 W/m²）*很可能*比 $CH_4$ 浓度增加产生的辐射强迫大（约 0.5 W/m²），因为 $CH_4$ 浓度变化是多物种排放和随后的化学反应部分抵消作用的结果。另外，在全球尺度上，CO 的排放产生净的正辐射强迫，而 $NO_X$ 的排

www.climatechange.cn



放产生净的负辐射强迫。消耗卤代烃的排放很可能产生净的正辐射强迫，而它们本身正辐射强迫超过了平流层 $O_3$ 消耗产生的负辐射强迫。

气溶胶、$O_3$ 和地表反照率的变化具有高度的时空不均一性。其分布特征可以追溯到区域经济发展情况。在北美和北欧，气溶胶辐射强迫在20世纪初期就已经出现，而在亚洲、南美和南欧则在1980年左右出现。北美和北欧已经开始控制气溶胶污染，而亚洲、南美和南欧还没有开始这样做。整个20世纪，$O_3$ 的辐射强迫一直在增加，其峰值位于15°～30°N区域，这是由对流层$O_3$污染造成的。而南极洲上方的 $O_3$ 辐射强迫在20世纪末期则出现减小的趋势。这些特征和辐射强迫的空间变化，不仅影响着全球及区域温度响应，同时也影响着气候响应的其他方面，如水循环。

## 3　自然辐射强迫

1978—2011年的太阳总辐照度（TSI）的卫星观测资料显示，最近一个太阳周期的TSI最小值低于前两个周期。这可能导致了1986—2008年的−0.04 (−0.08～−0.00) W/m² 辐射强迫。由于TSI变化导致的1750—2011年间的正辐射强迫为0.05 (0.00～0.10) W/m²。这个结果明显小于AR4的估计结果，这是因为AR4及前几次报告中并没有考虑最近一个太阳周期的影响。关于未来太阳辐射强迫的估计具有*很低信度*，不过将来TSI辐射强迫的变化远小于温室气体增加引起的强迫的预估值却具有*高信度*。

火山气溶胶的辐射强迫在火山喷发后的短时期内（大约两年）达到最大。自1991年皮纳图博火山喷发之后，一直没有再出现大的火山喷发活动。不过几次小的喷发仍然导致2008—2011年间 −0.10 (−0.13～−0.07) W/m²的辐射强迫（与1750年比较），和−0.05 (−0.07～−0.03) W/m²的辐射强迫（与1999—2002年平均值比较）。自1750年至今，火山排放的 $CO_2$ 量比人类排放量至少小100倍。

除去几次大的火山喷发后的短暂时间外，自工业革命以来的自然强迫仅占人为强迫的很小部分（*很高信度*）。特别是，来自卫星观测的太阳辐射和火山气溶胶的强有力的证据表明[10]，在1980—2011年间，自然辐射强迫接近0 (−0.1～0.1) W/m²，而人为有效辐射强迫为1.0 (0.7～1.3) W/m²。过去15年的自然辐射强迫可能已经抵消相当部分（10%～95%）的人为辐射强迫。

## 4　未来的人为辐射强迫和排放指标

由图3可见，不同排放情景的辐射强迫之间的差别在2030年较小，但在2100年会变得很大，这些辐射强迫的差别是由 $CO_2$ 控制的。另外，RCP2.6、RCP4.5和RCP6.0在2100年 $O_3$ 的净有效辐射强迫与RCP8.5的气溶胶有效辐射强迫接近[11]。这些情景显示了气溶胶负有效总辐射强迫的大大减弱。其中硝酸盐气溶胶是个例外，其负有效辐射强迫的绝对值将大大增加。

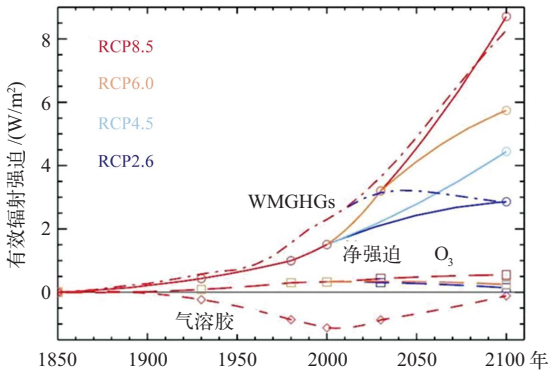


图3　ACCMIP模拟的全球平均人为有效辐射强迫随时间变化（带圆圈的实线表示净有效辐射强迫，带方形的长虚线代表$O_3$的有效辐射强迫，带菱形的短虚线表示气溶胶的有效辐射强迫，点划线代表充分混合的温室气体）[11]

Fig. 3　Global mean anthropogenic forcing with symbols indicating the times at which ACCMIP simulations were performed (Solid lines with circles are net, long dashes with squares are ozone, short dashes with diamonds are aerosol, and dash-dot lines are WMGHGs) [11]

排放指标主要指GWP和GTP，可以衡量不同物质排放、不同区域／国家或者不同来源／时间段排放对气候变化的相对和绝对贡献。目前被用于制定政策的指标是GWP，定义为选定时间段内，某种温室气体造成的辐射强迫与 $CO_2$ 造成的辐射强迫的比值。而GTP的含义为，在选定时间段内，某种温室

气体造成的全球平均地表温度的变化与$CO_2$造成的相应变化的比值。由于辐射强迫和温度响应也受所选时间段的影响，GWP和GTP均存在显著的不确定性，其中GTP的不确定性更大些。两者在反映间接效应和反馈时存在不一致性并均受到某种限制。其数值依赖于所用的指标类型和所选取的时间范围。

## 5 结 论

综上所述，AR5关于人为辐射强迫的几个主要结论是：混合温室气体的辐射强迫为2.83 (2.54～3.12) W/m$^2$，与AR4相比，增加了8%。自AR4以来，气溶胶强迫的数值在减小，其中由气溶胶－辐射相互作用产生的有效辐射强迫为−0.45 (−0.95～0.05) W/m$^2$，气溶胶－云相互作用产生的有效辐射强迫为−0.45 (−1.2～0.0) W/m$^2$，总的气溶胶有效辐射强迫估计值为−0.9 (−1.9～0.1) W/m$^2$。虽然自AR4以来在模式中包含了更多的气溶胶过程，但模式和观测之间存在的差异导致气溶胶强迫估计的不确定性与AR4相同。然而，仍有*很高信度*显示气溶胶已经抵消了很大部分由混合温室气体造成的全球平均辐射强迫。强有力的证据表明人类活动造成的土地利用变化增加了地表反射率，其辐射强迫为（−0.15 ± 0.10）W/m$^2$。

AR5关于自然辐射强迫的主要结论是：关于未来太阳辐射强迫的估计具有*很低信度*，而未来太阳总辐照度辐射强迫的变化远小于温室气体增加引起的强迫的预估值却具有*高信度*。除去几次大的火山喷发后的短暂时间外，自工业革命以来的自然强迫仅占人为强迫的很小部分（*很高信度*）。■

**致 谢**：国家气候中心的博士研究生赵树云、硕士研究生陈琪，南京信息工程大学的硕士研究生杨冬冬，国家卫星气象中心的杨冰韵硕士和兰州大学博士研究生何永利对IPCC AR5第8章执行摘要部分内容和图标进行了中文翻译工作。

**参考文献**

[1] Myhre G, Shindell D, Bréon F-M, *et al*. Anthropogenic and natural radiative forcing [M/OL]//IPCC. Climate change 2013: the physical science basis. Cambridge: Cambridge University Press, in press. 2013-09-30 [2013-09-30]. http://www.climatechange2013.org/images/uploads/WGIAR5_WGI-12Doc2b_FinalDraft_Chapter08.pdf

[2] Shindell D T, Pechony O, Voulgarakis A, *et al*. Interactive ozone and methane chemistry in GISS-E2 historical and future climate simulations [J]. Atmospheric Chemistry and Physics, 2013, 13: 2653-2689

[3] Lohmann U, Rotstayn L, Storelvmo T, *et al*. Total aerosol effect: radiative forcing or radiative flux perturbation? [J]. Atmospheric Chemistry and Physics, 2010, 10: 3235-3246

[4] Hansen J, Sato M, Ruedy R, *et al*. Efficacy of climate forcings [J]. Journal of Geophysical Research: Atmospheres, 2005, 110, D18104

[5] Isaksen I, Granier C, Myhre G, *et al*. Atmospheric composition change: climate-chemistry interactions [J]. Atmospheric Environment, 2009, 8: 5138-5192, doi:10.1016/j.atmosenv.2009.08.003

[6] Ashmore M R. Assessing the future global impacts of ozone on vegetation [J]. Plant Cell and Environment, 2005, 28: 949-964

[7] Pongratz J, Reick C, Raddatz T, *et al*. A reconstruction of global agricultural areas and land cover for the last millennium [J]. Global Biogeochemical Cycles, 2008, 22, Gb3018

[8] Kaplan J O, Krumhardt K M, Ellis E C, *et al*. Holocene carbon emissions as a result of anthropogenic land cover change [J]. Holocene, 2011, 21: 775-791

[9] Gaillard M J, Sugita S, Mazier F, *et al*. Holocene land-cover reconstructions for studies on land cover-climate feedbacks [J]. Climate of the Past, 2010, 6: 483-499

[10] Kopp G, Lean J. A new, lower value of total solar irradiance: evidence and climate significance [J].Geophysical Research Letter, 2011, 38, L01706

[11] Shindell D T, Lamarque J F, Schulz M, *et al*. Radiative forcing in the ACCMIP historical and future climate simulations [J]. Atmospheric Chemistry and Physics, 2013, 13: 2939-2974

# 多层四流球谐函数算法的构建及在大气辐射传输模式中的应用*

张 华[1,2] 卢 鹏[2,3]
ZHANG Hua[1,2] LU Peng[2,3]

1. 南京信息工程大学,气象灾害预报预警与评估协同创新中心,南京,210044
2. 中国气象局气候研究开放实验室,国家气候中心,北京,100081
3. 江苏省气候中心,南京,210008
1. *Collaborative Innovation Center on Forecast and Evaluation of Meteorological Disasters, Nanjing University of Information Science and Technology, Nanjing* 210044, *China*
2. *Laboratory for Climate Studies, China Meteorological Administration, National Climate Center, Beijing* 100081, *China*
3. *Jiangsu Climate Center, Nanjing* 210008, *China*

2013-11-19 收稿,2014-06-30 改回.

张华,卢鹏. 2014. 多层四流球谐函数的构建及在大气辐射传输模式中的应用. 气象学报, 72(6):1258-1269
**Zhang Hua, Lu Peng. 2014. Construction of the multi-layers four-stream spherical harmonic expansion algorithm and its application to atmospheric radiative model. *Acta Meteorologica Sinica*, 72(6):1258-1269**

**Abstract** In order to increase the accuracy of radiative transfer calculation without increasing calculation cost, a method using the single-layer four-stream spherical harmonic expansion approximation combining with the two-stream adding algorithm has been built in this paper. Then, the four-stream spherical harmonic expansion approximation was compared with the traditional Eddington approximation and the four-stream discrete ordinate approximation by using the 48-stream discrete-ordinate approximation method as a standard reference. The results of the upward and downward radiative fluxes as well as the heating rates in the real atmosphere have been shown. For clear sky, the differences between the Eddington method, four-stream spherical harmonic expansion approximation, four-stream discrete-ordinate approximation, and the standard results are all less than 0.3 K/d for heating rates, and less than 1% and 0.6% for the upward and downward radiative fluxes, respectively. It shows that the three methods have no large difference for heating rate calculations. The two four-stream approximations are a little more accurate than the Eddington method for flux calculation in clear sky. For cloudy sky, the differences of heating rates between the two four-stream methods and the standard results are all less than 1% at the top of the cloud, whereas these differences between the Eddington method and the standard results are large than 5%. Therefore, the four-stream spherical harmonic expansion approximation built in this paper can be applied to the radiative transfer model to improve the accuracies of the whole radiation calculation for clear sky and the heating rate calculation for cloudy sky without increasing large costs.

**Key words** Four-stream spherical harmonic expansion, Eddington approximation, Four-stream discrete ordinate method, Radiative heating rate, Radiative flux

**摘 要** 为了在不大幅度增加计算成本的情况下提高大气辐射传输计算的精度,利用单层四流球谐函数结合多层二流累加法,构造了可用于多层大气的四流球谐函数算法。为了比较与其他辐射传输算法的差异,引入48流离散纵坐标算法作为比较

* 资助课题:国家自然科学基金(41375080)、科技部公益性行业(气象)科研专项项目(GYHY201406023)和国家重点基础研究发展计划项目(2011CB403405)。
作者简介:张华,主要从事大气辐射传输模式、云-辐射相互作用及其气候影响等方面的研究。E-mail: huazhang@cma.gov.cn

标准,Eddington近似、四流离散纵坐标算法作为比较对象。在真实大气廓线条件下,计算了晴空和有云大气顶向上辐射通量、地表向下辐射通量以及加热率廓线。得出以下结论:在晴空情况下,与作为标准的48流离散纵坐标法相比,Eddington近似、四流离散纵坐标法和新构造的四流球谐函数方法加热率绝对误差都小于0.3 K/d;向上、向下辐射通量的相对误差分别小于1%和0.6%。这表明在晴空情况下,3种算法对加热率的计算精度差别不大;对辐射通量的计算精度,两种四流近似算法比传统的Eddington近似更为精确。在有云情况下,与48流离散纵坐标法相比,四流球谐函数和四流离散纵坐标法计算的云顶加热率相对误差小于1%,而Eddington近似计算的云顶加热率相对误差大于5%。结果表明:新构造的四流球谐函数算法可用于大气辐射传输模式,在不大幅度增加计算成本的同时,提高了晴空大气的整体辐射计算精度和有云大气辐射加热率的计算精度。

**关键词**　四流球谐函数,Eddington近似,四流离散纵坐标法,辐射加热率,辐射通量

**中图法分类号**　P422

## 1　引　言

辐射方案的精度差异会对大气模式模拟效果产生一定影响(杨学胜等,2009;许尤福等,2011;荆现文等,2012;张梦等,2014;Zhang,et al,2014)。在平行大气假设下,Stamnes等(1988)开发的离散纵标法(DISORT)程序包是目前使用最广泛的辐射传输模式之一。DISORT 32流或48流方案计算的辐射结果一般可以作为衡量其他辐射传输算法优劣的参考标准。但是高流(大于二流)DISORT程序的计算成本比较高,目前高性能计算机的运算能力尚不足以将高流DISORT算法应用于气候模式。目前大多数气候模式仍然采用二流辐射传输方法,其主要优点是计算速度快,且在晴空大气下的计算精度基本能满足气候模式的需求,但是在有云大气情况下误差较大。因此,对于有云大气情况,需要采用更为精确的辐射传输计算方法。随着高性能计算机的发展,四流辐射传输方案逐渐被应用于全球气候模式的计算。Shibata等(1992)研究表明利用四流矩阵算子法能将辐射传输计算的误差控制在10%以内。Chou(1992)利用单层四流离散坐标法结合二流累加法,计算了辐射通量和加热率,与通过求解线性方程组的传统四流离散坐标法相比,明显地节省了计算时间。Kay等(2001)比较了二流和四流离散纵坐标法以及矩阵求逆法。其结果表明在光化通量的计算中,四流离散纵坐标法略优于矩阵求逆法,而两者都要优于二流离散纵坐标法。而在辐射通量的比较中,四流离散纵坐标法要优于矩阵求逆法和二流离散纵坐标法。Ayash等(2008)在第3代加拿大气候中心大气环流模式(Scinocca,et al,2008)中引入了二流-四流混合离散纵坐标法(Liou,et al,1988),并比较了其与二流近似辐射传输算法对辐射通量计算结果的影响。Zhang等(2013a,2013b)分别利用四流离散纵坐标、四流球谐函数法结合四流累加法构造了多层四流离散纵坐标和多层四流球谐函数法,在有云情况下可以使得加热率和辐射通量的相对误差小于1%。

以上研究进展表明与二流辐射传输方案相比,四流方案在计算精度上有明显的优势。采用二流累加法和单层四流辐射传输方案相结合能够兼顾计算时间和精度。Li等(1996)的研究表明,对于求解单层辐射传输方程而言,四流球谐函数辐射传输算法计算的透过率和反射率精度要略优于四流离散纵标法,大幅度优于Eddington近似方法。因此,本研究利用Li等(1996)给出的单层四流球谐函数辐射传输算法的数值解析解结合累加法,构造了应用于非均匀大气辐射传输计算的四流球谐函数辐射传输算法,首先应用于北京气候中心辐射传输模式(BCC-RAD)(Zhang,et al,2003,2006a,2006b;Randles,et al,2013),并进行了检验。

## 2　单层四流球谐函数结合多层二流累加法的辐射传输算法介绍

### 2.1　单层四流球谐函数求解

一般的辐射传输方程可以写成以下形式(廖国男,2004)

$$\mu \frac{\mathrm{d}I}{\mathrm{d}\tau} = I - J \tag{1}$$

式中,$\mu$为局地天顶角,$I$是辐射强度,$\tau$是光学厚度,$J$是源函数。

Li等(1996)推导了单层四流球谐函数算法的

数值解

$$F^{\pm} = \pi(I_0 \pm 2I_1 \pm \frac{5}{4}I_2) \tag{2}$$

式中,$I_i$ 为辐射强度展开式的各项,$F^{\pm}$ 为向上和向下辐射通量。

### 2.2 多层二流累加法

Coakley 等(1983)给出了计算 2 层大气总的反射率和透射率的公式

$$r_{12}(\mu_0) = r_1(\mu_0) + \frac{\bar{t}_1[t_1(\mu_0) - \mathrm{e}^{-\tau_1/\mu_0}\bar{r}_1 + \mathrm{e}^{-\tau_1/\mu_0} r_2(\mu_0)]}{1-\bar{r}_1\bar{r}_2} \tag{3}$$

$$t_{12}(\mu_0) = \mathrm{e}^{-\tau_1/\mu_0} t_2(\mu_0) + \frac{\bar{t}_2[t_1(\mu_0) - \mathrm{e}^{-\tau_1/\mu_0} + \mathrm{e}^{-\tau_1/\mu_0} r_2(\mu_0)\bar{r}_1]}{1-\bar{r}_1\bar{r}_2} \tag{4}$$

$$\overline{r_{12}} = \overline{r_1} + \frac{\bar{t}_1\bar{r}_2\bar{t}_1}{1-\bar{r}_1\bar{r}_2} \tag{5}$$

$$\overline{t_{12}} = \frac{\bar{t}_1\bar{t}_2}{1-\bar{r}_1\bar{r}_2} \tag{6}$$

式中,$r_i$、$\bar{r}_i$、$t_i$、$\bar{t}_i$ 分别表示第 $i$ 层的反射率、漫反射率、透过率/漫射透过率;$r_{12}$、$\bar{r}_{12}$、$t_{12}$、$\bar{t}_{12}$ 分别表示总反射率、总漫反射率、总透过率、总漫射透过率;$\mu_0$ 是入射太阳天顶角余弦,$\tau_1$ 表示光学厚度。

通过式(3)—(6),可以得到任意两层的反射率和透过率,从而得到每层大气的向上和向下的辐射通量。

单层四流球谐函数方法在辐射强度的计算上采用了更多的展开项,在精度上优于单层二流辐射传输方案。利用式(3)—(6)计算的任意层的反射率和透过率,采用的是二流累加法,在时间上优于多层四流辐射传输方案。因此,单层四流球谐函数和多层二流累加法的组合方式,一方面单层计算具有四流方法的精度;另一方面可以节约部分计算时间。

### 2.3 BCC-RAD 介绍

BCC-RAD 采用 Zhang 等(2003,2006a,2006b)研发的相关 $k$ 分布算法;原短波辐射传输方案采用二流 Eddington 算法。波长范围 10—49000 $\mathrm{cm}^{-1}$,分为 17 个波段(长波 8 个波段,短波 9 个波段)。共包含了 8 种主要温室气体(水汽、二氧化碳、臭氧、氧化亚氮、甲烷和氟氯烃等),其气体吸收系数和吸收截面数据取自 HITRAN2000 光谱数据库(Rothman,et al,2001)。水汽、二氧化碳、臭氧和氧气的连续吸收系数数据来源于 CKD_2.4 (Zhang,et al,2003)。水云和冰云光学性质来自 Nakajima 等(2000);气溶胶光学性质取自卫晓东等(2011)、Zhang 等(2012)。详细介绍可参见 Randles 等(2013)。

## 3 四流球谐函数结合二流累加法在大气辐射模式中的应用

### 3.1 晴空大气情况

将 48 流 DISORT 算法、Eddington 近似、四流球谐函数和四流离散纵坐标算法加入 BCC-RAD,主要比较四流球谐函数方法与传统的 Eddington 近似算法对大气辐射计算的影响。由于四流离散纵坐标法被广泛应用于大气辐射传输模式中,因此,文中也将该算法加入比较。同时将 48 流 DISORT 辐射传输算法的结果作为参考标准。4 种辐射传输方案的相函数展开式采用 Henyey 等(1941)提出的公式

$$P_{\mathrm{HG}}(\cos\theta) = \sum_{l=0}^{N}(2l+1)g^l P_l(\cos\theta)。$$

式中,$P_{\mathrm{HG}}(\cos\theta)$ 为项函数,$P_l(\cos\theta)$ 为勒让德函数展开式,$g$ 为非称的因子,$\theta$ 为太阳天项角。

48 流 DISORT 辐射传输算法相函数展开为 48 项,Eddington 近似将相函数展开成两项,四流球谐函数和四流离散纵坐标法将相函数展开成 4 项。在进行辐射传输计算之前对光学厚度、单次散射比和相函数采用了 δ 函数调整(廖国男,2004)。

首先在晴空情况下比较了 Eddington 近似、四流球谐函数、四流离散纵坐标法与 48 流 DISORT 算法计算的辐射通量以及加热率的差别。在计算中,大气廓线采用的中纬度夏季大气廓线与张华等(2005)相同,模式的垂直分辨率为 1 km,在计算中模式顶选取在 70 km,因为 50 km 以上需要考虑非局地热力学,因此,作图时仅显示 50 km 以下的结果。地表反照率采用 Nakajima 等(2000)的方案,在短波第 9、10 波段分别取 0.1 和 0.26;在短波 11—17 波段取为 0.3。

图 1 给出了晴空加热率的比较结果。与 48 流 DISORT 辐射传输方案的加热率相比,Eddington 近似、四流球谐函数和四流离散纵坐标 3 种辐射传输方案在 40 km 以下高度的绝对误差都小于 0.3 K/d;太阳天顶角为 60° 时小于 0.15 K/d。20 km 以下高度,3 种辐射传输方案的加热率计算结果的绝对误差都小于 0.03 K/d;20 km 以上高度,3 种辐射传输方案计算的加热率误差有所增大,但相对误差不超过 2%。

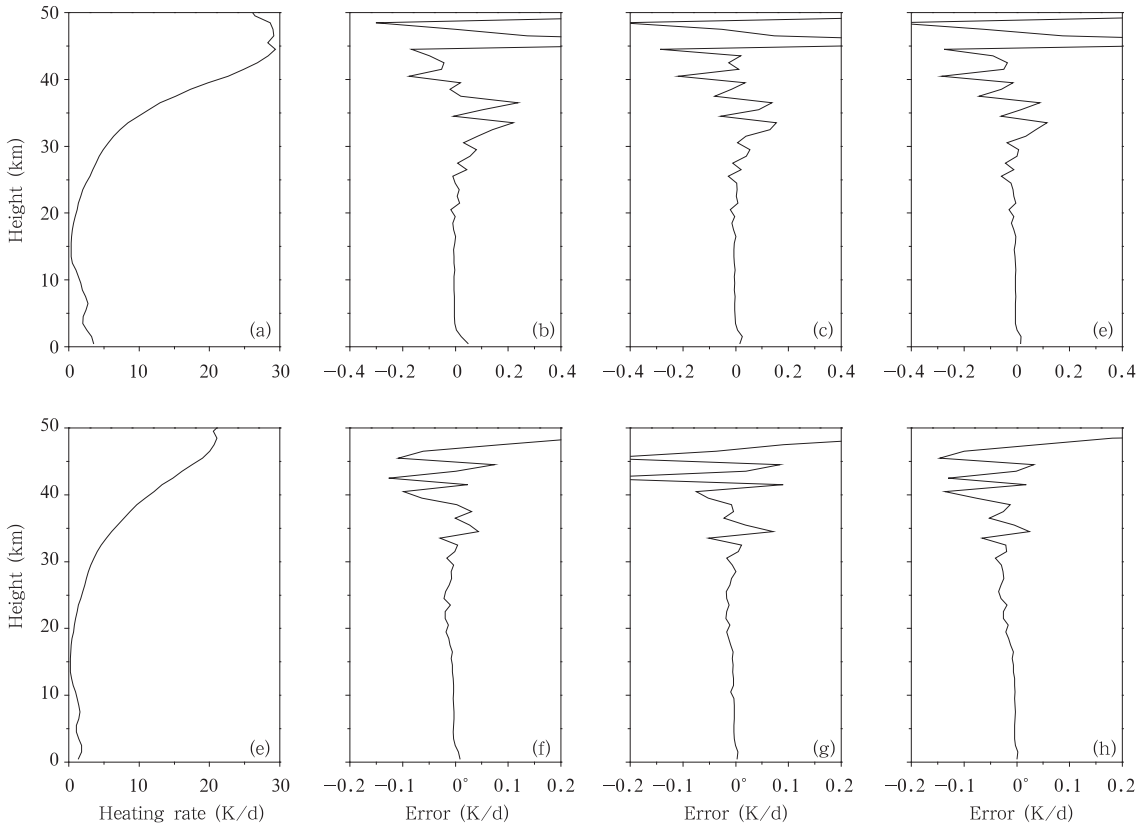


图 1　晴空短波加热率

(a、e. 48 流 DISORT 辐射传输方案的参考结果,b、f. Eddington 近似,c、g. 四流球谐函数,d、h. 四流离散纵坐标辐射传输方案与 48 流 DISORT 辐射传输方案的差值;(a)—(d)为太阳天顶角为 0°时的结果,(e)—(h)为太阳天顶角为 60°时的结果)

Fig. 1　Shortwave heating rate in clear sky

((a), (e) is the results of the 48-stream discrete-ordinate approximation method, the others are the differences between the Eddington method ((b), (f)), four-stream spherical harmonic expansion approximation ((c), (g)), four-stream discrete-ordinate approximation ((d), (h)) and 48-stream discrete-ordinate approximation method, respectively. (a) - (d) are for the solar zenith angle of 0°; and (e) - (h) are for the solar zenith angle of 60°)

图 2 给出了短波向下辐射通量的比较结果,与 48 流 DISORT 辐射传输方案的向下辐射通量结果相比,当太阳天顶角为 0°时,Eddington 近似、四流球谐函数、四流离散纵坐标 3 种辐射传输方案中,Eddington 近似的最大误差为 - 6.3 W/m$^2$;四流球谐函数法的最大误差为 - 1.5 W/m$^2$;四流离散纵坐标法的最大误差为 2.8 W/m$^2$。太阳天顶角为 60°时,Edington 近似的最大误差为 - 1.44 W/m$^2$;四流球谐函数法的最大误差为 - 1.1 W/m$^2$;四流离散纵坐标法的最大误差为 1.14 W/m$^2$。从中可以看出,当太阳天顶角为 0°时,两种四流辐射传输算法的结果要优于 Eddington 近似。太阳天顶角为 60°时,3 种辐射传输算法的误差相差不大,其中 Eddington 近似和四流球谐函数的误差曲线的形状相似,只是四流球谐函数的误差要略小。Eddington 近似是球谐函数的二流展开。因此,与四流球谐函数的误差曲线形状相似,而由于四流球谐函数的辐射强度展开式比 Eddington 近似的展开式多两项,因此计算误差要略小。对于晴空向下辐射通量而言,3 种辐散传输算法的误差相差不大,相对误差都在 0.6%以内。

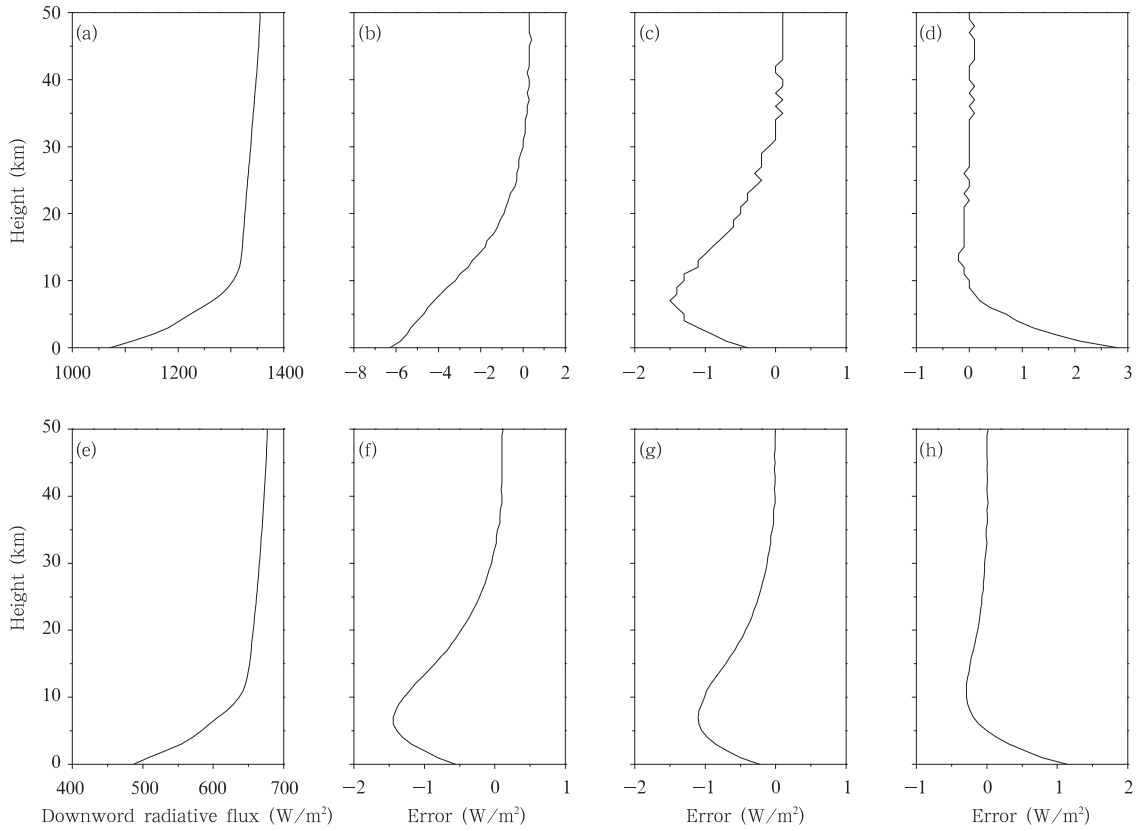


图 2 同图 1,但为晴空向下辐射通量的结果

Fig. 2 As in Fig. 1 but for the downward radiative flux in clear sky

图 3 给出了短波向上辐射通量的比较。与 48 流 DISORT 辐射传输方案的结果相比,太阳天顶角为 0°时,Eddington 近似、四流球谐函数、四流离散纵坐标 3 种辐射传输方案中 Eddington 近似的最大误差为 -1.92 W/m²,四流球谐函数法的最大误差为 -1.62 W/m²,四流离散纵坐标法的最大误差为 2.17 W/m²。太阳天顶角为 60°时,Eddington 近似的最大误差为 -1.11 W/m²,四流球谐函数法的最大误差为 -0.92 W/m²,四流离散纵坐标法的最大误差为 -0.9 W/m²。对于晴空向上辐射通量而言,3 种辐散传输算法的误差相差不大,相对误差都在 1%以内。

### 3.2 有云大气情况

在有云情况下,仍然采用中纬度夏季大气廓线进行计算。云水含量和云滴有效半径的设置与 Fu 等(1997)中的设置一致,本文选取的低云位于 1—2 km,云水含量为 0.22 g/m³,云滴有效半径为 5.89 μm;中云位于 4—5 km,云水含量为0.28 g/m³,云滴有效半径为 6.2 μm。由于着重关注云的辐射传输计算,因此在计算有云大气情况时,将模式的垂直分辨率加密到 0.25 km,同时只显示 16 km 以下有云时的计算结果,垂直分辨率设置与 Fu 等(1997)一致。

图 4 给出了低云情况下短波加热率的比较。可以看出,与 48 流 DISORT 辐射传输方案加热率结果相比,太阳天顶角为 0°时,Eddington 近似、四流球谐函数、四流离散纵坐标 3 种辐射传输方案中,Eddington 近似在云顶的加热率最大误差为 -1.57 K/d,而四流球谐函数和四流离散纵坐标方法在云顶的加热率绝对误差都在 0.3 K/d 以内;太阳天顶角为 60°时,Eddington 近似、四流球谐函数、四流离散纵坐标 3 种辐射传输方案计算的云顶加热率的绝对误差都小于 0.2 K/d。这表明在太阳天顶角比较小时,Eddington 近似引起的云顶加热率的相对误差可以达到 5%,而同样情况下的四流球谐函数和四流离散纵坐标方案的相对误差小于 1%。

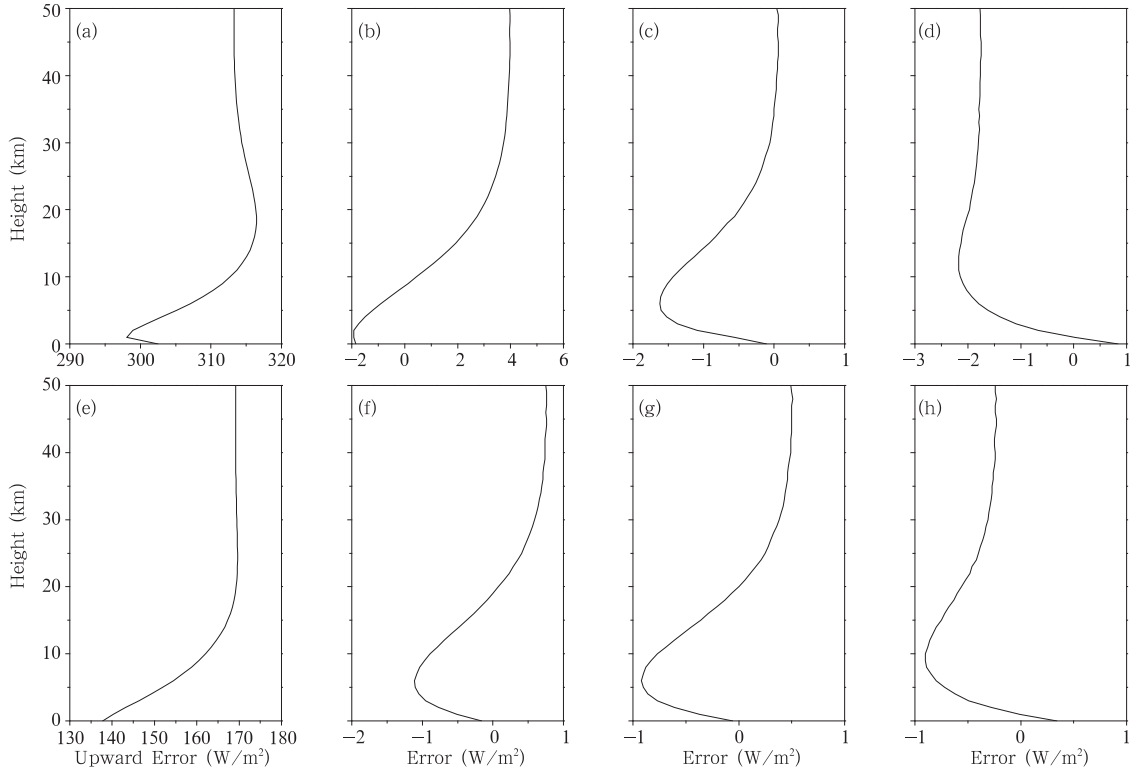


图 3　同图 1,但为晴空向上辐射通量的结果

Fig. 3　As in Fig. 1 but for the upward radiative flux in clear sky

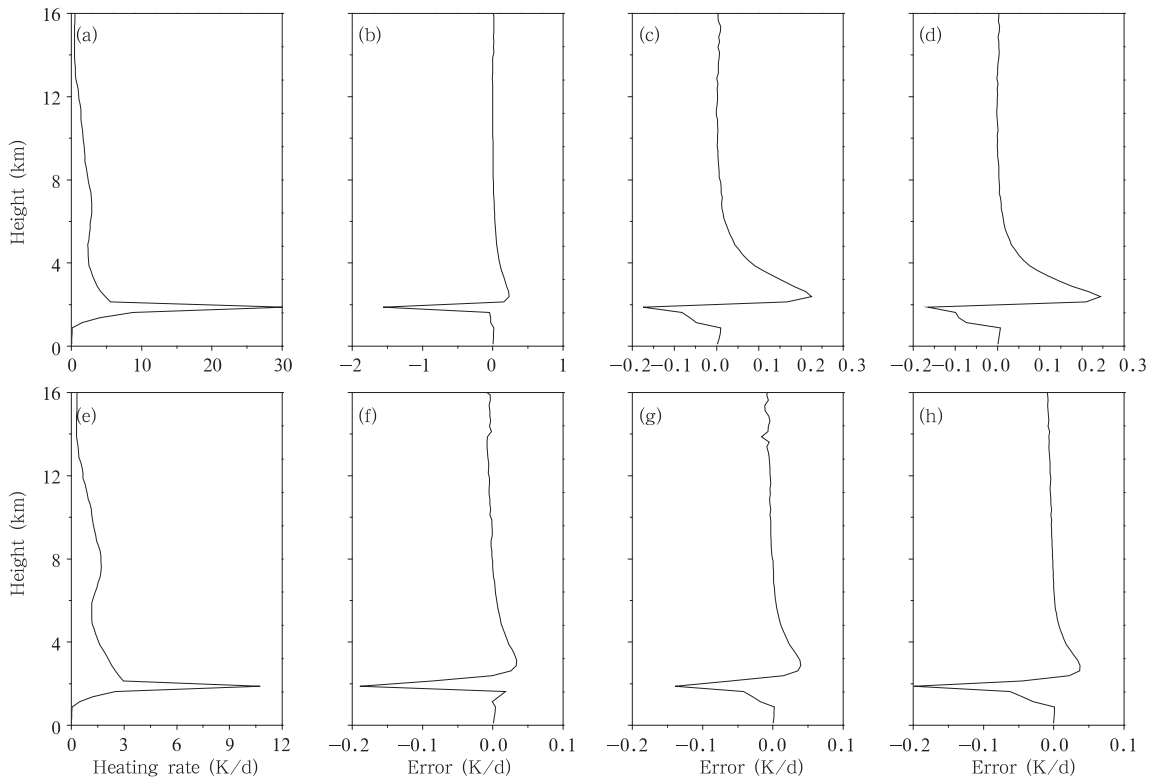


图 4　同图 1,但为有云大气短波加热率的结果

Fig. 4　As in Fig. 1 but for the shortwave heating rate in cloudy sky

图5给出了有云大气短波向下辐射通量的比较。可以看出,与48流DISORT辐射传输方案向下辐射通量结果相比,太阳天顶角为0°时,Eddington近似、四流球谐函数、四流离散纵坐标3种辐射传输计算方案中,Eddington近似的最大误差为-13.6 W/m$^2$,四流球谐函数法最大误差为5.13 W/m$^2$,四流离散纵坐标法的最大误差为40.87 W/m$^2$。而太阳天顶角为60°时,Eddington近似的最大误差为-6.64 W/m$^2$,四流球谐函数法的最大误差为-13.26 W/m$^2$,四流离散纵坐标法的最大误差为9.82 W/m$^2$。当太阳天顶角为0°时,3种辐射传输方案计算的短波向下辐射通量的最大差别都出现在云顶的下一层大气,同时Eddington方案的最大差别为负值,而两种四流辐射传输算法的最大差别为正值。出现这种差别的原因可能与相函数的展开式有关。两种四流方案都将相函数展开成4项,与Eddington二流方案相比多展开了两项,因此可能造成更多的前向散射,从而造成云顶下一层的辐射通量相对较大,而在进行辐射传输计算时由于仍然采用与二流方案相匹配的累加法,因此计算的总的辐射通量,会由于单层四流方案与多层二流累加法的不匹配造成比较大的误差。而当太阳天顶角为60°时,Eddington近似和四流球谐函数法计算的短波向下辐射通量的最大误差都出现在云顶所在层大气,最大误差为负值;而四流球谐函数算法计算的向下辐射通量的最大误差出现云顶下一层大气,最大误差为正值。

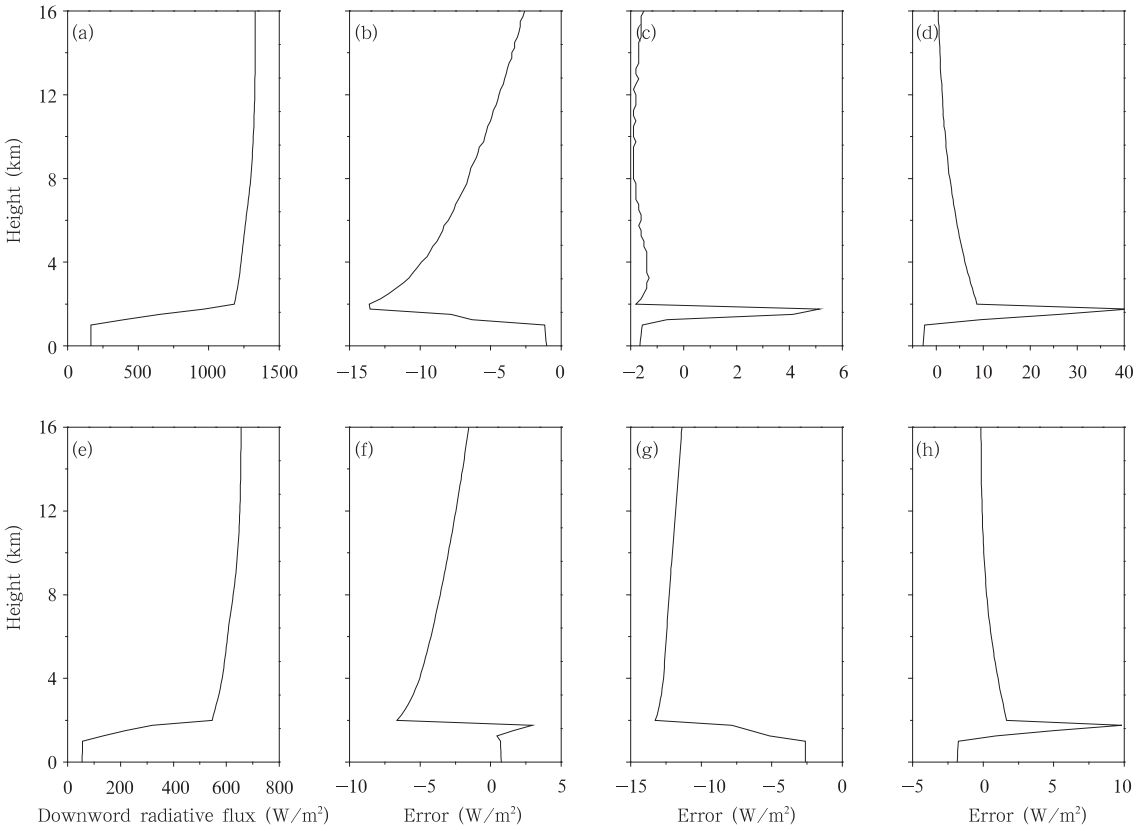


图5 同图1,但为有云大气短波向下辐射通量的结果

Fig. 5 As in Fig. 1 but for the downward radiative flux in cloudy sky

图6给出有云大气短波向上辐射通量的比较。可以看出,与48流DISORT辐射传输方案向上辐射通量结果相比,太阳天顶角为0°时,Eddington近似、四流球谐函数、四流离散纵坐标3种辐射传输方案中,Eddington近似的最大误差为-12.63 W/m$^2$,四流球谐函数法的最大误差为6.79 W/m$^2$,四流离散

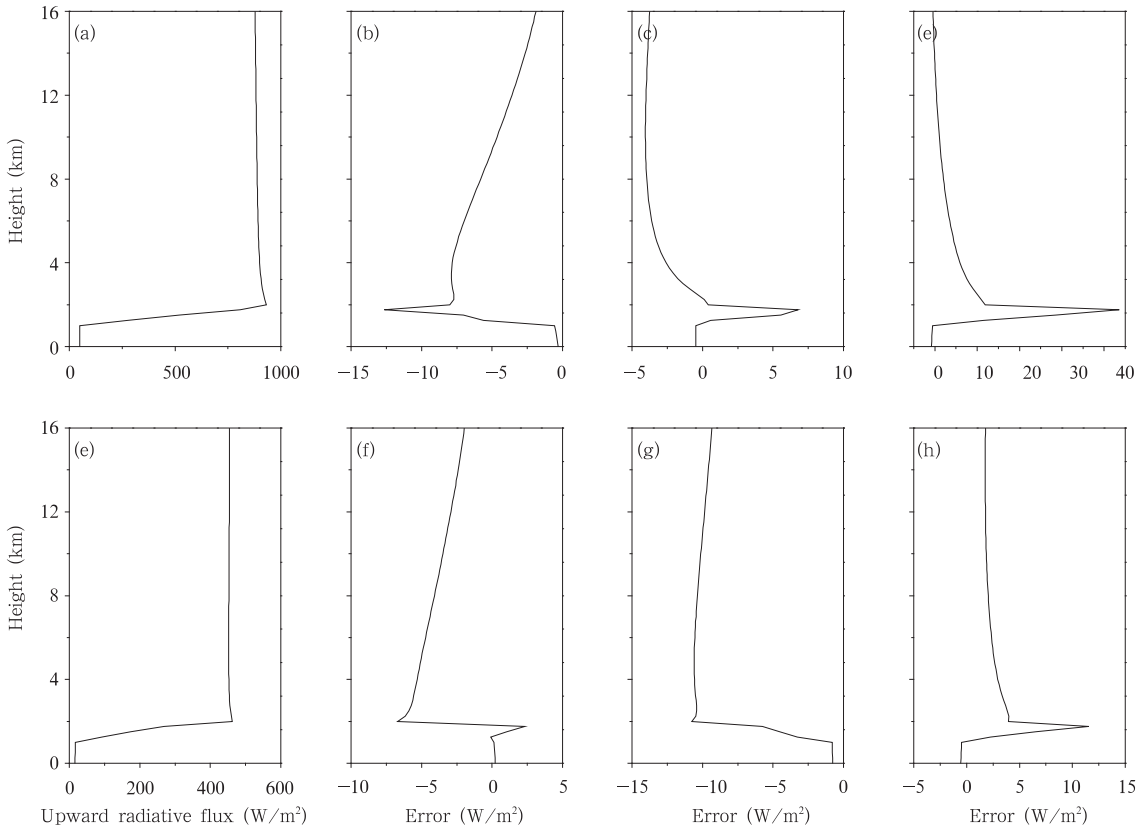


图 6　同图 1,但为有云大气短波向上辐射通量的结果

Fig. 6　As in Fig. 1 but for the upward radiative flux in cloudy sky

纵坐标法的最大误差为 43.57 W/m²;太阳天顶角为 60° 时,Eddington 近似的最大误差为 −6.71 W/m²,四流球谐函数法的最大误差为 −10.76 W/m²,四流离散纵坐标方法的最大误差为 11.53 W/m²。最大误差出现的位置与正负和短波向下辐射通量的情况一致。

从图 5 和 6 可以看出,与 48 流 DISORT 辐射传输方案结果相比,Eddington 近似、四流球谐函数、四流离散纵坐标 3 种辐射传输方案在云顶附近的辐射通量的误差较大,但是向上辐射通量和向下辐射通量的误差是一致的。气候模式中辐射模块的输出量主要是大气顶和地表的辐射通量以及加热率,而加热率是由相邻两层的净辐射通量决定的,因此在图 7 中给出了 48 流 DISORT 算法计算的短波净辐射通量以及 Eddington 近似、四流球谐函数、四流离散纵坐标算法计算的短波净辐射通量分别与 48 流 DISORT 算法的差值。可以看出,以上 3 种辐射传输方案与 48 流 DISORT 辐射传输方案的结果相比,在太阳天顶角为 0°时,Eddington 近似的最大误差为 −5.6 W/m²,四流球谐函数法的最大误差为 −2.22 W/m²,四流离散纵坐标法的最大误差为 −3.19 W/m²;太阳天顶角为 60°时,Edington 近似的最大误差为 0.62 W/m²,四流球谐函数法的最大误差为 −2.66 W/m²,四流离散纵坐标法的最大误差为 −2.42 W/m²。从中可以看出,当太阳天顶角为 0°时,两种四流辐射传输方案计算的净辐射通量要优于 Eddington 近似;而当太阳天顶角为 60°时,Eddington 近似计算的净辐射通量结果要优于这两种四流方案。

表 1 给出了晴空大气情况大气顶和地表的净辐射通量的比较结果,大气顶取 50 km。从表 1 中可以看出太阳天顶角为 0°时,四流球谐函数法的结果远好于其他两种方法;太阳高度角为 60°时,四流球谐函数法也略好于其他两种方法。

表 2 给出了有云大气的比较结果,可以看出,太阳天顶角为0°时,对大气顶的净辐射通量的计算,

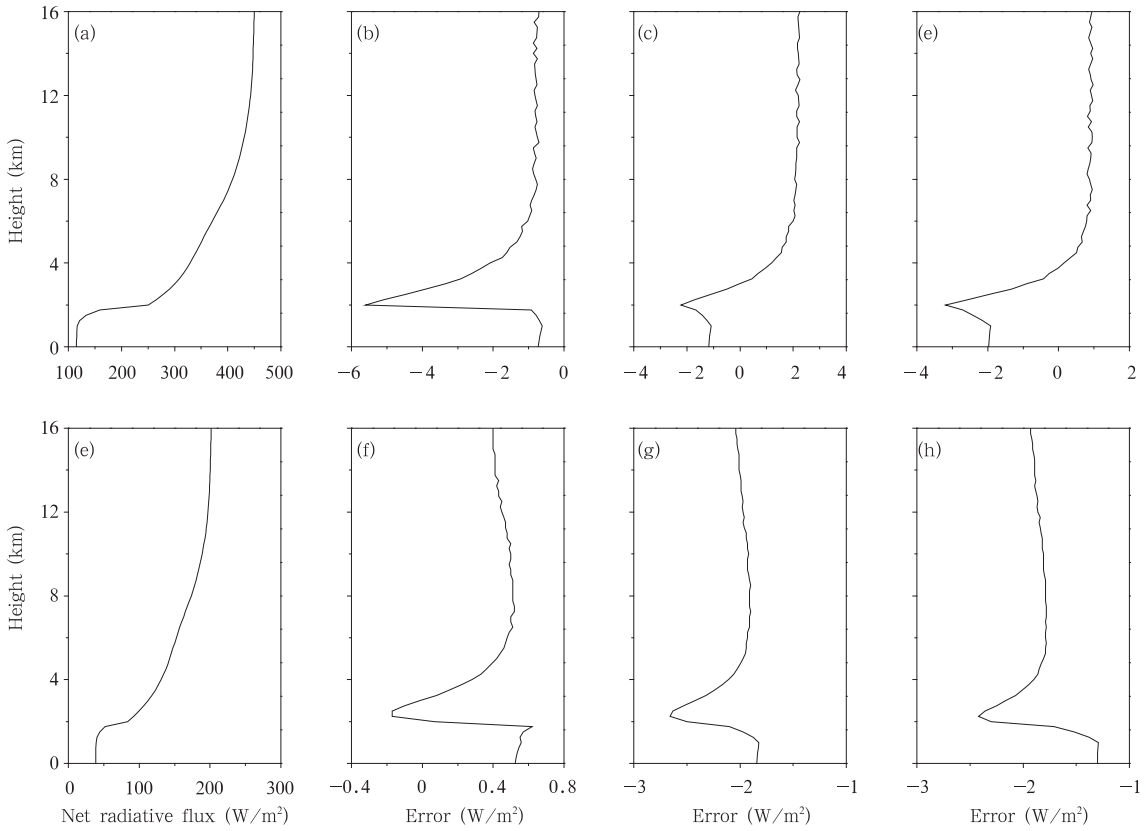


图 7 同图 1,但为有云大气净辐射通量的结果

Fig. 7 As in Fig. 1 but for the net radiative flux in cloudy sky

表 1 晴空条件下大气顶和地表净辐射通量比较(单位:W/m²)

Table 1 Comparison of the net flux at TOA with that at the surface among the different algorithms for clear sky (unit: W/m²)

| 晴空大气 | 太阳天顶角 0° | | 太阳天顶角 60° | |
|---|---|---|---|---|
| | 大气顶 | 地表 | 大气顶 | 地表 |
| DISORT | 1041.5 | 769.2 | 507.4 | 349.2 |
| Eddington | -3.7 | -4.4 | -0.1 | -0.5 |
| 四流球谐函数 | 0.3 | -0.4 | -0.1 | -0.3 |
| 四流离散纵坐标 | 1.8 | 2.0 | 0.3 | 0.8 |

表 2 有云大气情况下大气顶和地表净辐射通量比较(单位:W/m²)

Table 2 As in Table 1 but for cloudy sky (unit: W/m²)

| 有云大气 | 太阳天顶角 0° | | 太阳天顶角 60° | |
|---|---|---|---|---|
| | 大气顶 | 地表 | 大气顶 | 地表 |
| DISORT | 498.9 | 159.3 | 218.6 | 53.5 |
| Eddington | -1.6 | -0.6 | 0.9 | 0.7 |
| 四流球谐函数 | 1.6 | -1.2 | -3.3 | -1.9 |
| 四流离散纵坐标 | -0.3 | -2.8 | -2.3 | -1.5 |

四流离散纵坐标法的结果较好,而对地表的净辐射通量的计算,Eddington 方法结果较好;太阳天顶角为 60°时,Eddington 方法的结果要优于两种四流方法,可能是由于后两者单层辐射方程求解与多层二流累加法不匹配造成的;但两种四流方法的最大误差都小于 3.3 W/m²。

图 8 给出了低云和中云情况下的云顶加热率随太阳天顶角的变化。从中可以看出,随着太阳天顶角的减小(对应太阳天顶角的余弦的增大),云顶的向下辐射能量增大,因此云顶的加热率也随之增大。不论是低云还是中云情况,当太阳天顶角大于 60°时,Eddington 近似计算的云顶加热率略高于两种四流方案;当天顶角小于 60°时,Eddington 近似计算的云顶加热率开始低于两种四流方案。与 48 流辐射传输方案计算的云顶加热率相比,两种四流方案计算的短波加热率在绝大多数太阳天顶角情况

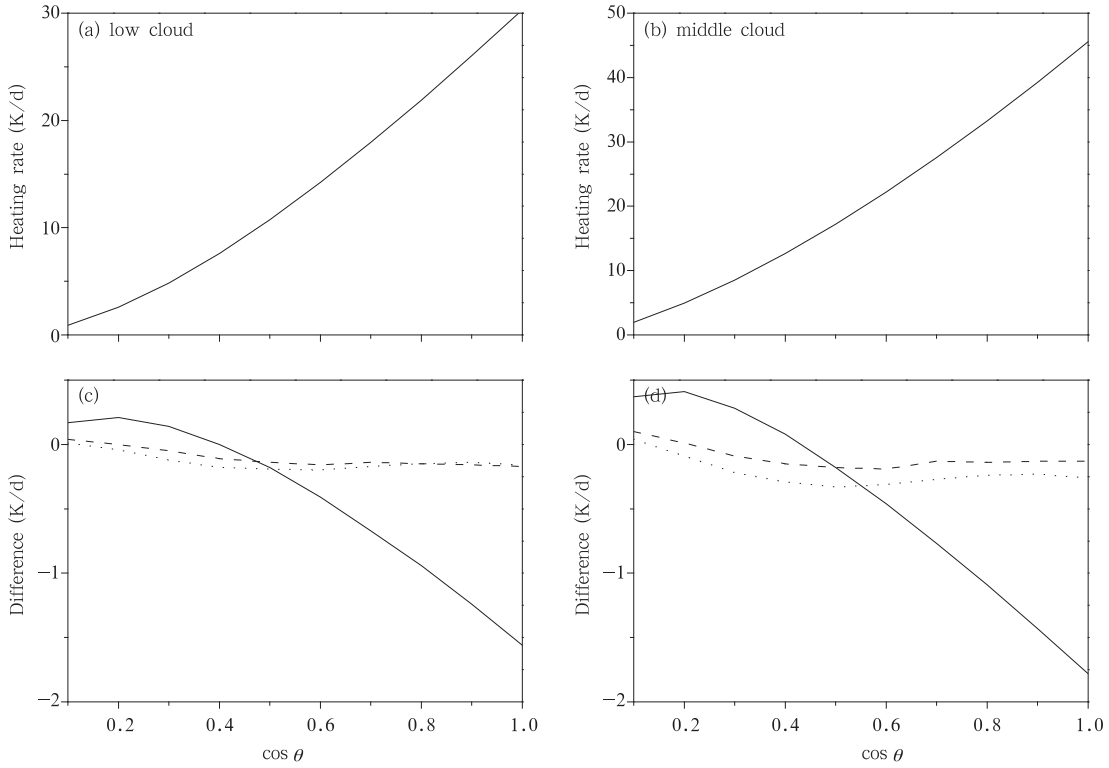


图 8　低云(a、c)和中云(b、d)情况下的云顶加热率随太阳天顶角变化

(a、b. 48 流 DISORT 计算的云顶加热率,c、d. 实线、虚线和点线分别表示 Eddington 近似、四流球谐函数法、四流离散纵坐标法计算的云顶加热率与 48 流 DISORT 结果的差值)

Fig. 8　Changes in the heating rate at the top of cloud with the solar zenith angle for low (a,c) and middle (b,d) cloud cases

((a), (b) are the results of the 48-stream discrete-ordinate approximation method; and (c), (d) are the differences between the Eddington method (solid line), four-stream spherical harmonic expansion approximation (dashed line) and four-stream discrete-ordinate approximation (dotted line), and the 48-stream discrete-ordinate approximation method, respectively)

下都优于 Eddington 近似的结果。特别是在太阳天顶角小于 60°时,两种四流算法要明显优于 Eddington 近似。由于中云的云水含量比低云高,造成的云顶加热率比低云大,因此其云顶加热率的误差比低云情况有所增大。

图 9 给出低云和中云情况下云顶加热率随云水含量的变化。可以看出,随着云水含量的增大,水云的光学厚度随之增大,云顶的加热率也随之增大。不论是低云还是中云情况,两种四流方案的短波云顶加热率误差都要远小于 Eddington 近似的误差。

从表 3 可以看出,DISORT48 方法最费时,运行一次单气柱辐射传输的时间是 Eddington 方法的 3000 多倍,可以用于一般辐射传输模式计算,尚不能应用于气候模式;而四流球谐函数和四流离散纵坐标法的运行时间仅为 Eddington 近似的 2 倍左右,都在百分之一秒的量级,可以用于通常的辐射传输模式,也可以应用于全球气候模式的辐射过程计算。

## 4　结　论

利用单层四流球谐函数结合二流累加法,构造了可用于多层大气的四流球谐函数算法,并将四流球谐函数应用于大气辐射模式中。结果表明:在未大幅度增加计算成本的情况下,所构造的四流球谐函数结合二流累加法方案,在晴空大气情况下,无论是对加热率的计算还是对辐射通量的计算都要优于传统的 Eddington 近似。在有云大气情况下,四流球谐函数和四流离散纵坐标法计算的加热率与标准结果相比优于传统的 Eddington 近似;对有云大气辐射通量的计算,当太阳天顶角为 60°时,两种四流方案的向上和向下辐射通量的最大误差要大于

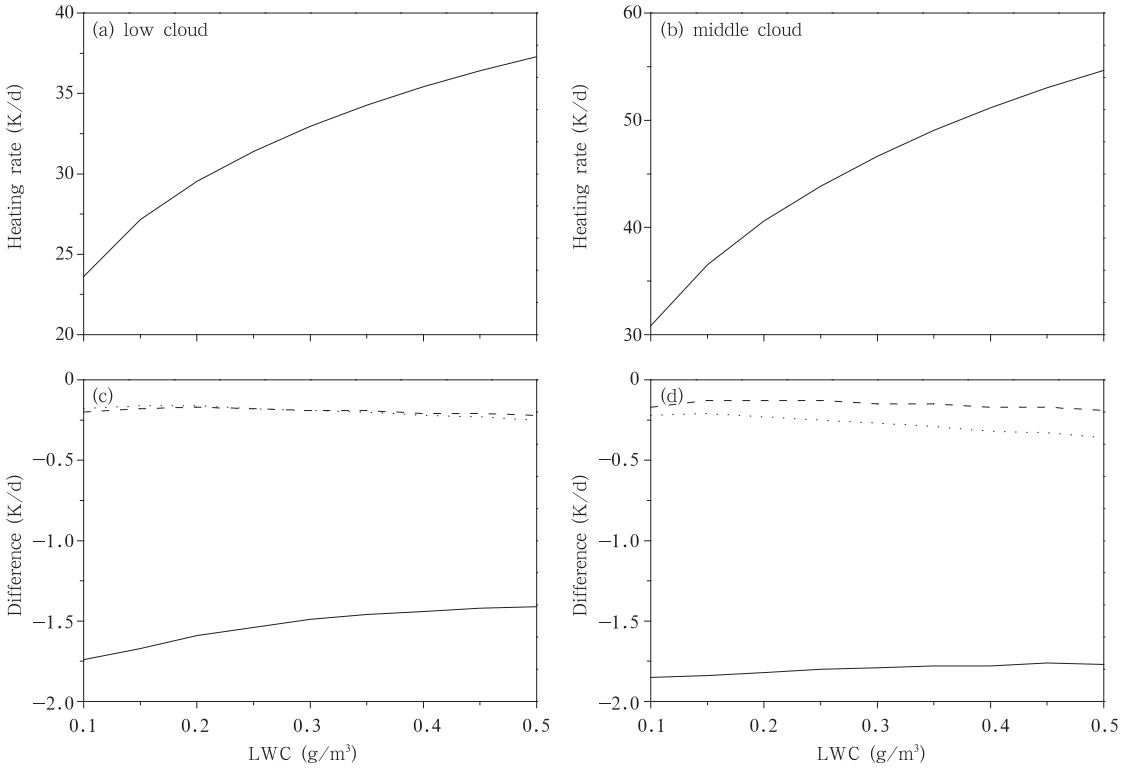


图 9 太阳天顶角 0°,低云(a、c)和中云(b、d)情况下的云顶加热率随云水含量的变化

(a、b. 48 流 DISORT 计算的云顶加热率,c、d. 实线、虚线和点线分别表示 Eddington 近似、四流球谐函数法、四流离散纵坐标法计算的云顶加热率与 48 流 DISORT 结果的差值)

Fig. 9 Changes in the heating rate at the top of cloud with among the liquid water content for low (a,c) and middle (b,d) cloud cases

((a), (b) are the results of the 48-stream discrete-ordinate approximation method; and (c), (d) are the differences between the Eddington method (solid line), four-stream spherical harmonic expansion approximation (dashed line) and four-stream discrete-ordinate approximation (dotted line), and the 48-stream discrete-ordinate approximation method, respectively)

表 3 运行时间比较

Table 3 Comparison among the running times

| | DISORT | Eddington | 四流球谐函数 | 四流离散纵坐标 |
|---|---|---|---|---|
| 运行时间(s) | 57.6 | $1.56\times10^{-2}$ | $3.12\times10^{-2}$ | $3.12\times10^{-2}$ |

Eddington 方法;当太阳天顶角为 0°时,四流算法计算的向上和向下辐射通量的精度也没有传统的 Eddington 方法高。经分析发现这可能是由于单层精确的四流球谐函数计算与大气辐射传输二流累加法的不匹配造成的,这种不匹配使得单层计算的辐射通量的精度在逐层传输过程中损失了一部分。因此,单层精确的辐射计算也需要精确的辐射传输算法匹配才能达到提高整个辐射计算精度的目的。总体而言,本研究构建的四流球谐函数及二流累加法可以应用于大气辐射传输模式来改进晴空大气的整体辐射计算精度和有云大气的加热率计算精度,而不会大幅度增加计算成本。

## 参考文献

荆现文,张华. 2012. McICA 云-辐射方案在国家气候中心全球气候模式中的应用与评估. 大气科学,36(5):945-958

廖国男. 2004. 大气辐射导论. 北京:气象出版社,614pp

卫晓东,张华. 2011. 非球形沙尘气溶胶光学特性的分析. 光学学报,31(5):D0501002,doi:10.3788/AOS201131.0501002

许尤福,赵凤生,闵玉秋. 2011. 平面平行大气中偏振辐射传输的数值计算. 气象学报,69(5):912-921

杨学胜,沈元芳,徐国强. 2009. 辐射方案对 GRAPES 全球模式的影响. 大气科学,33(3):593-599

张华,石广玉,刘毅. 2005. 两种逐线积分辐射模式大气吸收的比较研究. 大气科学,29(4):581-594

张梦,王宏,黄兴友. 2014. NASA/Goddard 长波辐射方案在 GRAPES_Meso 模式中的应用研究. 大气科学,38(3):603-614

Ayash T, Gong S L, Jia C Q. 2008. Implementing the delta-four-stream approximation for solar radiation computations in an atmosphere general circulation model. J Atmos Sci, 65(7): 2448-2457

Chou M D. 1992. A solar radiation model for use in climate studies. J Atmos Sci, 49(9): 762-772

Coakley J A, Cess R D, Yurevich F B. 1983. The effect of tropospheric aerosols on the Earth's radiation budget: A parameterization for climate models. J Atmos Sci, 40(1): 116-138

Fu Q, Liou K N, Cribb M C, et al. 1997. Multiple scattering parameterization in thermal infrared radiative transfer. J Atmos Sci, 54(24): 2799-2812

Henyey L C, Greenstein J L. 1941. Diffuse radiation in the galaxy. Astrophys J, 93: 70-83

Kay M J, Box M A, Trautmann T, et al. 2001. Actinic flux and net flux calculations in radiative transfer: A comparative study of computational efficiency. J Atmos Sci, 58(24): 3752-3761

Li J, Ramaswamy V. 1996. Four-stream spherical harmonic expansion approximation for solar radiative transfer. J Atmos Sci, 53(8): 1174-1186

Liou K N, Fu Q, Ackerman T P. 1988. A simple formulation of the delta-four-stream approximation for radiative transfer paramterization. J Atmos Sci, 45(13): 1940-1947

Nakajima T, Tsukamoto M, Tsushima Y, et al. 2000. Modeling of the radiative process in an atmospheric general circulation model. Appl Opt, 39(27): 4869-4878

Randles C A, Kinne S, Myhre G, et al. 2013. Intercomparison of shortwave radiative transfer schemes in global aerosol modeling: results from the AeroCom Radiative Transfer Experiment. Atmos Chem Phys, 13(5): 2347-2379

Rothman L S, Barbe A, Benner D C, et al. 2001. The HITRAN molecular spectroscopic database: Edition of 2000 including updates of 2001. J Quant Spectrosc Radiat Transfer, 82(1): 5-44

Scinocca J F, McFarlane N A, Lazare M, et al. 2008. Technical Note: The CCCma third generation AGCM and its extension into the middle atmosphere. Atmos Chem Phys, 8(23): 7055-7074

Shibata K, Uchiyama A. 1992. Accuracy of the delta-four-stream approximation in inhomogeneous scattering atmospheres. J Meteor Soc Japan, 70(6): 1097-1109

Stamnes K, Tsay S C, Wiscombe W, et al. 1988. A numerically stable algorithm for discrete-ordinate-method radiative transfer in multiple scattering and emitting layered media. Appl Opt, 27(12): 2502-2509

Zhang F, Shen Z P, Li J G, et al. 2013a. Analytical delta-four-stream doubling-adding method for radiative transfer parameterizations. J Atmos Sci, 70(3): 794-808

Zhang F, Li J. 2013b. Doubling-adding method for delta-four-stream spherical harmonic expansion approximation in radiative transfer parameterization. J Atmos Sci, 70(10): 3084-3101

Zhang H, Nakajima T, Shi G Y, et al. 2003. An optimal approach to overlapping bands with correlated k-distribution method and its application to radiative calculations. J Geophy Res, 108(D20): doi: 10.1029/2002JD003358

Zhang H, Shi G Y, NakajimaT, et al. 2006a. The effects of the choice of the k-interval number on radiative calculations. J Quant Spectrosc Radiat Transfer, 98(1): 31-43

Zhang H, Suzuki T, Nakajima T, et al. 2006b. Effects of band division on radiative calculations. Optical Eng, 45(1): D016002, doi: 10.1117/1.2160521

Zhang H, Shen Z P, Wei X D, et al. 2012. Comparison of optical properties of nitrate and sulfate aerosol and the direct radiative forcing due to nitrate in China. Atmos Res, 113: 113-125

Zhang H, Jing X W, Li J. 2014. Application and evaluation of a new radiation code under McICA scheme in BCC_AGCM2.0.1. Geosci Model Dev, 7(3): 737-754

Theor Appl Climatol (2014) 115:365–373
DOI 10.1007/s00704-013-0894-0

ORIGINAL PAPER

# Effect of data homogenization on estimate of temperature trend: a case of Huairou station in Beijing Municipality

**Lei Zhang · Guo-Yu Ren · Yu-Yu Ren · Ai-Ying Zhang · Zi-Ying Chu · Ya-Qing Zhou**

Received: 16 February 2013 / Accepted: 27 March 2013 / Published online: 25 April 2013
© The Author(s) 2013. This article is published with open access at Springerlink.com

**Abstract** Daily minimum temperature (Tmin) and maximum temperature (Tmax) data of Huairou station in Beijing from 1960 to 2008 are examined and adjusted for inhomogeneities by applying the data of two nearby reference stations. Urban effects on the linear trends of the original and adjusted temperature series are estimated and compared. Results show that relocations of station cause obvious discontinuities in the data series, and one of the discontinuities for Tmin are highly significant when the station was moved from downtown to suburb in 1996. The daily Tmin and Tmax data are adjusted for the inhomogeneities. The mean annual Tmin and Tmax at Huairou station drop by 1.377°C and 0.271°C respectively after homogenization. The adjustments for Tmin are larger than those for Tmax, especially in winter, and the seasonal differences of the adjustments are generally more obvious for Tmin than for Tmax. Urban effects on annual mean Tmin and Tmax trends are −0.004°C/10 year and −0.035°C/10 year respectively for the original data, but they increase to 0.388°C/10 year and 0.096°C/10 year respectively for the adjusted data. The increase is more significant for the annual mean Tmin series. Urban contributions to the overall trends of annual mean Tmin and Tmax reach 100% and 28.8% respectively for the adjusted data. Our analysis shows that data homogenization for the stations moved from downtowns to suburbs can lead to a significant overestimate of rising trends of surface air temperature, and this necessitates a careful evaluation and adjustment for urban biases before the data are applied in analyses of local and regional climate change.

L. Zhang
College of Atmospheric Science, Nanjing University of Information Science & Technology, Nanjing, China

G.-Y. Ren (✉) · Y.-Y. Ren
Laboratory for Climate Studies, National Climate Center, CMA, Beijing, China
e-mail: guoyoo@cma.gov.cn

A.-Y. Zhang · Z.-Y. Chu
Beijing Meteorological Bureau, CMA, Beijing, China

Y.-Q. Zhou
Jinzhong Meteorological Bureau of Shanxi Province, CMA, Jinzhong, China

## 1 Introduction

The homogeneous time series of climate variables are defined as those which contain only climatic variation and regional trend information. It is generally recognized that only by using homogenized data series can the long-term climatic trends be accurately detected. However, due to changes in observing sites, instruments, observing schedule, observing habits and micro-environment around the observational grounds, discontinuous points in the observational records can be created, especially for surface air temperature (SAT) records. The inhomogeneous data may bring certain deviation for estimating climatic trends, leading to inaccurate analyses for regional climate change detection in some circumstances (Jones et al. 1986; Easterling and Peterson 1995a; Yan et al. 2001; Ren et al. 2005; Menne et al. 2010). Therefore, researchers commonly examine and adjust the inhomogeneities before going to analyze long-term SAT trends at single sites or on regional scales, by combining varied mathematical methods and station metadata (e.g., Jones et al. 1986; Easterling and Peterson 1995a, b; Alexandersson and Moberg 1997; Aguilar et al. 2003; Menne and Williams 2005).

The inhomogeneities caused by observing schedule, instrumentation, and relocation were adjusted in SAT data of the United States USHCN (US Historical Climate Network)

(Karl and Williams 1987; Quayle et al. 1991; Easterling and Peterson 1995a, b; Menne and Williams 2009). Vincent (1998) and Vincent et al. (2002) adjusted the Canadian Tmin and Tmax series using multiple linear regression method. Researchers from other countries and regions also created their own homogeneous SAT dataset using methods such as Easterling and Peterson method, Standard Normal Homogeneity Test, Two-Phase Regression, Penalized Maximal *t* Test, and Multiple Analysis of Series for Homogenization (MASH) (Wang et al. 2007a; Aguilar et al. 2003; Reeves et al. 2007).

Chinese researchers made studies of SAT data homogenization (Song et al. 1995; Zhai and Eskridge 1996; Liu 2000; Yan et al. 2001; Yan and Jones 2008; Li et al. 2004; Li and Dong 2009; Li and Yan 2010). Using three different tests for undocumented change points, for example, Li et al. (2009) estimated the artificial discontinuities in annual mean daily Tmin and Tmax in southeastern China and found that there are more discontinuity points in annual mean Tmin series; Li and Yan (2010) apply MASH method to detect and to adjust inhomogeneities for daily SAT series of 1960–2006 at Beijing station.

Given the adjustments are accurate and applicable for monitoring and detecting regional climate change, however, there remain still a few of issues to be solved. One is what effect the homogenization will have on the estimated long-term SAT trends at a single station or in a large region. If the SAT trends are significantly different between the prior and aft adjusted data series, then what are the underlying causes? Does the adjustment for inhomogeneities significantly recover the urban bias when the breakpoints are mostly caused by the moves of stations from urban areas to rural areas, as previously suggested by Winkler et al. (1981) and Hansen et al. (2001) for the United States and recently by Ren et al. (2010) for mainland China? To answer these questions will certainly deepen our understanding of the systematic biases of the SAT data and their influences on the estimates of magnitude and rate of local and regional temperature change.

In this paper, we examine the effect of data homogenization on the estimate of Tmin and Tmax trends at Huairou station of Beijing Municipality (BM). We first make an examination of inhomogeneities of temperature data and adjust the breakpoints identified to obtain a homogenized SAT data; we then compare the linear trends of the original and adjusted SAT series and analyze the urban effects on the linear trends of the original and adjusted SAT series using the temperature data of the same reference stations.

## 2 Data and methods

The original daily Tmin and Tmax data of Huairou, Xiayunling, and Shangdianzi stations from 1960 to 2008 are obtained from the National Meteorological Information Center of the China Meteorological Administration. The locations of the stations are shown in Fig. 1, and the basic information of the stations is listed in Table 1. The station history records are from the Beijing Meteorological Bureau (BMB) (2009), and the population data for the residential areas near the stations are from the China Statistic Bureau (2002).

As a rapidly grown small city, Huairou is located in the northern mountainous areas of the BM, with a population of ~75 thousands in the urban area in 2000 (Fig. 1a). Huairou

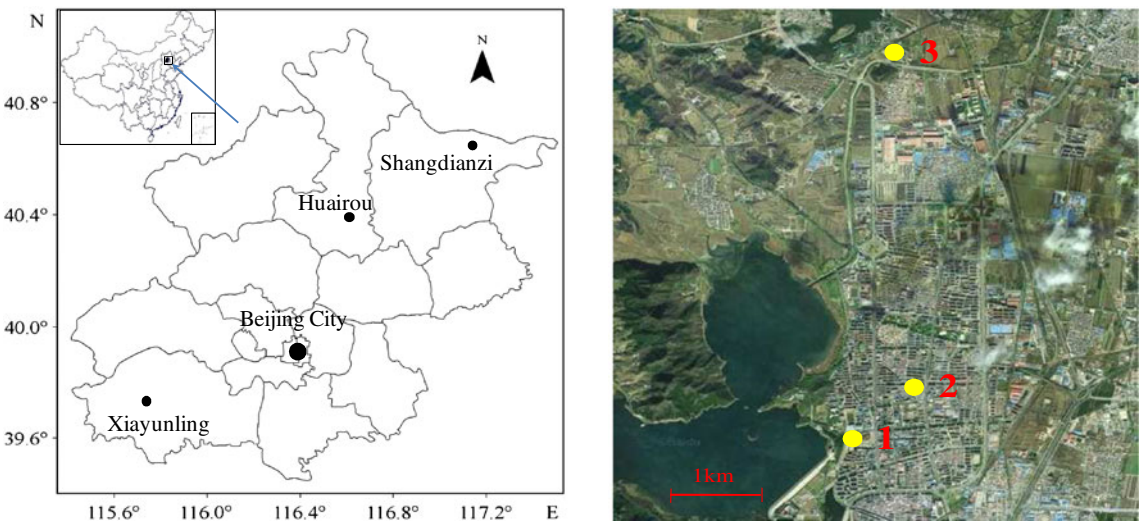


**Fig. 1** Locations of the weather stations used in the study. **a** Huairou station and reference stations in present; **b** present and historical locations of Huairou station. Numbers *1*, *2*, and *3* in **b** indicate the locations before 1964, 1964–1996, and after 1996

weather station is a typical urban station (Fig. 1b), and the recent 49-year records from the station are evaluated in this paper for the data inhomogeneities and urbanization effects on the SAT trends as a target observational site. Although Xiayunling and Shangdianzi stations are also located in the mountainous areas, they are both far from larger residential areas, with the former being on a valley in the southwest and the latter on a slope near a small village having a population of no more than a thousand in the northeast (Fig. 1a). The two observational sites are chosen as the reference stations from 20 weather stations with over 30-year records in the BM. In addition to the small population of the residential areas near stations and the similar physiographic characteristics to the target station, the reference stations are also required to have the continuous observation records with as possible as less the missing observational values. The two weather stations were ever used as reference stations in previous studies of urbanization effect on the SAT trends of Beijing station (Chu and Ren 2005; Ren et al. 2007).

Inhomogeneities of SAT data can be caused by such factors as instrumentation, relocation, change in observational time, and modified statistical methods for daily averages. The introduction of the Autonomous Weather Stations (AWS) to operational observations around 2004 in mainland China may in certain extent have resulted in additional inhomogeneities in SAT records. Wang et al. (2007b) indicated, however, that the SAT of AWS has certain difference from that of manual weather stations, but overall the difference is small and not significant. No change in observational time and statistical methods of daily mean SAT occurred during the last 50 years, and these will not cause any detectable inhomogeneities of the SAT data. It has been realized that the most important factor causing the inhomogeneities of SAT data is the frequent relocations of stations in mainland China (Yan et al. 2001; Li et al. 2004; Ren et al. 2005).

Huairou station experienced relocation twice. It was moved for the first time from West Gate of the old town (Site 1 in Fig. 1b) to Beitumenzi (Site 2 in Fig. 1b) at the East Gate Road outside the old town on 1 August 1964. The second move occurred on 1 July 1996, from Beitumenzi to a suburban village called Liugezhang (Site 3 in Fig. 1b), about 5.5 km from the center of the old town (BMB 2009). For the two reference stations, on the other hand, the only move occurred for Shangdianzi station on 1 September 1989, but the horizontal distance of the movement was 750 m, and the observational grounds changed from 255 m above sea level (ASL) to 293 m ASL, increasing by 38 m in altitude.

The data are quality-controlled with the following steps: (1) if the maximum temperature (Tmax) values are lower than the minimum temperature (Tmin) values, they are registered as unreasonable readings. There is no unreasonable record in the SAT dataset of Huairou station; (2) the values beyond four times of standard deviation are marked as outliers. If outliers are detected, the reasonable records are retained, and unreasonable ones are corrected or regarded as missing values, based on the comparison to the records of the neighboring stations. There is only one outlier found in the dataset, but it is not unreasonable; (3) missing values, which account for less than 0.25% of the total records, are filled in by using the means of the same stations for the reference time period 1971–2000.

The monthly mean Tmin and Tmax series $T_{i,j}$ are calculated based on the daily records, and the monthly change-in-temperature time series $\mathrm{d}T/\mathrm{d}t$ for Huairou station are then created referring to Easterling and Peterson (1995a). The $i$ and $j$ indicate number of year and month respectively.

$$(\mathrm{dT/dt})_{i,j} = T_{i+1,j} - T_{i,j} \tag{1}$$

The monthly reference change-in-temperature time series $(\mathrm{dT/dt})'$ are constructed by averaging the two reference station data with squares of correlation coefficients with Huairou station series as weights. We thus get the reference series $T'$.

$$T'_{i+1,j} = T'_{i,j} + (\mathrm{dT/dt})'_{i,j} \tag{2}$$

Discontinuous points in annual difference series of the target station and the reference stations are detected by using method of moving $t$ test. As mentioned above, Huairou station was moved in 1964 and 1996. In order to effectively identify the discontinuities due to the relocations, the son series length is set as 3 years since the dataset started in 1960. Therefore, the series length $n$=49, the son series length $n1$=$n2$=3, and the significance level $\alpha$=0.01. The metadata are used to validate the existence of the inhomogeneous points, and they are adjusted if proved to be real and caused by relocation. Otherwise, the original records are kept as they were.

The 5-year averages of monthly mean SAT difference between the target station and the reference series is taken as the adjustment values. If the records are less than 5 years before or after discontinuous points, then all the years of record available are used to determine the adjustment values. The adjustments for inhomogeneities are made on basis of daily SAT data. The daily adjustment values are obtained by a linear interpolation method, with the monthly mean adjustment values being assigned to the mid-month days (15th or 14th) of the neighboring months.

The sections of data after the last documented inhomogeneous points are taken as the base series, and they remain unchanged. Before the inhomogeneous points, the adjustment values are added to the original records for every day.

Urban effect ($\Delta T_{ur}$) is defined as the SAT trends caused by the changing Urban Heat Island (UHI) intensity and/or

other factors (such as aerosols) related to urbanization near the specific locations of urban weather stations (Chu and Ren 2005; Ren et al. 2008). It is estimated by formula:

$$\Delta T_{ur} = T_u - T_r \quad (3)$$

where $T_u$ is the SAT trend of urban station and $T_r$ is the SAT trend of reference (rural) station (series). $\Delta T_{ur}$ is larger than 0 if the urbanization raises the SAT trend at urban station, and it is smaller than 0 if the urbanization reduces the SAT trend at urban station.

$\Delta T_{ur}$ can also be estimated by calculating the annual and monthly mean SAT differences between urban station and reference series and the linear trend of the difference series over the time period analyzed. In this paper, the annual mean SAT difference series of Tmin and Tmax between Huairou station and the average reference series are constructed, and their linear trends for the time period 1960–2008 are estimated by using least-square method and are examined for statistical significance by $t$ test.

Urban contribution ($E_u$) is defined as a proportion that the statistically significant urban effect accounts for the total SAT trend at urban station (Chu and Ren 2005; Ren et al. 2008). It can be expressed as:

$$E_u = \left|\frac{\Delta T_{ur}}{T_u}\right| \times 100\% = \left|\frac{T_u - T_r}{T_u}\right| \times 100\% \quad (4)$$

Generally, $\Delta T_{ur}/T_u$ is a positive value less than 100% ($0 \le E_u \le 100\%$); absolute value is taken because it, in certain circumstances, assumes negative value due to the effects other than increasing UHI intensity. If $E_u$=100%, then it shows that the SAT trend of the urban station is entirely caused by urbanization; if $E_u$ is more than 100%, it implies that the extra trend might have been caused by other local factors not yet identified or the errors of data, but it is regarded as 100% in this study. As the definition implies, urban contribution is not calculated if the urban effect is not statistically significant.

## 3 The results

### 3.1 Detection and adjustment of data inhomogeneities

There is no discontinuous point detected in the SAT data series of the two reference stations, despite the relocation of Shangdianzi station in September 1989. This happens mainly due to the relatively small change in the altitude and the environment. No adjustment is done, therefore, and the quality-controlled data are used for producing a single and average reference series.

However, the inhomogeneities are more evident in the SAT data series of Huairou station. Figure 2 shows curves of the moving $t$ statistics of Tmin and Tmax at Huairou station. There are three discontinuous points in the Tmin series in 1963, 1991, and 1996, respectively, and three discontinuous points in the Tmax series in 1974, 1996, and 2000, respectively. By checking the metadata, the discontinuous points in 1963 and 1996 occurred most probably due to the station moves of 1 August 1964 and 1 July 1996 (Table 1). The two discontinuous points are more significant statistically for the Tmin series than those for Tmax series, and they have to be

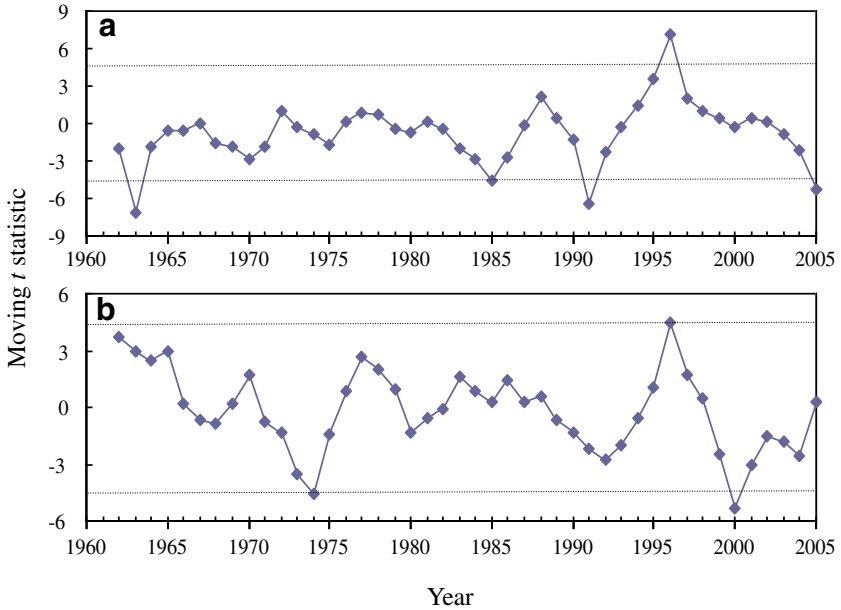


**Fig. 2** The moving $t$ statistics of Tmin (**a**), Tmax (**b**) at Huairou station (the *dotted straight lines* denote that the values are statistically significant at 0.01 confidence level)

**Table 1** Information of the weather stations used in this study

| Station code | Station name | Longitude (°E) | Latitude (°N) | Altitude (m) | Start time of record | Relocation (d/m/y) | Population in 2000 ($10^3$) |
|---|---|---|---|---|---|---|---|
| 54419 | Huairou | 116.62 | 40.37 | 76 | 1959 | 1/8/1964<br>1/7/1996 | 74.6 |
| 54597 | Xiayunling | 115.72 | 39.72 | 408 | 1959 | | 0 |
| 54421 | Shangdianzi | 117.12 | 40.65 | 293 | 1958 | 1/9/1989 | Less than 1.0 |

adjusted for homogeneity. However, the discontinuous points statistically detected for Tmin in 1991 and for Tmax in 1974 and 2000 cannot be validated by the station historical records and have been kept as they are.

The daily mean adjustment values of Tmin and Tmax for the two discontinuous points validated are shown in Fig. 3. The monthly and daily mean adjustment values are all positive in 1964 and 1996. For the discontinuous point in 1996, however, the Tmin adjustment values are significantly larger than the Tmax adjustment values, and the Tmin adjustment values are significantly larger in winter than those in summer. It suggests that the daily Tmin and Tmax all dropped when the station was moved from within the town to outside the town, with the drop in Tmin more significant. There are also obvious seasonal differences in the Tmin adjustment values, with those in winter larger than in summer. The seasonal differences for Tmax adjustment values are smaller.

Figure 4 gives the annual mean Tmin and Tmax of the original and the homogeneity-adjusted data series at Huairou station and of the average reference data series. It is obvious that the adjusted temperature series, especially for Tmin, are more homogeneous and continuous than the original ones, and they are more consistent with the average reference series in inter-annual variability. The annual mean Tmin for the whole period analyzed decreases by 1.377°C after the adjustment, while the annual mean Tmax decreases by 0.271°C (Table 2). The average adjustment magnitudes of mean Tmin are significantly larger than those of mean Tmax.

A notable phenomenon is that the linear trends of the original annual mean Tmin and Tmax series of Huairou station are −0.006°C/10 year and 0.204°C/10 year, respectively, while the linear trends of the adjusted annual mean Tmin and Tmax series are increased to 0.385°C/10 year and 0.335°C/10 year, respectively (Table 3 and Fig. 4). The trends of annual mean Tmin and Tmax both increase obviously after the adjustment, with the former regaining 0.391°C/10 year and the latter 0.131°C/10 year, respectively. It is obvious that the increase of annual mean Tmin trend is larger and more significant, indicating that Tmin records are more sensitive to the station relocations and the data homogenizations than Tmax records. The reasons for the regains of the SAT trends will be discussed below.

The annual mean Tmin and Tmax values are all reduced after the adjustments, and the reasons for the decrease are that the adjustments are made with the section of data series at the present location of observation as baseline, and also the sections of data series adjusted before the last relocation are longer in combination than the latest section of records. Once again, the reduction of the annual mean Tmin is significantly larger than that of the annual mean Tmax.

### 3.2 Urban biases in adjusted and original data series

Figure 5 shows changes in annual mean SAT difference values between Huairou station and the average reference

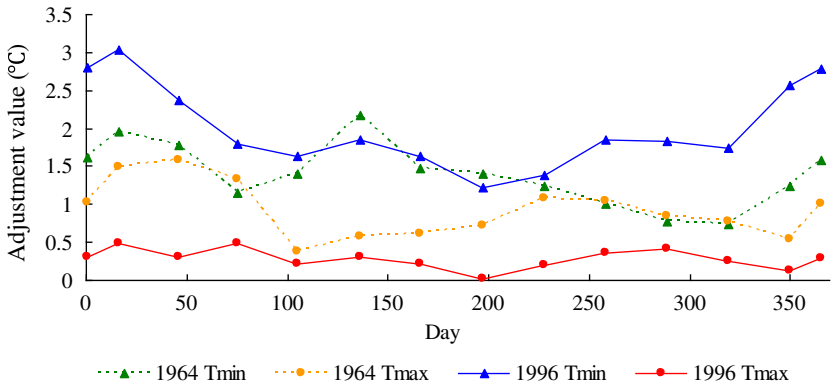


**Fig. 3** The daily mean adjustment values of Tmin and Tmax at Huairou station in 1964 and 1996

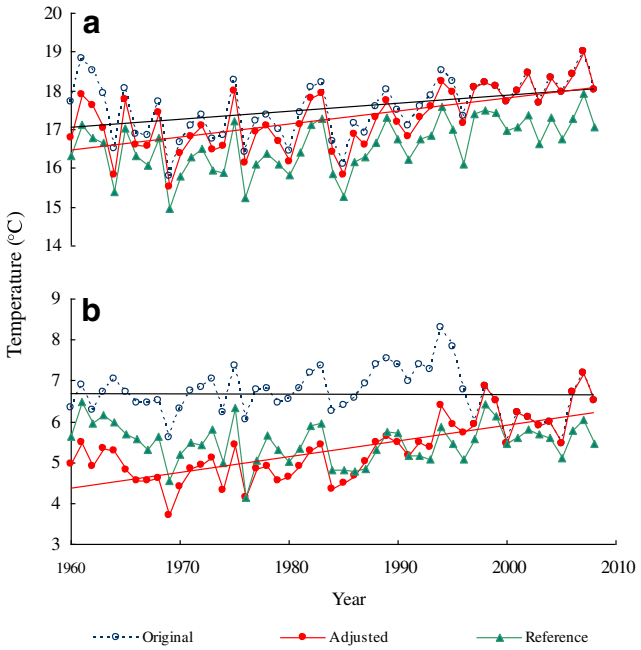


**Fig. 4** The annual mean Tmax (**a**) and Tmin (**b**) of original and adjusted data series at Huairou station and of reference series during 1960–2008. The *solid straight lines* denote linear trends

series. The two SAT difference series of annual mean Tmin and Tmax for the original and homogeneity-adjusted data have highly similar inter-annual variability, but their linear trends are obviously different, with those for the adjusted data witnessing larger increasing trends, especially for Tmin series. Therefore, the relocations of Huairou station from the downtown to the suburb produced breakpoints or inhomogeneities, but they at the same time also largely reduced the urban warming trends, as seen in the original temperature series, while the data homogenization performed for welding the breakpoints now results in a recovery of the urban effect as shown in the adjusted temperature series.

Table 3 gives the urban effects and urban contributions of Huairou station for the time period 1960–2008 for the data series before and after the data adjustments. The urban effects are −0.004°C/10 year and −0.035°C/10 year, respectively, for the Tmin and Tmax before the adjustments, all non-significant statistically, but they increase to 0.388°C/10 year and 0.096°C/10 year, respectively, after the adjustments, both statistically significant at the 0.01 confidence level. The adjusted Tmin series witnesses a more significant increase in the annual mean urban warming trend.

Urban contributions to the overall temperature trends for Huairou station are not estimated for the original annual mean Tmin and Tmax series due to the non-significance of the urban effects, but they reach 100% and 28.8% for the adjusted annual mean Tmin and Tmax series, respectively. After the data adjustment for inhomogeneities, the positive trend of annual mean Tmin at Huairou station during 1960–2008 can be totally explained by the urban effect, and almost a third of the warming trend observed for annual mean Tmax at the station can be attributed to the urban effect.

## 4 Discussion

Relocations of weather stations from downtowns to suburbs are a common practice in mainland China during the past decades, especially for the national reference climate stations and national basic meteorological stations (Li et al. 2004; Ren et al. 2010), which have been mostly frequently applied for analyses of regional climate change. This occurs mainly due to the closeness of the weather stations to built-up areas of cities and towns and the unprecedented urbanization process over the past decades in mainland China under the rapid growth of economy (Ren et al. 2008). Our analysis and the findings of Huairou station in this paper therefore are in some extent of representativeness to the SAT datasets commonly used in studies for the country.

The frequent relocations of stations usually cause obvious inhomogeneities in SAT data, which require a homogenization before long-term trends of temperature can be analyzed. However, the adjustment may change the estimates of mean SAT trends at single stations or even in regional scale and may lead to an overestimate of the warming rates for the stations or the regions. This phenomenon were pointed out in previous studies (Hansen et al. 2001; Menne et al. 2009; Ren et al. 2010) but have not been exclusively examined. Winkler et al. (1981) found, however, that the homogeneity-adjusted SAT data depict a larger UHI intensity and UHI extent in the urban area of Minneapolis–St. Paul, Minnesota. They adjusted the data inhomogeneities induced by changes in observational time and station location. Our analysis for Huairou station in this paper shows that the increased warming rates as estimated

**Table 2** The mean and variance of annual Tmin and Tmax of Huairou station before and after adjustment during 1960–2008 (degrees Centigrade)

| | | Before adjustment | After adjustment | Difference |
|---|---|---|---|---|
| Tmin | Mean | 6.683 | 5.306 | −1.377 |
| | Variance | 0.339 | 0.577 | 0.238 |
| Tmax | Mean | 17.561 | 17.290 | −0.271 |
| | Variance | 0.542 | 0.629 | 0.087 |

**Table 3** Urban effects on the Tmin and Tmax trends of the Huairou station (degrees Centigrade per 10 years) and the urban contribution to the overall temperature trends (percent) for the data series before and after adjustment for period 1960–2008

| | | Before adjustment | After adjustment | Difference |
|---|---|---|---|---|
| Tmin | Linear trend | −0.006 | 0.385[a] | 0.391 |
| | Urban effect | −0.004 | 0.388 [a] | 0.392 |
| | Urban contribution | | 100 | |
| Tmax | Linear trend | 0.204 [a] | 0.335 [a] | 0.131 |
| | Urban effect | −0.035 | 0.096 [a] | 0.131 |
| | Urban contribution | | 28.8 | |

[a] Significant at the 0.01 confidence level

from the homogeneity-adjusted data series compared with the original data series mainly result from the recovery of the urban warming trends. The regained warming trends, especially for the annual mean Tmin, are caused by enhanced urban effect near the first location of the city station, which now has been located in the center of the built-up areas due to the urbanization. The overall trend and the urban effect in the annual mean Tmax series also increase after the homogenization, but the changes are much smaller.

Figure 6 gives a conceptual illustration of the effects of homogenization on estimates of SAT trends with those occurred at Huairou station as a case. The first move of the station from West Gate of the old town to Beitumenzi of East Gate Road in 1964 resulted in a relatively small drop of annual mean Tmin due to the short distance between the two sites, but the second move from Beitumenzi to Liugezhang in 1996 caused a tremendous drop of annual mean Tmin due to the long distance of the relocation and the radically different settings around the two sites (also see Fig. 1b). The positive linear trend of annual mean Tmin for the unadjusted data series, as shown by the black dotted line, is small and statistically insignificant as a result of the two plunges caused by the relocations. When the SAT data is adjusted for the inhomogeneities, however, the larger positive trend of annual Tmin at the station has been recovered, as shown by the red dotted line, because the annual mean Tmin values before the two breakpoints are successively lowered by subtracting the adjustment values from the original data series.

Further investigations are needed to understand to what extent the data homogenization of the national reference climate stations and national basic meteorological stations in mainland China has affected the estimates of the large scale SAT trends. It is reasonable to assume that the effect of the data homogenization on the estimates of SAT trends and urban biases for the country on a whole would be more moderate than that reported for Huairou station in this paper,

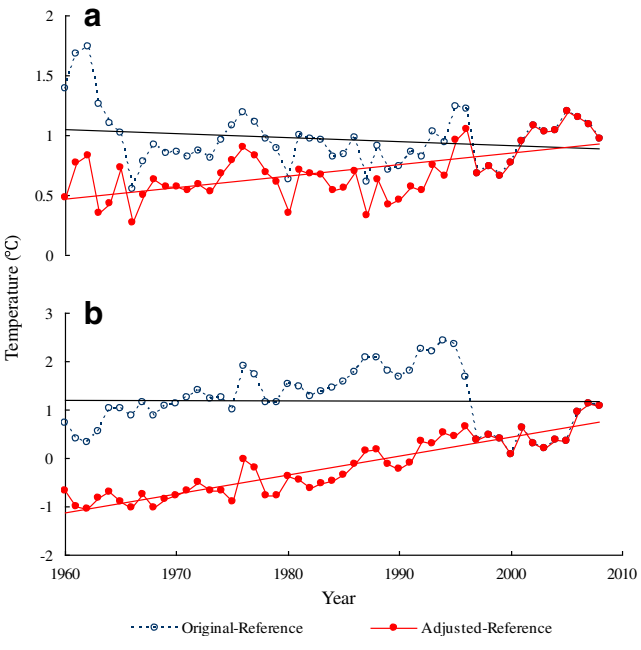


**Fig. 5** The differences of annual mean Tmax (**a**) and Tmin (**b**) between Huairou station and reference data for original (dotted lines) and adjusted (solid lines) data series during 1960–2008. The *solid straight lines* denote linear trends

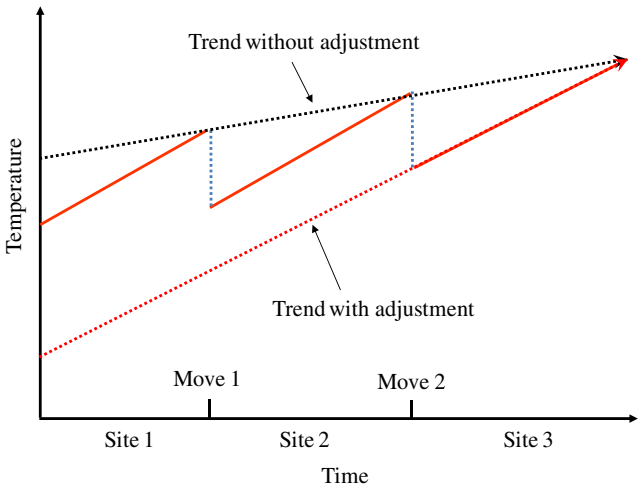


**Fig. 6** A sketch of effects of Huairou station relocations on annual mean minimum temperature trends of the adjusted and unadjusted data series

but it would not be overlooked considering that a common practice is to relocate the weather stations within built-up areas to suburbs or countryside when they are regarded as being less representative for monitoring baseline climate, and this will result in obvious inhomogeneities in the SAT data series in mainland China, which has been consensually regarded as improper for applications in studies of climate change and requires a homogeneity-adjustment before they could be used in studies. If the homogenization significantly affects the SAT trends for part or even majority of the stations in the country, the urban biases in the homogenized SAT data series of the stations have to be more carefully assessed and adjusted before they are to be confidently used in analyses of climate change.

The issue is also relevant to a few of questions baffling the researchers of climate change. One is the understanding of the different trends of Tmin and Tmax in continents. The "asymmetry" in increases of Tmin and Tmax series and the resulting decline of the Diurnal Temperature Range (DTR) were reported for many regions (e.g., Karl et al. 1993; Xie and Cao 1996; Zhai and Pan 2003; Qian and Lin 2004; Choi et al. 2009; Zhou and Ren 2011). The changes were related to the increase in cloud coverage and precipitation worldwide and aerosols over some regions (Dai et al. 1999; Easterling et al. 2000). However, Zhou and Ren (2009, 2011) found a larger urban contribution to the "asymmetry" in the Tmin and Tmax increases and in the decrease of the DTR in North China. The analysis result based on the homogeneity-adjusted data in this paper also shows that the significant increase in annual mean Tmin at Huairou station might have been completely explained by urbanization, and the increase in annual mean Tmax might have been partially caused by urbanization, generally consistent with the conclusions drawn by Zhou and Ren (2009, 2011) for North China and by Zhang et al. (2011) for Beijing station.

## 5 Conclusions

In this paper, the daily Tmin and Tmax data at Huairou station, Beijing Municipality, from 1960 to 2008 are examined and adjusted for inhomogeneities caused by relocations of station, and the temperature trends before and after the adjustments are compared. Following conclusions are drawn:

1. The adjusted annual mean Tmin and Tmax drop by 1.377°C and 0.271°C, respectively, and the adjustment values for Tmin are significantly larger than those for Tmax. The location changes of Huairou station from downtown to the suburb, especially the second move in 1996, cause more significant drop in annual mean Tmin. The drops in monthly mean Tmin values are larger during winter than those during summer.
2. The data homogenization for the station relocations from downtown to suburb at Huairou station leads to an increase in mean SAT trends, and the increase is more significant for Tmin than for Tmax. The urban effects on annual mean Tmin and Tmax trends are statistically insignificant (−0.004°C/10 year and −0.035°C/10 year, respectively) for the original data series, but they reach 0.388°C/10 year and 0.096°C/10 year, respectively, for the homogeneity-adjusted data series. The urban contributions to the overall positive SAT trends are 100% and 28.8%, respectively, for Tmin and Tmax for the homogeneity-adjusted data.
3. The larger effects of relocations, homogenization, and urbanization on Tmin data series than on Tmax data series in a larger extent explain the "asymmetry" in daytime and nighttime SAT trends at Huairou station, and the urban effect is also a major contributor to the DTR decline as implied in the "asymmetry" changes of the annual mean Tmin and Tmax for the homogeneity-adjusted data at the station.

**Acknowledgments** This work is financially supported by the Ministry of Science and Technology of China (GYHY201206012). Thanks are also due to Mr. G.H. Li. at the Huairou Meteorological Bureau, Beijing Municipality, for providing the information of station history.

**Open Access** This article is distributed under the terms of the Creative Commons Attribution License which permits any use, distribution, and reproduction in any medium, provided the original author(s) and the source are credited.

## References

Aguilar E, Auer I, Brunet M, Peterson TC, Wieringa J (2003) Guidelines on climate metadata and homogenization. WMO-TD No.1186, WCDMP No.53. Geneva, Switzerland: World Meteorological Organization, 55

Alexandersson H, Moberg A (1997) Homogenization of Swedish temperature data. Part I: homogeneity test for linear trends. Int J Climatol 17:25–34

Beijing Meteorological Bureau (2009) The history of meteorological stations in Beijing. 147 pp., China Meteorological Press, Beijing, China (in Chinese)

China Statistic Bureau (2002) Population data of China towns and city districts. 949 pp., China Statistic Press, Beijing, China (in Chinese)

Choi G, Collins D, Ren GY, Trewin B, Baldi M, Fukuda Y, Afzaal M, Pianmana T, Gomboluudev P, Huong PTT, Lias N, Kwon WT, Boo KO, Cha YM, Zhou YQ (2009) Changes in means and extreme events of temperature and precipitation in the Asia-Pacific Network region, 1955–2007. Int J Climatol 29:1960–1925

Chu ZY, Ren GY (2005) Chang in urban heat island magnitude and its effect on mean air temperature record in Beijing region. Acta Meteor Sin 63(4):534–540 (in Chinese)

Dai A, Trenberth KE, Karl TR (1999) Effects of clouds, soil moisture, precipitation, and water vapor on diurnal temperature range. J Climate 12:2451–2473

Easterling DR, Peterson TC (1995a) A new method for detecting undocumented discontinuities in climatological time series. Int J Climatol 15:369–377

Easterling DR, Peterson TC (1995b) The effect of artificial discontinuities on recent trends in minimum and maximum temperatures. Atmos Res 37:19–26

Easterling DR, Evans JL, Groisman PY, Karl TR, Kunkel KE, Ambenje P (2000) Observed variability and trends in extreme climate events: a brief review. Bull Amer Meteor Soc 81:417–425

Hansen J, Ruedy R, Sato M, Imhoff M, Lawrence W, Easterling D, Peterson T, Karl T (2001) A closer look at United States and global surface temperature change. J Geophys Res 106(D20):23947–23963

Jones PD, Raper SCB, Bradley RS, Diaz HF, Kelly PM, Wigley TML (1986) Northern Hemisphere surface air temperature variations: 1851–1984. J Climate Appl Meteor 25(2):161–179

Karl TR, Williams CN (1987) An approach to adjusting climatological time series for discontinuous inhomogeneities. J Climate Appl Meteor 26:1744–1763

Karl TR, Jones PD, Knight RW, Kukla G, Plummer N (1993) A new perspective on recent global warming: asymmetric trends of daily maximum and minimum temperature. Bull Amer Meteor Soc 74(6):1007–1023

Li QX, Liu XN, Zhang HZ, Peterson TC, Easterling DR (2004) Detecting and adjusting on temporal inhomogeneity in Chinese mean surface air temperature data. Adv Atmos Sci 21(2):260–268

Li QX, Dong WJ (2009) Detection and adjustment of undocumented discontinuities in Chinese temperature series using a composite approach. Adv Atmos Sci 26(1):143–153

Li Z, Yan ZW (2010) Application of multiple analysis of series for homogenization to Beijing daily temperature series 1960–2006. Adv Atmos Sci 27(4):777–787

Liu XN (2000) The homogeneity test on mean annual wind speed over China. Quart J Appl Meteor 11(1):27–34 (in Chinese)

Menne MJ, Williams CN (2005) Detection of undocumented changepoints using multiple test statistics and composite reference series. J Climate 18:4271–4286

Menne MJ, Williams CN (2009) Homogenization of temperature series via pairwise comparisons. J Climate 22:1700–1717

Menne MJ, Williams CN, Palecki MA (2010) On the reliability of the U.S. surface temperature record. J Geophys Res 115, D11108

Qian WH, Lin X (2004) Regional trends in recent temperature indices in China. Clim Res 27:119–134

Quayle RG, Easterling DR, Karl TR, Hughes PY (1991) Effects of recent thermometer changes in the cooperative station network. Bull Amer Meteor Soc 72(11):1718–1723

Ren GY, Zhang AY, Chu ZY, Zhou JX, Ren YY, Zhou YQ (2010) Principles and procedures for selecting reference surface air temperature stations in China. Meteorol Sci Technol 38(1):78–85 (in Chinese)

Ren GY, Xu MZ, Chu ZY, Guo J, Li QX, Liu XN, Wang Y (2005) Changes of surface air temperature in China during 1951–2004. Clim Environ Res 10(4):717–727 (in Chinese)

Ren GY, Zhou YQ, Chu ZY, Zhou JX, Zhang AY, Guo J, Liu XF (2008) Urbanization effects on observed surface air temperature trends in north China. J Climate 21:1333–1348

Ren GY, Chu ZY, Chen ZH, Ren YY (2007) Implications of temporal change in urban heat island intensity observed at Beijing and Wuhan stations. Geophys Res Lett 34, L05711. doi:10.1029/2006GL027927

Reeves J, Chen J, Wang XL, Lund R, Lu QQ (2007) A review and comparison of changepoint detection techniques for climate data. J Appl Meteor Climatol 46:900–915

Song CH, Liu XN, Li JM (1995) A study of testing methods on inhomogeneity of temperature sequences. Quart J Appl Meteor 6(3):289–296 (in Chinese)

Vincent LA (1998) A technique for the identification of inhomogeneities Canadian temperature series. J Climate 11:1094–1104

Vincent LA, Zhang X, Bonsal BR, Hogg WD (2002) Homogenization of daily temperatures over Canada. J Climate 15:1322–1334

Wang XL, Wen QH, Wu Y (2007a) Penalized maximal *t* test for detecting undocumented mean change in climate data series. J Appl Meteor Climatol 46:916–931

Wang Y, Liu XN, Ju XH (2007b) Differences between automatic and manual observation. J Appl Meteorol Sci 18(6):849–855 (in Chinese)

Winkler JA, Skaggs RH, Baker DG (1981) Effect of temperature adjustments on the Minneapolis–St. Paul urban heat island. J Appl Meteor 20:1295–1300

Xie Z, Cao HX (1996) Asymmetric changes in maximum and minimum temperature in Beijing. Theor Appl Climatol 55:151–156

Yan ZW, Yang C, Jones P (2001) Influence of inhomogeneity on the estimation of mean and extreme temperature trends in Beijing and Shanghai. Adv Atmos Sci 18(3):309–322

Yan ZW, Jones PD (2008) Detecting inhomogeneity in daily climate series using wavelet analysis. Adv Atmos Sci 25(2):157–163

Zhai PM, Eskridge RE (1996) Analyses of inhomogeneities in radiosonde temperature and humidity time series. Int J Climatol 9:884–894

Zhai PM, Pan XH (2003) Trends in temperature extremes during 1951–1999 in China. Geophys Res Lett 30(17):1913. doi:10.1029/2003GL018004

Zhang L, Ren GY, Liu J, Zhou YQ, Ren YY (2011) Urban effect on trends of extreme temperature indices at Beijing Station. Chin J Geophys 54(5):1150–1159 (in Chinese)

Zhou YQ, Ren GY (2009) The effect of urbanization on maximum, minimum temperatures and daily temperature range in north China. Plateau meteorology 28(5):1158–1166 (in Chinese)

Zhou YQ, Ren GY (2011) Change in extreme temperature events frequency over mainland China during 1961–2008. Clim Res 50:125–139

# 武汉异常强降水水汽来源、输送路径分析

张 灵[1]，杜良敏[1]，陈丽娟[2]，高正旭[1]

（1. 武汉区域气候中心，武汉 430070；2. 国家气候中心中国气象局气候研究开放实验室，北京 100081）

**摘 要**：采用百分位法挑选出武汉站 63 次强降水事件，使用 Hysplit 模型模拟强降水事件不同高度上后向 168 h的运动轨迹并进行空间聚类分析，结果发现：武汉强降水发生时底层暖湿气流主要来自南海，自南方路径输送；中层水汽主要来源于孟加拉湾，以西南路径输送，其中青藏高原东南侧和南海充当水汽输送通道；较高层水汽输送路径以偏西路径为主，源地位于青藏高原。此外，稳定、持续的大尺度环流配置有利于强降水的发生，如副高南侧的暖湿气流沿着南支槽前向北影响长江中游。850 hPa 上，马斯克林高压西侧的西南气流，汇入亚洲地区低涡南侧的偏西气流中，越过印度半岛、孟加拉湾和中南半岛，与来自澳大利亚越赤道后转向的偏南气流自我国南端北上抵达长江中游。

**关键词**：Hysplit；异常强降水；百分位法；水汽输送；后向轨迹

**中图分类号**：P434⁺.5 **文献标识码**：A **文章编号**：1673－7148(2014)01－0069－06

## 引 言

武汉地处长江中游，夏季降水深受季风影响。已有研究表明，季风区的异常强降水与洪涝的发生有着紧密的联系[1-2]，可引发泥石流、山体滑坡等灾害，给社会经济和人民生命财产带来重大的损失和负面影响。异常强降水发生的原因多样[3-8]，而其根本原因与大尺度环流背景下的水汽来源和输送密不可分。目前，有关水汽输送、通道和源地的研究主要是致力于分析某次暴雨[4-5]，研究方法主要采用湿位涡诊断分析、水汽通量计算和比较等[6-8]，较少使用后向轨迹模型对异常强降水水汽源地进行分析。虽有学者从气候角度统计不同区域不同月份的水汽输送路径，但并非针对异常强降水[7]。例如，崔玉琴[8]分析发现西北内陆上空水汽主源地是北冰洋陆缘海域、大西洋和欧洲南方大陆；周长艳等[9]指出了9—11月中国大陆的主要水汽来源；周晓霞等[10]研究得出华北汛期水汽主要来自亚洲季风水汽输送，其次是西风带的水汽输送。也有少数学者从气候态上讨论异常强降水事件的水汽输送和环流特征[11]，但主要针对华北地区。长江中游是降水集中度和集中期变率最大的区域之一[12]，其异常强降水的水汽输送、通道等气候特征尤其值得深入探讨，迄今为止暂无相关的统计诊断分析，无法为监测、预测武汉异常强降水提供有利的分析诊断信息。因此从气候角度加大对其研究力度，可加深对于武汉站及长江中游异常强降水的水汽输送以及环流配置等气候特征的认识。本文通过定义武汉站异常强降水事件，计算挑选出1978—2011年期间异常强降水事件，然后采用混合型单粒子拉格朗日综合轨迹模型 Hysplit（Hybrid Single-Particle Lagrangian Integrated Trajectory Model）依据异常强降水事件统计出强降水发生的气团来源地及气团输送路径，并通过空间轨迹聚类分析找出气团运行的几种可能路径和规律，总结影响武汉异常强降水发生应关注的重点区，给出气团源地、输送通道及相应的高低空环流形势配置。

## 1 Hysplit 以及异常强降水的定义

Hysplit 模型是由美国国家海洋与大气管理局（NOAA）空气资源实验室 ARL（Air Resources Laboratory）和澳大利亚墨尔本气象研究中心联合研发的

**收稿日期**：2012－12－29；**修订日期**：2013－05－21

**基金项目**：国家科技支撑计划项目（2009BAC51B05）；公益性行业（气象）科研专项（GYHY201306024、GYHY201306033）资助

**作者简介**：张灵（1985－），女，湖北武汉人，助理工程师，硕士，从事短期气候预测研究. E-mail：zhanglingwh2011@163.com

一种用于计算和分析气团输送、扩散轨迹的模型。此模型有两种运行轨迹,为前向轨迹和后向轨迹,其中后向轨迹是指到达研究点之前的模拟运行路径。该模型更多的是被广泛地应用于多种污染物在各个地区的传输和扩散的研究中[13],较少利用其分析水汽输送路径和通道。鉴于它能处理多种气象要素输入场、多种物理过程较为完整的输送[14],可为直观分析武汉地区不同高度上气团运行的轨迹提供有力支持,本文尝试采用 Hysplit 来模拟分析,并通过现有水汽输送路径、源地的常用研究方法——水汽通量来验证模拟效果,以期最终阐述 Hysplit 模拟水汽路径和源地的可行性。

该模型可以实时预报风场形势,研究轨迹。它的平流和扩散计算采用 Lagrangian 方法。方程为

$$P(t+\Delta t)=P(t)+0.5[V(P,t)+V(P',t+\Delta t)] \quad (1)$$

$$P'(t+\Delta t)=P(t)+V(P,t)\Delta t \quad (2)$$

式(1)中, $\Delta t$ 为可变时间步长,$\Delta t$ 小于 0.75 个格距/$U$max($U$max 为最大风速 ),即一个时间步长内气团的移动不超过 0.75 个格距。模式的水平网格与输入的气象场相同,垂直方向分为 28 层,将气象要素线性内插到各 σ 层上[15]。采用的气象场资料为 NOAA 的 GBL 的日资料。

通常将日降水量超过 50 mm 降水事件称为暴雨,而事实上,对于不同地区来说,异常强降水事件是不能完全用全国统一固定的日降水量简单定义的[16]。因此采用文献[17]所用方法,其具体方法是将1981—2010年逐年日降水量序列的第 99 个百分位值的 30 a 平均值定义为异常强降水事件的阈值。通过此定义,计算由湖北省气象信息与技术保障中心提供的武汉站逐日降水资料,得知阈值为 77 mm。武汉站历史上超过此阈值的异常强降水事件有 63 次。最强异常强降水事件发生于 1982 年 6 月 20 日,日降水量为 298.5 mm,占武汉站气候平均年降水量(1317.84 mm)的 22.7%。其中超过 200 mm 的有 3 次,150 ~ 199.9 mm 的有 4 次,100 ~ 149.9 mm 的有 28 次。这 63 次强降水事件集中于夏半年,发生于4—10月。其中 4 月发生 4 次,5 月 11 次,6 月 20 次, 7 月 17 次, 8 月 5 次, 9 月 4 次,10 月发生最少,仅有 2 次(图 1)。发生于6—8月的异常降水事件达总事件的 66.7%,这与武汉地处季风区,夏季降水主要受季风环流影响有关。63 次事件中,有 49 次事件(77.8%)发生当日的平均气温低于历史同期均温,其中 30 次(47.62%)强降水异常日的最高气温低于气候同期均温,表明异常强降水发生同时,气温相对同期而言偏低,这与大多异常强降水的发生有较强的北方偏冷气流南下配合有必然关系。此外,1978—2011年异常强降水次数呈现出较为显著的年际和年代际变化。其中 1978 年和 1994 年无异常强降水发生,2006—2010年连续 5 a 异常强降水发生次数都持续偏低,仅为 1 次。而 1991 年和 2004 年发生次数最多,为 5 次;1998 年其次,为 4 次。

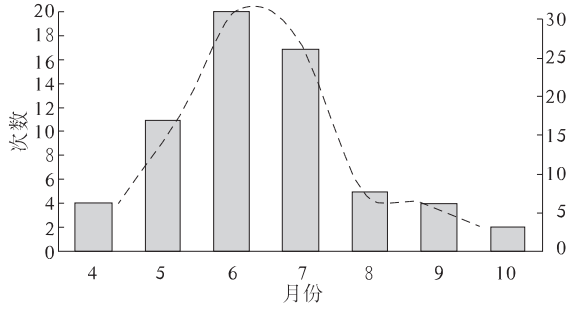


**图 1 强降水在各月出现次数统计**

柱状图:次数;虚线:百分率

## 2 Hysplit 模拟不同高度的后向轨迹

依据异常强降水发生日期,采用 Hysplit 模拟事件当日气团输送路径,模拟的开始时间为每次事件当日 18 时,模拟 6 个高度,依次为 100 m、750 m、1500 m、3000 m、4000 m 和 5500 m(分别代表 1000 hPa 、925 hPa 、850 hPa、700 hPa、600 hPa 和 500 hPa)的后向 168 h(鉴于模型积分时间的限制和短中期天气预报时效性,选定后向轨迹运行时间为 168 h)的运行轨迹。将各高度上 63 条后向轨迹路径采用聚类分析,遵循类与类之间差异极大而同一类的内部差异极小的原则[18],得知各高度上各类的后向轨迹如图 2,路径数依次为 3、5、3、3、5 和 2 条。

100 m 高度上,气团的第一路径为东北路径,占 38%,源自渤海海域,以反气旋路径越过黄海到达武汉;第二、三条路径为南方路径,分别占 35% 和 27%,源自南海,其中第二路径源于南海中沙群岛,第三路径源于南海南端,近南沙群岛。

750 m 高度上,第一、二路径为偏西南路径,分别占 30% 和 27%,各自来源于中南半岛南端的泰国湾和中南半岛,西南气流受中南半岛地形影响转为偏南气流,途经海南岛;第三、四路径源于我国东海,分别占 20% 和 13%,以反气旋路径运行;第五路径占 10%,源于贝加尔湖地区,东移南下,越过山东半岛最终抵达武汉。

1500 m 高度上,第一路径占 46%,来自于孟加拉湾东南部,向北向东推进,经青藏高原东南边缘;第二、三路径同为 27%,其中一条路径自台湾岛附近洋面以反气旋路径运行,途经中国大陆东南沿岸。

3000 m 高度上,第一、二路径为西南路径,分别占 33% 和 38%,分别来自于孟加拉湾西部和东南海面,绕过青藏高原东南侧边缘;第三路径为偏东路径,来源于青藏高原的雅鲁藏布江地区。

4000 m 高度上,第一至第四路径都为西南路径,只是源地略有差异,分别占 35%、22%、32% 和 5%,第一、二路径源自孟加拉湾区;第三路径源自印度半岛;第四路径源自青藏高原东部,以气旋路径到达长江中游;第五路径占 5%,来自巴尔喀什湖地区的气流越过天山山脉,东移南下,抵达武汉站。

5500 m 高度上,第一路径为偏西路径,来自于青藏高原,占 62%;第二路径占 38%,为西南路径,来自印度半岛。

结合不同高度上各路径后向轨迹的结束点(endpoint,也就是此轨迹的起始点)位置(表略)得知,各高度上来自东北路径的冷空气都源自更高层,而西南路径、南方路径都来自低层。表明异常强降水的发生,必定是南方路径、东南路径和西南路径输送的暖湿气团逐渐向北推进并在推进过程中不断向上抬升,而来自北方或东北路径的冷干气团自高层逐渐向南扩散并在南下过程中不断下沉造成的。通过 Hysplit 模拟能简单地揭示出异常强降水发生的条件,即暖湿气团的上升、冷干气团的下沉以及冷暖气团的交汇。

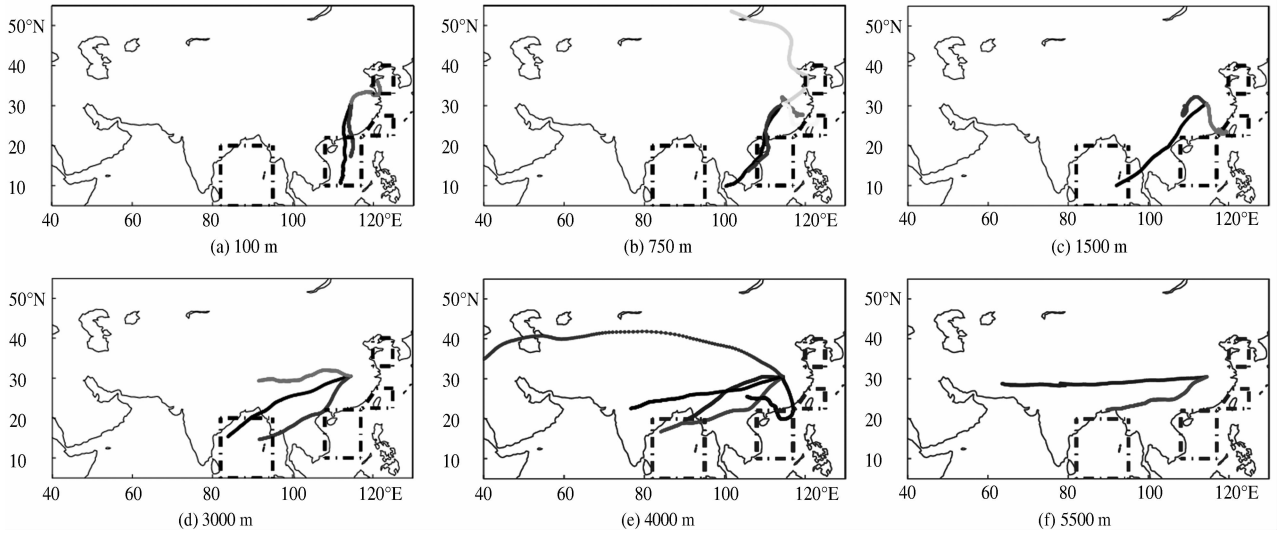


**图 2　6 个高度上的异常降水后向 168 h 的轨迹聚类路径及重点关注区**

结合图 2 各路径百分率可知,武汉异常强降水发生时低层气流(750 m 及其以下)主要来自于我国南海,其中南沙群岛、泰国湾地区是重点关注区域;750—1500 m 高度上,我国东南侧的西太平洋以及东北侧的渤海也是较为重要的气团输送地;750—4000 m 孟加拉湾地区是重要的水汽源地,其中孟加拉湾东南部的安达曼海及孟加拉湾西侧的水汽输送尤其值得研究,而南海和青藏高原东南侧在此充当着重要水汽通道的角色。此外,在 3000 m 及其以上层次主要是来自青藏高原雅鲁藏布江地区的偏西气流。上述分析表明,青藏高原既发挥着水汽通道的作用,同时也是水汽源地之一,印证了青藏高原在水汽输送中的重要、复杂作用,因此以后在研究异常降水时应从 3000 m 及其以上高度关注青藏高原的“转运”和输送的作用[19]。这些结论与陶杰和丁一汇[20-21]等的研究结论较为相近。

## 3　不同高度水汽通量对比验证

图 3 为 6 个高度上异常降水发生日的水汽通量和水汽通量散度。

NCEP/NCAR 提供的再分析资料中,300 hPa 以上大气比湿为 0,大气中的水汽主要集中于对流层低层(低层为地面至 700 hPa,中层为700—500 hPa,高层为500—300 hPa),一般认为最大水汽输送量出现在距离地面 2000 m 高度上[22]。对比图 3,1000 hPa 上来自澳大利亚的东南气流越过赤道转为偏南气流,查看对应水汽通量的大小得知,此偏南气流将携带南海地区的水汽输送至武汉。此结论与 Hysplit 模拟出 100 m 高度上气团的偏南路径一致。同样 750 hPa 和 850 hPa 上,来自澳大利亚的越赤道气

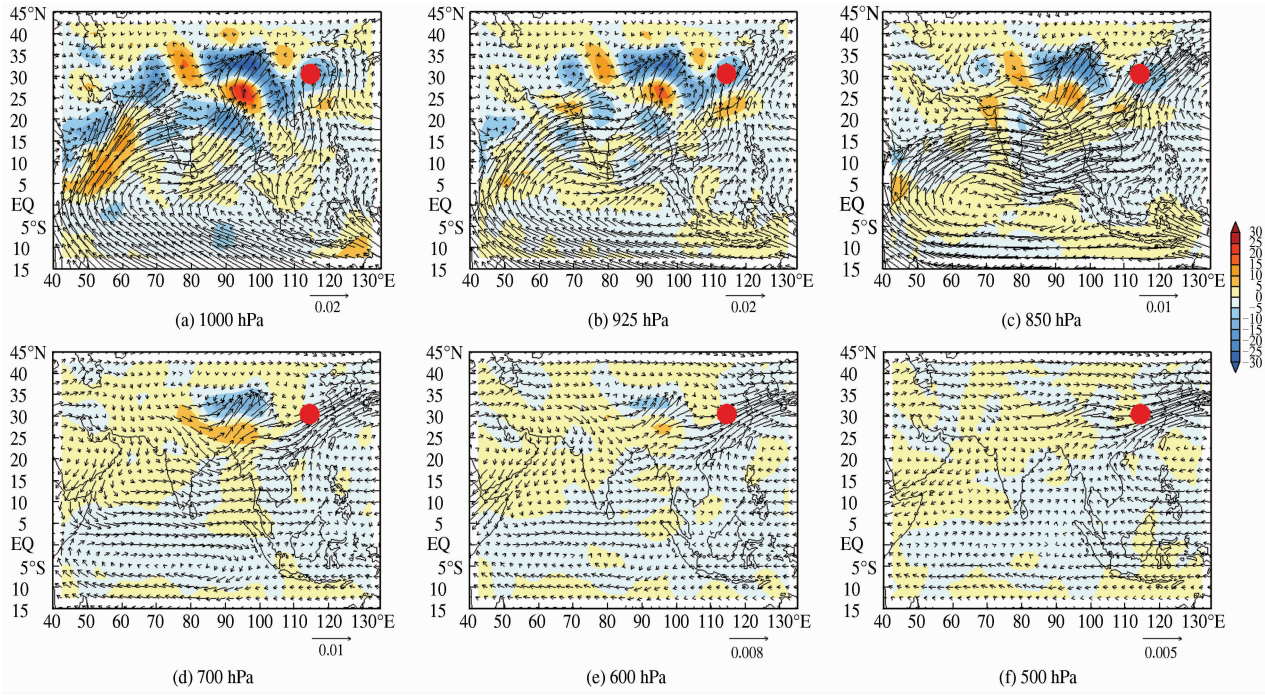


**图 3　6 个层次上异常强降水发生当日的水汽通量和水汽通量散度**

水汽通量单位：$g \cdot cm^{-1} \cdot hPa^{-1} \cdot s^{-1}$，水汽通量散度单位：$10^{-9} \cdot g \cdot cm^{-2} \cdot hPa^{-1} \cdot s^{-1}$

流已减弱，主要是来源于索马里的越赤道气流转向，经阿拉伯海、孟加拉湾携带大量水汽越过中南半岛以西南路径到达武汉，说明 Hysplit 也能模拟出以上提到的水汽集中层上的主要水汽输送路径。700 hPa 上的水汽通量输送路径有三条，依次为沿青藏高原西侧的偏西北气流南下至孟加拉湾，汇入中印半岛的偏西气流转向为西南气流，自青藏高原南侧绕过以西南路径输送；高原北侧的偏西气流；西太平洋副高外围的偏南气流。3000 m 高度上 Hysplit 模拟的结果虽没能体现出西太平洋副高外围的偏南气流，但有效地反映了此层主要的水汽输送路径。600 hPa 的水汽通量和散度类似于 700 hPa 的分布，当然 600 hPa 上还有来自高纬度的气流（不排除是北冰洋或者北大西洋的冷湿气流），对应 4000 m 高度上的后向轨迹路径能识别出以上提到的西南、南方和东北路径。5500 m 高度上的模拟路径能体现出 500 hPa 上西太平洋副高外围的西南气流和偏西气流。以上结论都印证了 Hysplit 模型能简单、直观地模拟异常强降水气团主要来源地和通道。

## 4　异常强降水发生当天及前 6 d 的典型大气环流形势

将 63 次异常强降水事件发生当日的环流进行合成，高低空环流配置如图 4。850 hPa 上，在青藏高原西北侧存在一个范围较广的西北—东南走向的低涡，此外以武汉西侧的四川盆地为中心也存在着低涡，此低涡中心以北地区的中高纬以及我国东面太平洋都被高压中心控制，武汉正处于低涡东侧偏南气流与高压北侧的偏西偏北气流的汇合区。此汇合区北侧 200 hPa 上存在着明显的高空急流，长江中游不仅受到 500 hPa 副高南侧来自于西太平洋的暖湿气流的影响，同时还处于南支槽前，短波槽明显。850 hPa 上，位于赤道印度洋上空的马斯克林高压明显，高压西侧的西南气流，汇入亚洲地区低涡气旋南侧的偏西气流中，依次越过印度半岛、孟加拉湾和中南半岛，与来自澳大利亚越过赤道后转向的偏南气流自我国南端北上抵达长江中游。图 4 反映出自高空至低空，各种有利的环流配置为武汉发生异常强降水提供非常有利的条件。

当然，在强降水发生前 6 ~ 7 d，有利强降水的环流配置（图略）一直处于稳定、持续并缓慢发展的状态。在强降水发生前 6 d 时，西脊点位于 125°E 附近，850 hPa 上低涡位于青藏高原西侧。之后，西太平洋副高西脊点逐渐西伸至 115°E 附近，副高面积东扩，同时南支槽底部加深，槽区范围扩大，同时 850 hPa 低涡东扩，最终在四川盆地为中心形成低涡，武汉站受到更明显的西南气流的影响。

6—9月发生的异常强降水对应的环流配置与4—

10月发生的异常强降水的环流配置大体相似,但500 hPa 上南支槽相对更深,850 hPa 的西南气流更强盛,对于降水的形成愈加有利。

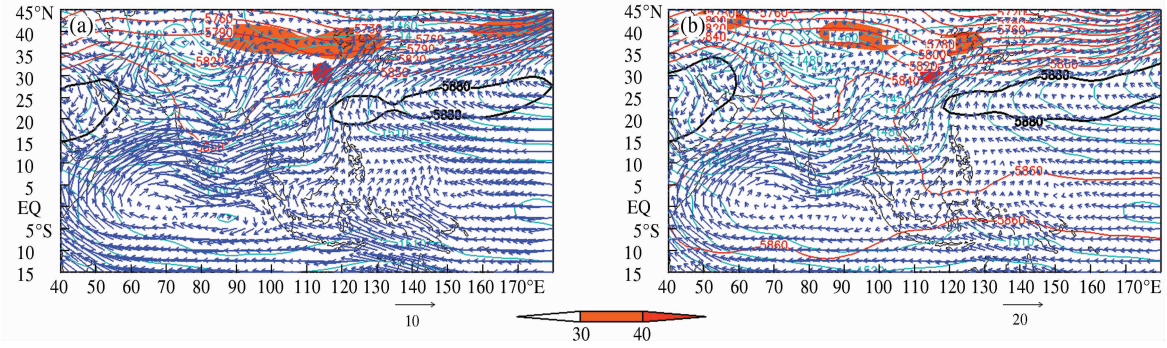


**图 4　4－10 月异常强降水(a)和 6－9 月异常强降水(b)发生日的环流形势配置**

彩色填图为 200 hPa 纬向风,黑色粗线为 5880 gpm 线,红色实线为 500 hPa 等值线,蓝绿色等值线为 850 hPa 高度场,蓝色矢量风图为 850 hPa 矢量风;风速单位:m/s,高度单位:gpm;红色实心圆:武汉站位置

## 5　结论与讨论

本文采用百分位法挑选出武汉站异常强降水事件,根据事件发生时间,使用 NOAA 提供的 Hysplit 模型模拟出不同高度后向 168 h 的 63 条轨迹并进行空间聚类分析,找出异常强降水对应的水汽输送路径、通道等信息,并通过水汽通量来验证 Hysplit 的模拟效果,最后还明确了武汉站异常强降水发生时大气环流的高低空配置,主要结论如下。

(1)Hysplit 能较为有效地模拟出不同层次对应高度上的气团来源。此外,相比通常计算水汽来源和路径的方法,它更直观、快捷和客观。

(2)武汉站异常强降水发生时,底层暖湿气流主要来自南海,自南方路径输送;中层水汽来源于孟加拉湾,自西南路径输送为主;较高层则主要是偏西路径和东北路径。而在水汽较为集中的中下层,值得关注的水汽通道和水汽源地有 4 处,分别是东北侧的东海、黄海,东南侧的西太平洋,南侧的南海,西南侧的孟加拉湾,可为研究异常强降水发生的关键区的监测、分析提供参考。

(3)异常强降水发生前 168 h,大尺度的环流配置已稳定存在。武汉地区北侧 200 hPa 上存在着明显的高空急流,长江中游不仅受到 500 hPa 副高南侧来自于西太平洋的暖湿气流的影响,同时还处于南支槽前,短波槽明显。850 hPa 上,位于赤道印度洋上空的马斯克林高压明显,高压西侧的西南气流,汇入亚洲地区低涡气旋南侧的偏西气流中,依次越过印度半岛、孟加拉湾和中南半岛,与来自澳大利亚越过赤道后转向的偏南气流自我国南端北上抵达长江中游。

Hysplit 模拟异常强降水的水汽输送路径还存在一定的缺陷,例如 Hysplit 自身的模拟存在积分误差,会导致模拟的路径与实际路径存在微弱差异,但这种差异对于结果的影响在本文看来是可以接受的。目前还无法明确识别出各高度上不同水汽源地输送的水汽在武汉总水汽中所占比重。当然可通过对不同水汽源地的水分子进行追踪,但在资料获取上存在困难。此外,本文挑选出的异常强降水事件发生时间跨度大(自 4 月至 10 月),模糊了主要影响异常强降水发生的因子。实际上导致异常强降水发生的因素较多,例如西风急流、局地强对流、西南低涡等形成的强降水,在此没有单独进行分类讨论,仅统计了全年所有类型异常强降水发生时的综合环流配置,对于以后监测或者预测异常强降水没有提供较为明确的分类信息,在未来值得进一步分月、分季和分类型的细化分析和研究。

## 参考文献

[1]鲍名,黄荣辉. 近 40 年我国暴雨的年代际变化特征[J]. 大气科学,2006,30(6):1057－1067.

[2]李吉顺,王昂生,陈家田. 降水时空分布变化是长江流域水旱灾害加重的主要原因[J]. 中国减灾,1999,9(4):27－40.

[3]朱乾根,周伟灿,张海霞. 高低空急流耦合对长江中游强暴雨形成的机理研究[J]. 南京气象学院学报,2001,24(3):308－314.

[4]姚文清,徐祥德. 一次特大暴雨形成中天气尺度和次天气尺度系统的作用[J]. 应用气象学报,2003,14(3):287－298.

[5]Xu X D,Zhou L,Zhang S J,et al. Characteristics of the correlation between regional water vapor transport along with the convective action and variation of the Pacific subtropical high in 1998[J]. Advances in Atmospheric Sciences,2003,20(2): 269－283.

[6]邓国,周玉淑,崔晓鹏. 2003 年梅雨期湿位涡异常诊断分析[J]. 中国科学院研究生学报,2005,22(6):712－728.

[7]蒋兴文,李跃清,王鑫. 中国地区水汽输送异常特征及其与长江

流域旱涝的关系[J]. 地理学报,2008,63(5):482 - 490.
[8]崔玉琴. 西北内陆上空水汽输送及其源地[J]. 水利学报,1994(9):79 - 87.
[9]周长艳,李跃清,李薇,等. 东亚地区秋季水汽输送特征及水汽源地分析[J]. 热带气象学报,2006,22(4):380 - 385.
[10]周晓霞,丁一汇,王盘兴. 影响华北汛期降水的水汽输送过程[J]. 大气科学,2008,32(2):345 - 357.
[11]梁萍,何金海,陈隆勋,等. 华北夏季强降水的水汽来源[J]. 高原气象,2007,26(3):460 - 465.
[12]张录军,钱永甫. 长江流域汛期降水集中程度和洪涝关系研究[J]. 地球物理学报,2004,47(4):622 - 630.
[13]黄健,颜鹏,Draxler R R. 利用 Hysplit_4 模式分析珠海地面 $SO_2$ 浓度的变化规律[J]. 热带气象学报,2002,18(4):407 - 414.
[14]HYSPLIT-Hybrid single particle lagrangian integrated trajectory model [EB/OL]. (2012 - 08 - 12)[2012 - 12 - 10]. http://ready. arl. noaa. gov/HYSPLIT. php.
[15]Draxler R R, Hess G D. An overview of HYSPLIT_4 modeling system for trajectories, disperse on and deposition[J]. Australian Meteorological Magazine,1998,47(2): 295 - 308.
[16]杨金虎. 中国极端强降水事件特征研究及其成因分析[D]. 南京:南京信息工程大学,2007.
[17]翟盘茂,潘晓华. 中国北方近 50 年温度和降水极端事件变化[J]. 地理学报,2003,58(增刊):1 - 10.
[18]HYSPLIT Tutorial Table of Contents[EB/OL]. (2012 - 08 - 12)[2012 - 12 - 10]. http://www. meteozone. com/tutorial/html/index. html.
[19]蒋兴文,李跃清. 长江流域地区水汽输送及其对旱涝影响研究综述[J]. 气象科学,2009,29(1):138 - 142.
[20]陶杰,陈久康. 江淮梅雨暴雨的水汽源地及其输送通道[J]. 南京气象学院学报,1994,17(4):443 - 447.
[21]丁一汇,胡国权. 1998 年中国大洪水时期的水汽收支研究[J]. 气象学报,2003,61(2):146 - 163.
[22]张学文. 气流对物质和能量输送量的垂直分布[J]. 沙漠与绿洲气象,2009(2):1 - 5.

# Analysis of Water Vapor Source and Transport Path of Abnormal Heavy Rain in Wuhan

Zhang Ling[1], Du Liangmin[1], Chen Lijuan[2], Gao Zhengxu[1]

(1. Wuhan Regional Climate Center, Wuhan 430070, China;
2. Laboratory for Climate Studies, National Climate Center, CMA, Beijing 100081, China)

**Abstract**: Using percentile method, 63 heavy rain events in Wuhan station are selected, the backward trajectory in 168 hours on different heights are simulated by Hysplit model and analyzed by the spatial clustering analysis. The results show that: when heavy rain events occur in Wuhan, warm-moist air current at the bottom mainly comes from South China Sea and transfers along the southern route; water vapor at middle level primarily derives from Bengal Bay and transfers along southwest route, and the transmission channels are at the southeast side of Tibet Plateau and the South China Sea; water vapor at high level chooses westward route as the main transmission channel and the source place is Tibet Plateau. In addition, stable and sustainable large-scale circulation stimulates the occurrence of heavy rainfall. For example, the warm-moist air current in the southern side of western pacific subtropical high moves forward to the north along the south trough, and influence regions are in middle reaches of Yangtze River. In 850 hPa, southwest air current in the western side of Mascarene high joins in the westward air current in the southern side of Asian vortex, crosses over India peninsula, Bengal Bay and the Indo-china peninsula and arrives in middle reaches of Yangtze River from the south to the north together with the southward airflow from Australia which turn after crosses the equator.

**Key words**: Hysplit; abnormal heavy rain; percentile method; water vapor transmission; backward trajectory

张媛,任国玉. 2014. 无参考序列条件下地面气温观测资料城市化偏差订正方法:以北京站为例. 地球物理学报,57(7):2197-2207,doi:10.6038/cjg20140715.

Zhang Y, Ren G Y. 2014. Correcting urban bias for surface air temperature series of Beijing Station over time period 1915—2012. *Chinese J. Geophys.* (in Chinese),57(7):2197-2207,doi:10.6038/cjg20140715.

# 无参考序列条件下地面气温观测资料城市化偏差订正方法:以北京站为例

张媛[1,2],任国玉[2*]

1 中国气象科学研究院,北京 100081

2 中国气象局气候研究开放实验室,国家气候中心,北京 100081

**摘要** 本文以北京气象站长期地面气温观测资料为例,发展了一种无早期参考序列条件下城镇站城市化偏差评价和订正方法.首先对北京站逐月平均最高、最低气温资料进行质量控制和均一化处理,并借助卫星遥感亮度温度资料遴选附近乡村站;然后利用最近 3 年逐时地面气温资料,计算观象台和 5 个乡村站各月平均地面气温的差值,把其作为北京站 1915—2012 年期间的城市化累积影响;最后假设城市化累积影响在整个研究时期呈匀速增长,采用线性订正法对地面月平均气温序列中的城市化偏差进行订正.分析表明:资料均一化处理后,北京站近百年最高、最低和平均气温多年平均值有所下降,气温日较差则有所提高,但三种年平均气温序列增温趋势和年平均气温日较差序列下降趋势有所增强.北京站年平均最低气温、平均气温和气温日较差序列中均存在较大的城市化累积影响,其中最低气温和平均气温四个季节均为正值,冬季最大,秋季次之,夏季最小,四季和年平均气温日较差均为较大的负值.订正城市化偏差后,最低气温和平均气温增加速率均明显下降,年平均气温日较差下降趋势则明显变弱.

**关键词** 北京站;城市化累积影响;城市化偏差;订正方法;最高气温;最低气温;平均气温;气温日较差

doi:10.6038/cjg20140715 **中图分类号** P423 **收稿日期** 2013-07-02,2014-04-11 收修定稿

# Correcting urban bias for surface air temperature series of Beijing Station over time period 1915—2012

ZHANG Yuan[1,2], REN Guo-Yu[2*]

1 *Chinese Academy of Meteorological Sciences, Beijing* 100081, *China*

2 *Laboratory for Climate Studies, National Climate Center, China Meteorological Administration, Beijing* 100081, *China*

**Abstract** In this paper, a new method of evaluating and correcting urban bias of surface air temperature is developed in case of no reference climate series, taking Beijing Station as an example. After quality control of the data, the discontinuities resulting from relocations are examined and adjusted using a statistical procedure in combination with the station's history information. The 5 rural stations around the urban station are selected by using the data of remote sensing to determine the relative locations of the Automatic Weather Stations (AWS) in the spatial distribution of surface brightness temperature. Applying surface air temperature data of AWS and Beijing Station for the last 3 years, the accumulated urbanization effect and its

**基金项目** 国家公益性行业专项项目(GYHY201206012)资助.



**作者简介** 张媛,女,硕士生,主要从事气候变化研究. E-mail: mepink2013@163.com

* **通讯作者** 任国玉,研究员,从事气候变化和古气候研究. E-mail: guoyoo@cma.gov.cn

contribution are calculated. With an assumption that the accumulated urbanization effect increases at a constant rate, a linear correction method is used to correct the urban bias for the surface air temperature series of Beijing Station over 1915—2012. Analysis of the homogenized data of Beijing Station indicates that the increasing trend in annual mean temperature and the decreasing trend in annual mean diurnal temperature range (DTR) get larger than those of the original data. The accumulated urbanization effects for mean minimum, average temperature and DTR of the homogenized series are all large positive values, in spite of the small negative value for annual mean maximum. We correct the urban bias for the time series of Beijing Station. After that, the increasing rate of the annual mean minimum and average temperature, and the decreasing rate of annual mean DTR, are all brought down significantly.

**Keywords** Beijing Station; Accumulated urbanization effect; Urban bias; Adjustment; Maximum temperature; Minimum temperature; Average temperature; DTR

## 1 引言

城市化因素对中国等国家和地区的地面气温观测序列有很大的影响(Chung et al.,2004;Ren et al.,2008;Fujibe,2009),只有客观评价并消除这种影响,才能更好地认识长期气候变化趋势,为检测和预估全球和区域气候变化奠定科学基础.

北京观象台(简称"北京站")是我国有正式观测记录最早的地面气象站.对具有长序列观测记录的北京站地面气温资料中的观测误差特别是城市化偏差进行研究,采用合理方法对其进行评价和订正,提升地面气温观测资料的可信性,对于区域和全球气候变化研究具有十分重要的意义.

前人对北京站地面气温观测序列中的城市化影响进行过很多研究(宋艳玲和张尚印,2003;初子莹和任国玉,2005;林学椿和于淑秋,2005;司鹏等,2009;张雷等,2011),他们发现北京站地面气温观测记录中存在明显的城市化影响.但已有研究全部集中在最近半个世纪,对20世纪50年代以前的城市化影响没有开展评价.目前的单站和区域尺度城市化影响偏差评价和订正,一般通过城乡站气温序列的趋势差异来估算,这要求乡村站与目标城市站具有相同长度的时间序列,但在20世纪50年代以前难以遴选出与目标站序列长度相当的参考序列,对许多类似北京站具有长时间观测记录的城镇站地面气温序列的城市化影响无法进行研究.在这种情况下,如何正确评价和订正具有长序列资料的目标站地面气温观测记录中的城市化影响,是需要深思的一个问题.

本文以北京站为例,发展了一种基于当前城市热岛强度空间分布规律的城镇站地面气温资料城市化偏差评价和订正方法.该方法利用北京站较长的历史观测记录资料,借助卫星遥感资料空间分辨率高、自动气象站空间分布密度大等优势,在对原始长序列资料质量控制和均一化处理,得到相对均一的目标站长序列资料的基础上,选取自动站观测记录计算当前城市站的平均城市化影响,将其作为北京站近百年城市化累积影响和其贡献的替代指示,评价和订正北京站地面气温资料序列.

## 2 资料和方法

### 2.1 资料质量控制、插补和均一化

选取1915—2012年北京站的月平均最高、最低和平均气温地面观测资料.该站在观测时次、时制、日平均气温统计方法、站点位置等有多次变化,在不同程度上影响到资料的均一性(Yan et al.,2001).本文采用月平均最高、最低气温求算月平均气温(Jones et al.,2003),同时对资料进行了均一化处理.1950年以前的数据质量较差且缺测现象严重,故对原始资料进行质量控制和缺测值插补.从华北地区的国家基准站、基本站网中选取用于数据订补和均一化订正的候选参考站.资料来自国家气象信息中心,其中1950年以后资料已经过质量控制,本文对1950年以前各站月平均最高气温($T_{max}$)、月平均最低气温($T_{min}$)和月平均气温($T_{ave}$)资料进行了初步质量检验.

北京站月平均最高、最低气温记录中缺测数据均为43个,占各自总数的3.7%,缺测年月为:1915/01—1915/04、1917/12、1926/12—1927/06、1927/10、1928/01、1928/05—1928/12、1929/02—1929/

06、1937/09—1938/12. 采用差值订正法订补缺测数据,参考站选取根据北京站与华北地区其他站年平均气温的相关程度、站点距离及平行观测记录情况确定(表 1). 在计算相关系数时,采用第一差分序列,因为对于原始数据,台站迁移将改变迁站后所有年月的值,而对于差分序列将只改变当年值,对计算的相关系数影响不大. 这些站和北京站 1961—1990 年间均无缺测值,将其作为参考期.

**表 1　插补缺测值所用参考站与北京站的相关系数和直线距离**

**Table 1　The correlation coefficient and distance between Beijing Station and its reference stations**

| 站名(站号) | 记录起始年 | 相关系数 | | 与北京站距离/km |
|---|---|---|---|---|
| | | 最高气温 | 最低气温 | |
| 营口(54471) | 1905 | 0.80 | 0.78 | 493.0 |
| 天津(54527) | 1890 | 0.94 | 0.89 | 94.3 |
| 大连(54662) | 1905 | 0.78 | 0.80 | 454.8 |

如果北京站某年月缺测值为 $P$,对应月参考期平均气温为 $X$,参考站相同年月平均气温为 $Q_r$,对应月参考期平均气温为 $Y_r$,北京站与参考站的相关系数为 $CORR_r$,得到插补公式:

$$P = \sum_{r=1}^{3} [(X - Y_r + Q_r) \times CORR_r^2] \Big/ \sum_{r=1}^{3} CORR_r^2. \quad (1)$$

利用(1)式插补了缺测记录后,建立了北京站 1915—2012 年完整的地面月平均最高、最低气温序列.

表 2 给出北京站迁站的历史沿革情况. 参照建立国家基本基准站均一化气温数据集所用的方法,以当前站址位置为基准,利用滑动 t 检验法检测资料的非均一性断点(Li et al.,2004).

**表 2　1915—2012 年北京站迁站情况**

**Table 2　Information of relocations of Beijing Station during 1915—2012**

| 序号 | 时间(年/月) | 地点 | 纬度/N, 经度/E | 海拔/m |
|---|---|---|---|---|
| 1 | 1915/04—1930/07 | 建国门泡子河畔 | 39°54′,116°28′ | 37.5 |
| 2 | 1930/08—1939/12 | 不详 | 不详 | 不详 |
| 3 | 1940/01—1953/05 | 西郊公园 | 39°56′,116°20′ | 51.3 |
| 4 | 1953/06—1964/12 | 西郊五塔寺 7 号 | 39°57′,116°19′ | 53.3 |
| 5 | 1965/01—1968/12 | 大兴县东黑垡村 | 39°35′,116°19′ | 29.4 |
| 6 | 1969/01—1970/06 | 西郊彰化农场 | 39°56′,116°16′ | 53.3 |
| 7 | 1970/07—1980/12 | 南郊大兴县旧宫东 | 39°48′,116°28′ | 31.2 |
| 8 | 1981/01—1997/06 | 西郊北洼路又一村 | 39°56′,116°17′ | 54.0 |
| 9 | 1997/07—2012/12 | 南郊大兴旧宫东 | 39°48′,116°28′ | 31.3 |

检测非均一性所用参考站是 3 个站,主要考虑参考站在北京站迁址时间前后没有迁站,气温起始记录不晚于 1915 年,与北京站相关系数较高且直线距离较近. 这 3 个站分别是天津、熊岳和青岛站,其中青岛站距北京站最远,为 535.3 km,但三站与北京站最高、最低气温相关系数均大于 0.72. 将参考站序列的加权平均值作为参考序列,权重系数根据第一差分序列相关系数的平方确定;然后用标准化处理后的北京站原始序列与其参考序列的差值序列作为滑动 t 检验的待检序列,对于有迁站历史数据支持的间断点,即检测出的突变点出现时间与迁站时间记录接近一致(相差不超过 6 个月),确定该点为序列的人为不连续点;对于没有迁站数据支持的间断点,不做处理. 结果发现最高气温序列中有 2 个断点是人为不连续点,对应的时间分别是 1981 和 1997 年;最低气温序列中有 4 个断点是人为不连续点,对应的时间分别是 1965、1969、1981 和 1997 年. 由于这些人为不连续点时间都出现在 1960 年后,为使后续订正结果更可靠,采用与前述相同的方法,重新选取了与北京站相关系数更大、距离更近的参考站,用于非均一性订正. 新的参考站记录起始年、迁站历史以及与北京站的距离、相关系数见表 3.

**表 3　参考站有气温记录的起始年、迁站历史、与北京站相关系数和直线距离**

**Table 3　The starting year and information of relocations for the reference stations′ temperature, the correlation coefficient and distance between Beijing Station and its reference stations**

| 站名(站号) | 记录起始年 | 迁站时间(年/月) | 相关系数 | | 距离/km |
|---|---|---|---|---|---|
| | | | 最高气温 | 最低气温 | |
| 密云(54416) | 1957 | 1988/07 | 0.97 | 0.89 | 72.9 |
| 廊坊(54518) | 1957 | 无 | 0.96 | 0.89 | 76.0 |
| 天津(54527) | 1890 | 1992/01 | 0.94 | 0.89 | 94.3 |

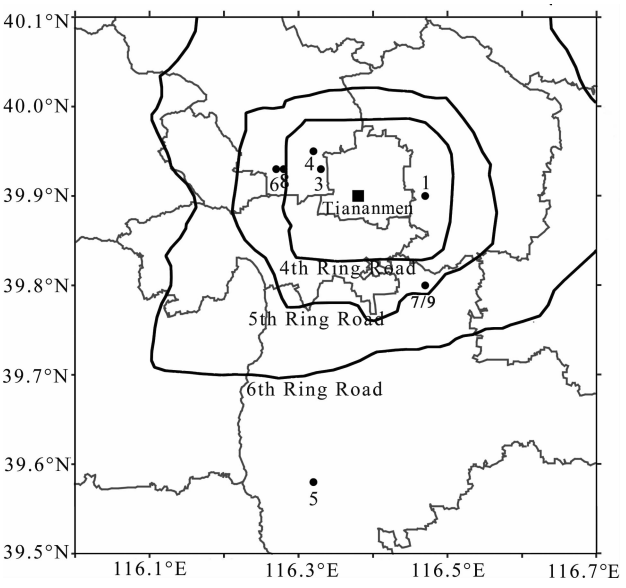


图1 1915—2012年北京站位置变化

圆圈代表站址位置,数字和表2中序号对应.

Fig. 1 Locations of Beijing Station for different time periods of 1915—2012

Circles stand for locations of Beijing Station, the numbers correspond to the ones from the table 2

图1是与表2对应的北京站不同时期位置示意图.1915年4月的迁站发生在原始序列中的第一年,很难对其检测,但也不会对整个序列的均一性产生显著影响.1965年的断点是由西郊五塔寺7号(位置4)迁至大兴县东黑垡村(位置5)导致的;1968和1969年的断点是由大兴县东黑垡村(位置5)迁至西郊彰化农场(位置6)造成的;1980年的断点是由南郊大兴县旧宫东(位置7)迁至西郊北洼路又一村(位置8)引起的;1997年的断点与从西郊北洼路又一村(位置8)迁回原来的南郊大兴县旧宫东(位置9)有关.以上迁站距离都大于20 km,伴随着周围环境较明显的变化,使得气温序列出现不连续性断点.本文检测并证实的断点时间与郑祚芳(2011)利用逐日气温资料检测出的断点时间大体相同,证明台站较大距离的迁移是造成气温序列非均一性的主要原因(李庆祥等,2003).

在对检测出的人为不连续断点进行订正时,分别求算北京站序列和参考序列的差值序列在断点前后3年的平均值,以及前后平均值的差值,将其作为订正值,逐个订正序列的断点,得到北京站均一化的地面月最高、最低气温资料序列.表4为滑动t检验结果及其对应的迁站时间、距离和订正值.北京站月平均气温资料序列中非均一性断点的订正值介于−1.17 ℃至0.97 ℃之间.

采用订正后的月最高、最低气温序列计算得到月平均气温序列和气温日较差序列,最后建立了经过质量控制和均一化处理的1915—2012年北京站地面月最高、最低、平均气温和气温日较差序列.

图2是1915—2012年北京站年最高、最低、平均气温和气温日较差均一化序列及其与原始序列的比较.均一化后气温序列比原始序列表现出略强的增温趋势,其中最高、最低和平均气温序列趋势分别由原来的0.014 ℃/10a、0.260 ℃/10a和0.137 ℃/10a变为0.022 ℃/10a、0.274 ℃/10a和0.148 ℃/10a,分别增加0.008 ℃/10a、0.014 ℃/10a和0.011 ℃/10a;平均气温日较差序列趋势由原来的−0.246 ℃/10a变为−0.251 ℃/10a,减少0.005 ℃/10a.

Cao等(2013)最近发现,中国中东部地区站点1901—2010年平均气温变化趋势由均一化前的0.05～0.15 ℃/10a变为均一化后的0.15～0.42 ℃/10a,也证实资料均一化处理致使地面气温增加趋势得到加强.当观测点从城市中心位置向郊区迁移时,通常会使地面平均气温值比迁站前减小(Li and Yan,2009),均一化处理后长期气温上升趋势一般会比原来加强(任国玉等,2010; Zhang et al.,2014).本文的订正结果表明,迁站对最低气温的均一性影响大于最高气温,这和前人研究中发现的台站迁移对最高气温影响没有对最低气温影响大的结论一致(李庆祥等,2005; Zhang et al.,2014).

**表4 滑动t检验结果、迁站时间和水平距离以及订正值**

**Table 4 The result of moving t test, time and distances of relocations, and the adjustment values**

| 最高气温 | | | | 最低气温 | | | |
|---|---|---|---|---|---|---|---|
| 断点时间(年/月) | 迁站时间(年/月) | 迁站距离/km | 订正值/(℃) | 断点时间(年/月) | 迁站时间(年/月) | 迁站距离/km | 订正值/(℃) |
| 1997/07 | 1997/07 | 21.6 | −0.63 | 1997/07 | 1997/07 | 21.6 | −1.17 |
| 1980/08 | 1981/01 | 21.6 | 0.32 | 1981/01 | 1981/01 | 21.6 | 0.97 |
| — | — | — | — | 1969/01 | 1969/01 | 39.2 | 0.39 |
| — | — | — | — | 1965/01 | 1965/01 | 40.8 | −0.70 |

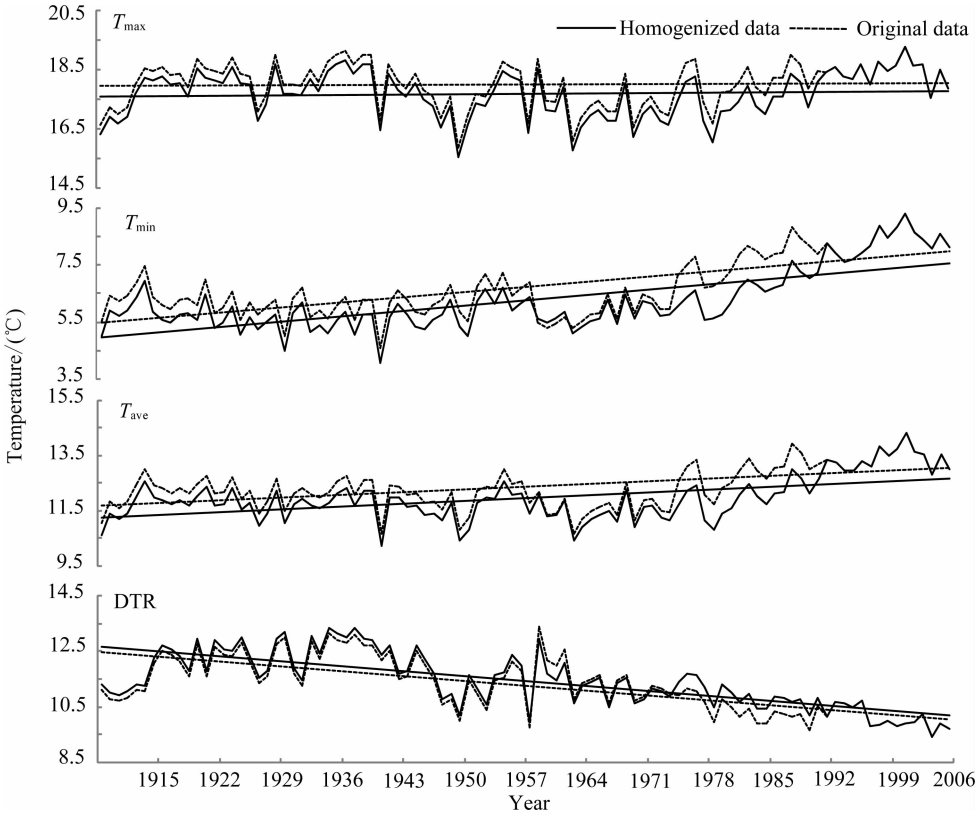


图 2　1915—2012 年北京站年最高($T_{max}$)、最低($T_{min}$)、平均气温($T_{ave}$)和气温日较差(DTR)序列均一化前后比较

Fig. 2　The maximum ($T_{max}$), minimum ($T_{min}$), average temperature ($T_{ave}$) and DTR time series of Beijing Station before and after homogenization for time period 1915—2012

## 2.2　城市化偏差评价和订正方法

先前研究已证实，北京地区城市化影响存在着显著的随时间增强趋势(初子莹和任国玉，2005；陈正洪等，2005；林学椿等，2005；张雷等，2011；Zhang et al.，2014)．本文假设城市站所经历的城市化影响是线性递增的，可以把当前几年城市站附近的平均城市化影响程度(即平均城市热岛强度)作为该站从有记录开始至今的城市化影响历史累积值．通过线性回归的方法可估算不同年份的城市化影响偏差，进而对原有序列进行偏差订正．

为区别前人使用等长参考序列定量评价城市化对地面气温记录影响时所用的术语(周雅清和任国玉，2005；初子莹和任国玉，2005；张爱英等，2010)，本文做如下定义：

城市化累积影响：当前城市站气温与相似高度和环境条件下的乡村站气温的差值，代表了城市站长期以来的城市化增温累积值，亦即当前城市站附近的城市热岛强度．

城市化累积影响用 $\Delta T_{ur}$ 表示：

$$\Delta T_{ur} = T_u - T_r, \tag{2}$$

其中，$T_u$ 代表当前城市站地面气温；$T_r$ 代表城市站周围与其相似高度和环境条件下乡村站地面气温．当 $\Delta T_{ur} > 0$ 时，表示城市化累积影响使地面气温上升；当 $\Delta T_{ur} < 0$ 时，表示城市化累积影响使地面气温下降．

城市化影响贡献率：城市化累积影响对城市站长期地面气温变化总体趋势的相对贡献，即城市化累积影响在城市站长期地面气温变化趋势中所占的百分比率．城市站长期地面气温变化总体趋势用 $T_t$ 表示，则城市化影响贡献率 $R_u$ 为

$$R_u = |\Delta T_{ur}/T_t| \times 100\%. \tag{3}$$

为使城市化影响贡献率满足 $0 \leqslant R_u \leqslant 100\%$，故上式取绝对值．当 $R_u = 0$ 时，表示城市化累积影响对城市站地面气温的变化趋势没有贡献；当 $R_u = 100\%$ 时，表示城市站地面平均气温的趋势变化完全由城市化累积影响造成．

乡村站的选取利用卫星遥感反演的地表亮度温度资料，根据自动气象台站在地表亮度温度场中的位置来确定(Ren et al.，2011)．北京地区城市热岛强度一般在冬季夜晚最强(季崇萍等，2006；谢庄等，2006；Yang et al.，2013)．采用 NASA 提供的 MOD11A2 数据集中 2010 年 12 月 3 日至 2011 年 3 月 5 日期间 8 日夜晚陆表温度资料，绘制平均地表

亮度温度等值线.把在地表亮度温度场中处于闭合等值线外围背景气候条件下的站点看作乡村站,同时参照以下原则:(1)与北京站距离不超过 60 km,保证与北京站处于相同的大尺度环流和气候背景下;(2)与北京站海拔高差小于 30 m,避免由于高度差异带来的影响;(3)Google Earth 和其他手段证实周围观测环境开阔.

据此选取 5 个乡村站,分别是小汤山站(站号 A1401)、大孙各庄站(站号 A1553)、高丽营站(站号 A1561)、大王古站(站号 A2407)和下伍旗站(站号 A2461).图 3 给出了北京站和 5 个乡村站的具体位置.5 个乡村站海拔高度介于 5.0～44.0 m 之间,平均 26.0 m,与北京站海拔高度 31.3 m 相差 5.3 m,不存在因海拔高度造成的地面气温差异.

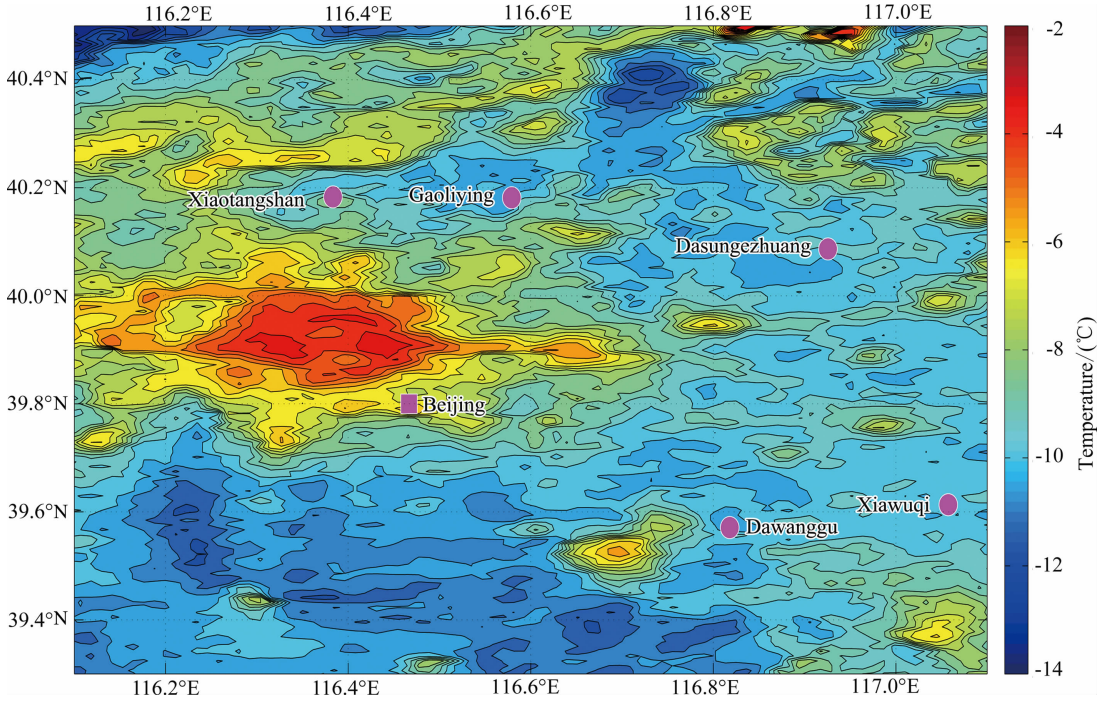


图 3 北京地区地表亮度温度分布等值线(等值线间隔为 0.05 ℃)
其中实心正方形代表北京站当前位置,实心圆代表 5 个乡村站位置.

Fig. 3 Distribution of Beijing Station and its five reference stations, the contour lines indicate land surface brightness temperature retrieved from MOD11A2 data

计算城市化累积影响时,所用资料为 5 个乡村站和北京站 2010 年 1 月至 2012 年 12 月 3 年时期逐小时自动站观测气温资料.为和北京站长序列资料统计方法一致,用月最高、最低气温的算术平均计算月平均气温.月最高、最低气温所依据的日值,采用自动气象站观测 24 个时次中的最高小时平均气温,日最低气温取 24 个时次中的最低小时平均气温.

气温序列的变化趋势估计采用最小二乘法,并用 t 检验法对线性趋势进行显著性检验.变化速率或趋势表示为每 10 年的气温变化值.季节划分方法:冬季为上一年 12、当年 1、2 月;春季为 3、4、5 月;夏季为 6、7、8 月;秋季为 9、10、11 月;年平均是全年 12 个月的平均.

在订正城市化影响偏差时,本文假设:均一化后的北京站地面气温序列 1915 年的观测记录未受到城市化影响,但从 1916 年开始逐渐受到城市热岛效应影响,同时假设北京站城市化影响在整个观测序列中呈线性递增.根据观测序列的时间长度和城市化累积影响,可由以下公式计算平均每年的城市化增温速率.

$$r = \Delta T_{ur}/N, \tag{4}$$

其中,$N$ 代表序列的长度,即 98 a,$\Delta T_{ur}$ 代表在该时间内城市化累积影响(℃),$r$ 为该段时间内城市化增温速率(℃/a),可称作城市化偏差订正系数.因此,城市化偏差订正公式为

$$A_i = B_i - r \times (Y_i - Y_1), \tag{5}$$

其中,$Y_i$ 为 1915—2012 年中的任一年(a),$Y_1$ 为 1915 年,$B_i$ 为订正前的气温(℃),$A_i$ 为订正后的气温(℃).

633

## 3　均一化资料序列及其城市化偏差

表 5 给出均一化处理后 1915—2012 年北京站年、季平均气温变化趋势及其显著性检验结果. 年最高、最低和平均气温增温速率分别为 0.02 ℃/10a、0.27 ℃/10a 和 0.15 ℃/10a，年平均气温日较差减小趋势为 0.25 ℃/10a，除年最高气温外，其他变化趋势均通过 0.01 的显著性检验. 从季节上看，最高气温冬季上升明显，春季上升缓慢，夏、秋季有微弱下降趋势；对最低气温和平均气温，除夏季平均气温外，其他季节增温趋势都通过了 0.01 的显著性检验，冬季增温最明显，春季次之，夏季最小；气温日较差四季均出现下降趋势，且都通过了 0.01 的显著性检验. 对整个分析时段，年平均最高、最低、平均气温和气温日较差趋势分别为 0.22 ℃、2.68 ℃、1.45 ℃和−2.46 ℃，其中最低气温和平均气温表现出非常显著的上升趋势，比全国和全球陆地平均增暖趋势高出 1 倍左右(Solomon et al.，2007；Ren et al.，2012). 最低气温比最高气温上升速率快，冬、春季比夏、秋季增温明显，这些特征与同期和近 60 年全国平均地面气温变化完全一致(唐国利和任国玉，2005；Ren et al.，2012).

图 4 给出了北京站 1915—2012 年均一化气温资

**表 5　北京站 1915—2012 年地面年、季平均气温和气温日较差变化趋势(单位：℃/10a)**

**Table 5　Linear trends of annual and seasonal mean maximum, minimum, average temperature and DTR during 1915—2012 (Unit: ℃/10a)**

| | 最高气温 | 最低气温 | 平均气温 | 日较差 |
|---|---|---|---|---|
| 春季 | 0.05 | 0.30** | 0.17** | −0.25** |
| 夏季 | −0.07 | 0.17** | 0.05 | −0.24** |
| 秋季 | −0.03 | 0.24** | 0.11** | −0.28** |
| 冬季 | 0.14** | 0.38** | 0.26** | −0.24** |
| 年 | 0.02 | 0.27** | 0.15** | −0.25** |

注：** 表示通过 0.01 显著性水平检验，* 表示通过 0.05 显著性水平检验.

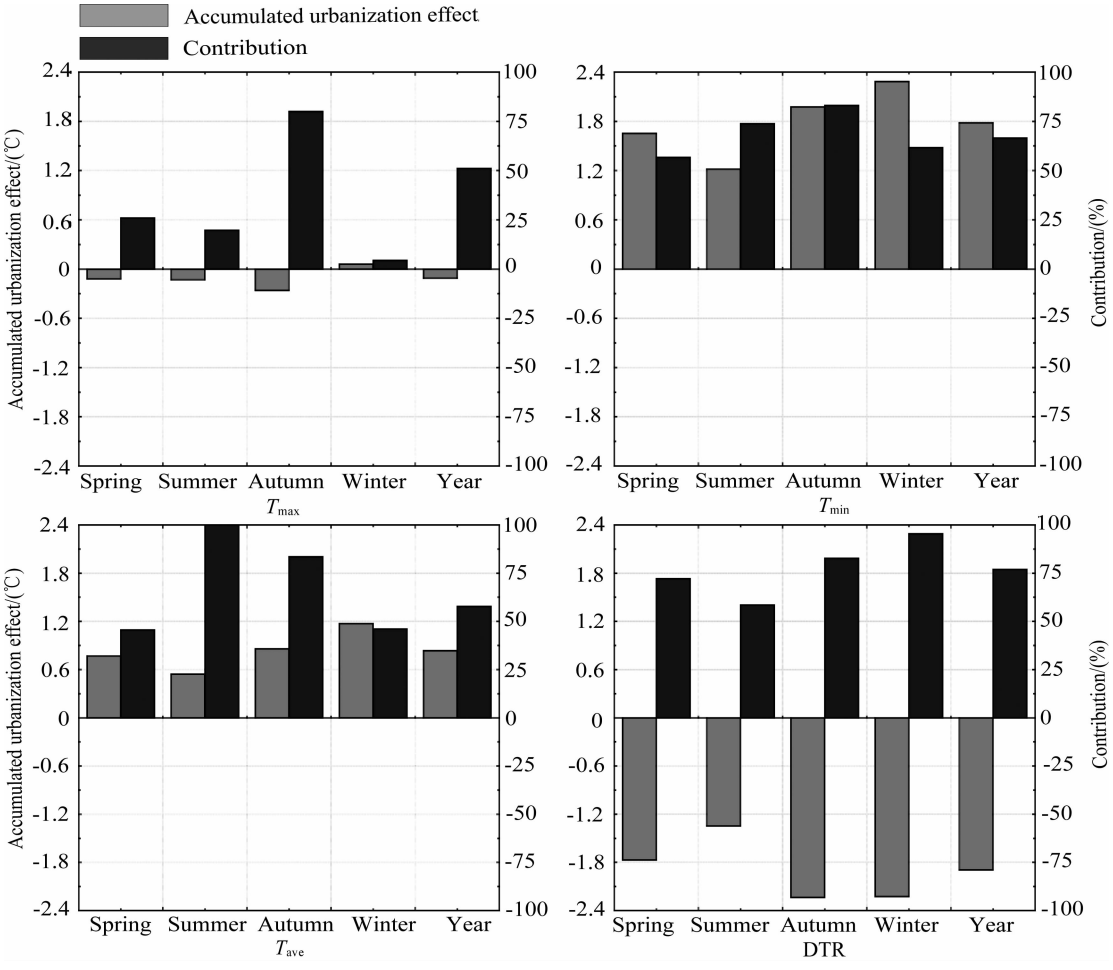


图 4　1915—2012 年北京站地面年、季最高($T_{max}$)、最低($T_{min}$)、平均($T_{ave}$)气温和气温日较差(DTR)的城市化累积影响及城市化影响贡献率

Fig. 4　Accumulated urbanization effects and the contributions to overall temperature trends and DTR for Beijing Station during 1915—2012

料序列中的年、季平均城市化累积影响及其贡献率.年最高、最低、平均气温和气温日较差序列中的城市化累积影响分别为－0.11 ℃、1.78 ℃、0.84 ℃和－1.90 ℃,对应的城市化影响贡献率分别为51.1%、66.5%、57.7%和77.0%.把上述城市化累积影响转化为城市化增温率,分别是－0.01 ℃/10a、0.18 ℃/10a、0.09 ℃/10a和－0.19 ℃/10a.因此,在近百年内,北京站年最高、最低、平均气温和年气温日较差序列均表现出较大的城市化影响偏差,这种系统偏差占同期总体变化趋势的50%以上.

从四季的城市化累积影响来看,最高气温序列很小,除冬季外,其他季节均为负值,秋季绝对值最高,为0.26 ℃;最低气温序列较大,介于夏季的1.22 ℃到冬季的2.29 ℃之间;平均气温序列也较大,冬季最大,为1.17 ℃,夏季最小;气温日较差序列均为负值,秋、冬季约－2.23 ℃,春、夏季较小,但绝对值也在1.30 ℃以上.四季的城市化累积影响贡献率,最高气温秋季达80%,其余三季均在30%以下;最低气温秋季最大,为83%,其他三季均在50%以上;平均气温夏季最大,为100%,秋季次之,春季和冬季均接近50%;气温日较差冬季最大,为95.4%,夏季最小,但也达58.4%.

## 4 城市化偏差订正结果及其分析

对1915—2012年北京站月气温资料进行了城市化偏差订正,利用订正后资料建立了年、季平均地面气温序列.消除了城市化偏差后,最高气温趋势改变不明显,最低气温和平均气温上升趋势都有不同程度的减小,气温日较差下降趋势也有明显减弱.

图5表示均一化资料序列与城市化偏差订正后资料序列逐年值及其线性趋势.城市化偏差订正后,年平均最高气温增加趋势略有上升,增温趋势由均一化序列的0.02 ℃/10a上升为0.03 ℃/10a;年平均最低气温和平均气温增加趋势有不同程度下降,分别由均一化序列的0.27 ℃/10a和0.15 ℃/10a下降到0.09 ℃/10a和0.06 ℃/10a;年气温日较差趋势由均一化序列的－0.25 ℃/10a变为－0.05 ℃/10a,绝对值出现较大幅下降.

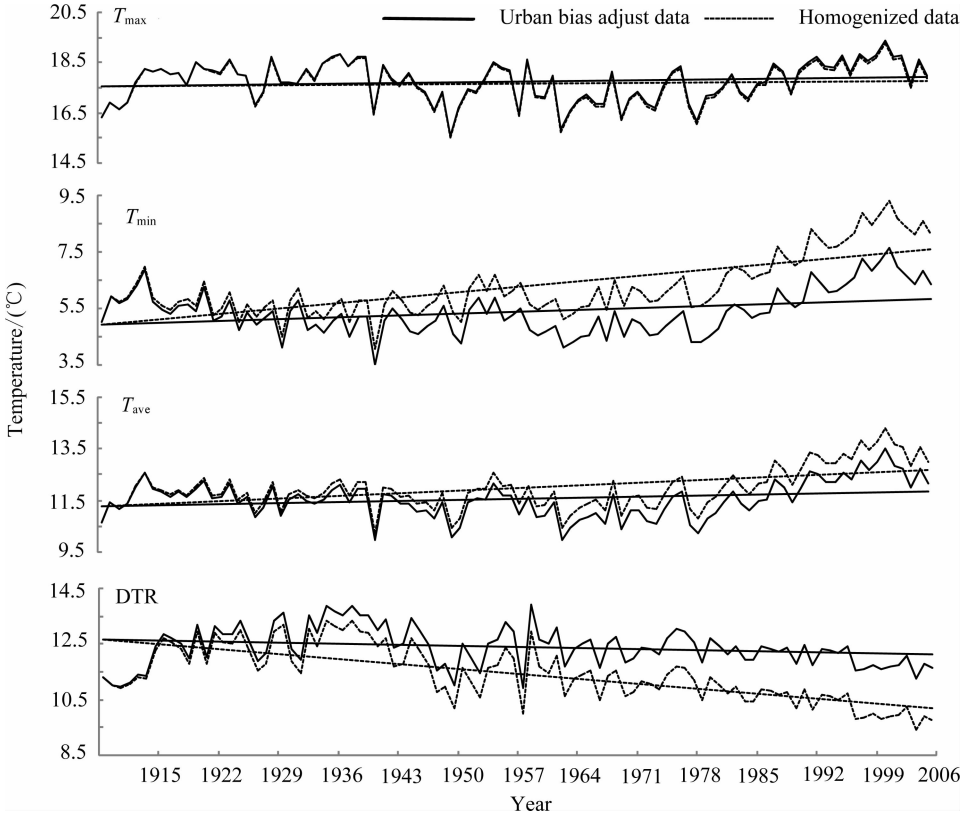


图5 1915—2012年北京站城市化偏差订正前、后年最高($T_{max}$)、最低($T_{min}$)、平均气温($T_{ave}$)和气温日较差(DTR)变化趋势比较

Fig. 5 Annual maximum ($T_{max}$), minimum ($T_{min}$), average temperature ($T_{ave}$) and DTR series before and after urban bias correction

表 6 给出了 1915—2012 年北京站最高、最低、平均气温和气温日较差城市化偏差订正前后年、季变化趋势的差值. 城市化偏差订正前后年、季最高气温趋势变化不明显,最低气温和平均气温趋势减弱较明显,气温日较差趋势变弱很明显.

**表 6　1915—2012 年北京站年、季平均最高、最低、平均气温和气温日较差城市化偏差订正前后的线性趋势的差值(单位:℃/10a)**

**Table 6　The difference of linear trends of annual and seasonal mean temperature and DTR before and after urban bias correction (Unit: ℃/10a)**

| | 春 | 夏 | 秋 | 冬 | 年 |
|---|---|---|---|---|---|
| 最高气温 | 0.01 | 0.01 | 0.03 | −0.01 | 0.01 |
| 最低气温 | −0.17 | −0.13 | −0.20 | −0.24 | −0.18 |
| 平均气温 | −0.08 | −0.06 | −0.09 | −0.12 | −0.09 |
| 日较差 | 0.18 | 0.14 | 0.23 | 0.23 | 0.20 |

## 5　讨论

利用均一化处理后的地面气温资料,本文得到北京站 1915—2012 年年最高、最低和平均气温,其气温变化趋势分别为 0.02 ℃/10a、0.27 ℃/10a 和 0.15 ℃/10a. 季节平均气温增加趋势按从大到小排序分别是冬、春、秋、夏季. 以上结果与先前分析(唐国利和任国玉,2005;Ren et al.,2012)获得的过去百余年中国大陆平均地面气温变化趋势比较,数值偏高,但季节性特征完全一致. Yan 等(2001)在对资料进行均一化处理后,得出 1915—1998 年间北京站年平均气温显示出更明显的上升趋势,而且增温主要表现在 20 世纪 60 年代以后,与本文的结果大体一致. 此外,本文分析结果也同谢庄和曹鸿兴(1996)发现的北京站最低气温比最高气温上升趋势明显的结论一致.

本文在资料均一化的基础上,进一步评价了城市化对长期地面气温变化趋势的影响,发现由于均一化过程致使观测序列中的城市热岛效应影响得以恢复,订正后的气温资料序列中存在更明显的城市化偏差. 徐祥德和汤绪(2002)在总结国内外热岛研究结果时指出,百万人口以上的大城市平均气温一般约高于郊区 0.5～1.0 ℃,本文年平均气温序列中的城市化累积影响为 0.84 ℃. Yang 等(2013)根据迄今最密集观测站点资料的研究指出,北京六环以内的城区年平均城市热岛强度达到 1.63 ℃,四环以内中心城区冬季平均城市热岛强度高达 2.40 ℃以上,夜间和清晨城市热岛强度明显大于白天,表明近百年来大部分时间处于或接近城区的北京站地面气温记录中包含着明显的城市化累积影响.

尽管分析时期不同,本文对平均气温序列中的城市化影响估算结果与先前研究(Ren et al.,2008;张爱英等,2010)得到 1961—2004 年间华北地区城市化引起的国家基准站和基本站增暖偏差约为 0.08 ℃/10a到 0.11 ℃/10a 的结果可以对比;但与多数研究(宋艳玲和张尚印,2003;初子莹和任国玉,2005;林学椿和于淑秋,2005;司鹏等,2009;Yan et al.,2010)得出的 1960 年后北京站的城市化影响程度范围 0.16～0.54 ℃/10a 相比,本文结果偏低,原因可能是城市化影响在早期较弱,改革开放后明显增大(林学椿等,2005). 关于最高、最低气温城市化影响的估算与司鹏等(2009)针对 1960—2006 年的分析结果具有可比性,最高、最低气温的城市化影响比后者明显偏低,可能也与早期城市化影响偏弱有关. 张雷等(2011)对北京 1960—2008 年地面平均和极端气温指数序列的城市化影响进行了分析,发现年最低气温和气温日较差序列的城市化影响分别为 0.70 ℃/10a 和−0.73 ℃/10a,其对应的城市化影响贡献率均为 100%,是目前报告的最高估计值. 造成不同研究结果差异的原因,可能主要与所选乡村站的代表性以及所分析时间段不同等有关.

本文发展的无早期参考序列条件下城镇站城市化偏差评价和订正方法,只要求参考站具有最近几年的气温记录,因而只能得到当前城市化影响程度,无法细分城市化进程快(慢)阶段对不同时期地面气温变化的具体贡献,这是该方法的一个局限. 但气候变化研究主要关注某一时期气候要素的长期线性趋势,对于该时期各个阶段的具体城市化影响偏差可以忽略.

## 6　结论

本文发展了一个无早期参考序列条件下城市化偏差评价和订正方法,在对资料进行非均一性检验和订正的基础上,分析了北京站 1915—2012 年最高、最低和平均气温的变化趋势,评价了城市化对气温序列变化趋势的影响,并对城市化偏差进行了订正,得到以下结论:

(1)北京站最高、最低和平均气温的均一化资料序列表现出比原始资料序列更明显的上升趋势,气

温日较差序列均一化后下降趋势略变大,均一化后年最高、最低、平均气温和气温日较差变化速率分别为 0.02 ℃/10a、0.27 ℃/10a、0.15 ℃/10a 和 −0.25 ℃/10a.

(2)北京站平均气温序列受到很大的城市化影响.年最高、最低、平均气温和气温日较差序列中的城市化累积影响分别为−0.11 ℃、1.78 ℃、0.84 ℃和−1.90 ℃,其对应的城市化影响贡献率分别为51.1%、66.5%、57.7%和 77.0%.城市化累积影响在最高气温序列中只有冬季为正值,在最低和平均气温序列中四季均为正值,冬季最大,夏季最小;在气温日较差序列中四季均为负值.

(3)订正城市化偏差后,最高气温序列的增温速率变化不明显,最低和平均气温序列的增温速率均有明显下降,气温日较差下降趋势明显变弱.

## References


Cao L J, Zhao P, Yan Z W, et al. 2013. Instrumental temperature series in eastern and central China back to the nineteenth century. *Journal of Geophysical Research: Atmospheres*, 118 (15): 8197-8207.

Chen Z H, Hu J L, Zhang D S, et al. 2005. Correction of urban "Heat Island" strength and forecast of heat load. *Meteorology* (in Chinese), 31(1): 69-71.

Chu Z Y, Ren G Y. 2005. Effect of enhanced urban heat island magnitude on average surface air temperature series in Beijing region. *Acta Meteor. Sinica* (in Chinese), 63(4): 534-540.

Chung U, Choi J, Yun J I. 2004. Urbanization effect on the observed change in mean monthly temperatures between 1951—1980 and 1971—2000 in Korea. *Climatic Change*, 66(1-2): 127-136.

Fujibe F. 2009. Detection of urban warming in recent temperature trends in Japan. *International Journal of Climatology*, 29 (12): 1811-1822.

Li Q X, Liu X N, Zhang H Z, et al. 2003. Homogeneity study of in situ observation climate series. *Meteorological Science and Technology* (in Chinese), 31(1): 3-10.

Li Q X, Liu X N, Zhang H Z, et al. 2004. Detecting and adjusting temporal inhomogeneity in Chinese mean surface air temperature data. *Advances in Atmospheric Sciences*, 21(2): 260-268.

Li Q X, Menne M J, Williams C N Jr, et al. 2005. Detection of discontinuities in Chinese temperature series using a multiple test approach. *Climatic and Environmental Research* (in Chinese), 10(4): 736-742.

Li Z, Yan Z W. 2009. Homogenized daily mean/maximum/minimum temperature series for China from 1960—2008. *Atmos. Oceanic Sci. Lett.*, 2(4): 237-243.

Lin X C, Yu S Q. 2005. Interdecadal changes of temperature in the Beijing region and its heat island effect. *Chinese J. Geophys.* (in Chinese), 48(1): 39-45.

Lin X C, Yu S Q, Tang G L. 2005. Study on the relation between urbanization and Beijing UHI intensity. *Progress in Natural Science* (in Chinese), 15(7): 882-886.

Ji C P, Liu W D, Xuan C Y. 2006. Impact of urban growth on the heat island in Beijing. *Chinese J. Geophys.* (in Chinese), 49(1): 69-77.

Jones P D, Moberg A. 2003. Hemispheric and large-scale surface air temperature variations: An extensive revision and an update to 2001. *Journal of Climate*, 16(2): 206-223.

Ren G Y, Zhou Y Q, Chu Z Y, et al. 2008. Urbanization effects on observed surface air temperature trends in North China. *Journal of Climate*, 21(6): 1333-1348.

Ren G Y, Zhang A Y, Chu Z Y, et al. 2010. Principles and procedures for selecting reference surface air temperature stations in China. *Meteorological Science and Technology* (in Chinese), 38(1): 78-85.

Ren G Y, Ding Y H, Zhao Z C, et al. 2012. Recent progress in studies of climate change in China. *Advance in Atmospheric Sciences*, 29(5): 958-977.

Ren Y Y, Ren G Y. 2011. A remote-sensing method of selecting reference stations for evaluating urbanization effect on surface air temperature trends. *Journal of Climate*, 24(13): 3179-3189.

Si P, Li Q X, Xuan C Y, et al. 2009. Contribution of urbanization to change of air temperature in Beijing. *Journal of Natural Disasters* (in Chinese), 18(4): 138-144.

Solomon S, Qin D, Manning M, et al. 2007. Climate Change 2007: The Physical Science Basis. Contribution of Working Group I to the Fourth Assessment Report of the Intergovernmental Panel on Climate Change. New York: Cambridge University Press.

Song Y L, Zhang S Y. 2003. The study on heat island effect in Beijing during last 40 years. *Chinese Journal of Eco-Agriculture* (in Chinese), 11(4): 126-129.

Tang G L, Ren G Y. 2005. Reanalysis of surface air temperature change of the last 100 years over China. *Climatic and Environmental Research* (in Chinese), 10(4): 791-798.

Xie Z, Cao H X. 1996. The asymmetric trend of change in maximum and minimum temperature in Beijing. *Acta Meteor. Sinica* (in Chinese), 54(4): 501-507.

Xie Z, Cui J L, Chen D G, et al. 2006. The annual, seasonal and monthly characteristics of diurnal variation of urban heat island intensity in Beijing. *Climatic and Environmental Research* (in Chinese), 11(1): 69-75.

Xu X D, Tang X. 2002. An Introduction to Meteorology in Urbanization Environment (in Chinese). Beijing: China Meteorological Press.

Yan Z W, Yang C, Jones P. 2001. Influence of inhomogeneity on the estimation of mean and extreme temperature trends in Beijing and Shanghai. *Advances in Atmospheric Sciences*, 18 (3): 309-322.

Yan Z W, Li Z, Li Q X, et al. 2010. Effects of site change and urbanization in the Beijing temperature series 1977—2006. *International Journal of Climatology*, 30(8): 1226-1234.

Yang P, Ren G Y, Liu W D. 2013. Spatial and temporal characteristics of Beijing urban heat island intensity. *Journal of Applied Meteorology and Climatology*, 52(8): 1803-1816.

Zhang A Y, Ren G Y, Zhou J X, et al. 2010. On the urbanization effect on surface air temperature trends over China. *Acta Meteorologica Sinica* (in Chinese), 68(6): 957-966.

Zhang L, Ren G Y, Liu J, et al. 2011. Urban effect on trends of extreme temperature indices at Beijing Meteorological Station. *Chinese J. Geophys.* (in Chinese), 54(5): 1150-1159.

Zhang L, Ren G Y, Ren Y Y, et al. 2014. Effect of data homogenization on estimate of temperature trend: a case of Huairou station in Beijing Municipality. *Theoretical and Applied Climatology*, 115(3-4): 365-373.

Zheng Z F. 2011. Characteristics of extreme temperature variation and their response to urbanization in Beijing. *Scientia Geographica Sinica* (in Chinese), 31(4): 459-463.

Zhou Y Q, Ren G Y. 2005. Indetifying and correcting urban bias for regional surface air temperature series North China over period of 1961—2000. *Climatic and Environmental Research* (in Chinese), 10(4): 743-753.

## 附中文参考文献

陈正洪，胡江林，张德山等. 2005. 城市热岛强度订正与供热量预报. 气象，31(1)：69-71.

初子莹，任国玉. 2005. 北京地区城市热岛强度变化对区域温度序列的影响. 气象学报，63(4)：534-540.

李庆祥，刘小宁，张洪政等. 2003. 定点观测气候序列的均一性研究. 气象科技，31(1)：3-10.

李庆祥，Menne M J，Williams C N Jr 等. 2005. 利用多模式对中国气温序列中不连续点的检测. 气候与环境研究，10(4)：736-742.

林学椿，于淑秋. 2005. 北京地区气温的年代际变化和热岛效应. 地球物理学报，48(1)：39-45.

林学椿，于淑秋，唐国利. 2005. 北京城市化进程与热岛强度关系的研究. 自然科学进展，15(7)：882-886.

季崇萍，刘伟东，轩春怡. 2006. 北京城市化进程对城市热岛的影响研究. 地球物理学报，49(1)：69-77.

任国玉，张爱英，初子莹等. 2010. 我国地面气温参考站点遴选的依据、原则和方法. 气象科技，38(1)：78-85.

司鹏，李庆祥，轩春怡等. 2009. 城市化对北京气温变化的贡献分析. 自然灾害学报，18(4)：138-144.

宋艳玲，张尚印. 2003. 北京市近 40 年城市热岛效应研究. 中国生态农业学报，11(4)：126-129.

唐国利，任国玉. 2005. 近百年中国地表气温变化趋势的再分析. 气候与环境研究，10(4)：791-798.

谢庄，曹鸿兴. 1996. 北京最高和最低气温的非对称变化. 气象学报，54(4)：501-507.

谢庄，崔继良，陈大刚等. 2006. 北京城市热岛效应的昼夜变化特征分析. 气候与环境研究，11(1)：69-75.

徐祥德，汤绪. 2002. 城市化环境气象学引论. 北京：气象出版社.

张爱英，任国玉，周江兴等. 2010. 中国地面气温变化趋势中的城市化影响偏差. 气象学报，68(6)：957-966.

张雷，任国玉，刘江等. 2011. 城市化对北京气象站极端气温指数趋势变化的影响. 地球物理学报，54(5)：1150-1159.

郑祚芳. 2011. 北京极端气温变化特征及其对城市化的响应. 地理科学，31(4)：459-463.

周雅清，任国玉. 2005. 华北地区地表气温观测中城镇化影响的检测和订正. 气候与环境研究，10(4)：743-753.

（本文编辑　胡素芳）

ADVANCES IN ATMOSPHERIC SCIENCES, VOL. 31, SEPTEMBER 2014, 1167–1180

# The Boreal Summer Intraseasonal Oscillation Simulated by Four Chinese AGCMs Participating in the CMIP5 Project

ZHAO Chongbo*[1], ZHOU Tianjun[2], SONG Lianchun[3], and REN Hongli[1]

[1]*Laboratory for Climate Studies, National Climate Center, China Meteorological Administration, Beijing* 100081

[2]*State Key Laboratory of Numerical Modeling for Atmospheric Sciences and Geophysical Fluid Dynamics, Institute of Atmospheric Physics, Chinese Academy of Sciences, Beijing* 100029

[3]*National Climate Center, China Meteorological Administration, Beijing* 100081

(Received 25 October 2013; revised 30 December 2013; accepted 10 February 2014)

ABSTRACT

The performances of four Chinese AGCMs participating in the Coupled Model Intercomparison Project Phase 5 (CMIP5) in the simulation of the boreal summer intraseasonal oscillation (BSISO) are assessed. The authors focus on the major characteristics of BSISO: the intensity, significant period, and propagation. The results show that the four AGCMs can reproduce boreal summer intraseasonal signals of precipitation; however their limitations are also evident. Compared with the Climate Prediction Center Merged Analysis of Precipitation (CMAP) data, the models underestimate the strength of the intraseasonal oscillation (ISO) over the eastern equatorial Indian Ocean (IO) during the boreal summer (May to October), but overestimate the intraseasonal variability over the western Pacific (WP). In the model results, the westward propagation dominates, whereas the eastward propagation dominates in the CMAP data. The northward propagation in these models is tilted southwest–northeast, which is also different from the CMAP result. Thus, there is not a northeast–southwest tilted rain belt revolution off the equator during the BSISO's eastward journey in the models. The biases of the BSISO are consistent with the summer mean state, especially the vertical shear. Analysis also shows that there is a positive feedback between the intraseasonal precipitation and the summer mean precipitation. The positive feedback processes may amplify the models' biases in the BSISO simulation.

**Key words**: boreal summer intraseasonal oscillation, AGCM, simulation, feedback

**Citation**: Zhao, C. B., T. J. Zhou, L. C. Song, and H. L. Ren, 2014: The boreal summer intraseasonal oscillation simulated by four Chinese AGCMs participating in the CMIP5 project. *Adv. Atmos. Sci.*, **31**(5), 1167–1180, doi: 10.1007/s00376-014-3211-7.

## 1. Introduction

The intraseasonal oscillation (ISO) is one of the most prominent large-scale sources of variability in the tropics and it undergoes a peculiar seasonal variation (Seo et al., 2005). While the strongly eastward propagating ISO (the Madden–Julian oscillation) is primarily observed in the boreal winter, the ISO in the boreal summer from May to October is dominated by the northward propagation over the Indian and western Pacific (Jiang et al., 2004). This boreal summer subseasonal mode significantly affects the active and break phases of the summer monsoon (Yasunari, 1979, 1980; Li et al., 2001). The wet and dry spells of the boreal summer intraseasonal oscillation (BSISO) strongly influence the extreme hydro-meteorological events, which cause about 80% of natural disasters (Lau and Waliser, 2005). The intraseasonal oscillation also has an effect on the formation, intensity, and course of the tropical cyclones (Nakazawa, 1986; Liebmann et al., 1994). Therefore, the BSISO is important for weather forecasting and climate prediction.

Numerical weather prediction results have shown that a model capable of simulating ISO may have a better overall forecasting ability (Li et al., 2006). However, attempts to simulate the BSISO have met with poor results (Slingo et al., 1996; Waliser et al., 2003; Lin et al., 2008; Sperber et al., 2013). This is because the BSISO shows a complex propagation process due to a prominent northeastward propagation associated with the monsoon over the Indian Ocean (IO) and the western Pacific (WP), as well as the formation of the summertime intertropical convergence zone off the equator (Sikka and Gadgil, 1980; Lau and Chan, 1986; Wang and Rui, 1990; Annamalai and Sperber, 2005; Seo et al., 2007). How to reliably simulate the BSISO has been a challenge to the climate-modeling community.

Over the Asian summer monsoon region, precipitation is an important forecast variable in model simulation. The outgoing longwave radiation (OLR) and the real-time multi-

* Corresponding author: ZHAO Chongbo
Email: chongbozhao@mail.iap.ac.cn

© Institute of Atmospheric Physics/Chinese Academy of Sciences, and Science Press and Springer-Verlag Berlin Heidelberg 2014

variate MJO (Madden–Julian oscillation) index (Wheeler and Hendon, 2004) focus on the deep convection and large-scale circumnavigate mode. During the boreal summer, the variability of the ISO is weaker than the MJO in the winter and propagates as far north as the Asian continent. The evaluation of precipitation is helpful in comprehensively examining the convective parameterization and topography description of the AGCMs. Lin et al. (2008) evaluated the intraseasonal precipitation during the boreal summer in the models participating in the IPCC Fourth Assessment Report (AR4). The results showed that the GCMs still have difficulties and display a wide range of ability in simulating the subseasonal variability. Our analysis is based on the atmospheric component of the four Chinese AGCM simulations, which were submitted to the ongoing Coupled Model Inter-comparison Project—Phase 5 (CMIP5). Specifically, the models we use are forced by the same observed SST, sea ice fractions, $CO_2$ concentrations, and other external forcing as defined in the Atmospheric Model Inter-comparison Project (AMIP) framework (Taylor et al., 2009). The aim of the study is to assess the performances of four new generation Chinese AGCMs in the simulation of BSISO and to understand the strengths and weaknesses of the models.

The remainder of the paper is organized as follows. The models and validation datasets used in this study are described in section 2. The results of the BSISO simulation are presented in section 3. A discussion of the model bias analysis and the relationship between the simulated mean state and BSISO are given in section 4. A summary is given in section 5.

## 2. Data, model, and analysis method

### 2.1. *Data*

To check the reliability of the model simulations, the pentad precipitation datasets are obtained from the Climate Prediction Center (CPC) Merged Analysis of Precipitation (CMAP) (Xie and Arkin, 1997) and the Global Precipitation Climatology Project (GPCP) Precipitation (Xie et al., 2003). The 3D zonal wind, meridional wind, and specific humidity datasets are used for analysis. These are obtained from the Climate Forecast System Reanalysis (CFSR; Saha et al., 2006; Saha et al., 2010) of the National Centers for Environmental Prediction (NCEP). Prior to the analysis, the pentad data are interpolated to daily values. We use nineteen (1979–97) summers (May to October) data for validating the simulations and discussing the biases.

### 2.2. *Models*

This analysis is based on 19 years of AMIP simulations from four Chinese AGCMs. In the AMIP run, the observed SST and sea ice temperature served as the boundary forcing of the numerical experiments. In addition, other conditions ($CO_2$ concentrations, solar constant, and aerosols) are also included during the integration.

Table 1 shows the acronyms, names, atmospheric models, resolutions, and convection parameterization schemes.

The BCC-CSM (Climate System Models developed by Beijing Climate Center) is a coupled climate system model including atmosphere, ocean, land surface, and sea ice components. There are two versions of this model with different horizontal resolutions, BCC-CSM1-1 and BCC-CSM1-1-m, that are participating in the CMIP5 (Jiang et al., 2012). In this paper, we focus on the former one. For the atmosphere, it uses an atmospheric general circulation model, BCC-AGCM2.1, developed by the Beijing Climate Center (BCC; Wu et al., 2008, 2010). This is a spectral model with horizontal T42 truncation ($\sim 2.8125^\circ$ horizontal resolution) and 26 layers in the vertical direction.

The BNU-ESM (Beijing Normal University-Earth System Model) is developed at the College of Global Change and Earth System Science at Beijing Normal University (Wu et al., 2013; http://esg.bnu.edu.cn/BNU_ESM_webs/htmls/index.html). For the atmosphere, BNU AGCM's horizontal resolution is T42 and the vertical resolution is 26 layers.

FGOALS-g2 (Flexible Global Ocean-Atmosphere-Land System Model, Grid-point Version 2) is developed at the State Key Laboratory of Numerical Modeling for Atmospheric Sciences and Geophysical Fluid Dynamics (LASG) at the Institute of Atmospheric Physics (IAP), Chinese Academy of Sciences (hereafter LASG/IAP) and Tsinghua University. The atmospheric component of FGOALS-g2 is the Grid Atmospheric Model of IAP/LASG (GAMIL), which employs a horizontal resolution of 2.8° between 65.58°N and 65.58°S

**Table 1.** List of models.

| Modeling center | Abbreviation | Atmospheric model | Resolution | Convection parameterization scheme |
|---|---|---|---|---|
| Beijing Climate Center | BCC-CSM1-1 | BCC_AGCM 2.1 | T42, L26 | Wu Scheme (Wu et al., 2010) |
| College of Global Change and Earth System Science, Beijing Normal University | BNU-ESM | BNU_AGCM | T42, L26 | Standard Zhang–McFarlane with Convective Momentum Transports (Richter and Rasch, 2008) |
| LASG, Institute of Atmospheric Physics, Chinese Academy of Sciences and CESS, Tsinghua University | FGOALS-g2 | GAMIL 2.0 | $\sim 2.8^\circ \times 2.8^\circ$, L26 | New Zhang–Mcfarlane (Zhang and Mu, 2002) |
| LASG, Institute of Atmospheric Physics, Chinese Academy of Sciences | FGOALS-s2 | SAMIL 2.0 | R42, L26 | Tiedtke (1989) |

and has 26 vertical layers. The details of the model are found in Li et al. (2013).

FGOALS-s2 (Flexible Global Ocean-Atmosphere-Land System Model, Spectral Version 2) is also developed at LASG/IAP. The atmospheric component of FGOALS-s2 is version 2.4.7 of Spectral Atmospheric Model in IAP/LASG (SAMIL; Bao et al., 2010, 2013), a spectral transform model with 26 atmospheric layers extending from the surface to 2.19 hPa, and with a horizontal resolution of R42 [$\sim 2.81^\circ$ (lon) $\times 1.66^\circ$ (lat)].

These models have updated their physical schemes to incorporate state-of-the-art research results. For example, the parameterizations for the deep cumulus convection, dry adiabatic adjustment, latent heat and sensible heat fluxes over the ocean surface, and the snow cover fraction were replaced with new schemes in BCC_AGCM2.0.1 Wu et al. (2010). In GAMIL2.0, the convection parameterization scheme was replaced by the Zhang–McFarlane scheme (Zhang and Mu, 2005), and a two-moment bulk stratiform cloud microphysics scheme (Morrison and Gettelman, 2008) was added to the microphysical processes (Li et al., 2013). Therefore, it is of interest to assess the simulations of BSISO in this new generation of climate models to look at the effects of the updated physical processes.

### 2.3. *Analysis method*

First, we estimate the reproduction quality of the BSISO's intensity, period, and propagation in turn. To extract the BSISO signal, daily precipitation, evaporation, specific humidity, and wind during 1979–97 are subject to a 20–100-day bandpass filtering based on harmonic decomposition (Kemball-Cook and Wang, 2001; Teng and Wang, 2003; Jiang et al., 2004). The 20–100-day bandpass filtered data from May to October in each year are then used as the intraseasonal component in the following analyses.

Next, to investigate the positive feedback between BSISO and the summer mean state, the moisture budget analysis are calculated according to Ray and Li (2013). To examine

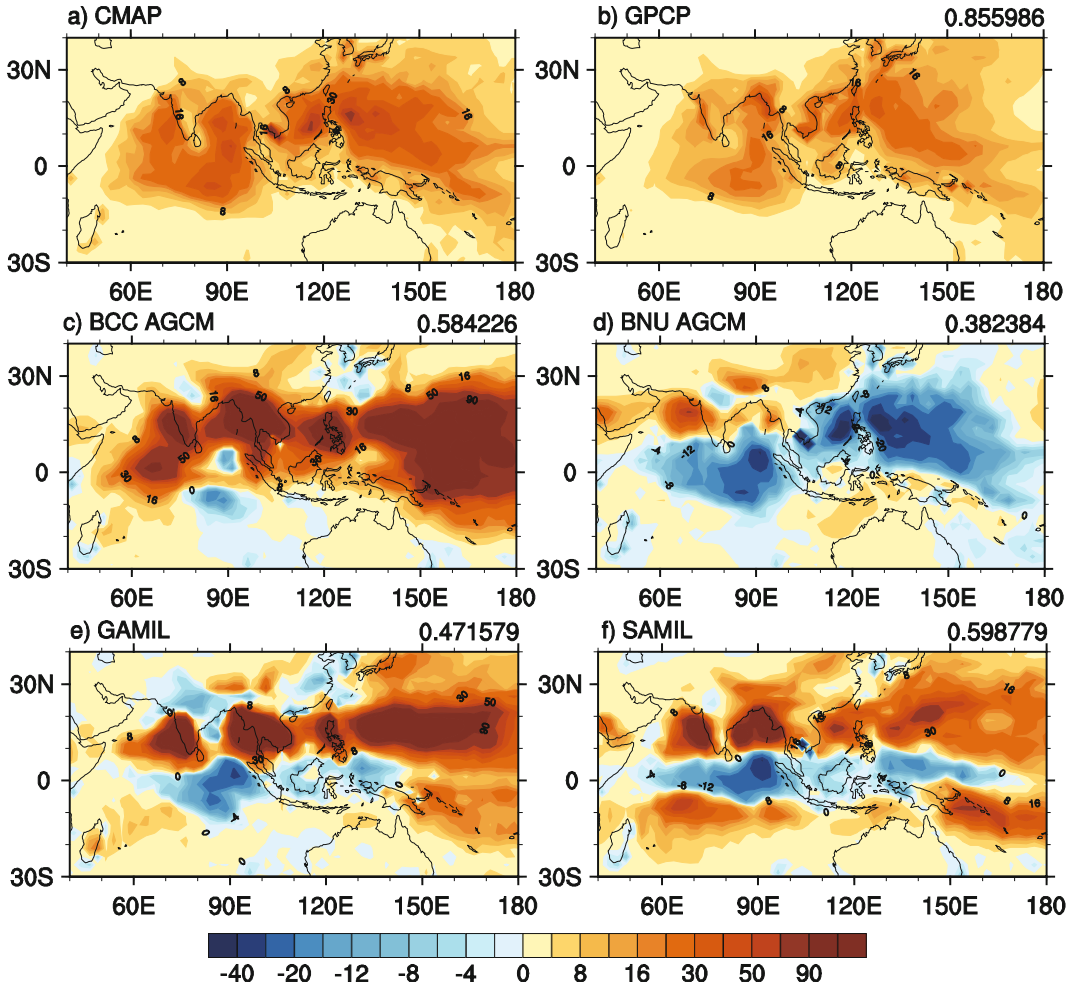


**Fig. 1.** Horizontal distribution of 20–100 day filtered precipitation variance of (a) CMAP, (b) GPCP and (c–f) the difference between models and CMAP (units: $mm^2\ d^{-2}$) during the boreal summer. The pattern correlations between models and CMAP are given at the top-right corner of each panel.

changes in precipitation, the summer mean vertically integrated moisture budget equation can be written as

$$\overline{\mathrm{Pr}} = \overline{E} + \overline{\langle -\boldsymbol{V}\cdot\nabla q\rangle} + \overline{\langle -q\nabla\cdot\boldsymbol{V}\rangle} + \overline{R}\,, \tag{1}$$

where Pr is precipitation, $E$ is evaporation, $\boldsymbol{V}$ is horizontal velocity, $q$ is specific humidity, and $R$ is the residual term. $\langle -\boldsymbol{V}\cdot\nabla q\rangle$ is the advection of moisture term, $\langle -q\nabla\cdot\boldsymbol{V}\rangle$ is the moisture convergence term. The overbar, "–", represents the summer mean and "$\langle\ \rangle$" means the vertical integration and indicates a mass integration through the troposphere:

$$\langle\ \rangle = \int_{P_s}^{P_t} \frac{dP}{g}\,, \tag{2}$$

here $P_t$ is 100 hPa, $P_s$ is 1000 hPa, and $g$ is gravity.

The summer mean moisture advection term, $\overline{\langle -\boldsymbol{V}\cdot\nabla q\rangle}$, can be further separated into two terms (Adv1 and Adv2)

$$\overline{\langle -\boldsymbol{V}\cdot\nabla q\rangle} = \langle -\overline{\boldsymbol{V}}\cdot\nabla\overline{q}\rangle + \overline{\langle -\boldsymbol{V}'\cdot\nabla q'\rangle} = \mathrm{Adv1} + \mathrm{Adv2}\,, \tag{3}$$

and the summer mean convergence term, $\overline{\langle -q\nabla\cdot\boldsymbol{V}\rangle}$, also can

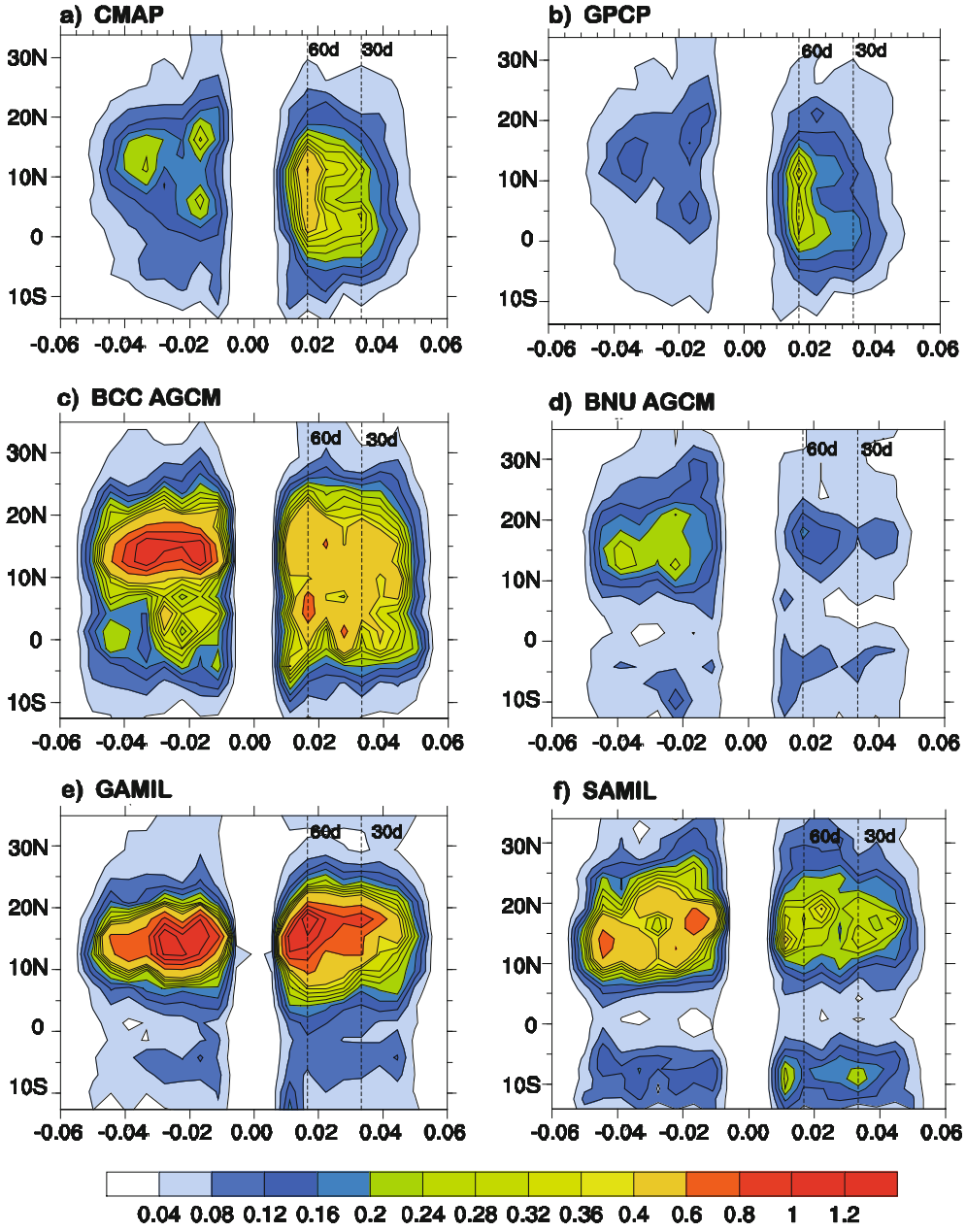


**Fig. 2.** Spectrum distribution of the eastward and westward propagating BSISO (units: $\mathrm{mm^2\ d^{-2}}$) as a function of latitude and period for zonal wavenumber 1 (40°–180°E) from precipitation of CMAP, GPCP, BCC AGCM, BNU AGCM, GAMIL, and SAMIL.

be further separated into two terms (Con1 and Con2)

$$\overline{\langle -q\nabla\cdot\boldsymbol{V}\rangle} = \langle -\overline{q}\nabla\cdot\overline{\boldsymbol{V}}\rangle + \overline{\langle -q'\nabla\cdot\boldsymbol{V}'\rangle} = \mathrm{Con1} + \mathrm{Con2}\ , \quad (4)$$

here, the prime, "′", denotes the boreal summer intraseasonal perturbation, Adv1 represents the advection of the moisture by the summer mean wind, and Adv2 represents the summer mean advection of the intraseasonal moisture by the intraseasonal wind. Con1 denotes the convergence of summer mean moisture by the summer mean wind, and Con2 denotes the summer mean convergence of the intraseasonal moisture by the intraseasonal wind.

Through calculating the equations above during the boreal summer, the feedback correlation between the BSISO and the summer mean state can be derived.

## 3. Results of BSISO simulation

The reproduction quality of the BSISO's major characteristics is estimated first. Figure 1 shows the variance of the 20–100 day bandpass filtered precipitation anomaly during the boreal summer from 1979 to 1997. The most conspicuous

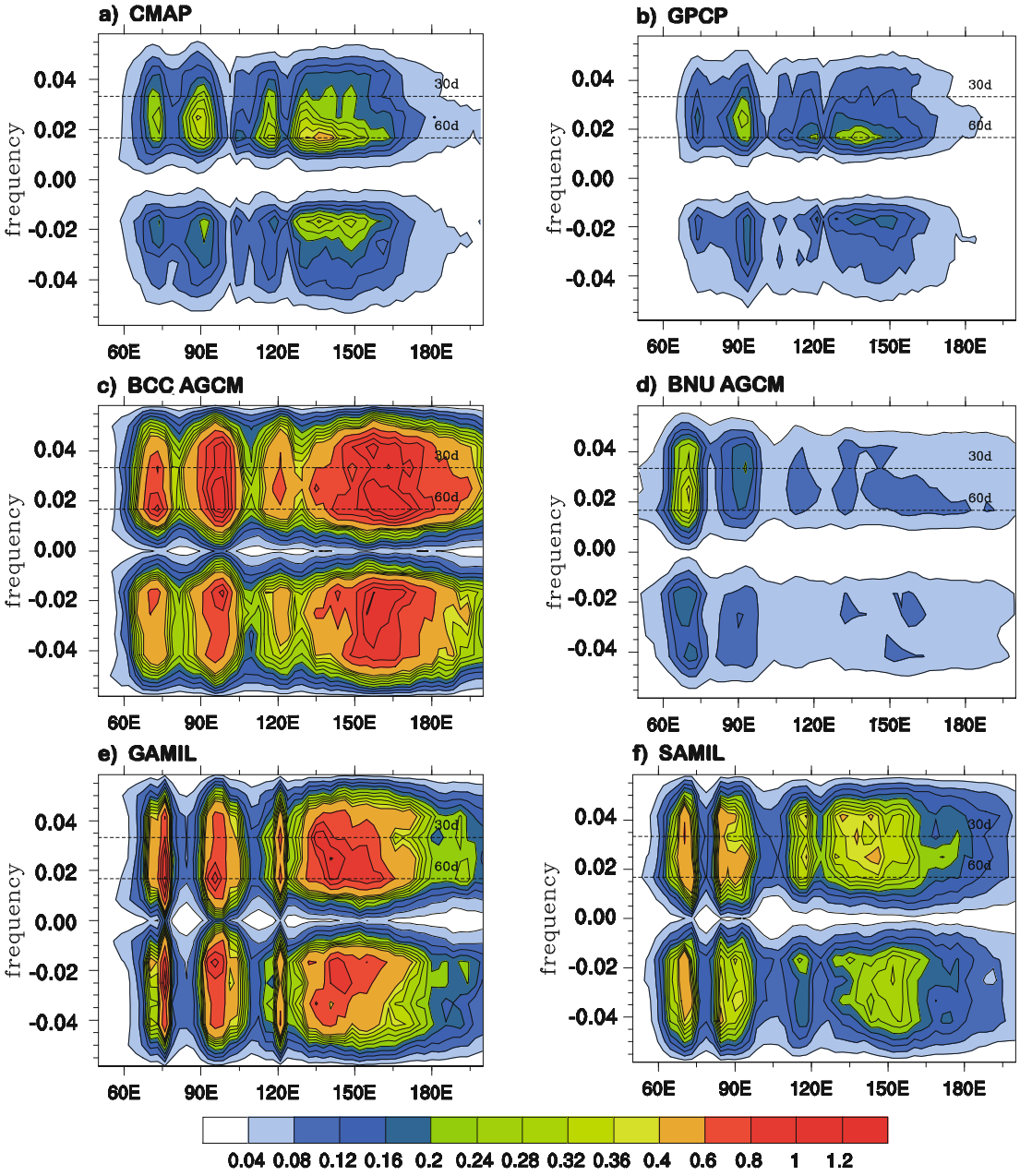


**Fig. 3.** Spectrum distribution of the northward and southward propagating BSISO (units: $mm^2\ d^{-2}$) as a function of longitude and period for meridional wavenumber 1 (15°S–25°N) from precipitation of CMAP, GPCP, BCC AGCM, BNU AGCM, GAMIL, and SAMIL.

feature of the precipitation intraseasonal variability in CMAP is two maxima: the tropical eastern IO and the WP. The horizontal distribution of the BSISO in the GPCP looks similar and has pattern correlations of 0.93 with the CMAP result. The models can replicate the BSISO signals; however there are still intensity biases in the two maxima areas. The four models all underestimate the variability over the tropical eastern IO. Three models (BCC AGCM, GAMIL, and SAMIL) overestimate the variability over the WP, but the BSISO is weaker in the BNU AGCM model than in the observation.

To provide a comprehensive evaluation of the period and propagation simulations on the BSISO, Figs. 2 and 3 show the zonal and meridional spectrum distribution at wavenumber 1 of the 20–100 days filtered precipitation anomaly. In the observation, separation of the eastward propagation and the westward propagation show that the eastward propagation of the BSISO is dominant and the strongest energy spectrum appears in the period of 30–90 days at zonal wavenumber 1 (corresponding to a wavelength from 40°E to 180°E) along the equator and 10°N. The highest westward propagation energy spectrum is concentrated at the 30–60 day period, and the location of the maxima is shifted northward compared with the eastward propagation. This indicates the northwestward propagation of the large-scale convection system in the WP, which is consistent with previous studies (Lau and Chan, 1986; Knutson and Weickmann, 1987). Models can reproduce the 30–90 day signals with the peak of 60 days, but the amplitude of the westward propagating mode of the BSISO is larger than the eastward counterpart.

In the observation, the northward propagation of the BSISO has its maxima over the IO and WP (Fig. 3). The significant period is around 40 days over the IO and 60 days over the WP, which means the BSISO propagates faster over the IO than over the WP. In the models' results, the northward propagation is well simulated, but the northward propagation is southwest–northeast tilted, which is also different from the

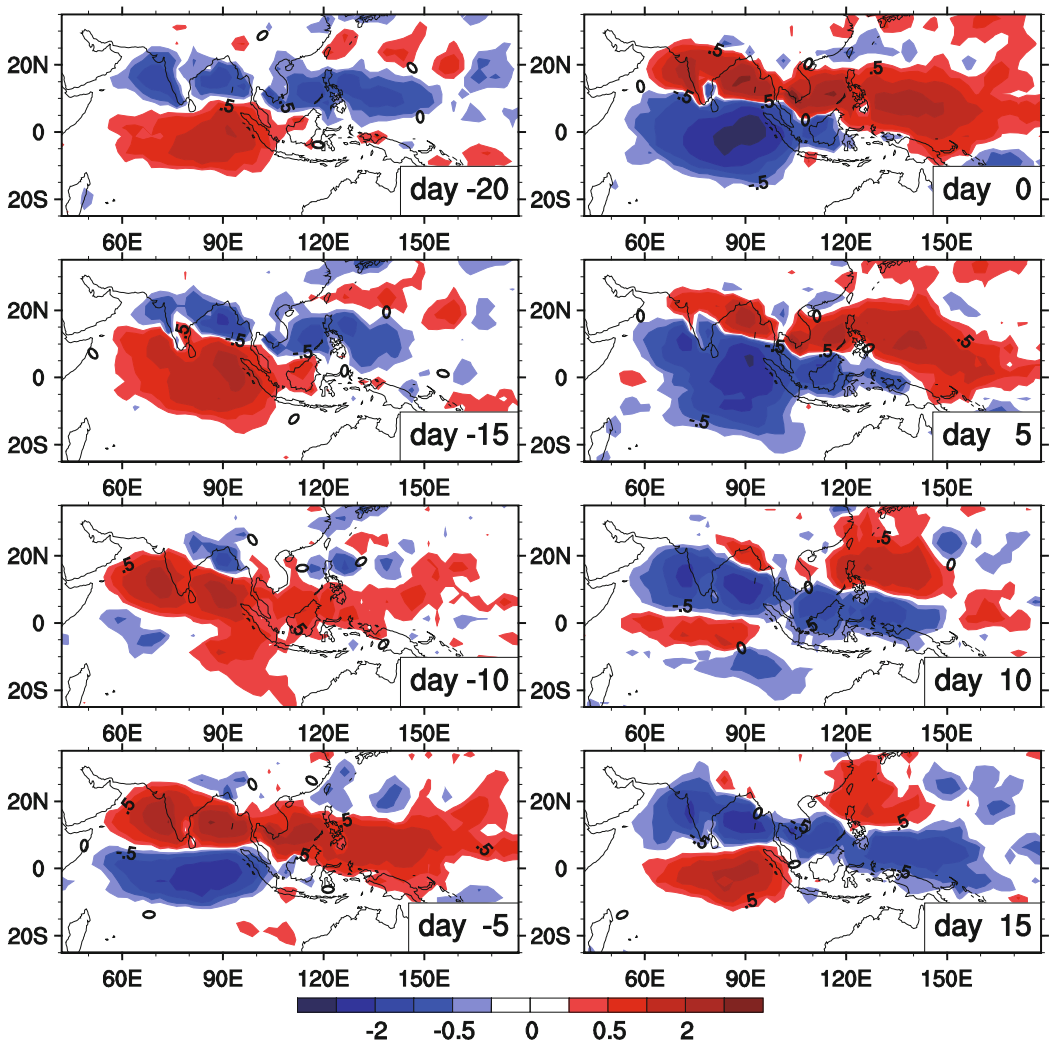


**Fig. 4.** Lag regression of 20–100 day bandpass filtered precipitation with PC-1 from day −20 to day 15 with 5-day intervals. The lag regressions have been scaled by one standard deviation of PC-1 to give units of mm $d^{-1}$.

CMAP result. This also can be seen in the lifecycle of the BSISO.

The time series of the first EOF mode that spans from 30°S to 30°N and 40°E to 180°E was used as the BSISO index (Jiang and Li, 2005; Zhao et al., 2013). Figure 4 shows the lag regressions of the 20–100 day filtered rainfall anomalies with PC-1. The regressions have been scaled by one standard deviation of PC-1. The pattern at day 0 resembles the first EOF mode pattern, as expected. During the observed BSISO lifecycle, rainfall is initiated over the southwestern IO around day −10, with a suppressed convective anomalies belt poleward over the IO and WP that propagates eastward. By day 10, the enhanced convection is mostly concentrated over the northern IO and tropical WP. At this time the suppressed BSISO phase dominates over the tropical Indian Ocean. The entire northwest–southeast tilted rainfall anomalies belt propagates northward (black line in Fig. 4).

Figure 5 shows the BSISO lifecycle patterns obtained from the BCC AGCM. The northward propagation of the rainfall anomalies band tilts southwest–northeast, though the essential evolution features seen in the lifecycle of CMAP are well represented. It is clear to see that the onset of positive rainfall anomalies occurs over the central Indian Ocean at day −10, and then propagates westward instead of eastward at day −5. The BSISO in the model result propagates more slowly over the IO than over the WP, which is opposite to the observation. This is also true with BNU AGCM, GAMIL, and SAMIL models (figure not shown). When the BSISO propagates northward faster over the WP than over the IO, positive rainfall anomalies first occur over the WP then the IO and the westward propagation is more significant than the eastward propagation.

These results demonstrate that the four Chinese models have the ability to capture the BSISO signals, but they are not perfect. The variance distribution shows a negative bias over the eastern IO. Over the WP, the variance in three of the models is larger than that in the observation, but is smaller in BNU AGCM. All the models show an overly strong west-

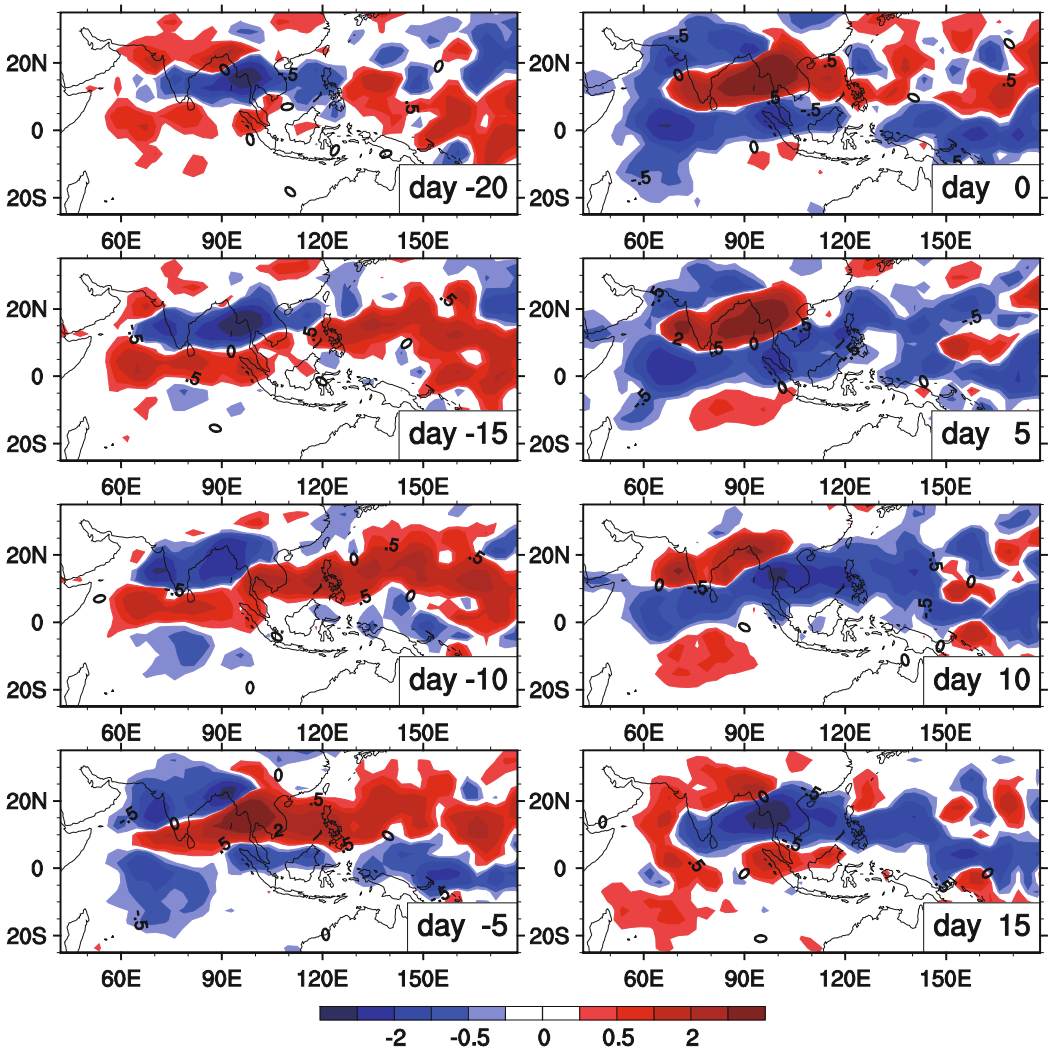


**Fig. 5.** The same as Fig. 4, except for BCC AGCM.

ward propagation and a southwest–northeast titled rainfall belt, which both have a relationship with the different northward propagation speed over the IO and WP. Next we present the possible cause of the models' bias.

## 4. Relationship between the simulated mean state and BSISO

### 4.1. *The effect of summer mean state on BSISO*

Previous observational studies indicate that the intensity of the ISO is highly correlated with the mean precipitation intensity (Wheeler and Kiladis, 1999; Ray and Li, 2013; Yang et al., 2013). The ability to reproduce the mean state is important for the models in simulating the ISO (Maloney and Hartman, 2001; Inness et al., 2003; Zhang et al., 2006). We assess the summer mean state in the model results and analyze the correlation between the BSISO and the summer mean state.

Figure 6 shows the summer mean precipitation. The observed summer precipitation (Figs. 6a and b) has two maxima: the tropical IO and WP. In the models, the summer mean precipitation is weaker over the tropical IO than it is in CMAP. BCC AGCM, GAMIL, and SAMIL overestimate the summer mean precipitation over the WP, whereas BNU AGCM underestimates it. This is consistent with the bias of the BSISO variance simulation. Since the greater precipitation along the Pacific Intertropical Convergence Zone may lead to a stronger Rossby wave response and a suppressed Kelvin wave, the westward propagation is excessive in the models.

There is a close relationship between the easterly shear and the precipitation intensity over the tropical IO and WP, since the strength of the zonal wind along the convective center's sides is synchronous with the tropical convection activity. The CFSR reanalysis result (Fig. 7a) has lower tro-

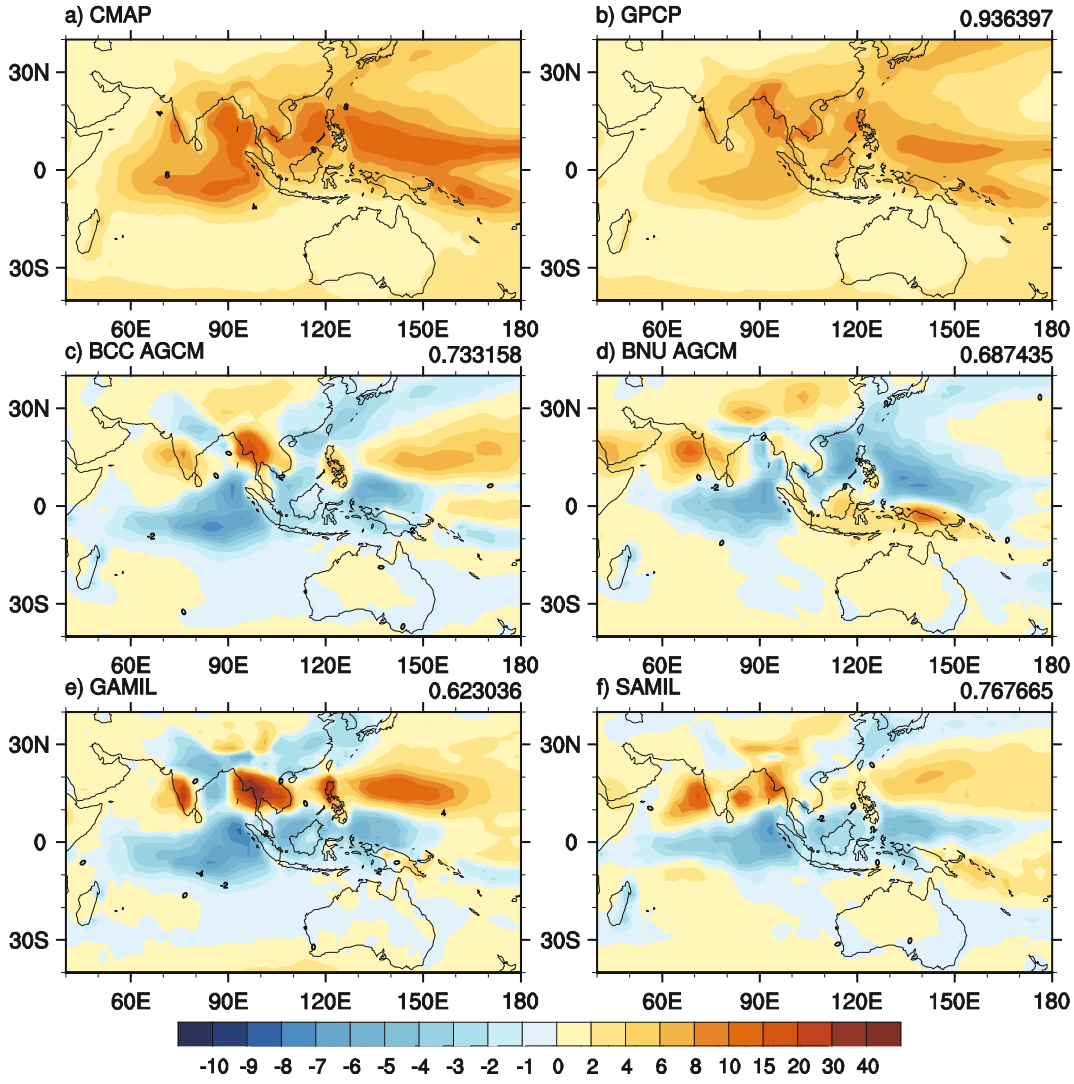


**Fig. 6.** Summer mean precipitation of (a) CMAP, (b) GPCP and (c–f) the difference between models and CMAP (units: mm $d^{-1}$). The pattern correlations between models and CMAP are given at the top-right corner of each panel.

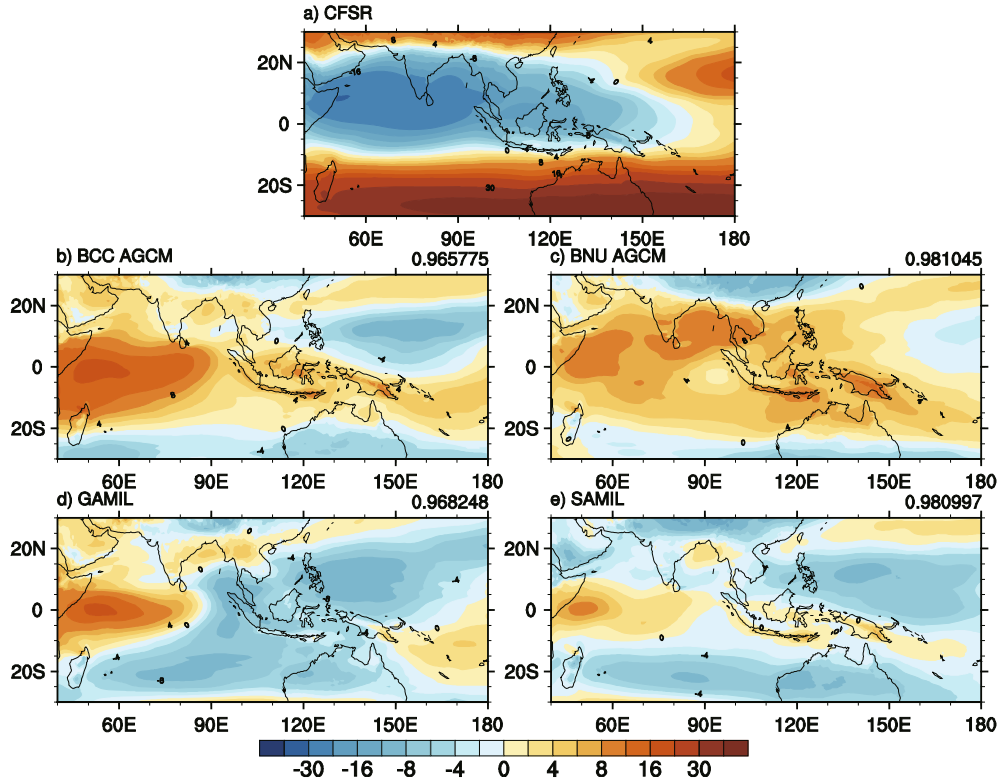


**Fig. 7.** Summer mean vertical shear ($U_{200} - U_{850}$) of (a) CFSR and (b–e) the difference between models and CFSR (units: m $s^{-1}$). The pattern correlations between models and CFSR are given at the top-right corner of each panel.

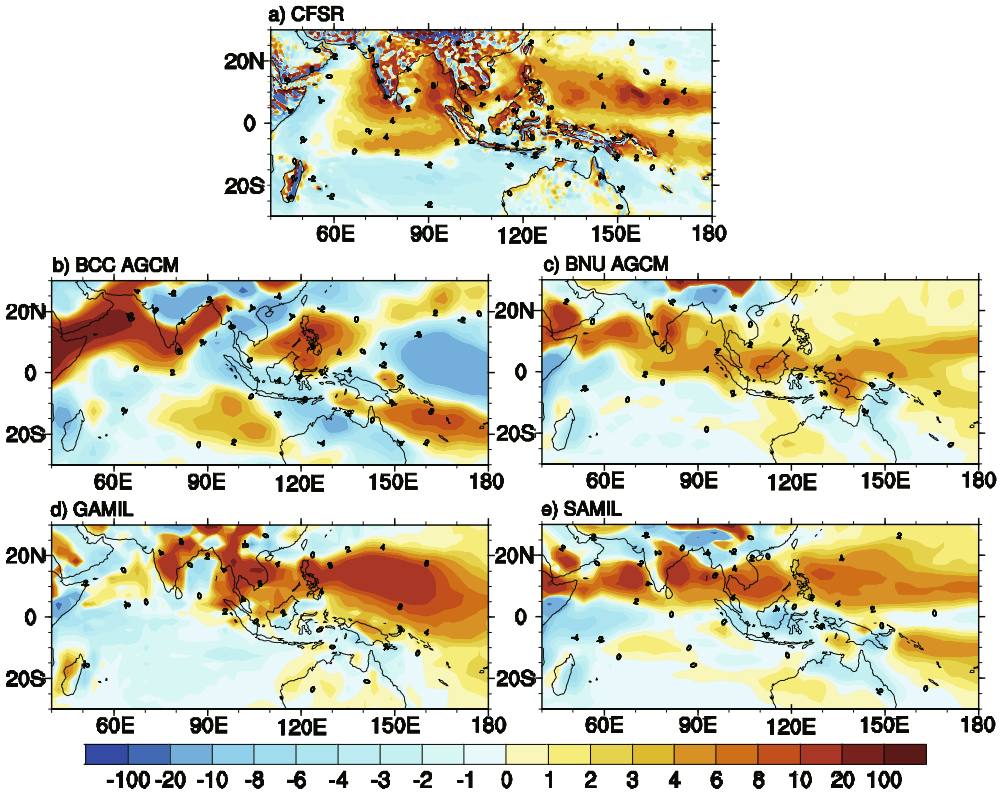


**Fig. 8.** Summer mean moisture convergence ($\overline{\langle -q\nabla \cdot \boldsymbol{V} \rangle}$) of CFSR, BCC AGCM, BNU AGCM, GAMIL, and SAMIL (units: mm $d^{-1}$).

pospheric westerlies and upper tropospheric easterlies over the IO and WP during the boreal summer. The models capture the observed summer mean wind well; however, both the westerlies in the lower troposphere and the easterlies in the upper troposphere are underestimated over the IO. Therefore, the summer mean vertical shear ($U_{200} - U_{850}$) is weak in the model results (Figs. 7b–d). Over the WP, the vertical shear is too strong in these models, apart from BNU AGCM. The summer mean easterly shear biases may exercise a great influence on the BSISO simulation. Wang and Xie (1997) found that the easterly vertical shear can remarkably enhance the Rossby wave emanation in the western North Pacific and their development in the monsoon region, playing an essential role in sustaining the ISO in the off-equatorial monsoon regions. Jiang et al. (2004) proposed that the key process associated with the BSISO is the generation of barotropic vorticity due to the coupling between the free-atmosphere baroclinic and barotropic modes in the presence of the vertical shear of the mean flow. The induced barotropic vorticity in the free atmosphere further causes a moisture convergence in the planetary boundary layer, leading to the northward shift of the convective heating.

With a reduced easterly shear over the IO in the four Chinese models, the tropical intraseasonal activity is reduced and the northward propagation is also suppressed. With an increased easterly shear over the WP in BCC AGCM, GAMIL, and SAMIL, the intraseasonal activity is increased and the northward propagation is favored.

### 4.2. *BSISO upscale feedback to summer mean state*

We further investigate the BSISO feedback to the summer mean state which is responsible for the BSISO simulation biases through the moisture budget analysis. Figure 8 shows the distribution of the boreal summer mean moisture convergence term ($\overline{\langle -q\nabla\cdot\boldsymbol{V}\rangle}$) in Eq. (1). In the CFSR result, the marked precipitation maxima are primarily attributed to this positive moisture convergence term (Fig. 8a), and it has a similar distribution to the summer mean precipitation. In the model results, the moisture convergence pattern (Figs. 8b–e) is also very similar to the distribution of the summer mean precipitation, suggesting that moisture convergence plays a key role in explaining the summer mean precipitation biases.

Figure 9 shows the contributions from the moisture convergence decomposition term Con2 [see Eq. (4)]. The calculation suggests that the convergence of the intraseasonal moisture by intraseasonal winds is conducive to the positive boreal summer mean moisture convergence in the region with

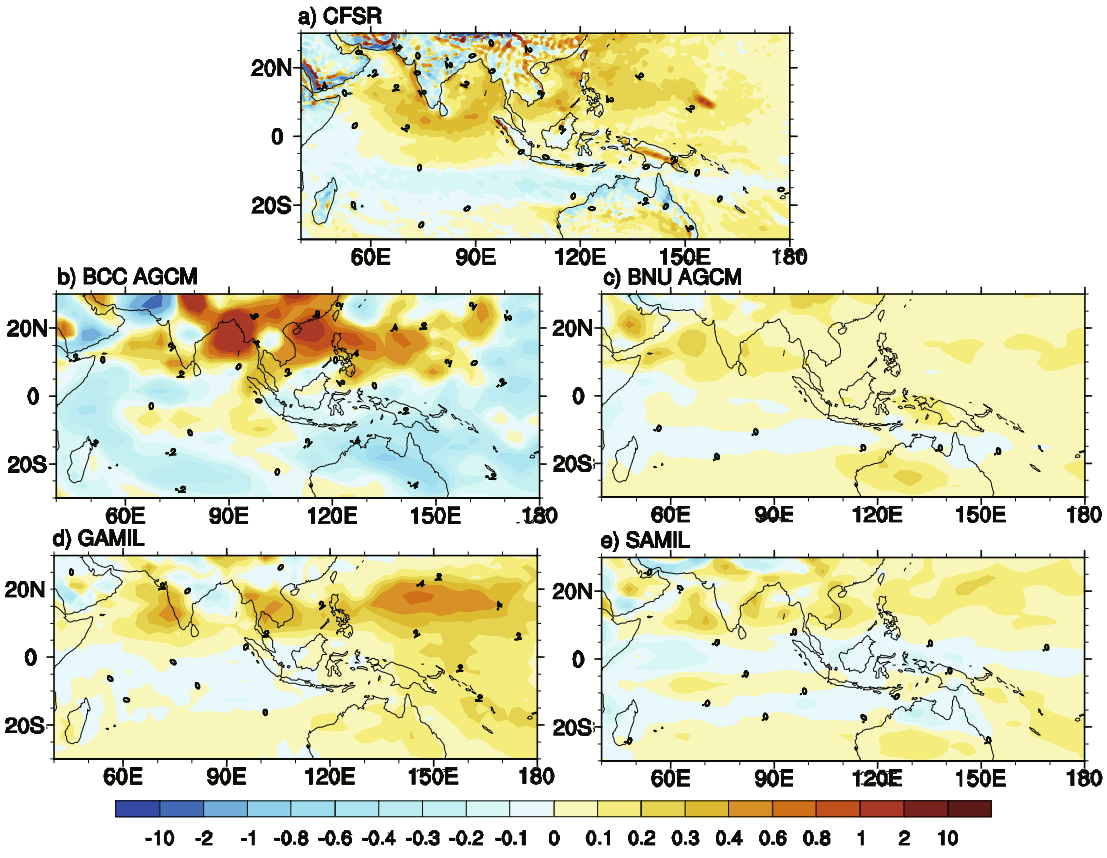


**Fig. 9.** Summer mean term Con2 ($\overline{\langle -q'\nabla\cdot\boldsymbol{V}'\rangle}$) of CFSR, BCC AGCM, BNU AGCM, GAMIL, and SAMIL (units: mm d$^{-1}$).

maxima precipitation (Fig. 9). The nonlinear interaction between the intraseasonal fields plays a positive role in the summer mean precipitation, and the Con2 term accounts for about 5% of the summer mean precipitation over the IO. This positive feedback of the BSISO on the summer mean state may further influence the BSISO simulation itself.

The in-phase relationship between the intraseasonal moisture and intraseasonal convergence can affect the summer mean precipitation (Ray and Li, 2013). The intraseasonal convergence and wet anomaly accompany the positive phase (enhanced convection) of ISO, and vice versa, the intraseasonal and dry anomalies accompany the negative phase (suppressed convection) of ISO (Hsu and Li, 2012). As a result, the summer mean Con2 is positive and conducive to promoting a positive contribution to the summer mean precipitation. The synchronous relationship is significant over the IO and WP where the summer mean precipitation and moisture convergence are overly underestimated or overestimated in the model results (Fig. 10).

## 5. Summary and concluding remarks

The performance of four Chinese AGCMs in reproducing the intraseasonal precipitation during boreal summer has been assessed.

Compared with the CMAP data, over the eastern tropical IO all the models produce insufficient BSISO amplitude, whereas over the WP, BCC-CSM1-1, GAMIL, and SAMIL give an excessive BSISO amplitude, and BNU AGCM gives an inadequate BSISO amplitude. Also, an overly westward propagation and a southwest–northeast tilted northward propagation are found in the model results.

By comparing the models with each other, both BCC AGCM and SAMIL have higher correlations with the observation in the BSISO variance pattern simulation. BNU AGCM and SAMIL both have a greater ratio between the eastward and westward propagations. BNU AGCM reproduces more reasonable periodicity over the IO and WP regions (Fig. 11).

The possible reason for the bias for both the summer mean tropical precipitation and the BSISO variance in the models is analyzed by calculating the vertical shear and diagnosing the time-averaged vertically integrated moisture budget equation. The major results are summarized below.

In the models, the background easterly vertical shear is weaker (stronger), accompanied by a weaker (stronger) summer mean precipitation than the observation. This decrease (increase) causes the decrease (increase) of intraseasonal activity and the suppression (enhancement) of the BSISO northward propagation. The induced weaker (stronger) BSISO humidity and wind further leads to less (more) contribution to the summer mean precipitation, through the nonlinear interaction of the intraseasonal moisture and intraseasonal convergence term. This positive feedback between the summer mean state and the BSISO may eventually lead to a significant deviation of the BSISO variance.

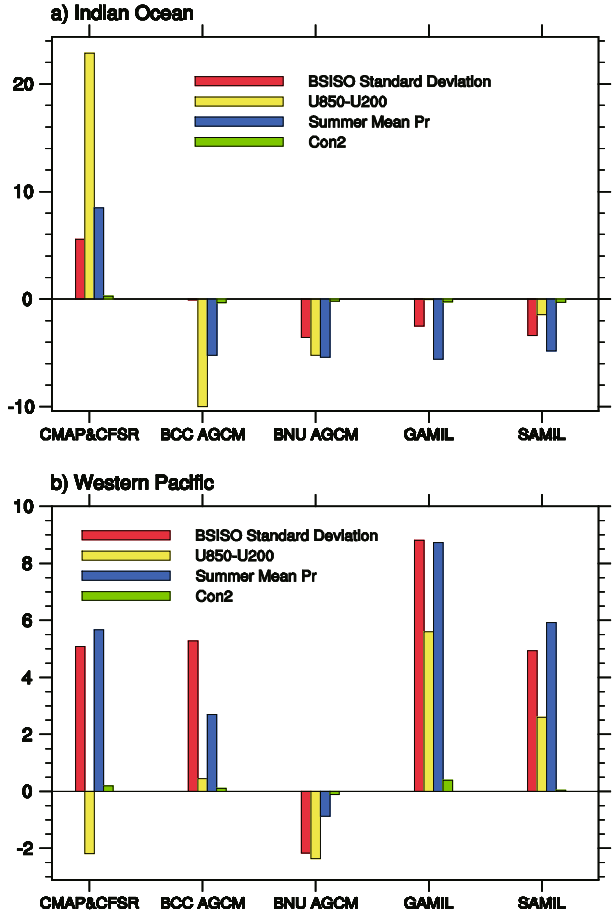


**Fig. 10.** The BSISO standard deviation (units: $mm^2\ d^{-2}$), vertical shear (units: $m\ s^{-1}$), summer mean precipitation (units: $mm\ d^{-1}$), and Con2 term (units: $mm\ d^{-1}$) of CMAP/CFSR and the difference between models and CMAP/CFSR over (a) IO (2°N, 87°E) and (b) WP (20°N, 145°E).

To improve the model simulation of the BSISO, the mean state calibration is not enough. The ratio between ISO variability and other subseasonal variability also needs to be adjusted. Compared with the observation, the BSISO in the models is not the dominant signal in the total subseasonal variation. Both of the observational datasets (CMAP and GPCP) have prominent spectral peaks between the 10- and 60-day periods over the IO, and the 10- and 75-day periods over the WP. In the models' results, compared to the BSISO signal, the higher and lower frequency signals are more significant in the total subseasonal perturbation (Fig. 11). The results reveal two common biases in the four models, i.e., a higher frequency and too strong persistence of equatorial precipitation. In the models, the higher and lower frequency signals are overpowered due to the easy initiation and overly strong persistence of equatorial precipitation. These biases may be ascribed to the convection parameterization process, model resolution, and vertical heating profile in atmospheric models, which are essential for the BSISO simulation (Lin et al., 2008; Jia et al., 2009; Li et al., 2009).

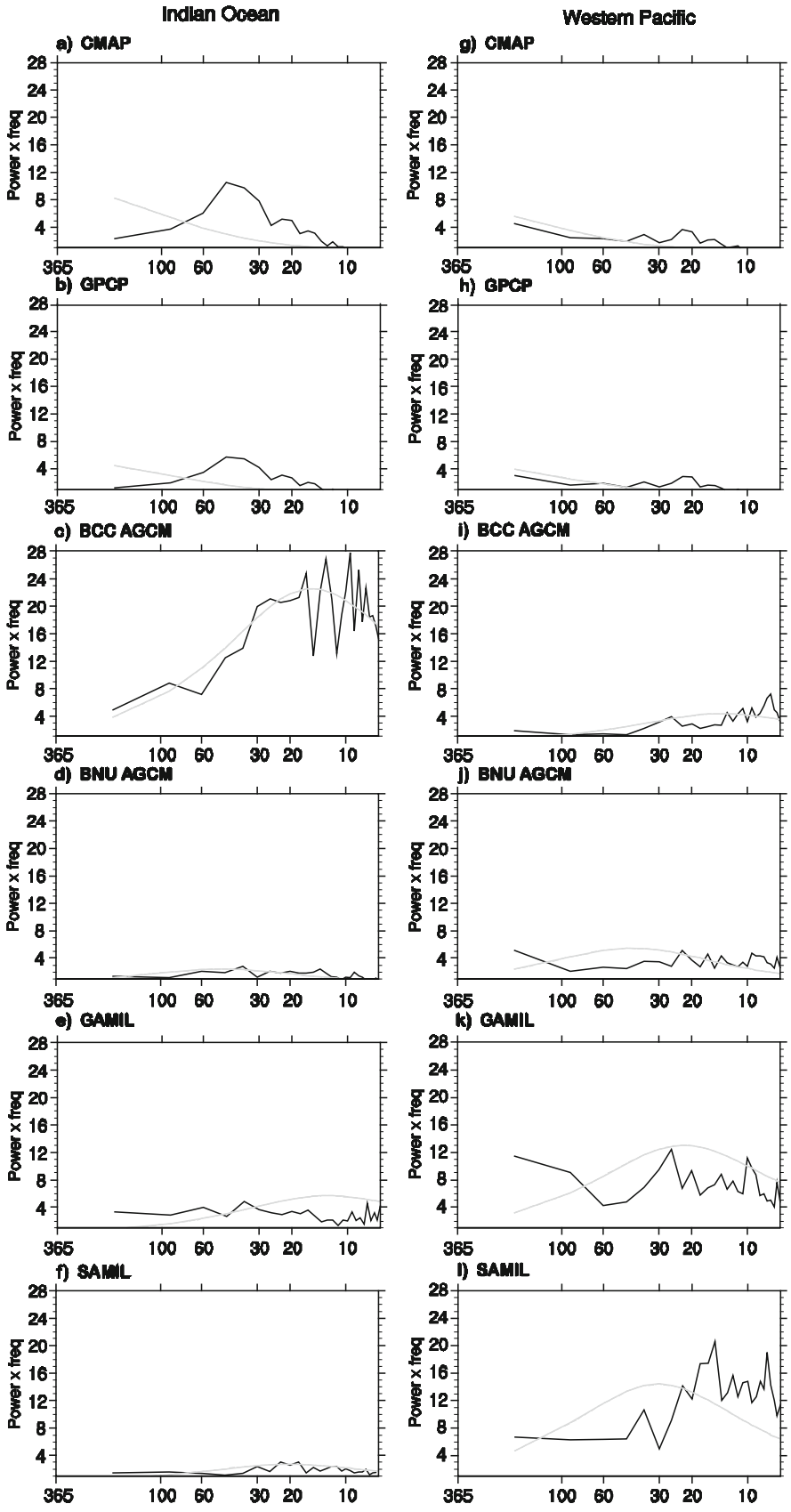


**Fig. 11.** Spectrum of precipitation over (a–f) IO (5°S–0°N, 50°–100°E) and (g–l) WP (10°–15°N, 110°–160°E) for CMAP, GPCP, BCC AGCM, BNU AGCM, GAMIL, and SAMIL (units: $mm^2\ d^{-2}$).

***Acknowledgements.*** This study is jointly supported by the National Basic Research and Development (973) Program of China (Grant No. 2012CB955902), China Meteorological Special Project (Grant Nos. GYHY201206016 and GYHY 201406022), National Natural Science Foundation of China (Grant No. 41125017) and the Public science and technology research funds projects of ocean (Grant No. 201105019-3).

## REFERENCES

Annamalai, H., and K. R. Sperber, 2005: Regional heat sources and the active and break phases of boreal summer intraseasonal (30–50 day) variability. *J. Atmos. Sci.*, **62**, 2726–2748.

Bao, Q., G. X. Wu, Y. M. Liu, J. Yang, Z. Z. Wang, and T. J. Zhou, 2010: An introduction to the coupled model FGOALS1.1-s and its performance in East Asia. *Adv. Atmos. Sci.*, **27**, 1131–1142, doi: 10.1007/s00376-010-9177-1.

Bao, Q., and Coauthors, 2013: The flexible global ocean-atmosphere-land system model, spectral version 2: FGOALS-s2. *Adv. Atmos. Sci.*, **30**, 561–576, doi: 10.1007/s00376-012-2113-9.

Hsu, P. C., and T. Li, 2012: Role of the boundary layer moisture asymmetry in causing the eastward propagation of the Madden-Julian Oscillation. *J. Climate*, **25**, 4914–4931.

Inness, P. M., J. M. Slingo, E. Guilyardi, and J. Cole, 2003: Simulation of the Madden-Julian oscillation in a coupled general circulation model. Part II: The role of the basic state. *J. Climate*, **16**, 365–382.

Jia, X. L., C. Y. Li, N. F. Zhou, and J. Ling, 2009: The MJO in an AGCM with three different cumulus parameterization schemes. *Dyn. Atmos. Oceans*, **49**, 141–163.

Jiang, J. H., and Coauthors, 2012: Evaluation of cloud and water vapor simulations in CMIP5 climate models using NASA "A-Train" satellite observations. *J. Geophys. Res.*, **117**, D14105, doi: 10.1029/2011JD017237.

Jiang, X., and T. Li, 2005: Reinitiation of the boreal summer intraseasonal oscillation in the tropical Indian Ocean. *J. Climate*, **18**, 3777–3795.

Jiang, X., T. Li, and B. Wang, 2004: Structures and mechanisms of the northward propagating boreal summer intraseasonal oscillation. *J. Climate*, **17**, 1022–1039.

Kemball-Cook, S., and B. Wang, 2001: Equatorial waves and air-sea interaction in the boreal summer intraseasonal oscillation. *J. Climate*, **14**, 2923–2942.

Knutson, T. R., and K. M. Weickmann, 1987: 30–60-day atmospheric oscillations: Composite life cycles of convection and circulation anomalies. *Mon. Wea. Rev.*, **115**, 1407–1436.

Lau, K. M., and P. H. Chan, 1986: Aspects of the 40–50 day oscillation during the northern summer as inferred from the outgoing longwave radiation. *Mon. Wea. Rev.*, **114**, 1354–1367.

Lau, W. K. M., and D. E. Waliser, Eds., 2005: *Intraseasonal Variability of the Atmosphere-Ocean Climate System*. Springer, Heidelberg, 614 pp.

Li, C. Y., Z. X. Long, and Q. Y. Zhang, 2001: Strong/weak summer monsoon activity over the South China Sea and atmospheric intraseasonal oscillation. *Adv. Atmos. Sci.*, **18**, 1146–1160.

Li, C. Y., X. L. Jia, J. A. Ling, W. Zhou, and C. D. Zhang, 2009: Sensitivity of MJO simulations to convective heating profiles. *Climate Dyn.*, **32**, 167–187.

Li, L. J., and Coauthors, 2013: The flexible global ocean-atmosphere-land system model, Grid-point Version 2: FGOALS-g2. *Adv. Atmos. Sci.*, **30**, 543–560, doi: 10.1007/s00376-012-2140-6.

Li, T., X. Jia, and M. Dong, 2006: The importance of the atmospheric intraseasonal oscillation in the prediction of the weather and climate. *Acta Meteorologica Sinica*, **64**, 412–419. (in Chinese)

Liebmann, B., H. H. Hendon, and J. D. Glick, 1994: The relationship between tropical cyclones of the western Pacific and Indian Oceans and the Madden-Julian oscillation. *J. Meteor. Soc. Japan*, **72**, 401–411.

Lin, J. L., K. M. Weickman, G. N. Kiladis, B. E. Mapes, S. D. Schubert, M. J. Suarez, J. T. Bacmeister, and M. I. Lee, 2008: Subseasonal variability associated with Asian summer monsoon simulated by 14 IPCC AR4 coupled GCMs. *J. Climate*, **21**, 4541–4567.

Maloney, E. D., and D. L. Hartman, 2001: The sensitivity of intraseasonal variability in the NCAR CCM3 to changes in convective parameterization. *J. Climate*, **14**, 2015–2034.

Morrison, H., and A. Gettelman, 2008: A new two-moment bulk stratiform cloud microphysics scheme in the community atmosphere model, version 3 (CAM3). Part I: Description and numerical tests. *J. Climate*, **21**, 3642–3659.

Nakazawa, T., 1986: Intraseasonal variations of OLR in the tropics during the FGGE year. *J. Meteor. Soc. Japan*, **64**, 17–34.

Ray, P., and T. Li, 2013: Relative roles of circumnavigating waves and extratropics on the MJO and its relationship with the mean state. *J. Atmos. Sci*., **70**, 876–893.

Saha, S., and Coauthors, 2006: The NCEP climate forecast system. *J. Climate*, **19**, 3483–3517.

Saha, S., and Coauthors, 2010: The NCEP climate forecast system reanalysis. *Bull. Amer. Meteor. Soc.*, **91**, 1015–1057.

Seo, K.-H., J.-K. Schemm, C. Jones, and S. Moorthi, 2005: Forecast skill of the Tropical Intraseasonal Oscillation in the NCEP GFS dynamical extended range forecasts. *Climate Dyn.*, **25**, 265–284.

Seo, K.-H., J.-K. E. Schemm, W. Wang, and A. Kumar, 2007: The boreal summer intraseasonal oscillation simulated in the NCEP Climate Forecast System (CFS): The effect of sea surface temperature. *Mon. Wea. Rev.*, **135**, 1807–1827.

Sikka, D. R., and S. Gadgil, 1980: On the maximum cloud zone and the ITCZ over Indian longitudes during the southwest monsoon. *Mon. Wea. Rev.*, **108**, 1840–1853.

Slingo, J. M., and Coauthors, 1996: Intraseasonal oscillation in 15 atmospheric general circulation models: Results from an AMIP diagnostic subproject. *Climate Dyn.*, **12**, 325–357.

Sperber, K. R., H. Annamalai, I.-S. Kang, A. Kitoh, A. Moise, A. Turner, B. Wang, and T. Zhou, 2013: The Asian summer monsoon: An intercomparison of CMIP5 vs. CMIP3 simulations of the late 20th century. *Climate Dyn.*, **41**, 2711–2744, doi: 10.1007/s00382-012-1607-6.

Taylor, K. E., R. J. Stouffer, and G. A. Meehl, 2009: A summary of the CMIP5 experiment design. [Available online at http://cmip-pcmdi.llnl.gov/cmip5/docs/Taylor-CMIP5-design.pdf]

Teng, H., and B. Wang, 2003: Interannual variations of the boreal summer intraseasonal oscillation in the Asian-Pacific region. *J. Climate*, **16**, 3572–3584.

Waliser, D. E., and Coauthors, 2003: AGCM simulations of intraseasonal variability associated with the Asian summer monsoon. *Climate Dyn.*, **21**, 423–446.

Wang, B., and H. Rui, 1990: Synoptic climatology of transient tropical intraseasonal convection anomalies. *Meteor. Atmos. Phys.*, **44**, 43–61.

Wang, B., and X. Xie, 1997: A Model for the Boreal Summer Intraseasonal Oscillation. *J. Atmos. Sci.*, **54**, 72–86.

Wheeler, M. C., and G. N. Kiladis, 1999: Convectively coupled equatorial waves: Analysis of clouds and temperature in the wavenumber-frequency domain. *J. Atmos. Sci.*, **56**, 374–399.

Wheeler, M. C., and H. Hendon, 2004: An All-Season Real-Time multivariate MJO index: Development of an index for monitoring and prediction. *Mon. Wea. Rev.*, **132**, 1917–1932.

Wu, Q. Z., J. M. Feng, W. J. Dong, L. N. Wang, D. Y. Ji, and H. Q. Cheng, 2013: Introduction of the CMIP5 experiments carried out by BNU-ESM. *Progressus Inquisitiones de Mutatione Climatis*, **9**, 291–294.

Wu, T. W., R. C. Yu, and F. Zhang, 2008: A modified dynamic framework for the atmospheric spectral model and its application. *J. Atmos. Sci.*, **65**, 2235–2253.

Wu, T. W., and Coauthors, 2010: The Beijing climate center for atmospheric general circulation model (BCC AGCM 2.0.1): Description and its performance for the present-day climate. *Climate Dyn.*, **34**, 123–147.

Xie, P., and P. A. Arkin, 1997: Global precipitation: A 17-year monthly analysis based on gauge observations, satellite estimates, and numerical model outputs. *Bull. Amer. Meteor. Soc.*, **78**, 2539–2558.

Xie, P., and Coauthors, 2003: GPCP pentad precipitation analyses: An experimental dataset based on gauge observations and satellite estimates. *J. Climate*, **16**, 2197–2214.

Yang, J., Q. Bao, and X. C. Wang, 2013: Intensified eastward and northward propagation of tropical intraseasonal oscillation over the equatorial Indian Ocean in a global warming scenario. *Adv. Atmos. Sci.*, **30**, 167–174, doi: 10.1007/s00376-012-1260-3.

Yasunari, T., 1979: Cloudiness fluctuations associated with the northern hemisphere summer monsoon. *J. Meteor. Soc. Japan*, **57**, 227–242.

Yasunari, T., 1980: A quasi-stationary appearance of 30 to 40 day period in the cloudiness fluctuations during the summer monsoon over India. *J. Meteor. Soc. Japan*, **58**, 225–229.

Zhang, C, M. Dong, S. Gualdi, H. H. Hendon, E. D. Maloney, A. Marshall, K. R. Sperber, and W. Wang, 2006: Simulations of the Madden-Julian oscillation by four pairs of coupled and uncoupled global models. *Climate Dyn.*, **27**, 573–592.

Zhang, G. J., and M. Mu, 2005: Effects of modifications to the Zhang-McFarlane convection parameterization on the simulation of the tropical precipitation in the national center for atmospheric research community climate model, version 3. *J. Geophys. Res.*, **110**, D09109, doi: 10.1029/2004JD005617.

Zhao, C. B., T. Li, and T. J. Zhou, 2013: Precursor signals and processes associated with MJO initiation over the Tropical Indian Ocean. *J. Climate*, **26**, 291–307.

INTERNATIONAL JOURNAL OF CLIMATOLOGY
*Int. J. Climatol.* (2014)
Published online in Wiley Online Library
(wileyonlinelibrary.com) DOI: 10.1002/joc.4093

RMetS
Royal Meteorological Society

# Simulating direct effects of dust aerosol on arid and semi-arid regions using an aerosol–climate coupled system

Shuyun Zhao,[a,b,c] Hua Zhang,[c]* Song Feng[d] and Qiang Fu[e]

[a] *Chinese Academy of Meteorological Sciences, Beijing, China*
[b] *University of Chinese Academy of Sciences, Beijing, China*
[c] *Laboratory for Climate Studies, National Climate Center, China Meteorological Administration, Beijing, China*
[d] *Department of Geosciences, University of Arkansas, Fayetteville, AR, USA*
[e] *Department of Atmospheric Sciences, University of Washington, Seattle, Washington, DC, USA*

**ABSTRACT:** This work uses an aerosol–climate coupled system to study the direct climatic effects of dust aerosol on global arid (including hyper-arid) and semi-arid regions. Results show that dust aerosol can cause surface cooling over these regions. The cooling effects of dust aerosol are larger in the Northern Hemisphere (NH) than in the Southern Hemisphere (SH). This asymmetric cooling leads to a severer reduction in evaporation over the low latitudes of the NH compared with their counterpart areas in the SH. In addition, air descent is enhanced (or ascent is weakened) by dust aerosol over the low latitudes of the NH, whereas the reverse happens in the SH. With the anomalous in evaporation and circulation, precipitation is decreased (increased) over the arid and semi-arid areas in the NH (SH) by dust aerosol. Dust aerosol can decrease the potential evapotranspiration in arid and semi-arid regions mainly by decreasing the net radiation flux at the top of the atmosphere, which compensates for the decrease in precipitation caused by dust aerosol. Therefore, as the dominant aerosol in the arid and semi-arid regions, dust aerosol does not exacerbate the aridity over most of these regions. The effects of dust aerosol are indiscernible in the expansion of arid and semi-arid areas on a global scale.

KEY WORDS dust aerosol; arid and semi-arid; AGCM

*Received 3 July 2013; Revised 3 March 2014; Accepted 28 May 2014*

## 1. Introduction

Dust aerosol, as an abundant type of aerosol in the atmosphere, can scatter and absorb solar and terrestrial radiation, influencing the regional and global climate (Foster *et al.*, 2007). Miller *et al.* (2004) pointed out that dust aerosol could reduce global evaporation and precipitation by reducing surface temperature, but overall acts as a negative feedback to desertification. Through its effect on atmospheric circulation, dust aerosol can also influence the activity of monsoon. For instance, Lau *et al.* (2006) and Lau and Kim (2006) suggested that the absorption of elevated dust aerosol accompanied with black carbon led to an earlier onset and intensification of the Indian Monsoon, through an 'elevated heating pump' mechanism. This 'elevated heating pump' mechanism of dust aerosol also enhanced the West African Monsoon in boreal summer, leading to an increase of rainfall over the West Africa/Eastern Atlantic inter-tropical convergence zone (ITCZ) and a decrease of rainfall over the Western Atlantic and Caribbean regions (Lau *et al.*, 2009). Zhao *et al.* (2012) found that dust aerosol from Western America may cause an eastward migration of moisture convergence driven by North America Monsoon and a sequent increase in precipitation over Arizona-New Mexico-Texas regions.

Some studies specially investigated the impact of dust aerosol on arid and semi-arid regions, where surface is bare or poorly vegetated (Islam and Almazroui, 2012; Sun *et al.*, 2012). Since dust aerosol originated mainly in these regions (Marticorena and Bergametti, 1995; Zender *et al.*, 2003), it might exert more influence on the climate in these regions than in other regions. Arid (including hyper-arid) and semi-arid areas account for about one-third of the earth's land surface and are an important part of the earth's major ecosystems (Reynolds *et al.*, 2007). Owing to excessive grazing/deforestation (Schlesinger *et al.*, 1990), ecosystems over these regions are vulnerable and sensitive to climate changes (Emanuel *et al.*, 1985). Islam and Almazroui (2012) suggested that dust aerosol might increase the wet season precipitation in Arabian Peninsula based on the simulation of ICTP-RegCM4. Using the same model as Islam and Almazroui (2012), Sun *et al.* (2012) suggested that dust aerosol tends to increase summer precipitation around its source areas but suppress summer precipitation in its downward areas in East Asia. However, the study of dust aerosol on the climate change in the arid and semi-arid regions is still rare, and most previous studies are focused on its climatic effects over a specific arid or semi-arid region. No attempts have been made to investigate the effects of dust aerosol on arid and

* Correspondence to: H. Zhang, Laboratory for Climate Studies, National Climate Center, China Meteorological Administration, Beijing 100081, China. E-mail: huazhang@cma.gov.cn.

© 2014 Royal Meteorological Society

semi-arid areas over the entire globe, as well as their effects on the aridity and areal extent of arid and semi-arid regions.

By using an aerosol-climate coupled system BCC_AGCM2.0.1_CAM (Zhang *et al.*, 2012), this study evaluated the effects of dust aerosol on arid and semi-arid regions by examining their direct interaction with radiation from a global perspective. Special attention was paid to the influence of dust aerosol on the aridity and spatial distribution of arid and semi-arid areas, by examining the anomaly in aridity index (AI; UNEP, 1992) induced by dust aerosol. The UNEP (1992) AI was defined as the ratio of precipitation to potential evapotranspiration (PET), which is a quantitative indicator of the degree of water scarcity at a given region. Thus, gaining knowledge on the changes in aridity may lead to better understanding of the impact of climate change and human activities on arid and semi-arid regions.

This article is organized as follows. Models and model experiments as well as the methods to define arid and semi-arid areas are described in Section 2. Changes in temperature, precipitation, and aridity caused by dust aerosol over arid and semi-arid regions are investigated in Section 3, followed by conclusions and discussion in Section 4.

## 2. Models and methods

### 2.1. Models and model experiments

We use the general circulation model developed at the National Climate Centre of the Chinese Meteorological Administration (BCC_AGCM2.0.1; Wu *et al.*, 2010). The model is based on Community Atmospheric Model version 3.0 from the National Centre for Atmospheric Research (NCAR). The model was further developed to be coupled online with the Canadian Aerosol Model (CAM; Gong *et al.*, 2002, 2003a), with updated aerosol emission sources (Zhou *et al.*, 2012), as described by Zhang *et al.* (2012). In addition, a new method of Monte Carlo Independent column approximation (McICA) dealing with the cloud overlapping was introduced by Jing and Zhang (2012) and Zhang *et al.* (2014), and the radiation scheme BCC-RAD developed by Zhang *et al.* (2003a, 2006a, 2006b) was adopted.

The CAM is a size-segregated aerosol model that includes the processes for the emission, transport, chemical transformation, cloud interaction, and deposition of five typical aerosols, sulfate, black carbon, organic carbon, dust, and sea salt. The radii of aerosols fall into 12 bins: 0.005-0.01, 0.01-0.02, 0.02-0.04, 0.04-0.08, 0.08-0.16, 0.16-0.32, 0.32-0.64, 0.64-1.28, 1.28-2.56, 2.56-5.12, 5.12-10.24, and 10.24-20.48 μm. The emission data were primarily from AeroCom, which includes the surface emission rate of black and organic carbon (Bond *et al.*, 2004; Van der Werf *et al.*, 2004), $SO_2$ and sulfate (Van der Werf *et al.*, 2004; Cofala *et al.*, 2005), and DMS (Kettle and Andreae, 2000; Nightingale *et al.*, 2000). Other emission data were from the Emission Database for Global Atmospheric Research (EDGAR) version 3.2, 1995, database (Olivier *et al.*, 2002; http://www.mnp.nl/edgar). The sea-salt module was developed by Gong *et al.* (2002). An online sulfur chemistry module was included in CAM, in which $H_2S$, DMS, $SO_2$, and $H_2SO_4$ are prognostic variables, whereas OH, $O_3$, $H_2O_2$, and $NO_3$ are prescribed offline from the MOZART/NCAR model (Brasseur *et al.*, 1998; Hauglustaine *et al.*, 1998). The soil dust emission scheme was developed by Marticorena and Bergametti (1995), in which the surface velocity and roughness were the main factors that determined the vertical flux of dust aerosol. Three lognormal population distributions for dust in China were used, and the mass median diameters and standard deviations of these three populations were determined by considering the soil features in China and source region dust size-distribution measurements (Gong *et al.*, 2003b; Zhang *et al.*, 2003b). Out of China, the two-mode size distribution for dust from the observation by Chatenet *et al.* (1996) was used.

To couple aerosols with atmospheric radiative processes, the optical properties of the aerosols (e.g. extinction coefficient, single scattering *albedo*, and asymmetry parameter) were calculated according to the band division of the BCC-RAD based on Mie theory. The refractive indices of dry aerosols were adopted from D'Almeida *et al.* (1991), and the Mie scattering code of Wiscombe (1980) was used. The effects of water vapour on the size distributions and optical properties of three hygroscopic aerosols, sulfate, organic carbon, and sea salt, have been considered. In this study, 10 relative humidities were considered: 0.0, 0.45, 0.5, 0.6, 0.7, 0.8, 0.9, 0.95, 0.98, and 0.99. In the calculations, first, the radii of the 12-size bins of wet particles for each relative humidity were obtained. The effective refractive indices of the wet particles were then computed using a volume-weighted method. The optical properties of the aerosols were obtained for the 12-size bins with 10 relative humidities in 17 spectral bands, and these properties were used to form the look-up tables (Wei and Zhang, 2011; Wang *et al.*, 2013). The optical properties of the aerosols for any relative humidity could therefore be easily obtained using linear interpolation in the climate model. It has been noted that the non-sphericity of dust aerosols has little effect on their radiative forcing (Fu *et al.*, 2009; Wang *et al.*, 2013), and the optical properties can therefore be derived from the Mie theory.

The aerosol–climate coupled system BCC_AGCM2.0.1 _CAM was run for 50 years with and without considering the radiative effect of dust aerosol, named RUN + DUST and RUN-DUST for short, respectively. To examine the interaction between dust aerosol and the global climate, a slab ocean model (Hansen *et al.*, 1984) was coupled in both runs. The horizontal resolution of the model was set at T42 ($\sim 2.8 \times 2.8°$), with 26 vertical layers on the hybrid $\sigma$-pressure coordinate. All other model parameters in both experiments were identical, meaning that any differences between the two experiments are a result of the impact of dust aerosol on the simulated climate.

In this study, we analysed the model results of the past 30 years using the first 20 years as the spin-up data. It is important to evaluate a model's capacity before using it to perform studies. The evaluation focusing on the capability

© 2014 Royal Meteorological Society

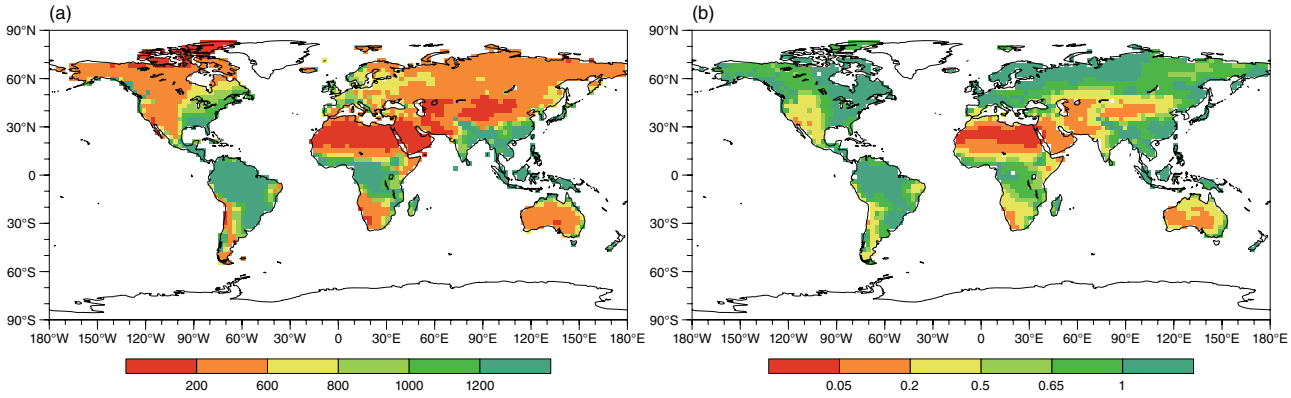


Figure 1. Global distributions of (a) calibrated annual mean precipitation (unit: mm $yr^{-1}$) and (b) aridity index, based on the model calibrated results of RUN + DUST (unit: 1).

of BCC_AGCM2.0.1 to reproduce meteorological fields had been given in detail by Wu *et al.* (2010), whereas the evaluation focusing on the capability of the model to reproduce the dust aerosol had been given in detail by Zhang *et al.* (2012), Wang *et al.* (2013), and Zhao *et al.* (2014).

### 2.2. Definitions of the arid and semi-arid areas

The areal extent of the arid and semi-arid areas must be identified before examining the effects of dust aerosol on these regions. Different criteria have been used to define arid and semi-arid regions, including annual precipitation (Huang *et al.*, 2012) and a combination of annual precipitation and PET (UNEP, 1992; Feng and Fu, 2013). The criteria based on merely precipitation are simple and may reasonably define the arid and semi-arid areas in the middle and low latitudes (e.g. Sahara Desert, Arabian Peninsula, and Western Australia). The precipitation criteria, however, also classify the higher latitudes (north of 50°N) as arid and semi-arid (Figure 1(a)), which is inconsistent with Koppen–Geiger climate classification (Kottek *et al.*, 2006; Feng *et al.*, 2014)

This study defines the arid and semi-arid regions using the (AI (UNEP, 1992), which is based on the ratio between the annual mean precipitation (P) and annual mean PET. The global land surface can be classified as hyper-arid ($AI < 0.05$), arid ($0.05 \le AI < 0.2$), semi-arid ($0.2 \le AI < 0.5$), dry sub-humid ($0.5 \le AI < 0.65$), sub-humid ($0.65 \le AI < 1$), or humid ($AI \ge 1$). In this article, PET is calculated using the Penman–Monteith method, as described in the Food and Agriculture Organization (FAO) Irrigation and Drainage Paper (Allen *et al.*, 1998). The Penman–Monteith method simultaneously accounts for the effects of radiation, temperature, wind speed, and humidity:

$$PET = \frac{0.408\Delta\left(R_n - G\right) + \gamma\frac{900}{T+273}u_2\left(e_s - e_a\right)}{\Delta + \gamma\left(1 + 0.34u_2\right)} \quad (1)$$

where $R_n$ is the net radiation at the surface (MJ $m^{-2}$ $day^{-1}$); $G$, the soil heat flux density (MJ $m^{-2}$ $day^{-1}$); $T$, the air temperature at 2-m height (°C); $u_2$, the wind speed at 2-m height (m $s^{-1}$); $e_s$ and $e_a$ are the saturation and actual vapour pressure, respectively (kPa); $\Delta$, the slope vapour-pressure curve (kPa °$C^{-1}$); and $\gamma$, a psychrometric constant (kPa °$C^{-1}$). Figure 1(b) indicates the wide distribution of arid (including hyper-arid) and semi-arid areas around the world. Large arid and semi-arid regions appear in North Africa, the Arabian Peninsula, Central Asia, Northwestern China, Southwest North America, and central and Western Australia. Arid and semi-arid regions are also seen over the west Namibia and South Africa, and highlands in the eastern and southern parts of South America. Most areas north of 50°N in Figure 1(b) are classified as sub-humid and humid regions, suggesting a more realistic classification using AI than just using annual precipitation.

## 3. Climate effects of dust aerosol on arid and semi-arid areas

As shown in Figure 2(a), higher dust aerosol burden is distributed in the tropical and sub-tropical regions in both hemispheres, with peaks in arid and semi-arid areas and their downwind regions. The simulated total burden of dust aerosol in the atmosphere is 30.8 Tg, which is slightly larger than the simulations from the Goddard Institute for Space Sciences (GISS) model (29.0 Tg) and the Goddard Global Ozone Chemistry Aerosol Radiation and Transport (GOCART) model (29.5 Tg) (Huneeus *et al.*, 2011). These differences are likely because only the GISS and GOCART models consider dust aerosol with diameter smaller than 10 μm, whereas our model considers dust aerosol smaller than 20.48 μm. Of the total content of atmospheric dust aerosol, more than 90% is located in the Northern Hemisphere, which is mostly attributed to the dust emission from the Sahara Desert. The climate effects of this asymmetric distribution of dust aerosol about the equator will be discussed in the following sections. Dust aerosol can reduce the net incoming radiation flux at the top of atmosphere (TOA) because it reflects solar radiation, leading to a decrease in surface temperature. The total effect of dust aerosol on the net radiation flux (shortwave + longwave) at the TOA is

© 2014 Royal Meteorological Society

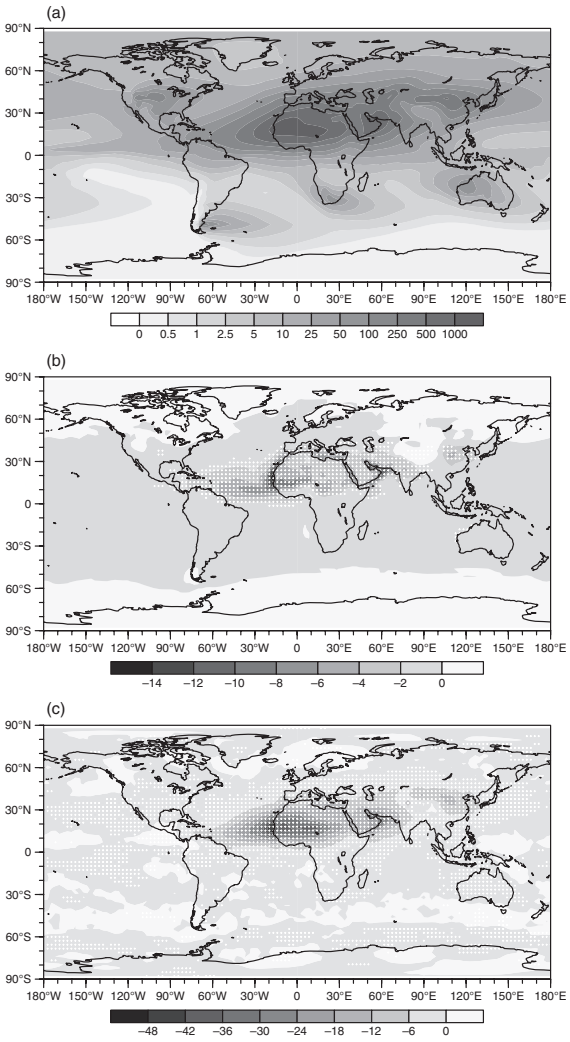


Figure 2. Distributions of (a) the column burden of dust aerosol (unit: mg $m^{-2}$), (b) the effects of dust aerosol on the net radiation (shortwave + longwave) at the TOA (unit: W $m^{-2}$), and (c) the effects of dust aerosol on the net radiation (shortwave + longwave) at the surface. White dots indicates results below the significance cutoff of 0.05.

shown in Figure 2(b). The dust aerosol can reduce incoming radiation energy in most terrestrial areas, especially over arid and semi-arid areas and their downward regions. The global average effect of dust aerosol on the net radiation at the TOA is −0.62 (−0.68 ∼ −0.56) W $m^{-2}$, and −2.83 (−3.01 ∼ −2.65) W $m^{-2}$ at the surface, respectively. The value at the TOA is slightly larger than the adjusted radiative forcing from spherical dust aerosol calculated by Wang *et al.* (2013), which used the same model configuration as in this study but used a fixed sea surface temperature instead of the slab ocean model.

### 3.1. Temperature

The radiative effects of dust aerosol lead to a global decrease in surface temperature (Figure 3(a)), except for a small portion of the Northern Europe and Central America. The cooling effect is especially pronounced in the arid and semi-arid areas such as Sahara Desert, where dust aerosol can cool the surface temperature by up to 4 K. The changes in surface temperature in most areas can be explained by the direct radiative effects of dust aerosol. Dust aerosol can absorb and scatter shortwave radiation, leading to the reduction of solar radiation reaching the surface and consequently causing surface cooling. A few exceptions (e.g. the Central America) suggest that cloud feedback to aerosol direct effect may be important in the coastal regions of the tropics.

The surface cooling induced by dust aerosol varies seasonally (Figure 4, left panel). In North China, dry and windy springs are in favour of dust emission and transportation. The decrease of surface temperature over this area and its downwind areas in spring is more obvious than in other seasons (Figure 4(b)). The extensive cooling around Arabian Peninsula in summer (Figure 4(c)) is consistent with the main dry season mainly from June to September in this area (Islam and Almazroui, 2012). In Sahara region, the band of temperature decrease shifts north in summer and south in winter (Figure 4(a) and (c)), mainly relate to the match of the subtropical high. The change of surface temperature caused by dust aerosol is −0.503 K in boreal summer and −0.475 K in winter, and the values for spring and fall are in the between.

### 3.2. Precipitation

Compared to temperature, the response of precipitation to dust aerosol is more inhomogeneous (Figure 3(b) and Figure 4, right panel), suggesting that the effects of dust aerosol on precipitation are more complex. On a global

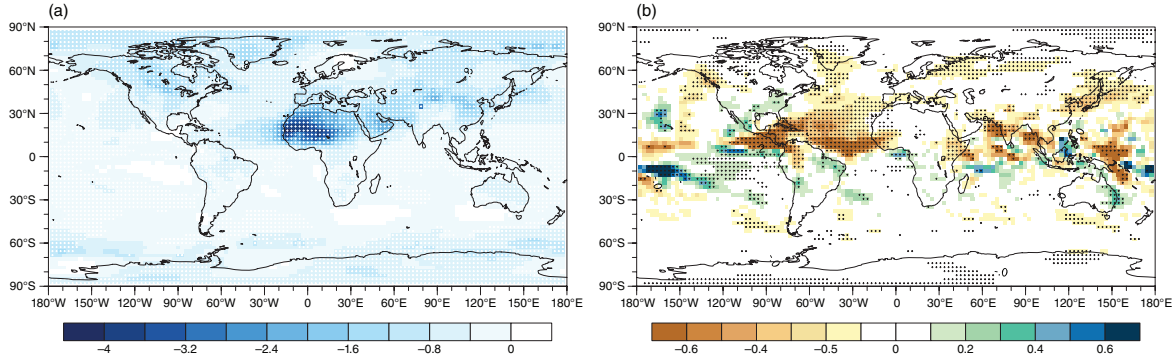


Figure 3. Changes in (a) annual mean surface temperature (unit: K) and (b) annual mean precipitation (unit: mm $day^{-1}$) caused by soil dust, with white dots and black dots indicating results below the significance cutoff of 0.05.

© 2014 Royal Meteorological Society

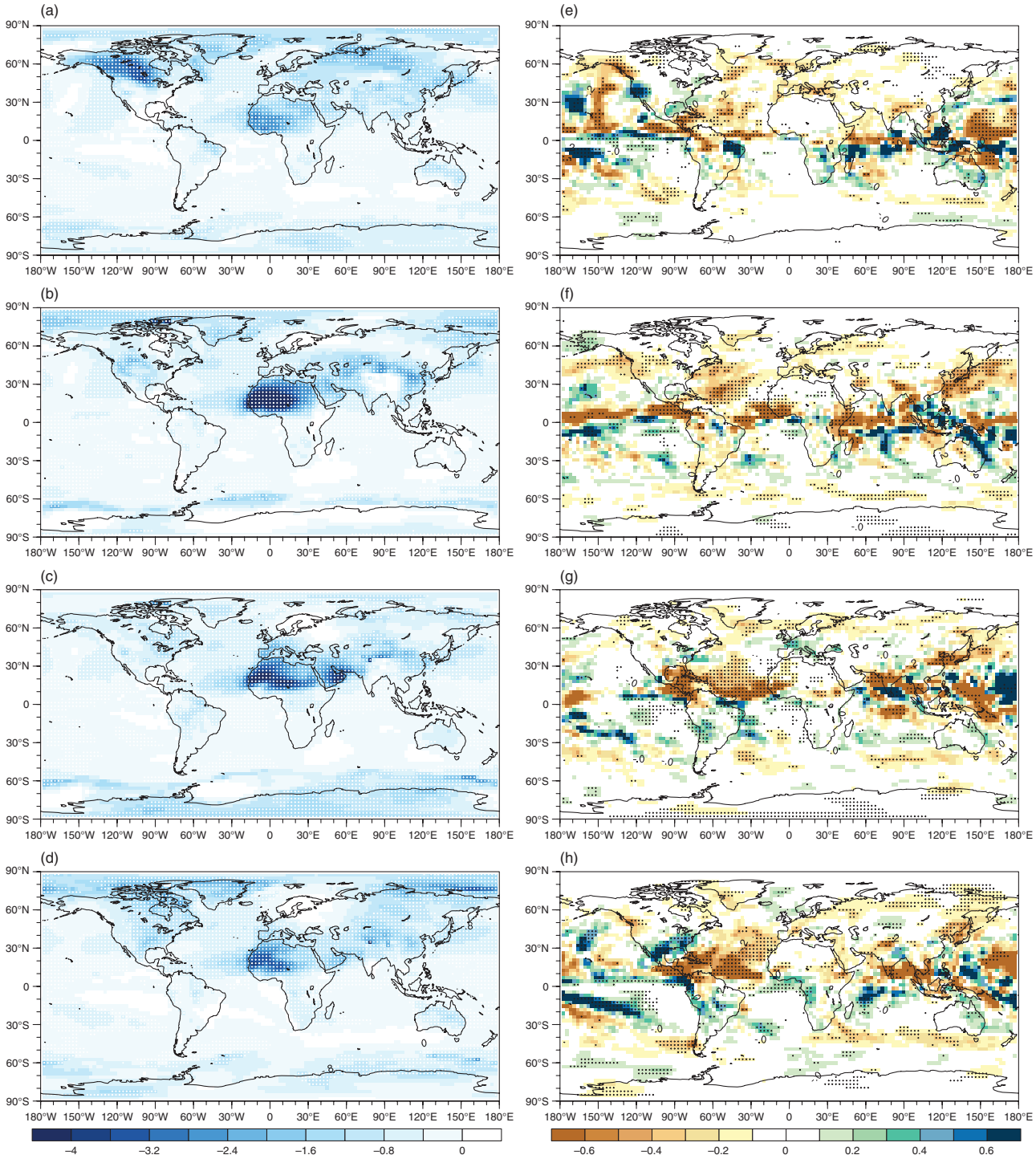


Figure 4. Anomalies in (left panel) seasonal mean surface temperature (unit: K) and (right panel) seasonal mean precipitation (unit: mm day$^{-1}$) induced by dust aerosol, with white dots and black dots indicating results below the significant cutoff of 0.05. (a) and (e) for December to February (DJF), (b) and (f) for March to May (MAM), (c) and (g) for June to August (JJA), and (d) and (h) for September to November (SON).

average, the simulated change of rainfall induced by dust aerosol is $-0.075$ mm day$^{-1}$ and $-0.061$ mm day$^{-1}$ in boreal spring and summer, respectively. The values for winter and fall are slightly larger than $-0.05$ mm day$^{-1}$.

Over arid and semi-arid areas, where the effects of dust aerosol are much more important than over the rest of the terrestrial regions, dust aerosol may either suppress (e.g. the Sahara Desert) or enhance the precipitation (e.g. central and Western Australia). In general, the annual precipitation is decreased in most parts of the arid and semi-arid areas in the Northern Hemisphere, whereas is increased in the Southern Hemisphere (Figure 3(b)).

Compared with the cooling in the tropical Southern Hemisphere, there is much stronger surface cooling in the lower latitudes of the Northern Hemisphere, which induces a strong northward temperature gradient

© 2014 Royal Meteorological Society

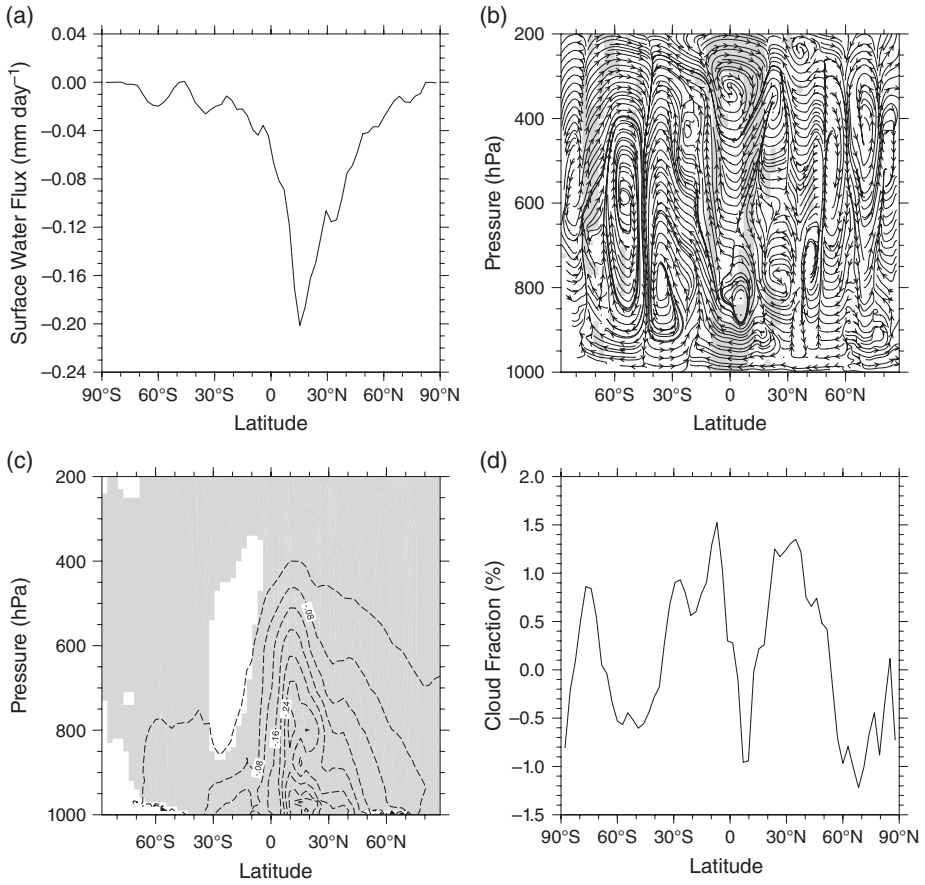


Figure 5. Changes in (a) evaporation (mm day$^{-1}$), (b) meridional circulation, (c) specific humidity (g kg$^{-1}$) and (d) (high + median + low) cloud fraction (unit: %) caused by dust aerosol, with shaded areas (b and c) indicating levels below the significance cutoff of 0.05.

(Figure 3(a)). This is mainly caused by the asymmetric distribution of dust aerosol about the equator (Figure 1(b) and Figure 2(a)). Correspondingly, the evaporation is reduced most severely over the low latitude areas of the Northern Hemisphere than elsewhere (Figure 5(a)), with a zonal mean reduction up to about 0.20 mm day$^{-1}$ between 10°N and 20°N. Owing to the heterogeneous change in surface temperature, there is a northerly trend of wind in the lower atmospheric levels, whereas a southerly trend of wind in the upper atmospheric levels, between 30°S and 30°N. In addition, air tends to ascend more strongly (or descend more weakly) in the Southern Hemisphere near 30°S and tends to descend more strongly (or ascend more weakly) in the Northern Hemisphere near 30°N, suggesting that dust aerosol can enhance the general circulation in the Northern hemisphere and weaken it in the Southern Hemisphere.

With these anomalous in evaporation and circulation, a strong reduction in specific humidity is observed between 30°N and the equator than elsewhere (Figure 5(c)). In the low levels of tropical Northern Hemisphere, the zonal mean specific humidity is reduced as much as 0.4 g kg$^{-1}$. The northward gradient of specific humidity is enhanced by dust aerosol above the equatorial area. It can be seen in Figure 5(d) that the cloud is inhibited over the low latitudes of the Northern Hemisphere and enhanced over the low latitudes of the Southern Hemisphere. The change in precipitation (Figure 3(b)) is consistent with that in cloud fraction (Figure 5(d)).

In general, the enhanced cooling over the Northern Hemisphere caused by the abundant dust aerosol load can not only depress the evaporation, but also inhibit the cloud. The humidity and dynamical conditions are not in favour of the formation of precipitation over the low latitudes of the Northern Hemisphere. Over the low latitudes of the Southern Hemisphere, the changes in evaporation and humidity are relatively small (Figure 5(a) and (d)), but the weakened air descent facilitates cloud development and precipitation. These responses of precipitation to the asymmetric change of temperature about the equator are consistent with the findings of Broccoli *et al.* (2006) and Wang *et al.* (2013).

### 3.3. Aridity and areal extent of arid and semi-arid regions

Dust aerosol leads to increased AI (reduced aridity) over the middle of Sahara Desert, Northwestern China and Central Asia, West North America, and most arid and semi-arid areas in the Southern Hemisphere (Figure 6). However, AI is decreased (increased aridity) over the west and east coasts of North Africa, the Arabian Peninsula, and the highlands from Iran to North India. Changes in AI can be caused by the changes in precipitation and/or the PET.

© 2014 Royal Meteorological Society

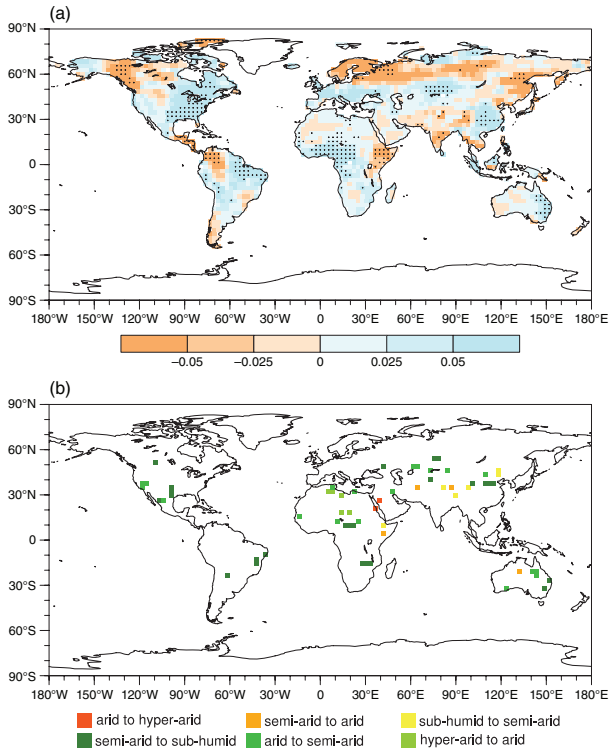


Figure 6. Changes in (a) AI, with dots indicating results below the significance level of 0.05 and (b) areas of arid and semi-arid regions (AI $< 0.5$) by dust aerosol radiative effects. Different colours in (b) show the change in areal extent of the arid and semi-arid regions caused by dust aerosol.

The change in AI can be written as follows:

$$\Delta AI_{\mathrm{U}} = \frac{P}{PET}\left(\frac{1}{P}\Delta P - \frac{1}{PET}\Delta PET\right) \qquad (2)$$

The above-mentioned equation clearly suggests that the change in AI is dependent on the relative changes in P and PET. Taking the middle of Sahara Desert as an example, dust aerosol suppresses precipitation (Figure 3(b)) by inhibiting vertical movement and cools the surface, lessening the water demand (i.e. decreasing the PET, Figure 7), causing a collective increase in AI and a reduction in aridity (Figure 6(a)). Similar changes in precipitation, PET, and AI can be found over the Northwestern China and Central Asia. However, in western North America and the most arid and semi-arid areas in the Southern Hemisphere, the change in precipitation and PET both favour increased AI. Overall, dust aerosol does not lead to the expansion of the total areal extent of the earth's arid and semi-arid areas. Dust aerosol may reduce the hyper-arid areas in the north of Africa and arid and semi-arid areas in western North America, Central Asia, northwestern China, and Australia (Figure 6(b)). However, it is worth noting that dust aerosol may degrade some arid places on both sides of the Red Sea into hyper-arid areas and enlarge arid and semi-arid areas in some parts of northern and western China and the Somalia Peninsula.

Similar results are found when classifying arid and semiarid region using the Koppen–Geiger climate classification (not shown), which suggests that our results

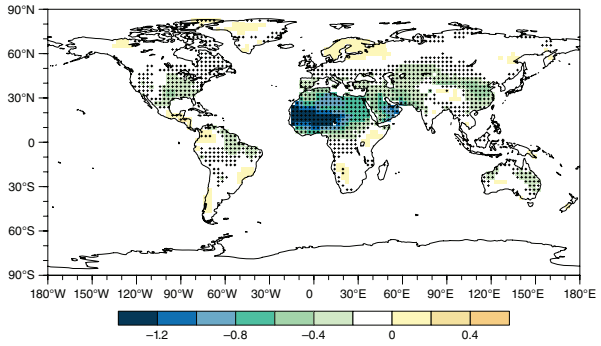


Figure 7. Change in PET caused by dust aerosol, with dots indicating results below the significance level of 0.05; unit: mm day$^{-1}$.

are robust. Although dust aerosol neither exacerbates the dryness over arid and semi-arid areas nor leads to the global expansion of arid and semi-arid areas, the effort towards anti-desertification is not useless. Dust aerosol can cause high latitudes to become drier (Fig. 6a). In addition, dust aerosol can work as cloud condensation nuclei and change the global microphysics of clouds and climate (Rosenfeld *et al.*, 2001; IPCC, Foster *et al.*, 2007). Because of these effects, controlling the process of desertification is an urgent task for climate scientists.

PET is an important variable to quantify the potential water requirement for crops. As discussed previously, changes in PET play an important role in causing changes in AI in some places. The changes in PET caused by dust aerosol are shown in Figure 7. PET is reduced in most parts of arid and semi-arid areas, except for some small patches such as the east coast of North Africa. The global average change in PET is $-0.230$ mm day$^{-1}$.

The change in PET is controlled by surface temperature, net radiation, humidity, and wind speed, as described in Allen *et al.*, 1998. To quantitatively understand how dust aerosol may impact PET, we recalculated PET with one specific variable from the RUN + DUST and the other variables from the RUN-DUST. The difference between this recalculated PET and the original PET from the RUN-DUST is regarded as the contribution of the specific variable to the total change in PET caused by dust aerosol. The average 30 model years' annual and global mean contributions of these variables are shown in Table 1. Clearly, the total change in PET is not a linear combination of the contributions of surface temperature, net radiation flux, humidity, and wind on a global scale. In addition, the effects of dust aerosol on PET are primarily determined by the changes in net radiation, to a lesser extent by changes in the surface temperature and relative humidity, and least by changes in the surface wind.

## 4. Conclusion

The climate effects of dust aerosol on arid and semi-arid areas were evaluated using the aerosol–climate coupled system BCC_AGCM2.0.1_CAM. The arid and semi-arid regions were defined according to the criteria by UNEP (1992).

© 2014 Royal Meteorological Society

Table 1. Global average PET (unit: mm day$^{-1}$) and PET changing one variable at a time and keeping other variables the same.

| Changing variables | Change of PET |
|---|---|
| Surface temperature | −0.079 |
| Net radiation flux on the surface | −0.114 |
| Relative humidity | −0.068 |
| Surface wind | −0.018 |
| Total | −0.280 |

Mainly due to its extinction of shortwave radiation, dust aerosol leads to surface cooling, especially over arid and semi-arid areas. However, the asymmetric distribution of dust aerosol about the equator has different effects on precipitation over arid and semi-arid areas in the two hemispheres, through its different effects on evaporation and general circulation, between 30°S and 30°N. Dust aerosol can either alleviate or exacerbate the dryness over some arid and semi-arid areas, depending on the comparative importance of its effects on precipitation and PET. As a net effect, dust aerosol does not enlarge the areal extent of arid and semi-arid regions on a global scale.

Dust aerosol both influences and responds to climate change. This work may provide some additional information about the role of dust aerosol on the climate change. However, this study only considered the direct effects of dust aerosol. Additional work is still needed to evaluate the indirect climate effects of dust aerosol. And the effects of anthropogenic aerosols on arid and semi-arid areas should be investigated in future work.

## Acknowledgements

This work was financially supported by the National Basic Research Programme of China (2012CB955303 and 2011CB403405).

## References

Allen RG, Pereira LS, Raes D, Smith M. 1998. Crop Evapotranspiration-Guidelines for Computing *Crop water Requirements-FAO Irrigation and Drainage Paper 56*. FAO, Rome, Retrieved July 9, 2014. http://www.fao.org/publications/card/en/c/5de3a877-5547-5b23-9e6f-0c8951c54b5e/.

Brasseur GP, Hauglustaine DA, Walters S, Rasch PJ, Muller JF, Granier C, Tie XX. 1998. MOZART, a global chemical transport model for ozone and related chemical tracers 1. Model description. *J. Geophys. Res.* **103**: 28265–28289.

Bond T, Streets D, Yarber K, Nelson S, Wo JH, Klimont Z. 2004. A technology-based global inventory of black and organic carbon emissions from combustion. *J. Geophys. Res.* **109**: D14203, DOI: 10.1029/2003JD003697.

Broccoli AJ, Dahl KA, Stouffer RJ. 2006. Response of the ITCZ to Northern Hemisphere cooling. *Geophys. Res. Lett.* **33**: L01702, DOI: 10.1029/2005GL024546.

Chatenet B, Marticorena B, Gomes L, Bergametti G. 1996. Assessing the size distribution of desert soils erodible by wind. *Sedimentology* **43**: 901–911.

Cofala J, Amann M, Klimont Z, Schopp W. 2005. Scenarios of world anthropogenic emissions of $SO_2$, $NO_x$ and CO up to 2030. *Internal Report of the Transboundary Air Pollution Programme,* International Institute for Applied Systems Analysis, Laxenburg, Austria, 17 pp, Retrieved July 9, 2014. http://www.iiasa.ac.at/rains/global_emiss/global_emiss.html.

D'Almeida GA, Koepke P, Shettle EP. 1991. *Atmospheric Aerosols: Global Climatology and Radiative Characteristics*. Deepak Publishing: Hampton, VA.

Emanuel WR, Shugart HH, Stevenson MP. 1985. Climatic change and the broad-scale distribution of terrestrial ecosystem complexes. *Clim. Change* **7**(1): 29–43, DOI: 10.1007/BF00139439.

Foster P, Ramaswamy V, Artaxo P, Berntsen T, Betts R, Fahey DW, Haywood J, Lean J, Lowe DC, Myhre G, Nganga J, Prinn R, Raga G, Schulz M, Dorland RV. 2007. Changes in atmospheric constituents and in radiative forcing. *In Climate Change 2007: The Physical Science Basis. Contribution of Working Group I to the Fourth Assessment Report of the International Panel on Climate Change*, Solomon S, Qin D, Manning M, Chen Z, Marquis M, Averyt KB, Tignor M, Miller HL (eds). Cambridge University Press: Cambridge, UK and New York, NY.

Fu Q, Thorsen TJ, Su J, Ge JM, Huang JP. 2009. Test of Mie-based single-scattering properties of non-spherical dust aerosols in radiative flux calculations. *J. Quant. Spectrosc. Radiat. Transf.* **110**(14): 1640–1653, DOI: 10.1016/j.jqsrt.2009.03.010.

Feng S, Fu Q. 2013. Expansion of global drylands under a warming climate. *Atmos. Chem. Phys.* **13**: 14637–14665, DOI: 10.5194/acpd-13-14637-2013.

Feng S, Hu Q, Huang W, Ho CH, Li R, Tang Z. 2014. Projected climate regime shift under future global warming from multi-model multi-scenario CMIP5 simulations. *Glob. Planet. Chang.* **112**: 41–52.

Gong SL, Barrie LA, Lazare M. 2002. Canadian Aerosol Module (CAM): a size-segregated simulation of atmospheric aerosol processes for climate and air quality models 2. Global sea-salt aerosol and its budgets. *J. Geophys. Res.* **107**(D24): 4779, DOI: 10.1029/2001JD002004.

Gong SL, Barrie LA, Blanchet JP, von Salzen K, Lohmann U, Lesins G, Spacek L, Zhang LM, Girard E, Lin H, Leaitch R, Leighton H, Chylek P, Huang P. 2003a. Canadian Aerosol Module: a size-segregated simulation of atmospheric aerosol processes for climate and air quality models 1. Module development. *J. Geophys. Res.* **108**(D1): 4007, DOI: 10.1029/2001JD002002.

Gong SL, Zhang XY, Zhao TL, McKendry IG, Jaffe DA, Lu NM. 2003b. Characterization of soil dust aerosol in China and its transport and distribution during 2001 ACE-Asia: 2. Model simulation and validation. *J. Geophys. Res.* **108**(D9): 4262, DOI: 10.1029/2002JD002633.

Hansen J, Lacis A, Rind D, Russell G, Stone P, Fung I, Ruedy R, Lerner J. 1984. Climate sensitivity: analysis of feedback mechanisms. In *Climate processes and climate sensitivity, Geophysical Monograph Series 29*, Hansen JE, Takahashi T (eds). AGU: Washington, DC, 130–163, DOI: 10.1029/GM029p0130.

Hauglustaine DA, Brasseur GP, Walters S, Rasch PJ, Muller J-F, Emmons LK, Carroll MA. 1998. MOZART, a global chemical transport model for ozone and related chemical tracers 2. Model results and evaluation. *J. Geophys. Res.* **103**: 28291–28335.

Huang J, Guan X, Ji F. 2012. Enhanced cold-season warming in semi-arid regions. *Atmos. Chem. Phys.* **12**: 5391–5398, DOI: 10.5194/acp-12-5391-2012.

Huneeus N, Schulz M, Balkanski Y, Griesfeller J, Prospero J, Kinne S, Bauer S, Boucher O, Chin M, Dentener F, Diehl T, Easter R, Fillmore D, Ghan S, Ginoux P, Grini A, Horowitz L, Koch D, Krol MC, Landing W, Liu X, Mahowald N, Miller R, Morcrette JJ, Myhre G, Penner J, Perlwitz J, Stier P, Takemura T, Zender CS. 2011. Global dust model intercomparison in AeroCom phase I. *Atmos. Chem. Phys.* **11**: 7781–7816, DOI: 10.5194/acp-11-7781-2011.

Islam MN, Almazroui M. 2012. Direct effects and feedback of desert dust on the climate of the Arabian Peninsula during the wet season: a regional climate model study. *Clim. Dyn.* **39**: 2239–2250, DOI: 10.1007/s00382-012-1293-4.

Jing X, Zhang H. 2012. Application and evaluation of McICA cloud-radiation framework in the AGCM of the National Climate Center. *Chinese J. Atmos. Sci.* **36**(5): 945–958 (in Chinese).

Kettle AJ, Andreae MO. 2000. Flux of dimethysulfide from the oceans: a comparison of updated data sets and flux models. *J. Geophys. Res.* **105**: 26793–26808.

Kottek M, Grieser J, Beck C, Rudolf B, Rubel F. 2006. World map of the Köppen-Geiger climate classification updated. *Meteorol. Z.* **15**(3): 259–263.

Lau KM, Kim KM. 2006. Observational relationships between aerosol and Asian monsoon rainfall, and circulation. *Geophys. Res. Lett.* **33**: L21810, DOI: 10.1029/2006GL027546.

Lau KM, Kim MK, Kim KM. 2006. Asian summer monsoon anomalies induced by aerosol direct forcing: the role of the Tibetan Plateau. *Clim. Dyn.* **26**(7–8): 855–864, DOI: 10.1007/s00382-006-0114-z.

© 2014 Royal Meteorological Society 

Lau KM, Kim KM, Sud YC, Walker GK. 2009. A GCM study of the response of the atmospheric water cycle of West Africa and the Atlantic to Sahara dust radiative forcing. *Ann. Geophys.* **27**: 4023–4037, DOI: 10.5194/angeo-27-4023-2009.

Marticorena B, Bergametti G. 1995. Modeling the atmospheric dust cycle: 1. Design of a soil-derived dust emission scheme. *J. Geophys. Res.* **100**(D8): 16415–16430, DOI: 10.1029/95JD00690.

Miller RL, Tegen I, Perlwitz J. 2004. Surface radiative forcing by soil dust aerosols and hydrologic cycle. *J. Geophys. Res.* **109**: D04203, DOI: 10.1029/2003JD004085.

Nightingale P, Malin G, Law C, Watson A, Liss P, Liddicoat M, Boutin J, Upstill-Goddard RC. 2000. In situ evaluation of air-sea gas exchange parameterizations using novel conservative and volatile tracers. *Glob. Biogeochem. Cycles* **14**: 373–387.

Olivier J, Berdowski J, Peters J, Bakker J, Visschedijk A, Bloos J. 2002. Applications of EDGAR including a description of ENDGAR V3.0: reference dataset with trend data for 1970-1995. NRP Report, 410200 051, RIVM, Bilthoven, the Netherlands.

Rosenfeld D, Rudich Y, Lahav R. 2001. Desert dust suppressing precipitation: a possible desertification feedback loop. *Proc. Natl. Acad. Sci. U. S. A.* **98**(11): 5975–5980, DOI: 10.1073/pnas.101122798.

Reynolds JF, Smith DMS, Lambin EF, Turner BL, Mortimore M, Batterbury SPJ, Downing TE, Dowlatabadi H, Fernández RJ, Herrick JE, Sannwald EH, Jiang H, Leemans R, Lynam T, Maestre FT, Ayarza M, Walker B. 2007. Global desertification: building a science for dryland development. *Science* **316**: 847–851, DOI: 10.1126/science.1131634.

Schlesinger WH, Reynolds JF, Cunningham GL, Huenneke LF, Jarrell WM, Virginia RA, Whitford WG. 1990. Biological feedbacks in global desertification. *Science* **247**: 1043–1048.

Sun H, Pan Z, Liu X. 2012. Numerical simulation of spatial-temporal distribution of dust aerosol and its direct radiative effects on East Asian climate. *J. Geophys. Res.* **117**(D13206), DOI: 10.1029/2011JD017219.

UNEP. 1992. *World Atlas of Desertification*. Edward Amold: London.

Van der Werf GR, Randerson JT, Collatz GJ, Giglio L, Kasibhatla PS, Arellano AF, Olsen SC, Kasischke ES. 2004. Continental-scale partitioning of fire emissions during the 1997 to 2001 El Nino/La Nina period. *Science* **303**: 73–76.

Wiscombe WJ. 1980. Improved Mie scattering algorithms. *Appl. Opt.* **19**: 1505–1509.

Wu T, Yu R, Zhang F. 2010. The Beijing Climate Center atmospheric general circulation model: description and its performance for the present-day climate. *Clim. Dyn.* **34**: 123–147, DOI: 10.1007/s00382-008-0487-2.

Wei X, Zhang H. 2011. Analysis of optical properties of non-spherical dust aerosols. *Acta. Opt. Sin.* **31**(5): 0501002 (in Chinese).

Wang Z, Zhang H, Jing X, Wei X. 2013. Effect of non-spherical dust aerosol on its direct radiative forcing. *Atmos. Res.* **120**: 112–126, DOI: 10.1016/j.atmosres.2012.08.006.

Zender CS, Bian H, Newman D. 2003. The mineral dust entrainment and deposition (DEAD) model: description and 1990s dust climatology. *J. Geophys. Res.* **108**(D14): 4416, DOI: 10.1029/2002JD002775.

Zhang H, Nakajima T, Shi G. 2003a. An optical approach to overlapping bands with correlated *k* distribution method and its application to radiative calculations. *J. Geophys. Res.* **108**(D20): 4641, DOI: 10.1029/2002JD003358.

Zhang XY, Gong SL, Shen ZX, Mei FM, Xi XX, Liu LC, Zhou ZJ, Wang D, Wang YQ, Cheng Y. 2003b. Characterization of soil dust aerosol in China and its transport and distribution during 2001 ACE-Asia: 1. Network observations. *J. Geophys. Res.* **108**(D9): 4261, DOI: 10.1029/2002JD002632.

Zhang H, Suzuki T, Nakajima T, Shi G, Zhang X, Liu Y. 2006a. Effects of band division on radiative calculations. *Opt. Eng.* **45**(1): 016002, DOI: 10.1117/1.2160521.

Zhang H, Shi G, Nakajima T, Suzuki T. 2006b. The effects of the choice of the *k*-interval number on radiative calculations. *J. Quant. Spectrosc. Radiat. Transf.* **98**(1): 31–43, DOI: 10.1016/j.jqsrt.2005.05.090.

Zhang H, Wang Z, Wang Z, Liu Q, Gong S, Zhang X, Shen Z, Lu P, Wei X, Che H, Li L. 2012. Simulation of direct radiative forcing of aerosols and their effects on East Asian climate using an interactive AGCM-aerosol coupled system. *Clim. Dyn.* **38**: 1675–1693, DOI: 10.1007/s00382-011-1131-0.

Zhang H, Jing X, Li J. 2014. Application and evaluation of a new radiation code under McICA scheme in BCC_AGCM2.0.1. *Geosci. Model Dev.* **7**: 737–754, DOI: 10.5194/gmd-7-737-2014.

Zhou CH, Gong SL, Zhang XY, Liu HL, Xue M, Cao GL, An XQ, Che HZ, Zhang YM, Niu T. 2012. Towards the improvements of simulating the chemical and optical properties of Chinese aerosols using an online coupled model CUACE/Aero. *Tellus B.* **64**: 18965, DOI: 10.3402/tellusb.v64i0.18965.

Zhao C, Liu X, Leung LR. 2012. Impact of the desert dust on the summer monsoon system over southwestern North America. *Atmos. Chem. Phys.* **12**: 3717–3731, DOI: 10.5194/acp-12-3717-2012.

Zhao S, H Zhang, X Zhi, Z Wang, Z Wang. 2014. A primary assessment of the simulated climatic state by a coupled aerosol-climate model BCC_AGCM2.0.1_CAM. *Clim. Env. Res.* **19**(3): 265–277, DOI: 10.3878/j.issn.1006-9585.2012.12015 (in Chinese).

© 2014 Royal Meteorological Society 

赵树云, 智协飞, 张华, 等. 2014. 气溶胶－气候耦合模式系统 BCC_AGCM2.0.1_CAM 气候态模拟的初步评估 [J]. 气候与环境研究，19 (3): 265−277, doi: 10.3878/j.issn.1006-9585.2012.12015. Zhao Shuyun, Zhi Xiefei, Zhang Hua, et al. 2014. Primary assessment of the simulated climatic state using a coupled aerosol－climate model BCC_AGCM2.0.1_CAM [J]. Climatic and Environmental Research (in Chinese), 19 (3): 265−277.

# 气溶胶—气候耦合模式系统 BCC_AGCM2.0.1_CAM 气候态模拟的初步评估

赵树云[1,2] 智协飞[1] 张华[2] 王志立[3] 王在志[2]

1 南京信息工程大学大气科学学院，南京 210044
2 中国气象局气候研究开放实验室，国家气候中心，北京 100081
3 中国气象科学研究院，北京 100081

**摘 要** 本文讨论了国家气候中心第二代大气环流模式 BCC_AGCM2.0.1 和加拿大气溶胶理化模式 CAM 所组成的耦合模式系统对 5 种典型气溶胶（硫酸盐、黑碳、有机碳、沙尘和海盐）和气候要素的模拟效果。结果表明，耦合系统对 5 种典型气溶胶的模拟总体上比较合理，尤其是对硫酸盐、沙尘和海盐的模拟比 BCC_AGCM2.0.1 原有的月平均气溶胶资料有很大的改进。耦合系统模拟的全球平均气候态参量与观测/再分析资料比较一致，在总云量、陆地表面温度和降水等方面要略优于原月平均气溶胶资料的模拟结果。耦合系统对沙尘和海盐气溶胶模拟的改进使得撒哈拉沙漠和南半球中纬度海洋大气顶净太阳辐射的模拟也有所改进，而这将直接影响地表温度尤其是陆地表面温度。而不同气溶胶方案在赤道海洋上引起的云反馈不仅引起辐射的改变，还将对降水产生明显影响。

**关键词** 气溶胶 BCC_AGCM2.0.1_CAM 耦合模式系统 模式评估
**文章编号** 1006−9585（2014）03−0265−13 **中图分类号** P461.8 **文献标识码** A
doi: 10.3878/j.issn.1006-9585.2012.12015

# Primary Assessment of the Simulated Climatic State Using a Coupled Aerosol−Climate Model BCC_AGCM2.0.1_CAM

ZHAO Shuyun[1,2], ZHI Xiefei[1], ZHANG Hua[2], WANG Zhili[3], and WANG Zaizhi[2]

1 *Department of Atmospheric Science*, *Nanjing University of Information Science and Technology*, *Nanjing* 210044
2 *Laboratories for Climate Studies*, *Chinese Meteorological Administration*, *National Climate Center*, *Beijing* 100081
3 *Chinese Academy of Meteorological Sciences*, *Beijing* 100081

**Abstract** Using the coupled model system of the second generation Global Circulation Model of the National Climate Center (BCC_AGCM2.0.1) and Canadian Aerosol Model (CAM), the simulation of five typical aerosols (sulfate, black carbon, organic carbon, soil dust, and sea salt) and possible effects on the modeled climate are discussed in this paper. The results show that in general, the coupled system simulates the five aerosols reasonably well, and there are obvious improvements in sulfate, dust, and sea salt aerosols compared to the original monthly mean aerosol data used in BCC_AGCM2.0.1. The climatic statistics simulated by the coupled system mainly agree well with observational/reanalyzed data, and are a little better than the monthly mean aerosol data in terms of the total cloud amount, land surface temperature, and precipitation rate. The enhanced representation of dust and sea salt improves the

**收稿日期** 2012−02−01 收到，2013−06−19 收到修定稿
**资助项目** 国家重点基础研究发展计划项目 2011CB403405、2012CB955303，科技部公益性行业（气象）科研专项课题 GYHY201406023，国家自然科学基金 41205116
**作者简介** 赵树云，女，1985 年出生，硕士研究生，主要从事气溶胶辐射强迫与气候效应研究。E-mail: shuyun_z@aliyun.com
**通讯作者** 张华，E-mail: huazhang@cma.gov.cn

simulation of net solar radiation at the top of the atmosphere in the Sahara Desert and mid-latitude ocean in the Southern Hemisphere and also affects the land surface temperature. The cloud feedback above the tropical ocean caused by the change in aerosol scheme not only alters radiation but also markedly influences precipitation.

**Keywords** Aerosol, BCC_AGCM2.0.1_CAM coupled model system, Assessment of model

# 1 引言

气溶胶是大气中的重要成分之一，能够吸收或散射长、短波辐射，从而影响大气的辐射平衡，对当前的气候状态以及未来的气候变化有着比较显著的作用。但是目前对气溶胶的研究还不够深入，有很多待解决的问题（如气溶胶光学性质的精确观测、混合问题、气溶胶在气候模式中的模拟等），因此成为气候研究领域的一个热点。

气溶胶的成分、分布和含量不是一成不变的，其受下垫面特征、人类活动、气象条件等诸多因素的影响，和这些因素存在着广泛的相互作用。而气候模式一般使用月平均或者季节平均的固定气溶胶数据作为模式的气溶胶输入场（Miller and Tegen，1998；王志立等，2009a，2009b；Zhang et al., 2009）。固定的气溶胶资料虽然能够体现过去某个时间段气溶胶的分布特征，但是却丢失了气溶胶和模式其他过程相互作用的环节，对于研究气溶胶对气候的影响和随气候的演变等问题，这种做法显然不够合理。出于这种考虑，越来越多的研究开始寻求大气环流模式和能描述气溶胶产生、扩散和演变的气溶胶理化模式的耦合，目前国际上成功耦合气溶胶模式的大气环流模式主要有 ARQM（Zhang and McFarlane, 1995）、DLR（Roeckner et al., 1996）、GISS（Schmidt et al., 2006）、KYU（Numaguti et al., 1995; Hasumi and Emori, 2004）、LSCE（Sadourny and Laval, 1984; Hourdin and Armengaud, 1999）、LOA（Sadourny and Laval, 1984; Hourdin and Armengaud, 1999）、MPI_HAM（Roeckner et al., 2003, 2004; Stier et al., 2005）、PNNL（Kiehl and Gent, 2004）、UIO_GCM（Hack, 1994; Kiehl et al., 1998）、BCC_AGCM2.0.1（Zhang et al., 2012）等。

在大气环流模式中耦合气溶胶模式是研究气溶胶气候影响最理想的方式（Gong et al., 2003）。Zhang et al.（2012）在国家气候中心第二代大气环流模式 BCC_AGCM2.0.1 中耦合了加拿大气溶胶理化模式 CAM，并做了初步分析，但是还没有对新耦合系统的整体模拟情况进行研究。因此本文将对新耦合系统从气溶胶本身到常规气候态变量的模拟情况进行初步的探讨，一方面深化对耦合系统气溶胶模拟性能的了解，另一方面揭示新气溶胶模式 CAM 的引入对气候态模拟的影响。这将为未来利用该耦合系统进行气溶胶气候效应的研究及其他相关研究提供重要的参考依据。

# 2 模式和方法简介

## 2.1 大气环流模式

国家气候中心第二代大气环流模式 BCC_AGCM2.0.1 由 CAM3.0/NCAR 发展而来，改进后的模式整体模拟能力比原来 CAM3.0 有所提高，特别是对热带和副热带降水、风场、海洋上感热和潜热通量的模拟（Wu et al., 2010）。该模式在水平方向采用 42 波三角截断方案[T42，约 2.8°（纬度）× 2.8°（经度）]，垂直方向为混合$\sigma$−压力坐标系，共 26 层，模式顶气压约为 2.9 hPa，刚性边界。相对于 CAM3.0，BCC_AGCM2.0.1 在动力和物理过程上进行了许多调整。在动力方面，主要的调整体现在参考大气温度和参考地面气压的应用上，这种变化导致了相关的诊断方程和求解方法发生了根本改变（Wu et al., 2008）。物理过程调整主要包含以下几个方面：1）将原来的 Zhang and Mcfarlane（1995）对流方案调整为 Zhang and Mu（2005）方案，并且在对流触发条件中加入相对湿度＞75%和垂直速度$\upsilon$＜0 的限制，将云水向雨水的转化系数调低；2）干绝热调整方案采用颜宏（1987）的方案；3）海洋表面（动量、潜热、感热）湍流通量计算过程中所用粗糙度采用 Smith（1988）的计算方法，并且将海面波动和海浪飞沫的影响进行了参数化；4）陆地模式中冰覆盖量的计算公式采用 Wu and Wu（2004）的经验公式。该模式用由 1971～2000 年 NCEP 再分析资料得到的多年平均大气状态作为初始场，海温和海冰密度是由 1981～2001 年实测数据得到的逐月平均海温和海冰资料（Hurrell et al., 2008）。

## 2.2 气溶胶模式

Zhang et al.（2012）在 BCC_AGCM2.0.1 的基

础上耦合了一个气溶胶理化数值模式 CAM（Gong et al., 2003）。CAM 包含 5 种典型气溶胶（硫酸盐、海盐、黑碳、有机碳、沙尘）的排放、传输、化学转化、与云的相互作用、干沉降和湿沉降等过程，气溶胶按粒径大小分为 12 档，最小粒径为 0.005 μm，最大粒径为 20.48 μm。气溶胶的排放（包括自然排放和人为排放）来自气溶胶观测和模式比较项目 AeroCom（http://aerocom.met.no/aerocomhome.html [2012-04-23]），包括黑碳和有机碳（Van der Werf et al., 2004; Bond et al., 2004）、$SO_2$ 和硫酸盐（Van der Werf et al., 2004; Cofala et al., 2005）、二甲基硫（Dimethyl Sulfide，DMS）（其中海洋资料：Kettle and Andreae, 2000；大气－海洋转换资料：Nightingale et al., 2000）。其它排放数据来自 EDGAR3.2（the Database for Global Atmospheric Research）1995 年资料（Olivier et al., 2002）。海盐排放方案来自 Gong et al.（2002），沙尘排放方案来自 Marticorena and Bergametti（1995）。该模式包含一个在线的硫化学模块，其中 DMS、$SO_2$、$H_2S$、$H_2SO_4$ 气体浓度为预报量，而 OH、$O_3$、$H_2O_2$ 和 $NO_3$ 的浓度为给定的离线值，来自 MOZART/NCAR（Brasseur et al., 1998；Hauglustaine et al., 1998）。该模式在 Zhang et al.（2012）中有详细说明。

### 2.3 方法及试验设计

本文利用上述国家气候中心第二代大气环流模式 BCC_AGCM2.0.1 和加拿大气溶胶理化模式 CAM 的耦合系统运行 22 年，取后 18 年结果平均得到典型种类气溶胶柱含量和光学厚度等变量以及典型气候态变量的分布，并与观测/再分析资料进行对比。BCC_AGCM2.0.1 模式原来采用的气溶胶资料是由大气化学传输模式（MATCH）和一个卫星反演气溶胶光学厚度的同化系统生成的一组月平均气溶胶浓度值（Collins et al., 2001, 2002）。作为对比试验，利用原有的月平均气溶胶资料作为 BCC_AGCM2.0.1 的气溶胶输入量同样运行 22 年，取其后 18 年的结果分析。两组试验分别记为“BCC_int”（取 interactive aerosols 之意）和“BCC_pre”（取 prescribed aerosols 之意）。两次模式运行均只考虑气溶胶的直接辐射效应。

## 3 气溶胶柱含量和光学厚度的模拟

由于耦合系统对气溶胶方案进行了替换，大气环流模式中的气溶胶输入发生了很大的变化，这里首先对耦合系统模拟的气溶胶柱含量和光学厚度进行分析，将本文的模拟结果和参与“AeroCom”的多模式中值 AEROCOM_MEDIAN 相比较，以了解 BCC_int 模拟的气溶胶水平在国际同类研究中所处的位置。

### 3.1 气溶胶柱含量

硫酸盐气溶胶来源于化石燃料燃烧排放的 $SO_2$（72%），海洋生物排放的 DMS（19%），火山喷发的 $SO_2$（7%）等的氧化以及生物质燃烧排放的 $SO_4$（2%）（Forster et al., 2007）。从各种源所占比例可见，硫酸盐气溶胶的排放和不同国家和地区的工业化程度密切相关。由图 1a1 可以发现，BCC_int 模拟的硫酸盐大值区分别出现在美国东南部、欧洲东部、印度和中国东部，其分布形势基本与 AEROCOM_MEDIAN（图 1b1）相同，但数值上普遍较 AEROCOM_MEDIAN 有所偏大。BCC_pre 给出的硫酸盐柱含量比前两者均大一倍以上。全球平均硫酸盐柱含量 BCC_int 为 1.770 mg $m^{-2}$，AEROCOM_MEDIAN 为 1.248 mg $m^{-2}$，而 BCC_pre 为 3.397 mg $m^{-2}$。可见，不同模式和方法得到的硫酸盐气溶胶柱含量还有很大的不确定性，BCC_int 模拟的硫酸盐柱含量更接近 AEROCOM_MEDIAN 的中值水平。

黑碳气溶胶主要由含碳物质不完全燃烧产生，因其对可见光到近红外波段的太阳辐射均有很强的吸收性而引起人们的广泛关注（张华等，2008；Zhang et al., 2009；王志立等，2009b；杨溯等，2010）。黑碳气溶胶在全球有 4 个主要的排放源区，分别在中国东部、西欧、非洲中部和南美（Bond et al., 2007）。由图 1a2 可见，耦合系统基本模拟出了黑碳的几个大值区，但是和 AEROCOM_MEDIAN 的分布（图 1b2）相比，黑碳柱含量大值区的分布范围明显偏小。从全球平均来看，BCC_int 模拟的黑碳柱含量为 0.138 mg $m^{-2}$，比 AEROCOM_MEDIAN 结果（0.345 mg $m^{-2}$）小将近 2/3。BCC_int 模拟的黑碳气溶胶柱含量偏小原因可能有两方面：首先耦合系统的黑碳气溶胶排放强度在参与 AeroCom 的模式中处于较低的水平（Zhang et al., 2012）；另一个原因可能和 BCC_int 中黑碳的老化时间有关，CAM 中不可溶性碳类气溶胶的存在时间只有一个积分步长（Gong et al., 2003），这使得黑碳很快地老化为吸湿性气溶胶而参与湿沉降。

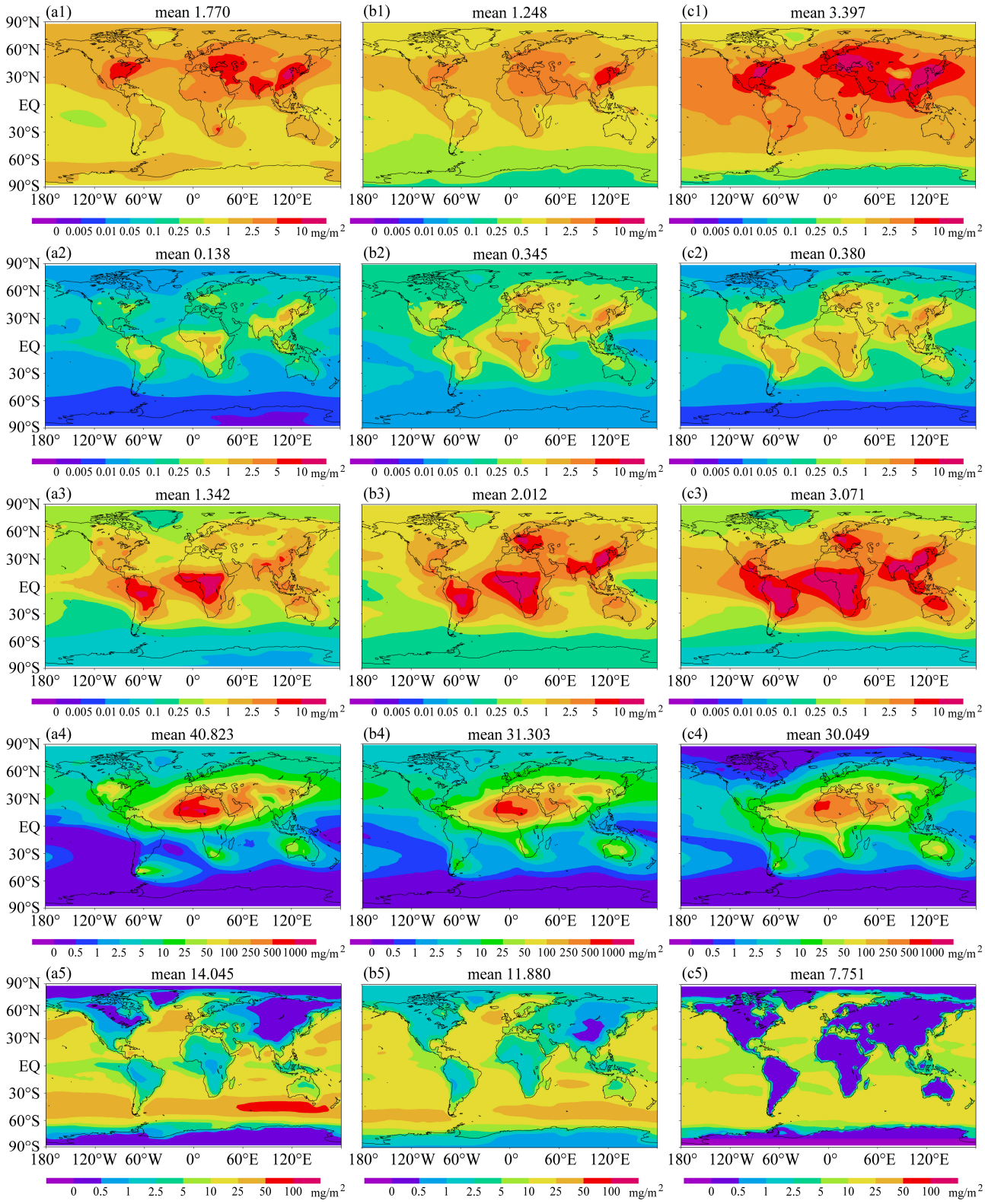


图 1 BCC_int（左列）、AEROCOM_MEDIAN（中列）、BCC_pre（右列）得到的（a1−c1）硫酸盐、（a2−c2）黑碳、（a3−c3）有机碳、（a4−c4）沙尘和（a5−c5）海盐 5 种典型种类气溶胶年平均柱含量的全球分布

Fig. 1 Global distributions of column burden of typical aerosols (a1−c1) sulfate, (a2−c2) black carbon, (a3−c3) organic carbon, (a4−c4) soil dust, and (a5−c5) sea salt from BCC_int (left panel), AEROCOM_MEDIAN (middle panel), and BCC_pre (right panel)

有机碳气溶胶和黑碳气溶胶是同源的，所以许多方案把一定种类化石燃料或植物的有机碳和黑碳排放率设定为一个固定比值（Liousse et al., 1996; Cooke et al., 1999）。图 1a3、1b3、1c3 所示的有机碳模拟情形与黑碳基本相似，耦合系统模拟值仍然偏低，其原因也与黑碳气溶胶偏低相同。

沙尘气溶胶也称矿物沙尘，主要源于干旱、半干旱地区的风蚀过程（钱云等，1999）。全球 4 个沙尘暴多发区（中亚、北美、中非和澳大利亚）主要分布在赤道两侧（25°S～25°N）的副热带地区（马井会等，2007）。从图 1a4 和 1b4 可以看出，BCC_int 模拟的沙尘气溶胶柱含量的分布形势基本与 AEROCOM_MEDIAN 相似，且与 BCC_pre 相比，耦合系统更好地模拟了沙尘气溶胶的南北传输，这在沙尘气溶胶在北半球高纬度地区的分布上表现得最为明显。但是，BCC_int 模拟的全球平均值（40.823 mg $m^{-2}$）比 AEROCOM_MEDIAN（31.303 mg $m^{-2}$）偏大。耦合系统的沙尘排放率（10.641 g $m^{-2}$ $a^{-1}$)远远大于 AEROCOM_MEDIAN（2.208 g $m^{-2}$ $a^{-1}$），这可能是 BCC_int 沙尘柱含量比较大的主要原因。

海盐气溶胶主要由海浪飞沫破裂生成，主要排放源在海洋。从图 1a5、1b5 可以看出，BCC_int 模拟的海盐气溶胶柱含量分布与 AEROCOM_MEDIAN 比较相似，尤其是在中低纬度地区；在高纬度地区，耦合系统的海盐柱含量较 AEROCOM_MEDIAN 偏低可能是由于其南北方向传输较弱。BCC_int 在南北纬 30°～60°之间的海洋上有两个非常明显的柱含量大值带，这可能是造成耦合系统全球平均海盐柱含量（14.045 mg $m^{-2}$）稍大于 AEROCOM_MEDIAN 全球平均（11.88 mg $m^{-2}$）的主要原因。值得注意的是，图 1c5 中显示的月平均气溶胶资料的海盐柱含量分布，陆地上几乎没有海盐气溶胶，这表明原有的月平均气溶胶资料在计算大气中海盐含量的时候没有通过动力过程处理海洋向陆地的输送。从这点来说，耦合系统的海盐方案较月平均气溶胶资料有明显的改进。

综上所述，BCC_AGCM2.0.1 与 CAM 耦合系统对 5 种典型种类气溶胶柱含量的模拟总体上比较合理，尤其是对硫酸盐、沙尘和海盐的模拟都较月平均气溶胶资料有所改进。但是，耦合系统对碳类气溶胶的模拟相对 AEROCOM_MEDIAN 总体偏低，这需要从黑碳的排放方案、物理参数化和大气环流过程多方面进行更深入的探讨，同时应该注意 AEROCOM_MEDIAN 仅仅代表了多模式的中值水平，各模式之间也存在很大的差异。要对耦合系统碳类气溶胶的模拟进行改进，需要在观测方面有可靠的数据支持。

### 3.2 气溶胶光学厚度

气溶胶光学厚度是影响气溶胶辐射效应最重要的物理量。图 2 给出了耦合系统和月平均气溶胶资料模拟的气溶胶光学厚度（550 nm，下同）的全球分布。从全球平均来看，BCC_int 模拟值（0.070）和 BCC_pre（0.064）相差不大。但是从空间分布来看，两者差别是比较明显的。首先，在撒哈拉沙漠、30°S～60°S 海洋上和北极附近，BCC_int 的气溶胶光学厚度相对 BCC_pre 偏大；而在美国东部、南美、西欧、非洲南部，情况正好相反。对比图 1 气溶胶柱含量的分布，两者在非洲撒哈拉地区的气溶胶光学厚度差别主要是沙尘造成的；而海洋上空，远离大陆地区（比如 30°S～60°S）的气溶胶光学厚度差异主要归因于海盐；西欧、北美等工业程度较高的

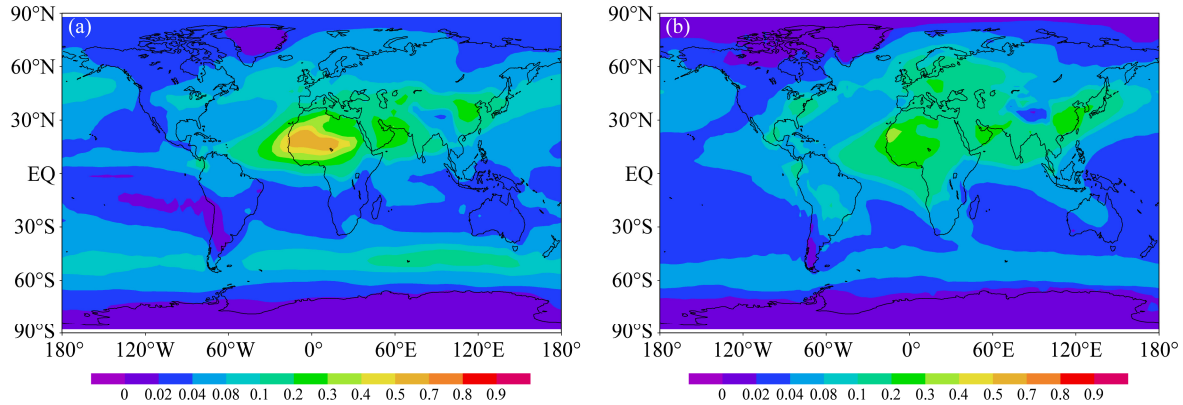


图 2 （a）BCC_int 和（b）BCC_pre 得到的总光学厚度的全球分布对比

Fig. 2 Comparisons of the global distribution of total aerosol optical depth from (a) BCC_int and (b) BCC_pre

地区，气溶胶光学厚度差别的主要贡献者为硫酸盐；非洲南部和南美的差异主要由碳类气溶胶产生。对比 AEROCOM_MEDIAN（http://aerocom.met.no/cgi-bin/aerocom/surfobs_annualrs.pl [2012-04-23]），BCC_int 对于撒哈拉地区和中纬度海洋上空的气溶胶光学厚度的模拟都有较大的改进。

Zhang et al.（2012）利用 CARSNET 和 AERONET 站点资料对比了耦合系统模拟的气溶胶光学厚度，发现除了在某些受硝酸盐和铵盐影响较大的站点（CAM 里没有考虑硝酸盐和铵盐）外，耦合系统对气溶胶光学厚度的量级和季节变化模拟是比较好的。本文为了说明 BCC_int 气溶胶光学厚度相对于 BCC_pre 的变化，选取了以下 8 个站点与 AERONET 比较：中国两个[北京（40.0°N，116.4°E），敦煌（40.0°N，94.8°E）]，北非两个[Tamanrasset（22.8°N，5.5°E），Dahkla（23.7°N，15.9°W）]，欧洲 1 个[Hamburg（53.6°N，10.0°E）]、北美洲 1 个[Bondville（40.0°N，88.4°W）]、南美洲 1 个[Brasilia（15.9°S，47.9°W）]、南印度洋 1 个[Amsterdam_Island（37.8°S，77.6°E）]，主要考虑了各个站点所处区域的主导性气溶胶不同。

如图 3 所示，除了北非两个站点春季气溶胶光学厚度过大外，BCC_int 模拟的气溶胶光学厚度均在 AERONET 资料的变化范围内。在中国的两个站点，BCC_pre 模拟的春季气溶胶光学厚度普遍偏小，而 BCC_int 对这种情况有所改善；而在 Hamburg 站（受硫酸盐气溶胶影响较大），BCC_int 对其季节变化趋势模拟得很好；另外，在 Amsterdam 岛（位于海盐气溶胶的大值区），BCC_int 模拟的气溶胶光学厚度与 AERONET 非常吻合，较月平均气溶胶资料有很大的改进。在 Tamanrasset（位于撒哈拉沙漠腹地）和 Dahkla 站（位于撒哈拉大西洋沿岸），BCC_int 对其春季气溶胶光学厚度模拟偏大，其原因可能与春季该地区地表风速模拟偏大有关；在 Bondville 站（位于美国中东部）对光学厚度季节变化趋势模拟稍差；在 Brasilia 站（位于巴西内陆地区），BCC_int 模拟结果接近观测的最小值，这主要是 BCC_int 对碳类气溶胶模拟偏小造成的。

表 1 给出了 BCC_int 和 BCC_pre 模拟的总气溶胶光学厚度、各类气溶胶光学厚度和对总气溶胶光学厚度的贡献。从中可以看出，耦合系统和月平均气溶胶资料模拟的总气溶胶光学厚度分别为 0.070 和 0.064，两者均比 AEROCOM_MEDIAN 结果（约 0.11）小，与 GEOSCHEM（Yu and Luo, 2009）结果（0.069）接近。其中，耦合系统总气溶胶光学厚度的最大贡献来源于沙尘，其次来源于海盐，两者贡献了气溶胶光学厚度的约 77%；而月平均气溶胶资料中，光学厚度最大的是硫酸盐，贡献了总光学厚度的 43.8%，沙尘和海盐的贡献分别只有 22.2% 和 13.4%。由于各类气溶胶吸收和散射性存在差异，另外，各类气溶胶的主要分布区域不同，因此各类气溶胶在总光学厚度中比例配置的不同将导致各地区大气和地表辐射收支发生变化，进而影响到各地区的气候。

## 4 常规气候场的模拟

### 4.1 全球平均量

表 2 列出了 BCC_int 和 BCC_pre 模拟的全球年平均气候态参量以及相应的观测或再分析资料。从表 2 中可以看出，BCC_int 较好地模拟了大气顶净太阳辐射通量和向上长波辐射通量，净辐射通量比 BCC_pre 减小了约 0.4 W $m^{-2}$，使其更接近 ERBE 观测结果。在地面，BCC_int 模拟的净太阳辐射较 ISCCP 资料偏小、净长波辐射较 ISCCP 资料偏大，使模拟的地表总辐射（约 99 W $m^{-2}$）比观测值（约 116 W $m^{-2}$）偏小约 17 W $m^{-2}$，这可能与模拟的赤道和两极地区到达地表的短波辐射偏低有关（Wu et al., 2010）；与 BCC_pre 相比，BCC_int 的地表净短波辐射和净长波辐射都有一定的增加，但两者地表总辐射收支差别很小，仅有约 0.1 W $m^{-2}$。

对于地表潜热和感热通量，BCC_int 模拟的两者之和与 NCEP 资料结果比较接近，但是潜热和感热通量分别比 NCEP 资料偏小和偏大，说明

**表 1 气溶胶总光学厚度、各种气溶胶光学厚度及其对总光学厚度的贡献**

**Table 1 Total aerosol optical depth (AOD), each AOD and their contributions to total AOD**

| | | 硫酸盐 | | 黑碳 | | 有机碳 | | 沙尘 | | 海盐 | |
|---|---|---|---|---|---|---|---|---|---|---|---|
| | 总光学厚度 | 光学厚度 | 贡献 | 光学厚度 | 贡献 | 光学厚度 | 贡献 | 光学厚度 | 贡献 | 光学厚度 | 贡献 |
| BCC_int | 0.070 | 0.010 | 14.30% | 0.000604 | 0.86% | 0.0055 | 7.90% | 0.0280 | −40.00% | 0.0260 | 37.10% |
| BCC_pre | 0.064 | 0.028 | 43.80% | 0.00208 | 3.30% | 0.0104 | 16.30% | 0.0142 | 22.20% | 0.0087 | 13.40% |

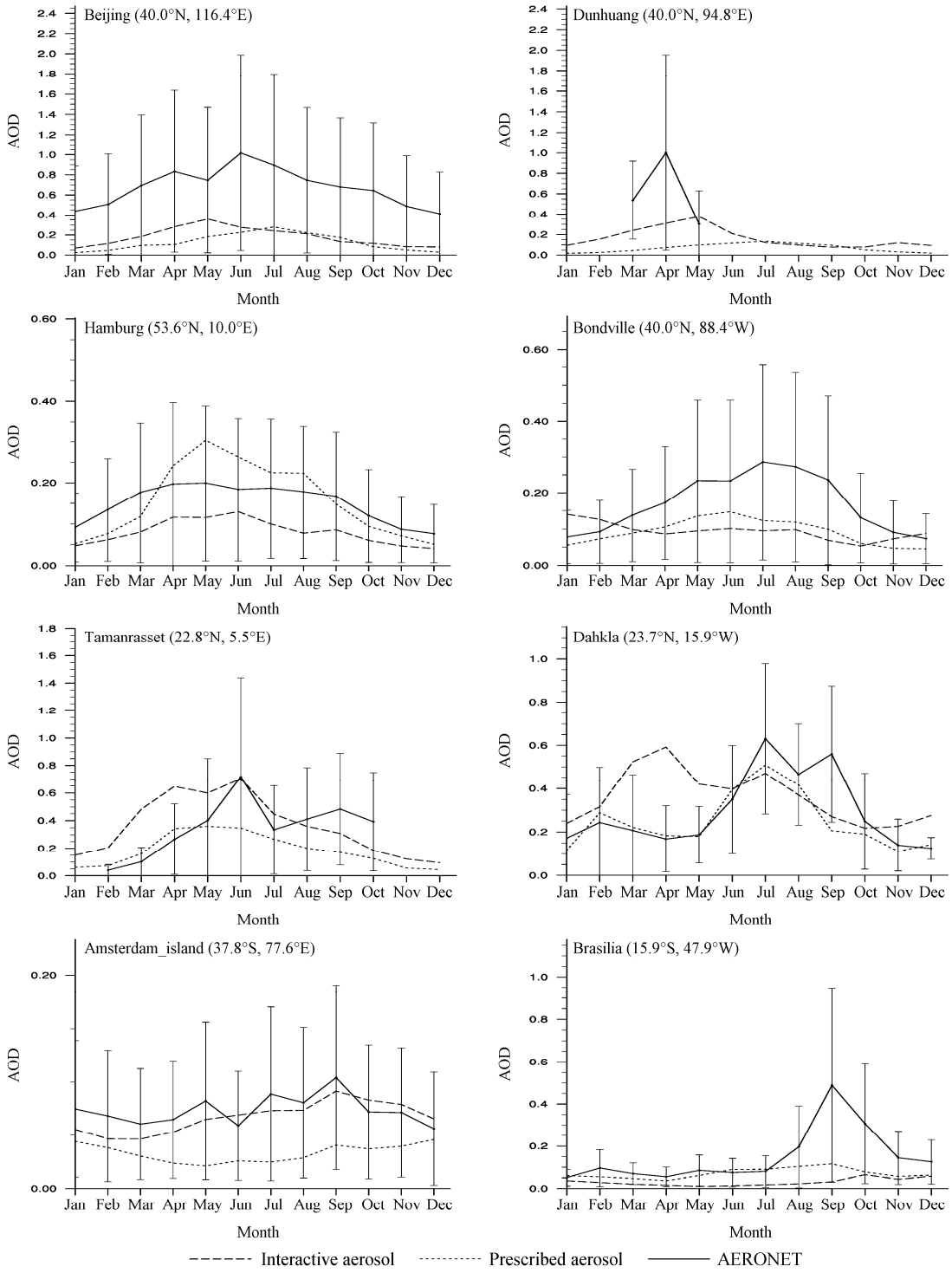


图 3 BCC_int 和 BCC_pre 模拟的 550 nm 气溶胶光学厚度和 AERONET 平均结果的对比（误差棒代表观测光学厚度的标准差）

Fig. 3 Comparisons of BCC_int and BCC_pre simulated AOD at 550 nm and AERONET mean level (the error bar indicates the standard deviation of observed optical depth)

BCC_int 模拟的地表蒸发偏弱、地表温度偏高，BCC_pre 与 BCC_int 情形相似。但气溶胶方案的改变对潜热和感热通量的改变比较明显，BCC_int 相比 BCC_pre 减少了 0.6 W $m^{-2}$ 潜热通量、而增加了约 0.9 W $m^{-2}$ 感热通量，超过了两者辐射通量的差异。潜热和感热与大气温度、水汽输送和降水有着密切联系，因此气溶胶的变化引起这二者的明显改变是值得关注的。

**表 2 BCC_int 和 BCC_pre 的全球年平均气候态变量和相应的观测/再分析资料值比较**

**Table 2 Comparisons of globally and annually mean climate variables among BCC_int, BCC_pre, and observational/reanalyzed data**

| 物理量 | 观测 | BCC_int | BCC_pre |
|---|---|---|---|
| 大气顶 | | | |
| 辐射能量收支/W m$^{-2}$（向下为正） | 0.059[a] | 2.006 | 2.421 |
| 净太阳辐射通量/W m$^{-2}$ | 234.004[a] | 235.324 | 235.956 |
| 向上长波辐射通量/W m$^{-2}$ | 233.946[a] | 233.317 | 233.534 |
| 地面 | | | |
| 辐射能量收支/W m$^{-2}$ | 116.458[b] | 98.924 | 99.038 |
| 净太阳辐射通量/W m$^{-2}$ | 165.893[b] | 158.838 | 158.407 |
| 净长波辐射通量/W m$^{-2}$ | 49.425[c] | 59.914 | 59.369 |
| 潜热通量/W m$^{-2}$ | 80.922[e] | 76.911 | 77.523 |
| 感热通量/W m$^{-2}$ | 15.795[c] | 21.971 | 21.051 |
| 其它量 | | | |
| 总云量 | 66.715%[b] | 59.185% | 58.879% |
| 可降水量/mm | 24.575[d] | 23.686 | 23.657 |
| 降水率/mm d$^{-1}$ | 2.607[e] | 2.635 | 2.657 |
| 陆地表面温度/K | 281.31[c] | 282.23 | 282.24 |
| 云短波辐射强迫/W m$^{-2}$ | −54.163[a] | −54.655 | −54.312 |
| 云长波辐射强迫/W m$^{-2}$ | 30.355[a] | 29.088 | 28.966 |

注：[a]−ERBE：地球辐射收支试验；[b]−ISCCP：国际人造成卫星云气候学项目；[c]−NCEP：美国国家环境预报中心；[d]−NVAP：美国国家航空航天局水蒸气项目；[e]−GPCP：全球降水气候学计划

BCC_int 模拟的总云量较 ISCCP 总云量偏小，但相对于 BCC_pre 的模拟值略有提高，这里仅仅考虑了气溶胶的直接辐射效应。模式对云的模拟是一个公认的难题，其水平的提高需要发展更为精细的云处理方案，另外，气溶胶和云的相互作用也值得进一步研究。BCC_int 模拟的云短波和长波辐射强迫和 ERBE 资料比较一致。BCC_int 的可降水量较 NVAP 偏小，但是相对于 BCC_pre 略有增加，这意味着相对于 BCC_pre，BCC_int 模拟的大气总的水汽含量有所增加。BCC_int 模拟的降水率和陆地表面温度均较 BCC_pre 更接近观测/再分析结果。

从以上模式结果与观测/再分析资料的对比分析可以发现，新气溶胶方案的加入虽然没有从根本上消除模式存在的偏差，但是使得模拟结果相比较月平均气溶胶资料向观测/再分析资料靠近。

### 4.2 辐射通量

气溶胶主要通过影响辐射影响气候，气溶胶的辐射效应是研究其气候影响的基础，因此，应该对新的气溶胶—气候耦合系统模拟的辐射场有所了解。从表 2 可以看出，BCC_int 和 BCC_pre 模拟的大气顶净太阳辐射通量相差 0.6 W m$^{-2}$，地面净太阳辐射通量相差 0.4 W m$^{-2}$。图 4 对比了模式模拟与 ERBE 观测资料的大气顶净太阳辐射通量的全球分布。从图 4a 和 4b 可以看出，除了青藏高原、撒哈拉沙漠和阿拉伯地区存在明显的差异外，BCC_int 模拟的大气顶净太阳辐射通量的分布与观测资料基本一致。图 4 d 给出了两者差异的全球分布，可以看出，BCC_int 模拟的赤道附近、青藏高原和北半球高纬度大陆上的大气顶净太阳辐射通量相对 ERBE 偏小，在撒哈拉和中纬度大洋上则相对 ERBE 偏大，这主要是大气环流模式本身的误差（Wu et al., 2010）造成的，需要模式的进一步完善。BCC_pre 模拟结果也存在同样的特点（见图 4e）。但是从 BCC_int 和 BCC_pre 模拟结果的对比（图 4f）可以看出，在撒哈拉沙漠、阿拉伯半岛和 30°S～60°S 洋面上，BCC_int 对模拟结果存在的正偏差有明显的纠正效果，这表明耦合系统的海盐方案在南半球洋面上，以及沙尘方案在撒哈拉和阿拉伯半岛较月平均气溶胶资料有一定的优越性。从中亚经中国西北到中国东部地区，BCC_int 模拟的大气顶净太阳辐射较 BCC_pre 偏低，比较图 1a4 和图 1c4，这主要是耦合系统模拟的沙尘气溶胶相对于月平均气溶胶资料偏多造成的。但在有些地区，如南中国海和赤道太平洋地区，两种气溶胶方案的气溶胶光学厚度差异不明显（图 2），而且在晴空条件下，以上地区大气顶净太阳辐射通量的差异也不明显（图略）。对比云水含量差异的分布，这些地区大气顶净太阳辐射通量的差异主要与云对气溶胶直接辐射效应的反馈有关。

### 4.3 地表温度与降水

地表温度和降水是最典型的两个气候态变量，也是讨论气溶胶气候效应最重要的两个变量。图 5 对比了模式模拟和 NCEP 再分析资料地表温度的全球分布。从图 5a 和图 5b 可以看出，BCC_int 模拟的地表温度全球分布形势和 NCEP 再分析资料基本相同。图 5 d 显示了二者差异的分布，由于模式在运行时用的是固定的 NCEP 再分析海温资料（2.1 节），因此在海洋上的差异很小；在非洲和南美洲大陆，耦合系统普遍存在温度正偏差，而在亚欧大陆大部分地区和北美大陆高纬度地区，耦合系统存在着负偏差。这种偏差的分布形式在 BCC_pre 结果中有同样的体现（图 5e）。图 5f 显示了 BCC_int 与 BCC_pre 地表温度差异的分布形势，从中可以看出，

在撒哈拉沙漠地区，耦合系统对模式模拟的正温度偏差有明显的改进作用，这主要是沙尘气溶胶的贡献；在西欧和美国东部，BCC_int 温度负偏差相对 BCC_pre 较小，这主要是耦合系统在这些地区的硫酸盐气溶胶相对月平均气溶胶资料较少造成的；从中亚到我国西北和华北地区，耦合系统的地表温度

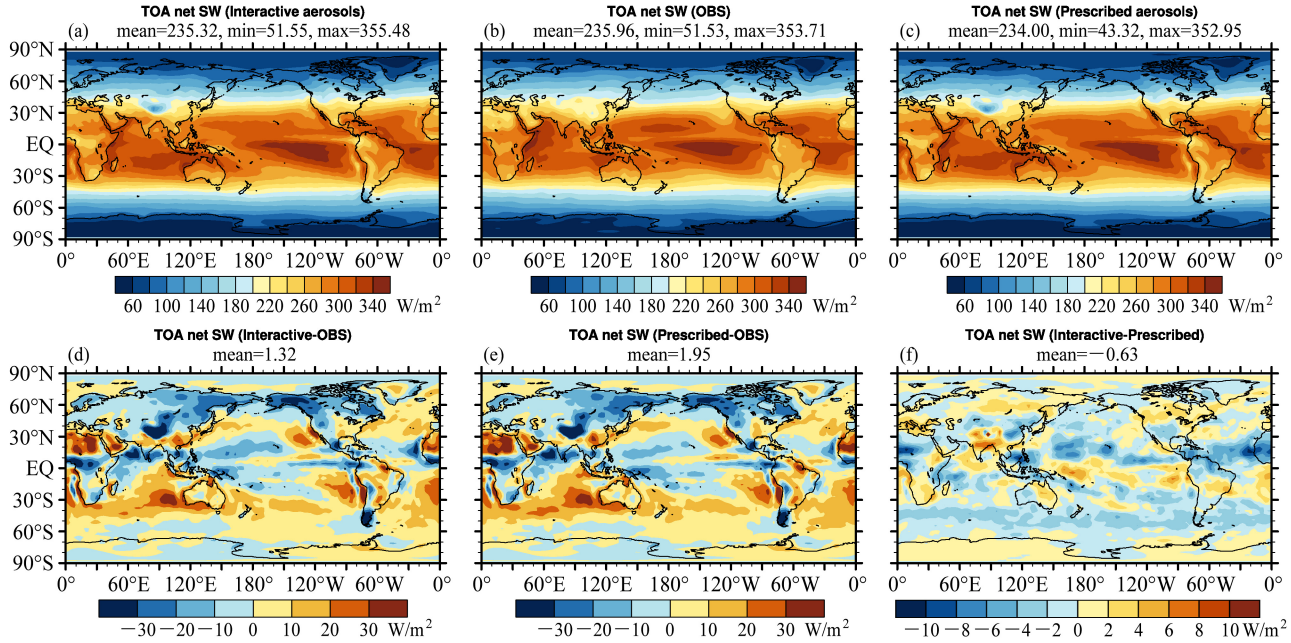


图 4　（a）BCC_int、（b）ERBE、（c）BCC_pre 大气顶净太阳辐射通量及差异（d）BCC_int−ERBE、（e）BCC_pre−ERBE、（f）BCC_int−BCC_pre 的分布

Fig. 4　The distributions of net solar radiation at the top of atmosphere from (a) BCC_int, (b) ERBE, (c) BCC_pre, and their differences (d) BCC_int minus ERBE, (e) BCC_pre minus ERBE, and (f) BCC_int minus BCC_pre

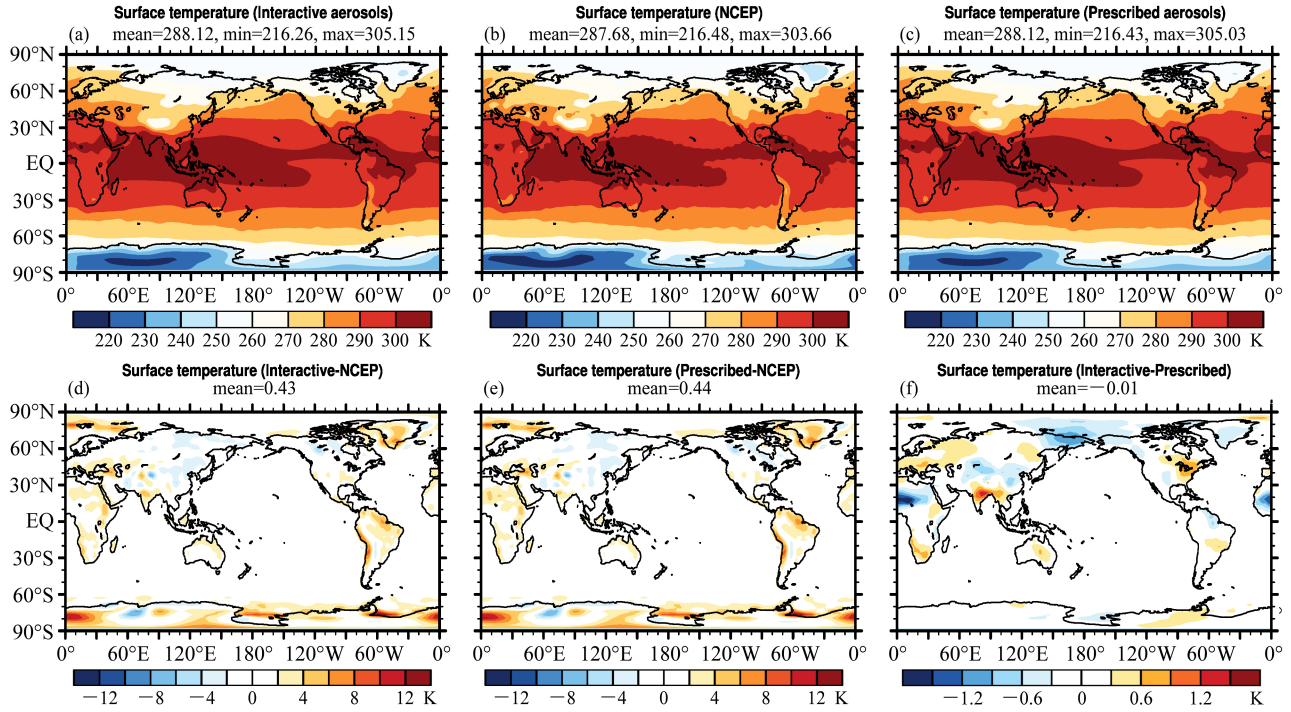


图 5　（a）BCC_int、（b）NCEP、（c）BCC_pre 得到的地表温度及差异（d）BCC_int−NCEP、（e）BCC_pre−NCEP、（f）BCC_int−BCC_pre 的全球分布

Fig. 5　The distributions of temperature at the surface form (a) BCC_int, (b) NCEP, (c) BCC_pre, and their differences (d) BCC_int minus NCEP, (e) BCC_pre minus NCEP, and (f) BCC_int minus BCC_pre

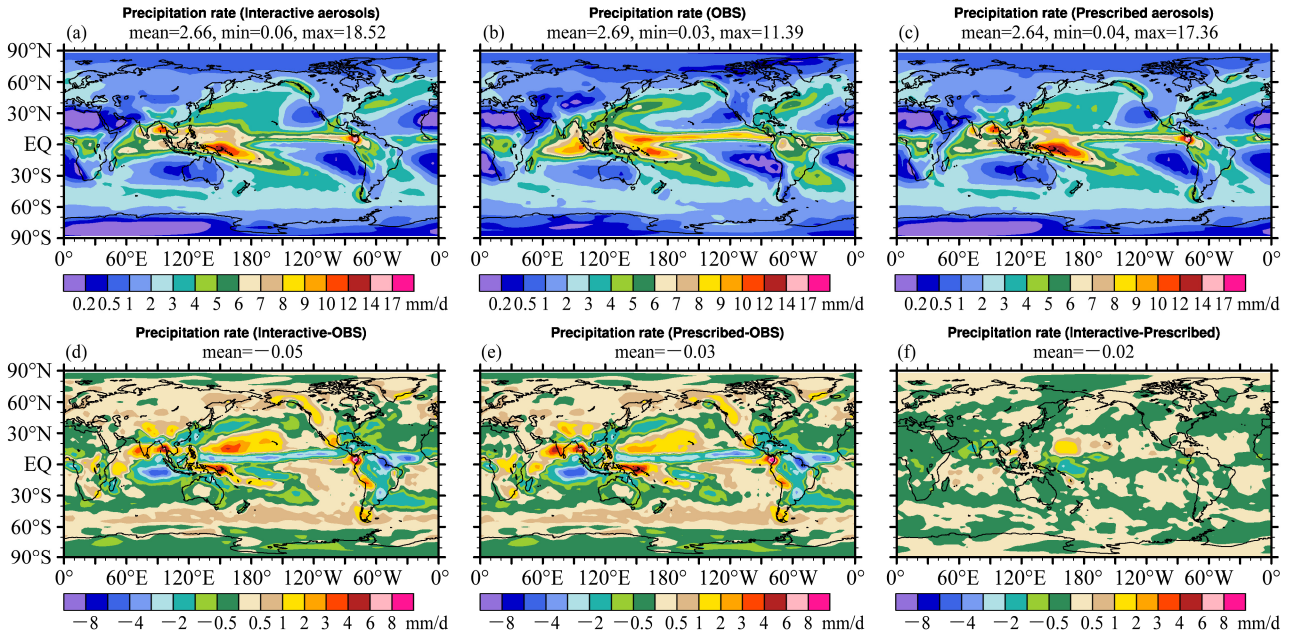


图 6 （a）BCC_int、（b）GPCP、（c）BCC_pre、（d）BCC_int−GPCP、（e）BCC_pre−GPCP、（f）BCC_int−BCC_pre 得到的降水率及其差异的全球分布

Fig. 6 The distributions of precipitation rate at the surface from (a) BCC_int, (b) GPCP, (c) BCC_pre, and their differences (d) BCC_int minus GPCP, (e) BCC_pre minus GPCP, and (f) BCC_int minus BCC_pre

负偏差相对月平均气溶胶资料增大基本是沙尘气溶胶相对后者偏多造成的。

图 6 给出了模式模拟的降水率全球分布形势以及和 GPCP 资料的对比。从图 6a 和图 6b 中可见，BCC_int 模拟出了降水率空间分布的基本形势，但在热带地区，其降水率明显偏大。图 6d 给出了 BCC_int 和观测结果差异的分布，从中可以看出在印度和孟加拉湾季风降水区和西太平洋的赤道两侧 BCC_int 的降水率偏差较大，BCC_pre 模拟的降水率偏差分布与此类似（图 6 e）。图 6f 显示了气溶胶方案的不同造成的降水率差异的分布，从中可以看出比较明显的特征：首先，在印度和孟加拉湾地区 BCC_int 的降水率相对 BCC_pre 有所减小，在一定程度上减小了模拟结果与观测的偏差；其次，在西太平洋赤道南北两侧 BCC_int 的降水率相对于 BCC_pre 分别有明显的减少和增加，这种变化使南侧降水率的模拟偏差有所减小，而使北侧降水率的模拟偏差有所增大。气溶胶对降水的影响比对地表温度的影响更复杂，要通过一系列反馈过程来实现，其中最重要的是云反馈。气溶胶影响云，进而影响降水的途径主要有两个，即影响地气辐射平衡和作为云凝结核或者冰核影响云微物理性质进而影响云和降水。但目前还无法准确获得气溶胶与云及降水的确切关系（杨慧玲等，2011）。本文仅考

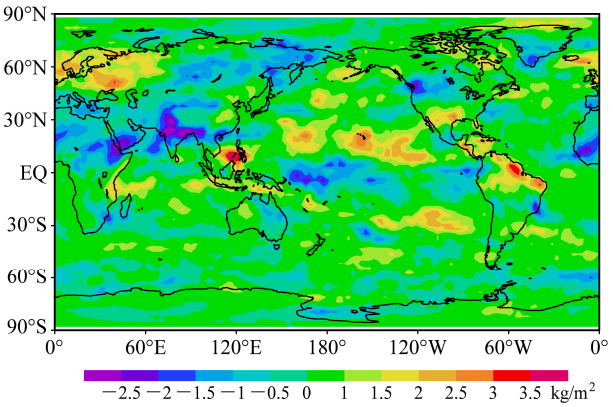


图 7 BCC_int−BCC_pre 得到的云水（包括液水和冰水）路径差异

Fig. 7 The difference of in-cloud water (liquid and ice) from BCC_int minus BCC_pre

虑气溶胶的直接辐射作用，而没有考虑气溶胶与云的微物理过程，因此这里的云反馈主要是指云对气溶胶辐射作用的反馈，即气溶胶作用于大气辐射过程，而影响温度、环流等气候特征，云的形成和分布随着这些特征的改变而变化，云的变化进而对辐射场、降水等产生影响，构成气溶胶—辐射—云—气候的复杂反馈过程。从图 7 可以看出，在印度地区，BCC_int 使得该地区云水路径相比 BCC_pre 有所减小，与降水率的变化有很好的对应；而在西太平洋赤道两侧，气溶胶的改变造成的降水率变化与云水路径的变化同样有着很好的对应关系。如果对

整层大气进行水汽通量的积分（图略），在印度地区，BCC_int 使得由陆地向海洋的水汽通量明显增加，这不利于云和降水的形成；而在西太平洋赤道南、北两侧，BCC_int 分别减弱和增加了水汽的辐合，从而减弱和增加了降水。同时我们发现，印度和西太平洋赤道附近既不是气溶胶光学厚度最大的地区，也不是气溶胶改变最明显的地区（图 2），但是气溶胶方案的改变对这些地区降水率的影响最大。这一方面是因为这些地区的降水率本身比较大，另一方面也可能与这些地区降水对气溶胶比较敏感有关。由此可见，准确模拟气溶胶和其辐射效应，对于提高降水，尤其是印度和西太平洋赤道附近地区的降水模拟非常重要。

## 5 结论

通过对气溶胶－气候耦合模式系统 BCC_AGCM2.0.1_CAM 的气溶胶和气候态模拟情况的初步评估，得到以下结论：

耦合系统对 5 种典型种类气溶胶的柱含量和光学厚度的模拟总体上是合理的，尤其是对硫酸盐、沙尘和海盐的模拟相比 BCC_AGCM2.0.1 原有的月平均气溶胶资料有很大改进，但是碳类气溶胶处于 AeroCom 的较低水平。

耦合系统对全球平均气候态变量的模拟和观测/再分析资料比较一致，且对总云量、陆地表面温度和降水等的模拟比月平均气溶胶资料模拟结果略有改进，虽然并没有从根本上降低误差。从大气顶净太阳辐射通量、地表温度和降水率的全球分布来看，耦合系统模拟的分布形势和观测/再分析资料比较相似，其误差主要是 BCC_AGCM2.0.1 本身误差造成的。耦合系统在撒哈拉、阿拉伯和南半球海洋上模拟的大气顶净短波辐射比原有月平均气溶胶资料有所改进，而在赤道太平洋上，气溶胶的改变引起了云和其它反馈，不仅影响了辐射场，而且对降水产生了重要的影响。

### 参考文献（References）

Bond T C, Streets D G, Yarber K F, et al. 2004. A technology-based global inventory of black and organic carbon emissions from combustion [J]. J. Geophys. Res., 109, D14203, doi: 10.1029/2003JD003697.

Bond T C, Bhardwaj E, Dong R, et al. 2007. Historical emissions of black and organic carbon aerosol from energy-related combustion, 1850–2000 [J]. Global Biogeochemical Cycles, 21, doi: 10.1029/2006GB002840.

Brasseur G P, Hauglustaine D A, Walters S, et al. 1998. MOZART: A global chemical transport model for ozone and related chemical tracers, 1, Model description [J]. J. Geophys. Res., 103: 28265–28289.

Cofala J, Amann M, Klimont Z, et al. 2005. Scenarios of world anthropogenic emissions of $SO_2$, $NO_x$, and CO up to 2030, internal report of the Tran Boundary Air Pollution Programme [R]. International Institute for Applied Systems Analysis. Laxenburg, Austria, 17pp.

Collins W D, Rasch P J, Eaton B E, et al. 2001. Simulating aerosols using a chemical transport model with assimilation of satellite aerosol retrievals: Methodology for INDOEX [J]. J. Geophys. Res., 106 (D7): 7313–7336.

Collins W D, Rasch P J, Eaton B E, et al. 2002. Simulation of aerosol distributions and radiative forcing for INDOEX: Regional climate impacts [J]. J. Geophys. Res., 107 (D19): 8082, doi: 10.1029/2000JD000032.

Cooke W F, Liousse C, Cachier H, et al. 1999. Construction of a 1°×1° fossil fuel emission data set for carbonaceous aerosol and implementation and radiative impact in the ECHAM4 model [J]. J. Geophys. Res., 104 (D18): 22137–22162.

Forster P, Ramaswamy V, Artaxo P, et al. 2007. Change in atmospheric constituents and in radiative forcing [M]// Climate Change 2007: The Physical Science Basis. Contribution of working Group I to the Fourth Assessment Report of the Intergovernmental Panel on Climate Change. Solomon S, Qin D, Manning M, et al., Eds. Cambridge, United Kingdom and New York, NY, USA: Cambridge University Press.

Gong S L, Barrie L A, Lazare M. 2002. Canadian Aerosol Module (CAM): A size-segregated simulation of atmospheric aerosol processes for climate and air quality models 2, Global sea-salt aerosol and its budgets [J]. J. Geophys. Res., 107 (D24): 4779, doi: 10.1029/2001JD002004.

Gong S L, Barrie L A, Blanchet J P, et al. 2003. Canadian aerosol module: A size-segregated simulation of atmospheric aerosol processes for climate and air quality models 1, Module development [J]. J. Geophys. Res., 108 (D1), doi: 10.1029/2001JD002002.

Hack J J. 1994. Parameterization of moist convection in the National Center for Atmospheric Research community climate model (CCM2) [J]. J. Geophys. Res., 99: 5551–5568.

Hasumi H, Emori S. 2004. K-1 coupled GCM (MIROC) description [R]. Center for Climate System Research, University of Tokyo, National Institute for Environmental Studies, Frontier Research Center for Global Change, Tokyo, Japan, 38.

Hauglustaine D A, Brasseur G P, Walters S, et al. 1998. MOZART: A global chemical transport model for ozone and related chemical tracers, 2, Model results and evaluation [J]. J. Geophys. Res., 103: 28291–28335.

Hourdin F, Armengaud A. 1999. The use of finite-volume methods for atmospheric advection of trace species, Part 1. Test of various formulations in a general circulation model [J]. Mon. Wea. Rev., 127: 822–837.

Hurrell J W, Hack J J, Shea D, et al. 2008. A new sea surface temperature and sea ice boundary dataset for the community atmosphere model [J]. J. Climate, 21 (19): 5145–5153.

Kettle A J, Andreae M O. 2000. Flux of dimethylsulfide from the oceans: A comparison of updated data sets and flux models [J]. J. Geophys. Res.,

105: 26793–26808.

Kiehl J T, Hack J J, Bonan G B, et al. 1998. The national center for atmospheric research community climate model: CCM3 [J]. J. Climate, 11: 1131–1149.

Kiehl J T, Gent P R. 2004. The community climate system model, version two [J]. J. Climate, 17: 3666–3682.

Liousse C, Penner J E, Chuang C, et al. 1996. A global three-dimensional model study of carbonaceous aerosols [J]. J. Geophys. Res., 101 (D14): 19411–19432.

马井会, 张华, 郑有飞, 等. 2007. 沙尘气溶胶光学厚度的全球分布及分析 [J]. 气候与环境研究, 12 (2): 156–164. Ma Jinghui, Zhang Hua, Zheng Youfei, et al. 2007. The optical depth global distribution of dust aerosol and its possible reason analysis [J]. Climatic and Environmental Research (in Chinese), 12 (2): 156–164.

Marticorena B, Bergametti G. 1995. Modeling the atmospheric dust cycle, 1: Design of a soil-derived dust emission scheme [J]. J. Geophys. Res., 100: 16415–16430.

Miller R L, Tegen I. 1998. Climate response to soil dust aerosols [J]. J. Climate, 11: 3247–3267.

Nightingale P D, Malin G, Law C S, et al. 2000. Upstill-Goddard RC in situ evaluation of air−sea gas exchange parameterizations using novel conservative and volatile tracers [J]. Global Biogeochemical Cycles, 14: 373–387.

Numaguti A, Takahashi M, Nakajima T, et al. 1995. Development of an atmospheric general circulation model [R]. CCSR, Tokyo, Reports of a new program for creative basic research studies, studies of global environment change with special reference to Asia and Pacific regions, Rep. 1−3, pp27.

Olivier J, Berdowski J, Peters J, et al. 2002. Applications of EDGAR including a description of EDGAR V3.0: Reference database with trend data for 1970–1995 [R]. NRP Report, 410200051, RIVM, Bilthoven, The Netherlands.

钱云, 符淙斌, 王淑瑜. 1999. 沙尘气溶胶与气候变化 [J]. 地球科学进展, 14 (4): 391–394. Qian Yun, Fu Congbin, Wang Shuyu. 1999. Soil dust aerosol and climate change [J]. Advances in Earth Science (in Chinese), 14 (4): 391–394.

Roeckner E, Arpe K, Bengtsson L, et al. 1996. The atmospheric general circulation model (ECHAM-4): Model description and simulation of the present-day climate [R]. Max-Planck-Institute für Meteorologie, Hamburg, Germany.

Roeckner E, Bäuml G, Bonaventura L, et al. 2003. The atmospheric general circulation model ECHAM5, Part I: Model description [R]. Max-Planck-Institute for Meteorology, Report No. 349, Hamburg, Germany.

Roeckner E, Brokopf R, Esch M, et al. 2004. The atmospheric general circulation model ECHAM5 Part II: Sensitivity of simulated climate to horizontal and vertical resolution [R]. Max-Planck-Institute for Meteorology, Report No. 354, Hamburg, Germany.

Sadourny R, Laval K. 1984. January and July performance of the LMD general circulation model [M] // Berger A, Nicolis C. New Perspectives in Climate Modelling. New York: Elsevier, 173–198.

Schmidt G A, Ruedy R, Hansen J E, et al. 2006. Present day atmospheric simulations using GISS Model E: Comparison to in-situ, satellite and reanalysis data [J]. J. Climate, 19: 153–192.

Smith S D. 1988. Coefficient for sea surface wind stress, heat flux, and wind profiles as a function of wind speed and temperature [J]. J. Geophys. Res., 93: 15467–15472, doi: 10.1029/JC093iC12p15467.

Stier P, Feichter J, Kinne S, et al. 2005. The aerosol−climate model ECHAM5-HAM [J]. Atmos. Chem. Phys., 5: 1125–1156.

Van der Werf G R, Randerson J T, Collatz G J, et al. 2004. Continental-scale partitioning of fire emissions during the 1997 to 2001 El Niño/La Niña period [J]. Science, 303: 73–76.

王志立, 张华, 郭品文. 2009a. 南亚地区黑碳气溶胶对亚洲夏季风的影响 [J]. 高原气象, 28 (2): 419–424. Wang Zhili, Zhang Hua, Guo Pinwen. 2009a. Effects of black carbon aerosol in South Asia on Asian summer monsoon [J]. Plateau Meteorology (in Chinese), 28 (2): 419–424.

王志立, 郭品文, 张华. 2009b. 黑碳气溶胶直接辐射强迫及其对中国夏季降水影响的模拟研究 [J]. 气候与环境研究, 14 (2): 161–171. Wang Zhili, Guo Pinwen, Zhang Hua. 2009b. A simulation study of effect of direct radiative forcing due to black carbon aerosol on the summer precipitation in China [J]. Climate and Environment Study (in Chinese), 14 (2): 161–171.

Wu T W, Wu G X. 2004. An empirical formula to compute snow cover fraction in GCMs [J]. Adv. Atmos. Sci., 21: 529–535, doi: 10.1007/BF02915720.

Wu T, Yu R, Zhang F. 2008. A modified dynamic framework for the atmospheric spectral model and its application [J]. J. Atmos. Sci., 65: 2235–2253, doi: 10.1175/2007JAS2514.1.

Wu T W, Yu R C, Zhang F, et al. 2010. The Beijing Climate Center atmospheric general circulation model: Description and its performance for the present-day climate [J]. Climate Dyn., 34: 123–147, doi: 10.1007/s00382-008-0487-2.

颜宏. 1987. 复杂地形条件下嵌套细网格模式的设计（二）：次网格物理过程参数化 [J]. 高原气象, 6（增刊）: 64–139. Yan Hong. 1987. Design of a nested fine-mesh model over the complex topography, Part two: Parameterization of the subgrid physical processes [J]. Plateau Meteorology (in Chinese), 6 (Suppl.): 64–139.

杨慧玲, 肖辉, 洪延超. 2011. 气溶胶对云宏微观特性和降水影响的研究进展 [J]. 气候与环境研究, 16 (4): 525–542. Yang Huiling, Xiao Hui, Hong Yanchao. 2011. Progress in impacts of aerosol on cloud properties and precipitation [J]. Climatic and Environmental Research (in Chinese), 16 (4): 525–542.

杨溯, 张武, 史晋森, 等. 2010. 半干旱地区黑碳气溶胶特征初步分析 [J]. 气候与环境研究, 15 (6): 756–764. Yang Su, Zhang Wu, Shi Jinsen, et al. 2010. Preliminary analyses of the characteristics of black carbon in the semi-arid area [J]. Climatic and Environmental Research (in Chinese), 15(6): 756–764.

Yu F, Luo G. 2009. Simulation of particle size distribution with a global aerosol model: Contribution of nucleation to aerosol and CCN number concentrations [J]. Atmos. Chem. Phys., 9: 7691–7710.

Zhang G J, McFarlane N A. 1995. Sensitivity of climate simulations to the parameterization of cumulus convection in the Canadian Climate Centre general circulation model [J]. Atmos. Ocean, 33: 407–446.

Zhang G J, Mu M Q. 2005. Effects of modifications to the Zhang McFarlane

convection parameterization on the simulation of the tropical precipitation in the National Center for Atmospheric Research Community Climate Model, version 3 [J]. J. Geophys. Res., 110: D09109, doi: 10.1029/2004JD005617.

张华, 马井会, 郑有飞. 2008. 黑碳气溶胶辐射强迫全球分布的模拟研究 [J]. 大气科学, 32 (5): 1147–1158. Zhang Hua, Ma Jinghui, Zheng Youfei. 2008. A modeling study of the global distribution of the radiative forcing of black carbon aerosol [J]. Journal of Atmospheric Science (in Chinese), 32 (5): 1147–1158.

Zhang H, Wang Z L, Guo P W, et al. 2009. A modeling study of the effects of direct radiative forcing due to carbonaceous aerosol on the climate in East Asia [J]. Adv. Atmos. Sci., 26 (1): 57–66.

Zhang H, Wang Z L, Wang Z Z, et al. 2012. Simulation of direct radiative forcing of aerosols and their effects on East Asian climate using an interactive AGCM−aerosol coupled system [J]. Climate Dyn., 38: 1675–1693, doi: 10.1007/s00382-011-1131-0.

周雅清，任国玉. 城市化对华北地区极端气温事件频率的影响[J]. 高原气象，2014，33(6)：1589－1598，doi：10.7522/j.issn.1000-0534.2013.00153.

# 城市化对华北地区极端气温事件频率的影响

周雅清[1]， 任国玉[2]

（1. 山西省晋中市气象局，晋中 030600；2. 中国气象局气候研究开放实验室/国家气候中心，北京 100081）

**摘要**：通过分析和对比华北区域(33°N－43°N，108°E－120°E)国家站和乡村站 1961－2008 年极端气温指数的变化趋势发现，近 48 年与最低气温相关的指数的时间序列变化趋势国家站较乡村站明显，与最高气温相关的指数两者时间演变基本一致。气温指数中冷指数突变一般发生在 20 世纪 80 年代末，暖指数突变要晚一些，出现在 90 年代中后期。城市化加剧了冷指数日数的减少和暖指数日数的增加，同时也使最低气温的极值明显升高。与最低气温相关的指数城市化影响比与最高气温相关的更显著，两者城市化影响贡献率都在 50% 以上。极值指数和冷夜日数城市化增温效应一般在春、冬季更明显，而冷(暖)昼日数和暖夜日数则是夏季受城市化影响更显著。

**关键词**：极端气温指数；城市化影响；最高气温；最低气温

**文章编号**：1000-0534(2014)06-1589-10 **中图分类号**：P467 **文献标志码**：A

**doi**：10.7522/j.issn.1000-0534.2013.00153

## 1 引言

近 100 年，全球的年平均表面温度升高了 0.74℃[1]，同期中国大陆地区年平均地面气温增加 0.6℃左右[2]。全球大部分陆地地区极端冷事件发生频率显著减少，而极端暖事件发生频率明显增加，其中极端冷事件频率的变化趋势比极端暖事件更为明显[3－6]。针对中国地区的研究表明，影响中国的寒潮和低温事件频率和强度有显著下降趋势；异常冷夜(昼)天数、霜冻日数一般显著减少，偏冷的气候极值减轻；与异常偏暖相关的暖夜(昼)日数明显增加，但与高温相关的极端气候事件频率和强度变化一般较弱，高温事件频数和偏热的气候极值未见显著趋势变化[7－16]。

对于全球和区域气温变化的原因，目前已有共识，一般认为主要和人类活动长期向大气中排放温室气体有关，但其他因子也起到一定作用[1]。在气温变化原因的识别过程中，还有很多问题需要解决。其中一个重要的问题是，城市热岛效应的影响究竟在多大程度上还保留在目前的近地面气温序列中[17]。不少学者评价了全球、半球和不同尺度区域平均气温序列城市化影响问题，尽管在全球尺度上仍存在不同看法[18－19]，但在东亚东区和中国大陆地区，目前已经积累了充分的证据，表明城市化对基于现有观测资料的近地面气温趋势变化产生了显著的影响[20－29]。张爱英等[28]研究指出，1961－2004 年期间中国范围内国家基准气候站和基本气象站地面年平均气温序列中的城市化增温贡献达到 27.33%。

目前城市化对地面气温观测记录的影响研究多针对平均气温和平均最高、最低气温，对基于最高和最低气温资料的极端气温指数的研究较少。张雷等[30]分析发现，城市化因素对北京观象台记录的 20 世纪 60 年代初以来主要极端气温指数趋势变化具有控制性的影响。Zhou et al[15] 在对中国大陆 1961－2008 年极端气温指数变化进行分析后，简要讨论了华北地区平均极端气温指数序列中的城市化偏差，发现在利用国家基准气候站和基本气象站(下称国家站)资料获得的与最低气温相关的冷(暖)指数序列中，存在明显的城市化影响。

本文在以前分析工作[15]的基础上，进一步比较分析华北地区国家站和乡村站极端气温指数的时

**收稿日期**：2013-06-21；**定稿日期**：2013-10-21
**资助项目**：公益性行业(气象)专项(GYHY201206012)；山西省科技攻关项目(20110311041)；山西省自然科学基金(2009011045-1)
**作者简介**：周雅清(1971－)，女，山西原平人，高级工程师，主要从事气候变化研究. E-mail：zhouyqsx@126.com

间演变特征，评价主要极端气温指数序列中的城市化影响性质和程度，为开展区域性气候变化监测和检测研究提供科学认识和基础资料。

## 2 资料和方法

### 2.1 研究区域和资料

所用国家站逐日最高、最低气温资料取自国家气象信息中心整编的近 50 年中国均一化历史气温数据集[31-32]，资料时段为 1961－2008 年，研究区域在 33°N－43°N，108°E－120°E 之间(图 1)。乡村站的选取依据任国玉等[33]地面气温参考站点遴选的原则和方法，并对乡村站中一般站资料按照国家站整编资料时采用的质量控制和均一化方法进行处理。根据序列长度不少于 48 年、缺测不超过 2% 的原则，选取国家站 84 个，乡村站 24 个，如图 1 所示。

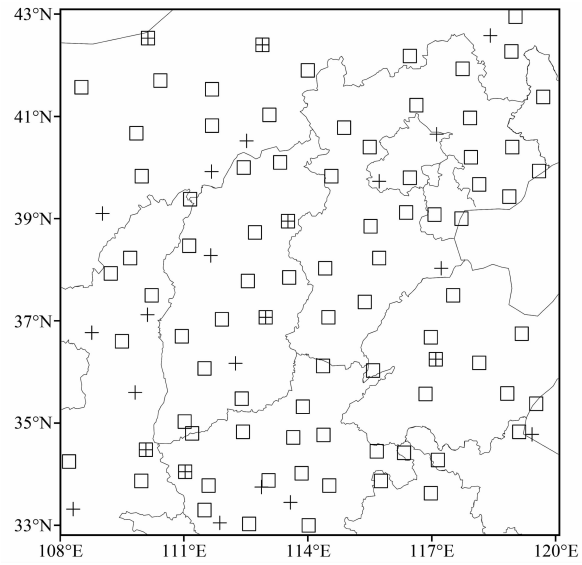


图 1 所选华北地区气象台站分布
方框为国家站，十字为乡村站

Fig. 1 Distribution of the selected weather stations in North China. Squares indicate the national stations and crosses are the rural stations

### 2.2 极端气温指数定义

采用的 12 个极端气温指数沿用 ETCCDMI(气候变化检测、监测和指数专家小组)的定义。以 1971－2000 年为参考期，使用 Rclimdex 软件[34]计算逐站极端气温指数时间序列和线性趋势，并对趋势的统计显著性进行评估。

将极端气温指数分为三种类型[12]。第一类是基于原始观测数据和固定阈值的指数，简称绝对指数，包括霜冻日数、夏季日数、结冰日数和炎热夜数。该 4 项指数中，当某站在 48 年中有 2/3 的年份没有出现某项极端气温事件记录时，该站不参与该项指数的趋势和时间序列的统计分析。在华北地区，霜冻日数和结冰日数不存在以上情况，夏季日数有 2 站，炎热夜数有 11 站符合以上条件，在相关指数计算中被剔除；第二类为日最高(低)气温的极值，简称极值指数，包括日最高(低)气温的极大(小)值；第三类为基于相对(浮动)阈值的指数，简称相对指数，包括冷昼(夜)、暖昼(夜)日数等。为了方便与其他研究结果的对比，将原来定义中超过(低于)上(下)阈值的百分比转换为超过(低于)上(下)阈值的日数。

### 2.3 分析方法

线性趋势的计算采用最小二乘法，趋势统计显著性检验采用 Kendall-Tau 非参数检验方法，气候突变检测采用 Mann-Kendall 方法[35-36](下称 M－K 检验)，判断城市化影响是否显著采用相关系数显著性检验[36]。华北地区区域平均极端气温指数时间序列参照 Jones 网格面积加权平均法[37]建立，经纬度网格为 2.5° × 2.5°。季节的划分采用春季(3－5 月)、夏季(6－8 月)、秋季(9－11 月)和冬季(12 月—次年 2 月)。

### 2.4 城市化影响

为了定量评价城市化对国家站极端气温指数变化趋势的影响，参照文献[25]定义下列术语。

城市化影响是指国家站极端气温指数线性趋势中城市热岛效应因素导致的变化，用 $\Delta X_{ur}$ 表示，即：

$$\Delta X_{ur} = X_u - X_r \quad , \tag{1}$$

其中：$X_u$ 为国家站极端气温指数的变化趋势；$X_r$ 为乡村站极端气温指数的变化趋势。

城市化影响贡献率是指通过显著性检验的城市化影响在国家站极端气温指数趋势变化中所占的比率，用 $E_u$ 表示，即：

$$E_u = | \Delta X_{ur}/X_u | \times 100\% = | (X_u - X_r)/X_u | \times 100\% \quad . \tag{2}$$

## 3 结果分析

### 3.1 极端气温指数趋势变化

利用上述资料和方法计算得到近 48 年华北地区极端气温指数的变化趋势，可见霜冻和结冰日数显著减少，夏季日数和炎热日数明显增加；极端最高(最低)气温的极大(极小值)都呈现出升高趋势；冷夜(昼)日数减少、暖夜(昼)日数增加。国家站

**表 1　1961－2008 年华北区域极端气温指数城市化影响年变化**

**Table 1　Urbanization effect on trends of extreme temperature indices in North China during 1961－2008**

| 指数类型 | 指数名称 | 指数代码 | 线性趋势 | | 城市化影响 | 城市化影响贡献率/% |
|---|---|---|---|---|---|---|
| | | | 国家站 | 乡村站 | | |
| 绝对指数 | 霜冻日数 | FD0 | －4.232＊＊ | －1.855＊＊ | －2.377＊＊ | 56.2 |
| | 夏季日数 | SU25 | 2.375＊＊ | 2.209 | 0.166 | － |
| | 结冰日数 | ID0 | －2.468＊＊ | －2.590＊＊ | 0.122 | － |
| | 炎热夜数 | TR20 | 2.298＊＊ | 0.459 | 1.839＊＊ | 80.0 |
| 极值指数 | 极端最高气温 | TXx | 0.051 | 0.084 | －0.033 | － |
| | 最低气温极大值 | TNx | 0.268＊＊ | 0.118＊ | 0.150＊＊ | 56.0 |
| | 最高气温极小值 | TXn | 0.338＊ | 0.300 | 0.038 | － |
| | 极端最低气温 | TNn | 0.615＊＊ | 0.225 | 0.390＊＊ | 63.4 |
| 相对指数 | 冷夜日数 | TN10p | －8.870＊＊ | －4.427＊＊ | －4.443＊＊ | 50.1 |
| | 冷昼日数 | TX10p | －3.440＊＊ | －3.291＊＊ | －0.149 | － |
| | 暖夜日数 | TN90p | 8.362＊＊ | 3.854＊＊ | 4.508＊＊ | 53.9 |
| | 暖昼日数 | TX90p | 4.076＊＊ | 4.308＊＊ | －0.232 | － |

注：绝对指数、相对指数的线性趋势和城市化影响的单位为 d·(10a)$^{-1}$；极值指数的线性趋势和城市化影响的单位为℃·(10a)$^{-1}$；＊、＊＊分别表示通过 0.05、0.01 显著性水平检验；“－”表示城市化影响未通过 0.05 显著性水平检验，则不计算城市化影响贡献率

的变化趋势与乡村站是同向的，对于大多数极端指数而言，国家站指数变化幅度要大(表 1)。

从绝对指数距平的时间演变(图 2)中可看出，霜冻日数在国家站和乡村站随时间都是减少的，国家站减少更显著；经 M－K 检验发现(图 3)，国家站霜冻日数从 20 世纪 80 年代开始呈现减少趋势，90 年代初减少趋势达到 0.05 显著性水平，1994 年前后出现突变点。乡村站则是90年代之前以波动

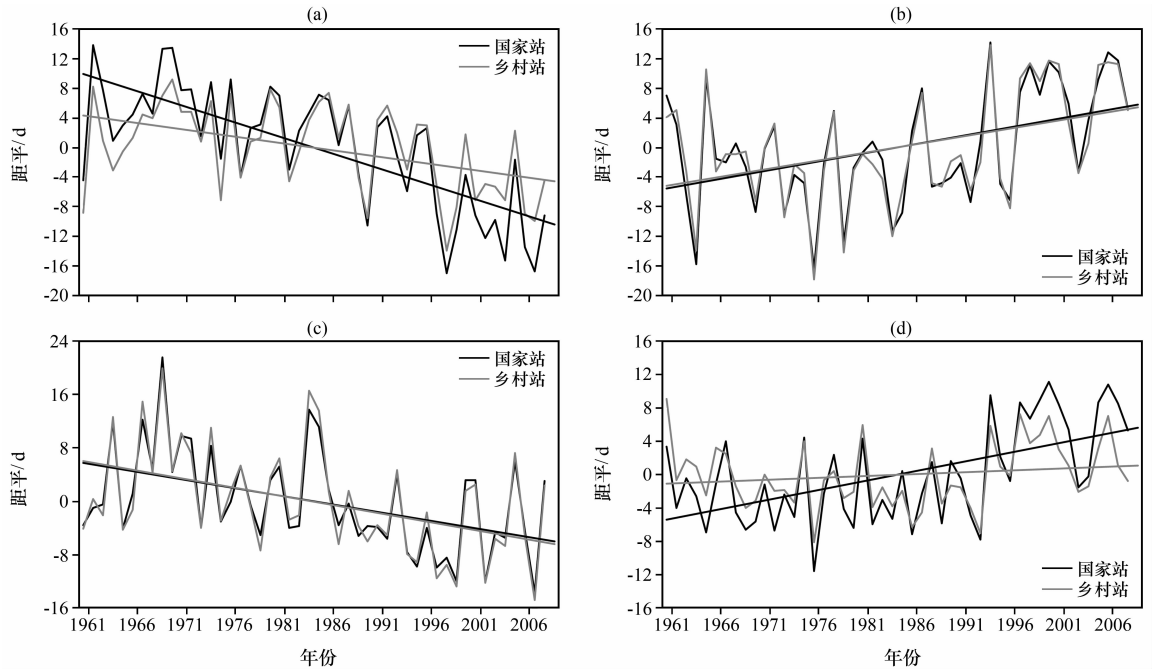


图 2　1961－2008 年华北地区国家站和乡村站绝对极端气温指数距平序列时间演变

(a) 霜冻日数，(b) 夏季日数，(c) 结冰日数，(d) 炎热夜数，直线为趋势线

Fig. 2　Anomalies of absolute indices of national stations and rural stations in North China during 1961－2008. (a) frost days, (b) summer days, (c) ice days, (d) tropical nights. Straight lines are linear trends

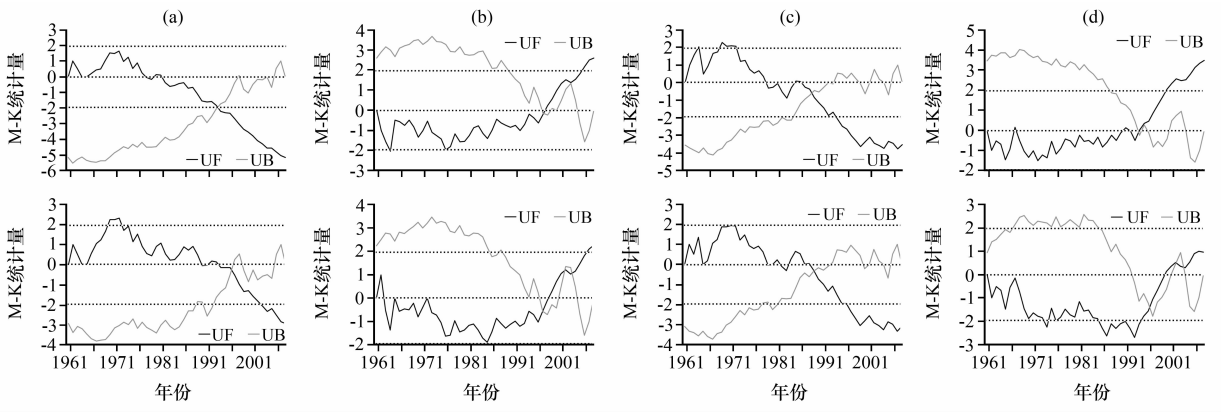


图 3 1961－2008 年华北地区国家站(上)和乡村站(下)绝对极端气温指数序列的 M－K 统计量曲线

(a) 霜冻日数,(b) 夏季日数,(c) 结冰日数,(d) 炎热夜数

Fig. 3 The Mann-Kendall abrupt detection of absolute indices of national stations(up) and rural stations(down) in North China during 1961－2008. (a) frost days, (b) summer days, (c) ice days, (d) tropical nights

变化为主,之后开始减少,21 世纪减少显著,1996 年前后存在突变。夏季日数是增多的趋势,国家站和乡村站时间演变基本一致,都是在 20 世纪 60－90 年代为振荡变化,90 年代末后发生多次突变,出现了增长趋势,但趋势都不显著。结冰日数在国家站和乡村站表现出一致的减少趋势,从 M－K 曲线看,两者 20 世纪 80 年代前趋势变化都不明显,从 80 年代后期开始减少,90 年代中期减少趋势达到 0.05 显著性水平,其突变点都出现在 1989 年前后。炎热夜数在国家站是增多趋势,从 20 世纪 90 年代中期突变后增多,21 世纪突破 0.05 显著性水平;在乡村站趋势不明显,从 M－K 的曲线也可以看出,21 世纪前期振荡变化,之后有一个上升趋势,但没有达到 0.05 显著性水平。

从极值指数距平的时间演变(图 4)和 M－K 统计值曲线(图 5)看,极端最高气温在国家站和乡村

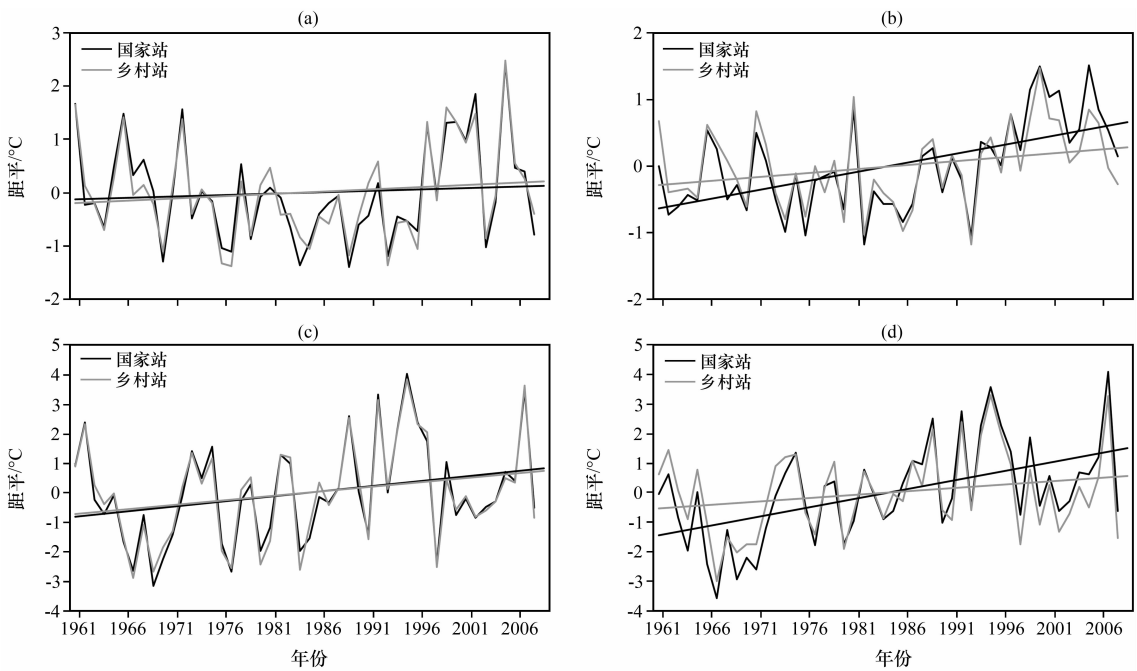


图 4 1961－2008 年华北地区国家站和乡村站极值指数距平时间演变

(a) 极端最高气温,(b) 最低气温极大值,(c) 最高气温极小值,(d) 极端最低气温,直线为趋势线

Fig. 4 Anomalies of extreme value indices of national stations and rural stations in North China during 1961－2008. (a) the maximum of daily maximum temperature $T_{max}$, (b) the maximum of daily minimum temperature $T_{min}$, (c) the minimum $T_{max}$, (d) the minimum $T_{min}$. Straight lines are linear trends

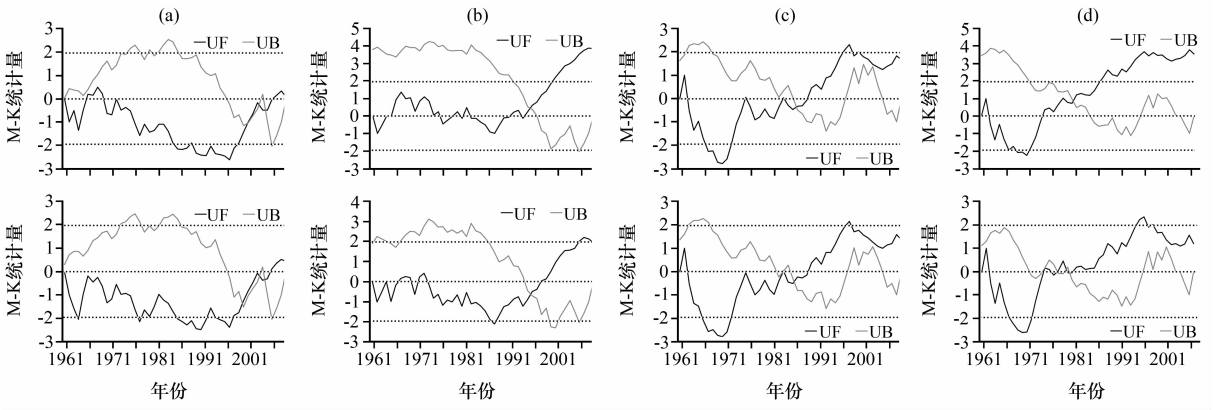


图 5　1961－2008 年华北地区国家站(上)和乡村站(下)极值指数的 M－K 统计量曲线

(a) 极端最高气温，(b) 最低气温极大值，(c) 最高气温极小值，(d) 极端最低气温

Fig. 5　The Mann-Kendall abrupt of extreme value indices of national stations(up) and rural stations(down) in North China during 1961－2008. (a) the maximum $T_{max}$, (b) the maximum $T_{min}$, (c) the minimum $T_{max}$, (d) the minimum $T_{min}$

站都没有明显变化趋势。最高气温极小值有弱的升高趋势，但基本未达到显著性水平。最低气温极大值在国家站和乡村站都有微弱上升，国家站上升趋势相对明显，开始上升的时间也偏早，从 20 世纪 90 年代中期开始呈增长趋势，进入 21 世纪后增长趋势明显，突变时间出现在 1994 年前后；乡村站则是从 20 世纪 90 年代后期开始增长，21 世纪增长趋势明显，突变时间也出现在 1994 年前后。极端最低气温在国家站自 20 世纪 70 年代以来升高，1981 年前后发生突变，80 年代后期升高趋势达到 0.05 显著性水平；在乡村站开始升高时间偏晚，且存在多个突变点，但大部分时段没有达到 0.05 显著性水平，其时间演变较国家站平缓得多。

从相对指数距平的时间演变(图 6)看，冷夜日数在国家站和乡村站都明显减少，但乡村站变化趋势较缓。根据M－K统计值曲线(图 7)可以看出，

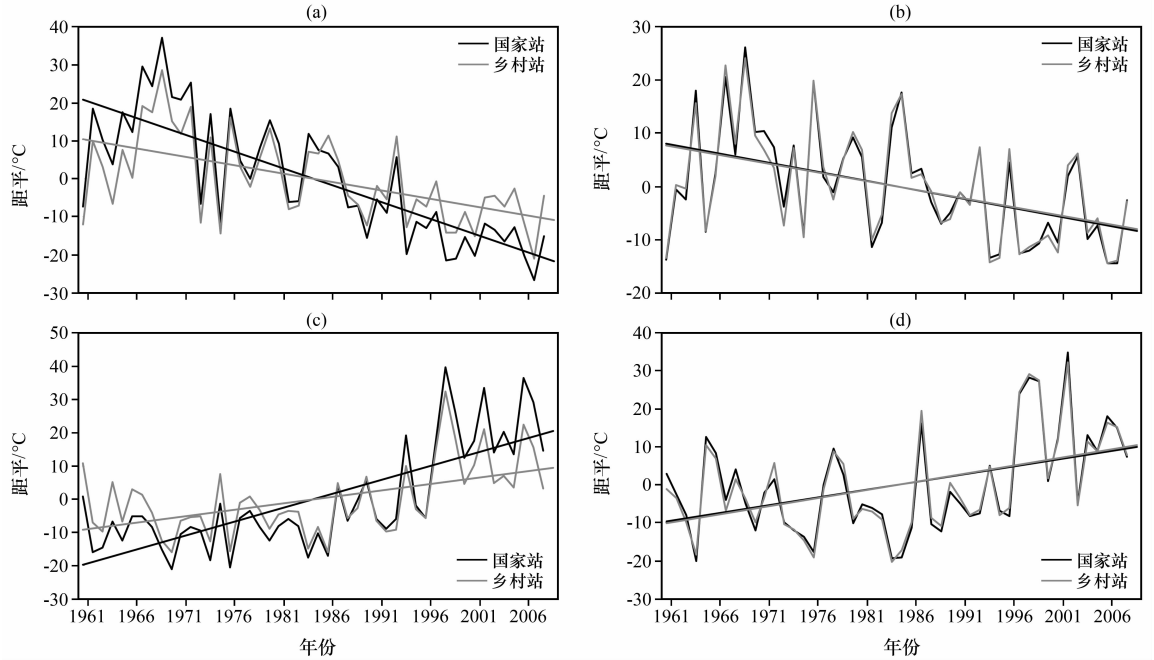


图 6　1961－2008 年华北地区国家站和乡村站相对指数距平时间演变

(a) 冷夜日数，(b) 冷昼日数，(c) 暖夜日数，(d) 暖昼日数，直线为趋势线

Fig. 6　Anomalies of relative indices of national stations and rural stations in North China during 1961－2008. (a) cool nights, (b) cool days, (c) warm nights, (d) warm days. Straight lines are linear trends

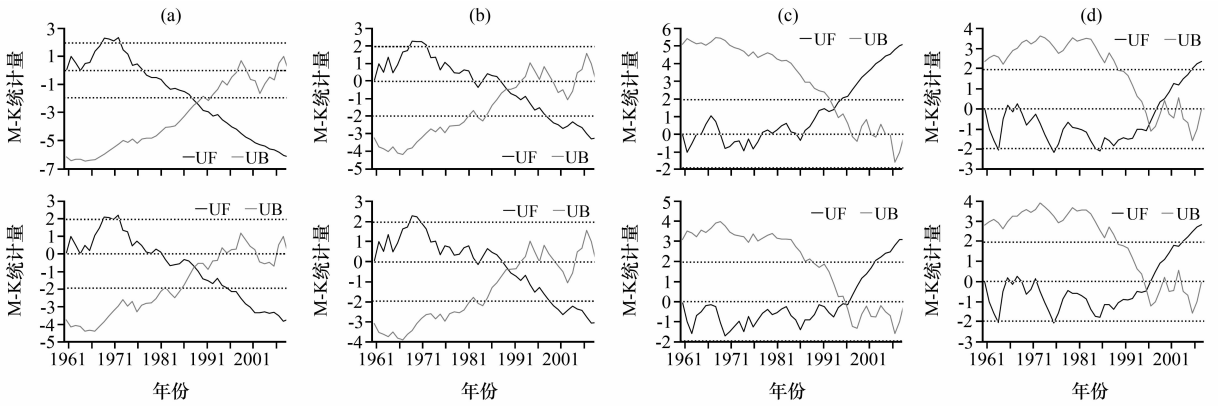


图 7 1961－2008 年华北地区国家站(上)和乡村站(下)相对指数的 M－K 统计量曲线
(a) 冷夜日数,(b) 冷昼日数,(c) 暖夜日数,(d) 暖昼日数

Fig. 7 The Mann-Kendall abrupt of relative indices of national stations(up) and rural stations(down) in North China during 1961－2008. (a) cool nights, (b) cool days, (c) warm nights, (d) warm days

国家站和乡村站冷夜日数都是从 20 世纪 70 年代减少，在 1989 年前后发生突变，但国家站冷夜日数减少自 80 年代后期就达到 0.05 显著性水平，而乡村站则是到 90 年代中期才达到 0.05 显著性水平。冷昼日数在国家站和乡村站随时间变化较为一致，都是自 20 世纪 80 年代后期开始减少，90 年代后期减少趋势显著，突变点都在 1989 年前后。暖夜日数为增加的趋势，在国家站是从 20 世纪 80 年代后期开始增加，1994 年前后出现突变，1995 年以后增加的趋势都达到 0.05 显著性水平；乡村站则是在 20 世纪 90 年代后期才开始增加，1997 年前后出现突变，进入 21 世纪后达到 0.05 显著性水平，显著增加的时间偏晚，且其增加趋势也比国家站弱。暖昼日数在国家站和乡村站都表现出明显的增加趋势，且两者的时间变化也较一致，都是从 20 世纪 90 年代后期开始增加，21 世纪以后达到 0.05 显著性水平，突变点在 1997 年前后。

综上所述，近 48 年华北区域极端暖指日数明显增加，冷指日数明显减少，而极端指数的极值都呈上升的趋势，与最低气温相关的指数的变化一般比与最高气温相关的指数变化要显著；国家站的时间变化趋势也较乡村站明显。气温指数中冷指数突变一般发生在 20 世纪 80 年代末，暖指数突变要晚一些，出现在 90 年代中后期。

### 3.2 国家站极端气温指数序列中的城市化影响

由上述分析可知，近 48 年华北区域国家站极端气温指数趋势变化一般较乡村站幅度更大。通过对比该区域内国家站和乡村站极端气温指数趋势的变化，期待定性、定量了解城市化对华北极端气候变化的影响，为进一步检测、识别中国以及更大区域极端气候变化原因进行试验性研究。

从表 1 中还可看出，绝对指数中国家站霜冻日数减少比乡村站明显，城市化影响为负值，城市化影响贡献率为 56.2%，表明城市化加剧了霜冻日数的减少，国家站霜冻日数的减少有一半以上是由城市化造成的。国家站夏季日数增加比乡村站明显，城市化影响为正值，但未达到 0.05 显著性水平，表明城市化对夏季日数影响不显著。国家站结冰日数和乡村站差异不大，城市化影响也不显著。国家站炎热夜数明显增多，乡村站变化不大，城市化影响为正值，城市化影响为 80%，表明国家站炎热夜数的增多有 80% 是由城市化影响增强导致的。

就极值指数而言，在国家站和乡村站极端最高气温和最高气温极小值趋势变化差异不大，城市化影响都不明显。最低气温极大值和极端最低气温的城市化影响为正值，贡献率分别为 56% 和 63.4%，表明最低气温受城市化影响较大，其极值的升高有 6 成左右是城市化影响造成的。

就相对指数而言，冷(暖)夜日数的城市化影响都显著，城市化影响贡献率都在 50% 以上，表明城市化使冷夜日数的减少和暖夜日数的增多更显著，而冷(暖)昼日数的趋势变化中没有检测到明显的城市化影响。

综上所述，城市化加剧了冷指日数的减少和暖指日数的增加，同时也使最低气温的极值明显升高。与最低气温相关的指数城市化影响较与最高气温相关的要显著许多，其城市化影响贡献率都在 50% 以上，且都达到 0.01 显著性水平。这说明在

**表 2　1961－2008 年华北区域城市化影响代表台站个例分析**

**Table 2　Case analysis of the urbanization effect in North China during 1961－2008**

| 测站 | 经度/°E | 纬度/°N | 变化趋势 | | | | | | | | | | | |
|---|---|---|---|---|---|---|---|---|---|---|---|---|---|---|
| | | | 绝对指数/[d·(10a)$^{-1}$] | | | | 极值指数/[℃·(10a)$^{-1}$] | | | | 相对指数/[d·(10a)$^{-1}$] | | | |
| | | | 霜冻日数 | 夏季日数 | 结冰日数 | 炎热夜数 | 极端最高气温 | 最低气温极大值 | 最高气温极小值 | 极端最低气温 | 冷夜日数 | 冷昼日数 | 暖夜日数 | 暖昼日数 |
| 北京 | 116.47 | 39.80 | −4.33* | 2.44* | −2.39* | 4.15* | 0.24 | 0.21* | 0.43* | 0.95* | −13.21* | −4.64* | 10.91* | 7.08* |
| 霞云岭 | 115.73 | 39.73 | 0.12 | 1.72 | −2.61* | −2.32* | 0.09 | −0.10 | 0.40 | 0.18 | 1.17 | −3.10* | −1.79 | 5.62* |
| 上甸子 | 117.12 | 40.65 | −1.10 | 1.99 | −3.67* | −0.84 | 0.29 | −0.01 | 0.38 | 0.06 | −0.29 | −2.74 | 2.08 | 6.97* |
| 太原 | 112.55 | 37.78 | −4.14* | 3.7* | −3.51* | 1.67* | 0.28* | 0.33* | 0.09 | 0.65* | −8.87* | −5.15* | 9.82* | 7.08* |
| 岚县 | 111.65 | 38.28 | −1.26 | 3.37* | −5.03* | − | 0.25 | 0.24* | 0.36 | −0.18 | −4.85* | −4.74* | 2.63* | 6.97* |
| 五台山 | 113.52 | 38.95 | −2.38* | − | −1.94* | − | 0.19 | 0.07 | 0.78* | 1.01* | −5.73* | −2.12 | 4.56* | 4.45* |
| 呼和浩特 | 111.68 | 40.82 | −5.44* | 3.85* | −3.96* | 2.08* | 0.20 | 0.57* | 0.27 | 1.25* | −15.95* | −4.75* | 13.51* | 7.08* |
| 凉城 | 112.52 | 40.52 | −3.06* | 3.42* | −2.99* | − | 0.08 | 0.13 | 0.08 | 0.06 | −8.03* | −4.42* | 5.77* | 5.66* |
| 朱日和 | 112.90 | 42.40 | −3.41* | 3.19* | −3.56* | 1.62* | 0.25 | 0.32* | 0.46 | 0.67* | −8.54* | −3.65* | 6.64* | 3.91* |

注：“－”表示该台站没有该项指数，＊表示达到 0.05 显著性水平

华北区域国家站与最低气温相关的气温极端指数的变化中，城市化影响显著，如果剔除城市化的影响，这些指数的变化幅度将显著减小。而与最高气温相关的指数中未检测出明显的城市化影响。

选取华北区域 3 个大城市站为代表，分析其与周围乡村站极端指数的差异(表 2)。从表 2 中可看出，城市站绝对指数中冷指数明显减少，暖指数明显增加，对应的乡村站大致也呈现相应变化，但变化幅度大部分相对要小；城市站极值指数均为上升趋势，且大部分达到 0.05 显著性水平，而对应的乡村站虽然也以上升趋势为主，但大部分没有达到 0.05 显著性水平，其增幅一般比城市站小；相对指数城乡差异尤其明显，城市站冷昼(夜)明显减少，暖昼(夜)显著增多，其增(减)趋势都达到 0.05 显著性水平；乡村站冷昼(夜)和暖昼(夜)变化与城市站基本一致，但趋势明显比城市站弱。

考察极端指数线性趋势的四季变化发现(图略)，国家站极值指数除夏季最高气温极小值略降低外，其余均为升高趋势，与最低气温相关的指数所有季节的变化趋势都达到 0.01 显著性水平，而与最高气温相关的指数仅秋季的极端最高气温和冬季的最高气温极小值分别达到 0.01 和 0.05 显著性水平。乡村站极值指数四季变化与国家站基本相似，但通过显著性检验的比国家站少，与最低气温相关的指数升高幅度较国家站小。

国家站相对指数冷指数明显减少，暖指数明显增多，与最低气温相关的指数所有季节的变化趋势都达到 0.01 显著性水平，与最高气温相关的指数除夏季冷(暖)昼日数外，其余都达到 0.05 显著性水平。乡村站除夏季冷昼日数增多外，其余指数的四季变化与国家站相似，冷(暖)夜变化趋势较国家站弱。

从城市化影响(表 3)中可看出，极值指数中极端最高气温城市化影响四季均为负值，但仅冬季达到 0.05 显著性水平。最高气温极小值城市化影响以正值为主，仅春季达到 0.05 显著性水平。最低气温极大值的城市化影响四季均为正值，除秋季以外，其余季节城市化影响均达到 0.01 显著性水平。极端最低气温城市化影响都是正值，且都达到 0.01 显著性水平。极值指数城市化增温效应春、冬季相对显著。

相对指数中冷(暖)昼日数的城市化影响仅夏季达到 0.05 显著性水平。而冷(暖)夜日数四季城市化影响都达到 0.01 显著性水平。冷夜日数城市化影响冬季最大，春、秋季次之，但城市化影响贡献率以秋季最大，达 62.6%，表明秋季冷夜日数的减少有 6 成以上是由城市化增温效应造成的；暖夜日数城市化影响则是夏季最显著。值得注意的是，城市化对夏季暖昼日数的增加起到明显的抑制作用。究其原因，考虑与城市热岛环流导致上升气流加强、城市污染严重、上空含有较多凝结核等导致市区云量多、白天最高温度升不上去有关。

综上所述，国家站极值指数四季变化基本以升高趋势为主，相对指数则是冷指日数减少、暖指日

表 3 1961－2008 年华北区域极值指数和相对指数城市化影响四季变化

Table 3 Urbanization effects for seasonal extreme value index and relative index in North China during 1961－2008

| 极值指数 | 季节 | 城市化影响 /[℃·(10a)$^{-1}$] | 城市化影响贡献率/% | 相对指数 | 季节 | 城市化影响 /[d·(10a)$^{-1}$] | 城市化影响贡献率/% |
|---|---|---|---|---|---|---|---|
| 极端最高气温 | 春季 | －0.069 | － | 冷夜日数 | 春季 | －4.643** | 51.9 |
| | 夏季 | －0.050 | － | | 夏季 | －2.981** | 44.0 |
| | 秋季 | －0.057 | － | | 秋季 | －4.593** | 62.6 |
| | 冬季 | －0.099* | －33.3 | | 冬季 | －4.977** | 36.9 |
| 最低气温极大值 | 春季 | 0.218** | 75.2 | 冷昼日数 | 春季 | －0.219 | － |
| | 夏季 | 0.118** | 48.0 | | 夏季 | －0.746** | 100.0 |
| | 秋季 | 0.070 | － | | 秋季 | 0.051 | － |
| | 冬季 | 0.154** | 24.7 | | 冬季 | 0.151 | － |
| 最高气温极小值 | 春季 | 0.079* | 34.3 | 暖夜日数 | 春季 | 5.068** | 52.7 |
| | 夏季 | 0.011 | － | | 夏季 | 5.503** | 69.8 |
| | 秋季 | －0.004 | － | | 秋季 | 3.871** | 54.7 |
| | 冬季 | 0.012 | － | | 冬季 | 3.552** | 38.6 |
| 极端最低气温 | 春季 | 0.383** | 80.3 | 暖昼日数 | 春季 | －0.469 | － |
| | 夏季 | 0.242** | 41.7 | | 夏季 | －0.825* | －39.6 |
| | 秋季 | 0.212** | 30.7 | | 秋季 | 0.354 | － |
| | 冬季 | 0.343** | 48.0 | | 冬季 | 0.071 | － |

注：*、**分别表示达到 0.05 和 0.01 显著性水平；“－”表示城市化影响未达到 0.05 显著性水平的不计算城市化影响贡献率

数增多，与最低气温相关的指数变化更为显著。城市化对与最高气温相关的指数影响不明显，却显著加剧了与最低气温相关的指数变化趋势，极值指数和冷夜日数城市化增温效应一般在春、冬季更明显，冬季气候逐渐变得温和，冷(暖)昼日数和暖夜日数则是夏季受城市化影响更显著。

## 4 结论和讨论

利用经过非均一性检验和订正的华北区域 84 个国家站和 24 个乡村站逐日最高、最低气温，分析了 1961－2008 年该区域极端气温指数的变化趋势及城市化影响对这些指数的影响情况，得到以下主要结论：

(1) 极端暖指日数明显增加，冷指日数明显减少，而极端指数的极值都呈上升趋势，与最低气温相关的指数变化一般比与最高气温相关的指数变化要显著；国家站的时间变化趋势也较乡村站明显。气温指数中冷指数突变一般发生在 20 世纪 80 年代末，暖指数突变要晚一些，在 90 年代中后期。

(2) 从年变化来看，城市化加剧了冷指日数的减少和暖指日数的增加，同时也使最低气温的极值明显升高。与最低气温相关的指数城市化影响较与最高气温相关的要显著许多，其城市化影响贡献率都在 50% 以上，且都达到 0.01 显著性水平。这说明在华北地区国家站与最低气温相关的气温极端指数变化中，城市化影响显著，如果剔除城市化的影响，这些指数的变化幅度将显著减小。而与最高气温相关的指数中未检测出明显的城市化影响。

(3) 从四季变化来看，国家站极值指数四季变化基本以升高趋势为主，相对指数则是冷指日数减少，暖指日数增多，与最低气温相关的指数变化更为显著。城市化对与最高气温相关的指数影响不明显，却显著加剧了与最低气温相关的指数的变化趋势，极值指数和冷夜日数城市化增温效应一般在春、冬季更明显，冷(暖)昼日数和暖夜日数则是夏季受城市化影响更显著。

从 Zhou et al[15] 和本文的研究都可以看出，华北地区与最低气温相关的极端气温指数变化趋势中存在明显的城市化影响。城市热岛增强效应使得该区域冷指日数的减少和暖指日数的增加更加明显，并使得最低气温的极值显著升高。与 Zhou et al[15] 研究结果相比，本文城市化影响在数值上略有差异，主要原因在于本文计算各指数区域平均的趋势的方法与前者不同。本文是先将逐站指数的时间序

列区域平均后求取趋势作为区域的趋势，而 Zhou et al[15] 则是将逐站各指数的趋势直接区域平均得到整个区域的趋势。

根据本文结论，华北区域国家站与最低气温相关的极端气温指数的年变化趋势中城市化影响贡献率都在 50% 以上，如果去掉城市热岛影响，那么这部分极端气温指数的变化将明显减弱。需要指出的是，由于作为背景站的乡村站选取非常困难，真正没有受到城市化影响的台站很少，目前能够做到的只能是尽最大可能，选择那些代表性相对较好的站点，但一些参考站仍不可避免地坐落于乡镇甚至小城市等居民区附近，其气候也不免要受到一些城市化的影响。因此本文给出的国家站极端气温变化中城市热岛增温贡献率只是最低估计值。准确估计城市化对区域极端气温序列的影响还需要进一步深入研究。

## 参考文献：


[1] IPCC. Climate Change 2007. The Physical Science Basis[R]. Solomon S, Qin D, Manning M, et al. eds. Cambridge, UK and New York, USA: Cambridge University Press, 2007: 996.

[2] 气候变化国家评估报告编委会. 气候变化国家评估报告[M]. 北京：科学出版社, 2007：80－105.

[3] Alexander L V, Zhang X, Peterson T C, et al. Global observed changes in daily climate extremes of temperature and precipitation [J]. J Geophys Res, 2006, 111, D05109, doi:10.1029/2005JD006290.

[4] Alexander L V, Tapper N, Zhang X, et al. Climate extremes: Progress and future directions[J]. Int J Climatol, 2009, 29: 317－319.

[5] Zhang X, Zwiers F W, Hegerl G C, et al. Detection of human influence on twentieth-century precipitation trends[J]. Nature, 2007, 448: 461－465.

[6] Choi G, Collins D, Ren G, et al. Changes in means and extreme event s of temperature and precipitation in the Asian－Pacific network region, 1955－2007[J]. Int J Climatol, 2009, 29(13): 1906－1925.

[7] Zhai P, Pan X. Trends in temperature extremes during 1951－1999 in China[J]. Geophys Res Lett, 2003, 30, doi: 10.1029/2003 Gl018004.

[8] 胡宜昌，董文杰，何勇. 21 世纪初极端天气气候事件研究进展[J]. 地球科学进展, 2007, 22(10): 1066－1075.

[9] 丁一汇，任国玉. 中国气候变化科学概论[M]. 北京：气象出版社, 2008：281.

[10] 郭军，任国玉，任雨. 近 100 年天津平均气温与极端气温变化[J]. 高原气象, 2011, 30(5): 1399－1405.

[11] 陈少勇，王劲松，任燕，等. 近49 年中国西北地区极端低温事件的演变特征[J]. 高原气象, 2011, 30(5): 1266－1273.

[12] 周雅清，任国玉. 中国大陆 1956－2008 年极端气温事件变化特征分析[J]. 气候与环境研究, 2010, 15(4): 405－417.

[13] 任国玉，封国林，严中伟. 中国极端气候变化观测研究回顾与展望[J]. 气候与环境研究, 2010, 15(4): 337－353.

[14] Ren G, Chen Y, Zou X, et al. Change in climatic extremes over mainland China based on an integrated extreme climate index[J]. Climate Res, 2011, 50: 113－124, doi: 10.3354/cr01023.

[15] Zhou Y, Ren G. Change in extreme temperature event frequency over mainland China, 1961－2008[J]. Climate Res, 2011, 50: 125－139, doi: 10.3354/cr01053.

[16] 段春锋，缪启龙，曹雯，等. 以高山站为背景研究城市化对气温变化趋势的影响[J]. 大气科学, 2012, 36(4): 811－822.

[17] 任国玉，初子莹，周雅清，等. 中国气温变化研究最新进展[J]. 气候与环境研究, 2005, 10(4): 701－716.

[18] Jones P D, Groisman P Y, Coughlan M, et al. Assessment of urbanization effects in time series of surface air temperature over land[J]. Nature, 1990, 347: 169－172.

[19] Peterson T C. Assessment of urban versus rural in situ surface temperatures in the contiguous United States: No difference found [J]. J Climate, 2003, 16(18): 2941－2959.

[20] Kalnay E, Cai M. Impact of urbanization and land－use change on climate[J]. Nature, 2003, 423: 528－531.

[21] Ren G, Zhou Y, Chu Z, et al. Urbanization effect on observed surface air temperature trend in North China[J]. J Climate, 2008, 21(6): 1333－1348.

[22] 郑祚芳，高华，王在文，等. 北京地区降水空间分布及城市效应分析[J]. 高原气象, 2014, 33(2): 522－529, doi: 10.7522/j.issn.1000-0534.2012.00193.

[23] 初子莹，任国玉. 北京地区城市热岛强度变化对区域温度序列的影响[J]. 气象学报, 2005, 63(4): 534－540.

[24] 周雅清，任国玉. 华北地区地表气温观测中城镇化影响的检测和订正[J]. 气候与环境研究, 2005, 10(4): 743－753.

[25] 周雅清，任国玉. 城市化对华北地区最高、最低气温和日较差变化趋势的影响[J]. 高原气象, 2009, 28(5): 1158－1166.

[26] 李书严，陈洪滨，李伟. 城市化对北京地区气候的影响[J]. 高原气象, 2008, 27(5): 1102－1110.

[27] 白虎志，任国玉，张爱英，等. 城市热岛效应对甘肃省温度序列的影响[J]. 高原气象, 2006, 25(1): 90－94.

[28] 张爱英，任国玉，周江兴，等. 中国地面气温变化趋势中的城市化影响偏差[J]. 气象学报, 2010, 68(6): 957－966.

[29] 杜予罡，唐国利，王元. 近 100 年中国地表平均气温变化的误差分析[J]. 高原气象, 2012, 31(2): 456－462.

[30] 张雷，任国玉，刘江，等. 城市化对北京气象站极端气温指数趋势变化的影响[J]. 地球物理学报, 2011, 54(5): 1150－1169.

[31] Liu X N, Li Q X. Research of the inhomogeneity test of climatological data series in China[J]. Acta Meteor Sini, 2003, 17(4): 492－502.

[32] Li Q X, Liu X N, Zhang H Z, et al. Detecting and adjusting temporal inhomogeneity in Chinese mean surface air temperature data[J]. Adv Atmos Sci, 2004, 21(2): 260－268.

[33] 任国玉，张爱英，初子莹，等. 我国地面气温参考站点遴选的依据、原则和方法[J]. 气象科技, 2010, 38(1): 79－85.

[34] Zhang X B, Yang F. RClimDex (1.0) user manual[Z]. http://cccma.seos.uvic.ca/ETCCDI/software.shtml, 2004.
[35] Von Storch H, Zwiers F W. Statistical analysis in climate research[M]. New York: Cambridge University Press, 2003: 484.
[36] 魏凤英. 现代气候统计诊断与预测技术[M]. 第2版. 北京: 气象出版社, 2007.
[37] Jones P D, Hulme M. Calculating regional climatic time series for temperature and precipitation: Methods and illustrations[J]. Int J Climatol, 1996, 16: 361 - 377.

# Urbanization Effect on Long - Term Trends of Extreme Temperature Events in North China

ZHOU Yaqing[1], REN Guoyu[2]

(1. *Jinzhong Meteorological Bureau of Shanxi Province*, *Jinzhong* 030600, *China*;
2. *Laboratory for Climate Studies*, *National Climate Center*, *China Meteorological Administration*, *Beijing* 100081, *China*)

**Abstract**: An analysis of urbanization effect on the long-term trends of extreme temperature events as observed from the national meteorological stations over North China is made in the period of 1961 －2008. It is found that the minimum-related extreme temperature indices of both the national stations and the rural stations exhibit statistically significant trends, but those from the national stations are more significant. The abrupt shifts of the cold extreme temperature indices generally occur in 1980s, and those of the warm extreme temperature indices mostly occur in middle to late 1990s. Urbanization leads to significant decrease(increase) in days of cold(warm) extreme indices and significant increase in extreme values of minimum temperature for the national stations. More significant urbanization effects are registered for the extreme indices related to minimum temperature than for those related to maximum temperature, with the urbanization contributions for the formers all above 50%. Urbanization effects on trends of extreme value indices and cold nights are generally larger in spring and wintertime. Changes in cold(warm) days and warm nights due to urbanization, however, are more significant in summertime.

**Key words**: Extreme temperature indices; Urbanization effect; Maximum temperature; Minimum temperature

# 冬季大气遥相关和海温关键区的复杂网络性质*

左冬冬[1)] 龚志强[2)†] 冯爱霞[3)] 支蓉[2)]

1) (扬州大学物理科学与技术学院, 扬州 225002)

2) (国家气候中心气候研究开放实验室, 北京 100081)

3) (国家气象信息中心资料服务室, 北京 100081)

( 2013 年 10 月 14 日收到; 2013 年 11 月 6 日收到修改稿 )

基于大气遥相关指数和海表温度关键区, 以各关键区高度场平均值和海表温度关键区平均值之间的相关系数作为连边条件, 建立体现大气遥相关和海表温度关键区相互作用的关联网络, 进而给出了大气和海洋关键区相互作用的空间图像. 同时基于网络的结构特征量, 研究了该网络的基本性质, 给出了关键区中的网络关键节点, 并分析了关键节点对网络性质的影响. 研究结果表明: 大气遥相关和海温关键区关联网络具有一定的小世界性质, 即网络具有小的平均路径长度和较大的集群系数; 网络的平均路径长度在阈值为 0.1—0.4 时系统基本保持稳定, 即网络的性质保持不变, 进而证明了以信度为 0.01 下的相关系数 0.19 作为连边阈值的有效性. 对于网络中的单个节点网络特征分析发现, 东亚-太平洋遥相关 1 区和 2 区以及太平洋-北美遥相关 1 区和 4 区在网络中具有较大的节点度, 即大气中这 4 个区域在大气遥相关和海表温度关键区中作用较强; 北太平洋涛动区域 1, 东亚-太平洋遥相关区域 3 的节点度则相对最小, 即这个区域在大气遥相关和海表温度关键区相互作用中的影响较小. 通过依次去除网络中度大的节点进一步证明了网络具有一定的鲁棒性. 该研究对于重点把握遥相关和海温的一些重要区域具有一定指示意义, 也从另一角度提供了研究海气相互作用新方法.

**关键词**: 关联网络, 遥相关区域, 海洋关键区域

**PACS:** 92.60.Wc **DOI:** 10.7498/aps.63.049201

## 1 引 言

自 Wattsk 和 Strogatz[1] 在《Nature》杂志上发表关于小世界 (small world) 网络以及 Barabasi 和 Albert[2] 在《Science》上发表“无标度网络”以来, 近十几年间, 全球范围内开展了复杂网络的相关研究. 该方法为其他学科提供了一种看问题的全新视角. 一些科研工作者将复杂网络的理论与方法成功地运用到其他学科领域 [3,4] 来研究复杂现象, 例如: 生物网、因特网、社会网等, 并取得了许多的成果.

由于气候系统的非线性和复杂性, 对该系统的研究具有挑战性. 目前气象工作者对该方向的研究已经取得了丰硕的成果 [5−15]. 复杂网络的发展为复杂科学问题研究提供了一种全新的视角, 为此许多气象工作者也利用该方法来研究气象上的一些问题, 也取得了不少的进展. 如: Tsonis 等 [16−18] 利用太平洋十年涛动 (Pacific decadal oscillation, PDO), 北大西洋涛动 (the North Atlantic oscillation, NAO), 厄尔尼诺/南方涛动 (the El Nino/southern oscillation, ENSO) 和北太平洋涛动 (the north pacific oscillation, NPO) 的指数来构建网络, 研究了它们之间的同步协调关系; Yamasaki 等 [19] 研究了 La Nina 事件对全球温度关联网的影响; 龚自强等 [20,21] 研究了基于环流系统关联网的北半球各种遥相关年代际尺度的变化特征和全球温度关联网络动力学统计性质; 王晓娟等 [22] 研究了极端事件对温度关联网络稳定性的影响; Feng

* 国家重点基础研究发展计划 (批准号: 2012CB955903) 和国家自然科学基金 (批准号: 41205040, 41105055) 资助的课题.

† 通讯作者. E-mail: gzq0929@126.com

© 2014 中国物理学会 Chinese Physical Society 

等[23]研究了海气双层网络的拓扑结构和动力行为.

目前已经有较多有关遥相关和海温场关键区域的研究, 应用的方法比较多[24−26], 而利用复杂网络研究气象问题却更多的是从单层面、单节点上来分析单个要素的网络行为特征. 气候系统往往更多的是区域之间的相互影响、相互作用, 不仅是单个节点上的相互作用, 构建区域之间网络更能体现出一种稳定的、更深层次上的相互作用关系, 通过对这种区域构建的网络来理解它们之间的动力学行为. 而在复杂的气候系统中大气中的遥相关和海洋中的一些具有指示意义的海洋区域常是受关注较多的, 而某个遥相关常包含多个区域, 在相互作用中并不是所有的区域都发挥着相当的作用地位, 而是一些区域影响较大, 一些区域影响较小. 因此本文根据文献[27]提出的遥相关指数, 按照遥相关指数定义选取该遥相关的代表的区域与海洋中的一些关键区建立连接, 来理解它们的空间结构特征, 并比较这些区域对网络性质的影响, 从而从网络这一层面上加强对遥相关和海洋关键区域的理解.

## 2 资料与方法

### 2.1 资 料

高度场(500 hPa)、海平面气压场资料来源[28]是NCEP再分析格点逐月月平均资料, 分辨率为2.5° × 2.5°; 海温场的资料来源[29]是NOAA格点逐月月平均资料, 分辨率为2° × 2°. 时间都为1953年12月至2013年2月, 由于环流系统中的各种遥相关在冬季相对更稳定, 为此只分析12月至2月即冬季构成的时间序列.

### 2.2 研究方法

根据Wallace和Gutzler[27]提及的遥相关, 选取其中比较典型的6个遥相关分别为: NAO, NPO, 东亚/太平洋遥相关 (the east Asia/Pacific, EAP)、太平洋/北美遥相关 (the Pacific/north American pattern, PNA)、西大西洋遥相关(the western Atlantic pattern, WA)、欧亚遥相关(the Eurasian pattern, EU). 按照各遥相关的指数定义选取出各遥相关类型的代表区域, 共16个. 另外在海洋上选取常关注的7 个区域分别为: 北印度洋(north Indian Ocean, NIO)、西太平洋(west Pacific, WP)、赤道中东太平洋(middle east Pacific, MEP)、北太平洋(north Pacific, NP)、北大西洋(north Atlantic, NA)、大西洋赤道区域(equatorial Atlantic, EA)、南大西洋(south Atlantic, SA). 表1给出了上述23个区域的经纬度区间.

根据表1列出的各区域范围求出该范围内所对应要素的平均值, 构成区域平均的时间序列$H_i(j)$, 并对该序列进行标准化, 计算公式如下:

$$H_i'(j)=\frac{H_i(j)-\langle H_i\rangle}{\sqrt{\langle H_i^2\rangle-\langle H_i\rangle^2}}, \tag{1}$$

其中$H_i(j)$表示$i$区域的时间序列第$j$个值, $\langle H_i\rangle$为$i$区域的时间序列的平均值. 利用标准化后的时间序列数据计算任意两个区域的相关系数$C_{ij}$为

$$C_{ij}=\frac{1}{180}\sum_{k=1}^{180}H_i'(k)H_j'(k), \tag{2}$$

$C_{ij}$的范围为 $-1\leqslant C_{ij}\leqslant 1$, $C_{ij}=1$表示完全正相关, $C_{ij}=-1$表示完全负相关, $C_{ij}=0$表示不相关. 把区域看成网络的节点, 通过(2)式计算两两区域间的相关系数$C_{ij}$, 利用$C_{ij}$的绝对值大小是否超过指定的阈值作为判断两节点之间是否存在连边的条件, 这样便建立起23个区域之间的关联网络.

对网络的分析, 通常借助网络性质的统计量[30,31], 通过计算统计量的大小并结合网络的特性进行分析, 为此下文将逐个介绍常见的几个网络特征量.

节点度计算公式如下:

$$k_i=\sum_j a_{ij}, \tag{3}$$

其中, $a_{ij}$为网络的邻接矩阵的元素, 描述$i$, $j$两节点是否存在连接, $a_{ij}=1$表示点$i$和点$j$之间存在连边, 反之则无. 度在网络中代表节点在网络中的影响力或重要程度, 度越大表征其影响力越大, 在整个网络中的作用越强, 反之亦然.

网络的平均路径长度计算公式如下:

$$\langle l\rangle=\frac{2}{N(N+1)}\sum_{i\geqslant j}d_{ij}, \tag{4}$$

其中, $N$为网络的节点总数, $d_{ij}$表示$i$节点到$j$节点的最短路径长度. 平均路径长度描述了网络中任意两节点之间的距离平均值, 用来描述网络的传输效率.

表 1 类似于大气遥相关和部分海洋区域计算范围

| | 区域 1 | 区域 2 | 区域 3 | 区域 4 |
|---|---|---|---|---|
| | | | 大气部分 | |
| NAO | W35°—W5° | W35°—W5° | | |
| | N55°—N75° | N20°—N40° | | |
| NPO | E155°—W175° | E150°—180° | | |
| | N55°—N75° | N15°—N35° | | |
| EAP | E110°—E140° | E110°—E140° | E110°—E140° | |
| | N10°—N30° | N30°—N50° | N50°—N70° | |
| PNA | W175°—W145° | 180°—W150° | W130°—W100° | W100°—W70° |
| | N10°—N30° | N35°—N55° | N45°—N65° | N20°—N40° |
| WA | W70°—W40° | W70°—W40° | | |
| | N45°—N65° | N20°—N40° | | |
| EU | E5°—E35° | E60°—E90° | E130°—E160° | |
| | N45°—N65° | N45°—N65° | N30°—N50° | |
| | | | 海洋部分 | |
| NIO | E70°—E100° | | | |
| | S15°—N15° | | | |
| WP | E135°—E165° | | | |
| | S10°—N10° | | | |
| MEP | W150°—W90° | | | |
| | S5°—N5° | | | |
| NP | E175°—W135° | | | |
| | N40°—N50° | | | |
| NA | W45°—W15° | | | |
| | N50°—N60° | | | |
| EA | W45°—W15° | | | |
| | S10°—N10° | | | |
| SA | W30°—0° | | | |
| | S40°—S25° | | | |

注: 例如 PNA 的指数定义为: $\mathrm{PNA}=1/(4[z^*(20°\mathrm{N},160°\mathrm{W})-z^*(45°\mathrm{N},165°\mathrm{W})+z^*(55°\mathrm{N},115°\mathrm{W})-z^*(30°\mathrm{N},85°\mathrm{W})])$, 根据该指数定义中所包含的 4 项, 分别以该 4 项对应的经纬度为中心选取 4 个区域.

节点的集群系数计算公式:

$$C_i=\frac{2E_i}{k_i(k_i-1)}, \tag{5}$$

其中, $E_i$ 表示与 $i$ 节点连接的两节点也相连接的个数, $k_i$ 为 $i$ 节点的度大小. 整个网络的集群系数 $C$ 是各节点的集群系数的平均值, 显然 $0\leqslant C\leqslant 1$, $C=0$ 表示当且仅当所有的节点均为孤立节点, 即没有任何连接边; $C=1$ 表示当且仅当网络是全局耦合的, 即网络中的任意两节点都相连. 集群系数描述了网络节点的群居或集团现象.

节点的中介系数计算公式如下:

$$BC_k=\frac{\sigma_{ij}(k)}{\sigma_{ij}}, \tag{6}$$

其中, $\sigma_{ij}(k)$ 表示从 $i$ 节点到 $j$ 节点经过 $k$ 节点的最短路径个数, $\sigma_{ij}$ 表示 $i$ 节点到 $j$ 节点的最短路径个数. $k$ 节点的中介系数的平均值为: $k$ 点对任意一对节点的中介系数的平均值. 节点中介系数是网络中心性的一个衡量指标.

## 3 区域关联网结构性质分析

### 3.1 阈值选取与网络整体性质分析

由于连边阈值对网络的后续计算有较大的影响, 选择合理和可信的阈值是后续研究结论的正确性保证. 为此图 1 给出了在不同阈值下网络结构统计量的变化情况.

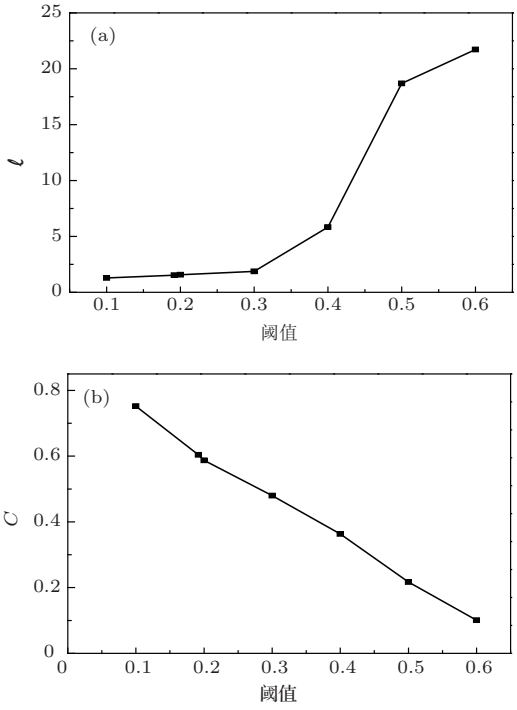


图 1 网络的统计量随阈值的变化 (a) 网络的平均路径长度 $l$ 随阈值的变化; (b) 网络的集群系数 $C$ 随阈值的变化

从图 1 (a) 可以看出, 网络的平均路径长度 $l$ 在阈值小于 0.4 时变化较小, 但当阈值大于 0.4 后平均路径长度迅速地变大; 集群系数的大小变化 (图 1 (b)) 表现为: 随着阈值的变大集群系数逐渐减小. 平均路径长度和集群系数是描述复杂网络的两个基本统计量, 他们的变化大致反映了网络结构的变化情况. 从图 1 可以看出, 在阈值为 0.4 前后网络的结构发生了明显的变化. 利用大于 0.4 的值作为阈值来分析网络会因选值的差异导致结果存在较大的差异. 另外由于区域间存在的是稳定的相互作用, 为此阈值应取在小于 0.4 的范围内, 同时在考虑到相关系数的信度检验后, 本文以达到 0.01 信度的 0.19 作为连边阈值进行讨论. 图 2 则是阈值为 0.19 时得到的网络空间连接图像.

从图 2 的节点连接情况可以看出, 海洋中的节点主要与其上方周围的大气节点连接, 而较少与较远的节点连接, 该点直观地说明区域之间的相互作用首先表现为与该区域附近的区域相互作用, 然后再间接地和相离较远区域进行相互作用. 另外, 根据计算得到网络的平均路径长度大小为 1.53, 由网络的平均路径长度大小定义可知其值表示了网络中任意两节点之间最短路径长度的平均值, 从此可看出网络中节点之间的连接是十分紧密的, 任意两节点之间的连接只要经过少于两个节点就能将一节点的波动传到另一节点, 即具有高效的传输效率. 区域之间的交流紧密性有利于将一区域的不稳定快速地传递到其他区域, 从而保持该区域的稳定. 同时按照集群系数计算公式计算得到集群系数的大小为 0.6. 集群系数表征了网络中节点之间的区域结构特征, 其大小为 0 至 1 之间, 1 表示任意两点都相连, 即全耦合网络, 0 表示网络中的任意三节点无三角形结构. 集群系数为 0.6 表明该网络具有较强的社区结构特征, 具有该特征的网络在信息传输方面表现出: 当其中的一个区域受到外胁迫作用后会带动整个社区成员一起变化, 然后再通过该社区结构向整个网络传播, 同时该网络还具有在受到外界干扰下能够保持网络的结构不变性, 即维持网络的稳定性. 这种具有较小平均路径长度和较大集群系数的网络又被称为小世界网络 [1].

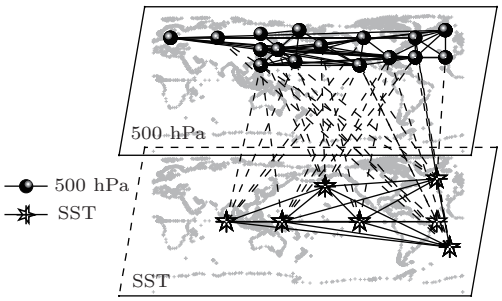


图 2 阈值为 0.19 时的网络空间连接图 (图中标注的 SST 平面表示海温层, SST 层中的五角星为表 1 所述海温区域的中心点 (代表点), 500 hPa 层含义类似; 同层间的连线用实线表示, 用虚线表示层与层间的连线; 定义在海平面气压的 NPO, NAO, 为简化图像将该点画至 500 hPa 层中)

另外, 从图 2 中可以看到, 赤道区域的海温与中高纬度的大气建立了较多连接, 把连接看成是一种作用关系, 则二者间的关系是密切的, 该关系可能是直接的作用关系, 也有可能是间接式的相互作用关系. 图中的连接现象同较多学者的研究有着较多的符合. 例如, 周波涛等 [32] 指出, Haley 环流与 NPO 存在着密切关系, 当 Hadley 环流位于正位相时, NPO 偏强, 反之则弱. 而赤道地区海温偏高会加强 Hadley 环流, 反之减弱, 为此, 赤道区

域的海温变化便可通过Hadley环流间接地影响到NPO, 然后再将变化通过大气内部作用传递给其他类型的遥相关区域. 本文也得到了低纬度地区的中东太平洋区域与NPO区域2建立有连接. Pozo-Vazquez 等[33]认为太平洋-北美遥相关型可能是联系热带强迫和北大西洋地区热带外环流变化的机制. 另外, 还有研究[34]指出黑潮的输送与PDO及ENSO有较好的关系, 并且在年际尺度上, 黑潮输送异常滞后于PDO及ENSO变化, 且呈现负相关. 而黑潮输运的变化将会直接影响其上空的大气环流的变化, 从而影响到遥相关的变化.

图2中还可看出, 大气中有较多的区域与中纬度的海洋连接, 而较多的研究认为冬季中纬度地区的海洋对大气的作用较小, 为此图2中显示的连线应是大气对海洋的强迫作用. 该点能较多地从他人研究中得到, 如: 李博等[35]利用模式分析指出北太平洋冬季大尺度的大气环流异常能通过影响湍流热通量从而决定SST的变率, 该文也进一步证明了热带外地区大气环流与海洋的相互关系中大气对海洋的强迫可能是主要的. 另外, 周天军等[36,37]利用一个耦合模式讨论了北大西洋冬季的海气相互作用特征, 证实了大气对海洋的强迫作用. 综上可得到, 图2中的连线暗含的区域作用关系是多样的, 对于各区域间详细的物理机制值得进一步深入探讨和研究. 以上仅简单地分析了一些连线可能代表的含义, 图2中的连线情况能较直观地反映出区域与区域间存在作用关系, 可为其他研究提供一种整体上对区域作用的把握, 具有较强的指示作用.

### 3.2 网络单节点性质分析

对复杂网络的描述不仅包含对整体网络性质的描述量, 同时也有对单节点的描述统计量. 例如, 节点度、中介系数和集群系数等. 利用王小凡等[30]和邹勇等[31]的定义描述分析了代表网络中各个区域的节点性质, 并在表2中列出了排序后得到的前4项和后4项对应区域.

表2 网络单节点性质排序表

| | 区域 | 节点度 | 区域 | 中介系数 | 区域 | 集群系数 |
|---|---|---|---|---|---|---|
| 前4位 | EAP-1 | 18 | EAP-1 | 0.0775 | EA | 0.857 |
| | PNA-1 | 16 | PNA-1 | 0.0639 | NAO-2 | 0.762 |
| | EAP-2 | 15 | EAP-2 | 0.0506 | NAO-1 | 0.714 |
| | PNA-4 | 15 | PNA-4 | 0.0505 | EU-1 | 0.694 |
| | ··· | | ··· | ··· | ··· | ··· |
| 后4位 | NAO-2 | 7 | NAO-1 | 0.0044 | PNA-4 | 0.495 |
| | EA | 7 | NAO-2 | 0.0026 | PNA-1 | 0.467 |
| | NPO-1 | 6 | EAP-3 | 0.0026 | EU-2 | 0.444 |
| | EAP-3 | 4 | EA | 0.0016 | PNA-3 | 0.444 |

注: 上述EAP-1表示表1中叙述的EAP区域1, 其他类同.

从表2中的节点度排序可以看出, 在EAP遥相关包含的3个区域中, 区域1和区域2都有着较大的度, 而EAP 区域3的度大小仅为4, 是其他两个区域的近1/4. 另外, PNA遥相关包含有4个区域, 其中的1区和4区的度较大, 另外两个区域的节点度分别为10和8. 以上表明, 同一遥相关包含的区域之间是有差异的, 即有的区域作用强些, 有的则弱些. 该观点也体现在中介系数中的PNA和EAP的区域差异. 节点度描述了节点的连接数, 度大的节点连接的节点数多, 这样的节点变化可以很快地影响网络的整体变化, 而度小的点就必须经过它的连接点甚至是次连接点才能把自身的波动信息传开, 另外对于具有损耗的系统, 信息在多次传输的过程中强度会逐渐减弱甚至湮灭. 所以度大的节点在一定程度上影响了整个网络的性质, 是值得关注的节点.

网络节点的中介性描述了节点在网络中的输运性质, 该含义可类似比于交通枢纽的特性. 从表2的中介系数排序可以看到, 度大的节点多数也是中介系数大的点, 度小的点也有着较小的中介系数, 另外中介系数最大值与最小值之间相差近23倍, 该点亦体现区域之间的差异性.

从表2的集群系数栏可以看出, EA区域、NAO遥相关包含的两个区域和EU区域1都有着较大的

集群系数, 另外海洋中的几个区域都具有较高的集群系数, 该点在一定程度上阐释了海洋相对于大气更稳定. 为了更直观地理解关键区域和其他区域的作用空间图像, 图3给出了大气中和海洋中度靠前的两个区域空间连接图.

图3 (a) 和 (b) 给出了500 hPa高度场上度大的两个区域的空间连接图. 从图中可以直观得到两个度大的区域在海洋中主要都与北印度洋、西太平洋和大西洋的赤道区域建立连接, 说明该区域的变化和这三个区域的变化存在较大关系. 海洋中度靠前的两个区域连接如图3 (c) 和 (d) 所示, 图3 (c) 中的南大西洋连接有较多的区域, 海洋部分仅大西洋的赤道部分未有连接. 从图3 (d) 的连接情况可以看到, 尽管北大西洋存在较多的连接, 但未与具有较大度的EAP遥相关区域建立连接.

### 3.3 网络鲁棒性分析

根据复杂网络理论, 网络的鲁棒性指: 如果在移走少量节点后网络中的绝大部分节点仍是连通的, 那么就称该网络的连通性对节点故障具有鲁棒性. 一般对节点的干扰又可以分为随机干扰和蓄意干扰. 对鲁棒性的度量一般采用“去除节点数和网络中的总节点数的比例 $f$”与“网络的平均路径长度 $l$”之间的关系来度量. 图4 (a) 为网络受到随机干扰和依次去除度大的蓄意干扰条件下得到的 $f$-$l$ 关系规律图. 当网络受到随机攻击后, 网络的平局路径长度在 $f < 0.4$ 时基本不变化, 当 $f > 0.4$ 后, 网络出现先增加后迅速减小. 而在蓄意攻击下的网络平均路径变化在一开始就出现明显增加, 在 $f$ 为0.5 左右后平均路径长度迅速减小. 从两者的对比可以看出, 蓄意攻击度大节点迅速破坏了网络的拓扑连接完整性, 使得网络的连通效率的降低, 另外也从侧面表明度大的节点对网络的拓扑性质有着较大影响. 虽然在现实中无法实现把该网络中的节点移除, 但是通过该方法却能明显地看出度大的节点在该网络中的重要性, 另外为了更好地对比单节点对网络的影响, 图4 (b) 给出了在去除网络单节点后集群系数和平均路径长度相对于原网络的变化量. 从图4 (b) 可以看出, 随着去除节点度的增大, 网络的平均路径大小增加, 而集群系数是减少的. 表明在该网络中度大的点, 不仅利于网络间的信息传输, 而且有益于形成社区结构增强网络的稳定性.

由此可见, 区域关联网络具有一定的鲁棒性, 并且网络中度大的节点不仅有利于网络间的信息传输. 而且还有利于形成具有稳定性的社区结构. 为此这些度大的节点是值得高度关注的关键区域.

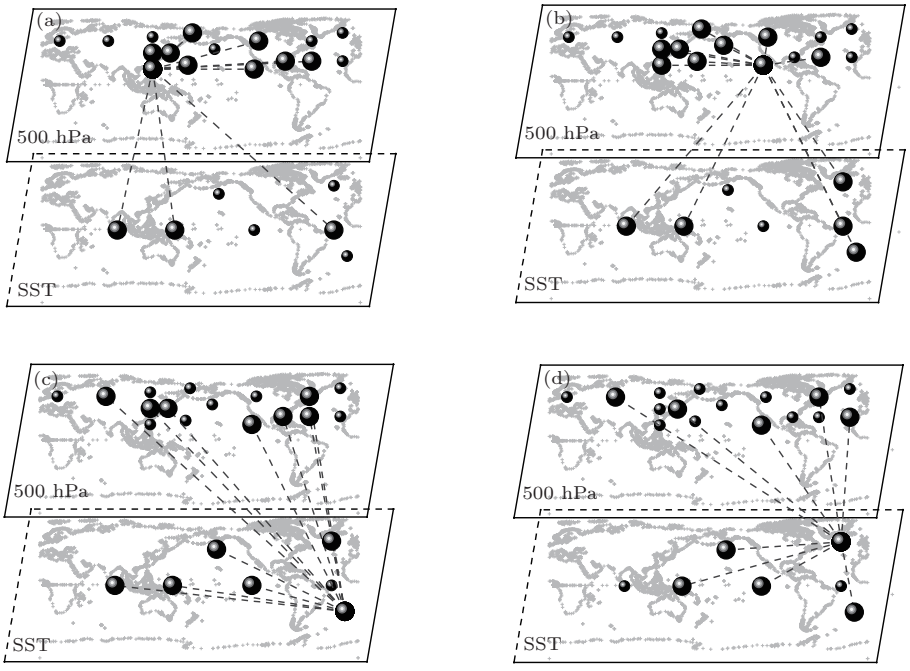


图3 大气和海洋中关键区域空间连接图 (a) EAP区域1的空间连接图像; (b) PNA区域1的空间连接图像; (c) 南大西洋的空间连接图像; (d) 北大西洋的空间连接图像 (图中点和层的含义介绍如图2所述, 另外在该图中都用虚线描述节点间的连线, 大圆圈表示有连接的节点, 小圆圈表示未连接的节点)

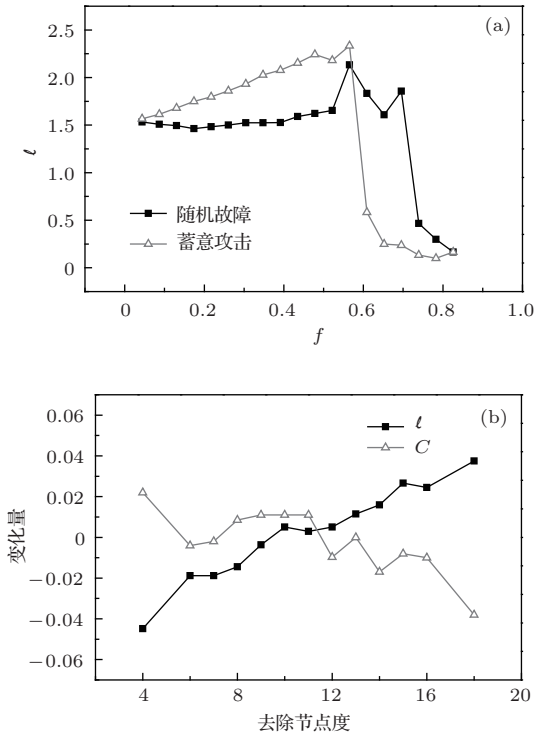


图 4 网络鲁棒性分析 (a) 平均路径长度对随机故障和蓄意攻击的响应; (b) 去除单节点对网络集群系数和平均路径长度的影响

## 4 结 论

利用复杂网络的基本原理与方法, 构建起遥相关包含的区域和海温关键区的关联网络, 根据建立的网络计算网络的基本统计量. 从计算的结果得到以下结论:

1) 平均路径长度在阈值小于0.4时基本不变, 大于0.4后平均路径长度开始迅速增大, 而集群系数随阈值的增大是逐渐减小的, 综合考虑该变化和信度约束下, 以0.19构建区域关联网络, 进一步计算得到该网络具有一定的小世界性质;

2) 单节点的对比分析得到: EAP遥相关1区、2区和PNA遥相关1区、4区在网络中不仅有着较大的度, 同时也有较大的中介系数, 而EAP区域3和NPO区域1则较小; 在对比分析后得到, 区域之间的差异较大, 另外大西洋的赤道部分和NAO的区域1和区域2有着较大的集群系数, 但是其他两个量都较小; 由于这些节点在网络中的特殊性, 所以一些值大的节点值得较高的关注;

3) 网络的鲁棒性分析得到, 该网络具有一定的鲁棒性特征, 另外去除网络的单节点分析得出, 网络的集群系数和平均路径长度对度大小的敏感度是不一样的, 度大的节点和度小的节点变化较大.

## 参考文献


[1] Watts D J, Strogatz S H 1998 *Nature* **393** 440

[2] Barabasi A L, Albert R 1999 *Science* **286** 509

[3] Ren G, Lu L L, Wang W 2012 *Acta Phys. Sin.* **61** 144501 (in Chinese) [任刚, 陆丽丽, 王炜 2012 物理学报 **61** 144501]

[4] Gao X Y, An H Z, Liu H H, Ding Y H 2011 *Acta Phys. Sin.* **60** 068902 (in Chinese) [高湘昀, 安海忠, 刘红红, 丁颖辉 2011 物理学报 **60** 068902]

[5] Feng G L, Hou W, Dong W J 2006 *Acta Phys. Sin.* **55** 962 (in Chinese) [封国林, 侯威, 董文杰 2006 物理学报 **55** 962]

[6] Feng G L, Dai X G, Wang A H, Chou J F 2001 *Acta Phys. Sin.* **50** 606 (in Chinese) [封国林, 戴新刚, 王爱慧, 丑纪范 2001 物理学报 **50** 606]

[7] Feng G L, Dong W J, Jia X J, Cao H X 2002 *Acta Phys. Sin.* **51** 1181 (in Chinese) [封国林, 董文杰, 贾晓静, 曹鸿兴 2002 物理学报 **51** 1181]

[8] Da C J, Chou J F 2008 *Acta Phys. Sin.* **57** 2595 (in Chinese) [达朝究, 丑纪范 2008 物理学报 **57** 2595]

[9] Da C J, Feng A X, Gong Z Q, Song J 2013 *Acta Phys. Sin.* **62** 039202 (in Chinese) [达朝究, 冯爱霞, 龚志强, 宋健 2013 物理学报 **62** 039202]

[10] Chou J F 1997 *Bull. Chin. Acad. Sci.* **5** 325 (in Chinese) [丑纪范 1997 中国科学院院刊 **5** 325]

[11] Feng G L, Dong W J, Gong Z Q, Hou W, Zhi R 2006 *Nonlinear Theories and Methods on Spatial-Temporal Distribution of the Observational Data* (Beijing: Metrological Press) pp1–227 (in Chinese) [封国林, 董文杰, 龚志强, 侯威, 支蓉 2006 观测数据非线性时空分布理论和方法 (北京: 气象出版社) 第1—227页]

[12] He W P, Feng G L, Wu Q, Wan S Q, Chou J F 2008 *Nonlinear Processes in Geophysics* **15** 601

[13] He W P, Feng G L, Dong W J, Li J P 2004 *Acta Phys. Sin.* **53** 3258 (in Chinese) [何文平, 封国林, 董文杰, 李建平 2004 物理学报 **53** 3258]

[14] Wan S Q, Feng G L, Zhou G H, Wang B M, Qin M R, Xu X Z 2005 *Acta Meteorol. Sin.* **63** 516 (in Chinese) [万仕全, 封国林, 周国华, 王冰梅, 秦铭荣, 许遐桢 2005 气象学报 **63** 516]

[15] Zhi R, Lian Y, Feng G L 2007 *Acta Phys. Sin.* **56** 1837 (in Chinese) [支蓉, 廉毅, 封国林 2007 物理学报 **56** 1837]

[16] Tsonis A A, Swanson K, Kravtsov S 2007 *Geophys. Res. Lett.* **34** 13705

[17] Wang G L, Swanson K L, Tsonis A A 2009 *Geophys. Res. Lett.* **36** 07708

[18] Tsonis A A, Swanson K L 2011 *Int. J. Bifurc. Chaos* **21** 3549

[19] Yamasaki K, Gozolchiani A, Havilin S 2008 *Phys. Rev. Lett.* **100** 228501

[20] Gong Z Q, Zhi R, Hou W, Wang X J, Feng G L 2012 *Acta Phys. Sin.* **61** 029202 (in Chinese) [龚志强, 支蓉, 侯威, 王晓娟, 封国林 2012 物理学报 **61** 029202]

[21] Gong Z Q, Zhou L, Zhi R, Feng G L 2008 *Acta Phys. Sin.* **57** 5351 (in Chinese) [龚志强, 周磊, 支蓉, 封国林 2008 物理学报 **57** 5351]

[22] Wang X J, Gong Z Q, Zhou L, Zhi R 2009 *Acta Phys. Sin.* **58** 6651 (in Chinese) [王晓娟, 龚志强, 周磊, 支蓉 2009 物理学报 **58** 6651]

[23] Feng A X, Gong Z Q, Wang Q G, Feng G L 2012 *Theor. Appl. Climatol.* **10** 704

[24] Zong H F, Zhang Q Y, Chen L T 2008 *Chin. J. Atmosph. Sci.* **32** 220 (in Chinese) [宗海锋, 张庆云, 陈烈庭 2008 大气科学 **32** 220]

[25] Jin D C, Guan Z Y, Cai J X, Jiang L L 2010 *Chin. J. Atmosph. Sci.* **34** 947 (in Chinese) [金大超, 管兆勇, 蔡佳熙, 江丽俐 2010 大气科学 **34** 947]

[26] Gong Z Q, Wang X J, Zhi R, Feng A X 2011 *Chin. Phys. B* **20** 079201

[27] Wallace J M, Gutzler D S 1981 *Monthly Weather Review* **109** 784

[28] Kistler R, Kalnay E, Kanamitsu M 2001 *Bull. Amer. Meteor. Soc.* **82** 247

[29] Smith T M, Reynolds R W 2003 *J. Climate* **16** 1495

[30] Wang X F, Li X, Chen G R 2006 *Complex Network Theory and Its Application* (Vol. 1) (Beijing: Tsinghua University Press) pp9–11 (in Chinese) [王小帆, 李翔, 陈关荣 2006 复杂网络理论及应用第 1 版 (北京: 清华大学出版社) 第 9—11 页]

[31] Zou Y, Donges F J, Kurths J 2011 *Complex Systems and Complexity Science* **8** 27 (in Chinese) [邹勇, Donges F J, Kurths J 2011 复杂系统与复杂性科学 **8** 27]

[32] Zhou B T, Wang H J, Cui X 2008 *Chin. J. Geophys.* **51** 999 (in Chinese) [周波涛, 王会军, 崔绚 2008 地球物理学报 **51** 999]

[33] Pozo-Vazquez D, Esteban-Parra M J, Rodrigo F S, Castro-diez Y 2001 *J. Climate* **14** 3408

[34] Gu D J, Wang D X, Yuan J N 2004 *J. Tropical Oceanography* **23** 30 (in Chinese) [谷德军, 王东晓, 袁金南 2004 热带海洋学报 **23** 30]

[35] Li B, Zhou T J, Lin P F, Bao Q 2011 *Acta Meteorol. Sin.* **69** 52 (in Chinese) [李博, 周天军, 林鹏飞, 包庆 2011 气象学报 **69** 52]

[36] Zhou T J, Yu R C, Gao Y Q, Drange H 2006 *Acta Meteorol. Sin.* **64** 1 (in Chinese) [周天军, 宇如聪, 郜永祺, Drange H 2006 气象学报 **64** 1]

[37] Zhou T J, Yu R C, Gao Y Q, Drange H 2006 *Acta Meteorol. Sin.* **64** 18 (in Chinese) [周天军, 宇如聪, 郜永祺, Drange H 2006 气象学报 **64** 18]

# Properties of complex network between atmospheric teleconnection and the key areas of SST in winter*

Zuo Dong-Dong[1)] Gong Zhi-Qiang[2)†] Feng Ai-Xia[3)] Zhi Rong[2)]

1) (*Department of Physics, Yangzhou University, Yangzhou 225002, China*)

2) (*Laboratory for Climate Studies, National Climate Center, China Meteorological Administration, Beijing 100081, China*)

3) (*Data Service Space, National Meteorological Information Center, China Meteorological Administration, Beijing 100081, China*)

( Received 14 October 2013; revised manuscript received 6 November 2013 )

**Abstract**

Based on the index of atmospheric teleconnection and the key areas of the sea, taking the relationship between the average of the height fields of the key areas and the average of the key areas of SST as boundary condition, the associated network that embodies the interaction between atmospheric teleconnection areas and the key areas of SST is constructed. Then the image of the interaction between atmospheric and ocean is given. Based on the structural characteristics of network, the basic nature of the network and the key nodes of the interaction network are studied and the influence of the key nodes on network is analysed. The Results show that the associated network belongs to the small world that has a smaller average path length and a lager clustering coefficient. Besides, the average path length has a stable value in the threshold less than 0.4. In other words, in this case the characteristics of network remain unchanged, and then it is proved that using the correlation 0.19 as the condition of edge connection is effective. The single node characteristic is analysed in the network and the results show that the areas of the East Asia-Pacific 1 and 2 and the Pacific/North American pattern 1 and 4 have lager node degrees. That is to say, these four atmosphere regions have stronger effect than other regions in the atmosphere and sea, the North Pacific Oscillation 1 and the East Asia-Pacific 3 have low node degrees, so these two regions have low effects on the region interaction. In addition, it is proved that the network has certain robustness by removing nodes in turn. The study is of significance to grasp some important areas of the teleconnection and the sea, and also it provides a new method to study air-sea interaction.

**Keywords:** associative network, teleconnection regions, key areas of the sea

**PACS:** 92.60.Wc **DOI:** 10.7498/aps.63.049201

* Project supported by the National Basic Research Program of China (Grant No. 2012CB955903) and the National Natural Science Foundation of China (Grant Nos. 41205040, 41105055).

† Corresponding author. E-mail: gzq0929@126.com

# 论文编目索引


1. Bao, B. and G. Y. Ren. 2014: Climatological characteristics and long-term change of SST over the marginal seas of China. *Continental Shelf Research*, 77 (1): 96-106.
2. Bian, T., G. Y. Ren, B. X. Zhang, L. Zhang, Y. X. Yue. 2014: Urbanization effect on long-term trends of extreme temperature indices at Shijiazhuang station, North China. *Theoretical and Applied Climatology*, DOI 10.1007/s00704-014-1127-x.
3. Chen Ajiao, Weiping Li, Weijing Li, and Xin Liu. 2014: An observational study of snow aging and the seasonal variation of snow albedo by using data from Col de Porte. *France. Chin. Sci. Bull.* 59(34): 4881-4889.
4. 达朝究，穆　帅，马德山，等. 2014：基于 Lorenz 系统的数值天气转折期预报理论探索. *物理学报*，63(2)：029201-14.
5. 董思言，徐　影，周波涛，侯美亭. 2014：基于 CMIP5 气候模式的中国地区未来高温风险预估. *气候变化研究进展*，10(5)：365-369.
6. 段居琦，徐新武，高清竹. 2014：IPCC 第五次评估报告关于适应气候变化与可持续发展的新认知. *气候变化研究进展*，10(3)：197-202.
7. 房一禾，龚志强，等. 2014：中国东北区域盛夏雨季的客观识别研究. *物理学报*，63(20)：209202.
8. Gong Z Q, Zhao J H, Feng G L, Chou J F., 2014: Dynamic-statistics combined forecast scheme based on the abrupt decadal change component of summer precipitation in East Asia. *Sci. China: Earth Sci.*, doi: 10.1007/s11430-014-4967-4.
9. GU wei, Lin WANG, Weijing LI, Lijuan CHEN. 2014: Influence of the tropical Pacific east-west thermal contrast on the autumn precipitation in South China. *Int. J. Climatol*, DOI:10.1002/joc.4075.
10. 韩荣青，高　辉，李维京. 2014：旋转经验正交函数分解回归方法在东北夏季气温季节预测和成因诊断中的应用. *气象学报*，72(2)：291-305.
11. 胡　泊，乔少博，封国林. 2014：20 世纪 90 年代末东亚夏季降水年代际变化及其成因初探. *物理学报*，63(20)：209204.
12. JIA Xiaolong, CHEN Lijuan, LUO Jingjia, 2014: Climate Prediction experiment for tropical cyclone genesis frequency using the large0scale circulation forecast by a coupled global circulation model. *Journal of Tropical Meteorology*, 20(2):103-111.
13. Li Weijing, Jingpeng Liu, Lijuan Chen, et al, 2014: Spatiotemporal distribution and decadal change of the monthly temperature predictability limit in China. *China Sci Bull*, 59(34): 4864-4872.
14. 李维京，刘景鹏，陈丽娟，张培群，任宏利. 2014：中国月平均气温可预报性的时空特征及其年代际变化. *科学通报*，59(25)：2520-2527.
15. 李　娇，任国玉，任玉玉，张　雷. 2014：资料均一化对沈阳站气温趋势和城市化偏差分析的影响. *大气科学学报*，37(3)：297-303.
16. Liu Yunyun, Li Weijing, Zuo Jinqing, Hu Zeng-Zhen. 2014: Simulation and projection of the western Pacific subtropical high in CMIP5 models. *J. Meteor. Res.*, 28(3): 327-340.

17. 刘芸芸，李维京，左金清，胡增臻. 2014：CMIP5 模式对西太平洋副热带高压的模拟和预估. 气象学报，72(2)：277-290.
18. Liu，Xiangwen，Tongwen Wu，Song Yang，et al.，2014：Relationships between interannual and intraseasonal variations of the Asian-western Pacific summer monsoon hindcasted by BCC_CSM1.1(m). *Advances in Atmospheric Sciences*，31 (5)：1051-1064.（LCS Youth Fund，2014）
19. Liu，Y. and Fan，K.，2014：An application of hybrid downscaling model to forecast summer precipitation at stations in China. *Atmospheric Research*，143：17-30.
20. Liu，Y. and Ren，H.-L. 2014：A hybrid statistical downscaling model for prediction of winter precipitation in China. *International Journal of Climatology*，doi：10.1002/joc.4058.
21. 马　琴，刘　新，李伟平，等. 2014：青藏高原夏季土壤有机质及砾石影响水热传输特性的数值模拟. 大气科学，38(2)：337-351.
22. Jie PENG，Hua ZHANG，Zhanqing Li. 2014：Temporal and spatial variations of global deep cloud systems based on CloudSat and CALIPSO Satellite observations. *Adv. in Atmos. Sci.*，31(3)：593-603.
23. 祁　莉，王晓芳，何金海，张文君，吴　捷. 2014：前期西太平洋暖池热含量异常影响长江中下游夏季降水的可能途经. *地球物理学报*，57(6)：1769-1781.
24. 乔少博，沈柏竹，王晓娟，封国林. 2014：欧亚北部 2004 年以来频繁冷冬的特征分析及机理初探. 气象学报，72(6)：1143-1154.
25. Ren，G. and Y. Zhou. 2014：Urbanization effects on trends of extreme temperature indices of national stations over mainland China，1961－2008. *Journal of Climate*，27(6)：2340-2360.
26. 任国玉，任玉玉，李庆祥，徐文慧. 2014：全球陆地表面气温变化研究现状、问题和展望. *地球科学进展*，29(8)：934-946.
27. Ren，Hong-Li，Fei-Fei Jin，and Jong-Seong Kug. 2014：Eddy-induced growth rate of low-frequency variability and its mid-late winter suppression in the northern hemisphere. *Journal of the Atmospheric Sciences*，71(7)：2281-2298.
28. Ren，Hong-Li，Ying Liu，Fei-Fei Jin，Yu-Ping Yan，and Xiang-Wen Liu. 2014：Application of the analogue-based correction of errors method in ENSO prediction. *Atmospheric and Oceanic Science Letters*，7(2)：157-161，doi：10.3878/j.issn.1674-2834.13.0080.
29. 任宏利，张培群，李维京，陈丽娟. 2014：提高月预报业务水平的动力相似集合方法. 气象学报，72(4)：723-730.
30. 任霄玉，任国玉，魏明建. 2014：我国北方 TOMS 气溶胶光学厚度与地面沙尘天气频数的比较. 干旱区研究，31(5)：874-881.
31. Su T，Feng G L，Zhou J，Ye M. 2014：The response of actual evaporation to global warming in China based on six reanalysis datasets. *International Journal of Climatology*，doi：10 1002/joc 4203.
32. SU T，Feng G L. 2014：Spatial-temporal variation characteristics of global evaporation revealed by eight reanalyses. *Science China Earth Sciences*，doi：10 1007/s11430-014-4947-8.
33. 苏　涛，封国林. 2014：中国夏季大气水分循环特征及再分析资料对比分析. *物理学报*，63(24)：249201.
34. 司　东，袁　媛. 2014：2013 年海洋和大气环流异常对中国气候的影响. 气象，40(4)：1-10.
35. Tan，Gui-Rong，Fei-Fei Jin，Hong-Li Ren，and Zhao-Bo Sun. 2014：The role of eddy feedback in the exci-

tation of NAO. *Meteorological Applications*, DOI: 10.1002/met.1415.

36. 汪　雷，王彰贵，凌铁军，左金清. 2014：海洋模式中垂直混合参数化方案介绍. *海洋预报*，31(5)：93-104.

37. Y.J. Wang, F. M. Ren. 2014: Spatial and Temporal Variations of Regional High Temperature Events in China. *International Journal of Climatiology*, 34: 3054-3065.

38. 王艳姣，高　蓓，周　兵，姜　彤，等. 2014：2013 年全球重大天气气候事件及其成因. 气象，40(6)：759-768.

39. Zhili Wang, Hua Zhang, and Peng Lu, 2014: Improvement of cloud microphysics in the aerosol-climate model BCC_AGCM2.0.1_CUACE/Aero, evaluation against observations and updated aerosol indirect effect. *Journal Geophysical Research*,119, 8400-8417, doi:10.1002/2014JD021886.

40. 谢　冰，张　华. 2014：关于大气臭氧问题的主要研究进展. *科学技术与工程*,14(8)：1671-181508-0000-05.

41. 杨冰韵，张　华，彭　杰，王志立，荆现文. 2014：利用 CloudSat 卫星资料分析云微物理和光学性质的全球分布特征. *高原气象*，33(4)：1105-1118.

42. 尹宜舟，罗　勇，肖风劲，等. 2014：1971—2011 年中国县级行政区域热带气旋基本气候特征. *热带气象学报*,30(6)：089-097.

43. You, Q.L., K. Fraedrich, F. Sielmann, J. Min, S.C. Kang, Z.M. Ji, X.H. Zhu, G.Y. Ren. 2014: Present and projected degree days in China from observation, reanalysis and simulations. *Clim Dyn*. 1449-1462. DOI 10.1007/s00382-013-1960-0.

44. YU Haipeng, HUANG Jiangping, LI Weijing, Feng Guolin. 2014: Development of the Analogue-Dynamical Method for Error Correction of Numerical Forecasts. *J. Meteor. Res.*,28(5): 934-943.

45. 于海鹏，黄建平，李维京，封国林. 2014：数值预报误差订正技术中相似—动力方法的发展. 气象学报，72(5)：1012-1022.

46. 尤焕苓，刘伟东，任国玉. 2014：1981—2010 年北京地区极端降水变化特征. *气候与环境研究*，19(1)：69-71.

47. 尤煥玲，任国玉，等. 2014：北京“7·21”特大暴雨过程时空特征解析. 气象*科技*，42(5)：856-864.

48. 曾宇星，封国林，等. 2014：春季马斯克林高压对中国东北地区夏季气温的影响. *高原气象*，33(5)：1374-1382.

49. H. Zhang, X. Jing J. Li, 2014: Application and evaluation of a new radiation code under McICA scheme in BCC_AGCM2.0.1. *Geosci. Model Dev.* 7, 737-754.

50. ZHANG H., XIE B., ZHAO S.-Y., CHEN Q., 2014: PM2.5 and tropospheric $O_3$ in China and an analysis of the impact of pollutant emission control. *Advances in Climate Change Research*, 5(2014)136-141.

51. 张　华，陈　琪，谢　冰，赵树云. 2014：中国的 PM2.5 和对流层臭氧及污染物排放控制对策的综合分析. *气候变化研究进展*，10(4)：289-296.

52. 张　华，黄建平. 2014：IPCC 第五次评估报告关于人为和自然辐射强迫的解读. *气候变化研究进展*，10(1)：40-44.

53. 张　华，卢　鹏. 2014：多层四流球谐函数的构建及在大气辐射传输模式中的应用. 气象学报，72(6)：1257－1268.

54. Zhang, L., G.Y. Ren, Y.Y. Ren, A.Y. Zhang, Z.Y. Chu, Y.Q. Zhou, 2014: Effect of data homogeni-

zation on estimate of temperature trend: a case of Huairou station in Beijing Municipality. *Theor Appl Climatol*, 115 (3): 365-373.

55. 张　灵, 杜良敏, 陈丽娟, 高正旭. 2014: 武汉异常强降水水汽来源、输送路径分析. 气象与环境科学, 37 (1):69-74.

56. 张　媛, 任国玉. 2014: 无参考序列条件下地面气温观测资料城市化偏差订正方法:以北京站为例. *地球物理学报*, 57(7): 2197-2207.

57. Zhao,Chongbo, Tianjun Zhou, Lianchun Song, Hongli Ren, 2014: The Boreal Summer Intraseasonal Oscillation Simulated by Four Chinese AGCMs Participated in the CMIP5 Project. *Advances in Atmospheric Sciences*, 31(5): 1167-1180.

58. Shuyun Zhao, Hua Zhang, Song Feng, and Qiang Fu, 2014: Simulating direct effects of dust aerosol on arid and semi-arid regions using an aerosol-climate coupled system. *International Journal of Climatology*, *in press*, C11DOI: 10.1002/joc.4093.

59. 赵树云,智协飞,张　华. 2014: 气溶胶-气候耦合模式系统 BCC_AGCM2.0.1_CAM 气候态模拟的初步评估.*气候与环境研究*,19(3):265-277.

60. 周雅清,任国玉. 2014: 城市化对华北地区极端气温事件频率趋势变化的影响. 高原气象, 33(6): 1589-1598.

61. 左冬冬, 龚志强, 等. 2014: 冬季大气遥相关和海温关键区的复杂网络性质. *物理学报*,63(4): 049201-9.



LCS

气候研究开放实验室